ENCYCLOPEDIA OF THE ALKALINE EARTH COMPOUNDS

R. C. Ropp

ELSEVIER

AMSTERDAM • BOSTON • HEIDELBERG • LONDON
NEW YORK • OXFORD • PARIS • SAN DIEGO
SAN FRANCISCO • SINGAPORE • SYDNEY • TOKYO

Elsevier
The Boulevard, Langford Lane, Kidlington, Oxford OX5 1GB, UK
Radarweg 29, PO Box 211, 1000 AE Amsterdam, The Netherlands

Copyright © 2013 Elsevier B.V. All rights reserved

No part of this publication may be reproduced, stored in a retrieval system or transmitted in any form or by any means electronic, mechanical, photocopying, recording or otherwise without the prior written permission of the publisher

Permissions may be sought directly from Elsevier's Science & Technology Rights Department in Oxford, UK: phone (+44) (0) 1865 843830; fax (+44) (0) 1865 853333; email: permissions@elsevier.com. Alternatively you can submit your request online by visiting the Elsevier web site at http://elsevier.com/locate/permissions, and selecting *Obtaining permission to use Elsevier material*

Notice
No responsibility is assumed by the publisher for any injury and/or damage to persons or property as a matter of products liability, negligence or otherwise, or from any use or operation of any methods, products, instructions or ideas contained in the material herein.

British Library Cataloguing in Publication Data
A catalogue record for this book is available from the British Library

Library of Congress Cataloging-in-Publication Data
A catalog record for this book is available from the Library of Congress

ISBN: 978-0-444-59550-8

For information on all **Elsevier** publications
visit our web site at store.elsevier.com

Printed and bound in Spain

13 14 15 16 17 10 9 8 7 6 5 4 3 2 1

Working together to grow
libraries in developing countries
www.elsevier.com | www.bookaid.org | www.sabre.org
ELSEVIER BOOK AID International Sabre Foundation

This book is dedicated to my wife,
Francisca Margarita, who has
staunchly supported my efforts for
more years than I wish to remember.

Preface

This book is designed to document all of the alkaline earth compounds known to date in the scientific literature. It is a reference book intended to bring together, in an organized fashion, information difficult to find, or dispersed in many published journals and books. Many of these references are obscure and not easily discovered except by persistent searching. This is the main value of this content. As such, the previously published subject matter has been the source of information presented here. The author has assembled results and conclusions, published by various researchers in the open literature, regarding a particular compound. He then used his personal knowledge and experience to discuss various viewpoints and judgments reached by various authors concerning the physical and chemical properties for each compound presented within this volume. The reader then has a starting point concerning whether a particular compound is known to exist and what properties it may exhibit. Although there are many other resources for inorganic compounds like the Wiley encyclopedia, Scifinder, Scopus/Scirus, the Gmelin Handbooks, PubMed, Springer/Link, the NIMS Materials database and the Web of Science, they cover a vast multitude of compounds and are, in some cases, difficult to access. In contrast, the present book is limited to alkaline earth compounds. This is the major worth of the book—a place to determine what alkaline earth compounds are known to exist.

However, the reader will soon discover that references to the literature, including tables, drawings and figures, are not given. There is a good reason for this. Early in the writing of the manuscript, the author assembled known data and results published as papers and books in the open literature. He then described succinctly was known about a particular alkaline earth compound and added references. Since his description was based upon the compilation and personal assessment of what several authors had published in the past, just one compound required 6–8 citations. Many compounds required 8–10 references and sometimes even more. Therefore, the decision was made not to include citations because the reference pages would consume a large part of the book. If the reader wishes to ascertain which authors discovered the properties of a particular compound, a good starting point is the Internet.

Concerning figures, the author has drawn all of these, starting with figures published within various articles and books. In many cases, more than one author(s) published essentially the same result, each a refinement of the previous one. The author then formed the figure (such as a crystal structure) according to the latest results known to date. For example, the author redrew many phase diagrams which were not complete and added known data to complete the diagram. Because most of the figures had several contributors, no citations have been included since they, like the information presented for each compound, would consume a considerable space within the manuscript.

Most of the tables are compilations of previously published data derived from books and journals. For example, some tables present unit-cell occupancies for a specific crystal structure. These were derived from the literature but have many authors. No specific citations are presented for these tables as well.

R.C. Ropp - October 2012

CHAPTER

1

The Alkaline Earths as Metals

OUTLINE

1.1. General Properties 1

1.2. Properties of the Alkaline Earth Metals 4

1.2.1. Beryllium 4

1.2.2. Magnesium 8

1.2.3. Calcium 12

1.2.4. Strontium 15

1.2.5. Barium 18

1.2.6. Radium 19

The alkaline earth metals comprise Group 2 of the periodic table and include the elements Be, Mg, Ca, Sr, Ba and Ra. These metals form cations with a formal charge of +2 in solution and are the second most electropositive metals of all of the elements (the alkali metals are the most electropositive). The name of this specific group in the periodic table stems from the fact that their oxides produce basic alkaline solutions and that these elements melt at such high temperatures that they remain solid (earths) in fires. The alkaline earth metals provide a good example of group trends in chemical properties within the periodic table, with well-characterized homologous behavior as one goes down the group. With the exception of Be and Mg, the metals have a distinguishable flame color, orange-red for Ca, magenta-red for Sr, green for Ba and crimson-red for Ra.

1.1. GENERAL PROPERTIES

Like other groups, the members of this family show specific patterns in their electron configuration, especially the outermost shells, that results in trends in chemical behavior (Table 1.1).

Another way to depict the electronic structure of these elements is shown in Table 1.2.

All of the alkaline earth metals have two electrons in their outer valence shell, so the energetically preferred state of achieving a filled electron shell is to lose two electrons to form doubly charged cations, M^{2+}. The alkaline earth metals are silver-colored, soft metals that react readily with halogens to form ionic salts. They also react with water, though not as rapidly as the alkali metals, to form strongly alkaline (basic) hydroxides. For example,

TABLE 1.1

Z	Element	No. of electrons/shell
4	Beryllium	2, 2
12	Magnesium	2, 8, 2
20	Calcium	2, 8, 8, 2
38	Strontium	2, 8, 18, 8, 2
56	Barium	2, 8, 18, 18, 8, 2
88	Radium	2, 8, 18, 32, 18, 8, 2

TABLE 1.2

Element	Symbol	Electronic configuration
Beryllium	Be	$[He]2s^2$
Magnesium	Mg	$[Ne]3s^2$
Calcium	Ca	$[Ar]4s^2$
Strontium	Sr	$[Kr]5s^2$
Barium	Ba	$[Xe]6s^2$
Radium	Ra	$[Rn]7s^2$

Encyclopedia of the Alkaline Earth Compounds
http://dx.doi.org/10.1016/B978-0-444-59550-8.00001-6

Copyright © 2013 Elsevier B.V. All rights reserved.

whereas Na and K react with water at room temperature, Mg reacts only with steam and Ca with hot water:

$$\mathrm{Mg(solid) + 2\ H_2O(gas)} \Rightarrow \mathrm{Mg(OH)_2(solid) + H_2(gas)}$$

Be is an exception. It does not react with water or steam, and its halides are covalent.

The alkaline earth metals are named after their oxides, the *alkaline earths*, whose old-fashioned names were Beryllia, Magnesia, Lime, Strontia and Baryta. "Earth" is the old term applied by early chemists to nonmetallic substances that were insoluble in water and resistant to heating, properties shared by these oxides. The realization that these earths were not elements but compounds is attributed to the chemist Antoine Lavoisier. In his "Traité Élementaire de Chemie" (*Elements of Chemistry*) of 1789, he called them "salt-forming" earth elements. Later, he suggested that the alkaline earths might be metal oxides, but admitted that this was mere conjecture. In 1808, acting on Lavoisier's idea, Humphrey Davy became the first to obtain samples of the metals by electrolysis of their molten "earths".

If the alkaline earths are compared to the alkalis, many similarities are apparent. The main difference is the electron configuration, which is ns^2 for alkaline earth metals and ns^1 for alkali metals. But for the alkaline earth metals, the nucleus also contains an additional positive charge. Also, the elements of Group 2 (alkaline earths) have much higher melting points and boiling points compared to those of Group 1 (alkali metals). The alkalis are softer and more lightweight than the alkaline earth metals that are much harder and denser.

The second valence electron is very important when it comes to comparing chemical properties of the alkaline earth and the alkali metals. The second valence electron is in the same "sublevel" as the first valence electron. Therefore, the Z_{eff} is much greater. This means that the elements of Group 2 have a smaller atomic radius and much higher ionization energy than those of Group 1. Even though the Group 2 contains a much higher ionization energy, they still form ionic compounds containing 2+ cations. Beryllium, however, behaves differently. This is due to the fact that in order to remove two electrons from this particular atom, significantly more energy is required. It never forms the Be^{2+} cation and its bonds are polar covalent.

Atomic and ionic radii increase smoothly down the Group. The ionic radii are all much smaller than the corresponding atomic radii. This arises because the atom contains two electrons in an s level relatively far from the nucleus. It is these electrons that are removed to form the ion. Remaining electrons are thus in levels closer to the nucleus, and in addition the increased effective nuclear charge attracts the electrons toward the nucleus and decreases the size of the ion.

These elements are all found in the Earth's crust, but not in the elemental form because they are so reactive. Instead, they are widely distributed in rock structures. The main minerals in which magnesium is found are "Carnellite", "Magnesite" and "Dolomite". Calcium is found in "Chalk", "Limestone", "Gypsum" and "Anhydrite". Magnesium is the eighth most abundant element in the Earth's crust, and calcium is the fifth.

Some of the physical properties of the alkaline earth metals are shown in Table 1.3.

The metals of Group 2 are harder and denser than sodium and potassium, and have higher melting points. These properties are due largely to the presence of two valence electrons on each atom, which leads to stronger metallic bonding than occurs in Group 1.

Three of these elements give characteristic colors when heated in a **flame**:

$$\mathrm{Mg} = \text{brilliant white} \qquad \mathrm{Ca} = \text{brick} - \text{red} \qquad \mathrm{Sr} = \text{crimson}$$

In all their compounds, these metals have an oxidation number of +2 and, with few exceptions, their compounds are ionic in nature. The reason for this can be seen by examination of the electron configuration, which always has two electrons in an outer quantum level. These electrons are relatively easy to remove, but removing the third electron is much more difficult, as it is close to the nucleus and in a filled quantum shell. This results in the formation of M^{2+}. The ionization energies reflect this electron arrangement. The first two ionization energies are relatively low, and the third very much higher.

In general, the chemical properties of Group 2 elements are dominated by the strong reducing power of the metals. The elements become increasingly electropositive as one descends within the Group. In direct contact with oxygen or chlorine gas, little or no reaction occurs. However, once started, the reactions with oxygen and chlorine are vigorous:

$$\mathrm{2Mg(solid) + O_2(g)} \Rightarrow \mathrm{2MgO(solid)} + \text{heat}$$

$$\mathrm{Ca(solid) + Cl_2(gas)} \Rightarrow \mathrm{CaCl_2(solid)} + \text{heat}$$

All the metals except beryllium form oxide layers in air at room temperature that dulls the surface of the metal. Barium is so reactive that it is stored under oil. All of the metals except beryllium reduce water and dilute acids to hydrogen:

$$\mathrm{Mg(solid) + 2H^+(aq)} \Rightarrow \mathrm{Mg(aq) + H_2(gas)}$$

Magnesium reacts only slowly with water unless the water is boiling, but calcium reacts rapidly even at room temperature, and forms a cloudy white suspension of sparingly soluble calcium hydroxide.

TABLE 1.3

Element	Atomic number	Relative atomic mass	Melting point, °C	Density in kgm/m^3
Be	4	9.012	1551	1847.7
Mg	12	24.31	922	1738
Ca	20	40.08	1112	1550
Sr	38	87.62	1042	2540
Ba	56	137.33	1002	3594

	Ionization energies in kJ/mol		
	1st	2nd	3rd
Be	899.4	1757.1	14,848
Mg	737.7	1450.7	7732.6
Ca	589.7	1145	4910
Sr	549.5	1064.2	4210
Ba	502.8	965.1	3600

	Atomic radius/Å	Ionic radius/Å (M^{2+})	Standard electrode potentials/V
Be	1.13	0.34	−1.85
Mg	1.60	0.78	2.36
Ca	1.97	1.06	−2.87
Sr	2.15	1.27	−2.89
Ba	2.17	1.43	−2.90

Calcium, strontium and barium can reduce hydrogen gas when heated, forming the hydride:

$$Ca(solid) + H_2(gas) \Rightarrow CaH_2(solid)$$

The hot metals are also sufficiently strong reducing agents to reduce nitrogen gas and form nitrides:

$$3Mg(solid) + N_2(gas) \Rightarrow Mg_3N_2(solid)$$

Magnesium can reduce, and burn, in carbon dioxide:

$$2Mg(solid) + CO_2(gas) \Rightarrow 2MgO(solid) + C(solid)$$

This means that magnesium fires cannot be extinguished using carbon dioxide fire extinguishers.

The oxides of alkaline earth metals are normally prepared by heating the hydroxide or carbonate to release carbon dioxide gas. They have high lattice enthalpies and melting points. Peroxides, MO_2, are known for all these elements except beryllium. It appears that the Be^{2+} cation is too small to accommodate the peroxide anion.

Calcium, strontium and barium oxides react with water to form hydroxides:

$$CaO(solid) + H_2O(liq) \Rightarrow Ca(OH)_2(solid)$$

Calcium hydroxide is known as "slaked lime". It is sparingly soluble in water and the resulting mildly alkaline solution is known as "limewater" which is used to test for the acidic gas, carbon dioxide.

The Group 2 halides are normally found in the hydrated form. They are all ionic except beryllium chloride. Anhydrous calcium chloride has such a strong affinity for water that it is used as a drying agent.

Of the elements in this Group only magnesium is produced on a large scale. It is extracted from seawater by the addition of calcium hydroxide, which precipitates out the less soluble magnesium hydroxide. This hydroxide is then converted to the chloride with HCl, which is electrolyzed in a "Downs Cell" to extract magnesium metal. The metal is used in flares, tracer bullets and incendiary bombs as it burns with a brilliant white light. It has also been alloyed with aluminum to produce a low-density, strong material used in aircraft. Magnesium oxide has such a high melting point that it is used to line furnaces.

The alkaline earth elements are found in all living organisms. However, beryllium's low aqueous solubility means that it is rarely available to biological systems. That is, it has no known role in living organisms. It is generally highly toxic if encountered by them.

In contrast, magnesium and calcium are ubiquitous and essential to all known living organisms. These elements are involved in more than one role. For example, Mg/Ca ion pumps play a pivotal role in some cellular processes, where magnesium functions as the active center in some enzymes, while calcium salts take a structural role (e.g. bones and teeth) in animals.

Strontium and barium display a lower availability in the biosphere. Strontium plays an important role in marine aquatic life, especially hard corals. They use strontium to build their exoskeleton. These elements also have some uses in medicine, for example "barium meals" in radio graphic imaging, while strontium compounds are employed in some toothpastes. Radium has a low availability and is highly radioactive, making it toxic to life.

1.2. PROPERTIES OF THE ALKALINE EARTH METALS

Each of these metals display specific properties which differ from the others but have some characteristics that are nearly the same.

1.2.1. Beryllium

The name *beryllium* comes from the Greek word for *bérullos*, *beryl*, and from the Prakrit *veruliya*, in allusion "to become pale", in reference to the pale semiprecious gemstone "Beryl". For about 160 years, beryllium was also known as **glucinium** (with the accompanying chemical symbol **Gl**), the name coming from the Greek word for "sweet", due to the sweet taste of its salts. A bivalent element, beryllium is found in nature as a combination with other elements in minerals. Notable gemstones which contain beryllium include "Beryl" (Aquamarine, Emerald) and "Crysoberyl". The free element is a steel-gray, strong, lightweight, brittle, alkaline earth metal with an atomic weight of 9.01218 g/mol. It is primarily used as a hardening agent in alloys, notably beryllium–copper. Structurally, beryllium's very low density (1.85 times that of water), high melting point (1278 °C), high temperature stability, and low coefficient of thermal expansion, make it in many ways an ideal aerospace material, and it has been used in rocket nozzles and is a significant component of future-planned space telescopes. Because of its relatively high transparency to X-rays and other ionizing radiation types, beryllium metal also has a number of uses as filters and windows for radiation and particle physics experiments.

Commercial use of beryllium metal presents technical challenges due to the toxicity (especially by inhalation) of beryllium-containing dusts. Beryllium produces a direct corrosive effect to human tissue, and can cause a chronic life-threatening allergic disease called "Berylliosis" in susceptible persons. The author has had direct contact with such persons who present skeletal aspects of facial appearance and torso as the disease progresses.

TABLE 1.4

Location	ppb by weight	ppb by atoms
Universe	1	0.1
Sun	0.1	0.01
Meteorite (carbonaceous)	30	70
Crustal rocks	4900	4300
Seawater	0.0006	0.00041
Streams	0.1	0.01
Humans	0.4	0.3

Beryllium is a relatively rare element in both the Earth and the Universe because it is not formed in conventional stellar nucleosynthesis. It more accurately was formed during the "Big Bang", and later from the action of cosmic rays on interstellar dust.

The abundance of beryllium is shown in Table 1.4.

The beryllium content of the earth's surface rocks is about 4–6 ppm. Beryllium is a constituent in about 100 out of about 4000 known minerals, the most important of which are "Bertrandite" ($Be_4Si_2O_7(OH)_2$), "Beryl" ($Al_2Be_3Si_6O_{18}$), "Crysoberyl" (Al_2BeO_4), and "Phenakite" (Be_2SiO_4). Precious stone forms of beryl are "Aquamarine", "Bixbite" and "Emerald".

Beryllium has one of the highest melting points of any of the light metals. It has exceptional elastic rigidity (Young's modulus = 316 GPa). The modulus of elasticity of beryllium is approximately 50% greater than that of steel. The combination of this modulus plus beryllium's relatively low density gives it an unusually fast conduction of sound at standard conditions (about 12.9 km/s).

Other significant properties are the high values for specific heat (1925 J/kg K) and thermal conductivity (216 W/m K). This makes beryllium the metal with the best heat dissipation characteristics per unit weight of all of the metals. In combination with the relatively low coefficient of linear thermal expansion (11.4×10^{-6}/K), these characteristics ensure that beryllium demonstrates a unique degree of dimensional stability when heated. At STP (standard temperature and pressure), beryllium resists oxidation when exposed to air (its ability to scratch glass is due to the formation of a thin layer of the hard oxide BeO). It also resists corrosion by concentrated HNO_3.

Beryllium has a large scattering cross section for high-energy neutrons, thus effectively slowing the neutrons to the thermal energy range where the cross section is low (0.008 b). The predominant beryllium isotope, ^9Be, also undergoes a (n, 2n) neutron reaction to form ^8Be, i.e. beryllium is a neutron multiplier, releasing more neutrons than

TABLE 1.5

Known isotopes of beryllium

Nuclide	Z	N	Isotopic mass	Half-life	Decay mode
^{5}Be	4	1	5.04079	No data available	Proton emission
^{6}Be	4	2	6.019726	4.06848×10^{-21} s [0.092 MeV]	Alpha decay
^{7}Be	4	3	7.01692983	53.22 days	Electron capture
^{8}Be	4	4	8.00530510	6.72206×10^{-17} s [6.8 eV]	Alpha decay
^{9}Be	4	5	9.0121822	Stable	Stable
^{10}Be	4	6	10.0135338	1.51×10^{6} years	β-minus decay
^{11}Be	4	7	11.021658	13.81 s	β-minus decay
^{12}Be	4	8	12.026921	21.31 ms	β-minus decay
^{12}Be	4	8	12.026921	2.71×10^{-21} s	Neutron emission
^{14}Be	4	10	14.04289	4.84 ms	β-minus decay
^{15}Be	4	11	15.05346	<200 ns	No data
^{16}Be	4	12	16.06192	<200 ns	No data

it absorbs. Beryllium is highly permeable to X-rays and neutrons are liberated when it is struck by alpha particles.

Of beryllium's isotopes, only ^{9}Be is stable and the others are relatively unstable or rare. It is thus a "mono-nuclide" element. "Cosmogenic" ^{10}Be is produced in the atmosphere by cosmic ray spallation of oxygen and nitrogen. Cosmogenic ^{10}Be accumulates at the soil surface, where its relatively long half-life (1.51 million years) permits a long residence time before decaying to ^{9}Be. Thus, ^{10}Be and its daughter products have been used to examine soil erosion and soil formation from "regolith" (which is soil formed by material originating through rock weathering or plant growth), the development of lateritic soils as well as variations in solar activity, and the age of ice cores. Solar activity is inversely correlated with ^{10}Be production, because the solar wind decreases the flux of galactic cosmic rays which reach the Earth (Table 1.5).

Beryllium-10 is also formed in nuclear explosions by a reaction of fast neutrons with ^{13}C in the carbon dioxide in air, and is one of the historical indicators of past activity at nuclear test sites.

The fact that ^{7}Be and ^{8}Be are unstable has profound cosmological consequences as it means that elements heavier than beryllium could not have been produced by nuclear fusion in the "Big Bang" since there was insufficient time during the nucleosynthesis phase of the Big Bang expansion to produce carbon by fusion of ^{4}He nuclei. The other factor was the relatively low concentrations of ^{8}Be available because of its short half-life. Astronomer Fred Hoyle first showed that the energy levels of ^{8}Be and ^{12}C allow carbon production by a triple-alpha process in helium-fueled stars where more synthesis time is available. ^{7}Be decays by electron capture. Therefore, its decay rate is dependent upon its electron configuration—a rare occurrence in nuclear decay.

The shortest-lived known isotope of beryllium is ^{13}Be which decays through neutron emission. It has a half-life of 2.7×10^{-21} s. ^{6}Be is also very short lived with a half-life of 4.96×10^{-21} s. The exotic isotopes ^{11}Be and ^{14}Be are known to exhibit a "nuclear halo".

Beryllium has the electronic configuration $[He]2s^2$ and exhibits only the +2 oxidation state. The only evidence of a lower valence state of beryllium is in the fact that Be is soluble in $BeCl_2$. The small atomic radius ensures that the Be^{2+} ion is highly polarizing, a fact leading to significant covalent character in beryllium's bonding within various compounds. Beryllium is 4 coordinate in complexes e.g. $[Be(H_2O)_4]^{2+}$ and tetrahaloberyllates, BeX_4^{2-}. This characteristic is used in analytical techniques for determining Be using EDTA as a ligand which preferentially forms octahedral complexes, thus absorbing other cations such as Al^{3+} which might interfere in the solvent extraction of a complex formed between Be^{2+} and acetylacetone.

Beryllium metal lies above aluminum in the electrochemical series and would be expected to be a reactive metal. However it is passivated by an oxide layer and does not react with air or water even at red heat. Once ignited however, beryllium burns brilliantly in air forming a mixture of BeO and Be_3N_2.

Beryllium dissolves readily in nonoxidizing acids, such as HCl and H_2SO_4, but not in nitric acid as this forms the oxide on the surface of the metal. This behavior is similar to that of aluminum metal. Another strange feature is that Be is **amphoteric**. This means that it has the properties of both an acid and a base. The following two reactions show this factor:

$$Be(OH)_2(solid) + H_2SO_4(aq) \Rightarrow BeSO_4(solid) + 2\,H_2O(liq)$$

$$Be(OH)_2(solid) + 2\,NaOH(aq) \Rightarrow Na_2Be(OH)_4(aq) \Leftrightarrow 2\,Na^+(aq) + Be(OH)_4^{2-}(aq)$$

Beryllium, again similarly to aluminum, dissolves in warm alkali to form the berylliate anion, $Be(OH)_4^{2-}$ and hydrogen gas. The solutions of salts, e.g. beryllium sulfate and beryllium nitrate are acidic because of hydrolysis of the $[Be(H_2O)_4]^{2+}$ ion. For example:

$$BeSO_4(solid) + 4\,H_2O(liq) \Rightarrow [Be(H_2O)_4]^{2+}(aq) + SO_4^{2-}(aq)$$

$$[Be(H_2O)_4]^{2+}(aq) + H_2O \Rightarrow [Be(H_2O)_3(OH)]^{+}(aq) + H_3O^{+}(aq)$$

The hydrolytic reactions of beryllium(II) ions have been calorimetrically studied at 25 °C in aqueous solution and dioxane–water mixtures, both containing 3.0 mol/dm^3 Li_2ClO_4 as a constant ionic medium. On the basis of the formation constants determined, the enthalpy and entropy changes for the reaction:

$$x\ Be^{2+} + y\ H_2O \Rightarrow (Be_x(OH)_y)^{2(x-y)+} + y\ H^+,$$

were estimated for the Be_2OH^{3+} and $Be_3(OH)_3^{3+}$ complexes in aqueous solution and 0.1 mol fraction dioxane–water mixture and for Be_2OH^{3+}, $Be_3(OH)_3^{3+}$, and $Be_2(OH)_2^{2+}$ complexes in 0.2 mol fraction dioxane–water mixture. The enthalpy and entropy changes of formation of the $Be_x\ (OH)_y)^{2(x-y)+}$ complex in solutions of various mole fractions of dioxane were obtained and shown to abide by the following reaction:

$$2Be^{2+} + H_2O \Rightarrow Be_2OH^{3+} + H^+$$

Thus, it is clear that the Be^{2+} cation in aqueous solution never appears but is an "aquo-complex". This illustrates the amphoteric nature of beryllium salts.

Beryllium differs from its brothers (or sisters) in Group 2 in that it usually forms covalent bonds. But, unlike other covalent molecules, it is soluble in organic solvents and is a poor conductor when molten.

Because of its high affinity for oxygen at elevated temperatures and its ability to reduce water when its oxide film is removed, the extraction of beryllium from its compounds is very difficult. Although electrolysis of a fused mixture of beryllium and sodium fluorides was used to isolate the element in the nineteenth century, the metal's high melting point makes this process more energy intensive than the corresponding production of alkali metals by the Down's Process. Early in the twentieth century, the production of beryllium by the thermal decomposition of BeI_2 was investigated following the success of a similar process for the production of zirconium, but this proved to be uneconomic for volume production. Beryllium metal is available commercially and is never normally made in the laboratory. Its extraction from ores is complex.

The mineral beryl, $[Be_3Al_2(SiO_3)_6]$ is the most important source of beryllium. It is roasted with sodium hexafluorosilicate, Na_2SiF_6, at 700 °C to form beryllium fluoride. This salt is water soluble and beryllium may be precipitated as the hydroxide $Be(OH)_2$ by adjustment of the pH to 12.

Pure beryllium may be obtained by electrolysis of molten $BeCl_2$ containing some NaCl. Salt is added since molten $BeCl_2$ conducts very poorly. Another method involves the reduction of beryllium fluoride with magnesium at 1300 °C:

$$BeF_2 + Mg \Rightarrow MgF_2 + Be$$

Although emeralds and beryl were known to ancient civilizations, they were first recognized as the same mineral ($Be_3Al_2(SiO_3)_6$) by Abbé Haüy in 1798. Later that year, Louis-Nicholas Vauquelin, a French chemist, discovered that an unknown element was present in emeralds and beryl. Attempts to isolate the new element finally succeeded in 1828 when two chemists, Friedrich Wölhler of Germany and A. Bussy of France, independently produced beryllium by reducing beryllium chloride ($BeCl_2$) with potassium metal in a platinum crucible. Today, beryllium is primarily obtained from the minerals Beryl ($Be_3Al_2(SiO_3)_6$) and Bertrandite ($4BeO\cdot 2SiO_2\cdot H_2O$) through a chemical process or through the electrolysis of a mixture of molten beryllium chloride ($BeCl_2$) and sodium chloride (NaCl).

Beryllium metal did not become readily available until 1957. Currently, the metal is produced by reducing BeF_2 with Mg metal. The price on the US market for vacuum-cast beryllium ingots was $338 per pound ($745/kg) in 2001.

The metal, beryllium, has had many uses and applications in Industry. Among these are the following:

- Because of its low atomic number and very low absorption for X-rays, the oldest and still one of the most important applications of beryllium is in radiation windows for X-ray tubes. Extreme demands are placed on purity and cleanliness of Be to avoid artifacts in the X-ray images. Thin beryllium foils are used as radiation windows for X-ray detectors, and the extremely low absorption minimizes the heating effects caused by high intensity, low energy X-rays typical of synchrotron radiation.
- Vacuum-tight windows and beam tubes for radiation experiments on synchrotrons are manufactured exclusively from beryllium. In scientific setups for various X-ray emission studies, the sample holder is usually made of beryllium because its emitted X-rays have much lower energies (~100 eV) than the X-rays from most studied materials.
- Because of its low atomic number, beryllium is almost transparent to energetic particles. Therefore it is used to build the "beam pipe" around the collision region in "Collider Particle Physics" experiments. Notably all four main detector experiments at the Large Hadron Collider Accelerator in Berne, Switzerland use a beryllium beam pipe.
- Beryllium's low density allows collision products to reach the surrounding detectors without a significant interaction. Its stiffness allows a powerful vacuum to be produced within the pipe to minimize interaction with gases. Its thermal stability allows it to function correctly at temperatures of only a few degrees above the absolute zero, and its diamagnetic nature keeps it from interfering with the complex multipole

magnet systems used to steer and focus the particle beams.

- Due to its stiffness, lightweight, and dimensional stability over a wide temperature range, beryllium metal is used in the defense and aerospace industries for lightweight structural components in high-speed aircraft, missiles, space vehicles and communication satellites. Several liquid-fueled rockets use nozzles of pure beryllium.
- Beryllium is used as an alloying agent in the production of beryllium–copper, which contains up to 2.5% beryllium. Beryllium–copper alloys are used in many applications because of their combination of high electrical and thermal conductivity, high strength and hardness, nonmagnetic properties, along with good corrosion and fatigue resistance. These applications include the making of spot-welding electrodes, springs, non-sparking tools and electrical contacts.
- The excellent elastic rigidity of beryllium has led to its extensive use in precision instrumentation, e.g. in gyroscope inertial guidance systems, and in support structures for optical systems.
- Beryllium mirrors are a field of particular interest in astronomical applications. Large-area mirrors, frequently with a honeycomb support structure, are used. For example, in meteorological satellites where low weight and long-term dimensional stability are critical, the use of beryllium is essential. Smaller beryllium mirrors are used in optical guidance systems and in fire control systems, as in the German "main-battle" tanks of World War II. In these systems, very rapid movement of the mirror is required which again dictates low mass and high rigidity. Usually the beryllium mirror is coated with hard electroless nickel that can be more easily polished to a finer optical finish than beryllium. In some applications, though, the beryllium blank is polished without any coating. This is particularly applicable to a cryogenic operation where any thermal expansion mismatch can cause the coating to buckle.
- The James Webb Space Telescope (JWST), a planned infrared space observatory (which will replace, in part, the Hubble Space Observatory), will have 18 hexagonal beryllium sections for its mirrors. Because JWST will face a temperature of 33 K, the mirror is made of beryllium, because it is capable of handling extreme cold better than glass. Beryllium contracts and deforms less than glass and remains more uniform at such temperatures. For the same reason, the optics of the Spitzer Space Telescope, launched by NASA in 2003, are entirely built of beryllium metal.
- An earlier major application of beryllium was in brakes for military aircraft because of its hardness, high melting point and exceptional heat dissipation. Environmental and toxicity considerations have since led to substitution by other materials.
- Cross-rolled beryllium sheet is an excellent structural support for printed circuit boards in surface-mounted technology. In critical electronic applications, beryllium is both a structural support and a heat sink. The application also requires a coefficient of thermal expansion that is well matched to that of alumina and polyimide glass substrates. The beryllium–beryllium oxide composite "E-Materials" have been specially designed for these electronic applications and have the additional advantage that the thermal expansion coefficient can be tailored to match diverse substrate materials.
- Due to their non-magnetic properties, beryllium-based tools are often used by military naval personnel when working on or around sea-mines, as these devices often have fuses that detonate on direct magnetic contact or when influenced by a magnetic field.
- Beryllium-based tools are used for maintenance and construction near MRI scanners. Magnetic tools would be pulled by the scanner's strong magnetic field. Apart from being difficult to remove once magnetic items are stuck in the scanner, the induced missile effect can have dangerous consequences.
- In the telecommunications industry, tools made of beryllium are used to tune the highly magnetic klystrons used for high-power microwave applications.
- Beryllium is used in nuclear weapon designs as the outer layer of the "pit" (the core of an implosion weapon—the fissile material and any reflector or tamper bonded to it) of the primary stage, surrounding the fissile material. It is a good implosion pusher and a very good neutron reflector, and is used in certain moderated reactors such as "Molten-salt Reactors".
- Beryllium is sometimes used as a neutron source in which the beryllium is mixed with an alpha emitter such as ^{210}Po, ^{226}Ra, ^{239}Pu or ^{241}Am.
- Beryllium has also been proposed as a cladding material for nuclear fuel, due to its combination of mechanical, chemical, and nuclear properties.
- Beryllium's characteristics (low weight and high rigidity) make it useful as a material for high-frequency audio-drivers in audio applications. Until recently, most beryllium tweeters used an alloy of beryllium and other metals. This was due to beryllium's high cost and difficult formability. These challenges, coupled with the high performance of beryllium, caused some manufacturers to falsely claim that they used pure beryllium. Some high-end audio companies now manufacture pure beryllium tweeters or speakers using such tweeters. Because beryllium is many times more expensive than titanium, hard to shape due to its brittleness,

and toxicity if mishandled, these tweeters are limited to high-end and "public address" applications.

- Beryllium is an effective p-type dopant in III–V semiconductors. It is widely used in materials such as GaAs, AlGaAs, InGaAs, and InAlAs grown by "Molecular Beam Epitaxy".
- BeO is useful for many applications that require the combined properties of an electrical insulator, an excellent heat conductor with high strength and hardness, with a very high melting point. Beryllium oxide is frequently used as an insulator base plate in high-power transistors in RF transmitters for telecommunications. Beryllium oxide is also being studied for use in increasing the thermal conductivity of UO_2 nuclear fuel pellets.
- Beryllium compounds were once used in fluorescent lamps as zinc beryllium silicate phosphor, but this use was discontinued because of berylliosis induced in the workers manufacturing the phosphor and fluorescent lamps. Although the use of beryllium compounds in fluorescent lighting was discontinued in 1949, potential for exposure to beryllium still exists in the nuclear and aerospace industries and in the refining of beryllium metal and melting of beryllium-containing alloys, the manufacturing of electronic devices, and the handling of other beryllium-containing material.

Early researchers tasted beryllium and its various compounds for sweetness in order to verify its presence. Modern diagnostic equipment no longer necessitates this highly risky procedure and no attempt should be made to ingest this highly toxic substance. Beryllium and its compounds should be handled with great care and special precautions must be taken when carrying out any activity that could result in the release of beryllium dust (causing lung cancer is a possible result of prolonged exposure to beryllium laden dust). This substance can be handled safely if certain procedures are followed. No attempt should be made to work with beryllium before familiarization with correct handling procedures.

A successful test for beryllium in air and on surfaces was developed and published (2006) as an international voluntary consensus standard (ASTM D7202; www.astm.org). The procedure uses dilute ammonium bifluoride for dissolution and fluorescence detection with beryllium bound to sulfonated hydroxybenzoquinoline, allowing detection up to 100 times lower than the recommended limit for beryllium concentration in the workplace. Fluorescence increases with increasing beryllium concentration. This procedure has been successfully tested on a variety of surfaces and is effective for the dissolution and ultratrace detection of refractory beryllium oxide and siliceous beryllium (Table 1.6).

TABLE 1.6

Physical properties of beryllium metal	
CAS number	7440-41-7
Phase	Solid
Density at rt	1.85 g/cm^3
Liquid density at MP	1.690 g/cm^3
Melting point	1560 K, 1287 °C, 2349 °F
Heat of fusion	7.895 kJ/mol
Heat of vaporization	297 kJ/mol
Specific heat capacity	16.443 J/mol K
Electronegativity	1.57 (Pauling scale)
Ionization energies	1st: 899.5 kJ/mol
	2nd: 1757 kJ/mol
	3rd: 14,848 kJ/mol
Atomic radius	1.12 Å
Covalent radius	0.96 Å
Van der Waals radius	1.53 Å
Crystal structure	Hexagonal
Magnetic ordering	Diamagnetic
Thermal conductivity	200 W/mol K (at 300 K)
Thermal expansion	11.3 μm/mol K (25 °C)
Speed of sound (thin rod)	12,870 ms (at rt)
Young's modulus	287 Gpa
Shear modulus	132 Gpa
Bulk modulus	130 Gpa
Poisson ratio	0.032
Mohs hardness	5.5
Vickers hardness	1670 Mpa
Brinell hardness	600 MPa

1.2.2. Magnesium

Magnesium is a Group 2 element (Group IIA in older labeling schemes). This element has the symbol Mg, atomic number 12, atomic weight of 24.305 g/mol and common oxidation number +2. It is the eighth most abundant element in the earth's crust by mass, although ninth in the Universe as a whole. This preponderance of magnesium in the Universe is related to the fact that it is easily built up in supernova stars from a sequential addition of three helium nuclei to carbon (which in turn is made from three helium nuclei). Magnesium constitutes about 2% of the Earth's crust by mass, which makes it the eighth most abundant element in the crust.

TABLE 1.7

Location	ppb by weight	ppb by atoms
Universe	600,000	30,000
Sun	700,000	30,000
Meteorite (carbonaceous)	120,000,000	100,000,000
Crustal rocks	29,000,000	25,000,000
Seawater	1,326,000	337,000
Stream	4,100	170
Humans	270,000	70,000

Magnesium ion's high solubility in water helps to ensure that it is the third most abundant element dissolved in seawater.

The name originates from the Greek word for a district in Thessaly called "Magnesia". It is related to the terms "magnetite" and "manganese", which also originated from this area, and required differentiation as separate substances. Magnesium is the seventh most abundant element in the Earth's crust by mass and eighth by molarity. It is found in large deposits of Magnesite, Dolomite and other minerals, and in mineral waters, where the magnesium ion is soluble. The abundance of magnesium is shown in Table 1.7.

In 1618 a farmer at Epsom in England attempted to give his cows water from a well. They refused to drink because of the water's bitter taste. However the farmer noticed that the water seemed to heal scratches and rashes. The fame of "Epsom Salts" spread. Eventually the compound was recognized to be hydrated magnesium sulfate, $MgSO_4$.

The first person to propose that magnesium was an element was Joseph Black of Edinburgh in 1755. In 1792, an impure form of metallic magnesium was produced by Anton Rupprecht who heated magnesia (magnesium oxide, MgO) with charcoal. He named the element "Austrium" after his native Austria. In 1808, a small sample of the *pure* metal was isolated by Humphry Davy by the electrolysis of moist MgO. He proposed the name "magnium" based on the mineral Magnesite ($MgCO_3$) that came from Magnesia in Greece. Neither name survived and eventually the metal was called magnesium. The metal itself was first produced in quantity in England by Davy in 1808 using then the new method of electrolysis of a mixture of molten magnesia and mercuric oxide. Antoine Bussy prepared it in a consistent form in 1831.

The known isotopes of magnesium are listed in Table 1.8.

Magnesium has three stable isotopes: ^{24}Mg, ^{25}Mg and ^{26}Mg. All are present in significant amounts (see Table 1.8). About 79% of Mg is ^{24}Mg. The isotope ^{28}Mg is radioactive and in the 1950s to 1970s was made commercially by several nuclear power plants for use in scientific experiments. This isotope has a relatively short half-life (21 h) and so its use was limited by shipping times. ^{26}Mg has found application in isotopic geology, similar to that of aluminum. ^{26}Mg is a radiogenic daughter product of ^{26}Al, which has a half-life of 717,000 years. Large enrichments of stable ^{26}Mg have been observed in the Ca–Al-rich inclusions of some carbonaceous chrondrite meteorites. The anomalous abundance of ^{26}Mg is attributed to the decay of its parent ^{26}Al in the inclusions. Therefore, the meteorite must have formed in the solar nebula before the ^{26}Al had decayed. Hence, these fragments are among the oldest objects in the solar system and have preserved information about its early history.

It is conventional to plot $^{26}Mg/^{24}Mg$ against an Al/Mg ratio. In an isochronic dating plot, the Al/Mg ratio plotted is $^{27}Al/^{24}Mg$. The slope of the isochron has no age significance, but indicates the initial $^{26}Al/^{27}Al$ ratio

TABLE 1.8

Nuclide	Z	N	Isotopic mass	Half-life	Nuclear spin
^{19}Mg	12	7	19.03547	Not known	1/2−
^{20}Mg	12	8	20.018863	90.8 ms	0+
^{21}Mg	12	9	21.011713	122 ms	(5/2, 3/2)+
^{22}Mg	12	10	21.9995738	3.8755 s	0+
^{23}Mg	12	11	22.9941237	11.317 s	3/2+
^{24}Mg	12	12	23.98504170	Stable (79%)	0+
^{25}Mg	12	13	24.98583692	Stable	5/2+
^{26}Mg	12	14	25.982592929	Stable	0+
^{27}Mg	12	15	26.98434059	9.458 min	1/2+
^{28}Mg	12	16	27.9838768	20.91 h	0+
^{29}Mg	12	17	28.988600	1.30 s	3/2+
^{29}Mg	12	17	28.988600	1.30 s	3/2+
^{31}Mg	12	19	30.996546	230 ms	3/2+
^{32}Mg	12	20	31.998975	86 ms	0+
^{33}Mg	12	21	33.005254	90.5 ms	7/2−
^{34}Mg	12	22	34.00946	20 ms	0+
^{35}Mg	12	23	35.01734	70 ms	(7/2−)
^{36}Mg	12	24	36.02300	3.9 ms	0+
^{37}Mg	12	25	37.03140	40 ms	7/2−
^{38}Mg	12	26	38.03757	1.0 ms	0+
^{39}Mg	12	27	39.04677	<260 ns	7/2−
^{40}Mg	12	28	40.05393	1.0 ms	0+

in the sample at the time when the systems were separated from a common reservoir.

Magnesium is a rather tough metal. Elemental magnesium is a moderately strong, silvery-white, lightweight metal (two-thirds the density of aluminum). Magnesium tarnishes slightly in air, and finely divided magnesium readily ignites upon heating in air and burns with a dazzling white flame, making it a useful ingredient in flares. Normally, magnesium is coated with a layer of oxide, MgO, that protects magnesium from air and water.

Like its neighbor, Ca, magnesium reacts with water at room temperature, though it reacts much more slowly than calcium. When it is submerged in water, hydrogen bubbles will almost unnoticeably begin to form on the surface of the metal. If powdered, it will react much more rapidly. The reaction occurs much faster at higher temperatures. Magnesium also reacts exothermically with most acids, such as hydrochloric acid (HCl). As with aluminum, zinc and many other metals, the reaction with hydrochloric acid produces the chloride of the metal and releases hydrogen gas.

Magnesium is a highly flammable metal, but, while it is easy to ignite when powdered or shaved into thin strips, it is difficult to ignite in mass or bulk. Once ignited, it is difficult to extinguish, being able to burn in both nitrogen (forming magnesium nitride), and also in CO_2 (forming magnesium oxide and carbon). This property was used in incendiary weapons used in the "fire bombing" of cities in World War II, the only practical civil defense being used to smother a burning flare under dry sand to exclude the atmosphere. On burning in air, magnesium produces a brilliant white light. Thus, magnesium powder (as "flash powder") was used as a source of illumination in the early days of photography. Later, magnesium ribbon was used in electrically ignited flash bulbs.

Magnesium powder is used in the manufacture of fireworks and marine flares where a brilliant white light is required. Flame temperatures of magnesium and magnesium alloys can reach 1371 °C (2500 F), although flame height above the burning metal is usually less than 300 mm (12 in). Magnesium may be used as an ignition source for "thermite", or otherwise difficult to ignite mixture of aluminum and iron oxide powder.

Magnesium compounds are typically white crystals. Most are soluble in water, providing the sour-tasting magnesium ion, Mg^{2+}. Small amounts of dissolved magnesium ion contribute to the tartness and taste of natural waters. Magnesium ion in large amounts is an ionic laxative, and magnesium sulfate (known as "Epsom Salts") is sometimes used for this purpose. So-called "milk of magnesia" is a water suspension of one of the few insoluble magnesium compounds, $Mg(OH)_2$. The undissolved particles give rise to its appearance and name. Milk of magnesia is a mild base commonly used as an antacid.

The metal is now mainly obtained by electrolysis of magnesium salts obtained from brine. Commercially, the chief use for the metal is as an alloying agent to make Al–Mg alloys, sometimes called "magnalium" or "magnelium". Since magnesium is less dense than aluminum, these alloys are valued for their relative lightness and strength.

Magnesium is an important element for plant and animal life. Chlorophylls are porphyrins (a class of pigments including heme and chlorophyll) whose molecules contain a flat ring of four-linked heterocyclic groups, based upon magnesium. The adult human daily requirement of magnesium is about 0.3 g/day. Magnesium is the 11th most abundant element by mass in the human body. Its ions are essential to all living cells, where they play a major role in manipulating important biological polyphosphate compounds like ATP, DNA and RNA. Hundreds of enzymes thus require magnesium ions in order to function. Magnesium, being the metallic ion at the center of chlorophyll, is thus a common additive to fertilizers. Magnesium compounds are used medicinally as common laxatives, antacids (i.e. "Milk of Magnesia"), and in a number of situations where stabilization of abnormal nerve excitation and blood vessel spasm is required (i.e. to treat eclampsia). Magnesium ions are sour to the taste, and in low concentrations help to impart a natural tartness to fresh mineral waters.

Magnesium metal can be made commercially by several processes and would not normally be made in the laboratory because of its ready availability. There are massive amounts of magnesium in seawater. This can be recovered as magnesium chloride, $MgCl_2$ through reaction with calcium oxide, CaO:

$$CaO + H_2O \Rightarrow Ca^{2+} + 2OH^-$$

$$Mg^{2+} + 2OH^- \Rightarrow Mg(OH)_2$$

$$Mg(OH)_2 + 2HCl \Rightarrow MgCl_2 + 2H_2O$$

Electrolysis of hot molten $MgCl_2$ produces magnesium as a liquid. This is poured off and chlorine gas is recovered:

$$\text{cathode: } Mg^{2+}(liq) + 2e^- \Rightarrow Mg(solid)$$

$$\text{anode: } Cl^-(liq) \Rightarrow {}^1/_2\, Cl_2(gas) + e^-$$

The other method used to produce magnesium involves Dolomite, i.e. $MgCa(CO_3)_2$, an important magnesium mineral, and involves a non-electrolytic method. In this process, Dolomite is "calcined" by heating to form the oxide, "calcined dolomite" = $MgO \cdot CaO$, and this product is then reacted with ferrosilicon alloy:

$$2[MgO \cdot CaO] + FeSi \Rightarrow 2Mg + Ca_2SiO_4 + Fe$$

Magnesium, as the metal, may be distilled out from this mixture of solid products (BP = 1091 °C). Although magnesium is found in over 60 minerals, only Dolomite-($MgCa(CO_3)_2$), Magnesite-($MgCO_3$), Brucite-($Mg(OH)_2$), Carnallite-($KMgCl_3 \cdot 6H_2O$), Talc-($Mg_3Si_4O_{10}(OH)_2$) and Olivine-($(Mg,Fe)_2SiO_4$) are of commercial importance.

The Mg^{2+} cation is the second most abundant in seawater (occurring at about 12% of the mass of sodium cations), which makes seawater and sea-salt an attractive commercial source of Mg. To extract the magnesium, $Ca(OH)_2$ is added to seawater to form $Mg(OH)_2$ as a precipitate:

$$MgCl_2(aq) + Ca(OH)_2(solid) \Rightarrow Mg(OH)_2(solid) + CaCl_2(aq)$$

Magnesium hydroxide is insoluble in water so it can be filtered out and then reacted with hydrochloric acid to obtain concentrated magnesium chloride:

$$Mg(OH)_2(solid) + 2\,HCl(aq) \Rightarrow MgCl_2(aq) + 2\,H_2O$$

From molten magnesium chloride, an electrolysis process produces magnesium.

In the United States, magnesium is principally obtained by electrolysis of fused magnesium chloride from brines, wells, and seawater. The United States has traditionally been the major world supplier of this metal, supplying 45% of world production even as recently as 1995. Today, the US market share is at 7%, with a single domestic producer left, "US Magnesium", a company born from the now-defunct "Magcorp". As of 2005, China has taken over as the dominant supplier, pegged at 60% world market share, which increased from 4% in 1995. Unlike the above-described electrolytic process, China is almost completely reliant on a different method of obtaining the metal from its ores, the so-called "Silicothermic Pidgeon" process which involves the reduction of the oxide at high temperatures with silicon.

Magnesium is the third most commonly used structural metal, following steel and aluminum. Magnesium, in its purest form, can be compared with aluminum, and is strong and light so that it is used in several high-volume part manufacturing applications, including automotive and truck components.

Specialty, high-grade car wheels of magnesium alloy are called "mag wheels". In 1957 a Corvette SS, designed for racing, was constructed with magnesium body panels. An earlier Mercedes-Benz race car model had a body made from "Elektron", a magnesium alloy; these cars ran (with successes) at Le Mans and other world-class race events in 1955. Volkswagen Group has used magnesium in its engine components for many years. For a long time, Porsche AG has used a magnesium alloy for its engine blocks due to the weight advantage. There is renewed interest in magnesium engine blocks, as featured in the 2006 BMW 325i and 330i models. The application of a magnesium alloy in the 2006 Corvette engine cradle has advanced the technology of designing robust automotive parts using magnesium. These alloys, recent developments in high-temperature low-creep metals, are becoming competitive to aluminum because of lower costs.

The second application field of magnesium is in electronic devices. Due to low weight, good mechanical and electrical properties, magnesium is widely used for manufacturing of mobile phones, laptop computers, cameras, and other electronic components.

Historically, magnesium was one of the main aerospace construction metals and was used for German military aircraft as early as World War I and extensively for German aircraft in World War II. The Germans coined the name "Elektron" for the magnesium alloy that is still used today. Due to perceived hazards with magnesium parts in the event of fire, the application of magnesium in the commercial aerospace industry was generally restricted to engine-related components. Currently the use of magnesium alloys in aerospace is increasing, mostly driven by the increasing importance of fuel economy and the need to reduce weight. The development and testing of new magnesium alloys continues, notably Elektron-21, which has successfully undergone extensive aerospace testing for suitability in engine, internal and airframe components. The European Community currently runs three R&D magnesium projects in its Aerospace Priority agenda called "Six Framework Program".

Magnesium is flammable, burning at a temperature of approximately 1371 °C (1644 K; 2500 °F). The autoignition temperature of magnesium ribbon is approximately 510 °C (783 K; 950 °F) in air. The high temperature at which magnesium burns makes it a handy tool for starting emergency fires during outdoor recreation. Other related uses include flashlight photography, flares, pyrotechnics and fireworks sparklers.

Magnesium is also used:

- To remove sulfur from iron and steel.
- To refine titanium in the "Kroll" process.
- To photoengrave plates in the printing industry.
- To combine in alloys, where this metal is essential for airplane and missile construction.
- In the form of turnings or ribbons, to prepare "Grignard Reagents", which are useful in organic synthesis.
- As an alloying agent, improving the mechanical, fabrication and welding characteristics of aluminum.
- As an additive agent in conventional propellants and the production of "nodular graphite" in cast iron.
- As a reducing agent for the production of uranium and other metals from their salts.
- As a desiccant, since it easily reacts with water.
- As a sacrificial (galvanic) anode to protect underground tanks, pipelines, buried structures, and water heaters.

TABLE 1.9

Physical constants of magnesium	
CAS number	7439-95-4
Phase	Solid
Density	1.738 g/cm^3
Liquid density at MP	1.584 g/cm^3
Melting point	923 K, 650 °C, 1202 °F
Boiling point	1363 K, 1091 °C, 1994 °F
Heat of fusion	8.48 kJ/mol
Heat of vaporization	128 kJ/mol
Specific heat capacity	24.869 J/mol/K
Electronegativity	1.31 (Pauling scale)
Atomic radius	1.60 Å
Covalent radius	1.41 Å
Van der Waals radius	1.73 Å
Crystal structure	Hexagonal
Magnetic ordering	Paramagnetic
Electrical resistivity	43 nΩ m
Thermal conductivity	156 W/m K (at 300 K)
Speed of sound (thin rod)	4940 ms
Young's modulus	45 Gpa
Shear modulus	17 Gpa
Bulk modulus	46 Gpa
Poisson ratio	0.29
Mohs hardness	2.5
Brinell hardness	260 Mpa

Stable isotopes		
^{24}Mg	78.99%	^{24}Mg is stable with 12 neutrons
^{25}Mg	10%	^{25}Mg is stable with 13 neutrons
^{26}Mg	11.01%	^{26}Mg is stable with 14 neutrons

Magnesium metal and its alloys are explosive hazards. They are highly flammable in their pure form when molten or in powder or in ribbon form. Burning or molten magnesium metal reacts violently with water. When working with powdered magnesium, safety glasses for eye protection are employed, because the bright white light produced by burning magnesium contains UV light that can permanently damage human eye retinas.

Physical constants of Mg metal are listed in Table 1.9.

1.2.3. Calcium

Calcium is the chemical element with the symbol **Ca** and atomic number 20. It has an atomic weight of 40.078 g/mol. Calcium is the fifth most abundant dissolved ion in seawater by both molarity and mass, after Na^+, Cl^-, Mg^{2+} and SO_4^{2-}. Calcium metal is quite reactive. It readily forms a white coating of calcium nitride (Ca_3N_2) in air at room temperature. It reacts with water and the metal burns in air with an orange-red flame, forming largely the nitride, but some oxide.

In the visible portion of the spectrum of many stars, including the Sun, strong absorption lines of singly ionized calcium ions are evident. Prominent among these are the H line at 3968.5 Å and the K line at 3933.7 Å of singly ionized calcium, or Ca II. For the Sun, and stars with low temperatures, the prominence of the H and K lines is an indication of strong magnetic activity in the chromosphere. Measurement of periodic variations of these active regions can also be used to deduce the rotational periods of these stars.

Calcium as the element is a gray silvery metal. The metal is relatively hard. Calcium is an essential constituent of leaves, bones, teeth, and shells in the Earth's environment. Calcium is the fifth most abundant element in the earth's crust and makes up more than 3% of the crust by weight. Calcium does not occur as the metal itself in nature and instead is found in various minerals including Limestone and Fluorite. Stalagmites and stalactites contain calcium carbonate ($CaCO_3$). Calcium occurs most commonly in sedimentary rocks in the minerals "Calcite", "Dolomite" and "Gypsum". It also occurs in igneous and metamorphic rocks chiefly in the silicate minerals: "Plagioclase"-($CaAl_2Si_2O_8$), "Amphiboles"-($Ca_2Mg_5Si_8O_{22}(OH)_2$), "Pyroxenes"-($CaMg(Si,Al)_2O_6$) and "Garnets"-($Ca_3Al_2(SiO_4)_3$. The abundance of calcium is shown in Table 1.10.

Calcium (Latin word *calcis* meaning "lime") was known as early as the first century when the Ancient Romans prepared lime as calcium oxide from limestone and used "slaked lime" as a "whitewash" on various homes and buildings. Literature dating back to 975 AD notes that "Plaster-of-Paris" (calcium sulfate), is useful for setting broken bones. The metal was not isolated until 1808 when Sir Humphrey Davy of England electrolyzed a mixture of lime and mercuric oxide, using then the new "Voltaic Cell" as an energy source. Davy was trying to isolate calcium. When he heard that Swedish chemist Jöns Berzelius and his colleague, Pontin, had prepared calcium amalgam by electrolyzing lime in mercury, he set up a similar system and was successful. He worked with electrolysis throughout his life and also

TABLE 1.10

The abundance of calcium		
Location	**ppb by weight**	**ppb by atoms**
Universe	70,000	2000
Sun	70,000	2000
Meteorite (carbonaceous)	11,000,000	5,200,000
Crustal rocks	50,000,000	26,000,000
Seawater	4220	650
Stream	1500	38
Humans	14,000,000	2,200,000

discovered/isolated boron, sodium, potassium, magnesium, calcium, strontium and barium. Calcium metal was not available on a large scale until the beginning of the twentieth century.

Calcium, with a density of 1.55 g/cm^3, is the lightest of the alkali earth metals. Magnesium (1.74) and beryllium (1.84) are heavier although they are *lighter* in atomic mass. Both strontium and barium metals get heavier along with the heavier atomic mass. Calcium has a higher resistivity than copper or aluminum. Yet, weight for weight, allowing for its much lower density, it is a better conductor than either. However, its use in terrestrial applications is usually limited because of its high reactivity when exposed to air.

Chemically, calcium is reactive and soft for a metal (though harder than lead, it can be cut with a knife with some difficulty). It is a silvery metallic element that must be extracted by electrolysis from a molten salt like $CaCl_2$. Once produced, it is not stable when exposed to air. It is somewhat difficult to ignite, unlike magnesium, but when lit, the metal burns in air with a brilliant high-intensity reddish light.

Calcium metal reacts with water, evolving hydrogen gas at a rate rapid enough to be noticeable, but not fast enough at room temperature to generate much heat. In powdered form, however, the reaction with water is extremely rapid, as the increased surface area of the powder accelerates the reaction with the water. Part of the slowness of the calcium–water reaction results from the metal being partly protected by an insoluble white $Ca(OH)_2$ layer. In acid solutions where the salt product is water soluble, calcium reacts vigorously. Calcium has 24 known isotopes, as shown in Table 1.11.

Calcium has four stable isotopes (^{40}Ca and ^{42}Ca through ^{44}Ca), plus two more isotopes (^{46}Ca and ^{48}Ca) that have such a long half-lives that for all practical purposes they can be considered stable. It also has a cosmogenic isotope, radioactive ^{41}Ca, with a half-life of 103,000 years. Unlike cosmogenic isotopes that are produced in the atmosphere, ^{41}Ca is produced by neutron activation of ^{40}Ca. Most of its production is in the upper meter or so of the soil column, where the cosmogenic neutron flux is still sufficiently strong. ^{41}Ca has received much attention in stellar studies because it decays to ^{41}K, a critical indicator of solar system anomalies.

A major part (97%) of naturally occurring calcium is in the form of ^{40}Ca. This isotope is one of the daughter products of ^{40}K decay, along with ^{40}Ar. While K/Ar dating has been used extensively in the geological sciences, the prevalence of ^{40}Ca in nature has impeded its use in dating. Techniques using mass spectrometry and a "double-spike" isotope dilution have been used for K/Ca age dating.

TABLE 1.11

Nuclide	Z	N	Isotopic mass	Half-life	Nuclear spin
^{34}Ca	20	14	34.01412	<35 ns	0+
^{35}Ca	20	15	35.00494	25.7 ms	1/2+
^{36}Ca	20	16	35.99309	102 ms	0+
^{37}Ca	20	17	36.985870	181.1 ms	(3/2+)
^{38}Ca	20	18	37.976318	440 ms	0+
^{39}Ca	20	19	38.9707197	859.6 ms	3/2+
^{40}Ca	20	20	39.96259098	Stable $>5.9 \times 10^{21}$ years (96.941%)	0+
^{41}Ca	20	21	40.96227806	1.03×10^5 years	7/2−
^{42}Ca	20	22	41.95861801	Stable (0.467%)	0+
^{43}Ca	20	23	42.9587666	Stable (0.135%)	7/2−
^{44}Ca	20	24	43.9554818	Stable (2.026%)	0+
^{45}Ca	20	25	44.9561866	162.67 days	7/2−
^{46}Ca	20	26	45.9536926	Stable [$>100 \times 10^{15}$ years] (0.004%)	0+
^{47}Ca	20	27	46.9545460	4.536 day	7/2−
^{48}Ca	20	28	47.952534	43.1×10^{18} years (0.187%)	0+
^{49}Ca	20	29	48.955674	8.718 min	3/2−
^{50}Ca	20	30	49.957519	13.9 s	0+
^{51}Ca	20	31	50.96151	10.0 s	3/2−
^{52}Ca	20	32	51.96510	4.6 s	0+
^{53}Ca	20	33	52.97005	90 ms	3/2−
^{54}Ca	20	34	53.97435	50 ms	0+
^{55}Ca	20	35	54.98055	30 ms	
^{56}Ca	20	36	55.98557	10 ms	0+
^{57}Ca	20	37	56.99236	5 ms	5/2−

The most abundant isotope, ^{40}Ca, has a nucleus of 20 protons and 20 neutrons. This is the heaviest stable isotope of any element known that has equal numbers of protons and neutrons. In supernova explosions, calcium is formed from the reaction of carbon with various numbers of alpha particles (helium nuclei), until this most common calcium isotope (containing 10 helium nuclei) has been formed.

Calcium salts are colorless (unless the anion is colored) and ionic solutions of calcium (Ca^{2+}) are colorless as well. Many calcium salts are not soluble in water. When in solution, the calcium ion to the human taste varies remarkably, being reported as mildly salty, sour, "mineral like" or even "soothing". It is apparent that many animals can taste, or develop a taste, for calcium, and use this sense to detect the mineral in "salt licks" or other sources. In human nutrition, soluble calcium salts may be added to tart juices without much effect to the average palate.

Calcium is essential for living organisms, particularly in cell physiology, where the movement of the calcium ion, Ca^{2+}, into and out of the cytoplasm operates as a signal for many cellular processes. As a major material used in mineralization of bones and shells, calcium is the most abundant metal by mass in many animals. Calcium is the fifth most abundant element by mass in the human body, where it is a common cellular ionic messenger for many bodily functions, and serves also as a structural element. The relatively high atomic number of calcium in the skeleton causes bone to be radioopaque. Of the human body's solid components after drying (as for example, after cremation), about a third of the total mass is approximately 1 kg of calcium that composes the average skeleton (the remainder being mostly phosphates and oxides).

Calcium is an important component of a healthy diet and a necessary mineral for maintaining life. Calcium plays an important role in building stronger, denser bones early in life and keeping bones strong and healthy later in life. Approximately 99% of the body's calcium is stored in the bones and teeth. The rest of the calcium in the body has other important uses, such as "neurotransmitter release", muscle contraction and "exocytosis" (a durable process by which a cell directs the contents of secretory vesicles out of the cell membrane). Especially important are "neurotransmitter release", and muscle contraction. In the electrical conduction system of the heart, calcium replaces sodium as the mineral that depolarizes the cell, thereby proliferating the action potential. In cardiac muscle, sodium influx commences an action potential, but during potassium efflux, the cardiac myocyte experiences calcium influx, prolonging the action potential and creating a plateau phase of dynamic equilibrium.

Long-term calcium deficiency can lead to rickets and poor blood clotting. In case of a menopausal woman, it can lead to "Osteoporosis", in which the bone deteriorates and an increased risk of fractures develops. While a lifelong deficit can affect bone and tooth formation, over-retention can cause "hypercalcemia" (elevated levels of calcium in the blood), impaired kidney function and decreased absorption of other minerals. High calcium intakes or high calcium absorption was previously thought to contribute to the development of kidney stones. However, recent research has indicated that a high calcium intake is associated with a lower risk for kidney stones. Vitamin D is needed to absorb calcium.

Calcium metal is readily available commercially. Commercially it is made by the electrolysis of molten calcium chloride, $CaCl_2$:

$$\text{cathode: } Ca^{2+}(\text{liq}) + 2e^- \Rightarrow Ca(\text{solid})$$

$$\text{anode: } Cl^-(\text{liq}) \Rightarrow {}^1/_2\,Cl_2(\text{gas}) + e^-$$

in the same way that magnesium is produced. The calcium chloride is made by the action of hydrochloric acid upon calcium carbonate. Calcium chloride is also a by-product in the Solvay process used to make sodium carbonate:

$$CaCO_3 + 2\,HCl \Rightarrow CaCl_2 + H_2O + CO_2$$

Alternatively, and on a small scale, calcium can be made through the reduction of CaO with aluminum or of $CaCl_2$ with sodium metal:

$$6CaO + 2Al \Rightarrow 3Ca + Ca_3Al_2O_6$$

$$CaCl_2 + 2Na \Rightarrow Ca + 2NaCl$$

Some important uses of calcium metal are:

- Use as a reducing agent in the extraction of other metals, such as uranium, zirconium and thorium.
- Use as a deoxidizer, desulfurizer, or decarbonizer for various ferrous and nonferrous alloys.
- Use in the making of cements and mortars to be used in construction.
- Calcium is also used to remove oxygen, sulfur and carbon from certain alloys.
- Calcium can be alloyed with aluminum, beryllium, copper, lead and magnesium.
- Calcium is also used in vacuum tubes as a getter, a material that combines with and removes trace gases from vacuum tubes.
- Use in dehydrating oils, decarburization and desulfurization of iron and its alloys.
- Also used in fertilizer, concrete and plaster of paris (Table 1.12).

TABLE 1.12

Physical constants of calcium	
CAS number	7440-70-2
Phase	Solid
Atomic mass	40.078
Density	1.55 g/cm^3
Liquid density at MP	1.378 g/cm^3
Melting point	1115 K; 842 °C; 1548 °F
Boiling point	1757 K; 1448 °C; 2703 °F
Heat of fusion	8.54 kJ/mol
Heat of vaporization	154.7 kJ/mol
Specific heat capacity	25.929 J/mol K
Electronegativity	1.00 (Pauling scale)
Ionization energies	1st: 589.8 kJ/mol
	2nd: 1145.4 kJ/mol
	3rd: 4912.4 kJ/mol
Atomic radius	2.23 Å
Covalent radius	1.76 Å
Van der Waals radius	2.31 Å
Atomic volume	29.9 cm^3/mol
Crystal structure	Face-centered cubic
Magnetic ordering	Diamagnetic
Electrical resistivity	33.6 nΩ m (20 °C)
Thermal conductivity	204 W/m K
Thermal expansion	22.3 μm/m K
Speed of sound (thin rod)	3810 m/sex (20 °C)
Young's modulus	20 Gpa
Shear modulus	7.4 Gpa
Bulk modulus	17 Gpa
Poisson ratio	0.31
Mohs hardness	1.75
Brinell hardness	167 Gpa
Cross section (thermal neutron capture)	0.432 b
Electrochemical equivalent	0.7477 g/amp h
Heat of fusion	8.54 kJ/mol
Ionization potential	Ist: 6.113 eV
	2nd: 11.871 eV
	3rd: 50.908 eV
Coefficient of linear expansion	K = 22 × 10^{-6}
Conductivity	Electrical: 0.298 × 10^6/cm
	Thermal: 2.01 W/cm K
Enthalpy of atomization:	184 kJ/mol at 25 °C
Enthalpy of vaporization:	153.6 kJ/mol
Enthalpy of fusion:	8.54 kJ/mol
Vapor pressure	254 Pa at 839 °C
Abundance of calcium	Earth's crust: 41.000 ppm
	Seawater: 390 ppm
	Sun = 2.24 × 10^6 (relative to H = 10^{12})
Main isotopes of calcium	^{40}Ca = 96.941% ^{41}Ca = trace
	^{42}Ca = 0.647% ^{43}Ca = 0.135%
	^{44}Ca = 2.086% ^{48}Ca = 0.187%

Due to its high reactivity with common materials like water, there is very little demand for metallic calcium.

1.2.4. Strontium

Strontium has the symbol **Sr**, the atomic number 38 and an atomic weight of 87.623 g/mol. As an alkaline earth metal, strontium is a soft silver-white or yellowish metallic element that is highly reactive chemically. Due to its extreme reactivity with oxygen and water, this element occurs naturally only in compounds with other elements. The metal turns yellow when exposed to air. It occurs naturally in the minerals "Celestine" ($SrSO_4$) and "strontianite" ($SrCO_3$). The isotope, ^{90}Sr, is present in "radioactive fallout" and has a half-life of 28.90 years.

The following table presents the abundance of strontium. Strontium commonly occurs in nature, the 15th most abundant element on earth, averaging 0.034% in all igneous rock. It is found chiefly as the form of the sulfate mineral "Celestite" ($SrSO_4$) and the carbonate "Strontianite" ($SrCO_3$) (Table 1.13).

Of the two, Celestite occurs much more frequently in sedimentary deposits of sufficient size to make the development of mining facilities attractive. Strontianite is more useful of the two common minerals because strontium is used most often in the carbonate form, but few deposits have been discovered that are suitable for development. The metal can be prepared by electrolysis of melted $SrCl_2$ containing a small amount of KCl (to assist conductivity):

$$Sr^{2+} + 2e^- \Rightarrow Sr$$

$$2Cl^- \Rightarrow Cl_2(gas) + 2e^-$$

TABLE 1.13

Abundance of strontium		
Location	**ppb by weight**	**ppb by atoms**
Universe	40	0.6
Sun	50	0.7
Meteorite (carbonaceous)	8900	2000
Crustal rocks	360,000	85,000
Seawater	8100	570
Streams	60	0.7
Humans	4600	330

This is similar to those methods used for the other alkaline earth metals. Alternatively it is made by reducing strontium oxide with Al metal in vacuum at a temperature at which strontium distills off. Three allotropes of the metal exist, with transition points at 235 °C ($\alpha \Rightarrow \beta$) and 540 °C ($\beta \Rightarrow \gamma$). The largest commercially exploited deposits are found in England.

Both strontium and "Strontianite" are named after Strontian, a village in Scotland near which the mineral was first discovered in the ores taken from the lead mines. In 1787, an intriguing mineral came to Edinburgh from a Lead mine in a small village on the shores of Loch Sunart, Argyll, in the western highlands of Scotland. At that time, the substance was thought to be some sort of Barium compound. It was 3 years later that Scott's Irish chemist, Adair Crawford, published a paper claiming that the mineral held a new species including a new chemical element. Other chemists later prepared a number of compounds with the element, noting that it caused the candle's flame to burn red, while barium compounds gave a green color. The new mineral was named "Strontite" in 1793 by Thomas Hope, another professor of medicine at the University of Glasgow.

This element was eventually isolated by Humphrey Davy in 1808 during his studies of the electrolysis of various "alkaline earths" containing molten chloride such as $SrCl_2$ and mercuric oxide. He announced his work in a lecture to the Royal Society on 30 June 1808. In keeping with the naming of the other alkaline earths, he changed the name to *Strontium*.

Strontium is a gray/silvery metal that is softer than Ca. It is even more reactive in water, and reacts on contact to produce $Sr(OH)_2$ and hydrogen gas. It burns in air to produce both SrO and Sr_3N_2. But since it does not react with nitrogen below 380 °C, it only forms the oxide spontaneously at room temperature. It should be kept under kerosene to prevent oxidation. Freshly exposed strontium metal rapidly turns a yellowish color as the oxide forms. Finely powdered strontium metal will ignite spontaneously in air at room temperature. Volatile strontium salts impart a crimson color to flames, and these salts are used in pyrotechnics and in the production of flares.

Strontium has four naturally occurring isotopes ^{84}Sr (0.56%), ^{86}Sr (9.86%), ^{87}Sr (7.0%) and ^{88}Sr (82.58%), but there are 33 known isotopes (Tables 1.14 and 1.15).

This element (**Sr**) has four stable, naturally occurring isotopes: ^{84}Sr (0.56%), ^{86}Sr (9.86%), ^{87}Sr (7.0%) and ^{88}Sr (82.58%). Only ^{87}Sr is radiogenic since it is produced by decay from the radioactive alkali metal ^{87}Rb, which has a half-life of 4.88×10^{10} years. Thus, in any material, there are two sources of ^{87}Sr. That formed during primordial nucleosynthesis along with ^{84}Sr, ^{86}Sr and ^{88}Sr, and that formed by radioactive decay of ^{87}Rb. The ratio $^{87}Sr/^{86}Sr$ is the parameter typically reported in geologic investigations. The ratios reported in minerals and rocks have values ranging from 0.7 to greater than 4.0. Because strontium has an electronic configuration similar to that of calcium, it readily substitutes for Ca in minerals.

Sixteen unstable isotopes are known to exist. Of greatest importance are strontium-89 (^{89}Sr) with a half-life of 50.57 days, and strontium-90 (^{90}Sr) with a half-life of 28.78 years. They decay by emitting an electron and an anti-neutrino (ν_e) in beta-minus decay (β^- decay) to become yttrium, ^{90}Y (half-life = 64 h). ^{89}Sr is an artificial radioisotope that is used in the treatment of bone cancer. In circumstances where cancer patients have widespread and painful bony metastases, the administration of ^{89}Sr results in the delivery of β-particles directly to the area of the bony problem, where calcium turnover is greatest. ^{90}Sr is a by-product of nuclear fission found in "nuclear fallout" and presents a health problem since it substitutes for calcium in bone, preventing its expulsion from the body. Significant absorption usually results in death.

Because it is a long-lived high-energy beta-emitter, ^{90}Sr is used in SNAP (Systems for Nuclear Auxiliary Power) devices. These devices hold promise for use in spacecraft, remote weather stations, navigational buoys, etc., where a lightweight, long-lived, nuclear-electric power source is required.

According to the latest records, China was the top producer of strontium in 2007, with over two-thirds world share, followed by Spain and Mexico. Annual worldwide production is around 137,000 t. Primary mining areas are UK, Tunisia, Russia, Germany, Mexico and USA.

Several uses for radioactive strontium have emerged:

- The species, ^{89}Sr, is the active ingredient in Metastron, a radiopharmaceutical used for bone pain secondary to metastatic bone cancer. The strontium acts like

TABLE 1.14

Nuclide	Z	N	Isotopic mass	Half-life	Nuclear spin
^{73}Sr	38	35	72.96597	>25 ms	1/2−
^{74}Sr	38	36	73.95631	50 ms	0+
^{75}Sr	38	37	74.94995	88(3) ms	(3/2−)
^{76}Sr	38	38	75.94177	7.89 s	0+
^{77}Sr	38	39	76.937945	9.0 s	5/2+
^{78}Sr	38	40	77.932180	159 s	0+
^{79}Sr	38	41	78.929708	2.25 min	3/2(−)
^{80}Sr	38	42	79.924521	106.3 min	0+
^{81}Sr	38	43	80.923212	22.3 min	1/2−
^{82}Sr	38	44	81.918402	25.36 days	0+
^{83}Sr	38	45	82.917557	32.41 h	7/2+
^{84}Sr	38	46	83.913425	Stable (0.56%)	0+
^{85}Sr	38	47	84.912933	64.853 days	9/2+
^{86}Sr	38	48	85.9092602	Stable (9.86%)	0+
^{87}Sr	38	49	86.9088771	Stable (7.00%)	9/2+
^{88}Sr	38	50	87.9056121	Stable (82.58%)	0+
^{89}Sr	38	51	88.9074507	50.57 days	5/2+
^{90}Sr	38	52	89.907738	28.90 years	0+
^{91}Sr	38	53	90.91020	9.63 h	5/2+
^{92}Sr	38	54	91.911038	2.66 h	0+
^{93}Sr	38	55	92.914026	7.423 min	5/2+
^{94}Sr	38	56	93.915361	75.3 s	0+
^{95}Sr	38	57	94.919359	23.90 s	1/2+
^{96}Sr	38	58	95.921697	1.07 s	0+
^{97}Sr	38	59	96.926153	429 ms	1/2+
^{98}Sr	38	60	97.928453	0.653 s	0+
^{99}Sr	38	61	98.93324	0.269 s	3/2+
^{100}Sr	38	62	99.93535	202 ms	0+
^{101}Sr	38	63	100.94052	118 ms	(5/2−)
^{102}Sr	38	64	101.94302	69 ms	0+
^{103}Sr	38	65	102.94895	50 ms	
^{104}Sr	38	66	103.95233	30 ms	0+
^{105}Sr	38	67	104.95858	20 ms	

calcium and is preferentially incorporated into bone at sites of increased "Osteogenesis". This localization focuses the radiation exposure on the cancerous lesion.

- ^{90}Sr has been used as a power source for radioisotope thermoelectric generators (RTGs). ^{90}Sr produces about

TABLE 1.15

Physical constants of strontium	
CAS number	7440-24-6
Phase	Solid
Atomic mass	87.621 g/mol
Density	2.64 g/cm^3
Liquid Density at MP	2.375 g/cm^3
Melting point	1050 K; 777 °C; 1431 °F
Boiling point	1655 K; 1382 °C; 2520 °F
Vapor pressure at 769 °C	253 Pa
Heat of fusion	7.43 kJ/mol
Heat of vaporization	136 kJ/mol
Specific heat capacity	26.4 J/mol K
Electronegativity	0.95 (Pauling scale)
Atomic radius	2.45 Å
Covalent radius	1.91 Å
Thermal neutron capture cross section	Barns = 1.28
Atomic volume: 33.7 cm^3/mol	Covalent radius: 1.91 Å
Crystal structure: Cubic face centered	Electrochemical equivalent: 1.635 g/amp h
Electron work function = 2.59 eV	Heat of fusion: 8.3 kJ/mol
Valence electron potential in eV	25.7
Ionization potential	Ist: 5.695
	2nd: 11.03
	3rd: 43.6
Coefficient of linear expansion	23×10^{-6} (per K)
Magnetic ordering	Paramagnetic
Electrical resistivity	(20 °C) 132 nΩ m
Thermal conductivity	35.4 W/m K
Thermal expansion	22.5 μm/m K
Elastic modulus	Rigidity: 6.1 Gpa
	Bulk: 12 Gpa
	Young's: 15.7 Gpa
Poisson ratio	0.28
Conductivity	Electrical: 0.0795×10^6/cm
	Thermal: 0.353 W/cm K
Hardness scale	1.5 Mohs
Abundance of Sr	Earth's Crust = 370 ppm
	Seawater = 7.6 ppm
	Sun (relative to H at $10^{12} = 790$)

0.93 W of heat per gram (it is lower for the form of ^{90}Sr used in RTGs, which is SrF_2). But, ^{90}Sr has a lifetime approximately three times shorter and has a lower density than ^{238}Pu, another RTG fuel. The main advantage of ^{90}Sr is that it is cheaper than ^{238}Pu and can be recovered from nuclear waste.

- ^{90}Sr is also used in cancer therapy. Its beta emission and long half-life are ideal for superficial radiotherapy.
- $^{87}Sr/^{86}Sr$ ratios are commonly used to determine the likely source in areas of sediment in natural systems, especially in marine and fluvial environments. Dasch (1969) showed that surface sediments of Atlantic displayed $^{87}Sr/^{86}Sr$ ratios that could be regarded as bulk averages of the $^{87}Sr/^{86}Sr$ ratios of geological terranes from adjacent landmasses. A good example of a fluvial marine system to which Sr isotope provenance studies have been successfully employed is the River Nile–Mediterranean Sea system.
- Due to the differing ages of the rocks that constitute the majority of the Blue and White Nile catchment areas reaching the River Nile delta and East Mediterranean Sea, the changing provenance of sediment can be discerned through Sr isotopic studies. Such changes have been climatically controlled in the Late Quaternary eras.
- More recently, $^{87}Sr/^{86}Sr$ ratios have also been used to determine the source of ancient archaeological materials such as timbers and corn in Chaco Canyon, New Mexico.
- $^{87}Sr/^{86}Sr$ ratios in teeth may also be used to track animal migrations or in criminal forensics.
- A recent in vitro study conducted in the NY College of Dental Sciences using strontium to stimulate "osteoblasts" showed marked improvement of bone-building by osteoblasts.

As a pure metal, Sr is used in strontium 90%–aluminum 10% alloys of an eutectic composition for the modification of aluminum–silicon casting alloys. The AJ62 alloy, a durable creep-resistant magnesium alloy used in car and motorcycle engines by BMW Motor Car company contains 2% by weight of strontium metal.

Other than its usage as radioactive tracers and radioactive sources for human body treatment, the only other usage has been in fireworks where the crimson red color is due to strontium.

1.2.5. Barium

Barium has the symbol **Ba**, atomic number 56, and is the fifth element in Group 2. Its atomic weight is 137.332 g/mol. Barium is a soft silvery metal. It is never found in nature in its pure form due to its reactivity with air. Its oxide is historically known as "Baryta" but because it reacts with water and carbon dioxide, it is not found as a mineral. The most common naturally occurring minerals are the very insoluble barium sulfate, $BaSO_4$ (Barite), and barium carbonate, $BaCO_3$ (Witherite). Barium's name originates from the Greek word "bary", meaning "heavy", describing the high density of some common barium-containing ores. Alchemists in the early Middle Ages knew about some barium minerals. Smooth pebble-like stones of mineral Baryte found in Bolona, Italy were known as "Bologna Stones". After exposed to light, they would glow for years (probably because they contained some barium sulfide (BaS) formed during the calcination of the "stone" with charcoal carbon). It was this quality that attracted them to witches and alchemists.

Though barium minerals are dense, barium metal itself is comparatively light. Its cosmic abundance is estimated as 3.7 atoms (on the same basis, Si = 106 atoms). Barium constitutes about 0.03% of the Earth's crust, chiefly as the minerals "Barite" (also called barytes or heavy spar) and "Witherite". The abundance of barium is 0.0425% in the Earth's crust and 13 μg/l in seawater. A rare gem containing barium is known, called "Benitoite" ($BaTiSi_3O_9$). Large deposits of Barite are found in China, Germany, India, Morocco, and in the US. Because barium quickly oxidizes in air, it is difficult to obtain the free metal and it is never found free in nature. The following table lists the abundance of barium as found in nature (Table 1.16).

Barium is a soft and ductile metal. Its simple compounds are notable for their relatively high specific gravity (as compared to the other alkaline earth elements). Barium, which is slightly harder than lead, has a silvery white luster when freshly cut.

The Swedish chemist Carl Wilhelm Scheele discovered (1774) a new base (baryta, or barium oxide) as a minor constituent in "Pyrolusite", but could not isolate barium as the metal. From this base, he prepared some crystals of barium sulfate, which he sent to Johan

TABLE 1.16

Abundance of Barium

Location	ppb by weight	ppb by atoms
Universe	10	0.09
Sun	10	0.1
Meteorite (carbonaceous)	2800	410
Crustal rocks	340,000	51,000
Seawater	30	1.4
Streams	25	0.2
Humans	300	14

Gottlieb Gahn, the discoverer of manganese. A month later Gahn found that the mineral Barite is composed of barium sulfate. Only after the electric battery became available could Sir Humphry Davy finally isolate (1808) the element itself by electrolysis. Oxidized barium was at first called "barote", by Guyton-de Morveau, a name that was changed by Lavoisier to *baryta*. Barium was first isolated by electrolysis of molten barium salts in 1808, by Davy, who, by analogy with calcium named "barium" after baryta, with the "-ium" ending signifying a metallic element.

Because barium quickly oxidizes in air, it is difficult to obtain the free metal and it is never found free in nature. The metal is primarily found in, and extracted from, Barite. Because Barite is so insoluble, it cannot be used directly for the preparation of other barium compounds, or barium metal. Instead, the ore is heated with carbon to reduce it to barium sulfide:

$$BaSO_4 + 2\,C \;\Rightarrow\; BaS + 2\,CO_2$$

The barium sulfide is then hydrolyzed or treated with acids to form other barium compounds, such as the chloride, nitrate or carbonate.

Barium is commercially produced through the electrolysis of molten barium chloride ($BaCl_2$):

$$\text{(Cathode reaction)}\ Ba^{2+}(liq) + 2e^- \;\Rightarrow\; Ba(solid)$$

$$\text{(Anode reaction)}\ 2\,Cl^- \;\Rightarrow\; Cl_2(gas) + 2\,e^-$$

This process is similar to that of the other alkaline earth metals. Barium metal is also produced by the reduction of barium oxide with finely divided aluminum at temperatures between 1100 and 1200 °C:

$$4\,BaO + 2\,Al \;\Rightarrow\; BaO{\cdot}Al_2O_3 + 3\,Ba(gas)$$

The barium vapor is cooled by means of a water jacket and condensed into the solid metal. The solid block may be cast into rods or extruded into wires. This is the most effective method i.e. the reduction of the oxide by heating with aluminum or silicon in a high vacuum, to produce the metal. A mixture of barium monoxide and peroxide can also be used in the reduction. Being a flammable solid, it is packaged under Argon gas in steel containers or plastic bags. Only a few tons of the metal are produced each year.

Barium reacts exothermically with oxygen at room temperature to form both BaO and BaO_2. The reaction is violent if the barium is powdered. It also reacts violently with dilute acids, alcohol and water:

$$Ba + 2\,H_2O \;\Rightarrow\; Ba(OH)_2 + H_2(gas)$$

At elevated temperatures, barium combines with chlorine, nitrogen and hydrogen to produce $BaCl_2$, Ba_3N_2 and BaH_2, respectively. Barium reduces oxides, chlorides and sulfides of less reactive metals. For example:

$$Ba + CdO \;\Rightarrow\; BaO + Cd$$

$$Ba + ZnCl_2 \;\Rightarrow\; BaCl_2 + Zn$$

$$3\,Ba + Al_2S_3 \;\Rightarrow\; 3\,BaS + 2\,Al$$

When heated with nitrogen and carbon, it forms the cyanide:

$$Ba + N_2 + 2\,C \;\Rightarrow\; Ba(CN)_2$$

Barium combines with several metals, including aluminum, zinc, lead and tin, forming intermetallic compounds and alloys.

About 40 isotopes of barium have been isolated as shown in Table 1.17.

Naturally occurring barium is a mixture of seven stable isotopes: barium-138 (71.66%), barium-137 (11.32%), barium-136 (7.81%), barium-135 (6.59%), barium-134 (2.42%), barium-130 (0.101%), and barium-132 (0.097%). About six times this many radioactive isotopes have been prepared with mass numbers ranging from 114 to 153. Of the 40 isotopes known, most are highly radioactive and have half-lives in the several milliseconds to a few days range. The only notable exceptions are ^{133}Ba with a half-life of 10.51 years, ^{128}Ba (2.43 days), ^{141}Ba (11.50 days) and ^{140}Ba (12.75 days).

The element is used in metallurgy, and its compounds in pyrotechnics, petroleum mining, and radiology. Metallic barium has few industrial uses. It has been historically used to scavenge air in vacuum tubes. There, the metal is used as a getter in electron tubes to perfect the vacuum by combining with final traces of gases. It is also used as a deoxidizer in copper refining, and as a constituent in certain alloys. The alloy with nickel readily emits electrons when heated and, for this reason, is used in electron tubes and in spark plug electrodes. The presence of barium (atomic number 56), observed after uranium (atomic number 92) had been bombarded by neutrons, was the clue that led to the recognition of nuclear fission (1939).

The most important use of elemental barium is as a scavenger removing last traces of oxygen and other gases in television and other electronic tubes. Additionally, an isotope of barium, ^{133}Ba, is routinely used as a standard source in the calibration of gamma ray detectors in nuclear physics studies.

Physical properties of Ba metal shown in Table 1.18.

1.2.6. Radium

Radium has the symbol Ra and atomic number 88. Its atomic weight is 226.0254 g/mol. Radium is an alkaline

TABLE 1.17

Nuclide	Z	N	Mass	Decay time	Spin
^{114}Ba	56	58	113.95068	530 ms	0+
^{115}Ba	56	59	114.94737	0.45 s	(5/2+)
^{116}Ba	56	60	115.94138	1.3 s	0+
^{117}Ba	56	61	116.93850	1.75 s	(3/2)+
^{118}Ba	56	62	117.93304	5.2 s	0+
^{119}Ba	56	63	118.93066	5.4 s	(5/2+)
^{120}Ba	56	64	119.92604	24 s	0+
^{121}Ba	56	65	120.92405	29.7 s	5/2(+)
^{122}Ba	56	66	121.91990	1.95 min	0+
^{123}Ba	56	67	122.918781	2.7 min	5/2(+)
^{124}Ba	56	68	123.915094	11.0 min	0+
^{125}Ba	56	69	124.914473	3.5 min	1/2+
^{126}Ba	56	70	125.911250	100 min	0+
^{127}Ba	56	71	126.911094	12.7 min	1/2+
			80.33(12) keV		
^{128}Ba	56	72	127.908318	2.43 days	0+
^{129}Ba	56	73	128.908679	2.23 h	1/2+
				8.42(6) keV	
^{130}Ba	56	74	129.9063208	Stable (0.106%) [$>4.0 \times 10^{21}$ years]	0+
^{131}Ba	56	75	130.90694	11.50 days	1/2+
				187.14(12) keV	
^{132}Ba	56	76	131.9050613	Stable (0.101%) [$>300 \times 10^{18}$ years]	0+
^{133}Ba	56	77	132.9060075	10.51 years	1/2+
^{134}Ba	56	78	133.9045084	Stable (2.417%)	0+
^{135}Ba	56	79	134.9056886	Stable (6.592%)	3/2+
^{136}Ba	56	80	135.9045759	Stable (7.854%)	0+
^{137}Ba	56	81	136.9058274	Stable (11.232%)	3/2
^{138}Ba	56	82	137.9052472	Stable (71.698%)	0+
^{139}Ba	56	83	138.9088413	83.06 min	7/2−
^{140}Ba	56	84	139.910605	12.752 day	0+
^{141}Ba	56	85	140.914411	18.27 min	3/2−
^{142}Ba	56	86	141.916453	10.6 min	0+
^{143}Ba	56	87	142.920627	14.5 s	5/2−
^{144}Ba	56	88	143.922953	11.5 s	0+
^{145}Ba	56	89	144.92763	4.31 s	5/2−
^{146}Ba	56	90	145.93022	2.22 s	0+
^{147}Ba	56	91	146.93495	0.893 s	(3/2+)

TABLE 1.17 (*cont'd*)

Nuclide	Z	N	Mass	Decay time	Spin
^{148}Ba	56	92	147.93772	0.612 s	0+
^{149}Ba	56	93	148.94258	344 ms	3/2−
^{150}Ba	56	94	149.94568	300 ms	0+
^{151}Ba	56	95	150.95081	200 ms	3/2−
^{152}Ba	56	96	151.95427	100 ms	0+
^{153}Ba	56	97	152.95961	80 ms	5/2−

TABLE 1.18

Physical properties of barium metal	
Name, symbol and atomic number	Barium, Ba, 56
Atomic weight	137.331 g/mol
Phase	Solid
Density	3.51 g/mol (20 °C)
Liquid density at MP	3.338 g/cm^3
Melting point	1000 K; 727 °C: 1341 °F
Boiling point	2170 K; 1897 °C; 3447 °F
Heat of fusion	7.12 kJ/mol
Heat of vaporization	140.3 kJ/mol
Specific heat capacity	8.07 J/mol K
Electronegativity	0.89 (Pauling scale)
Ionization energies	1st: 502.9 kJ/mol
	2nd: 965.1 kJ/mol
	3rd: 3600 kJ/mol
Atom radii	Atomic- 2.22 Å
	Covalent- 2.15 Å
	Van der Waals- 2.68 Å
Magnetic ordering	Paramagnetic
Electrical resistivity	332 nωm
Thermal conductivity	18.5 W/m K
Thermal expansion	20.6 μm/m K
Crystal structure	Body-centered cubic
Speed of sound (thin rod)	1620 ms
Modulus	Young's- 13 GPa
	Shear- 4.9 GPa
	Bulk- 9.6 GPa
Mohs hardness	1.25
CAS number	7440-39-3

earth metal that is found in trace amounts in uranium ores. Its most stable isotope, ^{226}Ra, has a half-life of 1602 years and decays into radon gas.

The heaviest of the alkaline earth elements, radium is intensely radioactive and resembles barium in its chemical behavior. This metal is found in tiny quantities in the uranium ore "Pitchblende", and various other uranium minerals. Radium preparations are remarkable for maintaining themselves at a higher temperature than their surroundings, and for their radiations, which are of three kinds: alpha particles, beta particles and gamma rays.

When freshly prepared, pure radium metal is almost pure white, but blackens when exposed to air (probably due to nitride formation). Radium is luminescent when struck by electromagnetic radiation of the proper wavelength (giving a faint blue color). It reacts violently with water to form radium hydroxide and is slightly more volatile than barium. The normal phase of radium is a solid. Since all the isotopes of radium are radioactive and short-lived on the geological time scale, any primeval radium would have disappeared long ago. Therefore, radium occurs naturally only as a disintegration product in the three natural radioactive decay series (Thorium, Uranium, and Actinium series). Radium-226 is a member of the uranium decay series. Its parent is Thorium-230 and its daughter Radon-222. The following lists the known abundance of radium (Table 1.19).

Radium is a decay product of uranium and is therefore found in all uranium-bearing ores. (One ton of Pitchblende yields one seventh of a gram of radium). Radium was originally acquired from pitchblende ore from the Czech Republic. Carnotite ($K_2(UO_2)_2(VO_4)_2 \cdot 3H_2O$) sands in Colorado provide some of the element, but richer ores are found in the Democratic Republic of Congo and the Great Lakes area of Canada. Radium can also be extracted from uranium processing waste. Large radium-containing uranium deposits have been located in Canada (Ontario), the United States (New Mexico, Utah and Virginia), Australia, and in other places.

TABLE 1.19

Abundance of Radium

Location	ppb by weight	ppb by atoms
Universe	0	No data
Sun	No data	No data
Meteorite (carbonaceous)	No data	No data
Crustal rocks	0.00010	0.00001
Seawater	0.00000001	0.0000000003
Streams	0.0000004	0.000000002
Humans	0.0000011	0.00000003

Radium (Ra) has no stable isotopes. A standard atomic mass cannot be given (but is usually given as 226.0 g/mol). The longest lived, and most common, isotope of radium is ^{226}Ra that occurs in the disintegration chain of ^{238}U (often referred to as the radium series). Radium (Ra) has 33 different known isotopes, four of which are found in nature, with ^{226}Ra being the most common. ^{223}Ra, ^{224}Ra, ^{226}Ra and ^{228}Ra are all generated naturally in the decay of either Uranium (U) or Thorium (Th). ^{226}Ra is a product of ^{238}U decay, and is the longest-lived isotope of radium with a half-life of 1602 years. The next longest is ^{228}Ra, a product of ^{232}Th breakdown, with a half-life of 5.75 years (Table 1.20).

Radium is over 1 million times more radioactive than the same mass of uranium. Its decay occurs in at least seven stages. The successive main products have been studied and were called "radium emanation" or "exradio" (now identified as radon), radium A (polonium), radium B (lead), radium C (bismuth), etc. Radon is a heavy gas in contrast to the others (which are solids). These solid products are themselves radioactive elements, each with an atomic weight a little lower than its predecessor.

The chemistry of radium is what would be expected of the heaviest of the alkaline earths, but the intense radioactivity is its most characteristic property. One gram of radium-226 undergoes 3.7×10^{10} disintegrations per second, producing energy equivalent to 6.8×10^{-3} calories, sufficient to raise the temperature of a well-insulated sample at the rate of 1 °C every 10 s. The practical energy release is even greater than this due to the production of a large number of short-lived radioactive decay products. The alpha particles emitted by radium may be used to initiate nuclear reactions. Radium loses about 1% of its activity in 25 years, being transformed into elements of lower atomic weight with lead being the final product of disintegration.

The SI unit of radioactivity is the "Becquerel" (Bq), equal to one disintegration per second. The "Curie" is a non-SI unit defined as the amount of radioactivity which has the same disintegration rate as 1 g of Ra-226 (3.7×10^{10} disintegrations per second, or 37 GBq).

Radium (Latin *radius*, ray) was discovered by Pierre Curie, Marie Curie, and an assistant, G. Bémont. This occurred after Marie Curie had observed that the radioactivity of pitchblende was four or five times greater than that of the uranium it contained and was not fully explained on the basis of radioactive polonium, which she had just discovered in pitchblende residues originating from North Bohemia, in the Czech Republic. While studying pitchblende the Curies removed uranium from it and found that the remaining material was still radioactive. They then separated out

TABLE 1.20

Nuclide	Z	N	Isotopic mass	Decay time	Spin
^{202}Ra	88	114	202.00989	2.6 ms	0+
^{203}Ra	88	115	203.00927	4.0 ms	(3/2−)
^{204}Ra	88	116	204.006500	60 ms	0+
^{205}Ra	88	117	205.0062	220 ms	(3/2−)
^{206}Ra	88	118	206.003827	0.24 s	0+
^{207}Ra	88	119	207.00380	1.3 s	(5/2−, 3/2−)
^{208}Ra	88	120	208.001840	1.3 s	0+
^{209}Ra	88	121	209.00199	4.6 s	5/2−
^{210}Ra	88	122	210.000495	3.7 s	0+
^{211}Ra	88	123	211.000898	13 s	5/2(−)
^{212}Ra	88	124	211.999794	13.0 s	0+
^{213}Ra	88	125	213.000384	2.74 min	1/2−
^{214}Ra	88	126	214.000108	2.46 s	0+
^{215}Ra	88	127	215.002720	1.55 ms	(9/2+)#
^{216}Ra	88	128	216.003533	182 ns	0+
^{217}Ra	88	129	217.006320	1.63 μs	(9/2+)
^{218}Ra	88	130	218.007140	25.2 μs	0+
^{219}Ra	88	131	219.010085	10 ms	(7/2)+
^{220}Ra	88	132	220.011028	17.9 ms	0+
^{221}Ra	88	133	221.013917	28 s	5/2+
^{222}Ra	88	134	222.015375	38.0 s	0+
^{223}Ra	88	135	223.0185022	11.43 days	3/2+
^{224}Ra	88	136	224.0202118	3.6319 days	0+
^{225}Ra	88	137	225.023612	14.9 days	1/2+
^{226}Ra	88	138	226.0254098	1600 years	0+
^{227}Ra	88	139	227.0291778	42.2 min	3/2+
^{228}Ra	88	140	228.0310703	5.75 years	0+
^{229}Ra	88	141	229.034958	4.0(2) min	5/2(+)
^{230}Ra	88	142	230.037056	93(2) min	0+
^{231}Ra	88	143	231.041221	103 s	(5/2+)
^{232}Ra	88	144	232.04364	250 s	0+
^{233}Ra	88	145	233.04806	30 s	1/2+
^{234}Ra	88	146	234.05070	30 s	0+

a radioactive mixture consisting mostly of barium that produced a brilliant green flame color and crimson-carmine spectral lines that had never been documented before. The Curies announced their discovery to the French Academy of Sciences on 26 December 1898.

TABLE 1.21

Radium emanation	^{222}Rn
Radium A	^{218}Po
Radium B	^{214}Pb
Radium C	^{214}Bi
Radium C_1	^{214}Po
Radium C_2	^{210}Tl
Radium D	^{210}Pb
Radium E	^{210}Bi
Radium F	^{210}Po

In 1910, radium was isolated as a pure metal by Curie and Debierne through the electrolysis of a pure radium chloride solution by using a mercury cathode and distilling it in an atmosphere of hydrogen gas. The separation was followed by the increase in intensity of the new lines in the ultraviolet spectrum and by a steady increase in the apparent atomic weight of the material until a value of 225.18 was obtained, remarkably close to the accepted value of 226.03. By 1902, 0.1 g of pure radium chloride was prepared by refining several tons of pitchblende residues, and by 1910 Marie Curie and André-Louis Debierne had isolated the metal itself.

Radium was first industrially produced in the beginning of the twentieth century by Birac, a subsidiary company of UMHK in its Olen plant in Belgium. This company offered to Marie Curie her first gram of radium. Historically the decay products of radium were known as radium A, B, C, etc. These are now known to be isotopes of other elements as shown in Table 1.21.

On February 4, 1936 radium E became the first radioactive element to be made synthetically. Since all the isotopes of radium are radioactive and short-lived on the geological time scale, any primeval radium would have disappeared long ago. Therefore, radium occurs naturally only as a disintegration product in the three natural radioactive decay series (thorium, uranium, and actinium series). Radium-226 is a member of the uranium decay series. Its parent is thorium-230 and its daughter radon-222.

Radium was formerly used in self-luminous paints for watches, nuclear panels, aircraft switches, clocks, and instrument dials. More than 100 former watch-dial painters who used their lips to shape the paintbrush died from the radiation from the radium that had become stored in their bones. Soon afterward, the adverse effects of radioactivity became widely known. Nevertheless, radium was still used in dials as late as the 1950s. Although the beta-radiation from tritium is

TABLE 1.22

Physical constants of radium	
CAS number	7440-14-4
Atomic weight	226.0 g/mol
Electronic configuration	(Rn) $7s^2$
Phase	Solid
Density at 20 °C	5.51 fm/cm^3
Melting point	973 K: 700 °C: 1292 °F
Boiling point	2010 K; 1727 °C; 3159 °F
Heat of fusion	8.5 kJ/mol
Heat of vaporization	113 kJ/mol
Electronegativity	0.9 (Pauling scale)
Ionization energies	1st: 509.3 kJ/mol
	2nd: 979.3 kJ/mol
Covalent radius	2.21 Å
Van der Waals radius	2.83 Å
Magnetic ordering	Non-magnetic
Electrical resistivity	1.0 μΩ m
Crystal structure	Body-centered cubic
Thermal conductivity	18.6 W/m K

potentially dangerous if ingested, it has replaced radium in these applications.

Radium was also put in some foods for taste and as a preservative, but this also exposed many people to radiation. Radium was once an additive in products like toothpaste, hair creams, and even food items due to its supposed curative powers. Such products soon fell out of vogue and were prohibited by authorities in many countries, after it was discovered they could have serious adverse health effects. In the United States, nasal radium irradiation was also administered to children to prevent middle ear problems or enlarged tonsils from the late 1940s through early 1970s.

TABLE 1.23

Isotope	Abundance	Half-life	Decay mode	Decay energy (MeV)	Decay product
^{223}Ra	Trace	11.43 days	Alpha	5.99	^{219}Rn
^{224}Ra	Trace	3.6319 days	Alpha	5.789	^{220}Rn
^{226}Ra	~100%	1602 years	Alpha	4.871	^{222}Rn
^{228}Ra	Trace	5.75 years	Beta$^-$	0.046	^{228}Ac

In 1909, the famous Rutherford experiment used radium as an alpha source to probe the atomic structure of gold. This experiment led to the Rutherford model of the atom and revolutionized the field of nuclear physics.

Radium (usually in the form of $RaCl_2$) was used in medicine to produce radon gas which in turn was used as a cancer treatment. For example, several radon sources were used in Canada in the 1920s and 1930s. The isotope ^{223}Ra is currently under investigation for its use in cancer treatment of bone metastasis.

Some of the few practical uses of radium are derived from its radioactive properties. More recently discovered radioisotopes, such as ^{60}Co and ^{137}Cs are replacing radium in even these limited uses because several of these isotopes are more powerful emitters, safer to handle, and available in more concentrated form. The current price for radium metal is ~$40 million per lb (Table 1.22).

The major isotopes of Radium as a metal are listed in Table 1.23.

In the next chapters, we will survey the properties of the alkaline earths as they form compounds. We will begin with the Halides of Group 17 since they are the most electronegative elements in the Periodic Table. This will be followed by a description of the compounds formed with succeeding Groups in the Periodic Chart encompassing Groups 16, 15, 14, and 13.

CHAPTER

2

Group 17 (H, F, Cl, Br, I) Alkaline Earth Compounds

OUTLINE

2.1. Hydride Compounds of the Alkaline Earths 26
- *2.1.1. Types of Hydrides* 26
- *2.1.2. Ionic Hydrides (Groups 1 and 2)* 26
  - Beryllium Hydride 27
  - Magnesium Hydride 27
  - Calcium Hydride 29
  - Strontium Hydride 30
  - Barium Hydride 30
  - Radium Hydride 30

2.2. Halogen Compounds of the Alkaline Earths 31
- *2.2.1. Halogen Acids* 31
  - Hydrofluoric Acid 31
  - Hydrochloric Acid 32
  - Hydrobromic Acid 35
  - Hydroiodic Acid 36
- *2.2.2. Halide Compounds of Beryllium* 37
  - Beryllium Fluoride 38
  - Beryllium Chloride 39
  - Beryllium Bromide 40
  - Beryllium Iodide 41
- *2.2.3. Halide Compounds of Magnesium* 41
  - Magnesium Fluoride 41
  - Magnesium Chloride 43
  - Magnesium Bromide 46
  - Magnesium Iodide 47
- *2.2.4. Halide Compounds of Calcium* 49
  - Calcium Fluoride 49
  - Calcium Chloride 51
  - Calcium Bromide 53
  - Calcium Iodide 55
- *2.2.5. Halide Compounds of Strontium* 56
  - Strontium Fluoride 56
  - Strontium Chloride 57
  - Strontium Bromide 58
  - Strontium Iodide 59
- *2.2.6. Halide Compounds of Barium* 60
  - Barium Fluoride 60
  - Barium Chloride 62
  - Barium Bromide 65
  - Barium Iodide 66
- *2.2.7. Halide Compounds of Radium* 68
  - Radium Fluoride 68
  - Radium Chloride 69
  - Radium Bromide 69
  - Radium Iodide 70

2.3. Oxy-Chlorine Compounds of the Alkaline Earths 70
- *2.3.1. Oxy-Chlorine Acids* 70
- *2.3.2. Oxy-Chlorine Acid Anhydrides* 71
  - Dichlorine Pentoxide 72
- *2.3.3. Alkaline Earth Oxy-Chlorine Compounds* 73
  - Alkaline Earth Hypochlorites 73
  - Alkaline Earth Chlorites 76
  - Alkaline Earth Chlorates 78
  - Alkaline Earth Perchlorates 83

2.4. Alkaline Earth Oxy-Bromine Compounds 86
- *2.4.1. Oxy-Bromine Acids* 87
- *2.4.2. Alkaline Earth Hypobromites* 88
  - Beryllium Hypobromite 88
  - Magnesium Hypobromite 88
  - Calcium Hypobromite 88
  - Strontium Hypobromite 88
  - Barium Hypobromite 89
  - Radium Hypobromite 89
- *2.4.3. Alkaline Earth Bromite Compounds* 89
  - Beryllium Bromite 89
  - Magnesium Bromite 89
  - Calcium Bromite 89
  - Strontium Bromite 90
  - Barium Bromite 91

Encyclopedia of the Alkaline Earth Compounds
http://dx.doi.org/10.1016/B978-0-444-59550-8.00002-8

Copyright © 2013 Elsevier B.V. All rights reserved.

Radium Bromite 92
2.4.4. *Alkaline Earth Bromate Compounds* 92
Beryllium Bromate 92
Magnesium Bromate 92
Calcium Bromate 92
Strontium Bromate 93
Barium Bromate 94
Radium Bromate 94
2.4.5. *Alkaline Earth Perbromates* 94
Beryllium Perbromate 94
Magnesium Perbromate 95
Calcium Perbromate 95
Strontium Perbromate 95
Barium Perbromate 95
Radium Perbromate 96
2.5. Alkaline Earth Metals Oxy-Iodine Compounds 96
2.5.1. *Oxy-Iodine Acids* 96
2.5.2. *Alkaline Earth Iodates* 97
Beryllium Iodate 97
Magnesium Iodate 97
Calcium Iodate 98
Strontium Iodate 98
Barium Iodate 99
Radium Iodate 99
2.5.3. *Alkaline Earth Periodates* 99
Beryllium Periodate 99
Magnesium Periodate 100
Calcium Periodate 101
Strontium Periodate 102
Barium Periodate 103
Radium Periodate 104
2.6. Actinium and the Alkaline Earths 104
Radium Periodate 104

2.1. HYDRIDE COMPOUNDS OF THE ALKALINE EARTHS

Hydrogen forms compounds with less electronegative elements, such as most of the metals and the metalloids such as B, Si, Ge, As, Sb, Te and Po. These compounds are known as hydrides. In inorganic chemistry, hydrides can also serve as bridging ligands that link two metal centers in a coordination complex. This function is particularly common in Group 13 elements such as boranes (boron hydrides) and aluminum complexes. The term "hydride" implies that the H atom has acquired a negative or anionic character, denoted H^-, and is used when hydrogen forms a compound with a more electropositive element. The existence of the hydride anion, first suggested by G.N. Lewis in 1916 for Group 1 and 2 salt-like hydrides, was demonstrated by Möers in 1920 by the electrolysis of molten lithium hydride (LiH). This reaction produced a *stoichiometric quantity* of hydrogen at the anode. For hydrides other than Group 1 and Group 2 metals, the term is quite misleading, considering the low electronegativity of hydrogen. An exception in Group 2 hydrides is BeH_2, which is polymeric. In $[AlH_4]$, the anion carries hydridic centers firmly attached to the Al(III) ion. Although hydrides can be formed with almost all main group elements, the number and combination of possible compounds varies widely. For example, there are over 100 binary borane hydrides known, but only one binary aluminum hydride.

2.1.1. Types of Hydrides

There are four main groups (or types) of hydrides known. These are: ionic hydrides, covalent hydrides, interstitial hydrides and transition-metal complexes.

Saline hydrides (Groups 1 and 2) have significant ionic character.
Covalent hydrides (Groups 13, 14 and 15) include the hydrocarbons and many other compounds.
Interstitial hydrides (Group 11 and part of Groups 4, 10 and 12) may be described as having metallic bonding.
Transition metal hydrido complexes (which are not true hydrides).

The following diagram shows their location in the periodic chart (Fig. 2.1).

2.1.2. Ionic Hydrides (Groups 1 and 2)

Ionic or saline hydrides, consists of a hydrogen atom bound to an extremely electropositive metal, generally one of the **alkali** metals or the **alkaline earths**. In these compounds, the metal has donated an electron to the 1s orbital of protium, producing the following:

$$M^+H^- \text{ or } M^{2+}H_2^-$$

Saline hydrides are insoluble in conventional solvents, reflecting their nonmolecular structures. Most ionic hydrides exist as "binary" materials involving only including hydrogen and another element. Ionic hydrides are used as heterogeneous bases and reducing reagents in organic syntheses. An example is given in Fig. 2.2.

Typical solvents for such reactions are ethers. Water and other protic solvents are not able to serve as

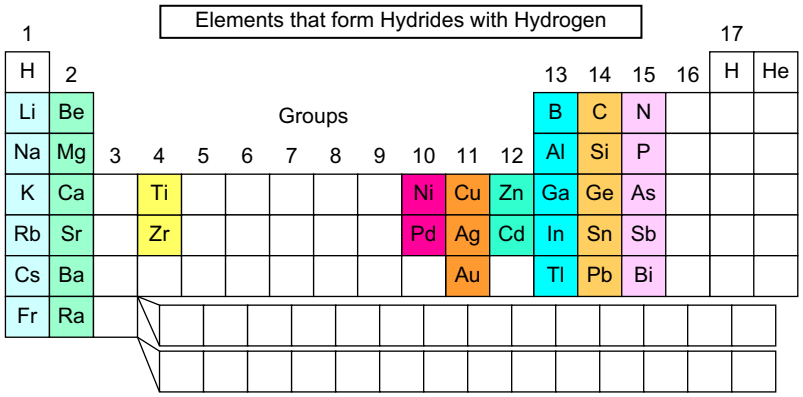

FIGURE 2.1

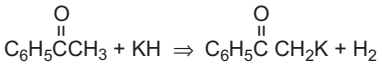

FIGURE 2.2

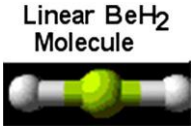

FIGURE 2.3

a solubilizing medium for pure ionic hydrides because the hydride ion is a stronger base than hydroxide and most other hydroxyl anions. Hydrogen gas is liberated in a typical acid–base reaction.

$$NaH + H_2O \Rightarrow H_2\ (gas) + NaOH\ \Delta H = -83.6\ kJ/mol,\ \Delta G = -109.0\ kJ/mol$$

Beryllium Hydride

BeH_2 was first synthesized in 1951 by reacting dimethylberyllium, $Be(CH_3)_2$, with lithium aluminum hydride, $LiAlH_4$. A purer grade of BeH_2 can also be formed from the pyrolysis of di-tert-butylberyllium, $\{Be(C(CH_3)_3)_2\}$ at 210 °C. The purest beryllium hydride is obtained by the reaction of triphenylphosphine, i.e. PPh_3, with beryllium borohydride, $Be(BH_4)_2$ by the reaction:

$$Be(BH_4)_2 + 2PPh_3 \Rightarrow 2Ph_3PBH_3 + BeH_2$$

Note that unlike the other elements in Group IIA where the hydride can be prepared by reaction of the elements, the reaction of the metal with hydrogen to produce beryllium hydride has not proved possible.

BeH_2 is usually formed as an amorphous white solid, but a hexagonal crystalline form with a higher density (~0.78 g/cm^3) has also been reported. This was prepared by heating amorphous BeH_2 under pressure, with 0.5–2.5% LiH as a catalyst. A more recent investigation found that crystalline beryllium hydride has a body-centered orthorhombic unit cell, containing a network of corner-sharing BeH_4 tetrahedra (there are 12BeH_2 molecules in the unit cell) in contrast to the flat, hydrogen-bridged, infinite chains previously thought to exist in crystalline BeH_2. Studies of the amorphous form also find that it consists of a network of corner-shared tetrahedra. The density is 0.755 g/cm3.

Molecular BeH_2 has been confirmed in a recent study as a linear structure with a Be–H bond length of 1.33376 Å. Because of the long-term toxicity of Be toward the human body, no actual uses of beryllium hydride have been promulgated. The structure is shown in Fig. 2.3.

The actual structure has the form shown in Fig. 2.4.

Cell parameters are: $a = 4.161$ Å, $b = c = 6.3084$ Å, $\alpha = \beta = \gamma = 70.748°$, cell volume = 145.59 Å3, cell occupancy is shown in Table 2.1.

Physical properties of BeH_2 are listed in Table 2.2.

Beryllium hydride is not used in Industry and remains an Academic oddity.

Magnesium Hydride

MgH_2 contains 7.66% by weight of hydrogen and has been studied as a potential hydrogen-storage medium. It was discovered in 1912, during the pyrolysis of ethyl magnesium iodide (a Grignard reagent), which produced small amount of MgH_2. In 1951, preparation from the elements was first reported involving direct hydrogenation of Mg metal at high pressure and temperature (200 atmospheres, 500 °C) with magnesium iodide as a catalyst:

$$Mg + H_2 \Rightarrow MgH_2$$

Lower temperature production from Mg and H_2 using nano-crystalline Mg produced in ball mills has been investigated. Other preparations include:

1. The hydrogenation of magnesium anthracene under mild conditions:

$$Mg(anthracene) + H_2 \Rightarrow MgH_2 + C_{14}H_{10}$$

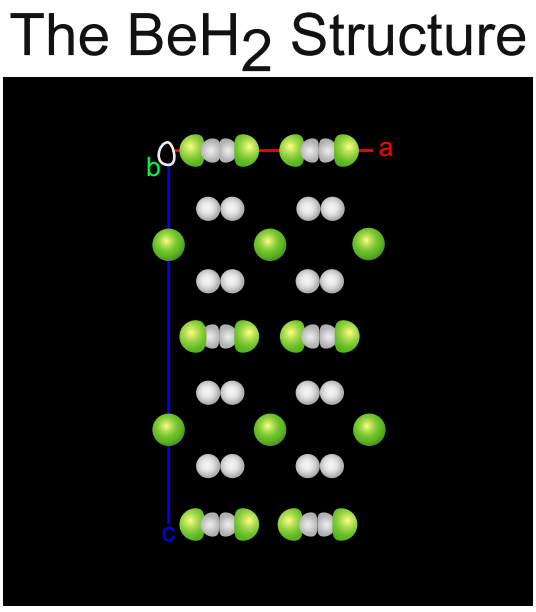

FIGURE 2.4

2. The reaction of diethyl magnesium with $LiAlH_4$
3. An adduct of complexed MgH_2, e.g. $MgH_2 \cdot THF$ by the reaction of phenylsilane (C_6H_8Si) and dibutyl magnesium in ether or hydrocarbon solvents in the presence of THF (C_4H_8O) using TMEDA (Tetramethylethylenediamine = $(CH_3)_2NCH_2CH_2N(CH_3)_2$) as a ligand.

The room temperature form, β-MgH_2, has a rutile structure. There are two high temperature forms, α-MgH_2 with the α-PbO_2 structure and γ-MgH_2. Additionally, a nonstoichiometric $MgH_{(2-\delta)}$ has been characterized. The bonding in the rutile form has been sometimes described as being covalent in nature rather than purely ionic. However, charge density determination by synchrotron X-ray diffraction indicates that the magnesium atom is fully ionized and spherical in shape and the hydride ion is elongated. Molecular forms of magnesium hydride such as MgH, MgH_2, Mg_2H, Mg_2H_2, Mg_2H_3, and Mg_2H_4 molecules were identified in matrix isolated samples at <10 K by their vibrational spectra. They were formed following laser ablation of magnesium in the presence of hydrogen. The Mg_2H_4 molecule has a bridged structure analogous to dimeric aluminum hydride, i.e. Al_2H_6. The structure of magnesium hydride is shown in Fig. 2.5.

This is the TiO_2 type of structure with cell parameters of: $a = 3.025$ Å, $b = c = 4.520$ Å, $\alpha = \beta = \gamma = 90°$. Cell volume = 61.80 Å^3, cell occupancy is shown in Table 2.3 and physical properties are shown in Table 2.4.

TABLE 2.2 Physical properties of BeH_2

Molar mass = 11.0334 g/mol
Appearance—amorphous white solid
Density = 0.65 g/cm^3
Melting point = 250 °C with decomposition
Solubility in water—decomposes

TABLE 2.1

No	Site notation	Atom	Multiplicity	Wyckoff	Site symmetry	*x*	*y*	*z*	Occupancy
1	H1	H	16	k	1	0.1949	0.089	0.1515	1.0
2	Be2	Be	8	j	..m	0.1253	0.170	0	1.0
3	H2	H	8	j	..m	0.2823	0.306	0	1.0
4	Be1	Be	4	a	222	0	0	1/4	1.0

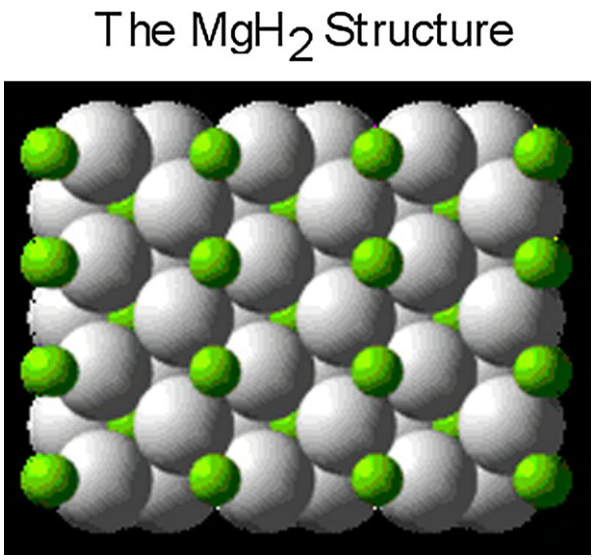

FIGURE 2.5

MgH_2 readily reacts with water to form hydrogen gas:

$$MgH_2 + 2H_2O \Rightarrow 2H_2 + Mg(OH)_2$$

At 300 °C, it decomposes to produce H_2 at 1 bar pressure. The high temperature required is seen as a limitation in the use of MgH_2 as a reversible hydrogen-storage medium. Its potential as reversible-"storage" medium for hydrogen has lead to interest in improving the hydrogenation and dehydrogenation reaction kinetics. An alternative approach under investigation is the production of a pumpable slurry of MgH_2 (which is safe to handle), the release of H_2 by the reaction with water and a reprocessing of the $Mg(OH)_2$ into MgH_2. Physical properties of MgH_2 are shown in Table 2.4.

No significant Industrial usage of magnesium hydride has yet arisen.

TABLE 2.4

Physical properties of MgH_2
Molar mass = 26.3209 gm/mol
Appearance—white crystals
Density = 1.45 gm/cm^3
Melting point = 327 °C
Solubility in water = decomposes

Calcium Hydride

Calcium hydride is a gray powder (white if pure, which is rare). It reacts vigorously with water liberating H_2 gas. CaH_2 is thus used as a drying agent, i.e. a desiccant. It is prepared directly from the metal or by reacting $CaCO_3$ with hydrogen at elevated temperatures. The overall reaction is shown as follows:

$$CaCO_3 + \text{heat} + H_2 \Rightarrow CaH_2 + H_2O + CO_2$$

CaH_2 is a saline hydride, meaning that its structure is salt-like. The alkali metals and the alkaline earth metals all form saline hydrides. These species are insoluble in all solvents with which they do not react because they have extended structures. CaH_2 crystallizes in the $PbCl_2$ structural pattern.

The reaction of CaH_2 with water can be represented as follows:

$$CaH_2 + 2H_2O \Rightarrow Ca(OH)_2 + 2H_2$$

The two hydrolysis products, H_2, a gas, and $Ca(OH)_2$, an aqueous mixture of solid plus liquid (i.e. a slurry), are

TABLE 2.3

No	Site notation	Atom	Multiplicity	Wyckoff	Site symmetry	x	y	z	Occupancy
1	H1	H	4	f	m.2m	0.30478	0.305	0	1.0
2	Mg1	Mg	2	a	m.mm	0	0	0	1.0

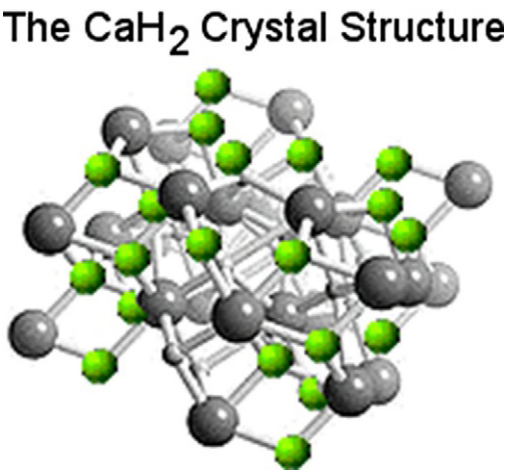

FIGURE 2.6

readily separated from the solvent by distillation, filtration, or decantation.

Calcium hydride is a relatively mild desiccant. It is safer than the more reactive agents such as sodium metal. Calcium hydride is widely used as a desiccant for basic solvents such as amines and pyridine in organic syntheses. It is also used to pre-dry solvents prior to the use of a more reactive desiccant. The compound has, however, been widely used for decades as a safe and convenient means to inflate weather balloons. Likewise, it is regularly used in laboratories to produce small quantities of highly pure hydrogen for experiments. The crystal structure is shown in Fig. 2.6.

Cell parameters are: $a = 3\ 602$ Å, $b = 5.957$ Å, $c = 6.809$ Å, $\alpha = \beta = \gamma = 90°$, Cell volume $= 146.31$ Å^3, cell occupancy is shown in Table 2.5.

Physical properties of CaH_2 are listed in Table 2.6.

Strontium Hydride

This hydride, SrH_2, is formed from the metal in the presence of hydrogen, under similar reaction conditions to that of calcium. Because of its great resemblance to calcium, little practical usage has evolved. It is an electronically neutral reagent chemical. In contact with water, it decomposes to form hydrogen:

$$SrH_2 + H_2O \Rightarrow Sr(OH)_2 + H_2$$

TABLE 2.6

Physical properties
Molecular formula = CaH_2
Molar mass = 42.094 g/mol
Appearance = gray powder (colorless when pure)
Density = 1.70 g/cm^3, solid
Melting point = 816 °C
Solubility in water = reacts violently

TABLE 2.7

Formula weight (molecular mass) = 89.635 g/mol
White rhombic crystals
Melting point = 675 °C decomposes
Density = 3.72 g/cm^3
Solubility: organic liquids = insoluble; water = decomposes
Melting point = 675 °C (decomposes)
Boiling point = sublimes at 1000 °C (in H_2)

The following lists the physical and chemicals properties of this compound (Table 2.7).

SrH_2 has the same type of structure as CaH_2 except that the cell parameters are: $a = 3.875$ Å, $b = 6.364$ Å, $c = 7.343$ Å, $\alpha = \beta = \gamma = 90°$, cell volume = 181.08 Å^3, cell occupancy is shown in Table 2.8.

Barium Hydride

BaH_2 forms in a manner similar to that of strontium hydride with the $PbCl_2$ type of structure. It too has found little usage in Industry. Cell parameters are: $a = 4.168$ Å, $b = 6.792$ Å, $c = 67.858$ Å, $\alpha = \beta = \gamma = 90°$, Cell volume $= 222.45$ Å^3, cell occupancy is shown in Table 2.9.

Known physical properties are listed in Table 2.10.

Radium Hydride

No hydride of radium is known.

TABLE 2.5

No	Site notation	Atom	Multiplicity	Wyckoff	Site symmetry	*x*	*y*	*z*	Occupancy
1	H1	H	4	c	.m.	0.0227	1/4	0.6621	1.0
2	H2	H	4	c	.m.	0.1425	1/4	0.0745	1.0
3	Ca1	Ca	4	c	.m.	0.2393	1/4	0.4045	1.0

TABLE 2.8

No	Site notation	Atom	Multiplicity	Wyckoff	Site symmetry	x	y	z	Occupancy
1	HII	H	4	c	.m.	0.004	1/4	0.758	1.0
2	HI	H	4	c	.m.	0.240	1/4	0.070	1.0
3	Sr	Sr	4	c	.m.	0.240	1/4	0.390	1.0

TABLE 2.9

No	Site notation	Atom	Multiplicity	Wyckoff	Site symmetry	x	y	z	Occupancy
1	H2	H	4	c	.m.	0.04	1/4	0.67	1.0
2	H1	H	4	c	.m.	0.15	1/4	0.086	1.0
3	Ba	Ba	4	c	.m.	0.26029	1/4	0.3886	1.0

TABLE 2.10

Physical properties of BaH_2

Formula weight (molecular mass) = 139.36 g/mol

Gray crystals

Density = 3.21 g/cm^3

Solubility: organic liquids = insoluble; water = decomposes

Melting point = 665 °C (decomposes)

Boiling point = no data

2.2. HALOGEN COMPOUNDS OF THE ALKALINE EARTHS

The chemical properties of the halo-acids such as HF and HCl are relevant to the type of compounds that the alkaline earths can form.

2.2.1. Halogen Acids

Hydrofluoric Acid

HF is a solution of hydrogen fluoride in water. While this acid is extremely corrosive and difficult to handle, it is technically a weak acid. Hydrogen fluoride, often in the aqueous form as hydrofluoric acid, is a valued source of fluorine, being the precursor to numerous pharmaceuticals such as fluoxetine (Prozac), diverse polymers such as polytetrafluoroethylene (Teflon), and most other synthetic materials that contain fluorine. Hydrofluoric acid is best known to the public for its ability to dissolve glass by reacting with SiO_2 (silicon dioxide), the major component of most glass, to form silicon tetrafluoride gas and hexafluorosilicic acid. This property has been known since the seventeenth century, even before hydrofluoric acid had been prepared in large quantities by Scheele in 1771. Because of its high reactivity toward glass, hydrofluoric acid must be stored (in small quantities) in polyethylene or Teflon containers. It is also unique in its ability to dissolve many metal and semimetal oxides. Hydrofluoric acid attacks glass by reaction with silicon dioxide to form gaseous or water-soluble silicon fluorides. This dissolution process proceeds as follows:

$$SiO_2\ (\text{solid}) + 4HF\ (\text{aq}) \Rightarrow SiF_4\ (\text{gas}) + 2H_2O\ (\text{liq})$$

$$SiO_2\ (\text{solid}) + 6HF\ (\text{aq}) \Rightarrow H_2SiF_6\ (\text{aq}) + 2H_2O\ (\text{liq})$$

Hydrofluoric acid is very dangerous to handle, because the human skin becomes easily saturated with the acid. Even though skin absorption of small areas of only 25 square inches (160 cm^2) may be relatively painless, yet the exposure may be ultimately fatal. High concentrations of hydrofluoric acid and hydrogen fluoride gas will also quickly destroy the corneas of the eyes.

Hydrogen fluoride ionizes in aqueous solution in a similar fashion to other common acids:

$$HF + H_2O \Rightarrow H_3O^+ + F^-$$

Due to its low degree of ionization in dilute solution, hydrofluoric acid is the only hydrohalic acid that is not considered a strong acid.

When the concentration of HF approaches 100%, the acidity increases dramatically due to the following shift in equilibrium:

$$2HF \Rightarrow H^+ + FHF^-$$

The FHF^- anion is stabilized by very strong hydrogen–fluorine hydrogen bonds. Industrially, hydrofluoric acid is produced by treatment of the mineral Fluorite (CaF_2) with concentrated sulfuric acid. When combined at 250 °C, these two substances react to produce hydrogen fluoride and calcium sulfate according to the following reaction:

$$CaF_2 + H_2SO_4 \Rightarrow 2HF\ (gas) + CaSO_4\ (solid)$$

Although bulk fluorite is a suitable precursor, most HF is produced as a by-product of the production of phosphoric acid, which is derived from the mineral Apatite. Apatite sources typically contain a few percent of fluorite. The acid hydrolysis of fluorite-containing minerals generates an impure gas stream consisting of SO_2 (from the H_2SO_4), water, and HF, as well as particulates. After separation from the solids, the gases are treated with sulfuric and oleum to afford anhydrous HF. Owing to the corrosive nature of HF, its production is accompanied by the dissolution of silicate minerals, and in this way a significant amount of fluorosilicic acid is generated.

Diluted hydrofluoric acid (1–3 %wt) is used in the "Oil Patch" in a mixture with other acids (HCl or organic acids) in order to stimulate the production of water, oil and gas wells specifically where sandstone is involved. HF is also used in oil refining. In a standard oil-refinery process known as Alkylation, isobutane is alkylated with low-molecular weight alkenes (primarily a mixture of propylene and butylene) in the presence of a strong acid catalyst, hydrofluoric acid. The catalyst is able to protonate the alkenes (propylene, butylene) to produce reactive "carbo-cations", which cause alkylation of isobutane. The reaction is carried out at mild temperatures (0 and 30 °C) in a two-phase reaction. It is important to keep a high ratio of isobutane to alkene at the point of reaction to prevent side reactions that lead to a lower octane product, so the plants have a high recycle of isobutane back to feed. The phases separate spontaneously, so the acid phase is vigorously mixed with the hydrocarbon phase to create sufficient contact surface.

Hydrofluoric acid (HF) is used principally in organofluorine chemistry. Many such compounds are prepared using HF as the fluorine source, including "Teflon™", fluoropolymers, fluorocarbons and "Freon™" refrigerants.

Additionally, most high-volume inorganic fluoride compounds are prepared from hydrofluoric acid. Foremost are Na_3AlF_6, (Cryolite), and AlF_3(aluminum trifluoride). A molten mixture of these solids serves as a high-temperature solvent for the production of metallic aluminum. Concerns about fluorides in the environment have led to a search for alternative technologies. Other inorganic fluorides prepared from hydrofluoric acid include NaF and UF_6.

The ability of hydrofluoric acid to dissolve metal oxides is the basis of several applications. It removes oxide impurities from stainless steel in a process called *pickling*. Surface oxides are removed from silicon with hydrofluoric acid in the Semiconductor Industry. For this purpose, dilute hydrofluoric acid is sold as a household rust stain remover. Recently, it has even been used in "Car-Wash" facilities in "wheel cleaner" compounds.

Due to its ability to dissolve oxides, hydrofluoric acid is useful for dissolving rock samples (usually powdered) prior to analysis. Similarly, this acid has been used to extract organic fossils from silicate rocks. Fossiliferous rock may be immersed directly into the acid, or a cellulose nitrate film may be applied (dissolved in amyl acetate), which adheres to the organic component and allows the rock to be dissolved around it.

Hydrochloric Acid

This acid is the result of solution of HCl gas in water. It is a highly corrosive, strong mineral acid and has many major industrial uses. It is found naturally in "gastric acid" of the human body. Historically, it has been called **muriatic acid** or **spirits of salt**. Hydrochloric acid was first produced from vitriol (H_2SO_4 or "oil of vitriol") and salt. The Alchemist, Jabir ibn Hayyan, formally described it in the eighth century. During the Middle Ages, alchemists used it in the quest for the "Philosophers Stone", and later by European scientists including Glauber, Priestley and Davy in their scientific research.

Major production of HCl started during the Industrial Revolution of the 1800s where hydrochloric acid was used in the chemical industry. Today, it is used in a wide variety of industrial applications as a chemical reagent. It has numerous smaller scale applications, including household cleaning, production of gelatin and other food additives, removal of scale from metals and leather processing. About 20 million metric tons of hydrochloric acid is produced annually.

Hydrochloric acid was first discovered around AD 800 by the alchemist Jabir ibn Hayyan, who mixed salt with sulfuric acid (vitriol) to form gaseous HCl. He discovered many important chemicals, and recorded his findings in over 20 books. His chemical knowledge of hydrochloric acid and other basic chemicals remained the foundation of chemistry for hundreds of years. Jabir's invention of the gold-dissolving "aqua-regia", consisting of hydrochloric acid and nitric acid, was of great interest to alchemists searching for the Philosopher's Stone.

In the Middle Ages, hydrochloric acid was known to European alchemists as *spirits of salt* or *acidum salis* (salt acid). Both names are still deployed, notably in non-English languages, such as German: *Salzsäure* and

Dutch: *Zoutzuur*. Gaseous HCl was called *marine acid air*. The old name *muriatic acid* has the same origin (*muriatic* means "pertaining to brine or salt"), and this name is still sometimes used. In the seventeenth century, Glauber, used sodium chloride and sulfuric acid for the preparation of sodium sulfate, releasing hydrogen chloride gas. Priestley prepared pure hydrogen chloride in 1772, and in 1818, Davy proved that the chemical composition included hydrogen and chlorine.

During the Industrial Revolution in Europe, demand for acidic and alkaline substances increased. A new industrial process by LeBlanc enabled cheap large-scale production of sodium carbonate (soda ash). In this process, common salt is converted to soda ash, using sulfuric acid, limestone, and coal, releasing hydrogen chloride gas as a by-product. Until the British Alkali Act of 1863 and similar legislation in other countries, the excess HCl was vented to the air. After the passage of the act, soda ash producers were obliged to absorb the waste gas in water, producing hydrochloric acid on an industrial scale.

In the twentieth century, the Leblanc process was effectively replaced by the Solvay Process without a hydrochloric acid by-product. Since hydrochloric acid was already fully settled as an important chemical in numerous applications, the commercial interest initiated other production methods, some of which are still used today. After the year 2000, hydrochloric acid is mostly made by absorbing by-product hydrogen chloride from industrial production of organic compounds.

The latest method consists of synthesis of hydrogen chloride by burning hydrogen gas and chlorine gas in graphite acid-synthesis equipment. This has proved to be an economical and reliable operation. This is true particularly in those processes where chlorine gas is produced as a by-product or where hydrogen chloride or hydrochloric acid is required for on-site use. Typical uses occur in brine electrolysis, vinyl chloride manufacture, paper and pulp production and various metallurgical processes.

Since 1988, hydrochloric acid has been listed as a Table II precursor under the 1988 UN Convention—Illicit Traffic in Narcotic Drugs because of its use in the production of heroin, cocaine and methamphetamine.

Hydrogen chloride (HCl) is a monoprotic acid. In aqueous hydrochloric acid, the H^+ joins a water molecule to form a hydronium ion, H_3O^+:

$$HCl + H_2O \Rightarrow H_3O^+ + Cl^-$$

The other ion formed is Cl^-. Hydrochloric acid can therefore be used to prepare chloride salts. Hydrochloric acid is a strong acid, since it is essentially completely dissociated in water.

For a strong acid like HCl, the K_a is large. When chloride salts such as NaCl are added to aqueous HCl they have practically no effect on pH, indicating that the Cl^- aqueous ion is an exceedingly weak conjugate base and that HCl is fully dissociated in aqueous solution. For intermediate to strong solutions of hydrochloric acid, the assumption that the H^+ molarity equals the HCl molarity is excellent, agreeing to four significant digits.

Of the seven common strong mineral acids in chemistry, hydrochloric acid is the monoprotic acid least likely to undergo an interfering oxidation–reduction reaction. It is one of the least hazardous of the strong acids to handle. Despite its acidity, it consists of the nonreactive and nontoxic chloride ion. Intermediate-strength hydrochloric acid solutions are quite stable upon storage, maintaining their concentrations over time. These attributes, plus the fact that it is available as a pure reagent, mean that hydrochloric acid makes an excellent acidifying reagent.

Hydrochloric acid is the preferred acid in titration for determining the amount of bases present. Strong acid titrants give better results due to a more distinct endpoint. Azeotropic or "constant-boiling" hydrochloric acid can be used as a primary standard in Quantitative Analysis, although its exact concentration depends on the pressure of the atmosphere when it is prepared (because of Henry's Law).

Hydrochloric acid is frequently used in digest samples for analysis. Concentrated hydrochloric acid dissolves many metals and forms oxidized metal chlorides and hydrogen gas, and it reacts with basic compounds such as calcium carbonate or cupric oxide forming the dissolved chlorides that can be analyzed.

The physical properties of hydrochloric acid, such as boiling point or melting point, density and pH depend on the molarity of HCl in the acid solution. They range from those approaching 0% HCl to values for fuming hydrochloric acid at over 40% HCl. The following table summarizes some of these values (Table 2.11).

Hydrochloric acid, as the binary (two-component) mixture of HCl and H_2O, has a constant-boiling azeotrope at 20.2% HCl and 108.6 °C (227 F).

There are four "constant-crystallization" eutectic points for hydrochloric acid, which form crystals which the solution is cooled:

$HCl \cdot H_2O$ (68% HCl)

$HCl \cdot 2H_2O$ (51% HCl)

$HCl \cdot 3H_2O$ (41% HCl)

$HCl \cdot 6H_2O$ (25% HCl)

and Ice (0% HCl).

TABLE 2.11

Conc as % HCl per kg	kg HCl/m^3	Density kg/L	Molarity in Mols/dm^3	pH	Viscosity (mPa·s)	Vapor pressure (Pa)	BP °C	MP °C
10%	104.80	1.048	2.87	−0.5	1.16	0.527	103	−18
20%	219.60	1.098	6.02	−0.8	1.37	27.3	108	−59
30%	344.70	1.149	9.45	−1.0	1.70	1410	90	−52
32%	370.88	1.159	10.17	−1.0	1.80	3130	84	−43
34%	397.46	1.169	10.90	−1.0	1.90	6733	71	−36
36%	424.44	1.179	11.64	−1.1	1.99	14,100	61	−30
38%	451.82	1.189	12.39	−1.1	2.10	28,000	48	−26

There is also a metastable eutectic point at 24.8% between ice and the $HCl{\cdot}3H_2O$ crystallization point. However, these crystals cannot be separated and used since they are unstable and give rise to HCl gas and water.

Hydrogen chloride can be generated in many ways, and thus several precursors to hydrochloric acid exist. The large-scale production of hydrochloric acid is almost always integrated with the industrial scale production of other compounds.

Hydrochloric acid is produced in solutions up to 38% HCl (concentrated grade). Higher concentrations are possible up to about 40% but the evaporation rate of HCl gas is then so high that storage and handling need extra precautions, such as pressure and low temperature. Bulk industrial grade is therefore 30%–34%, as optimized for effective transport and limited product loss by HCl vapors. Solutions for household purposes in the US, mostly cleaning, are typically 10%–12%, with strong recommendations to dilute before use. In the United Kingdom, where it is sold as "Spirits of Salt" for domestic cleaning, the potency is the same as the US industrial grade.

Major producers worldwide include Dow Chemical at 2 million metric tons annually (2 Mt/year), calculated as HCl gas. FMC and Georgia Gulf Corporation in the U.S., Tosoh Corporation (Japan), Akzo Nobel, and Tessenderlo (Europe) each produce about 0.5 to 1.5 Mt/year each. Total world production, for comparison purposes expressed as HCl, is estimated at 20 Mt/year, with 3 Mt/year from direct synthesis, and the rest as a secondary product from organic and similar syntheses. By far, most hydrochloric acid is consumed captively by the producer. The open world market size is estimated at 5 Mt/year.

One of the most important applications of hydrochloric acid is in the "pickling of steel" to remove rust or iron oxide scale from iron or steel before subsequent processing, such as extrusion, rolling, galvanizing, and other techniques. Technical quality HCl at typically 18% concentration is the most commonly used pickling agent for the pickling of carbon-steel grades:

$$Fe_2O_3 + Fe + 6HCl \Rightarrow 3FeCl_2 + 3H_2O$$

The spent acid has long been reused as iron(II) chloride (also known as ferrous chloride) solutions, but high heavy-metal levels in the pickling liquor have decreased this practice.

The steel-pickling industry has developed hydrochloric acid regeneration processes, such as the "spray roaster" or the fluidized bed HCl regeneration process, which allow the recovery of HCl from spent pickling liquor. The most common regeneration process is the "pyrohydrolysis process", applying the following reaction:

$$4FeCl_2 + 4H_2O + O_2 \Rightarrow 8HCl + 2Fe_2O_3$$

By recuperation of the spent acid, a closed acid loop is established. The iron(III) oxide by-product of the regeneration process is valuable and used in a variety of secondary industries.

Another major use of hydrochloric acid is in the production of organic compounds such as vinyl chloride, used to form the plastic, PVC. This is often captive-use, consuming locally produced hydrochloric acid that never actually reaches the open market. Other organic compounds produced with hydrochloric acid include Biphenol-A for polycarbonate plastic, activated carbon, and ascorbic acid, as well as numerous pharmaceutical products:

$$2CH_2 = CH_2 + 4HCl + O_2 \Rightarrow 2ClCH_2CH_2Cl + 2H_2O$$

(vinyl chloride by oxchlorination)

$$\text{wood} + HCl + \text{heat} \Rightarrow \text{activated carbon}$$

(chemical activation)

Numerous products can be produced with hydrochloric acid in normal acid–base reactions, resulting in various inorganic compounds. These include water treatment chemicals such as ferric chloride and polyaluminum trichloride (PAC).

$$Fe_2O_3 + 6HCl \Rightarrow 2FeCl_3 + 3H_2O$$

(iron(III)chloride from magnetite)

Both iron(III) chloride and PAC are used as flocculation and coagulation agents in sewage treatment, drinking water treatment, and paper production.

Other inorganic compounds produced with hydrochloric acid include road application salts such as $CaCl_2$, $NiCl_2$ for electroplating, and $ZnCl_2$ for the galvanizing industry and battery production:

$$CaCO_3 + 2HCl \Rightarrow CaCl_2 + CO_2 + H_2O$$

(calcium chloride from limestone)

Hydrochloric acid can be used to regulate the basicity (pH) of solutions:

$$OH^- + HCl \Rightarrow H_2O + Cl^-$$

In industries demanding purity (food, pharmaceutical, drinking water), high-quality hydrochloric acid is used to control the pH of process water streams. In less-demanding industry, technical-quality hydrochloric acid suffices for neutralizing waste streams and swimming pool treatment.

High-quality hydrochloric acid is used in the regeneration of ion-exchange resins used for "water-softening". A cation-exchange mechanism is widely used to remove ions such as Na^+ and Ca^{2+} from water, producing "demineralized" water. The acid is used to rinse the cations from the resins:

$$Na^+ \text{ is replaced by } H^+$$

$$Ca^{2+} \text{ is replaced by } 2H^+$$

Ion exchangers and demineralized water are used in all chemical industries for drinking water production, and many food industries.

Hydrochloric acid is also used for a large number of small-scale applications, such as leather processing, household cleaning, and building construction. In the crude-oil industry, oil production may be stimulated by injecting hydrochloric acid into the limestone rock formation of an oil well, dissolving a portion of the rock, and creating a large-pore structure. Oil well acidizing is a common process in the North Sea oil production industry.

Many chemical reactions involving hydrochloric acid are applied in the production of food, food ingredients, and food additives. Typical products include aspartame, fructose, citric acid, lysine, hydrolyzed vegetable protein as a food enhancer, and in gelatin production. Food-grade (extra-pure) hydrochloric acid can be applied when needed for the final product.

Gastric acid is one of the main secretions of the stomach. It consists mainly of hydrochloric acid and acidifies the stomach content to a pH of 1–2. Gastric acid acts as a barrier against microorganisms to prevent infections and is important for the digestion of food. Its low pH denatures proteins and thereby makes them susceptible to degradation by enzymes.

Concentrated hydrochloric acid (fuming hydrochloric acid) forms acidic mists. Both the mist and the solution have a corrosive effect on human tissue, with the potential to damage respiratory organs, eyes, skin, and intestines. Upon mixing hydrochloric acid with common oxidizing chemicals, such as bleach (NaClO) or potassium permanganate ($KMnO_4$), the toxic gas, chlorine is produced:

$$NaClO + 2HCl \Rightarrow H_2O + NaCl + Cl_2$$

$$2KMnO_4 + 16HCl \Rightarrow 2MnCl_2 + 8H_2O + 2KCl + 5Cl_2$$

Rubber or PVC gloves, protective eye goggles, and chemical-resistant clothing and shoes are used to minimize risks when handling hydrochloric acid. The hazards of solutions of hydrochloric acid depend on its concentration. The properties of commercial HCl can be summarized as in Table 2.12.

Hydrobromic Acid

This is a strong acid formed by dissolving the diatomic molecule HBr in water. "Constant-boiling" hydrobromic acid is an aqueous solution that distills at 124.3 °C and contains 47.6% HBr by weight. Hydrobromic acid has a pK_a of −9, making it a stronger acid than hydrochloric acid, but not as strong as HI, hydroiodic acid. Hydrobromic acid is one of the strongest mineral acids known.

TABLE 2.12

CAS number = 7647-01-0
Molar mass = 36.46 g/mol (as HCl)
Appearance: Clear colorless to light-yellow liquid
Density = 1.18 g/cm^3 (variable, value for assay = 36−38% w/w)
Miscible in water
Soluble in diethyl ether, ethanol and methanol
Acidity (pKa) = 8.0
Refractive index, (n_D) = 1.342
Viscosity = 1.9 MPa at 25 °C

Hydrobromic acid is mainly used for the production of inorganic bromides, especially the bromides of zinc, calcium, and sodium. It is a useful reagent for generating organobromine compounds. Certain ethers are cleaved with HBr. It also catalyzes alkylation reactions and the extraction of certain ores. Industrially significant organic compounds prepared from hydrobromic acid include allyl bromide, tetrabromobis(phenol), and bromoacetic acid.

Hydrobromic acid can be prepared in the laboratory via the reaction of Br_2, SO_2 and water. Another laboratory preparation involves the production of anhydrous HBr, which is then dissolved in water.

Hydrobromic acid has commonly been prepared industrially by reacting bromine with either sulfur or phosphorous and water. However, it can also be produced electrolytically. It can also be prepared by treating bromides with nonoxidizing acids like phosphoric or acetic acids. Hydrobromic acid is available commercially in various concentrations and purities.

The properties of hydrobromic acid can be summarized as in Table 2.13.

Hydroiodic Acid

This is a strong acid, made by dissolving HI gas in water. However, hydrogen iodide and hydroiodic acid differ in that the former is a gas under standard conditions whereas the other is an aqueous solution of said gas. They are noninterconvertible. That is, once the acid is formed with water, it cannot be recovered like HCl or HBr. Hydroiodic acid is used in organic and inorganic synthesis as one of the primary sources of iodine and as a reducing agent.

With moist air, HI gas gives a mist (or fumes) of hydroiodic acid. It is exceptionally soluble in water. One liter of water will dissolve 425 L of HI, the final solution containing only four water molecules per molecule of HI. As stated, although chemically related, hydroiodic acid is not pure HI but a mixture containing it. Commercial "concentrated" hydroiodic acid usually contains 90–98% HI by mass.

The solution forms an azeotrope boiling at 127 °C containing 57% HI, 43% water. Hydroiodic acid is one of the strongest of all the common halide acids due to the high stability of its corresponding conjugate base. The iodide ion is much larger than the other common halides. This results in the negative charge being dispersed over a larger space. By contrast, a chloride ion is much smaller, meaning its negative charge is more concentrated, leading to a stronger interaction between the proton and the chloride ion. This weaker H^+–I^- interaction in HI facilitates dissociation of the proton from the anion, and is the reason HI is the strongest acid of the hydrohalides:

$$HI_{(gas)} + H_2O_{(liq)} \Rightarrow H_3O^+_{(aq)} + I^-_{(aq)} \quad K_a \approx 10^{10}$$

$$HBr_{(gas)} + H_2O_{(liq)} \Rightarrow H_3O^+_{(aq)} + Br^-_{(aq)} \quad K_a \approx 10^{9}$$

$$HCl_{(gas)} + H_2O_{(liq)} \Rightarrow H_3O^+_{(aq)} + Cl^-_{(aq)} \quad K_a \approx 10^{8}$$

The industrial preparation of HI involves the reaction of I_2 with hydrazine, which also yields nitrogen gas:

$$2I_2 + N_2H_4 \Rightarrow 4HI + N_2$$

When performed in water, the HI must be distilled to obtain the anhydrous form. HI can also be distilled from a solution of NaI or other alkali iodide in concentrated H_3PO_4 (note that sulfuric acid will not work for acidifying iodides as it will oxidize the iodide to elemental iodine).

Another way HI may be prepared is by bubbling a hydrogen sulfide steam through an aqueous solution of Iodine, forming hydroiodic acid (which is then distilled) and elemental sulfur (this is filtered):

$$H_2S + I_2 \Rightarrow 2HI + S$$

Additionally, HI can be prepared by simply combining H_2 and I_2. This method is usually employed to generate high-purity samples:

$$H_2 + I_2 \Rightarrow 2HI$$

For many years, this reaction was considered to involve a simple bimolecular reaction between molecules of H_2 and I_2. However, when a mixture of the gases is irradiated with the wavelength of light equal to the dissociation energy of I_2, (about 578 nm), the rate increases significantly. This supports a mechanism whereby I_2 first dissociates into two iodine atoms, which each attach themselves to a side of an H_2 molecule and break the H–H bond:

$$H_2 + I_2 + 578\text{ nm radiation} \Rightarrow H_2 + 2I \Rightarrow I\text{–}H\text{–}H\text{–}I \Rightarrow 2HI$$

TABLE 2.13

CAS number	10035-10-6
Molecular formula	HBr
Molar mass	80.91 g/mol
Appearance	Colorless liquid
Density	Variable
Melting point	Variable
Boiling point	Variable
Solubility in water	Aqueous solution
Acidity (pK_a)	−9

The HI is then dissolved in water to form the acid. In the laboratory, another method involves the hydrolysis of PI_3, the iodine equivalent of PBr_3. In this method, I_2 reacts with phosphorous to create phosphorous triiodide, which then reacts with water to form HI and phosphorous acid:

$$3I_2 + 2P + 6H_2O \Rightarrow 2PI_3 + 6H_2O \Rightarrow 6HI + 2H_3PO_3$$

Hydroiodic acid will undergo oxidation if left open to air according to the following pathway:

$$4HI + O_2 \Rightarrow 2H_2O + 2I_2$$

$$HI + I_2 \Rightarrow HI_3$$

HI_3 is dark-brown in color, which makes aged solutions of HI often appear dark brown. Like HBr and HCl, HI adds to alkene compounds:

$$HI + H_2C{=}CH_2 \Rightarrow H_3CCH_2I$$

HI is also used in organic chemistry to convert primary alcohols into alkyl halides. This reaction is an S_N2 substitution, in which the iodide ion replaces the "activated" hydroxyl group (water). HI is preferred over other hydrogen halides because the iodide ion is a much better nucleophile than bromide or chloride. Thus, the reaction can take place at a reasonable rate without much heating. This reaction also occurs for secondary and tertiary alcohols, but substitution occurs via the S_N1 pathway (Fig. 2.7).

HI (or HBr) can also be used to cleave ethers into alkyl iodides and alcohols, in a reaction similar to the substitution of alcohols. This type of cleavage is significant because it can be used to convert a chemically stable and inert ether into more reactive species. In the following example, diethyl ether is cleaved into ethanol and iodoethane. The reaction is regioselective, as iodide tends to attack the less sterically hindered ether carbon (Fig. 2.8).

HI reduces certain α-substituted ketones and alcohols replacing the α-constituent with a hydrogen atom.

Hydroiodic acid is currently listed as a Federal DEA List 1 Chemical. Owing to its usefulness as a reducing agent, reduction with HI and red phosphorus has become the most popular method to produce methamphetamine in the United States. Clandestine chemists react pseudo-ephedrine (recovered from decongestant pills) with hydroiodic acid and red phosphorus under heat, HI reacts with pseudoephedrine to form iodoephedrine, an intermediate which is reduced primarily to methamphetamine.

The properties of this acid may be summarized as in Table 2.14.

TABLE 2.14

CAS number	10034-85-2
Molecular formula	HI
Molar mass	127.904 g/mol
Appearance	Colorless gas
Density	2.85 g/ml (−47 °C)
Melting point	−50.80 °C (184.55 K)
Boiling point	−34.36 °C (237.79 K)
Acidity (pK_a)	−10
Refractive index (n_D)	1.466
Molecular shape	Terminus
Dipole moment	0.38 D
Standard enthalpy of formation $\Delta H^\circ_{f_{298}}$	0.2072 kJ/g
Specific heat capacity, C_p	0.2283 J/g K

2.2.2. Halide Compounds of Beryllium

The hydrolytic reactions of beryllium(II) ions have been calorimetrically studied at 25 °C in aqueous solution and dioxane–water mixtures, both containing 3.0 mol/dm^3 Li_2ClO_4 as a constant ionic medium. The formation constants, on the basis of the enthalpy and entropy changes, for the reaction:

$$x\mathrm{Be}^{2+} + y\mathrm{H_2O} \Rightarrow \{\mathrm{Be}_x\,(\mathrm{OH}_y)\}^{(2x-y)+} + y\mathrm{H}^+,$$

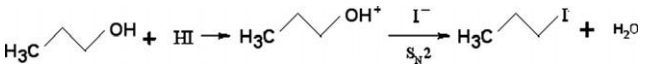

FIGURE 2.7

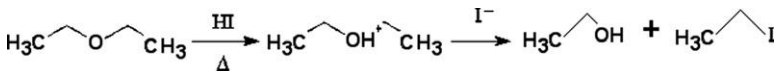

FIGURE 2.8

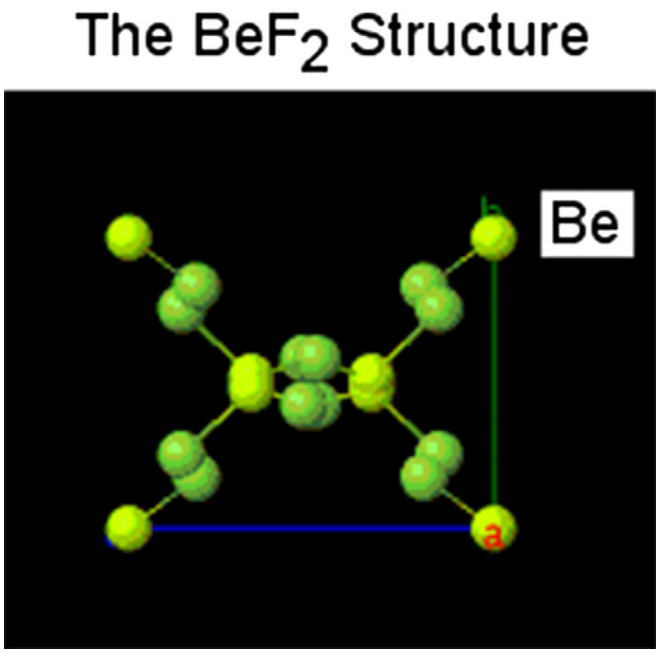

FIGURE 2.8A

were determined for the Be_2OH^{3+} and $Be_3(OH)_3^{3+}$ complexes in aqueous solution, for the 0.1 mol fraction dioxane–water mixture, and for Be_2OH^{3+}, $Be_3(OH)_3^{3+}$, and $Be_2(OH)_2^{2+}$ complexes in 0.2 mol fraction dioxane–water mixture. The enthalpy and entropy changes of formation of the $Be_x(OH)_y^{(2x-y)+}$ complex in solutions of various mole fractions of dioxane were obtained and shown to abide by the following reaction:

$$2Be^{2+} + H_2O \Rightarrow (Be_2OH)^{3+} + H^+$$

Thus, it is clear that the Be^{2+} cation in aqueous solution never appears but is an "aquo-complex". Therefore, if one desires the halide and oxo-halogen compounds of beryllium, they are usually prepared via a solid-state method, not an aqueous one.

Beryllium Fluoride

Beryllium fluoride has the formula, BeF_2, and is a hygroscopic, **amorphous** solid with a melting point of 800 °C. It is soluble in water and is used in beryllium metallurgy in which the metal, Be, is employed as an alloy. It is the binary Be compound with the greatest amount of ionic character (due to the high electronegativity of fluorine), but even so it is not considered ionic but covalent by many chemists. This synthetic material is the principal precursor for the manufacture of beryllium metal, which is obtained by reduction of BeF_2 at 1300 °C:

$$BeF_2 + Mg \Rightarrow Be + MgF_2$$

Solid crystalline BeF_2 has a silica-like structure with beryllium in a four-coordinate position. The structure has the form shown in Fig. 2.8A.
with cell parameters of: $a = b = 4.802$ Å, $c = 5.240$ Å, $\alpha = \beta = 90°$, $\gamma = 120°$, cell volume = 104.82 Å^3, cell occupancy is shown in Table 2.15.

Molecular BeF_2, is isoelectronic with CO_2 and SiO_2. As determined in the gas phase above 1160 °C, beryllium fluoride is a linear molecule with a Be–F distance of 1.77 Å. The condensed form adopts a number of different polymeric structures similar to those formed by silica {namely α-quartz, β-quartz, "Crystobalite" (a polymorph of quartz) and "Tridymite" (a high-temperature polymorph of quartz stable between 870 and 1470 °C)}. The difference between the ambient temperature structures of BeF_2 and CO_2 reflects the decreased tendency of alkali metals to form multiple bonds. An analogy exists between BeF_2 and AlF_3. Both adopt extended structures at mild temperatures. The following illustrates the various polymeric structures of BeF_2 which exist as a function of temperature:

$$\alpha Q - BeF_2 \overset{220^\circ C}{\Leftrightarrow} \beta Q - BeF_2 \overset{420-450^\circ C}{\Leftrightarrow} T - BeF_2$$

$$\overset{552^\circ C}{\Leftrightarrow} \text{melt} \overset{690^\circ C}{\Leftrightarrow} \beta C - BeF_2 \overset{730^\circ C}{\Leftrightarrow} \alpha C - BeF_2$$

where "Q" is the quartz structure, "T" is the tridymite structure, and "C" is the Crystobalite structure. Note that the allotropic changes of Crystobalite occur in the melt. The melt does not recrystallize upon cooling but forms an amorphous glass-like silica.

Beryllium fluoride is used in biochemistry, particularly protein crystallography, since it binds in some of the same ways as phosphate does in human tissues. ADP and beryllium fluoride together tend to bind to ATP sites and inhibit protein action, making it possible to crystallize proteins in the bound state.

Beryllium fluoride forms a basic constituent of the preferred fluoride salt mixture used in liquid-fluoride nuclear reactors. Typically, beryllium fluoride is mixed

TABLE 2.15

No	Site notation	Atom	Multiplicity	Wyckoff	Site symmetry	*x*	*y*	*z*	Occupancy
1	F	F	12	k	1	0.4204	0.171	0.1856	0.5
2	Be	Be	6	g	2.	0.4806	0	0	0.5

TABLE 2.16 Physical constants of beryllium fluoride

CAS number	7787-49-7
Molecular formula	BeF_2
Molar weight	47.008988 g/mol
Appearance	Colorless lumps
Density	1.986 g/cm^3
Melting point	554 K; 927 °C; 1029 F
Boiling point	1169 K; 1442 °C; 2136 F
Solubility	Very soluble in water; sparingly soluble in alcohol
Standard enthalpy of formation	$\Delta H^{\circ}_{f_{298}} = -21.84$ kJ/g
Specific heat capacity	1.102 J/°K
Specific free energy of formation	$\Delta G^0_f = -20.83$ kJ/g
Specific heat of formation	$\Delta H^0_f = -21.84$ kJ/g
Specific heat of fusion	0.10147 kJ/g

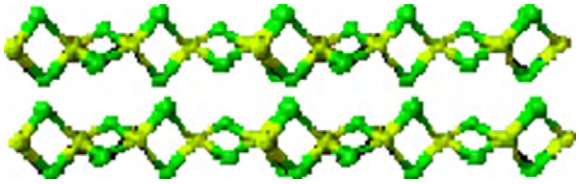

FIGURE 2.8B

with LiF to form a base solvent, into which fluorides of uranium and thorium are introduced. Beryllium fluoride is exceptionally chemically stable and LiF/BeF_2 mixtures have low melting points and the best neutronic properties of any of the fluoride salt combinations appropriate for reactor use (Table 2.18).

Beryllium Chloride

Beryllium chloride has the formula $BeCl_2$ with a molecular weight of 79.9176 g/mol. Beryllium chloride, $BeCl_2$, melts at 405 °C and boils at 520 °C. That compares with 714 °C and 1412 °C for magnesium chloride. The solid is a one-dimensional polymer consisting of edge-shared tetrahedra. In contrast, BeF_2 is a three-dimensional polymer, with a structure akin to that of quartz. In the gas phase, $BeCl_2$ exists both as a linear monomer and a bridged dimer with two bridging chlorine atoms where the beryllium atom is 3-coordinate. This linear shape contrasts with the monomeric forms of some of the dihalides of the heavier members of group 2, e.g. CaF_2, SrF_2, BaF_2, $SrCl_2$, $BaCl_2$ and Ba that are all nonlinear.

The linear chain structure of the solid is illustrated as Fig. 2.8B.

In the solid, the $BeCl_2$ molecules polymerize to make long chains. They do this by forming coordinate bonds (dative covalent bonds) between lone pairs on chlorine atoms and adjacent beryllium atoms. The orthorhombic unit, $a_0 = 9.86$, $b_0 = 5.36$, $c_0 = 5.26$ Å contains four beryllium chloride molecules. The structure consists of continuous chains with an essentially tetrahedral configuration about beryllium. The Cl–Be–Cl bond angle within the four-membered rings is 98.2° which is less than the tetrahedral angle, as is found in SiS_2, instead of more, as in dimethylberyllium. The bond angles indicate that all bonds in beryllium chloride contain an electron pair, so that chlorine uses an unshared pair in forming bridge bonds. Hence, chlorides isomorphic with electron-deficient metal alkyls are not to be classified as electron-deficient compounds.

Although early workers (1798) obtained the chloride in solution, the pure salt was not made until about 1827 when one worker of the time prepared it in the sublimed anhydrous state by passing chlorine gas over a heated mixture of carbon and beryllium oxide. Finally (1885), it was prepared as the pure chloride in very pure form for the purpose of determining its vapor density by the action of dry hydrochloric acid gas on the metal, but the pure salt was not produced until 1898 when one worker made it by heating the double fluoride of ammonium and beryllium, which had previously been dried over phosphoric anhydride, in a current of dry carbon dioxide and cooled in an atmosphere of the same gas. He also prepared it by the action of hydrofluoric acid gas on the carbide. No matter what method is used, it was determined that the materials must be absolutely dry if a pure chloride is to be obtained.

The pure chloride is a glassy, transparent mass having a specific gravity of 2.01 at 15 °C. It becomes fluid toward 440 °C, passing through a viscous condition, but above 800 °C it begins to volatilize, yielding white and very deliquescent crystals. It dissolves readily in water, but is only slightly soluble in absolute alcohol. By cooling an alcoholic solution to −23 °C, one can obtain a white crystalline mass which, however, melts easily as the temperature rises. It is also soluble in a mixture of ether and alcohol. The majority of metalloids like copper or titanium do not react with the chloride. It is insoluble in anhydrous hydrofluoric acid and is not altered by it. It is readily attacked by sulfuric acid. The alkali metals and magnesium reduce it. With potassium, the reaction begins below 500 °C. Lithium and magnesium act at about 650 °C. Aluminum fuses it without alteration. The anhydrous chloride is a white crystalline solid having a melting point about 440 °C. The boiling point is about 520 °C.

$BeCl_2$ can be prepared by treating Be metal with hydrogen chloride:

$$Be + 2HCl \Rightarrow BeCl_2 + H_2$$

It is said to hydrolyze upon contact with water to give the aquo complex, $[Be(H_2O)_4]Cl_2$. It is also readily soluble in alcohol, and yields a crystalline compound with it, but is almost insoluble in benzene, chloroform, carbon tetrachloride and sulfur dichloride.

Beryllium chloride reacts vigorously and exothermically with water with the evolution of acidic, steamy hydrogen chloride gas. This is typical of covalent chlorides. Beryllium chloride dissolves in water with great avidity and, unless special precautions are taken, with loss of chlorine as hydrochloric acid. In this case, it reacts to give hydrated beryllium ions, $[Be(H_2O)_4]^{2+}$, HCl and chloride ions. The question concerning whether the solvation is water molecules or hydroxy ions remains unsolved.

Beryllium chloride is stable in dry air, but absorbs moisture in air forming the tetrahydrate, $BeCl_2 \cdot 4H_2O$. It readily dissolves in water undergoing hydrolysis and evolving hydrochloric acid:

$$BeCl_2 + 2H_2O \Rightarrow Be(OH)_2 + 2HCl$$

A cold aqueous solution of beryllium chloride reacts with hydrogen sulfide to form beryllium sulfide that decomposes on heating in air:

$$BeCl_2\ (aq) + H_2S \Rightarrow BeS\ (aq) + 2HCl$$

$$BeS + \text{heat}\ Be + SO_2$$

Beryllium chloride, an electron-deficient compound similar to aluminum chloride, is a Lewis acid. The anhydrous salt is used as a catalyst in organic reactions. Physical constants are presented in Table 2.17 and thermochemical data are presented in Table 2.18.

TABLE 2.17

Physical constants of $BeCl_2$

CAS number	7787-47-5
Molecular formula	$BeCl_2$
Molar mass	79.9182 g/mol
Appearance	White or yellow crystals
Density	1.899 g/cm^3, solid
Melting point	399 °C, 672 K, 750 F
Boiling point	482 °C, 755 K, 900 F
Solubility	Soluble: alcohol, ether and pyridine Insoluble: benzene, chloroform, acetone and ammonia
Molecular shape	Linear
Standard enthalpy of formation	$\Delta H^{\circ}_{f_{298}} = -6.136$ kJ/g
Specific heat capacity	7.808 J/g K
Standard free energy of formation	$\Delta G^0_f = -5.576$ kJ/g
Standard heat of formation	$\Delta H^0_f = -6.136$ kJ/g
Specific heat of fusion	0.108 kJ g

TABLE 2.18

Thermochemical data for $BeCl_2$

$\Delta_f H^{\circ}_{gas}$ (Heat of formation)	−360.24 kJ/mol
$S^{\circ}_{gas,\ 1\ bar}$	252.13 J/mol K
$\Delta_f H^{\circ}_{liquid}$	−491.31 kJ/mol
$S^{\circ}_{liquid,\ 1\ bar}$	79.71 J/mol K
$\Delta_f H^{\circ}_{solid}$	−496.22 kJ/mol

Beryllium Bromide

Beryllium bromide has the formula $BeBr_2$. It is very hygroscopic and is soluble in water. It has the molecular weight of 168.821 g/mol. The structure has not been documented. Beryllium bromide can be prepared by reacting Be metal with elemental bromine at temperatures of 500 °C–700 °C:

$$Be + Br_2 \Rightarrow BeBr_2$$

Beryllium bromide is also formed when beryllium oxide with HBr in aqueous solution or hydrogen bromide in the gas phase:

$$BeO + 2HBr \Rightarrow BeBr_2 + H_2O$$

This bromide compound was first prepared by Wohler (1828) by the action of bromine vapor on the metal and also upon a mixture of carbon and beryllium oxide. Berthemot (1831) obtained it in solution by dissolving the oxide in hydrobromic acid. Humpridge (1883) also prepared it by acting on a mixture of the oxide and carbon with dry bromine.

The anhydrous bromide is always obtained by sublimation as colorless white crystals. Its vapor density determined by Humpridge (1886) is in accord with the formula $BeBr_2$. Its melting point is about 490 °C where it fuses and begins to sublime. It also sublimes somewhat below this temperature. The fused salt does not conduct electricity so that it cannot be used to make Be metal. It dissolves in water with avidity, losing hydrobromic acid on evaporation. It is soluble in absolute alcohol and forms a crystalline compound therewith. It combines with ammonia and with the organic bases, Physical properties of $BeBr_2$ are shown in Table 2.19.

TABLE 2.19

CAS number	7787-46-4
Molar formula	$BeBr_2$
Molar mass	168.821 g/mol
Appearance	Colorless, white crystals
Density	3.465 g/cm^3 (20 °C)
Melting point	508 °C (sublimes—473 °C)
Boiling point	520 °C
Solubility	Water: highly soluble Ethanol: soluble
Crystal structure	Orthorhombic
Standard enthalpy of formation	$\Delta H^{\circ}_{f_{298}} = -2.094$ kJ/g
Standard molar entropy	$\Delta S = 9.5395$ J/K
Specific heat capacity	$C_p = 0.4111$ J/g
Specific heat of formation	$\Delta_f H^0 = -2.094$ kJ/g
Specific heat of fusion	0.1103 kJ/g

Beryllium Iodide

Beryllium iodide has the formula BeI_2. It is very hygroscopic and reacts violently with water, forming hydroiodic acid. Beryllium iodide can be prepared by reacting Be metal with elemental iodine at temperatures of 500 °C–700 °C:

$$Be + I_2 \Rightarrow BeI_2$$

Beryllium iodide is also formed when beryllium carbide reacts with hydrogen iodide in the gas phase:

$$Be_2C + 4HI \Rightarrow 2BeI_2 + CH_4$$

The iodine in beryllium iodide is easily replaced with the other halogens. It reacts with F_2 gas giving beryllium fluoride and fluorides of iodine, or with Cl_2 gas giving beryllium chloride, or with Br_2 gas giving beryllium bromide. Beryllium iodide also reacts violently with oxidizing agents such as chlorate and permanganate to give the purple vapor of iodine. The solid and vapor are both flammable in air.

Beryllium Iodide, BeI_2, was first prepared by Wöhler (1828) and Debray (1855) who prepared the iodide by the action of iodine upon the metal. Lebeau (1898), was the first to prepare large quantities (for the time) by the action of gaseous hydroiodic acid, or a mixture of hydrogen and iodine vapor, on the carbide at about 700 °C.

Beryllium iodide, as obtained in the sublimed state, consists of colorless crystals, which are quickly decomposed in moist air. Its specific gravity at 15 °C is close to 4.20 g/cm^3. It begins to sublime below its melting point which is 510 °C. The melted iodide boils between 585 and 595 °C. It is insoluble in benzene, toluene, spirits of turpentine, and but slightly soluble in carbon disulphide. The slightest trace of water attacks it immediately, but if it is first fused, its sensitivity to water is much less. It can be distilled without alteration in dry hydrogen, nitrogen or carbon dioxide. At this point in time, the structure BeI_2 has not been published.

Reaction of BeI_2 with fluorine gas forms fluorides of both beryllium and of iodine. The reaction of fluorine and chlorine with BeI_2 occurs even when cold, giving off heat and light. Cyanogen acts upon it at about a red heat, producing a white material, less volatile than the iodide, which with water gives a clear solution reacting for cyanides. Heated in oxygen, it burns at a red heat and the vapor itself will burn even in air. Heated with sulfur it yields a sulfide of beryllium, which is readily decomposed by water. The vapor of phosphorus also attacks it, probably forming a phosphide of beryllium.

Sodium, potassium and lithium metals reduce BeI_2 at about 350 °C. Magnesium reduces it at about 450 °C. Aluminum, silver, copper and mercury are without action below the temperature of the softening temperature (~585 °C) of glass. Hydrogen sulfide acts upon it, but only at elevated temperatures and yields a white sulfide, BeS. It absorbs large amounts of ammonia gas and forms compounds which melt easily and can be crystallized on cooling.

Ammoniated Beryllium Iodide is classified as an explosive and propellant (However, these compounds have not been fully characterized). It reacts with a large number of organic compounds, particularly amines. It is soluble in alcohol and produces a crystalline compound therewith. It also combines with ether. It differs from the iodide of aluminum in not reacting with cold tetrachloride of carbon. Acetic anhydride and anhydrous chloral give energetic reactions with beryllium iodide. Ammonium compounds and organic bases, especially aniline and, produce crystalline compounds with it Physical properties of BeI_2 are shown in Table 2.20.

2.2.3. Halide Compounds of Magnesium

Magnesium Fluoride

Magnesium fluoride (MgF_2) is a white crystalline salt. It is used in the electrolysis of aluminum ore to produce metallic aluminum and also as a reflective coating on various types of optical components. It is a tetragonal, birefringent crystal with the TiO_2 type of structure shown in Fig. 2.9.

Cell parameters are: $a = 3.052$ Å, $b = c = 4.612$ Å. $\alpha = \beta = \gamma = 90°$, cell volume = 64.82 Å3, cell occupancy is shown in Table 2.21.

TABLE 2.20

CAS number	7787-53-3
Molecular formula	BeI_2
Molecular weight	262.82112 g/mol
Density	4.21 g/cm^3
Appearance	Colorless, needle-like crystals
Density	4.325 g/cm^3
Melting point	480 °C
Boiling point	590 °C
Solubility in water	Reacts violently with water
Solubility	Slightly soluble in CS_2 Soluble in ethanol
Specific heat capacity	$C_p = 0.27055$ J/g·K
Standard enthalpy of formation	$\Delta_f H^0 = -0.7324$ kJ/g
Standard heat of formation	$\Delta_f H^0 = -2.094$ kJ/g
Specific heat of fusion	0.0798 kJ/g

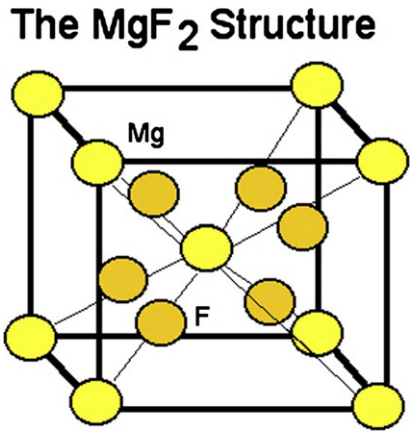

FIGURE 2.9

Magnesium fluoride is transparent over an extremely wide range of wavelengths. Windows, lenses, and prisms made of this material can be used over the entire range of wavelengths from 0.120 μm (vacuum UV) to 8.0 μm (IR). The range of transmission is shown in Fig. 2.10.

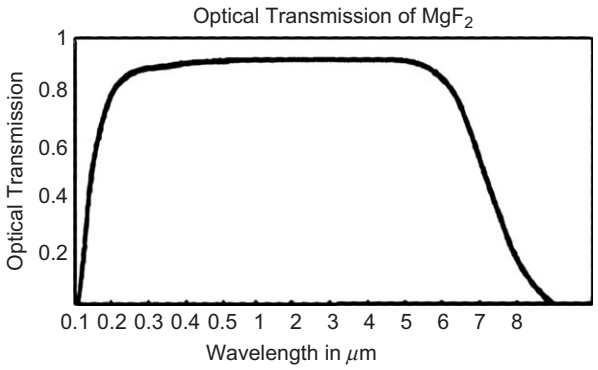

FIGURE 2.10

Good synthetic VUV grade MgF_2, without vacancies or other structural defects, is quite expensive, in the region of $3000/kg (2007). But the real cost of optics in this material is due to relatively low-volume manufacture. Nevertheless, similar to LiF, it is one of the two materials that will transmit in the vacuum ultraviolet range at 121 nm and this is where it finds its application. Lower grade MgF_2 is sometimes used in the IR but it is inferior to calcium fluoride.

MgF_2 is tough and works and polishes well. Since it is slightly birefringent, it should be cut with the optic axis perpendicular to the plane of the window or lens {i.e. so that the Verdet Constant of MgF_2 at 632.8 nm is 0.00810 arc-min/g/cm}.

Thin layers of MgF_2 are frequently applied to the surfaces of optical elements as part of optical coatings such as antireflective coatings. It is the only optical material that combines wide spectral band transmittance with the birefringence phenomenon. Magnesium Fluoride has superior features such as its hardness and resistance to mechanical shock and water. The material is sensitive to thermal shock but does not cleave.

Irradiation does not lead to color centers. This Vacuum UV material is the least susceptible to radiation-induced color centers of any known material. Magnesium Fluoride is a proven material for high-energy lasers, and in particular for lasers operating in UV and VUV range. Generally, all optical elements are manufactured with working surface perpendicular to the *c* axis of the crystal.

The following table lists some of the parameters that are used to form thin layers of MgF_2 on various substrates (Table 2.22).

TABLE 2.21

No	Site notation	Atom	Multiplicity	Wyckoff	Site symmetry	*x*	*y*	*z*	Occupancy
1	F1	F	4	f	m.2m	0.30478	0.305	0	1.0
2	Mg1	Mg	2	a	m.mm	0	0	0	1.0

TABLE 2.22

Container	Graphite, Ta, Mo or Al_2O_3
Evaporation temperature	~950 °C
Substrate temperature	150–250 °C
Evaporation pressure	10^{-5}–10^{-6} Torr

Vacuum-melted MgF_2 granules can be evaporated by either electron beam or resistance heating. Graphite or tantalum containers are suggested. They are loaded to the top with material. For thermal evaporation, a large heater-shaped like an open boat is used. The power should be increased slowly, and in the case of E-beam sources, the beam should be swept for even heating. Preconditioning for granules of MgF_2 consists of fully melting the charge. The shutter should remain closed until the melt is uniformly red hot. No outgassing is experienced during the preconditioning cycle or during evaporation with MgF_2-coating material.

The pressure should be in the low 10^{-6} Torr range. When completely melted, the material can be evaporated at a smooth rate of 20 Å/s without spitting. The temperature of the substrate should be at least 250 °C for high-film hardness and density on glass or zinc sulfide substrates. In difficult cases, a thin, initial bonding layer of yttrium oxide, Y_2O_3, can promote nucleation and adhesion. Films will grow and adhere to glass substrates heated to as low as 150 °C. Glow discharge cleaning is recommended for low temperature depositions. The melt can be reused until reaction with the holder begins. The factor that limits MgF_2 layer thickness to ~1 μm is internal stress. MgF_2 can be doped with BaF_2 to reduce this stress and permit thicker layers to be grown.

Films of MgF_2 that have been deposited on high-temperature substrates (250–300 °C) using E-beam deposition are mechanically hard but grow with densities only ~80% of bulk density. Voids in the microstructure admit water upon exposure to air, increasing the mean refractive index of the film. Absorption bands are seen in the UV spectra at 3 and 6 μm. Multilayers that include MgF_2 will shift in wavelength upon venting the deposition system to room air. Films that are bombarded by high-energy ions during growth achieve higher densities, since an amorphous structure is created. This produces an environmentally stable film with a higher refractive index. Excessively high-ion energies can, however, deplete the fluorine content and produce absorption in the UV (Table 2.24).

TABLE 2.23

CAS number	7783-40-6
Molecular formula	MgF_2
Molar mass	62.3018 g/mol
Appearance	White tetragonal crystals
Density	3.177 g/cm^3
Melting point	1251 °C
Boiling point	2260 °C (decomposes)
Solubility in water	<0.007325 g/100 ml at 0 °C
Solubility product	$K_{SP} = 5.16 \times 10^{-11}$
Refractive index	$\eta_D = 1.37397$
Crystal structure	Rutile (tetragonal) Space group = P_42/mmm
Lattice constants	$a = 4.60$ Å; $c = 3.06$ Å
Standard molar entropy	$S_{298} = 57.2$ kJ/mol
Standard enthalpy of formation	$\Delta H_f = -1124.2$ kJ/mol
Specific heat in cal/g·K	0.24 at 298 K 0.362 at 1700 K
Knoop hardness, kg/mm^2	415
Young's modulus, GPa	138.5
Shear modulus, GPa	54.66
Bulk modulus, GPa	101.32
Apparent elastic limit, MPa	49.64
Poisson ratio	0.276
Thermal expansion	Parallel = 14×10^{-6} Perpendicular = 8.9×10^{-6}
Refractive index	$\eta_o = 1.3796$, $\eta_e = 1.3852$ at 1.0 mm
Transmission band	0.11 − 7.5 mm
Specific heat capacity, J/(kg) at 18 °C	920.0
Reflection loss, % for two surfaces in the visible	4.8
Dielectric constant for 95×10^{-3} cm at 42×10^6 Hz	5.45
Thermal conductivity, W/(m K) at 300 K	14–15
Band gap	10.8 eV

Magnesium Chloride

Magnesium chloride is chemically represented as $MgCl_2$. It is usually obtained from seawater and is generally found in a hydrated form. Magnesium chloride in its pure state is colorless, odorless, highly soluble in water and bitter to taste. Magnesium chloride has the molecular weight of 95.221 g/mol. It occurs as a white

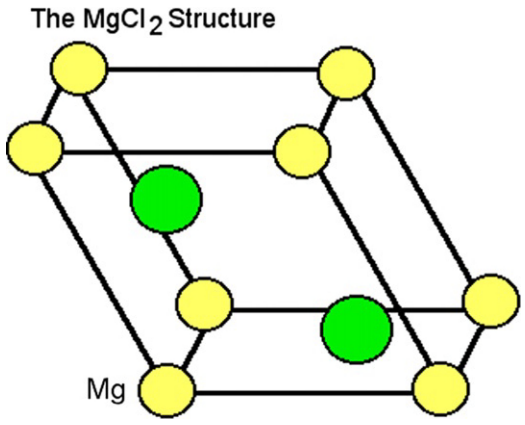

FIGURE 2.11

powder and its CAS number is 7791-18-6. Its density is 2325 kg/m^3, its melting point is 714 °C and its boiling point is 1412 °C. However, it generally is obtained as the hexahydrate, $MgCl_2 \cdot 6H_2O$, which has a molecular weight of 203.3 g/mol and a CAS number of 7791-18-6. Its water solubility is 2350 g/l (20 °C).

Various hydrates occur, denoted as $MgCl_2 \cdot (H_2O)_x$. These salts are typical ionic halides, being highly soluble in water. Hydrated magnesium chloride can be extracted from brine or seawater. Magnesium chloride as the natural mineral "bischolite" is also extracted (solution mining) out of ancient seabeds, for example in the Zechstein seabed in NW Europe or the Permian Period seabed in the central parts of the US. Anhydrous magnesium chloride is the principal precursor to magnesium metal which is produced on a large scale.

It also occurs as the mineral "carnolite". Carnolite is an important source of potash, an invaluable fertilizer. "Sylvite" is the more important source of potash, but Carnallite makes a significant contribution. Carnallite's magnesium output is of much lesser importance worldwide but is still Russia's most significant source.

Metallic magnesium was first produced in 1828 by the French scientist A. B. Bussy. His work involved the reduction of molten magnesium chloride by metallic potassium. In 1833, the English scientist Michael Faraday was the first to produce magnesium by the electrolysis of molten magnesium chloride. $MgCl_2$ crystallizes in the CdI_2 structure, which features an octahedral Mg coordination. The structure has the form shown in Fig. 2.11.

Cell parameters are: $a = b = 3.641$ Å, $c = 5.927$ Å, $\alpha = \beta = 90°$, $\gamma = 120°$. Cell volume = 68.05 Å^3, cell occupancy is shown in Table 2.24.

A variety of hydrates are known with the formula $MgCl_2 \cdot (H_2O)_x$, and each loses water with increasing temperature:

$x = 12$ (−16.4 °C), 8 (−3.4 °C), 6 (116.7 °C), 4 (181 °C), 2 (ca. 300 °C).

In the hexahydrate, the Mg^{2+} remains octahedral, but is coordinated to six water ligands. The thermal dehydration of the hydrates $MgCl_2(H_2O)_x$ ($x = 6$, 12) does not occur straight forwardly since HCl gas begins to form at those temperatures. As suggested by the existence of these hydrates, anhydrous $MgCl_2$ is a Lewis acid, although a relatively weak one.

In the "Dow Process" (which is the electrolytic method of extracting bromine from brine), magnesium chloride is regenerated from magnesium hydroxide by hydrochloric acid:

$$Mg(OH)_2\ (s) + 2HCl \Rightarrow MgCl_2\ (aq) + 2H_2O$$

It can also be prepared from $MgCO_3$ by a similar reaction. Magnesium chloride is ionic and so will undergo ***electrolysis*** when it is molten. Electricity is carried by the movement of the ions within the melt and their discharge at the electrodes. However, solid magnesium chloride is a nonconductor of electricity because the ions are immobile. In most of its derivatives, $MgCl_2$ forms octahedral complexes. Derivatives with tetrahedral Mg^{2+} are less common. Examples include salts of $(Et_4N)_2MgCl_4$ and adducts such as $MgCl_2$(TMEDA = Tetramethylethylenediamine).

When magnesium ions are broken off the solid lattice and go into solution, there is enough attraction between the 2+ ions and the water molecules to get coordinate (dative covalent) bonds formed between the magnesium ions and lone pairs on surrounding water molecules. Hexa-aqua-magnesium ions are formed, $[Mg(H_2O)_6]^{2+}$. Ions of this sort are acidic, the degree of acidity depending on how much the electrons in the water molecules are pulled toward the metal at the center of the complex. The hydrogen atoms are made more positive than they would otherwise be, and more easily removed by a base. In the case of magnesium, the amount of distortion is quite small,

TABLE 2.24

No	Site notation	Atom	Multiplicity	Wyckoff	Site symmetry	x	y	z	Occupancy
1	Cl	Cl	2	d	3m.	1/3	2/3	0.25	1.0
2	Mg	Mg	1	a	-3m.	0	0	0	1.0

and only a small proportion of the hydrogen is removed by a base—in this case, by water molecules in the solution.

The presence of the hydroxonium ions in the solution causes it to be acidic. The fact that there are not many of them formed (the position of equilibrium lies well to the left), means that the solution is only weakly acidic. This is shown in the following equilibrium:

$$\{Mg(H_2O)_6\}^{2+}\,(aq) \Leftrightarrow \{Mg(H_2O)_5(OH)\}^{+}\,(aq) + H_3O^{+}$$

Magnesium chloride serves as precursor to other magnesium compounds, for example by precipitation:

$$MgCl_2\,(aq) + Ca(OH)_2\,(aq) \Rightarrow Mg(OH)_2\,(solid) + CaCl_2\,(aq)$$

It can be electrolyzed by melting the salt to give Mg metal:

$$MgCl_2\,(liq) \Rightarrow Mg\,(solid) + Cl_2\,(gas)$$

This process is practiced on a large scale commercially to produce Mg metal.

Magnesium chloride is used for a variety of other applications besides the production of Mg metal. It is used in the manufacture of textiles, paper, fireproofing agents, cements and refrigeration brine. It has also been used in dust and erosion control. Mixed with hydrated magnesium oxide, magnesium chloride forms a hard material called "Sorel-cement". The cement is a mixture of MgO (burnt magnesia) with $MgCl_2$ with the approximate chemical formula $Mg_4Cl_2(OH)_6(H_2O)_8$, corresponding to a weight ratio of 2.5–3.5 parts MgO to one part $MgCl_2$. This usage of magnesium chloride is unmatched by any other compound. $MgCl_2$ was one of the earlier antiseptics, first used for that purpose by Dr Pierre Delbert in 1915. One veterinary study in 1989 indicated some effectiveness against tumors when used as a feed additive.

The fact that it can store hydrogen gas is a unique property of this compound. A single molecule of ammonia is rich in hydrogen atoms. Ammonia can be absorbed on the surface of solid magnesium chloride as $Mg(NH_3)_6Cl_2$. On application of mild heat, ammonia is easily released from magnesium chloride and when it is made to pass through a catalyst, hydrogen gas is obtained.

Magnesium chloride in liquid form acts as an anti-icer on roadways. During winter months, it is sprayed on pavements before precipitation. As a result, snow and ice formation is reduced on the surface of the road. Thus, it prevents the vehicles from skidding and ensures road safety. Magnesium chloride is the more preferred deicer than sodium chloride because the former is a less corrosive substance, as compared to the latter, and does not cause much harm to plant life, road concrete or the steel electric poles on the roads. It is also used in crystalline form to deice sidewalks and driveways of home and offices. The crystals are applied, after precipitation, on the accumulated ice.

A commercial form of liquid $MgCl_2$ called "DustGard Liquid" is used to control dust on unpaved roads, construction sites and similar surfaces. Because it is produced from naturally occurring minerals, it improves air quality and visibility with minimal environmental impact. It also decreases vehicle maintenance costs, prevents soil erosion and reduces the need for blading, watering and gravel replacement. Road departments and private industry may apply liquid or powdered magnesium chloride to control dust and erosion on unimproved (dirt or gravel) roads and dusty job sites such as quarries. Its hygroscopicity makes it absorb moisture from the air, controlling the number of small particles which become airborne. Similarly, owners of indoor arenas (e.g. for horse riding) may apply magnesium chloride to sand or other floor materials to control dust. When it is applied in, either liquid or powdered form on dusty places, then the dust get suppressed onto the floor. Thus, it prevents small dust particles from spreading into the air. This is commonly used in places like excavation sites, indoor sport arenas, racecourses etc.

Magnesium ion Mg^{2+} (usually added as the chloride) is an important component in the polymerase chain reaction (PCR), a procedure used to amplify DNA fragments. Magnesium ions (Mg^{2+}) from $MgCl_2$ are an important component of PCR reactions where they interact with the DNA template, dNTPs and the *Taq* DNA Polymerase. It is generally used in experimental biology whenever RNA and DNA and their enzymes are to function in vitro, since Mg^{2+} is a necessary associate ion for nucleotides in biology, such as ATP.

Magnesium chloride is also used in several medical and topical (skin-related) applications. It has been used in pills as supplemental sources of magnesium, where it serves as a soluble compound which is not as laxative as $MgSO_4$, and more bio-available than $Mg(OH)_2$ and MgO, since it does not require stomach acid to produce soluble Mg^{2+} ion. It can also be used as an effective anesthetic for cephalopods, some species of crustaceans, and several species of bivalves, including oysters.

Magnesium chloride is an important coagulant used in the preparation of "tofu" from soy milk. In Japan, it is sold as *"Nigari"*, (derived from the Japanese word for "bitter"). It is a white powder produced from seawater after the sodium chloride has been removed, and the water evaporated. In China, it is called "Lushui", Nigari or Lushui and consists mostly of magnesium chloride, with some $MgSO_4$ and other trace elements. It is also an ingredient in baby formula milk.

TABLE 2.25

		g/100 ml of water								
Substance	**Formula**	**0 °C**	**10 °C**	**20 °C**	**30 °C**	**50 °C**	**60 °C**	**80 °C**	**90 °C**	**100 °C**
Magnesium chloride	$MgCl_2$	52.9	53.6	54.6	55.8	57.5	61	66.1	69.5	73.3

A number of state highway departments throughout the United States have decreased the use of rock salt and sand on roadways and have increased the use of solutions of magnesium chloride as a deicer or anti-icer. Magnesium chloride is much less toxic to plant life surrounding highways and airports, and is less corrosive to concrete and steel (and other iron alloys) than salt. The liquid magnesium chloride is sprayed on dry pavement (tarmac) prior to precipitation or on wet pavements prior to freezing temperatures in the winter months to prevent snow and ice from adhering and bonding to the roadway. The application of deicers is utilized in an effort to improve highway safety. Magnesium chloride is also sold in crystal form for household and business use to deice sidewalks and driveways. In these applications, the compound is applied after precipitation has fallen or ice has formed, instead of previously.

Magnesium chloride has shown promise as a storage material for hydrogen gas. Ammonia can be effectively adsorbed onto solid magnesium chloride, forming $Mg(NH_3)_6Cl_2$. When the ammonia is released by mild heat, and is then passed through a catalyst, hydrogen gas is retrieved. The solubility of magnesium chloride in water is shown in Table 2.25.

Physical properties of $MgCl_2$ are listed in Table 2.26.

TABLE 2.26

CAS number	7786-30-3 7791-18-6 (hexahydrate)
Molecular formula	$MgCl_2$
Molar mass	95.2111 g/mol (anhydrate) 203.2914 g/mol (hexahydrate)
Appearance	White crystalline solid
Density	2.32 g/cm^3 (anhydrate) 1.569 g/cm^3 (hexahydrate)
Melting point	Anhydrate 714 °C; 1312 F (987 K)—rapid heating: slow heating leads to decomposition at 300 °C Hexahydrate 118 °C—decomposes at 300 °C
Boiling point	1412 °C; 2496 F (1685 K)
Solubility in water	Anhydrate = 54.3 g/100 ml (20 °C) Hexahydrate = 157 g/100 ml (20 °C)
pH of solution	7.00
Specific heat capacity	$C_p = 0.7499$ cal/g K
Standard heat of fusion	$\Delta H_f = 0.453$ kJ/g
Specific free energy of formation	$\Delta G_f = -0592.5$ kJ/g
Specific heat of formation	$\Delta_f H^0 = -641.8$ kJ/g
Standard entropy	$S_0 = 89.5$ kJ/g

Magnesium Bromide

Magnesium bromide ($MgBr_2$) has a molecular weight of 184.11 g/mol and a CAS number of 7789-48-2. It is white powder that is very deliquescent. It is often used as a mild sedative and as an anticonvulsant for treatment of nervous disorders. It is an electrolytic component in certain dry-cell batteries. The melting point of the anhydrous form is 711 °C.

Magnesium bromide occurs in seawater, surface and subterranean brines. The Dead Sea is significantly different from that of ocean water, consisting of approximately 53% $MgCl_2$, 37% potassium chloride and 8% sodium chloride (common salt) with the remainder consisting of other alkali ions. The sulfate, SO_4^{2-}, content is very low, but the bromide ion concentration is the highest of all dormant waters on Earth.

A number of hydrates occur. The decahydrate, $MgBr_2 \cdot 10H_3O$ is known but it easily loses waters of hydration to form the more stable hexahydrate. This salt, $MgBr_2 \cdot 6H_2O$, is deliquescent, colorless, and the crystals are bitter tasting. They melt at 172 °C (dissolving in their own "water of hydration"), are soluble in water and are slightly soluble in alcohol. This compound has also been used in medicine and in the synthesis of organic chemicals. Its molecular weight is 292.20 g/mol, density is 3.72 g/cm^3 and its CAS number is 13446-53-2.

Thermodynamic Properties of $MgBr_2 \cdot 6H_2O$ include:

$$\Delta_f H^0 \text{ (gas)} = -74.0 \text{ kcal/mol}$$

$$\Delta_f H^0 \text{ (crystal)} = -125 \text{ kcal/mol}$$

$$\Delta_f H^0 \text{ (aqueous)} = -169.7 \text{ kcal/mol}$$

TABLE 2.27

No	Site notation	Atom	Multiplicity	Wyckoff	Site symmetry	x	y	z	Occupancy
1	Br	Br	2	d	3m.	1/3	2/3	0.25	1.0
2	Mg	Mg	1	a	-3m.	0	0	0	1.0

TABLE 2.28

		gm/100 ml of water								
Substance	**Formula**	**0 °C**	**10 °C**	**20 °C**	**30 °C**	**40 °C**	**60 °C**	**80 °C**	**90 °C**	**100 °C**
Magnesium bromide	$MgBr_2$	98	99	101	104	106	112	118	121	125

$$\Delta_f G^0 \text{ (crystal)} = -120.4 \text{ kcal/mol}$$

$$S^0 \text{ (crystal)} = 28.0 \text{ cal/°C/mol}$$

Magnesium bromide is prepared by treating MgO with hydrobromic acid and then crystallization above 0.0 °C in solution. The product is the hexahydrate salt:

$$MgO + 2HBr \Rightarrow MgBr_2 + H_2O \Rightarrow MgBr_2 \cdot 6H_2O$$

The anhydrous form may also be prepared by heating the hexahydrate with dry HBr gas. This compound can also be formed directly from the elements:

$$Mg + Br_2 \Rightarrow MgBr_2$$

This salt has the same type of structure as $MgCl_2$ except that the unit cell parameters are elongated: $a = b = 3.851$ Å, $c = 6.256$ Å, $\alpha = \beta = 90°$, $\gamma = 120°$. Cell volume = 78.85 Å^3, cell occupancy is shown in Table 2.27.

The major use of $MgBr_2$ has been in the commercial production of bromine. The **Dow process** is an electrolytic method of bromine extraction from brine, and was Herbert Dow's second revolutionary process for generating bromine commercially (1889).

Before Dow got into the bromine business, bromine-rich brine was evaporated by heating brine with wood chips. This crystallized sodium chloride that was removed by filtration. An oxidizing agent was added, and bromine formed in the solution was then distilled. This was a very complicated and costly process. Dow's first process involved eliminating the heating. First he oxidized the bromine with a bleaching agent, then dripped it onto burlap, and blew air under the burlap. The air contained bromine gas, which was then reacted with iron (or alkalis) producing $FeBr_2$. In the second method, Dow became the first to use an electrolytic method of extracting bromine from brine in a commercial process. He used a 15-V generator powered by a steam engine. He later established the "Dow Chemical Co." which remains one of the major chemical companies in the U.S.

Current processes involving production of bromine gas involve treating bromide-rich brines with chlorine gas while simultaneously flushing through with air. In this treatment, bromide anions are oxidized to bromine by the chlorine gas:

$$2Br^- + Cl_2 \Rightarrow 2Cl^- + Br_2$$

Magnesium bromide has also been used in organic syntheses. An efficient and environmentally friendly procedure for the one-pot synthesis of tetrahydropyrimidines from aldehydes, α-diketones and urea/thiourea by using magnesium bromide as an inexpensive and easily available catalyst under solvent-free conditions has been described. Compared with the classical Biginelli reaction conditions, this new method has the advantage of good to excellent yields (74%–94%) and short reaction times (45–90 min). The structure of the Biginelli reaction product from α-diketone, salicylaldehyde and urea has been proposed to possess an oxygen bridge by cyclization (intramolecular Michael addition). The solubility of magnesium bromide is shown in Table 2.28.

Physical properties of $MgBr_2$ are listed in Table 2.30.

Magnesium Iodide

Magnesium iodide has the formula MgI_2 and forms various hydrates, expressed as $MgI_2 \cdot (H_2O)_x$. These salts are typical ionic halides, being highly soluble in water. $MgI_2 \cdot 8H_2O$ is a crystalline powder, white and deliquescent, discoloring in air; soluble in water, alcohol, and ether. This salt has been used in medicine. The anhydrous compound has a molecular weight of 278.1139 g/mol,

TABLE 2.29

CAS number	7789-48-2 (anhydrate) 13446-56-2 (hexahydrate) 75198-45-7 (decahydrate)
Molecular formula	$MgBr_2$ (anhydrate) $MgBr_2 \cdot 6H_2O$ (hexahydrate)
Molar mass	184.113 g/mol (anhydrate) 292.204 g/mol (hexahydrate)
Appearance	Anhydrate—white hygroscopic hexagonal crystals Hexahydrate—colorless monoclinic crystals
Density	3.72 g/cm^3 (anhydrate) 2.07 g/cm^3 (hexahydrate)
Melting point	711 °C (anhydrate) 172.4 °C (hexahydrate)
Boiling point	1158 °C (2116.4 F)
Solubility in water	102 g/100 ml (anhydrate) 316 g/100 ml at 0 °C (hexahydrate)
Solubility in ethanol	6.9 g/100 ml at 20 °C
Crystal structure	Rhombohedral Space group = P-3m1
Standard enthalpy of formation	$\Delta_f H_{298} = -524.3$ kJ/mol
Standard molar entropy	$S_0 = 117.2$ J/mol K

a melting point of 637 °C, a density of 4.43 g/cm^3 and a water solubility of 1480 g/l at 18 °C. MgI_2 has the same type of structure (CdI_2) as the chloride and bromide except that the cell parameters differ. Its crystal structure is shown in Fig. 2.12.

Cell parameters are: $a = b = 4.412$ Å, $c = 6.884$ Å, $\alpha = \beta = \gamma = 90°$, cell volume = 102.12 Å^3, cell occupancy is shown in Table 2.30.

Magnesium iodide can be prepared from MgO, $Mg(OH)_2$, and $MgCO_3$ by treatment with HI:

$$MgO + 2HI \Rightarrow MgI_2 + H_2O$$

$$Mg(OH)_2 + 2HI \Rightarrow MgI_2 + 2H_2O$$

$$MgCO_3 + 2HI \Rightarrow MgI_2 + CO_2 + H_2O$$

Magnesium iodide is stable at high heat under a hydrogen atmosphere, but decomposes in air at normal temperatures, turning brown due to the release of elemental iodine. When heated in air, it decomposes completely to magnesium oxide, releasing iodine vapor.

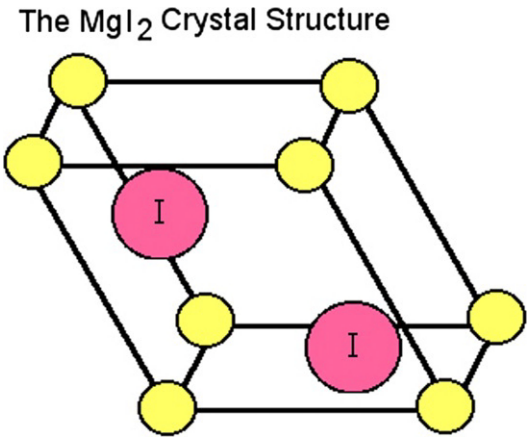

FIGURE 2.12

Magnesium iodide is known to form three hydrates, $MgI_2 \cdot 6H_2O$, $MgI_2 \cdot 8H_2O$ and $MgI_2 \cdot 10H_2O$ of which the decahydrate is claimed to be the most stable.

Magnesium iodide has few commercial uses but can be used to prepare many compounds for organic synthesis. Usage of magnesium iodide in the "Baylis–Hillman" reaction (an organic reaction of an aldehyde and an α,β-unsaturated electron-withdrawing group catalyzed by MgI_2) tends to give vinyl-specific compounds.

Another example of the usage of MgI_2 as a catalyst involves the reaction of 2,3,4,6-tetra-O-benzyl-D-gluconolactone or 2,3,4,6-tetra-O-benzyl-D-mannono-lactone with MgI_2 in EtOH which afforded the respective C-2 epimer.

Anhydrous magnesium iodide (MgI_2) has been shown to be an effective promoter of the homo 3 + 2 dipolar cyclo-addition of nitrones with 1,1-cyclopropane diesters. In almost all cases, the products, tetrahydro-1,2-oxazines, are formed in excellent yields. These reactions are highly dia-stereoselective for a cis relationship between the constituents at the 3- and 6-positions on the tetrahydro-oxazine ring. As an alternative to using a preformed nitrone, the reaction may be performed in a 3-component sense by combining an aldehyde,

TABLE 2.30

No	Site notation	Atom	Multiplicity	Wyckoff	Site symmetry	x	y	z	Occupancy
1	I	I	2	d	3m.	1/3	2/3	0.25	1.0
2	Mg	Mg	1	a	-3m.	0	0	0	1.0

TABLE 2.31

Quantity	Value	Units
$\Delta H^{\circ}_{f\ gas}$	24.61	kJ/mol
$S^{\circ}_{gas,\ 1\ bar}$	252.65	J/mol K

a hydroxylamine, and the cyclopropane in the presence of catalytic MgI_2.

The following lists some of the known thermodynamic constants for MgI_2 (Table 2.31).

Its solubility in water is shown in Table 2.32.

The following is a summary of the physical constants of MgI_2 (Table 2.33).

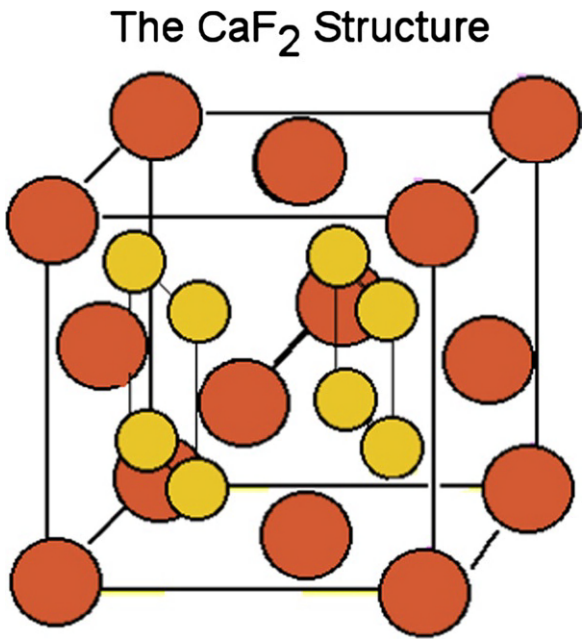

FIGURE 2.13

TABLE 2.33

CAS number	10377-58-9 (anhydrate) 75535-11-4 (hexahydrate) 7790-31-0 (octahydrate)
Molar mass	278.1139 g/mol (anhydrate) 386.2005 g/mol (hexahydrate) 422.236 g/mol (octahydrate)
Appearance	White crystalline solid
Density	4.43 g/cm^3 (anhydrate) 2.353 g/cm^3 (hexahydrate) 2.098 g/cm^3 (octahydrate)
Melting point	637 °C (anhydrate—decomposes) 41 °C (octahydrate—decomposes)
Solubility in water	54.7 g/100 ml (anhydrate at 0 °C) 81 g/100 ml (octahydrate at 20 °C)
Solubility	Soluble in ether, alcohol and ammonia
Crystal structure	Hexagonal (anhydrate) Monoclinic (hexahydrate) Orthorhombic (octahydrate)

2.2.4. Halide Compounds of Calcium

Calcium Fluoride

Calcium fluoride (CaF_2) is an insoluble ionic compound composed of Ca^{2+} and F^- ions. It occurs naturally as the mineral "Fluorite" (also called fluorspar) and as "Blue-John". This salt is the source of most of the world's fluorine. This insoluble solid adopts a cubic structure wherein calcium is coordinated to eight fluoride anions and each F^- ion is surrounded by four Ca^{2+} ions (Fig. 2.13).

The structure is face centered in Ca^{2+} ions. Cell parameters are: $a = b = c = 3.865$ Å, $\alpha = \beta = \gamma = 60°$, cell volume $= 40.83$ Å^3, cell occupancy is shown in Table 2.34.

Although the pure material is colorless, the mineral is often deeply colored due to the presence of "F-centers"

TABLE 2.32

		gm/100 ml of water								
Substance	**Formula**	**0 °C**	**10 °C**	**20 °C**	**40 °C**	**60 °C**	**70 °C**	**80 °C**	**90 °C**	**100 °C**
Magnesium iodide	MgI_2	120		140	173			186		

TABLE 2.34

No	Site notation	Atom	Multiplicity	Wyckoff	Site symmetry	*x*	*y*	*z*	Occupancy
1	F	F	8	c	−43m.	1/4	1/4	1/4	1.0
2	Ca	Ca	4	a	m−3m.	0	0	0	1.0

(which are electrons trapped by a vacancy in the crystal structure). Fluorite, the mineral, is well known and prized for its glassy luster and rich variety of colors. The range of common colors for fluorite starting from the hallmark color purple, then blue, green, yellow, colorless, brown, pink, black and reddish orange is amazing and is only rivaled in color range by quartz. Intermediate pastels between the previously mentioned colors are also possible. It is easy to see why fluorite earns the reputation as *"The Most Colorful Mineral in the World"*.

Naturally occurring CaF_2 is the principal source of hydrogen fluoride, a commodity chemical used to produce a wide range of materials. Fluoride is liberated from the mineral by the action of concentrated sulfuric acid:

$$CaF_2\,(\text{solid}) + H_2SO_4\,(\text{liq}) \Rightarrow CaSO_4\,(\text{solid}) + 2HF\,(\text{gas})$$

The resulting HF is converted into fluorine, fluorocarbons, and diverse fluoride materials. As of the late 1990s, 5 billion kilograms were mined annually.

CaF_2 is used as an optical component because of its chemical stability under adverse conditions. Exposure to 100% relative humidity at room temperature does not fog polished surfaces even after 1 month. In normal working conditions, polished surfaces will not degrade. For temperatures exceeding 600 °C, calcium fluoride surfaces will degrade in the presence of moisture. In dry environments, calcium fluoride can be used up to 1000 °C, and it does not begin to soften at 800 °C. Calcium fluoride is inert to organic chemicals and many acids, including HF. It will slowly dissolve in nitric acid.

Hughes Aircraft observed that the mean modulus of rupture for 900 °C forgings was 74.2 MPa for a 77% reduction. Rupture always occurred with no evidence of yield, indicating that the ultimate strength is still higher. This is shown in Table 2.35.

The thermodynamic properties of CaF_2 are presented in Tables 2.36 and Table 2.37.

Calcium fluoride is commonly used as a window material for both infrared and ultraviolet wavelengths, since it is transparent in these regions (about 0.15 to 9 μm) and exhibits an extremely low-refractive index.

TABLE 2.35

Elastic constants	Elastic compliance	Elastic stiffness
3×10^{-2}/GPa	2×10^2 GPa	$S_{11} = 0.6867$
$C_{11} = 1.6420$	$S_{12} = 0.1451$	$C_{12} = 0.4398$
$S_{44} = 2.9764$	$C_{44} = 0.3370$	$E_0 = 6.81$ at 27 °C
Dielectric constant: 0.26	Hardness: 158.3 Knoop [for both (100) and (110) directions]	

TABLE 2.36

Quantities per gram

Specific heat capacity |solid|, 0.8582 J/(g K)	Specific free energy of formation, $\Delta_f G_f$ deg |solid| −15.06 kJ/g
Specific heat of formation ΔH_f deg |solid| −15.73 kJ/g	Specific heat of vaporization |4.305 kJ/g|
Specific heat of fusion = 0.41 kJ/g	

This material is fairly inert chemically so that these windows are not attacked. Nevertheless, at wavelengths as low as 157 nm, which are useful for semiconductor manufacturers, the refractive index of calcium fluoride exceeds tolerable limits. This problem can be mitigated through an optimized growth process. It is particularly important as an ultraviolet optical material for "integrated circuit lithography". The camera manufacturer, Canon, also uses artificially crystallized calcium fluoride components in some of its L-Series lenses to reduce light dispersion. As an infrared optical material, calcium fluoride is sometimes known by the Eastman Kodak Co. trademarked name "Irtran-3," although this designation is now obsolete.

Its transmission spectrum is shown in Fig. 2.14.

Calcium Fluoride is a water insoluble calcium source for use in oxygen-sensitive applications, such as metal production. In extremely low concentrations (ppm), fluoride compounds are used in health applications. Fluoride compounds also have significant uses in synthetic organic chemistry. They are also commonly used to alloy metal and for optical deposition. Thus, it is useful from the far-UV to the near-IR, both as a coating and as an optical element. CaF_2 is superior in such applications because of its exceptional hardness and inertness. Only MgF_2 exhibits a wider and useful range of transmission wavelengths.

TABLE 2.37

Quantities per mole

Quantity	Value	Units
$\Delta_f H^\circ_{\text{gas}}$	−784.50	kJ/mol
$S^\circ_{\text{gas, 1 bar}}$	273.77	J/mol K
$S^\circ_{\text{gas, 1 bar}}$	273.77	J/mol K
$\Delta_f H^\circ_{\text{liquid}}$	−1186.07	kJ/mol
$S^\circ_{\text{liquid, 1 bar}}$	92.60	J/mol K
$\Delta_f H^\circ_{\text{solid}}$	−1225.91	kJ/mol
S°_{solid}	68.63	J/mol K

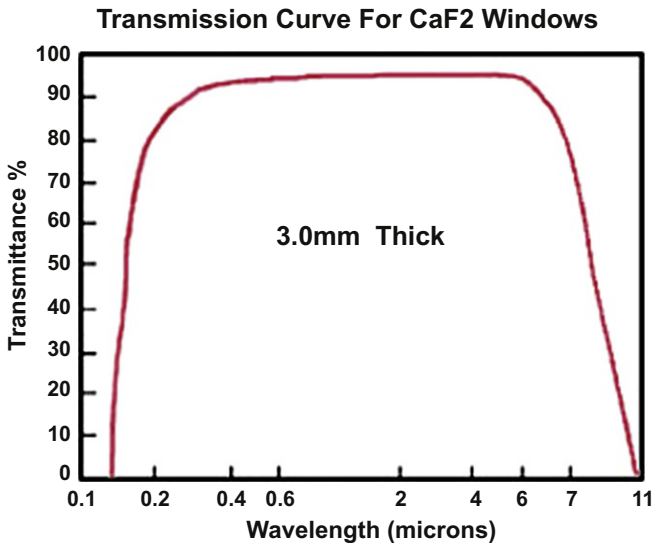

FIGURE 2.14

It is an optical material used in place of crown glass to produce lenses with extraordinary correction of chromatic aberrations. Its high coefficient of thermal expansion and its tendency to absorb moisture limit its range of application.

Uranium-doped calcium fluoride was the second type of solid-state laser invented, in the 1960s. Peter Sorokin and Mirek Stevenson at IBM's laboratories in Yorktown Heights (US) achieved lasing at 2.5 μm shortly after Maiman's ruby laser.

It is also used as a flux for melting and liquid processing of iron, steel and their composites. Its action is based on its similar melting point to iron, on its ability to dissolve oxides and on its ability to wet oxides and metals.

Physical properties are listed in Table 2.38.

Calcium Chloride

Calcium chloride, $CaCl_2$, is a typical ionic halide and is a solid at room temperature. Its molecular weight is 110.98 g/mol and its melting point is 772 °C. Very few natural minerals occur. The occurrence of a dihydrate (mineral "Sinjarite") and hexahydrate ("Antarcticite") is very rare and is connected mainly with dry lakes and brines. "Chlorocalcite", $KCaCl_3$, is a related mineral (also very rare).

It has a unique structure as exemplified by MgF_2 except for cell parameters of: $a = 4.166$ Å, $b = 6.264$ Å, $c = 6.436$ Å, $\alpha = \beta = \gamma = 90°$, cell volume $= 167.87$ Å^3, cell occupancy is shown in Table 2.39 and the crystal structure is shown in Fig. 2.15.

Calcium chloride, being very soluble, can serve as a source of calcium ions in a solution, unlike many other calcium compounds, which are insoluble:

$$3CaCl_2 + 2K_3PO_4\ (aq) \Rightarrow Ca_3(PO_4)_2\ (solid) + 6KCl\ (aq)$$

Molten $CaCl_2$ can be electrolyzed to produce Ca metal and chlorine gas:

$$CaCl_2\ (liq) \Rightarrow Ca\ (solid) + Cl_2\ (gas)$$

Calcium chloride is one of the most versatile of the basic chemicals. It has been produced commercially for over 100 years. The properties and characteristics of $CaCl_2$ make it useful in a large number of applications. It has several common applications such as brine for refrigeration plants, ice and dust control on roads, and in concrete. The anhydrous salt is also widely used as a desiccant, where it will absorb so much water that it will eventually dissolve in its own crystal lattice water (water of hydration). It can be produced directly from limestone, but large amounts are also produced as a by-product of the "Solvay Process" (which is a process to produce soda ash from brine). Because of its hygroscopic nature, the anhydrous form must be kept in tightly sealed containers.

Because the anhydrous salt is strongly hygroscopic, air or other gases can be channeled through a column of calcium chloride to remove moisture. In particular, calcium chloride is usually used to pack "drying tubes" to exclude atmospheric moisture from a reaction setup while allowing gases to escape. It cannot, however, be used to dry alkaline gases such as ammonia because it will form addition products. It is used to dry kelp, which

TABLE 2.38

CAS number	7789-75-5
Molecular formula	CaF_2
Molecular weight	78.07 g/mol
Appearance	White crystalline solid (single crystals are transparent)
Density	3.18 g/cm^3
Melting point	1418 °C; 1619 K; 2584 F
Boiling point	2533 °C; 2806 K; 4591 F
Solubility	Water = 0.00161 g/100 ml at 20 °C Insoluble in acetone
Solubility product	$K_{SP} = 3.9 \times 10^{-11}$
Refractive index	$\eta_D = 1.4328$
Space group	Fm3m (#225)
Crystal structure	Cubic
Free energy of formation	$\Delta_f G^0 = -1146$ kJ/mol
Heat of formation	$\Delta_f H_0 = -741$ kJ/mol
Specific heat of fusion	$\Delta H_f = 80.3$ kJ/mol

TABLE 2.39

No	Site notation	Atom	Multiplicity	Wyckoff	Site symmetry	*x*	*y*	*z*	Occupancy
1	Cl1	Cl	4	g	..m	0.275	0.325	0	1.0
2	Ca1	Ca	2	a	..2/m	0	0	0	1.0

is then used to produce soda ash. It can also be added to liquids to remove suspended or dissolved water.

The dissolving process is highly exothermic and rapidly produces temperatures of around 60 °C (140 F). In this capacity, it is known as a drying agent or desiccant. It is converted to a brine as it absorbs the water or water vapor from the substance to be dried:

$$CaCl_2 + 2H_2O \Rightarrow CaCl_2 \cdot 2H_2O$$

Aided by the intense heat evolved during its dissolution, calcium chloride is also used as an ice-melting compound. Unlike the more common NaCl (rock salt or halite), it is relatively harmless to plants and soil. However, recent observations in Washington state suggest it may be particularly harmful on roadside evergreen trees It is also more effective at lower temperatures as a "deicer" than sodium chloride.

Used for its hygroscopic property, it can be applied to keep a liquid layer on the surface of the roadway, which holds dust down. It is used in concrete mixes to help speed up the initial setting, but chloride ion leads to corrosion of steel "rebar", so it is not be used in reinforced concrete. Anhydrous calcium chloride, used for this purpose, can provide a measure of the moisture present in concrete.

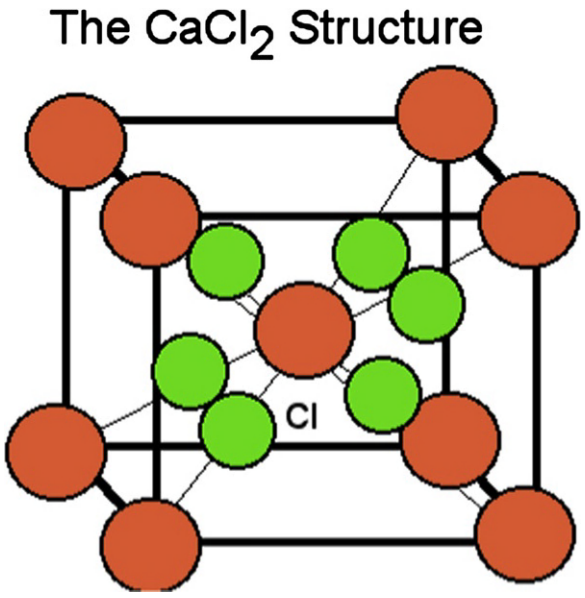

FIGURE 2.15

Aqueous calcium chloride (in solution with water) lowers the freezing point as low as −52 °C (−62 °F), making it ideal for filling agricultural implement tires as a liquid ballast, aiding traction in cold climates.

Calcium chloride is also commonly used as an additive in swimming pool water as it increases the "calcium hardness" value for the water. Low calcium hardness values in pool water cause pool water to be corrosive on equipment, pumps and metal fittings.

Other industrial applications include use as an additive in plastics, as a drainage aid for wastewater treatment, as an additive in fire extinguishers, as an additive in control scaffolding in blast furnaces, and as a thinner in "fabric softeners". North American consumption in 2002 was 1,687,000 tons (3.7 billion pounds). A Dow chemical company manufacturing facility in Michigan produces about 35% of the total U.S. production of calcium chloride.

As an ingredient, it is listed as a permitted food additive in the European Union for use as a sequestrant and "firming agent" with the number E509, and considered as generally recognized as safe (GRAS) by the U.S. Food and Drug Administration (FDA). The average intake of calcium chloride as food additives has been estimated to be 160–345 mg/day for individuals. Ingestion of concentrated or pure calcium chloride products may cause gastrointestinal irritation or ulceration. The anhydrous form has been approved by the FDA as a packaging aid to ensure dryness.

Solutions of pure calcium chloride above 69% cannot be prepared by boiling a solution at 760 mm pressure because a eutectic causes the dihydrate to separate as a solid phase and the solution remains constant boiling. Four hydrates have been identified in the open literature. Their properties are shown in the following Table 2.40.

Its solubility in water is shown in Table 2.41.

Calcium chloride is commonly used as an "electrolyte" and has an extremely salty taste, as found in sports drinks and other beverages such as Nestle bottled water. It can also be used as a preservative to maintain firmness in canned vegetables or in higher concentrations in pickles to give a salty taste while not increasing the food's sodium content. It is even found in snack foods, including Cadbury chocolate bars.

It has been used to make a substitute "caviar" from vegetable or fruit juices or added to processed milk to

TABLE 2.40

Property	$CaCl_2 \cdot 6H_2O$	$CaCl_2 \cdot 4H_2O$	$CaCl_2 \cdot 2H_2O$	$CaCl_2 \cdot H_2O$	$CaCl_2$
Composition (% $CaCl_2$)	50.66	60.63	75.49	86.03	100
Molecular weight	219.09	183.05	147.02	129	110.99
Melting point (°C)	29.9	45.3	176	187	773
Melting point (F)	85.8	113.5	349	369	1424
Boiling point[2] (°C)	—	—	174	183	1935
Boiling point (F)	—	—	345	361	3515
Density at 25 °C (77 F), g/cm^3	1.71	1.83	1.85	2.24	2.16
Heat of fusion (cal/g)	50	39	21	32	61.5
Heat of fusion (Btu/lb)	90	70	38	58	110.6
Heat of solution[3] in H_2O (cal/g) (to infinite dilution) (Btu/lb)	17.2	−14.2	−72.8	−96.8	−176.2
	31.0	−25.6	−131.1	−174.3	−317.2
Heat of formation[3] at 25 °C (77 F), kcal/mol	−623.3	−480.3	−335.58	−265.49	−190.10
Heat capacity at 25 °C (77 F), cal/g °C or Btu/lb F	0.34	0.32	0.28	0.20	0.16

TABLE 2.41

		g/100 ml of water							
Substance	**Formula**	**0 °C**	**10 °C**	**15 °C**	**20 °C**	**30 °C**	**50 °C**	**70 °C**	**90 °C**
Ca chloride	$CaCl_2$	59.5	64.7	74.5	100	128	137	147	159

restore the natural balance between calcium and protein for the purposes of making cheese such as Brie and Stilton. Calcium chloride's exothermic properties are exploited in many "self-heating" food products where it is activated (mixed) with water to start the heating process, providing a nonexplosive, dry fuel that is easily activated.

In brewing beer, calcium chloride is sometimes used to correct mineral deficiencies in the brewing water. It affects flavor and chemical reactions during the brewing process, and it can also affect yeast function during fermentation.

Calcium chloride can be injected as intravenous therapy for the treatment of "hypocalcemia" (low serum calcium). It can be used for insect bites or stings (such as Black Widow spider bites), sensitivity reactions, particularly when characterized by "urticaria" (hives). It has also been used in the treatment of:

- Magnesium intoxication.
- As an aid in the management of the acute symptoms in lead colic.
- In cardiac resuscitation, particularly after open heart surgery.
- It can help to protect the myocardium from dangerously high levels of serum potassium in "hypercalcemia".
- Calcium chloride can be used to quickly treat "calcium channel blocker" toxicity, from the side effects of drugs such as Diltiazem, helping avoid potential heart attacks.
- The aqueous form of calcium chloride is used in genetic transformation of cells by increasing the cell membrane permeability, inducing competence for DNA uptake (allowing DNA fragments to enter the cell more readily) (Table 2.42).

Physical constants of $CaCl_2$

Calcium Bromide

Calcium bromide has the chemical formula $CaBr_2$. It was first prepared by Pfeiffer, Klossmann and Angern in 1924. It is a deliquescent salt that has the form of colorless hexagonal crystals that are soluble in water

TABLE 2.42

CAS number	1004-82-4 (anhydrate) 22691-02-7 (monohydrate) 10035-04-8 (dihydrate) 25094-02-4 (tetrahydrate) 7774-34-7 (hexahydrate)
Molecular formula	$CaCl_2$
Molecular weight	110.98 g/mol (anhydrate) 128.993 g/mol (monohydrate) 147.014 g/mol (dihydrate) 183.045 g/mol (tetrahydrate) 219.089 g/mol (hexahydrate)
Density	2.15 g/cm^3 (anhydrate) 1.835 g/cm^3 (dihydrate) 1.832 g/cm^3 (tetrahydrate) 1.71 g/cm^3 (hexahydrate)
Melting point	772 °C (anhydrate) 260 °C (monohydrate) 176 °C (dehydrate) 45.5 °C (tetrahydrate) 30 °C (hexahydrate)
Boiling point	1965 °C (anhydrate)
Solubility in water	74.5 g/100 ml (20 °C) (soluble in alcohol)
Acidity	$pK_a = 8-9$ (anhydrate) 6.5–8.5 (hexahydrate)
Crystal structure	Orthorhombic (deformed rutile)
Space group	Pnnm, #58
Coordination chemistry	Octahedral-6-coordinate
Specific free energy of formation	$\Delta G = -750.2$ kJ/mol
Standard heat of formation	$\Delta_f H = -798.4$ kJ/mol

and absolute alcohol. Its molecular weight is 199.90 g/mol for the anhydride. When strongly heated in air, calcium bromide will produce CaO (lime) and Br_2. It is generally obtained as the dihydrate, $CaBr_2 \cdot 2H_2O$, in the form of a white crystalline powder. A hexahydrate, $CaBr_2 \cdot 6H_2O$, is also known. Anhydrous calcium bromide is obtained by dehydration (250 °C, vacuum) of the dihydrate $CaBr_2 \cdot 2H_2O$. On contact with hot surfaces or flames, $CaBr_2$ decomposes forming bromine as a toxic and corrosive fume. It also reacts with strong acids to produce corrosive fumes of bromine. It adopts the $CaCl_2$ structure with the cell

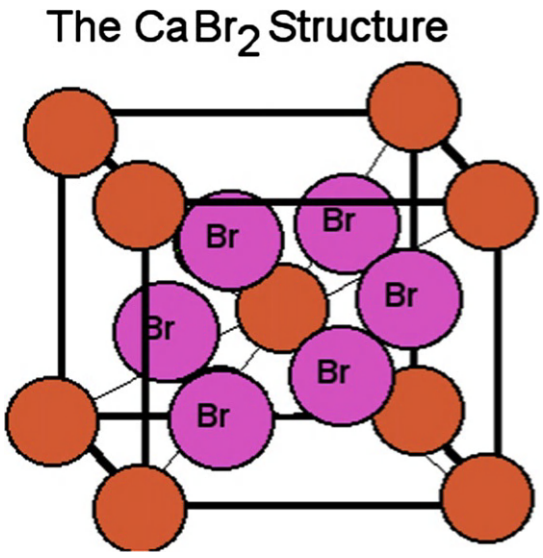

FIGURE 2.16

parameters of: $a = 4.342$ Å, $b = 6.584$ Å, $c = 6.871$ Å, $\alpha = \beta = \gamma = 90°$, cell volume $= 196.43$ Å^3, cell occupancy is shown in Table 2.43 and Fig. 2.16.

In its solid anhydrous state, it is a white powder. $CaBr_2$ can be found in drilling muds, neuroses medication, freezing mixtures, food preservatives, photography and fire retardants. The anhydride has a melting point of 730 °C and a boiling point of 810 °C where it decomposes. Its density is 3.41 g/cm^3. It is moderately soluble in water at 142 g/100 ml of water.

$CaBr_2 \cdot 2H_2O$ has a melting point of 38 °C where it dissolves in its own waters of hydration. Its density is 2.290 g/cm^3. It can be prepared by reaction in solution with HBr on the carbonate:

$$CaCO_3\ (solid) + HBr\ (liq) \Rightarrow CaBr_2\ (liq) + CO_2\ (gas)$$

An improved method for producing calcium bromide has been developed by reacting hydrogen bromide with calcium hydroxide in the presence of water.

Calcium bromide has a number of useful applications. Used in the oil and gas fields, the compound is a true working example. At almost every stage of the oil and gas extraction process, calcium bromide has found extensive usage. Stability, dependability and ease of use distinguish calcium bromide in the drilling process. There, it is used in "drilling muds" worldwide.

Because of this, bromine has recently become a tracked sector of the financial markets. The cost of

TABLE 2.43

No	Site notation	Atom	Multiplicity	Wyckoff	Site symmetry	x	y	z	Occupancy
1	Br	Br	4	g	..m	0.2636	0.342	0	1.0
2	Ca	Ca	2	a	..2/m	0	0	0	1.0

TABLE 2.44

		g/100 cc of water							
Substance	**Formula**	**0 °C**	**10 °C**	**15 °C**	**30 °C**	**50 °C**	**60 °C**	**70 °C**	**80 °C**
Calcium bromide	$CaBr_2$	125	132	143	213	278		295	

TABLE 2.45

CAS number	7789−41-5
Molecular formula	$CaBr_2$
Molecular weight	199.89 g/mol (anhydrate) 235.98 g/mol (dihydrate)
Density	3.363 g/cm^3
Melting point	750 °C
Boiling point	810 °C (anhydrate) 38 °C (dihydrate)
Solubility in acetone and alcohol	Soluble
Acidity	$pK_a = 9.0$
Heat of formation	$\Delta H^0 = -682.8$ kJ/mol
Free energy of formation	$\Delta G = -663.6$ kJ/mol
Standard entropy	130 kJ/mol

calcium bromide, as one of the bromines, has thus become subject to a variety of market pressures. Worldwide production of calcium bromide exceeds 15 megatons. Speculation in the bromine market now contributes to the cost of dollars spent on calcium bromide, not just the cost of the chemicals themselves. In addition to these speculative increases, the price of calcium bromide has also jumped due to increases in the price of calcium. Thus, the increased cost of exploration for oil and gas reserves has skyrocketed. As the cost of multiple components that make up the drilling operation continue to move upward, each cost must be examined closely for ways in which it can be most effectively exploited. To mitigate the damage due to the increased chemical costs have on an overall drilling budget, it is necessary to choose the correct fluids from the start of the project. Calcium bromide solutions are used in site preparation to increase the overall productivity of an oil or gas well. The compound is also widely found to be one of the most effective completion fluids currently used in the industry. Calcium bromide can be adjusted to meld seamlessly with the specific characteristics of individual drill holes. In addition, it protects the inner surface of the drill lines and can actually aid in the repair of the interior surfaces of the drill hole.

Calcium bromide reduces seepages and damage to the productive zone of the original drill site. Use of calcium bromide-based fluids also makes it easier to go back into the original drill zone and branch out into secondary productivity zones. Accessing the hardpan or rock-layers with low permeabity to get at lesser oil and gas reserves greatly increases the productivity of a well overall. The solubility of $CaBr_2$ in water is shown in Table 2.44.

Physical properties are listed in Table 2.45.

Calcium Iodide

Calcium iodide has the formula, CaI_2. This colorless, deliquescent solid is highly soluble in water. Its properties, including structure, are similar to those for related salts, such as $MgCl_2$ or $CaCl_2$. Its cell parameters are: $a = b = 4.482$ Å, $c = 6.963$ Å, $\alpha = \beta = \gamma = 90°$, cell volume = 120.98 Å^3, cell occupancy is shown in Table 2.46.

It is used in photography but the specific usage is not clear. CaI_2 is not stable and reacts in air with carbon dioxide to form the carbonate and iodine. For this reason, calcium iodide has not found many usages in Industry. The tetrahydrate, $CaI_2 \cdot 4H_2O$, is known but is no more stable than the anhydrate. A hexahydrate, $CaI_2 \cdot 6H_2O$, is also known which has a melting point of 42 °C.

In 1808, an impure form of calcium metal was prepared by H. Davy. The pure metal was later made by H. Moissan in 1898 by reducing calcium iodide with sodium:

$$CaI_2 + 2Na \Rightarrow 2NaI + Ca$$

TABLE 2.46

No	**Site notation**	**Atom**	**Multiplicity**	**Wyckoff**	**Site symmetry**	***x***	***y***	***z***	**Occupancy**
1	I	I	2	d	3m.	1/3	2/3	0.25	1.0
2	Ca	Ca	1	a	-3m.	0	0	0	1.0

TABLE 2.47

Substance	Formula	0 °C	15 °C	20 °C	30 °C	50 °C	70 °C	100 °C
Calcium iodide	CaI_2	64.6	66	67.6	70.8	74	78	81

TABLE 2.48

CAS number	10102-68-8 (anhydrate) 13640-62-5 (tetrahydrate)
Molecular weight	293.887 g/mol (anhydrate) 365.952 g/mol (tetrahydrate)
Appearance	White solid
Density	3.956 g/cm^3
Melting point	779 °C (anhydrate)
Boiling point	1115 °C (anhydrate)

Calcium iodide can be formed by treating calcium carbonate with hydroiodic acid:

$$CaCO_3 + 2HI \Rightarrow CaI_2 + H_2O + CO_2$$

The reaction is reversible in the air, liberating iodine, which is responsible for the faint yellow color of impure samples. This salt has a specific gravity of 3.956 g/cm^3, a melting point of 630–740 °C (depending upon purity) and a boiling point of 708–719 °C. It is soluble in water, ethyl alcohol and amyl alcohol.

Bromine replaces the iodine in calcium iodide to form calcium bromide and free iodine. The equation for this reaction is:

$$CaI_2 + Br_2 \Rightarrow CaBr_2 + I_2$$

CaI_2 has been used for measuring low-energy X-ray scintillation as a CaI_2:Eu^{2+} single-crystal detector. It is shown that on account of their layered structure, perfect cleavage, and high-light output, calcium iodide scintillators can be used to fabricate thin-film detectors for long-wavelength X-rays.

The solubility of CaI_2 in water is shown in Table 2.47.

Physical properties are listed in Table 2.48.

2.2.5. Halide Compounds of Strontium

Strontium Fluoride

Strontium fluoride, SrF_2, also called "strontium difluoride" and "strontium (II) fluoride", is a stable, brittle, white crystalline solid with a melting point of 1477 °C and a boiling point of 2460 °C. Its molecular weight is 125.62 g/mol. Its density is 4.24 g/cm^3. Its melting point has also been given as 1463 °C and a boiling point of 2489 °C. It is virtually insoluble since its solubility in water is 0.00012 g/100 ml of water at 18 °C.

The solid adopts the fluorite structure of CaF_2 with the cell parameters of: $a = b = c = 4.1012$ Å, $\alpha = \beta = \gamma = 60°$, cell volume = 48.78 Å^3, cell occupancy is shown in Table 2.49.

In the vapor phase, the SrF_2 molecule is nonlinear with an F–Sr–F angle of approximately 120°. This is an exception to the model generally used to predict the shape of individual molecules since it would predict a linear structure {This is called the "Gillespie–Nyholm" theory, named after its two main developers which is based upon the extent of electron-pair electrostatic repulsion}. Ab-initio calculations have been cited that propose the contributions from d-orbitals of the Sr atom in the shell below the valence shell are responsible for the nonlinear conformation.

SrF_2 is almost insoluble in water (its K_{SP} value is approximately 4.33×10^{-9} at 25 °C). It irritates eyes and skin, and is harmful when inhaled or ingested.

Similar to other alkaline earth fluorides like CaF_2 and BaF_2, SrF_2 presents "superionic conductivity" when heated to elevated temperatures. This phenomenon involves the electrical conductivity exhibited by a small group of solids that show high **ionic** conductivity and negligible electronic conductivity in the solid state unless heated beyond a specific temperature. In

TABLE 2.49

No	Site notation	Atom	Multiplicity	Wyckoff	Site symmetry	x	y	z	Occupancy
1	F	F	8	c	−43m	1/4	1/4	1/4	1.0
2	Sr	Sr	4	a	m−3m	0	0	0	1.0

TABLE 2.50

Refractive index: 1.439 at 0.55 μm	Transmission range: 0.15–11 μm
Reflection loss: 6.3% at 0.55 μm (2 surfaces)	Absorption coefficient: $<1 \times 10^{-3}$/cm at 5 μm
Restrahlen peak: 46 μm	dn/dT : -12×10^{-6}/°C
Thermal conductivity: 1.42 W/m/K at 298 K	Thermal expansion: 18.4×10^{-6}/°C at 293 K
Hardness: Knoop 154 (100) and 140 (110)	Specific heat capacity: 543 J/Kg/K
Dielectric constant: 7.69 at 2 MHz	Youngs modulus (E): 89.91 GPa
Shear modulus (G): 34.6 GPa	Bulk modulus (K): 24.65 GPa
Elastic coefficients: $C_{11} = 124$; $C_{12} = 45$; $C_{44} = 31.7$	Apparent elastic limit: 36.5 MPa (5300 psi)
Poisson ratio: 0.25	Class/structure: Cubic FCC, CaF_2, Fm3m

TABLE 2.51

CAS number	7783-48-4
Molecular weight	125.62 g/mol
Density	4.24 g/cm^3
Melting point	1477 °C
Boiling point	2460 °C
Solubility in water	0.0394 g/100 ml
Solubility product	$K_{SP} = 4.33 \times 10^{-9}$
Refractive index	$\eta_D = 1.439$ at 580 nm
Crystal structure	Cubic = cF12
Space group	Fm2m, #225

general, ionic conductivity is due to the motion of ions, whereas the electronic conductivity results from the flow of electrons within the solid. For superionic conductors, also called fast ion conductors or solid electrolytes, the specific conductivity is usually within the range from about 10^{-3} to 10 S/cm (or mhos) whereas metals have typical values ranging from 10 to 10^5 S/cm. These values are very high for a crystalline ionic solid, but are still an order of magnitude lower than many electronic conductors such as metals or semiconductors.

Strontium fluoride is transparent to light in the wavelengths from the vacuum UV (150 nm) to the near IR (11 μm). Its optical properties are intermediate to CaF_2 and BaF_2. Strontium fluoride is used as an optical material for a small range of special applications, for example, as an optical coating on lenses and also as a thermoluminescent dosimeter crystal. Another use is as a carrier of the ^{90}Sr radioisotope in thermoelectric generators. SrF_2 is also used as a single crystal for lasers. Some optical properties of single-crystal SrF_2 are listed in Table 2.50.

Strontium fluoride can be prepared by the reaction of strontium chloride with fluorine gas, or by action of hydrofluoric acid on strontium carbonate:

$$SrCl_2\ (aq) + F_2\ (gas) \Rightarrow SrF_2\ (solid) + Cl_2\ (gas)$$

$$SrCO_3 + 2HF \Rightarrow SrF_2 + CO_2 + H_2O$$

Note that the first reaction depends upon the insolubility of SrF_2 in water. Strontium fluoride is a water-insoluble source for use in oxygen-sensitive applications, such as metal production since it in nonhygroscopic (Table 2.51).

Strontium Chloride

Strontium chloride has the formula $SrCl_2$ and the molecular weight of 247.43 g/cm^3. It is a typical salt, forming neutral aqueous solutions.

Strontium chloride can be prepared by treating strontium hydroxide or strontium carbonate with hydrochloric acid:

$$Sr(OH)_2 + 2HCl \Rightarrow SrCl_2 + 2H_2O$$

$$SrCO_3 + 2HCl \Rightarrow SrCl_2 + CO_2 + H_2O$$

Crystallization from a cold aqueous solution gives the hexahydrate, $SrCl_2 \cdot 6H_2O$. Dehydration of this salt occurs in stages, commencing above 61 °C and ending at 320 °C, where full dehydration occurs. The dihydrate, $SrCl_2 \cdot 2H_2O$, is a metastable form before the anhydrate begins to form at 200 °C. The hydrates formed in solution have one, two or six waters of crystallization.

$SrCl_2 \cdot 6H_2O$ is a hexagonal system consisting of colorless long-needle crystals. It loses four crystal waters of hydration at 61.4 °C to form plate crystals of $SrCl_2 \cdot 2H_2O$ which become the monohydrate at 100 °C and anhydrate at 200 °C.

The solid anhydrate adopts a deformed rutile structure as well as the CaF_2 type of structure. Cell parameters for the CaF_2 type are: $a = b = c = 4.9321$ Å, $\alpha = \beta = \gamma = 60°$, cell volume = 84.84 Å^3, cell occupancy is shown in Table 2.52.

The structure is shown in Fig. 2.17.

In the vapor phase, the $SrCl_2$ molecule is nonlinear with a Cl–Sr–Cl angle of approximately 130°, similar to that of $CaCl_2$. Apparently, the same rules (Gillespie–Nyholm) apply.

TABLE 2.52

No	Site notation	Atom	Multiplicity	Wyckoff	Site symmetry	x	y	z	Occupancy
1	Cl	Cl	8	c	−43m	1/4	1/4	1/4	1.0
2	Sr	Sr	4	a	m−3m	0	0	0	1.0

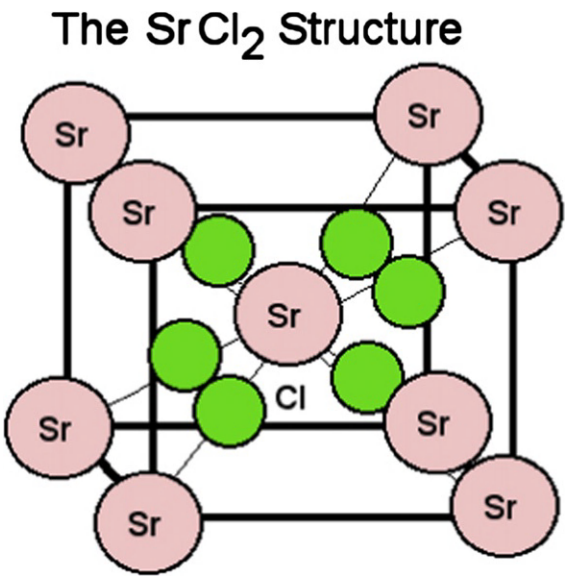

FIGURE 2.17

Strontium chloride is the precursor to other compounds of strontium, such as yellow $SrCrO_4$, which is used as a corrosion inhibitor for aluminum. The precipitation proceeds analogously to the related isostructural sulfate:

$$SrCl_2 + Na_2CrO_4 \Rightarrow SrCrO_4 + 2NaCl$$

Like all compounds of Sr, this salt emits a bright red color in a flame. Its optical and chemical properties are intermediate between those found for its neighbors in Group 2, such as $BaCl_2$ (which is more toxic), and calcium chloride (which is more common). Strontium chloride is the compound usually used as a red coloring agent in fireworks. It imparts a much more intense red color to the flames than other alternatives. It is employed in small quantities in glass making and metallurgy. The radioactive isotope, strontium-89, used for the treatment of bone cancer. It is usually administered in the form of strontium chloride. Seawater aquaria require small amounts of strontium chloride, which is consumed in the production of the exoskeletons of certain planktons.

$SrCl_2$ is useful in reducing tooth sensitivity by forming a barrier over microscopic tubules in the dentin-containing nerve endings that have become exposed by gum recession. Known in the US as "Sensodyne", these products are called "strontium chloride toothpastes," although most now use KNO_3 instead which works as a nerve calming agent rather than a barrier.

Another common hydrate, $SrCl_2 \cdot 2H_2O$, is composed of white, crystalline needles which have a sharp, bitter taste. It can be prepared by fusing $SrCO_3$ with $CaCl_2$ at high temperature and then extracting the melt with water. The solution is then concentrated and then crystallized to form $SrCl_2 \cdot 6H_2O$, which is then dehydrated at 68 °C to form the dihydrate.

Anhydrous strontium chloride is a colorless crystal or a white powder with a molecular weight of 158.53 g/mol and a density of 3.05 g/cm^3. Its melting point is 875 °C and its boiling point is 1250 °C. It is easily soluble in water but slightly soluble in anhydrous alcohol and acetone. It is not soluble in liquid ammonia. Its solubility in water is shown in Table 2.53.

Physical properties are listed in Table 2.54.

Strontium Bromide

Strontium bromide has the formula $SrBr_2$. At room temperature, it is a white, odorless, crystalline powder with the molecular weight of 247.43 g/mol. Strontium bromide burns bright red in a flame test. It is used in flares and also has some pharmaceutical uses. Several hydrates have been characterized including the monohydrate and the hexahydrate, $SrBr_2 \cdot 6H_2O$. This salt is a white, hygroscopic powder soluble in water and alcohol. It loses water at 180 °C, melts at 643 °C and is used in medicine and as an analytical reagent.

The structure of $SrBr_2 \cdot 6H_2O$ is tetragonal with $a_o = 11.633$ Å and $c_o = 7.155$ Å. Density measurements

TABLE 2.53

		g/100 ml of water								
Substance	Formula	0 °C	10 °C	15 °C	20 °C	30 °C	50 °C	70 °C	90 °C	10 °C
Sr chloride	$SrCl_2$	43.5	47.7	52.9	58.7	65.3	81.8	90.5	101	

TABLE 2.54

CAS number	10476-85-4 (anhydrate) 10025-70-4 (hexahydrate)
Molecular weight	158.53 g/mol (anhydrate) 266.62 g/mol (hexahydrate)
Appearance	White crystalline solid
Density	3.052 g/cm^3 (anhydrate, monoclinic form) 2.672 g/cm^3 (dihydrate) 1.930 g/cm^3 (hexahydrate)
Melting point	874 °C (anhydrate) 61 °C (hexahydrate)
Boiling point	874 °C (anhydrate)
Solubility in water	Anhydrate = 53.8 g/100 ml (20 °C) Hexahydrate = 106 g/100 ml (0 °C) Hexahydrate = 206 g/100 ml (40 °C)
Solubility	Very slightly soluble in ethanol Very slightly soluble in acetone Insoluble in ammonia
Refractive index	$\eta_D = 1.650$ (anhydrate) 1.594 (dihydrate) 1.536 (hexahydrate)
Crystal structure	Deformed rutile
Coordination chemistry	Octahedral (6-coordinate)

are consistent with 10 molecular units per cell. The space group is $D_{4n}^{7}-P_n^{4mm}$ or $C_{4h}^{3}-P_n^{4}$. $SrBr_2 \cdot 6H_2O$ is a white, hygroscopic powder soluble in water and alcohol which loses water at 180 °C when heated, and the resulting anhydrate melts at 643 °C and decomposes at 1135 °C to form the oxide plus Br_2 gas.

The anhydrate, $SrBr_2$, is a colorless, transparent, crystal, odorless, having a bitter, saline taste. It is very deliquescent and soluble in water and is readily soluble in alcohol and amyl alcohol. The specific gravity of $SrBr_2$ is 4.210 g/cm^3. It can be prepared by treating $SrCO_3$ with a hydrogen bromide solution. Alternatively, a strontium salt (carbonate, sulfate, chloride, etc.) is treated with bromine or hydrobromic acid in presence of a reducing agent. It has the structure as shown in Fig. 2.18.

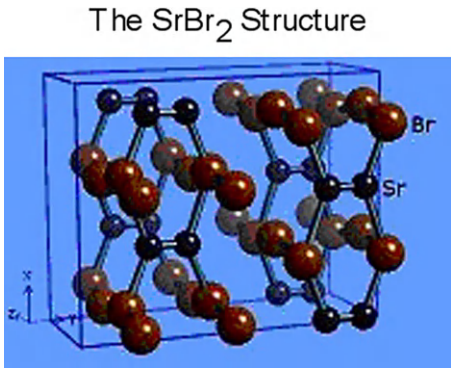

FIGURE 2.18

Cell constants are: $a = 7.133$ Å, $b = c = 11.645$ Å, $\alpha = \beta = \gamma = 90°$, cell volume = 962.30 Å^3 cell occupancy is shown in Table 2.55.

Its solubility in water is shown in Table 2.56.

Very little use has been found for this salt in Industry. Physical properties of this salt are given in the following Table 2.57.

Strontium Iodide

Strontium iodide (SrI_2) is an ionic, water-soluble, deliquescent compound that has been used in medicine as a substitute for potassium iodide. Strontium iodide crystals are colorless, transparent, hexagonal in structure, and have a bitter, saline taste. Soluble in 0.6 part of water at 15 °C, they are also soluble in alcohol.

Strontium iodide can be prepared by reacting strontium carbonate with hydroiodic acid:

$$SrCO_3 + 2HI \Rightarrow SrI_2 + H_2O + CO_2$$

Strontium iodide turns yellow when exposed to air due to the formation of iodine at the surface of the crystals. At high temperatures (when in the presence of air), strontium iodide completely decomposes to form strontium oxide and free iodine.

TABLE 2.55

No	Site notation	Atom	Multiplicity	Wyckoff	Site symmetry	*x*	*y*	*z*	Occupancy
1	Br(2)	Br	8	g	1	0.0428	0.161	0.5963	1.0
2	Sr(1)	Sr	8	g	1	0.0856	0.605	0.2524	1.0
3	Br(1)	Br	8	g	1	0.1531	0.041	0.1253	1.0
4	Sr(2)	Sr	2	c	4..	1/4	1/4	0.3483	1.0
5	Br(3)	Br	2	b	−4..	1/4	3/4	1/2	1.0
6	Br(4)	Br	2	a	−4..	1/4	3/4	0	1.0

TABLE 2.56

		g/100 ml of water							
Substance	**Formula**	**0 °C**	**10 °C**	**15 °C**	**20 °C**	**30 °C**	**50 °C**	**70 °C**	**90 °C**
Sr bromide	$SrBr_2$	85.2	93.4	102	112	123	150	182	223

TABLE 2.57

CAS number	10476-81-0
Molecular formula	$SrBr_2$
Molecular weight	247.43 g/mol
Appearance	White crystalline powder
Density	4.216
Melting point	643 °C
Boiling point	Hexahydrate: Melting point: 88 °C Boiling point: 100 °C
Crystal structure	Tetragonal

Three types of structures are known (Fig. 2.19).

CELL PARAMETERS

$Sr(OH)_2$ type: $a = 4.921$ Å, $b = 8.394$ Å, $c = 12.328$ Å, $\alpha = \beta = \gamma = 90°$, cell volume = 508.52 Å^3, cell occupancy is shown in Table 2.58.

$PbCl_2$ type: $a = 4.632$ Å, $b = 8.889$ Å, $c = 11.232$ Å, $\alpha = \beta = \gamma = 90°$, cell volume = 462.18 Å^3, cell occupancy is shown in Table 2.59.

SrI_2 type: $a = 7.896$ Å, $b = 8.251$ Å, $c = 15.268$ Å, $\alpha = \beta = \gamma = 90°$, cell volume = 994.71 Å^3, cell occupancy is shown in Table 2.60.

Several hydrates are known including $SrI_2 \cdot 6H_2O$. This salt is a white crystalline substance composed of small plates. It decomposes in moist air due to its deliquescence. Its specific gravity varies from 4.415 g/cm^3 to 4.549 g/cm^3, depending upon how the crystals are formed. It loses water at 78 °C and the anhydrate forms above 200 °C. The melting point of SrI_2 is 507 °C and its boiling point is 645 °C where it decomposes to the oxide and iodine. It is soluble in water as shown in Table 2.61.

Researchers have grown and characterized scintillation crystals of strontium iodide (SrI_2). Scintillation energy resolution and light yield proportionality surpass NaI and are similar to $LaBr_3$. The SrI_2 scintillators doped with europium (Eu) exhibit very high light yields (>100,000 photons/MeV), extremely good energy resolution (<3% at 662 keV) and excellent light yield proportionality. Europium-activated strontium and barium iodide single crystals have been found to be readily formed by the Bridgman method and are used to produce crystals having high scintillation light yields. SrI_2:Eu^{2+} emits in the blue Eu^{2+} band, centered at 435 nm, with a decay time of 1.2 μs and a light yield of ~90,000 photons/MeV. It offers an energy resolution better than 4% full width at half maximum at 662 keV, and exhibits excellent light yield proportionality. An additional broad impurity-mediated recombination band is present at 550 nm (>3 μs decay), and is probably due to the presence of Tb^{3+} unless high-purity feedstock is used. Physical properties are listed in Table 2.62.

2.2.6. Halide Compounds of Barium

Barium Fluoride

Barium fluoride (BaF_2), also known as barium(II) fluoride, is a solid which can also be a transparent crystal. Its molecular weight is 175.34 g/mol. It occurs in nature as the mineral "Frankdicksonite". It occurs as a white powder with a melting point of 1290 °C and a boiling point of 2259 °C. It is slightly soluble in water (0.159 at 0.0 °C and 0.162 g/100 ml of water at 20 °C).

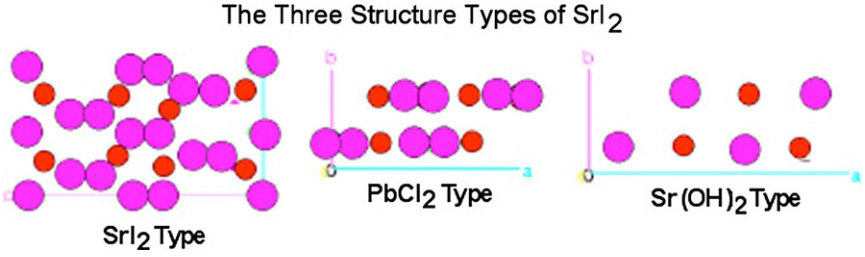

FIGURE 2.19

TABLE 2.58

No	Site notation	Atom	Multiplicity	Wyckoff	Site symmetry	x	y	z	Occupancy
1	I1	I	4	c	.m.	0.108	1/4	0.123	1.0
2	I2	I	4	c	.m.	0.12	1/4	0.617	1.0
3	Sr	Sr	4	c	.m.	0.33	1/4	0.37	1.0

TABLE 2.59

No	Site notation	Atom	Multiplicity	Wyckoff	Site symmetry	x	y	z	Occupancy
1	I1	I	4	c	.m.	0.0227	1/4	0.6621	1.0
2	I2	I	4	c	.m.	0.1425	1/4	0.0745	1.0
3	Sr1	Sr	4	c	.m.	0.2393	1/4	0.4045	1.0

TABLE 2.60

No	Site notation	Atom	Multiplicity	Wyckoff	Site symmetry	x	y	z	Occupancy
1	I(2)	I	8	c	1	0.0054	0.034	0.2318	1.0
2	Sr	Sr	8	c	1	0.2236	0.390	0.0495	1.0
3	I(1)	I	8	c	1	0.337	0.298	0.3923	1.0

TABLE 2.61

		g/100 ml of water							
Substance	Formula	0 °C	15 °C	30 °C	50 °C	60 °C	70 °C	80 °C	90 °C
Sr iodide	SrI_2	165	178	192	218		270	365	383

The solid generally assumes the fluorite structure, but when subjected to high pressure, changes to the $PbCl_2$ structure. In the vapor phase, the BaF_2 molecule is nonlinear with an F–Ba–F angle of approximately 108° (Fig. 2.20).

CELL PARAMETERS

$PbCl_2$ type (SG = 0P12): $a = 3.979$ Å, $b = 6.159$ Å, $c = 7.853$ Å, $\alpha = \beta = \gamma = 90°$, cell volume = 192.45 Å^3, cell occupancy is shown in Table 2.63.

CaF_2 type: $a = b = c = 4.3842$ Å, $\alpha = \beta = \gamma = 60°$, cell volume = 59.58 Å^3 (Table 2.64).

Barium fluoride crystal is transparent from the ultraviolet to the infrared, i.e. from 150–200 nm to 11–11.5 μm, and can be used as a material to make optical components such as lenses. It is used, for example, in windows for infrared spectroscopy. Its transmittance at 200 nm is relatively low (0.60), but at 500 nm it goes up to 0.96–0.97 and stays at that level until 9 μm, then it starts falling off (0.85 for 10 μm and 0.42 for 12 μm). The refractive index is about 1.46 from 700 nm to 5 μm (Table 2.65).

Barium fluoride is also a common, very fast (one of the fastest) scintillator for the detection of X-rays, gamma rays and other high-energy particles (That is, its decay time is very short). One of its applications lies in the detection of 511 keV gamma photons in measurements of "positron emission" tomography. {The other material used in this application is "bismuth germanate", $Bi_4Ge_3O_{12}$ ("Evlitine" structure)}. Its measured crystal properties are included in the following Table 2.66.

BaF_2 as a crystal responds also to alpha and beta particles, but, unlike most scintillators, it glows in ultraviolet light. It can also be used for detection of high-energy (10–150 MeV) neutrons, and for use as

TABLE 2.62

CAS number	10476-86-5 (anhydrous)
Molecular formula	SrI_2 (anhydrous) $SrI_2 \cdot 6H_2O$ (hexahydrate)
Molecular weight	341.43 g/mol (anhydrous)
Appearance	Colorless to white crystalline plates
Density	5.459 g/cm^3 (anhydrous) 4.415 g/cm^3 (hexahydrate)
Melting point	507−645 °C
Boiling point	1773 °C (decomposes)
Solubility in ethanol	3.1 g/100 ml (4 °C) [2]
Crystal structure	Orthorhombic, *oP24*
Space group	Pbca, No. 61

a "pulse shape" discriminator to separate them from simultaneously occurring gamma photons.

It is corroded by water vapor, even up to 500 °C, but in a dry environment, it can be used up to 800 °C. Prolonged exposure to moisture degrades its transmission in the vacuum UV range. It is less resistant to water than calcium fluoride. However, it is the most resistant of all the optical fluorides to high-energy radiation, though its far ultraviolet transmittance is lower than theirs. It is quite hard, but is very sensitive to thermal shock.

Barium fluoride is used as a "pre-opacifying" agent in enamel and glazing frits in the production of ceramic products. Its other use is in the production of welding agents:

- as an additive to some welding fluxes,
- a component of coatings,
- for welding rods,
- in welding powders.

It is also used in metallurgy, as a molten bath for refining aluminum metal (Table 2.67).

Barium Chloride

Barium chloride has the formula, $BaCl_2$ and is an ionic chemical compound. It is one of the most important water-soluble salts of barium-containing compounds. Like other barium salts, it is toxic and imparts a yellow-green coloration to a flame. It is also hygroscopic. Barium chloride was the by-product of the discovery of radium by Madame Curie (1898).

The Two BaF_2 Crystal Structures

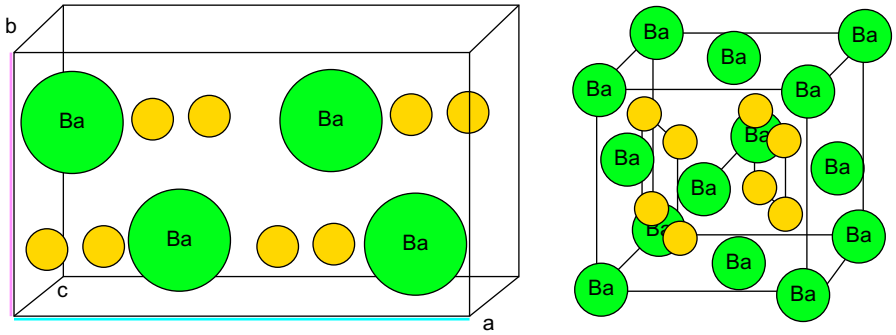

FIGURE 2.20

TABLE 2.63

No	Site notation	Atom	Multiplicity	Wyckoff	Site symmetry	*x*	*y*	*z*	Occupancy
1	F2	F	4	c	.m.	0.039	1/4	0.68	1.0
2	F1	F	4	c	.m.	0.139	1/4	0.067	1.0
3	Ba	Ba	4	c	.m.	0.241	1/4	0.388	1.0

TABLE 2.64

No	Site notation	Atom	Multiplicity	Wyckoff	Site symmetry	x	y	z	Occupancy
1	F	F	8	c	−43m	1/4	1/4	1/4	1.0
2	Ba	Ba	4	a	m−3m	0	0	0	1.0

TABLE 2.65 Optical properties

Transmission range: 150 nm − 11.5 μm
Refractive index: 1.46 at 3.2 μm
Reflection loss: 6.8% at 3.0 μm (2 surfaces)
Hardness (Knoop): 82 psi
Young's modulus: 53.07 GPa
Modulus of rupture: 3900 psi
Structure: Cubic—111 cleavage plane

When refining radium, the final separation resulted in barium chloride and radium chloride.

$BaCl_2$ crystallizes in both the cubic "fluorite" and "lead chloride" crystal structures, both of which accommodate the preference of the large Ba^{2+} ion for coordination numbers greater than six. There are four structure types known (Fig. 2.21).

CELL PARAMETERS

Fe_2P type: $a = 4.059$ Å, $b = c = 7.083$ Å, $\alpha = 120°$, $\beta = \gamma = 90°$, cell volume = 176.31 Å, cell occupancy is shown in Table 2.68.

TABLE 2.66

Chemical formula	BaF_2
Crystal class	Cubic
Lattice constant, Å	6.196
Density, g/cm^3 (20 °C)	4.89
Knoop hardness, kg/mm^2	82
Young's modulus, GPa	53.05
Shear modulus, GPa	25.4
Bulk modulus, GPa	56.4
Apparent elastic limit, MPa	26.89
Poisson ratio	0.343
Dielectric constant for 2.0×10^6 Hz	7.33
Specific heat, cal/(g K) at 274 K	0.096
Thermal conductivity, W/(m K) at 286 K	11.7
Thermal expansion, 1/K at 300 K	19.9×10^{-6}

$PbCl_2$ type, SG = mP24: $a = 4.604$ Å, $b = 8.613$ Å, $c = 11.901$ Å, $\alpha = 92.6°$, $\beta = \gamma = 90°$, cell volume = 471.48 Å^3, cell occupancy is shown in Table 2.69.

$PbCl_2$ type, SG = 0P12: $a = 4.732$ Å, $b = 7.872$ Å, $c = 9.425$ Å, $\alpha = \beta = \gamma = 90°$, cell volume = 651.08 Å^3, cell occupancy is shown in Table 2.70.

In aqueous solution, $BaCl_2$ behaves as a simple salt. In water, it is a 1:2 electrolyte and the solution exhibits a neutral pH. Electrolysis of molten barium chloride produces barium metal. This can be used for obtaining barium salts for commercial uses. Barium chloride reacts with sulfate ion to produce a thick white, insoluble precipitate of barium sulfate:

$$Ba^{2+}(aq) + SO_4^{2-}(aq) \Rightarrow BaSO_4\ (solid)$$

Oxalate effects a similar reaction:

$$BaCl_2\ (aq) + Na_2C_2O_4\ (aq) \Rightarrow BaC_2O_4\ (solid) + 2NaCl\ (aq)$$

Barium chloride can be prepared from barium hydroxide or barium carbonate, the latter being found naturally as the mineral "Witherite". These basic salts react to give hydrated barium chloride. On an industrial scale, it is prepared via a two-step process from the mineral "Baryte":

$$BaSO_4 + 4C \Rightarrow BaS + 4CO\ (gas)$$

This first step requires high temperatures. The second step requires fusion of the reactants:

$$BaS + CaCl_2 \Rightarrow BaCl_2 + CaS$$

The $BaCl_2$ is then be leached out from the mixture with water. From water solutions of barium chloride, the dihydrate can then be crystallized as white crystals, $BaCl_2 \cdot 2H_2O$, which are colorless, translucent rhomboidal tablets or lamellae. The dihydrate is stable in the air at room temperature, but loses one-half of its water above 55 °C (131 °F), and becomes anhydrous at 121 °C (250 F). As a cheap, soluble salt of barium, barium chloride finds wide application in the laboratory. It is commonly used as a test for sulfate ion. In industry, barium chloride is mainly used chiefly in the synthesis of pigments and in the manufacture of rodenticides and pharmaceuticals. It is also used:

- In the purification of brine solution in caustic chlorine plants,

TABLE 2.67 Physical properties

CAS number	7787-32-8
Molecular formula	BaF_2
Molecular weight	175.34 g/mol
Appearance	White cubic crystals
Density	4.893 g/cm^3
Melting point	1368 °C
Boiling point	2260 °C
Solubility in water	0.16 g/100 ml (20 °C)
Other solubility	Soluble in methanol, ethanol
Crystal structure	Fluorite (cubic), *cF12*
Space group	Fm3m, No. 225

- In the manufacture of heat treatment salts,
- For case hardening of steel,
- In the manufacture of pigments,
- In the manufacture of other barium salts such as barium hydroxide,
- In fireworks to give a bright green color. However, its toxicity limits its applicability,
- As a flux in the manufacture of magnesium metal,
- For making color kinescope glass ceramics,
- In wastewater treatment,
- For the production of PVC stabilizers, oil lubricants, barium chromate and barium fluoride,
- For stimulating the heart and other muscles for medicinal purposes,
- For softening water,
- For manufacturing of other barium salts used as pesticides, pigments, boiler detergent,
- As a mordant in dyeing and printing textiles,

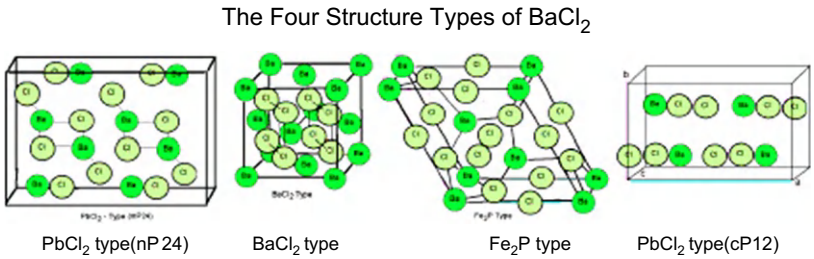

FIGURE 2.21

TABLE 2.68 Cell occupany is:

No	Site notation	Atom	Multiplicity	Wyckoff	Site symmetry	*x*	*y*	*z*	Occupancy
1	Cl1	Cl	3	g	m2m	0.25683	0	1/2	1.0
2	Cl2	Cl	3	f	m2m	0.59461	0	0	1.0
3	Ba1	Ba	2	d	−6..	1/3	2/3	1/2	1.0
4	Ba2	Ba	1	a	−62m	0	0	0	1.0

TABLE 2.69

No	Site notation	Atom	Multiplicity	Wyckoff	Site symmetry	*x*	*y*	*z*	Occupancy
1	Cl2	Cl	4	e	1	0.07	0.227	0.072	1.0
2	Ba1	Ba	4	e	1	0.12	0.27	0.334	1.0
3	Cl4	Cl	4	e	1	0.165	0.727	0.24	1.0
4	Ba2	Ba	4	e	1	0.38	0.273	0.13	1.0
5	Cl1	Cl	4	e	1	0.455	0.273	0.355	1.0
6	Cl3	Cl	4	e	1	0.71	0.227	0.03	1.0

TABLE 2.70

No	Site notation	Atom	Multiplicity	Wyckoff	Site symmetry	x	y	z	Occupancy
1	Cl1	Cl	4	c	.m.	0.0227	1/4	0.6621	1.0
2	Cl2	Cl	4	c	.m.	0.1425	1/4	0.0745	1.0
3	Ba1	Ba	4	c	.m.	0.2393	1/4	0.4045	1.0

TABLE 2.71

Substance	Formula	0 °C	10 °C	15 °C	20 °C	30 °C	50 °C	70 °C	80 °C	90 °C
Barium chloride	$BaCl_2$	31.2	33.5	35.8	38.1	40.8	46.2	52.5	55.8	59.4

TABLE 2.72

CAS number	10361-37-2 10326-27-9 (dihydrate)
Molecular formula	$BaCl_2$
Molecular weight	208.23 g/mol (anhydrous) 244.26 g/mol (dihydrate)
Appearance	White solid
Density	3.856 g/cm^3 (anhydrous) 3.0979 g/cm^3 (dihydrate)
Melting point	962 °C
Boiling point	1560 °C
Solubility in water	31.2 g/100 ml (0 °C)
Other solubility	Soluble in methanol, insoluble in ethanol, ethyl acetate
Crystal structure	Orthogonal (anhydrous) Monoclinic (dihydrate)
Coordination geometry	7–9
Thermodynamic properties of gas, liquid and solid	
Standard Heat (solid) of formation	$\Delta_f H^{\ominus}_{solid} = -855.56$ kJ/mol
Standard molar entropy	$S^{\ominus}_{solid} = 123.70$ J/(mol K)
Heat capacity	$C_p = 71.2$ J/(mol K)
Standard Heat (liquid) of formation	$\Delta_f H^{\ominus}_{liquid} = -832.47$ kJ/mol
Standard molar entropy	$S^{\ominus}_{liquid} = 143.52$ J/(mol K)
Standard Heat (gas) of formation	$\Delta_f H^{\ominus}_{gas} = -498.73$ kJ/mol
Standard molar entropy	$S^{\ominus}_{gas} = 325.73$ J/(mol K)

- In the manufacture of caustic soda, polymers, and stabilizers.

Its solubility in water in grams per 100 ml of water is shown in Table 2.71.

Physical properties are listed in Table 2.72.

Barium Bromide

Barium bromide has the molecular formula of $BaBr_2$. Like barium chloride, it is soluble in water but is toxic if ingested. $BaBr_2$ crystallizes in a $PbCl_2$ motif, as white orthorhombic crystals that are deliquescent. In aqueous solution, $BaBr_2$ behaves as a simple salt. It adopts the same type of $PbCl_2$ type of structures as $BaCl_2$ (Fig. 2.22).

CELL PARAMETERS

$PbCl_2$ type, SG = 0P12: $a = 4.935$ Å, $b = 8.252$ Å, $c = 9.915$ Å, $\alpha = \beta = \gamma = 90°$, cell volume = 402.77 Å^3, cell occupancy is shown in Table 2.73.

$PbCl_2$ type, SG = mP24: $a = 4.896$ Å, $b = 9.302$ Å, $c = 12.773$ Å, $\alpha = 92.6°$, $\beta = \gamma = 90°$, cell volume = 581.36 Å^3, cell occupancy is shown in Table 2.74.

Barium bromide reacts with the SO_4^{2-} ion to produce insoluble $BaSO_4$ as a precipitate:

$$BaBr_2\ (aq) + SO_4^{2-} \Rightarrow BaSO_4\ (solid) + 2Br^-\ (aq)$$

Similar reactions occur with oxalic acid, HF and H_3PO_4. Barium bromide can be prepared from barium sulfide or barium carbonate by reaction with hydrobromic acid to give hydrated barium bromide:

$$BaS + HBr \Rightarrow BaBr_2 + H_2S$$

$$BaCO_3 + HBr \Rightarrow BaBr_2 + CO_2 + H_2O$$

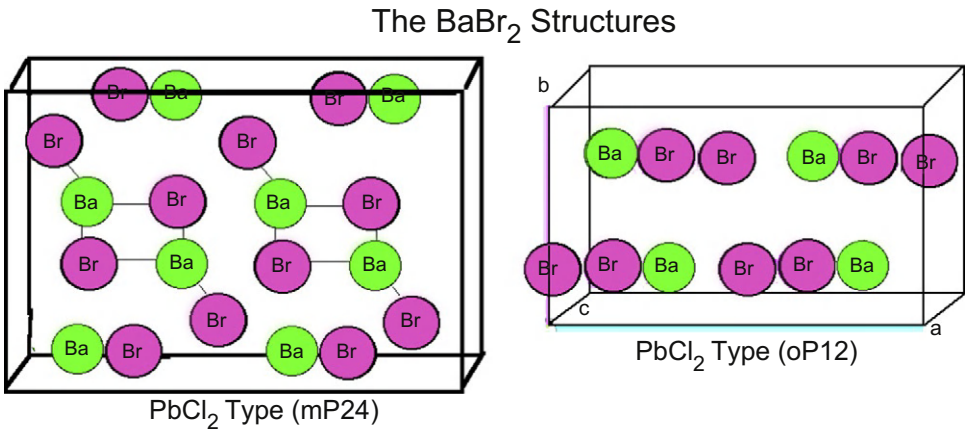

FIGURE 2.22

TABLE 2.73

No	Site notation	Atom	Multiplicity	Wyckoff	Site symmetry	x	y	z	Occupancy
1	Br1	Br	4	c	.m.	0.0227	1/4	0.6621	1.0
2	Br2	Br	4	c	.m.	0.1425	1/4	0.0745	1.0
3	Ba1	Ba	4	c	.m.	0.2393	1/4	0.4045	1.0

TABLE 2.74

No	Site notation	Atom	Multiplicity	Wyckoff	Site symmetry	x	y	z	Occupancy
1	Br2	Br	4	e	1	0.07	0.227	0.072	1.0
2	Ba1	Ba	4	e	1	0.12	0.27	0.334	1.0
3	Br4	Br	4	e	1	0.165	0.727	0.24	1.0
4	Ba2	Ba	4	e	1	0.38	0.273	0.13	1.0
5	Br1	Br	4	e	1	0.455	0.273	0.355	1.0
6	Br3	Br	4	e	1	0.71	0.227	0.03	1.0

Barium bromide can be crystallized from its solution as a dihydrate, $BaBr_2 \cdot 2H_2O$ (molecular weight: 333.19), which forms the anhydrate by heating to 120 °C. It dissolves in its own water-of-hydration at 75 °C before decomposing to the anhydrate. Barium bromide is a precursor to chemicals used in photography as well as to form other bromides.

Historically, barium bromide was used to purify radium in a process of fractional crystallization devised by Marie Curie. Since radium precipitates preferentially in a solution of barium bromide, the ratio of radium to barium in the precipitate was found to be higher than the ratio in the solution.

The solubility of barium bromide in water is shown in Table 2.75.

Physical properties are listed in Table 2.76.

Barium Iodide

Barium iodide occurs in two forms, one anhydrous and the other as a dihydrate. Both are white solids. There are three forms of the anhydrous salt (Fig. 2.23).

CELL PARAMETERS

Fe_2P type: $a = 5.173$ Å, $b = c = 9.142$ Å, $\alpha = 120°$, $\beta = \gamma = 90°$, cell volume = 374.42 Å^3, cell occupancy is shown in Table 2.77.

$PbCl_2$ type (SG = mP24): $a = 5.022$ Å, $b = 9.572$ Å, $c = 13.501$ Å, $\alpha = 91°$, $\beta = \gamma = 90°$, cell volume = 648.90 Å^3, cell occupancy is shown in Table 2.78.

$PbCl_2$ type (SG = mP12): $a = 5.298$ Å, $b = 8.904$ Å, $c = 10.685$ Å, $\alpha = \beta = \gamma = 90°$, cell volume = 504.05 Å^3, cell occupancy is shown in Table 2.79.

TABLE 2.75

		g/100 ml of water							
Substance	**Formula**	**0 °C**	**10 °C**	**15 °C**	**20 °C**	**30 °C**	**50 °C**	**70 °C**	**90 °C**
Barium bromide	$BaBr_2$	98	101	104	109	114	123	135	149

TABLE 2.76

CAS number	10553-31-8 (anhydrous) 7791-28-8 (dihydrate)
Molecular formula	$BaBr_2$ (anhydrous)
Molecular weight	297.14 g/mol
Density	4.78 g/cm^3 (anhydrous)
Melting point	857 °C
Boiling point	1835 °C
Crystal structure	Orthorhombic, oP12 Space group = Pnma, No. 62
Standard enthalpy of formation	$\Delta_f H\ominus_{298} = -181.1$ kcal/mol

This salt is stable, but air and light sensitive. It is also hygroscopic and moisture sensitive. Barium iodide is incompatible with strong oxidizing agents. Barium iodide is made by the neutralization of barium carbonate with HI in water:

$$BaCO_3 + 2HI\ (aq) \Rightarrow BaI_2\ (aq)$$

It is also made by the reaction of BaH_2 with ammonium iodide in pyridine:

$$BaH_2 + 2NH_4I\ (aq) \Rightarrow BaI_2\ (aq) + 2NH_3\ (gas) + H_2\ (gas)$$

The product crystallizes as the hydrate $BaI_2 2H_2O$. If this heated, dehydration to anhydrous BaI_2 occurs. The dihydrate dehydrates at 539 °C to form BaI_2.

Another view of one of the structures is shown as follows. Europium-doped barium iodide was found to be readily growable by the Bridgman method and to produce high **scintillation** light yields. BaI_2:Eu^{2+} produces >30,000 photons/MeV as the divalent Eu^{2+} emission band at 420 nm (Fig. 2.24).
that has a decay time less than 1.0 μs. High-Z crystal barium iodide is less prone to crack, as compared to lanthanum halides.

In another report, barium iodide crystals, activated by Eu^{2+} were also grown. Radioluminescence spectra and time-resolved decay were measured. BaI_2:Eu exhibits luminescence from both Eu^{3+} at 420 nm (with a 450- ns

TABLE 2.77

No	**Site notation**	**Atom**	**Multiplicity**	**Wyckoff**	**Site symmetry**	***x***	***y***	***z***	**Occupancy**
1	I(1)	I	3	g	m2m	0.2563	0	1/2	1.0
2	I(2)	I	3	f	m2m	0.5918	0	0	1.0
3	Ba(2)	Ba	2	d	−6..	1/3	2/3	1/2	1.0
4	Ba(1)	Ba	1	a	−62m	0	0	0	1.0

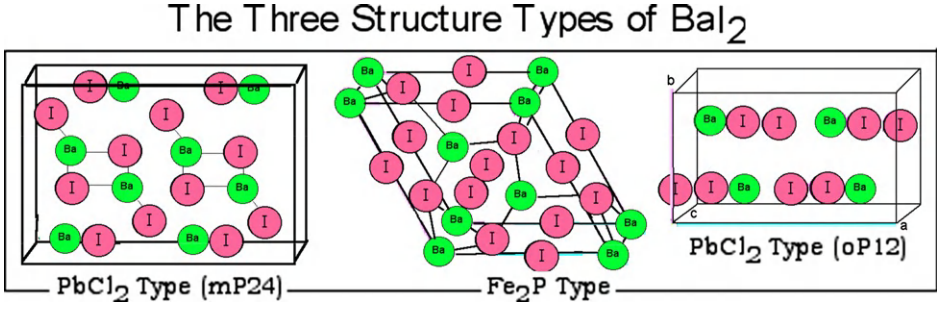

FIGURE 2.23

TABLE 2.78

No	Site notation	Atom	Multiplicity	Wyckoff	Site symmetry	x	y	z	Occupancy
1	I2	I	4	e	1	0.07	0.227	0.072	1.0
2	Ba1	Ba	4	e	1	0.12	0.27	0.334	1.0
3	I4	I	4	e	1	0.165	0.727	0.24	1.0
4	Ba2	Ba	4	e	1	0.38	0.273	0.13	1.0
5	I1	I	4	e	1	0.455	0.273	0.355	1.0
6	I3	I	4	e	1	0.71	0.227	0.03	1.0

TABLE 2.79

No	Site notation	Atom	Multiplicity	Wyckoff	Site symmetry	x	y	z	Occupancy
1	I(2)	I	4	c	.m.	0.029	1/4	0.6613	1.0
2	I(1)	I	4	c	.m.	0.1393	1/4	0.0735	1.0
3	Ba	Ba	4	c	.m.	0.2366	1/4	0.3785	1.0

decay), and a broad band at 550 nm (about a 3- μs decay) that was assigned to a trapped exciton. The 550 nm luminescence decreases relative to the Eu^{2+} luminescence when the barium iodide is zone refined prior to crystal growth.

Solubility in water is shown in Table 2.80.

Physical properties are listed in Table 2.81.

2.2.7. Halide Compounds of Radium

Radium and radium halide compounds find utilization in many areas in making commercial products and for medical applications. Radium is utilized in creating radon gas and this product is used for medical radiation treatment for diseases such as cancer. There are many compounds such as radium fluoride, radium chloride, radium bromide, radium iodide, radium oxide, and radium nitride. These compounds are regarded as very dangerous for humans and are not allowed in products that people use for normal consumption.

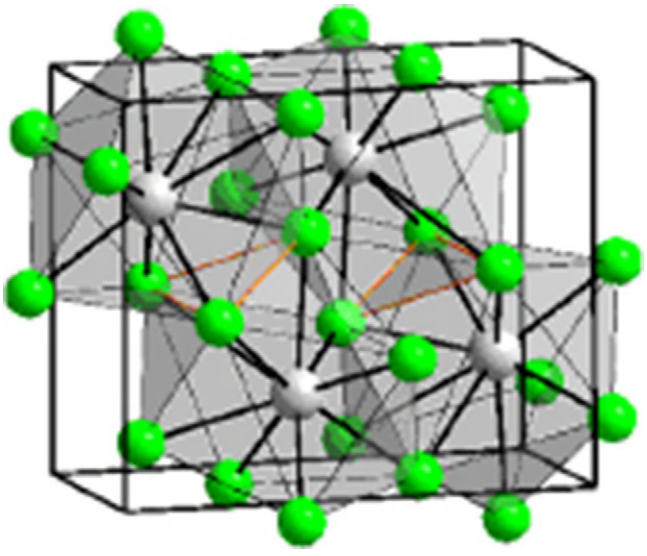

FIGURE 2.24

Radium and radium halide compounds are utilized in the nuclear and atomic areas for the production of weapons and also for creating electrical power. Radium bromide is employed in the extraction and separation of radium from the naturally occurring mineral ore of uranium. Radium chloride is used in the process of chemical extraction of radium from the naturally occurring ores such as pitchblende. The products had been used before 1950 to make dials for watches but now this practice is stopped because the items are deadly.

Radium Fluoride

This compound has the chemical formula of RaF_2 and a molecular weight of 263.8214 g/mol. Its structure is similar to that of CaF_2, the cubic fluoride. It can be prepared by reaction of HF gas on the metal:

$$Ra + 2HF \Rightarrow RaF_2 + H_2$$

Although this compound is listed as a viable salt of radium, no scientific studies of the properties of this material are readily available. Furthermore, RaF_2 is not offered for sale nor are there any descriptions of its physical and chemical properties. However, this compound

TABLE 2.80

		g/100 ml of water							
Substance	**Formula**	**0 °C**	**10 °C**	**15 °C**	**20 °C**	**50 °C**	**60 °C**	**80 °C**	**90 °C**
Barium iodide	BaI_2	182	201	223	250	264		291	301

has been given a CAS number of 20610-49-5, presumably because of its dangerous inherent radioactivity.

Radium Chloride

Radium chloride, $RaCl_2$, was the first radium compound to be prepared in a pure state and was the basis of Marie Curie's original separation of radium from Barium. The first preparation of radium metal was by the electrolysis of a solution of radium chloride using a mercury cathode. The structure remains unknown.

Radium chloride is soluble and crystallizes from solution as the dihydrate. It may be dehydrated by heating to 100 °C in air for 1 h followed by 5 h at 520 °C under Argon gas. If the presence of other anions is suspected, the dehydration may be effected by fusion under hydrogen chloride gas.

Radium chloride is a white solid having a blue-green luminescence, especially when heated. It is less soluble in water than other alkaline earth chlorides, a fact which is used in the first stages of the separation of radium from barium by fractional crystallization. It is only sparingly soluble in azeotropic HCl (20.2% HCl) and virtually insoluble in concentrated hydrochloric acid.

Gaseous radium chloride exists as $RaCl_2$ molecules, as do the other alkaline earth metal halides. The gas shows strong absorptions in the visible spectrum at 676.3 nm and 649.8 nm (red). The dissociation energy of the radium–chlorine bond is estimated as 2.9 eV, and its length is 2.92 Å.

Radium chloride is still used for the initial stages of the separation of radium from barium during the extraction of radium from the mineral "Pitchblende". The large quantities of material involved (tons of ore for milligrams of radium) favor this less costly (but less efficient) method over those based on radium bromide or radium chromate (used for the later stages of the separation).

$RaCl_2$ is used to produce radon gas that in turn is used as a cancer treatment in medicine. This compound is not offered for sale to the general public. Physical properties are listed in Table 2.82.

TABLE 2.81

CAS number	13718-50-8 (anhydrous) [7787-33-9] (dihydrate)
Molecular formula	BaI_2 (anhydrate) $BaI_2 \cdot 2H_2O$ (dihydrate)
Molecular weight	391.136 g/mol (anhydrous) 427.167 g/mol (dihydrate)
Appearance	White orthorhombic crystals (anhydrous) colorless crystals (dihydrate)
Density	5.15 g/cm^3 (anhydrous), 5.01 g/cm^3 (dihydrate)
Melting point	711 °C (anhydrous) decomposes at 740 °C (dihydrate)
Boiling point	2027 °C (decomposes)
Other solubility	Soluble in ethanol, acetone
Crystal structure	Othorhombic, oP12 Space group = Pnma, No. 62
Standard enthalpy of formation	$\Delta_f H^{\ominus}_{298} = -602.1$ kJ/mol

Radium Bromide

Radium bromide is the bromide salt of Ra with the formula $RaBr_2$. It is used primarily in separating radium from uranium ore. $RaBr_2$ is a water-soluble, poisonous, radioactive white powder or white orthorhombic crystals that is corrosive to skin or flesh. It melts at 728 °C used in medicine, physical research, and luminous paint. Its structure remains unknown.

Radium bromide has been used for skin complaints such as acne, moles, skin, cancer, eczema, dermatitis, and acne–rosacea. It is also used in research projects but is not offered for sale to the general public. Known physical properties are listed in Table 2.83.

TABLE 2.82

CAS number	10025-66-8
Molecular formula	$RaCl_2$
Molecular weight	296.094 g/mol
Solubility in water	19.6 g/100 ml (20 °C)
Melting point	1000 °C

TABLE 2.83

CAS number	10031-23-9
Molecular formula	$RaBr_2$
Molecular weight	386.23 g/mol
Appearance	White orthorhombic crystals
Melting point	728 °C
Boiling point	Sublimes at 900 °C
Solubility in water	70.6 g/100 g at 20 °C
Density	5.79 g/cm^3

TABLE 2.84

CAS number	7790-92-3
Molecular formula	HClO
Molecular weight	52.46 g/mol
Appearance	Colorless aqueous solutions
Density	Variable
Solubility in water	Very soluble
Acidity	$pK_a = 7.497$

Radium Iodide

This compound has the molecular formula of RaI_2 and a molecular weight of 479.834 g/mol. Its CAS number is 20610-52-0. It can be prepared by reaction of the metal with hydroiodic acid:

$$Ra + 2HI \Rightarrow RaI_2 + H_2$$

Little is available concerning its physical or chemical properties. As with radium fluoride, no scientific studies are easily accessed. Its structure has not been determined. RaI_2 is not offered for sale to the general public.

2.3. OXY-CHLORINE COMPOUNDS OF THE ALKALINE EARTHS

The alkaline earths do not form oxy-fluoride types of compounds. They do form a number of different types of compounds with the other oxy-halide acids. The compositions obtained are based upon the types of acids that can form. The following presents the characteristics of these oxy-acids in relation to the type of alkaline earth compounds that are known.

2.3.1. Oxy-Chlorine Acids

Hypochlorous acid is a weak acid where the chlorine atom is in the +1 oxidation state and has the formula HClO. It forms when Cl_2 dissolves in water. It cannot be isolated in pure form due to rapid equilibration with its precursor. Addition of chlorine to water gives both hydrochloric acid (HCl) and hypochlorous acid:

$$Cl_2 + H_2O \Rightarrow HClO + HCl$$

Physical properties are listed in Table 2.84.

Chlorous acid has the formula $HClO_2$. It is a weak acid. The chlorine atom possesses oxidation state +3 in this acid. The pure substance is unstable and disproportionates to hypochlorous acid (Cl oxidation state +1) and chloric acid (chlorine oxidation state +5).

$$2HClO_2\ (aq) \Rightarrow HClO\ (aq) + HClO_3\ (aq)$$

Chlorite salts such as sodium chlorite are stable conjugate bases derived from this acid. These salts are sometimes used in the production of chlorine dioxide, ClO_2 (Table 2.85).

Chloric acid, $HClO_3$, is an oxoacid of chloride, and the formal precursor of chlorate salts. It is a strong acid ($pK_a = -1$) and a strong oxidizing agent. It is stable in cold aqueous solution up to a concentration of approximately 30%, and solution of up to 40% can be prepared by careful evaporation under reduced pressure. Above these concentrations, and on warming, chloric acid solutions decompose to give a variety of products, for example:

$$8HClO_3 \Rightarrow 4HClO_4 + 2H_2O + 2Cl_2 + 3O_2$$

Note that it disproportionates into perchloric acid in which the chlorine atom has a +7 oxidation state and also the zero oxidation state of chlorine gas (an oxidation–reduction reaction). Thus, under the proper conditions, it can also be used to make perchloric acid (Table 2.86).

$$3HClO_3 \Rightarrow HClO_4 + H_2O + 2ClO_2$$

Perchloric acid, $HClO_4$, is a colorless liquid soluble in water. It is a strong acid comparable in strength to sulfuric and nitric acids. It is useful for preparing perchlorate salts, but it is also dangerously corrosive and readily forms explosive mixtures. Perchloric acid

TABLE 2.85

CAS number	13898-47-0
Molecular formula	$HClO_2$
Molecular weight	68.46 g/mol
Acidity (pK_a)	1.96

TABLE 2.86

CAS number	7790-93-4
Molecular formula	$HClO_3$
Molecular weight	84.45914 g/mol
Appearance	Colorless solution
Density	1 g/mL, solution (approximate)
Solubility in water	>40 g/100 ml (20 °C)
Acidity (pK_a)	ca.−1
Molecular shape	Pyramidal

TABLE 2.88

Chlorine mon—ooxide = ClO
Chlorine dioxide = ClO_2
Chlorine trioxide = ClO_3
Dichlorine monooxide = Cl_2O
Dichlorine dioxide = Cl_2O_2
Dichlorine trioxide = Cl_2O_3
Dichlorine tetroxide = Cl_2O_4
Dichlorine heptoxide = Cl_2O_7

is produced by the treatment of sodium perchlorate with sulfuric acid and by the electrochemical oxidation of aqueous chlorine (Table 2.87).

2.3.2. Oxy-Chlorine Acid Anhydrides

Each of the above acids has an "anhydride" which is a member of the chlorine–oxygen family. Chlorine and oxygen form a number of differing compounds. These are included in Table 2.88.

Of these, the following are "anhydrides" of the known oxy-chlorine acids (Table 2.89).

Dichlorine monoxide, Cl_2O, is one of the "chlorine-oxide" creators of the oxy-chlorine acids. It is a brownish yellow gas at room temperature that can explode at high concentrations when heated or subjected to sparks. It is best prepared by treating fresh yellow mercuric oxide with Cl_2 gas:

$$2Cl_2 + 2HgO \Rightarrow HgCl_2 \cdot HgO + Cl_2O$$

It can also be prepared by reaction of Cl_2 gas with moist sodium carbonate, Na_2CO_3. Dichlorine monoxide is very water soluble. It is the anhydride of hypochlorous acid. Much of the Cl_2O manufactured industrially is used to make hypochlorites. It is also the unstable decomposition product of calcium hypochlorite (Fig. 2.25).

TABLE 2.87

CAS number	7601-90-3
Molecular formula	$HClO_4$
Molecular weight	100.46 g/mol
Appearance	Colorless liquid
Density	1.67 g/cm^3
Melting point	−112 °C
Boiling point	19 °C (decomposes)
Solubility in water	Miscible

The shape of dichlorine monoxide is bent, due to the two lone pairs of electrons orbiting the nucleus of the oxygen atom that are not used to bond with the chlorine atoms. Its molecular weight is 86.9054 g/mol. Its melting point is –130 °C (−153 K, −185 F) and its boiling point is 2.2 °C (275 K, 36 F). It is a strong oxidizer when added to a water solution. The crystal structure is shown in Fig. 2.26.

Lately, it has been determined that it is best to generate dichlorine oxide for use commercially rather than use one of the salts of the alkalis or the alkaline earths. As a matter of fact, only the calcium salt has seen extensive usage in Industry or domestically as "bleaching powder". This accounts for the paucity of data concerning the various alkaline earth hypochlorites. The advantage of Cl_2O for bleaching paper pulp

TABLE 2.89

Acids	Anhydrides
Hypochlorous acid (HClO)	= Dichlorine monoxide (Cl_2O)
Chlorous acid ($HClO_2$)	= Dichlorine trioxide (Cl_2O_3)
Chloric acid ($HClO_3$)	= Dichlorine pentoxide (Cl_2O_5)
Perchloric acid ($HClO_4$)	= Dichlorine heptoxide (Cl_2O_7)

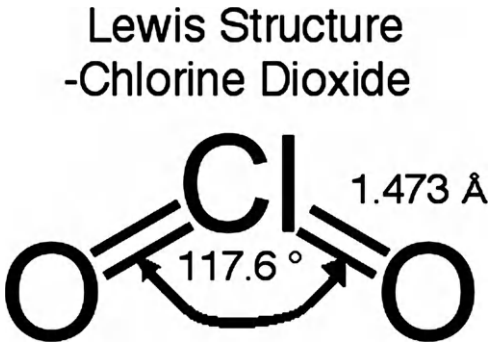

FIGURE 2.25

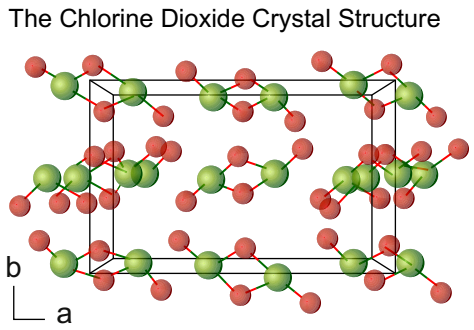

FIGURE 2.26

lies in the fact that it is a gas and can be manipulated much easier than a solid like sodium hypochlorite or its solution. The disadvantage is that Cl_2O reacts with any water vapor present and must be kept anhydrous until it is used. The amount of Cl_2O gas used for oxidation of paper pulp, for example, in the U.S. is in the many tons per year area. Physical properties are listed in Table 2.90.

Dichlorine trioxide, Cl_2O_3, is a chlorine oxide that is the anhydride of chlorous acid. It is a dark brown gas discovered in 1967 which is explosive even below 0 °C. It is formed by the low-temperature photolysis of ClO_2 and is formed along with Cl_2O_6, Cl_2 and O_2. Its structure is believed to be OCl–ClO_2 with possible isomers such as Cl–O–ClO_2. It is very soluble and forms chlorous acid if dissolved in water:

$$Cl_2O_3\ (gas) + H_2O \Rightarrow 2H_2ClO_2\ (aq)$$

It is less stable than chlorous acid, its more stable product, and therefore is not used commercially as an oxidizing agent. Its solubility in water is low, about 3.42 g/100 ml of water but it slowly reacts to form chlorous acid at room temperature. Raising the temperature causes it to decompose to form chlorine gas that remains soluble in aqueous solution (Table 2.91).

TABLE 2.90

CAS number	7791-21-1
Molecular formula	Cl_2O
Molecular weight	86.9054 g/mol
Melting point	−120.6 °C, 153 K, −185 F
Boiling point	2.2 °C, 275 K, 36 F
Solubility in water	Slightly soluble
Solubility in other solvents	Hydrolyses
Dipole moment	0.78 ± 0.08 D
Standard heat of formation $\Delta_f H^{\circ}_{298}$	+80.3 kJ/mol
Standard molar entropy S°_{298}	265.9 J/K/mol

TABLE 2.91

CAS number	17496-59-2
Molecular formula	Cl_2O_3
Molecular weight	118.903 g/mol
Appearance	Dark brown gas
Melting point	Explodes below 0 °C

Dichlorine Pentoxide

This compound has not been characterized and its physical and chemical properties remain unknown.

Dichlorine Hexoxide, Cl_2O_6, is the mixed oxide of chloric and perchloric acids.

It is produced by reaction between chlorine dioxide and excess ozone:

$$2ClO_2 + 2O_3 \Rightarrow 2ClO_3 + 2O_2 \Rightarrow Cl_2O_6 + 2O_2$$

It is a dark red fuming liquid at room temperature that crystallizes as an ionic compound, chloryl perchlorate, $[ClO_2]^+[ClO_4]^-$. It was originally reported to exist as the monomeric chlorine trioxide ClO_3 in gas phase, but was later shown to remain an oxygen-bridged dimer after evaporation and until thermal decomposition into chlorine perchlorate, Cl_2O_4, and oxygen. Cl_2O_6 is diamagnetic and is a very strong oxidizing agent. Although stable at room temperature, it explodes violently on contact with organic compounds and reacts with Au to produce the chloryl salt $[ClO_2]^+[Au(ClO_4)_4]^-$. Many other reactions involving Cl_2O_6 reflect its ionic structure, $[ClO_2]^+[ClO_4]^-$, including the following:

$$NO_2F + Cl_2O_6 \Rightarrow NO_2ClO_4 + ClO_2F$$

$$NO + Cl_2O_6 \Rightarrow NOClO_4 + ClO_2$$

$$2V_2O_5 + 12Cl_2O_6 \Rightarrow 4VO(ClO_4)_3 + 12ClO_2 + 3O_2$$

$$SnCl_4 + 6Cl_2O_6 \Rightarrow [ClO_2]_2[Sn(ClO_4)_6] + 4ClO_2 + 2Cl_2$$

Nevertheless, it can also react as a source of the ClO_3 radical:

$$2AsF_5 + Cl_2O_6 \Rightarrow 2ClO_3AsF_5$$

Dichlorine Heptoxide is a chemical compound with the formula Cl_2O_7. Dichlorine heptoxide is the anhydride of perchloric acid and is related to perchlorates in general. It is produced by the careful distillation of perchloric acid in the presence of a dehydrating agent such as phosphorus pentoxide:

$$2HClO_4 + P_4O_{10} \Rightarrow Cl_2O_7 + H_2P_4O_{11}$$

It is also produced by the careful distillation of perchloric acid that has been dehydrated with P_2O_5.

The distillation is usually safe at atmospheric pressure if it is truly free of perchloric acid. It is slowly hydrolyzed back into perchloric acid if allowed to sit in air. This can be dangerous since the resulting acid will be anhydrous, and anhydrous perchloric acid can detonate without reason.

It may also be formed by illumination of mixtures of chlorine and ozone. It slowly hydrolyzes back to perchloric acid, if allowed to contact moisture in any way. Dichlorine heptoxide melts at −91.5 °C and boils at 82 °C. It is highly explosive and can be set off with flame, mechanical shock, and on contact with organic substances. Cl_2O_7 is an endothermic molecule, which means that it is intrinsically unstable:

$$2Cl_2O_7 \Rightarrow 2Cl_2 + 7O_2 \ (\Delta H = +135 \text{ kJ/mol})$$

The Cl_2O_7 molecule is bent with a Cl–O–Cl angle of 118.6° giving the molecule C_2 symmetry. The terminal Cl–O distances are 1.709 Å and the Cl–O distances are 1.405 Å. In this compound, chlorine exists in its highest formal oxidation state of +7, although the bonding in this hypervalent molecule is significantly covalent (Fig. 2.27).

Dichlorine heptoxide reacts with primary and secondary amines in carbon tetrachloride solution to yield *N*-perchloryls:

$$2RNH_2 + Cl_2O_7 \Rightarrow 2RNHClO_3 + H_2O$$

$$2R_2NH + Cl_2O_7 \Rightarrow 2R_2NClO_3 + H_2O$$

It also reacts with olefins to give alkyl perchlorates. For example, it reacts with propene in carbon tetrachloride solution to yield isopropyl perchlorate and 1-chloro-2-propyl perchlorate.

Although it is the most stable chlorine oxide, Cl_2O_7 is strong oxidizer as well as an explosive that can be set off with flame or mechanical shock, or by contact with iodine. Nevertheless, it is less strongly oxidizing than the other chlorine oxides, and does not attack sulfur, phosphorus, or paper when cold. It has the same effects on the human body as elemental chlorine.

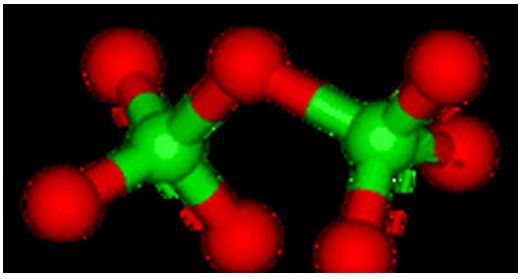

FIGURE 2.27

2.3.3. Alkaline Earth Oxy-Chlorine Compounds

The alkaline earths all form oxy-chlorine compounds with all of these complexes, $Ae(ClO_x)_2$ where x varies from 1 to 4, i.e. the acids discussed above. These compounds are strong oxidizers and corrosive to most materials with which they react. Of the four classes of chlorine-based oxidizers, the hypochlorous salts (ClO^-) have found the most usage commercially in Industry and domestically where they are used to bleach (whiten) wood pulp, paper, textiles and as cleaning, sanitizing and antibacterial aids for wastewater, sewage industrially and in the home. A large number of research papers can be found in the scientific literature concerning their properties and chemical reactions upon materials.

The chlorites (ClO_2^-) have not been employed to any great extent and relevant scientific literature is sparse whereas the chlorates (ClO_3^-) have found a number of commercial and domestic niches of usages. A number of research investigations are readily available concerning their properties. In contrast, the perchlorates (ClO_4^-) have found little applications industrially and have not been explored extensively as to their properties in the research literature.

There are only three oxyanions that form anhydrous salts: chlorites (ClO_2^-), chlorates (ClO_3^-) and perchlorates (ClO_4^-). Their stability increases with the increasing oxidation state of the halogen. There is no clear evidence of the existence of stable, stoichiometric, anhydrous hypochlorites since there is an evidence of the odor of chlorine, indicating continuous decomposition at room temperature.

Alkaline Earth Hypochlorites

BERYLLIUM HYPOCHLORITE

The stability and formulation of beryllium hypochlorite remain in question since the Be^{2+} cation is not formed in solution. The chemical formula would be $Be(ClO)_2$ if it did. Thus, since Be is amphoteric in solution and forms anions, the existence of a beryllium salt in solution like the hypochlorite remains in doubt. It may be that the small size of the Be atom precludes formation of a stable compound with the larger hypochlorite radical. Of course, the possibility of formation of a cation like $Be(OCl)^+$ exists but it has never been characterized. It could be prepared by reacting a hypochlorite salt like sodium hypochlorite with beryllium chloride in the solid state:

$$BeCl_2 + 2NaOCl \Rightarrow 2Be(OCl)_2 + 2NaCl$$

Of course, one would have to separate the two salts but any difference in solubility of the hypochlorite remains unknown. However, there is no data available

for such a reaction nor is there any description of the physical properties of beryllium hypochlorite.

Beryllium hypochlorite is not offered for sale nor is there any scientific data in the literature concerning its properties. The reason for this lies in its amphoteric nature in solution where the following reaction:

$$2Be^{2+} + H_2O \Rightarrow (Be_2OH)^{3+} + H^+$$

has been documented. Thus, it is clear that the Be^{2+} cation in aqueous solution never appears but is an "aquo-complex", and any formulation depicting "waters of hydration" in an oxy-chlorine compound is not completely accurate and valid.

MAGNESIUM HYPOCHLORITE

Magnesium hypochlorite has the chemical formula of $Mg(OCl)_2$ and the molecular weight of 127.286 g/mol. Its assigned CAS number is 10233-03-1. It can be prepared by reaction of hypochlorous acid upon magnesium carbonate in water. However, the product is not stable in water and decomposes to form basic magnesium hypochlorite, $Mg(OCl)_2 \cdot 2Mg(OH)_2$, which is useful in bleaching and sanitizing applications. The structure of this compound remains unknown.

A better process for the production of pure dibasic magnesium hypochlorite is said to comprise the reaction of a solid magnesium salt and a solid hypochlorite where one of the solid reactants is in the hydrate form. The process produces dibasic magnesium hypochlorite with excellent recovery of chlorine values and with reduced requirements for the disposal of solutions containing available chlorine. In this case, the reactants are magnesium chloride hexahydrate with calcium hypochlorite and its hydrates as preferred solid hypochlorite reactants:

$$MgCl_2 \cdot 6H_2O + Ca(ClO)_2 \Rightarrow Mg(ClO)_2 + CaCl_2 \cdot 6H_2O$$

wherein the solid components are reacted together by fusion at an elevated temperature. In general, the product is a mixture of compounds that is similar to the compound known as "bleaching powder"

Basic magnesium hypochlorite, $Mg(OCl)_2 \cdot 2Mg(OH)_2$, is a solid compound having an available chlorine content in the range of from about 50 to 60%. Textiles are bleached by immersing them in an aqueous solution of this salt. Bleaching takes place at any suitable temperature such as those in the range of about 10 – 100 °C, but preferably from about 30 to 80 °C. Textiles are held in contact with the aqueous solution of dibasic magnesium hypochlorite for a period of time sufficient to provide the materials with the desired degree of bleaching.

This salt is available commercially but has not found widespread usage since the calcium hypochlorite salt is cheaper and just as effective in these applications.

CALCIUM HYPOCHLORITE

Calcium hypochlorite has the molecular formula of $Ca(ClO)_2$ and a molecular weight of 142.974 g/mol. Its CAS number is 7778-54-3. Its specific gravity is 1.21 g/cm^3. When dissolved in water, it can provide nascent chlorine and oxygen to sterilize pool water or industrial wastewater. The structure of calcium chlorite, $Ca(ClO_2)_2$, has been refined from X-ray powder diffraction data using the Rietveld method. The compound crystallizes in the orthorhombic space group *Ccca* (*Ccce*), with $Z = 4$. The structure is based on separate layers parallel to the *ac* plane, consisting of calcium cations that are coordinated by chlorite anions; the O atoms form almost ideal square antiprisms. Within the layers, each anion bridges four metal cations. The Ca atoms are located on special positions of 222 symmetry, the Cl atoms lie on twofold axes and the O atoms are in general positions. The compound is isostructural with strontium chlorite, $Sr(ClO_2)_2$, and lead chlorite, $Pb(ClO_2)_2$.

It is manufactured by two main processes, the so-called "calcium process" and the "sodium process". These are essentially the same as described for the $Mg(ClO)_2$ salt method given above except that a sodium hypochlorite salt is used in one case and a calcium chloride salt in the other. The products are nearly the same. It is manufactured by the calcium process:

$$2Ca(OH)_2 + 2Cl_2 \Rightarrow Ca(ClO)_2 + CaCl_2 + 2H_2O$$

Bleaching powder is actually a mixture of calcium hypochlorite ($Ca(ClO)_2$) and the basic chloride $CaCl_2$, H_2O with some slaked lime, $Ca(OH)_2$. The product is generally called "**bleaching powder**". It consists of a mixture of calcium chloride ($CaCl_2$), calcium hypochlorite ($Ca(OCl)_2$), and calcium chloride hypochlorite (CaCl(OCl)).

In another method developed for the manufacture of $Ca(ClO)_2$, chlorine gas is reacted with calcium hydroxide:

$$Ca(OH)_2 + 2Cl_2 \Rightarrow Ca(ClO)_2 + 2HCl$$

In this method, it is claimed that the excess HCl is neutralized by excess $Ca(OH)_2$ to form $CaCl_2$. The product is said to be more "neutral" chemically and more stable than that produced by other methods.

Bleaching powder is white or gray white granular material, with a strong irritative odor. Its main component is calcium hypochlorite that exhibits several hydrates, the dihydrate, the trihydrate and the tetrahydrate.

The anhydrate releases a great deal of heat (heat of solution = 150 kcal/mol) and nascent oxygen and chlorine when solved in water:

$$Ca(ClO)_2 + H_2O \Rightarrow Ca^{2+}(aq) + ClO_2\,(aq)$$
$$\Rightarrow Cl + 2O\cdot + 2H^+$$

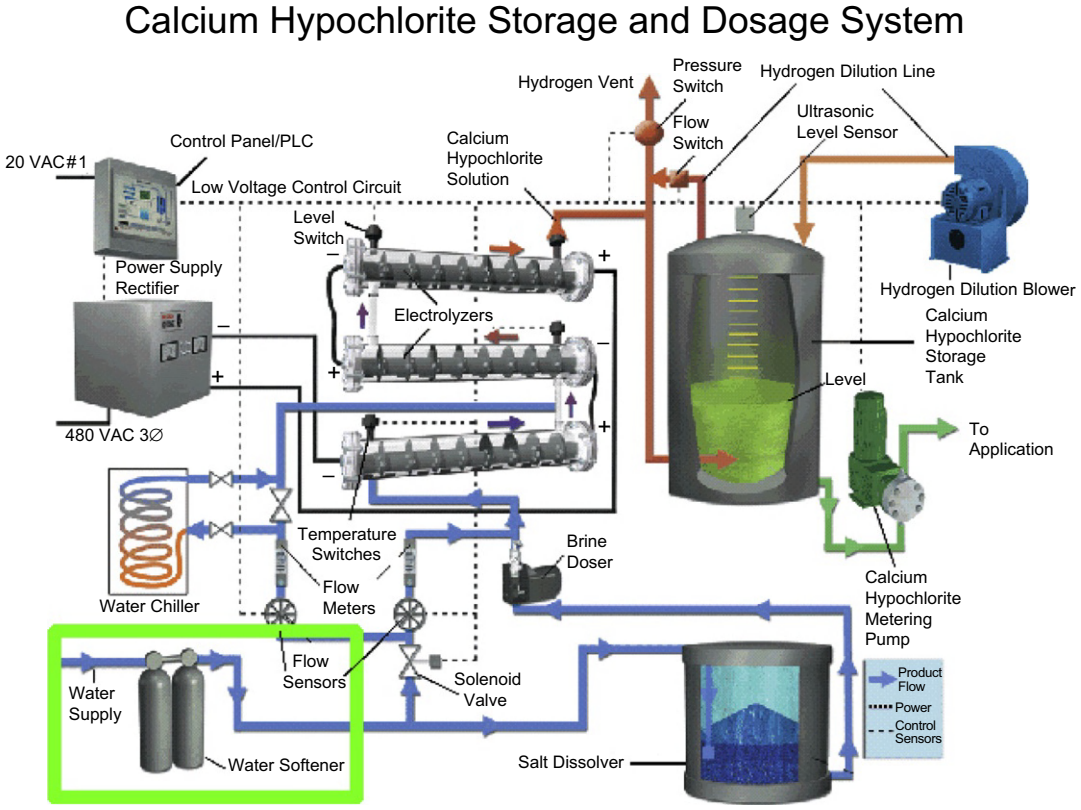

FIGURE 2.28

If the solid salt, calcium hypochlorite, is heated, its decomposition may cause an explosion. Reaction of the solid calcium hypochlorite with an acid may release chlorine, reaction of solid calcium hypochlorite with organics and oils may cause burning, and calcium hypochlorite tends to decompose and explode at high temperature. When stored at normal temperature, calcium hypochlorite is stable, with the effective chloride loss not more than 10% for sodium method. This salt is generally supplied to the public as a 3% solution. Specific methods of storage for large users (such as textile manufacturers) have been developed, as shown in Fig. 2.28.

Calcium hypochlorite is a powerful oxidizing agent, particularly in the presence of water or at higher temperature as it decomposes to release oxygen and chlorine gases. Therefore, it is necessary to contain the solution until it is used. When large quantities become necessary upon short notice, the above equipment becomes economical. As strong oxidant, calcium hypochlorite may react with vigor in combination with carbon compounds, and combination with finely divided carbon particles forms an explosive mixture. Reaction with acetylene leads to creation of explosive chloroacetylenes. Contact with organic matter, oil, hydrocarbons and alcohols such as methanol or ethanol may cause a violent explosion. Reaction with nitromethane causes a delayed violent reaction. Organic sulfur compounds such as sulfides react by self-ignition and explosion. Iron oxide in metal containers catalyze oxygen-evolving decomposition of the oxidant.

It forms highly explosive NCl_3 on contact with urea. This salt produces highly toxic gaseous chlorine gas when heated or on contact with acids. Mixture of damp sulfur with hypochlorite caused a violent reaction, that ejected molten sulfur.

$Ca(ClO)_2$ is used in industrial wastewater treatment, sanitation and cleaning, epidemic prevention and household sanitation facilities, as well as for disinfection and sterilization of swimming pools, drinking water, cleaning vegetables, and sanitizing fishponds.

The development of bleaching powder (calcium hypochlorite) by Scottish chemist Charles Tennant in the early 1800s, based on the discoveries of French chemist Claude Louis Berthollet, revolutionized the bleaching processes in the textile industry of that time by dramatically reducing the time required (from months to days) for the traditional process then in use. This outdated process required repeated exposure to the sun in bleach fields after soaking the textiles with alkali or sour milk.

Bleaching of textile fabrics with solid chlorine-containing compounds such as calcium hypochlorite or sodium chlorite has been practiced for many years. Calcium hypochlorite has had limited use in this manner as it can produce pinholes in fabrics. The use of calcium chlorite in bleaching processes requires the generation of chlorine dioxide which is toxic to humans and corrosive to equipment. Calcium hypochlorite has been used for bleaching of cotton, hemp, fiber, pulp and starch, disinfection of surfaces, and as a sterilant for water treatment. It has also been proposed as a solid fire extinguisher. This composition comprises a mixture of hydrated calcium hypochlorite with at least two hydrated inorganic salts, having an enthalpy, ΔH_0, of at least 150 cal/g, and having a phase transition temperature, as defined by the melting point of 19 °C–200 °C, whereby said mixture provides water release in an endothermic reaction to sufficiently quench dangerous reactions and reduce potential for a conflagration while providing increased chlorine stability as compared to blends containing a single-hydrated inorganic hypochlorite salt.

Calcium hypochlorite is available commercially but is most often generated in situ at the site of usage.

STRONTIUM HYPOCHLORITE

Strontium hypochlorite has the molecular formula $Sr(ClO)_2$ and the molecular weight of 190.514 g/mol. It is offered commercially for sale but the scientific literature concerning its uses or physical and chemical properties is not readily available. Its CAS number is 14674-76-1. The structure of the solid has not been determined.

BARIUM HYPOCHLORITE

Barium hypochlorite has the formula, $BaClO_2$ and the molecular weight of 240.234 g/mol. Its CAS number is 13477-10-6. It is white-colored crystalline solid that is denser than water. Contact may irritate skin, eyes and mucous membranes. It may be toxic by ingestion. It will accelerate the burning of combustible materials. Prolonged exposure to heat or flames may result in an explosion. It reacts with acids, evolving chlorine, an irritating, corrosive and toxic gas. It reacts fiercely with cyanides when heated or by friction. It may form explosive mixtures with combustible material, powdered metals or ammonium compounds. It is not offered commercially for sale nor is the scientific literature concerning its uses or physical and chemical properties readily available.

RADIUM HYPOCHLORITE

Radium hypochlorite remains unknown and the scientific literature remains devoid of any description of such a salt. Presumably, it can be prepared by the same method used for barium hypochlorite but no data are available concerning radium hypochlorite. Presumably, this is due to the difficulty in handling radioactive ^{226}Ra and the lack of interest in Industry for any uses of this salt.

Alkaline Earth Chlorites

BERYLLIUM CHLORITE

Beryllium chlorite has the molecular formula of $Be(ClO_2)_2$ and a molecular weight of 143.9158 g/mol. It is a white solid with a melting point of 1278 °C and a boiling point of 2970 °C. Its density is 1.85 g/cm^3 and it is insoluble in water.

Because chlorous acid is so unstable, it is difficult, if not impossible, to prepare beryllium chlorite by the use of dichlorine trioxide or chlorous acid. Furthermore, because of the amphoteric nature of beryllium, the existence of this compound in solution is questionable. It is said to have been prepared via the solid-state method but its physical and chemical properties have not been studied extensively. It is not offered for sale commercially due, perhaps, to the toxicity of beryllium to humans. Again, this beryllium salt is subject to restrictions concerning its degree of "hydration". The reason for this lies in its amphoteric nature in solution where the following reaction has been observed:

$$2Be^{2+} + H_2O \Rightarrow (Be_2OH)^{3+} + H^+$$

Thus, it is clear that the Be^{2+} cation in aqueous solution never appears alone but is an "aquo-complex", and any formulation depicting "waters of hydration" in an oxy-chlorine compound of beryllium is not completely accurate nor valid.

MAGNESIUM CHLORITE

Magnesium chlorite has the molecular formula of $Mg(ClO_2)_2$ and a molecular weight of 81.757 g/mol. As a solid, it has a melting point of 648 °C and a boiling point of 1090 °C. Its density is 1.738 g/cm^3. It reacts in water to produce dichlorine oxide, the anhydride of hypochlorous acid.

$$Mg(ClO_2)_2 + H_2O \Rightarrow Mg(OH)_2 + Cl_2O$$

Magnesium chlorite can be prepared by reaction of chlorous acid with magnesium carbonate:

$$MgCO_3\ (\text{solid}) + 2HClO_2\ (\text{aq}) \Rightarrow Mg(ClO_2)_2 \cdot 6H_2O$$

It crystallizes as the hexahydrate which has a tetragonal crystal structure with space group of $P4_2/nmc$. The lattice parameters are: $a_0 = 7.471$ Å and $c_0 = 7.780$ Å.

There is a paucity of data regarding this salt and it is offered for sale only in research quantities. Its solid structure has not been documented.

CALCIUM CHLORITE

Calcium chlorite, $Ca(ClO_2)_2$, has the molecular weight of 174.98 g/mol. Its density is 2.71 g/cm^3. Its CAS number is 14674-72-7. Calcium chlorite can be prepared by reaction of chlorous acid with calcium carbonate:

$$CaCO_3\ (solid) + 2HClO_2\ (aq) \Rightarrow Ca(ClO_2)_2 \cdot 6H_2O$$

It is a white granular solid and if formed in solution, crystallizes as the hexahydrate. Calcium hypochlorite, hydrated, is a white granular solid having an odor of chlorine. It is noncombustible and accelerates the burning of combustible materials. It is decomposed by water with evolution of chlorine gas and heat. Prolonged exposure to fire or heat may result in an explosion. It is decomposed by water to form calcium hydroxide and chlorine dioxide, an explosive oxidizing gas:

$$Ca(ClO_2)_2 + H_2O \Rightarrow Ca(OH)_2 + 2ClO_2$$

It has the structure shown in Fig. 2.29.

Calcium chlorite is a strong oxidizing agent. It ignites on contact with potassium thiocyanate and reaction with chlorine yields explosive chlorine dioxide gas. Reaction with ammonia produces ammonium chlorite, which is shock sensitive and explodes. If mixed with finely divided metallic or organic substances, the combination is highly flammable and may be ignited by friction.

A three-dimensional structure is shown in Fig. 2.30.

The structure of calcium chlorite, $Ca(ClO_2)_2$, has been refined from X-ray powder diffraction data. The compound crystallizes in the orthorhombic space group *Ccca* (*Ccce*), with $Z = 4$. The structure is based on separate layers parallel to the *ac* plane, consisting of calcium cations that are coordinated by chlorite anions; the O atoms form almost ideal square antiprisms. Within the layers, each anion bridges four metal cations. The Ca atoms are located on special positions of 222 symmetry, the Cl atoms lie on twofold axes and the O atoms are in general positions. The compound is isostructural with strontium chlorite, $Sr(ClO_2)_2$, and lead chlorite, $Pb(ClO_2)_2$.

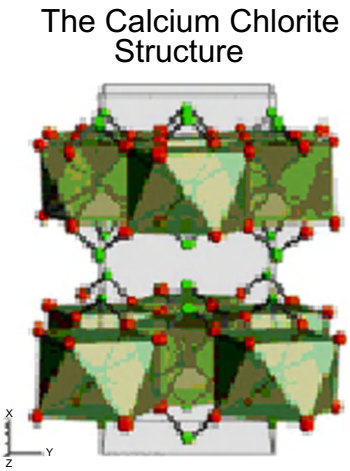

FIGURE 2.29

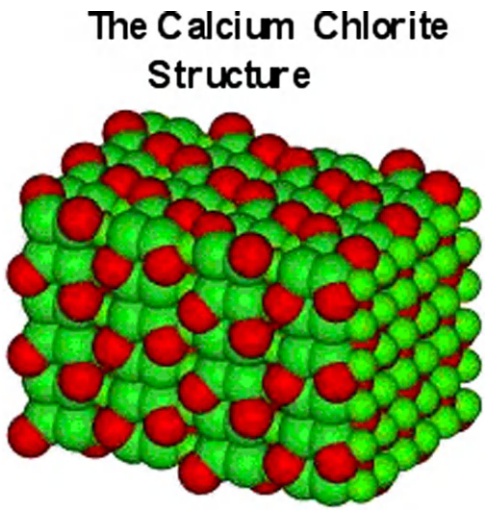

FIGURE 2.30

Currently, no manufacturer is registered for the product CALCIUM CHLORITE [CAS 14674-72-7]. There is a paucity of data concerning the physical properties of this salt and they are not easily accessible.

STRONTIUM CHLORITE

Strontium chlorite, $Sr(ClO_2)_2$, has the molecular weight of 155.072 g/mol. Its density is 2.61 g/cm^3. Its CAS number is 14674-72-7. Its melting point is 757 °C and it has a boiling point of 1484 °C. Strontium chlorite can be prepared by reaction of chlorous acid with strontium carbonate:

$$SrCO_3\ (s) + 2HClO_2\ (aq) \Rightarrow Sr(ClO_2)_2 \cdot 6H_2O$$

It is a white granular solid and, if formed in solution, crystallizes as the hexahydrate. Like its calcium homologue, strontium chlorite is a strong oxidizing agent. It accelerates the burning of combustible materials, ignites on contact with potassium thiocyanate and reaction with chlorine yields explosive chlorine dioxide gas. Reaction with ammonia produces ammonium chlorite, which is shock sensitive. If mixed with finely divided metallic or organic substances, the

combination is highly flammable and may be ignited by friction.

The structure of strontium chlorite, $Sr(ClO_2)_2$, has been refined from X-ray powder diffraction data using the Rietveld method. The compound crystallizes in the orthorhombic space group *Ccca* (*Ccce*), with $Z = 4$. The structure is based on separate layers parallel to the *ac* plane, consisting of strontium cations that are coordinated by chlorite anions; the O atoms form almost ideal square antiprisms. Within the layers, each anion bridges four metal cations. The Sr atoms are located on special positions of 222 symmetry, the Cl atoms lie on twofold axes and the O atoms are in general positions.

Strontium chlorite is not offered for sale commercially, due in part to the cost of strontium as compared to the same calcium salt which is just as effective as an oxidizing agent.

BARIUM CHLORITE

Barium chlorite, $Ba(ClO_2)_2$, is a solid with the molecular weight of 204.779 g/mol. Its density is 3.61 g/cm^3. Its CAS number is 14674-74-9. Its melting point is 727 °C and it has a boiling point of 1640 °C. Barium chlorite can be prepared by reaction of chlorous acid with barium carbonate:

$$BaCO_3\ (s) + 2HClO_2\ (aq) \Rightarrow Ba(ClO_2)_2 \cdot 7H_2O$$

It is a white granular solid and if formed in solution, crystallizes as the heptahydrate. Like its strontium homologue, barium chlorite is a strong oxidizing agent. It accelerates the burning of combustible materials, ignites on contact with potassium thiocyanate and reaction with chlorine yields explosive chlorine dioxide gas. Reaction with ammonia produces ammonium chlorite, which is shock sensitive. If mixed with finely divided metallic or organic substances, the combination is highly flammable and may be ignited by friction.

The structure of barium chlorite hydrate, $Ba(ClO_2)_2 \cdot 3.5H_2O$, has been determined by single-crystal X-ray analysis at 150 K. The structure is monoclinic, space group $C2/c$, with $Z = 8$. It contains layers of Ba^{2+} cations coordinated by ClO_2^- anions and water molecules. There are also solvate water molecules involved only in hydrogen bonding of the layers. Three solvate water oxygen atoms are on sites of twofold symmetry, while all other atoms are in general positions. The full coordination environment of the Ba^{2+} cation consists of 10 O atoms belonging to six chlorites and three water molecules, forming a bicapped square antiprism. Its solubility in water is:

Substance	Formula	0 °C	10 °C	15 °C	30 °C	50 °C	70 °C	90 °C
Barium chlorite	$Ba(ClO_2)_2$	43.9	44.6	45.4	47.9	53.8	66.6	80.8

Barium chlorite is not offered for sale commercially, due in part to the cost of barium as compared to the same calcium salt which is just as effective as an oxidizing agent. Very little data is available regarding its physical properties.

RADIUM CHLORITE

Radium chlorite remains unknown and the scientific literature remains devoid of any description of such a salt. Presumably, it can be prepared by the same method used for barium chlorite but no data is available concerning radium chlorite. This is probably due to lack of interest by those who use radioactive salts as well as the fact that the isotope, ^{226}Ra, is a very strong radioactive species.

Alkaline Earth Chlorates

The structure of alkaline earth chlorates is unique in that the chlorine atom is in the +5 valence state but the chlorate anion is triangular and mononegative in nature, i.e. Fig. 2.31.

In this case, the negative charge and the double bonds are not one Lewis structure but is a combination of all three where the negative charge is in resonance with all three oxygen atoms and the double bonds shift accordingly (Fig. 2.32).

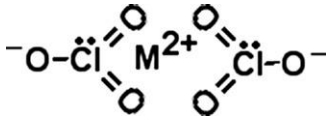

FIGURE 2.31

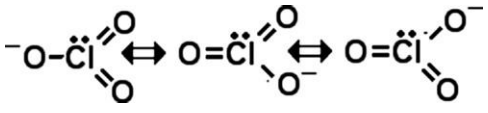

FIGURE 2.32

BERYLLIUM CHLORATE

Beryllium Chlorate, $Be(ClO_3)_2$ has the molecular weight of 92.4632 g/mol and is a solid having a melting point of 1278 °C and a boiling point of 2970 °C. Its density is 1.85 g/cm^3 and it is insoluble in water.

It is a strong oxidizer and reacts with organic compounds if mixed intimately. Because of its insolubility in water, its reactivity is much lower than corresponding soluble homologues like the magnesium or calcium salt. Little data is available concerning its physical properties. In view of the amphoteric nature of beryllium ion, the formula given above may not be completely accurate but may include hydroxy groups when formed from solution:

$$BeCl_2\ (aq) + 2HClO_4 + xH_2O \Rightarrow Be(OH)_x(ClO_4) + (x+2)\ H_3O^+$$

The reason for this lies in its amphoteric nature in solution where the following reaction has been observed:

$$2Be^{2+} + H_2O \Rightarrow (Be_2OH)^{3+} + H^+$$

Thus, it is clear that the Be^{2+} cation never appears in aqueous solution but is an "aquo-complex", and any formulation depicting "waters of hydration" in a beryllium oxy-chlorine compound is not completely accurate and valid.

Beryllium chlorite is not offered for sale nor is there a listed manufacturer of this salt. It has no CAS number. No structural data are available.

MAGNESIUM CHLORATE

Magnesium chlorate has a molecular weight of 299.33 g/mol and a CAS number of 10326-21-3. It is composed of white deliquescent crystals (or as a powder) that is soluble in water. It is denser than water. It poses a dangerous fire risk when in contact with organic materials or heat. This salt is irritating to skin, eyes and mucous membranes. It can be prepared by reaction of chloric acid upon magnesium carbonate:

$$MgCO_3 + 2HClO_3 \Rightarrow Mg(ClO_3)_2 + CO_2 + H_2O$$

Two hydrates are formed in solution and may be crystallized from solution, the dihydrate has a CAS number of 36355-97-2 while that of the hexahydrate, $Mg(ClO_3)_2 \cdot 6H_2O$, has a CAS number of 10326-21-3. The hexahydrate is a colorless rhomboidal needle-like crystal powder with a density of 1.80 g/cm^3, a 35 °C melting point and a boiling point of 120 °C where decomposition takes place. It is a water-soluble white powder, bitter tasting and hygroscopic. It is soluble in acetone and alcohol. At 35 °C, it loses two waters of hydration to form the tetrahydrate. This salt is deliquescent. It is stable, not explosive, but when mixed with sulfur, phosphorus or organic matter, friction, impact or other detonations causes an explosion. Its molecular weight is 407.402 g/mol.

If the hydroxide is reacted with chlorine gas in water, a mixture of compounds results:

$$6Mg(OH)_2\ (solid) + 6Cl_2\ (gas) \Rightarrow 5MgCl_2\ (aq) + Mg(ClO_3)_2\ (aq) + 6H_2O$$

The magnesium chlorate formed can then be extracted with acetone. This salt can also be prepared from magnesium chloride by an electrochemical method:

$$MgCl_2\ (aq) + 6H_2O\ (aq) + e^- \Rightarrow Mg(ClO_3)_2 + 6H_2$$

in which a platinum anode and a rotating stainless steel cathode are used. Yields up to 68% have been achieved.

Magnesium chlorate is a powerful oxidizer. There is an explosive reaction with copper(I) sulfide, an incandescent reaction with antimony(III) sulfide, arsenic(III) sulfide, tin(II) sulfide, and tin(IV) sulfide. This salt is incompatible with Al, As, C, Cu, MnO_2, organic matter, organic acids, phosphorus or sulfur. Mixtures with ammonium salts, with powdered metals, silicon, sulfur, or sulfides are readily ignited and potentially unstable, even at room temperature.

A combination of finely divided aluminum and magnesium chlorate can explode by heat, percussion, or friction. The solubility of $Mg(ClO_3)_2$ is shown in Table 2.92.

Magnesium chlorate is readily available commercially.

CALCIUM CHLORATE

Calcium chlorate $Ca(ClO_3)_2$ is the chemical compound formed from calcium and the chlorate anion. Like $KClO_3$, it is a strong oxidizer and can be used in pyrotechnic formulations. Its molecular weight is 206.98 g/mol. Its

TABLE 2.92

		g/100 ml of water								
Material	**Formula**	**0 °C**	**10 °C**	**20 °C**	**30 °C**	**49 °C**	**50 °C**	**60 °C**	**80 °C**	**100 °C**
Magnesium chlorate	$Mg(ClO_3)_2$	114	123	135	155	178		242		268

solubility in water is 209 g/100 ml at 20 °C. It is slightly soluble in alcohol. Calcium chlorate has a melting point of 325 °C and its density is 2.71 g/cm^3. Its CAS number is 10017-74-3. A dihydrate, $Ca(ClO_3)_2 \cdot 2H_2O$, forms as white monoclinic crystals, which are decomposed by heating above 150 °C. No structural data is available.

Calcium chlorate can be prepared by the Liebig process which is also used to prepare the alkali chlorates. In Liebig's process, chlorine is passed into milk of lime, at or above a temperature of 1000 °C, the apparent reaction being:

$$6Ca(OH)_2 + 6Cl_2 \Rightarrow 5CaCl_2 + Ca(ClO_3)_2 + 6H_2O.$$

But this may comprise two minor reactions:

$$2Ca\ (OH)_2 + 2Cl_2 \Rightarrow CaCl_2 + Ca(OCl)_2 + 2H_2O;$$

$$3Ca(OCl)_2 \Rightarrow 2CaCl_2 + Ca(ClO_3)_2$$

where the hypochlorite undergoes a redox reaction. It is possible, however, that the hypochlorite may decompose thus:

$$Ca(OCl)_2 \Rightarrow CaCl_2 + O_2,$$

causing a waste of chlorine and a double salt in the final product. To prevent this, an excess of chlorine must always be present. Theoretically, only one molecule of calcium chlorate is obtained from 12 atoms of ch1orine. The other product is the dichloride of calcium, $CaCl_2$. This salt can also be prepared from calcium chloride by an electrochemical method:

$$CaCl_2\ (aq) + 6H_2O\ (aq) + e^- \Rightarrow Ca(ClO_3)_2 + 6H_2$$

using a platinum anode and a rotating stainless steel cathode. Yields of the dihydrate up to 78% have been achieved. The hydrogen produced can be "burned" to reform water.

Calcium chlorate undergoes the same type of reactions with other compounds like that described for the magnesium chlorate salt. It is a strong oxidizer. There is an explosive reaction with copper(I) sulfide, an incandescent reaction with antimony(III) sulfide, arsenic(III) sulfide, tin(II) sulfide, and tin(IV) sulfide.

This salt is incompatible with Al, As, C, Cu, MnO_2, organic matter, organic acids, phosphorus or sulfur. Mixtures with ammonium salts, with powdered metals, silicon, sulfur, or sulfides are readily ignited and potentially unstable. A combination of finely divided aluminum and calcium chlorate can explode by heat, percussion, or friction.

Calcium chlorate is used as a herbicide in agriculture, in making fireworks and is available commercially.

The physical properties of calcium chlorate may be summarized as in Table 2.93.

TABLE 2.93

CAS number	10017-84-3
Molecular formula	$Ca(ClO_3)_2$
Molecular weight	206.98 g/mol
Appearance	White solid
Density	2.71 g/cm^3
Melting point	325 °C
Solubility in water	209 g/100 ml (20 °C)

STRONTIUM CHLORATE

Strontium chlorate, $Sr(ClO_3)_2$, has a molecular weight of 254.52 g/mol. It is a white solid with a melting point of 120 °C and a density of 3.152 g/cm^3. It is soluble in water (174 g/100 ml at 20 °C). Its CAS number is 7791-10-8.

$Sr(ClO_3)_2$ is shock sensitive, and is highly flammable if allowed to sit in air. These white, water-soluble crystals decompose at 120 °C. It is used in pyrotechnics and tracer bullets. There are two coexisting crystal hydrates that undergo interconversion, the dihydrate and the hexahydrate. These compounds are not as shock sensitive as the anhydrate.

Strontium chlorate can be produced by the Liebig method which consists of passing chlorine gas through a solid such as $Sr(OH)_2$:

$$6Sr(OH)_2 + 6Cl_2 \Rightarrow 5SrCl_2 + Sr(ClO_3)_2 + 6H_2O.$$

However, separating the two salts remains problematic since both are soluble in water. Strontium chloride solubility is 42.9 g/100 ml of water at 20 °C while that of strontium chlorate is 174.9 g/100 ml of water at 20 °C.

Strontium chlorate is a strong oxidizing agent. It forms a flammable mixture with combustible materials (can be ignited by friction). Such mixtures may be explosive. Contact with concentrated sulfuric acid can cause fires or explosions. When mixed with ammonium salts, spontaneous decomposition and ignition may result. This compound liberates explosive chlorine dioxide gas in the presence of strong acid; heating with a dibasic organic acid in the presence of moisture liberates chlorine dioxide and carbon dioxide. Mixtures with ammonium salts, powdered metals, silicon, sulfur, or sulfides are readily ignited and potentially explosive.

Paramagnetic color centers produced by irradiation of $Sr(ClO_3)_2$ single crystals have been studied by electron spin resonance. The products of *x*- or δ-irradiation at 298 K are ClO_2 and O^{3-} centers. ClO_2 is trapped at six magnetically inequivalent sites in the crystal lattice, forming three pairs. The magnetic parameters for two of the pairs, that is, ClO_2(B) and ClO_2(C), are in close agreement

with ClO_2 centers reported in other systems; while the third pair, that is ClO_2(A), has slightly different hyperfine parameters. The principal g-values of this center (A) are $g_{xx} = 1.9984$, $g_{yy} = 2.0170$ and $g_{zz} = 2.0142$ and those of the A tensor are $A_{xx} = 90.0$ G, $A_{yy} = -8.7$ G and $A_{zz} = -5.0$ G. The chlorine centers that are trapped at six magnetically inequivalent sites produced by radiation damage reveal hexagonal symmetry among themselves. UV or thermal bleaching (at 90 °C) removes all the chlorine centers, giving a single anisotropic line, trapped at two magnetically inequivalent sites with a $g_{av} = 2.0092$. This new center is identified as an O^{3-} center.

Strontium chlorate is extremely volatile and is used mainly for pyrotechnics and selected fireworks. It is available commercially, worldwide.

BARIUM CHLORATE

Barium chlorate has the molecular formula of $Ba(ClO_3)_2$ and a molecular weight of 304.229 g/mol. Its density is 3.18 g/cm^3 and its melting point is 413.9 °C. It is a white crystalline solid, a skin irritant and if consumed can cause nausea, vomiting, and diarrhea. Its CAS number is 13477-00-4. It is used in fireworks to produce a green color. It also forms a monohydrate, $Ba(ClO_3)_2 \cdot H_2O$ whose CAS number is 10294-38-9.

The structure of the monohydrate crystal is monoclinic with lattice parameters of $a = 8.86$ Å, $b = 7.80$ Å and $c = 9.85$ Å with $\beta = 93°\ 30'$. The space group is C2/c. The lattice structure of $Ba(ClO_3)_2$ differs from that of the monohydrate and most probably belongs to the space group F$d2d$ with a crystal structure of orthorhombic face centered. The monohydrate begins to decompose to the anhydrate when heated to 85 °C.

Shock-sensitive compounds are formed with organic compounds, reducing agents, ammonia-containing agents, and metal powders. The substance decomposes violently on heating, producing oxygen, toxic fumes, and causing fire and explosive hazards. This salt is a strong oxidant and reacts with most combustible and reducing materials.

Barium chlorate can be produced through a double replacement reaction of barium chloride and sodium chlorate:

$$BaCl_2 + 2NaClO_3 \Rightarrow Ba(ClO_3)_2 + 2NaCl$$

It can also be produced through a more complicated process involving barium carbonate and ammonium chlorate, both of which are produced in situ. There are four separate reactions used to produce this salt:

$$BaCl_2 + Na_2CO_3 \Rightarrow BaCO_3 + 2NaCl$$

or

$$BaCl_2 + 2NaHCO_3 \Rightarrow BaCO_3 + 2NaCl + H_2O + CO_2 \quad (1)$$

In a separate step, ammonium chlorate is produced by reaction of tartaric acid, $C_4H_6O_6$, to produce ammonium bitartrate. This is then reacted with potassium chlorate which produces potassium bitartrate and ammonium chlorate:

$$C_4H_6O_6 + NH_4OH \Rightarrow NH_4C_4H_5O_6 + H_2O \quad (2)$$

$$NH_4C_4H_5O_6 + KClO_3 \Rightarrow KC_4H_5O_6 + NH_4ClO_3 \quad (3)$$

The produced barium carbonate is then reacted with ammonium chlorate:

$$2NH_4ClO_3 + BaCO_3 + \text{heat} \Rightarrow Ba(ClO_3)_2 + 2NH_3 + H_2O + CO_2 \quad (4)$$

The final product is obtained without having to handle the chlorate solutions or product before the final product is obtained. The potassium bitartrate remains soluble while the barium chlorate crystallizes from solution as the monohydrate. The reason that such a method is used is to mitigate the potential for an explosive mixture causing a serous fire and injury during its manufacture

It can also be produced via the Liebig process similar to that of the strontium homologue which consists of passing chlorine gas through a solid such as $Ba(OH)_2$:

$$6Ba(OH)_2 + 6Cl_2 \Rightarrow 5BaCl_2 + Ba(ClO_3)_2 + 6H_2O$$

However, separating the two salts remains problematic since both are soluble in water. Barium chloride solubility is 33.9 g/100 ml of water at 20 °C while that of barium chlorate is 35.9 g/100 ml of water at 20 °C. However, the solubilities change at 100 °C, being 104.9 g/100 ml of water for barium chlorate and 59.4 g/100 ml of water for barium chloride. Thus, one runs the risk that the chlorate will decompose. It is for this reason that the Liebig method is not used for the commercial production of barium chlorate.

Its solubility in water is shown in Table 2.94.

Polycrystalline $Ba(ClO_3)_2 \cdot (H_2O)_x$, with x between zero and one, and $Ba(ClO_3)_2 \cdot D_2O$ have been

TABLE 2.94

		g/100 ml of water								
Material	**Formula**	**0 °C**	**10 °C**	**20 °C**	**30 °C**	**40 °C**	**50 °C**	**60 °C**	**80 °C**	**100 °C**
Barium chlorate	$Ba(ClO_3)_2$	20.3	26.9	33.9	41.6	49.7		66.7	84.8	105

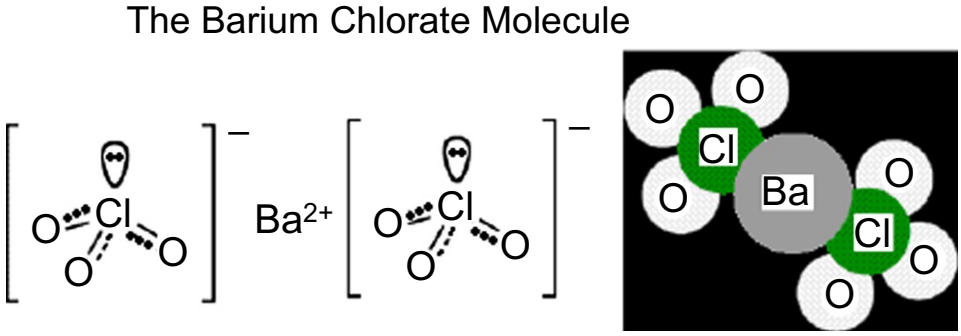

FIGURE 2.33

investigated by ^{35}Cl nuclear quadrupole resonance and X-ray diffraction experiments. Frequency, line width, and intensity of the chlorine resonance signal change with increasing loss of water and the quadrupole effects become less distinct as the hydrate decomposes to form anhydrous barium chlorate. X-ray diffraction and Raman measurements show that the lattice structure of $Ba(ClO_3)_2$ differs from that of the monohydrate and it most probably belongs to the space group F*d*2*d*. The dehydration of the monoclinic fully hydrated $Ba(ClO_3)_2 \cdot H_2O$ transforms into the orthorhombic face centered (ofc) fully anhydrous $Ba(ClO_3)_2$. The dehydration process begins at 85 °C and the transition proceeds through intermediate steps, where the two phases coexist with a gradual dominance of the anhydrous phase as the temperature increases. The role of the loss of the water of crystallization in the process is clarified by invoking a two-step mechanism for the accomplishment of the structural changes within the crystal. This comprises random nucleation and growth of clusters of vacancies, left by the exit of H_2O molecules, which, up to a certain critical size, can retain the original crystal structure. This is followed by a sudden onset of the phase transition within each of the overcritically sized clusters. As this process goes on, the concentration of clusters increases and the transition is further enhanced by cluster–cluster interactions. Barium Chlorate is a powerful oxidizer, due in part to the presence of the two lone-pair electrons on the chloride atom (Fig. 2.33).

Barium chlorate is used in the pyrotechnics industry to give a bright light for illumination (especially green light) (Fig. 2.34).

The crystalloluminescence and mechanoluminescence of $Ba(ClO_3)_2 \cdot H_2O$ crystals has been investigated. The crystalloluminescence spectra are almost similar to the photoluminescence spectra. However, they differ completely from the mechanoluminescence spectra. The crystalloluminescence excitations is believed to take place due to the various chemical processes: (i) the recombination of ions, (ii) from amorphous to crystalline transition, (iii) from the phase change during the crystallization, and (iv) from the dielectric breakdown by the electric field produced due to the creation of microfracture during the crystal growth. It is concluded that the crystalloluminescence excitation in $Ba(ClO_3)_2 \cdot H_2O$ crystals is probably chemical in origin.

$Ba(ClO_3)_2 \cdot H_2O$ is a powerful oxidizing agent. It is used to manufacture explosives and matches because of its ability to produce oxygen. This salt is available commercially. Physical properties are listed in Table 2.95.

RADIUM CHLORATE

Radium chlorate, $Ra(ClO_3)_2$, is a white solid with a molecular weight of 303.451 g/mol. Its melting point is 703 °C and its boiling point is 1737 °C. Its density is

FIGURE 2.34

TABLE 2.95

CAS number	13477-00-4
Molecular formula	$Ba(ClO_3)_2$
Molecular weight	304.23 g/mol
Appearance	White solid
Density	3.18 g/cm^3
Melting point	414 °C

5.10 g/cm^3. It is insoluble in water. It can be prepared by methods similar to those used for the other alkaline earth chlorates.

Radium chlorate is a strong oxidizer and the same precautions, already described for chlorate salts, apply. Additionally, radium itself is highly radioactive so that its uses, both Industrial and domestic, are miniscule to none. It is available commercially but only in research quantities.

Alkaline Earth Perchlorates

With the exception of Be, the alkaline earth perchlorates (Mg, Ca, Sr & Ba) have been shown to be extraordinarily soluble in water with the solubility specified in terms of mols per liter of water rather than in g/l. The freezing point of these solutions has been of special interest where the actual solubility is given as kg/l. For example, the strontium salt solution shows a freezing point of −67°C at a concentration of 1.15 kg/l. But at 0°C, the saturated solution of 8.16 mols/l (2.34 kg/l) was reported to be −2°C. A similar situation was determined also for the Mg, Ca and Ba salts, i.e.- $M(ClO_4)_2$, except that the differences were not as extreme.

BERYLLIUM PERCHLORATE

Beryllium perchlorate has the molecular formula of $Be(ClO_4)_2$ and a molecular weight of 207.012 g/mol. Its CAS number is 13597-95-0. It can be prepared by reaction of beryllium oxide in a water solution of an alkali perchloric salt or perchloric acid itself. The reaction is very slow and there is some doubt as to whether the oxide actually dissolves but is converted directly to the perchlorate directly.

The hydrolytic reactions of beryllium(II) ions have been calorimetrically studied at 25 °C in aqueous solution and dioxane–water mixtures, both containing 3.0 mol/dm^3 Li_2ClO_4 as a constant ionic medium. On the basis of the formation constants determined, the enthalpy and entropy changes for the reaction:

$$x\ Be^{2+} + y\ H_2O \Rightarrow \{Be_x\ (OH)_y\}^{(2x-y)+} + y\ H^+,$$

were estimated for the Be_2OH^{3+} and $Be_3(OH)_3^{3+}$ complexes in aqueous solution and 0.1 mol fraction dioxane–water mixture and for Be_2OH^{3+}, $Be_3(OH)_3^{3+}$, and $Be_2(OH)_2^{2+}$ complexes in 0.2 mol fraction dioxane–water mixture. The enthalpy and entropy changes of formation of the $Be_x(OH)_y^{(2x-y)+}$ complex in solutions of various mole fractions of dioxane were obtained and shown to abide by the following reaction:

$$2Be^{2+} + H_2O \Rightarrow (Be_2OH)^{3+} + H^+$$

Thus, it is clear that the Be^{2+} cation never appears in aqueous solution but is an "aquo-complex".

Beryllium forms what is called a "tetrahydrate" which probably is a hydroxy complex. Its solubility in water is 146.6 g/100 ml at 20 °C. These are very hygroscopic crystals that hold their "waters of hydration" very tenaciously. That is, when heated to higher temperatures, they do not lose water molecules to form the anhydrate. The reason for this may be seen by examining the following formula:

$$\{Be_2\ (OH)^{3+}\}_2\{Cl(OH)O_3\}^{6-}$$

Here, the chlorine atom is in the +7 oxidation state, i.e. it is the central atom in a peroxide anion. Thus, when heated, these salts cannot eject a water molecule, leaving the rest of the molecule intact, unlike the other alkaline earth perchlorates which form anhydrates, but breaks down to form chlorine gas and an oxide. These results were discussed in connection with interactions between the hydroxo complexes and the solvent molecules and with those between solvent molecules in the mixed solvents of the solvent beryllium cation. This concept may be better understood by examining the following diagram where the tetrahedral nature of the perchlorate anion is depicted (Fig. 2.35).

The introduction of a hydroxy group in the tetrahedron changes the oxidation state of the chlorine atom. Therefore, it is unlikely that such an anion exists for the beryllium perchlorate salt.

Beryllium perchlorate is not employed in industry, medicine or other domestic usages. It is not available commercially. It has no CAS number.

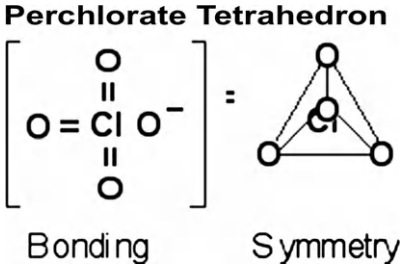

FIGURE 2.35

MAGNESIUM PERCHLORATE

Magnesium perchlorate is a powerful oxidizing agent, with the formula $Mg(ClO_4)_2$. Magnesium perchlorate decomposes at 250 °C. The heat of formation is −568.90 kJ/mol. The following table lists the CAS numbers assigned, the molecular formulas and the molecular weights of these compounds (Table 2.96).

If water is added to magnesium perchlorate, the reaction is highly exothermic and may cause damage to the eyes. Thus, this salt should be added to a sufficient amount of water in order to form a dilute solution. It can be prepared by reacting magnesium carbonate with a solution of perchloric acid:

$$MgCO_3 + HClO_4 \Rightarrow Mg(ClO_4)_2 + CO_2$$

This salt can also be prepared by an electrochemical method in water whereby magnesium perchlorate is formed from magnesium chlorate in which a platinum anode and a rotating stainless steel cathode are employed. The effect of electrolyte concentration, cathode and anode current densities, pH and temperature of the electrolyte and cathode rotation on current efficiency for the preparation of magnesium perchlorate has been studied. A maximum current efficiency of 65–72% was achieved. When formed from an aqueous solution, the hexahydrate is obtained. However, a tetrahydrate and a dihydrate are also known.

The previously unknown crystal structure of magnesium perchlorate anhydrate, determined and refined from laboratory X-ray powder diffraction data, represents a new structure type. The compound was obtained by heating magnesium perchlorate hexahydrate at 523 K for 2 h under vacuum. It crystallizes in the monoclinic space group $P2_1/c$. The asymmetric unit contains one Mg (site symmetry on special position 2*a*), one Cl and four O sites (on general positions 4*e*). The structure consists of a three-dimensional network resulting from the corner sharing of MgO_6 octahedra and ClO_4 tetrahedra. Each MgO_6 octahedron share corners with six ClO_4 tetrahedra (Fig. 2.36).

Each ClO_4 tetrahedron shares corners with three MgO_6 octahedra, with one O-atom corner dangling. The ClO_4 tetrahedra are oriented in such a way that one-dimensional channels parallel to [100] are formed between the dangling O-atoms.

$Mg(ClO_4)_2 \cdot 6H_2O$ is composed of white, deliquescent crystals which are soluble in water and alcohol but explosive when in contact with reducing materials. This compound is used as a drying agent for gases. This salt is highly exothermic when added to water and releases steamy HCl gas. It can be dried to form the anhydrate by heating to 250 °C under vacuum. The hexahydrate losses two molecules of water at 244 °C in air and further decomposes to the dihydrate at 336 °C and the anhydrate at 438 °C.

Electron paramagnetic resonance of Mn^{2+} doped $Mg(ClO_4)_2 \cdot 6H_2O$ crystals has been studied from room temperature (300 K) down to liquid nitrogen temperature at *X*-band. The room temperature results show three inequivalent sites for Mn^{2+} in the crystal. Hyperfine forbidden transitions are observed when the magnetic field is not oriented along one of the principal axes. Two structural phase transitions have been observed at temperatures of 272 ± 1 and 103 ± 1 K, respectively. The transition occurring at 272 ± 1 K has been observed for the first time. The transition occurring at 103 ± 1 K is the one detected earlier through Mössbauer studies.

The anhydrate has been used as a desiccant to dry gas streams or air samples. However, it is no longer used since perchlorates tend to form explosive compounds with a variety of organic materials as well as other substances. Physical properties are listed in Table 2.97.

TABLE 2.96

Compound	CAS number	Formula	g/mol
Magnesium perchlorate	10034-81-8	$Mg(ClO_4)_2$	223.21
Magnesium perchlorate hexahydrate	13446-19-0	$Mg(ClO_4)_2 \cdot 6H_2O$	331.31

CALCIUM PERCHLORATE

Calcium perchlorate has the formula, $Ca(ClO_4)_2$ with a molecular weight of 238.9792 g/mol and a CAS number of 13477-36-6. It can be prepared by reacting calcium carbonate with a solution of perchloric acid:

$$CaCO_3 + HClO_4 \Rightarrow Ca(ClO_4)_2 + CO_2$$

This salt can also be prepared by an electrochemical method in water whereby calcium perchlorate is formed from calcium chlorate in which a platinum anode and a rotating stainless steel cathode is employed. The effect of electrolyte concentration, cathode and anode current densities, pH and temperature of the electrolyte and cathode rotation on current efficiency for the preparation of calcium perchlorate was studied. A maximum current efficiency of 65–72% was achieved. When formed from an aqueous solution, the tetrahydrate is obtained, $Ca(ClO_4)_2 \cdot 4H_2O$. Its CAS number is 15627-86-8.

The anhydrate is a white to yellow crystalline solid with a density of 2.651 g/cm^3. Contact with this salt will irritate the eyes, skin and mucus membranes. If ingested, it is toxic in sufficient quantities. The structure of the molecule is shown as a Lewis structure where the actual shape of the molecule is a tetrahedron (Fig. 2.37).

When formed from an aqueous solution, the tetrahydrate is obtained. Calcium perchlorate tetrahydrate has the formula $Ca(ClO_4)_2 \cdot 4H_2O$ and the CAS number 15627-86-8. Its molecular weight is 311.04 g/mol and

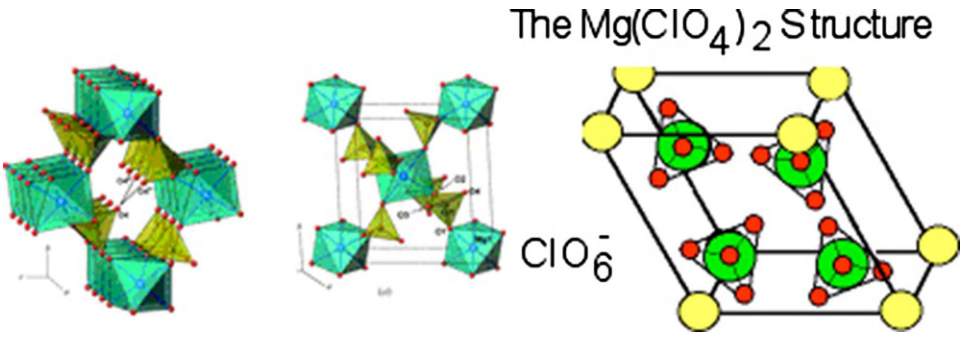

FIGURE 2.36

its density is 2.651 g/cm^3. Its solubility in water is 188 g/100 ml at 20 °C.

Melting processes and the thermal decomposition of $[Ca(H_2O)_4](ClO_4)_2$ was studied by thermogravimetry analysis (TG) and differential scanning calorimetry (DSC). The gaseous products of the decomposition were identified by a quadruple mass spectrometry. The loss process for waters of hydration starts at ca. 340–350 K and continues up to about 600 K. Tetra-aqua-calcium perchlorate dissolves in own waters-of-hydration (melts) at $T_m = 350$ K. The decomposition of the sample proceeds in three main stages. In stage I (351–602 K), dehydration of $[Ca(H_2O)_4](ClO_4)_2$ to anhydrous $Ca(ClO_4)_2$ undergoes two steps, in which two molecules of water are liberated consecutively forming the dihydrate and then the anhydrate. In stage II (602–701 K), anhydrous $Ca(ClO_4)_2$ has one solid-solid phase transition at $T_c = 619$ K and then melts at $T_m = 689$ K. Stage III (above 700 K) is connected with decomposition of melted $Ca(ClO_4)_2$ to oxygen and solid $CaCl_2$.

Very little physical data is available for this salt, although it has been the subject of a number of research studies. It is available commercially.

TABLE 2.97

CAS number	10034-81-8
Molecular formula	$Mg(ClO_4)_2$
Molecular weight	223.206 g/mol
Appearance	White powder, deliquescent
Density	2.21 g/cm^3
Melting point	251 °C
Boiling point	Decomposes at 400 °C
Solubility in water	99.3 g/100 ml
Solubility in ethanol	24.0 g/100 ml

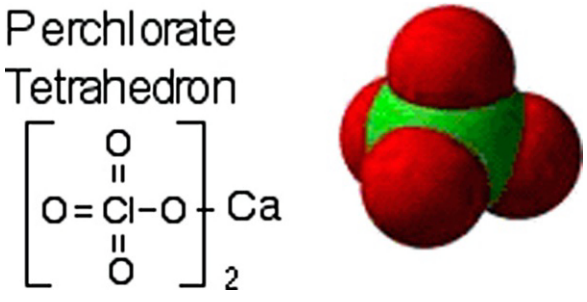

FIGURE 2.37

STRONTIUM PERCHLORATE

Strontium perchlorate has the formula, $Sr(ClO_4)_2$ and a molecular weight of 286.52 g/mol. It is a white solid with a melting point of 100 °C. Its density is 2.073 g/cm^3 and it is lightly soluble in water (3.21 g/100 ml at 20 °C). It can be prepared by reaction of strontium carbonate with a solution of perchloric acid or ammonium perchlorate:

$$SrCO_3 + 2HClO_4 \Rightarrow Sr(ClO_4)_2 + H_2O + CO_2$$

In an aqueous solution, the hexahydrate results. $Sr(ClO_4)_2 \cdot 6H_2O$ has the molecular weight of 394.63 g/mol and a CAS number of 13450-97-0. A trihydrate, $Sr(ClO_4)_2 \cdot 3H_2O$ is also known, having the molecular weight of 340.57 g/mol and a CAS number of 15650-09-6. The features of the solubility polytherm of strontium perchlorate, that distinguish it from those of other Group II metal perchlorates, can be explained in terms of these two coexisting interconverting crystal hydrates. The anhydrate can be formed by careful heating of these hydrates to about 155 °C. But the anhydrate is unstable and is likely to explode due to external shock whereas the hydrates are relatively stable.

Strontium perchlorate can be prepared by an electrolytic method. The electrochemical preparation of strontium perchlorate, $Sr(ClO_4)_2$, from strontium chlorate, employing a platinum anode and a rotating stainless steel cathode, has been studied. The effect of electrolyte concentration, current density, pH and temperature of the electrolyte and cathode rotation on current efficiency for the

preparation of strontium perchlorate was measured. A maximum current efficiency of 42% was achieved corresponding to an energy consumption of 6.1 (kilowatt-hours)./Kg.

The solubility of strontium perchlorate in water is shown in Table 2.98.

Very little physical data is available for this salt, although it has been the subject of a number of research studies. Several hydrates exist, the dihydrate and possible a monohydrate. $3Sr(ClO_4)_2{:}2H_2O$ also exists. Its molecular weight is (anhydrous) 286.52 g/mol.

Currently, no manufacturer is registered for the product **STRONTIUM PERCHLORATE** [13450-97-0]. It is not available commercially.

BARIUM PERCHLORATE

Barium perchlorate has the molecular formula of $Ba(ClO_4)_2$ and the molecular weight of 336.228 g/mol with a density of 3.21 g/cm^3. Its CAS number is 1346595-7. The following lists some of its physical properties:

Melting point: 505 °C	Density: 3.2 g/cm^3 at 25 °C
Flash point: 21 °C	Storage temperature: 2–8 °C
Shock sensitive	Hygroscopic
Appearance: white crystalline powder.	

It may be prepared by reaction of barium carbonate with a solution of perchloric acid or ammonium perchlorate:

$$BaCO_3 + 2HClO_4 \Rightarrow Ba(ClO_4)_2 + H_2O + CO_2$$

In an aqueous solution, several hydrates result as shown in the following Table 2.99.

TABLE 2.98 Solubility of strontium perchlorate

Temperature, °C	Mols $Sr(ClO_4)_2$ per 1000 g of water
0	8.16
5	8.57
10	9.03
15	9.49
20	10.18
25	10.54
30	11.43
35	12.02
40	12.70

The tetrahydrate, $Ba(ClO_4)_2{\cdot}4H_2O$ forms colorless hexagons which are used in pyrotechnics. The trihydrate, $Ba(ClO_4)_2{\cdot}3H_2O$, is hexagonal, space group-$P6_3/m$, $a = 7.277$ Å, $c = 9.656$ Å, $V = 442.9$ Å^3, $Z = 2$. The calculated density is 2.93 g/cm^3. The barium atoms in this structure are coordinated by six water oxygen atoms (O_3) at 2.919 Å and by six perchlorate oxygens (O_2) at 3.026 Å in a slightly distorted icosahedral arrangement. The Cl–O bond length is 1.433 Å and each axial (O_1) perchlorate oxygen is hydrogen bonded to three water molecules.

The thermal decomposition of the anhydrate to barium chloride and oxygen was studied gasometrically at 718 K. The amount decomposed (α) vs t plot for the salt alone displays (i) initial gas evolution, (ii) an induction period, (iii) a short acceleratory stage and (iv) a long-decay stage. The most pronounced features of the (a)-(t) curves are an initial acceleratory period, which is succeeded by an approximately linear period and then, after a sharp break (reduction in rate), by a deceleratory period which conforms to the contracting-volume kinetic law. The latter stage is associated with the decomposition of barium chlorate and has an activation energy of 59 kcal/mol. The first two stages comprise the decomposition:

$$3ClO_4^- \Rightarrow = 2ClO_3^- + C1^- + 3O_2$$

The succeeding reactions all follow this mode of reaction.

The enthalpy of formation of barium perchlorate has been determined to be:

$$\Delta_f H_m^0(BaClO_4, \text{crystal}) = -796.26 \text{ kJ/mol}.$$

Its solubility in water is shown in Table 2.100.

Very little physical data is available for this salt, although it has been the subject of a number of research studies. It is available commercially.

RADIUM PERCHLORATE

No data is available for this salt. It apparently has not been synthesized or studied. Its physical properties remain unknown. It is not available commercially, perhaps due to the radioactivity of radium and the extreme oxidation properties of the perchlorate anion.

2.4. ALKALINE EARTH OXY-BROMINE COMPOUNDS

The alkaline earths form a number of compounds with the oxy-bromine acids, of which there are four.

TABLE 2.99

Name	CAS number	Formula	MW
Barium perchlorate tetrahydrate	15318-52-2	$Ba(ClO_4)_2 \cdot 4H_2O$	408.30 g/mol
Barium perchlorate trihydrate	10294-39-0	$Ba(ClO_4)_2 \cdot 3H_2O$	390.29
Barium perchlorate anhydrous	13465-95-7	$Ba(ClO_4)_2$	336.24

TABLE 2.100

		g/100 ml of water								
Material	Formula	0 °C	10 °C	20 °C	30 °C	40 °C	50 °C	60 °C	80 °C	100 °C
Barium perchlorate	$Ba(ClO_4)_2$	239		336		416		495	575	653

2.4.1. Oxy-Bromine Acids

Hypobromous acid is a weak, unstable acid with the chemical formula HBrO, where the bromine atom is in the +1 oxidation state. It is also called "bromanol" or "hydroxidobromine". It occurs only in solution and has chemical and physical properties that are very similar to those of hypochlorous acid, HClO. In aqueous solution, hypobromous acid only partially dissociates into the hypobromite anion BrO^- and the cation, H^+. The salts of hypobromous acid are called **hypobromites**. Like the acid, these salts are unstable and when evaporated or boiled to dryness, they undergo a disproportionation reaction, yielding the respective bromate and bromide salts.

If bromine is dissolved in water, not only bromide anion (Br^-) is formed, but also the hypobromite anion (OBr^-). This hypobromite anion is responsible for the bleaching abilities of bromine solutions. In warm solutions, the disproportion reaction of the hypobromite is quantitative. The resulting bromate is a strong oxidizing agent and very similar to the chlorate:

$$3BrO^- \Rightarrow BrO_3^- + 2Br^-$$

Very few salts of these alkaline earth compounds have been characterized.

Bromous acid with the formula $HBrO_2$ contains bromine in the +3 oxidation state. The salts of bromous acid are called **bromites**. The acid is not stable and only occurs as an intermediate, for example in the oxidation of hypobromites. If bromine gas is added to an aqueous hydroxide (such as sodium or potassium hydroxide), at 20 °C, the reaction is rapid:

$$Br_2(aq) + 2OH^-(aq) \Rightarrow Br^-(aq) + BrO^-(aq) + H_2O(l)(1)$$

In this reaction, the bromine disproportionates (undergoes both reduction and oxidation) from oxidation state 0 (Br_2) to oxidation state –1 (Br^-) and oxidation state +1 (BrO^-).

Bromous acid can thus be produced by a classical chemical or an electrochemical method in which hypobromite is oxidized to the bromite anion:

$$HBrO + HClO \Rightarrow HBrO_2 + HCl$$

or

$$HBrO + H_2O + e^- \Rightarrow HBrO_2 + H_2$$

Also disproportioning of hypobromous acid will give bromous acid and hydrobromic acid:

$$2HBrO + \text{heat} \Rightarrow HBrO_2 + HBr$$

In addition, a rearrangement reaction of bromic acid and hydrobromic acid will produce bromous acid:

$$2HBrO_3 + HBr \Rightarrow 3HBrO_2$$

Bromic acid or the **bromate** anion, BrO_3^-, is a bromine-based oxoanion where the bromine atom is in the +5 oxidation state. The acid is bromic acid, $HBrO_3$. Examples of bromates include sodium bromate ($NaBrO_3$) and potassium bromate ($KBrO_3$).

Perbromic acid or **perbromate** ion is BrO_4^- and the acid is **perbromic acid**, $HBrO_4$, where the bromine atom is in the +7 oxidation state. A **perbromate** is a compound that contains this group. Perbromic acid is unstable and cannot be formed by displacement of chlorine from perchlorate, as some periodates are prepared.

The acid was discovered when a sample of radioactive selenate, SeO_4^{2-}, was left to decay. It is a strong acid, and strongly oxidizing, and is the least stable of the halogen(-VII) acids. It decomposes rapidly on standing to bromic acid and oxygen, with the evolution of brown bromine vapor. The perbromates are not accessible through electrolysis like the perchlorates, but only by reacting bromate solutions with fluorine or ozone.

2.4.2. Alkaline Earth Hypobromites

Because of the unstable nature of hypobromous acid, only a few of these compounds have been prepared. They are not, in general, offered for sale and only a few scientific studies are available. Their physical properties have not been documented.

Hypobromous acid is a very weak acid and oxidizing agent, unlike the hypochlorites, and has not found extensive usage in Industry or domestically.

Beryllium Hypobromite

This substance, $Be(OBr)_2$, appears to be unknown. This is not surprising in view of the solution behavior of beryllium salts. If bromine vapor or liquid is dissolved in water, hypobromous acid results. If beryllium is present, the cation formed is a aquo-based cation or a hydroxy-based anion and all species remain soluble. The possibility of extracting a compound like $Be(OBr)_2$ and measuring its properties is remote.

Nonetheless, a compound like $Be(OH)^+(OCl)^-$ is possible but has never been reported.

Magnesium Hypobromite

Magnesium hypobromite has the molecular formula of $Mg(BrO)_2$ and the molecular weight of 127.2098 g/mol. When bromine is added to an aqueous hydroxide (such as sodium or potassium hydroxide) at 20 °C the reaction is rapid:

$$Br_2(liq) + 2OH^-(aq) \Rightarrow Br^-(aq) + BrO^-(aq) + H_2O(liq)$$

In this reaction, the bromine disproportionates (undergoes both reduction and oxidation) from oxidation state 0 (Br_2) to oxidation state –1 (Br^-) and oxidation state +1 (BrO^-). However, if the reaction is carried out at 0 °C, the reaction is slow and in the presence of magnesium chloride in solution, the salt $Mg(ClO)_2$ forms. Removing this salt from solution is problematic since a secondary reaction, where hypobromite spontaneously disproportionates to **bromide** (bromine oxidation state –1) and **bromate** (bromine oxidation state +5) takes place rapidly at 20 °C and slowly at <0 °C:

$$3BrO^-(aq) \Rightarrow 2Br^-(aq) + BrO_3^-(aq)$$

Hence, the formation and proportions of the –1, +1 and +5 bromine oxidation state products can be controlled by temperature.

Because of the instability of the hypobromite anion, magnesium hypobromite is always supplied as a solution. Although the pH could be raised by the addition of NaOH or the like, the resulting solution is no more stable than NaClO (which is cheaper and easier to prepare). Thus, although the magnesium salt can be prepared to form a stable solution, the solid form cannot be isolated from solution. This accounts for its limited usage in Industry.

The scientific literature is completely lacking concerning the physical properties of this salt, except for papers published in the late 1880s to 1920s (whose content may not be entirely correct or consistent). Magnesium hypobromite is available commercially in limited quantities.

Calcium Hypobromite

Calcium hypobromite has the molecular formula of $Ca(BrO)_2$ and the molecular weight of 142.9778 g/mol. It can be prepared by the same methods as the magnesium salt, namely—the addition of bromine to a basic solution at a temperature <0 °C:

$$Br_2(liq) + 2OH^-(aq) \Rightarrow Br^-(aq) + BrO^-(aq) + H_2O(liq)$$

If $CaCl_2$ is present, a soluble salt, $Ca(ClO)_2$ results. However, removal of the salt by vacuum evaporation causes a disproportionation reaction in which the bromide and bromate are obtained. Because of this redox reaction, even at 0 °C, calcium hypobromite is always supplied as a solution. The holding container must be carefully sealed since bromine vapor will escape from the solution. Because of this instability, calcium hypobromite has found little usage in Industry. Alkali solutions are more basic than alkaline earth solutions (i.e. NaOH vs $Ca(OH)_2$) and have proven more useful.

A discussion of the physical and chemical properties of this salt is completely lacking in the scientific literature.

Calcium hypobromite is available commercially in limited quantities. However, it is usually prepared in situ as needed at the site of usage.

Strontium Hypobromite

Strontium hypobromite has the molecular formula of $Sr(BrO)_2$ and the molecular weight of 190.5248 g/mol. It may be prepared by the same methods given above for the magnesium or calcium salts.

$$Br_2(liq) + 2OH^-(aq) \Rightarrow Br^-(aq) + BrO^-(aq) + H_2O(liq)$$

If $SrCl_2$ is present, a soluble salt, $Sr(ClO)_2$ results. However, removal of the salt by vacuum evaporation causes a disproportionation reaction in which the bromide and bromate are obtained. Because of this redox reaction, even at 0 °C, strontium hypobromite is always supplied as a solution. The holding container must be carefully sealed since bromine vapor will escape from the solution.

Because of this instability, strontium hypobromite has found little usage in Industry. Alkali solutions are more basic than alkaline earth solutions (i.e. NaOH vs

$Sr(OH)_2$) and have proven more useful. No CAS number is available and this salt is not available commercially.

Barium Hypobromite

Barium hypobromite has the molecular formula of $Ba(BrO)_2$ and the molecular weight of 240.2348 g/mol. It is known only in solution and is prepared by the same methods given for the Mg and Ca salts. $Ba(OH)_2$ is generally used and bromine is added to an aqueous solution thereof:

$$Br_2(liq) + 2Ba(OH)_2\ (aq) \Rightarrow BaBr\ (aq) + Ba(BrO)_2\ (aq) + 2H_2O(liq)$$

However, removal of the salt by vacuum evaporation causes a disproportionation reaction in which the bromide and bromate are always obtained. Because of this redox reaction, even at 0 °C, barium hypobromite is always supplied as a solution or is made in situ as needed.

Barium hypobromite has been used in several research studies to oxidize specific organic molecules to form another type. One example is the conversion of leucine to valeric aldehyde. The reason is that barium compounds like $BaCO_3$ or $Ba(OH)_2$ are much more insoluble than the homologous compounds of the alkaline earths so that they can be removed by filtration from the reaction mixture (Fig. 2.38).

Barium hypobromite is unstable and so is not available commercially.

Radium Hypobromite

Radium hypobromite is expected to possess the molecular formula of $Ra(ClO)_2$ and the molecular weight of 328.9282 g/mol. However, in view of the extreme degree of radioactivity of ^{226}Ra, it is clear that this compound has never been prepared. Whether the compound is stable enough to be prepared in solution remains a conjecture because of cost as well as difficulty in handling. There is no demand or reason to obtain this unstable salt.

It is not available commercially.

2.4.3. Alkaline Earth Bromite Compounds

Beryllium Bromite

Beryllium bromite has the molecular formula of Be(OH)BrO_2 and the molecular weight of 137.9223 g/mol. It can be prepared by a reaction of bromous acid or sodium bromite:

$$Be(OH)_2 + NaBrO_2 \Rightarrow Be(OH)BrO_2 + NaOH$$

The most stable method to produce this salt involved the use of sodium bromate and HBr gas:

$$3Be(OH)_2\ (solid) + 2NaBrO_3\ (aq) + HBr\ (gas) \Rightarrow 3Be(OH)BrO_2\ (aq) + 2NaOH\ (aq) + 4H_2O$$

Nevertheless, there are no reports of the preparation of this salt and any such description of its physical and chemical properties remain a conjecture. It is not offered commercially nor does it have a CAS number.

Magnesium Bromite

Magnesium bromite has the molecular formula of $Mg(BrO_2)_2$ and a molecular weight of 248.1106 g/mol. It can be prepared by a number of means including the disproportionation of hypobromous acid, prepared by dissolving bromine in water:

$$Mg(OH)_2 + 2HBrO \pm heat \Rightarrow Mg(BrO_2)_2$$

However, a by-product of the reaction is likely to be MgBr. The best way to prepare the pure salt, uncontaminated by other forms is to react sodium bromate with HBr gas in solution:

$$3Mg(OH)_2\ (solid) + 2NaBrO_3 + 6HBr\ (gas) \Rightarrow 3Mg(BrO_2)_2\ (aq) + 2NaBr\ (aq)$$

Whether this salt can be isolated from solution remains a mystery since no research papers have appeared describing its physical or chemical properties.

Magnesium bromite is not available commercially nor does it have a CAS number.

Calcium Bromite

Calcium bromite has the molecular formula of $Ca(BrO_2)_2$ and the molecular weight of 263.8836 g/mol. It can be prepared by reacting calcium chloride with sodium bromite:

$$CaCl_2 + NaBrO_2 \Rightarrow Ca(BrO_2)_2 + 2NaCl$$

However, calcium bromite is much less stable than the sodium analogue so that it is used to prepare the sodium salt which is used extensively in Industry to bleach and desize cellulose fabrics like rayon. The main attractive attribute of calcium bromite is that it can be isolated as a solid which is relatively stable and

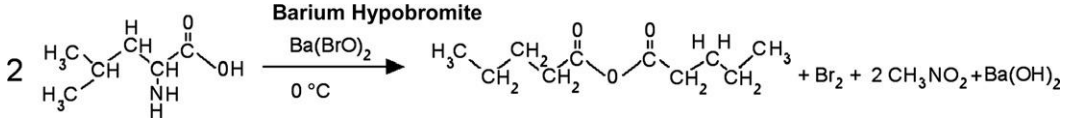

FIGURE 2.38

can be shipped with little fear of decomposition or danger of fire.

One method to produce **solid** calcium bromite has been described as:

> "Calcium hydroxide or "milk of lime" was first added to water in the reaction chamber to form a relatively insoluble hydroxide layer. This bottom layer was cooled to 5 °C, and bromine was added therein while stirring; then milk of lime and bromine were alternately added at controlled feed rates so that the stoichiometric excess of lime relative to the bromine present did not exceed 0.7% by weight of mixture and that, during the addition of bromine, the pH did not fall below 10. After all the milk of lime was introduced into the reaction vessel, the pH of the medium approached 10.05. Bromine was then added very slowly so as to adjust the pH to 9.62. The weight ratio of $Ca(OH)_2$/water in the mixture was 32.5%. The bromite content of the reaction mixture was 64% relative to the total oxidizing power. The mixture was stirred continuously for another 125 min while the temperature was maintained at 5 °C. The bromite yield then reached 71%, and the hypobromite content of the mixture decreased to 9.6%. The solid precipitate is then separated from the mother liquor by filtration and a moist product is obtained having the following composition in percent by weight: $Ca(BrO_2)_2 = 57.5$; $Ca(BrO)_2 = 1.4$; $Ca(BrO_3)_2 = 1.2$; $CaBr_2 = 9.6$ and $Ca(OH)_2 = 1.8$. If a substantially pure salt is desired, the washed product is dissolved in alkaline water, and the bromite is recrystallized by evaporation and cooling. There obtained is a crystalline calcium bromite with 3.0 mols of water $Ca(BrO_2)_2 \cdot 3H_2O$ substantially free from calcium hypobromite and bromide and containing only 0.2% of 30 calcium bromate. The composition of this salt after 165 h in a closed bottle away from light at a temperature of 35 °C was practically unchanged. Calcium bromite, as with all other bromites prepared heretofore, is an excellent oxidizing agent in alkaline media".

In a patent issued in 1963, a method of preparing alkaline earth bromites, particularly calcium bromite, was published. The method consisted of the steps shown in the following diagram (Fig. 2.39) and was applicable to all types of bromite salts.

Nonetheless, this salt has not been characterized extensively and most of the available data was generated in the early work by investigators in the 1890s to 1910s. Calcium bromite does not have a CAS number but is not available commercially. It is usually made "in situ" as needed.

Strontium Bromite

Strontium bromite has the molecular formula of $Sr(BrO_2)_2$ and the molecular weight of 311.4256 g/mol. Only the dihydrate is known but there may be others. This salt has not been the subject of any research and only a few patents mention it. No papers can be found in the open literature.

Alkaline earth bromites such as strontium bromite can be produced by various processes as described below:

$$3Sr(OH)_2\ (\text{solid}) + 2NaBrO_3 + 6HBr\ (\text{gas}) \Rightarrow 3Sr(BrO_2)_2\ (\text{aq}) + 2NaBr\ (\text{aq})$$

Before isolation of the pure solid crystalline strontium bromite, a solid composition of matter is obtained containing a major proportion of the crystalline strontium bromite, together with impurities such as the hypobromite or bromide, or bromate or hydroxide or carbonate

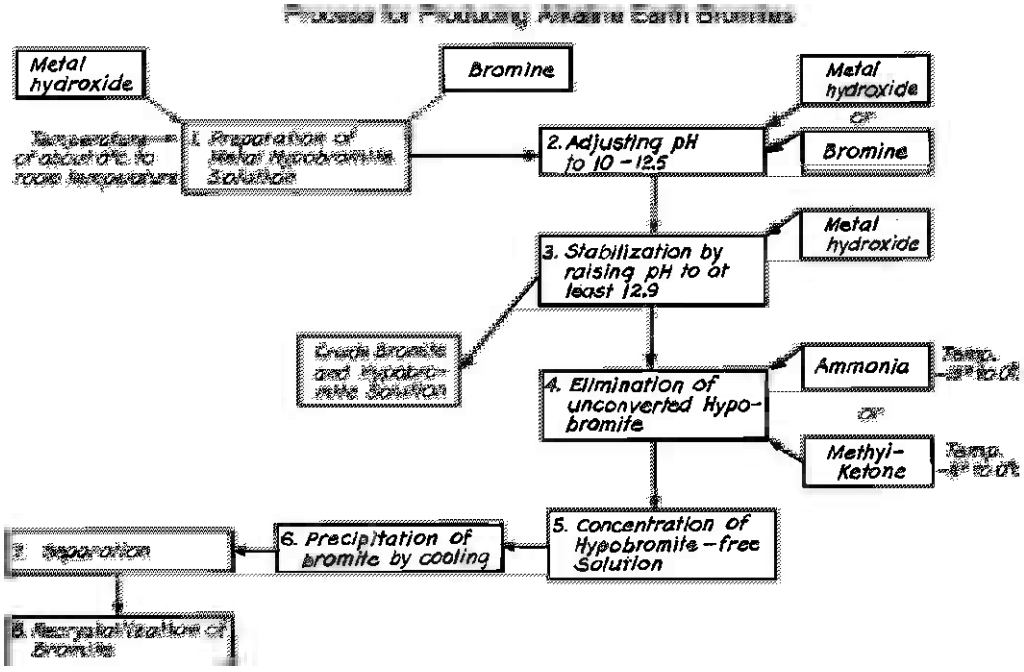

FIGURE 2.39

and mixtures thereof, of the respective alkaline earth metal. The pure solid crystalline strontium bromite is $Sr(BrO_2)_2 \cdot 2H_2O$. This bromite is definitely identifiable under X-ray examination wherein *d*-values are available.

Strontium bromite is a surprisingly stable compound in the solid state, thus being particularly suitable for relatively inexpensive transportation. For example, strontium bromite crystals have been heated to 58 °C under reduced pressure for about 3 h without noticeable decomposition. When heated to 80 °C under reduced pressure for 3 h, about 40% of the initially present bromite is decomposed. The composition of the crystallized solid held under vacuum at 0 °C remains practically unchanged for 6 months and longer.

It has further been found that a saturated solution of strontium bromite containing about 80 g of active bromine per liter, remains unchanged when exposed to daylight at room temperature for at least 3 months. Strontium bromites is an excellent starting materials for the preparation of the alkali metal bromites by cation exchange reaction, for instance, with sodium carbonate. The resultant sodium bromite can then be advantageously employed as a desizing agent in textile operations.

It is also to be noted that strontium bromites are also useful as oxidizing agents, in general, and are particularly advantageous because of their relative stability under atmospheric conditions.

The impure solid can be purified by dissolving it in water at about 0 °C in order to obtain an aqueous solution saturated in strontium bromite, which is then concentrated at ambient temperature (20–25 °C). The precipitate so formed is filtered, washed with an aqueous solution saturated in strontium hydroxide, and dried. There is obtained pale yellow crystals of substantially pure strontium bromite containing 99.2% of $Sr(BrO_2)_2$–$2H_2O$. The solid strontium bromite is a stable compound, its decomposition begins when heated at about 80 °C. By heating at 81 °C during 3 h, about 3% of the initially present strontium bromite is decomposed.

For numerous industrial uses (for instance as oxidizing agent), it is not necessary to dispose of substantially pure strontium bromite. In this case, the impure solid obtained after evaporation of water and containing 37.8% of $Sr(BrO_2)_2$ is merely washed with 0.10 N strontium hydroxide as an aqueous solution at a temperature of about 0 °C, the quantity of washing solution being about 40% by weight of the solid to be treated. After washing and drying, a product is obtained with a higher content of strontium bromite.

In spite of the stability of strontium bromite as a solid, little research has occurred concerning its physical or chemical properties as an oxidizing agent.

This salt has no CAS number nor is it offered for sale commercially.

Barium Bromite

Barium bromite has the molecular formula of $Ba(BrO_2)_2$ and the molecular weight of 361.1356 g/mol. Only the dihydrate is known but there may be others. This salt has not been the subject of any research and only a few patents mention it. No papers can be found in the open literature. Like its strontium analogue, barium bromite can be prepared as a stable compound and so has found favor in Industry for preparing sodium bromite in situ for use as a bleaching process for rayon fibers. Barium bromite has the added advantage, unlike the strontium salt, of being able to remove all traces of Ba^{2+} ions by forming $BaSO_4$ and washing it out of the fabric or plastic rayon fibers. In order to obtain a pure solid, devoid of other forms of soluble oxy-bromine components, it is necessary to form the barium bromite (which contains a significant amount of unstable bromite compounds such as hypobromite or bromide, or bromate or hydroxide or carbonate and mixtures thereof, of the respective alkaline earth metal:

$$BaCl_2 + NaBrO_2 \Rightarrow Ba(BrO_2)_2 + 2NaCl$$

Barium bromite forms as a solid which is removed by filtration and then resuspended in water to recrystallize it. The pure solid crystalline barium bromite is $Ba(BrO_2)_2 \cdot H_2O$, and can be identified by X-ray powder patterns.

Barium and strontium bromites are surprisingly stable compounds in the solid state, with the barium compound being the most stable. Thus, it is very suitable for relatively inexpensive transportation since the oxidation properties are suppressed. For example, barium bromite crystals have been heated to 58 °C under reduced pressure for about 3 h without noticeable decomposition. When heated to 80 °C under reduced pressure for 3 h, about 40% of the initially present bromite is decomposed. The composition of the crystallized solid held under vacuum at 0 °C remains practically unchanged for 6 months and longer.

It has further been found that a saturated solution of barium bromite containing about 130 g of active bromine per liter, remains unchanged when exposed to daylight at room temperature for at least 3 months.

Both barium and strontium bromites are excellent starting materials for the preparation of the alkali metal bromites by cation exchange reaction, for instance, with sodium carbonate. The resultant sodium bromite can then be advantageously employed as a desizing agent in textile operations.

The moist solid mass can be recrystallized directly without washing, by adding water to obtain a solution saturated in barium bromite at 0 °C. The soluble barium bromate is eliminated by filtration. By slow evaporation

of water at about 30 °C under reduced pressure (15–20 Torr), and after separation of the crystals from the solution by decantation or filtration and subsequent washing with an aqueous saturated barium bromite solution, there is obtained a practically pure barium bromite of the following composition:

$$Ba(BrO_2)_2 \cdot H_2O = 98.1\%$$

$$Ba(BrO_3)_2 \cdot H_2O = 1.0\%$$

$$BaBr_2 = \text{Traces}$$

It is also to be noted that barium bromite is also useful as an oxidizing agent, in general, and is particularly advantageous because of its relative stability under atmospheric conditions. In spite of this, barium bromite has found little usage in Industry since the bromates are more stable and easier to prepare.

Radium Bromite

Radium bromite has the molecular formula of $Ra(BrO_2)_2$ and the molecular weight of 449.8311 g/mol. In view of the intense radioactivity of ^{226}Ra, there has been little incentive to prepare this salt. It can be prepared by the same methods used for its barium homologue, namely:

$$RaCl_2 + NaBrO_2 \Rightarrow Ra(BrO_2)_2 + 2NaCl$$

According to one literature source, radium bromite (also known as "Radium-Bromatum") has been used to treat mange-spots on dogs. The reason to use a radioactive chemical is not known except that radium bromite is both radioactive and oxidative. Radium bromite is not available commercially and does not have a CAS number.

2.4.4. Alkaline Earth Bromate Compounds

Beryllium Bromate

Beryllium bromate has the molecular formula of $Be(OH)BrO_3$ and the molecular weight of 153.9217 g/mol. It can be prepared by a reaction of bromic acid or sodium bromate:

$$Be(OH)_2 + NaBrO_3 \Rightarrow Be(OH)BrO_3 + NaOH$$

The most stable method to produce this salt involved the use of sodium bromate and HBr gas:

$$3Be(OH)_2\ (\text{solid}) + 2NaBrO_3\ (aq) + HBr\ (\text{gas}) \Rightarrow 3Be(OH)BrO_3\ (aq) + 2NaOH\ (aq) + 4H_2O$$

Nevertheless, there are no reports of the preparation of this salt in the technical literature and any such description of its physical and chemical properties remains a conjecture. It is not offered commercially nor does it have a CAS number

Magnesium Bromate

Magnesium bromate has the molecular formula of $Mg(BrO_3)_2$ and the molecular weight of 280.1094 g/mol. It has the CAS number of 14519-17-6. It can be prepared by the reaction of bromic acid and magnesium carbonate:

$$MgCO_3 + 2HBrO_3 \Rightarrow Mg(BrO_3)_2 + CO_2 + H_2O$$

However, magnesium bromate is not stable in an acidic environment and tends to decompose if one attempts to remove it from solution. Thus, the best method of preparation involves the use of sodium bromate which is basic enough to prevent such decomposition in solution:

$$Mg(OH)_2 + 2NaBrO_3 \Rightarrow Mg(BrO_3)_2 + 2NaOH$$

The product is a hexahydrate, $Mg(BrO_3)_2 \cdot 6H_2O$ whose molecular weight is 388.201 g/mol. This salt is soluble in water (58.2 g/100 ml) and must be recrystallized by vacuum evaporation at 15–20 °C in order to obtain a crystalline solid (which is the stable form). This salt can also be prepared by adding a solution of magnesium sulfate to a suspension of barium bromate:

$$MgSO_4\ (aq) + Ba(BrO_3)_2\ (s) \Rightarrow Mg(BrO_3)_2\ (aq) + BaSO_4\ (s)$$

The solution is then evaporated to recrystallize the hexahydrate, $Mg(BrO_3)_2 \cdot 6H_2O$.

These occur as large, colorless, octahedral crystals which melt in their own waters of hydration. It loses the water molecule above 60 °C and decomposes when heated to a higher temperature, forming MgO and bromine.

Magnesium bromate hexahydrate is a white crystalline compound that is insoluble in alcohol, but soluble in water. It reacts with methyl alcohol to form a complex. It is a fire hazard but is used as an analytical reagent. Its CAS number is 7789-36-8 and its density is 2.29 g/cm^3. On heating to 50–60 °C, magnesium bromate first decomposes to form the dihydrate. It loses the other two waters of hydration at 105 °C. The anhydrate then decomposes at 200 °C and forms the oxide plus bromine and oxygen:

$$2Mg(BrO_3)_2 + \text{heat} \Rightarrow 2MgO + 2Br_2 + 5O_2$$

This mechanism differs from that of the other alkaline earth bromates which decompose to form the bromide plus oxygen. Its water solubility is shown in Table 2.101.

Magnesium bromate has found little usage in Industry because there are better oxidizing agents available. It is offered for sale commercially but in limited quantities.

Calcium Bromate

Calcium bromate has the molecular formula of $Ca(BrO_3)_2$ and the molecular weight of 295.8824 g/mol.

TABLE 2.101

		g/100 ml of water							
Material	**Formula**	**0 °C**	**10 °C**	**20 °C**	**30 °C**	**50 °C**	**65 °C**	**75 °C**	**81 °C**
Magnesium bromate	$Mg(BrO_3)_2 \cdot 6H_2O$	42.3	45.6	48.7	51.4	57.3	62.5	66.8	70.1

Its CAS number is 5743-36-2 and it is soluble in water (125 g/100 ml at 20 °C). It may be prepared by reacting calcium hydroxide with sodium bromate or by reacting calcium sulfate with barium bromate:

$$Ca(OH)_2 + 2NaBrO_3 \Rightarrow Ca(BrO_3)_2 + 2NaOH$$

$$CaSO_4\ (aq) + Ba(BrO_3)_2\ (solid) \Rightarrow Ca(BrO_3)_2\ (aq) + BaSO_4\ (solid)$$

Of the two methods, the latter seems to be more stable one since the temperature can be as high as 80 °C in solution. The usual product is a monohydrate, $Ca(BrO_3)_2 \cdot H_2O$; F.W.: 313.90 g/mol; CAS number: 10102-75-7.

Calcium bromate monohydrate occurs as colorless, monoclinic crystals or prismatic plates which are soluble in water. This salt loses its water below 180 °C and decomposes above that temperature to form calcium bromide plus oxygen.

The solubility of calcium bromate monohydrate in water from −20 to +100 °C has been determined. Its solubility in water is: 230 g/100 ml at 20 °C and 181.3 g/100 ml at 80 °C. Differential thermal analysis (DTA) indicates a loss of water at 130–150 °C and decomposition to calcium bromide at 270–300 °C. In contact with acids such as HCl or HNO_3, the bromate decomposes forming HBr as a gas.

A proton magnetic resonance spectrum of calcium bromate monohydrate showed that there are two orientations of the water molecule in the crystal. The *p–p* distances are 1.58 ± 0.02 and 1.59 ± 0.02 Å, respectively. Their orientations with respect to the crystallographic axes were measured as functions of orientation at room temperature and of temperature in a single crystal of calcium bromate monohydrate. The *b* crystallographic axis was the axis of rotation of the crystal. The proton-resonance relaxation time was essentially independent of orientation of the crystal in the external magnetic field. The temperature dependence was characteristic of 180° flipping motion of the H_2O molecule whose activation energy was 6.7 ± 0.4 kcal/mol. The H_2O molecules were determined to be hydrogen bonded to the O(5) and O(2) atoms in the crystal.

Calcium bromate is used as a maturing agent and dough conditioner in bromated flours. However, it is relatively expensive at $252 for 5 kg. About 75 ppm is used as a bromating agent which costs about $20/100 lb of flour.

Other than this usage, this salt is not utilized in Industry. It is available commercially.

Strontium Bromate

Strontium bromate has the chemical formula of $Sr(BrO_3)_2$ and the molecular weight of 343.4244 g/mol. Its CAS number is 10102-75-7. It can be prepared by reacting strontium hydroxide with sodium bromate or by reacting strontium sulfate with barium bromate:

$$Sr(OH)_2 + 2NaBrO_3 \Rightarrow Sr(BrO_3)_2 + 2NaOH$$

$$SrSO_4\ (aq) + Ba(BrO_3)_2\ (solid) \Rightarrow Sr(BrO_3)_2\ (aq) + BaSO_4\ (solid)$$

Of the two methods, the latter seems to be more stable since the temperature can be as high as 80 °C in solution. The usual product is a monohydrate, $Sr(BrO_3)_2 \cdot H_2O$; F.W.: −361.4397 g/mol; CAS number: 14519-18-7. Strontium bromate is about 40 times more soluble in water than barium bromate. The increased solubility plus the greater stability of the barium compound allows the formation of the strontium bromate-monohydrate to be recrystallized easily. The monohydrate decomposes at 76 °C to form the anhydrate.

$Sr(BrO_3) \cdot H_2O$ occurs as small, colorless but lustrous, monoclinic crystals which are prismatic in nature. It is somewhat soluble in water and loses its water of hydration if heated to about 110 °C. It decomposes at 240 °C forming strontium bromide and oxygen.

Chemically this salt is soluble in water (30.9 g/100 ml at 20 °C), and is a moderately strong oxidizing agent. It is also toxic if ingested and irritates the skin and respiratory tract if come into contact with or inhaled, respectively.

The crystal structures of the isostructural halates $Sr(BrO_3)_2 \cdot H_2O$, $Ba(BrO_3)_2 \cdot H_2O$, $Ba(IO_3)_2 \cdot H_2O$, $Pb(ClO_3)_2 \cdot H_2O$, and $Pb(BrO_3)_2 \cdot H_2O$ were determined using X-ray single-crystal data (monoclinic space group $C2/cC$, $Z = 4$). The mean bond lengths and bond angles of the halate ions in the $Ba(ClO_3)_2 \cdot 1H_2O$-type compounds, which correspond to those of other halates, are ClO, 149.0, BrO, 165.9, IO, 180.2 pm, ClO_3^-, 106.4, BrO_3^-, 104.0, and IO_3^-, 99.6°. The structure data obtained were discussed in terms of possible orientation disorder of the water molecules, strengths of the hydrogen bonds, influence of the lead ions on the structure, and site group distortion of the halate ions.

Strontium bromate is rarely used in the laboratory or in Industry. It is available commercially but in limited quantities.

Barium Bromate

Barium bromate has the molecular formula of $Ba(BrO_3)_2$ and the molecular weight of 393.1344 g/mol. It may be prepared by reaction of the hydroxide with sodium bromate:

$$Ba(OH)_2 + 2NaBrO_3 \Rightarrow Ba(BrO_3)_2 + 2NaOH$$

Barium bromate is relatively insoluble, and has a value of 0.782 g/100 ml of water at 298 K; its enthalpy of solution is +54 kJ/mol and the solubility product is 2.43×10^{-4}. If recrystallized, it forms a monohydrate, $Ba(BrO_3)_2 \cdot H_2O$, which occurs as white or colorless, prismatic crystals. Its solubility in hot water increases but it is decomposed by strong acids, forming HBr and the corresponding salt:

$$Ba(BrO_3)_2 + 2HCl \Rightarrow 2HBr + BaCl_2 + 3O_2$$

$Ba(BrO_3)_2 \cdot H_2O$ loses its water of hydration at about 190 °C and decomposes to the bromide at 265 °C, forming the bromide plus oxygen:

$$Ba(BrO_3)_2 \cdot H_2O + \text{heat} \Rightarrow BaBr_2 + H_2O + 3O_2$$

A new and general method of inducing a precipitation from homogeneous solution has been applied to the separation of barium and strontium. The precipitation of barium bromate, a water-soluble compound, is brought about by a gradual change in the composition of the solvent media. An organic compound, such as methanol or tetrahydrofuran, is allowed to diffuse into the original water solution, thus slowly converting the solution into a water–organic mixture. Strontium bromate is about 40 times more soluble in water than barium bromate. The increased solubility plus the greater stability of the strontium MEDTA chelate tend to hold the strontium in solution. The chief advantage of this method over the separation of Sr from Ba by precipitation of barium chromate is in the preparation of barium compounds. Usually, barium must be separated from the chromate before proceeding. However, barium bromate can be easily converted to the oxide, eliminating this separation step.

Barium bromate-monohydrate has a molecular weight of 411.1734 g/mol and is monoclinic in structure with a space group of I2/c, $a = 9.0696$ Å, $b = 7.8952$ Å, $c = 9.695$ Å, $\beta = 93.26°$, $V = 688.4$ Å^3, $Z = 4$. Each Ba atom has 11 oxygen neighbors at 2.702 Å – 3.057 Å. The average bond length is 1.652 Å and the O…O bond length is 2.832 Å in a hydrogen bond.

The results of proton magnetic resonance absorption spectrum of barium bromate monohydrate indicate that there is only one orientation of the water molecule in the crystal. The p–p distance is 1.61 ± 0.01 Å and direction angles of the p–p vector are $\alpha_0 = 30°$, $\beta_0 = 95°$, and $\gamma_0 = 122°$.

Barium bromate is used extensively to form other bromates, including the alkali metal bromates which are used extensively in Industry. $HBrO_3$, a colorless liquid, is made by the addition of dilute sulfuric acid to barium bromate. It dissociates extensively in aqueous solution and is a strong acid.

The solubility of barium bromate-monohydrate is shown in Table 2.102.

The scientific literature contains a few studies of barium bromate chiefly due to interest in Industry for its use to prepare other bromate salts.

This salt is available commercially, worldwide.

Radium Bromate

Radium bromate would have the molecular formula $Ra(BrO_3)_2$ and the molecular weight of g/mol. There is no report for the preparation of radium bromate. Perhaps this is due to the fact that the thermodynamic data for the bromates of the other alkaline earths are incomplete. This salt could be prepared by the reaction of sodium bromate and radium chloride:

$$RaCl_2 + 2NaBrO_3 \Rightarrow Ra(BrO_3)_2 + 2NaCl$$

In view of the extreme degree of radioactivity of ^{226}Ra, there is no industrial or commercial demand for this salt and it has no CAS number.

2.4.5. Alkaline Earth Perbromates

Beryllium Perbromate

Beryllium perbromate has the molecular formula of $BeOHBrO_4$ and the molecular weight of grams per mole. This salt can be prepared by the reaction of sodium perbromate and the hydroxide salt in aqueous solution:

$$Be(OH)_2 + NaBrO_4 \Rightarrow BeOHBrO_4 + NaOH$$

TABLE 2.102

		g/100 ml of water									
Material	**Formula**	**0 °C**	**10 °C**	**20 °C**	**30 °C**	**40 °C**	**50 °C**	**60 °C**	**80 °C**	**90 °C**	**100 °C**
Barium bromate monohydrate	$Ba(BrO_3)_2H_2O$	0.29	0.44	0.65	0.95	1.31	1.75	2.27	3.65	4.45	5.71

A description of the preparation and properties of this salt is completely lacking in the literature. Whether an attempt to prepare such a salt has been accomplished remains a mystery.

It has no CAS number and it is not offered for sale commercially.

Magnesium Perbromate

Magnesium perbromate has the molecular formula of $Mg(BrO_4)_2$ and the molecular weight of gm/mol. This salt can be prepared by the reaction of sodium perbromate and the chloride salt in aqueous solution:

$$MgCl_2 + 2NaBrO_4 \Rightarrow Mg(BrO_4)_2 + 2NaCl$$

The solution is then evaporated slowly under partial pressure to produce the hexahydrate, $Mg(BrO_4)_2 \cdot 6H_2O$. Little is known concerning this salt. The physical parameters describing this salt have not been documented. Presumably, $Mg(BrO_4)_2 \cdot 6H_2O$ loses its six waters sequentially below about 240 °C where it decomposes at 250 °C to form $MgBr_2$ plus oxygen. It may form the oxide, MgO plus bromine and oxygen but this has not been the subject of a research investigation.

$Mg(BrO_4)_2 \cdot 6H_2O$ is not used in Industry but it is mentioned in a few patents concerning a Ziegler–Natta catalyst and part of a gas-generating mixture for automotive air bags. Whether this compound has ever been used commercially remains unknown. It does not have a CAS number and is not offered for sale commercially.

Calcium Perbromate

Calcium perbromate has the molecular formula of $Ca(BrO_4)_2$ and the molecular weight of gm/mol. It can be prepared by the reaction of sodium perbromate and the chloride salt in aqueous solution:

$$CaCl_2 + 2NaBrO_4 \Rightarrow Ca(BrO_4)_2 + 2NaCl$$

The solution is then evaporated slowly under partial pressure to produce the tetrahydrate, $Ca(BrO_4)_2 \cdot 4H_2O$. This salt is very slightly soluble in water and is not as stable as the barium salt. Therefore, it is recrystallized from solution and stored under dry conditions.

The structure of calcium perbromate is similar to other perbromates. There are columns of Ca^{2+} cations surrounded by four columns of perbromate anions and four columns of water molecules. The eight coordinating O atoms in the CaO_8 complex form a polyhedron of a square antiprism. In this complex, Ca is coordinated by four water molecule oxygens at 2.37 Å and four anion O atoms at 2.57 Å.

The literature of calcium perbromate is sparse. A comprehensive description of physical, as well as chemical, properties of this salt is lacking in the technical literature or reference books.

This salt is not used in Industry and does not have a CAS number.

Strontium Perbromate

Strontium perbromate has the molecular formula of $Sr(BrO_4)_2$ and the molecular weight of gm/mol. It can be prepared by the reaction of sodium perbromate and the chloride salt in aqueous solution:

$$SrCl_2 + 2NaBrO_4 \Rightarrow Sr(BrO_4)_2 + 2NaCl$$

The solution is then evaporated slowly under partial pressure to produce the trihydrate, $Sr(BrO_4)_2 \cdot 3H_2O$. Its structure is very likely like that of its barium homologue and is hexagonal in structure. However, the specific lattice parameters have not been documented in the open literature.

Very little data concerning the physical properties of this salt exist. It too is mentioned in a few patents concerning catalytic converters for automobiles. Strontium perbromate does not have a CAS number and is not offered for sale commercially.

Barium Perbromate

Barium perbromate has the molecular formula of $Ba(BrO_4)_2$ and the molecular weight of gm/mol. It can be prepared by the reaction of sodium perbromate and the chloride salt in aqueous solution:

$$BaCl_2 + 2NaBrO_4 \Rightarrow Ba(BrO_4)_2 + 2NaCl$$

The solution is then evaporated slowly under partial pressure to produce the trihydrate, $Ba(BrO_4)_2 \cdot 3H_2O$. It is very slightly soluble even in boiling water. This salt has a molecular weight of 479.1926 g/mol and is hexagonal in structure. Lattice parameters include: $a = 7.414$ Å, $c = 9.965$ Å, $V = 474.4$ Å^3, $Z = 2$ and density $= 3.35$ g/cm^3 (Fig. 2.40).

The Ba atoms in this structure are coordinated by 12 oxygen atoms in a near-icosahedral arrangement, with an average Ba–O bond length of 2.987 Å. The perbromate ion has regular tetrahedral symmetry and an average Br–O bond length of 1.608 Å. Each perbromate

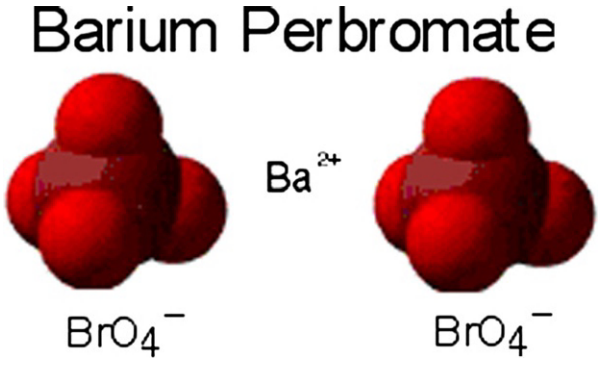

FIGURE 2.40

ion in the structure is hydrogen bonded to three water molecules.

This salt has been the subject of a few research papers but has no CAS number. It is not offered for sale commercially.

Radium Perbromate

Radium perbromate is expected to have the molecular formula of $Ra(BrO_4)_2$ and the molecular weight of gm/mol. This salt can be prepared by the reaction of sodium perbromate and the chloride salt in aqueous solution:

$$RaCl_2 + 2NaBrO_4 \Rightarrow Ra(BrO_4)_2 + 2NaCl$$

The solution is then evaporated slowly under partial pressure to produce the trihydrate, $Ra(BrO_4)_2\ 3H_2O$. It is expected to be very slightly soluble even in boiling water. However, there is no description of its physical or chemical properties in the technical literature. It has no CAS number and is not offered for sale commercially.

2.5. ALKALINE EARTH METALS OXY-IODINE COMPOUNDS

The alkaline earths all form oxy-iodine compounds of assorted compositions. These are based upon the oxy-acids of iodine.

2.5.1. Oxy-Iodine Acids

Iodous acid, HIO_2, with the iodine atom in the +3 oxidation state apparently does not exist. Thus, alkaline earth "Iodites" cannot exist (Neither do "hypo-iodites" or "per-iodites").

Iodic acid, HIO_3, can be obtained as a white solid. It dissolves in water very well, but it also exists in the pure state, as opposed to chloric acid or bromic acid. Iodic acid contains iodine in the oxidation state +5 and it is one of the most stable oxo-acids of the halogens in its pure state. When iodic acid is carefully heated, it dehydrates to iodine pentoxide. On subsequent heating, the iodine pentoxide further decomposes, giving a mixture of iodine, oxygen and lower oxides of iodine.

Iodic acid is a relatively strong acid with a pK_a of 0.75. It is strongly oxidizing in acidic solution, less so in basic solution. When iodic acid acts as oxidizer, then the product of the reaction is either iodine, or iodide ion. Under some special conditions (very low pH and high concentration of chloride ion, e.g. in concentrated hydrochloric acid), iodic acid is reduced to iodine trichloride, a golden yellow compound in solution and no further reduction occurs. In the absence of chloride ions, when there is an excess amount of reducing agent, then all iodate is converted to iodide ion. When there is an excess amount of iodate, then only part of the iodate is converted to iodine.

Iodic acid can be produced by oxidizing I_2 with chlorine in an aqueous solution. Iodic acid can be used to synthesize sodium or potassium iodate salts (which are used in salt as a source of iodine in the human body.

Periodic acid, or **iodic(VII) acid is** an oxoacid of iodine having a chemical formula HIO_4 or H_5IO_6. In dilute solution, periodic acid exists as H^+ and IO_4^-. When more concentrated, **orthoperiodic acid**, H_5IO_6, is formed. Note that this compound is essentially a dihydrate, $HIO_4 \cdot 2H_2O$. This can be obtained as a crystalline solid. O-periodic acid can be dehydrated to **metaperiodic acid**, m-HIO_4. Further heating gives di-iodine pentoxide (I_2O_5) and O_2. The anhydride *di-iodine heptoxide*, i.e. I_2O_7, does not exist in nature but can be formed synthetically.

Thus, two forms of periodates exist. One relating to the acid m-HIO_4, the other relating to o-H_5IO_6. The former results in metaperiodates (meta—meaning less water) and the latter, orthoperiodates (ortho—meaning more water). Metaperiodates have solubilities and chemical properties similar to perchlorates (similar but larger ion size) though they are less oxidizing than perchlorates. The reason that these homologues are cited refers to their behavior when dissolved in water:

$$HIO_4(\text{solid}) \Rightarrow H^+ + IO_4^-$$

$$H_5IO_6(\text{solid}) \Rightarrow H^+ + H_4IO_6^-$$

Thus, two differing anions form in aqueous solution. These act chemically in a similar manner even though the anionic complex differs. A probable structure for the O-periodate anion is shown in Fig. 2.41.

In this anion, the iodine atom remains in the +7 oxidation state but the complex is not a "dihydrate" but is similar to its tellurium analogue in alkali tellurates.

Periodic acid is also used in organic chemistry for structural analysis. Periodic acid will cleave a vicinal

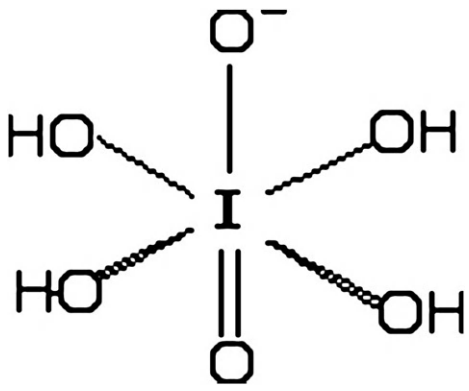

FIGURE 2.41

diol into two aldehyde fragments. This can be useful in determining the structure of carbohydrates.

2.5.2. Alkaline Earth Iodates

Beryllium Iodate

Beryllium iodate is expected to have the molecular formula, $Be(IO_3)_2$ and the molecular weight of 374.1104 g/mol. In view of the hydrolysis of the Be^{2+} cation in other compounds prepared in aqueous solution, the composition is expected to be $Be(OH)IO_3$. However, beryllium forms a complex iodate in solution which has been characterized by X-ray analysis as $Be(IO_3)_2 \cdot 2HIO_3$ It can be prepared by reaction of iodic acid and beryllium hydroxide:

$$Be(OH)_2 + 3HIO_3 \Rightarrow Be(IO_3)_2 \cdot 2HIO_3 + H_2O$$

The product is expected to be relatively insoluble like the other alkaline earth iodates. The compound $Be(IO_3)_2 \cdot 2HIO_3 \cdot 6H_2O$ has been identified by quantitative analysis, IR spectra and X-ray diffraction analysis. On the basis of the absorption bands in the IR spectra of the compound and its partially deuterated analogue, the basic structural units making up the compound were shown to be $Be(H_2O)_4(IO_3)_2 \cdot 2HIO_3 \cdot 2H_2O$, as well as the existence of two kinds of nonequivalent water molecules (whether this is actually the compound, $Be(OH)_4(IO_3)_2 \cdot 2HIO_3 \cdot 2H_2O$, i.e. the OH-radical or an actual water molecule coordinated to the Be atom in the structure, remains a conjecture). Nonetheless, it is this compound which results if HIO_3 is in excess, i.e. the $Be(OH)_2$ is added to the acid. If HIO_3 is added to the $Be(OH)_2$ slurry, then the "normal" salt results:

$$Be(OH)_2 + 2HIO_3 \Rightarrow Be(IO_3)_2 \cdot 8H_2O + H_2O$$

The thermal decomposition of $Be(IO_3)_2 \cdot 2HIO_3 \cdot 6H_2O$ was studied by means of DTA and DSC methods. The important phase transitions were determined to involve $Be(IO_3)_2 \cdot I_2O_5$ that was isolated and identified as an intermediate.

The thermal decompositions of two beryllium periodate hydrates, $Be(IO_4)_2 \cdot 8H_2O$ and $Be(H_4IO_6)_2 \cdot 2H_2O$, were studied by DTA and TGA in the temperature range from 298 to 1073 K, and by DSC from 298 to 723 K. The intermediates of the thermal decompositions were identified via quantitative analysis, IR spectroscopy and the TG curves. The data obtained to show that the two periodates decompose via an anhydrous beryllium iodate, and the final residue is beryllium oxide. This is the mechanism expected for this type of iodate.

Beryllium iodate has found little usage in Industry but has been available commercially in limited quantities. Perhaps, this is due to the toxicity of beryllium in general.

Magnesium Iodate

Magnesium iodate has the molecular formula, $Mg(IO_3)_2$ and the molecular weight of 374.1104 g/mol. It can be prepared by reaction of iodic acid and magnesium hydroxide:

$$Mg(OH)_2 + 2HIO_3 \Rightarrow Mg(IO_3)_2 + H_2O$$

A tetrahydrate results that is relatively insoluble.

This salt has the CAS number 7790-32-1 and a molecular weight of 446.1715 g/mol. It is soluble in water as shown in Table 2.103.

Magnesium iodate tetrahydrate occurs as well-defined monoclinic crystals of high luster. It is easily soluble in sulfuric acid. When heated, it loses two waters of hydration at 510 °C and the other two at 620 °C. The anhydrate is stable to 680 °C where it decomposes into MgO, iodine and oxygen:

$$Mg(IO_3)_2 + \text{heat (580 °C)} \Rightarrow MgO + I_2 + 3O_2$$

The phase transitions of $Mg(IO_3)_2 \cdot 4H_2O$ crystals occurring in the heating process have been investigated by means of thermal analyses and X-ray diffraction at high room temperature. There are two phases observed on heating or cooling, a high temperature one, β-$Mg(IO_3)_2$ and a low-temperature one, α-$Mg(IO_3)_2$. The crystal structure of β-$Mg(IO_3)_2 \cdot 4H_2O$ has been determined by means of the method of single-crystal diffraction, it has been found that the space group of $Mg(IO_3)_2 \cdot 4H_2O$ is P2 or Pm. There are two formula units per unit cell. Lattice parameters are: $a = 8.307$ Å, $b = 6.627$ Å, $c = 8.541°$, $\beta = 100.5°$. The crystal structure of α-$Mg(IO_3)_2$ has been determined by X-ray powder method. The unit cell of α-$Mg(IO_3)_2$ is hexagonal, with $a = 5.4777$ Å, $c = 5.1282$ Å, $c/a = 0.9362$ at 14 Å. There is one formula unit per unit cell. The space group is $P6_3$. 6-0^{II} are situated at the 6(c) positions, 2-I^{V} are situated at 2(b) positions, and Mg^{+2} ion is disorderly distributed at half of 2(a) positions. The atomic parameters found to be $X_c = 0.096$, $Y_c = 0.344$, $Z_c = 0.162$, $Z_b = 0$, $Z_a = 0.981$. The crystal structure of α-$Mg(IO_3)_2$ is isomorphic with α-$LiIO_3$. α-$Mg(IO_3)_2$ is different from α-$LiIO_3$ only in that the Mg^{++}-ion is disorderly distributed at one-half of 2(a) positions and the other half is vacant.

TABLE 2.103

Material	Formula	0 °C	10 °C	20 °C	30 °C	40 °C	60 °C	80 °C	90 °C
Magnesium iodate—tetrahydrate	$Mg(IO_4)_2 \cdot 4H_2O$	2.9	7.2	10.0	11.7	15.2	15.5		15.6

TABLE 2.104

		g/100 ml of water						
Compound	**Formula**	**0 °C**	**20 °C**	**40 °C**	**50 °C**	**65 °C**	**80 °C**	**100 °C**
Calcium iodate monohydrate	$Ca(IO_3)_2 \cdot H_2O$	0.09	0.24	0.52	0.59	0.65	0.80	0.95

A DTA and DSC study was made of the thermal dehydration and decomposition of $Mg(IO_3)_2 \cdot 4H_2O$ and $Mg(IO_3)_2 \cdot 4D_2O$. The data obtained show that the dehydration takes place in one stage. The ΔH°_{deh} values obtained were used to calculate ΔH°_{f}, and comparisons were made with the literature data. It was confirmed that the thermal decomposition passes through an intermediate $Mg_5(IO_6)_2$, which is unstable and immediately decomposes to MgO (note that this salt is an ortho-iodate). An isotope effect is observed in both DTA and DSC curves. Thermogravimetric data on $Mg(IO_3)_2 \cdot 4H_2O$ showed that the thermal decomposition of magnesium iodate was a two-step reaction which starts at 588 and 615 °C, respectively. It is noted that the enthalpy change of magnesium iodate to intermediate orthoperiodate—$Mg_5(IO_6)_2$—is 65.4 kcal/mol and that of orthoperiodate to magnesium oxide is 99.0 kcal/mol.

The anhydrate, $Mg(IO_3)_2$, is a monoclinic structure. It crystallizes in the monoclinic crystal system, space-group type $P2_1$ (no.4) with a pseudo-hexagonal lattice, as shown by the lattice parameters of $Mg(IO_3)_2$ for example: $a = 11.247$ Å, $b = 5.045$ Å, $c = 11.246$ Å, $\beta = 120.02°$, $V = 552.5$ Å^3, $Z = 4$. This monoclinic symmetry with a to c and $\beta = 120°$ leads to a three-individual pseudo-hexagonal twin by pseudo-merohedry. The structure reveals a three-dimensional network in which each octahedrally coordinated cation is linked to ten others via iodate bridges.

Magnesium iodate is not employed extensively in Industry but is available commercially.

Calcium Iodate

Calcium iodate has the molecular formula, $Ca(IO_3)_2$, and the molecular weight of 389.8834 g/mol where iodine atom is in the +5 oxidation state. This composition occurs as a mineral "**Lautarite** (*Calcium Iodate·Monohydrate*). It can be prepared by the reaction of iodic acid upon the carbonate:

$$CaCO_3 + 2HIO_3 \Rightarrow Ca(IO_3)_2 + CO_2 + H_2O$$

The monohydrate formed has limited solubility in water and can be separated by filtration. Its CAS number is 40563-56-2 (anhydrate) and 7789-80-2 (monohydrate). The slurry can be evaporated to increase the yield. The monohydrate has a density of 4.519 g/cm^3 and a solubility of 0.24 g at 20 °C.

The solubility, as a function of temperature is shown in Table 2.104.

This salt also occurs as the hexahydrate whose crystals are efflorescent, rhombic and occur as microprisms. This salt too is very slightly soluble in hot water but more soluble in HNO_3. It is insoluble in sulfuric acid or alcohol but is decomposed by HCl where it forms $MgCl_2$ plus iodine and oxygen. Whether I_2O_5 is an intermediate in the decomposition has not been determined.

The monohydrate loses its water of hydration at 160 °C and decomposes at 560 °C to form the oxide plus iodine and oxygen. The hexahydrate, $Ca(IO_3)_2 \cdot 6H_2O$, has a solubility product of $K_{SP} = 7.10 \times 10^{-7}$. When heated to 130 °C, the hexahydrate loses five waters of hydration to form the more stable monohydrate. However, if the monohydrate is then exposed to water, then the hexahydrate is again obtained (Fig. 2.42).

Calcium iodate (also called **Lautarite**) is used as an oxidant added to lotions and ointments as an antiseptic and deodorant. It is also used in the food industry in animal feed, and the manufacture of disinfectants.

The forms of iodine most commonly used in animal feed are **calcium iodate**, ethylenediamine dihydriodide (EDDI), and potassium iodide. Calcium iodate is usually the most stable source of iodine. All three major sources of iodine (calcium iodate, EDDI, and potassium iodide) are roughly equivalent in biological availability.

Crude iodine (99.9% iodine) is refined as a coproduct from brines associated with underground gas and oil wells in Japan and the U.S. In Chile, it is refined as a coproduct with potassium nitrate from Caliche deposits which are mined by open pit methods. Iodine salts are manufactured from crude iodine and are very pure. There are three major converters of crude iodine to feed grade salts in the U.S. and Canada.

Calcium iodate is available commercially.

Strontium Iodate

Strontium iodate has the molecular formula, $Sr(IO_3)_2$ and the molecular weight of 437.4254 g/mol. Its CAS

$$Ca(IO_3)_2 \cdot 6H_2O \underset{H_2O}{\overset{110°C}{\rightleftharpoons}} Ca(IO_3)_2 \cdot H_2O$$

FIGURE 2.42

number is 13470-01-4. It can be prepared by the reaction of iodic acid upon the carbonate:

$$SrCO_3 + 2HIO_3 \Rightarrow Sr(IO_3)_2 + CO_2 + H_2O$$

The product is either a monohydrate or a hexahydrate (like the calcium homologue). Its occurs as a triclinic crystal with a density of 5.045 g/cm^3 and a solubility of 0.165 g/100 ml of water at 20 °C. Strontium iodate monohydrate, $Sr(IO_3)_2 \cdot H_2O$ has the solubility product of 3.77×10^{-7} while the value of strontium iodate hexahydrate, $Sr(IO_3)_2 \cdot 6H_2O$, is 4.55×10^{-7}.

The hexahydrate is a crystalline powder that is slightly soluble in water but is soluble in dilute nitric acid where it forms the nitrate plus iodine. The solubility of this salt in water is 0.19 g/100 ml at 20 °C and 0.35 g/100 ml at 100 °C. The magnetic susceptibility of the salt is 108 g/10^{-6} cm^3/mol.

Strontium iodate, $Sr(IO_3)_2$, has been prepared by hydrothermal reactions at 170 °C. The X-ray single-crystal structural analysis showed that it crystallizes in a new structure type with space group $P1$, $a = 7.0130$ Å, $b = 7.0520$ Å, $c = 13.088$ Å, $\alpha = 84.12°$, $\beta = 84.80°$, $\gamma = 63.48°$, $Z = 4$. The crystal structure of $Sr(IO_3)_2$ consists of pyramidal IO_3^- anions and Sr^{2+} cations, which are alternately arranged along the a-axis in a 2:1 ratio to form a layer-like structure. Infrared spectra further confirmed that the compound contains low-symmetric IO_3^- groups. This salt has found little usage in Industry, but is offered for sale commercially.

Barium Iodate

Barium iodate has the molecular formula, $Ba(IO_3)_2$ and the molecular weight of 487.1354 g/mol. It can be prepared by the reaction of iodic acid upon the carbonate:

$$BaCO_3 + 2HIO_3 \Rightarrow Ba(IO_3)_2 + CO_2 + H_2O$$

The product is either a monohydrate or a hexahydrate (like the calcium homologue). The monohydrate occurs as lustrous, monoclinic crystals or a white crystalline powder. It is somewhat soluble in hot water but slightly in cold water. It is insoluble in sulfuric acid or alcohol. It loses its water of hydration at 130 °C.

The solubility of barium iodate in water is shown in Table 2.104.

The solubility product of the monohydrate at 25 °C is 2.7×10^{-9}. This salt is not used in Industry but is offered for sale commercially in limited quantities.

Radium Iodate

Radium iodate has the molecular formula, $Ra(IO_3)_2$ and the molecular weight of 575.8308 g/mol. It can be prepared by the reaction of iodic acid upon the hydroxide of radium:

$$Ra(OH)_2 + HIO_3 \Rightarrow Ra(IO_3)_2 + CO_2 + H_2O$$

It occurs as the monohydrate with a solubility product of 1.16×10^{-9}. Its solubility in water is 0.04 g/100 ml at 20 °C. Very little data is available concerning the physical or chemical properties of this salt. Little use has been found by Industry and it is not offered for sale commercially.

2.5.3. Alkaline Earth Periodates

There are two forms of periodates, the "meta-" (m^-) and the "ortho-" (o^-). Metaperiodates have the formula m-HIO_4 whereas that of the orthoperiodates is o-H_5IO_6. Metaperiodates have solubilities and chemical properties similar to perchlorates (similar but larger ion size) though they are less oxidizing than perchlorates. In general, the O-periodates form the $H_4IO_6^-$ anion in solution while the m-periodates form the IO_4^- anion in solution. However, both types of anion behave similarly chemically even though the two types of differ in chemical constitution. Both contain the iodide atom in the +7 oxidation state but differ stereochemically, i.e. Fig. 2.43.

Little information in the literature is available for these salts.

Beryllium Periodate

Beryllium periodate has the molecular formula of $Be(H_4IO_6)_2$ and a molecular weight of gm/mol. It can be formed by reacting periodic acid with beryllium hydroxide:

$$Be(OH)_2 + HIO_4 \Rightarrow Be(H_4IO_6)_2$$

This is an orthoperiodate with the structure shown in Fig. 2.44.

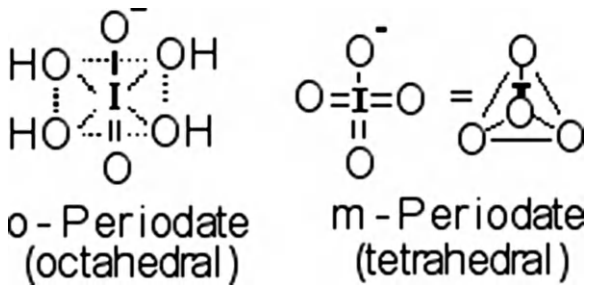

FIGURE 2.43

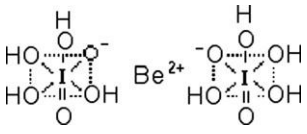

FIGURE 2.44

Note that $Be(H_3IO_6)_2$ and $Be_2(HIO_6)$ are also possible (Fig. 2.45).

At least one of these compositions has been reported in the literature.

Phase relationships and thermal decomposition of beryllium iodates and periodates were studied by X-ray and spectroscopic (IR and Raman) measurements. $Be(IO_3)_2 \cdot 4H_2O$, $Be(IO_3)_2$, and $Be(H_4IO_6)_2 \cdot 4H_2O$ have been characterized. $Be(H_4IO_6)_2 \cdot 4H_2O$ (hitherto claimed in the literature to be a metaperiodate) dehydrates on heating with decomposition to form $Be(IO_3)_2$. Anhydrous beryllium periodate was not obtained in this study.

In another research paper, the thermal decompositions of two beryllium periodate hydrates, $Be(IO_4)_2 \cdot 8H_2O$ and $Be(H_4IO_6)_2 \cdot 2H_2O$, were studied by DTA and TGA in the temperature range from 298 to 1073 K, and by DSC from 298 to 723 K. The intermediates of the thermal decompositions were identified via quantitative analysis, IR spectroscopy and the TG curves. The data obtained were utilized to suggest a scheme for the thermal decompositions of the two periodates. Both compounds decomposed via an anhydrous beryllium iodate, $Be(IO_3)_2$, and the final residue was beryllium oxide, i.e.

$$Be(IO_4)_2 \cdot 8H_2O + \text{heat} \Rightarrow Be(IO_4)_2 + 8H_2O$$
$$\Rightarrow Be(IO_3)_2 + O_2 \Rightarrow BeO + I_2 + 3O_2$$

The enthalpies of the phase transitions were determined from the DSC curves.

In another study, a new beryllium periodate hydrate has been synthesized whose composition was $Be_2HIO_6 \cdot 6.5H_2O$. It was identified by DTA, TG, DSC, IR spectra and X-ray powder diffraction. The compound is thermally stable up to 60 °C, followed by a three-step dehydration and decomposition to form BeO. The IR spectra proved the presence of the following structural groups: HIO_4^{6-}, BeO_4 and H_2O.

$Be(H_4IO_6)_2 \cdot 4H_2O$, beryllium tetrahydrogen-hexaoxoiodate(VII) tetrahydrate, is built up from slightly deformed $Be(OH_2)_4$ tetrahedra (*a,b*) and $IO_2(OH)_4$ octahedra (*A,B*) with *cis* configuration of the oxo ligands. They are arranged along the [001] direction, forming layers with stacking *aBAbABaBAbAB*. The $[H_4IO_6]^-$ and $Be(OH_2)_4^{2+}$ ions are held together by a network of eight independent hydrogen bonds of different strength. Two of the H atoms of $[H_4IO_6]^-$ are disordered over O–H H–O split positions.

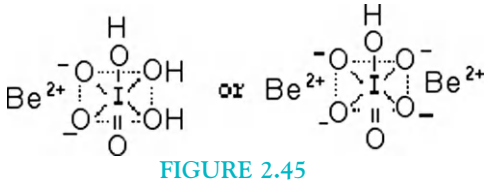

FIGURE 2.45

Beryllium periodate has found little usage in Industry but is available in limited quantities commercially.

Magnesium Periodate

m-Magnesium periodate has the molecular formula, $Mg(IO_4)_2$ and the molecular weight of 406.1092 g/mol. It may be prepared by reaction of magnesium hydroxide and periodic acid:

$$Mg(OH)_2 + 2HIO_4 \Rightarrow Mg(IO_4)_2$$

The product is an octahydrate, $Mg(IO_4)_2 \cdot 8H_2O$. The products differ depending upon the mode of addition. If the acid is added to the $Mg(OH)_2$ slurry, i.e. the Mg^{2+} cation is in excess, then the meta-salt results. In the opposite in which the acid is in excess, the ortho-salt, $Mg(H_4IO_6)_2$, results.

A composition, $Mg_2I_2O_9 \cdot 11H_2O$, has been reported and its thermal decomposition was studied in the temperature interval of 20–600 °C by means of emanation thermal analysis (ETA) and DTA. This composition differs from that which is usually presented. According to a Lewis structure analysis of this composition, the formula should be $Mg_2(H_4I_2O_9)_2 \cdot 9H_2O$ (Fig. 2.46).
where the waters of hydration are omitted. This would be a metaperiodate and orthoperiodate salt. Whether this is correct remains unknown at this point in time. It too decomposes to form MgO and iodine plus oxygen.

Additionally, in another study, it was claimed that the compositions, $Mg(H_4IO_6)_2 \cdot 4H_2O$ and $Mg(IO_4) \cdot 8H_2O$, are wrong and that the dimesoperiodate composition, $Mg(H_4I_2O_{10})_2 \cdot 6H_2O$, is the correct one. The Lewis structure would be (minus the waters of hydration) (Fig. 2.47).

This would mean that a direct bond between the iodine atoms had to exist. Whether this is true remains unsolved. Direct bonds in compounds like these are extremely rare and have not been documented. In addition, the molecular formula is described as $Mg(H_4I_2O_{10})_2 \cdot 6H_2O$ whereas it would have to be $Mg(H_6I_2O_{10})_2 \cdot 6H_2O$ if only one Mg^{2+} cation is present.

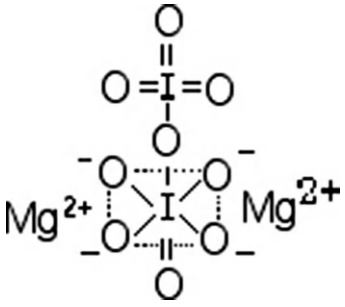

FIGURE 2.46

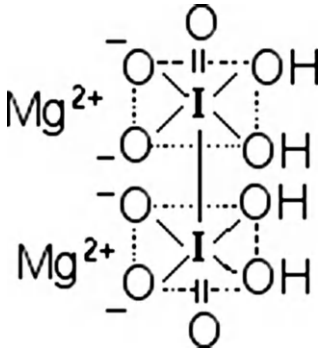

FIGURE 2.47

In this study, crystal structure, DRIFT, Infrared and Raman spectra were employed, and the results of thermal analyses of the hitherto wrongly described dimesoperiodate, $Mg_2(H_4I_2O_{10})_2 \cdot 6H_2O$, were reported. This compound crystallizes in the monoclinic space group $P2_1$ ($Z = 2$) with $a = 10.710$ Å, $b = 5.470$ Å, $c = 11.949$ Å, and $\beta = 112.58°$. The structure, which was refined from X-ray single-crystal data of the magnesium compound ($R_1 = 2.72\%$, 3824 independent reflections), is built up from isolated distorted $M(H_2O)_6^{2+}$ octahedra and dimesoperiodate ions, $H_4I_2O_{10}^{2-}$, connected by a network of hydrogen bonds formed by the $H_4I_2O_{10}^{2-}$ ions and six crystallographically different hydrate H_2O molecules. The strength of the hydrogen bonds ranges from unusually weak bonds corresponding to uncoupled (isotopically dilute samples) OD stretching modes of >2600/cm and very strong ones (OD <2200/cm). The IO stretching modes of the *trans*-configured $H_4I_2O_{10}^{2-}$ ions are assigned to terminal I–O groups (816/cm), I–OH groups (746 and 762/cm) and bridging I–O groups (618 and 647/cm). On heating, $Mg_2(H_4I_2O_{10})_2 \cdot 6H_2O$ undergoes dehydration in the range of 373–485 K (DSC) to two different polymorphs of magnesium metaperiodate, $Mg(H_4I_2O_{10})_2 \cdot 2(IO_4) + 2(H_2O)$. Anhydrous $Mg(IO_4)_2$ is unstable. Above 423 K (high-temperature Raman data), it decomposes to magnesium iodates and finally MgO.

However, another study confutes the above finding:

> "Crystals of hexaaquomagnesium trihydrogenhexaoxoiodate(VII), $[(Mg(OH_2)_6][H_3IO_6]$, are monoclinic, space group Pc1. The unit-cell constants are $a = 5.180$ Å, $b = 9.886$ Å, $c = 10.625$ Å, $\beta = 116.90°$, $Z = 2$. The structure consists of octahedral cations, $[Mg(OH_2)_6]^{2+}$, and octahedral anions, $(H_3IO_6)^{2-}$. The iodine–oxygen bond lengths range from 2.01 to 1.78 Å and the magnesium–water bond lengths range from 2.15 to 2.06 Å. The hexa-aquo-cations and the trihydrogenhexaoxo-iodato (VII) anions are held together by a dense network of hydrogen bonds. There are 14 independent possible hydrogen bonds 0…0, shorter than 2.86 Å, the shortest being 2.65 Å".

The Lewis structure for this octahedrally coordinated compound is shown as follows, where the waters of hydration are shown as well as that of the $(H_3IO_6)^{2-}$ anion (Fig. 2.48).

Thus, the question of the actual composition of magnesium periodate has not been answered satisfactorily.

Magnesium periodate is not used in Industry but is offered for sale in limited quantities commercially.

Calcium Periodate

m-Calcium periodate has the molecular formula, $Ca(IO_4)_2$, and the molecular weight of 421.8822 g/mol. O-calcium periodate has the molecular formula of $Ca(H_4IO_4)_2$ and the molecular weight of 425.9140 g/mol. They can be prepared by the reaction of periodic acid and calcium hydroxide:

$$Ca(OH)_2 + 2HIO_4 \Rightarrow Ca(HIO_4)_2 + H_2O$$

As in the case of the Mg^{2+} cation, the nature of the periodate compound produced depends upon concentration of the components, the temperature of precipitation and the mode of addition of the two solutions, including that of the $(Ca(OH))_2$ slurry. The meta-salt is formed when the acid is in excess and the ortho-salt when the hydroxide is in excess. However, a detailed study of these conditions upon the product produced has not been available.

The precipitate formed is relatively insoluble but no specific data has been presented. The meta-salt forms a monohydrate whereas the ortho-salt forms either a monohydrate or a tetrahydrate. The CAS number of m-$Ca(HIO_4)_2$ is 13478-04-1 while that of the ortho-salt is 77353-51-6. Calcium periodate is offered commercially as a variety of salts (Table 2.105 and Table 2.106).

A variety of molecular weights and molecular formulas are presented in the literature. The correct Lewis structure and formulas for these salts are shown in Fig. 2.49.

Note that at least one of the formulas given for the ortho-salt is incorrect. In addition, these salts are only offered in small quantities and are expensive.

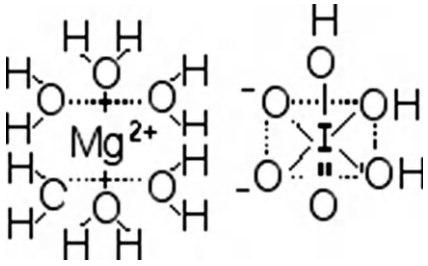

FIGURE 2.48

TABLE 2.105

		g/100 ml of water						
Compound	**Formula**	**0 °C**	**10 °C**	**20 °C**	**30 °C**	**60 °C**	**80 °C**	**100 °C**
Barium iodate monohydrate	$Ba(IO_3)_2 \cdot H_2O$	0.022	0.035	0.046	0.057	0.08	0.19	0.22

TABLE 2.106

CAS number and formula weight None given	**Formula $Ca_2HIO_6 \cdot H_2O$**	**Price 100 g—$254.12**
F.W.: 322.08 g/mol	$Ca_2HIO_6 \cdot H_2O$	100 g—$222.04
CAS#: 77353-51-6 F.W.: 640.1165 g/mol	$Ca_3(H_2IO_6)_2 \cdot 4H_2O$	500 g—$173.80
F.W.: −421.89 g/mol		100 g—$67.40
CAS#: 22700-17-0 F.W.: −439.8975 g/mol	$Ca(IO_4)_2 \cdot H_2O$	100 g—$145.85

According to the "Code of Federal Regulations", the food additive "calcium periodate" may be safely used in accordance with the following prescribed conditions:

(a) The additive is produced by reacting calcium iodate with calcium hydroxide or calcium oxide to form a substance consisting of not less than 60% by weight of penta calcium orthoperiodate containing 28%–31% by weight of iodine.

(b) It is used or intended for use in salt for livestock as a source of iodine.

This is the only commercial usage identifiable in the literature.

Additionally, a combination salt, calcium meta-orthoperiodate has been studied. Details on its preparation have not been forthcoming. Thermal decomposition of $Ca_2I_2O_9 \cdot 8H_2O$ in the temperature interval of 20–600 °C was studied by means of ETA and DTA. The calcium dimesoperiodate octahydrate upon thermolysis forms a hexavalent iodate, $CaIO_4$ as an intermediate product which with increasing temperature decomposes to its orthoperiodate, $Ca_5(10_6)_2$ via presumably the formation of $Ca_2I_2O_7$-type compounds. Its Lewis structure is shown in Fig. 2.50.

$CaIO_4$ compounds can be made from dimesoperiodates by heating at 220–240° for 2 h. The hexavalent state of iodine in $CaIO_4$ has been verified by chemical analysis, magnetic moment measurement and EPR spectra. These compounds undergo hydrolytic decomposition to metal iodate and hydroxide accompanied by the evolution of oxygen. The energy of activation, the order of reaction and the enthalpy change for the conversion of the iodates to the orthoperiodates have been evaluated by nonisothermal kinetic study.

As stated above, calcium periodate is available commercially and is used in Industry as a food additive for animals and some food products for humans.

Strontium Periodate

m-Strontium periodate has the molecular formula, $Sr(IO_4)_2$, and the molecular weight of 469.4242 g/mol. It has no CAS number. It can be formed by the reaction of periodic acid on strontium hydroxide:

$$Sr(OH)_2 + 2HIO_4 \Rightarrow Sr(IO_4)_2$$

A mono-hydrate of the metaperiodate, $Sr(IO_4)_2 \cdot H_2O$, is generally obtained. By crystallization from a strong acidic aqueous solution strontium-tetrahydrogen-hexaoxoperiodate-trihydrate $Sr(H_4IO_6)_2 \cdot 3H_2O$ has been obtained. In the structure of this compound (space group = P1, lattice parameters: $Z = 2$, $a = 6.361$ Å,

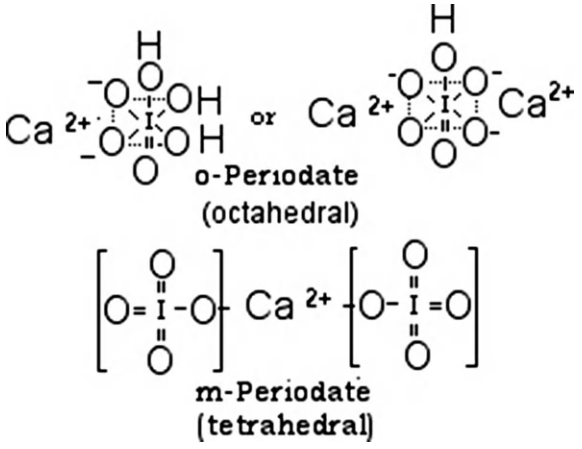

FIGURE 2.49

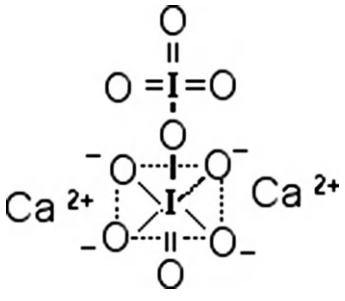

FIGURE 2.50

$b = 9.939$ Å, $c = 10.445$ Å, $\alpha = 114.54°$, $\beta = 95.61°$, and $\gamma = 97.11°$), two crystallographically different $H_4IO_6^-$ anions are linked by two and three common oxygen atoms, respectively, to $SrO_5(H_2O)_4$ polyhedra which are of the form of monocapped distorted square antiprisms. The IR- and Raman-spectra of this compound are analyzed with respect to the internal vibrations of the periodate anion and the O–H vibrations of the hydrogen bonds. The dehydration and decomposition of the compound, studied by thermal analysis, high-temperature Raman experiments and mass spectrometric analysis of the evolved gases, takes place via a metaperiodate $Sr(IO_4)_2$, results at 265 °C in the formation of $Sr(IO_3)_2$ in an exothermic reaction and finally $Sr_5(IO_6)_2$ is formed in a disproportionation reaction.

The dimesoperiodate of strontium, $Sr_2I_2O_9 \cdot 3H_2O$ on thermolysis forms a hexavalent iodate, $SrIO_4$, as an intermediate product which with increasing temperature decomposes to its orthoperiodate, $Sr_5(I0_6)_2$, via presumably the formation of $Sr_2I_2O_7$ type of compound. $SrIO_4$ compounds can be made from dimesoperiodates by heating at 220–240° for 2 h. The hexavalent state of iodine in $SrIO_4$ has been verified by chemical analysis, magnetic moment measurement and EPR spectra. This compound undergoes hydrolytic decomposition to metal iodate and hydroxide accompanied by the evolution of oxygen. Anhydrous strontium iodate prior to its decomposition undergoes a phase transition that is not observed in calcium iodate. The energy of activation, the order of reaction and the enthalpy change for the conversion of the iodate to the orthoperiodate has been evaluated by nonisothermal kinetic study.

Strontium periodate has not found usage in Industry and is not offered for sale commercially.

Barium Periodate

m-Barium periodate has the molecular formula, $Ba(IO_4)_2$, and the molecular weight of 519.1342 g/mol. It can be prepared by the reaction of periodic acid on barium hydroxide:

$$Ba(OH)_2 + 2HIO_4 \Rightarrow Ba(IO_4)_2$$

Its CAS number is 13718-58-6. This salt is relatively insoluble and can be removed from solution by filtration. It is a white powder and is a strong oxidizing agent that will explode if mixed with organics or other oxidizable compounds. By crystallization from strongly acidic aqueous solutions barium-tetrahydrogen-decaoxodiperiodatedihydrate, $BaH_4IO_{10} \cdot 2H_2O$ has been obtained (space group: C2/c, no. 15) with the lattice constants $a = 12.728$ Å, $b = 7.987$ Å, $c = 9.459$ Å, and $\beta = 94.07$). Its CAS number is 26946-37-2. IR and Raman spectra are given and analyzed with respect to the internal vibrations of the $H_4I_2O_{10}^{2-}$ ion and the hydrogen bond system. According to high-temperature Raman spectra and DTA and TGA measurements, the compound decomposes via unknown salts with the anion IO_4^- above 230 °C to the corresponding iodate which above 575 °C starts to disproportionate to the periodate $Ba_5(IO_6)_2$.

This would have the Lewis structure of Fig. 2.51.

Thermal decomposition of $Ba_2I_2O_9 \cdot 9H_2O$ (which is a combination of meta-orthoperiodate) in the temperature interval of 20–600° was studied by means of ETA and DTA. Its Lewis structure is shown in Fig. 2.52.

The dimesoperiodate of $Ba_2I_2O_9 \cdot 3H_2O$ on thermolysis form a hexavalent iodate, $BaIO_4$ as an intermediate product which with increasing temperature decomposes to its di-orthoperiodate, $Ba_5(IO_6)_2$, via presumably the formation of $Ba_2I_2O_7$-type compounds. $BaIO_4$ compounds can be made from di-mesoperiodates by heating at 220–240° for 2 h. The hexavalent state of iodine in $BaIO_4$ has been verified by chemical analysis, magnetic moment measurement and EPR spectra. These compounds undergo hydrolytic decomposition to metal iodate and hydroxide accompanied by the evolution of oxygen. Anhydrous barium iodate prior to its decomposition undergoes a phase transition, this change is less defined in the strontium compound and is not observed in calcium iodate. The energy of activation, the order of reaction and the enthalpy change for the conversion of

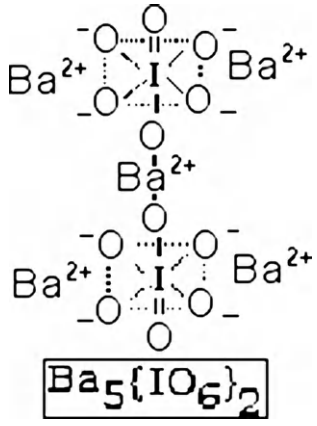

FIGURE 2.51

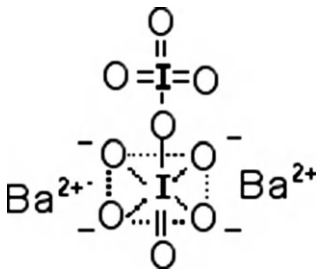

FIGURE 2.52

the iodates to the orthoperiodates have been evaluated by nonisothermal kinetic study.

Barium periodates are offered commercially for sale but only in limited quantities.

Radium Periodate

m-Radium periodate has the molecular formula, $Ra(IO_4)_2$, and the molecular weight of 607.8296 g/mol. It could be formed by the reaction of periodic acid on radium hydroxide:

$$Ra(OH)_2 + 2HIO_4 \Rightarrow Ra(IO_4)_2$$

However, there is no record of such a preparation and radium periodate remains unknown both to Industry and to commercial sales. Perhaps this is due to the radioactivity of ^{226}Ra and the lack of potential usage of such a compound.

2.6. ACTINIUM AND THE ALKALINE EARTHS

Although actinium is a member of the halide series of the periodic table, it is too electropositive and does not form any compounds with alkaline earths. Actinium is a radioactive element with the symbol **Ac** and atomic number of 89. It was discovered in 1899 by Andre Debeime, a French chemist. It was the first nonprimordial radioactive element to be isolated. Po, Ra and radon were observed before actinium, but they were not isolated until 1902. It was actinium that gave the name to the "Actinide" series of elements, a group of 15 similar elements between actinium and lawrencium in the periodic table.

A soft, silvery-white metal, actinium reacts rapidly with oxygen and moisture in air forming a white coating of actinium oxide that prevents further oxidation. As does most lanthanides and actinides, actinium assumes the +3 oxidation state in nearly all its chemical compounds and does not form any known compounds with the alkaline earths. Actinium is found only in traces in uranium ores as the ^{227}Ac isotope. This decays with a half-life of 21.772 years, predominantly emitting β-rays. About 0.2 mg of actinium is contained from 2000 lbs of uranium ore (907,600 g) or 22 ppb (parts per billion). The close similarity of physical and chemical properties of actinium and lanthanum makes separation of actinium from the uranium ore impractical. Instead, the element is prepared, in milligram amounts, by the neutron irradiation of ^{226}Ra in a nuclear reactor. Owing to its scarcity, high price and radioactivity, actinium has no significant industrial use. Its current applications include uses as a neutron source and an agent for radiation therapy, targeting cancer cells in the body. Only a limited number of actinium compounds are known including AcF_3, $AcCl_3$, $AcBr_3$, AcOF, AcOCl, AcOBr, Ac_2S_3, Ac_2O_3 and $AcPO_4$. Except for $AcPO_4$, they are all similar to the corresponding lanthanum compounds and contain actinium in the oxidation state +3.

CHAPTER

3

Group 16 (O, S, Se, Te) Alkaline Earth Compounds

OUTLINE

3.1. Oxides and Hydroxides of the Alkaline Earths 106
3.1.1. Alkaline Earth Oxides 106
Beryllium Oxide 106
Magnesium Oxide 108
Calcium Oxide 109
Strontium Oxide 112
Barium Oxide 113
Radium Oxide 115
3.1.2. Alkaline Earth Hydroxides 116
Beryllium Hydroxide 116
Magnesium Hydroxide 118
Calcium Hydroxide 120
Strontium Hydroxide 122
Barium Hydroxide 123
Radium Hydroxide 124
3.1.3. Alkaline Earth Peroxides 124
Beryllium Peroxide 125
Magnesium Peroxide 125
Calcium Peroxide 126
Strontium Peroxide 128
Barium Peroxide 129
Radium Peroxide 130
3.1.4. Hyperoxides of the Alkaline Earths 130
Beryllium Hyperoxides 130
Magnesium Hyperoxides 130
Calcium Hyperoxides 130
Strontium Hyperoxides 131
Barium Hyperoxides 132
Radium Hyperoxides 132

3.2. Alkaline Earth Oxy-Sulfur Compounds 132
3.2.1. Oxy-Sulfur Acids 132
Hydrogen Sulfide 132
Sulfurous Acid 133
Sulfuric Acid 133
Thiosulfuric Acid 136
Pyrosulfuric Acid or Disulfuric Acid 136
Dithionic Acid 137
3.2.2. Alkaline Earth Sulfides 137
Beryllium Sulfide 137
Magnesium Sulfide 138
Calcium Sulfide 138
Strontium Sulfide 140
Barium Sulfide 141
Radium Sulfide 142
3.2.3. Alkaline Earth Sulfites and Bisulfites 142
Beryllium Sulfite 143
Magnesium Sulfite 143
Calcium Sulfite or Bisulfite 145
Strontium Sulfite 149
Barium Sulfite 149
Radium Sulfite 150
3.2.4. Alkaline Earth Sulfates 150
Beryllium Sulfate 150
Magnesium Sulfate 150
Calcium Sulfate 152
Strontium Sulfate 155
Barium Sulfate 156
Radium Sulfate 158
3.2.5. Alkaline Earth Thiosulfates 158
Beryllium Thiosulfate 158
Magnesium Thiosulfate 158
Calcium Thiosulfate 159
Strontium Thiosulfate 159
Barium Thiosulfate 160
Radium Thiosulfate 160

Encyclopedia of the Alkaline Earth Compounds
http://dx.doi.org/10.1016/B978-0-444-59550-8.00003-X

Copyright © 2013 Elsevier B.V. All rights reserved.

3.2.6. Alkaline Earth Pyrosulfates or Disulfates 160
Beryllium Pyrosulfate 160
Magnesium Pyrosulfate 161
Calcium Pyrosulfate 161
Strontium Pyrosulfate 161
Barium Pyrosulfate 162
Radium Pyrosulfate 162
3.2.7. Alkaline Earth "Thionites and Thionates" 162
Beryllium Thionates 163
Magnesium Thionates 164
Calcium Thionates 165
Strontium Thionates 167
Barium Thionates 168
Radium Thionates 170
3.2.8. Alkaline Earth Peroxysulfites and Peroxysulfates 170
Peroxy Acids 170
Alkaline Earth Metabisulfites or Pyrosulfites 170
Alkaline Earth Peroxymonosulfates 171
Alkaline Earth Peroxydisulfate Salts 171

3.3. Alkaline Earth Selenides and Oxy-Selenium Compounds 172
3.3.1. Alkaline Earth Selenides 173
Beryllium Selenide 173
Magnesium Selenide 174
Calcium Selenide 175
Strontium Selenide 176
Barium Selenide 177
Radium Selenide 177
3.3.2. Alkaline Earth Selenites 178
Beryllium Selenite 178
Magnesium Selenite 178
Calcium Selenite 179
Strontium Selenite 180
Barium Selenite 180
Radium Selenite 181
3.3.3. Alkaline Earth Selenates 181
Beryllium Selenate 181
Magnesium Selenate 182
Calcium Selenate 183
Strontium Selenate 184
Barium Selenate 184
Radium Selenate 184

3.4. Alkaline Earth Tellurium Compounds 184
3.4.1. Tellurium Acids 185
Hydrogen Telluride 185
Tellurous Acid 185
Telluric Acid 185
3.4.2. Alkaline Earth Tellurides 186
Beryllium Telluride 186
Magnesium Telluride 187
Calcium Telluride 187
Strontium Telluride 188
Barium Telluride 188
Radium Telluride 190
3.4.3. Alkaline Earth Tellurites 190
Beryllium Tellurite 190
Magnesium Tellurite 190
Calcium Tellurite 190
Strontium Tellurite 192
Barium Tellurite 193
Radium Tellurite 194
3.4.4. Alkaline Earth Tellurates 194
Beryllium Tellurate 194
Magnesium Tellurate 195
Calcium Tellurate 195
Strontium Tellurate 196
Barium Tellurate 196
Radium Tellurate 197
3.4.5. Alkaline Earth Teflates 197

3.5. Polonium-Based Alkaline Earth Compounds 197

3.1. OXIDES AND HYDROXIDES OF THE ALKALINE EARTHS

The alkaline earth metals all form oxides, hydroxides, peroxides and superoxides. These compounds are used extensively in industry and are readily available commercially. A few, such as beryllium peroxide, are unknown. Most of the oxo-alkaline earth compounds are ubiquitous on the Earth and have been used for centuries, both domestically and industrially.

3.1.1. Alkaline Earth Oxides

Beryllium Oxide

Beryllium oxide (**BeO**) is a white crystalline oxide. It occurs in nature as the mineral "Bromellite". Historically, beryllium oxide was called **glucina** or glucinium oxide. It is an electrical insulator and its thermal conductivity is such that it is higher than any other nonmetal except diamond, and actually exceeds that of some metals. Its high melting point leads to its use as a refractory.

Beryllium oxide can be prepared by calcining beryllium carbonate, dehydrating the hydroxide or igniting the metal with oxygen gas, as shown in the following reactions:

$$BeCO_3 \Rightarrow BeO + CO_2$$

$$Be(OH)_2 \Rightarrow BeO + H_2O$$

$$2Be + O_2 \Rightarrow 2BeO$$

Igniting beryllium in air gives a mixture of BeO and the nitride Be_3N_2. Its CAS number is 1304-56-9 and its molecular weight is 25.0116 g/mol. It is a white solid with a density of 3.02 g/cm^3. Its melting point is 2507 °C, its boiling point is 3905 °C and its band gap (electronic) is 10.6 eV.

The heat of formation, $\Delta H_{f(solid)}$ is −609.4 kJ/mol while the standard molar entropy, $S_{\Theta(solid)}$ is 13.8 J/mol·K. Its heat capacity, C_p, is 25.6 J/mol·K. Beryllium oxide formed at high temperatures (>800 °C) is inert but may be easily dissolved in hot aqueous ammonium bifluoride (NH_4HF_2) or a hot solution of concentrated sulfuric acid (H_2SO_4) and ammonium sulfate ($(NH_4)_2SO_4$).

BeO is polymorphic. The low-temperature form is hexagonal (hP4) and its space group is $P6_3/mc$ (#186). The high temperature form, β-BeO, is tetragonal (c/2) and space group of Im3m. It is highly toxic to the human body. BeO at normal temperatures has the hexagonal wurtzite, from which differs from those of other members of Group 2, whose oxides have the cubic rock salt structure shown in Fig. 3.1.

The resulting structure has a BeO bond distance of 1.659 ± 0.003 Å parallel to the *c* axis and three distances of 1.645 ± 0.003 Å completing the tetrahedral coordination. The difference of 0.014 Å appears statistically significant and indicates that the long bond has slightly more ionic character than the other three. At high temperature, the structure transforms to a tetragonal form. BeO is a unique metallic compound in that it is a nonionic oxide. Lattice parameters are:

α-BeO: $a = 0.2288$ Å; $c = 0.4377$ Å (21 °C)

β-BeO: $a = 0.4751$ Å; $c = 0.2741$ Å (2103 °C)

Beryllium oxide is extracted from the naturally occurring minerals "Beryl"-$Be_3Al_2(SiO_3)_6$ and "Bertrandite"—$Be_4Si_2O_7(OH)_2$, and produced as a powder by the thermal decomposition of $Be(OH)_2$.

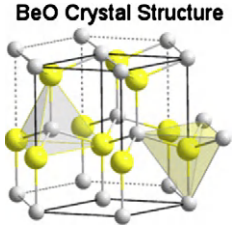

FIGURE 3.1

Sintered beryllium oxide, which is very stable, is used for rocket engines, catalysts, semiconductors, moderators-of-atomic-reactors, and neutron reflectors. When it is evaporated at temperatures around 2500 °C, as studied using graphite furnace atomic absorption spectrometry (GFAAS), beryllium has an atomization mechanism similar to the other alkaline earth elements with one significant difference. For the alkaline earth elements (Mg, Ca, Sr and Ba), the species preceding the appearance of the free element has been the simple oxide, MO. Beryllium, on the other hand, forms a polymeric oxide, $(BeO)_n$ and then release of the free element proceeds as follows:

$$BeO + \text{heat} \Rightarrow (BeO)_n\,(ad) \Rightarrow (BeO)_{n-1}(gas) + \cdots + BeO(gas)$$

$$BeO(ad) \Rightarrow Be(gas) + O(gas)$$

Beryllium oxide is used in many high-performance semiconductor parts for applications such as radio equipment because of its good thermal conductivity while also being a good electrical insulator. It is used as a filler in some thermal interface materials such as "THERMAL GREASE". Some high-powered semiconductor devices have used beryllium oxide ceramic between the silicon chip and the metal mounting base of the package in order to achieve a higher degree of thermal conductivity than for a similar construction made with Al_2O_3. It is also used as a structural ceramic for high-performance microwave devices, vacuum tubes, magnetrons and gas lasers. Currently, there are only two companies in the United States that manufacture beryllium oxide. These are American Beryllium Inc. in Haskell, NJ and Brush Ceramics in Tucson, AZ.

Beryllium oxide has a number of physical properties that are very attractive to industry (Table 3.1).

Beryllium oxide (BeO) is a space age technical ceramic material that offers a combination of desirable properties not found in any other material. Distinguished by excellent high heat and thermal conductivity, it retains dielectric constant, loss factor and dielectric strength in the range of most electrical insulators. Along with good mechanical strength and stiffness to weight ratios, this unique combination of properties provides designers with a material that can reduce the size of heat-generating circuitry while retaining essential high-power capability and improved thermal stability.

For certain applications, the use of a single-crystal of BeO is more appropriate. However, the very high melting point of BeO has been a deterrent. Recently, a method, which circumvents this difficulty, has come to the forefront. A process for growing large single crystals substantially free of surface inclusions within

TABLE 3.1

Thermal conductivity = 265 W/M·K
Specific heat = 0.25 cal/°C g (25 °C)
Thermal expansion = 8.0×10^{-6} in/in/°C (25 to 1000 °C)
Density = 2.85 g/cc, min.
Hardness = 60 on rockwell 45 N
Permeability, liquid = impervious
Permeability, gas = impervious
Flexural strength = 35,000 psi = 242 MPa
Tensile strength = 20,000 psi = 138 MPa
Compressive strength = 225,000 psi = 1.55 GPa
Young's modulus = 50 × 106 psi = 345 GPa
Shear modulus = 25 × 106 psi = 173 GPa
Poisson's ratio = 0.26
Dialectic constant = 6.6 at 1 Mhz; 6.7 at 10 GHz
Dissipation factor = 0.0003 at 2 MHz; 0.0009 at 10 GHz
Resistivity = 1015 ohm/cm
Dialectic strength = 300 V/mil (1/8″ thick)
Impact resistance = 6 inch-lbs.
Maximum use temperature = 1800 °C

several days involves the concept of promoting further growth on seed crystals from a melt composition of suitable oxides which form a lower temperature eutectic. Growth occurs as the crystal seed is rotated and pulled slowly from the melt composition. The temperature decrease of such a melt is such that the temperature can be defined by the liquidus curve of the melt composition phase diagram. Growing single crystal beryllium oxide at a temperature of about 1980 °C from a melt composition having 56 wt% beryllium oxide and 44 wt% calcium oxide is an example of this process. The single crystal can be cut into thin slices for use in integrated circuitry.

Sintered beryllium oxide is a promising thermoluminescent material with a very low sensitivity to thermal neutrons (0.2 gamma rays equivalent per 1010 neutrons/cm^2). It has a fairly high sensitivity to gamma rays, and a good energy response. These properties enable beryllium oxide to be used successfully in mixed fields of thermal neutrons and gamma rays, such as exist in nuclear reactor facilities.

Beryllium and/or beryllium oxide in any form is quite expensive, and this fact limits their use. The current price (2004) for the powder metal was $375 per pound, and for copper master alloy, $160 per pound of Be content.

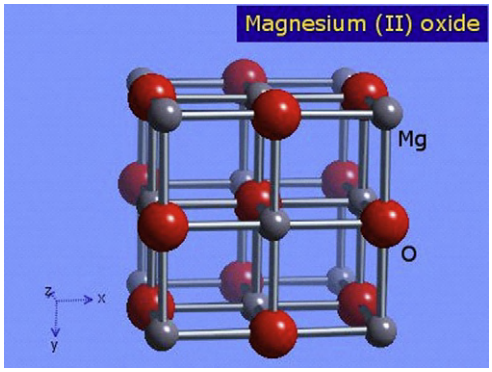

FIGURE 3.2

Magnesium Oxide

Magnesium oxide has the formula of MgO and can be formed by reacting the metal with oxygen gas. Magnesium oxide is easily formed by burning magnesium metal ribbon. Mg oxidizes and emits a bright white light, rich in ultraviolet and hard to extinguish. Extreme care must be taken if MgO is to be prepared by this method. Magnesia is a white solid mineral that occurs naturally as "Periclase" and is used as a source of magnesium metal. Magnesium oxide is hygroscopic in nature and care must be taken to protect it from moisture. It reacts with water and forms the hydroxide:

$$MgO + H_2O \Rightarrow Mg(OH)_2$$

However, this reaction can be reversed by heating it to remove moisture. MgO has the CAS number of 1309-48-2 and its molecular weight is 40.3044 g/mol. Its density is 3.58 g/cm^3. Its melting point is 2852 °C (3125 K, 5166 °F) and its boiling point is 3610 °C (3873 K, 6512 °F). It is slightly soluble in water at 0.0086 g/100 ml at 20 °C. MgO is an excellent insulator both electrically and electronically (with a band gap of 7.8 eV). It has a halite cubic structure (cF8) and a space group of Fm3 m (No. 225). Both Mg^{2+} and $O^{=}$ occupy octahedral positions in the structure in Fig. 3.2.

MgO is a very stable molecule. When it is evaporated, as studied using GFAAS. Mg oxide (MgO) and Ca oxide (CaO) vaporize from the graphite surface as oxides and in the vapor phase dissociates giving atoms.

The thermal conductivity of polycrystalline magnesium oxide has been measured over the temperature range from 400 to 1300 K using a modified guarded hot plate design. Three different thicknesses of specimens having 93% of theoretical density were tested to verify the operation, accuracy, and reproducibility of the apparatus. The measured thermal conductivity ranges from 30 W/m·K down to 8 W/m·K.

MgO is an efficient moisture absorbent used by many libraries for preserving books. It is also one of the raw materials for making cement in dry process plants;

specifically, Portland cement. If too much of MgO is added, the cement may become expansive.

In medicine, magnesium oxide is used for relief of heartburn and sore stomach, as an antacid, magnesium supplement, and as a short-term laxative. It is also used to improve symptoms of indigestion. Side effects of magnesium oxide may include nausea and cramping.

There are several grades of MgO supplied commercially. These are:

DEAD-BURNED MAGNESIUM OXIDE

Temperatures used when calcining to produce refractory grade magnesia will range between 1500 °C and 2000 °C and the magnesium oxide is referred to as "dead-burned" since most, if not all, of the reactivity has been eliminated. Refractory grade MgO is used extensively in steel production to serve as both protective and replaceable linings for equipment used to handle molten steel.

HARD-BURNED MAGNESIUM OXIDE

A second type of magnesium oxide produced from calcining at temperatures ranging from 1000 °C to 1500 °C is termed "hard-burned". Due to its narrow range of reactivity, this grade is typically used in applications where slow degradation or chemical reactivity is required such as with animal feeds and fertilizers.

LIGHT-BURNED MAGNESIUM OXIDE

The third grade of MgO is produced by calcining at temperatures ranging from 700 °C to 1000 °C and is termed "light-burn" or "caustic" magnesia. Due to the material's wide reactivity range, industrial applications are quite varied and include plastics, rubber, paper and pulp processing, steel boiler additives, adhesives, and acid neutralization to name just a few.

Using relatively simple chemistry, it is also possible to add certain ingredients to magnesium oxide to generate a broad range of new magnesium-based compounds. As in the high-purity magnesium oxide process, magnesium hydroxide slurry is a convenient medium for these additions. Examples of typical reactions are included in Table 3.2.

TABLE 3.2

Slurry reactants	Slurry + additive	End-product
$2MgO + 2H_2O \Rightarrow$	$2Mg(OH)_2 + 4HNO_3 \Rightarrow$	$2Mg(NO_3)_2 + 4H_2O$
$2MgO + 2H_2O \Rightarrow$	$2Mg(OH)_2 + 2H_2SO_4 \Rightarrow$	$2MgSO_4 + 4H_2O$
$2MgO + 2H_2O \Rightarrow$	$2Mg(OH)_2 + 2CO_{2(gas)} \Rightarrow$	$2MgCO_3 + 2H_2O$

MgO is used in many industrial areas, as shown in Table 3.3, presented on the next page.

- Magnesium oxide's ancient usage was mostly in masonry construction. It was used primarily as a mortar component and stabilizer for soil bricks. MgO has also been identified in the Great Wall of China and other ancient landmarks. Roman cement is reported to have contained high levels of MgO. In the U.S., Portland cement has replaced MgO for masonry uses.
- Due to its fire resistance and safety ratings, New York and New Jersey were early adopters of MgO board. Florida has adopted MgO for its mold/mildew resistance. It is hurricane and impact tested and approved in Florida.
- MgO board for building construction is available in various sizes and thickness. It is a nonpaper-covered material and generally light gray, white or beige in color. It comes in various grades, such as smooth finishes, rough textures, and utility grades.
- It is used as a reference white color in colorimetry, owing to its good diffusing and reflectivity properties. It may be smoked onto the surface of an opaque material to form an integrating sphere.
- It is used extensively in electrical heating as a component of "CalRod"-styled heating elements. There are several types available and most commonly used ones are 40 and 80 mesh, as per the American Foundry Society. The extensive use is due to its high dielectric strength and average thermal conductivity. MgO is usually crushed and compacted with minimal air gaps or voids. The electrical heating industry also experimented with Al_2O_3, but it is not used anymore.
- Pressed MgO is used as an optical material. It is transparent from 0.3 to 7 μm. The refractive index is 1.72 at 1 μm and the Abbe number is 53.58. It is sometimes known by the Eastman Kodak Co. trademarked name **Irtran-5**, although this designation is long since obsolete. Crystalline pure MgO is available commercially and has small use in infrared optics.

MgO is manufactured in a number of areas around the world, primarily near areas where MgO ore ("periclase" = MgO) deposits are mined. Major deposits are found in China, Europe, and Canada. MgO ore deposits in the US are negligible. Estimates put the use of MgO board products at 8 million SQF in Asia alone. It is gaining popularity in the US, particularly near coastal regions.

MgO is available in large quantities commercially.

Calcium Oxide

Calcium oxide (CaO), commonly known as **quicklime**, is a widely used material. It is a white, caustic, alkaline solid at room temperature. As a commercial

TABLE 3.3

Area of industry	Usage
Abrasives	As a binder in grinding wheels
Animal feed supplement	Source of magnesium ions for chickens, cattle and other animals
Boiler (oil-fired) additives	Raises melting point of ash generated to produce a friable material that is easily removed; reduced corrosion of steel pipes holding steam as well as sulfur emissions into the environment
Boiler feedwater treatment	Reduces iron, silica and solids
Chemicals	Starting point for the production of other magnesium salts such as sulfate and nitrate
Coatings	Pigment extender in paint and varnish
Construction	Basic ingredient of oxychloride cements used for flooring, wallboard, fiber board, and tile
Electrical	Semiconductors; heating elements insulating filler between wire and outer sheath
Fertilizers	Source of essential magnesium for plant nutrition
Foundries	Catalyst and water acceptor in shell molding
Glass manufacture	Ingredient for specialty, scientific and decorative glassware and fiberglass
Insulation	Light, flexible mats for insulating pipes
Lubricating oils	Additive to neutralize acids
Pharmaceuticals	Special grades of magnesium hydroxide, oxide and carbonate are used in antacids, cosmetics, toothpaste, and ointments
Plastics manufacture	Filler, acid acceptor, thickener catalyst and pigment extender
Refractory and ceramics	Basic ingredient in product formulations for the steel industry
Rubber compounding	Filler, acid acceptor, antiscorch ingredient, curing aid, pigment
Steel industry	Annealing process; coating for grain-oriented silicon steel used in electrical transformers
Sugar refining	Reduces scale build-up when used in juice clarification and precipitation
Sulfite wood pulping	Source of base for cooking liquors
Uranium, gallium and boron processing	Precipitation initiator by acid neutralization
Wastewater treatment	Acid stream neutralizer; precipitates heavy metals
Building construction	MgO is a versatile material used in residential and commercial building Construction. It is suitable for a wide range of general building board usages and for applications requiring a fire rating as well as mold and mildew control as well as sound control applications. MgO boards were approved for construction use in the US around 2003.

product, lime often also contains MgO, silicon oxide (sand) and smaller amounts of aluminum oxide and iron oxide. This is due to the fact that "limestone" contains these impurities. It is primarily $CaCO_3$ which when fired at high temperatures forms CaO:

$$CaCO_3 + \text{heat} \Rightarrow CaO + CO_2$$

This is accomplished by heating the material to about 825 °C, a process called "calcination" or *lime burning*, to liberate a molecule of CO_2, leaving "quicklime". This process is reversible, since once the quicklime product has cooled, it immediately begins to absorb carbon dioxide from the air, until, after enough time, it is completely converted back to calcium carbonate. The CAS number of CaO is 1305-78-8 and its molecular weight is 56.0768 g/mol. It is a white to pale yellow powder with a density of 3.35 g/cm^3. Its melting point is 2572 °C and its boiling point is 2853 °C. It is soluble in acids, glycerol and a sugar solution. If dissolved in water ($Ca(OH)_2$) exhibits a pH of 12.5. CaO has the cubic "halite" structure. Calcium oxide transforms from the B1 (sodium chloride type) to the B2 (cesium chloride type) structure at 60 to 70 GPa (0.6 to 0.7 megabar) pressure with a volume decrease of 11%.

The CaO molecule is relatively stable even in the vapor state. When the evaporation of CaO was using GFAAS, Ca oxide (CaO) vaporized from the graphite surface as oxides and in the vapor phase dissociated, thereby giving atoms.

Quicklime is very corrosive and reacts violently with water. A relatively inexpensive substance, quicklime produces heat energy by the formation of the hydrate, calcium hydroxide, as in the following equation:

$$\mathrm{CaO(solid) + H_2O(liq) \Rightarrow Ca(OH)_2\ (aq)} \times (\Delta H_f = -63.7\ \mathrm{kJ/mol\ of\ CaO})$$

The hydrate can be reconverted to quicklime by removing the water in the reversible equation. If the hydrated lime is heated to redness, the quicklime will be regenerated to reverse the reaction. As it hydrates, an exothermic reaction results. One liter of water combines with approximately 3.1 kg of quicklime to give calcium hydroxide plus 3.54 MJ of energy. This process can be used to provide a convenient portable source of heat, as for on-the-spot food warming in a self-heating can.

The production of calcium oxide from limestone is one of the oldest chemical transformations produced by man. Its use predates recorded history. Most ancient languages have a word for calcium oxide. In Latin it is *calx*, from which the name of the element calcium is taken. In Old English, its name is *lïm*, which is the origin of the modern commercial name for calcium oxide, namely lime. The abundance of limestone in the Earth's crust and the ease of its transformation to calcium oxide do not alone explain why the lime is one of the oldest products of chemistry. Lime has many properties that make it quite valuable. It is so useful, that it is today produced industrially on a vast scale; over 20 million metric tons were produced in the U.S. in 2000.

Lime is produced in several grades or types. If the limestone is fired at about 850 °C, a "Standard Quicklime" grade is produced which is used in most applications.

The use of powdered calcium oxide with a surface area of about 4 cm^2/g, obtained by calcining calcium carbonate at 1250 °C, yields dense, defect-free specimens. Firing then at 1700–1750 °C yields nearly fully sintered ceramics of relative density 0.91–0.92 with an open porosity of about 0.5%.

An increase in the firing temperature to 2000 °C in a vacuum furnace in argon, or an increase in the sintering period in a flame furnace, leads to a certain further densification (relative density 0.93–0.94). The sintered, defect-free specimens of CaO of enhanced purity can be stored in air without damage for long periods (for a period of a month).

In contrast, if 325-mesh (43 μm) particles of $Ca(OH)_2$, formed by precipitation from solution, are fed slowly into a hot (750–780 °C) fluidized-bed furnace, nanosized quick lime results which is extremely reactive to air and moisture. Nanoscale calcium oxide particles are typically 20–80 nm with specific surface area (SSA) in the 15−50 m^2/g range and also available in with an average particle size of 100 nm range with a SSA of approximately 5−10 m^2/g. Nano calcium oxide particles are available in ultrahigh and high purity, transparent, and coated and dispersed forms. They are available as a nanofluid as well. Nanofluids are generally defined as suspended nanoparticles in solution either using surfactant or surface charge technology. Nanofluid dispersion and coating selection technical guidance is also available. Nanostructures available include nanorods, nanowhiskers, nanohorns, nanopyramids and other nanocomposites. Surface functionalized nanoparticles allow for the particles to be preferentially adsorbed at the surface interface using chemically bound polymers. Development research is underway in nano electronics and photonics materials, such as MEMS and NEMS, bio-nano materials, such as bio-markers, biodiagnostics and bio-sensors, and related nano materials, for use in polymers, textiles, fuel-cell layers, composites and solar energy materials. The most important usage today is in dental work where implants are positioned.

Quicklime or CaO, as hydrated or "slaked lime" $Ca(OH)_2$ (mineral "portlandite"), is used in mortar and plaster. Lime is also used in glass production and its ability to react with silicates is also used in modern metal production industries (steel in particular) to remove impurities as "slag".

Lime is also used in water and sewage treatment to reduce acidity, as a flocculent in swimming pools to remove phosphates and other impurities; in paper making to dissolve lignin, and in paper bleaching as a coagulant; in agriculture to improve acidic soils; and in gas scrubbers to desulfurize waste gases and to treat many liquid effluents. It has traditionally been used in the burial of bodies in open graves, to hide the smell of decomposition, as well as in forensic science, to reveal fingerprints.

Perhaps the most commercially important property of lime is its ability to form solutions with silicates. When lime is heated with silica sand (SiO_2) and sodium carbonate (Na_2CO_3), a solution is formed that does not crystallize when it is cooled. Instead, it hardens to an amorphous, clear, and nearly colorless solid, namely "soda lime" glass. Because it is a mixture and not a pure compound, glass does not have a distinct melting point; it gradually softens as it is heated. Therefore, it can be molded and blown into many useful shapes. The production of glass from lime is another of the ancient uses of lime and dates back at least 12,000 years.

The most important modern use of lime also relies on its ability to form solutions with silicates. Nearly, 45% of lime produced is used in the steel industry. Steel and iron are smelted from ores, which are rocks that contain iron oxides. Many of these ores also contain a large amount of silicates. When lime is mixed with the ore

and the mixture melted, these silicates combine with the lime, forming a liquid solution called slag. Slag is immiscible with molten iron, so the silicates can be removed from the iron by draining off the slag. Approximately, 80 kg of lime is used in the production of each metric ton (1000 kg) of iron. Lime is also used in the production of other metals. For example, it is used to remove silicates from alumina (Al_2O_3) before the alumina is reduced to aluminum metal.

Lime is also an important material in the manufacture of chemicals. Its major use here is in the production of calcium carbide, CaC_2. Calcium carbide is manufactured by heating lime with coke:

$$2CaO(solid) + 5C(solid) \Rightarrow 2CaC_2(solid) + CO_2(gas)$$

Calcium carbide reacts with water, releasing acetylene:

$$CaC_2(solid) + H_2O(liq) \Rightarrow C_2H_2(gas) + Ca(OH)_2(solid)$$

Acetylene is an important fuel for welding and is also a starting material for a range of organic compounds, including vinyl chloride, neoprene, and acrylonitrile, all of which are raw materials for polymers. Pollution control is a rapidly expanding consumer of lime. Lime is also used in stack gas scrubbers to reduce sulfur dioxide emissions from power plants. Sulfur dioxide reacts with lime to form solid calcium sulfite:

$$SO_2(gas) + CaO(solid) \Rightarrow CaSO_2(solid)$$

Lime is added to sewage to remove phosphates as well:

$$3CaO(solid) + 3H_2O(liq) + 2PO_4^{3-}(aq) \Rightarrow Ca_3(PO_4)_2(solid) + 6OH^-$$

The pretreatment of water supplies involves the use of lime to decrease the acidity, to soften, and to clear drinking water.

A variety of other industrial processes also make extensive use of lime. It is used as an opacifier in plastics. The paper industry uses it in pulping wood; because lime is highly alkaline, it dissolves the lignin that binds the fibers together in wood. Precipitated calcium carbonate (PCC), calcium oxide, and calcium hydroxide have a diverse range of functionality in the paper industry. Calcium carbonates are used in both paper coating and as a paper filler, while calcium oxide and calcium hydroxide are used in pulp/PCC manufacturing applications. In the refining of sugar, lime causes coagulation of plant material, allowing it to be more easily separated from the sugar syrup.

When quicklime is heated to 2400 °C (4300 F), it emits an intense glow. This form of illumination was known as a "limeLight", and was used broadly in theatrical productions prior to the invention of electric lighting.

Annual worldwide production of quicklime is around 283 million metric tons. China is by far the world's largest producer, with a total of around 170 million metric tons per year. The United States is the next largest with around 20 million metric tons per year in 2000.

Calcium oxide is available in large quantities commercially.

Strontium Oxide

Strontium oxide has the formula of SrO and the molecular weight of 103.6225 g/mol. Strontium oxide or **strontia**, SrO, is formed when Sr metal reacts with oxygen:

$$2Sr + O_2 \Rightarrow 2SrO$$

Burning strontium in air results in a mixture of strontium oxide and strontium nitride. It also forms from the decomposition of strontium carbonate $SrCO_3$. It is a strongly basic oxide. SrO has the CAS number of 1314-11-0 and a density of 4.70 g/cm^3. Its melting point is 2531 °C and its boiling point exceeds 3000 °C. It reacts with moisture forming the hydroxide and with carbon dioxide in the air to form the carbonate. However, the latter reaction is much slower than that of MgO. SrO has the halite (cubic-NaCl) structure with both Sr^{2+} and $O^{=}$ atoms in octahedral positions within the structure. The space group is Fm3M (#25). The enthalpy of formation, ΔH_f, is –592.036 kJ/mol (−141.50 kcal/mol) and the entropy S_0, is 55.5271 J/K. (−13.271 cal/mol) (Fig. 3.3).

Specific heat capacity, C_P, is 44.41 J/mol·K and the Gibbs Free energy, ΔG_f^0, is –562.4133 kJ/mol, (−134.42 kcal/mol).

SrO is a relatively stable molecule. When evaporated above 2500 °C, it first forms SrO molecules in the vapor state (as determined by GFAAS). SrO vaporizes from the graphite surface as oxides and in the vapor phase dissociates giving atoms.

There has been some uncertainty surrounding the vaporization of Sr oxide. It was suggested that SrO(s) vaporizes directly to SrO(g). However, mass spectrometric studies by others suggested direct formation of the gaseous elements from the solid oxide. Nagdaev and Bukreev (using a graphite rod atomizer) showed that the most probable mechanism for free Sr and Ba atom formation is

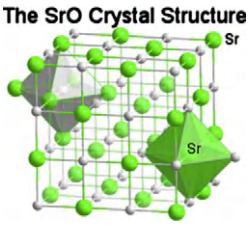

FIGURE 3.3

sublimation of the oxide with dissociation in the gas phase which directly preceded the appearance of free Sr atoms.

SrO decomposes above 3000 °C. A quadrupole mass filter was used to establish the partial pressures of Sr(g) and SrO(g) over strontium oxide heated on a platinum-ribbon filament. The ion currents of $^{88}Sr^{+}$ and $^{88}Sr^{16}O^{+}$ were measured while the filament temperature was continuously increasing at a heating rate of about 14 °C/min; the calculations of the partial pressures were carried out by the integral method for Sr(g) and by the sensitivity-calibration method for SrO(g). The data are represented by:

$$\log P_{Sr(g)}(\text{mm Hg}) = 6.633\text{–}2.536 \times 10^4/T$$

in the temperature range of 1643–1851 K, and by:

$$\log P_{SrO(g)}(\text{mm Hg}) = 6.707\text{–}2.793 \times 10^4/T$$

in the 1747–1850 K range. From the values of the partial pressures, the dissociation energy of strontium oxide was determined to be $D_0^\circ(\text{SrO}) = 96.2$ kcal/mol by the third-law treatment and $D_0^\circ(\text{SrO}) = 102 \pm 5$ kcal/mol by the second-law treatment.

About 8% by weight of TV picture tube glass is strontium oxide, which has been the major use of strontium since 1970. Color televisions and other devices containing color CRT's sold in the United States are required by law to use strontium in the faceplate to block X-ray emission. (PbO can be used in the neck and funnel, but causes discoloration when used in the faceplate.)

SrO is also used in medicine, pyrotechnics, pigments, greases, soaps, and as a chemical intermediate. It is also produced as high-purity strontium oxide rotatable sputtering targets with the highest possible density and smallest possible average grain sizes for use in semiconductor, photovoltaic, and coating applications by chemical vapor deposition and physical vapor deposition and optical applications. Most oxide compounds are not conductive to electricity. However, certain perovskite-structured oxides are electronically conductive finding application in the cathode of solid oxide fuel cells and oxygen-generation systems. "Sputtering" allows for thin film deposition of an ultra high-purity sputtering oxide material onto another solid substrate by the controlled removal and conversion of the target material into a directed gaseous/plasma phase through ionic bombardment.

One of the reasons why rare metals are restrained from wide use in production is their high cost. Strontium and its oxide are an exception: 1 kg of strontium oxide costs no more than 1 dollar. Low price and unique characteristics of strontium, its oxide and salts are in favor of their wide use in metallurgy, mechanical engineering and other branches of industry. Promising branches of industry in which strontium is being used are automobile construction, production of modifiers for aluminum casting, electronics (photomagnetic elements of memory), laser technology (active material for solid lasers), and manufacturing of high-temperature superconducting ceramics.

Samples of strontium oxide on nickel alloy or platinum substrates show a blue-green luminescence when excited at 100 K with photons of energy greater than 3·9 eV (318 nm). The emission spectrum shows peaks at 2·1 (591 nm), 2·8 (443 nm) and 3·1 eV (400 nm), the 3·1 eV peak increasing in intensity as the oxide sample is subjected to thermion activation. In SrO samples, luminescence maxima were observed at photon energies of 4.9 eV (253 nm), 3.7 eV (335 nm), 3.2 eV (388 nm), and 2.4 eV (517 nm). The 4.9-eV band intensity increases with the thermion activity of the sample whereas that of the 3.2-eV band decreases.

In vacuum tubes, a "hot" cathode is an electrode which emits electrons due to "thermion emission" ("Cold" cathodes emit electrons by "field emission" and do not require heating). The heating element is usually a coiled tungsten electrode. SrO has long been used in "Triple-Carbonate" mixtures applied to such electrodes that are used in electronic devices such as TV guns which emit electrons to excite a phosphor screen in color TV tubes or fluorescent lamps. In all of these, the electrode, made from coiled-coil tungsten wire, is heated to incandescence (~800–900 °C). The coil is first coated with a mixture of Ba–Sr–Ca carbonates which decompose to the oxides when the coil is "activated" by applying an electrical current. A maximum of 750 °C (dull red heat) is used for decomposition to prevent loss of barium during the activation stage. The oxide coating thereby formed lowers the "work-function" of the tungsten surface and allows a longer life of the electrode during the ionic emission of electrons during the life of the device. Typically made of a selected mixture of barium, strontium and calcium oxides, the coating is sputtered away through normal use, eventually resulting in failure of the device.

Strontium oxide is readily available for sale commercially in large lots. Its usage in industry is expanding every year.

Barium Oxide

Barium oxide has the molecular formula of BaO. It is a white, hygroscopic formed by the burning of Ba metal in oxygen or the decomposition of the carbonate salt:

$$2\text{Ba} + \text{O}_2 \Rightarrow 2\text{BaO}$$

$$\text{BaCO}_3 \Rightarrow \text{BaO} + \text{CO}_2$$

It transforms into the hydroxide on contact with water.

$$\text{BaO} + \text{H}_2\text{O} \Rightarrow \text{Ba(OH)}_2$$

Its CAS number is 1304-28-5 and its molecular weight is 153.3328 g/mol. Its density is 5.72 g/cm^3 and its melting point is 1924 °C. Its boiling point is close to 2000 °C. Its solubility in water is 3.48 g/100 ml but it rapidly transforms to the hydroxide. It is soluble in ethanol, dilute acids and alkalis but insoluble in acetone and liquid ammonia. BaO has the cubic structure (cF8) and the space group–Fm3m (#225).

Three oxides of barium are known, namely, the monoxide, BaO, the peroxide, BaO_2, and a suboxide, obtained by heating BaO with Mg in a vacuum to 1100 °C. The monoxide is formed when the metal burns in air, but is usually prepared by the ignition of the nitrate, oxygen and oxides of nitrogen being liberated. It can also be obtained by the ignition of an intimate mixture of the carbonate and carbon, and in small quantities by the ignition of the iodate. It is a grayish-colored solid, which combines very energetically with water to form the hydroxide, much heat being evolved during the combination; on heating to redness in a current of oxygen it combines with the oxygen to form the dioxide, which at higher temperatures breaks up again into the monoxide and oxygen.

The following are thermodynamic values determined for BaO (Table 3.4).

BaO is a stable molecule even in the gaseous phase. It has been studied using GFAAS. For Ba, the oxide is thought to exist predominately in the vapor phase as a gas. Free Ba is formed from the gas phase thermal dissociation of the oxide and thermodynamic calculations show that the hydroxide (gaseous and liquid) and the gaseous oxide are the precursors to gaseous Ba atom formation. One investigator added oxygen to the purge gas to produce signal shifts giving evidence in support of the gaseous oxide dissociation hypothesis. The final analysis showed BaO as the precursor to Ba atom formation during the evaporation of this oxide.

Barium oxide is used as a coating for "hot cathodes" in a variety of electronic devices such as TV's and lamps. It replaced lead oxide in the production of certain kinds of glass. While lead oxide raised the refractive index of the glass, it also raised the dispersion, i.e refraction of various colors of light resulting in distortion of images which barium oxide does not alter. Barium oxide also has use as an ethoxylation catalyst in the reaction of ethylene oxide and alcohols which takes place between 150 and 200 °C. Nanoscale Barium Oxide Particles are typically 20–80 nm with SSA in the $10-50$ m^2/g range and also available in with an average particle size of 100 nm range with a SSA of approximately $7-10$ m^2/g. Nano barium oxide particles are also available in ultrahigh purity and high purity, transparent, and coated and dispersed forms. They are also available as a nanofluid through the AE Nanofluid production group. Nanofluids are generally defined as suspended nanoparticles in solution either using surfactant or surface charge technology. Applications for barium oxide nanocrystals include as a flame retardant in coatings, plastics, fiber and textiles and in certain alloy and catalyst applications.

In vacuum tubes, a "hot" cathode is an electrode that emits electrons due to "thermionic emission" ("cold" cathodes emit electrons by "field emission" (application of an electric field) and do not require heating). The heating element is usually a coiled tungsten electrode. SrO has long been used in "triple-carbonate" mixtures applied to such electrodes that are used in electronic devices such as TV guns that emit electrons to excite a phosphor screen in color TV tubes or fluorescent lamps. In all of these, the electrode, made from coiled-coil tungsten wire, is heated to incandescence (~800–900 °C). The coil is first coated with a mixture of Ba–Sr–Ca carbonates which decompose to the oxides when the coil is "activated" by applying an electrical current. A maximum of 750 °C (dull red heat) is used for decomposition to prevent loss of barium during the activation stage. The oxide coating thereby formed lowers the "work-function" of the tungsten surface and allows a longer life of the electrode during thermionic emission of electrons during the life of the device. Typically made of a selected mixture of barium, strontium and calcium oxides, the coating is sputtered away through normal use, eventually resulting in failure of the device.

The thermionic emission from thin evaporated films of barium oxide has been studied extensively. Thin barium oxide films have a good emission following evaporation. The emission improves a little during heat treatment, and is then similar to that from a sprayed cathode coating of barium oxide. There is a maximum emission at a thickness of 10^{-5} cm. The method of

TABLE 3.4

State of matter, Gibbs free energy		Enthalpy of formation			Entropy of formation	
	(kcal/mol)	(kJ/mol)	(cal/K)	(J/K)	(kcal/mol)	(kJ/mol)
(s)	−131.0	−548.104	17.23	72.09032	−124.38	−520.40592
(l)	−117.50	−491.62	23.08	96.56672	−112.63	−471.24392
(g)	−29.60	−123.8464	56.25	235.35	−34.61	−144.80824

Knudsen has been applied to this problem. In this method, the oxide escapes through a small aperture in the wall of a "blackbody'" at a rate so small that the equilibrium vapor pressure is not sensibly disturbed. The final results are in agreement with those of Claassen and Veenemans. The vapor pressure of barium oxide is given by:

Log_{10} p (mm Hg) $= 8.63 - 19.400 \times 10^3/\mathrm{T}$ (1200–1800 K).

In another paper, it was determined that excess barium, which is indispensable to a well-activated oxide cathode, can exist in two forms in BaO crystal: oxygen vacancies and barium ultrafine particles (UFPs). When the density of the oxygen vacancies exceeds the critical value, the formation and the growth of the barium UFPs take place. Some experimental results related to BaO crystal with excess barium are interpreted, and the role of barium UFPs is accentuated. The optical absorption of BaO around photon energy 2.0 eV is attributed to barium UFPs embedded in BaO, and the low work function of the oxide cathode is considered to arise from the presence of oxygen vacancies. The physical origin of the photoemission from the oxide cathode bears a resemblance to that of the photoemission from Ag–O–Cs cathode in visible and infrared region.

The field emission microscope has been used to investigate the state of adsorption of barium oxide molecules deposited on tungsten by evaporation. Precautions are taken so as to keep the tube pressure at ultra high vacuum. Pulse method is adopted to protect the state of adsorption from changing with steady application of intense fields. Surface migration of adsorbed molecules over the entire surface is pronounced only above 700 °C and its activation energy is about 4.6 eV. Work function decreases very rapidly for the first 0.15 layer with the rate which can be explained quantitatively by considering the adsorbed molecules as oriented dipoles. The mean dipole moment of an adsorbed molecule is estimated to be $(13.5 \pm 8.1) \times 10\text{^}<-18>$ esu. Crystallites of barium oxide are formed when covering factor amounts to about unity.

BaO is a critical component of "high-temperature" superconductors, discovered in 1987. The following describes how this material is prepared.

PREPARATION OF THE CERAMIC OXIDE SUPERCONDUCTORS

The most common method of making the yttrium-barium-copper oxide superconductors is to mix dry powders of yttrium oxide, barium carbonate, and cupric oxide in the proper molecular ratios. (Barium carbonate is used instead of barium oxide because commercially available barium oxide is very impure. Also, much of the barium oxide tends to be converted into barium hydroxide and barium carbonate upon exposure to air.)

After the chemicals are thoroughly mixed, they are heated in a furnace at about 950 °C for about 18 h. This forms the basic crystal structure and eliminates the carbon dioxide from the barium carbonate. The chemical reaction that occurs in this step is:

$$0.5Y_2O_3 + 2BaCO_3 + 3CuO \Rightarrow YBa_2Cu_3O_{6.5} + 2CO_2$$

This first firing results in a porous dark gray or black clump. If the powders are not mixed well enough, a green phase will appear as well. This mass is ground into a fine powder and placed again in the furnace. This time an oxygen flow is maintained as the material is heated to about 950 °C for about 18 h. After this firing, the sample will show some signs of superconductivity. But an additional grinding and firing under flowing oxygen is usually necessary to obtain a good quality superconductor. In the process of being heated under oxygen flow, the oxygen content of each crystal unit is increased from 6.5 atoms of oxygen to approximately 7. There was considerable uncertainty during much of 1987 about the "ideal" oxygen content. One early report showed that a good yttrium-based superconductor had an oxygen content of 6.72[5]. It is now generally believed that the compound should have an oxygen content that is as close to 7 as possible. The chemical formula of the superconducting compound is:

$$YBa_2Cu_3O_7$$

The rate of cooling in this final firing must not exceed 100°/h until the temperature of the material is below 500 °C. This slow rate of cooling is an absolute necessity for producing superconductors with a critical temperature above the temperature of liquid nitrogen.

Barium oxide is available in large lots commercially and is being used in industry in new applications each year.

Radium Oxide

Radium oxide has the molecular formula of RaO and a molecular weight of 241.9994 g/mol. Its CAS number is 12143-02-1. It can be prepared by heating radium metal in air to give a mixture of white radium oxide, RaO, and radium nitride, Ra_3N_2. The superoxide RaO_2 is also likely to form in this reaction. Radium, four places below magnesium in the periodic table is more reactive with air than magnesium:

$$2Ra(solid) + O_2(gas) \Rightarrow 2RaO(solid)$$

$$Ra(solid) + O_2(gas) \Rightarrow RaO_2(solid)$$

$$3Ra(solid) + N_2(gas) \Rightarrow Ra_3N_2(solid)$$

Radium reacts very readily with water to form radium hydroxide, $Ba(OH)_2$ and hydrogen gas (H_2).

The reaction is expected to be more violent than that of barium:

$$Ra(solid) + 2H_2O(gas) \Rightarrow Ra(OH)_2(aq) + H_2(gas)$$

Reported are the mechanism of vaporization and optimum experimental conditions for the determination of Ra by electrothermal vaporization inductively coupled plasma mass spectrometry (ETV-ICP-MS). Calculated and published data along with new experimental results suggest that this element is vaporized from the surface of the graphite tubes oxides. These oxides are then transported to the argon plasma where dissociation and ionization take place. Appearance temperatures and maximum pyrolysis temperatures obtained experimentally generally agree with values obtained using GFAAS. For Ra, the optimum pyrolysis and vaporization temperatures were 1400 and 2500 °C, respectively.

Radium oxide is often used as a precursor to the formation of other radium compounds which are used in radiotherapy of humans.

3.1.2. Alkaline Earth Hydroxides

All of the alkaline earths form hydroxides, many of which are used extensively in industry. "Slaked Lime" is just one example where $Ca(OH)_2$ is used in paper making. The alkaline earth hydroxides can be divided into two groups depending on the hydration of the solid. First, the sparingly soluble anhydrous beryllium, magnesium and calcium hydroxides, whose freshly precipitated solids are poorly crystalline and show decreasing solubility with aging, and whose solubility in water decreases with increasing temperature. Second, the soluble strontium and barium hydroxide octahydrates that form crystalline precipitates which do not show changes in solubility on aging, and whose solubility in water increases with increasing temperature.

Beryllium Hydroxide

Beryllium hydroxide has the formula $Be(OH)_2$ and the molecular weight of 43.0268 g/mol. A more likely formula is $Be(OH)^+OH^-$. It can be prepared by reacting the oxide with water:

$$BeO + H_2O \Rightarrow Be(OH)_2$$

It is a white solid with a density of 1.92 g/cm^3. Its heat of formation, ΔH_f, is –20.98 kJ/g and its specific heat capacity, C_p, is 1.443 J/K. If heated, it decomposes at 1273 °C. Its solubility in water is slight and its solubility product $K_{sp(H_2O)}$ is 6.92×10^{-22}. It is soluble in acids and bases. The enthalpy of formation, ΔH_f, is –902.5 kJ/mol; the Gibbs free energy, ΔG_f^0, is –815.0 kJ/mol; Entropy of formation, S_0, is 45.5 J/mol and the heat capacity, C_P, is 62.1 J/mol. Its vapor pressure at 25 °C is 24.5 mm Hg, probably because there is a negligible enthalpy of vaporization of 45.5 J/mol K.

Beryllium hydroxide, $Be(OH)_2$, is an amphoteric hydroxide, dissolving in both acids and alkalis. Industrially it is produced as a by-product in the extraction of beryllium metal from the ores, "beryl" and "bertrandite" When alkali is added to beryllium salt solutions, the α-form (a gel) is formed. If this left to stand or boiled the rhombic β-form precipitates. This has the $Zn(OH)_2$ structure with tetrahedral beryllium centers. The alkali dissolution forms a "beryllate":

$$2NaOH(aq) + Be(OH)_2(solid) \Rightarrow Na_2Be(OH)_4(aq)$$

With acids, beryllium salts are formed involving the $Be(OH)^+$ cation. With sulfuric acid, H_2SO_4:

$$2Be(OH)_2 + H_2SO_4 \Rightarrow [Be(OH)]_2SO_4 + 2H_2O$$

Thus, the probable formula for beryllium hydroxide is Be(OH)OH. However, this has never been reported. Beryllium hydroxide dehydrates completely at 400 °C to form a white powder of acid soluble beryllium oxide:

$$Be(OH)_2 + heat \Rightarrow BeO + H_2O$$

Further heating at higher temperature produces acid insoluble BeO.

Proton magnetic resonance spectra of beryllium hydroxide β-$Be(OH)_2$ and products of its thermal decomposition were studied at room temperature and 123 K. It was shown, based on these spectra and differential thermal analysis (DTA) and X-ray diffractometry data, that, heated to above 500 K, β-$Be(OH)_2$ decomposes into a finely dispersed BeO and H_2O to convert finally to an amorphous beryllium oxyhydroxide. At a temperature above 600 K, a crystalline BeO is formed involving dehydration of the finely dispersed BeO and amorphous oxyhydroxide phase.

Beryllium hydroxide is a strategic component concerning the usage of beryllium metal and its compounds in industry. The following narrative illustrates this fact:

> "One company in Utah mined Bertrandite ore and recovered beryllium hydroxide from this ore and from domestic beryl. Beryllium hydroxide was shipped to a plant in Ohio, where it was converted into beryllium metal, alloys, and oxide. Another company in Pennsylvania purchased beryllium oxide and converted this material into beryllium alloys. Small quantities of beryl were recovered as a by-product of U.S. pegmatite mining operations in various states. Beryllium consumption of 205 tons was valued at more than $70 million, based on the producer price for beryllium-copper master alloy. The use of beryllium (as an alloy, metal, and oxide) in electronic and electrical components, and aerospace and defense applications accounted for more than 80% of consumption".

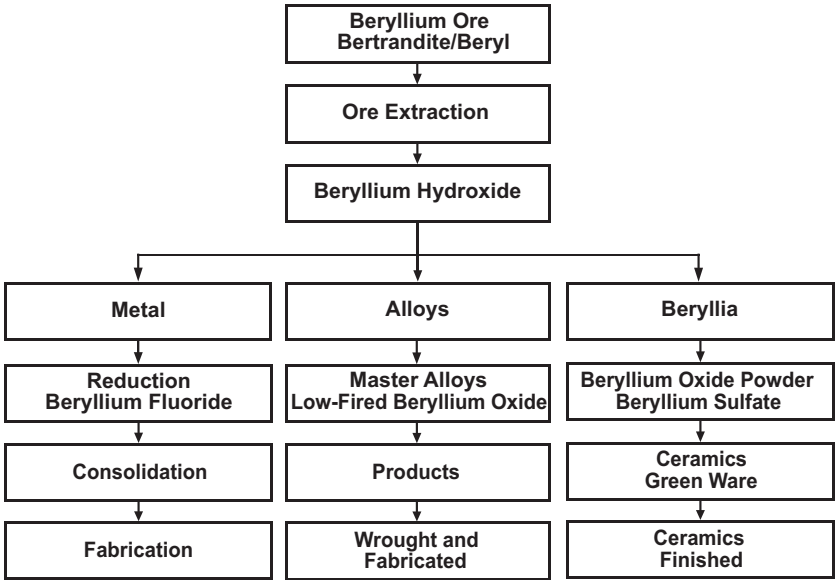

FIGURE 3.4

Beryllium hydroxide is the key compound used to prepare a variety of beryllium products. One method used to extract it from an ore like beryl is:

1. Grind up the ore and add sodium silicofluoride and soda ash. Press the mixture into briquettes. Heat the briquettes to 700 °C in a rotating hearth furnace until they become a coherent mass. Crush, mill and leach the heated briquettes to remove any remaining water.
2. Remove the red mud waste from the resulting material, which will leave a high concentration of sodium beryllium fluoride in solution. Add sodium hydroxide until the pH of the solution is 12 and allow beryllium hydroxide to precipitate out, leaving beryllium fluoride. The major portion will be beryllium hydroxide.
3. Add magnesium to the beryllium fluoride and heat to 1300 °C. The beryllium fluoride will be reduced to pure beryllium by the following equation: $BeF_2 + Mg \Rightarrow MgF_2 + Be$.

These steps are summarized in Fig. 3.4.

Note that $Be(OH)_2$ is the primary product used to prepare the metal and various beryllium salts.

The United States has very little beryl that can be economically hand sorted from pegmatite deposits. The Spor Mountain area, Utah, an epithermal deposit, contains a large reserve base of Bertrandite, which was being mined. Proven Bertrandite reserves in Utah total about 16,000 tons of contained beryllium. World beryllium reserves and reserve base are not sufficiently well delineated to report consistent figures for all countries (Table 3.5).

TABLE 3.5

World production of beryllium ores in tons

	2004	2005
United States	900	900
China	200	200
Mozambique	30	30
Other countries	10	10
World total	1140	1140

Beryllium hydroxide exists in three forms: as a metastable tetragonal crystalline solid (α-$Be(OH)_2$; as a stable orthorhombic crystalline solid (β-$Be(OH)_2$); and in a slightly basic pH, it appears as a slimy, gelatinous substance ($Be(OH)_4^{2-}$). It is soluble in acids and alkalis but insoluble in water. Beryllium oxide (BeO) occurs as a white amorphous powder or gel which is insoluble in both cold and hot water but is soluble in acids, alkalis, and ammonium carbonate. It is BeO that has found most usage in industry in electronic components but it is the hydroxide from which it is prepared. One method to produce an oxide suitable for this purpose is:

> "This method provides a process for producing beryllium oxide with a controlled mean particle size and morphology. Powdered beryllium hydroxide is admixed with a calcination additive, and the mixture is calcined to directly convert the beryllium hydroxide to beryllium oxide. Calcination additives include any calcium and/or magnesium compound which forms the corresponding oxide when subject to calcination. These additives facilitate the calcination reaction and recrystallization of the beryllium oxide product. Preferred calcination additives are magnesium basic carbonate and calcium

carbonate, present in amounts of 0.10% to 0.70% by weight relative to the beryllium oxide. Calcination is preferably accomplished in air at 1000° to 1300 ° C. Nitrogen, argon and hydrogen are also suitable calcination atmospheres. Mean particle size and morphology are controlled by the type and quantity of calcinations additive, final calcination temperature and, to a limited degree, by the initial morphology of beryllium hydroxide. The resultant beryllium oxide is characterized by low fluorine content, preferably not more than about 100 ppm, low surface area, preferably not more than about 1.5 m^2/g, and a mean particle size in the range of 2 μm to 25 μm. Surface area depends on the precise quantity of magnesium additive and the final calcination temperature. It reflects the morphology and particle size distribution of the beryllium oxide, e.g., a low surface area powder is normally well crystallized with a large mean size. High surface area powders are less crystallized and have lower mean particle sizes. Known ceramic comminuting treatments may be applied to change the final size distribution of BeO powder".

Maleic and phthalic acids are found to react with $Be(OH)_2$, generated in situ from $BeSO_4$ and $Ba(OH)_2$, in aqueous solution at pH 3.0 or 4.4, respectively (25 °C), to give solutions containing the complexes:

$$(H_2O)_2Be[(OOCCH)_2] \quad (1)$$

$$(H_2O)_2Be[(OOC)_2C_6H_4] \quad (2)$$

The products can be isolated in high yield and identified by microanalytical data. With two equivalents of the dicarboxylic acids and the pH adjusted to 5.5 and 5.9, respectively, by addition of ammonia, the following bis-chelate complexes are obtained, which can also be isolated:

$$[(NH)_4)^+]_2\{[Be[(OOCCH)_2]_2\}^-_2 \quad (3)$$

$$[(NH)_4)^+]_2\{[Be[(OOC)_2C_6H_4)_2]_2\}^-_2 \quad (4)$$

The compounds show distinct ^9Be, ^1H, and ^{13}C resonances in their NMR spectra in aqueous solutions. Layering of an aqueous solution of compound-4 with acetone at ambient temperature leads to the precipitation of single crystals suitable for an X-ray structure determination. This salt was found to contain the bis-chelated dianion, $\{[Be[(OOC)_2C_6H_4)_2]_2\}^-_2$ with the beryllium atom in the spiro-center of two seven-membered rings and an overall geometry approaching closely C_2 symmetry. These anions are associated with two crystallographically independent but structurally similar counter ions $[MeC_O)CH_2CMe_2NH_3]^+$, which are the product of a condensation reaction of the ammonium cation with the acetone solvent. In the crystal, the ammonium hydrogen atoms of the cations form N–H–O hydrogen bonds with the oxo-functions of the dianion.

The largest usage of beryllium hydroxide is to make the oxide or the metal that is used in many industries. The total tonnage is not large but substantial.

Beryllium hydroxide is available commercially in large quantities.

Magnesium Hydroxide

Magnesium hydroxide has the chemical formula $Mg(OH)_2$ and the molecular weight of 58.3197 g/mol. Its CAS number is 1309-42-8 and its density is 2.345 g/cm^3. It decomposes when heated to 360 °C and forms the oxide, MgO. It is very slightly soluble in water at 0.00122 g/100 ml and has a solubility product of 5.61×10^{-12}. Crystals of $Mg(OH)_2$ have a refractive index of 1.559. Its heat of formation is –925 kJ/mol with an entropy of 63 J/mol·K.

As a suspension in water, it is often called **milk of magnesia** because of its milk-like appearance. The solid mineral form of magnesium hydroxide is known as "brucite". It can be prepared by the metathesis reaction between any soluble magnesium salts and an alkali hydroxide such as sodium or even ammonium:

$$Mg^{2+}(aq) + 2OH^-(aq) \Rightarrow Mg(OH)_2(solid)$$

Magnesium hydroxide is a common component of antacids and laxatives. It interferes with the absorption of folic acid and iron. Magnesium hydroxide has low solubility in water, with a K_{SP} of 1.5×10^{-11}. All of magnesium hydroxide that does dissolve does dissociate into ions. Since the dissociation of this small amount of dissolved magnesium hydroxide is complete, magnesium hydroxide is considered a strong electrolyte. Its low solubility makes it a weak base.

In 1829, Sir James Murray used a fluid magnesia preparation of his own design to treat the Lord Lieutenant of Ireland, the Marquis of Anglesey. This was so successful (advertised in Australia and approved by the Royal College of Surgeons in 1838) that he was appointed resident physician to Anglesey and two subsequent Lords Lieutenants, and knighted. His fluid magnesia product was patented 2 years after his death in 1873.

The term *milk of magnesia* was first used for a white-colored, aqueous, mildly alkaline suspension of magnesium hydroxide formulated at about 8% by weight by Charles Phillips in 1880 and sold under the brand name *Phillips' Milk of Magnesia* for medicinal usage.

Suspensions of magnesium hydroxide in water (milk of magnesia) are used as an antacid to neutralize stomach acid, and a laxative. This may cause diarrhea and loss of potassium with concomitant muscle cramps. Magnesium hydroxide is also used as an antiperspirant armpit deodorant. Milk of magnesia is useful against "canker sores" (aphthous ulcer) when used topically. Milk of magnesia is sold for medical use to alleviate constipation, but also to relieve indigestion and heartburn. Milk of magnesia is also used as a folk remedy, applied and massaged in (a few minutes before washing), to relieve symptoms of "seborrhea" and "dandruff". It is also said to be used for seborrheic dermatitis, which is

a drying and flaking of the skin similar to dandruff but often occurring on the face.

Magnesium hydroxide powder is used industrially as a nonhazardous alkali to neutralize acidic wastewaters. Solid magnesium hydroxide has also smoke suppressing and fire retarding properties. This is due to the endothermic decomposition it undergoes at 332 °C (630 °F):

$$Mg(OH)_2 \Rightarrow MgO + H_2O$$

The heat absorbed by the reaction acts as a retardant by delaying ignition of the associated substance. The water released dilutes any combustible gases and inhibits oxygen from aiding the combustion.

The commercial production of $Mg(OH)_2$ involves brines and dolomite ores. The following reaction is an example:

$$\underset{\text{brine}}{[CaCl_2 + MgCl_2](aq)} + H_2O + \underset{\text{magnesium hydroxide}}{[CaO\cdot MgO]} + 2H_2O$$
$$\Rightarrow 2\underset{\text{calcined dolomite}}{Mg(OH)_2(solid)} + 2CaCl_2(aq) + H_2O$$

The magnesium hydroxide and calcium chloride produced from this reaction exist together but in two distinct physical states: magnesium hydroxide is formed as solid particles while the calcium chloride is dissolved in the liquid or watery phase. The bottom solids are then filtered to remove any remaining water and given a series of water washes to remove chlorides from the material. This results in a damp filter cake which is finally directed to a source of heat, such as a rotary kiln, where it is thermally decomposed (calcined) to produce magnesium oxide:

$$2Mg(OH)_2 - \text{heat} \Rightarrow 2MgO + 2H_2O(\text{steam})$$

Common uses of magnesium hydroxide as a fire retardant include plastics, roofing, and coatings. Magnesium hydroxide, $Mg(OH)_2$, as a flame retardant functions in the same manner as ATH, however, there is one important difference: it undergoes endothermic decomposition with water release at 330 °C (626 F). Magnesium hydroxide is marketed as a slurry for use as a neutralizing agent in the treatment of acidic wastewaters.

The basic structure of magnesium hydroxide consists of stacked sheets of octahedrons of magnesium hydroxide. The octahedrons are composed of magnesium ions with a +2 charge bonded to six octahedrally coordinated hydroxides with a −1 charge. Each hydroxide is bonded to three magnesium atoms. The result is a neutral sheet since $+2/6 = +1/3$ (+2 charge on the magnesium atoms divided among six hydroxide bonds) and $-1/3 = -1/3$ (−1 charge on the hydroxides divided among three magnesium atoms); Thus, the charges cancel.

Another method of commercial manufacture of magnesium hydroxide involves the chloride obtained from seawater. After the chloride is recrystallized several times to obtain a level of purity, it is calcined at about 1000 °C:

$$MgCl_2\cdot 6H_2O \Rightarrow MgCl_2 + 6H_2O$$
$$\Rightarrow Mg(OH)_xCl_{2-x} + xHCl$$
$$\Rightarrow MgO + (2-x)HCl$$

The chloride first dissolves in its own waters of hydration, then forms a basic chloride before decomposing to the oxide. It is the oxide which is reacted in water to form a hydroxide slurry. Although NaOH could be added to the chloride itself, contamination by sodium ion, Na^+, is, in many cases, undesirable. The use of ammonia, NH_4OH, is not feasible since the pH of the solution must exceed 10.5.

Crystallization of magnesium hydroxide by a continuous mixed suspension mixed product removal crystallizer was conducted to make clear the characteristics of reactive crystallization kinetics of magnesium hydroxide, which was produced by the precipitation from magnesium chloride with calcium hydroxide. The following operating factors affecting the crystallization kinetics were investigated:

- the initial concentration of feeds,
- residence time of reactants,
- feed ratio of reactants,
- concentrations of hydroxide and chloride ions.

It was determined that the nucleation rate and the growth rate are correlated by the power law model and that the kinetic order in the power law model is correlated with concentrations of OH^- and Cl^-.

Because $Mg(OH)_2$ belongs to the bivalent metal hydroxides group with a layered CdI_2-type structure (space group P3m1), systematic studies to produce nanoparticles have been presented. In such materials, successive hexagonal Mg^{2+} ion layers and OH^- ion layers are stacked one upon another, favoring the formation of the plate-like crystals but being difficult to induce. However, by careful control of the process parameters, such as the reactants, the temperature, the supersaturation, the solvent, the template and the surfactant etc., it was reported that:

- $Mg(OH)_2$ nanoneedles with a length of 100–4000 nm and a diameter of 10–95 nm were prepared by the orderly addition of ammonia and NaOH solution to $MgCl_2$ solution to maintain the one-dimensional morphology and increase the yield of $Mg(OH)_2$.
- $Mg(OH)_2$ nanorods with a length of 3 μm, a diameter of 30 nm and a coarse surface were obtained by hydrothermal treatment (160 °C, 16 h) of the mixture containing 0.1 mol/l $MgSO_4$ and ammonia at pH = 12.

- $Mg(OH)_2$ nanorods with a length of 200–450 nm and a diameter of 8–20 nm were also synthesized by hydrothermal treatment (180 °C, 20 h) of Mg or MgSO4 in the presence of ethylenediamine, where ethylenediamine acted as a template for the formation of platelet-like $Mg(OH)_2$ via the interaction of bidentate ligand and Mg^{2+}.
- $Mg(OH)_2$ nanoneedles, having a length of 50–100 nm and a diameter of 3–5 nm, coexisted with some nanosheets that were produced by hydrothermal treatment (180 °C, 6 h) of a mixture containing $Mg(CH_3COO)_2$ and NaOH in the presence of citrate, where the preferential adsorption of citrate on the (001) surface of $Mg(OH)_2$ inhibited the growth of $Mg(OH)_2$ along the [001] direction.
- $Mg(OH)_2$ nanotubes with a length of 5–10 μm, an outer diameter of 80–150 nm and a wall thickness of 30–50 nm were obtained via hydrothermal conversion (180 °C, 6 h) of $Mg_{10}(OH)_{18}Cl_2 \cdot 5H_2O$ nanowires in ethylenediamine.

These nanoparticles have found usage as flame retardants in plastics and the like where they exhibit superior properties not found in other flame retardants.

Magnesium hydroxide is available commercially in large quantities.

Calcium Hydroxide

This salt has the molecular formula of $Ca(OH)_2$ and the molecular weight of 74.0931 g/mol. It may be prepared by the reaction of "lime" and water, where the product is called "slaked lime":

$$CaO + H_2O \Rightarrow Ca(OH)_2$$

the solubility of calcium hydroxide is 0.185 g/100 ml at 0 °C and 0.077 g/100 ml at 100 °C. Its $K_{sp} = 4.68 \times 10^{-6}$ at 25 °C. Its CAS number is 1305-62-0 and a density of 2.211 g/cm^3. It is a colorless crystal or white powder, obtained when CaO (called *lime* or *quicklime*) is mixed, or "slaked" with water. It can also be precipitated by mixing $CaCl_2$ and NaOH. The name of the natural, mineral form is "portlandite". It is a relatively rare mineral, known from some volcanic, plutonic, and metamorphic rocks. It has also been known to be formed in burning coal dumps.

The structure of calcium hydroxide is trigonal, space group = P3m1, with $a = 3.589$ Å, $C = 4.911$ Å and $V = 64.8$ Å^3 ($Z = I$). The positions of the Ca, O and H atoms are at: 1(a) (0,0,0,), 2(d) (1/3,2/3, $z_0 = 0.234$) and 2(d) (1/3,2/3, $z_0 = 0.425$), respectively in space group P3m1. Ca(OH)2 is a layered compound with the layers being builtup with distorted, edge-sharing CaO_6 octahedra. Each hydroxyl group is linked to three Ca atoms in its layer and surrounded by three (3) other hydroxyl groups belonging to the adjacent layer. A view of the structure is given in Fig. 3.5.

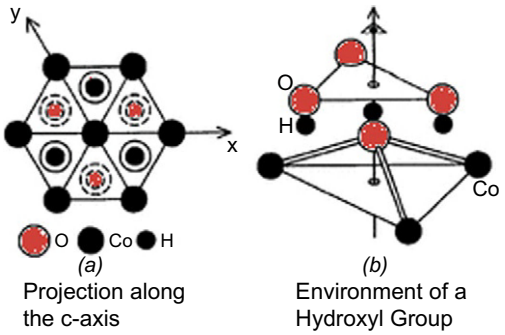

FIGURE 3.5

When heated to 512 °C, calcium hydroxide decomposes into calcium oxide and water. A suspension of fine calcium hydroxide particles in water is called milk of lime. The solution is called "lime water". It is important to differentiate between these two terms (which have been confused in the past. Lime water is a medium strength base that reacts violently with acids and attacks many metals in presence of water. It turns milky if CO_2 is passed through the solution, due to precipitation of $CaCO_3$.

Calcium hydroxide, a weak base, has many diverse uses. Among the most important ones are:

FLOCCULANTS

This salt is a flocculent, used in water and sewage treatment where, in sewage treatment, it is used to control acidity and to help remove soluble phosphates from the sewage stream. It is also used in improvement of acid soils.

PAINTS AND SEALANTS

Whitewash (also known as **calcimine**, **kalsomine**, or **calsomine)** is a very low-cost type of paint made from slaked lime (calcium hydroxide) and chalk (whiting). Various other additives have also been used. Whitewash cures through a reaction with CO_2 in the atmosphere to form calcium carbonate in the form of "calcite", a reaction known as "carbonization". When the paint initially dries it is uncured, and has almost no strength. It takes up to a few days, depending on climate, to harden. It is usually applied to exteriors—however, it is traditionally used internally in food preparation areas—particularly rural dairies—for its mildly antibacterial properties. In Britain and Ireland, whitewash was used historically, both externally and internally—in workers' cottages and still retains something of this association with rural poverty.

Whitewash is especially effective on adobe-like materials because it is absorbed easily and the resultant chemical reaction hardens the substrate. In addition,

whitewash and adobe are both very low-cost building materials. In the early to middle of the twentieth century, when dairy-barns in the mid-West were common, whitewash was a necessary part of routine barn maintenance. A traditional animal barn contains a variety of extremely rough surfaces that are difficult to wash and keep clean. Whitewash aids in sanitation by coating and smoothing over the rough surfaces. Successive applications of whitewash buildup layers of scale which flake off and in the process remove surface debris with it. In addition, it "sweetened" the offal which was carried out to the fields as fertilizer.

Lime wash is pure slaked lime in water. It produces a unique surface glow due the to refraction of calcite crystals. Lime wash and whitewash both cure to become the same material. When lime wash is initially applied it has very low opacity, which can lead novices to overthicken the paint. Drying increases opacity, and subsequent curing increases opacity again.

MORTAR

Mortar is a workable paste composed of calcium hydroxide and other ingredients used to bind construction blocks together and fill the gaps between them. The blocks may be stone, brick, cinder blocks etc. Mortar becomes hard when it sets, resulting in a rigid aggregate structure. Modern mortars are typically made from a mixture of sand, a binder such as lime (and sometimes cement) and water. Mortar can also be used to fix, or *point*, masonry when the original mortar has washed away. Originally, lime mortars were used.

PORTLAND CEMENT MORTAR

This was often known simply as cement mortar and was invented in 1794 by Joseph Aspdin and patented on 18 December 1824, largely as a result of various scientific efforts to develop stronger mortars than existed at the time. It was popularized during the late nineteenth century, and, owing to the First World War, by 1930 it had superseded lime mortar for new construction. The main reasons for this were that Portland cement sets hard and quickly, allowing a faster pace of construction, and requires less skilled workers. However, as a general rule, Portland cement should not be used for the repair of older buildings constructed in lime mortar, which require the flexibility, softness and breathability of lime if they are to function correctly.

LIME PLASTER

Lime plaster is a mixture of calcium hydroxide and sand (or other inert fillers). Carbon dioxide in the atmosphere causes the plaster to set by transforming the calcium hydroxide into calcium carbonate (limestone). To make lime plaster, limestone (calcium carbonate) is heated to produce quicklime (calcium oxide). Water is then added to produce slaked lime (calcium hydroxide), which is sold as a white powder. Additional water is added to form a paste prior to use. The paste may be stored in airtight containers. Once exposed to the atmosphere, the calcium hydroxide turns back into limestone, causing the plaster to set.

Lime plaster was a common building material for wall surfaces in a process known as "lath and plaster", whereby a series of wooden strips on a studwork frame was covered with a semidry plaster that hardened into a surface. The plaster used in most lath and plaster construction was mainly lime plaster, with a cure time of about a month. To stabilize the lime plaster during curing, small amounts of plaster of paris were incorporated into the mix. Because plaster of paris sets quickly, "retardants" were used to slow setting time enough to allow workers to mix large working quantities of lime putty plaster. A modern form of this method uses expanded metal mesh over wood or metal structures, which allows a great freedom of design as it is adaptable to both simple and compound curves. Today, this building method has been partly replaced with "drywall", also composed mostly of gypsum plaster. In both methods, a primary advantage of the material is that it is resistant to a fire within a room and so can assist in reducing or eliminating structural damage or destruction provided the fire is promptly extinguished.

Lime plaster is used for true "frescoes". Pigments, diluted in water, are applied to the still wet plaster. Lime plaster is not to be confused with "plaster of paris" which is a calcium sulfate composition.

Other uses that have occurred in industry include:

- An alkali used as a lye substitute (NaOH) in no-lye hair relaxers.
- A chemical depilatory agent found in Nair™.
- A calcium supplement in mineral fortified baby formulas.
- A chemical reagent used to form a long-lasting fungicide.
- In "reef-aquariums" for adding bio-available calcium in solution for calcium-using animals such as algae, snails, tube worms and corals and also to increase the alkalinity of the water.
- In the tanning industry for neutralization of acid, the liming of hides and skins and the flocculation of resultant wastewater.
- In the oil industry for the manufacture of oil additives (salicatic, sulphatic, fenatic).
- In the chemical industry for manufacture of calcium stearate.
- In the food industry for processing water (for alcoholic and soft drinks).
- Used in the separation of sugar from sugar cane in the sugar industry.

- Used in the processing of Norwegian "Lutefisk". Dried cod fish is soaked in a mixture of slaked lime and soda to produce a soft-fleshed fish fillet that is steamed or baked and served with potato "Lefse".
- In the manufacture of brake = pads, ebonite and pesticides.
- In dentistry, it is used as dressing in paste form used for antimicrobial effect during a dental root canal procedure. Calcium hydroxide is known to have a strong antimicrobial effect and is a bone-regeneration stimulant.
- In the production of metals, lime is injected into the waste gas stream to neutralize acids, such as fluorides and chlorides prior to being released to atmosphere.

Calcium hydroxide is readily available commercially in large lots.

Strontium Hydroxide

Strontium hydroxide has the molecular formula of $Sr(OH)_2$ and the molecular weight of 121.6324 g/mol. It occurs as an anhydrate whose prismatic, colorless crystals are deliquescent. A monohydrate and octahydrate are also known. The respective molecular weights are: 139.6523 g/mol and 265.7634 g/mol. The CAS numbers are: 311-10-0 (Octahydrate); 18480-07-4 (Anhydrate). Densities are: 3.625 g/cm^3 (anhydrate) and 1.91 g/cm^3 for the octahydrate. The melting point of the anhydrate is 375 °C and its boiling point is 710 °C, a point where it decomposes to the oxide. Solubility in water for the anhydrate is 0.41 g/100 ml at 0 °C, 1.77 g/100 ml at 20 °C and 21.83 g/100 ml at 100 °C. The anhydrate is insoluble in acetone but soluble in acids and ammonia chloride.

It can be prepared by the reaction of water upon the oxide but because $Sr(OH)_2$ is very slightly soluble in water, its preparation can be easily carried out by the addition of a strong base such as NaOH or KOH to a solution of any strontium salt, most commonly the nitrate, $Sr(NO_3)_2$. $Sr(OH)_2$ crystals will precipitate out as a fine white powder. From here, the solution is filtered, and the $Sr(OH)_2$ is washed with cold water and dried. However, strontium hydroxide is sufficiently soluble that a major part remains in solution.

Evaporating the solution causes the octahydrate, $Sr(OH)_2 \cdot 8H_2O$ to crystallize. The octahydrate may also be obtained by precipitating the hydroxide from strontium nitrate solution with NaOH and washing the precipitate with cold ethyl alcohol.

Strontium hydroxide octahydrate $Sr(OH) \cdot 8H_2O$ crystallizes in the tetragonal space group $P4/ncc$ with cell constants $a = 9.017$ Å and $c = 11.603$ Å. The crystal structure has been refined and it was possible to localize the positions of all hydrogen atoms for the first time and to describe the hydrogen-bonding scheme in detail. The Sr^{2+} ions are square antiprismatically coordinated by eight water molecules. These $\{Sr(H_2O)_8\}^{2+}$ coordination polyhedra are linked with each other via hydrogen bonds in a way that linear columns parallel to the c axis result. The two hydroxyl anions of the asymmetric unit are linked by weak hydrogen bonds and are not coordinated to strontium atoms. Like the strontium atoms, they form linear chains parallel to the c axis. Both, $\{Sr(H_2O)_8\}^{2+}$ columns and OH^- chains, are interconnected through two types of additional hydrogen bonds. The structure is reminiscent of the calcium homologue (see above), except that the coordination is octagonal, not hexagonal.

Strontium hydroxide is slightly soluble in water but, surprisingly, the octahydrate is much more soluble. It is the latter that is supplied commercially for most applications. A comparison of water solubilities may be seen in Table 3.6.

When the octahydrate is heated, seven waters of hydration are lost to form the monohydrate and finally the oxide:

$$Sr(OH)_2 \cdot 8H_2O + \text{heat} \Rightarrow Sr(OH)_2 \cdot H_2O + \text{heat} \Rightarrow SrO + H_2O$$

The thermal behavior of strontium hydroxide octahydrate was studied by thermal analysis, an X-ray diffraction technique and optical microscopy. Up to 210°, this compound transforms to the hexahydrate and then to the monohydrate. Anhydrous strontium hydroxide crystallizes in the tetragonal system and a polymorphic transformation may occur at 480°. From 530° on, it decomposes in three stages. Amorphous strontium oxide is obtained at 700°.

Strontium hydroxide is used chiefly in the refining of beet sugar and as a stabilizer in plastic. It may be used as

TABLE 3.6

G/100 ml of water									
Compound	**Formula**	**0 °C**	**10**	**20**	**40**	**60**	**80**	**90**	**100**
Octahydrate	$Sr(OH)_2 \cdot 8H_2O$	0.91	1.25	1.77	3.95	8.42	20.2	44.5	91.2
Anhydrate	$Sr(OH)_2$	0.41		1.77					21.8

a source of strontium ions when the Cl^- ion is undesirable. Strontium hydroxide absorbs carbon dioxide from the air to form strontium carbonate.

This salt is available commercially in sizable quantities.

Barium Hydroxide

Barium hydroxide has the molecular formula of $Ba(OH)_2$ and the molecular weight of 121.6324 g/mol. It occurs as an anhydrate whose prismatic, colorless crystals are very deliquescent. Barium hydroxide can be prepared by dissolving barium oxide (BaO) in water:

$$BaO + 9H_2O \Rightarrow Ba(OH)_2 \cdot 8H_2O$$

It crystallizes as the octahydrate, which converts to the monohydrate upon heating in air. Barium oxide has been found to react with water vapor at temperatures from 1443 to 1593 K to form gaseous $Ba(OH)_2$ according to the reaction:

$$BaO(solid) + H_2O(gas) \Rightarrow Ba(OH)_2(gas)$$

The standard free energy of formation is given by the equation, $\Delta G_r^{\circ} = 49{,}400 - 16.6\ T$ (cal/mol) in the present temperature range. From the thermodynamic cycle, the bond energy between barium and two hydroxyl groups has been found to be 196.8 kcal/mol.

A better method of preparation involves addition of NaOH to the nitrate. Since barium hydroxide is fairly soluble, it is necessary to evaporate the solution to crystallize $Ba(OH)_2 \cdot 8H_2O$. Ethanol is added to aid in this crystallization. The crystals are washed in cold ethanol to remove sodium ions and then dried. Barium hydroxide octahydrate forms crystalline precipitates which do not show changes in solubility on aging and whose solubility in water increases with increasing temperature.

When heated, the octahydrate decomposes to the monohydrate at about 78 °C and to the anhydrate at about 375 °C. The thermal dehydration of crystalline barium hydroxide octahydrate has been studied. The octahydrate first dissolves in its own waters of hydration (78 °C) and then loses four waters to form the trihydrate at about 125 °C. The trihydrate is not stable and it is the monohydrate which is obtained at 180 °C. Gradual thermal treatment in air leads to the formation of anhydrous barium hydroxide at 375 °C. Barium oxide is formed at about 410 °C in an inert atmosphere. The hydroxide is converted directly to the peroxide in the temperature range 400–600 °C.

Physical properties of these barium hydroxide compounds are listed in Table 3.7.

Barium hydroxide is used in analytical chemistry to titrate weak acids, particularly organic acids. It forms clear aqueous solutions that are free from carbonate, unlike those of the alkali hydroxides, since barium carbonate is insoluble in water. This allows the use of indicators such as phenolphthalein or thymophthalein (with alkaline color changes) without the risk of titration errors due to the presence of weakly basic CO_3^{2-} ions.

TABLE 3.7

CAS Number	Anhydrate-17194-00-2
	Monohydrate-22326-55-2
	Octahydrate-12230-71-6
Molecular weight	Anhydrate-171.3422 g/mol
	Monohydrate-189.3925 g/mol
	Octahydrate-315.4636 g/mol
Density	Anhydrate-4,495 g/cm^3
	Monohydrate-3.743 g/cm^3
	Octahydrate-2.18 g/cm^3
Melting point	78 °C—octahydrate
	407 °C—Anhydrate
Boiling point	780 °C—Anhydrate
Basicity	$PK_d = -2.02$
Refractive index	$\eta_D = 1.51$ (octahydrate)
Enthapy of formation	$\Delta_f H = -944.7$ kJ/mol
Standard entropy	$S^0_{solid} = 100 \pm 6$ J/mol·K
Heat of fusion	$\Delta H_f = 93.38$ kJ (anhydrate)

Barium hydroxide is used in organic synthesis as a strong base, for example for the hydrolysis of esters and nitriles (Fig. 3.6).

It has been used to hydrolyze one of the two equivalent ester groups in dimethyl endecanedioate. It is also used in the preparation of cyclopentanone, diacetone alcohol and d-Gluonic γ-lactone (Fig. 3.7).

Barium hydroxide is used as an additive in thermoplastics (such as phenolic resins), rayon and PVC stabilizers to improve plastic properties. This material is used as a general-purpose additive for lubricants and greases. Other industrial applications for barium hydroxide include sugar fabrication, manufacturing soaps, fat saponification, fusing of silicates and chemical synthesis of other barium compounds and organic compounds.

Barium hydroxide is an important component in the preparation of "high-temperature superconductors". High-quality bulk $YBa_2Cu_3O_{7-x}$ was synthesized by fusing stoichiometric amounts of yttrium and copper nitrates and barium hydroxide in air, using an ordinary Bunsen burner. The starting materials go through a short-lived liquid phase yielding a solid black product which was subsequently heat treated (900 °C, 18–24 h in air, followed by 500 °C, 5 h in O_2). These materials were greater than 99% phase-pure with CuO as the only other

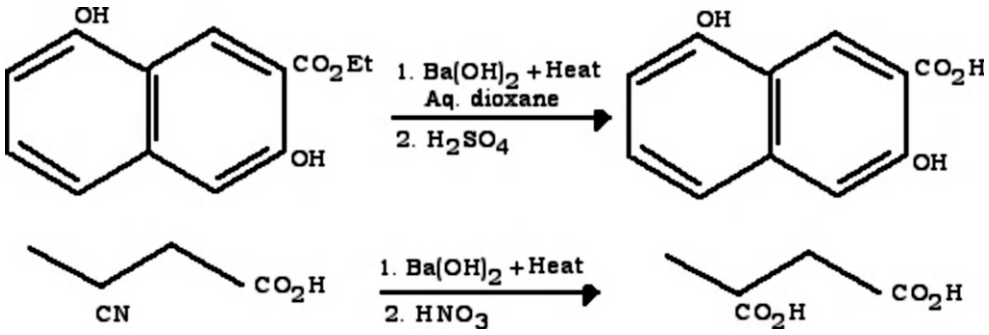

FIGURE 3.6

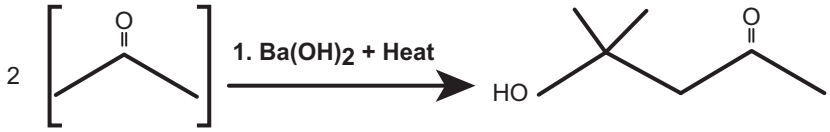

FIGURE 3.7

phase and they exhibited a transition temperature of 92 K, a 15.5% perfect diamagnetic response (field cooled). This synthesis represents an improvement over the much more labor and time intensive conventional methods in that it allows high-quality superconducting materials of varied compositions to be prepared quickly.

The structure of barium hydroxide trihydrate has been determined. It is orthorhombic; space group = Pnma with $a = 7.640$ Å, $b = 11.403$ Å, $c = 5.965$ Å, $V = 519.7$ Å^3, $Z = 4$ and density = 2.88 g/cm^3. The water molecules exhibit strong hydrogen bonds to the hydroxide anion with H–O distances of 1.693 Å (H_2O-I), 1.672 Å (H_2O-II) and 1.667 Å (H_2O-III). The hydroxide anions themselves are not hydrogen bonded. The OH bond lengths are 0.99–1.01 Å (H_2O) and 0.948 Å (OH^-). The HOH angles are 102° (H_2O-I) and 107.6° (H_2O-II).

This salt has been used as a catalyst for the oxidative coupling of methane to form higher molecular weight hydrocarbons. The catalytic performance of the alkaline earths, Be, Mg, Ca, Sr, and Ba, was studied for the oxidative coupling of methane to form $(C_xH_y)_n$ hydrocarbons ($n \geq 2$). To compare the various catalytic compounds, normalized reaction conditions were applied: $T = 740$ °C, $PoCH_4 = 660$ mbar, $PoO_2 = 80$ mbar, $PoN_2 = 260$ mbar at a total pressure of 1 bar. C_{2+} selectivity increased from BeO (22%) via MgO (22 to 53%) and CaO (47 to 55%) to SrO and BaO (70 to 72%) with $Ba(OH)_2$ being the most promising.

Barium hydroxide is offered for sale both as the octahydrate and the monohydrate. It is available in large quantities commercially.

Radium Hydroxide

Radium hydroxide has the formula, $Ra(OH)_2$ and the molecular weight of grams per mole. Radium hydroxide is the most soluble of the alkaline earth hydroxides and more basic than barium hydroxide. It may be prepared by the reaction of BeO added to water. The reaction is violent with evolution of considerable heat:

$$RaO + H_2O \Rightarrow Ra(OH)_2$$

It may also be prepared by reacting the nitrate with NaOH in solution. There is no record of this salt actually having been prepared. However, it is expected that beryllium hydroxide is soluble so that the solution needs to be evaporated at a low temperature (with vacuum) in the presence of ethanol to crystallize the salt, $Be(OH)_2 \cdot 8H_2O$. The crystals are then washed in cold ethanol to remove traces of sodium ions and then dried. The crystals are strongly absorbent of carbon dioxide from the air, forming the carbonate as an end-product.

The CAS number of radium hydroxide is 98966-86-0. When an aqueous solution of radium salt is kept in a closed flask, there is a continuous evolution of radon, hydrogen, and oxygen. The last two are produced by the decomposition of water by the radium, as well as the radon.

There is no demand for this salt and it is not available commercially.

3.1.3. Alkaline Earth Peroxides

The peroxides of the alkali metals and Ca, Sr and Ba are ionic in electronic character. The peroxides of a number of other electropositive metals such as Mg

show an intermediary character, between ionic and covalent.

Beryllium Peroxide

Beryllium peroxide is expected to have a molecular formula of Be(OH)OOH. There is no experimental proof documented in the literature for the existence of any beryllium peroxide compound. All recent pertinent preparative attempts described in such work, using a range of beryllium salts with various peroxides as reagents under mild conditions, were equally unsuccessful. $^{(1)}$H and $^{(9)}$Be NMR investigations of aqueous solutions containing beryllium salts and hydrogen peroxide in a broad pH range also gave no definite evidence for the presence of peroxoberyllates as components of the manifold equilibria in such solutions. Quantum chemical calculations have therefore been carried out to delineate the energetics and structures of various beryllium peroxide model compounds.

Standard Hartree–Fock and density functional methods were employed at various levels of sophistication. The series of prototypes considered consists of $[BeOH]^+$, $Be(OH)_2$, Be(OH)(OOH), $Be(OOH)_2$, $(BeO_2)_2^{2-}$, $BeO_2(OH_2)_2$, and $Be_2(O_2)_2(OH_2)_4$ (all in the gas phase). Surprisingly, the triatomic cation $[BeOH]^+$ has been found to have a linear structure. All the Be–O (peroxide) bonds are found to be rather long, suggesting weaker bonding compared to the Be–O bonds in aquo, hydroxo, or oxo complexes. Hydrogen peroxide or anions derived thereof are therefore not able to compete successfully with water (hydroxide anions) in aqueous solution. In the mononuclear beryllium peroxide molecules, the peroxide groups form chelating units at tetrahedrally 4-coordinate metal atoms. The binuclear compound $Be_2(O_2)_2(OH_2)_4$ has a puckered six-membered ring structure, close to the standard chair conformation. A significant lengthening of the O–O bonds upon coordination to the Be^{2+} centers has been calculated, but it is unlikely that the polarization of the peroxide group by the high-positive charge density at $Be^{2+}$is significant to cause an intrinsic instability of beryllium peroxides. All structures represent distinct local minima on the potential energy surface and are predicted to be (meta)stable species in nonaqueous media. The field of aluminum peroxides is a similar gray area on the map of metal and metalloid peroxides and is reminiscent of the well-established "diagonal-relation" of Be and Al in the periodic table of the elements.

Beryllium peroxide and similar salts have not been described in the literature and they are not available commercially.

Magnesium Peroxide

Magnesium peroxide has the molecular formula of MgO_2 and the molecular weight of 56.3038 g/mol.

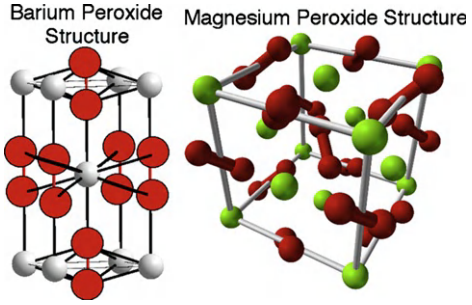

FIGURE 3.8

Magnesium peroxide is a fine powder with a white to off-white color. It is similar to calcium peroxide because magnesium peroxide also releases oxygen by breaking down at a controlled rate when in contact with a hydrous fluid. It is used in bleaching, disinfecting, and deodorizing. In contact with water, it decomposes by the reactions:

$$MgO_2 + 2H_2O \Rightarrow Mg(OH)_2 + H_2O_2$$

$$2H_2O_2 \Rightarrow 2H_2O + O_2$$

Its CAS number is 1335-26-8. A high-purity product is also offered for sale as an "analytical reagent". Its CAS number is 14452-57-4. MgO_2 has a density of 3.04 g/cm^3 and a melting point of 223 °C. Its boiling point is 353 °C, a temperature at which it decomposes. It is not very soluble in water. Its structure is cubic, cP12 (#205). This structure differs from that of the other alkaline earth peroxides, as shown in Fig. 3.8.

The peroxide-"dumbbells" are in-line on the (100), (001) and (010) directions of the lattice while the O–O dumbbells are at (002) points in the BaO_2 lattice.

Magnesium peroxide is used for enhanced aerobic bioremediation. This is a process in which organic contaminants found in soil and/or groundwater are degraded by indigenous or inoculated microorganisms, transforming them to harmless end-products. Magnesium peroxide has a very low solubility in water that allows the product to continue to release its active oxygen content for many months. The duration of oxygen release depends upon many factors including soil type, its pH and buffering capacity, kind of contaminants and their concentration, the presence of other organics or metals in the soil, etc. Because of its stable oxygen release rate and environmentally benign character, magnesium peroxide is widely used in agricultural, environmental, pharmaceutical and cosmetic industries. Magnesium peroxide is primarily used as the main oxygen source for in situ bioremediation. It was the first inorganic peroxide to be used for this purpose. It was originally introduced into wells or drilled holes as a permeable "sock" where it is slowly dissolved in water to remediate the enhanced

bio-remediation of many organic pollutants by indigenous bacteria. Later technology evolved in the injection of an MgO_2 slurry containing about 7–10% of "active", i.e. nascent, oxygen. The addition of oxygen releasing compounds to groundwater can be an effective treatment technology capable of reducing the levels of contaminants in groundwater. Magnesium peroxide is applied to aid in the remediation of petroleum hydrocarbons and other similar contaminants found in groundwater. Magnesium peroxide is very effective for the bioremediation of contaminated soils and improvement of soil quality for plant growth and metabolism.

The thermal stability of magnesium peroxide, using preparations containing up to 75% MgO_2 has been studied using DTA. It has been shown, by an interpretation of the thermograms, that these preparations release bulk of water of the adsorbed mother liquor at 110° and are entirely dehydrated at 260°. In this case, there is a partial decomposition of MgO_2 with evolution of oxygen and the formation of $Mg(OH)_2$. The mixture of MgO_2 and $Mg(OH)_2$ formed decomposes exothermically within the range 360–375°, liberating oxygen and forming MgO. The following reactions are responsible for the exothermicity of the effect on the heating curves of magnesium peroxide preparations:

$$MgO_2 + 2H_2O \Rightarrow Mg(OH)_2 + H_2O_2$$

$$H_2O_2 \Rightarrow H_2O + \tfrac{1}{2}O_2.$$

The heating curve is characterized by the presence of two exothermic effects. The first, beginning at 50 °C passes through a maximum at 105 °C and ends at 125 °C. This corresponds to the decomposition to form hydrogen peroxide. The second effect, beginning at 305 °C, passes through a maximum at 330 °C and ends at 345 °C. This pertains chiefly to the decomposition of H_2O_2 and MgO_2 and has been confirmed by measurement of oxygen evolution.

The major advantage that MgO_2 possesses over other oxidative agents is its steady long-term release of oxygen. It was determined that the MgO_2(s) decomposition, followed a rate law derived from a shrinking-core model for fixed-size particles. The rate of the reaction was controlled by diffusion through the $Mg(OH)_2$(s) product layer rather than by chemical reaction at the core surface. Compared with ionic peroxides, MgO_2(s) was found to be a potential O_2-generating agent for generating oxygen gas during a relatively long period of time. For this reason, MgO_2 has appeared in many "teeth-whitening" products of late.

Magnesium peroxide has also been used to "dehair" cattle hides prior to conversion to "cowhide" leather. Dehairing reaction conditions that rapidly removed 80% or greater of hair from cattle hide pieces were observed for magnesium peroxide (5%, 15% NaOH, 200% float, 45 °C, 8 min, hair-burn process) and potassium peroxymonosulfate (5%, 15% NaOH, 200% float, 45 °C, 7 min, hair-burn process). Leather produced from matched side pieces that were subjected to these oxidative dehairing treatments was determined to take up less chromium yet was tougher than leather produced using conventional hairburn with sodium sulfide.

Additionally, magnesium peroxide has been developed into a form suitable for use as an antibacterial agent for cotton and cotton-blend fabrics. Development of environmentally benign antibacterial agents for application to textiles and other materials is necessary and desirable because many of the older, effective antibacterial agents have been or are in the process of being removed from commercial use. The new antibacterial agent has been characterized by elemental and functional group analysis, infrared spectroscopy and thermal analysis as magnesium dihydroperoxide (MDHP), i.e. $MgO_2 \cdot 2H_2O$. This agent is water insoluble, but dispersible and may be applied as dispersions to fabrics and affixed by conventional pad-cure methods. Aqueous dispersions of this agent are remarkably stable since it retains more than 75% of its peroxide activity after 6 months. Cotton-and cotton/polyester-blend fabrics containing the agent are antibacterial to representative gram-positive and gram-negative bacteria after curing. This activity is retained for 30 launderings on the blend fabrics and up to 50 launderings on cotton fabrics.

This salt is readily available commercially from many manufacturers.

Calcium Peroxide

Calcium peroxide (CaO_2) is a solid peroxide with a white or yellowish color. Its molecular weight is 72.0772 g/mol and its CAS number is 1305-79-9. Its density is 2.91 g/cm^3 and its melting point is 196 °C. For all practical purposes, calcium peroxide is insoluble in water but will dissolve in acid to form H_2O_2. When in contact with water, it will immediately begin to decompose releasing oxygen. It is a tetragonal crystal with a space group of I4/mmm and point group D_{4h}^{17} (Fig. 3.9).

Calcium peroxide is manufactured to varying specifications and purity and has been used in different areas of

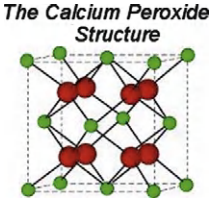

FIGURE 3.9

TABLE 3.8

Salt	Hydrogen peroxide	Magnesium peroxide	Calcium peroxide
Appearance	Liquid	Powder	Powder
Concentration	Dilute	25–35%	60–75%
Active oxygen	0.5–3.0%	7–10%	14–17%
Solubility in water	Soluble	Low solubility	Low solubility
Rate of oxygen release	Instantaneous	3–9 months, based on soil conditions	3–9 months, based on soil conditions

industry and agriculture. In agriculture, it is used as a fertilizer and is also used in the presowing treatments of rice seed. Also, calcium peroxide has found use in the "aqua-culture" industry where it is used to oxygenate and disinfect water, and in the ecological restoration industry as it is used in the treatment of soils. Calcium peroxide is used in a similar manner to MgO_2 for environmental restoration programs. It is used to restore soil and groundwater contaminated with petroleum hydrocarbons by stimulating aerobic microbial degradation of the contaminants in a process known as "Enhanced-Insitu-Bioremediation". Lately, calcium peroxide has begun to replace MgO_2 for this treatment because of its greater availability of nascent oxygen and lower cost. The following table shows a comparison (Table 3.8).

Additionally, calcium peroxide has found use in a coating to supply oxygen to rice seeds during germination. Rice seeds coated with CaO_2, held in place with sodium silicate, were reported to produce more seedlings of better quality and faster growth due to the availability of oxygen over a period of time. Prior practice has involved planting seedlings directly (of which only a fraction survived) whereas more seeds can be planted in submerged soil at a cheaper cost and better seedling plant features than previous methods used for centuries in far East countries.

Calcium peroxide is an ecologically pure substance that has been used in various fields of industry and agriculture.

In environmental protection, it is used:

- For treating wastewater and remediation of groundwater
- For decontaminating soil

In agriculture, it is used:

- As a fertilizer rich with oxygen
- For stimulating seed growth and their germination capability
- For presowing treatment of rice seed, which allows to do planting not by seedlings, but by dry seeds, coated with calcium peroxide. Such a technique sufficiently decreases the work expenditure and increases crop capacity.

In aquaculture, it is used:

- To provide sufficient dissolved oxygen
- To adjust pH value
- To reduce the subaqueous content of ammonium and nitrogen
- To eliminate carbon dioxide and sulfureted hydrogen
- To prevent anaerobic bacteria from proliferation and application to manure heaps to kill disease-carrying bacteria originating from animal defecation.

In poultry raising, it is used:

- To decontamination of fodder
- To increase productivity, safety from disease in hens and improving their eggs.

In cattle breeding, it is used:

- For prophylaxis of casein-stone formation in the abdomen and to prevent diarrhea with newborn calves
- As an antimicrobic agent to prevent disease
- For stimulating protective organism strength
- For normalizing activity of the alimentary canal
- For activating digestion work
- For great increasing live-stock safety.

In the bakery industry, it is used:

- To improve bread crumb and its porosity
- To keep moisture in dough during its baking
- To initiate yeast growth.

The alkaline earths, with the exception of Be and Mg, all form octahydrates in a manner similar to those of the hydroxides. By slow diffusion of NH_3 gas into a very cold solution of the nitrate and hydrogen peroxide, crystals of these compounds have been obtained. Calcium peroxide octahydrate is tetragonal with a space group of D_h^2-P4/mmc. The crystal lattice parameters are: $a = 6.202$ Å and $c = 5.502$ Å. Ca^{2+} atoms reside at (0,0,0) and O′ atoms are at (1/2, 1/2, ±w). H_2O molecules are shown in Fig. 3.10.

(x,y,z) $(\bar{x},\bar{y},z)$ $(x,y,\bar{z})$ $(\bar{x},\bar{y},\bar{z})$ $(x,\bar{y},z)$ $(\bar{x},y,z)$ $(x,\bar{y},\bar{z})$ $(\bar{x},y,\bar{z})$

FIGURE 3.10

where $w = 0.12$, $x = 0.32$, $y = 0.11$ and $z = 0.25$ within the unit cell.

In connection with an investigation on the formation and structure of certain alkaline-earth peroxides and superoxides, the dehydration of the compound $CaO_2 8H_2O$ has been studied. It has been proved that drying this hydrate with phosphorus pentoxide at room temperature will not yield pure CaO_2, but a substance with the following approximate composition:

$$Ca^{2+}\ [(O_2^{2-})_{0.87}\ (O_4^{-})_{0.16}\ (H_2O)_{0.10}]$$

Thus, the formation of a "superoxide" is involved as well as the peroxide.

Calcium peroxide may be used to rapidly de-hair cattle hides with efficiency similar to that of sodium sulfide. Under alkaline conditions (pH $\geq$ 13), a 5–15% (w/w) calcium peroxide mixture, applied in two back-to-back applications, afforded either complete or nearly complete unhairing within 10 min of total reaction time at a reaction temperature of 45 °C. Most of the removed hair was essentially broken down or dissolved in this rapid oxidative hairburn process. Alternatively, intact long strands of hair could be removed and recovered (hairsave) with a single application of the calcium peroxide solution (solids removed) followed by rapid adjustment of the hair solids to an approximately neutral pH. However, hair stubble remained on the hide after subjected to this latter "hairsave" process. The study revealed that shrinkage temperature, physical testing, dye shading, dye levelness and grain appearance were comparable to the sulfide process. In addition, several commercially available nonsulfide sharpening agents, added during "reliming" of hide pieces, were demonstrated to remove residual hair stubble that remained after the rapid oxidative hairburn.

The peroxidation of lime to CaO_2 was studied as a possible step in the commercial production of H_2O_2. Experiments were made with commercial grade CaO, which averaged about 60% CaO initially, and with high-purity (90 to 95%) CaO at oxygen pressures of 1000 and 1525 psia. The equilibrium temperatures of the CaO–CaO_2–O system for these two pressures were determined to be 106 °C and 111 °C, respectively. Only traces of CaO_2 were formed from CaO and oxygen gas. The experimental results indicated that the equilibrium relationships of this system are not favorable for the peroxidation of lime.

Calcium peroxide is available commercially both as a powder and a slurry.

Strontium Peroxide

Strontium peroxide has the molecular formula of SrO_2 and the molecular weight of 119.6194 g/mol. It is an oxidizing agent that is used for bleaching. It has also been used in some pyrotechnic displays to provide a vivid-red color. Its CAS number is 1314-18-7 and its density is 4.56 g/cm^3. When heated to 215 °C, it decomposes. Like the other alkaline earth peroxides, it can be prepared by reaction of the nitrate and sodium peroxide in a cold solution:

$$Sr(NO_3)_2 + Na_2O_2 + xH_2O \Rightarrow SrO_2 \cdot xH_2O + 2NaNO_3$$

The hydrated form is usually the octahydrate. If the anhydrate is desired, the hydrated peroxide is dried and then sintered at 350 °C for 10 min or less:

$$SrO_2 \cdot xH_2O + \text{heat} \Rightarrow SrO + SrO_2 + H_2O$$

About equal amounts of oxide and peroxide form. The ratio is a function of the time and temperature of heating. To separate the two forms, the heated mass is plunged into a large volume of water where the oxide forms the hydroxide. The peroxide is insoluble whereas the hydroxide is soluble, allowing the separation of the two by filtration. The peroxide is then vacuum dried. If desired, the hydroxide solution can be mixed with hydrogen peroxide to form the octahydrate that is then dehydrated as described.

Like its calcium homologue, strontium peroxide octahydrate is insoluble in water but will dissolve in acid to form H_2O_2. When in contact with water, it will immediately begin to decompose releasing oxygen. It is a tetragonal crystal with a space group of D_{4h}^{17} I4/mmm. The crystal lattice parameters are: $a = 6.322$ Å and $c = 5.552$ Å. Sr^{2+} atoms reside at (0,0,0) and O′ atoms are at (1/2, 1/2, ±w). H_2O molecules are shown in Fig. 3.11.

(x,y,z) ($\bar{x}$,$\bar{y}$,z) (x,$\bar{y}$,z) ($\bar{x}$,y,$\bar{z}$) ($\bar{x}$,y,z) ($\bar{x}$,y,z) ($\bar{x}$,y,$\bar{z}$) ($\bar{x}$,y,$\bar{z}$)

FIGURE 3.11

where $w = 0.11$, $x = 0.32$, $y = 0.13$ and $z = 0.27$ within the unit cell. The following diagram presents the structure of SrO_2 as the anhydrate.

Eight single crystals of strontium peroxide as the anhydrate were prepared and the crystal structure was characterized by X-ray diffraction. The crystallographic data were successfully refined as the calcium carbide structure (space group $I4/mmm$, $Z = 2$). The results clearly indicate that the peroxide is a nonstoichiometric compound, MO_{2-x} (M = Sr), with a peroxide deficiency and **that oxide ions are present on interstitial lattice sites** (Fig. 3.12).

The composition rage extends from near stoichiometry to compounds with a total oxygen content of 1.90 in the anhydrous strontium peroxide. It was found that the oxide ions, replacing the peroxide molecular ions, occupy an interstitial position that is in the middle of the replaced peroxide molecular ion. A decrease of peroxide content in the crystal results as well as a decrease in the c axis of the tetragonal unit cell of the

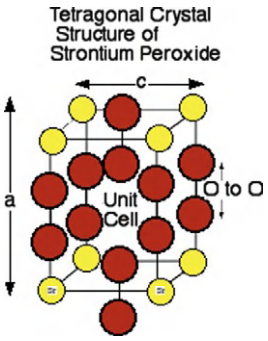

FIGURE 3.12

structure. But, the *a* axis remains almost constant. Furthermore, the peroxide bond length decreases, as confirmed by Raman spectroscopy. Thus, the nonstoichiometry results due to the size of the Sr^{2+} atom in the structure.

Strontium peroxide is available commercially.

Barium Peroxide

Barium peroxide has the chemical formula of BaO_2 and the molecular weight of 169.3324 g/mol. Its CAS number is 1304-29-6. Its density is 5.68 g/cm^3 and its melting point is 450 °C. Its boiling point is 810 °C, a point where it decomposes to BaO and oxygen. It is relatively insoluble in water. This gray-white solid is one of the most common of the inorganic peroxides since it has been traditionally used to prepare them. The original method to prepare oxygen gas was based upon the "Brin process". It was noted by Boussingault (1878), that when Baryta (BaO) is heated to low redness (~700 °C) in a current of air, it takes up oxygen and becomes barium dioxide (BaO_2). Further heating of this dioxide at a higher temperature converts it into free oxygen and Baryta, the latter being ready for use again. It was L. D. Brin who perfected a commercial process to produce oxygen gas. He discovered that, by heating the dioxide in a partial vacuum, the temperature necessary to drive off its oxygen was much reduced. He also found that by supplying the air to the Baryta under a moderate pressure, its absorption of oxygen was greatly assisted. Under these conditions, and by carefully purifying the air before use, it became possible to use the Baryta an indefinite number of times. Thus, the process became practical, as it was theoretically, continuous.

Barium peroxide is best prepared by reacting barium nitrate with sodium peroxide in a cold solution:

$$Ba(NO_3)_2 + Na_2O_2 + xH_2O \Rightarrow BaO_2 \cdot xH_2O + 2NaNO_3$$

The hydrated form is usually the octahydrate. If the anhydrate is desired, the hydrated peroxide is dried and then sintered at 350 °C for 10 min or less:

$$4BaO_2 \cdot xH_2O + \text{heat} \Rightarrow 2BaO + 2BaO_2 + xH_2O + O_2$$

About equal amounts of oxide and peroxide form. The ratio is a function of the time and temperature of heating. To separate the two forms, the heated mass is plunged into a large volume of water where the hydroxide is formed. The peroxide is insoluble whereas the hydroxide is soluble, allowing the separation of the two by filtration. The peroxide is then vacuum dried. If desired, the hydroxide solution can be mixed with hydrogen peroxide to form the octahydrate that is then dehydrated as described.

BaO_2 is an iron gray or white powder. It is slowly decomposed in air, forming the hydroxide and oxygen. It does not dissolve in water, but can slowly hydrolyze, forming hydrogen peroxide in solution. It is a strong oxidizing agent and will explode if direct contact with organic matter occurs. Therefore, barium peroxide is always diluted to form a slurry before usage.

Barium peroxide is a strong oxidizing agent that is used for bleaching. Barium peroxide contains O_2^{2-} subunits wherein the oxygen atoms bond to each other as well as to the barium.

Hydrogen peroxide can also be prepared via the related reaction:

$$BaO_2 + H_2SO_4 \Rightarrow H_2O_2 + BaSO_4$$

Thus, barium peroxide will react in solution with a soluble sulfate salt to produce other peroxides:

$$BaO_2(\text{solid}) + Na_2SO_4(aq) \Rightarrow 2NaO_2(aq) + BaSO_4(\text{solid})$$

$BaO_2 \cdot 8H_2O$ has the tetragonal lattice structure. The crystal lattice parameters are: $a = 6.508$ Å and $c = 5.752$ Å. Ba^{2+} atoms reside at (0,0,0) and O' atoms are at (1/2, 1/2, ±w). H_2O molecules are shown in Fig. 3.13.

$$(x,y,z)\ (\bar{x},\bar{y},z)\ (\bar{x},y,z)\ (\bar{x},y,\bar{z})\ (x,y,\bar{z})\ (\bar{x},y,z)\ (\bar{x},\bar{y},z)\ (\bar{x},y,\bar{z})$$

FIGURE 3.13

where $w = 0.10$, $x = 0.32$, $y = 0.12$ and $z = 0.27$ within the unit cell. The unit cell has the tetragonal crystal structure, as shown for the SrO_2 compound. In this structure, Ba^{2+} is bound to ten oxygen atoms, eight at 2.788 Å and two at 2.648 Å. The bond length in the peroxide anion is 1.482 Å.

The crystal structures of eight single crystals of barium peroxide, prepared by high-pressure, high-temperature synthesis, were determined by X-ray diffraction. The crystallographic data were successfully refined in the calcium carbide structure (space group $I4/mmm$, $Z = 2$). The results clearly indicate that this peroxide is a nonstoichiometric compound, BaO_{2-x}, with a peroxide deficiency and that oxide ions are present on interstitial lattice sites. The composition rage extends from near stoichiometry to compounds

with a total oxygen content of 1.72 in the barium peroxide. The oxide ions, replacing the peroxide molecular ions, occupy an interstitial position that is in the middle of the replaced peroxide molecular ion. A decrease of the peroxide content in the crystal results in a decrease of the *c* axis of the tetragonal unit cell of the structure, while the *a* axis remains almost constant. Furthermore, the peroxide bond length decreases, as confirmed by Raman spectroscopy.

Barium peroxide is used as a hydrogen peroxide source and oxygen oxidant, as well as a bleaching agent. Its main usage has been for making hydrogen peroxide and oxygen, in organic syntheses, fabric printing and dyeing.

Barium peroxide is available commercially, primarily as the oxctahydrate (which is the more stable form of this peroxide).

Radium Peroxide

Radium peroxide is expected to have the molecular formula of RaO_2 and the molecular weight of 258.0242 g/mol. It could be prepared by the reaction of $Ra(OH)_2$ with sodium peroxide in a cold solution:

$$Ra(OH)_2 + Na_2O_2 \Rightarrow RaO_2 + 2NaOH$$

The octahydrate is the expected product but there is no record of this compound ever having been prepared because of the lack of interest by industry and academia. RaO_2 is expected to have a tetragonal structure but it has not been measured. Whether the Ra^{2+} cation is too large to fit into the Ca_2C structure, like the Sr and Ba homologues, remains unknown.

3.1.4. Hyperoxides of the Alkaline Earths

The term "hyperoxide" is meant to include literature data on the molecular oxygen anions O_2^{2-}, O_2^-, and O_3^- that characterize the structures of simple peroxy-compounds: peroxides, superoxides, and ozonides. Most of the alkaline earth compounds are not stable in comparison to those of the alkali metals. In general, the superoxide and ozonide salts of magnesium are stable at room temperature while those of calcium are stable up to about 0 °C and those of strontium and barium up to about –70 °C.

Beryllium Hyperoxides

In view of the fact that beryllium (Be^{2+}) does not form peroxides, there is little likelihood that a superoxide can be produced. Thus, a compound like the superoxide, $Be(O_2)_2$ or $Be(OH)(O_2)_2$, {BeO_4 or $Be(OH)O_4$} is implausible. Even an ozonide like $Be(O_3)_2$ or $Be(OH)(O_3)_2$, {BeO_6 or $Be(OH)O_6$} is questionable. The fact that the peroxide does not form is related to the small size of the Be^{2+} cation, compared to the oxide ($O^=$) anion.

Magnesium Hyperoxides

Magnesium forms both superoxides and ozonides having a general formula: $Mg(O_2)_2$ or MgO_4. They may be prepared by the reaction of the peroxide, suspended in Freon-12 (Cl_2F_2C = dichloro-difluoro-methane) with a solution of ozone in the same medium:

$$2MgO_2 + 2O_3 \Rightarrow Mg(O_2)_2 + Mg(O_3)_2$$

The superoxide is more stable than the ozonide which will decompose to form the superoxide. Magnesium superoxide has a rhombohedral lattice with $\alpha_{hex} = 11.44$ Å, $c/a/ = 1.12$ ($\alpha_{rhombohedron} = 7.88$ Å, $\alpha = 93°$). Above 10 °C, magnesium ozonide decomposes to the superoxide which then decomposes to the peroxide (Fig. 3.14).

Optical and resonance Raman spectra of the reaction products of Mg, Ca, Sr, and Ba with ozone were observed in argon and nitrogen matrices. The visible spectra were characterized by strong, vibronically structured absorptions between 540 and 350 nm, and are assigned to the alkaline earth metal ozonides, $M(O_3)_2$. Vibrational analysis yielded ω_1- and $\omega_1 x_1$ values of about 900 and 6/cm, respectively, with only slight variation from metal to metal. Resonance Raman spectra consisted of a strong fundamental near 1020/cm and two overtones with decreasing intensity. Oxygen-18 substitution confirmed the vibrational assignments, which agree very well with the alkali metal ozonide spectra.

Magnesium superoxides are not stable enough to be available commercially.

Calcium Hyperoxides

Calcium forms at least two hyperoxides, an ozonide, CaO_3 and a di-superoxide, CaO_4 or O_2CaO_2. The usual method for making such compounds involves the use of liquid ammonia or Freon-12, but calcium ozonide does not form under such conditions. The best method involves the use of potassium ozonide in a reaction with calcium peroxide:

$$CaO_2 + 2KO_3 \Rightarrow Ca(O_3)_2 + KO_2$$

Originally, attempts to prepare CaO_4 have centered around the reaction between CaO and aqueous hydrogen peroxide, illustrated as follows:

$$CaO + 3H_2O_2 \Leftrightarrow CaO_4 + 3H_2O$$

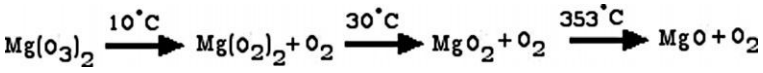

FIGURE 3.14

The removal of the water posed problems and resulted in low yields of CaO_4. In view of this problem of water removal inherent in the use of hydrogen peroxide, other methods were sought searching for an improved method of making superoxides in a water-free system. During these investigations, it was discovered that the superoxides could be prepared by the ozonation of alkaline earth metal oxides, usually in the presence of an alkali metal compound as a catalyst or ozone carrier, with subsequent thermal decomposition of the resulting alkaline earth metal ozonide to the superoxide.

The following is a description of a method used to prepare calcium ozonide:

> "The alkaline earth metal starting material needs to be substantially free of water at the start of the ozonation treatment. For example, lime may be dried by use of an inert gas heated as high as 400–500 ° C. Also, traces of water in CaO may be removed by mixing, with this starting material, alkali metal in the form of an oxide, such as the peroxides Na_2O_2 or K_2O_2 which absorb the moisture to form the hydroxide. Thus, the alkali metal compound is present usually as the hydroxide. The peroxides are most often used, as may be also the hydroxides. Enough of the alkali metal peroxide or hydroxide is employed to give a catalytic effect, at least 0.1 to 10% by weight of the reaction mass, preferably about 0.5 to 6%".
>
> Ozone may be supplied by any convenient means and in a concentration suitable for the desired conversion to oxonide. Usually, the ozone is supplied as a 1 to 5% concentration in oxygen, e.g. about 3%. This gas mixture is readily obtained by passing relatively pure oxygen through an electric arc. Since the instability of ozone increases at higher temperatures and is quite pronounced at above about 100 °C, ambient temperature (20 °C) is often chosen for the reaction to form ozonide. The gas should be substantially anhydrous.
>
> The ozonide is decomposed to alkaline earth metal superoxide by a gentle treatment with oxygen at a slightly elevated temperature. Usually, the temperature should be kept below 100 °C. The oxygen may be diluted with inert gases, but the presence of nitrogen should be avoided to obviate nitride formation. The end of the reaction is often signaled by a color change in the treated solid. For example, calcium superoxide is yellow.

In another method, the following description was made:

> "About 10 g of dry commercially obtained calcium peroxide was mixed with 0.5 g KOH and heated to about 400–500 °C to thoroughly dry it by passing oxygen through it. After cooling, the powder was subjected to a stream of dry 3% ozone for about 2 h at room temperature. At this time, the reaction mixture containing calcium ozonide is subjected to a stream of dry oxygen and the temperature is raised to about 100 °C. After about 1 h, the reaction mixture is cooled and the resulting calcium superoxide is recovered and maintained free from moisture".
>
> About 100 g of calcium nitrate mixed with about 1 g Na_2O_2 is first heated to about 350–400 °C in flowing oxygen for several minutes. The dry calcium nitrate is then allowed to cool and is subjected to a stream of a dry 3% ozone–oxygen mixture at room temperature. After about 2 h, the resulting calcium ozonide is subjected to oxygen at about 60–80 °C and the calcium superoxide is recovered.

Both the superoxide and ozonide products of calcium are decomposed by water so that moisture should be excluded from the reaction site and from the product obtained. Thus, the ozone–oxygen mixture should be free from moisture, and storage containers should be blanketed with a dry gas. Ordinary ambient temperatures, about 20–30 °C, can be used, but because of the tendency of the ozonides to decompose at even moderately elevated temperatures, it is preferred to use low temperatures. Temperatures as low as −80 °C and lower are feasible for use in carrying out the process, but the reaction at such low temperatures is quite slow. The preferred temperature is about 0 °C, where the reaction takes place at a satisfactory rate while little or no decomposition is ordinarily encountered. Temperatures higher than 30 °C. should be avoided.

In the case of $Ca(O_2)_2$, the reaction gives primarily the 3_B2 open bent O_2CaO_2 superoxide product, but the reaction in condensed N_2 favors the 1_A1 cyclic CaO_2 peroxide species. Calcium superoxide, O_2CaO_2, is characterized as a D_{2d} species with +1.12 charge on Ca and −0.28 on each O, in contrast to calcium peroxide, CaO_2, a C_{2v} molecule with +1.05 charge on Ca and −0.525 on each oxygen atom.

Calcium ozonide, CaO_6 or $Ca(O_3)_2$, decomposes appreciably at 25 °C, strontium ozonide a little below 0 °C, and barium ozonide at 0 °C. Calcium and oxygen isotopic data (^{44}Ca and ^{18}O) strongly support the observation of rhombic CaO_4 and isosceles triangular CaO_6 species.

Neither calcium ozonide nor calcium superoxide is available commercially.

Strontium Hyperoxides

The reaction of a solution of ozone in Freon 12 with a suspension of strontium peroxide in the same medium at a negative temperature gives a mixture of the ozonide $Sr(O_3)_2$ and the superoxide $Sr(O_2)_3$. The ozonide is not formed above –70 °C, and the superoxide is not formed above –20 °C. The heating curve for the preparation obtained at –100 °C is characterized by the presence of one endothermic effect which begins at –173 °C and is accompanied by a vigorous evolution of oxygen. This decomposition effect, corresponding to the ozonide transforming into the superoxide, could not be separated. Thus, the decomposition relates to the formation of a mixture of the two compounds:

$$2SrO_2 + 2O_3 \Rightarrow Sr(O_3)_2 + Sr(O_2)_2$$

and is caused by the transfer of an electron from the negatively doubly charged O_2^{2-} ion to ozone.

Strontium peroxide forms a hydrogen peroxide "hydrate", i.e. $SrO_2 \cdot 2H_2O_2$ which decomposes at 50 °C to form a series of compounds, including the superoxide:

$$SrO_2 \cdot 2H_2O_2 \Rightarrow Sr(O_2)_2\ (36\%) + SrO_2\ (56\%) + Sr(OH)_2\ (8\%)$$

ESR spectroscopy showed that the product obtained as the result of the disproportionation of SrO_2 $2H_2O_2$ contains strontium superoxide [$Sr(O_2)_2$] with a paramagnetic O_2^- molecular anion.

Strontium ozonide has been synthesized, starting from cesium ozonide, via cation exchange in liquid ammonia. From these solutions, if kept at −78 °C for 14 days, an ammoniate, $Sr(O_3)_2 \cdot 9NH_3$, crystallizes. The coarse, ruby red crystals decompose above the boiling temperature of ammonia and are extremely sensitive to moisture. According to a single-crystal structure determination (P4/nmm; $a = 7.597$ Å, $Z = 2$); $Sr(O_3)_2 \cdot 9NH_3$ consists of ozonide anions and strontium cations. The complex cations form an virtual cubic close packing, where the octahedral and half of the tetrahedral interstices are occupied by ozonide anions. The anions are orientationally disordered.

There are no listed suppliers for either the ozonide or superoxide of strontium.

Barium Hyperoxides

The reaction of a solution of ozone in Freon 12 with a suspension of barium peroxide in the same medium at a negative temperature gives a mixture of the ozonide $Ba(O_3)_2$ and the hyperoxide $Ba(O_2)^2$. The ozonide is not formed above –70°, and the superoxide is not formed above –40°. The formation of barium ozonide $Ba(O_3)_2$ with a yield of 82% of the basic substance by the reaction of ozone dissolved in Freon-12 with a suspension of barium peroxide in the same medium at –100 to –105° was demonstrated. It was determined that barium ozonide is thermally stable below –70° and that the primary decomposition product of barium ozonide is the superoxide $Ba(O_2)_2$. The thermal stability of these hyperoxide compounds is illustrated in Fig. 3.15.

There is no listed commercial supplier for these compounds and they are not available for sale.

Radium Hyperoxides

No radium hyperoxide compounds are known.

3.2. ALKALINE EARTH OXY-SULFUR COMPOUNDS

The alkaline earths form a series of compounds with sulfur, including sulfides, sulfites and sulfates. These are primarily based upon the acids, H_2S, H_2SO_3 H_2SO_4, and variations thereof. sulfur forms a large number of oxy-sulfur anions including those provided in Table 3.9.

Many of these anions are the result of decomposition of one phase into another. We will describe only those salts that form from the acids or those that have been studied in the scientific literature. Many of these acids, such as dithionic acid, are not stable and are only known in solution. However, it is possible to form stable compounds from the stable acids in solution even though the acids cannot be formed separately.

3.2.1. Oxy-Sulfur Acids

Hydrogen Sulfide

Hydrogen sulfide has the chemical formula of H_2S. It is a colorless, very poisonous, flammable gas with the characteristic foul odor of rotten eggs. It often results from the bacterial breakdown of organic matter in the absence of oxygen, such as in swamps and sewers where anaerobic digestion can take place. It also occurs in volcanic gases, "natural gas", and some well waters. Hydrogen sulfide has numerous names, some of which are archaic.

Hydrogen sulfide is slightly heavier than air with a specific gravity of 1.363 g/l. The CAS number is 7788-06-4 and its molecular weight is 34.0822 g/mol. Its melting point is –80.3 °C and its boiling point is –60.3 °C. A mixture of H_2S and air is explosive. Hydrogen sulfide and oxygen burn with a blue flame to form SO_2 and H_2O. In general, this compound acts as a reducing agent. It is soluble in water at 0.41 g/100 ml (20 °C) and 0.255 g/100 ml (90 °C). H_2S is soluble in carbon disulfide, methanol, acetone and alkanolamines. The heat of formation, ΔH_f, is –20.599 kJ/mol.

Hydrogen sulfide is somewhat soluble in water and acts as a weak acid, giving both the hydrosulfide ion HS^- ($pK_a = 6.9$ in 0.01–0.1 mol/l solutions at 18 °C) and the sulfide anion S^{2-} ($pK_a = 11.96$):

$$H_2S \Leftrightarrow HS^- + H^+ \Leftrightarrow S^= + H^+$$

A solution of hydrogen sulfide in water is initially clear but over time turns cloudy. This is due to the slow reaction of hydrogen sulfide with the oxygen

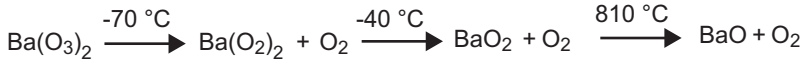

FIGURE 3.15

TABLE 3.9

Name	Formula
Peroxomonosulfate	SO_5^{2-}
Sulfate	SO_4^{2-}
Sulfite	SO_3^{2-}
Peroxodisulfate	$S_2O_8^{2-}$
Pyrosulfate	$S_2O_7^{2-}$
Dithionate	$S_2O_6^{2-}$
Metabisulfite	$S_2O_4^{2-}$
Dithionite	$S_2O_4^{2-}$
Thiosulfate	$S_2O_3^{2-}$
Tetrathionate	$S_4O_6^{2-}$

dissolved in water, yielding elemental sulfur, which precipitates out.

Small amounts of hydrogen sulfide occur in crude oil, but natural gas can contain up to 90%. About 10% of the total global emission of H_2S is due to human activity. By far the largest industrial route to H_2S occurs in petroleum refineries. The "hydrodesulfurization" process liberates sulfur from petroleum by the action of hydrogen. The resulting H_2S is converted to elemental sulfur by partial combustion via the Claus process that is a major source of elemental sulfur (In the Claus process, hydrogen sulfide is catalytically reacted with oxygen from the air to produce sulfur and sulfur dioxide). Other anthropogenic sources of hydrogen sulfide include coke ovens, paper-mills (using the sulfate method), and tanneries, where Na_2S is used for processing cowhide to form leather. H_2S arises from virtually anywhere where elemental sulfur comes in contact with organic material, especially at high temperatures.

Hydrogen sulfide is extremely lethal and 0.0047 ppm (4.7 ppb) in the air is the "recognition threshold", the concentration at which 50% of humans can detect the characteristic odor of hydrogen sulfide: less than 10 ppm has an exposure limit of 8 h per day; 10–20 ppm is the borderline concentration for eye irritation; 50–100 ppm leads to eye damage; at 150–250 ppm the olfactory nerve is paralyzed after a few inhalations, and the sense of smell disappears, often together with awareness of danger; 320–530 ppm leads to pulmonary edema with the possibility of death; 530–1000 ppm causes strong stimulation of the central nervous system and rapid breathing, leading to loss of breathing; 800 ppm is the lethal concentration for 50% of humans for 5-min exposure; and concentrations over 1000 ppm cause immediate collapse with loss of breathing, even after inhalation of a single breath.

Sulfurous Acid

Sulfurous acid has the formula H_2SO_3 and the molecular weight of 82.075 g/mol. Its CAS number is 7782-99-2. There is no clear evidence that sulfurous acid exists in solution, but the molecule has been detected in the gas phase. The conjugate bases of this elusive acid are, however, common anions: bisulfite (or hydrogensulfite) = HSO_3^- and sulfite, $SO_3^=$. Bisulfite salts are typically prepared by treatment of alkaline solutions with excess sulfur dioxide:

$$SO_2 + NaOH \Rightarrow NaHSO_3$$

HSO_3^- is the conjugate base of sulfurous acid, H_2SO_3 and its appearance is a function of solution pH:

$$H_2SO_3 \Leftrightarrow HSO_3^- + H^+$$

Sulfurous acid has not been isolated as a separate compound and does not appear to exist in solution either. An equilibrium that is much more consistent with spectroscopic evidence is given as:

$$SO_2 + H_2O \Leftrightarrow HSO_3^- + H^+$$

HSO_3^- is a weak acidic species with a pK_a of 6.97. Its conjugate base is the sulfite anion, SO_3^{2-}:

$$HSO_3^- \Leftrightarrow SO_3^{2-} + H^+$$

Bisulfites are reducing agents, as are all sulfites and sulfur dioxide, which contains sulfur in the same oxidation state of +5. Raman spectra of solutions of sulfur dioxide in water show only signals due to the SO_2 molecule and the bisulfite ion, HSO_3^-. The intensities of the signals are consistent with the following equilibrium:

$$SO_2 + H_2O \Leftrightarrow HSO_3^- + H^+$$

$$K_a = 1.54 \times 10^{-2};\ pK_a = 1.81.$$

Aqueous solutions of sulfur dioxide, which sometimes are referred to as "sulfurous acid" are used as reducing agents and as disinfectants, as are solutions of bisulfite and sulfite salts. They are also mild bleaches, and are used for materials that may be damaged by chlorine-containing bleaches.

Sulfuric Acid

Sulfuric (or sulfuric) acid, H_2SO_4, is a strong mineral. It is soluble in water at all concentrations. Sulfuric acid has many applications, and is one of the top products of the chemical industry. World production in 2001 was 165 million tons, with an approximate value of $8 billion.

Sulfuric acid is produced from sulfur, oxygen and water via the conventional contact process (DCDA) or the wet sulfuric acid process (WSA). Principle uses include lead acid batteries for cars and other vehicles,

ore processing, fertilizer manufacturing, oil refining, wastewater processing, and chemical synthesis.

Pure (undiluted) sulfuric acid is not encountered naturally on Earth, due to its great attraction for water. Sulfuric acid is a constituent of acid rain, which is formed by oxidation of sulfur dioxide by oxygen in the air in the presence of water—i.e. oxidation of sulfurous acid to sulfuric acid. Sulfur dioxide is the main by-product produced when sulfur-containing fuels such as coal or oil are burned.

Sulfuric acid is formed naturally on the Earth by the oxidation of certain sulfide minerals, such as iron sulfide. The resulting water can be highly acidic and is called acid-mine-drainage or acid-rock-drainage. This acidic water is capable of dissolving metals present in sulfide ores, which results in brightly colored, toxic streams. Sulfuric acid is produced in the upper atmosphere of the planet Venus by a photochemical reaction induced by the Sun's rays on carbon dioxide, sulfur dioxide and water vapor. Ultraviolet photons of wavelengths less than 169 nm can photodissociate carbon dioxide into carbon monoxide and atomic oxygen. The atomic oxygen is highly reactive and reacts with the SO_2 to produce SO_3 that can combine with water vapor, another trace component of Venus's atmosphere, to yield sulfuric acid. In the upper, cooler portions of Venus's atmosphere, sulfuric acid exists as a liquid, and thick sulfuric acid clouds completely obscure the planet's surface when viewed from above. The main cloud layer extends from 45 to 70 km above the planet's surface, with thinner hazes extending as low as 30 and as high as 90 km above the surface. The permanent Venusian clouds produce a concentrated acid rain, just as the clouds in the atmosphere of Earth produce water rain.

The discovery of sulfuric acid is credited to the eighth century Muslim alchemist, Jabir ibn Hayyan. The acid was later studied by the ninth century Persian and alchemist Ibn Zakariya (Rhazes), who obtained the substance by dry distillation of minerals including iron(II) sulfate heptahydrate, $FeSO_4 \cdot 7H_2O$, and copper(II) sulfate pentahydrate, $CuSO_4 \cdot 5H_2O$. When heated, these compounds decompose to Fe_2O_3 and CuO, respectively, giving off water and sulfur trioxide, which combine to produce a dilute solution of sulfuric acid. This method was popularized in Europe through translations of Arabic and Persian treatises, as well as books by European alchemists, such as the thirteenth century German Albertus Magnus.

Sulfuric acid was known to medieval European alchemists as *oil of vitriol*, *spirit of vitriol*, or simply *vitriol*, among other names. The word vitriol derives from the Latin vitreus, "glass", referring to the glassy appearance of the hydrated sulfate salts, which also carried the name vitriol. Salts called by this name included $CuSO_4$ (blue vitriol, or rarely Roman vitriol), $ZnSO_4$ (white vitriol), $FeSO_4$ (green vitriol), $Fe_2(SO_4)_3$ (vitriol of Mars), and $CoSO_4$ (red vitriol). However, red vitriol is also a twentieth century technical name for a grade of sulfuric acid.

In the seventieth century, sulfuric acid was prepared by burning sulfur together with KNO_3, in the presence of steam. As saltpeter decomposes, it oxidizes the sulfur to SO_3, which combines with water to produce sulfuric acid. This method was used in 1736, to begin the first large-scale production of sulfuric acid.

In 1746 in Birmingham, John Roebuck adapted this method to produce sulfuric acid in lead-lined chambers, which were stronger, less expensive, and could be made larger than the previously used glass containers. This "lead-chamber" process allowed the effective industrialization of sulfuric acid production. After several refinements, this method remained standard for sulfuric acid production for almost two centuries. This method used "lead chambers" where sulfur dioxide was introduced along with steam and oxides of nitrogen into three large chambers lined with sheet lead where the gases are sprayed down with water and chamber acid. The sulfur dioxide and nitrogen dioxide dissolved and over a period of a few tens of minutes, the sulfur dioxide oxidized to sulfuric acid. The presence of nitrogen dioxide was necessary for the reaction to proceed. The process is highly exothermic, and a major consideration of the design of the chambers was to provide a way to dissipate the heat formed in the reactions. Early manufacturing plants used very large wooden rectangular chambers (Faulding box chambers) that were cooled by ambient air. Around the turn of the nineteenth century, such plants required about half a cubic meter of volume to process the sulfur dioxide equivalent of a kilogram of burned sulfur. In 1831, British merchant Peregrine Phillips patented the "Contact method", which was a far more economical process for producing sulfur trioxide and concentrated sulfuric acid. Today, nearly all of the world's sulfuric acid is produced using this method. Sulfuric acid is produced today from sulfur, oxygen and water either by the conventional "Contact process" or the "wet sulfuric acid" process.

In the first step of the **Contact process**, sulfur is burned to produce sulfur dioxide:

$$S(\text{solid}) + O_2(\text{gas}) \Rightarrow SO_2(\text{gas})$$

This is then oxidized to sulfur trioxide using oxygen in the presence of a vanadium(V) oxide catalyst.

$$2SO_2 + O_2(\text{gas}) \Rightarrow 2SO_3(\text{gas}) \text{ (in the presence of } V_2O_5)$$

The sulfur trioxide is absorbed into 97–98% H_2SO_4 to form "oleum" ($H_2S_2O_7$), also known as "fuming sulfuric

acid". The oleum is then diluted with water to form concentrated sulfuric acid. The reactions are:

$$H_2SO_4(liq) + SO_3(gas) \Rightarrow H_2S_2O_7(liq)$$

$$H_2S_2O_7(liq) + H_2O(liq) \Rightarrow 2H_2SO_4(liq)$$

Note that directly dissolving SO_3 in water is not practical due to the highly exothermic nature of the reaction between sulfur trioxide and water. The reaction forms a corrosive aerosol that is very difficult to separate, instead of a liquid.

$$SO_3(gas) + H_2O(liq) \Rightarrow H_2SO_4(gas\ and\ liq)$$

In the first step of the **wet sulfuric acid** method, sulfur is burned to produce sulfur dioxide:

$$S(solid) + O_2(gas) \Rightarrow SO_2(gas)$$

or, alternatively, H_2S gas is incinerated to SO_2 gas:

$$2H_2S(gas) + 3O_2(gas) \Rightarrow 2H_2O(gas) + 2SO_2(gas)\ (+518\ kJ/mol)$$

This is then oxidized to sulfur trioxide using oxygen with V_2O_5 as a catalyst.

$$2SO_2(gas) + O_2(gas) \Rightarrow 2SO_3(gas)\ (+99\ kJ/mol)$$

The sulfur trioxide is hydrated into sulfuric acid H_2SO_4:

$$SO_3(gas) + H_2O \Rightarrow H_2SO_4(gas)\ (+101\ kJ/mol)$$

The last step is the condensation of the sulfuric acid to liquid 97–98% H_2SO_4:

$$H_2SO_4(gas) \Rightarrow H_2SO_4(liq)\ (+69\ kJ/mol)$$

The overall process can be summarized as shown in Fig. 3.16.

The technology is able to treat one or more sulfur-containing streams such as:

- H_2S gas from amine-gas treating units.
- Off-gas from sour water strippers (SWS gas).
- Spent acid from alklyation units.
- Claus process tail gas.
- Heavy residue or petcoke-fired utility boiler off-gas.
- Boiler flue gases from various processes.
- Metallurgical process gas.

Prior to 1900, most sulfuric acid was manufactured by the lead chamber process.

The current process (2005) used to manufacture H_2SO_4 is shown in Fig. 3.17.

This process takes advantage of the fact that several steps in the manufacturing are highly exothermic. The heat is absorbed in water and then transferred to the steps that are more endothermic. The process starts with dry air from the drying tower and sulfur which is "burned" in air to form a gas containing about 10% SO_2 at a temperature of 950–1000 °C. The first boiler removes some of that heat so that the gas entering the #1 catalytic section of the catalytic converter is about 420 °C (the optimum temperature for conversion) where about 60–65% of the SO_2 is converted to SO_3. The reaction is very exothermic and the gas remainder is cooled in the #2 boiler before entering the #2 section of the converter. From there, the gas stream is directed to the "hot-heat" exchanger before entering the #3 section. From there, the gas stream is directed through the "cold-heat" exchanger and then through the "first-absorber" where the SO_3 is allowed to react with water to form the acid. The gas stream, at about 80 °C, is directed back through the "hot-heat" exchanger where its temperature is adjusted and then through the final stage #4 section of the converter.

The gas stream, which is now essentially all SO_3 gas (>99.5%), goes to the final absorber and the depleted gas stream is directed to the stack. The liquid stream is directed among various stages of acid pumps and water is added. The acid stream is finally cooled and directed to the "drying-tower" and then to "acid-storage".

This manufacturing design process was mandated by the legislation regarding "acid rain", therein, all stack emissions must contain no more than 0.5% SO_2 in their emissions to the atmosphere. Sulfuric acid is a very important commodity chemical, and indeed, a nation's sulfuric acid production is a good indicator of its industrial strength.

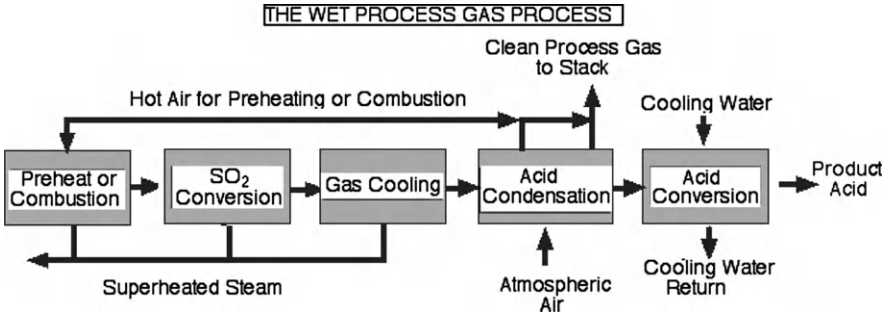

FIGURE 3.16

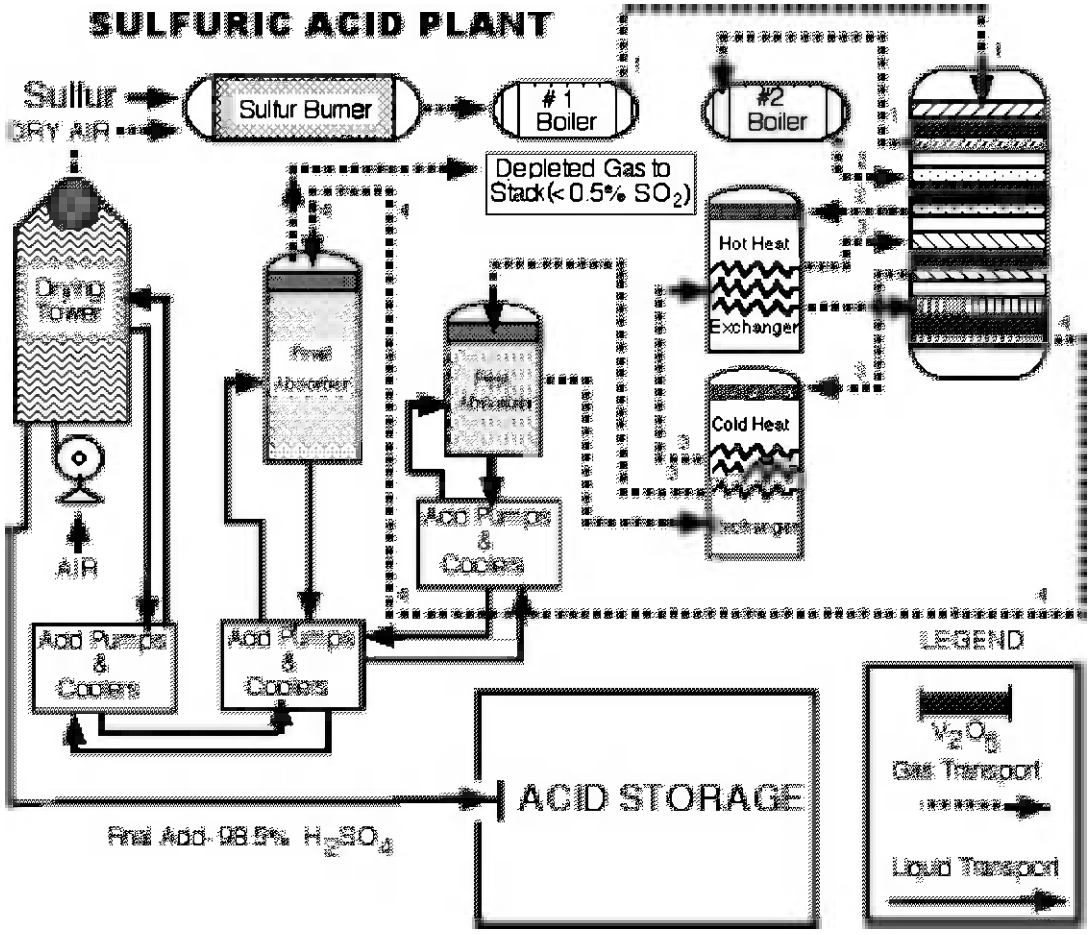

FIGURE 3.17

Thiosulfuric Acid

Thiosulfuric acid is a sulfur oxoacid. The free acid cannot be prepared by acidifying thiosulfate salts as the acid readily decomposes in water. The decomposition products can include S, SO_2 H_2S, H_2SO_4, polysulfanes $= H_2S_n$ and polythionates such as the tetrathionate anion, $S_4O_6^{2-}$, depending on the exact reaction conditions. Anhydrous methods of producing the acid are:

$$H_2S + SO_3 \Rightarrow H_2S_2O_3 \cdot n Et_2O \text{ (in diethyl ether at } -78\ ^\circ C)$$

$$Na_2S_2O_3 + 2HCl \rightarrow 2NaCl + H_2S_2O_3 \cdot 2Et_2O$$
(in diethyl ether at $-78\ ^\circ C$)

$$HSO_3Cl + H_2S \Rightarrow HCl + H_2S_2O_3 \text{ (low temperature)}$$

The anhydrous acid also decomposes below 0 °C:

$$H_2S_2O_3 \Rightarrow H_2S + SO_3$$

There is another isomeric form, a white crystalline adduct of hydrogen sulfide and sulfur trioxide, $H_2S \cdot SO_3$, which can also be prepared at low temperature. Thiosulfuric acid contains the sulfur in the +6 oxidation state and has the Lewis structure shown in Fig. 3.18.

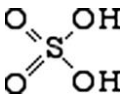

FIGURE 3.18

where the molecule is tetrahedral. The CAS number is 13686-28-7 and its molecular weight is calculated to be 114.145 g/mol. It decomposes below 0 °C in nonaqueous media and goes directly to sulfur and sulfur dioxide in water.

Pyrosulfuric Acid or Disulfuric Acid

Although the salts are called pyrosulfates, the acid is called disulfuric acid. Disulfuric acid has the molecular formula of $H_2S_2O_7$ where the S-atom is in the +5 oxidation state and a Lewis structure shown in Fig. 3.19.

Its CAS number is 7783-05-3 and its molecular weight is 178.1417 g/mol. It melts at 36 °C. It is a major

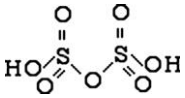

FIGURE 3.19

constituent of fuming sulfuric acid (also known as "oleum") described by the formula $ySO_3 \cdot H_2O$ where y is the total molar sulfur trioxide content. The value of y can be varied, to include different types of "oleum". They can also be described by the formula: $H_2SO_4 \cdot xSO_3$, which are also minor constituents of liquid anhydrous sulfuric acid due to the equilibria:

$$H_2O + SO_3 \Leftrightarrow H_2SO_4 + SO_3 \Leftrightarrow H_2S_2O_7$$

Thus, the disulfuric acid is prepared by reacting excess SO_3 with sulfuric acid:

$$H_2SO_4 + SO_3 \Rightarrow H_2S_2O_7$$

Disulfuric acid is a strong acid and protonates sulfuric acid in the (anhydrous) sulfuric acid solvent system. An alternative IUPAC name is *(sulfo-oxy)sulfonic acid*.

Dithionic Acid

Dithionic acid, $H_2S_2O_6$, is a chemical compound known only in solution. This acid is dibasic and salts called dithionates are known. All dithionates are readily soluble in water. They are mild oxidizing and mild reducing agents. The structure of dithionate ion is like ethane, but two SO_3 groups adopt an almost eclipsed conformation. The S–S length is 2.15 Å; S–O bonds are rather short with bond length of 1.43 Å. The Lewis structure is shown in Fig. 3.20.

The sulfur atoms are in the +6 oxidation state and are directly bonded to each other. In the pyrosulfate molecule, they are separated by an oxygen atom. Only a few dithionates are known, including barium dithionate. All of the other alkaline earth dithionates are less stable and have not been studied extensively. Thus, for the alkaline earths combined with sulfur-containing compounds, one would expect to find sulfides and salts of the oxo-sulfur acids:

Sulfides = MS
Sulfites
Hydrogen sulfites (Bisulfites)
Sulfates
Thiosulfates
Pyrosulfates or disulfates
Dithionates or tetrathionates

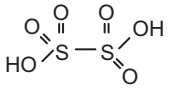

FIGURE 3.20

3.2.2. Alkaline Earth Sulfides

Beryllium Sulfide

Beryllium sulfide has the molecular formula of BeS and the molecular weight of 41.077182 g/mol. It can be prepared by the direct reaction of the elements, calcined in an inert atmosphere, at a 1.0:1.05 molecular ratio:

$$Be + S + \text{heat} \Rightarrow BeS$$

Beryllium does not form a polysulfide. Its CAS number is 13598-22-6. Its density is 2.36 g/cm^3 and its refractive index is 1.741. Its crystals are isometric and the structure is of the cubic-sphalerite type. The space group is $F\bar{4}3m$ (T_4^2) with the unit-cell dimension of $a = 4.862$ Å. There are four BeS units per cell. Crystals are isotropic (Fig. 3.21).

Due to their large energy gap and hardness, beryllium sulfides and selenides are interesting materials for improving the lifetime of optical devices made of other II-VI-semiconductors by forming multicombinatory alloys, notably with ZnS or CdS. Among them, beryllium sulfide (BeS) is an indirect semiconductor with a band gap of 7.4 eV direct and 4.7 eV indirect. BeS, which has only been prepared in powder form, is the only sulfur-containing II-VI-compound without any published experimental information about its electronic structure. This is due to the fact that the commonly employed method of choice (photoelectron spectroscopy) cannot be applied to this insulating powder because of charging effects, the lack of a suitable surface preparation method, and the fact that no sufficiently large single crystals have been available. According to theory, BeS is an indirect semiconductor material with the highest valence band edge at Γ and the lowest conduction band edge at X. The electrical conductivity of BeS has been found to be p-type. This has been attributed to Be vacancies or $S^=$ interstitials.

Thermodynamic properties of BeS are:

$$\Delta H_f = -234.3 \text{ kJ/mol}$$

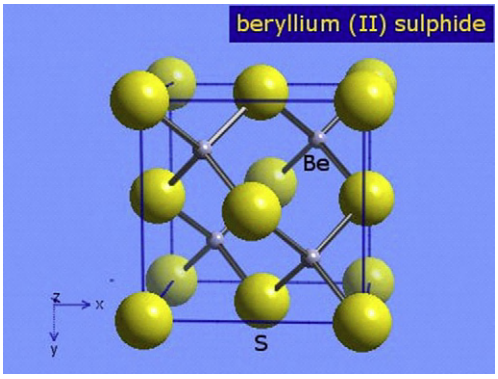

FIGURE 3.21

$$S_0 = 34.0\ \mathrm{J/mol\cdot{}^\circ K}$$

$$C_p = 34\ \mathrm{J/mol\cdot{}^\circ K}$$

Danalite is an iron, beryllium sulfo-silicate mineral with the formula: $(Fe^{2+})_4Be_3(SiO_4)_3S$. It is a rare mineral that occurs in various types of granites, pegmatites, and gneisses. It has been found at a number of places in the U.S., Canada, England, Russia, Australia and Japan.

Beryllium sulfide is available in limited quantities commercially.

Magnesium Sulfide

Magnesium sulfide has the molecular formula of MgS and the molecular weight of 58.3826 g/mol. It can be prepared by the direct reaction of the elements, calcined in an inert atmosphere, at a 1:1.1 molecular ratio:

$$\mathrm{Mg + S + heat \Rightarrow MgS}$$

Its CAS number is 12032-36-9. Its density is 2.68 g/cm^3 and its melting point is 2085 °C. MgS also forms by the reaction of hydrogen sulfide gas with soluble magnesium salts in solution. Aside from being a component of some slags, MgS is a rare **nonterrestial** mineral "niningerite" detected in some meteorites. MgS is also found in the circumstellar envelopes of certain evolved "carbon-stars", i.e. C/O > 1. Magnesium polysulfide, MgS_x, does not exist at ambient temperature and pressure.

MgS is a white crystalline material but is often encountered in an impure form that is a brown noncrystalline powder. It crystallizes in the rock salt structure (cubic-cF8 and space group = $Fm\bar{3}m$ (#225). The lattice parameters are: $a = 5.20182$ Å, $V = 140.76$ Å^3, $Z = 4$. The effective radius and electron density of the Mg atom in the crystal was found to be 1.28 Å, yielding a net charge of +1.50 (Fig. 3.22).

The chemical properties of MgS resemble those of related ionic sulfides such as those of Na, Ba, and Ca. It reacts with oxygen to form the corresponding sulfate, magnesium sulfate. MgS reacts with water to give hydrogen sulfide and magnesium hydroxide.

It is generated industrially in the production of metallic iron. In the BOS steel-making process, sulfur is the first element that needs to be removed. Sulfur is removed from the impure blast furnace iron by the addition of several hundred kilograms of magnesium powder. Magnesium sulfide is formed, which then floats on the molten iron and is then removed.

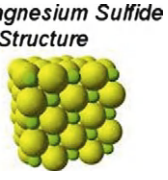

FIGURE 3.22

MgS is a wide band gap direct semiconductor of interest as a blue-green emitter, a property that has been known since the early 1900s. Although MgS has been considered as a phosphor for television and the like, its efficiency as a cathode ray emitter is not as great as those of its calcium and strontium homologues.

Atomic and bulk properties of rare earth doped wide band gap semiconductors, particularly alkaline earth sulfides, have been tailored and a novel storage technique, "power-gated hole burning", has been devised. It has been demonstrated that this combination of materials and method of storage allows for ultradense, fast, persistent, and rewriteable spectral memories. The improvement in performance parameters has been by orders of magnitude, and more importantly, all favorable characteristics of spectral storage have been combined in a single material, magnesium sulfide doped with Europium. It has been demonstrated that with the exception of low-temperature operation, the performance of this materials matches or exceeds the standards of current commercial memories. On the basis of these investigations, it is apparent that almost all barriers to a commercially viable device based on spectral hole burning can be removed.

The lattice energy for MgS has been calculated:

$$\mathrm{Mg^{2+}(gas) + S^{2-}(gas) \Rightarrow MgS(solid)}$$

$$\Delta H^\circ_{\mathrm{MgS}} = -3406\ \mathrm{KJ/mol}$$

Magnesium sulfide is available commercially from a number of suppliers.

Calcium Sulfide

Calcium sulfide has the molecular formula of CaS and the molecular weight of 74.1432 g/mol. It can be prepared by the direct reaction of the elements, calcined in an inert atmosphere, at a 1:1.05 molecular ratio:

$$\mathrm{Ca + S + heat \Rightarrow CaS}$$

This white material crystallizes in a cubic structure-like rock salt and the bonding is highly ionic. This is consistent with its description as an ionic solid.

In the crystal, each S^{2-} ion is surrounded by an octahedron of six Ca^{2+} ions, and complementarily, each Ca^{2+} ion surrounded by six S^{2-} anions. Like many salts containing sulfide ions, CaS typically has an odor of hydrogen sulfide, a foul-smelling gas, which results from a small amount of this gas being formed from hydrolysis of the salt by atmospheric moisture (Fig. 3.23).

Its CAS number is 20548-54-3 and its density is 2.59 g/cm^3. Its melting point is 2528 °C and it is slightly soluble in water but insoluble in alcohol. It

TABLE 3.10

Thermodynamic values for MgS

Enthalpy of formation		Entropy of formation		Gibbs free energy		State of matter
(kcal/mol)	(kJ/mol)	(cal/K)	(J/K)	(kcal/mol)	(kJ/mol)	(s)
−82.7	−346.0168	12.03	50.33352	−81.7	−341.8328	

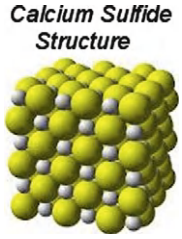

FIGURE 3.23

reacts with acids, producing hydrogen sulfide gas. Calcium sulfide is pale yellow to light gray with a bitter taste. It is hygroscopic, producing an odor of H_2S in moist air. Its refractive index is 2.137 and Mohs hardness is 4.0.

Thermochemical properties
ΔH_f° − 115.30 kcal/mol
ΔG_f° − 114.10 kcal/mol
S° − 13.50 cal/degree·mol
C_P − 11.33 cal/degree·mol

CaS can also be produced by the "carbothermic reduction" of calcium sulfate, which entails the conversion of carbon, usually as charcoal, to CO_2:

$$CaSO_4 + 2C \Rightarrow CaS + 2CO_2$$

This can react further:

$$3CaSO_4 + CaS \Rightarrow 4CaO + 4SO_2$$

Thus, this type of preparation cannot be used to prepare a pure CaS salt. Calcium sulfide decomposes upon contact with water, including moist air, giving a mixture of $Ca(SH)_2$, $Ca(OH)_2$, and Ca(SH)(OH):

$$CaS + H_2O \Rightarrow Ca(SH)(OH)$$

$$Ca(SH)(OH) + H_2O \Rightarrow Ca(OH)_2 + H_2S$$

"Milk of lime", $Ca(OH)_2$, reacts with elemental sulfur to produce a "lime sulfur", which has been used extensively as an insecticide. The active ingredient is probably a calcium polysulfide, not CaS. This salt, CaS_6, has been used in the remediation of Cr(VI) ions in groundwater where the Cr_2S_3 produced is insoluble in water and is easily removed.

A major usage of CaS has been its behavior as a phosphor for CRT and for flat-panel display usage. Although the alkaline earth sulfides have been known to provide excellent hosts as CRT phosphors, their main drawback has been the deleterious hydrolysis behavior experienced when one tries to prepare a CRT screen. That is, they are chemically unstable in water and other solutions generally used in the manufacture of CRTs. Thus, none of these compositions received much attention until the recent past. Of all of these sulfides, only CaS and SrS are stable enough to be used, and only if they are prepared in a suitable manner.

Dry $CaSO_4 \cdot 2H_2O$ is fired in an open silica boat in a tube furnace in an atmosphere of H_2 gas (at about 50 cc per minute gas flow for a 4-inch tube) for 0.5 to 1.0 h at 1000 °C. At the end of this period, the gas flow is changed to that of H_2S (about 100 cc per minute for a 4-inch tube) and the firing continues for another 45 min at 1000 °C. At the end of this period, the boat is pushed into the cool zone and allowed to cool in the H_2S atmosphere. The result is a white, very fluffy CaS powder with no traces of oxide, sulfate, etc. (Note that the use of the H_2S atmosphere is very dangerous and adequate air-scrubbing equipment must be used).

The nominal composition of one phosphor is: $CaS:Ce^{3+}_{0.010}:Cl_{0.050}$. If chloride (or other halide) is not used in the formulation, the resulting composition will be nonluminescent. The emission is green (bands at 520 and 560 nm) and the decay is classified as medium short ($t_{10} = 70$ μs). A good red phosphor can be made using the following composition: $CaS:Ce^{3+}_{0.01}:Eu^{2+}_{0.10}$. The resulting phosphor has its emission peak near to 6500 Å. In this case, the broad emission band is due to the Eu^{2+} activator in the CaS host. Note that the usual blue emission band of Eu^{2+} is shifted to the red region of the spectrum due to the very strong crystal field of the CaS lattice. Although it had a deep red saturation in color and a high screen brightness due its high cathode ray efficiency, it has not been used as a CRT screen to any great extent.

However, $CaS:Eu^{2+}$ and variations thereof is beginning to find usage with blue-emitting light-emitting

diodes (LEDs) to manufacture "white" LED lamps. The highly efficient red-emitting phosphors $(Ca_{1-x}Sr_x)S:Eu^{2+}$ and $(Ca_{1-x}Sr_x)Se:Eu^{2+}$, in combination with commercial green phosphor $SrGa_2S_4:Eu^{2+}$ and a blue LED are proposed for a three-band white LED.

"Oldhamite" is the name for mineralogical form of CaS. It is a rare component of some meteorites and has scientific importance in solar nebula research. Burning of the coal dumps can also produce such compound. Calcium sulfide has several applications. The "luminous" calcium sulfide is used in phosphors, luminous paints and varnishes. Calcium sulfide is also used as an additive to lubricants and as a flotation agent in ore extraction.

When heated in dry air or oxygen, the compound is oxidized to calcium sulfite and then to the sulfate, $CaSO_4$:

$$2CaS + 3O_2 \Rightarrow 2CaSO_3 + O_2 \Rightarrow 2CaSO_4$$

Partial decomposition occurs in hot water with the evolution of H_2S.

Evaporation and crystallization of the solutions give corresponding calcium salts:

$$CaS + 2HCl \Rightarrow CaCl_2 + H_2S$$

Vigorous to violent reactions can occur with oxidizing agents, such as potassium chlorate, potassium nitrate or lead dioxide.

Calcium sulfide is available commercially as the pure sulfide as well as the polysulfide due to its extensive usage in the past as an insecticide both agriculturally and in home gardens.

Strontium Sulfide

Strontium sulfide has the molecular formula of SrS and the molecular weight of 119.6852 g/mol. It can be prepared by the direct reaction of the elements, calcined in an inert atmosphere, at a 1:1.05 molecular ratio:

$$Sr + S + \text{heat} \Rightarrow SrS$$

SrS can also be produced by the "carbothermic reduction" of calcium sulfate, which entails the conversion of carbon, usually as charcoal, to CO_2:

$$SrSO_4 + 2C \Rightarrow SrS + 2CO_2$$

This can react further:

$$3SrSO_4 + SrS \Rightarrow 4SrO + 4SO_2$$

A mixture of oxide–sulfide is the result. Thus, this type of preparation cannot be used to prepare a pure SrS salt. Strontium sulfide has the CAS number of 1314-96-1 and is a gray powder with a density of 3.73 g/cm^3. Its melting point is 2078 °C and it is slightly soluble in water. It decomposes in acids, forming

FIGURE 3.24

hydrogen sulfide gas. It has the cubic halite structure (cF8) and the space group of $Fm\bar{3}m$. Both Sr^{2+} and $S^{=}$ occupy octahedral coordination positions in the lattice and there are four molecules per unit cell (Fig. 3.24).

Strontium sulfide has long been known as a phosphor. It is prepared in the same manner as the calcium sulfide salt. $SrCO_3$ is placed in a silica boat and is fired in a flowing argon atmosphere in a tube furnace (about 200 cc of gas per minute) for about 1.0 h at 1100 °C. At the end of this period, the argon gas is replaced by H_2S gas, using a flow of about 100 cc per minute through a 4-inch tube, and the firing is continued for at least 1.0 more hour. At the end of the firing period, the boat is pushed into a cool zone and allowed to cool. (The same safety precautions discussed above apply).

The result is again a fluffy white powder devoid of oxide, etc. However, it may still contain some Mn^{2+} which imparts a weak yellow fluorescence under either 2537 Å or 3650 Å excitation (This property may be used to detect its presence).

A better way to prepare SrS completely free from Mn^{2+} is as follows. One starts by dissolving $Sr(NO_3)_2 \cdot 4H_2O$ in water. The solution is then heated to near boiling. A few pieces of Mg metal ribbon are added to the solution with stirring. The Mg does not dissolve entirely, but causes heavy metal impurities left in the solution to precipitate preferentially on the metal or to precipitate as hydroxides due to the $Mg(OH)_2$ present in solution. This method is especially successful in removing any Mn^{2+} that may be present which would cause a deviation in the expected spectral properties of the SrS phosphors.

The solution is then filtered and diluted H_2SO_4 is added to precipitate $SrSO_4 \cdot 2H_2O$. The white precipitate is then allowed to settle, is washed with pure water several times, and the supernatant liquid is decanted. Washing continues until the excess sulfate is no longer detected. The precipitate is then filtered, washed in alcohol, and then dried in a vacuum oven at about 100–125 °C overnight.

Dry $SrSO_4 \cdot 2H_2O$ is fired in an open silica boat in a tube furnace in an atmosphere of H_2 gas for 0.5 to 1.0 h at 1000 °C. At the end of this period, the gas flow is changed to that of H_2S and the firing continues for another 45 min at 1000 °C. At the end of this period, the boat is pushed into the cool zone and allowed to

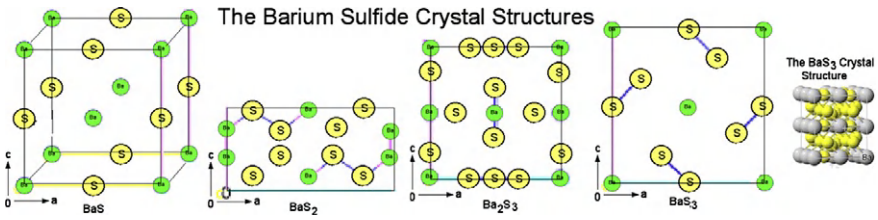

FIGURE 3.25

cool in the H_2S atmosphere. The result is a white, very fluffy SrS powder with no traces of oxide, sulfate, etc. (Note that the use of the H_2S atmosphere is very dangerous and adequate air-scrubbing equipment must be used.)

It is important to store the SrS powder under dry conditions before it is used to prepare the phosphor compositions. SrS itself is somewhat hygroscopic before use and needs to be protected from the atmosphere. A satisfactory formula for SrS is SrS = 1.0 mol; CeO_2 = 0.0050 mol; NH_4Cl = 0.0055 mol; S = 0.0624 mol. The mix is then placed in a covered silica crucible and fired in a tube furnace with a flowing H_2S atmosphere for 2 h at 1200 °C. After firing, when the phosphor cakes are cool, they are inspected under ultraviolet light and crushed. This green-emitting phosphor is then sifted through a 325-mesh screen and then is washed in alcohol. It is then filtered and dried at 125 °C in air for 12 h. The best phosphor is composed of: $Ca_{0.5}Sr_{0.4}S{:}Ce_{0.01}{:}Cl_{0.0075}$.

Strontium sulfide is available commercially but not in a "phosphor-grade".

Barium Sulfide

Barium sulfide has the molecular formula of BaS and the molecular weight of 169.3942 g/mol. It can be prepared by the direct reaction of the elements, calcined in an inert atmosphere, at a 1:1.05 molecular ratio:

$$Ba + S + \text{heat} \Rightarrow BaS$$

Its CAS number is 21109-95-5. If the sulfur is in excess, barium also forms several other sulfides. Among them are:

Barium hydrosulfide, $Ba(SH)_2$ [CAS = 25417-81-6]

Barium disulfide, BaS_2 [CAS = 12230-99-8]

Dibarium trisulfide, Ba_2S_3 [CAS = 53111-28-7]

Barium trisulfide, BaS_3 [CAS = 12231-01-5]

Barium pentasulfide, BaS_5 [CAS = 12448-68-9]

If the precipitation occurs in an aqueous solution, the product will be:

Barium tetra-sulfide monohydrate, $BaS_4 \cdot H_2O$ [CAS = 12248-67-8].

A two-dimensional structural comparison of some of these compounds is shown in the above diagram where a three-dimensional structure is also included (Fig. 3.25).

The change in arrangement of the sulfide atoms within the unit cells is typical of the alkaline earth sulfide systems in general.

BaS is a colorless crystalline solid with a density of 4.25 g/cm^3; its refractive index is 2.155 and it melts at 1200 °C. BaS is soluble in water (decomposes) but is insoluble in alcohol.

Thermochemical properties

ΔH_f^0 −110 kcal/mol
ΔG_f^0 −109 kcal/mol
S^0 −18.7 cal/degree mol
C_P −11.8 cal/degree mol

Barium sulfide is prepared commercially by heating barite (BaO) with coal or petroleum coke in a rotary kiln at 1000 °C to 1250 °C in an oxygen-free atmosphere. The product, black ash, is a gray or black powder containing carbonaceous impurities and unreacted barite. Barium sulfide is separated from impurities by extraction with hot water and filtration. It is obtained as an aqueous solution of 15–30% strength. The commercial product is 80% to 90% BaS. Barium sulfide may also be made by high temperature reduction of barium sulfate with methane.

Barium sulfide dissolves in water, dissociating to about 10%, forming barium hydrosulfide and barium hydroxide:

$$2BaS + 2H_2O \Rightarrow Ba(SH)_2 + Ba(OH)_2$$

The solution is highly alkaline. When the aqueous solution is cooled, crystals of barium hydroxide appear first. The aqueous solution of barium sulfide oxidizes slowly in the air forming elemental sulfur and various anions of sulfur including sulfite, thiosulfate, polysulfides and sulfate. The yellow color of barium sulfide solution is attributed to the presence of dissolved elemental sulfur that results from its slow oxidation in the air. In the presence of an oxidizing agent, barium sulfate is formed.

Violent to explosive oxidation may occur when BaS is heated with strong oxidants such as phosphorus pentoxide or potassium chlorate. Barium sulfide undergoes double decomposition reactions with hydrochloric acid

and nitric acid, giving barium chloride and barium nitrate, respectively, when the solution is evaporated. Reaction with carbon dioxide produces barium carbonate and hydrogen sulfide:

$$BaS + CO_2 + H_2O \Rightarrow BaCO_3 + H_2S$$

Barium sulfide is available commercially in large lots from many manufacturers.

Radium Sulfide

Radium sulfide has the molecular formula of RaS and the molecular weight of grams per mole. It can be prepared by the direct reaction of the elements, calcined in an inert atmosphere, at a 1:1.05 molecular ratio:

$$Ra + S + \text{heat} \Rightarrow RaS$$

It has no CAS number. If the sulfur is in excess, radium undoubtedly forms several other sulfides. However, this aspect has never been studied. There is very little information available for RaS and there is no qualified manufacturer of radium sulfide.

3.2.3. Alkaline Earth Sulfites and Bisulfites

Sulfurous acid is a diprotic acid and the anions involve either the HSO_3^- ("Bisulfite") or the SO_3^{2-} (sulfite) ion. The appearance of these two anions in solution is a function of pH and the manner in which they are prepared. If a basic salt such as sodium sulfite is used, the product will be a sulfite because of the basicity of Na^+ in solution. The ratio of **bisulfite to sulfite** at pH 6.0 is 8:1. At pH 8, the opposite is true. The pure sulfite ion is obtained at pH 10–11. To obtain such a pH, sodium sulfite is usually added to sodium sulfite before the solution is used to prepare an alkaline earth sulfite. Ammonium sulfite may be added to achieve an intermediate pH and bisulfite anions. A diagram illustrating this behavior follows (Fig. 3.26).

All of the alkaline earths form bisulfites and sulfites. The cations added to achieve a certain pH are shown in the upper part of this diagram. The addition of SO_2 gas to sodium hydroxide first generates sodium sulfite. The addition of excess SO_2 gas to sodium sulfite serves to reverse the pH in the solution, thus forming bisulfite:

$$2NaOH + SO_2 \Rightarrow Na_2SO_3 + H_2O$$

$$Na_2SO_3 + SO_2 + H_2O \Rightarrow 2NaHSO_3$$

Thus, sulfur dioxide forms both sulfite and bisulfite anions in water:

$$SO_2(aq) \Leftrightarrow H^+ + HSO_3^-$$

$$pK_a = 1.98\ (K_a = 1.05 \times 10^{-2})$$

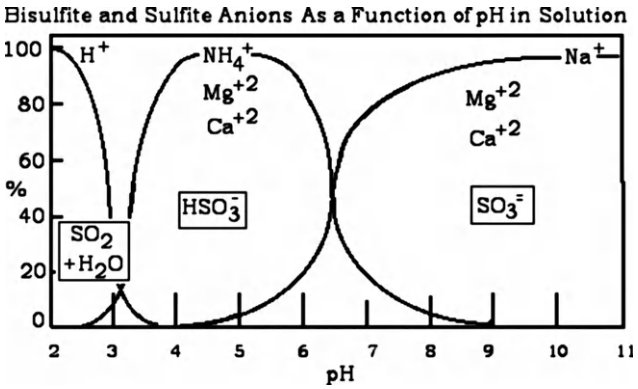

FIGURE 3.26

$$HSO_3^- \Leftrightarrow H^+ + SO_3^{2-} \quad pK_a = 7.30\ (K_a = 5.02 \times 10^{-8})$$

and at very high concentrations:

$$HSO_3^- + SO_2(aq) \Leftrightarrow HS_2O_5^-$$

$$K_a = 1.55 \times 10^{-2};\ pK_a = 1.81$$

Such ratios of bisulfite/sulfite are particularly important in the "wood-pulping" industry to manufacture paper.

The solubilities of the alkaline earth sulfites vary greatly as one progresses down the Group 2 series:

If one wishes to determine the dependence of the distribution of ionic species as a function of pH for a diprotic acid such as H_2SO_3, the simplest approach is to express the concentration of the three forms (H_2SO_3, HSO_3^-, and SO_3^{2-}) in terms of any one of them. The relevant equation is:

$$H_2SO_3 \Leftrightarrow H^+ + HSO_3^+ \Leftrightarrow H^+ + SO_3^{2-}$$

We then find the fraction of each by dividing by their sum. Since bisulfite is intermediate between these anions, we express the concentrations in terms of $HSO_3^- = 1.0$, to produce:

$$H_2SO_3 = [(HSO_3)(H^+)]/K_1 \quad (1)$$

$$SO_3^{2-} = [(HSO_3)(K_2)]/(H^+) \quad (2)$$

(where $K_1 = 1.05 \times 10^{-2}$ and $K_2 = 5.02 \times 10^8$). The term $[H_2SO_3]$ is taken to be equal to the actual H_2SO_3 present plus the dissolved (hydrated) SO_2 that has not

TABLE 3.11

Gram/100 ml of water				
Sulfite	**Mg**	**Ca**	**Sr**	**Ba**
	27.1	0.0044	0.0033	0.0022
Relative to Ba	1240×	2.0×	1.5×	1.0

reacted to form H_2SO_3. Now, if the total sulfite in all different forms is denoted by s, then:

$$s = [H_2SO_3 + HSO_3^- + SO_3^{2-}] \quad (3)$$

Combining these three equations, we obtain:

$$s = [H^+/K_1 + 1.0 + K_2/H^+][HSO_3^-]$$

where we have defined the relative proportion of the busulfite anion as 1.0. Thus, the relative proportions of the three species in solution are therefore:

$$[H_2SO_3]:\ [HSO_3^-]:\ [SO_3^{2-}] = [H^+/K_1]:\ 1/0:\ [K_2/H^+]$$

At any solution pH, the ratio of bisulfite to sulfite ions in solution is:

$$[HSO_3]:\ [SO_3^{2-}] = 1:\ K_2/H^+ = [5.1 \times 10^{-8}]/[10^{pH}]$$

and pH = 10 produces a ratio of 1:500 of bisulfite to sulfite anions in solution. We can then calculate relative bisulfite concentration form from near 0 to near 100% as shown in the above curve. To calculate the SO_3^{2-} concentration, we use the same approach except that we define SO_3^{2-} as 1.0. The result is given in the diagram presented above.

Beryllium Sulfite

Beryllium sulfite would have the formula of $[Be(OH)]_2SO_3$ and the molecular weight of 132.0824 g/mol. It could be prepared by the reaction of a magnesium hydroxide slurry and SO_2 gas:

$$Be(OH)_2 + SO_2(gas) + H_2O \Rightarrow BeSO_3 \cdot 6H_2O$$

No article on "beryllium sulfite" can be found in the scientific literature. There is no scientific data that beryllium sulfite even exists as no studies have documented such a salt. The same may be said for the compound "beryllium bisulfite".

Magnesium Sulfite

Magnesium sulfite has the formula of $MgSO_3$ and the molecular weight of 104.3682 g/mol. It can be prepared by the reaction of a magnesium hydroxide slurry and SO_2 gas:

$$Mg(OH)_2 + SO_2(gas) + H_2O \Rightarrow MgSO_3 \cdot 6H_2O$$

If the solution temperature is kept below 40 °C, the hexahydrate results. Above 40 °C, the trihydrate, $MgSO_3 \cdot 3H_2O$, is the usual product. Magnesium sulfite may also be prepared by adding a solution of sodium sulfite to a solution of magnesium chloride. The mix is kept at 25 °C for 1–2 h and the solid phase which forms is separated and washed with isopropanol and dried at 60 °C. Again, the hexahydrate results.

The anhydrous form is hygroscopic. The CAS number is 7757-88-2 (hexahydrate) and its molecular weight is 212.4599 g/mol. The solubility of the hexahydrate in water is less than that of the anhydrate (Fig. 3.27).

The structure of magnesium sulfite hexahydrate is rhombohedral, space group—R3, and $a = 5.911$ Å, $\alpha = 96.52°$, $V = 202.6$ Å^3, $Z = 1$. The sulfite $O^=$ atoms carry a negative charge and are considerably expanded compared to free oxygen atoms. An extended lone pair of electrons is observed at the apex of the sulfur atom pyramid. The net charge on the sulfite group was estimated at –1.0 e^-. The shape of the hydrate oxygen lone-pair lobes is clearly affected by cation and hydrogen bond interactions. The dimensions of the SO_3^{2-} ion are S to O = 1.528Å and the angle of O to S to O = 104°. The O–H distances in the water molecules are in the range of 0.957–0.980 Å.

$MgSO_3 \cdot 6H_2O$ is thermally decomposed to $MgSO_3 \cdot 3H_2O$ at about 78 °C or to $MgSO_3 \cdot 2H_2O$ at about 120 °C. $MgSO_3 \cdot 3H_2O$ (and other lower hydrates of $MgSO_3$), decomposes to amorphous anhydrous $MgSO_3$ at about 395 °C. A crystalline compound of $MgSO_3 \cdot xH_2O$ with $x = 1/2$ forms from the dihydrate. Thermoanalytical data (DTA, TG, DTG, high- and low-temperature X-ray diffraction patterns), IR and Raman spectroscopic data of these hydrates have been reported. The crystal data are:

$MgSO_3 \cdot 3H_2O\ (P4_12_12)$, $(CoSO_3 \cdot 2H_2O$ type);
$a = 9.444$ and $c = 10.255$ Å, $Z = 8$

$MgSO_3 \cdot 2H_2O\ (P2_1/n)(ZnSeO_3 \cdot 2H_2O$ type):
$a = 6.359$, $b = 8.54.7$, $c = 7.544$ Å, and $\beta = 98.72°$,
$Z = 4$

$MgSO_3 \cdot ½H_2O\ (P2_1/n)$, $(MnSO_3 \cdot ½H_2O$ type):
$a = 4.699$, $b = 12.823$, $c = 5.63.2$Å, ß = 90.26°,
$Z = 4$.

Solubilities of $MgSO_3$-$6H_2O$ in Water

t, °C	gm of $MgSO_3$/liter	t, °C	gm of $MgSO_3$/liter
43.0	11.04	79.0	40.17
51.4	14.19	84.1	53.73
61.4	19.30	88.0	71.21
71.5	28.87	94.0	95.19

FIGURE 3.27

Magnesium sulfite has found usage in the "Kawasaki process" as first developed in Japan. It involves absorption of SO_2 gas from gaseous effluents of coal-burning electrical generating power plants ("flue gas") using a slurry composed of magnesium and calcium sulfites plus magnesium hydroxide, which forms soluble magnesium sulfite and insoluble calcium bisulfite. The following diagram presents one design of such as flue-gas plant (Fig. 3.28).

Here, the spent slurry is continuously withdrawn and sent to an air oxidizer where the sulfites and bisulfites are converted to their corresponding sulfates. This results in the production of magnesium sulfate and gypsum. The gypsum is removed by thickening and centrifugation for sale in commercial applications such as "dry-wallboard" manufacturing. The recovered liquid is returned to the scrubbing tower while the remainder is sent to the magnesium hydroxide regeneration tank where it is reacted with lime to convert $MgSO_4$ back into $Mg(OH)_2$ along with precipitation of additional gypsum. The regenerated slurry is then fed back into the scrubber.

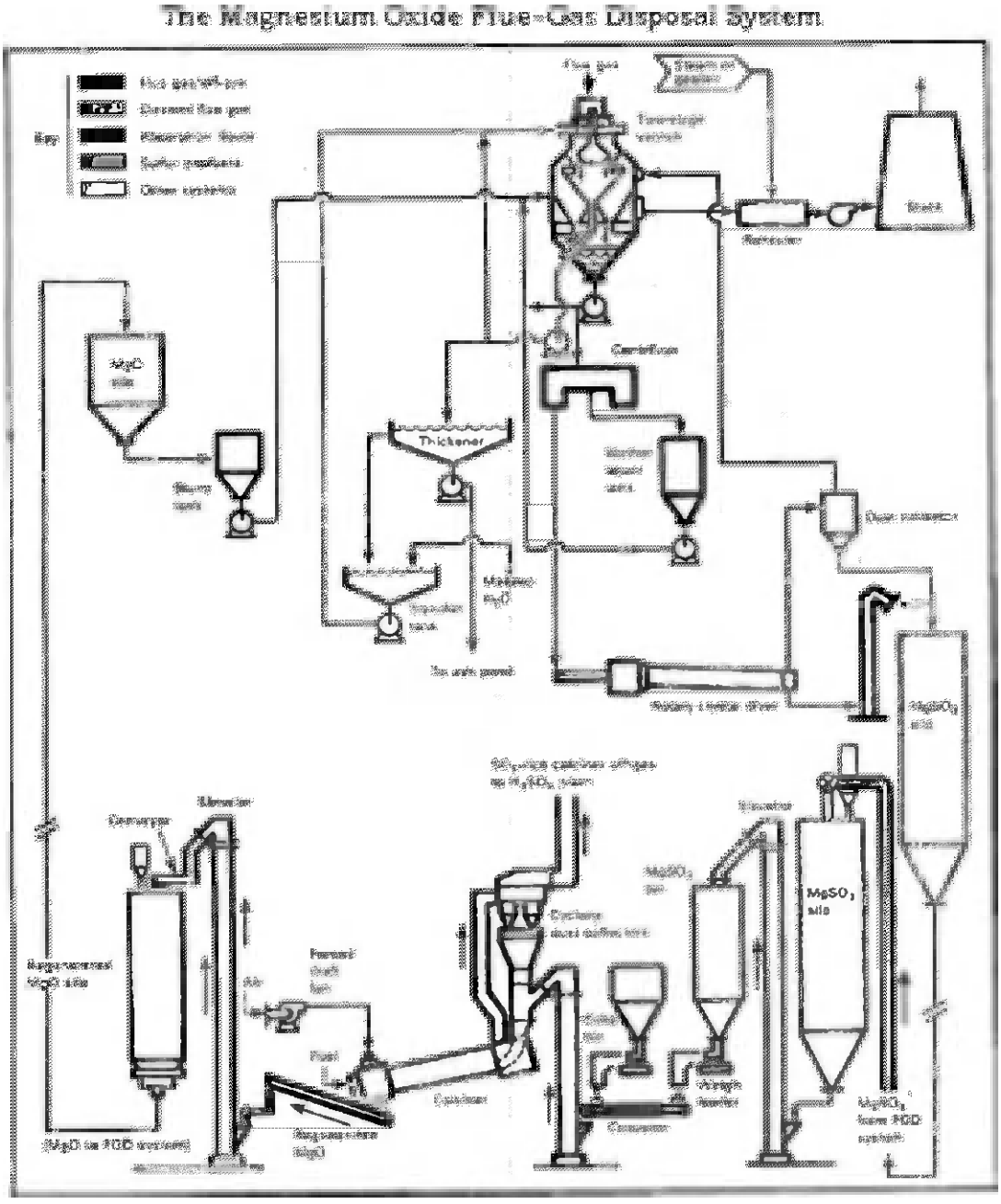

FIGURE 3.28

Although magnesium sulfite has found a number of usages in industry, it is the bisulfite compound that is used extensively in the wood-pulping process. Originally, it was the calcium salts, both bisulfite and sulfite that were used in the wood-pulp industry because of the low cost of lime and limestone. Dolomite can contain up to 40% magnesium and it was determined that calcium was more proficient in the "sulfite process" whereas magnesium bisulfite is used in the "Kraft process" of making wood pulp used to manufacture paper and cardboard products used extensively today. The sulfite process, SO_3^{2-}, involving calcium sulfite, has been used in the past but it is the magnesium bisulfite (Kraft Process) that is used today. "Kraft woodpulp" manufacturing plants have almost supplanted "sulfite woodpulp" plants nowadays because of environmental motives, even though magnesium salts cost more than the corresponding calcium salts. However, the history of pulp making from wood and trees involves the use of limestone and lime, because of availability of magnesium compounds at that time. For this reason, the detailed description of the paper-pulping processes is given in the next sectional discussion of calcium sulfites and bisulfites.

Magnesium sulfite and/or magnesium bisulfite are readily available commercially, although many paper-pulping industries make their own from readily available magnesium chemicals.

Calcium Sulfite or Bisulfite

Calcium sulfite has the molecular formula of $CaSO_3$ and the molecular weight of grams per mole. It can be prepared by the reaction of sodium sulfite with calcium chloride:

$$CaCl_2 + Na_2SO_3 \Rightarrow CaSO_3 + 2NaCl$$

The dihydrate, $CaSO_3 \cdot 2H_2O$ is formed. This salt is white powder that is soluble in dilute sulfurous acid to form the bisulfite. It may be dehydrated at 150 °C to form the anhydrous salt. It is used in the sulfite process for the manufacture of wood pulp. The anhydrate has the CAS number of 10257-55-3 and a melting point of 604 °C. It is slightly soluble in water at 0.0043 g/100 ml. If the hydroxide is used instead of the chloride, a hemihydrate is formed: $(CaSO_3)_2 \cdot H_2O$. The crystal data for calcium sulfite hemihydrate are: orthorhombic, space group-Pmna, $a = 9.808$, $b = 10.676$, $c = 6.496$ Å, and $Z = 8$. The structure consists of two alternating layers. The calcium ions are coordinated by six O atoms: five originate from the sulfite ions, and one from the water molecule.

A major use of calcium sulfite in the past has been the use of "lime" ($Ca(OH)_2$) in "flue-gas" desulphurization (removal of SO_2 gas) at "fossil-fuel" electrical power generating plants. Since calcium sulfite is relatively insoluble in water, it can be removed from the slurry by filtration and converted to gypsum, $CaSO_4 \cdot 2H_2O$. This has been superseded by magnesium bisulfite absorption processes (as described above).

The other usage of calcium sulfite or bisulfite compounds has been in the "wood-pulping" industry. Chemical wood pulping involves the extraction of cellulose from wood by dissolving the lignin that binds the cellulose fibers together. The four processes principally used in chemical pulping have been:

"Soda"
"Sulfite"
"Kraft"
"Neutral sulfite semi-chemical"

arranged in order of initial usage. The first three display the greatest potential for causing air and water pollution. The Kraft process alone accounts for over 80% of the chemical pulp produced in the United States today. The choice of pulping process is determined by the desired product, by the wood species available, and by economic considerations.

There have been two major competing processes, the "Kraft process" and the "sulfite process" to manufacture wood pulp for paper making. The former employs calcium or magnesium sulfite or bisulfite (at basic pH) while the latter uses calcium or magnesium bisulfite (at a more acidic pH).

Originally, domestic or financial transactions were stored on baked-clay tablets (about 5000 years ago). The Chinese developed a form of paper from crushed plants about 4000 years ago. With the coming of papyrus (made from flattened stems of a water plant) in Egypt on which permanent records could be stored (about 3000 years ago), the modern notion of paper was born. Parchment, made from animal skins, was used in the Middle ages in Europe from about 50 to 1600 AD. The use of wood to make pulp for paper did not begin until about 1840 with the development of mechanical pulping in Germany. The use of chemicals to aid this process soon followed. Caustic (NaOH) was the first, followed by the use of sulfur dioxide in water (sulfites and bisulfites)

TABLE 3.12

Kraft process	Sulfite process
Produces highest strength pulp	Produces brighter unbleached pulp
Utilized proven technology for efficient chemical recovery	Pulp is easier to bleach to full brightness
Handles wide variety of wood species	Produces higher yield of bleached pulp
Tolerates bark in the pulping process	Pulp is easier to refine

and then by the use of calcium bisulfite, $Ca(HSO_3)_2$, to pulp wood in 1867.

The first process used was the "soda process" which used NaOH or Na_2CO_3 to process wood chips and to make wood pulp for paper. This process was developed in 1851. The action of caustic soda on wood is very appreciable at ordinary temperatures, and is much more rapid and complete as the temperature is raised. It is, therefore, customary to cook the wood in the form of chips in closed digesters at high temperature and pressure. A major fault of the Soda Process was that acidic constituents in the wood tended to neutralize the caustic so that it could only process a certain amount of wood chips.

The second chemical method for pulp making was the "sulfite" process, invented by Benjamin C. Tilghman, who experimented with the effect of sulfurous acid on wood shortly after the Civil War in 1867. Almost a decade later, the first commercial Sulfite Mill was built in Sweden. It used magnesium as the counter ion. By 1900, sulfite pulping had become the dominant means of producing wood pulp, surpassing mechanical pulping methods. The amount of wood processed with the sulfite process was 11.1 million tons (dry wt) but there are virtually no Plants in the U.S. today using the calcium sulfite or bisulfite chemicals, derived from lime or limestone. The problem is that these calcium salts are more insoluble than the corresponding magnesium or ammonium homologues that dissolve more easily and are more soluble at the pH values required for dissolving lignin in the wood chips to make wood pulp.

In the sulfite process, a mixture of sulfurous acid and the bisulfite ion are used to attack and solubilize in the cooking liquor, and the chemical structure of the lignin is left largely intact. The chemical base for the bisulfite can be ionic calcium, magnesium, sodium, or ammonium. Sulfite pulping can be carried out over a wide range of pH. "Acid sulfite" denotes pulping with an excess of free sulfurous acid (pH 1–2), while "bisulfite" cooks are carried out under less acidic conditions (pH 4–6).

The cooking liquor for the acid-sulfite process is made by burning sulfur to form sulfur dioxide. This is then absorbed in water in the presence of calcium hydroxide or carbonate to form calcium sulfite, which is relatively insoluble, but which dissolves as calcium bisulfite when more sulfur dioxide is added. Care must be taken to avoid the formation of SO_3 since it produces sulfuric acid. Sulfuric acid is undesirable since it promotes hydrolysis of cellulose without contributing to delignification. The solution containing calcium bisulfite and an excess of sulfur dioxide forms the usual cooking liquor, or "acid," for the sulfite process. Sulfite pulping is carried out between pH 1.5 and 5, depending on the counter ion to sulfite (bisulfite) and the ratio of base to sulfurous acid. The pulp is in contact with the pulping chemicals for 4 to 14 h and at temperatures ranging from 130 to 160 °C. The spent cooking liquor from sulfite pulping is called "red or brown liquor" (compared to "black liquor" from the Kraft process). Ammonia-based processes do not allow recovery of the pulping chemicals since ammonia or ammonium salts are oxidized to N_2 or NO_x products when burned. The earliest process used calcium, obtained as inexpensive limestone and there was little incentive to recover the inorganic materials. Sodium-based processes use a recovery system similar to that used in the Kraft process, except that there is no "lime cycle".

In some plants, a high magnesia lime, containing about 40% magnesia, is used; in others a high calcium lime which contains about 92–95% calcium oxide. An acid solution prepared with a sodium base instead of calcium can be used equally well, and even has an advantage in cooking those woods which do not permit "ordinary acid" to penetrate easily. An all-magnesia base acid "Kraft process" is now being used in many mills, as is also an ammonia base acid. These last three—soda, magnesia and ammonia—enable the waste liquors to be treated for recovery of the base constituent, and so aid in avoiding stream pollution, which is becoming a more and more serious problem.

The sulfite pulping process depends on two principal reactions, which probably take place simultaneously to a considerable extent. These are the splitting of the cellulose–lignin complex of the wood by hydrolysis, and the combination of the lignin with the calcium bisulfite to form calcium lignosulfonate, which is soluble in the hot cooking liquor, and can be easily washed out at the end of the cook. The hydrolytic reaction also causes the easily decomposable hemicelluloses to dissolve with the formation of sugars. Fortunately, the chief portion of the cellulose is relatively stable under conditions of cooking, though it is not entirely unattacked.

These reactions are less drastic than those of the alkaline pulping (Kraft) processes, so the wood must be selected more carefully. The woods most commonly used for sulfite pulp are spruce, hemlock, balsam and the true firs; the woods of many deciduous trees can be cooked by this process, but are not largely used because their short fibers impart low strength to papers in which they are employed. Sulfite pulps are lighter in color than Kraft pulps and can be bleached more easily, but the paper sheets are weaker than equivalent Kraft sheets. The sulfite process works well for such softwoods as spruce, fir, and hemlock, and for such hardwoods as poplar and eucalyptus. Resinous softwoods and tannin-containing hardwoods, however, are more difficult to handle. This sensitivity to wood species, along with the weaker strength and the greater difficulty

in chemical recovery, are the major reasons for the decline of sulfite pulping relative to Kraft. The trend toward whole-tree chipping puts sulfite at a further disadvantage because of its intolerance to bark.

The competing chemical pulping process, the bisulfate or "Kraft process" started (in Sweden) in 1890. It was the invention of the "recovery boiler" in the 1930s that allowed Kraft Mills to recycle almost all of their pulping chemicals. It enabled the recovery and reuse of the inorganic pulping chemicals such that a Kraft mill is nearly a closed cycle with respect to inorganic chemicals, apart from those used in the bleaching process. For this reason, in the 1940s, the Kraft process surpassed the sulfite process as the dominant method for producing wood pulp. This, along with the ability of the Kraft process to accept a wider variety of types of wood and produce stronger fibers that made it become the dominant pulping process starting in the 1940s. Sulfite pulps now account for less than 10% of the total chemical pulp production and the number of Sulfite Mills continues to decrease.

A diagram of a typical magnesium-base process is shown in Fig. 3.29.

Pulp washers, using counter-current flow, remove the spent cooking chemicals and degraded lignin and hemicellulose. The extracted brown liquor is concentrated in multiple-effect evaporators. The concentrated brown liquor can be burned in the recovery boiler to generate steam and recover the inorganic chemicals for reuse in the pulping process or it can be neutralized to recover the useful by-products of pulping. The recovery process used in magnesium-based sulfite pulping the "magnetite" process is well developed. The concentrated brown liquor is burned in a recovery boiler, producing MgO and SO_2, both of which are recovered from the flue gases. Magnesium oxide is converted in a wet scrubber to give a slurry of $Mg(OH)_2$. This magnesium hydroxide slurry is then used in another scrubber to produce a magnesium bisulfite solution that is clarified, filtered and used as the pulping liquor.

Digestion is carried out under high pressure and high temperature, in either batch mode or continuous digesters, and in the presence of a sulfurous acid/bisulfite cooking liquid. When cooking is completed, either the digester is discharged at high pressure into a blow pit, or its contents are pumped into a dump tank at lower pressure. The spent sulfite liquor (also called red liquor) then drains through the bottom of the tank and is treated and discarded, incinerated, or sent to a plant for recovery of heat and chemicals. The pulp is then washed and processed through screens and centrifuges to remove knots, bundles of fibers, and other material. It subsequently may be bleached, pressed, and dried in papermaking operations.

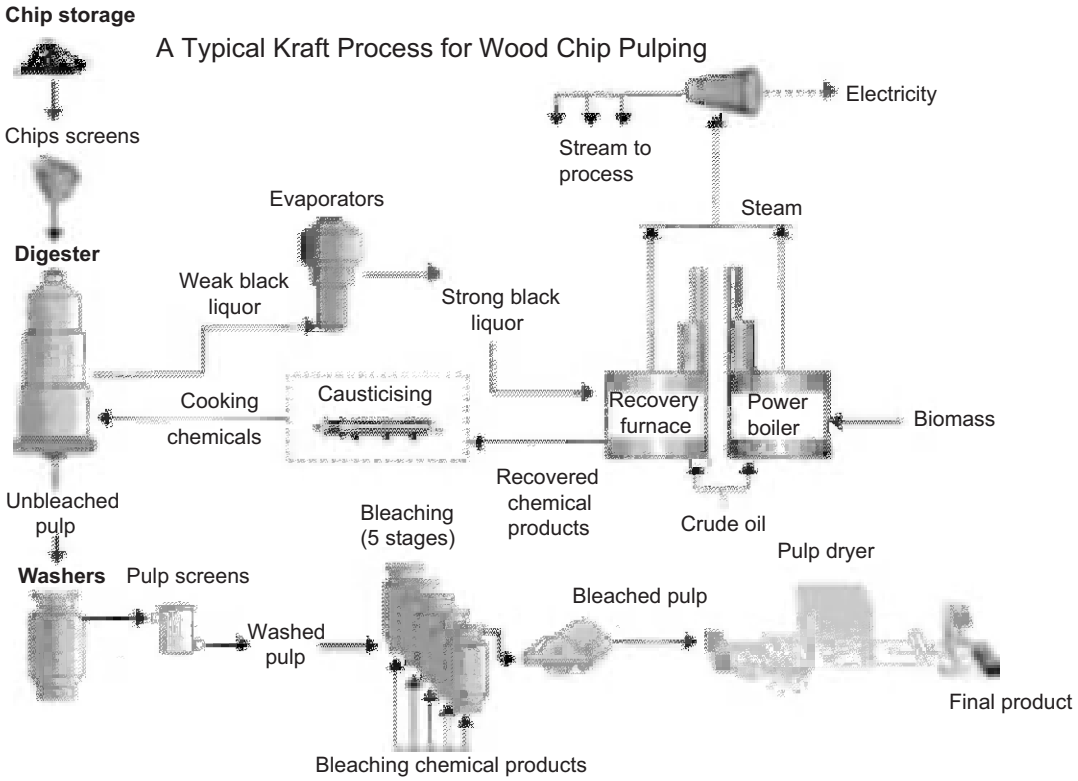

FIGURE 3.29

Because of the variety of cooking liquor bases used, numerous schemes have evolved for heat and/or chemical recovery. In calcium-based systems, found mostly in older mills, chemical recovery is not practical, and the spent liquor is usually discharged or incinerated. In ammonium base operations, heat can be recovered by combusting the spent liquor, but the ammonium base is thereby consumed. In sodium or magnesium base operations, the heat, sulfur, and base all may be feasibly recovered.

In the magnesium bisulphite wood pulping process, recovery of the spent process chemicals is of both economical and environmental importance. One part of the complex recovery system of the acid magnesium sulphite pulping process is the absorption unit, which is attached to the recovery burner. There, the waste gas from the thick liquor burning is cleaned from SO_2 by reaction to magnesium bisulphite. The main part of the SO_2 absorption recovery system of absorption system is a four-stage scrubber, operating according to the venturi principle, working at 65 °C and at pH values from 7 to 8. In a two-step reaction, where the flue gas is exposed to $Mg(OH)_2$, magnesium bisulphite is formed, which is reintroduced in the washing solution pulping process as cooking liquor.

Oxidation of lignosulfonates was used to produce "vanillin" (artificial vanilla), and this process is still used by one supplier (Borregaard, Norway) while all North American production by this route ceased in the 1990s. Acid hydrolysis of cellulose during sulfite pulping produces monosaccharides, predominanently mannose, which can be fermented to produce ethanol.

In order to transform wood chips into a NBSK pulp, wood fibers undergo a multistep process involving the following principal stages: wood chips, screening, cooking, pulp washing and screening, bleaching and drying, and finally, chemical recovery.

The following diagram is a brief description of such a process (which includes the steps necessary for chemical recovery) (Fig. 3.30).

WOOD CHIP SCREENING

This Kraft-mill currently uses a mix of softwood fibers composed of approximately 70% of Black Spruce and 30% of Jack Pine and other softwoods. In the initial processing stage, wood chips are screened to remove oversized chips and sawdust:

WOOD CHIPS COOKING

After the screening stage, the accepted chips are conveyed to a pressurized digester where they are heated and cooked with chemicals. This process softens and eventually dissolves the phenolic material called lignin that binds the fibers together in the wood.

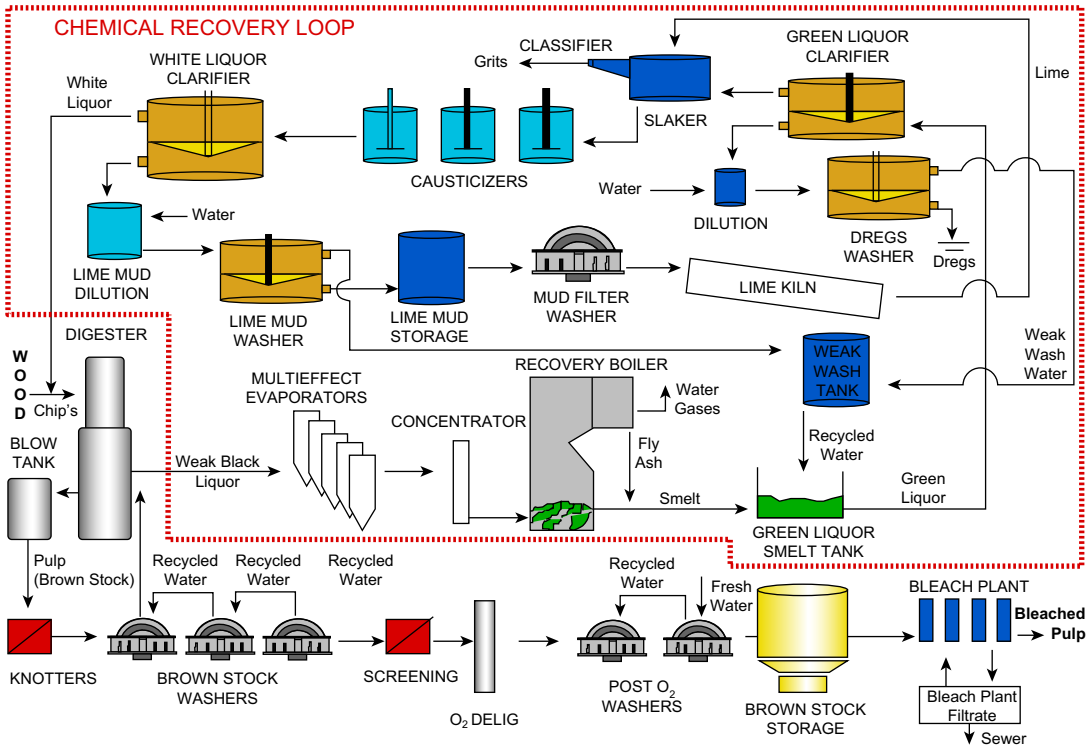

FIGURE 3.30

PULP WASHING AND SCREENING

When the cooking process is completed, the pulp is pressure blown out of the digester. The pulp is then washed and screened to remove most of the residual spent chemicals, called black liquor, and partially cooked wood chips.

BLEACHING AND DRYING

As pulp is initially brown in color when it exits the digester, it must undergo a series of bleaching stages where the brightness of the pulp is gradually increased to 95% ISO brightness. The Saint-Félicien Mill's bleaching process is elemental chlorine free. Finally, the bleached pulp is sent to the pulp machine where it is dried to achieve a dryness level of 93% air dry.

EXPEDITION

The pulp is then ready to be cut in sheets, baled and shipped to customers, by truck, railed car or boat depending on the destination.

RECUPERATION

A significant feature of Kraft pulping technology is the recovery system, whereby chemicals used in the process are captured and extracted for reuse, which reduces raw material costs and improves the mill's environmental performance. During the cooking stage, dissolved organic wood materials and chemicals are extracted from the digester through the weak black liquor. After undergoing an evaporation process, black liquor, now called strong black liquor, is burned in a recovery boiler. The heat produced by the recovery boiler is used to generate high-pressure steam. The chemical compounds of the black liquor are collected from the recovery boiler and reconstituted into cooking chemicals used in the cooking stage through additional processing in the recaustisizing plant. Additional steam is generated by the mill's power boiler through the combustion of biomass consisting of bark and other residues, including the ones generated by the mill's effluent treatment system. Bunker C (a type of crude oil) can also be used as needed. The steam produced by the recovery and power boilers is used to meet the mill's steam requirements, and to generate electricity through two turbo generators.

Calcium sulfite and bisulfite are available commercially in large quantities from a number of manufacturers worldwide.

Strontium Sulfite

Strontium sulfite has the molecular formula of $SrSO_3$ and the molecular weight of 167.6832 g/mol. It may be prepared by the reaction of sodium sulfite and strontium hydroxide:

$$Sr(OH)_2 + Na_2SO_3 \Rightarrow SrSO_3 + 2NaOH$$

This salt is sparingly soluble in water at 0.0033 g/100 ml at 20 °C, 0.00025 g/100 ml at 60 °C and 0.001525 g/100 ml at 100 °C. It solubility product is 4.2×10^{-8} and its CAS number is 13451-02-0. The question of the existence of hydrates remains unanswered. Strontium sulfite occurs as colorless, crystallites which decompose upon heating to 380 °C to the oxide plus SO_2 gas. It is soluble in sulfuric acid and HCl.

There is virtually no literature concerning the physical properties of this salt and the chemical properties have not been delineated except in general terms.

Strontium sulfite is, however, available in limited quantities commercially.

Barium Sulfite

Barium sulfite has the molecular formula of $BaSO_3$ and the molecular weight of 217.3912 g/mol. It can be prepared by reacting sodium sulfite with barium chloride:

$$BaCl_2 + Na_2SO_3 \Rightarrow BaSO_3 + 2NaCl$$

Its CAS number is 7787-39-5. It occurs as white, monoclinic crystals with a density of 4.44 g/cm^3. Its solubility in water is low (0.001125 g/100 ml) and it is insoluble in ethanol. When heated, it decomposes at 480 °C to the oxide and SO_2 gas.

It has been used as a weighting material on oil-drilling rigs to prevent "blow out" during drilling operations. This salt is used for such purposes, presumably because of its ability to absorb SO_2 and H_2S gases trapped in the rocks as drilling proceeds. The demand for barium sulfite is low.

Very little scientific studies of barium sulfite have ensued in the literature. The physical properties of this salt remain unspecified. One paper presents the formation of spherulites of $SrSO_3$ and $BaSO_3$, synthesized in agar–agar gels (0–40 °C). The reactants were sodium sulfite and the chloride of the respective metals. Each spherulite consists of fibrous crystals which are arranged minutely in a radial manner from the center. A linear relation was recognized between (mean diameter)^2 and reaction time in the same manner as the $CaSO_3$ $0.5H_2O$ spherulite reported. The slopes of the lines, namely the growth rates of the spherulites, were greater in the order of calcium sulfite > strontium sulfite > barium sulfite. The ratio of (mean diameter)^2/time was dependent upon the concentration of the agar–agar gel (0.5%–2.0%) and the reaction temperature (0–40 °C); the ratios decreased linearly with an increase of the gel concentration and increased with an increase of temperature.

Barium sulfite is available in limited quantities, commercially.

Radium Sulfite

Radium sulfite would have the molecular formula of $RaSO_3$ and the molecular weight of 306.0866 g/mol. It could be prepared by the reaction of RaO and gaseous SO_2 at an elevated temperature of about 650 °C:

$$RaO(solid) + SO_2(gas) \Rightarrow RaSO_3(solid)$$

However, there is no report of this salt ever having been prepared.

There is no demand for this salt and it is not clear whether it has ever existed. It is not available commercially.

3.2.4. Alkaline Earth Sulfates

Beryllium Sulfate

Beryllium sulfate has the molecular formula of $[Be(OH)]_2SO_4$ and the molecular weight of 105.0852 g/mol. Beryllium sulfate may be prepared by treating an aqueous solution of any beryllium salt with sulfuric acid, followed by evaporation of the solution and crystallization. The hydrated product may be converted to anhydrous salt by heating at 400 °C. The anhydrate may also be prepared by reacting the oxide with SO_2 gas at elevated temperature. Its CAS number is 13510-49-1. If the solution method is used, a tetrahydrate forms, $(BeOH)_2SO_4 \cdot 4H_2O$ whose molecular weight is 177.1462 g/mol with a CAS number of 7787-56-6.

Beryllium sulfate is a colorless crystalline solid with a tetragonal crystal system. It is hygroscopic and its density is 2.50 g/cm^3 (tetrahydrate = 1.71 g/cm^3). The tetrahydrate salt loses water of crystallization on heating to about 110 °C to form a dihydrate. Upon heating to 400 °C, it then forms the anhydrate. Further heating to 550 °C causes decomposition of the anhydrate to BeO and SO_2 and O_2.

Beryllium sulfate is soluble in water, tetrahydrate being more soluble in water (30.5 g/100 ml at 30°) than the anhydrous salt; both are insoluble in alcohol.

Thermochemical properties of this salt include:

Thermochemical properties

$\Delta H_f^\circ = -288.2$ kcal/mol
$\Delta G_f^\circ = -261.5$ kcal/mol
$S^\circ = 18.63$ cal/degree mol
$C_P = 20.49$ cal/degree mol

No major commercial application of beryllium sulfate is known and it has not been offered for sale.

Magnesium Sulfate

Magnesium sulfate has the molecular formula of $MgSO_4$ and the molecular weight of 120.3662 g/mol. It may be prepared by the reaction of sodium sulfate and any soluble magnesium salt:

$$MgCl_2 + N_2SO_4 \Rightarrow MgSO_4 + 2NaCl$$

Hydrated magnesium sulfate occurs in nature as the minerals "kieserite" and "epsomite". The salt is mined in large scale from these and other naturally occurring minerals. The salt is also prepared in the laboratory by the action of sulfuric acid on magnesium oxide, hydroxide, or carbonate followed by evaporation and crystallization:

$$MgO + H_2SO_4 \Rightarrow MgSO_4 + H_2O$$

$$Mg(OH)_2 + H_2SO_4 \Rightarrow MgSO_4 + 2H_2O$$

$$MgCO_3 + H_2SO_4 \Rightarrow 4 + CO_2 + H_2O$$

Crystallization at temperatures between 1.8 and 48 °C yields the heptahydrate, $MgSO_4 \cdot 7H_2O$. Below 1.8 °C, a dodecahydrate, $MgSO_4 \cdot 12H_2O$ crystallizes out. Above 48 °C, a lower hydrate crystal forms. The anhydrous salt is obtained by heating the heptahydrate at about 500 °C or dehydrating above 150 °C in the presence of sulfuric acid. The heptahydrate, $MgSO_4 \cdot 7H_2O$, is commonly called **Epsom salt**. A number of hydrates have been prepared and assigned CAS numbers. These are shown as follows along with their mineral names and CAS numbers:

Hydrate	Mineral name	Formula	CAS No.
Monohydrate	Kieserite	$MgSO_4 \cdot H_2O$	[14168-73-1]
Tetrahydrate	Starkeyite	$MgSO_4 \cdot 4H_2O$	[24378-31-2]
Pentahydrate	Pentahydrite	$MgSO_4 \cdot 5H_2O$	[15553-21-6]
Hexahydrate	Hexahydrite	$MgSO_4 \cdot 6H_2O$	[13778-97-7]
Heptahydrate	Epsomite	$MgSO_4 \cdot 7H_2O$	[10034-99-8]

In their hydrated form, these salts have a pH of 6.0 (5.5 to 6.5) in solution. These magnesium sulfates are white crystalline solids. Their densities are: 2.66 g/cm^3 (anhydrous); 2.445 g/cm^3 (monohydrate); 1.68 g/cm^3 (heptahydrate). Solubilities in water are: *anhydrous* = 26.9 g/100 ml (0 °C); *monohydrate* = 25.5 g/100 ml (20 °C); *heptahydrate* = 71 g/100 ml (20 °C).

Magnesium sulfate is found in nature in many salt deposits and mineral waters, occurring as hydrates or double salts. The heptahydrate or Epsom salt was discovered in 1695, found in the mineral water at Epsom. Kieserite and epsomite are the two most important minerals. Other than these and the above hydrates, magnesium sulfate is also found in several other minerals, including:

Langbeinite, $K_2SO_4 \cdot 2MgSO_4$ [CAS #13826-56-7]

Leonite, $K_2SO_4 \cdot MgSO_4 \cdot 4H_2O$ [15226-80-9]

Vanthoffite, $3Na_2SO_4 \cdot MgSO_4$ [15557-33-2]

Bloedite, $Na_2SO_4 \cdot MgSO_4 \cdot 4H_2O$ [15083-77-9]

Kainite, $4KCl \cdot 4MgSO_4 \cdot 11H_2O$ [67145-93-1]

Polyhalite, $K_2SO_4 \cdot MgSO_4 \cdot 2CaSO_4 \cdot 2H_2O$ [15278-29-2].

The anhydrous salt, $MgSO_4$, consists of colorless rhombohedral crystals with a density of 2.66 g/cm^3; it decomposes at 1124 °C. It is soluble in water (269 g/100 ml at 0 °C). It is also soluble in ethanol and glycerol but sparingly soluble in ether (1.16 g/ml at 18 °C); it is insoluble in acetone.

The monohydrate $MgSO_4 \cdot H_2O$, as the mineral Kieserite, consists of colorless monoclinic crystals, having a refractive index of 1.523, a density of 2.445 g/cm^3. It becomes anhydrous on heating at 200 °C; it is soluble in water.

Epsom salt, or heptahydrate $MgSO_4 \cdot 7H_2O$, constitutes colorless, monoclinic or rhombohedral crystals with a refractive index of 1.433; a density of 1.68 g/cm^3. It loses six molecules of water of crystallization at 150 °C and converts to the anhydrous form at 200 °C. The heptahydrate is highly soluble in water (71 g/100 ml at 20 °C) but slightly soluble in alcohol and glycerol.

Thermochemical properties

$\Delta H_f^0(MgSO_4)$ −307.1 kcal/mol

$\Delta H_f^0(MgSO_4 \cdot 2H_2O)$ −453.2 kcal/mol

$\Delta H_f^0(MgSO_4 \cdot 4H_2O)$ −596.7 kcal/mol

$\Delta H_f^0(MgSO_4 \cdot 6H_2O) = -737.8$ kcal/mol

$\Delta H_f^0(MgSO_4 \cdot 7H_2O) = -809.9$ kcal/mol

$\Delta G_f^0(MgSO_4) = -279.8$ kcal/mol

$\Delta G_f^0(MgSO_4 \cdot 6H_2O) = -629.1$ kcal/mol

$\Delta G_f^0(MgSO_4 \cdot 7H_2O) = -686.4$ kcal/mol

$S^0(MgSO_4) = 21.9$ cal/degree mol

$S^0(MgSO_4 \cdot 6H_2O) = 83.2$ cal/degree mol

$S^0(MgSO_4 \cdot 7H_2O) = 89.0$ cal/degree mol

$C_P(MgSO_4) = 23.0$ cal/degree mol

$C_P(MgSO_4 \cdot 6H_2O) = 83.2$ cal/degree mol

The anhydrous salt decomposes at elevated temperatures to magnesium oxide, oxygen, sulfur dioxide, and sulfur trioxide. The decomposition commences around 900 °C and is complete at about 1100 °C. The overall reaction is:

$$MgSO_4 + \text{heat} \Rightarrow MgO + O_2 + SO_2 + SO_3$$

On the other hand, heating hydrated sulfate above 150 °C yields magnesium oxysulfate, a hydrolysis reaction. No dehydration or thermal decomposition occurs. The anhydrous salt may be reduced to magnesium oxide when heated with carbon at 750 °C:

$$MgSO_4 + C \Rightarrow MgO + SO_2 + CO$$

Magnesium sulfate undergoes three important types of reactions in aqueous solution. These are:

Double decomposition,
Double salt formation,
Formation of oxysulfate cements.

Many insoluble magnesium salts may be precipitated out by double decomposition reactions:

$$MgSO_4 + 2NaOH \Rightarrow Mg(OH)_2 + 2Na^+ + SO_4^{2-}$$

$$3MgSO_4 + 2Na_3PO_4 \Rightarrow Mg_3(PO_4)_2 + 6Na^+ + 3SO_4^{2-}$$

Magnesium sulfate forms several double salts having varying stoichiometric compositions. When gaseous ammonia is bubbled through magnesium sulfate solution, several hydrated double salts are obtained by crystallization. Magnesium sulfate double salts have the compositions:

$$MgSO_4 \cdot NH_3 \cdot 3H_2O$$

$$MgSO_4 \cdot 2NH_3 \cdot 4H_2O$$

$$MgSO_4 \cdot 2NH_3 \cdot 2H_2O$$

Similarly, in sulfuric acid, crystals of double salts form:

$$MgSO_4 \cdot H_2SO_4 \cdot 3H_2O$$

$$MgSO_4 \cdot H_2SO_4$$

$$MgSO_4 \cdot 3H_2SO_4$$

Addition of magnesium oxide to magnesium sulfate solutions yields crystalline oxy-sulfates at varying stoichiometric compositions, such as:

$$MgSO_4 \cdot 3MgO \cdot 11H_2O$$

$$MgSO_4 \cdot 5MgO \cdot 8H_2O.$$

Treatment of barium peroxide, BaO_2, with a concentrated solution of magnesium sulfate, yields magnesium peroxide MgO_2, a white powdery material used as a bleaching and oxidizing agent, and as an antacid in medicine.

Anhydrous magnesium sulfate is used as a drying agent since it is highly hygroscopic. This property limits its usefulness and the hydrate is generally preferred when weighing out the material for preparing solutions,

for example in medical preparations. Epsom salt has been traditionally used as a component of bath salts.

Magnesium sulfate is used widely in several industries including fertilizer, cement, textile, chemicals, and medicine. In the cement industry, it is used in manufacturing oxysulfate cement. In medicine, it is an analgesic and cathartic. An important application of anhydrous magnesium sulfate in the laboratory involves drying organic solvents required for syntheses and GC analysis. In the textile industry, magnesium sulfate is used in finishing composition for dressing cotton; for weighting and sizing silk; as a mordant for fixing basic dyestuffs on wool; and in fireproofing fabrics. It is also a component of certain types of electrolytic plating baths; of various photographic solutions; of cosmetic lotions. It is a catalyst carrier; a dietary supplement in cattle feed; a coagulant for rubber and plastic; and is used in making citric acid and several magnesium salts, such as magnesium stearate.

Both are, however, not the highest known hydrates of $MgSO_4$ due to the recent terrestrial find of Meridianite, $MgSO_4 \cdot 11H_2O$, which is thought to also occur on Mars.

In agriculture and gardening, magnesium sulfate is used to correct magnesium deficiency in soil, since magnesium is an essential element in the chlorophyll molecule. It is most commonly applied to potted plants, or to magnesium-hungry crops, such as potatoes, tomatoes, peppers, and roses. The advantage of magnesium sulfate over other magnesium compounds (such as dolomitic limestone) is its high solubility. $MgSO_4$ has been used in organic synthesis to remove water from nonaqueous solutions before the organic reaction is started. Since it is insoluble in most organic solvents, its addition forms hydrates that can be easily removed.

Epsom salt is also used to prepare footbaths, intended to soothe sore feet. The reason for the inclusion of the salt is partially cosmetic. However, magnesium sulfate can also be absorbed into the skin, reducing inflammation. It is also sometimes found in bottled mineral water, and accordingly is sometimes listed in the contents thereof. Magnesium sulfate heptahydrate is also used to maintain the magnesium concentration in marine aquaria which contain large amounts of stony corals as it is slowly depleted in their calcification process, precipitation into calcium carbonate. Oral Epsom salt is used as a saline laxative as well as for replacement therapy in "hypomagnesaemia" (lack of Mg^{2+}) in animals and humans. Magnesium sulfate paste has been used as an agent for dehydrating (drawing) boils, carbuncles or abscesses. Magnesium sulfate solution has also been shown to be an effective aid in the fight against blemishes and acne when applied directly to problematic areas. Magnesium sulfate, when used through soaking, can soothe muscle pains and help improve rough patches in the skin. Soaking in a warm bath containing Epsom salt (magnesium sulfate) can be beneficial to soothe and relieve herpes outbreak symptoms, such as itching and lesions relating to genital herpes or shingles.

Magnesium sulfate salts are available commercially in large lots in a variety of compositional hydrates for varied uses in the home and in industry.

Calcium Sulfate

Calcium sulfate has the molecular formula of $CaSO_4$ and the molecular weight of 136.1452 g/mol. It may be prepared by the addition of a soluble calcium salt to a solution of sodium sulfate:

$$CaCl_2 + Na_2SO_4 \Rightarrow CaSO_4 + 2NaCl$$

The product is generally a dihydrate although other hydrates are also known. The CAS numbers of these materials are: 7778-18-9 (anhydrite); 10034-76-1 (hemihydrate); 10101-41-4 (dihydrate). The molecular weight of the hydrates is: 145.15 g/mol (hemihydrate); 172.172 g/mol (dihydrate). These white solids are odorless. Known densities are: 145.15 g/mol (hemihydrate); 172.172 g/mol (dihydrate). The anhydrate melts at 1462 °C. It is a basic salt with a pK_a of 10.4 (anhydrous); 7.3 (dihydrate). The thermochemical constants for the three forms of calcium sulfate are:

Thermochemical properties

ΔH_f° (anhydrite) −342.76 kcal/mol

ΔG_f° (anhydrite) = −315.93 kcal/mol

S° (anhydrite) = 25.50 cal/degree mol

C_p (anhydrite) = 23.82 cal/*degree mol*

ΔH_f° (hemihydrate) = −376.85 kcal/mol

ΔG_f° (hemihydrate) = −343.41 kcal/mol

S° (hemihydrate) = 31.20 cal/degree mol

C_p (hemihydrate) = 28.54 cal/degree mol

ΔH_f° (dihydrate) = −483.42 kcal/mol

ΔG_f° (dihydrate) = −429.60 kcal/mol

S° (dihydrate) = 46.40 cal/degree mol

C_p (dihydrate) = 44.46 cal/degree mol

The structure of the "anhydrite" is shown in Fig. 3.31.

Its crystal symmetry is orthorhombic, 2/m 2/m 2/m, with unit cell parameters of: $a = 6.245(1)$ Å, $b = 6.995(2)$ Å, $c = 6.993(2)$ Å; $Z = 4$. Calcium sulfate is a common laboratory and industrial chemical. It is most often used as "gypsum" which is the dihydrate. In the form of β-anhydrite (the nearly anhydrous form), it is used

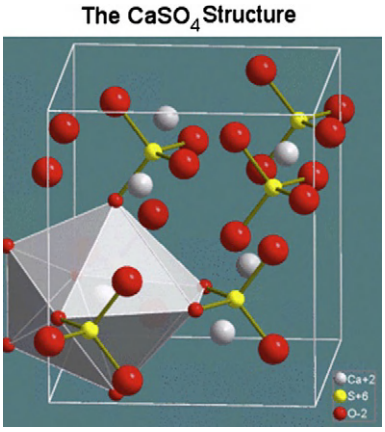

FIGURE 3.31

as a desiccant. It is also used as a coagulant in products like "tofu", which is a "bean curd". When sold as a color-indicating variant under the name "Drierite™", it appears blue or pink due to impregnation with cobalt chloride, which functions as a moisture indicator.

Gypsum is moderately water soluble (~2.0–2.5 g/l at 25 °C) and, in contrast to most other salts, it exhibits a retrograde solubility, becoming less slightly less soluble at higher temperatures (Table 3.13).

As for β-anhydrite, its solubility in saline solutions and in brines is also strongly dependent on the salt concentration. Because gypsum dissolves over time in water, gypsum is rarely found in the form of sand. However, the unique conditions of the "White Sands National Monument" in New Mexico have created a 710-sq. km (270 sq. mile) expanse of white gypsum sand, enough to supply the construction industry with dry wall for 1000 years. Commercial exploitation of the area, strongly opposed by area residents, was permanently prevented in 1933 when the gypsum dunes were declared a protected national monument.

In its natural state, unrefined calcium sulfate is a translucent, crystalline white rock. Many forms are known, including "Alabaster" and "Gypsum". Selenite, Satin spar, Desert rose, and Gypsum flower are four varieties of Gypsum minerals; all four varieties are crystalline. The four "crystalline" varieties of gypsum are sometimes grouped together and called selenite. All have the same chemical formulation, $CaSO_4 \cdot 2H_2O$. All varieties of gypsum are very soft minerals (hardness: 2 on Mohs scale). This is the most important identifying characteristic of gypsum, as any variety of gypsum can be easily scratched with a fingernail.

TABLE 3.13

Gram/100 ml of water									
		0 °C	10	20	30	40	60	80	100
Calcium sulfate	$CaSO_4 \cdot 2H_2O$	0.223	0.244	0.255	0.264	0.265	0.244	0.234	0.205

The origin of the word, "Alabaster", comes from Middle English, through Old French *alabastre*, in turn derived from the Latin, *Alabaster* and that from the Greek. This substance, the "alabaster" of the ancient Egyptians and the Bible, often is termed *Oriental alabaster*, since the early examples came from the far East. This name may derive further from the ancient Egyptian word *a-labaste*, which refers to vessels of the Egyptian goddess "Bast", who was represented as a lioness or it may have been derived from the town of Alabastron in Egypt where the stone was quarried. Additionally, an Arabic etymological origin has also been suggested. However, the origin of the mineral name remains obscure. Thousands of gypsum alabaster artifacts dating to the late fourth millenium BC also have been found in Mesopotamia (Syria) which dates back into the first half of the third millennium BC.

The finest mineral alabaster deposits occur in England in many places. Deposits at all of these localities have been worked extensively. In the fifteenth century, its carving into icons and altarpieces was a valuable local industry, as well as a major English export. Alabaster is also found, although in subordinate quantity, in Spain and Scandinavia. *Black Alabaster* is a rare form of the gypsum-based mineral. This black form is only found in three veins in the world, one each in Oklahoma (USA), Italy, and China.

The hemihydrate, $CaSO_4 \cdot 1/2H_2O$ is better known as "plaster of paris" while the dihydrate ($CaSO_4 \cdot 2H_2O$) occurs naturally as Gypsum. The anhydrous form occurs naturally as β-Anhydrite. Anhydrite is a mineral—anhydrous $CaSO_4$. It is not to be confused with "anhydride" which is the hemihydrate. It has the orthorhombic crystal system, with three directions of perfect cleavage parallel to the three planes of symmetry. It is not isomorphous with the orthorhombic barium or strontium sulfates, as might be expected from the chemical formulas. Distinctly developed crystals are somewhat rare, the mineral usually presenting the form of cleavage masses. The hardness is 3.5 and the specific gravity is 2.9. The color is white, sometimes grayish, bluish or purple. When exposed to water, anhydrite readily transforms to the more commonly occurring $CaSO_4 \cdot 2H_2O$ by the absorption of water. Depending on the method of calcination of calcium sulfate dihydrate, specific hemihydrates are sometimes distinguished: α-hemihydrate and β-hemihydrate. They appear to differ only in crystal size. α-hemihydrate crystals are more prismatic than β-hemihydrate crystals and, when mixed with water, form a much stronger and harder superstructure.

Heating gypsum to between 100 °C and 150 °C (302 F) partially dehydrates the mineral by driving off

approximately 75% of the water contained in its chemical structure. The temperature and time needed depend on ambient partial pressure of H_2O. Temperatures as high as 170 °C are used in industrial calcination, but at these temperatures β-anhydrite begins to form. The reaction for the partial dehydration is:

$$CaSO_4 \cdot 2H_2O + \text{heat} \Rightarrow CaSO_4 \cdot 1/2H_2O + 1.5H_2O \text{ (steam)}$$

The partially dehydrated mineral is called calcium sulfate hemihydrate or calcined gypsum (commonly known as plaster of paris = $CaSO_4 \cdot nH_2O$, where n is in the range 0.5 to 0.8). The dehydration begins at approximately 80 °C (176 °F), although in dry air, some dehydration will take place already at 50 °C. The heat energy delivered to the gypsum at this time (the heat of hydration) tends to go into driving off water (as water vapor) rather than increasing the temperature of the mineral, which rises slowly until the water is gone, then increases more rapidly. The endothermic property of this reaction is exploited in "drywalls" to confer fire resistance to residential and other structures. In a fire, the structure behind a sheet of drywall will remain relatively cool as water is lost from the gypsum. This prevents (or substantially retards) damage to the wood framing (through combustion of wood or loss of strength of steel members at high temperatures) and consequent structural collapse.

In contrast to most minerals, which when rehydrated simply form liquid or semiliquid pastes, or remain powdery, calcined gypsum has an unusual property: when mixed with water at normal (ambient) temperatures, it quickly reverts chemically to the preferred dihydrate form, while physically "setting" to form a rigid and relatively strong gypsum crystal lattice:

$$CaSO_4 \cdot \tfrac{1}{2}H_2O + 1.5H_2O \Rightarrow CaSO_4 \cdot 2H_2O$$

This reaction is exothermic and is responsible for the ease with which gypsum can be cast into various shapes including sheets (for Drywall), sticks (for blackboard chalk), and molds (to immobilize broken bones, or for metal casting). Mixed with polymers, it has been used as a bone repair cement. Small amounts of calcined gypsum are added to earth to create strong structures directly from bricks, an alternative to adobe (which loses its strength when wet). The conditions of dehydration can be changed to adjust the porosity of the hemihydrate, resulting in the so-called alpha and beta hemihydrates (which are more or less chemically identical).

On heating to 180 °C, the nearly water-free form, called γ-anhydrite ($CaSO_4 \cdot nH_2O$ where $n = 0$ to 0.05) is produced. β-Anhydrite reacts slowly with water to return to the dihydrate state, a property exploited in some commercial desiccants. On heating above 250 °C, the completely anhydrous form called β-anhydrite or "natural" anhydrite is formed. Natural anhydrite does not react with water, even over geological timescales, unless very finely ground.

The variable composition of the hemihydrate and β-anhydrite, and their easy interconversion, is due to their possessing nearly identical crystal structures, containing "channels" that can accommodate variable amounts of water, or other small molecules such as methanol.

When exposed to water, anhydrite readily transforms to the more commonly occurring gypsum ($CaSO_4 \cdot 2H_2O$), by the absorption of water. Anhydrite is commonly associated with the minerals, calcite, halite, galena, chalcopyrite and pyrite in vein deposits. The word gypsum is derived from the Greek word for "chalk" or "plaster". Because the gypsum from the quarries of the Montmarte district of Paris has long furnished burnt gypsum used for various purposes, this material has been called "plaster of paris".

Gypsum and β-anhydrite have been used as "plaster" throughout the centuries as a building material. The Sumerians who lived in Mesopotamia (Ancient Iraq) from the mid-sixth millennium to the second millennium BC used plaster to face off dried mud bricks to preserve them and lengthen their lifetime in construction. The story of Sumerian architecture is overwhelmingly one of clay masonry and of increasingly complex forms of stacked bricks. Because these bricks were sun baked, Sumerian buildings eventually deteriorated. They were periodically destroyed, leveled, and rebuilt on the same spot.

Common materials of Greek architecture were wood, used for supports and roof beams; plaster, used for sinks and bathtubs; unbaked brick, used for walls, especially for private homes, limestone and marble used for columns, walls, and upper portions of temples and public buildings; terracotta, used for roof tiles and ornaments; and metals, especially bronze, used for decorative details. Gypsum was used as "Stucco" for a variety of purposes. As a building material, stucco is a durable, attractive, and weather-resistant wall covering. It was traditionally used as both an interior and exterior finish applied in one or two thin layers directly over a solid brick or stone surface. The finish coat usually contained an integral color and was typically textured for appearance. A stucco face from the ancient Greek city of Al Khanoum I, Afghanistan, third-second century BC is known. Stucco has also been used as a sculptural and artistic material. Baroque and Rococo architecture made heavy use of stucco. Examples can be found in churches and palaces from the eighth to sixteenth century, where stucco is mostly used to provide a smooth, decorative transition from walls to ceiling, decorating and giving measure to ceiling surfaces. Since stucco can be used for decoration

as well as for figurative representation, it provides an ideal transitive link from architectural details to wall paintings such as the typically Baroque ceilings. Here, the real architecture of the church is visually extended into a heavenly architecture with a depiction of Christ or the Virgin Mary at the center. Stucco is used to form a semiplastic extension of the real architecture that merges into the painted architecture. Many of the greatest paintings in Europe, like Michelangelo's Sistine Chapel ceiling are executed or painted on a thin layer of wet plaster, called intonaco (in fact the general term for plaster in Italian); the pigments sink into this layer so that the plaster itself becomes the medium holding them, which accounts for the excellent durability of fresco. Additional work may be added *"a-secco"* on top of the dry plaster, though this is generally less durable.

Stucco is still used today as a building material. It is applied as a cover coat to wallboard and stylized. A major usage has occurred with the introduction and development of light wood-framed construction methods, in which stucco was adapted for a new use by adding a reinforcement lattice, or lath, attached to and spanning between the structural supports, thereby increasing the thickness and number of layers of the total system. The lath added support for the wet plaster and tensile strength to the brittle, cured stucco; while the increased thickness and number of layers helped control cracking. The traditional application of stucco and lath occurs in three coats—the scratch coat, the brown coat and the finish coat. The two base coats of plaster are either hand applied or machine sprayed. The finish coat can be troweled smooth, hand textured, floated to a sand finish or sprayed.

Plaster may be cast directly into a damp clay mold. In creating this *piece molds* (molds designed for making multiple copies) or *waste molds* (for single use) would be made of plaster. This "negative" image, if properly designed, may be used to produce clay productions, which when fired in a kiln become terra-cotta building decorations, or these may be used to create cast concrete sculptures. Plaster expands while hardening, then contracts slightly just before hardening completely. This makes plaster excellent for use in molds, and it is often used as an artistic material for casting. Plaster is also commonly spread over an armature (form), usually made of wire, mesh or other materials, a process called *direct plaster*.

Plaster is widely used as a support for broken bones; a bandage impregnated with plaster is moistened and then wrapped around the damaged limb, setting into a close fitting yet easily removed tube. Plaster is also used within radiotherapy when making immobilization casts for patients. Plaster bandages are used when constructing an impression of the patient's head and neck, and liquid plaster is used to fill the impression and produce a plaster bust. Perspex is then vacuum formed over this bust creating an immobilization shell. In dentistry, plaster is used for mounting casts or models of oral tissues. These diagnostic and working models are usually made from dental stone, a stronger, harder and denser derivative of plaster which is manufactured from gypsum under pressure. Plaster is also used to invest or flask wax dentures, the wax being subsequently removed and replaced with the final denture base material which is cured in the plaster mold.

The main sources of calcium sulfate are naturally occurring gypsum and anhydrite that occur at many locations worldwide as "evaporites". These may be extracted by open cast quarrying or by deep mining. World production of natural gypsum is around 127 million tons per year. In addition to natural sources, calcium sulfate is produced as a by-product in a number of chemical processes. In "flue gas" desulfurization, exhaust gases from fossil fuel burning power plants and other processes (e.g. cement manufacture) are scrubbed to reduce their sulfur dioxide content, by injecting finely ground limestone or lime. This produces an impure calcium sulfite, which oxidizes on storage to calcium sulfate. In the production of H_3PO_4 from phosphate rock, calcium phosphate is treated with sulfuric acid and calcium sulfate precipitates. Over 200 million tons per annum of calcium sulfate waste is produced by the phosphate industry worldwide. In the production of HF, calcium fluoride is treated with sulfuric acid, precipitating calcium sulfate. Calcium sulfate can also be recovered and reused from scrap drywall at construction sites.

Strontium Sulfate

Strontium sulfate has the molecular formula of $SrSO_4$ and the molecular weight of 183.6842 g/mol. It can be prepared by the reaction of sodium sulfate and strontium chloride:

$$Na_2SO_4 + SrCl_2 \Rightarrow SrSO_4 + 2NaCl$$

Strontium sulfate occurs in nature as "celestite" and is mined from its natural deposits. Also, the sulfate can be made by reacting strontium oxide, hydroxide, or carbonate with dilute hydrochloric acid:

$$SrO + H_2SO_4 \Rightarrow SrSO_4 + H_2O$$

$$SrCO_3 + H_2SO_4 \Rightarrow SrSO_4 + CO_2 + H_2O$$

No hydrates are known. Its CAS number is 7759-02-6. It is a white, orthorhombic crystal with a refractive index of 1.622 and a density of 3.96 g/cm^3. Its hardness is 3.3 Mohs. It melts at 1608 °C. Its solubility in water is 0.015 g/100 ml at 25 °C and 0.014 g at 35 °C. It is insoluble in ethanol and acetone, but slightly soluble in acids and alkalis. It is soluble in alkali chloride solutions. The

heat of formation, ΔH_f, is –1453 kJ/mol with an entropy value, S_0, of 117.0 J/mol K. Its Mohs Hardness is 3.0–3.5. A water solution has a pH of 7.5. Its specific gravity ranges from 3.8 to 4.0 g/cm^3.

Thermochemical properties

$$\Delta H_f = -347.3 \text{ kcal/mol}$$

$$\Delta G_f = -320.05 \text{ kcal/mol}$$

$$S_0 = 28 \text{ cal/deg mol}$$

It occurs in nature as the mineral "celestine". Celestite is a favorite among mineral collectors. Its sky blue (or *celestial*) color is very pretty, and is unique in the mineral kingdom. Celestite also forms with other colorful minerals, making very nice combinations. Blue celestite with bright yellow sulfur is one of the most famous colorful combinations of minerals. Color is usually blue but can also be colorless, yellow and tints of red, green and brown. The luster is vitreous. Crystals can vary from transparent to translucent. Crystal system is orthorhombic; 2/m 2/m 2/m. The name Celestine comes from a Latin word meaning "heaven." This refers to the sky blue, "celestial" color often seen in this mineral. Since celestine is the most common mineral that contains the metal strontium, it is the predominate ore for that element. Compounds of strontium color a flame red, and they sometimes are used in the manufacture of fireworks.

Celestite has been found in various places in Europe and North America, but the state of Ohio is famous for having many of the best deposits. This mineral has been reported in 11 of Ohio's counties. Northwestern Ohio produces crystals of this mineral in colors ranging from white to a beautiful pale blue. Crystal cave on South Bass Island is a large jug filled with very large crystals of celestine. In the southwestern part of the state, it occasionally found in the area of Serpent Mound State Memorial where an unusual geological disturbance occurred.

Strontium sulfate is a polymeric material, isostructural with barium sulfate. Under certain conditions, it grows as "dendrites" which are layered (Fig. 3.32).

The compound, $SrSO_4$, is orthorhombic, with a space group *Pnma* ($a = 8.359$, $b = 5.351$, $c = 6.869$ Å, $Z = 4$), with 11 variable atomic positional parameters, and gives a fairly complex powder pattern with many overlapping peaks. Accurate high-resolution synchrotron X-ray powder diffraction (XRD) data were obtained at three energies: 14, 225 and 5133 eV below the Sr *K* edge. From combinations of two of the three data sets, partial Patterson densities were derived and used to phase the 71 uniquely resolved reflections, allowing a complete solution of the rest of the structure.

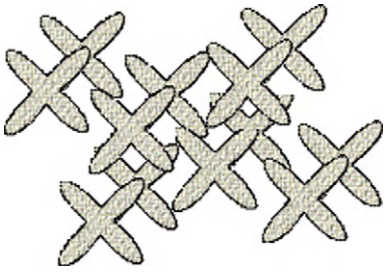

FIGURE 3.32

The crystal habits of $SrSO_4$ crystals grown from 0.015 M solution with and without the addition of polyvinyl sulfonate have been compared. Pure strontium sulfate precipitate consists of single crystals, about some tens of microns long, with distinctly visible growth steps. Crystals grown with polyvinyl sulfonate in stirred solutions show a striking change of habit: they are sponge-like structures, composed of minute crystallites, of size in the nanometer range.

The thermoluminescence of $SrSO_4$ and $BaSO_4$ doped with dysprosium and thulium has been studied. The phosphors were crystallized from H_2SO_4 solution by evaporation. $SrSO_4$:Dy and $SrSO_4$:Tm exhibit the same glow curve, both having a major glow peak at 140 °C. $BaSO_4$:Dy and $BaSO_4$:Tm also exhibit identical glow peaks at 130 °C which are similar to the $SrSO_4$ peaks except for the small shift in temperature. The sensitivities of $SrSO_4$:Dy and $BaSO_4$:Dy relative to $CaSO_4$:Dy are 90 and 27%, respectively, for ^{60}Co irradiation.

Crystallized strontium sulfate is utilized by a small group of protozoa as a main constituent of their skeleton. It is sometimes used to impart iridescence to glass and pottery glazes or used as a fining agent in crystal glass.

There is very little demand for this salt in industry. It is available in limited quantities commercially.

Barium Sulfate

Barium sulfate has the molecular formula of $BaSO_4$ and the molecular weight of 233.3896 g/mol. It can be prepared by the reaction of barium carbonate and sulfuric acid:

$$BaCO_3 + H_2SO_4 \Rightarrow BaSO_4 + CO_2 + H_2O$$

Barium sulfate is a soft crystalline solid. It is a rhombic crystal. The pure salt is white but the color of the mineral "barite" can vary between red, yellow, gray or green, depending on impurities. Its density is 4.50 g/cm^3 and its refractive index is 1.64. It melts around 1580 °C but decomposes above 1600 °C. Its hardness is 4.3 to 4.6 Mohs. It is virtually insoluble in water (285 mg/l at 30 °C) and insoluble in alcohol. Its K_{sp} is 1.1×10^{-10}. It is soluble in concentrated sulfuric acid. The crystal structure of BaSO4 is known to be rhombic, with a space group pnma. The lattice

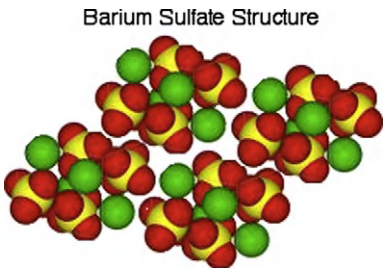

FIGURE 3.33

parameters are: $a = 8.896$ Å, $b = 5.462°$, $c = 7.171$ Å, $V = 348.4$ Å^3. Its three-dimensional structure is shown in Fig. 3.33.

Strontium sulfate has an identical structure. Thernodynamic constants are given by the following table. These values are for 293 K (Table 3.14).

Natural barium sulfate is widely distributed in nature and occurs as the mineral "barite" (also known as barytes or heavy spar). It often associated with other metallic ores, such as fluorspar. Barites containing over 94% $BaSO_4$ can be processed economically. It also contains silica, ferric oxide and fluoride impurities. Silica is the prime impurity that can be removed as sodium fluorosilicate by treatment with hydrofluoric acid followed by caustic soda. Very pure barium sulfate may be obtained by treating an aqueous solution of a soluble barium salt with sodium sulfate:

$$BaCl_2 + Na_2SO_4 \Rightarrow BaSO_4 + 2NaCl$$

Barium sulfate is one of the most insoluble salts of the alkaline earths. It does not undergo double decomposition reactions in aqueous phase like its Mg homologue. It dissolves in concentrated H_2SO_4 to form an acid sulfate that breaks down to $BaSO_4$ upon dilution. Reduction with coke under heating produces barium sulfide:

$$BaSO_4 + 3C \Rightarrow BaS + 2CO + CO_2$$

The accidental discovery of this conversion many centuries ago led to the discovery of the first luminescent material in 1803. The sulfide, unlike the sulfate, is water soluble. Sometime prior to the autumn of 1803, the Englishman John Dalton was able to explain the results of some of his studies by assuming that matter is composed of atoms and that all samples of any given compound consist of the same combination of these atoms. Dalton also noted that in a series of compounds like barium sulfate, the ratios of the masses of the second element that combine with a given weight of the first element can be reduced to small whole numbers (the law of multiple proportions). This was further evidence for the existence of "atoms".

TABLE 3.14

Thermochemical properties
$\Delta H_f = -352.3$ kcal/mol
$\Delta G_f = -325.7$ kcal/mol
$S^0 = 31.6$ cal/degree mol
$C_p = 24.3$ cal/degree mol
$\Delta H_{fusion} = 9.71$ kcal/mol

$BaSO_4$ reacts violently when heated with aluminum or explosively when mixed with potassium. Sulfamic acid, HSO_3NH_2 is a moderately strong acid. Water solutions are unstable and slowly hydrolyze to NH_4HSO_4. It has been used to produce nanosized barium sulfate particles.

Barium sulfate has many commercial applications. It is used either as natural barite, or precipitated $BaSO_4$. The precipitated salt in combination with equimolar amount of co-precipitated zinc sulfide formerly was used as a white protective coating pigment, known as "lithopone". Similarly, in combination with sodium sulfide, it is used to produce fine pigment particles of uniform size, known as "blanc fixe". Natural barite, however, has greater commercial application than the precipitated salt. It is used as an additive in drilling mud in crude oil, well drilled to lubricate and cool the drilling bit, and to plaster the walls of the drill hole to prevent caving. It is used as a filler in automotive paints, plastics and rubber products. It also is used as a filler in polyurethane foam floor mats, white sidewall rubber tires and as a flux and additive to glass to increase the refractive index.

Barium sulfate is frequently used clinically as a contrast agent for X-ray imaging and other diagnostic procedures. It is most often used in imaging of the gastrointestinal tract. It is administered, orally or by enema, as a suspension of fine particles in an aqueous solution. Although barium, and its water-soluble compounds are often highly toxic, the extremely low solubility of barium sulfate protects the patient from absorbing harmful amounts of the metal. Barium sulfate is also readily removed from the body, unlike prior compounds, which it replaced. Its absorbance of X-rays is also higher.

Barium sulfate mixtures are used as white pigment for paints. In oil paint, barium sulfate is almost transparent, and is used as a filler or to modify consistency. One major manufacturer of artists' oil paint sells "permanent white" that contains a mixture of titanium white pigment and barium sulfate. Barium sulfate itself is called *blanc fixe* (French for "permanent white").

A scientific-grade, barium sulfate-based paint is offered for sale that exhibits near-perfect diffuse reflectance at levels up to 98% in the UV-VIS-NIR wavelength

range. It is applied by spray painting to almost any substrate (metals, plastics, glass) for use in integrating spheres, laser cavities, lamp reflectors and display backlights. It is characterized by a near-perfect Lambertian (i.e. diffuse) reflectance of up to 98% in the spectral range from 250 to 2500 nm.

Other chemical applications of barium sulfate are used as a pigment for photographic paper. It is also used to prepare many other barium salts. It is available in many forms commercially.

Radium Sulfate

Radium sulfate has the molecular formula of $RaSO_4$ and the molecular weight of 322.0626 g/mol. It can be prepared by dissolving radium oxide in sodium sulfate solution:

$$RaO + Na_2SO_4 + H_2O \Rightarrow RaSO_4 + NaOH$$

Radium sulfate is insoluble in water with a solubility product of 3.66×10^{-11}. The solubility of **radium sulfate** would appear as at least 100-fold less than barium sulfate. Thus, it is the most insoluble sulfate known. Its CAS Number is 7446-16-4. It appears as white crystals. Since radium is a decay product in the ^{238}U series which then allows radon to accumulate in household basements, it is $RaSO_4$ that has received some attention in the scientific literature.

There is absolutely no demand for this salt and there are no listed suppliers commercially.

3.2.5. Alkaline Earth Thiosulfates

The thiosulfate ion, $S_2O_3^{2-}$, is a structural analog of the SO_4^{2-} ion in which one oxygen atom is replaced by one S atom. However, the two sulfur atoms in $S_2O_3^{2-}$; are not equivalent. One of the S atoms is a sulfide-like sulfur atom that gives the thiosulfate its reducing properties and complexing abilities. Thiosulfates readily oxidize to dithionate, then tetrathionate and finally to sulfates. A representation of the S–SO_3 molecule is given in Fig. 3.34.

Beryllium Thiosulfate

Beryllium thiosulfate would have the molecular formula of $[Be(OH)]_2S_2O_3$ and the molecular weight of 155.1571 g/mol. It can be prepared by the reaction of sodium thiosulfate upon the chloride:

$$BeCl_2 + Na_2S_2O_3 \Rightarrow [Be(OH)]_2S_2O_3 + 2NaCl$$

Since this thiosulfate is expected to be soluble in water, the solution must be evaporated at a low temperature to crystallize the product [salt-out temperature ~15 °F (−9.4 °C)]. However, there is absolutely no description in the scientific literature of the preparation of this compound, either by the use of sodium thiosulfite (basic solution) or the use of thiosulfuric acid (acidic solution).

Beryllium thiosulfate is not commonly mentioned in the literature or reference books. Only a few articles prevail, mostly in patents, which discuss technically specific physical uses along with many other similar compounds.

There is no designated supplier of beryllium thiosulfate and it is not available commercially, even in limited quantities.

Magnesium Thiosulfate

Magnesium thiosulfate has the molecular formula of MgS_2O_3 and the molecular weight of 136.4352 g/mol. It is also known as "hyposulfite". It can be prepared by the reaction of sodium thiosulfate upon the chloride in water:

$$MgCl_2 + Na_2S_2O_3 \Rightarrow MgS_2O_3 + 2NaCl$$

Since magnesium thiosulfate is soluble in water (50 g/100 ml at 20 °C), the solution must be evaporated at a low temperature to crystallize the product (salt-out temperature ~15 °F (−9.4 °C). A hexahydrate, $MgS_2O_3 \cdot 6H_2O$, is the result. Its CAS number is 13446-30-5 while that of the anhydrate is 10124-53-5. Thiosulfuric acid could also be used to prepare this salt at an acidic pH. The expected result is the hexahydrate. However, there is no report of an investigation concerning the product(s) formed as a function of pH of precipitation.

These are colorless crystals that lose water at 170 °C to form the trihydrate. Further heating to 420 °C then forms the anhydrate. Further heating to 600 °C will cause the production of magnesium sulfate, sulfur and oxides of sulfur:

$$2MgS_2O_3 + 2O_2 + \text{heat} \Rightarrow 2MgSO_4 + S + SO_2$$

The anhydrate has a density of 1.236 g/cm^3 and a melting point of 1710 °C while the density of the hexahydrate is 1.818 g/cm^3.

Magnesium thiosulfate hexahydrate has the rhombic structure with: space group = Pnma; $a = 9.324$ Å, $b = 14.461$ Å, $c = 6.862$ Å, $V = 925.2$ Å^3, $Z = 4$. Both neutron and X-ray diffraction were used to determine this structure. Peaks of about 0.25 e/Å^3 were observed at the midpoints of the S–O and S–S bonds. Extended

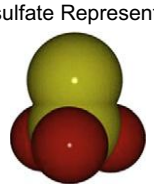

FIGURE 3.34

lone-pair electron regions up to 0.30 e/Å^3 were found at the back of the sulfate oxygen atoms. These were rather diffuse. Three of the water molecules are directly associated with the Mg^{2+} cations. The three independent water molecules show O–H bond peaks of 0.35–0.40 e/Å^3. Their lone-pair peaks amount to 0.30–0.37 e/Å^3 and are considerably extended normal to the H–O–H plane.

Magnesium thiosulfate is considered to have a low toxicity to humans. It has been used to remove ozone from either a water stream, such as a drinking water or wastewater stream being treated with ozone, or scrubbing ozone from a gaseous stream by contacting the gaseous stream with solid magnesium thiosulfate. It has also been used to remove chlorine gas from a water stream by contacting the stream with magnesium thiosulfate solution. In yet another aspect, a method of scrubbing chlorine from a gaseous stream comprises contacting the gas stream with solid magnesium thiosulfate.

Magnesium thiosulfate is not commonly referenced in scientific literature. The few articles that prevail discuss technically specific physical properties of the end product itself. Synthetic methods are described in some Japanese patents and there is mention of MgTS in a short German description in Handbuch der Anorganischen Chemie, vol. 11, 1984. Both refer to adding sulfur to magnesium sulfite to produce magnesium thiosulfate. Neither reference describes the pH nor physical consistency of the "sulfite" intermediate, although the German article does note the "color change" observed as SO_2 is purged into MgO: the slurry becomes yellow.

Magnesium thiosulfate is available in limited quantities commercially.

Calcium Thiosulfate

Calcium thiosulfate has the molecular formula of CaS_2O_3 and the molecular weight of 152.2082 g/mol. It can be prepared by the reaction of sodium thiosulfate upon the chloride:

$$CaCl_2 + Na_2S_2O_3 \Rightarrow CaS_2O_3 + 2NaCl$$

Since calcium thiosulfate is soluble in water (50.2 g/100 ml at 20 °C), the solution must be evaporated at a low temperature to crystallize the product (salt-out temperature ~15 °F (−9.4 °C). A hexahydrate, $CaS_2O_3 \cdot 6H_2O$, is the result. Its CAS number is 10124-43-3 while that of the anhydrate is 10124-41-1. Its density is 1.87 g/cm^3 and it loses four waters of hydration at 45 °C and the other two at about 85 °C. Further heating to 112 °C causes it to decompose, forming S, SO_2 and calcium sulfate:

$$2CaS_2O_3 + \text{heat} \Rightarrow 2CaSO_4 + S + SO_2$$

Thiosulfuric acid could also be used to prepare this salt at an acidic pH. The expected result is the hexahydrate. However, there is no report of an investigation concerning the product(s) formed as a function of pH of precipitation. A high-purity calcium thiosulfate can be prepared by a metathesis reaction of ammonium thiosulfate and calcium hydroxide or calcium oxide. Aqueous solutions of high-purity calcium thiosulfate, in concentrations up to about 30% by weight, are prepared by removing substantially all of the co-product ammonia under conditions that minimize the decomposition of the thiosulfate ion. Heating the reaction mixture to a temperature of about the boiling point at atmospheric pressure is used to prepare aqueous solution of about 10% by weight calcium thiosulfate, and lower reaction temperatures are employed to prepare more concentrated aqueous solutions of calcium thiosulfate up to about 30% by weight, which is the saturation point.

Calcium thiosulfate is supplied as a solution commercially. The clear solution has little odor, and the pH is in the range of 6.5–7.5. It is used in dechlorination, ozone and hydrogen peroxide quenching, concrete and cement formulations, photographic processes, coatings, stabilizers, and reactant for precious and nonprecious metals. It is also used as a "liquid lime" in agriculture.

Calcium thiosulfate is a reducing agent. It is routinely used as a titrant to determine concentrations of oxidants such as hypochlorite in bleach and dissolved oxygen in water. It instantly dechlorinates water, and is used to stop a bleaching action in the paper making industry.

Triclinic $CaS_2O_3 \cdot 6H_2O$ is builtup from $[Ca(H_2O)_6(S_2O_3)]$ chains, parallel to the [100] direction, of alternating S_2O_3 and $Ca(H_2O)_6O_2$ groups sharing common O atoms. It crystallizes centrosymmetrically in the pinacoidal class (point group 1). The structure is characterized by chains, parallel to [100], of alternating S_2O_3 and $Ca(H_2O)_6O_2$ groups sharing common O atoms. The composition of each chain link is $[Ca(H_2O)_6(S_2O_3)]$. The geometry has been analyzed and compared in detail with the structural features of monoclinic strontium(II) thiosulfate pentahydrate. Calcium thiosulfate is offered commercially, mostly as a solution of up to 30% by weight.

It is available commercially in large quantities.

Strontium Thiosulfate

Strontium thiosulfate has the molecular formula of SrS_2O_3 and the molecular weight of 199.7502 g/mol. It can be prepared by the reaction of sodium thiosulfate upon the chloride:

$$SrCl_2 + Na_2S_2O_3 \Rightarrow SrS_2O_3 + 2NaCl$$

It is moderately soluble in water (12.5 g/100 ml at 15 °C) so that the solution must be evaporated at a low

temperature to crystallize the product (salt-out temperature ~15 °F (−9.4 °C). A pentahydrate, $SrS_2O_3 \cdot 5H_2O$, is the result. Its CAS number is 15123-90-7 while that of the anhydrate is 10124-40-1. Its density is 2.17 g/cm^3 and it loses four waters of hydration at 100 °C and decomposes at 225 °C. In air, it forms sulfur plus strontium sulfate but the decomposition in an inert atmosphere remains unknown.

It is insoluble in ethanol and acetone. Its solubility in water varies with temperature (Table 3.15).

Monoclinic $SrS_2O_3 \cdot 5H_2O$ consists of $[Sr(H_2O)_3 O(S_2O_3)]$ layers of alternating S_2O_3 and $Sr(H_2O)_4O_5$ groups, parallel to (100), sharing O atoms and O-O edges. Strontium (II) thiosulfate pentahydrate, $SrS_2O_3 \cdot 5H_2O$, forms layers, parallel to (100), of alternating S_2O_3 and $Sr(H_2O)_4O_5$ groups connected via common O atoms and O-O edges. Each layer contains $[Sr(H_2O)_3 O(S_2O_3)]$ as the unique repeat unit.

Very little information is available for this salt in the scientific literature. It is classified as a "rare" chemical commercially and is available only in small quantities. There are no reference books which discuss this salt in depth. It is mentioned "in passing" as an alkaline earth salt.

It has no CAS number and there is no listed supplier for this salt.

Barium Thiosulfate

Barium thiosulfate has the molecular formula of BaS_2O_3 and the molecular weight of 249.4602 g/mol. It can be prepared by the reaction of sodium thiosulfate in water with the chloride of barium:

$$BaCl_2 + Na_2S_2O_3 \Rightarrow BaS_2O_3 + 2NaCl$$

It is not very soluble in water (0.25 g/100 ml at 15 °C) so that the solution does not need to be evaporated at a low temperature to crystallize the product. A monohydrate is the result. $BaS_2O_3 \cdot H_2O$ has the CAS number of 35112-53-9. It is insoluble in ethanol. It is a white, crystalline, water-insoluble, poisonous solid. It loses the water of hydration at 110 °C and decomposes at 228 °C to form the sulfate, sulfur and SO_2. The CAS number of the anhydrate is 7787-40-8.

$BaS_2O_3 \cdot H_2O$ is used chiefly in the manufacture of explosives, matches, paints, and varnishes. However, the demand for this chemical is not substantial and it is classified as a "rare" chemical.

Barium thiosulfate monohydrate is available in small quantities commercially.

TABLE 3.15

Gram/100 ml of water									
Material	**Formula**	**0 °C**	**10**	**20°**	**30**	**40°**	**60°**	**80°**	**100**
Strontium thiosulfate	$SrS_2O_3 \cdot 5H_2O$	8.78		15.6	21.1	26.8		30.4	

Radium Thiosulfate

Radium sulfate would have the molecular formula of RaS_2O_3 and the molecular weight of 338.1556 g/mol. It could be prepared by the reaction:

$$RaCl_2 + Na_2S_2O_3 \Rightarrow RaS_2O_3 + 2NaCl$$

It is expected to be insoluble in water so that the solution does not need to be evaporated at a low temperature to crystallize the product. The question of hydrate formation remains unknown as there is no record of this salt ever having been prepared. It has no CAS number. It is expected to be insoluble in ethanol. It is expected to be a white, crystalline, water-insoluble, poisonous, radioactive material.

Almost no information is available for this salt in the technical literature and it is not offered commercially.

3.2.6. Alkaline Earth Pyrosulfates or Disulfates

Although the salts are called pyrosulfates, the acid is called disulfuric acid. Disulfuric acid has the molecular formula of $H_2S_2O_7$ where the S-atom is in the +6 oxidation state. The structure of the acid, and of the alkaline earth compounds, consists of two sulfate tetrahedral directly connected by one oxygen. Thus, the acid would have the following Lewis structure while the magnesium (and other alkaline earths) would have the appearance shown in Fig. 3.35.

However, the actual structure is tetrahedral (Fig. 3.36).

Beryllium Pyrosulfate

Beryllium pyrosulfate is not stable in aqueous solution and so must be prepared via a solid-state reaction. It would have the molecular formula of BeS_2O_7 and

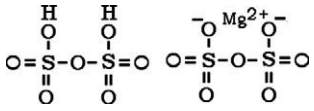

FIGURE 3.35

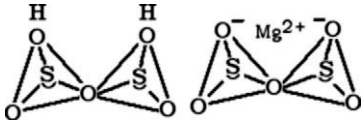

FIGURE 3.36

the molecular weight of 185.1401 g/mol. It could be prepared by the reaction involving "fuming" sulfuric acid (oleum) with beryllium sulfate:

$$[Be(OH)]_2SO_4 + (H_2SO_4)_n \Rightarrow 2BeS_2O_7 + (n+2)\ H_2O$$

The $[Be(OH)]_2SO_4$ salt is added to the oleum and allowed to dissolve in an excess of acid. The acid is heated to 150–175 °C to drive off the water. This is an equivalent of using $H_2S_2O_7$. The solution is allowed to equilibrate and crystals of the anhydrous salt appear. These are separated and allowed to dry. Beryllium disulfate is stable and may be heated to a red heat before it begins to decompose to the sulfate and SO_3.

There is no data or description of this salt in the open literature and its physical and chemical properties have not been studied. It has no CAS number and is not described in the industrial or commercial literature, including patents.

Magnesium Pyrosulfate

Magnesium pyrosulfate has the molecular formula of MgS_2O_7 and the molecular weight of 200.4328 g/mol. Almost no data concerning this salt is available either in patents, scientific or technical literature, or in reference books. Since this salt is not stable in water, it must be prepared by a solid-state reaction. One such reaction involves heating ammonium pyrosulfate with the oxide:

$$MgO + (NH_4)_2S_2O_7 + \text{heat} \Rightarrow MgS_2O_7 + 2H_2O + 2NH_3$$

It is known that the lower molecular weight alkaline earth pyrosulfates are not very stable in moist air or aqueous solution and hydrolyze to sulfate:

$$S_2O_7^{2-} + H_2O \Rightarrow 2SO_4^{2-} + 2H^+$$

$$MgS_2O_7 + H_2O \Rightarrow 2MgSO_4 + 2H^+$$

This may explain why the data on the Mg salt is sparse to nonexistent. The use of pyrosulfuric acid (as an acid solution) to form this compound is not feasible and solid state is required. When the solid persulfate is heated, it loses oxygen to form pyrosulfate:

$$2MgS_2O_8 \Rightarrow 2MgS_2O_7 + O_2$$

The evolved oxygen contains a small amount of ozone, which is identifiable by its smell. The pyrosulfate further decomposes into magnesium sulfate and sulfur trioxide, but the reaction only takes place when sulfuric acid is present:

$$MgS_2O_7 + H_2SO_4 \Rightarrow MgSO_4 + SO_3$$

The sulfuric acid plays the role of a catalyst in that it does not take part in the overall reaction, but without its presence, no SO_3 is formed.

Magnesium pyrosulfate, once formed, is relatively stable in dry air and can be heated to about 750 °C before it decomposes to the sulfate. It has no CAS number and is not offered for sale commercially.

Calcium Pyrosulfate

Calcium pyrosulfate has the molecular formula of CaS_2O_7 and the molecular weight of 216.2078 g/mol. There are few references in the scientific literature concerning this salt. This salt is not expected to be stable in aqueous solution and is expected to decompose to the sulfate. This may explain why the data on the Ca salt is sparse to nonexistent. It can be prepared via a solid-state reaction with ammonium pyrosulfate:

$$CaCl_2 + (NH_4)_2S_2O_7 + \text{heat} \Rightarrow CaS_2O_7 + 2NH_3(\text{gas}) + H_2O(\text{gas})$$

The solubility of this salt has not been reported. The existence of hydrates is unlikely. However, if one heats the persulfate, a pyrosulfate salt can be obtained:

$$2CaS_2O_8 \Rightarrow 2CaS_2O_7 + O_2$$

Further heating then forms the sulfate plus oxygen. These reactions have not been studied critically and no decomposition temperatures can be quoted. Another method of preparation involves the sulfate. If calcium sulfate is mixed with fuming sulfuric acid (to minimize the water present), it dissolves, forming a syrup which upon heating to 150 °C deposits the pyrosulfate crystals which are stable. Further heating removes the excess acid. These crystals are stable to about 720 °C where they decompose to form the sulfate plus sulfur trioxide.

Calcium pyrosulfate has no CAS number and is not offered for sale commercially.

Strontium Pyrosulfate

Strontium pyrosulfate has the molecular formula of SrS_2O_7 and the molecular weight of 263.7478 g/mol. It is expected to be more stable to decomposition in water than the Be, Mg and Ca homologues but no specific data on this aspect has appeared in the literature. There are no references in the scientific literature concerning this salt. Whether this salt is stable in aqueous solution remains unknown. This may explain why the data on strontium pyrosulfate (disulfate) is sparse to nonexistent. It can be prepared via a solid-state reaction with ammonium pyrosulfate:

$$SrCl_2 + (NH_4)_2S_2O_7 + \text{heat} \Rightarrow SrS_2O_7 + 2NH_3(\text{gas}) + H_2O(\text{gas})$$

The solubility of this salt has not been reported. The existence of hydrates is unknown. However, if one heats the persulfate, a pyrosulfate salt can be obtained:

$$2SrS_2O_8 \Rightarrow 2SrS_2O_7 + O_2$$

Further heating then forms the sulfate plus oxygen. These reactions have not been studied critically and no decomposition temperatures can be quoted. Another method of preparation involves the sulfate. If strontium sulfate is mixed with fuming sulfuric acid (to minimize the water present), it dissolves forming a syrup which upon heating to 150 °C deposits the pyrosulfate crystals which are stable. Further heating removes water and the excess acid. These crystals are stable to about 720 °C where they decompose to form the sulfate plus sulfur trioxide.

Strontium pyrosulfate is not offered commercially and has no CAS number.

Barium Pyrosulfate

Barium pyrosulfate has the molecular formula of BaS_2O_7 and the molecular weight of 313.4578 g/mol. There is no data concerning this salt is available either in patents, scientific or technical literature, or in reference books. Indeed, it has been stated that "This salt does not exist—it was first prepared by J.J. Berzelius in 1843 …." "It is decomposed by water … Apart from some doubt as to its precise structure, the compound is of little interest, and has never been more than a chemical curiosity—1933". However, this salt can be prepared by the solid-state reaction of ammonium pyrosulfate with barium chloride:

$$BaCl_2 + (NH_4)_2S_2O_7 + \text{heat} \Rightarrow BaS_2O_7 + 2HCl(\text{gas}) + 2NH_3(\text{gas})$$

However, a better method of preparation involves reaction of the sulfate with fuming sulfuric acid (Oleum):

$$BaSO_4 + H_2SO_4 \Rightarrow BaS_2O_7 + H_2O$$

The syrupy solution is heated to >150–175 °C to drive off the water and allow crystals to appear. Once formed, barium pyrosulfate is stable to about 720 °C where it decomposes to the sulfate plus sulfur trioxide gas. It can also be prepared by heating the persulfate:

$$2BaS_2O_8 + \text{heat} \Rightarrow 2BaS_2O_7 + O_2$$

The persulfate is also called peroxodisulfate. Further heating will form the sulfate, $BaSO_4$ plus sulfur trioxide. It is expected that this salt will be unstable in water. However, the solubility of this salt has not been reported.

Barium pyrosulfate has no CAS number and remains unknown commercially as there is no demand for this salt.

Radium Pyrosulfate

Radium pyrosulfate would have the molecular formula of RaS_2O_7 and the molecular weight of 402.1532 g/mol. However, there is no demand for this salt and it is not mentioned in the scientific literature. It could be prepared by dissolving radium sulfate in oleum and then heating the syrupy liquid to >150 °C to drive off the water:

$$RaSO_4 + H_2SO_4 \Rightarrow RaS_2O_7 + H_2O$$

A description of its physical or chemical properties remains unavailable and it has no CAS number. It is not available commercially.

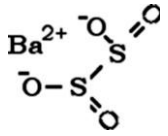

FIGURE 3.37

3.2.7. Alkaline Earth "Thionites and Thionates"

The **dithionite** anion, $S_2O_4^{2-}$, is an anion formally derived from the hypothetical compound "dithionous acid", $H_2S_2O_4$. Dithionous acid has not been detected either as a pure compound or in solution. Its IUPAC name is *sulfinatosulfinate*, the name of its corresponding acid is *sulfinosulfinic acid*. Dithionite anions are prepared by the reaction of sulfurous acid and a bisulfite. They undergo both acid and alkaline hydrolysis to thiosulfate and bisulfite, and sulfite and sulfide, respectively:

$$2S_2O_4^{2-} + 2H^+ \Leftrightarrow S_2O_3^{2-} + 2HSO_3^-$$

$$3S_2O_4^{2-} + 6OH^- \Leftrightarrow 5SO_3^{2-} + S^{2-} + 3H_2O$$

The alkali salts are well known. The sodium salt of dithionous acid, sodium dithionite, finds widespread use in industry as a reducing agent. Of the alkaline earths, only the barium salt has received any attention in technical studies or industrial usage. It has the Lewis structure shown in Fig. 3.37.

The decomposition of dithionite produces reduced species of sulfur that can be very aggressive for the corrosion of steel and stainless steel.

The **dithionate** anion, $S_2O_6^{2-}$, is derived from "dithionic acid", $H_2S_2O_6$. Its IUPAC name is *sulfonatosulfonate*. It has the Lewis structure shown in Fig. 3.38. where the barium salt is shown. The sulfur atoms of

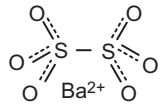

FIGURE 3.38

the dithionate ion are in the +5 oxidation state due to the presence of the S–S bond. Note that the individual bonds are resonant bonds, not double bonds. In general,

only the barium compound has been studied intensively. Generally, dithionates form stable compounds that are not readily oxidized or reduced. Strong oxidants oxidize them to sulfates and strong reducing agents reduce them to sulfites and dithionites:

$$S_2O_6^{2-} + H_2O_2 \Rightarrow 2SO_4^{2-} + H_2O$$

$$3S_2O_6^{2-} + 4H_2 \Rightarrow 2SO_3^{2-} + 2S_2O_4^{2-} + 4H_2O$$

Aqueous solutions of dithionates are quite stable and can be heated to 250 °C without decomposition. The alkali dithionates are well known but the alkaline earths compounds have not been explored.

The **tetrathionate** anion, $S_4O_6^{2-}$, is derived from the compound tetrathionic acid, $H_2S_4O_6$. Two of the sulfur atoms present in the ion are in the +2 oxidation state and two are in oxidation state +5. Alternatively, the compound can be viewed as the adduct resulting from the binding of the sulfide to sulfite. Tetrathionate is one of the polythionates, a family of anions with the formula $[S_n(SO_3)_2]^{2-}$. Its IUPAC name is (sulfonatodisulfanyl) sulfonate; the name of its corresponding acid is (sulfodisulfanyl)sulfonic acid. Tetrathionate is the product of the oxidation of thiosulfate, $S_2O_3^{2-}$, by iodine, I_2:

$$2S_2O_3^{2-} + I_2 \Rightarrow S_4O_6^{2-} + 2I^-$$

The tetrathionates of the alkalis are well known but those of the alkaline earths, with the exception of Ba, remain relatively unknown in the scientific literature. A comparison of these types of compounds is shown in Fig. 3.39.

Beryllium Thionates

Beryllium dithionite is expected to have the molecular formula of BeS_2O_4 and the molecular weight of 153.1412 g/mol. The "thionite" and "thionate" salts of beryllium would include:

Beryllium dithionite = BeS_2O_4
Beryllium dithionate = BeS_2O_6
Beryllium tetrathionate = BeS_4O_6

Beryllium dithionite could be prepared in solution by the reaction of beryllium chloride with sodium dithionite:

$$BeCl_2 + Na_2S_2O_4 \Rightarrow [Be(OH)]_2S_2O_4 + 2NaCl$$

However, there is no record of this reaction ever having been attempted. Alternatively, it may be prepared by the solid-state reaction of SO_2 gas upon the sulfite:

$$Be(HSO_3)_2 + SO_2(gas) + heat \Rightarrow BeS_2O_4 + H_2O$$

This reaction could probably be carried out in solution as well. But, the product would differ due to the hydrated-solution characteristics of the beryllium cation in water. However, the reaction would be dependent upon the pH of the solution and a pH of about 5.0 would produce the hydrosulfite:

$$BeCl_2 + 2(NH_4)_2SO_3 + SO_2 + H_2O \Rightarrow [Be(OH)]_2S_2O_4 + 2NH_4Cl$$

The description of the physical and chemical properties of this salt are completely lacking in the scientific and technological literature. Only barium dithionite is mentioned in a few patents as a reducing agent. Indeed, Parsons in "The Chemistry and Literature of Beryllium"-1909 states "The normal dithionite salt has not been produced". The older reference books like Sidgewick or Remy (1933 or 1950) do not list such a compound as being known.

It has no CAS number and has no commercial value.

Beryllium dithionate, BeS_2O_6, would have the molecular weight of 297.4538 g/mol. It could be prepared by the following method:

$$NH_3(gas) + SO_2(gas) + H_2O \Rightarrow (NH_4)_2SO_3(liq)$$

$$(NH_4)_2SO_3(liq) + MnO_2(solid) \Rightarrow MnS_2O_6(liq)$$

$$MnS_2O_6(liq) + Be(OH)_2(solid) \Rightarrow [Be(OH)]_2S_2O_6(liq) + Mn(OH)_2(solid)$$

In the first reaction, sulfur dioxide gas was passed through a cooled, continuously agitated solution to produce the ammonium compound. The solution was heated to remove excess sulfur dioxide. In the second reaction, the MnO_2 was allowed to dissolve over a period of 2–5 h and was then diluted. The third reaction served to form the insoluble manganese hydroxide that was removed by filtration and the resulting solution was evaporated at a low temperature to form dihydrate crystals. On allowing the solution to evaporate at a moderate temperature, rhombic dihydrate crystals are obtained.

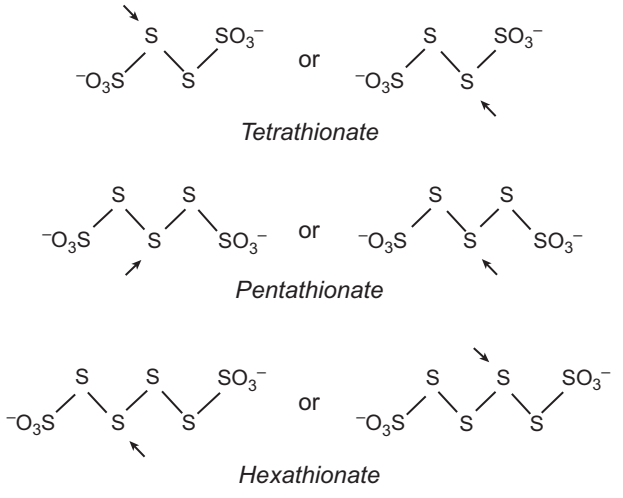

FIGURE 3.39

Beryllium dithionate dihydrate crystallizes as orthorhombic crystals; $a = 1.482$ Å, $b = 6.660$ Å, $c = 9.195$ Å, $\beta = 111.1°$, $Z = 4$, $V = 710.3$ Å^3. There are four molecules per unit cell. The space group is C2/c.

Other than the crystal data, no further description of the physical and chemical properties of beryllium dithionate has been forthcoming. This salt has no interest in industry and is not available commercially. It has no CAS number.

Beryllium Tetrathionate, BeS_4O_6, would have the molecular weight of 233.2726 g/mol. It could be prepared by the reaction of beryllium thiosulfate with iodine:

$$2BeS_2O_3 + I_2 \Rightarrow BeS_4O_6 + BeI_2$$

The tetrathionate is expected to be insoluble in ethanol and addition of alcohol to the reaction mixture serves to cause precipitation. If this is done slowly, crystals of the dihydrate should appear. However, there is no record of this reaction ever being tried or accomplished. In another method, the chloride is reacted with ammonium tetrathionate:

$$BeCl_2 + (NH_4)_2S_2O_6 \Rightarrow BeS_4O_6 + 2NH_4Cl$$

The tetrathionate can be crystallized as a dihydrate from solution by slow evaporation and the addition of alcohol.

Orthorhombic and triclinic **beryllium pentathionate** dihydrate, $BeS_5O_6 \cdot 2H_2O$, crystals have been reported. The presence of unbranched and nonplanar sulfur chains have been demonstrated in this compound. The penta-thionate chain contains three divalent sulfur atoms, together with terminal sulfur atoms to each of which are attached three oxygen atoms, respectively. The sulphonate groups, together with the adjacent divalent sulfur atoms, constitute thiosulfate groups, which have the shape of distorted tetrahedrons. The pentathionate compound is thus built of two thiosulfate groups linked by one divalent sulfur atom. The Lewis structure thus appears as in Fig. 3.40.

The structure actually consists of $S(S_2O_3^{2-})_2$ units in this salt. The structure of the hexa-thionate salt has not been determined.

Beryllium tetrathionate is available in small commercial quantities. Its usage in industry has not been established to date.

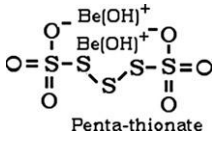

FIGURE 3.40

Magnesium Thionates

Magnesium dithionite has the molecular formula of MgS_2O_4 and the molecular weight of 168.4341 g/mol. The "thionite" and "thionate" salts of magnesium include:

Magnesium dithionite = MgS_2O_4
Magnesium dithionate = MgS_2O_6
Magnesium tetrathionate = MgS_4O_6

Magnesium dithionite, MgS_2O_4, may be prepared by the reaction of magnesium chloride with sodium dithonite:

$$MgCl_2 + Na_2S_2O_4 \Rightarrow MgS_2O_4 + 2NaCl$$

Alternatively, it may be prepared by the solid-state reaction of SO_2 gas upon the sulfite:

$$Mg(HSO_3)_2 + SO_2(gas) + heat \Rightarrow MgS_2O_4 + H_2O$$

This reaction could probably be carried out in solution as well. However, the reaction would be dependent upon the pH of the solution and a pH of about 5.0 would produce the hydrosulfite:

$$MgCl_2 + 2(NH_4)_2SO_3 + SO_2 \Rightarrow MgS_2O_4 + 2NH_4Cl + H_2O$$

This method is mentioned in a patent where all of the other alkaline earths are cited as well. The description of the physical and chemical properties of this salt are completely lacking in the scientific and technological literature. Magnesium dithionite is mentioned in a few patents as a reducing agent to decolorize wood pulp. The older reference books like Sidgewick or Remy (1933 or 1950) do not list such a compound as being known. It has no CAS number and has no commercial value.

Magnesium dithionate, MgS_2O_6, has the molecular weight of 297.4538 g/mol. It has been prepared by the following method:

$$NH_3(gas) + SO_2(gas) + H_2O \Rightarrow (NH_4)_2SO_3(liq)$$

$$(NH_4)_2SO_3(liq) + MnO_2(solid) \Rightarrow MnS_2O_6(liq)$$

$$MnS_2O_6(liq) + MgCO_3(solid) \Rightarrow MgS_2O_6(liq) + MnCO_3(solid)$$

In the first reaction, sulfur dioxide gas was passed through a cooled, continuously agitated solution to produce the ammonium sulfite compound. The water was cooled to 10 °C and then saturated with gaseous ammonia and sulfur dioxide. In the second reaction, the MnO_2 was added over several hours such that the temperature remained between 10 °C and 15 °C. The finely powdered MnO_2 reacted rapidly with a slight exotherm. Upon completion of the MnO_2 addition, the excess SO_2 was removed by heating the solution to 40 °C under a N_2 (g) sparge for 8 h. The third reaction served to form the insoluble manganese

carbonate by adding an aqueous solution of sodium magnesium carbonate to the well-stirred solution of manganese dithionate over 30 min. The precipitated manganese carbonate was removed by vacuum filtration, using a 1-μ glass microfibre pad, and the aqueous magnesium dithionate filtrate was collected. The filtrate was reduced in-vacuo to a solid. The product was isolated as the solid heptahydrate is greater than 95% yield based on MnO_2. On allowing the remaining solution to evaporate at a moderate temperature, rhombic crystals were obtained. The product is a heptahydrate, $MgS_2O_6 \cdot 7H_2O$. It has the CAS number of 13845-15-3 and the molecular weight of 184.4312 g/mol. The decomposition of $MgS_2O_6 \cdot 7H_2O$ has been studied using TG and DTG. Magnesium dithionate heptahydrate dehydrates in three separate steps, first forming the tetrahydrate at about 78 °C and then the dihydrate at 120 °C. The anhydrate is formed by 155 °C which decomposes at >650 °C to form the sulfate plus sulfur dioxide gas.

A description of the physical properties of this salt is not available. It has been cited in several patents as being useful in metal surface cleaning since it is water soluble and is a good reducing agent. Rust is easily dissolved. Nonetheless, the sodium compound is just as efficient and much cheaper. Other than the references cited (6 in all), no citations are given in the technical or scientific literature regarding this salt.

It is available in limited quantity commercially for sale.

Magnesium tetrathionate, MgS_4O_6, has the molecular weight of 248.56 grams per mole.

Magnesium tetrathionate can been prepared by reaction of magnesium thiosulfate with iodine:

$$2MgS_2O_3 + I_2 \Rightarrow MgS_4O_6 + BaI_2$$

The tetrathionate is insoluble in ethanol and addition of alcohol serves to cause precipitation. If this is done slowly, crystals of the octahydrate appear. In another method, the chloride is reacted with ammonium tetrathionate:

$$MgCl_2 + (NH_4)_2S_2O_6 \Rightarrow MgS_4O_6 + 2NH_4Cl$$

The tetrathionate can be crystallized from solution by slow evaporation and the addition of alcohol. The crystals of this salt are prismatic. Upon heating, the octahydrate loses 4 waters at about 105 °C and two other water molecules at about 160 °C. The last two water molecules are lost at about 185 °C.

The penta- and hexa-thionate chains contain three and four divalent sulfur atoms, respectfully, together with terminal sulfur atoms to each of which are attached three oxygen atoms. The sulphonate groups, together with the adjacent divalent sulfur atoms, constitute thiosulfate groups, which have the shape of distorted tetrahedrons. The pentathionate compound is thus built of two thiosulfate groups linked by three divalent sulfur atoms.

Magnesium tetrathionate is available in small commercial quantities. Its usage in industry has not been established to date.

Calcium Thionates

Calcium dithionate has the molecular formula of CaS_2O_4 and the molecular weight of grams per mole. The "thionite" and "thionate" salts of calcium include:

Calcium dithionite = CaS_2O_4
Calcium dithionate = CaS_2O_6
Calcium tetrathionate = CaS_4O_6

Calcium **dithionite**, CaS_2O_4, may be prepared by the reaction of calcium chloride with sodium dithonite:

$$CaCl_2(solid) + (NH_4)_2S_2O_4(solid) + heat \Rightarrow CaS_2O_4(solid) + 2NH_3(gas) + HCl(gas)$$

Alternatively, it may be prepared by the solid-state reaction of SO_2 gas upon the sulfite:

$$Ca(HSO_3)_2(solid) + SO_2(gas) + heat \Rightarrow CaS_2O_4(solid) + H_2O$$

This reaction could probably be carried out in solution as well. However, the reaction would be dependent upon the pH of the solution and a pH of about 4.5 would produce the hydrosulfite:

$$CaCl_2 + 2(NH_4)_2SO_3 + SO_2 \Rightarrow CaS_2O_4 + 2NH_4Cl + H_2O$$

The description of the physical and chemical properties of this salt are completely absent in the scientific and technological literature. Calcium dithionite is mentioned in a few patents as a reducing agent. The older reference books like Sidgewick or Remy (1933 or 1950) do not list such a compound as being known. It has no CAS number and has no commercial value. However, it is offered for sale either as "dithionite" or "hydrosulfite".

There is some confusion in the commercial literature concerning calcium dithionite, CaS_2O_4. Most manufacturers list the dithionite as synonymous with "hydrosulfite", $Ca(H_2SO_3)_2$. Its CAS number is 15512-36-4. However, the two are completely different compounds.

Calcium hydrosulfite is supplied as a colorless or slightly yellow colored liquid with a strong sulfur odor. It is a strong reducing agent. It is corrosive to skin and eyes and may be toxic by ingestion or inhalation. It is spontaneously combustible upon exposure to air or moisture. In contrast, calcium dithionite is stable in air and reacts slowly with moisture, releasing SO_2 gas. But, it dissolves in water, forming calcium hydrosulfite:

$$CaS_2O_4 + 2H_2O \Rightarrow Ca(HSO_3)_2 + 2H^+ \Rightarrow Ca(OH)_2 + 2SO_2$$

Both compounds react with oxidizing agents to generate heat and products that may be flammable, combustible, or otherwise reactive. These reactions may be violent. Sulfites generate gaseous sulfur dioxide in contact with oxidizing acids and nonoxidizing acids.

Calcium dithionate, CaS_2O_6, has the molecular weight of 297.4538 g/mol. It has been prepared by the following method:

$$NH_3(gas) + SO_2(gas) + H_2O \Rightarrow (NH_4)_2SO_3(liq)$$

$$(NH_4)_2SO_3(liq) + MnO_2(solid) \Rightarrow MnS_2O_6(liq)$$

$$MnS_2O_6(liq) + Ba(OH)_2(solid) \Rightarrow BaS_2O_6(liq) + Mn(OH)_2(solid)$$

In the first reaction, sulfur dioxide gas was passed through a cooled, continuously agitated solution to produce the ammonium compound. The solution was heated to remove excess sulfur dioxide. In the second reaction, the MnO_2 was allowed to dissolve over a period of 2–5 h and was then diluted. The third reaction served to form the insoluble manganese hydroxide that was removed by filtration and the resulting solution was evaporated at a low temperature to form dihydrate crystals. On allowing the solution to evaporate at a moderate temperature, rhombic crystals are obtained. The product is a tetrahydrate, $CaS_2O_6 \cdot 4H_2O$.

It can also be prepared from the sodium salt:

$$CaCl_2 + Na_2S_2O_6 \Rightarrow CaS_2O_6 + 2NaCl$$

The addition of alcohol to a cooled solution, while slow evaporation occurs, serves to form the tetrahydrate salt. It has the CAS number of 13813-19-9.

It is expected to be soluble in water but no data has been forthcoming. It occurs as white crystals that lose water of hydration at about 145 °C. Its density is 3.54 g/cm^3. It is slightly soluble in alcohol. Solid dithionate(V) salts when heated decompose to the corresponding sulfates with loss of sulfur dioxide. With these hydrated salts and complexes, it is often possible to distinguish two separate stages. For example with $CaS_2O_6 \cdot 4H_2O$, losses take place (a) between 120 and 200 °C and (b) between 250 and 320 °C, corresponding to loss of water and sulfur dioxide, respectively.

The lattice parameters and crystal structure of calcium dithionate tetrahydrate are: space group = $P6_422$, $a = 12.706$ Å, $c = 39.636$ Å, $V = 627$ Å^3, $Z = 3$. This structure is a superstructure of the strontium salt with doubling of all three axes where the $S_2O_6^{2-}$ anions occupy two sites on either side of a two-fold axis along [110] plus three sites around [001]. The water oxygen atoms occupy three sites around [001]. The Lewis structure is shown in the following diagram where the molecule is bent at the S–S bonds and the Ca^{2+} ion is bonded to the two oxygen ions (Fig. 3.41).

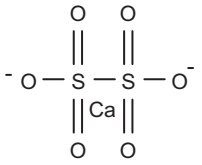

FIGURE 3.41

However, the two SO_3^-—groups are not tetrahedrally bonded in the strict sense of the configuration (which is actually a "strained" type of tetrahedra).

The optical rotatory dispersion (ORD) issue was discovered in 1867 by Pape (which is the main reason why these compounds have received some attention in the Literature). The origin of ORD was attributed to the dithionate grouping in this compound in 1987. Only the calcium and strontium dithionates as the tetrahydrates appear to possess the ORD characteristics. It seems to be absent in the Be, Mg and Ba compounds of a similar nature.

Calcium dithionate tetrahydrate is available commercially in limited quantities.

Calcium tetrathionate, CaS_4O_6, has the molecular weight of grams per mole. It has been prepared by the reaction of the thiosulfate with iodine:

$$2CaS_2O_3 + I_2 \Rightarrow CaS_4O_6 + CaI_2$$

It is advertised for sale with the CAS number 19188-83-1. However, its composition is not specified. There is no current information existing on the properties of this salt and whether it actually exists is not known. According to prior work in the late 1870s, only the trithionate was found. When the reaction with calcium thiosulfate with SO_2 was attempted, the product was identified as the trithionate:

$$4CaS_2O_3 + SO_2 \Rightarrow 2CaS_3O_5 + CaI_2$$

This was reported early in 1877 but has not been confirmed to date. If calcium thiosulfite is reacted with HCl, the thiosulfate (hyposulfite) is not split into calcium sulfite and sulfur but forms the trithionate:

$$5CaS_2O_3 + 6HCl \Rightarrow 2CaS_3O_6 + 3CaCl_2 + 4S + 3H_2O$$

A secondary reaction was said to occur:

$$2CaS_2O_3 + 3SO_2 \Rightarrow 2CaS_3O_6 + S$$

On heating, it was stated that the trithionate decomposes to $CaSO_4$ plus S and SO_2. Nevertheless, the physical properties of the calcium trithionate salt remain unknown. It appears that Ca^{2+} as a cation tends to form only the trithionate compound and not the pentathionate or hexathionates similar to the strontium or barium cations.

In another early source in the literature, it was stated:

> "Trithionate of calcium is generally the most stable polythionate, and often is found among the products of oxidation reduction of thiosulfate. In acid media, trithionate slowly hydrolyzes to sulfuric acid, colloidal sulfur, and sulfur dioxide. In alkaline media, it hydrolyzes to sulfate and thiosulfate. Trithionate is produced by reaction of thiosulfate with oxygen, catalyzed by copper compounds".

Calcium "tetrathionate" is offered for sale under the CAS number of 19188-83-1, and stated to have a molecular weight = 264.3344 g/mol or CaS_2O_6. Calcium tetrathionate is said to be an effective fungicide against powdery mildew.

Strontium Thionates

The "thionite" and "thionate" salts of strontium include:

Strontium dithionite = SrS_2O_4
Strontium dithionate = SrS_2O_6
Strontium tetrathionate = SrS_4O_6

Strontium dithionite, SrS_2O_4, may be prepared by the reaction of strontium chloride with sodium dithonite:

$$SrCl_2 + Na_2S_2O_4 \Rightarrow SrS_2O_4 + 2NaCl$$

Alternatively, it may be prepared by the solid-state reaction of SO_2 gas upon the sulfite:

$$Sr(HSO_3)_2(solid) + SO_2(gas) + heat \Rightarrow SrS_2O_4(solid) + H_2O$$

This reaction could probably be carried out in solution as well. However, the reaction would be dependent upon the pH of the solution and a pH of about 4.5 would produce the compound:

$$SrCl_2 + 2(NH_4)_2SO_3 + SO_2 \Rightarrow SrS_2O_4 + 2NH_4Cl + H_2O$$

The description of the physical and chemical properties of this salt are completely lacking in the scientific and technological literature. Strontium dithionite is mentioned in a few patents as a reducing agent to decolorize certain plastics. The older reference books like Sidgewick or Remy (1933 or 1950) do not list such a compound as being known. It has no CAS number and has no commercial value.

Strontium **dithionate**, SrS_2O_6, has the molecular weight of 297.4538 g/mol. It has been prepared by the following method:

$$NH_3(gas) + SO_2(gas) + H_2O \Rightarrow (NH_4)_2SO_3(liq)$$

$$(NH_4)_2SO_3(liq) + MnO_2(solid) \Rightarrow MnS_2O_6(liq)$$

$$MnS_2O_6(liq) + Sr(OH)_2(solid) \Rightarrow SrS_2O_6(liq) + Mn(OH)_2(solid)$$

In the first reaction, sulfur dioxide gas was passed through a cooled, continuously agitated solution to produce the ammonium compound. The solution was heated to about 40 °C to remove excess sulfur dioxide. In the second reaction, the MnO_2 was allowed to dissolve over a period of 2–5 h and was then diluted. The third reaction served to form the insoluble manganese hydroxide that was removed by filtration and the resulting solution was evaporated at a low temperature to form crystals. On allowing the solution to evaporate at a moderate temperature, prismatic crystals are obtained. The product is a tetrahydrate, $SrS_2O_6 \cdot 4H_2O$ with a molecular weight of 319.8422 g/mol.

Strontium dithionate tetrahydrate crystallizes as a hexagonal structure with $a = 6.3529$ Å and $c = 19.218$ Å, $Z = 3$, and $V = 671.7$ Å^3. The space group assigned, $P6_422$, is indicative of a dextro-rotative crystal. The structure is disordered about the twofold axis along the [110] direction. Disorder arises from the fact that the $S_2O_6^{2-}$ anion occupies two sites on either side of this axis. The dithionate anions are located in symmetry centers and the strontium cations lie in special positions along the twofold axes. Each strontium ion is ten coordinated to four water molecules and six oxygen atoms from six dithionate groups.

It is soluble in water at 22.2 g/100 ml at 16 °C and 64.5 m/100 ml at 100 °C. Its CAS number is 13845-17-5. It occurs as white crystals that decompose at about 145 °C. Its density is 2.373 g/cm^3. It is slightly soluble in alcohol. Dehydration of $SrS_2O_6 \cdot 4\ H_2O$ takes place in two steps. When the hydrate is heated to 90 °C, loss of four molecules of water of hydration occurs. On further heating to 210 °C, it decomposes to $SrSO_4$.

The description of the physical and chemical properties of this salt are sparse in the scientific and technological literature. Strontium dithionite is mentioned in a few patents as a reducing agent. The older reference books like Sidgewick or Remy (1933 or 1950) do not list such a compound as being known.

Strontium dithionate is available commercially in limited quantities.

Strontium tetrathionate, SrS_4O_6, has the molecular weight of 311.87 grams per mole. This salt has been prepared by reaction of strontium thiosulfate with iodine:

$$2SrS_2O_3 + I_2 \Rightarrow SrS_4O_6 + SrI_2$$

The tetrathionate is insoluble in ethanol and addition serves to cause precipitation. If this is done slowly, crystals of the hexahydrate appear. In another method, the chloride is reacted with ammonium tetrathionate:

$$SrCl_2 + (NH_4)_2S_2O_6 \Rightarrow SrS_4O_6 + 2NH_4Cl$$

The tetrathionate can be crystallized from solution by slow evaporation and the addition of alcohol to form the hexahydrate. The crystals of this salt are

prismatic but its lattice parameters have not been published. Presumably, it resembles the structure of the barium homologue and is hexagonal. It is expected that there are four molecules per unit cell and that the sulfur chain of the tetrathionate anion is unbranched and nonplanar. The space group is expected to be C_{2h}^5 – $P2^1/c$.

Orthorhombic and triclinic strontium pentathionate dihydrate, $SrS_5O_6 \cdot 2H_2O$, structures have also been reported. The presence of unbranched and nonplanar sulfur chains has been demonstrated in these compounds. The penta- and hexa-thionate chains contain three and four divalent sulfur atoms, respectfully, together with terminal sulfur atoms to each of which are attached three oxygen atoms. The sulphonate groups, together with the adjacent divalent sulfur atoms, constitute thiosulfate groups, which have the shape of distorted tetrahedrons. The pentathionate compound is thus built of two thiosulfate groups linked by three divalent sulfur atoms. The Lewis structure thus appears as in Fig. 3.42.

The structure of the hexa-thionate salt has not been determined. The structure actually consists of $S(S_2O_3^{2-})_2$ and $S_2(S_2O_3^{2-})_2$ units in these salts.

Strontium tetrathionate is available in small commercial quantities. Its usage in industry has not been established to date.

Barium Thionates

The "thionite" and "thionate" salts of barium include:

Barium dithionite = BaS_2O_4
Barium dithionate = BaS_2O_6
Barium tetrathionate = BaS_4O_6

Barium dithionite, BaS_2O_4, may be prepared by the reaction of barium chloride with sodium dithonite:

$$BaCl_2 + Na_2S_2O_4 \Rightarrow BaS_2O_4 + 2NaCl$$

Alternatively, it may be prepared by the solid-state reaction of SO_2 gas upon the sulfite:

$$Ba(HSO_3)_2(\text{solid}) + SO_2(\text{gas}) + \text{heat} \Rightarrow BaS_2O_4(\text{solid}) + H_2O(\text{gas})$$

This reaction could probably be carried out in solution as well. However, the reaction would be dependent upon the pH of the solution and a pH of about 5.0 would produce the hydrosulfite and then the dithionite:

$$BaCl_2 + 2(NH_4)_2SO_3 + SO_2 \Rightarrow BaS_2O_4 + 2NH_4Cl + H_2O$$

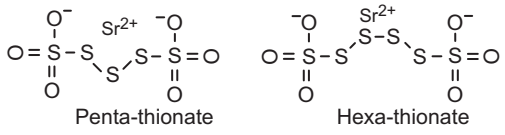

FIGURE 3.42

The description of the physical and chemical properties of this salt are completely lacking in the scientific and technological literature. Barium dithionite is mentioned in a few patents as a reducing agent. The older reference books like Sidgewick or Remy (1933 or 1950) do not list such a compound as being known. It has no CAS number and has no commercial value.

Barium dithionate, BaS_2O_6, has the molecular weight of 297.4538 g/mol. It has been prepared by the following method:

$$NH_3(\text{gas}) + SO_2(\text{gas}) + H_2O \Rightarrow (NH_4)_2SO_3(\text{liq})$$

$$(NH_4)_2SO_3(\text{liq}) + MnO_2(\text{solid}) \Rightarrow MnS_2O_6(\text{liq})$$

$$MnS_2O_6(\text{liq}) + Ba(OH)_2(\text{solid}) \Rightarrow BaS_2O_6(\text{liq}) + Mn(OH)_2(\text{solid})$$

In the first reaction, sulfur dioxide gas was passed through a cooled, continuously agitated solution to produce the ammonium compound. The solution was heated to remove excess sulfur dioxide. In the second reaction, the MnO_2 was allowed to dissolve over a period of 2–5 h and was then diluted. The third reaction served to form the insoluble manganese hydroxide that was removed by filtration and the resulting solution was evaporated at a low temperature to form dihydrate crystals. On allowing the solution to evaporate at a moderate temperature, rhombic crystals are obtained. The product is a dihydrate, $BaS_2O_6 \cdot 2H_2O$. It is soluble in water at 24.4 g/100 ml (18 °C) and 50.2 g/100 ml at 100 °C. Its CAS number is 13845-17-5. It occurs as white crystals that decompose at about 145 °C, its density is 4.54 g/cm^3, its solubility in water is 22.1 g/100 ml and it is slightly soluble in alcohol. When the dihydrate is heated to 90 °C, loss of the two molecules of water of hydration occurs. On further heating, it decomposes to $BaSO_4$:

$$BaS_2O_4 + \text{heat} \Rightarrow BaSO_4 + BaS$$

Barium dithionate dihydrate crystallizes as orthorhombic crystals; $a = 12.482$ Å, $b = 6.660$ Å, $c = 9.195$ Å, $\beta = 111.1°$, $Z = 4$, $V = 710.3$ Å^3. Its density is 3.118 g/cm^3. There are four molecules per unit cell. The space group is C2/c. The dithionate anions are located in symmetry centers and the barium cations lie in special positions along the twofold axes. Each barium ion is ten-coordinated to four water molecules and six oxygen atoms from six dithionate groups. The systematic absences may be summarized as: hkl when $h + k = 2n + 1$; h0l when $l = 2n + 1$ and $h = 2\pi + 1$; 0k0 when $k = 2n + 1$.

The γ-irradiation of crystalline dithionates produces sulfite [SO_3^-] anions. The unpaired electron in the SO_3^- radical can be detected by electron paramagnetic resonance (EPR) means and barium dithionate has been proposed as the basis for a radiation detector. Crystalline barium dithionate dihydrate ($BaS_2O_6 \cdot 2H_2O$) is thought to be a promising material for manufacturing dosimetric

EPR sensors for detection of gamma and beta radiation. For the purposes of EPR dosimetry, barium dithionate powder specimens are used, since it has been shown that a single narrow line of SO_3 radicals results, the intensity of which is proportional to the exposure dose. This has been confirmed in the irradiated powders concerned.

The results of EPR studies dealing with the accumulation of SO_3^- radicals in gamma-irradiated powder specimens have been reported, and the values of some parameters of their EPR spectra were presented; in particular, $g_{powder} = 2.0036$, the EPR line halfwidth $\Delta H_{powder} = 0.55$ mT and the isotropic constant of superfine interaction with the nuclear spin of the sulfur isotope 33S $A_{powder} \approx 11.5$ mT. SO_3^- radicals in natural $BaSO_4$ single crystals were also studied. These crystals have the same orthorhombic symmetry as $BaS_2O_6 \cdot 2H_2O$ crystals do. This work showed that there are several types of paramagnetic centers in this material, and some of them can occupy two magnetically nonequivalent states. But their spectra are described by different EPR parameters. This work aimed at studying, by the method of EPR spectroscopy, the radiation-induced centers in powder specimens of crystalline barium dithionate dihydrate, which emerge under the influence of gamma and UV irradiation, as well as due to the annealing of initial and irradiated specimens, and form the spectrum that is used in EPR dosimetry.

Barium dithionate is available commercially for sale in limited quantities.

Barium tetrathionate, BaS_4O_6, has the molecular weight of grams per mole. Barium tetrathionate has been prepared by reaction of barium thiosulfate with iodine:

$$2BaS_2O_3 + I_2 \Rightarrow BaS_4O_6 + BaI_2$$

The tetrathionate is insoluble in ethanol and addition serves to cause precipitation. If this is done slowly, crystals of the dihydrate appear. This salt was first isolated by Fordos and Gëlis in 1842. In another method, the chloride is reacted with ammonium tetrathionate:

$$BaCl_2 + (NH_4)_2S_2O_6 \Rightarrow BaS_4O_6 + 2NH_4Cl$$

The tetrathionate can be crystallized from solution by slow evaporation and the addition of alcohol. The crystals of this salt are prismatic and monoclinic with cell parameters of $a = 5.17$ Å, $b = 9.46$ Å, $c = 19.07$ Å, $\beta = 96°$. There are four molecules per unit cell. The sulfur chain of the tetrathionate anion is unbranched and nonplanar. Three oxygen atoms are arranged in approximately tetrahedral positions around each of the terminal sulfur atoms, at an average distance of 1.41 Å, the length of the sulfur–sulfur bond is 2.02 Å and that of the terminal S to S bonds is 2.12 Å, the bond angle between the two divalent sulfur atoms is 103° and the dihedral angle is 90°. The space group is $C_{2h}^5 - P2^1/c$.

TABLE 3.16

Crystal structure parameters

Salt	*a*	*b*	*c*	*α*	*β*	*γ*	Space group	*Z*
$BaS(S_2O_3)_2 \cdot 2H_2O$	5.01	10.37	11.54	109°	97°	97°	P1	2
$BaS(S_2O_3)_2 \cdot 2H_2O$	5.01	10.31	21.81		—		Pnma	4
$BaS(S_2O_3)_2 \cdot H_2O$	5.04	10.47	13.61		104°		$P2_1/m$	
$BaS(S_2O_3)_2 \cdot 2H_2O$	9.18	13.27	21.25		—		A2/m	
$BaS(S_2O_3)_2 \cdot 2H_2O$	5.04	10.56	13.81		108°		$2P_1/m$	

Two dimorphs of barium pentathionates exist, orthorhombic and triclinic barium pentathionate dihydrate, $BaS_5O_6 \cdot 2H_2O$ and barium hexathionate, BaS_6O_7 has also been reported. There are five dihydrates, which crystallize in three different space groups, a triclinic, an orthorhombic and a monoclinic one. The following lists the crystal parameters of some of these compounds (Table 3.16).

The presence of unbranched and nonplanar sulfur chains have been demonstrated in these compounds. The penta- and hexa-thionate chains contain three and four divalent sulfur atoms, respectfully, together with terminal sulfur atoms to each of which are attached three oxygen atoms. The sulphonate groups, together with the adjacent divalent sulfur atoms, constitute thiosulfate groups, which have the shape of distorted tetrahedrons. The pentathionate compound is thus built of two thiosulfate groups linked by three divalent sulfur atoms.

The Lewis structures thus appear as thiosulfates in which one of the sulfur atoms is divalent (Fig. 3.43).

The structure of the hexa-thionate salt has not been determined. The structure actually consists of $S(S_2O_3^{2-})_2$ and $S_2(S_2O_3^{2-})_2$ units in these salts.

Barium tetrathionate is available in small commercial quantities. Its usage in industry has not been established to date.

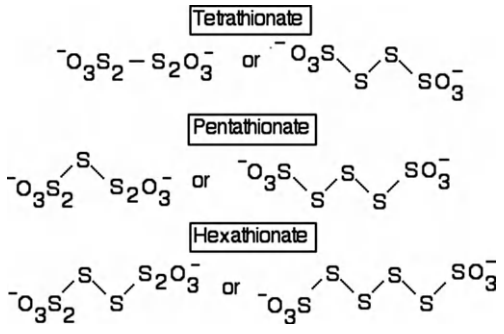

FIGURE 3.43

Radium Thionates

Radium dithionate would have the molecular formula of RaS_2O_4 and the molecular weight of grams per mole. The "thionite" and "thionate" salts of radium would include:

Radium dithionite = RaS_2O_4
Radium dithionate = RaS_2O_6
Radium tetrathionate = RaS_4O_6

Radium dithionite, BaS_2O_4, could be prepared by the reaction of radium chloride with sodium dithonite:

$$RaCl_2 + Na_2S_2O_4 \Rightarrow RaS_2O_4 + 2NaCl$$

Radium tetrathionate could be prepared by reaction of barium thiosulfate with iodine:

$$2RaS_2O_3 + I_2 \Rightarrow RaS_4O_6 + BaI_2$$

However, there is absolutely no industrial or domestic usage for these compounds and it is doubtful that they have been, or ever will be, prepared. They have no commercial value at this time and they have no CAS number.

3.2.8. Alkaline Earth Peroxysulfites and Peroxysulfates

The alkaline earths do not form many peroxy-sulfites or peroxy-sulfates.

Peroxy Acids

The acids involved include:

Oxydisulfuric acid is a chemical compound having the formula $H_2S_2O_5$. In structural terms, it can be written as $HO_3S–SO_2H$. The salts are commonly called "metabisulfites". Essentially, this acid is a "sulfate–sulfite acid". It is related to the "dithionites" except for the addition of an extra oxygen atom to the molecule. The **dithionite** anion, $S_2O_4^{2-}$, is an anion formally derived from the hypothetical compound "dithionous acid", $H_2S_2O_4$.

Although the alkalis such as Na and K form metabisulfites, very few alkaline earths do. Such compounds are commonly used as food preservatives. Metabisulfite compounds have been demonstrated to cause asthma and other allergic reactions in sensitive individuals.

Peroxymonosulfuric acid, also known as persulfuric acid, peroxysulfuric acid, or as **Caro's acid**, has the formula, H_2SO_5, a liquid at room temperature. In this acid, the S(VI) center adopts its characteristic tetrahedral geometry; the connectivity is indicated by the formula HO-O-S(O)$_2$-OH. H_2SO_5 is sometimes confused with $H_2S_2O_8$, known as "peroxydisulfuric acid". The disulfuric acid, which appears to be more widely used as its alkali metal salts, has the structure HO-S(O)$_2$-O-O-S(O)$_2$-OH.

The laboratory scale preparation of Caro's acid involve the combination of chlorosulfuric acid and hydrogen peroxide:

$$H_2O_2 + ClSO_2OH \Rightarrow H_2SO_5 + HCl$$

Large-scale production of Caro's acid is usually done on site, due to its instability. According to the patent by Martin, Caro's acid is produced by reacting >85% sulfuric acid and >50% hydrogen peroxide (also known as "Piranha solution"):

$$H_2O_2 + H_2SO_4 \Rightarrow H_2SO_5 + H_2O$$

H_2SO_5 has been used for a variety of disinfectant and cleaning applications, e.g. swimming pool treatment and denture cleaning. Alkali metal salts of H_2SO_5 show promise for the "pulping" of wood. Caro's acid is a strong oxidizing agent but few alkaline earth compounds have been prepared.

Peroxydisulfuric acid has the formula $H_2S_2O_8$. It is also called Marshall's acid. In structural terms, it can be written as HO_3SOOSO_3H. It is one of a group of sulfur oxoacids. Its salts, commonly known as persulfates, are industrially important but the acid itself is not. Alkali salts are commonly used but most alkaline earth peroxydisulfates remain unknown.

The Lewis structure for these acids is shown in Fig. 3.44.

Alkaline Earth Metabisulfites or Pyrosulfites

Beryllium metabisulfite—this salt is unknown.

Magnesium metabisulfite has the formula MgS_2O_5 and the molecular weight of 168.4342 g/mol. It is mentioned in a few patents as an oxidizing agent for fabric stabilization of dyes and is offered for sale as the tetrahydrate, $MgS_2O_5 \cdot 5H_2O$. These suppliers tend to mislabel the bisulfite, MgS_2O_6, as the metabisulfite.

Calcium metabisulfite has the formula CaS_2O_5 and the molecular weight of 1184.2072 g/mol. It is mentioned in a few patents as a catalyst for synthesis

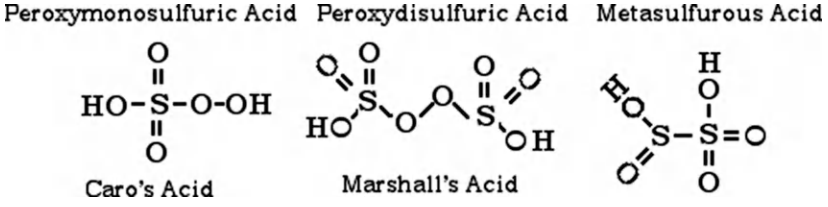

FIGURE 3.44

of certain indoles and for the treatment of coconut meat. It is offered for sale by certain commercial suppliers but it is often confused with calcium hydrosulfite (which is the product of SO_2 gas and calcium hydroxide in water).

The following "pyrosulfites" or "metabisulfites" are unknown:

Beryllium metabisulfite = BeS_2O_5 = Beryllium Pyrosulfite

Strontium Metabisulfite = SrS_2O_5 = Strontium Pyrosulfite

Barium Metabisulfite = BaS_2O_5= Barium Pyrosulfite

Radium Metabisulfite = RaS_2O_5 = Radium Pyrosulfite

Alkaline Earth Peroxymonosulfates

Many of the peroxymonosulfates have never been formed. An example is beryllium peroxymonosulfate.

Magnesium peroxymonosulfate has the molecular formula of $MgSO_5$ and the molecular weight of 136.3682 g/mol. It can be produced by the reaction of magnesium hydroxide, fuming sulfuric acid and hydrogen peroxide:

$$Mg(OH)_2 + H_2O_2 + H_2SO_4 \Rightarrow MgSO_5 + 3H_2O$$

The hexahydrate results upon evaporation and recrystallization of the solution at a low temperature of ~15 °C. This salt is offered for sale as $MgSO_5 \cdot 6H_2O$ and is used as a fumigant and biocide in hospitals. It is a very strong oxidizing agent and care must be taken in handling. This compound provides powerful non-chlorine oxidation for a wide variety of industrial and consumer uses. Its applications may be found in pool and spa shock and disinfection, oral hygiene formulations, polymerization initiator and oxygen-releasing agent in aquiculture.

Strontium peroxymonosulfate would have the molecular formula of $SrSO_5$ and the molecular weight of 152.1412 g/mol. It could be produced by the reaction of calcium hydroxide, fuming sulfuric acid and hydrogen peroxide:

$$Sr(OH)_2 + H_2O_2 + H_2SO_4 \Rightarrow SrSO_5 + 3H_2O$$

Upon evaporation and recrystallization of the solution at a low temperature of ~15 °C, it is expected that a hexahydrate would result. However, the scientific literature is completely devoid of mention of the preparation of such a salt and no physical or chemical properties have been documented. It is not known whether this salt or others like it could be prepared or are stable. Since both Mg and Ba form stable compounds, the mystery of why this salt has not been described remains unknown. No interest has been shown by industry or academia to detail the properties of this salt.

Barium peroxy-monosulfate has the molecular formula of $BaSO_5$ and the molecular weight of 249.3932 g/mol. It can be produced by the reaction of barium hydroxide, fuming sulfuric acid and hydrogen peroxide:

$$Ba(OH)_2 + H_2O_2 + H_2SO_4 \Rightarrow BaSO_5 + 3H_2O$$

The question of the existence of hydrates remains unknown since this salt is soluble, is very toxic and is used as a solution. It is referred to in a few patents that describe methods of producing pyrrolidine derivatives. The Lewis structure would be shown in Fig. 3.45.

This salt is sometimes mistaken for the persulfate which has the Lewis formula shown in Fig. 3.46.

These groups are aligned in a cubic array to form the structure shown in Fig. 3.47.

The following peroxysulfates remain unknown:

Beryllium peroxysulfate = $BeSO_5$
Calcium peroxysulfate = $CaSO_5$
Strontium peroxysulfate = $SrSO_5$
Radium peroxysulfate = $RaSO_5$

Alkaline Earth Peroxydisulfate Salts

Beryllium peroxydisulfate remains unknown.

Magnesium peroxydisulfate has the molecular formula of MgS_2O_8 and the molecular weight of

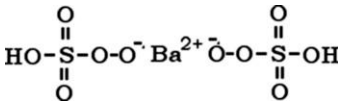

FIGURE 3.45

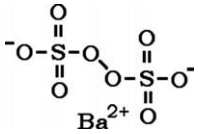

FIGURE 3.46

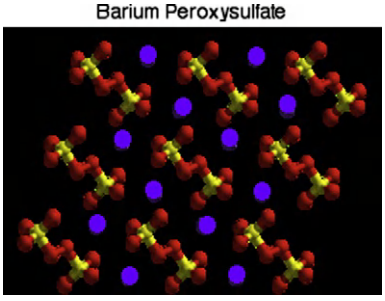

FIGURE 3.47

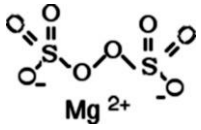

FIGURE 3.48

216.4322 g/mol. It can be prepared by the reaction of barium peroxydisulfate with magnesium sulfate in solution:

$$BaS_2O_8(aq) + MgSO_4(aq) \Rightarrow BaSO_4(solid) + MgS_2O_8(aq)$$

The barium sulfate precipitate is removed by filtration and the solution is evaporated at a low temperature of about 15–20 °C to produce the hexahydrate, $MgS_2O_8 \cdot 6H_2O$. The Lewis structure is shown in Fig. 3.48.

It has no CAS number and is not offered for sale by any commercial manufacturer.

STRONTIUM PEROXODISULFATE

Strontium peroxodisulfate has the molecular formula of SrS_2O_8 and a molecular weight of 279.7472 g/mol. It has been synthesized by the reaction of solid $Sr(OH)_2$, taken in 30% excess, with an aqueous solution of $(NH_4)_2S_2O_8$:

$$Sr(OH)_2 + (NH_4)_2S_2O_8 \Rightarrow SrS_2O_8 + 2NH_4OH$$

This solution is then evaporated at low temperature to form crystals of the tetrahydrate. Strontium peroxydisulfate has been used to etch copper circuits in the manufacture of integrated circuits for computers and the like. However, it is only mentioned in patents and there are no papers in the scientific literature describing its physical properties.

It is not offered for sale nor does it have a CAS number.

BARIUM PEROXODISULFATE

Barium peroxodisulfate has the molecular formula of BaS_2O_8 and a molecular weight of 329.4572 g/mol. It has been synthesized by the reaction of solid $Ba(OH)_2$, taken in 30% excess, with an aqueous solution of $(NH_4)_2S_2O_8$:

$$Ba(OH)_2 + (NH_4)_2S_2O_8 \Rightarrow BaS_2O_8 + 2\,NH_4OH$$

This solution is then evaporated at low temperature to form crystals of the tetrahydrate.

Barium peroxydisulfate has been used to etch copper circuits in the manufacture of integrated circuits for computers and the like. However, it is only mentioned in patents and there are no papers in the scientific literature describing its physical properties.

Barium peroxydisulfate, BaS_2O_8, in sharp contrast with the sulfate, is soluble in water. Among the uses of this compound is the saponification of fats and of soap, the oxidation of some dyestuffs and the promotion of certain polymerization processes, especially in the synthetic rubber industry. It is offered for sale by several suppliers but does not have a CAS number.

The following compounds remain unknown:

Beryllium peroxydisulfate = BeS_2O_8
Calcium peroxydisulfate = CaS_2O_8
Radium peroxydisulfate = RaS_2O_8

They are not offered for sale nor do they have a listed commercial supplier or CAS number.

3.3. ALKALINE EARTH SELENIDES AND OXY-SELENIUM COMPOUNDS

The seleno-oxo compounds of the alkaline earths include the compositional states of Se^{2-}, SeO_3^{2-} and SeO_4^{2-}, i.e. the selenides, selenites and the selenates, respectively. Selenium occurs in several valence states: −2 (hydrogen selenide and selenides), 0 (elemental selenium), +4 (selenium dioxide, selenious acid and selenites) and +6 (selenic acid and selenates).

Selenides are chemical compounds in which the Se atom has the valence state (oxidation state) of –2, similar to that of sulfur in sulfides. The chemistry of the selenides parallels that of the sulfides. Similar to sulfide, the selenide ion, Se^{2-}, is prevalent only in very basic conditions. In neutral conditions, hydrogen selenide anion, HSe^-, is most common. Under acid conditions, hydrogen selenide, H_2Se, is formed. It is a colorless, flammable gas under standard conditions. It is the most toxic selenium compound known with an exposure limit of 0.3 ppm over an 8-h period. This compound has the very irritating smell of decayed "horseradish". Its CAS number is 7783-07-5 and its molecular weight is 80.9832 g/mol. Its density is 3.553 g/cm^3. It has a melting point of –55.7 °C (207.4 K) and a boiling point of 41.2 °C (232 K).

H_2Se adopts a "bent" structure with a H–Se–H bond angle of 91°. Consistent with this structure, three infrared active vibrational bands are observed at 2358, 2345, and 1034/cm (Fig. 3.49).

The properties of H_2S and H_2Se are similar, although the selenide is more acidic with $pK_a = 3.89$, and the second $pK_a = 11.0$ at 25 °C. Reflecting its acidity, H_2Se is soluble in water.

H_2Se is usually prepared by the action of water on Al_2Se_3, which produces aluminum hydroxide. A related reaction involves the acid hydrolysis of FeSe.

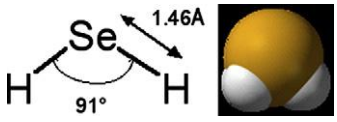

FIGURE 3.49

$$Al_2Se_3 + 6H_2O \Rightarrow 2Al(OH)_3 + 3H_2Se$$

According to the Sonoda method, H_2Se is generated from the reaction of H_2O and CO on Se in the presence of triethyl-amine. H_2Se can also be synthesized by the direct reaction of H_2 with elemental Se at temperatures greater than 300 °C. Elemental selenium can be recovered from H_2Se through a reaction with aqueous sulfur dioxide (SO_2):

$$2H_2Se + SO_2 \Rightarrow 2H_2O + Se + S$$

Selenous acid (also known as **selenious acid**) has the formula H_2SeO_3, written perhaps more descriptively as $(HO)_2SeO$. Selenous acid is the principal oxoacid of selenium when the Se atom is in the +4 oxidation state.

Selenous acid is analogous to sulfurous acid, but it is more readily isolated. Selenous acid is easily formed upon the addition of selenium dioxide gas to water. As a crystalline solid, the compound appears as pyramidal molecules that are interconnected with hydrogen bonds. In solution, it is a diprotic acid:

$$H_2SeO_3 \Rightarrow H^+ + HSeO_3^- \ (pK_a = 2.62)$$
$$\Rightarrow H^+ + SeO_3^{2-} \ (pK_a = 8.32)$$

It is moderately oxidizing in nature, but kinetically slow to react in aqueous solutions. In 1 M H^+, the following reaction occurs:

$$H_2SeO_3 + 4H^+ + 4e^- \Rightarrow Se + 3H_2O \ E\ominus = +0.74 \text{ V}$$

In 1 M OH^-, the following reaction occurs:

$$SeO_3^{2-} + 4e^- + 3\ H_2O \Rightarrow Se + 6OH \ (E\ominus = -0.37 \text{ V})$$

Thus, instead of selenites as a product, one sometimes obtains elemental selenium. Selenious acid has been used in organic synthesis for the synthesis of 1,2-diketones (e.g. glyoxal).

Selenic acid has the formula H_2SeO_4 where Se is in the +6 oxidation state. Oxoacid is more descriptively written as $(HO)_2SeO_2$, which emphasizes that the Se atom is attached to four oxygen atoms. Thus, the selenium center is tetrahedral. Selenic acid has the molecular weight of 144.9734 g/mol and the density of 2.95 g/cm^3. Its CAS number is 7783-08-6. It is a colorless crystal with a melting point of 58 °C and a boiling point of 261 °C (533 K) where it decomposes. Its solubility in water is 130 g/100 ml at 30 °C. The crystals have a refractive index of $\eta_d = 1.5174$.

Selenic acid can be prepared by oxidation of selenium dioxide with hydrogen peroxide:

$$SeO_2 + H_2O_2 \Rightarrow H_2SeO_4$$

To obtain the anhydrous acid as a crystalline solid, the resulting solution is evaporated at temperatures below 140 °C (413 K; 284 F) in a vacuum.

Like H_2SO_4, selenic acid is a strong acid that is hygroscopic and extremely soluble in water. Concentrated solutions are viscous. Crystalline mono- and di-hydrates are known. Unlike sulfuric acid, H_2SeO_4 is a sufficiently strong oxidizer to liberate chlorine from chloride ions, while being reduced to H_2SeO_3 (selenium[IV] acid). Selenic acid reacts with barium salts to precipitate $BaSeO_4$, analogous to the sulfate. Calcium selenate is more soluble than the sulfate.

Treatment of selenic acid with fluorosulfuric acid gives the dioxydifluoride (whose BP = −8.4 °C):

$$H_2SeO_4 + 2HO_3SF \Rightarrow SeO_2F_2 + 2H_2SO_4$$

Hot, concentrated selenic acid is capable of dissolving gold, forming a reddish-yellow solution of gold(III) selenate.

3.3.1. Alkaline Earth Selenides

Beryllium Selenide

Beryllium selenide has the molecular formula of BeSe and the molecular weight of 87.9722 g/mol. Its CAS number is 12232-25-6. The literature concerning BeSe is very sparse and the physical constants such as melting point have not been published. It can be prepared by reacting the elements at about 650 °C in an inert atmosphere:

$$Be + Se \Rightarrow BeSe$$

Beryllium selenide crystallizes in the zincblende unit cell with a lattice parameter of 5.1521 Å. Space group = F43m-T_d^2. It is not very stable in air and tends to hydrolyze with moisture to form H_2Se gas (which is toxic to humans). Because of this instability, BeSe has not been employed by itself as a semiconductor even though its band gap is classified as wide. A three-dimensional structure is shown in Fig. 3.50.

Interest in BeSe originates from the fact that formation of ternary BeZnSe or BeMgZnSe compositions allows the formation of deposited layers that can be matched to silicon substrates.

They can also be used to form a blue-green emitting ZnSe-based laser diode grown on GaSe.

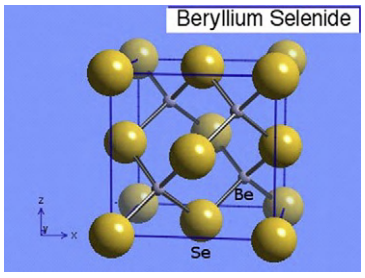

FIGURE 3.50

BeSe is an indirect band gap material with the highest edge at Γ, the top of the valence band, and X, the excitation edge at the bottom of the band gap, making the direct band gap 5.6 eV (221 nm) at 20 °C and the indirect band gap at $E_g \sim 3.5$ eV (354 nm) for the Γ ⇒ X transition.

Beryllium selenide telluride $BeSe_{0.41}Te_{0.59}$ is a zinc-blende semiconductor lattice matched to silicon with indirect band gap $E_G \sim 3.5$ eV. The high-stacking fault energy, thermal stability, and chemical compatibility of BeSeTe allow good crystalline quality epitaxial growth on silicon. The silicon substrates are vicinal (100), offcut 4° toward (011), annealed to form a double-stepped surface and arsenic passivated. Si regrowth on BeSeTe is done by solid-phase epitaxy. Deposition of ~30 Å amorphous Si at low substrate temperatures near room temperature, followed by crystallization anneal to 660 °C, yields a smooth double-stepped silicon surface as shown by the streaky single-domain pattern.

BeSe is available commercially in target form for sputtering in small quantities.

Magnesium Selenide

Magnesium selenide has the molecular formula of MgSe and the molecular weight of 103.2652 g/mol. It is a stable, light gray to brown crystalline powder with a refractive index, $\eta_D = 2.44$. Its density is 4.21 g/cm^3 and it decomposes in water:

$$MgSe + 2H_2O \Rightarrow Mg(OH)_2 + H_2Se$$

Thus, it cannot be prepared by bubbling H_2Se gas through a soluble Mg^{2+} aqueous solution. MgSe can be prepared by a variety of other methods. Among the easiest are the reaction of magnesium oxide and selenium. Alternately, the two elements can be reacted together to form the selenide:

$$MgO(solid) + Se(solid) + heat \Rightarrow MgSe(solid) + SeO_2(gas)$$

$$Mg(solid) + Se(solid) + heat \Rightarrow MgSe(solid)$$

In the first reaction, Se melts at 225 °C while the MgO is stable. Selenium dioxide sublimes at 320 °C. The reaction is carried out in an inert atmosphere at about 550 °C. If a tube furnace is used, crystals of SeO_2 appear at the cool end of the tube. In the second reaction, an inert atmosphere is mandatory and the reaction temperature is also 550 °C (which is below the melting point of Mg metal).

Magnesium selenide has the CAS number of 1313-04-8. It is not stable in air and reacts with moisture to form H_2Se, a foul-smelling and toxic gas:

$$MgSe + H_2O \Rightarrow Mg(OH)_2 + H_2Se$$

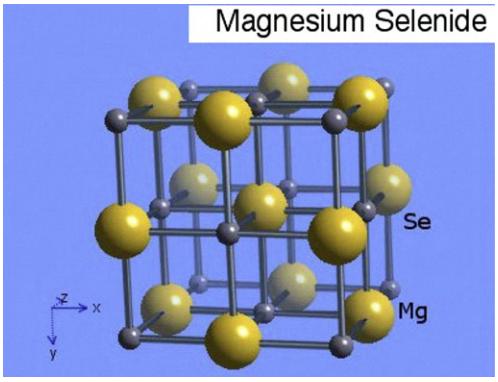

FIGURE 3.51

MgSe has the rock salt structure with $a = 5.462$ Å and a dielectric constant of 3.8 and a band gap of 4.05 eV. It is a wide-band semiconductor but is not very stable by itself. Other data concerning this salt, such as thermodynamics constants, are not available. A three-dimensional structure is shown in Fig. 3.51.

MgSe has the rock salt structure. It has been shown that, for MgSe, a transition under pressure occurs from the rock salt to the iron silicide structure at about 107 GPa. Industrial and academic interest in MgSe stems from the fact that the realization of a high p-type conductivity can be significantly improved by alloying ZnTe with ZnSe. Moreover, the ZnSe–ZnTe alloys, particularly alloy compositions near $ZnSe_{0.7}Te_{0.3}$ have excellent *p*-type and *n*-type doping properties without MgSe but with a band gap lower than that of ZnSe.

The addition of MgSe to the ZnSe–ZnTe alloy makes it possible to realize band gaps equal to and larger than that of ZnSe, while maintaining the superior n-type and p-type doping properties of the solid-state compound.

The vertical Bridgman method[1] was used to obtain crystals of $Zn_{1-x}Mg_xSe$ solid solutions ($0.03 \leq x \leq 0.55$). The composition of the samples was determined by means of electron probe microanalysis (EPMA). The methods of optical microscopy and X-ray analysis were used to investigate the structure of the crystal and to determine their lattice parameters. Investigated were the microhardness and microbrittleness of the grown crystals, as well as their polarizational, optical, photoelectric and dielectric properties depending on Mg concentration. The obtained crystals were found to possess anisotropy of physical properties. The largest anisotropy of their mechanical, polarizational and optical properties is observed in the crystals containing 5–6 atomic percentage of Mg. The samples with such a concentration of Mg are believed to be applicable as a base for making thermostable

[1]See: "Luminescence and the Solid State–2nd Ed." by R C Ropp, p298, Elsevier, (2004) – ISBN 0 444 51661 1.

multifunctional IR optical elements that can operate within a wide IR spectral region.

Further studies have established the temperature dependency of the refractive index of wide-gap $Zn_{1-x}Mg_xSe$ ($x = 0.5$) single crystals. It was established that, in the temperature range 300–530 K, the value of dn/dT for such crystals grown by the vertical Bridgman method is 9.31×10^{-5} at $x = 0.63$ m and 5.29×10^{-5} at $x = 10.6$ m. The obtained values of the coefficients dn/dT for hexagonal Zn_{1-x} Mg_xSe single crystals are close to the corresponding values for cubic ZnSe single crystals and are much lower than those for hexagonal CdS. Examples of practical application of single crystals of the ZnMgSe substitutional solid solution as a thermostable material for polarization optical elements in the IR range have been presented.

The XRD patterns for three bulk $Zn_{1-x}Mg_xSe$ crystals have been reported. The data were obtained with the help of an automated Bragg–Brentano diffractometer using Ni-filtered Cu *K* radiation. One of the samples is of the sphalerite structure type, and it has the magnesium content slightly below the sphalerite–wurtzite phase transition. The two remaining ones are of the wurtzite type with low and high magnesium content. The lattice constant for the sphalerite $Zn_{0.86}Mg_{0.14}Se$ is $a_0 = 5.701$ Å. For the wurtzite alloys, the lattice constants are $a_0 = 4.0540$ Å, $c_0 = 6.6270$ Å (for $Zn_{0.72}Mg_{0.28}Se$), $a_0 = 4.1195$ Å, $c_0 = 6.6941$ Å (for $Zn_{0.37}Mg_{0.63}Se$).

MgSe is available commercially as a sputtering or plasma targets for preparing thin-layer electronic structures for diodes, solid-state lasers and the like. MgSe has been assigned a CAS number of 1313-04-8.

Calcium Selenide

Calcium selenide has the molecular formula of CaSe and the molecular weight of 119.0452 g/mol. Its CAS number is 1305-84-6. It is a white to brown cubic crystal with a melting point of 1408 °C (where it decomposes, in air, to CaO and SeO_2). Its density is 3.81 g/cm^3 and it is unstable in air or moisture. Its refractive index is 2.274. Because of its instability in the presence of water, it cannot be prepared in an aqueous solution. Its structure is shown in Fig. 3.52.

CaSe can be prepared by the reaction of calcium oxide and selenium:

$$CaO(solid) + Se(solid) + heat \Rightarrow CaSe(solid) + SeO_2(gas)$$

Alternately, the two elements can be reacted together to form the selenide:

$$Ca(solid) + Se(solid) + heat \Rightarrow CaSe(solid)$$

In the first reaction, Se melts at 225 °C while the CaO is stable. Selenium dioxide sublimes at 320 °C. The reaction is carried out in an inert atmosphere at about 550 °C. If a tube furnace is used, crystals of SeO_2 appear at the cool end of the tube. In the second reaction, an inert atmosphere is mandatory and the reaction temperature is also 550 °C (which is below the melting point of Ca metal). However, the reaction does not go to completion and only about 50% of theoretical CaSe is formed. To achieve close to 100% reaction, the selanate can be reduced to form CaSe:

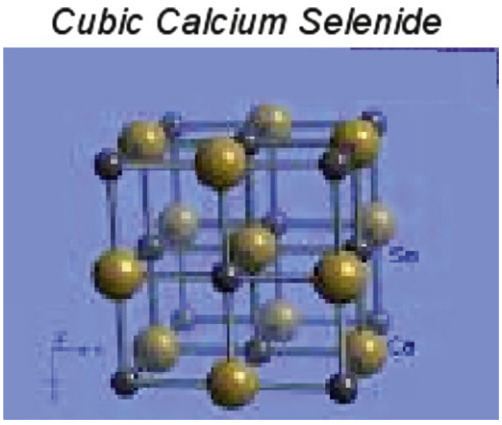

FIGURE 3.52

$$CaSeO_4 + H_2 + heat \Rightarrow CaSe + H_2O$$

The major usage of CaSe has been as a phosphor. Lenard and Pauli first described this phosphor, CaSe:Sm^{3+}, as an infrared stimulable material about 100 years ago. CaSe:Ce^{3+} is a blue-emitting (~4500 Å) phosphor. However, due to its instability, CaSe was never used in the lighting industry. More recently, it has been combined with the strontium compound to form phosphors.

$(Ca_{1-x},Sr_x)Se:Eu^{2+}$, which is an efficient red-emitting phosphor, was prepared by solid-state reaction at high temperatures in CO atmosphere. These phosphors can be excited efficiently by visible light from 430 to 490 nm and emit red light with broadband excitation from blue LED chips. If the Sr/Ca ratio is decreased, the lattice parameters get smaller, and the emission wavelength shows a red shift. A suitable wavelength can be obtained by adjusting the Sr/Ca ratio. Because of the commercial afterglow exhibited by calcium sulfide phosphor, these synthesized phosphors have higher emission efficiency and are a good choice for manufacturing white LED lamps. These phosphors are promising candidates for emitting red light for LEDs. When mixed with a green phosphor on a InGaN-based blue chip, the as-synthesized red phosphors generated white light for LEDs.

Additionally, a phosphorescent (long glow time) phosphor comprising a crystalline matrix including sulfur or a combination of sulfur and selenium, one or more metals including Sr or combination of Sr and Ca, and first and second activators consisting essentially of Eu and Cu, has been prepared. Its general composition

is $Ca_{1-x}Sr_xSe:Eu^{2+}:Cu^{+}$. This phosphor is capable of storing energy upon exposure of the phosphor to visible or ultraviolet exciting light and emitting said stored energy in the form of visible light after cessation of said exposure of said phosphor to said exciting visible light.

In contrast to MgSe, CaSe is a direct band gap semiconductor. However, under pressure, CaSe shows a progressive transition from a direct to an indirect gap semiconductor at a pressure of about 2 GPa, in the rocksalt phase. An insulator–conductor change was also observed at 70 GPa, in the zinc-blende phase. The structure is identical to that of MgSe except for the lattice dimensions.

CaSe is available commercially in both high purity and chemical grades.

Strontium Selenide

Strontium selenide has the molecular formula of SrSe and the molecular weight of 166.5852 g/mol. It is a white cubic crystal whose CAS number is 1315-07-7. Its melting point is 1605 °C and its density is 4.54 g/cm^3. It reacts with water and so cannot be prepared by an aqueous precipitation method. It can be prepared by the reaction of the oxide with Se metal:

$$2SrO + Se + Heat \Rightarrow SrSe + SeO_2$$

It can also be prepared by reducing the selenate with hydrogen gas:

$$SrSeO_4 + 4H_2 + heat \Rightarrow SrSe + 4H_2O$$

Strontium selenide and barium selenide both have a simple cubic structure, with cube edges equal to 3.117 Å and 3.308 Å, respectively. In the case of SrSe, the ions at the corners are Sr^{++} and Se^{--}, and the calculated density is 4.53 (Fig. 3.53).

The major usage of SrSe has been as an infrared stimulable phosphor. Photoluminescent materials useful for detection of infrared light are prepared using a base material, such as SrSe. Up to three dopants, Sm^{3+}, cerium, Ce^{3+} and Eu^{2+} compounds are used for the purpose of providing electron traps. The base material can be a combination of alkaline earth metal selenides such as strontium selenide, calcium selenide, or a mixture of these. Luminescence is a long known phenomenon of nature reaching back very far in history. Recorded observations reach back to the last century. Seeback and Becquerel observed momentary visible afterglow in certain materials. In 1889, Klatt and Lenard also observed some effects with infrared. During this time period, words like "phosphor" and "luminescence" appeared. In 1904, Dahms distinguished between "stimulation" and "quenching"; meaning inducing or stopping afterglow. Much of the later work is associated with Lenard, who received the Nobel Prize in 1905 in physics for cathode ray emission. He studied different phosphors until at least 1918. Later work can be found by Urbach in 1926 through 1934. These early scientists basically observed very small luminescent effects.

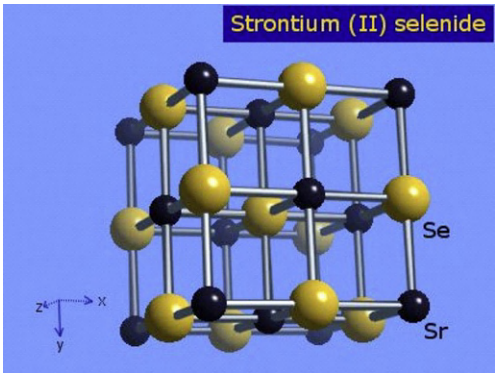

FIGURE 3.53

Phosphors can be categorized in accordance with their behavior as fluorescent, phosphorescent or stimulable. As used in this disclosure, such categories should be understood as based upon the predominant behavior of the phosphor at about room temperature, i.e at about 20 °C.

- A "stimulable" phosphor is one that, at room temperature, stores energy absorbed upon exposure to excitation by electromagnetic radiation and releases the predominant portion of the stored energy upon exposure to stimulating electromagnetic radiation.
- A phosphorescent phosphor at room temperature will store absorbed energy for an appreciable time but will release the predominant portion of the stored energy spontaneously.
- A fluorescent phosphor will release the predominant portion of the absorbed energy as emission radiant energy substantially simultaneously with exposure to the exciting radiant energy.

Typical IR-stimulable phosphors include:

$$SrSe:Sm^{3+}:Eu^{2+}$$

$$SrSe:Bi^{3+}:Eu^{2+}$$

This material will absorb and store energy upon exposure to ultraviolet or blue visible exciting radiation and will emit the stored energy as orange visible light upon stimulation by infrared radiation. One method of preparing such phosphors is:

STRONTIUM SELENIDE–SAMARIUM–EUROPIUM PHOSPHOR

To 3 gram of pure strontium chloride, solutions of samarium(III) and europium(III) chlorides are added

to give 0.5 mg of europium ion and 1.2 mg of samarium ion per gram of strontium chloride. The water is evaporated and the mixture dried at 200 °C. Twenty-five grams of strontium selenide and 2.5 g of the strontium chloride containing the activators are ground together in a porcelain mortar in a dry box. The mixture is heated in a platinum boat for 56 h at 1050 °C in a stream of purified nitrogen and cooled in the same nitrogen stream. Its excitation characteristics are the same as those of the corresponding sulfide phosphor, but the emission color is yellowish green.

The preferred phosphorescent phosphors have absorption and emission spectra similar to those of the IR-stimulable phosphors referred to above. Thus, the absorption spectrum typically extends from about 220 nm to about 540 nm, with peaks at about 300–350 nm and about 400–450 nm. The emission spectrum typically is between about 500 to about 700 nm, most preferably about 510 to 630 nm, with an emission peak at about 550 to about 600 nm, most preferably at about 560–570 nm. Eu and Cu together form an activator system for incorporation into an activated SrSe or (Sr,Ca)Se phosphor to provide phosphorescent behavior. This activator system is especially useful in phosphors wherein the base matrix incorporates sulfur and selenium, and particularly those in which the alkaline earth component of the base matrix is strontium or a combination of strontium and calcium, (Sr,Ca)(Se,S):Eu^{2+}:Cu^{+}.

Strontium selenide is available commercially from several suppliers.

Barium Selenide

Barium selenide has the molecular formula of BaSe and the molecular weight of 216.2956 g/mol. Its CAS number is 1304-39-8. It is a white crystalline powder having a melting point of 1782 °C. Its density is 5.02 g/cm^3. It reacts with water so that an aqueous method of precipitation cannot be used to prepare this compound. Barium selenide is very moisture sensitive, and must be handled under inert conditions. It can be prepared by reaction of the oxide or carbonate with Se, or by the reduction of the selenate with hydrogen gas:

$$2BaCO_3 + 5Se + Heat \Rightarrow 2BaSe + 3SeO_2 + CO_2$$

$$BaSeO_4 + 4H_2 \Rightarrow BaSe + 4H_2O$$

Strontium selenide and barium selenide both have a simple cubic structure, with cube edges equal to 3.117 Å and 3.308 Å, respectively.

In contrast to the other alkaline earth selenides, barium forms at least three other selenide compounds shown in Table 3.17.

TABLE 3.17

Compound	Symbol	Space group	Structure type
BaSe	cF8	Fm3m	NaCl-cubic
Ba_2Se_3	—	—	Unknown
$BaSe_2$	mC12	C2/c	ThC_2—monoclinic
$BaSe_3$	hP3	$P3_121$	Tetragonal

The last three compounds form by peritetic reactions at 930 °C, 840 °C and 760 °C, respectively. BaSe is formed at 712 °C. These reactions occur if an excess of Se is present. Ba metal melts at 727 °C while Se melts at 223 °C. Thus, the reactions take place in a selenium melt and form at the indicated temperatures shown in the following phase diagram (Fig. 3.54).

Barium selenide has been used to construct a photocell that has been used extensively to measure the solar irradiance of the Sun at various points on the globe. It is used because other photocell elements like selenium tend to decline in output and saturate under the intense radiance of the Sun. BaSe remains quasi-linear and can be used to measure intensity from 2000 Å to 7200 Å using a double monochrometer as a spectrum analyzer. As a portable unit, it uses narrowband (20–50 Å halfwidth) interference glass filters in 14 steps as a spectrum analyzer over the range 3100 Å to 16,300 Å, but the recording is manual. The field of view is $<3°$ of the solar irradiance over the face of the Sun.

BaSe is available commercially as a sputtering target or in limited quantities as a powder.

Radium Selenide

Radium selenide has the molecular formula of RaSe and the molecular weight of 304.984985 g/mol. It has the CAS number of 23320-14-1. It reacts with water so that an aqueous method of precipitation cannot be used to prepare this compound. Radium selenide is very moisture sensitive, and must be handled under inert conditions. It can be prepared by reaction of the oxide or carbonate with Se, or by the reduction of the selenate with hydrogen gas:

$$2RaO + 3Se \Rightarrow 2RaSe + SeO_2$$

$$2RaCO_3 + 5Se + Heat \Rightarrow 2RaSe + 3SeO_2 + CO_2$$

$$RaSeO_4 + 4H_2 \Rightarrow RaSe + 4H_2O$$

Radium selenide is expected to have a simple cubic structure but the crystal lattice parameters have never been published.

RaSe has been used in the past (1920s–1930s) in the treatment of certain types of cancer, primarily mammography where it was injected directly into tissue. It is no longer used in the U.S. but is employed in some European countries. RaSe is available commercially in selected dosages and quantities.

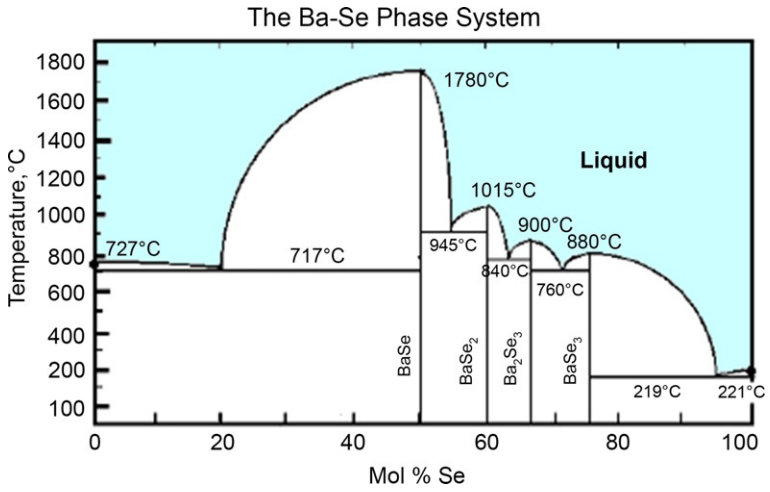

FIGURE 3.54

3.3.2. Alkaline Earth Selenites

A number of selenites are known.

Beryllium Selenite

Beryllium selenite has the molecular formula of $BeSeO_3$ and the molecular weight of 135.969 grams per mole. It can be prepared by adding sodium selenite to a solution of beryllium chloride:

$$BeCl_2(aq) + Na_2SeO_3(aq) \Rightarrow (BeOH)_2SeO_3 \cdot 2H_2O(solid)$$

It can also be prepared by treating a solution of beryllium chloride with selenous acid and adding sodium carbonate to start precipitation. By heating the dihydrate to 100 °C, one obtains the monohydrate, $(BeOH)_2SeO_3 \cdot H_2O$.

The monohydrate and dihydrate of **beryllium selenite** have not found usage in industry and they have no CAS number. These compounds are not commercially available.

Magnesium Selenite

Magnesium selenite has the molecular formula of $MgSeO_3$ and the molecular weight of 151.2658 g/mol. Its melting point is 557 °C. Its CAS number is 15593-61-0. It is relatively insoluble in water at 0.05454 g/100 ml. However, the most common form is the hexahydrate obtained by adding sodium selenite to a solution of magnesium chloride:

$$MgCl_2(aq) + Na_2SeO_3(aq) \Rightarrow MgSeO_3 \cdot 6H_2O(solid)$$

It can also be prepared by treating a solution of magnesium chloride with selenous acid and adding sodium carbonate to start precipitation. The hexahydrate is a colorless crystal with a density of 2.09 g/cm^3 that is insoluble in water. It is soluble in dilute acids. It is orthorhombic in crystal structure and when heated in a sealed tube to 150 °C forms monoclinic prisms of the dihydrate, when heated to 100 °C in air, it loses 5.0 mol of water to form the monohydrate. The monohydrate then loses the last water of hydration around 190 °C to form the anhydrate.

The dihydrate has been the subject of further investigation. Hydrothermally prepared $MgSeO_3 \cdot 2H_2O$ consists of pairs of edge-sharing MgO_6 (4O, $2H_2O$) octahedra [d_{av}(Mg–O) = 2.095 Å]. These are linked by pyramidal SeO_3 units [d_{av}(Se–O) = 1.697 Å] and hydrogen bonds forming a three-dimensional network (Fig. 3.55).

A 7.5 hydrate has also been discovered. The crystal structure of magnesium selenite as the 7.5-hydrate, $Mg(SeO_3) \cdot 7.5H_2O$ (space group = $P6_3/mmc$), is characterized by two crystallographically distinct $[Mg(H_2O)_6]^{2+}$ octahedra, one of which is disordered over two different orientations. The selenite groups and water molecules (with partially disordered H atoms) bridge the octahedra via hydrogen bonds. All the atoms are located on special positions, except for one water molecule (Fig. 3.56).

The selenites, in general, have several versatile and practical applications. The Mg and Ca salts are used as

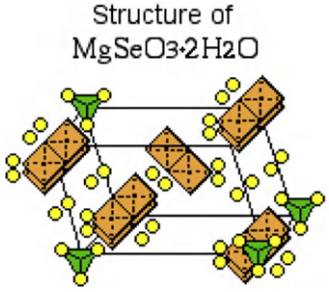

FIGURE 3.55

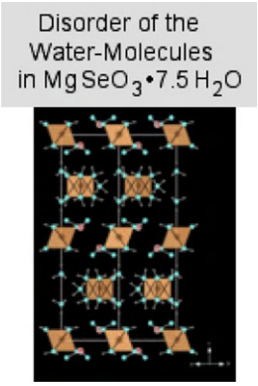

FIGURE 3.56

microfertilizers and repellants in agriculture. They are also used as catalysts in organic synthesis and they are precursors for the preparation of pure selenides of stoichiometric proportion. They are also important intermediate products in the production and purification of selenium metal itself.

$MgSeO_3$ is available commercially from a number of suppliers.

Calcium Selenite

Calcium selenite has the molecular formula of $CaSeO_3$ and the molecular weight of 167.0410 g/mol. It can be prepared by the addition of sodium selenite to a solution of magnesium chloride:

$$CaCl_2(aq) + Na_2SeO_3(aq) \Rightarrow CaSeO_3 \cdot H_2O(solid)$$

It can also be prepared by treating a solution of calcium chloride with selenous acid and adding sodium carbonate to start precipitation. The monohydrate is a colorless crystal with a density of 2.09 g/cm^3 that is insoluble in water. The K_{sp} is $1.2 \times 10^{-7.27}$. It is soluble in dilute acids. A dihydrate has also been observed whose molecular weight is 203.0669 g/mol. The monohydrate has a molecular weight of 185.0569 g/mol and is a monoclinic crystal with $a = 7.622$ Å, $b = 6.745$ Å, $c = 7.922$ Å, $\beta = 108.46°$, $V = 386.4$ Å^3, $Z = 4$ with a density of 3.18 g/cm^3. The polyhedron around the calcium atoms is pentagonal bipyramidal and the selenite group forms a trigonal pyramid with Se and O atoms at the apices. These pyramids form layers parallel to the *bc* plane which are connected by hydrogen bonds involving crystal water. The selenite group acts as a bidentate ligand.

The chemistry of the system CaO–SeO_2–H_2O has been investigated at 23 and 80 °C. The existence of four major phases in this system:

$$CaSeO_3 \cdot H_2O$$

$$Ca(HSeO_3) \cdot 2H_2O$$

$$Ca_2(SeO_3)(Se_2O_5)$$

$$Ca_2(HSeO_3)_2 \quad (5)$$

These have been confirmed, and the equilibria among them determined. At 23 °C, $CaSeO_3 \cdot H_2O$ and $Ca(HSeO_3) \cdot 2H_2O$ are the stable calcium selenites. $CaSeO_3 \cdot H_2O$ exists over the pH range 12.5–3.7, making it the most important phase for natural systems as well as most technological applications. $Ca(HSeO_3) \cdot 2H_2O$ is the more acidic phase; it exists over the pH range 3.7–0.4. Incongruent dissolution of $Ca(HSeO_3) \cdot 2H_2O$ forms $CaSeO_3 \cdot H_2O$. These results indicate $Ca_2(HSeO_3)_2(Se_2O_5)$ is not a stable phase at 23 °C. At 80 °C, $CaSeO_3 \cdot H_2O$, $Ca_2(SeO_3)(Se_2O_5)$, and $Ca_2(HSeO_3)_2(Se_2O_5)$ are the stable calcium selenite phases. $Ca(HSeO_3) \cdot 2H_2O$ has not been observed. Thus, $CaSeO_3 \cdot H_2O$ exists over the broadest pH range, 11.0–3.9. $Ca_2(SeO_3)(Se_2O_5)$ and $Ca_2(HSeO_3)_2(Se_2O_5)$ dissolve incongruently. The formation of $Ca_2(SeO_3)(Se_2O_5)$ and $Ca_2(HSeO_3)_2(Se_2O_5)$ at 80 °C demonstrates the increasing stability of the $Se_2O_5^{2-}$ ion and the decreasing stability of the $HSeO^{3-}$ ion with increasing temperature.

Calcium hydrogen selenite monohydrate and dicalcium diselenite {bis(hydrogenselenite)} were synthesized and their crystal structures determined:

Crystal data for **$Ca(HSeO_3)_2 \cdot H_2O$** were: $a = 6.911$, $b = 7.369$, $c = 6.739$ Å, $\alpha = 90.51°$, $\beta = 90.93°$, $\gamma = 107.46°$, $V = 327.3$ Å^3, space group (No. 2), $d_{calcd} = 3.19$ g/cm^3, $Z = 2$, and $R = 0.036$ for 1503 reflections.

Data for **$Ca_2(HSeO_3)_2(Se_2O_5)$**: $a = 14.719$, $b = 7.059$, $c = 11.793$ Å, $\beta = 117.96°$, $V = 1082.3(4)$ Å^3, space group $C2/c$ (No. 15), $d_{calcd} = 3.52$ Mg/m^3, $Z = 4$, and $R = 0.047$ for 1251 reflections.

Both structures form a three-dimensional network. The coordination polyhedron around calcium is a monocapped trigonal prism in dicalcium diselenite bis(hydrogenselenite) and a bicapped trigonal prism in calcium hydrogenselenite monohydrate. The Ca–O distance varies from 2.368 to 2.615 Å. Thermal behavior was investigated and the infrared spectrum assigned for dicalcium diselenite bis(hydrogenselenite).

In another study, selenious acid solutions containing a suspension of CaO were held under mild shaking for 1 month at 25 °C. The original analytical data for the solutions, wet residues and precipitates were presented graphically as the ternary phase diagram for the CaO–SeO_2–H_2O system. It was obvious from this graphical procedure that two compounds, $Ca(HSeO_3)_2 \cdot H_2O$ and $CaSeO_3 \cdot H_2O$ existed. Also, the chemical analysis of three precipitates obtained at around pH = 12.0 gave a mole ratio of Ca/Se(IV) of 2.0, corresponding to the $Ca_2SeO_3(OH)_2 \cdot 2H_2O$ species with CaO = 40.47 wt%, SeO_2 = 40.04 wt% and H_2O = 19.49 wt%. In this system, there are three invariant points. The first invariantvv point lies at the point where $Ca(HSeO_3)_2 \cdot H_2O$ and

$CaSeO_3 \cdot H_2O$ coexist. The second lies at the point E ($CaO = 0.06$ wt%, $SeO_2 = 0.003$ wt%) where $CaSeO_3 \cdot H_2O$ and $Ca_2SeO_3(OH)_2 \cdot 2H_2O$ coexist. The third lies at the point ($CaO = 0.08$ wt%, $SeO_2 = 0.00004$ wt%) where $Ca_2SeO_3(OH) \cdot 2H_2O$ and $Ca(OH)_2$ coexist. It was noted that $Ca(HSeO_3)_2 \cdot H_2O$ with a Ca/Se(IV) mole ratio of 0.5 is stable at a pH below 3.5, $CaSeO_3 \cdot H_2O$ with Ca/Se(IV) mole ratio of 1.0 in the pH range 3.5–12.3 and $Ca_2SeO_3(OH)_2 \cdot 2H_2O$ with Ca/Se(IV) mole ratio of 2.0 in the pH range 12.3–12.5. In this system, there are three invariant points at pH 3.5, 12.3 and 12.5, and at each point, a two-point solid phase coexists:

$$Ca(HSeO_3)_2 \cdot H_2O \text{ and } CaSeO_3 \cdot H_2O$$

$$CaSeO_3 \cdot H_2O \text{ and } Ca_2SeO_3(OH)_2 \cdot 2H_2O$$

$$Ca_2SeO_3(OH)_2 \cdot 2H_2O \text{ and } Ca(OH)_2$$

Calcium selenite is available as the monohydrate from a number of commercial suppliers.

Strontium Selenite

Strontium selenite has the molecular formula of $SrSeO_3$ and the molecular weight of 214.5782 g/mol. It can be prepared by adding strontium hydroxide or carbonate to selenous acid which has been stabilized by sodium carbonate to form the sodium salt:

$$Sr(OH)_2(\text{solid}) + Na_2SeO_3(\text{aq}) \Rightarrow SrSeO_3 \cdot 7H_2O(\text{solid}) + H_2O$$

The product is a heptahydrate whose CAS number is 14590-38-6. This compound is insoluble in water but soluble in dilute acids. An acid selenite, $Sr(HSeO_3)_2$, has been reported that is soluble in water. However, its existence has not been confirmed. If it exists, it would be obtained by low temperature evaporation of the solution at an acid pH (~pH = 5.5) and would probably require the presence of ammonium hydroxide during the evaporation to form the crystals. The existence of a hydrate remains unknown.

Another method of preparation of strontium selenite has been given:

A solution of 77 g of sublimed selenium(1 V) oxide in 154 ml of distilled water is added to 500 ml of pure strontium nitrate solution prepared as previously described. The solution is heated to boiling and fresh ammonium hydroxide solution is added until no further precipitation of strontium selenite occurs. The precipitate is drained and washed six times with 300-ml portions of hot distilled water. The nitrate content should be less than 5 parts per million as determined by the diphenylamine-sulfuric acid test. The strontium selenite is dried at 200° for several hours. The yield is about 125 g.

During synthesis of the monazite-type strontium selenate, $SrSeO_4$, a new compound $SrSe_2O_5$ was obtained. This compound was formed by the reaction of hydrogen peroxide upon a mixture of strontium oxide plus selenous acid at a 1:2 molar ratio:

$$2SrO + 4H_2SeO_3 + 2H_2O_2 \Rightarrow 2SrSe_2O_5 + 6H_2O + O_2$$

Essentially this "diselenite" is a mixed compound, $SrSeO_3 \cdot SeO_2$, whose molecular weight is 325.54 g/mol. It is triclinic with a space group of P1 and the lattice parameters of $a = 6.916°$, $b = 6.971°$, $c = 10.875$ Å, $\alpha = 85.07°$, $\beta = 81.46°$, $\gamma = 79.56°$, $V = 509.0$ Å^3, $Z = 4$. The mean Sr–O distance for the eight-coordinated Sr(1) atom is somewhat shorter than that for the nine-coordinated Sr(2) atom. The two crystallographically different diselenite groups have Se–O bond lengths to the bridging O-atoms ranging from 1.822 to 1.879 Å, and others from 1.645 to 1685 Å. The Se–O–Se angles are 120.7° and 122.5°.

Strontium selenite has been used to prepare the selenide by heating it in a hydrogen atmosphere:

$$2SrSeO_3 \cdot 7H_2O + 6H_2 + \text{heat} \Rightarrow 2SeSe + 13H_2O$$

Strontium selenite is available commercially from several manufacturers.

Barium Selenite

Barium selenite has the molecular formula of $BaSeO_3$ and the molecular weight of 264.2865 g/mol. Its CAS number is 13718-59-7. It is a white solid that is insoluble in water. It can be prepared by the addition of sodium selenite to a solution of barium chloride:

$$BaCl_2(\text{aq}) + Na_2SeO_3(\text{aq}) \Rightarrow BaSeO_3(\text{solid})$$

It can also be prepared by treating a solution of barium chloride with selenous acid and adding sodium carbonate to start precipitation. There is no record of a hydrate and the anhydrate is stable upon heating to over 950 °C.

The heat of formation of barium selenite is:

$$\Delta_f H_{298} - BaSeO_3 = 2230.6 \text{ kcal/mol } (-964.7 \text{ kJ/mol}).$$

The precipitate of barium selenite is not oxidized by air during drying at 110 °C. In air, however, it oxidizes to the selenate at about 700–750 °C:

$$2BaSeO_3 + O_2 + \text{heat} \Rightarrow 2BaSeO_4$$

Barium selenite is a fine white crystalline powder that is mainly used in the glass industry to color and decolor glass. Barium selenite is primarily chosen for producing special glass and leads to the formation of glass with high index of refraction. Barium selenite has weak oxidizing or reducing powers. Redox reactions can however still occur. The majority of compounds in this class are slightly soluble or insoluble in water. Noncombustible, the substance itself does not burn but may decompose upon heating to produce corrosive and/or toxic fumes of SeO_2.

A study of the ternary phase diagram for the BaO–SeO_3–H_2O system at 25 °C has been made. In this equilibrium experiment, $Ba(OH)_2 \cdot 8H_2O$ was used as the starting material. The results indicated the existence of two solid phases, $BaSe_2O_5$ and $BaSeO_3$. At one invariant point, (BaO = 0.56 wt%, SeO_2 = 0.83 wt%), these two solid phases are in equilibrium. The stability and solubility regions for barium selenites as a function of pH at 25 °C indicated that $BaSe_2O_5$ having Ba/Se(IV) mole ratio = 1/2 is stable at a pH below 4.6 and $BaSeO_3$ having Ba/Se(IV) = 1/1 is stable in the pH range 4.6 to 13.7. Furthermore, the system Ba–Se(IV)–H_2O at pH 4.6 has two invariant points where $BaSe_2O_5$ and $BaSeO_3$ coexist and at pH 13.7 where $BaSeO_3$ and $Ba(OH)_2.H_2O$ coexist.

The volatility of selenium in making selenium ruby glass has been studied. About 75% of the selenium added to the batch was lost by volatilization. Sodium selenite and barium selenite were stable at 950 °C and are probably stable at higher temperatures. Regardless of whether selenium or the compounds studied are used, the resulting glass contains about equal amounts of selenium. Methods of preparing sodium and barium selenites are described. An outline is given of an analytical procedure by which selenium is determined in glass.

Barium selenite is available commercially as $BaSeO_3$ from a number of suppliers.

Radium Selenite

Radium selenite has the molecular formula of $RaSeO_3$ and the molecular weight of 352.9832 g/mol. It can be prepared by the addition of sodium selenite to a solution of radium chloride:

$$RaCl_2(aq) + Na_2SeO_3(aq) \Rightarrow RaSeO_3(solid)$$

It can also be prepared by treating a solution of radium chloride with selenous acid and adding sodium carbonate to start precipitation. There is no record of a hydrate. $RaSeO_3$ has been administered in the past as a irradiative treatment of certain tumors but there is no substantive evidence concerning its efficacy in this regard. $RaSeO_3$ has no CAS number and is not available commercially.

3.3.3. Alkaline Earth Selenates

Only a few selenates are known.

Beryllium Selenate

Beryllium selenate has the molecular formula of $BeSeO_4$ and the molecular weight of 224.0354 g/mol. Its density is 2.03 g/cm^3. If prepared in solution, the formula is likely to be $(BeOH)_2SeO_4 \cdot 4H_2O$. Nevertheless, the literature persists in relating the compound produced as $BeSeO_4$. The addition of beryllium carbonate and sodium carbonate to a selenic acid solution is sufficient to form the tetrahydrate:

$$BeCO_3(solid) + Na_2CO_3(solid) + H_2SeO_4(aq) \Rightarrow (BeOH)_2SeO_4 \cdot 4H_2O(solid) + 2NaOH(aq) + CO_2(gas)$$

It is soluble in water and the solution must be evaporated to obtain the crystalline salt. Beryllium selenate tetrahydrate has the CAS number of 10039-31-3 and a molecular weight of 267.0582 g/mol. Its density is 2.032 g/cm^3 and it is very soluble in water (49.6 g/100 ml at 20 °C). It is isomorphous to the sulfate and it has been determined to have three indices of refraction at 4681 Å (F-line) which depend upon the orientation of the crystal:

$$\eta_{d(a)} = 1.5105,\ \eta_{d(b)} = 1.5084,\ \eta_{d(c)} = 1.4725$$

The crystal and molecular structure of $BeSeO_4 \cdot 4H_2O$, as determined by single crystal X-ray diffraction and infrared spectroscopy have been determined. $BeSeO_4 \cdot 4H_2O$ crystallizes in the orthorhombic space group *Cmca* (at 295 K), $a = 11.920$ Å, $b = 11.449$ Å, $c = 10.764$ Å, $V = 1468.8$ Å^3, $Z = 2$, $R_2 = 0.057$ for 2035 reflections and 68 variables. The crystal structure is composed of isolated $Be(H_2O)_4$ and SeO_4 tetrahedra which are interconnected by strong hydrogen bonds with O–O lengths between 2.619 and 2.661 Å. Contrary to expectation, the cell volume and the mean Be–O and Se–O distances increase with decreasing temperature. The structure is closely related with that of accentric tetragonal $BeSO_4 \cdot 4H_2O$, but differs in pronounced polyhedral rotations and a partial rearrangement of the hydrogen bonding scheme.

The infrared spectrum of $BeSeO_4 \cdot 4H_2O$ in the region of the uncoupled order-disorder (OD) modes (matrix-isolated HDO molecules) reveals that very strong hydrogen bonds are formed in this compound, analogical to other hydrated beryllium salts due to the strong synergetic effect of the Be^{2+} ions. The appearance of two bands only (2327 and 2239/cm) corresponding to OD stretches instead of four expected was attributed to both the similar O…O hydrogen bond distances and the strong Be–OH_2 and O–O–SeO_3 interactions. The water librations that couple intensively with the translatory modes of the Be^{2+} ions (BeO_4 skeleton vibrations) are also discussed.

The thermal dehydration of $BeSeO_4 \cdot 4H_2O$ has been studied by the use of TG, DTA and DSC analysis methods. The tetrahydrate first decomposes to form the dihydrate. The dehydration occurs in four steps and intermediate hydrates $BeSeO_4$ $2H_2O$, $BeSeO_4$ H_2O and $BeSeO_4$ $0.5H_2O$ are formed at 101 °C, 142 °C, and 182 °C, respectively.

$BeSeO_4 \cdot 2H_2O$ and $BeSeO_4$ have been studied via X-ray methods: $BeSeO_4 \cdot 2H_2O$ forms orthorhombic

crystals with lattice constants: $a = 5.843$ Å; $b = 9.790$ Å; $c = 4.692$ Å; $V = 268.4$ Å^3. The crystals of $BeSeO_4$ are tetragonal: $a = 4.648(1)$ Å; $c = 7.084$ (3) Å; $V = 153.1(1)$ Å^3, SG I. The enthalpies of dehydration of the observed dehydration processes have been determined. The higher value of H_{deh} of $BeSeO_4 \cdot 4H_2O$ as compared to those of other metal selenate tetrahydrates is discussed in terms of the strong Be–H_2O interaction. The enthalpies of formation of $BeSeO_4$ $4H_2O$ and $BeSeO_4$ $2H_2O$ have been calculated.

This salt is available commercially as $BeSeO_4 \cdot 4H_2O$.

Magnesium Selenate

Magnesium selenate has the molecular formula of $MgSeO_4$ and the molecular weight of 167.2566 g/mol. It can be prepared by reacting sodium selenate with magnesium chloride in solution:

$$MgCl_2(aq) + Na_2SeO_4(aq) \Rightarrow MgSeO_4 + 2NaCl(aq)$$

It is soluble in water and the solution must be evaporated to obtain crystals of the hexahydrate, $MgSeO_4 \cdot 6H_2O$. Its molecular weight is 275.3641 g/mol. It is a white, monoclinic crystal with a density of 1.928 g/cm^3. Its CAS number is 13446-58-1 and it is soluble in water (55.52 g/100 ml at 60 °C). The anhydrate is stable upon heating to 1338 °C the heat of formation, $\Delta H_f^\circ = -968.5$ kJ/mol.

Its solubility in water as a function of temperature is shown in Table 3.18.

$MgSeO_4 \cdot 6H_2O$ is isostructural with its sulfate analog and the corresponding cobalt(II) salt. The structure is based on alternating layers of $Mg(H_2O)_6$ octahedra and SeO_4 tetrahedra parallel to (001), connected via hydrogen bonds. All atoms are on general positions except Mg1 and Mg2 (site symmetries 2 and $\bar{1}$, respectively). The average Mg–O and Se–O bond lengths are 2.066 and 1.639 Å, respectively. The structure is shown on the next page.

A number of studies concerning the dehydration of magnesium selenate hexahydrate have been conducted:

I. "The thermal dehydration of the compounds, $MgSeO_4 \cdot 6H_2O$, $MgSeO_4 \cdot 4H_2O$ and $MgSeO_4 \cdot 2H_2O$, has been studied by TG, DTA and DSC. The dehydration of the hexahydrate occurs in steps and the intermediate hydrates $MgSeO_4 \cdot 5H_2O$, $MgSeO_4 \cdot 4H_2O$, $MgSeO_4 \cdot 2H_2O$ and $MgSeO_4 \cdot H_2O$ are produced at 78 °C, 110 °C, 205 °C and 235 °C, respectively. The enthalpies of dehydration of the observed stages have been determined. The enthalpies of formation of $MgSeO_4 \cdot 6H_2O$, $MgSeO_4 \cdot 4H_2O$, $MgSeO_4 \cdot 2H_2O$ and $MgSeO_4 \cdot H_2O$ have also been calculated from the DSC data" (Fig. 3.57).

TABLE 3.18

G/100 ml of water									
Compound	**Formula**	**0 °C**	**10**	**20**	**30**	**40**	**60**	**80**	**100**
Magnesium selenate	$MgSeO_4 \cdot 6H_2O$	20.2	30.4	38.3	44.3	48.6	55.8		

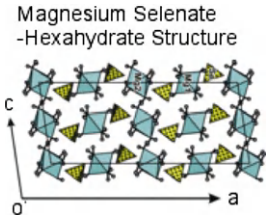

FIGURE 3.57

II. The dehydration of **$MgSeO_4 \cdot 6H_2O$** has been studied using an XRD method at elevated temperatures. Five different crystalline phases have been identified in the temperature interval of 20–450 °C:

$MgSeO_4 \cdot 6H_2O$

$MgSeO_4 \cdot 5H_2O$ (with a small amount of $MgSeO_4 \cdot 4H_2O$)

$MgSeO_4 \cdot 2H_2O$

Magnesium selenate(VI) monohydrate, $MgSeO_4 \cdot H_2O$

Crystalline $MgSeO_4$

Amorphous $MgSeO_4$

$MgSeO_4 \cdot 5H_2O$ crystallizes in the triclinic system with the lattice parameters: $a = 6.403$ Å, $b = 10.576$ Å, $c = 6.196$ Å, $\alpha = 98.63°$, $\beta = 110.36°$, $\gamma = 75.25(3)°$, space group = P1.

$MgSeO_4 \cdot 2H_2O$ forms orthorhombic crystals with lattice parameters: $a = 10.304$ Å, $b = 10.351$ Å, $c = 9.138$ Å.

$MgSeO_4 \cdot H_2O$ has been prepared and studied roentgeno-graphically. It is a monoclinic system with the lattice constants: $a = 6.064$ Å, $b = 13.773$ Å, $c = 8.062$ Å, $\beta = 91.82(7)°$, space group = $P2_1/n$.

The crystalline anhydrous magnesium selenate, **$MgSeO_4$** crystallizes in the orthorhombic system with the lattice parameters: $a = 4.925$ Å, $b = 9.026$ Å, $c = 6.816$ Å.

According to expectation, the magnesium selenate hydrates are determined to be isomorphous with the corresponding magnesium sulfate hydrates.

III. "$MgSeO_4 \cdot 6H_2O$ is isostructural with its sulfate analog and the corresponding cobalt(II) salt (monoclinic, space group = C2/c with eight formula units per unit cell and $a = 10.224$ Å, $b = 7.370$ Å, $c = 24.866$ Å, $\beta = 98.5°$, $V = 211.4$ Å^3, $Z = 4$). The structure is based

on alternating layers of $Mg(H_2O)_6$ octahedra and SeO_4 tetrahedra parallel to (001), connected via hydrogen bonds. All atoms are on general positions except Mg1 and Mg2 (site symmetries 2 and 4, respectively). The average Mg–O and Se–O bond lengths are 2.066 and 1.639 Å, respectively".

IV. "The crystal structure of a new compound $[Mg(H_2O)_4(SeO_4)]_2(H_2O)$ (monoclinic, $P2_1/a$, $a = 7.2549$ Å, $b = 20.059$ Å, $c = 10.3934$ Å, $\beta = 101.989$, $V = 1479.5$ Å^3) has been solved by direct methods and refined to $R_1 = 0.059$ for 2577 observed reflections with $|F\ hkl| \geq 4 \leq |F\ hkl|$. The structure consists of $[Mg(H_2O)_4(SeO_4)]^0$ chains formed by alternating corner-sharing Mg octahedrons and $(SeO_4)^{2-}$ tetrahedrons. O atoms of Mg octahedrons that are shared with selenate tetrahedrons are in a *trans* orientation. The heteropoly-hedral octahedral-tetrahedral chains are parallel to the *c*-axis and undulate within the (010) plane. The adjacent chains are linked by hydrogen bonds involving H_2O molecules not bound with M^{2+} cations."

Magnesium selenate has found little usage in industry but is available commercially by several manufacturers.

Calcium Selenate

Calcium selanate has the molecular formula of $CaSeO_4$ and the molecular weight of 201.0598 g/mol. It can be prepared by reacting sodium selenate with calcium chloride in solution:

$$CaCl_2(aq) + Na_2SeO_4(aq) \Rightarrow CaSeO_4 + 2NaCl(aq)$$

The result is calcium selenate dihydrate $CaSeO_4 \cdot 2H_2O$ whose CAS number is 7790-74-1. It is slightly soluble in water at 9.22 g/100 ml at 20 °C.

Evaporating the solution serves to form white, monoclinic crystals whose molecular weight is 219.07 g/mol, with a density of 2.75 g/cm^3. The solubility varies with temperature (Table 3.19).

The structure of the high-temperature form of $CaSeO_4$, formed by dehydration of the gypsum-type structure dihydrate has been presented. The material is equivalent to that described previously as a $P2_12_12_1$ form, but is however, a monazite with unit cell $a = 6.8566$ Å, $b = 7.04962$ Å, $c = 6.68817$ Å and $\beta = 104.2675°$ in space group $P12_1/n_1$. Also presented was evidence for two intermediate trigonal and pseudo-trigonal phases related to the structurally similar minerals rhabdophane, bassanite, and α-$CaSO_4$. This result permits closer comparisons between intermediate-temperature structures of the selenate with related sulphates, and orthophosphates with a view to extending structural stability via synthesis of solid solutions.

TABLE 3.19

G/100 ml of water

Compound	Formula	0 °C	10	20	30	40	60	80	90	100
Calcium selenate	$CaSeO_4 \cdot 2H_2O$	9.73	9.77	9.22	8.79	7.14				

Various compounds can be formed by adjusting the pH of the solution. Four calcium selenates have been found which are represented by the formulas, $CaSe_2O_7$, $CaSeO_4$, $CaSeO_4 \cdot 2H_2O$ and $Ca_2SeO_3(OH)_2$. The X-ray data for $CaSeO_4 \cdot 2H_2O$ are known. On the other hand, the XRD data for three compounds, $CaSe_2O_7$, $CaSeO_4$ and $Ca_2SeO_4(OH)_2$ are not listed in the ICCD Cards.

The stability and solubility regions for calcium selenates as a function of pH at 25 °C were established. It was noted that $CaSeO_4 \cdot 2H_2O$ having Ca/Se(VI) mole ratio of 1.0 is stable over a wide range of pH, while $Ca_2SeO_3(OH)_2$ having Ca/Se(VI) mole ratio of 2.0 is stable in the very narrow range of pH 11.8 to 12.2. Also, there are two invariant points where $CaSeO_4 \cdot 2H_2O$ and $Ca_2SeO_3(OH)_2$ coexist at pH 12.0 and $Ca_2SeO_3(OH)_2$ and $Ca(OH)_2 \cdot H_2O$ coexist at pH 12.2. It was determined that the calcium concentration in solutions in equilibrium with $CaSeO_4 \cdot 2H_2O$ stayed constant at 0.42 mol/l in the pH range 0.6 to 12.0 and then decreased to 0.14 mol/l. The selenium(VI) concentration slightly decreases with increasing pH from 0.6 to 1.4 and then remains constant at same value of calcium concentration in the same pH range. A further increase in pH leads again to a decreased selenium(VI) concentration until it is reached to 11.1 g/l (0.14 mol/l). The free energy of formation for these compounds was determined to be:

$$\Delta_f G^\circ_{298} - CaSeO_3 \cdot H_2O = -284.2 \text{ kcal/mol} \quad (-1189.1 \text{ kJ/mol})$$

$$\Delta_f G^\circ_{298} - Ca_2SeO_3(OH)_2 \cdot 2H_2O = -556.9 \text{ kcal/mol} \quad (-2330.1 \text{ kJ/mol})$$

$$\Delta_f G^\circ_{298} - CaSeO_4 \cdot 2H_2O = -352.7 \text{ kcal/mol} \quad (-1475.6 \text{ kJ/mol})$$

$$\Delta_f G^\circ_{298} - Ca_2SeO_4(OH)_2 = 453.1 \text{ kcal/mol} \quad (-1895.9 \text{ kJ/mol})$$

SeO_4^{2-} ions can substitute for sulfate in the gypsum structure. In this work, crystals of different $Ca(SO_4,SeO_4) \cdot 2H_2O$ solid solutions were precipitated by mixing a $CaCl_2$ solution with solutions containing different ratios of Na_2SO_4 and Na_2SeO_4. The compositions of the precipitates were analyzed by EDS and the cell parameters were determined by XRD. Moreover, a comparative study on dehydration behavior of selenate-rich and sulfate-rich $Ca(SO_4,SeO_4) \cdot 2H_2O$ solid solutions was carried out by thermogravimetry. The

experimental results show that the $Ca(SO_4,SeO_4)\cdot 2H_2O$ solid solution presents a symmetric miscibility gap for compositions ranging from $X_{CaSO_4 2H_2O} = 0.23$ to $X_{CaSO_4 2H_2O} = 0.77$. By considering a regular solution model, a Guggenheim parameter $a_0 = 2.238$ was calculated. The solid phase activity coefficients obtained with this parameter were used to calculate a Lippmann diagram for the system $Ca(SO_4,SeO_4)\cdot 2H_2O$–$H_2O$.

A major use for calcium selenate has been the formation of CaSe by reduction with hydrogen gas. This salt is readily available commercially by several manufacturers.

Strontium Selenate

Strontium selanate has the molecular formula of $SrSeO_4$ and the molecular weight of 230.5798 g/mol. It can be prepared by reacting sodium selenate with strontium chloride in solution:

$$SrCl_2(aq) + Na_2SeO_4(aq) \Rightarrow SrSeO_4 + 2NaCl(aq)$$

The result is strontium selenate whose CAS number is 7446-21-1. It is slightly soluble in water at 0.656 g/100 ml at 20 °C. Evaporating the solution serves to form white, orthorhombic crystals, with a density of 4.25 g/cm^3. It is less soluble in hot water at 0.1152 g/100 ml at 100 °C and soluble in hot HCl.

$SrSeO_4$ is monoclinic with a space group of $P2_1/n$ and lattice parameters of: $a = 6.853°$, $b = 7.352°$, $c = 7.102°$, $\beta = 0.7107°$, $V = 348.0$ Å^3, $Z = 4$. The major use for this compound has been to form SrSe by reduction:

$$SrSeO_4(solid) + H_2(gas) + heat \Rightarrow SrSe(solid) + H_2O(gas)$$

Strontium selenate is available commercially from several manufacturers.

Barium Selenate

Barium selanate has the molecular formula of $BaSeO_4$ and the molecular weight of 280.2748 g/mol. It can be prepared by reacting sodium selenate with barium chloride in solution:

$$BaCl_2(aq) + Na_2SeO_4(aq) \Rightarrow BaSeO_4 + 2NaCl(aq)$$

Barium selenate is slightly soluble in water at 0.0052 g/100 ml at 20 °C. Its CAS number is 7787-41-9. It is a white rhombic crystal which decomposes when heated beyond about 425 °C. It is slightly soluble in water at 0.0152 g/100 ml at 20 °C. Its solubility product is 3.40×10^{-8}.

The heat of formation of barium selenate is:

$$\Delta H_{298}\ BaSeO_4 = -249.0\ \text{kcal/mol}\ (-1041.8\ \text{kJ/mol}).$$

As a result of the measurements, it has been found that for the reaction:

$$Ba_{solid} + Se_{solid} + 2O_2 = BaSeO_4$$

$$\Delta H_{298} = -279.2\ \text{cal/mol}$$

$$\Delta F_{298} = -249.1\ \text{cal/mol}$$

From the thermodynamic data for H_2SeO_4, $SrSeO_4$, and $BaSeO_4$, the average value of the entropy of the aqueous SeO_4^{2-} ion is $\Delta S = 5.5 \pm 0.3$ entropy units.

A ternary phase diagram for the system BaO–SeO_3–H_2O at 25 °C was constructed. It was obvious from this diagram that two compounds can be identified. These are represented by the formulas $BaSe_2O_7$ and $BaSeO_4$. At the invariant point, the two solid phases are in equilibrium and the liquid has a low concentration of BaO between 0.40 and 0.47 wt% and a high concentration of SeO_3 between 75.53 and 77.30 wt%. The XRD pattern for the compound, $BaSe_2O_7$, could not be identified, whereas the XRD patterns for the other compound were matched with that for $BaSeO_4$. The stability and solubility regions for barium selenates as a function of pH at 25 °C. It was noted that $BaSeO_4$ having Ba/Se(VI) mole ratio = 1/1 is stable over the wide range of pH and at the invariant point of pH 13.7, $BaSeO_4$ and $Ba(OH)_2\cdot H_2O$ coexist. It was also noted that the barium concentration in solution in equilibrium with $BaSeO_4$ increases with an increase in pH and then remains constant at 2×10^{-3} mol/l in the pH range 5.4 to 10.9 and increases again until the solution is saturated with $Ba(OH)_2\cdot H_2O$. The selenium(VI) concentration reversely decreases with an increase in pH and then remains constant at 1×10^{-3} mol/l in the same pH range (5.4–10.9) as well as the barium content. A further increase in pH leads again to a decreased selenium(VI) concentration until it is reached to about 16 mg/l. This lowest concentration of selenium (VI) is much higher than the limit of industrial wastewater regulation for selenium (0.1 mg/l).

Barium selenate has not found much usage in industry but is available from a few manufacturers commercially.

Radium Selenate

Radium selanate has the molecular formula of $RaSeO_4$ and the molecular weight of 368.9826 g/mol. It can be prepared by reacting sodium selenate with radium chloride in solution:

$$RaCl_2(aq) + Na_2SeO_4(aq) \Rightarrow RaSeO_4 + 2NaCl(aq)$$

Radium selenate is expected to be insoluble in water but there is no record of this compound ever having been prepared. It had no CAS number. There is no demand for this compound and it is not available commercially.

3.4. ALKALINE EARTH TELLURIUM COMPOUNDS

The alkaline earths form a series of compounds with tellurium. These are based primarily upon the acids,

tellurous, H_2TeO_3 and telluric, H_2TeO_4. They also form tellurides, H_2Te. As is the case for selenium, tellurium only forms the –2, +4 and +6 oxidation states in this series of compounds. In comparison to S and Se, Te in these compounds shows less anionic and more cationic behavior. That is, Te has a far greater cationic character and tends to form compounds in which it is the cation. Thus, oxy-sulfur and oxy-selenate compounds are stable and easy to prepare, but not oxy-tellurium compounds (particularly when the cation is large like Sr or Ba). Compounds include metatellurates and orthotellurates. Metatellurates are analogous to sulfates, but they are rare. Orthotellurates are much more common and this forms most of the chemistry of tellurates.

3.4.1. Tellurium Acids

A number of acids based upon tellurium exist.

Hydrogen Telluride

Hydrogen telluride has the formula, H_2Te. The simplest hydride of Te, it is rarely encountered because of its tendency to decompose to the constituent elements. Most compounds with Te–H bonds are unstable with respect to loss of H_2. H_2Te is chemically and structurally similar to H_2S, and both are acidic species with H–X–H angles approaching 90°. The tellurides of the alkaline earth metals tend to immediately decompose on exposure to air, with liberation of tellurium.

H_2Te is prepared by the acidification of salts of Te^{2-}, such as Al_2Te_3 and Na_2Te. Na_2Te can be generated by the reaction of Na and Te in anhydrous ammonia. The intermediate in the acidification, the HTe^- is a stable anion.

H_2Te is an endothermic compound, and is unstable in air, rapidly decomposing into water and elemental tellurium:

$$2H_2Te + O_2 \Rightarrow 2H_2O + 2Te$$

It is almost as acidic as phosphoric acid ($pK_a = 8.1 \times 10^{-3}$), having a pK_a value of about 2.3×10^{-3}. It reacts with many metals to form tellurides. However, many of these are unstable relative to their decomposition to the elements. Its CAS number is 7783-09-7 and its molecular weight is 129.6158 g/mol. It is a colorless gas and is toxic if breathed. Its density is 3.310 g/cm^3 and its melting point is –49 °C with a boiling point of –2.2 °C. Its solubility in water is 0.701 g/100 ml of water at 20 °C.

Tellurous Acid

H_2TeO_3 has been synthesized as a solid but it is not well characterized. If tellurium dioxide, TeO_2, is added to water, tellurous acid does not easily form, but it can be made other ways. Its CAS number is 10049-23-7.

Tellurous acid can be formed from the chlorides. Two chlorides are known, the *dichloride*, $TeCl_2$, and the *tetrachloride*, $TeCl_4$. They are both obtained by passing chlorine over tellurium, the product being separated by distillation (the tetrachloride is the less volatile). The dichloride is an amorphous, readily fusible, almost black solid. It is decomposed by water with formation of tellurium and tellurous acid:

$$2TeCl_2 + 3H_2O \Rightarrow Te + H_2TeO_3 + 4HCl$$

However, pure tellurous acid, H_2TeO_3, can be obtained when the tetrachloride is decomposed by water, or on dissolving tellurium in nitric acid and pouring the solution into water. It is a colorless solid and behaves as a dibasic acid. The alkali tellurites are soluble in water. They also gives rise to super acid salts, such as $KHTeO_3 \cdot H_2TeO_3$.

Telluric Acid

Telluric acid, H_6TeO_6, is obtained in the form of its salts when tellurium is fused with potassium nitrate plus carbonate, or by the oxidizing action of chlorine on a tellurite in alkaline solution. The free acid may be obtained by decomposing the barium salt with sulfuric acid and concentrating the solution. Originally, this crystalline mass was thought to have the composition $H_2TeO_4 \cdot 2H_2O$ but it was soon determined to possess the form shown in Fig. 3.58.

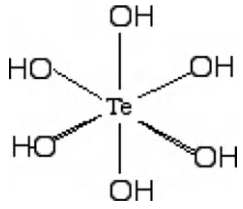

FIGURE 3.58

where tellurium is in an octahedral coordination. Telluric acid, $Te(OH)_6$, has the CAS number of 7803-68-1 and a molecular weight of 229.6425 g/mol. It is a white, monoclinic crystal with a density of 3.07 g/cm^3. Its melting point is 136 °C and its solubility in water is 50.1 g/100 ml.

It is also formed when tellurium dioxide is oxidized by hydrogen peroxide in caustic solution (A. Gutbier, *Zest. Anorg. Chem.*, 1904, 40, p. 260), and perhaps best of all by oxidizing tellurium with a mixture of nitric and chromic acids. It crystallizes as prisms, which lose their water of hydration at 160 °C. The tellurates of the alkaline earth metals are more or less soluble in water, those of the other metals being very sparingly or almost insoluble in water. Some tellurates exist in two forms, a colorless form soluble in water and acids, and a yellow form insoluble in water and acids.

Telluric acid itself is a white solid made up of octahedral $Te(OH)_6$ molecules and this structure persists in aqueous solution as $Te(OH)_4O^{-2}$. There are two crystalline forms of telluric acid, rhombohedral and monoclinic, and both contain octahedral $Te(OH)_6$ molecules. Telluric acid is a weak acid, is dibasic, and forms tellurate salts with strong bases like the alkali metals.

Telluric acid can also be formed by the oxidation of Te or TeO_2 with a powerful oxidizing agent such as hydrogen peroxide, chromium trioxide or sodium peroxide:

$$TeO_2 + 2H_2O_2 + 2H^+ \Rightarrow Te(OH)_6$$

Crystallization of telluric acid solutions below 10 °C gives $Te(OH)_6 \cdot 4H_2O$.

The anhydrous acid is stable in air at 100 °C but, above this temperature, it dehydrates to form polymetatelluric acid, a white hygroscopic powder (approximate composition $(H_2TeO_4)_{10}$), and allotelluric acid, an acid syrup of unknown structure (approximate composition $(H_2TeO_4)_3(H_2O)_4$). Strong heating above 300 °C produces the alpha-crystalline modification of tellurium trioxide, α-TeO_3. Reaction with diazomethane gives the hexamethyl ester, $Te(OMe)_6$.

Telluric acid and its salts mostly contain hexacoordinate Te. This is true even for salts such as magnesium tellurate, $MgTeO_4$, which is isostructural with magnesium molybdate and contains TeO_6 octahedra. It is oxidizing, as shown by the electrode potential for the reaction below, although it is kinetically slow in its oxidations:

$$H_6TeO_6 + 2H^+ + 2e^- \Rightarrow TeO_2 + 4\,H_2O \quad E\ominus = +1.02\ V$$

Metatelluric acid, H_2TeO_4, the tellurium analog of sulfuric acid, H_2SO_4, is unknown. Allotelluric acid, of approximate composition $(H_2TeO_4)_3(H_2O)_4$, is not well characterized and may be a mixture of $Te(OH)_6$ and $(H_2TeO_4)_n$. The meta-tellurates are based upon this acid even though it cannot be isolated.

There is also a related acid, Teflic acid, with the formula $HOTeF_5$. This strong acid is related to orthotelluric acid, $Te(OH)_6$. Teflic acid has octahedral geometry and, ignoring its bent Te–O–H bond, has point group symmetry C_{4v}. It has no CAS number but its molecular weight is 239.6512 g/mol. Teflic acid is a colorless solid that melts at 39.1 °C and has a boiling point of 59.7 °C (Fig. 3.59).

Many elements form teflates but only Barium appears to be large enough in atomic radius to form a stable compound.

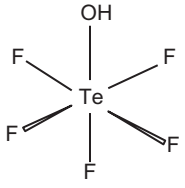

FIGURE 3.59

3.4.2. Alkaline Earth Tellurides

Beryllium Telluride

Beryllium telluride (BeTe) is a chemical compound whose molecular weight is 136.6122 g/mol. Its CAS number is 12232-27-8 and it has a density of 5.12 g/cm^3. Its structure is one of the sphalerite cF8 group with a space group of F43m (#216). It is a crystalline solid with face-centered symmetry, $a = 5.615$ Å at 300 K (Fig. 3.60).

It can be prepared by heating the elements together in an inert atmosphere:

$$Be + Te + \text{heat} \Rightarrow BeTe$$

Te melts at 450 °C and Be melts at 1287 °C. A heating temperature of 750 °C is sufficient to cause complete reaction. BeTe is a crystalline solid with the lattice constant of 0.5615 nm. It is a semiconductor with a large energy gap of around 3 eV. Toxicity is unknown, but both beryllium and tellurium are toxic. Toxic H_2Te gas is evolved on exposure to water.

BeTe, like ZnTe, tends toward p-type conductivity. Using plasma-assisted doping of nitrogen, very high *p*-type concentrations above 10^{20}/cm^3 have been achieved. *N*-type conductivity has not been reported. The composite wave variational version of the APW method has been used in conjunction with the LCAO interpolation scheme to compute the energy bands and the joint density of states of the compounds BeS, BeSe and BeTe at various symmetry points and axes of the brillouin zone. From these computed bands, all three materials are found to be semiconductors having band gaps of 6.10 eV, 4.75 eV and 1.49 eV, respectively. From the joint density of state characteristics, various optical transitions have also been predicted. The results have been favorably compared with those of Stükel. Since BeTe is found to be a small gap semiconductor, its possible technological importance has also been

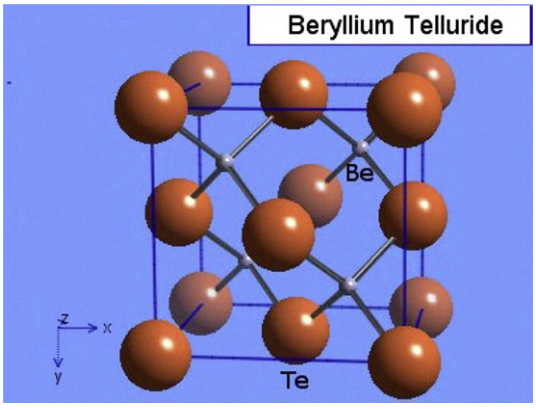

FIGURE 3.60

emphasized. BeTe has been used in efficient pseudomorphic p-contacts for ZnSe laser diodes.

BeTe is available commercially in small quantities as a sputtering target.

Magnesium Telluride

Magnesium telluride has the molecular formula of MgTe and the molecular weight of 151.9146 g/mol. It can be prepared by heating the elements together in an inert atmosphere:

$$\mathrm{Mg} + \mathrm{Te} + \mathrm{heat} \Rightarrow \mathrm{MgTe}$$

Te melts at 450 °C and Mg melts at 650 °C. A heating temperature of 750 °C is sufficient to cause complete reaction. MgTe powder can also be prepared by reaction of stoichiometric quantities of Mg and Te in a pure graphite crucible in vacuum at 480 °C during 48 h. MgTe single crystals were grown by vacuum sublimation in a two-zone furnace at a sublimation temperature of 960 °C. The crystals are transparent hexagonal columns with a length up to 12 mm and extremely hygroscopic. They have a high index of refraction. The lattice parameters are: $a = 4{,}5303$ Å, $c = 7.4056$ Å and the band gap, $E_g = 3.49$ eV. MgTe is a direct gap semiconductor. It tends toward *p*-type conductivity and very high concentrations above 10^{21} have been achieved.

MgTe in its stable (wurtzite) and high-pressure phases (NiAs) has been studied. The latter provided the ground-state properties such as lattice parameter, bulk modulus and its pressure derivatives. The transition pressure at which this compound undergoes the structural phase transition from the NiAs to CsCl phase is calculated as 69.6 Gpa.

The NiAs-type (*B*8) MgTe structure is shown in Fig. 3.61.

The electronic structure, the charge density, and the total energy of MgTe in the wurtzite (B4), nickel arsenide ($B8_1$), and iron silicide (B28) structures have been determined, using first-principles self-consistent local-density calculations in a large plane wave basis employing soft nonlocal pseudopotentials. For MgTe, the experimental ground state is the wurtzite (cubic) structure, while the nickel arsenide structure obtained at 1.1–3.5 GPa persists after unloading to normal pressure. Up to 60 Gpa, no other transition was observed. Theoretically, the ground state is a nickel arsenide structure with a transition to the cesium chloride structure at 69.6 GPa. The wurtzite and nickel arsenide structures are energetically very close. The difference at the minimal energy in these two structures is only 20.3 meV per atom.

In another study, *Ab Iinitio* phonon calculations on NiAs-type (*B*8) MgTe are performed to probe the structural behaviors of MgTe under high pressure. We predicted an unstable transverse acoustic mode and a phase transition of *B*8 ⇒ orthorhombic *Pnma* (*B*31) driven by this soft mode is thus identified. The polymorph of *B*31 in MgTe adopts MnP-type structure containing chains of metal atoms and is stable above 42.7 GPa through the enthalpy calculations. With the discovery of the *B*31 phase, the previously theoretical high-pressure structures of the tetragonal *P*4/*nmm* (*PH*4*I*) and the CsCl (*B*2) are ruled out.

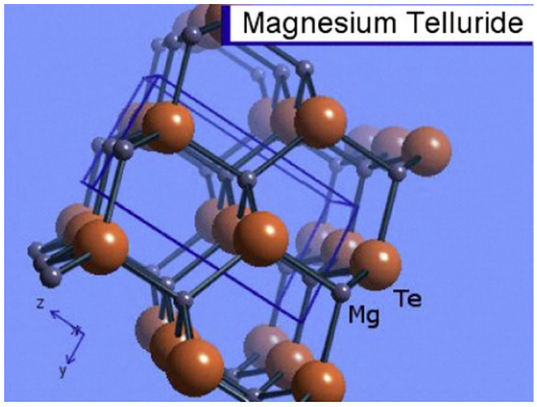

FIGURE 3.61

Theoretical modeling of two-junction tandem solar cells shows that for optimal device performance, the band gap of the top cell should be in the range of 1.6 to 1.8 eV. $Cd_{1-x}Mg_xTe$ (CMT) alloys have a lattice constant close to that of CdTe, and the addition of a small amount of MgTe changes the band gap considerably. Work on developing CMT for solar cell applications has shown considerable promise. CMT films were prepared by vacuum deposition with co-evaporation of CdTe and MgTe on substrates heated to 300–400 °C. Films with a composition in the range of $x = 0$ to 0.66 were fabricated, and optical analysis of the films showed that the band gap of the samples ranged from 1.5 to 2.3 eV and varied linearly with composition. All the $Cd_{1-x}Mg_xTe$ alloy films deposited at substrate temperature of 300 °C exhibit the sphalerite structure characteristic of CdTe, and only a small variation in lattice constant as expected for these alloys. Optical and structural properties of these samples show that CMT alloy films are well behaved in the composition range covered in this study. Devices fabricated using these films show promising device performance and attest to the device quality of polycrystalline CMT thin films.

Magnesium telluride is available commercially.

Calcium Telluride

Calcium telluride has the molecular formula of CaTe and the molecular weight of 167.6782 g/mol. It can be prepared by heating the elements together in an inert atmosphere:

$$\mathrm{Ca} + \mathrm{Te} + \mathrm{heat} \Rightarrow \mathrm{CaTe}$$

Te melts at 450 °C and Ca melts at 842 °C. A heating temperature of 750 °C is sufficient to cause complete reaction. CaTe powder can also be prepared by reaction of stoichiometric quantities of Ca and Te in a pure graphite crucible in vacuum at 480 °C for 48 h. Its molecular weight is 119.04 g/mol. Calcium telluride has the CAS number of 12013-57-9. It is a crystalline solid with a density of 4.872 g/cm^3. It has the rock salt structure with octahedral coordination of the Ca^{2+} cation. Its refractive index is 2.51. If heated to 1605 °C, it decomposes (Fig. 3.62).

The ternary compound, PbCaTe, has been grown using the technique of molecular beam epitaxy. Source ovens containing Ca, Te, PbTe, Tl_2Te (p dopant) and Bi_2Te_3 (n dopant) were used to grow films on (111) oriented BaF_2 substrates or on (100) oriented PbTe substrates. Auger electron spectroscopy studies of $Pb_{1-x}Ca_xTe$ films have shown that the incorporation of calcium is independent of substrate growth temperature in the range 300–400 °C, despite the relatively high vapor pressure of elemental calcium in this temperature range. The diffusion coefficient of Ca in PbTe is 3×10^{-17} cm^2/s at 370 °C. The energy band gap increases as $dE_g/dx = 2.5$ eV for small x, as determined by infrared transmission studies at room temperature. For $x = 0.15$, the energy gap is 0.65 eV. The index of refraction decreases with increasing calcium concentration up to $x \sim 0.15$, but increases anomalously for $x = 0.26$. The electron and hole mobilities at 80 K are comparable and decrease to a few hundred cm^2/V s for $x = 0.15$. From X-ray diffraction studies, the crystal lattice constant is almost independent of x for $x < 0.15$. These results suggest that PbCaTe may be a useful material for long wavelength (>2 μm) diode lasers.

CaTe has found very little usage in industry and the only available information academically deals with its usage to form ternary tellurides. It is available commercially in limited quantities.

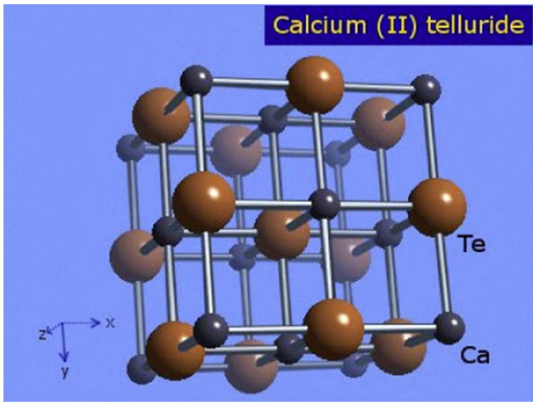

FIGURE 3.62

Strontium Telluride

Strontium telluride has the molecular formula of SrTe and the molecular weight of 215.2238 g/mol. It can be prepared by heating the elements together in an inert atmosphere:

$$Sr + Te + \text{heat} \Rightarrow SrTe$$

Te melts at 450 °C and Sr melts at 778 °C. A heating temperature of 750 °C is sufficient to cause complete reaction. SrTe powder can also be prepared by the reaction of stoichiometric quantities of Sr and Te in a pure graphite crucible in vacuum at 480 °C during 48 h. Its molecular weight is 166.58 g/mol. Strontium telluride has the CAS number of 12040-08-3. It is a white, crystalline solid with a density of 4.83 g/cm^3. It has the rock salt structure with octahedral coordination of the Sr^{2+} cation. Its refractive index is 2.408. If heated to 1605 °C, it decomposes.

$Pb_{1-x}Sr_xTe$ films were prepared by hot-wall epitaxy on BaF_2(111) substrates. X-ray diffraction analysis, optical transmission measurement, Hall measurement and EPMA were performed on the films. It was observed that the increasing rate of the lattice constant of the $Pb_{1-x}Sr_xTe$ films with the SrTe content was considerably larger than that estimated from Vegard's law. $Pb_{1-x}Sr_xTe$/PbTe double-heterostructure (DH) and multiple quantum well (MQW) lasers were also prepared for the first time by hot-wall epitaxy. Pulsed laser operations were obtained up to 227 K (4.1 μm) for the DH laser and up to 220 K (3.5 μm) for the MQW laser. Large output energy shifts due to misfit strain in the active layer were observed.

Strontium telluride is not used in industry for any purpose and the scientific literature concerning it has been very scattered. Most of the known data concerning this compound originated in the 1900s. SrTe is mentioned in a few patents where complete coverage of all possibilities was desired.

SrTe is available commercially in small quantities as a sputtering target.

Barium Telluride

Barium telluride has the molecular formula of BaTe and the molecular weight of 264.9270 g/mol. It can be prepared by heating the elements together in an inert atmosphere:

$$Ba + Te + \text{heat} \Rightarrow BaTe$$

Te melts at 450 °C and Ba melts at 728 °C. A heating temperature of 750 °C is sufficient to cause complete reaction. BaTe powder can also be prepared by reaction of stoichiometric quantities of Ba and Te in a pure graphite crucible in vacuum at 480 °C during 48 h. Its molecular weight is 216.31 g/mol. The heat of formation, ΔH^o at that temperature is 9.29 kJ/mol. Barium telluride can also be prepared by direct reduction of barium tellurate.

Barium telluride has the CAS number of 12009-36-8. It is a white, crystalline solid with a density of 4.94 g/cm^3. It has the rock salt structure with octahedral coordination of the Ba^{2+}cation. Its refractive index is 2.408. The melting point of barium telluride was found to be 2070 ± 10 °C.

A fast-growing interest in solid-state telluride chemistry has taken place during the past several years. Research in this area has been primarily on the development and applications of several synthetic techniques that can be applied to the synthesis of the tellurides over a wide temperature range (100–1200 °C). These techniques include chemical vapor transport, molten-salt, and hydro(solvo)thermal methods. A number of binary, ternary, and quaternary metal tellurides, $BaTe_2$, $TaCu_3Te_4$, $RbTaCu_2Te_4$, $K_2BaSnTe_4$, and $K_2Ag_2SnTe_4$, synthesized by the molten-salt (alkali-metal polytelluride flux) reactions at intermediate temperatures (400–550 °C). The crystal structures of these compounds have been determined by single-crystal X-ray diffraction techniques. Crystal data: $BaTe_2$, space group $I4/mcm$ (No. 140), $a = 7.181$ Å, $c = 8.898$ Å, $Z = 4$, $R1 = 1.55\%$, $wR^2 = 3.46\%$; $RbTaCu_2Te_4$, space group $P2_1cn$ (No. 33), $a = 5.982(2)$, $b = 20.316(3)$, $c = 8.192(2)$ Å, $Z = 4$, $R1 = 7.13\%$, $wR^2 = 4.95\%$; $TaCu_3Te_4$, space group P-43m (No. 215), $a = 5.930(2)$ Å, $Z = 1$, $R1 = 2.40\%$, $wR^2 = 6.48\%$; $K_2BaSnTe_4$, space group I-43m (No. 217), $a = 8.393(1)$ Å, $Z = 2$, $R1 = 2.52\%$, $wR^2 = 3.56\%$; $K_2Ag_2SnTe_4$, space group I-42m (No. 121), $a = 8.732(5)$, $c = 7.425(3)$ Å, $Z = 2$, $R1 = 3.06\%$, $wR^2 = 7.25\%$.

The compound, barium ditelluride, $BaTe_2$, was grown by a flux-growth technique, the first alkaline earth metal dichalcogenide prepared by this method. The crystal structure of $BaTe_2$ was determined by single-crystal X-ray diffraction methods. It belongs to the tetragonal space group I4/mcm (No. 140) with lattice constants $a = 7.181$ Å, $c = 8.898$ Å, $V = 458.8$ Å^3, and $Z = 4$. The final residual index is converged to $R = 1.5\%$, $wR^2 = 3.5\%$. $BaTe_2$ is a Zintl-type compound isostructural to SrS_2. Pairs of tellurium atoms form dimeric units $(Te_2)^{2-}$ with a Te–Te separation of 2.7722 Å. The synthesis of $BaTe_2$ at relatively low temperature has provided an alternative and convenient route for preparing new compounds in this category.

Single crystals of barium telluride were grown in graphite crucibles using a Bridgman–Stockbarger technique. A procedure for seeding the melt with a portion of a previously grown crystal was used. The lattice constant for barium telluride was found to vary, depending on the history of the sample, from a value of 7.000 Å for freshly prepared powder to as low as 6.950 Å for samples melted in an open crucible.

The photoelectric emission from barium telluride has been investigated by measuring the total photoelectric-yield spectra and the distributions in kinetic energy of the emitted electrons, using a magnetic velocity analyzer tube. From the threshold for photoelectric emission from the valence band, the energy of the top of the valence band was estimated to be 4.8 eV below the vacuum level. Using an estimate of 3.4 eV for the band gap, the electron affinity was estimated to be 1.4 eV. The kinetic energy distributions showed two peaks which were interpreted as being associated with direct ionization of defect levels located approximately 2.9 and 3.6 eV below the vacuum level. At photon energies above about 4.1 eV, these fast peaks were observed to become distorted. No evidence was seen for an exciton-induced component in the photoelectric emission.

Long wavelength diode lasers operating in the 3–10 μm wavelength range are of interest as optical sources for future fiber optics communications and sensor systems. PbEuSeTe large optical cavity single quantum well diode lasers have so far attained the highest operating temperatures (174 K cw, 280 K pulsed) in this wavelength range. Two alternative materials systems PbSrTe and PbBaTe have now been grown for the first time by molecular-beam epitaxy. The choice of these ternaries was motivated by the fact that SrTe and BaTe have the same face centered cubic crystal structure as PbTe and roughly comparable lattice constants, but much larger energy band gaps. In the $Pb_{1-x}Ba_xTe$ system, X-ray diffraction studies show clear evidence of phase segregation for $x \geq 0.05$. The carrier mobilities decrease monotonically with barium concentration in the single-phase region, which suggests that disorder-related scattering is dominant. The energy band gap increases approximately as $dE_g/dx = 3.2$ eV for small x, and the index of refraction decreases monotonically with increasing x. A combination of X-ray diffraction, energy band gap and other data clearly demonstrate that the solubility of BaTe in PbTe is limited to about 4%, possibly because of the relatively large difference in lattice constants between PbTe (6.460 Å) and BaTe (7.001 Å). These results imply that PbSrSeTe grown lattices matched to PbTe is a promising material system for long wavelength diode lasers and LEDs but that BaTe is too large in lattice size for this application.

A new binary material, $BaTe_2$, the first alkaline earth metal dichalcogenide prepared using flux-growth technique, has been prepared. It belongs to the tetragonal space group I4/mcm (No. 140) with lattice constants: $a = 7.81$ Å, $c = 8.898$ Å, and $Z = 4$. $BaTe_2$ is a Zintl-type compound isostructural to SrS_2. Pairs of tellurium atoms form dimeric units $(Te_2)^{2-}$ with a Te–Te separation of 2.7722(8) Å. The synthesis of $BaTe_2$ at relatively low temperature has provided an alternative and convenient route for preparing new compounds in this category.

Barium telluride has been sadly overlooked in industry but not as a research subject in the literature. According to early sources, BaTe ought not to exist but a few workers have found methods to prepare it.

However, the physical data such as melting point for this compound have not been available. It is, however, readily available commercially.

Radium Telluride

Radium telluride has the molecular formula of RaTe and the molecular weight of 353.6254 g/mol. It can be prepared by heating the elements together in an inert atmosphere:

$$\mathrm{Ra + Te + heat \Rightarrow RaTe}$$

Te melts at 450 °C and Ra melts at 695 °C. A heating temperature of 750 °C is sufficient to cause complete reaction. RaTe powder can also be prepared by reaction of stoichiometric quantities of Ra and Te in a pure graphite crucible in vacuum at 480 °C during 48 h. Its molecular weight is 305.36 g/mol. Radium telluride has no CAS number. It is expected to be a white, crystalline solid with the rock salt structure. However, it has never been prepared. Moreover, there is no report of such a compound in the scientific literature and there is no demand for this material. It is not available commercially.

3.4.3. Alkaline Earth Tellurites

Beryllium Tellurite

Beryllium tellurite has the molecular formula of $BeTeO_3$ and the molecular weight of 184.61 grams per mole. It can be prepared by means of the solid-state reaction:

$$\mathrm{BeO + TeO_2 + heat \Rightarrow BeTeO_3}$$

An inert atmosphere is required. This salt is a metatellurite but its formation and physical properties have not been reported in the literature. If a solution method is used, the result is likely to be quite different in that a hydroxy-tellurite is formed:

$$\mathrm{BeCl_2 + Na_2TeO_3 \Rightarrow [Be(OH)]_2TeO_3}$$

Additionally, this compound can be prepared by reacting tellurium dichloride in a solution of beryllium chloride:

$$\mathrm{BeCl_2 + 2TeCl_2 + 4H_2O \Rightarrow Te + [Be(OH)]_2TeO_3 + 6HCl}$$

Nonetheless, there is absolutely no description of these compounds in the literature and whether a hydrate appears remains unknown.

Beryllium tellurite has no CAS number and no manufacturer is listed as a commercial source.

Magnesium Tellurite

Magnesium tellurite has the molecular formula of $MgTeO_3$ and the molecular weight of 199.9032 g/mol. It can be formed by the solid-state reaction:

$$\mathrm{MgO + TeO_2 + heat \Rightarrow MgTeO_3}$$

An inert atmosphere is required. This salt is a metatellurite. If a solution method is used, the result is likely to be quite different in that a hydrate is formed:

$$\mathrm{MgCl_2 + Na_2TeO_3 \Rightarrow MgTeO_3}$$

Additionally, this compound can be prepared by reacting tellurium dichloride in a solution of magnesium chloride:

$$\mathrm{MgCl_2 + 2TeCl_2 + 3H_2O \Rightarrow Te + MgTeO_3 + 6HCl}$$

In all cases involving solution chemistry, the product is either a pentahydrate or hexahydrate, $MgTeO_3 \cdot 5H_2O$ or $MgTeO_3 \cdot 6H_2O$. The former results if the solution temperature is ~80 °C while the hexahydrate results at T_{Soln} °C < 25 °C.

The molecular weights of these compounds are 289.9799 g/mol and 307.9952 g/mol, respectively. If the hexahydrate is heated, a loss of water of hydration occurs at about 105 °C. The further loss of water has not been published in the literature but is estimated to be:

$$\mathrm{MgTeO_3 \cdot 5H_2O \xrightarrow{180^\circ C} MgTeO_3 \cdot H_2O \xrightarrow{240^\circ C} MgTeO_3}$$

Magnesium tellurite occurs as a mineral, **zemannite** (*Hydrated magnesium zinc iron tellurite*) = $Mg_{0.5}[Zn^{2+}\ Fe^{3+}\ (TeO_3)_3] \cdot 4.5\ H_2O$ whose molecular weight is 741.25 g/mol.

Polycrystalline samples of $MgTeO_3$ have been prepared by a conventional solid-state reaction technique at 750 °C. The XRD analysis showed the formation of a single-phase $MgTeO_3$ compound with cell parameters $a = 4.421$ Å, $b = 14.916$ Å and $c = 12.289$ Å in an orthorhombic crystal system. Detailed studies of dielectric and electrical properties confirmed that the compound has a sharp ferroelectric phase transition of first order.

The structure of the hexahydrate has also been studied. It is rhombohedral with a space group of R3 and $a = 3.011$ Å, $c = 5.965°$, $\alpha = 97.36°$, $V = 211.3$ Å^2, $Z = 1$. Its density is 2.42. The structure is isomorphous with $MgSO_3 \cdot 6H_2O$.

Magnesium tellurite has no CAS number. Only a few manufacturers are listed as a supplier of this compound.

Calcium Tellurite

Calcium tellurite has the molecular formula of $CaTeO_3$ and the molecular weight of 233.6015 g/mol. It can be formed via the solid-state reaction:

$$\mathrm{CaO + TeO_2 + heat \Rightarrow CaTeO_3}$$

An inert atmosphere is required. This salt is a metatellurite. If the solution method is used, a monohydrate is formed:

$$\mathrm{CaCl_2 + Na_2TeO_3 \Rightarrow CaTeO_3 \cdot H_2O + 2NaCl}$$

Additionally, this compound can be prepared by reacting tellurium dichloride in a solution of calcium chloride:

$$CaCl_2 + 2TeCl_2 + 3H_2O \Rightarrow Te + CaTeO_3 \cdot H_2O + 6HCl$$

In all cases involving solution chemistry, the product is a monohydrate. Its CAS number is 13812-57-2 and its molecular weight is 233.6915 g/mol.

Calcium tellurite occurs in mineral form:

Carlfriesite (*calcium tellurite*) = $CaTe_3O_8$ or $CaTe^{4+}Te^{6+}O_8$

Crystal system: monoclinic

Class (H-M): $2/m$ – prismatic

Space group: B_2/b {B_112/b} {C_2/c} {C_12/c_1}

Cell parameters: $a = 12.576$ Å, $b = 5.662$ Å, $c = 9.994$ Å, $\beta = 115.56°$

Ratio: a:b:c = 2.221:1:1.765

Unit cell volume: $V = 641.98$ Å^3 (calculated from unit cell), Z**:** 4

Mroseite (calcium tellurite carbonate oxide)

$CaCO_3 \cdot TeO_2 = \{CaTe^{4+}(CO_3)O_2\}$

Molecular weight = 259.69 g/mol

$a = 6.93$ Å, $b = 11.16$ Å, $c = 10.54$ Å, $Z = 8$, $V = 815.15$ Å^3, Density = 4.23 g/cm^3

Orthorhombic-dipyramidal, symbol (2/m 2/m 2/m), space group: Pbca

In the solid-state method of synthesis, an excess of TeO_2 produces a combined product of tellurium dioxide and the tellurite that has a different composition and structure from the tellurite:

$$CaO + 2TeO_2 \Rightarrow CaTe_2O_5 = CaTeO_3 \cdot TeO_2$$

In contrast to the tellurite, this compound, a "ditellurite", has received some attention in the literature. When the oxides, $0.30[MgO_xCaO_{30-x}] - 0.70[TeO_2]$, with $0 \leq x \leq 30$ mol %, were heated together at 750 °C for 4 h, the resulting compounds were identified by means of X-Ray diffraction, Raman and infrared spectroscopy. The X-ray diffraction results showed that two phases are observed in the samples, which have the separate compositions: $MgTe_2O_5$ and $CaTe_2O_5$. Raman spectroscopy studies showed that the vibrations of the samples are identical with α-TeO_2 vibrations, with a shift of about 40–50/cm. Strong bands are observed around 435, 616, 689, 785, and 807/cm. As the concentration of the modifier, MgO and CaO increased, the coordination of TeO_4 was transformed from the corner-sharing structure, α-TeO_2, to the edge sharing, β-TeO_2, structure.

The phase diagram of the CaO–TeO_2 system has been experimentally determined in the composition range 50–100 mol% TeO_2 employing DTA, room temperature and high-temperature XRD and quenching techniques. Only two intermediate compounds, $CaTeO_3$ and $CaTe_2O_5$, melting congruently at 1072 °C and 876 °C, respectively, were observed. $CaTeO_3$ exhibited two high temperature polymorphs, β and γ, with corresponding transition temperatures at 882 and 894 °C while $CaTe_2O_5$ showed three phase transformations at 802, 845 and 857 °C. The system has one eutectic reaction between $CaTeO_3$ and $CaTe_2O_5$ at 870 °C and 62.5 mol% TeO_2, that is: α-$CaTeO_3$ + $CaTe_2O_5$ and another one between $CaTe_2O_5$ and TeO_2 at 650 °C and 87 mol% TeO_2, that is: β-$CaTe_2O_5$ + TeO_2.

Single crystals and microcrystalline samples of the calcium tellurite(IV) phases α, β, β′ and γ-$CaTeO_3$ as well as of two solid solutions $Ca_xSr_{1-x}TeO_3$ ($x = 0.55$ and 0.77) have been synthesized and characterized by X-ray diffraction and thermal analysis. A comparative description of the structures and the relations between the polymorphs is given. The main building units of the hitherto unknown structures are isolated $[Te^{IV}O_3]^{2-}$ units and [(Ca,Sr)O_x] (x = 6–8) polyhedra. All structures exhibit channels in which the Te^{IV} electron lone pairs protrude. The low-temperature phase, α-$CaTeO_3$, is stable up to 1168 K. It exhibits nearly cylindrical channels (diameter = 4 Å) and differs structurally from the other phases, whereas the metastable high-temperature phases are closely related to each other. They feature oval channels (shortest and longest diameter = 2 and 8 Å). γ-$CaTeO_3$ can be described as an OD structure of two nonpolar layers with layer groups $p12_1/m1$ and $p12_11$. The γ-$CaTeO_3$ crystal under investigation consists of two polytypes with a maximum degree of order. The two phases $CaxSr_1$-$xTeO_3$ ($x = 0.55$ and 0.77) are isostructural to the MDO_1 polytype of γ-$CaTeO_3$. β-$CaTeO_3$ shows a distinct reversible phase transition at 293 K. The low-temperature modification β′-$CaTeO_3$ as well as its high-temperature modification β-$CaTeO_3$ can be considered as three-fold superstructures along [100] based on the MDO_1 polytype of γ-$CaTeO_3$.

The crystalline phases of **glasses** in TeO_2–CaO system revealed α-TeO_2 phase which transforms into the stable β-TeO_2 phase up to 500 °C. IR and Raman studies show the transition of TeO_4, TeO_{3+1} and TeO_3 units with increasing CaO content. The value of refractive index and density of glasses have been measured.

Single crystals of a new compound $Ca_4Te_5O_{14}$, were obtained during phase formation experiments in the systems Ca–Te–O. The crystal structure {$Ca_4Te_5O_{14}$: *Pbca*, $Z = 8$, $a = 10.9536$ Å, $b = 16.556$ Å, $c = 15.779$ Å}, was determined and refined from single-crystal X-ray diffraction data. This compound exhibits a new structure type consisting of complex frameworks between the main building units; one-dimensional channels with cavities about 4.0 Å in size are observed. Calcium tellurite(IV), $Ca_4Te_5O_{14}$, is made up of [CaO_7] polyhedra and $Te^{IV}O_3$ and $Te^{IV}O_4$ groups.

The compounds $CaTe_2O_5$ and $SrTe_2O_5$ were obtained as mica-like plates by slowly cooling their melts.

Dielectric properties were similar to those of mica. Optical and infrared spectra showed appreciable transmittance from 0.33 to 7 μm on with a cutoff at 10 μm. The compounds have refractive indices greater than 2. X-ray diffraction studies showed that the calcium and strontium compounds are not isomorphous.

Calcium tellurite is available commercially from several manufacturers.

Strontium Tellurite

Strontium tellurite has the molecular weight of 215.6761 g/mol and the molecular formula of $SrTeO_3$. It can be formed via the solid-state reaction:

$$SrO + TeO_2 + \text{heat} \Rightarrow SrTeO_3$$

An inert atmosphere is required. This salt is a metatellurite. If a solution method is used, a monohydrate is formed:

$$SrCl_2 + Na_2TeO_3 \Rightarrow SrTeO_3 \cdot H_2O + 2NaCl$$

Additionally, this compound can be prepared by reacting tellurium dichloride in a solution of strontium chloride:

$$SrCl_2 + 2TeCl_2 + 3H_2O \Rightarrow Te + SrTeO_3 \cdot H_2O + 6HCl$$

In all cases involving solution chemistry, the product is a monohydrate. Its CAS number is 13812-57-2 and its molecular weight is 233.6915 g/mol. Strontium tellurite ($SrTeO_3$) has been shown by Yamada and Iwasaki (1972) to possess ferroelectric properties (ferroelectric = a substance exhibiting permanent electric polarization that varies in strength with the applied electric field).

The crystal structure of strontium tellurite, $SrTeO_3$, has been determined at room temperature using X-ray diffraction data obtained from single crystals grown by the Czochralski method. Selection of a noncentrosymmetric (*C*2) structure model was confirmed by the second harmonic generation (SHG) test. The structure of strontium tellurite is built up of three types of distorted [SrO_x] polyhedra ($x = 6$, 7 and 8) that share their oxygen anions with TeO_3 pyramidal units. These main anionic polyhedra are responsible for establishing two types of tunnels required for the electron lone pairs of the Te^{4+} cation.

In another systematic investigation of strontium tellurite, $SrTeO_3$, with particular emphasis on crystal chemistry and phase transitions, the structure of the γ-phase has been determined at 583 K using a single-crystal analysis. Both structural and nonlinear optical measurements indicate a β ⇒ γ first-order phase transition temperature that is close to 563 K. The structure of the γ-phase is monoclinic (*C*2) and does not differ essentially from the α-phase (*C*2). Comparison of the α and γ structures shows that the main atomic shifts and tilting are connected with Te_4, Te_5 and Te_6 pyramids.

$SrTeO_3$ has also been studied by powder neutron diffraction (PND) experiments and by SHG method at a series of temperatures between 20 and 560 °C. The $SrTeO_3$ low temperature (22 °C) form was found to crystallize in space group C2/c with the unit-cell parameters, $a = 28.133°$, $b = 5.904$ Å, $c = 28.418$ Å, $\gamma = 114.303°$. The Sr atoms are coordinated by six, seven, or eight oxygen atoms. Each Te atom has a similar "pyramidal" geometry, coordinated by three oxygen atoms having similar TeO bond lengths. The Te^{4+} lone-pair (E) plays an active stereochemical role. The SrO polyhedra form an open framework with two types of channels. Inside the channels the tellurium atoms are located. The TeO_3E pyramids do not connect to each other; instead they share their oxygen atoms with Sr polyhedra. The discontinuous change of the $SrTeO_3$ lattice parameters in the region 260–310 °C and abrupt growth of SHG signal in this temperature region correspond to the onset of the ferroelectric phase in a first-order phase transition. However, from the diffraction data acquired at 410 °C, no evidence of lowering of the symmetry was found. The structure model of the $SrTeO_3$ high temperature (410 °C) modification is proposed in the same space group C2/c. The plausible reasons of the discrepancy between the PND and SHG results have been discussed.

The compound, $SrTe_2O_5$, was obtained as mica-like plates by slowly cooling its melt. Dielectric properties were similar to those of mica. Optical and infrared spectra showed appreciable transmittance from 0.33 to 7 μm on with a cutoff at 10 μm. The compound has a refractive index greater than 2.

Single crystals of $Sr_3Te_4O_{11}$ were grown from $SrTeO_3$–TeO_2 melts. $Sr_3Te_4O_{11}$ crystallizes in the triclinic system, space group *P*1 (No. 1). The lattice parameters are $a = 7.531$, $b = 9.240$, $c = 9.546$ Å, $\alpha = 98.07(1)°$, $\beta = 109.55(1)°$, $\gamma = 102.19(1)°$, $Z = 2$. The $Sr_3Te_4O_{11}$ crystal structure has been solved by X-ray single-crystal techniques up to a final R value 0.0455 and wR^2 value 0.1245, using 2490 observed reflections. $Sr_3Te_4O_{11}$ forms a three-dimensional lattice consisting of trigonal TeO_3 pyramids, trigonal TeO_4 bipyramids, and irregular polyhedra (with 7, 8, or 9 apices) of Sr.

Aluminate sodalites containing the telluride and tellurite ions have been synthesized for the first time. The structures of $Sr_8[AlO_2]_{12}(TeO_3)_2$ and its reduced product $Sr[AlO_2]_{12}Te_2$ have been determined using Rietveld refinement of powder neutron-diffraction (PND) data. In $Sr_8[AlO_2]_{12}Te_2$, the anion occupies a position at the sodalite cage center, while in $Sr_8[AlO_2]_{12}(TeO_3)_2$ the larger tellurite ion is displaced to allow reasonable coordination to the strontium ions.

$Sr_{1-x}Pb_xTeO_3$ ($0 < x < 0.2$) and $Sr_{1-x}La_{2x}Te_{1+2x}O_{3+6x}$ ($0 < x < 0.15$) solid solutions are synthesized (the latter, for the first time), and their properties are studied. The

results demonstrate that partial substitutions of Pb and La for Sr extend the temperature stability range of ferroelectric $SrTeO_3$.

Although a number of research papers have been published, its usage in industry is miniscule. It is, however, available commercially by several manufacturers.

Barium Tellurite

Barium tellurite has the molecular formula of $BaTeO_3$ and the molecular weight of 265.4015 g/mol. Its CAS number is 58440-17-8. It can be formed via the solid-state reaction:

$$BaO + TeO_2 + \text{heat} \Rightarrow BaTeO_3$$

An inert atmosphere is required. This salt is a metatellurite. A series of $BaO–TeO_2$ binary ceramic compounds were explored for microwave dielectric applications with ultralow processing temperatures. During the calcination of mixed $BaCO_3$ and TeO_2 raw powders, $BaTe_4O_9$, $BaTe_2O_6$, $BaTeO_3$, and Ba_2TeO_5 phases were obtained through the sequential phase formations from Te-rich to Ba-rich phases at temperatures ranging from 500 to 850 °C. Sintering temperatures were as low as only 550 °C for the Te-rich phases. Barium tellurate ceramics exhibited excellent microwave dielectric properties with intermediate dielectric permittivities and high-quality factors (Q). The dielectric properties at microwave frequencies were:

$$\varepsilon_r = 10^{-21},\ Q \times f = 34{,}000–55{,}000\ \text{GHz, and}$$
$$TCf = -51 \text{ to } -124\ \text{ppm/°C},$$

depending upon compositions. The structure of the compound, Ba_4TeO_{11} has been solved: It is monoclinic, space group = P1 with $a = 9.4245$ Å, $b = 9.9759$ Å, $c = 7.8877$ Å, $\alpha = 110.58°$, $\beta = 103.27°$, $\gamma = 97.80°$, $V = 658.5$ Å^3, $Z = 2$. The structure consists of TeO_3^{2-} and $Te_3O_8^{4-}$ anions which form $Te_8O_{22}^{12-}$ rings around a center of symmetry with Te–O bonds of about 2.7 Å in length. The Ba^{2+} cations couple these rings together. The TeO_3^{2-} has the usual pyramidal shape while the $Te_3O_8^{4-}$ anion has a pseudo two-fold axis.

If a solution method is used, a trihydrate is formed:

$$BaCl_2 + Na_2TeO_3 \Rightarrow BaTeO_3 \cdot 3H_2O + 2NaCl$$

Additionally, this compound can be prepared by reacting tellurium dichloride in a solution of strontium chloride:

$$BaCl_2 + 2TeCl_2 + 3H_2O \Rightarrow Te + BaTeO_3 \cdot 3H_2O + 6HCl$$

In all cases involving solution chemistry, the product is either a trihydrate or a monohydrate. The trihydrate CAS number is 28557-54-2 and its molecular weight is 319.4477 g/mol. The trihydrate is obtained at ~20 °C and the monohydrate at >80 °C solution temperature.

The crystal structure of barium tellurite monohydrate has been solved. The crystals are monoclinic, $P2_1/a$ (C_{2h}^5), with $a = 8.582$ Å, $b = 7.631$ Å, $c = 7.704$ Å, $\beta = 106.2°$, $V = 478.1$ Å^3, $Z = 4$ with a density of 4.62 g/cm^3. The structure contains TeO_3 pyramids with Te–O distances of 1.864 Å. The water molecule is loosely coordinated to a Te atom. The Te–O distance being 3.33 Å. One other oxygen atom has a second Te atom as a neighbor at a distance of 3.03 Å. There are systematic absences at: k0l for h-odd and 0h0 for k-odd.

The standard molar Gibbs energy of formation of barium tellurite, $BaTeO_3$(s), was determined by the transpiration technique using pure oxygen as the carrier gas in the temperature range 1133 to 1260 K. The condensate was exclusively identified as TeO_2(s) by chemical analysis. From a quantitative chemical analysis of the condensed TeO_2(s), the vapor pressure of TeO_2(g) over pure $BaTeO_3$(s) was calculated and is given by: $\ln \{p(TeO_2,g)/\text{kPa} \pm 0.1\} = 18.64 - 30863.2 \cdot (K/T)$. The Gibbs energy of formation of $BaTeO_3$(s) was computed from the values of ln {p(TeO_2, g)/kPa} and the values of $\Delta_f G_m^\circ$ for BaO(s) and TeO_2(g) taken from the literature. This is given by $\{\Delta_f G_m^\circ(BaTeO_3,(s),T)/\text{kJ/mol}\} = -856.5 + 0.2067$ (T/K). The enthalpy increments of $BaTeO_3$(s) were measured using a high-temperature Calvet microcalorimeter in the temperature range 304 to 1000 K. Enthalpy increment values are represented by a polynomial of the form $\{\Delta H°(T) - \Delta H°(298.15\ K)\}/(J_{mot\text{-}1}) = -39{,}190 + 118.96$ (T/K) + [4.235×10^{-3} (T/K)]^2 + 9.975×10^5 (K/T), with an accuracy of ±0.4% over the interval: (304° ≤ T/K ≤ 1000°).

It is possible to achieve a "zero-stress" glass with barium selenite (defined as a glass that no internal strain due to external stress during its formation). Zero stress-optic glasses are achieved traditionally through a high content of lead oxide or other closely related p-block metal oxide. It has been found that the underlying cause for this behavior is the combination of high metallicity and low coordination numbers adopted by compounds such as lead oxide. Barium tellurite glasses also show zero stress-optic and negative stress-optic response, at very low barium content. This response results from the fact that barium oxide bonds have very high metallicity, and at the same time barium modifies tellurite by lowering the Te coordination number. The two effects together are sufficient to produce zero stress-optic response.

The properties of novel ternary tellurite glasses, based on the $TeO_2–BaO–Bi_2O_3$ system, have been reported for their applications in online chemical sensing and process control by characterizing the fundamental frequencies of molecular vibrations in the 2–5 μm spectral region of mid-IR. The chemical sensing for process control also requires above room temperature operation (>100 °C) for prolonged periods of time. Bulk samples of ternary tellurite glasses with

a number of different compositions were prepared using the heavy molecular weight oxides of TeO_2, BaO, and Bi_2O_3. Infrared and Raman spectroscopic analysis were carried out together with DTA to study the relationship between glass structure and thermal and viscosity properties. The temperature dependence of the viscosities of the glasses was also reported.

The Mössbauer spectrum of tellurite glasses, containing 5-mol% Fe_2O_3 as a probe, consisted of a paramagnetic quadrupole doublet with an isomer shift of 0.39 ± 0.01/ms. This indicated that Fe^{3+} ions are present at substitutional sites of Te^{4+} ions constituting distorted TeO_4 trigonal bipyramids, each of which has one oxygen vacancy at an equatorial site. On increasing the K_2O content from O to 35 mol%, the quadrupole splitting (Λ) for potassium tellurite glasses decreases continuously from 0.76 to 0.44 mm/s. On the other hand, Λ for magnesium and barium tellurite glasses increases with increasing MgO and BaO content, respectively. When the alkali or alkaline earth oxide contents are the same as each other, Λ increases in proportion to the ionic potential (Z/r) of the alkali or alkaline earth metal ion. These results suggest that the glass matrices of alkali and alkaline earth tellurite glasses are continuously changed into chains or a three-dimensional network structure, respectively. DTA studies revealed that there exists a linear relationship between the glass transition temperature, T_g, and the quadrupole splitting, Λ, indicating that T_g is primarily determined by the magnitude of the distortion of TeO_4 trigonal bipyramids. This relationship is also applicable to several other oxide glasses.

Thermal resistance against crystallization, electronic polarizabilities and optical basicities of ternary tellurite glasses of R_2O–R′O–TeO_2 (R = Li, Na, K, R′ = Mg, Ba, Zn, $TeO_2 = 70$ to 80 mol%) having a high potential as new optical functional glasses are examined from differential thermal analyses, density and refractive index measurements. Ternary tellurite glasses containing ZnO or both Li_2O and BaO show a high resistance against recrystallization. Large electronic polarisabilities of oxide ions of 2.1–2.4 Å and large optical basicities of 0.9–0.97 are obtained even in the ternary tellurite glasses. Correlation between experimental optical basicities $\Lambda(n_0)$ estimated using refractive index and theoretical optical basicity σth calculated using optical basicity values of each oxide is examined. It is proposed that the modified optical basicity value for TeO_2 oxide, $\Lambda(TeO_2) = 0.93$ gives a good agreement between $\Lambda(n_0)$ and Λ_{th}. The effect of glass structure (i.e.−TeO_4 and TeO_3 network structural units) on the optical basicity of tellurite glasses and the validity of large electronic polarisabilities of oxide ions was also examined.

Barium tellurite has not found much usage in industry but is available commercially. In spite of the extensive study of barium tellurite as a component of tellurite glasses, the physical properties such as melting point, etc. are not available.

Radium Tellurite

Radium tellurite has the molecular formula of $RaTeO_3$ and the molecular weight of 354.0969 g/mol. It has no CAS number. It can be formed via the solid-state reaction:

$$RaO + TeO_2 + \text{heat} \Rightarrow RaTeO_3$$

An inert atmosphere is required. This salt is a meta-tellurite. It can also be formed by a solution method:

$$RaCl_2 + Na_2TeO_3 \Rightarrow RaTeO_3 + 2NaCl$$

Additionally, this compound can be prepared by reacting tellurium dichloride in a solution of strontium chloride:

$$RaCl_2 + 2TeCl_2 + 3H_2O \Rightarrow Te + RaTeO_3 + 6HCl$$

The question of a hydrate remains unknown. There is absolutely no mention of this compound in the scientific literature and its physical properties remain unknown. There is no listed supplier for this compound and it is doubtful that it has ever been prepared.

3.4.4. Alkaline Earth Tellurates

The two forms of telluric acid create *tellurate* salts containing the TeO_4^{2-} and TeO_6^{6-} anions. The former is tetrahedral in structure while the latter is octahedral. Salts of these are named "meta-" and "ortho-" tellurates.

Beryllium Tellurate

Beryllium tellurate has the molecular formula of $BeTeO_4$ and the molecular weight of 200.61 grams per mole. Its solubility is 6.72 g/100 ml at 20 °C. It can be prepared by the solid-state reaction of TeO_3 and BeO:

$$BeO + TeO_3 \Rightarrow BeTeO_4$$

This is the tetragonal composition. It can also be formed in the same manner by solid-state reaction of telluric acid:

$$BeO(\text{solid}) + H_2TeO_4(\text{solid}) \Rightarrow BeTeO_4(\text{solid}) + H_2O(\text{gas})$$

Telluric acid is soluble in water and produces $Te(OH)_4O^{2-}$ anions in solutions. If beryllium chloride is added, the product is a tetrahydrate:

$$BeCl_2(aq) + H_2Te(OH)_4(aq) \Rightarrow \{Be(OH)\}_2Te(OH)_4$$

The Lewis structure is shown in Fig. 3.63.

However, the literature presents the formulation as $BeSeO_4 \cdot 4H_2O$, i.e. the meta-tellurate. Note that a compound such as $\{Be(OH)\}_6TeO_6$ is possible or $\{Be(OH)\}_4 \cdot H_2TeO_6$. It is said to be isomorphous

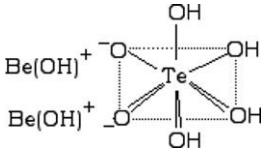

FIGURE 3.63

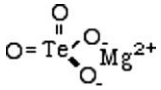

FIGURE 3.64

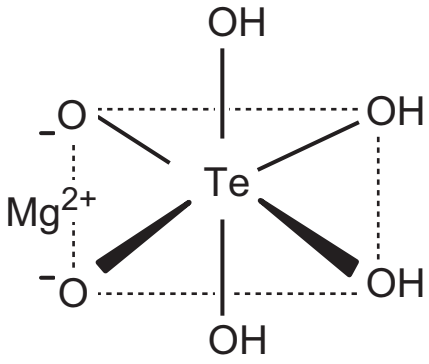

FIGURE 3.65

with the sulfate and loses water at 105 °C forming the dihydrate. If so, then the dehydration reaction involves:

$$\{Be(OH)\}_2Te(OH)_4 + \text{heat} \Rightarrow \{Be(OH)\}_2TeO_4 + 2H_2O$$

where the tellurate complex changes from an octahedral to a tetrahedral configuration. Although the chemistry of beryllium tellurate was studied earlier, it has received no attention in the current literature. According to Topsoe (1872), beryllium tellurate crystallizes in the rhombohedral system with a ratio of lattice parameters $a{:}b{:}c = 1{:}0.9602{:}0.9027$. More recently, this compound has been said to be cubic and have a structure very similar to spinel, $MgAl_2O_4$. A compound having the molecular formula of Be_4TeO_7 is said to be isomorphous to spinel as well. More likely, its composition is $Be(OH)_4H_2TeO_6$.

Beryllium tellurate has no CAS number and is not offered for sale commercially.

Magnesium Tellurate

Magnesium tellurate has the molecular formula of $MgTeO_4$ and the molecular weight of 215.9026 g/mol. Its CAS number is 15852-08-1. Its density is 3.16 g/cm^3 and it is sparingly soluble in water (4.07 g/100 ml of water at 20 °C). It can be prepared by the solid-state reaction of TeO_3 and MgO:

$$MgO + TeO_3 + \text{heat} \Rightarrow MgTeO_4$$

TeO_3 melts at 430 °C and a temperature of 550 °C serves to drive the reaction to completion. This is the tetragonal composition. It can also be formed in the same manner by solid-state reaction of telluric acid:

$$MgO(\text{solid}) + H_2TeO_4(\text{solid}) \Rightarrow MgTeO_4(\text{solid}) + H_2O(\text{gas})$$

This is also tetragonal (magnesium meta-tellurate) and the Lewis structure is shown in Fig. 3.64.

Telluric acid is soluble in water and produces $Te(OH)_4O^{2-}$ anions in solutions (Fig. 3.65).

If magnesium chloride is added, the product is a tetrahydrate:

$$MgCl_2(aq) + H_2Te(OH)_4(aq) \Rightarrow MgTeO_2(OH)_4$$

However, the literature presents the formulation as $MgTeO_4 \cdot 4H_2O$. Note that a compound such as Mg_3TeO_6 is possible or even $Mg_2H_2TeO_6$ (see diagram presented above). Mg_3TeO_6 is rhombohedral, space group R_3, with six molecules in a hexagonal unit cell, where $a = 8.58$ Å. The crystal structure is closely related to Y_6UO_{12} with octahedrally coordinated Mg and Te and mean Mg–O and Te–O bond lengths of 2.18 and 1.75 Å.

The salt, lead magnesium tellurate, Pb_2MgTeO_6, undergoes two structural phase transitions at about 194 and 142 K. The structures of the cubic and of the lower temperature phase have been refined by the Rietveld method at three different temperatures (350, 220 and 6 K). The relative simplicity of the structure has allowed the incommensurately modulated structure for powder samples to be characterized. The modulated displacements of O atoms give rise to a large spread of bond lengths. Pb atoms are disordered and their average positions are away from the threefold axis. The structural resolution is compared to that from the analysis of the symmetry-adapted coordinates of the optic modes becoming totally symmetric in the lower temperature phase.

The literature concerning magnesium tellurate is sparse and limited to structural studies in general.

Magnesium tellurate is available commercially but in limited quantities.

Calcium Tellurate

Calcium tellurate has the molecular formula of $CaTeO_4$ and the molecular weight of 231.68 grams per mole. Its CAS number is 712354-41-1 and its solubility in water is 0.727 g/100 ml at 20 °C. It can be prepared by the solid-state reaction of TeO_3 and CaO:

$$CaO + TeO_3 + \text{heat} \Rightarrow CaTeO_4$$

TeO_3 melts at 430 °C and a temperature of 600 °C serves to drive the reaction to completion. This is the tetragonal meta-tellurate composition. It can also be formed in the same manner by solid-state reaction of telluric acid:

$$CaO(\text{solid}) + H_2TeO_4(\text{solid}) \Rightarrow CaTeO_4(\text{solid}) + H_2O(\text{gas})$$

This is also tetragonal in structure, with the meta-tellurate configuration. Of the two possible configurations, the meta-tellurate is said to be the most stable.

Telluric acid is soluble in water and produces $Te(OH)_4O^{2-}$ anions in solutions: If calcium chloride is added, the product is a tetrahydrate:

$$CaCl_2(aq) + H_2Te(OH)_4(aq) \Rightarrow CaTeO_2(OH)_4$$

However, the literature presents the formulation as $CaTeO_4 \cdot 4H_2O$. If this compound is heated, it loses water at 120 °C to form the dihydrate and 180 °C to form the anhydrate, $CaTeO_4$. The tetrahydrate compound is orthorhombic with a space group of Pbcn and the lattice parameters: $a = 5.231$ Å, $b = 12.676$ Å, $c = 4.977$ Å, $V = 330.0$ Å^3, $Z = 4$ and a calculated density of 4.66 g/cm^3. It contains strings of TeO_6^{2-} octahedra similar to those of Na_2TeO_6. There are systematic absences of 0kl with $k = 2n$ +1, h0l with $l = 2n + 1$ and hk0 with $h + k = 2n + 1$, thus producing the space group Pbcn.

The structure of the dihydrate or the anhydrate has not been published.

Calcium tellurate has been used to isolate telluric acid by heating TeO_2 with and excess of CaO at 975 °C in air at a ration of 1:5 equivalents. The dioxide was completely oxidized and the product was $CaTeO_4$. Ratios less than this affected the overall yield. By adding nitric acid, soluble calcium nitrate and insoluble telluric acid were formed:

$$5CaO(solid) + TeO_2(solid) + heat \Rightarrow CaTeO_4(solid)$$

$$CaTeO_4(solid) + HNO_3(aq) \Rightarrow Ca(NO_3)_2(aq) + H_2TeO_4(solid)$$

If calcium tellurite(IV) is heated, in N_2 atmosphere, with stoichiometric amounts of CaO, the reaction product, proceeding at 380–620 °C, contained orthotellurate and telluride anions formed in disproportionation:

$$3CaTeO_3 + CaO + heat \Rightarrow CaTeO_4 + 2CaTe$$

The scientific literature concerning calcium tellurate is exceedingly limited and no data on its physical properties have been published. It has found little usage in industry but is available commercially in small quantities for use in research.

Strontium Tellurate

Strontium tellurate has the molecular formula of $SrTeO_4$ and the molecular weight of 279.216 grams per mole. Its CAS number is 15852-10-5. It can be prepared by the solid-state reaction of TeO_3 and SrO:

$$SrO + TeO_3 + heat \Rightarrow SrTeO_4$$

TeO_3 melts at 430 °C and a temperature of 600 °C serves to drive the reaction to completion. This is the tetragonal meta-tellurate composition. It can also be formed in the same manner by solid-state reaction of telluric acid:

$$SrO(solid) + H_2TeO_4(solid) \Rightarrow SrTeO_4(solid) + H_2O(gas)$$

This is also tetragonal in structure, with the meta-tellurate configuration. Of the two possible configurations, the meta-tellurate is said to be the most stable (Fig. 3.66).

Telluric acid is soluble in water and produces $Te(OH)_4O^{2-}$ anions in solutions. If strontium chloride is added, the product is a tetrahydrate:

$$SrCl_2(aq) + H_2Te(OH)_4(aq) \Rightarrow SrTeO_2(OH)_4$$

The orthotellurate, $SrTeO_2(OH)_4$, is orthorhombic with $a = 5.574$ Å, $b = 13.114$ Å, $c = 4.911$ Å, $V = 365.6$ Å^3, $Z = 4$ and density (calc) = 5.07 g/cm^3. Strings of Te–O octahedral complexes are apparent in the structure. The orthorhombic Sr_3TeO_6 (with a structure related to cryolite = Na_3AlF_6) forms a solid solution with Ba_3TeO_6 that is quadratic and changes to cubic. The quadratic phase exhibits highly anisotropic thermal expansion above the phase transformation to cubic as it changes between 370 and 670 °C (Fig. 3.67).

The literature concerning strontium tellurate is scattered and little has been published concerning the physical properties of the meta- or ortho-tellurate.

It is available commercially even though it has found little use in industry.

Barium Tellurate

Barium tellurate has the molecular formula of $BaTeO_4$ and the molecular weight of 328.9742 g/mol. Barium

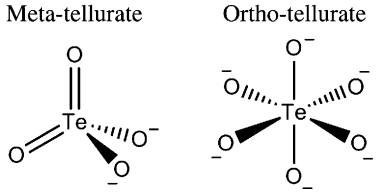

FIGURE 3.66

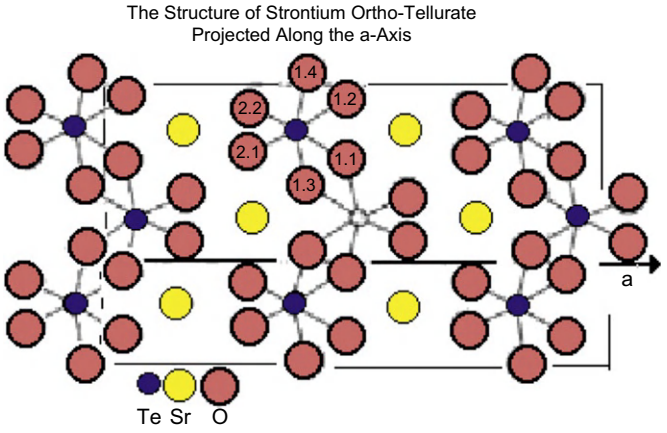

FIGURE 3.67

tellurate has the molecular formula of $BaTeO_4$ and the molecular weight of 328.936 grams per mole. Its CAS number is 13466-24-5 and its solubility in water is 0.727 g/100 ml at 20 °C. It can be prepared by the solid-state reaction of TeO_3 and BaO:

$$BaO + TeO_3 + \text{heat} \Rightarrow BaTeO_4$$

TeO_3 melts at 430 °C and a temperature of 650 °C serves to drive the reaction to completion. This is the tetragonal meta-tellurate composition. It can also be formed in the same manner by solid-state reaction of telluric acid:

$$BaO(\text{solid}) + H_2TeO_4(\text{solid}) \Rightarrow BaTeO_4(\text{solid}) + H_2O(\text{gas})$$

This is also tetragonal in structure, with the meta-tellurate configuration. Of the two possible configurations, the ortho-tellurate is said to be the most stable. A major usage for barium ortho-tellurate has been the production of other ortho-tellurates as well as ortho-telluric acid. Reduction of $BaTeO_4$ with hydrogen has been used to produce BaTe, used as a thermionic emitter in various types of cathodes in electronic instruments. If the ratio of TeO_3 and BaO is varied, it is possible to form a compound by solid-state reaction of:

$$BaO + TeO_3 + \text{Heat} \Rightarrow BaTeO_4$$

Telluric acid is soluble in water and produces $Te(OH)_4O^{2-}$ anions in solutions: If calcium chloride is added, the product is a trihydrate:

$$BaCl_2(aq) + H_2Te(OH)_4(aq) \Rightarrow BaTeO_2(OH)_4$$

However, the literature presents the formulation as $BaTeO_4 \cdot 3H_2O$. If this compound is heated, it loses water at 120 °C to form the dihydrate and 180 °C to form the anhydrate, $BaTeO_4$. This compound is essentially insoluble in water at 0.000523 g/100 ml at 20 °C. The trihydrate is slightly more soluble at 0.0056 g/100 ml but is more soluble in boiling water. It dissolves in most aqueous acids. Its CAS number is 28557-54-2.

The compound, $Ba_2Te(OH)_2O_2$, is known but specific data on its chemical and physical properties have not been clarified.

Barium tellurate is available as the trihydrate commercially.

Radium Tellurate

No data in the technical literature is available concerning this compound.

3.4.5. Alkaline Earth Teflates

Teflic acid can be prepared from barium tellurate and fluorosulfonic acid:

$$5HOSO_2F + BaO_2 \cdot Te(OH)_4 \Rightarrow HOTeF_5 + 4H_2SO_4 + BaSO_4$$

It is also the first hydrolysis product of tellurium hexafluoride:

$$TeF_6 + H_2O \Rightarrow HOTeF_5 + HF$$

The conjugate base of teflic acid is called the teflate anion, F_5TeO^- (not to be confused with "triflate"). Many teflates are known, examples being $B(OTeF_5)_3$ and the acid anhydride $O(TeF_5)_2$. Pyrolysis of the boron compound gives the dimer $(TeF_4O)_2$:

$$2B(OTeF_5)_3 + \text{heat} \Rightarrow 2B(OTeF_5)_2F + (OTeF_4)_2$$

The teflate anion is known to resist oxidation. This property has allowed the preparation of several highly unusual species such as the hexateflates $M(OTeF_5)_6^-$ (M = As, Sb, Bi).

Although some of the transition elements of Groups 3 to 12 do form teflate compounds, the alkaline earths do not. At least, there is no record of their formation or chemical and physical properties available. The following compounds remain unknown at this date:

$$Be(TeF_5O)_2 \cdot Mg(TeF_5O)_2$$

$$Ca(TeF_5O)_2Sr(TeF_5O)_2$$

$$Ba(TeF_5O)_2$$

3.5. POLONIUM-BASED ALKALINE EARTH COMPOUNDS

Polonium, Po, has 39 known isotopes, all of which are radioactive. The chemistry of polonium is similar to that of tellurium and bismuth. Polonium dissolves readily in dilute acids, but is only slightly soluble in alkalis. The hydrogen compound PoH_2 is liquid at room temperature (MP = −36.1 °C, BP = 35.3 °C). Halides of the structure PoX_2, PoX_4 and PoX_6 are known.

The two oxides PoO_2 and PoO_3 are the products of oxidation of polonium.

Fluorides

None listed

Chlorides

Polonium dichloride: $PoCl_2$
Polonium tetrachloride: $PoCl_4$

Bromides

Polonium tetrabromide: $PoBr_4$

Iodides

Polonium diiodide: PoI_2
Polonium tetraiodide: PoI_4

However, these compounds are the only ones that have been characterized in the available scientific literature. Polonium is too metallic in nature and forms no type of "polonites" or "polonates" with the alkaline earths.

CHAPTER

4

Group 15 (N, P, As, Sb and Bi) Alkaline Earth Compounds

OUTLINE

4.1. Alkaline Earth Nitrides and Oxo-Nitrogen Compounds **201**
4.1.1. Nitrogen Acids *201*
Trihydrogen Nitride 201
Nitrous Acid 201
4.1.2. Alkaline Earth Nitrides *201*
Beryllium Nitride 201
Magnesium Nitride 202
Calcium Nitride 205
Strontium Nitride 207
Barium Nitride 209
Radium Nitride 210
4.1.3. Alkaline Earth Nitrites *210*
Beryllium Nitrite 210
Magnesium Nitrite 210
Calcium Nitrite 211
Strontium Nitrite 212
Barium Nitrite 213
Radium Nitrite 215
4.1.4. Alkaline Earth Nitrates *215*
Beryllium Nitrate 215
Magnesium Nitrate 216
Calcium Nitrate 218
Strontium Nitrate 220
Barium Nitrate 221
Radium Nitrate 223

4.2. Alkaline Earth Phosphides and Oxo-Phosphorous Compounds **223**
4.2.1. Phosphorous Oxy-Acids *223*
Phosphorous Oxide Anhydrides 223
Phosphorous Acids 224
4.2.2. Alkaline Earth Phosphides *229*
Beryllium Phosphide 229
Magnesium Phosphide 230
Calcium Phosphide 231
Strontium Phosphide 232
Barium Phosphide 233
Radium Phosphide 234
4.2.3. Alkaline Earth Hypophosphites *234*
Beryllium Hypophosphite 234
Magnesium Hypophosphite 235
Calcium Hypophosphite 236
Strontium Hypophosphite 236
Barium Hypophosphite 237
Radium Hypophosphite 237
4.2.4. Alkaline Earth Phosphites *237*
Beryllium Phosphite 238
Magnesium Phosphite 238
Calcium Phosphite 239
Strontium Phosphite 239
Barium Phosphite 240
Radium Phosphite 241
4.2.5. Alkaline Earth Phosphates *241*
Beryllium Orthophosphates 242
Magnesium Orthophosphates 243
Calcium Orthophosphates 245
Calcium Hydroxyapatite 252
Calcium Fluoroapatite 254
Calcium Chloroapatite 254
Calcium Bromoapatite 255
Calcium Iodoapatite 255
Strontium Orthophosphates 255
Hydroxyapatite 257
Fluorapatite 257
Strontium Chloroapatite 258
Strontium Bromoapatite 259
Strontium Iodoapatite 259
Barium Orthophosphates 259
Barium Hydroxyapatite 262
Barium Fluorapatite 263
Barium Chloroapatite 264

Encyclopedia of the Alkaline Earth Compounds
http://dx.doi.org/10.1016/B978-0-444-59550-8.00004-1

Copyright © 2013 Elsevier B.V. All rights reserved.

Barium Bromoapatite 264
Barium Iodoapatite 264
Radium Orthophosphates 264
Radium Hydroxyapatite 265
Radium Fluorapatite 265
Radium Chloroapatite 265
Radium Bromoapatite 265
Radium Iodoapatite 266
4.2.6. Related Alkaline Earth Chalcogen Apatites 266
4.2.7. Alkaline Earth Pyrophosphates 266
Beryllium Pyrophosphate 266
Magnesium Pyrophosphate 266
Calcium Pyrophosphate 268
Strontium Pyrophosphate 270
Barium Pyrophosphate 271
Radium Pyrophosphate 271
4.2.8. Alkaline Earth Metaphosphates and Polyphosphates 272
Beryllium Metaphosphates and Polyphosphates 273
Magnesium Metaphosphates and Polyphosphates 273
Calcium Metaphosphates and Polyphosphates 274
Strontium Metaphosphate or Polyphosphates 278
Barium Metaphosphate or Polyphosphates 279
Radium Metaphosphates and Polyphosphates 280
4.2.9. Alkaline Earth Hypophosphates 281
Beryllium Hypophosphate 281
Magnesium Hypophosphate 281
Calcium Hypophosphate 282
Strontium Hypophosphate 282
Barium Hypophosphate 282
Radium Hypophosphate 282
4.2.10. Alkaline Earth Peroxyphosphates 282
Beryllium Peroxyphosphate 283
Magnesium Peroxyphosphate 283
Calcium Peroxyphosphate 283
Strontium Peroxyphosphate 284
Barium Peroxyphosphate 285
Radium Peroxyphosphate 285

4.3. Alkaline Earth Metal Oxo-Arsenic Compounds 286
4.3.1. Arsenic Acids 286
Arsenous Acid 286
4.3.2. Alkaline Earth Arsenides 287
Beryllium Arsenide 287
Magnesium Arsenide 287
Calcium Arsenide 288
Strontium Arsenide 289
Barium Arsenide 289
Radium Arsenide 290
4.3.3. Alkaline Earth Arsenites 291
Berylium Arsenite 291
Magnesium Arsenites 291
Calcium Arsenites 293
Strontium Arsenites 295
Barium Arsenites 295
Radium Arsenites 296
4.3.4. Alkaline Earth Orthoarsenates 297
Beryllium Arsenates 297
Magnesium Arsenates 298
Calcium Arsenates 302
Strontium Arsenates 304
Barium Arsenates 306
Radium Arsenates 309

4.4. Alkaline Earth Antimony Compounds 309
4.4.1. Alkaline Earth Antimonites 309
Beryllium Antimonite 309
Magnesium Antimonite 309
Calcium Antimonite 310
Strontium Antimonite 311
Barium Antimonite 311
Radium Antimonite 312
4.4.2. Alkaline Earth Antimonates 312
Beryllium Antimonate 312
Magnesium Antimonate 313
Calcium Antimonate 314
Strontium Antimonate 314
Barium Antimonate 315
Radium Antimonate 316
4.4.3. Alkaline Earth Antimonides 317
Beryllium Antimonide 317
Magnesium Antimonide 317
Calcium Antimonide 321
Strontium Antimonide 324
Barium Antimonide 325
Radium Antimonide 328

4.5. Alkaline Earth Bismuthate Compounds 328
4.5.1. Alkaline Earth Bismuthate Compounds 328
Beryllium Bismuthates 328
Magnesium Bismuthate 328
Calcium Bismuthate 329
Strontium Bismuthates 331
Barium Bismuthate 333
Radium Bismuthate 336
4.5.2. Alkaline Earth Bismuthides 337
Beryllium Bismuthides 337
Magnesium Bismuthides 337
Calcium Bismuthides 339
Strontium Bismuthides 343
Barium Bismuthides 347
Radium Bismuthide 350

4.1. ALKALINE EARTH NITRIDES AND OXO-NITROGEN COMPOUNDS

Nitrogen has three valence states, N^{3-}, N^{3+} and N^{5+} or "nitrides, nitrites" and "nitrates". The compounds formed with these anions are based upon the acids, H_3N, HNO_2 and HNO_3.

4.1.1. Nitrogen Acids

Trihydrogen Nitride

The hydride of nitrogen is NH_3, an azane known as ammonia. Nitrogen forms a quasi-like hydride, NH_3. It is normally encountered as a gas. However, it does not behave as a typical hydride in that it does not decompose in water to form hydrogen but dissolves in water to form a weak base:

$$NH_3 + H_2O \Rightarrow NH_4^+ + OH^-$$

Ammonia, as used commercially, is often called *anhydrous ammonia.* This term emphasizes the absence of water in the material. It is lighter than air, its density being 0.589 times that of air. It is easily liquefied due to the strong hydrogen bonding between molecules; the liquid boils at −33.3 °C, and solidifies at −77.7 °C (195 K, −108 F) to white crystals. Because NH_3 boils at −33.34 °C, the liquid must be stored under high pressure or at low temperature. Its solubility in water is 47% (0 °C), 31% (25 °C), 28% (50 °C). Its density is 0.86 g/cm^3 (1.013 bar at boiling point), 0.73 g/cm^3 (1.013 bar at 15 °C), 681.9 g/cm^3 at −33.3 °C (liquid), 817 g/cm^3 at −80 °C (transparent solid). It is a flammable gas with a flash point of 11 °C and an auto-ignition temperature of 651 °C. Nitrides of the alkaline earths are generally made by heating the metals in pure nitrogen gas.

Nitrous Acid

Nitrous acid (molecular formula = HNO_2) is a weak and monobasic acid known only in solution and in the form of nitrite salts. Nitrous acid rapidly decomposes into nitrogen oxide, nitric oxide and water when in solution:

$$2HNO_2 \Rightarrow NO_2 + NO + H_2O$$

It can also decompose into nitric acid and nitrous oxide and water.

$$4HNO_2 \Rightarrow 2HNO_3 + N_2O + H_2O$$

Nitric acid (HNO_3), also known as "aqua fortis" and "spirit of nitre", is a highly corrosive and toxic strong acid that can cause severe burns. It is colorless when pure and a slight yellow when "glacial". Older samples tend to acquire a yellow cast due to the accumulation of various oxides of nitrogen. If the solution contains more than 86% nitric acid, it is referred to as "fuming nitric acid". Fuming nitric acid is characterized as "white fuming nitric acid" and "red fuming nitric acid", depending on the amount of nitrogen dioxide present.

4.1.2. Alkaline Earth Nitrides

Beryllium Nitride

Beryllium nitride has the molecular formula of Be_3N_2 and the molecular weight of 55.0652 g/mol. It can be prepared from the elements at high temperature (1100–1500 °C). Be_3N_2 decomposes in vacuum into beryllium and nitrogen:

$$3Be + N_2 + \text{heat} \Rightarrow Be_3N_2 + \text{heat (Vac)} \Rightarrow 3Be + N_2$$

It is a white to yellow powder with a density of 2.71 g/cm^3. Its melting point is 2208 °C and a boiling point of 2240 °C. Its CAS number is 1304-54-7. It is soluble in water and is readily hydrolyzed forming beryllium hydroxide and ammonia:

$$Be_3N_2 + 3H_2O \Rightarrow 3Be(OH)_2 + 2NH_3$$

It has two polymorphic forms: cubic α-Be_3N_2 with a defect anti-bixbyite structure ($a = 8.1452$ Å), and hexagonal β-Be_3N_2. A three-dimensional structure is shown in the following Fig. 4.1.

It reacts with silicon nitride, Si_3N_4 in a stream of ammonia at 1800–1900 °C to form $BeSiN_2$. Calorimetric determinations of the heats of reaction of beryllium

FIGURE 4.1

TABLE 4.1

Enthalpy of formation energy		Entropy of formation			Gibbs free energy
(kcal/mol)	(kJ/mol)	(cal/K)	(J/K)	(kcal/mol)	(kJ/mol)
−140.6	−588.2704	8.16	34.14144	−127.4	−533.0416

and of α- and β-beryllium nitride with chlorine has produced the following heats of formation (Table 4.1):

$$\Delta H^{\circ}_{f_{298}}(\alpha\text{-}BeCl_2) = -117.1 \text{ kcal/mol}$$
$$\Delta H^{\circ}_{f_{298}}(\alpha\text{-}Be_3N_2) = -141.0 \text{ kcal/mol}$$
$$\Delta H^{\circ}_{f_{298}}(\beta\text{-}Be_3N_2) = -136.7 \text{ kcal/mol}$$

Another calorimetric determination of the heat of reaction of beryllium with ammonia gave a heat of formation of α-beryllium nitride, $\Delta H^{\circ}_{f_{298}}(\alpha\text{-}Be_3N_2) = -140.5 \pm 0.3$ kcal/mol. $\alpha\text{-}Be_3N_2$ has the space group of Ia3 while that of $\beta\text{-}Be_3N_2$ is $P6_3/mmm$. The low temperature heat capacity, C_p, of $\alpha\text{-}Be_3N_2$ at 0 °C is 15.39 cal/mol.

Beryllium nitride ($\beta\text{-}Be_3N_2$) vaporizes congruently in the range 1640° to 1960 K by the reaction:

$$Be_3N_2(\text{solid}) \Rightarrow 3Be(\text{gas}) + N_2(\text{gas}).$$

The equilibrium nitrogen partial pressure, in atmospheres, at the composition for congruent sublimation is given by the expression:

$$\log P_{N2} = [-1.952 \times 10^4/T] + 6.509$$

The measured enthalpy of decomposition (370 kcal at 298 K) yields an enthalpy of formation for Be_3N_2(s) of -136 ± 6 kcal/mol. The upper limit to the evaporation coefficient at 1600°–2000 K can be set as 10^{-4}. The apparent enthalpy of activation for the reaction is 409 ± 7 kcal/mol at 1800 K.

Beryllium nitride reacts with mineral acids producing ammonia and the corresponding salts of the acids:

$$Be_3N_2 + 6HCl \Rightarrow 3BeCl_2 + 2NH_3$$

Beryllium nitride is salt-like. The literature presents the formulations as containing Be^{2+} cations whereas they are, in reality, hydroxylated ($Be(OH)^{+}$) cations. The reaction, $Be(H_2O)_n^{2+} \Rightarrow Be(H_2O)_{n-1}^{+} + H^{+}$ is known. In strong alkali solutions, a beryllate forms, with evolution of ammonia:

$$Be_3N_2 + 6NaOH \Rightarrow 3Na_2BeO_2 + 2NH_3$$

Both the acid and alkali reactions are brisk and vigorous. Reaction with water, however, is very slow:

$$Be_3N_2 + 6H_2O \Rightarrow 3Be(OH)_2 + 2NH_3$$

Reactions with oxidizing agents are likely to be violent. It is oxidized when heated at 600 °C in air. Beryllium nitride (Be_3N_2) is used in refractory ceramics as well as in nuclear reactors and used to produce radioactive ^{14}C for tracer applications.

Extreme ultraviolet and soft X-ray optical systems require low absorbing materials for many technological applications. It has been determined that this compound can substitute for Be metal, a widely used material in this context. Thus, the dielectric function of Be and Be_3N_2 were determined in the 4–100 eV energy interval by means of reflection electron energy loss spectroscopy. It was found that the absorption coefficient of Be and Be_3N_2 are similar in the 40–100 eV energy range. Thereafter, the superior chemical stability and mechanical properties of Be_3N_2 makes it a promising substitute for Be as optical material in severe environments. Beryllium nitride thin films can be grown on silicon substrates by laser ablating a beryllium foil in a molecular nitrogen ambient. A low-absorption coefficient in the visible region and an optical band gap of 3.8 eV, determined by reflectance ellipsometry, were obtained for films grown at nitrogen pressures higher than 25 mTorr. The results showed that the reaction of beryllium with nitrogen is very effective using this preparation method in producing high-quality films.

The system, nitrides of beryllium, involving Be metal and N_2 gas, has not been investigated thoroughly. At a temperature between 500 and 900 °C, nitride formation is slow (from 24 to 60 h), but can be catalyzed if hydrogen is added to nitrogen, hydrogen (2–6%) being the catalyst for this reaction. Kinetics of the reaction of beryllium with nitrogen indicate that the reaction rate at temperatures up to 850 °C is slow; even at 950 °C, the reaction proceeds two times slower than the corresponding oxidation of beryllium.

To obtain a pure beryllium nitride powder, the metal was reacted with ammonia at a temperature of 1000 °C for 5 h at 800 °C and 17 h at 900 °C to produce a pure product. After subsequent processing of these products in a vacuum at 2000 °C, an X-ray of graphically pure beryllium nitride was obtained.

At temperatures up to 500 °C, Be_3N_2 is resistant to oxidation with dry oxygen but at 1000 °C is rapidly oxidized.

Beryllium nitride is available commercially from several manufacturers.

Magnesium Nitride

Magnesium nitride has the molecular formula of Mg_3N_2 and the molecular weight of 100.9494 g/mol. It can be prepared by the reaction of Mg metal in a pure stream of nitrogen gas:

$$3Mg + 2N_2 \Rightarrow Mg_3N_2$$

At room temperature and pressure, it is a greenish yellow powder. Its density is 2.712 g/cm^3 and it melts at about 1500 °C. Its CAS number is 12057-71-5. It reacts with water to produce ammonia gas, as do many metal nitrides:

$$Mg_3N_2 + 6H_2O \Rightarrow 3Mg(OH)_2 + 2NH_3$$

In fact, when magnesium is burned in air, some magnesium nitride is formed in addition to the principal product, MgO. The Lewis structure can be visualized as in Fig. 4.2.

Where two Mg^{2+} ions are directly linked together. The lattice parameter and coordinates of Mg_3N_2 were obtained. It is a cubic anti-bixbyite structure with lattice parameter $a = 9.9528$ Å. The metal (Mg) atoms are in general positions 48 e of space group *Ia*3 (*x; y; z*). There are two crystallographically different kinds of N atoms: N_1 is in positions 8b (1/4, 1/4, 1/4), and N_2 in positions 24d (x, 0, 1/4). In this structure, the N-arrays are fairly close to ideal cubic close packing. The 12 shortest N–N distances are in the range from 3.31 to 3.72 Å. Each nitrogen atom is coordinated by six Mg atoms. N_1 has six Mg neighbors with a distance of 2.145 Å, while N_2 is coordinated by six Mg with different N–Mg distances ranging from 2.084 to 2.179 Å. The Mg–Mg distances are 2.72 Å.

Formation of magnesium nitride was first discovered by Sainte-Claire Deville and Caron (1854) during a study of sublimation of magnesium in the air. Magnesium nitride is thus formed in the form of colorless needle-like crystals that are rapidly decomposed by water with formation of magnesium hydroxide and ammonia gas. The first systematic study (1885) of the process of formation of magnesium nitride was accomplished by heating magnesium powder in an atmosphere of ammonia. It was found that the reaction between magnesium and nitrogen begins at 450 °C, and proceeds most intensely at 600–700 °C, at atmospheric pressure of ammonia. Temperature dependence of the reaction rate was determined to be parabolic in nature, and the activation energy of the process was found to be 31.7 kJ/mol. It was also established that magnesium nitride is easily obtained by simply heating magnesium metal in a glass container in the air in the flame of a gas burner.

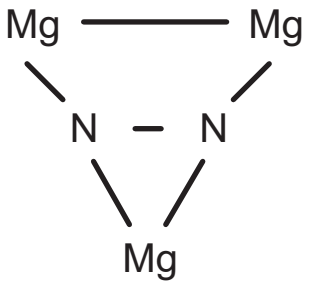

FIGURE 4.2

Most researchers suggested, at that time, a relatively high temperature nitriding of magnesium, in the range from 700 to 900 °C. The interaction of magnesium with nitrogen to form nitride begins at 780–800 °C, and, within 4–5 h at a temperature of 800–850 °C, forms a nitride whose nitrogen content is 27.3–27.6%, that almost exactly corresponds to the calculated content of nitrogen in Mg_3N_2 (which is equal to 27.74%).

The structural changes of Mg_3N_2 under pressure have been investigated up to 40.7 GPa at room temperature by means of angle-dispersive X-ray diffraction (XRD). A reversible, first-order structural phase transition from the ambient cubic phase (*Ia*) to a high-pressure monoclinic phase ($C2/m$) is found to start at 20.6 GPa and was said to be complete at 32.5 GPa. The equation of state determined yielded bulk moduli of 110.7 and 171.5 GPa for the cubic and monoclinic phases, respectively, indicating the higher incompressibility of the high-pressure phase of Mg_3N_2. In addition, a second-phase transition from the monoclinic phase to a hexagonal phase (Pm_1) was predicted around 67 GPa for Mg_3N_2. The electronic band structures of the three phases of Mg_3N_2 were also calculated.

The hydriding and dehydriding reactions occurring in mixtures of lithium and magnesium nitrides (Li_3N and Mg_3N_2) were investigated using fixed composition ratios. A mixture of 80-Li_3N–20 atom% of Mg_3N_2 after heat treatment at 833 K was hydrogenated at 523 K and a pressure of 35 MPa according to the following overall reaction:

$$4Li_3N + Mg_3N_2 + 12H_2 \Rightarrow 12LiH + 3Mg(NH_2)_2$$

This reaction is one of the candidates for reversible hydrogen-storage functions in which 9.1 mass% of hydrogen can be stored in the solid state.

Due to the rapid decomposition of Mg_3N_2 in the presence of water in the atmosphere, the synthesis of single-crystalline Mg_3N_2 nanowires has been a challenge. It has been demonstrated that carbon nanotubes may serve as nanoreactors for a simple thermal reaction process resulting in the fabrication of high-quality, large-yield, single-crystalline Mg_3N_2 nanowires. The Mg_3N_2 nanowires are homogeneously sheathed over their entire lengths with very thin graphitic carbon tubular layers, which effectively prevent their decomposition.

Magnesium nitride was the catalyst in the first practical synthesis of cubic boron nitride. Ab *initio* band structure calculations have been performed for $MgSiN_2$ and Mg_3N_2. Calculations show that both nitrides are semiconductors with direct energy gaps at 3.2 eV. The valence bands are composed mainly of N-2p states hybridized with s and p characteristics of the metals. The bottom of the conduction band consists of the "s" characters of Mg and N for Mg_3N_2, as well as for $MgSiN_2$, while the characters of Si are higher in energy.

The experimental optical-diffuse spectra show an energy gap of about 2.8 eV for Mg_3N_2 and 4.8 eV for $MgSiN_2$, in agreement with the calculated values.

The phase interactions in the Mg_3N_2–BN system at high pressures were refined. Along with the known compound, Mg_3BN_3, Mg_6BN_5 is formed in this system (hexagonal crystal lattice: $a = 5.397$ Å and $c = 10.585$ Å, $Z = 2$). At atmospheric pressure and 900 °C, Mg_6BN_5 breaks down to Mg_3BN_3 and Mg_3N_2. In the range 500–1150 °C, the conductivity of the solid solutions increases with Mg_3N_2 concentration. The ionic transference number is close to unity, and the ionic transport is mainly due to boride ions.

$MgSiN_2$ is noted as an alternative ternary compound for high-temperature applications, showing good physical properties such as a reasonable thermal conductivity, a rather good fracture toughness and hardness, and a good oxidation resistance up to 920 °C. $MgSiN_2$ is also promising as a substrate material with an electrical resistivity at room temperature comparable to (and at high temperature greater than) that of AlN. $MgSiN_2$:Eu has not only luminescence properties similar to AlN, but also a quantum yield for the green band as high as 40%, as compared to 8% for AlN. $MgSiN_2$ crystallizes in an orthorhombic structure, which is derived from the Wurtzite structure. The hexagonal structure is distorted because of the presence of the two metal atoms and the displacement of the nitrogen atoms from the ideal positions in the Wurtzite structure.

Most studies of $MgSiN_2$ have concentrated on its preparation, characterization, mechanical and thermal properties. There has been almost no work performed relating to the electronic properties, except the optical reflectance experiments, which showed $MgSiN_2$ has an energy gap of about 4.8 eV.

Mg_3N_2 is widely used as a catalyst in the preparation of some nitrides, such as silicon nitride ceramics and cubic boron nitride. It was found in 1933 that some alkaline earth metal nitrides M_3N_2 (M = Be, Mg, Ca) have the anti-bixbyite structure. However, it was not until 1997 that the fully refined structure for Mg_3N_2 was demonstrated by use of the neutron time-of-flight diffraction data. In this refined structure, the Mg atoms are at the tetrahedral sites of an approximately cubic close-packed array of N atoms (MgN_4). $MgSiN_2$ is orthorhombic, with lattice parameters: $a = 5.2708$ Å, $b = 10.4692$ Å and $c = 4.9840$ Å. All the atoms are at general positions 4a of the space group *Pna*21. Both Mg^{2+} and Si^{4+} atoms are tetrahedrally coordinated by N^{3+} atoms. The average Mg–N distance is 2.090 Å, which is shorter than that in Mg_3N_2 (2.141 Å). The Si–N distances range from 1.728 to 1.766 Å. The average Si–N distance is 1.752 Å, longer than that in Si_3N_4 (1.732 for α-Si_3N_4, 1.738 Å for β-Si_3N_4). The Mg–Mg distances are about 3.09 to 3.11 Å, which are also longer than those in Mg_3N_2, but shorter than those (about 3.20 Å) in the Mg metal. The shortest N–N distance is about 2.829 Å, larger than that in β-Si_3N_4 (2.77 Å). A three-dimensional structure is shown in the following Fig. 4.3.

Experiments in the system RE–Mg–N (RE = La, Ce, Gd) have been accomplished to explore the possible synthesis of nitrides using Mg as reactive melt and to extend the number of known nitride compounds containing Mg. Since these experiments produce only binary nitrides, mixed Na/Mg melts were used and the quaternary nitrides:

$$BaMg_{3.33}Nb_{0.67}N_4 \quad (1)$$

$$BaMg_{3.33}Ta_{0.67}N_4 \quad (2)$$

$$Eu_4TaMgN_5 \quad (3)$$

were discovered. These were characterized by single-crystal structure analysis. The $BaMg_{3.33}M_{0.67}N_4$ compounds are isotypic to UCr_4C_4 which is a filled $MoNi_4$

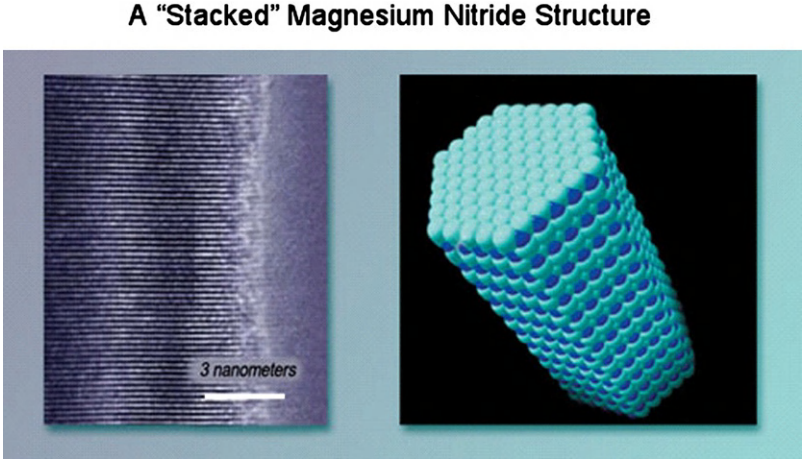

FIGURE 4.3

type and crystallize in the space group I4/*m* (#87) with the lattice parameters $a = 8.5640$ Å and $c = 3.5390$ for (**1**), and $a = 8.5961$ Å and $c = 3.5421$ Å for (**2**). The third type crystallizes in a new structure type in the acentric orthorhombic space group $Pna2_1$ (#33) and with the lattice parameters $a = 12.655$ Å, $b = 10.159$ Å and $c = 6.925$ Å.

The published literature concerning magnesium nitride itself is very sparse and a description of its physical properties is not extensive. There is little demand for this compound in industry. It is, however, available commercially.

Calcium Nitride

Calcium nitride has the formula of Ca_3N_2 and the molecular weight of grams per mole. It can be prepared by the reaction of Ca metal in a pure stream of nitrogen gas:

$$3Ca + 2N_2 \Rightarrow Ca_3N_2$$

A second method is the decomposition of an amide:

$$3Ca(NH_2)_2 + \text{heat} \Rightarrow Ca_3N_2 + 4NH_3$$

This must be accomplished in an inert atmosphere (not nitrogen gas). It is a reddish-brown powder. Its CAS number is 12013-82-0 and its density is 2.76 g/cm^3. It melts at 1195 °C (2183 F). α-Calcium nitride is the commonly encountered form. It has an anti-bixbyite structure similar to Mn_2O_3, except that the positions of the ions are reversed: calcium (Ca^{2+}) ions take the oxide (O^{2-}) positions and nitride ions (N^{3-}) that of the manganese (Mn^{3+}). If Ca metal is burned in air, it forms the oxide, CaO, and the nitride, Ca_3N_2. The latter reacts with atmospheric moisture to produce the hydroxide of calcium and ammonia:

$$Ca_3N_2 + 6H_2O \Rightarrow 3Ca(OH)_2 + 2NH_3$$

It absorbs hydrogen above 350 °C. The Lewis structure diagram is shown in Fig. 4.4.

Calcium is a unique element, as it is the only element in the s-block that forms both ionic and subnitrides with nitrogen. For a long time, it was believed that there were many compounds in the Ca–N system, including α-Ca_3N_2, β-Ca_3N_2 and γ-Ca_3N_2, calcium pernitride, Ca_3N_4 and a compound of composition $Ca_{11}N_8$. α-Ca_3N_2 is the only compound that has been extensively characterized. Further published work has practically ruled out the existence of all other forms of calcium nitride. Those compounds all appear to be a calcium nitride cyanamide, $Ca_4N_2(CN_2)$ or $Ca_{11}N_6(CN_2)_2$. The carbon contamination most likely was derived from steel in crucibles and reactors or even from the calcium metal itself.

α-Ca_3N_2 has been characterized by X-ray powder diffraction and its structure confirmed by a crystal structure refinement using the Rietveld method. A three-dimensional structure is presented as shown on the next page. Ca_3N_2 and the isostructural Mg_3N_2 crystallize in the anti-bixbyite structure of the mineral $(Mn,Fe)_2O_3$ in the body-centered space group of $Ia3(T_7h)$. It has a distorted form of this structure, in which Ca is tetrahedrally coordinated to N, whereas N is octahedrally coordinated to Ca. The general appearance of their infrared and Raman spectra resembles that of the sesquioxides belonging to the same space group. Both compounds decompose into $Mg(OH)_2$ and NH_3, when exposed to the atmosphere. The presence of NH_4^+ vibrational bands in the decomposition products was explained in terms of the existence of Brønsted acid centers on the surface of the solid (Fig. 4.5).

During the initial stages of decomposition, infrared bands characteristic of adsorbed NH_3 were observed, showing that Lewis centers also exist on the surface. The decomposition product $Mg(OH)_2$ has weaker proton-donating centers than that of $Ca(OH)_2$. The kinetics of the decomposition of Mg_3N_2, which is a much slower reaction than that of α-Ca_3N_2, has been studied with Fourier transformation-infrared (FT-IR) microspectrometry. It was shown that the formation of $Mg(OH)_2$ involves a three-dimensional diffusion process

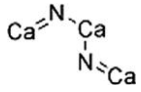

FIGURE 4.4

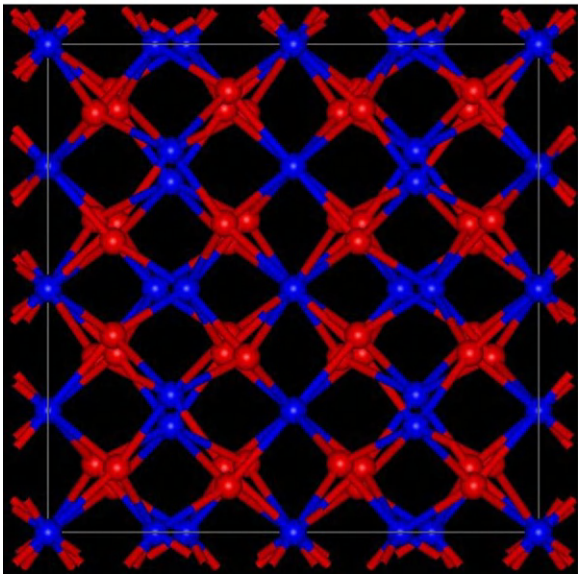

FIGURE 4.5

while the proton donation by the hydroxide to adsorbed NH_3 to form NH_4^+ ions is a quasi-first-order reaction.

It has been found that aluminum nitride single crystals of reproducibly good quality and large size can be grown by a novel technique that involves the use of calcium nitride as a solvent system in the solution growth of these crystals. In general, the method involves the use of calcium nitride (Ca_3N_2) as a solvent for aluminum nitride at elevated temperatures. Aluminum nitride is dissolved by calcium nitride and then recrystallized from solution as a single crystal. The synthesis of single crystals by this method is known as the Solution Growth Method. For example, to synthesize the aluminum nitride material as a crystal, the general procedure is to intimately mix from about 8 to 40 mol % aluminum nitride (AlN) and from about 92 to 60 mol% calcium nitride. The mixture is heated in an appropriate crucible to a temperature above the melting point of the mixture which is generally in the range of about 1525 to 1650 °C. After the temperature of the molten solution is maintained from 1 to 2 h, the solution temperature is slowly cooled to a temperature slightly below its saturated solubility temperature at a programmed rate of from about 0.5 to about 3 °C/h.

Recent advances in the utilization of single crystals for a wide variety of purposes, especially in various electronic surveillance and detection applications, has generated considerable research in the development of improved techniques for growing single crystalline materials. A problem has arisen, however, in that many of the methods relied upon heretofore fail to grow crystals having a reproducibly high quality. Calcium nitride as a high temperature solvent has been used in the recrystallization of refractory aluminum nitride, that is growing single crystals of aluminum nitride from a molten solution containing the refractory material as the solute, and calcium nitride as the solvent. Crystallization is accomplished by the precipitation or crystallization of the solute, the solute being the desired crystal, from the molten solution.

Large, water white aluminum nitride single crystals have never been grown from its melt because of the following reasons. First, aluminum nitride sublimes and decomposes according to the reaction $2AlN(s) \Rightarrow 2Al\,(g) + N_2\,(g)$ at temperatures far below (c.a. 1723 K) the temperature range (3023 K) in which AlN is reported to melt. Secondly, materials that could be used as crucible materials to contain aluminum nitride in its melting temperature range are violently attacked, particularly under high pressures. Thirdly, the state of materials science, as far as crystal growth is concerned, has not developed high-pressure chamber materials capable of sustaining pressures greater than 100 atmospheres for long periods (3 weeks) at elevated temperatures (2000 °C). It is highly improbable, therefore, that in the near future, large, good quality aluminum nitride single crystals will be grown from its own melt at least by present day techniques. The use of molten calcium nitride as a solvent has solved most of these problems.

The sublimation pressure of calcium nitride was measured, based upon the reaction:

$$Ca_3N_2\,(\text{solid}) \Rightarrow Ca\,(\text{gas}) + N_2\,(\text{gas})$$

The second-law and third-law heats of sublimation were found to be 217.3 and 227.9 kcal/mol, respectively. The free-surface vapor pressure of calcium nitride in the temperature range of 1152–1479 K was: $\log P_L \pm 1.108 \times 10^4/T + 3.528$, where P is in atmospheres and T is the absolute temperature.

The high-pressure behavior of Ca_3N_2 was studied up 100 GPa using density functional theory. Evaluation of many hypothetical polymorphs of composition A_3X_2 led to the proposal of four high-pressure polymorphs for both α- and β-Ca_3N_2: (1) an anti-Rh_2O_3(II) structure at 5 GPa, (2) an anti-B-sesquioxide structure at 10 GPa, (3) an anti-A-sesquioxide structure at 27 GPa, and (4) a hitherto unknown hexagonal structure ($P6_3/mmc$), derived from the post-perovskite structure of $CaIrO_3$, at 38 GPa. However, only α-Ca_3N_2 has been confirmed to date.

α-Ca_3N_2 belongs to the series of curious alkaline earth nitride salts that are constrained by their stoichiometry of 3-to-2 divalent alkaline earth cations to trivalent nitride anions, to form odd cubic crystals containing cation vacancies ordered along their <111> axes, in a $2 \times 2 \times 2$ supercell of an anti-fluorite arrangement, that nonetheless exists in a high space group symmetry of Ia-3 [3]. In a high-pressure study using a conventional diamond anvil cell, the nature of these cation vacancies was probed as a function of pressure to a maximum pressure, as measured by the equation of state of Au [5], of 137 Kb. No phase transition was observed in the α-Ca_3N_2 salt to 137 Kb but a compression of the unit cell was observed in diffraction photographs taken of the sample at several pressures, by conventional Debye-Scherrer powder methods.

A similar compound, Ca_2N, has also been discovered. It can be synthesized by heating α-Ca_3N_2 in vacuum. Ca_2N adopts the anti-$CdCl_2$ structure in which two sheets of calcium ions enclose a sheet of N^{3-} ions, with each calcium bonded to three N^{3-} at 2.4500 Å and each nitrogen octahedrally coordinated by six calcium atoms. Within one calcium sheet, each metal has three others at 3.2944 Å and a further six at 3.6271 Å. The distance between two calcium layers with no intervening nitrogen layer is 4.3221 Å, and this intervening region contains no observable electron density. Neutron and X-ray powder diffraction studies have shown that the *c*-axis dimension changes with the synthetic method employed. In the single crystal, *c* is significantly lower, reflecting the higher temperature employed in its formation.

Calcium nitride hydride (Ca_2NH) was obtained as a single-phase material by reacting either calcium metal or calcium hydride (CaH_2) in an argon atmosphere containing 5–7% H_2 and 1–7% N_2. Imide ions substituting for hydride and nitride ions constitute a major chemical defect in this material. Long-range ordering of the nitride and hydride ions occurs, giving rise to a double cubic crystal symmetry. This order breaks down at 600–650 °C. Applying the same reaction conditions to strontium metal results in a mixed phase of strontium nitride hydride and imide. No long-range order in the nitride hydride phase could be observed. Doping Ca_2NH with lithium hydride (LiH) causes the appearance of a second calcium imide phase, whereas doping with sodium hydride (NaH) increases the amount of imide ions as a defect in the nitride hydride structure, thereby decreasing the long-range ordering of nitride and hydride ions.

Closely related to calcium nitride hydride, Ca_2NH, are calcium imide, CaNH, and calcium amide, $Ca(NH_2)_2$. Calcium imide has the rock salt structure, with calcium octahedrally coordinated to nitrogen in a cubic closest packed array of nitrogen ions. Hydrogen is positioned close to the nitrogen ion with a large degree of disorder. Calcium amide has the tetragonal Anatase structure, which is closely related to calcium imide. It can roughly be viewed as two imide unit cells stacked on top of each other, with only half of the calcium ions now occupied. The hydrogen in the amide ions was shown to have a large degree of disorder by assuming in and out of plane movements relative to the nitrogen ion. The compounds have been synthesized via the following reactions:

Ca_2NH has previously been synthesized either by reacting Ca_3N_2 in hydrogen atmosphere or by reacting Ca_3N_2 with CaH_2 in vacuum, both at high temperatures:

$$4Ca_3N_2 \Rightarrow 6Ca_2NH + N_2 \text{ (Reacted in } H_2 \text{ and } T > 850\ ^\circ\text{C)}$$
$$Ca_3N_2 + CaH_2 \Rightarrow 2Ca_2NH \text{ (Vacuum } T > 950\ ^\circ\text{C)}$$

Calcium imide is traditionally obtained by thermally decomposing calcium amide, which in its turn is obtained by thermally decomposing calcium hexaammonia complex (calcium metal dissolved in ammonia):

$$Ca(NH_3)_6 \Rightarrow Ca(NH_2)_2 + 4NH_3 + H_2$$
$$Ca(NH_2)_2 \Rightarrow CaNH + NH_3$$

A great deal of work is currently being undertaken to provide phosphors which absorb the blue emission of (In,Ga)N or (Al,Ga,In)P light-emitting diodes (LEDs). The work has centered around alkaline earth silicide–nitride compositions which have a sufficient crystal field strength to "Stokes Shift" the intrinsic UV absorption of the Eu^{2+} ion to the blue region of the spectrum where the LED emits. A synthetic $Ca_2Si_5N_8$:Eu^{2+} phosphor was prepared through a solid-state reaction and its structural and luminescent properties investigated. Refinement of the crystal structure of $Ca_{1.9}Eu_{0.1}Si_5N_8$ revealed that Eu atoms substituting for Ca atoms occupy two crystallographic positions. Between 10 and 300 K, $Ca_2Si_5N_8$:Eu^{2+} phosphor shows a broad red emission band centered at ~1.97–2.01 eV (617–629 nm). The gravity center of the excitation band is located at 3.0–3.31 eV (374 nm). The centroid shift of the 5*d* levels of Eu^{2+} is determined to be ~1.17 eV (1059 nm), and the red shift of the lowest absorption band to be ~0.54 eV (2296 nm) due to the crystal field splitting. The temperature dependence of photoluminescence (PL) was analyzed by using a configuration coordinate model. The Huang–Rhys parameter $S = 6.0$, the phonon energy $hv = 52$ meV, and the Stokes shift, $S = 0.57$ eV, were obtained. The emission intensity maximum occurring at ~200 K can be explained by a trapping effect. Both PL emission intensity and decay time decrease with temperature increasing beyond 200 K due to the nonradiative process.

However, the main focus of research on LED–phosphor modifiers involves the $(Ba,Sr,Ca)_2Si_5N_8$:Eu^{2+} family which can be "fine-tuned" to emit in specific ranges from green, yellow, orange and red and can be pumped with any blue emitter in the 425–480 nm range very efficiently LED = Light emitting diodes.

Calcium nitride is a minor part of such compositions. Calcium nitride is available from a number of commercial suppliers.

Strontium Nitride

Strontium nitride should have the molecular formula of Sr_3N_2 and the molecular weight of 290.8752 g/mol. However, according to some sources, Strontium does not form the ionic compound Sr_3N_2 and Sr_2N is the only compound that has been properly characterized to date. The reaction of Sr metal in a pure stream of nitrogen gas produces the "subnitride":

$$4Sr + N_2 \Rightarrow 2Sr_2N$$

A second method would be the decomposition of an amide:

$$2Sr(NH_2)_2 + \text{Heat} \Rightarrow 2Sr_2N + 2NH_3 + H_2$$

This must be accomplished in an inert atmosphere (not nitrogen gas). Sr_2N was shown to be iso-structural to Ca_2N. The excess electron is mobile and gives these subnitride materials their electronic conductivity. The electronic conductivity is highly an isotropic and they can therefore be seen as two-dimensional metals, with reasonable conductivity in the direction parallel to the N–A layers.

However, some commercial sources offer "strontium nitride" as Sr_3N_2 (CAS number = 12033-82-8). It is apparently prepared by reaction of Sr metal in a nitrogen atmosphere. Strontium nitride is described as Sr_3N_2,

produced by burning strontium metal in air (resulting in a mixture with strontium oxide) or in nitrogen. Like other alkaline earth metal nitrides, it reacts with water to give strontium hydroxide and ammonia:

$$Sr_3N_2 + 6H_2O \Rightarrow 3Sr(OH)_2 + 2NH_3$$

In air, it strontium metal burns and produces strontium oxide and strontium nitride. But, since it does not react with nitrogen below 380 °C, it will only form the oxide spontaneously at room temperature. To produce the pure nitride, it is necessary to maintain the temperature above 380 °C in air or to heat the metal in pure nitrogen gas. In air, the molten mass, as it cools from 380 °C, tends to convert some of the nitride to oxide. However, a prominent supplier of "Materials Used in the Manufacture of Tomorrow's Phosphor Formulations" (Cerac, Milwaukee, Wisc 53201) offers Ca_3N_2 and Ba_3N_2 for sale but not Sr_3N_2.

The alkaline earth metal nitride compounds: Sr_2N, $(Sr_{0.48}Ba_{0.52})_2N$, Ba_2N, Sr_2NCl and Sr_2NBr have been synthesized and investigated by the means of XRD. These compounds all have crystal structures closely related to the anti-α-$NaFeO_2$ structure type. The reaction products obtained from the nominal starting compositions "Sr_2NH_x" ($0 \leq x \leq 1$) were also analyzed by X-ray powder diffraction. With $x \geq 0.75$, Sr_2NH_{1-x} is the only product observed, but for $x \leq 0.75$, Sr_2N is found in equilibrium with Sr_2NH_{1-x}.

A number of new, layered nitride mixed halides have been synthesized in the quaternary phase systems Sr–N–Cl–Br and Sr–N–Br–I. The variation in structure with composition has been investigated by powder X-ray and powder neutron diffraction techniques and the structure of strontium nitride iodide, Sr_2NI, has been determined for the first time (rhombohedral space group $R-3m$, $a = 4.0103$ Å, $c = 23.1138$ Å, $Z = 3$). A continuous solid solution exists between Sr_2NCl and Sr_2NBr with intermediate compounds adopting the same *anti*-α-$NaFeO_2$ structure (rhombohedral, space group = R-3m) as the ternary end members. A similar smooth and linear relationship between structure and composition is seen from Sr_2NBr to Sr_2NI and hence cubic close packing of metal–nitrogen layers is adopted regardless of halide. While nitride and halide anions occupy distinct crystallographic sites, there is no ordering of the halides in the quaternary materials irrespective of stoichiometry or temperature (between 3 and 673 K).

Sr_2N has been used to produce other subnitrides. Bulk thermal- or filament-initiated reactions of mixed powders of transition metal chlorides and Sr_2N produces transition metal nitrides (TiN, ZrN, HfN, VN, V_2N) in good yield. The products were characterized by X-ray powder diffraction, scanning electron microscopy (SEM)/EDAX, FT-IR, microelemental analysis and imaging XPS. The effect of diluting the reaction by the addition of LiCl was used to lower reaction temperatures and in the case of WCI_4 and Li_3N produced WN. Reaction propagation was investigated by using various mixtures of nitriding reagent (Li_3N, Mg_3N_2, Ca_3N_2), this was correlated with $T_{ad(s)}$ the maximum adiabatic combustion temperature for salt formation only.

A major effort is currently being conducted to produce white-emitting LED (light emitting diode) lights for both outdoor and interior lighting, thereby replacing the "standard" light sources. These LED lights have the advantage of long-life (~30,000 h) and low wattage compared to conventional lamps.

A simple, inexpensive, and high-yield synthetic route to $Sr_2Si_5N_8$:Eu^{2+}-based red nitridosilicate phosphors for white LEDs has been described. Through the chemical reaction of $SrCO_3$, Eu_2O_3, and Si_3N_4 rather than the air-sensitive Sr, Eu, Si(NH), Sr_3N_2, and EuN powders, a complex phosphor consisting of $Sr_2Si_5N_8$:Eu^{2+} (64 wt%) and Sr_2SiO_4:Eu^{2+} (36 wt%) were obtained by firing the powder mixture at 1600 °C under 0.5 MPa N_2. The structural characterization, luminescence spectra, quantum efficiency, and thermal quenching of the synthesized phosphor were investigated and compared with those of $Sr_2Si_5N_8$:Eu^{2+} prepared by the conventional method. It was shown that the emission of the existing Sr_2SiO_4:Eu^{2+} is extremely low (about 0.04% of that of $Sr_2Si_5N_8$:Eu^{2+}) under ultraviolet light irradiation, and it is not responsive under the blue light excitation ($\lambda_{Ex} = 400$–480 nm); therefore, it was concluded that the luminescence of the complex phosphor solely arises from $Sr_2Si_5N_8$:Eu^{2+}. The $Sr_2Si_5N_8$:Eu^{2+}-based phosphor is orange-red in color and emits strongly in the red region of 616–670 nm depending on the Eu^{2+} concentration when excited at $\lambda_{Ex} = 450$ nm. Furthermore, the $Sr_2Si_5N_8$:Eu^{2+}-based phosphor synthesized by this novel method shows equal optical properties, such as high emission intensity, high quantum efficiency, and very low thermal quenching, when compared to those prepared by the conventional approaches. This makes it a promising red luminescent material for white LEDs".

In another research paper, undoped and Eu^{2+}-doped $M_2Si_5N_8$ (M = Ca, Sr, Ba) materials were obtained by a solid-state reaction of MN_x, EuN_x and α-Si_3N_4 powder at 1300–1400 °C under an N_2–H_2 (10%) atmosphere. The maximum solubility of Eu^{2+} is about 7 mol% in the $Ca_2Si_5N_8$ lattice. In contrast, Eu^{2+} can be completely incorporated into the $M_2Si_5N_8$ (M = Sr, Ba) lattice because the $M_2Si_5N_8$ (M = Sr, Ba) compounds are isostructural with $Eu_2Si_5N_8$. Eu-doped $M_2Si_5N_8$ shows a typical broad-band emission of Eu^{2+} in the spectral range from orange to red (570–680 nm) due to the 4f65d ⇒ 4f7 transition. With increasing Eu^{2+} concentration, the emission band shifts to longer wavelength depending on the type of M ion and the Eu content. This was found to be proportional

to the changes of the unit cell volume for M = Sr and Ba. This red shift is related to an increase of the Stokes shift and possibly can also be attributed to some reabsorption by Eu^{2+}. The absorption and excitation bands of $M_2Si_5N_8$:Eu^{2+} materials ranging from 370 to 460 nm perfectly match with the emission of InGaN-based LEDs making them attractive as conversion phosphors for white LED applications. The best material for this purpose was shown to be $Sr_2Si_5N_8$:Eu^{2+} with a conversion (i.e. quantum) efficiency of 75–80% for 465 nm excitation and a very favorable thermal quenching behavior.

A number of nitride-containing compounds have also been studied. These include:

> "Strontium nitride carbodiimide, $Sr_4N_2(CN_2)$, is isostructural with the calcium analog and consists of a framework of edge- and vertex-sharing Sr_6N octahedra forming channels within which almost linear and almost symmetrical carbodiimide anions reside, surrounded by eight strontium ions".
>
> "Single crystals of Sr_2NI have been grown for the first time. Redetermination from single-crystal XRD data confirms the anti-α$NaFeO_2$ structure, previously found from powder diffraction data [Bowman, Smith and Gregory (2006). *J. Solid State Chem.* **179**, 130–139]. Iodide ions occupy octahedral voids between layers of edge-sharing NSr_6 octahedra".
>
> "The synthesis of single crystals of Sr_2NiN_2 has been accomplished in a liquid sodium flux from strontium or strontium nitride, nickel, and sodium azide. The decomposition of sodium azide provides additional nitrogen for the synthesis. The structure of Sr_2NiN_2 is derived from the Na_2HgO_2 structure type. However, Sr_2NiN_2 forms with a twinned superstructure. Single crystal XRD was used to determine the structure of the tetragonal subcell: **I4/mmm**, $a = 3.8874$ Å, $c = 13.992$ Å, $Z = 2$, with the Ni and N positions split into two sites, each half occupied. The superstructure can be modeled as a $2 \times 1 \times 1$ ordering of the subcell in **Pnma**. The physical properties are unusual since Sr_2NiN_2 displays metallic conductivity and Pauli paramagnetism even though it is comprised of isolated NiN_2 units. In addition, Sr_2NiN_2 possesses a Ni^{2+} formal charge, whereas the oxidation states for nickel nitrides are typically Ni^{+} and Ni^{0}".
>
> "The synthesis of calcium, strontium and barium–nitride–fluorides has been accomplished by using a 3 to 1 mol ratio of the metal to metal fluoride for the Sr_2NF and Ba_2NF syntheses, and a 4 to 1 mol ratio for Ca_2NF syntheses. The reaction mixtures were annealed in an inert argon environment at a temperature of 1000 °C for 24 h and then reacted in nitrogen gas for 5 h at 450 °C. Following this treatment, the calcium, strontium, and barium reaction mixtures were sintered in a nitrogen gas flow for 24 h at 1000, 950, 700 °C, respectively. The Ca_2NF that was found was a light yellow color, although colors of the other two phases were not reported. The products were reportedly characterized using Debye-Scherrer powder XRD. The resulting patterns suggested the presence of both the MF_2 and M_2NF phases (where M is a symbol for the appropriate metal) in representative lines".

Strontium nitride is available commercially from several suppliers.

Barium Nitride

Barium nitride purportedly has the molecular formula of Ba_3N_2 and the molecular weight of 439.9944 g/mol. Its CAS number is 12047-79-9. It is offered for sale by several reputable manufacturers but the actual composition and identity may not coincide with the formula presented. Although Mg, Ca (and to some extent Sr) forms a number of compounds based upon the general formula M_3N_2, there is no report in the literature that or Ba forms such compositions. The literature is devoid of any data relating to Ba_3N_2 and the subnitride is mentioned only in the presence of Sr_2N.

Barium nitride has been reported to be metastable and sublimes in the 915 to 1050 °C temperature range. The reported equation for this behavior is: $\log P = 6.38 \times 10^4/T(\mathrm{K})$ and it decomposes when heated beyond this range to form the metal and nitrogen gas, i.e. it is metastable. Thus, the existence of barium nitride is doubtful and no report of its formation or properties exists to date.

The metal combines with nitrogen and hydrogen at elevated temperatures producing barium nitride hydride, Ba_2NH:

$$4Ba + N_2 + H_2 \Rightarrow 2Ba_2NH$$

Barium–nitride–hydride is one of the few documented H^--ionic conductors. It crystallizes in the α-$NaFeO_2$ structure (space group R_m) with distorted Ba-octahedra centered alternately by H^- and N^{3-}. Neutron diffraction shows that the hydrogen ions are distributed independent of temperature over lattice sites: 85% on (3a) and 15% on (6c). At $T > 525$ K a sharp increase of the ionic conductivity can be observed. The diffusion process takes place by uncorrelated jumps of hydrogen ions between regular lattice sites. Using quasielastic neutron scattering techniques and a planar jump diffusion model, we were able to determine the mean residence time on a H^--site to be $\tau = 20 \pm 2$d ps and the diffusion constant D to be 2.1×10^{-5} cm^2/s at $T = 823$ K.

Ba_2N has been used to produce other subnitrides. Bulk thermal or filament-initiated reactions of mixed powders of transition metal chlorides and Ba_3N_2 produces transition metal nitrides (TiN, ZrN, HfN, VN, V_2N) in good yield. The products were characterized by X-ray powder diffraction, SEM/EDAX, FT-IR, microelemental analysis and imaging XPS. The effect of diluting the reaction by the addition of LiCl was used to lower reaction temperatures and in the case of WCI_4 and Li_3N produced WN. Reaction propagation was investigated by using various mixtures of nitriding reagent (Li_3N, Mg_3N_2, Ca_3N_2), this was correlated with $T_{ad(s)}$, the maximum adiabatic combustion temperature for salt formation only

The latest innovation has been the invention of a new class of red-emitting nitride phosphors $M_2Si_5N_8$:Eu^{2+} (M = Ca, Sr, Ba) that has triggered a renewal in the field of luminescent materials. Subsequently, a number of new nitride-based phosphors has been found and

investigated. For $M_2Si_5N_8$:Eu^{2+} (M = Ca, Sr, Ba), it has been reported that unusual long-wavelength Eu^{2+} emission (620–660 nm) with absorption bands in the visible range can be achieved. The long-wavelength emission is attributed to a large covalency and crystal-field splitting effect on the Eu^{2+} 5d band due to the presence of coordinating nitrogen. Later, studies presented the luminescence properties in a series of $Ba_{2-x}Eu_xSi_5N_8$ compounds which revealed two emission maxima peaking at about 600 nm, corresponding to two crystallographic Ba(Eu) sites in the $Ba_2Si_5N_8$ host lattice. The emission maxima shift to longer wavelength with increasing Eu content due to reabsorption processes of Eu^{2+}.

Further work has clarified the solubility of Eu^{2+} in these lattices. It has been established that Eu^{2+} forms the same type of compounds with the Si_5N_8 lattice with corresponding Sr or Ba Si_5N_8 lattices while that of Ca differs. This limits the amount of Eu^{2+} that can be dissolved in the calcium compound as shown in the following Table 4.2.

Barium nitride is offered for sale commercially but the exact nature of its composition remains in doubt.

Radium Nitride

It is doubtful whether such a compound such as Ra_3N_2 could be prepared. Furthermore, there is absolutely no demand or usage in industry for such a compound because of the radioactivity of ^{226}Ra. Whether Ra could form a compound like the nitride hydride, Ra_2NH, remains a mystery.

4.1.3. Alkaline Earth Nitrites

Nitrites are usually prepared by addition of a soluble salt to sodium nitrite. Of this, $NaNO_2$ = sodium nitrite, is usually prepared by electrolytic reduction of the nitrate.

Beryllium Nitrite

According to Sidgwick, Beryllium nitrite cannot be prepared, owing to the weakness of the acid, HNO_2. Parsons states that beryllium nitrite has never been prepared. The efforts of Vogel (1903) proved fruitless as the solution immediately hydrolyzed with loss of the oxides of nitrogen. It might possibly be prepared in nonaqueous solutions. However, there is no record of this having ever been done.

If beryllium nitrite is to be prepared by the usual double decomposition reaction of sodium nitrite and $BeCl_2$:

$$2NaNO_2\,(aq) + BeCl_2 \Rightarrow Be(NO_2)_2\,(aq) + 4NaCl\,(aq)$$

The product is likely to be $Be(OH)NO_2$ if it is obtained under vacuum evaporation at 10 °C. Whether a hydrate forms or not remains unknown. Furthermore, the product probably will not be stable in air and will decompose at room temperature unless protected from the atmosphere.

It has no CAS number and is not listed as available commercially.

Magnesium Nitrite

Magnesium nitrite has the formula of $Mg(NO_2)_2$ and the molecular weight of 116.3164 g/mol. It can be made by the usual double decomposition reaction of sodium nitrite and $CaCl_2$:

$$2NaNO_2\,(aq) + MgCl_2 \Rightarrow Mg(NO_2)_2\,(aq) + 4NaCl\,(aq)$$

It forms a trihydrate having a molecular weight of 170.3626 g/mol. Magnesium nitrite is soluble in water and the solution must be evaporated at very low temperatures to obtain crystals. The solution is stable and is slightly hydrolyzed in the cold but at 60° and above it evolves oxides of nitrogen. Its CAS number is 15070-34-5 and it occurs as white, hydroscopic crystals that must be protected from moisture to prevent decomposition. The trihydrate, when heated, forms the monohydrate at 100 °C and then decomposes to $NO + NO_2$ and MgO at >130 °C. It is soluble in alcohol.

The instability of magnesium nitrite, even when dissolved in water, has not engendered any usage in

TABLE 4.2

Crystal system	$Ca_2Si_5N_8$ Monoclinic Cc	$Sr_2Si_5N_8$ Orthorhombic Pmn21	$Ba_2Si_5N_8$ Orthorhombic Pmn21
Maximum solubility of Eu2+	$x = 0.14$	$x = 2.0$	$x = 2.0$
5d excitation band (nm)	297, 355, 394, 460, 496	294, 334, 395, 465, 505	295, 334, 395, 460, 504
Emission band (nm)	605–615	609–680	570–680
Center of gravity (cm^{-1})	25,800	26,000	26,100
Crystal-field splitting (cm^{-1})	13,500	14,200	14,100
Stokes shift (cm^{-1})	3800	3700	3500
Conversion efficiency (%)	50–55	75–80	75–80

industry. Although it has a CAS number, no research papers dealing with its physical or chemical properties are currently accessible. Most of the known data comes from early (before 1890) work in the technical literature.

Magnesium nitrite is available in small quantities commercially.

Calcium Nitrite

Calcium nitrite has the formula of $Ca(NO_2)_2$ and the molecular weight of 132.0894 g/mol. It can be made by the usual double decomposition reaction of sodium nitrite and $CaCl_2$. It forms a tetrahydrate that is isomorphous with the strontium and barium salts:

$$2Na_2NO_2\,(aq) + CaCl_2 \Rightarrow Ca(NO_2)_2\,(aq) + 4NaCl\,(aq)$$

Calcium nitrite, $Ca(NO_2)_2$, has the CAS number of 13780-06-8 and occurs as yellow-white crystals. It is very hygroscopic. Its density is 2.23 g/cm^3 and it decomposes at 392 °C to form nitrogen oxides and CaO. It is slightly soluble in alcohol. $Ca(NO_2)_2 \cdot 4H_2O$ loses two waters of hydration at about 80 °C and one at 105 °C to form the monohydrate. It loses the other at about 155 °C. The anhydrate, if further heated, is unstable and oxidizes to the nitrate in air above 220 °C:

$$Ca(NO_2)_2 + O_2 + \text{heat} \Rightarrow Ca(NO_3)_2$$

Calcium nitrite monohydrate, $Ca(NO_2)_2 \cdot H_2O$ and has the CAS number of 10031-34-2. It occurs as colorless crystals. The Lewis structure is shown in Fig. 4.6.

Industrially, calcium nitrite is manufactured by reacting "NOX" gas with "lime":

$$Ca(OH)_2 + NO + NO_2 \Rightarrow Ca(NO_2)_2 + H_2O$$

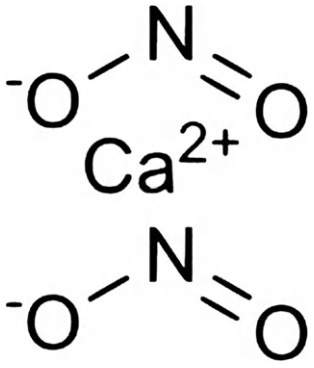

FIGURE 4.6

By carefully controlling calcium nitrite conditions, the selectivity on converted lime, on a molar basis, is over 95% pure. It is soluble in water (98.2 g/100 ml at 20 °C) and the solution must be evaporated at low temperature to obtain the tetrahydrate. If heated with NO_2 gas, it also form the nitrate:

$$Ca(NO_2)_2 + NO_2 \Rightarrow Ca(NO_3)_2 + NO$$

Anhydrous calcium nitrite is unstable and slowly oxidizes in air to form the nitrate. It is also soluble in alcohol at 0.97 g/100 ml at 20 °C. It has the CAS number of 13780-06-8. Its solubility is shown in Table 4.3.

This product is supplied as a clear, light yellow to colorless solution which has a slight sweet odor. It is a mild reducing agent and the CAS number of the commercial solution is 10124-37-5. Two major manufacturers in the world produce this product with plants in Wilmington, NC and Augusta, Ga and the other in China. The calcium nitrite plant in Wilmington, NC was based on technology Grace had licensed from the Japanese chemical firm, Nissan. The Nissan process utilized three (3) reactors. In this scheme, the so-called Rich NOX gas entered the first reactor, and so-called Lean NOX gas from the first reactor went to the second reactor (Fig. 4.7).

Calcium nitrite has several industrial uses:

1. Calcium nitrite has high solubility, so can be used as a solution or powder in concrete as an "anti-freeze" during winter months as needed. Using this antifreeze at negative temperature can promote the hydration of minerals in cement, and the freezing point of operative temperature can be reduced to –25 °C.
2. This salt is a steel rust inhibitor: calcium nitrite can clean steel and protect it from rust, and can protect steel material in concrete used to construct buildings and structures, to extend the useful life of concrete in buildings.
3. In concrete, $Ca(NO_2)_2$ acts as a coagulator: calcium nitrite is free of chlorine and alkali, capable to reduce alkali aggregation of concrete and improve its early strength and compressive resistance. The calcium nitrite protects steel reenforcing bars from chloride-induced corrosion. One advantage to calcium nitrite is that its protection mechanism is well defined. Data are known that show the levels of chloride to which given levels of calcium nitrite will protect. Once

TABLE 4.3

		g/100 ml of water								
Compound	**Formula**	**0 °C**	**10 °C**	**20 °C**	**30 °C**	**60 °C**	**70 °C**	**80 °C**	**90 °C**	**100 °C**
Calcium nitrite	$Ca(NO_2)_2 \cdot 4H_2O$	63.9		84.5	104	134		151	166	178

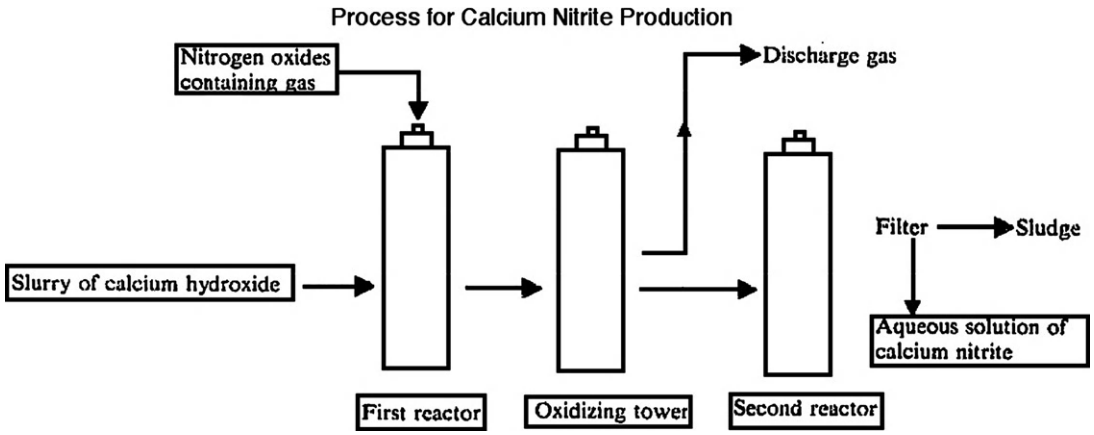

FIGURE 4.7

corrosion initiates, the rates are lower with calcium nitrite present. These results have been used to produce reinforced concrete structures with durability in excess of 50–100 years.

4. Calcium nitrite can be used as corrosion inhibitor when added to lubricating agents.
5. Calcium nitrite can also be used in pharmaceutical, dyes and metallurgy industries, as a mild reducing agent.

Calcium nitrite is readily available commercially in large quantities.

Strontium Nitrite

Strontium nitrite has the formula of $Sr(NO_2)_2$ and the molecular weight of 179.6311 g/mol. It can be made by the usual double decomposition reaction of sodium nitrite and $SrCl_2$. It forms a tetrahydrate which is isomorphous with the calcium and barium salts:

$$Na_2NO_2\,(aq) + SrCl_2 \Rightarrow SrNO_2\,(aq) + 2NaCl\,(aq)$$

Anhydrous strontium nitrite, $Sr(NO_2)_2$, has the CAS number of 13780-06-8 and occurs as yellow-white crystals. It is very hygroscopic. Its density is 2.23 g/cm^3 and it decomposes at >650 °C to form nitrogen oxides and SrO. It is slightly soluble in alcohol (0.04 g/100 ml at 20 °C) but soluble in water at 72.1 g/100 ml at 20 °C.

$Sr(NO_2)_2 \cdot 4H_2O$ loses two waters of hydration at about 80 °C and one at 105 °C to form the monohydrate. It loses the other at about 155 °C. The anhydrate, if further heated, is unstable and oxidizes to the nitrate in air above 240 °C:

$$Sr(NO_2)_2 + O_2 + \text{heat} \Rightarrow Sr(NO_3)_2$$

Strontium nitrite monohydrate, $Sr(NO_2)_2 \cdot H_2O$, has the CAS number of 13470-06-9 and a molecular weight of 197.6464 g/mol. It occurs as yellow-white crystals which are hygroscopic. Its density is 2.84 g/cm^3. In air, the crystals begin to decompose at about 245 °C. It is soluble in water at about 58.5 g/100 ml at 20 °C.

When heated in a nitrogen atmosphere, $Sr(NO_2)_2 \cdot H_2O$, undergoes a single loss of water at around 150 °C followed by a $\text{solid}_1 \Rightarrow \text{solid}_2$ phase transition in the anhydrous solid $Sr(NO_2)_2$ phase at around 265 °C with subsequent melting at about 365 °C. There is a very slight decomposition commencing even before melting which becomes more significant at 500 °C and very rapid above 650 °C. The final product is cubic SrO as identified by powder XRD. EGA (evolved gas analysis) studies of the decomposition in a vacuum were consistent but indicated lower temperatures of dehydration and particularity of decomposition. The quantities of product gases evolved during the complex decomposition region followed the order $NO > NO_2 \approx O_2 > N_2 > N_2O$. $Sr(NO_3)_2$ is a probable intermediate species during the decomposition.

$Sr(NO_2)_2 \cdot H_2O$ is a newly characterized material with pyroelectric coefficient $p_2 = 20\ \mu C/m^2/K$ and second-order nonlinear dielectric susceptibility about 0.06×10^{-12}/V/m at room temperature. Its space group is $P2_1$. The monoclinic unit cell has dimensions $a = 12.5831$ Å, $b = 8.94941$ Å, $c = 4.4860$ Å, and $\beta = 99.111°$ at 295 K. The linear thermal expansion coefficients at room temperature are $\alpha_1 = 37 \times 10^{-6}$/K, $\alpha_2 = 41 \times 10^{-6}$/K, and $\alpha_3 = 25 \times 10^{-6}$/K.

In another study, it was determined that a new phase transition at 538 K occurs in $Sr(NO_2)_2$ with an entropy gain, on passing from phase II to phase I, of 18.9 J/mol/K. On quenching, phase I is metastable to 296 K but reverts on heating to phase II at about 467 K. Phase II is orthorhombic, with lattice constants at 296 K of $a = 7.5320$ Å, $b = 8.1496$ Å, $c = 6.4820$ Å, and four $Sr(NO_2)_2$ molecules per unit cell. Thermal expansion coefficients, as given by $a_T = a_{296}\ [1 + \alpha\Delta T + \beta(\Delta T)^2]$, are: $\alpha(a) = 33$, $\alpha(b) = 39$, and $\alpha(c) = 62 \times 10^{-6}$/K, $\beta(a) = -119$, and $\beta(b) = 61 \times 10^{-9}/K^2$, i.e. the thermal expansion of the a and b axes is nonlinear, that of the

c-axis is linear (Here, a, b & c are lattice directions while α, β & γ are expansion coefficients). The volume expansion, as given by $V_T = V_{296}\ [1 + \beta\Delta T]$, is linear with $\beta(V) = 123 \times 10^{-6}$/K. Phase I is cubic with $a = 7.5752$ Å at 538 K, $\alpha(a) = 29 \times 10^{-6}$/K; crystals of phase I melt at 637 K. The increase in volume at the phase transition is 6.0%. The postulate of threefold positional disorder by the nitrite ions about the cubic body diagonals results in an expected entropy increase of $R \ln 9 = 18.27$ J/mol/K.

If strontium nitrite is added to a mixture of magnesium–strontium nitrate, normally used in pyrotechnic formulations, it prevents aging of the nitrate mixture in the presence of water until usage in fireworks. Studies by isothermal microcalorimetry show that the addition of strontium nitrite to a 50% magnesium–50% strontium nitrate composition eliminated the induction reaction normally observed in closed ampoule studies in air at 50 °C and relative humidity in the range 65–69%.

Strontium nitrite is available commercially from several manufacturers, notably Chinese.

Barium Nitrite

Barium Nitrite has the molecular formula of $Ba(NO_2)_2$ and the molecular weight of 247.3532 g/mol. Barium *nitrite* is made by double decomposition from barium chloride and sodium nitrite:

$$BaCl_2 + 2NaNO_2 \Rightarrow Ba(NO_2)_2 + 2NaCl$$

It is soluble so that the solution must be evaporated at low temperature to obtain crystals. The product is a monohydrate whose molecular weight is 247.4356 g/mol and whose CAS number is 7787-38-4. It loses water at about 100 °C and the anhydrous salt melts with decomposition at 217 °C. It occurs as yellowish-white crystals whose solubility is 75.3 g/100 ml. It is insoluble in ethanol.

Barium nitrite, $Ba(NO_2)_2$ has the CAS number of 13465-94-6 and the molecular weight of 229.338 g/mol. It occurs as colorless hexagonal crystals which decompose upon heating at about 267 °C. Its density is 3.234 g/cm^3 and it is soluble in water at 79.525 g/100 ml at 25 °C (Table 4.4).

$Ba(NO_2)_2 \cdot H_2O$ is hexagonal with a space group of $P6_1$ and $a = 7.070$ Å, $c = 17.886$ Å, $V = 774.3$ Å^3, $Z = 4$. $Ba(NO_2)_2 \cdot H_2O$ undergoes a sluggish reversible phase transition on heating to 350 K, followed by water loss to form the hemihydrate at about 425–435 K. The final half-molecule of water is lost by 455 K. Differential thermal analysis (DTA), thermogravimetry, differential scanning calorimetry (DSC), infrared spectroscopy, XRD, and optical microscopic techniques were used to characterize this salt. The entropy change of 36 J/K/mol measured at the phase transition is consistent with five new orientations becoming available to each water molecule above 350 K (77 °C), accompanied by related reorientations of the two independent NO_2^- ions as new hydrogen bonds are formed. Both the high-temperature monohydrate and the hemihydrate phases are unstable.

Further work has shown that phase transitions at 462 K and 495 K occur in $Ba(NO_2)_2$. The increase in entropy at each transition is about 13 J/mol/K. A gain of two orientations per independent NO^{-2} ion at each transition corresponds to an entropy increase of 11.5 J/mol/K. The crystal melts at 516 K. The high-temperature phase I is metastably retained at 298 K on rapid solidification, reverting to phase III on reheating above 350 K. Phase III is orthorhombic with lattice constants at 298 K of $a = 7.657$, $b = 8.355$, and $c = 6.742$ Å and four $Ba(NO_2)_2$ in the unit cell. The linear thermal expansion coefficients are 30.7, 14.0, and -5.9×10^{-6} Å/K for the a, b, and c axes, respectively. The powder pattern for phase II has not been indexed. Phase I may be fitted by a monoclinic unit cell with $a = 6.692$, $b = 7.052$, and $c = 9.638$ Å and $\beta = 104.61°$ at 507 K with four $Ba(NO_2)_2$ in the unit cell. A dielectric anomaly is observed at 468 K in the frequency range 0.1–1 MHz: dielectric losses obscure the anomaly at lower frequencies.

The phase relation and the dehydration behavior of barium nitrite hydrates have been examined by DTA under various external pressures, and by thermogravimetry and differential thermal analysis (TG–DTA) in air. The equilibrium water vapor pressures of the mono-, hemi-, and 1/3-hydrates have been measured. The temperatures of III ⇒ II and II ⇒ I phase transitions and melting point of the anhydrate are 469, 497 and 542 K, respectively (196, 224, 269 °C). The dehydration in air atmosphere proceeds as in Fig. 4.8.

A phase transition has been observed at 211 K in crystalline barium nitrite hemihydrate, $Ba(NO_2)_2 \cdot 1/2H_2O$, by DTA and dielectric measurements. A dielectric relaxation phenomenon was also found and the activation energies governing the relaxation were determined to

TABLE 4.4

		g/100 ml of water								
Compound	**Formula**	**0 °C**	**10 °C**	**20 °C**	**30 °C**	**40 °C**	**60 °C**	**80 °C**	**90 °C**	**100 °C**
Barium nitrite	$Ba(NO_2)_2$	50.3	60	72.8		102	151	222	261	325

$$\text{monohydrate} \xrightarrow{(372\ \text{K})} \text{hemihydrate} \xrightarrow{(425\ \text{K})} 1/3\text{-hydrate} \xrightarrow{(457\ \text{K})} \text{anhydrate}$$

FIGURE 4.8

be 23 kJ/mol and 41 kJ/mol below and above the transition temperature, respectively. Some discussions have been made on the nature of the phase transition.

Neutron diffraction studies of barium nitrite monohydrate [$Ba(NO_2)_2 \cdot H_2O$] have been made at 20, 102, and 298 K on the same crystal. Intensities of 954 (20 K), 2179 (102 K), and 2393 (298 K) reflections were measured at the Brookhaven National Laboratory high-flux beam reactor. The structures were refined on the basis of the hexagonal space group $P6_5$ to yield agreement factors R (F^2) = 0.028 (20 K), 0.034 (102 K), and 0.061 (298 K). The thermal expansion is nonlinear along both the a and c axes, with $\alpha_1 = 3.8 \times 10^{-6}/\text{K}$, $\beta_1 = 2.8 \times 10^{-8}/\text{K}^2$, $\alpha_3 = 21.3 \times 10^{-6}/\text{K}$, $\beta_3 = 10.9 \times 10^{-8}/\text{K}^2$. The cell dimensions are:

$$a = 7.0524\ \text{Å},\ c = 17.6372\ \text{Å at 20 K}$$
$$a = 7.0559\ \text{Å},\ c = 17.6810\ \text{Å at 102 K}$$
$$a = 7.07492\ \text{Å},\ c = 17.89087\ \text{Å at 298 K.}$$

The mean-square amplitude of thermal motion of Ba is proportional to temperature in the range 298–20 K, with small departures from linearity for the O and N amplitudes and larger departures for the H nuclear amplitudes. The Ba^{2+} cation is coordinated by nine oxygen atoms and one nitrogen atom at an average distance of 2.881 Å at 20 K, 2.884 Å at 102 K, and 2.902 Å at 298 K. The increase in length corresponds completely to the lattice expansion. A maximum difference within a nitrite ion of 0.015 Å in N–O bond lengths, observed at 298 K, is reduced to 0.008 Å at 20 K for a mean N–O distance of 1.254 Å. One O–H bond of 0.958 Å, which forms a bifurcated hydrogen bond with two oxygen atoms, is identical in length to that in the free water molecule; the other is slightly elongated by formation of a nearly linear hydrogen bond to a nitrogen atom. The largest nuclear displacement between 298 and 20 K in this pyroelectric crystal is only 0.038 Å along the polar axis.

In another study, Barium nitrite monohydrate, $Ba(NO_2)_2 \cdot H_2O$, was found to be strongly pyroelectric at room temperature and crystallizes in the hexagonal system with space group $P6_5$, or the enantiomorphous (mirror-like) $P6_1$, with six formulas in the unit cell. The lattice constants at 298 K are $a = 7.07490$ Å and $c = 17.89087$ Å ($CuK\alpha_1 = 1.540598$ Å). The integrated intensities of most reflections within a quadrant of reciprocal space having radius $(\sin\theta)/-1.15$ or $1.08/\text{Å}$ were measured on two different crystals, each with different diffractometer, resulting in 3218 F_{meas} for one set and 3671 F_{meas} for the second set of independent structure factors. The crystal structure was solved from Patterson and Fourier series, and refined by the method of least squares. The final agreement factor $R = 0.026$ for the first set, 0.018 for the second set of F_{meas} (Fig. 4.9).

The two sets of F_{meas} and the derived structural parameters are compared using normal probability plot analysis. The two NO^{2-} ions have a mean N–O distance of 1.246 ± 0.002 Å and O–N–O angle of $114.2 \pm 0.2°$. The Ba^{2+} ion is coordinated by nine-oxygen and one-nitrogen atoms at an average distance of 2.899 Å. The water molecule has a weighted mean O–H distance of 1.04 ± 0.03 Å and H–O–H angle of $102.7 \pm 4.3°$: it is hydrogen bonded to two independent NO_2^- ions by an O–H to O bond of 2.878 Å and an O–H to N bond of 2.951 Å.

Using ^{1}H nuclear magnetic resonance (NMR), the diffusive properties of the pyroelectric and piezoelectric compound, $Ba(NO_2)_2 \cdot H_2O$, were investigated. Spin-lattice relaxation times of the quiesecent and the rotating frames (T_1 and T_{1q}) as well as the dipolar relaxation times (T_{iD}) were measured. Single crystals were used for measuring these spin-lattice relaxation times and polycrystalline samples for the temperature dependencies. $Ba(NO_2)_2 \cdot H_2O$ undergoes a reversible phase transition at 350 K (77 °C), followed by a water loss upon further heating. In the room temperature phase, two major processes were found to be responsible for the relaxation. These dominate the relaxation in separate temperature regions. The activation energies, E, associated with the low-and high-temperature regions are 25 kJ/mol and 57 kJ/mol, respectively. The high activation energy process is clearly a 180° flip motion of the water molecules. The other process could not be clearly defined. The pre-exponential factor

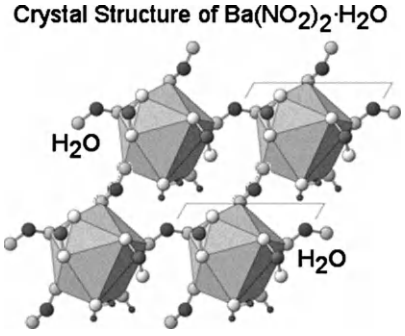

FIGURE 4.9

for the correlation times of the H_2O flip motion is 1.1×10^{-15} s.

The infrared spectra of crystalline barium nitrite monohydrate and of the deuterium substituted or anhydrous counterparts were investigated at various temperatures up to the melting point of the anhydride 516 K (243 °C). Samples were prepared as mineral oil mulls, single-crystal plates, and oriented polycrystalline sheets and were measured in polarized or unpolarized radiation. In addition to observations of the dehydration occurring near 430 K (167 °C) as temperature is increased and transitions among the three forms of anhydride (I, II, and III) known from X-ray and thermal measurements, a new transition near 348 K (75 °C) in the monohydrate was investigated, and a new, room temperature form of anhydride (IV) was discovered.

In another paper, infrared and Raman spectroscopy and normal coordinate analysis were used to investigate the detailed forms of the internal vibrations and the librations of the water molecule in $Ba(NO_2)_2 \cdot H_2O$. The asymmetric bonding situation is shown to result in normal vibrations that tend to give displacements more or less localized to one O–H bond of the water molecule. Thus, the mixing of twisting and wagging produces two normal modes which are more like H(1) and H(2) out-of-plane displacement, respectively. The corresponding mixing of bending and rocking also occurs, but to a smaller extant. Vibrational amplitudes for the hydrogen nuclei of the water molecule are derived in two ways; from earlier diffraction studies and from the normal coordinate analysis. The agreement between the two sets of amplitude is found to be very good in the O–H bond directions and in the out-of-plane direction, but somewhat poorer in the in-plane direction which is perpendicular to the O to H bonds. Some systematic deviations from the equilibrium geometry of the water molecule as obtained by neutron diffraction were discussed in view of the calculated normal vibrations and the vibrational model used in the diffraction experiment.

The IR spectra of undeuterated and partially deuterated $Ba(NO_2)_2 \cdot H_2O$ were recorded between 4000 and 1000/cm. The single HOH bending frequency confirms that the six H_2O molecules in the unit cell are equivalent. The splitting of the fundamentals of isotopically dilute HDO shows that the water molecules are asymmetrically hydrogen bonded, with one strong and one weak hydrogen bond. The asymmetry decreases gradually with increasing molecular motion at higher temperatures. The nonequivalence of the two hydrogen atoms shows that the space group $P6_122$-D_6^2 (or $P6_522$-D_6^3) proposed on the basis of XRD studies is incorrect. The space group is one of lower symmetry, probably $P6_1$-C_6^2 (or $P6_5$-C_6^3). The considerable asymmetry of the water molecules may explain the discrepancy, reported by Tramer and Mathieu, between the directions of the experimental transition moments and those calculated on the assumption that the water molecules are symmetric.

Barium nitrite monohydrate is available commercially from several suppliers. No CAS numbers have been assigned to date.

Radium Nitrite

There are no reports on the experimental preparation of **radium nitrite.** It could be prepared by the aqueous reaction between sodium nitrite and radium chloride:

$$RaCl_2 + 2NaNO_2 \Rightarrow Ra(NO_2)_2 + 2NaCl$$

However, this preparation has likely never been attempted since the industrial demand for this salt is zero. The question of a hydrate and how it is obtained remain unknown. It has no CAS number and is not available commercially or otherwise.

4.1.4. Alkaline Earth Nitrates

Since nitric acid, in contrast to nitrous acid, is stable in aqueous solution, the acid can be used to prepare these salts. Thus, the pH of solution can be controlled from acidic to basic, as required, by the use of acid, ammonia salts or alkali salts.

Beryllium Nitrate

Beryllium nitrate is said to have the molecular formula of $Be(NO_3)_2$ and the molecular weight of grams per mole. It is very soluble in water (Table 4.5).

It could be prepared by the action of nitric acid on beryllium carbonate, oxide or hydroxide:

$$BeCO_3 + 2HNO_3 \Rightarrow Be(NO_3)_2 + CO_2 + H_2O$$
$$Be(OH)_2 + 2HNO_3 \Rightarrow Be(NO_3)_2 + 2H_2O$$

It is described as $Be(NO_3)_2 \cdot 4H_2O$, a compound that forms colorless, deliquescent crystals that are soluble in water, and used to introduce beryllium oxide into

TABLE 4.5

		g/100 ml of water						
Compound	**Formula**	**0 °C**	**10 °C**	**20 °C**	**30 °C**	**40 °C**	**60 °C**	**100 °C**
Beryllium nitrate	$Be(NO_3)_2$	97	102	108	113	125	178	Decomposes

materials used in incandescent mantles. However, in view of recent developments concerning the behavior of the Be^{3+} cation in solution, the more likely reactions are:

$$BeCO_3 + 2HNO_3 \Rightarrow Be(OH)NO_3 + CO_2 + 1/2H_2O$$
$$Be(OH)_2 + 2HNO_3 \Rightarrow Be(OH)NO_3 + 3/2H_2O$$

The result is either the tetrahydrate at low HNO_3 concentrations or the trihydrate or the monohydrate at more concentrated nitric acid solutions. The trihydrate is usually the commercial product. These would have the molecular formula of:

$Be(H_2O)_3(OH)NO_3$—tetrahydrate
$Be(H_2O)_2(OH)NO_3$—trihydrate
$Be(H_2O)(OH)NO_3$—monohydrate

It is notable that these hydrates are "quasi-stable" and heating them up to $\geq$100 °C causes decomposition and evolution of nitrogen oxides.

DTA analysis of the tetrahydrate showed that it dissolves in its own waters of hydration at about 60.4 °C. Heating above 101 °C causes decomposition with loss of water and oxides of nitrogen plus formation of the oxide. The decomposition is complete at 250 °C. Thermal decomposition of these salt hydrates occurs by release of nitric acid which then breaks down to form the nitrogen oxides, rather than break down of the nitrate anion itself. The anhydrate has been prepared by the reaction of beryllium chloride with N_2O_4 dissolved in ethylacetate. If heated in a vacuum above 50 °C, the product, $Be(NO_3)_2 \cdot 2N_2O_4$, evolves oxides of nitrogen to produce the anhydrate.

The tetrahydrate has a CAS number of 13597-99-4 and molecular weight is grams per mole. Anhydrous beryllium nitrate is a white to pale yellow crystalline solid. Beryllium nitrate trihydrate (CAS number = 7787-55-5) forms slightly yellow crystals with a vapor pressure 49.8 mm Hg at 25 °C. Its melting point is 60.5 °C and it decomposes completely at 102.3 °C. Its Enthalpy of vaporization = 37.72 kJ/mol and its boiling point is 83 °C at 760 mm Hg where it becomes anhydrous. Beryllium nitrate is a tumorigen, mutagen and reproductive effector in rats and, presumably in humans.

Beryllium metal dissolves readily in nonoxidizing acids such as HCl and H_2SO_4, but not in nitric acid as this forms the oxide (this behavior is similar to that of aluminum metal). Beryllium, again similarly to aluminum, dissolves in warm alkali to form the beryllate anion, $Be(OH)_4^{2-}$, and hydrogen gas.

The solutions of salts such as beryllium nitrate are acidic because of hydrolysis of the $[Be(H_2O)_4]^{2+}$ ion, for example:

$$[Be(H_2O)_4]^{2+} + H_2O \Rightarrow [Be(H_2O)_3(OH)]^{+} + H_3O^{+}$$

Thus, the chemistry of soluble beryllium salts is dominated by the formation of hydroxy-complexes.

The vaporization of 20–50 g of beryllium from nitrate solution was observed in graphite furnace atomizers using pyro-coated and Ta-lined tubes. A charge coupled device (CCD) spectrometer was employed to follow the evolution of absorption spectra (200–475 nm), light scattering and emission. Molecular bands of NO and NO_2 were observed below 1000 °C. Beryllium absorption at 234.9 nm was prominent in spectra above 2200 °C and 1900 °C, respectively. The most intense Be atomic absorption, light scattering and emission were observed when the maximum temperature reached 400 °C.

The study of beryllium nitrate has not been extensive and even the decomposition of the tetrahydrate has not been fully elucidated. Beryllium nitrate is offered commercially as trihydrate crystals or as a solution containing 35% by weight beryllium nitrate of 99.99% purity.

Magnesium Nitrate

Magnesium nitrate has the molecular formula of $Mg(NO_3)_2$ and the molecular weight of 148.3152 g/mol. It is very soluble in water (Table 4.6).

Magnesium nitrate is prepared by the action of nitric acid on magnesium carbonate, oxide or hydroxide:

$$MgCO_3 + 2HNO_3 \Rightarrow Mg(NO_3)_2 + CO_2 + H_2O$$
$$Mg(OH)_2 + 2HNO_3 \Rightarrow Mg(NO_3)_2 + 2H_2O$$

The salt crystallizing at room temperature after evaporation is the hexahydrate, $Mg(NO_3)_2 \cdot 6H_2O$. Two stable hydrates are formed, the hexahydrate [CAS number =13446-18-9] and the dihydrate, $Mg(NO_3)_2 \cdot 2H_2O$ [CAS number = 15750-45-5].

The magnesium nitrate used in commerce has been synthesized in a variety of ways. The reaction between nitric acid and magnesium metal is one way and reaction with MgO is another. Magnesium hydroxide and

TABLE 4.6

		g/100 ml of water							
Compound	**Formula**	**0 °C**	**10 °C**	**20 °C**	**30 °C**	**40 °C**	**60 °C**	**80 °C**	**90 °C**
Magnesium nitrate	$Mg(NO_3)_2$	62.1	66	69.5	73.6	78.9	78.9	91.6	106

ammonium nitrate also form the product but ammonia is released as a by-product:

$$2HNO_3 + Mg \Rightarrow Mg(NO_3)_2 + H_2$$
$$2HNO_3 + MgO \Rightarrow Mg(NO_3)_2 + H_2O$$
$$Mg(OH)_2 + 2NH_4NO_3 \Rightarrow Mg(NO_3)_2 + 2NH_3 + 2H_2O$$

Since magnesium nitrate has a high affinity for water, heating the hexahydrate does not result in the dehydration of the salt. Instead, it decomposes into magnesium oxide, oxygen and nitrogen oxides:

$$4Mg(NO_3)_2 \cdot 6H_2O + \text{heat} \Rightarrow 4MgO + 2NO_2 + 2N_2O + O_2 + 6H_2O$$

Heating the hexahydrate above its melting point first forms basic nitrates, such as $Mg(NO_3)_2 \cdot 4Mg(OH)_2$. It is this salt that decomposes at 400 °C, forming magnesium oxide and oxides of nitrogen. The absorption of these nitrogen oxides in water is one possible way to synthesize HNO_3. Although it is inefficient, it does not require the use of another strong acid and the mineral, nitromagnesite, can be used in this context. This mineral is monoclinic with space group = $P2_1/c$ (2/m) and $a = 6.194$, $b = 12.71$, $c = 6.6$, $Z = 2$; $\beta = 93°$, $V = 518.88$ Å^3, density (Calc) = 1.64 g/cm^3.

The anhydrous salt (CAS number = 10377-60-3) consists of white cubic crystals whose density is 2.32 g/cm^3 and is very soluble in water. It is very hygroscopic and in air quickly forms the hexahydrate with the formula $Mg(NO_3)_2 \cdot 6H_2O$. The dihydrate (CAS number = 15750-45-5) is a white crystalline solid having a density of 1.456 g/cm^3. It decomposes at about 100 °C and is soluble in water and ethanol. The hexahydrate, $Mg(NO_3)_2 \cdot 6H_2O$ (CAS number = 13446-18-9 and molecular weight of 256.41 g/mol), is a colorless solid having monoclinic crystal structure and density of 1.464 g/cm^3. The salt is hygroscopic and very soluble in water and moderately soluble in ethanol. Of these salts, the hexahydrate is the most stable in air at room temperature. It melts in its own waters of hydration at 88.9 °C (362 K) and begins to decompose at 330 °C (Table 4.7).

The nonahydrate has not received much attention whereas the hexahydrate, $Mg(NO_3)_2 \cdot 6H_2O$, occurs in mines and caverns as the mineral *"Nitromagnesite"*. This form is not common, although it may be present where in caves where guano contacts magnesium-rich rock. It is used in the ceramics, printing, chemical and agricultural industries. It is a fertilizer and is listed as 11-0-0 (%N-P-K) grade with 9.4% Mg (which is an essential fertilizer as well). Fertilizer blends containing magnesium nitrate plus ammonium nitrate, and calcium nitrate are used in the greenhouse and hydroponics trade. Magnesium nitrate is also used in pyrotechnics; and in the manufacture of concentrated nitric acid where it removes water and concentrates the acid vapors to 90–95% HNO_3. It is also used to aid coating and prilling in production of ammonium nitrate. The salt is also used as an analytical standard for magnesium and a matrix modifier in furnace atomic absorption spectroscopic analysis. It also finds some limited application as a nitrogenous fertilizer.

TABLE 4.7

Thermochemical properties of the hexahydrate
$\Delta H_f^0 = -189.0$ kcal/mol
$\Delta G_f^0 = -147.4$ kcal/mol
$S_0 = 39.2$ cal/degree mol
$C_P = 33.9$ cal/degree mol

A phase diagram of the relation of these hydrated salts is shown in the following Fig. 4.10 and Fig. 4.11.

$Mg(NO_3)_2 \cdot 6H_2O$ shows a two-stage melting process including an additional phase transition. It has been investigated as a phase-change material for storing waste energy from urban waste heat emerging from co-generation systems, typically available at temperatures of 60–100 °C. Several authors have investigated latent heat storage by these materials with phase change temperatures in the above range, and focused on a mixture of magnesium nitrate hexahydrate as a base material and magnesium chloride hexahydrate as an

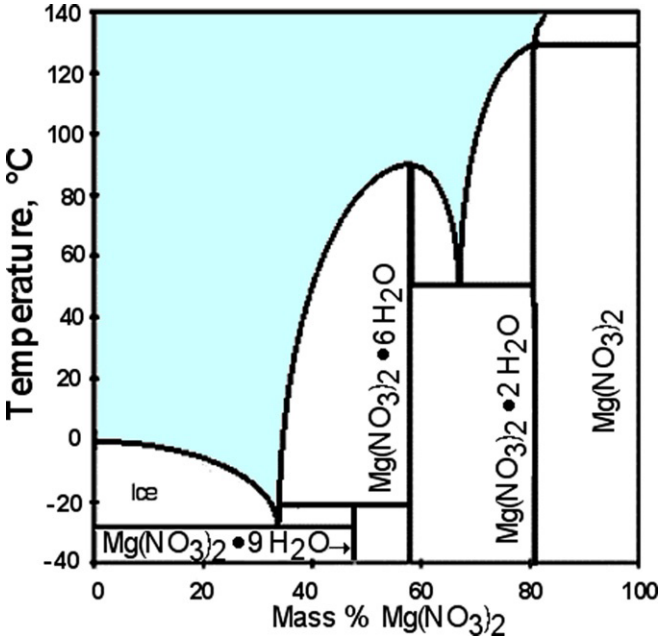

FIGURE 4.10

Salt Hydrate	Melting Temp., °C	Melting Entropy	Behavior
$Ca(NO_3)_2 \cdot 4H_20$	42	265 kJ /dm^3 or 140 kJ / kg	Melts Congruently
$LiNO_3 \cdot 3H_20$	29	459 kJ /dm^3 or 298 kJ / kg	Melts Congruently
$Mg(NO_3)_2 \cdot 6H_2O$	89	262 kJ /dm^3 or 160 kJ / kg	Melts Congruently

FIGURE 4.11

additive to modulate the melting point. Addition of 5–10 wt% of the latter resulted in a modulated melting point of around 80 °C and a heat of fusion of about 150 kJ/kg. Increasing the mix ratio had little effect on heat of fusion, but allowed the melting point to be reduced to about 60 °C. Repeated melting and solidification tests showed that the heat of fusion and melting point retained their original values even after 1000 cycles.

The structural results for $Mg(NO_3)_2 \cdot H_2O$ at the low temperature of 173 K using neutron single-crystal diffraction confirmed the monoclinic space group $P2_1/c$ and yielded lattice constants: $a = 6.190(2)$ Å, $b = 12.614(4)$ Å, $c = 6.56(1)$ Å, and $\beta = 93.72(1)°$, which is exactly those of the hexahydrate at room temperature.

The salt, cerium magnesium nitrate, $Mg(NO_3)_2 \cdot Ce(NO_3)_3$, has been of interest in low-temperature physics, largely because of its use as a coolant in adiabatic demagnetization experiments. Magnetic interactions of the Ce^{3+} magnetic moments are smaller in this matrix than in any other known salt and this, together with the extreme anisotropy in the ground state g-factor makes it ideal for use in experiments below 1 K. This salt has also been used to establish an absolute temperature scale in the range of 0.0100–0.0010 K. Systematic deviations were found below 0.003 K in the temperature dependence of nuclear orientation of Ce^{137} in cerous magnesium nitrate, using the temperature scale proposed by Daniels and Robinson. The temperature scale below 0.006 K was redetermined using a new method: nuclear orientation. This has the advantage over the γ-ray heating method of having high sensitivity at the lowest temperature. The most striking result is that a value of 1/T of 520 was found, rather than the previously accepted 324, obtained by demagnetization from initial conditions of 18.8 kG/deg. The useful absolute temperature range is thus extended by at least 60% in 1/T. Auxiliary experiments on oriented Pm^{144} gave similar results and provided independent confirmation both of the inadequacy of the old temperature scale and of the validity of the new one.

There are over 3 million registered exporters of this salt and it is readily available commercially.

Calcium Nitrate

Calcium nitrate has the molecular formula of $Ca(NO_3)_2$ and the molecular weight of 164.0935 g/mol. Its CAS number is 10124-37-5. Calcium nitrate may be prepared by the reaction of nitric acid with calcium carbonate or calcium sulfide:

$$CaCO_3 + 2HNO_3 \Rightarrow Ca(NO_3)_2 + CO + H_2O$$
$$CaS + 2HNO_3 \Rightarrow Ca(NO_3)_2 + H_2S$$

It is very soluble and forms a tetrahydrate, $Ca(NO_3)_2 \cdot 4H_2O$ if the solution is evaporated to dryness. The CAS number of the anhydrate is 10124-37-5 while that of the tetrahydrate is 13477-34-4. As with the beryllium nitrate salts, variation of the nitric acid concentration affects the type of hydrate produced. The trihydrate is known (CAS number 10124-37-5) but not the monohydrate. The anhydrate is a white cubic crystal that is hygroscopic; its density is 2.504 g/cm^3 and it melts at 561 °C. This salt is highly soluble in water and also dissolves in alcohols and acetone. The tetrahydrate melts in its own waters of hydration at 42.7 °C and loses $4H_2O$ molecules at 132 °C. It decomposes to form nitrogen oxides and CaO similar to the behavior of the other alkaline earth nitrates. The anhydrous salt is soluble at 121.2 g/100 ml at 20 °C and 271.2 g/100 ml at 40 °C (Table 4.8).

Synonyms include: Lime nitrate; Lime saltpeter; Norwegian saltpeter, Nitrocalcite. The anhydrate salt absorbs moisture from the air to form the tetrahydrate, which is the stable form of this salt. It is mainly used as a component in fertilizers. Nitrocalcite is the name for a mineral which is a hydrated calcium nitrate that

TABLE 4.8

		g/100 ml of water						
Compound	**Formula**	**0 °C**	**10 °C**	**20 °C**	**30 °C**	**40 °C**	**80 °C**	**100 °C**
Calcium nitrate tetrahydrate	$Ca(NO_3) \cdot 4H_2O$	102	115	129	152	191	358	363

forms as an efflorescence in places where manure contacts limestone (or concrete) in a dry environment such as caverns or stables.

Norgessalpeter was the first synthetic nitrogen fertilizer to be manufactured. Production began at Notodden, Norway in 1905. It was produced by treating limestone with nitric acid, followed by neutralization with ammonia:

$$CaCO_3 + 2HNO_3 \Rightarrow Ca(NO_3)_2 + CO_2 + H_2O$$

It is also a by-product of the "ODDA Process" invented in 1925 for the extraction of calcium phosphate:

$$Ca_3(PO_4)_2 + 6HNO_3 + 12H_2O \Rightarrow 2H_3PO_4 + 3Ca(NO_3)_2 + 12H_2O$$

The mixture is cooled to below 0 °C, where the calcium nitrate crystallizes and can be separated from the phosphoric acid:

$$2H_3PO_4 + 3Ca(NO_3)_2 + 12H_2O \Rightarrow 2H_3PO_4 + 3Ca(NO_3)_2 \cdot 4H_2O$$

The resulting calcium nitrate produces nitrogen fertilizer. The filtrate is composed mainly of phosphoric acid with some nitric acid and traces of calcium nitrate, and this is neutralized with NH_3 gas to produce a compound fertilizer:

$$Ca(NO_3)_2 + 4H_3PO_4 + 8NH_3 \Rightarrow CaHPO_4 + 2NH_4NO_3 + 3(NH_4)_2HPO_4$$

If KCl or K_3PO_4 is added, the result will be NPK fertilizer. This early process was an innovation for requiring neither the expensive H_2SO_4 nor producing gypsum waste.

Like related alkaline earth nitrates (as well as $LiNO_3$), calcium nitrate decomposes upon heating to release nitrogen dioxide:

$$2Ca(NO_3)_2 \Rightarrow 2CaO + 4NO_2 + O_2 \quad \Delta H = 369 \text{ kJ/mol}$$

Calcium nitrate is used in explosives, matches and pyrotechnics. Other applications are in the manufacture of incandescent mantle; and as an additive to diesel fuel for corrosion inhibition (Table 4.9).

TABLE 4.9

Thermochemical properties
$\Delta H_f^\circ = -244.24$ kcal/mol
$\Delta G_f^\circ = -177.53$ kcal/mol
$S^\circ = 46.18$ cal/degree mol
$C_p = 35.71$ cal/degree mol

The hydration structure of calcium nitrate tetrahydrate, $Ca(NO_3)_2 \cdot 4H_2O$, which melts at 328 K (55.1 °C) has been investigated by an X-ray scattering method. Analysis of the radial distribution function and model fitting revealed that in the hydrate melt, a Ca^{2+} ion is surrounded by about six oxygen atoms, 4.1 of which come from water molecules at the average distance of 2.41 Å, 2.0 coming from the nitrate ions at the average distance of 2.54 Å. In the first coordination shell of the melt, the formation of a direct Ca^{2+}–NO^{3-} correlation, such as contact ion pairs, was suggested. The hydration structure of the melt analyzed was compared with that of $Ca(NO_3)_2 \cdot 3H_2O$ melt previously reported, and the decrease from nine of the reported melt to six in this melt was observed in the number of the nearest neighbor oxygen atoms around a Ca^{2+} ion. This implies that in the highly concentrated aqueous solution, the structure of the first coordination shell around the cation changes markedly with a small difference in the water molecule content.

Calcium nitrate tetrahydrate exists in two monoclinic crystalline forms (alpha, specific gravity 1.93 and beta, specific gravity 1.82). The melting point of α-$Ca(NO_3)_2 \cdot 4H_2O$ is 44 °C with a boiling point of 83 °C at 760 mm Hg. Enthalpy of vaporization is 37.72 kJ/mol at a vapor pressure of 49.8 mm Hg at 25 °C. β-Calcium nitrate tetrahydrate is a white columnar shape crystal of the monoclinic system whose specific density is 1.82 g/cm^3. Melting point is 39.7 °C. It decomposes at 40 °C or so, and converts into anhydrous calcium nitrate due to thorough dehydration when heated at 151 °C. When heated further to 500 °C, calcium nitrate will first break down in vacuum to calcium nitrite accompanied with emission of oxygen gas, then degrade to calcium oxide and nitrogen oxide. β-Calcium nitrate tetrahydrate dissolves in water, methanol, ethanol, acetone, methyl acetate and liquid ammonia. This calcium nitrate is useful as an oxidizer but its hygroscopic nature, results in extreme deliquescence in air. The unit-cell parameters of these two isomers are shown in Table 4.10.

TABLE 4.10

Crystal system = monoclinic		
Lattice parameter	**α-$Ca(NO_3)_2 \cdot H_2O$**	**β-$Ca(NO_3)_2 \cdot H_2O$**
a	6.277 Å	6.268 Å
b	9.157 Å	9.116 Å
c	14.484 Å	14.830 Å
β	98.6°	106.5°
Z	4	4
Density	1.91 g/cm^3	1.88 g/cm^3
Space group	$P2_1/n$	$P2_1/c$

The structure contains mostly of $Ca_2(NO_3)_4 \cdot (H_2O)_8$ dimers joined by hydrogen bonding, (i.e. $[Ca(NO_3)_2 \cdot (H_2O)_4]$–$[Ca(NO_3)_4 \cdot (H_2O)_4]$.

Calcium nitrate is mainly used as a flocculent in rubber latex and in refrigerant manufacture. And it is also employed in oil exploratory wells and sewage treatment. In agriculture, it is used in hydroponic culture and as a fast-effective fertilizer for acid soil. It can also be used to make fireworks, to produce explosives in national defense industry, and to paint negative poles in the electronic instrument industry. It is also a raw material in making other nitrates. It is this usage that calcium nitrate finds most of its employment in industry, other than its use in agriculture.

Calcium nitrate is a strong oxidizing agent. Mixing it with organic substances such as fuel oil or hydrocarbons or other oxidizable compounds can cause an explosion.

Calcium nitrate has been evaluated as a component for heat storage devices. Enthalpy of melting can be used to store heat in a simple way for time periods of hours and days. The storage capacity first of all depends on the volume-specific enthalpy of melting. At temperatures below 423 K, the largest values are found for salt hydrates. However, for practical performance besides the heat storage capacity, appropriate melting–crystallization temperatures within a few degrees are crucial for intended applications. Also, reversible phase changes over many heating–cooling cycles have to be ensured, which is easier with congruent melting than with incongruent melting hydrates.

Applications of salt hydrates require fine-tuned melting temperatures, which can be achieved by using mixtures. The best mixture found to date consists of $LiNO_3$–$Mg(NO_3)_2$–$Ca(NO_3)_2$.

Calcium nitrate has been found to be an excellent host and solvent for dissolving organic compounds which then react within the waters of hydration, with calcium nitrate acting as a catalyst for the reactions (Fig. 4.12).

The synthesis of 1,2,3,4-dihydropyrimidinone/thione derivatives was achieved in good to excellent yields using calcium(II) nitrate as a catalyst to promote Biginelli three-component condensation reactions from a diversity of aromatic aldehydes, -keto compounds and urea or thiourea. The reaction was carried out under solvent-free conditions. This represents a new usage of such salts and further work to elucidate the exact mechanisms is currently being conducted at various laboratories.

Calcium nitrate is manufactured in tonnage quantities and is offered commercially for sale, by many industrial chemical firms. Major production occurs in Norway for distribution throughout the World.

Strontium Nitrate

Strontium nitrate has the molecular formula of $Sr(NO_3)_2$ and the molecular weight of 211.6327 g/mol. Strontium nitrate is prepared by treating strontium carbonate with nitric acid. The solution is evaporated and crystallized:

$$SrCO_3 + HNO_3 \Rightarrow Sr(NO_3)_2 + CO_2 + H_2O$$

Crystallization yields the tetrahydrate, $Sr(NO_3)_2 \cdot 4H_2O$, which, on heating, melts at 31.3 °C in its own waters of hydration and then decomposes >100 °C to form the anhydrous nitrate. The anhydrate melts at 570 °C (It begins to decompose as low as 545 °C), is soluble in water (70.3 gm/100 ml at 20 °C) and is very slightly soluble in ethanol. These colorless crystals, or white powder, have a density of 2.986 g/cm^3 and its CAS number is 10042-76-9. It is very soluble in water, as shown in Table 4.11 on the following

TABLE 4.11

		g/100 ml of water							
Compound	**Formula**	**0 °C**	**10 °C**	**20 °C**	**30 °C**	**40 °C**	**60 °C**	**80 °C**	**90 °C**
Strontium nitrate	$Sr(NO_3)_2$	39.5	52.9	69.5	88.7	89.4	93.4	96.9	98.4

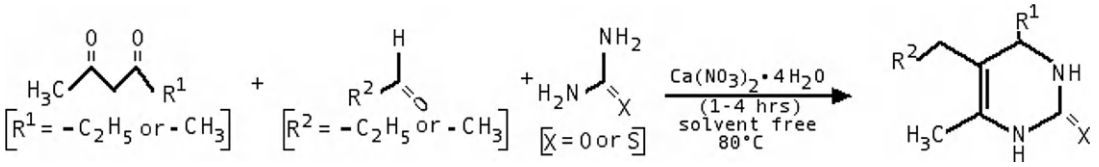

FIGURE 4.12

page. Strontium nitrate apparently forms only the tetrahydrate when a solution is evaporated below 80 °C. Otherwise it decomposes at higher solution temperatures to $Sr(OH)_2$ and nitrogen oxides. The nitric acid concentration makes little difference in the hydrate produced, in contrast to other alkaline earths like Ca and Mg.

The anhydrate is cubic with $a = 7.7813$ Å and space group = Pa3, $Z = 4$.

The tetrahydrate, $Sr(NO_3)_2 \cdot 4H_2O$, has a molecular weight of 283.69 g/cm^3 and a density of 2.21 g/cm^3. It is composed of colorless monoclinic crystals but loses all water of crystallization at 100 °C. The anhydrate is stable to 1100 °C where it converts to strontium oxide, SrO, at 1100 °C. There are three (3) allotropes of the anhydrate known. When $Sr(NO_3)_2$ is heated to 547 °C, a change in structure occurs, i.e. γ-$Sr(NO_3)_2 \Rightarrow \beta$-$Sr(NO_3)_2$ (547 °C). Two other transitions are known: β-$Sr(NO_3)_2 \Rightarrow \alpha$-$Sr(NO_3)_2$ (547 °C) and α-$Sr(NO_3)_2 \Rightarrow$ liq-$Sr(NO_3)_2$ (918 °C). ΔH for liquidification is 44.6 kcal/mol. Decomposition to nitrogen oxides takes place at about 1110 °C. It is very soluble in water, 60.4 g/100 ml at 0 °C, 206 g/100 ml at 100 °C. It is also soluble in liquid ammonia and very slightly soluble in ethanol and acetone (Table 4.11).

The growth behavior of the primary α-phase ($Sr(NO_3)_2$ and the secondary β-phase ($Sr(NO_3)_2 \cdot 4H_2O$) in a $Sr(NO_3)_2$–H_2O peritectic system was observed in situ in a solution flow system. The two phases grew simultaneously below the peritectic temperature in the solution with the composition near the peritectic point. The β-phase grew much faster than the α-phase due to the difference in both supersaturation and kinetic property for two phases. This resulted in the peritectic structure that the β-phase engulfed the α-phase. Using Michelson interferometry, growth rate was measured on the most widely developed faces, the (1 1 1) face of the α-phase and the (1 1 0) face of the β-phase. The β-phase had the larger growth rate and step velocity and the smaller hillock slope than the α-phase at a given supersaturation. The kinetic coefficient β_s and the edge-free energy, α_s, of steps were evaluated as follows: $\beta_s = 5.1 \times 10^{-2}$ cm/s and $\alpha_s = 3.6$ mJ/m^2 for the α-phase; $\beta_s = 5.3 \times 10^{-1}$ cm/s and $\alpha_s = 18$ mJ/m^2 for the β-phase. This indicates that the step kinetics influences the growth of the two phases more significantly than that of the surface energy of step edge.

Industrial uses of strontium nitrate are rather limited and have rather limited commercial value because the corresponding calcium and barium compounds serve the same purpose yet are cheaper. A few, however, have found application in industry and elsewhere. Strontium nitrate, $Sr(NO_3)_2$, and strontium chlorate, $Sr(ClO_3)_2$, are extremely volatile and impart a brilliant crimson color to flames; they are thus used in fireworks and similar displays.

Studies have been made of the band-spectra produced by strontium in an oxy-hydrogen flame, in a "vacuum arc" in water vapor, in a "vacuum arc" in heavy water vapor (D_2O), and in an arc in air at atmospheric pressure. For Sr^{2+}, a band with some structure at 6050 Å and diffuse bands with maxima at 6460, 6590, 6675 and 6820 Å are attributed to SrOH, in agreement with James and Sugden's suggestion, the assignment being supported by small isotopic displacements with SrOD. Bands at 5950 Å, 6050 Å and the far red, obtained best in the arc at 1 atmosphere, have a very complex structure suggesting a polyatomic emitter and variation of strength with concentration when strontium nitrate solution is sprayed into a flame supports assignment to the dimer of the oxide, Sr_2O_2.

Recent clinical studies demonstrate that when strontium nitrate is applied to the facial skin, it significantly reduces skincare-induced burning, stinging and facial redness. These findings are very important to Rosacea sufferers, who report facial burning and flushing to topical skincare products and environmental insults such as wind, sun, heat and cold. This is the first compound that selectively blocks the irritation-producing nerve endings (type C nociceptors) that become activated when itching, burning and stinging occur from any cause. Glycolic acid removes the upper layer of old and dead skin cells, while encouraging the growth of younger, smoother and evenly pigmented looking skin. Strontium nitrate is a substance capable of inhibiting tingling sensations and irritations associated with peels containing glycolic acid. It reduces irritations, inflammations, and redness caused by glycolic acid peels.

Strontium nitrate is available as the tetrahydrate and as a solution from several manufacturers.

Barium Nitrate

Barium nitrate has the molecular formula of $Ba(NO_3)_2$ and the molecular weight of 261.3745 g/mol. It is also known as "nitrobarite". Its CAS number is 10022-31-8. It is soluble in water (Table 4.12).

It can be prepared by a number of methods. The reaction between nitric acid and barium metal is one way and reaction with BaO or $BaCO_3$ is another. Barium hydroxide and ammonium nitrate also form the product but ammonia is released as a by-product:

$$2HNO_3 + Ba \Rightarrow Ba(NO_3)_2 + H_2$$
$$2HNO_3 + BaO \Rightarrow Ba(NO_3)_2 + H_2O$$
$$Ba(OH)_2 + 2NH_4NO_3 \Rightarrow Ba(NO_3)_2 + 2NH_3 + 2H_2O$$

TABLE 4.12

		g/100 ml of water							
Compound	**Formula**	**0 °C**	**10 °C**	**20 °C**	**30 °C**	**40 °C**	**60 °C**	**80 °C**	**100 °C**
Barium nitrate	$Ba(NO_3)_2$	4.95	6.67	9.02	11.5	14.1	20.4	27.2	34.4

Barium nitrate can also be prepared by the reaction of barium carbonate or barium carbonate with nitric acid:

$$BaCO_3 + 2HNO_3 \Rightarrow Ba(NO_3)_2 + CO_2 + H_2O$$

In this method, barium carbonate is suspended in nitric acid. The solution is filtered and the product crystallizes out. Alternatively, barium carbonate and nitric acid are added to a saturated solution of barium nitrate. The product is then obtained by crystallization. It may also be prepared by adding sodium nitrate to a saturated solution of barium chloride. Barium nitrate precipitates out from the solution. The precipitate is filtered, washed with alcohol and dried.

Barium nitrate is always anhydrous. It is slightly soluble in water and alcohols (water = 9.1 g/100 ml at 20°; methyl alcohol = 0.057 g/100 ml at 25° and ethyl alcohol = 0.0033 g/100 ml at 20 °C). It is a white, cubic crystal with $a = 8.1184$ Å, space group = Pa3 and a density of 3.24 g/cm^3. Its melting point has been stated as 595.2 °C. However, the exact number is in doubt since 262 °C and 284 °C have been cited. When heated, some decomposition begins as low as 256 °C. The most probable melting point (formation of a liquid) is about 610 °C. The thermolysis of $Ba(NO_3)_2$ has been studied by thermogravimetric analysis (TGA) and DTA. It has been determined that a complex reaction, involving melting, decomposition to produce BaO_2 and BaO, and the transformation of BaO_2 to produce BaO occurs in three stages. This suggested that the thermal decomposition of $Ba(NO_3)_2$ at temperatures higher than 800 °C would be required to obtain BaO directly.

$$Ba(NO_3)_2(\text{solid}) \Rightarrow BaO_2(\text{solid}) + 2NO(\text{gas}) + O_2(\text{gas}) \quad (1)$$

$$Ba(NO_3)_2(\text{solid}) \Rightarrow BaO(\text{solid}) + 2NO(\text{gas}) + 3/2O_2(\text{gas}) \quad (2)$$

Because the BaO_2 decomposes during these temperature intervals, the following overall reaction also occurs:

$$BaO_2\ (\text{solid}) = BaO(\text{solid}) + 1/2O_2(\text{gas}) \quad (3)$$

Barium nitrate is used to produce green color in flares, pyrotechnic devices, in green signal lights; and in tracer bullets. Barium nitrate is used in industry in the production of green signal lights, to remove gases from vacuum tubes, and in the production of barium oxide. The following shows the color of a flare at night (Fig. 4.13). Thermochemical properties are shown in Table 4.13.

TABLE 4.13

Thermochemical properties
$\Delta H_f^o = -237.11$ kcal/mol
$\Delta G_f^\circ = -190.42$ kcal/mol
$S^o = 51.1$ cal/degree mol
$C_P = 36.2$ cal/degree mol

A $Ba(NO_3)_2$ crystal, 60 mm long, was activated by a Q-switched Nd:YAG laser pulses at 1.067 μm with intracavity energies of up to 10 mJ. Intracavity Raman shifting of the barium nitrate crystal led to pulses with energies of 2.5 mJ at 1197 nm. The output pulse duration

FIGURE 4.13

was reduced to 8.5 ns compared to 50 ns at the fundamental wavelength. Beam quality improvement was observed. The Raman radiation was frequency doubled into the yellow spectral region from 580 to 599 nm, which is difficult to reach with other solid-state lasers.

A high-efficiency eye-safe Raman laser was demonstrated by use of the third Stokes radiation in a $Ba(NO_3)_2$ crystal pumped by a 1064 nm Nd:YAG laser. The output wavelength of the Raman laser was 1598.5 nm with a full-width at half-maximum of 1.5 nm. With an incident pump energy of 140 mJ, a maximum of 18-mJ Raman output energy was generated at a repetition rate of 30 Hz, corresponding to an optical-to-optical conversion efficiency of 12.9%. The Raman pulse duration was shortened to 2.9 ns compared with that of the pump pulse of 19.3 ns. The eye-safe solid-state Raman laser is expected to have wide applications in range finding, telemetry, laser radar, and other aspects.

At elevated temperatures above 800 °C, barium nitrate decomposes to barium oxide, nitrogen dioxide, and oxygen, In an atmosphere of nitric oxide, thermal decomposition produces barium nitrite, $Ba(NO_2)_2$. Reactions with soluble metal sulfates or sulfuric acid yield barium sulfate. Many insoluble barium salts, such as the carbonate, oxalate and phosphate of the metal, are precipitated by similar double decomposition reactions. $Ba(NO_3)_2$ is an oxidizer and reacts vigorously with common reducing agents. The solid powder, when mixed with many other metals such as aluminum or zinc in their finely divided form, or combined with alloys such as aluminum–magnesium, ignites and explodes on impact.

This salt is available commercially both as a solid and a solution from many suppliers.

Radium Nitrate

Radium nitrate had the molecular formula of $Ra(NO_3)_2$ and the molecular weight of 350.0343 g/mol. It can be prepared by a number of methods. The reaction between nitric acid and radium metal is one way and reaction with Ra RaO or $RaCO_3$ is another. Radium hydroxide and ammonium nitrate also form the product but ammonia is released as a by-product:

$$2HNO_3 + Ra \Rightarrow Ra(NO_3)_2 + H_2$$
$$2HNO_3 + RaO \Rightarrow Ra(NO_3)_2 + H_2O$$
$$Ra(OH)_2 + 2NH_4NO_3 \Rightarrow Ra(NO_3)_2 + 2NH_3 + 2H_2O$$

Radium nitrate can also be prepared by the reaction of radium carbonate with nitric acid. The product is soluble but can be isolated by evaporation of the solution at low temperature. It occurs as the anhydrate, like barium nitrate, but is slightly more soluble at 12.1 g/100 ml at 20 °C. Its CAS number is 10213-12-4. When heated, $Ra(NO_3)_2$ decomposes at about 280 °C to form RaO. A number of other oxides have been proposed but this decomposition mechanism has not been thoroughly studied. Like the barium analog, the decomposition is probably complex and may involve the peroxides as well. Temperatures above 820 °C are probably required to obtain an oxide. Whether the nitrite is involved during the decomposition is not known.

Little interest has been shown for this compound in industry. The main academic and scientific interest in radium nitrate has been the fact that, since it is soluble (and the ^{226}Ra isotope has a 1600 year half-life), the presence of radium nitrate, even in pico-gram quantities (10^{-12} g/ml) of ingested water is sufficient to cause health problems in the human body because it accumulates in the bones while continuing to emit energetic γ-rays.

Radium nitrate is available commercially in very small quantities.

4.2. ALKALINE EARTH PHOSPHIDES AND OXO-PHOSPHOROUS COMPOUNDS

The alkaline earths form a continuous series of compounds with phosphorous. The valence state of phosphorous can vary from –3, +1, +3, to +5 in the associated acids, H_3P, H_3PO_2, H_3PO_3, HPO_3, $H_5P_3O_{10}$, $H_4P_2O_7$, and H_3PO_4. The oxides are used to prepare the corresponding acids in some cases.

4.2.1. Phosphorous Oxy-Acids

Phosphorous Oxide Anhydrides

The formation of phosphorus oxides is complex. Phosphorus forms two well-defined oxides, namely, diphosphorous trioxide and diphosphorous pentoxide, having the empirical formula P_2O_3 and P_2O_5, respectively. An intermediate oxide, diphosphorous tetroxide, P_2O_4, and possibly the suboxide P_4O (phosphorous tetrioxide) are known.

DIPHOSPHOROUS TRIOXIDE

P_2O_3 has been prepared by the action of the trichloride on phosphorous acid, thus:

$$H_3PO_3 + PC1_3 \Rightarrow P_2O_3 + 3HC1$$

It is also produced when phosphorous trichloride is used to replace the hydroxyl group of anhydrous acetic acid, thus:

$$3CH_3COOH + 2PC1_3 = P_2O_3 + 3HC1 + 3CH_3C(O)C1_3$$

The trioxide sublimes as a mist of solid particles that are difficult to condense completely. The condensate forms a snow-like mass of minute crystals, or large feathery crystals, which is very fusible, deliquescent

and inflammable. The trioxide can be crystallized from dry carbon disulphide in an atmosphere of carbon dioxide at −18 °C. The crystals are filtered off and washed with petroleum ether.

PHOSPHOROUS(III) TETRAOXIDE

P_4O_6 (also called tetraphosphorous hexoxide) is an acid anhydride of phosphorous acid and hence readily reacts with water. P_4O_6 is formed by the combustion of phosphorus in a limited supply of oxygen or air. It contains traces of free phosphorus, which can be removed by dissolving it in carbon disulphide and exposing the solution to the light so that the free phosphorus goes over into the insoluble red form, filtering, and recrystallizing the product as P_4O_6. It melts at 23.8 °C, and boils at 173 °C. It can also be formed by heating the vapor of P_2O_3 above 210 °C. It has the same composition as hypophosphoric acid ($H_4P_2O_6$) but does not form this acid when dissolved in solution. The structure of P_4O_6 is like that of P_4 with an oxygen atom inserted between each of the P–P bonds. The structure of P_4O_{10} is like that of P_4O_6 with the addition of one oxygen bond to each phosphorus atom via a double bond and protruding away from the tetrahedral structure (Fig. 4.14).

PHOSPHOROUS(V) PENTOXIDE

P_2O_5, diphosphorous pentoxide (or P_4O_{10}—called tetraphosphorous decaoxide) may be prepared by direct combustion, in a full supply of air or oxygen, of white phosphorus (ignition temperature about 60 °C), or from phosphorous (III) oxide (50–70 °C), or from red phosphorus (about 260 °C). This solid has long been known to be polymorphic. The form first produced by the combustion of phosphorus has a vapor pressure of 1.0 atmosphere at 359 °C, but if heated to 400° or so, it soon changes into another form with a far smaller vapor pressure. The relations of the various forms are: (I) hexagonal, the volatile form first produced, (II) orthorhombic, [obtained by heating (I)], and (III) tetragonal, obtained by further heating. Once formed, the tetragonal form (III) is the stable modification at all temperatures. Phosphorous pentoxide dissolves in water, first forming metaphosphoric acid HPO_3 and then transforms to the pyro- and ortho-acids. P_4O_{10} is particularly a good dehydrating agent that can even remove water from concentrated nitric acid, HNO_3. It is the most efficient drying agent known (magnesium perchlorate is nearly as good). It is always practically the first (hexagonal) form that is used for drying because it naturally has the largest surface. It has been shown, however, that for equal surfaces all three modifications absorb moisture from the air at about the same rate. But on addition to liquid water, the hexagonal reacts violently, the orthorhombic reacts very slowly even at 100 °C, and the tetragonal at once forms a jelly, which then slowly liquefies. Phosphorous pentoxide is as efficient as drying agent at 90° as it is at 0°. For the most part, these oxides can be used to form "oxy-acids".

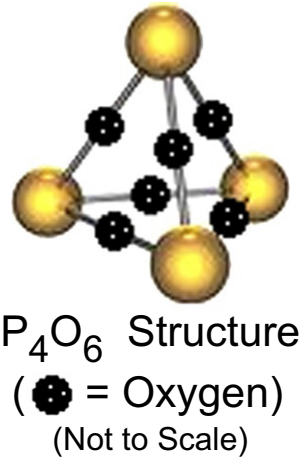

FIGURE 4.14

Phosphorous Acids

Phosphorous acids can have acidic protons bound to oxygen atoms and nonacidic protons which are bonded directly to the phosphorus atom. Although many oxy-acids of phosphorus are formed, only six are important and three of them, hypophosphorous acid, phosphorous acid, and phosphoric acid are the particularly important ones. Two other "peroxy"-acids are included since there properties have been described in the literature.

A summary of these acids is given in the Table 4.14.

HYDROGEN PHOSPHIDE AS AN ACID

Liquid Hydrogen Phosphide: Analysis of this compound shows that it is hydrogen hemiphosphide, $(PH_2)_X$, and the molecular weight corresponds to tetrahydrogen diphosphide, P_2H_4. This liquid, which is the cause of the spontaneous inflammability of phosphine, PH_3, is prepared by passing the gas resulting from the action of water upon calcium phosphide through a freezing mixture. The condensate is a mobile liquid having a density of about 1.01 g/cc that vaporizes between 30 and 40 °C. The boiling point at 735 mm was found to be 57 to 58 °C.

The compound is unstable and decomposes when heated. It is also unstable upon standing and changes, slowly in the dark and quickly in the light, into gaseous and solid hydrides. Since 100 parts by weight produces 38 parts of the solid and 62 parts of the gaseous hydride, this decomposition may be represented by the equation:

$$5P_2H_4 \Rightarrow 6PH_3 + P_4H_2$$

TABLE 4.14

Oxidation state	Formula	Name	Acidic protons	Compounds
+1	H_3PO_2	Hypophosphorous acid	1	Acid and salts
+3	H_3PO_3	(ortho)Phosphorous acid	2	Acid and salts
+5	H_3PO_4	(ortho)Phosphoric acid	3	Acid and salts
+5	$(HPO_3)_n$	Metaphosphoric acids	n	Salts ($n = 3,4$)
+5	$H_4P_2O_7$	Pyrophosphoric acid	4	Acid and salts
+5	$H_4P_2O_6$	Hypophosphoric acid	4	Acid and salts
+5	H_3PO_5	Peroxophosphoric acid	3	Acid and salts
+5	$H_5P_3O_{10}$	Triphosphoric acid	3	Salts

The diphosphide is a yellow powder, which is tasteless, odorless and insoluble in most solvents. It decomposes in the light giving phosphine, and is easily decomposed by heating in an atmosphere of hydrogen. It ignites in air at temperatures between 100 and 200 °C. The empirical formula is $(P_2H)_n$. The molar weight, deduced from the lowering of the freezing point of white phosphorus, corresponds to the formula $P_{12}H_6$. The density is 1.83 g/cm^3 at 19 °C. The heat of formation from white phosphorus and hydrogen is given as +35.4 cal/mol. $P_{12}H_6$ is dissociated when heated in an inert gas into its elements at 175 °C or into phosphorus and phosphine at 215 °C. The ignition temperature in air is 120 to 150 °C. The only liquids that dissolve it without decomposition are phosphorus and PH_3. It dissolves in ammonia at −40 °C with evolution of phosphine. When the diphosphide is gradually heated to 175 °C in vacuo, or when its ammoniate is heated, a reddish powder is formed.

HYPOPHOSPHOROUS ACID

Hypophosphorous acid is a powerful reducing agent with a molecular formula of H_3PO_2. Inorganic chemists refer to the free acid by this name although its IUPAC name is dihydridohydroxidooxidophosphorus, or the acceptable name of phosphinic acid. It is a colorless low-melting compound, which is soluble in water, dioxane, and alcohols. The formula for hypophosphorous acid is generally written H_3PO_2, but a more descriptive presentation is $HOP(O)H_2$ which highlights its monoprotic character. Salts derived from this acid are called **phosphinates** (hypophosphites). Its Lewis structure is shown in Fig. 4.15.

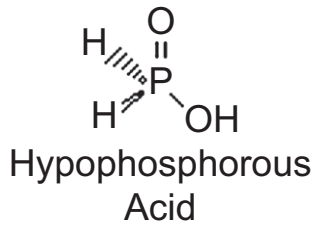

FIGURE 4.15

PHOSPHOROUS ACID

Phosphorous acid, H_3PO_3, is diprotic (readily ionizes two protons), not triprotic as might be suggested by this formula. Phosphorous acid is as an intermediate in the preparation of other phosphorous compounds. Because preparation and uses of "phosphorous acid" actually pertain more to the major tautomer, phosphonic acid, it is more often referred to as "phosphorous acid". Phosphorous acid has the chemical formula H_3PO_3, which is best expressed as $HPO(OH)_2$ to show its diprotic character. $P(OH)_3$ (IUPAC: phosphorous acid) has CAS number 10294-56-1. It has been shown to be a stable tautomer.

Its Lewis structure is shown as in Fig. 4.16.

Diphosphorous acid is made by condensation:

$$2P(OH)_3 \Leftrightarrow (OH)_2POP(OH)_2 + H_2O$$

For phosphorous acid, an **oligophosphorous acid** refers to a few molecules condensed into a molecule with the loss of H_2O as each unit of $P(OH)_3$ is added on. The general formula is $(HO)_2PO[P(OH)O]_{n-2}P(OH)_2$,

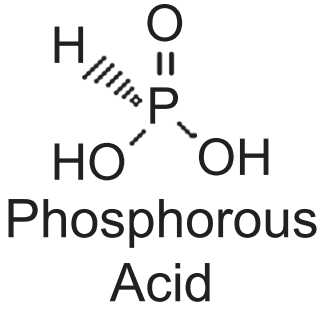

FIGURE 4.16

where $n = 2$, 3, 4, etc. = oligo-. Here, as with phosphonic acid, the repeat unit is $(HPO_2)_{n-2}$. This repeat unit (HPO_2) is called phosphenous acid.

PHOSPHORIC ACID

Chemists refer to orthophosphoric acid as *phosphoric acid*, which is the IUPAC name for this compound. The prefix "ortho" is used to distinguish the acid from other phosphoric acids, which are generally called polyphosphoric acids. Orthophosphoric acid is a nontoxic, rather weak triprotic acid. When pure, it is a solid at STP. Orthophosphoric acid is a very polar molecule which makes it highly soluble in water. The valence state of phosphorous in orthophosphoric acid and other phosphoric acids is +5. Triprotic means that the orthophosphoric acid molecule can dissociate up to three times, producing a hydrogen cation, H^+, each time. This typically combines with H_2O, as shown in the following ionization reactions:

$$H_3PO_4\ (\text{solid}) + H_2O\ (\text{liq}) \Rightarrow H_3O^+\ (\text{aq}) + H_2PO_4^-\ (\text{aq})$$

$$K_{a_1} = 7.25 \times 10^{-3}$$

$$H_2PO_4^-\ (\text{aq}) + H_2O_{(l)} \Rightarrow H_3O^+\ (\text{aq}) + H_2PO_4^{2-}\ (\text{aq})$$

$$K_{a_2} = 6.31 \times 10^{-8}$$

$$HPO_4^{2-}\ (\text{aq}) + H_2O\ (\text{liq}) \Rightarrow H_3O^+\ (\text{aq}) + PO_4^{3-}\ (\text{aq})$$

$$K_{a_3} = 3.98 \times 10^{-13}$$

The anion produced after the first dissociation, $H_2PO_4^-$, is the *dihydrogen phosphate* anion. The salt produced is "monobasic phosphate". The anion after the second dissociation, HPO_4^{2-}, is the *hydrogen phosphate* anion (dibasic phosphate). The anion after the third dissociation, PO_4^{3-}, is the orthophosphate anion (tribasic phosphate). For each of the dissociation reactions shown above, there is a separate "acid-dissociation constant", called K_{a_1}, K_{a_2}, and K_{a_3}. Associated with these three dissociation constants are corresponding values, $pK_{a_1} = 2.12$, $pK_{a_2} = 7.21$, and $pK_{a_3} = 12.67$ values at 25 °C. Even though all three hydrogen (H^+) atoms are equivalent in the molecule, the successive K_a values differ because it is energetically less favorable to lose another H^+ if one (or more) has already been lost so as to cause the molecule/ion to become more negatively charged.

Because of the triprotic dissociation of orthophosphoric acid, its conjugate bases (the phosphates mentioned above) cover a wide pH range, and, because phosphoric acid/phosphate solutions are, in general, nontoxic, mixtures of these types of phosphates are often used as buffering agents or to make buffer solutions, where the desired pH depends on the proportions of the phosphates in the mixtures. Phosphates are found pervasively in biology, especially in the compounds derived from phosphorylated sugars, such as DNA, RNA and adenosine triphosphate (ATP), which are found in all of the cells comprising the human body.

Upon heating orthophosphoric acid, condensation of the phosphoric units, i.e. driving off the water formed from condensation of the molecules produces polyphosphates. When one molecule of water has been removed for each two molecules of phosphoric acid, the result is pyrophosphoric acid, $H_4P_2O_7$. When an average of one molecule of water per phosphoric unit has been driven off, the resulting substance is a glassy solid having an empirical formula of HPO_3 and is called metaphosphoric acid.

Metaphosphoric acid is a singly anhydrous version of orthophosphoric acid and is sometimes used as a water- or moisture-absorbing reagent. Further dehydration is very difficult, and can be accomplished only by means of an extremely strong desiccant (and not by heating alone). This produces "phosphoric anhydride", which has an empirical formula P_2O_5, although the actual molecule has a chemical formula of P_4O_{10}. Phosphoric anhydride is a solid, which is very strongly moisture absorbing and is mainly used as a desiccant.

METAPHOSPHORIC ACID

When an average of one molecule of water per phosphoric unit has been driven off from phosphoric acid, H_3PO_4, the resulting substance is a glassy solid having an empirical formula of **HPO_3** and is called metaphosphoric acid. Metaphosphoric acid is a singularly anhydrous version of orthophosphoric acid and is sometimes used as a water- or moisture-absorbing reagent. Metaphosphoric acid has phosphorus in the formal oxidation state of +5. Although it has several CAS numbers: 10343-62-1, 135306-83-1, 13566-25-1, and 37267-86-0, only the last two are associated with the IUPAC name "phosphenic acid".

Metaphosphoric acid units can be bonded together in rings (cyclic structures), chains (catena), or branched by condensation yielding water as each acid unit is added. These structures consist of linked metaphosphoric acid molecules. For example, trimetaphosphoric acid is the simplest cyclophosphoric acid. Metaphosphoric acid would need to share the doubly bonded oxygen with neighboring phosphorus atoms to form polymers itself. Many oligamers are possible with the alkaline earths but the trimetaphosphates and hexametaphosphates seem to be the most prevalent. These would have the general formula of MHP_3O_9 and $M_2HP_6O_{18}$. Trimetaphosphates are often moderately soluble, e.g. $Ag_3(PO_3)_3 \cdot H_2O$ and $Ba(HPO_3)_3 \cdot 6H_2O$.

Monometaphosphates are known but only with alkali cations. Dimetaphosphates form with transition elements like Zn^{2+} and Mn^{2+} while tetrametaphosphates form compounds with the alkaline earths like Ba^{2+}. Calcium,

strontium and barium salts, when added to solutions of pentametaphosphates, gave gummy or flocculent precipitates of uncertain character. Hexametaphosphates of the alkaline earths are also known. The complex basic phosphates such as $5CaO \cdot 3P_2O_5$, which was made by passing the vapor of phosphorus pentoxide over anhydrous calcium oxide, are supposed to be derived from more hydrated condensed acids such as $H_5P_6O_{20}$. However, this has never been confirmed in the current literature.

PYROPHOSPHORIC ACID

Pyrophosphoric acid, also known under the name **diphosphoric acid**, is colorless, odorless, hygroscopic and is soluble in water, diethyl ether and ethyl alcohol. It is produced from phosphoric acid by dehydration. Pyrophosphoric acid slowly hydrolyzes in the presence of water into phosphoric acid.

$$H_4P_2O_7 + H_2O \Rightarrow 2H_3PO_4$$

Pyrophosphoric acid is a medium strong acid. It has the Lewis structure shown in Fig. 4.17.

Upon heating, phosphoric acid loses water, being converted successively, and to some extent concurrently, into the pyro- and meta-acids:

$$2H_3PO_4 \Rightarrow H_4P_2O_7 + H_2O$$
$$nH_3PO_4 \Rightarrow (HPO_3)_n + [H_2O]_n$$

According to early investigators, the pyro-acid is formed as low as 100 °C, and the conversion is complete between 255 and 260 °C. Phosphorous oxychloride reacts with phosphoric acid in the following manner:

$$5H_3PO_4 + POC1_3 \Rightarrow 3H_4P_2O_7 + 3HC1$$

A mixture of the ortho- and meta-acids may be condensed together to form the pyro-acid by heating on the water bath:

$$nH_3PO_4 + [HPO_3]_n \Rightarrow [H_4P_2O_7]_n$$

The concentrated acid, prepared by dehydration of orthophosphoric acid, is a highly viscous liquid and probably is polymerized.

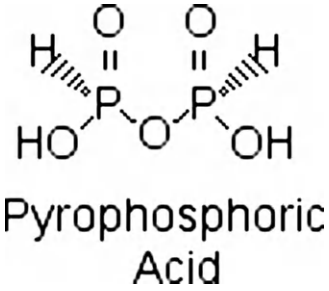

FIGURE 4.17

The heats of transformation by means of liquid water were found to be:

$$H_4P_2O_7 \text{ (solid)} + H_2O \Rightarrow 2H_3PO_4 \text{ (solid)} \quad \Delta H_{Trans} = +6.97 \text{ cal/mol}$$
$$H_4P_2O_7 \text{ (liq)} + H_2O = 2H_3PO_4 \text{ (liq)} \quad \Delta H_{Trans} = +9.09 \text{ cal/mol}$$
$$H_4P_2O_7 \text{ (aq).} = 2H_3PO_4\text{(aq)} \quad \Delta H_{Trans} = +4.25 \text{ cal/mol}$$

All the evidence shows that pyrophosphoric acid is tetrabasic and that each hydrogen is that of a stronger acid, i.e. more dissociated at the same dilution, than orthophosphoric acid.

Salts of these acids are prepared by heating the orthophosphates to form the pyrophosphate.

HYPOPHOSPHORIC ACID

This acid has the general formula of $H_4P_2O_6$ and differs from the other oxy-phosphorous acids. It has many peculiarities. It is formed along with phosphorous and phosphoric acids, when phosphorus is oxidized by moist air. If white phosphorus is exposed to air, and sodium acetate is added to the liquid which forms, the somewhat insoluble sodium hypophosphate, $Na_2H_2P_2O_6 \cdot 6H_2O$ separates. The sodium hypophosphate monohydrate, however, is very soluble and deliquescent at ~98.7 g/100 ml.

$H_4P_2O_6$ can also be prepared by (I) treating red phosphorus with concentrated sodium hydroxide and hydrogen peroxide, and (II) also by the action of alkaline hydrogen peroxide on P_2I_4, or by the hydrolysis of phosphorous trichloride or tribromide in presence of iodine. It is to be noticed that methods I and II start with a material containing P–P links. Hypophosphoric acid is not formed by the hydration of P_4O_8, which only yields phosphorous and phosphoric acids. Lead and barium hypophosphates are insoluble, and the free acid can be obtained from them by means of hydrogen sulfide or sulfuric acid. It forms a hydrate $H_4P_2O_6 \cdot 2H_2O$, M.P. = 70°most chemists know that M.P. = melting point. The anhydrous acid can be formed on standing *in vacuo* in the presence of a dehydrating agent like phosphorous pentoxide.

The best method seems to be the addition of hydrogen peroxide to a suspension of red phosphorus in water. The peroxide is added slowly over a period of time because an intense, explosive reaction will occur. When most of the P_4 has dissolved, then NaOH is added to pH 4.5. Cooling causes the crystallization of $Na_2H_2P_2O_6 \cdot 6H_2O$. Ethyl alcohol is added to aid in the formation of the crystals. The final pH is adjusted to 5.2. All alkaline earths hypophosphates are insoluble. If the oxidation reaction is carried out in an alkaline medium, the products include phosphite, phosphate diphosphate and hypophosphate.

Hypophosphoric acid has far less reducing power than phosphorous acid, and it is hydrolyzed in strongly

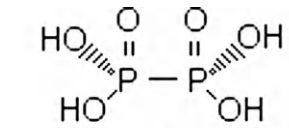

Hypophosphoric Acid

FIGURE 4.18

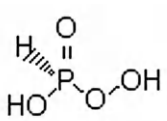

Peroxyphosphoric Acid

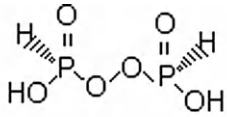

Peroxydiphosphoric Acid

FIGURE 4.19

acid solution at elevated temperature to phosphorous and phosphoric acid:

$$H_4P_2O_6 + H_3O^+ \Rightarrow H_3PO_4 + H_3PO_3$$

The double formula $H_4P_2O_6$ was established by molecular weight determinations by the freezing point of solutions in water of the free acid and of the salt $Na_2H_2P_2O_6 \cdot 6H_2O$. Also the rate of hydrolysis of the acid by hydrogen ion to $H_3PO_4 + H_3PO_3$ is strictly monomolecular for $H_4P_2O_6$. It is thus clear that the acid is $H_4P_2O_6$, and probable Lewis structure for this acid is shown in Fig. 4.18, where a direct bond between the two P-atoms is evident.

PEROXOPHOSPHORIC ACID

Two of these acids have been prepared, a peroxymonophosphoric acid H_3PO_5 and a peroxydiphosphoric acid $H_4P_2O_8$. Note that the latter is related to pyrophosphoric acid. Both are formed with 30% hydrogen peroxide, the first with phosphorous pentoxide:

$$P_2O_5 + 2H_2O_2 + H_2O \Rightarrow 2H_3PO_5$$

The reaction is very violent, but it can be moderated by using acetonitrile as a solvent. At higher concentrations, the peroxydiphosphoric acid can be produced. This is a stronger oxidizing agent than peroxymonosulphuric acid. With silver salts, it forms oxygen plus silver phosphate Ag_3PO_4. It converts aniline into nitroso- and nitrobenzene, and manganous salts quickly in the cold into permanganates. If pyrophosphoric acid is treated with hydrogen peroxide the diperoxy-acid $H_4P_2O_8$ is formed along with the monoacid. The two behave differently with potassium iodide: the monoacid separates iodine at once, and the other acid only slowly. In water, the two acids go over into one another, the mono- predominating in acid and the di-(peroxy-) in alkaline solution. Their Lewis structures are shown in Fig. 4.19.

TRIPOLYPHOSPHORIC AND TETRAPOLYPHOSPHORIC ACID

Triphosphoric acid, also tripolyphosphoric acid, with formula $H_5P_3O_{10}$, is a condensed form of phosphoric acid. In the series, polyphosphoric acids, it is the next after pyrophosphoric acid, $H_4P_2O_7$, which is also called diphosphoric acid. It can be made by condensing pyrophosphoric acid with phosphoric acid:

$$H_3PO_4 + H_4P_2O_7 + \text{heat} \Rightarrow H_5P_3O_{10} + H_2O$$

Both tripolyphosphoric and tetrapolyphosphoric acids are known. The tripoly acid is related to the trimetaphosphoric acid as shown in the Lewis structures (Fig. 4.20).

Three orthophosphoric acid molecules can condense in a line to obtain **tripolyphosphoric acid** ($H_5P_3O_{10}$), as shown in the illustration. This condensation process can continue with additional orthophosphoric acid units to obtain **tetrapolyphosphoric acid** ($H_6P_4O_{13}$) and so on. Note that each extra phosphoric unit adds one extra H-atom, one extra P-atom, and three extra O-atoms. The "backbone" chain of these types of molecules consists of alternating P and O atoms covalently bonded together. Polyphosphoric acid molecules can have dozens of such phosphoric units bonded in a row. A general formula for such poly-acid compounds is $HO(PO_2OH)_xH$, where x = number of phosphoric units in the molecule. The four oxygen atoms bonded to each phosphorus atom are in a tetrahedral configuration with the phosphorus in the center of the tetrahedron and the oxygens in each of the four corners. While the diagrams show the linkage of the tetrahedral $[P(=O)\text{-}O_2\text{-}OH]_n$ units as linear, they can also form branched units in the tetrapolyphosphate.

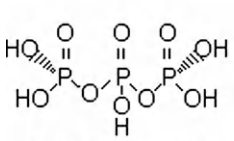

Tripolyphosphoric Acid

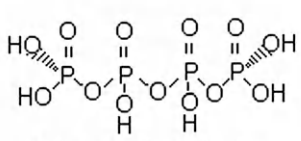

Tetrapolyphosphoric Acid

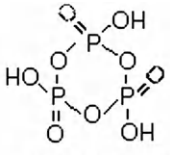

Trimetaphosphoric Acid

FIGURE 4.20

For the alkaline earths, we shall be interested in the following acids and their products:

HYPOPHOSPHOROUS ACID

$H_3PO_2 = HO\text{-}P(=O)(OH)$, a monobasic acid in valence state +1. One (1) salt is possible with the alkaline earths that form hypophosphites.

PHOSPHOROUS ACID

$H_3PO_2 = H\text{-}P(=O)(OH)_2$, a dibasic acid in valence state +3. Two (2) salts are possible with the alkaline earths that form phosphates.

PHOSPHORIC ACID

$H_3PO_4 = HO\text{-}P(=O)(OH)_2$, a dibasic acid in valence state +5. Three (3) salts are possible with the alkaline earths that form phosphates.

METAPHOSPHORIC ACID

$HPO_3 = HOP(=O)O$, the trimetaphosphoric state= $H_2(HPO_3)_3$, is a dibasic acid in valence state +5. One (1) salt is possible with the alkaline earths that form such compounds. The hexametaphosphoric state = $H_4(HPO_3)_6$ forms two salts with certain alkaline earths.

PYROPHOSPHORIC ACID

$H_4P_2O_7 = (HO)_2(O=)P\text{-}O\text{-}P(=O)(OH)_2$ is a tetrabasic acid in valence state +5. Two (2) salts are possible with the alkaline earths.

HYPOPHOSPHORIC ACID

$H_4P_2O_6 = (HO)_2P(=O)\text{-}P(=O)\text{-}(OH)_2$ is a tetrabasic acid with P in the +5 valence state. Two (2) salts are possible with the alkaline earths.

PEROXOPHOSPHORIC ACID

H_3PO_5 or $H_4P_2O_8 = HO\text{-}P(=O)\text{-}O\text{-}OH$ or $(HO)P(=O)\text{-}O\text{-}OP(=O)\text{-}OH$ is a monobasic acid with P in the +5 valence state. One or two compounds are possible with the alkaline earths.

TRIPOLYPHOSPHORIC ACID

$H_5P_3O_{10}$ or $H_6P_4O_{12} = (HO)_2\text{-}P(=O)\text{-}O\text{-}P(=O)(OH)\text{-}O\text{-}P(=O)(OH)\text{-}O\text{-}P(=O)\text{-}(OH)_2$ is a hexabasic acid with P in the +5 valence state. Three (3) compounds are possible with the alkaline earths.

4.2.2. Alkaline Earth Phosphides

Although there are a number of ways to prepare phosphides, the most general method is to heat stoichiometric amounts of the metal and red phosphorus to high temperature in an inert atmosphere or a vacuum. Alkali and alkaline earth metal phosphides are inert metallic-looking solids with high melting points and electrical conductivities. Many are semiconductors.

There are many metal phosphides, M_3P_2, which can be considered Zintl phases with phosphorus as a negative anion, P^{-3}. Zintl phases are ionic in contrast to covalent P to P bonding. They can be made by reaction of red or white phosphorus at high temperature in the absence of air. They can also be made using solvents such as tetrahydrofuran (C_4H_8O), monoglyme (1,2-Dimethoxyethane) or dimethylformamide (C_3H_7NO). Such phosphides can include: P^{3-}, P_2^{4-}, P_3^{4-}, P_3^{4-}, P_5^{4-}, P_6^{4-}, P_7^{4-}, P_{11}^{4-}, P_{14}^{6-}, P_{16}^{4-}, P_{19}^{4-}, P_{21}^{4-}, P_{26}^{4-}, $[P^-]_x$, $[P_5^-]_x$, $[P_6^{4-}]_x$, $[P_7^-]_x$, and $[P_{15}^-]_x$. The structure of Sr_3P_{14} and Ba_3P_{14} features discrete P_7^{3-} cages.

Monophosphides = P^{3-} which are formed by Mg, Ca, Sr and Ba (M_3P_2)

Diphosphides = P_2^{4-} which are formed by Ca and Sr (M_2P_4) as Zintl phases

Triphosphides = P_3^{5-} which are not known with the alkaline earths

Tetraphosphides = P_4^{6-} which is formed by Ba (Ba_3P_4)

Beryllium Phosphide

Beryllium phosphide has the formula of Be_3P_2 and the molecular weight of 88.9841 g/mol. It can be prepared by reaction of the elements, but not from aqueous solution:

$$12Be + 2P_4 \Rightarrow 4Be_3P_2$$

Red phosphorus melts at 317.3 °C and the boiling point is 553 °C so that addition of Be metal serves to form the phosphide. By adding Be to P_4 at about 350 °C, but less than the phosphorus sublimation temperature of 415 °C in an inert atmosphere, the melt readily forms the phosphide. A better way is to sublime the P_4 at 450 °C in an inert gas stream and react it with Be metal at 750 °C. Be_3P_2 has the CAS number 58127-61-0. It is a brown powder having a slight odor of garlic. Once formed, Be_3P_2 is very stable. However, it reacts slowly with moisture to form phosphine, PH_3 (which is toxic and flammable), and must be stored under dry conditions.

Beryllium phosphide is a semiconductor and has been studied by XRD methods using powder or a crystal, and by neutron diffraction from powder. The cell is tetragonal with $a = 10.22$ Å, $c = 20.39$ Å, Group I_{41}/a, $Z = 32$. The structure is like a superstructure of anti-fluorite with an ordering of vacancies and beryllium atoms.

Be_3P_2 is a direct band gap material with an eV of about 1.60. This is centered at about 775 nm which is too small to be of use in formulating semiconductors for LEDs or the like. The band gap of Mg_3P_2, for

example, is 160% wider. It is for this reason that beryllium phosphide films or composites have found little usage in the industry.

Furthermore, it has been shown that Be_3P_2 microcrystals are formed preferentially when Be was used as a dopant in phosphorus-based semiconductor compounds grown by chemical beam epitaxy. An example is an epilayer of $In0_{0.53}Ga_{0.47}As$ sandwiched between undoped InP epilayers to form InGaAs/InP interfaces. When Be was added as an electronic doping agent, the results showed that microcrystal formation occurs when high Be concentrations ($>10^{18}/cm^3$) and temperatures higher than 500 °C are used for crystal growth. The main consequence of Be_3P_2 formation is a high phosphorus consumption close to these microcrystals that causes a large density of P vacancies in the semiconductor layer. Experimental data shows that neutral Be interstitials in InGaAs and singly positively charged Be interstitials in InP result. This creates reduced electrical mobility, lattice parameter reduction, and poor crystallinity of the film in general.

A novel beryllium phosphide has been reported when a Au/AuBe/Au/p-GaP(111) thin-film system was rapidly annealed at 500 °C. The beryllium phosphide appeared having the crystal structure of a fcc lattice. The lattice constant of this beryllium phosphide is about 4.996 Å. The formation of beryllium phosphide was confined to the cubic-to-cubic orientation of GaP as a relationship with this cubic compound. The crystal structure of this beryllium phosphide does not pertain to those of any known binary beryllium phosphide systems. Thus, it was concluded that this cubic beryllium phosphide, was a new discovery.

Beryllium phosphide is offered by several manufacturers commercially for sale. Since it reacts slowly with water, it must be stored under dry conditions until usage.

Magnesium Phosphide

Magnesium phosphide has the formula of Mg_3P_2 and the molecular weight of 134.9456 g/mol. It can be prepared by reaction of the elements, but not from solution:

$$12Mg + 2P_4 \Rightarrow 4Mg_3P_2$$

Red phosphorus melts at 317.3 °C and the boiling point is 553 °C so that addition of Mg metal serves to form the phosphide. By adding Mg to P_4 at about 350 °C, but less than the sublimation temperature of 415 °C in an inert atmosphere, the melt readily forms the phosphide. A better way is to sublime the P_4 at 450 °C in an inert gas stream and react it with Mg metal at 750 °C. Mg_3P_2 has the CAS number of 12057-74-8 and is marketed as magnesium phosphide. It is a yellow cubic crystal having a density of 2.06 g/cm. It reacts violently with water and may ignite upon contact with air. It is toxic by ingestion. It has a slight odor of garlic. It is not combustible but forms a flammable gas on contact with water or damp air:

$$Mg_3P_2\,(solid) + 6H_2O\,(liq) \Rightarrow 3Mg(OH)_2\,(solid) + 2PH_3\,(gas)$$

Mg_3P_2 burns in air or oxygen at a dull red heat to form a phosphate, and reacts with chlorine gas to form:

$$Mg_3P_2\,(solid) + Cl_2 \Rightarrow MgCl_2 + PCl_3$$

The cubic structure of Mg_3P_2 has a D_{3h} symmetry and trigonal bipyramidal geometry. The antibixbyite structure of Mg_3P_2 is derived from the cubic bixbyite structure of the metal sesquioxide by switching the metal and nonmetal positions. The lattice constant is 6.06 Å.

A systematic study of the Mg–P system has revealed that only two compounds exist in the phase diagram: Mg_3P_2 and MgP_4. The latter compound was prepared using the former plus an excess of phosphorus:

$$2Mg_3P_2\,(solid) + 5P_4\,(gas) \Rightarrow 6MgP_4$$

The preparation of MgP_4 occurred from the reaction of gaseous P with Mg_3P_2 at 600 °C in a sealed silica tube. Powder XRD methods found that the structure of the MgP_4 to be isostructural with CdP_4. The crystal structure refinement from X-ray data produced the lattice constants: $a = 5.141$ Å, $b = 5.079$ Å, $c = 7.518$ Å,= 98.64°; $Z = 2$; space group $P2_1/c$. Among the distances between the P-atoms, there are three distinctly smaller ones than the others in the unit cell. Two of them are 2.18 Å and 2.19 Å in size between the P(1) and P(2) atoms and form a helical chain around a screw axis at $[x = 1/2, z = 1/4]$ and $[x = 1/2, z = 3/4]$ in the unit cell. These helices are joined with P to P bonds of 2.24 Å and the P-atoms are tetrahedrally distorted. The Mg atoms, which are all in centers of symmetry, have a distorted octahedral coordination.

The ^{31}P solid-state NMR spectra of Mg_3P_2 and MgP_4 were reported. Static and magic angle spinning (MAS) spectra were obtained for each compound. In all cases, chemical shift anisotropy and the effects of dipolar broadening were sufficiently reduced by the MAS method to reveal the isotropic chemical shifts for each crystallographically distinct phosphorus atom. The observed resonances were assigned to the different types of phosphorus by considering the structural details of each compound. In Mg_3P_2, two chemical resonance shifts from the 24*d* and 8*a* site P atoms were observed at −262.3 and −239.6 ppm, respectively. In MgP_4, two types of phosphorus, one type coordinated to two Mg and two P and the other to three P and one Mg, gave chemical shifts of −109.2 and −6.1 ppm, respectively.

Magnesium phosphide has found several uses in industry. It reacts with moisture in the atmosphere to produce phosphine gas which is the substance that is

active as a pesticide to control insects and rodents. It is primarily used for indoor fumigation of raw agricultural commodities, animal feeds, processed food commodities, and nonfood commodities in sealed containers or structures, and for outdoor fumigation of burrows to control rodents and moles in nondomestic areas, noncropland, and agricultural areas. Aluminum and magnesium phosphide are formulated as tablets, pellets, impregnated materials and dusts. Aluminum and magnesium phosphide are restricted use chemicals.

Tobacco was fumigated to control the cigarette beetle "*Lasioderma serricorne*" with a fumigant based on magnesium phosphide (Detiaphos-R™) in hogsheads and cartons at temperatures held almost constantly below freezing point and alternatively at temperatures which increased or decreased very slowly in the course of the fumigation. The dosage was 1.0 g PH_3/m^3 and the fumigation lasted 96 h in all cases. Gas concentration measurements in the tobacco and under sheeting showed that PH_3 developed rapidly in lethal concentrations from magnesium phosphide at low temperatures. Complete mortality of the interred test insects was registered after 96 h of the fumigation period. With magnesium phosphide, a fumigant is available which can be used for fumigating tobacco even at low temperatures.

Magnesium phosphide treatment of dried-fig stacks at 600 and 1000 ppm phosphine for 3 days under tarpaulin were compared with the standard method of control, Methyl bromide. The tested concentrations and exposure periods for Mg_3P_2 provided 100% mortality in test insects and no negative effect on fruit quality for 9 months in storage under ambient conditions. In contrast, fruit quality with CH_3Br did not match that of PH_3-treated fruit.

Magnesium phosphide has also been used to control insects in stored almonds, barley, brazil nuts, cashews, cocoa beans, coffee beans, corn, cottonseed, dates, filberts, flower seed, grass seed, millet, oats, peanuts, pecans, pistachio nuts, popcorn, rice, rye, sorghum, soybeans, sunflower seed, triticale, walnuts, wheat, vegetable seed, animal feed or feed ingredients.

Electronic structure calculations for Mg_3P_2 have been performed. Mg_3P_2 is predicted to be a direct semiconductor with the gap value of about 2.55 eV. The band gap widens in the alkaline earth series:

$$Be_3P_2 = 1.60 \text{ eV}; Mg_3P_2 = 2.55 \text{ eV}; Ca_3P_2 = 1.73 \text{ eV}$$

Whereas the complex polymeric structures of the Ca, Sr and Ba **polyphosphides** have received considerable attention in the literature, that of the Mg complex is almost nonexistent.

Magnesium phosphide is readily available from a number of manufacturers worldwide but is a restricted usage chemical and its importation is controlled in the U.S.

Calcium Phosphide

Calcium phosphide has the molecular formula of Ca_3P_2 and the molecular weight of 182.1825 g/mol. Its CAS number is 1305-99-3. It is a red-brown crystalline material with a melting point of 1605 °C. Its density is 2.51 g/cm^3. It readily reacts with water to form phosphine, PH_3, but is insoluble in ethanol.

It is easily prepared by reacting the metal with red phosphorus at high temperature. The best way is to sublime the P_4 at 450 °C in an inert gas stream and react it with Mg metal at 750 °C:

$$6Ca + 2P_4 \Rightarrow 2Ca_3P_4$$

Metal phosphides, primarily Ca_3P_2, have been used as rodenticides. Calcium phosphide baits have strong, pungent garlic-like odor characteristic for phosphine liberated by hydrolysis. The odor attracts rodents, but has a repulsive effect on other animals, who are not receptive to the smell. This salt has uses in incendiary bombs and other explosives. On contact with acids or water, calcium phosphide releases phosphine, which ignites spontaneously. It is also used in fireworks, torpedoes, self-igniting naval pyrotechnic flares, and various water-activated ammunition.

Early work (1845) separated diphosphine from phosphine that had been generated from Ca_3P_2, thereby demonstrating that P_2H_4 is responsible for the spontaneous flammability associated with PH_3, and also for the characteristic orange/brown color that can form on surfaces, which is a polymerization product. Ca_3P_2 produces more P_2H_4 than other phosphides because of the preponderance of P–P bonds in the starting material.

It has been established that CaO and P_4 react stoichiometrically at the temperature of 1100 °C to form the phosphide and orthophosphate:

$$24CaO + 4P_4 \Rightarrow 5Ca_3P_2 + 3Ca_3(PO_4)_2$$

Although the complete phase diagram for Ca–P has not been completely established, the reaction of excess P with calcium phosphide is sufficient to form the compound, CaP:

$$Ca_3P_2 + P_4 \Rightarrow 3Ca_2P_2 \text{ (CaP)}$$

or "calcium monophosphide". The term "calcium phosphide" describes the composition Ca_3P_2. CaP and Ca_3P_2 are completely different materials. CaP is black, but Ca_3P_2 is red-brown. The monophosphide is unstable and decomposes to Ca_3P_2 at about 600 °C.

$$12CaP \Rightarrow 4Ca_3P_2 + P_4$$

The structures of CaP and sodium peroxide (Na_2O_2) are very similar. The solid is described as a salt: $(Ca^{2+})_2P_2^{4-}$, or Ca_2P_2. Since the bonding is ionic (as a Zintl phase), the diphosphide centers carry a negative

charge and are easily protonated. Upon hydrolysis, this material releases diphosphine (P_2H_4):

$$Ca_2P_2 + 4H_2O \Rightarrow 2Ca(OH)_2 + P_2H_4$$

In this case, diphosphine spontaneously ignites in air. Thus, CaP must be protected from air or moisture. The thermal decomposition of calcium phosphohydride, $Ca(PH_2)_2$, prepared in liquid ammonia from calcium hydride and PH_3, was shown by X-ray analysis to decompose to first form Ca_2P_2 at 650 °C and then at 800 °C to form Ca_3P_2 plus P_4.

CaP and SrP, crystallize with the Na_2O_2 structure type, characterized by groups of P_2^{4-}. The magnetic susceptibility and the lattice constants of CaP show that P is divalent in this compound. The corresponding phase, BaP, is said not to exist. Calcium also forms a dicalcium hexaphosphide. The structure of Ca_2P_6 has been shown to consist of the P_6^{4-} groups bonded together to form a specific pattern (Fig. 4.21).

This is a polyphosphide which is a member of the polyphosphides referred to at the beginning of this section. In some of these positions in the structure, some of the P-atoms have only 2-bonds plus a negative charge. This accounts for the alkaline earth bonds that make up the total charge and bonding in the structure. This compound has been predicted to be a semiconductor with the direct band gap of 2.62 eV (473.3 nm).

A salt with the formula, $Na_{22}Ca_{13}P_{16}$ is said to exist but corroborating data is scanty.

A Knudsen-effusion technique in combination with a mass spectral analysis of the vapor phase has been applied to study thermodynamic properties of $(Ca_x + P_{1-x})$ alloys $(0.5 \leq x \leq 1)$ over the temperature range 650 K to 1537 K (377 °C to 1264 °C). The compound CaP was found to be unstable and to decompose at low temperatures (~600 °C) into Ca_3P_2 and gaseous phosphorus. Evaporation of the phosphide

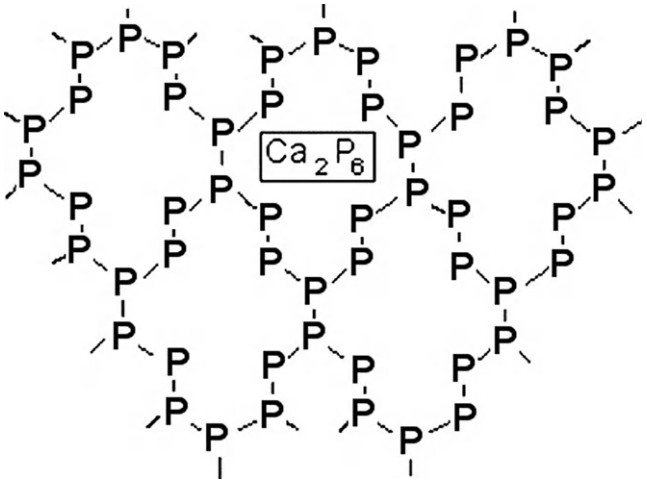

FIGURE 4.21

Ca_3P_2 was followed by congruent decomposition. The standard molar Gibbs energy of formation of Ca_3P_2 from red phosphorus and solid calcium, over the range of 1000 to 1300 °C, has been expressed by the equation:

$$3Ca(liq) + P_2(gas) = Ca_3P_2(solid) \quad \Delta G^\circ = -653{,}460 + 144.01T \text{ (J/mol)}$$

Thermodynamic functions of $[x\ Ca + (1-x)\ P]$ have been estimated with help of $\Delta_f G_m$ (Ca_3P_2) values and the coordinates of a point on the line of the two-phase equilibrium $(Ca_3P_2 + 1)$. It has been shown that the liquid solution can be described by the ideal associated solution model if complexes of the Ca_3P_2 type are assumed to exist.

Calcium phosphide is readily available as a fumigant and insecticide from many manufacturers worldwide commercially.

Strontium Phosphide

Strontium phosphide has the molecular formula of Sr_3P_2 and the molecular weight of 324.8075 g/mol. Its CAS number is 12504-13-1. It is a black crystalline material with a melting point of 1205 °C. Its density is 2.71 g/cm^3. It readily reacts with water to form phosphine, PH_3, but is insoluble in ethanol.

It is easily prepared by reacting the metal with red phosphorus at high temperature. The best way is to sublime the P_4 at 450 °C in an inert gas stream and react it with Sr metal at 650 °C:

$$6Sr + 2P_4 \Rightarrow 2Sr_3P_4$$

Strontium phosphide is a solid which will evolve flammable and toxic gases on contact with water. It also can react vigorously with oxidizing materials. In general, materials in this group are incompatible with oxidizers such as atmospheric oxygen. They are violently incompatible with acids, particularly oxidizing acids.

Strontium phosphide has not been utilized in industry due to cost and the fact that the calcium salt is just as efficacious.

Strontium also forms polyphosphides such as Sr_2P_6 which has been shown to have a structure similar to that of Ca_2P_6 except that a cyclic P_6^{2-} group is situated between the P_{13}^{4-} groups (Fig. 4.22).

In some of these positions in the structure, the P-atoms have only 2-bonds plus a negative charge. This accounts for the alkaline earth bonds that make up the total charge and bonding in the structure.

The compounds $CaFe_2P_2$, $SrFe_2P_2$ and $BaFe_2P_2$ have been studied because of their magnetic properties. They crystallize in the $ThCr_2Si_2$ structure that is a ternary variant of the $BaAl_4$ structure. For the three compounds, densities of states (DOS), local partial DOS and electron

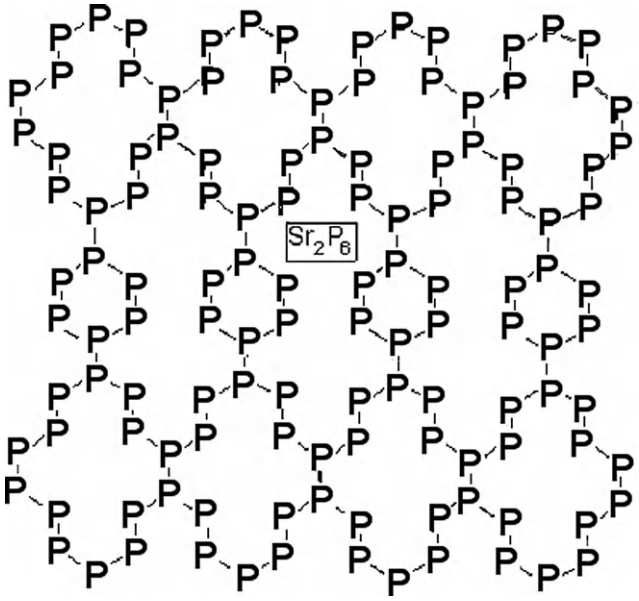

FIGURE 4.22

densities have been calculated. Compared to $CaNi_2P_2$ with a P–P distance of 2.30 Å (a value very close to that for a P–P single bond), the distance found for is 2.71 Å for $CaFe_2P_2$. While in this compound one still observes pronounced P–P (s–s and p–p) σ-bonds, this is not the case for $SrFe_2P_2$ and $BaFe_2P_2$ (P–P distances: 3.43 Å and 3.84 Å, respectively). Despite their different c/a ratios, the Sr and Ba compounds show fairly similar bonding properties, in particular as far as the Fe–Fe and Fe–P interactions are concerned. In $BaFe_2P_2$, however, non-negligible interactions of the semicore [Ba(5p)] states with the P(3s) states are found.

Strontium phosphide is available in limited quantities from domestic manufacturers. It is a restricted usage chemical, monitored by the EPA.

Barium Phosphide

Barium phosphide has the molecular formula of Ba_3P_2 and the molecular weight of 182.1825 g/mol. Its CAS number is 12380-72-2. It is a red-brown crystalline material with a melting point of 1585 °C. Its density is 2.51 g/cm^3. It readily reacts with water to form phosphine, PH_3, but is insoluble in ethanol.

It is easily prepared by reacting the metal with red phosphorus at high temperature. The best way is to sublime the P_4 at 450 °C in an inert gas stream and react it with Ba metal at 600 °C:

$$6Ba + 2P_4 \Rightarrow 2Ba_3P_4$$

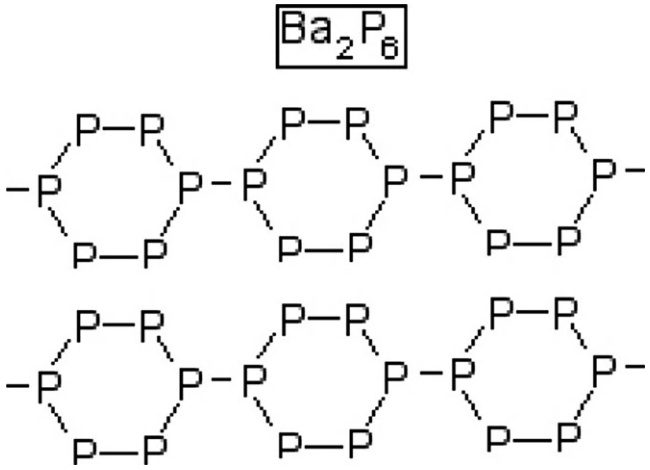

FIGURE 4.24

Barium Phosphide is a semiconductor used in high-power, high-frequency applications and in laser diodes. It crystallizes in the body-centered cubic mode.

The standard Gibbs energies of formation of barium phosphide was determined by a chemical equilibration technique yielding the following results:

$$3Ba(1iq) + P_2(gas) \Rightarrow Ba_3P_2(solid) \quad \Delta G^\circ = -732{,}000 + 156.1\,T(\pm 12{,}800)\ (J/mol)$$

This relates to the stability and the thermodynamic behavior of barium compounds as reaction products of dephosphorous reactions with steel.

Stoichiometric compounds BaP and Ba_3P_2 as well as alloys with compositions belonging to the two-phase equilibrium region ($BaP + Ba_3P_2$) were studied. The standard molar Gibbs energies of formation of BaP and Ba_3P_2 from gaseous phosphorus and liquid barium in the temperature range investigated have been expressed by the equations (Fig. 4.23).

Barium also forms one or more polyphosphide whose structure consists of a type of cage consisting of P_6^{4-} units as shown in the following diagram. This structure is linear in contrast to the cages shown for the calcium and strontium polyphosphide structures that are actually three-dimensional cages (Fig. 4.24).

In some of these positions in the structure, the P-atoms have only 2-bonds plus a negative charge. This accounts for the alkaline earth bonds that make up the total charge and bonding in the structure.

The Zintl phases Ba_3P_2 with isolated P^{3-} ions or Ba_4P_3 which contains P^{3-} ions and P_2^{4-} dumbbells, react

$$\Delta_f G_m^\circ(BaP)/(J \cdot mol^{-1}) = -(306804 \pm 1180) + (79.42 \pm 0.89) \cdot (T/K),$$

$$\Delta_f G_m^\circ(Ba_3P_2)/(J \cdot mol^{-1}) = -(736708 \pm 3014) + (171.43 \pm 2.21) \cdot (T/K).$$

FIGURE 4.23

with iodine in a direct way to **$Ba_3P_3I_2$** and BaI_2 (Eqns 1 and 2). A characteristic detail of the new compound is P_3 chains; therefore, an oxidation of the anionic partial structure results. The consequence is a P–P bonding formation and an enlargement of the phosphorus chains. The reaction was carried out at 1050 K, which is obviously below the melting points of the binary phosphides. Thus, the planned oxidation of a Zintl anion in the solid phase could be successfully realized. To avoid the formation of BaI_2 as a by-product, a mixture with the composition "BaP", containing Ba_3P_2, Ba_4P_3 and Ba_3P_4 can be used, too (Eqn 3). The use of P_2I_4 as an oxidation reagent is also possible (Eqn 4).

$$3Ba_3P_2 + 5I_2 \Rightarrow 2Ba_3P_3I_2 + 3BaI_2 \quad (1)$$

$$Ba_4P_3 + 2I_2 \Rightarrow Ba_3P_3I_2 + BaI_2 \quad (2)$$

$$3BaP + I_2 \Rightarrow Ba_3P_3I_2 \quad (3)$$

$$2Ba_3P_2 + P_2I_4 \Rightarrow 2Ba_3P_3I_2 \quad (4)$$

Reducing the amount of iodine has a direct influence on the anionic partial structure. Therefore one obtains, when using the composition $Ba_3P_3I_{1.8}$ the new compound **$Ba_5P_5I_3$**, which contains additional P_4 chains besides P_3.

The new compounds $Ba_3P_3I_2$ and $Ba_5P_5I_3$ are sensitive to air and moisture. They crystallize in new structure types: $Ba_3P_3I_2$ (*oP*32; *Pnma*; $a = 1719.5(5)$ pm; $b = 462.4(2)$ pm; $c = 1427.2(4)$ pm; $Z = 4$, $Ba_5P_5I_3$ (*mC*52; *C*2/*m*; $a = 4266.4(13)$ pm; $b = 456.3(2)$ pm; $c = 943.1(3)$ pm; $b = 92.20(3)°$; $Z = 4$). Both can be described as double salts of hypothetic Zintl phases ('Ba_2P_3" or "Ba_7P_{10}") and a halide (BaI_2). Characteristic structural features are P_3 and P_4 chains, corresponding to $Ba_3[P_3]I_2$ and $Ba_{10}[P_3]_2[P_4]I_6$, respectively (Figs. 4.25 and 4.26).

Barium phosphide is offered commercially in limited quantities for use as a target for deposition to form various semiconductor configurations.

Radium Phosphide

Radium phosphide would have the molecular formula of Ra_3P_2 and the molecular weight of

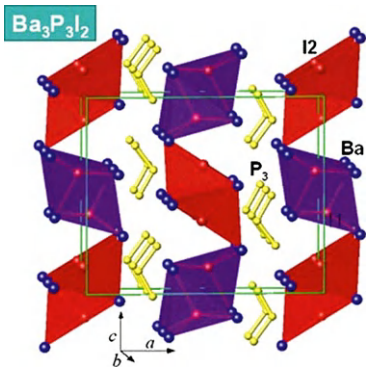

FIGURE 4.25

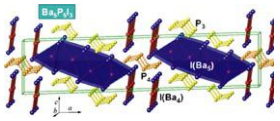

FIGURE 4.26

740.0237 g/mol. It has no CAS number. It has never been prepared but could be formed by reacting the metal with red phosphorus at high temperature. The best way is to sublime the P_4 at 450 °C in an inert gas stream and react it with Ra metal at 600 °C:

$$6Ra + 2P_4 \Rightarrow 2Ra_3P_4$$

It is expected to be a red–brown crystalline material with a high melting point and to readily react with water to form phosphine, PH_3. There is absolutely no demand for such a compound and it is likely that it will never be prepared and its physical properties measured.

4.2.3. Alkaline Earth Hypophosphites

Hypophosphorous acid is a powerful reducing agent with a molecular formula of H_3PO_2. Inorganic chemists refer to the free acid by this name although its IUPAC name is dihydridohydroxidooxidophosphorus, or the acceptable name of phosphinic acid. It is a colorless low-melting compound, which is soluble in water, dioxane, and alcohols. The formula for hypophosphorous acid is generally written H_3PO_2, but a more descriptive presentation is $HOP(O)H_2$ which highlights its monoprotic character. Salts derived from this acid are called **phosphinates** (hypophosphites).

Beryllium Hypophosphite

Beryllium hypophosphite has the molecular structure of $Be(H_2PO_2)_2$ or $Be(OH)H_2PO_2$, depending upon how the crystal is prepared. If an aqueous method is used, the latter is the result. The use of "monoglyme = 1,2 dimethoxy-ethane" or dimethylformamide (DMF) as a solvent allows the usage of an organic compound (such as acetylacetonate = Pentane-2,4-dione = $C_5H_8O_2$ = Acac) of Be to react with hypophosphorous acid to form the desired compound:

$$BeCl_2(aq) + H_3PO_2(aq) \Rightarrow Be(OH)H_2PO_2(solid)$$

$$Be(Acac)_2(DMF) + H_3PO_2(DMF) \Rightarrow Be(H_2PO_2)_2(solid)$$

The product is an anhydride and hydrates apparently do not exist.

The structure of tetragonal ($P4_12_12$) beryllium bis(dihydrogen phosphite), $Be(H_2PO_2)_2$, has been determined by single-crystal XRD. The method of preparation was

not presented. The structure consists of layers of hypophosphite anions and metal cations held in tetrahedral coordination by O atoms. Within the layers, the anions bridge two Be^{2+} cations. This structure is related to LiH_2PO_2, in which the Li atom lies on a twofold axis and the $H_2PO_2^-$ anion has the PO_2 atoms on a mirror plane. In $Be(H_2PO_2)_2$, the Be atom lies on a twofold axis and the $H_2PO_2^-$ anion is in a general position.

Polymers are frequently rendered flame resistive by adding phosphorus and halogen compounds or mixtures thereof to them. Some polymers are processed at high temperatures, for example at 250 °C or higher. For this reason, many known flame retardants are unsuitable for such applications, since they are too volatile or are not sufficiently heat resistant.

Beryllium forms a great number of organo-phosphinates which have been studied extensively. Such materials have potential as a catalyst in controlling the growth and size of polymers in general and in the production of fire-resistant polymers by incorporation of a metallic cation like Be^{2+}. An example is the preparation and measurement of the physical properties of such materials using infrared, DTA, and TGA methods of analysis. Data have been given for beryllium dimethyl-, tetramethylene-, di-*n*-butyl-, di-*n*-pentyl-, di-*n*-heptyl-, methylphenyl-, diphenyl-, and bis-pentafluorophenylphosphinates. Synthesis of dimeric beryllium acetylacetonyl phenyl-[*o*-methylcarboranyl phosphinate is reported. The beryllium phosphinates were prepared by the reaction of beryllium acetylacetonate with the appropriate hypophosphorus acid in dimethylformamide.

The general structure of these organo-phosphinates has been proposed to be a linear but three-dimensional cyclic structure of phosphinate groups to which "R groups = dimethyl, tetramethylene, di-*n*-butyl, etc." are attached (Fig. 4.27).

The characterization of beryllium phosphinates of stoichiometry, $Be(Bu_2^nPO_2)_2$ and $Be(Ph_2PO_2)_2$, and of some mixed-ligand species $Be[(Bu_2^nPO_2)_{2-2x}(Ph_2PO_2)_{2x}]$ has also been reported. The compounds richer in alkyl groups give stable solutions in hydrocarbon and halogenated solvents. Solution properties indicate that these compounds are linear polymers which undergo a reversible degradation influenced by the nature of the solvent, concentration, and temperature. The mixed-ligand species can be crystallized and are formulated as random copolymers. Isomorphous replacement of the two kinds of phosphinate groups within the crystal lattice of the related homopolymers is observed. The XRD fiber photographs indicate that the homopolymer $[Be(Bu_2^nPO_2)_2]_n$ and the copolymers $\{Be[(Be_2^nPO_2)_{2-x}(Ph_2PO_2)_{2x}]\}_n$ ($x = 0{\cdot}20$ or $0{\cdot}33$) have a backbone structure with alternate single and triple bridging phosphinate groups between tetrahedral metal atoms. The same chain-type structure is proposed for the homopolymer $[Be(Ph_2PO_2)_2]_n$ and the copolymers richer in diphenylphosphinate groups. It has been discovered that the phenyl type of beryllium phenylphosphinate (i.e.- R = phenyl) is sensitive to water vapor and decomposes. Thus, magnesium salts of a similar composition have not been used for this same usage.

Beryllium hypophosphite is available commercially but only from a few manufacturers and in limited quantities.

Magnesium Hypophosphite

Magnesium hypophosphite or phosphinate has the molecular formula of $Mg(H_2PO_2)_2$ and the molecular weight of 154.2546 g/mol. Its CAS number is 10377-57-8. This salt can be prepared by the aqueous reaction of the carbonate or oxide with H_3PO_2:

$$MgO + 2H_3PO_2 \Rightarrow Mg(H_2PO_2)_2$$

The salt is soluble in water (20 g/100 ml at 20 °C) so that the solution must be evaporated to obtain the hexahydrate crystals. $Mg(H_2PO_2)_2{\cdot}6H_2O$ has the CAS number of 26264-58-4 and the density of 1.59 g/cm^3. It is composed of white square crystals that are water soluble. It is insoluble in alcohol or ether. If heated to about 101 °C, five (5) waters of crystallization are lost, leaving the monohydrate. This decomposes at 182 °C to form the anhydrate. Further heating to about 345 °C causes decomposition to phosphine, PH_3, and $MgHPO_3$:

$$Mg(H_2PO_2)_2 + \text{heat} \Rightarrow PH_3 + MgHPO_3$$

If mixed with strong oxidants, a fire may result. It decomposes into H_3P, H_3PO_4, H_3PO_3 and H_2:

$$Mg(H_2PO_2)_2 + 2HNO_3 \Rightarrow PH_3 + MgHPO_3 + H_2 + N_2O_4$$

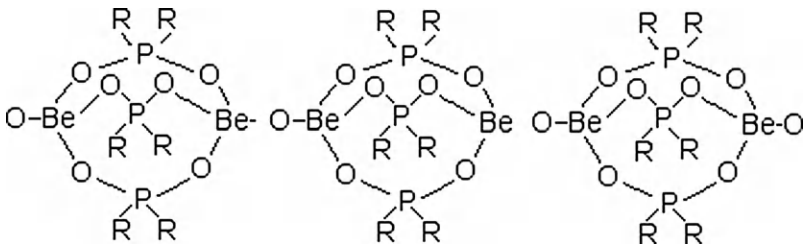

FIGURE 4.27

Two modifications of hexaaquamagnesium hypophosphite $[Mg(H_2O)_6](H_2PO_2)_2$ have been synthesized and structurally characterized. One of these forms is tetragonal with $a = 6.789$ Å and $c = 9.873$ Å. The geometrical characteristics of hexaaqua cations, hypophosphite anions, and nets of hydrogen bonds between the hypophosphite anions and the coordinated water molecules are analyzed. The packing motif of the structure-forming fragments was found to be the same for the two structures, except that modification of the inner structure of the complex cation leads to different nets of hydrogen-bonded cations and anions.

This salt has found several industrial applications. It is used as a reducing agent in the plating of polymers and in the preparation of finely supported catalysts in the production of oxide ceramics. A process for treating paper to prevent discoloration when exposed to light which comprises adding 1% to 10% by weight of magnesium hypophosphite to prevent discoloration when exposed to light. This addition can be added to the paper at any stage during or after papermaking.

However, the major use of magnesium phosphinate has been for the treatment of calcium and magnesium deficiency in cattle, swine, goats and sheep. This salt has been approved by numerous Agencies, including the FDA and Veterinary Association for this purpose. It is injected as a pure solution along with a sugar, calcium gluconate.

There are over 1 million registered importers–exporters in the world and this salt is readily available commercially.

Calcium Hypophosphite

Calcium hypophosphite has the molecular formula of $Ca(H_2PO_2)_2$ and the molecular weight of 170.0631 g/mol. This salt can be prepared by the aqueous reaction of the carbonate or oxide with H_3PO_2:

$$CaO + 2H_3PO_2 \Rightarrow Ca(H_2PO_2)_2$$

The salt is soluble in water (20 g/100 ml at 20 °C) so that the solution must be evaporated to obtain crystals. $Ca(H_2PO_2)_2$ has the CAS number of 7789-79-9 and the density of 1.59 g/cm^3. It is composed of white square monoclinic crystals which are water soluble. It is insoluble in alcohol or ether. When heated to about 305 °C, it disproportionates, forming calcium phosphate and phosphine:

$$Ca(H_2PO_2)_2 + \text{heat} \Rightarrow CaHPO_3 + PH_3$$

This salt is used in electroplating and protecting metals from corrosion (because it is a strong reducing agent). Its Lewis structure is shown in Fig. 4.28.

Recent patent and technical publications indicate a growing interest in halogen-free solutions with the predominance of the literature focusing on phosphorus-based flame retardants. Patents published on

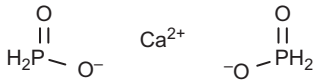

FIGURE 4.28

the flame retardancy of polycarbonate and its blends significantly exceed the number of patents on flame retardancy of any other polymer. Bridged aromatic diphenyl calcium phosphinates, especially as resorcinol bis(diphenyl phosphinate) and bisphenol A bis(diphenyl calcium phosphinate) have found broad application because of their good thermal stability, high efficiency, and low volatility.

Another actively reported group of compounds are the metal salts of dialkylphosphonic acid as well as calcium hypophosphite, which have recently been found to be particularly effective in poly(utylenes terephthalate) and polycarbonate. These products are synergistic with a number of phosphorus and nitrogen-containing compounds, such as melamine salts, which seem to be very efficient and commercially useful as fire retardants in nylons.

Calcium hypophosphite is relatively soluble in water, and when added to a solution of sodium hypophosphite, forms a double salt. Crystals were obtained by slow evaporation of the solution to form dodecahedra with well-developed {110} faces. The crystal structure of $CaNa(H_2PO_2)_3$ belongs to the cubic system with space group, $P2_13$, $Z = 4$ and $a = 9.721$ Å. The structure consists of two kinds of octahedral groups, one with a calcium atom and the other with a sodium atom. Each atom of the hypophosphite ions is coordinated to each one of the calcium and sodium atoms to form the octahedral. This structure is, in general, typical of the salts of hypophosphorous acid.

Calcium hypophosphite is readily available commercially since its main usage, both industrially and in Research, has proven to be as a source of hypophosphite anions to form other hypophosphites.

Strontium Hypophosphite

Strontium hypophosphite has the molecular formula of $Sr(H_2PO_2)_2$ and the molecular weight of 170.0631 g/mol. This salt can be prepared by the aqueous reaction of the carbonate or oxide with H_3PO_2:

$$SrO + 2H_3PO_2 \Rightarrow Sr(H_2PO_2)_2$$

The salt is soluble in water (16 g/100 ml at 20 °C) so that the solution must be evaporated to obtain crystals.

The structure of monoclinic strontium dihydrogenphosphinate, $Sr(H_2PO_2)_2$ consists of layers of hypophosphite anions and metal cations exhibiting square

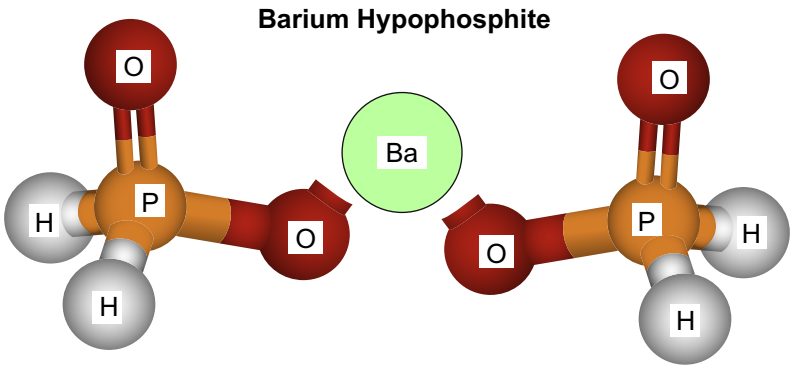

FIGURE 4.29

antiprismatic coordination by O atoms. The Sr atoms are located on sites with point symmetry 2_1. Within the layers, each anion bridges four metal cations.

Although strontium hypophosphite is mentioned in many patents concerning metal surface finishing, electroplating, chemical intermediates and as a source of hypophosphite anions, it is the calcium salt that is preferred since it is lower in cost and easier to use.

$Sr(H_2PO_2)_2$ is available in limited quantities commercially.

Barium Hypophosphite

Barium hypophosphite has the formula, $Ba(H_2PO_2)_2$, and the molecular weight of 267.30388 g/mol. This salt can be prepared by the aqueous reaction of the carbonate or oxide with H_3PO_2:

$$BaO + 2H_3PO_2 \Rightarrow Ba(H_2PO_2)_2$$

The salt is slightly soluble in water (3.62 g/100 ml at 20 °C) so that the solution must be evaporated to obtain crystals. This procedure forms barium hypophosphite monohydrate, $Ba(H_2PO_2)_2 \cdot H_2O$, whose CAS number is 14871-79-5. Its molecular weight is 285.320 g/mol. It occurs as monoclinic plates with a density of 2.94 g/cm^3. It is soluble in water but insoluble in alcohol. Therefore, the addition of alcohol during evaporation serves to hasten the crystallization process from aqueous solution. Heating to about 110 °C causes the loss of the water of hydration to form the anhydrate. The anhydrate is soluble in water at about 35 g/100 ml at 20 °C but only 30 g/100 ml at 100 °C.

The structure of orthorhombic barium bis(dihydrogenphosphinate), $Ba(H_2PO_2)_2$, consist of layers of hypophosphite anions and metal cations exhibiting square antiprismatic coordination by O atoms. The Ba atoms are on sites with point symmetry 222. Within the layers, each anion bridges four metal cations. A "ball and stick" model (like a Lewis structure) is shown in Fig. 4.29.

The major usage of barium hypophosphite has been as a source of hypophosphorous acid because the addition of H_3PO_4 to a solution allows the separation of the very insoluble $BaSO_4$. Although this salt is mentioned in a few patents concerning metal surface finishing, electroplating, chemical intermediates and as a source of hypophosphite anions, it is the calcium salt that is preferred since it is lower in cost and easier to use.

However, a number of Chinese manufacturers offer "barium phosphinate" as BaP_2O_4. This would have the Lewis structure shown in Fig. 4.30.

This is likely a mistake since the Lewis dot-structure formulation does not show a full complement of electrons for the phosphorus atoms.

Barium hypophosphite is readily available commercially from a number of manufacturers, notably Chinese.

Radium Hypophosphite

Radium hypophosphite would have the molecular formula of $Ra(H_2PO_2)_2$ and the molecular weight of 740.0237 g/mol. It has no CAS number. It has never been prepared but could be formed by reacting the oxide with hypophosphorous acid:

$$RaO + 2H_3PO_2 \Rightarrow Ra(H_2PO_2)_2 + H_2O$$

It would expected to be water soluble and would have strong reducing properties. In view of the intense radioactivity of ^{226}Ra, it is unlikely that this compound will ever be synthesized.

4.2.4. Alkaline Earth Phosphites

Phosphorous acid is a diprotic acid, since the hydrogen bonded directly to the central phosphorus

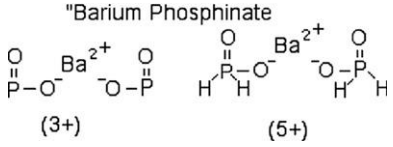

FIGURE 4.30

atom is not readily ionizable. $HP(O)_2(OH)$ is moderately a strong acid:

$$HP(O)(OH)_2 \Leftrightarrow HP(O)_2(OH)^- + H^+ \quad pK_a = 1.3$$
$$HP(O)_2(OH)^- \Leftrightarrow HPO_3^{2-} + H^+ \quad pK_a = 6.7$$

The $HP(O)_2(OH)^-$ species is called the hydrogen phosphite, and the HPO_3^{2-} the phosphite ion. Thus, two species are possible with the alkaline earths but only one, the hydrogen phosphite, is usually prevalent.

Beryllium Phosphite

Beryllium phosphite can have the formulas of either $Be(OH)HPO_3$ or $Be(OH)(H_2PO_3)_2$. It is the former that appears when phosphorous acid is reacted with the oxide, hydroxide or carbonate:

$$BeO\,(s) + H_3PO_3\,(aq) \Rightarrow [Be(OH)]_2HPO_3$$

The product is the hydrogen phosphite. If the sodium salt is employed, then the product is likely to be the phosphite:

$$BeO\,(s) + Na_3PO_3 \Rightarrow [Be(OH)]_3PO_3$$

On heating, it decomposes around 400 °C to form the pyrophosphite:

$$3[Be(OH)]_3PO_3 + \text{heat} \Rightarrow Be_3(PO_3)_2 = \{Be_3P_2O_6\} + 3H_2 + PH_3$$

It would also be possible to form a dihydrogen phosphite:

$$BeO\,(s) + H_3PO_3\,(aq) \Rightarrow [Be(OH)]H_2PO_3$$

However, there is no defining literature showing the properties of any of these possible salts of Be. Very little information is available in the literature regarding beryllium phosphite salts. The actual structure of beryllium hydrogen phosphite is not known. Nor has the structure of the phosphite or pyrophosphite been examined. The effect of pH in solution on the formation of these salts also remains unknown.

However, a mixed organophosphite has been studied. An organically templated beryllophosphite, $[H_3N(CH_2)_3NH_3]\cdot[Be_3(HPO_3)_4]$ **1**, was synthesized under mild hydrothermal conditions and characterized by single-crystal XRD. It is the first beryllophosphite formed using an organic amine as a structure-direction agent. Compound **1** crystallizes in a monoclinic system, space group $P2_1/c$ with cell parameters: $a = 8.5983$ Å, $b = 13.1561$ Å, $c = 13.460$ Å, $\beta = 92.470°$, and $Z = 4$. The three-dimensional framework is built up from strictly alternating (BeOH) tetrahedra and $[HPO_3^{2-}]$ pseudopyramids by sharing vertices. A new type of network containing 4-, 6-, 8-, 10-, 12-membered rings makes up the inorganic framework. The 1,3-diammonium propane template molecules are located in 8-membered ring windows. The compound was characterized by IR spectroscopy, inductively coupled plasma (ICP), and differential thermal and thermogravimetric analyses.

Beryllium phosphite has no CAS number and it is not offered for sale by a registered manufacturer. However, it is offered commercially by a few Chinese firms. Its quality remains questionable.

Magnesium Phosphite

Magnesium phosphite can have the molecular formula of the hydrogen phosphite, $MgHPO_3$ or the dihydrogen phosphite, $Mg(H_2PO_3)_2$. It is the former that appears when a solution of phosphorous acid is reacted with the oxide, hydroxide or carbonate:

$$MgO + H_3PO_3 \Rightarrow MgHPO_3 + H_2O$$

The product is a hexahydrate. It can also be prepared by the action of ammonium phosphite on magnesium chloride:

$$MgCl_2\,(aq) + NH_4HPO_3\,(aq) \Rightarrow MgHPO_3\cdot 6H_2O + NH_4Cl_2\,(aq)$$

If a sodium phosphite is used in the preparation, then the dihydrogen phosphite, $Mg(H_2PO_3)_2$, is produced. However, the full effect of pH during the formation of these phosphite salts of magnesium has not been fully defined in the scientific literature.

The nature of the hydrates of these hydrogen-phosphite salts is controlled, to some extent, by the solution temperature employed. The hexahydrate, $MgHPO_3\cdot 6H_2O$, is obtained at room temperature (15–25 °C). At 30–50 °C, the tri-hydrate occurs whereas at >85 °C, the monohydrate is most stable. This is due in part to the solubilities of these three salts. The hexahydrate is rather soluble at 16.4 g/100 ml of water (20 °C) whereas the trihydrate is most stable at 50 °C. It has been shown that at reaction temperatures less than about 60 °C a crystalline magnesium hydrogen phosphite trihydrate, $MgHPO_3\cdot 3H_2O$, whose solubility increased from 8.9 at 20 °C to 11.2 g/100 ml at 50 °C and then to 6.5 at 95 °C temperature. If formed at >85 °C, a magnesium hydrogen phosphite with about 0.5 waters of hydration, $MgHPO_3\cdot 0.5H_2O$, is produced. The CAS number of the trihydrate is 7757-86-0.

If heated to about 85 °C, the hexahydrate loses two water molecules to form the trihydrate. Further heating causes the trihydrate to decompose to the hemihydrate at about 110 °C and then the anhydrate at 185 °C. The anhydrate is stable in air up to about 300 °C where it decomposes:

$$3MgHPO_3 + \text{heat} \Rightarrow PH_3 + Mg(PO_3)_2$$

The anhydrate has a molecular weight of 103.2769 g/mol.

The crystal structure of magnesium hydrogen phosphite hexahydrate has been determined to be rhombohedral (Trigonal class) with $a, b, c = 5.96$ Å, $\alpha, \beta, \gamma = 96°24'$. The space group is R3 and the Mg, P and H atoms lie on the unique linear axis. The structure is built from discrete tetrahedral $(HPO_3)^{2-}$ ions and octahedral $\{Mg^{2+}(H_2O)_6\}$ groups that are linked together in three dimensions by a continuous system of hydrogen bonds.

It also forms a series of double salts. One example is that of the sodium–magnesium hydrogen phosphite. The structure of $NaMg(H_2PO_3)_3 \cdot H_2O$ belongs to the isotypic dihydrogen phosphite monohydrate series $NaMg(H_2PO_3)_3 \cdot H_2O$ with alternating NaO_6 [d_{av}(Na–O) = 2.466 (2) Å] and MgO_6 [d_{av}(Mg–O) = 2.086 (2) Å] octahedra, cross-linked by H_2PO_3 pseudo-pyramids [d_{av}(P–OMg) = 1.530 (2) Å and d_{av}(P–OH) = 1.575 (2) Å].

Magnesium apparently forms only the $MgHPO_3$ type of compounds (magnesium hydrogen phosphite) and the $Mg(H_2PO_3)_2$ type has not been studied. Although the hexahydrate as a crystal is known to be strongly pyroelectric, it has not found any usage in industry and has received little to no attention in the scientific literature.

The hexahydrate is available commercially as a powder from a few manufacturers.

Calcium Phosphite

Calcium phosphite can have the molecular formula of $CaHPO_3$ or $Ca(H_2PO_3)_2$. It is the former that appears when a solution of phosphorous acid is reacted with the oxide, hydroxide or carbonate:

$$CaO + H_3PO_3 \Rightarrow CaHPO_3 \cdot H_2O + H_2O$$

The product is a monohydrate. It can also be prepared by the action of ammonium phosphite on calcium chloride:

$$CaCl_2\,(aq) + NH_4HPO_3\,(aq) \Rightarrow CaHPO_3 \cdot H_2O + NH_4Cl_2\,(aq)$$

A white, crystalline powder is obtained. The solubility of $CaHPO_3 \cdot H_2O$ has apparently not been determined exactly. If heated to about 250 °C, the anhydrate results. This is stable when heated further up to about 320 °C where it decomposes to form phosphine and hydrogen:

$$3CaHPO_3 + \text{heat} \Rightarrow 2PH_3 + 3Ca(PO_3)_2 + H_2$$

$CaHPO_3 \cdot H_2O$ has the CAS number of 25232-60-4 and a molecular weight of 138.073 g/mol. It is a colorless, monoclinic crystal which loses water at about 150 °C and is slightly soluble in water but insoluble in alcohol. The anhydrate, calcium phosphite ($CaHPO_3$), is stable in air even when heated at 95 °C for 2 months. The CAS number of $CaHPO_3$ is 21056-98-4 and its molecular weight is 119.0479 g/mol.

The dihydrogen phosphite compound is prepared by reaction of calcium carbonate and sodium phosphite:

$$CaCO_3 + 2NaH_2PO_3\,(aq) \Rightarrow Ca(H_2PO_3)_2\,(aq) + 2NaOH\,(aq) + CO_2$$

The solution is evaporated via vacuum. This water-soluble dihydrogen phosphite monohydrate, $Ca(H_2PO_3)_2 \cdot H_2O$, loses its water of crystallization at about 150 °C.

This salt has been used to provide a coating composition useful for increasing the corrosion resistance of a surface. The final layer comprises the anticorrosive agent, calcium phosphite. The composition may also include fillers and other conventional additives. A process for protecting a surface from corrosion is also provided.

The crystal structures of two-layered metal phosphites $M(HPO_3) \cdot H_2O$ where M = Ca and Sr have been reported. These compounds are the first examples of inorganic phosphates, structurally related to metal phosphonates, with the general formula of $M(HPO_3) \cdot H_2O$. They crystallize in a monoclinic system with space group $P2_1/c$ and are isostructural with $a = 6.778$ Å, $b = 7.928$ Å, $c = 8.097$ Å, $\alpha = 67.9°$, $\beta = 84.8°$, $\gamma = 84.2°$, $V = 354.99$ Å^3 The structures consist of two-dimensional sheets formed by linked metal and phosphorus polyhedra, which are held together by O–H···O hydrogen bonds.

The crystal structure of the dihydrogen compound, $Ca(H_2PO_3)_2 \cdot H_2O$, exhibits two-dimensional sheets formed by linked Ca and P polyhedra. The layers are held together by O–H–O hydrogen bonds (Fig. 4.31).

Neither of the two types of calcium phosphite compounds have been utilized extensively in industry. Nor have they been studied academically except in general terms. The literature concerning them is exceptionally sparse.

Both the hydrogen and dihydrogen phosphite of calcium are available commercially. They are made in small quantities for sale.

Strontium Phosphite

Strontium phosphite can have the molecular formula of $SrHPO_3$ or $Sr(H_2PO_3)_2$. It is the former that appears when a solution of phosphorous acid is reacted with the oxide, hydroxide or carbonate:

$$SrO + H_3PO_3 \Rightarrow SrHPO_3 + H_2O$$

The product is a hemimonohydrate, i.e. $SrHPO_3 \cdot 1.5H_2O$. It can also be prepared by the action of ammonium phosphite on strontium chloride:

$$SrCl_2\,(aq) + NH_4HPO_3\,(aq) \Rightarrow SrHPO_3 \cdot 1.5H_2O + NH_4Cl_2\,(aq)$$

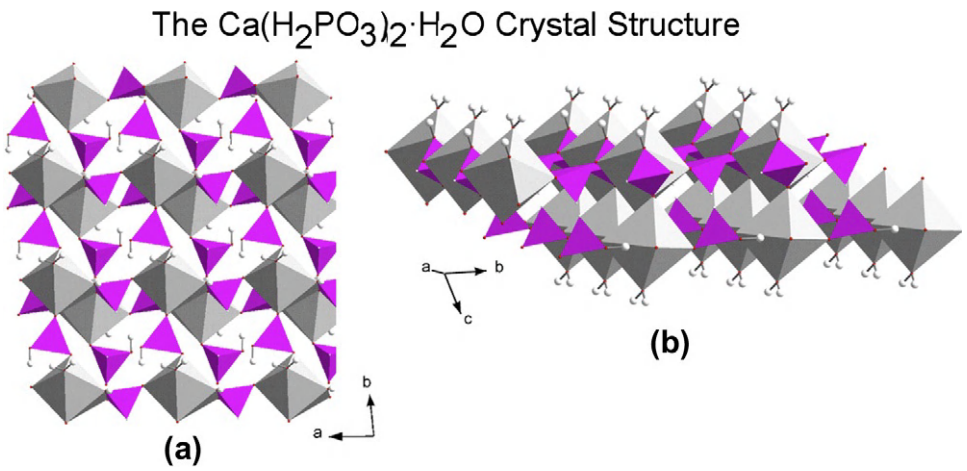

FIGURE 4.31

A white, crystalline powder is obtained. The dihydrogen phosphite compound is prepared by reaction of strontium carbonate and sodium phosphite:

$$SrCO_3 + 2NaH_2PO_3\ (aq) \Rightarrow Sr(H_2PO_3)_2\ (aq) + 2NaOH\ (aq) + CO_2$$

The salt is soluble in solution and is evaporated via vacuum. In contrast, the monohydrogen compound is relatively insoluble in water.

Very little information on these compounds is available in the scientific or technical literature. Papers dealing directly with strontium phosphite or similar salts are few and far between. Strontium phosphite is not used in industry although it is mentioned in several patents which generally employ the magnesium or calcium salt but cite the strontium salt as possibly functional in the usage

$Sr(H_2PO_3)_2$ has been characterized by means of single-crystal XRD and FT-IR absorption spectroscopy. The IR spectra exhibit split AB band systems in the OH stretching mode region due to Fermi resonance interactions of the (OH) with the in-plane bending modes of the hydroxyl groups. The compounds crystallize in a new structure type and are isotypic, if the P-bonded hydrogen atoms of $Sr(H_2PO_3)_2$ and the lone electron pairs are considered to be equivalent. The coordination of Sr is that of a distorted square antiprism. These SrO_8 polyhedra share three common edges and are additionally connected via O–X–O bonds of the isolable XO_2OH^- ions ($X = HP^{IV}$) of tetrahedral configuration. The resulting layers $^2[Sr(XO_2OH)_2]$ are connected via circular hydrogen bond systems of tetrameric $[XO_2OH^-]_4$ groups of a cyclooctane-like chair topology. Both the P-bonded hydrogen atoms and the lone electron pairs of the $HP^{IV}O_2OH^-$ form channels along [001] and induce the same crystal structure. This is a new configuration for acid salts of the type $M^{II}(XO_2OH)_2 \cdot nH_2O$ with $X = HP^{IV}$.

$Sr(HPO_3) \cdot H_2O$ crystallizes in a monoclinic system with space group $P2_1/c$ with $a = 6.778$ Å, $b = 7.928$ Å, $c = 8.097$ Å, $\alpha = 67.9°$, $\beta = 84.8°$, $\gamma = 84.2°$, $V = 354.99$ Å^3. The structure consists of two-dimensional sheets formed by linked metal and phosphorus polyhedra, which are held together by O–H···O hydrogen bonds, similar to the ca-compound.

Strontium phosphite has no CAS number and is not offered for sale by any registered manufacturer.

Barium Phosphite

Barium phosphite can have the molecular formula of $BaHPO_3$ or $Ba(H_2PO_3)_2$ with molecular weights of 216.3021 and 296.2739 g/mol, respectively. It is the latter that appears when a solution of phosphorous acid is reacted with the carbonate:

$$BaCO_3 + H_3PO_3 \Rightarrow Ba(H_2PO_3)_2 + H_2O + CO_2$$

The product is soluble in water so that a vacuum evaporation is needed to form the hemihydrate, $Ba(H_2PO_3)_2 \cdot 0.5H_2O$. It can also be prepared by the action of ammonium phosphite on barium chloride:

$$BaCl_2\ (aq) + 2NH_4HPO_3\ (aq) \Rightarrow Ba(H_2PO_3)_2 \cdot 0.5H_2O + 2NH_4Cl\ (aq)$$

After evaporation, a white, crystalline powder is obtained. The solubility of $Ba(H_2PO_3)_2 \cdot 0.5H_2O$ has apparently not been determined exactly. If heated to about 130 °C, the anhydrate results. This is stable when heated further up to about 320 °C where it decomposes:

$$6Ba(H_2PO_3)_2 + \text{heat} \Rightarrow 2PH_3 + 2Ba_3(PO_3)_2 + 10H_2$$

$Ba(H_2PO_3)_2 \cdot 0.5H_2O$ contains ninefold-coordinated Ba^{2+} ions connected by dihydrogen phosphite anions to form a three-dimensional network. The asymmetric unit contains two Ba^{2+} ions, four $[H_2PO_3]^-$ ions and

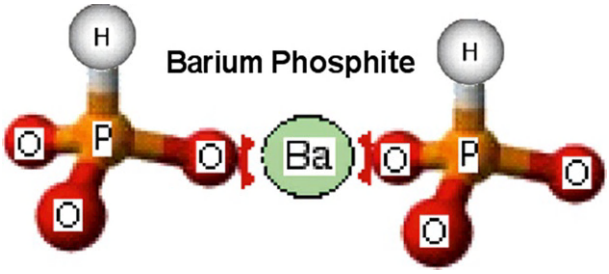

FIGURE 4.32

one water molecule. A ball and stick molecule are presented as follows. This may be compared to that of barium hypophosphite (Fig. 4.32).

The hydrogen phosphite compound is prepared by reaction of barium chloride and sodium phosphite:

$$BaCl_2 + 2NaHPO_3\,(aq) \Rightarrow Ba(HPO_3)\cdot H_2O\,(s) + 2NaOH\,(aq) + CO_2$$

The salt is substantially insoluble in water at 0.687 g/100 ml at 20 °C. This salt decomposes in boiling water to form phosphorous acid:

$$BaHPO_3\,(s) + 2H_2O\,(100\,^\circ C) \Rightarrow H_2PHO_3 + Ba(OH)_2$$

The literature regarding these barium phosphite salts is scarce and they have found little to no use in industry. Barium phosphite has no CAS number and is not offered for sale by a registered manufacturer. A few Chinese manufacturers state that they have a limited quantity available.

Radium Phosphite

Radium hypophosphite would have the molecular formula of $Ra(H_2PO_3)_2$ and $Ra(HPO_3)$ with the molecular weight of 383.6963 and 304.9974 g/mol, respectively. These salts have no CAS number and have never been prepared but could be formed by reacting the oxide with phosphorous acid:

$$RaO + 2H_3PO_3 \Rightarrow Ra(H_2PO_3)_2 + H_2O$$

In view of the intense radioactivity of ^{226}Ra, it is unlikely that these salts will ever be prepared.

Radium phosphite is not available commercially.

4.2.5. Alkaline Earth Phosphates

Alkaline earth orthophosphates are based upon phosphoric acid, H_3PO_4, in which the phosphorus atom has the oxidation state of +5. Orthophosphates are ubiquitous in Nature and "phosphate rock" is found in all parts of the world because the (PO_4^{3-}) cation is most stable of the phosphate species which includes hypo-ite, -ite, -ate, pyro-, meta- and poly- variations of -phosphates in which the P-atom is in the +1, +3, +5, +5, +5, +5 states, respectively.

If phosphoric acid is condensed to a solid by removing most of the water in which it is dissolved, it forms two solid hydrates. The thermal phase diagram shows two melting points, that of H_3PO_4 (40 °C) and that of $2H_3PO_4\cdot H_2O$ (28 °C), and two eutectics, that of H_8PO_4 (40 °C) and $2H_3PO_4\cdot H_2O$ (−85 °C) plus that of ice (0 °C). The heat of solution was found to be positive, +42.69 cals/mol of the crystalline acid dissolved. The heat of dilution in 11.4 mol of water/mol of acid was found to be +33.4 cals. Thus, it is clear that the acid, solid or liquid must be added to water and not the reverse.

The alkaline earths form three types of compounds based upon the number of hydrogen atoms in the phosphate complex, monobasic = $H_2PO_4^{3-}$, dibasic = HPO_4^{3-}, and tribasic = PO_4^{3-}. These arise dependant upon the pH and ionization constant of the acid in aqueous solution:

$$H_3PO_4\,(s) + H_2O\,(l) \Rightarrow H_3O^+\,(aq) + H_2PO_4^-\,(aq)$$
$$K_{a_1} = 7.25 \times 10^{-3}$$
$$H_2PO_4^-\,(aq) + H_2O_{(l)} \Rightarrow H_3O^+\,(aq) + H_2PO_4^{2-}\,(aq)$$
$$K_{a_2} = 6.31 \times 10^{-8}$$
$$HPO_4^{2-}\,(aq) + H_2O\,(l) \Rightarrow H_3O^+\,(aq) + PO_4^{3-}\,(aq)$$
$$K_{a_3} = 3.98 \times 10^{-13}$$

The regions of formation as a function of pH are shown in Fig. 4.33.

Thus, all of the monobasic salts are soluble and the solution must be evaporated to obtain the salt whereas the dibasic salts are insoluble and are easily separated from the solution. The ammonium dibasic salts generally provide the proper pH. The tribasic salts are insoluble in aqueous solution but the high pH demands the use of a soluble alkali salt. If a pure salt, free from the alkali cation, is desired, the best way is to sinter the dibasic salt with an oxide, hydroxide or carbonate.

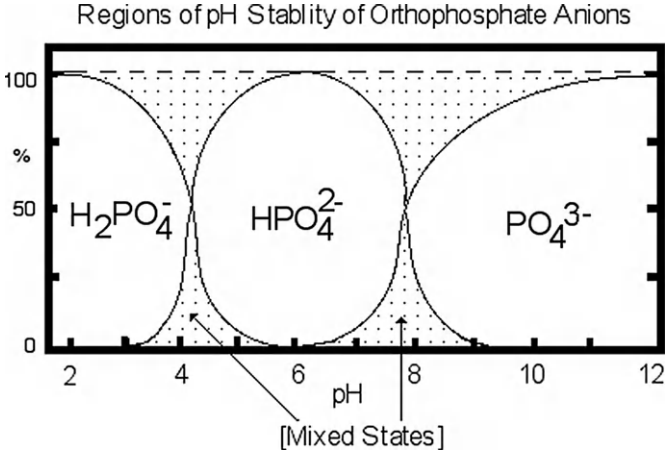

FIGURE 4.33

Beryllium Orthophosphates

The literature concerning the normal phosphates of beryllium is very far from clear. A few investigators who have taken up the subject have found the material they produced to be of a gelatinous nature very difficult to identify as an individual salt. The properties of the monobasic and dibasic salts have remained unknown. Their exact solubility in water is unknown. The formula for the monobasic salt ought to be $[Be(OH)]H_2PO_4$ while that of the dibasic salt should be $[Be(OH)]_2HPO_4$. However, it is listed and offered for sale as "Beryllium hydrogen phosphate—$BeHPO_4$—CAS number = 23598-15-7" with a molecular weight of 104.991 g/mol. It is described as insoluble in water.

The best-known phosphate is the compound $BeNH_4PO_4 \cdot 5H_2O$. It is prepared by adding diammonium phosphate to $BeCl_2$ at pH = 5.2–5.5. If the pH is lower than this, $Be(OH)HPO_4$ is also obtained. Heating $BeNH_4PO_4$ releases 4 waters of hydration at 60 °C and the final one at 250 °C. Ammonia is released at 400 °C and water of constitution at 500 °C to form the pyrophosphate at 700 °C. $BeNH_4PO_4$ crystallizes in the tetragonal system with $a = 12.96$ Å and $c = 9.65$ Å. $BeHPO_4$ is also tetragonal with $a = 9.05$ Å and $c = 9.65$ Å.

The only other salt identified and confirmed has been the tribasic salt, $[Be(OH)]_3PO_4$, which is described as a soluble salt. It is prepared by the reaction of trisodium phosphate and a soluble beryllium salt:

$$Be(OH)Cl_2\ (aq) + Na_3PO_4\ (aq) \Rightarrow [Be(OH)]_3PO_4$$

Upon evaporating the solution, a trihydrate is obtained as colorless crystals. $[Be(OH)]_3PO_4 \cdot 3H_2O$ loses one water of hydration at about 100 °C and the other two by 140 °C. Further heating presumably forms the pyrophosphate but there is no record of this in the literature.

Beryllium tribasic phosphate is said to form the heptahydrate, $[Be(OH)]_3PO_4 \cdot 7H_2O$ when alcohol was added to cause the formation of crystals. This preparation (1878) involved precipitating and growing crystals from a phosphoric acid solution of beryllium hydroxide with alcohol. However, this preparation and data obtained have never been confirmed. It is likely that the trihydrate dominates.

So-called "low-dimensional" beryllium phosphates have received some attention in the literature. They are composed of:

$$[C_5H_{14}N_2]_2[Be_3(HPO_4)_5] \cdot H_2O \quad \text{(I)}$$

and

$$[C_6H_{18}N_2]_{0.5}[Be_2(PO_4)(HPO_4)OH] \cdot 0.5H_2O \quad \text{(II)}$$

They were synthesized under mild hydrothermal/solvothermal conditions. The first is built up from strict alternation of BeO_4 and HPO_4 tetrahedra forming a unique one-dimensional double chains with 12-ring apertures. There are pseudo-10-ring apertures enclosed by two double chains through H-bonds. This compound can also be viewed as a pseudo two-dimensional layered structure stabilized by strong H-bonds. The diprotonated 2-methylpiperazium cations are located at three positions (i.e. inside the 12-ring aperture, inside the pseudo-10-ring aperture, and in the interlayer of the inorganic pseudo-layers.

The second is constructed by the alternation of Be-centered tetrahedra (including BeO_4 and $HBeO_4$) and P-centered tetrahedra (including PO_4 and HPO_4) resulting in a two-dimensional layered structure parallel to the (011) direction. The complex layer is composed of coupled 4.8 net-sheets. The diprotonated 1,6-hexandiamine cations and water molecules reside in the interlayer regions and interact with the inorganic layers through H-bonds.

Crystal data are shown in Table 4.15.

TABLE 4.15 Crystal Parameters of Two "Low-Dimensional" Beryllium Phosphates

			Angstroms				Degrees		
Type	Structure	Space Group	a	b	c	V (A^3)	α	β	γ
I	Triclinic	P_1 (No. 2)	8.1000	8.4841	18.6650	1321.9	89.683	78.182	87.932
$[C_5H_{14}N_2]_2\ [Be_3(HPO_4)_5] \cdot H_2O$ (I)									

			Angstroms				Degrees		
Type	Structure	Space Group	a	b	c	V (A^3)	α	β	γ
II	Orthorhombic	Pccn (No.56)	26.011	8.431	9.598	2105	—	—	—
$[C_6H_{18}N_2]_{0.5}[Be_2(PO_4)(HPO_4)OH] \cdot 0.5H_2O$ (II)									

Beryllium phosphates are found as minerals in several parts of the world. These include:

$$\text{Beryllonite} = NaBePO_4$$
$$\text{Hurlbutite} = CaBe_2(PO_4)_2$$
$$\text{Hydroxylherderite} = CaBe[(OH,F)|PO_4]$$
$$\text{Glycine} = CaBe_4[(OH)_2|PO_4]_2\cdot 0.5H_2O$$
$$\text{Fransoletite} = Ca_3Be_2[HPO_4]_2\cdot 4H_2O$$
$$\text{Moraesite} = Be(OH)_2PO_4\cdot 3H_2O$$

Moraesite, a hydrous beryllium phosphate from the Sapucaia pegmatite mine, Minas Gerais, Brazil, has the composition $Be_2PO_4(OH)\cdot 4H_2O$. It occurs in spherulitic masses, as distinct crystals, and as crusts with a coarse fibrous structure. Crystals are singly terminated needles, acicular [001] with forms [100] and {130} and faces (131) and (131). Moraesite is monoclinic and prismatic (2/m, C_n) Lattice constants are: $a_0 = 8.55$ Å, $b_0 = 36.90$ Å, $c_0 = 7.13$ Å, $\beta = 97°41''$, $V = 2{,}229$ Å^3, $Z = 4$. It is biaxial negative, $2Y = 65''$; $\eta_\alpha = 1.462$, $\eta_\beta = 1.482$, $\eta_\gamma = 1.490$.

Beryllonite, $NaBePO_4$, is a rare beryllium mineral. It is found at only a few places around the world. It can be cut as gems, but lacks color, fire and hardness to be a popular gemstone. The first and some of the best specimens of beryllonite have come from McKean Mt., Stoneham, Maine. It forms from pegmatitic dikes and can be easily confused with more common pegmatite minerals. Crystals are colorless, white to pale yellow.

The mineral, **herderite**, $CaBePO_4(F,OH)$, calcium beryllium phosphate fluoride hydroxide is an attractive and, except in some mines in New England, a rather scarce phosphate mineral. It forms regular crystals and can have a nice yellow or light blue color. Its twinned crystals are its most noteworthy form although its simple prismatic crystals can have quite complex and interesting terminations

There is no demand for any of these compounds in industry. The tribasic salt has been given a CAS number of 35089-00-0. This salt is offered for sale by a few registered manufacturers. The dibasic salt, listed as $BeHPO_4$, has been assigned a CAS number of 23598-15-7. It is said to be insoluble in water. It is also offered for sale by few producers, notably Chinese. The actual constitution of this salt remians questionable and unknown.

Magnesium Orthophosphates

Magnesium forms all three of the orthophosphates salts rather easily. These are the monobasic, dibasic and tribasic varieties.

MONOBASIC SALT: $Mg(H_2PO_4)_2$

This is prepared by dissolving the oxide, the hydroxide or the carbonate in excess phosphoric acid. The best acid to cation ratio appears to be at least 2.5 to 1.0. If the pH is allowed to climb more than about 3.5, the insoluble dibasic salt begins to appear. Addition of acid causes it to redissolve. All alkaline earth monobasic salts are water soluble so that the solution must be evaporated to obtain the salt. The result is the monobasic salt, $Mg(H_2PO_4)_2\cdot 3H_2O$. Its molecular weight is 175.3025 g/mol while that of the anhydrate is 121.2563 g/mol. Its CAS number is 13092-66-5. It is also known as: magnesium biphosphate; primary magnesium phosphate; acid magnesium phosphate; magnesium tetrahydrogen phosphate.

Monobasic magnesium phosphate decomposes upon heating and loses waters of hydration at 145, 168 and 173 °C, respectively. The formation of the anhydrate is complete by 200 °C. The conversion to the acid pyrophosphate, $MgH_2P_2O_7$ is complete by 450 °C. This compound then forms a metaphosphate glass whose composition depends upon the cycle of heating.

Such glasses have been studied.[1] The XRD profile of magnesium glasses have been measured and the pair function distributions were calculated. Using the pair function method, distance and coordination numbers for the pairs of P–O, O–O, and Mg–O were determined. A fundamental unit of the structure in this phosphate glass is confirmed to be a PO_4 tetrahedron. It is found that in the structures of the abnormal-type magnesium phosphate glasses consist of long chains with many branches, and most of Mg^{2+} atoms are surrounded by four oxygens. Thus, the distinct structural difference for abnormal-type phosphate glasses was recognized by XRD results. However, an abrupt change of an oxygen coordination number around a metallic ion at the metaphosphate concentration was not observed, which is previously considered to be a main reason for the abnormal behavior of these abnormal-type phosphate glasses.

Monobasic magnesium phosphate has found limited usage in industry. It has been evaluated in fireproofing wood. As a food additive, it is used as an acidity regulator.

This salt is available commercially from several listed manufacturers.

DIBASIC SALT: $MgHPO_4$

Magnesium phosphate dibasic has the formula of $MgHPO_4$ and the molecular weight of 120.2626 g/mol. It is also called magnesium hydrogen phosphate; secondary magnesium phosphate. Its CAS number is 7757-86-0. It may be prepared by reacting the oxide,

[1]see "Inorganic Polymeric Glasses" by RC Ropp, ISBN 0-444-89500-0- Elsevier, 1992

hydroxide or carbonate in phosphoric acid at a pH of about 5.6–6.0. (Ammonia cannot be used to control the pH since it forms a double salt $MgNH_4PO_4$.) The result is a stable trihydrate, $MgHPO_4 \cdot 3H_2O$. Its density is 2.123 g/cm^3. It is slightly soluble in water, soluble in acid but insoluble in ethanol. The heptahydrate also forms at low solutions concentrations. $MgHPO_4 \cdot 7H_2O$ is a white monoclinic needlelike compound with a density of 1.728 g/cm^3 at 15 °C. It is also sparingly soluble in water (0.3 g/100 ml at 20 °C), soluble in acids but insoluble in ethanol.

If ammonia is used, the magnesium present is precipitated in highly alkaline solution as the hydrated crystal, $MgNH_4PO_4 \cdot 6H_2O$. When calcined at 1100 °C, it decomposes to the pyrophosphate $Mg_2P_2O_7$. Various mechanisms have been proposed for the course of decomposition of the magnesium-ammonium salt. It has been shown that a loss of 5 mols of water but no ammonia occurs at about 105 °C. The simultaneous decomposition and loss of the monohydrate and the ammonium radical itself occurs above 250 °C.

The dibasic magnesium phosphate trihydrate is a white crystalline powder with an orthorhombic structure. Its refractive index is 1.514 and density is 2.123 g/cm^3 at 15 °C. When heated, it loses a molecule of water at 105 °C and one more at 165 °C. The anhydrate is formed at 205 °C by losing the last molecule of water. It is stable to about 650 °C where it reacts to form the pyrophosphate:

$$2MgHPO_4 + \text{heat} \Rightarrow Mg_2P_2O_7 + H_2O$$

The pyrophosphate is stable at least to 1200 °C.

The dibasic magnesium phosphate trihydrate crystal is Orthorhombic with the space group = *mmm* (2/*m* 2/*m* 2/*m*)—Dipyramidal. The cell parameters are: $a = 10.23$ Å, $b = 10.68$ Å, $c = 10.01$ Å, $V = 1090.45$ Å^3, $Z = 6$. It is a biaxial (+) crystal with refractive indices of $\eta_\alpha = 1.514$, $\eta_\beta = 1.517$, $\eta_\gamma = 1.533$. Another source gave the cell parameters as: $a = 10.203$ Å, $b = 10.678$ Å, $c = 10.015$ Å, $Z = 8$, space group Pbca.

The trihydrate is found in nature as the mineral, "Newberyite" ($Mg(PO_3OH) \cdot 3H_2O$)—found in caves, formed directly from bat guano and as "Phosphoroesleriite" ($MgHPO_4 \cdot 7H_2O$). The latter mineral has a density of 1.721–1.729 g/cm^3. It is Monoclinic with the space group 2/m—prismatic.

A number of magnesium phosphate dibasic minerals have been found throughout the world. They are quite numerous. Some of these are:

$$\text{Dittmarite} = MgNH_4PO_4 \cdot H_2O$$
$$\text{Struvite} = MgNH_4PO_4 \cdot 6H_2O$$
$$\text{Hannayite} = Mg_3(NH_4)_2(PO_4) \cdot 8H_2O$$

Note that these are double salts. Dibasic magnesium phosphate is used as a food additive and also as a laxative. It also has been used as a stabilizer in certain plastics.

This salt is available commercially from several manufacturers, both domestically and foreign.

TRIBASIC SALT: $Mg_3(PO_4)_2$

This salt can be formed by the addition of a soluble salt like magnesium chloride to a solution of sodium phosphate:

$$3MgCl_2\ (aq) + 2Na_3PO_4\ (aq) \Rightarrow Mg_3(PO_4)_2 + 3NaCl$$

This forms the stable hydrate, $Mg_3(PO_4)_2 \cdot 4H_2O$ whose CAS number is 7757-87-1 and molecular weight is 239.6124 g/mol. Other hydrates have been formed by varying the solution concentration before precipitation. Those that have been studied include $Mg_3(PO_4)_2 \cdot 8H_2O$ and $Mg_3(PO_4)_2 \cdot 22H_2O$. The octahydrate occurs naturally as the mineral "Bobierrite", $Mg_3(PO_4)_2 \cdot 8H_2O$. The tribasic salt is also known as "magnesium orthophosphate", "neutral magnesium phosphate", and "tri-magnesium phosphate".

All basic magnesium phosphates find applications in plastics as stabilizers. The tribasic phosphate is an antacid and a nutritional food supplement. The compound also is an adsorbent and a polishing agent in dental work.

The tetrahydrate of the tribasic phosphate, $Mg_3(PO_4)_2 \cdot 4H_2O$ is a bulky and soft white powdery material. It forms monoclinic crystals with a density of 1.64 g/cm^3 at 15 °C. It is slightly soluble in water (0.02 g/100 ml at 20 °C) and soluble in acids. The naturally occurring octahydrate, "Bobierite", is a white crystalline solid, containing monoclinic plates with a refractive index of 1.510, has a density of 2.195 g/cm^3 at 15 °C. When heated, it loses two molecules of water of crystallization at 150 °C and loses all water at 400 °C. This salt is insoluble in water but soluble in dilute mineral acids.

The crystal structure was solved from powder XRD data. $Mg_3(PO_4)_2 \cdot 4H_2O$ crystallizes in the orthorhombic space group $Cmc2_1$ (No. 36) with $a = 8.41087(9)$ Å, $b = 17.3850(2)$ Å, $c = 12.8034(1)$ Å, $V = 1872.15(4)$ Å^3 and $Z = 8$. The structure consists of sheets stacked along [010], which are linked by edge-sharing octahedral $Mg_2O_6(H_2O)_4$ dimers. Within the sheets, there are infinite edge-sharing chains of Mg octahedra along [100]. The compound has been further characterized by ^{31}P MAS-NMR spectroscopy and TGA. The crystal structure of two dehydrated variants existing around 200 °C ($Mg_3(PO_4)_2 \cdot 2.5H_2O$) and 275 °C ($Mg_3(PO_4)_2 \cdot 2H_2O$) remains unknown.

The anhydrate, magnesium orthophosphate $Mg_3(PO_4)_2$ forms rhombic crystals; melts at 1184 °C, is insoluble in water but soluble in ammonium salt solution.

THERMOCHEMICAL PROPERTIES [$Mg_3(PO_4)_2$]

$$\Delta H_f^0 = -903.6 \text{ kcal/mol}$$
$$\Delta G_f^0 = -845.8 \text{ kcal/mol}$$
$$S^0 = 45.2 \text{ cal/degree mol}$$
$$C_P = 51.0 \text{ cal/degree mol}$$

The basic phosphates that occur naturally may be extracted from their respective minerals. They are formed by reactions of phosphoric acid with intrinsic magnesium oxide and/or hydroxide followed by crystallization from solution. Tribasic magnesium phosphate can be prepared by treating magnesium ores with phosphoric acid at high temperature. Some of these natural phosphates include:

$$\text{Farringtonite} = Mg_3(PO_4)_2$$
$$\text{Holtedahlite} = Mg_2(OH)PO_4$$
$$\text{Althausite} = Mg_2[(OH,F)|PO_4]_2$$

Tribasic magnesium phosphate is available as an impure salt from a number of commercial suppliers as well as the pure salt used as a food supplement and additive to dental pastes.

APATITES OF MAGNESIUM

Magnesium does not form the usual haloapatite formulation of 5:3 cation to anion ratio. Instead, the compound, $Mg_4O(PO_4)_2$ is known. This is not an apatite per se but is related in structure. The mineral, "Althausite" = $Mg_2(PO_4)(OH, F, O)$" is orthorhombic with Point Group: 2/m 2/m 2/m. It was found at Tingelstadtjern Quarry, Norway, its Space Group is Pnma and lattice parameters of: $a = 8.258$ Å, $b = 6.054$ Å, $c = 14.383$ Å, $Z = 8$, $V = 719.06$ Å^3, density = 2.98 g/cm^3.

A similar mineral, "Raadeite" = $Mg_7(PO_4)_2(OH)_8$ was found within the Tingelstadtjern serpentinite body, Norway. It is colorless, transparent, biaxial (−) [for = 589 nm], with refractive indices of $\eta_x = 1.5945$, $\eta_y = 1.6069$, $\eta_z = 1.6088$, $2V_{meas} = 45.6°$, $2V_{calc} = 43°$; strong dispersion $r > v$. The infrared spectrum shows prominent OH stretching bands at 3375, 3475, 3540 and 3580/cm. Raadeite is monoclinic, space group $P2_1/n$, $a = 5.250(1)$, $b = 11.647(2)$, $c = 9.655(2)$ Å, $\beta = 95.94(1)°$, $Z = 2$.

Magnesium can be incorporated into the structures of calcium or strontium haloapatites. Magnesium was incorporated in the compound according to the formula $(Ca_{10-x}Mg_x)_{10}(PO_4)_6(OH)_2$, where $x = 0$, 0.50, 1.00, 1.50 and 2.00. The magnesium hydroxyapatite should be described as $(Ca_{0.86}Mg_{0.14})_{10}(PO_4)_6(OH)_2$.

0.01w?>Ionic activity data were used to determine the phase relationships existing under aqueous conditions along the $Mg_5F(PO_4)_3 \cdot Mg_5OH(PO_4)_3$ join of the system $MgOP_2O_5 \cdot MgF_2 \cdot H_2O$. The results indicated that magnesium analog of fluoroapatite $Ca_5F(PO_4)_3$ and hydroxyapatite $Ca_5OH(PO_4)_3$ are unlikely to be found under aqueous conditions.

Magnesium does form a series of similar compounds with the sodium salt. The $MgO–Mg_3(PO_4)_2–Mg_4Na(PO_4)_3–Na_4P_2O_7$ subsystem of the ternary system $MgO–Na_2O–P_2O_5$ was investigated using thermal analysis (heating and cooling), XRD techniques and microscopy in reflected light. Three intermediate compounds: $Mg_4Na(PO_4)_3$, $MgNaPO_4$ and $MgNa_4(PO_4)_2$ occur in the partial system. $Mg_4Na(PO_4)_3$ melts incongruently at 1155 °C, $MgNa_4(PO_4)_2$ melts congruently at 1655 °C, whereas $MgNaPO_4$ exists only in the solid phase and decomposes at 950–960 °C. A phase diagram for the partial system was proposed. It has been established that the $MgNa_4(PO_4)_2$ phosphate forms a binary system with $Na_4P_2O_7$. A phase diagram of this specific system has been constructed. It was found that a ternary peritectic ($t_P = 1145 \pm 3.0$ °C) and two ternary eutectics ($t_{E1} = 984 \pm 3.0$ °C, $t_{E2} = 732 \pm 1.5$ °C) occur in the $MgO–Mg_3(PO_4)_2–Mg_4Na(PO_4)_3–Na_4P_2O_7$ system.

In another study, the partial system $Mg_3(PO_4)_2–Mg_4Na(PO_4)_3–Na_4P_2O_7–Mg_2P_2O_7$ in the ternary system $MgO–Na_2O–P_2O_5$ was investigated using thermal and XRD analyses and microscopy, and its phase diagram has been determined. In this range of composition, two binary phosphates occur: $Mg_4Na(PO_4)_3$ and $Mg_6Na_8(P_2O_7)_5$. The former melts incongruently (at 1155 °C) and the latter does so congruently (at 808 °C). In the partial system of interest, the two sections $Mg_4Na(PO_4)_3–Mg_2P_2O_7$ and $Mg_4Na(PO_4)_3–Mg_6Na_8(P_2O_7)_5$ were studied, and their phase diagrams were established. The partial system is divided into three partial ternary systems in which two ternary eutectics and one ternary peritectic occur.

None of these compounds are offered for sale commercially. The only interest in their properties has been academic, not industrial. No CAS numbers are available.

Calcium Orthophosphates

All of the possible calcium phosphates are known and can be prepared from phosphoric acid and calcium carbonate.

CALCIUM PHOSPHATE, MONOBASIC

This salt has the formula, $Ca(H_2PO_4)_2$ and the molecular weight of 137.0293 g/mol. Its CAS number is 3358-23-8. It is easily prepared by dissolving calcium carbonate in an excess of H_3PO_4. A ratio of at least 3:1 mol of acid is required:

$$CaCO_3 + 2H_3PO_4 \Rightarrow Ca(H_2PO_4)_2 + CO_2 + H_2O$$

If the pH exceeds about 3.8, the dibasic salt begins to precipitate. The monobasic salt is soluble so that the

solution must be evaporated, usually at high temperature, >80–90 °C. A monohydrate, $Ca(H_2PO_4)_2 \cdot H_2O$, readily forms acicular crystals.

The CAS numbers are: anhydrous: 7758-23-8, monohydrate: 10031-30-8. Their molecular weight is: anhydrous: 238.0122 g/mol, monohydrate: 256.0264 g/mol. Synonyms are: monocalcium orthophosphate; calcium biphosphate; primary calcium phosphate, calcium dihydrogen phosphate.

The monohydrate occurs as colorless shiny crystals, granules or powder. The impure material is hygroscopic due to the presence of traces of phosphoric acid and other impurities. The density of the monohydrate is 2.22 g/cm^3. It is moderately soluble in water (1.82 g/100 ml at 20 °C) and more so in dilute acids. The monohydrate loses water at 191 °C to form the anhydrate. Upon further heating, the acid pyrophosphate is formed at 291 °C and a series of metaphosphates are formed at 342, 361, 383, 400 and 553 °C before the final stage at 637 °C to form a polymeric metaphosphate, $[Ca(PO_3)_2]_n$.

$Ca(H_2PO_4)_2 \cdot H_2O$ crystallizes in the space group PI with the triclinic unit cell parameters of $a = 5.6261$ Å, $b = 11.8891$ Å, $c = 6.473$ Å, β = 98"633, $V = 118.262$ $Å^3$, and $\beta = 83.344$ ° at 25 °C with $Z = 2$. The hydrogen positions have been determined by neutron diffraction and no evidence of disorder was found. The two crystallographically distinct $H_2PO_4^-$ ions are hydrogen bonded to each other and to the water molecule. The distances of Ca···O and H···O bonds are 2.479 and 1.679 Å, respectively.

$Ca(H_2PO_4)_2$ crystallizes in the triclinic unit cell with $a = 7.5577$ Å, $b = 8.2561$ Å, $c = 5.5504$ Å, $\alpha = 109.87°$, $\beta = 93.68°$, $\gamma = 109.15°$, $V = 302.5$ $Å^3$ with $Z = 2$. The structure consists of rudimentary chains of Ca–$[P_{(1)}O_4]$-$H_{(1)}$)–$[P_{(2)}O_4]$… that run parallel to the (110) direction. Adjacent chains are joined by Ca···O bonds on one side and by $O_{(8)}$–$H_{(5)}$···$O_{(8')}$ hydrogen bonds on the other. These layers are held together by hydrogen bonds on one side and Ca···O bonds on the other. There are two very strong bonds in the structure: $O_{(7)}$–$H_{(4)}$–$O_{(7')}$ and $O_{(8)}$–$H_{(5)}$–$O_{(8')}$. These very strong hydrogen bonds join the $(P_{(2)}O_4)$ groups together to form an infinite chain and are centers of symmetry.

Monobasic calcium phosphate is primarily used in fertilizers. It has been called "superphosphate" since it is slightly soluble and more easily available to plants in the soil. It is also used in baking powders and as a mineral supplement in food. It is a buffer for pH control and as a stabilizer for plastics. A fertilizer grade product can be obtained by dissolving pulverized phosphate rock (tricalcium phosphate) in phosphoric or sulfuric acid and then evaporating the solution.

Calcium dihydrogen phosphate is also used in the food industry as a leavening agent to cause baked goods to rise. Because it is acidic, when combined with an alkali ingredient—commonly $NaHCO_3$ (baking soda)—it reacts to produce CO_2 and a salt. The carbon dioxide gas is what leavens the baked goods. When combined in a ready-made baking powder, the acid and alkali ingredients are included in the right proportions such that they will exactly neutralize each other. Apart from acting as leavening agent, it also inhibits microbial activity because of the phosphate ions present in the molecule.

Calcium dihydrogen phosphate is readily available commercially in tonnage quantities. There are 22 suppliers in the U.S. alone and over 3 million exporters and importers worldwide.

CALCIUM PHOSPHATE, DIBASIC

Dibasic calcium has the formula $CaHPO_4$ and the CAS number 7757-93-9. Its molecular weight is 136.0658 g/mol. It also occurs as the dihydrate, $CaHPO_4 \cdot 2H_2O$, known as "Brushite" (CAS number = 7789-77-7). The anhydrate is "Monetite"—$CaHPO_4$. Synonyms are: calcium hydrogen phosphate; secondary calcium phosphate; bicalcium phosphate. The most prevalent use of dibasic calcium phosphate has been in the manufacture of "Halophosphate" phosphors, $Ca_5(F,Cl)(PO_4)_3$:$Sb^{3=}$:Mn^{2+}, used as the main ingredient in all fluorescent lamps. Halophosphate phosphors were introduced about 1940 to replace zinc beryllium orthosilicate phosphors which were found to induce "Berylliosis" in Humans who handled it during the manufacture of fluorescent lamps.

It was determined that brushite could be converted to Monetite (both are slightly soluble in water) after the brushite had been formed by the addition of diammonium phosphate to a calcium chloride solution:

$$CaCl_2 + (NH_4)_2HPO_4 \Rightarrow CaHPO_4 \cdot 2H_2O$$

This is usually accomplished at room temperature. Dicalcium Phosphate Dihydrate (DCPD), also known as Brushite, is a hydrated calcium phosphate mineral with the composition $CaHPO_4 \cdot 2H_2O$. The structure of DCPD is almost identical to that of gypsum with their respective unit cell dimensions very similar. The phosphate of DCPD is isomorphous with arsenate, which forms instead, the mineral Pharmacolite. The backbone of DCPD is made up of alternating calcium and phosphorus atoms which form chains via the sharing of oxygens (the four phosphate oxygens). These chains run perpendicular to the ***b***-axis in the plane formed by the ***a*** and ***c*** axes (Fig. 4.34).

The phosphorus atoms have fourfold coordination forming phosphate tetrahedra while the calcium atoms have eightfold coordination. Four of calcium's bonds are with these phosphate tetrahedra, forming the backbone chains, while two more of the calcium bonds are

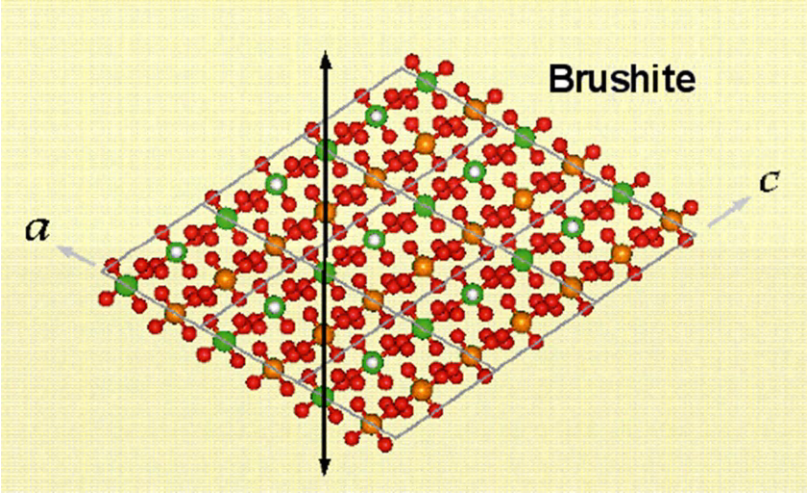

FIGURE 4.34

with oxygens from neighboring chains. These last bonds which link the chains together result in a zigzag pattern or corrugated sheet. The last two calcium bonds are with the water molecules. These water molecules are what hold the sheets together.

A continuous process has arisen in industry to convert brushite to Monetite. The equipment used to manufacture $CaHPO_4$ is shown in Fig. 4.35.

CONTINUOUS PROCESS FOR $CaHPO_4$

1. This process is used to manufacture the halophosphate phosphor and is made in tonnage quantities each month. $CaHPO_4$ is dimorphic in that it forms "brushite", i.e. $CaHPO_4 \cdot 2H_2O$ at precipitation temperatures below about 35 °C and "Monetite", i.e. $CaHPO_4$, above about 65–70 °C. The brushite crystals, formed at 25 °C, are "poorly-crystalline" to amorphous while the monetize crystals, formed at 65 °C are also not very crystalline. By a separate conversion in solution, brushite is first formed and then redissolved to form Monetite, a very crystalline product.
2. Brushite is converted to Monetite from a slurry suspension by reheating the suspension. Brushite crystals are of indeterminate size and crystallinity.

   The conversion produces flat plates or diamond-shaped crystals. Since the solubility product of $CaHPO_4$ is $K_{SP} = 3.4 \times 10^{-14}$, the solution equilibrium is a dynamic one:

$$Ca^{2+} + HPO_4^{=} \Leftrightarrow CaHPO_4 \Downarrow$$

3. In this process, a series of processing and holding tanks are used to purify both the $CaCl_2$ and the $(NH_4)_2HPO_4$ solutions, whereupon each solution stored is ready for use. Sulfide is added on a continuous basis.
4. These solutions are then pumped into a precipitation tank to form the $CaHPO_4 \cdot 2H_2O$ on a continuous basis. Then, the slurry is fed to a drum filter where the mother liquor is separated. The wet cake is then reslurried at a specific ratio of solid to water (sometimes containing a small amount of soluble phosphate) and the pH of the slurry is adjusted.
5. Thereupon, it is pumped to a conversion tank wherein the particles undergo a change from brushite to Monetite of predetermined size and proportions via the reaction:

$$[CaHPO_4]_{\text{brushite}} \Rightarrow Ca^{2=} + HPO_4^{2-} \Rightarrow [CaHPO_4]_{\text{Monetite}}$$

6. As stated above, a thick slurry will form the diamond-shaped crystals, whereas a thinner slurry forms the square crystals. The same general precipitation procedure is then followed. The type of crystals being formed during conversion is important. Increasing the solid content of the slurry gives diamond-shaped crystals while decreasing it tends to form elongated cubes rather than flat square crystals.
7. Product desired = flat, platy diamond-like crystals of about 7–9 μ (microns) in size. If a truly diamond-shaped crystal is desired, i.e. the procedure for making $CaHPO_4$ is modified (since crystal habit forms basis for final shape of phosphor crystals; Fig. 4.36).
8. Particle size should be about 8.0 μ. Most manufacturers have chosen to prepare flat square platy crystals to form the particulate film. This is referred to as "covering power". It is now well established that particles less than about 3.0 μ and greater than 35–40 scatter the ultraviolet and generated visible light within the film to such

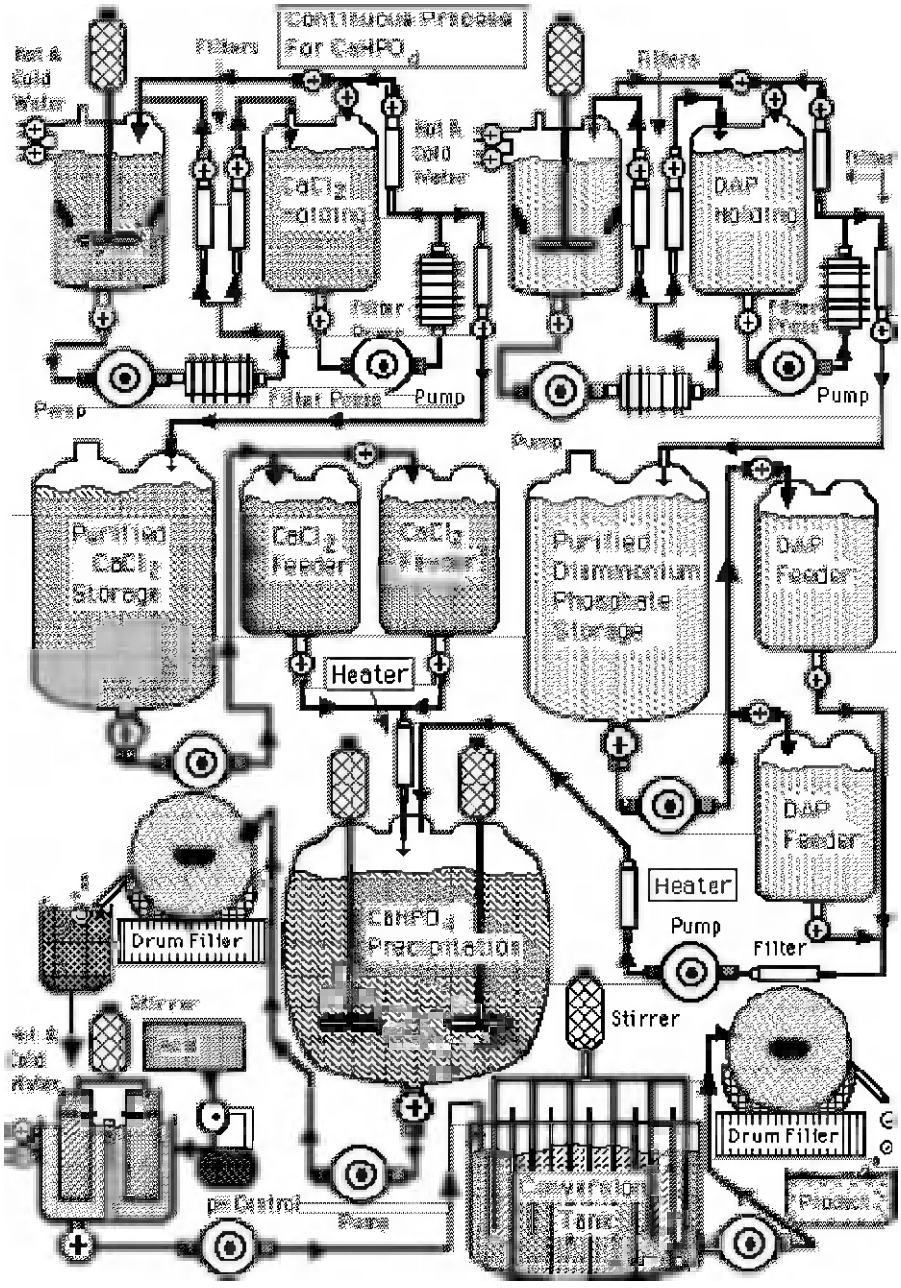

FIGURE 4.35

a degree that a loss of output of the fluorescent lamp results. Thus, the optimum particle size has been determined to be:

$$3.0\ \mu < \text{optimal particle size} < 35\text{–}40\ \mu$$

Dibasic calcium phosphate is found in nature as the mineral "Monetite". This mineral is triclinic (pinacoidal) and has the lattice parameters of: $a = 6.92$ Å, $b = 7.12$ Å, $c = 6.65$ Å, $Z = 4$; $\alpha = 96.35°$, $\beta = 91.267°$, $\gamma = 76.1°$, $V = 309.80$ Å^{33} and a density of 2.92 g/cm^3.

Dibasic calcium phosphate is also used as a food supplement and source of calcium, both in human food and animal feed. It is used in dough conditioner; in several dental products and in medicine.

Calcium hydrogen phosphate crystallizes as a double salt, $CaNaPO_4$. This salt has found some application in Dentistry and as a Medical bone graft. The use of biodegradable bone substitutes is advantageous in Dentistry for alveolar ridge augmentation, since it avoids second-site surgery for autograft harvesting. This study examines the effect of novel, rapidly resorbable calcium

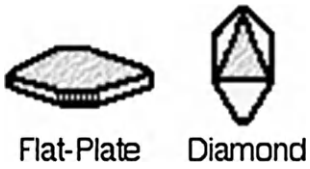

FIGURE 4.36

phosphates on the expression of bone-related genes and proteins by human bone-derived cells (HBDCs) and compares this behavior to that of tricalcium phosphate (TCP). Test materials were α-TCP, and four materials which were created from α-Rhenanite and its derivatives: R_1-α-Rhenanite ($CaNaPO_4$); R_1/M_2 composed of $CaNaPO_4$ and $MgNaPO_4$; $R_1 + SiO_2$ composed of $CaNaPO_4$ and 9% SiO_2 (wt%); and R_{17}-$Ca_2KNa(PO_4)_2$. HBDC were grown on the substrata for 3, 5, 7, 14 and 21 days, counted and probed for various mRNAs and proteins (Type I collagen, osteocalcin, osteopontin, osteonectin, alkaline phosphatase and bone sialoprotein). All substrata supported continuous cellular growth for 21 days. At day 21, surfaces of $R_1 + SiO_2$ and R_{17} had the highest number of HBDC. At 14 and 21 days, cells on R_1 and on $R_1 + SiO_2$ displayed significantly enhanced expression of all osteogenic proteins. Since all novel calcium phosphates supported cellular proliferation together with expression of bone-related proteins at least as much as TCP, these ceramics can be regarded as potential bone substitutes. R_1 and $R_1 + SiO_2$ had the most effect on osteoblastic differentiation, thus suggesting that these materials may possess a higher potency to enhance osteogenesis than TCP.

Other applications are in fertilizers, plastics and in the manufacture of glass. The salt used is less pure than those employed directly for human or animal consumption.

$CaHPO_4$, synthetic monetite, crystallizes in the triclinic unit cell $a = 6$–910 Å, $b = 6.627$ Å, $c = 6''998$ Å, $\alpha = 96'34°$, $\beta = 103''82°$, $\gamma = 88.33$ ° at 25 °C with cell contents of 4[$CaHPO_4$]. This structure may be regarded as $CaHPO_4$ chains bonded together by Ca···O bonds and three types of hydrogen bonds. These vary across the "normal" range, 2.565–2.669 Å. The P···O bond is about 2.567 Å. Ca(1) is coordinated to seven oxygen atoms with distances ranging from 2.2951 to 2.763 Å and Ca(2)–O distances are 2.379–2.5718 Å. Monetite is a white triclinic crystal; density 2.31 g/cm^3 (dihydrate). It is soft (3.5 Moh) and decomposes on heating to form the pyrophosphate.

Dibasic calcium phosphate can also be prepared by the reaction of phosphoric acid with tribasic calcium phosphate:

$$\underset{\text{Sl.Sol.}}{Ca_3(PO_4)_2} + \underset{\text{Sol.}}{Ca(H_2PO_4)_2} \Leftrightarrow \underset{\text{Insol.}}{4CaHPO_4}$$

This salt is readily available commercially in tonnage quantities from many manufacturers worldwide.

Both Monetite and Brushite are available in tonnage quantities from numerous sources, worldwide.

CALCIUM PHOSPHATE, TRIBASIC

Tricalcium phosphate has the formula $Ca_3(PO_4)_2$. It is also known as *tribasic calcium phosphate* or *"bone ash"* (calcium phosphate being one of the main products when bone is heated). It has an alpha and a beta crystal form, the alpha state being formed at high temperatures. As a mineral, it is found in "Whitlockite", which is a complex hydroxyapatite = $Ca_9(Mg,Fe)(PO_4)_6(PO_3OH)$. Its CAS number is 7758–87–4. Its molecular weight is 310.2045 g/cm^3. It is also known as "calcium orthophosphate; calcium phosphate; tricalcium phosphate; tertiary calcium phosphate; precipitated calcium phosphate; bone ash (technical product).

Tribasic calcium phosphate can be prepared by the reaction of calcium chloride added to a solution of trisodium phosphate. However, it is very difficult to obtain a pure product since this combination of solutions tends to form the hydroxyapatite, $Ca_5OH(PO_4)_3$ rather than the tribasic compound, $Ca_3(PO_4)_2$:

$$8CaCl_2\ (aq) + 5Na_3PO_4\ (aq) + H_2O \Rightarrow Ca_5OH(PO_4)_3\ (solid) + Ca_3(PO_4)_2 + 15NaCl_2 + HCl$$

The best way to prepare a pure product is to react monetite with calcium carbonate via a solid-state reaction:

$$2CaHPO_4 + CaCO_3 + heat \Rightarrow Ca_3(PO_4)_2 + CO_2$$

Calcium phosphate, tribasic, has the CAS number of 7758-87-4 and the molecular weight of 310.3346 g/mol. Its solubility in water is 0.00012 g/100 ml at 20 °C. It is a whiter, amorphous powder with a density of 3.14 g/cm^3 and a melting point of 1670 °C. Its solubility product is: $K_{sol} = 2.07 \times 10^{-33}$. The following thermodynamic constants of $Ca_3(PO_4)_2$ are known:

Enthalpy of formation: −4120.8 kJ/mol	Entropy: 236.0 J/mol K
Gibbs energy of formation: −3884.7 kJ/mol	Heat capacity: 227.8 J/mol K

It has been determined that the formation of tribasic calcium phosphate in solution is somewhat dependant upon the presence of $Ca(OH)_2$. If the monobasic salt is reacted with calcium hydroxide, the product is substantially the tribasic salt:

$$Ca(H_2PO_4)_2\ (aq) + 2Ca(OH)_2\ (solid) \Rightarrow Ca_3(PO_3)_2\ (solid) + 4H_2O$$

The solution is initially acidic but is shifted to just slightly alkaline as the calcium hydroxide dissolves and the tribasic salt forms as a precipitate. Nonetheless, it is possible to obtain a small fraction of hydroxyapatite as well.

The formation of tricalcium phosphate (TCP) from thermal reaction of dicalcium phosphate and calcium carbonate has been investigated using DTA, TGA, and powder XRD. DTA showed three distinct thermal events attributed to dehydration of DCPD (brushite) to dicalcium phosphate anhydrous (monetite, DCPA), the formation of beta-calcium pyrophosphate (β-$Ca_2P_2O_7$), and the calcination of calcium carbonate. TGA showed three weight losses corresponding to the three thermal events, respectively. XRD analysis showed that β-TCP formed, beginning at about 900 °C, by the reaction of β-$Ca_2P_2O_7$ with CaO and β-TCP changed to α-TCP above 1200 °C. Further examination of the formation of TCP from calcium hydroxide ($Ca(OH)_2$) and DCPA showed that β-TCP would form only after the decomposition of $Ca(OH)_2$ to CaO and from the reaction of CaO with β-$Ca_2P_2O_7$ at a fairly low temperature of 800 °C. In addition, by naturally cooling α-TCP, formed at 1300 °C within the heating furnace, to room temperature, it was difficult to obtain a pure phase of β-TCP. The proposed mechanism of the reaction to form TCP may include the dehydration of brushite to monetite, dehydration of monetite to beta-calcium pyrophosphate, decomposition of calcium carbonate, the formation of β-TCP, and phase transition.

The phase, α-$Ca_3(PO_4)_2$, is thermodynamically stable between the temperature range of 1120 and 1470 °C but is metastable at room temperature. It crystallizes in the monoclinic space group $P2_1/a$ with $a = 12.887$ Å, $b = 27.280$ Å, $c = 15.219$ Å, $\beta = 126.2°$ and $Z = 24$. The structure consists of columns of cations plus columns of anions and cations with compensating cation vacancies, and is closely related to the mineral "Glasserite", $K_3Na(SO_4)_2$. The calcium ions in α-$Ca_3(PO_4)_2$ exhibit a wide range of coordination numbers and geometries.

A related salt, an oxotetracalcium diphosphate, $Ca_4O(PO_4)_2$, is also known and is related to calcium hydroxyapatite. It crystallizes in the monoclinic unit cell of $a = 7.023$ Å, $b = 11.986$ Å, $c = 9.473$ Å, $\beta = 90.90°$ and space group of $P2_1$. The unit-cell dimensions of this salt and hydroxyapatite are similar and related. Although this three-dimensional relationship in the unit-cell shapes is not carried over in the details of the actual structures, $Ca_4O(PO_4)_2$ does contain a layer which is similar to that of hydroxyapatite. In this structural relationship, the oxide ions are "extra". One is weakly coordinated to the face of a PO_4-group, a feature that has been only observed in the β-$Ca_3(PO_4)_2$ structure as a distorted cation site. The two crystallographically discrete oxide ions are surrounded by tetrahedra of Ca^{2+} ions with Ca···O distances in the range of 2.136–2.277 Å. Thus, the oxide ions do not lie in the channel formed by cations in the structure and $Ca_4O(PO_4)_2$ cannot be considered to be an oxyapatite. The positions of the P atoms and those of the Ca atoms lie close to those required by the space group Pmcn. This explains the appreciable twinning exhibited by $Ca_4O(PO_4)_2$.

Tribasic calcium phosphate occurs in nature as the minerals:

$$\text{Oxyapatite} = Ca_{10}O(PO_4)_6$$
$$\text{Whitlockite} = Ca_9(Mg,Fe)(PO_4)_6(PO_3OH)$$
$$\text{Voelicherite} = (Ca,Mg,Fe)_{10}O(PO_4)_6$$
$$\text{Apatite} = Ca_5(PO_4)_3(OH,F,Cl)$$
$$\text{Phosphorite} = Ca_5(OH,F,Cl)(PO_4)_3\text{—amorphous}$$

The tribasic salt has many industrial applications. Some are similar to the monobasic and dibasic salts. It is used in fertilizers, dental products, ceramics and polishing powder. Some other important applications are in plastics as a stabilizer; as an anticaking agent; as a nutrient supplement in cattle food; for clarifying sugar syrup; as a mordant in dyeing textiles; and as a buffer to control pH.

Tricalcium phosphate is used in powdered spices as an anticaking agent. Calcium phosphate is an important raw material for the production of H_3PO_4 and fertilizers. In 1927, a process was invented wherein phosphate rock was processed to form a mixed fertilizer. The process involves acidifying the rock with nitric acid to produce a mixture of phosphoric acid and calcium nitrate:

$$Ca_3(PO_4)_2 + 6HNO_3 + 12H_2O \Rightarrow 2H_3PO_4 + 3Ca(NO_3)_2 + 12H_2O$$

The mixture is cooled to below 0 °C, where the calcium nitrate crystallizes and can be separated from the phosphoric acid:

$$2H_3PO_4 + 3Ca(NO_3)_2 + 12H_2O \Rightarrow 2H_3PO_4 + 3Ca(NO_3)_2 \cdot 4H_2O$$

The resulting calcium nitrate produces nitrogen fertilizer. The filtrate is composed mainly of phosphoric acid with some nitric acid and traces of calcium nitrate, and this is neutralized with NH_3 gas to produce a compound fertilizer:

$$Ca(NO_3)_2 + 4H_3PO_4 + 8NH_3 \Rightarrow CaHPO_4 + 2NH_4NO_3 + 3(NH_4)_2HPO_4$$

This method is now obsolete but was called the "ODDA Process".

Calcium phosphate is also a raising agent (food additives). It is a mineral salt found in rocks and bones. It is

used in cheese products. It is also a nutritional supplement and occurs naturally in cow's milk.

It is commonly used in porcelain and dental powders, and medically as an antacid or calcium supplement. It has been tried as a bony defect tissue replacement for repairing bony defects when autogenous bone graft is not possible.

Another practical application of the compound is its use in gene transfection. Calcium ions can make a cell porous to exogenous genes that can then enter the cell by diffusion. A heat shock afterward then invokes the cell to repair itself.

Thermochemical properties

$$\Delta H_f^0 = -984.9 \text{ kcal/mol}$$
$$\Delta G_f^0 = -928.5 \text{ kcal/mol}$$
$$S^0 = 56.4 \text{ cal/degree mol}$$
$$C_p = 54.4 \text{ cal/degree mol}$$

Tribasic calcium phosphate is available from many manufacturers worldwide. However, many of these actually supply the hydroxyapatite or a mixture of the two compounds.

CALCIUM APATITE COMPOUNDS

Calcium forms all of the apatite compounds possible, including the fluoro-, chloro-, hydroxy-, bromoapatites and iodoapatites. They all have the same composition, namely $Ca_5X(PO_4)_3$ where X is one of the halogens. They cannot, with the exception of the hydroxyapatite, be prepared from an aqueous solution but must be made by solid-state reaction. The overall enthalpy of formation of these apatite compounds has been determined. The standard ($p = 0.1$ MPa) molar enthalpies of formation in the crystalline state of hydroxyapatite, chlorapatite and a preliminary value for bromapatite, at $T = 298.15$ K, were determined by reaction-solution calorimetry as:

$$Ca_5OH(PO_4)_3 = -12{,}969 \text{ kcal/mol}$$
$$Ca_5Cl(PO_4)_3 = -13{,}231 \text{ kcal/mol}$$
$$Ca_5Br(PO_4)_3 = -13{,}063 \text{ kcal/mol}$$
$$Ca_5I(PO_4)_3 = -12{,}969 \text{ kcal/mol}$$

Those of Sr and Ba are similar. What this means is that the formation by solid-state reaction is energetically and thermodynamically driven and occurs rather easily under the right conditions. The general structure of haloapatites is hexagonal. The following diagram shows the two sites for the metal cations as well as the halogen sites in the lattice (Fig. 4.37).

This structure is indigenous to the apatite compounds and is found as a general composition, $M_{10}X_2(PO_4)_6$, where M is any of the alkaline earths (except Mg^{2+}) and X is any of the halogens including OH^-.

It is possible to estimate the lattice energy of these haloapatites. Experimentally based lattice energies are calculated for the apatite family of double salts $M_5X(PO_4)_3$, where M is a divalent metal cation (Ca, Sr, Ba) and X is hydroxide or a halide. These values are also shown to be estimable, generally to within 4%, using the recently derived Glasser-Jenkins equation:

$$U_{pot} = A \cdot I_{ion}/(2I_{ion}/V_m)^{1/3}$$

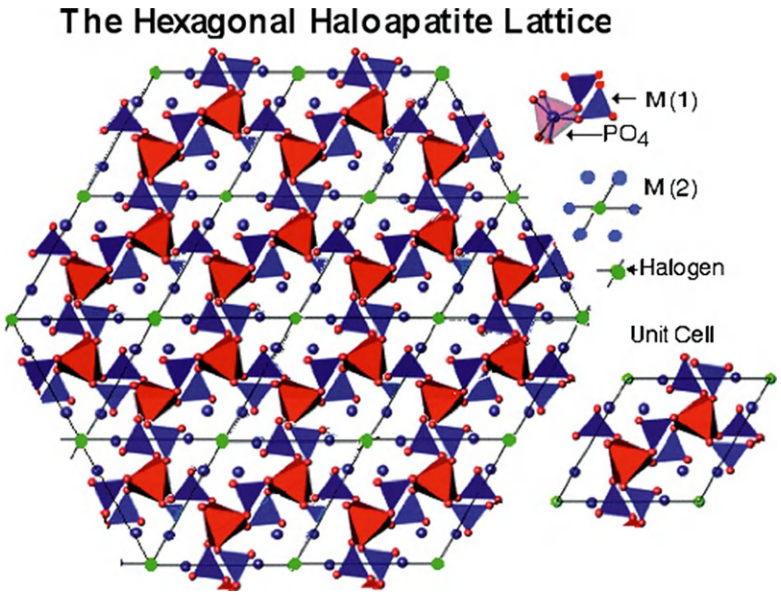

FIGURE 4.37

where A = 121.39 kJ/mol and M = Pb, Cd, etc. are less well reproduced but are within 8% of the experimentally based value. The lattice energy for ionic apatites (having identical lattice ionic strengths, I_{ion}) takes the particularly simple form which reproduces cycle values of U_{pot} well when V_m is estimated by ion volume summation and employing a volume for the PO_4^{3-} ion (not previously quantified with an associated error) of $0.063 \pm 0.003\ nm^3$.

$$U_{pot}/kJ/mol = 26680/(V_m/nm^3)^{1/3}$$

This allows one to compare the lattice stability of the various haloapatites. Because of the extensive usage of haloapatite phosphors in the lamp industry, the practical and theoretical knowledge of these compounds are broad. For example, the reactions that form apatites in general are:

Overall reaction:

$$6CaHPO_4 + 3CaCO_3 + CaF_2 + CaCl_2 \Rightarrow Ca_{10}(F,Cl)_2(PO_4)_6 + 3CO_2 + 3H_2O$$

Partial reactions:

a. $2CaHPO_4 \Rightarrow$ ß-$Ca_2P_2O_7$ (monoclinic) + H_2O
b. $CaCO_3 \Rightarrow CaO + CO_2$
c. $Ca_2P_2O_7 + CaO \Rightarrow$ ß-$Ca_3(PO_4)_2$ (triclinic)
d. ß-$Ca_3(PO_4)_2 + CaF_2 + CaCl_2 \Rightarrow Ca_5(F,Cl)(PO_4)_3$ (Hexagonal)

Probably, the most important fact concerning calcium apatite is that the hydroxyapatite is the dominant crystallite in human and animal bones.

Calcium Hydroxyapatite

This compound, also called hydroxylapatite, is a naturally occurring mineral form of calcium apatite with the formula $Ca_5(PO_4)_3(OH)$, but is usually written $Ca_{10}(PO_4)_6(OH)_2$ to denote that the crystal unit cell comprises two molecules. Pure hydroxyapatite powder is white. Naturally occurring hydoxyapatites can, however, also have brown, yellow, or green colorations, comparable to the discolorations of "dental-fluorosis".

Up to 50% of human bone is made up of a modified form of the inorganic mineral hydroxylapatite (known as bone mineral). Carbonated calcium-deficient hydroxylapatite is the main mineral of which dental enamel and dentin are comprised. Hydroxyapatite crystals are also found in the small calcifications (within the pineal gland and other structures) known as corpora arenacea or "brain sand". Hydroxyapatite is commonly used as a filler to replace amputated bone or as a coating to promote bone ingrowth into prosthetic implants. It has been suggested that this may promote osseointegration.

$Ca_{10}(PO_4)_6(OH)_2$ has the molecular weight of 502.3145 g/mol and the density of $3.16\ g/cm^3$. It has a hexagonal structure and the refractive index of $\eta_\omega = 1.651$, $\eta_\varepsilon = 1.644$. Birefringence, $\delta = 0.007$. It has been prepared by reaction of calcium chloride and trisodium phosphate:

$$CaCl_2\ (aq) + Na_3PO_4\ (aq) \Rightarrow Ca_5(PO_4)_3OH\ (solid) + NaCl\ (aq)$$

The chloride (45 °C) is added to the phosphate solution at 95 °C and the precipitate is allowed to recrystallize while stirring. It is then filtered, washed with water and dried. The system needs to be protected from the atmosphere since CO_2 will form a "carbonato-hydroxyapatite". Hydroxyapatites containing two levels of sodium and carbonate have been investigated by IR absorption spectroscopy and X-ray powder pattern fitting methods. Results confirm that both compounds relate to the apatite family crystallizing in a hexagonal system, space group $P6_3/m$. The cell parameters of the lower carbonate content apatite are $a = 9.3892$ Å and $c = 6.9019$ Å, while those of the higher one are $a = 9.3249$ Å and $c = 6.9213$ Å. Occupancy factors show that sodium is localized mainly in a 6h cationic site. Furthermore, carbonate ions occupy phosphate sites leading to a B-type carbonate apatite. These simultaneous substitutions affect the OH^- position in the channel, as well as the metal–oxygen interatomic distances. The substitution mechanism can be described using two of the six known elementary reaction mechanisms.

If the exactly pure hydroxyapatite is desired, $Ca(OH)_2$ is suspended in 100 °C water, protected from CO_2 by a NaOH trap, and 2.5 molar H_2PO_4 is added until the hydroxide disappears. The slurry of precipitate is then boiled until the pH exceeds 6.0 where any traces of $CaHPO_4$ are converted to hydroxyapatite. This apatite is hexagonal with $a = 9.424$ Å, $c = 6.885$ Å, $V = 446.73$ Å^3, $Z = 2$.

In another route of hydroxyapatite synthesis, a solution of calcium nitrate tetrahydrate ($Ca(NO_3)_2 \cdot 4H_2O$) and dibasic ammonium phosphate ($(NH_4)_2HPO_4$), of proper concentrations, were reacted with each other at high pH values in the presence of ammonium hydroxide (NH_4OH). The solution was held at 25 °C to prevent loss of the hydroxide during precipitation. The solution was protected, as before from CO_2 from the air. The solubility constant is *K*sp $(HA) = (2.03 \pm 0.04) \times 10^{-59}$.

Since hydroxyapatite has an affinity for proteins and other organic compounds, it can be used in combination with TiO_2 as an adsorbent. The TiO_2 regions and hydroxyapatite regions can function as photocatalysts and adsorbents for organic contaminants, respectively,

allowing simultaneous decomposition of organic contaminants by the photocatalysis of TiO_2 under irradiation. Therefore, the TiO_2coated hydroxyapatite crystals can favorably be applied for antibacterial applications and environmental purification.

DTA and TG data indicate that the presence of one water molecule in $Ca_5(PO_4)_3OH$ which, when heated, is lost at 110 °C:

$$2Ca_5(PO_4)_3OH + \text{heat} \Rightarrow Ca_{10}O(PO_4)_6 + H_2O$$

Calcium hydroxyapatite has a unique structure in that it is conductive along the hydroxide channels. OH^- ions lie at (1/4/,1/4,1/4) and (3/4/,3/4,3/4) on the *c*-axis and charge-carrying protons are responsible for the observed conductivities in $M_{10}(PO_4)_6(OH)_2$. The H^+ migration between the electroattractive ion (O^{2-}) to give molecular H_2O in matrix channels carries charge and the resulting conductivity. The structure of this salt is shown in the following Fig. 4.38.

The unit cell consists of two triangular prismatic subcells forming a rhombic prism with vertical sides. There are two horizontal mirror planes at the OH levels of 1/4 and 3/4 of the *c*-axis. In addition, there is a center of inversion exactly in the center of each vertical face of each subcell.

In a study of the high-temperature behavior of hydroxyapatite (HAp), it was found in relation to its ionic conduction properties that HAp underwent partial dehydration of its lattice hydroxide ions. Considering that HAp ceramics are sintered above 1200 °C without destruction of the apatitic structure, the dehydration was reflected in the time-dependent characteristics of conductivity, which exhibited up-and-down change of 10^3 S/cm above 700 °C.

The conduction was proved purely protonic by measurements of a hydrogen concentration cell, and it was noted that the protonic conductivity was increased to a high value of 10^{-3} S/cm at the initial stage of the dehydration. This phenomenon was demonstrated to be reversible in that the deuteration of fully dehydrated Hap could be accomplished; the uptake of OD^- inside the specimen was confirmed by infrared spectroscopic analysis after exposure to deuterium oxide vapor. Based on those results, a conduction model was proposed consistent with the dehydration phenomenon. This study also showed the importance of the supply of H_2O vapor to the ambient during sintering, for the lattice hydroxide ions of ceramic HAp were considerably dehydrated in sintering in air at high temperatures.

In the 1970s, it was found that sintered calcium hydroxyapatite, $(Ca_{10}(PO_4)_6(OH)_2$ (abbreviated as CaHap), possessed excellent biocompatibility and nontoxicity with femur and mandible bones. Since then, CaHap has been used as a biomaterial for artificial teeth and bones and as a filler for cements and polymers. Today, bone fillers made of CaHap are widely used in the medical and dental fields. In the 1980s, it was found that sintered CaHap has a good compatibility with skin tissues. Hence, percutaneous devices based on CaHap have been developed and applications have included continuous ambulatory peritoneal dialysis and intravenous hyperalimentation systems, blood pressure measurement and blood access for nutrition. Recently, many researchers have studied the chemistry of apatites, particularly CaHap, and have found various applications, such as artificial teeth and bones, ion exchangers, adsorbents for chromatography to separate proteins and enzymes, catalysts, ionic conductors, temperature and gas sensors, etc. In many of the applications, HA is applied by coating replacement hip joints with this chemical, so that the body may be more likely to accept the artificial joint, forming new bone that bonds the joint to the original leg bone. CaHA deposited by laser ablation in vacuum adheres to the substrate better at high temperatures of up to 700 °C.

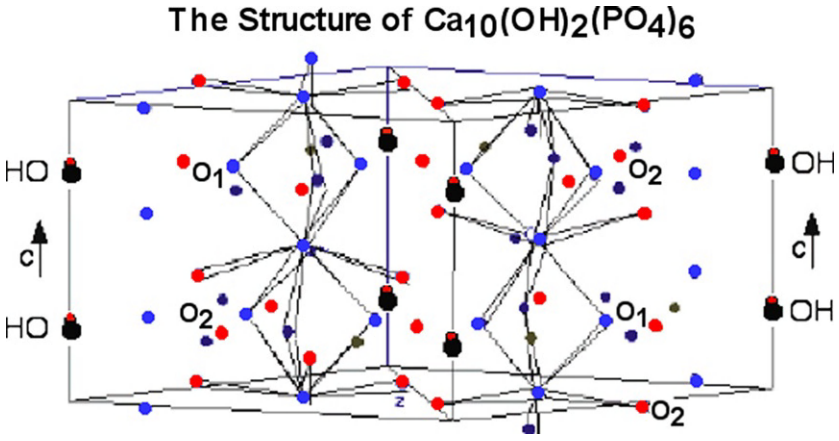

FIGURE 4.38

Calcium Fluoroapatite

This compound crystallizes in a hexagonal crystal system. It is often combined as a solid solution with hydroxyapatite ($Ca_5(PO_4)_3OH$) in biological matrices. Calcium fluorapatite is the most common phosphate mineral. It occurs widely as an accessory mineral in igneous rocks and in calcium-rich metamorphic rocks. It commonly occurs as a detritus mineral in sedimentary rocks and is an essential component of "Phosphorite" ore deposits. It occurs as a residual mineral in lateritic (clayey) soils. $Ca_5F(PO_4)_3$ is hexagonal with lattice parameters of $a = 9.367$, $c = 6.884$, $Z = 2$; $V = 523.09$ Å^3, its density $= 3.20$ g/cm^3. It is bipyramidal with point group 6/m and space group = P6/m. Single crystals are Uniaxial (−), $\varepsilon = 1.6325$, $\omega = 1.63$, birefringence = 0.0025. The most common source of fluoride (F^-) in the environment is the natural mineral fluorapatite.

Carbonate-fluorapatite ("Francolite") is the principal mineral of "Phosphorites", the sedimentary rock phosphates. The nature of the carbonate content, (whether it is part of the apatite, or adsorbed on the surface of the mineral, or even due to admixture with $CaCO_3$), and its structural position, or if it is part of the apatite lattice, has been a subject of considerable controversy in the past. This now appears to be resolved. The CO_3^- group is now considered to be a part of the fluorapatite structure, substituting for PO_4^- groups in the naturally occurring mineral.

The structure of carbonate-fluorapatite is probably triclinic (pseudohexagonal), and upon heating it decomposes according to the following reaction:

$$\underset{\text{(carbonate-fluroapatite)}}{Ca_{5-1/2x}\{(PO_4)_{3-x}(CO_3)_x(F,OH)\}} + \text{heat}$$
$$\Rightarrow \underset{\text{(fluroapatite)}}{Ca_5(OH,F)(PO_4)_3} + xCO_2 + CaO$$

The presence of CaO as a separate phase in the product has been confirmed by the X-ray powder pattern of CaO in the heated sample.

In the 1940s, calcium fluorapatite ($Ca_{10}(PO_4)_6F_2$) was the sole industrial resource for the production of phosphorus, phosphorus compounds, and fertilizers.

Calcium Chloroapatite

This has the empirical formula of $Ca_5(PO_4)_3Cl$ and the molecular weight of 520.7645 g/mol. It is formed by the same methods given for the fluoroapatite and is wholly soluble with it in solid-state solution:

$$[Ca_5(PO_4)_3F]_{1-x} \cdot [Ca_5(PO_4)_3Cl]_x$$

where x can vary from 0 to 100. When this series of compounds was activated with Sb^{3+} and Mn^{2+}, the resulting phosphors were used extensively in fluorescent lamps until about 1990 when the so-called "three-line emitting" rare-earth activated alkaline earth aluminates replaced them. Thus, the "broadband" emitting phosphors were replaced by line-emitting phosphors which could withstand high-energy discharge in lamps. This resulted in thinner fluorescent lamps that could be operated at much higher wattages.

Calcium chlorapatite has the following crystal parameters. Crystal system = hexagonal, bipyramidal with point group 6/m and space group $P6_3/m$. Lattice constants are: $a = 9.598$ Å, $c = 6.776$ Å, $Z = 2$; $V = 540.59$ Å^3, Density $= 3.20$ g/cm^3.

Calcium chlorapatite, as a mineral, is relatively much rarer than fluorapatite or hydroxylapatite, and is formed primarily in F-deficient environments. It is found as a mineral in calcium silicate marble, is an accessory mineral in layered mafic intrusions, occurs in veins such as "Diabase" and replaces "Triphylite" in some granite pegmatites. Such deposits are found in the USA, Quebec in Canada, in the Bushveld complex of Transvaal, South Africa, at the Angarf-Sud Tazenakht Plain of Morocco, at Rajagarh, India, at Kurokura in Japan, and from Snarum, Norway.

The values of the free energy of formation ΔG_f^0 of $Ca_5Cl(PO_4)_3$ has been calculated as $-1483 \cdot 2$ kcal/mol utilizing ionization activity data obtained from the hydrolysis of $CaHPO_4 \cdot 2H_2O$ in water. The concentration was 10^{-3} M for both F^- and Cl^-. The activity data was used to obtain the variation of ΔG_f^0 with composition along the $Ca_5F(PO_4)_3$–$Ca_5Cl(PO_4)_3$ and Ca_5OH–$(PO_4)_3$–$Ca_5Cl(PO_4)_3$ joins of the system CaO–$CaCl_2 \cdot CaF_2$–P_2O_5–H_2O. The phase relationships of solid solutions along these joins under aqueous conditions relative to pH and to either (a_{Ca}^{2+}), ($aH_2PO_4^-$) or (a_{Cl}^- was determined for equilibrium at 25 °C). It was then suggested that the $Ca_5Cl(PO_4)_3$–$Ca_5F(PO_4)_3$ solid solution shows considerable departure from ideal behavior. However, details are not available.

Normally, calcium apatites are expected to be hexagonal. However, a nearly stoichiometric synthetic chloroapatite has been found to be pseudo-hexagonal with a monoclinic space group of $P2_1/b$ and lattices parameters of $a = 9.628$ Å, $b = 19.256$ Å, $c = 6.754$ Å, $\gamma = 120°$. The monoclinic and hexagonal forms are very similar, the most significant feature of the monoclinic structure being an ordered arrangements of the Cl^- ions above and below $Z = 1/2$ on the pseudo-hexagonal axis with the doubling of one cell dimension. The Cl^- ion lies above and below the ordered oxygen triangle along the vertical planes, thus tilting the associated phosphate tetrahedral and resulting in a distortion throughout the structure.

Calcium Bromoapatite

This compound can be formed by the same methods of the chloro compound, namely:

$$6CaHPO_4 + 3CaCO_3 + CaBr_2 + \text{heat} \Rightarrow Ca_{10}(Br)_2(PO_4)_6 + 3CO_2 + 3H_2O$$

The bromoapatite has been of academic interest because, if it is stoichiometric, it must contain two Br^- ions of 1.98 Å along the *z*-axis which would produce an elongated *c*-axis greater than that measured. The bromoapatite is hexagonal with space group $P6_3/m$ and $a = 9.761$ Å, $c = 6.739$ Å, $V = 556.06$ Å^3, $Z = 2$ and has a density of 3.374 g/cm^3. Calcium bromoapatite has the typical hexagonal structure with most of the Br^- ions at (0,0,0) but about 2% at (0,0,0–1,0,3) positions. The packing of Br^- ions requires an apparent radius of 1.68 Å, which is appreciably smaller than the traditional free-ion radius of 1.98 Å.

The value found for $\Delta G^{\circ}_{(Ca_5Br(PO_4)_3)}$ was –1475.2 kcal/mol. Calcium bromoapatite is a soft crystal and has not found much usage in industry or commercially. It does not have a CAS number and is not offered for sale commercially. It is mentioned in a few patents but usually in conjunction with the chloroapatite.

Calcium Iodoapatite

Calcium iodoapatite, $Ca_5\ I\ (PO_4)_3$, does not exist as a separate phase but as an "oxoapatite". Iodo-oxyapatite [pentadecacalcium iodide oxide nonaphosphate, $Ca_{15}(PO_4)_9(I,O)$] was synthesized by a flux method and the structure was solved from single-crystal X-ray data. The crystal structure was refined in the space group $P6_3/m$ with lattices parameters of: $a = 9.567$ Å, $c = 20.754$ Å and $Z = 2$. Iodo-oxyapatite has a typical hexagonal apatite structure but the unit cell is tripled along the hexad direction owing to the size and ordering of the iodide and oxide ions along this direction.

Strontium Orthophosphates

All of the possible strontium compounds have been prepared.

STRONTIUM PHOSPHATE, MONOBASIC

This salt has the formula, $Sr(H_2PO_4)_2$ and the molecular weight of 137.0293 g/mol. Its CAS number is 3358-23-8. It is easily prepared by dissolving strontium carbonate in an excess of H_3PO_4. A ratio of at least 3:1 moles of acid is required:

$$SrCO_3 + 2H_3PO_4 \Rightarrow Sr(H_2PO_4)_2 + CO_2 + H_2O$$

If the pH exceeds about 3.8, the dibasic salt begins to precipitate. The monobasic salt is soluble so that the solution must be evaporated, usually at high temperature, >80–90 °C. An anhydrate, $Sr(H_2PO_4)_2$, readily forms acicular crystals. Its molecular weight is 164.5713 g/mol. Substantially pure **strontium dihydrogen phosphate** was found to act as a catalyst for the production and conversion of hydroxyethylpiperazine to triethylenediamine (Fig. 4.39).

N-(2-Hydroxyethyl)piperazine) is used in the synthesis of triethylenediamine which is an important catalyst in the production of polyurethane foams.

Monobasic strontium phosphate has not found usage in industry due to the fact that it is very similar in physical and chemical properties to the calcium analog but is more expensive. It has been used to make a polymeric glass which is almost as stable to atmospheric moisture and dissolution in boiling water as sodalime plate glass. The hydrolysis stability of sodalime glass is 5.7×10^{-5} g/cm^2/h in boiling water (96 h) while that of the $(SrPO_3)_n$ glass was 13.0×10^{-5} g/cm^2/h in boiling water. However, the calcium glass had a value of 8.3×10^{-5} g/cm^2/h in boiling water (96 h) while that of the magnesium glass was 5.5×10^{-5} g/cm^2/h in boiling water (96 h). The corresponding ratios to sodalime glass were: Sr = 2.28 X, Ca = 1.48 X and Mg = 1.04 X.

Strontium phosphate, monobasic is available commercially from several manufacturers.

STRONTIUM PHOSPHATE, DIBASIC

Owing to similarity in both ionic size and polarity, strontium (Sr^{2+}) is known to behave in a comparable way to calcium (Ca^{2+}), and its role in bone metabolism has been well documented as both antiresorptive and bone forming. Dibasic strontium phosphate, or strontium hydrogen phosphate as it is sometimes known, can easily be prepared by the addition of diammonium orthophosphate to a soluble strontium solution:

$$SrCl_2 + (NH_4)_2HPO_4 \Rightarrow SrHPO_4 + 2NH_4Cl$$

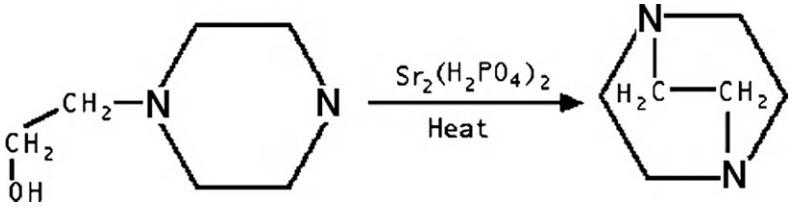

FIGURE 4.39

There is one of two dimorphs formed, α-$SrHPO_4$ and β-$SrHPO_4$, depending upon the temperature of precipitation. The beta salt is obtained below 25 °C and the alpha salt above about 40 °C. Between the two temperatures, a mixture is obtained. Both are anhydrates. α-$SrHPO_4$ has the CAS number of 250716-88-3 while that of β-$SrHPO_4$ is 13450-99-2. In addition, a new hydrogen orthophosphate has been reported.

"The hydrothermal synthesis, initial characterization (EDX analysis, IR, X-ray powder pattern), and X-ray single-crystal structure are reported for a new form of strontium hydrogen phosphate (γ-$SrHPO_4$). The cell is orthorhombic, space group Pbca (No. 61) with $a = 8.131$ Å, $b = 9.258$ Å, $c = 18.084$ Å, $V = 1361.31$ Å^3, and $Z = 16$. The structure was determined from 1272 observed reflections to a final R value of 0.039. The atomic arrangement consists of two kinds of anionic layers (P(1) and P(2)) lying parallel to (001), formed by closed dimers and infinite chains of H-bonded HPO_4^{2-} groups, respectively. These sheets are linked to each other via Sr^{2+} cations".

In addition, a compound, $SrNaPO_4$, has been reported. The crystal structure of $SrNaPO_4 \cdot 9H_2O$ is cubic with $a = 10.554$ Å, space group = P_23 and $Z = 4$. All cations and anions are surrounded by water molecules. All nine H_2O molecules are coordinated to the same Sr^{2+} cation, forming a tricapped trigonal prism. The Na^+ ion is coordinated to six water molecules forming a distorted octahedron. Extensive edge sharing of $Sr(H_2O)_9$ and $Na(H_2O)_6$ polyhedra exists. The environment of the PO_4^{3-} ion consists of 15 water molecules, all of which are hydrogen bonded to PO_4^{3-} oxygen atoms. There is considerable disordering of the phosphate-oxygen atoms, somewhat similar to those of SO_4^{2-} groups in Alums.

The main usage of the dibasic strontium phosphate salt has been to form various phosphors used in fluorescent lamps. $Sr_2P_2O_7$:Sn^{2+} is a blue-emitting phosphor as is $Sr_5(F)(PO_4)_3$:Sb^{3+}. The advent of LED lighting fixtures promises to eliminate the usage of these phosphors from the marketplace.

Strontium phosphate, dibasic is available commercially from many manufacturers worldwide.

STRONTIUM PHOSPHATE, TRIBASIC

The tribasic salt, $Sr_3(PO_4)_2$, can be prepared in a number of ways. If the tribasic sodium phosphate salt is used, the product is likely to be the hydroxyapatite, $Sr_5OH(PO_4)_3$ (which will be contaminated with sodium ion). The best method of preparation seems to be the use of the hydroxide with the monobasic salt in solution to carefully control the solution pH to about 7.5:

$$Sr(H_2PO_4)_2\ (aq) + 2Sr(OH)_2\ (s) \Rightarrow Sr_3(PO_4)_2\ (s) + 4H_2O$$

Since the monobasic salt is acidic, the hydroxide slowly dissolves into solution, and the pH must be monitored. Strontium phosphate, tribasic has the CAS number of 847870-28-4, and the molecular weight of 452.8027 g/mol. This type of preparation has been studied in detail.

Strontium phosphate precipitates were formed by mixing different amounts of $Sr(OH)_2$ and H_3PO_4. A solubility diagram was prepared from the analysis of the supernatant in equilibrium with the precipitate. XRD patterns indicated that there were two other compounds formed, $SrHPO_4$ and $Sr_{10}(PO)_6(OH)_2$. From the solubility diagram, it is estimated that the K_{sp} of $SrHPO_4$ is 4.2×10^{-7}. At high ratios of $Sr(OH)_2$ to H_2PO_4, the initial precipitate is $Sr_3(PO_4)_2 \cdot 4H_2O$, which then converts to a phase having the XRD pattern of strontium hydroxyapatite, but having a strontium: phosphorus ratio that depends somewhat on the initial ratio of $Sr(OH)_2$ to H_3PO_4 used in the precipitation.

Anhydrous $Sr_3(PO_4)_2$ is rhombohedral and the unit cell contains one molecule. The space group is R3m with $a = b = c = 7.280$ Å and $\alpha = 42°35'$. Its density is 5.25 g/cm^3. The atomic positions are; one Sr^{2+} in (0,0,0), 2 Sr^{2+} in ± (u_1, u_1, u_1), 2 P in ± (u_2, u_2, u_2), 2 O in ± (u_3, u_3, u_3), 6 O in ± (x, x, z) (x, z, x) (z, x, x), with parameters of $u_1 = 0.218$, $u_2 = 0.412$, $x = 0.285$ and $z = 0.742$.

The salt, "distrontium triphosphate", CAS number = 14414-90-5, is offered for sale by several manufacturers (notably overseas) but it is not likely that it is the tribasic salt since the formulation, $Sr_2(PO_4)_3$ is both energetically and Lewis electron charge-compensation impossible as a formula.

The tetrahydrate, $Sr_3(PO_4)_3 \cdot 4H_2O$, has been reported if strontium nitrate, $Sr(NO_3)_2$ is added to a large excess of K_2HPO_4 at 10 °C and then made basic with KOH to pH = 7.7 prevent hydrolysis to the hydroxyapatite:

$$Sr(NO_3)_2\ (aq) + K_3HPO_4\ (xs\text{-}aq) \Rightarrow Sr_3(PO_4)_2 \cdot 4H_2O + 3KNO_3$$

This product loses waters of hydration around 175 °C and 280 °C to form the anhydrate which is stable to >900 °C.

$M_3(PO_4)_2$ phosphates of divalent elements with a larger radius (M = Sr, Ba, Pb) are known to crystallize in the $K_2Pb(SO_4)_2$ or palmierite structure. The palmierite- and whitlockite-type structures are very similar and are made up of isolated PO_4^{3-} tetrahedra, which connect the Mon polyhedra into a three-dimensional framework via common vertices.

The following figure shows the [1120] projections of the palmierite-type $Sr_3(PO_4)_2$ (d) structure (Fig. 4.40).

Along the c-axis in these structures, it is possible to differentiate two types of columns: A and B. In the

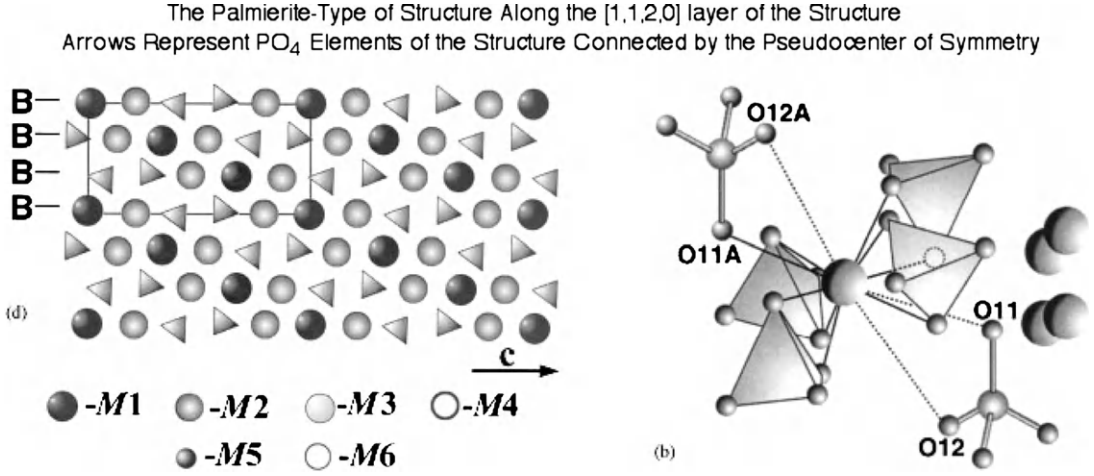

FIGURE 4.40

B-type column, three MOn polyhedra and two tetrahedra PO3 alternate. The A-type column consists of a sequence of polyhedra and cavities. All layers in the palmierite-type structure are built up by B columns. Sr^{2+} cations occupy two crystallographically different positions and B columns can be presented as [–$M2O_{10}$–$M1O_{12}$–$M2O_{10}$–PO_4–PO_4–].

$Sr_3(PO_4)_2$ has not found any uses in industry except as a matrix for phosphors. A thermoluminescence (TL) investigation has been reported for $Sr_3(PO_4)_2$:Eu^{2+}, which is a commercially available X-ray phosphor. Its TL emission spectrum is dominated by a single-emission band centered at 420 nm, that is characteristic of Eu^{2+}. The glow curve of the Eu^{2+} band has two well-separated peaks, a feature which rarely occurs in dosimetric materials. Owing to the above properties, $Sr_3(PO_4)_2$:Eu^{2+} seems to be the best choice for studying TL kinetics and the relation between radioluminescence and TL.

Sb^{3+}-doped $Sr_3(PO_4)_2$ crystals have been synthesized and the phosphor exhibits excitation peaks at 250 and 215 nm and an emission peak at 396 nm. The emission is attributed to $^3P_1$-$^1S_0$ transition and the excitation is attributed to $^1S_0$-$^3P_1$ and $^1S_0$-$^1P_1$ transition (as is usual for this activator). It was also observed that the intensity of PL is thermally stable up to 673 K (400 °C).

Tribasic strontium phosphate is available commercially in limited quantities from several manufacturers worldwide.

STRONTIUM APATITES

The strontium halophosphates or strontium apatites comprise the compound, $Sr_5X(PO_4)_3$ where X is OH, F, Cl Br or I. All can be formed (with the exception of the hydroxyapatite which must be formed in solution) by solid-state reaction:

$$6SrHPO_4 + 3SrCO_3 + SrX_2 + \text{heat} \Rightarrow Sr_{10}X_2(PO_4)_6 + 3CO_2 + 3H_2O$$

Hydroxyapatite

This salt is prepared by the aqueous reaction of a soluble strontium salt with trisodium phosphate:

$$10SrCl_2\ (aq) + 6Na_3PO_4\ (aq) \Rightarrow Sr_{10}(OH)_2(PO_4)_6\ (solid) + 18NaCl\ (aq) + 2HCl$$

Alternately, it can be prepared by the aqueous reaction of the monobasic salt and the hydroxide at about 60–80 °C with addition of NaOH to control pH to a minimum of 10–11.

$$3Sr(H_2PO_4)_2\ (aq) + 2Sr(OH)_2\ (solid) \Rightarrow Sr_5OH(PO_3)_3\ (solid) + 8H_2O$$

Its molecular weight is 1479.8162 g/mol. Strontium readily forms mixed hydroxyapatites with both calcium and barium hydroxyapatites. The strontium hydroxyapatite crystal is hexagonal with $a = 9.745$ Å, $c = 7.265$ Å, $Z = 2$. The phosphate tetrahedra are less distorted than in the isostructural calcium hydroxyapatite ($a = 9.23$ Å, $c = 6.875$ Å). These hydroxyapatites can be OH deficient, with the charge balance maintained by Sr^{2+} or Ca^{2+} vacancies.

This salt can also be prepared by a series of solid-state reaction in an atmosphere of steam (Fig. 4.41).

Strontium hydroxyapatite has not found extensive usage in industry since the calcium analog is just as useful and is less expensive. It has been intensively studied since it will form nanosized particles via the sol-gel method. Nevertheless, it does not have a CAS number and is not offered for sale commercially.

Fluorapatite

This apatite is formed by the same methods as the calcium apatite analog. The solid-state reaction required is:

$$6SrHPO_4 + 3SrCO_3 + SrF_2 + \text{heat} \Rightarrow Sr_{10}F_2(PO_4)_6 + 3CO_2 + 3H_2O$$

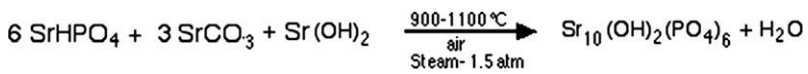

FIGURE 4.41

It has also been prepared by the solution method:

$$10SrF_2\ (aq) + 6Na_3PO_4\ (aq) \Rightarrow Sr_{10}(F)_2(PO_4)_6\ (solid) + 18NaF\ (aq) + 2HCl$$

However, the product is contaminated by Na^+ ions and must be washed thoroughly to obtain a pure product. A small amount of hydroxyapatite may also be present.

Strontium fluoroapatite is hexagonal with the space group = P6/m and unit-cell parameters of $a = 9.415$ Å and $c = 6.924$ Å, $Z = 2$ with the point group of $\underline{P3}$. Optical properties are: transparent, colorless, with the optical class = Uniaxial (–). $\omega = 1.651$, $\varepsilon = 1.637$.

It readily forms solid solutions with all of the calcium apatite analog and so is found as a partial substitute in those materials used in industry. This includes some formulations from various manufacturers of "Halophosphate" phosphors (while others only use the unadulterated calcium apatite). $Sr_5F(PO_4)_3{:}Sb^{3+}$ is a widely used phosphor employed for many years in fluorescent lamps. $Sb_5F(PO_4)_3$ has been stated as "an ideal substrate to demonstrate the emission characteristics of all of the Rare Earths, including, Ce^{3+}, Pr^{3+}, Sm^{3+}, Eu^{3+}, Gd^{3+}, Tb^{3+}, Dy^{3+}, Ho^{3+}, Er^{3+}, Tm^{3+}, and Yb^{3+}. These trivalent cations are large but seem to fit into the Sr^{2+} sites with a minimum of energy, including a negative vacancy, $V_{\overline{Sr}}$ or an associated F^- ion. The exact combination has not been exactly determined.

A number of fluoroapatite glass ceramics have been studied for medical and dental applications. These bioceramics have consist of both calcium–strontium fluoroapatites as well as those based upon strontium apatite glass crystal combination themselves. Such glass ceramics have consisted of an aluminum silicate in which the apatite is suspended as a ceramic. The influence of substituting strontium for calcium in a glass of the following composition: $4.5SiO_2 3Al_2O_3 1.5P_2O_5$ 3CaO2CaF$_2$, having a Ca:P ratio of 1.67 corresponding to calcium fluorapatite ($Ca_5(PO_4)_3F$) has been studied. The glasses were characterized by magic angle spinning-nuclear magnetic resonance (MAS-NMR), by DSC and X-ray powder diffraction (XRD). The ^{29}Si, ^{27}Al and ^{31}P NMR spectra for the glasses with different strontium contents were identical. The ^{19}F spectra indicated the presence of F–Ca(n) and Al–F–Ca(n) species in the calcium glasses and F–Sr(n) and Al–F–Sr(n) in the strontium glasses. It can be concluded that strontium substitutes for calcium with little change in the glass structure as a result of their similar charge to size ratio.

Strontium fluorapatite has been shown to be one of the best hosts for Nd^{3+} doping among apatite crystals. Neodymium-doped strontium fluorapatite crystal has been grown by the Czochralski method. The data of thermal expansion and specific heat of the crystal have been measured. The thermal expansion coefficients along X and Z direction are $\alpha_1 = 11.4 \times 10^{-6}/K$ and $\alpha_3 = 12.3 \times 10^{-6}/K$, respectively. The specific heat is 110 cal/mol K at 330 K. The measured absorption spectra from 400 to 850 nm showed that the crystal has absorption peaks around 805.5 nm, and the absorption coefficients at 805.5 nm are 16.05/cm and 5.59/cm for π and α-polarization, respectively. The polarization fluorescence spectra at room temperature showed that the strongest fluorescence is centered at 1058.8 nm. The lifetime of $^4F_{3/2}$ is 175 μs for 1 atom% Nd^{3+} doped in the crystal. The laser at 1058.8 nm was demonstrated pumped by a 3 W CW laser diode at 805.5 nm, and the slope efficiency was 31.7%.

Strontium occurs in several minerals but never as the major cation in these apatites:

$$\text{Belovite} = (LaSr_3NaCe)_5(PO_4)_3(F,OH)$$
$$\text{Deloneite} = (NaCa_2SrCe)_5(PO_4)_3F$$
$$\text{Fluorcaphite} = (CaSrCeNa)_5(PO_4)_3F$$

Strontium fluoroapatite does not have a CAS number even though it is still used as a phosphor for compact and standard fluorescent lamps. It has been the subject of numerous academic studies but has found little or no usage in industry except those already mentioned.

Strontium Chloroapatite

This salt is prepared by the solid-state reaction of:

$$6SrHPO_4 + 3SrCO_3 + SrCl_2 + heat \Rightarrow Sr_{10}Cl_2(PO_4)_6 + 3CO_2 + 3H_2O$$

It has the molecular weight of 1516.7183 g/mol. It is hexagonal, as expected, with $a = 9.859$ Å and $c = 7.205$ Å. The general features of the structure are the same as the fluoroapatite or hydroxyapatite except the Cl^- atoms are at the (0,0,1/2) point along the c-axis between the two Sr triangles on the mirror planes at $z = 1/4$ and $z = 3/4$. This structure is almost identically the same as the calcium analog.

The major use of strontium chloroapatite has been as a matrix for forming "SCAP" which is a phosphor having the formula of $Sr_5Cl(PO_4)_3{:}\ Eu^{2+}$ in which the divalent

europium activator emits a blue band peaking at 450 nm. It is used extensively in "Tri-Color" fluorescent lamps. This phosphor is imported from Japan and China.

This salt has a CAS number of 68784-77-0 as the phosphor or luminophor. It is offered for sale as the phosphor but not as the compound, $Sr_5Cl(PO_4)_3$.

Strontium Bromoapatite

This apatite is formed by the same methods as the chloroapatite analog. The solid-state reaction required is:

$$6SrHPO_4 + 3SrCO_3 + SrBr_2 + \text{heat} \Rightarrow Sr_{10}Br_2(PO_4)_6 + 3CO_2 + 3H_2O$$

It has also been prepared by the solution method:

$$10SrBr_2\ (aq) + 6Na_3PO_4\ (aq) \Rightarrow Sr_{10}(Br)_2(PO_4)_6\ (solid) + 18NaCl\ (aq) + 2HCl$$

However, the product is contaminated by Na^+ ions and must be washed thoroughly to obtain a pure product. A small amount of hydroxyapatite may also be present.

Strontium bromoapatite is a softer crystal than the fluorapatites or chloroapatites of strontium and has not been used in forming phosphors for use in the lighting industry as it is not stable under the mercury-vapor discharge in fluorescent lamps. It has no CAS number.

It is not offered for sale commercially by many suppliers but is available in small quantities from a few manufacturers, notably Chinese.

Strontium Iodoapatite

Strontium iodoapatite is of academic interest because of the large size of the I^- ion compared to the other halide ions. However, the thermodynamic functions determined for the alkaline earth apatite series preclude the formation of a stable iodoapatite because of the cationic size of Sr^{2+} or Ba^{2+} is too small relative to that of the iodide ion which must fit upon the *c*-axis of the structure next to the triads of Sr^{2+} or Ba^{2+} at (000), (010), (011), and (001) positions in the lattice. Such crystals relevant to radioactive waste management include fluorapatite, and, in the end, iodoapatite, which should be able to immobilize the radioactive species, ^{129}I.

However, a lead vanado-iodoapatite $Pb_{10}(VO_4)_6I_2$ has been synthesized as a potential waste form to immobilize radioactive iodine and some thermal, mechanical and chemical properties were measured. TG–DTA showed that the apatite was stable up to about 800 K.

Barium Orthophosphates

Barium forms all of the normal orthophosphates, including the mono-, di-, tribasic compounds and the apatites.

MONOBASIC BARIUM PHOSPHATE

This salt has the formula, $Ba(H_2PO_4)_2$ and the molecular weight of 137.0293 g/mol. Its CAS number is 10048-98-3. It is easily prepared by dissolving barium carbonate in an excess of H_3PO_4. A ratio of at least 3:1 mol of acid is required:

$$BaCO_3 + 2H_3PO_4 \Rightarrow Ba(H_2PO_4)_2 + CO_2 + H_2O$$

If the pH exceeds about 3.8, the dibasic salt begins to precipitate. The monobasic salt is soluble so that the solution must be evaporated, usually at high temperature, >80–90 °C. An anhydrate, $Ba(H_2PO_4)_2$, readily forms acicular crystals. Its molecular weight is 331.3057 g/mol and its CAS number is 13517-08-3.

Monobasic barium phosphate forms two related crystalline dimorphs. One is monoclinic and the other orthorhombic. The monoclinic structure has the cell parameters of: $a = 7.0335$ Å, $b = 8.043$ Å, $c = 7.2158$ Å, $\alpha = \beta = 90°$, $\gamma = 96.02°$, $Z = 2$, density $= 2.99$ g/cm^3. The orthorhombic cell has the parameters of $a = 7.7926$ Å, $b = 10.2574$ Å, $c = 8.5653$ Å, $\alpha = \beta = \gamma = 90°$. The space group is Pccn and density is 3.03 g/cm^3. In both of these polymorphs, a corrugated network of hydrogen-bonded phosphate groups lies parallel to the *a*–*c* plane with Ba···O coordination bonds running between the phosphate layers. The eight Ba···O distances range from 2.579 Å to 2.903 Å. The phosphate distances are: P···OH = 1.579 Å and 1.576 Å and P···O = 1.495 Å and 1.490 Å.

The anhydrate, when heated, decomposes to form the acid pyrophosphate ($Ba(H_2P_2O_7)_2$ at 350 °C and the metaphosphate, $Ba(PO_3)_2$ at about 430 °C. These dehydrations occur in two distinct stages as shown in the following Fig. 4.42.

Further heating results in three internal rearrangements of the metaphosphate groups to final form of the polymerized phase, $\{Ba(PO_3)_2\}_n$ which melts at 830 °C. The glass, once formed and cooled, melts at 743 °C. The polymerized glass phase has several interesting characteristics among which is the existence of two thermal expansion coefficients, a lower one and an upper one, having a value of 115 and 127×10^{-7} in/in/°C, respectively.

Although monobasic barium phosphate has received considerable academic attention, little has occurred in industry.

It is available in moderate quantities commercially from a number of manufacturers worldwide.

BARIUM ORTHOPHOSPHATE, DIBASIC

Dibasic barium phosphate has the formula of $BaHPO_4$ and the molecular weight of 233.30933 g/mol and the CAS number of 10048-98-3. It is sometimes

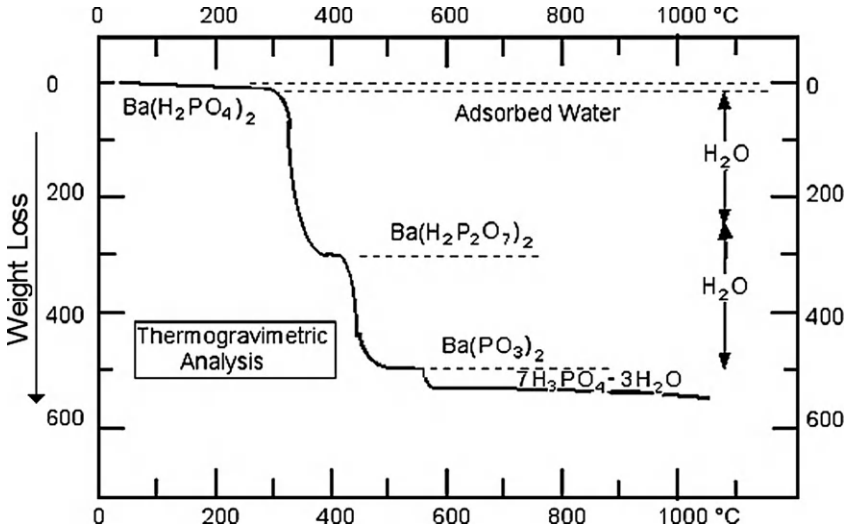

FIGURE 4.42

referred to as "barium hydrogen phosphate (BHP)". It is easily prepared by reacting diammonium phosphate with a soluble solution of barium, such as the chloride:

$$BaCl_2 + (NH_4)_2PO_4 \Rightarrow BaHPO_4 + 2NH_4Cl$$

To obtain a pure salt, the phosphate is always added to the barium solution.

Otherwise, one obtains a salt contaminated with a slight excess of phosphate. The solubility of $BaHPO_4$ is 0.013 g/100 ml at 20 °C. It is important to monitor the pH as the precipitation proceeds, as shown in the following diagram, in order to obtain the pure product (Fig. 4.43).

It has been shown that the size and shape of the product produced can be controlled by the use of an organic soluble polymer. By the use of a double-hydrophilic copolymer, poly(ethylene glycol)-acrylate-copoly(methacrylic acid), the morphology of BHP crystals produced can be controlled. This gives different shapes at different pH values: hexagon (pH = 7.26), sphere cluster (pH = 8), sphere with rough surface (pH = 9), sphere with relatively smooth surface (pH = 10), and small sphere (pH = 11). The results of XRD indicate that the morphology of the particles, as controlled by copolymers, contain mainly $BaHPO_4$ when pH < 11. Weak diffraction peaks of $Ba_5(PO_4)_3OH$ (112) and (211) appear when pH = 11, which means that precipitates are also mainly $BaHPO_4$ but with minor amounts of $Ba_5(PO_4)_3OH$.

The X-ray single-crystal structure of $BaHPO_4$ was refined in the centric space group Pbnm (No. 62) with $a = 4.609$ Å, $b = 14.195$ Å, $c = 17.214$ Å, $V = 1126.3$ Å^3, $Z = 12$ and a final R value of 0.036 for 1261 independent

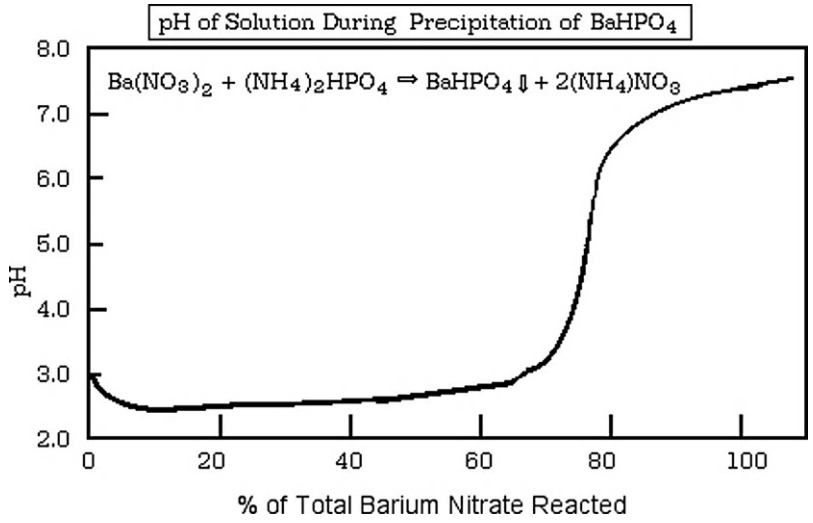

FIGURE 4.43

reflections. The atomic arrangement consists of anionic linear chains lying parallel to the a-direction and strongly linked by hydrogen bonds. Two successive chains are separated by Ba^{2+} cations. A comparison of the anionic networks for some similar compounds is also given. The polarized Raman and infrared absorption spectra are investigated. A factor group analysis leads to determination of internal modes of the PO_4^{3-} anions. The vibrational study confirmed the strong H–OP hydrogen bonds to the phosphate groups and indicated notably strong hydrogen bridges in the $BaHPO_4$ compound. The arrangement of the phosphate groups around the Ba^{2+} cations has been determined to be a dodecaheadral cage as shown in the following Fig. 4.44.

In addition, it has been determined that $BaHPO_4$ is dimorphic, the high-temperature phase being formed at precipitation temperatures <95–100 °C. This phase, α-$BaHPO_4$, was synthesized as a single-phase crystalline powder starting from an aqueous solution of barium hydroxide and phosphorus pentoxide at 373 K. α-$BaHPO_4$ crystallizes in a new structure type in which the Ba^{2+} ions form a distorted body-centered arrangement with the HPO_4^- anions in the quasi-octahedral voids ($BaHPO_4$, space group = Aem2, $Z = 16$, $a = 4.5996$ Å, $b = 22.809$ Å, $c = 14.081$ Å). The crystal structures of α-$BaHPO_4$ and β-$BaHPO_4$ are related. The infrared spectrum and a thermal and TGA of α-$BaHPO_4$ has also been reported.

Hydrothermal synthesis, IR characterization and X-ray single-crystal structure is reported for $CaBa(HPO_4)_2$. It crystallizes in the monoclinic system, space group $P2_1/a$ (N14) with $a = 9.470$ Å, $b = 7.930$ Å, $c = 9.865(1)$ Å, $\beta = 115.78°$, $V = 667.1$Å^3 and $Z = 4$. The crystal structure of $CaBa(HPO_4)_2$ is built up from corner-and/or edge-sharing BaO_9 polyhedra, CaO_7 pentagonal bipyramids and $(H)PO_4$ tetrahedra giving rise to a three-dimensional network. The HPO_4^{2-} groups are located in layers parallel to the a and b plane at $z \sim 0$ and $z \sim 1/2$. Interleaved barium and calcium cations ensure the cohesion between these sheets. Hydrogen bonds contribute to the stability of the structure.

BHP single crystals have gained considerable interest on account of their ferroelectric, dielectric and electro-optical properties. $BaHPO_4$ is ferroelectric and also shows intrinsic conductivity due to the hydrogen atom. The DC conductivity of the ferroelectric, $BaHPO_4$, was measured and found to lie between usual conductivities of semiconductor and insulator. Its temperature dependence shows intrinsic conduction in defective crystals due to H^+ ions. The AC conductivity calculated from the measured dielectric constant follows a power law. A frequency of 20 kHz was used to resolve the resistivity peak of AC conduction into two Gaussians. The ln σ vs f plots at different temperatures show an exponential dependence and existence of a focal point. An infrared spectroscopic study on pelletized BHP has been made. The distinct bands observed seem to be related with the P=O bond of PO_4 group. Around the ferroelectric transition at 315 K (32 °C), the interionic band at 2650/cm disappears on account of BaO ionic bond being broken. For the sample prepared at 500 K (227 °C), the bands around 2000 and 2500/cm appear intense, while broadening of bands due to various deformations like P=O and P=O–H takes place.

Barium hydrogen orthophosphate was first used for phosphor preparation, notably barium titanium phosphate, $Ba_2P_2O_7$:$TiFO_2$, by Ropp and first made commercially at Sylvania Electric Products, Inc at Towanda, Pa. because it was not available commercially in 1955. Since that time, a number of suppliers offer this chemical commercially in large lots.

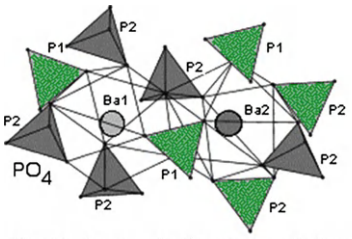

The Environment of the Barium Cations in the Barium Hydrogen Orthophosphate Structure

FIGURE 4.44

BARIUM ORTHOPHOSHATE, TRIBASIC

Tribasic barium orthophosphate has the molecular formula of $Ba_3(PO_4)_2$ and the molecular weight of 601.9327 g/mol. Its CAS number is 13517-08-3. It can be prepared by a number of methods including solution and solid-state methods. The best way to prepare a pure salt is to react the dibasic salt with the carbonate:

$$2BaHPO_4 + BaCO_3 + \text{heat} \Rightarrow Ba_3(PO_4)_2 + CO_2 + H_2O$$

If a solution method is desired, the reaction of the soluble monobasic salt with the hydroxide seems to be superior to any other method:

$$Ba(H_2PO_4)_2\,(aq) + 2Ba(OH)_2\,(s) \Rightarrow Ba_3(PO_4)_2\,(s) + 4H_2O$$

Since the monobasic salt is acidic, the hydroxide slowly dissolves into solution, but the pH must be monitored so that it does not exceed pH = 9.5. Otherwise, the hydroxyapatite begins to appear.

The crystal structure refinement of rhombohedral $Ba_3(PO_4)_2$ [$a = 7.698$ Å, $\alpha = 42°35'$ and space group R-3m] have been carried out by means of the single-crystal diffraction data. The rod sequence of coordination polyhedra,

$$PO_4–M(2)O_{10}–M(1)O_{12}–M(2)O_{10}–PO_4,$$

where M = Sr or Ba, is characteristic in these structures. The $M(1)O_{12}$ and $M(2)O_{10}$ polyhedra show smaller distortion with increase in the ionic radius of the constituent elements. Atomic positions are: one Ba in (000), 2 Ba in ± (u_1, u_1, u_1), 2P in ± (u_2, u_2, u_2), 2 O in ± (u_3, u_3, u_3), and 6 O in (x, x, z) (x, z, x) (z, x, x) with $u_1 = 0.208$, $u_2 = 0.412$, $u_3 = 0.337$, $x = 0.285$, $z = 0.742$.

PL and electroluminescence (EL) in blue-violet emission were observed in newly developed phosphate phosphor thin films such as $Ba_3(PO_4)_2$:Eu and $Ba_3(PO_4)_2$:Ti. These phosphate phosphor thin films were first deposited on thick $BaTiO_3$ ceramic sheets by RF magnetron sputtering using powder targets and then post-annealed in various atmospheres. Blue-violet PL and EL emissions were obtained in $Ba_3(PO_4)_2$:Eu and $Ba_3(PO_4)_2$:Ti phosphor thin films that were deposited in an $Ar + H_2$ (10%) gas atmosphere and then post-annealed above about 900 °C in an $Ar + H_2$ (10%) gas atmosphere. In particular, the EL observed in $Ba_3(PO_4)_2$:Eu thin films exhibited two peaks, a red emission peaking at about 615 nm and a blue-violet emission peaking at about 420 nm. A luminance of 2.0 cd/m^2 in blue-violet emission was obtained in a thin film EL device using a two-step post-annealed $Ba_3(PO_4)_2$:Eu thin film emitting layer: step 1, post-annealing at 1000 °C in air for 1 h, and step 2, post-annealing at 1000 °C in an $Ar + H_2$ atmosphere.

Barium orthophosphate doped with Ce^{3+}, Pr^{3+}, Gd^{3+}, or Tb^{3+} acts as an efficient X-ray storage phosphor. The four compositions have different thermal stimulation properties; the thermally stimulated luminescence (TSL) occurs at higher temperatures than in $Ba_3(PO_4)_2$:La^{3+}. Similar to this latter compound, atomic hydrogen is present after irradiation in $Ba_3(PO_4)_2$:Ce^{3+} and $Ba_3(PO_4)_2$:Gd^{3+}, but its electron paramagnetic resonance signal disappears before the TSL takes place. In $Ba_3(PO_4)_2$:Pr^{3+} and $Ba_3(PO_4)_2$:Tb^{3+}, no H^0 is found. In the four cases studied, codoping with Eu^{2+} changes the TSL properties. In view of these results, it is concluded that the storage mechanism is different for barium phosphate doped with luminescent trivalent rare earth ions on the one hand, and barium phosphate with La^{3+} or Y^{3+} on the other.

Tribasic barium phosphate is offered for sale by several manufacturers worldwide. The CAS number of one may be 182259-25-2 while another is 13463-10-0. These materials vary according to the method of preparation (which is not disclosed). The former material is said to involve the use of H_3PO_4 and may be a barium hydroxyapatite.

BARIUM APATITES

All but the iodoapatite have been prepared. The barium halophosphates or barium apatites comprise the compound, $Ba_5X(PO_4)_3$ where X is OH, F, Cl Br or I. All can be formed (with the exception of the hydroxyapatite which must be formed in solution) by solid-state reaction:

$$6BaHPO_4 + 3BaCO_3 + BaX_2 + \text{heat} \Rightarrow Ba_{10}X_2(PO_4)_6 + 3CO_2 + 3H_2O$$

Barium Hydroxyapatite

This salt is prepared by the aqueous reaction of a soluble barium salt with trisodium phosphate:

$$10BaCl_2\ (aq) + 6Na_3PO_4\ (aq) \Rightarrow Ba_{10}(OH)_2(PO_4)_6\ (s) + 18NaCl\ (aq) + 2HCl$$

Alternately, it can be prepared by the aqueous reaction of the monobasic salt and the hydroxide at about 60–80 °C with addition of NaOH to control pH to a minimum of 10–11.

$$3Ba(H_2PO_4)_2\ (aq) + 2Ba(OH)_2\ (solid) \Rightarrow Ba_5OH(PO_4)_3\ (solid) + 8H_2O$$

Its molecular weight is 1728.3662 g/mol and the CAS number of 12356-34-2. Barium readily forms mixed hydroxyapatties with both calcium and strontium hydroxyapatites. These hydroxyapatites can be OH deficient, with the charge balance maintained by Ba^{2+}, Sr^{2+} or Ca^{2+} vacancies. It has been found that Ba^{2+} ions are more difficult to be incorporated into hydroxyapatite crystals compared to Sr^{2+}ions. In a mixture with increasing Ba^{2+}content, the particles grew and finally turned into pure rod-shaped barium hydroxyapatite particles with a size of ca. 0.2 μ.

When barium hydroxyapatite, $(Ba_{10}(PO_4)_6(OH)_2$, (abbreviated-BaHAp) was synthesized by a wet method using $Ba(OH)_2 \cdot 8H_2O$ and $(NH_4)_2HPO_4$ as starting materials, the Ba-HAp obtained had a Ba/P atomic ratio of 1.76 and contained CO_3 groups. Thus, any solution method to prepare this compound must be protected from the ambient atmosphere in order to obtain a pure salt.

Carbonated barium hydroxyapatite $Ba_{10}(PO_4)_6(OH)_{2-2x}(CO_3)_x$, where $X = 0.30$–0.57, produced BaHAP particles with different Ba/P molar ratios. These were prepared by a wet method and CO_3^{2-} ions were incorporated into OH^- sites of a BaHAP lattice during the preparation at high pH solution. The obtained BaHAP particles were well crystallized and showed a high thermostability. On elevating the mixing temperature of the H_3PO_4 and $Ba(OH)_2$ solutions, the mean particle size of BaHAP particles decreased and their specific surface area increased. The amount of CO_2 adsorbed irreversibly on BaHAP particles increased as their Ba/P molar ratio increased.

In another study, carbonate-containing barium hydroxyapatite was prepared by solid-state reactions

in air at 950 °C. Obtained samples were investigated by X-ray powder diffraction and IR spectroscopy. The stoichiometry of these samples conforms to $Ba_5(PO_4)_{3-x}(CO_3)_x(OH)_{1-x}O_x$ as the result of CO_3^{2-} and O_{2-} substitution for PO_4^{3-} and OH_- in the hydroxyapatite lattice under the scheme:

$$PO_4^{3-} + OH^- \Rightarrow CO_3^{2-} + O^-$$

The crystal structure of some carbonated barium hydroxyapatite patterns were refined by the Rietveld method using X-ray powder diffraction data. The analysis of the crystallographic site occupation has shown that the single-phase range of $Ba_5(PO_4)_{3-x}(CO_3)_x(OH)_{1-x}O_x$ is limited by $x = 0.32$.

The properties of barium hydroxyapatite (BaHAp) as an ion-exchange medium with Pb^{2+}, Cu^{2+}, Zn^{2+}, Cd^{2+} and Co^{2+} in solution have been investigated, with particular emphasis on the former two cations. Under similar conditions, the exchange capacities followed the order $Cu^{2+} > Pb^{2+} > Zn^{2+} > Cd^{2+} > Co^{2+}$. After exchange with Pb^{2+}, lead hydroxyapatite was identified in the solid phase but with Cu^{2+} no copper analog of BaHAp was found, although $Ba_3(PO_4)_2$ was formed. With solutions containing either Pb^{2+} or Cu^{2+}, only the former exchanged into BaHAp. With HCl in the exchanging solutions, the capacity of BaHAp for both Pb^{2+} and Cu^{2+} was enhanced, while copper hydroxyapatite was not found in the solid.

Barium hydroxyapatite is hexagonal with the point group of 6/m. The space group is P_63/m, $a = 10.1327(3)$ Å and $c = 7.7526(3)$ Å. The ionic conductivity measurement of $Ba_5(PO_4)_3OH$ showed its ionic conductivity reached the maximum of 2.0×10^{-6} S/cm at 400 °C with an activation energy as low as 0.43 eV due to the activity of OH groups along the channels.

Although barium hydroxyapatite has received considerable attention in the literature, it has not found many applications in industry. It is offered for sale by several manufacturers worldwide.

Barium Fluorapatite

This salt is generally prepared by solid-state reaction:

$$2BaHPO_4 + BaCO_3 + BaF_2 \Rightarrow Ba_{10}(F)_2(PO_4)_6$$

It is hexagonal with space group P63/m and $a = 10.153$ Å, $c = 7.733$ Å with $V = 607.142$ Å^3 and $Z = 2$.

Recently, neodymium-doped barium fluorapatite (Nd: B-FAP) of laser quality and dimension has been synthesized and has been shown to possess excellent qualities as a laser. High-quality single crystals of neodymium-doped barium fluorapatite have been grown by the Czochralski technique and evaluated as an optical gain medium. A product of the emission cross-section and lifetime of Nd^{3+} luminescence of more than 1.8×10^{-22}/cm^2/sex at 1055 nm, and laser performance with slope efficiency up to 65% have been obtained.

The vibrations of phosphate (PO_4^{-3}) ions in single crystals of hexagonal $Ba_5(PO_4)_3F$ (B-FAP) have been investigated by means of polarized Raman scattering and compared to Raman frequencies observed in fluorapatite analogs $Sr_5(PO_4)_3F$ (S-FAP) and $Ca_5(PO_4)_3F$ (FAP). The Raman vibrational frequencies decrease upon substitution of Ba^{2+} for Sr^{2+} or Ca^{2+} in the lattice, asymptotically approaching the Raman frequencies for vibrations of the free ion. The observed splitting is in accord with predictions made by a group theory analysis of the factor group of the unit cell. The effects of the host lattice environment on the magnitude of the Davydov splittings and frequency shifts of phosphate ions within different crystals with the fluorapatite structure are demonstrated to be inversely proportional to the unit cell volume.

Ultrafine $M_5(PO_4)_3F{:}Dy^{3+}$ (M = Ca, Ba) phosphors were prepared via a combustion process using metal nitrates as precursors. The formation of the crystalline phosphate was confirmed by XRD pattern. The PL excitation spectra show the excitation peaks observed at 250–400 nm due to $f \Rightarrow f$ transition of Dy^{3+} ion, which are useful for solid-state lighting purpose (mercury-free excitation). The PL emission of Dy^{3+} ion by 348 nm excitation gave an emission at 489 nm (blue), 582 nm (yellow) and 675 nm (red). All the characteristics of BYR emissions like BGR indicate that Dy doped $Ca_5(PO_4)_3F$ and $Ba_5(PO_4)_3F$ phosphors are good candidates that can be applied as solid-state lighting phosphors (mercury-free excited lamp phosphor) and white light LED.

The phosphors, fluorapatites $M_5(PO_4)_3F$ (M = Sr, Ba) activated with Dy^{3+} ions, were prepared by a high-temperature solid-state reaction technique. The VUV–UV excitation spectra and emission spectra under VUV/UV excitation were measured. The phosphors show broad and strong absorption near 172 nm and intensive emission with the chromaticity coordinates entering the white light region. Hence, the phosphors may be considered as suitable candidates for LED's and Hg-free lamps.

Additionally, barium fluoroapatite activated by Ce^{3+}, $Ba_5F(PO_4)_3{:}Ce^{3+}$ has been determined to be a good scintillator. Its luminosity is 450 photons/Mev with a decay time of 24 ns and an emission band peaking at 358 nm.

Other than its use as a phosphor for solid-state lighting, barium fluoroapatite has received little attention in industry. Whether these phosphors will receive actual usage remains to be seen. It is offered for sale commercially.

Barium Chloroapatite

This salt is easily prepared by the solid-state reaction:

$$6BaHPO_4 + 3BaCO_3 + BaCl_2 + \text{heat} \Rightarrow Ba_{10}(Cl)_2(PO_4)_6 + 3CO_2 + 3H_2O$$

Barium chloroapatite is hexagonal with space group of P63/m and $a = 10.284$ Å, $c = 7.651$ Å, $V = 602.003$ Å^3, $Z = 2$ and point group of 6/m. The following table shows the position of the various ions in the hexagonal structure. Thus, the Cl^- ion is located at (000) and (1/2, 1/2, 1/2) while the others lie at points in between. Ba_1 lies at (0.3333, 0.6667, 0.6667) while Ba_2 is at (0.2445, 0.2606, 0.2500).

This salt occurs as a natural mineral having the same composition, except the ore is contaminated by other metallic minerals as well. "Alforsite", ideally $Ba_5(PO_4)_3CI$ is a new member of the apatite group occurring in contact with metamorphosed vaporitic rocks from Fresno and Mariposa Counties, California, associated with fluorapatite and many other rare barium minerals previously described by Alfors et al (1965). It is optically uniaxial, negative, with $\omega, \varepsilon = 1.70$. The density is calculated to be 4.83 g/cm^3 for the end member composition. It is hexagonal, space group = p63/m, with $a = 10.25$ Å and $c = 7.64$ Å.

Single crystals of neodymium-doped barium chloroapatite have been grown by the Czochralski technique and evaluated as a laser medium. Among the known Nd-doped apatites, the material studied is characterized by the longest luminescence lifetime, $\tau = 0.375$ ms, and one of the largest emission cross-sections known, $\chi = 6 \times 10^{-19}$/cm^2. The product $\tau\chi$ in this crystal, which is equal to 2.3×10^{-22}/cm^2/s, is apparently the largest of those of all Nd-doped laser crystals. Laser operation at 1053.8 nm with a slope efficiency of 25% and an intrinsic slope efficiency of 49% was obtained.

It has been determined that this compound exhibits strong luminescence when excited by X-rays. $Ba_5Cl(PO_4)_3$ and the bromoapatite showed a broad emission band with the emission peak centered at about 400 nm while no luminescence from $Ba_5(PO_4)_3OH$ has been observed.

Yb^{2+} ion-doped $Ba_5(PO_4)_3Cl$ phosphor was synthesized by solid-state reaction. Four distinct absorption bands were observed in the UV light region due to the electronic transitions of Yb^{2+} ion from the $^1S_0$ ground state to $2F_5/2(t_{2g})$, $2F_5/2(eg)$, $2F_7/2(t_{2g})$, and $2F_7/2(eg)$ excited states. The main emission wavelength of the phosphor was around 630 nm. The optimized Yb^{2+} ion concentration was 0.2 mol% ($k_{exc} = 400$ nm). The calculated critical distance was about 8.729 Å and concentration quenching was observed above 0.2 mol% due to an electric dipole–dipole interaction of the adjacent activator sites.

Other than its potential uses as a matrix for phosphors and solid-state lasers, barium chloroapatite has received little attention in the literature or in academia. Industrially, it is used as a low-power but efficient laser for various purposes. It is available commercially.

Barium Bromoapatite

This salt can be prepared by the solid-state reaction:

$$6BaHPO_4 + 3BaCO_3 + BaBr_2 + \text{heat} \Rightarrow Ba_{10}(Br)_2(PO_4)_6 + 3CO_2 + 3H_2O$$

It has also been prepared by the solution method:

$$10BaBr_2\ (aq) + 6Na_3PO_4\ (aq) \Rightarrow Ba_{10}(Br)_2(PO_4)_6\ (solid) + 18NaCl\ (aq) + 2HCl$$

However, the product is contaminated by Na^+ ions and must be washed thoroughly to obtain a pure product. A small amount of hydroxyapatite may also be present.

Barium bromoapatite is a softer crystal than the fluorapatites or chloroapatites of barium and has not been used in forming phosphors for use in the lighting industry as it is not stable under the mercury-vapor discharge in fluorescent lamps.

This salt has received little attention academically except as an adjunct to study of other haloapatites. It has no CAS number but is offered for sale commercially.

Barium Iodoapatite

Barium iodoapatite would have the formula, $Ba_5(PO_4)_5I$ if it could be formed. Barium iodoapatite, which has not been prepared, would have a small positive Gibbs energy of dissolution, and a small enthalpy of formation. This is probably due to the large size of the I^- ion as it would enter the lattice. Speculations on the existence of a possible fifth member of the alkaline earth apatite family, Iodoapatite, have been withdrawn due to energetic considerations. Whether an oxy-iodo-apatite, similar to the calcium analogue exists remains speculative.

Radium Orthophosphates

The main concern about radium as a phosphate has been its intense radioactivity (^{226}Ra) as a component of phosphate-rock minerals. Little or no description of these phosphate compounds can be found in the scientific literature. Yet, the chemistry of Ra should closely resemble that of the corresponding barium salts. Therefore, the following descriptions are those which will form the desired radium phosphate compound, even though these salts have apparently not been prepared heretofore nor have their physical and chemical properties been described.

MONOBASIC RADIUM PHOSPHATE

This salt could be easily prepared by dissolving radium carbonate in an excess of H_3PO_4. A ratio of at least 3:1 mol of acid is required:

$$RaCO_3 + 2H_3PO_4 \Rightarrow Ra(H_2PO_4)_2 + CO_2 + H_2O$$

If the pH exceeds about 3.8, the dibasic salt begins to precipitate. The monobasic salt is expected to be soluble so that the solution must be evaporated, usually at high temperature, >80–90 °C. An anhydrate, $Ra(H_2PO_4)_2$, readily forms acicular crystals. Its molecular weight would be 422.0011 g/mol. If heated, it should form a metaphosphate, then a polymeric radioactive glass.

RADIUM ORTHOPHOSPHATE, DIBASIC

Dibasic radium phosphate would have the formula of $RaHPO_4$ and the molecular weight of 322.0047 g/mol. It is sometimes referred to as "radium hydrogen phosphate". It would be easily prepared by reacting diammonium phosphate in solution with a soluble solution of radium, such as the chloride:

$$RaCl_2 + (NH_4)_2PO_4 \Rightarrow RaHPO_4 + 2NH_4Cl$$

To obtain a pure salt, the phosphate is always added to the radium solution. Otherwise, one obtains a salt contaminated with a slight excess of phosphate. Whether radium hydrogen phosphate is dimorphic or not remains speculative. It may be ferroelectric in the crystalline state as well as intrinsically conductive.

RADIUM ORTHOPHOSHATE, TRIBASIC

Tribasic radium orthophosphate would have the molecular formula of $Ra_3(PO_4)_2$ and the molecular weight of 690.6281 g/mol. It could be prepared by a number of methods including solution and solid-state methods. The best way to prepare a pure salt would be to react the dibasic salt with the carbonate:

$$2RaHPO_4 + RaCO_3 + \text{heat} \Rightarrow Ra_3(PO_4)_2 + CO_2 + H_2O$$

If a solution method is desired, the reaction of the soluble monobasic salt with the hydroxide seems to be superior to any other method:

$$Ra(H_2PO_4)_2\ (aq) + 2Ra(OH)_2\ (solid) \Rightarrow Ra_3(PO_4)_2\ (solid) + 4H_2O$$

Since the monobasic salt is expected to be acidic, the hydroxide slowly dissolves into solution, but the pH must be monitored so that it does not exceed pH = 9.5. Otherwise, the hydroxyapatite begins to appear. The crystal structure is expected to be rhombohedral $Ra_3(PO_4)_2$ with the space group *R*-3*m*.

RADIUM APATITES

None of these compounds have been prepared. The radium halophosphates or radium apatites comprise the compounds, $Ra_5X(PO_4)_3$ where X is OH, F, Cl Br or I. All of these should be easily formed (with the exception of the hydroxyapatite which must be formed in solution) by solid-state reaction:

$$6RaHPO_4 + 3RaCO_3 + RaX_2 + \text{heat} \Rightarrow Ra_{10}X_2(PO_4)_6 + 3CO_2 + 3H_2O$$

Radium Hydroxyapatite

This salt is expected to be obtained by the aqueous reaction of a soluble barium salt with trisodium phosphate:

$$10RaCl_2\ (aq) + 6Na_3PO_4\ (aq) \Rightarrow Ra_{10}(OH)_2(PO_4)_6\ (solid) + 18NaCl\ (aq) + 2HCl$$

Alternately, it should be easily prepared by the aqueous reaction of the monobasic salt and the hydroxide at about 60–80 °C with addition of NaOH to control pH to a minimum of 10–11.

$$3Ra(H_2PO_4)_2\ (aq) + 2Ra(OH)_2\ (solid) \Rightarrow Ra_5OH(PO_4)_3\ (solid) + 8H_2O$$

Its molecular weight would be 1817.0616 g/mol.

Radium Fluorapatite

This salt is probably best prepared by solid-state reaction:

$$6RaHPO_4 + 3RaCO_3 + RaF_2 \Rightarrow Ra_{10}(F)_2(PO_4)_6 + 3CO_2 + 3H_2O$$

It is expected to be hexagonal with space group P63/m.

Radium Chloroapatite

This salt should be easily prepared by the solid-state reaction:

$$6RaHPO_4 + 3RaCO_3 + RaCl_2 + \text{heat} \Rightarrow Ra_{10}(Cl)_2(PO_4)_6 + 3CO_2 + 3H_2O$$

Radium chloroapatite is expected to be hexagonal with a space group of P63/m and point group of 6/m.

Radium Bromoapatite

This salt could be prepared by the solid-state reaction:

$$6RaHPO_4 + 3RaCO_3 + RaBr_2 + \text{heat} \Rightarrow Ra_{10}(Br)_2(PO_4)_6 + 3CO_2 + 3H_2O$$

It could also be prepared by the solution method:

$$10RaBr_2\ (aq) + 6Na_3PO_4\ (aq) \Rightarrow Ra_{10}(Br)_2(PO_4)_6\ (solid) + 18NaCl\ (aq) + 2HCl$$

However, the product is expected to be contaminated by Na^+ ions and must be washed thoroughly to obtain a pure product.

Radium Iodoapatite

Radium iodoapatite would have the formula, $Ra_5(PO_4)_5I$ if it could be formed. Radium iodoapatite, which has not been prepared, has great interest in academia since the size of the lattice may be sufficient to allow the formation of the iodoapatite phase. This salt is probably best prepared by solid-state reaction:

$$6RaHPO_4 + 3RaCO_3 + RaI_2 \Rightarrow Ra_{10}(I)_2(PO_4)_6 + 3CO_2 + 3H_2O$$

Whether this compound can be formed remains speculative.

4.2.6. Related Alkaline Earth Chalcogen Apatites

Four new apatitic phases have been prepared and their structures determined. The structure of $Ca_{10}(PO_4)_6S$ was refined from single-crystal X-ray data and the structures of $Sr_{10}(PO_4)_6S$, $Ba_{10}(PO_4)_6S$ and $Ca_{10}(PO_4)_6Se$ from powder X-ray data using the Rietveld method. The four apatites are isostructural and crystallize in the trigonal space group P3 with the chalcogenide ion positioned at (000) in the structure. The sulfoapatites show no ability to absorb H_2S in the way that oxyapatite absorbs H_2O at elevated temperatures. This can be attributed to the position of the sulfide ion and the way it influences the crystal structure around the vacant chalcogenide position at (000).

4.2.7. Alkaline Earth Pyrophosphates

The alkaline earths form at least two pyrophosphates, based on the acid, $H_4P_2O_7$. These are the acid pyrophosphate, $M(HP_2O_7)_2$ and the basic salt, $M_2P_2O_7$. The former salt is rare and it is the latter most often seen.

Beryllium Pyrophosphate

This salt has the formula, $Be_2P_2O_7$ or $(BeOH)_4P_2O_7$ depending upon the method of preparation. The compound, $(BeOH)_2H_2P_2O_7$, is also possible if a solution method is employed:

$$4(BeOH)Cl\ (aq) + Na_4P_2O_7 \Rightarrow (BeOH)_4P_2O_7 + 4NaCl$$

It is said to occur as the pentahydrate but more likely it is the monohydrate, $(BeOH)_4P_2O_7 \cdot H_2O$. If BeO is calcined with solid pyrophosphoric acid, the result is:

$$2BeO + H_4P_2O_7 + heat \Rightarrow Be_2P_2O_7 + 2H_2O$$

By precipitating a solution of sodium pyrophosphate with a basic solution of beryllium nitrate, a white pulverable precipitate was obtained, $(BeOH)_2H_2P_2O_7$. On analysis, this salt yielded results close to the theoretical formula for the pyrophosphate. However, the salt was completely dissolved for analysis and did not take into account the hydroxy-groups attached to the Be atom.

Once formed, $Be_2P_2O_7$ has been found to be dimorphic, the high-temperature form, α-$Be_2P_2O_7$ being stable above about 68 °C.

Beryllium dihydrogen pyrophosphate is unknown. There is absolutely no mention of use of these salts in industry and the number of papers dealing with them is very sparse in the scientific literature. Beryllium pyrophosphate has no CAS number and is not offered for sale commercially.

Magnesium Pyrophosphate

Magnesium pyrophosphate has the molecular formula of $Mg_2P_2O_7$ and the molecular weight of grams per mole. It may be prepared by the solid-state reaction of the dibasic orthophosphate, or alternately by the precipitation of a soluble Mg salt with aqueous pyrophosphoric acid:

$$2MgHPO_4\ (\text{or } MgNH_4PO_4) + heat \Rightarrow Mg_2P_2O_7 + H_2O\ (+NH_3)$$

$$MgCl_2\ (aq) + H_4P_2O_7\ (aq) \Rightarrow Mg_2P_2O_7\ (solid) + 2HCl\ (aq)$$

In the solution method, the result is the hexahydrate, $Mg_2P_2O_7 \cdot 6H_2O$. This is a white powder with a CAS number of 13478-16-5 and a molecular weight of 245.4073 g/mol. Its density is 1.71 g/cm^3 and it is relatively insoluble in water or ethanol but soluble in acids. Its structure may be visualized as in Fig. 4.45.

The angle between the tetrahedra is about 120°. The compound, $Mg_2P_2O_7$, has long been used for the quantitative determination of magnesium in the field of analytical chemistry. The magnesium is precipitated in highly alkaline solution as the hydrated crystal, $MgNH_4PO_4 \cdot 6H_2O$, calcined at 1100 °C, and weighed as $Mg_2P_2O_7$. It is for

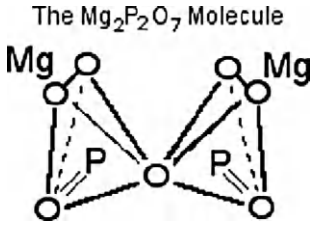

FIGURE 4.45

this reason that the decomposition of magnesium ammonium orthophosphate has been studied intensely.

Various mechanisms have been proposed for the course of decomposition of the magnesium-ammonium salt. It has been shown that $MgNH_4PO_4 \cdot 6H_2O$ loses 5 mols of water at about 105 °C but no ammonia below 150 °C. The simultaneous decomposition of the monohydrate and of the ammonium salt itself occurs above 250 °C. Rapid heating will destroy this sequence of the decomposition due to the formation of primary ammonium salts, which volatilize slowly at these temperatures. Once formed, the ignited compound $Mg_2P_2O_7$ first showed a contraction slightly above room temperature before the normal positive movement due to reversible thermal expansion took place. This unusual behavior showed that an inversion temperature took place. By means of thermal analyses, thermal expansions, and X-ray data, a solid-phase inversion of $Mg_2P_2O_7$ has been placed at approximately 68 °C. X-ray data indicate an accuracy of ±2 °C for the rapid low to high inversion, i.e.

$$\beta\text{-}Mg_2P_2O_7 \Leftrightarrow \alpha\text{-}Mg_2P_2O_7$$

The melting point of α-$Mg_2P_2O_7$ is 1668 K (1395 °C) ± 5 K with a heat of fusion of 32.1 kcal/mol. The transition at 342.2 K (69.2 °C) due to the change in crystal structure requires 729 cal/mol. The Raman spectra were measured and analyzed for both β- and α-$Mg_2P_2O_7$. The IR and Raman spectra were interpreted for both phases using factor-group analyses. The spectral features predicted with factor groups arising from the X-ray crystallographic space groups $P2_1/c$-c_{2h}^5 and $C2/m$-C_{2h}^3 for α-$Mg_2P_2O_7$ and β-$Mg_2P_2O_7$, respectively, fit the observed results. Bands observed in the Raman spectrum for β-$Mg_2P_2O_7$ are consistent with a linear bond angle while those for α-$Mg_2P_2O_7$ are consistent with a bent P–O–P bond angle. No soft modes were observed in the Raman spectra indicating that the phase transition between the two phases is not a second-order process.

The lattice parameters of the low temperature phase, β-$Mg_2P_2O_7$, are $a = 13.198$ Å, $b = 8.295$ Å, $c = 9.072$ Å, $\beta = 104.9°$ and $Z = 8$. The space group, $C2_1/c$ allows an easy comparison of the α- and β-phases of this compound. A primitive cell with the same space group could be chosen with cell parameters of $a = 6.981$ Å, $b = 8.295$ Å, $c = 9.072$ Å, $\beta = 113.0°$ and $Z = 2$. In contrast to with the apparently linear P···O···P group found for the α-phase, stable above 70 °C, the β-phase P···O···P group is bent at an angle of 144°. The $P_2O_7^{4-}$ ion has nearly C_2 symmetry with an average inner and outer P···O bond distances of 1.59 and 1.52 Å, respectively. The phase-diffuse transition appears to be related to the fact that the cations show both five and six coordination in the β-phase whereas in the α-phase, all cations are equivalent and sixfold coordinated.

The crystal structures of various hydrates of magnesium pyrophosphate have been studied. The thermal dehydration of $Mg_2P_2O_7 \cdot 6H_2O$ were studied, in the range 25–800 °C, by TGA (TG-DSC), XRD, and infrared spectroscopy. According to the TG-DSC curves, the dehydration of this salt takes place in two stages. The results of thermal analysis, X-ray patterns, and infrared spectra of this compound heated at different temperatures showed that, after dehydration, $Mg_2P_2O_7 \cdot 6H_2O$ decomposes into dihydrate $Mg_2P_2O_7 \cdot 2H_2O$ then to an amorphous $Mg_2P_2O_7$ product which crystallizes at 665 °C to give anhydrous diphosphate $Mg_2P_2O_7$. The enthalpy of the dehydration of $Mg_2P_2O_7 \cdot 6H_2O$ and of the formation of $Mg_2P_2O_7$ have been calculated from thermogravimetric data. An infrared spectroscopic study of $Mg_2P_2O_7 \cdot 6H_2O$ and of its heated products, revealed the existence of the characteristic bands of the P_2O_7 group and showed that the P···O···P angle is bent in these salts.

The crystal structure of the hexahydrate has been determined and is compared with the known structures of the dihydrate and two forms of the anhydrous compound. Comparisons among the structures provide some insight as to the structural role of Mg^{2+} as a cofactor in the ATP-ADP hydrolysis reactions of bioenergetics. Crystal data for dimagnesium pyrophosphate hexahydrate: $Mg_2P_2O_7 \cdot 6H_2O$, M(r) = 330.66, monoclinic, P2(1)/n, $a = 7.189$ (2) Å, $b = 18.309$ (8) Å, $c = 7.665$ (5) Å, $\beta = 92.360$ (14) degrees, $V = 1008.1$ A^3, $Z = 4$. "Struvite" is the name for the mineral with the same composition.

The room temperature variant with composition $Mg_2P_2O_7 \cdot 3.5H_2O$ crystallizes in the monoclinic space group $P2_1/c$ (No. 14) with $a = 10.9317(1)$, $b = 8.05578(9)$, $c = 9.2774(1)$ Å, $\beta = 90.201(1)°$, $V = 816.99(2)$ $Å^3$ and $Z = 4$. The structure consists of sheets stacked along [100] which are linked through $MgO_2(H_2O)_4$ pillars into a three-dimensional framework with cavities containing water molecules. Within the sheets, there are infinite edge-sharing chains of Mg octahedra along [010] which are cross-linked by $P_2O_7^{4-}$ groups. A high-temperature variant exists around 200 °C. The crystal structure of this compound with composition $Mg_2P_2O_7 \cdot H_2O$ was solved and refined in the monoclinic space group $C2/c$ (No. 15) with $a = 18.6596$ Å, $b = 7.9769$ Å, $c = 8.9757$ Å, $\beta = 107.378°$, $V = 1275.01$ $Å^3$, $Z = 8$. The transformation to $Mg_2P_2O_7 \cdot H_2O$ involves removal of the water molecules in the cavities and the water molecules of the Mg octahedral pillars in $Mg_2P_2O_7 \cdot 3.5H_2O$. The sheets in $Mg_2P_2O_7 \cdot 3.5H_2O$ however remain unchanged during the transformation as the water molecule coordinating Mg here is retained. These sheets are linked through tetrahedral MgO_4 pillars into a three-dimensional structure containing infinite 10-membered ring channels along [001]. Both compounds have been further

characterized by ^{31}P MAS-NMR spectroscopy, TGA and high-temperature powder XRD.

The dihydrate, $Mg_2P_2O_7 \cdot 2H_2O$, has the space group of $P2_1/n$ with $a = 7.367$, $b = 13.906$ Å, $c = 6.277$ Å, $\beta = 94°34'$, $Z = 4$, with a density of 2.66 g/cm^3. The structure consists of $P_2O_7^{4-}$ radicals linked by two kinds of Mg atoms. The Mg atoms have six nearest neighbors and share edges of the coordination octahedral to form infinite chains. One of the H atoms makes an O–H···O defined hydrogen bond. The other three form bifurcated hydrogen bonds.

Although the various magnesium pyrophosphate hydrates have received considerable attention in the literature, this has arisen because this compound is formed in the human body. This salt is also a plant virus inhibitor and has been used in industry as such. The only other usage has been as a matrix for forming phosphors. For example, Magnesium pyrophosphate, double activated with cerium and thorium, has been developed as an ultraviolet-emitting phosphor. However, magnesium is generally used as a minor ingredient in phosphors such as $(Sr,Mg)_3(PO_4)_2{:}Sn^{2+}$.

Magnesium pyrophosphate is available commercially in two varieties. It is offered for sale as $Mg_2P_2O_7 \cdot 2H_2O$ with the CAS number of 10102-34-8. The CAS number of 13446-24-7 refers to the hexahydrate.

Calcium Pyrophosphate

Calcium pyrophosphate has the molecular formula of $Ca_2P_2O_7$ and the molecular weight of 254.1378 g/mol. It has the CAS number of 7790-76-3. It may be prepared by the solid-state reaction of the dibasic orthophosphate, or alternately by the precipitation of a soluble Ca salt with aqueous pyrophosphoric acid:

$$2CaHPO_4 + \text{heat} \Rightarrow Ca_2P_2O_7 + H_2O$$

$$CaCl_2\,(aq) + H_4P_2O_7\,(aq) \Rightarrow Ca_2P_2O_7\,(solid) + 2HCl\,(aq)$$

The solid-state reaction produces an amorphous crystal at 240–500 °C. β-$Ca_2P_2O_7$ forms >750 °C and α-$Ca_2P_2O_7$ forms in the temperature range of 1140 to 1350 °C. The free energy of formation, $\Delta G_f = -3132$ kcal/mol.

The product of the aqueous method is the dihydrate, $Ca_2P_2O_7 \cdot 2H_2O$. It is a white powder and has the CAS number of 7790-76-3. It is insoluble in water but soluble in dilute acids. The anhydrate decomposes at 1353 °C to form a metaphosphate:

$$Ca_2P_2O_7 + \text{heat} \Rightarrow Ca(PO_3)_2 + CaO$$

The dihydrate is triclinic with $a = 7.365$ Å, $b = 8.287$ Å, $c = 6.691$ Å, $\alpha = 102.96°$, $\beta = 72.73°$, $\gamma = 95.01°$ with a space group of $P\underline{1}$. There are two units per unit cell. The six P···O_T (terminal) bond lengths range from 1.499 to 1.538 Å. The two bridge lengths, P···O_B, are equal to 1.623 Å. Average angles are O_B···P···$O_T = 107°$, O_T···P···$O_T = 112.1°$ and the P···O_B···P angle = 123.1°. The two water molecules form one interwater hydrogen bond and three hydrogen bonds to the pyrophosphate-oxygen atoms. Both calcium atoms are seven-coordinated at Ca…O distances less than 2.71 Å.

Calcium pyrophosphate is dimorphic. The phase transformation and sintering behaviors of $Ca_2P_2O_7$ with different phase composition has been investigated by using X-ray powder diffraction (XRD), dilatometery and SEM techniques. It was found that although α-$Ca_2P_2O_7$ (high-temperature form) could be maintained during its cooling process, it was metastable and retransformed into β-$Ca_2P_2O_7$ (low-temperature form) at about 950 °C during its reheating process. This reversible phase transformation was discussed from the point view of polyhedral distortion. The sample from β-$Ca_2P_2O_7$ calcined at 1000 °C/2 h densifies much faster than that from α-$Ca_2P_2O_7$ or the β + α mixture, and bulk density as high as 98% TD can be obtained as it is sintered at 1150 °C. A dense α-$Ca_2P_2O_7$ free of microcracks could not be obtained whatever using a powder of α-$Ca_2P_2O_7$, or of β-$Ca_2P_2O_7$, or of β + α mixture. Such different sintering behavior was explained in relation to the reversible phase transformation between the two forms, α- and β-$Ca_2P_2O_7$.

β-$Ca_2P_2O_7$ is composed of $P_2O_7^{4-}$ groups linked through Ca^{2+} cations. The P···O_B bonds involving the bridging O atoms are longer (average—1.650 Å) than the others (average—1.517 Å). As the PO_4 tetrahedra are almost regular, the displacement of the P-atoms involves two sets of O···P···O angles: O···P···O = 112.7° and O···P···O_B = 106°.

Raman spectra and middle infrared absorption spectra (4000–200/cm) were measured for α-$Ca_2P_2O_7$. No coincidences in the infrared and Raman spectra of α-$Ca_2P_2O_7$ indicated that this material possesses the centrosymmetric space group D_{2h}^{16}-Pnma rather than the noncentrosymmetric space group, C_{2v}^{9}-Pna2$_1$. Differences were noted in the vibrational spectra of monoclinic α-$Ca_2P_2O_7$ and the two orthorhombic α-phases, α-$Sr_2P_2O_7$ and α-$Ba_2P_2O_7$, which were related to differences in their crystal structures. The $P_2O_7^{4-}$-anions of both compounds contained nonlinear P–O–P bond angles. Microwave dielectric properties of β- and α-$Ca_2P_2O_7$ ceramic materials were investigated, using a network analyzer at the frequency of 10 GHz. It was found that β-$Ca_2P_2O_7$ could be sintered at 1150 °C for 2 h to produce a high-bulk density (98% TD) and α-$Ca_2P_2O_7$ could be sintered at 1290 °C/4 h with bulk density of 95.8% TD. The dielectric constant (ε_r) of β-$Ca_2P_2O_7$ sintered at 1150 °C/2 h is 8.4, the temperature coefficient of resonant frequency (τ_f) is −53 ppm/°C, and the *Qxf* value is 53,500 GHz. α-$Ca_2P_2O_7$ sintered at 1290 °C/4 h has ε_r of 7.8, τ_f of −97 ppm/°C and *Qxf* value of 14,115 GHz.

The Raman and IR spectra of triclinic $Ca_2P_2O_7 \cdot 2H_2O$ was interpreted using factor group analysis. Solid-state

effects, factor group splitting and two-site splitting, must be considered to explain the spectra; site group or free ion group models are inadequate. The simple unit cell of this pyrophosphate allows unambiguous assignment of the eight P–O stretching modes in order of decreasing energy: $4\,v^{a}_{PO} > v^{s}_{PO} > v^{a}_{PO} > v^{a}_{POP} > v^{s}_{POP}$. Comparison of these spectra with those for pyrophosphates such as Sr or Ba exhibiting larger unit cells demonstrates that the number of factor group split symmetric P–O stretching modes, v^{s}_{PO}, in the Raman spectra is proportional to the unit cell size. These spectra uniquely characterize this medically interesting material which can cause in vivo crystal-induced inflammation in tissues.

β-$Ca_2P_2O_7\cdot 4H_2O$ is monoclinic, $P2_1/c$, $a = 12.287$ Å, $b = 7.511$ Å, $c = 10.775$ Å, and $\beta = 112.54°$. Five of the terminal O atoms from a pyrophosphate group bind to Ca atoms, together with O atoms from three of the water molecules. The fourth H_2O forms only hydrogen bonds. Both Ca atoms have coordination number 7 and show characteristics between those of a capped octahedron and a pentagonal bipyramid. The analysis of coordination distortions suggests that regularity and volume efficiency of a Ca coordination polyhedron increases with the number of bound water O atoms. The structure is layered after {100}, reflected also in the morphology of crystals which are formed as extremely thin plates. The central parts of the layers are formed by chains of Ca coordination polyhedra that run along the *b*-axis and are interconnected by pyrophosphate groups. Water molecules form the surfaces of the layers. A peculiar auto-inhibition of growth from supersaturated solutions is supposed to be caused by a direct attachment of $CaP_2O_7^{2-}$ and $P_2O_7^{4-}$ to the water molecules on the surfaces of layers. $Ca_2P_2O_7\cdot 4H_2O$ is known in two polymorphs. The unit cell volume of the β-form compared with that of the α-form suggests that the former is a low-temperature modification.

The high-temperature form of calcium pyrophosphate, α-$Ca_2P_2O_7$, crystallizes in the monoclinic space group P2(1)/n. The structure is closely related to that of β-$Sr_2P_2O_7$, although the latter has orthorhombic symmetry. Both cations show coordination numbers of eight with average cation-oxygen atom bond lengths of 2.54 and 2.51 Å for the individual cation sites. The diffraction pattern shows a marked orthorhombic character suggesting a high-temperature phase with Pbnm symmetry.

The ultimate goal of implantation of biomaterials in the skeleton is to reach full integration of the nonliving implant with the living bone. The biomaterial can be used much as a bone graft, resorbing or dissolving as bone growth occurs, and the end result is a new remolded bone. Calcium pyrophosphate, $Ca_2P_2O_7$, is one of the intermediate products of bone mineralization. β-Dicalcium pyrophosphate (β-CP) doped with certain amounts of $Na_4P_2O_7\cdot 10H_2O$ was prepared as the developed material. $Na_4P_2O_7\cdot 10H_2O$ was used as a liquid-phase additive to improve the sintering process and promote physiological bioresorbability. Compressive strength and four-point bending strength were measured by the Bionix test system 858. The mechanical strength of the sintered β-CP increased with the addition of $Na_4P_2O_7\cdot 10H_2O$ up to 5 wt%, but thereafter decreased. The microstructure and crystal structure were analyzed by the techniques of SEM, EPMA, transmission electron microscopy (TEM) and XRD. The relationship between the mechanical strength of the sintered bioceramics and the $Na_4P_2O_7\cdot 10H_2O$ dopant was examined in terms of the presence of $NaCa(PO_3)_3$ (which is the fired product of the mixture), grain growth and abnormal grain coalescence while the dopant increased. A newly produced bioceramic, β-$Ca_2P_2O_7$ with addition of $Na_4P_2O_7\cdot 10H_2O$ (SCP), was implanted into the femoral condyle of rabbits. Within 6 weeks after implantation, most of the bioceramic is replaced by new woven bone. On the contrary, block form hydroxyapatite (HA) and β-tricalcium phosphate (β-TCP), which are osteoconductible, do not resorb within a short period of time. It appears that the biodegradable behavior of SCP may occur in two steps. The first and most important step is the digestion of particles and migration of the particles by phagocytosis. The object of this study was to examine the change in morphologies, chemical compositions and crystal structure of SCP after soaking in distilled water for a certain period of time. The SCP ceramic was also cocultured with leucocytes to observe how the SDCP particles were digested by the leucocytes, so that the mechanism of biodegradable behavior of SCP ceramic *in vivo* might be clarified. Four types of sintered calcium phosphate ceramics were tested in the experiment: SCP, pure α-$Ca_2P_2O_7$ (CP), HA and β-TCP. They were soaked in distilled water at 37 °C for up to 30 days. The microstructure and morphology of crystals deposited on the surface were observed using SEM. Sodium, calcium and phosphorus ion contents in the supernatant solution were detected by atomic absorption analysis and ion-coupled plasma. In summary, HA and DCP showed no significant evidence of dissolution in distilled water. In static distilled water, calcium ions may be released from β-TCP into solution during the initial 7 days and then converted into HA by reprecipitation. The results showed that the SCP was firstly dissolved into small grains or fragments by the solution.

A single-phased β-$Ca_2P_2O_7$:Eu^{2+}:Mn^{2+} phosphor has been synthesized for application to white-emitting LEDs. The enhancive orange emission of Mn^{2+} observed in α-$Ca_2P_2O_7$:Eu^{2+}:Mn^{2+} upon UV excitation is due to the energy transfer of $Eu^{2+} \Rightarrow Mn^{2+}$. The energy transfer efficiency can be as high as 65%. The white LED is formed by integrating the 400 nm emission of the blue-emitting chip with that of the phosphor

β-$Ca_2P_2O_7$:$Eu_{0.04}$:$Mn_{0.12}$ blue-orange phosphor and a Ba_2SiO_4:0.03Eu^{2+} green phosphor. The results show a color rendering index of 78 and a good luminescent efficiency of 9 lm/W. β-$Ca_2P_2O_7$:Eu^{2+}:Mn^{2+} appears to be a promising candidate phosphor for the production of white LEDs.

A new pyrophosphate long-lasting (phosphorescent) phosphor (LLP) with the composition of $Ca_{1.96}P_2O_7$:0.02Eu^{2+}:0.02Y^{3+} was synthesized via a high-temperature solid-state reaction method. The phosphor emits blue light that is related to the characteristic emission of Eu^{2+} due to 5d–4f transitions. For the optimized sample, bright-blue long-lasting phosphorescence could be observed by naked eyes even 8 h after the excitation source is removed. The TL spectra showed that the doping of Y^{3+} ions greatly enhanced the intensity of 335 K peak and created new TL peak at about 373 K that is also responsible for the blue LLP.

$Ca_2P_2O_7$ is an important product finding applications in the manufacture of oral care products like toothpaste and the like. Calcium pyrophosphate is available commercially from several manufacturers.

Strontium Pyrophosphate

Strontium pyrophosphate has the molecular formula of $Sr_2P_2O_7$ and the molecular weight of 349.1833 g/mol. Its CAS number is 765305-66-6. It may be prepared by the solid-state reaction of the dibasic orthophosphate, or alternately by the precipitation of a soluble Mg salt with aqueous pyrophosphoric acid:

$$2SrHPO_4 + \text{heat} \Rightarrow Sr_2P_2O_7 + H_2O$$

$$SrCl_2\ (aq) + H_4P_2O_7\ (aq) \Rightarrow Sr_2P_2O_7\ (solid) + 2HCl\ (aq)$$

The solution method produces a hemihydrate, $Sr_2P_2O_7 \cdot 1/2H_2O$. This salt decomposes at 575 °C to form β-$Sr_2P_2O_7$. The transition to the high temperature form, α-$Sr_2P_2O_7$ takes place at about 760–780 °C.

In the $Sr_2P_2O_7$ system, the unit-cell parameters of orthorhombic β-$Sr_2P_2O_7$ are: $a = 8.9839$ Å, $b = 13.163$ Å, and $c = 5.403$ Å. The crystallographic data of $Sr_2P_2O_7$ are reported to contain two types of sites for Sr^{2+} ions in the unit cell.

Single crystals in the $Sr_2P_2O_7 \cdot Mg_2P_2O_7$ system have been prepared in conjunction with crystallographic and electron spin resonance studies of α-$Ca_2P_2O_7$ and α-$Sr_2P_2O_7$. In an attempt to resolve the site of preferred solubility for Mn^{2+}, $(Sr,Mn)_2P_2O_7$ was prepared. When this phase was found to be triclinic, emphasis was then directed toward the $Sr_2P_2O_7 \cdot Mg_2P_2O_7$ system. $(Sr,Mg)_2P_2O_7$ was prepared and found to have the α-$Ca_2P_2O_7$ structure. The results of a study of the single-crystal diffraction patterns were reported

Raman spectra and middle infrared absorption spectra (4000–200/cm) were measured for α-$Ca_2P_2O_7$, α-$Sr_2P_2O_7$, and α-$Ba_2P_2O_7$. These spectra were interpreted using factor group analyses, and band assignments were made. Noncoincidences in the infrared and Raman spectra of α-$Sr_2P_2O_7$ indicated that this material possesses the centrosymmetric space group D_{2h}^{16} Pnma rather than the noncentrosymmetric space group, C_{2v}^{9}-Pna2$_1$. The similarities between the vibrational spectra of α-$Ba_2P_2O_7$ and α-$Sr_2P_2O_7$ suggested that α-$Ba_2P_2O_7$ is isostructural with α-$Sr_2P_2O_7$. Differences were noted in the vibrational spectra of monoclinic α-$Ca_2P_2O_7$ and the two orthorhombic α-phases, α-$Sr_2P_2O_7$ and α-$Ba_2P_2O_7$, which were related to differences in their crystal structures. The $P_2O_7^{4-}$-anions of all three compounds contained nonlinear P–O–P bond angles.

α-$Sr_2P_2O_7$ has an orthorhombic unit cell that contains four molecules per cell with space group = Pnma and cell parameters of: $a = 8.9104$ Å, $b = 5.4035$ Å, $c = 13.1054$ Å, $V = 631.1$ Å^3, the structure contains ecliptic diphosphate groups of m-symmetry with a P···O_{bridge}···P angle of 130.7°, the average bond distances are: P···$O_{Bridge} = 1.60$ Å and P···$O_{Terminal} =$ 1.50 Å. The Sr^{2+} atoms have nine oxygen neighbors.

Strontium pyrophosphate has long been used as a matrix for phosphors used in fluorescent lamps in the lamp industry. Tin-activated $Sr_2P_2O_7$ was introduced by Ropp in 1957. This same matrix has been used to incorporate divalent Eu^{2+} as a phosphor useful in producing white-emitting LED lamps. Such lamps promise to completely replace fluorescent lamps in the near future.

The phosphors in the system $Sr_2P_2O_7$:$x$$Eu^{2+}$:$y$$Mn^{2+}$ were synthesized by solid-state reactions and their PL properties were investigated. These phosphors have strong absorption in the near UV region, which is suitable for excitation of ultraviolet light-emitting diodes (UV-LEDs). The orange-reddish emission of Mn^{2+} in these phosphors can be used as a red component in the tri-color system and may be enhanced by adjusting the Mn^{2+}/Eu^{2+} ratio. The energy transfer from Eu^{2+} to Mn^{2+} is observed with a transfer efficiency of 0.45 and a critical distance of 10 Å. The results reveal that $Sr_2P_2O_7$:$x$$Eu^{2+}$,$y$$Mn^{2+}$ phosphors could be used in white light UV-LEDs.

By introducing the Y^{3+} cation into $Sr_2P_2O_7$:Eu^{2+} (which has divalent cation sites in the lattice), a kind of new phosphor with blue long-lasting phosphorescence was successfully prepared by a high-temperature solid-state reaction method. The properties of $Sr_2P_2O_7$:Eu^{2+}:Y^{3+} were investigated utilizing XRD, PL, luminescence decay, long-lasting phosphorescence and TL spectra. The phosphor emitted blue light that was related to the $4f^6 5d1–8S_{7/2}$ transition of Eu^{2+}. The bright blue phosphorescence could be observed by naked eyes even 8 h after the excitation source was removed. Two

TL peaks at 317 and 378 K related to two types of defects appeared in the TL spectrum. By analyzing the TL curve, the depths of traps were calculated to be 0.61 and 0.66 eV.

Strontium pyrophosphate activated by divalent europium has been used in fluorescent lamps for photocopying and has enabled higher reproduction rates to be achieved.

Other than the applications mentioned above, the literature concerning strontium pyrophosphate is sparse indeed. Few papers concerning this salt can be found in the scientific literature and little is available from industry, perhaps due to the higher cost of this salt, compared to the calcium variety.

It is commercially available from a number of suppliers both in the U.S. and other countries.

Barium Pyrophosphate

Barium pyrophosphate has the molecular formula of $Ba_2P_2O_7$ and the molecular weight of 448.5973 g/mol. It has the CAS number of 13466-21-2 and may be prepared by the solid-state reaction of the dibasic orthophosphate, or alternately by the precipitation of a soluble Ba salt with aqueous pyrophosphoric acid:

$$2Ba\ HPO_4 + \text{heat} \Rightarrow Ba_2P_2O_7 + H_2O$$

$$BaCl_2\ (aq) + H_4P_2O_7\ (aq) \Rightarrow Ba_2P_2O_7\ (s) + 2HCl\ (aq)$$

The solution method produces a dihydrate, $Ba_2P_2O_7 \cdot 2H_2O$.

The thermal dehydration in air of this hydrate and α-$Ba^2P^2O^7$ crystallization in air, vacuum, and a water vapor atmosphere was studied using thermal analysis, X-ray powder diffraction, IR spectroscopy, and low-temperature air adsorption. In vacuum, α-$Ba_2P_2O_7$ crystallizes at higher temperatures, and in a water vapor atmosphere, at lower temperatures than in air. The specific surface area of samples decreases systematically, because of caking, as the temperature was elevated. The applicability of the Kolmogorov model with $n = 4$ is an evidence of a three-dimensional growth of α-$Ba^2P^2O^7$ nuclei and their steady-state generation during growth. The appearance of crystallization centers within the induction period requires a relatively high value of the activation energy (387.1 kJ/mol). No experimental evidence of the existence of the low-temperature phase β-$Ba_2P_2O_7$ was found.

Anhydrous barium pyrophosphate is a white powder with a density of 3.91 g/cm^3. It is not very soluble in water at 0.008820 g/100 ml but is soluble in dilute acids. It melts at 1430 °C.

Raman spectra and middle infrared absorption spectra (4000–200/cm) were measured for α-$Ba_2P_2O_7$. These spectra were interpreted using factor group analyses, and band assignments were made. Noncoincidences in the infrared and Raman spectra of α-$Ba_2P_2O_7$ indicated that this material possesses the centrosymmetric space group D_{2h}^{16}-Pnma rather than the noncentrosymmetric space group, C_{2v}^{9}-Pna2$_1$. Differences were noted in the vibrational spectra of monoclinic α-$Ca_2P_2O_7$ and the two orthorhombic α-phases, α-$Sr_2P_2O_7$ and α-$Ba_2P_2O_7$, which were related to differences in their crystal structures. The $P_2O_7^{4-}$-anions of this compound contained nonlinear P–O–P bond angles. The structure of α-$Ba_2P_2O_7$ is shown in Fig. 4.46.

Parameters of the monoclinic cell of $BaMgP_2O_7$ are $a = 5.483$ Å, $b = 8.561$ Å, $c = 12.626$ Å and $\beta = 91.32°$ space group is P2$_1$/n, $Z = 4$. Although $Mg_2P_2O_7$, cannot be activated by tin, combination with $Ba_2P_2O_7$ (Ba < 25 mol%) produces a very efficient phosphor, $(Mg,Ba)_2P_2O_7$:Sn, emitting at 3970 Å. This last phase, combined with δ-$Ba_2P_2O_7$, forms a solid solution of limited stability, $(Ba,Mg)_2P_2O_7$:Sn, whose emission band appears at 5120 Å when excited by 2537 Å. A ternary phase can be formed $(Mg_{1.5}Ba_{0.5-x}Srx)P_2O_7$:Sn, whose ultraviolet emission peak changes with composition.

Titanium-activated barium pyrophosphate has long been used in fluorescent lamps as a wideband emitting bluish phosphor. It was introduced to the lighting industry by Ropp in 1953. Other than this application, barium pyrophosphate has found little usage in the lighting industry.

Few papers concerning this salt can be found in the scientific literature. It is available from a number of suppliers commercially, worldwide.

Radium Pyrophosphate

Radium pyrophosphate would have the molecular formula of $Ra_2P_2O_7$ and the molecular weight of 448.5973 g/mol. It has no CAS number. It may be prepared by the solid-state reaction of the dibasic

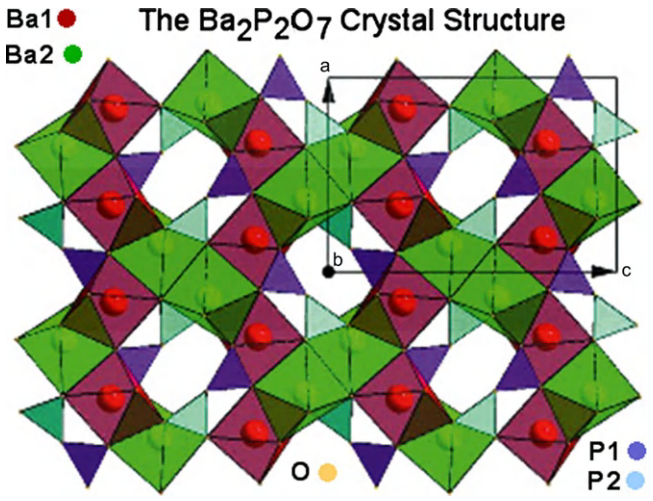

FIGURE 4.46

orthophosphate, or alternately by the precipitation of a soluble Ba salt with aqueous pyrophosphoric acid:

$$2RaHPO_4 + \text{heat} \Rightarrow Ra_2P_2O_7 + H_2O$$

$$RaCl_2\,(aq) + H_4P_2O_7\,(aq) \Rightarrow Ra_2P_2O_7\,(\text{solid}) + 2HCl\,(aq)$$

Radium coprecipitates with all barium compounds (and to a lesser extent with most strontium and lead compounds) even though the solubility product of the radium compound itself may not be exceeded. Because radium was one of the first radioactive elements utilized in tracer research, it was used in the development of the coprecipitation laws. Thus, in view of the intense radioactivity of ^{226}Ra, the formation of $(Ba,Ra)_2P_2O_7$ is probably the best method of forming the pyrophosphate.

The only usage of radium pyrophosphate has been in the medical field as a radioactive tracer and catalyst. Removal of ADP ribose from the iron protein of nitrogenase by activating enzyme resulted in the activation of the inactive iron protein. A radioassay that directly measured the initial velocity of the activation was developed using iron protein radiolabeled with radium pyrophosphate and either [8-3H]- or [G-3ZP]ADP-ribose. The release of radiolabeled ADP ribose by activating enzyme was linearly correlated with the increase in specific activity of the iron protein as measured by acetylene reduction.

The physical properties of radium pyrophosphate remain unknown. Whether a hydrate can be formed remains unknown. Furthermore, whether this salt is monomeric like the Ba salt or dimorphic like the Ca and SR salts remains to be determined.

Radium pyrophosphate is available in small lots commercially from several suppliers.

4.2.8. Alkaline Earth Metaphosphates and Polyphosphates

Metaphosphoric acid, HPO_3, is a singularly anhydrous version of orthophosphoric acid and is sometimes used as a water- or moisture-absorbing reagent. Metaphosphoric acid has phosphorus in the formal oxidation state of +5. Although it has several CAS numbers: 10343-62-1, 135306-83-1, 13566-25-1, and 37267-86-0, only the last two are associated with the IUPAC name **phosphenic acid**. The salts are called "metaphosphates" or "phosphenates". The phosphoric acid units can be bonded together in rings (cyclic structures) forming **metaphosphoric acid** molecules. The simplest such compound is **trimetaphosphoric acid** or **cyclo-triphosphoric acid** having the formula $H_3P_3O_9$. Its structure is shown in the following illustration. Since the ends are condensed, its formula has one less H_2O (water) than tripolyphosphoric acid. A general formula for such cyclic

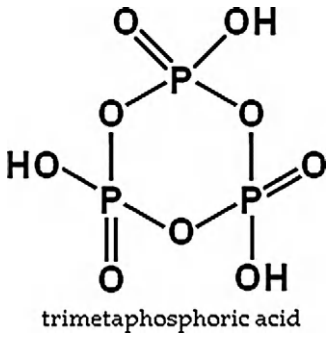

FIGURE 4.47

compounds is $(HPO_3)_x$ where x = number of phosphoric units in the molecule (Fig. 4.47).

One of the main differences in "metaphosphates" and "tripolyphosphates" lies in the fact that the former is cyclic whereas the latter is a linear structure. That is, there are 3-OH groups present in the above Lewis presentation while 6-OH groups are present in the tripolyphosphate. Yet many authors call one salt a polyphosphate when it actually is a metaphosphate and vice versa.

In a pyrophosphoric acid molecule, there are four hydrogens bonded to oxygens, and one, two, three, or all four can be lost as H^+ ions. When all four are lost from pyrophosphoric acid, a **pyrophosphate** ion is formed. The situation with higher order polyphosphoric acids and polyphosphates continues in a similar way. Tripolyphosphoric acid can lose up to five H^+ ions to form a **tripolyphosphate** ion, tetrapolyphosphoric acid can lose up to six H^+ ions to form **tetrapolyphosphate**, etc. As more dissociations per molecule are possible, the intervals between individual pK_a and pK_b values now start becoming smaller on the pH scale. As the polyphosphoric molecules grow increasingly larger and more complex, practically any number of the somewhat acidic −OH groups in them can dissociate to become negatively charged oxygens, forming numerous combinations of multiple-charged polyphosphoric/polyphosphate anions. Generally, in an aqueous solution, the degree or percentage of dissociation depends on the pH of the solution. Tripolyphosphoric acid has two more hydroxy groups in its molecule than the trimetaphosphate. A comparison of the two Lewis structures is shown in Fig. 4.48.

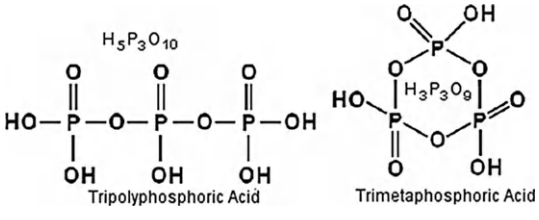

FIGURE 4.48

Tripolyphosphate compounds, especially alkali-based compounds, have been commonly used in detergents (i.e. cleaners) formulations. Sometimes pyrophosphate, tripolyphosphate, tetrapolyphosphate, etc. are called **diphosphate**, **triphosphate**, **tetraphosphate**, etc. especially when they are part of phosphate esters in biochemistry.

Beryllium Metaphosphates and Polyphosphates

Beryllium metaphosphate can be prepared by the solid-state reaction of metaphosphoric acid and the hydroxide, oxide or carbonate of calcium:

$$BeCO_3\ (s) + HPO_3\ (s) + \text{heat} \Rightarrow Be(PO_3)_2\ (s) + H_2O + CO_2$$

The best temperature to use is about 700 °C. It can also be prepared by the aqueous reactions:

$$NaPO_3\ (aq) + (BeO)Cl\ (aq) \Rightarrow (BeOH)(PO_3)\ (s) + NaCl\ (aq)$$

or

$$Be(OH)_2\ (s) + HPO_3\ (aq) \Rightarrow (BeOH)(PO_3)\ (s) + H_2O$$

The dissolution and reaction involving HPO_3 is slow and should be carried out in a hot solution. Evaporation at a low temperature (<15 °C) serves to form the crystals. The product is a monohydrate, $(BeOH)(PO_3)\cdot H_2O$. This salt loses its water of hydration at about 105 °C. Anhydrous beryllium metaphosphate is a white porous powder or granular material that is insoluble in water. If it is heated above about 450 °C, it forms a polymeric glass:

$$nBe(PO_3)_2 + \text{heat} \Rightarrow \{Be(PO_3)_2\}_n$$

If the cooled glass is then reheated, it devitrifies to form a high-temperature form, β-$Be(PO_3)_2$ (II) above 600 °C. This transformation is reversible. The so-called low-temperature form, γ-$Be(PO_3)_2$ (I) never appears but can be formed from the monohydrate, heated to above 250 °C.

The glassy and crystalline β-$Be(PO_3)_2$ (II) has a highly polymerized quartz-like structure with a mixed Be-metaphosphate skeleton where the Be-modifier also plays the role of the vitrifier. In this metaphosphate matrix, Be atoms merge into the quartz-like matrix with threefold coordinated oxygen atoms. Analogous elements are well known in "Phenacite"-orthosilicate lattices.

Four crystalline forms of $Be(PO_3)_2$ are known to date. The first form γ-(I) can be prepared at temperatures lower than 400 °C and β-(II) occurs above this temperature. The unit cell and space group have been determined. A third form α-(III), it was determined that this form has two modifications with a transition temperature of 96 °C. That is, one cooled the stable α-$Be(PO_3)_2$ form undergoes a further transformation when reheated to 96 °C. The stable higher temperature form of α-$Be(PO_3)_2$ (III) has an atomic arrangement closely related to that of "Keatite" which is an allotropic form of silica.

The major difference in these phases lies in the differences in bond lengths and bond angles of the various phases that results in differences in their crystal structure.

The following measurements have been made: (Table 4.16).

β-$Be(PO_3)_2$ (II) is a tetrapolyphosphate with a monoclinic cell: $a = 6.959$ Å, $b = 12.853$ Å, $c = 4.839$ Å, $\beta = 106.79°$, $Z = 4$, and space group = P2. Infinite PO_3 chains, with a period of four tetrahedra, run along the *a*-direction. BeO_4 tetrahedra link the different chains to form a three-dimensional network of tetrahedra.

Single crystals of γ-$Be(PO_3)_2$ (I) have been grown from a $BeCO_3 + (NH_4)_2HPO_4$ mixture, heated to about 600 °C. Its IR absorption spectrum is characteristic of linear polyphosphate. This beryllium polyphosphate variety crystallizes with a tetragonal unit cell, $a = b =$ 9.217 Å, $b = 21.082$ Å, $V = 1790.98$ Å^3, $Z = 16$, space group $P4/nnc$ and *density* = 2.48 g/cm^3.

Beryllium metaphosphate has limited use as a raw material in special ceramic compositions and as a catalyst carrier. It has been used as a component in a mixed-glass element used as a dosimeter. The combination of 80% ($Be(PO_3)_2 + LiPO_3$) and 20% $AgPO_3$ is melted to form a glass. The glass element, when exposed to radiation and excited by UV radiation, emits fluorescence directly proportional to the dose of the applied radiation. The dose is measured by the intensity of the emission.

Beryllium metaphosphate is available in limited quantities from selected suppliers. No polyphosphates of beryllium are listed.

Magnesium Metaphosphates and Polyphosphates

Magnesum metaphosphate can be prepared by the solid-state reaction of metaphosphoric acid and the hydroxide, oxide or carbonate of magnesium:

$$MgCO_3 + HPO_3 + \text{heat} \Rightarrow Mg(PO_3)_2 + H_2O + CO_2$$

TABLE 4.16

Phase	P–P (Å)	P–O–P (°)	P–P–P (°)	Period	Fs
β-$Be(PO_3)_2$ (II)	2.957	129.6	98.7	4	0.702
	2.887	139.9	108.1		
α-$Be(PO_3)_2$ (III)	2.933	139.8	105.2	8	1.000
	2.951	137.4	103.5		

Fs, Stretching coefficient.

The best temperature to use is about 700 °C. It can also be prepared by the aqueous reactions:

$$2NaPO3\ (aq) + MgCl_2\ (aq) \Rightarrow Mg(P_3O_9)_2 \cdot xH_2O\ (s) + 2NaCl$$

or

$$Mg(OH)_2\ (s) + 6\ HPO_3\ (aq) \Rightarrow Mg(P_3O_9)_2 \cdot xH_2O\ (s)$$

The reaction involving HPO_3 is slow and should be carried out in a hot solution. Evaporation at a low temperature (<15 °C) serves to form the crystals. The exact degree of hydration is not known. Magnesium trimetaphosphate is used as a coronary perfusing agent in Medicine (at a concentration of 15 mM) as a standard to estimate the absolute value of the phosphate-containing metabolites. The amounts of inorganic phosphate (Pi), phosphocreatinine (PCr) and ATP in the myocardium were determined by planimetry of the areas under individual peaks and were corrected for saturation factors.

A previously unreported metastable intermediate phase during the crystallization of magnesium metaphosphate ($Mg(PO_3)_2$) glasses to the equilibrium ring phase, $Mg_2P_4O_{12}$. It appears that the metastable phase contains polyphosphate chains, as in other crystalline alkaline earth polyphosphates. This type of phase appears to form by low-energy rearrangement of the polyphosphate chains in the glass structure to form the cyclic metaphosphate.

An investigation into the structure of glasses made from $Mg(PO_3)_2$ metaphosphate has been made. The phosphate network was found to consist of long linear chains of PO_4 tetrahedral units. This type of structure exists in many polyphosphate glasses, indicating that the cation modifier has little effect on the structure of the phosphate backbone. A study of the Mg^{2+} networks revealed that the modifier's field strength plays a significant role in determining the short-range order of the metal ions.

One paper reports a systematic structure investigation of alkaline earth metaphosphate glasses $Me(PO_3)_2$ with Me = Zn, Mg, Ca, Sr, Ba by neutron diffraction. The total structure factor S(Q) was measured up to Q = 170/nm. The total atomic distribution functions of most of the glasses show well-defined maxima for short distances which can be attributed to distinct atomic pairs. By a peak separation procedure, partial coordination numbers and mean distances for the atomic pairs P–O, O–O, Me–O, and P–P as well as the distribution of bond angles P–O–P were determined. The experimental data are compatible with the following model of the glass structure. The basic elements are PO_4 tetrahedra that are interconnected via two oxygens in chains. The chains are not straight. Metal ions are located between the chains and have oxygens in the first coordination shell. The metal-oxygen coordination number is 4 for Mg, Ca and 8 for Ba.

Binary magnesium phosphate glasses have been investigated by XRD to extract information on their short- and intermediate-range order. In these glasses, the Mg^{2+}/PO_4^{2-} ratio was varied. In order to study the intermediate-range order primarily, the main diffraction peak of the structure factors, S(s), was examined. The metaphosphate glass and crystalline compound, MgP_4O_{11}, exhibits a remarkably different structure from that of the related crystal $Mg_2P_4O_{13}$ which is a polyphosphate. Comparison of the X-ray scattering structure factors of the glasses experimentally obtained and calculated from the related crystal structures supports these findings. Thus, one is a metaphosphate and the other is a polyphosphate.

Magnesium polyphosphate glasses have been examined using X-ray and neutron scattering and ^{31}P MAS-NMR spectroscopy to extract information on their short-range, intermediate-range and submicroscopic structure. The depolymerization of the PO_4 chains with rising MgO content is quantitatively described by the increasing concentration of Q^1 and Q^0 groups determined by NMR. In the pyrophosphate region, the Q^1 sites disproportionate to Q^0 and Q^2 groups, whereas there is no disproportionation of the Q^2 sites at metaphosphate composition. The shortening of the real-space distances, r_m, indicates that the structure of the glasses becomes more compact with progressive depolymerization which is due to the increasing connection of the MgO_n polyhedra by the sharing the nonbridging oxygen atoms. The Mg–O coordination sphere was found to change insignificantly as composition changed.

The crystal structure of $Mg_2P_4O_{12}$ has been determined. This salt crystallizes in the monoclinic space group, C2/c with: $a = 11.756$ Å, $b = 8.285$ Å, $c = 9.917$ Å, $\beta = 118.96°$, $Z = 4$, $V = 845$ Å^3. The PO_4 tetrahedra in the structure are linked together in a ring to form $P_4O_{12}^{4-}$ ions with P···O···P angles of 134.2° and 138.8°. The Mg^{2+} ions are always 6-coordinated. Most "metaphosphate" compounds have previously been thought to be linked together in infinite chains (technically making them polyphosphates). Only a few "metaphosphates" with such anions have been found to date. The Mg^{2+} ions in $Mg_2P_4O_{12}$ are always surrounded by regular MgO_6 octahedra of two differing types: one with 2-point symmetry (around Mg_1) and the other with $\bar{1}$ symmetry (around Mg_2). The Mg···O distances range from 1.990 to 2.161 Å.

Magnesium metaphosphate and magnesium polyphosphate salts have listed no manufacturer or supplier. These salts have no CAS numbers listed.

Calcium Metaphosphates and Polyphosphates

Calcium metaphosphate (CMP) has the molecular formula of $Ca(PO_3)_2$ and the molecular weight of 198.0219 g/mol. Its CAS number is 13477-39-9.

This salt is also offered commercially as Calcium dimetaphosphate ($Ca(PO_3)_2$) with the CAS number of 53801-86-8. Another manufacturer has a calcium bismetaphosphate with the CAS number 53806-80-7. It is not clear what differences may exist, if any, between these salts or the method of their preparation. CMP can be prepared by the solid-state reaction of metaphosphoric acid and the hydroxide, oxide or carbonate of calcium:

$$CaCO_3 + HPO_3 + \text{heat} \Rightarrow Ca(PO_3)_2 + H_2O + CO_2$$

The best temperature to use is about 700 °C. Anhydrous β-$Ca(PO_3)_2$ is monoclinic, space group = $P2_1/a$ with $a = 16.960$ Å, $b = 7.7144$ Å, $c = 6.9963$ Å, $\beta = 90.394°$, $V = 915.40$ Å^3, $Z = 8$. The density is 2.874 g/cm^3. The crystal structure of $Ca(PO_3)_2$ consists of meandering chains of PO_4 tetrahedra along the [001] direction, connected by Ca atoms. Thus, it is a polyphosphate. P···O distances average 1.584 Å for bridging and 1.487 Å for terminal atoms. $Ca(O_1)$ has coördination number 8 with Ca···O distances ranging from 2.381 to 2.696 Å; the polyhedron is close to a tetragonal antiprism. $Ca(O_2)$ has coördination number 7 with Ca···O distances from 2.339 to 2.638 Å; the polyhedron is a capped trigonal prism (Fig. 4.49).

This salt can also be obtained by the thermal degradation of the monobasic phosphate:

$$Ca(H_2PO_4)_2 + \text{heat} \Rightarrow \beta\text{-}Ca(PO_3)_2 + 2H_2O$$

The monobasic firing product has been tested for biocompatibility using alkali salts additions. The purpose of this study was to investigate biocompatibility, osteoconduction capacity and biodegradability of Na_2O and/or K_2O-added CMP. Biodegradability of CMP, Na_2O–CMP and K_2O–CMP in Tris-buffer solution and simulated body fluid (SBF) for 30 days was measured. Graft materials were placed in rabbit parietal bone defects and sacrificed at 3 and 6 months. The amount of new bone formation was measured under LM. Biodegradability of Na_2O–CMP and K_2O–CMP was greater than that of CMP. All CMP grafts were biocompatible and osteoconductive. Histomorphometric data showed that there was no significant difference in new bone formation between all the CMP groups and Bio-Oss group. It was concluded that 5% Na_2O–CMP and 5% K_2O–CMP would be good candidates for bone substitution materials.

Chemical preparation, thermal behavior, kinetic and IR studies have been presented for the cyclotriphosphate $Ca_3(P_3O_9)_2 \cdot 10H_2O$. It is prepared by an aqueous method:

$$2NaPO_3\ (aq) + CaCl_2\ (aq) \Rightarrow Ca(P_3O_9)_2 \cdot 10H_2O(\text{solid}) + 2NaCl$$

or

$$Ca(OH)_2\ (\text{solid}) + 6\ HPO_3\ (aq) \Rightarrow Ca(P_3O_9)_2 \cdot 10H_2O\ (\text{solid})$$

The reaction involving HPO_3 is slow and should be carried out in a hot solution. Evaporation at a low temperature (<15 °C) serves to form the hydrate crystals. $Ca_3(P_3O_9)_2 \cdot 10H_2O$ is monoclinic $P2_1/n$ with the

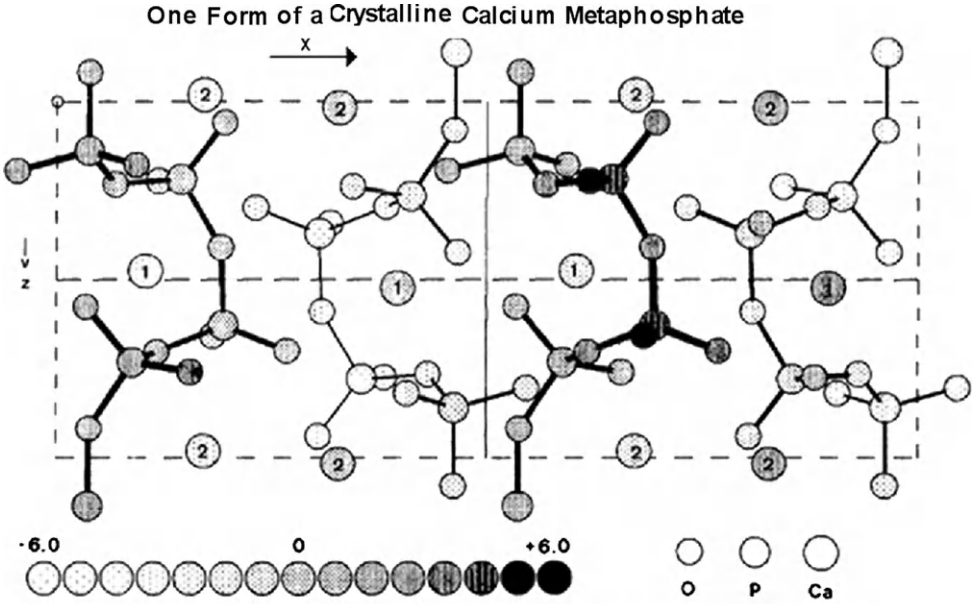

FIGURE 4.49

following unit-cell dimensions: $a = 9.332$ Å, $b = 18.132$ Å, $c = 7.841$ Å, $\beta = 106.69°$ and $Z = 2$. $Ca_3(P_3O_9)_2 \cdot 10H_2O$ has never been studied except for its crystallographic characterization. The thermal behavior of $Ca_3(P_3O_9)_2 \cdot 10H_2O$ has been studied and interpreted by comparison with IR absorption spectrometry, XRD experiments, chemical analyses, thermal analyses (TGA-DTA) and DSC. $Ca_3(P_3O_9)_2 \cdot 10H_2O$ is stable, under standard conditions of temperature and pressure, until 80 °C. It is impossible to dehydrate $Ca_3(P_3O_9)_2 \cdot 10H_2O$ without breaking its rings $P_3O_9^{3-}$ into chains that leads to amorphous compounds according to XRD and IR absorption spectrometry. The final product of the dehydration and calcination of $Ca_3(P_3O_9)_2 \cdot 10H_2O$, under atmospheric pressure is its long-chain polyphosphate form, β $[Ca(PO_3)_2]_8$. β$[Ca(PO_3)_2]_8$ is stable until its melting point at 1097 °C. On the other hand, α$[Ca(PO_3)_2]_8$ is prepared in a dry way. α$[Ca(PO_3)_2]_8$ has many applications in industry such as a humidity sensor and corrosion inhibitor. Also, quantum chemical calculations have been performed for the P_3O_9 rings.

$Ca_2[P_4O_{12}] \cdot 4H_2O$ crystallizes in the monoclinic space group $P2_1/n$, $a = 7.668$ Å, $b = 12.895$ Å, $c = 7.144$ Å, 107.00°, $D_x = 2.28$ g/cm^3, $Z = 2$. In the structure, there are ring-like anions, which are composed of $4PO_4^{3-}$ tetrahedra connected by oxygen bridges. The Ca^{2+} are surrounded by seven oxygen atoms. Each two-cation polyhedra are connected by a common edge to pairs which are isolated from one another. The water molecules form hydrogen bridges with one another and with the anion rings. The H_2O molecules of hydration are lost at about 120–140 °C.

If anhydrous CMP, $(Ca(PO_3)_2$, is heated to about 1150 °C, a glass is formed. Glasses were prepared with water content between 0.005 and 0.16 mol/l. Properties measured vary in a characteristic way in dependence on the water content. An interpretation for the shift of the absorption edge to shorter wavelength with increasing OH-group concentration, which also explains the change of the glass transition and the recrystallization temperature, is proposed. Dispersion calculations for the wavelength dependence of the refractive index refer to an additional absorption band caused by the OH-groups on the short wavelength side of the absorption determining the UV edge.

The short range structure of $Ca(PO_3)_2$ glass has been studied using X-ray and neutron diffraction and modeled using the reverse Monte Carlo method. Using this, combination of techniques has allowed six interatomic correlations to be distinguished and fitted to obtain a set of bond lengths and coordination numbers that describe the structure of the glass. The glass consists of metaphosphate chains of phosphate tetrahedra and each phosphate unit has two nonbridging oxygen atoms available for coordination with Ca. The Ca···O correlation was fitted with two peaks at 2.35 and 2.86 Å, representing a broad distribution of bond lengths. The total Ca···O coordination is 6.9 and is consistent with distorted polyhedral units such as capped octahedra or capped trigonal prisms. It is found that most nonbridging oxygen atoms are bonded to two calcium atoms. All of these observations are consistent with Hoppe's model for phosphate glasses. Furthermore, the medium-range order is revealed to consist of phosphate chains intertwined with apparently elongated clusters of Ca ions, and the Ca–O and Ca–P correlations contributed significantly to the first sharp diffraction peak in XRD.

CMP is trimorphic. The following table shows some of the differences determined for the bond lengths and bond angles for two of these phases (Table 4.17).

Unidirectionally crystallized $CaO–P_2O_5$ glass ceramics were produced by reheating glass rods between 450 and 580 °C (glass transition temperature = 500 °C) under a temperature gradient of 30 °C/cm. These glass ceramics exhibit high-bending strength (~650 MN/m^2) and toughness. Sample preparation is described and compared with conventional unidirectional solidification of melts. The characteristic mechanical properties were discussed in terms of the texture of the glass ceramics.

The facile synthesis and structural characterization of γ-$Ca(PO_3)_2$, a novel polymorph of CMP was reported. The single-step synthesis of this potential biomaterial was achieved using flux methods at 250 °C, yielding a single-phase product stable at room temperature. Single-crystal XRD determined the structure to be of monoclinic symmetry ($a = 9.5669$ Å, $b = 9.5023$ Å, $c = 10.3717$ Å, and $\beta = 93.474°$, space group = Cc), with layers of helical polyphosphate chains directed alternately along the [110] and [−110] unit cell directions to produce a unique arrangement of criss-cross polyphosphate layers separated by calcium ions. Further structural characterization by MAS-NMR and FT-IR was found to be consistent with this structure. Thermal studies indicated that γ-$Ca(PO_3)_2$ is stable up to 690 °C, whereupon it irreversibly converts to the β-$Ca(PO_3)_2$ polymorph. The actual arrangement of the PO_4 tetrahedra are shown in the following Fig. 4.50.

TABLE 4.17

Phase	P—P (Å)	P—O—P (°)	P—P—P (°)	Period	Fs
β-$Ca(PO_3)_2$	2.947	140.6	111.6	4	0.705
	2.978	135.9	93.1		
	2.939	135.9	88.2		
	2.980	141.5	116.7		
γ-$Ca(PO_3)_2$	2.898	124.6 133.9	102.2	2	0.909

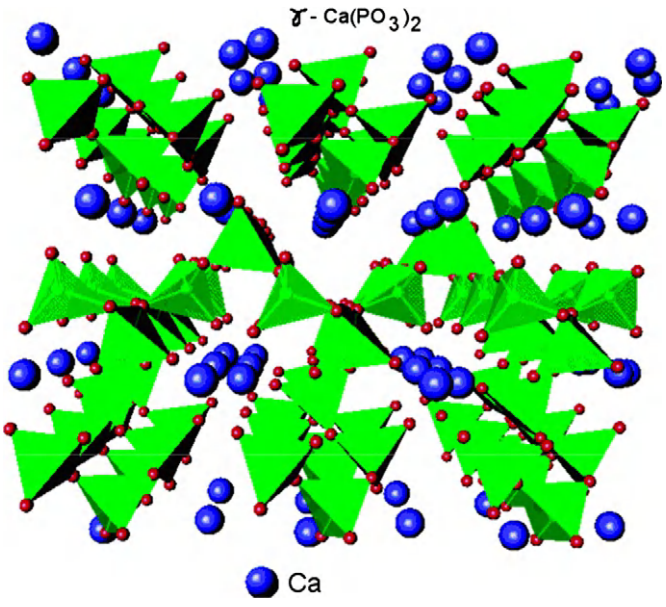

FIGURE 4.50

CMP has been prepared by reaction of CaO and gaseous white phosphorus, P_2O_5. The CaO/P_2O_5 ratio of starting materials was changed from 5.06 to 0.64, and the reaction was carried out at 400–1100 °C. These calcium phosphates were investigated using X-ray diffractometry and scanning electron microscope. By gas–solid reaction of $CaO–P_2O_5$, β-CMP was only synthesized at 400–500 °C, β-CMP, hydroxyapatite, and β- pyrophosphate at 600–700 °C, and α-CMP, hydroxyapatite, α-pyrophosphate, and α-tricalcium phosphate above 800 °C. Synthesized calcium phosphates were independent of the CaO/P_2O_5 ratio of starting materials but highly dependent on the reaction temperature. Nevertheless, a pure salt was never achieved in any of these preparations.

Although pure glassy compounds, that are colorless transparent polymers $[Ca(PO_3)_2]_n$, can be prepared, they remain hygroscopic and atmospheric moisture decomposes them over a period of time. The presence of water vapor can cause them to rapidly break down into calcium dihydrogen phosphate. Ropp has solved this problem and has samples that have remained stable for over 40 years. Their resistance to boiling water is equal or surpasses that of "window glass". They have many physical properties not found in "ordinary" glasses.

The porosity and slow solubility of "ordinary" calcium polyphosphates (CPPs) has led to its testing as a bone substitute. Porous structures were formed by gravity sintering CPP particles of either 106–150 or 150–250 μ size to form samples with 30–45 vol% porosity with pore sizes in the range of 100 micron (40–140 μ). Tensile strength of the samples assessed by diametric compression testing indicated relatively high values for porous ceramics with a maximum strength of 24.1 MPa for samples made using the finer particles (106–150 μ). XRD studies of the sintered samples indicated the formation of crystalline β-CPP from the starting amorphous powders. In vitro aging in 0.1 M tris-buffered solution (pH 7.4) or 0.05 M potassium hydrogen phthalate buffered solution (pH 4.0) at 37 °C for periods up to 30 days indicated an initial rapid loss of strength. Elution of P over 14 days was followed by a more gradual continuing strength but P loss resulted in strengths at 30 days equal to about one-third the initial value. The observed structures, strengths and in vitro degradation characteristics of the porous CPP samples suggested their potential usefulness as bone substitute materials. Subsequent in-vivo behavior assessment was not reported.

Further studies revealed that CPP bone substitutes could be prepared by gravity sintering crystal transformations. The crystalline structure of CPP was analyzed by Raman spectroscopy and in situ variable temperature XRD. In addition, the variation of CPP in SBF considered as degradation was characterized by monitoring the changes of its compressive strength and weight loss. The results revealed that CPP was inorganic condensed phosphate with a linear long-chain structure. Amorphous CPP (γ-CPP) was initially transformed to crystalline β-CPP, then crystalline α-CPP with the increase of sintering temperature. The transformation of β-CPP to α-CPP occurred from 650 to 670 °C. Compressive strength decreased quickly at initial stage for all specimens after immersed in SBF, and thereafter, continued to decrease at a slower rate subsequently. After immersion for 15 and 30 days, the compressive strength of β-CPP decreased from 13.5 to 7.6 and 4.8 MPa, while α-CPP decreased from 16 to 12 and 8 MPa, respectively. The degradation rate of γ-CPP, β-CPP and α-CPP decreased with time after immersed in SBF. γ-CPP had highest degradation rate, which would have been completely degraded in 10 days, and the weight loss ratio of β-CPP was 28% for 15 days and 35% for 30 days, but the weight loss of α-CPP was only 11% for 30 days. The results therefore revealed that CPPs with different degradation rates could be obtained by controlling the crystalline structure.

A novel biodegradable nanocomposite porous scaffold, comprising a β-TCP matrix and hydroxylapatite (HA) nanofibers, was developed and studied for load-bearing bone tissue engineering. HA nanofibers were prepared with a biomimetic precipitation method. The composite scaffolds were fabricated by a method combining the gel casting and polymer sponge techniques. The role of HA nanofibers in enhancing the mechanical properties of the scaffold was investigated. Compression tests were performed to measure the compressive strength, modulus and toughness of the

porous scaffolds. The identification and morphology of HA nanofibers were determined by XRD and TEM, respectively. SEM was used to examine the morphology of porous scaffolds and fracture surfaces to reveal the dominant toughening mechanisms. The results showed that the mechanical property of the scaffold was significantly enhanced by the inclusion of HA nanofibers. The porous composite scaffold attained a compressive strength of 9.870.3 MPa, comparable to the high-end value (2–10 MPa) of cancellous bone. The toughness of the scaffold increased from 1.0070 ± 0.04 to 1.7270 ± 0.02 kN/m, as the concentration of HA nanofibers increased from 0 to 5 wt%.

CMP is used as a mild abrasive and as neutralizing agent in toothpastes.

A galvanic cell-type humidity sensor has been constructed from sintered β-$Ca(PO_3)_2$ which is a proton conductive solid. The e.m.f. response as a function of the logarithm of water vapor is linear, reversible, reproducible, and very fast over a wide range of vapor pressure measured at 578, 678 and 776 °C, respectively. The variation of observed e.m.f. versus logarithm of water vapor is in good agreement with the theoretical e.m.f. expected from the Nernst equation. Experimental results of steam-oxygen and steam-hydrogen concentration cells, respectively, employing β-$Ca(PO_3)_2$ as an electrolyte confirm proton conductivity and suggest the potential application of this material for high-temperature galvanic cell-type humidity sensing.

CPP has been used as a food additive. Among the many direct uses are as an Acidity regulator, Emulsifier (emulsifier), Emulsifying salt (sequestrant), Raising agent (in Bakeries) and Stabilizer (moisture/water retention agent). Calcium tripolyphosphate was proven to inhibit steel corrosion when incorporated in a paint film. Good protection was achieved by employing only 10% volume of the pigment, instead of 30%, as was suggested in the case of phosphates. Calcium tetrapolyphosphate, $Ca_3P_4O_{13}$, has also been proven to be a good detergent. Upon heating, it decomposes to the tripolyphosphate plus orthophosphate and pyrophosphate:

$$3Ca_3P_4O_{13} + \text{heat} \Rightarrow 2Ca_2HP_3O_{10} + Ca_3(PO_4)_2 + Ca_2P_2O_7$$

Calcium metaphosphates and polyphosphates are available from many suppliers and manufacturers worldwide.

Strontium Metaphosphate or Polyphosphates

Strontium metaphosphate can be prepared by the solid-state reaction of metaphosphoric acid and the hydroxide, oxide or carbonate of strontium:

$$SrCO_3 + HPO_3 + \text{heat} \Rightarrow Sr(PO_3)_2 + H_2O + CO_2$$

The best temperature to use is about 600 °C. Strontium metaphosphate has the CAS number of 13762-75-9 and a density of 2.61 g/cm^3. It melts at 757 °C and its boiling point is 1384 °C. It is somewhat soluble in water.

It can also be prepared by the aqueous reactions:

$$2NaPO_3\,(aq) + SrCl_2\,(aq) \Rightarrow Sr(PO_3)_2\,(solid) + 2NaCl\,(aq)$$

or

$$Sr(OH)_2\,(solid) + HPO_3\,(aq) \Rightarrow Sr(PO_3)_2\,(solid) + H_2O$$

The dissolution and reaction involving HPO_3 are slow and should be carried out in a hot solution. Evaporation at a low temperature (<15 °C) serves to form the crystals. Hydrated alkaline earth cyclo-octaphosphates were made by adding an aqueous solution of alkaline earth chlorides into an aqueous solution of sodium cyclo-octaphosphate. Thermal properties of the compounds were studied by TG-DTA analysis. The water of crystallization was removed below 200 °C. The cyclo-octaphosphates decomposed to produce many phosphate species up to about 500 °C, and they finally reorganized to metaphosphates. The overall thermal reaction of alkaline earth cyclo-octaphosphates can be written by the equation:

$$Sr_4(PO_3)_8 \cdot nH2O \Rightarrow 4Sr(PO_3)_2 + nH_2O$$

Strontium trimetaphosphate heptahydrate, $Sr_3(P_3O_9)_2 \cdot 7H_2O$, is orthorhombic. The unit cell, with $a = 16.05$ Å, $b = 12.33$ Å, $c = 10.87$ Å, contains four formula units with the space group Pnma. It is a cyclic metaphosphate in structure. Strontium cyclotetraphosphate $Sr_2(P_4O_{12}) \cdot 6H_2O$ has also been successfully characterized. This hydrate was synthesized as a single-phase crystalline powder starting from an aqueous solution of barium hydroxide and phosphorus pentoxide at 300 K. $Sr_2(P_4O_{12}) \cdot 6H_2O$ crystallizes in a new structure type in which the Sr^{2+} ions form a distorted hexagonal diamond-like arrangement with the $(P_4O_{12})^{4-}$ anions in the trigonal prismatic voids with the point group, $C2/c$, $Z = 4$, $a = 7.773$ Å, $b = 12.976$ Å, $c = 13.461$ Å, $\beta = 95.38°$.

Three forms of $Sr(PO_3)_2$ have been observed. The low-temperature form, γ-$Sr(PO_3)_2$ (originally formed at 583 °C) is transformed to the β-crystal at 400 °C and finally to the high temperature form α-$Sr(PO_3)_2$ at 850 °C. The low temperature form is possibly a cyclotriphosphate. The β-form is the only one well characterized.

Two polymorphic phases of strontium polyphosphate were prepared by solid-state reactions. The structure of β-$Sr(PO_3)_2$ is a redetermination. The structure of γ-$Sr(PO_3)_2$ was solved and contains $(PO_3)_n$ chains and SrO_8 polyhedra. $(PO_3)_n$ chains cross the cell along the a direction. Their repeat unit is two PO_4 tetrahedra. SrO_8 polyhedra are connected by edge sharing to form

infinite chains, which are further interconnected by edge sharing to form double chains parallel to a. The $(PO_3)_n$ groups link these double chains to build three-dimensional networks. This, it is a polyphosphate.

The phosphate α-$Sr(PO_3)_2$ was synthesized as a single-phase crystalline powder starting from strontium carbonate and phosphorous acid at a temperature of 1150 °C. α-$Sr(PO_3)_2$ crystallizes in a novel structure type in which helical *catena*-polyphosphate ions interpenetrate a substructure of Sr^{2+} closely related to cubic diamond ($Sr_4(PO_3)_8$, $P2_1$, $Z = 2$, $a = 7.354$ Å, $b = 7.354$ Å, $\beta = 90.02°$. The catena-polyphosphate chains form helices running along [010]. Their chain periodicity is 16 and the length of the repeating unit complies with $b = 18.68$ Å, the chain stretching factor amounts to $f_s = 0.48$ and the pitch to radius ratio is $\xi = 2.49$. The vibrational spectra of α-$Sr(PO_3)_2$ are also reported. The structure of α-$Sr(PO_3)_2$ is shown in the following Fig. 4.51.

The coordination of the Sr^{2+} ions can be clearly seen as well as those of the PO_3^- tetrahedral which form chains. The structure of γ-$Sr(PO_3)_2$ consists of $(Sr_4O_{22})_n$ double chains and infinite $(PO_3)_n$ chains linked together by polyphosphate sharing edges and corners. The structure of β-$Sr(PO_3)_2$ has been redetermined.

The polyphosphates β-$Sr(PO_3)_2$ and $BaCa(PO_3)_4$ have been doped with Eu^{2+}. $BaCa(PO_3)_4$ was structurally characterized for the first time. Both phosphors were analyzed by fluorescence spectroscopy. β-$Sr(PO_3)_2$:Eu and $BaCa(PO_3)_4$:Eu were found to emit blue light at 424 nm and 418 nm, respectively, with a broader emission band compared with α-$Sr(PO_3)_2$:Eu. Both phosphors can be excited at 330 nm, i.e. an UV-LED emission. The crystal structure of $BaCa(PO_3)_4$ has been determined based on single-crystal data [$P2_1/n$, $Z = 4$, $a = 7.230$ Å, $b = 9.171$ Å, $c = 15.247$ Å, $\beta = 90.995(12)°$, $R_1 = 0.050$, $wR_2 = 0.099$, 1748 reflections, 164 parameters]. $BaCa(PO_3)_4$ is not homeotypic with β-$Sr(PO_3)_2$ and α-$Sr(PO_3)_2$ but isotypic with $BaCd(PO_3)_4$. The vibrational spectra of $Sr_2(PO_3)_4$ are also presented and discussed.

Strontium metaphosphates and polyphosphates are readily available commercially, even though only one CAS number is available. Whether the salt purchased is a metatype or polytype depends upon the method of manufacture.

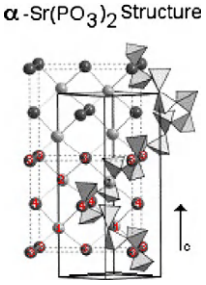

FIGURE 4.51

Barium Metaphosphate or Polyphosphates

Barium metaphosphate can be prepared by the solid-state reaction of metaphosphoric acid and the hydroxide, oxide or carbonate of barium:

$$BaCO_3 + HPO_3 + \text{heat} \Rightarrow Ba(PO_3)_2 + H_2O + CO_2$$

The best temperature to use is about 700 °C. It has the CAS number of 13762-83-9 and the molecular weight of 295.2709 g/mol. If diammonium phosphate is used instead of solid metaphosphoric acid, the product is not pure. Colored glasses are obtained caused by the reduction of P-atoms in the phosphate anion by hydrogen released from NH_3 to form colloidal dispersions of P_4 which produce various colors in the glass. β-$Ba(PO_3)_2$ is the final product. This compound can also be prepared by the aqueous reactions:

$$NaPO_3\,(aq) + BaCl_2\,(aq) \Rightarrow Ba(PO_3)_2\,(solid) + NaCl\,(aq)$$

or

$$Ba(OH)_2\,(solid) + 2HPO_3\,(aq) \Rightarrow Ba(PO_3)_2\,(solid) + 2H_2O$$

The dissolution and reaction involving HPO_3 are slow and should be carried out in a hot solution. Evaporation at a low temperature (<15 °C) serves to form the crystals. The product involves several hydrates depending upon the conditions of precipitation. Anhydrous barium metaphosphate is a white porous powder or granular material that is insoluble in water. If it is heated to about 950 °C, it forms a polymeric glass:

$$nBa(PO_3)_2 + \text{heat} \Rightarrow \{Ba(PO_3)_2\}_n$$

If the cooled glass is then reheated, it devitrifies to form α-$Ba(PO_3)_2$ above 600 °C. This transformation is reversible.

There are three form of $Ba(PO_3)_2$, a γ-form, a β-form and an α-form (Fig. 4.52).

The major difference between these phases lies in the P···P distances and P···O···P angles of the bonds. For example, the γ-phase and β-phase have the following parameters in the crystal where the bending angles are shown in Table 4.18.

Most of these compounds are true cyclic metaphosphates. This includes the trimeta- and tetrameta salts which form hydrates.

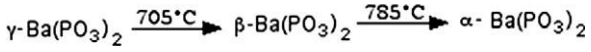

FIGURE 4.52

TABLE 4.18

Phase	P–P (Å)	P–O–P (°)	P–P–P (°)	Period	Fs
γ-$Ba(PO_3)_2$	2.818	120.7	127.3	4	0.695
	3.022	143.4	93.0		
β-$Ba(PO_3)_2$	2.898	124.6	102.2	2	0.909
		133.9			

(Fs = Stretching Coefficient)

Barium tetrametaphosphate hydrate $Ba_2(P_4O_{12})\cdot 3.5H_2O$ was synthesized as a single-phase crystalline powder starting from an aqueous solution of barium hydroxide and metaphosphoric acid at 30 °C. $Ba_2(P_4O_{12})\cdot 3.5H_2O$ crystallizes in a new structure type in which the Ba^{2+} ions form a distorted hexagonal diamond-like arrangement with the $(P_4O_{12})^{4-}$ anions in the trigonal prismatic voids. The ubit cell parameters are: $C2/c$, $Z = 4$, $a = 7.773$ Å, $b = 12.976$ Å, $c = 13.461$ Å, $\beta = 95.38°$, ($wR_2 = 0.071$, $R_1 = 0.018$, 1180 reflections, 118 parameters). The vibrational spectra of $Ba_2(P_4O_{12})\cdot 3.5H_2O$ and its thermal behavior up to 720 K have been reported.

The salt, barium cyclotriphosphate hexahydrate, $Ba_3(P_3O_9)_2\cdot 6H_2O$, is triclinic with the space group P-1 and the following unit-cell dimensions: $a = 7.547$ Å, $b = 11.975$ Å, $c = 13.068$ Å, $\alpha = 108.58°$, $\beta = 100.35°$, $\gamma = 95.54°$, $Z = 2$. $Ba_3(P_3O_9)_2\cdot 6H_2O$ is stable in the air and moisture until heated to about 80 °C. It is impossible to dehydrate $Ba_3(P_3O_9)_2\cdot 6H_2O$ without breaking its rings. $P_3O_9^{3-}$ a condition leading an amorphous compound. The final product of the dehydration and calcination of $Ba_3(P_3O_9)_2\cdot 6H_2O$, under atmospheric pressure, is its long chain polyphosphate form β-$Ba(PO_3)_2$. This compound is stable until it reaches its melting point of 870 °C.

The dehydration of the cyclotriphosphate hexahydrate of barium, $Ba_3(P_3O_9)_2\cdot 6H_2O$, occurs in two steps in two temperature ranges 69–198 °C and 274–456 °C. In the thermogravimetric (TG) curve, the first stage between 69 and 198 °C corresponds to the elimination of 5.5 water molecules and the second stage from 274 to 456 °C is due to the elimination of 0.5 water molecule. The derivative of the TG curve, DTG, of $Ba_3(P_3O_9)_2\cdot 6H_2O$ under atmospheric pressure and at a heating rate of 10 °C/min contains two peaks due to the dehydration of $Ba_3(P_3O_9)_2\cdot 6H_2O$. The first intensive peak in the domain 69–198 °C, at 165 °C is due to the departure of 5.5 water molecules. The second weak peak in the range of 274–456 °C, at 403 °C is due to the evolution of 0.5 remaining water molecules.

The preparation and determination of the crystalline structure of $Ba_3(P_3O_9)_2\cdot 4H_2O$ has been made. It has the space group of C2/m and is monoclinic. There is a mirror-plane symmetry of the anions P_3O_9 stretched along the c-axis and a localization of all Ba^{2+} in the mirror planes. Two of them are located in the mirror plane while the other two are distributed statistically within the entire cavity in a centrosystematic manner.

A systematic structure investigation of alkaline earth metaphosphate glasses, using $Me(PO_3)_2$ including Mg, Ca, Sr and Ba, was carried out using neutron diffraction. The total structure factor $S(Q)$ was measured up to $Q = 170/nm$. The total atomic distribution functions of most of the glasses show well-defined maxima for short distances which can be attributed to distinct atomic pairs. By a peak separation procedure, partial coordination numbers and mean distances for the atomic pairs P–O, O–O, Me–O, and P–P as well as the distribution of bond angles P–O–P were determined. The experimental data are compatible with the following model of the glass structure. The basic elements are PO_4 tetrahedra which are interconnected via two oxygens in chains. The chains are not straight. Metal ions are located between the chains and have oxygens in the first coordination shell. The metal–oxygen coordination number is 4 for Mg, Ca and 8 for Sr and Ba.

The salt, tribarium hexametaphosphate octahydrate, $Ba_3P_6O_{18}\cdot 8H_2O$, is monoclinic: space group = C2/c, $a = 20.98$ Å, $b = 7.227$ Å, $c = 17.44$ Å, $V = 2300.1$ Å^3, $Z = 4$ and density = 2.974 g/cm^3. The atomic arrangement can be described as being built of two layers of BaO_8 and BaO_{10} polyhedra approximately centered at the planes, $z = 1/4$ and 3/4, interconnected through the external O-atoms of the large $P_6O_{18}^{6-}$ groups. Inside a given layer, the Ba polyhedra assemble to form rings of 8-polyhedra which cover the available space as tiles. The phosphoric ring anions have a twofold internal symmetry rarely observed in the crystal chemistry of cyclophosphates. Other than the alkali compounds, the only other known cyclophosphates are $Cd_3P_6O_{18}\cdot 16H_2O$ $Mn_3P_6O_{18}\cdot 9H_2O$ and $Cu_3P_6O_{18}\cdot 14H_2O$.

Uses for barium metaphosphates or polyphosphates are few in industry. A few phosphors utilizing $Ba(PO_3)_2$ have been tried but this compound is usually a minor component. The polyphosphate glasses of barium, when activated by various rare earth cations have not proven to be as efficient as those of the other alkaline earths. $Ba(PO_3)_2$ has also been combined with BaF_2 to form optical glasses with a high refractive index (nD) 1.67–1.70, high transmission in the near infrared part of the spectra (to 6 micron) and a wide glass-forming domain. However, these glasses have not become commercial.

$Ba(PO_3)_2$ is available commercially from a few suppliers in limited quantities.

Radium Metaphosphates and Polyphosphates

Radium metaphosphate would have the formula of $Ra(PO_3)_2$ and the molecular weight of gm/mol. There is no record of either of these salts ever having been

prepared, although they could be made by several methods. The best one would be to react metaphosphoric acid and the hydroxide, oxide or carbonate of radium in the solid state:

$$RaCO_3 + HPO_3 + \text{heat} \Rightarrow Ra(PO_3)_2 + H_2O + CO_2$$

The best temperature to use is about 700 °C. It has no CAS number. The molecular weight is expected to be 383.9663 g/mol. This compound can also be prepared by the aqueous reactions:

$$NaPO_3\,(aq) + RaCl_2\,(aq) \Rightarrow Ra(PO_3)_2\,(solid) + NaCl\,(aq)$$

or

$$Ra(OH)_2\,(solid) + 2HPO_3\,(aq) \Rightarrow Ra(PO_3)_2\,(solid) + 2H_2O$$

Whether hydrates form remains unknown at this date. The only reference in the scientific literature concerns the removal of radioactive ^{226}Ra from drinking water by the addition of sodium polyphosphate. Radium polyphosphate is sufficiently insoluble so that all of the radium polyphosphate could be filtered out and subjected to proper disposal.

4.2.9. Alkaline Earth Hypophosphates

Hypophosphoric acid has the general formula of $H_4P_2O_6$ and differs from the other oxy-phosphorous acids. Lead and barium hypophosphates are insoluble, and the free acid can be obtained from them by means of hydrogen sulfide or sulfuric acid. It forms a hydrate $H_4P_2O_6 \cdot 2H_2O$. All alkaline earths hypophosphates are insoluble. Hypophosphoric acid has far less reducing power than phosphorous acid, and it is hydrolyzed in strong acid solution at elevated temperature to phosphorous and phosphoric acid:

$$H_4P_2O_6 + H_3O^+ \Rightarrow H_3PO_4 + H_3PO_3$$

The double formula $H_4P_2O_6$ was established by molecular weight determinations by the freezing point of solutions in water of the free acid and of the salt $Na_2H_2P_2O_6 \cdot 6H_2O$. Also the rate of hydrolysis of the acid by hydrogen ion to $H_3PO_4 + H_3PO_3$ is strictly monomolecular for $H_4P_2O_6$. It is thus clear that the acid is $H_4P_2O_6$, and the probable Lewis structure for this acid is shown in Fig. 4.53.

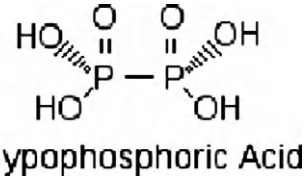

FIGURE 4.53

Where a direct bond between the two P-atoms is evident.

Beryllium Hypophosphate

Beryllium hypophosphate should have the molecular formula of $Be_2P_2O_6$ if it were to be formed by a solid-state reaction between hypophosphoric acid and BeO:

$$BeO + H_4P_2O_6 + \text{heat} \Rightarrow Be_2P_2O_6 + 2H_2O$$

However, there is no record that the preparation of this salt has ever been attempted. It could also be formed via an aqueous solution of hypophosphorus acid and a soluble beryllium salt:

$$2(BeOH)Cl\,(aq) + H_4P_2O_4\,(aq) \Rightarrow (BeOH)_2P_2O_4\,(solid) + 2HCl\,(aq)$$

Alternatively, sodium hypophosphate could be used to produce a basic solution instead of an acidic pH. A product from a basic solution, prepared in 1916, was said to have the formula, $Be_2P_2O_6 \cdot 1.5H_2O$ but this has never been confirmed. This compound was stated to lose its waters of hydration between 230 and 240 °C.

The formation of an "acid" salt-like $BeH_2P_2O_6$ or $(BeOH)H_2P_2O_6$ remains speculative. The formation of hydrates is not known nor has the structure of such compounds been delineated.

There are absolutely no academic studies concerning beryllium hypophosphate in the scientific literature nor is it mentioned in industrial circles. It has no CAS number nor is it offered for sale commercially by any manufacturer.

Magnesium Hypophosphate

Magnesium hypophosphate has the molecular formula of $Mg_2P_2O_4$. It can be formed by an aqueous solution of hypophosphorus acid and a soluble magnesium salt:

$$2MgCl_2\,(aq) + H_4P_2O_4\,(aq) \Rightarrow Mg_2P_2O_4\,(solid) + 2HCl\,(aq)$$

The magnesium salt solution is added until no precipitate results. Alternatively, sodium hypophosphate can be used to produce a basic solution instead of acidic. The acidic product is a magnesium hydrogen hypophosphate, $MgH_2P_2O_6 \cdot 4H_2O$. This salt is much more soluble in water (~0.05 g/100 ml) than the basic product that is a decahydrate, $Mg_2P_2O_4 \cdot 12H_2O$. The latter compound is much less soluble at 0.00072 g/100 ml. Neither of these salts has a CAS number.

The crystal structure of the anhydrate or the hydrates has not been determined. The thermal decomposition of either of these two salts has not been determined.

Only a few manufacturers and sellers of this salt are known. Whether the acid and/or basic salt is readily available remains to be determined by the buyer.

Calcium Hypophosphate

Calcium hypophosphate has the molecular formula of $Ca_2P_2O_4$. It can be formed by an aqueous solution of hypophosphorus acid and a soluble calcium salt:

$$2CaCl_2\ (aq) + H_4P_2O_4\ (aq) \Rightarrow Ca_2P_2O_4\ (solid) + 2HCl\ (aq)$$

The calcium salt solution is added until no precipitate results. Alternatively, sodium hypophosphate can be used to produce a basic solution instead of acidic. The basic product is a hexahydrate, $Ca_2P_2O_4 \cdot 6H_2O$. The acidic product is a dihydrate, $CaH_2P_2O_4 \cdot 2H_2O$. The former salt is insoluble in water but slightly soluble in acetic acid. It redissolves in excess hypophosphoric acid. Its CAS number is 75499-50-2. The acidic salt is more soluble in water at 16.8 g/100 ml at 20 °C. If this salt is heated, it loses the two waters of hydration at about 125–130 °C. The crystal structure of the anhydrate or the hydrate has not been determined.

Calcium hypophosphate has been used as a root-desensitizing agent in Dentistry. It has been prescribed as a source of calcium and phosphorus in the human body by Homopathic practioners until it was discovered that this compound crystallizes in tissues and may add to kidney stones and gall stones.

The literature concerning this salt is almost nonexistent and little attention from academia has occurred. It is available commercially in modest quantities.

Strontium Hypophosphate

Strontium hypophosphate would have the molecular formula of $Sr_2P_2O_4$, if it were to be produced. It can be formed by an aqueous solution of hypophosphorus acid and a soluble strontium salt:

$$2MgCl_2\ (aq) + H_4P_2O_4\ (aq) \Rightarrow Mg_2P_2O_4\ (solid) + 2HCl\ (aq)$$

The strontium salt solution is added until no precipitate results. Alternatively, sodium hypophosphate can be used to produce a basic solution instead of acidic.

However, there is categorically no record of preparation of this salt, unlike that of barium. It would be expected to mimic the properties of the homologous barium salts but no such descriptions can be found in any of the textbooks or scientific literature concerning the properties of this salt. Whether it forms hydrates or an acid salt remains unknown. It is expected to be rather insoluble in water but soluble in acids. It does not have a CAS number.

The crystal structure of the anhydrate or the possible hydrates has not been determined. It is not offered for sale commercially.

Barium Hypophosphate

Barium Magnesium hypophosphate has the molecular formula of $Ba_2P_2O_4$ and the molecular weight of 432.8235 g/mol. It can be formed by an aqueous solution of hypophosphorus acid and a soluble barium salt:

$$2BaCl_2\ (aq) + H_4P_2O_4\ (aq) \Rightarrow Ba_2P_2O_4\ (solid) + 2HCl\ (aq)$$

The barium salt solution is added until no precipitate results. Alternatively, sodium hypophosphate can be used to produce a basic solution instead of acidic. The basic product apparently is anhydrous since no record of a hydrate is known. The acidic product is a barium hydrogen hypophosphate, $BaH_2P_2O_6 \cdot 2H_2O$. This salt is slightly soluble in water at 1.1 g/100 ml at 20 °C. The basic salt is much less soluble at 0.00067 g/100 ml. Neither of these salts have a CAS number.

The crystal structure of the anhydrate or the hydrates has not been determined. The thermal decomposition of either of these two salts has not been determined.

No usage of either of these salts has appeared in industry. There are no commercial sources for these salts.

Radium Hypophosphate

Radium hypophosphate has the molecular formula of $Ra_2P_2O_4$. It can be formed by an aqueous solution of hypophosphorus acid and a soluble radium salt:

$$2RaCl_2\ (aq) + H_4P_2O_4\ (aq) \Rightarrow Ra_2P_2O_4\ (solid) + 2HCl\ (aq)$$

Alternatively, sodium hypophosphate can be used to produce a basic solution instead of acidic. The acidic product is expected to be a radium hydrogen hypophosphate, $RaH_2P_2O_6$. Neither of these salts have a CAS number. Whether hydrates form or not remains unknown.

The crystal structure of the anhydrate or the hydrates has not been determined. The thermal decomposition of either of these two salts has not been determined.

4.2.10. Alkaline Earth Peroxyphosphates

Two of these acids have been prepared, a peroxymonophosphoric acid H_3PO_5 and a peroxydiphosphoric acid $H_4P_2O_8$. Note that the latter is related to pyrophosphoric acid. Both are formed with 30% hydrogen peroxide, the first with phosphorous pentoxide:

$$P_2O_5 + 2H_2O_2 + H_2O \Rightarrow 2H_3PO_5$$
$$2H_3PO_5 + (P_2O_5 + H_2O_2) \Rightarrow 2H_4P_2O_8$$

The latter is the stronger oxidizing agent of the two acids. In aqueous solution, monoperoxyphosphoric

acid exists as H_3PO_5, $H_2PO_5^-$, HPO_5^{2-} and PO^{3-} at different pH values.

$$K_1 = H_3PO_5 \Leftrightarrow H_2PO_5^- + H^+ \quad (1)$$

$$K_2 = H_2PO_5^- \Leftrightarrow H_2PO_5^{2-} + H^+ \quad (2)$$

$$K_3 = HPO_5^{2-} \Leftrightarrow PO^{3-} + H^+ \quad (3)$$

The dissociation constants K_1, K_2, and K_3 are 8.0×10^{-2}, 4.2×10^{-6}, 1.6×10^{-13}, respectively at 298 K and $\mu = 0.2$ mol/dm^3.

Beryllium Peroxyphosphate

The chemistry of beryllium phosphates is far from complete. Beryllium peroxyphosphate has never been prepared. The chemistry involved and the physical properties of these compounds remain little known. Only a few references in the literature are available and most of these are dated before 1900. The compounds were identified by analysis, i.e. %Be, %P and %O as an oxidant. Parsons wrote a monograph "The Chemistry of Beryllium and Its Compounds" in 1910 but had little to add to what was already known.

Beryllium peroxyphosphates could be prepared by both solid-state or solution methods. However, it is likely that the two sets of compounds would differ. For the monoperoxyphosphates, one would get $Be(HPO_5)_2$ for the former method and $(BeOH)(HPO_5)$ for an aqueous solution. The question of hydrates remains unknown.

In the solution method, one could use the acid, H_3PO_5 or the potassium salt K_2HPO_5. Whether the solution should be acidic or basic is not known. Like the other alkaline earths, it is probably best to prepare the acid in a nonaqueous solution like carbon tetrachloride and ;then add the potassium compound for the basic solution:

$$P_2O_5 + 2H_2O_2 + H_2O \Rightarrow 2H_3PO_5$$
$$2H_3PO_5 + KOH \Rightarrow K_2HPO_5$$

To either of these is added to the beryllium compound to form the monoperoxyphosphate. Note that an aqueous solution could be used but the reaction product will undoubtedly differ in overall composition.

For the diperoxy compounds, the potassium monoperoxyphosphate compound is transformed to the diperoxyphosphate compound, in a nonaqueous solution at low temperature:

$$K_2HPO_5 + P_2O_5 \Rightarrow K_2P_2O_8$$

For beryllium, the probable compounds that will be formed are:

$$BeHPO_5 \text{ (or } (BeOH)HPO_5)$$
$$Be_2P_2O_8 \text{ (or } (BeOH)_2P_2O_8)$$

The nature of these compounds has never been explored. Beryllium peroxyphosphate has no CAS number and no listed manufacturers offer it for sale.

Magnesium Peroxyphosphate

Magnesium peroxyphosphate has remained unknown and little to no publications concerning this salt are available on the scientific literature. Like the other alkaline earths, magnesium peroxyphosphates could be prepared by both solid-state or solution methods. The two sets of compounds would likely differ. For the monoperoxyphosphates, one would get $MgHPO_5$ for the former method and perhaps a hydrate for an aqueous solution. The question of degree of hydration remains unknown.

In the solution method, one could use the acid, H_3PO_5 or the potassium salt K_2HPO_5. Whether the solution should be acidic or basic is not known. Like the other alkaline earths, it is probably best to prepare the acid in a nonaqueous solution like carbon tetrachloride and then add the potassium compound for the basic solution:

$$P_2O_5 + 2H_2O_2 + H_2O \Rightarrow 2H_3PO_5$$
$$2H_3PO_5 + KOH \Rightarrow K_2HPO_5$$

To either of these is added the magnesium compound to form the monoperoxyphosphate:

$$Mg(OH)_2 + K_2PO_5 \Rightarrow MgHPO_5 + H_2O$$

For the diperoxy compounds, the potassium monoperoxyphosphate compound is transformed to the diperoxyphosphate compound, in a nonaqueous solution at low temperature:

$$K_2HPO_5 + P_2O_5 \Rightarrow K_2P_2O_8$$

For magnesium, the probable compounds that will be formed are:

$$MgHPO_5 \text{ or } Mg_2P_2O_8$$

Other possible compounds are:

$$Mg(H_2PO_5)_2$$
$$Mg(H_2P_2O_8)_2$$

The nature of these compounds has never been explored. Magnesium peroxyphosphate has no CAS number and no listed manufacturers offer it for sale.

Calcium Peroxyphosphate

Calcium peroxyphosphate has the formula of $CaHPO_5$ as the monooxyphosphate or $Ca_2P_2O_8$ as the dioxyphosphate. For preparation of the monooxyphosphate, the acid is first prepared by adding P_2O_5 to 30%

hydrogen peroxide and then adding the hydroxide or carbonate to the acid:

$$P_2O_5 + 2H_2O_2 + H_2O \Rightarrow 2H_3PO_5$$
$$Ca(OH)_2 + H_3PO_5 \Rightarrow CaHPO_5 + H_2O$$

The phosphorus pentoxide powder was suspended in carbon tetrachloride under stirring while cooled in an ice bath. Aqueous hydrogen peroxide was added drop wise to this suspension to form H_3PO_5. Calcium carbonate or calcium hydroxide slurry was added slowly to the formed inorganic concentrated peroxymonophosphoric acid layer in an ice bath. The precipitate was then filtered. The result is a dihydrate, $CaHPO_5 \cdot 2H_2O$.

In an alternate Preparation of Calcium Peroxymonophosphate, the following recipe was given:

> "Suspend 2.22 g of calcium hydroxide in 50 ml of water. To this suspension, slowly add 2.28 g of concentrated peroxymonophosphoric acid, to be prepared as described in Example 1, in order to precipitate calcium peroxymonophosphate. Filter the resulting slurry and wash it with distilled water. The solid to be recovered is a basic calcium peroxymonophosphate, possibly also containing one or more calcium phosphate compounds."
>
> "To prepare diperoxyphosphate, dissolve 3.46 g of potassium peroxydiphosphate in 10 ml of water. To this solution, add 2.94 g of calcium chloride dihydrate under stirring, in order to precipitate calcium peroxydiphosphate. Filter the resulting slurry and wash it with distilled water. The solid to be recovered contains calcium peroxydiphosphate".

Note that the diperoxy compound is prepared from a monoperoxy compound. Still another method has been given:

> "To Prepare diperoxymonophosphoric acid by the action of hydrogen peroxide on pyrophosphoryl chloride. Maintain this inorganic diperoxy-phosphoric acid in an ice bath under stirring and slowly add a calcium carbonate slurry until the pH of the resulting solution is 3.3 and calcium diperoxyphosphate precipitates. Filter the resulting slurry and then wash it with distilled water. The solid to be recovered contains calcium diperoxymonophosphates and possibly also contains one or more calcium phosphate compounds".

The industrial interest stems from its use as a "dental whitener" in toothpaste and the like. Calcium peroxyphosphate compounds and dental compositions combine both whitening/stain removal of teeth with remineralization. The calcium peroxyphosphate compounds are capable of releasing, in an aqueous environment, whitening and reminiralization effective amounts of calcium ion, phosphate ion, and active oxygen. Preferred compounds are calcium peroxymonophosphate or calcium diperoxymonophosphate compounds. These compounds may be used in humans and other animals, including other mammals.

Yet, the only mention of calcium monoperoxy- or diperoxy-phosphate to be found in the technical literature is in patents several years old. These patents list a number of compounds as products of such preparations, as shown in the following:

Calcium monoperoxyphosphate
$CaHPO_5$
$Ca_3(PO_5)_2$
$Ca(H_2PO_5)_2$
$Ca_5(PO_5)_3OH$
Calcium diperoxyphosphate
$CaH_2(P_2O_8)$
$Ca_2P_2O_8$

Of these, only the physical properties of $CaHPO_5$ and $Ca_2P_2O_8$ have been documented. The scientific literature has been particularly devoid and publications from those in industry are exceedingly sparse, except for patents.

Diperoxyphosphoric acid, $H_4P_2O_8$, a starting material in the preparation of calcium diperoxymonophosphate, is less well known than H_2PO_5. However, this peroxy acid may be prepared, for example, in a manner similar to that for preparation of H_2PO_5, namely by the action of hydrogen peroxide on either P_2O_5 or pyrophosphoryl chloride ($P_2O_3Cl_2$). In general, the use of a peroxygenated phosphoric acid starting material allows for the preparation of various types of calcium peroxyphosphate compounds described herein. While the above procedures may generate a single calcium peroxyphosphate compound, generally a mixture of compounds is obtained. For example, a mixture of the peroxygenated forms $Ca(H_2\ PO_5)_2$ and $CaHPO_5$ may be obtained in the preparation of calcium peroxymonophosphates. Any of the calcium peroxyphosphates and calcium diperoxyphosphates described above may be in their respective hydrated or peroxyhydrated forms without adversely affecting their ability to release calcium ions, phosphate ions, and peroxide. Thus, as an example, a hydrated form of calcium peroxymonophosphate may be represented as $CaHPO_5 \cdot nH_2O$, indicating the association of "n" water molecules per molecule of calcium peroxymonophosphate.

Strontium Peroxyphosphate

Strontium peroxyphosphate has remained unknown and little to no publications concerning this salt are available on the scientific literature. Like the other alkaline earths, strontium peroxyphosphates could be prepared by both solid-state or solution methods. The two sets of compounds would likely differ. For the monoperoxyphosphates, one would get $SrHPO_5$ for the former method and perhaps a hydrate for an aqueous solution. The question of degree of hydration remains unknown.

In the solution method, one could use the acid, H_3PO_5 or the potassium salt K_2HPO_5. Whether the solution should be acidic or basic is not known. Like the other alkaline earths, it is probably best to prepare the acid in a nonaqueous solution like carbon tetrachloride and then add the potassium compound for the basic solution:

$$P_2O_5 + 2H_2O_2 + H_2O \Rightarrow 2H_3PO_5$$
$$2H_3PO_5 + KOH \Rightarrow K_2HPO_5$$

To either of these is added a soluble strontium compound to form the monoperoxyphosphate:

$$Sr(OH)_2 + K_2PO_5 \Rightarrow SrHPO_5 + H_2O$$

For the diperoxy compounds, the potassium monoperoxyphosphate compound is transformed to the diperoxyphosphate substance in a nonaqueous solution at low temperature:

$$K_2HPO_5 + P_2O_5 \Rightarrow K_2P_2O_8$$

For strontium, the probable compounds that will be formed are:

$$SrHPO_5$$
$$Sr_2P_2O_8$$

Other possible compounds are:

$$Sr(H_2PO_5)_2$$
$$Sr(H_2P_2O_8)_2$$

The nature of these compounds has never been explored. Strontium peroxyphosphate has no CAS number and no listed manufacturers offer it for sale.

Barium Peroxyphosphate

Barium peroxyphosphate has remained unknown and little to no publications concerning this salt are available on the scientific literature. Like the other alkaline earths, Barium peroxyphosphates could be prepared by both solid-state or solution methods. The two sets of compounds would likely differ. For the monoperoxyphosphates, one would get $BaHPO_5$ for the former method and perhaps a hydrate for an aqueous solution. The question of degree of hydration remains unknown.

In the solution method, one could use either the acid, H_3PO_5 or the potassium salt K_2HPO_5. Whether the solution should be acidic or basic is not known. Like the other alkaline earths, it is probably best to prepare the acid in a nonaqueous solution like carbon tetrachloride and then add the potassium compound for the basic solution:

$$P_2O_5 + 2H_2O_2 + H_2O \Rightarrow 2H_3PO_5$$
$$2H_3PO_5 + KOH \Rightarrow K_2HPO_5$$

To either of these is added a barium compound to form the monoperoxyphosphate:

$$Ba(OH)_2 + K_2PO_5 \Rightarrow BaHPO_5 + H_2O$$

For the diperoxy compounds, the potassium monoperoxyphosphate compound is transformed to the diperoxyphosphate compound, in a nonaqueous solution at low temperature:

$$K_2HPO_5 + P_2O_5 \Rightarrow K_2P_2O_8$$

For barium, the probable compounds that will be formed are:

$$BaHPO_5$$
$$Ba_2P_2O_8$$

Other possible compounds are:

$$Ba(H_2PO_5)_2$$
$$Ba(H_2P_2O_8)_2$$

The nature of these compounds has never been explored. Barium peroxyphosphate has no CAS number and no listed manufacturers offer it for sale.

Radium Peroxyphosphate

Radium peroxyphosphate has remained unknown and no publications concerning this salt are available in the scientific literature. This is not surprising in view of the intense radioactivity of ^{226}Ra. Like the other alkaline earths, radium peroxyphosphates could be prepared by both solid-state or solution methods. For the monoperoxyphosphates, one would get $RaHPO_5$ for the former method. The question of degree of hydration remains unknown.

In the solution method, one could use the acid, H_3PO_5 or the potassium salt K_2HPO_5. Whether the solution should be acidic or basic is not known. Like the other alkaline earths, it is probably best to prepare the acid in a nonaqueous solution like carbon tetrachloride and then add the potassium compound for the basic solution:

$$P_2O_5 + 2H_2O_2 + H_2O \Rightarrow 2H_3PO_5$$
$$2H_3PO_5 + KOH \Rightarrow K_2HPO_5$$

To either of these is added the radium compound to form the monoperoxyphosphate:

$$Ra(OH)_2 + K_2PO_5 \Rightarrow RaHPO_5 + H_2O$$

To prepare radium diperoxy compounds, the potassium monoperoxyphosphate compound is transformed to the diperoxyphosphate compound, in a nonaqueous solution at low temperature:

$$K_2HPO_5 + P_2O_5 \Rightarrow K_2P_2O_8$$

For radium, the probable compounds that will be formed are:

$$RaHPO_5$$

$$Ra_2P_2O_8$$

Other possible compounds are:

$$Ra(H_2PO_5)_2$$

$$Ra(H_2P_2O_8)_2$$

The nature of these compounds has never been explored. Radium peroxyphosphate has no CAS number and no listed manufacturers offer it for sale.

4.3. ALKALINE EARTH METAL OXO-ARSENIC COMPOUNDS

The alkaline earths form a series of compounds based upon the arsenic acids. The element, Arsenic, with the symbol As, forms a limited series of compounds called "arsenides" with the alkaline earth metals. The reason for this lies in the fact that arsenic is on the border line between those elements that are purely cationic (metallic in nature) and those that form anionic compounds. Even though the alkali metals have the highest degree of cationic behavior and form ionic bonds easily, arsenic exhibits both ionic and covalent character in its compounds and is classified as one of the "metalloids". There are two major forms of the acids, one having As either in the +3 state, i.e. H_3AsO_3, or the +5 valence state, H_3AsO_4 plus the arsenides in which the arsenic atom is in a trivalent state, i.e. As^{3+}.

4.3.1. Arsenic Acids

The following acids of Arsenic are known.

Arsenous Acid

This compound, also known as **arsenious acid**, is the hydrolyzed form of As_2O_3 and has the formula $As(OH)_3$. $As(OH)_3$ occurs in aqueous solutions and has not been isolated as a pure material, although this fact does not detract from the significance of $As(OH)_3$. This compound is essentially the "hydroxide" of the arsenic ion but is not basic in character. The molecular weight of arsenous acid is 125.94 g/mol. $As(OH)_3$ is a pyramidal molecule consisting of three hydroxyl groups connected by single bonds to arsenic. In contrast, the nominally related phosphorous species H_3PO_3 mainly adopts the structure $HPO(OH)_2$ in which $P(OH)_3$ is a very minor equilibrium component of such solutions (if it exists at all). The differing behaviors of the As and P compounds reflect a trend whereby high oxidation states are more stable for lighter members of main group elements than their heavier congeners like As where the +3 valance state dominates.

Arsenous acid [13464-58-9], AsH_3O_3, is known to exist only in solution. It is a weak acid with a dissociation constant of 8×10^{-16} at 25 °C. The free acid apparently has three OH groups attached directly to the arsenic atom and hence is not analogous to phosphorous acid. A number of complex arsenites are known, among which are copper acetate arsenite [12002-03-8], $Cu_2(C_2H_3O_2)(AsO_3)$, Paris green, and cupric hydrogen arsenite [10290-12-7], $CuHAsO_3$, Scheele's green. These have been used mainly as insecticides in the past.

$As(OH)_3$ is a weak acid with a pK_a of 9.2. The preparation of $As(OH)_3$ involves a slow hydrolysis of hydolysis of arsenic trioxide in water. Addition of a base such as one of the alkali cations converts arsenous acid to the arsenite ions $[AsO(OH)_2]^-$, $[AsO_2(OH)]^{2-}$, and $[AsO_3]^{3-}$. In other words, arsenous acid is "amphoteric" and easily forms anions in the presence of more cationic species like the alkali metals. Note that these anions are analogous to the mono, di and tri-basic anions of phosphate. Reactions attributed to aqueous arsenic trioxide are due to arsenous acid and its conjugate bases.

Arsenic acid has the molecular formula H_3AsO_4. More descriptively written as $AsO(OH)_3$, this colorless acid is the arsenic analog of phosphoric acid. Arsenate and phosphate salts behave very similarly. Arsenic acid as such has not been isolated, but only found in solution where it is largely ionized. Its hemihydrate form ($H_3AsO_4 \cdot 1/2H_2O$) does form stable crystals. Crystalline samples dehydrate with condensation at 100 °C. The difference in molecular structure between arsenous and arsenic acids is shown in Fig. 4.54.

Arsenic acid is a tetrahedral species of idealized symmetry C_{3v} with As–O bonds lengths ranging from 1.66 to 1.71 Å. Being a triprotic acid, its acidity is described by three equilibria:

$$H_3AsO_4 \Leftrightarrow H_2AsO_4^- + H^+ \quad (pk_1 = 10^{-2.19})$$

$$H_2AsO_4^- \Leftrightarrow HasO_4^{2-} + H^+ \quad (pk_2 = 10^{-6.94})$$

$$HasO_4^{2-} \Leftrightarrow AsO_4^{3-} + H^+ \quad (pk_3 = 10^{-11.5})$$

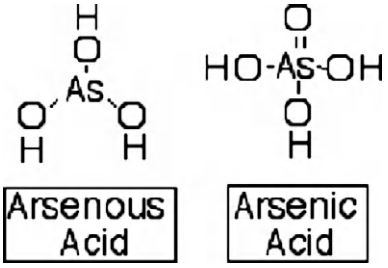

FIGURE 4.54

These K_a values are close to those for phosphoric acid. The highly basic arsenate ion (AsO_4^{3-}) is the product of the third ionization. Unlike phosphoric acid, arsenic acid is **strongly oxidizing**, illustrated by its ability to convert iodide to iodine. Thus, some compounds with the alkali metal ions are not stable.

Arsenic acid is prepared by treating arsenic trioxide with concentrated nitric acid or by combination of arsenic acid with water. The latter reaction is very slow. It is also formed when metaarsenic or pyroarsenic acid is treated with cold water.

4.3.2. Alkaline Earth Arsenides

Elemental arsenic combines with electropositive metals to form their arsenides, i.e. Mg_3As_2. It also combines with hydrogen to form arsine, a colorless gas; garlic-like unpleasant odor; liquefies at –55 °C; solidifies at –116.3 °C; heavier than air; gas density 2.695 (air = 1). Arsenic sublimes at 887 K, (615 °C, 1139 F) but does not melt. Thus, reaction with the liquid alkaline earths in an inert atmosphere serves to form the arsenides.

Beryllium Arsenide

Beryllium arsenide should have the molecular formula of Be_3As_2 and the molecular weight of 176.8801 g/mol. However, this is a doubtful compound that has never been prepared. Be melts at 1287 °C and the reaction at that temperature apparently does not occur:

$$3Be + 2As + \text{heat} \not\longrightarrow Be_3As_2$$

The reason for this is not clear but may lie in the difference in atomic radii of the two species (Be = 1.05 Å; As = 1.15 Å = ±10%). This behavior remains a mystery since the other alkaline earths all form arsenide compounds. However, a compound having a Be···As bond has been found. This compound was described as:

> "The compound (η^5-C_5Me_5)BeAs(*t*-Bu)$_2$ (**1**) was prepared by the reaction of (η^5-C_5Me_5)BeCl with LiAs(*t*-Bu)$_2$ in diethyl ether at 0 °C. The structure of **1** has been determined by X-ray crystallography and is the first structurally characterized diorganoarsenide derivative of beryllium. It is monomeric in the solid state with the As-*t*-Bu$_2$ ligand acting as a one electron donor".

This anomaly has been studied theoretically. The electronic structure and spectroscopic properties of a manifold of states of a new molecular species, Be···As, have been investigated theoretically using the "complete active space self-consistent field/multireference single and double excitations configuration interaction (CASSCF/MRSDCI)" approach, using the aug-cc-pV5Z-PP basis set for arsenic, which includes a relativistic effective core potential, and the cc-pV5Z set for beryllium. Potential energy curves of five quartet and eight doublet (L + S) states correlating with the five lowest-lying dissociation limits were constructed. The effect of spin–orbit coupling was also included in the description of the ground state, and of the doublet states correlating with the second dissociation channel. Dipole moment functions and vibrationally averaged dipole moments are also evaluated. The similarities and differences between BeAs, BeP, and BeN were analyzed. Spin–orbit effects are small for the ground state close to the equilibrium distance, but avoided crossings between $\Omega = 1/2$ states, and between $\Omega = 3/2$ states which changes significantly the L + S curves for the lowest-lying doublets.

Beryllium arsenide is not well known in either academic circles or industry. It is not available commercially and does not have a CAS number.

Magnesium Arsenide

Magnesium arsenide has the molecular formula of Mg_3As_2 and the molecular weight of 223.6592 g/mol. It may be prepared by direct reaction between the elements. Since As sublimes at 614 °C and Mg melts at 650 °C, the latter is melted at about 675 °C in an inert atmosphere like argon (not N_2 which would form nitrides) and arsenic vapors are carried into the reaction zone by a stream of Ar gas:

$$3Mg + 2As + \text{heat} \Rightarrow Mg_3As_2$$

Mg_3As_2 is obtained by this method as a deep-brown, X-ray amorphous powder. Magnesium arsenide has the CAS number of 12044-49-4. This compound decomposes in contact with water:

$$Mg_3As_2 + 3H_2O \Rightarrow 2AsH_3 + 3Mg(OH)_2$$

Thus, it must be stored under dry conditions. Its density is 3.15 g/cm^3. This compound is dimorphic with the low temperature form, β-Mg_3As_2 being cubic ($a = 12.33$ Å) and the high-temperature form, α-Mg_3As_2 being hexagonal. It crystallizes in the anti-La_2O_3 crystal structure, with unit-cell parameters of: $a = 4.264$ Å, $c = 6.738$ Å, c/a = 1.580. Both of these compounds are semiconductors. The latter has a band gap, E_g, of 2.2 eV (564 nm).

The phase diagram for the Mg–As system has been presented and is shown in the following Fig. 4.55.

In addition to the α- and β-phases, a compound, $MgAs_4$, is known to form. Paar first reported the existence of the Mg_3As_2 compound in 1867. It is a deep-red color when crystalline. The low-temperature form undergoes an allotropic transformation between 1000 and 1100 °C to form α-Mg_3As_2 (whose melting point is above 1200 °C.

These magnesium arsenide compounds have a narrow stability and homogeneity range (just like Mg_3Bi_2 and Mg_3Sb_2). The $MgAs_4$ compound was first

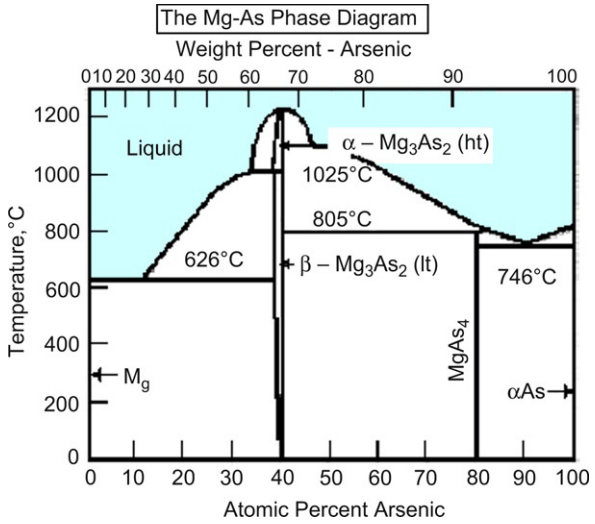

FIGURE 4.55

reported in 1874. Upon heating, it decomposes to Mg_3As_2 and As:

$$6MgAs_4 + \text{heat} \Rightarrow 2Mg_3As_2 + 5As_4$$

$MgAs_4$ crystallizes in the tetragonal space group $P4_12_12$ with $a = b = 5.385$ Å, $c = 15.798$ Å and $Z = 4$. The Mg atoms are octahedrally coordinated by six As atoms and the two types of As atoms are tetrahedrally bonded to two Mg and two As atoms or one Mg and three As atoms, respectively. The coordination of MgP_4 and $MgAs_4$ is similar in these structures.

Electronic structure calculations for Mg_3As_2 (low and high temperature modifications) have been performed. Mg_3As_2 with a high temperature modification is predicted to be a semiconductor with the gap value of about 1.1 eV (1127 nm), and Mg_3As_2 (low-temperature phase) is a semiconductor with 1.57 eV (790 nm).

Magnesium arsenide decomposes rapidly on exposure to air. It reacts with ethyl alcohol at the boiling point and at 180′ to 205 °C ethyl- and diethyl-arsines, with a trace of triethylarsine, are formed. The crystal structure of the arsenide has been investigated by the X-ray powder method. It resembles the corresponding zinc arsenide and has a cubic, lattice containing two molecules of Mg_3As_2 in the unit cell, the side of which is 6.10 Å, the calculated density being 3.26 g/cm^3. The structure of magnesium arsenide is not ionic but covalent.

Magnesium arsenide was used as a rodenticide and insecticide. Its toxicity to humans has led to its prohibition in the US and Europe. Yet, it is available commercially from a number of suppliers worldwide.

Calcium Arsenide

Calcium arsenide has the molecular formula of Ca_3As_2 and the molecular weight of 270.0772 g/mol. It may be prepared by reacting the elements together. Since As sublimes at 614 °C and Ca melts at 839 °C, the latter is melted at about 875 °C in an inert atmosphere like argon (not N_2 which would form nitrides) and arsenic vapors are carried into the reaction zone by a stream of Ar gas:

$$3Ca + 2As + \text{heat} \Rightarrow Ca_3As_2$$

Its CAS number is 12255-53-7. The standard Gibbs energies of formation of Ca_3As_2 was determined by a chemical equilibration technique yielding the following results:

$$3Ca + 2As \Rightarrow Ca_3As_2 \text{ (solid)}$$
$$\Delta G^\circ = -723{,}800 + 172.8T \text{ (J/mol)}$$
$$(T = 1273 \text{ to } 1573 \text{ K})$$

Calcium arsenide has the zinc-blende (cubic) structure with $a = 6.751$ Å. It can also be prepared by the reduction of calcium arsenate by carbon:

$$2Ca_3AsO_4 + 5C + \text{heat} \Rightarrow Ca_3As_2 + 2CaO + 3CO_2$$

When a mixture of hydrogen and arsenic vapor is passed over heated quicklime the product is mainly arsenite, only a little arsenide being formed. It has been shown that calcium arsenate is reduced by carbon slowly at 800 °C and rapidly at 850 °C, the arsenite being first produced and finally calcium oxide and arsenic; in order to obtain the arsenide, rapid heating to 1500 to 1600 °C is necessary. If the heating is slow, loss of arsenic occurs.

The arsenide is obtained as a crystalline mass, small fragments of which are transparent or reddish-brown in color. Its density is 2.54 g/cm^3, and it is harder than calcite. It is readily attacked by the halogens, but the higher the atomic number of the latter, the higher the temperature necessary for reaction to occur. It remains unchanged in dry air or oxygen at room temperature, but when heated in the latter it burns brilliantly to form a calcium arsenate. Hydrogen does not attack the arsenide, even at 700 to 800 °C. Water decomposes it in the cold with formation of calcium hydroxide and evolution of arsine; it is consequently unstable in moist air. It is also soluble in acids:

$$Ca_3As_2 + 6HCl \Rightarrow 2AsH_3 + 3\ CaCl_2$$

It is attacked by sulfur or hydrogen sulfide at dull red heat. Cold concentrated sulfuric acid is reduced to sulfurous acid. The gaseous halogen acids react at red heat giving arsenic and a calcium salt. Fuming nitric acid does not attack it in the cold, but there is a rapid reaction on heating. Carbon and boron are without action at 1000 °C, but the former can decompose it completely at the temperature of the electric furnace. Many metallic salts are decomposed when heated with the arsenide.

Calcium arsenide also forms several types of compounds, some of which are "Zintl" compounds (Zintl compounds consist of anionic elements which bind first to each other to form complex geometries like hexagonal bipyramids and then to the cations present). The compound, $Ca_{14}GaAs_{11}$ is such a compound. It is tetragonal with the space group $I4_1/acd$ and the lattice parameters of $a = 15.642$ Å, $c = 21.138$ Å. Its structure is composed of isolated $GaAs_4$ tetrahedra that are separated by As_3 linear units and isolated As and Ca atoms. The As_3 units are situated between the tetrahedral and alternate by 90° down the *c*-axis. This unit has essentially a –7 charge (similar to the isoelectronic hypervalent I_3^- anion). That is, there are seven bonds associated with the bonding of this unit to the other atoms in the structure. This compound is a semiconductor as well.

Another, similar compound is Ca_3AsCl_3, prepared as a grayish white, microcrystalline powder by the reaction of Ca, As, and $CaCl_2$ in the molar ratio 3:2:3 or by the reaction of Ca_3As_2 and $CaCl_2$ in the molar ratio 1:3. Colorless single crystals of the compound were obtained. Ca_3AsCl_3 begins to decompose reversibly at 1025 °C by forming the phase $Ca_{2x}As_{1x}Cl_{1+x}$, where x is about 0.1, and the second product is $CaCl_2$. Single crystal investigations show that Ca_3AsCl_3 is isotypic with Mg_3NF_3.

Calcium arsenide will also combine with CaO to form Ca_4As_2O (yellow). It was prepared by reaction of "Ca_3As_2" with CaO in a molar ratio 1:1 in steel ampoules under argon. This compound was obtained as a well-crystallized, easily hydrolyzed powder. It crystallizes in the anti-K_2NiF_4 tetragonal structure.

In industrial settings, arsine poisoning generally results from the accidental formation of arsine gas. Most reported cases of exposure to arsine have occurred during the smelting and refining of metals. However, there are many other situations where exposures to lethal concentrations of the gas have been reported including galvanizing, soldering, etching and lead plating operations. Arsine can be produced by Fungi (especially in sewage) when arsenic is present. The renewed interest in coal as a source of energy causes concern for a possible increase in the number of exposures to arsine, because coal contains considerable quantities of arsenic. The processes for converting coal to gas and other by-products should include preventative measures aimed at reducing the chance of transformation of the arsenic impurities into arsine.

Calcium arsenide has been used as a fungicide as well as a rodenticide. Ca_3As_2, treated with water gives a 14% yield of arsine. Better yields (60–90%) are obtained by decomposing a solution of acid. However, its toxicity has precluded extensive usage in the U.S. and less poisonous compounds are now being used. It is used in Research to develop new types of semiconductors but not in industry.

Calcium arsenide is still available commercially as crushed chunks and flakes from a number of suppliers worldwide.

Strontium Arsenide

Strontium Arsenide, Sr_3As_2, may be prepared by the reaction of the elements or by the reduction of strontium arsenate. The latter method is best accomplished by rapidly heating with carbon to 1500 to 1600 °C. If the heating is slow, reduction begins at about 800 °C yielding first the arsenite, arsenic then being lost and strontium oxide formed:

$$3Sr + 2As + \text{heat} \Rightarrow Sr_3As_2$$

$$2Sr_3AsO_4 + 4C + \text{heat} \Rightarrow Sr_3As_2 + 3SrO + 3CO + CO_2$$

Strontium arsenide forms reddish-brown crystals, transparent in thin sections, with a density of 3.23 g/cm^3. It has the CAS number 39297-24-0. Its molecular weight is 1167.9668 g/mol. It decomposes in contact with water, forming strontium hydroxide with liberation of arsine. It burns brilliantly when heated in oxygen or sulfur vapor. It reacts with fluorine at room temperature with incandescence and formation of arsenic trifluoride. Similar reactions occur with chlorine at 160 °C, with bromine at 200 °C, and with iodine vapor at a higher temperature. It is a powerful reducing agent and attacks most metallic oxides and oxidizing agents.

It is considered as a "Dangerous Substance for the Environment" and is prohibited in Europe by the EEC. Only one or two research papers exist in the scientific literature concerning this salt. The structure of strontium arsenide remains to be determined. Whether it is cubic like the calcium homologue remains unknown. It well may be hexagonal because of the size difference of the Sr^{2+} cation.

There are no uses listed in industry and the calcium and magnesium arsenides have found favor over this salt because of cost. Nevertheless, strontium arsenide is offered for sale commercially by a number of suppliers worldwide.

Barium Arsenide

Barium arsenide has the molecular formula of Ba_3As_2. By passing arsine over barium oxide, at red heat, a mixture of arsenide and arsenite is obtained. The best way is to react the elements together at red heat:

$$3Ba + 2Ar \Rightarrow Ba_3As_2$$

Since Ba metal melts at 729 °C, the metal is melted at 750 °C and vapors of As are passed over it in a stream of argon gas. Crystals of Ba_3As_2 slowly form in cooler parts of the enclosed tube furnace. It can also be prepared in

a pure form by reduction of barium arsenate with carbon in an electric furnace:

$$2Ba_3AsO_4 + 3C + \text{heat} \Rightarrow Ba_3As_2 + 3BaO + 2CO_2 + CO$$

The oxide produced may be removed by washing in an acid like HCl to solubilize it. The crystals obtained are deep brown with a density of 4.16 g/cm^3. Its molecular weight is 561.9324 g/mol.

Barium arsenide is very similar in chemical properties to the arsenides of calcium and strontium. Its CAS number is 12255-50-4. It is slightly darker in color, more readily fusible and more reactive chemically. It burns spontaneously in fluorine, chlorine or bromine vapor. In oxygen, it burns at about 300 °C to form the orthoarsenate and in sulfur vapor at dull red heat to form thioarsenates. Ba_3As_2 has the body-centered cubic structure with $a = 9.846$ Å, where 1/9 of the anion sites are empty.

Barium arsenide also forms double salts such as $Li_4Ba_3As_4$ (Orthorhombic space group = *Immm*) which is isostructural with $Li_4Sr_3Sb_4$ and $Li_4Ba_3Sb_4$. It contains two anionic moieties, namely As_2^{4-} dumbbells and As^{3-}, and consists of planes of $BaAs_6$ octahedra separated by corrugated sheets of Li and Ba atoms.

The ternary iron arsenide $BaFe_2As_2$ becomes superconducting by hole doping, which was achieved by partial substitution of the barium site with potassium. Bulk superconductivity has been discovered at $T_c = 38$ K in $(Ba_{1-x}K_x)Fe_2As_2$ with $x \approx 0.4$. The parent compound $BaFe_2As_2$ crystallizes in the tetragonal $ThCr_2Si_2$-type structure, which consists of $(FeAs)^-$ iron arsenide layers separated by Ba^{2+} ions. $BaFe_2As_2$ is a poor metal and exhibits a spin density wave anomaly at 140 K. Substituting Ba^{2+} for K^+ ions introduces holes in the $(FeAs)^-$ layers, which suppress the anomaly and induces superconductivity. The T_c of 38 K in $(Ba_{0.6}K_{0.4})Fe_2As_2$ is the highest in hole-doped iron arsenide superconductors known to date.

The barium–scandium–iron arsenide oxide, Ba_2ScO_3FeAs was synthesized by high-temperature solid-state reactions and its crystal structure determined by X-ray powder diffraction. Its structure is tetragonal (*P*4/*nmm*; Ba_2ScO_3FeAs: $a = 4.1266$ Å, $c = 16.800$ Å, $Z = 2$) and isotypic to Sr_2GaO_3CuS. This compound is vaguely similar to barium arsenide. Iron arsenide layers are sandwiched between perovskite-like metal oxide layers and separated by ~16.00 Å, which is much larger compared to the ZrCuSiAs-type "1111" iron arsenide superconductors. The structure is shown in the following Fig. 4.56.

The bond lengths and angles within the FeAs layers are adapted to the space requirements of the oxide blocks. Measurements of the magnetic susceptibility, electrical resistivity and temperature-dependent crystal structure show no hint for a structural phase transition

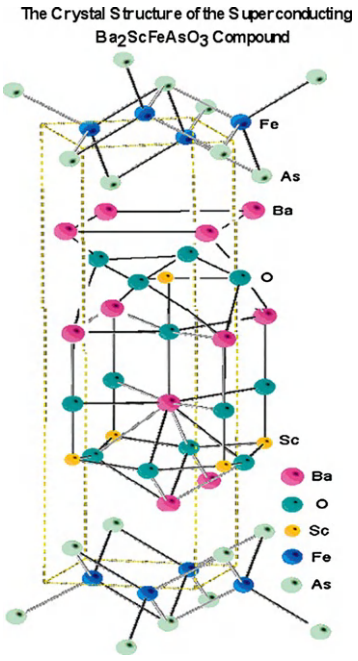

FIGURE 4.56

or magnetic anomaly in this compound. Ba_2ScO_3FeAs shows Curie–Weiss paramagnetism above 160 K with an effective magnetic moment of 3.83 KB in good agreement with the theoretical value of 3.87 KB for Cr3+ ($S = 3/2$). Antiferromagnetic ordering was detected below $T_N \sim 31$ K. ^{57}Fe-Mossbauer spectra of Ba_2ScO_3FeAs show single signals which are only subject to weak quadrupole splitting.

Barium arsenide itself has not been the subject of investigation of its physical properties of late. This compound was discovered in the 1800s and was well scrutinized in the twentieth century. However, the physical properties such as melting point and boiling point have not been documented. This salt is available in pure form commercially for use in the sputtering and vapor formation of mixed arsenides.

Radium Arsenide

Radium arsenide has not been prepared. It could be prepared by reaction of the elements. Ra melts at 700 °C (973 K) and the vapors of As could be carried into a reaction zone of 750 °C to form the compound. Yet, no record of this salt is available in the literature. Perhaps this is due the radioactive decay of ^{226}Ra and the fact that no demand in industry exists. The reaction would be:

$$3Ra + 2As + \text{heat} \Rightarrow Ra_3As_2$$

However, whether this compound exists and could be prepared remains unknown. It has no CAS number and there are no listed manufacturers of this salt.

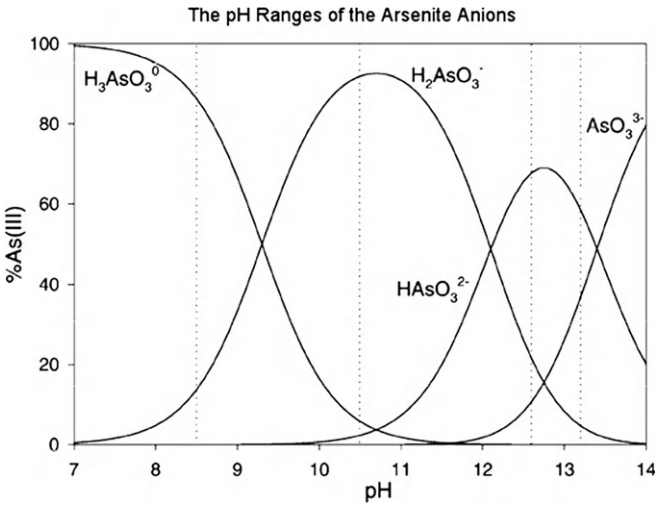

FIGURE 4.57

4.3.3. Alkaline Earth Arsenites

The alkaline earth arsenites can be prepared by precipitation from arsenous acid or from an alkali metaarsenite salt such as potassium arsenite. Above pH 9.0, As(III)behaves like a weak acid and its speciation is the result of the following equilibria:

$$As(OH)_3 \Leftrightarrow H^+ + AsO(OH)_2^- \quad pKa_1 = 9.32 \quad (1)$$

$$As(OH)_2^- \Leftrightarrow H^+ + AsO_2(OH)^{2-} \quad pKa_2 = 12.10 \quad (2)$$

$$AsO_2(OH)^{2-} \Leftrightarrow H^+ + AsO_3^{3-}(OH)^{2-} \quad pKa_3 = 13.41 \quad (3)$$

At pH 7.5, the neutral $As(OH)_3^\circ$ species predominates. The others appear as a function of pH. Thus, all arsenites must be prepared at a basic pH.

The pH ranges at which various arsenites appear is shown in the following Fig. 4.57.

The structures of all alkaline earth arsenites are based upon a triangular molecule as shown in the following Lewis structure (Fig. 4.58).

Berylium Arsenite

Beryllium Arsenite could be prepared by the solid-state reactions of the oxide and solid arsenous acid:

$$BeO + H_3AsO_3 + \text{heat} \Rightarrow BeHAsO_3 + H_2O$$

At a 2:1 ratio and a pH of 13.5, one would expect to obtain $Be_3(AsO_3)_2$. However, there is no record of this having been attempted. Attempts to prepare definite compounds of beryllium with arsenious acid in aqueous solution have not been successful. When beryllium hydroxide is precipitated from solutions containing arsenious oxide, much of the latter is adsorbed but a product has never been isolated and identified. The literature is devoid of any references and the only citations are dated in the 1860–1880s. Perhaps this is due to the fact that beryllium cations in aqueous solution are dominated by hydroxy groups which attach themselves to Be^{2+} to form species like $Be(OH)^+$. These do not react the same in solution as the other alkaline earths do.

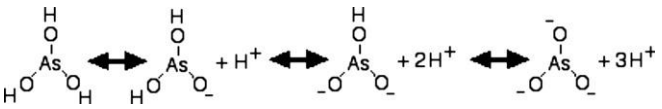

FIGURE 4.58

There are no uses that have developed for beryllium arsenites and they do not have any CAS numbers.

Magnesium Arsenites

Magnesium forms a series of compounds with arsenious acid similar to those of phosphorous acid. These include the monobasic, dibasic and tribasic forms as well as a pyro- and tetraärsenite. The Lewis structural formula for these compounds included in Fig. 4.59.

Note that these structures are based upon a linear triangular AsO_3^{3-} anion.

Basic magnesium arsenite cannot be prepared by reacting the oxides together either in a solid-state reaction in an inert atmosphere or in an aqueous reaction. An investigation of the system $MgO–As_2O_3–H_2O$ at 25 °C gave no evidence of chemical combination, but considerable adsorption of arsenious oxide by the magnesium hydroxide occurred. The key to forming this compound lies in controlling the pH around 7.5–8.0. Combination of the two oxides occurs at higher solution temperatures where some of the MgO dissolved to form the hydroxide and some basic metarsenite was formed.

However, the composition was mostly a basic arsenite of composition, $MgHAsO_3 \cdot 3H_2O$. This has the Lewis structure shown in Fig. 4.60.

A solution of soluble magnesium chloride and arsenious acid forms a dibasic salt which then results in an insoluble hexahydrate, $MgHPO_3 \cdot 6H_2O$. The pH then needs to be around 12.5 to maximize the formation of the compound. The dimensions of the hexagonal cell are $a = 8.88$ Å, $c = 9.10$ Å. The corresponding rhombohedral structure unit-cell parameters are $a_R = 5.96$ Å, $\alpha = 96°24'$. The space group is R3 and the Mg, P and H-atoms lie on the unique axis. The structure is built from discrete tetrahedral $(HPO_3)^{2-}$ ions and octahedral $Mg(H_2O)_6^{2+}$ groups which are linked together in three dimensions by a continuous system of hydrogen bonds. This compound is isomorphous with $MgSO_3 \cdot 6H_2O$. Its CAS number is 14332-25-3. Its molecular weight is 188.1007 g/mol. A trihydrate is also known which can be formed by heating the hexahydrate to 100 °C. This salt has few references in the scientific literature. The physical properties have not been studied.

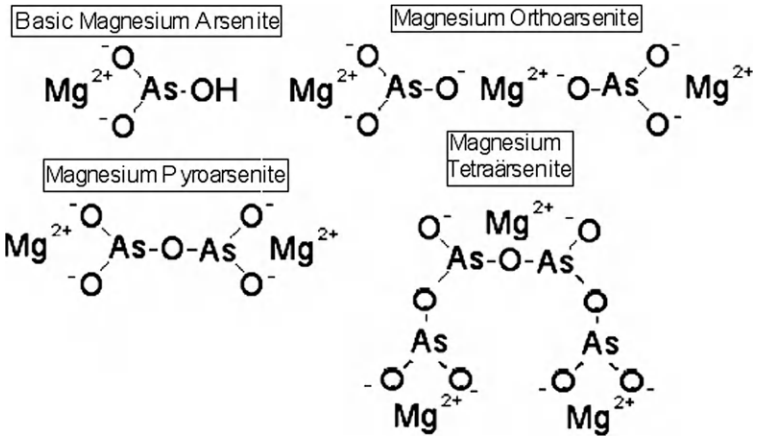

FIGURE 4.59

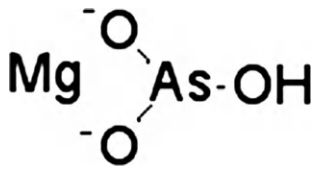

FIGURE 4.60

The monobasic salt, $Mg(H_2AsO_3)_2$ can be formed by the addition of $MgCl_2$ to an excess of arsenious acid or potassium arsenite and the evaporating the solution. The pH needs to around 10.5. Monobasic magnesium arsenite is soluble at 25 °C at 20 g/100 ml of water. Evaporation of the solution at low temperature (preferably vacuum evaporation) serves to form the hexahydrate. This salt, $Mg(H_2AsO_3)_2 \cdot 6H_2O$, when heated loses 5 waters of hydration at 105 °C and the other at 115 °C. Very little information is available concerning this salt. It is not listed in any textbooks and, with the exception of a few papers, the only references to it date back to the 1900s. Even Remi and Sidgewick do not categorize it. It has no CAS number and is not listed by any manufacturers for sale. Perhaps, this is due to the lack of knowledge regarding the requirement that the pH needs to be controlled. The pH data was not obtained and published until 2002.

Magnesium hydrogen arsenite forms a hydrate, $MgHPO_3 \cdot 0.5H_2O$ when precipitated from aqueous solution:

$$MgCl_2 + H_3AsO_3 \Rightarrow (MgHAsO_3)_2 \cdot H_2O + 2HCl$$

The solution is made neutral with sodium acetate. Ammonium arsenite forms the ammonium salt, $MgNH_4AsO_3$. Dibasic magnesium arsenite hemihydrate is essentially insoluble in water. Other hydrates include $MgHAsO_3 \cdot 5H_2O$ and $MgHAsO_3 \cdot 6.5H_2O$. Thus, the temperature of precipitation plays a large part in determining which hydrate forms. $(MgHAsO_3)_2 \cdot 13H_2O$ is formed at temperatures close to or less than 15 °C while the hemihydrate is obtained at 85 °C. If this salt is heated, it loses waters of hydration at about 85 °C and then at 120 °C. The exact sequence has not been studied intensively.

Magnesium orthoarsenite, $Mg_3(AsO_3)_2$, can be obtained as a white precipitate, easily soluble in water and in dilute acids, by adding a solution of magnesium chloride in 50% alcohol to a solution of potassium orthoarsenite made just neutral with acetic acid. The pH is around 13.5. Its molecular weight is 383.1666 g/mol. It is also formed when a solution of potassium tetraärsenite is added slowly to an aqueous solution of a magnesium salt. When heated in an inert atmosphere, the salt decomposes forming arsenious oxide and magnesium oxide:

$$Mg_3(AsO_3)_2 + \text{heat} \Rightarrow 3MgO + As_2O_3$$

Yet, this reaction is not reversible and the arsenite cannot be formed by reheating these ingredients together, either in an inert atmosphere or in air. However, if the mixture is heated in steam, then the reaction does occur. The mechanism of this reaction has not been studied in detail. This salt has found little usage in industry but is offered for sale by a number of manufacturers and suppliers, notably Chinese. It has no CAS number. There are few to no scientific publications that deal with this compound. Its physical properties like melting point have not been documented. This salt was described in the early work in the 1800s concerning inorganic salts. Since that time, the orthoarsenite of magnesium has received little attention for industry or academia. Very little information is available concerning this salt. It is not listed in any textbooks and, with the exception of a few papers, the only references to it date back to the 1900s. Even Remi and Sidgewick do not categorize it. It has no CAS number and is not listed by any manufacturers for sale.

Magnesium pyroarsenitc, $Mg_2As_2O_5 \cdot 4H_2O$, is a white, granular, hygroscopic, amorphous powder, soluble in water and dilute acids; on heating it undergoes decomposition and darkens in color. It is produced by the double decomposition between barium pyroarsenite and magnesium sulfate:

$$Ba_2As_2O_5\ (aq) + MgSO_4\ (aq) \Rightarrow Mg_2As_2O_5\ (aq) + BaSO_4\ (solid)$$

Crystals are formed when the filtered solution is evaporated. At low temperature, i.e. $<15\,^{\circ}C$, the 18-hydrate is obtained. At higher temperatures, the 13-hydrate and the 3-hydrate are also known, each a product of the crystallization temperature used. Like most of the magnesium arsenites, this salt has found little usage in industry but is offered for sale by a small number of manufacturers and suppliers, notably Chinese. It has no CAS number. There are few to no scientific papers which deal with this compound. Its physical properties like melting point have not been documented. This salt was described in the early work in the 1800s concerning inorganic salts. Since that time, the orthoarsenite of magnesium has received little attention for industry or academia.

Magnesium tetraärsenite, $Mg_3As_4O_9 \cdot 3H_2O$, is formed when a solution of magnesium sulfate or magnesia mixture is added to an aqueous solution of arsenious oxide or acid:

$$3MgSO_4\ (aq) + 4H_3AsO_3\ (aq) \Rightarrow Mg_3As_4O_9 \cdot 3H_2O\ (solid) + 3H_2SO_4$$

Very little information is available concerning this salt. It is not listed in any textbooks and, with the exception of a few papers, the only references to it date back to the 1900s. Even Remi and Sidgewick do not categorize it. It has no CAS number and is not listed by any manufacturers for sale. The metaarsenite can also be formed by adding a chloride slurry to sodium trimeta- or tetrameta-arsenite:

$$2MgCl_2 + Na_3(H_3AsO_{2n+1})_3 \Rightarrow 2Mg(H_3AsO_{2n+1})_3 + 6NaCl$$

Little is known in the literature or reference books concerning these salts. $MgHAsO_3$ is insoluble but whether it forms a hydrate remains unknown. The metaarsenites have not been studied extensively.

The above five salts of magnesium and arsenite ions have received little attention from academia and even less from industry. None of these compounds have found usage even though some of them are offered for sale commercially.

Calcium Arsenites

Divalent calcium forms the same type of arsenite compounds as its homologue, magnesium. The basic salt

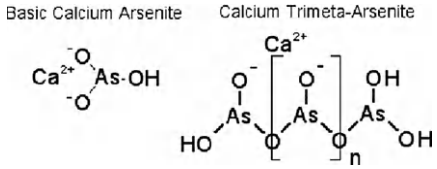

FIGURE 4.61

is $CaHAsO_3$ or $CaAsO_2(OH)$. It is referred to as a "metaarsenite" even though it is not polymeric (Fig. 4.61).

It is also known as: "calcium hydrogen arsonite" and **CAS Registry Number:** 52740-16-6. Synonyms: Calcium arsonite, Calcarin arsenicosa, Calcium arsenicosum, Calcium metaarsenite, Monocalcium arsenite, CALCIUM ARSENITE, Calcium arsenite (1:1), Calcium arsonate (1:1)".

Basic calcium arsenite can be prepared by adding a slurry of calcium hydroxide (slaked lime) to a solution of arsenious acid. The hydroxide dissolves and is basic enough to form the rather insoluble basic arsenite. The metaarsenite is formed by adding the same slurry to sodium trimeta- or tetrameta-arsenite:

$$CaCl_2 + H_3AsO_3 \Rightarrow CaHAsO_3$$

$$2CaCl_2 + Na_3(H_3AsO_{2n+1})_3 \Rightarrow 2Ca(H_3AsO_{2n+1})_3 + 6NaCl$$

Little is known in the literature or reference books concerning these salts. $CaHAsO_3$ is insoluble but whether it forms a hydrate remains unknown. The metaarsenites have not been studied extensively.

Calcium dihydrogen arsenite, $Ca(H_2AsO_3)_2$, is formed when excess of $Ca(OH)_2$ is added to an ammoniac solution of arsenious oxide, or when a solution of calcium chloride, is added to aqueous ammonium metarsenite, keeping the latter in excess. It is obtained as a white powder or as a gelatinous mass, and contains 5 to 11 waters of hydration. It is fairly soluble in water so that the solution must be evaporated to obtain crystals. The degree of hydration depends upon the temperature used during evaporation, the lower temperatures producing the highest degree of hydration. The pH should be slightly basic but if it becomes strongly acidic, no crystals will result during evaporation. A gelatinous mass results if the solution is strongly alkaline. It is insoluble in absolute alcohol and addition of ethyl alcohol aids in the crystallization process. Monobasic calcium arsenite has been used as an insecticide. It is soluble in water and can be sprayed onto plants. If sprayed on apricot, cherry or pear trees, it retards the ripening of the fruit. It has also been used in the manufacture of latex products. Its CAS number is 15194-98-6.

The ternary system $CaO–As_2O_3–H_2O$ was investigated at 0, 25, and 99 °C by the method wherein the

components were suspended in water and then heated. The pH was not controlled. The results indicated the formation of two arsenites, $CaHAsO_3$ and $Ca(H_2AsO_3)_2$. The former is a dibasic compound, calcium hydrogen arsenite, $CaHPO_3$, having the molecular weight of 120.0579 g/mol. It is slightly soluble in water (~1.2 g/100 ml), and practically insoluble in alcohol. It can also be prepared by adding H_3AsO_3 to a suspension of $Ca(OH)_2$ in water. It is well known that $CaHAsO_3$ is very stable under the high pH (12–13) values provided by lime water. The product is calcium arsenite monohydrate ($CaHPO_3 \cdot H_2O$). The CAS number of the $CaHAsO_3$ salt is 21056-98-4. That of the monohydrate is 138.073 g/mol. It is a colorless monoclinic crystal. Heating this salt to 150 °C causes the loss of the water of hydration. Its CAS number is 52740-16-6.

Calcium Metaärsenite, $Ca(H_2AsO_3)_2$, is an amorphous white powder, anhydrous at 100 °C, obtained by precipitation of calcium chloride with ammonium arsenite in ammoniac solution. It is also produced as a commercial preparation by the interaction of milk of lime and arsenious oxide with vigorous stirring at 100 °C, or by heating together at 60 to 70 °C arsenious oxide and slaked lime. The product produced is somewhat impure, containing calcium arsenate and a trace of free lime. Its solubility in water at 15 °C is about 0.044 to 0.051/100 ml. When strongly heated in an inert gas it decomposes, forming calcium and arsenious oxides and a little arsenic. This salt is best prepared by adding milk of lime to a sodium tri- or tetra-metaarsenite. The tetrameta salt may be considered to be a basic calcium metaarsenite polymer having the Lewis structure of Fig. 4.62.

Note that this compound is not the "monobasic" one but is related and differs in the number of hydroxyl groups present in the compounds structure. The general formula is $Ca_{n-2}(H_{2n}As_nO_{2n+1})_{2n-2}$.

Tribasic calcium arsenite can be formed by a solid-state reaction in which steam acts as a catalyst:

$$3CaO\ (solid) + As_2O_3\ (solid) + steam \Rightarrow Ca_3(AsO_3)_2\ (solid)$$

Apparently, the steam causes the formation of the hydroxide which is basic enough to cause the formation of the compound. If aqueous conditions are used where the concentrations of the reactants and the pH are much lower, then the dibasic salt, $CaHPO_3$ results.

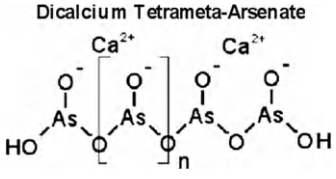

FIGURE 4.62

When mixtures of solid arsenious oxide and CaO are heated, reaction commences at about 300 °C and at 465 °C considerable heat is evolved and calcium orthoarsenite, $Ca_3(AsO_3)_2$, is formed. An industrial process for the manufacture of this compound consists of treating a dry mixture of quicklime (3 mol) and arsenious oxide (1 mol) with dry steam. It may also be obtained by precipitation of dilute calcium chloride solution with potassium orthoarsenite, 3 or of lime water (i.e. $CaCl_2$) with boiling aqueous arsenious acid. It is a white amorphous powder, which may be dried at 100 °C. It is only slightly soluble in water, but dissolves in acids. At red heat, it decomposes with volatilization of arsenic, leaving calcium arsenate. The latter is also formed when the arsenite is heated in oxygen. Its major usage in the past has been as an insecticide. Calcium arsenite ($Ca_3As_2O_6$) has a CAS number of 27152-57-4. Another is listed as 7778-44-1 while a third CAS number 52740-16-6 also exists. These CAS numbers may exist due to the method used to prepare the salt. Its molecular weight is 366.0748 g/mol.

Calcium Pyroarsenite, $Ca_2As_2O_5$, is a white powder obtained by slowly precipitating a solution of arsenious acid with excess of lime water, or by adding calcium chloride or sulfate to aqueous ammonia in the air at room temperature. The monohydrate is obtained. The pyroarscnite is only slightly soluble in water at 0.025 g/100 ml. It is more soluble in the presence of alkali chlorides and some ammonium salts, such as the nitrate, sulfate, acetate and succinate. It also dissolves in dilute acids. It has the CAS number of 13765-19-0. The pyroarsenite can also be prepared by firing arsenic trioxide with calcium hydroxide:

$$2Ca(OH)_2 + As_2O_3 + heat \Rightarrow Ca_2As_2O_5 + 2H_2O$$

A salt of composition $Ca_3As_4O_9 \cdot 3H_2O$, which may be regarded as consisting of three molecules of metaarsenite, $Ca\{AsO_2(OH)_2\}_2$, or as a derivative of a hypothetical tetraärsenous acid derived thus:

$$2As_2O_3\ (solid) + 6NH_4OH\ (solid) \Rightarrow H_6As_4O_9\ (solid) + 6NH_3\ (gas)$$

has been prepared by adding a solution of the corresponding potassium salt, $K_4H_2As_4O_9$, to a concentrated solution of calcium chloride. The white precipitate, after washing with alcohol, was dried in the air. At 100 °C, it loses one molecule of water. It is somewhat soluble in water. Very little is available in the literature concerning this salt. No description of its physical or chemical properties has been presented.

The above five salts of calcium and arsenite ions have received little attention from academia and even less

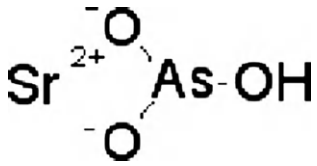

FIGURE 4.63

from industry. None of these compounds have found usage even though some of them are offered for sale commercially.

Strontium Arsenites

Strontium forms the same type of compounds expected for arsenious acid derivatives. The basic meta-arsenite has the formula, $Sr(As(OH)O_2)$ and the molecular weight of gm/mol. Its CAS number is 15195-06-9. It has the Lewis structure of Fig. 4.63.

Monobasic strontium arsenite can be prepared by heating a slurry of strontium hydroxide and adding a solution of arsenious acid:

$$Sr(OH)_2 + 2H_3AsO_3 \Rightarrow Sr(H_2PO_3)_2 + 2H_2O$$

The pH needs to be about 9.5–10.0. Strontium arsenite tetrahydrate, $Sr(H_2AsO_3)_2 \cdot 4H_2O$, has a molecular weight of 373.5234 g/mol and a CAS number of 10378-48-0. It is a white powder that is slightly soluble in H_2O but insoluble in EtOH. It is soluble in dilute acids. When heated, it loses two waters of hydration at 105 °C and the other two at 155 °C. The crystal structure of strontium dihydrogen phosphite, $Sr(H_2PO_3)_2$, contains eightfold-coordinated Sr ions connected by dihydrogenphosphite anions so that a layer structure is formed.

Tribasic strontium arsenite has the CAS number of 10378-48-0. Strontium arsenite is a white powder. It is slightly soluble in water. It is toxic by inhalation and by ingestion. Strontium arsenite is a white powder. It is slightly soluble in water. It is toxic by inhalation and by ingestion. An impure strontium orthoarsenite, containing more strontium that corresponds to the formula $Sr_3(AsO_3)_2$, was obtained as a white flocculent precipitate by treating strontium chloride solution with potassium orthoarsenite in the cold. The pH needs to be maintained around 13.5. Little is known about tribasic strontium arsenite. It is probably the most stable of this family of compounds. Yet, its physical properties have not been properly documented.

If the precipitate is dissolved in a dilute solution of acetic acid, on evaporation strontium hydrogen orthoarsenite, $SrHAsO_3 \cdot H_2O$, is obtained. Its CAS number is 15195-06-9.

Strontium Pyroarsenite. $Sr_2As_2O_5 \cdot 2H_2O$, may be prepared by adding an aqueous arsenious acid solution to strontium chloride dissolved in alcohol. The solution is filtered after standing for a time, and the white flocculent precipitate is dried at 100 °C. It is easily soluble in water and in acids. A better method is to fire the dibasic salt, $SrHAsO_3$ in a solid-state reaction under an inert gas atmosphere:

$$2SrHAsO_3 + \text{heat} \Rightarrow Sr_2As_2O_5 + H_2O$$

Little is known concerning this salt in the literature. It has not been studied extensively and is rarely mentioned for sale commercially. Although it is known to be rather insoluble, its physical properties have not been studied in detail.

Strontium dimetaärsenite, $Sr(H_3AsO_5)_{n=2}$, may be obtained as the tetrahydrate by the action of ammonium arsenite on a cold solution of a strontium salt. This salt has three hydroxy groups present and thus is a basic strontium arsenite. The precipitation is helped by the addition of alcohol, since the arsenite is fairly soluble in water. When dried at 100 °C it has the composition $Sr(H_3AsO_5)_{n=2} \cdot 3H_2O$. Further heating causes loss of hydrate water molecules at 120 and 150 °C. At higher temperatures, it decomposes to form strontium oxide, arsenious oxide and a little arsenic. Its CAS number is 91724-16-2. A salt, $Sr(HAsO_{2.5})_{n=2}$ (or $SrH_2As_2O_5$) is also possible but has not been documented. The trimeta- and tetrameta-salts, similar to those of Mg or Ca are not known.

The above five salts of strontium and arsenite ions have received little attention from academia and even less from industry. None of these compounds have found usage even though some of them are offered for sale commercially.

Barium Arsenites

Barium forms the same type of compounds with arsenite anions as the other alkaline earths. The most stable compounds are the dibasic and tribasic species, $BaHAsO_3$ and $Ba_3(AsO_3)_2$, respectively. In an investigation of the ternary system $BaO–As_2O_3–H_2O$ in which the two oxides in varying proportions were shaken with water at the temperatures 25 and 50 °C, the solution and solid phases were subsequently analyzed. Evidence of the formation of only two arsenites was obtained: a dibasic arsenite, $BaHAsO_3 \cdot 2H_2O$, and an arsenite of composition $3BaO \cdot 2As_2O_3 \cdot 4H_2O$ or $Ba_3(AsO_3)_2 \cdot 4H_2O$.

Tribasic barium arsenite, $Ba_3(AsO_3)_2$, has been prepared by the addition of potassium orthoarsenite to an aqueous solution of barium chloride and drying the precipitate at 100 °C in a current of hydrogen gas. The pH needs to at least 13.5. It is obtained as a white amorphous powder, readily soluble in hot water and in dilute

acids. When heated rapidly to about 730 °C in an inert atmosphere, it decomposed into arsenic and the arsenate. This is a double oxidation–reduction reaction in which part of the tribasic arsenite is oxidized and part reduced:

$$4Ba_3(AsO_3)_2 + \text{heat} \Rightarrow 12BaO + 4As_2O_3 + 4As$$
$$4As_2O_3 \Rightarrow 2As_2O_5 + 4As + 2O_2$$
$$4Ba_3(AsO_3)_2 + \text{heat} \Rightarrow 12BaO + 2As_2O_5 + 8As + 2O_2$$

Slow heating below 300 °C causes loss of arsenious oxide if heated in hydrogen or arsenic pentoxide if heated in air:

$$Ba_3(AsO_3)_2 + \text{Heat } (H_2) \Rightarrow 3BaO + As_2O_3$$

The monobasic salt, barium dihydrogen arsenite, $Ba(H_2AsO_3)_2$, can be obtained:

(1) by adding an excess of barium hydroxide to aqueous arsenious acid,
(2) by treating an ammonical solution of arsenious oxide with excess of barium chloride,
(3) by adding potassium pyroarsenite to a barium chloride solution and adjusting the solution pH to around pH = 10.5. The solution is then evaporated at a low temperature to recrystallize the salt.

This salt has the CAS number of 125687-68-5 and the molecular weight of 657.82 g/mol. In (1), the hydroxide is basic enough to afford the formation of the monobasic salt that is then obtained by low temperature evaporation of the solution. Very little is known concerning this salt and few papers are available in the literature. Even the contemporary reference books like Remy or Sidgwick do not mention it. The only references known date back to the middle 1800s and the data found there are probably not reliable. Barium dihydrogen arsenite is said to form a dihydrate when it is prepared from aqueous solution. It was observed to lose waters of hydration when exposed to air. The loss of water from this compound has never been studied. It is slightly soluble in cold water, more readily in hot water, the solution having a slightly alkaline reaction.

The dibasic salt is to be regarded as $BaHAsO_3$. It is best prepared from a solution of arsenious acid whose pH has been adjusted to about 12.5 with potassium acetate. If the precipitate is dried at low temperature, it has been determined that an octahydrate results. If dried at 100 °C, the dihydrate, $BaHAsO_3 \cdot 2H_2O$, is the stable compound. This salt has no CAS number and there is no registered supplier or manufacturer of this salt. The molecular weight is 261.2577 g/mol.

Barium pyroarsenite, $Ba_2As_2O_5$, is best prepared by heating barium hydrogen arsenite in an inert atmosphere at about 450 °C:

$$2BaHAsO_3 + \text{heat} \Rightarrow Ba_2As_2O_5 + H_2O$$

Very little is known concerning this salt and few papers are available in the literature. Even the current reference books like Remy or Sidgwick do not mention it. The only known references date back to the middle 1800s and the data found there is probably not reliable.

Barium metaärsenite, $Ba(H_3AsO_3)_{n=2}$, may be obtained as the tetrahydrate by the action of ammonium arsenite on a cold solution of a barium salt. This salt has three hydroxy groups present and thus is a basic barium arsenite. The precipitation is helped by the addition of alcohol, since the arsenite is fairly soluble in water. When dried at 100 °C it has the composition $Ba(H_3AsO_3)_{n=2} \cdot 3H_2O$. Further heating causes loss of hydrate water molecules at 105 and 130 °C. At higher temperatures, it decomposes to form barium oxide, arsenious oxide and a little arsenic. It has no CAS number.

The tetrameta-arsenite would have the Lewis structure of Fig. 4.64.

Where $n = 4$. The dimeta salt (which is the beginning of the series) would have the formula: $Ba(AsO_3(OH)_2)$. Early work (1844–1850) tried to prepare barium metaarsenite by warming barium chloride with a solution ammonium arsenite to which acetic acid had been added until arsenious acid was on the point of precipitation. The precipitate was then dried at 100 °C. It was said to be a white powder, easily soluble in water, but it was also obtained as a gelatinous mass when a mixture of barium chloride and potassium trimetaarsenite in solution was left to stand for a few hours. It is not clear what the degree of polymerization was in these preparations and they deserve further study.

The above five salts of barium and arsenite ions have received little attention from academia and even less from industry. None of these compounds have found usage in industry even though some of them are offered for sale commercially.

Radium Arsenites

Radium is expected to form the same type of compounds as the Sr and Ba homologues. That is, the monobasic-, dibasic- and tribasic compounds could be prepared using arsenious acid and radium hydroxide or oxide. The solution pH would have to be adjusted to: pH = 10.5, 12.5 or pH = 13.5 with potassium acetate and ammonia to obtain the corresponding arsenites.

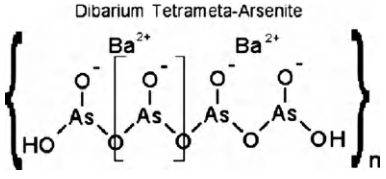

FIGURE 4.64

The pyroarsenite could be obtained by firing the dibasic salt, radium hydrogen arsenite in a solid-state reaction. The metaarsenite compounds could be obtained using the potassium metaarsenite compounds. However, there is absolutely no record of such work to be found in the scientific literature. Even the notable references books such as the CRC "Handbook of Chemistry and Physics" do not list such compounds. Of course, no early work exists since radium was not discovered until after the year 1900.

4.3.4. Alkaline Earth Orthoarsenates

Arsenious acid, H_3AsO_3, [As(III)] behaves as a monobasic acid and arsenic acid [As(V)] behaves as a tribasic acid. It is for this reason that arsenious acid shows quite different areas of pH stability than the corresponding phosphorous acid, H_2PO_3. Arsenic acid has ionization constants in aqueous solution very close to that of phosphoric acid, H_3PO_4:

$$H_3AsO_4 \Rightarrow H_2AsO_4^- + H^+ \ (pK_1 = 10^{-2.19})$$

$$H_2AsO_4^- \Rightarrow HAsO_4^{2-} + H^+ \ (pK_2 = 10^{-6.94})$$

$$HAsO_4^{2-} \Rightarrow AsO_4^{3-} + H^+ \ (pK_3 = 10^{-11.5})$$

These K_a values are close to those for phosphoric acid. Thus, the areas of pH stability are shown in the following Fig. 4.65.

The dotted lines show the area of greatest stability for the three states of ionization.

Beryllium Arsenates

Beryllium arsenate salts are less stable than those of magnesium and readily form basic salts. This is due to the fact that Be^{2+} preferentially forms hydroxy complexes of the type, $Be(OH)^+$ in association with water molecules. Species such as $Be_2(OH)^{3+}$ and $Be_3(OH)_3^{2+}$ are known to exist. The hydroxylation reaction has been given as:

$$xBe^{2+} + yH_2O \Rightarrow Be_x(OH)_y^{(2x-y)+} + yH^+$$

where x and y can vary from 1 to 8. Species such as $Be_3(OH)_7^{3+}$ and $Be_4(OH)_8^{4+}$ are known. Thus, the prior literature may be in doubt as to exact formulas for beryllium compounds prepared from aqueous solutions.

Beryllium orthoarsenate, $Be_3(AsO_4)_2 \cdot 15H_2O$, is obtained by drying in air the precipitate formed on mixing aqueous solutions of sodium monohydrogen arsenate and beryllium sulfate. The pH is maintained at 13.5. The precipitate itself is probably beryllium monohydrogen ortho-arsenate, $BeHAsO_4$, but this is readily hydrolyzed and unless immediately removed from the solution forms the tribasic salt, $Be_3(AsO_4)_2 \cdot 15H_2O$.

Dibasic beryllium arsenate has been obtained in the form of a dihydrate, $BeHAsO_4 \cdot 2H_2O$, as a viscous solid by dissolving beryllium hydroxide in arsenic acid and then precipitating with alcohol, and in the anhydrous form by heating arsenic pentoxide and beryllium hydroxide together in a sealed tube at 220 °C.

Beryllium dihydrogen orthoarsenate, $Be(H_2AsO_4)_2$, is obtained as colorless hygroscopic platelets by the action of a hot saturated solution of arsenic acid on beryllium hydroxide and vacuum evaporation.

By stirring beryllium oxide or carbonate with aqueous arsenic acid under carefully regulated conditions of concentration, acidity and temperature, two arsenates of definite composition have been isolated in a crystalline state, namely, $Be_4As_2O_9 \cdot 9H_2O$ and $Be_4As_2O_9 \cdot 10H_2O$. These are probably pyro-beryllium arsenates containing the hydroxy-Be cation (Fig. 4.66).

Thus, the correct formula is probably $(BeOH)_4As_2O_7 \cdot 6H_2O$ (hexahydrate or heptahydrate). The physical properties of this compound have never been documented or examined systematically.

The high-temperature/high-pressure hydrothermal synthesis and X-ray single-crystal structure of $Be_3(AsO_4)_2 \cdot 2H_2O$ has been described. The compound contains a three-dimensional network of BeO_4− and AsO_4-tetrahedra. Its structural motif includes infinite layers of "bridged" tetrahedral 3- and 4-rings. ^{9}Be NMR data are consistent with those derived from Be atom environments in the crystal structure (lattice parameters are: $Be_3(AsO_4)_2 \cdot 2H_2O$, molecular weight = 170.4528 g/mol), monoclinic, space group = C2/c,

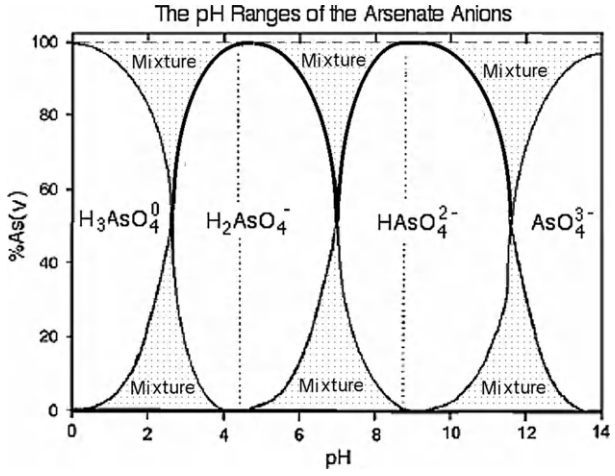

FIGURE 4.65

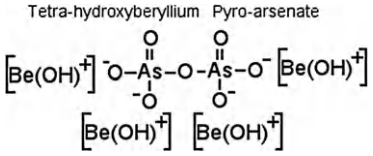

FIGURE 4.66

$a = 16.318$ Å, $b = 4.6664$ Å, $c = 9.8755$ Å, $\beta = 93.777°$, $V = 750.37$ Å^3, $Z = 4$).

This compound was prepared by a high-temperature/high-pressure hydrothermal reaction. $Be(OH)_2$, H_2O and H_3AsO_4 solution were sealed in a gold tube and heated to 550 °C for 135 h. Upon cooling, numerous needle- and shard-like crystals were recovered from the mother liquor (pH = 2) by vacuum filtration. $Be_3(AsO_4)_2 \cdot 2H_2O$ is built up from BeO_4 and AsO_4 subunits. This connectivity of tetrahedral nodes in $Be_3(AsO_4)_2 \cdot 2H_2O$ leads to a three-dimensional network, built up from infinite b···c plane layers of As(l) and Be(2) tetrahedral groups, which are linked together by the Be(1) groups. The As(1)/Be(2) layers are built up from infinite tetrahedral "bridged" 3- and 4-rings. The "backbone" of the layer is an edge-sharing chain of 4-rings, each of configuration L-[Be(2)–As(1)–Be(2)–As(l)]-J, which propagates in the *b*-direction. Adjacent 4-ring chains are fused together by 3-rings (configuration L-[Be(2)–As(1)–Be(2)]-J), which are fused edge-to-edge themselves, resulting in an infinite sheet structure. A notable feature of this connectivity is the fact that each Be(2) atom makes contact with *six* nearest-neighbor tetrahedral atoms [four distinct As(1)'s and two distinct Be(2)'s], and each As(l) atom bonds to six different Be(2) atoms.

The following diagram does not show the water molecules (for the sake of simplicity) (Fig. 4.67).

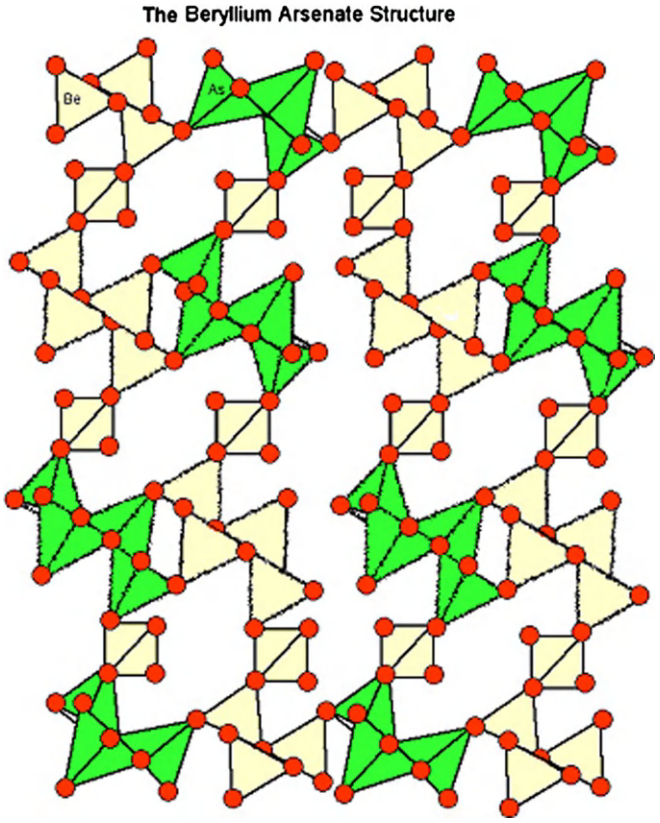

FIGURE 4.67

In another paper, $(BeOH)_2(AsO_4)_2OH \cdot 3H_2O$ was found to contain 3-ring groupings of tetrahedra as part of a one-dimensional chain of $(BeOH)AsO_4$ groups. Crystal data for this compound were: MW = 246.0124 g/mol, monoclinic, space group = $P2_1/a$, Unit cell: $a = 7.2349$ Å, $b = 12.6861$ Å, $c = 8.6545$ Å, $\beta = 98.439°$, $Z = 4$. The compound contains 1-dimensional stacks of interconnected BeO_4 and AsO_4 tetrahedra, including alternating 3-ring and 4-ring groups, the former containing Be···OH···Be bonds. The tetrahedral columns are connected by water molecules via a network of H-bonds.

Although studies of the tribasic beryllium orthoarsenate compound have been conducted, there has been no systematic investigation of the other arsenates of Be, including the basic-, monobasic-, dibasic, pyro- and metaarsenates. No data exists except that of early work whose results are subject to interpretation.

None of these compounds have CAS numbers and there is no record of them having been recently prepared. Little interest has resulted in industry or academia and they are not offered for sale commercially.

Magnesium Arsenates

Magnesium forms the same sequence of ortho-arsenates as the ortho-phosphates. Tribasic magnesium arsenate ($As_2Mg_3O_8$), has the CAS number 13464-38-5 while that of dibasic magnesium arsenate trihydrate, $MgHAsO_4 \cdot 3H_2O$, is 7757-86-0.

Magnesium forms a dibasic salt, $MgHAsO_4 \cdot H_2O$, that is insoluble in water:

$$MgCl_2\ (aq) + Na_2HAsO_4\ (aq) \Rightarrow MgHAsO_4 \cdot H_2O\ (solid)$$

The pH needs to be about 9.0. Other hydrates include $MgHAsO_4 \cdot 5H_2O$. Thus, the temperature of precipitation plays a large part in determining which hydrate forms. $(MgHAsO_3)_2 \cdot 8H_2O$ is formed at a temperature close to or less than 15 °C while the monohydrate is obtained at 85 °C. If this salt is heated in air, it loses waters of hydration at about 85 °C and then at 120 °C. The mode of dehydration of the octa-hydrate salt has never been documented.

In another method, magnesium monohydrogen orthoarsenate, $MgHAsO_4 \cdot 7H_2O$, was said to have been prepared by adding a calculated amount of magnesium sulfate to a solution of sodium monohydrogen arsenate neutralized with acetic acid. The amorphous precipitate was kept in contact with the solution for some days, during which time it became crystalline. It loses water when heated. The hepta-hydrate occurs in Nature as "Rösslerite" or "Roesslerite", a fibrous mineral consisting of monoclinic crystals with $a : b : c = 0–4473:1:0.2598$ and $\beta = 94°\ 26'$. A hemihiydrate, $(MgHAsO_4)_2 \cdot H_2O$ is obtained in the form of prismatic crystals by heating

Rösslerite
("Im Lochborn") Copper
mine, Bieber, Gelnhausen,
Spessart, Hesse, Germany

FIGURE 4.68

a solution of magnesium carbonate in excess of arsenic acid at 225 °C in a sealed tube (Fig. 4.68).

$MgHAsO_4 \cdot 4H_2O$ or "Brassite", which may occur as a dehydration product of "Rösslerite", crystallizes in the monoclinic system with Space Group C2/c and $a = 6.6918$ Å, $b = 25.744$a, $c = 11.538$ Å, $\beta = 95.15°$, $Z = 8$. The two crystallographically independent Mg-atoms are coordinated by 6 water molecules. The seventh water molecule is linked by hydrogen bonds only. No oxygen atoms are shared by coordination polyhedra and the crystal structure can be described in terms of layers parallel to (010) or to (001) lattice directions.

$MgAsO_3(OH) \cdot 4H_2O$ may recrystallize in the orthorhombic system with $a = 7.47$ Å, $b = 10.89$ Å, $c = 16.58$ Å, Space Group = Pbca, point group = 2m 2m 2m, $Z = 8$, Unit cell volume: V =1348.75 Å^3 and density = 2.326 g/cm^3. The structure is built up with $AsO_3(OH)$ tetrahedral linked together with $MgO_2(H_2O)_4$ octahedra to make chains parallel to (010). A two-dimensional net of hydrogen bonds between tetrahedral and octahedral belonging to different chains exists. They include O···O and O···H_2O bonds define layers parallel to (001).

Tribasic magnesium orthoarsenate may be obtained in various hydrated forms. When solutions containing equivalent quantities of magnesium sulfate and normal sodium ortho-arsenate are mixed, an amorphous precipitate forms which, on prolonged keeping in contact with the solution, becomes crystalline. Upon drying at 100 °C, the composition $Mg_3(AsO_4)_2 \cdot 2H_2O$ results:

$$MgSO_4\ (aq) + Na_3AsO_4\ (aq) \Rightarrow Mg_3(AsO_4)_2 \cdot 2H_2O\ (solid)$$

The crystals are monoclinic and isomorphic with the corresponding phosphate. The density at 15 °C is 1.788 g/mol, and the indices of refraction along the three axes $x = 1.548$ to 1–563, $z = 1.556$ to 1.571 and $y = 1.574$ to 1.596. The octahydrate, $Mg_3(AsO_4)_2 \cdot 8H_2O$, is obtained by mixing aqueous solutions of magnesium sulfate, sodium monohydrogcn arsenate and sodium bicarbonate and keeping the amorphous precipitate in contact with the solution for 24 h, when it becomes crystalline:

$$MgSO_4\ (aq) + Na_2HAsO_4\ (aq) \Rightarrow Mg_3(AsO_4)_2 \cdot 8H_2O\ (solid) + Na_2SO_4\ (aq)$$

$Mg_3(AsO_4)_2 \cdot 8H_2O$ has the molecular mass of 494.9458 g/mol and the CAS number of 10103-50-1. This hydrate is found in Nature as the mineral "Hornesite", the crystals of which are monoclinic and probably isomorphic with "Vivianite". The density of the mineral is 2.474 g/cm^3; that of the artificially prepared product is 2.609 g/cm^3. The mineral, "Roselite", $Ca_2(Co,Mg)(AsO_4)_2 \cdot 2H_2O$, is a beautifully colored mineral and varies from rose-red to pink. It would be a misguided assumption that its name came from its color. In fact it is named for a Germany eighteenth century mineralogist, Gustav Rose. The color of Roselite comes from the same coloring agent of many different colorful minerals, namely cobalt. Hoernesite [$Mg_3(AsO_4)_2 \cdot 8H_2O$] was originally found in arsenic-contaminated soils and in toxic waste sites. The solubility of this mineral is poorly known, but it must be not much different from the value determined for tribasic compound.

The heptahydrate, $Mg_3(AsO_4)_2 \cdot 7H_2O$, is obtained if sodium dihydrogen arsenate is substituted for the monohydrogen salt in the above preparation. The decahydrate, $Mg_3(AsO_4)_2 \cdot 10H_2O$ is formed when potassium or ammonium magnesium orthoarsenate is digested with water for several hours. On dehydration, hydrates containing 6. 5, 3, 2 and 2 can be obtained. The anhydrous salt decomposes when heated above 1100 °C in a vacuum, MgO, As_2O_3 and O_2 being formed.

A light form of magnesium arsenate may be obtained by heating a slurry of magnesium hydroxide with the theoretical quantity of arsenic acid and 15% of the equivalent amount of sodium hydroxide in an autoclave at 180 °C until the filtrate contains less than 0.2% of arsenic pentoxide. The solubility of magnesium arsenate is 5×10^{-5} mol/l. The solubility product constant is: $K_{SP} = 2 \times 10^{-20}$ for $Mg_3(AsO_4)_2$. The crystal structure of the anhydrate, $Mg_3(AsO_4)_2$, has been solved. It is tetragonal with: $a = 6.783$ Å, $c = 18.963$ Å, $V = 842.7$ Å^3, $Z = 6$ and space group = I $\bar{4}$ 2d. Crystals were obtained from a melt of $MgCO_3$ and As_2O_5 at 1450 °C. The structure contains two distinct AsO_4 groups with average bond lengths of 1.678 and 1.690 Å, respectively. Two of the three Mg ions are octahedrally coordinated and it is the third that occupies a site of $\bar{4}$ symmetry.

Atomic parameters for $Mg_3As_2O_8$

U_{ij}'s in Å² are computed from $\beta_{ij}=2\pi^2 b_i b_j U_{ij}$ where $T=\exp\{-[\beta_{11}h^2+2\beta_{12}hk+\ldots]\}$ appears in the structure-factor expression and b_j are reciprocal-lattice cell vectors.

		x	y	z	U_{11}	U_{22}	U_{33}	U_{12}	U_{13}	U_{23}
Mg(1)	8d	0·2416 (6)	¼	¼	0·008 (1)	0·005 (1)	0·008 (1)	—	—	−0·000 (1)
Mg(2)	8c	0	0	0·2284 (2)	0·011 (1)	0·007 (1)	0·007 (1)	−0·003 (1)	—	—
Mg(3)	4b*	0	0	½	0·014 (5)	U_{11}	0·013 (4)	—	—	—
As(1)	8d	−0·3446 (1)	¼	¼	0·0050 (3)	0·0045 (3)	0·0053 (3)	—	—	−0·0005 (3)
As(2)	4a	0	0	0	0·0036 (6)	U_{11}	0·0053 (4)	—	—	—
O(1)	16e	0·0566 (7)	0·2074 (7)	0·0438 (2)	0·009 (2)	0·004 (1)	0·010 (2)	0·000 (1)	−0·004 (1)	−0·002 (1)
O(2)	16e	0·4937 (9)	0·2883 (9)	0·1925 (2)	0·007 (2)	0·023 (3)	0·010 (1)	−0·001 (2)	0·005 (2)	−0·010 (2)
O(3)	16e	0·2206 (8)	0·5464 (8)	0·1017 (3)	0·009 (2)	0·006 (2)	0·017 (2)	−0·003 (1)	−0·003 (2)	0·000 (1)

* Site is half occupied.

FIGURE 4.69

The coordinates of the Mg, As and O atoms in the unit cell are shown in the following table labeled "Atomic parameters for $Mg_3As_2O_8$" (Fig. 4.69).

Stability diagrams derived for $Ca_3(AsO_4)_2$ and $Mg_3(AsO_4)_2$ show the comparatively high solubility of such compounds. The presence of CO_2 in the air has a pronounced effect in greatly increasing the water solubility of $Ca_3(AsO_4)_2$ and significantly affecting that of $Mg_3(AsO_4)_2$.

The relative stabilities of solid Ca and Mg arsenates were established by solubility experiments from the pH range and total aqueous Ca, Mg and As concentrations. The experimental data were consistent with the following solid phases defined as a function of the pH range:

$$Ca_3(AsO_4)_2\cdot 10H_2O \quad (7 < pH < 10)$$
$$CaNaAsO_4\cdot 7.5H_2O \quad (10 < pH < 12)$$
$$MgHAsO_4\cdot 4H_2O \quad (6.5 < pH < 7.1)$$
$$Mg_3(AsO_4)_2\cdot 8H_2O \quad (7.2 < pH < 9)$$

All the experimentation was performed at constant ionic strength in aqueous $NaClO_4$ solutions and at 25 °C, where the stoichiometric solubility products of the different solids were calculated. The corresponding thermodynamic solubility products of all the precipitates were computed by means of the Modified Bromley's Methodology that considers the variation of the activity coefficients of the ions involved in the precipitation equilibria with the medium and ionic strength. Moreover, all the solid arsenates obtained were characterized by FT-IR and FT-Raman spectroscopy and the hydration of each precipitate was confirmed by XRD data.

Several double arsenates of magnesium and the alkali metals, ammonium and calcium are known. The most important of these is magnesium ammonium ortho-arsenate, $MgNH_4AsO_4\cdot 6H_2O$ that is obtained as a crystalline precipitate when ammonium ortho-arsenate is added to a solution of a magnesium salt. It may be dried over sulfuric acid. It is also formed when an alkali arsenate is added to a solution of a magnesium salt in the presence of an ammonium salt and ammonia. When heated above 40 °C it loses ammonia and water. It is doubtful if any lower hydrate can be formed, although such are described in the literature. If heated above about 450 °C, it forms the pyroarsenate:

$$2MgNH_4AsO_4\cdot 6H_2O + \text{Heat} \Rightarrow Mg_2As_2O_7 + 2\,NH_3 + 14H_2O$$

Magnesium pyroarsenate, $Mg_2As_2O_7$, is monoclinic with space group C2/m.

It also forms a double salt with Ba^{2+}, as $BaMgAs_2O_7$ having the crystal structure parameters of: $a = 5.620$ Å, $b = 8.629$ Å, $c = 13.344$ Å, $\beta = 90.20°$, $V = 647.1$ Å^3, space group $P2_1/n$, $Z = 4$.

A number of magnesium ortho-arsenate minerals are known. Among these are:

$$\text{Manganberzeliite (TL)} = (Ca,Na)_3(Mn^{2+},Mg)_2[AsO_4]_3$$
$$\text{Manganohörnesite (TL)} = (Mn,Mg)_3(AsO_4)_2\cdot 8H_2O$$
$$\text{Guanacoite} = (Cu_{0.85}Mg_{0.15})_2Mg_2\,(Mg_{0.83}Cu_{0.17})(OH)_4(H_2O)_4(AsO_4)_2$$
$$\text{Arsenostruvite} = MgNH_4AsO_4\cdot 6H_2O$$

Magnesium dihydrogen orthoarsenate, $Mg(H_2AsO_4)_2$, has been described as a very deliquescent crystalline mass obtained by dissolving magnesium oxide in aqueous arsenic acid. The pH is set at 4.5 by the addition of ammonium acetate. A monohydrate results. It is soluble in water. To prepare the pyroarsenate, the dibasic compound is calcined at about 450 °C. If it is fired in air, it first decomposes to form the anhydrate at 150 °C and then the dimeta-arsenate between 200 and 206 °C and finally the pyro-arsenate at >600 °C.

A di-hydrate of the pyroarsenates, $Mg_2As_2O_7\cdot 2H_2O$ (dimagnesium diarsenic heptaoxide dihydrate) and $Zn_2As_2O_7\cdot 2H_2O$ (dizinc diarsenic heptaoxide dihydrate), have been synthesized. The two compounds are isotypic. Their frameworks are characterized by zigzag

infinite chains of edge-sharing MO_6 octahedra linked by As_2O_7 groups to form a three-dimensional architecture with intersecting tunnels. Water O-atoms are tightly bound to the Mg or Zn atoms with the H atoms directed into the tunnels. Both the MO_6 octahedra and the AsO_4 tetrahedra are more distorted in the zinc compound than in the magnesium compound.

To prepare the metaarsenate compounds, the monobasic compound is calcined at about 550 °C:

$$2Mg(H_2AsO_4)_2 + \text{heat} \Rightarrow Mg_2(AsO_3)_2 + 2H_2O$$

A tetrameric compound is said to be obtained, $Mg_2As_4O_{12}$ or a higher polymeric species such as $Mg_2(AsO_3)_6$. Very little is known concerning the metaarsenate compounds. Three different forms of condensed magnesium arsenatophosphates have been described but not that of the pure magnesium metaärsenates. One of these was the (As,P) analog of high-molecular magnesium polyarsenate, $[Mg(AsO_3)_2]_x \cdot H_2O$. A second form resembles the cyclic magnesium tetrametaphosphate, and a third one is either another modification of this tetrameta-arsenatophosphate or a salt with chain-like anions having an approximately regular As–P distribution. The Lewis structure of the magnesium tetrameta salt has been given as a cyclic one, rather than a linear chain as described for the calcium metaärsenate salt (Fig. 4.70).

Obviously, the exact formula depends upon the Mg/As ratio found in the metaarsenate compound. The only papers to be found date back to the 1950s.

A new compound, hepta-magnesium bis(arsenate) tetrakis(hydrogenarsenate), $Mg_7(AsO_4)_2(HAsO_4)_4$, was synthesized by a hydrothermal method. The structure is based on a three-dimensional framework of edge- and corner-sharing MgO_6, $MgO_4(OH)_2$, MgO_5, $AsO_3(OH)$ and AsO_4 polyhedra. Average Mg–O and As–O bond lengths are in the ranges 2.056–2.154 and 1.680–1.688 Å, respectively. Each of the two nonequivalent OH groups is bonded to both an Mg and an As atom. One OH group is involved in a very short hydrogen bond [OO = 2.468 (3) Å]. The formula unit is centro-symmetric, with all atoms in general positions except for one Mg atom, which has site symmetry. The compound is isotypic with $Mn_7(AsO_4)_2(HAsO_4)_4$ and $M_7(PO_4)_2(HPO_4)_4$, where M is Fe, Co or Mn. **Formula:** $Mg_7(AsO_4)_2(HAsO_4)_4$.

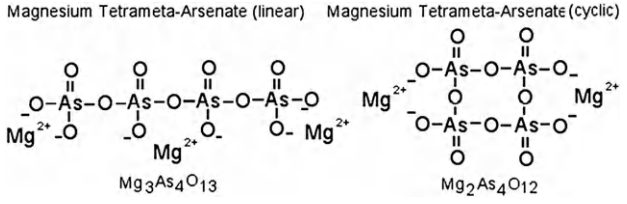

FIGURE 4.70

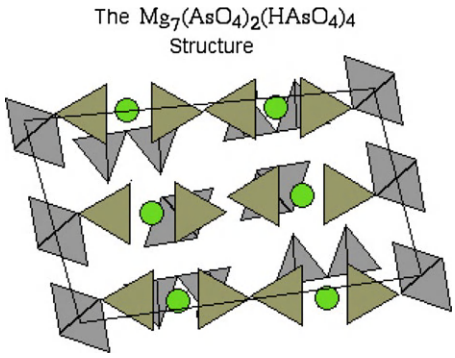

FIGURE 4.71

The structure is shown in (Fig. 4.71).

Single crystals of magnesium arsenate have been grown from a PbO–As_2O_5 eutectic by flux crystallization of a ceramic preparation having an initial composition of $6MgO \cdot As_2O_5$. The crystals are rhombohedral, space group P2/a, with hexagonal unit-cell parameters $a = 6.0278$ Å and $c = 27.600$ Å. The structure analysis indicated that magnesium arsenate has the composition $Mg_{8.5}As_3O_{16}$ and is isostructural with the previously reported $Co_8As_3O_{16}$. The structure is based upon a cubic close-packed oxygen array with charge balance achieved in magnesium arsenate through partial occupancy of a unique magnesium site occurring in an arsenic-substituted MgO-type layer.

In the system MgO–As_2O_5, there is a compound of the composition $6MgO \cdot 1As_2O_5$ or $Mg_6As_2O_{11}$. Products containing small concentrations of manganese show fluorescence upon excitation by cathode rays or by ultra-violet radiation. The band emitted depends on the valence of the manganese. Divalent manganese causes fluorescence in a broadband in the green, with a maximum at 5050 Å. Tetravalent manganese causes a red fluorescence in a band consisting of five narrow subbands at 6200, 6300, 6400, 6500 and 6580 Å. Both bands decay exponentially; the time constant at room temperature is 130/ms for the green band and 360/ms for the red band. For the red luminescent systems, the spectral distributions of the absorption, excitation and fluorescence and the temperature dependence of the intensity of the fluorescence, the fluorescence spectrum and the decay constant have been determined and a quantitative representation of several of these quantities has been given. This system has been studied intensively in a number of publications.

A number of United States patents cover processes for the manufacture of magnesium arsenates for use as insecticides. The magnesium arsenates tested as insecticides consisted generally of the dibasic magnesium arsenate, $MgHAsO_4$, the tribasic magnesium arsenate, $Mg_3(AsO_4)_2$, or the pyro-arsenate, $Mg_2As_2O_7$, with varying amounts of water of crystallization and excess

magnesium oxide or hydroxide. These magnesium arsenates have been tested against a large number of insects affecting fruits and vegetables and at one time were recommended for the control of the Mexican Bean Beetle but their use has declined due to the toxicity of As.

Various magnesium arsenates are available commercially but it is the dibasic and tribasic salts that are used in industry because of their relative stability.

Calcium Arsenates

In a basic form, calcium arsenate is an important commercial product and is used in the form of a spray or dust as an insecticide for plants. The commercial arsenates are usually mixtures and exhibit a wide variation in chemical and physical characteristics. The system $CaO–As_2O_5–H_2O$ has been investigated at various temperatures, and under various equilibrium data.

Microscopic and X-ray examination show that the following compounds are the most stable in water:

$$CaHAsO_4$$
$$Ca_5OH(AsO_4)_4\cdot 5H_2O$$
$$Ca_3(AsO_4)_2\cdot 2H_2O$$

The phase diagram for the ternary system $CaO–As_2O_5–H_2O$ at $23\pm1\,^{\circ}C$ has been determined. The calcium arsenates represented therein are:

$$Ca(H_2AsO_4)$$
$$CaHAsO_4\cdot H_2O$$
$$Ca_5H_2(AsO_4)_4\cdot 9H_2O$$
$$Ca_3(AsO_4)_2\cdot xH_2O\ (x=2/3 \text{ and } 3/4)$$
$$Ca_5(AsO_4)_3OH \text{ (apatite)}$$
$$Ca_4(OH)_2(AsO_4)_2\cdot 4H_2O$$

The solubility data indicate the following invariant points:

$$Ca(H_2AsO_4)_2–CaHAsO_4\cdot H_2O—\text{solution}$$
$$CaHAsO_4\cdot H_2O–Ca_5H_2(AsO_4)_4\cdot 9H_2O—\text{solution}$$
$$Ca_5H_2(AsO_4)_4\cdot 9H_2O–Ca_3(AsO_4)_2\cdot 41/4H_2O—\text{solution}$$
$$Ca_3(AsO_4)_2\cdot 31/3H_2O–Ca_4(OH)_2(AsO_4)_2\cdot 4H_2O—\text{solution}$$
$$Ca4(OH)_2(AsO_4)_2\cdot 4H_2O–Ca(OH)_2–\text{solution}.$$

The tricalcium arsenate, $Ca_3(AsO_4)_2\cdot 31/3H_2O$, or $[Ca_3(AsO_4)_2]_3\cdot 4H_2O$ was shown to be the only hydrate to dissolve congruently. The solubility of tribasic calcium arsenate dihydrate, precipitated at pH 7.0 and its dissolution in aqueous solutions at temperatures of 35, 40, 45 and 50 °C and a pH of between 3.0 and 8.0 was investigated. Temperature dependence of solubility is obtained by the equation:

$$-\log K_{TCA} = 9078.138/T - 34.0468 + 0.0821421\,T$$

where T is K. At 20 °C, its solubility is 0.0756 g/100 ml.

The normal salt, calcium orthoarsenate, $Ca_3(AsO_4)_2$, may be obtained by the action of lime water or milk of lime, $(Ca(OH)_2)$, on arsenic acid, or by addition of aqueous calcium chloride to aqueous sodium monohydrogen arsenate. In the latter case, if the solutions are alkaline (~pH = 9.0), a product of a high degree of purity is obtained. Drying at 100 °C gives the dihydrate, $CaHAsO_4\cdot 2H_2O$, which loses its water of crystallization at 175 °C. The anhydrous salt melts at 1455 °C. It is reduced by hydrogen at 400–450 °C to calcium oxide, arsenic and water. The density of the dihydrate is 3.28 g/cm^3, and of the anhydrous salt 3.62 g/cm^3. The solubility of the latter at 25 °C is 0.0133 g/100 ml of water. A mineral, "Adelite" [$CaMgAsO_4(OH)$] is known.

The commercial product made in the past was usually obtained either by adding arsenic acid to partly slaked lime containing sufficient quicklime to combine with the free water, thus yielding a dry product, or by heating a mixture of lime and white arsenic in the presence of an oxidizing medium, such as oxygen, chlorine or nitrates. It is essential that the product should contain a minimum of soluble arsenic and that the presence of the more soluble acid arsenates should be avoided. The commercial arsenate is generally slightly basic. Its actual composition is generally not known and varies from manufacturer to manufacturer. The results of analyses of 16 samples showed that the total As_2O_5 ranged only from 40.3 to 44.4% [As_2O_5 in $Ca_3(AsO_4)_2 = 57.7\%$], and the average molecular quotient CaO/As_2O_5 was 3/4. The average commercial product contains 80–85% of what is probably a mixture of the normal tribasic arsenate and a basic arsenate, probably $4CaO\cdot As_2O_5$, together with about 6.5% each of calcium hydroxide and calcium carbonate, and small quantities of other impurities. If varying quantities of arsenic acid are added to a saturated solution of lime, the ratio of $CaO:As_2O_5$ in the precipitate shows a continuous variation according to the quantity of arsenic acid added. Under these conditions, there is no evidence of the real existence or formation of tribasic calcium arsenate, $Ca_3(AsO_4)_2$.

The calcium arsenate that is sold commercially today as an insecticide is not a single chemical compound but a complex mixture of several calcium arsenates and an excess of calcium hydroxide. The material is made from arsenic trioxide by first oxidizing it to arsenic pentoxide with nitric acid and then reacting the solution of arsenic pentoxide or arsenic acid with a slurry of calcium hydroxide. The conditions of temperature,

concentration, and duration of reaction are important because of their influence on the physical nature of the product.

Commercial calcium arsenate generally is colored pink and is alkaline in reaction. It is a finely divided powder. It has been used extensively against certain insects affecting field crops, especially cotton. It cannot be used safely on apples, peaches, beans, and some other crops because of its burning effect on the foliage and fruit. It is banned by a number of countries.

A number of calcium orthoarsenate minerals are known. Some of these are shown in Table 4.19.

Groatite is isostructural with O'Danielite. The presence of the rare calcium arsenate minerals Weilite, Pharmacolite, Haidingerite, and Phaunouxite indicate that these minerals formed in locations where high concentrations of total dissolved arsenate existed. These minerals are isotypic and homologous: Phaunouxite, $Ca_3(AsO_4)_2\cdot 11H_2O$, is triclinic with $a = 12.563$ Å, $b = 12.181$ Å, $c = 6.205$ Å, $\alpha = 88.94°$, $\beta = 91.67°$, $\gamma = 113.44°$, $V = 807.77$ Å^3, MW = 596.2413 g/mol and $d = 2.28$ g/cm^3. Rauenthalite, $Ca_3(AsO_4)_2\cdot 10H_2O$, is triclinic with $a = 12.564$ Å, $b = 12.169$ Å, $c = 6.195$ Å, $\alpha = 89.09°$, $\beta = 79.69°$, $\gamma = 118.54°$, $V = 812.65$ Å^3, MW = 578.2264 g/mol and $d = 2.36$ g/cm^3. Space group for both is P1.

Raman and infrared (IR) spectroscopy have been used to study the mineral Pharmacolite $Ca(AsO_3OH)\cdot 2H_2O$. The mineral is characterized by an intense Raman band at 865/cm, assigned to the $(AsO_3)^{2-}$ symmetric stretching mode. The equivalent IR band is found at 864/cm. The low-intensity Raman bands is in the range from 844 to 886/cm provide evidence for 3 (AsO_3) antisymmetric stretching vibrations. A series of overlapping bands in the 300–450/cm region are attributed to 2- and 4(AsO_3)-bending modes. Prominent Raman bands at around 3187/cm are assigned to the OH stretching vibrations of hydrogen-bonded water molecules and the two sharp bands at 3425 and 3526/cm to the OH stretching vibrations of only weakly hydrogen-bonded hydroxyls in $(AsO_3OH)^{2-}$ units.

TABLE 4.19

Svabite = $Ca_5(AsO_4)_3F$

Tilasite (TL) = $CaMg[F|AsO_4]$

Turneaureite (TL) = $Ca_5(AsO_4)_3Cl$

O'Danielite = $Na(Zn,Mg)_3(AsO_4)[AsO_3(OH)]_2$

Weilite = $CaHAsO_4$

Pharmacolite = $CaHAsO_4\cdot 2H_2O$

Haidingerite = $CaHAsO_4\cdot H_2O$

Phaunouxite = $Ca_3(AsO_4)_2\cdot 11H_2O$

An old method involving electrolysis in solution for the manufacture of calcium arsenate is as follows. A solution of arsenious oxide in caustic soda (As_2O_3:NaOH = 198:250) is electrolyzed between iron electrodes. Hydrogen and a small quantity of metallic arsenic are liberated at the cathode and very little oxygen at the anode, the basic arsenite in solution being oxidized to arsenate. When this oxidation is complete, any arsenic is filtered off and the solution treated with milk of lime. A basic arsenate of extremely low solubility is precipitated and after removal, is washed and dried.

Calcium hydrogen orthoarsenate, $CaHAsO_4$, may be prepared by treating calcium carbonate with arsenic acid, or by precipitation from solutions of calcium salts with sodium monohydrogcn arsenate. Both solutions should be acidified to around pH = 9.0. When dried at 100 °C the monohydrate, $CaHAsO_4\cdot H_2O$, is obtained, but the water of crystallization is lost before the temperature of 175 °C is reached. By very slow addition of sodium monohydrogen arsenate solution to a vessel containing aqueous calcium nitrate, so that the two salts were able to mix by diffusion, well-defined monoclinic prisms of the dihydrate, $CaHAsO_4\cdot 2H_2O$ have been obtained. These two hydrates occur in Nature, the monohydrate as Haidingerite and the dihydrate as Pharmacolite. Calcium arsenate is a constituent of many other minerals. A saturated solution at 25 °C of calcium monohydrogen arsenate contains 0.3108 g, of the anhydrous salt per 100 ml of solution.

Calcium hydrogen arsenate trihydrate crystallizes in the orthorhombic system with space group = Pbca. Unit-cell parameters are: $a = 11.185$ Å, $b = 10.713$ Å, $c = 11.179$ Å, $Z = 8$. The hydrogen atoms were located and one of the three water molecules appears to be very weakly bonded. The structure is built from isolated Ca-octahedra sandwiched between As-tetrahedra. The resulting layers, parallel to (100), are connected by infinite zigzag chains of H-bonds along (100).

$CaHAsO_4\cdot 3H_2O$ is the most highly hydrated member of the group that includes:

$$CaHAsO_4\cdot 2H_2O = \text{Pharmacolite}$$
$$CaHAsO_4\cdot H_2O = \text{Haidingerite}$$
$$CaHAsO_4 = \text{Weilite}.$$

These hydrated species all form the same type of lattice structures except for the location of the water molecules and the ensuing point group. The tri-hydrate is probably D_{2h}^{14} while that of the monohydrate is C_{2v}^{6}. Weilite, the anhydrate, crystallizes in the triclinic system with space group P1 and unit-cell parameters of: $a = 7.0591$ Å, $b = 6.8906$ Å, $c = 7.2006$ Å, $\alpha = 97°26'$, $\beta = 103°33'$, $\gamma = 87°45'$, $Z = 4$. The structure has layers parallel to the (001) plane in which the two Ca atoms are crystallographically independent and coordinate

7- and 8-O atoms, respectively. The AsO_4 tetrahedra are on the layer surface. A series of hydrogen bonds exist between the tetrahedral and the Ca-positions.

The dihydrogen arsenate, $Ca(H_2AsO_4)_2$ is sparingly soluble in cold water and is decomposed by hot water, yielding the monohydrogen salt and arsenic acid. Calcium dihydrogen orthoarsenate has been obtained in the form of a monohydrate by adding nitric acid to a mixture containing equal proportions of calcium carbonate and arsenious oxide and allowing the solution to crystallize. It may also be prepared by adding excess of arsenic acid to calcium carbonate or to the normal or monohydrogen orthoarsenate. It forms colorless plates which lose their water at 180 and at 360 °C to yield calcium metaärsenate, $Ca(AsO_3)_2$, as a crystalline mass, insoluble in hydrochloric acid. Its molecular weight is 319.93 g/mol. It occurs in Nature as "Svenekite".

Calcium Pyroarsenate, $Ca_2As_2O_7$, as orthorhombic prisms, may be obtained by fusing calcium oxide with potassium monohydrogen arsenate at an elevated temperature or with a mixture of the latter with less than 40% of calcium chloride. When treated with cold water, the prisms break up into minute crystals of the hexahydrate, $Ca_2As_2O_7 \cdot 6H_2O$. By leaving it in contact with water, the salt is gradually transformed into calcium monohydrogen orthoarsenate, $CaHAsO_4 \cdot 2H_2O$. The pyroarsenate undergoes reduction when heated in hydrogen to above 400 °C to form arsenic and CaO. The best way to prepare the pyroarsenate is to calcine the dibasic salt, $CaHAsO_4 \cdot 2H_2O$, at about 650 °C.

Tribasic calcium arsenate was used extensively in the early 1900s as an insecticide on farm crops. In 1919, 1360 tons were manufactured, and 7270 tons (16 million lbs) were manufactured in 1922. Magnesium salts are used to a much lesser extent to promote arsenic fixation in soils, sediments, and wastes. In spite of magnesium arsenates being considered extremely insoluble solids, their solubilities are similar to the calcium arsenates.

The solubilities of some calcium arsenates are shown in the following Table 4.20.

TABLE 4.20

Solid phase	T/K	pH[a]	$Arsenate_{total}$/(mol/L)[a]
$CaHAsO_4 \cdot H_2O$	308	Acid	0.12–1.2
$Ca_3(AsO_4)_2$	293	6.90–8.35	1.5×10^{-2}–3.5×10^{-3}
$Ca_3(AsO_4)_2 \cdot 4.25H_2O$	296	7.32–7.55	1.1×10^{-2}–6.5×10^{-3}
$Ca_{10}(AsO_4)_6(OH)_2$	310	5.56–7.16	7.5×10^{-3}–4.4×10^{-4}
$Ca_{10}(AsO_4)_6Cl_2$	293	6.50–7.40	1.9×10^{-3}–3.7×10^{-5}

[a] *pH and total arsenate values are the highest and lowest numbers presented in the references, but a direct relation does not exist between the values of the two columns.*

The structure of the calcium arsenate compounds, precipitated from the mixing of soluble arsenic solutions with $Ca(OH)_2$ slurry was studied. The nature of the compounds formed depended on the pH and the Ca/As molar ratio. Three types of calcium arsenates, i.e. $Ca_3(AsO_4)_2 \cdot xH_2O$, $Ca_5(AsO_4)_3(OH)$ and $Ca_4(OH)_2(AsO_4)_2 \cdot 4H_2O$, were identified over a wide range of pH and for Ca/As molar ratios between 1.25 and 4.0.

The mixture of $Ca_3(AsO_4)_2 \cdot xH_2O$ and $Ca_4(OH)_2(AsO_4)_2 \cdot 4H_2O$ was observed to form at pH 3 to 7 and at Ca/As ratios of 1.0 and 1.25. The XRD and SEM analysis of 11 separate precipitation experiments for the Ca/As = 1.5 confirmed that four solid samples, precipitated at low initial pH values (3.06, 4.06, 4.75, 5.45) and low final pH (3.70, 4.13, 5.94, 5.54) were pure $Ca_3(AsO_4)_2 \cdot xH_2O$. Seven solids precipitated at initial pH values between pH = 6.84 to 12.94 and final pH values between 7.14 and 7.50 were mainly $Ca_3(AsO_4)_2 \cdot xH_2O$ with hydroxyarseanate apatite, $Ca_5(AsO_4)_3(OH)$, appearing as the solutions were in the process of precipitating. However, at equilibrium, the $Ca_3(AsO_4)_2 \cdot xH_2O$ solid appeared to be the most dominant at the final pH of 7.14 to 7.50.

At the Ca/As ratios of 1.67 and 4.0, the precipitated solids were comprised mainly $Ca_5(AsO_4)_3(OH)$ and some $Ca_3(AsO_4)_2 \cdot xH_2O$. The predominant compound formed at ratios of Ca/As = 2.0 was $Ca_4(OH)_2(AsO_4)_2 \cdot 4H_2O$, which appeared in conjunction with $Ca_5(AsO_4)_3(OH)$ and $Ca_3(AsO_4)_2 \cdot xH_2O$ but in minor amount. The XRD and SEM analysis indicated that the $Ca_3(AsO_4)_2 \cdot xH_2O$ compound found in all precipitates was independent on the Ca/As ratio and the pH of the mixing solution. These compounds were crystalline and had the distinct XRD pattern of $Ca_3(AsO_4)_2 \cdot xH_2O$. However, the structure and the grain size were related to the forming pH. For example, at the Ca/As = 1.25 and the initial pH = 4.09, and at the Ca/As = 1.5 and the initial pH = 3.04 and 4.06, the precipitated $Ca_3(AsO_4)_2 \cdot xH_2O$ was granular or platy. At the Ca/As = 1.5 and the initial pH = 4.75, the precipitated compound was equigranular and had a grain size of 5.40 μm. At the ratio Ca/As = 1.5 and the initial pH = 5.45, the small platy or leafy $Ca_3(AsO_4)_2 \cdot xH_2O$ with a grain size of 2.10 μm formed. In a word, the $Ca_3(AsO_4)_2 \cdot xH_2O$ solids precipitated at lower pH were more crystalline and had relatively larger grain size than those formed at higher pH.

Various calcium arsenates are still available commercially worldwide in spite of their toxicity. They are used mostly as insecticides.

Strontium Arsenates

Strontium forms several orthoarsenates of various degrees of ionization from arsenic acid.

Crystals of $M(AsO_3OH)$ (M = Sr and Ba) were synthesized under hydrothermal conditions. Single-crystal

X-ray structure investigations were performed. The average structure of $Sr(AsO_3OH)$ exhibits three crystallographically different hydrogen bonds; two of them are related by -1 symmetry [space group P-1, $a = 7.349(2)$ Å, $b = 7.057(2)$ Å, $c = 7.460(2)$ Å, $\alpha = 95.20(3)°$, $\beta = 104.78(3)°$, $\gamma = 88.11(3)°$, $Z = 4$]. Weak superstructure reflections were detected which are responsible for a larger cell volume [space group P-1, $a = 9.038(2)$ Å, $b = 11.732(2)$ Å, $c = 15.356(3)$ Å, $\alpha = 71.66(3)°$, $\beta = 75.16(3)°$, $\gamma = 89.11(3)°$, $Z = 16$]. All inversion centers restricting the hydrogen bonds are avoided in the supercell. As a result, a completely ordered atomic arrangement is obtained. The arsenate tetrahedra are linked by hydrogen bonds to polar chains with branches in [110] and [110], respectively. They are linked by the Sr atoms. The compounds $CaHPO_4$ (Monetite), $CaHAsO_4$ (Weilite), α-$SrHPO_4$ α-$NaHSO_4$, and $HgHPO_4$ have roughly the same arrangements of the cation and anion atoms. However, their hydrogen-bonding schemes are principally different. For the detailed comparison, the nonstandard unit cell was chosen for $Sr(AsO_3OH)$ [space group $F\bar{1}$, $a = 14.697$ Å, $b = 28.230$ Å, $c = 14.920$ Å, $\alpha = 95.20(3)°$, $\beta = 104.78(3)°$, $\gamma = 88.11(3)°$, $Z = 64$]. The structural refinement of $Ba(AsO_3OH)$ confirmed it as isotypic with γ-$Sr(PO_3OH)$, $K(SO_3OH)$, and $K(SeO_3OH)$ [space group Pbca $a = 8.581(2)$, $b = 9.896(2)$, $c = 19.417(4)$ Å, $Z = 16$]. $Sr(AsO_3OH)$ and $Ba(AsO_3OH)$ are characterized by short (strong) hydrogen bonds.

Strontium Orthoarsenate, $Sr_3(AsO_4)_2$, may be prepared by neutralizing aqueous arsenic acid with strontium hydroxide water slurry, or by adding ammonia to a solution of strontium monohydrogen arsenate in dilute hydrochloric acid. In either case, the precipitate is separated and well washed with water. The salt may also be obtained by fusing together at 450 °C equal quantities of sodium chloride and sodium orthoarsenate and adding the required proportion of strontium oxide. After cooling, the sodium salts are removed by washing with water. Colorless rhombic crystals, of density 4.601 g/cm^3, are obtained that are readily soluble in dilute acids. The salt melts at 1635 °C. When heated at 400–450 °C in hydrogen, reduction occurs to give strontium oxide, arsenic trioxide and water.

The previously uninvestigated atomic arrangements of six strontium arsenate(V) phases in the systems Sr–As–O–X (X = H, Cl) have been determined. These included in Table 4.21.

Single crystals of $Sr_3(AsO_4)_2$ and $Sr_5(AsO_4)_3Cl$ were grown from a borate and NaCl melt, respectively, whereas single crystals of α- and β-$SrAs_2O_6$ and of $Sr_5(AsO_4)_3OH$ were obtained under hydrothermal conditions. Microcrystalline samples of $Sr_2As_2O_7$ were prepared by solid-state reaction of As_2O_5 with $SrCO_3$ and, alternatively, by thermolysis of $SrHAsO_4$. Crystal structure determinations based on powder XRD data using the Rietveld method ($Sr_2As_2O_7$), and from single-crystal XRD data (all other phases) revealed isotypism with known structure types (except β-$SrAs_2O_6$ which represents a new structure type). $Sr_3(AsO_4)_2$ crystallizes in the $K_2Pb(SO_4)_2$ structure type. $Sr_2As_2O_7$ is isotypic with the high-temperature polymorphs of $Ca_2P_2O_7$ and $Sr_2V_2O_7$, but itself shows no polymorphism. $Sr_5(AsO_4)_3OH$ and $Sr_5(AsO_4)_3Cl$ crystallize with the hydroxylapatite and chloroapatite structure, respectively; $SrAs_2O_6$ is dimorphic. Like all other known $M^{II}As_2O_6$ metaärsenates (M = Mn, Co, Ni, Sr, Pd, Cd, Hg, Pb), the α-polymorph crystallizes in the $PbSb_2O_6$ structure type, whereas the novel β-polymorph is the first example of a $M^{II}As_2O_6$ superstructure with a doubled *c*-axis. Additional analytical methods using Raman spectroscopy and thermal analyses support the results of the X-ray structure work.

TABLE 4.21

$Sr_3(AsO_4)_2$
$Sr_2As_2O_7$
$Sr_5(AsO_4)_3OH$
$Sr_5(AsO_4)_3Cl$
α-$SrAs_2O_6$
β-$SrAs_2O_6$

In an early method, the following recipe was given: "Strontium Monohydrogen Arsenate, $SrHAsO_4$, may be prepared as follows: Strontium hydroxide is added slowly and with stirring to a solution of arsenic acid (containing 75 g As_2O_5 in 1.5 l H_2O) until a slight turbidity appears. Sodium hydroxide, free from carbonate, is then added to bring the pH to about 5.4, and the faintly turbid solution is heated and stirred until the monohydrogen orthoarsenate separates in fine crystals. The supernatant liquid is removed, again treated with sodium hydroxide and heated to give a further yield. The crystals are washed with alcohol and dried in air. They usually contain a slight excess of arsenic acid".

The salt, $SrHAsO_4$, may also be obtained by the action of hot water on strontium dihydrogen ortho-arsenate or on the pyroarsenate, where these salts hydrolyze to the more stable dibasic compound. It may also be obtained by mixing solutions of strontium chloride and sodium monohydrogen ortho-arsenate, adding HCl, heating the resulting solution and then adding ammonia to form the insoluble dibasic precipitate. In the last case, the anhydrous salt crystallizes out, but if the mother liquor is kept in an atmosphere of ammonia, the monohydrate, $SrHAsO_4 \cdot H_2O$, appears. The density of the latter is

3.606 g/cm^3 at 15 °C and of the anhydrous salt 4.035 g/cm^3. The monohydrate becomes anhydrous at 130 °C and at a higher temperature yields the pyroarsenate.

Strontium dihydrogen orthoarsenate, $Sr(H_2AsO_4)_2$, may be prepared by adding strontium hydroxide to an aqueous solution of arsenic acid and heating until a clear solution is obtained. On prolonged boiling, much of the monohydrogen salt crystallizes out and, after filtration, a further crop may be obtained from the mother liquor. The crystals should be washed with alcohol and dried.

The dihydrate, $Sr(H_2AsO_4)_2 \cdot 2H_2O$, may be obtained by treating strontium carbonate with an excess of arsenic acid. The crystals lose their water of crystallization at 240 to 250 °C and on further heating yields strontium meta-ärsenate, $Sr(AsO_3)_2$.

Monobasic strontium arsenate is triclinic with space group P1 and $a = 8.558$ Å, $b = 7.697$ Å, $c = 5.721$ Å, $\alpha = 92°35'$, $\beta = 109°59'$, $\gamma = 109°52'$, $V = 327.2$ Å^3, MW = 321.9321 g/mol, $d = 3.195$ g/cm^3, Z = 4. No piezoelectric effect has been noted. The four H-atoms were located. In one anion, two half-hydrogens, located at centers of symmetry, for symmetrical hydrogen bonds. The bond lengths of these O(H)–O(H) species vary between 2.436–2.444 Å. The other is relatively long at 2.875 Å. The angles between these hydrogen bonds is about 150° and the As···O bonds carrying the half-hydrogen species are 1.667 Å while the full hydrogen bonds are 1.727 Å.

Strontium pyroarsenate, $Sr_2As_2O_7$, is formed when the monohydrogen ortho-arsenate is heated above 360 °C or when potassium monohydrogen ortho-arsenate is fused with strontium oxide or carbonate. It is slightly soluble in mineral acids. A new related compound $Sr_5(As_2O_7)_2(AsO_3OH)$ was synthesized under hydrothermal conditions. It represents a previously unknown structure type and belongs to a group of a few compounds in the system $SrO–As_2O_5–H_2O$ $(As_2O_7)^{4-}$ besides $(AsO_3OH)^{2-}$ groups have not been described yet. The crystal structure of $Sr_5(As_2O_7)_2(AsO_3OH)$ was determined by single-crystal XRD (space group $P2_1/n$, $a = 7.146$ Å, $b = 7.142$ Å, $\beta = 93.67°$, $Z = 4$). One of the five symmetrically unique Sr atoms is in a trigonal antiprismatic coördination, whereas the other Sr atoms adopt the commonly observed coordination. The position of the hydrogen atom was located in a difference Fourier Map and subsequently refined with an isotropic displacement parameter. A very short hydrogen bond length O_h–HO(1) of 2.494 Å was noted. It belongs to the shortest known examples where the donor and acceptor atoms are crystallographically different. This hydrogen bond was confirmed by IR spectroscopy.

A basic arsenate of composition $Sr_3(AsO_4)_2 \cdot Sr(OH)_2$ has been obtained as a fine flaky precipitate by the action of sodium hydroxide and strontium hydroxide slurry water on an acidified solution of sodium monohydrogen orthoarsenate, care being taken to ensure the absence of carbonate. This salt is apparently not apatitic in nature since it does not have the molecular formula of $Sr_5(As)_4)_3OH$ but that of $\{Sr_2HAsO_4)_2$.

The crystal structure of the double salt, strontium potassium arsenate octahydrate, $SrKAsO_4 \cdot 8H_2O$, has been determined by single crystal XRD. The crystals are tetragonal, $a = 7.144$ Å, $c = 23.613$ Å, space group $I4_1/md$ (No. 109), $Z = 4$, $V = 1205.1$ Å^3, and $d = 2.258$ g/cm^3. All cations and anions in this compound are completely surrounded by water molecules. Sr^{2+} and K^+ ions are each coordinated to eight water molecules arranged in an approximately square antiprism. The $[Sr(H_2O)_8]^{2+}$ polyhedron shares one face of four water molecules with a $[K(H_2O)_8]^+$ polyhedron forming $O_4–Sr–O_4–K–O_4$ polyhedra. The $O_4–Sr–O_4–K–O_4$ units are linked together through a pair of edge-sharing linkages of the outer water molecules, alternating along the *a*-axis and *b*-axis. The hydrated-cation polyhedra define the host lattice, which accommodates the AsO_4^{3-} ion in the interstitial space. The environment of the AsO_4^{3-} ion consists of 16 water molecules; each oxygen atom is the acceptor in hydrogen bonds from four water molecules. Each water molecule is coordinated to one Sr and one K, and hydrogen bonded to two O atoms of two different AsO_4^{3-} ions. There is no hydrogen bonding between water molecules.

Very little is known concerning the metaarsenate compounds. If the monobasic compound is heated, a number of "meta"-compounds are formed but these have not been characterized:

$$nSr(H_2AsO_4)_2 + \text{heat} \Rightarrow Sr(AsO_3)_{2n} + H_2O$$

Whether strontium forms a cyclic or linear metaarsenate is still not known. The reaction can be used to form a pure glass $\Rightarrow [Sr(AsO_3)_2]_n$ whose physical properties have been described by Ropp but its molecular structure remains to be elucidated.

Although a considerable amount of attention has ensued concerning these five types of strontium orthoarsenates in the literature and academia, little awareness of them has resulted in industrial circles. None of them have found usage in products. The dibasic and tribasic salts are readily available commercially but only in small quantities.

Barium Arsenates

Tribasic barium orthoarsenate, $Ba_3(AsO_4)_2$, is formed as large colorless plates when a mixture of barium oxide, alkali chloride and alkali hydrogen orthoarsenate is fused at about 750 °C and allowed to cool. Early work concerning barium arsenates and their formation from solution did not control the pH of the solution (If the pH is controlled around 9.0, the dibasic compound results but

the tribasic compound is obtained at pH > 11.0). As a result, mixtures of compounds usually resulted. In one work, the following description was given:

> "The tribasic compound was formed by the action of ammonia on an aqueous solution of barium hydrogen arsenate. The product, however, varied in composition, barium ammonium arsenate sometimes being formed and barium orthoarsenate rarely. The latter salt retains water which may be lost at 150 °C. Definite hydrates were not obtained. The tribasic compound was found to be only slightly soluble in cold water. The anhydrous orthoarsenate had a density of 5.086 g/cm^3 and melted at 1605 °C. It was reduced by hydrogen at 400–450 °C to barium oxide, arsenic and water".

A study of the acid section of the system As_2O_5–BaO–H_2O at 30 °C suggested that the stable solid phases are barium monohydrogen orthoarsenate, $BaHAsO_4 \cdot H_2O$, barium dihydrogen orthoarsenate, $Ba(H_2AsO_4)_2 \cdot 2H_2O$, and the (3, 5)-hydrate of arsenic pentoxide, $3As_2O_5 \cdot 5H_2O$. Current thermodynamic data advocate barium arsenate $Ba_3(AsO_4)_2$ to be the highly stable phase. However, sufficient evidence is available to question the validity of the current data. In order to determine the solubility (pK_{sp}) and calculate the standard free energy of formation (ΔG_f) of $Ba_3(AsO_4)_2$, an equilibrium solubility study was conducted. The equilibrium experiments were carried out under three different ionic strength conditions for reaction times up to 45 days. Equilibrium was approached from both undersaturated and supersaturated initial conditions. The pK_{sp} for the dissolution of $Ba_3(AsO_4)_2$ was calculated to be 21.62. Correspondingly, a ΔG_f of -3101.2 ± 2.0 kJ/mol was calculated. This value is 166.9 kJ/mol more positive than the current literature value. Reevaluation of the solubility data from a previous work suggests that the pK_{sp} for the dissolution of $BaHAsO_4 \cdot H_2O$ is 24.64 and the corresponding ΔG_f is -1587.0 ± 2.5 kJ/mol. Tribasic barium arsenate has the CAS number of 56997-31-0.

Barium dihydrogen orthoarsenate, the monobasic salt, $Ba(H_2AsO_4)_2$, can be prepared by adjusting a solution of arsenic acid with sodium acetate to about 4.5 and then adding barium carbonate to precipitate the arsenate:

$$BaCO_3\ (\text{solid}) + 2H_3AsO_4\ (\text{aq}) \Rightarrow Ba(H_2PO_4)_2 \cdot 2H_2O\ (\text{solid}) + CO_2 + H_2O$$

The best way to form the monobasic barium arsenate is to dissolve the carbonate in an excess of arsenic acid and then to evaporate the solution at a low temperature to form the crystals. Both triclinic and orthorhombic barium dihydrogen arsenates are known. The triclinic form has the following unit-cell parameters: Space group = $\overline{1}$, $a = 7.0334$ Å, $b = 8.0437$ Å, $c = 7.2158$ Å, $\alpha = 104.45°$, $\beta = 109.46°$, $\gamma = 96.09°$, $Z = 2$, $d = 2.99$ g/cm^3. The crystal is built up of BaO_8 square antiprisms linked together along the axis, c. The AsO_4 tetrahedra are connected to the BaO_8 groups to constitute layers parallel to the (100) plane.

Two related arsenates with the general formula $Ba(ZnAsO_4)_2$ and $Ba(ZnPO_4)_2$ were synthesized by solid-state reaction. The divalent Zn^{2+} ions replace the two H^+ ions in the structures. X-ray structures of these compounds were indexed with a monoclinic unit cell, and their structures were refined by the Riewelt method, using reported atomic coordinates of Paracelsian, $Ba(AlSiO_4)_2$. The synthesis of the compounds was carried out by high-temperature sintering of stoichiometric amounts of $BaCO_3$, ZnO (first dried at 700 °C), NH_4HPO_4 and $As_2O_5 \cdot 0.6H_2O$ (a hygroscopic compound determined to be 3/5 by TGA analysis). The powder mixtures were thoroughly mixed, placed in a platinum crucible, and heated to 400 °C (with loss of H_2O, NH_3, CO_2). They were then reground and fired at 900 °C for 72 h with intermediate remixing. Finally, the samples were slowly cooled to room temperature.

Crystal parameters were shown in Table 4.22.

Phosphorus and arsenic are totally ordered in the tetrahedra. Each ZnO_4 tetrahedron shares its oxygen atoms with four PO_4 or AsO_4 and vice versa. The resulting structure may be described as a (100) pseudo-layered framework of 4- and 8-membered rings. One layer of the 4- and 8-membered rings of AsO_4 and ZnO_4 is shown in the following Fig. 4.72.

This structure is typical of the ortho-arsenates in general where the AsO_4 tetrahedra are coordinated with other MO_4 tetrahedra in any given structure.

The case of $Ba(ZnPO_4)_2$ seems very different in that the Paracelsian form was only obtained under hydrothermal conditions. The crystal form resulting from heating the initial mixture under atmospheric pressure is trigonal ($a = 5.32$ Å, $c = 8.02$ Å), with space group $P3m_1$, and may be related to the hexagonal form of Paracelsian by introducing complete Zn–P order among the tetrahedra.

TABLE 4.22

$Ba(ZnPO_4)_2$	$Ba(ZnAsO_4)_2$	
Crystal system	Monoclinic	Monoclinic
Space group	$P2_1/c$	$P2_1/c$
a in Å	8.5783	8.0883
b in Å	9.7383	9.9821
c in Å	9.1446	9.4089
β in degrees	91.394	91.465
V in cubic Å	763.69	827.00
Formula weight	458.024 g/mol	545.92 g/mol

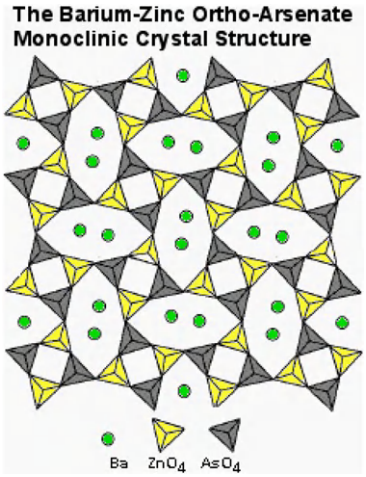

FIGURE 4.72

The change from one allotropic form to the other may be achieved either by pressure or temperature modification in agreement as shown in Fig. 4.73.

Barium Monohydrogen Orthoarsenate may be obtained as a gelatinous precipitate by adding barium hydroxide water slurry drop by drop to aqueous arsenic acid until the solution is alkaline to phenolphthalein (pH = 9.0). On shaking, the precipitate becomes crystalline. This salt can also be obtained in the form of small crystalline flakes by adding sodium hydrogen arsenate drop by drop to excess of barium chloride solution. The precipitate, $BaHAsO_4 \cdot H_2O$, is then dried at 100 °C. The crystals are transparent rhombic plates of density 3.926 g/cm^3 at 15 °C. If acetic acid is used, the crystals take the form of octahedra. When heated at 120 °C the salt loses its water of crystallization, and at 320 °C it loses constitutional water and forms barium pyroarsenate:

$$2\ BaHAsO_4 \cdot H_2O + \text{heat} \Rightarrow Ba_2As_2O_7 + 2\ H_2O$$

The monobasic salt, barium dihydrogen orthoarsenate, crystallizes as the dihydrate when tribasic barium orthoarsenate or barium monohydrogen orthoarsenate is dissolved in aqueous arsenic acid:

$$BaHAsO_4 \cdot H_2O\ (\text{solid}) + H_3AsO_4\ (\text{aq}) \Rightarrow Ba(H_2AsO_4)_2 \cdot 2H_2O\ (\text{solid})$$

This reaction was used in the past but was difficult to control. A better way to prepare the monobasic salt is to dissolve a $Ba(OH)_2$ or $BaCO_3$ slurry in excess arsenic acid solution. The crystals are monoclinic, with axial ratios $a{:}b{:}c = 1.100{:}1{:}0.625$ and $\beta = 108°34'$. The salt is only slightly soluble in water and in the presence of excess water changes to the monohydrogen arsenate:

$$Ba(H_2AsO_4)_2 + \text{x's } H_2O \Rightarrow BaHAsO_4\ (\text{solid}) + H_3AsO_4\ (\text{aq})$$

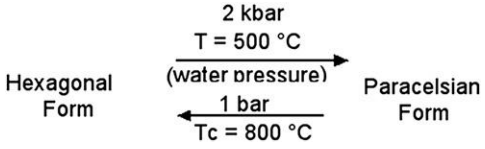

FIGURE 4.73

The solid product is readily soluble in hydrochloric acid but less soluble in acetic acid. When heated, it loses water, and above 230 °C barium metaärsenate, $Ba(AsO_3)_2$ remains. The latter may also be obtained by evaporation of a solution of the pyro-arsenate and calcination of the residue.

The anhydrate, $BaHAsO_4$ or $Ba(AsO_3OH)$ was synthesized under hydrothermal conditions and single-crystal X-ray structure investigations were performed. The average structure of $Ba(AsO_3OH)$ exhibits three crystallographically different hydrogen bonds. Two of them are related by $\bar{1}$ symmetry [space group $P\bar{1}$, $a = 7.349$ Å, $b = 7.057$ Å, $c = 7.460$ Å, $\alpha = 95.20°$, $\beta = 104.78°$, $\gamma = 88.11°$, $Z = 4$]. Weak superstructure reflections were detected which are responsible for a larger cell volume [space group $P\bar{1}$, $a = 9.038$ Å, $b = 11.732$ Å, $c = 15.356$ Å, $\alpha = 71.66°$, $\beta = 75.16°$, $\gamma = 89.11°$, $Z = 16$]. All inversion centers restricting the hydrogen bonds are avoided in the supercell. As a result, a completely ordered atomic arrangement is obtained. The arsenate tetrahedra are linked by hydrogen bonds to polar chains with branches in [110] and [110], respectively; they are linked by the Ba atoms. The compounds $CaHPO_4$ (monetite), $CaHAsO_4$ (weilite), β-$SrHPO_4$ β-$NaHSO_4$, and $HgHPO_4$ have roughly the same arrangements of the cation and anion atoms. However, their hydrogen-bonding schematics are predominantly different. For the detailed comparison, the nonstandard unit cell was chosen for $Sr(AsO_3OH)$ [space group F-1, $a = 14.697(3)$, $b = 28.230(5)$, $c = 14.920(3)$ Å, $\alpha = 95.20(3)°$, $\beta = 104.78(3)°$, $\gamma = 88.11(3)°$, $Z = 64$]. The structural refinement of $Ba(AsO_3OH)$ was confirmed isotropic with β-$Sr(PO_3OH)$, $K(SO_3OH)$, $K(SeO_3OH)$, and $Sr(AsO_3OH)$ and is characterized by short (strong) hydrogen bonds.

Barium Pyroarsenate, $Ba_2As_2O_7$, is formed when barium monohydrogen orthoarsenate is ignited, or when barium oxide is fused with an alkali hydrogen arsenate. In the latter case, it may be extracted with anhydrous glycerol. In contact with cold water, the hexahydrate, $Ba_2As_2O_7 \cdot 6H_2O$, is formed. Boiling water converts it to the ortho-arsenate.

Very little is known concerning the metaarsenate compounds. If the monobasic compound is heated, a number of "meta"-compounds are formed but these have not been characterized:

$$n\ Ba(H_2AsO_4)_2 + \text{heat} \Rightarrow Ba(AsO_3)_{2n} + H_2O$$

Whether barium forms a cyclic or linear metaarsenate is still not known. The reaction can be used to form a pure glass ⇒ $[Ba(AsO_3)_2]_n$ whose probable properties have been described by Ropp but its molecular structure remains to be elucidated.

Although the five above compounds have been described in the technical literature, they have not been well received from those in industry. There are no usages found for barium arsenates or for products that use any of these compounds. One of these compounds is offered for sale commercially but only from a few manufacturers worldwide.

Radium Arsenates

No radium arsenate compounds are known. This is likely due to the scarcity and high price of radioactive ^{222}Ra compounds and to the lack of interest in industry.

4.4. ALKALINE EARTH ANTIMONY COMPOUNDS

Antimony forms a limited number of compounds with the alkaline earths. This is due primarily to the fact that antimony, as Sb^{3+}, is almost as electropositive as any of the alkaline earth cations. The compounds that are stable are based upon the acids. Antimony is sufficiently electropositive in nature that acids such as "antimonous acid" ($H_3Sb^{3+}O_3$) or "antimonic acid" ($H_3Sb^{5+}O_4$) do not exist, or cannot be isolated from solution. In chemistry, an **antimonite** refers to salts of antimony(III), such as $NaSb(OH)_4$ (a double-salt) and $NaSbO_2$ (metaantimonite). Formally, these are salts of antimonous acid (antimonious acid—"$Sb(OH)_3$") whose existence in solution is dubious. Attempts to isolate it generally form $Sb_2O_3 \cdot xH_2O$, antimony(III) oxide hydrate, which slowly transforms into Sb_2O_3 (which is the more stable form).

The **antimonate** ion is $Sb(OH)^{6-}$ and an **antimonate** (compound) refers to a substance that contains the antimony(V) ion. In acid conditions, this forms antimony pentoxide, Sb_2O_5; in basic conditions, the antimonate ion, $Sb(OH)_6^-$ ion exists.

Like its horizontal neighbor in the periodic table, tellurium, Te and unlike the other elements in this Group, antimony(V) is commonly hexa-coordinate, for example in the unit $Sb(OH)_6^-$. Tetra-coordinate units, $Sb(OH)_4^-$, are not common. Thus, the known "antimonates" are usually prepared by solid-state reaction of Sb_2O_5 and the corresponding alkaline earth hydroxide. Even though many varying ratios of the two reactants have been attempted in an effort to form compounds similar to the phosphates and arsenates, only certain compositions of the individual alkaline earths have proven to be stable. Because antimony eschews aqueous solutions (due to the observed fact that the oxides, Sb_2O_3 and Sb_2O_5), are more stable than the acids themselves when contacted by water, it is the oxides that appear in many cases. Thus, antimonites and antimonates tend to decompose in contact with water to form the oxides, respectively. However, the alkali antimonates are stable in water and can be used to prepare some of these salts.

In addition, antimony metal forms a series of compounds with the alkaline earth metals, called antimonides.

4.4.1. Alkaline Earth Antimonites

Beryllium Antimonite

Beryllium antimonite can be prepared by firing BeO and Sb_2O_3 together in an inert atmosphere such as argon at about 1000 °C. However, this system has not been studied at all. The basic compounds that can be formed have not yet been identified. There is no description of the solution chemistry of beryllium antimonites in which sodium antimonite is reacted with a soluble beryllium salt like the chloride. Perhaps this is due to the fact that Be forms hydroxl complexes like $Be_x(OH)_y^{(2x-y)+}$ in solution. The technical literature is completely devoid of any description either by academia or industry in the form of structure determinations or products involving such compounds. Be is used but mostly in the form of the metal.

The beryllium antimonites, if they exist, have no CAS number nor are they offered for sale commercially.

Magnesium Antimonite

Magnesium antimonite can be prepared by the solid-state reaction of Sb_2O_3 and MgO or $MgCO_4$ wherein the reaction is carried out in an inert atmosphere like argon at about 1100 °C:

$$MgO + Sb_2O_3 \Rightarrow MgSb_2O_4$$

By varying the molecular ratio of MgO to Sb_2O_3, a number of compounds is expected to result. However, there is no record of this ever having been accomplished. The early work in the 1800s used an aqueous method to define the now known magnesium antimonites in which sodium or potassium antimonite, $K_2Sb_2O_4$, reacted to form the stable compound, $MgSb_2O_4$. This compound was reported in 1889 as the precipitation product, $Mg(SbO_2)_2 \cdot 12H_2O = MgO \cdot Sb_2O_3 \cdot 12H_2O$, but no corroborating evidence has since emerged.

The only available reference to magnesium antimonite identified the product of a 1:1 ratio of MgO and Sb_2O_3 as $MgSb_2O_4$. This compound was synthesized by a phase-equilibration technique and identified by XRD to be $MgSb_2O_4$. To determine the standard Gibbs energies of formation of this antimonite, the

e.m.f. values of the following galvanic cells were measured:

$$\text{Pt, Re/Sb (solid, liq), } Sb_2O_3 \text{ (solid, liq)/} ZrO_2 + \text{MgO(or } Y_2O_3\text{)/air, Pt,}$$

$$\text{Pt, Re/Sb (liq), } MgSb_2O_4 \text{ (solid), MgO (solid)/} ZrO_2 + \text{CaO/air, Pt,}$$

The resulting free energies of formation were determined:

$$\Delta G^0/\text{kJ/mol} = -687.7 + 0.2425\ T \text{ (773–904 K),}$$
$$[\text{for 2 Sb (solid)} + O_2 \text{ (gas)} \Rightarrow Sb_2O_3 \text{ (solid)}]$$
$$\Delta G^0/\text{kJ/mol} = -730.2 + 0.2895\ T \text{ (904–929 K),}$$
$$[\text{for 2 Sb (liq)} + O_2 \text{ (gas)} \Rightarrow Sb_2O_3 \text{ (solid)}]$$
$$\Delta G^0/\text{kJ/mol} = -683.1 + 0.2385\ T \text{ (929–1095 K),}$$
$$[\text{for 2 Sb (liq)} + O_2 \text{ (gas)} \Rightarrow Sb_2O_3 \text{ (liq)}]$$
$$\Delta G^0/\text{kJ/mol} = -78.9 + 0.0495\ T \text{ (929–1101 K),}$$
$$[\text{for } Sb_2O_3 \text{ (liq)} + \text{MgO (solid)} \Rightarrow MgSb_2O_4 \text{ (solid)}]$$

There are no publications that directly address the formation and properties of any magnesium antimonites in the scientific literature and no mention can be found in the current reference books. No products have found their way into industry and no CAS numbers exist at this time.

Calcium Antimonite

There are three calcium antimonites that have been established in the CaO–Sb_2O_3 system. These are: $CaSb_2O_4$, Ca_2SbO_5 and $Ca_4Sb_2O_7$. These compounds can be prepared by firing the carbonate or oxide with the appropriate ratio of CaO/Sb_2O_3 in argon at about 1000 °C:

$$\text{CaO} + Sb_2O_3 \Rightarrow CaSb_2O_4 \text{ (1:1)}$$

To determine the standard Gibbs energies of formation of this antimonite, e.m.f. values of the following galvanic cells have been measured:

$$\text{Pt, Re/Sb (solid, liq), } Sb_2O_3 \text{ (solid, liq)/} ZrO_2 + \text{CaO(or } Y_2O_3\text{)/air, Pt,}$$

$$\text{Pt, Re/Sb (liq), } Ca_4Sb_2O_7 \text{ (solid), CaO (solid)/} ZrO_2 + \text{CaO/air, Pt.}$$

Standard Gibbs free energies of formation of double oxides coexisting with liquid antimony from CaO (s) and Sb_2O_3 are derived as follows:

$$4\text{CaO(solid)} + Sb_2O_3\text{(liq)} = 4\text{CaO}\cdot Sb_2O_3\text{(solid);}$$
$$\Delta G^\circ/\text{kJ} = -130.3 \text{ to } 0.0031\ \text{T/K}$$
$$2\text{CaO(solid)} + Sb_2O_3\text{(l)} = 2\text{CaO}\cdot Sb_2O_3\text{(solid);}$$
$$\Delta G^\circ/\text{kJ} = -121.7 \text{ to } 0.00005\ \text{T/K}$$
$$\text{CaO(solid)} + Sb_2O_3\text{(l)} = \text{CaO}\cdot Sb_2O_3\text{(solid);}$$
$$\Delta G^\circ/\text{kJ} = -98.3 + 0.0197\ \text{T/K.}$$

The activities of Sb_2O_3 and CaO in the two-phase regions at 1000 and 1100 K were derived and the most stable double oxide was determined to be CaO·Sb_2O_3 in this system. By X-ray diffractometry, it was found that 3CaO·Sb_2O_3 (s) cannot coexist with Sb_2O_3.

In another work, the phase composition of crystalline mechanochemical synthesis products in the CaO–Sb_2O_3–Bi_2O_3 system was determined (Mechanochemical reactions consists of using a Rotary-Mill, equipped with "mill-stones", to grind the reactants together and cause a solid-state reaction to occur). Of the known phases in this system, only three could be prepared mechanochemically: $Ca_2Sb_2O_5$, $CaSb_2O_4$, and $Ca_2Bi_2O_5$ (all-fcc). A new metastable phase, "γ-Bi_2O_3", with an orthorhombic structure close to that of the high-temperature, fluorite phase α-Bi_2O_3, was obtained by mechanical processing at 30 °C. The mechanochemical yield of primary crystalline products was shown to be several times higher than that of secondary products. A broad composition range was found in which perovskite and fluorite phases are in mechanochemical equilibrium. The composition dependence of the lattice parameter of the metastable fluorite phase $Bi_{2-x}Sb_xO_3$ was found to be the opposite of the one predicted by Vegard's law. Metastable-mixed oxides undergo phase transformations during heating (starting at 280 °C in the case of the ternary perovskite phase). The compound, $Bi_{2\text{-}x}Ca_xO_{3-0.5x}$ (fluorite structure) experiences a transformation at 400 °C, accompanied by oxygen loss. During heating in air, Sb_2O_3-containing fluorite phases partially stabilize owing to oxidation but, nevertheless, undergo structural transformations above 480 °C. The transformation of $Sb_{2-x}Ca_xO_{3-0.5x}$ metastable fluorite solid solutions near 500 °C in air is accompanied by the formation of needle-like Sb_2O_3 crystals. A mechanism was proposed for the extremely rapid growth of such crystals. Extrusion of the Sb_2O_3 results from the fluorite decomposition in agglomerates through triple junctions of aggregates and through cracks in the surface layer of agglomerates.

Opacifiers, such as tin oxide and calcium antimonite, can be added to create opal-like or opalescent glass. Antimony reacts with the lime in the glass matrix to precipitate **calcium antimonite** crystals creating a white with high opacity. Indeed, there is evidence that early Egyptian craftsmen (1570–1292 BC), could have produced $Ca_2Sb_2O_5$ by using mixtures of Sb_2O_3 with calcium carbonates (atomic ratio Sb/Ca = 1) heat treated between 1000 and 1100 °C. This method has since been used to produce glass items for decorative items used in the home. A very opalescent glass can be produced. Since the glass making is usually done in air, there

is some question concerning whether the Sb is in the +3-state or the +5 state.

Calcium antimonite has no CAS number and is not used directly in industry. A paucity of technical papers concerning this compound(s) exists in the literature. It has only been described in conjunction with other antimonites, as detailed above (never by itself). Perhaps, this is due to its lack of stability in air. It is not offered for sale commercially.

Strontium Antimonite

Strontium antimonite can be prepared by the solid-state reaction of the oxides of Sr and Sb in an inert atmosphere at a temperature about 850 °C:

$$SrO + Sb_2O_3 \Rightarrow SrSb_2O_4$$

A detailed investigation of the $SrO–Sb_2O_3$ binary system was reported. The samples were prepared at 1200 °C under ambient inert gas pressure, and the binary compounds, $Sr_2Sb_2O_7$ and $SrSb_2O_4$, were confirmed. The former contains Sb(V) whereas the latter contains Sb(III), the stable compounds in this binary oxide system. A new mixed oxide, $Sr(Sr_{0.5}Sb_{0.5})O_{3-y}$, showing a double perovskite-related structure was described. It gives rise to $Sr_{(1.5-x)}Sb_{(0.5+x)}O_{3-y}$ solid solution ($0 \le x \le 0.64$), the lattice parameter of which was determined as a function of x by means of XRD.

The synthesis, structural and microstructural characterization of a strontium antimonite, $Sr_{1.5}Sb_{0.5}O_{3-y}$ (where $y = 0.25$), results in a cubic, double-perovskite structure and a large concentration of oxygen vacancies with no apparent long-range order. High-resolution electron microscopy indicates, however, that short-range ordering phenomena may occur. Electrical conductivity in this solid-state compound is independent of oxygen partial pressure (pO_2) for $pO_2 < 10^{-1.25}$ atmosphere, typical of ionic transport ($\sigma \sim 10^{-4}$ S/cm at 600 °C), whereas the conductivity is dominated by p-type charge carriers at higher pO_2 pressures. A number of substitutions have been made in this double-perovskite composition.

Several compositions in the system $Sr_{(1.45-x)}Ca_xSb_{0.55}O_{3-y}$ ($0 < x < 1.45$) have been synthesized by solid-state reaction at 1000 °C and investigated by powder XRD and EDS microanalysis. They exhibit good thermal stability up to 1200 °C. The solid solution range was delimited at the composition $0 < x < 1.1$. For quantities of Ca^{2+} higher than 1.1, the amount of solid solution decreases and another phase, $Ca_6Sb_2O_{10}$, appears.

A new phase, $Sr(Sr_{0.5}Sb_{0.5})O_{3-y}$ perovskite structure was discovered. This phase is the origin of a solid solution of SrO and $SrSb_2O_4 = Sr_{(1.5-x)}Sb_{(0.5+x)}O_{3-y}$, where x ranges between 0.00 and 0.64 ($0 \le x \le 0.64$) with the lattice parameter of a "double-perovskite", as determined by XRD. This is essentially a "strontium antimonite-strontiate". This oxygen-deficient and ordered perovskite-type structure was synthesized readily by a solid-state reaction in air at 1200 °C. The structure of the $Sr(Sr_{0.5}Sb_{0.5})O_{3-y}$ phase as determined by Rietveld analysis using XRD data, corresponds to an ordered perovskite with face-centered cubic symmetry, space group $Fm3m$ (No. 225) and lattice parameters, $a = 8.3136$ Å, $V = 574.602$ Å^3 and $Z = 8$. An important structural feature of $Sr(Sr_{0.5}Sb_{0.5})O_{3-y}$ is the oxygen deficiency and the displacements of oxygen atoms from their ideal positions toward the Sb^{5+} cations. This fact leads to an alternating arrangement of larger $[SrO_6]$ and smaller $[SbO_6]$ octahedra (B-sites), the remaining Sr^{2+} being in the larger 12-fold coordinated A-sites. The thermal stability of the $Sr(Sr_{0.5}Sb_{0.5})O_{3-y}$ phase was revealed because its melting point is 1480 °C, and it does not decompose at that point. Subsequent quenching of the liquid phase gives rise to a glassy material.

These double perovskites, as solid electrolytes at elevated temperature, are of interest for use in solid oxide fuel cells.

In another study, a penta-fluoroantimonite, $Sr_2Sb_2F_{10}$, in which all of the oxygen atoms (O^{2-}) have been replaced by (F^-) atoms has been synthesized. Strontium pentafluoroantimonite has the molecular weight of 354.8026 g/mol, and is orthorhombic with space group = Pbcm and $a = 4.378$ Å, $b = 8.853$ Å, $c = 11.233$ Å, $V = 435.3$ Å^3, $Z = 4$. The three-dimensional network consists of isolated SbF_5^{2-} units which are interconnected by ten-coordinated Sr^{2+} ions. The geometry of these pentafluoroantimonite ions is approximately square pyramidal with the Sr atom outside of the pyramid, below the four F^-atoms constituting the basal plane. Thus, $SrSbF_5$ is essentially an "Antimonite" in structure if not in chemical composition.

The literature is inadequate in terms of description of the physical and chemical properties of these strontium antimonites. No CAS numbers can be found. This class of salts has received little attention from academia and none from industry. No commercial suppliers offer these salts for sale.

Barium Antimonite

Barium antimonite can be prepared by firing the oxide with trivalent antimony oxide in an inert atmosphere at about 800–850 °C:

$$BaO + Sb_2O_3 \Rightarrow BaSb_2O_4$$

The system, $BaO \cdot Sb_3O_3$ has been investigated. The stable compounds are: $Ba_3Sb_2O_6$ and $Ba_2Sb_2O_5$. These compounds have been found to be triclinic and orthorhombic, respectively. The X-ray data are: barium antimonite(III)–$Ba_3[SbO_3]_2$, (triclinic, $P\bar{1}$, $a = 6.152$ Å,

$b = 9.814$ Å, $c = 12.154$ Å, $\alpha = 74.683°$, $\beta = 89.710°$, $\gamma = 71.464°$, $Z = 2$, $R_1 = 0.0802$) and $Ba_2[Sb_2O_5]$ (orthorhombic, Cmcm, $a = 4.010$ Å, $b = 14.506$ Å, $c = 6.366$ Å, $Z = 4$, $R_1 = 0.0589$). These compounds have been synthesized from melts of elemental barium and antimony oxide Sb_2O_3 at a temperature of 800 °C. Their oxoantimonite building units are strongly influenced by the stereochemically active lone pair electrons of the trivalent Sb(III) element. In the Ba-rich compound $Ba_3[SbO_3]_2$, isolated α-tetrahedra units, $[SbO_3]^{3-}$, are present; in $Ba_2[Sb_2O_5]$ which crystallizes with the $Sr_2Bi_2O_5$ structure type, two of these α-tetrahedra are condensed to form nuclear units $[Sb_2O_5]^{4-}$. The two compounds were compared in terms of structure and bonding with the alkali antimonites on one hand and with the alkaline earth bismutates on the other.

In another study, a penta-fluoroantimonite, $Ba_2Sb_2F_{10}$, in which all of the oxygen atoms (O^{2-}) have been replaced by (F^-) atoms has been synthesized. Barium pentafluoroantimonite has the molecular weight of 354.8026 g/mol, and is orthorhombic with space group = Pbcm and $a = 4.676$ Å, $b = 9.313$ Å, $c = 11.213$ Å, $V = 488.3$ Å^3, $Z = 4$. The three-dimensional network consists of isolated SbF_5^{2-} units which are interconnected by ten-coördinated Ba^{2+} ions. The geometry of these pentafluoroantimonite ions is approximately square pyramidal with the Ba atom outside of the pyramid, below the four F^-atoms constituting the basal plane. Thus, $BaSbF_5$ is essentially an "Antimonite" in structure if not in chemical composition.

The scientific literature concerning the barium antimonite salts are scarce indeed and no CAS numbers have been assigned to a commercial or academic product. None of these salts have been investigated in any detail other than those documented herein. There are no industrial products that use such antimonite salts and no patents concerning them.

Radium Antimonite

Radium antimonite could be prepared by firing the oxide with antimony trioxide in an inert atmosphere around 750–800 °C:

$$RaO + Sb_2O_3 \Rightarrow RaSb_2O_4$$

However, there is no record of anyone having done so. There is no demand for any of the possible or probable radium antimonites and the likelihood that they will ever be prepared is little to none because of the instability of such compounds in air and the intense radioactivity of ^{226}Ra atom.

4.4.2. Alkaline Earth Antimonates

These salts are generally prepared by reacting the oxides together in air.

Beryllium Antimonate

Beryllium antimonate can be prepared by firing BeO with Sb_2O_5:

$$BeO + Sb_2O_5 \Rightarrow BeSb_2O_6$$

The system, BeO/Sb_2O_5 has not been studied in any detail. Beryllium forms a mixed salt, $Na_2O{\cdot}8BeO{\cdot}Sb_2O_5 = Be_8Na_2Sb_2O_{14}$, which is a colorless, cubic compound with a density of 6.98 g/cc and a molecular weight of 585.6742 g/mol. Few papers are available describing the various salts of beryllium antimonate compositions.

Swedenborgite is a sodium-beryllium antimonate containing small amounts of Ca^{2+} ions which have been incorporated into the structure via the charge-compensation scheme:

$$Ca^{2+} + V^+ \Leftrightarrow 2Na^+$$

where "V" is a cation vacancy. Thus the molecular formula for Swedenborgite is:

$$(Na_{1-3x}Ca_xV_{2x})Be_4SbO_7$$

This mineral $[(Na_{0.88}Ca_{0.04}V_{0.08})Be_4SbO_7]$ is hexagonal, with unit-cell parameters: $a = 5.4317$ Å, $c = 8.8571$ Å, $V = 226.31$ Å^3, space group P63mc, $Z = 2$. The crystal structure was refined to an R index of 1.2. There is one *Sb* site occupied by Sb^{5+} and coordinated by an octahedron of O atoms, with a <Sb–O> distance of 1.97 Å. There are two *Be* sites that are each occupied by Be^{2+} and coordinated by a tetrahedron of O atoms, with a grand <Be–O> distance of 1.64 Å. There is one *Na* site, coordinated by 12 O atoms and occupied primarily by Na. The structure consists of layers of corner-sharing (BeO_4) tetrahedra and (SbO_6) octahedra that link together to form a dense framework. The resulting arrangement consists of (SbO_6) octahedra alternating with $[Be_4O_{13}]$ clusters that are fragments of the bromellite (BeO) structure. Small amounts of Ca are incorporated into the structure via the substitution $Ca + V_{Be} \Rightarrow 2Na$. The actual structure is shown in the following Fig. 4.74.

The structure can also be described as $[Be_4O_{13}]$ clusters and (SbO_6) octahedra placed at the vertices of a 6^3 net, and linked by sharing polyhedron vertices. Significant in this description is the fact that the $[Be_4O_{13}]$ cluster is a fragment of the bromellite (BeO) structure. Bromellite has the wurtzite structure and consists of identical layers of corner-sharing (BeO_4) tetrahedra that occupy the vertices of a 3^6-net. If we remove three Be and one O atoms per unit cell for such a layer, we obtain the pattern of (BeO_4) in the A layer of Swedenborgite. If we remove one Be atom per unit cell from a BeO layer, we obtain the B layer of Swedenborgite. Addition of Sb^{5+} and Na^+

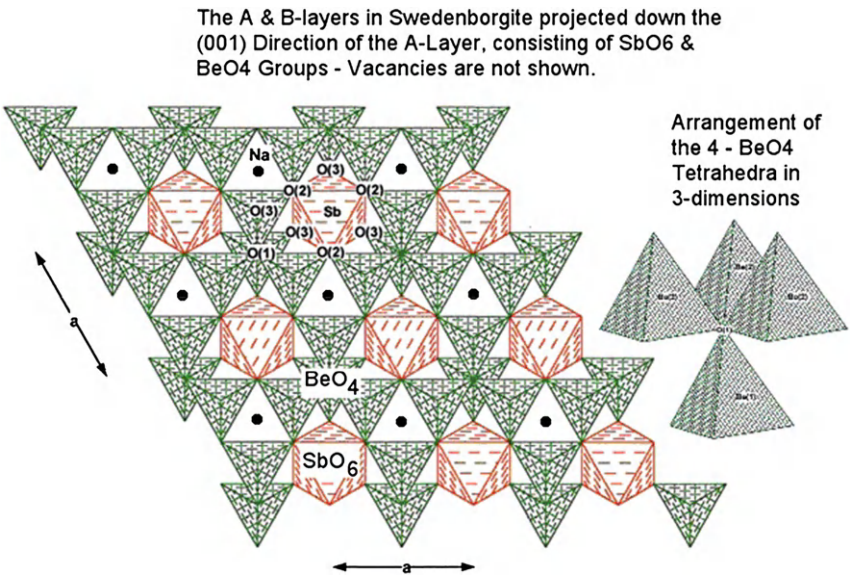

FIGURE 4.74

to the interstices of these layers results in the Swedenborgite structure:

$$Be_8O_8{-}Be_4{-}O + Sb_{5+} + Na \Rightarrow NaBe_4Sb^{5+}O_7.$$

Although several beryllium antimonate minerals have been studied, the system $BeO{\cdot}Sb_2O_5$ has not been studied in detail. No CAS number has been assigned and the papers dealing with beryllium antimonates are exceedingly rare. Even the early work of the 1880s do not list such compounds. No interest in industry has been shown in these compositions, due mainly to a lack of chemical and physical information concerning them. They are not available commercially.

Magnesium Antimonate

Magnesium antimonate can be prepared by firing MgO and antimony pentoxide in air at 1000 °C for 18 h:

$$MgO + Sb_2O_5 \Rightarrow MgSb_2O_6$$

The system $MgO{-}Sb_2O_5$ has not been studied in detail to establish the most stable antimonates. Indeed, the early literature cited compounds prepared in aqueous solution. The following compound was presented (1889), but no corroborating evidence has since emerged: $Mg(SbO_3)_2{\cdot}12H_2O$. It was said to be soluble in hot water.

In another preparation, $MgSb_2O_6$ samples were synthesized by a solution method, using Sb_2O_3 and H_2O_2 added to water and kept at 90 °C with stirring for 1.0 h to form Sb_2O_5. Stoichiometric $MgCl_2$ in aqueous solution was poured into the antimony pentoxide solution slowly and heated until evaporation of the solvent was achieved. After drying, the samples were pressed into pellets and sintered at 1320 K.

Single crystals of the compound, tetramagnesium diantimonate(V) $\{(MgO)_4[(Sb_2O_5)_2]$ or $Mg_4Sb_4O_{14}\}$, were obtained by a slow cooling method using K_2CO_3. The structure is isotypic with ilmenite, whose structure comprises the alternate stacking of layers consisting of metal–oxygen coordination octahedra. In each layer, the octahedra are connected by edge sharing so as to produce holes. One of the two nonequivalent metal sites is fully occupied by Mg (3-symmetry), while the second metal site (3-symmetry) is disordered and occupied by Mg and Sb with occupation factors of 1/3 and 2/3, respectively.

Other than this tetramagnesium diantimonate compound, no description of other Mg-antimonates has ensued to date. However, several antimonate minerals have been described.

"Bystromite" occurs in the antimony deposits of El Antimonio district as a tetragonal (ditetragonal dipyramidal) compound with lattice parameters of: $a = 4.68$ Å, $c = 9.21$ Å, $Z = 2$; $V = 201.72$ Å^3, $d = 5.9$ g/cc, Tetragonal-Bi-tetragonal Di-pyramidal, Point Group: (4/m,2/m,2/m), Space Group: $P4_1/mnm$, with two formula groups in the unit cell. The structure is of the trirutile type, and the mineral is isomorphous with the mineral, Tapiolite.

"Brandholzite", a magnesium antimony hydroxide hydrate mineral, $Mg(H_2O)_6[Sb(OH)_6]_2$, has been discovered in Au–Sb–Quartz veins of the former mining district of Brandholz-Goldkronach, Fichtelgebirge, Germany. This mineral is associated with stibnite and antimony ochers and forms colorless, plate-like crystals

up to ~1 mm in size. Natural as well as synthetic samples obtained by slow evaporation of an aqueous solution exhibit {100} twinning, leading to a pronounced I_m pseudo-symmetry. The crystal structures of Brandholzite and its synthetic analogue were investigated using single-crystal X-ray CCD data. It is trigonal, space group $P3$, $Z = 6$, $a = 16.119$ Å, $c = 9.868$ Å, (Brandholzite), and $a = 16.113$ Å, $c = 9.868$ Å, (synthetic analog). The structures are isotypic with "Bottinoite", $Ni(H_2O)_6[Sb(OH)_6]_2$, and are built up by nearly regularly shaped, isolated $Mg(H_2O)_6$ and $Sb(OH)_6$ octahedra which are interconnected by hydrogen bonds only.

Other than the above described compounds, no other combinations of $MgO \cdot Sb_2O_5$ have been found. No CAS numbers have been issued for any of these compounds and none of them is available commercially.

Calcium Antimonate

Calcium antimonite can be prepared by the solid-state reaction in air of the oxides. **A major study of the $CaO \cdot Sb_2O_5$ system had led to a seminal discovery**, namely that the stable phases obtained depend upon the firing temperature employed and less upon the ratio of CaO/Sb_2O_5 used. For the 1Ca:1Sb composition, a calcination at 1300 °C led to a pure $Ca_2Sb_2O_7$ weberite phase as the stable compound. Thus, the stable products obtained were: $1Ca:1Sb = CaSb_2O_4$ at 873 K (600 °C), $2Ca:1Sb = Ca_2Sb_2O_7$ at1073 K (800 °C) that is stable at 1573 K(1300 °C).

A study of the preparation of these two compounds has been made and it has been established that $Ca_2Sb_2O_7$ is orthorhombic. Calcium fluoantimonate was also synthesized for the first time and found to have the cubic structure of the mineral "Romeite". The probable formula is $Ca_4Sb_4O_{11}F_2$.

Actually, the early literature cited compounds prepared in aqueous solution. The following compounds were presented (1889), but no corroborating evidence has since emerged: $Ca(SbO_3)_2 \cdot 5H_2O$. Sodium meta-antimonate was used as the source but no mention of the pH or concentrations used was forthcoming.

Metastable antimony(V) oxide compounds were prepared via mechanochemical reactions in mixtures of CaO and the antimonite, Sb_2O_3, followed by mild oxidizing heat treatment and calcium leaching in a hydrochloric acid solution. They were characterized by XRD and thermal analysis. The synthesized compounds have the pyrochlore structure or a monoclinic pyrochlore-like structure ($Ca_{16}Sb_8^{3+}Sb_8^{5+}O_{48}$).

During the eighteenth Egyptian dynasty (1570–1292 BC), opaque white, blue and turquoise glasses were opacified by calcium antimonate crystals dispersed in a vitreous matrix. The technological processes as well as the antimony sources used to manufacture these crystals remain unknown. A new light on glass making history has been demonstrated in that, contrary to what was thought, Egyptian glassmakers did not use in situ crystallization but first synthesized calcium antimonate opacifiers, which do not exist in nature, and then added them to the molten glass. By using TEM for the first time in the study of Egyptian opaque glasses, it was shown that these opacifiers were nanocrystals. Prior to this research, such a process for glassmaking had not been suggested for any kind of ancient opaque glass production. Studying various preparation methods for calcium antimonate, it is supposed that Egyptian craftsmen (1570–1292 B.C.), could have produced $Ca_2Sb_2O_7$ by using mixtures of Sb_2O_3 or Sb_2O_5 with calcium carbonates (atomic ratio $Sb/Ca = 1$) heat treated between 1000 and 1100 °C.

Nonetheless, the literature is sparse and few papers dealing directly with calcium antimonates, their physical and chemical properties and uses in industry are rare.

Calcium antimonate as $CaSb_2O_4$ has the CAS number of 55200-87-8 and is offered for sale commercially.

Strontium Antimonate

Strontium antimonite can be prepared by the reaction of the oxides in proper proportion: For the 1:1:compound, the reaction takes place at 850 °C:

$$SrO + Sb_2O_5 \Rightarrow SrSb_2O_6 = Sr(SbO_3)_2$$

The system, SrO/Sb_2O_5 has not been thoroughly explored. Several different samples were prepared in the open air at a temperature of 1200 °C by varying the SrO/Sb_2O_5 ratio. The binary compounds $Sr_2Sb_2O_7$ and $SrSb_2O_6$ have been found and appear to be the most stable of those likely to form. Indeed, the early literature cited compounds prepared in aqueous solution. The following compound was presented (1889), but no corroborating evidence has since emerged of the existence of a hydrate, $Sr(SbO_3)_2 \cdot 6H_2O$. $SrSb_2O_6$ was synthesized by solid-state reactions between $Sr(NO_3)_2$ and Sb_2O_3 in air at 1150 °C for 24 h. This compound is essentially a meta-antimonate.

The Weberite, $Sr_2Sb_2O_7$ has been synthesized by reacting 2 mols of SrO to 1 mol of Sb_2O_5 at 1000 °C. Its molecular weight is 530.7432 g/mol. It is orthorhombic with space group = Imma and unit-cell parameters of $a = 7.4557$ Å, $b = 10.3708$ Å, $c = 7.6860$ Å, $V = 594.289$ Å^3, $Z = 4$. Although the Ca and Cd-salts form both the pyrochlore and weberite structure, Sr forms only the weberite modification. This compound shows high "photo-catalytic" activity in the presence of certain organic compounds like benzene and has been used to destroy such compounds when the mixture is exposed to UV light such as quartz-mercury lamps that emit 254 nm radiation.

This solid-state-prepared $Sr_2Sb_2O_7$ showed high photo-catalytic activity for benzene degradation under 254 nm UV irradiations, and no deactivation was observed during the prolonged photo-catalytic reaction. However, the photo-catalytic performance of a hydrothermally synthesized $Sr_2Sb_2O_7$ was superior to both P25 and the $Sr_2Sb_2O_7$ prepared by the conventional solid-state reaction. In the presence of the surfactant, cetyltrimethyl ammonium bromide (CTAB) or poly (vinyl pyrrolidone) (PVP), different three-dimensional hierarchical flower-like architectures of $Sr_2Sb_2O_7$, $Sr_2Sb_2O_7$ (CTAB) and $Sr_2Sb_2O_7$ (PVP) were successfully synthesized via a facile hydrothermal process using Sb_2O_5 as the starting material. The obtained samples were characterized by XRD, N_2-sorption BET surface area, UV-Visible diffuse reflectance spectroscopy, SEM, TEM, high-resolution transmission electron microscopy, and FT-IR spectroscopy. These are shown in Fig. 4.75.

"a" shows one form in which the micelles direct the antimonate "rods" into a loosely held particle while "b" shows another form in which the nanoparticles grow into a larger state before the particles agglomerate. The formation mechanisms for $Sr_2Sb_2O_7$ (CTAB) and $Sr_2Sb_2O_7$ (PVP) were proposed. Both $Sr_2Sb_2O_{7(CTAB)}$ and $Sr_2Sb_2O_{7(PVP)}$ show obvious photo-catalytic activity for the decomposition of salicylic acid under UV light illumination. $Sr_2Sb_2O_7$ (PVP) shows the best photo-catalytic activity for the degradation of salicylic acid due to its higher band gap energy and larger BET-specific surface area. Compared to samples prepared without the surfactant, both $Sr_2Sb_2O_7$ (CTAB) and $Sr_2Sb_2O_7$ (PVP) can be more readily separated from the slurry system by filtration or sedimentation after the photo-catalytic reaction and reused. This makes them ideal photo-catalysts for aqueous phase photo-catalytic reactions (Table 4.23).

It was shown that the light absorbance starts at about 350 nm for all these antimonate samples, while a uniform red shift of absorbance edge is observed in the order of $CaSb_2O_6$ ($\lambda = 346$ nm), $SrSb_2O_6$ ($\lambda = 349$ nm), and $BaSb_2O_6$ ($\lambda = 358$ nm). So the intrinsic band gaps of $CaSb_2O_6$, $SrSb_2O_6$ and $BaSb_2O_6$ are estimated at 3.59, 3.55 and 3.46 eV, respectively, using the widely applied equation: $Eg\ (eV) = 1241/\lambda\ (nm)$.

In spite of the potential uses of strontium antimonates as solid-state aqueous phase photo-catalytic reactants to destroy organic contaminants in soils and mixtures of organic compounds, these

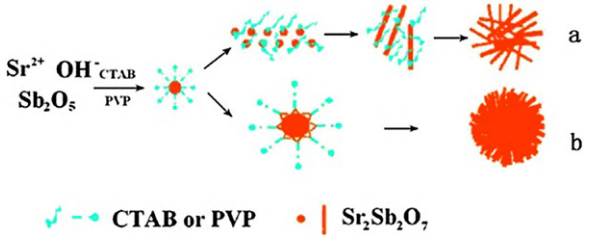

FIGURE 4.75

antimonates have not had a CAS number assigned. Little attention has ensued in industry and they are not being used in any capacity at this moment. The advent of fuel cells in the near future may change all of that. Certain types of Stand-Alone electrical-power generators, based on Fuel Cells, have been installed in certain manufacturing facilities. However, the solid-state conductance layer is not based upon strontium antimonates.

Barium Antimonate

Barium antimonate can be prepared by the solid-state reaction of BaO or $BaCO_3$ with Sb_2O_5 in air at about 1200 °C.

$$BaO + Sb_2O_5 \Rightarrow BaSb_2O_6$$

By changing the ratio of BaO/Sb_2O_5 during firing, a series of compounds is expected to result. However, there is no record in the literature concerning this possibility or even probability. No recent work is available although certain textbooks and reference books do cite $BaSb_2O_6$ as a stable compound. Indeed, the early literature cited compounds prepared in aqueous solution. The following compounds were presented (1889), but no corroborating evidence has since emerged:

$$Ba(SbO_3)_2 = BaO{\cdot}Sb_2O_5\text{—sl. soluble.}$$

$$Ba(SbO_3)_2{\cdot}2H_2O\text{—somewhat soluble (soluble in HCl)}$$

$$BaSb_4O_{11}{\cdot}5H_2O = BaO{\cdot}2Sb_2O_5\text{ (soluble in HCl)}$$

$$BaO{\cdot}3Sb_2O_5\text{ (insoluble in water–soluble in HCl)}$$

$$BaO{\cdot}4Sb_2O_5{\cdot}15H_2O$$

$$9BaO{\cdot}10Sb_2O_5{\cdot}18H_2O\text{ (insoluble in HCl)}$$

The salt, $Ba(SbO_3)_2$ or $BaSb_2O_6$ is offered for sale with the CAS number of 15600-59-6.

TABLE 4.23

Space	Catalyst	*Eg* (eV)	Crystal system	PF (%)	Method	Activity	Reference	Group
$Ca_2Sb_2O_7$	4.02	Orthorhombic	Imma	65.41	UV	MO	Sr > Ca	S30
$Sr_2Sb_2O_7$	3.86	Orthorhombic	Imma	64.45	Degrades	–	–	–

Nanoparticles of barium gadolinium antimonate, (Ba_2GdSbO_6), a complex perovskite-type oxide, have been synthesized using an autoignition combustion process. The nanoparticles thus obtained were characterized by powder XRD, TGA, DTA, Fourier transform infrared spectroscopy and TEM. The XRD studies showed that the as-prepared powder is phase-pure Ba_2GdSbO_6 and has a complex cubic perovskite crystalline structure with a lattice constant, $a = 8.449$ Å. The TEM image revealed that the particle size of the as-prepared nanopowder was in the range 30–60 nm. The nanocrystals of Ba_2GdSbO_6, synthesized by the combustion technique, could be sintered to 96% of the theoretical density by heating at a temperature of 1560 °C for a short duration of 3 h. The surface morphology of the sintered pellet was studied by use of a SEM. The dielectric constant ($\sigma_{\mu r}$) was 20 and the loss factor (tan θ) was ≈ 0.03 at 3 MHz. Using the present combustion technique, a phase-pure nanopowder of Ba_2GdSbO_6 could be obtained by a single-step process without the need of any calcination step.

Other rare-earth combinations studied include the Sm^{3+} ion. Nanoparticles of samarium barium antimonate (Ba_2SmSbO_6), a complex perovskite were also synthesized by the autoignition combustion process. The nanoparticles thus obtained were characterized in a similar manner. The XRD studies showed that the as-prepared powder is a phase-pure Ba_2SmSbO_6 and has the complex cubic perovskite ($A_2BB'O_6$) crystalline structure with a lattice constant of $a = 8.491$ Å. The particle size of the as-prepared powder was in the range 20–50 nm. The nanocrystals of Ba_2SmSbO_6 synthesized by the combustion technique could be sintered to 97% of the theoretical density by heating at a temperature of 1550 °C for 2 h. A similar study showed that Yttrium could also be incorporated into a powder which was phase pure Ba_2YSbO_6 with the complex cubic perovskite ($A_2BB'O_6$) crystalline structure and the lattice constant of $a = 8.402$ Å.

In another similar study, the crystal structure of the ordered perovskites $Ba_2(R,Sb)O_6$ (R = Y, Ho) was refined from neutron powder diffraction data in the space group *Fmm*(No. 225), $Z = 4$, with Ba at 8(*c*), R at 4(*b*), Sb at 4(*a*), oxygen at 24(*e*), oxygen positional parameter $x = 0.2636$ for R = Y and Ho, and unit-cell dimensions of $a = 8.4240$ Å and 8.4170 Å for R = Y and Ho, respectively. Bond valence analysis explains how the highly covalent Sb–O bonds determine the overall structure of these perovskites in which R–O and Ba–O bonds are under compressive and tensile stresses, respectively. The magnetic susceptibility of $Ba_2(HoSb)O_6$ has been measured in the temperature range 2–350 K. From an apriori estimation of the crystal-field parameters corresponding to the point site symmetry of the rare earth, O_h, and using the wave functions associated with the energy levels obtained, the paramagnetic susceptibility and its evolution vs temperature is simulated according to the van Vleck formalism. The observed deviation from the Curie–Weiss behavior at low temperature, very well reproduced, reflects the splitting of the ground state of this type of cation under the influence of the crystal field. These compositions were studied in relation to their possible superconducting properties relative to the copper-based compound, yttrium barium copper oxide = $YBa_2Cu_3O_7$.

Barium antimonate, $BaSb_2O_6$, has been tested as an opacifier in enamels used on cast iron. Antimonates of potassium, lithium, barium, calcium, magnesium, strontium, zinc, aluminum, lead, and tin were substituted for sodium antimonate in an acid-resisting dry process enamel for cast iron. The sodium antimonate content of this high-lead enamel was also varied to permit comparisons of all antimonates with sodium antimonate, as a standard, on an equivalent antimony pentoxide basis. In acid-resisting enamels, antimonates of potassium and barium compared reasonably well with sodium antimonate in opacifying power without introducing objectionable colors. Barium antimonate also produced improved acid resistance. Barium antimonate most closely approaches sodium antimonate in effectiveness. The behavior of the antimonates suggests an explanation for the variations often encountered with antimony oxide enamels.

Barium antimonate has been found to be a useful additive to varistor-ceramic compositions. When BaO was added to the usual $ZnO–Bi_2O_3–Sb_2O_3$ mixture and then fired, it was found that a new grain-boundary phase was formed consisting of $BaSb_2O_6$ besides the known Bi_2O_3 and $Zn_{2.33}Sb_{0.67}O_4$ grain-boundary phases. The barium antimonite phase was thermally stable and markedly improved the degradation tendencies of the varistor ceramic. The long-duration load voltage and surge current stability of the varistor were enhanced by this addition which improved the antidegradation properties (longer life).

The above five salts of barium and antimonate ions have received little attention from academia and even less from industry. None of these compounds have found marketable usage even though some of them are offered for sale commercially.

Radium Antimonate

Radium antimonate could be prepared by firing the oxide with antimony pentoxide in an air atmosphere around 750–800 °C:

$$RaO + Sb_2O_5 \Rightarrow RaSb_2O_6$$

However, there is no record of anyone having done so. There is no demand for any of the possible or probable radium antimonates and the likelihood that they

will ever be prepared is essentially zero because of the instability of such compounds in air and the intense radioactivity of ^{226}Ra atom.

4.4.3. Alkaline Earth Antimonides

Antimonides are generally prepared by solid-state reaction of the elements in an inert atmosphere. Whereas Be and Mg obey the basic electronic charge rules when reacted with Sb to form an alloy, i.e. $Mg_2^{2+}Sb_2^{3-}$, the heavier alkaline earths, Ca, Sr and Ba, form what appear to be "fractional-charge" compounds. They are, in reality, "Zintl phases" and obey the Zintl-Klemm electron counting rules and concept of covalent bonding in one-, two- or three-dimensions. The alkali and alkaline earth metals combine with the semimetals to form not only compounds with salt-like stoichiometries but also numerous compounds in which clustering of the semimetals occurs. Chains, rings, and cages of different lengths and sizes, as well as infinite sheets and porous frameworks are encountered. Such compounds as $Ca_{11}Sb_{10}$ and Ba_2Sb have been explained in terms of ionicity and charge assignment to each atom in the compound alloy. Zintl phases are a subgroup of brittle, high-melting point intermetallic compounds which are diamagnetic or exhibit temperature-independent paramagnetism, are poor conductors or are semiconductors. Zintl (1931) noted that there was an atomic volume contraction when these compounds were formed and realized this could indicate cation formation. He suggested that the structures of Zintl phases were ionic, where there was complete electron transfer from the more electropositive element. The structure of the anion (nowadays called the **Zintl ion**) should then be considered on the basis of the resulting electronic state. These ideas were further developed to become the **Zintl rules** or **Zintl-Klemm concept**, where the polyanion structure should be similar to an isoelectronic element.

Beryllium Antimonide

Beryllium antimonide has been prepared by the reaction of Be and Sb metals. Be melts at 1287 °C and is stable in an inert atmosphere until its boiling point of 2469 °C. Since Sb melts at 630.6 °C and is stable in an inert atmosphere until its boiling point of 1587 °C, the reaction is best carried out by evaporating Sb metal at about 1600 °C onto Be metal:

$$3Be + 2Sb \Rightarrow Be_3Sb_2$$

Although this is the expected reaction of these elements, it apparently does not always occur. Geach, Knapton and West (1958) observed no reaction between Be and Sb, but evaporation and electrical-resistivity measurements made by Ugai, Gordin and Anokhin (1964) indicated the existence of a compound with the formula Be_3Sb_2. Another study was undertaken to clarify the actual condition of beryllium antimonide and found that the stable form was $SbBe_{13}$, a material with space group = Fm3c, cubic with $a = 10.046$ Å, $Z = 8$, density = 3.13 g/cc, and $V = 1013$ Å^3. This compound has the $NaZn_{13}$ type of structure. Apparently, the Be^{3+} cation is too small to fit into a viable structure but requires 13-ions to form a stable one.

However, a patent (1968) stated that if Sb metal powder is "hot-pressed" with a large excess of Be-metal powder at about 1075 °C, a compound believed to be Be_3Sb_2 is formed. This cubic phase readily undergoes ordering which creates a distorted cubic structure, possibly tetragonal, with the *a*-axis only slightly different than the *b*-axis. Based upon X-ray examination, Be_2Sb_3 appeared to be the only compound in the binary Sb–Be system. The disordered structure is face-centered cubic with $a = 11.82$ Å. The point group was found to be T_h^7 with a density of 6.71 g/cc. Its melting point was stated to be 630 °C. Nonetheless, the pure compound could not be obtained but only as $(Be_3Sb_3)_{0.178} \cdot Be_{0.822}$ since the maximum content of Sb that could be incorporated was 0.16 of the weight of Be. However, the use of antimony to form the "beryllide" markedly improved the physical and mechanical properties of the Be metal so-treated and remains in use for some applications involving beryllium metal.

Although a phase diagram has been published, it is incomplete and is not included here.

Be_3Sb_2 has no CAS number and is not offered for sale by any manufacturer or supplier of beryllium or its compounds.

Magnesium Antimonide

Magnesium antimonide has been prepared by the reaction of Mg and Sb metals. Mg melts at 652 °C and is stable in an inert atmosphere until its boiling point of 1091 °C is reached. Since Sb melts at 630.6 °C and is stable in an inert atmosphere until its boiling point of 1587 °C, the reaction is best carried out by evaporating Mg metal at about 680 °C onto molten Sb metal:

$$3Mg + 2Sb \Rightarrow Mg_3Sb_2$$

Its molecular weight is 316.4351 g/mol and its CAS number is 12057-75-9. Mg_3Sb_2 melts at 1245 °C. Structural stabilities elastic properties and electronic structures have been determined from first-principles calculation by using Castep and Dmol computer programs based on the density functional theory given for the Mg_3Sb_2 phase. The calculation results of heat of formation and cohesive energy indicate that Mg_3Sb_2 has a strong alloying ability as well as the highest

structural stability of those compounds studied. The calculations of thermodynamic properties show that the Gibbs free energy of Mg_3Sb_2 changes with elevated temperature when the temperature is below 423 K (150 °C).

β-Mg_3Sb_2 crystallizes with an anti-La_2O_3-type structure with a space group of $P\bar{3}\,m1$. There is one formula unit in a hexagonal cell of $a = 4.558$ Å, $c = 7.229$ Å and a density of 4.02 g/cc. The existence of a polymorphic transition of β-Mg_3Sb_2 to cubic α-Mg_3Sb_2 has been suggested wherein the latter is isotypic La_2O_3. A phase diagram has been established (Fig. 4.76).

Layers of Mg_3Sb_2 evaporated in vacuo were found to exhibit semiconducting properties, although both constituents are normally metals. Under suitable conditions, the layers are photosensitive. Measurements were carried out on the spectral distribution of sensitivity, and showed bands with long wavelength edges at 1.5, 2.6 and 3.5 μ. The former is identified with intrinsic conductivity, and the two latter with impurity levels. Activation energies found from resistance-temperature measurements are very similar to the optical activation energies corresponding to the above wavelengths. Single-phase samples of Mg_3Sb_2 were prepared and found to contain oxygen at the grain boundaries. This compound was found to lose Mg and oxidize at temperatures above 900 K. Thermoelectric properties were characterized by Seebeck, electrical resistivity, and thermal conductivity measurements from 300 to 1023 K, and the maximum zT was found to be 0.21 at 875 K. Dimensionless figure of merit for Mg_3Sb_2 hot pressed and sintered at 873 K. The inset illustrates the crystal structure of Mg_3Sb_2 along the [100] direction (white = Mg, black = Sb).

In contrast, when zinc is added to Mg_3Sb_2, the result is a compound with metal-like conductivity. The $Mg_{3-x}Zn_xSb_2$ phases with $x = 0.00$–1.34 were prepared by direct reactions of the elements in tantalum tubes (Fig. 4.77).

According to the X-ray single crystal and powder diffraction, the $Mg_{3-x}Zn_xSb_2$ phases crystallize in the same $P\bar{3}m1$ space group as the parent Mg_3Sb_2 phase. The $Mg_{3-x}Zn_xSb_2$ structure is different from the other substituted structures of Mg_3Sb_2, such as (Ca, Sr, Ba) Mg_2Sb_2 or $Mg_{5.23}Sm_{0.77}Sb_4$. That is, in $Mg_{3-x}Zn_xSb_2$, it is the Mg_{tetr} atoms on the tetrahedral sites that are replaced, while in the other structures the Mg_{octa} on the octahedral sites is replaced. Thermoelectric performance for the two members of the series, Mg_3Sb_2 and $Mg_{2.36}Zn_{0.64}Sb_2$, was evaluated from low to room temperatures through the measurements of resistivity, Seebeck coefficient and thermal conductivity. In contrast to Mg_3Sb_2 which is a semiconductor, $Mg_{2.36}Zn_{0.64}Sb_2$ is metallic and exhibits an 18-times larger dimensionless figure-of-merit, ZT, at 20 °C. However, thermoelectric performance of $Mg_{2.36}Zn_{0.64}Sb_2$ is still poor and it is mostly due to its development of increased electrical resistivity at the higher temperatures.

In another study, the results of near infrared and visible optical studies on thin amorphous Mg–Sb alloy films were briefly reported. Excess Sb in the amorphous semiconductor Mg_3Sb_2 is found to change the band gap

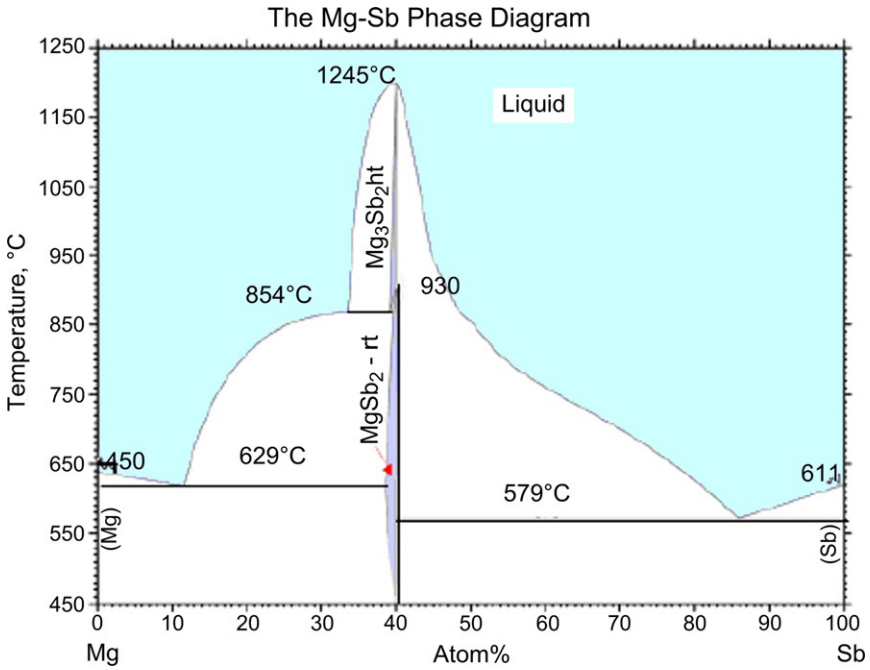

FIGURE 4.76

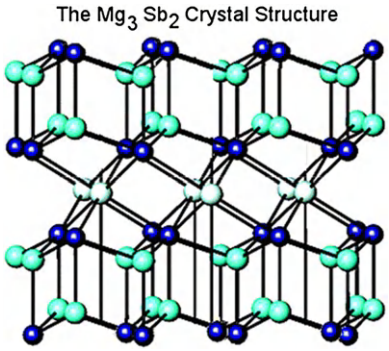

FIGURE 4.77

smoothly from about 1.05 for Mg_3Sb_2 to 0.24 eV for amorphous Sb. In contrast, excess Mg contributes localized states to Mg_3Sb_2 that fill in the band gap. The electrical properties of amorphous Mg–Sb alloys are discussed in terms of a model of a pseudogap containing localized states with the electrons moving by thermally activated hopping. However, in the Mg–Sb alloys on the Sb-rich side of the intermetallic compound, it appears that the density of states in the pseudogap is too low for hopping between localized states to be of importance, and the alloy behaves more like an extrinsic semiconductor with electrons being excited into acceptor states a few tenths of an electron volt above the valence band.

Mechanical alloying plus hot pressing was employed to prepare nanocrystalline Mg_3X_2 (X = Bi, Sb) compounds that were characterized by microstructural examinations and DC electrical resistance measurements. The results indicated that Mg_3Sb_{2+y} compounds with mean grain size 30 nm and with solute Sb atoms as much as 5 atom % in the powder specimens were successfully prepared. By comparison, $Mg_{3+x}Bi_2$ compound with solute Mg atoms as much as 13 atom% could be fabricated with similar grain sizes. Hot pressing at 673 K (400 °C for 20–50 min) only led to a limited grain growth (<10 nm) for both compound systems. However, experiments showed that hot pressing could further facilitate alloying of the elements in Mg–Bi system. In contrast, an elementary Sb phase formed gradually in the Mg_3Sb_{2+y} system with supersaturated solute Sb atoms incorporated during hot pressing, presumably due to its high ionicity and a large number of intragranular imperfections, as revealed by large lattice strain. DC-resistance measurements indicated that a semimetal–metal transition occurred in $Mg_{3+x}Bi_2$ system as solute $3+x$ reached 3.72; while in Mg_3Sb_{2+y} system a transition of its conduction behavior from logarithmic law to Mott's $T^{1/4}$ law was observed at $T < 190$ K (−83 °C) as solute Sb-content y exceeded 0.097, suggesting that phonon-assisted hopping occurred in the Mg_3Sb_{2+y} at the low temperatures.

The ternary polar intermetallic phase, $Mg_{5.231}Sm_{0.769}Sb_4$ has been obtained from solid-state reactions at 700–850 °C in sealed Ta or Nb containers wherein the synthetic conditions took into account its characteristic incongruent melting point. The compound crystallizes in the trigonal space group P ($Z = 1$) with $a = 4.618$ Å and $c = 14.902$ Å in a structure that derives from that of Mg_3Sb_2 (anti-La_2O_3 type). This composition appears to be near the lower limit of the Sm content, and solutions with appreciably higher Sm contents are also stable ($Mg_{6-x}Sm_xSb_4$ with $x \leq 1$). The structure has been presented in the literature, shown in Fig. 4.78.

The result provides the first example of a superstructure of a Mg_3Sb_2-like structure with a doubled c-axis induced by ordering a mixture of the larger trivalent and divalent Sm and Mg ions separately within alternate layers of octahedral sites of Sb^{3+} ions. Still larger proportions of Sm also give rise to a second solid solution region in the parent Mg_3Sb_2-type structure ($Pm1$), $Mg_{6-x}Sm_ySb_4$, ($0 \leq y \leq 1$). Retention of the same $3e^-$ valence electron counts per antimony in all of these phases suggests that the compounds remain electron precise and Zintl phases. Analogous compounds with Ca, Sr, or Ba substitution have evidently not been investigated.

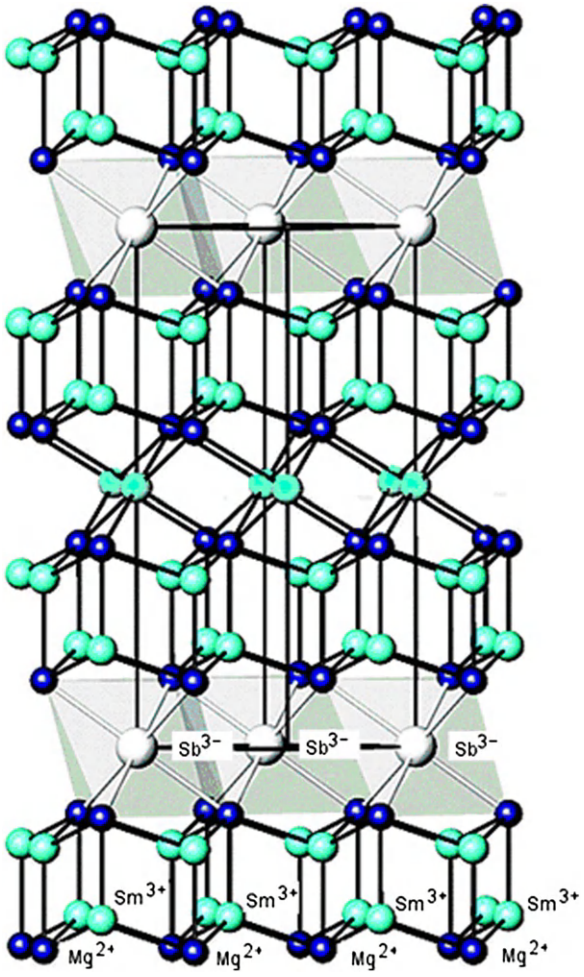

FIGURE 4.78

Magnesium and calcium antimonites, which can coexist with MgO and CaO, respectively, were synthesized by a phase-equilibration technique and identified by XRD to be $MgSb_2O_4$ and $Ca_4Sb_2O_7$. To determine the standard Gibbs energies of formation of those antimonites, e.m.f. values of the following galvanic cells have been measured:

$$\text{Pt, Re/Sb (solid,liq), } Sb_2O_3\text{(solid,liq)/}ZrO_2 + \text{CaO(or } Y_2O_3\text{)/air, Pt}$$

$$\text{Pt, Re/Sb (liq), } MgSb_2O_4 \text{ (solid), MgO (solid)/}ZrO_2 + \text{CaO/air, Pt}$$

$$\text{Pt, Re/Sb (liq), } Ca_4Sb_2O_7 \text{ (solid), CaOA(solid)/}ZrO_2 + \text{CaO/air, Pt.}$$

The following free energies of formation were determined:

$$\Delta G^0/\text{kJ/mol} \pm 0.4 = -687.7 + 0.2425\ T \text{ (773–904 K),}$$
$$\text{for 2Sb (solid)} + 3/2O_2 \text{ (gas)} = Sb_2O_3 \text{ (solid)}$$
$$\Delta G^0/\text{kJ/mol} \pm 0.3 = -730.2 + 0.2895\ T \text{ (904–929 K),}$$
$$\text{for 2Sb (solid)} + 3/2O_2 \text{ (gas)} = Sb_2O_3 \text{ (solid)}$$
$$\Delta G^0/\text{kJ/mol} \pm 0.2 = -683.1 + 0.2385\ T \text{ (929–1095 K),}$$
$$\text{for 2Sb (liq)} + 3/2O_2\text{(gas)} = Sb_2O_3 \text{ (ℓ)}$$
$$\Delta G^0/\text{kJ/mol} \pm 0.7 = -78.9 + 0.0495\ T \text{ (929–1101 K),}$$
$$\text{for } Sb_2O_3 \text{ (liq)} + \text{MgO (solid)} = MgSb_2O_4 \text{ (solid)}$$
$$\Delta G^0/\text{kJ/mol} \pm 0.7 = -134.7 + 0.0017\ T \text{ (972–1101 K),}$$
$$\text{for } Sb_2O_3 \text{ (liq)} + 4\text{CaO (solid)} = Ca_4Sb_2O_7 \text{ (solid).}$$

Magnesium antimonide has also been used in an electrochemical and device apparatus for high-amperage electrical energy storage. It features a high-temperature, all-liquid chemistry. The batteries are simply tanks filled with three separate layers of liquid that float on top of one another at 700 °C: the top layer is molten magnesium, the bottom is antimony, and the middle layer is a salt containing magnesium antimonide, a dissolved compound of the two metals. When the battery is being charged, magnesium antimonide in the middle layer breaks down into the pure elements and so the upper and lower layers deepen. Discharging the battery reverses the process and releases electrons to provide power. Once heated up to its operating temperature, the battery generates enough heat on its own to keep the liquids molten. The reaction products created during charging remain part of the electrodes during storage for discharge on demand.

In a simultaneous ambipolar electrodeposition cell, a reaction compound is electrolyzed to effect transfer from an external power source; the electrode elements are electro-dissolved during discharge. A cell containing molten metal layer of: magnesium (density 1.5 g/ml, melting point 650 °C), a liquid metalloid layer of antimony (density 6.5 g/ml, melting point 630 °C) and an appropriate electrolyte containing magnesium antimonide (density 4.1 g/ml, melting point 1245 °C) was found to be a system of immiscible liquids having the requisite conductivity modes that could self-assemble into the layers shown in the following figure. These, upon melting, provided for simple manufacture and assembly of a cell from billets. A cell containing these constituents preferably operates around 700 °C. The design of such a cell is shown in Fig. 4.79.

With reference to this cell, an energy storage cell **10** of the invention houses three liquid constituents: a molten metal layer **14** that serves as negative electrode; a liquid metalloid layer **16** that serves as positive electrode; and an intervening ionically conductive electrolyte **20**. The liquid constituents are housed in a conductive container **22** which provides mechanical support to an inner sheath **24**. The sheath **24** prevents shorting by electronic conduction between the negative electrode **14** and the positive electrode **16** through the container **22**. The sheath **24** also protects the conductive container **22** from chemical attack by corrosive salts in the electrolyte **20**. The cell is covered by a conductive lid **26**. An insulating seal **29** electrically insulates the lid **26** from the container **22** and confines molten constituents and vapors to the container **22**. The portion of the lid **26** in contact with the negative electrode **14** functions as a negative current collector **27**, through which electrons pass between the molten electrode **14** and an external source or sink by way of a negative terminal **28**. The portion of the container **22** in contact with the positive electrode **16** functions as a positive current collector **23**, through which electrons pass between the molten electrode **16** and an external source or sink by way of a positive terminal **30**. The placement of the

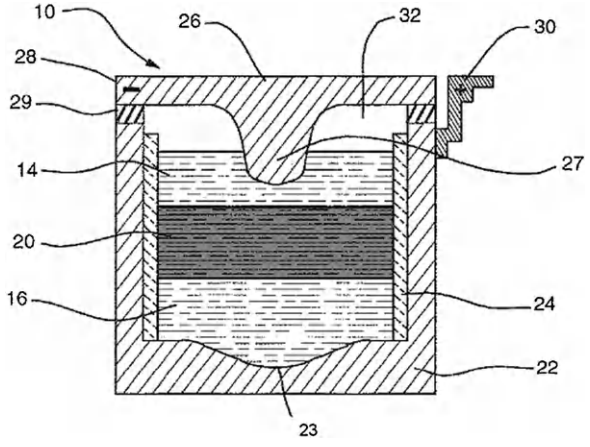

FIGURE 4.79

negative terminal **28** and the positive terminal **30** facilitates arranging individual cells in series by connecting the positive terminal of one cell to the negative terminal of another cell. An inert gas layer **32** overlaying the negative electrode **14** accommodates volume changes in the three-constituent system during charging and discharging. Optionally, the lid **26** or seal **29** incorporates a safety pressure valve.

In the case of the magnesium–antimony cell system, a lower melting supporting electrolyte was needed to bring the liquid range of the electrolyte **20** down from the melting point of magnesium antimonide and within the liquid range of magnesium, which boils at 1090 °C. Preferably, the liquid electrolyte **20** has a liquid range permitting a cell operating temperature close the melting temperatures of the electrode elements. Prime candidates for supporting electrolyte in a magnesium–antimony magnesium–antimonide system are sodium sulfide, lithium sulfide, calcium sulfide, magnesium sulfide and potassium sulfide. Other additives may include sodium selenide, lithium selenide, sodium antimonide and small amounts of other selenides, tellurides and/or halides.

Structural stabilities, elastic properties and electronic structures have been determined from first-principles calculation by using Castep and Dmol computer programs based on the density functional theory for the aluminum alloy, $Mg_{17}Al_{12}$ as well as those of Mg_3Bi_2 and Mg_3Sb_2 phases. The calculation results of heat of formation and cohesive energy indicated that Mg_3Sb_2 has the strongest alloying ability as well as the highest structural stability. The calculations of thermodynamic properties showed that the Gibbs free energy of formation for $Mg_{17}Al_{12}$, Mg_3Bi_2 and Mg_3Sb_2 change with elevated temperature. When the temperature is below 423 K (150 °C), Mg_3Sb_2 and Mg_3Bi_2 are more stable than the $Mg_{17}Al_{12}$ phase and Sb or Bi addition to the Mg–Al-based alloys can improve the heat resistance. The elastic parameters were calculated, then the bulk modulus, shear modulus, Young's modulus and Poisson ratio value were derived. All the results of the analysis indicate that adding Sb to Mg–Al alloy could improve the ductility and plasticity by forming Mg_3Sb_2 phases.

Laboratory experiments to test Mg_3Sb_2 as a reagent to disperse thick fog by condensation of water have shown that when this substance sublimes in a supercooled fog, the upper temperature limit for the occurrence of the ice phase is about −10–11 °C. The temperature limit increases to −8 or –9 °C when Mg_3Sb_2 in aqueous suspension is sprayed into the fog. Hence, Mg_3Sb_2 is, basically, an effective reagent for crystallizing a supercooled fog. However, there are some practical difficulties involved in employing this substance, e.g the instability of the substance and the difficulty of producing and dispersing it.

There are no vendors are listed for this material even though it has been assigned a CAS number. There are several potential commercial usages for this compound that have not materialized as yet. This includes high-amperage electrical energy storage.

Calcium Antimonide

Calcium antimonide can be prepared by the reaction of Ca and Sb metals. Ca melts at 842 °C and is stable in an inert atmosphere until its boiling point of 1484 °C is reached. Since Sb melts at 630.6 °C and is stable in an inert atmosphere until its boiling point of 1587 °C, the reaction is best carried out by evaporating Ca metal at about 880 °C onto molten Sb metal:

$$3Ca + 2Sb \Rightarrow Ca_3Sb_2$$

However, the product(s) is not the expected 3:2 compound but a series of Zintl products whose composition is dependent upon the initial Ca:Sb atomic ratio. Ca_3Sb_2 itself does not exist but Ca_5Sb_3 does. The most stable compound was determined to be $Ca_{11}Sb_{10}$. It was only after the Zintl-Klemm electron counting rules and concept of covalent bonding in one-, two- or three-dimensions became a reality that such compounds could be explained in terms of ionicity and charge assignment to each Atom in the compound alloy. A phase diagram has been established (Fig. 4.80).

The early work on calcium antimonides as intermetallic compounds involved determination of standard Gibbs energies of formation of Ca_3Sb_2, and Ca_3Bi_2 by a chemical equilibration technique yielding the following results:

$$3Ca\ (liq) + 2Sb\ (liq) = Ca_3Sb_2\ (solid)$$

$$\Delta G^\circ = -726{,}300 + 159.3\ T\ (\pm 24{,}600)\ (J/mol)$$

$$(1273\ to\ 1573\ K)$$

$$3Ca\ (liq) + 2Bi\ (liq) = Ca_3Bi_2\ (solid)$$

$$\Delta G^\circ = -696{,}400 + 195.6\ T\ (\pm 23{,}200)\ (J/mol)$$

$$(1148\ to\ 1323\ K)$$

The stabilities of these compounds were also discussed by using the critical oxygen partial pressures calculated from the above equations.

A Knudsen effusion technique combined with mass-spectrometric analysis of the evaporated species was used to investigate the gaseous phase and to determine the thermodynamic properties of alloys of calcium with antimony in the temperature range from 933 to 1669 K (660–1396 °C). Concentration of antimony varied from 50.2 to 63.5 mol%. The thermodynamic properties of the liquid phase were approximated by

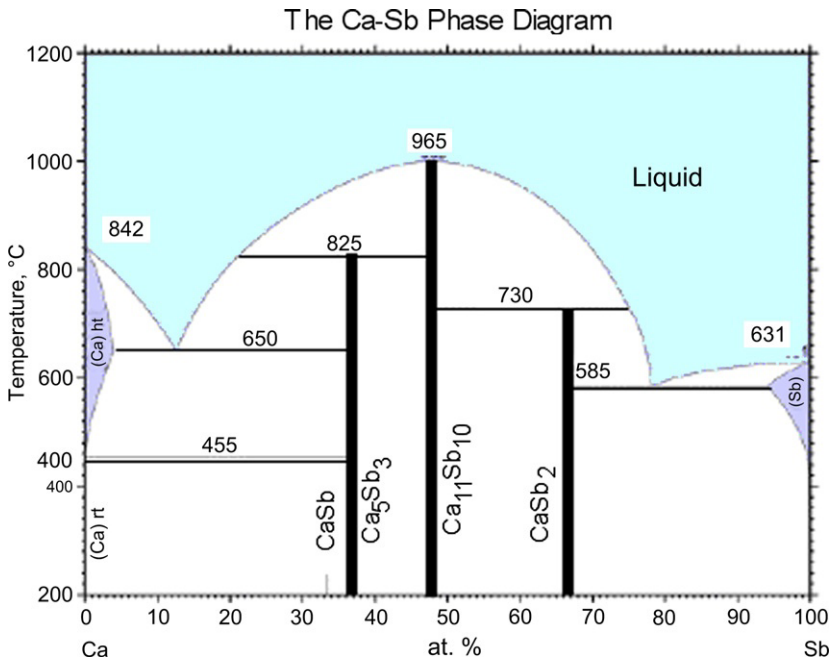

FIGURE 4.80

the association solution model, assuming that four types of associates Ca_3Sb_2, Ca_3Sb, Ca_2Sb and CaSb can exist in the melt. The Gibbs energies of formation of compounds from solid components were expressed by the equations:

$$\Delta_f G\ (Ca_{11}Sb_{10}) = (218{,}844 \pm 14595) - (43.47 \pm 12.34)\ T, \text{J/mol}$$

$$\Delta_f G(Ca_5Sb_3) = -(919{,}276 \pm 5110) + (34.24 \pm 4.75)\ T, \text{J/mol}$$

The obtained data were used for the computation of the part of the Ca–Sb phase diagram, corresponding to the composition range studied.

The latest data are shown in the above phase diagram where the congruently melting compound is $Ca_{11}Sb_{10}$, which melts at 965 °C. The other three compounds, Ca_2Sb, Ca_5Sb_3 and $CaSb_2$ all melt incongruently with corresponding horizontal eutectics of 455, 825 and 730 °C.

Data concerning the compositions forming in the Ca–Sb system have been controversial. CaSb was reported to melt congruently (985 °C) while the compounds Ca_3Sb_2 and $CaSb_3$ were reported to melt with decomposition. The corresponding horizontal peritectics were reported as 825 and 730 °C, respectively. The corresponding thermodynamic constants have not always been consistent. The standard enthalpy of formation, $\Delta H_{f(298)}$, has been given as 728 kJ/mol and the standard entropy, S^0_{298} as 157.3 J/mol. In the range of 1000–1300 °C, the Gibbs free energy of formation for the reaction to form Ca_3Sb_2 has been given as:

$$\Delta G^0_f = -726{,}300 + 159.6\ T \pm 24{,}000$$

However, this stoichiometric compound is not stable and is supplanted by the compound, Ca_2Sb. Furthermore, the most stable compound is $Ca_{11}Sb_{10}$, not the conventional Ca_3Sb_2 where the ionic charges on the latter are Ca^{2+} and Sb^{3-} whereas the formal charges on the former appear to be Ca^{2+} and $Sb^{2.2-}$. This relates to the fact that the stable compounds in the Ca–Sb system adhere to the Zintl-Klemm electron counting rules and concept of covalent bonding in one-, two- or three-dimensions. That is, linear chains, square two-dimensional boxes or three-dimensional networks are the norm. Thus, the optimal electron count for a linear chain is seven electrons per atom, six electrons per atom for a square lattice and five electrons per atom for a simple cubic lattice.

The basic concept behind the Zintl-Klemm concept is the transfer of electrons from more electropositive elements to more electronegative elements like Sb. This protocol usually works well with the alkaline earths as electron donors but as the atomic weight and number of electrons increase, as in Ca, Sr and Ba, things are not so simple. Thus, a "fractional-valence" seems to appear as in $Ca_{11}Sb_{10}$. Isolated Sb_4 squares are quite common within antimony phases. If the electron-octet is completed around the Sb_4 squares, then this leads to

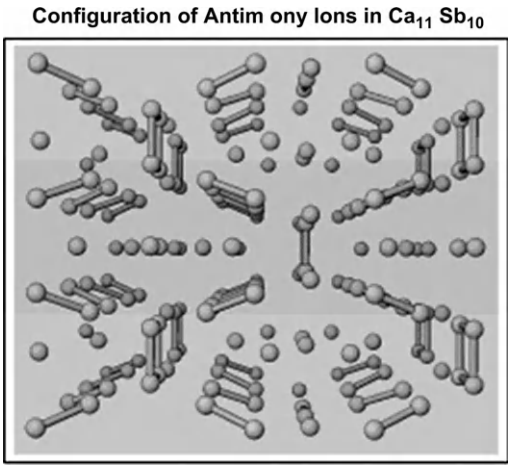

FIGURE 4.81

a –1 charge on each Sb atom in the square. $Ca_{11}Sb_{10}$ contains one isolated Sb_4 square, four Sb_2 pairs and eight Sb atoms per two formula units. This is shown in the following Fig. 4.81.

This gives the following assignment of charge to this Zintl phase:

$$(Ca_{22})^{44+}(Sb_4^{square})^{4-}(Sb_8^{pair})^{16-}.$$

In contrast, $CaSb_2$ consists of planar zigzag helical chains as shown in the following Fig. 4.82.

Thus, the charge assignment is:

$$Ca^{2+}(Sb^{atom})^{-}(Sb^{helix})^{-}.$$

The lattice parameters for CaS_2 are: $a = 4.746$ Å, $b = 4.177$ Å, $c = 9.084$ Å, $\beta = 106.3°$, Space Group = $P2_1/m$, $Z = 2$. In the helix, the Sb···Sb bond distances vary from 2.92 and 2.94 Å.

The compound, Ca_5Sb_3, appears to have two modifications. Hexagonal Ca_5Sb_3 and Ba_5Bi_3 belong to the hexagonal Mn_5Si_3 type; Sr_5Bi_3 is isostructural with orthorhombic β-Yb_5Sb_3. The orthorhombic form of

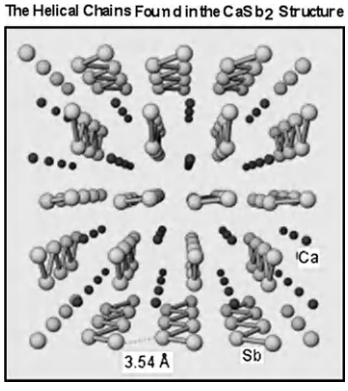

FIGURE 4.82

Ca_5Sb_3 (β-Yb_5Sb_3 type) has already been reported in the literature as stable at room temperature. It crystallizes as: Space Group = Pnma, with four formula units in a cell of: $a = 12.502$ Å, $b = 9.512$ Å, $c = 8.287$ Å, $d = 3.81$ g/cc, $Z = 4$. The Zintl-Klemm charge assignment is:

$$Ca_5^{10+}(Sb_2^{pair})^{4-}(Sb^{atom})^{2-}$$

Ca_2Sb can be obtained by the thermal decomposition of $Ca_2Sb_{1-x}I_x$. It crystallizes in the tetragonal system with $a = 4.69$ Å, $C = 16.39$ Å and Space group = 14 mm. The structure can be described as an arrangement of cubes with Sb atoms at each corner. The faces are centered by Ca atoms. These cubes build infinite layers along the x- and y-axes. A glide plane appears along the sequence of these layers along the z-axis. The corners of the upper cubes project at the center of the faces of the lower cubes. The Zintl-Klemm charge assignment for this compound is thus:

$$Ca_4^{8+}(Sb_2^{cube})^{8-}$$

The relation of these calcium antimonates has been somewhat elucidated by a study involving the addition of iron to this Ca–Sb system. This is shown in the following phase Fig. 4.83.

Samples of $Ca_{11}Sb_{10}$ have been synthesized using a high-temperature (1075–1275 °C) flux method. This compound is iso-structural to $Ho_{11}Ge_{10}$, crystallizing in the body-centered, tetragonal unit cell, space group I4/mmm, with $Z = 4$. The structure consists of antimony dumbbells and squares, reminiscent of Zn_4Sb_3 and filled "Skutterudite" (e.g. $LaFe_4Sb_{12}$) structures. In addition, this structure can be considered a Zintl compound and are valence precise semiconductors with ionic contributions to the bonding. DSC, thermogravimetry (TG),

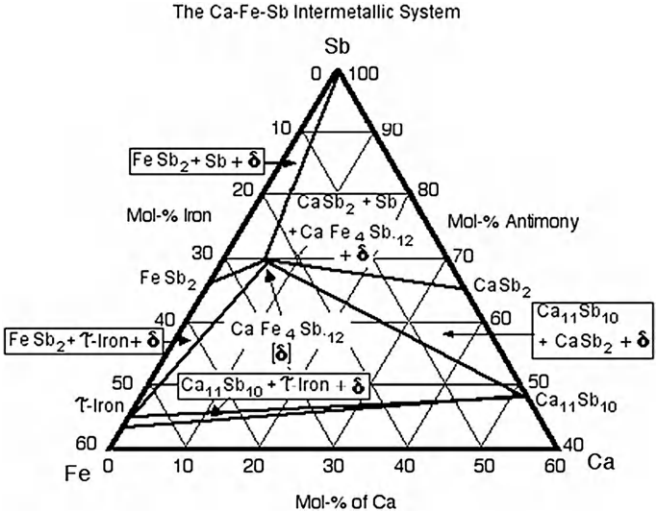

FIGURE 4.83

resistivity ([ρ]), Seebeck coefficient ([α]), thermal conductivity ([κ]), and thermoelectric figure of merit (zT) from room temperature to a minimum of 700 °C are presented for $Ca_{11}Sb_{10}$. DSC/TG were measured to 1250 °C and reveal the stability of these compounds. This compound exhibits remarkably low-lattice thermal conductivity (~10 mW/cm K) for $Ca_{11}Sb_{10}$ that can be attributed to the complex crystal structure. $Ca_{11}Sb_{10}$ is a semiconductor suggesting that a gradual metal–insulator transition may be possible upon the addition of a trivalent ion like Yb^{3+} or Y^{3+}. The low values and the temperature dependence of the Seebeck coefficients for this compound suggest that bipolar conduction produces a compensated Seebeck coefficient and consequently a low zT.

Calcium antimonide is particularly unstable in the presence of water and releases the volatile Stibine gas (Ayhan et al. 1982):

$$Ca_{11}Sb_{10} + 6H_2O \Rightarrow 2SbH_3\ (gas) + 3Ca(OH)_2$$

Perhaps this is the reason that no calcium antimonides have found usage in industry. None of these compounds have received CAS numbers and there are no listed suppliers commercially.

Strontium Antimonide

The compounds formed by solid-state reaction of strontium and antimony are lesser known than those of Ca or Ba. Perhaps this is due to the higher cost of Sr. Nonetheless, Sr forms the same type of Zintl phases and these compounds have been mentioned in conjunction with discussion of the Ca and Ba Zintl-Klemm analyses. The known strontium intermetallic phases include:

$$Sr_{11}Sb_{10}\quad Sr_2Sb\quad Sr_5Sb_4\quad Sr_2Sb_3\quad SrSb_3$$

Thus, the conventional Sr_3Sb_2 compound, where the ionic charges are Sr^{2+} and Sb^{3-} is not known. Since Sr melts at 777 °C and is stable in an inert atmosphere until its boiling point of 1382 °C is reached. Since Sb melts at 630.6 °C and is stable in an inert atmosphere until its boiling point of 1587 °C, the reaction is best carried out by evaporating Sr-metal at about 787 °C onto molten Sb metal in an inert atmosphere:

$$xSr + yBe \Rightarrow Sr_xSb_y$$

where x can vary from 1 to 11 and y varies from 1 to 10.

$SrSb_3$, $Sr_{11}Sb_{10}$, Sr_3Sb_2 and Sr_2Sb have melting points of 680 °C, 935 °C, 880 °C and 840 °C. All except $Sr_{11}Sb_{10}$ melt incongruently. Thus, the phase diagram is quite similar to that of calcium and its antimonides, as shown in the following Fig. 4.84.

Sr_2Sb crystallizes in the tetragonal system, space group I4/mmm, with four formula units in a cell of dimensions of $a = 5.002$ Å and $c = 17.405$ Å. The point group is tP_t6 and the space group is P4/nmm with atoms in the positions of 2 (*a*) O,O,O; 2(c_i) (0, 1/2, z_i) and 2(z_2) (O, 1/2, Zn).*i*. There are uncommonly short

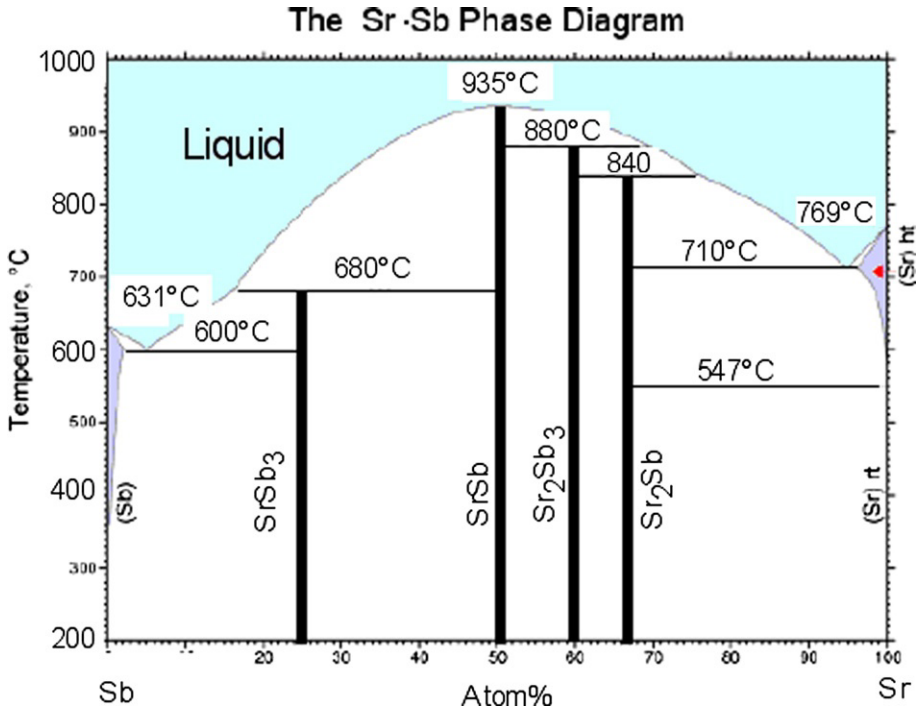

FIGURE 4.84

Sr···Sr distances in layers perpendicular to the *x*-axis. The positional cell coordinates of these are: Sr(1) at (0,1.2,)-($B = 0.85$ Å^2), Sr(2) at (0,0,0.328)-($B = 1.24$ Å^2), and Sr(3) at (0,0,0.137)-($B = 0.94$ Å^2). Single crystals can be prepared using a 2:1 ratio of these are crystallographically important points in the crystal lattice Sr:Sb. The crystals are black and have a laminar shape, the *c*-axis being perpendicular to the length. Because of their extreme sensitivity to air, they have to be kept under argon atmosphere.

Sr_2Sb_3 crystallizes in the monoclinic system with lattice parameters $a = 6.670$ Å, $b = 12.973$ Å, and $c = 15.208$ Å, with $\beta = 90.03°$, space group P21/c. The structure is characterized by Sb_6^{chains} and the compound belongs to the Zintl phases. The empirical formula is Sr_4Sb_6 and the Zintl charge-density formula is $Sr_4^{8+}(Sb_6^{chains})^{8-}$.

Sr_5Sb_3 crystallizes both in a tetragonal and orthorhombic phase. Single crystals of Sr_5Sb_3 can be prepared by cooling a melt of 3 Sr/2Sb from 1350 °C to room temperature. Isolated crystals are black and unstable to air. It crystallizes as a Mn_5Si_3 type (tetragonal) with space group $P6_3/mcm$ and two formula units per cell with dimensions of: $a = 9.496$ Å, $c = 7.422$ Å. The density is 4.602 gm/cc. This compound has a chain-structure like Ba_2Sb_3 except that the chains are linear, not zigzag. The assigned electrical Zintl-Klemm charge is:

$$(Sr5)^{10+}(Sb)^{3-}(Sb)^{4-}(Sb)^{3-}$$

There is one unusually-short Sr···Sr bond distance in the crystal.

Both tetragonal and orthorhombic phases have been identified. The tetragonal phase has the unit-cell constants of: $a = 5.002$ Å, $c = 17.405$ Å with density = 1.740 g/cc and Sr(1) at (0,0,0.137) and Sr(2) at (0,0,0.328).

In another study (1990), four phases were synthesized and their crystal structures determined by powder diffraction methods. $Sr_{11}Sb_{10}$ ($a = 12.581$ Å, $c = 18.098$ Å) and $Sr_{11}Bi_{10}$ ($a = 12.801$ Å, $c = 18.451$ Å), space group = I4/mmm, are of the $Ho_{11}Ge_{10}$ type. Relatively few compounds crystallize with this structure type. The structure consists of square-planar Sb_4 rings which are interconnected three-dimensionally by Sb_2 dumbbells. Therefore, the Zintl-Klemm designation is:

$$(Sr_{11})^{22+}(Sb_4^{square})_2^{8-}(Sb_6^{pair})^{12-}(Sb_2^{single})^{2-}.$$

Thus, the structure resembles that of the barium compound. The crystal structure of a fifth compound Sr_2Bi_3 was determined by single-crystal diffractometry: $M_r = 802.18$, orthorhombic, *Pnna*, $a = 15.631$ Å, $b = 6.793$ Å, $c = 6.599$ Å, $V = 700.4$ Å^3, $Z = 4$, $d_x = 7.60$ g/cm^3, Sr_2Bi_3 is of a new type and is closely related to the monoclinic Sr_2Sb_3 and Ca_2As_3 structures.

A new Zintl compound strontium tin antimonide, $SrSn_3Sb_4$, has been synthesized, and its structure has been determined by single-crystal XRD methods. It crystallizes in the orthorhombic space group—Pnma with $a = 10.060(2)$ Å, $b = 4.361(1)$ Å, $c = 22.934(4)$ Å, and $Z = 4$ at 22 °C. The structure of $SrSn_3Sb_4$ may be described as consisting of large, narrow channels running along [010] defined by 30-membered rings constructed from an anionic framework of linked $SnSb_4$ tetrahedra, $SnSb_3$ trigonal pyramids, and zigzag Sb–Sb chains. Sr^{2+} cations are situated within these channels. The channel structures of $SrSn_3Sb_4$ and $Ba_2Sn_3Sb_6$ are closely related. The relation of these strontium antimonides has been somewhat elucidated by a study involving the addition of iron to this Sr–Sb system. This is shown in the following phase Fig. 4.85.

Although $Sr_{11}Sb_{10}$ melts congruently and is featured prominently in the Ca–Sb–Fe phase diagram, it does not appear in the Sr–Sb–Fe phase diagram. The reason for this remains unknown. The stable phases are: Sr_2Sb_3, $SrSb_2$, and $FeSb_2$. Strontium antimonite is not listed for sale in general although $SrSb_2$ is offered for sale commercially. None of these Sr–Sb compounds have CAS numbers.

Barium Antimonide

Barium antimonide can be prepared by the reaction of Ba and Sb metals. Ba melts at 727 °C and is stable in an inert atmosphere until its boiling point of 1897 °C is reached. Since Sb melts at 630.6 °C and is stable in an inert atmosphere until its boiling point of 1587 °C, the reaction is best carried out by evaporating Ba-metal at about 780 °C onto molten Be metal:

$$xBa + ySb \Rightarrow Ba_xSb_y$$

where $0 < x < 12$ and $0 < y < 12$. Its CAS number is 12057-75-9.

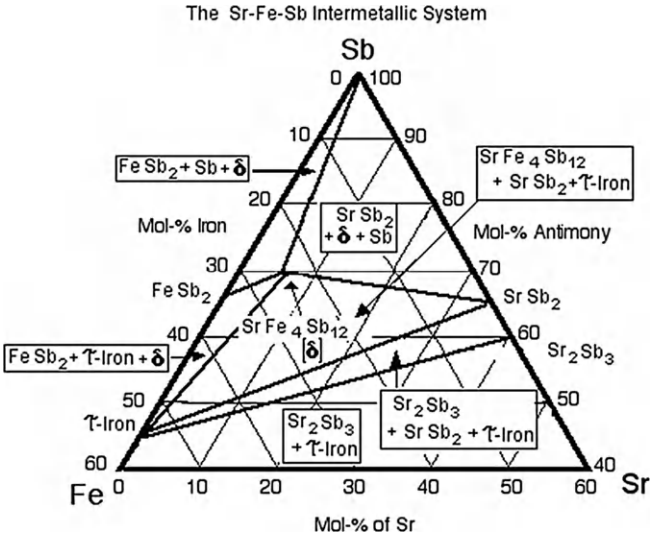

FIGURE 4.85

The $Ba_{11}Sb_{10}$ compound melts at 945 °C. $BaGa_2Sb_2$ was obtained from a direct element combination reaction in a sealed graphite tube at 950 °C, and its structure was determined by single-crystal XRD methods. It crystallizes in the orthorhombic space group Pnma (No. 62) with $a = 25.454(5)$ Å, $b = 4.4421(9)$ Å, $c = 10.273(6)$ Å, and $Z = 8$. The anionic $[Ga_2Sb_{6/3}]^{2-}$ framework is assembled by the ethane-like dimeric $[Sb_3Ga–GaSb_3]$ units sharing Sb atoms, forming parallel tunnels with a 26-membered ring cross section. These tunnels are filled with Ba atoms. The three-dimensional $[Ga_2Sb_{6/3}]^{2-}$ framework features a new structure type. The compound satisfies the classical Zintl concept. Band structure calculations indicate that the material is a semiconductor, and this is confirmed by spectroscopic experiments which show $E(g)$ approximately 0.35 eV. The calculations also suggest that the structure is stabilized by strong Ga–Ga covalent bonding interactions. Polycrystalline ingots of $BaGa_2Sb_2$ show room-temperature electrical conductivity of approximately 65 S/cm and a Seebeck coefficient of +65 μV/K.

Barium antimonides are Zintl complexes involving a numbers of types of Ba···Ba bond configurations. For example, Ba_5Sb_4 forms a series of one-dimensional pairs (dumbbells) plus isolated atoms. $BaSb_3$ on the other hand forms two-dimensional nets which are interconnected (2,3-connected nets). Still another configuration involves Ba_2Sb_3 with linear Ba_6 zigzag units (also Sb_2Sb_3). $Ba_{11}Sb_{10}$ forms a series of linear Sb_4 squares, plus pairs, and separated atoms.

The most commonly occurring in barium antimonides is a Sb substructure with an Sb···Sb bond involving an Sb_2 pair, or dumbbell. In theory, the pair can have 7, 6 or 5 electrons per Sb atom that would formally be consistent to single, double or triple bonds. In Ba_5Sb_4, the charges can be assigned as $(Ba_5)^{10+}(Sb_2^{atom})^{6-}(Sb_2^{pair})^{4-}$.

The crystal structure of Ba_2Sb_3 contains isolated zigzag chains as shown in the following Fig. 4.86.

Thus, the charges in Ba_2Sb_3 can be assigned as $(Ba_2)^{4+}(Sb^{2-})(Sb^{-})(Sb^{-})$. These are isolated Sb_3 units in a zigzag chain. There is also a form with Sb_6^{8-} chains having the empirical formula Ba_4Sb_6 and the charge formula of $Ba_4^{8+}(Sb_6^{chain})^{8-}$ where chain consists of the zigzag chain pictured above.

$BaSb_3$ consists of a 2-dimensional 2,3-connected Sb-net, shown in Fig. 4.87.

The charges may be assigned as $Ba^{2+}Sb^0Sb_2^{2-}$.

Barium also forms an antimonide with Zn as $BaZnSb_2$. This is shown in the following Fig. 4.88.

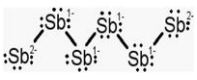

FIGURE 4.86

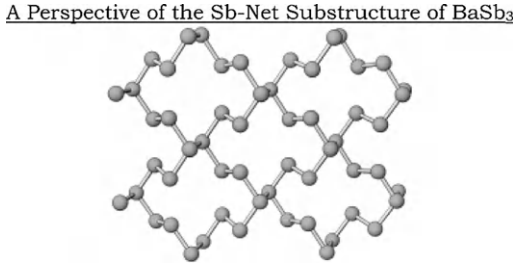

FIGURE 4.87

This structure has a 3-dimensional sheet-like structure in which the Zn ions are in a tetrahedral conformation, $ZnSb_4$. In the $(Ba,Zn)Sb_2$ compound, Ba ions are the small dark spheres, Zn is within the tetraheda setup by the Sb atoms and Sb-nets are the light large spheres. Perfectly square Sb sheets are present and the Zn atoms are surrounded by isolated Sb atoms forming the tetrahedral complex. This gives rise to the assignment: $Ba^{2+}Zn^{2+}(Sb^{sheet})^{-}(Sb^{atom})^{3-}$.

Ba_2Sb is tetragonal with $a = 5.22$ Å, $c = 18.46$ Å and a space group of I4mm. Ba(1) atoms are at (0,0,0), Sb atoms are at (0,0,0.136) and Ba(2) atoms are at (0,0,0.327) positions within the unit cell. The structure can be described as an arrangement of cubes with Sb atoms at each corner. The faces are centered by Ca atoms. These cubes build infinite layers along the x- and y axes. A glide plane appears along the sequence of these layers along the z-axis. The corners of the upper cubes project at the center of the faces of the lower cubes.

The Zintl-Klemm charge assignment for this compound is thus: $Ba_4^{8+}(Sb_2^{cube})^{8-}$.

The relation of barium antimonates has been somewhat elucidated by a study involving the addition of

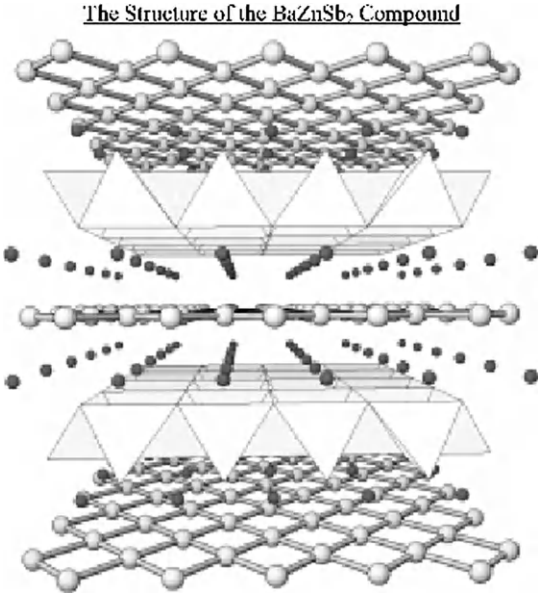

FIGURE 4.88

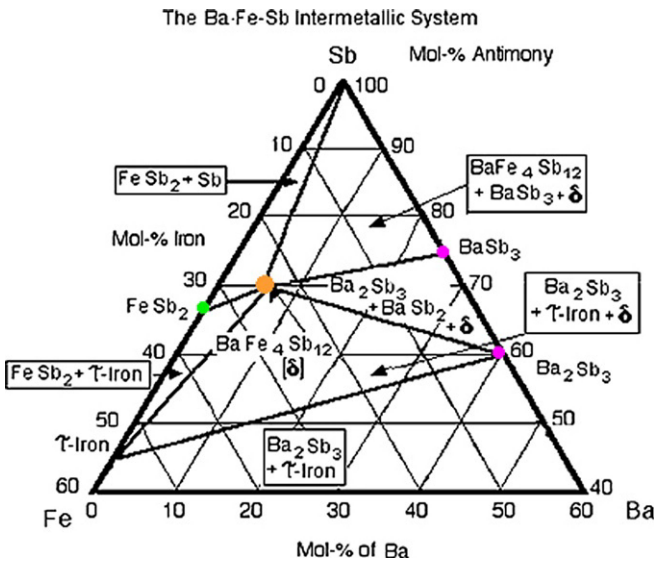

FIGURE 4.89

iron to this Ba–Sb system. This is shown in the following phase Fig. 4.89.

In the Ba–Fe system, the two metals do not dissolve or react with one another. Only when Sb is present is there a reaction to form specific compounds. Only Ba_2Sb_3 and $BaSb_3$ appear in this phase diagram of Ba–Fe–Antimonides. The other known phases do not. The reason for this behavior is not known.

$Ba_{11}Sb_{10}$ contains non electron-precise isolated dumbbells statistically composed of $(Sb_2^{pair})^{4+}$ charges, containing pentelide dumbbells among isolated Zintl anions. A redetermination of the structure of $Ba_{11}Sb_{10}$ has been made: Orthorhombic, Immm, $a = 12.653$ Å, $b = 13.161$ Å, $c = 19.472$ Å, $Z = 4$, $R_1 = 0.0724$, shows, that it represents a distorted variant of the tetragonal $Ho_{11}Ge_{10}$ structure type. This distortion is not only of crystallographic importance, as it results in a major change in the nature of the anions and their bonding, which is supported by DFT band-structure calculations. Likewise, the Zintl phase $BaSb_2$ is monoclinic, P21/m, $a = 11.679$ Å, $b = 4.381$ Å, $c = 12.571$ Å, $\beta = 100.53°$, $Z = 6$, $R_1 = 0.0648$. It crystallizes with a superstructure of the $CaSb_2$ type previously reported.

Ba_5Sb_4 crystallizes in the orthorhombic space group Cmca and is isostructural with Eu_5As_4 reported in the Ccmb alternate setting. β-$Ba_5Sb_4$is a new arrangement which is more symmetrical than α-Ba_5Sb_4 (1981) with space group Pnma, and isostructural with Sm_5Ge_4. The structure contains two anionic moieties, i.e. $(Sb_2^{pair})^{4-}$ dumbbells [Sb···Sb = 2.886 Å] and $(Sb_3^{atom})^{3-}$. The Sb(l) atom [$(Sb_3^{atom})^{3-}$] lies inside a monocapped distorted trigonal prism (6 × Ba(l) and 1 × Ba(2). The Sb(2) atom, which forms the $(Sb_2^{pair})^{4-}$dumbbells, sits inside a tricapped trigonal prism (6 × Ba(l), 2 × Ba(2) and 1 × Sb(2). β-Ba_5Sb_4 displays a more symmetrical arrangement than α-Ba_5Sb_4 (*Pnma*). It contains two anionic moieties, which are Zintl phases lying in tri-capped and distorted monocapped trigonal prisms of Ba atoms, respectively.

The antimonide oxide Ba_3Sb_2O consists of discrete $(Sb_2^{pair})^{4-}$ dumbbells and O^{2-} anions, and crystallizes with a new structure type. The Sb–Sb distances are comparable to those known from electron-precise Zintl phases and the tetrahedral coordination of the O^{2-} anion is also observed in some other Ba-rich metallide oxides.

A Zintl phase, dibarium-tritin-hexaantimonide, $Ba_2Sn_3Sb_6$ has been synthesized, and its structure has been determined by single-crystal XRD methods. It crystallizes in the orthorhombic space group—Pnma with $a = 13.351(1)$ Å, $b = 4.4100(5)$ Å, $c = 24.449(3)$ Å, and $Z = 4$ ($T = -50$ °C). The structure of $Ba_2Sn_3Sb_6$ comprises large channels [010] defined by 30-membered rings constructed from an anionic framework. This framework is built up from Sn-centered trigonal pyramids and tetrahedra, as well as zigzag chains of Sb atoms. Within the channels reside the Ba^{2+} cations and additional isolated zigzag Sb–Sb chains. The simultaneous presence of Sn trigonal pyramids and tetrahedra implies that $Ba_2Sn_3Sb_6$ is a mixed-valence compound whose oxidation state notation can be best represented as $(Ba^{2+})_2[(Sn^{II})_2(Sn^{IV})(Sb^{-III})_3(Sb^{-I})]^{2-}[(Sb^{-I})_2]^{2-}$. The structure has been given in Fig. 4.90.

Resistivity and AC magnetic susceptibility measurements on $Ba_2Sn_3Sb_6$ and $SrSn_3Sb_4$ indicate that these Zintl compounds display a transition to a superconducting phase at $T_C = 3.9$ K. The Meissner effect was observed for $Ba_2Sn_3Sb_6$ under an applied field of 25 Oe. The signatures for superconductivity, such as high- and low-velocity conduction electrons and lone pairs, are present for both of these compounds.

Only a few of these barium antimonides are offered for sale commercially. Ba_2Sb_3 has one supplier and has

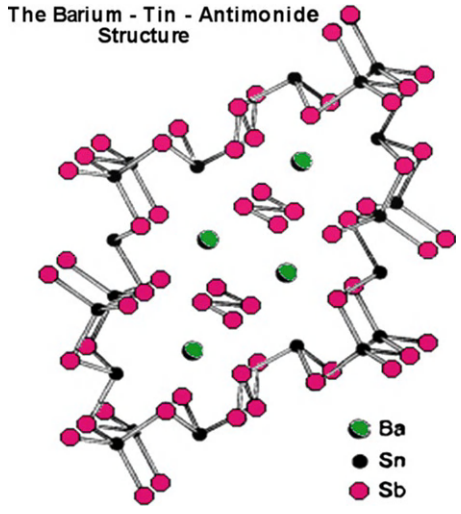

FIGURE 4.90

the CAS number of 55576-04-0. $BaSb_2$ is offered for sale by one or two Chinese manufacturers (CAS number = 12057-75-9).

Radium Antimonide

Radium antimonide could probably be prepared by the reaction of Ra and Sb metals. Ra melts at 700 °C and is stable in an inert atmosphere until its boiling point of 1737 °C is reached. Since Sb melts at 630.6 °C and is stable in an inert atmosphere until its boiling point of 1587 °C, the reaction is best carried out by evaporating Ra metal at about 680 °C onto molten Sb metal:

$$3Ra + 2Be \Rightarrow Ra_3Sb_2$$

However, this reaction has never been carried out due, perhaps, to the intense radioactivity of ^{226}Ra atom. It is probable that Ra forms the same type of antimonide compounds as Ba but there is no industrial or commercial interest and no academic interest in these compounds due to the care required in handling such compounds.

4.5. ALKALINE EARTH BISMUTHATE COMPOUNDS

According to some early sources, bismuth (either as Bi^{3+} or Bi^{5+}) is too electropositive to form "bismuthates" with the alkaline earths. However, this observation undoubtedly applied to solution chemistry. Even then, there were exceptions, notably that of barium, where soluble alkali bimuthates were used to form barium bismuthates. In recent years, bismuthates have been prepared by solid-state reaction and evaluated for various applications. The possible oxy-complexes include BiO_2^{1-} or $Bi_2O_4^{2-}$ (bismuthites), and BiO_3^{1-} or $Bi_2O_6^{2-}$ (bismuthates) and combinations like $Bi_2O_7^{4-}$. The major driving force has been the discovery of "high-temperature" superconducting compounds (1989) where liquid N_2 at 77 K is sufficient to maintain the superconducting state of these Sr or Ba bismuthate–cuprate compounds with a critical temperature of 113 K.

Bismuth has unusually low toxicity for a heavy metal. Bismuth is stable to both dry and moist air at ordinary temperatures. When red hot, it reacts with water to make bismuth(III) oxide. Bismuth forms trivalent and pentavalent compounds. The trivalent compounds are more common. Many of its chemical properties are similar to those of As and Sb, although they are less toxic than derivatives of those lighter elements. At elevated temperatures, the vapors of the metal combine rapidly with oxygen, forming the yellow trioxide, Bi_2O_3. On reaction with base, this oxide forms two series of oxy-anions: BiO_2^-, which is polymeric and forms linear chains, and BiO_3^{3-}. The anion in Li_3BiO_3 is actually a cubic octameric anion, $Bi_8O_{24}^{24-}$, whereas the anion in Na_3BiO_3 is tetrameric. The dark red bismuth(V) oxide, Bi_2O_5, is unstable, liberating oxygen gas upon heating. In aqueous solution, Bi^{3+}, as an anion, exists in various states of hydration, depending on the pH (Table 4.24).

Thus, in order to describe the alkaline earth bismuthate system, it is necessary to consider solution methods as well as solid-state reaction methods of combining the oxides. The valence state of Bi in the final solid will depend upon the nature of the alkaline earth whereas the trivalent Bi atom is almost always present in compounds formed from solution.

In general, the phase diagrams of the various AeO–Bi_2O_3 or AeO–Bi_2O_5 systems are not available and have not been thoroughly studied.

4.5.1. Alkaline Earth Bismuthate Compounds

Beryllium Bismuthates

There are no reports that deal with beryllium–bismuth compounds. None of the reference books like Remy, Sidgwick or Lange's Handbook of Chemistry list such compounds and their properties. It is highly probable that they do not exist. The literature is devoid of such references unlike the other alkaline earths.

Magnesium Bismuthate

Of the possible magnesium bismuthate (-ite) compounds, only $MgBi_2O_6$ has been reported. No phase diagram for the MgO–Bi_2O_3 or MgO–Bi_2O_5 systems are available. This compound is semiconducting and is employed in small batteries used in portable electronic devices. Magnesium bismuthate is prepared by the reaction of sodium bismuthate with a soluble Mg salt:

$$MgCl_2\ (aq) + 2NaBiO_3\ (aq) \Rightarrow MgBi_2O_6\ (solid) + 2NaCl\ (aq)$$

The preparation of magnesium bismuthate, $MgBi_2O_6$, was accomplished in a sealed PTFE-lined pressure

TABLE 4.24

pH range	Species
<3	$Bi(H_2O)^{3+}$
0–4	$Bi(H_2O)_5(OH)^{2+}$
1–5	$Bi(H_2O)_4(OH)_2^+$
5–14	$Bi(H_2O)_3(OH)_3$
>11	$Bi(H_2O)_2(OH)_4^-$

vessel. The pressure vessel and contents were heated to and held at 135 °C for 2.5 days. The pressure vessel was cooled to room temperature before opening. After separation of the solid by filtration and drying at 60 °C for 24 h, a dark brown powder was obtained. The powder was characterized using X-ray powder diffraction, chemical analysis, and thermal analysis. The X-ray powder diffraction pattern was consistent with that reported for trirutile $MgBi_2O_6$. The lattice parameters were refined in the tetragonal space group P42/mnm. The values obtained ($a = 4.82168$ Å and $c = 9.70194$ Å) corresponded closely to the reported values in the literature. The density of 7.51 g/cm^3 was determined by displacement of helium gas using a null-pycnometer. A Mg:Bi atom ratio of 1.02:2.00 was determined by ICP spectroscopy which is consistent with that expected for a trirutile structure. Thermal analysis of $MgBi_2O_6$ by DTA/TGA at a heating rate of 10 °C/min to 550 °C revealed a loss in weight starting below about 400 °C in flowing air. This was caused by the decomposition of $MgBi_2O_6$ to MgO and Bi_2O_3 accompanied by oxygen loss. The experimentally observed weight loss of 5.91 wt% is consistent with the calculated weight loss of 5.94 wt%.

$MgBi_2O_6$ can be classified as a transparent conducting oxide (TCO) that possess an unusual combination of properties; high transparency across most of the visible spectrum, coupled with high-electrical conductivity. TCO's have a wide variety of applications, including use in flat panel displays, solar cells, energy-efficient windows, gas sensors, antistatic coatings, and heating elements. $MgBi_2O_6$ reveals temperature-independent conductivity (0.01 S/cm^2), a negative Seebeck coefficient (20.025 mV/K), and an optical band gap that falls at the low-energy end of visible region (1.8 eV). This combination of attributes, indicating that this compound is a degenerate *n*-type semiconductor, a trait that has not previously been reported in a Bi^{5+} oxide.

The crystal structure is shown in the following Fig. 4.91.

It consists of a ring structure of octahedral BiO_6^{2-} octagonal units with interspersed Mg^{2+} cations. Characterization of polycrystalline samples of the trirutile oxide $MgBi_2O_6$ revealed temperature-independent conductivity (0.4 and 0.01 S/cm), a negative Seebeck coefficient (−0.035 and −0.025 mV/K), and an optical band gap that falls at the low-energy end of visible region (1.7 and 1.8 eV). This combination of attributes indicates that this compound is a degenerate *n*-type semiconductor, a property that has not previously been observed in a Bi^{5+} oxide.

Although this compound is thoroughly described in the scientific literature, it has no CAS number and is not offered for sale commercially.

Crystal Structure of Magnesium Bismuthate

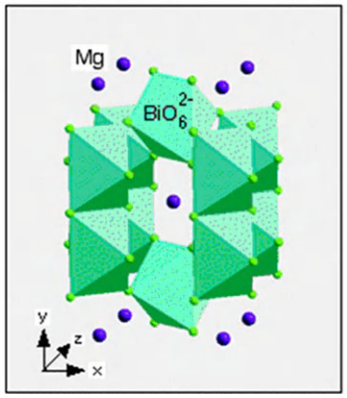

FIGURE 4.91

Calcium Bismuthate

Calcium forms a series of compounds with Bi_2O_3. Four stable phases with stoichiometric molar ratio, $Ca_6Bi_6O_{15}$, $Ca_4Bi_6O_{13}$, $CaBi_2O_4$ and $Ca_5Bi_{14}O_{26}$ have been prepared by conventional solid-state reaction methods. The reactions are:

$$x\mathrm{CaCO_3} + y\mathrm{Bi_2O_3} + \text{heat} \Rightarrow \mathrm{Ca}_x(\mathrm{Bi}_{2y}\,\mathrm{O}_{3y+5}) + x\mathrm{CO_2}$$

where x varies from 1 to 4 and y varies from 2 to 7. Thus, the above stable compounds are essentially variations of 6:3, 4:3, 1:1 and 5:7 mol ratios.

The details of the reaction processes have been investigated and the different intermediate products were identified by XRD before the pure phases were obtained. In the four phases, the valence of Bi was +3 and the lone-pair electrons of Bi^{3+} led to the formation of the Bi–O sheet structures. Bi–O polyhedrons with different coordination numbers and bond lengths were discussed. The optical properties of the four samples were also investigated. The band gaps of $Ca_6Bi_6O_{15}$, $CaBi_2O_4$, $Ca_4Bi_6O_{13}$ and $Ca_5Bi_{14}O_{26}$ were estimated from the absorption spectra as 3.34 (372 nm), 3.08 (402 nm), 2.76 (450 nm) and 2.60 eV (477 nm), respectively, and they were all direct transition semiconductors. Moreover, the Raman spectra of $Ca_6Bi_6O_{15}$, $Ca_4Bi_6O_{13}$ and $CaBi_2O_4$ were also investigated and the results suggested that some high-frequency phonon modes (Raman shift more than 450/cm) appeared in the crystals when Ca was being introduced into the three complex oxides.

Single crystals and powdered samples of the bismuth(III) calcium oxide $Ca_6Bi_6O_{15}$ have been synthesized and studied using both X-ray and neutron diffractometry. The compound crystallizes in the space group P with $Z = 2$. Cell parameters, obtained with the single-crystal X-ray diffractometer, were $a = 10.101$ Å, $b = 10.130$ Å, $c = 10.466$ Å, and $\alpha = 116.86°$, $\beta = 107.18$ Å, $\gamma = 92.90°$.

As with other materials in the series M–Bi–O (M = Ca, Sr) studied thus far, at least some Bi is found in threefold coordination with oxygen; the remaining Bi are fourfold coordinated. The structure is related to that of $Ca_4Bi_6O_{13}$, which has been studied using neutron powder diffraction. Both compounds are composed of layers containing alternating Bi- and Ca-rich segments. These layers stack to form Bi-rich slabs containing tunnels accommodating the Bi-$6s^2$ lone pairs.

$Ca_4Bi_6O_{13}$ has both a high-temperature (HT) and low temperature (LT) phase. The HT phase forms at 820 °C while the LT phase is stable up to 700 °C. The HT phase is a defect type with oxygen vacancies comprising a body-centered cubic structure ($a = 4.26$ Å) γ-type solid solution (ss-γ) phase as $(1-x)Bi_2O_3{\cdot}CaO_x$ ($0.50 < x < 0.60$) was investigated by electron diffraction. Instead of finding evidence for additional Bragg reflections at G_n^o as previously assumed in attempting to interpret powder neutron diffraction data, localized diffuse scattering was detected and described by G_q^0, where $q \sim 0.2$ <211>*gamma as a (diffuse) modulation wave vector. A crystal structural relationship between the cation arrays in the ssγ phase and the low-temperature (LT) line phase, $Ca_4Bi_6O_{13}$, was established. The unit cell of the LT phase can be expressed as $a_{LT} = a_\gamma - c_\gamma$, $b_{LT} = 5/3(a_\gamma - 2b_\gamma + c_\gamma)$ and $c_{LT} = \cong (a_\gamma + b_\gamma + c_\gamma)$. From the cation ordering in the LT phase and the reciprocal space relation $2b \times LT = 0.2$<121>*γ ≅ q, the localized diffuse scattering in the ssγ phase was linked to cation ordering into layers perpendicular to <121>γ.

The crystal structure of the 1:1 CaO–Bi_2O_3 compound ($CaBi_2O_4$) has been determined by single-crystal X-ray and neutron powder diffraction techniques. The compound crystallizes with the symmetry of the monoclinic space group C2/c and lattice parameters $a = 16.6130$ Å, $b = 11.5900$ Å, $c = 13.9939$ Å, $\beta = 134.048°$ (Fig. 4.92).

The structure consists of sheets parallel to the b–c plane and connected by Ca–O bonds. There is a structural unit in each layer consisting of four Bi atoms, ten oxygen atoms, and two calcium atoms. The Bi atoms are fourfold coordinated and the coordination polyhedron may be described as a short distorted pyramid, open on one end to accommodate the lone-pair electrons of the bismuth atoms. Calcium is seven-coordinated and the coordination polyhedron may be described as a monocapped trigonal prism.

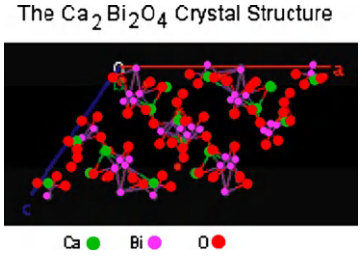

FIGURE 4.92

The electronic structure of $CaBi_2O_4$ was calculated by a GGA approach. The valence-band maximum is approximately located at the Γ-point or the *Y*-point and the conduction band minimum at the *V*-point. This means that $CaBi_2O_4$ is an indirect energy gap material. The conduction band is composed of Bi 6p–O 2p interaction. On the other hand, the valence band can be divided into two energy regions ranging from −9.92 to −7.40 eV (lower valence band) and −4.69 to 0 eV (upper valence band). The former is mainly constructed from Bi-6s states interacting slightly with O-2s and O-2p states, and the latter consists of O-2p states hybridizing with Bi-6s and Bi-6p states. The states near the valence band maximum are strongly localized and the mobility of holes generated by band gap excitation is predicted to be fairly low.

Organic contaminants such as volatile organic compounds and dyes (e.g. acetaldehyde and methylene blue (MB)) can be photo-catalytically degraded over a novel $CaBi_2O_4$ catalyst. The reaction is environmentally friendly (O_2 oxidant) and proceeds at room temperature under visible-light irradiation of wide-ranging wavelengths. An example is the conversion of CH_3CHO into CO_2.

Lithium forms a series of glasses with Bi_2O_3 in which electrical conductivity is supported by transmission of Li^+ cations. The addition of Ca^{2+} improves and stabilizes the conductivity. Ion transport in Li_2O–CaO–Bi_2O_3 glasses has been studied in the frequency range from 10 Hz to 2 MHz and in the temperature range from 293 to 543 K. The variation of the DC conductivity and the activation energy of these glasses with composition have been compared with those of binary lithium bismuthate glasses. It has been observed that the introduction of CaO in small amounts does not effect the DC conductivity and the corresponding activation energy, but a larger amount of CaO changes them to some extent. The frequency-dependent conductivity has been studied using both conductivity and modulus formalisms. The values of the nonexponential parameter and frequency exponent are found to differ for the Li_2O–CaO–Bi_2O_3 glasses from those for the binary Li_2O–Bi_2O_3 glasses. Mobile Li^+ ion concentration does not change appreciably with a change in the Li_2O content or the CaO content in the compositions. The increasing amount of CaO in the glass compositions for fixed Li_2O content shows that it is the fact that CaO dilates the glass network, thus enhancing the rate and migration of Li^+ ions.

Calcium bismuthates have no CAS numbers and they are not offered for sale commercially.

Strontium Bismuthates

The known data for the phases $Sr_6Bi_2O_9$, $Sr_3Bi_2O_6$, $Sr_2Bi_2O_5$, $Sr_{18}Bi_{22}O_{51}$, $Sr_6Bi_{14}O_{27}$, $SrBi_4O_7$, $Sr_2Bi_6O_{11}$, $SrBi_2O_4$, $Sr_8Bi_{10}O_{23}$, $Sr_8Bi_2O_{11}$, $Sr_5Bi_6O_{14}$, $Sr_6Bi_2O_{11}$, $Sr_6Bi_4O_{15}$ and $Sr_{24}Bi_{14}O_{52}$ have been revised, corrected, and unknown data have been estimated. The values of ΔH^0_{298}, S^0_{298}, H^0_{297}-H^0_0, the T and ΔH values for the phase transformations, $Cp(T)$ for the crystalline state, Cp at $T > T_{ph,tr}$, and also the polynomial approximating a reduced Gibbs have been presented (G. Moseev et al—1996). In the phase diagram of SrO and Bi_2O_3, four compounds are known. These are:

$SrBiO_4$—monoclinic

$Sr_2Bi_2O_5$—tetragonal

$Sr_3Bi_2O_6$—orthorhombic

$Sr_6Bi_2O_9$—type not known

Note that the tribasic compound, Bi_2O_3 is specified. Strontium bismuthate can be prepared by firing the oxides, SrO and Bi_2O_5, in air. The reaction is:

$$2SrCO_3 + Bi_2O_5 + \text{heat} \Rightarrow 2SrBiO_3$$

where the bismuth oxide is in reality the acid salt, $Bi_2O_5 \cdot 3.67H_2O$ (or $3Bi_2O_5 \cdot 11H_2O$). $SrBiO_3$ is a mixed-valence type of compound where the actual formula is $Sr(Bi^{3+},Bi^{5+})O_{3-x}$ signifies an oxygen deficiency. Varying the Sr:Bi(V) ratio always results in the formation of this mixed-valence perovskite salt and the pyrochlore salts never appear. It is for this reason that many preparations have used sealed ampoules where the contents are under pressure when heated and in many cases employ an oxidizing agent such as $KClO_4$ to ensure that the oxidized form results. However, the preparation is not always successful. It is this fact that accounts for the scarcity of data concerning both strontium and barium bismuthates.

According to another paper, new cubic pyrochlore oxides of the type $(RM)(Bi)_2O_7$ (M = Ba, Sr, R = rare earth) could be prepared by solid-state reactions at 850 °C under 3 kbar pressure, starting from Bi_2O_3, R_2O_3 and peroxides of Ba, Sr or Ca in sealed gold ampoules. In the case of Sr, attempts to synthesize $Sr_2Bi_2O_7$ pyrochlores under high-oxygen pressure always resulted in the formation of the perovskite $SrBiO_{3-x}$ where Bi(III&V) is always the resultant.

Interest in these types of compounds stems from the fact that a copper–Sr (or Ba) bismuthate is a superconductor with a transition temperature, T_c, of 113 K. The general formula of the "2212" phase is $Sr_2Ca_{n-1}Cu_nBi_2O_{2-n}+4$, where n is the number of copper-oxide planes in the structure. The above diagram shows such a structure. In this diagram, Sr is shown but the composition with Ba has a higher critical temperature, T_c, number (Fig. 4.93).

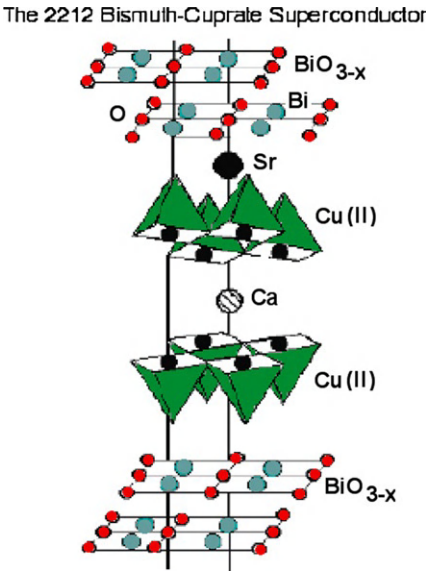

FIGURE 4.93

In this diagram, layers of $Cu(II)O_6$ are bordered by layers of bismuthates, BiO_{3-x} and interspersed with isolated Sr^{2+} (Ba^{2+}) or Ca^{2+} cations.

The "pyrobismuthate" has been difficult to obtain owing to the difficulty of bismuth to form stable Bi^{5+} compounds. The brownish-orange product obtained by heating an intimate mixture of $SrBiO_{3-x}$ and $KClO_4$, for 15 min at 730 °C and 60 kbar was a mixture of KC1 and a relatively well-crystallized phase whose XRD pattern could be indexed on an orthorhombic unit cell with $a = 7.70$ Å, $b = 7.91$ Å, and $c = 10.58$ Å. There is little doubt that this phase was the weberite $Sr_2Bi_2O_7$. Its "a-value", 5.44 Å, is about 2.6% larger than that of the perovskite phase, $Sr_2Sb_2O_7$. The loss of as much as one oxygen per $Sr_2Bi_2O_7$ (corresponding to $Sr_2Bi(III)Bi(V)O_7$) would amount to a weight loss of only 2.3%. The $Sr_2Bi_2O_7$ weberite appears to be one of the few genuinely stoichiometric oxygen compounds of Bi(V). It is noted that barium forms a mixed-valence compounds related to $Sr_2Bi_2O_7$, the golden $Ba_4Bi(III)Bi(V)O_{13}$.

The compound, $SrBi_2O_4$, has the following lattice parameters: $M_w = 569.58$ g/mol, monoclinic space group = C2/m, $a = 19.300$ Å, $b = 4.358$ Å, $c = 6.106$ Å, $\beta = 94.801(4)°$, $V = 511.7$ Å^3, $Z = 4$, $d_x = 7.39$ g/cm^3. The structure has been refined by Rietveld analyses of XRD data recorded at room temperature.

The $Ca_2Sb_2O_7$ compound crystallizes with a structure of both the pyrochlore (P) and the weberite (W) type, but $Sr_2Sb_2O_7$ is only known as a weberite. Its orthorhombic unit-cell parameters are: $a = 7.452$ Å, $b = 7.687$ Å, $c = 10.381$ Å, $Z = 4$. It is pseudo-cubic with "$a = 8.297$ Å". The structures are given in Fig. 4.94.

In the SrO–Bi_2O_3 system, several compounds were found to adopt an unusual structure. For example, in the structure of $Sr_2Bi_2O_5$, all Bi atoms are in unusual

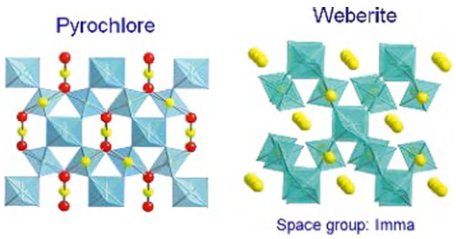

FIGURE 4.94

threefold coordination with respect to oxygen. The compound crystallizes with the space group *Amam*, and with cell parameters of $a = 6.1715(6)$ Å, $b = 14.3066(13)$ Å, $c = 3.8261(4)$ Å, $V = 338.1$ Å^3 and $Z = 2$.

The basic structure consists of the intergrowth of two simple structural elements. The first element is the anti-nickel arsenide structure. Each Sr atom is surrounded by six nearest neighbors in a trigonal prismatic arrangement. The second structural element can be regarded as $Bi_2O_4^{4+}$ chains which are inserted between the anti-NiAs slabs, Bi in 3-coordination with oxygen appears to exist only in systems containing the electropositive alkaline earth cations Ca and Sr. These Sr and Ca atoms appear to allow the Bi–O bonds to be more covalent in nature and therefore more directional. Ordering of oxygen and vacancies is also visible along the *c*-direction and results in displacements of the Bi atoms along *c*. The lone-pair electrons associated with the Bi can be envisioned as being directed toward the vacant site. The unit cell of $Sr_2Bi_2O_5$ showing the SrO_6 trigonal prisms and the position of $[Sr_2O_4]^{4+}$ groups is given in Fig. 4.95.

The Sr^{2+}(I) positions in the lattice are occupied by the $Sr_2O_4^{4+}$ groups while the Sr^{2+}(II) positions are occupied by the SrO_6 trigonal prisms. The two layers are separated by a channel caused by the $6s^2$ electrons of the $Bi_2O_4^{2-}$ groups.

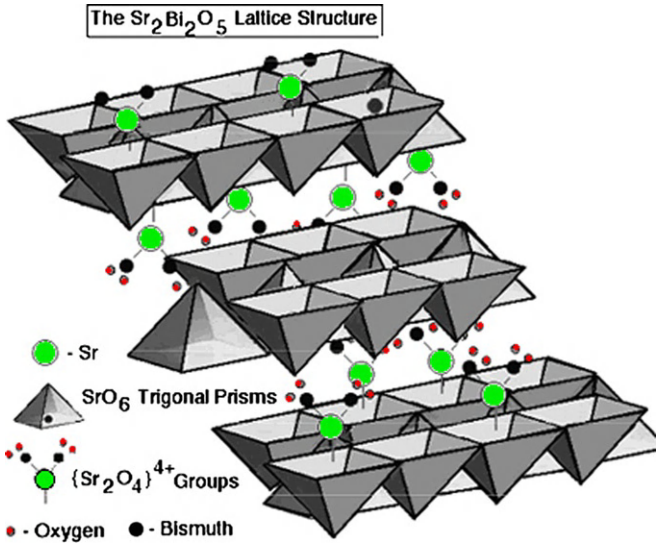

FIGURE 4.95

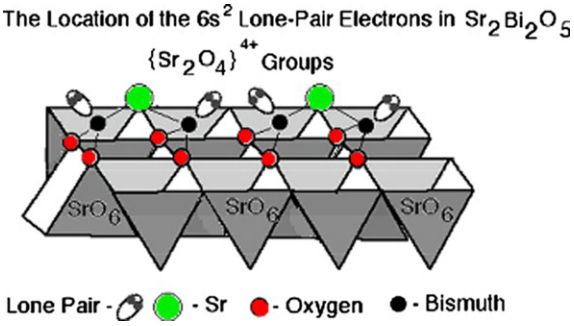

FIGURE 4.96

A better detail is shown in the following diagram showing the bond attachments and the two-electron lone-pairs of Bi^{3+} (Fig. 4.96).

The lone pairs, $6s^2$ of Bi^{3+} dominate all of the bismuthite compounds and cause noticeable channels within the structure of these compounds wherein they are coordinated. Perhaps it is this factor that makes pentavalent bismuth compounds so hard to achieve since the $6s^2$ electrons must be transferred to the relevant anion in order to achieve the pentavalent degree of ionization.

Ion transport in Li_2O–Bi_2O_3–SrO glasses has been studied in the frequency range 10 Hz–2 MHz and in the temperature range 263–483 K. The variation of the DC conductivity and the activation energy of these glasses with composition have been compared with those of bismuthate and lead bismuthate glasses. The frequency-dependent conductivity has also been studied using both modulus and conductivity formalisms. In the strontium glasses, Li_2O–Bi_2O_3–SrO, the variation of the power law exponent with Li_2O content is in contrast to that for the Li_2O–Bi_2O_3 and Li_2O–Bi_2O_3–PbO glasses. The values of the nonexponential parameter for the Li_2O–Bi_2O_3–SrO glasses are lower than those for the binary Li_2O–Bi_2O_3 glasses.

The conductivity increases and the activation energy decreases with the increase of SrO content in the glass compositions with fixed Li_2O content. The estimated mobile ion concentration is almost independent of temperature and SrO content in the compositions. The results have been interpreted on the basis of the modification of the bismuthate network by the addition of SrO, which enhances the mobility of Li ions, without altering the mobile Li+ ion concentration. It has also been shown that the conductivity relaxation in these glasses is independent of temperature and composition, and the non-exponential parameter is less than that for the lithium bismuthate glasses without SrO.

A new bismuth-based oxide, (Sr,K)BiO_3, was synthesized. Superconductivity was induced by the K-doping of $SrBiO_{3-x}$, performed under high pressure. The maximum T_c achieved was about 12 K (for 45–60% of K). This new compound has a distorted perovskite-based

structure. Powder synchrotron and neutron diffraction studies have shown that, as a function of K doping, the symmetry changes from monoclinic (space group $P2_1/n$) to tetragonal (space group I4/mcm) and remains the same down to 4 K. Above room temperature, $SrBiO_3$ keeps the same structure until decomposition around 700 °C, whereas the K-doped phases decompose around 300 °C with a progressive loss of oxygen until the $(Sr,K)BiO_{2.5}$ stoichiometry is reached. The oxygen loss is accompanied by a decrease of T_c. An increase of T_c was observed when resistivity was measured as a function of pressure. Powder synchrotron studies indicated that, for K-doped samples, pressure induces an increase of the tetragonal distortion, as well as a change of the tilt angle of the octahedra until the pressure corresponding to T_{cmax} is reached. The (Sr,K) site is more affected by the pressure effect than the Bi one. In the case of $SrBiO_3$, no noticeable change was observed under pressure.

The compound, $Sr_3Bi_2O_6$, has been studied because it is related to a superconducting compound, Bi_3O_3–PbO–SrO–CaO–CuO. Phase equilibria of the quasi-quinary system were studied between 650 and 900 °C in air with emphasis on the high-temperature superconducting phase ($T_c = 110$ K). $(Bi,Pb)_{2+x}Sr_2Ca_2Cu_3O_{10+d}$ (2223). The 2223 phase lies in equilibrium with a number of non-superconducting phases and also with the superconducting phase $(Bi,Pb)_2Sr_2CaCu_2O_{8+d}$ (2212). The single-phase region was found to be very limited. The Pb solubility of the 2223 phase is strongly temperature dependent. The phase relations are very sensitive to variations of the cation concentration and temperature. This effect significantly influences the preparation of 2223 ceramics.

In another paper, the compound $Sr_2Bi_2CuO_6$ should nominally be the phase with $n = 1$ of the high T_c superconducting series $Sr_2Bi_2Ca_nO_{4+2n}$. However, the superconducting phase with $n = 1$ (with no CaO) occurs only with a gross deficiency in SrO content. Instead, at the composition $Sr_2Bi_2CuO_6$, a different phase is formed with an XRD pattern considerably different from that expected for the $n - 1$ member of the series. This phase has been found, by a combination of electron diffraction and single-crystal and powder XRD, to have a commensurate lattice with monoclinic symmetry, space group $C2/m$ or Cm, $a = 24.473$ Å, $b = 5.4223$ Å, $c = 21.959$ Å, and $ß = 105.40°$. The actual composition of this phase may be deficient in CuO by as much as 1.0 mol%.

The phase equilibria of the systems SrO–CuO and $SrO\text{-}1/2Bi_2O_3$ were studied by XRD analysis of quenched powder samples. The compounds $SrCuO_2$ and Sr_2CuO_3 melt incongruently at 1085 and 1225 °C, respectively. The newly found compound $Sr_6Bi_2O_9$ decomposes at 965 °C into SrO and $Sr_3Bi_2O_6$ melts incongruently into SrO and liquid at 1210 °C. $SrBi_2O_4$ undergoes a phase transition at 825 °C, and although both are nonstoichiometric, the low-temperature phase is slightly poorer in SrO with 33.5 mol% SrO than the high-temperature phase. The decomposition of $SrBi_2O_4$ into $Sr_5Bi_2O_9$ at 780 °C for the $SrBi_2O_4$ composition has to be associated to the decomposition into two solid solutions. The $Sr_6Bi_2O_9$ compound is not part of the Bi_2O_3–SrO system but, due to a necessary stabilizing Bi^{III}–Bi^{V} oxidation phenomenon, it must be formulated $Sr_6Bi^{V}_yBi^{III}_{2-y}O_{9+y}$ with $y > 0$.

Another reported compound was designated $SrBi_3O_{5.5}$ or $Sr_2Bi_6O_{11}$. The crystal structure of the rhombohedral (R/m) $Bi_{0.75}Sr_{0.25}O_{1.375}$ phase has been determined at room and high temperature using single-crystal neutron diffraction. It can be described at all temperatures as the regular repetition of three fluorite-like sheets shifted with respect to one another by a vector $\gamma = 2\,(a/3 + b/3 + c/3)$ and thus separated by an intersheet space free of anions. Interstitial anions partially occupy delocalized sites in the vicinity of the unsubstituted interface Bi-layers and are responsible for the high ionic conductivity of this phase. They are mainly located on the fluorite-like sheet side of this Bi-layer at room temperature. At high temperature, they partly migrate to the opposite side, i.e. the intersheet side, a phenomenon which results in the $\gamma_2 \Rightarrow \gamma_1$ transition and a sudden increase of the conductivity. In light of these and previous results, the different behavior of various alkaline earth-doped rhombohedral phases (Ca, Sr, Ba) and of the La-doped homologue is analyzed and rationalized.

Strontium bismuthates have no CAS numbers and they are not offered for sale commercially.

Barium Bismuthate

Metal oxides containing Bi^{5+} are relatively rare. Those of $BaO \cdot Bi_2O_5$ are not easily formed due to the same restrictions already mentioned for $SrO \cdot Bi_2O_5$. Thus, those of $BaO \cdot Bi_2O_3$ are much more stable due to the presence of the $6s^2$ lone pairs of the ion, Bi^{3+}. $BaBiO_3$ is a mixed-valency type of compound where the actual formula is $Ba(Bi^{3+},Bi^{5+})O_{3-x}$ signifies an oxygen deficiency. Varying the Ba:Bi(V) ratio always results in the formation of this mixed-valency perovskite salt and the pyrochlore salts never appear under usual chemical conditions. It is for this reason that many preparations have used sealed ampoules where the contents are under pressure when heated and in many cases employ an oxidizing agent such as $KClO_4$ to ensure that the oxidized form results. However, the preparation is not always successful. It is this fact that accounts for the scarcity of data concerning barium bismuthates. The correct formulation for $BaBiO_3$ is believed to be:

$$Ba{Bi^{3+}}_{0.5+x}{Bi^{5+}}_{0.5-x}O_{3-x}$$

which is accurately a "Bismuthite". $BaBiO_{3-x}$ occurs as a distorted monoclinic type of structure with a breathing- and a tilting-mode lattice distortion of

BiO_6 octahedra, and it shows semiconducting behavior despite the theoretical calculation predicting metallic behavior. The compound crystallizes monoclinic in the space group I2/m, with $a = 6.181$ Å, $b = 6.136$ Å, $c = 8.670$ Å, $\beta = 90.17°$, and $Z = 4$. The calculated density of the valence electrons is 0.3041 electrons per $Å^3$. The compound undergoes two structural phase transitions, a first-order transition to a rhombohedral structure near 425 K (152 °C) and a second-order transition to a cubic structure, the transition temperature being estimated as 893 K (620 °C).

In order to clarify the effect of oxide ion vacancy on electronic structure of $BaBiO_{3-x}$, the electrical conduction property at high temperature under various oxygen partial pressures, $P(O_2)$, was investigated. At 775 °C, in dependence of electrical conductivity on log $P(O_2)$, three phases were observed. This behavior shows agreement with oxygen nonstoichiometry data measured by thermogravimetry. Under log P (O_2) higher than −1.75, *n*-type semiconducting property was observed which could be attributed to charge density waves originating from two kinds of Bi sites in crystal structure. In the log $P(O_2)$ region between −1.75 and −2.45, electrical conductivity almost independent of log $P(O_2)$ was observed. This suggested semimetallic electronic structure with itinerant electrons that could originate from single Bi site in $BaBiO_{3-x}$ with ideal perovskite structure (as clarified by neutron diffraction). Below log $P(O_2)$ of −2.45, abrupt decrease of electrical conductivity was observed, suggesting localization of electron in Bi orbitals, which could also be speculated from low symmetry around the Bi site in $BaBiO_{2.5}$.

If a ratio of $2BaO:Bi_2O_3$ is used, a compound, $Ba_2(BiO_3)_2$ or $(BaBiO_3)_2$ results. This identical compound shows that the most stable configuration of the $Bi^{3+}Bi^{5+}$ complex is an ordered supercell, but there are no big variations in energy between different $Ba_2Bi^{3+}Bi^{5+}O_{6-x}$ configurations. If divalent or trivalent cations are added to $BaBi^{3+}Bi^{5+}O_{3-x}$, it has been reported that the results are quite different. With the aid of infrared spectroscopy, it was shown that the bismuth ions in $BaBiO_{3-x}$ are equivalent and that the charge distribution is $Ba_2Bi^{3+}Bi^{5+}O_6$. In addition, it was demonstrated that the bismuth ions are pentavalent in Ba_2TbBiO_6, but tetravalent in $Ba_3PbBi_2O_9$.

Doping $BaBiO_{3-x}$ with alkali ions transforms the larger monoclinic parent lattice into a more compact cubic or nearly cubic lattice. This lattice contraction favors the transition from semiconductor to metal. It also leads to superconductivity. Doping $BaBiO_3$ with both K and Rb raises the onset resistivity T_c above those obtained by doping with either K or Rb alone. $BaBiO_{3=x}$ keeps the same structure until decomposition around 750 °C, whereas the K-doped phases decompose around 300 °C with a progressive loss of oxygen until the (Ba, K, Rb)$BiO_{2.5}$ stoichiometry is reached. The oxygen loss is accompanied by a decrease of T_c. An increase of T_c was observed when resistivity was measured as a function of pressure. Both, Bismuth and Barium have a distorted coordination sphere. Bismuth and oxygen occupy two different crystallographic positions, the 2(a)- and 2(c)-positions and the 4(i)- and 8(j)-positions.

Following the initial discovery, $BaBiO_{3-x}$ has been doped with a variety of cations in efforts to increase the T_c of the product. Two such examples were:

> "The structure, nonstoichiometry, and electrical conductivity of compositions in the $BaBiO_{3-x} \Rightarrow Ba(Ce_{1-x}Gd_x)O_{3-x/2}$ system have been investigated in an attempt to prepare new mixed (ionic-electronic) conducting oxides. The substitution of Bi into $Ba(Ce_{1-x}Gd_x)O_{3-x/2}$ decreases the concentration of oxygen-ion vacancies, and the effective negative charge of the Gd dopant is compensated by the mixed valence of Bi (3+, 5+). For low Bi contents, a decrease in ionic conductivity decreases the overall conductivity; however, higher levels of Bi introduce significant electronic conductivity, and for $Ba(Bi_{0.5}Ce_{0.5})O_3$, $<> s_{total}$ at 1 S/cm^2 at 800 °C in air was observed. Compositions in the $Ba(Bi_{0.5}Ce_{0.5-x}Gd_x)O_3$ pseudobinary system undergo a B-cation site order-disorder transformation at 1300–1350 °C for $x = 0.5$ and at 1250 °C for $x = 0.4$; all other compositions retain a disordered B-site arrangement. These disordered perovskites exhibit oxygen nonstoichiometry under reducing conditions at elevated temperatures, with the extent of reduction decreasing with increasing Gd content. However, their ordered counterparts remain close to stoichiometric proportion. The electronic conductivities of this nonstoichiometric pseudobinary could be fitted to a 3-band type-2 model, and, despite the presence of oxygen vacancies for the lower values of x, no significant ionic conductivity was observed".
>
> "Changes in the electronic states for $Ba_{1-y}K_yBiO_{3-x}$ ($y = 0$ and 0.5) due to various surface treatments (fracturing, scraping and ion sputtering) have been studied by X-ray photoelectron spectroscopy. It is found that marked spectral changes occur as a result of scraping and sputtering; the core levels are broadened and the intensity at the top of the valence bands is reduced. These results are discussed in terms of the reduction of elements and damage in the surface region. The above results cause the authors to conclude that fracturing these samples is suitable as a cleaning procedure for this system. The Bi-4f, Ba-4d and O-1s core levels have very low binding energies and are shifted by 0.2–0.4 eV to lower binding energies on 50% substitution of K for Ba. The Bi-4f line seems to contain a single chemical state for $BaBiO_{3-x}$, and more than one chemical state for $Ba_{0.5}K_{0.5}BiO_{3-x}$. The top of the valence band is found to be 0.5 eV below the Fermi level for $BaBiO_{3-x}$, while a clear Fermi edge appears for the K-doped material in the valence band spectra from both X-ray and ultraviolet photoelectron spectroscopy. The electronic states of $BaBiO_{3-x}$ and K doping effects are discussed and compared with band calculations".

The compound $Ba_{1-y}K_yBiO_{3-x}$ shows superconductivity at $T_c \approx 30$ K (−243 °C). One such study shows that in $BaBiO_3$, Bi^{3+} sites can trap two holes from the valence band to form Bi^{5+} cations. The trapping is accompanied by large local lattice distortions; therefore the composite particle consisting of the electronic hole and the local lattice phonon field forms a polaron. This study clearly shows that even "sp" elements can trap carriers at

lattice sites, if the local lattice relaxations are sufficiently large to screen the localized hole. The derived model describes all relevant experimental results, and settles the issue of why hole-doped $BaBiO_{3-x}$ remains semiconducting upon moderate hole doping.

The structure of the valence ordered perovskite-like compound $BaBiO_{3-x}$ has been studied at five temperature intervals between room temperature and 923 K (650 °C) using high-resolution synchrotron X-ray powder diffraction methods. The compound undergoes two structural phase transitions, a first-order transition to a rhombohedral structure near 425 K (152 °C) and a second-order transition to a cubic structure, the transition temperature being estimated as 893 K (620 °C). The perovskite-like compound $BaBiO_{3-x}$ system has been studied by first-principles molecular dynamics and the relation between phase-transition properties and different valence of bismuth has been discussed. A successful match between theoretical and experimental results has been achieved. It is found that irrespective of which bismuth valence, $Bi^{4+}Bi^{4+}$ or $Bi^{3+}Bi^{5+}$, is used, the structural transformation is present and is basically a size effect. The calculation also shows that the most stable configuration of the $Bi^{3+}Bi^{5+}$, is an ordered supercell, but there are no big variations in energy between different $Ba_2Bi^{3+}Bi^{5+}O_6$ configurations.

In an effort to study the effect of reduction on the oxygen content in $BaBiO_{3-x}$, the following observations have been made. The reduction isobar T vs x ($pO_2 = 0.21$ atm) of $BaBiO_{3-x}$ between 750 and 1050 °C shows a trend with three near linear sections in the ranges 750–850 °C, 850–1000 °C, and 1000–1045 °C, respectively. The quenching in liquid N_2 of first-section solids (phase I) does not prevent the transformations $Fm\bar{3}\,m \Rightarrow R3 \Rightarrow I2/m$ (which are typical of the stoichiometric compound) and their XRD patterns at room temperature are not different from that of the stoichiometric $BaBiO_3$. The quenching of the cubic structure $Pm\bar{3}\,m$ of solids in the second section (phase II) still originates a monoclinic structure, but one strongly perturbed by the high concentration of oxygen vacancies. As determined by neutron diffraction at high temperatures, the phase II to phase III transition (third section of the isobar) occurs unusually in a gradual way, and it is nearly complete as the melting temperature (1045 °C) is approached. The close resemblance of the XRD patterns of the terms of the Aurivillius series with those of $BaBiO_{2.56}$ (phase III) leads to the conclusion that this last phase is the term limit of the above series. Its structure would therefore be characterized by a random distribution of Ba and Bi ions in the perovskite A and B sites. The reduction of $BaBiO_3$ in high purity N_2 ($pO_2 \approx 10^{-6}$ atm) yields the polymorphous solid $BaBiO_{2.50}$. At 1000 °C, it still shows a structure with the tetragonal symmetry of phase III. Between 1000 and 800 °C, this bright red solid shows a pseudocubic perovskite-type structure, while for lower temperatures it assumes a bright yellow color and a structure with monoclinic "no-longer-perovskite"-type symmetry. The equilibria between the solids of the examined system were also studied through annealing and quenching in water of solids with $x = 0.2$, 0.3, and 0.44, sealed in silica glass tubes. The eutectoid decomposition of phase II ($x = 0.2$) to phase I and phase III (at $T = 668 \pm 2$ °C) and the subsequent decomposition of phase III to phase I plus the yellow phase $BaBiO_{2.5}$ (at 663 ± 2 °C) disagrees with the results of other authors. The results of the simultaneous DTA, TG, and DTG analyses on the stoichiometric $BaBiO_3$ at $pO_2 = 0.21$ and 1 atm leads to the conclusion that the monophasic region II ($Pm\bar{3}\,m$) for adequate pO_2 ($pO_2 > 1$ atm) extends as far as the stoichiometric solid itself ($x = 0$).

Barium bismuthate, $BaBiO_3$, has a CAS number of 12785-50-1 and a molecular weight of 394.305 g/mol. It is a bronze crystal which decomposes at 1040 °C. It has found usage in industry in alkaline batteries. The incorporation of small amounts (1–5 wt%) of semiconducting $BaBiO_{3-x}$ and metallic $Ba_{0.6}K_{0.4}BiO_3$ additives on the rechargeability of electrolytic manganese dioxide cathodes in alkaline cells in the one-electron regime has been investigated. Both the $BaBiO_3$ and $Ba_{0.6}K_{0.4}BiO_3$ additives lead to better recyclability compared to the previously known binary oxide additive Bi_2O_3. XRD patterns recorded before and after 30 cycles as well as cyclic voltammograms recorded after first and 30 cycles reveal that the better recyclability in the presence of $BaBiO_3$ and $Ba_{0.6}K_{0.4}BiO_3$ additives is due to the suppression of the formation of unwanted, electrochemically inactive "Birnessite" and "Hausmannite" phases and a shifting of the second-electron capacity of Mn to higher potentials.

The synthesized oxide $BaBiO_{3-x}$ can absorb light with wavelength below 650 nm, which almost covers the region from UV through all strong visible light in the sunlight, as well as that of an indoor lamp. The material demonstrates highly photocatalytic properties for the decompositions of hazardous chemicals such as gaseous acetaldehyde and methylene-blue dye even under light irradiation with wavelength longer than 600 nm. These optical effects have been explained in terms of "excitons". The energy splitting due to Charge Density Wave formation in the 6s band of Bi is found to be very large (2.0 eV), whereas, the minimum gap is much smaller (0.55 eV) than it. This large optical gap appears in the visible region as a dominant peak of the optical conductivity, and it is mainly due to the direct formations of excitons. The smaller gap appears in the infrared region, and is due to an indirect exciton mechanism. This theory well agrees with the results of recent optical experiments on $BaBiO_{3-x}$.

A Bi-based photocatalyst ($BaBiO_{3-x}$) was prepared by the solid-state reaction of BaO and $Bi_2O_3 \cdot (OH)_4$ and its

optical absorption properties were determined by UV-visible diffuse reflectance spectrum. The photocatalytic properties of the oxide for decomposition of acetaldehydes were investigated. The results show that this Bi-based material is very active in photocatalytic organic decomposition under visible light irradiation.

$BaBiO_{3-x}$ and modifications thereof are now being used as solid-state ceramic conducting membranes for the separation of oxygen from air. These membranes are heated to about 700 °C and involves transport of O^{2-} atoms across the membrane to form O_2 atoms. They can deliver oxygen fluxes in excess of 5 ml/min/cm^2.

$BaBiO_3$ is a semiconducting material and shows a good negative temperature coefficient (NTC) effect. NTC thermistors are thermally sensitive resistors whose resistance decreases with increasing temperature. They are mainly used in electronics for the suppression of in-rush current, for temperature measurement and control, and for compensation for other circuit elements.

Although $BaBiO_{3-x}$ remains the most studied compound in the $BaO \cdot Bi_2O_3$ series, other compounds have been discovered. $BaBi_2O_6 \cdot 4H_2O$ is an orange crystal which can be precipitated from solution by the reaction:

$$BaCl_2\ (aq) + NaBiO_3\ (aq) \Rightarrow Ba(BiO_3)_2 \cdot 4H_2O\ (s)$$

This compound, when heated to about 80 °C, loses two waters of hydration and the other two at 180 °C. Further heating to about 420 °C then causes loss of oxygen and formation of the compound, $BaBiO_{3-x}$.

$Ba_2Bi_2O_5$ actually has the formula of $Ba_2Bi_2O_{5+y}$ where an excess of oxygen is present. It has been found useful in the dehydrogenation of olefins where the double bond is changed from 2(C=C) to (C-C-C-C) a saturated hydrocarbon useful in fuels. Bi_2O_5 has traditionally been used in this context but $Ba_2Bi_2O_{5+y}$ has proven to be superior as a catalyst. To prepare this compound, the stoichiometric compound, $Ba_2Bi_2O_6$ is first prepared. A mixture of the nitrates are first fired together in air for 2 h at 400 °C, followed by regrinding and heating at 800 °C for 24 h. This compound was brownish-red in color. It was then reheated at 850 °C in flowing oxygen (100 ppm or 0.0001 atm) + argon. The product is magenta in color. It is sensitive to moisture in air. The product was analyzed as $Ba_2Bi_2O_{5.0 \pm 0.02}$. Its structure was pseudo-cubic with $a = 8.892$ Å. The actual formula is probably: $Ba_2Bi^{3+}Bi^{5+}O_{5+y}$.

To prepare other degrees of oxygen-rich barium bismuthate, $Ba_2Bi_2O_6$ is heated in a flowing oxygen argon at the following temperatures and oxygen concentrations (Table 4.25).

Further modifications have been made by the addition of Y^{3+} and Ln^{3+} ions which substitute for the Bi^{3+} ion in the structure. Such catalysts are used in Refinery processes for treating various fractions of crude oils, particularly "heavy crude". Such a process includes the heterogenetic-catalytic oxidative gaseous phase dehydrogenation of alkyl aromatics or aliphatics (educts) to form the corresponding alkenyl aromatics or olefins. In a first reaction step, the educt is dehydrogenated with a bismuth-containing redox catalyst (oxygen carrier) in the absence of molecular oxygen, and, in a second reaction step, the reduced catalyst is reoxidized with an oxidizing agent. The reaction steps are chronologically or spatially decoupled, and at least one reducible bismuthate like $Ba_2La^{3+}Bi^{5+}O_{5+y}$ on a basic or neutral carrier is used as the bismuth-containing catalyst. The process further concerns a Ba-bismuthate(5) having the composition $Ba_9Bi_3O_{14}$ as a novel substance.

$Ba_2Bi^{3+}Bi^{5+}O_6$ has been synthesized. High-resolution neutron powder diffraction has been used to investigate the structures and phase transitions in the double perovskites $Ba_2Bi^{3+}Bi^{5+}O_6$ (dibarium dibismuth hexaoxide) in the temperature ranges 4.2–973 K (−269 to 700 °C). The charge-ordered bismuthate adopts four structures in the temperature range—monoclinic in $P2_1/n$, monoclinic in I2/m, rhombohedral in $R\bar{3}$, and finally cubic in $\bar{b}$. The low-temperature monoclinic structure has been determined for the first time. The transitions from $P2_1/n \Rightarrow$ I2/m, at 132 K (−141 °C), and $R\bar{3} \Rightarrow Fm\bar{3}$ at 820 K (547 °C), are tricritical in nature; the transition from I2/m $\Rightarrow \bar{b}$ at ≈ 430 K (157 °C) is discontinuous. The behavior of Ba_2BiSbO_6 is very similar, except that the transition temperatures are lower at 250 K for I2/m $\Rightarrow R\bar{3}$ and 515 K for $R\bar{3} \Rightarrow Fm\bar{3}$ and the low-temperature structure is not formed at all.

Although $BaBiO_{3-x}$ has a CAS number, its availability is commercially limited to small quantities suitable for CVD studies. Only a few manufacturers offer it for sale.

Radium Bismuthate

There are no known publications concerning $RaBi_2O_4$- or $RaBi_2O_6$-type compounds. The most likely stable compound would be $RaBiO_{3-x}$ but even this composition has apparently not been synthesized. The systems, $xRaO \cdot yBi_2O_3$ or $xRaO \cdot yBi_2O_5$, remain unknown.

TABLE 4.25

$Ba_2Bi_2O_{5.10 \pm 0.04}$	Tetragonal, $a = 8.784$ Å; $c = 8.977$ Å	3 h at 765 °C	1000 ppm = 0.001 Atm	Black
$Ba_2Bi_2O_{5.62 \pm 0.04}$	Perovskite	58 h at 715 °C	1000 ppm = 0.001 Atm	Dark brown

The chemistry of Ra^{2+} ought to follow that of Ba^{2+}. However, in view of the difficulty in forming similar compounds of barium and the radioactivity of ^{226}Ra, it is apparent why this line of research has not been followed. If one were to initiate such a program, one would follow that of barium.

Metal oxides containing Bi^{5+} are relatively rare. Those of $RaO \cdot Bi_2O_5$ are not expected to be easily formed due to the same restrictions already mentioned for $SrO \cdot Bi_2O_5$. Thus, those of $RaO \cdot Bi_2O_3$ would be much more stable due to the presence of the $6s^2$ lone pairs of the ion, Bi^{3+}. $RaBiO_3$ would be a mixed-valency type of compound where the actual formula is $Ra(Bi^{3+},Bi^{5+})O_{3-x}$ signifies an oxygen deficiency. Varying the Ra:Bi(V) ratio would always result in the formation of this mixed-valency perovskite salt and the pyrochlore salts would never appear under usual chemical conditions. It is for this reason that many preparations would require sealed ampoules where the contents are under pressure when heated and in many cases employ an oxidizing agent such as $KClO_4$ to ensure that the oxidized form results. However, the preparation is not expected to always be successful. It is this fact that probably accounts for the scarcity of data concerning radium bismuthates. The correct formulation for $RaBiO_3$ is believed to be:

$$RaBi^{3+}_{0.5+x}Bi^{5+}{}_{0.5-x}O_{3-x}$$

which is accurately a "Bismuthite".

4.5.2. Alkaline Earth Bismuthides

Bi metal forms a series of alloy compounds with the alkaline earths. Various compositions have been studied and the phase diagrams have been established. Some of these have unique structures.

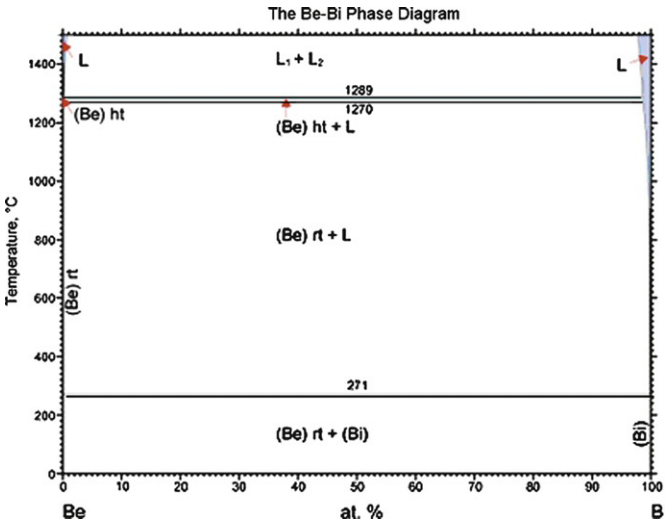

FIGURE 4.97

Beryllium Bismuthides

Be metal does not form any specific compounds with metallic Bi. The only phenomena found was the formation of alloys having the characteristics of Be metal itself, as shown in the following phase Fig. 4.97.

Magnesium Bismuthides

Mg metal forms a series of compounds with Bi metal, as shown in the following phase Fig. 4.98.

Only one compound has been established which is dimorphic. The crystal parameters of the system are: The crystal structure of Mg_3Bi_2 has the form shown as follows, which is a La_2O_3 type of structure (Fig. 4.99).

Cell parameters are: $a = 4.62$ Å, $b = 4.62$ Å, $c = 7.41$ Å, $\alpha = \beta = 90°$, $\gamma = 120°$, cell volume = 136.97 Å^3, $Z = 1$. Site occupancy is shown in Table 4.26.

In addition, the high-temperature phase changes and has the Ag_2S type of structure (Fig. 4.100).

TABLE 4.26

No	Site notation	Atom	Multiplicity	Wyckoff	Site symmetry	*x*	*y*	*z*	Occupancy
1	Mg1	Mg	2	d	3m.	1/3	2/3	0.2467	1.0
2	Bi1	Bi	2	d	3m.	1/3	2/3	0.6470	1.0
3	Bi2	Bi	1	a	-3m.	0	0	0	1.0

Material	Structure type	Pearson group	Space group	Melting temperature, °C	Physical character
(Bi)	As	hR6	166	271	No data
Mg_3Bi_2 rt	La_2O_3	hP5	164	703	No data
$Mg_{1.5}Bi$ ht	Ag_2S	cI20	229	821	No data
(Mg)	Mg	hP2	194	650	No data

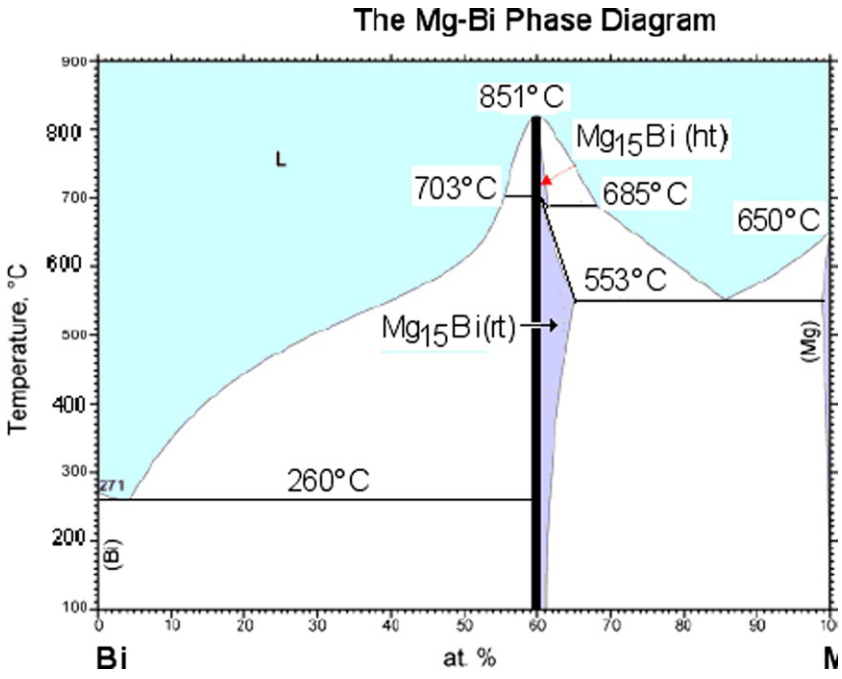

FIGURE 4.98

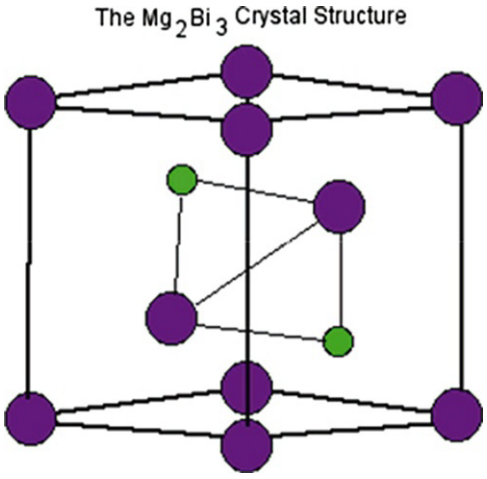

FIGURE 4.99

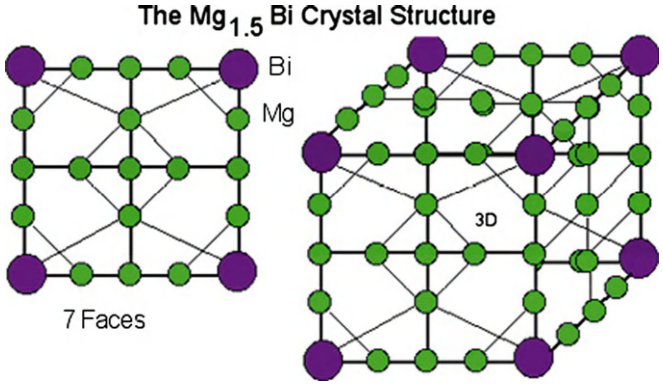

FIGURE 4.100

The $Mg_{1.5}Bi$ structure, actually α-Mg_3Bi_2, consists of seven (7) unilateral faces, one on each side of the cube and one hidden in the middle. The low-temperature phase, β-Mg_3Bi, shows a much simpler structural design. Cell parameters of α-Mg_3Bi_2 are: $a = b = c = 4.5673$ Å, $\alpha = \beta = \gamma = 109.471°$, cell volume $= 74.31$ Å^3, $Z = 2$. Cell occupancy is shown in Table 4.27.

The structure of β-Mg_3Bi_2 has been determined by neutron powder diffraction. The results show that it is a super-ionic phase, with a fixed body-centered cubic bismuth sublattice and mobile Mg^{2+} ions. From the analysis of the radial distribution function obtained from the diffraction pattern, it is concluded that the magnesium ions occupy the tetrahedral and triangular symmetry sites of the bismuth lattice in a similar way to the silver

TABLE 4.27

No	Site notation	Atom	Multiplicity	Wyckoff	Site symmetry	x	y	z	Occupancy
1	Mg1	Mg	12	d	-4m.2	1/4	0	1/2	0.266
2	Mg2	Mg	6	b	4/mm.m	0	1/2	1/2	0.135
3	Bi1	Bi	2	a	m-3m	0	0	0	1.0

ions in the anion lattices of α-AgI and α-Ag2Se. This material is an example of a new type of super-ionic conductor in which the metallic mobile ion is small and doubly charged.

Structural stabilities, elastic properties and electronic structures have been determined from first-principles calculation by using Castep and Dmol program based on the density functional theory for $Mg_{17}Al_{12}$, Mg_3Bi_2 and Mg_3Sb_2 phases. The calculation results of heat of formation and cohesive energy indicate that Mg_3Sb_2 has the strongest alloying ability as well as the highest structural stability. The calculations of thermodynamic properties show that the Gibbs free energy of $Mg_{17}Al_{12}$, Mg_3Bi_2 and Mg_3Sb_2 change with the elevated temperature, when the temperature is below 423 K, Mg_3Sb_2 and Mg_3Bi_2 are more stable than $Mg_{17}Al_{12}$ phases and Sb or Bi addition to the Mg–Al-based alloys can improve the heat resistance. The DOS of these compounds have been given. The elastic parameters are calculated, then the bulk modulus, shear modulus, Young's modulus and Poisson ratio value are derived. All the results of the analysis indicate that adding Sb or Bi to Mg–Al alloy could improve the ductility and plasticity by forming Mg_3Sb_2 and Mg_3Bi_2 phases.

Calcium Bismuthides

Calcium forms a number of compounds with Bi as can be seen by examination of the phase diagram shown in Fig. 4.101.

$CaBi_3$ does not appear in the phase diagram and has not been characterized separately. The reason for this remains unknown. Very little information concerning this compound is available in the literature and its structure has not been determined. Its physical properties are the only ones described (in one paper). It has no CAS number.

The other compounds are: Ca_2Bi, Ca_5Bi_3, and $Ca_{11}Bi_{10}$.

The system parameters are shown in Table 4.28.

The crystal structure of Ca_5Bi_3 is shown as follows where a view of the *c*-direction is shown. The cell parameters are: $a = 8.437$ Å, $b = 9.706$ Å, $c = 12.66$ Å, $\alpha = \beta = \gamma = 90°$, $Z = 4$, cell volume $= 104.640$ Å^3 (Fig. 4.102).

Cell occupancy by the 32 atoms in the unit cell is shown in Table 4.29.

The Mn_5Si_3 structure arrangement is virtually unique. The active component in this hexagonal structure ($P6_3/mcm$) is a confacial chain of $A_6/2B_6/2$ units; that is, a chain of A_6 trigonal antiprisms (octahedra) that are condensed with like units by sharing basal faces. The shared faces in these condensed units are then each bridged by three B atoms to give what can be described as $[A_{6/2}\text{-}B_{6/2}]$ chains. Each of these A atoms (crystallographically A_2) has six other A neighbors, two in the shared face and two in each of the two adjoining shared faces. The A atoms likewise have four B neighbors, two around the shared face plus one above and one below in the staggered planar A_5B_3 units. The active site for binding of an interstitial atom (Z) is the center of each trigonal antiprismatic A_6 unit. A better diagram shows the hexagonal network of the Ca_5Bi_3 structure that is endemic to all Yb_2Si_3-type of compounds (Fig. 4.103).

In contrast, the structure of Ca_2Bi is much simpler as shown in the following Fig. 4.104.

The unit-cell parameters are: $a = b = 4.722$ Å, $c = 8.918$ Å, $\alpha = \beta = 105.345°$, $\gamma = 90°$, cell volume $= 184.24$ Å^3. Cell occupancy of the 12 atoms is shown in Table 4.30.

This compound has been reported not to exist. Reported were the structure refinements and the electronic structure calculations for the ternary

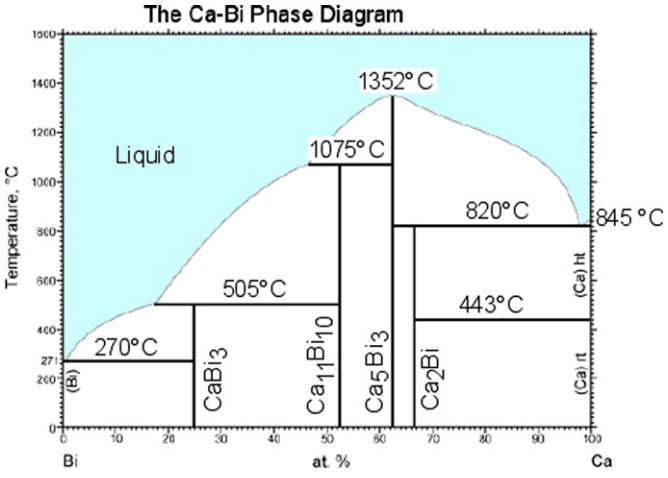

FIGURE 4.101

TABLE 4.28

Compound	Structure type	Pearson group	Space group	Melt temperature	Physical parameters
(Ca) rt	Cu	cF4	225	443	No data
(Ca) ht	W	cI2	229	842	No data
Ca_5Bi_3 (H)	Yb_5Sb_3	oP32	62	1352	No data
$Ca_{11}Bi_{10}$	$Ho_{11}Ge_{10}$	tI84	139	1075	No data
Ca_2Bi	La_2Sb	tI12	139	820	No data
$CaBi_3$	—	—	—	505	No data
(Bi)	As	hR6	166	271	No data

TABLE 4.29

No	Site notation	Atom	Multiplicity	Wyckoff	Site symmetry	*x*	*y*	*z*	Occupancy
1	Ca1	Ca	8	d	1	0.074	0.0421	0.1952	1.0
2	Bi1	Bi	8	d	1	0.3293	0.0144	0.0675	1.0
3	Ca2	Ca	4	c	.m.	0.0054	1/4	0.5354	1.0
4	Ca3	Ca	4	c	.m.	0.2295	1/4	0.8196	1.0
5	Ca4	Ca	4	c	.m.	0.2883	1/4	0.3492	1.0
6	Bi2	Bi	4	c	.m.	0.4834	1/4	0.5786	1.0

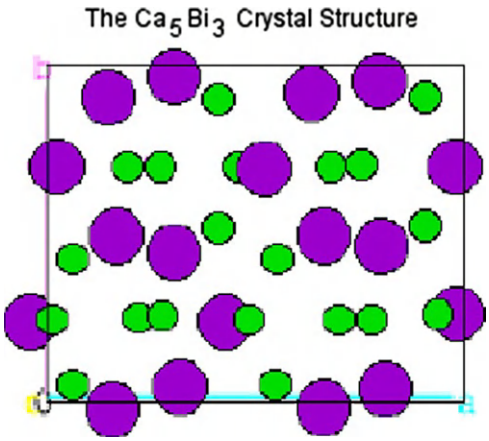

FIGURE 4.102

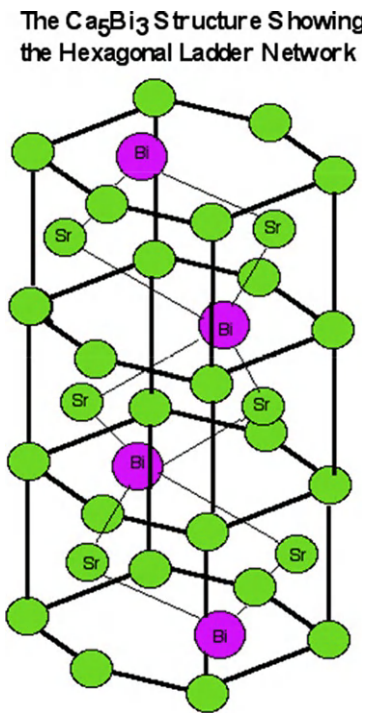

FIGURE 4.103

compound Ca_4Bi_2O, up until now stated to have been erroneously known as the binary $Ca_2Bi.\cdot Ca_4Bi_2O$ crystallizes in the body-centered tetragonal space group $I4/mmm$ (no. 139), with cell parameters $a = 4.719(2)$ Å and $c = 16.505(9)$ Å at 120 K, and its structure can be regarded as built of oxygen-centered octahedra of Ca, forming infinite layers via corner sharing, i.e. as an antitype of the perovskite-related

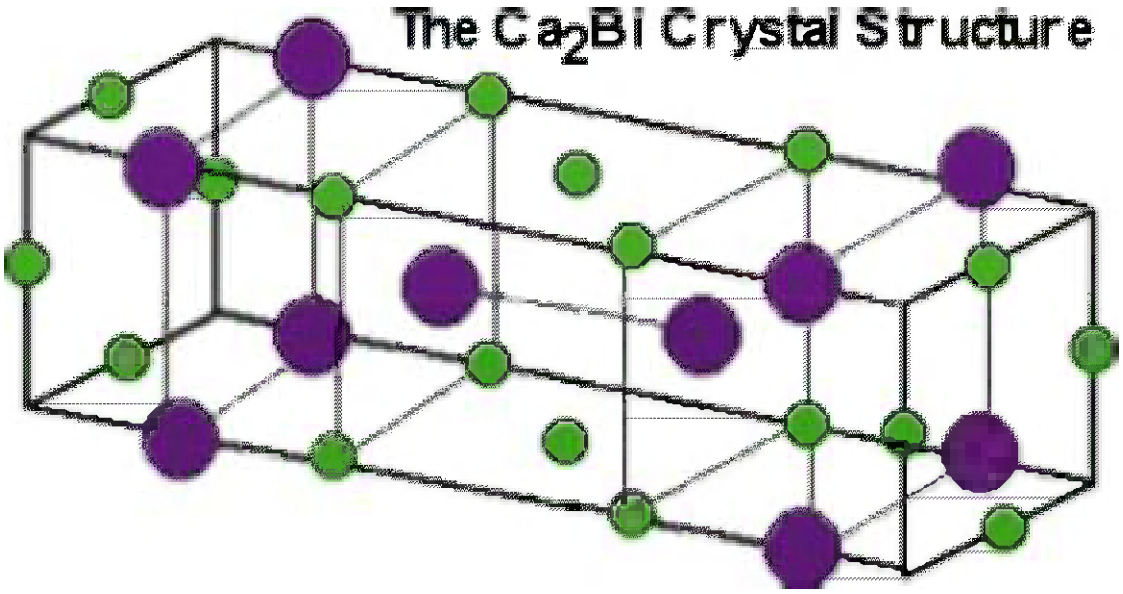

FIGURE 4.104

K_2NiF_4. The bonding in Ca_4Bi_2O has been further analyzed using electronic structure calculations (LMTO-ASA), which confirm that Ca_4Bi_2O and related phases, as expected, are closed-shell compounds. It is likely that both compounds exist, the latter being a product formed when the two metals are melted together in air.

The 11:10 compound has also been characterized. Its structure is shown in Fig. 4.105.

Lattice parameters are: $a = b = 12.22$ Å, $c = 12.40$ Å, $\alpha = \beta = 119.518°$, $\gamma = 90°$, cell volume $= 132.828$ Å^3, $Z = 4$. Cell parameters for the 84 atoms present in the unit cell are shown in Table 4.31.

In addition, a compound having the stoichiometry of $Ca_{16}Bi_{11}$ has been characterized. Its structure has the form shown in Fig. 4.106.

Cell parameters are: $a = 11.43$ Å, $b = \gamma = 12.495$ Å, $\alpha = \beta = \gamma = 90°$, cell volume $= 175.448$ Å^3, $Z = 2$. Site occupancy of the 58 atoms in the unit cell is shown in Table 4.32.

Zintl phases of type $M_{16}X_{11}$ (M = Ca and Yb; X = Sb and Bi) have been synthesized by both the flux and the solid-state reaction methods. In order to evaluate the potential of these phases for thermoelectrics, the electrical resistivity (δ), thermopower (σ) and thermal conductivity (η) have been measured on hot pressed samples over a wide temperature range of 10–1000 K. The δ and σ trends are typical of a degenerate semiconductor. However, δ remains low (30 μV/K or less). Hall measurements indicate a low-charge carrier mobility 3–7 cm^2/V s, except for $Ca_{16}Sb_{11}$. It is notable that low-thermal conductivity values ranging from 2.5 to 0.8 W/m K are measured for these phases at higher

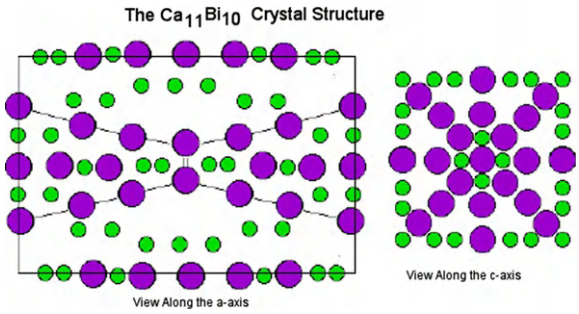

FIGURE 4.105

TABLE 4.30

No	Site notation	Atom	Multiplicity	Wyckoff	Site symmetry	x	y	z	Occupancy
1	Bi	Bi	4	e	4mm	0	0	0.14	1.0
2	CaII	Ca	4	e	4mm	0	0	0.334	1.0
3	CaI	Ca	4	c	mmm.	0	1/2	0	1.0

TABLE 4.31

No	Site notation	Atom	Multiplicity	Wyckoff	Site symmetry	*x*	*y*	*z*	Occupancy
1	Ca(1)	Ca	16	n	.m.	0	0.246	0.311	1.0
2	Ca(4)	Ca	16	n	.m.	0	0.34	0.103	1.0
3	Bi(5)	Bi	16	m	..m	0.2038	0.2038	0.1737	1.0
4	Bi(1)	Bi	8	j	m2m.	0.1553	1/2	0	1.0
5	Bi(3)	Bi	8	h	m.2m	0.131	0.131	0	1.0
6	Ca(2)	Ca	8	h	m.2m	0.345	0.345	0	1.0
7	Ca(3)	Ca	4	e	4mm	0	0	0.16	1.0
8	Bi(2)	Bi	4	e	4mm	0	0	0.3671	1.0
9	Bi(4)	Bi	4	d	-4m2	0	1/2	1/4	1.0

TABLE 4.32

No	Site notation	Atom	Multiplicity	Wyckoff	Site symmetry	*x*	*y*	*z*	Occupancy
1	Ca1	Ca	8	f	1	0.0706	0.2032	0.3159	1.0
2	Ca2	Ca	8	f	1	0.2078	0.0881	0.001	1.0
3	Ca3	Ca	8	f	1	0.5761	0.2903	0.2882	1.0
4	Ca4	Ca	4	e	..m	0.1313	0.6313	0.501	1.0
5	Bi1	Bi	4	e	..m	0.16398	0.66398	0.23649	1.0
6	Bi2	Bi	4	e	..m	0.17925	0.67925	0.7621	1.0
7	Bi3	Bi	4	e	..m	0.62692	0.12692	0.48675	1.0
8	Bi4	Bi	4	e	..m	0.64498	0.14498	0.03173	1.0
9	Bi5	Bi	4	d	2..	0	0	0.15037	1.0
10	Bi6	Bi	4	d	2..	0	0	0.4698	0.500
11	Ca5	Ca	2	c	2.mm	0	1/2	0.1401	1.0
12	Ca6	Ca	2	c	2.mm	0	1/2	0.7858	1.0

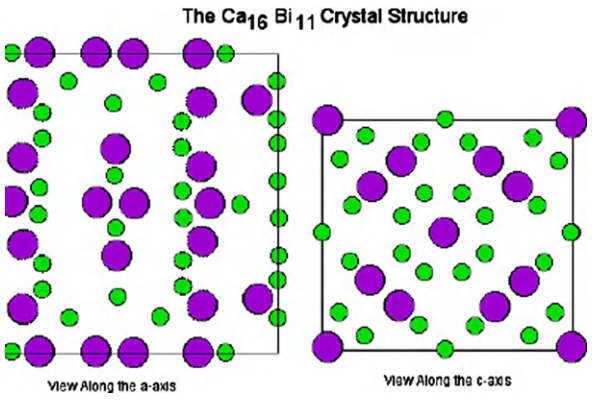

FIGURE 4.106

temperatures up to 1273 K. Particularly for $Yb_{16}Sb_{11}$, the lattice part of thermal conductivity is found to be between 0.5 and 0.7 W/m K. However, the challenge in this M16X11 system is to achieve high thermopower. In order to understand more fully the measured transport properties, band structure calculations have been performed. Consistent with experimental data, these calculations suggest that all the systems are indeed metallic. The electronic structures for Ca-based phases show one-dimensional metallic behavior with small and almost symmetric density of states around the Fermi level.

Calcium bismuthide compounds have not been developed sufficiently to warrant any usage in industry. This may be due to the fact that alkaline earth

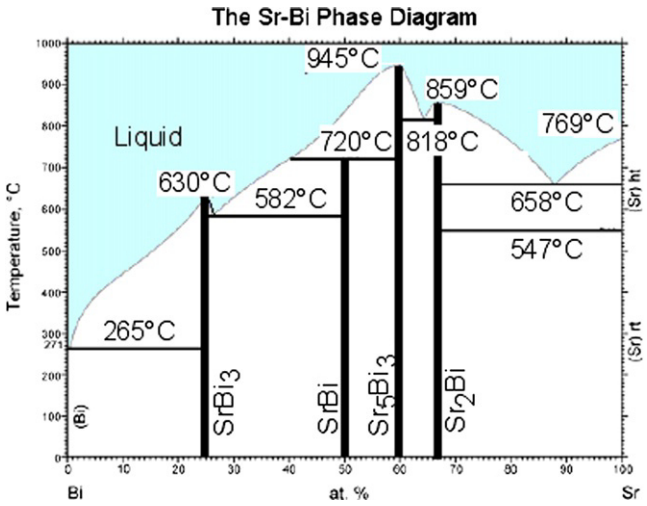

FIGURE 4.107

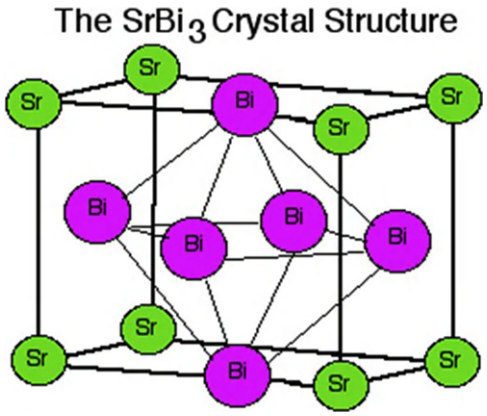

FIGURE 4.108

metals are not very stable in air or moisture and that the addition of Bismuth metal does not improve their instability.

Strontium Bismuthides

Sr metal also forms a number of compounds, as shown in Fig. 4.107.

Four compounds, $SrBi_3$, SrBi, Sr_5Bi_3 and Sr_2Bi are known.

The structure factors for these compounds are shown in Table 4.33.

The compound, $SrBi_3$, has the face-centered cubic structure, as shown on the next page. It has lattice parameters of: $a = b = c = 5.042$ Å, $\alpha = \beta = \gamma = 90°$, cell volume $= 128.18$ Å^3 (Fig. 4.108).

Cell occupancy is shown in Table 4.34.

This compound is a superconductor with $T_c = \sim 3.6$ K.

The compound Sr_5Bi_3 has the Mn_5Si_3 structure with point Group hP16 and space group $P6_3/mcm$. Its structure can be represented as in Fig. 4.109.

Unit-cell parameters are: $a = 7.523$ Å, $b = c = 9.651$ Å, $\alpha = 120°$, $\beta = \gamma = 90°$, cell volume $= 606.83$ Å^3. Site occupancy is shown in Table 4.35.

This compound is dimorphic and can assume the Yb_5Sb_3 structure with point group oP32 and space group Pnma (Fig. 4.110).

TABLE 4.33

Compound	Structure type	Pearson group	Space group	Melt temperature	Physical parameters
(Sr) rt	Cu	cF4	225	547	No data
(Sr) ht	W	cI2	229	769	No data
Sr_5Bi_3	Mn_5Si_3	hP16	193	945	No data
$SrBi_3$	Cu_3Au	cP4	221	630	No data
Sr_2Bi	La_2Sb	tI12	139	858	No data
SrBi	—	—	—	720	No data
(Bi)	As	hR6	166	271	No data

TABLE 4.34

No	Site notation	Atom	Multiplicity	Wyckoff	Site symmetry	*x*	*y*	*z*	Occupancy
1	Bi	Bi	3	c	4/mm.m	0	1/2	1/2	1.0
2	Sr	Sr	1	a	m-3m	0	0	0	1.0

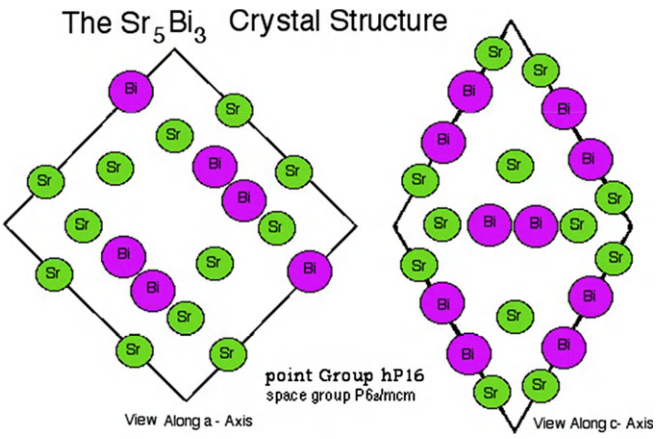

FIGURE 4.109

Cell parameters are: $a = 8.89$ Å, $b = 10.233$ Å, $c = 13.37$ Å, $\alpha = \beta = \gamma = 90°$, cell volume $= 1216.29$ Å^3. Site occupancy is shown in Table 4.36.

The compound, Sr_2Bi_3 does not appear in the phase diagram. It has the structure as in Fig. 4.111.

Cell parameters are: $a = 6.599$ Å, $b = 6.793$ Å, $c = 15.631$ Å, $\alpha = \beta = \gamma = 90°$, cell volume $= 700.69$ Å^3. Site occupancy is shown in Table 4.37.

If Ba is substituted for Sr in this structure, it changes to Fig. 4.112.

Crystals of the composition $Sr_{2-x}Ba_xBi_3$ $(0 \leq x \leq 1.3)$ were synthesized from the elements and were characterized by single-crystal and powder XRD methods. The compounds crystallize for $x = 0$, 0.45, 0.86, 1.08, 1.28 in the structure type of the parent compound Sr_2Bi_3 with

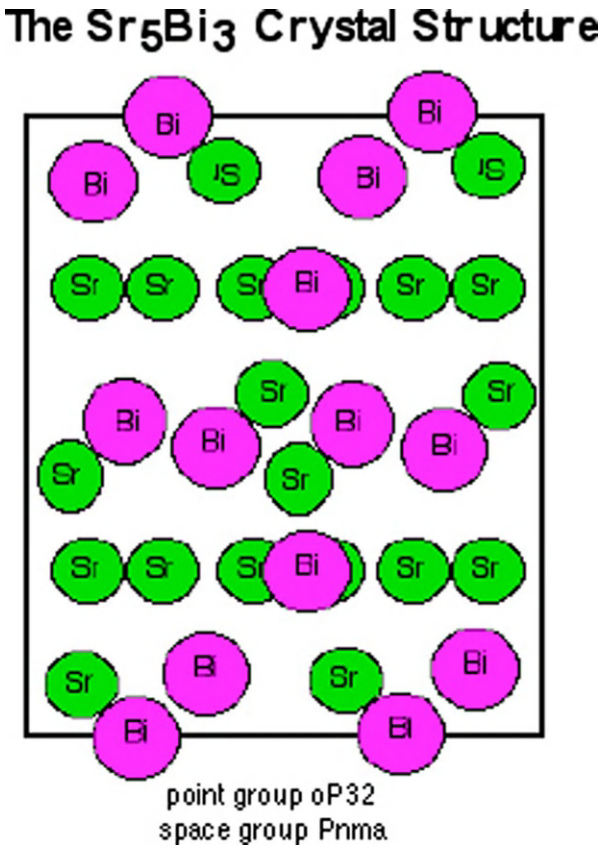

FIGURE 4.110

TABLE 4.35

No	Site notation	Atom	Multiplicity	Wyckoff	Site symmetry	x	y	z	Occupancy
1	Sr1	Sr	6	g	m2m	0.236	0	1/4	1.0
2	Bi1	Bi	6	g	m2m	0.5991	0	1/4	1.0
3	Sr2	Sr	4	d	3.2	1/3	2/3	0	1.0

TABLE 4.36

No	Site notation	Atom	Multiplicity	Wyckoff	Site symmetry	x	y	z	Occupancy
1	Sr1	Sr	8	d	1	0.074	0.0421	0.1952	1.0
2	Bi1	Bi	8	d	1	0.3293	0.0144	0.0675	1.0
3	Sr2	Sr	4	c	.m.	0.0054	1/4	0.5354	1.0
4	Sr3	Sr	4	c	.m.	0.2295	1/4	0.8196	1.0
5	Sr4	Sr	4	c	.m.	0.2883	1/4	0.3492	1.0
6	Bi2	Bi	4	c	.m.	0.4834	1/4	0.5786	1.0

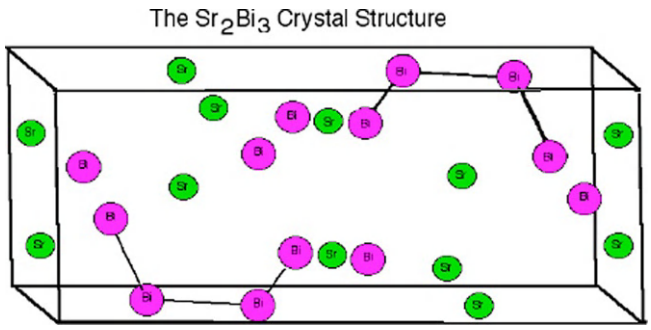

FIGURE 4.111

space group Pnna (No. 52) and $Z = 4$. Substitution of Sr by Ba leads to a site preference for Ba. The anionic Bi substructures in the pseudoternary system simultaneously distort under remarkable elongation of one distinct Bi–Bi contact. Magnetic measurements for samples with $x = 0$, 0.45 and 1.08 reveal superconducting transitions at low temperatures. Linear muffin-tin orbital band structure calculations of Sr_2Bi_3 show strong cation–anion interactions that greatly stabilize the structure. Besides showing characteristics of a typical metal, the band structure plot unveils the co-instantaneous

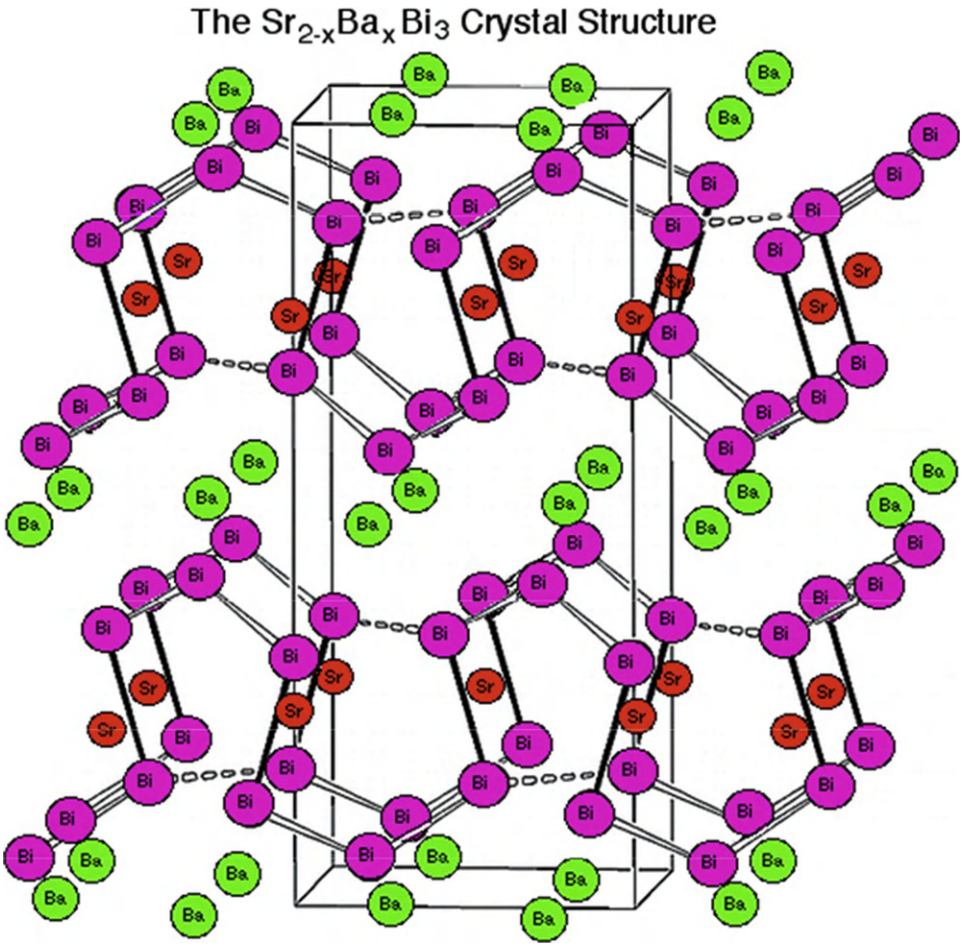

FIGURE 4.112

TABLE 4.37

No	Site notation	Atom	Multiplicity	Wyckoff	Site symmetry	*x*	*y*	*z*	Occupancy
1	Bi1	Bi	8	e	1	0.1539	0.0640	0.5788	1.0
2	Sr1	Sr	4	d	2..	0.0001	1/4	1/4	1.0
3	Bi2	Bi	4	d	2..	0.4294	1/4	1/4	1.0
4	Sr2	Sr	4	c	..2	1/4	0	0.0570	1.0

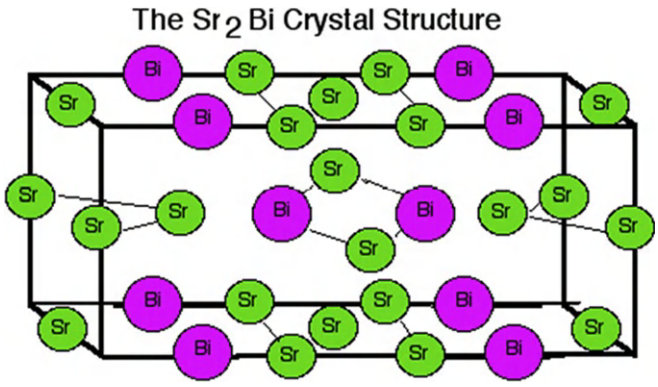

FIGURE 4.113

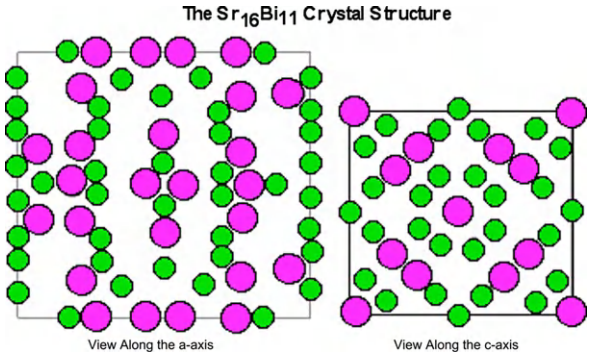

FIGURE 4.114

occurrence of flat and steep bands around the Fermi level indicative for superconductivity.

The compound, Sr_2Bi has the structure shown in the following Fig. 4.113.

The unit-cell parameters are: $a = b = 5.01$ Å, $c = 9.623$ Å, $\alpha = \beta = 105.25°$, $\gamma = 90°$, cell volume = 221.88 Å^3. Cell occupancy is shown in Table 4.38.

$Sr_{16}Bi_{11}$ has the same structure as the Ca-homologue (Fig. 4.114).

Cell parameters are: $a = 11.934$ Å, $b = 13.152$ Å, $c = 13.152$ Å, $\alpha = \beta = \gamma = 90°$, cell volume = 2064.29 Å^3. Cell occupancy is shown in Table 4.39.

When Sr metal and Bi metal in proper proportion is reacted in Ta containers at about 1100 °C and then annealed at 825–900 °C or slowly cooled, the $Sr_{16}Bi_{11}$ composition results. It is important to run particularly such reactions either under dynamic vacuum or to previously remove the pervasive hydrogen impurity from these metals. The complex structure is built of

TABLE 4.38

No	Site notation	Atom	Multiplicity	Wyckoff	Site symmetry	x	y	z	Occupancy
1	Bi	Bi	4	e	4mm	0	0	0.138	1.0
2	SrII	Sr	4	e	4mm	0	0	0.329	1.0
3	SrI	Sr	4	c	mmm.	0	1/2	0	1.0

TABLE 4.39

No	Site notation	Atom	Multiplicity	Wyckoff	Site symmetry	x	y	z	Occupancy
1	Sr1	Sr	8	f	1	0.0706	0.2032	0.3159	1.0
2	Sr2	Sr	8	f	1	0.2078	0.0881	0.001	1.0
3	Sr3	Sr	8	f	1	0.5761	0.2903	0.2882	1.0
4	Sr4	Sr	4	e	..m	0.1313	0.6313	0.501	1.0
5	Bi1	Bi	4	e	..m	0.1639	0.66398	0.2365	1.0
6	Bi2	Bi	4	e	..m	0.1793	0.67925	0.7621	1.0
7	Bi3	Bi	4	e	..m	0.6269	0.12692	0.48675	1.0
8	Bi4	Bi	4	e	..m	0.6449	0.14498	0.03173	1.0
9	Bi5	Bi	4	d	2..	0	0	0.15037	1.0
10	Bi6	Bi	4	d	2..	0	0	0.4698	0.50
11	Sr5	Sr	2	c	2.mm	0	1/2	0.1401	1.0
12	Sr6	Sr	2	c	2.mm	0	1/2	0.7858	1.0

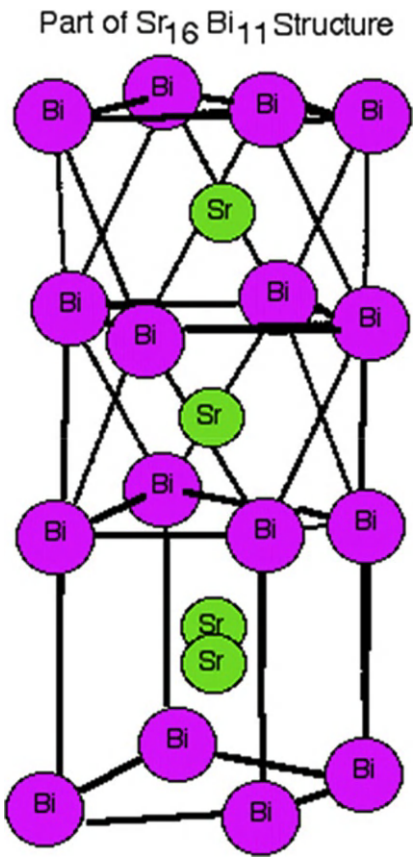

FIGURE 4.115

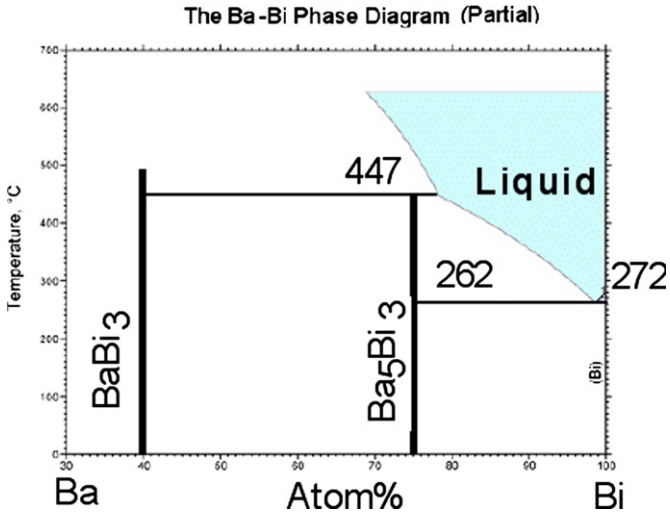

FIGURE 4.116

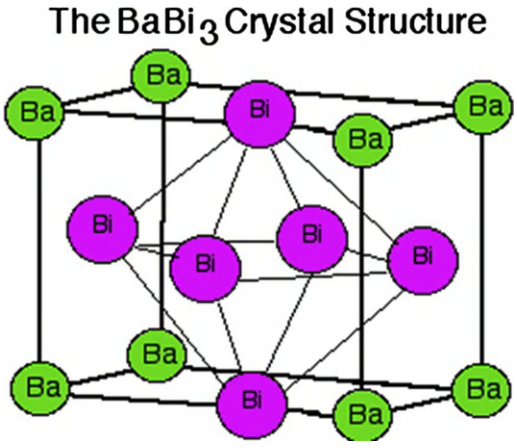

FIGURE 4.117

pairs of confacial Sr_5Bi_3-like slabs intergrown with single square-prismatic slabs along c in which Sr atoms in both define the polyhedra centered by Bi (Fig. 4.115).

This structure is missing the $n = 2$ member of the homologous series $A_{5n+6}B_{3n+5}$ (Parthé) with n:1 ratios of intergrown slabs. Four of five $Ae_{16}(Sb,Bi)_{11}$ examples studied are diamagnetic ($Ba_{16}Sb_{11}$ excepted), and $Ca_{16}Sb_{11}$ is a poor semiconductor. Accommodation of these Zintl-phase characteristics in the $Sr_{16}Bi_{11}$ structure requires that 50% of the Bi atom pairs centering the confacial square antiprisms be bonded ($d = 3.40$ Å) on a random basis. Ellipsoids on these atoms are elongated along the proposed bonds.

Strontium bismuthides are not used in industry and do not have assigned CAS numbers.

Barium Bismuthides

The phase diagram of the Ba–Bi system has only been partly examined. The atom-ratio between 30 and 100 At % are shown in the following Fig. 4.116.

However, four compounds are known: $BaBi_3$, Ba_5Bi_3, Ba_2Bi and $Ba_{16}O_{11}$. All of these have the same structure as that of the Sr homologues.

$BaBi_3$ has the structure shown in Fig. 4.117.

Cell parameters are: $a = 5.157$ Å, $b = c = 5.188$ Å, $\alpha = \beta = \gamma = 90°$, cell volume = 138.80 Å^3. Cell occupancy is shown in Table 4.40.

$BaBi_3$ has the assigned CAS number 91648-92-9 and is available commercially.

The compound, Ba_5Bi_3, has the structure shown in Fig. 4.118.

A better diagram of the structure is shown in Fig. 4.119.

Ba_5Bi_3 belongs to the hexagonal Mn_5Si_3 type while Sr_5Bi_3 is isostructural with orthorhombic α-Yb_5Sb_3. Unit-cell parameters are: 7.768 Å, $b = c = 10.098$ Å, $\alpha = 120°$, $\beta = \gamma = 90°$, cell volume = 658.98 Å^3. Cell occupancy is shown in Table 4.41.

Resistivity measurements have been performed for electronic characterization of the compounds Ba_5Bi_3 with the Mn_5Si_3 structure type, along with Ca_5Bi_3 and

TABLE 4.40

No	Site notation	Atom	Multiplicity	Wyckoff	Site symmetry	x	y	z	Occupancy
1	Bi2	Bi	2	e	mmm.	0	1/2	1/2	1.0
2	Bi1	Bi	1	c	4/mmm	1/2	1/2	0	1.0
3	Ba	Ba	1	a	4/mmm	0	0	0	1.0

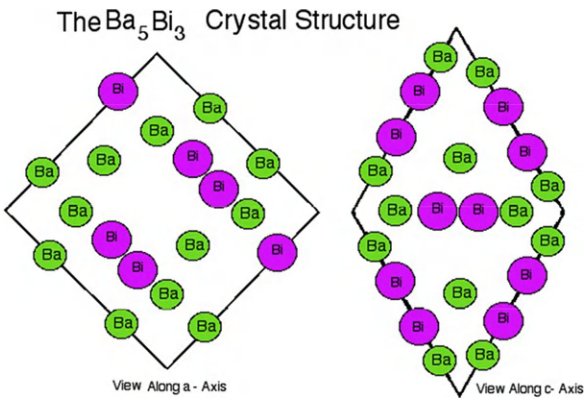

FIGURE 4.118

Ca_5Bi_3F, with the β-Yb_5Sb_3 structure type. Ba_5Bi_3 was found to be a semiconductor ($Eg = 0.30$ eV) with a larger band gap than its corresponding chloride ($Eg = 0.09$ eV).

A new ternary phase $Ba_5In_4Bi_5$ has been synthesized by direct reaction of the corresponding elements at high temperature. It crystallizes in a noncentrosymmetric space group and represents a new structure type (tetragonal, P4nc with $a = 10.620(2)$ and $c = 9.009(2)$ Å, $Z = 2$). The structure is built of interconnected heteroatomic clusters of In_4Bi_5, square pyramids with In_4-bases and four exo-bonded bismuth atoms (bonded to the In atoms). According to Wade's rule, the compound is electron deficient with one electron per cluster, that is, $[In_4Bi_5]_{10}$ instead of the expected $[In_4Bi_5]$ for a closed shell species. The clusters were discussed also in light of the known

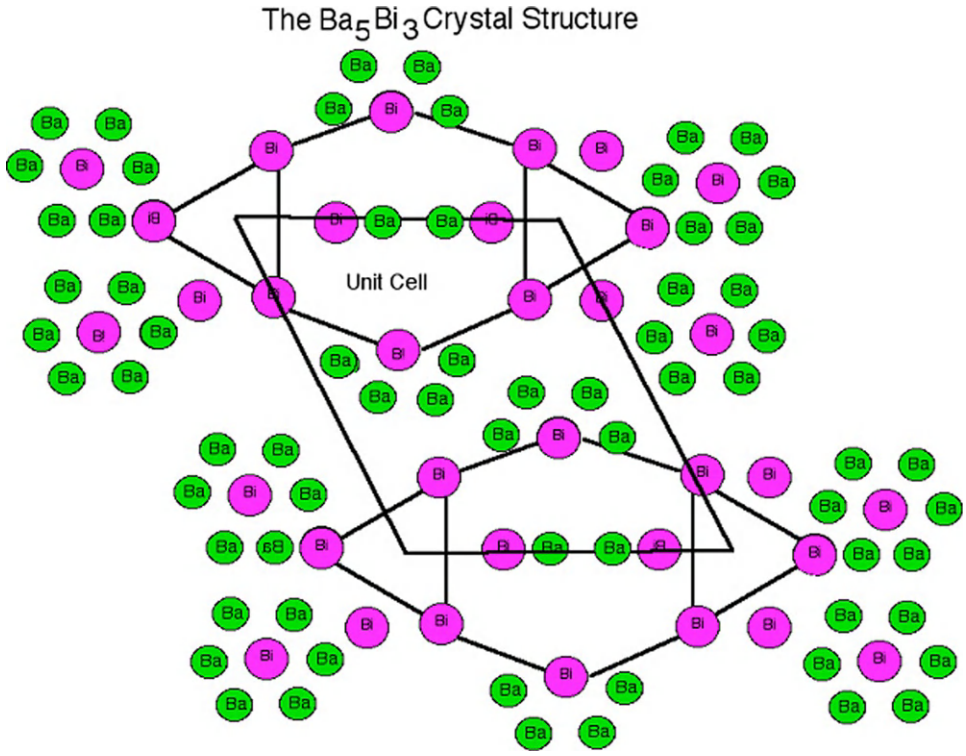

FIGURE 4.119

TABLE 4.41

No	Site notation	Atom	Multiplicity	Wyckoff	Site symmetry	*x*	*y*	*z*	Occupancy
1	Ba1	Ba	6	g	m2m	0.236	0	1/4	1.0
2	Bi1	Bi	6	g	m2m	0.5991	0	1/4	1.0
3	Ba2	Ba	4	d	3.2	1/3	2/3	0	1.0

TABLE 4.42

No	Site notation	Atom	Multiplicity	Wyckoff	Site symmetry	*x*	*y*	*z*	Occupancy
1	Bi	Bi	4	e	4mm	0	0	0.13661	1.0
2	Ba(2)	Ba	4	e	4mm	0	0	0.32679	1.0
3	Ba(1)	Ba	4	c	mmm.	0	1/2	0	1.0

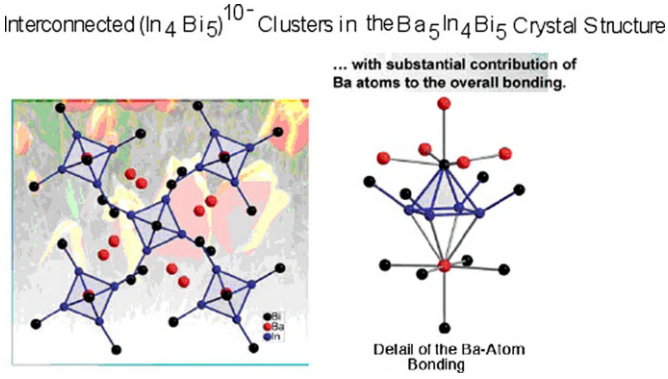

FIGURE 4.120

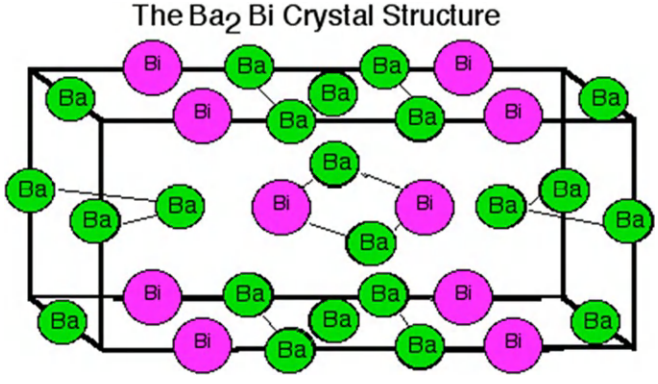

FIGURE 4.121

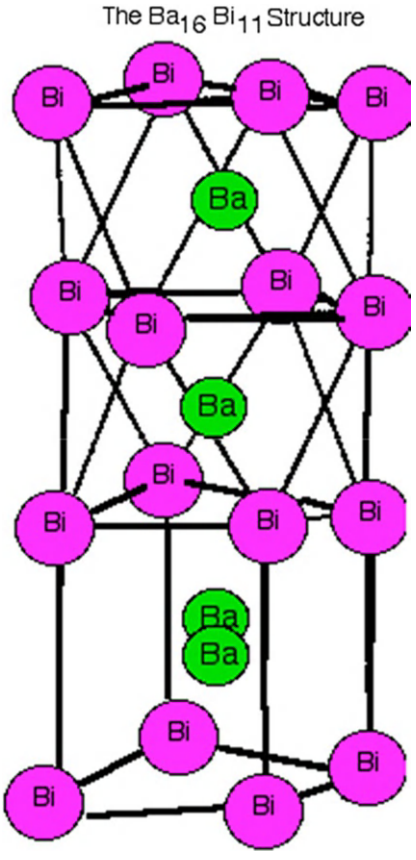

FIGURE 4.122

TABLE 4.43

No	Site notation	Atom	Multiplicity	Wyckoff	Site symmetry	*x*	*y*	*z*	Occupancy
1	Ba1	Ba	8	f	1	0.0706	0.2032	0.3159	1.0
2	Ba2	Ba	8	f	1	0.2078	0.0881	0.001	1.0
3	Ba3	Ba	8	f	1	0.5761	0.2903	0.2882	1.0
4	Ba4	Ba	4	e	..m	0.1313	0.6313	0.501	1.0
5	Bi1	Bi	4	e	..m	0.16398	0.6639	0.2365	1.0
6	Bi2	Bi	4	e	..m	0.17925	0.6793	0.7621	1.0
7	Bi3	Bi	4	e	..m	0.62692	0.1269	0.4868	1.0
8	Bi4	Bi	4	e	..m	0.64498	0.1449	0.0317	1.0
9	Bi5	Bi	4	d	2..	0	0	0.1504	1.0
10	Bi6	Bi	4	d	2..	0	0	0.4698	0.500
11	Ba5	Ba	2	c	2.mm	0	1/2	0.1401	1.0
12	Ba6	Ba	2	c	2.mm	0	1/2	0.7858	1.0

heteroatomic deltahedral clusters with the same composition but different charge, $[In_4Bi_5]^{3-}$. Band structure calculations on the new compound suggested substantial participation of barium in the overall bonding of the structure that accounts for the electron shortage (Fig. 4.120).

Ba_2Bi has the structure shown in Fig. 4.121.

Cell parameters are: $a = b = 5.263$ Å, $c = 10.063$ Å, $\alpha = \beta = 105.16°$, $\gamma = 90°$, cell volume $= 256.99$ Å^3. Cell occupancy is shown in Table 4.42.

Single crystals of Ba_2Bi can be prepared by cooling a melt of stoichiometry $3Ba + 2Bi$ with a small excess of Ba from 1350 °C to room temperature. It is orthorhombic.

$Ba_{16}Bi_{11}$ has the structure shown in Fig. 4.122.

Cell parameters are: $a = 12.568$ Å, $b = 13744$ Å, $c = 13.744$ Å, $\alpha = \beta = \gamma = 90°$, cell volume $= 2374.06$ Å^3. Cell occupancy is shown in Table 4.43.

Only $BaBi_3$ is offered for sale. The other compounds have not found usage in industry.

Radium Bismuthide

Radium bimuthide could probably be prepared by the reaction of Ra and Bi metals. Ra melts at 700 °C and is stable in an inert atmosphere until its boiling point of 1737 °C is reached. Since Bi melts at 272 °C and is stable in an inert atmosphere until its boiling point of 1564 °C, the reaction is best carried out by evaporating Ra metal at about 680 °C onto molten Bi metal:

$$3Ra + 2Bi \Rightarrow Ra_3Bi_2$$

However, this reaction has never been carried out due, perhaps, to the intense radioactivity of ^{226}Ra atom. It is probable that Ra forms the same type of antimonide compounds as Ba but there is no industrial or commercial interest and no academic interest in these compounds due to the care required in handling such compounds.

CHAPTER

5

Group 14 (C, Si, Ge, Sn, and Pb) Alkaline Earth Compounds

OUTLINE

5.1. Alkaline Earth Oxy-Carbon Compounds 352
- *5.1.1. Carbonic Acid 352*
- *5.1.2. Alkaline Earth Carbides 353*
  - Beryllium Carbides 353
  - Magnesium Carbides 354
  - Calcium Carbides 355
  - Strontium Carbides 357
  - Barium Carbides 358
  - Radium Carbide 359
- *5.1.3. Alkaline Earth Carbonates and Bicarbonates 359*
  - Beryllium Carbonates 359
  - Magnesium Carbonates 360
  - Calcium Carbonate 362
  - Strontium Carbonate 366
  - Barium Carbonate 368
  - Radium Carbonate 370

5.2. Alkaline Earth Oxy-Silicon Compounds 371
- *5.2.1. Acids Based on Silicon 371*
- *5.2.2. Silicides of the Alkaline Earths 371*
  - Beryllium Silicides 371
  - Magnesium Silicide 372
  - Calcium Silicides 375
  - Strontium Silicide 377
  - Barium Silicide 381
  - Radium Silicides 386
- *5.2.3. Alkaline Earth Silicates 386*
  - Beryllium Silicates 389
  - Magnesium Silicates 392
  - Calcium Silicates 395
  - Strontium Silicates 398
  - Barium Silicates 400
  - Radium Silicates 403

5.3. Alkaline Earth Oxy-Germanium Compounds 403
- *5.3.1. Alkaline Earth Oxo-Germanium Compounds 403*
  - Beryllium Germanates 403
  - Magnesium Germanates 404
  - Calcium Germanates 406
  - Strontium Germanates 409
  - Barium Germanates 410
  - Radium Germanate 412
- *5.3.2. Other Related Oxo-Germanium Compounds, Including Bismuth 413*
- *5.3.3. Alkaline Earth Germanides 413*
  - Beryllium Germanides 413
  - Magnesium Germanides 413
  - Calcium Germanides 414
  - Strontium Germanides 419
  - Barium Germanides 423
  - Radium Germanides 428

5.4. Alkaline Earth Oxy-Tin (Stannum) Compounds 428
- *5.4.1. Stannides of the Alkaline Earths 428*
  - Beryllium Stannides 428
  - Magnesium Stannides 428
  - Calcium Stannides 432
  - Strontium Stannides 436
  - Barium Stannides 441
  - Radium Stannides 446
- *5.4.2. Acids and Bases of the Stannite or Stannic Anions 446*
- *5.4.3. Alkaline Earth Orthostannates, Metastannates and Stannites 447*
  - Beryllium Stannates 447
  - Magnesium Stannates 447
  - Calcium Stannates 450
  - Strontium Stannates 452

Encyclopedia of the Alkaline Earth Compounds
http://dx.doi.org/10.1016/B978-0-444-59550-8.00005-3

Copyright © 2013 Elsevier B.V. All rights reserved.

Barium Stannates 454
Radium Stannates 458
5.5. Alkaline Earth Oxy-Plumbate Compounds 458
5.5.1. Oxides of Lead, Pb_xO_y 458
5.5.2. Plumbides of the Alkaline Earths 459
Beryllium Plumbides 459
Magnesium Plumbides 459
Calcium Plumbides 461
Strontium Plumbides 464
Barium Plumbides 469
Radium Plumbides 472
5.5.3. Oxy-Plumbates of the Alkaline Earths 472
Beryllium Plumbates 472
Magnesium Plumbates 473
Calcium Plumbates 473
Strontium Plumbates 475
Barium Plumbates 476
Radium Plumbates 480

5.1. ALKALINE EARTH OXY-CARBON COMPOUNDS

Among the possible oxy-carbon compounds known are the carbides, carbonates and "bicarbonates". Carbonates are related to carbonic acid which in turn is related to carbon dioxide, CO_2.

5.1.1. Carbonic Acid

Carbonic acid has the formula H_2CO_3 (equivalently $OC(OH)_2$). It is also a name sometimes given to solutions of CO_2 in water, where it exists in equilibrium:

$$CO_2 + H_2O \Leftrightarrow H_2CO_3$$

At room temperature, only small amounts of carbonic acid are present. The salts of carbonic acids are called bicarbonates (or hydrogen carbonates) and carbonates. They are weak acids. The hydration equilibrium constant for carbonic acid at 25 °C is $K_h = [H_2CO_3]/[CO_2] = 1.70 \times 10^{-3}$. Hence, the majority of the carbon dioxide is not converted into carbonic acid, but remains as CO_2 molecules. In the absence of a catalyst, the equilibrium is reached quite slowly. The rate constants are 0.039/s for the forward reaction ($CO_2 + H_2O \Rightarrow H_2CO_3$) and 23/s for the reverse reaction ($H_2CO_3 \Rightarrow CO_2 + H_2O$). Carbonic acid is used in the manufacture of soft drinks, inexpensive and artificially carbonated sparkling wines, and other bubbly drinks. If two equivalents of water could add to CO_2, this would give orthocarbonic acid, $C(OH)_4$, which is virtually unimportant in aqueous solution.

Carbonic acid is diprotic in that it has two protons, which may dissociate from the molecule. Thus, there are two dissociation constants, the first one for the dissociation into the bicarbonate ion, HCO_3^-, (also called hydrogen carbonate):

$$H_2CO_3 \Rightarrow HCO_3^- + H^+$$

$$K_{a_1} = 2.5 \times 10^{-4};\ pK_{a_1} = 3.60 \text{ at } 25\ ^\circ C$$

This indicates that H_2CO_3 is a stronger acid than acetic acid or formic acid. Its high acidity reflects the influence of the electronegative oxygen constituent. The second constant for the dissociation of the bicarbonate ion into the carbonate ion is:

$$HCO_3^- \Rightarrow CO_3^{2-} + H^+$$

$$K_{a_2} = 5.61 \times 10^{-11};\ pK_{a_2} = 10.33 \text{ at } 25\ ^\circ C \text{ and ionic strength} = 0.0$$

Care must be taken when quoting and using the first dissociation constant of carbonic acid. In aqueous solution, carbonic acid only exists in equilibrium with carbon dioxide, and the concentration of H_2CO_3 is much lower than the dissolved CO_2 concentration. Since it is not possible to distinguish between H_2CO_3 and dissolved CO_2 (referred to as CO_2 (aq) by conventional methods), $H_2CO_3^-$ is used to represent the two species when writing the aqueous chemical equilibrium equation. The equation may be rewritten as follows:

$$H_2CO_3^- \Rightarrow HCO_3^- + H^+$$

$$K_a = 4.6 \times 10^{-7};\ pK_a = 6.352 \text{ at } 25\ ^\circ C \text{ and ionic strength} = 0.0$$

Whereas this is the pK_a quoted as the dissociation constant of carbonic acid, it is ambiguous. It might better be referred to as the acidity constant of dissolved carbon dioxide, as it is particularly useful for calculating the pH of CO_2–containing solutions. At a given temperature, the composition of a pure carbonic acid solution (or of a pure CO_2 solution) is completely determined by the partial pressure of carbon dioxide above the solution. To calculate this composition, account must be taken of the above equilibria between the three different carbonate forms (H_2CO_3, HCO_3^- and CO_3^{2-}) as well as of the hydration equilibrium between dissolved CO_2 and H_2CO_3 with the constant:

$$K_h = H_2CO_3/CO_2$$

and of the following equilibrium between the dissolved CO_2 and the gaseous CO_2 above the solution:

$$CO_2(\text{gas}) \Leftrightarrow CO_2(\text{dissolved}) \text{ where the Henry constant, } k_H = 29.76 \text{ atm/(mol/l) at } 25\ ^\circ\text{C}$$

The corresponding equilibrium equations together with the relation and the charge neutrality condition result in six equations for the six unknowns $[CO_2]$, $[H_2CO_3]$, $[H^+]$, $[OH^-]$, $[HCO_3^-]$ and $[CO_3^{2-}]$, showing that the composition of the solution is fully determined by these. The equation obtained for $[H^+]$ is a cubic whose numerical solution yields the following values for the pH and the different species concentrations (Table 5.1).

- We see that in the total range of pressure, the pH is always largely lower than pK_{a_2} so that the CO_3^{2-} concentration is always negligible with respect to HCO_3^- concentration. In fact CO_3^{2-} plays no quantitative role in the present calculation.
- For vanishing PCO_2, the pH is close to the one of pure water (pH = 7) and the dissolved carbon is essentially in the HCO_3^- form.
- For normal atmospheric conditions ($PCO_2 = 3.5 \times 10^{-4}$ atm), we get a slightly acid solution (pH = 5.7) and the dissolved carbon is now essentially in the CO_2 form. From this pressure on, $[OH^-]$ becomes also negligible so that the ionized part of the solution is now an equimolar mixture of H^+ and HCO_3^-.
- For a CO_2 pressure typical of the one in soda drink bottles ($PCO_2 \sim 2.5$ atm), we get a relatively acid medium (pH = 3.7) with a high concentration of dissolved CO_2. These features contribute to the sour and sparkling taste of these drinks.
- Between 2.5 and 10 atm, the pH crosses the pK_{a_1} value (3.60) giving a dominant H_2CO_3 concentration (with respect to HCO_3^-) at high pressures.
- CO_2 gas solidifies at –78 °C and boils at –57 °C.

5.1.2. Alkaline Earth Carbides

These compounds are generally prepared by the high-temperature sintering of the alkaline earth metals (AEMs) with an excess of carbon. These compounds can be classified according to the type of hydrocarbon that appears when the carbide compound is hydrolyzed:

$$\text{Methanides} = C^{4-} = CH_4$$

$$\text{Acetylides} = C_2^{4-} = HC{\equiv}CH$$

$$\text{Sesquicarbides} = C_3^{4-} = CH_3C{\equiv}CH$$

These are essentially "salt-like" carbides in contrast to covalent carbides like SiC or B_4C.

Beryllium Carbides

This compound has the molecular formula of Be_2C and the molecular weight of 30.0351 g/mol. It is a very hard compound. Beryllium carbide is prepared by heating the elements at elevated temperatures (above 900 °C). It also may be prepared by reduction of BeO with carbon at a temperature above 1500 °C:

$$2BeO + 3C \Rightarrow Be_2C + 2CO$$

TABLE 5.1

P_{O2} (atm)	pH	$[CO_2]$	(mol/l)	$[H_2CO_3]$	CO_3^{2-}
10^{-8}	7.00	3.36×10^{-10}	5.71×10^{-13}	1.42×10^{-9}	7.90×10^{-13}
10^{-7}	6.94	3.36×10^{-9}	5.71×10^{-12}	5.90×10^{-9}	1.90×10^{-12}
10^{-6}	6.81	3.36×10^{-8}	5.71×10^{-11}	9.16×10^{-8}	3.30×10^{-11}
10^{-5}	6.42	3.36×10^{-7}	5.71×10^{-9}	3.78×10^{-7}	4.53×10^{-11}
10^{-4}	5.92	3.36×10^{-6}	5.71×10^{-9}	1.19×10^{-6}	5.57×10^{-11}
3.5×10^{-4}	5.65	1.18×10^{-5}	2.00×10^{-8}	2.23×10^{-6}	5.60×10^{-11}
10^{-3}	5.42	3.36×10^{-5}	5.71×10^{-8}	3.78×10^{-6}	5.61×10^{-11}
1.0×10^{-2}	4.92	3.36×10^{-4}	5.71×10^{-7}	1.19×10^{-5}	5.61×10^{-11}
1.0×10^{-1}	4.42	3.36×10^{-3}	5.71×10^{-6}	3.78×10^{-5}	5.61×10^{-11}
10^{0}	3.92	3.36×10^{-2}	5.71×10^{-5}	1.20×10^{-4}	5.61×10^{-11}
2.5×10^{0}	3.72	8.40×10^{-2}	1.43×10^{-4}	1.89×10^{-4}	5.61×10^{-11}
1.0×10^{1}	3.42	3.36×10^{-1}	5.71×10^{-4}	3.78×10^{-4}	5.61×10^{-11}

Beryllium oxide (BeO) and carbon react at 2000 °C (3600 F) to produce the brick-red beryllium carbide. Beryllium carbide has a CAS number of 506-66-1 and a density of 1.91 g/cc (15 °C). Its melting point is 2110 °C. It is a yellow to brick-red crystal whose color depends upon the amount of excess carbon present. Be_2C has the anti-CaF_2 cubic structure with $a = 4.341$ Å, $Z = 2$ and $V = 81.7$ Å^3. It decomposes very slowly in water, but is stable in air if it is compacted:

$$Be_2C + 2H_2O \Rightarrow 2BeO + CH_4\ (gas)$$

The rate of decomposition and evolution of methane are faster in mineral acids:

$$Be_2C + 4H^+ \Rightarrow 2Be^{2+} + CH_4\ (gas)$$

However, in hot concentrated alkali, the reaction is very rapid, forming alkali metal beryllates and methane:

$$Be_2C + 4OH^- \Rightarrow 2\ BeO_2^{2-} + CH_4\ (gas)$$

Beryllium carbide is hard (Knoop = 2410) and compares favorably with tungsten carbide (Knoop = 1800) and silicon carbide (Knoop = 2480). As a refractory, beryllium carbide has several disadvantages. It tends to hydrolyze in atmospheric moisture and to react with both oxygen and nitrogen when heated. Because of its refractory nature and chemical instability in the presence of moisture, methods of fabricating beryllium carbide are definitely limited. Considerable success has, however, been achieved by hot-pressing techniques, and by means of cold-pressing followed by sintering under controlled conditions. Additions of graphite or of beryllium oxide to the carbide considerably facilitate fabrication. BeC_2 has no value as a ceramic since it is attacked by N_2 above 1100 °C, by oxygen above 800 °C and by sulfur above 1000 °C. When stored under ambient conditions in air, it loses its crystallinity and cannot be identified by X-ray diffraction (XRD).

The vapor pressure of beryllium carbide has been measured over the temperature range 1388–1763 K (1115–1490 °C) using Knudsen-effusion mass spectrometry. Vaporization occurs incongruently according to the reaction:

$$Be_2C\ (solid) \Rightarrow 2Be\ (gas) + C\ (solid)$$

The equilibrium vapor pressure above the mixture of Be_2C and C over the experimental temperature range is:

$$(R/J/K\ mol)\ Ln(p/Pa) = -(3.610 \pm 0.009) \times 10^5 (K/T) + (221.43 \pm 1.06)$$

The third-law enthalpy change for the above reaction obtained from the vapor pressures present is $\Delta H^o(298\ K) = (740.5 \pm 0.1)$ kJ/mol. The corresponding second-law result is $\Delta H^o(298\ K) = (732.0 \pm 1.8)$ kJ/mol. The enthalpy of formation for Be_2C (solid) is $\Delta H_f^o(298\ K) = -(92.5 \pm 15.7)$ kJ/mol [calculated from the third-law vaporization enthalpy and the enthalpy of formation of Be (gas)].

The kinetics of the oxidation of electrolytic flake beryllium in carbon dioxide, in carbon monoxide and in carbon monoxide–carbon dioxide mixtures have been measured at temperatures from 500 to 750 °C. In carbon dioxide, at temperatures up to 700 °C, the rate of oxidation continuously decreases with time to reach a very small value (e.g. at 700 °C, 0.13 μg/cm^2 h after 300 h). This is due to formation of a protective oxide layer on the metal. At 750 °C, the rate first decreases and then increases, indicating that a breakaway occurs. If the carbon dioxide is admitted to the preheated sample, the oxidation is very rapid at first and most of the carbon deposition occurs over this initial period. In carbon monoxide, the oxidation is nonprotective above 550 °C, and the rate of oxidation being considerably greater than in carbon dioxide. When beryllium is heated at 650 °C in carbon monoxide–carbon dioxide mixtures containing up to 7.5% of carbon monoxide, the kinetics are the same as in pure carbon dioxide.

Preparation of a beryllium dicarbide, BeC_2, has been reported. It is formed by passing acetylene over Be metal powder at 450–550 °C in an inert atmosphere:

$$Be + HC{\equiv}CH \Rightarrow BeC_2 + H_2$$

This carbide is offered for sale as "beryllium carbide" with a CAS number of 12070-28-9. Other manufacturers list Be_2C for sale with the CAS number of 506-66-1.

Magnesium Carbides

There are two known carbides of magnesium, MgC_2 and the sesquicarbide, Mg_2C_3. The sesquicarbide ion is linear and is isoelectronic with CO_2. The C≡C distance in Mg_2C_3 is 1.333 Å. Mg_2C_3 yields methylacetylene, $CH_3C{\equiv}CH$, on hydrolysis which, when it was first synthesized, was the first indication that it may contain the ion, C_3^{4-}. This salt can be prepared by the reaction of methane with the oxide at temperatures above 2100 °C:

$$5\ CH_4 + 2MgO \Rightarrow Mg_2C_3 + 6H_2 + CO$$

The sesquicarbide reaction has potential for upgrading natural gas by using the solid metal carbide to generate useful acetylenes for manufacture of olefins and subsequent plastics. The acetylene can also be converted into a useful fuel. This potential is based, of course, upon relative costs of the process.

A similar reaction at 450–600 °C produces the acetylide, MgC_2, which has a fcc cubic structure. The reaction is endothermic with $\Delta G_f = +15$ kJ/mol. Most of the reactions between carbon and the metals to form carbides are exothermic. Thus, the difficulty in forming a stable MgC_2 stems from the fact that the structure is not thermodynamically stable as a solid. Even the Mg_2C_3

compound is not thermodynamically inclined and its free energy of formation is only $\Delta G_f = -15$ kJ/mol. However, it is the more stable of the two salts that form in this system.

If MgC_2 is heated to about 1100 °C, it decomposes to form the sesquicarbide:

$$2MgC_2 + \text{heat} \Rightarrow Mg_2C_3 + C$$

Carbon crystals having high structural order, of macrocrystalline size (>0.25 μm) and monocrystalline character were prepared by decomposition of this magnesium carbide between 950 and 1200 °C. CaC_2 was the source of carbon; this was dissolved in and reacted with $MgCl_2$. Crystalline carbon was formed by conversion of MgC_2 to Mg_2C_3 and subsequent decomposition of the latter to its elements. Magnesium metal formed in situ appeared to catalyze rearrangement of carbon atoms to a higher degree of order. The maximum yield of graphite was 86% of the carbon present.

The self-hydrogenation of propyne and propadiene to propene on evaporated magnesium films has been studied at 100 and 150 °C. The species retained in the solid state in the course of the reaction were then desorbed by deuterium oxide and characterized as deuterated hydrocarbons. The structures of these hydrocarbons (mainly propyne = HC≡CH and propene = H_2C=CH_2) and the variations in their deuterium distributions with temperature and contact time of the previous self-hydrogenation reaction are consistent with a mechanism involving two parallel processes:

(a) Dehydrogenation of propyne and propadiene into methylated propyne CH_3C≡CH–Mg (or deuterolyzed to [$^2H_1$]-propyne), that was stable at 373 K but rapidly further dehydrogenated at 423 K to the magnesium carbide Mg_2C_3 (or deuterolyzed to [$^2H_4$]propyne).

(b) Two-step hydrogenation of the reagent to propene, via half-hydrogenated intermediates, stable at 373 K and deuterolyzed to [$^2H_1$]-propene.

In an AC type of plasma-display panel, "PDP", an electrode for the main discharge is generally covered with a dielectric layer, and performs memory driving to reduce a driving voltage. When the dielectric layer deteriorates due to an impact of ions generated by the discharge and hitting the layer, the driving voltage may increase. To prevent this from increasing, a protective layer for protecting the dielectric layer is formed on a surface of the dielectric layer. The protective layer, made of MgO and magnesium carbide, reduces a variation of the discharge delay time against temperature. Thus, the protective layer has excellent electron emission ability hardly changing against temperature. This allows the PDP to preferably display images regardless of environmental temperature.

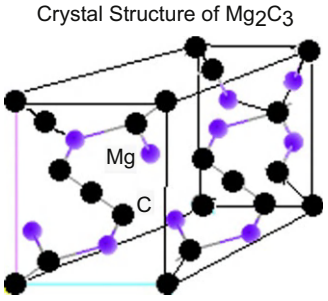

FIGURE 5.1

Magnesium carbide, Mg_2C_3 has the CAS number of 12151-74-5 and is also offered for sale commercially. It has a quasi-cubic structure, distorted along the *c*-axis with unit-cell parameters of: $a = 3.7283$ Å, $b = 5.2786$ Å, $c = 6.4108$ Å, $\alpha = 90°$, $\beta = 90°$, $\gamma = 90°$, cell volume = 126.17 Å^3, $Z = 2$.

MgC_2 has the CAS number of 12122-46-2 and is offered for sale commercially. Its crystal parameters are: $a = 3.9342$ Å, $b = 3.9342$ Å, $c = 5.021$ Å, $\alpha = 90°$, $\beta = 90°$, $\gamma = 90°$, $V = 77.71$ Å^3, $Z = 2$.

The structure of Mg_2C_3 is shown in the above diagram. The structure is quasi-cubic (rhombohedral) with a distortion in the *c*-direction (Fig. 5.1).

Under pressure, this compound reverts to the acetylide, Mg_2C_2 (designated MgC in the literature). It is known that Mg reacts with hydrocarbons in the temperature range of 450–700 °C at atmospheric pressure, producing the known magnesium carbides, MgC_2 and Mg_2C_3. The interaction of Mg and graphite was studied under pressures up to 7.7 Gpa and temperatures up to 1800 °C. Differential thermal analysis (DTA) was used, under pressure, to determine what reactions were taking place as the carbon content was changed. With C-concentrations above 15% by weight, the acetylide Mg_2C_2 was formed. This compound was cubic (FFC) with $a = 5.635$ Å. As the C was increased, the rhombic lattice of Mg_2C_3 appeared at C-concentrations of 50–67% by weight.

Magnesium carbides are available commercially but calcium carbides remain the leader in industrial usage.

Calcium Carbides

Calcium carbide has the nominal formula of CaC_2 and the molecular weight of 64.0992 g/mol. The pure material is colorless, but most samples have a color ranging from black to grayish-white, depending on the grade. Its density is 2.22 g/cc and it melts at 2160 °C with a boiling point (under an inert atmosphere) of 2300 °C, where it decomposes. Its main use industrially is in the production of acetylene and calcium cyanamide, $CaCN_2$. Calcium carbide is produced industrially in an electric-arc furnace from a mixture of $CaCO_3$ and

coke (carbon) at approximately 2000 °C. This method has not changed since its invention in 1888:

$$CaCO_3 + 3C \Rightarrow CaC_2 + CO + CO_2$$

The high temperature required for this reaction is not practically achievable by traditional combustion, so the reaction is performed in an electric-arc furnace where the electrodes are graphite. The carbide product produced generally contains around 80–85% calcium carbide by weight. The carbide is crushed to produce small lumps that can range a few millimeters up to 50 mm. The impurities are concentrated in the finer fractions. The CaC_2 content of the product is assayed by measuring the amount of acetylene produced on hydrolysis. As an example, the U.S. standard for the content of the coarser fractions is 295–300 l/kg. Impurities present in the carbide include phosphide, which produces PH_3 (a poisonous gas) when hydrolyzed to produce HC≡CH, i.e. acetylene.

This reaction was an important part of the industrial revolution in chemistry, and was made possible in the U.S. as a product of massive amounts of cheap hydroelectric power generated at Niagara falls before the turn of the twentieth century. The method for the production of CaC_2 in an electric-arc furnace was discovered independently by two researchers in Europe in 1888 and 1892. The following diagram is an illustration of how CaC_2 has been manufactured (Fig. 5.2).

The common crystalline form at room temperature is a distorted rock salt structure with the C_2^{4-} units lying parallel. The structure is tetragonal with point group $= D_{4h}^{17}$ and space group = I4/mmm. Actually, there are several forms of calcium carbide (Table 5.2).

TABLE 5.2

Number	Composition	Space group	Point group	SG #
1	Ca_6C_{60}	cP	—	—
2	CaC_2	aP12	P-1	2
3	CaC_2	mS12	C2/c	15
4	CaC_2	tI6	I4/mmm	139
5	CaC_2	cF36	Fm-3m	225
6	CaC_6	hR21	R-3m	166

In the following diagram, the a ⇒ c vector plane of the structures of calcium carbides are shown as a function of the space groups that form due to differences in how the CaC_2 was created (Fig. 5.3).

In calcium carbide, CaC_2, the C≡C triple bond length is about 1.092 Å (similar to ethyne).

$$CaC_2 + 2\,H_2O \Rightarrow HC{\equiv}CH + Ca(OH)_2$$

This reaction is the basis of the industrial manufacture of acetylene, and is the major industrial use of calcium carbide in industrial circles.

In China, acetylene derived from calcium carbide remains a raw material for their chemical industry, in particular for the production of polyvinyl chloride. Locally produced acetylene is more economical than using imported oil. Production of calcium carbide in

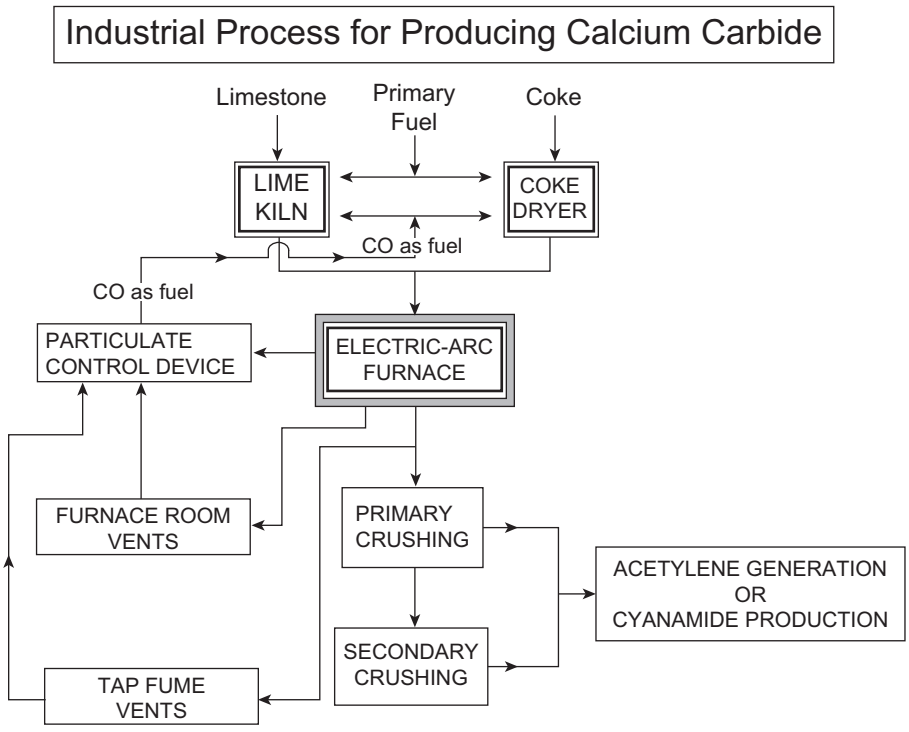

FIGURE 5.2

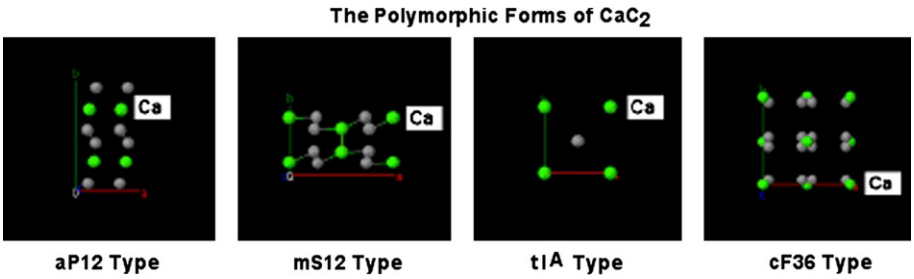

FIGURE 5.3

China has been increasing. In 2005, output was 8.94 million tons, with the capacity to produce 17 million tons. In the USA, Europe and Japan consumption is generally declining. Production levels in the USA in 1990s were 236,000 tons per year.

Calcium carbide reacts with nitrogen at high temperature to form calcium cyanamide:

$$CaC_2 + N_2 \Rightarrow CaCN_2 + C$$

Calcium cyanamide is used as fertilizer. It is hydrolyzed to cyanamide, $H_2N{=}C{=}N$, in the soil and is readily available to plants as a nitrogen plant food.

Calcium carbide has been used:

- in the "desulfurization" of iron (pig iron, cast iron and steel).
- as a fuel in steelmaking to extend the scrap ratio to liquid iron, depending on economics.
- as a powerful deoxidizer in steel at ladle treatment facilities.
- was used in carbide lamps, in which water drips on the carbide and the acetylene formed is ignited. These lamps were usable but dangerous in coal mines, where the presence of the flammable gas methane made them a serious hazard. The presence of flammable gases in coal mines led to the miner "safety lamp". However, carbide lamps were used extensively in slate, copper and tin mines, but most have now been replaced by electric lamps. Carbide lamps are still used for mining in some less wealthy countries, such as in the silver mines near Potosi, Bolivia. Carbide lamps are also still used by some in exploring caves and other underground areas, though they are increasingly being replaced in this use by the new LED lamps. They were also used extensively as headlights in early automobiles, motorcycles and bicycles, although in this application they are also obsolete, having been replaced entirely by electric lamps, and in some cases, by LED lamps.
- in the ripening of fruit. Calcium carbide is used as source of acetylene gas, which is a ripening agent.
- in toy cannons where the acetylene is set off by an applied spark to create a loud "boom".
- as floating, self-igniting naval flares for use as signals.

Thermodynamic constants for CaC_2 are:

$$\Delta H_f^\circ = -14.29 \text{ kcal/mol}$$

$$\Delta G_f^\circ = -15.51 \text{ kcal/mol}$$

$$S^\circ = 16.73 \text{ cal/degree mol}$$

$$C_p = 14.99 \text{ cal/degree mol}$$

The standard Gibbs energies of formation of CaC_2 was determined by an equilibration technique at temperatures ranging from 1223 to 1673 K, yielding the following results:

$$\text{Ca (liq)} + 2\text{C (solid)} \Rightarrow CaC_2 \text{ (solid)},$$
$$\Delta G^\circ = -90,100 - 11.0\,T \text{ [J/mol]}$$

Calcium carbides are available commercially in tonnage lots.

Strontium Carbides

Strontium carbide has the molecular formula of SrC_2 and the molecular weight of 111.644 g/mol. It is obtained by heating strontium carbonate with carbon in the electric furnace. It resembles calcium carbide, decomposing rapidly in the presence of water or moisture, producing acetylene. SrC_2 has the CAS number of 12071-29-3. It is a black, tetragonal crystal whose melting point is in excess of 1700 °C. Its density is 3.19 g/cc. A number of polymorphs exist as shown in the following Fig. 5.4.

The a ⇒ c vector plane is shown for these polymorphs. SrC_2 has been used in a metathetical reaction to produce transition elements carbides. These carbides are difficult to produce by any other means. Examples of such reactions are:

$$NaVO_3 + SrC_2 \Rightarrow V_8C_7 \ (a = 4.165 \text{ Å})$$

$$Nb_2O_5 + SrC_2 \Rightarrow Nb_2C_2 \ (a = 4.462 \text{ Å})$$

$$Ta_2O_5 + SrC_2 \Rightarrow Ta_2C_2 \ (a = 4.446 \text{ Å})$$

The standard Gibbs energy of formation of SrC_2 was determined by an equilibration technique at

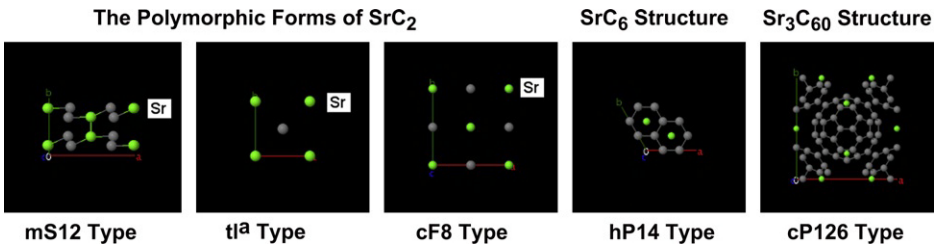

FIGURE 5.4

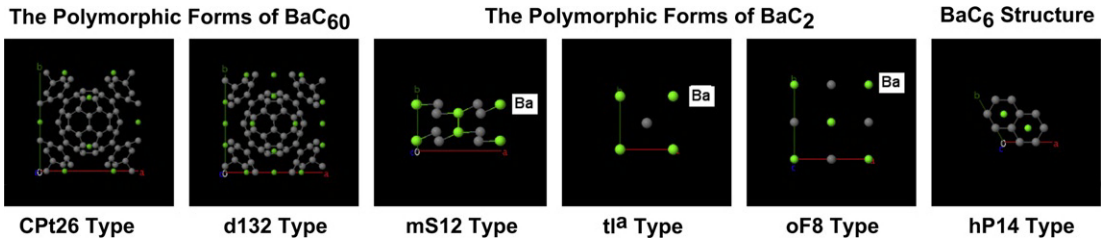

FIGURE 5.5

temperatures ranging from 1223 to 1673 K, yielding the following results:

$$\mathrm{Sr\ (Liq) + 2\,C\ (solid) = SrC_2\ (solid)},$$
$$\Delta G_f^\circ = -104{,}000 - 8.04\,T\ \ [\mathrm{J/mol}]$$

Its CAS number is 12071-29-3. Strontium carbide is available in numerous forms and custom shapes including ingot, rod, plate and sputtering target. High-purity forms also include carbide powder, submicron powder and nanoscale, single crystal or polycrystalline forms. Strontium carbide is generally immediately available in most manufactured volumes.

Barium Carbides

In the system, Ba–C, seven barium carbides are known. These have the following crystal parameters (Table 5.3).

These have the form as shown in Fig. 5.5.

The a ⇒ c plane is shown for these polymorphs that arise due to differences in how they were formed. The difference for BaC_2 is due to stability at a given temperature. The face-centered cubic form is stable above 150 °C while the face-centered tetragonal (rhombohedral) form is stable below 150 °C. BaC_2 has the molecular weight of 161.348 g/mol and the CAS number of 50813-65-5. It is a gray cubic to rhombohedral crystal with a density of 3.74 g/cc. Only two types of barium carbide appears in the phase diagram of Ba–C, that of BaC_2 and BaC_6. The BaC_2 compound melts incongruently at about 1065 °C.

The standard Gibbs energy of formation of BaC_2 was determined by an equilibration technique at temperatures ranging from 1223 to 1673 K, yielding the following results:

$$\mathrm{Ba\ (Liq) + 2C\ (solid) \Rightarrow BaC_2\ (solid)},$$
$$\Delta G_f^\circ = -115{,}000 + 3.53\mathrm{T}\ [\mathrm{J/mol}]$$

TABLE 5.3

Number	Composition	Type	Space group	Point group	SG #
1	Ba_3C_{60}	Ba_3C_{60}	cP126	Pm-3b	223
2	Ba_3C_{60}	Ba_3C_{60}	oL	Immm	71
3	Ba_3C_{60}	Cs_3C_{60}	cL132	Im-3	204
4	BaC_2	ThC_2	mS12	C2/c	15
5	BaC_2	CaC_2	tI6	I4/mmm	139
6	BaC_2	NaCl	cF8	Fm-3m	225
7	BaC_6	BaC_6	hP14	$P6_3/mmc$	194

An intercalated compound of Ba metal and graphite has been reported. Ba metal was evaporated and diffused into well-oriented pyrolytic graphite (PG) and formed the compound, BaC_8. This material was shiny gold in color, brittle and had a hardness about five times that of graphite. Resistivity and thermoelectric power measurements indicated that it is metallic in nature. However, it could not be separated from the bulk graphite in a pure form.

Data concerning the barium carbides are scarce in the scientific literature. Little work concerning potential compounds can be found. The binary phase diagram is not to be found although a ternary phase diagram of Ba–C–The is available.

Barium carbide, BaC_2, is available commercially for sale but not in the quantities that CaC_2 is offered. BaC_6 is offered for sale as CAS #50813-65-5.

Radium Carbide

Radium carbide is not listed in the literature. No published report for the preparation of radium carbides can be found. This is probably due to difficulties in handling the ^{226}Ra radioactivity as well as lack of interest. Because of the closeness of the chemistry of Ba and Ra, and the fact that it is the end-member of the alkaline earth series (Group 2), an acetylide having the formula RaC_2 is expected. Carbides of elements in the radioactive actinide series, The, Pa, U, Nap and Up, are known and have been discussed in the literature. Thus, the absence of data concerning radium carbide compounds is probably due to lack of interest.

5.1.3. Alkaline Earth Carbonates and Bicarbonates

Alkaline earth carbonates are based upon carbonic acid, H_2CO_3 whose properties have been discussed above. Since this acid is dipodic, bicarbonates, i.e. HCO_3^-, are also possible salts.

Beryllium Carbonates

Beryllium carbonate has the molecular formula of $BeCO_3$ and the molecular weight of 69.0211 g/mol. Beryllium carbonates are less stable than those of magnesium and readily form basic salts. This is due to the fact that Be^{2+} preferentially forms hydroxyl-complexes of the type, $Be(OH)^+$ in association with water molecules. Species such as $Be_2(OH)^{3+}$ and $Be_3(OH)_3^{2+}$ are known to exist. The hydroxylation reaction has been given as:

$$xBe^{2+} + yH_2O \Rightarrow Be_x(OH)_y^{(2x-y)+} + hype^+$$

where x and y can vary from 1 to 8. Species such as $Be_3(OH)_7^{3+}$ and $Be_4(OH)_8^{4+}$ are also known. Thus, the prior literature listing of the formulation, $BeCO_3$, may be in doubt concerning exact formulas for beryllium carbonate compounds prepared from aqueous solutions.

The preparation of beryllium carbonate can be accomplished by heating BeO at about 1000 °C in a current of CO_2 gas. The reaction is slow and requires several hours:

$$BeO\ (solid) + CO_2\ (gas) + heat \Rightarrow BeCO_3(solid)$$

There are three forms reported in the literature, an anhydrous, a tetra hydrate and a "basic" beryllium carbonate. The anhydrous form is reported to be unstable, decomposing to BeO and CO_2 in air, and requiring storage under CO_2 for stability. It is not clear whether "basic" refers to the bicarbonate or not. The anhydrous form, $BeCO_3$, is said to have a "melting point" of 54 °C and a "boiling point" of 100 °C where it decomposes to the oxide and carbon dioxide. The enthalpy of formation, ΔH_f^0, is —14.85 kJ/mol and the specific heat capacity, C_p, is 0.9417 J/K. The tetra hydrate is said to be formed when CO_2 is bubbled through a solution of $Be(OH)_2$ and is also reported to be similarly unstable.

Basic beryllium carbonate is a mixed salt that can be prepared by the reaction of beryllium sulfate and ammonium carbonate, and contains both carbonate and hydroxide ions, with a formula said to be $Be_2CO_3(OH)_2$. In the older literature, this is probably what was referred to as beryllium carbonate. However, in view of more recent work, the most likely formula is $(BeOH)_2CO_3$. This is not a basic carbonate but a "hydroxyl-based" beryllium carbonate. This compound is offered for sale as CAS #66104-24-3. $BeCO_3$, formed by dehydration of the hydroxyl-salt, is offered as CAS #1319-43-3.

Soluble beryllium carbonate complexes can be produced by dissolving $BeCO_3$ in ammonium carbonate solutions. This solution has the stoichiometry of $(NH_4)_4Be(CO_3)_2$. This salt can be separated from solution by vacuum evaporation at a low temperature. Hydrolysis of the salt by heating the solution produces:

$$BeCO_3 + (NH_4)_2CO_3\ (aq) \Rightarrow (NH_4)_4Be(CO_3)_2\ (aq) + Evap \Rightarrow (NH_4)_4Be(CO_3)_2\ (solid)$$

$$(NH_4)_4Be(CO_3)_2\ (aq) + heat \Rightarrow (BeOH)_2CO_3\ (solid)$$

Heating this salt at about 400 °C then produces BeO. Note that when the pH of the solution is greater than about pH = 9.5–10, beryllates compounds tend to form. These are based upon the acid, beryllic acid:

$$H_4BeO_4 \Leftrightarrow H^+ + H_3BeO_4^- \Leftrightarrow H^+ + H_2BeO_4^{-2} \Leftrightarrow H^+ + HBeO_4^{-3} \Leftrightarrow H^+ + BeO_4^{-4}$$

The major usage in industry for beryllium carbonate has been as an intermediate in processing beryllium ores to obtain Be metal. This is due to the instability of the various Be carbonates that tend to decompose to

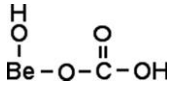

FIGURE 5.6

the oxide when stored in air over long periods of time. Thus, it is the hydroxide which forms by a second hydrolysis of the carbonate while still in solution. The hydroxide is more soluble than the carbonate (basic carbonate = 0.00036 g/100 ml vs hydroxide = 0.029 g/100 ml at 20 °C).

Beryllium carbonate occurs in nature as the mineral, "niveolinite", with the formula, $NaBe(CO_3)(OH)\cdot 2H_2O$. It is tetragonal with $a = 13.087$ Å, $c = 5.404$ Å, $V = 925.54$ Å^3, $Z = 8$, space group = P4/mmc, density = 2.09 g/cc. The crystals are fibrous and snow white or pearl white. They are deliquescent—when removed from their natural habitat, these crystals absorb water from the air and melt or otherwise deteriorate. Its structure includes isolated, infinite chains of $BeO_2(OH)_2$ tetrahedra linked via common OH^- groups; two other vertices of each Be tetrahedron are shared with (CO_3) groups, and Na cations occupy sevenfold polyhedra $[NaO_6(H_2O)]$, forming columns. Chains of Be tetrahedra and columns of Na polyhedra are aligned along the *c*-axis, as broad channels in which H_2O molecules are located. The structural formula is: $\{(Na_{0.9}Ca_{0.1})[(H_2O)_{0.9}(OH)_{0.1}]\}\{Be(OH)\}(CO_3)\cdot 0.1H_2O$. The idealized formula is: $NaBe(CO_3)(OH)\cdot 2H_2O$.

Beryllium bicarbonate, $Be(OH)(HCO_3)$ remains unknown but would have the Lewis structure shown in Fig. 5.6.

This structure is apparently not stable as well.

Beryllium carbonate compounds are not generally available commercially because of their instability in air and moisture.

Magnesium Carbonates

Magnesium carbonate has the molecular formula of $MgCO_3$ and the molecular weight of 84.3145 g/mol. For the most part, Mg^{2+} forms several hydrated and basic carbonates that are stable and occur in nature. The types, names, formulas and CAS numbers of anhydrous, hydrated and basic magnesium carbonates are tabulated as in Table 5.4.

These compounds are also available commercially, and, in many cases, directly extracted from the minerals themselves. The two principal minerals are magnesite, $MgCO_3$ and dolomite, a double salt, $CaCO_3\cdot MgCO_3$. Both minerals are used as source materials in the production of magnesium metal. Also, they are calcined to produce basic refractory bricks for use in furnaces and the like.

There are two main branches of sedimentary petrology. One branch deals with carbonate rocks, namely limestones and dolomites, composed principally of calcium carbonate (calcite) and calcium magnesium carbonate (dolomite). Much of the complexity in classifying carbonate rocks stems partly from the fact that many limestones and dolomites have similar properties. Both are used extensively as a secondary fertilizer to "sweeten acid-soils". Dolomite has been used as a building material for centuries.

In 1701, M. B. Valentine prepared "heavy" magnesium carbonate from mother liquors obtained in the manufacture of potassium nitrate. Magnesia was confused with lime until 1754 when J. Black showed that the two substances were entirely different. Deposits of natural magnesium carbonate were discovered in Moravia in 1803 and were described by C. F. Ludwig as "talcum carbonatum". The term "magnesite" was first restricted to the natural carbonate in 1808 by Dr L. G. Karsten and was generally accepted gradually although the term "globertite" was used in France for some time thereafter.

The most common magnesium carbonate forms available on the open market are the anhydrous salt magnesite ($MgCO_3$) and the di, tri, and pentahydrate minerals known as barringtonite ($MgCO_3\cdot 2H_2O$), nesquehonite ($MgCO_3\cdot 3H_2O$), and lansfordite ($MgCO_3\cdot 5H_2O$),

TABLE 5.4

Compound	Mineral	Formula	CAS No.
Anhydrous salt	Magnesite	$MgCO_3$	[13717-00-5]
Dihydrate	Barringtonite	$MgCO_3\cdot 2H_2O$	[5145-48-2]
Trihydrate	Nesquehonite	$MgCO_3\cdot 3H_2O$	[14457-83-1]
Pentahydrate	Lansfordite	$MgCO_3\cdot 5H_2O$	[61042-72-6]
Basic carbonate	Artinite	$MgCO_3\cdot Mg(OH)_2\cdot 3H_2O$	[12143-96-3]
Basic carbonate	Hydromagnesite	$4MgCO_3\cdot Mg(OH)_2\cdot 4H_2O$	[12072-90-1]
Basic carbonate	Dypingite	$4MgCO_3\cdot Mg(OH)_2\cdot 5H_2O$	[12544-02-4]
Basic carbonate	—	$4MgCO_3\cdot Mg(OH)_2\cdot 8H_2O$	[75300-49-1]

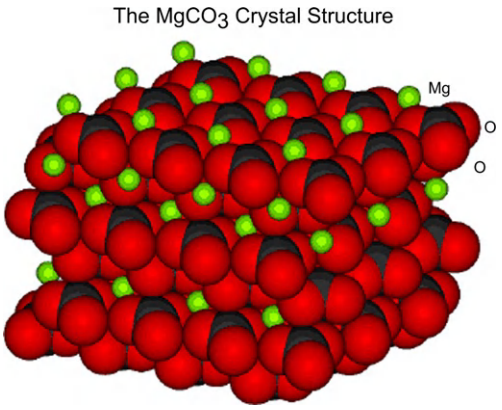

FIGURE 5.7

respectively. All forms of magnesium carbonate react with acids. The calcite structure of magnesium carbonate has the form wherein Mg^{2+} is surrounded by six O^{2-} atoms. The dihydrate composition has a triclinic structure, while the trihydrate has a monoclinic structure. References to "light" and "heavy" magnesium carbonates actually refer to the magnesium hydroxycarbonates. A space-filling structure of the anhydrous salt is seen in the above diagram where the triangular CO_3^{2-} groups are clearly visible (Fig. 5.7).

This anhydrous salt consists of white trigonal crystals with a refractive index of 1.717 and a density 2.958 g/cm^3. It decomposes at 540 °C to form the oxide. It is practically insoluble in water (0.0106 g/100 ml at room temperature) with a K_{sp} of 1.1×10^{-5}. Under partial pressure of CO_2 in water, it has an increased solubility (3.5 and 5.9 g $MgCO_3$/100 g of saturated solution at CO_2 pressures of 2 and 10 atm, respectively). It is insoluble in acetone and ammonia but dissolves in acids.

The di- and trihydrates, $MgCO_3 \cdot 2H_2O$ and $MgCO_3 \cdot 3H_2O$ are colorless crystals having triclinic and monoclinic structures, respectively; the refractive index of 1.458 and 1.412, respectively; and their densities are 2.825 and 1.837 g/cm^3.

The pentahydrate, $MgCO_3 \cdot 5H_2O$, occurring naturally as the mineral "lansfordite", is a white crystalline solid consisting of monoclinic crystals. Its refractive index is 1.456 and has a density of 1.73 g/cc. It is not stable and decomposes in air to the trihydrate. The pentahydrate is slightly soluble in water (0.375 g/100 ml at 20 °C). Its density is 1.73 g/cc. The K_{SP} of magnesium carbonate trihydrate, $MgCO_3 \cdot 3H_2O$, is 2.38×10^{-6} while that of magnesium carbonate pentahydrate, $MgCO_3 \cdot 5H_2O$, is 3.79×10^{-6}.

All three basic carbonates, artinite, hydromagnesite and dypingite, are white crystalline substances having monoclinic crystal structures and refractive indices of 1.488, 1.523 and 1.508, respectively. The index of refraction for the basic carbonate octahydrate is 1.515 while the densities are 2.02 and 2.16 g/cc for artinite and hydromagnesite. These basic carbonates are all practically insoluble in water.

Thermochemical properties

$$\Delta H_f^0\ (MgCO_3) = -261.9\ \text{kcal/mol}$$

$$\Delta G_f^0\ (MgCO_3) = -241.9\ \text{kcal/mol}$$

$$\Delta G_f^0\ (MgCO_3 \cdot 3H_2O) = -412.6\ \text{kcal/mol}$$

$$\Delta G_f^0\ (MgCO_3 \cdot 5H_2O) = -525.7\ \text{kcal/mol}$$

$$S^0\ (MgCO_3) = 15.7\ \text{cal/degree mol}$$

$$C_p\ (MgCO_3) = 18.05\ \text{cal/degree mol}$$

Magnesium carbonate is obtained mainly by mining the natural mineral magnesite. The trihydrate salt, $MgCO_3 \cdot 3H_2O$, is prepared by mixing solutions of magnesium and carbonate ions in the presence of carbon dioxide. Alternatively, it may be produced by carbonation of magnesium hydroxide slurry with carbon dioxide under pressure (3.5 to 5 atm) and at a temperature below 50 °C which yields soluble magnesium bicarbonate:

$$Mg(OH)_2 + 2CO_2 \Rightarrow Mg(HCO_3)_2$$

The solution is filtered to remove impurities and the filtrate is subjected to vacuum or aeration to yield insoluble magnesium carbonate as a hydrated salt:

$$Mg^{2+}\,(aq) + 2HCO_3^-\,(aq) \Rightarrow MgCO_3\,(solid) + CO_2\,(gas) + H_2O$$

Under ordinary conditions, anhydrous magnesium carbonate cannot be prepared in aqueous systems. The anhydrous salt, however, can be made under very high partial pressures of carbon dioxide.

Basic magnesium carbonate occurs in nature as the mineral, "Hydromagnesite". The basic salt is obtained by mining the ore followed by purification. The basic carbonates also can be made by drying the magnesium carbonate trihydrate at about 100 °C. Alternatively, it can be prepared by simply boiling a solution of magnesium bicarbonate. The bicarbonate is obtained by carbonation of a magnesium hydroxide slurry below 50 °C and under a CO_2 partial pressure of 3.5 to 5 atm. Composition of the basic carbonate produced by the above methods is $4MgCO_3 \cdot Mg(OH)_2 \cdot 4H_2O$.

Another basic salt, $MgCO_3 \cdot Mg(OH)_3 \cdot 3H_2O$ is precipitated when magnesium salt solution is treated with sodium carbonate solution. The reactions are:

$$CO_3^{2-} + H_2O \Rightarrow HCO^{3-} + OH^-$$

$$2Mg^{2+} + CO_3^{2-} + 2OH^- \Rightarrow MgCO_3 \cdot Mg(OH)_2$$

When magnesium carbonate dissolves in dilute mineral acids, it evolves carbon dioxide:

$$MgCO_3 + HCl \Rightarrow MgCl_2 + CO_2\,(gas) + H_2O$$

$$MgCO_3 + H_2SO_4 \Rightarrow MgSO_4 + CO_2\,(gas) + H_2O$$

When heated above 360 °C, CO_2 and magnesium oxide are formed:

$$MgCO_3 \Rightarrow MgO + CO_2$$

The trihydrate, $MgCO_3 \cdot 3H_2O$ or other hydrates when heated form basic magnesium carbonates, the product compositions depending on degree of water of crystallization and the temperature employed. At a temperature range between 250 and 800 °C, $MgCO_3$ decomposes with a reaction enthalpy of 118 kJ/mol. Above 540 °C, the process reaches a decomposition rate of 100% MgO.

Magnesium carbonate forms several double salts with salts of alkali and AEMs and ammonium ion. Some examples are:

$$MgCO_3 \cdot Na_2CO_3$$

$$MgCO_3 \cdot K_2CO_3 \cdot 8H_2O$$

$$MgCO_3 \cdot KHCO_3 \cdot 4H_2O \text{ (Engle's salt)}$$

$$MgCO_3 \cdot (NH_4)_2CO_3 \cdot 4H_2O$$

$$MgCO_3 \cdot MgCl_2 \cdot 7H_2O$$

$$MgCO_3 \cdot MgBr_2 \cdot 7H_2O$$

Ammonium magnesium carbonate tetrahydrate, $MgCO_3 \cdot (NH_4)_2CO_3 \cdot 4H_2O$, crystallizes with an orthorhombic unit cell, $a = 7.697$, $b = 10.287$, $c = 6.639$ Å, $Z = 2$; $D_x = 1.595$, $D_M = 1.61$ mg/m^3.

Some applications of magnesium carbonate are uses in flooring, fireproofing and fire-extinguishing compositions; as a filler material and smoke suppressant in plastics; as a reinforcing agent in neoprene rubber; as a drying agent and for color retention in foods; in cosmetics. Magnesium carbonate is used as an antacid in medicine and as an additive to table salt. Another important application of magnesium carbonate is as a starting material in producing a number of magnesium compounds.

Because of its water-insoluble, hygroscopic properties, $MgCO_3$ was first added to salt in 1911 to make the salt flow more freely. Magnesium carbonate, most often referred to as "chalk", is used as a drying agent for hands in gymnastics, weight lifting and rock climbing. Magnesium carbonate is also used in taxidermy for whitening skulls. It can be mixed with hydrogen peroxide to create a paste, which is then spread on the skull to give it a white finish. Basic magnesium carbonate is used as a clay in face masks and it has mild astringent properties and helps to smooth and soften skin. It is recommended for use on normal to dry skins.

Magnesium carbonate is readily available commercially from a large number of suppliers worldwide.

Calcium Carbonate

Calcium carbonate has the molecular formula of $CaCO_3$ and the molecular weight of 100.0924 g/mol. It is a common substance found in rock in all parts of the world, and is the main component of the shells of many marine organisms such as snails and conches. It is the main ingredient in eggshells of birds and pearls obtained from oysters. Calcium carbonate is the active ingredient in "limestone" used as "agricultural lime" and is the principal cause of "hard water" since most subterranean streams used for fresh water come from wells where underground water flows through limestone beds which are eroded due to its passage.

Calcium carbonate occurs in nature as limestone in various forms, such as marble, chalk, and coral. It is probably the most widely used raw material in the chemical industry. It has numerous applications, primarily to produce cement, mortars, plasters, refractories, and glass as building materials. It is also used to produce quicklime, hydrated lime and a number of calcium compounds. Calcium carbonate is found naturally as the following polymorphs:

Aragonite
Calcite
Vaterite (μ-$CaCO_3$).

The trigonal crystal structure of calcite is the most common mineral. A transparent variety of calcite called "Iceland Spar" exhibits a "double refraction" wherein light is broken into two parts as it passes through the crystal. This double-refraction occurrence is one of the strongest of all minerals. The difference in refractive index of the ordinary part ($\eta_0 = 1.658$) and that of the extraordinary part ($\eta_0 = 1.4860$) is 0.172 (Fig. 5.8).

Few minerals can be found which approach this distinction.

In addition, this type of calcite crystal polarizes the light rays vertically as they pass through. This phenomenon was exploited in 1828 by the Englishman, William Nicol, who bisected an Iceland double-spar crystal, realigned them and cemented the two parts together with Canada balsam. He thus obtained a simple polarization

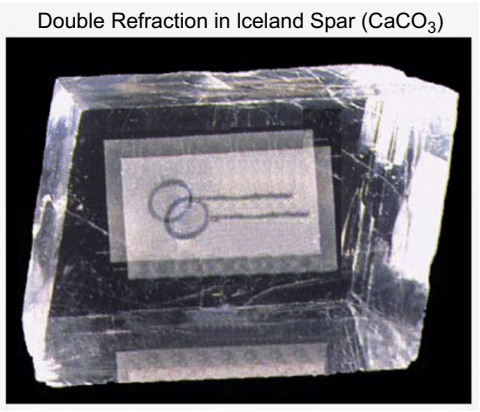

FIGURE 5.8

optical filter that we call today a "Nicol Prism". Large transparent calcite crystals can also be used for this purpose.

The following rocks are composed primarily of $CaCO_3$:

Calcite
Chalk
Limestone
Carbonatite
Marble
Tufa
Travertine.

These minerals have been mined extensively over the eons and used by man.

Calcite, which gets its name from "*chalix*" the Greek word for lime, is a most amazing and yet, most common mineral. The structure of cubic calcite is shown in the following Fig. 5.9.

It is one of the most common minerals on the face of the earth, comprising about 4% by weight of the earth's crust and is formed in many different geological environments. Calcite can form rocks of considerable mass and constitutes a significant part of all three major rock classification types. It forms oolitic, fossiliferous and massive limestones in sedimentary environments and even serves as the internal cement for many sandstones and shales. Calcite is even a major component in the igneous rock called carbonatite and forms the major portion of many hydrothermal veins. Not necessarily a variety of calcite, cave formations are certainly a unique aspect of calcite's story. Calcite is the primary mineral component in cave formations. Stalactites and stalagmites, cave veils, cave pearls, "soda straws" and the many other different cave formations that millions of visitors to underground caverns enjoy are made of calcite. It is the fact that calcite is readily dissolved or worn away by water that these formations occur. Overlying limestones or marbles are dissolved away by years and years of slightly acidic ground water that percolates into the caverns below. In fact, the caverns themselves may have been the result of water dissolving away the calcite-rich rock. As the calcite-enriched water enters a relatively dry cavern, the water starts to evaporate and thus reprecipitate as the calcite. The resulting accumulations of calcite are generally extremely pure and are colored, if at all, by very small amounts of iron or other impurities. Mexican onyx is a variety of calcite that is used extensively for ornamental purposes. It is easily carved into figurines and is so popular that almost every child in the USA owns a small onyx animal or two. Carvings such as vases, bookends, plates, eggs, obelisks, pyramids and statues are all popular. It is not the same onyx as the quartz variety of onyx which is a little more precious (it is used in jewelry) and is banded white and black. To avoid confusion, it is best to refer to it as *Mexican* onyx. Mexican onyx is banded with multiple orange, yellow, red, tan, brown and white colors that have marble-like texture. The carvings are quite attractive and affordable; a rare combination!

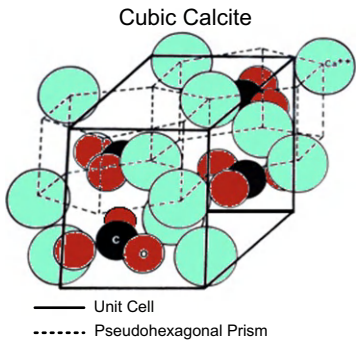

FIGURE 5.9

Chalk is a sedimentary rock of biochemical origin. It is soft, white and porous.

It formed in the deep ocean far from land via the gradual accumulation of the calcite shells of coccolithophores. Layers of chalk are known that are hundreds of feet thick, indicating extremely long periods of accumulation. This mineral of $CaCO_3$, is similar in composition to limestone, but softer. It is characteristically a marine formation and sometimes occurs in great thickness; the chief constituents of these chalk deposits are the shells of minute animals called "Foraminiferans". Chalk has been laid down in all periods of geologic time, but most of the best-known deposits, e.g. the cliffs of the English channel (known as "The Cliffs of Dover") date from the Cretaceous period of geological time. Chalk is used directly in the manufacture of putty, plaster, cement, quicklime, mortar, and also for blackboard chalk. Harder forms are used as building stones. Poor soils containing an excessive proportion of clay are frequently improved and "sweetened" by mixing chalk into them. Extensive deposits occur in Western Europe south of Sweden and in England, notably in the chalk cliffs of Dover along the English Channel. Other extensive deposits occur in the U.S. from South Dakota to Texas and eastward to Alabama. Chalk is used for making lime and Portland cement and as a soil additive. Finely ground and purified chalk is known as whiting and is used as a filler, extender, or pigment in a wide variety of materials, including ceramics, putty, cosmetics, crayons, plastics, rubber, paper, paints, and linoleum.

Limestone is a very common sedimentary rock of biochemical origin. It is composed mostly of the mineral calcite. Sometimes it is almost pure calcite, but most limestones are filled with lots of other minerals and sand and as such are called dirty limestones. The calcite

present is derived mostly from the remains of organisms such as clams, brachiopods, bryozoa, crinoids and corals. These animals live on the bottom of the sea and when they die their shells accumulate into piles of shelly debris. This debris can then form beds of limestone. Some limestones may have been derived from nonbiogenic calcite formation. Although some limestones can be nearly pure calcite, there is often a large amount or sand or silt that is included in the shelly debris. Limestones are important rocks. They can be used for building materials but are not quite as strong as sandstone and are easily weathered by acidic conditions. Limestones are the primary source of lime for cements. Cement is considered one of the most important construction materials ever invented by man. Limestone can be crushed and used as road ballast. Significant quantities of limestone are quarried around the world for these purposes. Limestone is usually the type of rock that gives us caves. Most caves are the result of dissolution of calcite by acidic waters. Ground water can dissolve portions of massive limestone formations and yield extremely large caverns. Large caves and numerous sinkholes are often found in areas that have significant limestone formations.

Carbonatite is an igneous rock that may be either intrusive or extrusive and is composed of at least 20% carbonate minerals. The rock known as "Natrocarbonatite" primarily consists of two carbonate minerals, nyerereite and gregoryite. Carbonatites are defined by mineralogic composition consisting of greater than 50% carbonate minerals. Carbonatites may be confused with marble, and may require geochemical verification. Carbonatites usually occur as small plugs within zoned alkali-like intrusive complexes, or as dikes, sills, breccias and veins. They are, almost exclusively, associated with continental rift-related tectonic settings. The majority of carbonatites are Proterozoic or Phanerozoic in age. It seems that there has been a steady increase in the carbonatitic igneous activity throughout the Earth's history, from Archean to present. Nearly, all carbonatite occurrences are intrusives or subvolcanic intrusives. This occurs because carbonatite lava flows are unstable and react quickly in the atmosphere. Carbonatite lavas may be more common than has been thought, but have been poorly preserved through weathering throughout the Earth's history.

Marble is a rock resulting from the metamorphism of sedimentary rocks such as limestone or dolemite rocks. Metamorphism causes variable recrystallization of the original carbonate mineral grains. The resulting marble rock is typically composed of an interlocking mosaic of carbonate crystals. Primary sedimentary textures and structures of the original carbonate rock (protolith) have typically been modified or destroyed. Pure white marble is the result of metamorphism of a very pure (silicate-poor) limestone or dolomite protolith. The characteristic swirls and veins of many colored marble varieties are usually due to various mineral impurities such as clay, silt, sand, iron oxides, or chert which were originally present as grains or layers in the limestone. Green coloration is often due to serpentine resulting from initial contamination of high magnesium limestone or "dolostone" with silica impurities. These various impurities may have been mobilized and recrystallized by the intense pressure and heat of the metamorphism mechanism. White marble has been valued for its use in creating sculptures since classical times. This preference has to do with the softness and relative isotropy and homogeneity, and a relative resistance to shattering of marble. Also, the low index of refraction of modified calcite within marble allows light to penetrate several millimeters into the stone before being scattered out, resulting in the characteristic "waxy" look which gives "life" to marble sculptures of the human body. The word "marble" derives from the Greek mármaron (mármaros), "crystalline rock", "shining stone", perhaps from the verb (marmaír), "to flash, sparkle, gleam". This linguistic stem is also the basis for the English word *marmoreal*, meaning "marble-like." Colorless or light-colored marbles are a very pure source of calcium carbonate, which is used in a wide variety of industries. Finely ground marble or calcium carbonate powder is a component in paper, and in consumer products such as toothpaste, plastics and paints. Ground calcium carbonate can be made from limestone, chalk, and marble; about three-quarters of the ground calcium carbonate worldwide is made from marble. Ground calcium carbonate is used as a coating pigment for paper because of its high brightness and as a paper filler because it strengthens the sheet and imparts high brightness. Ground calcium carbonate is used in consumer products such as a food additive, in toothpaste, and as an inert filler in pills. It is used in plastics because it imparts stiffness, impact strength, dimensional stability, and thermal conductivity. It is used in paints because it is a good filler and extender, has high brightness, and is weather resistant. However, the growth in demand for ground calcium carbonate in the last decade has mostly been for a coating pigment in paper. U.S. dimension marble production in 2006 was 46,400 tons valued at $18.1 million, compared to 72,300 tons valued at $18.9 million in 2005. Crushed marble production (for aggregate and industrial uses) in 2006 was 11.8 million tons valued at $116 million, of which 6.5 million tons was finely ground marble. As the favorite medium for Greek and Roman sculptors and architects, marble has become a cultural symbol of tradition and refined taste. Its extremely varied and colorful patterns make it a favorite decorative material. Sculptures of marble

FIGURE 5.10

are shown below that are typical of the type of detail that can be obtained with marble forms.

Pure white marble is the result of metamorphism of a very pure (silicate-poor) limestone or dolomite protolith. The characteristic swirls and veins of many colored marble varieties are usually due to various mineral impurities which were originally present as grains or layers in the limestone (Fig. 5.10).

Tufa is a variety of limestone, which is formed by carbonate mineral precipitation from ambient temperature water bodies. One example is from geothermally heated hot springs where such mechanisms sometimes produce similar (but less porous) carbonate deposits known as **travertine**. Tufa is sometimes referred to as (meteogene) travertine. Care must be taken when searching through literature to prevent confusion with hot spring (thermogene) travertine. Calcareous tufa should not be confused with Tuff, a porous volcanic rock with similar etymological origins. Modern and fossil tufa deposits abound in areas with wetland plants. As such many tufa deposits are characterized by their large macrobiological components and are highly porous. Tufa forms either in fluvial channels or in lacustrine settings. Tufa columns are an unusual form of tufa typically associated with saline lakes. It is generally thought that such features form from $CaCO_3$ precipitated when carbonate-rich source waters emerge into alkaline soda lakes. They have also been found in marine settings.

Calcium carbonate is produced commercially either as powdered or precipitated calcium carbonate. The latter consists of finer particles of greater purity and more uniform size. They also have many important commercial applications. Various grades of precipitated calcium carbonate are used in several products, such as textiles, papers, paints, plastics, adhesives, sealants, and cosmetics. The industrial equipment used to make pure $CaCO_3$ is shown in Fig. 5.11.

This diagram shows an array of equipment that has been used commercially for preparing salts such as calcium carbonate. The aim is to produce very high-purity $CaCO_3$ using ordinary purity commercial-grade $CaCl_2$ and ammonium carbonate. Both are dissolved and additives such as sodium sulfide and/or heavy-metal complexing agents like ammonium dithiocarbamate and the like are added to remove heavy metals so as to obtain pure $CaCO_3$ containing only a few parts per million of impurities. The crystal sizes required for various commercial applications can be controlled by regulation of temperature, pH, concentrations, and mixing rate.

Calcium carbonate may also be produced by mixing solutions of calcium chloride and sodium carbonate. In some cases, the presence of sodium is objectionable so that the ammonium carbonate salt is preferable.

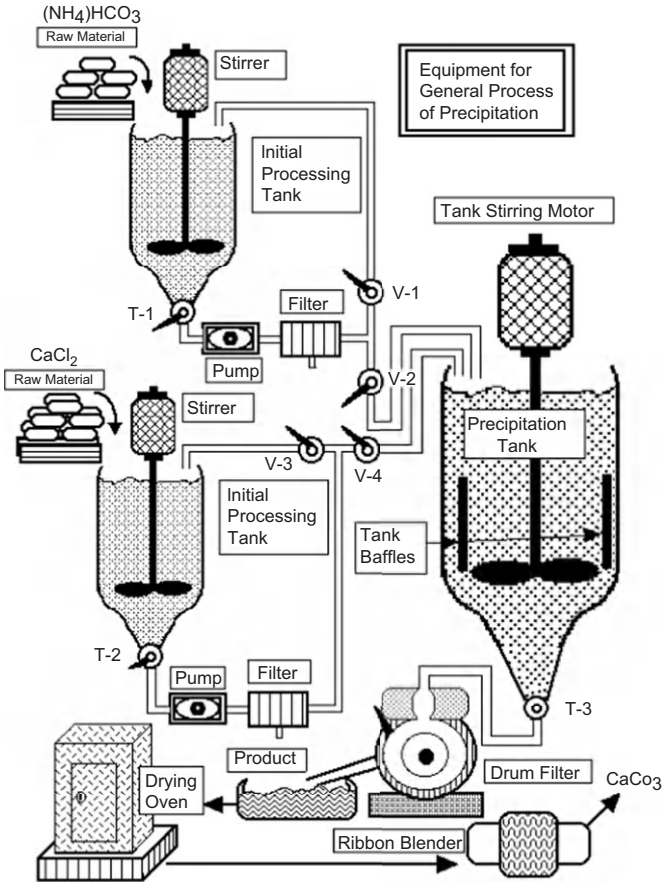

FIGURE 5.11

Calcium carbonate occurs in two main forms—the hexagonal crystal known as calcite, and the orthorhombic form, aragonite. Calcite decomposes on heating at 825 °C, aragonite melts at 1339 °C (at 102.5 atm. pressure). A comparison of the two structures is seen in the following diagram shown below (Fig. 5.12).

Densities are:

2.71 g/cc (calcite)
2.83 g/cc (aragonite).

Both are insoluble in water (0.0015 g/100 ml at 25 °C); $K_{sp} = 4.8 \times 10^{-9}$. Both forms are soluble in dilute mineral acids. It has already been found that calcium carbonate exists in one stable form, β-$CaCO_3$ (calcite), and two less stable forms, λ-$CaCO_3$ (aragonite) and μ-$CaCO_3$ (or vaterite), in the ordinary temperature range. Aragonite is formed if precipitation is carried out at a temperature approaching the boiling point of water (higher than 85 °C), whereas when precipitation is carried out at room temperature only calcite results. The third form of calcium carbonate, μ-$CaCO_3$, is formed by precipitation at 60 °C.

Thermochemical properties

$$\Delta H_f^\circ = -288.6 \text{ kcal/mol}$$
$$\Delta G_f^\circ = -269.9 \text{ kcal/mol}$$
$$S^\circ = 21.92 \text{ cal/degree mol}$$
$$C_p = 19.9 \text{ cal/degree mol}$$

Calcium carbonate is obtained from natural limestone deposits. The purified compound, known as precipitated calcium carbonate, is synthesized from limestone. Limestone is calcined to calcium oxide and carbon dioxide in a kiln. The products are recombined after purification. Calcium oxide is hydrated with water to give a slurry called milk of lime, which is then carbonated by bubbling CO_2 through it. The reactions involved in the process are as follows:

$$CaCO_3 + \text{heat} \Rightarrow CaO + CO_2$$

$$CaO + H_2O \Rightarrow Ca(OH)_2$$

$$Ca(OH)_2 + CO_2 \Rightarrow CaCO_3 + H_2O$$

Calcium carbonate is used to produce other calcium compounds. Treatment with dilute mineral acids produces corresponding calcium salts with liberation of CO_2 gas:

$$CaCO_3 \text{ (solid)} + 2HCl \text{ (aq)} \Rightarrow CaCl_2 \text{ (aq)} + H_2O + CO_2 \text{ (gas)}$$

$$CaCO_3 \text{ (solid)} + 2H_2SO_4 \text{ (aq)} \Rightarrow CaSO_4 \text{ (aq)} + H_2O + CO_2 \text{ (gas)}$$

$$CaCO_3 \text{ (solid)} + 2HNO_3 \text{ (aq)} \Rightarrow Ca(NO_3)_2 \text{ (aq)} + H_2O + CO_2 \text{ (gas)}$$

In the presence of CO_2, it dissolves in water with the formation of bicarbonate:

$$CaCO_3 \text{ (solid)} + H_2O + CO_2 \text{ (gas)} \Rightarrow Ca^{2+} + 2HCO_3^-$$

Limestone has been used by man since ancient times. Calcination of limestone using charcoal fires to produce "quicklime" or CaO has been practiced since antiquity by cultures all over the world. The quicklime is generally slaked to form what is called "whitewash" or $Ca(OH)_2$ as a slurry in water (see alkaline earth hydroxides presented above). Some of the earliest known examples of lime use for building purposes are in early Egyptian buildings (primarily monuments). Some of these examples in the chambers of the pyramids, which date back to around 2000 BC, are still hard and intact.

Calcium bicarbonate ($Ca(HCO_3)_2$), also known as calcium hydrogen carbonate, does not refer to a known solid compound. It exists only in aqueous solution containing the ions calcium (Ca^{2+}), dissolved carbon dioxide (CO_2), bicarbonate (HCO_3^-), and carbonate (CO_3^{2-}). It cannot be separated from solution in a stable form. The relative concentrations of these carbon-containing species depend on the pH. Bicarbonate anions predominate within the range 6.36–10.25 in fresh water. Attempts to prepare compounds such as calcium bicarbonate by evaporating its solution to dryness invariably yield the solid carbonate instead:

$$Ca(HCO_3)_2 \text{ (aq)} \Rightarrow CO_2 \text{ (gas)} + H_2O \text{ (Liq)} + CaCO_3 \text{ (solid)}$$

Very few solid bicarbonates other than those of the alkalis and ammonium ions are known to exist. This is due to the fact that bicarbonate is stable at basic pH values in solution. Calcium bicarbonate is moderately soluble in water with the following values:

16.1 g/100 ml (0 °C)
16.6 g/100 ml (20 °C)
18.4 g/100 ml (100 °C)

Calcium carbonate has the CAS number of 471-34-1. It is available commercially all over the world in large quantities.

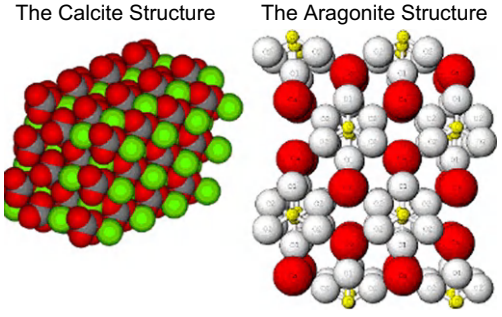

FIGURE 5.12

Strontium Carbonate

Strontium carbonate has the formula of $SrCO_3$ and the molecular weight of 147.6326 g/mol. Its CAS

number is 1633-05-2. Strontium carbonate occurs in nature as the mineral "strontianite". The name strontianite comes from a famous location for the mineral, Strontian, Scotland. Strontianite is strontium carbonate as found naturally. Significant deposits are found in Germany, Scotland and the US at Strontium Hills, California. It occurs as white or slightly gray orthorhombic crystals with a refractive index of 1.518. The unit-cell parameters are: $a = 5.107$ Å, $b = 8.414$ Å, $c = 6.029$ Å, $Z = 4$; $V = 259.07$ Å^3, Den(Calc) = 3.78. The crystal system is orthorhombic with space group Pmcn and point group 2/m, 2/m, 2/m. Strontium carbonate has only one stable form (aragonite-type structure) and temperature of precipitation has no effect on crystal form, unlike that of calcium or magnesium carbonates. However, it undergoes transitions as it is heated, before it decomposes at 1290 °C. Thermal decomposition studies (TG, DTG and DTA) in air showed $SrCO_3$ was formed at ca. 500 °C through the formation of transient intermediate of a mixture of $SrCO_3$ and SrC_2O_4 around 455 °C. A sharp phase transition from γ-$SrCO_3$ to β-$SrCO_3$ was indicated by a distinct endothermic peak at 900 °C in DTA.

The aragonite structure is shown in the following Fig. 5.13.

Aragonite, in contrast to calcite, has strontium ions coordinated by nine oxygen atoms and each oxygen is bonded to three strontium atoms. Aragonite has a more compact atomic arrangement than calcite and is the stable phase at high pressures and low temperatures.

$SrCO_3$ is slightly hygroscopic with a hardness of 3.5 Mohs and a density of 3.5 g/cc. It is almost insoluble in water (0.0011 g/100 ml at 18 °C) but soluble in dilute acids with liberation of carbon dioxide. It is stable in air but when heated decomposes at 1290 °C.

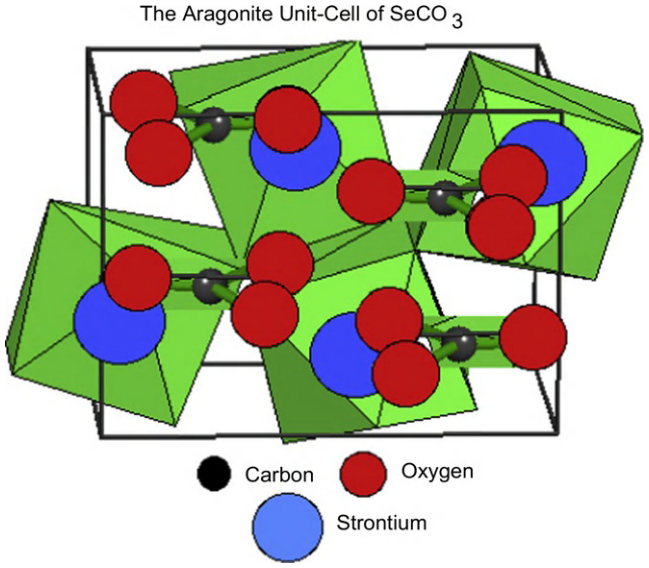

FIGURE 5.13

Thermochemical properties

$$\Delta H_f^0 = -291.6 \text{ kcal/mol}$$
$$\Delta G_f^0 = -272.5 \text{ kcal/mol}$$
$$S^0 = 23.2 \text{ cal/deg mol}$$
$$C_p = 19.5 \text{ cal/deg mol}$$

The solubility is increased if $SrCO_3$ is suspended in water and CO_2 gas is introduced. Such measurements of the solubility of strontianite were used to evaluate the equilibrium constant for the reaction:

$$SrCO_3 \text{ (solid)} \Rightarrow Sr^{2+} \text{ (aq)} + CO_2^{3-} \text{ (aq)}$$

between 2 and 91 °C. The temperature dependence of the equilibrium constant is given by the expression: $\log K = 155.0305 - 7239.594/T - 56.58638 \log T$ where T is in degrees Kelvin. The log K of strontianite, the Gibbs energy, and enthalpy of the reaction at 25 °C are:

$$\log K = -9.271 \pm 0.020,\ 52.919 \pm 0.08 \text{ kJ/mol}$$
$$\Delta G_f^0 = -1.67 \pm 1.30 \text{ kJ/mol}$$
$$\Delta H_f^0 = -183.1 \pm 4.0 \text{J/mol/K}$$

The equilibrium constants are consistent with an aqueous model that includes the ion pairs $SrHCO_3^+$ (aq) and $SrCO_3^0$ (aq) which were evaluated by potentiometric methods between 5 and 80 °C. The equilibrium constant for the association reaction:

$$Sr^{2+} \text{ (aq)} + HCO_3^- \text{ (aq)} \Rightarrow SrHCO_3^+ \text{ (aq)}$$

is given by the expression: $\log K\ (SrHCO_3^+) = -3.248 + 0.014867\ T$. The log of the association constant, the Gibbs energy, enthalpy and entropy of the reaction at 25 °C are:

$$\log K = 1.18$$
$$\Delta G_f^0 = -6.76 \text{ kJ/mol}$$
$$\Delta H_f^0 = 25.30 \text{ J/mol}$$
$$C_p = 107.5 \text{ J/mol/K}$$

The equilibrium constant for the association reaction:

$$Sr^{2+} \text{ (aq)} + CO_3^{-2} \text{ (aq)} \Rightarrow SrCO_3^0 \text{ (aq)}$$

is given by the expression: $\log K\ (SrCO_3^0) = -1.019 + 0.012826\ T$. The log of the association constant, the Gibbs energy, enthalpy, and entropy of the reaction at 25 °C are:

$$\log K = 2.81$$
$$\Delta G_f^0 = -16.01 \text{ kJ/mol}$$
$$\Delta H^0 = 21.83 \text{ J/mol}$$
$$C_p = 126.9 \text{ J/mol/K}$$

These results lead to reliable calculation of the aqueous speciation and solubility of strontianite in the system $SrCO_3$–CO_2–H_2O from 0 °C to more than 90 °C.

Strontium carbonate occurs in nature as strontianite and can be mined from its deposit. It is, however, usually made commercially from the mineral "celestite". Celestite is fused with sodium carbonate at elevated temperatures or boiled with a solution of ammonium carbonate:

$$SrSO_4\,(aq) + Na_2CO_3\,(aq) \Rightarrow SrCO_3\,(solid) + Na_2SO_4\,(aq)$$

$$SrSO_4\,(aq) + (NH_4)_2CO_3\,(aq) \Rightarrow SrCO_3\,(solid) + 2NH_3\,(gas) + CO_2\,(gas) + H_2O$$

Strontium carbonate is insoluble in water. It precipitates from the product mixture in the second reaction. If fused with sodium carbonate, the product mixture is leached with water. Insoluble carbonate separates from the water-soluble sodium sulfate.

Crystal structures of the so-called "triple carbonates" of Ba, Sr and Ca were studied where co-precipitated powders were studied by the X-ray powder method, using an X-ray Geiger counter spectrometer. There exist three kinds of solid solutions: aragonite type crystal (l-carbonate), calcite type crystal (β-carbonate) and vaterite type crystal (μ-carbonate); in the $BaCO_3$–$SrCO_3$–$CaCO_3$ system. The phase domains of these three crystal forms are affected somewhat by the temperature at which the precipitation is carried out. The triple diagrams are obtained at two stages of precipitation temperatures.

The compound, $SrCO_3$, is used in pyrotechnics and ceramic ferrites. It is also used in making iridescent glass for color television tubes. Other uses are in refining sugar and preparing other strontium salts. The most common use is as an inexpensive fireworks colorant. Strontium and its salts emit a brilliant red color in flame. Unlike other strontium salts, the carbonate salt is generally preferred because of its cost and the fact that it is not hygroscopic. Its ability to neutralize acid is also very helpful in pyrotechnics. Another similar application is in road flares. Strontium carbonate is used for electronic applications. It is used for manufacturing glass color-television tubes to absorb X-rays resulting from the bombardment of the cathode rays on the glass enclosure of the cathode-ray gun. With the advent of PDP and LCD panels as TV displays, this application is not so important anymore. $SrCO_3$ is used in the preparation of iridescent glass, luminous paints such as $SrS{:}Ce^{3+}$, strontium oxide or strontium salts and in refining sugar. It is widely used in the ceramics industry as an ingredient in glazes. It acts as a flux and also modifies the color of certain metallic oxides. It is also used in the manufacturing of strontium ferrites for permanent magnets that are used in loudspeakers and door-magnets. Strontium carbonate can be used to produce many different strontium compounds by simply dissolving it in the corresponding acid.

Strontium bicarbonate has not been isolated. It exists only in aqueous solution containing the ions strontium (Sr^{2+}), dissolved carbon dioxide (CO_2), bicarbonate (HCO_3^-), and carbonate (CO_3^{2-}). It cannot be separated from solution in a stable form. The relative concentrations of these carbon-containing species depend on the pH. Bicarbonate anions predominate within the range 6.36–10.25 in fresh water. Attempts to prepare compounds such as strontium bicarbonate by evaporating its solution to dryness invariably yield the solid carbonate instead. Ammonium or sodium bicarbonates can be used to prepare $Sr(HCO_3)_2$ as a solid only if the pH is >9.5.

Strontium carbonate is readily commercially available worldwide.

Barium Carbonate

Barium carbonate has the molecular formula of $BaCO_3$ and the molecular weight of 197.3359 g/mol. Its CAS number is 513-77-9. Barium carbonate has only one stable form (aragonite-type structure) and temperature of precipitation has no effect on crystal form, unlike that of calcium or magnesium carbonates. Barium carbonate is made commercially from barium sulfide either by treatment with sodium carbonate or ammonium carbonate at 60 to 70 °C or by passing CO_2 gas through a soluble Ba^{2+} solution at 40 to 90 °C:

$$BaS + Na_2CO_3 \Rightarrow BaCO_3\,(solid) + Na_2S$$

$$BaS\,(aq) + CO_2\,(gas) + H_2O \Rightarrow BaCO_3\,(solid) + 2H_2S$$

In the soda ash process, solid or dissolved sodium carbonate is added to barium sulfide solution, and the barium carbonate precipitate is filtered, washed to remove sodium nitrate, and dried. A barium sulfide solution is reacted with sodium carbonate in a suitable vessel in which barium carbonate is precipitated. The precipitate is then separated from the sodium sulfide solution except that greater difficulty is qualified in washing the precipitate free of the sodium salt. For the process to be economical, it is also necessary to work up the by-product, sodium sulfide, into a salable product. It is frequently sold as crystals containing 30% sodium sulfide or as a fused, broken mass. The Na_2S solution can be treated with nitric acid to oxidize the H_2S released to sulfur:

$$Na_2S\,(aq) + HNO_3\,(aq) \Rightarrow NaNO_3\,(aq) + S\,(solid)$$

A precipitated barium carbonate can be made from a barium sulfide solution, by precipitation with carbon

dioxide or with soda ash. The barium sulfide is made on the same premises by the high-temperature reduction of barites, $BaSO_4$ with coke in rotary kilns. The product commonly known as black ash is lixiviated or leached with water to form an impure barium sulfide solution. The solution may be evaporated to yield a crude technical grade product in the form of a brownish to grayish product and contains 80% to 90% barium sulfide.

Either the solution from the black ash leaching or the redissolved solid barium carbonate is then treated with carbon dioxide, often from the black-ash kiln, by bubbling the gas through the barium sulfide solution in a suitable vessel. The resulting slurry of barium carbonate is sent to a filter, where it is separated from the mother liquor and washed free of soluble salts. Then it is dried and ground to the required size. The mother liquor may be used as makeup in the next batch. In this process, only one-half of the barium is converted to barium carbonate. If desired, the reaction may be carried further by application of either of the reactions. In both cases, a higher conversion of barium ion to barium carbonate is effected, but a by-product disposal problem arises.

A similar process has been proposed to treat "mine-tailings". Mining is a significant contributor to water pollution. Effluents need to be treated to remove sulfate to less than 200 mg/l and for metal removal. The use of barium carbonate as a process can meet these requirements. A study was conducted to demonstrate the performance of an integrated barium carbonate process, consisting of the following stages:

(a) Sulfate precipitation as $BaSO_4$ by treatment of sulfate-rich water with $BaCO_3$.
(b) Thermal reduction of $BaSO_4$ to BaS.
(c) Conversion of BaS to $BaCO_3$ and H_2S by passing CO_2 through a solution of BaS.
(d) The stripped H_2S is converted to elemental sulfur.

A major constituent of mine tailings is pyrites. When pyrites (FeS_2) is exposed to air, it is oxidized by a biologically catalyzed reaction mediated by bacteria *Thiobacillus ferrooxidans*. The primary pollutants of acid mine drainage are the hydrogen ion (acidity), iron, sulfate, manganese, magnesium and sometimes aluminum. Sulfate needs to be removed from effluents to prevent or reduce salination of surface water, gypsum scaling, biocorrosion and acid corrosion. The proposed equipment consisted of a series of tanks in which the acidic mine tailings are treated in stages to reduce soluble sulfate from sulfide ores, using CO_2 derived from limestone, and barium carbonate to form $BaSO_4$ and then BaS and finally sulfur.

Barium carbonate is a white powder with an orthorhombic crystal structure. Its density is 4.286 g/cc and has a refractive index of 1.603. Its hardness is 3.50 Mohs. It is almost insoluble in water (0.00141 g/100 ml at 25 °C) and its K_{sp} is 2.04×10^{-9}. Its melts at 811 °C with subsequent decomposition to the oxide plus CO_2.

Barium carbonate decomposes to barium oxide and carbon dioxide when heated at 1300 °C. In the presence of carbon, decomposition occurs at lower temperatures. Barium carbonate dissolves in dilute HCl and HNO_3 liberating CO_2. A similar reaction occurs in acetic acid. The solid salts, chloride, nitrate and acetate that are water soluble may be obtained by evaporation of the solution. Dissolution in HF, followed by evaporation to dryness, and then heating to red heat, yields barium fluoride.

Barium carbonate forms barium iodide on treatment with ferrous iodide solution:

$$BaCO_3 + FeI_2 \Rightarrow BaI_2 + FeCO_3$$

Barium carbonate produces barium potassium chromate, a pale yellow pigment, known as pigment E, when heated with potassium dichromate. Calcination at 1300 °C with titanium dioxide yields barium metatitanate, $BaTiO_3$:

$$BaCO_3 + TiO_2 \Rightarrow BaTiO_3 + CO_2$$

Barium carbonate is found in nature as the mineral "witherite". The mineral is named after William Withering, who in 1784 recognized it to be chemically distinct from "barites". It occurs in lead-ore veins in Northumberland, England and in Lancaster, England and a few other localities there. It was also reported in Tsumeb, Namibia. There is only one region in North America that is a good producer of this mineral. That is the area of the Fluorite mines in Hardin Co., Illinois. Small deposits also exist in El Portal, Mariposa Co., California, Castle Dome District, Yuma Co., Arizona, and in Canada at Thunder Bay, Ontario.

Natural witherite ($Ba_{0.99}Sr_{0.01}CO_3$) has been studied by single-crystal XRD in a diamond anvil cell at eight pressures up to 8 GPa. At ambient pressure, cell dimensions are $a = 5.3164$ Å, $b = 8.8921$ Å, $c = 6.4279$ Å. The structure was refined to space group Pmcn with $R(F) = 0.020$ from 2972 line-intensity data. The unit-cell and atom position parameters for the orthorhombic cell were refined at pressures of 1.2, 2.0, 2.9, 3.9, 4.6, 5.5, 6.2, and 7.0 GPa. At approximately 7.2 GPa, a first-order transformation to space group $P\bar{3}/c$ was observed. Cell dimensions of the high-pressure phase at 7.2 GPa are $a_1 = 5.258$ Å, $c_1 = 5.64$ Å. The high-pressure structure was determined and refined to $R(F) = -0.06$ using 83 intensity data, of which 15 were unique. This high-pressure phase appears to be more compressible than the orthorhombic phase with an estimated initial bulk modulus ($K = 7.2$ GPa) of 10 GPa.

Barium carbonate has many major commercial applications in brick, glass, ceramics, oil-drilling, photographic and chemical industries. It is mixed with wet clay to immobilize many water-soluble salts in making uniform red bricks. In the glass industry, barium is added to glass as barium carbonate or barium oxide to improve the refractive index of optical glass and also to promote sintering and lower the viscosity of melted glass to make glass bead formation easy. It is used in the manufacture of television picture tubes and photographic paper. Another important application involves its use as a fluxing ingredient in ceramic industry for enamels, glazes and ceramic bodies. Barium carbonate is used in oil well drilling to insolubilize gypsum and inhibit coagulation; in ferrous metallurgy for steel carburizing; in chlor-alkali cells for treating salt brines to remove sulfates; and to make ferrites, and barium titanate. Many barium salts are prepared from barium carbonate.

The so-called "triple carbonates" of Ba, Sr and Ca have long been used to lower the work function of a variety of heated electrodes used in television tube guns and the like. Upon heating (breakdown), the carbonate coatings are converted to semiconductor oxides of Ba, Sr, and Ca. These oxides are characteristically *n*-type and exhibit high-electron conductivity paralleling the high-functional activity of the hot cathodes. The electron emissivity is multiplied many times and lower voltages on the electrodes can be used, resulting in multiplying the lifetimes of such electrodes in TV tubes, fluorescent lamps and other electronic equipment. Crystal structures of Ba, Sr and Ca carbonates were co-precipitated and studied by X-ray powder method using an X-ray Geiger counter spectrometer. There exist three kinds of solid solutions: aragonite type crystal (l-carbonate), calcite type crystal (β-carbonate) and vaterite type crystal (μ-carbonate); in the $BaCO_3$–$SrCO_3$–$CaCO_3$ system. The phase domains of these three crystal forms are affected somewhat by the temperature at which the precipitation is carried out. The triple diagrams are obtained at two stages of precipitation temperatures.

Barium carbonate ($BaCO_3$) was examined in a diamond anvil cell up to a pressure of 73 GPa using an in situ angle-dispersive XRD technique. Three new phases of $BaCO_3$ were observed at pressures >10 GPa. From 10 to 24 GPa, $BaCO_3$-IV had a post-aragonite structure with space group *Pmmn*. There are two molecules in a single unit cell ($Z = 2$) of the orthorhombic phase, which is same as the high-pressure phases of $CaCO_3$ and $SrCO_3$. The isothermal bulk modulus of $BaCO_3$-IV is $K_0 = 84$ GPa, with $V_0 = 129.0$ Å^3 when $K_0 = 4$. The *c* axis of the unit-cell parameter is less compressible than the *a* and *b* axes. The relative change in volume that accompanies the transformation between $BaCO_3$-III and $BaCO_3$-IV is −6%. $BaCO_3$-V, which has an orthorhombic symmetry, was synthesized at 50 GPa. As the pressure increases, $BaCO_3$-V is transformed into tetragonal $BaCO_3$-VI. This transformation is likely to be second order, because the diffraction pattern of $BaCO_3$-V is similar to that of $BaCO_3$-VI, and some single peaks in $BaCO_3$-VI become doublets in $BaCO_3$-V. After decompression, the new high-pressure phases transform into $BaCO_3$-II. These findings resolve a dispute regarding the stable high-pressure phases of $BaCO_3$

Only a few research papers concerning $BaCO_3$ are available in the current scientific literature. This salt is used primarily to make other barium compounds and in glazes for pottery.

Barium bicarbonate is a compound, $Ba(HCO_3)_2$, which is stable only in solution. It can be formed by the action of carbon dioxide on a suspension of barium carbonate in cold water:

$$BaCO_3\,(\text{solid}) + CO_2\,(\text{gas}) + H_2O\,(\text{liq}) \Rightarrow Ba(HCO_3)_2\,(\text{aq})$$

On heating, this reaction is reversed.

Barium carbonate is readily available commercially, both in an impure form and as a highly purified compound.

Radium Carbonate

Radium carbonate has the molecular formula of $RaCO_3$ and the molecular weight of grams per mole. Most of the compounds of radium are more insoluble than the corresponding barium compounds and concentrate in the precipitate upon fractional precipitation of barium–radium mixtures. One notable exception is radium carbonate, which is more soluble than barium carbonate and, hence, concentrates in the soluble fraction (filtrate) when barium–radium carbonate mixtures are fractionally separated.

Radium carbonate is soluble in dilute acids, and more soluble in concentrated ammonium carbonate solution than $BaCO_3$. In general, $RaCO_3$ is prepared in conjunction with $BaCO_3$ and then separated. Radium sulfate is the most insoluble of the alkaline earth sulfates and probably the most insoluble radium compound known. Its volubility is 2.1×10^{-4} g/100 ml of water at 18 °C. For this reason, precipitation as the sulfate is a common practice for the recovery of radium, particularly with the addition of barium carrier. Precipitation is readily accomplished by adding dilute sulfuric acid to a solution of a soluble radium compound. Radium sulfate may be dehydrated completely by heating it in dry air at 300 °C. The compound is soluble in concentrated sulfuric acid, but precipitates upon dilution of the acid. It is converted to radium carbonate by fusion with sodium carbonate (a technique frequently used for the dissolution of radiferous barium sulfate because the resulting barium–radium carbonates are soluble in any dilute mineral acid).

Radium carbonate may also be prepared by precipitation from neutral or weakly alkaline solutions of radium salts with a solution of ammonium carbonate. Gram quantities of radium have been recovered from a concentrated solution of radium nitrate by precipitation as the carbonate. The radium nitrate solution was adjusted to pH 9.2–9.5 with concentrated ammonium hydroxide. Carbon dioxide gas was bubbled into the solution until the pH was just slightly above 7.0. To insure complete precipitation of radium carbonate, ethyl alcohol and some additional ammonium hydroxide solution were added. The radium carbonate was filtered and washed with 90% ethyl alcohol. It was first dried at 110 °C to remove the alcohol and weighed as $RaCO_3$. Mixtures of radium and barium have been separated by fractional precipitation from homogeneous solution as carbonates.

When a mixture of chemically similar cations such as radium and barium is present in the solution, the one which forms the least soluble carbonate concentrate in the precipitate. Consequently, a radium–barium mixture radium is concentrated in the liquor and barium in the precipitate. It appears that the separation of radium and barium by fractional carbonate precipitation is more efficient at higher temperatures. The logarithmic distribution coefficient at 90 °C is 0.1830, whereas at 20 °C, it is about 0.51. Radium and barium carbonates probably show an increasing volubility differential with increasing temperature.

The principal use of radium carbonate has been in medicine and to prepare other radium compounds. Research papers concerning the properties of $RaCO_3$ are scarce and the physical data are scanty. Radium occurs in the mineral "davidite", $La_{0.7}Ce_{0.2}Ra_{0.02}Ca_{0.1}Y_{0.75}U_{0.25}Ti_{15}Fe^{3+}{}_5O_{38}$, which occurs at the Radium-Hill mine in Southern Australia. ^{226}Ra is separated via a $RaSO_4 \Rightarrow RaCO_3$ method. The latter finds employment in medicine.

5.2. ALKALINE EARTH OXY-SILICON COMPOUNDS

Silicon has but one electronic state, that of Si^{4+} in compounds. With the alkaline earths, it forms silicides, M_2Si and "silicates" based on various "silicic acids", composed of oxygen, silicon and the alkaline earth.

5.2.1. Acids Based on Silicon

Silicic acid is a general name for a family of chemical compounds of the elements, Si, H and O, with the general formula $[SiO_x(OH)_{4-2x}]_n$. Some simple silicic acids have been identified in very dilute aqueous solution, such as *metasilicic acid* (H_2SiO_3), *orthosilicic acid* (H_4SiO_4, $pK_{a1} = 9.84$, $pK_{a2} = 13.2$ at 25 °C), *disilicic acid* ($H_2Si_2O_5$), and *pyrosilicic acid* ($H_6Si_2O_7$). However, in the solid state, these forms are not generally stable and condense to form polymeric silicic acids of complex structure. Silicic acids may be obtained by acidifying certain silicate salts like sodium silicate in aqueous solution. When heated they lose water to form silica gel.

In the oceans, silicon exists primarily as orthosilicic acid (H_4SiO_4), and its biogeochemical cycle is regulated by the group of algae known as "diatoms". These algae polymerize the silicic acid to so-called "biogenic silica", used to construct their cell walls (called "frustules").

Orthosilicic acid is the form predominantly absorbed by humans and is found in numerous tissues including bone, tendons, aorta, liver and kidney. Persuasive data suggest that silica is essential for health although no RDI has been established. However, a deficiency of silica induces deformities in skull and peripheral bones, causes poorly formed joints, reduced contents of cartilage, collagen, and disruption of mineral balance in the femur and vertebrae.

5.2.2. Silicides of the Alkaline Earths

Similar to borides and carbides, the composition of silicides cannot be easily specified as covalent molecules. The chemical bonds in silicides range from conductive metal-like structures to ionic or covalent. Silicides of all nontransition metals, with exception of beryllium, have been described. Group 1 and 2 silicides, e.g. Na_2Si and Ca_2Si, react with water to yield hydrogen and/or silanes.

Electronic structures and densities of states of the following AEM silicides have been calculated using a first-principle pseudopotential method: Mg_2Si, $BaSi_2$, Ca_2Si, and Sr_2Si. Mg_2Si and $BaSi_2$ were predicted to be indirect semiconductors while Ca_2Si and Sr_2Si were predicted to be direct semiconductors. Estimated band gaps are about 50% or less of the observed values. The valence bands of these are composed of Si (3s,3p) as well as of Mg (3s,3p), Ca (4s,4p,3d), Sr (5s,5p,4d) or Ba (6s,6p,5d) electrons. The conduction bands are mainly composed of AEM s, p, d states and the contributions of Si(3s,3p) were relatively small. Formation energy of stoichiometric Mg_2Si was successfully foretold.

Beryllium Silicides

Beryllium silicide has the molecular formula of Be_2Si and the molecular weight of 46.1094 g/mol. Be_2Si has never been identified and its existence remains questionable. Although Si has a melting point of 1414 °C and a boiling point of 3265 °C, the melting and boiling points

of Be are nearly as high at 1287 °C and 2469 °C, respectively. Thus, fusion of the elements is not feasible because of lack of equipment that will withstand such temperatures during fusion. Thus, the system Be–Si has never been studied and it is not known whether Be_2Si exists or not. It may be that this compound is not stable thermodynamically due to the sizes of the Be^{2+} and Si^{4-} ions. The reaction of SiC with the oxide was studied:

$$SiC + 2BeO \Rightarrow Be_2Si + CO_2$$

But no beryllium silicide formation was observed.

Although the existence of beryllium silicide has never been reported, a paper describing the evaporation of Be metal upon the surface of silicon has resulted in the formation of "rings" during the growth of epitaxial single-crystal (0001) hcp Be on (111) Si substrates using molecular beam epitaxy. The ring structure is believed to be constructed from 4-Be atoms arranged in a square on the surface of the Si substrate arranged at a distance commensurate with that of 2-Si atoms, i.e. Be_4Si_2, as determined from scanning tunneling microscopy and photoelectron spectroscopy. These methods showed that the nucleation, growth, and structure of beryllium on Si (111) by a chemical reaction that occurs at temperatures as low as 120 K, resulting in a nano-cluster of Be_4Si_2 on the surface. The Be is oriented with Be[1010] parallel to Si[110] and Be[1120] parallel to Si[211]. Crystalline quality of the layer improved with increasing deposition temperature T, where $T = 100$, 200, 300, 400, and 500 °C for the results reported. The films deposited at $T \leq 300$ °C are smooth while those deposited at $T \geq 400$ °C are rough. A superstructure was observed on the surface, probably $\sqrt{3} - \sqrt{3}$, $R30°$, for films grown at $T = 300$ °C.

The physical properties of beryllium silicide remain unknown and it is unavailable commercially due to lack of demand for such a material.

Magnesium Silicide

Magnesium silicide has the molecular formula of Mg_2Si and the molecular weight of 76.6955 g/mol. Its CAS number is 22861-39-6. Its density is 1.998 g/cc and its melting point is 1102 °C. It is a black powder. Since the melting and boiling points of Mg metal are 651 °C and 1091 °C, respectively, this salt can be formed by the reaction of Mg, mixed with Si, at 800 °C in an inert atmosphere:

$$2Mg\ (gas) + Si\ (solid) \Rightarrow Mg_2Si\ (gas)$$

Magnesium silicide is unstable in air and reacts with moisture to form silane. When magnesium silicide is placed into aqueous HCl, the gas silane, SiH_4, is produced. This gas is the silicon analogue of methane, CH_4, but is more reactive. Silane is pyrophoric, that is due to the presence of O_2 in the air, i.e. it spontaneously combusts in air:

$$Mg_2Si\ (solid) + 4HCl\ (aq) \Rightarrow SiH_4\ (gas) + 2MgCl_2\ (solid)$$

$$SiH_4 + 2O_2 \Rightarrow SiO_2 + 2H_2O$$

These reactions are typical of a Group-2 silicide. Mg_2Si reacts similarly with sulfuric acid.

As a powder, magnesium silicide is dark blue or slightly purple in color. SiO_2, found in sand and glass, when heated with Mg metal forms magnesium silicide. The first product in this reaction is silicon, which then reacts further with magnesium to produce Mg_2Si:

$$SiO_2 + 2Mg \Rightarrow 2MgO + Si$$

$$Si + 2Mg \Rightarrow Mg_2Si$$

Magnesium silicide can also be formed by the reaction between magnesium hydride and silicon with the evolution of hydrogen gas at temperatures above 250 °C:

$$2MgH_2 + Si \Rightarrow Mg_2Si + 2H_2$$

Magnesium silicide is dimorphic and has the following cell parameters:

Cubic—cF12 type

$a = b = c = 4.4908$ Å, $\alpha = \beta = \gamma = 60°$, cell volume = 64.04 Å^3, cell occupancy is shown in Table 5.5.

Tetragonal—hP18 type

$a = 6.422$ Å, $b = c = 12.453$ Å, $\alpha = 120°$, $\beta = \gamma = 90°$, cell volume = 961.80 Å^3, cell occupancy is shown in Table 5.6.

Mg_2Si crystallizes in a cubic CaF_2 (fluorspar)-type lattice with $a = 4.49$ Å. The centers of this lattice are analogous to that of diamond. Each Si atom forms four covalent sp^3 bonds. The Mg subshells are only half-filled. There is no bonding between the two Mg atom sites. The distance between the Mg and Si atoms is 2.77 Å. Bonding in this compound is essentially covalent. The heat of formation ΔH_f^0 is –6380 cal/g atom. Mg_2Si is an n-type semiconductor with a forbidden band gap of 0.78 eV at 0 °C. Its conductivity can be expressed by:

Extrinsic: $Q_E = [13 \times 10^3] \exp [0.011/2KT]$
Intrinsic: $Q_I = [10^4/3150] \exp [0.48/2KT]$

A three-dimensional crystal model is shown in the following diagram presented below. Mg_2Si is an ionic crystal composed of Mg^{2+} and Si^{4-} ions that have very different ionic radii, 0.6 Å and 2.1 Å, respectively. This compound exhibits n-type electric conductivity which originates from formations of positively charged Mg ions at interstitial sites, regardless of the chemical composition in crystal growth. Thus, the vacancy model includes V_{Mg}^{2+} and $Mg_{Interstit}^{2+}$ (Fig. 5.14), a Frenkel type.

Magnesium silicide (Mg_2Si) undergoes a transformation from a cubic (fluorite)-type lattice to a hexagonal lattice at pressures above about 25 kilobars and

TABLE 5.5

No	Site notation	Atom	Multiplicity	Wyckoff	Site symmetry	x	y	z	Occupancy
1	Mg	Mg	8	c	-43m	1/4	1/4	1/4	1.0
2	Si	Si	4	a	m-3m	0	0	0	1.0

TABLE 5.6

No	Site notation	Atom	Multiplicity	Wyckoff	Site symmetry	x	y	z	Occupancy
1	Mg	Mg	8	c	-43m	1/4	1/4	1/4	1.0
2	Si	Si	4	a	m-3m	0	0	0	1.0

temperatures above 900 °C. There is an increase of density of about 15% associated with this structure change. Both the parent and product substances are semiconductors, but of different resistivities. The high-pressure phase may be recovered and is indefinitely metastable at normal ambient conditions.

Mg_2Si is not attached by alkali solutions but reacts vigorously with acids to form silanes. This substance also slowly reacts with ammonium chloride solution:

$$2Mg_2Si\ (\text{solid}) + 8NH_4Cl + 3H_2O \Rightarrow 4MgCl_2 + H_2Si_2O_3 + 8NH_3\ (\text{gas}) + 6H_2\ (\text{gas})$$

In a hydrogen atmosphere at 1000–1220 °C, magnesium silicide decomposes with the vaporization of Mg metal. Heating this compound in a N_2 stream forms a black mass which is unstable in air and moisture, forming ammonia, NH_3, as a result of the formation of magnesium nitride.

This compound is a thermoelectric material. That is, upon exposure to heat, it converts heat energy to an electric current. Efficient, inexpensive and nontoxic thermoelectric elements such as silicides are being developed for large-scale applications such as recovering the combustion heat of municipal solid waste, that are well suited for thermoelectric power generation. The characterization and thermoelectric properties of undoped and doped *n*-type magnesium silicide processed by the powdered elements spark plasma sintering (SPS) method were investigated. The patterns by powder X-ray diffractometry showed that it had typical polycrystalline phase. The temperature dependence of thermoelectric properties such as the Seebeck coefficient and electrical conductivity were measured for the temperature range from 300 to 773 K. As a result, a power factor value of $6.0 \times 10^{-4}\ W/(m\ K)^2$ was obtained at 773 K for a doped sample. Mg_2Si demonstrates semiconductor conductivity *n*-type character with an energy band gap $E_g = 0.78$ eV and a solid solution based on the Mg_2Si–Mg_2Sn composition has a figure of merit of $ZT > 1$. The magnesium silicide films grown on a silicon substrate by reactive diffusion method and their thermoelectric properties were also investigated.

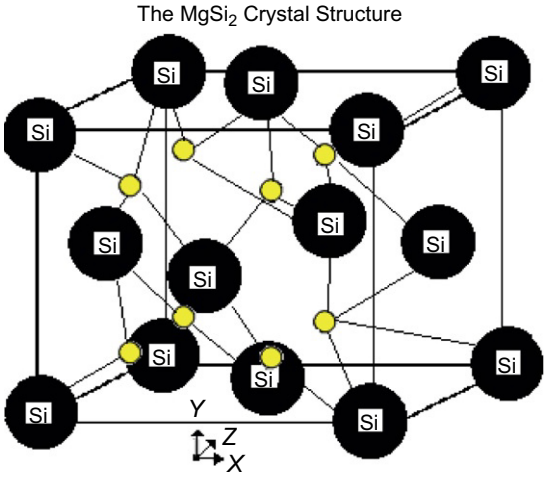

FIGURE 5.14

Bulk Mg_2Si crystals can be grown using a vertical Bridgman melt growth method. The *n*-type and *p*-type dopants, bismuth (Bi) and silver (Ag), respectively, were incorporated during the growth. X-ray powder diffraction analysis revealed clear peaks of Mg_2Si with no peaks associated with the metallic Mg and Si phases. Residual impurities and process-induced contaminants were explored by using glow discharge mass spectrometry (GDMS). A comparison between the results of GDMS and Hall effect measurements indicated that electrical activation of the Bi doping in the Mg_2Si was sufficient, while activation of the Ag doping was relatively smaller. It was shown that an undoped *n*-type specimen contained a certain amount of aluminum (Al), which was due either to residual impurities in the

Mg source or the incorporation of process-induced impurities. Thermoelectric properties such as the Seebeck coefficient and the electrical and thermal conductivities were measured as a function of temperature up to 850 K. The dimensionless figures of merit for Bi-doped and Ag-doped samples were 0.65 at 840 K and 0.1 at 566 K, respectively. Temperature dependence of the observed Seebeck coefficient was well fitted by the two-carrier model. First-principles calculations were carried out, using the all-electron band structure calculation package (ABCAP) in which the full-potential linearized augmented plane-wave method was employed. The ABCAP calculation adequately presents characteristics of the Seebeck coefficients for the undoped and heavily Bi-doped samples over the whole measured temperature range from room temperature to 850 K. The agreement between theory and experiment is poorer for the Ag-doped *p*-type samples.

Vacancies play a great part in the thermoelectric properties of Mg_2Si. The formation energy of vacancies in Mg_2Si has been studied. The calculation of the formation energy for vacancies on different sublattices using the ab initio method SIESTA have yielded specific values. While the values for the silicon (1.04 eV) and the magnesium vacancy (1.74 eV) lie in the expected range, the formation energy of the di-vacancy and the stoichiometric tri-vacancy turns out to be just 0.68 and 0.78 eV, respectively. This is smaller than the value for both mono-vacancies. Thus, this type of vacancies is preferred.

Polycrystalline, 10-μ size magnesium silicide was prepared by alloying 99.9% purity polycrystalline silicon obtained from rice husk ash and a high-purity magnesium metal powder. The material in sintered pellet form was characterized for its structural, electrical, thermal, thermoelectric and other properties. A typical sintered pellet exhibited a room temperature (30 °C) thermoelectric power of 565 μV/K and an electrical resistivity of 35 Ω cm. On the other hand, the material was found to be thermally quite stable up to 650 °C with a room temperature thermal conductivity of 6.3×10^{-3}/cals/cm/K (2.6 J/s/m/K). These properties of the material indicate that the material can find potential applications as a thermoelectric generator and in other semiconductor devices. Furthermore, an indigenous technology for large-scale production of silanes (SiH_4) can be developed using the Mg_2Si that could be prepared in large quantities by a simple and low-cost process.

In another paper, magnesium silicide has been regarded as a candidate for an advanced thermoelectric material used in the temperature range of 500–800 K that corresponds to that of vehicle exhaust emission. It is also a nontoxic substance, compared with other thermoelectric materials, such as PbTe and $CoSb_n$ that operate in the same conversion temperature range. The efficiency of a thermoelectric device is characterized by measurement of the dimensionless figure of merit, $ZT = S^2 \cdot \alpha / {}^\circ T / \hat{U}$, of its constituent thermoelectric material, where S is the Seebeck coefficient, α is the electrical conductivity, $\hat{U}$ is the thermal conductivity, and T is the absolute temperature.

For thermoelectric device operation, the use of a material with ZT more than unity is needed to realize a conversion efficiency of $\geq$10%. The optimization of doping in Mg_2Si is required in order to realize a value of unity for ZT. Mg_2Si single crystals have been grown (along with doping elements of Bi and Al) using a vertical Bridgman method. Mg (99.99%) and Si (99.99999%) with a stoichiometric Mg: Si ratio of 67:33 were mixed and melted to form Mg_2Si. Prior to the growth, Bi (99.999%) powder at the ratio from 0.5 to 3 at-% for Mg_2Si and the presynthesized polycrystalline Mg_2Si powder were mixed, and Mg_2Si crystals were grown at a rate of 3 mm/h by the vertical Bridgman method. Grown samples were characterized by XRD patterns and electron-probe microanalysis. Both analyses indicated that Mg_2Si crystals result. Hall carrier concentrations were evaluated at room temperature. The electrical conductivity, the Seebeck coefficient, and the thermal conductivity were estimated in the temperature range from RT to 850 K. The grown crystals exhibited *n*-type conductivity in undoped and all Bi-doped conditions. All the Bi-doped crystals showed high electrical conductivity and high carrier concentration compared with that of the undoped crystal. On the other hand, the thermal conductivity was lowered as the amount of Bi increased. Consequently, the thermal conductivity for the crystal that was Bi doped at 3 at-% was 0.021 W/cm/K at 842 K, and its ZT reached 0.99 at 842 K, which is near the unity of ZT that is regarded as a standard of practical use for thermoelectric materials. The solid solubility limit of Bi to Mg_2Si was determined to be around 3 at-%.

The development of advanced rechargeable batteries for efficient energy storage finds one of its keys in the lithium-ion concept. The optimization of the Li-ion technology urgently needs improvement for the active material of the negative electrode, and many recent papers in the field support this tendency. Mg_2Si was synthesized by mechanically activated annealing and evaluated as a negative electrode material. A maximum discharge capacity of 830 mA h/g was observed by cycling over a wide voltage window of 5–650 mV versus Li, but capacity fade was rapid. Cycling over the range 50–225 mV versus Li produced a stable discharge capacity of approximately 100 mA h/g. XRD experiments showed that lithium insertion converts Mg_2Si into Li_2MgSi after lithium intercalation into Mg_2Si. Electrochemical evidence of Li–Si reactions indicated

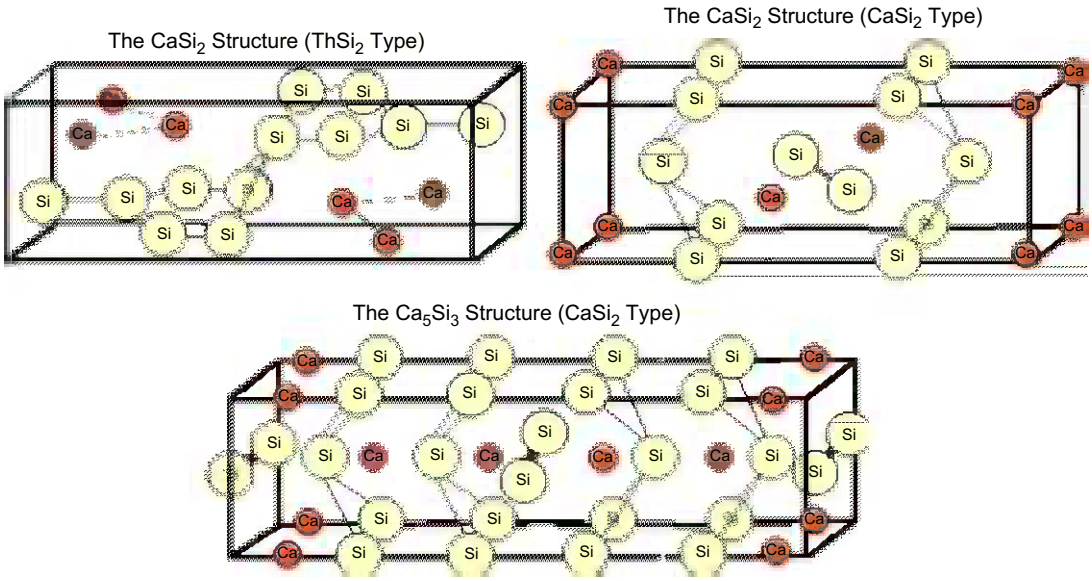

FIGURE 5.15

that the Li_2MgSi structure could be converted to binary lithium alloys with extensive charging.

Magnesium silicide is available commercially in small lots worldwide.

Calcium Silicides

Calcium silicide has the molecular formula of Ca_2Si and the molecular weight of 96.2514 g/mol. It has the CAS number of 12013-56-8. This salt can be formed by the reaction of Ca metal, mixed with Si, at 850 °C in an inert atmosphere:

$$2Ca\ (gas) + Si\ (solid) \Rightarrow Ca_2Si\ (gas)$$

The metal, Ca has a normal melting point of 842 °C and a normal boiling point of 1484 °C. Calcium silicide, also called calcium disilicide, is an inorganic compound, a silicide of calcium. It is a whitish or dark gray to black solid matter with melting point between 700 and 935 °C. It is insoluble in water, but may decompose when subjected to moisture, evolving hydrogen and producing calcium hydroxide. It decomposes in hot water. It is flammable and may ignite in air by producing silane that spontaneously ignites.

Calcium hydride and silicon react with the evolution of hydrogen gas at temperatures above 250 °C:

$$2CaH_2 + Si \Rightarrow Ca_2Si + 2H_2$$

This reaction can also produce a hydro-silicide, $CaSiH_2$, that has been assigned a CAS number of 12013-55-7.

The reaction of silica with excess Ca metal also produces the disilicide:

$$SiO_2 + 2Ca \Rightarrow 2CaO + Si$$

$$Si + 2Ca \Rightarrow Ca_2Si$$

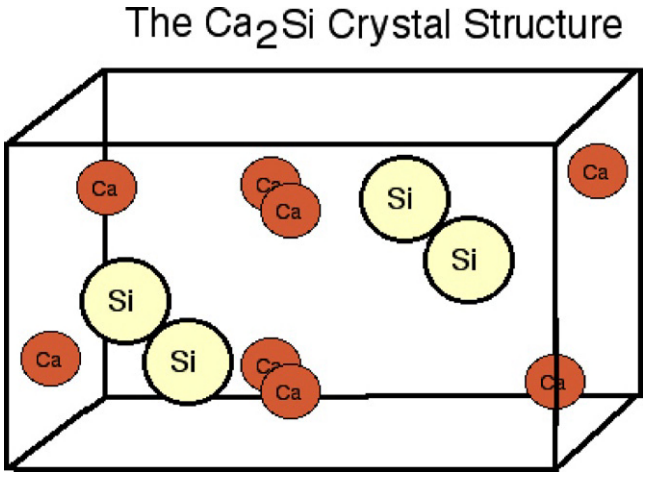

FIGURE 5.16

Calcium di-silicide is tri-morphic and the three structures are compared in the Fig. 5.15 given above.

Dicalcium silicide is dimorphic and readily forms two compounds, Ca_2Si as well as Ca_3Si_5. However, other forms have also been discovered. The cubic phase Ca_2Si film and the tetragonal phase Ca_5Si_3 film can be grown directly and individually on the different Si(100) substrates.

The Ca_2Si structure has the form shown in Fig. 5.16.

The phase diagram of the Ca–Si system has been investigated across almost the whole composition range (0 to 70 at% Si) using DTA, metallographic analysis, XRD and electron microscopy. Six intermediate phases have been found: $CaSi_2$ ($CaSi_2$-type), $Ca_{14}Si_{19}$ ($Ca_{14}Si_{19}$-type), Ca_3Si_4 (Ca_3Si_4-type), CaSi (CrB-type), Ca_5Si_3 (Cr_5B_3-type) and Ca_2Si (anti-$PbCl_2$-type). Ca_3Si_4, not

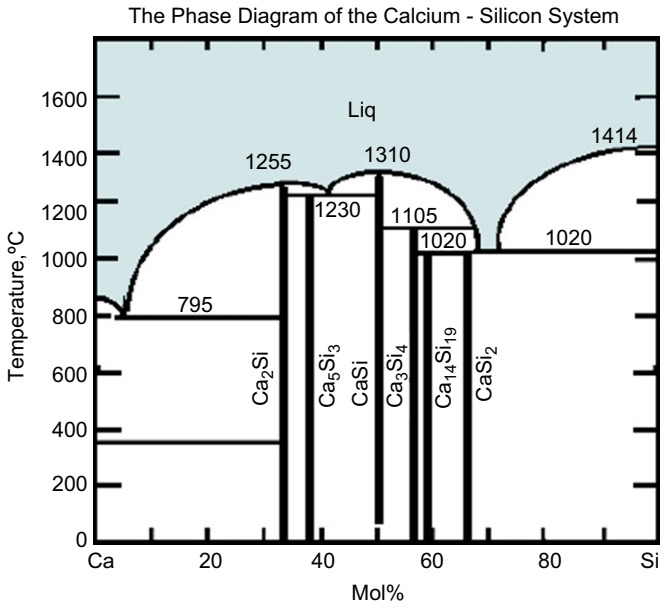

FIGURE 5.17

previously known, is a Zintl phase representative of a new structural type: hexagonal $hP42$, $a = 8.541$, $c = 14.906$ Å, space group $P6_3/m$. Three eutectics occur in this system: at about 3.5 at% Si and 795 °C, 42.5 at% Si and 1230 °C, 72.0 at% Si and 1020 °C.

The phase diagram is shown in Fig. 5.17.

Vaporization thermodynamics in this binary system of calcium–silicon has been studied by Knudsen effusion mass spectrometry and vacuum microbalance techniques. The equilibrium partial pressure of Ca (g) over the two-phase regions in the composition range 20–75 at.% Si has been measured and the standard enthalpy changes for the appropriate vaporization reactions were determined from the temperature dependence of the measured vapor pressures. The standard reaction enthalpy changes were also evaluated by the third-law method using the pressure data in conjunction with estimated Gibbs energy functions.

Standard enthalpies of formation of the calcium silicides were derived from the standard reaction enthalpy values at room temperature. The results obtained for $\Delta_f H^\circ_{298}$ were the following:

$$Ca_2Si = -56.1,\ Ca_5Si_3 = -55.3,\ CaSi = -49.6,$$

$$Ca_3Si_4 = -40.6,\ Ca_{14}Si_{19} = -44.4,\ CaSi_2 = -37.8$$

(all in kJ/mol atoms).

The results for Ca_2Si, CaSi and $CaSi_2$ may be compared with previous measurements. All other results were first determinations.

Trigonal/rhombohedral $CaSi_2$(I) ($CaSi_2$-type structure) with corrugated layers of three-connected Si atoms can be transformed by a high-pressure high-temperature treatment into a tetragonal $CaSi_2$(II) (α-$ThSi_2$-type structure) with a three-dimensional net of three-connected Si atoms. The silicon net of $CaSi_2$(II) is slightly distorted from the topologically simplest tetragonal three-dimensional three-connected net derived on a geometrical basis. In order to correlate crystal chemical with thermochemical data, the transformation between both polymorphs of $CaSi_2$ has been studied at equilibrium and nonequilibrium conditions. The pressure–temperature phase diagram of $CaSi_2$ has been investigated by X-ray technique in quenched samples. From the slope of the equilibrium line and the change in molar volume, the approximate values of the entropy and energy of transformation $CaSi_2(I \Rightarrow II)$ have been determined $\Delta S = 3.2$ e.u., $\Delta U = 4.9$ kcal/mol. Under nonequilibrium conditions, the transformation $CaSi_2(II \Rightarrow I)$ yielded $\Delta H = -4.2$ kcal/mol at 500 °C and ambient pressure in a DTA apparatus. Complete transformation of metastable $CaSi_2$(II) can be achieved within 5 min at a heating rate of 20 °C/min. Due to the relatively high speed of transformation, simple structural relations between both polymorphs of $CaSi_2$ were discussed.

The structure and phase variation of Ca_5Si_3 upon hydrogenation were systematically investigated using combined neutron powder diffraction (NPD), neutron vibrational spectroscopy, and first-principles calculations. The hydrogen absorption equilibrium was first attained with formation of $Ca_5Si_3{\cdot}H(D)_{0.53}$ ($I4/mcm$) with H exclusively located in Ca_4-tetrahedral sites. More hydrogen absorbed into the system under higher pressure leads to dissociations into CaH_2 (an amorphous hydride at higher pressures) and CaSi. The hydrogen-induced formation of an amorphous phase under higher pressures is very unusual in Cr_5B_3-type compounds and the observed formation of CaH_2 upon hydrogen absorption confirmed the proposed composition equilibrium. Ca_2Si was found to reversibly absorb and desorb hydrogen in a moderate temperature range of 473–573 K. Ca_2Si showed even more rapid absorption kinetics with the formation of a reversible amorphous hydride phase in the temperature range of 473–523 K. Further studies led to investigation of hydrogen storage properties of Ca_5Si_3 and structural variations upon the hydrogenation/dehydrogenation of Ca_5Si_3, another important intermetallic phase in the Ca–Si system. The crystal structure of Ca_5Si_3, belongs to the frequently encountered tetragonal Cr_5B_3-type structure, which features an equal number of monomeric and dimeric hydride anions so that the divalent cations formally meet the structure criterion for Zintl phases, in terms of oxidation states. The presence of a significant Ca_4-tetrahedral cavity in this structure type allows a ready incorporation of small quantities of hydrogen or fluorine into the structure, resulting in oxidation of the substrate.

A [1,0,0] view of the tetragonal structures of Ca_5Si_3 and $Ca_5Si_3{\cdot}D_{0.53}$ with empty and filled Ca_4-tetrahedral cavities.

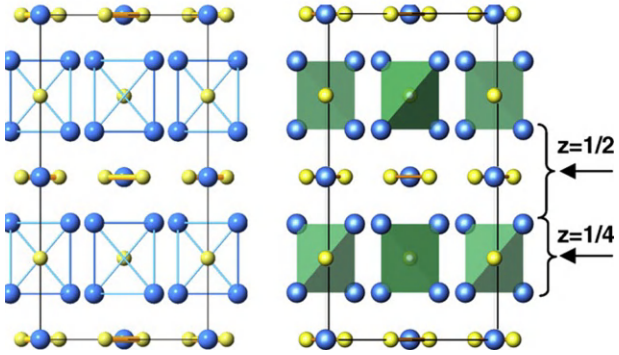

FIGURE 5.18

A representation of this phenomenon is shown in Fig. 5.18.

This compound has considerable potential for storing hydrogen at ambient temperatures for release thereof by heating. It would be used in automobiles or buses in lieu of natural or synthetic gas. Another possible usage is as the source for fuel-cell electrical generators in "electric-automobiles".

A newly discovered Ca_3Si_4 compound is said to be a semiconductor. It is characterized by an indirect transition of 0.35 eV. In fact, the phase diagram of the Ca–Si system was reinvestigated by Manfrinetti et al and a new compound—Ca_3Si_4—was found. It crystallizes in the hexagonal structure (space group $P63/m$) and has the following lattice constants: $a = 8.541$ Å and $c = 14.906$ Å. The unit cell consists of six formula units where Ca and Si atoms are grouped, respectively, into four inequivalent sites.

A peculiar dispersion of the last valence band and the first conduction band, displaying a loop of extrema, has been found. This feature leads to large anisotropy of the mobility of holes and electrons. A comparison of the dielectric function of this material was made with data for another semiconducting calcium silicide Ca_2Si.

Industrial calcium silicide usually contains iron and aluminum as the primary contaminants, and low amounts of carbon and sulfur. Calcium silicide is used for manufacture of special metal alloys, e.g. for removing phosphorus and as a deoxidizer. In pyrotechnics, it is used as fuel to make special mixtures, e.g. for production of smokes, in flash compositions, and in percussion caps. Specification for pyrotechnic calcium silicide is MIL-C-324C. In some mixtures, it may be substituted by ferrosilicon. Silicon-based fuels are used in some time-delay mixtures, e.g. for controlling of explosive bolts, hand grenades, and infrared decoys. Smoke compositions often contain hexachloroethane. During burning they produce silicon tetrachloride, It, like titanium tetrachloride used in smoke screens, reacts with air moisture and produces a dense white fog. Gum arabic is used in some mixtures to inhibit calcium silicide decomposition.

Self-heating cans of military food rations developed during the World War II used a thermite-like mixture of 1:1 of Fe(II,III) oxide and calcium silicide. Such mixture, when ignited, generates a moderate amount of heat and no gaseous products. There is also a calcium silicide CaH_2Si, CAS number 12013-55-7.

The uses of calcium silicide are many. Some of these include:

- Calcium silicide is used for manufacture of special metal alloys, e.g. for removing phosphorus and as a deoxidizer.
- In pyrotechnics, it is used as fuel to make special mixtures, e.g. for production of smokes, in flash compositions, and in percussion caps.
- Calcium silicide is used in the manufacture of certain initiatory, pyrotechnic and smoke compositions.
- The silicon and calcium alloy is mainly used as desulfurizing agent and deoxidizer for steel industry and casting industry.
- Calcium silicide has been found to be extremely corrosive to all metals including the refractory metals. It has been successfully contained in boron nitride for 36 h.
- The formation of calcium silicide ($CaSi_2$) intermetallic through the simultaneous reduction of calcium oxide from the electrolyte and of the silica pellet and reduction of dissolved carbon dioxide.

China has increased the selling price of calcium silicide continuously, especially in the products manufactured in Shaanxi, Shanxi and Inner Mongolia provinces within the past 2 years. The annual production of silicon and calcium alloy is about 130,000 tons all over world and international market demand is about 160,000 tons. Calcium silicon is made in shaft-type electric furnaces.

The "Calcium Silicide Manufacturers Directory" lists over 3,000,000 registered importers and exporters

Strontium Silicide

Strontium silicide has the molecular formula of Sr_2Si and the molecular weight of gm/mol. This salt can be prepared by the reaction of the elements in an inert atmosphere at about 850 °C:

$$2Sr + Si \Rightarrow Sr_2Si$$

Its CAS number is 12138-28-2. Di-strontium silicide has the structure shown below and that of mono-strontium silicide is shown next to it. Up to four other strontium silicides are known.

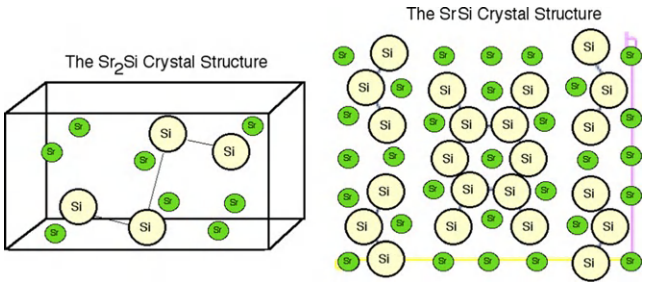

FIGURE 5.19

Thermodynamic modeling of the Si–Sr system was carried out using the CALPHAD method (Fig. 5.19).

Crystal parameters are given in Table 5.7.

The unit-cell parameters are:

Sr_2Si

$a = 5.162$ Å, $b = 8.133$ Å, $c = 9.544$ Å, $\alpha = \beta = \gamma = 90°$, cell volume $= 400.21$ Å^3, cell occupancy is shown in Table 5.8.

Sr_5Si_3

$a = b = 8.089$ Å, $c = 9.726$ Å, $\alpha = \beta = 114.72°$, $\gamma = 90°$, cell volume $= 513.72$ Å^3, cell occupancy is shown in Table 5.9.

SrSi—oP12 type

$a = 4.042$ Å, $b = 4.826$ Å, $c = 6.138$ Å, $\alpha = 113.15°$, $\beta = \gamma = 90°$, cell volume $= 110.09$ Å^3, cell occupancy is shown in Table 5.10.

SrSi—oI40 type

$a = 4.892$ Å, $b = c = 11.374$ Å, $\alpha = 69.584°$, $\beta = \gamma = 77.587°$, cell volume $= 572.20$ Å^3, cell occupancy is shown in Table 5.11.

$SrSi_2$—$ThSi_2$-type

$a = 4.438$ Å, $b = 4.438$ Å, $c = 7.594$ Å, $\alpha = \beta = 106.99°$, $\gamma = 90°$, cell volume $= 136.20$ Å^3, cell occupancy is shown in Table 5.12.

$SrSi_2$—$SrSi_2$ type

$a = b = c = 6.715$ Å, $\alpha = \beta = \gamma = 90°$, cell volume $= 302.79$ Å^3, cell occupancy is shown in Table 5.13.

In this system, three of the intermetallic compounds, Sr_2Si, Sr_5Si_3, SrSi, were considered to be stoichiometric

TABLE 5.7

Number	Compound	Type	Space group	Point group	SG number
1	Sr_2Si	Co_2Si	oP12	Pnma	62
2	Sr_5Si_3	Cr_5B_3	tl32	I4/mcm	140
3	SrSi	Tll	oS8	Cmcm	63
4	SrSi	SrSi	oI40	Immm	71
5	$SrSi_2$	$ThSi_2$	tl12	$I4_1/amd$	141
6	$SrSi_2$	$SrSi_2$	cP12	$P4_132$	213

TABLE 5.8

No	Site notation	Atom	Multiplicity	Wyckoff	Site symmetry	x	y	z	Occupancy
1	Sr1	Sr	4	c	.m.	0.038	1/4	0.718	1.0
2	Sr2	Sr	4	c	.m.	0.174	1/4	0.062	1.0
3	Si1	Si	4	c	.m.	0.202	1/4	0.389	1.0

TABLE 5.9

No	Site notation	Atom	Multiplicity	Wyckoff	Site symmetry	x	y	z	Occupancy
1	Sr2	Sr	16	l	..m	0.1785	0.6785	0.1416	1.0
2	Si2	Si	8	h	m.2m	0.6081	0.1081	0	1.0
3	Sr1	Sr	4	c	4/m..	0	0	0	1.0
4	Si1	Si	4	a	422	0	0	1/4	1.0

TABLE 5.10

No	Site notation	Atom	Multiplicity	Wyckoff	Site symmetry	*x*	*y*	*z*	Occupancy
1	Si1	Si	4	c	m2m	0	0.108	1/4	1.0
2	Sr1	Sr	4	c	m2m	0	0.367	1/4	1.0

TABLE 5.11

No	Site notation	Atom	Multiplicity	Wyckoff	Site symmetry	*x*	*y*	*z*	Occupancy
1	SrV	Sr	8	l	m..	0	0.164	0.19	1.0
2	SiII	Si	8	l	m..	0	0.180	0.368	1.0
3	SiI	Si	8	l	m..	0	0.345	0.429	1.0
4	SiIII	Si	4	j	mm2	1/2	0	0.145	1.0
5	SrIV	Sr	4	j	mm2	1/2	0	0.342	1.0
6	SrIII	Sr	4	g	m2m	0	0.304	0	1.0
7	SrII	Sr	2	c	mmm	1/2	1/2	0	1.0
8	SrI	Sr	2	a	mmm	0	0	0	1.0

TABLE 5.12

No	Site notation	Atom	Multiplicity	Wyckoff	Site symmetry	*x*	*y*	*z*	Occupancy
1	Si	Si	8	e	2mm.	0	1/4	0.2908	0.99
2	Sr	Sr	4	a	-4m2	0	3/4	1/8	1.0

TABLE 5.13

No	Site notation	Atom	Multiplicity	Wyckoff	Site symmetry	*x*	*y*	*z*	Occupancy
1	Si1	Si	8	c	.3.	0.0769	0.0769	0.0769	1.0
2	Sr1	Sr	4	a	.32	3/8	3/8	3/8	1.0

and $SrSi_2$ was modeled as a nonstoichiometric phase. For the liquid phase, two different models were used. In one case, Sr and Si were assumed to constitute a random solution, with its excess Gibbs energy being described through the Redlich–Kister polynomial. In the second case, the liquid phase was described through the associate model, considering the species Si, Sr and SrSi. The terminal solid solutions, (β-Sr), (α-Sr) and (Si), are treated as having negligible solubility. A set of self-consistent thermodynamic parameters were obtained by considering experimental phase equilibria, measurements of the mixing enthalpy in the liquid phase, as well as measured and calculated–via first-principles methods based on density functional theory–formation enthalpies of the intermetallic compounds.

The phase diagram determined is shown in Fig. 5.20.

Four intermediate phases exist: Sr_2Si ($PbCl_2$-type), Sr_5Si_3 (Cr_5B_3-type), SrSi (CrB-type) and the dimorphic $SrSi_2$ compound (for a total of five known forms).

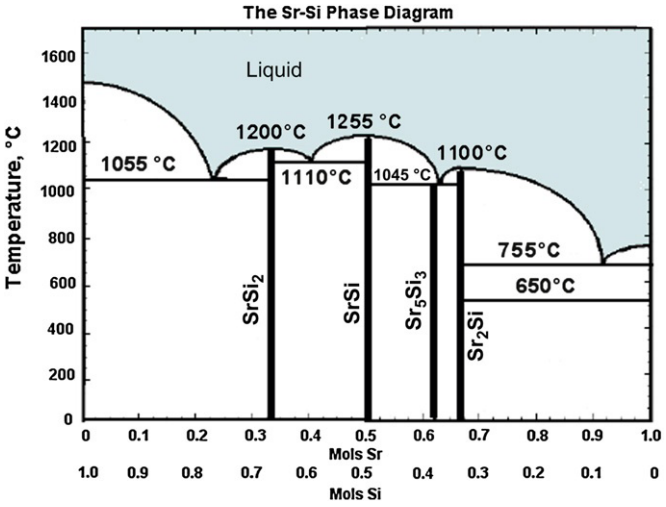

FIGURE 5.20

The low-temperature form α-$SrSi_2$ is cubic, $SrSi_2$-type, and the high-temperature form β-$SrSi_2$ is tetragonal with the α-$ThSi_2$ structure type. For this last phase, a solid solubility range, from about 62.0 to 66.7 at.% Si, has also been found. Four eutectics occur in the system: at about 3 at.% Si and 745 °C, 44 at.% Si and 1110 °C, 61 at.% Si and 1055 °C, 74 at.% Si and 1045 °C.

Strontium silicides have recently been found to have potential applications in electronic devices. Renewed research efforts have led to a reevaluation of the phase equilibria in this system, resulting in the discovery of previously undetected stable intermetallic compounds.

Dimorphic $SrSi_2$ is the first compound found that has the two simplest three-dimensional three-connected nets in its polymorphs. The cubic net of three-connected silicon atoms ($SrSi_2$ type of structure) can be transformed into the tetragonal one (α-$ThSi_2$ type of structure) by a high-pressure and high-temperature treatment. The tetragonal phase is quenchable. Heating of this phase to 600–700 °C at ambient pressure results in transformation into the cubic one. At a heating rate of 20 °C/min, complete transformation can be achieved within 5 min in a DTA apparatus. The energy of transformation, Δh_{Trans}, has been obtained from the peak areas of the DTA curves to be -1.6 ± 0.3 kcal/mol. Although the transformation between the three-dimensional three-connected sets in $SrSi_2$ must be formally classified as a reconstructive one, a relatively small entropy change ($\Delta S = 1.2$ cal/deg mol) has been calculated from the change in molar volume and *p-T* equilibrium conditions. The two structures look like in Fig. 5.21.

The pressure–temperature phase diagram of dimorphic $SrSi_2$ was investigated in the pressure range 10–40 kbar and temperature range 600–1200 °C in a belt-type apparatus. The phase boundary between cubic $SrSi_2$I ($SrSi_2$-type) and tetragonal $SrSi_2$II (α-$ThSi_2$-type) was studied by X-ray techniques in quenched samples. The curvature of the equilibrium line was not resolved. Molar volumes of both polymorphs have been measured in the temperature range 20–400 °C at ambient pressure. From the slope of the equilibrium line in the pressure–temperature diagram and the change in molar volume, approximate values of the entropy and heat of transition $SrSi_2$(I–II) have been calculated. In the silicon sublattice of both polymorphs of $SrSi_2$, the topologically simplest three-dimensional three-connected nets are found to be slightly distorted from their ideal configurations. The ideal $SrSi_2$-type net represents the three-connected analogy to the four-connected diamond net. The Sr_2Si, Sr_5Si_3 and SrSi phases have been predicted to undergo high-pressure transitions. The lattice transitions shown here have been calculated to occur at 5.5, 19.9, 11.8 and 60 GPa, respectively:

$$Sr_2Si\ (oP12 \Rightarrow hP6)$$

$$Sr_5Si_3\ (tI32\text{-}Cr_5B_3 \Rightarrow tI32\text{-}Mo_5Si_3)$$

$$SrSi(oC8 \Rightarrow oP8 \Rightarrow tP2)$$

Electronic structure of the computed ground states and the predicted four new high-pressure polymorphs of Sr_2Si, Sr_5Si_3 and SrSi phases are calculated and discussed in relation with their corresponding crystal structures and heats of formation.

The high-temperature vaporization processes of strontium silicides were studied by means of the Knudsen effusion mass spectrometry and Knudsen effusion

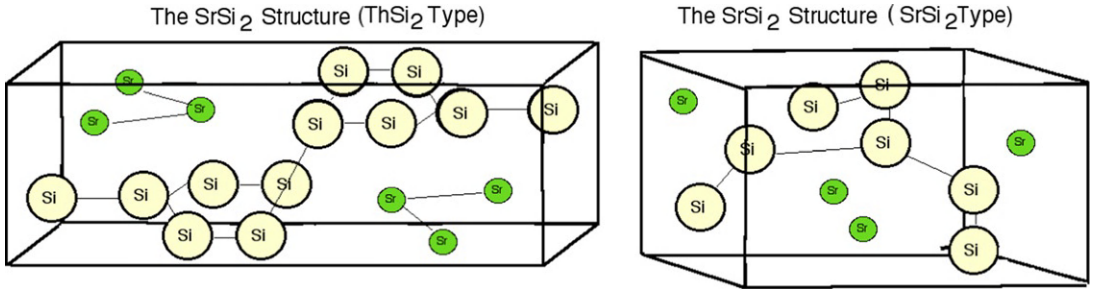

FIGURE 5.21

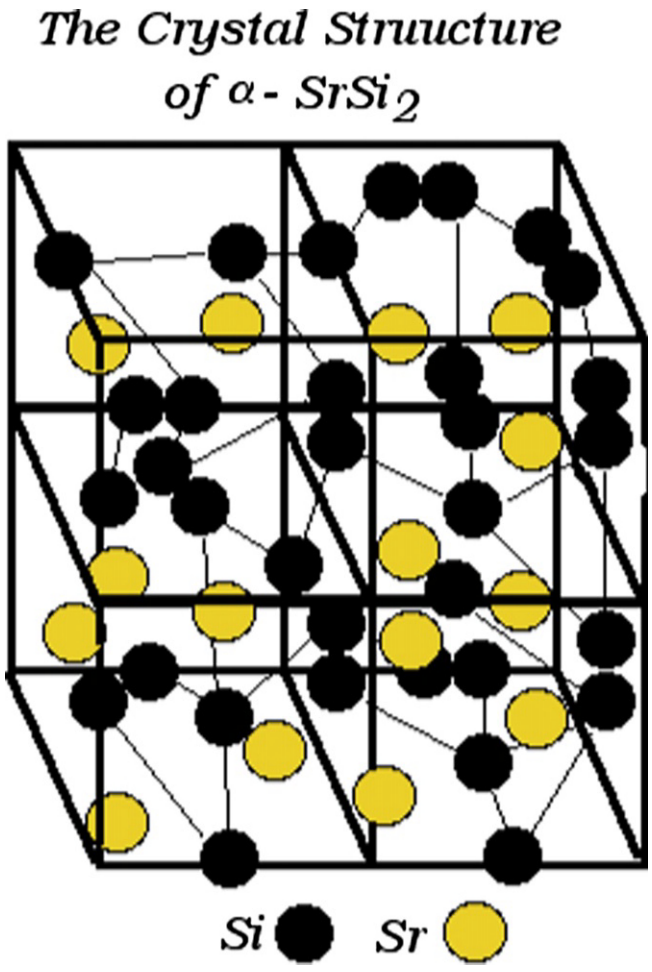

FIGURE 5.22

weight loss techniques in the temperature range 665–1300 K, with reference to the recent reinvestigation of the Sr–Si phase diagram. The only species detected in the vapor phase equilibrated with two-phase solid mixtures was monoatomic gaseous strontium. The vapor pressure of Sr (g) was measured as a function of the temperature, and the enthalpy changes associated with the decomposition processes were thereafter derived. The enthalpies of formation of the strontium silicide phases reported in the Palenzona reference (namely Sr_2Si, Sr_5Si_3, SrSi and α-$SrSi_2$), were finally obtained as, respectively (values in kJ/mol atoms, ($T = 298$ K): $\Delta H_f^0 = -39.7 \pm 3.2$; -43.8 ± 3.6; -51.7 ± 4.1; -40.3 ± 3.7). These results are definitely at variance with the scattered, strongly exothermic calorimetric data reported for some phases in the old literature, while they are in satisfactory agreement with recent density functional theory calculations. The crystal structure of α-$SrSi_2$ is shown in Fig. 5.22.

Strontium silicide has been explored as a possible thermoelectric material because it is a semiconductor. A study of the thermoelectric properties of $BaSi_2$, $SrSi_2$, and LaSi was conducted. The polycrystalline samples were prepared by SPS. The electrical resistivity (ρ), Seebeck coefficient (S), and thermal conductivity (κ) were measured above room temperature. The power factor (S^2/ρ) is quite low (below 10^{-5}/Wm/κ^2) over the whole temperature range for $BaSi_2$ and LaSi, while relatively high (1.19×10^{-3} Wm^{-1}/κ^2 at 331 K) for $SrSi_2$. $BaSi_2$ exhibits quite low κ. The κ values at room temperature are 1.56, 5.25, and 6.71/Wm/κ for $BaSi_2$, and $SrSi_2$, respectively. The maximum values of the dimensionless figure of merit, $ZT = S^2T/\rho/\kappa$, are 0.01 at 954 K for $BaSi_2$, and 0.09 at 417 K for $SrSi_2$.

Strontium silicide is available in all grades ranging from commercial to 99.999% purity. A large number of suppliers are available commercially.

Barium Silicide

Barium silicide has the molecular formula of Ba_2Si and the molecular weight of gm/mol. Its CAS number is 1304-40-1. This salt has been prepared by the reaction of the elements in an inert atmosphere at 850 °C:

$$2Ba + Si + \text{heat} \Rightarrow Ba_2Si$$

The reaction is slow. Melt growth of $BaSi_2$ by the vertical Bridgman (VB) technique is difficult, particularly when the elements are melted together. Because Ba is highly reactive at the growth temperature (≈1500 K), the crucible materials were chosen to avoid chemical reactions and sticking between the crucibles and the molten and vapor phases of Ba. Crucibles made of molybdenum, quartz, alumina, SiNx-coated quartz, chemical vapor deposition (CVD), PG, and CVD SiC-coated graphite were examined, and the semiconductor, orthorhombic $BaSi_2$, was obtained in quartz, alumina, and molybdenum crucibles. The crystalline forms of the grown crystals depend on the crucible materials and growth conditions.

Ba_2Si is a semiconductor that has been studied as a thermoelectric element for use in converting waste heat into electricity. To date, measurements have shown that $BaSi_2$ exhibits quite low-thermal conductivity and a comparative value of 0.01 when compared to conventional thermoelectrics which exhibit values of >0.10 in conversion efficiency.

Its structure is identical to that of Ca_2Si (Fig. 5.23).

The crystal parameters are given in Table 5.14.

The unit-cell parameters are:

Ba_2Si

$a = 5.214$ Å, $b = 8.443$ Å, $c = 9.634$ Å, $\alpha = \beta = \gamma = 90°$, cell volume = 422.21 Å^3, cell occupancy is shown in Table 5.15.

Ba_3Si_4

$a = b = 8.523$ Å, $c = 11.824$ Å, $\alpha = \beta = \gamma = 90°$, cell volume = 859.47 Å^3, cell occupancy is shown in Table 5.16.

Ba_4Si_{23}

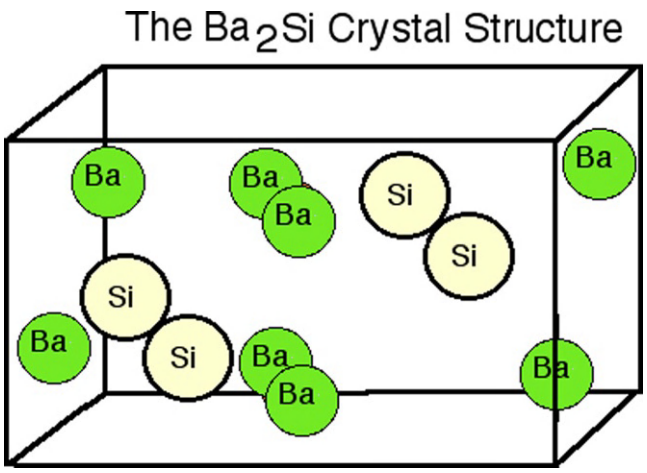

FIGURE 5.23

$a = b = c = 10.328$ Å, $\alpha = \beta = \gamma = 90°$, cell volume = 1101.47 Å^3, cell occupancy is shown in Table 5.17.

Ba_5Si_3

$a = b = 8.465$ Å, $c = 16.448$ Å, $\alpha = \beta = \gamma = 90°$, cell volume = 1178.47 Å^3, cell occupancy is shown in Table 5.18.

BaSi

$a = 4.142$ Å, $b = 5.042$ Å, $c = 6.494$ Å, $\alpha = 112.84°$, $\beta = \gamma = 90°$, cell volume = 124.99 Å^3, cell occupancy is shown in Table 5.19.

$BaSi_2$

$a = 6.733$ Å, $b = 8.942$ Å, $c = 11.555$ Å, $\alpha = \beta = \gamma = 90°$, cell volume = 695.69 Å^3, cell occupancy is shown in Table 5.20.

$BaSi_2$—$EuGe_2$ type

$a = b = 4.047$ Å, $c = 5.332$ Å, $\alpha = \beta = \gamma = 90°$, cell volume = 75.60 Å^3, cell occupancy is shown in Table 5.21.

TABLE 5.14

Number	Compound	Type	Space group	Point group	SG number
1	Ba_2Si	Co_2Si	OP12	Pnma	62
2	Ba_3Si_4	Ba_3Si_4	TP28	$P4_2/mnm$	136
3	Ba_4Si_{23}	Na_4Si_{23}	CP54	Pm-3n	223
4	Ba_5Si_3	Ba_5Si_3	TP32	P4/nnc	130
5	BaSi	TII	OS8	Cmcm	63
6	$BaSi_2$	$BaSi_2$	OP24	Pnma	62
7	$BaSi_2$	$SrSi_2$	CP12	$P4_132$	213
8	$BaSi_2$	$EuGe_2$	HP3	P-3m1	164

TABLE 5.15

No	Site notation	Atom	Multiplicity	Wyckoff	Site symmetry	*x*	*y*	*z*	Occupancy
1	Ba(2)	Ba	4	c	.m.	0.017	1/4	0.677	1.0
2	Ba(1)	Ba	4	c	.m.	0.153	1/4	0.084	1.0
3	Si	Si	4	c	.m.	0.252	1/4	0.403	1.0

TABLE 5.16

No	Site notation	Atom	Multiplicity	Wyckoff	Site symmetry	*x*	*y*	*z*	Occupancy
1	Si2	Si	8	j	..m	0.296	0.296	0.144	1.0
2	Si1	Si	8	i	m..	0.108	0.298	0	1.0
3	Ba1	Ba	4	g	m.2m	0.333	0.667	0	1.0
4	Ba2	Ba	4	e	2.mm	0	0	0.170	1.0
5	Ba3	Ba	4	d	−4..	0	1/2	1/4	1.0

TABLE 5.17

No	Site notation	Atom	Multiplicity	Wyckoff	Site symmetry	*x*	*y*	*z*	Occupancy
1	Si3	Si	24	k	m..	0	0.1199	0.3055	1.0
2	Si2	Si	16	i	.3.	0.1864	0.1864	0.1864	1.0
3	Si1	Si	6	d	−4m.2	1/4	1/2	0	1.0
4	Ba2	Ba	6	c	−4m.2	1/4	0	1/2	1.0
5	Ba1	Ba	2	a	m-3.	0	0	0	1.0

TABLE 5.18

No	Site notation	Atom	Multiplicity	Wyckoff	Site symmetry	*x*	*y*	*z*	Occupancy
1	Ba2	Ba	16	g	1	0.0799	0.5799	0.1069	1.0
2	Si2	Si	8	f	..2	0.3518	0.6482	1/4	1.0
3	Si1	Si	4	c	4..	1/4	1/4	0.0095	1.0
4	Ba1	Ba	4	c	4..	1/4	1/4	0.2271	1.0

TABLE 5.19

No	Site notation	Atom	Multiplicity	Wyckoff	Site symmetry	*x*	*y*	*z*	Occupancy
1	Si	Si	4	c	m2m	0	0.059	1/4	1.0
2	Ba	Ba	4	c	m2m	0	0.36	1/4	1.0

TABLE 5.20

No	Site notation	Atom	Multiplicity	Wyckoff	Site symmetry	*x*	*y*	*z*	Occupancy
1	Si1	Si	8	d	1	0.310	0.078	0.353	1.0
2	Si2	Si	4	c	.m.	0.076	1/4	0.409	1.0
3	Ba1	Ba	4	c	.m.	0.161	1/4	0.095	1.0
4	Si3	Si	4	c	.m.	0.295	1/4	0.531	1.0
5	Ba2	Ba	4	c	.m.	0.486	1/4	0.806	1.0

TABLE 5.21

No	Site notation	Atom	Multiplicity	Wyckoff	Site symmetry	*x*	*y*	*z*	Occupancy
1	Si1	Si	2	d	3m.	1/3	2/3	0.405	1.0
2	Ba1	Ba	1	a	-3m.	0	0	0	1.0

TABLE 5.22

No	Site notation	Atom	Multiplicity	Wyckoff	Site symmetry	x	y	z	Occupancy
1	Si1	Si	8	c	.3.	0.0769	0.0769	0.0769	1.0
2	Ba1	Ba	4	a	.32	3/8	3/8	3/8	1.0

$BaSi_2$—$SrSi_2$type

$a = b = c = 6.535$ Å, $\alpha = \beta = \gamma = 90°$, cell volume $= 279.09$ Å^3, cell occupancy is shown in Table 5.22.

These structures are compared in the following a ⇒ c vector diagrams (Fig. 5.24).

The high-temperature decomposition of the intermediate phases of the Ba–Si system (namely, Ba_2Si, Ba_5Si_3, BaSi, Ba_3Si_4 and $BaSi_2$) has been investigated by means of Knudsen effusion mass spectrometry and Knudsen effusion weight loss techniques. All barium silicides decompose at high temperature by loss of monatomic gaseous barium. The standard enthalpy changes of the decomposition reactions were derived from vapor pressure measurements by the second- and third-law methods of analysis. From these values, the heats of formation of all the barium silicides were calculated. First-principles electronic structure calculations for the same compounds were also performed by the density functional theory approach, in the generalized gradient approximation, using plane wave basis functions and Vanderbilt ultrasoft pseudopotentials. The experimental ground state lattices of the barium silicides have been studied: structures have been relaxed and total energy values derived. These were used in combination with calculated total energies of diamond–silicon and fcc-barium to derive the heats of formation of the barium silicides. First-principles predictions and experimental heats of formation are in satisfactory agreement. The selected values of the heats of formation of the intermediate phases of the Ba–Si system, ΔH_f^0, are (in kJ mol-at.$^{-1}$): $Ba_2Si = -35.8 \pm 7.0$; $Ba_5Si_3 = -42.4 \pm 5.2$; $BaSi = -50.1 \pm 2.9$; $Ba_3Si_4 = -50.7 \pm 3.1$; and $BaSi_2 = -46.7 \pm 3.5$.

The phase diagram is presented as shown in Fig. 5.25.

The phase diagram of the Ba–Si system has been completely revised from a thermal point of view. All the already-known intermediate phases have been confirmed: Ba_2Si (Co_2Si type), Ba_5Si_3 (Ba_5Si_3 type), BaSi (CrB type), Ba_3Si_4 (Ba_3Si_4 type) and $BaSi_2$ ($BaSi_2$ type). Save for Ba_5Si_3, which forms peritectically, all other compounds melt congruently. The five eutectic compositions occurring in the system are at 11, 40, 52.5, 60 and 83 at.% Si, respectively.

$BaSi_2$ crystals were grown from a near-stoichiometric melt containing mixtures of Ba (99.9%) and Si (99.99999%) with Ba:Si at.% ratios of 36:64 (Ba-rich) and 30:70 (Si-rich) by the vertical Bridgman growth method. XRD analysis revealed that the grown crystals were semiconducting orthorhombic $BaSi_2$. The samples produced were polycrystalline consisting of single-crystal grains. Optical absorption measurements were carried out to identify the different types of optical transition at room temperature. All of the bulk orthorhombic $BaSi_2$ grown exhibited an indirect transition with an indirect band gap energy ($E_G^{Indirect}$) of 1.13 eV.

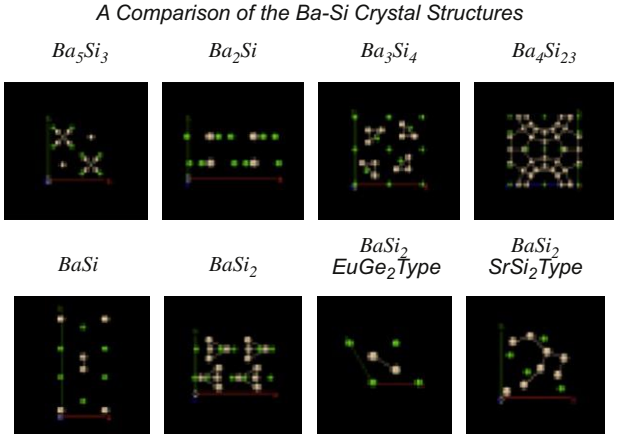

FIGURE 5.24

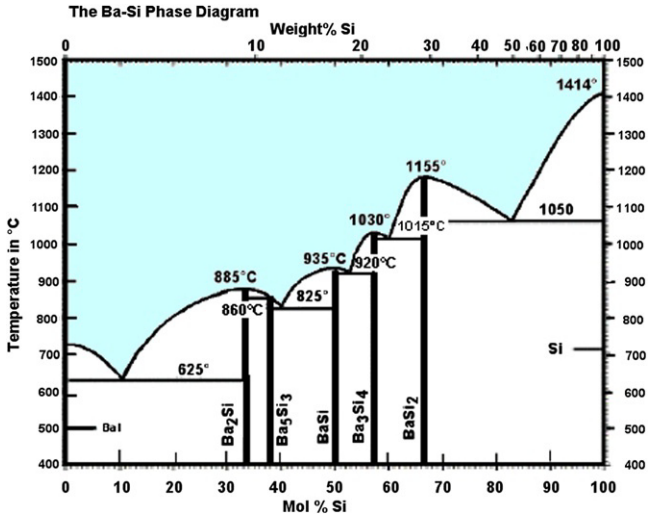

FIGURE 5.25

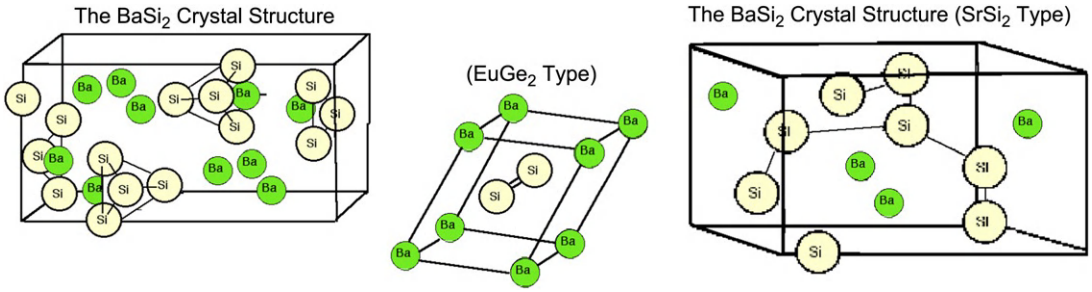

FIGURE 5.26

The structure of barium di-silicide may be represented as shown in Fig. 5.26.

Emission from photoluminescence measurements made at 15 K, seemed to be due to indirect transitions, and revealed that there were probably impurities and crystal defects present. To understand the experimental results, the electronic band structure from first principles using a local density approximation in the all-electron full potential linearized augmented plane wave method was calculated. The calculation is consistent with the experimental indirect band gap results giving an indirect band gap of 0.72 eV and a direct gap of 0.81 eV. The band gap arises from the Si-3p orbitals, while Ba-5d orbitals are strongly hybridized with the Si-3p orbitals in the conduction band.

In situ XRD measurements revealed the transition sequence of cubic and trigonal $BaSi_2$ from orthorhombic $BaSi_2$ at high pressures and high temperatures. The electrical resistivity measurements of three polymorphs show that the electrical properties depend on the crystal structure: orthorhombic $BaSi_2$ is an *n*-type semiconductor as previously reported; cubic $BaSi_2$ is an *n*-type semiconductor; trigonal $BaSi_2$ is a "hole-metal" conductor that shows superconductivity with an onset temperature of 6.8 K. $BaSi_2$ has three high-pressure, high-temperature phases: a trigonal, a cubic, and an additional phase, at pressures up to 7 GPa and temperatures up to 1300 K. All transformations between orthorhombic $BaSi_2$I with isolated Si-tetrahedra, trigonal $BaSi_2$II with corrugated Si-layers, and cubic $BaSi_2$III with a three-dimensional three-connected Si-net can be performed in approximately 5 min at high-pressure and high-temperature conditions. At ambient conditions, the difference in molar volume between $BaSI_2$I and $BaSi_2$III is relatively large ($\Delta V_{\text{I-III}} = -6.79\ \text{cm}^3/\text{mol}$) and that between $BaSi_2$III and $BaSi_2$II very small ($\Delta V_{\text{III-II}} = -0.05\ \text{cm}^3/\text{mol}$). Consequently, in the pressure–temperature phase diagram, the boundary (I-III) shows a strong pressure dependence contrary to that of (III-II) which is less dependent on variation of pressure. The triple point between the three solid phases is near 11 kbar and 925 °C. Substitution of divalent metal and quadrivalent metalloid can easily influence the phase relations in $BaSi_2$.

Over the past few years, compounds with clathrate structures have been the focus of much attention due to their good thermoelectric properties, their promising mechanical properties, their potential for optoelectronic applications correlated to their wide band gap [and the recent discovery of superconductivity in type I Ba intercalated Si clathrates, with a maximum superconducting critical temperature obtained for pure Ba_8Si_{46} ($T_c = -9$ K)]. The discovery of a superconducting transition in these doped column-IV sp^3 semiconductors bears much analogy with the superconducting transition in boron-doped diamond. Only recently, the full intercalation of Ba in type I Si-based clathrate compounds has been achieved under high pressure (3 GPa) and high temperature (HP-HT) conditions (800 °C). At lower pressure, around 1.5 GPa and high temperature, a new type of clathrate (type III), $Ba_{24}Si_{100}$, was also obtained [14], which is isotypic with $Ba_{24}Ge_{100}$.

This new type of clathrate structure is closely related to the type I structure. The unit cell contains three different kinds of cages surrounding the Ba guest atoms: eight "closed" Si_{20} cages, 12 "open" Si_{20} cages and four cages composed of eight silicon atoms. It should be noted that the Si atoms forming this last class of cages have sp^2 bonding. Therefore, in each unit cell, 68 Si atoms have sp^3 bonding while 32 Si atoms have sp^2 bonding. Thus, contrary to the type I clathrate which is only composed of sp^3 silicon atoms, this type III clathrate structure possesses both sp^2 and sp^3 bondings.

Because superconductivity with strong covalent bonding is atypical, the study of such kinds of superconducting compounds is of great interest. Within this class of compounds, the alkali-doped fullerenes, MgB_2 or the highly B-doped diamond and Si-based superconductors are found. Among the Ba-based silicide compounds, it should be noted that only type I Ba-based clathrate compounds and the metastable trigonal phase of $BaSi_2$ (synthesized under high-temperature and high-pressure conditions) have been found to be superconducting and both possess a sp^3 Si lattice. The two other forms of $BaSi_2$, the orthorhombic and the cubic ones, have sp^2 type Si bonds, are *n*-type semiconductors and do not superconduct. The compound, Ba_3Si_4, has the structure shown in Fig. 5.27.

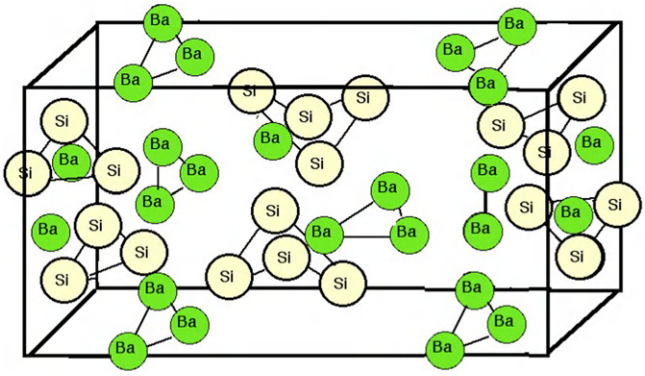

FIGURE 5.27

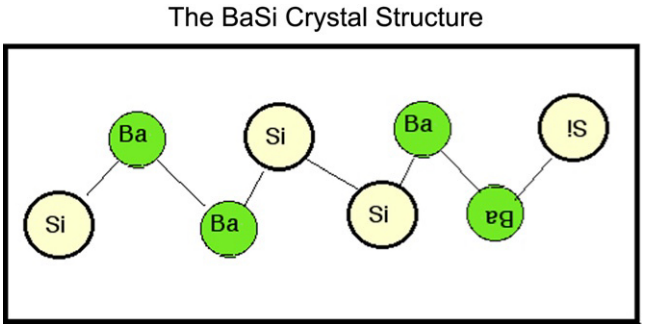

FIGURE 5.28

In addition, it is superconducting. In contrast, the compound, BaSi, is not superconducting and has the structure shown in Fig. 5.28.

The superconductivity of the type III helical cubic clathrate $Ba_{24}Si_{100}$ was investigated. The onset of the superconducting transition is observed at $T_c = 1.55 \pm 0.05$ K. This is the first observation of a Si-based superconductor having both sp^2 and sp^3 bondings. The magnetic superconducting state is investigated from the determination of the critical fields H_{c1} and H_{c2} by AC susceptibility measurements. It was determined that $Ba_{24}Si_{100}$ is a type II superconductor with moderate electron–phonon coupling. The comparison with the other superconducting clathrate Ba_8Si_{46}, based only on sp^3 silicon atoms and which superconducts at 8 K, points out that the presence of sp^2 Si bondings in $Ba_{24}Si_{100}$ is an important parameter to take into account for explaining the moderate electron–phonon coupling and the lower superconducting critical temperature in $Ba_{24}Si_{100}$ (Table 5.23).

Single crystals of the Ba-containing silicon clathrate superconductor $Ba_{7.76}Si_{46}$ were prepared using a high-pressure and high-temperature condition (3 GPa, 1300 °C). It crystallized in the cubic space group *Pm*-3*n* with $a = 10.3141(7)$ Å and $Z = 1$. There are two crystallographically different types of Ba sites, at the centers of Si dodecahederal (Ba at Si_2O) and Si tetrakaidecahedral (Ba at Si24) cages. On evacuation at 527 °C, a part of Ba atoms were removed from the Ba at Si_2O sites. The superconducting transition temperature (T_c) decreased from 9.0 to 6.0 K with the decrease of the Ba content from 7.76 to 6.63 Ba/Si_{46}. The Ba-deficient sites and the deficiency were determined by the structural refinement in the single-crystal X-ray analyses. The structure is shown in Fig. 5.29.

Although barium silicides have many interesting physical properties, their usage in industry has not yet materialized. Perhaps this is due to the higher cost and the fact that no superior aspect of quality has emerged over the other alkaline earth silicides. Nevertheless, barium silicides, in high purity, are offered for sale commercially.

Radium Silicides

Radium silicide has the molecular formula of Ra_2Si and the molecular weight of gm/mol. There have been no reports on the preparation of radium silicide. A variety of alkaline earth silicides has been prepared but there is insufficient evidence that any of the possible radium silicides have ever been synthesized. The expected compounds would include:

Ra_2Si(Co_2Si type) Ra_5Si_3(Ba_5Si type)
RaSi(CrB type)
Ra_3Si_4(Ba_3Si_4 type)
$RaSi_2$($BaSi_2$ type)

However, in view of the radioactive nature of ^{226}Ra, and the lack of demand for such a salt, the likelihood that they will ever be prepared is nil to none.

5.2.3. Alkaline Earth Silicates

The alkaline earths form an enormous number of compounds with oxy-silicon anions, i.e. Si_xO_y

TABLE 5.23 Fundamental Superconducting Parameters of Barium-based Type III and Type I Group IV Clathrates

Compound	T_c (K)	$\lambda_{e\text{-}ph}$	λ (Å)	ξ (Å)
Ba_8Si_{46}	8.0	1.05	4000	72
$Ba_{24}Si_{100}$	1.55 ± 0.05	0.4–0.7	6500	310
$Ba_{24}Ge_{100}$	0.24	0.31	—	280–350

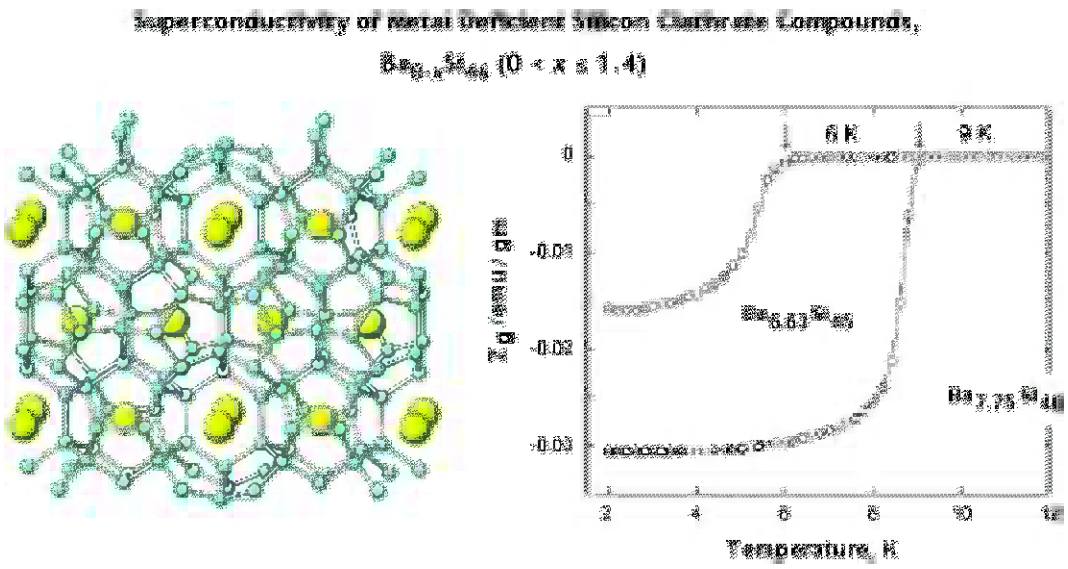

FIGURE 5.29

compounds (where x and/or y can range from 1 to 25 or more). In some silicates, the Si atoms clearly show an amphoteric character so that some Si atoms act as donors (bases) adopting an octahedral coordination, whereas most of the others behave as acceptors (acid), adopting a tetrahedral coordination. The chemistry of silica and silicates has been widely studied. Silicates are the most interesting and the most complicated class of all minerals. Approximately, 30% of all minerals are silicates and some geoscientists estimate that 90% of the earth's crust is made up of silicates. They also play an important role in daily life. Thus, silicates are present in raw materials and many industrial products such as glass, concrete and many ceramic materials. Their widespread application is due to the large variability of their properties and this, in turn, is due to the very large number of different silicate phases and the diversity of their structures.

Concerning the structural chemistry of silicates, the Inorganic Crystal Structure Database (ICSD), Release 2004, contains 3192 entries of binary, ternary and quaternary silicates. Silicates have often been described on the basis of an ionic model, i.e. a dense packing of O^{2-} anions in which Si^{4+} cations seem to fit into interstitial tetrahedral voids. However, several experimental studies of the electron density distribution clearly indicate that the Si–O bond has a considerable covalent character. Thus, a model that considers silicates as formed by either isolated or condensated [SiO_4] tetrahedra seems to be more appropriate. Thus, following this descriptive model, silicates have been classified into monosilicates, oligosilicates, ring silicates, chain silicates, layer silicates and tectosilicates according to the type of polyanion present in the structure. One of the major problems (from our viewpoint) is that most of the alkalis and transition elements cations readily substitute into these structures and are major contributors to their physical and chemical properties. Thus, any given formula can be quite lengthy.

In view of this difficulty in describing the alkaline earth silicates, we shall limit the current discussion to **"Binary"** silicates like Ca_2SiO_4 ($2CaO{\cdot}SiO_2$) or $CaSiO_3$ ($CaO{\cdot}SiO_2$), that is—the so-called "ortho-" or "meta-" silicates, etc.

The book "*Structural Chemistry of Silicates*" is an ornately and profusely illustrated survey of the structures of crystalline silicates which contains an extensive study of the bonding and structures of these compounds [Friedrich Liebau, (1985) *Structural Chemistry of Silicates*. Springer Publ. Co., Berlin, Heidelberg, New York—Library of Congress #- QD181.S6 L614 1985]. In it, the structures are classified and described following a criterion of increasing complexity of the silicate polyanions. However, it should be pointed out that the reasons why these polyanions adopt a given structure are far from being explained. This is the reason why the so-called "rich variety" of condensated silicate polyanions has been considered, in many instances, as "capricious".

The structures of monosilicates, oligosilicates, ring silicates, chain silicates, layer silicates and tectosilicates are shown in the following Fig. 5.30.

The mineral wadsleyite is a high-pressure phase having the composition, Mg_2SiO_4, a monosilicate. Disilicates are characterized by isolated $[Si_2O_7]^{6-}$ anions. $Ca_3Si_2O_7$ (the mineral rankinite) is such a compound.

Oligosilicates consist of "bound" $Si_2O_7^{6-}$ groups within an overall structure of "oxy-" groups such as belkovite = $Ba_3Nb_6[Si_2O_7]_2{\cdot}O_{12}$, or baghdadite = Ca_3Zr

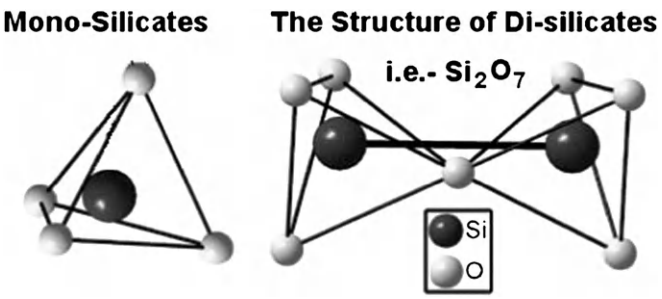

FIGURE 5.30

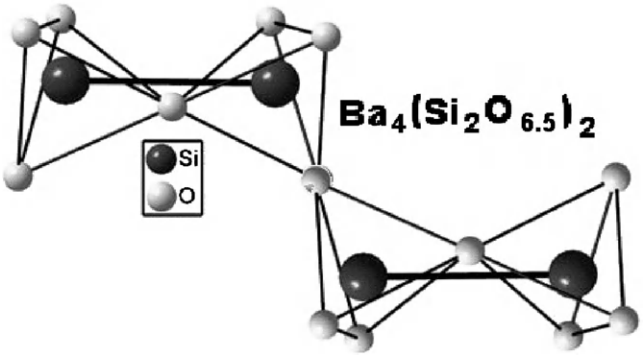

FIGURE 5.31

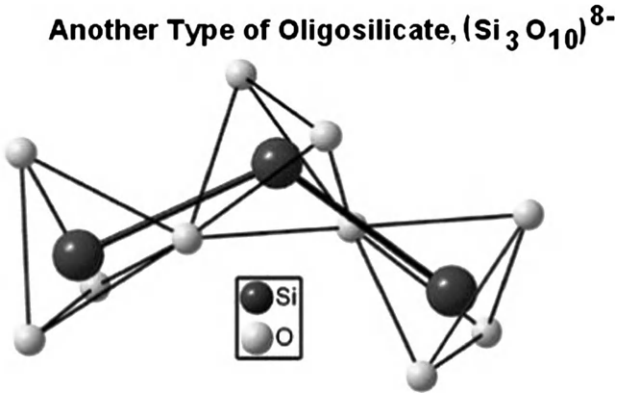

FIGURE 5.32

$[Si_2O_7]\cdot O_2$ while other disilicates consist of isolated $[Si_2O_7]^{6-}$ anions within the structure. Another oligosilicate has the formula of $Ba_4[Si_4O_{13}]$ wherein the two $[Si_2O_7]$ groups are connected by an oxygen atom (Fig. 5.31).

Still another type of oligosilicate is shown in Fig. 5.32.

Ring silicates are illustrated as shown. The structures of the ring silicate anions $[Si_3O_9]^{6-}$, $[Si_4O_{12}]^{8-}$, $[Si_6O_{18}]^{12-}$ and $[Si_{12}O_{36}]^{24-}$ are shown in Fig. 5.33.

The mineral "papagoite", $Sr_4[Si_4O_{12}]$, has such a structure. Double-ring structures such as $Si_6O_{15}^{6-}$ are also known.

Chain structures are illustrated by wollastonite, $Ca_3[Si_3O_9]$. Both "chain-branched" and "loop-branched" silicate structures have been established.

The following diagram shows the internal structure of such SiO_4^{4-} chain-tetrahedra (Fig. 5.34).

In addition, chain silicates are compiled according to their chain multiplicity into single-, double-, triple-, quadruple- and quintuple-chain silicates. Within each of these groups, the tetrahedra are arranged with regard to "branchedness" (unbranched, open-branched and loop-branched), and further classified according to their chain periodicity. The mineral, "tremolite" has the molecular structure of $Ca_2Mg_5Si_8O_{22}(OH)_2$ and this "double-looped single-chain" structure.

"Layered" structures are just what the word implies. A layered structure is seen in the following Fig. 5.35.

An example is the mineral "sanbornite"—$Ba[Si_2O_5]$. A whole variety of "layered silicates" are known which we will not elaborate upon. All silicates in which $[XO_4]$ tetrahedra form 3D tetrahedron frameworks by sharing oxygen atoms are called tectosilicates. The vast majority of tectosilicates contain only four-connected tetrahedra so that each framework oxygen atom is linked to two X atoms and is, therefore, two-connected. As a consequence, the ratio between X atoms and framework O (or more generally T) atoms in the unit cell is $z = \sum n(O)/\sum n(X) = 2$. For such tectosilicates, the term "fully linked" tectosilicates has been suggested. There is relatively small number of tectosilicates which contain $[XO_4]$ tetrahedra that are linked to less than four others, i.e. which contain, exclusively or in addition to three-connected Q3 units, also Q4 units and, very rarely, also Q2 and Q1 tetrahedra. These silicates necessarily contain nonbridging framework O atoms and their atomic ratio z is higher than 2.

To summarize, the principal types of arrangement of silicon–oxygen radicals that we will address are:

(a) isolated tetrahedrons of $[SiO_4]^{4-}$ with octahedrons of Mg and Ca
(b) $[Si_2O_7]^{6-}$ groups formed from two tetrahedrons
(c) hexagonal rings of $[Si_3O_9]^{6-}$
(d) chains of $[SiO_3]^{2-}$
(e) double chains of $[Si_4O_{11}]^{6-}$
(f) sheets of hexagonal rings of $[Si_4O_{10}]^{4-}$

These are illustrated in the following Fig. 5.36.

Therefore, the type of compounds that we will address here are the binary silicates based upon the acids:

Metasilicic acid (H_2SiO_3) = metasilicates (monosilicates)

Orthosilicic acid (H_4SiO_4) = orthosilicates (monosilicates)

Disilicic acid $(H_2Si_2O_5)$ = phyllosilicates

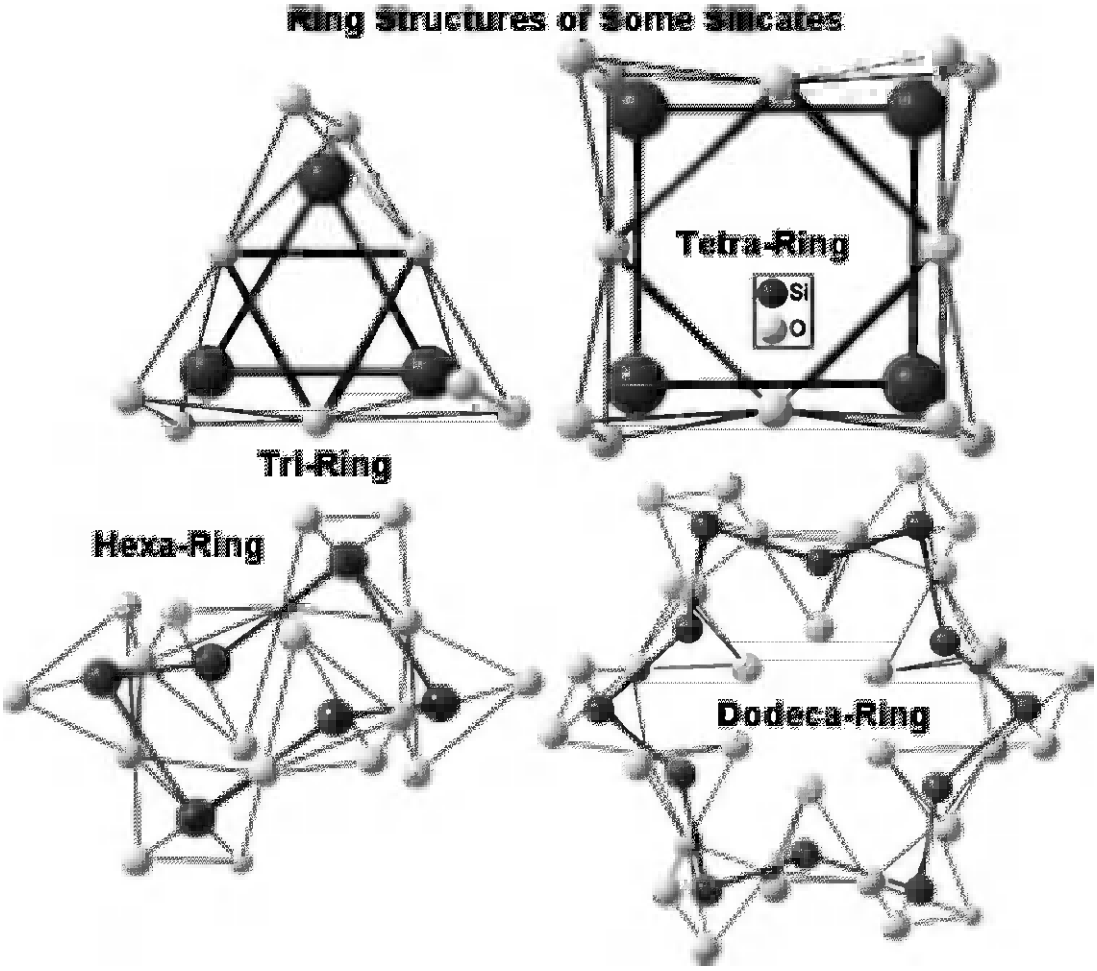

FIGURE 5.33

Pyrosilicic acid ($H_6Si_2O_7$) = pyrosilicates (disilicates)

$$Tri-ring\ structures\ =\ Si_3O_9{}^{6-}\ \text{etc.}$$

In addition, where known alkaline earth chain structures have been utilized in industry and/or studied in Academia, these types of compounds are included in this survey (but only if they conform to the binary $MO{\cdot}SiO_2$ motif).

In general, the alkaline earths form a number of silicates including the "orthosilicates = $M_2SiO_4 = 2MO{\cdot}SiO_2$" and the "metasilicates = $MSiO_3 = MO{\cdot}SiO_2$". The terms "meta-" and "ortho-" are now regarded as obsolete. The following diagram, presented on a following page, summarizes the types of known silicates (which are numerous). These silicates are synthesized by varying the ratio of MO to SiO_2 in a solid-state reaction (SSR) (Fig. 5.37).

$$x\text{MO} + y\text{SiO}_2 + \text{heat} \Rightarrow \text{M}_x(\text{SiO}_3)_y$$

Mg is anomalous and is plotted separately as part of the diagram (making it a ternary one). Melting points of some of the calcium silicates are given to show the range of melting points of these compounds. Not all of these possible silicates are formed by either Ca or Sr. Only Ba forms all of these (plus one more—1:3).

Beryllium Silicates

Beryllium silicate can be prepared by calcining the oxide with silica, SiO_2, at an elevated temperature:

$$\text{BeO} + \text{SiO}_2 + \text{heat} \Rightarrow \text{BeSiO}_3$$

The so-called "metasilicate" results. This compound appears in nature as beryl, $(BeSiO_3)_3{\cdot}Al_2(SiO_3)_3 = Be_3Al_2(SiO_3)_6$, which is a double salt. This is a chain silicate related to a ring-silicate structure. When two oxygen of SiO_4^{4-} units share bonds with other SiO_4^{4-} units, the silicates form a ring or an infinite chain. The stoichiometry of the silicate becomes $(SiO_3)_n^{2n-}$. Single-chain structures have the empirical formula $MSiO_3$ and were often called "metasilicates" in the older literature, a term that lingers in industrial usage but should now be regarded as obsolete. In natural minerals, these chains are ionically bound together by interstitial metal ions such as Be^{2+}, Mg^{2+}, Fe^{2+}, or Al^{3+}.

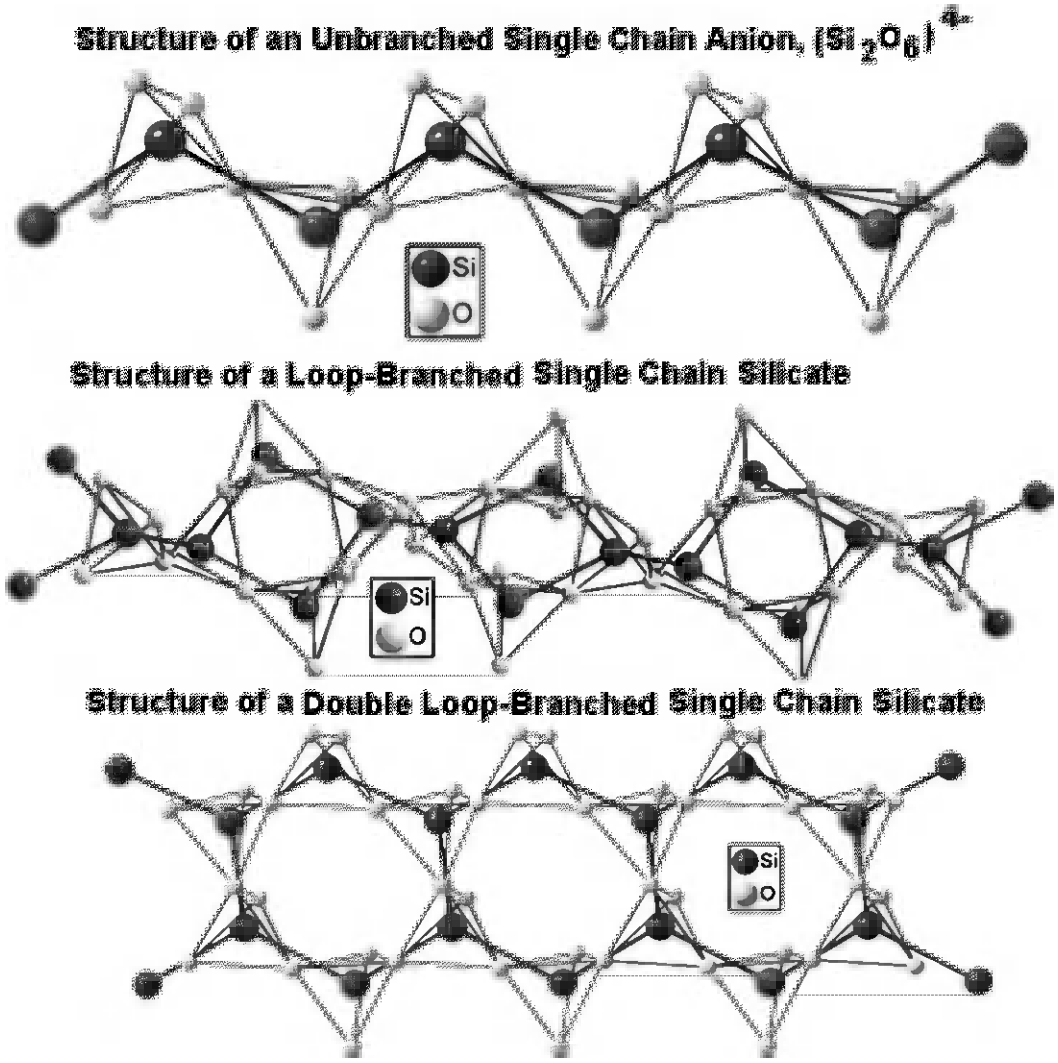

FIGURE 5.34

Beryllium used in industry begins as a silicate ($BeSiO_3$) in beryl and bertrandite ores. More than 20 minerals containing beryllium are known but most of them are rare. The most important are bertrandite ($Be_4Si_2O_7(OH)_2$), Beryl ($3BeO{\cdot}Al_2O_3{\cdot}6SiO_2$), phenacite ($2BeO{\cdot}SiO_2 = Be_2SiO_4$), and chrysoberyl ($BeO{\cdot}Al_2O_3 = BeAl_2O_4$), of which beryl is the most abundant and in fact is the only one of commercial importance. The beryllium aluminate, chrysoberyl, which can be obtained directly from the ore, has interesting possibilities because of its high-melting temperature (about 1880 °C). In a very pure crystalline form, beryl occurs as gems such as blue-green aquamarine and green emerald.

In the system, $BeO–SiO_2$, only two compounds appear in the phase diagram shown here. Both melt congruently (Fig. 5.38).

Phenacite is a fairly rare nesosilicate mineral consisting of beryllium orthosilicate, Be_2SiO_4. The name "phenacite", or the alternate spelling, "phenakite", was named in 1833 by Nordenskiold from the Greek for "deceiver" because it was often mistaken for quartz. In 1811, 20 years before, it was recognized as a new mineral, phenacite was identified as "White Tourmaline". Phenacite is trigonal–rhombohedral in structure with the point group, $\bar{3}$, space group = R $\bar{3}$ and unit-cell parameters of: $a = 12.472$, $c = 8.252$, $Z = 18$; $V = 1111.63$ Å^3, Den(Calc) = 2.96. Occasionally, used as a gemstone, phenacite occurs as isolated crystals, which are rhombohedral in structure with parallel-faced hemihedrism, and are either lenticular or prismatic in habit. The hardness is high, being 7.5–8 Mohs; the specific gravity is 2.96 g/cc. The crystals are sometimes perfectly colorless and transparent, but more often they are grayish or yellowish and only translucent; occasionally they are pale rose-red (Fig. 5.39).

Phenacite is found in high-temperature pegmatite veins and is associated with quartz, chrysoberyl and

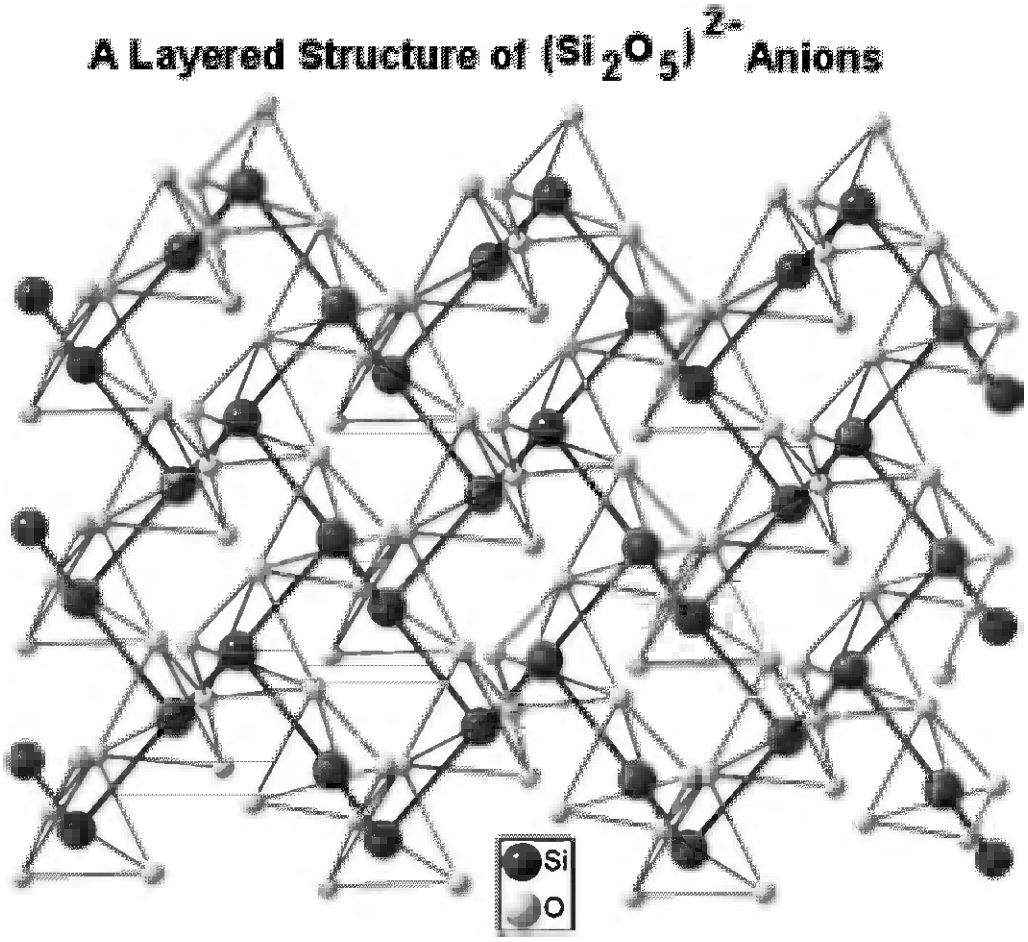

FIGURE 5-35

topaz. It has long been known from the Chrysoberyl mine on the Takovaya stream in Russia, where large crystals occur in mica-schist. It is also found with topaz and amazon stone in Colorado and Maine, USA. Large crystals of prismatic habit have been found in a Norway. The structure of phenacite is illustrated in the following diagram, presented below. The structure consists of a three-dimensional network of corner-linked, slightly distorted BeO_4 and fairly regular SiO_4 tetrahedra. The lattice of these materials consists of SiO_4 and BeO_4 tetrahedra, which are bound to each other and form chains oriented along the principal crystallo-graphic axis C_3. The chains form voids in the form of wide channels ~4.5 Å in diameter. In this diagram, the lighter tetrahedrons are oriented upward while the darker ones are oriented downward. A specific feature of phenacite-structure crystals is that the [SiO_4] tetrahedra are separated, i.e. they do not touch each other. All oxygen atoms on the phenacite lattice are three-coordinated, and each of them is shared by three tetrahedra, namely, two [BeO_4] and one [SiO_4].

The compound, Be_2GeO_4, has a similar structure. The heat of formation for Be_2SiO_4 has been found to be: $\Delta H_f^0 = -497.57$ kcal/mol and $\Delta G_f^0 = -470.22$ kcal/mol at 298 K. When heated above 700 °C, phenacite decomposes to BeO and SiO_2. Thermal expansion and high-temperature crystal structures of phenakite and chrysoberyl have been determined by X-ray methods at several temperatures to 690 °C. Phenakite (hexagonal, space group $R\bar{3}$) has a slightly anisotropic thermal expansion and average expansions between 25 and 690 °C perpendicular and parallel to the c axis are $\eta_1 = 5.2 \times 10^{-6}/°C$ and $\eta_2 = 6.4 \times 10^{-6}/°C$, respectively. The unit-cell volume of phenakite over this temperature range is given by the polynomial expression: $V = 1102.9 + 0.010\,T + 1.1 \times 10^{-5}\,T^2$. Chrysoberyl (orthorhombic, space group Pbnm) has nearly isotropic thermal expansion, with maximum expansivity of $8.5 \times 10^{-6}/°C$ parallel to the b axis, and minimum expansivity $7.4 \times 10^{-6}/°C$ parallel to a axis. The c axis expansivity is $8.3 \times 10^{-6}/°C$. Chrysoberyl volume between 25 and 690 °C may be represented by: $V = 227.1 + 0.003\,T + 4 \times 10^{-6}\,T^2$. The thermal expansion of beryllium, aluminum, and silicon cation coordination polyhedra in phenakite and chrysoberyl are similar to values found in previous studies of minerals

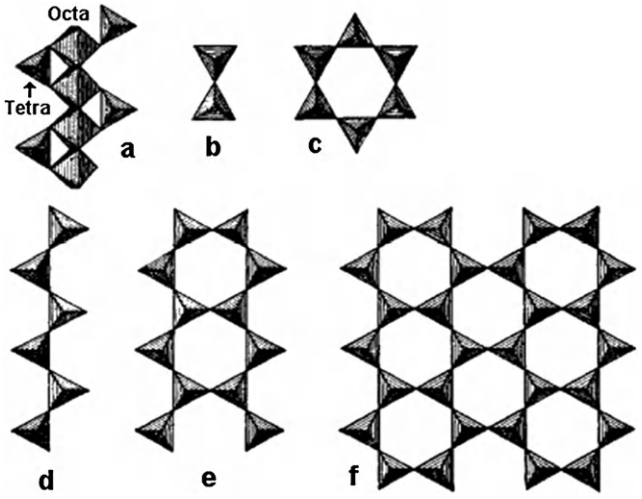

FIGURE 5.36

in the $BeO–Al_2O_3–SiO_2$ system. High-temperature structure studies of bromellite (BeO), beryl ($Be_3Al_2Si_6O_{18}$), phenakite and chrysoberyl all have beryllium tetrahedra that display the same near-zero expansion at room temperature, but increasing expansion at higher temperatures.

Beryllium silicates are available commercially but are usually processed to obtain the oxide and metal.

Magnesium Silicates

Magnesium silicate is very important in the earth sciences because it is the material that makes up most of the volume of the Earth. Magnesium silicate can be prepared by calcining the oxide with silica, SiO_2, at an elevated temperature:

$$MgO + SiO_2 + \text{heat} \Rightarrow MgSiO_3$$

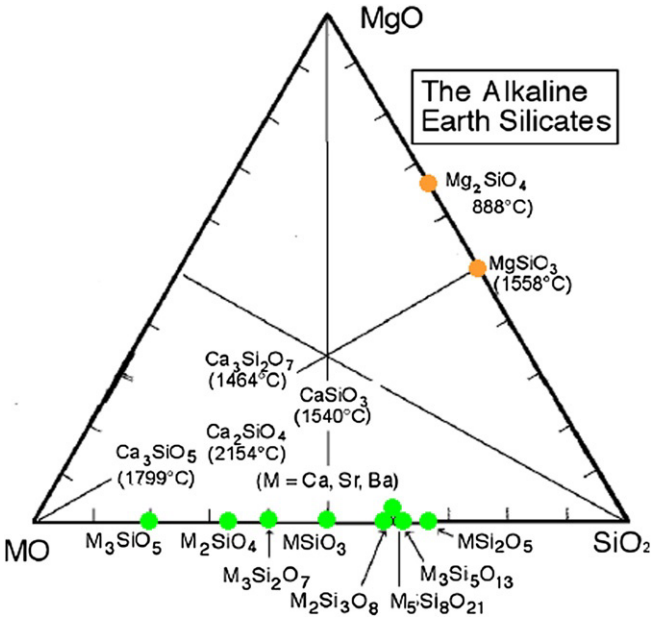

FIGURE 5.37

The so-called "metasilicate" results. In the phase diagram of $MgO–SiO_2$, only two compounds are seen whereas in the $CaO–SiO_2$ phase system, five compounds are apparent.

Magnesium is a major and ubiquitous "rock-forming" entity and magnesium silicates and expanded silicates are found in a majority of rocks and minerals. The relationships in the ternary diagram of $CaO–MgO–SiO_2$ are shown in the following Fig. 5.40.

The optimized $CaO–MgO–SiO_2$ system at 1 bar (Jung, 2003) is shown. Temperatures in parentheses are congruent melting points. The other temperatures are critical points in the ternary system. The abbreviations used include: Ak = Akermanite; Crs = Cristobalite;

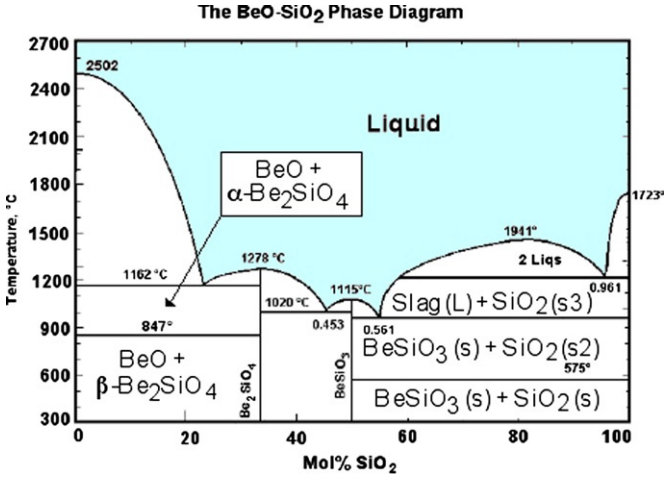

FIGURE 5.38

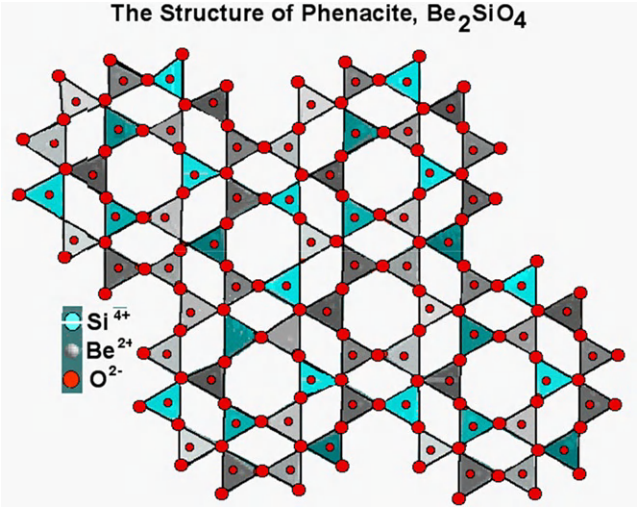

FIGURE 5.39

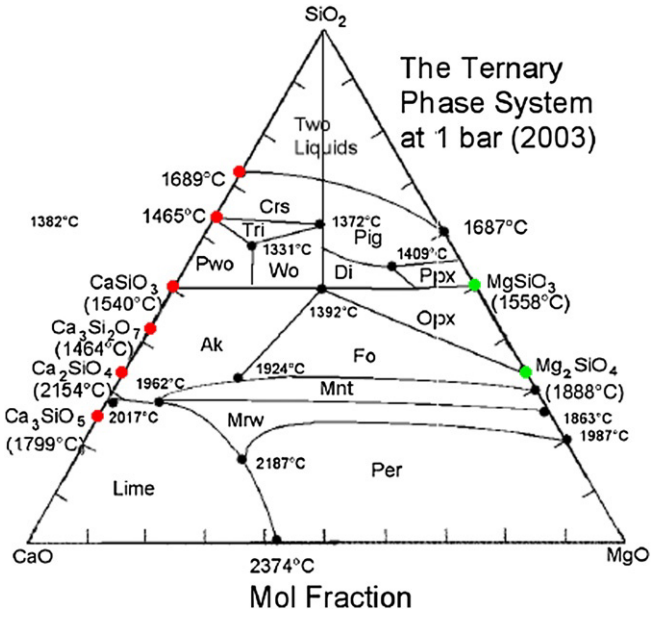

FIGURE 5.40

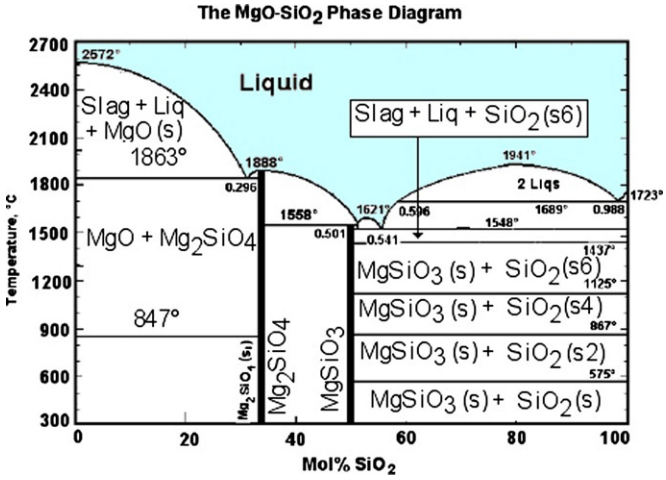

FIGURE 5.41

Di = Diopside; Fo = Forsterite; Mnt = Monticellite; Mrw = Merwinite; Opx = Orthopyroxene; Per = Periclase; Pig = Pigeonite; Ppx = Protopyroxene; Pwo = Pseudowollastonite; Tri = Tridymite; Wo = Wollastonite.

This diagram covers most of the known minerals found within the earth's crust. The system CaO–MgO–SiO_2 has been extensively studied in the past at low (Bowen, 1914; Schairer and Yoder, 1962; Kushiro, 1972; Longhi and Boudreau, 1980) and high pressures (Kushiro, 1969) because it includes forsterite, enstatite and diopside, which are major constituents of peridotitic (85%) and basaltic rocks.

The subsystem diopside–forsterite–silica has been very useful in providing a framework for the understanding of complex phase equilibria of natural basaltic rocks. The recognition that silica-saturated liquids may be generated by partial melting of peridotites at pressures up to 2.0 GPa pH_2O (Kushiro, 1969) is an excellent example of how experiments in this subsystem (dry and wet) have provided insight into the petrogenesis of igneous rocks.

Only two magnesium silicates appear in the binary phase diagram. These are $MgSiO_3$ and Mg_2SiO_4. This phase diagram is shown in Fig. 5.41.

Forsterite (Mg_2SiO_4) is the magnesium-rich end-member of the Olivine solid solution series. Forsterite crystallizes in the orthorhombic system (space group = Pbnm) with cell parameters $a = 4.75$ Å (0.475 nm), $b = 10.20$ Å (1.020 nm) and $c = 5.98$ Å (0.598 nm).

Forsterite is associated with igneous and metamorphic rocks and has also been found in meteorites. In 2005, it was also found in cometary dust returned by the "Stardust" probe in space. Experimental studies have shown that a number of dense hydrous magnesium silicates are stable at mantle pressures, corresponding to depths greater than 200 km: e.g. phase A, phase B, phase E, super hydrous phase B but also hydrous Wadsleyite and Ringwoodite, the high-pressure modifications of forsterite.

Two polymorphs of forsterite are known: "Wadsleyite" (also orthorhombic) and "Ringwoodite" (isometric). Both are mainly known from meteorites. Peridot is the Forsterite gemstone found in the mineral "olivine". Forsterite reacts with silica to form the orthopyroxene mineral "enastite" as shown in the following reaction:

$$Mg_2SiO_4 + SiO_2 + \text{heat} \Rightarrow 2MgSiO_3$$

The structure of Forsterite involves both octahedral and tetrahedral sites, as shown in the following Fig. 5.42.

In the diagram, the SiO_4^{2-} groups are clearly shown as well as the two Mg octahedral sites in green colors. The cations occupy two different octahedral sites generally labeled as and form isolated ionic bonds with the silicate

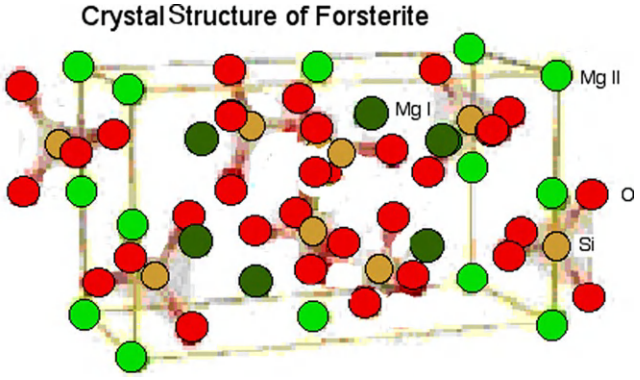

FIGURE 5.42

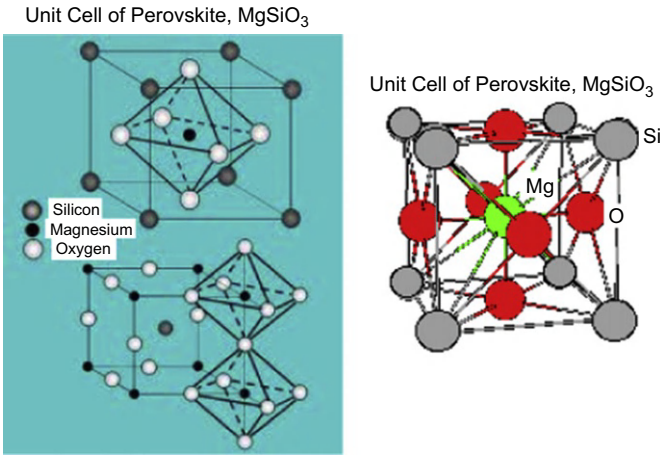

FIGURE 5.43

anions. MgI and MgII are slightly different. The MgII site is larger and more regular than MgI. The packing in forsterite structure is dense. The space group of this structure is Pbnm and the point group is 2/m, 2/m, 2/m which is an orthorhombic crystal structure.

Magnesium silicate perovskite ($MgSiO_3$) is thought to be the major phase in the earth's lower mantle (660–2900 km depth). It is orthorhombic. The structure is presented in the following Fig. 5.43.

The MgO_6 octahedra are shown both in the unit cell and in the environments of the SiO_4 tetrahedra. The Forsterite and Perovskite structures are related. A molecular dynamics simulation of the perovskite $MgSiO_3$ gave evidence for a phase transition from the orthorhombic to a tetragonal phase at about 2600 K on heating the crystal under a constant pressure of 310 kbar. Enstatite (orthorhombic—$a = 18.228$ Å, $b = 8.805$ Å, $c = 5.185$ Å, $Z = 8$; $V = 832.18$ Å^3, Den(Calc) = 3.20 g/cc) is the magnesium end-member of the pyroxene silicate mineral series "enstatite" ($MgSiO_3$)—"ferrosilite" ($FeSiO_3$).

The magnesium-rich members of the solid-solution series are common rock-forming minerals found in igneous and metamorphic rocks. The intermediate composition, $(Mg,Fe)SiO_3$, has historically been known as "hypersthene", although this name has been formally abandoned and replaced by "orthopyroxene". When determined petrographically or chemically, the composition is given as relative proportions of enstatite (En) and ferrosilite (Fs) (e.g. $En_{80}Fs_{20}$). Most natural crystals are orthorhombic (space group = Pbca) although four polymorphs are known. The high-temperature, low-pressure polymorphs are protoenstatite and protoferrosilite (also orthorhombic, space group = Pbcn) while the low-temperature, low-pressure forms, clinoenstatite and clinoferrosilite, are monoclinic (space group = P21/c).

Glasses made from the magnesium silicate minerals enstatite ($MgSiO_3$) and forsterite (Mg_2SiO_4) and three intermediate compositions can be considered as analogues of quenched melts from the earth and lunar mantle. Combined neutron and XRD data show an abrupt change in glass structure in the narrow compositional range 38% SiO_2 to 33% SiO_2 (Mg_2SiO_4). These structural changes reflect a change from a glass characterized by corner-shared SiO_4 tetrahedra and an approximately equal mixture of MgO_4 and MgO_5 polyhedra, to one in which the average coordination of magnesium by oxygen is increased from 4.5 ± 0.1 to 5.0 ± 0.1. Both these local environments are very different from that of their crystalline counterparts. The change in structure is associated with a discontinuous change in the rheological properties of these glass-forming liquids close to the forsterite composition.

Diopside is a monoclinic pyroxene mineral with composition $MgCaSi_2O_6$. It is an important rock-forming mineral in several metamorphic and basic to ultrabasic igneous rocks, and is also found in meteorites. It forms complete solid-solution series with "hedenbergite" ($FeCaSi_2O_6$) and "augite" $[(Ca,Na)(Mg,Fe,Al)(Si,Al)_2O_6]$ and partial solid solutions with "orthopyroxene" $[(Mg,Ca)(Si,Al)_2O_6]$ and "pigeonite" $[(Ca,Mg,Fe)(Mg,Fe)Si_2O_6)]$. The diopside–hedenbergite series is analogous to the amphibole series. Diopside has several varieties, including a chromium-rich gem variety called chrome diopside. Diopside forms variably colored, but typically dull green crystals in the monoclinic prismatic class. It has two distinct prismatic cleavages at 87 and 93° typical of the pyroxene series. It has a Mohs hardness of six, a Vickers hardness of 7.7 GPa at a load of 0.98 N, and a density of 3.25 to 3.55 g/cc. It is transparent to translucent with indices of refraction of $\eta_1 = 1.663–1.699$, $\eta_2 = 1.671–1.705$, and $\eta_3 = 1.693–1.728$. Violan is a rare blue variety found in some localities in Italy. There is also a green "cat's-eye" variety that contains minute inclusions, that reflect light in such a way as to produce a lively linear luminescence within the crystal.

Magnesium forms a series of phyllosilicates (from the Greek *phyllon*, leaf), or sheet silicates, and forms parallel sheets of silicate tetrahedra with Si_2O_5 of a 2:5 ratio. Hydroxy silicates are known. These minerals have the formula of $Mg_3Si_2O_5(OH)_4$ but differ in the actual lattice construction. "Antogorite" $[(Mg, Fe)_3Si_2O_5(OH)_4]$, lizardite $\{Mg_3[(OH)_4Si_2O_5]\}$ and "crysotile" all belong to the "serpentine" group of minerals. It is not clear whether these compositions are actually double salts of $2Mg(OH)_2 \cdot MgSi_2O_5$ or not. They definitely are not hydrates. Most of these minerals form as rocks. Rock composed primarily of these minerals is called "serpentinites".

Serpentines find use in industry for a number of purposes, such as railway ballast, building materials, and the asbestos-form types find use as thermal and

electrical insulation (chrysotile asbestos). The asbestos content can be released to the air when serpentine is excavated from the mine and if it is used as a road surface, forms a long-term health hazard to humans by breathing. Asbestos from serpentine can also appear at low levels in water supplies through normal weathering processes, but there is as yet no identified health hazard associated with use or ingestion. In its natural state, some forms of serpentine react with carbon dioxide and re-release oxygen into the atmosphere. Antigorite is the polymorph of serpentine that most commonly arises during metamorphism of wet ultramafic rocks and is stable at the highest temperatures—to over 600 °C at depths of 60 km or so in the earth. In contrast, lizardite and chrysotile typically form near the earth's surface and break down at relatively low temperatures, probably well below 400 °C. It has been suggested that chrysotile is never stable relative to either of the other two serpentine polymorphs.

Talc (derived from the Persian word for talk) is a mineral composed of hydroxy magnesium silicate with the chemical formula of $H_2Mg_3(SiO_3)_4$ or $Mg_3Si_4O_{10}(OH)_2$. In loose form, it is the widely used substance known as "talcum powder". It occurs in nature as foliated to fibrous masses. It is monoclinic but so rare that as to be almost unknown. It is very soft and can be easily cut with a knife. As the defining mineral for the value of 1,0 on the Mohs-hardness scale, it can be easily scratched by a fingernail. It has a density of 2.5–2.8 g/cc, a clear or dusty "luster", and is translucent to opaque. Talc is not soluble in water, but it is slightly soluble in dilute mineral acids. Its color ranges from white to gray and it has a distinctly greasy feel. Soapstone is a metamorphic rock composed predominantly of talc.

A hydrated magnesium silicate has been examined at 20 GPa and 1200 °C. The single crystal has composition $Mg_{1.11}Si_{1.89}H_{2.22}O_6$ (ideal formula: $MgSi_2H_2O_6$ or $MgSiO_5 \cdot H_2O$), trigonal, cell parameters $a = 4.7453$, $c = 54.3450$ Å, and $V = 5\ \ 84.74$ Å^3, and space group = P31m. The crystal structure is relatively simple with all the Si-occupying octahedral sites in a layer similar to that of brucite, but with one of every three Mg octahedra vacant. The MgO_6 octahedra are located above and below each vacant octahedral site. All O–H bonding occurs between SiO_6 octahedral layers. This is the only high-pressure hydrous magnesium silicate structure reported to date that contains all octahedrally coordinated Si. The calculated density of phase D ($d_{cal} = 5\ \ 3.50$ g/cm^3) is substantially greater than any other high-pressure hydrous magnesium silicate phase.

A synthetic magnesium silicate adsorbent is offered for sale as a white fine powder, amorphous, with vesicular structure and huge specific area. It is an amphoteric compound capable of absorbing either acid or alkali metal catalyst. It is an efficient refining and purifying agent in the production of polyols for its excellent depicking, deodorizing, potassium ion absorbing effects and function as a filter medium.

Magnesium silicate is offered for sale with a CAS number of 1343-88-0 but the actual composition has not been forthcoming. A number of differing compositions have been listed. Asbestos is a fibrous silicate of magnesium and calcium. However, the "extender", known as "asbestine", that has come to the forefront in paint making, is really a ring silicate of magnesia and slightly alkaline, but without the fibrous texture of asbestos or amianth. Asbestine pulp (as a certain variety of the material mined at the foot of the Adirondack mountains is known to the trade), although it is sold in the dry powdered form, belongs really to the soapstone or talc variety. But it is not as unctuous as either of those, has a harder texture, and is of whiter color than either soapstone or talc.

Soapstone or talc is used for toilet powder and as a lubricant by shoemakers, also on dancing floors, in fillers, Putties and cements, but not as a rule in paints for general usage. Asbestine pulp or asbestine in its various varieties has been used for many years by manufacturers of paints, not so much as an adulterant, but rather to make the paint more buoyant in order to keep it from settling to any extent, as this compound is of very low-specific gravity and a great oil absorber. This feature, however, depends on the location where it is mined, as there is a wide divergence in that respect. Its specific gravity varies between 2.3 and 2.7 and its oil absorption is between 30 and 36%, or in other words, to make a paste in oil will require 70 pounds of the heavier asbestine to 30 pounds of oil or 64 of the lighter asbestine pulp to 36 pounds of oil. Asbestine is used to some extent in making liquid fillers for soft wood, and certainly much better than silica. Mixed with silicate of soda (water glass) it makes a very good fireproof coating. Asbestine is as inert as barytes or silica, and does not undergo a chemical combination with oil or water, but will be found sometimes more or less alkaline, and while it may be safely used as an extender with almost any color.

A number of magnesium silicates are offered for sale commercially, worldwide from many manufacturers.

Calcium Silicates

The term, calcium silicate, is often used to refer to a group of chemical compounds formed from CaO and silica, SiO_2. In general, calcium silicates are not prepared by dissolving a soluble calcium salt and adding a solution of sodium silicate. One of the reasons is that sodium silicate is not well defined and contains a variety of silicate chains and structures. A hydrate is known and is the product formed when Portland cement "cures" as

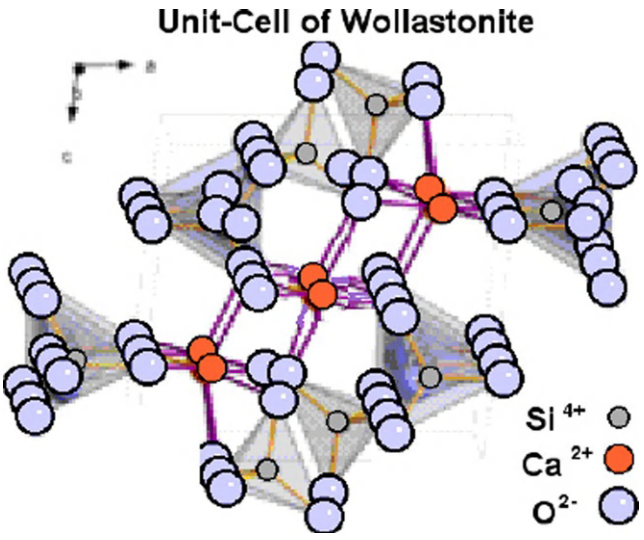

FIGURE 5.44

a result of the reaction between the contained silicate phases and water. This reaction typically is expressed as:

$$2Ca_3SiO_5 + 7H_2O \Rightarrow 3CaO{\cdot}2SiO_2{\cdot}4H_2O + 3Ca(OH)_2 + 173.6\ kJ$$

The stoichiometry of the hydrate in cement paste is variable and the state of the chemically and physically bound water in its structure is not clear.

Thus, calcium silicate can be prepared by calcining the oxide with silica, SiO_2, at an elevated temperature:

$$CaO + SiO_2 + heat \Rightarrow CaSiO_3$$

At a molar ration of 1:1, the metasilicate, $CaSiO_3$ results. "Wollastonite" occurs as a calcium inosilicate mineral that may contain small amounts of Fe, Mg and Mn substituting for calcium. An "inosilicate" is a chain silicate (from the Greek, Inos = fiber). The structure involves interlocking chains of silicate tetrahedra with either SiO_3, 1:3 ratio, for single chains or Si_4O_{11}, 4:11 ratio, for double chains. The manufactured salt is usually white. It forms within the earth when impure limestone is subjected to high temperature and pressure, sometimes in the presence of silica-bearing fluids as in metamorphic rocks. It is named after the English chemist and mineralogist William Wollaston (1766–1828). The structure is shown above in Fig. 5.44.

Some of the properties that make wollastonite so useful are its high brightness and whiteness, low moisture and oil absorption, and low-volatile content. Wollastonite is used primarily in ceramics, friction products (brakes and clutches), metalmaking, paint filler, and plastics. Despite its chemical similarity to the compositional spectrum of the Pyroxene group of minerals, it is structurally very different, with a third SiO_4 tetrahedron in the linked chain (as opposed to two in the pyroxenes). Wollastonite crystallizes as a triclinic crystal with

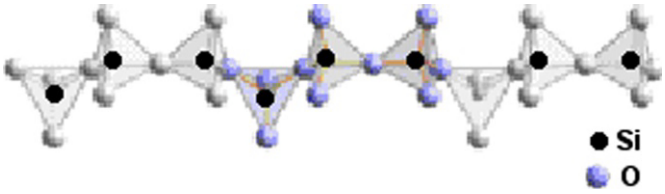

FIGURE 5.45

the space group, 1, and the lattice constants: $a = 7.94$ Å, $b = 7.32$ Å, $c = 7.07$ Å; $\alpha = 90.03°$, $\beta = 95.37°$, $\gamma = 103.43°$ and six formula units per cell (Fig. 5.44).

This is a chain structure and the arrangement of the SiO_4^{4-} tetrahedral are shown in Fig. 5.45.

Wollastonite was once classed structurally among the pyroxene group, because both of these groups have a ratio of Si:O = 1:3. In 1931, Warren and Biscoe showed that the crystal structure of wollastonite differs from minerals of the pyroxene group, and they classified this mineral within a group known as the pyroxenoids. It has been shown that the pyroxenoid chains are more kinked than those of pyroxene group, and exhibit longer repeat distance. The structure of wollastonite contains infinite chains of $[SiO_4]$ tetrahedra sharing common vertices, running parallel to the *b*-axis. The chain motif in wollastonite repeats after three tetrahedra, whereas in pyroxenes only two are needed. The repeat distance in the wollastonite chains is 7.32 Å and equals the length of the crystallographic *b*-axis. Wollastonite occurs as bladed crystal masses, single crystals can show an acicular particle shape and usually it exhibits a white color, but sometimes cream, gray or very pale green. The melting point of wollastonite is about 1540 °C.

In 2005, China was the top producer of wollastonite with at least 50% world share followed by India and the USA. In the United States, wollastonite is mined in New York state. Deposits have also been mined commercially in Northwestern Mexico. Wollastonite has industrial importance worldwide. It is used in many industries, mostly by tile factories that have incorporated it into the manufacturing of ceramic to improve many aspects, and this is due to its fluxing properties, freedom from volatile constituents, whiteness, and acicular particle shape. It can also be used in paint, paper, and vinyl tile manufacture. In some industries, it is used in different percentages of impurities such as its use as, a fabricator of mineral wool insulation, or as an ornamental building material. Wollastonite usually occurs as a common constituent of a thermally metamorphosed impure limestone, it also could occur when the silicon is due to metamorphism in contact altered calcareous sediments, or to contamination in the invading igneous rock. In most of these occurrences, it is the result

of the following reaction between calcite and silica with the loss of carbon dioxide:

$$CaCO_3 + SiO_2 \rightarrow CaSiO_3 + CO_2$$

Wollastonite may also be produced in a diffusion reaction in "skarn". It develops when limestone within a sandstone is metamorphosed by a "dyke", which results in the formation of wollastonite in the sandstone as a result of outward migration of Ca.

The chemical compound, Ca_2SiO_4, is also known as calcium orthosilicate and sometimes formulated $2CaO \cdot SiO_2$. Calcium orthosilicate is a white powder with a low-bulk density and absorbs water freely. It is used as an anticaking agent and an antacid. A free-flowing powder derived from limestone and silica, calcium silicate has no known adverse effects to health. It is used in roads, insulation, bricks, roof tiles, table salt and occurs in cements. Calcium orthosilicate is commonly used as a safe alternative to asbestos for high-temperature insulation materials. Industrial grade piping and equipment insulation are often fabricated from calcium orthosilicate. This compound has the CAS number of 1344-95-2 and the molecular weight of 116.1578 g/mol.

The phase diagram of this binary system is shown in the following Fig. 5.46.

Four compounds are relatively stable:

1:1 = $CaSiO_3$ = monosilicate
3:2 = $Ca_3Si_2O_7$ = disilicate
2:1 = Ca_2SiO_4 = orthosilicate
3:1 = Ca_3SiO_5 = layered structure

The compound, $Ca_2Si_3O_7$, is unstable and is not shown here. $CaSiO_3$ melts congruently at 1540 °C while $Ca_3Si_2O_7$ melts incongruently at 1464 °C. The compound, Ca_2SiO_4 is trimorphic and undergoes structural transformations at 847°, 1300°, and 1437°. It melts congruently at 2154 °C. At 25 mol% with CaO, the compound, Ca_3SiO_5, forms but only if the temperature reaches >1300 °C. It melts incongruently and decomposes into CaO and Ca_2SiO_4 at 1799 °C. $Ca_3Si_2O_7$ appears in nature as the mineral "rankinite". It is monoclinic with unit-cell constants of: space group: P21/, $a = 10.557$ Å, $b = 8.885$ Å, $c = 7.858$ Å, $V = 1195.86$ Å^3, $Z = 4$. Point Group = 2/m. It is found in Scawt Hill, near Larne, Co. Antrim, Ireland, found near Kilchoan, Ardamurchan, Argyllshire, and Camas Mor, Isle of Muck, Scotland. It appears in Golden Gully, Tokatoka district, Auckland, New Zealand at Fuka, near Bicchu, Okayama Prefecture, Japan. In the Christmas Mountains, Brewster Co., Texas, USA, in the Hatrurim Formation, at Hatrurim and Ma'aleh Adumim, Israel and in the Lower Tunguska River basin, central Siberia, Russia. Another variant, Kilchoanite, is orthorhombic with cell constants of: space group: Imam or Ima2: $a = 11.42$ Å, $b = 5.09$ Å, $c = 21.95$ Å, $Z = 8$, point group: 2/m 2/m 2/m or mm2. It is found solely in Kilchoan, Scotland and is isomorphous with rankinite. It has apparently formed in limestones, thermally metamorphosed by invasion of gabbro and is thought to have formed during retrograde metamorphism following decarbonation of limestone and thus under low pressure of CO_2. It is a retrograde replacement of rankinite that is a disilicate and has the structure shown in Fig. 5.47.

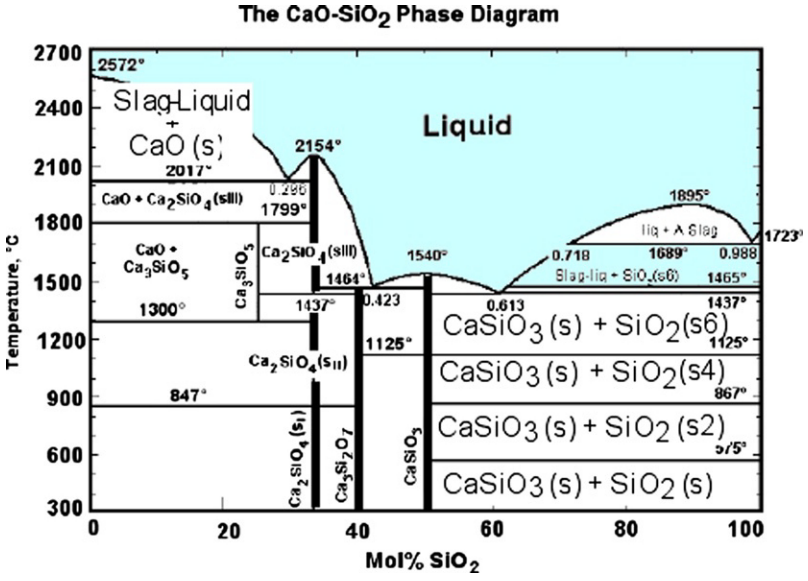

FIGURE 5.46

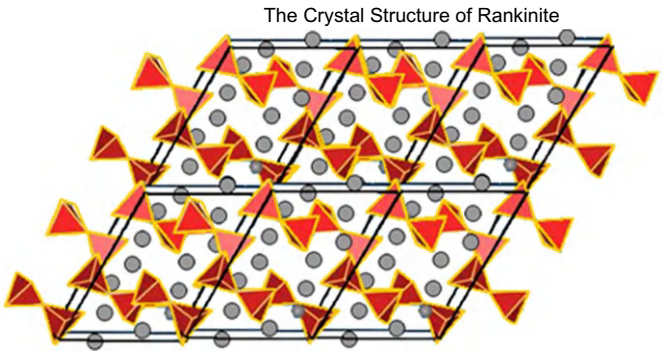

FIGURE 5.47

In this structure involving dimers, a series of disilicate chains interspersed with calcium atoms exists. Rankinite is unstable at the temperature 1510 °C and dissociates through diffusion mechanisms[1] according to the formula:

$$Ca_3Si_2O_7 + \text{heat} \Rightarrow 2CaSiO_3 + CaO$$

Thus, it is clear that wollastonite ($CaSiO_3$) is more thermodynamically stable than rankinite ($Ca_3Si_2O_7$).

A green emitting phosphor was prepared by SSR and its structure was confirmed to be $Ca_3Si_2O_7$:Eu^{2+} by XRD. The photoluminescence (PL) results showed that this phosphor is efficiently excited by ultraviolet (UV)–visible light in the wavelength range from 250 to 450 nm and emits intensely green light with a broad peak at around 521 nm, causing it to exhibit a bright green emission.

Ca_3SiO_5 occurs in nature as "Hatrurite". It contains small amounts of Al^{3+} and Ti^{4+} as cations. The structure is trigonal–ditrigonal pyramidal with point group (3m) and space group: R 3m. Unit cell dimensions are: $a = 7.151$ Å, $c = 25.562$ Å, $Z = 9$; $V = 1131.63$ Å^3, Den(Calc) = 3.02 g/cc. It is a brownish-red to colorless crystal with a hardness of 6 Mohs.

The thermal decomposition of pure Ca_3SiO_5 has been studied at temperatures between 1025 and 1210°. The results show that decomposition is initiated by formation of nuclei of Ca_2SiO_4 and CaO at the surface of Ca_3SiO_5 grains. The presence of CaO or Ca_2SiO_4 increases the apparent rate of decomposition, largely by eliminating the need for a separate nucleation period. A Ca_3SiO_5:Eu^{2+} phosphor was synthesized by the sol-gel reaction method. The emission spectrum exhibits one asymmetric band centered at 505 nm, under 365 nm excitation, and the excitation spectrum for 505 nm indicates two bands centered at 374 and 397 nm, respectively. The effect of synthesis condition, such as synthesis temperature, synthesis time and Eu^{2+} concentration, on the emission spectrum of Ca_3SiO_5:Eu^{2+} phosphor was investigated. The results show that the emission peak intensity of Eu^{2+} first increases, then decreases with the increase in synthesis temperature or synthesis time or Eu^{2+} concentration, and reaches the maximum value at 1100 °C, for 4 h and 0.5 mol% Eu^{2+}. Ca_3SiO_5 has the CAS number of 71396-54-8.

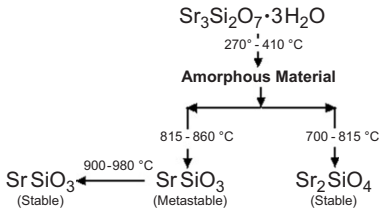

FIGURE 5.48

Calcium silicates are readily available commercially in several forms on a worldwide basis.

Strontium Silicates

Strontium silicate can be prepared by calcining the oxide with silica, SiO_2, at an elevated temperature:

$$SrO + SiO_2 + \text{heat} \Rightarrow SrSiO_3$$

The metasilicate composition results. Three forms of strontium silicate are known: $SrSiO_3$ (monoclinic), the ortho-salt, Sr_2SiO_4 (monoclinic) and the phyllo-salt, Sr_3SiO_5 (tetragonal) that has a layered structure. Only the ortho-salt has a CAS number = 12712-63-9.

Very few studies of strontium silicate hydrate precipitations have been reported. A hydrate can be prepared through an "alkoxy-process". Therein, Si–OC_2H_5 and Sr–OCH_3 were mixed together at a 2:3 molar ratio in an aqueous ammonia solution and heated to 85 °C. The resulting precipitate consisted of $Sr_3SiO_5 \cdot 3H_2O$. This compound was then heated and the products were identified as $SrSiO_3$ and Sr_2SiO_4. A diagram showing the preparation steps involved in heating the pyrosilicate compound to form the metasilicate and/or orthosilicate compound is shown above in Fig. 5.48.

In the SrO–SiO_2 binary system, there are three transition compounds including: $SrSiO_3$, Sr_2SiO_4 and Sr_3SiO_5. The phase diagram is presented as shown in Fig. 5.49.

The pyrosilicate is not seen in the solid-state preparation method. The melting temperature of the Sr_2SiO_4 compound is 2325 °C. The eutectic temperature between Sr_2SiO_4 and Sr_3SiO_5 is 2150 °C at 27 mol% SiO_2. The phase diagrams of the systems Sr_2SiO_4–$SrSiO_3$ and $SrSiO_3$–SiO_2 have been determined experimentally using DTA. The eutectic compositions and temperatures of the Sr_2SiO_4–$SrSiO_3$ and $SrSiO_2$ subsystems are estimated to be 49.3 mol% SiO_2, 1567 °C and 65.8 mol% SiO_2, 1342 °C, respectively. The known compounds,

[1]For a discussion of diffusion mechanisms in silicates, see "Solid-State Chemistry" by RC Ropp, Elsevier (2003), pp 161–168.

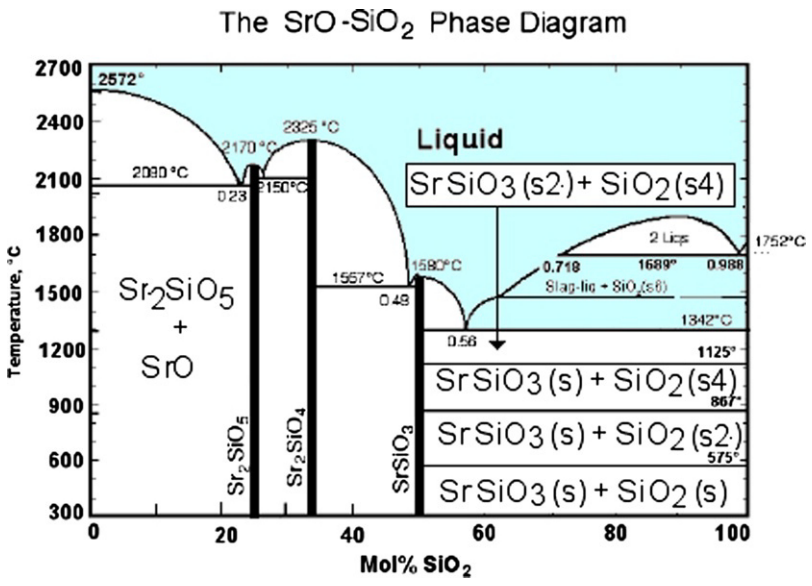

FIGURE 5.49

$SrSiO_3$, Sr_2SiO_4, and Sr_3SiO_3, melt congruently at 1580 ± 15 °C, 2325 ± 15 °C, and 2170 ± 15 °C, respectively. Simple binary eutectics exist between (1) Sr_2SiO_4 and Sr_3SiO_5 at 2150 ± 15 °C and 27 mol% SiO_2 and (2) Sr_3SiO_5, and SrO at 2080 ± 15 °C and 23 mol% SiO_2.

A new type of strontium silicate has been discovered. High-pressure synthesis of the new $SrSi_2O_5$ phase was performed at 16 GPa and 900 °C by using a Kawai-type multianvil apparatus. The powder XRD pattern of the compound was analyzed by Rietveld refinement based on the structure of a high-pressure polymorph of $BaGe_2O_5$, as $BaGe_2O_5$ III. The structure is orthorhombic with space group *Cmca* and cell parameters of $a = 5.2389$ Å, $b = 9.2803$ Å, $c = 13.4406$ Å, $V = 653.46(2)$ Å^3, $Z = 8$, dens $= 4.549$ g/cm^3. The structure consists of layers containing SiO_6 octahedra and SiO_4 tetrahedra. In a unit layer, oxygen and strontium atoms are arranged in an approximation to hexagonal close packing. The strontium atom is accommodated in a 12-coordinated site. Each SiO_6 octahedron shares four corners with SiO_4 tetrahedra and the other two corners with another SiO_6 octahedra. The SiO_6 octahedra are linked to each other to form SiO_6 chains along the *a*-axis. This is the first known example of a silicate with a $BaGe_2O_5$ III-type structure.

A Eu^{2+}-activated strontium silicate (Sr_3SiO_5:Eu^{2+}) yellow-emitting phosphor was prepared by conventional SSR (solid state reaction) techniques in a reducing atmosphere with starting materials of $SrCO_3$, SiO_2 and Eu_2O_3. The phase, morphology and luminescence properties of the samples were analyzed. XRD analysis showed the main phase in all samples to be tetragonal Sr_3SiO_5. With Eu^{2+} ions doped into the host lattice, the Sr_3SiO_5:Eu^{2+} phosphors absorb light energy in the near-UV–visible spectrum region and show an intense broad emission band in the yellow color range (around 570 nm) and a weak band in the blue region (around 470 nm). The excitation and the emission bands originate from the 4f ⇒ 5d transition of Eu^{2+} ions. As the concentration of Eu^{2+} ions increases, the emission peaks of phosphors shift to longer wavelengths. The effective emission in the yellow color indicates that the phosphor has potential usage for preparation of white light-emitting diodes.

The enthalpies of solution, ΔH_{sol}, of $SrSiO_3$ and Sr_2SiO_4 in 3.035 mol/dm^3 HF (aq) + 3.019 mol/dm^3 HCl (aq) have been measured.

From these results, the standard molar enthalpies of formation of $SrSiO_3$(s) and Sr_2SiO_4(s) have been calculated. The values obtained are −1635.3 kJ/mol and −2305.7 kJ/mol, respectively.

The aqueous phase interaction of divalent Sr with silicate-containing solutions was studied over a range of pH values, as a function of dissolved silica, Sr concentrations, and extended to basic solution (0.2 M NaOH) at room temperature (22–23 °C). Formation of an amorphous Sr silicate phase of variable composition was observed, beginning at approximately pH 10. The precipitate became quasi-crystalline at higher base concentrations and with aging time. The phase that formed at high-base concentration (beginning at pH 11.5–12.0) was identified by total chemical analysis, XRD, and thermogravimetric analysis to have a chemical formula of $Sr_5Si_6O_{16}(OH)_2 \cdot 5H_2O$, with a tobermorite-like structure. The $Sr_5Si_6O_{16}(OH)_2 \cdot 5H_2O$ phase has not been previously reported.

In another case, light-brown crystals were discovered growing from the interface of a strontium silicate melt and the containing platinum crucible. The compound turned out to be $Sr_4(PtO_6)\cdot 2Sr_2SiO_4$ with a molecular weight of 1176.21 g/mol. It is monoclinic with $a = 18.830$ Å, $b = 5.744$ Å, $c = 7.172$ Å, $\beta = 110.72°$, $V = 725.547$ Å^3, $Z = 2$ and density = 5.383 g/cc. The structure involves isolated SiO_4 tetrahedra and PtO_6 octahedra. Three of the four nonequivalent Sr atoms are coordinated by o-atoms in distorted trigonal prisms. The fourth is located in a square antiprism that has one small and one large face, i.e. 1/2 of a cubooctahedron. Two of the small faces are shared which produces a short Sr–Sr distance of 3.28 Å.

Strontium silicate is offered for sale as STRONTIUM METASILICATE; strontium silicate(1:1); CAS = 13451-00-8 by several suppliers, notably Chinese. Another type, CAS = 12712-63-9, is offered as "strontium silicate" but is probably the orthosilicate Sr_2SiO_4 (2:1).

Barium Silicates

Barium silicate can be prepared by calcining the oxide with silica, SiO_2, at an elevated temperature:

$$BaO + SiO_2 + \text{heat} \Rightarrow BaSiO_3$$

The so-called "metasilicate" results. Barium silicate has been given the CAS number of 13255-26-0.

The phase diagram of the system BaO–SiO_2 has been studied as shown in the following Fig. 5.50.

Whereas three compounds have been reported in most of the other alkaline earth silicate systems, seven (7) separate compounds were found in this system. The compounds were prepared by varying the molar ratio of BaO to SiO_2 as the 3:1, 2:1, 1:1, 2:3, 5:8, 3:5, and 1:2 before the calcination step.

Ba_3SiO_5 is tetragonal with the space group I4/mcm (D) isotypical with Cs_3CoCl_5. The unit-cell parameters are: $a = 7.3068$ Å, $c = 11.2275$ Å. It is a disilicate. It is stable up to 1800 °C where it decomposes to the orthosilicate:

$$Ba_3SiO_5 + \text{heat} \Rightarrow Ba_2SiO_4 + BaO$$

Ba_3SiO_5 has been used as a host to prepare a yellow-emitting phosphor using the activator, Eu^{2+}. It is easily activated by blue-light of an LED diode to produce a white-emitting LED lamp. The phosphor is formed at 1050 °C but the emission becomes green due to the formation of the Ba_2SiO_4:Eu^{2+} phosphor.

In general, barium containing silicate compounds are of great interest for practical luminescent materials due to higher luminous efficiency of Eu^{2+} in this kind of host lattices. Under UV excitation, Eu^{2+}-doped barium silicates can be roughly classified into two groups according to the emitting color: bluish-green emission, i.e. Ba_2SiO_4:Eu^{2+} ($\lambda_{em} = 504$ and 510 nm), $BaSi_2O_5$:Eu^{2+} ($\lambda_{em} \sim 520$ nm), and $Ba_2Si_3O_8$:Eu^{2+} ($\lambda_{em} \sim 485$ nm); and greenish-yellow emission, i.e.$BaSiO_3$:Eu^{2+} ($\lambda_{em} \sim 550$ nm) and Ba_3SiO_5:Eu^{2+} ($\lambda_{em} = 504$ and 566 nm or 560 and 590 nm). The position of the emission band mainly depends on the chemical composition and crystal structure.

Ba_2SiO_4, the orthosilicate, has the orthorhombic structure, Pnam (62), $Z = 4$, isostructural with α-K_2SO_4, and the unit-cell dimensions of $a = 7.508$ Å, $b = 10.214$ Å, $c = 5.8091$ Å.

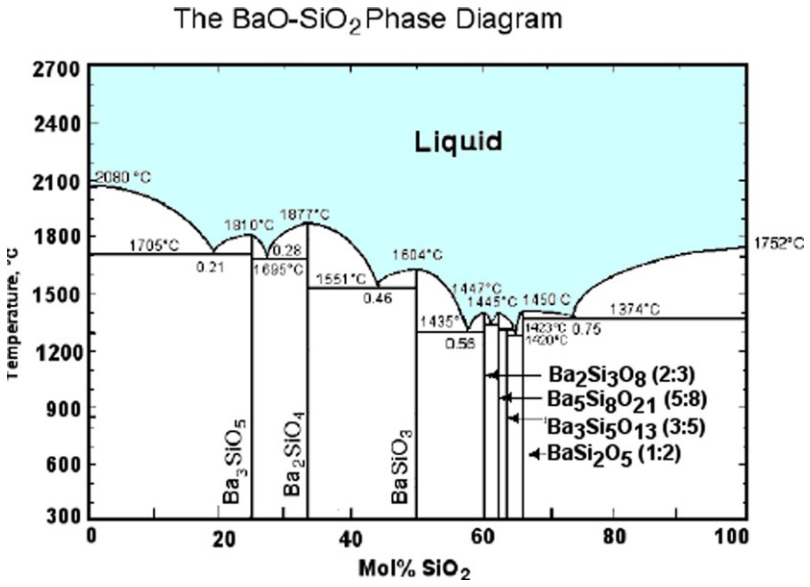

FIGURE 5.50

The enthalpy of solution of Ba_2SiO_4 in 3.15 mol/dm^3 HF + 8.13 mol/dm^3 HCl has been measured. From the results, the standard molar enthalpy of formation of Ba_2SiO_4(s) was been calculated. The value obtained was -2292.2 ± 4.2 kJ/mol.

The system Ba_2SiO_4–Ca_2SiO_4 was studied by heating mixtures of Ba_2SiO_4 and Ca_2SiO_4 at 1723 K. Six distinct phases resulted; they were examined by both XRD and DTA. The phases α-$(Ba_{0.05}Ca_{1.95})SiO_4$ and β-$(Ba_{0.15}Ca_{1.85})SiO_4$ are isostructural with corresponding high-temperature modifications of Ca_2SiO_4. The X phase ($Ba_{0.48}Ca_{1.52}SiO_4$) is orthorhombic and is a pure phase rather than a solid solution. The phase ($Ba_{1.31}Ca_{0.69}SiO_4$) is hexagonal and interpreted in terms of a unit cell with a doubled c parameter, in contrast with literature data.

This salt also forms a double salt with BaO, as $Ba_2SiO_4 \cdot BaO$. It is tetragonal with space group I4/mcm and $a = 7.3023$ Å, $c = 11.2178$ Å, $Z = 4$. Ba_3O-SiO_4 is isostructural with $Cs_3ClCoCl_4$. The SiO_4 tetrahedra are slightly distorted with O–Si–O angles of 110.6° and 107.6°, respectively and a distance of 1.639 Å for the Si–O bonds. The two crystallographically different Ba atoms are coordinated by ten Ba(I) and eight O-atoms at Ba(II) with mean Ba–O distances of 2.988 Å and 2.81 Å, respectively. The structure looks like in Fig. 5.51.

Numerous studies of Eu^{2+}-activated Ba_2SiO_4 have been performed. In one study, Eu^{2+}-activated Ba_2SiO_4 phosphors were synthesized at 1300 °C by SSRs under a weak reductive atmosphere and systematically investigated by photoluminescence excitation and emission spectra, diffuse reflectance spectra, concentration quenching process and lifetime. The intensive green LEDs were fabricated by combining the synthesized phosphors with near-ultraviolet InGaN chips ($\lambda_{em} = 395$ nm). The Commission Internationale de I'Eclairage color coordinate of the fabricated LEDs was calculated to be $x = 0.1904$, $y = 0.4751$ under 20 mA forward-bias current. The dependence of the green LEDs on forward-bias current shows that as the current increases, the relative intensity simultaneously increases and the color coordinates maintain excellent stability, falling in the standard area of the Institute of Transportation Engineers for traffic lights and the Society of Automotive Engineers for automotive displays. These results indicate that the fabricated phosphor-converted green LEDs show great potential for traffic lights and automotive display applications.

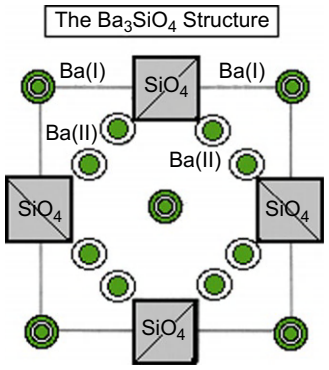

FIGURE 5.51

$BaSiO_3$ is orthorhombic with unit-cell dimensions of $a = 5.6182(5)$ Å, $b = 12.445(1)$, $c = 4.5816$ Å. It is dimorphic with α-$BaSiO_3$ stable below about 990 °C but forms β-$BaSiO_3$ above 1000 °C. A 1:1 mol ratio of BaO–SiO_2 fired at 850 °C and 1050 °C serves to form the two dimorphs.

The enthalpy of solution of $BaSiO_3$ in (3.15 mol/dm^3 HF + 8.13 mol/dm^3 HCl) has been measured. From the results, the standard molar enthalpy of formation of $BaSiO_3$ (s) was calculated. The value obtained was -1606.4 ± 2.6 kJ/mol.

$Ba_5Si_8O_{21}$ is not listed as to structure in the NBS Standard XRD powder patterns monograph.

β-$Ba_2Si_3O_8$ is monoclinic with space group P2i/a (14), $Z = 4$ and lattice constants of $a = 13.960$ Å, $b = 4.6895$ Å, $c = 12.486$ Å, $\beta = 93.54°$. A reversible transformation of β-$Ba_2Si_3O_8$ occurs when heated above 1009 °C to form α-$Ba_2Si_3O_8$.

$Ba_3Si_5O_{13}$ is monoclinic, P2j/c (14), $Z = 4$, with lattice parameters of: $a = 20.208$ Å, $b = 4.7106$ Å, $c = 13.854$ Å, $\beta = 98.62°$.

Sanbornite, **β-$BaSi_2O_5$**, previously described in the literature as triclinic, is orthorhombic with space group Pmmm. The unit cell is: $a_o = 4.6336$ Å, $b_o = 7.6922$ Å, $c = 13.525$ Å, $Z = 4$. There is a high-temperature phase, α-$BaSi_2O_5$, that is stable above 1350 °C. The unit-cell contains four $BaSi_2O_5$ molecules. The structure is a silicate sheet structure with two Si + oro-a sheets per unit cell lying parallel to (001) at 7/4 and 3/4, and two barium ions lying roughly half-way between each successive pair of sheets. Each sheet consists of continuously linked, distorted, six-membered rings of SiO_4 tetrahedra. Unshared vertices of tetrahedra lie on both sides of each sheet. Each barium ion is surrounded by seven near-oxygen ions. Interionic distances are of expected magnitude. The structure is shown in the following Fig. 5.52.

The mineral sanbornite, $BaSi_2O_5$, was first described by Rogers (1932). Only one occurrence in the U.S. is known, near Incline, Mariposa County, California, where it is found with the rare mineral gillespite ($BaFeSi_4O_{10}$) and other minerals. It is known from only one other locality. Sanbornite occurs as white to colorless, translucent to transparent, anhedral plates. The sanbornite deposits at Big Creek and Rush Creek, Fresno County, California are host to many rare barium silicates, including "bigcreekite", UK6, "walstromite" and "verplanckite". Bigcreekite, ideally $BaSi_2O_5 \cdot 4H_2O$, is

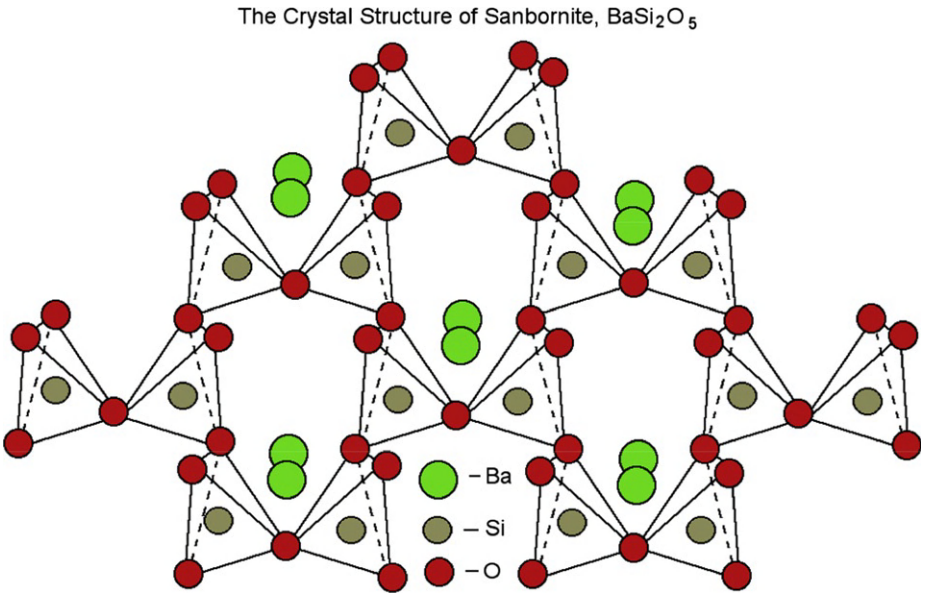

FIGURE 5.52

a newly identified mineral species that occurs along very thin transverse fractures in fairly well-laminated quartz-rich sanbornite portions of the rock.

Bigcreekite is biaxial negative, with indices of refraction $\eta_1 = 1.537(2)$, $\eta_2 = 1.538(2)$, $\eta_3 = 1.541(2)$; $X = b$, $Y = a$, $Z = c$ and $2V_{[submeas]} = 59.2°$, $2V_{[sub\ calc]} = 60.1°$. The crystal structure of bigcreekite was solved as space group Pnma, with cell parameters $a = 5.038$ Å, $b = 9.024$ Å, $c = 18.321$ Å, and $Z = 4$. Bigcreekite is a hydrous chain silicate containing four-membered rings which form chains of silica tetrahedra, parallel to [100] and staggered in the [001] direction. Water molecules fill the large spaces between the rows of silicon tetrahedra. The structure of "bigcreekite" has been solved and is shown in the following diagram shown as Figure 5.53. BigCreekite is a hydrous sheet silicate containing four-membered rings that form chains of silica tetrahedra, $Si_2O_5^{2-}$, parallel to the *a*-axis and staggered along the *c*-axis, with a repeat distance of two tetrahedra. The tetrahedra are connected to the Ba-polyhedra, BaO_9, which form sheets along the (001) direction, resulting in perfect cleavage of the mineral in that direction. The BaO_9 polyhedra are joined together by four-oxygen atoms at the corners. Parts of the O-atoms are those associated with water molecules (Fig. 5.53).

Bigcreekite has similarities to sanbornite and gillespite. Bigcreekite was named for Big Creek, California, its typical locality. Krauskopfite, $BaSi_2O_4(OH)_2 \cdot 2H_2O$, one of the rarer species at the deposits, is restricted to a single site above Rush Creek, where it occurs with macdonaldite in white veinlets up to 5-mm thick (Site 3). Krauskopfite is opaque to translucent white, and occurs as cleavage masses and occasional elongated tabular cleavages on fracture surfaces. Sanbornite is the most abundant of the barium silicates at Big Creek and Rush Creek. Bodies of this mineral host many of the other species. Walstromite, $BaCa_2Si_3O_9$, is the coarsest-grained mineral in the deposits, and is second only to sanbornite in abundance. It occurs widely as clots and layers of interlocking masses and also as isolated anhedral crystals in sanbornite-quartz rock, more frequently within the

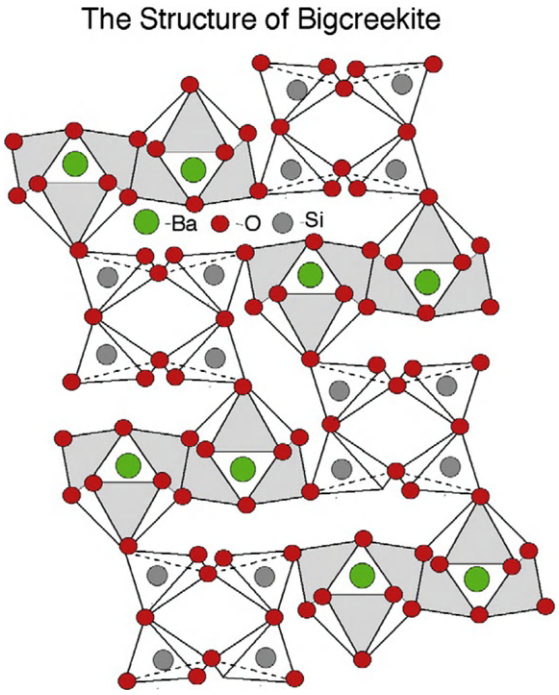

FIGURE 5.53

quartz-rich zones. Walstromite is white to gray with three perfect cleavages, but otherwise is similar in appearance to sanbornite. Twenty-three barium species have been identified from the sanbornite deposits at Big Creek and Rush Creek. Ten are type-locality minerals; the others occur elsewhere and are common to extremely rare. In addition, seven potentially new species are currently known and several are under study.

Barium and strontium silicates have nearly identical physical and chemical characteristics. Thus, studies have been conducted concerning the ternary system: $BaO–SrO–SiO_2$. Phase equilibria in the system $BaO–SrO–SiO_2$ in air were established using conventional solid-state techniques. The phase relations in the boundary system $SrO–SiO_2$ were completed by determining the liquidus temperatures for the SrO-rich portion of the diagram. The known compounds, $SrSiO_3$, Sr_2SiO_4, and Sr_3SiO_3, melted congruently at 1580 ± 15, 2325 ± 15, and 2170 ± 15 °C, respectively. Simple binary eutectics exist between (1) Sr_2SiO_4 and Sr_3SiO_5 at 2150 ± 15 °C and ~27 mol% SiO_2 and (2) Sr_3SiO_5, and SrO at 2080 ± 15 °C and ~23 mol% SiO_2. All alkemade lines were established for the ternary system; two of these joins were examined in detail because of extensive solid-solution regions. On the $Ba_2SiO_4–Sr_2SiO_4$ join, a maximum solubility of ~70 mol% Sr_2SiO_4 in Ba_2SiO_4 appears to exist at 2100 ± 15 °C, the eutectic reaction temperature. A two-phase region apparently connects the eutectic reaction isotherm with a high-temperature polymorphic transition ($\alpha \Rightarrow \beta$) of Sr_2SiO_4. Below this transition temperature, a complete solid-solution series exists between Ba_2SiO_4 and β-Sr_2SiO_4. The $BaSiO_3–SrSiO_3$, join contains limited solid-solution regions at the extremities which arise from the solid solubility of 40 mol% $SrSiO_3$ in the high-temperature (α) polymorph of $BaSiOs_3$ and 20 mol% $BaSiO_3$ in $SrSiO_3$ at 1210 ± 15 °C. The only ternary compound isolated, $BaSrSi_3O_8$, has a lower limit of stability at 1220 ± 3 °C and melts incongruently at 1275 ± 3 °C.

Barium silicates are readily available for sale commercially.

Radium Silicates

Radium silicate can be prepared by calcining the oxide with silica, SiO_2, at an elevated temperature:

$$RaO + SiO_2 + \text{heat} \Rightarrow RaSiO_3$$

The so-called "metasilicate" results. There have been no reports on the preparation of radium silicate. A variety of alkaline earth silicates has been prepared but there is insufficient evidence that any of the possible radium silicates have ever been synthesized. The most likely compound would be the $RaSiO_3$ composition but this synthesis and the physical and chemical properties remain unknown. Perhaps this is due to the lack of interest industrially since the oxide, carbonate and chloride salts are adequate for the purposes to which ^{226}Ra is employed.

5.3. ALKALINE EARTH OXY-GERMANIUM COMPOUNDS

In general, germanium is too electropositive in nature to form anions, i.e. "germanates", in solution. It is possible to fire the oxides together to form a germanate-like $CaGeO_3$ but the possibility of formation of alkaline earth germanates by a solution method is essentially zero. Germanium has but one valence state, that of Ge^{4+} so that GeO_3^{2-} and GeO_4^{4-} anions are possible. However, germanium does not form extensive anions in solution as silicon does.

5.3.1. Alkaline Earth Oxo-Germanium Compounds

Beryllium Germanates

Beryllium germanate can be formed by firing the oxides together at about 650–700 °C:

$$BeO + GeO_2 + \text{heat} \Rightarrow BeGeO_3$$

This is the metagermanate. Three beryllium germanate compounds appear in the phase diagram. They are: $BeGeO_3 = 1{:}1$, $Be_2GeO_4 = 2{:}1$, and $BeGe_2O_5 = 1{:}2$. They all mimic the corresponding silicate in structure. The metagermanate has the perovskite structure shown in Fig. 5.54.

The lattice parameters for the phyllo-compound, $BeGe_2O_5$ (as a type-3 $SrSi_2O_5$ structure), were found to be: $a = 5.2376$ Å, $b = 9.2751$ Å and $c = 13.4352$ Å, orthorhombic, space group: Cmca.

The complex oxide Be_2GeO_4 is a wide band gap insulator crystallizing in the phenacite structure ($BeSiO_4$).

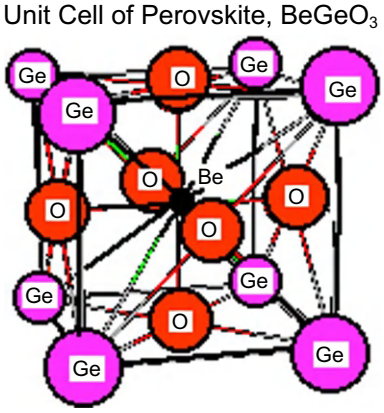

FIGURE 5.54

These compounds are crystallochemical analogs and belong to the nesosilicate class (germanates). The crystal lattice of these materials consists of [SiO_4/GeO_4] or [BeO_4] tetrahedra, which are bound to each other and form chains oriented along the principal crystallographic axis C_3. The chains form voids in the form of wide channels ~4.5 Å in diameter. A specific feature of phenacite-structure crystals is that the [SiO_4] tetrahedra (or [GeO_4] in the case of Be_2GeO_4) are separated, i.e. they do not touch each other. All oxygen atoms on the phenacite lattice are three-coordinated, and each of them is shared by three tetrahedra, namely, two [BeO_4] and one [Si(Ge)O_4]. Be_2GeO_4 is a trigonal phenakite structural analog. It relates to a class of island silicates which feature separated tetrahedrons, GeO_4 and BeO_4. Polycrystalline Be2GeO_4 can be prepared by reacting 2 mol of BeO and 1 mol of GeO_2 by a high-temperature SSR like that given above for the metagermanate. Be_2GeO_4 is hexagonal with $a = 12.79$ Å, $c = 8.42$ Å.

The luminescence emission of $(Zn,Be)_2GeO_4$:Mn phosphors at room temperature and near liquid nitrogen temperature is qualitatively similar to that of the $(Zn,Be)_2SiO_4$:Mn phosphors (which were used extensively for fluorescent lamps in the 1940s). In both the silicate and germanate, a green emission band is observed with low manganese content and beryllium concentrations. Increase in the concentration of either of these two constituents causes the growth of a new band in the red region of the spectrum. Certain differences in properties are noted, however, between the germanate and the silicate. The most important of these is the absence of any clear-cut "red" band in the low-temperature emission of Zn_2GeO_4 containing large manganese concentrations. Corresponding Zn_2SiO_4 phosphors clearly show the red band. The results of the emission measurements have been discussed in the light of two hypotheses that have been proposed to explain the dependence of the luminescence of manganese on the nature and composition of the host crystal.

Be_2GeO_4 polycrystalline samples preliminarily irradiated by fast neutrons ($E \sim 1.0$ MeV, $\phi = 4.5 \times 10^{17}/cm^2$) were studied by photoluminescence spectroscopy using synchrotron radiation pulses for excitation. The neutron-induced luminescence band observed at 1.7 eV (1033 nm) in the spectra of the irradiated samples is assigned to the radiative relaxation of a molecular ion O^{2-}. The luminescence of these point defects in the Be_2GeO_4 structure is effectively excited by 4.7 eV (263 nm) and 5.2 eV (238 nm) photons. It is most likely that, in the Be_2GeO_4 structure, the center is located in hollow channels oriented parallel to the C_3 axis. Thus, the vibrational structure of the point-defect O^{2-} center PL spectra in Be_2GeO_4 reflects the presence of predominantly intramolecular interactions. In other words, the O^{2-} defect center can be considered, in a certain sense, an almost free ion whose intrinsic vibrations are disturbed by the interaction with the Be_2GeO_4 lattice.

The possibilities of exoelectron spectroscopy to investigate defects in dielectrics have been demonstrated for the phenakite, Be_2SiO_4, and its structural analog Be_2GeO_4, and the solid solution, $Be_2Si_{1-x}Ge_xO_4$ ($0 < x < 1$). The optical sensitivity of BeO-based luminophores is well known for many years. Thermoluminescent emission maxima at 330 (57 °C) and 670 K (397 °C) in phenakite solid solution have been found to be due to $[GeO_4]^{5-}$ and E′ centers, respectively.

Beryllium germinates are not generally available commercially since the demand is not great. They do not have assigned CAS numbers but are considered hazardous due to the Be content in these salts.

Magnesium Germanates

Magnesium germanate can be formed by firing the oxides together at about 900 °C.

$$MgO + GeO_2 \Rightarrow MgGeO_3$$

This salt has the perovskite structure. The lattice parameters are: $a = 4.9375$ Å, $c = 13.743$ Å, $V = 290.15$ Å^3. It occurs as the mineral, "majorite", with lattice parameters of: $a = 11.051$ Å, $b = 11.051$ Å, $c = 11.480$ Å, $\alpha = \beta = \gamma = 90°$, space group = $I4_1/A$. There are four (4) magnesium germanates known as shown in the following phase diagram of the system, MgO–GeO_2 where each compound can be obtained by varying the MgO/GeO_2 mol ratios before firing (Fig. 5.55).

$MgGeO_3$ is polymorphic. It forms several types of pyroxenes. Pyroxene is one of the important constituent minerals of the earth's crust and upper mantle. Three kinds of $MgGeO_3$ pyroxene single crystals of l–10 mm size were grown by the flux method: an orthopyroxene, a clinopyroxene and a "clino-form-proto" phase. The lattice parameters and the space groups for the three are:

(1) Orthopyroxene: $a = 18.8099$ Å, $b = 8.9484$ Å, $c = 5.3451$ Å, $V = 899.69$ Å^3, orthorhombic, Pbca, $Z = 16$.

(2) Clinopyroxene: $a = 9.6010$ Å, $b = 8.9323$ Å, $c = 5.1592$ Å, $\beta = 101.034°$, $V = 434.27$ Å^3, $Z = 8$, monoclinic, C2/c.

The phase relationships of $MgGeO_3$ were studied in the temperature range 655–1030 °C and in the pressure range 0–55 kbar. The boundary between orthopyroxene and clinopyroxene was determined as 1810 °C + 3.8 P (in kbar), where both the high-pressure and low-temperature phase is monoclinic. Single crystals of ilmenite-type $MgGeO_3$ were also grown in association with the pyroxene–ilmenite transformation at 55 kbar, using the flux-grown millimeter-size orthopyroxene or

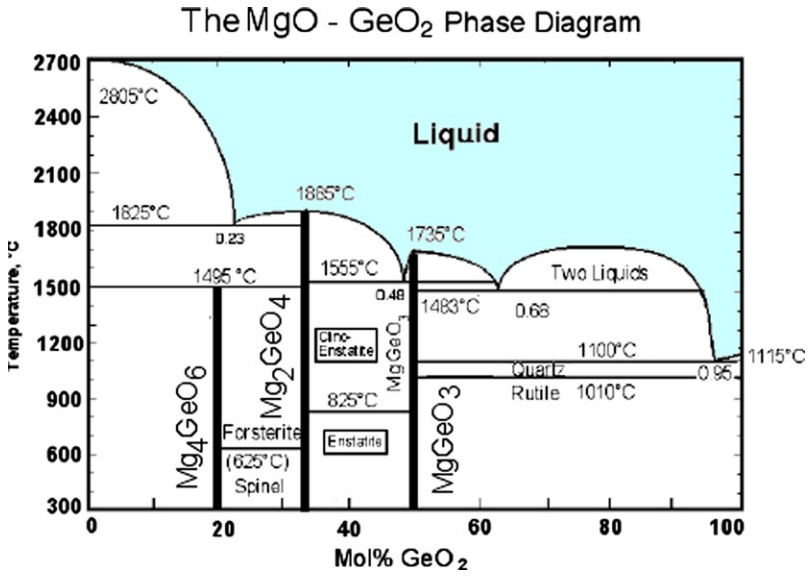

FIGURE 5.55

clinopyroxene $MgGeO_3$ single crystals as starting materials.

The orthogermanate, Mg_2GeO_4, has the molecular weight of 185.2476 g/mol and the CAS number of 12025-13-7. Study of the olivine-like compound, magnesium germanate, Mg_2GeO_4, showed that it has polymorphs that have both olivine and spinel structures. The free energies of transformation from the olivine to the spinel structure at 1200 °C are estimated to be +1.6 kcal/mol for Mg_2GeO_4. In the spinel structure, $a = 8.2496$ Å and the oxygen atoms are arranged in cubic closest packing (in which the position of every third layer repeats that of the initial layer) instead of hexagonal closest packing (in which the position of every second layer repeats that of the initial layer of the olivine structure).

Synthetic polycrystals of α-Mg_2GeO_4 (with the olivine structure) and γ-Mg_2GeO_4 (with the spinel structure) that deformed at high temperature and pressure in their respective stability fields were investigated by analytical transmission electron microscopy. Specimens with a mean grain size of 20–30 μm deform by dislocation glide and/or climb. The predominance of glide versus climb depends on stress and grain orientation. The defect microstructures of both polymorphs are very similar to those observed in their respective silicate analogues, α- and γ-$(Mg,Fe)_2SiO_4$, and, in the case of the spinel phase, very similar to those observed in magnesium aluminate spinels. These observations suggest that Mg_2GeO_4 is a good rheological analogue for the earth's upper mantle. A spinel specimen deformed under the same conditions of temperature and strain rate as an olivine specimen was approximately three times stronger than olivine. In specimens of both phases deformed at or above 1400 K, a thin amorphous film composed of Mg, Ge, and O was detected along some grain boundaries. Grains ≤ 10-μm diameter surrounded by a film of amorphous phase (>10-nm thick) exhibited low dislocation densities, and deformation appeared to have occurred by grain boundary sliding.

Magnesium germanate, when activated by manganese has long been used in fluorescent lamps. The emission spectrum of Mg_4GeO_6:0.01Mn^{2+} has been found to depend on the temperature of preparation. The spectrum of the sample prepared at 1275 °C shows four narrow bands at 6200 Å to 6600 Å; the spectrum of the sample prepared at 1475 °C consists of a broadband centered at 6150 Å. XRD patterns of the powders indicate the presence of an intermediate phase in the sample prepared at 127 °C. It was concluded that the valence of the manganese activator is different in the two samples. The emission of Mn^{4+} shows four brilliant narrow peaks in the red region of the spectrum (6200–6600 Å) whereas the Mn^{2+} ion emits in a broadband centered at about 6150 Å. Single crystals of magnesium germanate were obtained from a lead oxide flux crystallization of a ceramic preparation from an initial charge of $4MgO \cdot GeO_2$. The crystals are orthorhombic with $a = 14.512$ Å, $b = 10.219$ Å, and $c = 5.944$ Å and the unit-cell contents, $Mg_{28}Ge_{10}O_{48}$, conform to the symmetry requirements of the space group *Pbam*. The crystal structure was accurately determined by XRD analysis with a final residual $R = 0.044$. The structure, which is based upon a closest packed oxygen anion array, (*ABACBC*)*n*, involves a unique stacking of an olivine-type layer with a substituted MgO-type layer.

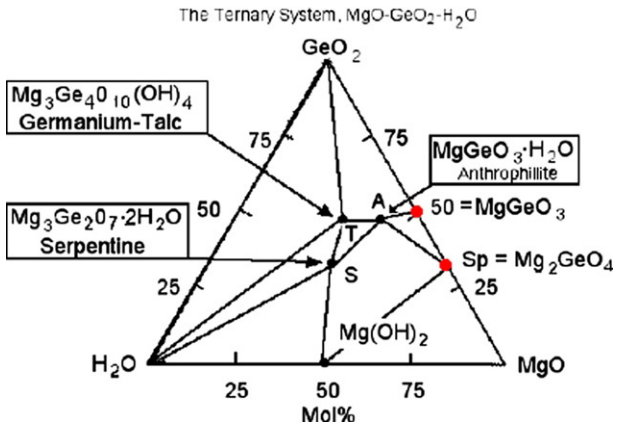

FIGURE 5.56

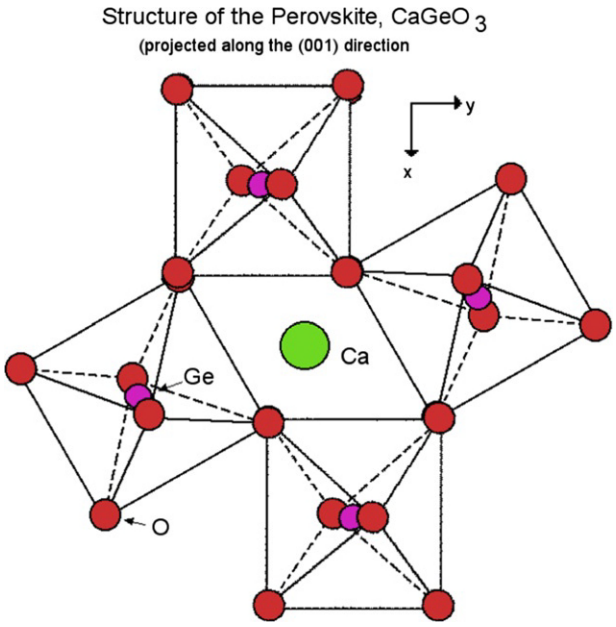

FIGURE 5.57

The germanium serpentine, $3MgO \cdot 2GeO_2 \cdot 2H_2O$ is formed easily from intimate mixtures of very fine MgO and the quartz form of GeO_2 under conditions similar to those under which the silicon analogue grows. The decomposition temperature was found to be 520 ± 15 °C at 10,000 psi. This phase gives a well-defined powder X-ray pattern not showing the diffuseness of the chrysotile pattern, and has a basal spacing of 7.47 Å and a mean refractive index for the basal section of 1.600. Above the decomposition temperature, the phases which appeared were $Mg_3Ge_4O_{10}(OH)_4$ (germanium talc) and Mg_2GeO_4. The ternary system phase diagram of $MgO–GeO_2–H_2O$ is shown as shown in Fig. 5.56.

This diagram summarizes all that is known concerning the hydrates of magnesium germanates. These salts are rare in nature and are only used to obtain the oxide, GeO_2, which is used in various electronic components manufactured in industry. Since Ge is a rare element, its costs prohibit extensive usage in industry and it is only used when its electrical properties are superior to any other combination of components.

Magnesium germanates are available commercially worldwide.

Calcium Germanates

Calcium germanate can be formed by firing the oxides together at about 750–800 °C:

$$CaO + GeO_2 \Rightarrow CaGeO_3$$

The result is a perovskite. This salt is polymorphic and exhibits three polymorphs. Phase boundaries for the reactions **$CaGeO_3$** (wollastonite ⇒ garnet) and $CaGeO_3$ (garnet ⇒ perovskite) were determined at high pressure and temperature. The enthalpies of these transitions were measured by high-temperature calorimetry. These studies indicate a positive dP/dT for the wollastonite ⇒ garnet transition and a negative dP/dT for the garnet ⇒ perovskite transition. These PT slopes are further supported by calculations of lattice vibrational entropies based on Kieffer's model and the infrared and Raman spectra of the three polymorphs. A single-crystal X-ray study indicates that the perovskite form of $CaGeO_3$ is orthorhombic (Pbnm) and isotypic with $GdFeO_3$. The cell dimensions are: $a = 5.2608$ Å, $b = 6.2688$ Å, $c = 7.4452$ Å, $V = 366.43$ Å^3, $Z = 4$, $d_{calc} = 5.17$ g/cc. The crystal structure is close to that of $SmAlO_3$. Although the unit cell of $CaGeO_3$ is pseudocubic, the structure itself is very distorted through the tilting and distortion of polyhedra. The oxygen polyhedra are less tilted and less distorted than those of other $GdFeO_3$-type perovskites. The structural deformation of the $GdFeO_3$ type of perovskite is determined primarily by the size ratio of two kinds of cation occupying A and B sites. Some structural characteristics such as O(2)-O(2F(2)) and A-O(1)-B angles and bond-length distortions exhibit systematic relationships as a function of the observed tolerance factor. The structure is shown in Fig. 5.57.

The GeO_6 octahedra are clearly seen and the CaO_{12} dodecahedra are indicated if one stacks this two-dimensional representation in the z-direction.

Single crystals of $CaGeO_3$ garnet were synthesized and the crystal structure was refined from single-crystal XRD data. This garnet is tetragonal with lattice parameters of $a = 12.535(2)$ Å, $c = 12.370(2)$ Å, $V = 1943.5(5)$ Å^3 and belongs to space group $I4_1/a$. The two dodecahedral sites are occupied only by Ca with mean Ca–O bond lengths of 2.480(4) and 2.467(4) Å. The Ca and Ge cations are completely ordered at two octahedral sites with mean Ca–O = 2.301(3) Å and mean Ge–O = 1.910(3) Å.

Three tetrahedral sites are occupied only by Ge, and their mean Ge–O bond lengths are 1.753(3), 1.787(4), and 1.764(4) Å. Furthermore, the present tetragonal garnet has an unusual feature in that the mean value [2.704 Å] of the shared edge lengths of GeO_6 octahedron is larger than that [2.699 Å] of the unshared ones, as has also been observed for other tetragonal garnets with $I4_1/a$. The equilibrium phase boundary between the garnet and perovskite phases was determined as P(GPa) = 6.9–0.0008T(°C). The negative P and T slope definitely established in the present study is in reasonable agreement with the value, −0.0023 GPa/°C, that was calculated from the thermochemical data on the enthalpy of transition. The molar volume change accompanied with this transformation was estimated to be about 13%.

The polymorphic transformation of pure $2CaO{\cdot}GeO_2$ (**Ca_2GeO_4**) and $3CaO{\cdot}GeO_2$ (**Ca_3GeO_5**) which are the nearest crystal chemical analogous with the main cement minerals $2CaO{\cdot}SiO_2$ and $3CaO{\cdot}SiO_2$ has been studied extensively by XRD. X-ray patterns of the polymorphic forms of Ca_3GeO_5 (2-layer and 24-layer) were obtained at ambient temperature, 820 °C and 1410 °C. The fragments of X-ray pattern of unstable modification were obtained at 1060 °C.

The binary system Ca_2SiO_4–Ca_2GeO_4 has been studied by means of XRD and DTA. For dicalcium silicate, Ca_2SiO_4, five modifications are known (α, α'_H, α'_L, γ and β); for dicalcium germanate, Ca_2GeO_4, only two (α and γ) were found at room temperature. Limited solubility has been found for α and for the metastable γ form, both of which occur only in the Si-rich part of the system. From single-crystal investigations, a new hexagonal structure with space group $P6_3mc$ was derived for the α form. These two modifications have a phase transition temperature of 1453 °C. The low-temperature phase (γ) is isostructural with forsterite and has the olivine structure with space group Pbnmn. The lattice parameters are: $a = 5.240$ Å, $b = 11.400$ Å, $c = 6790$ Å, $V = 670.32$ Å^3, $Z = 2$, $d = 3.53$ g/cc. Transition into phase-I forms the high-temperature phase (α) at 1470 °C which has a hexagonal structure ($P2_12_12_1$). Lattice parameters at 20 °C are: $a = 5.52$ Å, $c = 7.162$ Å, $V = 687.2$ Å^3, $Z = 2$. The melting point is 1901 °C.

Application of pressure and variation of temperature causes the formation of three more isotypes, labeled in the following diagram as II, III and IV. At $P = 11.3$ GPa and $T = 940$ °C, the triple point for the three isomers was found. Ca_2GeO_4 III is tetragonal with $a = 3.700$ Å, $c = 11.882$ Å. Ca_2GeO_4 IV is tetragonal as well (Fig. 5.58).

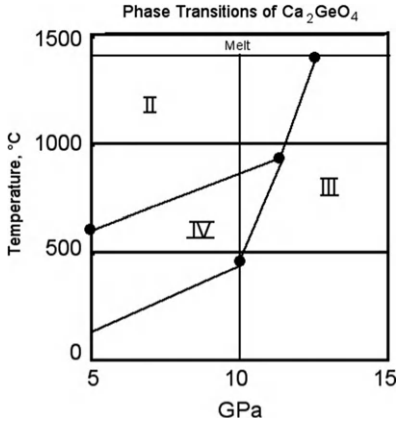

FIGURE 5.58

Ca_2GeO_4 has been tested as a host for lasers, using Nd^{3+} as the activator. Large crystals of highly doped Ca_2GeO_4:Cr^{4+} were grown by a top-seeded melt-solution growth method. Absorption and emission measurements for various crystal orientations have been performed. From the spectroscopic measurements, the only optically active center was identified as tetrahedrally coordinated Cr^{4+}. Gain switched, tunable laser operation of Ca_2GeO_4:Cr^{4+} crystal was demonstrated. Pulse energies of 0.4 mJ at 1.4 μm have been generated at a repetition rate of 100 Hz. Tunability over the 1348- to 1482-nm spectral range has been demonstrated.

A novel red phosphor Ca_2GeO_4:Eu^{3+} was prepared by the traditional SSR. X-ray powder diffraction (XRD) analysis suggested that there was no impurity phase. The study on the diffusion reflection spectra of the undoped and Eu^{3+}-doped Ca_2GeO_4 phosphors revealed an absorption band superposed of that of the host material and the Eu^{3+} ions. The excitation spectrum presented a dominating broadband at 250–300 nm which was attributed to both the host material absorption and the charge transfer band of the Eu^{3+} ions. The investigation on the excitation and diffusion spectra showed that there was an effective energy transfer from the host material to the Eu^{3+} ions. This was favorable to the red emission of the phosphor. Photoluminescence measurements indicated that the phosphor presents bright red emission at 611 nm under UV excitation. In addition, the Al^{3+} or Li^+ codoping enhanced the red emission from Ca_2GeO_4:Eu^{3+} by about 3 and 2 times, respectively under UV excitation.

Ce^{3+}-activated Ca_2GeO_4 phosphors were synthesized by a SSR method, and their photoluminescence properties were characterized. The excitation band of Ca_2GeO_4:Ce^{3+}:Li^+ ranges from 380 to 520 nm with a maximum intensity appearing at about 465 nm, which matches well with the emission of blue light-emitting diode chips. Through transitions from 5d to 4f ($^2F_{5/2}$ and $^2F_{7/2}$) in Ce^{3+}, Ca_2GeO_4:Ce^{3+}:Li^+ exhibits a broad yellow emission band in the wavelength range of 480–750 nm under 465-nm excitation. Compared to $Y_3Al_5O_{12}$:Ce^{3+} garnet, Ca_2GeO_4:Ce^{3+}:Li^+ shows a broader bandwidth (140 nm) and more saturation in

red, which is favorable for white light-emitting diode conversion phosphors.

By using a diamond anvil pressure cell coupled with laser heating, Ca_2GeO_4 has been found to decompose into the mixture $Ca_3Ge_2O_7$ plus CaO at pressures greater than 200 kbar and at about 1000 °C. The decomposition product, **$Ca_3Ge_2O_7$**, is a new compound which is isostructural with $Sr_3Ti_2O_7$ and has the lattice parameters of: hexagonal $a = 3.72 \pm 0.01$ and $c = 19.32 \pm 0.05$ Å at room temperature and 1 bar pressure.

$$2Ca_2GeO_4 + \text{heat (pressure)} \Rightarrow Ca_3Ge_2O_7 + CaO$$

Ca_3GeO_5 has the crystal structure of a 24-layer polytype with a molecular weight of 272.8 g/mol. It is rhombohedral, R3m, with $a = 7.228$ Å, $c = 76.72$ Å, $V = 3050$ Å^3, $Z = 24$. The structure consists of *two kinds of subunits*: one related to the structure of a two-layer polytype and the other to that of the nine-layer polytype. These alternate in the structure to form the 24-layered structure. Half of the eight independent GeO_4 tetrahedra show nearly perfect orientation disorder along the *c*-axis. The coordination numbers of the Ca atoms are in the range of 6.0 to 6.6, giving mean bond lengths of 2.34 to 2.51 Å. Slabs of CaO_6 and GeO_4 form a triangle mesh with single GeO_4 tetrahedra (partial orientation disorder) in $(h_2ch_4c)_3$ stacking. The formula may be represented as $Ca_3(GeO_4)O$. The two-layer polymorph is hexagonal ($P6_3mc$) with: $a = 7.223$ Å, $c = 5681$ Å, $V = 256.7$ Å^3, $Z = 2$, $d = 3.38$ g/cc. The structure may be regarded as a two-layer variant of the rhombohedral structure. It consists of isolated GeO_4 tetrahedra located on the threefold axes and separate anions on the mirror planes. Each tetrahedron takes a statistical orientation: 62% of the tetrahedra point in one *c*-direction while the other 38% point in the other. The separate cation sites, which are not coordinated to Ge sites.

Determination of the crystal structure of two polymorphic modifications of Ca_3GeO_5, one marked monoclinic C_3-G-3M (space group $P6_3mc$) and one rhombohedral denoted C_3-G-9R (space group R3m) was conducted. The relationships of atomic arrangements in both structures are closely the same. The deformations of polyhedra in C_3-G-3M are larger than in C_3-G-9R. The crystal structure of these 24-layer polytypes C3-G are: rhombohedral, $a = 7.228$ Å, $c = 76.42$ Å, $V = 3050$ Å^3, $Z = 24$. The structure consists of two kinds of subunits, one is related to the structure of the two-layer polytype and the other to that of the nine-layer polytype. These occur alternately in the structure. Half of the eight independent germanate tetrahedra are split, the separations being in the range of 0.34 to 0.69 Å. The coordination number of Ca is 8, each calculated as the sum of occupancy of the Ca–O bonds are in the range of 6.0–6.56 Å, giving a mean bond length of 2.34 to 2.51 Å.

If fluoride is substituted for oxygen in these structures (by substituting a small amount of CaF_2 for CaO in the oxide mixture before firing), the composition, $Ca_{3-x}GeO_4)(O_{1-2x}F_{2x})$ results. Instead of a 24-layer structure, a two-layer structure results. This salt is hexagonal with space group = $P6_3mc$, $a = 7.223$ Å, $c = 5.681$ Å, $V = 256.72$ Å^3, $Z = 2$. It is a variant of the rhombohedral structure of tribalism silicate (germanate) that has the nine-layer type of structure. It consists of isolated GeO_4 tetrahedra located on threefold axes and separate anions on the mirror planes. Each GeO_3 tetrahedron takes a statistical orientation—62% points in one *c*-direction while 38% point in the other direction. The separate anion sites that are not connected to the Ge were occupied by O–F complexed atoms 40.5% O–59.5% F). The resultant deficiency of minus charge is compensated by a distribution of vacancies at the Ca sites.

$CaGe_2O_5$, a new polymorph has been discovered via high-pressure experiments (above 8 GPa). The phase is orthorhombic, space group Pbam, with $a = 7.306$ Å, $b = 8.268$ Å, $c = 5.714$ Å, $V = 345.2$ Å^3, and $Z = 4$. This new phase, $CaGe_2O_5$, is the high-pressure polymorph of titanite $CaSi_2O_5$. The structure of this new polymorph is based on a network of 5- and 6-coordinated Ge polyhedra and 8-coordinated Ca atoms. Following the germanate analog to silicate, post-titanite $CaSi_2O_5$ could be expected to form at high-pressure conditions and thus might exist in earth's mantle.

The structure of $CaGe_2O_5$ between room temperature and 923 K has been determined by X-ray powder diffraction. A continuous phase transition from triclinic $C\bar{1}$ to monoclinic C2/c symmetry at $T_c = 714$ K was observed. The transition is accompanied by a weak heat capacity anomaly. This anomaly and the strain analysis based on the measured lattice parameters indicate a classical second-order phase transition. The order parameter, as measured by the strain component ε_{23}, is associated with the displacement of the Ca cation. Electronic structure optimization by density functional methods is used to verify the centric space group of the low-temperature structure of $CaGe_2O_5$.

Another new compound, octacalcium pentagermanium octadecaoxide **$Ca_8Ge_5O_{18}$**, represents a new intermediate phase between CaO and GeO_2, and had not previously been reported in the literature. The structure consists of three different Ge sites, two of them on general 8d positions, site symmetry 1, one on special position 4d, site symmetry 2. Three of the five Ca sites occur on 8d positions, site symmetry 1, one Ca is on 4b with site symmetry and one Ca is on 4c with site symmetry 2. All nine O atoms have symmetry 1 (8d position). By sharing common edges, the Ca sites form infinite bands parallel to the *c* axis. These bands are interconnected by isolated GeO_4 and Ge_3O_{10} units.

The (100) layers are stacked along *a* in an ABAB… sequence, with the B layer being inverted and displaced along b/2.

Although Ca_2GeO_4 is now being used commercially, there do not seem to be any suppliers offering these salts commercially. Primarily, the laser crystals are made from a melt of the oxides. No CAS numbers have been issued.

Strontium Germanates

Strontium germanate can be formed by firing the oxides together at about 850 °C:

$$SrO + GeO_2 + \text{heat} \Rightarrow SrGeO_3$$

The result is the metagermanate, β-$SrGeO_3$. The reaction of an equimolar mixture of SrO and GeO_2 at 1150 °C proceeds in five stages,

(1) $2SrO + GeO_2 \Rightarrow Sr_2GeO_4$
(2) $SrO + 4GeO_2 \Rightarrow SrGe_4O_9$
(3) $SrO + GeO_2 \Rightarrow$ β-$SrGeO_3$
(4) β-$SrGeO_3 \Rightarrow$ α-$SrGeO_3$
(5) $3Sr_2GeO_4 + SrGe_4O_9 \Rightarrow 7$ (α-$SrGeO_3$)

The overall reaction of [1], [2], and [3] forms ortho- and then the tetrameta- and finally the β-strontium metagermanate is formed directly at lower temperatures from amorphous material prepared by the simultaneous hydrolysis of strontium and germanium alkoxides which is the stable form at that temperature. This form has monoclinic rather than hexagonal symmetry. Two forms of $SrGeO_3$ are known at present: this monoclinic form and a triclinic form. β-$SrGeO_3$ transforms to α-$SrGeO_3$ at about 955 °C. The monoclinic structure has alternate stacking of ternary rings of GeO_4 groups and close-packed Sr atoms along [001], and is a six-layer polytype. The low-temperature form has the perovskite structure while the high-temperature form has the wollastonite form.

The $SrGeO_3$ perovskite crystal structure is formed by the Ge cations filling 25% of the octahedral holes in the cubic close-packed SrO_3 array as an octahedron. In the ideal cubic structure, each Sr cation is coordinated to 12 O-anions and each GE cation is coordinated to six O-anions. An example of this cubic structure is shown in Fig. 5.59.

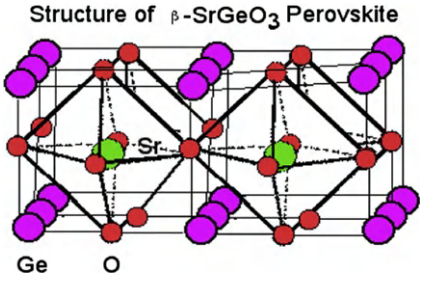

FIGURE 5.59

$SrGeO_3$ perovskite, like $CaSiO_3$ perovskite, forms at high pressure from a framework structure composed of vertex-sharing tetrahedra. It appears that when these frameworks condense with dramatic decreases in volume to form perovskite structures, the phase that is formed has quite a different nature than an ambient-pressure ideal perovskite such as $SrTiO_3$. Among the most important differences is the wide disparity in the covalency of the Ge–O and Ti–O bonds. While the octahedra themselves remain essentially intact and undistorted through the tilting and twisting motions required to form the distorted perovskite structures, the vertex-linking topology of the perovskite provides a flexible linkage whose resistance to bending varies widely with its covalency. In the silicate and germanate perovskites, high-pressure transformations to lower symmetry structures must overcome the significantly enhanced covalency of the vertex-linked octahedral chain, a process that makes observable phase transformations unlikely, particularly in the mantle of the earth.

In addition to the metagermanate, the orthogermanate, **Sr_2GeO_4** and the phyllo-germanate. **$SrGe_2O_5$**, have also been characterized. A stable monoclinic low-temperature (β) form of Sr_2GeO_4 was found which converts reversibly to the high-temperature α′ modification at 85 °C. The enthalpy of the β-α′ transition is 51 cal/mol. The high-temperature phases of Sr_2GeO_4 have been compared to those of the better-known $CaGeO_4$ homologues as shown in the following phase diagram shown on the next page as Fig. 5.60.

Sr_2GeO_4 melts at about 1800 °C but undergoes similar transitions from beta- to alpha-structures at about the same temperatures of the calcium homologues. However, the number of known polytypes is not as numerous as those of Ca_2GeO_4. Crystals of the orthorhombic phase of strontium germanate, Sr_2GeO_4, showing superstructure have been obtained. Crystal data are: $a = 5.8520$ Å, $b = 14.2991$ Å, $c = 9.9165$ Å, space group $Pbn2_1$ and $Z = 8$. The superstructure of this crystal was twice as large as the average structure ($a = 5.85$ Å, $b = 7.15$ Å, $c = 9.92$ Å). The dominant rule of differentiating two-layers superstructure type like this crystal and three-layers type like other crystals of the compounds α-Ca,Sr_2SiO_4 is the size effect of cations at the tetrahedral positions. This rule leads to the results that the two-layers type shows the space group $Pbn2_1$ and the three-layers type shows the space group $P2_1nb$ on account of the geometrical restriction.

Sr_3SiO_5 has the tetragonal structure and space group of P4/nnc with lattice parameters of: $a = 6.934$ Å, $c = 10.721$ Å, $Z = 4$. Systematic absences in hk0 for h + k-odd, in 0kl for l-odd, and in hkl for l-odd were seen. There is, in addition, a pronounced systemic flaw among the hkl reflections with h + k + l-odd, which makes it an approximately body-centered lattice.

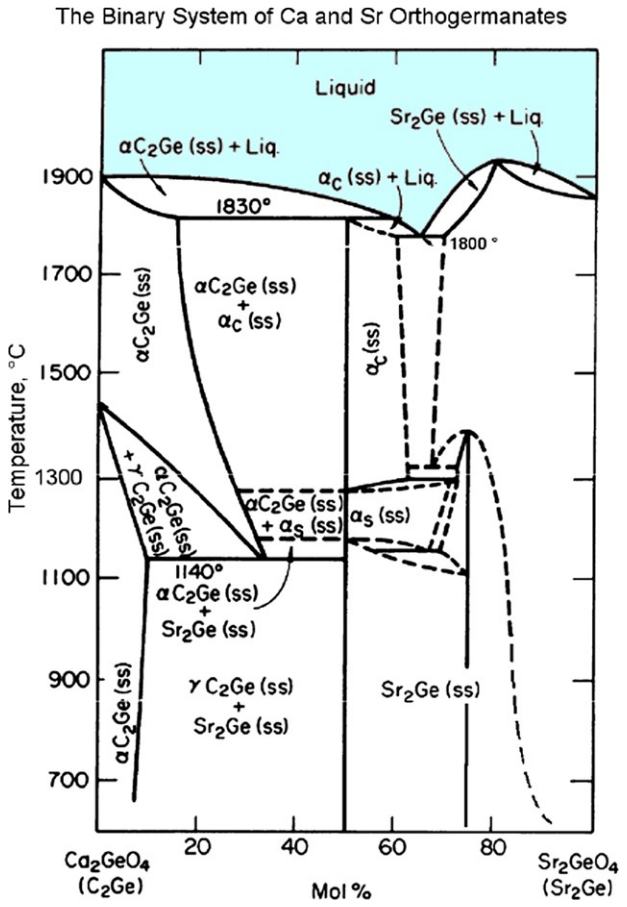

FIGURE 5.60

The devitrification behavior of strontium germanate glasses, examined by DTA, Fourier transform infrared spectroscopy (FTIR) and XRD, has been reported. The glass compositions are expressed by the general formula: $x\text{SrO}(1-x)\text{GeO}_2$ with $x = 0.050$, 0.125, 0.200 and 0.250. The glasses with $x = 0.050$ and 0.125 exhibit two glass transition temperatures due to a phase separation. The phases crystallizing during DTA runs were identified and devitrification mechanisms proposed. In all glasses, $SrGe_4O_9$ crystals grow from bulk nuclei.

Strontium also forms a 1:2 salt. The structure of tetragermanium strontium nonaoxide, $SrGe_4O_9$, comprises two different types of sheet structure stacked alternately along the c axis. One sheet comprises the GeO_6 octahedra and the SrO_8 polyhedra while the other sheet contains three-membered rings of GeO_4 tetrahedra.

Although other compounds like $SrSi_2O_5$, $Sr_3Si_2O_7$, $SrSi_3O_7$, $Sr_2Si_3O_8$, and $SrSi_2O_5$, are possible, the scientific literature and references make no mention of them. The phases possible in the SrO–GeO_2 system are: 1:1, 1;2, 1:3, 2:1, 3:1, 2:3 3:2, and 3:5, but only the 1:1 ($SrGeO_3$), 2:1 (Sr_2SiO_4) and 3:1 (Sr_3SiO_5) phases have been reported.

No CAS numbers have been assigned to strontium germanates, probably because they are primarily prepared from the oxides by the users and are not available as separate compounds commercially.

Barium Germanates

Phase equilibria in the system BaO–GeO_2 were studied using several complementary methods and a number of modifications made to the previously published phase Fig. 5.61.

The system contains four compounds, Ba_3GeO_5, Ba_2GeO_4, $BaGeO_3$ and $BaGe_4O_9$. Evidence was presented to show that the previously reported compounds $Ba_3Ge_2O_7$ and $BaGe_{19}O_{39}$ do not exist. However, other investigators have determined the structural

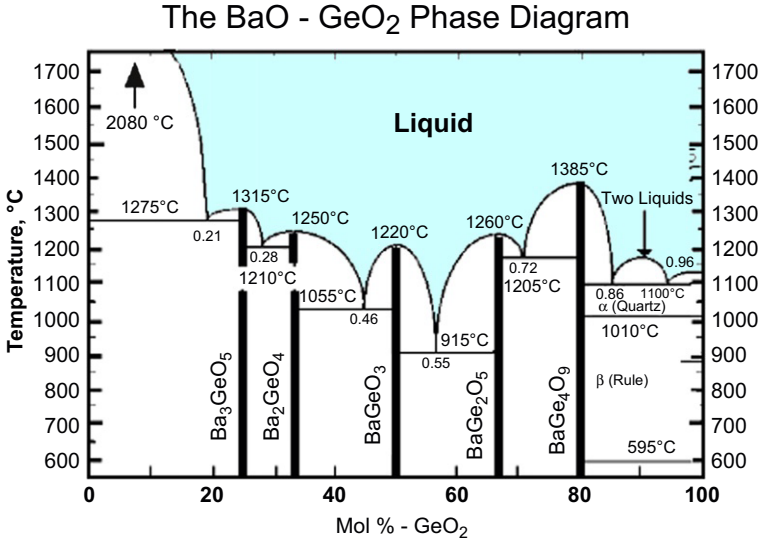

FIGURE 5.61

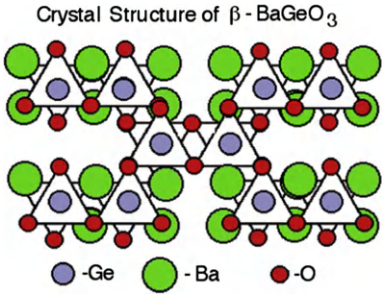

FIGURE 5.62

characteristics of the former but not the latter. Five invariant points were established in the system and defined as simple eutectics at: 1275 °C, 1210 °C, 1055 °C, 915 °C and 1205 °C at 0.21, 0.28, 0.46, 0.56, 0.72 and 0.80 mol of GeO_2.

Barium germanate can be formed by firing the oxides together at about 750–800 °C:

$$BaO + GeO_2 \Rightarrow BaGeO_3$$

The metagermanate results. This salt is dimorphic and forms both β- and α-$BaGeO_3$. β-$BaGeO_3$ is a pseudo-wollastonite which transforms at 1225 °C to α-$BaGeO_3$. The former consists of digermanate groups arranged in a chain structure. The packing is pseudo-cubic (Fig. 5.62).

The structure consists of alternating layers of Ba cations and triangular $[GeO_3]_3$ rings, and is closely related to pseudo-wollastonite. The rings show a twofold positional disorder owing to stacking faults. The stacking is not random, but can be rationalized by a twinning mechanism mapping the two noncongruent enantiomorphic polytypes of the structure onto each other. The compound is monoclinic with space group C2/c and unit-cell parameters of $a = 13.1877$ Å, $b = 7.6222$ Å, $c = 11.7190$ Å, $\beta = 112.295°$, $V = 1089.9$ Å^3 and $Z = 12$. The structure was found to consist of alternating layers of barium atoms and three-membered $[GeO_3]_3$ rings showing a twofold positional disorder. Apart from the disorder, the structure is very similar to the one of $SrGeO_3$; both are six-layer structures build from the same type of layers. The same structure type also appears in pseudo-wollastonite, forming four- or six-layer polytypes. Careful studies of possible structural variations using simulated annealing [did not reveal any deviation from symmetry C2/c]. The disorder of the ternary rings can be summarized as follows: ternary $[GeO_3]_3$ rings appear in only one out of two possible orientations and occupy only 2/3 of the positions compatible with this orientation. For six-layered structures of this type, there is only one distinct polytype with the inherent symmetry C2/c. There are, however, two noncongruent enantiomorphs of this structure. The disorder observed in $BaGeO_3$ can be

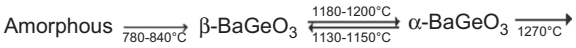

FIGURE 5.63

described as the simultaneous appearance of both possibilities.

In another study, $BaGeO_3$, was found to undergo a reversible phase transformation at 1100° from a low-temperature hexagonal polymorph to a medium-temperature polymorph. This had an unknown crystal structure, which experiences a further reversible transformation at 1200° to a high-temperature orthorhombic polymorph found to be stable up to the melting temperature of 1287°. On cooling from the melt, the high-temperature form can be retained as a metastable material at room temperature, but transforms to the low-temperature form at 900°. The structure of α-$BaGeO_3$ differs from that of β-$BaGeO_3$ in that the cubic form becomes a series of chains of triangular GeO_3 units, stacked in an orthorhombic fashion wherein 2 GeO_3—groups alternate with a single group in the structure.

α-Barium metagermanate ($BaGeO_3$), in its high-temperature form, was formed metastabely at 630–660 °C from an amorphous material prepared by the simultaneous hydrolysis of barium and germanium alkoxides. The transformation of $BaGeO_3$ was studied by thermal analysis and high-temperature XRD. The transformation of $BaGeO_3$ can be summarized as shown in Fig. 5.63.

On cooling from the melt, α- $BaGeO_3$ can be retained at room temperature.

A hydrate of barium metagermanate can also be obtained by the use of soluble compounds:

$$BaCl_2\ (aq) + Na_2GeO_3\ (aq) \Rightarrow BaGeO_3 \cdot 5H_2O\ (s) + 2NaCl$$

This salt, when heated to 100 °C loses three waters of hydration and then forms the β-$BaGeO_3$ composition at 460 °C. The hydrate has the structure of: monoclinic, space group = 2C/2, $a = 15.677$ Å, $b = 8.404$ Å, $c = 11.368$ Å, $\beta = 97.60°$, $V = 465.4$ Å^3, $Z = 4$.

The orthogermanate can be obtained by firing 2.0 mol of BaO with 1.0 mol of GeO_2. Ba_2GeO_4 is orthorhombic with space group: Pnma (62), crystal system: orthogonal unit cell parameters: $a = 7.585$, $b = 5.985$, $c = 10.43$.

Phase relations in the system BaO–GeO_2 were investigated in the pressure range 20–70 kbar in the temperature range 750–1200 °C. Several new phases were identified in this system which were modifications of $BaGe_2O_5$:

(a) An atmospheric phase of $BaGe_2O_5$ (monoclinic $BaGe_2O_5$ I)
(b) Two high-pressure phases of $BaGe_2O_5$ (monoclinic $BaGe_2O_5$ II and tetragonal $BaGe_2O_5$ III)
(c) A high-pressure phase of $Ba_2Ge_5O_{12}$.

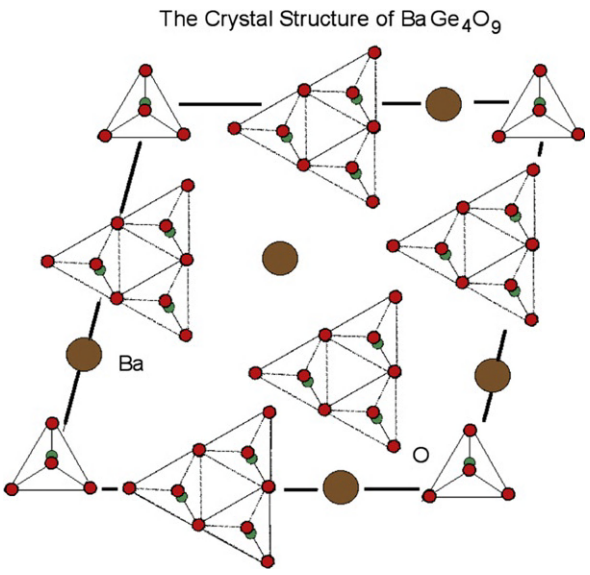

FIGURE 5.64

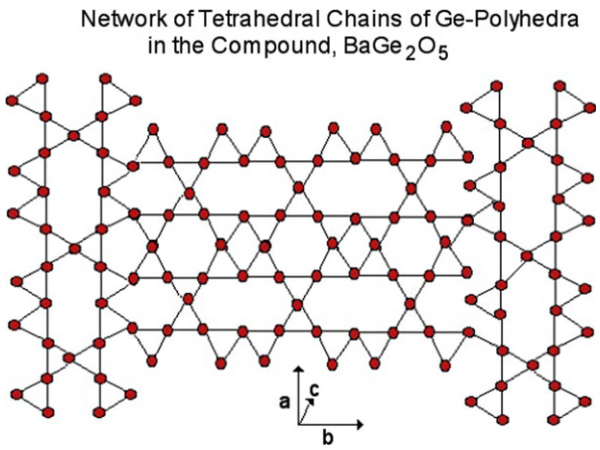

FIGURE 5.65

The phase boundary curve between $BaGe_2O_5$-II and $BaGe_2O_5$-III was preliminarily determined as P(kbar) = 7.7 + 0.047*T* (°C). The high-pressure phases of $BaGeO_3$, which were previously reported by Y. Shimizu et al (1970) in the pressure range 15–95 kbar, were interpreted to be not single-phase materials but complicated mixtures of more than two phases in the system BaO–GeO_2. X-ray powder diffraction data for the new compounds synthesized in this study are given. **$BaGe_3O_7$** does not exist as a single phase.

The compound, $BaGe_4O_9$ has the extraordinary structure shown in Fig. 5.64.

It consists of a tri-ring structure of GeO_4 tetrahedra arranged on a tetragonal lattice. There is a separated tetrahedron at the corners of the unit cell so that the formula should be designated as: $BaGeO_3(GeO_3)_3$. This is analogous to the compound $BaTi(SiO_3)_3$. BaGe $[Ge_3O_9]$ is trigonal, space group P3, with lattice constants $a = 11.61$, $c = 4.74$ Å, $V = 489.3$ Å^3 and $Z = 3$. The previously proposed structural relationship of this compound with benitoite, $BaTiSi_3O_9$, has been confirmed. The structure can be considered as composed of Ge_3O_9 rings, in which the Ge is tetrahedrally coordinated, linked through octahedrally coordinated Ge atoms to form a three-dimensional Ge–O network. All Ge polyhedra are linked by corner sharing. The Ba ions occupy positions in channels of the network.

The compound, $BaGe_2O_5$, has a molecular weight of 362.564 g/mol. It is monoclinic with space group = $P2_1/a$, the unit-cell parameters are: $a = 13.214$ Å, $b = 13.043$ Å, $c = 9.5501$ Å, $\beta = 94.006°$, $V = 1642.4$ Å^3 and $Z = 4$. There are three kinds of infinite chains of Ge polyhedra. One type, parallel to the *b*-axis, is connected to another chain of the same type by two other chains, parallel to the *a*-axis, so that two ladder-like sheets, parallel to the (201) and (201) directions, are formed. These are stacked in the *c*-direction (Fig. 5.65).

In this diagram, the Ba and Ge atoms have been omitted for clarity.

In the following diagram, they are shown in the unit cell of the compound (Fig. 5.66).

The compound, Ba_3GeO_5 is also known. It crystallizes in the tetragonal space group I4/mcm (D_{4h}^{18}) and is isostructural with Cs_3CoCl_5. Lattice constants of these compounds have been given. Sr_3SiO_5 shows a slight modification of the Cs_3CoCl_5 type of structure which causes a deviation from body centering; the space group is therefore P4/ncc (D).

In general, barium germanates are not offered for sale except as high-purity targets for sputtering and the like.

Radium Germanate

Radium germanate can be formed by firing the oxides together at about 750–800 °C:

$$RaO + GeO_2 + \text{heat} \Rightarrow RaGeO_3$$

In general, radium is expected to form the same type of compounds as its barium analogue. However, there is no record of the preparation of such compounds or

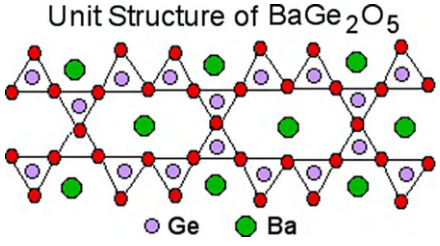

FIGURE 5.66

measurements of their properties, both physical and chemical. Perhaps this is due to the difficulty in handling radioactive ^{226}Ra compounds but more likely is due to the lack of interest in industry and academia.

5.3.2. Other Related Oxo-Germanium Compounds, Including Bismuth

In order to illustrate the concept of electronegativity as applied to the problem of whether a compound can be formed, the following discussion is presented. In this case, Bi^{3+} is sufficiently electropositive to be able to form a bismuth germanate. Bismuth germanate is a cubic crystal with the formula, $Bi_4Ge_3O_{12}$. It has the "evlitine" structure. A less common composition is $Bi_{12}GeO_{20}$ (Fig. 5.67).

The unit cell consists of three GeO_3 tetraheda arranged in a building block. These units are arranged in a cubic close-packed structure as shown in the above diagram.

The crystal structure of tetrabismuth tris(germanate), $Bi_4Ge_3O_{12}$ ($I3d$, $Z = 4$), is stable to at least 7.30 GPa, as demonstrated by hydrostatic single-crystal XRD measurements in a diamond anvil cell at room temperature. The highest pressure reached in this study was close to the onset of amorphous character at about 8 GPa. The Bi and Ge atoms are located at the 16*c* (3) and 12*a* (2) Wyckoff positions, respectively. The compression mainly affects the distorted BiO_6 octahedra, while the GeO_4 tetrahedra are relatively rigid. When compared with the values obtained under ambient conditions, the long Bi–O distances decrease with increasing pressure, while the short Bi–O distances do not change.

Its main use is as a scintillator crystal wherein it functions to absorb gamma rays (γ rays) and emit photons. Its emission band occurs at 480 nm with a band spread of 375–650 nm. It produces about 8500 photons per meV of the high-energy radiation absorbed. Thus, it can be used to count gamma-ray bursts, which are flashes of γ rays associated with extremely energetic explosions in distant galaxies. It has good "radiation hardness" (its parameters remaining stable up to 5×10^4 years) and a high "scintillation efficiency". It is mechanically strong, is not hygroscopic, and has a high density of 7.13 g/cc and a high "Z-value" (the *z*-value relates the resistance of a crystal to withstand differing temperatures without losing its scintillation efficiency). Its melting point is 1052 °C.

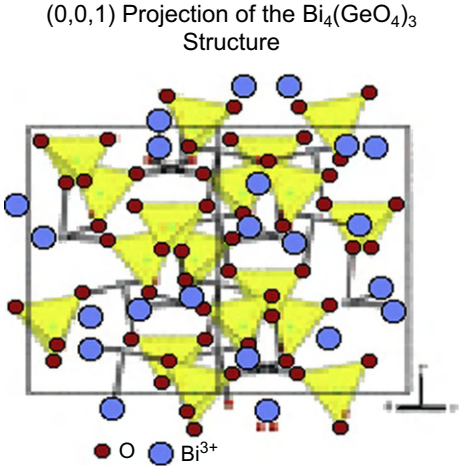

FIGURE 5.67

Bismuth germanate is used in detectors in particle physics, aerospace physics, nuclear medicine, geology exploration, and other industries. Bismuth germanate arrays are used for gamma pulse spectroscopy. BGO crystals are also used in detectors for positron emission tomography. Bismuth germanate has a high "electro-optic coefficient" (3.3 pm/V for $Bi_{12}GeO_{20}$) making it useful in nonlinear optics for building "Pockel cells". It can also be used for photorefractive elements useful in the ultraviolet part of the electromagnetic spectrum.

Commercially available crystals are grown by the Czochralski method and usually supplied in the form of cubes or cylinders. Large crystals are also available.

5.3.3. Alkaline Earth Germanides

In addition of forming oxy-germanate compounds with the alkaline earths, a series of "germanide" compounds have also been studied.

Beryllium Germanides

Beryllium does not form any compounds with germanium as shown in the following phase diagram shown as Fig. 5.68.

The structural factors are given in Table 5.24.

Perhaps, the lack of many compounds in this system is caused by the large disparity of atom sizes between the two metals.

Magnesium Germanides

Magnesium forms just one compound as shown in the following phase diagram shown as Fig. 5.69.

The structural factors are given in Table 5.25.

The dimagnesium germanide compound, Mg_2Ge, has the form shown as in Fig. 5.70.

The structure is cubic and has the fluorite arrangement. The unit-cell parameters are: $a = b = c = 4.5148$ Å, $\alpha = \beta = \gamma = 60°$, cell volume = 65.07 Å^3. Cell occupancy is shown in Table 5.26.

Two other structures have been presented that gave differing point groups and space groups:

$$Mg_2Ge\ (II) = cF12 = Fm\text{-}3m$$

$$Mg_2Ge\ (III) = hP45$$

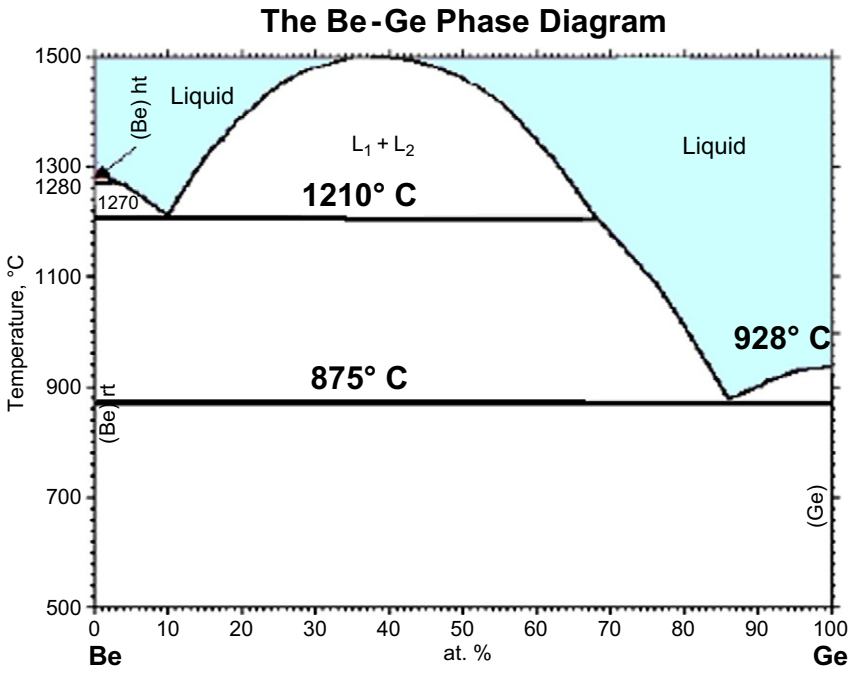

FIGURE 5.68

Large high-purity single crystals of the semiconductor Mg_2Ge have been grown by a modified Bridgman method. Crystals grown from stoichiometric melts were *p*-type with carrier concentrations at 77 K of about $10^{16}/cm^3$ and Hall mobilities near 1100 cm^5/V s. Excess magnesium placed in the melt acted as a donor and produced *n*-type material. Carrier concentrations of the compensated *n*-type material could be obtained ranging from 5×10^{14} to $5 \times 10^{17}/cm^3$ at 77 K. Mobilities for the *n*-type material were somewhat higher at about 1600 cm^5/V s than for the *p*-type crystals.

Infrared absorption spectra of several *n*-type Mg_2Ge single crystals were obtained in the wavelength regions from 1 to 13 μ and 1 to 7 μ, respectively, over the temperature range from 85–370 K. Free carrier absorption occurred in Mg_2Ge at the longer wavelengths. The absorption edges appeared to be due to indirect transitions and the shift of the optical energy gap with temperature is estimated to be ~6.5×10^{-4} eV/K for Mg_2Ge.

Magnesium germanide is readily available as Mg_2Ge and has a CAS number of 1310-52-7.

Calcium Germanides

Calcium metal readily forms a number of compounds with germanium metal, as can be seen in the phase diagram for the Ca–Ge system (Fig. 5.71).

Thermodynamic modeling of the Ca–Ge system has been carried out by means of the CALPHAD (calculation of phase diagrams) method and new experimental phase diagram data. The liquid phase and the intermetallic compounds Ca_2Ge, Ca_5Ge_3, Ca_7Ge_6 (new compound), CaGe and $CaGe_2$ are taken into consideration in this optimization. The substitutional solution model was used to describe the liquid phase. The five compounds were treated as stoichiometric phases. A consistent set of thermodynamic parameters has been obtained. The optimized phase diagram and thermodynamic properties were presented and compared with other calculated and experimental data obtained from the literature.

Associated structure factors are shown in Fig. 5.72.

TABLE 5.24

Compound	Structure type	Point group	Space group	Melting point, °C	Physical data
(Be) ht	W	cI2	229	1289	No data
(Be) rt	Mg	hP2	194	1270	No data
(Ge)	C	cF8	227	928	No data

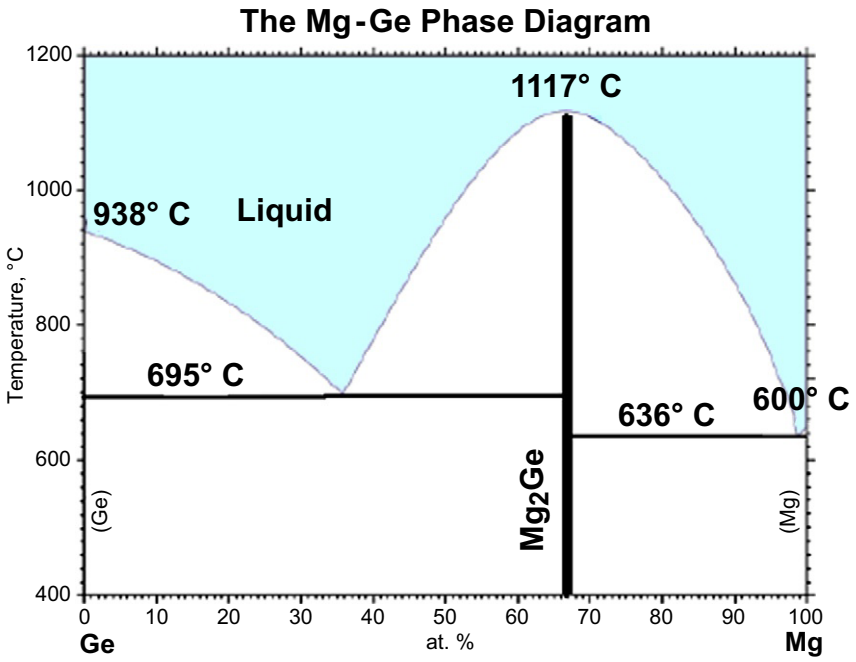

FIGURE 5.69

It was also found that CaGe is a mechanically unstable phase. Ca_2Ge is a direct band gap semiconductor with a band gap of 0.07 eV. In addition, it is found that the absolute values of heats of formation for all Ca–X intermetallics are larger than 30 kJ/mol-atom.

Dicalcium germanide, Ca_2Ge, has the structure shown in Fig. 5.73.

Cell parameters are: $a = 4.834$ Å, $b = 7.734$ Å, $c = 9.069$ Å, $\alpha = \beta = \gamma = 90°$, cell volume $= 339.06$ Å^3. Cell occupancy is: shown in Table 5.27.

The compound, CaGe, has the structure shown in Fig. 5.74.

Cell parameters are: $a = 4.005$ Å, $b = 4.565$ Å, $c = 5.880$ Å, $\alpha = 112.84°$, $\beta = \gamma = 90°$, cell volume $=$ 99.07 Å^3.

Cell occupancy is shown in Table 5.28.

Very little data is available for this compound. It has been stated that it is not stable and tends to decompose when subjected to moisture and/or oxygen in air.

Calcium digermanide has the structure shown in Fig. 5.75.

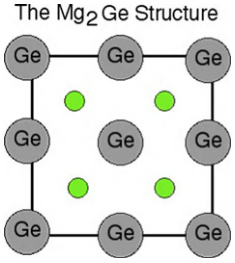

FIGURE 5.70

Cell parameters are: $a = b = 3.9492$ Å, $c = 10.493$ Å, $\alpha = \beta = 79.15°$, $\gamma = 60°$, cell volume $= 138.30$ Å^3. Cell occupancy is shown in Table 5.29.

The epitaxial growth of thin $CaGe_2$ films with reactive deposition epitaxy on Ge(1,1,1) substrates has been described. The films consisted in general of a mixture of the known trigonal rhombohedral tR6 modification and a hexagonal hR2 modification of $CaGe_2$ containing two Ca and two buckled Ge layers per unit cell in a twofold stacking sequence whose formation appears

TABLE 5.25

Compound	Structure type	Point group	Space group	Melting point, °C	Physical data
(Mg)	Mg	hP2	194	650	No data
Mg_2Ge	CaF_2	cF12	225	1117	No data
(Ge)	C	cF8	227	938	No data

TABLE 5.26

No	Site notation	Atom	Multiplicity	Wyckoff	Site symmetry	*x*	*y*	*z*	Occupancy
1	Mg	Mg	8	c	-43m	1/4	1/4	1/4	1.0
2	Ge	Ge	4	a	m-3m	0	0	0	1.0

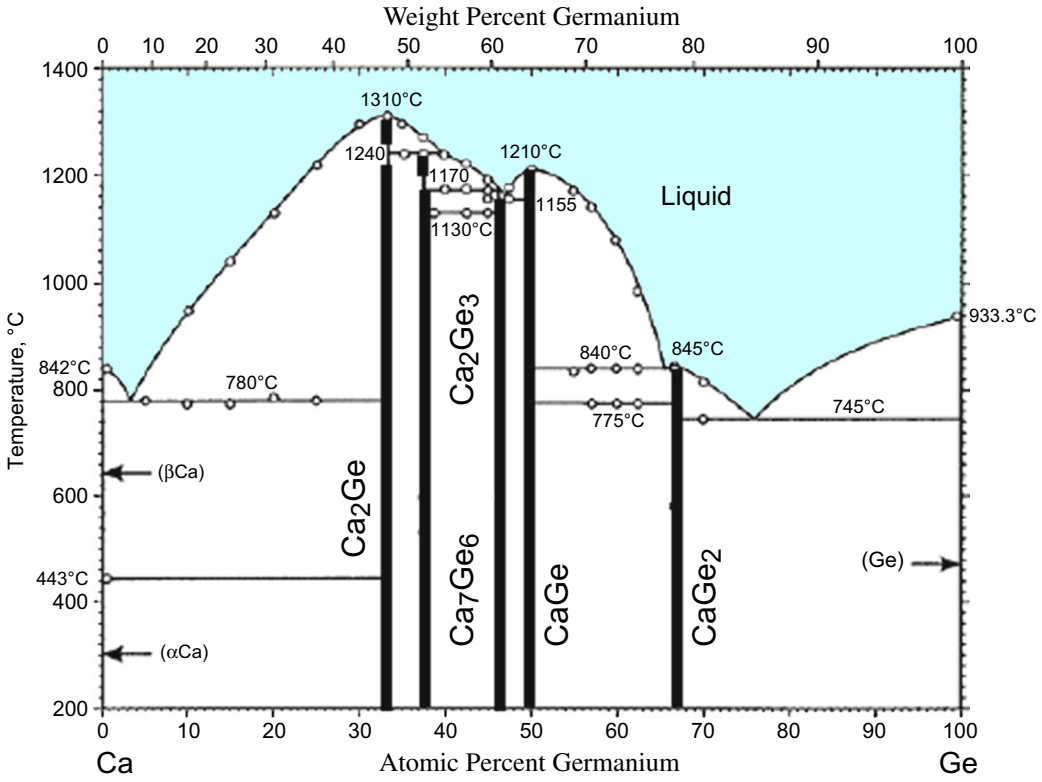

FIGURE 5.71

to be favored by strain. Epitaxial layers of both polytypes show remarkably higher crystalline quality compared to epitaxial $CaSi_2$ films grown on silicon substrates. The tr-6 modification is found to be unstable in air in contrast to the hR-2 modification.

This novel polymorph of $CaGe_2$, which crystallizes with the hexagonal space group $P6_3mc$ (no. 186) with cell parameters of $a = 3.9966$ and $c = 10.211$ Å ($Z = 2$; Pearson's code *hP6*) has been reported when formed by flux synthesis. The structure can be viewed as

Ca-Ge Crystal Structure Data

Phase	Composition, at.% Ge	Pearson Symbol	Space Group	Prototype
(βCa)	0	*cI*2	$Im\bar{3}m$	W
(αCa)	0	*cF*4	$Fm\bar{3}m$	Cu
Ca_2Ge	33.3	*oP*12	*Pnma*	Co_2Si
Ca_7Ge_6	12.5	*oP*52	*Pnma*	Ca_7Sn_6
Ca_5Ge_3	46.2	*tI*32	14/*mcm*	Cr_5B_3
CaGe	50	*oC*8	*Cmcm*	CrB
$CaGe_2$	66.7	*hR*6	$R\bar{3}m$	$CaSi_2$
(Ge)	100	*cF*8	$Fd\bar{3}m$	C (diamond)

FIGURE 5.72

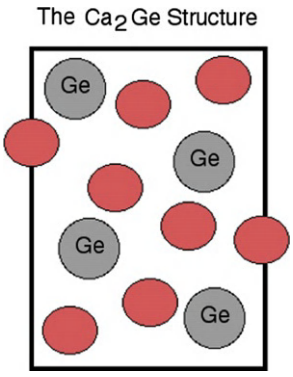

FIGURE 5.73

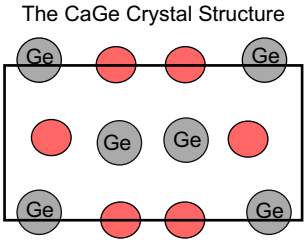

FIGURE 5.74

puckered layers of three-bonded germanium atoms, $^2{}_\infty[Ge_2]^{2-}$, which are stacked along the direction of the *c*-axis in an *ABAB*-fashion. The germanium polyanionic layers are separated by the Ca cations. As such, this structure is closely related to the structure of the other $CaGe_2$ polymorph, which crystallizes with the rhombohedral $CaSi_2$ type in the $R\bar{3}m$ space group (no. 166), where the $^2{}_\infty[Ge_2]^{2-}$ layers are arranged in an *AA'-BB'-CC'*-fashion, and are also interspaced by Ca^{2+} cations. LMTO calculations suggest that in spite of the formal closed-shell configuration for all atoms and the apparent adherence to the Zintl rules for electron counting, i.e. $Ca^{2+}[3b\text{-}^2{}_\infty[Ge_2]^{2-}]$, the phase will be a poor metal due to a small Ca-3*d*–Ge-4*p* band overlap. Magnetic susceptibility measurements as a function of the temperature indicate that the new $CaGe_2$ polymorph exhibits weak, temperature independent, Pauli paramagnetism. The hP6 structure can also be represented by Fig. 5.76.

The electrical resistivity of high-purity $CaGe_2$, $SrGe_2$, and $BaGe_2$ was measured in the temperature range from 20 to 800 °C by a four-point technique. $CaGe_2$ shows metallic behavior, while $SrGe_2$, and $BaGe_2$ are semiconducting. This difference can be explained by the change of the structure of the "anion" sublattices and the change of the metal distances in the metal sublattices.

Penta-calcium tri-germanide has the structure shown in Fig. 5.77.

Cell parameters are: $a = b = 7.74$ Å, $c = 9.148$ Å, $\alpha = \beta = 115.03°$, $\gamma = 90°$, cell volume $= 439.12$ Å^3. Cell occupancy is: Table 5.30.

Another view of the Ca_5Ge_3 structure may be seen in the following Fig. 5.78.

The electronic structure of Ca_5Ge_3 (Cr_5B_3 type), which can be formulated $(Ca^{+2})_5(Ge_2^{-6})Ge^{-4}$ in oxidation states, has been explored comparatively by means of semiempirical and first-principles density functional methods. The FP-APW calculations show that alkaline earth metal and germanium orbitals, particularly the d-orbitals on the cations and the p-π^* orbitals of the halogen-like dimeric Ge_2-6, mix considerably to form a conduction band. This covalency perfectly explains the unusual metallic properties of the nominally electron-precise Zintl phase Ca_5Ge_3 and its numerous relatives. Similar calculation results are obtained for Sr_5Ge_3, Ba_5Ge_3, and Ca_5Sn_3. Cation d-orbitals appear to be a common theme among Zintl phases that are also metallic.

TABLE 5.27

No	Site notation	Atom	Multiplicity	Wyckoff	Site symmetry	*x*	*y*	*z*	Occupancy
1	Ca2	Ca	4	c	.m.	0.022	1/4	0.676	1.0
2	Ca1	Ca	4	c	.m.	0.155	1/4	0.074	1.0
3	Ge	Ge	4	c	.m.	0.255	1/4	0.393	1.0

TABLE 5.28

No	Site notation	Atom	Multiplicity	Wyckoff	Site symmetry	*x*	*y*	*z*	Occupancy
1	Ge	Ge	4	c	m2m	0	0.076	1/4	1.0
2	Ca	Ca	4	c	m2m	0	0.362	1/4	1.0

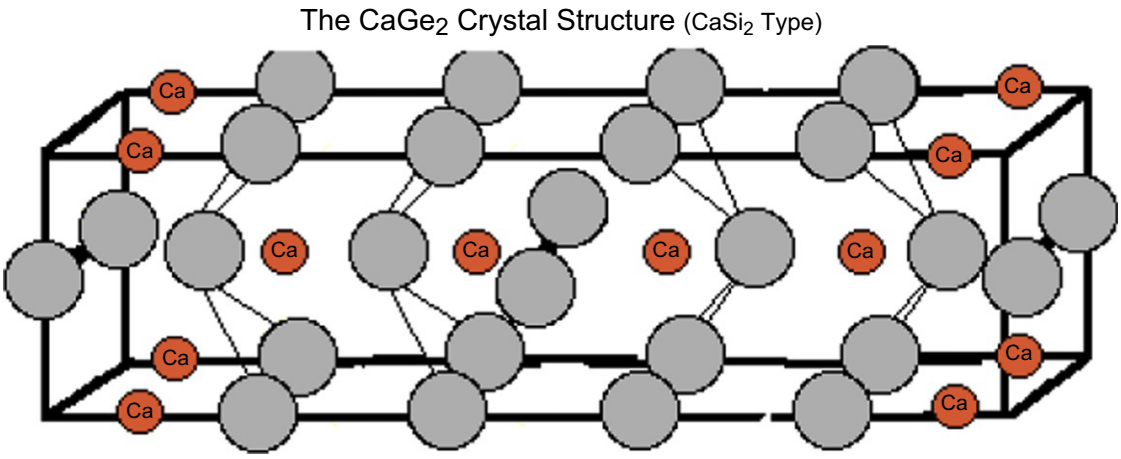

FIGURE 5.75

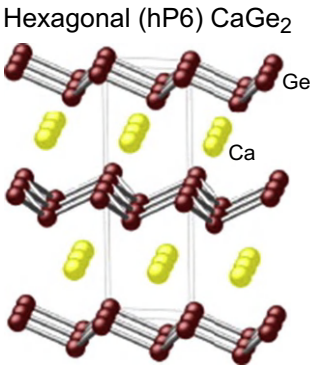

FIGURE 5.76

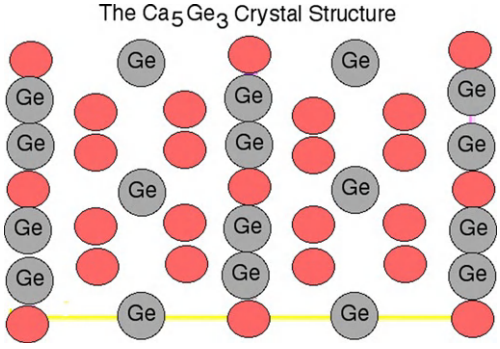

FIGURE 5.77

TABLE 5.29

No	Site notation	Atom	Multiplicity	Wyckoff	Site symmetry	*x*	*y*	*z*	Occupancy
1	Ca1	Ca	6	c	3m	0	0	0.083	1.0
2	Ge1	Ge	6	c	3m	0	0	0.183	1.0
3	Ge2	Ge	6	c	3m	0	0	0.35	1.0

TABLE 5.30

No	Site notation	Atom	Multiplicity	Wyckoff	Site symmetry	*x*	*y*	*z*	Occupancy
1	Ca1	Ca	16	l	..m	0.169	0.669	0.148	1.0
2	Ge1	Ge	8	h	m.2m	0.617	0.117	0	1.0
3	Ca2	Ca	4	c	4/m..	0	0	0	1.0
4	Ge2	Ge	4	a	422	0	0	1/4	1.0

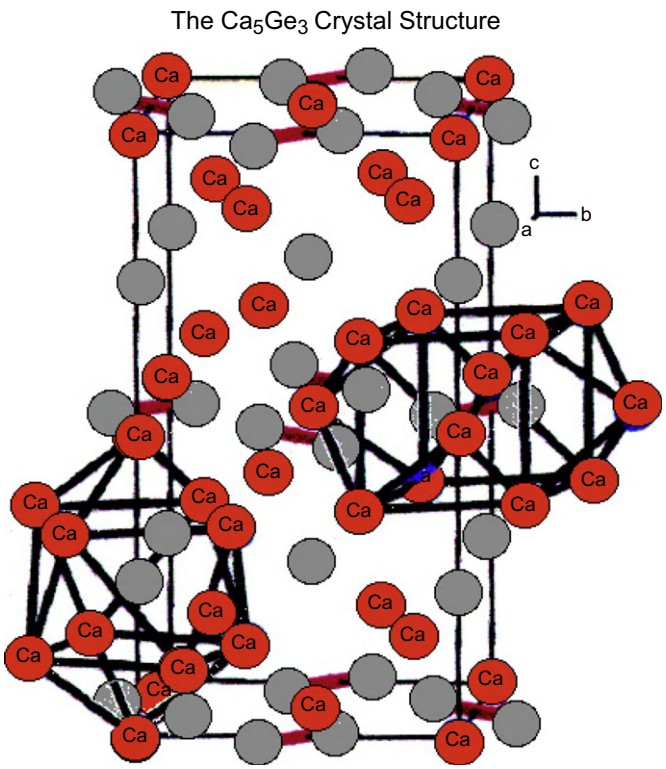

FIGURE 5.78

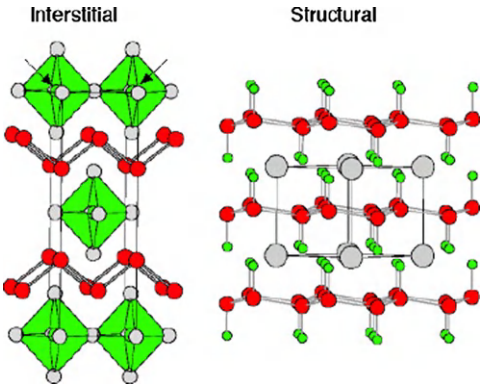

FIGURE 5.79

Hydrogen may be incorporated in Zintl phases in two different ways: either hydridic where H is exclusively coordinated by electropositive metals (interstitial hydrides), or as part of the polyanion where it acts as a covalently bonded ligand (polyanionic hydride). Both scenarios provide novel coordination environments and bonding scenarios for the atoms involved. This makes hydrogenous Zintl phases important model systems for fundamental studies of hydrogen–metal interactions. Simultaneously, hydrogen-induced chemical structure and physical property changes provide exciting prospects for materials science. In hydrogenous Zintl phases, hydrogen may occur hydridic or be part of the polymeric anion where it acts as a covalently bonded terminating ligand. This gives rise to the following structure types (Fig. 5.79).

Ca_5Ge_3 forms a structural type of hydride.

The compound, Ca_7Ge_6, is also known. It is isomorphous with Ca_7Sn_6 and melts at 1170 °C. However, little data concerning this compound has emerged in the open literature.

Calcium germanides, in general, have not been offered for sale commercially. They do not have an assigned CAS number. Stability in air and moisture is a critical factor for most of the compositions.

Strontium Germanides

Strontium metal forms a series of compounds with germanium metal as can be seen by examination of the phase Fig. 5.80.

The phase diagram of the Sr–Ge system has been investigated across almost the whole composition range (0–85 at.% Ge) using DTA and XRD. Four intermediate phases exist: Sr_2Ge ($PbCl_2$-type, orthorhombic oP12-Pnma), Sr_5Ge_3 (Cr_5B_3-type, tetragonal tI32-I4/mcm), SrGe (CrB-type, orthorhombic oC8-Cmcm) and $SrGe_2$ ($BaSi_2$-type, orthorhombic oP24-Pnma). A further intermediate phase, observed only at high temperature above 985 °C, crystallizes with a defective AlB_2-type structure. Four eutectics occur in the system: about 5 at.% Ge at 740 °C, 42 at.% Ge at 1100 °C, 61 at.% Ge at 965 °C and 85 at.% Ge at 755 °C. As a whole, the Sr–Ge system appears very similar to the Sr–Si one. The structure factors for the Sr–Ge system are given in Table 5.31.

Distrontium germanide has the structure shown in Fig. 5.81.

Lattice parameters are: $a = 5.166$ Å, $b = 8.153$ Å, $c = 9.593$ Å, $\alpha = \beta = \gamma = 90°$. Cell volume = 404.04 Å^3. Site occupancy is:

No	Site notation	Atom	Multiplicity	Wyckoff	Site symmetry	x	y	z	Occupancy
1	Sr1	Sr	4	c	.m.	0.038	1/4	0.718	1.0
2	Sr2	Sr	4	c	.m.	0.174	1/4	0.062	1.0
3	Ge1	Ge	4	c	.m.	0.202	1/4	0.389	1.0

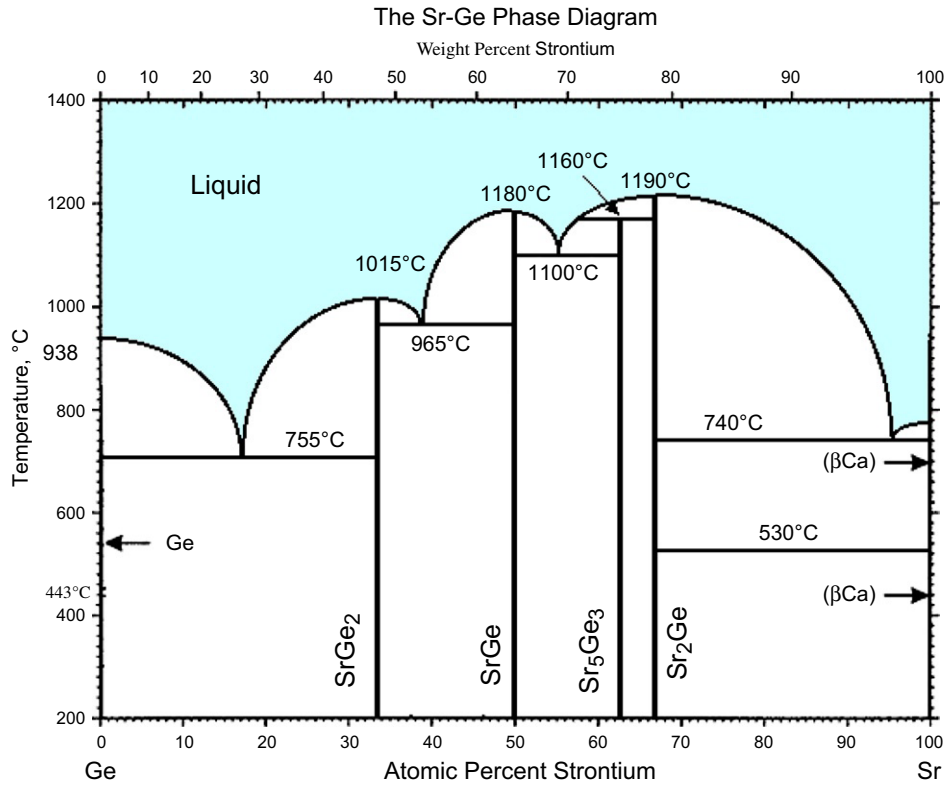

FIGURE 5.80

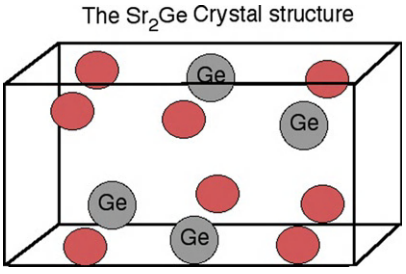

FIGURE 5.81

There is a dearth of information in literature concerning its physical properties.

The crystal **strontium monogermanide**, SrGe, has the structure shown in Fig. 5.82.

Lattice parameters are: $a = 4.17$ Å, $b = 4.82$ Å, $c = 6.18$ Å, $\alpha = 112.94°$, $\beta = \gamma = 90°$, cell volume $= 114.38$ Å^3. Site occupancy is shown in Table 5.32.

Other than structure data, little information concerning the physical properties of SrGe can be found.

Penta-strontium tri-germanide, Sr_5Ge_3, is dimorphic. One form has the same structure as that of its calcium homologue and is shown below. The other is orthorhombic and its structure is shown in Fig. 5.83.

Lattice parameters are: $a = b = 8.134$ Å, $c = 9.760$ Å, $\alpha = \beta = 114.626°$, $\gamma = 90°$, cell volume $= 521.172$ Å^3 (Table 5.33).

TABLE 5.31

Compound	Structure type	Point group	Space group	Melting temperature, °C	Physical properties
(Sr) ht	W	cI2	229	763	No data
(Sr) rt	Cu	cF4	225	420	No data
SrGe	TlI	oS8	63	1180	No data
$SrGe_2$	$BaSi_2$	oP24	62	1015	No data
Sr_2Ge	Co_2Si-b	oP12	62	1190	No data
Sr_5Ge_3	Sr_5Si_3	oI40	71	1160	No data
(Ge)	C	cF8	227	938	No data

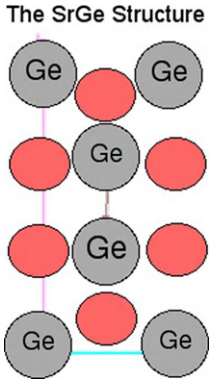

FIGURE 5.82

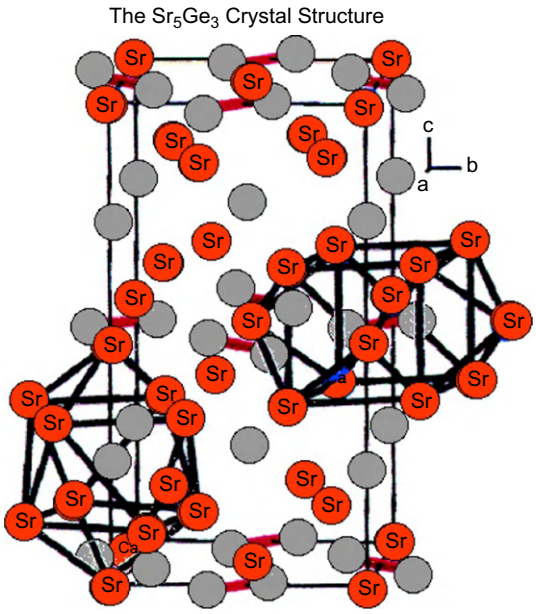

FIGURE 5.83

Lattice parameters are: $a = b = 8.134$ Å, $c = 9.760$ Å, $\alpha = \beta = 114.626°$, $\gamma = 90°$, cell volume $= 521.172$ Å^3. Site occupation is:

The orthorhombic form of Sr_5Ge_3 has the structure shown in Fig. 5.84.

Cell parameters are: $a = 8.134$ Å, $c = 9.7602$ Å, $\alpha = \beta = 114.626°$, $\gamma = 90°$, cell volume $= 521.72$ Å^3. Site occupancy is shown in Table 5.33.

Strontium di-germanide, $SrGe_2$, has the structure shown in Fig. 5.85.

Another form of the compound, $SrGe_2$, has the structure shown in Fig. 5.86.

Cell parameters are: $a = 6.82$ Å, $b = 8/63$ Å, $c = 11.15$ Å, $\alpha = \beta = \gamma = 90°$, cell volume $= 654.33$ Å^3. Site occupation is shown in Table 5.34.

A number of similar $SrGe_2$ compounds have been investigated by means of different ab initio methods. All materials are found to be indirect band gap semiconductors displaying almost equal dispersion of bands close to the gap region. The energy gaps of 0.83, 0.57

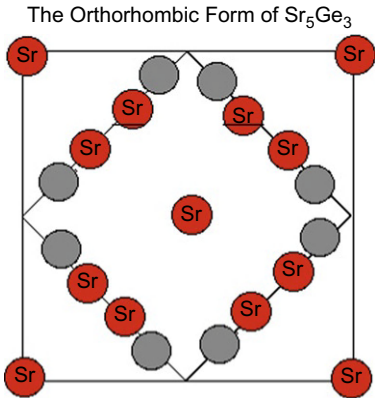

FIGURE 5.84

TABLE 5.32

No	Site notation	Atom	Multiplicity	Wyckoff	Site symmetry	x	y	z	Occupancy
1	Ge	Ge	4	c	m2m	0	0.07	1/4	1.0
2	Sr	Sr	4	c	m2m	0	0.365	1/4	1.0

TABLE 5.33

No	Site notation	Atom	Multiplicity	Wyckoff	Site symmetry	x	y	z	Occupancy
1	Sr2	Sr	16	l	..m	0.1739	0.6739	0.14441	1.0
2	Ge2	Ge	8	h	m.2m	0.6126	0.1126	0	1.0
3	Sr1	Sr	4	c	4/m..	0	0	0	1.0
4	Ge1	Ge	4	A	422	0	0	1/4	1.0

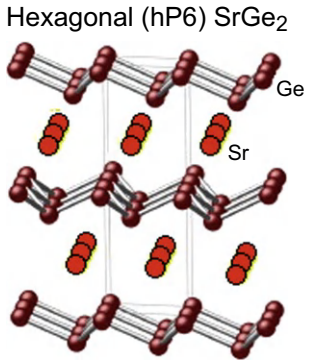

FIGURE 5.85

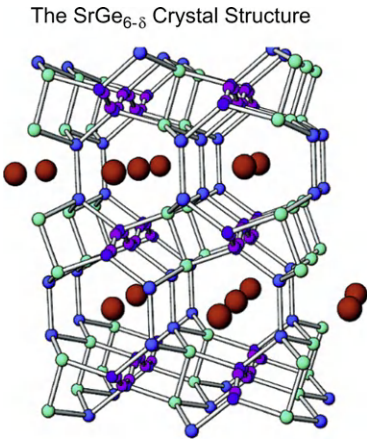

FIGURE 5.87

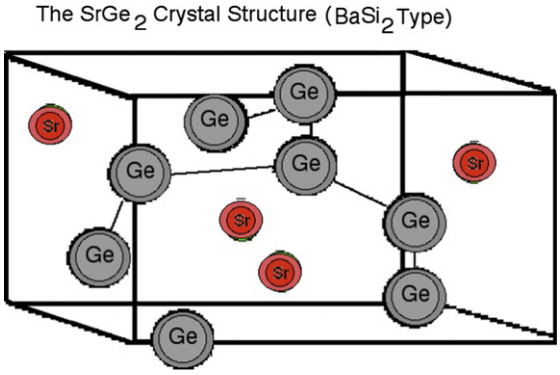

FIGURE 5.86

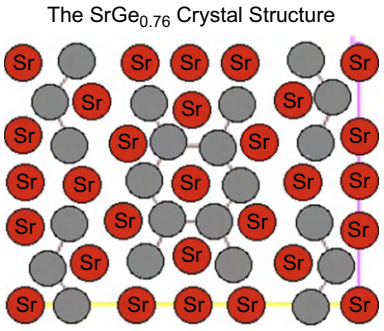

FIGURE 5.88

and 0.44 eV are estimated for $BaSi_2$, $BaGe_2$ and $SrGe_2$, respectively.

A new germanide, $SrGe_{6-\delta}$ ($\delta = 0.5$), was synthesized by the reaction of Sr and Ge mixtures under a pressure of 5 GPa at 1200 °C. It crystallized in the orthorhombic space group Cmcm (no. 63) with $a = 4.0981(6)$ Å, $b = 11.159(1)$ Å, $c = 12.6825(8)$ Å, $V = 580.0(1)$ Å^3, and $Z = 4$. $SrGe_{6-\delta}$ is composed of a Ge covalent network having a cage-like structure and Sr atoms situated in the cages. Each Ge atom is coordinated by four neighboring Ge atoms. The coordination polyhedra are fairly distorted from an ideal tetrahedron, and the Ge network contains vacancies and disordering. The resistivity shows metallic behavior down to 2 K, and the positive thermoelectric power indicates that the dominant carriers to be holes. The structure has been determined to be in Fig. 5.87.

In contrast, the compound, $SrGe_{0.76}$, has the structure shown in Fig. 5.88.

This structure appears to be related to the $SrGe_{6-\delta}$ compound in structure.

In addition to the compounds described above, Sr forms a differing set of materials if Mg is added to the mix. Synthetic investigations of the $Sr_xMg_{2-x}Ge$ section have been carried out in sealed Ta containers. These reveal, in addition to the known Mg_2Ge, MgSrGe, and Sr_2Ge, two new phases with the nominal compositions $Sr_2Mg_{12}Ge_7$ and $Sr_5Mg_{19}Ge_{12}$. The first is a line compound that is isostructural with $Zr_2Fe_{12}P_7$ (P6,

TABLE 5.34

No	Site notation	Atom	Multiplicity	Wyckoff	Site symmetry	x	y	z	Occupancy
1	Ge1	Ge	8	d	1	0.310	0.078	0.353	1.0
2	Ge2	Ge	4	c	.m.	0.076	1/4	0.409	1.0
3	Sr1	Sr	4	c	.m.	0.161	1/4	0.095	1.0
4	Ge3	Ge	4	c	.m.	0.295	1/4	0.531	1.0

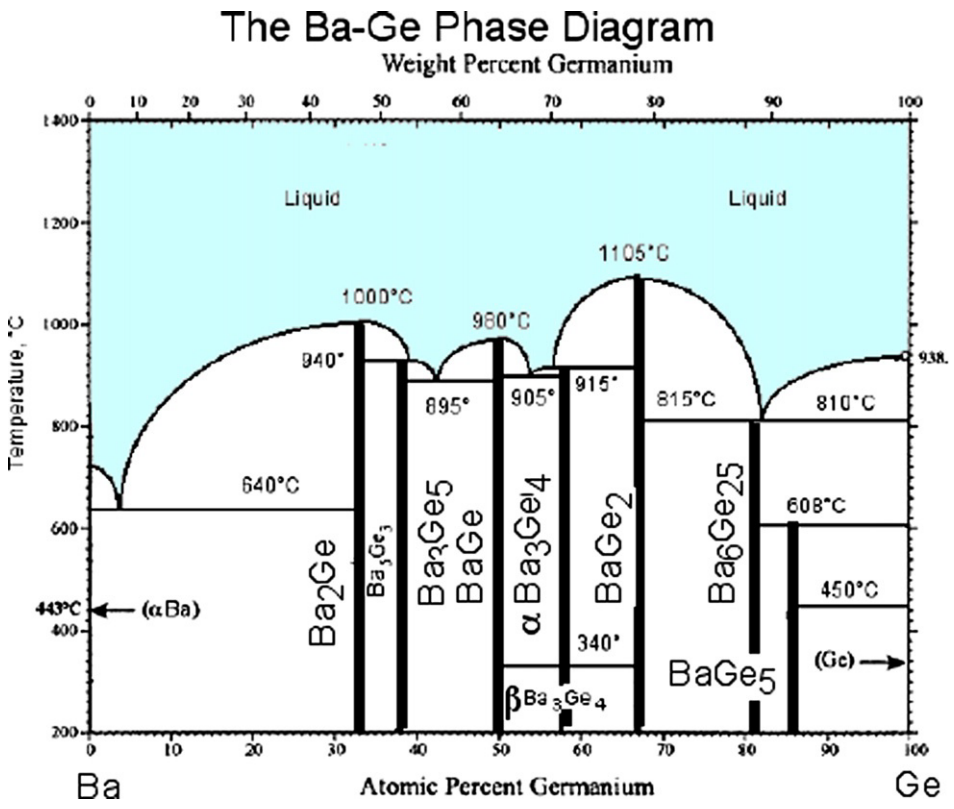

FIGURE 5.89

$Z = 1$, $a = 11.064$ Å, $c = 4.356$ Å, and has the refined composition $Sr_{2.17}Mg_{11.83}Ge_7$. About 6% strontium substitutes in the larger, five-coordinate magnesium site. The other phase is isostructural with $Ho_5Ni_{19}P_{12}$ or the very similar $Sc_5Co_{19}P_{12}$ according to Guinier powder diffraction and is nonstoichiometric, viz. $Sr_{5+y}Mg_{19-y}Ge_{12}$ with an approximate range of $-0.7 \leq y \leq 2.7$. Both structures feature tricapped trigonal prismatic units of metal about isolated germanium atoms, these prisms being condensed by sharing some prismatic edges and faces. The new compounds are the first valence (Zintl) examples of structures previously known only for metallic transition metal phosphides and arsenides.

Although a considerable amount of investigation concerning the strontium germanide intermetallic compounds has been published, little usage in industry has resulted. These compounds have not been assigned CAS numbers although a few are available commercially for sale in limited quantities.

Barium Germanides

Barium forms a number of compounds with Ge as can be seen in the above phase diagram shown as Fig. 5.89.

Structure factors are listed in Table 5.35.

Dibarium germanide, Ba_2Ge, has the structure shown in Fig. 5.90.

Unit cell parameters are: $a = 5.48$ Å, $b = 8.38$ Å, $c = 10.04$ Å, $\alpha = \beta = \gamma = 90°$, cell volume = 461.06 Å^3. Site occupancy is shown in Table 5.36.

The compound, Ba_2Ge, has not been studied thoroughly except for its structural relationship to other barium germanide compositions.

Barium digermanide, $BaGe_2$, is dimorphic. One form has the structure shown in Fig. 5.91.

This structure may be compared to the Ba_2Ge composition where an excess of Ba atoms is present. Unit cell parameters are: $a = b = 44.769$ Å, $c = 8.1035$ Å, $\alpha = \beta = 107.113$ Å, $\gamma = 90°$, cell volume = 167.58 Å^3. Site occupancy is shown in Table 5.37.

The alternative structure has the form shown in Fig. 5.92.

Tetrahedral units, Ge_4^{2-}, are present as well as triangular units, Ge_3^{2-} in the structure. Unit-cell parameters are: $a = 6.83$ Å, $b = 9.05$ Å, $c = 11.65$ Å, $\alpha = \beta = \gamma = 90°$, cell volume = 720.10 Å^3. Site occupancy is shown in Table 5.38.

Barium monogermanide, BaGe, has the crystal structure shown in Fig. 5.93.

The cell parameters are: $a = 4.341$ Å, $b = 5.058$ Å, $c = 6.502$ Å, $\alpha = 112{,}89°$, $\beta = \gamma = 90°$, cell volume = 130.28 Å^3. Cell occupancy is shown in Table 5.39.

This compound has not been thoroughly researched and its physical properties remain unknown, except for structure.

TABLE 5.35

Compound	Structure type	Point group	Space group	Melting temperature	Physical data
(Ba)	W	cI2	Im3m	738 °C	No data
BaGe	CrB	oC8	Cmcm	980	No data
$BaGe_2$	$BaSi_2$	oP24	Pmna	1105	No data
Ba_2Ge	Co_2Si-b	oP12	Pmna	1000	No data
Ba_5Ge_3	—	tP28	$P4_2/nmn$	940	No data
β-Ba_3Ge_4	—	tP28	$P4_2/nmn$	340	No data
α-Ba_3Ge_4	—	oC56	Cmmm	915	No data
Ba_6Ge_{25}	K_6Sn_{25}	oP124	P124	815	No data
(Ge)	C	cF8	227	938	No data

TABLE 5.36

No	Site notation	Atom	Multiplicity	Wyckoff	Site symmetry	*x*	*y*	*z*	Occupancy
1	Ba(I)	Ba	4	c	.m.	0.017	1/4	0.677	1.0
2	Ba(II)	Ba	4	c	.m.	0.153	1/4	0.084	1.0
3	Ge	Ge	4	c	.m.	0.252	1/4	0.403	1.0

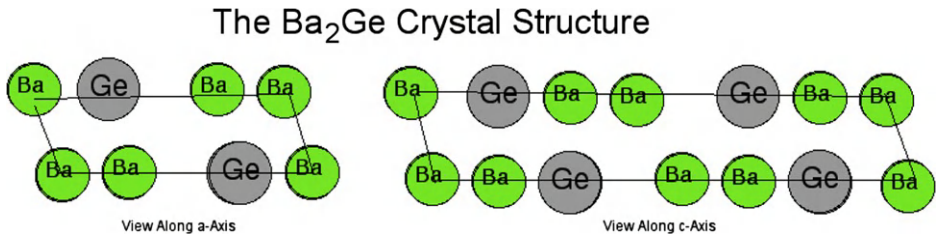

FIGURE 5.90

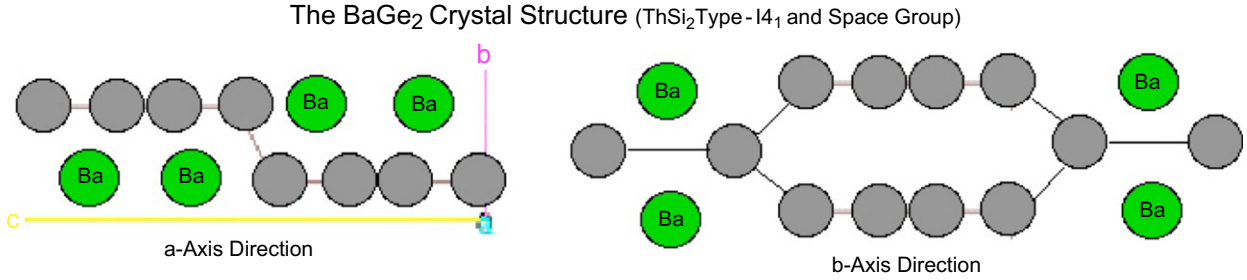

FIGURE 5.91

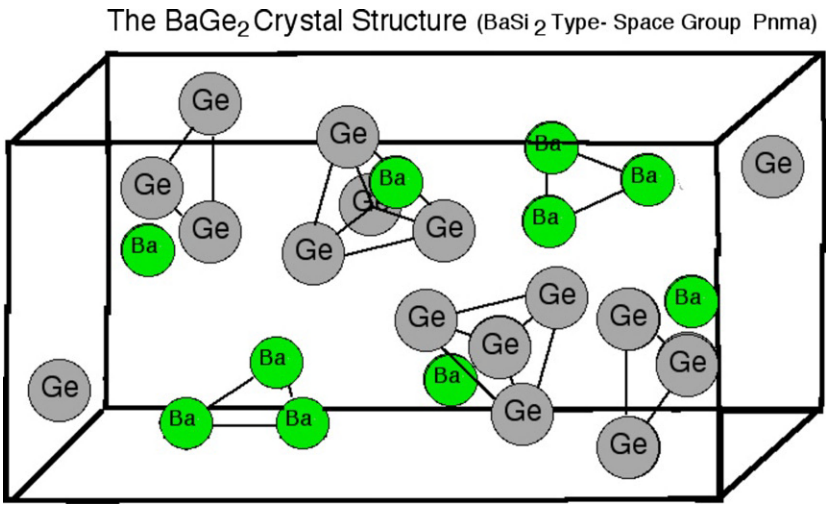

FIGURE 5.92

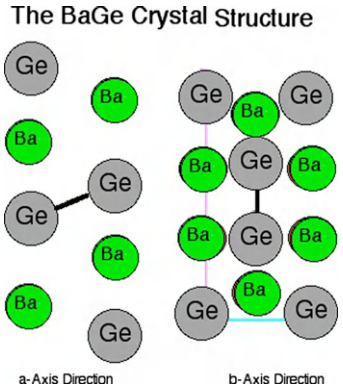

FIGURE 5.93

Penta-barium tri-germanide has the structure shown in Fig. 5.94.

Unit-cell parameters are: $a = b = 8.529$ Å, $c = 16.554$ Å, $\alpha = \beta = \gamma = 90°$, cell volume $= 1201.38$ Å^3. Site occupancy is shown in Table 5.40.

Barium also forms a tribarium tetragermanide that is dimorphic. One version has the form shown in Fig. 5.95.

Cell parameters are: $a = 11/799$ Å, $b = 12.21$ Å, $c = 12.097$ Å, $\alpha = \beta = \gamma = 90°$, cell volume $= 1742.76$ Å^3. Site occupancy is shown in Table 5.41.

The other has the form shown in Fig. 5.96.

Cell parameters are: $a = 8.621$ Å, $b = 8.624$ Å, $c = 12.031$ Å, $\alpha = \beta = \gamma = 90°$, cell volume $= 894.16$ Å^3. Site occupancy is shown in Table 5.42.

TABLE 5.37

No	Site notation	Atom	Multiplicity	Wyckoff	Site symmetry	*x*	*y*	*z*	Occupancy
1	Ge	Ge	8	e	2mm.	0	1/4	0.29178	0.98
2	Ba	Ba	4	a	-4m2	0	3/4	1/8	1.0

TABLE 5.38

No	Site notation	Atom	Multiplicity	Wyckoff	Site symmetry	*x*	*y*	*z*	Occupancy
1	Ge1	Ge	8	d	1	0.310	0.078	0.353	1.0
2	Ge2	Ge	4	c	.m.	0.076	1/4	0.409	1.0
3	Ba1	Ba	4	c	.m.	0.161	1/4	0.095	1.0
4	Ge3	Ge	4	c	.m.	0.295	1/4	0.531	1.0
5	Ba2	Ba	4	c	.m.	0.486	1/4	0.806	1.0

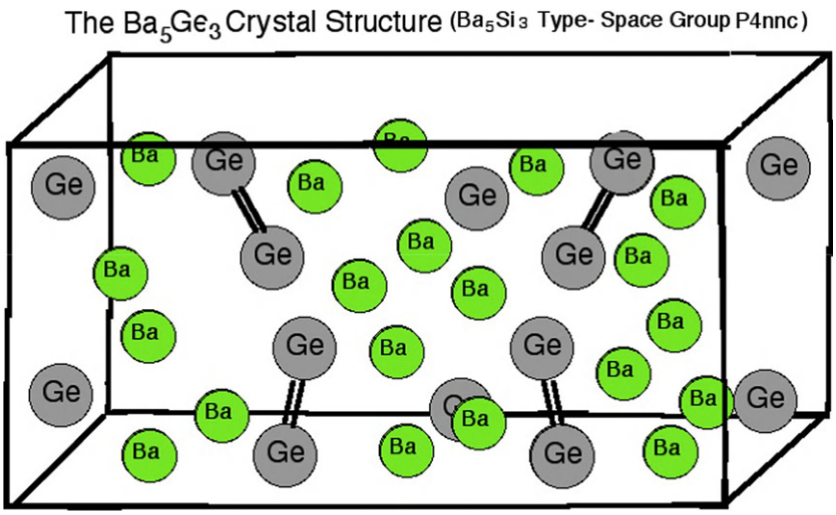

FIGURE 5.94

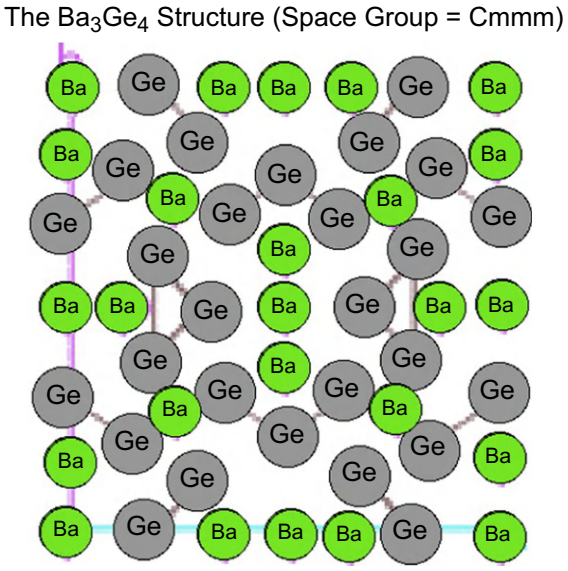

FIGURE 5.95

The composition, barium pentagermanide, $BaGe_5$, has been found to be semiconducting. $BaGe_5$ constitutes a new type of intermetallic clathrate obtained by decomposition of clathrate-I Ba_8Ge_{43}-3 at low temperatures. The crystal structure consists of characteristic layers interconnected by covalent bonds. $BaGe_5$ is a semiconducting Zintl phase (Fig. 5.97).

The reinvestigation of the crystal structure of $Ba_8Ge_{43\Delta 3}$ (space group, no. 230; $a = 21.3123(5)$ Å; $Z = 8$; Pearson symbol *cI*408) shows a full ordering of the vacancies (Δ) in the germanium framework. This ordered crystal structure can be considered as a derivative of an ideal "Ba_8Ge_{46}" clathrate-I-type structure (Pm3n, $a' = a/2$) in which three Ge vacancies (per formula unit) are allowed to order in a cubic superstructure with a doubled unit-cell parameter (Δ at the 24*c* site, space group Pm3n). In the resulting Ge framework, each vacancy Δ is surrounded by four three-bonded (3b)Ge^- species. The ordering in crystals of as-cast samples

TABLE 5.39

No	Site notation	Atom	Multiplicity	Wyckoff	Site symmetry	*x*	*y*	*z*	Occupancy
1	Ge	Ge	4	c	m2m	0	0.063	1/4	1.0
2	Ba	Ba	4	c	m2m	0	0.354	1/4	1.0

TABLE 5.40

No	Site notation	Atom	Multiplicity	Site symmetry	*x*	*y*	*z*	Occupancy
1	Ba2	Ba	16	1	0.06512	0.58295	0.10416	1.0
2	Ge2	Ge	8	..2	0.3564	0.6436	1/4	1.0
3	Ge1	Ge	4	4..	1/4	1/4	0.0081	1.0
4	Ba1	Ba	4	4..	1/4	1/4	0.2296	1.0

TABLE 5.41

No	Site notation	Atom	Multiplicity	Site symmetry	*x*	*y*	*z*	Occupancy
1	Ge1	Ge	8	q	0.30549	0.10568	1/2	1.0
2	Ge2	Ge	8	p	0.13872	0.20215	0	1.0
3	Ge4	Ge	8	o	0.1977	0	0.34901	1.0
4	Ge3	Ge	8	n	0	0.29357	0.13938	1.0
5	Ba5	Ba	8	m	1/4	1/4	0.2558	1.0
6	Ba4	Ba	4	l	0	1/2	0.3247	1.0
7	Ba3	Ba	4	k	0	0	0.1602	1.0
8	Ba1	Ba	4	j	0	0.1603	1/2	1.0
9	Ba2	Ba	4	g	0.3375	0	0	1.0

TABLE 5.42

No	Site notation	Atom	Multiplicity	Site symmetry	*x*	*y*	*z*	Occupancy
1	Ge2	Ge	8	j	0.3	0.3	0.1473	1.0
2	Ge1	Ge	8	i	0.0852	0.3076	0.3076	1.0
3	Ba1	Ba	4	M2m	0.3351	0.3351	0.6649	1.0
4	Ba2	Ba	4	2mm	0	0	0.170	1.0
5	Ba3	Ba	4	D	0	0	0	1.0

(cooled in argon atmosphere, nonannealed) is partially disrupted. For the "as-cast" crystals, a short-range model is proposed based on the partial distribution of Ge on the 24*c* and 24*d* sites. From the electron balance, Ba_8Ge_{43} can be considered as a metallic Zintl phase with four excess electrons per formula unit. The Ba_8Ge_{43} phase is stable in the temperature range 770–810 °C and exists in equilibrium with Ba_6Ge_{25} and Ge. By decomposition of under cooled (metastable) Ba_8Ge_{43}, a new metastable binary $BaGe_5$ phase is formed.

Further work has resulted in another Zintl-type semiconductor based upon the Ba–Cu–Ge system. Eight

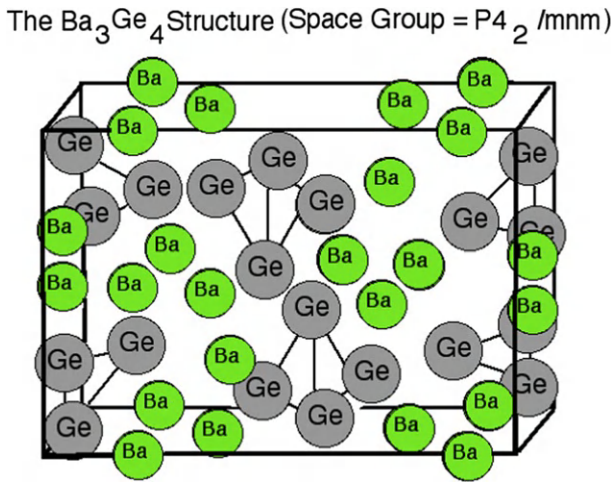

FIGURE 5.96

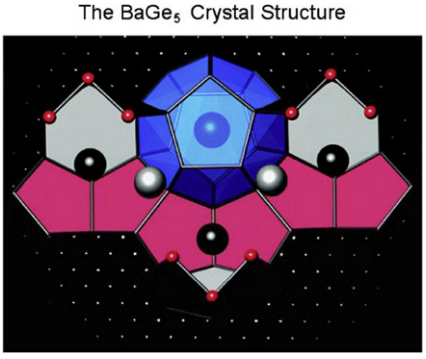

FIGURE 5.97

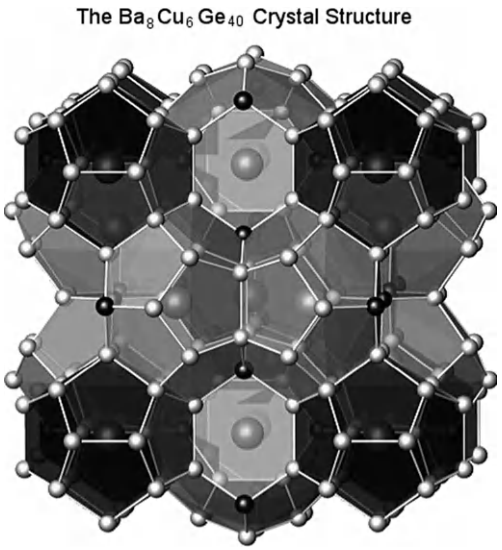

FIGURE 5.98

samples with nominal stoichiometry $Ba_8Cu_{6-x}Ge_{40+x}$ ($x = 0$ to 0.7) have been synthesized with a new method involving Ba_6Ge_{25} as an intermediate step. The new route provides fine control of the Cu:Ge ratio and allows systematic studies of the changes in the transport properties as a function of x. Resistivity, thermopower, and Hall carrier concentration all show systematic changes upon altering the Cu:Ge ratio. On the basis of density functional theory, we have calculated the electrical transport properties for fully ordered $Ba_8Cu_6Ge_{40}$. An optimal power factor is predicted for a Fermi level in the top of the valence band. Contrary to expectation, *n*-type behavior is observed in all samples, which appears to be due to small amounts of vacancies. Relatively low mobilities result in moderate thermoelectric properties with ZT = 0.07 at 400 K for the $x = 0.2$ sample. The structure determined was shown in Fig. 5.98.

Radium Germanides

Although radium germanides undoubtedly could be formed into the same type of compounds produced by the system Ba–Ge, there is no record of any work in the past or recent literature that has tried to characterize them. Without a doubt, this is due to the high cost of Ra metal as well as the high radioactive exposure level encountered.

5.4. ALKALINE EARTH OXY-TIN (STANNUM) COMPOUNDS

As a metal, tin forms alloys with a number of other elements. Alloys can be amorphous or crystalline. With the alkaline earths, it has been determined that there are a few crystalline alloy compounds of specific compositions. However, tin remains as a cation in these states, although it is not as electropositive as the alkaline earths. In both cases, both Sn and M (M = Be, Mg, Ca, Sr, Ba, Ra) remain in an elemental state, i.e. Sn^0 and M^0.

Tin has two valence states, Sn^{2+} and Sn^{4+}. Tin oxides are amphoteric and dissolve in aqueous solution under both acidic and basic conditions. As cations, they are sometimes called "Stannous" and "Stannic". As anions, chemical combination with any given cation is designated as a "stannite" or "stannate". These compounds are also called "metastannate" and "orthostannate", although this designation is not strictly correct. Stannic oxide, SnO_2, although insoluble in water, occurs in nature as the "Cassiterite" ore. It has been described as difficult to dissolve in acids and alkalis. "Stannic acid" refers to hydrated tin dioxide, $SnO_2 \cdot xH_2O$, which is also called "stannic hydroxide".

5.4.1. Stannides of the Alkaline Earths

The alkaline earths form a series of "Stannides" of the general formula "M_xSn_y, where both x and y can vary form 1 to 6, and combinations thereof.

Beryllium Stannides

The metal, Be, melts at 1287 °C while the metal, Sn, melts at 232 °C. However, the reaction:

$$Be(solid) + Sn(liq) \Rightarrow Be_xSn_y(solid)$$

does not occur. No beryllium stannides are known and there are no references in the literature that describe the physical or chemical properties of any possible compounds.

Magnesium Stannides

The metal, Mg, melts at 651 °C while the metal, Sn, melts at 232 °C.

The reaction:

$$Mg(solid) + Sn(liq) \Rightarrow Mg_xSn_y(solid)$$

forms a limited series of compounds like Mg_2Sn. However, combining the two metals above their melting temperatures usually results in an amorphous alloy combination, not a compound or series of compounds. The observed asymmetry in the properties of mixing of Mg–Sn alloy in molten state has been successfully explained on basis of the quasi-lattice model. This method has been utilized to determine the free energy of mixing, entropy of mixing, heat of mixing, the concentration–concentration structure factor in long wave length limit [Scc(0)] and the Warren Cowley short-range order parameter (α1) of the Mg_2Sn alloy in a molten state

at 1073 K (800 °C). The analysis suggests that hetero-coordination leading to the formation of a chemical complex-like Mg_2Sn is likely to exist in the melt but is weakly interacting in nature. The interaction energies between the species of the melt are found to depend considerably on temperature and the alloy is more ordered toward Mg-rich region. Only one compound can be formed from the melt as shown in the following phase Fig. 5.99.

Only one compound is shown, Mg_2Sn, but the compound, Mg_9Sn_5 has also been documented. The crystal parameters are given in Table 5.43.

A comparison of these structures can be seen in the following Fig. 5.100.

Cell parameters are:

Mg_2Sn

$a = b = c = 4.7496$ Å, $\alpha = \beta = \gamma = 60°$, cell volume = 77.21 Å^3, cell occupancy is shown in Table 5.44.

Mg_9Sn_5

$a = b = c = 8.8027$ Å, $\alpha = \beta = \gamma = 97.358°$, cell volume = 663.64 Å^3, cell occupancy is shown in Table 5.45.

$Mg_{0.974}Sn_{0.026}$

$a = b = 3.2058$ Å, $c = 5.2194$ Å, $\alpha = \beta = \gamma = 90°$, cell volume = 46.44 Å^3, cell occupancy is:

No	Site notation	Atom	Multiplicity	Wyckoff	Site symmetry	x	y	z	Occupancy
1	M	$Mg_{0.974} + Sn_{0.026}$	2	c	-6m2	1/3	2/3	1/4	1.0

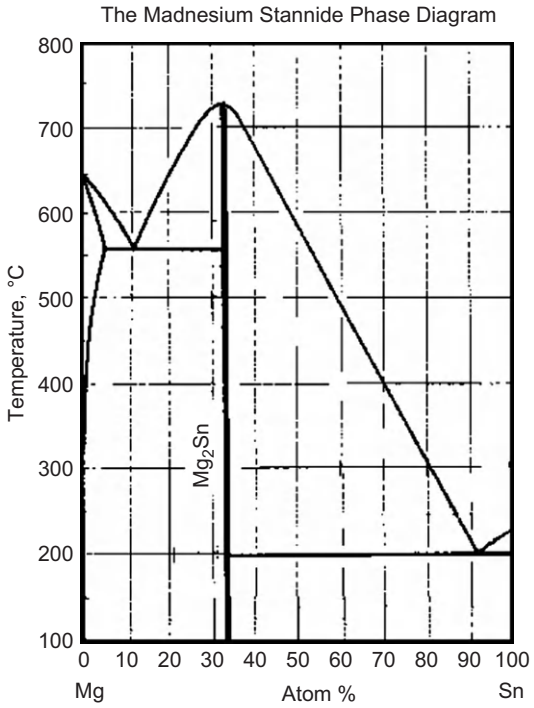

FIGURE 5.99

$Mg_{0.15}Sn_{0.85}$

$a = 3.011$ Å, $b = c = 3.189$ Å, $\alpha = 120°$, $\beta = \gamma = 90°$, cell volume = 26.47 Å^3, cell occupancy is shown in Table 5.46.

Single crystals of Mg_9Sn_5, a supposed high-pressure modification of Mg_2Sn, have been obtained from the elements by high-pressure and high-temperature reaction in a modified Belt-type apparatus (Ta capsule, 50 kbar, cooling = 1400 °C ⇒ 500 °C, and subsequent quenching to ambient conditions). The compound crystallizes trigonally, space group R3d, with $a = 13.222$, $c = 13.150$ Å, $c/a = 0.9946$ and $Z = 6$. Final residuals after refinement against F_2 were R1 = 0.0297, wR2 = 0.0811 and $S = 0.927$ for 85 refined parameters and 975 unique reflections. The crystal investigated showed obverse–reverse twinning and a pronounced pseudo-symmetry.

The crystal structure of Mg_9Sn_5 comprises a framework of magnesium atoms with an arrangement similar to that found in Fe_2P. The tin atoms are accommodated in tunnels running along the c-axis. Mg_9Sn_5 is at least very similar, perhaps even identical, with the "dense form of Mg_2Si", described by Cannon and Conlin (1964).

However, most of the published work has involved the Mg_2Sn type of compound. By varying the ratio of

TABLE 5.43

Number	Compound	Type	Space group	Point group	SG number
1	$Mg_{0.15}Sn_{0.85}$	$Hg_{0.1}Sn_{0.0}$	HP1	P6/mmm	191
2	$Mg_{0.975}Sn_{0.025}$	Mg	HP2	$P6_1/mmm$	194
3	Mg_2Sn	CaF_2	CF12	Fm-3m	225
4	Mg_9Sn_5	Mg_9Sn_5	HR84	R3	146

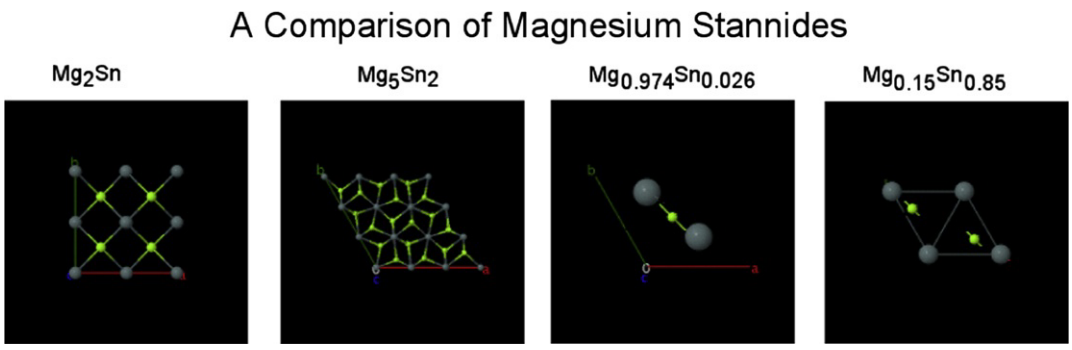

FIGURE 5.100

TABLE 5.44

No	Site notation	Atom	Multiplicity	Wyckoff	Site symmetry	*x*	*y*	*z*	Occupancy
1	Mg	Mg	8	c	-43m	1/4	1/4	1/4	1.0
2	Sn	Sn	4	a	m-3m	0	0	0	1.0

TABLE 5.45

No	Site notation	Atom	Multiplicity	Wyckoff	Site symmetry	*x*	*y*	*z*	Occupancy
1	Mg3	Mg	9	b	1	0.1506	0.2306	0.3656	1.0
2	Mg1	Mg	9	b	1	0.162	0.2402	0.0306	1.0
3	Mg5	Mg	9	b	1	0.1701	0.4273	0.2045	1.0
4	Mg2	Mg	9	b	1	0.2337	0.0774	0.1959	1.0
5	Sn1	Sn	9	b	1	0.3312	0.3345	0.1951	1.0
6	Sn2	Sn	9	b	1	0.3314	0.0007	0.0284	1.0
7	Mg6	Mg	9	b	1	0.4314	0.2601	0.0277	1.0
8	Mg4	Mg	9	b	1	0.5165	0.107	0.2005	1.0
9	Sn5	Sn	3	a	3.	0	0	0.0	1.0
10	Sn6	Sn	3	a	3.	0	0	0.2623	1.0
11	Sn4	Sn	3	a	3.	0	0	0.5044	1.0
12	Sn3	Sn	3	a	3.	0	0	0.7597	1.0

TABLE 5.46

No	Site notation	Atom	Multiplicity	Wyckoff	Site symmetry	*x*	*y*	*z*	Occupancy
1	M	0.85Sn + 0.15Mg	1	a	6/mmm	0	0	0	1.0

Mg/Sn in the Mg_2Sn melt, it is possible to obtain crystals with either *n*-type or *p*-type semiconducting properties. Resistivity and Hall measurements were carried out on Mg_2Sn crystals in the temperature range 300–60 K (−215 to 25 °C). Single crystals were grown by a modified Bridgman technique from stoichiometric melts and from melts containing 1, 2, 10, and 18 at.% excess Sn and 3 at.% excess Mg. In the mixed conduction and

extrinsic ranges, it was found possible to describe the calculated temperature dependence of the conduction mobility based on a combination of lattice vibration (acoustic mode) and ionized impurity scattering. A stoichiometry effect was observed. The Mg_2Sn crystals appear to dissolve the excess constituent producing *n*-type crystals (excess Sn) and *p*-type crystals (excess Mg). The observed effect corresponds to a solubility of 10^{-5} to 10^{-6} action excess constituent. This result was briefly discussed in terms of bonding in Mg_2Sn that has been found to consist of weak covalent bonds (Fig. 5.101).

By ball milling, a mixture of Mg–Sn metals, the mechanical alloying (MT) of a mixture of pure metals under argon or hydrogen atmosphere initially leads to the formation of the stable cubic structure of Mg_2Sn. Its transformation into the high-pressure and high-temperature phase of Mg_2Sn is produced during the course of milling. This metastable hexagonal structure transforms into the stable phase at 440 °C.

With the discovery of the MT method that produces stable compounds at room temperature, interest in industry has revived. Mg_2Sn has two relevant physical properties. It is an *n*-type semiconductor and it is a thermoelectric compound with a Seebeck coefficient that exceeds any other known compound, particularly when combined with Mg_2Si. Samples based on Mg_2Si–Mg_2Sn solid solutions, with a density exceeding 95% of theoretical density, have been prepared. The thermoelectric properties (Seebeck coefficient, electrical and thermal conductivities) have been measured in the temperature range 300–850 K (25–575 °C). Measurements of the thermoelectric properties from about 80 to 700 K show that the presence of excess Sn or Mg in the Mg_2Sn crystal decreases the absolute values of the Seebeck coefficient but causes the electrical conductivity to increase. The net effect of a small amount of finely dispersed inclusions leads to enhancement of the power factor, while larger amounts of free Mg or Sn or $Mg_2Sn + Mg$ eutectic can form interconnected microstructures which, while causing the electrical conductivity to increase, also lower the Seebeck coefficient and thus lead to a lower power factor. However, it is possible to disperse these coarse inclusions by powder metallurgy followed by hot pressing to produce bulk materials with nanoscale grain size and containing a large concentration of submicron inclusions of metal-like and semiconducting secondary phases which are effective in scattering phonons, i.e. decreasing the thermal conductivity, thus greatly enhancing the figure of merit.

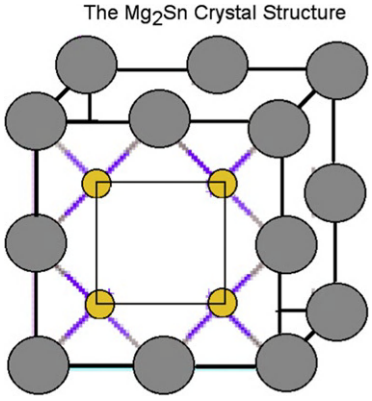

FIGURE 5.101

Phase relations in the Mg_2Sn–Sn system were studied by DTA at a pressure of 5.8 GPa and temperatures up to 1100 °C. A schematic *p*,*T* diagram for Mg_2Sn has been presented. Single crystals of the high-pressure phase of Mg_2Sn were obtained by growth from a molten solution under high pressure. Crystal data for Mg_2Sn(II) were determined using a Berger precession X-ray camera. The phase Mg_2Sn(II) crystallizes with a hexagonal unit cell, $a = 13.19 \pm 0.01$ Å, $c = 13.28 \pm 0.01$ Å, $c/a = 1.006$, $D_m = 4.1 \pm 0.2$ g/cm^3, $Z = 30$, $D_c = 4.17$ g/cm^3, space group $P3c1$ (no. 158) or (no. 163).

Positive electrodes for Li-ion and lithium batteries (also termed "cathodes") have been under intense scrutiny since the advent of the Li-ion cell in 1991. This is especially true in the past decade when Mg_2Sn came to the forefront. The electrochemical properties of Mg_2Sn were investigated to evaluate a new anode material for a lithium battery. A Mg_2Sn intermetallic compound was synthesized by the mechanical alloying (MA) method. As a result, it was found that the reversible insertion–extraction of a large amount of lithium can be electrochemically inserted in a mechanically alloyed Mg_2Sn. The Mg_2Sn changed its own crystal structure from cubic to orthorhombic with increasing MA time. The compound exhibiting a good performance as an anode had a mixture of cubic and orthorhombic phases. The discharge capacity of the Mg_2Sn electrode was still maintained at 250–300 mA h/g even after a 20 times charge–discharge cycle. The reaction proceeded without any phase separation and/or decomposition of the compound. Mg_2Sn is regarded as a promising anode material for lithium secondary batteries.

Further work has shown that the reversibility of alloying of lithium with the cubic phase of Mg_2Sn can be faulty in a lithium battery. Through in situ XRD measurements, the reactivity mechanisms of cubic Mg_2Sn toward lithium were deduced. It entails first a monophasic insertion of about one lithium per formula unit into the fcc Sn framework without extrusion of either Mg or Sn, then a biphasic process leading to the formation of cubic Li_2MgSn concomitant with a progressive expulsion of Mg, and finally the formation of

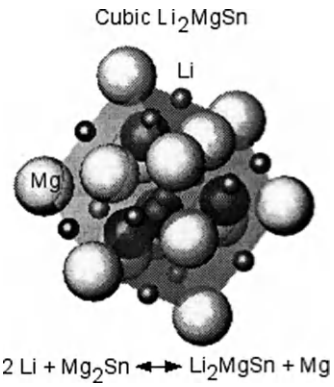

FIGURE 5.102

Li–Mg solid-solution alloys. Upon charging, the poor reversibility of the alloying reaction of Li with Mg leads to a deficit in free Mg, resulting in the formation of a $Mg_2Sn + Sn$ mixture, and accounting for the poor cyclability of Mg_2Sn/Li cells over the 0.0–1.5 V voltage window. Limiting the cycling to the monophasic process was shown to improve the cycling behavior. Finally, it was found that the electrochemical reaction of high-pressure Mg_2Sn(II) with Li leads to the same Li_2MgSn intermediate and the same subsequent sequence of transformations, resulting in similarly poor capacity retention upon cycling. The structure determined is shown in the following Fig. 5.102.

It is for this reason that Ag and/or Mg_2Si has been added to Mg_2Sn to improve this type of performance.

Mg_2Sn ingots, doped *p*-type by the addition of 0–1.0 at.% Ag, were prepared by the vertical Bridgman method at growth rates ~0.1 mm/min. The crystalline quality and microstructure of ingots were analyzed by XRD, scanning electron microscopy and energy-dispersive X-ray spectroscopy. The single-phase Mg_2Sn ingots consist of highly oriented large grains. Measurements of the Hall coefficient, Seebeck coefficient a, and electrical conductivity s in the temperature range 80–700 K were conducted to study the dependence on the silver content, and to determine the thermoelectric power factor a^2s which reached a maximum value 2.4×10^{-3} W/m/K^2 at 410 K (207 °C) for 1.0 at-% Ag content.

In another paper, $Mg_2Si_{1-x}Sn_x$ ($x = 0.2$, 0.4, 0.6 and 0.8) thermoelectric materials have been prepared by vacuum melting and melting/hot-pressing methods. The phase structures and electrical transport properties were measured. The relationships between electronic structures and electronic properties are discussed. XRD showed that the hot-pressed compounds were better formed. The electrical conductivity and Seebeck coefficient measurements showed that the properties of the compounds were dramatically affected by solid solubility. When $x = 0.2$, the highest electrical conductivity resulted in the highest power factor of 1.32×10^{-3}/Wm/K^2 at about 500 K, while the highest value of Seebeck coefficient of -459 μvk^{-1} was obtained at about 450 K for $x = 0.6$.

Mg_2Sn has the CAS number of 1313-08-2 and is available commercially.

Calcium Stannides

The metal, Ca, melts at 842 °C while Sn melts at 232 °C. The SSR of the metals produces:

$$2Ca + Sn \Rightarrow Ca_xSn_y$$

as a product, where x or y can vary from 1 to 30. The phase diagram of the Ca–Sn system has been investigated in the whole composition range using DTA, metallographic analysis, single-crystal and powder XRD. Seven intermediate phases have been found. Four of them have been confirmed: $CaSn_3$ ($AuCu_3$-type), CaSn (CrB-type), $Ca_{31}Sn_{20}$ ($Pu_{31}Rh_{20}$-type) and Ca_2Sn (Co_2Si-type). They melt congruently while Ca_7Sn_6 (Ca_7Sn_6-type), $Ca_{36}Sn_{23}$ ($Yb_{36}Sn_{23}$-type) and Ca_5Sn_3 (Cr_5B_3-type) have been identified and characterized as melting incongruently, as shown in the following phase Fig. 5.103.

Four eutectic points occur in this system: at about 5 at.% Sn and 780 °C, 48 at.% Sn and 995 °C, 68 at.% Sn and 610 °C, and at less than 1 at.% Ca and 225 °C. It was also found that $Ca_{36}Sn_{23}$ is a mechanically unstable phase. Results on the electronic energy band and densities of states also indicated that Ca_2Sn, is a direct band gap semiconductor with a band gap of 0.07 eV. In addition, it is found that the absolute values of heats of formation for all Ca–Sn intermetallics are larger than 30 kJ/mol atom.

The crystal structure data is shown in the following Table 5.47.

The following shows a comparison along the a ⇒ c vector plane of the structures (Fig. 5.104).

Unit-cell parameters for these compounds are:

$Ca_{0.15}Sn_{0.85}$

$a = 2.994$ Å, $b = c = 3.151$ Å, $\alpha = 120°$, $\beta = \gamma = 90°$, cell volume = 25.74 Å^3, cell occupancy is shown in Table 5.48.

$Ca_{31}Sn_{20}$

$a = b = 12.5422$ Å, $c = 21.8781$ Å, $\alpha = \beta = 106.66°$, $\gamma = 90°$, cell volume = 3146.02 Å^3, cell occupancy is shown in Table 5.49.

CaSn

$a = 4.349$ Å, $b = 4.841$ Å, $c = 6.244$ Å, $\alpha = 112.71°$, $\beta = \gamma = 90°$, cell volume = 120.77 Å^3, cell occupancy is shown in Table 5.50.

Ca_3Sn

$a = b = c = 4.732$ Å, $\alpha = 120°$, $\beta = \gamma = 90°$, cell volume = 105.96 Å^3, cell occupancy is shown in Table 5.51.

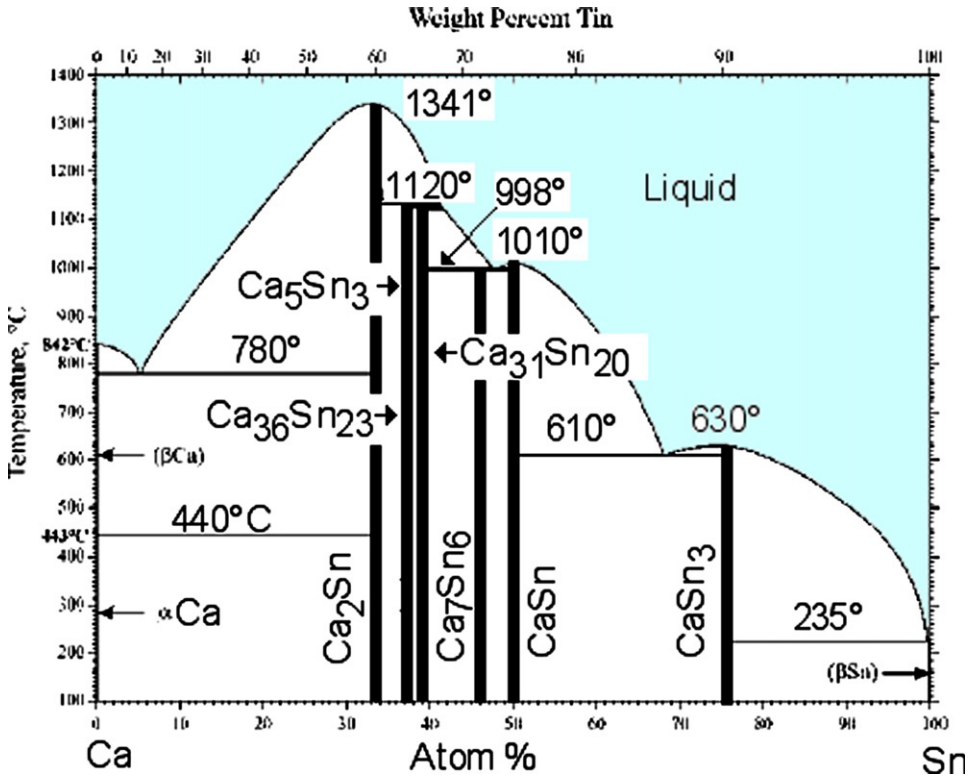

FIGURE 5.103

Ca_2Sn

$a = 5.044$, $b = 7.975$ Å, $c = 9.562$ Å, $\alpha = \beta = \gamma = 90°$, cell volume $= 384.64$ Å^3, cell occupancy is shown in Table 5.52.

The standard free energies of formation of dicalcium stannide were determined by a chemical equilibration technique, yielding the following results:

$$2Ca(liq) + Sn(liq) = Ca_2Sn(solid):$$

$$\Delta G° = -353{,}970 + 79.28\,T\ (J/mol)\ 1000\ °C \text{ to } 1300\ °C.$$

Dicalcium stannide is a thermoelectric material. Approximate room temperature values for the figures of merit of stoichiometric calcium stannide, and strontium stannide have been determined. The highest value obtained was about 7×10^{-5} (K), for the latter compound.

X-ray investigations have shown that Ca_2Sn is an isotype with Ca_2Si and Ca_2Ge ($PbCl_2$-structure, C23-type). Lattice constants, space group, and point parameters are: Ca_2Sn: $a = 9.562 \pm 0{,}004$; $b = 7.975 \pm 0.004$;

TABLE 5.47

Composition	at. % Sn	Pearson symbol	Space group	Designation	Prototype
β-Ca	0	C/2	$Im\bar{3}m$	A_1	W
α-Ca	0	CF/4	$Fm\bar{3}m$	A_2	Cu
Ca_2Sn	33.3	oP12	Pnma	C23	Co_2Si
Ca_5Sn_3	37.5	t/32	I4/mcm	$D8_f$	Cr_5B_3
$Ca_{31}Sn_{20}$	39.2	*tI*204	*I4/mcm*	1/4	$Pu_{31}Rh_{20}$
Ca_7Sn_6	46.2	*oP*52	*Pnma*	1/4	Ca_7Sn_6
CaSn	50	*oC*8	*Cmcm*	*Bf*	*Bf* CrB
$CaSn_3$	75	*cP*4	*Pm*$\bar{3}$*m*	*L*12	*L*12 $AuCu_3$
$Ca_{0.15}Sn_{0.85}$	85.0	*tP*118	*P4/mbm*	1/4	$Yb_{36}Sn_{23}$
βSn	100	*tI*4	$I4_1/amd$	*A*5	βSn

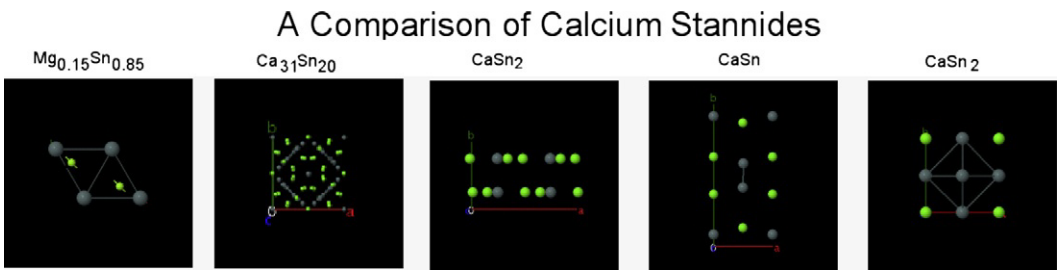

FIGURE 5.104

TABLE 5.48

No	Site notation	Atom	Multiplicity	Wyckoff	Site symmetry	*x*	*y*	*z*	Occupancy
1	M	0.85Sn + 0.15Ca	1	a	6/mmm	0	0	0	1.0

TABLE 5.49

No	Site notation	Atom	Multiplicity	Wyckoff	Site symmetry	*x*	*y*	*z*	Occupancy
1	Ca(2)	Ca	32	m	1	0.0519	0.2103	0.0533	1.0
2	Ca(6)	Ca	32	m	1	0.0861	0.2138	0.2125	1.0
3	Ca(4)	Ca	32	m	1	0.2161	0.0808	0.1365	1.0
4	Sn(7)	Sn	16	l	..m	0.1531	0.6531	0.2087	1.0
5	Sn(3)	Sn	16	l	..m	0.1981	0.6981	0.0748	1.0
6	Sn(5)	Sn	16	l	..m	0.6617	0.1617	0.1231	1.0
7	Ca(1)	Ca	8	h	m.2m	0.1595	0.6595	0	1.0
8	Sn(2)	Sn	8	h	m.2m	0.5859	0.0859	0	1.0
9	Ca(3)	Ca	8	g	2.mm	0	1/2	0.0716	1.0
10	Ca(5)	Ca	8	g	2.mm	0	1/2	0.1678	1.0
11	Sn(4)	Sn	8	f	4..	0	0	0.0949	1.0
12	Sn(6)	Sn	8	f	4..	0	0	0.1733	1.0
13	Sn(1)	Sn	4	c	4/m..	0	0	0	1.0
14	Ca(7)	Ca	4	b	-42m	0	1/2	1/4	1.0
15	Sn(8)	Sn	4	a	422	0	0	1/4	1.0

TABLE 5.50

No	Site notation	Atom	Multiplicity	Wyckoff	Site symmetry	*x*	*y*	*z*	Occupancy
1	Sn	Sn	4	c	m2m	0	0.084	1/4	1.0
2	Ca	Ca	4	c	m2m	0	0.367	1/4	1.0

TABLE 5.51

No	Site notation	Atom	Multiplicity	Wyckoff	Site symmetry	x	y	z	Occupancy
1	Sn	Sn	3	c	4/mm.m	0	1/2	1/2	1.0
2	Ca	Ca	1	a	m-3m	0	0	0	1.0

TABLE 5.52

No	Site notation	Atom	Multiplicity	Wyckoff	Site symmetry	x	y	z	Occupancy
1	Ca2	Ca	4	c	.m.	0.013	1/4	0.683	1.0
2	Ca1	Ca	4	c	.m.	0.155	1/4	0.067	1.0
3	Sn	Sn	4	c	.m.	0.253	1/4	0.389	1.0

$c = 5.044 \pm 0.003$ Å. The point group is D_{2h}^{14} and the space group is D-Pbnm; the atoms lie at:

$$4c \pm (x,y,1/4) \text{ and } (1/2 - x,1/2 + y,1/4)$$

The phase, $Ca_{31}Sn_{20}$, has a tetrahedral symmetry with: $a = 12.542$ Å, $c = 40.00$ Å, space group = I4/mcm, $V = 6292$ Å^3, $Z = 4$ and $d = 3.74$ g/cc.

Calcium distannide, $CaSn_2$ is not known.

The compound, **calcium tristannide**, $CaSn_3$, once formed, is immediately decomposed by air at room temperature. It has been observed to possess a pronounced singularity of orbital magnetic susceptibility. The degeneracy points of the electronic energy bands close to the Fermi level are found to be responsible for the anomalous diamagnetism in $CaSn_3$ alloys. The appearance and smearing of this anomaly with temperature and impurities were analyzed, and corresponding band structure and scattering parameters were determined. This compound, in argon gas atmosphere, melts congruently with:

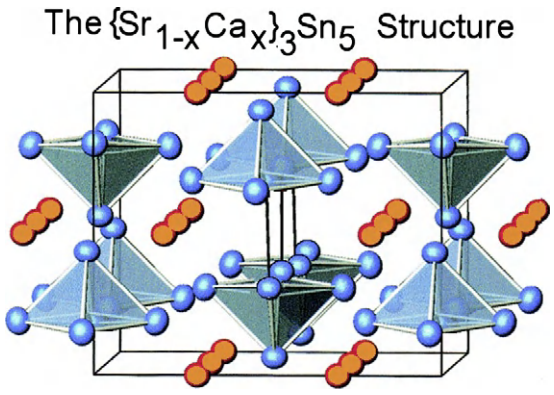

FIGURE 5.105

$$\Delta S \text{ melting } (Ca_{0.25}Sn_{0.75}) = 14.6 + 0.1 \text{ J/mol degree;}$$
$$T_{melting} = 891 \pm 1 \text{ K}$$

All attempts to obtain the pure Ca phase of **tricalcium pentastannide**, Ca_3Sn_5, have been unsuccessful. However, the compound, Sr_2CaSn_5, has been prepared. It was found to crystallize in the Pu_3Pd_5 structure type (SG = Cmcm) with cell dimensions of $a = 10.5179(9)$ Å, $b = 8.4789(8)$ Å, and $c = 10.7623(10)$ Å (Fig. 5.105).

The structure consists of isolated Sn_5^{6-} square-pyramidal units surrounded by cations that seem to play a crucial role in stabilizing the Zintl polyanions. The square pyramids contract at low temperatures (100 K = −173 °C) leading to the shortening of the basal intracluster Sn–Sn bond (2.74 Å), while the intercluster bonds become very large, indicating that features of bond-stretching isomerism are known for both Sr_3Sn_5 and Ba_3Ge_4. Study of different crystals shows a slight variation in the lattice parameters, suggesting the presence of a definite phase width which was substantiated by the successful synthesis of monophasic samples of $Sr_{3-x}Ca_xSn_5$ ($0.5 \le x \le 2.5$). The structure is shown in the following diagram which depicts the alkaline earth positions as "reddish-orange". The atom coordinates for this structure are given in Table 5.53.

The phase, $Ca_{31}Sn_{20}$ (which is related to Ca_3Sn_2—**tricalcium distannide**), can be obtained by allowing the pure elements to react in sealed Ta containers at 1100–1180 °C followed by slow cooling. It is isostructural with $Pu_{31}Pt_{20}$. The structure of $Ca_{31}Sn_{20}$ was redetermined (I4/mcm, $Z = 4$, $a = 12.5267$ Å, $c = 39.912$ Å). A description of the structure is given in terms of isolated tin atoms plus well-bonded tin dimers and linear pentamers (d(Sn–Sn) = 3.06–3.16 Å) in proportions of 5:5:1 within a rather distorted W_5Si_3-like framework. It was also found that $Ca_{36}Sn_{23}$ is a mechanically unstable phase.

TABLE 5.53

No	Site notation	Atom	Multiplicity	Wyckoff	Site symmetry	x	y	z	Occupancy
1	Sr1	Sr	16	l	..m	0.166	0.666	0.15	1.0
2	Sn1	Sn	8	h	m.2m	0.625	0.125	0	1.0
3	Sr2	Sr	4	c	4/m..	0	0	0	1.0
4	Sn2	Sn	4	a	422	0	0	1/4	1.0

The addition of hydrogen to these stannides forms a series of Zintl phases. The electronic structure of three recently discovered Zintl-phase hydrides: $SrAl_2H_2$, Ca_3SnH_2, and Ca_5Sn_3H have been analyzed. The energy bands and the total and partial densities of states were computed by means of the full-potential linearized augmented plane wave method. It was found that $SrAl_2H_2$ and Ca_5Sn_3H hydrides are metallic and Ca_3SnH_2 is a small-gap semiconductor.

Calcium stannides have no CAS number and are not offered for sale commercially.

Strontium Stannides

The metal, Sr, melts at 776 °C while Sn melts at 232 °C. The SSR of the two at 900 °C produces a compound with atomic ratios according to those of Sr/Sn used in the original mixture:

$$2Sr + Sn \Rightarrow Sr_2Sn$$

The phase diagram of the Sr–Sn system was investigated over the complete compositional range by means of DTA, XRD, optical microscopy (LOM). All the already known intermediate phases: Sr_2Sn ($PbCl_2$-type), Sr_5Sn_3 (Cr_5B_3-type), SrSn (CrB-type), Sr_3Sn_5 (Pu_3Pd_5-type), $SrSn_3$ ($PuGa_3$-type) have been confirmed. Also the very new compound, $SrSn_4$, recently determined, could be confirmed in this work. Three eutectics occur in the system: at about 2.5 at.% Sn and 752 °C, 45.5 at.% Sn and 1100 °C and about 99.0 at.% Sn and 230 °C (Fig. 5.106).

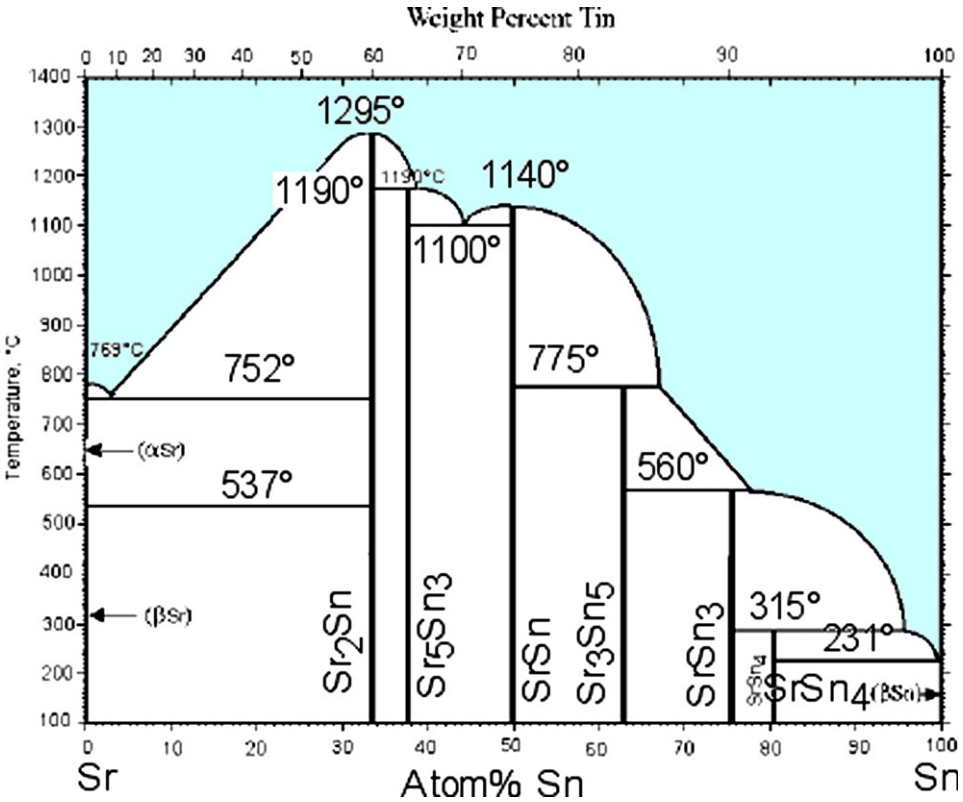

FIGURE 5.106

TABLE 5.54 Composition at-% Sn Pearson Symbol Space Group Designation Prototype

Composition	at. % Sn	Pearson symbol	Space group	Designation	Prototype
β-Sr	0	C/2	$Im\bar{3}m$	A_1	W
α-Sr	0	CF/4	$Fm\bar{3}m$	A_2	Cu
Sr_2Sn	33.3	oP12	Pnma	C23	Co_2Si
Sr_5Sn_3	37.5	t/32	I4/mcm	$D8_f$	Cr_5B_3
SrSn	50	*oC8*	*Cmcm*	*Bf*	CrB
Sr_3Sn_5	62.5	*OC32*	*Cmcm*	$D8_l$	Ca_7Sn_6
$SrSn_3$	75.0	*hR48*	*R3m*	—	Ga_3Pu
$SrSn_4$	80.0	*OC20*	*Cmcm*	—	Ga_3Pu
βSn	100	*tI4*	*$I4_1/amd$*	*A5*	βSn
αSn	100	*CF8*	*Fd3m*	*A_4*	C(diamond)

A part of the Sn–Sr phase diagram was investigated in 1981 and later by other investigators (1981). The entire phase diagram was reinvestigated in 2004 by means of DTA, XRD and optical microscopy. The result is shown below. The associated crystal structure data is shown in Table 5.54.

One paper reported that SnSr and SnSr2 were dimorphic. However, the 2004 investigation found no phase transitions in these compounds. The Sn_5Sr_3 phase was unknown.

Only two compounds, Sr_2Sn and SrSn, melt congruently. The other three melt incongruently, decomposing to the adjacent compound. For example, Sr_5Sn_3 decomposes to form Sr_2Sn and SrSn:

$$Sr_5Sn_3 + \text{heat} \Rightarrow 2Sr_2Sn + SrSn$$

$$Sr_3Sn_5 + \text{heat} \Rightarrow SrSn + SrSn_3$$

$$4SrSn_3 + \text{heat} \Rightarrow Sr_3Sn_5 + SrSn_4 + 3Sn$$

$$SrSn_4 + \text{heat} \Rightarrow SrSn_3 + Sn$$

A comparison of the a ⇒ c vector plane of four of these structures is shown in the following Fig. 5.107.

Unit-cell parameters are:

Sr_2Sn

$a = 5.378$, $b = 8.402$ Å, $c = 10.078$ Å, $\alpha = \beta = \gamma = 90°$, cell volume = 455.38 $Å^3$, cell occupancy is shown in Table 5.55.

Sr_2Sn

$a = b = 8.565$ Å, $c = 10.138$ Å, $\alpha = \beta = 114.99°$, $\gamma = 90°$, cell volume = 596.45 $Å^3$, cell occupancy is shown in Table 5.56.

SrSn

$a = 4.495$ Å, $b = 5.045$ Å, $c = 6.527$ Å, $\alpha = 112.74°$, $\beta = \gamma = 60°$, cell volume = 136.49 $Å^3$. Cell occupancy is shown in Table 5.57.

$SrSn_3$

$a = b = 6.945$ Å, $c = 11.710$ Å, $\alpha = \beta = 72.76°$, $\gamma = 60°$, cell volume = 458.96 $Å^3$. Cell occupancy is shown in Table 5.58.

Strontium tetrastannide, $SrSn_4$, is a superconducting stannide with localized and delocalized bond character.

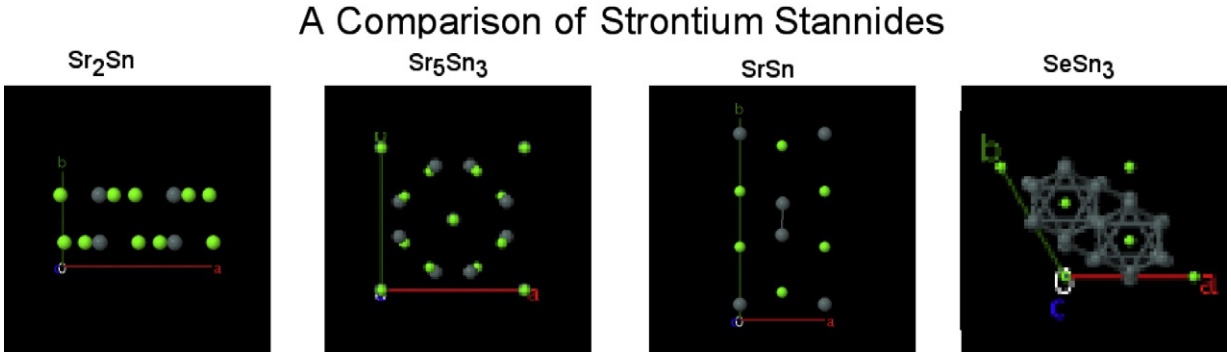

FIGURE 5.107

TABLE 5.55

No	Site notation	Atom	Multiplicity	Wyckoff	Site symmetry	*x*	*y*	*z*	Occupancy
1	Sr(2)	Sr	4	c	.m.	0.0213	1/4	0.6808	1.0
2	Sr(1)	Sr	4	c	.m.	0.1561	1/4	0.0723	1.0
3	Sn	Sn	4	c	.m.	0.2512	1/4	0.3932	1.0

TABLE 5.56

No	Site notation	Atom	Multiplicity	Wyckoff	Site symmetry	*x*	*y*	*z*	Occupancy
1	Sr1	Sr	16	l	..m	0.166	0.666	0.15	1.0
2	Sn1	Sn	8	h	m.2m	0.625	0.125	0	1.0
3	Sr2	Sr	4	c	4/m..	0	0	0	1.0
4	Sn2	Sn	4	a	422	0	0	1/4	1.0

TABLE 5.57

No	Site notation	Atom	Multiplicity	Wyckoff	Site symmetry	*x*	*y*	*z*	Occupancy
1	Sn	Sn	4	c	m2m	0	0.0788	1/4	1.0
2	Sr	Sr	4	c	m2m	0	0.3633	1/4	1.0

TABLE 5.58

No	Site notation	Atom	Multiplicity	Wyckoff	Site symmetry	*x*	*y*	*z*	Occupancy
1	Sn2	Sn	18	h	.m	0.4787	0.5213	0.1226	1.0
2	Sn1	Sn	18	h	.m	0.5060	0.4940	0.2914	1.0
3	Sr2	Sr	6	c	3m	0	0	0.1314	1.0
4	Sr1	Sr	6	c	3m	0	0	0.2904	1.0

This compound is the tin-richest phase in the system Sr–Sn and is obtained by stoichiometric combination of the elements. $SrSn_4$ decomposes in a peritectic manner with formation of $SrSn_3$ and Sn at 340 °C. The structure determined from a single crystal shows a new structure type with a novel structure motive in tin chemistry. It can be described by a corrugated, distorted quadratic net of tin atoms as the only building unit. The nets intersect at common Sn atoms, and the resulting channels host the Sr atoms (Fig. 5.108).

The structure can alternatively be described as an intergrowth structure of the AlB_2-type and W-type. The atoms that are connected by the two shortest Sn–Sn distances (2.900 and 3.044 Å) form a two-dimensional net consisting of hexagons of tin atoms. The hexagons have boat conformation in contrast to the rather similar alpha-As structure type, where hexagons have a chair conformation. Further tin atoms connect the two-dimensional net of Sn hexagons. Temperature-dependent magnetic susceptibility measurements show that $SrSn_4$ is superconducting with $T(c) = 4.8$ K at 10 G. LMTO band structure and density of states (DOS) calculations verify the metallic behavior of $SrSn_4$. An analysis of the electronic structure with the help of the electron localization function (ELF) shows that localized covalent bonds beside delocalized bonds

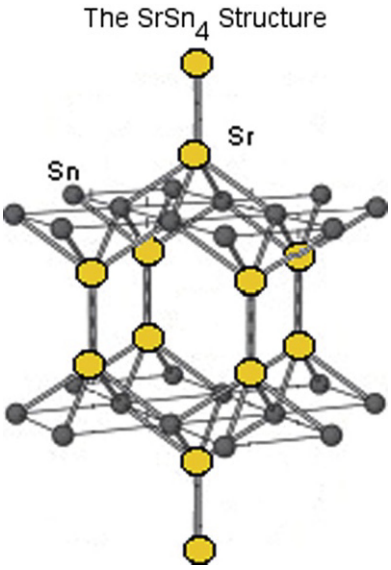

FIGURE 5.108

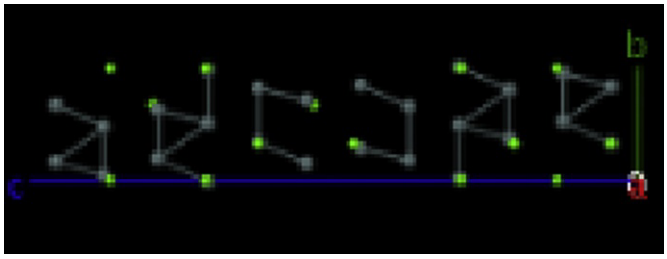

FIGURE 5.109

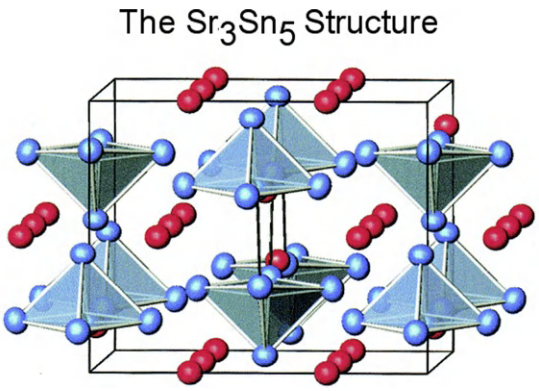

FIGURE 5.110

coexist in $SrSn_4$. The structure of $SrSn_4$ is characterized by regions, which can be described by covalent bonds between the Sn atoms and regions with higher coordination numbers for Sn, which are typical for intermetallic compounds. Therefore, $SrSn_4$ is an example for the structural transition between Zintl phases and intermetallics.

Strontium tristannide, $SrSn_3$, shows a transition to the superconducting state at 5.4 K and $SrSn_4$ at 4.8 K. $SrSn_3$ crystallizes in the Mg_3In-type, which consists of distorted hexagonal layers with AB_3 composition, similar to the above structure. In addition, a Zintl compound composed of $SrSn_3 \cdot SrSb_4$ has been synthesized and its structure has been determined by single-crystal XRD methods. It crystallizes in the orthorhombic space group—Pnma with $a = 10.060$ Å, $b = 4.361$ Å, $c = 22.934$ Å, and $Z = 4$ at 22 °C. The structure of $Sr_2Sn_3Sb_4$ may be described as consisting of large, narrow channels running along [010] defined by 30-membered rings constructed from an anionic framework of linked $SnSb_4$ tetrahedra, $SnSb_3$ trigonal pyramids, and zigzag Sb–Sb chains. Sr^{2+} cations are situated within these channels. This structure has the following symmetry where the coordination along the *a*-axis is shown in Fig. 5.109.

The atom coordinates for this structure are given in Table 5.59.

The structure of **tristrontium pentastannide**, Sr_3Sn_5 is isotypic to one of Pu_3Pd_5. The basic structural unit is a distorted square pyramid of Sn atoms. Those $[Sn_5]^{6-}$ anions can be regarded as a Wades cluster of the arachno type. The strontium and tin atoms are clearly seen in the above diagram, as shown in Fig. 5.110.

The electronic structure of the pyramidal Zintl anions and the influence of the number of skeletal electrons of these clusters were investigated using the ELF. The structural relationship between Sr_3Sn_5 and the Zintl phases Ba_3Si_4 and Ba_3Ge_4 are analyzed. Additionally, two new Zintl phases $Ba_3Ge_{2.82}Sn_{2.18}$ and $Ba_3Ge_{3.94}Sn_{0.06}$, have been synthesized and their structures are reported, which directly show that the exchange of tin against germanium leads to a change from the $M_{3\times5}$ to the $M_{3\times4}$ structure type. This effect

TABLE 5.59

No	Site notation	Atom	Multiplicity	Wyckoff	Site symmetry	*x*	*y*	*z*	Occupancy
1	Sn2	Sn	18	h	.m	0.4787	0.5213	0.1226	1.0
2	Sn1	Sn	18	h	.m	0.5057	0.4940	0.2914	1.0
3	Sr2	Sr	6	c	3m	0	0	0.1314	1.0
4	Sr1	Sr	6	c	3m	0	0	0.2904	1.0

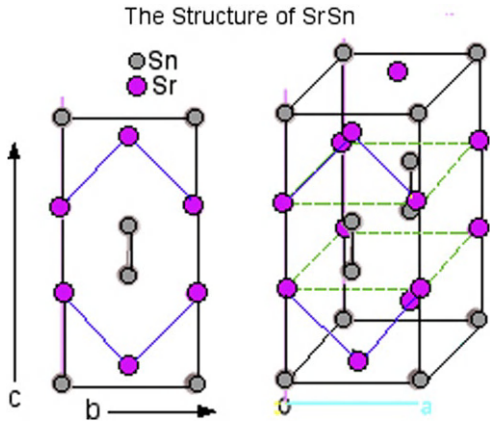

FIGURE 5.111

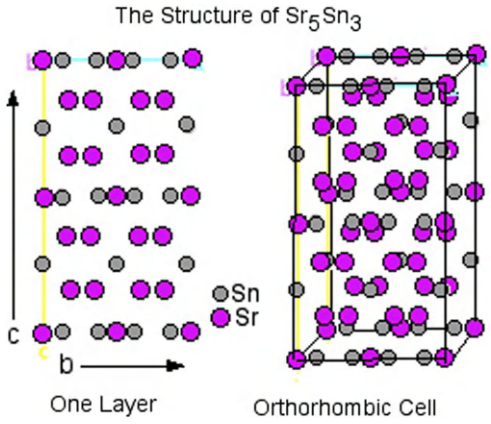

FIGURE 5.112

is traced back to the maximal charge acquisition property of the Zintl anions of heavier and lighter tetralides.

This compound contains square pyramidal Sn_5^{6-} polyanions and was been obtained by direct fusion of the elements at 570 °C, followed by slow cooling or annealing. The crystal structure was refined in the Pu_3Pd_5 structure type (orthorhombic, *Cmcm*, $Z = 4$) with cell dimensions of $a = 10.644$ Å, $b = 8.588$ Å, and $c = 10.895$ Å. Square pyramidal clusters of the tetrel elements are weakly interlinked into chains via two types of longer intercluster interactions that are mediated by bridging cations and substantially influenced by cation size and the free electron count. The new compounds are all metallic, in agreement with simple valence considerations that predict two and five extra electrons per formula unit. Extended Hückel tight-binding calculations on this compound reveal that bonding in the regions below and around the Fermi energies are dominated by general cation–anion interactions, that is, lattice covalency.

In another paper, the two binary Zintl phases, Sr_3Sn_5 and Ba_3Sn_5, have been synthesized and structurally characterized. The revised structure of Ba_3Pb_5 is also reported. All of these compounds are isotypic and crystallize with a modified Pu_3Pd_5 structure type. The anionic substructure is composed of Sn_5^{6-} square pyramidal clusters, which are described as arachno clusters according to the Wade–Mingos electron counting rules. The electronic structure of the pyramidal Zintl anions and the influence of the number of skeletal electrons of these clusters have been investigated using the ELF.

Although **strontium monostannide**, SrSn, has been synthesized, it has not been studied intensely. SrSn is a thermoelectric material but its Seebeck coefficient is lower than other known thermoelectrics. The highest value obtained was about 7×10^{-5}/K. The structure is presented shown in Fig. 5.111.

SrSn is orthorhombic with cell parameters of: $a = 5.045$ Å, $b = 12.04$ Å, $c = 4.494$ Å, $\alpha = 90°$, $\beta = 90°$, $\gamma = 90°$, cell volume $= 272.97$ Å^3, $d = 5.02$ g/cc, $Z = 4$. The atom coordinates for this structure are given in Table 5.60.

Pentastrontium tristannide, Sr_5Sn_3, also has not been the object of intense study academically. The phases Sr_5Sn_3 and Ba_5Sn_3 crystallize with the tetragonal Cr_5B_5 structure type and Sr_5Bi_3 is isostructural with orthorhombic β-Yb_5Sb_3. Single crystals of Sr_5Sb_3 in the orthorhombic form (β-Yb_5Sb_3 structure type) were obtained as a minor product of a reaction of the elements and Mn in a welded Nb container. To date only the hexagonal form (Mn_5Si_3-structure type) of Sr_5Sb_3 has been reported. The orthorhombic phase of Sr_5Sb_3 has synthesized in high yield by the reaction of stoichiometric amounts of the elements in an alumina crucible, sealed in a quartz tube. The structure is shown in the following Fig. 5.112.

The atom coordinates for this structure are given in Table 5.61.

Distrontium stannide, Sr_2Sn, also is orthorhombic but with differing cell parameters, as might be suspected. They are: $a = 8.402$ Å, $b = 5.378$ Å, $c = 10.078$ Å, $\alpha = 90°$, $\beta = 90°$, $\gamma = 90°$, cell volume $= 455.38$ Å^3. The structure is given in Fig. 5.113.

TABLE 5.60

No	Site notation	Atom	Multiplicity	Wyckoff	Site symmetry	*x*	*y*	*z*	Occupancy
1	Sn	Sn	4	c	m2m	0	0.0788	1/4	1.0
2	Sr	Sr	4	c	m2m	0	0.3633	1/4	1.0

TABLE 5.61

No	Site notation	Atom	Multiplicity	Wyckoff	Site symmetry	x	y	z	Occupancy
1	Sr1	Sr	16	l	..m	0.166	0.666	0.15	1.0
2	Sn1	Sn	8	h	m.2m	0.625	0.125	0	1.0
3	Sr2	Sr	4	c	4/m..	0	0	0	1.0
4	Sn2	Sn	4	a	422	0	0	1/4	1.0

TABLE 5.62

No	Site notation	Atom	Multiplicity	Wyckoff	Site symmetry	x	y	z	Occupancy
1	Sr(2)	Sr	4	c	.m.	0.0213	1/4	0.6808	1.0
2	Sr(1)	Sr	4	c	.m.	0.1561	1/4	0.0723	1.0
3	Sn	Sn	4	c	.m.	0.2512	1/4	0.3932	1.0

The atom coordinates for this structure are given in Table 5.62.

These three compounds may be compared to each other. Strontium stannides have no CAS number and are not available commercially.

Barium Stannides

Barium stannides can be formed through the reaction of the melted metals, provided that air is excluded from the reaction zone. The reaction that is used is:

$$x\mathrm{Ba} + y\mathrm{Sn} + \text{heat} \Rightarrow \mathrm{Ba}_x\mathrm{Sn}_y$$

where x and y usually varies from 1 to 6. In the phase diagram of the Ba/Sn system, the compounds Ba_2Sn, Ba_5Sn_3, Ba_3Sn_5, BaSn, $BaSn_2$, $BaSn_3$ and $BaSn_5$ have been recognized. The conditions for the synthesis of Ba_3Sn_5, $BaSn_3$, and $BaSn_5$ were optimized by DTA experiments of the corresponding stoichiometries of the binary phase system. Magnetic measurements showed that $BaSn_3$ and $BaSn_5$ become superconducting at 2.4 and 4.4 K, respectively. A partial substitution of Ba atoms by Sr atoms causes for $BaSn_3$ no significant change of the critical temperature. A higher transition temperature is observed in $BaSn_5$ if a part of Ba is replaced by Sr. The structural relationship between Ba_3Sn_5 and the Zintl phases, Ba_3Si_4 and Ba_3Ge_4, were analyzed. Additionally, two novel Zintl phases, $Ba_3Ge_{2.82}Sn_{2.18}$ and $Ba_3Ge_{3.94}Sn_{0.06}$, have been synthesized and their structures reported, which directly show that the exchange of tin against germanium leads to a change from the $M_{3\times5}$ to the $M_{3\times4}$ structure type. This effect is traced back to the maximal charge acquisition property of the Zintl anions of heavier and lighter tetralides. Although a number of barium stannide

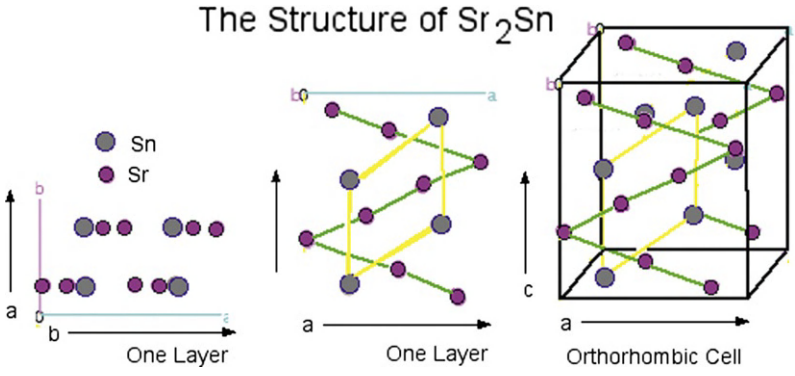

FIGURE 5.113

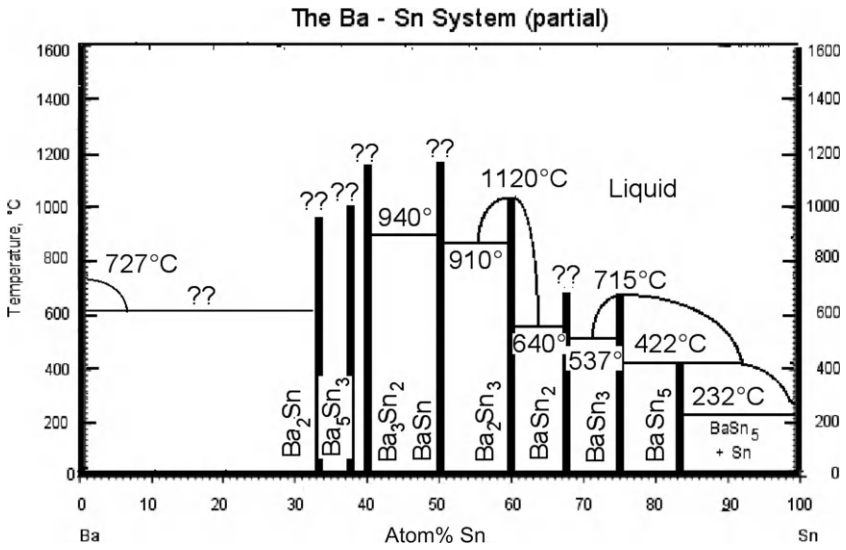

FIGURE 5.114

compounds are known, no complete phase diagram has been published. A partial phase diagram is shown in the following Fig. 5.114.

Instead of $BaSn_4$, the compound, $BaSn_5$, appears. Dibarium stannide, Ba_2Sn, is also known. The lack of melting-point data seems to be the reason why the full diagram has not been documented. All of the compounds that have been studied in regard to their crystal structure are included. However, melting points and mode of melting, as well as eutectics, are generally not available. Those compounds which have well-defined melting points are indicated in this diagram. It is clear that the high-barium compounds have not been studied in a thorough manner.

Barium monostannide, BaSn, contains zigzag chains of Sn^{2-} ions, along with Ba^{2+} ions. It is a Zintl compound. BaSn is orthorhombic with cell parameters of: $a = 7.065$ Å, $b = 14.041$ Å, $c = 4.484$ Å, $\alpha = 90°$, $\beta = 90°$, $\gamma = 90°$, cell volume = 444.81 Å^3, $d = 6.02$ g/cc, $Z = 4$. The structure is shown in Fig. 5.115.

Only a two-dimensional layout is shown so as to illustrate the Zintl layers which predominate in this structure. BaSn is metallic in electrical conductivity rather than being a semiconductor like many of the other Ba–Sn compounds. This may be the reason why BaSn has not received much attention in the scientific literature.

The atom coordinates for this structure are:

The compound, **barium distannide**, $BaSn_2$, is trigonal with space group $P3m1$ (no. 164), and lattice parameters of: $a = 4.652(2)$ Å, $c = 5.546(4)$ Å, $V = 103.9$ Å^3, $Z = 1$. $BaSn_2$ crystallizes in the $EuGe_2$ structure type ($c/a = 1.22$) with a c/a ratio of 1.19. The structure is shown in two-dimensions as in Fig. 5.116.

The structure is composed of 36 planar nets of Ba at $z = 0.5$ and corrugated 63 nets of three-bonded (3b) Sn atoms $\{[(3b)Sn]^{2-})_\infty\}$ with a Sn–Sn distance of 2.919(1) Å, which is slightly longer than the covalent bonds found in Sn (II) (2.80 Å). Such layers with 3b atoms are reminiscent of the element structure of (gray, rhombohedral) two-arsenic. The tin layers are made of condensed $\{Sn_6\}$ rings in chair conformation, which are arranged like in *trans*-decalin, and are primitively stacked along [001]. This is a contrast to the arsenic structure where the layers are displaced. Another difference is their clear separation with a shortest Sn–Sn interlayer contact of ca. 4.4 Å by Ba atoms. Another way of describing the Sn substructure is deriving it from the AlB_2 structure type by strong corrugation of the planar Ba-atom layers built of hexagons in AlB_2. The intralayer Sn–Sn distance is comparable to separations found in other Zintl phases, such as in Na_7Sn_{12} (2.83–3.09 Å). The valence angle of 105.7° in the layers is close to the ideal tetrahedral angle. The coordination by the six nearest Sn atoms (up to 4 Å) shows Ba residing in the center of a distorted $\{BaSn_6\}$

No	Site notation	Atom	Multiplicity	Wyckoff	Site symmetry	*x*	*y*	*z*	Occupancy
1	Sn	Sn	4	c	m2m	0	0.07	1/4	1.0
2	Ba	Ba	4	c	m2m	0	0.362	1/4	1.0

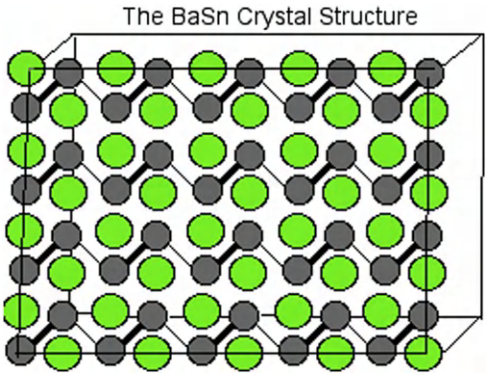

FIGURE 5.115

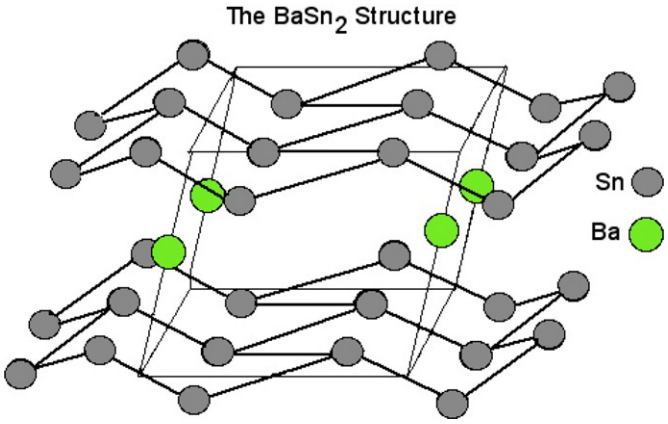

FIGURE 5.116

octahedron with a Ba–Sn distance of 3.473(2) Å. The latter description is consistent with Ba atoms populating the octahedral holes between two hexagonal Sn layers. Each octahedron shares six edges with its neighbors, resulting in edge-sharing layers of octahedra in the (001) plane. The tetrahedral holes are empty.

In the Ba/Sn system, **barium tristannide**, $BaSn_3$, could be isolated (Pearson symbol: hP6, space group: P63/mmc, $a = b = 7.253$ Å, $c = 5.496$ Å, $\beta = 120°$). $BaSn_3$ crystallizes in the structure of Ni_3Sn. The structure is shown in the following Fig. 5.117.

It is characterized by a chain of fused octahedra in which Sn_3 groups predominate. It contains linear chains of face sharing Sn octahedra. In between the octahedral chains, the Ba atoms can be found. The formula can be written as: Ba^{2+} $[Sn_3^{2-}]$. The atom coordinates for this structure are given in Table 5.63.

EH and LMTO investigations show that $BaSn_3$ is at the borderline of Zintl phases and intermetallic phases. Magnetometric investigations show that $BaSn_3$ becomes a superconductor at $T_C = 3.7$ K. Resistivity measurements reveal the metallic character of the compound. The electronic structure is shown in Fig. 5.118.

Molecular wires **2** are formed by the stacking of Sn triangles **1** in $BaSn_3$. The balanced interplay of interactions between localized and delocalized structural components is responsible for the superconductivity of **2**. The "fingerprint" in the band structure of this superconductor was discussed with the help of partial electron density introduced here as well as the ELF.

Barium pentastannide, $BaSn_5$, is the second compound obtained in the Ba/Sn system (Pearson symbol: hP5; space group: P6/mmm, $a = b = 5.357$ Å, $c = 7.065$ Å, $\beta = 120°$). The compound represents a new structure type. Its structure is shown in Fig. 5.119.

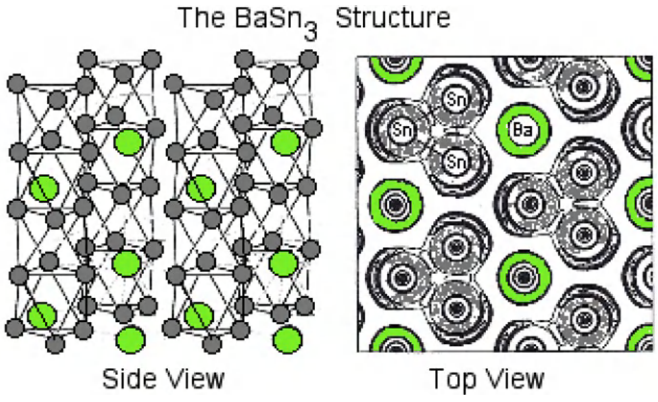

FIGURE 5.117

In this structure, a double layer of tin atoms can be found building hexagonal networks. The resulting hexagonal prisms are centered by tin atoms. The Ba atoms can be found between two double layers. $BaSn_5$ shows a two-dimensional slab of face-sharing hexagonal prisms which are formed by two superimposed graphite-like layers of Sn_6^{2-} clusters.

Tribarium pentastannide, Ba_3Sn_5, is a binary Zintl phase, not found in the phase diagram presented above. Sr_3Sn_5 and Ba_3Sn_5 were synthesized and structurally characterized. All compounds are isotypic and crystallize with a modified Pu_3Pd_5 structure type. The anionic substructure is composed of Sn_5^{6-} square pyramidal clusters, which are described as arachno clusters according

TABLE 5.63

No	Site notation	Atom	Multiplicity	Wyckoff	Site symmetry	x	y	z	Occupancy
1	Sn	Sn	6	h	mm2	0.1406	0.2812	1/4	1.0
2	Ba	Ba	2	d	-6m2	1/3	2/3	3/4	1.0

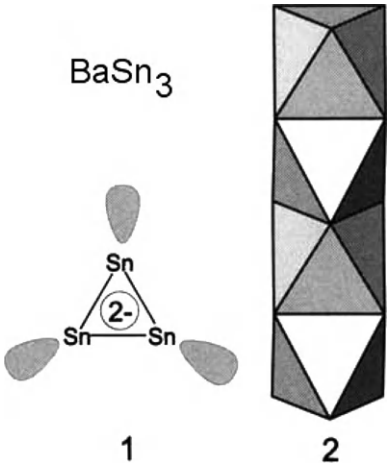

FIGURE 5.118

to the Wade–Mingos electron counting rules. The electronic structure of the pyramidal Zintl anions and the influence of the number of skeletal electrons of these clusters were investigated using the ELF. The structural relationship between Ba_3Sn_5 and the Zintl phases Ba_3Si_4 and Ba_3Ge_4 was also analyzed. Additionally, two new Zintl phases $Ba_3Ge_{2.82}Sn_{2.18}$ and $Ba_3Ge_{3.94}Sn_{0.06}$, have been synthesized and their structures were reported, which directly show that the exchange of tin against germanium leads to a change from the $M_{3\times5}$ to the $M_{3\times4}$ structure type. This effect is traced back to the maximal charge acquisition property of the Zintl anions of heavier and lighter tetralides.

The polar intermetallic compound, Ba_3Sn_5, has the crystal structure of Eu_3Sn_5 and crystallizes in an orthorhombic lattice, with a space group Cmcm and $a = 10.466$, $b = 8.445$, $c = 10.662$ Å, $V = 942.4$ Å^3, $Z = 4$, MW = 1049.33 g/mol, $D_{calc} = 7.396$ g/cc. Its structure belongs to the modified Pu_3Pd_5 type (Fig. 5.120).

It is isostructural with Sr_3Sn_5, featuring [Sn_5] square pyramidal clusters described as "arachno" according to the Wade–Mingos electron counting rules. The europium cations are located at the voids between the square pyramidal clusters. Results of the extended Hückel band structure calculations indicate that Ba_3Sn_5 is metallic. The structure is presented where the square pyramidal clusters are clearly evident.

The atom coordinates for this structure are given in Table 5.64.

Dibarium stannide, Ba_2Sn, is not well known in the technical literature. In contrast, interest in a like compound, dibarium tritin hexaantimonide, $Ba_2Sn_3Sb_6$, has been extensive because it is a superconductor. The novel Zintl phase dibarium tritin hexaantimonide, Ba_2Sn, has been synthesized, and its structure has been determined by single-crystal XRD methods. It crystallizes in the orthorhombic space group—*Pnma* with $a = 13.351(1)$ Å, $b = 4.4100(5)$ Å, $c = 24.449(3)$ Å, and $Z = 4$ ($T_c \cong 50$ °C). The structure can be represented as in Fig. 5.121. Where the arrangement of atoms in the *b*-direction of the lattice is shown. The atomic coordinates for this structure are given in Table 5.65.

The structure of $Ba_2Sn_3Sb_6$ comprises large channels [010] defined by 30-membered rings constructed from an anionic framework. This framework is built up from Sn-centered trigonal pyramids and tetrahedra, as well as zigzag chains of Sb atoms. Within the channels reside the Ba^{2+} cations and additional isolated zigzag Sb–Sb chains. The simultaneous presence of Sn trigonal pyramids and tetrahedra implies that $Ba_2Sn_3Sb_6$ is a mixed valence compound whose oxidation state notation can be best represented as $(Ba^{2+})_2[(Sn^{II})_2(Sn^{IV})$

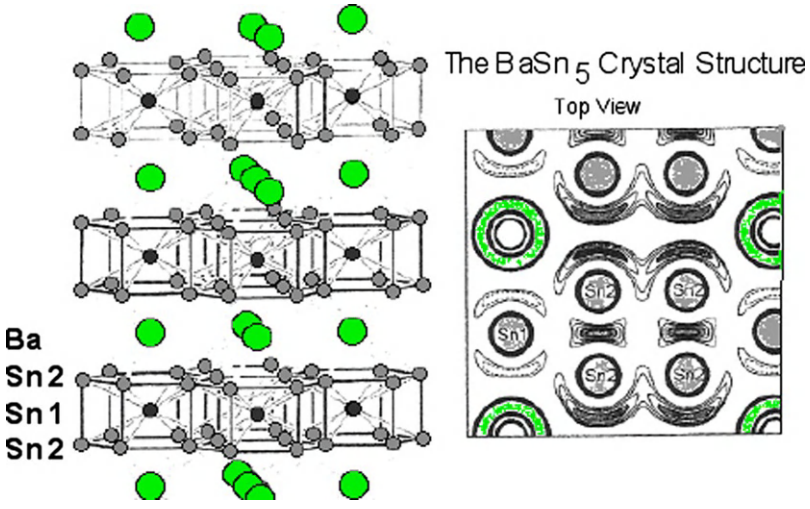

FIGURE 5.119

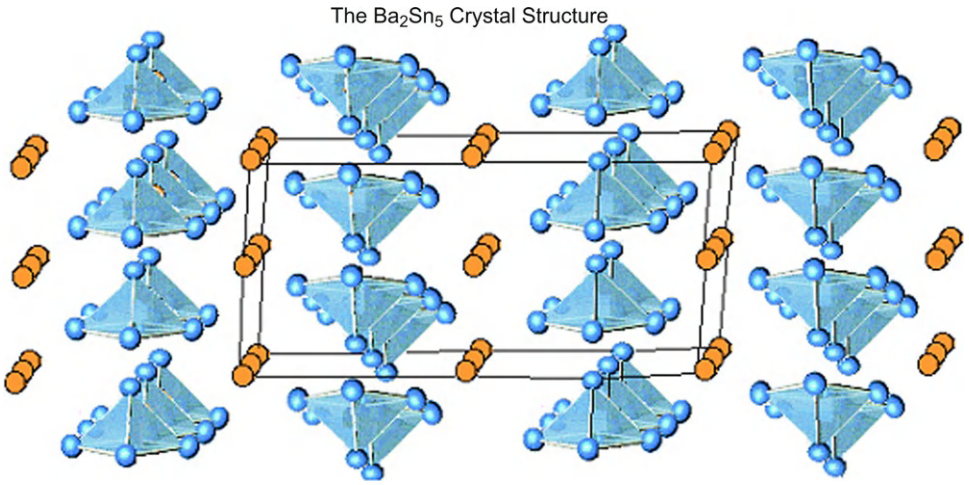

FIGURE 5.120

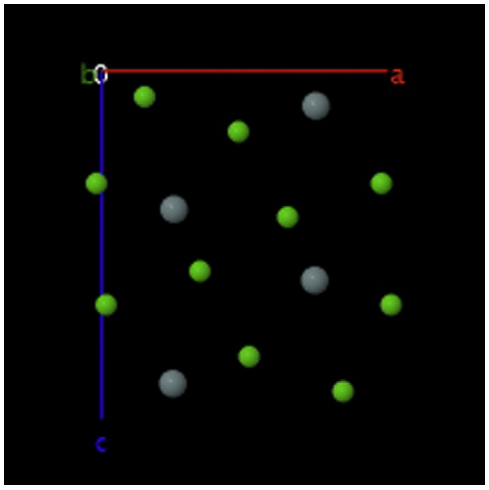

FIGURE 5.121

$(Sb^{-III})_3(Sb^{-I})]^{2-}[(Sb^{-I})_2]^{2-}$. The structure is shown in Fig. 5.122.

Resistivity and AC magnetic susceptibility measurements on $Ba_2Sn_3Sb_6$ and $SrSn_3Sb_4$ indicate that these Zintl compounds display a transition to a superconducting phase at $T_C = 3.9$ K. The Meissner effect was observed for $Ba_2Sn_3Sb_6$ under an applied field of 25 Oe. The signatures for superconductivity, such as high- and low-velocity conduction electrons and lone pairs, are present for both of these compounds.

Although **dibarium tristannide**, Ba_2Sn_3, is listed as a stable compound melting congruently at 1120 °C, the scientific literature is devoid of any mention of this compound except as already mentioned. Although it is crystalline, its unit-cell parameters are not listed nor is there any discussion of its physical or chemical properties.

Tribarium distannide, Ba_3Sn_2, is also listed as a crystalline component of the Ba–Sn series of compounds. However, its melting point and mode of melting (incongruent or congruent) have not been thoroughly investigated.

The lack of thermal behavior of the barium-rich series of compounds in the Ba–Sn system is the main reason why a description of these series of compounds cannot be provided. Since most of the Ba–Sn compounds are not stable to moisture and many are pyrophoric, the experimental conditions needed to investigate their physical and chemical properties have not been forthcoming. The work described above stems from the fact that several of these barium stannides are superconducting, even though their usage would be impractical due to their instability in air.

TABLE 5.64

No	Site notation	Atom	Multiplicity	Wyckoff	Site symmetry	*x*	*y*	*z*	Occupancy
1	Ba1	Ba	16	l	..m	0.166	0.666	0.15	1.0
2	Sn1	Sn	8	h	m.2m	0.625	0.125	0	1.0
3	Ba2	Ba	4	c	4/m..	0	0	0	1.0
4	Sn2	Sn	4	a	422	0	0	1/4	1.0

TABLE 5.65

No	Site notation	Atom	Multiplicity	Wyckoff	Site symmetry	x	y	z	Occupancy
1	Ba(2)	Ba	4	c	.m.	0.018	1/4	0.676	1.0
2	Ba(1)	Ba	4	c	.m.	0.153	1/4	0.077	1.0
3	Sn	Sn	4	c	.m.	0.252	1/4	0.398	1.0

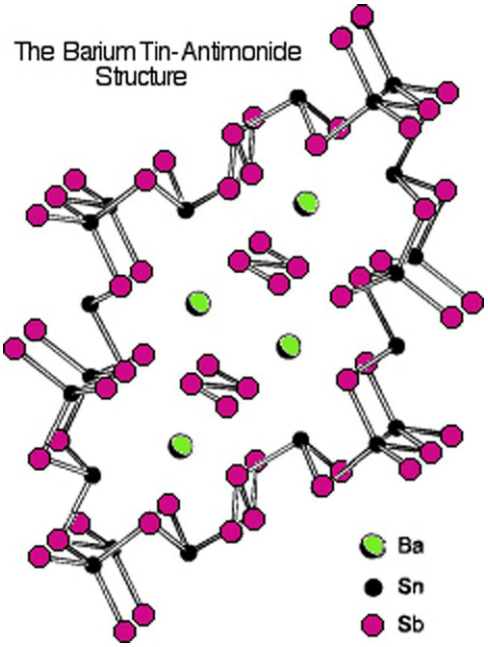

FIGURE 5.122

There are no CAS numbers for any barium stannides and they are not available commercially.

Radium Stannides

Although the likelihood of forming a series of compounds like:

Ra_2Sn
Ra_5Sn_3
RaSn
Ra_3Sn_5
$RaSn_3$
$RaSn_5$

is likely, no description of such work can be found in the technical literature. This may be due to the fact that ^{226}Ra is highly radioactive and not easy to work with chemically.

5.4.2. Acids and Bases of the Stannite or Stannic Anions

Tin oxides dissolve in acids. Certain halogen acids attack SnO_2 to give hexahalostannates, such as $[SnI_6]^{2-}$. One report describes reacting a sample in refluxing HI (hydroiodic acid) for many hours:

$$SnO_2 + 6HI \Rightarrow H_2SnI_6 + 2H_2O$$

HI is a colorless gas that reacts with oxygen to give water and iodine. With moist air, HI gives a mist (or fumes) of hydroiodic acid. It is exceptionally soluble in water. One liter of water will dissolve 425 l of HI gas, the final solution having only four water molecules per molecule of HI.

Similarly, SnO_2 dissolves in sulfuric acid to give the sulfate:

$$SnO_2 + 2H_2SO_4 \Rightarrow Sn(SO_4)_2 + 2H_2O$$

SnO_2 dissolves in strong base to give "stannates," with the nominal formula Na_2SnO_3. Dissolving the solidified SnO_2/NaOH melt in water gives $Na_2[Sn(OH)_6]_2$, "preparing salt," which is used in the dyeing industry. Blue-black SnO can be prepared by heating the tin(II) oxide hydrate, $SnO{\cdot}xH_2O$ $(x < 1)$ precipitated when a tin(II) salt is reacted with an alkali hydroxide such as NaOH. Metastable, red SnO can be prepared by gentle heating of the precipitate produced by the action of aqueous ammonia on a tin(II) salt. SnO may be prepared as a pure substance in the laboratory, by controlled heating of tin(II) oxalate (stannous oxalate) in the absence of air:

$$SnC_2O_4 \Rightarrow SnO + CO_2 + CO$$

Tin(II) oxide burns in air to form SnO_2. When heated in an inert atmosphere, a disproportion initially occurs giving Sn metal and Sn_3O_4 which further reacts to give SnO_2 and Sn metal:

$$4SnO \Rightarrow Sn_3O_4 + Sn$$

$$Sn_3O_4 \Rightarrow 2SnO_2 + Sn$$

SnO is amphoteric, dissolving in strong acid to give tin(II) salts and in strong base to give stannites containing $Sn(OH)_3^-$. It also dissolves in strong acid solutions to give the ionic complexes $Sn(OH_2)_3^{2+}$ and $Sn(OH)(OH_2)_2^+$, and in less acid solutions to give $Sn_3(OH)_4^{2+}$. Thus, the number of alkaline earth compounds formed in solution is strictly limited. Note that anhydrous stannites, e.g. $K_2Sn_2O_3$, K_2SnO_2, are also known. SnO is a reducing

agent and this appears to be its role in the manufacture of so-called "copper ruby glass".

The term **stannate** can refer to compounds:

- *orthostannates* which contain discrete SnO_4^{4-} units (e.g. K_4SnO_4) or have a "Spinel" structure (e.g. Mg_2SnO_4).
- *metastannates* with a stoichiometry $M^{II}Sn^{IV}O_3$ or $M^{I}{}_2Sn^{IV}O_3$ which may contain polymeric anions or may be sometimes better described as mixed oxides.

Note that stannic acid, the formal precursor to stannates, does not exist and is actually a hydrate of SnO_2. The term is also used as a suffix in naming conventions. For example, the hexachlorostannate ion is $SnCl_6^{2-}$.

In contrast, **stannite** is a mineral, a sulfide of copper, iron, zinc and tin with the chemical formula of Cu_2FeSnS_4. Zn commonly occurs and iron plus a trace of Ge may be present. Stannite is used as a source of tin, consisting of approximately 28% tin, 13% iron, 30% copper, 30% sulfur by mass.

Thus, "stannous" or "stannite" compounds of the alkaline earths are exceedingly rare.

5.4.3. Alkaline Earth Orthostannates, Metastannates and Stannites

Beryllium Stannates

The literature concerning beryllium and its oxy-tin compounds is not extensive. A description of the combination of a Be compound with a tin compound is completely lacking in the past or present technical literature. It should be possible to use the "peroxide method" to form these compounds but there is no record of anyone having done so. Thus, the physical and chemical properties of $BeSnO_3$ and Be_2SnO_4 have remained unknown.

The reactions for the peroxide method would be:

$$BeCl_2 + HCl(aq) \Rightarrow BeCl_3^- + H^+$$

$$SnCl_4 + 2HCl(aq) \Rightarrow SnCl_6^{2-} + 2H^+$$

$$BeCl_3^- + SnCl_6^{2-} + 3H^+ + NH_4OH + H_2O_2 \Rightarrow Be_2SnO_4 \text{ (or } BeSnO_3) + NH_3 + 3H_2O$$

In view of the propensity of beryllium to form hydroxy-compounds in solution, the Be precursor may actually be $(BeOH)Cl_2^-$. This propensity may actually depend upon the temperature and concentration of the solutions before the precipitation takes place. Thus, the likely composition of these compounds would be:

$(BeOH)_2SnO_3$—beryllium metastannate

$(BeOH)_4SnO_4$—beryllium orthostannate

These compounds would have the Lewis structure (Fig. 5.123).

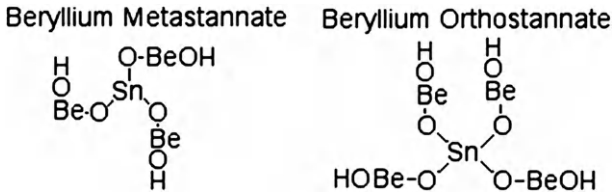

FIGURE 5.123

Since the SnO_4^{4-} anion is a tetrahedron in $(BeOH)_4SnO_4$, this compound is expected to have cubic close-packed perovskite structure containing SnO_6 octahedrons, similar to the barium compound. The metastannate is expected to consist of a network of SnO_3^{2-} trigonal prisms similar to that of the germanates. Alternatively, the cubic structure could form a series of chains of triangular SnO_3 units, stacked in an orthorhombic fashion wherein two SnO_3^{2-} groups alternate with a single group in the structure.

Beryllium stannates are not available commercially and no CAS numbers have been assigned.

Magnesium Stannates

Magnesium orthostannate Mg_2SnO_4 has the CAS number of 12032-29-0 and a molecular weight of 191.0145 g/mol. It can be synthesized at 900 °C with high purity using the peroxide route:

$$MgO_2 + SnO_2 + \text{heat} \Rightarrow MgSnO_4$$

The method involves mixed cation precursors, derived using magnesium chloride, tin tetrachloride and aqueous HCl. They are added to a basic solution of ammonia and hydrogen peroxide and the light-yellow precipitate is filtered, dried and calcined at relatively low temperatures of about 700–1200 °C to form homogeneous crystalline $MgSnO_3$ and Mg_2SnO_4. The powder produced shows a large specific surface area and small grain size, leading to a high sinterability. A peroxo-precursor is formed during the synthesis by a precipitation step from aqueous solution. The thermal decomposition of the X-ray amorphous precursor leads directly to Mg_2SnO_4. Magnesium metastannate, $MgSnO_3$, is formed after thermal degradation of a corresponding peroxo-precursor at temperatures below 700 °C. Further thermal treatment at temperatures above 700 °C leads to the decomposition of $MgSnO_3$ to Mg_2SnO_4 and SnO_2.

The above reaction, if the MgO compound is used, results in a "metastannate", $MgSnO_3$. Thus, these SSRs are dependent upon the molecular ratio of the oxides employed:

$$MgO + SnO_3 \Rightarrow MgSnO_3$$

$$2MgO + SnO_2 \Rightarrow Mg_2SnO_4$$

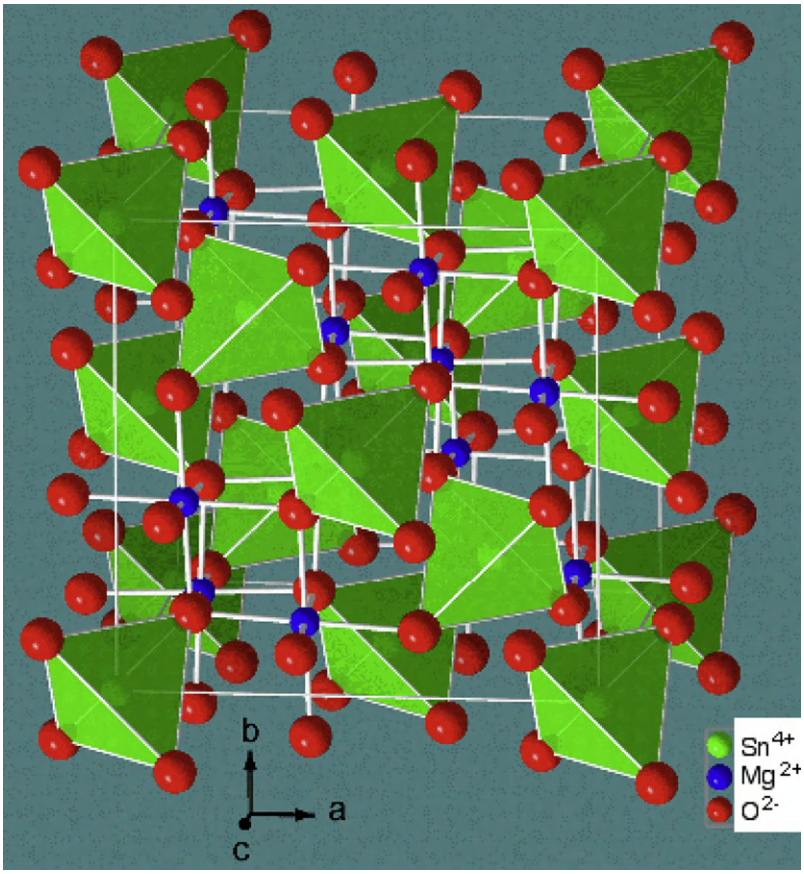

FIGURE 5.124

In the reaction, it is the chlorides, $MgCl_2$ and $SnCl_6^{2-}$, that are added to the basic hydrogen peroxide solution and MgO_2 is a fleeting prototype which forms the amorphous precursor. The cubic spinel structure of Mg_2SnO_4 is shown in Fig. 5.124.

It is easily seen that SnO_4 tetrahedra dominate with octahedra of MgO_6 arranged in a cubic unit cell with $a = 8.611$ Å. The dimensions of individual sites have also been measured (Fig. 5.125).

Interestingly, the behavior of magnesium metastannate ($MgSnO_3$) and orthostannate (Mg_2SnO_4) is very

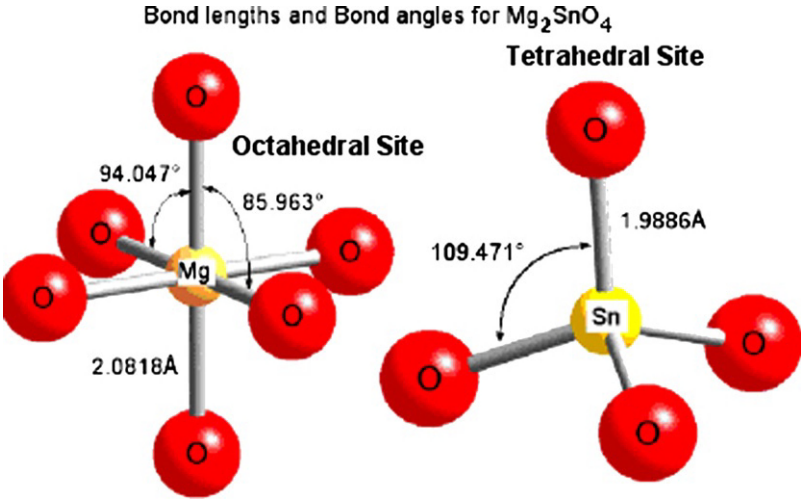

FIGURE 5.125

different from the corresponding Ca, Sr and Ba counterparts. The metastannates and orthostannates of calcium, strontium and barium are known to be stable independently up to very high temperatures without degradation. $MgSnO_3$ is unstable and disproportionates into orthostannate and tin oxide upon heating above 700 °C. In some cases, even the orthostannate cannot be synthesized as a single phase.

Phase stability of magnesium metastannate and orthostannate has been examined in samples synthesized via the traditional SSR and a novel self-heat-sustained (SHS) technique using 2 mol ratios of magnesium to tin (1:1 and 2:1). The powder mixtures were calcined over a wide temperature–time (*T*–*t*) span ranging from 600 to 1300 °C and 3 to 72 h. The powders obtained from the two preparative methods were processed and sintered under identical conditions. In the 2:1 molar mixtures, Mg_2SnO_4 was formed as a single phase upon calcination in both SRR and SHS methods. This phase remained the only compound in the sintered bodies as well. In the 1:1 composition, the ultimate reaction product was a mixture of Mg_2SnO_4 and SnO_2. Both SSR and SHS techniques with 2:1 molar mixture yielded a single phase, Mg_2SnO_4, in the sintered compacts. Compacts with near-zero porosity could be achieved in SSR-derived samples upon sintering up to 1600 °C, while significant porosity was an interesting feature of the SHS-derived samples.

Systematic microstructural evolution with the variation of sintering conditions has been discussed.

Magnesium orthostannate, Mg_2SnO_4, a potential candidate for applications in high-temperature and high-frequency domain as a ceramic capacitor element, was synthesized from metallic tin and magnesium powders. An alloy of composition Mg_2Sn was prepared by the conventional powder metallurgy route. This compound, upon heating in air under carefully designed ordinary and mild experimental conditions, yielded single-phase inverse spinel-type Mg_2SnO_4.

Uniform crystalline $MgSn(OH)_6$ nanocubes have been synthesized by a hydrothermal method. The influences of reaction conditions were investigated and the results showed that the solvent constituents significantly affected the shape and size of $MgSn(OH)_6 \cdot SnO_2$ crystals. Mg_2SnO_4 was obtained by thermal treatment at 850 °C for 8 h under a nitrogen atmosphere using $MgSn(OH)_6$ as the precursor. The electrochemical tests of SnO_2/Mg_2SnO_4 revealed that SnO_2/Mg_2SnO_4 has a higher capacity and better cyclability compared to pure SnO_2 or Mg_2SnO_4. The electrochemical performance of SnO_2/Mg_2SnO_4 was sensitive to the size of the nanoparticles. The lithium-driven structural and morphological changes of the electrode after cycling were also studied by the ex-situ XRD pattern and TEM tests. This work indicates that SnO_2/Mg_2SnO_4 is a promising anode material candidate for application in Li-ion batteries.

The thermodynamic properties of the spinel, Mg_2SnO_4, have been determined by e.m.f. measurements on the solid oxide galvanic cell:

$$\text{Pt, W, MgO} + \text{Mg}_2\text{SnO}_4 + \text{Sn}/\text{Y}_2\text{O}_3 - \text{ThO}_2/\text{Sn} + \text{SnO}_2, \text{ W, Pt}$$

in the temperature range 600 to 1000 °C. The Gibbs' free energy of formation of Mg_2SnO_4 from the component oxides can be expressed as:

$$2\text{MgO } (r.s) + \text{SnO}_2 \text{ (rut)} \rightarrow \text{Mg}_2\text{SnO}_4 \text{ (sp)},$$

$$\Delta G^\circ = 1420 - 2.96T \ (\pm 100) \text{ cal/mol}$$

These values are in good agreement with the information obtained by Jackson *et al.* (1974) concerning the high-pressure decomposition of magnesium stannate into component oxides at different temperatures. The thermodynamic data suggest that the spinel phase is entropy stabilized, and would be unstable below 207 (±25) °C at atmospheric pressure. Based on the information obtained in this study and trends in the stability of aluminate and chromite spinels, it was deduced that the stannates of nickel and copper(II) are unstable.

A new tin mineral named "schoenfliesite", magnesium hexahydroxostannate, $MgSn(OH)_6$, occurs as a late-stage hydrothermal alteration product in a contact metamorphic zone on Brooks Mountain, Seward Peninsula, Alaska. The chemical formula was derived from the analysis of a mixture, and electron microprobe study confirms the assigned composition. The mineral is soluble in HCl and slowly soluble in NaOH. The symmetry is cubic, space group Th^2–$Pn3$, $a = 7.759 \pm 0.006$ Å, $Z = 4$, density (calc.) $= 3.483$ g/cm^3. The four strongest lines in the XRD powder pattern are 3.88 Å (100), 4.48 Å (50), 2.74 Å (25), and 1.733 Å (25). Differential thermal analyses of natural and synthetic material are in agreement. The name is given in honor of the mathematical crystallographer, Artur Moritz Schoenflies. Some crystallographic data and the densities of magnesium orthostannate and magnesium metastannate are also presented.

The spinel phosphor, Mg_2SnO_4:Mn^{2+}, has been the object of intense study over the past 80 years. It was first described in 1935 and documented by Kröger in 1948. A number of current papers have appeared in the literature. One paper stated:

> "The photoluminescent (PL) spectrum of Mg_2SnO_4:Mn^{2+} at room temperature is dominated by a green band peaking at 500 nm, suggesting the existence of tetrahedral Mn^{2+} sites. When the phosphors are formed by a millimeter-wave heating method, the 500-nm band is very much more intense compared to that obtained by the electric furnace heating method. To clarify the origin of the PL enhancement, measurements of scanning electron microscope (SEM) and electron spin

resonance (ESR) were made. The SEM image reveals the growth of small round particles with an average size of 1.6 μm. Such well-grown micron-sized particles were not observed under the electric furnace heating. The ESR spectra exhibit six prominent lines, the intensity of which becomes greater for the phosphors obtained by the millimeter-wave heating method. From this observation, it is presumed that the PL enhancement is mainly due to the increase in the number of tetrahedral Mn^{2+} sites. Therefore, the millimeter-wave heating has an important advantage over the electric furnace heating in the synthesis of Mg_2SnO_4:Mn phosphors".

"Various stannate phosphors were prepared and some of their emissions were determined. Stannate phosphors based upon Mg_2SnO_4, Ca_2SnO_4, Sr_2SnO_4, emit green, blue or yellowish white light when activated by Mn^{2+}, blue, violet or red by Bi^{3+}, orange, green or blue by Pb^{2+}, while those activated by Ce^{3+} show blue or red emission. It is suspected that the activation by tin (Sn^{2+}) also occurs in some cases. This is supported by the fact that the emission of magnesium stannate activated by titanium changes as the flux is varied".

The latest work involves evaluation of Mg_2SnO_4:Mn^{2+} phosphor for use in "plasma-display" panels where very short UV is generated as an excitation medium. The Mg_2SnO_4:Mn phosphor exhibited green luminescence with the emission spectrum centered at 500 nm due to spin flip transition of the d-orbital electron associated with the Mn^{2+} ion. Optimum Mn concentration of Mg_2SnO_4:Mn under VUV excitation of 147 nm and electron beam excitation (with 800 V excitation voltage) are 0.25 and 0.6 mol%, respectively. The emission intensities of Mg_2SnO_4:Mn phosphors under the two excitation sources are higher than those of Zn_2SiO_4:Mn or $ZnGa_2O_4$:Mn phosphors. At 0.25 mol% of Mn concentration, the decay time is shorter than 10 ms, which makes it usable in plasma-display panels.

However, the same phosphor composition, i.e. Mg_2SnO_4:Mn, prepared in a different manner exhibits a long decay (phosphorescence). A novel long-lasting phosphorescence phosphor, Mn^{2+}-activated Mg_2SnO_4, was synthesized and its optical properties have been investigated. The Mg_2SnO_4:Mn^{2+}, upon UV irradiation, emits green light with high luminance centered at 499 nm from the spin forbidden transitions of the d-electrons in Mn^{2+} ions. The CIE chromaticity coordinates of the Mg_2SnO_4:Mn^{2+} phosphor are $x = 0.0875$ and $y = 0.6083$ under 254-nm UV excitation. The phosphorescence can be observed by the naked eyes (0.32 mcd/m^2) in the dark clearly for over 5 h after the 5-min UV irradiation. Its thermoluminescence has been studied and the mechanism of the long-lasting phosphorescence has been discussed.

Mg_2SnO_4 has recently been studied for use as a potential electronic ceramic for applications in the high-temperature and high-frequency domain such as thermally stable capacitors with low permittivity and small loss tangent. Uniform crystalline $MgSn(OH)_6$ nanocubes were synthesized by a hydrothermal method. The influences of reaction conditions were investigated and the results showed that the solvent constituents significantly affected the shape and size of $MgSn(OH)_6$/SnO_2. Mg_2SnO_4 was obtained by thermal treatment at 850 °C for 8 h under a nitrogen atmosphere using $MgSn(OH)_6$ as the precursor. The electrochemical tests of SnO_2/Mg_2SnO_4 revealed that SnO_2/Mg_2SnO_4 has a higher capacity and better cyclability compared to pure SnO_2 or Mg_2SnO_4. The electrochemical performance of SnO_2/Mg_2SnO_4 was sensitive to the size of the nanoparticles. The lithium-driven structural and morphological changes of the electrode after cycling were also studied by the ex-situ XRD pattern and TEM tests. This work indicates that SnO_2/Mg_2SnO_4 is a promising anode material candidate for application in Li-ion batteries.

Magnesium stannate is offered commercially in small lots by a number of manufacturers worldwide.

Calcium Stannates

A chemical route for the low-temperature synthesis of the calcium stannates, $CaSnO_3$ and Ca_2SnO_4, potential materials for dielectric applications, has been reported. Mixed cation precursor powders, derived using calcium chloride, tin tetrachloride and hydrogen peroxide, were calcined at relatively low temperatures of about 700–1200 °C to form homogeneous crystalline $CaSnO_3$ and Ca_2SnO_4. The reactions involved:

$$CaCl_2\,(HCl) + SnCl_6^{2-}(HCl) + H_2O_2(NH_4OH) \Rightarrow CaSnO_3 + 2HCl$$

This takes place in two stages involving the peroxide, CaO_2, as an intermediate. The structural evolution of the crystalline phases was studied using XRD, DTA, thermogravimetric analysis, scanning electron microscopy, Brunauer–Emmett–Teller (BET) measurements and chemical analysis. The thermal degradation of the X-ray amorphous peroxo precursors to the single-phase stannates occurs in two steps for the formation of $CaSnO_3$ and in three steps for the formation of Ca_2SnO_4. $CaSnO_3$ is one of the intermediate products formed during the final thermal decomposition to Ca_2SnO_4. The ultrafine powders resulting after the thermal degradation of the precursors contain a small amount of impurities. They show a high degree of sinterability at temperatures above 1000 °C which increases as Ca_2SnO_4 is formed from $CaSnO_3$. The highest densities reached for ceramic samples were about 97% of the theoretical value for $CaSnO_3$ and 95% for Ca_2SnO_4 by sintering at 1400 °C for 4 h.

In another method, a precursor $CaSn(OH)_6$ was prepared using tin tetrachloride, calcium chloride and sodium hydroxide at room temperature. Then the precursor was annealed at relatively low temperature

of 600 °C to obtain $CaSnO_3$. This compound has the CAS number of CAS 12013-46-6. Its molecular weight is 206.7218 g/mol.

The cubic compounds, denoted by $ASnO_3$ (A = Sr, Ba), adopt the cubic perovskite structure whereas Ca_2SnO_4 has the Sr_2PbO_4 structure.

The compounds $SrSnO_3$, $BaSnO_3$ and Ca_2SnO_4 were synthesized by solid-state and/or sol–gel methods, and characterized by XRD, X-ray photoelectron spectroscopy and SEM. Their electrochemical properties were studied as cathodes versus Li metal in the range 0.005–1.0 V for use in lithium batteries. The discharge capacities (mA-h/g) (moles of equivalent Li) on the 20th cycle at a current rate of 30 mA/g were found to be: $SrSnO_3$ (solid-state) (144 (1.4)), $SrSnO_3$ (sol–gel) (222 (2.1)), $BaSnO_3$ (solid-state) (190 (2.2)), $BaSnO_3$ (sol–gel) (156 (1.8)) and Ca_2SnO_4 (247 (2.4)). The $SrSnO_3$ (sol–gel) with nanoparticle morphology displays better galvanostatic cycling performance than $SrSnO_3$ (solid-state). The cycling behavior of $SrSnO_3$ and $BaSnO_3$ is inferior to that of Ca_2SnO_4 and $CaSnO_3$, which demonstrates that calcium is superior as a matrix element than Sr or Ba. The inferior electrochemical performance of Ca_2SnO_4 in comparison to $CaSnO_3$ reveals that the higher Ca:Sn ratio in the former is not advantageous and the perovskite structure is preferable to that of Sr_2PbO_4 structure. The coulombic efficiencies are >98% in all cases. Cyclic voltammetry (CV) results compliment the observed cycling behavior.

An ordered ilmenite phase of the stannate composition, $CaSnO_3$, was demonstrated from powder patterns. Two crystal forms were discovered. The hexagonal and rhombohedral unit-cell parameters are respectively: $a = 5.487$ (1), $c = 15.287$ (6) Å, $Z = 6$ and $a = 6.000$ (2) Å, $c = 54.42$ (3)°, $Z = 2$, $D_m = 5.16$, $D_x = 5.17$ g/cm^3.

The alkaline earth stannates having the general chemical formula $MSnO_3$ (M = Ca, Sr and Ba), have been projected as potential electronic ceramics (thermally stable capacitors, humidity sensors, carbon dioxide sensors, etc.). The nanocomposite "$CaO{\cdot}SnO_2$" and nano-$CaSnO_3$ were prepared by the thermal decomposition of $CaSn(OH)_6$ precursor and characterized by XRD, SEM, and high-resolution transmission electron microscopy (HR-TEM) along with selected area electron diffraction (SAED) and density measurements. Nanosize (3 to 6 nm) grains of CaO and SnO_2 in the X-ray amorphous $CaO{\cdot}SnO_3$ and particles of 60-nm size in nano-$CaSnO_3$ were obtained. Galvanostatic cycling of both phases vs Li metal was performed in the voltage ranges 0.005−1.0 V and 0.005−1.3 V at the current rate, 60 mA/g (0.12 °C). Stable and reversible capacities of 490 (±5) and 550 (±5) mA h/g was observed for nano-$CaO{\cdot}SnO_2$, respectively up to 50 cycles in the above voltage windows. These values correspond to 3.8 and 4.2 mol of cyclable Li per mole of $CaO{\cdot}SnO_2$ in comparison to the theoretical value of 4.4 mol of Li. A capacity of 420 (±5) mA h/g was observed at a rate of 0.4 °C. Nano-$CaSnO_3$ showed a stable capacity of 445 (±5) mA h/g (3.4 mol of Li) up to 50 cycles when cycled in the voltage window, 0.005 to 1.0 V. The average discharge and charge potentials are 0.2 and 0.5 V, respectively, for both the phases. The reasons for the superior Li-cycling performance of nano-$CaO{\cdot}SnO_2$ in comparison to nano-$CaSnO_3$ were discussed. Ex situ XRD, TEM, and SAED studies are carried out to support the reaction mechanism. Cyclic voltammetry and electrochemical impedance spectroscopy (EIS) data as a function of voltage were presented and discussed to complement the galvanostatic results. The "apparent" Li-ion diffusion coefficient (D^+_{Li}) estimated from EIS is 1.0×10^{-14} cm^2/s at $V \leq 1.0$ V during the first cycle and 11th discharge cycle. Thus, $CaSnO_3$ has been proven to be superior for use in lithium batteries over all of the alkaline earth metastannates and is being used commercially. The latest usage is a large rechargeable battery in electrically driven automobiles.

"Burtite", a calcium hexahydroxostannate, occurs as a latent mineral in a tin-rich garnet skarn in the vicinity of the El Hamman fluorite deposit. The surface of the altered "octahedral" crystal (up to 2 mm) is composed of pale yellow varlamoffite; the core is colorless and shows an apparently cubic cleavage. This unaltered core material has hardness 3; its density is 3.28 g/cc (meas.). It has a cubic symmetry with space group Pn3 or Pn3m, $a = 8.128$ Å and $Z = 4$. The optical orientation implies a rhombohedral departure from this symmetry. This leads to the most probable space group R3 with $a = 8.128$ Å, $\alpha = 90°$ and $Z = 4$. The mineral is colorless with a good cubic cleavage. It is very brittle and the hardness is about 3. The luster is vitreous, and there is no fluorescence under shortwave or longwave UV light. It is slowly soluble in cold, dilute HCl. In thin section, burtite is colorless, with the cubic cleavage traces visible. $CaSn(OH)_6$ is readily synthesized at room temperature by the reaction of $Na_2Sn(OH)_6$ or $K_2Sn(OH)_6$ with calcium chloride or nitrate in aqueous solution. It was found to be stable at 150 °C at 7 bar and 298 °C at 82 bar in the presence of H_2O; at a higher temperature, it converts to anhydrous calcium stannate (Christensen and Hazell 1969). The dehydration temperature at atmospheric pressure was 355 °C, according to the DTA data obtained by these authors.

Uniform and cubic-structured RE^{3+} (RE = Pr,Tb)-doped $CaSnO_3$ phosphors have been successfully synthesized by a two-step approach including the room-temperature synthesis of $CaSn(OH)_6$ precursors with the help of cetyltrimethylammoniumbromide surfactant and then converted to $CaSnO_3$ by calcination at 750 °C. The decomposition process of the $CaSn(OH)_6$ precursor, crystallization, and morphology of the

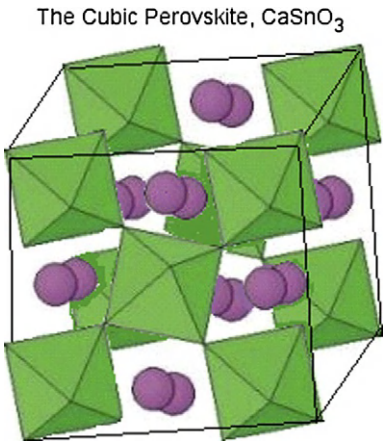

FIGURE 5.126

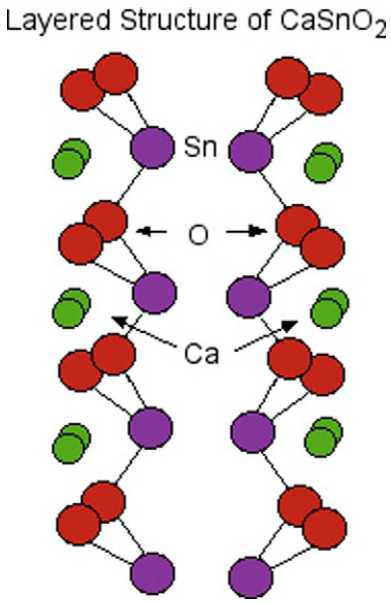

FIGURE 5.127

as-synthesized $CaSnO_3$ phosphors have been investigated using thermal analysis, XRD, and SEM. Furthermore, luminescence properties of $CaSnO_3/RE^{3+}$ (where RE = Pr or Tb) phosphors, including photoluminescence, fluorescence lifetime, afterglow decay, and thermoluminescence, were also systematically discussed in this paper. The as-synthesized Pr^{3+} and Tb^{3+}-doped $CaSnO_3$ phosphors show intense luminescence under ultraviolet excitation. Moreover, the afterglow emission from $CaSnO_3/RE^{3+}$ (RE = Pr,Tb) phosphors lasts for more than 3 h after the ultraviolet irradiation source has been removed. Both the fluorescence and afterglow decay curves of the $CaSnO_3/RE^{3+}$ (RE = Pr,Tb) phosphors contain one fast-decay component and another slow-decay process. Thermoluminescence spectra indicate that the incorporation of RE^{3+} ions into the $CaSnO_3$ host produces suitable trapping centers, which are the origin of the long-lasting phosphorescence phenomenon in this kind of material at room temperature.

The effect of high pressure upon phase stabilities of the $CaSnO_3$ system was investigated using density functional theory static lattice energy calculations. Six phase changes in this system were discovered:

Perovskite ⇒ post-perovskite,
Post-perovskite ⇒ B2 + cotunnite in $CaSiO_3$,
B1 ⇒ B2 in CaO,
Cassiterite ⇒ pyrite,
Pyrite ⇒ orthorhombic-I,
and orthorhombic ⇒ I-Cotunnite in SnO_2.

These results demonstrate a new high-pressure phase sequence of perovskite ⇒ post-perovskite ⇒ B2 + cotunnite. The post-perovskite transformation occurs at ~12 GPa with ~2.5% volume reduction and then it decomposes into the oxide mixture of B2 CaO and cotunnite SnO_2 at ~70 GPa with 8.1% volume reduction. The results also predict a few percent bulk velocity variations across these phase changes. The cubic structure of $CaSnO_3$ is shown in the following Fig. 5.126.

It is dominated by octahedrons of SnO_6^{2-} where Z = 10.

Calcium stannite, $CaSnO_2$, where tin is in the +2 state, i.e. Sn^{2+}, has been reported. It is believed that $CaSnO_2$ adopts a layered structure of SnO_2^{2-} groups but the crystallographic data only relates to the better known orthorhombic Na_2PbO_2. The probable structure is shown in Fig. 5.127.

The calcium stannates, $CaSnO_3$ and Ca_2SnO_4, are available commercially in small quantities. Hundred grams of $CaSnO_3$ is priced at $125.00 but the orthostannate price has not been given.

Strontium Stannates

Strontium tin oxide ($SrSnO_3$) is also known as strontium stannate or strontium tin trioxide. The strontium stannates, $SrSnO_3$ and Sr_2SnO_4, can be synthesized by the wet chemical peroxide route:

$$SrO_2(aq) + SnO(solid) \Rightarrow SrSnO_3$$

$$SrO_2(aq) + SnO_2(solid) \Rightarrow SrSnO_4$$

The first step of the preparation is the precipitation of stoichiometric peroxo precursors which can be transformed into the corresponding stannates by thermal degradation. The resulting very fine, single-phase strontium stannate powders have extremely small impurity contents. They show a very fast densification behavior during sintering at temperatures above 1200 °C. The phase, $Sr_3Sn_2O_7$, could not be prepared using the

peroxide route. This method involves dissolving $SrCl_2$ and $SnCl_4$ in dilute HCl and adding this to a solution of H_2O_2 and NH_4OH in water. Molar ratios used were 1:1:2.5 as $SrCl_2$, $SnCl_4$, and H_2O_2 and NH_4OH, respectively for $SrSnO_3$ and 2:1:2.5 for Sr_2SnO_4. Light yellow precipitates are formed. The ratios, 3:2:7, for $Sr_3Sn_2O_7$ did not produce a product. The precipitates were filtered and dried. The metastannate is first obtained as a trihydrate, $SrSnO_3 \cdot 3H_2O$ which can be calcined at 430 °C to obtain the anhydrate.

$SrSnO_3$ has the CAS number of 12143-34-9.

Alkaline earth stannates have received more and more attention in recent years as components of ceramic dielectric elements. $SrSnO_3$ has been employed in humidity sensors. Solid solutions of alkaline earth titanates plus stannates have been used in the fabrication of ceramic "boundary-layer" capacitors. The phase diagram shows the existence of two stable phases, $SrSnO_3$ and Sr_2SnO_4. $Sr_3Sn_2O_7$ is metastable at 1350 °C, decomposing to Sr_2SnO_4 and SrO. $SrSnO_3$, the most important of these compositions, is a dielectric of technological importance. It can be synthesized by a solid-state reaction between SrO and SnO_2 at 1000 °C. It is a cubic perovskite. Sr_2SnO_4 is a stable tetragonal K_2NiF_4 structure and forms a solid solution with Ba_2SnO_4. This compound decomposes to SrO and SnO_2 at >1250 °C. $Sr_3Sn_2O_7$ can be formed at <1150 °C by the reaction of 3SrO and $2SnO_2$. The phase diagram is similar to that of the barium analogues except for temperatures.

Strontium stannate is under study as an ultra-stable dielectric material for microelectronic applications at low temperatures. It is known to have a remarkably temperature-independent dielectric constant from 27 K to room temperature. However, anomalies in the Raman spectra, dielectric response, and DTA of strontium stannate exist, compatible with a structural phase transition at 160 K. Further anomalies are seen in calorimetric and Raman data (but not dielectric data) that suggest another phase transition at 270 K (−3 °C). An X-ray powder diffraction study confirms a small change in the pseudo-cubic lattice constant α (T) at the lower transition.

Hydroxide perovskites of $MSn(OH)_6$ (M = Ba, Sr, Ca, Mg) were synthesized by coprecipitation and sonochemical reaction routes. Some of the compounds were also prepared by the hydrothermal method. These were characterized by XRD, TGA/DTA, TEM and IR studies. The hydroxide perovskites are stable up to 523 K (250 °C) and all the compounds stabilize in cubic crystal system (SG = $Pn3m$) at 298–523 K except $BaSn(OH)_6$. The as-prepared powders of the above compositions show cubic square net in the reciprocal lattice of their electron diffraction patterns. Among these perovskites, $MgSn(OH)_6$ exhibits proton conduction at 298–500 K. Above 523 K, solid solutions of SnO_2 and the corresponding MO components were observed. On heat treatment at 850–950 K (577–677 °C) a defective $M_{2-x}(V_M)_xSnO_4$ (M-deficient spinel, $x \leq 1$) along with SnO_2 was observed. On further sintering to 1773 K (1500 °C) for a duration of 6–7 h, the $M_{2-x}(V_M)_xSnO_4$ phase was stabilized. The electrical properties of these compounds were measured by four-probe DC method. $SrSn(OH)_6$ does not show any type of electrical conduction at 298–850 K (25–577 °C). The loss of proton conduction above 523 K (250 °C) may be ascribed to dehydroxylation and subsequent decomposition to $SnO_2 + Mg_{2-x}SnO_4$ (defect spinel, or $MSnO_3$ (M = Ba, Sr, Ca).

The electrical conduction of rare earth-doped $SrSnO_3$ and $SrSnO_4$ has been ascribed to the formation of an oxygen vacancy, $V_{\bar{O}}^{\bar{=}}$. This shows that conduction occurs by hopping of charge carriers among localized sites. These sites are associated with Sn^{2+} and Sn^{4+} ions. Traces of divalent Sn^{2+} ions are probably present due to loss of oxygen during sintering in accordance with the reaction:

$$2O_O \Rightarrow O_2\,(\text{gas}) + V_{\bar{O}}^{\bar{=}} + 2e^-$$

the electrons released during the high-temperature sintering of these materials may be captured by the reaction:

$$Sn^{4+} + 2e^- \Rightarrow Sn^{2+}$$

Electrical conduction therefore seems to occur by hopping of charge carriers among the two tin sites.

Transparent and conductive oxide (TCO) films with a cubic perovskite structure, i.e. lanthanum-doped strontium stannate, $La_xSr_{1-x}SnO_3$ ($x = 0$–0.15) (LSSO), have been grown epitaxially on $SrTiO_3$ (001) substrates by a pulsed laser deposition method. The doping concentration and growth parameters were optimized based on the high-resolution XRD and electric transport measurements. It was found that the optimum doping level is around $x = 0.07$, and the epitaxial films can be grown at temperatures as low as 600 °C and in atmospheres compatible with many other perovskite oxide films. They are n-type TCO films, showing high optical transmittance in the visible range with a direct allowed band gap of 4.65 eV. They possess a weak metallic transport behavior with a low resistivity of ~4.0 mΩ cm within 10–300 K. Due to a very close lattice match with the ferroelectric $Pb(Zr_{0.52}Ti_{0.48})O_3$ (PZT) and multiferroic $BiFeO_3$ (BFO), all-perovskite LSSO(Pt)PZT(BFO)/LSSO capacitors and p-PZT($\leq$20 nm)/n-LSSO [p-BFO (100 nm)/n-LSSO] p–n junctions have also been fabricated and characterized. The square polarization versus electric field hysteresis loops, good rectifying characteristics, high optical transmittance, as well as the epitaxial growth exhibited by the heterostructures, strongly

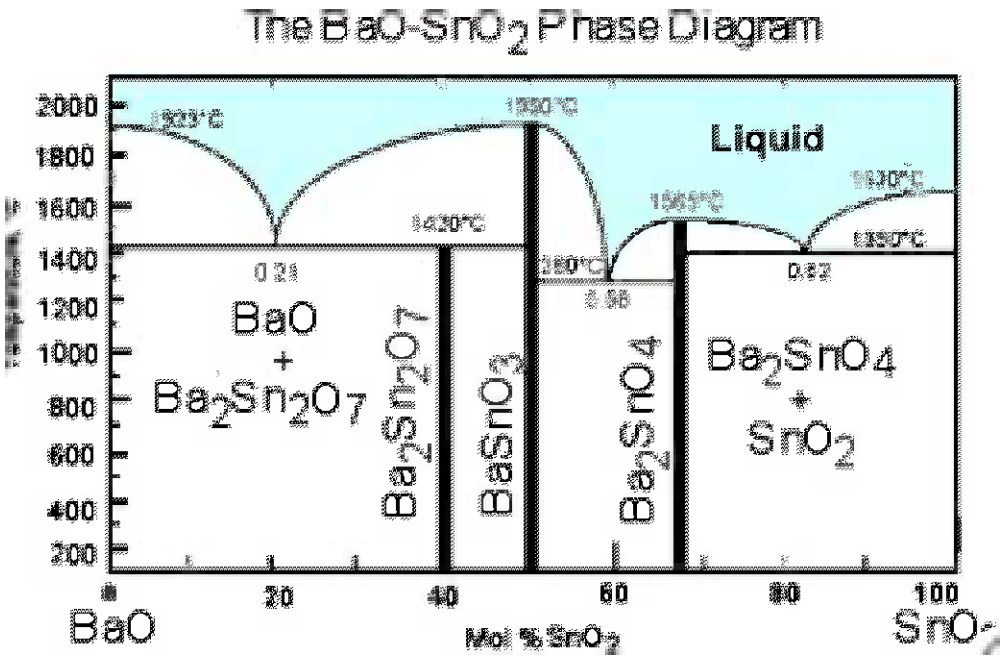

FIGURE 5.128

suggest that the LSSO films are potential candidates for use in transparent thin-film devices.

Intense green, orange or magenta luminescence was observed in rare-earth-doped alkaline earth (Ca, Sr, and Ba) stannates, particularly strontium stannates with perovskite-related structures. Tb–Mg codoped $SrSnO_3$ showed sharp emission lines corresponding to Tb ions as a green phosphor. Sm^{3+}-doped $Sr_3Sn_2O_7$ exhibited sharp pairs of emission lines corresponding to Sm ions as an orange phosphor. Eu–Ti codoped Sr_2SnO_4 as a magenta phosphor showed sharp red luminescent lines corresponding to Eu^{3+} ions as well as a broad blue emission band corresponding to Ti-related complexes. It was suggested that codoping and/or layered structures in these phosphors are closely related to the increase in luminescence intensity from these rare-earth ions.

Strontium stannates are available commercially from a number of suppliers worldwide.

Barium Stannates

There exist three oxostannate(IV) compounds in the BaO–SnO_2 binary system, $BaSnO_3$, $Ba_3Sn_2O_7$ and Ba_2SnO_4, but barium stannate is normally referred to as $BaSnO_3$ because $BaSnO_3$ is the best known among these, the most thoroughly investigated and the most useful compound. The phase diagram, shows the melting points and areas of temperature stability of these three compounds (Fig. 5.128).

$Ba_3Sn_2O_7$ melts incongruently, forming $BaSnO_3$ and BaO. The other two compounds are stable but $BaSnO_3$ is the preferred compound as a ceramic.

$BaSnO_3$ crystallizes in a cubic perovskite structure as shown in the following Fig. 5.129.

In this cubic structure, the Ba^{2+} ions (1.34 Å) occupy the corners of the Sn^{4+} ions (0.71 Å), the volume center, and the O^{2-} ions (1.40 Å), the surface center.

In this structure, the larger Ba^{2+} ions and the O^{2-} ions build a cubic, dense, ball by packing together. A quarter of the octahedral holes is filled with small Sn^{4+} ions. Each Ba^{2+} ion is coordinated with 12 O^{2-} ions and each O^{2-} ion is surrounded by four Ba^{2+} ions and two Sn^{4+} ions. Thus, the crystallochemical formula is $Ba^{[12]}Sn^{[6]}O_3^{[4+2]}$. The octahedrons of $[SnO_6]$ are linked by sharing corners to form a three-dimensional framework. It should be understood that this high-symmetry cubic structure can distort and deform under specific conditions so that the structure symmetry degree is lowered. The lattice constant of $BaSnO_3$ is $a = 4.1163$ Å.

The barium stannates, $BaSnO_3$ and Ba_2SnO_4, can be synthesized by the wet chemical peroxide route. The first step of the preparation is the precipitation of stoichiometric peroxo precursors which are transformable into the corresponding stannates by thermal decomposition. The resulting ultrafine, phase-pure barium stannate powders are generally very pure, >99.9%. They are very sinterable above 1200 °C. $BaSnO_3$ shows a better densification behavior than Ba_2SnO_4 during sintering. However, the phase, $Ba_3Sn_2O_7$, could not be synthesized using the peroxide method.

$BaSnO_3$ with cubic perovskite structure exhibits good dielectric properties. Because of these characteristic properties, $BaSnO_3$ ceramic is becoming more and more important in material technology. It can be

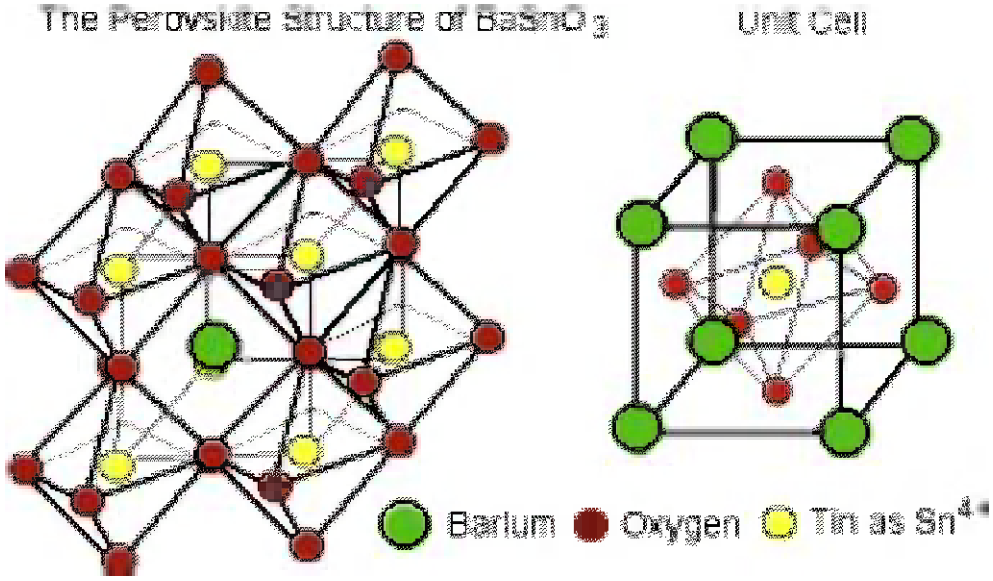

FIGURE 5.129

used to prepare thermally stable capacitors and to fabricate ceramic boundary layer capacitors. In recent years, $BaSnO_3$ has been found to be a very promising sensor material and has therefore received the most attention. In pure as well as doped forms, stannates have been investigated as potential solid-state sensor materials for many gases, including CO, NO_x, H_2 and CO_2. $BaSnO_3$ has also been used in the preparation of multifunctional temperature–humidity–gas sensors by combining it with $BaTiO_3$. Detection of gas in $BaSnO_3$ sensors is achieved by measurement of the electrical properties changes such as resistance and conductivity. The changes are induced in the semiconducting oxide form of $BaSnO_3$ following adsorption of any given gases on the solid surface. The gas sensitivity of this semiconducting oxide is related to the surface reaction process. Thus, a large surface area of the semiconducting oxide is of importance to its gas sensor devices.

Attempts to prepare $BaSnO_3$ by the hydrothermal method starting from $SnO_2 \cdot xH_2O$ gel and $Ba(OH)_2$ solution in Teflon-lined autoclaves at 150–260 °C invariably lead to the formation of a hydrated phase, $BaSn(OH)_6 \cdot 3H_2O$. On heating in air or on releasing the pressure at about 260 °C, $BaSn(OH)_6 \cdot 3H_2O$ converts to $BaSnO_3$ as a fine powder which involves the formation of an intermediate oxyhydroxide, $BaSnO(OH)_4$. TEM studies show that particle size of the resulting $BaSnO_3$ ranges from 0.2 to 0.6 μm. Solid solutions of Ba(Ti,Sn)O_3 were prepared from $(TiO_2 + SnO_2) \cdot xH_2O$ mixed gel and $Ba(OH)_2$ solutions. Single-phase perovskite Ba(Ti,Sn)O_3 was obtained up to 35 atom% Sn. Above this composition, the hydrothermal products are mixtures of $BaTiO_3$ (cubic) and $BaSn(OH)_6 \cdot 3H_2O$ which on heating at 260 °C give rise to $BaTiO_3 + BaSnO_3$. Annealing at 1000 °C results in monophasic Ba(Ti,Sn)O_3, in the complete range of Sn/Ti. Formation of the hydrated phase is attributed to the amphoteric nature of $SnO_2 \cdot xH_2O$ gel which stabilizes $Sn(OH)_6^{2-}$ anions under higher water pressures and elevated temperatures. The sintering characteristics and dielectric properties of ceramics prepared from these fine powders were also studied.

The electrical and optical properties of Ge-doped $BaSnO_3$ ceramics sintered at various temperatures have been investigated to determine their semiconductor behavior. The electrical conductivity of Ge-doped $BaSnO_3$ samples increases with increase in temperature, confirming that the samples exhibit a semiconductor behavior. A maximum conductivity value of 6.31×10^{-9} S/cm was observed for a sample sintered at 1200 °C. The optical band gaps of the Ge-doped $BaSnO_3$ samples were determined by means of reflectance spectra. The variation with optical band gap was analyzed using the $E_g(T) = Eg_o + \beta T$ equation. The rate of change of the band gap, β, of $BaSn_{0.99}Ge_{0.01}O_3$ was found to be 7.6×10^{-4} eV/°C. A minimum optical band gap value of 2.95 eV was observed for the sample sintered at 1400 °C. It was concluded that $BaSn_{0.99}Ge_{0.01}O_3$ is a wide band gap semiconductor and its semiconducting properties change with sintering temperature.

Nanocrystalline $BaSnO_3$ with a primary particle size of 40–60 nm was prepared through hydrolysis of a barium tin isopropoxide and a following crystallization. The thermal decomposition, the crystallization and the microstructure of the obtained powders were investigated with the help of TG-DTA, IR, XRD, HRSEM and HRTEM analytical methods. The organic groups in

the as-prepared powder decompose thermally at 350 °C, and is accompanied by the formation of $BaCO_3$ that disappears again at 600 °C. The crystallization of $BaSnO_3$ takes place at 500–600 °C. Single-phase $BaSnO_3$ powders have been obtained at a temperature as low as 600 °C. The amorphous as-prepared powder shows a cluster structure. Nucleation of $BaSnO_3$ beginning at 350 °C was observed under HRTEM, and the spherical nanoparticles of $BaSnO_3$ calcined at 760 °C crystallize well and are strongly aggregated. The presented results indicate a heterogeneous nucleation and growth mechanism as $BaSnO_3$ is formed.

The formation of solid solutions of the type $[Ba(HOC_2H_4OH)_4][Sn_{1-x}Ge_x\ (OC_2H_4O)_3]$ as a $BaSn_{1x}/Ge_xO_3$ precursor and the phase evolution during its thermal decomposition are described in this paper. The 1,2-ethanediolato complexes can be decomposed to nanosized $BaSn_{1-x}/Ge_xO_3$ pre-ceramic powders. Samples with $x = 0.05$ consist of only a $Ba(Sn,Ge)O_3$ phase, whereas powders with $x = 0.15$ and 0.25 show diffraction patterns of both the $Ba(Sn,Ge)O_3$ and $BaGeO_3$ phase. The sintering behavior on powders with a $BaGeO_3$ content of 5 and 15 mol% was investigated. These powders show a specific surface area of 15.4–15.9 m^2/g and were obtained from calcination temperatures above 800 °C. The addition of $BaGeO_3$ reduced the sintering temperature of the ceramics drastically. $BaSn_{0.95}Ge_{0.05}O_3$ ceramics with a relative density of at least 90% can be obtained by sintering at 1150 °C for 1.0 h. The ceramic bodies produced reveal a fine microstructure with cubical-shaped grains between 0.25 and 0.6 μm. To produce dense ceramics, the sintering temperature could be lowered down to 1090 °C, if the soaking time was extended up to 10 h.

In another paper, the same preparation of a nanometer-sized $BaSnO_3$ powder by calcination of a barium tin 1,2-ethanediolato complex precursor—$[Ba(HOC_2H_4OH)_4][Sn_{1-x}Ge_x(OC_2H_4O)_3]$ was employed. Its sintering behavior was studied. A linear rate-controlled calcination process to 820 °C led to a nanometer-sized $BaSnO_3$ powder with a BET-specific surface area of 15.1 m^2/g and a BET equivalent diameter of 55 nm. Crystallite-size measurements by XRD line broadening reveal a value of about 26 nm. The powder produced had a slightly larger cell parameter of $a = 4.1222$ Å compared to the single-crystal value, 4.1170 Å, that was caused by OH groups inside the lattice. The lattice parameter decreases with increasing calcination temperature and reaches the reference value above 1000 °C. The nanometer-sized powder consists of cubical-shaped particles. Corresponding powder compacts of the nano-sized $BaSnO_3$ achieve a relative density of 90% after sintering at 1600 °C for 1 h (grain size: 1.3–4 μm). At 1500 °C and a soaking time of 30 h, a grain size of 3–13 μm was observed, whereas coarse-grained powder compacts reach only 80% of the relative density at 1650 °C (10 h).

In another method, $BaSnO_3$ powder with a crystallite size of 27.6 nm was prepared through a hydrothermal reaction of a peptized $SnO_2 \cdot xH_2O$ and $Ba(OH)_2$ at 250 °C. This was followed by crystallization of this hydrothermal product at 330 °C. The peptization of the $SnO_2 \cdot xH_2O$ gel is dependent on the pH value. Through peptization, the mean particle size of $SnO_2 \cdot xH_2O$ in the aqueous solution has been decreased by a factor of 100 to 8 nm. A limited agglomeration in the sol-prepared powder was observed under the microscope. The structure evolution and crystallization behaviors of the sol-prepared powders were investigated by TG-DTA, IR and XRD. The $BaSn(OH)_6$ phase in the as-prepared powder transforms into an amorphous phase at 260 °C, from which the $BaSnO_3$ particles nucleate and grow with an increase in temperature. The single-phase $BaSnO_3$ powder has been obtained at a temperature as low as 330 °C. This sol-prepared powder is more sinterable than the gel-prepared powder and can be sintered to a ceramic at 340 °C with 90.7% of the theoretic density.

Because of its characteristic dielectric properties, $BaSnO_3$, has been used as a component of ceramic dielectric bodies to prepare thermally stable capacitors, and to fabricate ceramic boundary layer capacitors when combined with $BaTiO_3$. In recent years, more and more attention has been shifted to study of the application of barium metastannate as a sensor material. It has been found that the electrical properties of barium metastannate such as conductivity, resistance, capacitance or impedance are dependent on temperature, oxygen partial pressure, the nature of the measured gases and their concentrations. Based on these results, many gas sensor devices made from $BaSnO_3$ powder have been developed. $BaSnO_3$ and $BaSn_{1-x}Zr_xO_3$ ($x = 0.05$, 0.10 and 0.20) are also sensor materials for H_2S gas in ambient conditions. $BaSnO_3$ can also be used for fabricating a CO sensor. It is thought that the mechanism of CO detection sensitivity of this metal oxide is a surface reaction process. Thus, to achieve a high gas sensitivity, $BaSnO_3$ is fabricated as a thin film. The CO sensitivity shows a maximum in the temperature range of 600 to 700 °C under dry conditions. Humidity has a different influence on the CO sensitivity, which depends on the oxygen concentration. A gas sensor for detecting the presence of CO in polluted air, comprising a perovskite compound such as $Ba_{0.9}Gd_{0.1}SnO_3$, has been reported. $BaSnO_3$ as a semiconducting oxide is also a very promising sensor material for detecting nitric oxide. The sensitivity of the $BaSnO_3$ thin films to NO depends on the temperature and the oxygen concentration. The NO sensitivity, under dry conditions, shows a maximum in the range of 450 to 550 °C. A sensor comprising $BaSnO_3$ is found to be selectively sensitive to NO_2. Oxygen sensors used for

controlling air–fuel ratio in boilers or engines (sometimes called exhaust gas sensor or air–fuel ratio sensor) have been fabricated from sintered $BaSnO_3$. The application of $BaSnO_3$ to detect humidity has also been reported. The humidity sensitivity of $BaSnO_3$ is enhanced slightly by calcining barium tin hydroxides, which are prepared by a coprecipitation method. The partial substitution of the A-site element of the perovskite-type oxides with La produced an enhancement of the sensitivity.

Barium stannate behaves as a pure, *n*-type semiconductor below 900 °C. The measured band gap of $BaSnO_3$ is 3.4 eV. The behavior of this semiconducting oxide material can be controlled by manipulation of the crystallite size and specific surface area of the material exposed to the gas and of the concentration of electrically active donor species present in the lattice. This give characteristic changes either of *n*-type materials (resistance decreases in reducing gases and increases in oxidizing gases), or of *p*-type materials (resistance increases in reducing gases and decreases in oxidizing gases), or of a mixed behavior.

A ferroelectric ceramic based on Te-modified $BaSnO_3$ with a general formula $BaSn_{1-x}Te_xO_3$ ($x = 0$, 0.05, 0.10, 0.15) has been synthesized by a high-temperature SSR technique. Thermal analysis (DTA, TGA and DTG) was carried out to optimize the calcination temperature and other experimental conditions of material formation required. Preliminary structural analysis indicated that crystal structure of the material is basically cubic and remains unaffected even on Te doping. Microstructural analysis of the sample reveals polycrystalline nature and substantial modification of the surface properties of these materials on Te doping. Detailed studies of dielectric properties of the compounds produced as a function of temperature showed a ferroelectric to paraelectric phase transition. It has been observed that the value of peak dielectric constant (max) and Curie temperature are strongly dependent on frequency and dopant concentration. An evidence of a relaxation property has also been noticed for each concentration of the Te dopant. Studies of electrical conductivity of the Te-doped $BaSnO_3$ show a substantial improvement in its value at elevated temperatures.

The synthesis of $BaSn(OH)_6$ acicular crystals by precipitation at 100 °C from aqueous solutions and their transformation into the perovskite-like compound, $BaSnO_3$, has also been investigated. Single-acicular crystals 100–200 μm in length were obtained from a 0.05 M solution, whereas bundle-like aggregates of 20 to 40 μm were precipitated from 0.2 to 0.6 M solutions. The XRD pattern of barium hexahydroxostannate was indexed according to a monoclinic symmetry with cell parameters, $a = 11.029$ Å, $b = 6.340$ Å, $c = 10.563$ Å, $\beta = 128.51°$, $\alpha = \gamma = 90°$. The $BaSn(OH)_6$ particles decomposed to $BaSnO_3$ and water at approximately 270 °C and the original morphology was retained. The resulting product had a specific surface area of up to 30–40 m^2/g and consisted of 10- to 20-nm crystallites. The larger unit-cell edge in comparison to the single-crystal value and the continuous weight loss up to 1200 °C indicate that water is not completely released during decomposition and a substantial amount of proton defects (up to 0.4 mol per mole of $BaSnO_3$ is incorporated in the perovskite lattice as OH^- groups) remains. Normal crystallographic properties of $BaSnO_3$ are restored only after calcination at 1300 °C.

In still another paper, hydroxide perovskites of $BaSn(OH)_6$ were synthesized by coprecipitation and sono-chemical reaction routes. Some of the compounds were also prepared by the hydrothermal method. These were characterized by XRD, TGA/DTA, TEM and IR studies. The hydroxide perovskites are stable up to 523 K (300 °C) and all the compounds stabilize in cubic crystal system (space group = *Pn*3*m*) at 298–523 K (20–250 °C) except $BaSn(OH)_6$. The as-prepared powders of the above compositions show a cubic square net in the reciprocal lattice of their electron diffraction patterns. Among these perovskites, $BaSn(OH)_6$ exhibits proton conduction at 298–500 K (20–227 °C). Above 250 °C, solid solutions of SnO_2 and BaO components were observed. On heat treatment at 850–950 K (577–677 °C), an oxygen-deficient $Ba_{2-x}(V_M)_xSnO_4$ spinel, ($x < 1$) along with SnO_2 are observed. On further sintering to 1773 K (1500 °C) for a duration of 6–7 h, $M_{2-x}(V_M)_xSnO_4$ phase is stabilized. The electrical properties of these compounds were measured by four-probe DC method. The loss of proton conduction above 523 K may be ascribed to dehydroxylation and subsequent decomposition to $SnO_2 + Ba_{2-x}(V_M)_xSnO_4$.

Since $BaSnO_3$ crystallizes in a cubic perovskite structure and exhibits insulating behavior, the transformation into a semiconducting compound has been studied. It can be made conducting by reducing a small fraction of Sn^{4+} into Sn^{2+} under an O_2-free atmosphere. This can be achieved through the solid solution. $Ba_{1-x}La_xSnO_3$ is a mixed phase for $x > 0.02$ wherein a trivalent ion, La^{3+} substitutes for a divalent ion, Ba^{2+}. This behavior is readily understood in terms of the lone pair cation Sn^{2+}. The magnetic susceptibility was measured down to 4.2 K and is less than 1.7×10^{-5} emu cgs/mol consistent with a collective electron behavior. The Mössbauer spectrum exhibits a wide unsplit peak with a quadrupole doublet of 3.18 mm/s and an isomer shift of 0.12 mm/s characteristic of Sn^{4+} that corroborates the delocalization of the stereo chemical pair $5s^2$. The band gap, E_g, was found to be 3.12 eV with a further indirectly allowed interband transition occurring at 2.85 eV. The transport properties of $Ba_{0.98}La_{0.02}SnO_3$ indicate *n*-type conductivity ($\sigma_{300\ K} = 4.03$ Ω-cm), and little temperature dependence, with an activation energy ΔE of ~1 meV and an

electron mobility $\sigma_{300\ K} \sim 0.1\ cm^2/V/s$, thermally activated. The conduction occurs by small polaron hopping between mixed valence Sn^{4+}/Sn^{2+} ions. The observed conductivity is greater than that originating from La substitution, with one-electron doping implying the existence of oxygen vacancies. The electrons are believed to travel in the Sn-5s conduction band with an effective mass of $m(e,l) = 3.7m_{(0)}$ [where $m_{(0)} = 9.11 \times 10^{-31}$ kg]. The nonlinear dependence of ln σ versus T^{-1} at low temperatures could result from a predominant variable range hopping as suggested by the linear variation of log σ versus $T^{-0.25}$. The electron localization may be attributed to the random distribution of lanthanum as well as oxygen vacancies.

The AC conductivity, η_{ac} of $BaSnO_3$ has been measured in the temperature range 310–520 K (37–247 °C) and frequency range 100 Hz–1.0 MHz. Below 420 K (147 °C), the conductivity is almost independent of temperature while between 420 and 520 K, it is temperature dependent. At 100 kHz, the activation energy of these two regions is 0.08 and 0.35 eV, respectively. It has been proposed that in the low-temperature region, conduction is due to hopping of charge carriers among the Sn^{+2} and Sn^{+4} sites. In the high-temperature region, conduction is due to excitation of charge carriers at the edges of the conduction band and hopping at energies close to it.

The compound, barium stannite = $BaSnO_2$(II) remains unknown.

Barium stannate is available as $BaSnO_3$ commercially in small to medium lots worldwide.

Radium Stannates

There is no record of the preparation of any of these compounds. They could be prepared by the same methods used for the barium compounds, namely:

$$Ra^{2+}(HCl) + SnCl_6^{2-} \text{—the wet proxide method}$$

$$RaSn(OH)_6 \cdot 3H_2O \text{ method}$$

$$[Ra(HOC_2H_4OH)_4][Sn(OC_2H_4O)_3]$$

$$RaSn(OH)_6 \text{ method}$$

Three compounds are expected to be formed: $RaSnO_3$, Ra_2SnO_4 and $Ra_3Sn_2O_7$. Nonetheless, the reference books and chemical literature are devoid of any mention of any of these due, perhaps, to the intense radioactivity and danger of handling of ^{227}Ra compounds.

5.5. ALKALINE EARTH OXY-PLUMBATE COMPOUNDS

Plumbides can be formed when lead forms a Zintl phase compound with a more metallic element. The alkaline earths form a limited number of such compounds due to the large size of the lead ion. The structure of Pb_5^{2-} is presented as Fig. 5.130

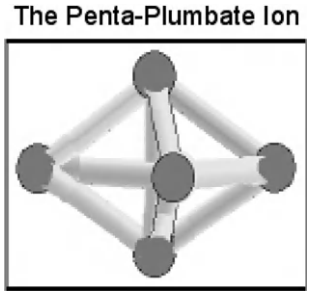

FIGURE 5.130

5.5.1. Oxides of Lead, Pb_xO_y

There are two valence states for the element, Pb^{2+} and Pb^{4+}. Lead oxides are amphoteric and dissolve in aqueous solution under both acidic and basic conditions. As cations, they are sometimes called "Plumbous" and "Plumbic". As anions, chemical combination with any given cation is designated as a "plumbite" or "plumbate". These compounds are also called "metaplumbate" and "orthoplumbate", although this designation is not strictly correct.

Divalent lead oxide has the formula PbO. Lead(II) oxide occurs in two polymorphs, red, having a tetragonal crystal structure and yellow, having an orthorhombic crystal structure. Both forms occur naturally as rare minerals. The red form is known as "Litharge" and the yellow form is known as "Massico".

Lead dioxide, PbO_2, also plumbic oxide, is an odorless dark-brown crystalline powder which is nearly insoluble in water. It exists in two crystalline forms. The α phase has orthorhombic symmetry, lattice constants $a = 0.497$ nm, $b = 0.596$ nm, $c = 0.544$ nm, $Z = 4$ (four formula units per unit cell). It was first synthesized in 1941 and identified in nature as a rare mineral "scrutinyite" in 1988. The prevailing, tetragonal β phase was first identified as the mineral "plattnerite" around 1845 and later produced synthetically. Its lattice parameters are: $P4_2/mnm$ (no. 136), tP6, $a = 0.491$ nm, $c = 0.3385$ nm, $Z = 2$. Lead dioxide is a strong oxidizing agent that is used in the manufacture of matches, pyrotechnics, dyes and other chemicals. It also has several important applications in the electrochemical industry, in particular as a component of lead–acid batteries used in almost all types of vehicles. Lead dioxide decomposes upon heating in air as follows:

$$PbO_2 \Rightarrow Pb_{12}O_{19} \Rightarrow Pb_{12}O_{17} \Rightarrow Pb_3O_4 \Rightarrow PbO$$

The stoichiometry of the end product can be controlled by changing the temperature—for example,

in the above reaction, the first step occurs at 290 °C, second at 350 °C, third at 375 °C and fourth at 600 °C. In addition, Pb_2O_3 can be obtained by decomposing PbO_2 at 580–620 °C under oxygen pressure of 1.4 kbar. Therefore, thermal decomposition of lead dioxide is a common industrial way of producing the various lead oxides.

Lead tetroxide, also called "minium", red lead or triplumbic tetroxide, is a bright red or orange crystalline pigment. Chemically, red lead is lead tetroxide, Pb_3O_4, or $2PbO \cdot PbO_2$. This compound's Latin name *Minium* originates from the Minius river in northwest Spain where it was first mined. Natural minium is uncommon, forming only in extreme oxidizing conditions of lead ore bodies. The best specimens known come from Broken Hill, New South Wales, Australia, where they were formed as the result of a mine fire.

Lead dioxide is an amphoteric compound with dominant acidic properties. It dissolves in strong bases to form the hydroxy-plumbate ion, $Pb(OH)_6^2$.

$$PbO_2 + 2NaOH + 2H_2O \Rightarrow Na_2[Pb(OH)_6]$$

It also reacts with basic oxides in the melt yielding orthoplumbates such as $K_4[PbO_4]$. Because of the instability of its Pb^{4+} cation, lead dioxide reacts with warm acids, converting to the more stable Pb^{2+} state and liberating oxygen:

$$2PbO_2 + 2H_2SO_4 \Rightarrow 2PbSO_4 + H_2O + O_2$$

$$2PbO_2 + 4HNO_3 \Rightarrow 2Pb(NO_3)_2 + H_2O + O_2$$

$$PbO_2 + 4HCl \Rightarrow PbCl_2 + 2H_2O + Cl_2$$

Plumbous acid, H_2PbO_3, does not exist per se. The divalent ion, Pb^{2+}, forms under weakly acidic conditions (~pH = 6.0–6.5) as $Pb(OH)_2$. In solution, lead(II) hydroxide is a somewhat weak base, forming the lead(II) cation, Pb^{2+}, under weakly acidic conditions. This cation hydrolyzes and, under progressively increasing alkaline conditions, forms $Pb(OH)^+$, $Pb(OH)_2$(aqueous), $Pb(OH)_3^-$, and $Pb(OH)_4^{2-}$.

Thus, the number of "plumbides", "plumbites" and "plumbates" of the alkaline earths is strictly limited and depends upon the nature of the alkaline earth. This is probably due to the large size of the lead atom which, when combined with the alkaline earths, limits the number of stable compounds. Thus, we would not expect to find many stable beryllium–lead compounds but barium would exhibit the greatest number of stable compounds.

5.5.2. Plumbides of the Alkaline Earths

Beryllium Plumbides

No beryllium plumbides are known to exist. It is not clear whether this is due to the fact that they are not stable or to the fact that preparation of such alloys have never been attempted experimentally. Be melts at 1287 °C while Pb melts at 232 °C. This disparity may be the reason why the Be–Pb phase system has not been explored. The lack of interest in industry to their physical or electrical properties is probably the primary reason why the Be–Pb system has not been explored.

Magnesium Plumbides

Magnesium (MP = 643 °C) and lead (MP = 232 °C) react to form but one compound:

$$2Mg + Pb + \text{heat} \Rightarrow Mg_2Pb$$

The stability and elastic properties of Mg_2Pb have been investigated by the first-principles method, using the method of ultrasoft pseudopotential within the generalized gradient approximation based on density functional theory. Cohesive energy and formation enthalpy show that Mg_2Pb is stable. Similar result is also obtained by the energy band structure and DOS analysis. The thermal data of Mg_2Pb have also been calculated using Debye's quasi-harmonic approximation, such as heat capacity and Gibbs free energy. Based on the C_V, it was found that the Debye temperature of Mg_2Pb is 247.2 K. Young's modulus and shear modulus for Mg_2Pb are 68.6 and 27.9 GPa calculated from the theoretical elastic constants by Voigt-Reuss-Hill averaging scheme. The phase diagram is shown in Fig. 5.131.

Following this work, the liquidus curve for the Mg–Pb system was redetermined, and its slope was used to assess phase transformations in the β′ + Pb-rich liquid phase field. A peritectic reaction occurred at 538.7 °C when Mg_2Pb decomposed into a Mg-rich liquid and β′ (a Mg–Pb compound containing 35.15 at% Pb, or 0.3515 N_{Pb}, the atomic fraction of Pb) which melted congruently at 548.5 °C, confirming the work of Eldridge et al. When β' was cooled, a series of reactions occurred with the progressive rejection of Pb, this catatectic reaction terminated at 249 °C, 4 °C below the temperature of the Pb-rich eutectic at 83.88 at% Pb and 252.6 °C. This finding was contrary to that of Eldridge et al [1967] as they reported that the catatectic reaction terminated at 291 ± 5 °C. The rejection of Pb from an ingot of β' was recorded as a time-lapse series of photographs. The phase transformations resulting from the catatectic reaction and several polymorphic transformations of the intermediate products have been identified in the temperature range 548.5 to 249 °C.

The identification of the reactions at 252.6 and 249 °C has clarified this region of the phase diagram, as both of these values have been reported as the eutectic temperature. Finally, two polymorphic transformations of Mg_2Pb at 229 and 208 °C were identified and provided a basis for the identification of the final stage of the

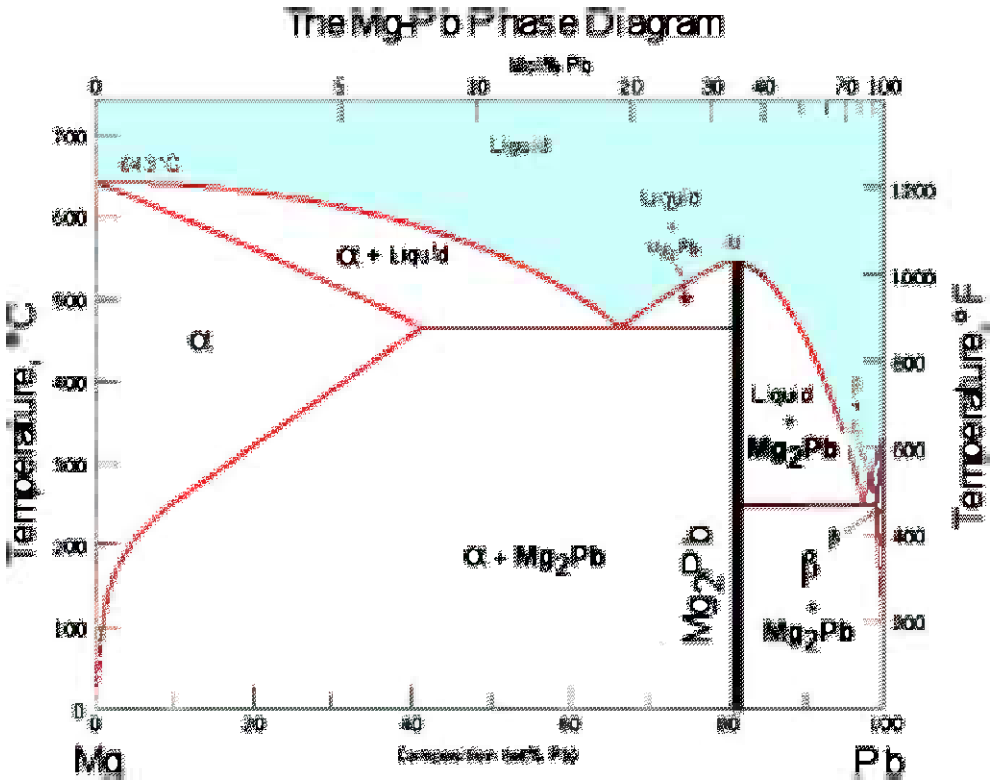

FIGURE 5.131

catatectic reaction at 249 °C. Mg_2Pb crystallizes in the "anti-fluorite" cubic structure with $a = 8.456$ Å (Fig. 5.132).

The thermal conductivity of a semimetal Mg_2Pb single crystal has been measured from 2 to 200 K (−271 to −73 °C). At low temperatures, thermal conduction is by phonons, but limited by phonon scattering from the heavy hole Fermi surface. At higher temperatures, the thermal conductivity contains both electronic and phonon contributions. A comparison of the thermal conductivity of Mg_2Pb with the thermal conductivities of the related semiconductors, Mg_2Si, Mg_2Ge, and Mg_2Sn, indicates that there is a significant bipolar contribution to the electronic thermal conductivity.

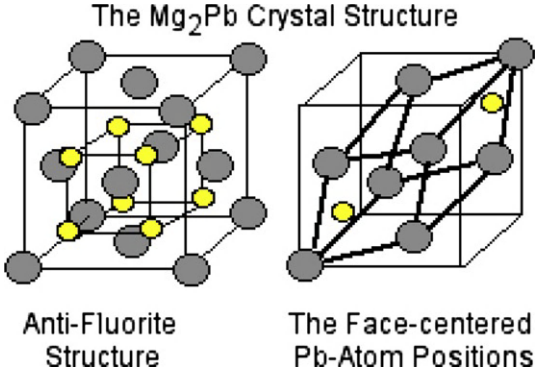

FIGURE 5.132

The sublimation of Mg_2Si, Mg_2Ge, Mg_2Sn and Mg_2Pb was studied by mass spectrometric observation of the vapor effusing from a Knudsen cell. Analysis of the temperature dependence of the partial pressure of Mg was used to obtain ΔH_{Mg}. The values of ΔH_{Mg} reported in this work are shown to correlate with the known melting points of the various compounds and to support metallic interpretation of the high conductivity of Mg_2Pb.

When Mg bismuthide and Mg plumbide react, the peritectic reaction changed from an even to odd reaction at 310 °C (0.14 wt% Bi and 4 wt% Mg). This was caused by the incorporation of 1.6 wt% Bi into Mg plumbide. This value was calculated from material balances of equilibrium studies of this reaction and confirmed by direct analysis of crystals using a "Cameca Microbeam" electron probe microanalyzer. A model was presented in which an atom of Pb in the unit cell, Mg_2Pb Mg_2Pb_5, was replaced by an atom of Bi which gives a concentration of 1.63 to 1.71 wt% Bi depending on the actual species of Mg plumbide present.

The phase boundary for double saturation of Pb and Mg plumbide has been established from the data of equilibrium tests. This shows a minimum temperature of 251.8 °C at 0.008 wt% Bi and 2.2 wt% Mg. Alloys in

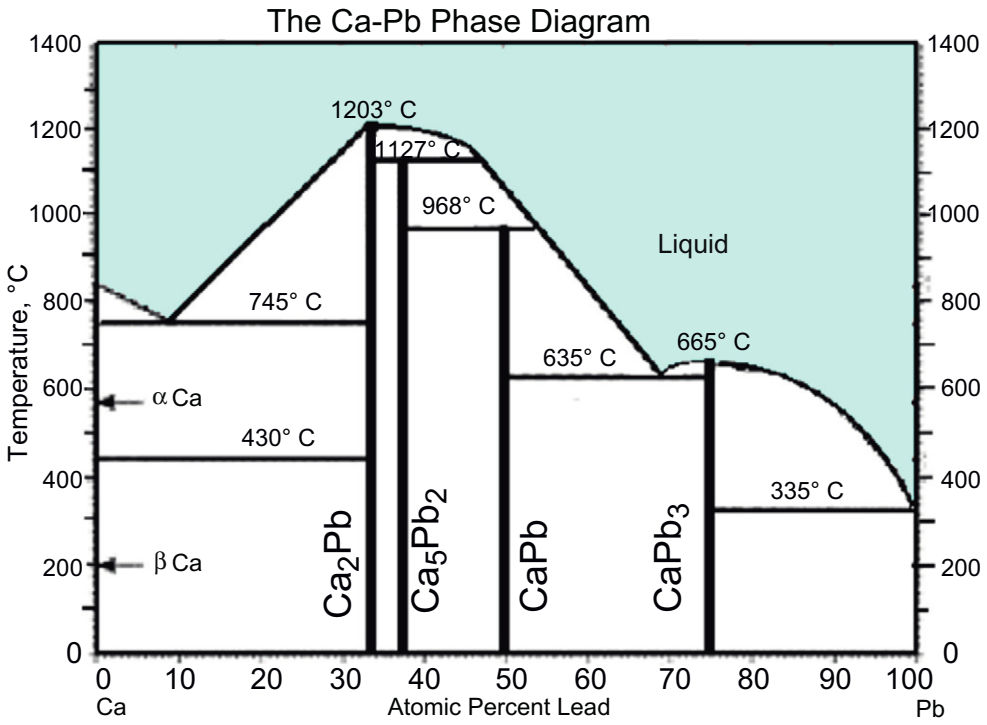

FIGURE 5.133

the primary Pb phase field adjacent to this boundary show undercooling to less than 248.5 °C, followed by one or two sharp temperature increases to 250.5 °C, with the initiation of the removal of Bi when the double saturation occurs, producing a final liquid phase containing less than 0.001 wt% Bi. Crystallization paths for alloys in the Mg plumbide phase field show a catatectic reaction and polymorphic transformations in the intermetallic compound. The removal of Bi is dependent on the concentration of Bi and Mg in the initial alloy. In systems containing sufficient Mg, a final alloy, containing less than 0.001 wt% Bi can be produced. These conditions have been used as the starting point for the development of a process for the removal of Bi from Pb. In addition, the crystallization paths show that there is a change in the thermal properties of the liquid alloy at 0.008 wt% Bi that is independent of the temperature and concentration of Mg. Further work is required to resolve this finding.

Mg_2Pb is offered for sale commercially even though no CAS number has apparently been assigned.

Calcium Plumbides

Calcium, Ca^0, melts at 842 °C and Pb^0 at 317 °C. Several compounds form from the melt. The reaction is:

$$xCa + yPb \Rightarrow Ca_xPb_y$$

where x and y can be 1 to 5.

The calcium–lead system has been investigated by thermal and X-ray methods. The Ca–Pb phase diagram, established as of 2004, is shown in Fig. 5.133.

Two compounds melt congruently: Ca_2Pb (1203 °C) and $CaPb_3$ (667 °C); two compounds form peritectically: Ca_5Pb_3 (1127 °C) and CaPb (968 °C).

Two eutectics occur at 90.5 at.% Ca (750 °C) and 36.5 at.% Ca (638 °C), respectively. The crystal structures of Ca_2Pb, Ca_5Pb_3 and $CaPb_3$ were confirmed. The compound CaPb was found to crystallize with the AuCu I-type structure ($a = 5.118$ Å, $c = 4.491$ Å). The same structure type was found for the phases EuPb ($a = 5.226$ Å, $c = 4.586$ Å) and YbPb ($a = 5.085$ Å, $c = 4.443$ Å), in which Eu and Yb behave as divalent elements similar to the alkaline earths. Crystal parameters are presented in the following Table 5.66.

Calcium triplumbide, $CaPb_3$, has been determined to be diamagnetic.

Diamagnetism is the property of an object which causes it to create a magnetic field in opposition to an externally applied magnetic field, thus causing a repulsive effect. Specifically, an external magnetic field alters the orbital velocity of electrons around their nuclei, thus changing the magnetic dipole moment. According to Lenz's Law, this opposes the external field. Diamagnetic materials cause lines of magnetic flux to curve away from the material, and superconductors can exclude them completely (except for a very thin layer at the

TABLE 5.66

Phase	Mol% Pb	Group symmetry	Lattice parameters			Space group	Type
			a	*b*	*c*		
β-Ca	0					$Im\bar{3}m$	W
α-Ca	0					$Fm\bar{3}m$	Cu
Ca_2Pb	33.3	Orthorhombic	8.035	5.067	9.617	—	Co_2Si
Ca_5Pb_3	37.5	Hexagonal	9.355	—	7.004	—	Mn_5Si_3
CaPb	50	Hexagonal	5.118	—	4.491	—	*Bf* CrB
$CaPb_3$	75	Cubic	4.897	—	—	—	$AuCu_3$
βPb	100					$I4_1/amd$	βPb

surface). The features of the band structure and orbital magnetic susceptibility of the intermetallic compound $CaPb_3$ have shown that the anomalous, strongly temperature-dependent diamagnetism observed earlier in experiments on these compounds is of an interband origin and is due to the presence of degenerate electronic states in the immediate vicinity of the Fermi level.

Ternary mixed Ca/Sr–Ba triplumbides of overall composition $M_{1.0}Pb_{3.0}$ were synthesized from stoichiometric mixtures of the elements. The structures of the compounds have been determined by means of single-crystal X-ray data. All structures exhibit close-packed ordered APb_3 layers containing Pb Kagomë nets, which are stacked in different orientations. Depending on the stacking sequences, the resulting lead polyanion resembles the oxygen nets of the hexagonal (face sharing octahedra, *h*-stacking, Ni_3Sn-type structure) or the cubic perovskites (corner-sharing octahedra, *c* stacking, Cu_3Au-type structure). The known binary compound, $BaPb_3$, the structure of which has been redetermined from single-crystal data (trigonal, space group $\bar{R}3m$, $a = 7.2906$ Å, $c = 25.6443$ Å, $Z = 9$), shows a $(hhc)_3$ stacking ($TaCo_3$-type structure). A small partial substitution of barium against calcium ($Ca_{0.03}Ba_{0.97}Pb_3$: trigonal, space group $\bar{R}3m$, $a = 7.260$ Å, $c = 34.43$ Å, $Z = 12$), or strontium ($Sr_{0.11}Ba_{0.89}Pb_3$: $a = 7.273$ Å, $c = 34.21$ Å, $Z = 12$) causes a structural change to the HT-$PuGa_3$ structure type with a $(hhcc)_3$-stacking sequence. At an approximate 1:1 ratio (35 to 53% Sr) of strontium and barium ($Sr_{0.56}Ba_{0.44}Pb_3$: trigonal, space group $P63/mmc$, $a = 7.1582$ Å, $c = 17.1791$ Å, $Z = 6$), the $PuAl_3$ structure type [$(hcc)_2$-stacking] has a distinct homogeneity range. The composition, $(Ba_{0.95},Sr_{0.05})Pb_3$ has a rhombohedral unit cell ($a = 12.80$ Å, $\alpha = 34.43°$). The series is terminated with the pure *cubic* stacking of $SrPb_3$ and $CaPb_3$. As already noted from the above series, the stacking of the closely-packed layers is influenced by the ratio of the atomic radii of the contributing elements. The electronic stability ranges, which are discussed on the basis of the results of FP-LAPW band structure calculations and in comparison to further compounds known from the literature, can be explained using Zintl/Wade rules. Still, due to the presence of only partially occupied steep Pb-*p* bands of σ-bonding characteristic, the compounds are metals exhibiting pseudo band gaps at or near the Fermi level. Thus, this structure family represents an instructive case of transition from polar ionic/covalent toward (inter)metallic chemistry.

The enthalpies of formation of liquid or solid Ca–Pb alloys have been measured by direct and indirect calorimetry, for example: DTA gave diagram lines. In particular, the peritectic invariant temperature of low-calcium alloys has been confirmed. The melting entropy of $CaPb_3$ (12.6 J/K/(mol at.)) was obtained by anisothermal calorimetry. All the enthalpy information and diagram lines have been included in a computer calculation. Numeric representation of the thermodynamic properties of the Ca–Pb system is given. The heat of formation of $CaPb_3$ is:

$$\Delta H_f\ (1/4\ CaPb_3\ (910\ K = 637\ °C)\ Ca(s)Pb\ (liq) = -35.1\ kJ/mol$$

Pentacalcium triplumbide, Ca_5Pb_3, has the Mn_5Si_3 structure. The many A_5B_3 phases that exhibit hexagonal Mn_5Si_3-type structures by and large have a nearly unique abilities to bind diverse heteratoms Z in a preformed cavity within a chain of confacial trigonal antiprisms of A. The historical development of this chemistry as interstitially stabilized Nowotny phases and recent research to clarify the necessity for Z and the range of Z possible in certain hosts are described. Some hosts may bind as many as 20 different interstitial Z. Structures, stoichiometric relationships, volume effects electronic guidelines, anomalies, Nowotny phases that require Z for stability, and a few band calculations are described. The special cases of hosts composed of divalent cations with pnictogens (As–Bi) and tetrels (Si–Pb) are complex cases of Nowotny phases.

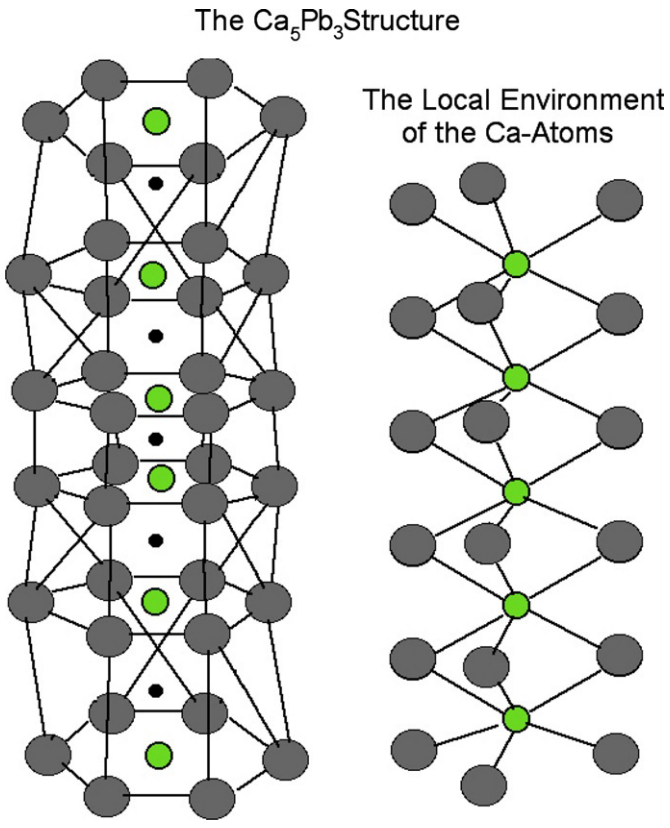

FIGURE 5.134

The structure of Ca_5Pb_3 is shown in Fig. 5.134.

The interstitial positions, referred to above, are shown as the black dots. Although the crystal structure and lattice constants have been measured, little data, other than its melting point, have been presented in the literature. It does form solid solutions with its Sr and Ba homologues but is only mentioned in passing when descriptions of those compounds are presented. The technical literature is almost devoid of mention of this compound except for structure.

The compound, **Monocalcium plumbide,** CaPb, was found to crystallize with the AuCu I-type structure. The Au–Cu system is one of the earliest systems for which several order–disorder-type transformations have been established. Much of the theory of order–disorder phenomenon has grown from an extensive study of these phases. In the case of CaPb, the structure is usually I-type which is a face-centered cubic structure where the Ca atoms are at the corners of the cube and Pb atoms lie at part of the face-centered positions. However, the occupartition can shift as shown in the accompanying diagram in which one row of the infinite structure is shown in Fig. 5.135.

The atom coordinates for this structure are presented in the following Table 5.67.

Although CaPb has been studied intensively concerning it structural abnormalities, little interest has been shown in industry due to the lack of interesting electrical properties.

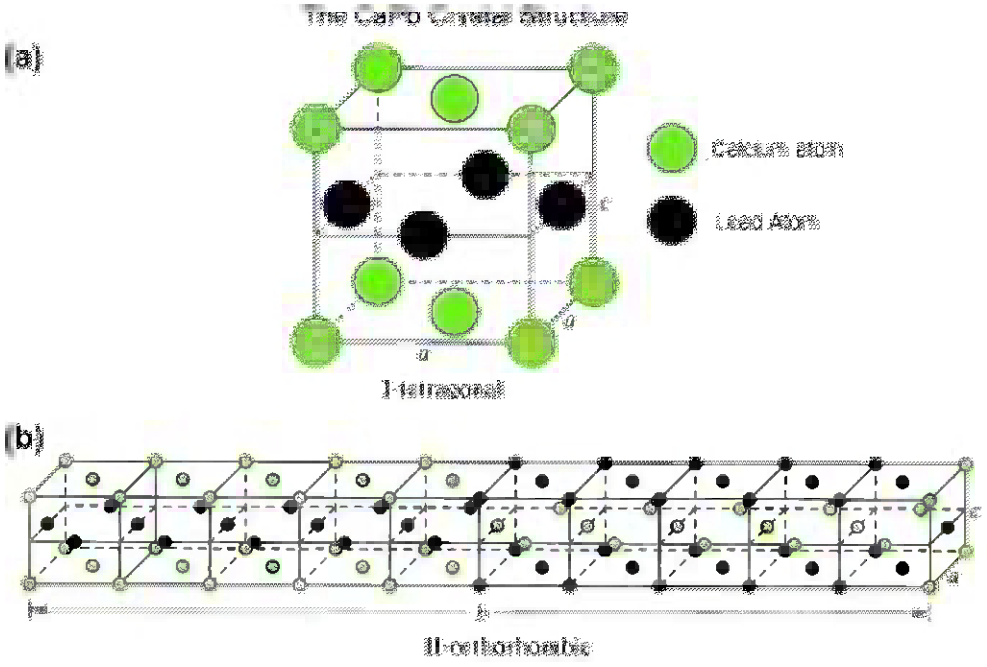

FIGURE 5.135

TABLE 5.67

No	Site notation	Atom	Multiplicity	Wyckoff	Site symmetry	x	y	z	Occupancy
1	Pb	Pb	1	d	4/mmm	1/2	1/2	1/2	1.0
2	Ca	Ca	1	a	4/mmm	0	0	0	1.0

Dicalcium plumbide, Ca_2Pb, is isotypic with Ca_2Si and Ca_2Ge ($PbCl_2$-structure, C-23-type). The lattice constants, space group, and point parameters are similar. The structure is shown in Fig. 5.136.

The lattices parameters are: Ca_2Pb: $a = 9.647 \pm 0.004$; $b = 8.072 \pm 0.004$; $c = 5.100 \pm 0.003$ Å, space group $= D_{2h}^{16}$.

The atoms occupy the point positions:

$$4(c) \pm (x, y, 1/4),\ (1/2 + y,\ 1/4).$$

The found parameters are the y values of the heavy metal atoms in both compounds and the same amount except: $x = x_{Pb} = 0.111$, $x = 0.067_{Ca1,Ca2} = 0.683$, $y_{Pb} = 0.250$, $y = 0.655_{Ca1}$, $y = 0.513_{Ca2}$.

Although Ca_2Pb has been studied concerning its structural properties, little interest has been shown in industry due to the lack of interesting electrical properties.

The **tricalcium plumbide** compound, Ca_3Pb, has been observed to be unstable yet it forms a hydride Zintl phase. Shiny crystals of the isotypic title compounds are obtained in high yield from suitable proportions of CaH_2, metal Ca, and Pb in welded Ta containers slowly cooled from 1100 °C. These were characterized by single-crystal XRD for Ca_3SnH_2 and Ca_3PbH_2 (orthorhombic, *Cmcm* (no. 63), $Z = 4$, $a = 8.866(1)$, 8.937(1) Å, $b = 11.371(2)$, 11.470(2) Å, $c = 5.220(1)$, 5.2551(7) Å, respectively). The structure is shown in Fig. 5.137.

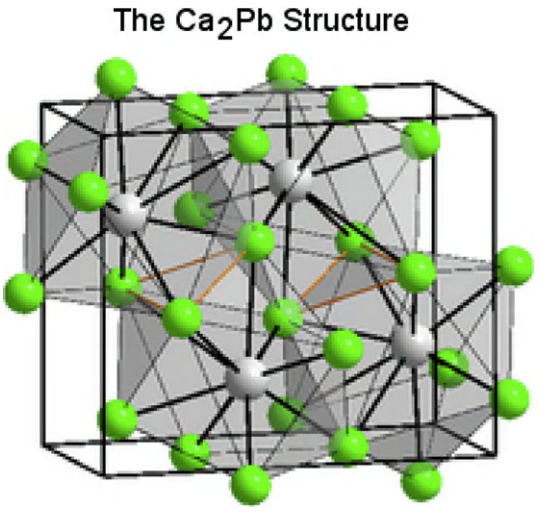

FIGURE 5.136

The structure contains distorted hcp layers of Ca_3Pb between which hydrogen occupies all tetrahedral voids formed by Ca atoms. These tetrahedra share three edges to form double chains along the c axis that are separated by Tt atoms. Both calcium compounds are diamagnetic semiconductors, and the family can all be formulated in terms of oxidation states as Zintl phases $(A^{+2})_3Tt^{-4}(H^-)_2$. Their structure may be derived from the hexagonal version of the cubic perovskite Ca_3SnO by distortions that split the octahedral site in the oxide into edge-sharing tetrahedral pairs shown below. Thus, although Ca_3Pb is not stable and does not form in a Ca–Pb melt, it is stable if CaH_2 is added to the melt.

In general, calcium plumbides are not available commercially and no CAS numbers have been assigned to any of these compounds.

Strontium Plumbides

Strontium, as a metal, forms a series of crystalline compounds with Pb. The Sr–Pb system was studied by thermal analysis and X-ray analysis. The phase diagram is shown in Fig. 5.138.

Seven intermediate phases were found to exist. Two of these phases melt congruently: Sr_2Pb (1155 °C); $SrPb_3$ (675 °C). The remaining five phases form peritectically: Sr_5Pb_3 (1054 °C); Sr_5Pb_4 (943 °C); SrPb (785 °C); Sr_2Pb_3 (717 °C); Sr_3Pb_5 (645 °C). Two eutectics are formed, at 87.5 at.% Sr (725 °C) and at 30.5 at.% Sr (627 °C). The crystal structures of the compounds Sr_2Pb (anti-$PbCl_2$ type), Sr_5Pb_3 (Cr_5B_3 type), SrPb (CrB type) and $SrPb_3$ (Ti_3Cu type) are confirmed; Sr_5Pb_4 crystallizes with the Gd_5Si_4-type structure.

Distrontium plumbide, Sr_2Pb, crystallizes in the "ordered" anti-$PbCl_2$ type and is therefore related to the binary compound Ca_2Pb, which forms the anti-$PbCl_2$ type as well.

The structure is given as follows. Lattice parameters are: $a = 8.445$ Å, $b = 5.391$ Å, $c = 10.139$ Å, $\alpha = 90°$, $\beta = 90°$, $\gamma = 90°$, cell volume $= 461.60$ Å^3, space group = Pnma, point group = oP12, $Z = 4$ (Fig. 5.139).

Little use has been found for this material in industry.

Strontium monoplumbide, SrPb, is tetragonal and has the lattice parameters of $a = 4.648$ Å, $b = 5.018$ Å, $c = 6.6097$ Å, $\alpha = 112.31°$, $\beta = 90°$, $\gamma = 90°$, cell

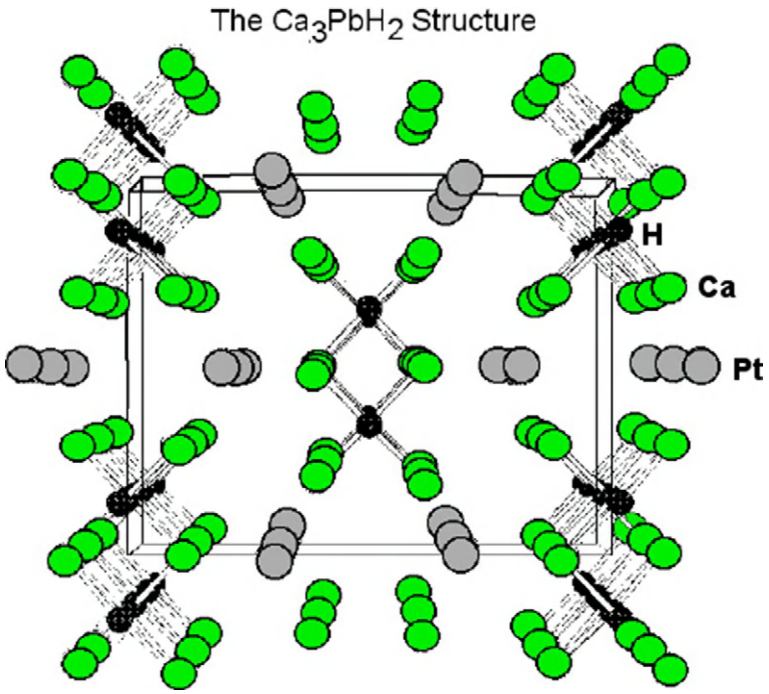

FIGURE 5.137

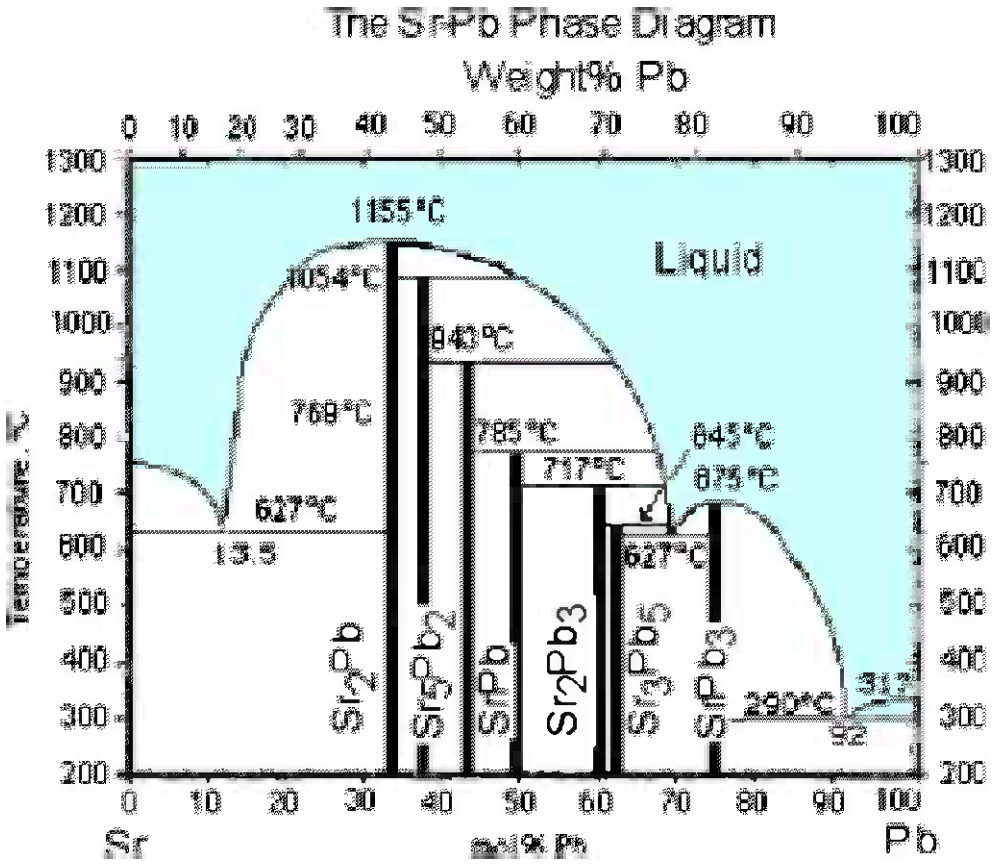

FIGURE 5.138

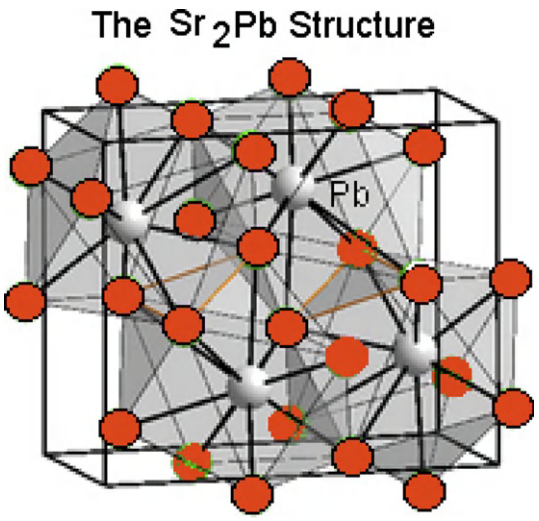

FIGURE 5.139

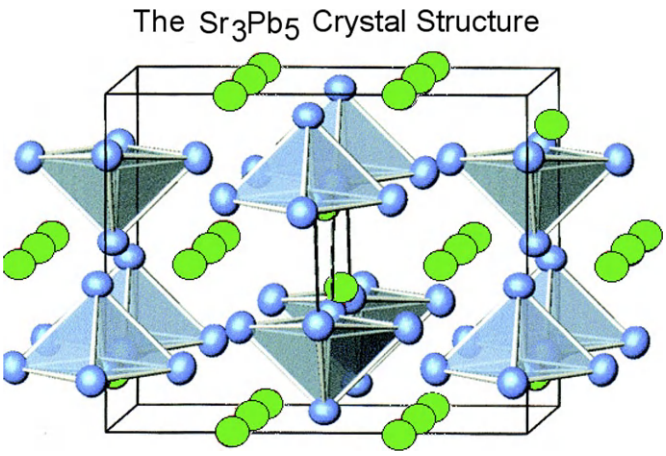

FIGURE 5.141

volume = 142.6 Å^3, $Z = 4$, space group = Cmcm, point group = oS8. Little usage for this compound has been found in industry. Hence, the technical literature is sparse. The structure of SrPb is shown in Fig. 5.140.

Tristrontium pentaplumbide, Sr_3Pb_5, has the same structure as its Ba homologue, and is shown in Fig. 5.141.

The cell parameters are: $a = 4.883$ Å, $b = 8.367$ Å, $c = 8.367$ Å, $\alpha = 90°$, $\beta = 90°$, $\gamma = 90°$, cell volume = 341.84 Å^3, $Z = 4$. It is orthorhombic with space group P4/mbm and point group tP10. In another modification, Sr_3Pb_5, is reported to be tetragonal with space group = P4/mbm, $a = 8.367$ Å, $c = 4.883$ Å, $Z = 2$.

Both binary Zintl phases, Sr_3Pb_5 and Ba_3Pb_5, were synthesized and structurally characterized. The revised structure of Ba_3Pb_5 is also reported. Both compounds are isotypic and crystallize with a modified Pu_3Pd_5 structure type. The anionic substructure is composed of Pb_5^{6-} square pyramidal clusters, which are described as arachno clusters according to the Wade–Mingos electron counting rules. The electronic structure of these pyramidal Zintl anions and the influence of the number of skeletal electrons of these clusters were investigated using the ELF.

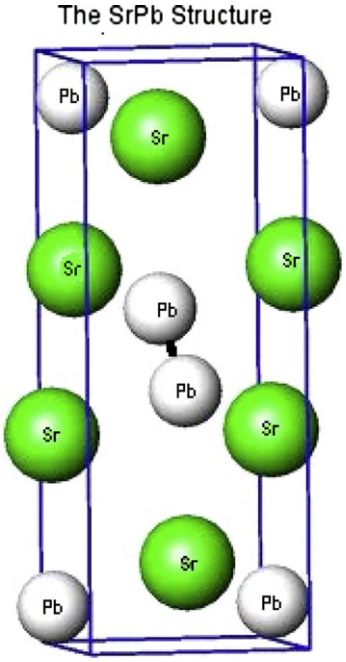

FIGURE 5.140

These compounds that contain square pyramidal polyanions of lead has been obtained in alkaline earth tetrel systems by direct fusion of the elements at 570 °C (Sr_3Pb_5), 1000 °C (Ba_3Pb_5), followed by slow cooling or annealing. The crystal structures have been refined in the Pu_3Pd_5 structure type (orthorhombic, *Cmcm*, $Z = 4$) with cell dimensions of $a = 10.644$, and 11.154 Å, $b = 8.588$ and 9.049 Å, and $c = 10.895$ and 11.370 Å, for Sr_3Pb_5 and Ba_3Pb_5, respectively. Square pyramidal clusters of the tetrel elements are weakly interlinked into chains via two types of longer intercluster interactions that are mediated by bridging cations and substantially influenced by cation size and the free electron count. The new compounds are all metallic ($\lambda_{298} = 10$ (Sr_3Pb_5) to 25 (Ba_3Pb_5) Ω cm), in agreement with simple valence considerations that predict two and five extra electrons per formula unit, respectively, beyond that necessary for closed-shell *nido*-Tt_5^{4-} anions. Extended Hückel tight-binding calculations on these new compounds reveal that bonding in the regions below and around the Fermi energies are dominated by general cation–anion interactions, that is, lattice covalency.

Strontium triplumbide, $SrPb_3$, [13c] crystallizes in the $AuCu_3$ type of structure with cell parameters of

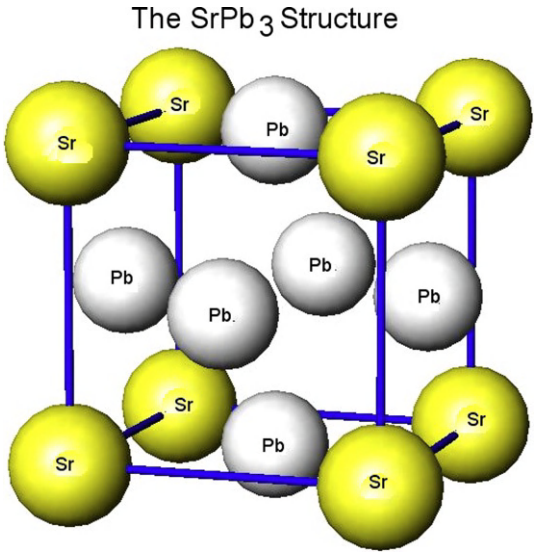

FIGURE 5.142

$a = 4.966$ Å, $b = 4.966$ Å, $c = 5.025$ Å, $\alpha = 90°$, $\beta = 90°$, $\gamma = 90$ °, cell volume = 123.92 Å^3, $Z = 2$, $d = 9.50$ g/cc, point group = tP4, space group = P4/mmm.

The structure is shown in Fig. 5.142.

Ternary mixed Sr/Ca–Ba triplumbides of overall composition $A^{II}Pb_3$ were synthesized from stoichiometric mixtures of the elements. The structures of the compounds have been determined by means of single-crystal X-ray data. All structures exhibit close-packed-ordered APb_3 layers containing Pb Kagomë nets, which are stacked in different orientations. Depending on the stacking sequences, the resulting lead polyanion resembles the oxygen nets of the hexagonal (face sharing octahedra, *h* stacking, Ni_3Sn-type structure) or the cubic perovskites (corner-sharing octahedra, *c* stacking, Cu_3Au-type structure). $SrPb_3$ is cubic but modification with barium causes change to a different structure: ($Sr_{0.11}Ba_{0.89}Pb_3$: $a = 7.273(2)$, $c = 3.421(2)$ Å, $Z = 12$, $R1 = 0.0424$) having the HT-PuGa3 structure type with a (*hhcc*)3-stacking sequence. At an approximate 1:1 ratio (35 to 53% Sr) of strontium and barium ($Sr_{0.56}Ba_{0.44}Pb_3$: trigonal, space group *P63/mmc*, $a = 7.1582(2)$, $c = 17.1791(7)$ Å, $Z = 6$, $R1 = 0.0309$) with the $PuAl_3$-structure type [(*hcc*)2-stacking] over a distinct homogeneity range.

Distrontium triplumbide, Sr_2Pb_3, crystallizes in the tetragonal system, P4/mbm group. This structure is highlighted by trigonal prismatic coordination and octahedral cubo atoms around the Pb atoms. Cell parameters are: $a = 4.883$ Å, $b = 8.367$ Å, $c = 8.367$ Å, $\alpha = 90°$, $\beta = 90°$, $\gamma = 90°$, cell volume = 341.84. The structure is shown in Fig. 5.143.

It consists of columns of 2 and 3 Pb atoms coordinated in a spiral fashion. A three-dimensional cell is shown along with a (100) plane and the positions of the columns along the *c*-axis [(001) plane]. This structure is unique among the alkaline earth plumbides. Little data exists concerning its physical properties and it has found no usage in industry at this moment.

Penta-strontium triplumbide, Sr_5Pb_3, crystallizes in the Cr_5B_3 type with point group of tl32 and space group of I4/mcm. Cell parameters are: $a = 8.67$ Å, $b = 8.67$ Å, $c = 10.0551$ Å, $\alpha = 115.539°$, $\beta = 115.539°$, $\gamma = 90°$, cell volume = 599.1 Å^3. The structure is shown in the following diagram. It consists of Zintl dumbbells of Pb, ⊙—⊙ which are interspersed among Sr-Pb_2 triangles along the (001) direction in the lattice (Fig. 5.144).

Both a three-dimensional view is shown along with an arrangement along the (100) plane (for simplicity). Little usage has developed for this Zintl phase whose conductivity is metallic in nature. The various Pb_2 dumbbells are slightly tilted away from the 90° angle in many of their positions in the lattice. Some of the Pb atoms form a localized $PbSr_4$ arrangement which is actually a *nido*-Tt_5^{4-} anion. This structure has the arrangement shown in Fig. 5.145.

Pentastrontium quadro-plumbide, Sr_5Pb_4, crystallizes in the Sm_5Ge_4 type of orthorhombic structure with cell parameters of: $a = 8.480$ Å, $b = 9.011$ Å,

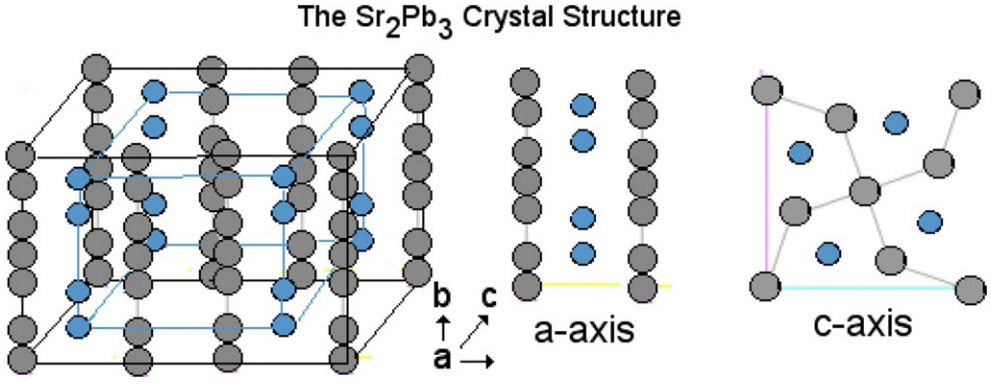

FIGURE 5.143

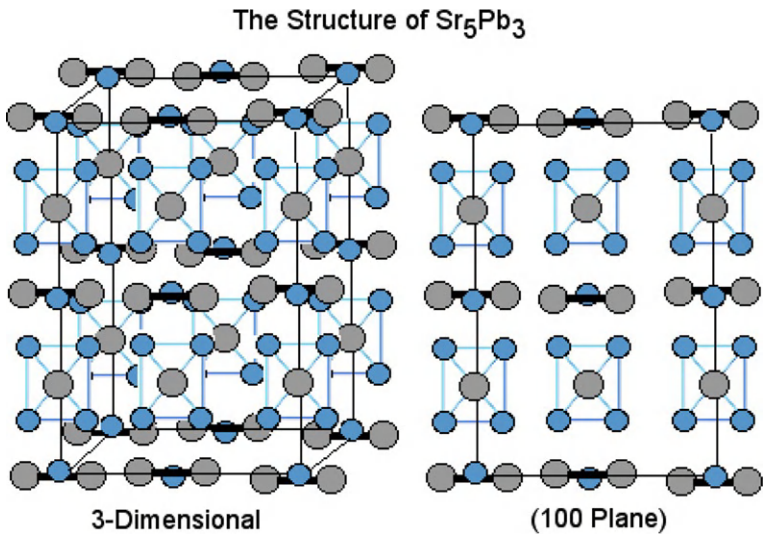

FIGURE 5.144

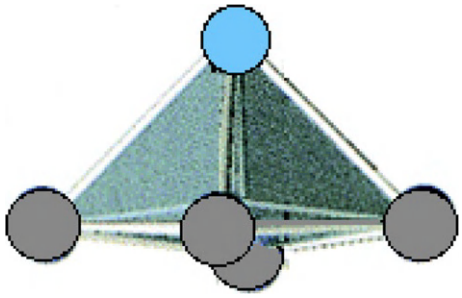

FIGURE 5.145

$c = 17.272$ Å, $\alpha = \beta = \gamma = 90°$, cell volume = 131.951 Å^3, point group = oP36, space group = Pnmna. There are six atoms in the asymmetric unit, one Sr in Wyckoff site 4*c*, two Sr in 8*d*, two Pb in 4*c* and one Pb in 8*d*. Two of the Pb sites are statistically occupied, with a lack of long-range ordering.

The arrangement of the individual atoms to each other in the slabs present are shown in Fig. 5.146.

The three-dimensional structure is shown with the three types of Sr atom symmetries (Fig. 5.147).

In addition to the seven compounds shown in the phase diagram, another composition has been found. Sr_7Pb_{12} has a unique crystal formation with cell parameters of: $a = 0.4.886$ nm, $b = 1.6.17$ nm, $c = 1.6.17$ nm, $\alpha = 90°$, $\beta = 90°$, $\gamma = 90°$, cell volume = 127.754 Å^3. The structure was determined as follows. Only the (100) plane is shown in the Fig. 5.148.

There are two kinds of Pb atoms, Pb1 forms a series of pentagonal nets while Pb2 forms triangles within the structure. Little is known concerning its physical properties. Only the structure has been determined.

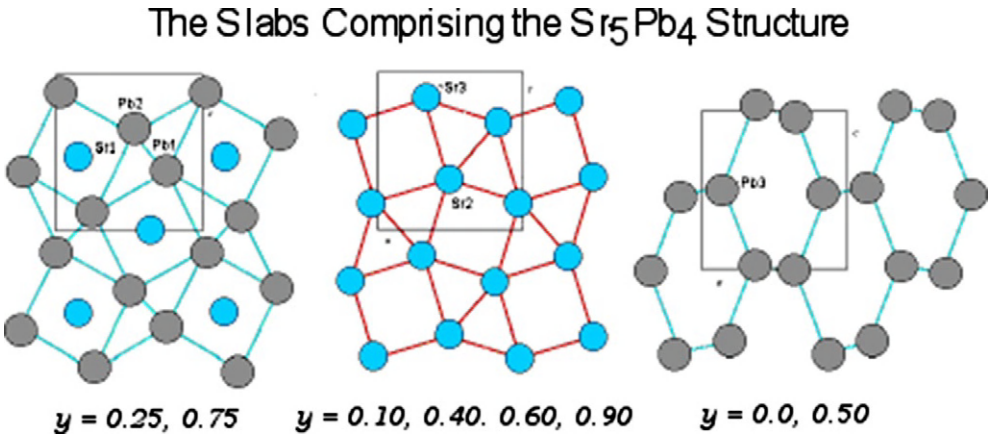

FIGURE 5.146

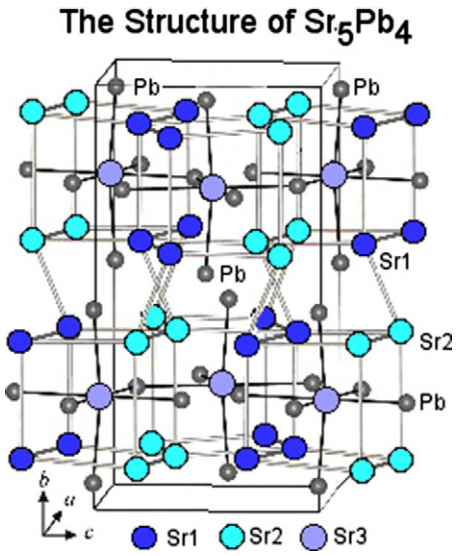

FIGURE 5.147

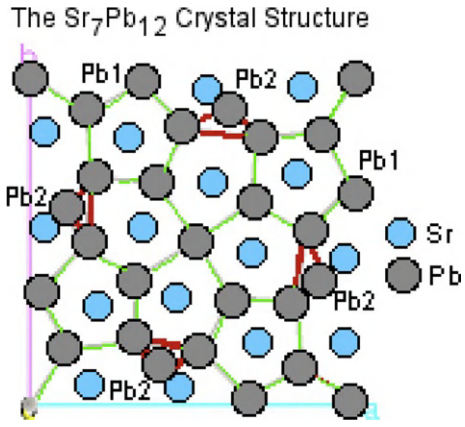

FIGURE 5.148

The strontium plumbides have not found usage in industry and they are not offered for sale commercially. No CAS numbers have been issued at this time.

Barium Plumbides

Barium forms a series of crystalline compounds with Pb. The complete phase diagram is shown in Fig. 5.149.

The structures of the compounds, Ba_5Pb_3, BaPb, and $BaPb_3$ have been determined. Ba_5Pb_3 has the body-centered tetragonal $D8_4$ structure with $a = 9.038$ Å, $c = 16.843$ Å, space group = I4/mcm, $Z = 4$. The room temperature modification of BaPb has the orthorhombic R_f structure with $a = 5.29$ Å, $b = 12.60$ Å, $c = 4.78$ Å, space group = Cmcm, $Z = 4$. $BaPb_3$ is rhombohedral with $a = 9.565°$, $\alpha = 44.78°$, $Z = 3$. Two other phases have been identified: Ba_3Pb_5 and Ba_2Pb. The former crystallizes in the Pu_3Pd_5-type structure

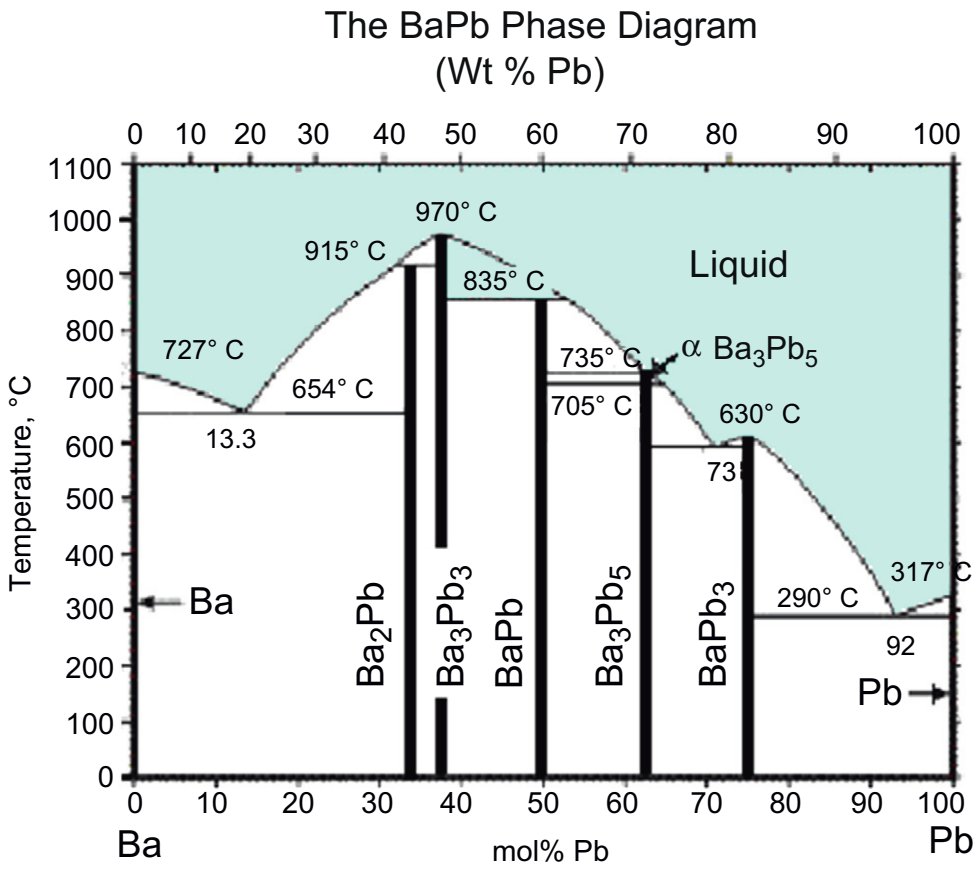

FIGURE 5.149

Ba-Pb Crystal Data

Compound	Mol%Pb	Pearson Symbol	Space Group	Prototype
Ba	0	c/2	Im3m	W
Ba_2Pb	33.3	oP12	Pnma	Co_2Si
Ba_5Pb_3	37.5	t/32	I4mcm	Cr_5B_3
BaPb	50.0	oC8	Cmmm	CrB
β-Ba_3Pb_5	62.5	...	.....	---
α-Ba_3Pb_5	62.5	oC32	Cmmm	Pu_3Pd_5
$BaPb_3$	75.0	hR12	R3m	....
Pb	100	cF4	Fm3m	Cu

FIGURE 5.150

The Ba_2Pb Structure

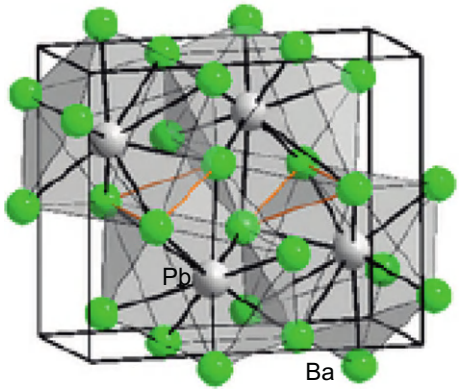

FIGURE 5.151

($a = 11.148$ Å, $b = 9.049$ Å, $c = 11.368$ Å) and the latter in the anti-$PbCl_2$-type structure ($a = 10.61$ Å, $b = 5.71$ Å, $c = 8.64$ Å). Crystal data for these compounds are shown in Fig. 5.150.

The barium plumbides have structures similar to those of calcium and strontium.

Dibarium plumbide, Ba_2Pb, has lattice unit-cell parameters of: $a = 5.71$ Å, $b = 8.64$ Å, $c = 10.61$ Å, $\alpha = 90°$, $\beta = 90°$, $\gamma = 90°$, cell volume = 823.44 Å^3, $Z = 4$. The lattice is of the Co_2Si type and is shown in Fig. 5.151.

Little information is available concerning this compound other than its crystal structure. It has found no usage in industry nor has its electrical properties been measured.

Tribarium pentaplumbide, Ba_3Pb_5, has the unit-cell parameters of: $a = 7.1792$ Å, $b = 7.1792$ Å, $c = 11.368$ Å, $\alpha = 90°$, $\beta = 90°$, $\gamma = 101.866°$, cell volume = 573.40 Å^3, $Z = 4$. It has the Pu_3Pd_5 type of structure shown in Fig. 5.152.

A series of compounds that contain square pyramidal Tt_5 polyanions of lead has been obtained in alkaline earth tetrel systems by direct fusion of the elements at 1000 °C (Ba_3Pb_5), followed by slow cooling or annealing.

The Ba_3Pb_5 Crystal Structure

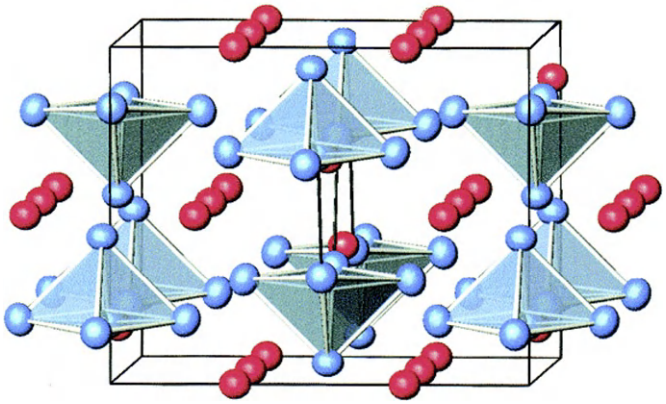

FIGURE 5.152

The crystal structures for all three have been refined in the Pu_3Pd_5 structure type (orthorhombic, Cmcm, $Z = 4$) with cell dimensions given above. Square pyramidal clusters of the tetrel elements are weakly interlinked into chains via two types of longer intercluster interactions that are mediated by bridging cations and substantially influenced by cation size and the free electron count. This new compound is all metallic in conductivity (~15–25 Ω cm), in agreement with simple valence considerations that predict two and five extra electrons per formula unit, respectively, beyond that necessary for closed-shell nido-Tt_5^{4-} anions. Extended Hückel tight-binding calculations reveals that bonding in the regions below and around the Fermi energies are dominated by general cation–anion interactions, that is, lattice covalency. Closed-shell bonding features for the classical PB_5^{4-} ion is also obvious but subsidiary to the heteroatomic interactions with the cations. The intercluster contacts are relatively unimportant in bonding.

Pentabarium triplumbide, Ba_5Pb_3, has the cell parameters of: $a = 9.04$ Å, $b = 9.04$ Å, $c = 10.562$ Å, $\alpha = 115.338°$, $\beta = 115.338°$, $\gamma = 90°$, cell volume = 687.11 Å^3, $Z = 6$. It is of the Cr_5B_3 type of structure shown in Fig. 5.153.

It consists of Zintl dumbbells of Pb, ⬬ which are interspersed among the Ba-Pb_2 triangles along the (001) direction in the lattice. There are four Ba_5Pb_3 groups per unit cell in a calculated density of 6.31 g/cc. General *hkl* reflections were observed only when $h + k + l = 2n$. Very little data is available for this compound other than its structure.

Barium monoplumbide, BaPb, has the cell parameters: $a = 4.822$ Å, $b = 5.289$ Å, $c = 6.8371$ Å, $\alpha = 112.755°$, $\beta = 90°$, $\gamma = 90°$, cell volume = 160.80 Å^3, $Z = 4$.

It has the CrB type of structure shown in Fig. 5.154.

This compound, BaPb, is stated to possess "incipient" ferroelectric properties but has not been researched

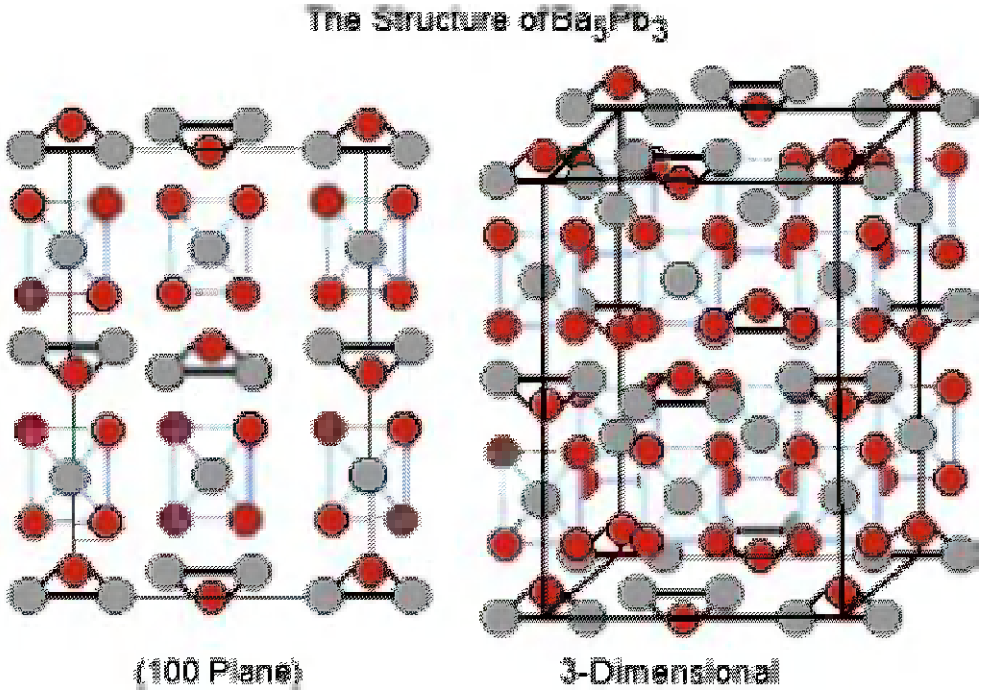

FIGURE 5.153

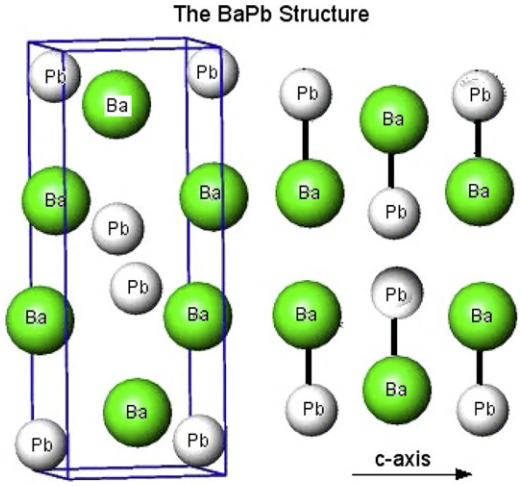

CrB. *Bf* type structure. Pearson symbol is *oC*8. Space group is *Cmcm*.

FIGURE 5.154

thoroughly. The only well-established property has been its structure. Its electrical properties remain unknown.

Barium triplumbide, $BaPb_3$, has the cell parameters of: $a = 7.298$ nm, $b = 7.298$ nm, $c = 9.5662$ nm, $\alpha = 67.577°$, $\beta = 67.577°$, $\gamma = 60°$, cell volume $= 396.14$ Å^3, $Z = 4$, space group = R3m. $BaPb_3$ is rhombohedral and has the Nb_3Sn type of structure as shown in Fig. 5.155.

Ternary-mixed Ca/Sr–Ba triplumbides of overall composition APb_3 were synthesized from stoichiometric mixtures of the elements. The structures of the compounds have been determined by means of single-crystal X-ray data. All structures exhibit closely-packed ordered APb_3 layers containing Pb Kagøme nets, which are stacked in different orientations. Depending on the stacking sequences, the resulting lead polyanion resembles the oxygen nets of the hexagonal (face-sharing octahedra, hexagonal (h) stacking, Ni_3Sn-type structure) or the cubic perovskites (corner-sharing octahedra, cubic (c) stacking, Cu_3Au-type structure). The known binary compound $BaPb_3$, the structure of which has been redetermined from single-crystal data (trigonal, space group R3m, shows a $(hhc)_3$ stacking, $TaCo_3$-type structure). A small partial substitution of barium against calcium ($Ca_{0.03}Ba_{0.97}Pb_3$: trigonal, space group R3m, $a = 7.260$ Å, $c = 34.43$ Å, $Z = 12$, $R_1 = 0.0542$) or strontium ($Sr_{0.11}Ba_{0.89}Pb_3$: $a = 7.273$ Å, $c = 34.21$ Å, $Z = 12$, $R_1 = 0.0424$) causes a structural change to the HT-$PuGa_3$ structure type with a $(hhcc)_3$ stacking sequence. At an approximate 1:1 ratio (35 to 53 % Sr) of strontium and barium ($Sr_{0.56}Ba_{0.44}Pb_3$: trigonal, space group P63/mmc, $a = 7.1582$ Å, $c = 17.1791$ Å, $Z = 6$, $R_1 = 0.0309$), the $PuAl_3$ structure type [$(hcc)_2$ stacking] has a distinct homogeneity range. The series is terminated with the pure c stacking of $SrPb_3$ and $CaPb_3$. As already noted from the above series, the stacking of the close-packed layers is influenced by the ratio of the atomic radii of the contributing elements. The electronic stability ranges, which are discussed on the basis of the results of FP-LAPW band structure calculations and in

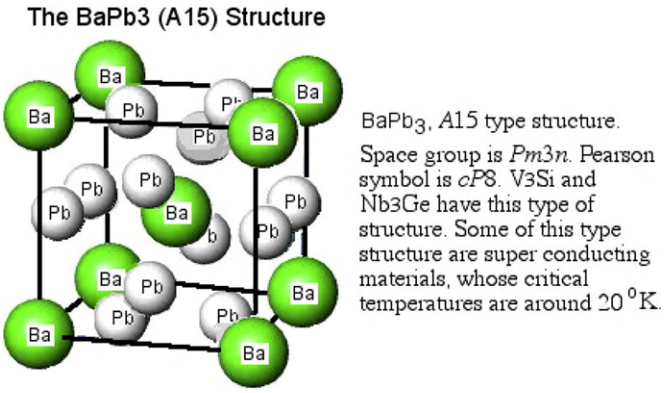

FIGURE 5.155

comparison to further compounds known from the literature, can be explained using Zintl/Wade rules. Still, due to the presence of only partially occupied steep Pb-p bands of σ bonding characteristic, the compounds are metals exhibiting pseudo band gaps at or near the Fermi level. Thus, this structure family represents an instructive case of transition from polar ionic/covalent toward (inter)metallic chemistry.

Tribarum pentaplumbide has been identified as a Zintl phase and the anionic substructure is composed of X_5^{6-} square pyramidal clusters (X = Pb), which are described as arachno clusters according to the Wade–Mingos electron counting rules. The electronic structure of the pyramidal Zintl anions and the influence of the number of skeletal electrons of these clusters are investigated using the ELF. The structural relationship between Ba_3Sn_5 and the Zintl phases Ba_3Si_4 and Ba_3Ge_4 were analyzed. Additionally, two new Zintl phases, $Ba_3Ge_{2.82}Sn_{2.18}$ and $Ba_3Ge_{3.94}Sn_{0.06}$, have been synthesized and their structures are reported, which directly show that the exchange of tin against germanium leads to a change from the $M_{3\times5}$ to the $M_{3\times4}$ structure type. This effect is traced back to the maximal charge acquisition property of the Zintl anions of heavier and lighter tetralides.

A series of compounds that contain square pyramidal Tt_5 polyanions of tin and lead has been obtained in alkaline earth or rare-earth metal tetrel systems by direct fusion of the elements at 1000 °C (Ba_3Pb_5), followed by slow cooling or annealing. The crystal structure has been refined in the Pu_3Pd_5 structure type (orthorhombic, Cmcm, $Z = 4$) with cell dimensions of $a = 11.154$ Å, $b = 9.049$ Å, and $c = 11.370$ Å. Square pyramidal clusters of the tetrel elements are weakly interlinked into chains via two types of longer intercluster interactions that are mediated by bridging cations and substantially influenced by cation size and the free electron count. This compound is all metallic in agreement with simple valence considerations that predict two and five extra electrons per formula unit, respectively, beyond that necessary for closed-shell nido-Tt_5^{4-} anions. Extended Hückel tight-binding calculations on the compound reveal that bonding in the regions below and around the Fermi energies are dominated by general cation–anion interactions, that is, lattice covalency.

Barium plumbide compounds have found little usage in industry and have no CAS numbers. They have received some attention in the technical literature but no specific usages have yet been found for these compounds.

Radium Plumbides

It is not surprising that no mention of any radium plumbide compounds can be found in the scientific literature because lead is the final decay product (^{208}Pb) of radium (^{228}Ra). It should be possible to form compounds similar to those of barium, namely:

RaPb
Ra_2Pb
Ra_5Pb_3
Ra_3Pb_5
$RaPb_3$

However, this has never been recorded in the literature to date. Nor it is likely that these compounds will ever be studied because of the radioactivity and long life of ^{226}Ra.

5.5.3. Oxy-Plumbates of the Alkaline Earths

Beryllium Plumbates

The technical literature concerning beryllium and its oxy-lead compounds is completely lacking. A description of any combination of a Be compound with a lead oxide compound is completely lacking in the past or present technical literature. It should be possible to use the thermal-heating method to form these compounds but there is no record of anyone having done so. Thus, the physical and chemical properties of $BePbO_3$ and Be_2PbO_4 have remained unknown. The reactions should involve:

$$BeO + PbO_2 \Rightarrow BePbO_3$$

$$2BeO + PbO_2 \Rightarrow Be_2PbO_4$$

A temperature of at least 1000 °C would be required. It is not certain whether these compounds are stable. The divalent Be^{2+} ion has a radius of 0.44 Å (0.31 Å in some references) whereas the size of the Pb^{4+} ion in PbO_3^{2-} is 1.19 Å. Thus, while the corresponding Ca (Ca^{2+} = 1.02 Å), Sr and Ba compounds have been well established ($Sr^{2+} = 1.18$ Å and $Ba^{2+} = 1.35$ Å), those of Be have not.

There are no CAS numbers assigned and these compounds are not available commercially.

Magnesium Plumbates

The technical literature concerning magnesium and its oxy-lead compounds is completely lacking. A description of any combination of a Mg compound with a lead oxide compound is completely lacking in the past or present technical literature. It should be possible to use the thermal-heating method to form these compounds but there is no record of anyone having done so. Thus, the physical and chemical properties of $MgPbO_3$ and Mg_2PbO_4 have remained unknown. The reactions should involve:

$$MgO + PbO_2 \Rightarrow MgPbO_3$$

$$2MgO + PbO_2 \Rightarrow Mg_2PbO_4$$

A temperature of at least 1000 °C would be required. $MgPbO_3$ would be expected to have the perovskite structure. It is not certain whether these compounds are stable. The divalent Mg^{2+} ion has a radius of 0.72 Å whereas the size of the Pb^{4+} ion in PbO_3^{2-} is 1.19 Å. That of Sr^{2+} is almost identical and the corresponding compounds have been well studied. If $MgPbO_3$ or Mg_2PbO_4 exists, either or both compounds would be expected to possess semiconducting or metallic-conducting properties due to the $Pb^{2+} \Leftrightarrow Pb^{4+}$ electron-exchange mechanism induced by a proper formation mechanism within the crystal.

Recent (2000) experimental investigations of phase equilibria and thermodynamic properties of the systems M–Pb–O, where M = Mg, Ca, Sr or Ba, indicate a regular increase in thermodynamic stability of ternary oxides, $MPbO_3$ and M_2PbO_4, with increasing basicity of the oxide of the alkaline earth metal. Number of stable interoxide compounds at 1100 K (827 °C) in the systems M–Pb–O (M = Mg, Ca, Sr, Ba) increases in unit increments from Mg to Ba. In this paper, experimentally determined standard Gibbs energies of formation of M_2PbO_4 (M = Ca, Sr, Ba) and $MPbO_3$ (M = Ca, Sr, Ba) from their component binary monoxides and oxygen gas are combined with an estimated value for $MgPbO_3$ to delineate systematic trends in thermodynamic stability of the ternary oxides. The trends are interpreted using concepts of tolerance factor and acid–base interactions. All the ternary oxides in these systems contain lead in the tetravalent state. The small Pb^{4+} ions polarize the surrounding oxygen ions and cause the formation of oxy-anions which are acidic in character. Hence, the higher oxidation state of lead is stabilized in the presence of basic oxides of alkaline earth group. A schematic subsolidus temperature-composition phase diagram is presented for the system BaO–PbO–O_2 to illustrate the change in oxidation states in binary and ternary oxides with temperature.

No CAS numbers have been assigned to any magnesium plumbates and they are not available commercially.

Calcium Plumbates

Phase relations in the system CaO–PbO at 1100 K (827 °C) in air and oxygen have been determined by equilibrating 18 compositions of varying ratios of these oxides and identifying the phases present in quenched samples by XRD and energy dispersive X-ray analysis (EDX). Only one binary compound, Ca_2PbO_4, was found to be present ($CaPbO_3$ was absent as was any other possible compounds). The compound coexists with CaO and PbO. The standard Gibbs energies of formation of Ca_2PbO_4 (880–1100 K) was determined using solid-state cells based on yttria-stabilized zirconia as the solid electrolyte. Pure oxygen gas at 0.1 MPa was used as the reference electrode. For measurements on Ca_2PbO_4, a novel cell design with three electrodes in series, separated by solid electrolyte membranes, was used to avoid polarization of the electrode containing three solid phases. Two three-phase electrodes were used. The first absorbs the electrochemical flux of oxygen from the reference electrode to the measuring electrode. The other three-phase electrode, which is unaffected by the oxygen flux through the solid electrolyte, is used for electromotive force (e.m.f.) measurement. The results from EMF studies were cross checked using thermogravimetry (TG) under controlled oxygen partial pressures. The results can be summarized by the following equations:

$$2CaO + PbO + 1/2O_2 \Rightarrow Ca_2PbO_4$$

$$\Delta G^0\,(\mathrm{J/mol}) = -128{,}340 + 93.21\,T/\mathrm{K} \pm 200$$

Single crystals of Ca_2PbO_4 were prepared by a flux technique and investigated by X-ray methods. It crystallizes with orthorhombic symmetry, space group D-Pbam ($a = 5.832$; $b = 9.766$; $c = 3.375$ Å, $Z = 2$). Ca_2PbO_4 belongs to the Sr_2PbO_4 type. It shows Ca^{2+} in a sevenfold and Pb^{4+} in octahedral coordination, as shown in the following Fig. 5.156.

Calcium orthoplumbate can be obtained by reaction of a homogeneous mixture of powdered oxides at 600–800° in the presence of air, or by heating compounds of calcium and lead which yield oxides and volatile products by dissociation. In the presence of excess oxygen, the kinetics of reaction between CaO and PbO to form calcium plumbate has been found to be governed by a diffusion process related to a specific kinetic model (Jander's model).

The energy of activation of the process, as calculated from the Arrhenius equation, was found to be 50 kcal/mol. In an air and nitrogen atmosphere (ratio 1:16), the reaction rate is 4–5 times slower than that obtained in a pure oxygen atmosphere:

$$2CaO + PbO + 1/2O_2 \Rightarrow Ca_2PbO_4$$

It has been shown that formation of calcium plumbate from pure CaO and PbO_2 occurs without formation of intermediate compounds between 600 and 800 °C.

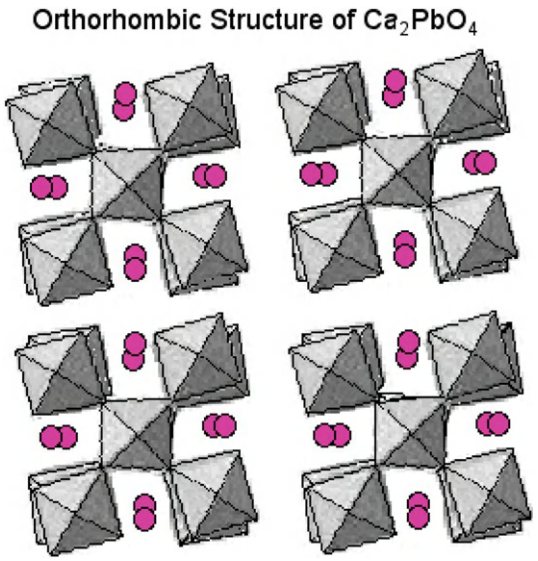

FIGURE 5.156

Calcium orthoplumbate, Ca_2PbO_4, can also be prepared by sol–gel methods (two varieties of the Pechini complex route and a water soluble polymer method) and by solid-state reaction. The sol–gel-prepared samples contained calcium orthoplumbate as the only phase as early as after 2 h annealing at 800 °C. Phase composition was detected by XRD measurement and by Raman spectroscopy. Annealing at 800 °C for 24 h induced small losses of Pb^{2+}, as confirmed by XRF measurement. The Pb losses were smaller for the sol–gel-prepared samples probably due to earlier formation of Ca_2PbO_4 as the samples were being heated. Microstructure and grain size were also established. Sol–gel-prepared samples had regularly distributed grains with a small distribution coefficient with a median value in order of 1 μm. Differences in microstructure of solid state and sol–gel samples were compared using SEM micrographs.

Calcium orthoplumbate is a powerful oxidizing agent that also prevents corrosion on iron and steel surfaces when added to paints. Its corrosion-inhibiting effect is a result of the pigment's capacity to oxidize soluble iron compounds formed in anodic areas, which then form an insoluble film of iron compounds at the anode. This neutralizes that element of the corrosion cell and restricts any further corrosion. In the meantime, calcium carbonate is formed at the cathodic region of the "corrosion cell".

Calcium orthoplumbate, like red lead, provides protection by a combination of basic and oxidizing characteristics, as well as film-forming properties by interaction with linseed oil. It is believed to pacify both cathodic and anodic areas on iron and steel, and in this respect differs from other rust-inhibitive pigments. In practice, it shows the behavior which on theoretical grounds might be expected to be associated with this type of inhibition. Linseed oil paints based on calcium plumbate have been found to be remarkably free from any tendency to crack, and their adhesion on galvanized iron and timber suggests the value of suck paints as primers with a wide variety of applications.

The metaplumbate, $CaPbO_3$, can be prepared by direct reaction at 800 °C of CaO and PbO_2. Its molecular weight is 295.2835 g/mol and its CAS number is 12744-29-7. The orthorhombic modification of $CaPbO_3$ can also be synthesized from a mixture of Ca_2PbO_4 and PbO_2 at high temperature and high pressure. Its structure was analyzed by Rietveld analysis of neutron diffraction data on the basis of space group Pbnm. It has a distorted perovskite structure of the $GdFeO_3$ type and a unit cell with dimensions of $a = 5.6710$ Å, $b = 5.8875$ Å, and $c = 8.1495$ Å. The Pb–O bond lengths in each PbO_6^{2-} octahedron are comparable to each other, whereas the PbO_6^{2-} octahedron tilts around [110]p and [001]p axes (p: perovskite subcell) by 18.50° and 20.28°, respectively. These tilt angles, which show great structural distortion in $CaPbO_3$ containing the smaller Ca^{2+} ion, are much larger than corresponding ones in crystal chemically isotypic $SrPbO_3$. The electric resistivity of $CaPbO_3$ at room temperature was as high as $3 \times 10^3\ \Omega$ cm, which is in sharp contrast to low resistivities observed in other perovskite-type oxides $BaPbO_3$ and $SrPbO_3$. The high resistivity of $CaPbO_3$ is explained as gap formation between 2p(O) nonbonding and 6s(Pb)-2p(O) sp-antibonding bands, which overlap with each other in $BaPbO_3$. Solid solutions, where Sr^{2+}, La^{3+}, Nd^{3+}, and Y^{3+} ions were partially substituted for Ca^{2+} ions, were also prepared to examine structural and electrical properties in perovskites based on $CaPbO_3$. Substitution of Sr^{2+} for Ca^{2+} led to reductions in the distortion and gap energy, whereas that of La^{3+}, Nd^{3+}, and Y^{3+} induced metallic conductivity owing to doping of electron carriers into the antibonding band, i.e. charged oxygen vacancies, V_O^+, causes electron hopping mechanisms to dominate.

A new structure type can be obtained under pressure. A new perovskite-type compound with nominal composition $CaPbO_3$ under about 6 GPa using a cubic-anvil-type apparatus from a mixed powder of high-purity CaO and PbO_2 was formed. The XRD pattern was indexed on the basis of an orthorhombic unit cell with $a = 5.667$ Å, $b = 5.879$ Å and $c = 8.147$ Å. This compound has a distorted perovskite-type structure, while two previously reported types of $CaPbO_3$ have a cubic fluorite-type structure and an ilmenite-type structure. EDX analysis and the unit-cell parameters suggest a deficiency in the Ca site. The electrical resistivity of this compound at room temperature was very high (>105 Ω cm) in contrast to the metallic and

semiconducting conductivity of $BaPbO_3$ and $SrPbO_3$, respectively.

Partial substitutions of La for alkaline earth elements of perovskite-type $CaPbO_3$ was studied in order to examine carrier-doping effects on the $CaPbO_3$ system. The solubility limit of La^{3+} was found to be about 10% for every alkaline earth element. The temperature dependencies of electrical resistivity and the Seebeck coefficient for the $Ca_{0.9}La_{0.1}PbO_3$ samples indicated that they were metallic conductors. This is in good contrast with the resistivity of $APbO_3$ (where A = Ca, Sr and Ba), which is strongly influenced by the ionic size of A, via the distortion of PbO_6 octahedra. The Seebeck coefficients (in V/K) for the $Ca_{1-x}La_xPbO_{3-\delta}$ ($x = 0$ and 0.1) samples were negative, and absolute values were reduced by the La^{3+} substitution, which implies that electron carriers were introduced into the conduction band. Superconductivity was not observed in these compounds down to 1.8 K, although the carrier density expected, based on the Seebeck coefficient, was comparable to the value for the superconducting $BaPb_{1-x}Bi_xO_3$.

Attempts to form calcium plumbite, $CaPbO_2$, have failed. If $CaCl_2$ (aq) is reacted with Na_2PbO_2 in solution, a precipitate is obtained. But upon separation from solution (by filtration and the like), it rapidly transforms in air to the metaplumbate:

$$2CaPbO_2 \Rightarrow CaPbO_3 + CaO$$

Ca_2PbO_4 has the CAS number of 12013-69-3. Both compounds, Ca_2PbO_4 and $CaPbO_3$, are available commercially.

Strontium Plumbates

The system SrO–PbO_2 has been shown to contain two compounds, $SrPbO_3$ and Sr_2PbO_4. $SrPbO_3$ is an orthorhombic distortion of the perovskite structure. Sr_2PbO_4 is considered in the literature, the type example of a newly described structure type. Precise unit cell and powder data have been presented for these phases. High-temperature diffractometry shows a transition from orthorhombic to tetragonal $SrPbO_3$ at 450 °C. This transition is not reflected in the dielectric constant. IR spectra for the compounds have been described. $SrPbO_3$ is orthorhombic with $a = 5.8595$ Å, $b = 5.9568$ Å, and $c = 8.3253$ Å. The probable space group is Pbnm.

To obtain $\Delta_f H^0$ of $SrPbO_3$ and Sr_2PbO_4, the enthalpies of solution of SrO, PbO_2, $SrPbO_3$, and Sr_2PbO_4 in 6 mol/dm^{-3} HCl were measured by isoperibolic solution calorimetry and the values of $\Delta_f H^0$ for the strontium plumbates were derived from Hess cycles. The values obtained were:

$$\Delta_f H^0_m(SrPbO_3 \text{ at } 298.15 \text{ K}) = -949.3 \pm 3.5 \text{ kJ/mol}$$

$$\Delta_f H^0_m(Sr_2PbO_4 \text{ at } 298.15 \text{ K}) = -1565.1 \pm 6.9 \text{ kJ/mol}$$

Strontium metaplumbate, $SrPbO_3$, samples were obtained by means of high-pressure synthesis and studied by means of the temperature (T) dependences of the resistivity δ and differential thermoelectric power, S. Thus, prepared samples were found to demonstrate a much steeper increase of δ for low T than those synthesized without high-pressure application. Moreover, the δ minimum observed earlier which indicated a proximity to the metal state completely disappeared. The sign of S (T) is positive in the whole T range, contrary to what has been observed earlier. Tunnel measurements were carried out using the in situ break-junction technique, revealing a correlation dielectric gap of 1.5 to 2 eV. The data can be explained if one assumes the existence of both holes (oxygen vacancies) and electrons in this oxide. The high-pressure application during synthesis leads to higher sample disorder, most probably inducing current carrier localization and a Coulomb gap emergence in the quasi-particle spectrum. Electrons do not survive this process, whereas the former minority holes reveal themselves in thermoelectric measurements. Meanwhile, the overall transport behavior loses its semimetallic features, characteristic of more conventionally produced lead oxide ceramics. Our results show how fragile the electron spectrum of this oxide is, being near the metal–semiconductor phase transition boundary.

$SrPbO_{3-\delta}$ is n-type, narrow band gap semiconductor crystallizing in a distorted perovskite structure (similar to that of its calcium homologue). The electrical conductivity varies with temperature but in a nonmonotonic manner. At high temperatures, the thermal evolution of the conductivity follows an Arrhenius-type law with an activation energy of 0.11 eV, which can be attributed to mixed valence states, Pb^{4+}/Pb^{2+}, and leads to a dielectric constant of 13.6. The sign of its thermopower, S, is negative, indicating that the mobile carriers are electrons, which is ascribed to oxygen extraction. The electron hopping occurs between similar electronic localized states in the vicinity of the mobility edge with an electron mobility of $2 \times 10^{-2}/cm^2/V/s$ that is thermally activated. The variation of $S(T)$ suggests a finite density of states at the Fermi level. At low temperatures, the conduction mechanism changes to a variable-range hopping. The weak hybridization of the Pb–O bond, due to the tilting of PbO_6 octahedra, lowers the energy of the antibonding conduction band resulting in a small optical gap E_g. The E_g value was found to be 1.76 eV and the transition is directly allowed; a further indirect transition occurs at 0.79 eV. The flat potential $V_f b$ measured from the Mott–Schottky plot was equal to –0.38 VSCE. The upper valence band edge, located at 6.8 eV below vacuum, is made from mainly the O:2p orbital, whereas the conduction band consists of empty 6s levels.

The transport properties of oxygen-deficient perovskite $SrPbO_{3-\delta}$ with mixed lead valence were investigated down to 4.2 K. The small δ-value (0.059), determined from iodometry, is due to the inert lone pair of Pb^{2+} that does not enjoy regular octahedral coordination in spite of collective electron behavior. The oxide exhibits a temperature-independent magnetic susceptibility consistent with itinerant electrons. The sign of carriers like polarons is that of *n*-type conductivity coming from the balance charge caused by oxygen extraction. The thermal variation of conductivity and thermopower reveal the existence of an energy gap. The conduction mechanism occurs by polaron hopping in conformity with a small activation energy. The metal-insulating transition seems to be of Anderson type, resulting from the disorder of oxygen vacancies. At low temperature, the conductivity was fitted to a variable hopping range, $\ln(1-p)\ T^{-1}$. A comparison with $SrSnO_{3-\delta}$ was reported. The covalency of the Sn–O bond raises the antibonding conduction state of its 5s parentage and increases the forbidden gap from 1.78 to 3.30 eV.

The subsolidus phase relationships of the PbO–SrO–CaO system in air were investigated at 830 to 835 °C. Complete solid solution exists between Ca_2PbO_4 and Sr_2PbO_4. Compatibility between $SrPbO_3$ and the $(Ca,Sr)_2PbO_4$ solid solution terminates at approximately $(Ca_{0.80}Sr_{0.20})_2PbO_4$. Tie-line relationships between $(Ca,Sr)_2PbO_4$ and PbO, $SrPbO_3$, and the solid solutions (Ca,Sr)O and (Sr,Ca)O were also determined. At 830 to 835 °C, SrO and CaO do not form a complete solid solution. Tie-lines were found to extend from the Ca-rich solid solution (CaO to $Ca_{0.89}Sr_{0.11}O$) to nearly the entire range of $(Ca,Sr)_2PbO_4$. Tie-lines were also found between $(Sr,Ca)_2PbO_4$ (from Sr_2PbO_4 to $Sr_{1.95}Ca_{0.5}PbO_4$) and (Sr,Ca)O (from SrO to $Sr_{0.83}Ca_{0.17}O$). No other ternary oxide phases were found in this system.

A comparative structural study of the tetravalent plumbates, $BaPbO_3$ and $SrPbO_3$, has been carried out by using a NPD technique. Both compounds are an orthorhombic distortion of the perovskite structure, with the lattice parameters related to that of the ideal cubic perovskite (ap) by $a \approx \sqrt{2}ap$, $b \approx \sqrt{2}ap$ and $c \approx \sqrt{2}ap$. The structure of $BaPbO_3$ (Ibmm) consists of the PbO_6 octahedra tilted around the primitive [110]p axis, whereas the tilts of the PbO_6 octahedra in $SrPbO_3$ (Pbnm) are about the [110]p and [001]p axis, respectively. These different tilts, necessary to keep the stable perovskite structure, are discussed and the influence of octahedral distortions on the physical properties of the relevant compounds are considered.

Strontium plumbates, both $SrPbO_3$ and Sr_2PbO_4, are available commercially in small lots.

Barium Plumbates

$BaPbO_3$ was prepared from high-purity powders of $BaCO_3$ and PbO_2 by a conventional solid-state procedure. Temperatures of 500–780 °C were used for the thermal treatment. Subsequent annealing was accomplished within a range of 530–1120 °C. The phase purity of $BaPbO_3$ was monitored by X-ray analysis. The data obtained by a full chemical analysis of samples showed this phase to have a barium deficit, and the composition of the phase was found to be $Ba_{0.80\pm0.03}PbO_{3.10\pm0.02}$. The structure is of rhombic perovskite type having the following unit-cell parameters: $a = 6.024$, $b = 6.065$ and $c = 8.506$ Å. The structure belongs to space group Imma and not to Pbnm ($GdFeO_3$) found for many other orthorhombic perovskite systems.

The structure of $BaPbO_3$ has been refined from powder neutron and synchrotron XRD data at both room temperature and 15 K. At room temperature, the structure is orthorhombic, space group = Imma and $a = 6.0299$ Å, $b = 8.5094$ Å, $c = 6.6094$ Å. On cooling, the structure transforms to a monoclinic form, space group C2/m, $a = 8.5548$ Å, $b = 8.4808$ Å, $c = 6.0118$ Å, $\beta = 134.806°$. $BaPbO_3$, which is a perovskite with a "pseudocubic [orthorhombic] symmetry". It is a true metal (its electrical conductivity at room temperature is 3448/ohm/cm, and at liquid helium temperature, 4.2 K, is 13,514/ohm/cm) with a bilayer metallic bond, so it has properties desirable for the layered composites.

A suggested electronic structure of BaPbO3, according to picture VB, is presented in the following Fig. 5.157.

The bilayer metallic bond in the compound would appear to be the lead $7p_{(y,z)}$ - oxygen $2P_{(y,z)}$ $2p_{(x,y)}$ $P_{(XO)}$ by this analysis. The $d_{(z)}2p_{(z)}$ lobes of the sp3ds octahedral hybrid orbital might be more voluminous and "bulge out" more than the sp-type lobes, thereby lengthening the *z*-axis of the cubic unit cell and making it orthorhombic, as is observed experimentally.

High-resolution X-ray powder diffraction studies have shown $BaPbO_3$ to transform from an orthorhombic Imma structure at room temperature, through an intermediate I4/mcm phase, to a cubic Pm3/m structure above 500 °C. The Imma to I4/mcm transition is first order and the I4/mcm–Pm3/m transition for $BaPbO_3$ is tricritical in nature. No evidence for any phase transitions in $SrPbO_3$ up to 760 °C was found, the structure remaining in Pnma from room temperature to 760 °C.

The preparation, structure and electrical properties of $Ba_{1-x}Sr_xPbO_{3-\delta}$ compounds have been reported. These phases all have orthorhombic perovskite structure whose space group, however, changes at around

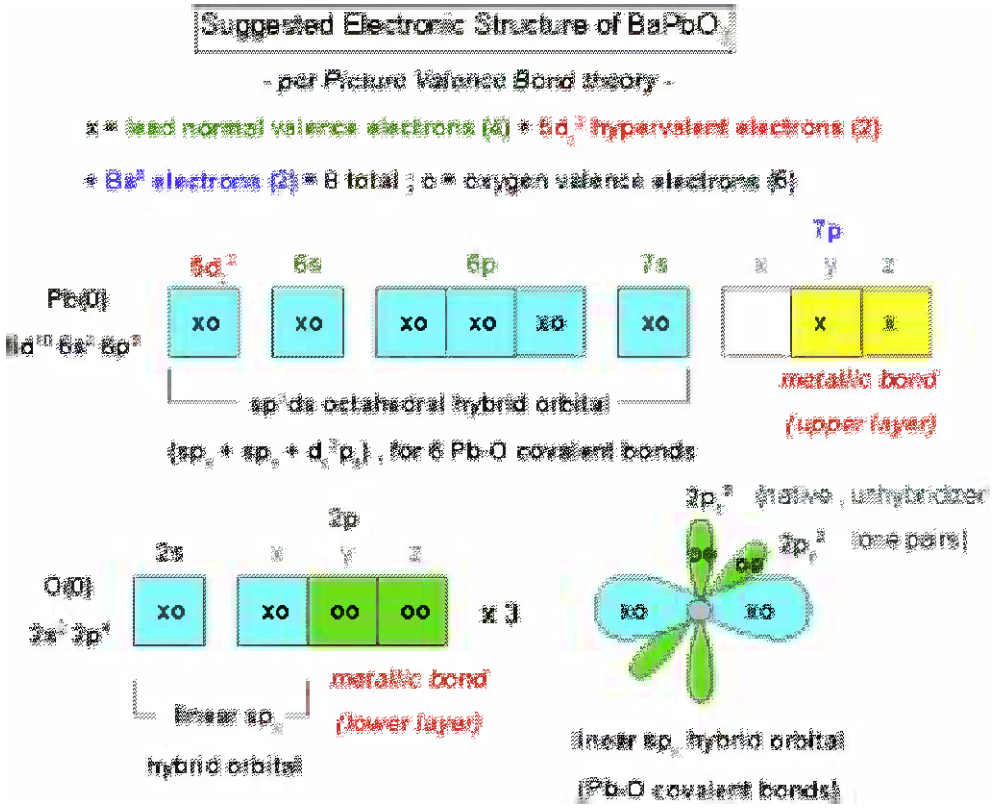

FIGURE 5.157

$x = 0.3$–0.4 from Inma ($BaPbO_3$ side) to Pnma ($SrPbO_3$ side). The transport property also changes from metallic (Inma) to semiconductive (Pnma) at this point. A wide range of oxygen deficiency was realized in this system by changing the synthetic oxygen pressure. With the increase of oxygen deficiency, the metallic conductivity region expanded to the Sr-rich side. The doping of La^{3+} into the A site was also effective to change the system to metallic conductivity.

$BaPbO_3$ ceramics were also fabricated using $BaCO_3$ and PbO powders. Phase transitions and the physical properties of $BaPbO_3$ fabricated with different Pb/Ba mol ratios were studied. The metallic conduction behavior of $BaPbO_3$ can be understood by either the unfilled d-orbital of Pb^{4+} or the substitution of Ba by Pb. However, the model of a unit-cell structure with PbO_2 layers "inserted" between BaO layers together with unfilled d orbital of Pb^{4+} seems to be the more appropriate mechanism. $BaPbO_3$ was also shown to be stable in water, but not so stable in the presence of both water and air (moisture). Increasing the Pb content can improve the resistance of $BaPbO_3$ to moisture.

Phase relations in the ternary system Ba–Pb–O have been studied by equilibrating 18 samples in the ternary in pure oxygen, inert gas or evacuated capsules at 1100 K. Phase identification of quenched samples was performed using optical and electron microscopy, XRD and energy dispersive analysis of X-rays. Three interoxide compounds, Ba_2PbO_4, $Ba_4Pb_3O_{10}$ and $BaPbO_3$ were found to be stable: tie-lines connect each of these compounds with PbO and oxygen gas. Lead is present in a tetravalent state in all the three interoxide compounds. All alloys and intermetallics (Ba_2Pb, Ba_5Pb_3 and BaPb) are in equilibrium with BaO. The oxygen chemical potential corresponding to the three-phase fields:

$$BaO + PbO + Ba_2PbO_4$$

$$PbO + Ba_2PbO_4 + Ba_4Pb_3O_{10}$$

$$PbO + Ba_4Pb_3O_{10} + BaPbO_3$$

These were measured using solid-state cells incorporating $(Y_2O_3)ZrO_2$ as the solid electrolyte in the temperature range 750–1080 K. A special cell design, with a buffer electrode in addition to the normal reference and measuring electrodes, was used to avoid polarization of the three-phase electrode. The standard Gibbs free energies of formation of the three ternary oxides were derived from the e.m.f. of three solid oxide

galvanic cells. The results were cross-checked by measuring the chemical potential of BaO in the three-phase field $PbO + BaPbO_3 + O_2$ (26.2 Pa) and Gibbs energy of formation of $BaPbO_3$ using a cell based on BaF_2 as the electrolyte. The following equations summarize the results:

$$2BaO + PbO + 1/2O_2 \Rightarrow Ba_2PbO_4;\ \Delta G^\circ = -202\,640 + 91.67\,T\ (J/mol)$$

$$4BaO + 3PbO + 3/2O_2 \Rightarrow Ba_4Pb_3O_{10};\ \Delta G^\circ = -556\,835 + 283.12\,T\ (J/mol)$$

$$BaO + PbO + 1/2O_2 \Rightarrow BaPbO_3;\ \Delta G^\circ = -165\,970 + 87.45\,T\ (J/mol)$$

The results obtained in this study differ significantly from data reported in the literature. The earlier investigators incorrectly assumed that BaO exists at unit activity under pure oxygen in the temperature range 700–875 K.

In another study, the phases, $BaPbO_3$ and Ba_2PbO_4, were produced using the sol–gel method, a method based around that described by Fan Wang. Precursors, $Pb(CH_3COO)_2 \cdot 3H_2O$ and $Ba(CH_3COO)_2$ were mixed and dissolved in water in stoichiometric amounts, and maintained at a temperature of 90 °C with stirring. A solution of PVA, a chelating agent, was added to the acetate solution in the ratio Ba: PVA = 0.01 mol:1 g. The resulting solution was heated, with stirring, at a temperature of 90 °C so as to allow partial evaporation of the water. The remaining gel was then dried at a temperature of 400 °C for 60 min before being fired at 500, 600 and 700 °C for 4 h at each temperature (with a heating and cooling rate of 5 °C/min), with intermediate grindings. For Ba_2PbO_4, final phase formation was observed at 1000 °C. For Sc-doped $BaPbO_3$, final phase formation was observed at 900 °C. Phase purity was confirmed by XRD.

Partial substitutions of La for alkaline earth elements of the type, $APbO_{3-\delta}$ (A = Ba, Sr, and Ca) were studied in order to examine carrier-doping effects on the $APbO_{3-\delta}$ system. The solubility limit of La was found to be about 10% for every alkaline earth element. The temperature dependencies of electrical resistivity and the Seebeck coefficient for $A_{0.9}La_{0.1}PbO_{3-\delta}$ samples indicated that they were metallic conductors, irrespective of the ionic size of the alkaline earth elements. This is in good contrast with the resistivity of $APbO_{3-\delta}$, which is strongly influenced by the ionic size of A, via the distortion of PbO_6 octahedra. The Seebeck coefficients for the $A_{1-x}La_xPbO_{3-\delta}$ ($x = 0$ and 0.1) samples were negative, and absolute values were reduced by the La substitution, which implies that electron carriers were introduced into the conduction band. Superconductivity was not observed in these compounds down to 1.8 K, although the carrier density expected, based on the Seebeck coefficient, was comparable to the value for the superconducting $BaPb_{1-x}Bi_xO_3$.

The perovskite-type compound $BaPbO_3$ in the Ba–PbO–O system is of considerable interest in materials science and technology owing to its wide-ranging electronic and chemical applications. To determine the thermodynamic stabilities of this compound and related plumbates, the e.m.f. of the galvanic cells using both oxide and fluoride solid electrolytes and with (a) $BaPbO_3$–$Ba_4Pb_3O_{10}$–PbO, (b) $Ba_4Pb_3O_{10}$–Ba_2PbO_4–PbO and (c) $BaPbO_3$–Pb_3O_4–Pb_3O_4–BaF_2 as the test electrodes have been studied over the temperature ranges 756–968, 797–1097 and 695–880 K, respectively. The least-squares analysis and further processing of the e.m.f data together with the standard Gibbs energies ΔG_f of formation of binary oxides from the literature have yielded the expressions:

$$\Delta G_f\ (BaPbO_3(s)\ (kJ/mol) = -901.56 + 0.26596\,T\ (K)$$

$$\Delta G_f\ (Ba_4Pb_3O_{10}(s)\ (kJ/mol) = -3278.95 + 0.89356\,T\ (K)$$

$$\Delta G_f\ (Ba_2PbO_4(s)\ (kJ/mol) = -1482.10 + 0.37421\,T\ (K)$$

These data together with phase equilibrium studies have been made use of in constructing the Ba–Pb–O phase diagram at 800 K.

The perovskite-type compound $BaPbO_3$ in the Ba–Pb–O system is of considerable interest in materials science and technology owing to its wide-ranging electronic and chemical applications. Barium plumbates have been studied extensively in recent years because of such interesting properties. $BaPbO_3$ is known to exhibit room temperature metallic conductivity, due to an overlap (~2 eV) of the O-2p nonbonding band with the (Pb-O)-sp antibonding band at the Fermi level. Another phase in the Ba–Pb–O system, Ba_2PbO_4, is known to adopt the K_2NiF_4 structure and behaves as a large-gap semiconductor (valence bands are separated by a ~1.7 eV semiconductor gap). The structures are shown in Fig. 5.158.

$BaPbO_3$ has a distorted perovskite structure, deviating from the normal cubic perovskite; it is an orthorhombic distortion of the perovskite structure with the space group Imma. This is only one of the possible structures that can result from a perovskite. The type of distortion seen is related to the radii of the cations and anions involved and while the 12-coordination of A is easily distorted, the 6 coordination octahedra is harder to distort. $BaPbO_3$ possesses lattice parameters related to that of the ideal cubic perovskite structure by $a \propto 2ap$, $b \propto 2ap$, $c \propto 2ap$ where ap is the lattice parameter of the ideal perovskite. The structure of $BaPbO_3$ consists of the PbO_6 octahedra tilted around the primitive [110]p axis. It is noted that the octahedra tilt differently when replacing the A site with Sr or Ca.

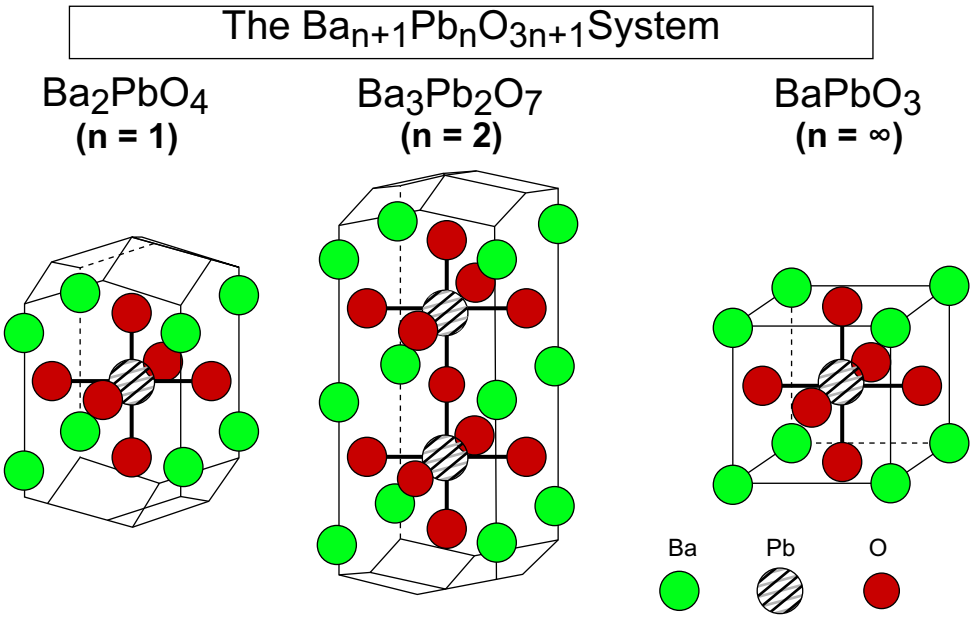

FIGURE 5.158

It is widely recognized that barium plumbate's room temperature metallic conductivity may be attributed to the overlap of the Pb-6s and O-2p orbitals at the Fermi level. Band structure calculations have shown the presence of such a strongly hybridized band at the Fermi level involving the energetic overlap of the previously mentioned orbitals. This broadband is only partially occupied by the available electrons and therefore metallic conductivity can occur. Thus, $BaPbO_3$ is not really a normal valence compound like its ionic insulating neighbor $BaSnO_3$, where such cation-oxygen hybridization apparently does not occur. The results of such a band structure calculation is shown in Fig. 5.159.

The overlap of the valence and conduction bands is clearly evident.

Unlike $BaPbO_3$ (which is a metallic conductor at room temperature), even though the valence state (4+) and coordination geometry around the Pb atom are the same (PbO_6 octahedra), the K_2NiF_4-type (tetragonal) Ba_2PbO_4 compound is a semiconductor with a band gap of ~1.7 eV. Band structure calculations have shown that a shortened axial Pb–O distance which induces sp interactions between Pb-6s and O-2p orbitals is instrumental in opening the band gap. $Ba_2Pb_{1-x}Bi_xO_{4-y}F_y$ compositions have been produced, aimed at modifying the coordination geometry around Pb in an attempt to induce metallic and/or superconducting properties in the system by possibly modifying the Pb–O/F orbital overlaps. However, the results were disappointing.

A new type of barrier layer capacitor was described utilizing thin glass layers on highly conducting ceramics of barium plumbate and barium bismuth plumbate. Barium metaplumbate ($BaPbO_3$) thin films were prepared using a chemical solution method. Films with different thicknesses, ranging from 100 nm to 1 μm, were deposited by a spin coating technique. After drying at 300 °C and firing between 600 and 700 °C in air, a room-temperature resistivity about 1 mΩ-cm was obtained, which is comparable to that of the ceramic bulk resistivity. The chemical reaction sequence during

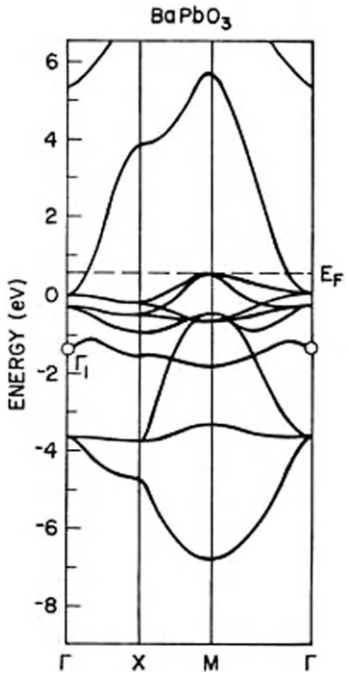

FIGURE 5.159

heating was investigated using XRD and thermal analysis. It was found that several reactions were involved in the temperature range from 200 to 600 °C. The crystallized films tended to decompose upon subsequent depositions, which resulted in the loss of conductivity of the films. However, the conductivity could be recovered by firing at higher temperatures than 600 °C. In addition, a thickness threshold about 1200 Å was observed to be required below which the resistivity of the films increased rapidly.

Barium plumbates are available commercially in small to medium-sized lots.

Radium Plumbates

The scientific literature is devoid of any description of radium plumbates. They could be prepared by the same methods as those used for barium but there is no record of anyone having done so. The expected, stable, compounds would be $RaPbO_3$ and Ra_2PbO_4. In addition, since barium forms a stable $Ba_3Pb_2O_{10}$ compound, there is a strong possibility that radium should also do so.

Perhaps the lack of any description of such salts can be ascribed to the intense radioactivity of the ^{226}Ra atom and the dangers of handling it improperly. Nonetheless, the chemistry of other radioactive cations have been reported so that this explanation does not seem valid. Little interest has been shown in industry or academia for radium plumbates and the corresponding alkaline earth plumbates are much cheaper and easier to handle than the radium salts.

CHAPTER

6

Group 13 (B, Al, Ga, In and Tl) Alkaline Earth Compounds

OUTLINE

6.1. Group 13 Acids and Bases 482
6.1.1. Boron, Boron Acids and Borates 482
6.1.2. Aluminates 483
6.1.3. Gallates 483
6.1.4. Indates 483
6.1.5. Thallates 484

6.2. Alkaline Earth Boron Compounds 484
6.2.1. Alkaline Earth Borides 484
Beryllium Boride 484
Magnesium Boride 485
Calcium Boride 488
Strontium Boride 490
Barium Borides 491
Radium Boride 492

6.3. Alkaline Earth Oxy-Boron Compounds 492
6.3.1. Beryllium Borates 493
Magnesium Borates 494
Calcium Borates 498
Strontium Borates 504
Barium Borates 511
Radium Borates 517

6.4. Aluminum Compounds of the Alkaline Earths 517
6.4.1. Alkaline Earth Aluminides 517
Beryllium Aluminides 517
Magnesium Aluminide 518
Calcium Aluminides 524
Strontium Aluminides 527
Barium Aluminides 529
Radium Aluminides 540
6.4.2. Oxy-Aluminum Compounds of the Alkaline Earths 540
Beryllium Aluminates 540
Magnesium Aluminates 543
Calcium Aluminates 547
Strontium Aluminates 553
Barium Aluminates 559
Radium Aluminates 566

6.5. Alkaline Earth Gallium Compounds 567
6.5.1. Alkaline Earth Gallide Compounds 567
Beryllium Gallide 567
Magnesium Gallide 567
Calcium Gallides 570
Strontium Gallides 578
Barium Gallides 581
Radium Gallides 584
6.5.2. Alkaline Earth Gallate Compounds 584
Beryllium Gallates 584
Magnesium Gallates 585
Calcium Gallates 586
Strontium Gallates 590
Barium Gallates 596
Radium Gallates 599

6.6. Alkaline Earth Indium-Compounds 599
6.6.1. Alkaline Earth Indides 599
Beryllium Indides 599
Magnesium Indides 599
Calcium Indides 603
Strontium Indides 606
Barium Indides 610
Radium Indides 612
6.6.2. Alkaline Earth Oxy-Indium Compounds 612
Beryllium Indates 612
Magnesium Indates 613
Calcium Indates 614
Strontium Indates 617
Barium Indates 618
Radium Indates 621

Encyclopedia of the Alkaline Earth Compounds
http://dx.doi.org/10.1016/B978-0-444-59550-8.00006-5

Copyright © 2013 Elsevier B.V. All rights reserved.

6.7. Alkaline Earth Thallium Compounds 621
6.7.1. Alkaline Earth Thallide Compounds 622
Beryllium Thallides 622
Magnesium Thallides 622
Calcium Thallides 623
Strontium Thallides 626
Barium Thallides 629
Radium Thallides 631
6.7.2. Alkaline Earth Thallates 631
Beryllium Thallates 631
Magnesium Thallates 631
Calcium Thallates 632
Strontium Thallates 633
Barium Thallates 633
Radium Thallates 635

6.1. GROUP 13 ACIDS AND BASES

A number of acids and bases of the Group 13 elements are known.

6.1.1. Boron, Boron Acids and Borates

Boron was not recognized as an element until it was isolated by Sir Humphrey Davy, Joseph Gay-Lussac and Louis Thénard in 1808 through the reaction of boric acid and potassium. Davy called the element boracium. Jöns Jacob Berzelius identified boron as an element in 1824. The first pure boron was arguably produced by the American chemist W. Weintraub in 1909. The alkaline earths form a number of compounds with boron, including borates as well as borides.

Boric acid, also called boracic acid or orthoboric acid or acidum boricum, is a weak acid often used as an antiseptic, insecticide, flame retardant, in nuclear power plants to control the fission rate of uranium, and as a precursor of other chemical compounds. It exists in the form of colorless crystals or as a white powder and is soluble in water. It has the chemical formula H_3BO_3, sometimes written $B(OH)_3$. As a mineral, it is called "sassolite".

Boric acid was first prepared by William Homberg (1652–1715) from borax, by the action of mineral acids, and was given the name "Sal Sedativum Hombergi" (sedative salt of Homberg). The presence of boric acid or its salts has been noted in seawater. It is also said to exist in plants and especially in almost all fruits. The free acid is found native in certain volcanic districts such as Tuscany, the Lipari Islands and Nevada, issuing mixed with steam from fissures in the ground. It is also found as a constituent of many minerals such as "borax", "boracite", "boronatrocaicite" and "colemanite".

Boric acid is soluble in boiling water. Its solubility in water is shown in Table 6.1:

Boric acid does not dissociate in aqueous solution, but is acidic due to its interaction with water molecules to form the tetrahydroxyborate ion:

$$B(OH)_3 + H_2O \Rightarrow B(OH)_4^- + H^+$$
$$(K_a = 5.8 \times 10^{-10}\ \text{mol/l};\ pK_a = 9.24)$$

Polyborate anions are formed at pH 7–10 if the boron concentration is higher than about 0.025 mol/l. The best known of these is the **tetraborate** ion, found in the mineral borax:

$$4B(OH)_4^- + 2H^+ \Rightarrow B_4O_7^{2-} + 9H_2O$$

Boric acid makes an important contribution to the absorption of low-frequency sound in seawater.

Colloidal suspensions of nanoparticles of boric acid dissolved in petroleum or vegetable oil can form a remarkable lubricant on ceramic or metal surfaces with a coefficient of sliding friction that decreases with increasing pressure to a value ranging from 0.1 to 0.02.

The primary industrial use of boric acid is in the manufacture of monofilament fiberglass usually referred to as "textile fiberglass". Textile fiberglass is used to reinforce plastics in applications that range from boats, to industrial piping to computer circuit boards.

Boric acid is used in nuclear power plants to slow-down the rate at which fission is occurring. Fission chain reactions are generally driven by the amount of neutrons present (as products from previous fissions). Natural boron is 20% boron-10 and about 80% boron-11. Boron-10 has a high cross-section for absorption of

TABLE 6.1

		G/100 ml of water								
Substance	**Formula**	**0 °C**	**10 °C**	**20 °C**	**30 °C**	**40 °C**	**50 °C**	**60 °C**	**80 °C**	**100 °C**
Boric acid	H_3BO_3	2.52		4.72		8.08	10.27	12.97	19.10	

low-energy (thermal) neutrons. By adding more boric acid to the reactor coolant which circulates through the reactor, the probability that a neutron can survive to cause fission is reduced. Therefore, boric acid concentration changes effectively regulate the rate of fissions taking place in the reactor. Boron is also dissolved into the spent fuel pools containing used uranium rods. The concentration is high enough to keep neutron multiplication at a minimum.

In the jewelry industry, boric acid is often used in combination with denatured alcohol to reduce surface oxidation and fire scale from forming on metals during annealing and soldering operations.

Boric acid is used in producing the glass faceplates of LCD flat panel displays.

In electroplating, boric acid is used as part of some proprietary formulas. It is also used in the manufacturing of "remming mass", a fine silica-containing powder used for producing induction furnace linings.

Borates including boric acid have been used since the time of the Greeks for cleaning, preserving food, and other activities. It is used in pyrotechnics to prevent the amide-forming reaction between aluminum and nitrates. A small amount of boric acid is added to the composition to neutralize alkaline amides that can react with the aluminum.

Boric acid dissolved in methane is popularly used among fire jugglers and fire spinners to create a deep green flame. Boric acid is added to salt in the curing of cattle hides, calfskins and sheepskins. Used in that way it helps to control bacteria development and also aids in the control of insects.

The alkaline earths form various types of borates as well as "borides". These include:

Metaborates—BO_2^-

Orthoborates—BO_3^{3-}

Pyroborates—$B_2O_5^{4-}$

Perborates—$B_2O_6^{6-}$

Diborates—$B_2O_5^{4-}$

Triborates—$B_3O_7^{5-}$

Tetraborates—$B_4O_9^{6-}$

The last three are examples of polymeric boron species. It should be recognized that species like "borites" do not exist (in deference to phosphorous species).

6.1.2. Aluminates

Aluminum forms intermetallic compounds known as aluminides. It does not form any acids. It is polymeric. Alumina exists as the phases, γ, δ, η, θ and χ. Each has a unique crystal structure and properties. The so-called β-alumina proved to be $NaAl_{11}O_{17}$. Since Al_2O_3 is amphoteric, it dissolves in a strong basic solution:

$$2NaOH + Al_2O_3 \Rightarrow Na_2Al_2O_4 + H_2O$$

This formula is also given as $NaAlO_2$ but the more exact one is $\{NaAlO_2\}_2$. The alkaline earths thus form aluminates as MAl_2O_4. There are other types of soluble "aluminates" such as discrete AlO_4^{5-} anions, or $Al_3O_8^{7-}$ and $Al_5O_{16}^{17-}$which contain complex polymeric anions. Whether a specific combination appears will depend upon the size and electropositivity of the alkaline earth.

6.1.3. Gallates

Gallium is found primarily in the +3 valence state. The +1 oxidation is also attested in some compounds, although they are known to disproportionate into elemental gallium and gallium(III) compounds. What are sometimes referred to as gallium(II) compounds are actually mixed-oxidation state compounds containing both gallium(I) and gallium(III). Gallium is amphoteric:

- β-Ga_2O_3 is prepared by heating nitrate, acetate, oxalate or other organic derivatives above 1000 °C.
- α-Ga_2O_3 can be obtained by heating β-Ga_2O_3 at 65 kbars and 1100 °C for 1 h giving a crystalline structure. The hydrated form can be prepared by decomposing precipitated and "aged" gallium hydroxide at 500 °C.
- γ-Ga_2O_3 is prepared by rapidly heating the hydroxide gel at 400–500 °C.
- δ-Ga_2O_3 is obtained by heating $Ga(NO_3)_3$ at 250 °C.
- ε-Ga_2O_3 is prepared by briefly heating δ-Ga_2O_3 at 550 °C for 30 min.

Strong acids dissolve gallium metal, forming gallium(III) salts such as $Ga_2(SO_4)_3$ and $Ga(NO_3)_3$. Aqueous solutions of gallium(III) salts contain the hydrated gallium ion, $[Ga(H_2O)_6]^{3+}$. $Ga(OH)_3$ may be precipitated from gallium(III) solutions by adding NH_4OH. Dehydrating $Ga(OH)_3$ at 100 °C produces gallium oxide hydroxide, GaO(OH).

Alkaline hydroxides such as NaOH solutions dissolve gallium, forming gallate salts containing the $Ga(OH)_4^-$ anion. Amphoteric gallium hydroxide also dissolves in alkali solutions to form alkaline earth gallate salts. Although earlier work had suggested $Ga(OH)_6^{3-}$ as a possible anion, later work has discredited this finding.

6.1.4. Indates

Indium is also amphoteric but less so than its homologues, Al^{3+} and Ga^{3+}. The oxide dissolves in NaOH to form the indate, $Na_2In_2O_4$, like its Al- or Ga-homologue.

There are no known acids containing the indate anion, $In_2O_4^{2-}$. Although indium is listed to possess a monovalent cationic state, In^+, it has been found that this valence state is unstable and it decomposes to In^0 and In^{3+}. Thus, no "indous" or "indite" compounds are known.

6.1.5. Thallates

The two main oxidation states of thallium are +1 and +3. In the oxidation state +1, most compounds closely resemble the K^+ compounds (the ionic radius of thallium(I) is 1.47 Å while that of potassium is 1.33 Å). For example, the water-soluble and very basic TlOH reacts with CO_2 forming water-soluble thallium carbonate, Tl_2CO_3. This carbonate is the only known water-soluble heavy metal carbonate.

The amphoteric nature of thallium oxide has been demonstrated. However, the reaction in solution does not follow the same rules as those for Al_2O_3 or Ga_2O_3. At 25 °C, it was established that the components, Na_2O, H_2O and Tl_2O_3, only react in systems containing thallium(I) and sodium hydroxides. They form with thallium(I) orthothallate with restricted solid solutions between thallium oxide and the orthothallate based on thallium oxide and sodium hydroxythallate $Na_3Tl(OH)_6$.

At elevated temperatures of 150 and 200 °C, it was established that potassium metathallate is formed in the K_2O–Tl_2O_3–H_2O system while sodium metathallate $Na_2Tl_2O_4$ and a hydrated thallate of the composition $4Na_2O{\cdot}Tl_2O_3{\cdot}(3–4)H_2O$ are formed in the Na_2O–Tl_2O_3–H_2O system at 150 °C. The thallates, Tl_3TlO_3, $Na_3Tl(OH)_6$, $Na_2Tl_2O_4$ and $K_2Tl_2O_4$ have been isolated in pure forms and identified by X-ray analysis.

6.2. ALKALINE EARTH BORON COMPOUNDS

In addition to forming borates, boron also forms borides with the alkaline earths.

6.2.1. Alkaline Earth Borides

Beryllium Boride

Beryllium forms a number of borides among which is BeB_2. This compound is copper-red in color and has a cubic fluorite structure with $a = 4.661$ Å. BeB_2 is readily hydrolyzed by dilute acids to produce beryllium hydrides. BeB_2 has the CAS number of 12429-94-6 and a molecular weight of 73.878 g/mol. This red solid melts at >1970 °C. The other beryllium borides are insoluble in acids. They do not melt below 1500 °C. Hydrochloric acid, when reacted with beryllium boride, was found to give higher yields of tetraborane (B_4H_{10}) than the corresponding reaction with magnesium boride.

There are four stable compounds in the Be–B system: Be_4Be, Be_2B, BeB_2 and BeB_6. They are prepared by heating the elements together at about 1400 °C. The BeB_6 compound has a salt structure in which the B_6^{2-} octahedra occupy the Cl^- sites and the Be^{2+} cations are on the Na^+ sites. Each octahedron is linked to six neighboring octahedra at a distance of 1.72 Å, which is also the interatomic distance within each octahedron.

Be_4B is a refractory solid with a melting point of 1160 °C, a molecular weight of 40.8601 g/mol, and a CAS number of 12536-52-6. At atmospheric pressure, Be_4B has a tetragonal structure with a space group of P4/nmm. It undergoes a polymorphic transformation to a rhombohedral structure at >50 GPa, but details of the lattice parameters have not been documented.

The following lists are some physical characteristics of these beryllium borides (Table 6.2).

Be_2B is a pink crystal with a melting point of 1560 °C, a molecular weight of 28.8351 g/mol, and a CAS number of 12536-51-5.

BeB_2 is a refractory copper-red solid with a melting point >1970 °C, a molecular weight of 30.3641 g/mol, and a CAS number of 12228-40-9.

BeB_6 is a red solid with a melting point >2070 °C, a molecular weight of 73.8782 g/mol, and a CAS number of 12429-94-6.

Though beryllium diboride has been known and studied for more than 40 years, there has been no firm evidence that this phase exists with stoichiometry

TABLE 6.2

Compound	Density	Structure	Melting temperature,°C	Hardness
Be_4B	1.94 g/cc	Tetragonal	1160 °C	1370 (HK_{100})
Be_2B	1.89	Cubic	1504	1300
BeB_2	2.42	Hexagonal	>1970	3180
BeB_3	2.35	Tetragonal	2020	2580
BeB_6	2.42	Hexagonal	—	—

BeB_2. The space group of a compound reported to be BeB_2 was hexagonal P6/mmm with lattice constants $a = 5.0979$ Å and $c = 5.0955$ Å, but a full structure determination was not carried out.

The actual composition of BeB_2 has been reported to be $Be_{29.5}B_{81}$. The space group of the unit cell is P-62m. In the unit cell, there are 12 inequivalent B sites and seven inequivalent Be sites, one of the latter being only half occupied. The refined structure produced a stoichiometry of $Be_{1.23}B_{3.38}$, i.e. $BeB_{2.75}$ with $a = 5.097738$ Å and $c = 5.095467$ Å. The structure has 81 B atoms and 29.5 Be atoms per unit cell. $BeB_{2.75}$ is a superconductor with a $T_c(^{10.8}B)$ of 0.72 K and that the ^{10}B sample has a slightly enhanced $T_c(^{10.0}B)$ of 0.79 K. This result can be explained in terms of "nanostructures". Small $(BeB_2)_n$ clusters ($n = 1$–6 and 8) as well as BeB_2 nanotubes and cages $(BeB_2)_n$, with $n = 10$, 12, 15, 18, and up to 30, have been studied using density functional theory. These nanostructures strongly resemble the ones formed by carbon, with ring-like geometries for very small clusters and closed cages for medium-sized clusters. The energetics for distortion and closure of planar sheets into cages and nanotubes prove favorable in comparison with carbon systems (Fig. 6.1).

However, by the time that the B atoms reach 80 (2×40) in the structure, the number of Be ions has shrunk to about 30 because of overlap of the wave functions.

Diberyllium boride, Be_2B, was prepared, and its crystal structure was studied. The structure of Be_8Be_5 was considered to be a compromise between a tendency for Be to adopt the fluorite arrangement and the tendency for B to form some sort of network containing B–B bonds. Be_8B_5 in contrast to Be_8B_4 had almost an identical number of valence electrons per unit cell as Be_8C_4. Thus, this series of compounds are subject to the same restraints as BeB_2 in that the actual compounds formed have the general formula, $(Be_2B)_n$, where n can vary from 2 to 10 (but the Be/B ratio does not remain at 2/1 at the higher numbers of n, i.e. $Be/B \leq 2/1$).

Both Be_2B and Be_4B have been of interest in the formation of light-weight armor. In general, the material selection should be a balance between low density, high incompressibility (high yield strength and impedance), and ability to dissipate tensile stresses without fracturing (ductility). Several ceramics (B_4C, $A1_2O_3$, B itself, etc.) possess the first two qualities, i.e. low density and high incompressibility, but ductility has been observed in only a few low-density ceramics (BeC, Be_2B,Be_4B, and MgO), even under high hydrostatic pressures. Exposure to moisture during handling and storage had little or no adverse effect on the Be_4B or Be_2B powders. Be_4B and Be_2B decompose below their melting points, 1165 and 1370 °C, respectively. The low-melting point of the Be_4B suggests the possibility of preparing a two-phase (~30 vol% Be_4B–Be_2B) armor material by casting. A method of casting lightweight armor material of Be_4B dispersed in a Be matrix was developed. This comprised the melting of a mixture of Be_4B and Be powder, cooling to induce a temperature gradient in the molten material, and recovering the solidified cermet. A phase diagram comprising these three compounds was prepared as a guide to forming lightweight armor by liquid casting (Fig. 6.2).

The phase equilibria of B from 70% to 100% are not shown here. Only BeB_2 melts congruently and Be_2B was determined to exist only above 950 °C and decomposes to BeB_2 and Be_4B below that temperature:

$$7Be_2B \Rightarrow 2BeB_2 + 3Be_4B$$

In order to obtain a compound stable at room temperature, the mixture was heated, $1400\,°C > T > 950\,°C$, and then rapidly quenched. Because of the toxicity of Be, the armor fittings are not used today, particularly with the advent of Kelvar™ body armor for use in military and police work.

Beryllium borides are available in limited quantities worldwide.

Magnesium Boride

Magnesium boride can be formed directly from the elements. Mg melts at 650 °C and boron melts at 2076 °C. Therefore, if a vapor of Mg metal at >750 °C (red-heat) is passed over crystals of boron, reaction forms the desired boride. However, to obtain a stoichiometric compositions, it is better to heat the well-mixed powders of Mg and B to obtain specific compounds:

$$Mg + 2B \Rightarrow MgB_2$$

Magnesium diboride (MgB_2) is a simple ionic binary compound that has proven to be an inexpensive and useful superconducting material. Its superconductivity was announced in March 2001 with a critical temperature of 39 K (−234 °C). This is the highest T_C found among conventional superconductors. This material was first synthesized and its structure confirmed in 1953, but its superconducting properties were not discovered until 2001. The discovery caused great

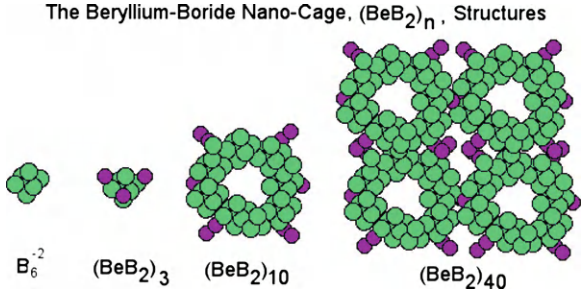

FIGURE 6.1

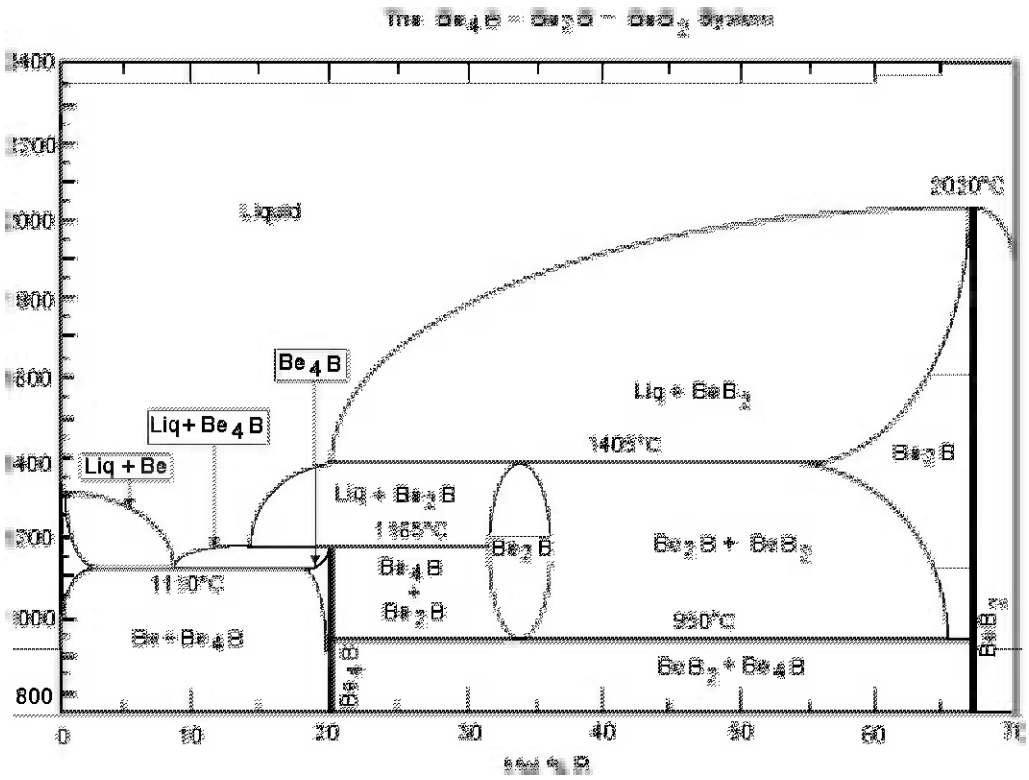

FIGURE 6.2

excitement. A large number of papers appeared in the scientific literature concerned with the physical and chemical properties of MgB_2 and its homologues. Its molecular weight is 45.9325 g/mol. It melts at 830 °C and is hexagonal with space group P6/mmm and lattice constants of $a = 3.0864$ Å, $c = 3.5215$ Å. The density is 2.625 g/cm^3 and the hardness is 1260 kg/mm^2. MgB_2 has the CAS number of 12007-25-9.

MgB_2 is a layered hexagonal crystal as shown in the following diagram. In this diagram, both Mg and B atoms are in a hexagonal coordination within the structure (Fig. 6.3).

The compounds of magnesium boride, such as the diboride MgB_2, are very promising materials for superconductivity applications. They represent a new class of low-cost and high-performance superconductors that are not oxides or fullerenes, but are characterized by relatively high Curie temperature. In addition to MgB_2, that has a honeycomb structure very similar to graphite, other thermodynamically stable borides such as MgB_4, MgB_7, MgB_{12} and MgB_{20} have been observed.

If Mg metal is heated with boric acid under a reducing (hydrogen) atmosphere, the product is:

$$Mg + 2H_3BO_3 + (\text{Heat} + H_2) \Rightarrow MgB_2 + 3H_2O$$

This compound appears even if the ratio of Mg/B approximates 3:2 (which is the stoichiometric composition expected between these two elements). In the Mg–B system, four boride phases were established in 1952: MgB_2, MgB_4, MgB_6 and MgB_{12}. More recent work found that the stable phases were MgB_2, MgB_4, and MgB_7. The diboride is hexagonal while the

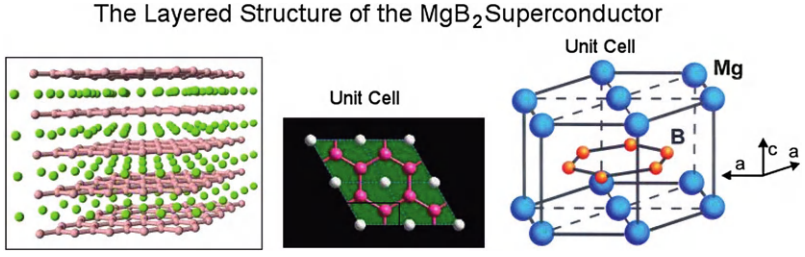

FIGURE 6.3

tetraboride is orthorhombic. At 800 °C, MgB_2 decomposes to the tetraboride:

$$2MgB_2 + \text{heat } (>800\ ^\circ C) \Rightarrow MgB_4 + Mg\ (gas)$$

$$3MgB_2 + \text{heat } (>1000\ ^\circ C) \Rightarrow MgB_6 + 2Mg\ (gas)$$

The vaporization behavior of MgB_2 and MgB_4 under thermodynamic conditions has been studied by the Knudsen effusion mass spectrometry technique. In the temperature range explored (883–1154 K or 610–887 °C), magnesium borides are observed to decompose by loss of gaseous Mg only. Above 1200 °C, both MgB_4 and MgB_6 decompose to form the decaboride:

$$3MgB_4 + \text{heat } (>1200\ ^\circ C) \Rightarrow MgB_{12} + 2Mg\ (gas)$$

$$2MgB_6 + \text{heat } (>1200\ ^\circ C) \Rightarrow MgB_{12} + Mg\ (gas)$$

At higher temperatures (>1700 °C), MgB_{12} decomposes to form gaseous Mg and B vapors which condense on a cool surface. A "normal" phase diagram cannot be presented as such since all of these magnesium borides decompose incongruently with a gas, Mg vapor, as the product. The temperature of decomposition of MgB_2 can be delayed up to >1500 °C by the application of an external, inert, atmosphere. The following diagram shows a type of phase diagram depicting this kind of behavior (Fig. 6.4).

The decomposition temperature of MgB_2 is dependant upon the external pressure present, whether it is air or an inert gas pressure. It is Mg metal gas that forms and the gaseous phase is retarded at higher external pressures.

The effect of external pressure on the formation of the various magnesium boride compositions is shown in Fig. 6.5.

It should be clear that the "melting temperatures" of these phases are dependant upon the external pressures used to formulate them. It is the volatility of Mg as the vapor which controls the apparent melting temperatures observed. This phenomenon appears to be the dominant

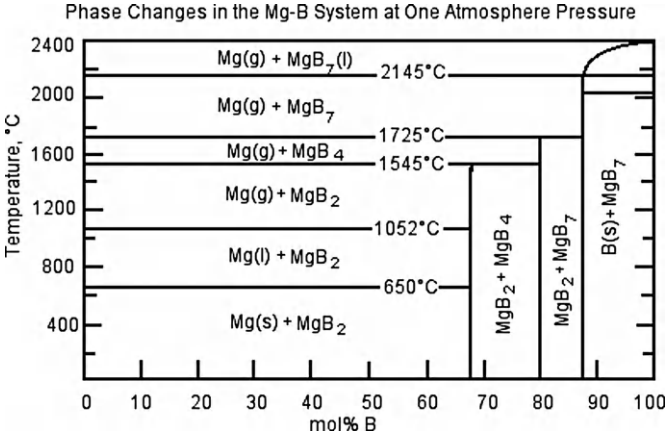

FIGURE 6.4

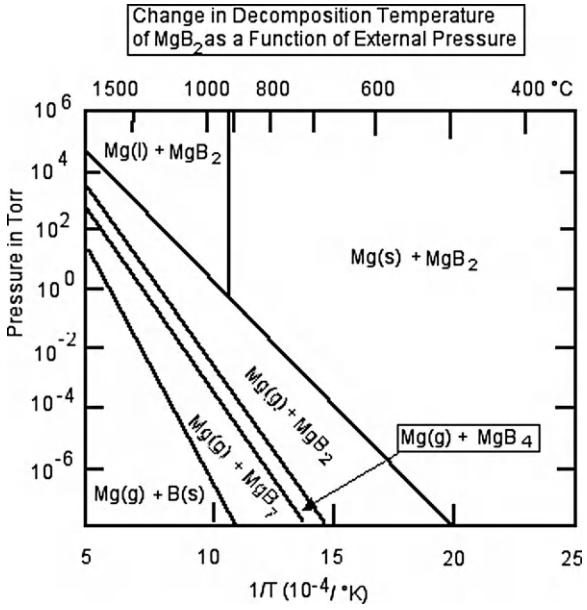

FIGURE 6.5

factor in the formation of all of the alkaline earths, but more so for magnesium borides.

A novel complex magnesium boride, Mg_2B_{25}, has been prepared and its crystal structure determined from laboratory X-ray powder diffraction data. It is an R-centered trigonal lattice (with $a = 11.0402$ Å, $c = 24.198$ Å, hexagonal setting), space group R-3m, which is isomorphous with β-boron and with the rhombohedral compounds of the boron-rich metal boride family. The magnesium atoms occupy interstitial sites with partial occupancies. The Mg atom in one site is vicariant with the B(4) atom and lies in a pseudo-metallic environmental site surrounded by the 10 nearest-neighbor B atoms. All other magnesium atoms are found in lattice cavities within the corrugated slabs normal to c, with Mg occupying two sites in the lattice that are similar to those populated in other metal borides. In addition, Mg also exists in a new type of site that has a different type of coordination not seen in other metal borides. Thus, a total of four interstitial sites of Mg exist. These slabs present two equiprobable, but self-excluding, configurations of ordered Mg atoms, which randomly stack along the *c*-axis. Mg_2B_{25} shows a significant increase in the *c*-axis of the rhombohedral lattice with respect to the other members of the family. This was attributed to both to the larger metallic radius and the anisotropic stacking of the Mg atoms, caused by the presence of the over-stuffed Mg sublattices.

MgB_2 reacts vigorously with acids, forming boron hydrides (like B_4H_{10}) and MgB_2 remains the chief source for preparing such compounds:

$$5MgB_2\ (s) + 14HCl\ (aq) \Rightarrow B_{10}H_{14}\ (\text{solid}) + 5MgCl_2\ (aq) + 2Cl_2\ (gas)$$

This borane is the final product of hydrolysis since diborane, tetraborane, are gases which are explosive in water and/or air and pentaborane and decaborane are liquids which are unstable in water and form explosive mixtures in air. Dodecaborane, $B_{12}H_{16}$, is also another possible product. The higher magnesium borides like the tetraboride are more stable and their hydrolysis is not accompanied by formation of boranes.

Magnesium aluminum boride ($MgAlB_{14}$), also known as BAM, is a ceramic alloy that is highly resistive to wear with a low coefficient of sliding friction. First reported in 1970, it has an orthorhombic structure with four icosahedral B12 units per unit cell. This ultra-hard material is also characterized by its high hardness and coefficient of thermal expansion comparable to other widely used materials. BAM alone is among the hardest nondiamond materials.

Magnesium diboride is available commercially worldwide.

Calcium Boride

Calcium boride can be formed directly from the elements. Ca melts at 842 °C and boron melts at 2076 °C. Therefore, if a vapor of Ca metal at >850 °C (red-heat) is passed over crystals of boron, a gas–solid reaction forms the desired boride. However, to obtain stoichiometric compositions, it is better to heat the well-mixed powders of Ca and B to obtain specific compounds:

$$Ca + 6B \Rightarrow CaB_6$$

The phase system of calcium and boron compounds is shown in the diagram as follows. Only one compound is known, CaB_6, which melts at 3162 °C (Fig. 6.6).

The intermediate fields in this diagram consist of various crystal states of Ca plus CaB_6. On the boron side, β-B changes to α-B at 2075 °C.

Other methods used to prepare calcium hexaboride **commercially** include high-temperature reactions of:

Reaction of calcium and boron at 1000 °C.
$Ca(OH)_2$ and boron in vacuum at about 1700 °C.
$CaCO_3$ and boron as B_4C in vacuum above 1600 °C.
Boron with calcium or calcium oxide (CaO) at 800–1800 °C.
CaO and H_3BO_3 and Mg at 1100 °C.

Calcium hexaboride (sometimes calcium boride) is a compound of calcium and boron with the chemical formula CaB_6.

Typical samples of CaB_6 are nonstoichiometric, i.e. the ratio of boron to calcium is not exactly 6:1, for example the ultra-fine powders of CaB_6 produced by some researchers had B:Ca ratio of 5.91:1. It is an important material due to its high electrical conductivity, hardness, chemical stability, and melting point. It is a black, lustrous, chemically inert powder with a low density. Calcium hexaboride is insoluble in H_2O, MeOH (methanol), and EtOH (ethanol) and dissolves slowly in acids. It has the cubic structure typical for metal hexaborides, with octahedral units of six boron atoms combined with calcium atoms. Lanthanum-doped CaB_6 show weak ferromagnetic properties, which is a remarkable fact because calcium and boron are neither magnetic, nor have inner 3d or 4f electronic shells, which are usually required for ferromagnetism. This structure is shown in the Fig. 6.7.

The crystal structure of calcium hexaboride is a cubic lattice with calcium at the cell centers and compact,

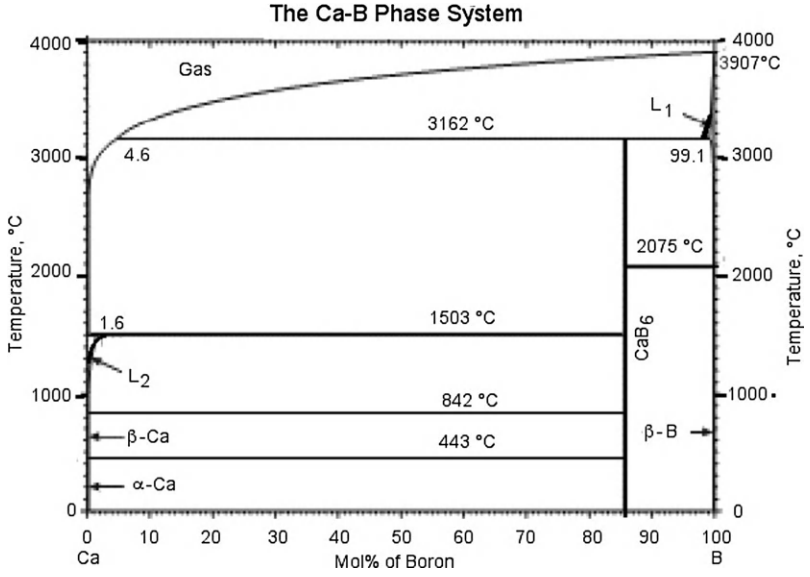

FIGURE 6.6

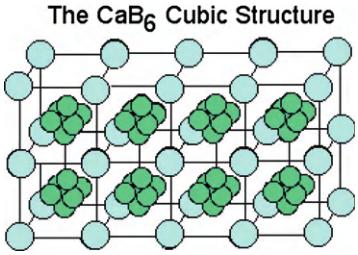

FIGURE 6.7

regular octahedrons of boron atoms linked at the vertices by B–B bonds to give a three-dimensional boron network.

The above diagram does not show this so that the relation of Ca^{2+} and B_6^{2-} ions could be shown simply. The B_6 ions should be linked three dimensionally. Each calcium has 24 nearest-neighbor boron atoms. The calcium atoms are arranged in simple cubic packing so that there are holes between groups of eight calcium atoms situated at the vertices of a cube. The simple cubic structure is expanded by the introduction of the octahedral B_6 groups and the structure is a CsCl-like packing of the calcium and hexaboride groups. Another way of describing calcium hexaboride is that a metal and a B_6^{2-} octahedral polymeric anions occupy a CsCl-type structure where the calcium atoms occupy the Cs sites and the B_6 octahedra in the Cl sites. The Ca–B bond length is 3.05 Å and the B–B bond length is 1.7 Å. The predicted lattice constant varies between 4.08 and 4.105 Å while it has been experimentally measured from 4.145 to 4.153 Å. The space group is P"m$\overline{3}$ m" and the point group is O_h. It is a semiconductor with an energy gap of 0.48 eV and a band gap of about 1.0 eV.

^{43}Ca NMR data contains a δ_{peak} at −56.0 ppm and δ_{iso} at −41.3 ppm where δ_{iso} is taken as peak max of +0.85 bandwidth and the negative shift is due to the high-coordination number.

Calcium hexaboride has three Raman peaks at 754.3, 1121.8, and 1246.9/cm due to the active modes A_{1g}, E_g, and T_{2g}, respectively.

Observed infrared vibration frequencies (in cm^{-1}) include: 1270 (strong) from A_{1g} stretch, 1154 (medium) and 1125 (shoulder) from E_g stretch, 526, 520, 485, and 470 from F_{1g} rotation, 775 (strong) and 762 (shoulder) from F_{2g} bend, 1125 (strong) and 1095 (weak) from F_{1u} bend, 330 and 250 from F_{1u} translation, and 880 (medium) and 779 from F_{2u} bend.

The microhardness is 27 GPa, $\Delta H_f = -120$ kJ/mol, and the resistivity is greater than 200 Ωm × 10^8. The magnetic moment is less than or equal to 0.07 μB per atom. The Curie temperature is ~600 K.

The ferromagnetic transition temperature of calcium hexaboride is around 900 K which is high for a molecule without partially filled d- or f-shell orbitals. It is a semiconductor with an energy gap of 0.48 eV and a band gap of about 1.0 eV. Ferromagnetic order (FM) have been observed at unexpectedly high temperatures in La-doped alkaline earth hexaboride compounds including calcium hexaboride. The origin of this high-temperature FM is the FM phase of a dilute electron gas, linkage to the presumed excitonic state in calcium boride, or external impurities on the surface of the sample. In fact, the impurities include iron and nickel probably coming from boron in sample preparation.

Hexaborides in general show a low work function, around 2.5 eV. They are also resistant to poisoning. Calcium hexaboride, as well as SrB_6 and BaB_6, has been used in this capacity. Boride cathodes are about 10 times as "bright" as the tungsten ones and have 10–15 times longer lifetime. For example, they are used in electron microscopes, microwave tubes, electron beam welding apparatus, X-ray tubes and free-electron lasers. However, these materials tend to be expensive.

The oxidation of CaB_6 powders at high temperatures was investigated. The sample oxidized at 873 to 973 K (600 to 700 °C) for 25 h exhibited weight gain with increasing oxidation temperature; the oxidation proceeded in accordance with the parabolic law during the initial oxidation stage. On the other hand, the weight gain of the sample oxidized at and above 1073 K for 4 h was approximately 80%; however, even if the oxidation time was prolonged, an additional weight change did not occur. Based on the results of the X-ray diffraction (XRD) analysis, calcium borate (CaB_4O_7) was found to be present on the surface of the sample oxidized at 1073 K (800 °C). The sample showed a good oxidation resistance at 1273 to 1373 K (1000 to 1100 °C), because the surface film of calcium borate (CaB_2O_4) formed by oxidation acted as an oxidation resistant layer:

$$CaB_6 + 5O_2 \Rightarrow CaB_4O_7 + B_2O_3$$

The optimum conditions for the preparation of pure calcium hexaboride by the borothermic and boroncarbide techniques are at temperature of 1600 °C and a holding time of 60 min; the charge should contain a 10% excess of calcium oxide.

A different calcium boride, CaB_3, was epitaxially grown on Al_2O_3 crystal on the (0001) lattice direction with a substrate temperature of 500 °C. Structural characterization by RHEED (Reflection high-energy electron diffraction) and XRD indicated that CaB_3 has a hexagonal cell with lattice parameters of $a = 4.008$ Å and $c = 4.098$ Å. No evidence for superconductivity was found down to 2 K.

Carbon hexaboride is used in the manufacturing of boron-alloyed steel. Also, calcium hexaboride is used as a deoxidation agent in production of oxygen-free copper, which results in higher conductivity than conventionally phosphorus-deoxidized copper owing to the low solubility of boron in copper. Also, it can serve

as a high temperature material, surface protection, abrasives, tools, and wear-resistant material. When used at elevated temperature, calcium hexaboride will oxidize degrading its properties and shortening its usable lifespan.

Calcium hexaboride is irritating to the eyes, skin, and respiratory system. This product should be handled with proper protective eyewear and clothing. Never put calcium hexaboride down the drain or add water to it.

Calcium hexaboride is available commercially in small to medium quantities worldwide.

Strontium Boride

Strontium boride can be formed directly from the elements. Sr melts at 777 °C and boron melts at 2076 °C. Therefore, if a vapor of Sr metal at >850 °C (red-heat) is passed over crystals of boron, reaction forms the desired boride. However, to obtain stoichiometric compositions, it is better to heat the well-mixed powders of Sr and B to obtain specific compounds:

$$Sr + 6B \Rightarrow SrB_6$$

Strontium boride appears as a crystalline black powder. Closer examination reveals slightly translucent dark red crystals capable of scratching quartz. It is very stable and has a high melting point and density. Although not thought to be toxic, it is an irritant to the skin, eyes, and respiratory tract. It has the formula of SrB_6, with a molecular weight of 152.49 g/mol. It is a black crystalline solid (15.0 °C) with a density of 3.39 g/cm^3, and a melting point of 2235.0 °C. Its CAS number is 12046-54-7.

Strontium boride, along with other alkali earth metal borides, has been shown to exhibit weak ferromagnetism at low temperatures. This is thought by some to be caused by slight impurities or aberrations in the crystal lattice, while others suggest different explanations are needed. Strontium boride has also been examined for semiconducting properties at lower temperatures. Strontium boride is used in insulation and nuclear control rods. A recent patent filed for aircraft windows uses SrB_6 nanoparticles in a transparent acrylic sheet. The IR-absorbing properties of these nanoparticles prevent the transmittance of infrared wavelengths while still allowing the transmittance of visible light. Strontium boride has the same cubic structure as CaB_6 except that the lattice parameters differ due to the larger size of the Sr^{2+} ion (Fig. 6.8).

Here, the interatomic bonding of the octagonal B_6^{2-} groups are shown. Only SrB_6 appears in the phase diagram which is similar to that of the calcium system except for the melting point of SrB_6 (Sr = 2235 °C and Ca = 3162 °C). It is a semiconductor at normal temperatures.

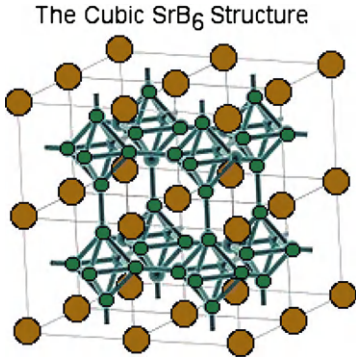

FIGURE 6.8

The NMR of this compound has been reported. Below 30 K, the NMR spectrum is temperature independent but the spin–lattice relaxation rate T_1^{-1} exhibits different features in two different temperature regimes. At high temperatures, between 30 K and a field-dependent crossover temperature T_B between 0.5 and 2 K, T_1^{-1} is almost temperature independent. For T in the crossover temperature range, the magnitude of T_1^{-1} of SrB_6 is distinctly larger than for LaB_6, a metal with a charge carrier concentration at least two orders of magnitude higher than that of SrB_6. A possible cause for this behavior may be the very weak itinerant ferromagnetism that has subsequently been established to occur in nominally pure SrB_6. At low temperatures, below T_B, T_1^{-1} decreases substantially with decreasing temperature confirming a crossover or phase transition phenomenon as observed by measurements of thermal and transport properties. It has been suggested that the ferromagnetism is due to a small amount of intrinsic defects in the lattice.

Growth of single-crystal strontium hexaboride (SrB_6) nanowires was achieved by pyrolysis of diborane (B_2H_6) over SrO powders at 760–800 °C and 400 mTorr in a quartz tube furnace. Raman spectra demonstrate that the nanowires are SrB_6, and transmission electron microscopy (TEM) along with selected area diffraction indicate that the nanowires consist of single crystals with a preferred [001] growth direction. Electron energy loss data combined with the TEM images indicate that the nanowires consist of crystalline SrB_6 cores with a thin (1 to 2 nm) amorphous oxide shell. The nanowires have diameters of 10–50 nm and lengths of 1–10 μm.

SrB_6 has been tested as a component in low-temperature emissive electron gun electrodes. LaB_6 has an emissive power of 29 A/cm^2/°C and a work function of 2.66 eV. The corresponding emissive power for SrB_6 is 0.14 A/cm^2/°C and a work function of 2.67 eV. In contrast, that for BaB_6 is 16 A/cm^2/°C and a work function of 3.45 eV. At 1700 °C, the currents obtained were: La = 1.0 A/cm^2; Sr = 140 mA/cm^2; Ba = 18 A/cm^2.

Strontium hexaboride is available commercially from a number of suppliers worldwide.

Barium Borides

Barium boride can be formed directly from the elements. Ba melts at 727 °C and boron melts at 2076 °C. Therefore, if a vapor of Ba metal at >750 °C (red-heat) is passed over crystals of boron, a chemical reaction forms the desired boride. However, to obtain stoichiometric compositions, it is better to heat the well-mixed powders of Ba and B to obtain specific compounds:

$$Ba + 6B \Rightarrow BaB_6$$

BaB_6 has the CAS number of 12046-08-1. It was established that a barium hexaboride with a composition approaching theoretical can be obtained by a so-called borothermic technique at a temperature of 1600 °C from a charge with a 40% excess of barium oxide. It is more economical to prepare BaB_6 by the reaction of barium carbonate with boron in two stages (30 min at 900 °C and 60 min at 1500 °C).

Barium hexaboride has the same cubic structure as Ca^{2+} and Sr^{2+} hexaborides. The following diagram shows two unit cells in the structure (Fig. 6.9).

Its melting point is 2543 °C and its density is 2.543 g/cc. Its molecular weight is 202.1973 g/mol. Barium hexaboride, BaB_6, has been obtained in the form of single crystals. Its crystal structure was refined in space group *Pmm* (no. 221), $a = 4.2615$ Å. The

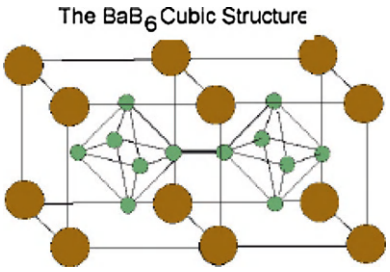

FIGURE 6.9

electronic situation of BaB_6 was discussed on the basis of different band structure calculations performed within the density functional theory (LMTO, plane wave). A comparison with CaB_6 and the molecular anion $[B_6H_6]^{2-}$ shows a similar band ordering. The different orbital contributions are strongly mixed and the inter-octahedral bonds are lower in energy than some of the intra-octahedral framework interactions.

Barium hexaboride has been considered as a candidate for manufacture of a "hot-cathode" electron gun for use in various instruments. The following diagram shows some of the results of their usage in this application (Fig. 6.10).

Note that lanthanum hexaboride can function up to 2200 °C and deliver a current as high as 75 A/cm^2. SrB_6 has been measured as limited to 0.14 A/cm^2 and BaB_6 has a limit of 18 A/cm^2 because of losses as they approach their melting point (see diagram). Only CaB_6

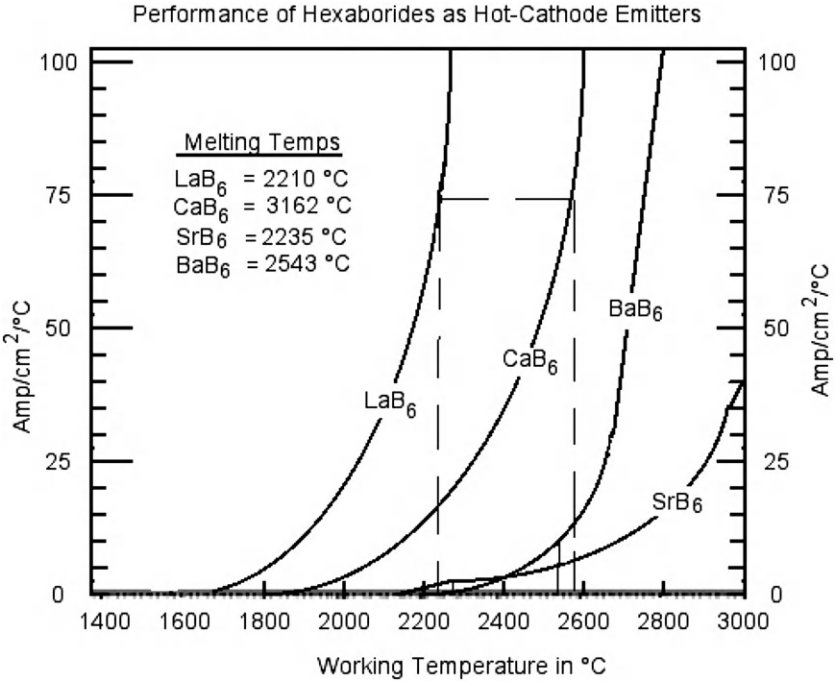

FIGURE 6.10

with a melting point of 3162 °C can approach and exceed the performance of LaB_6. However, to reach the same level of amperage output, the CaB_6 cathode gun must reach a temperature of 2580 °C whereas LaB_6 needs only a temperature of 2230 °C to do so. Thus, the CaB_6 electrode is not as efficient as the LaB_6 one. The difference lies in the fact that the LaB_6 crystal exhibits metallic conduction properties whereas the alkaline earths are semiconductors. The LaB_6 brightness is of the order of 15 to 20 times that of tungsten operated at 40-h life conditions, and it was stated that single-crystal cathodes are more reliable for producing high brightnesses of these electrodes.

The synthesis and formation mechanism of BaB_6 powder by the reaction of $BaCO_3$ with B_4C and carbon were investigated systematically. The influences of heating temperature and holding time on the reaction products were studied by X-ray diffractometry, and the morphologies of BaB_6 were investigated by scanning electron microscopy (SEM). The interaction in the $BaCO_3$–B_4C–C system by which BaB_6 is formed was found to be a solid-phase diffusion process that passes through $Ba_3B_2O_5$ and BaB_2O_4 transition phases. The optimal conditions for BaB_6 synthesis are a holding time of 2 h at 1400 °C, under a vacuum of 10^{-2} Pa of pressure.

Barium hexaboride (BaB_6) crystals can also be synthesized electrochemically using a molten salt technique. Barium carbonate ($BaCO_3$) and boron trioxide (B_2O_3) were used as reactants. Lithium fluoride (LiF) was used as the supporting electrolyte. Small single crystals could be separated from the molten mixture.

Single crystals of alkaline earth hexaborides, CaB_6, SrB_6 and BaB_6, have been grown from a molten aluminum metal flux. The size of crystals produced was up to 5 mm for CaB_6, 3 mm for SrB_6 and 1 mm for BaB_6 in the longest dimension. The color of single crystals is black for CaB_6, dark blue for SrB_6 and dark green for BaB_6. The optical reflectance of single crystals was measured over 1.5–5.5 eV photon energy range.

Barium hexaboride is available in small to medium lots commercially worldwide. It is also offered as single-crystal "whiskers" for sale for research into its properties.

Radium Boride

The scientific literature is devoid of any description of radium borides. The expected compound is RaB_6, the hexaboride. It could be prepared by the same methods as those used for barium but there is no record of anyone having done so. Perhaps the lack of any description of such salts can be ascribed to the intense radioactivity of the ^{226}Ra atom and the dangers of handling it improperly.

6.3. ALKALINE EARTH OXY-BORON COMPOUNDS

The alkaline earths form a series of compounds with the borate anions. These include:

Metaborites—$BO_2^- = M(BO_2)_2$

Orthoborates—$BO_3^{3-} = M_3(BO_3)_2$

Pyroborates—$B_2O_5^{4-} = M_2B_2O_5$

Perborates—$B_2O_6^{6-} = M_3B_2O_6$

Diborates—$B_2O_7^{8-} = M_4B_2O_7$

Triborates—$B_3O_7^{5-} = M_5(B_3O_7)_2$

Tetraborates—$B_4O_7^{2-} = M(B_4O_7)$

Not all of these compounds exist with any given alkaline earth. For example, the Be^{2+} ion is too small and perborates either do not exist or have never been explored. The last three types of compounds are polymeric in BO_3 groups and are stable with the larger alkaline earths like Sr^{2+} and Ba^{2+}. In that case, the valence of the group changes from −8 to −4 or −2, depending upon the nature of the corresponding alkaline earth. This stems from the fact that triangular BO_3^{3-} groups form bonds with tetrahedral BO_4^{5-} groups in the B_3O_7 structure by O to O sharing, as shown in the following Fig. 6.11.

These condensed polyanions have the Lewis structure shown in Fig. 6.12.

However, these BO_3 groups should not be confused with the $(BO_4)_2^{6-}$ groups of perborate. Unlike the percarbonate, and perphosphate, the sodium perborate compound is not simply an adduct with hydrogen peroxide, but contains a cyclic anion ($B_2O_4(OH)_4^{2-}$) with two peroxo bridges and does not contain the BO_3^- ion. This makes the substance more stable, and safer for handling and storage. The formulas of the monohydrates and tetrahydrates can therefore be written as

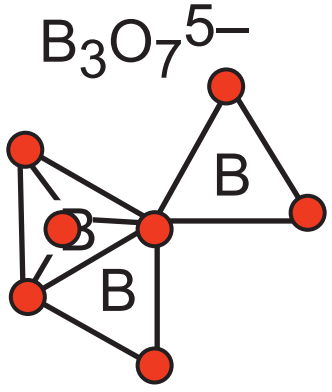

FIGURE 6.11

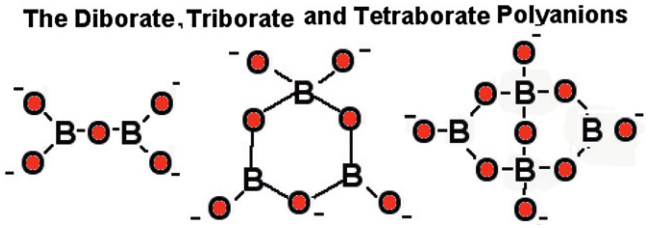

FIGURE 6.12

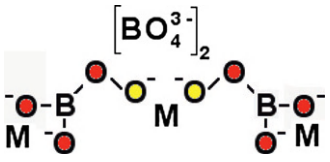

FIGURE 6.13

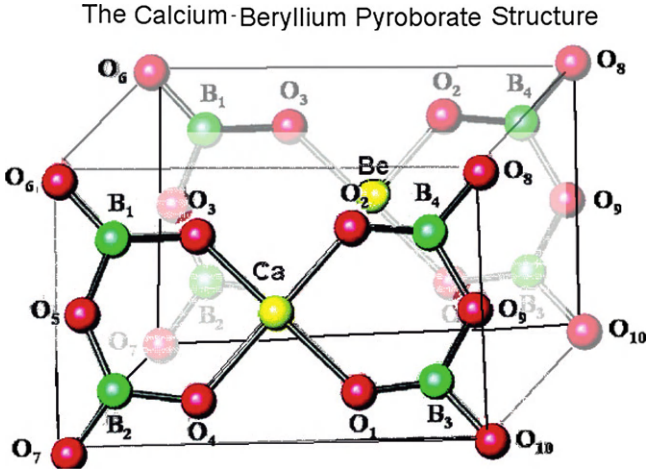

FIGURE 6.14

$H_4B_2O_6^{2-}$ (anhydrous) and $[H_2B_2O_8]^{4-}\cdot 4H_2O$, respectively. The Lewis structure is shown in Fig. 6.13.

The two types of oxygen atoms are clearly depicted.

6.3.1. Beryllium Borates

Beryllium borate can be synthesized by the reaction of the oxide with boric oxide:

$$BeO + B_2O_3 \Rightarrow Be(BO_2)_2$$

The metaborate is shown but a change in the molar ratio from 1:1 to 2:1, etc. produces other compositions. The **metaborate**, $Be(BO_2)_2$ or BeB_2O_4, is offered for sale with the CAS number of 14720-43-5. Another metaborate, $BeBO_2$, is offered for sale with the CAS number of 10682-18-3. It is actually a hydroxy compound with the composition $(BeOH)BO_2$ and was prepared by a solution method:

$$Be(OH)_2\ (aq) + NaBO_2\ (aq) \Rightarrow (BeOH)BO_2\ (solid)$$

A monohydrate is formed. The water of hydration is lost at 120 °C. In addition, the **orthoborate** has been prepared by a solid-state reaction (SSR):

$$3BeO + B_2O_3 + heat \Rightarrow Be_3(BO_3)_2$$

Its CAS number is 13701-63-8. Orthoborates have been used in the passivation of steel products but those containing Be have been shunned because of the potential toxicity.

In combination with other alkaline earths, beryllium forms a **pyroborate**, e.g. (Ca, Be)B_2O_5. Beryllium calcium diborate has the molecular weight of 150.7146 g/mol. It is monoclinic with: space group = $P2_1/n$; cell parameters of: $a = 5.167$ Å, $b = 3.756$ Å, $c = 17.161$ Å, $\beta = 98.12°$, $V = 329.7$ Å^3, $Z = 4$. The structure is formed from two intermingled networks—a CaO_9 polyhedral system and a Be complex constructed from 3- and 4-coordinate Be atoms. The extended coordinate complex results from a unique condensation of six-membered rings containing the triangular BO_3 and distorted tetrahedral BeO_4 groups. Although the formula would indicate a pyroborate group, i.e. 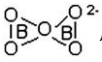 , a mixture of 3- and 4-coordinate boron atoms exists in a complex beryllium borate network. Crystals of (Ca,Be)B_2O_5 were grown from a melt of $Ca(BO_2)_2$ and BeO at 925 °C, as the melt was cooled slowly to 425 °C. The crystals were then washed in water to remove the excess flux. Similar compounds, such as (Sr,Be)B_2O_5 and (Ba,Be)B_2O_5 were also obtained. Part of the structure of the (Ca,Be)B_2O_5 is shown in Fig. 6.14.

Two layers are shown. These layers alternate to form the complete structure, as described above, to form the monoclinic structure where the cations exist in two differing, distorted, coordination states. This combination of $B_2O_5^{4-}$ with Sr and Ba to form mixed compounds has been studied for use as frequency-doubling crystals. Three new alkaline earth beryllium borates, built from unique two- and three-dimensional networks and frameworks, have been identified. $CaBeB_2O_5$ is constructed from a CaO_9 polyhedral network and a beryllium borate network.

The structure of $(Sr,Be)_3(BO_3)_2$ consists of layers of composition $(Be_2(BO_3))^{2-}$ interleaved by Sr atoms.

In $(BaBe)_2(BO_3)_2$, the structure is composed of a beryllium borate framework intermingled with a Ba-centered dodecahedral framework. While the work is not complete at this point in time, the barium beryllium borate is believed to be very useful as a frequency converter for YAG:Nd lasers to produce a collimated beam containing 155-nm photons used in the manufacturing of integrated circuits on silicon substrates.

Gaseous beryllium metaborate, $Be(BO_2)_2$, was identified mass spectrometrically in the vapor above the

beryllium–boron–oxygen system. A study of this system by differential thermal analysis (DTA) and Knudsen effusion using a vacuum balance and mass spectrometer, showed solid $Be_3B_2O_6$ to be the only condensed mixed oxide phase present with a melting point of 1495 ± 5 °C. The following thermodynamic values were obtained for the formation of gaseous beryllium metaborate from beryllium oxide and gaseous boron oxide:

$$BeO\ (solid) + B_2O_3\ (gas) = Be(BO_2)_2\ (gas);$$

$$\text{enthalpy, } \Delta H_f \text{ at } 1500\ ^\circ C = -22.5\ \text{kcal/mol};$$

$$\text{entropy, } S^0 \text{ at } 1500\ ^\circ C = 6.1\ \text{eu/mol}.$$

For the formation of solid $Be_3(BO_3)_2$ from the condensed oxides:

$$3BeO(solid) + B_2O_3\ (gas) \Rightarrow Be_3B_2O_6\ (gas);$$

$$\text{enthalpy } \Delta H_f = -23.5\ \text{kcal/mol};$$

$$\text{entropy, } S^0 = -13 = 2\ \text{eu/mol}.$$

The metal–anion bond strengths in the gaseous beryllium metaborates show the same relation to each other as the bond strengths in the corresponding chlorides, thus further confirming the pseudohalide character of the gaseous metaborates.

Only two beryllium borate minerals are known in which Be^{2+} is the major cation. They are:

Berborite (hydrated beryllium borate hydroxide fluoride),

Hambergite (beryllium borate hydroxide) $= (Be)_4B_4O_7(OH)_4$.

Beryllium perborate, $(BeOH)BO_3$, remains unknown. Presumably, it could be made by the reaction of:

$$Be(OH)_2\ (aq) + Na_4B_2O_8\ (aq) \Rightarrow (BeOH)_4B_2O_8\ (aq)$$

The solution is then evaporated to obtain crystals. The question of the hydrate(s) produced remains unknown. There is no record of anyone actually trying to prepare this compound.

Beryllium forms a beryllodiborate with sodium, $Na_2[BeB_2O_5]$. Single crystals of disodium beryllodiborate have been obtained by spontaneous nucleation from a high-temperature melt. $Na_2[BeB_2O_5]$ adopts a new structure type and contains $[BeB_2O_7]^{6-}$ rings as building units that are made up from one BeO_4 tetrahedron and two BO_3 triangles. These rings are further condensed and form $\{[BeB_2O_5]^{2-}\}_\infty$ two-dimensional layers extending parallel to the *ab* plane with the Na^+ cations in a $[6+1]$ coordination located between the layers. All atoms except Be and an O atom (both with site symmetry P.2) are in general positions.

The diborate, $Be_4B_2O_7$, has been said to have been prepared as a monohydrate by the reaction of the sodium salt in solution:

$$BeCl_2\ (aq) + Na_8B_2O_7\ (aq) \Rightarrow [Be(OH)]_8B_2O_7 \cdot H_2O + 6NaOH + 2NaCl$$

However, no specific data is available concerning this compound other than the statement that it had been prepared. In view of the fact that the **triborate**, $B_3O_7^{5-}$ and tetraborate, $B_4O_7^{2-}$ are known to be unstable, it is unlikely that this compound has ever been synthesized. The only known **tetraborate** of beryllium is the mineral "hambergite" which is described as a hydroxyborate. More likely, its actual formula is $(BeOH)_8B_4O_7 \cdot H_2O$.

A few beryllium borates are available commercially in small lots. The usage of these compounds in industry is nil to none. They have been of scientific interest only in Academia.

Magnesium Borates

Magnesium borate can be prepared by the SSR of boric oxide with MgO:

$$MgO + B_2O_3 \Rightarrow Mg(BO_2)_2$$

The metaborate is shown but the actual product obtained depends upon the molar ratio of the two components. If a solution method is used, then a hydrate results which is difficult to dehydrate by normal methods. The comparative effects of high-energy milling on solid-state thermal syntheses of different magnesium borate compounds from $MgO–B_2O_3$ and $MgO–B(OH)_3$ mixtures have been investigated using initial $MgO:B_2O_3$ mole ratios of 1:0.125, 1:0.25, 1:0.5, 1:1, 1:2 at temperatures between 500 and 900 °C. It was observed that magnesium oxide–boric acid mixtures react only by high-energy milling to form hydrous magnesium borates. Following high-energy milling of the initial solid mixtures, anhydrous magnesium borate compounds started to form at temperatures as low as 500 °C, and purer and more crystalline phases were obtained at higher temperatures compared to compositions that had not been milled.

Magnesium metaborate, $MgO \cdot B_2O_3{:}nH_2O$ was synthesized at 25 °C in solutions of the chlorides of sodium, potassium and magnesium in the presence of 3% boric acid and potassium hydroxide to a ratio $B_2O_3{:}K_2O{=}1$. The noncrystalline sediment which first precipitates is converted over the course of several weeks to crystalline magnesium metaborate, $Mg(BO_2)_2 \cdot nH_2O$, where *n* depends upon the temperature of the solution during this process.

Equilibrium in the system has been investigated for compositions from 0.6 to 75 wt% MgO. Three intermediate compounds were found. $MgO \cdot B_2O_3$ melts incongruently at 988 °C to form $2MgO \cdot B_2O_3$ and a liquid

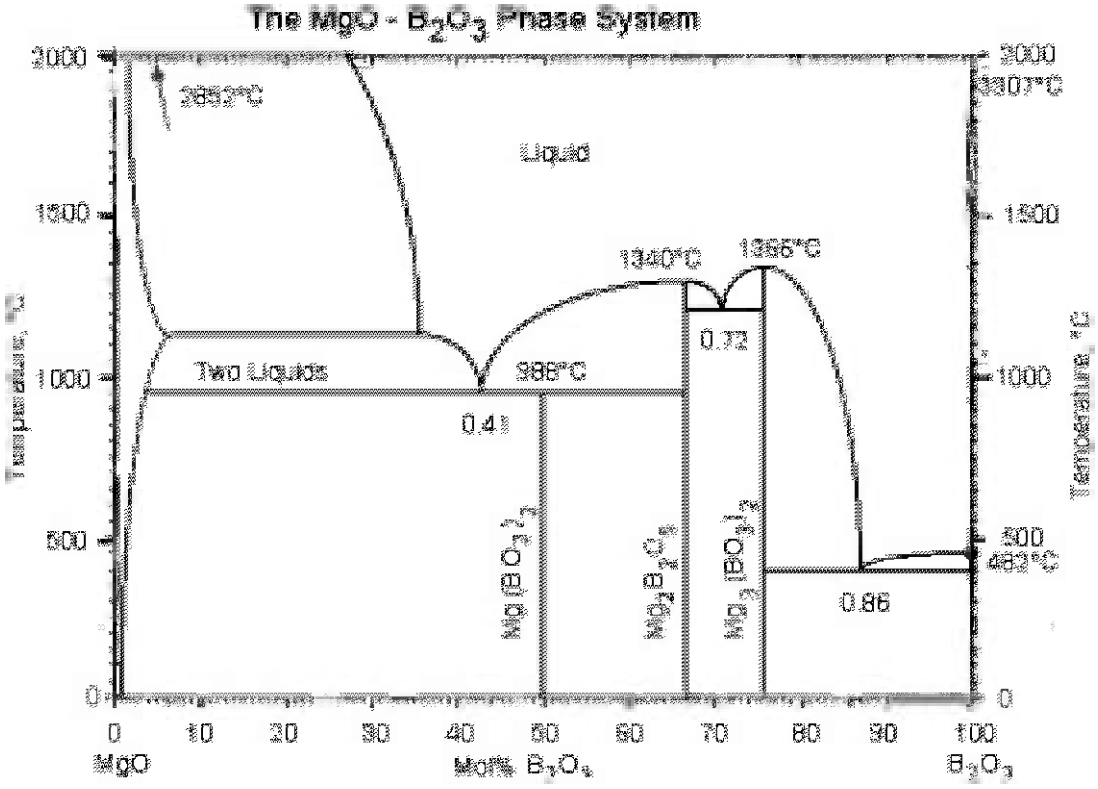

FIGURE 6.15

containing more than 99% B_2O_3. The other two compounds melt congruently: $2MgO \cdot B_2O_3$ at 1340 °C and $3MgO \cdot B_2O_3$ at 1366 °C. At 1142 °C, a region of liquid immiscibility extends from 0.6 to 36.0% MgO. The phase diagram is shown in Fig. 6.15.

Thus, at 1:1 molar ratio, a metaborate forms whereas at 3:1, an orthoborate is obtained. At a molar ratio of 2:1, the pyroborate forms. Thus, at 1:1 molar ratio, a metaborate forms whereas at 3:1, an orthoborate is obtained. At a molar ratio of 2:1, the pyroborate forms. The chemical properties of these three compounds differ from each other. The pyroborate anion, $B_2O_5^{4-}$, occurs in nature as the mineral "suanite" and has the formula, $Mg_2B_2O_5 \cdot xH_2O$.

If the metaborate is heated, single-crystalline magnesium borate nanowires of the form $Mg_2B_2O_5$ with typical diameter about 120–180 nm and length about 0.2 mm have been successfully synthesized by a new and simple method of heating the mixed tablet of $Mg(BO_2)_2$ and graphite directly in vacuum at 1200 °C for 1 h:

$$4Mg(BO_2)_2 + \text{heat (Vac)} \Rightarrow 2Mg_2B_2O_5 + 3O_2\ (\text{gas})$$

A number of magnesium borate minerals are known:

Hydroboracite, $CaMgB_6O_{11} \cdot 6H_2O$, is an uncommon borate mineral. It is one of the borate minerals that form silky, fibrous crystal clusters. Ulexite is another more common borate that forms similar fibrous aggregates and thus the two minerals are not easy to distinguish. Hydroboracite's silky luster is quite attractive.

"Ulexite" ($NaCaB_5O_6(OH)_6 \cdot 5(H_2O)$) (hydrated sodium calcium borate hydroxide) a.k.a. TV rock, is a mineral occurring in silky white rounded crystalline masses or in parallel fibers. The natural fibers of ulexite conduct light along their long axes, by internal reflection.

"Boracite" is a magnesium borate mineral with formula: $Mg_3B_7O_{13}Cl$. It occurs as blue green, colorless, gray, yellow to white crystals in the orthorhombic–pyramidal crystal system.

"Admontite" is a magnesium borate mineral with formula: $MgB_6O_{10} \cdot 7H_2O$. It is named after Admont, Austria. An alternate formula is $MgB_6O_7(OH)_6 \cdot 4H_2O$. Its crystal parameters are: space group: P21/c, $a = 12.68$ Å, $b = 10.07$ Å, $c = 11.32$ Å, $\beta = 109.68(10)$, $Z = 4$. It is generally found in gypsum deposits.

"Ludwigite" is a magnesium–iron borate mineral: Mg_2FeBO_5. Ludwigite typically occurs in magnesium–iron skarn and other metamorphic deposits. It occurs in association with magnetite, forsterite, clinohumite and the borates vonsenite and szaibelyite.

"**Warwickite"** is an iron magnesium titanium borate mineral with formula: $(Mg,Fe)_3Ti(O,BO_3)_2$ or $Mg(Ti,Fe^{3+},Al)(BO_3)O$. It occurs as brown to black prismatic orthorhombic crystals which are vitreous and transparent. It has a Mohs hardness of 3 to 4 and a density of 3.36 g/cc.

"**Teruggite"** is a mineral with the chemical formula of $Ca_4MgAs_2B_{12}O_{22}(OH)_{12}\cdot 12(H_2O)$. It is colorless. Its crystals are monoclinic prismatic. It is transparent. It is not radioactive. It has vitreous luster. Cell dimensions are: $a = 15.68$, $b = 19.9$, $c = 6.25$, $Z = 2$; $\beta = 100.083°$, $V = 1.920.08$, Den(Calc) $= 2.14$.

"**Chambersite**", a member of the borate mineral series that includes other minerals such as "ericacite", $Fe_3B_7O_{13}Cl$, and "boracite", $Mg_3B_7O_{13}Cl$. When chambersite was first discovered, it was the second chemical analog of boracite to be found in nature.

"**Admontite**" (hydrated magnesium borate) has the formula $MgB_6O_{10}\cdot 7H_2O$. Crystal data: monoclini, point group: 2/m; cell data: space group: P21/c, $a = 12.68$ Å, $b = 10.07$ Å, $c = 11.32$ Å, $\beta = 109.68°$, $Z = 4$.

"**Inderite**" or "kurnakovite" has the formula, $Mg_2B_6O_{11}\cdot 15H_2O$. It is monoclinic.

"**Macallisterite**", $2MgO\cdot 6B_2O_3\cdot 15H_2O$ [or $Mg_2(B_3O_5)_4\cdot 15H_2O$] is trigonal; the space group is R3c (nonpiezoelectric); hexagonal with $a = 11.546$ Å, $c = 35.562$ Å, c/a: 3.080; rhombohedral $a_{RH} = 13.600$ Å, $V = 4105$ Å^3, $Z = 6$.

Additional known minerals include:

Aksaite (hydrated magnesium borate hydroxide)
Boracite (magnesium borate chloride)
Fluoborite (magnesium borate fluoride hydroxide)
Halurgite (hydrated magnesium borate hydroxide)
Hungchaoite (hydrated magnesium borate hydroxide)
Kotoite (magnesium borate)
Inderite (hydrated magnesium borate hydroxide)
Mcallisterite (hydrated magnesium borate hydroxide)
Preobrazhenskite (magnesium borate hydroxide)
Pinnoite (hydrated magnesium borate)
Suanite (magnesium borate)
Wightmanite (hydrated magnesium borate oxide hydroxide)

If the metaborate, $Mg(BO_2)_2$, is dissolved in a solution of boric acid, a series of complex compounds, as hydrates, can be obtained. Conductivity and depression in freezing point of a series of solutions containing a fixed amount of boric acid and varying quantities of magnesium metaborate have been determined. The values obtained indicated the formation of three possible hydrated compounds:

$$MgO\cdot 4B_2O_3\cdot 9H_2O = MgB_4O_7\cdot 2B_2O_3\cdot 9H_2O$$

$$MgO\cdot 3B_2O_3\cdot 6H_2O = MgB_4O_7\cdot B_2O_3\cdot 6H_2O$$

$$2MgO\cdot 3B_2O_3\cdot 3H_2O = Mg_2B_2O_5\cdot 2B_2O_3\cdot 3H_2O$$

The first two are **tetraborates** and the last is a **pyroborate**. The results have been confirmed by quantitative estimation of magnesium and B_2O_3 in the precipitates obtained from solution. Thus, compounds corresponding to the above mentioned complexes have been formed in which a metaborate is transformed in solution to a tetraborate or pyroborate. In other words, the most stable compounds are the pyroborate and the tetraborate.

Magnesium borate of the **pyroborate** form, $Mg_2B_2O_5$, has been prepared and its structural and thermal properties were studied using XRD and DTA. An investigation of the electrical and optical properties of $Mg_2B_2O_5$ system has been carried out. The electrical resistivity of the sample was measured in the temperature range of 170–400 K. The data analysis revealed an extrinsic nature of the conductivity with two impurity levels located at 0.13 and 0.71 eV in the temperature ranges of 170–230 K and 240–400 K, respectively. The optical transmission and reflection were recorded at 300 K in the incident photon energy range of 3.0–6.0 eV. The absorption coefficient data analysis revealed an indirect optical energy band gap of 4.73 eV. In addition, two impurity levels located at 3.43 and 4.49 eV were observed in the absorption spectra.

Single-crystal triclinic $Mg_2B_2O_5$ and orthorhombic $Mg_3(BO_3)_2$ "nano-rods" were formed by a solvothermal method under supercritical conditions. Detailed microstructures of as-synthesized products were characterized by XRD, SEM, TEM, and X-ray photoelectron spectroscopy. It was found that the morphology and phase of the products were strongly dependent on the reaction conditions, such as the ratio of Mg/B, temperature, reaction time, and solvent media. The formation process of $Mg_2B_2O_5$ nano-rods was illustrated based on SEM observations of the different reaction stages. This technique may also have great potential in realizing other nanostructured materials. The following diagram shows the methods used to synthesize these "nano-rods" (Fig. 6.16).

In another method, magnesium borate "nano-belts" have been prepared by heating mixed powders of boron and MgO under flowing Ar/H_2O gases at 1100 °C. Typical widths with the nano-belts are in the range of 100–300 nm and lengths are up to tens of micrometers. XRD and selected area electron diffraction patterns show the nano-belts are of orthorhombic $Mg_3B_2O_6$ structure, having the **orthoborate** composition. Furthermore, high-resolution TEM identifies that the magnesium borate nano-belts are single crystal in nature.

A flux-assisted thermal conversion route to the pore-free high-crystallinity magnesium pyroborate ($Mg_2B_2O_5$) "nano-whiskers" with a length of 0.47–3.0 μm, diameter of 50–240 nm, and aspect ratio of 5/36 at a relatively low temperature of 650–700 °C (200–350 °C lower than that needed via the traditional method) was developed. Magnesium borate hydroxide [$MgBO_2(OH)$] nano-whiskers were first prepared by a coprecipitation–hydrothermal approach at 240 °C for 18 h by using $MgCl_2\cdot 6H_2O$, H_3BO_3 and NaOH (or

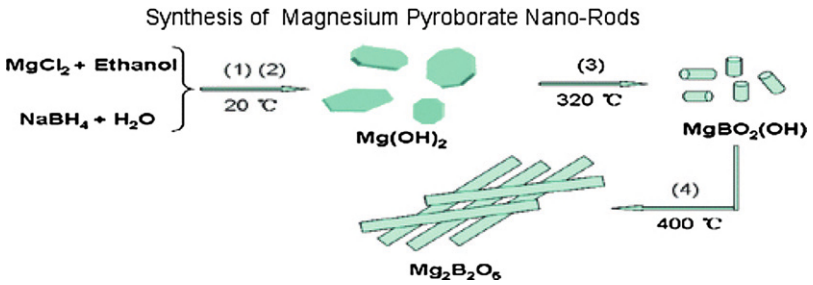

FIGURE 6.16

KOH) as the raw materials and the hydroxyborate was then calcined to produce $Mg_2B_2O_5$ nano-whiskers. The resultant NaCl (or KCl) in the coprecipitation served as the flux and played a key role in the thermal conversion of $MgBO_2(OH)$ nano-whiskers as the transport medium for the rearrangement of structural units of $Mg_2B_2O_5$, leading to the final formation of the pore-free $Mg_2B_2O_5$ nano-whiskers with uniform one-dimensional morphology, high-crystallinity, and twinned crystal structures.

It has been determined that a magnesium dibarium orthoborate, $MgBa_2(BO_3)_2$, is useful as an unconventional birefringent material with high transparency in the visible region and predicted that it is comparable to α-BBO in terms of the magnitude of birefringence. It usage as a frequency-doubling crystal for use with lasers is currently under investigation in that industry.

Magnesium pyroborate, $Mg_2B_2O_5$, when activated by trivalent dysprosium, has been studied as a phosphor for detection of radiation dosage. This thermoluminescent phosphor, $(Mg,V_{Mg}^{+})_2B_2O_5:Dy_{Mg}^{3+}$, has almost the same human-tissue equivalence and sensitivity to γ-rays but has the property of "fading" during usage as the vacancy defect is "repaired" in the lattice. If the tetraborate, MgB_4O_7, prepared from $Mg(NO_3)_2$ and ammonium tetraborate, $(NH_4)_2B_4O_7$, is activated by the addition of the Dy^{3+} ion, a phosphor, $(Mg,V_{Mg}^{+})B_4O_7:Dy_{Mg}^{3+}$, results that does not fade during multiple usages. The following figure shows the linear response obtained as a function of dosage (Fig. 6.17).

Magnesium perborate, $Mg(BO_3)_2$, can also be prepared by a solution method:

$$MgCl_2\ (aq) + Na_2BO_3\ (aq) \Rightarrow Mg(BO_3)_2 \cdot 7H_2O$$

The usual form is the heptahydrate and its CAS number is 17097-11-9. It is a bulky, white powder which gradually decomposes in air with loss of active oxygen. It is slightly soluble in water, with partial decomposition, so that it has been used in medicine as an oxidizing agent, antiseptic and antibacterial agent. It is soluble in dilute acids. The CAS number of the monohydrate is 14635-87-1. Its molecular weight is 141.9244 g/mol. Both of these salts are available commercially.

The perborates of magnesium were studied intensively in the early 1900s. There is little current work being accomplished on these salts. However, they are available in tonnage quantities worldwide. Their main usage has been in dental preparations and in laundry detergents as cleaning and bleaching agents.

Solid–liquid phase equilibria of the compound, $2MgO \cdot 2B_2O_3 \cdot MgCl_2 \cdot 14H_2O = Mg_2B_4O_7 \cdot 7H_2O$, when added to an aqueous 3.0% $H_3BO_3 + H_2O$ system have

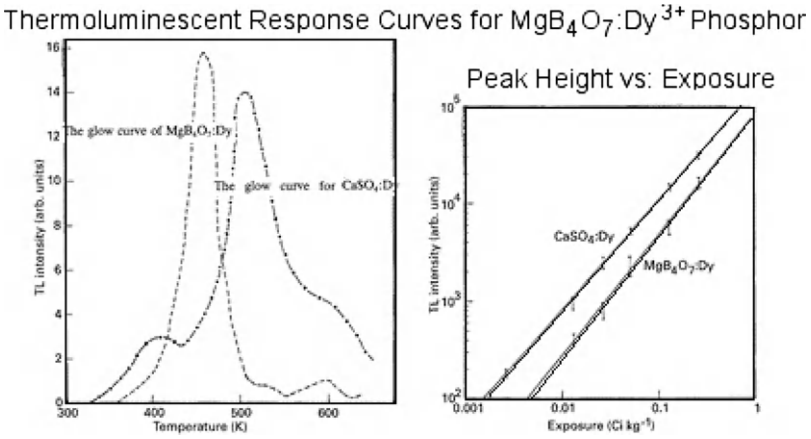

FIGURE 6.17

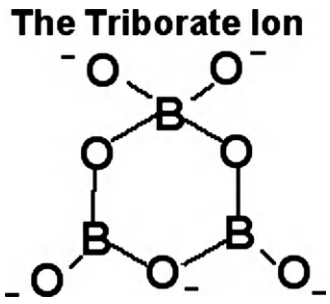

FIGURE 6.18

been studied at various temperatures of 0 to 200 °C. The solid phase equilibria identified by infrared spectra and X-ray powder diffraction were $MgB_4O_7 \cdot 9H_2O$ (a diborate) at 0 to 27 °C, $Mg_5(B_3O_7)_2 \cdot 15H_2O$ (a triborate) at 27 to 50 °C, $Mg_2B_6O_{11} \cdot 15H_2O$ (inderite) at 50 to 72 °C, $Mg(BO)_2 \cdot 3H_2O$ (a metaborate) at 72 to 98.5 °C, $Mg_2B_2O_5 \cdot 2H_2O$ (a pyroborate) at 98.5 to 190 °C, and $Mg_2B_2O_5 \cdot 1.5\ H_2O$ (a pyroborate) at 190 to 200 °C, respectively. The Lewis structure of the triborate ion is shown in Fig. 6.18.

The fundamental unit of these polyanionic structures is a trimeric ring containing both trigonal and tetrahedral boron atoms. The formation of the tetramer, pentamers, etc. and long-chain polyanions results from the fusion of two or more rings at the tetrahedral boron atoms, or from dehydration.

The structural mechanism of the thermal decomposition of "kaliborite", $HKMg_2B_{12}O_{16}(OH)_{10} \cdot 4H_2O$ has also been investigated. Kaliborite decomposition is an internal structural reconstitution process occurring in the whole volume of the crystal. The following stages of the process have been distinguished: (1) dehydroxylation; (2) dehydration; (3) recrystallization of the anhydrous amorphous substance and formation in succession of MgB_4O_7, $Mg_2B_2O_5$ and KB_5O_8. Dehydration precedes dehydroxylation and both of them consist of two independent stages: formation of free water molecules localized into the structural framework, and their release.

Magnesium borates are available commercially as several types of compounds.

Calcium Borates

Calcium forms all of the possible compounds based on "borates". This is based upon combination of CaO with B_2O_3. These two oxides are fired together at varying molecular ratios to obtain the various compounds. The phase diagram shows four separate compositions (Fig. 6.19).

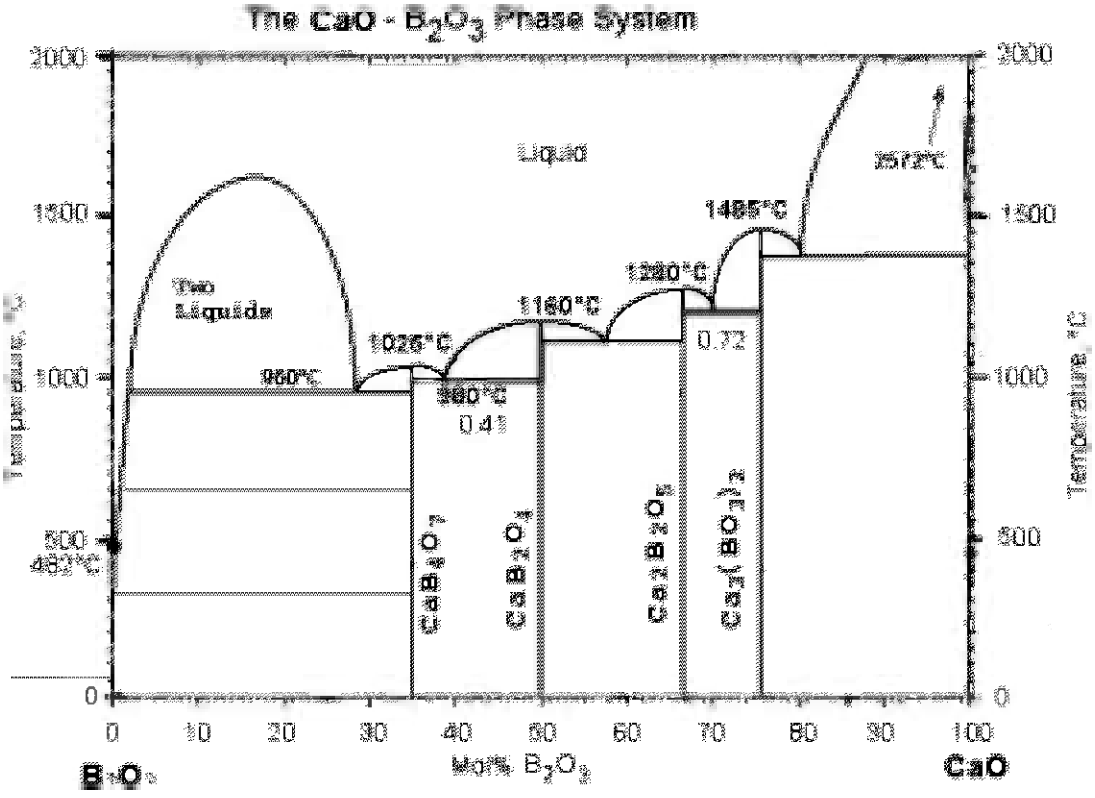

FIGURE 6.19

The tetraborate appears here in addition to the other compounds, meta-, pyro- and orthoborate that are also found in the Mg system. The melting points of these anhydrate compounds are given in the diagram. Additionally, a number of hydroxylated calcium borates have also been discovered. A great number of these occur as minerals throughout the world.

Calcium metaborate has the molecular formula of $Ca(BO_2)_2$ and the molecular weight of 125.7038 g/mol. It can be prepared by the aqueous reaction of sodium metaborate and a soluble calcium compound:

$$CaCl_2(aq) + Na_2BO_2\ (aq) \Rightarrow CaB_2O_4 \cdot xH_2O\ (aq)$$

where $x = 2$, 4 and 6. The solution is evaporated to obtain the salt. The most usual salt suppliers by manufacturers is $Ca(BO_2)_2 \cdot 2H_2O$ (whose CAS number is 13701-64-9). Some manufacturers supply the tetrahydrate, $CaB_2O_4 \cdot 4H_2O$ as white crystals. This hydrate, upon heating, loses two water molecules at 101 °C and lost two more water molecules at 120 °C. It changes from four water molecules at 300 °C when it is transformed into the dihydrate. In another method, a "fructoborate" complex is formed. The synthesis of calcium fructoborate was performed according to Miljkovic's procedure using boric acid, d-fructose, $CaCO_3$ and acetone. D-fructose was dissolved in distilled water at room temperature and boric acid was then added to this solution. Finally, calcium carbonate was added in small portions, under constant stirring. After the CO_2 evolution has ceased, 40 ml of acetone was added to the reaction mixture, whereupon a colorless oil was separated at the bottom of the reaction vessel. The two layers were separated and the lower oily layer, containing the crude boron complex was treated again with 40 ml of acetone. Upon standing for 1 h, crystallization was induced with a glass rod, and the oil slowly turned into a white crystalline solid. The product was filtered off, washed with small portions of acetone and air dried. Upon firing the product, $Ca(C_6H_{10}O_6BO)_2 \cdot 3.5H_2O$, a very pure $Ca(BO_2)_2$ product was obtained.

The anhydrate has the Lewis structure shown in Fig. 6.20.

Where a "double-bond" oxygen atom is present. The formula is sometimes written as: $Ca(BO_2)_2$. Its CAS number is 13701-64-9. This compound consists of infinite chains of $B_2O_4^{2-}$ ions held together by Ca^{2+} ions. Crystals of calcium metaborate are orthorhombic. The unit cell containing four molecules CaB_2O_4 was found to have the dimensions $a = 6.214$ Å, $b = 11.604$ Å, $c = 4.285$ Å. The space group is Pnca and the point group is V_h^{14}. The atoms are distributed among the available positions as:

$4Ca^{2+}$ on fold-axes: $\pm(1/4O_u)(1/4, 1/2, 1/2 + u)$

8 B. 8 O_1 and O_2: $\pm(x, y, z)(x, 1/2 - y, z + 1/2)(x + 1/2, 1/2 - y, 1.2 - z)(x + 1/2, y, z)$

In the lattice, each Ca^{2+} ion is surrounded by eight-oxygen atoms, two O_1 at 2.46 Å, two O_2 at 2.48 Å and two O_2 at 2.58 Å. Three oxygen atoms (two O_1 and one O_2) form an almost equilateral triangle around each boron atom. The B–O distances are: 1.35 Å, 1.35 Å and 1.38 Å. The edges of the oxygen triangle are 2.35 Å and 2.36 Å whereas each O_2 atom is linked to one boron and three calcium atoms. The following diagram shows one layer of the B_2O_4 chains which are linked three dimensionally (Fig. 6.21).

Each O_1 atom is linked to two boron atoms and one calcium atom, whereas each O_2 atom is linked to one boron and three calcium atoms. As all the BO_3 groups are oriented parallel to the *a*-face, strong negative birefringence has been found, the *a*-axis being the acute bisectrix. The observed perfect cleavage parallel to the *a*-face is accounted for by the structure; there is only one Ca–O bond per 12.5 A^2 crossing the *a*-face. The most interesting feature of the structure is the presence of endless strings of BO_3 groups parallel to the *c*-axis. The average composition of each string is BO_2.

Calcium metaborate has been evaluated as a wood preservative. Water-saturated wood specimens were first impregnated by a saturated borax solution and then diffuse-penetrated with Ca^{2+}, or Pb^{2+} solution. The precipitates of these metaborates in the wood proved to be insoluble or hardly soluble in water by a leaching test. A decay test was performed using a brown-rot fungus (*Fomitopsis palustris*) and a white-rot fungus (*Trametes versicolor*) and with the termite test using a virulent subterranean termite (*Coptotermes formosanus*). The metaborate-treated woods showed generally good decay and termite resistance with negligible mass loss of the specimens. Particularly, the lead metaborate formed in the wood provided superb biological resistance against decay and termite attacks.

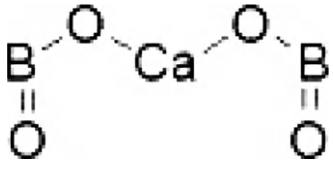

FIGURE 6.20

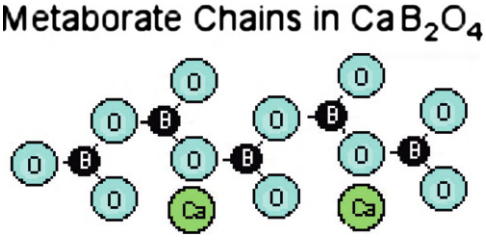

FIGURE 6.21

The tetrahydrate is soluble in water, acid and alkaline aqueous solutions. It is used in E-glass as a coating and is a new use for this industrial raw material. It is also used for antirust coatings, fire retardants, and in the fungicide and pharmaceutical industries.

Borate glasses present an absorption coefficient very close to that of human tissue. This fact makes some borate glasses ideal materials to develop medical and environmental dosimeters. Glass compositions with calcium tetraborate (CaB_4O_7) and calcium metaborate, such as the $(CaB_4O_7)_x \cdot (CaB_2O_4)_{100-x}$ system (0.6 to 100 wt%) were obtained by the traditional melting/quenching method. A phenomenon widely known as the "boron anomaly" was observed in thermal analysis measurements, as indicated by the increase of Tg (glass transition temperature) and the appearance of a maximum value in the composition with 40 wt% of CaB_2O_4. The Dy^{3+}-doped and Li co-doped 80 CaB_4O_7–20 CaB_2O_4 (wt%) glass samples were studied by the thermoluminescence technique. The addition of Dy improved the signal sensitivity in about three times with respect to the undoped glass sample. The addition of Li as a co-dopant in this glass caused a shift to a lower temperature of about 20 °C in the main glow peak.

Coatings of calcium metaborate have been found to protect iron against oxidation in the temperature range 750–1050 °C in oxygen. Protection is due to the compound iron boroferrite ($4FeO \cdot Fe_2O_3 \cdot B_2O_3$) that forms as a noncoherent, granular, blocking layer along the scale/metal interface, which effectively decreases the interfacial area for iron ion diffusion.

Calcium orthoborate, ($Ca_3(BO_3)_2$), also called Gerstley borate, is a bluish white crystal with a very defined structure. It can be prepared by reacting sodium borate in solution or by reacting Ca metal with boric acid. The resulting product is calcium orthoborate. A hydrate is obtained from the solution method.

Single crystals of $Ca_3(BO_3)_2$ have been obtained from the melt. The compound crystallizes in the rhombohedral system, space group R'3c, with six formula units in the hexagonal cell of dimensions $a = 8.6377$ Å and $c = 11\text{-}849$ Å. The BO_3 group appears as a nonplanar triangle with an O–B–O angle of 119.95° and a B–O distance of 1.3836 Å. The Ca^{2+} ions are surrounded by eight O-atoms, forming a distorted square antiprism. Analysis of calcium orthoborate, $Ca_3(BO_3)_2$, and recognize that the energy difference between oxygen nonbonding lone pair and B analysis on calcium orthoborate, $Ca_3(BO_3)_2$, and recognize that the energy difference between oxygen nonbonding lone pair and B–V_{Ca}–O–π bond states plays a crucial role in the origin of the large birefringence. With the aid of this mechanism, dibarium magnesium orthoborate, $Ba_2Mg(BO_3)_2$, has been proposed as an unconventional birefringent material with high transparency in the visible region and predicted that it will be comparable to α-BBO in terms of the magnitude of birefringence. O–π bond states play a crucial role in the origin of the large birefringence.

The luminescence properties of calcium orthoborate, $Ca_3(BO_3)_2$, doped with cerium (Ce^{3+}) were studied upon X-ray (~30 keV) and VUV (3.5–15 eV) synchrotron excitation. The emission bands peaked at 392 and 420 nm were attributed to interconfigurational transitions of Ce^{3+} ions. The short-wavelength emission band at 340 nm was said to be caused by radiative decay of exciton-like states. The fundamental absorption edge of $Ca_3(BO_3)_2$ was found to be near 7.1 eV. The introduction of a trivalent impurity into a divalent site causes formation of a positively charged vacancy, V^{+}_{Ca}. Based on thermoluminescence data and other information, the behavior of defects in the performance of $Ca_3(BO_3)_2$:Ce^{3+} as a thermoluminescent radiation detector was studied.

Calcium pyroborate has the molecular formula of $Ca_2B_2O_5$, it can be prepared by the reaction of:

$$2CaCl_2\ (\text{solid}) + 2H_2BO_3\ (\text{solid}) + \text{heat} \Rightarrow Ca_2B_2O_5 + 4HCl\ (\text{gas})$$

The structure consists of stacked double chains containing $Ca(1)O_7$ and $Ca(2)O_6$ polyhedra are linked to form a three-dimensional framework by B_2O_5 groups. The structure is shown in the following Fig. 6.22.

The structure in a unit cell contains four formula units or $[Ca_2B_2O_5]_4$. The structure contains Ca_4O_{19} tetramers which form double chains extending along the *a*-direction. The double chains are linked to form layers and the B_2O_5 groups bridge these adjacent chains and adjacent layers through O-atoms to form a three-dimensional network.

A hydrated calcium pyroborate has also been synthesized. A pure calcium borate, $Ca_2[B_2O_4(OH)_2] \cdot 0.5H_2O$, has been synthesized under hydrothermal condition and characterized by XRD, FT-IR and TG as well as by chemical analysis. The molar enthalpy of solution of $Ca_2[B_2O_4(OH)_2] \cdot 0.5H_2O$ in $HC1 \cdot 54.582H_2O$ was determined. From a combination of this result with measured

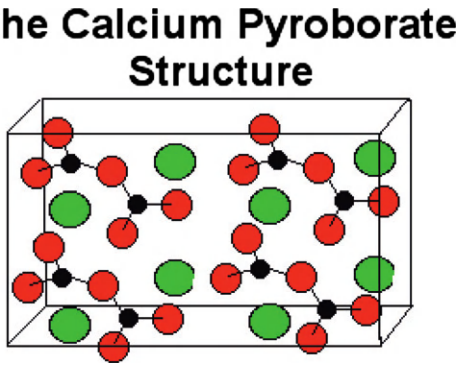

FIGURE 6.22

enthalpies of solution of H_3BO_3 in $HC1 \cdot 54.561H_2O$ and of CaO in $(HCl + H_3BO_3)$ solution, together with the standard molar enthalpies of formation of CaO(s), H_3BO_3(s) and H_2O(l), the standard molar enthalpy of formation of -3172.5 kJ/mol of $Ca_2[B_2O_4(OH)_2] \cdot 0.5H_2O$ was obtained. The thermal decomposition has revealed that it is a multistage internal process. The following stages have been distinguished: (1) a two-step release of interlayer water; (2) internal structure reconstruction; (3) dehydroxylation and amorphization of crystal structure; (4) recrystallization of amorphous solid and successive formation of CaB_2O_4 and then CaB_4O_7.

Microbiological fouling of plastic materials is an unwanted nuisance and a problem in many household and industrial environments. The humid and high-moisture environments where plastic materials are often used provide excellent growth environments for unwanted microorganisms such as mold, fungi, and mildew. In addition to degrading and fouling plastic materials, these microorganisms can cause unsightly stains and unpleasant odors. Calcium pyroborate has been employed in various plastic materials that contain a microbicidally effective amount of calcium pyroborate that protects plastic materials from microbiological attack. It is also used in fungicidal and corrosion inhibiting paint pigments.

Calcium perborate, CaB_2O_6, has the CAS number of 54630-47-6. Its Lewis formula is shown in Fig. 6.23.

It has been prepared by the reaction:

$$CaCl_2\ (aq) + Na_2B_4O_5 + H_2O_2 \Rightarrow Ca(BO_3)_2 \cdot 2H_2O + 2NaCl$$

This mixture was stirred, and the temperature was maintained at 20–25 °C. The solids were then filtered out, and the filter cake was reslurried with water and filtered again. Finally, the solids were dried overnight in a vacuum oven at 50 °C. The product thus obtained was a calcium perborate, $Ca(BO_3)_2$, containing the equivalent of 27.9% calcium oxide [CaO] and 10.0% active oxygen [O].

Calcium perborate has been used as an oxidizing and teeth-whitening agent in dentistry and in some applications in polyolefin polymer preparation.

Calcium triborate has been found to have the formulation of $CaB_3O_7(OH)_3$ and the Lewis structure of is shown in Fig. 6.24.

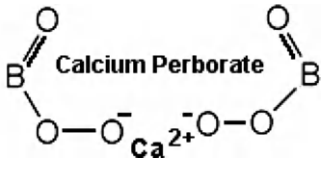

FIGURE 6.23

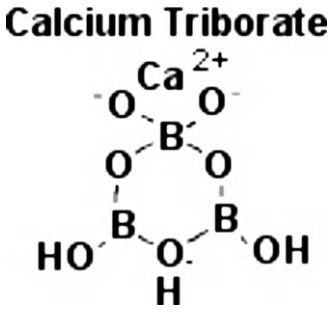

FIGURE 6.24

A monohydrate and a tetrahydrate are known.

Pentacalcium triborate fluoride has been studied in its relationship to fluoroapatite. $Ca_5F(BO_3)_3$ has the molecular weight of 395.8346 g/mol and is monoclinic with space group—Cm. Lattice parameters are: $a = 8.125$ Å, $b = 16.051$ Å, $c = 3.538$ Å, $\beta = 100.90°$, $V = 453.1$ Å^3, $Z = 2$.

Calcium tetraborate, CaB_4O_7, has the CAS number 27676-48-8. The monohydrate has the CAS number of 12007-56-6. Calcium tetraborate has been formed from the thermal decomposition of the mineral, "pandermite" $= Ca_2B_5O_8 \cdot 2H_2O$. Investigation has revealed that it is a multistage internal process, realized by gradual reconstitution of the mineral structure. The following stages have been distinguished: (1) a two-step release of interlayer water; (2) internal structure reconstruction; (3) dehydroxylation and amorphization of crystal structure; (4) recrystallization of amorphous solid and successive formation of CaB_2O_4 and then CaB_4O_7, the tetraborate. It has the monoclinic structure shown in Fig. 6.25.

Here, the calcium cations are in a face-centered position.

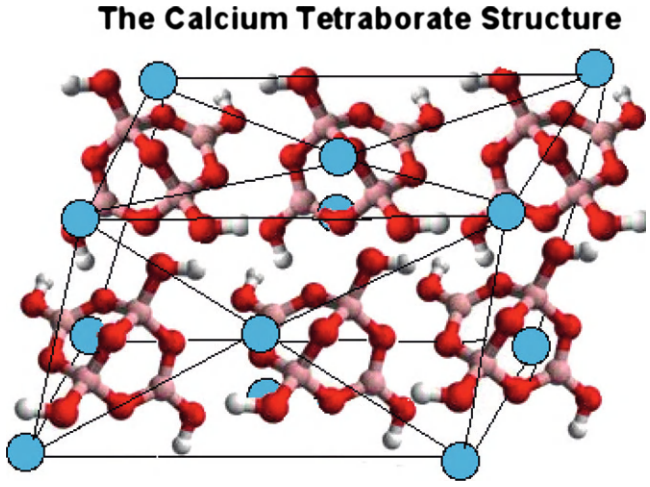

FIGURE 6.25

Thermal decomposition of "colemanite", Ca $[B_3O_4(OH)_3]H_2O$, monohydrate has been found to form calcium tetraborate when it is heated to high temperatures. The mode of decomposition was explored by thermal, X-ray, IR and optical microscopy methods at normal as well as at elevated temperatures. Investigation has revealed that thermal decomposition of colemanite occurs in the whole volume of the crystal and is divided into two independent stages: (1) formation of H_2O from OH groups and (2) breaking of H_2O and borate chains bonds and then removal of both kinds of water from the anhydrous phase of the preserved borate structure. Each process corresponds to a separate DTA peak, the second being accompanied also by loss of weight due to explosive water escape. This represents a rare event of dehydroxylation with distinct separation of H_2O formation and removal of water molecules from the parent substance.

The effect of mechanical treatment on the thermal decomposition of calcium borate, "colemanite"—$[CaB_3O_4(OH)_3]_2 \cdot H_2O$, a tetraborate, was studied by means of XRD, FTIR, SEM and thermal analysis methods. Grinding of colemanite causes the solid-state amorphization of this mineral, as a result of the destruction of its structure along the cleavage plane. The decrease in the particle size of the original material and the increase in its internal structural disorder affect the temperature and the magnitudes of the thermal effects accompanying the processes of dehydration and dehydroxylation. The diminishing values of the enthalpies of these processes may be a quantitative measure of the degree of amorphism of colemanite. This mineral is built of borate chains which are comprised of two tetrahedra and one triangle. Thermal decomposition proceeds within the temperature range of 300–370 °C by splitting off the hydroxy groups (−OH) to form water molecules at 320 °C. Next, the molecular water is removed at ca. 363 °C. This is accompanied by a gradual amorphism of the structure. "Pandermite", $Ca_2B_5O_8(OH)_3 \cdot 2H_2O$ belongs to the pentaborate group, which has a layered structure. The thermal decomposition of pandermite follows the same two-stage decomposition pattern. The first stage involves 3.5 mol of water at 438 °C, following by 0.5 mol of water at 438 °C. A rearrangement then takes place at 525 °C to form a tetraborate.

A pure calcium tetraborate, $Ca_2[B_2O_4(OH)_2] \cdot 0.5H_2O$, has been synthesized under hydrothermal conditions and characterized by XRD, FT-IR and TG as well as by chemical analysis. The molar enthalpy of solution of $Ca_2[B_2O_4(OH)_2] \cdot 0.5H_2O$ in $HC1 \cdot 54.582H_2O$ was determined. From a combination of this result with measured enthalpies of solution of H_3BO_3 in $HC1 \cdot 54.561H_2O$ and of CaO in $(HCl + H_3BO_3)$ solution, together with the standard molar enthalpies of formation of CaO(s), H_3BO_3(s) and H_2O(l), the standard molar enthalpy of formation of $Ca_2[B_2O_4(OH)_2] \cdot 0.5H_2O$ was obtained as −3,172.5 kJ/mol.

$(NH_4)_2Ca[H_4B_4O_9]_2 \cdot 8H_2O$ contains alternate layers of tetraborate anions and two of the water molecules. The structure is completed by the cations and the remaining water molecules. The space group and number of water molecules of hydration depend on the nature of the cation.

Calcium forms a number of borate minerals throughout the world. A hydrated form occurs naturally as the minerals:

"Ulexite" ($NaCaB_5O_6(OH)_6 \cdot 5H_2O$)
"Colemanite" ($CaB_3O_4(OH)_3 \cdot H_2O$)
"Nobleite" ($CaB_6O_9(OH)_2 \cdot 3H_2O$)
"Ginorite" [$Ca_2B_{14}O_{23} \cdot 8H_2O$]
"Fabianite" (CaB_3O_5OH)
"Calciborite" (CaB_2O_4)
and "priceite".

In addition, there are a large number of hydrolylated minerals containing calcium and borates. Some of these include:

Calciborite (calcium borate)
Chelkarite (hydrated calcium magnesium borate chloride)
Colemanite (hydrated calcium borate hydroxide)
Ekaterinite (hydrated calcium borate chloride hydroxide)
Fabianite (calcium borate hydroxide)
Frolovite (calcium hydroborate)
Ginorite (hydrated calcium borate)
Gowerite (hydrated calcium borate)
Hexahydroborite (hydrated calcium hydroborate)
Hilgardite (hydrated calcium borate chloride)
Hydroboracite (hydrated calcium magnesium borate hydroxide)
Hydrochlorborite (hydrated calcium borate chloride hydroxide)
Inderborite (hydrated calcium magnesium borate hydroxide)
Inyoite (hydrated calcium borate hydroxide)
Korzhinskite (hydrated calcium borate)
Kurnakovite (hydrated magnesium borate hydroxide)
Meyerhofferite (hydrated calcium borate hydroxide)
Nifontovite (hydrated calcium borate hydroxide)
Nobleite (hydrated calcium borate hydroxide)
Olshanskyite (calcium hydroborate)
Pentahydroborite (hydrated calcium hydroborate)
Priceite (calcium borate hydroxide)
Pringleite (hydrated calcium borate hydroxide chloride)
Probertite (hydrated sodium calcium borate hydroxide)

Ruitenbergite (hydrated calcium borate hydroxide chloride)
Shabynite (hydrated magnesium borate chloride hydroxide)
Sibirskite (calcium borate hydroxide)
Solongoite (calcium borate hydroxide chloride)
Takedaite (calcium borate)
Tertschite (hydrated calcium borate)
Tyretskite (hydrated calcium borate hydroxide)
Uralborite (calcium borate hydroxide)
Vimsite (calcium borate hydroxide)
Wardsmithite (hydrated calcium magnesium borate)
Vimsite—CaB_2O_2OH
Sibirskite—$Ca_2[(OH)(B_2O_4)(OH)]$
Parasibirskite—$Ca_2[B_2O_5]\cdot H_2O$
Fabianite—CaB_3O_5OH
Uralborite—$Ca_2[B_3O_3(OH)_5\cdot OB(OH)_3]$
Olshanskyite—$Ca_3\{(OH)(B[OH]_4])_2\}_2$
Frolovite—$Ca[B(OH)_4]_2$

Ulexite contains chains of sodium, water and hydroxide octahedrons linked in endless chains. The chains are linked together by calcium, water, hydroxide and oxygen polyhedra and massive boron units. The basic boron unit has a formula of $B_5O_6(OH)_6$ and a charge of -3. It is composed of three borate tetrahedrons and two borate triangular groups. The crystal system is triclinic and space group $\bar{1}$.

Colemanite, like other borates, is a complex mineral, that is found in playa lakes and other evaporite deposits. The basic structure of colemanite contains endless chains of interlocking $BO_2(OH)$ triangles and $BO_3(OH)$ tetrahedrons with the calcium ions, water molecules and extra hydroxides interspersed between the chains. The crystal system is monoclinic; 2/m.

Nobleite is monoclinic; space group is $P2_1/a$; lattice parameters are: $a = 14.56$ Å, $b = 8.01$ Å, $c = 9.83$ Å, $\beta = 111.75°$, $V = 1064.81$ Å^3 (calculated from unit cell) density = 2.095 g/cc.

Ginorite is monoclinic with $a = 13.37$ Å, $b = 14.36$ Å, $c = 12.26$ Å, $V = 2309.01$ Å^3, $\beta = 101.2°$.

Calcioborite is orthorhombic with $a = 8.38$ Å, $b = 13.82$ Å, $c = 5$ Å and $V = 579.06$ Å^3.

Takedaite has been proven to be a natural analog of synthetic $Ca_3B_2O_6$. The diffraction photographs showed takedaite to be trigonal with the possible space group of R3c or R3c. The unit-cell dimensions were $a = 8.638$ Å and $c = 11.850$ Å. Optically, the mineral was uniaxial negative with refractive indices omega = 1.726, $E = 1.630$, and the Vickers microhardness was 478 kg/mm^2.

Johachidolite, $CaAl[B_3O_7]$, (Cmma, $a = 9.767(2)$, $b = 11.723(3)$, $c = 4.3718(5)$ Å, $V = 408.3(1)$ Å^3, $Z = 4$) has been refined from a light-green gem-quality crystal from the Mogok gem-mining district in Myanmar. A fragment from the same gem was measured by electron microprobe and laser ablation inductively coupled plasma mass spectrometry, and is almost end-member composition with ca. 0.3 wt% ThO_2 and ca. 1000 ppm La^{3+} probably replacing Ca. Johachidolite has a very dense structure with all cations in maximum oxygen coordination. Boron is tetrahedrally coordinated and the tetrahedra form four- and six-membered rings that link to give a sheet, the only borate layer structure among minerals with only BO_4 tetrahedra. The interlayer space is filled by octahedrally coordinated Al and 10-coordinated Ca. Johachidolite, forming in boron-rich skarn or pegmatite, has never been synthesized. Other ternary compounds, synthesized from corresponding glass compositions, $CaAlBO_4$ and $CaAl_2B_2O_7$, are unknown as minerals and have B (three-coordinate), Al (tetrahedral), and Ca (octahedral) in their lowest known oxygen coordination. Johachidolite displays the structural characteristics of a mineral with high-pressure stability and has the triborate anion. $B_3O_7^{5-}$, as part of its structure.

Dirubidium calcium tetraborate octahydrate, $Rb_2Ca[B_4O_5(OH)_4]_2\cdot 8H_2O$, was prepared by reaction of Rb-borate aqueous solution with $CaCl_2$ and it's structure has been determined by single-crystal XRD data. It crystallizes in the orthorhombic system, space group $P2_12_12^1$ with unit-cell parameters, $a = 11.536$ Å, $b = 12.639$ Å, $c = 16.690$ Å; $Z = 4$, $V = 2433.5(8)$ Å^3. The structure contains alternate layers of $[B_4O_5(OH)_4]^{2-}$ polyanions separated by water molecules and Rb, Ca cations. The isolated $[B_4O_5(OH)_4]^{2-}$ is constructed from two $BO_3(OH)$ tetrahedron groups and two $BO_2(OH)$ triangular groups joined at common oxygen atoms. The two $BO_3(OH)$ tetrahedron groups are further linked by means of an oxygen bridge across the ring. The Ca^{2+} ion displays a coordination of seven, while the two nonequivalent Rb^+ ions display nine and seven coordination, respectively. Infrared and Raman (4000–400/cm) spectra of $Rb_2Ca[B_4O_5(OH)_4]_2\cdot 8H_2O$ were recorded at room temperature and analyzed. Fundamental vibration modes were identified and band assignments were made. The dehydration of this hydrated-mixed borate occurs in one step and leads to an amorphous phase which undergoes a crystallization at higher temperatures.

Calcium borates are available commercially in various sized lots. Most of the borates in the world are supplied by Rio Tinto Borax from the southern United States. The company was established by Francis Marion Smith in 1883 which was then known as The Harmony Borax Works. In 1872, Mr Smith found borates in the Nevada desert. Death Valley in California is famous for borate mining. The Atacama desert in Chile also contains mineable borate concentrations. Calcium borate's various forms are used as wood preservatives.

Strontium Borates

A number of various strontium borates are known. In general, alkaline earth metal borates exhibit framework structures made up of BO_4 tetrahedra and BO_3 triangles. Only a few compounds show isolated islands, and layered structural features and chain arrangements are generally absent. The structures of strontium and barium borates have been addressed in the past. Among the few strontium borates known are SrB_2O_4, the metaborate consisting of slightly puckered anionic layers with the composition $(B_2O_4)_n^{2n-}$, the tetraborate, SrB_4O_7, with a three-dimensional network structure, the pyroborate, $Sr_2B_2O_5$, composed of SrO_7 and SrO_6 polyhedra and isolated B_2O_5 groups, and the hexaborate, $Sr_3B_6O_9(OH)_6$, with infinite chains of composition $n[B_6O_9(OH)_6]^{6-}$.

Strontium metaborate can be synthesized by firing the oxides at 600 °C:

$$SrO + B_2O_3 + \text{heat} \Rightarrow Sr(BO_2)_2$$

The product has been assigned the CAS number of 13703-84-9. Its molecular weight is 173.2396 g/mol. Single crystals of strontium metaborate, SrB_2O_4, have been grown from the melt by the Czochralski method and a detailed structure analysis was carried out. The Sr atom is coordinated in a dodecahedral fashion by eight O atoms from the neighboring infinite planes consisting of borate molecules so that all O atoms in the borate molecules participate in the coordination with SrO distances ranging from 2.522 (7) to 2.728 (5) Å. It is orthorhombic with all boron atoms triangularly coordinated and the strontium atoms surrounded by eight oxygen polyhedra. The BO_3 groups lie in an infinite series of layers as shown in the following diagram shown on the next page. Here, the Sr atoms are dodecahedrally coordinated by eight O atoms from neighboring planes of borate molecules so that all of the O atoms in the BO_3 groups participate in the coordination (Fig. 6.26).

Sr–O distances range from 2.522 to 2.728 Å. Each B atom in the infinite chains is surrounded by three O atoms whose bond lengths vary from 1.328 to 1.395 Å. The BO_3 groups have an almost planar structure with B–O–B angles of 115.8 to 126.9°. The mean value is 120.0°. The BO_3 groups have almost a perfectly planar structure. The dihedral angle between planes is 161.1° so that the layers are slightly puckered. Thus, the strontium metaborate structure may be described as consisting of slightly puckered layers of $(B_2O_4)_n^{n2-}$ groups and Sr^{2+} atoms coordinated by eight neighboring O atoms from the $(B_2O_4)_n^{n2-}$ layers. The shortest Sr–Sr (x, $1-y$, $1.2+z$) distance is 3.8864 Å. The calcium homologue has the same structure except for distances.

This structure can be modified by application of pressure and temperature. SrB_2O_4 (III) and SrB_2O_4 (IV) are two high-pressure phases. The polycrystalline phase III was prepared at 15 kbar and 600 °C. It is orthorhombic with $a = 12.426$ Å, $b = 6.418$ Å and $c = 11.412$ Å, $d = 3.77$ g/cc, $Z = 12$ and has a symmetry of $Pna2_1$. It is isostructural with CaB_2O_4. The IV-phase, formed at 20 kbar and 600 °C, is cubic with $a = 8.222$ Å, $Z = 12$, $d = 4.38$ g/cc, and has the symmetry of Pa3. It, too, is isostructural with the Ca homologue. Further application of pressure causes decomposition to the tetraborate:

$$2\,SrB_2O_4 + \text{Pressure (600 °C)} \Rightarrow SrB_4O_7 + SrO$$

Both the III and IV-analogues could be reconverted to the low-pressure starting material by annealing them overnight at 750 °C in air. Crystals of the III-analog are birefringent whereas those of the IV-modification are isotropic.

The Raman spectra of these crystals, built solely of metaborate triangles, provide fingerprint identification of three distinct network types. Classified according to increasing cation field strength these are: rings with degenerate intra-annular bonds and D_3h symmetry, distorted rings with alternating intra-annular bonds and C_3h symmetry, as well as chains. The occurrence of

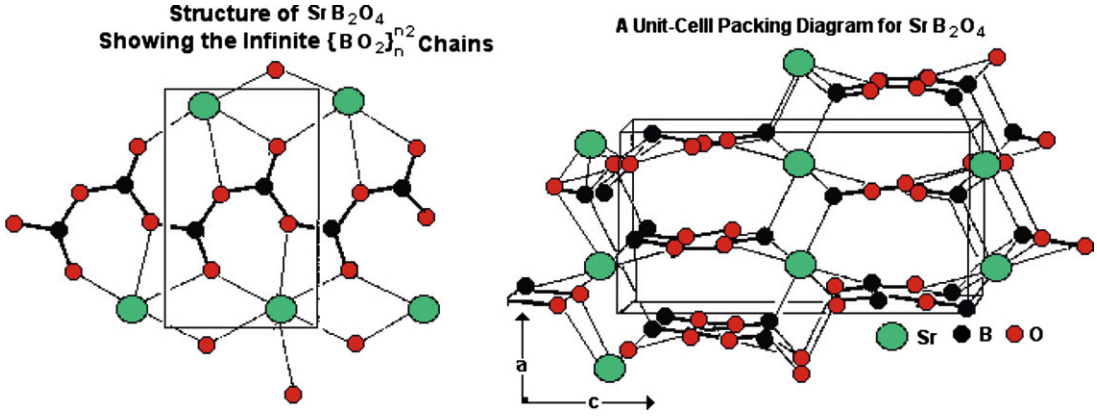

FIGURE 6.26

each network type has been associated with a characteristic range of cationic field strength. This approach led to the discovery of a hitherto unknown C_3h ring strontium metaborate crystal, with Sr^{2+} cations in 9- or 10-fold coordination to oxygen atoms. The Raman spectra of the mixed cation metaborates like $Ba_2Ca(B_2O_4)_3$ and $Ba_2Mg(B_2O_4)_3$ confirm their C_3h ring structure and clearly point to the fact that the synergetic effect of dissimilar cations to the metaborate network cannot be predicted by the additivity of their field strengths.

In another study, single crystals of strontium metaborate, SrB_2O_4, were obtained and their electrical and optical properties were studied. The wide optical transparency range of SrB_2O_4 extends from 100 to 3250 nm. The result of dielectric and thermal measurements confirms that no structural phase transition is exhibited in the temperature range from 50 to 1200 K (−223 to 927 °C). The dielectric dispersion above 600 K (327 °C) and a pronounced dielectric anomaly at 1136 K (863 °C), analyzed, using an equivalent circuit model, are a result of a low-frequency dielectric relaxation observed that gives rise to super ionic conduction at high temperature and by the space charge incurred by the softening, respectively.

Knudsen effusion mass spectrometry has been used to study the vaporization behavior of SrB_2O_4 (s or l) in the temperature range 1310 to 1442 K. Vapors of Sr(g), $SrBO_2$(g), BO(g), B_2O_2(g), and B_2O_3(g) have been identified. On the basis of their partial pressures, the molar enthalpies of formation and dissociation for $SrBO_2$(g) have been determined to be: $\Delta_f H_m$ ($SrBO_2$, gas, 298 K) = −(636 ± 19) kJ/mol and $\Delta_f H^0_m$ (Sr, gas, 298 K) + $\Delta_f H^o_m$ (BO_2, gas, 298 K) − $\Delta_f H^0_m$ ($SrBO_2$, gas, K) = (516 ± 17) kJ/mol, respectively. The molar enthalpies of formation for SrB_2O_4(s) formed from elements and from constituent oxides were found to be: $\Delta_f H^0_m$ ($SrBO_2$, s, 298.15 K) = −(2017 ± 29) kJ/mol and $\Delta_f H^0_m$ (SrB_2O_4, s, 298 K) − $\Delta_f H^0_m$ (SrO, s, 298 K) − $\Delta_f H^0_m$ (B_2O_3, s, 298 K) = −(153 ± 29) kJ/mol, respectively.

Two hydrated strontium borates, $SrB_2O_4 \cdot 4H_2O$ and $SrB_6O_{10} \cdot 5H_2O$, were synthesized by a liquid–phase precipitation method, and pure phase strontium tetraborate (SrB_4O_7) was obtained by high-temperature calcination. The phase compositions, morphology and the high-temperature sintering process of products were characterized by XRD, SEM, TG-DTA and chemical composition analysis. The effects of calcining temperature and holding time were investigated. The results showed that a process of dehydration, amorphization and crystallization exists in the calcination of these hydrated strontium metaborates. SrB_6O_{10} was unstable at 800 °C, and decomposed into SrB_4O_7 and liquid boric trioxide. Pure strontium tetraborate was obtained with $SrB_2O_4 \cdot 4H_2O$ and $SrB_6O_{10} \cdot 5H_2O$ compounds as raw materials, which were calcined for 4 h. With the increasing of reaction time, the degree of crystallization was improved at 900 °C, while the crystal structures were essentially unaffected.

Strontium orthoborate crystallizes in the rhombohedral system with two formula units in a cell of dimensions, $a = 6.695$ Å and $\alpha_R = 85.00°$ for $Sr_3B_2O_6$. The equivalent hexagonal lattice parameters are $a_H = 9.046$, $c_H = 12.566$ Å. In another study, the crystal parameters were determined as follows. The Rietveld refinement method was used to determine the structure of the compound $Sr_3(BO_3)_2$ and found it to be calcium orthoborate structure. The cell parameters are determined to be $a = b = 9.0405$ Å, $c = 12.5665$ Å, and Sr, B, and O occupy the 18e, 12c, 36f positions, respectively. It represents a new orthoborate structure type built of complex layers formed by BO_3 triangles sharing corners with Ga_2O_7 tetrahedral dimers and GaO_4OH square pyramids. The Sr atoms occupy both interlayer and intralayer sites (Fig. 6.27).

If a mixed crystal of Ba^{2+} and Sr^{2+} orthoborates is grown, the composition then varies from the normal orthoborate composition. Single crystals of strontium barium orthoborate, $(Sr_{1.36}Ba_{1.64})_3(B_3O_6)_2$, were grown by a high-temperature solution growth technique, and a detailed structure analysis was carried out. The orthoborate $(B_3O_6)^{3-}$ anion planar groups in this compound form infinite layers parallel to (001) plane, and Sr and Ba atoms are alternatively placed between the layers

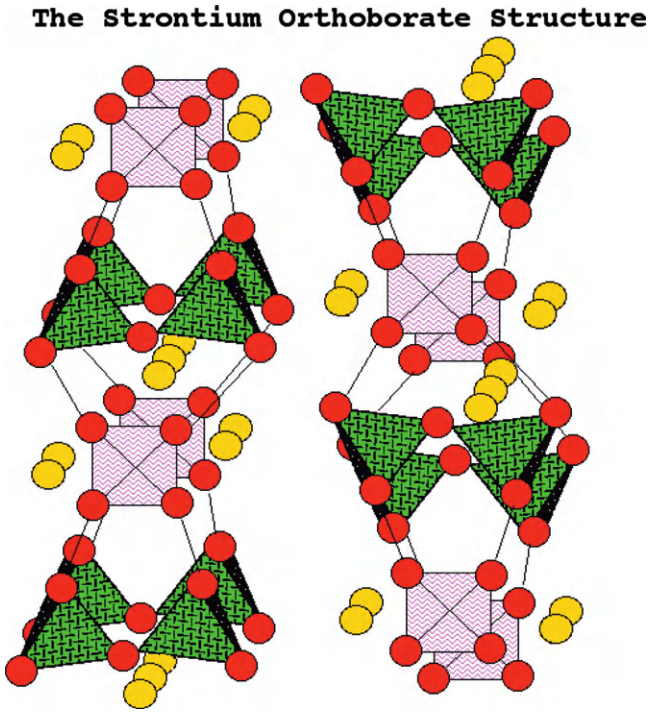

FIGURE 6.27

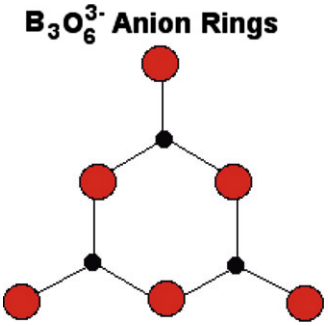

FIGURE 6.28

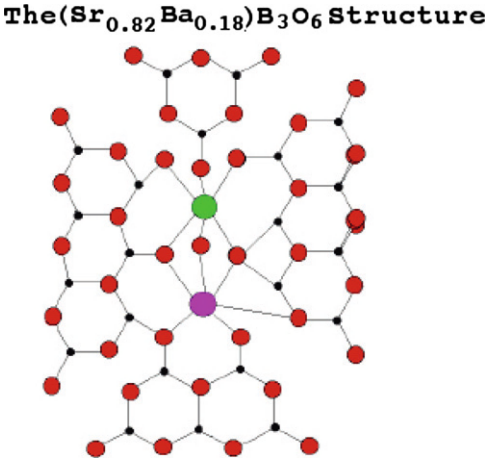

FIGURE 6.29

and are octahedrally coordinated by six O(2) atoms in the neighboring anion rings. This is shown in Fig. 6.28.

If a mixed crystal of Ba^{2+} and Sr^{2+} orthoborates is grown, the composition then varies from the normal orthoborate composition. Single crystals of strontium barium orthoborate, $(Sr_{1.36}Ba_{1.64})_3(B_3O_6)_2$, were grown by a high-temperature solution growth technique, and a detailed structure analysis was carried out. The orthoborate $(B_3O_6)^{3-}$ anion planar groups in this compound form infinite layers parallel to (001) plane, and Sr and Ba atoms are alternatively placed between the layers and are octahedrally coordinated by six O(2) atoms in the neighboring anion rings (Fig. 6.29).

In this structure, a metaborate molecule, $(B_3O_6)^{3-}$ anion ring, is completed by three BO_2 groups related by threefold rotation symmetry along the *c*-axis perpendicularly passing through the center of the molecular plane. The ring plane is planar within 0.078 Å with O_1-B = 1.410 Å, O_1-B_{ix} = 1.397 Å, and O_2-B = 1.306 Å showing double-bond character, whose geometry is very similar to that of $Sr_xBa_{3-x}(B_3O_6)_2$. The strontium atom is octahedrally coordinated by two O atoms in the anion groups with a $Sr\cdots O_2 = 2.5100$ Å, and the barium atom is also octahedrally coordinated by the same two O atoms but with two different coordination bond lengths $Ba\cdots O_2 = 2.7964$ Å and $Ba\cdots O_{2vi} = 2.738$ Å so that the two O atoms are participating in three coordinations with $Sr\cdots O_2\cdots Ba = 90.39°$, $Sr\cdots O_2\cdots Ba_{viii} = 131.05°$, $Ba\cdots O_2\cdots Ba_{viii} = 103°$. The sixfold coordination bond lengths of SrO_2 and $Ba\cdots O_2$ are very close to the respective 2.5801 Å and 2.76 Å bond lengths shown in international tables for X-Ray Crystallography (Vol III, Section 7). Therefore, the three-dimensional infinite molecular network is formed by the O_2 atom in the $(B_3O_6)^{3-}$ anion ring which plays a bridging role among Sr, Ba atoms, and the metaborate molecule.

Nonlinear optical crystals that enable to generate third and fourth harmonic generation of 1.064-mm wavelength of an Nd: YAG laser have become very important in providing UV light sources for the fabrication of very large scale integrated circuits by lithographic technique. For this purpose, much effort has been paid to develop borate crystals because the borates that are composed of BO_3 or BO_4 units are not only highly transparent in the UV spectral region, but also possess relatively large second-order nonlinear optical coefficients. A metaborate crystal containing $(B_3O_6)^{3-}$ anion-rings is one of such borates and is expected to show large second- and third-order nonlinear optical effects because of high nonlinearity of $(B_3O_6)^{3-}$ rings.

The physical and X-ray data of the $(Sr,Ba)_3(B_2O_3)_2$ compound as a crystal are given in the following Table 6.3.

Strontium pyroborate, $Sr_2B_2O_5$, has been synthesized by a high-temperature solution reaction. Crystals were grown from a mixture containing appropriate amounts of $SrCO_3$ and H_3BO_3, using KFB_4 as a flux. The mixture was thoroughly milled, heated in a platinum crucible in air to 1193 K (920 °C), and kept at that temperature for 15 h. The temperature was quickly quenched to 1053 K (880 °C) and slowly cooled from 1053 to 973 K (700 °C) at a rate of 0.011 K/h and then air quenched to room temperature. Colorless crystals were obtained.

Strontium pyroborate crystallizes in the monoclinic space group $P21/c$ with cell dimensions $a = 7.719$ Å, $b = 5.341$ Å, $c = 11.873$ Å, $\beta = 92.71°$, $V = 488.9$ Å^3, and $Z = 4$, $D_{calc} = 3.76$ g/cm^3. The structure comprises SrO_7 and SrO_6 polyhedra and B_2O_5 groups, as shown in the following Fig. 6.30.

The structure is based on Sr_4O_{19} tetramers and is composed of two $Sr(1)O_7$ and two $Sr(2)O_6$ polyhedra. These two polyhedra link by four shared O–O edges to form a double-chain extending along the *a*-direction. The double-chains link together to form sheets parallel to the *ac* plane by sharing O(4) atoms. These sheets stack along the *b*-direction to form the three-dimensional

TABLE 6.3

Color/shape = colorless/black	Empirical formula = $Ba_{0.82}Sr_{0.68}B_3O_6$
Formula weight = 300.54 g/mol	Temperature = 293 K
Wavelength = 0.71069 Å	Crystal system = Trigonal
Index ranges $-10 \leq h \leq 8$, $0 \leq k \leq 10$, $0 \leq l \leq 51$.	Unit-cell dimensions $a = 7.1584$ Å, $b = 7.1584$ Å, $c = 36.995$ Å, $\beta = 90°$, $\gamma = 120°$, volume = 1641.8 $Å^3$, $Z = 12$, calc. density = 3.648 g/cc, space group R3c
Absorption coefficient = 12.506 mm^{-1}	F(000) = 1617
Crystal size 0.429°—0.33°—0.231 mm	q range for data collection = 3.30 to 29.96°
Completeness to 100.0%: q = 29.96	Extinction coefficient = 0.00402
Maximum and minimum transmission = 0.1392 and 0.0466	Absorption correction Empirical (j-scan)

framework by sharing O(1), O(2), and O(3) atoms. The $[B_2O_5]$ group bridges the adjacent double chains and adjacent sheets together. A similar structure to this compound is $Mg_2B_2O_5$. It is built from the Mg_4O_{18} tetramer sharing three edges and connected by the B atom to form chains extending along [010]. However, the tetramer itself is discrete and forms an infinite chain only by B atoms.

The electronic structure of $Sr_2B_2O_5$ has been calculated by the ZINDO/S (Zerner's Intermediate Neglect of Differential Overlap) method for this compound, and the dynamic refractive indices have been obtained in terms of INDO/SCI following combination with the sum-over-states method. The calculated energy gap is 4.26 eV between the upper valence band and lower conduction band, and the calculated average refractive index is 1.791 at a wavelength of 1.065 lm. The charge transfers from O^{2-} anion orbitals to Sr^{2+} cation orbitals make the significant contributions to linear polarizability in terms of analyses of atomic state density contributing to the valence and conduction bands.

Strontium perborate can be made by the reaction of sodium perborate on strontium chloride in solution:

$$SrCl_2\ (aq) + Na_2BO_3\ (aq) \Rightarrow Sr(BO_3)_2 \cdot 2H_2O + 2NaCl$$

It has the probable Lewis structure shown in Fig. 6.31.

However, in view of its Mg and Ca homologues and its higher costs, little interest in this compound has been shown by industry. Hence, little effort by academia has been forthcoming. Thus, the physical and chemical properties of strontium perborate have not been thoroughly explored. The above formula shows boron having a double-bonded oxygen atom and a linear structure. It is clear that the BO_3^- anion is not an orthoborate, BO_3^{3-}, since the B atom would have to be in a +5 state. Nor is it a BO_3^- triangular species since two of the oxygen atoms are available as oxidizing agents. Perhaps it has a cyclic or linear structure shown in Fig. 6.32.

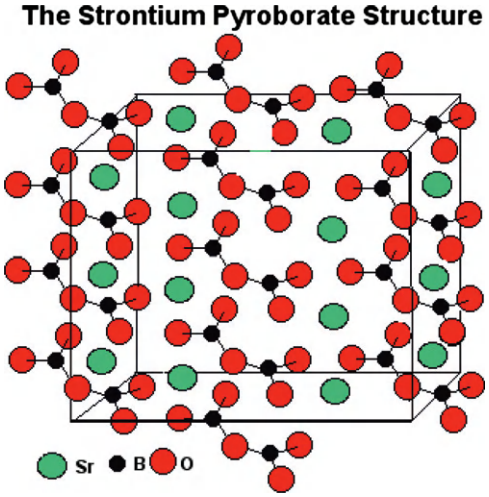

FIGURE 6.30

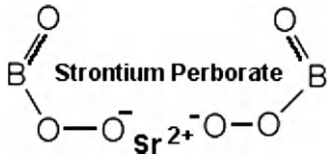

FIGURE 6.31

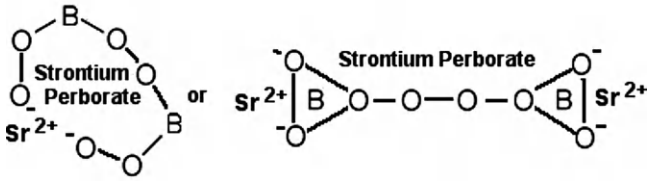

FIGURE 6.32

The actual formula would be $(SrBO_4)_2$, but this has not been firmly established.

Strontium tetraborate, SrB_4O_7, (SBO) has been investigated as a potential nonlinear optical material with excellent mechanical and optical properties such as a high power second harmonic generation (SHG) coefficient, high optical damage threshold, high hardness, etc. Additionally, the SBO crystals possess high UV transmittance at wavelengths down to about 130 nm. SrB_4O_7 congruently melts at 994 °C. The structure appears as a series of tetrahedrons (Fig. 6.33).

The structure consists of a three-dimensional borate network with channels parallel to the *a*- and *b*-axis with Sr ions located in these channels. All the boron atoms are tetrahedrally coordinated and all the tetrahedra are connected to each other by sharing corners. Four independent O atoms can be divided into two groups: O(1), O(2) and O(3) are linked to two B atoms with shorter O–B bonds (1.416–1.458 Å), while O(4) is linked to three B-atoms with longer O–B bonds (1.536–1.560 Å). The Sr atom is surrounded by nine oxygen atoms to form a capped cube-coordination environment (see Fig. 6.33). Although there are six-membered B–O rings in the borate network parallel to the *b*-axis, the rings do not belong to the "conjugated group" type. SBO crystals were not found to be hygroscopic.

SrB_4O_7 occurs in two polymorphs. The α-phase, $SrO{\cdot}2B_2O_3$ crystallizes below 1000 °C from a melt of the same composition. The orthorhombic crystals belong to the space group $Pmn2_1$ and have unit-cell dimensions $a = 10.711$ Å, $b = 4.427$ Å, $c = 4.235$ Å. The calculated density with two formula units in the cell is 4.02 g/cc. The asymmetric unit of β-SrB_4O_7, contains five Sr atoms (three located on a threefold rotation axis), 12 B and 21 O atoms. The structure is made up from BO_3 triangles and BO_4 tetrahedra in a 1:1 ratio. Pairs of BO_3 triangles are linked to BO_4 tetrahedra via common corners, forming chains. These chains are further linked to adjacent chains through corner sharing, leading to a three-dimensional framework with channels running parallel to [001]. The Sr^{2+} ions reside in the channels and exhibit strongly distorted polyhedra. The density of the β-polymorph is considerably lower than that of α-SrB_4O_7, which is constructed solely from BO_4 tetrahedra β-SrB_4O_7 has the molecular weight of 242.86 g/mol, it is trigonal with space group = P3, $a = 17.145$ Å, $c = 4.2527$ Å, $V = 1082.61$ Å^3, $Z = 9$. Strontium tetraborate is transparent across the far UV to far infra-red spectrum (Fig. 6.34).

Thus, it has great potential for use as lens components in optical devices such as those used for the fabrication of very large scale integrated circuits by a lithographic technique.

The luminescence properties of Ce^{3+} ions in strontium hexaborate $Sr(B_3O_5)_2$, excited in the 3.5- to 18-eV (68–365 nm) region, has been studied. At least two types of luminescent Ce^{3+} centers are observed in solid solutions of composition $Sr_{1-x}Ce_xB_6O_{10}$ ($x < 0.01$). One of them is formed by direct replacement of strontium ions without local charge compensation, and the second center is an associate of a Ce^{3+} cerium ion and a strontium vacancy, V_{Sr}^{+}. It is shown that the dominant charge-compensation mechanism on the cation sublattice includes the formation of one strontium vacancy for each two Ce^{3+} ions introduced into the lattice.

Strontium tetraborate compounds have been prepared by pouring slowly a concentrated solution of $Sr(NO_3)_2$ in water into another concentrated solution in water of $Na_2B_4O_7{\cdot}10H_2O$. The reaction brings about white flakes which precipitate. After vacuum filtration, the material has been dried in an oven at 100 °C for 12 h and afterward baked at 900 °C for 20 h. XRD experiments indicates that the final product is crystalline strontium tetraborate.

A number of phosphors based upon the matrix, SrB_4O_7, have been investigated. Strontium tetraborate when activated by Eu^{2+}, is used as a phosphor in "black-light" lamps for tanning salons. Its emission band is very narrow (~20 nm) as shown in the following Fig. 6.35.

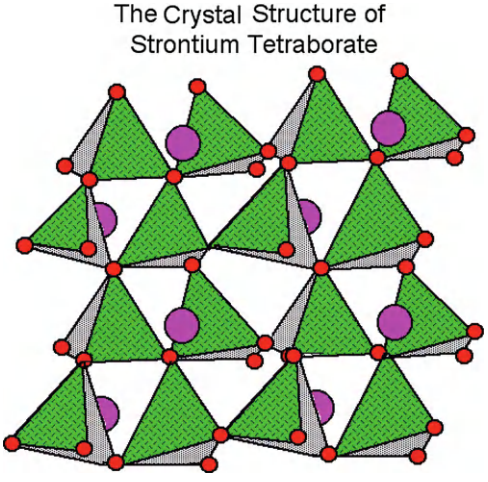

FIGURE 6.33

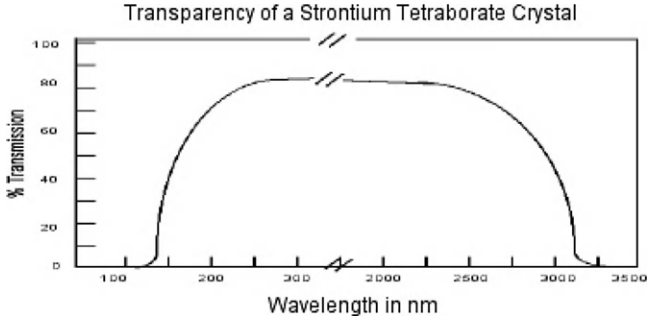

FIGURE 6.34

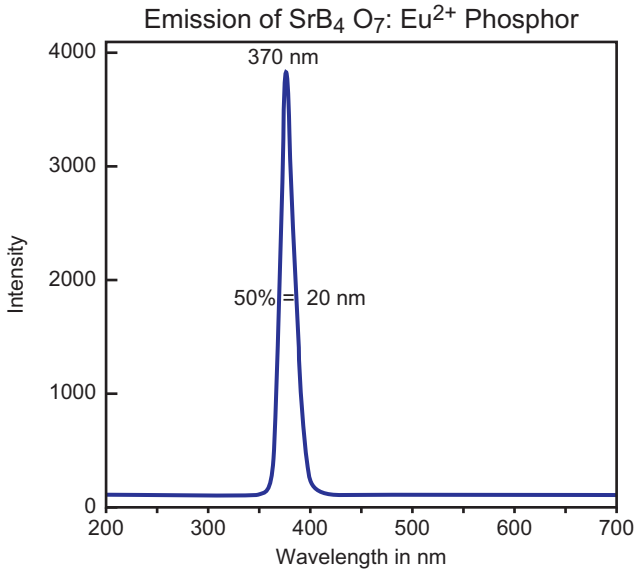

FIGURE 6.35

The luminescence properties of Eu(II) borates and Eu^{2+}-activated Sr borates have been studied, e.g. $Sr_{1-x}Eu_xB_2O_4$, $Sr_{1-x}Eu_xB_4O_7$ and $Sr_{1-x}Eu_xB_6O_{10}$. It was found that $Sr_{1-x}Eu_xB_4O_7$ consisting of a three-dimensional network of BO_4 tetrahedra gave a remarkably stronger emission than the other compounds consisting of BO_3^{3-} ions, $B_2O_5^{4-}$ ions, $(BO_2)\infty$ chains or a $(B_3O_5)\infty$ network. This was understood by considering their crystallographic properties and with help of the Dexter theory. The band emissions of the high-pressure phases of EuB_2O_4 and $SrB_2O_4Eu^{2+}$ are assigned to $(4f)^7$-$(4f)^6(5d)$ transitions of the Eu^{2+} ions.

The phosphor typically used for a near 368- to 371-nm UV emission peak is either europium-doped strontium fluoroborate ($SrB_4O_7F:Eu^{2+}$) or europium-doped strontium tetraborate ($SrB_4O_7:Eu^{2+}$) while the phosphor used to produce a peak at around 350–353 nm is lead-activated barium disilicate ($BaSi_2O_5:Pb^+$), sometimes called "Blacklight Blue" lamps that peak at 365 nm.

Bi^{2+}-doped SrB_4O_7 and SrB_6O_{10} for use as orange and red phosphors in white light-emitting diodes has been studied. In both compounds, absorption due to $^2P_{1/2}$–>$^2S_{1/2}$ in Bi^{2+} could be observed and quantified. The emission redshift from SrB_4O_7 to SrB_6O_{10} and their different phonon satellite spectra are attributed to the enhancement of phonon–electron interaction. Investigation of the reduction mechanism of Bi^{3+} to Bi^{2+} suggests that in oxidizing atmosphere, Bi^{2+} can only be stabilized on Sr^{2+} sites only in such lattices that are dominated by tetrahedrally coordinated boron.

A number of strontium borate minerals are known. Most of these are hydroxylated and/or hydrated.

Strontioborite (strontium borate hydroxide)
Strontioginorite (hydrated strontium calcium borate)
Sussexite (magnesium borate hydroxide)
Szaibelyite (magnesium borate hydroxide)
Tunellite (hydrated strontium borate hydroxide)
Veatchite (hydrated strontium borate hydroxide)

Tunellite, $(SrB_6O_9(OH)_2\cdot 3H_2O)$, is monoclinic with lattice parameters: space group = $P2_11a$; $a = 14.415(3)$ Å, $b = 8.213(1)$ Å, $c = 9.951(2)$ Å, $\beta = 114.05°$, $V = 1075.83$ Å^3. The crystal structure contains infinite sheets composed of polymerized borate polyanions, with Sr^{2+} cations and water molecules filling available spaces in and near the sheets. Each Sr^{2+} is coordinated by 10 oxygen atoms at an average distance of 2.74 Å. Adjacent sheets are held together solely by bonds to water molecules. The polymerized borate polyanions are composed of individual borate groups, each group containing three B–O tetrahedra and three B–O triangles. These polyhedra link at corners so that one oxygen is shared by all three tetrahedra, and three six-membered B–O rings result, each made up of two tetrahedra and one triangle. This compound has the same structure as that of the Ba analog (shown below).

Strontioborite has the empirical formula of $(SrB_8O_{11}(OH))_4$.

Strontioginorite has the empirical formula of $([Sr,Ca]B_{14}O_{23}\cdot 8H_2O)$.

Veatchite is an unusual strontium borate, with the chemical formula $Sr_2B_{11}O_{16}(OH)_5\cdot H_2O$. There are two known polymorphs, Veatchite-A and Veatchite-p. Veatchite was discovered in 1938, at the Sterling Borax mine in Tick Canyon, in California. Veatchite is named to honor John Veatch the first person to detect boron in the mineral waters of California.

A new compound, $Sr_4B_{14}O_{25}$ $(4SrO\cdot 7B_2O_3)$, corresponding to an oxide ratio of 4: 7 has been identified and synthesized in the $SrO–B_2O_3$ system. The crystal structure of the compound has been determined (space group $Cmc21$, $a = 7.734(5)$ Å, $b = 16.332(5)$ Å, $c = 14.556(5)$ Å, $Z = 4$). The borate anions form a three-dimensional framework consisting of borate groups of two types: three-ring structures (3B,6O) and BO_3 triangles (Fig. 6.36).

Layers formed by 14-membered rings composed of boron-oxygen tetrahedra and triangles packed within the layer according to the herringbone pattern can be distinguished in the framework. The strontium atoms

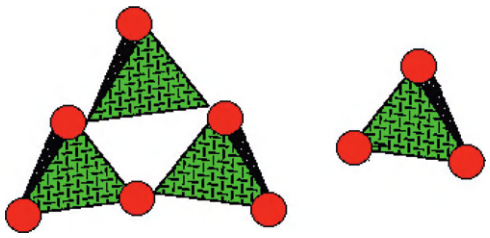

FIGURE 6.36

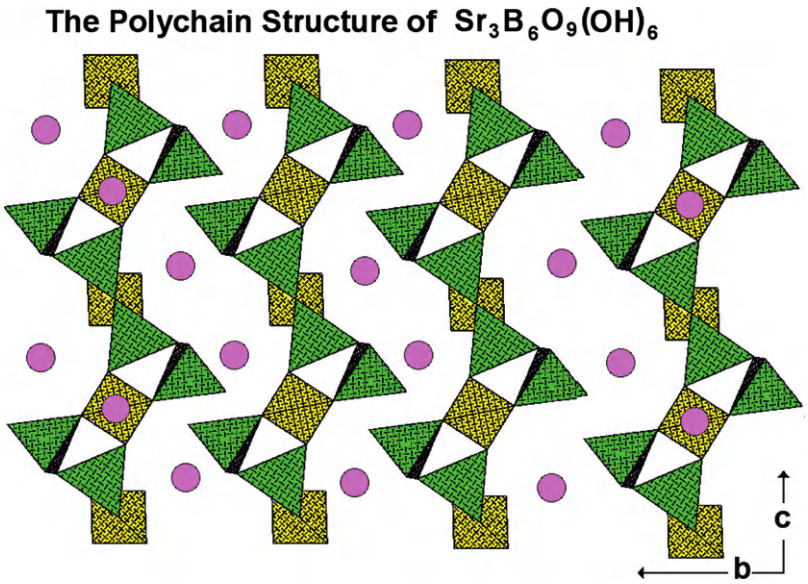

FIGURE 6.37

are located on the mirror symmetry planes between these layers. The compound is metastable and decomposes, on long-term storage, into strontium diborate and metaborate.

The compound, $(SrBe)_2B_2O_5$, (SBBO) has been reported to be transparent below 200 nm, and exhibits a large SHG coefficient. Significant difficulties in the flux growth of large, high-quality crystals have prevented this material from further development. Recently, large crystals of SBBO have been grown by a hydrothermal synthetic method for the first time, and their physical properties have been characterized. SBBO remains the best material found to date for this purpose.

Strontium also forms a number of hydrated borates. Among these is $Sr_3B_6O_9(OH)_6$, which is a polychain (Fig. 6.37).

This structure and composition has no analogues among the other alkaline earths except that of Ba which is identical. It is not a hydrate but is hydoxylated. The BO_3 triangles are actually $[BO_2(OH)]$ groups.

The following shows the arrangement of the individual borate anions $[BO_2(OH)]_2$ in $SrBO_2(OH)$ groups (Fig. 6.38).

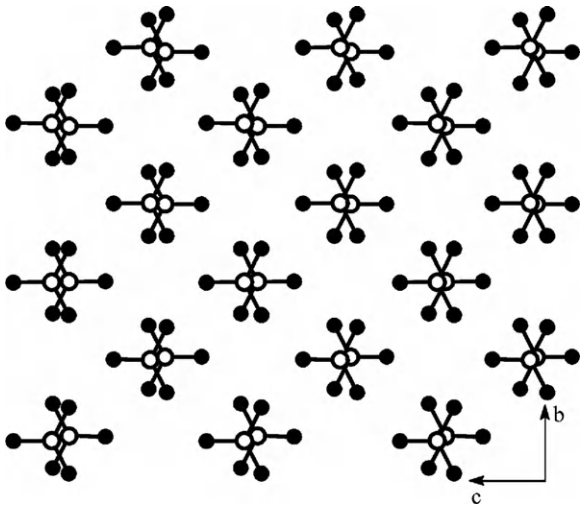

FIGURE 6.38

The open circles are boron atoms, the solid ones are oxygen atoms. Hydrogen atoms are not shown. The eightfold-coordinated Sr atom presents regular Sr–O bond distances between 2.557 and 2.862 Å (mean, 2.645 Å). Comparable values have been encountered in other Sr oxide structures. The B triangles are connected by common edges or corners to SrO_8 polyhedra. Each Sr shares only one edge of its coordination polyhedron with a neighboring BO_3 triangle, while all other O atoms of this particular SrO_8 polyhedron are corner shared with other BO_3 units. The structure of compound 2 contains anionic infinite chains extending along the *a*-direction, with a composition of $[B_6O_9(OH)_6]^{n6-}$ built up from nonplanar six-membered B_3O_3 rings, which are found to join together by sharing B atoms (Fig. 6.4). In each B_3O_3 ring, all the three B atoms are bonded to four oxygen atoms. The B–O bond distances range from 1.444(4) to 1.523(5) Å (average, 1.479 Å), comparable with the normal average tetrahedral B–O distance observed in the literature.

The crystallization of strontium borate glasses containing 16.7–43.0 mol% SrO was investigated. New crystalline compounds of the hypothetical compositions $2SrO{\cdot}3B_2O_3$ (metastable) and $SrO{\cdot}5B_2O_3$ (stable below

750 °C), as well as the metastable diborate modification β-$SrO \cdot 2B_2O_3$, were discovered, and their X-ray powder diffraction data are obtained. It was demonstrated that, with a deficit of strontium oxide, the $4SrO \cdot 7B_2O_3$ compound forms solid solutions. Strontium triborate $SrO \cdot 3B_2O_3$, which was previously prepared only through the dehydration of crystal hydrates, was produced by crystallizing certain glasses. The thermal stability of this compound was studied. The influence of the ease of dispersion on the stability of different crystalline phases was discussed. Variants of the phase diagram for the $SrO \cdot B_2O_3$ system in the case of monolithic and dispersed samples were proposed from analyzing the experimental results and data available in the literature.

Various strontium borates are available commercially from a number of suppliers worldwide.

Barium Borates

In general, alkaline earth metal borates exhibit framework structures made up of BO_4 tetrahedra and BO_3 triangles. Only a few compounds show isolated islands, and layered structural features and chain arrangements are usually absent. Previously reported barium borates include:

BaB_2O_4 containing isolated borate anions $(B_3O_6)^{3-}$
BaB_4O_7 and BaB_8O_{13}, with a framework structure
$Ba[B(OH)_4]2H_2O$
$Ba[B(OH)_4]_2$ containing discrete tetrahedral $B(OH)_4$ groups,
$Ba_2[B_5O_8(OH)_2](OH)$,
sheet structures of $Ba[B_5O_8(OH)](OH) \cdot H_2O$
$Ba_5[B_{20}O_{33}(OH)_4] \cdot H_2O$
Barium borate $Ba_3(B_6O_9)(OH)_6$, containing polyborate chains.

If BaO and B_2O_3 are heated together at various mol-ratios, four compounds are obtained. The phase diagram is shown in Fig. 6.39.

One compound is described as BaB_8O_{13} but appears to be a ditetraborate, $Ba(B_4O_7)_2$.

Barium metaborate, also called barium diborate, barium boron oxide, or (as an optical crystal) BBO (BaB_2O_4 or $Ba(BO_2)_2$) is available as a hydrate or dehydrated. Its molecular weight is 222.9526 g/mol and its density is 3.85 g/cc. Its melting point is 1051 °C and it is soluble in water. Barium diborate is a biocide registered in USA since 1960 as a broad-spectrum bactericide and fungicide. It is added to paints, coatings, adhesives, plastics, and paper and paper products. Barium metaborate can be prepared by reaction of an aqueous solution of boric acid with $Ba(OH)_2$. The prepared γ-BBO contains water of crystallization that cannot be completely removed by drying at 120 °C. Dehydrated γ-BBO can be prepared by heating to 300–400 °C. Further heating at about

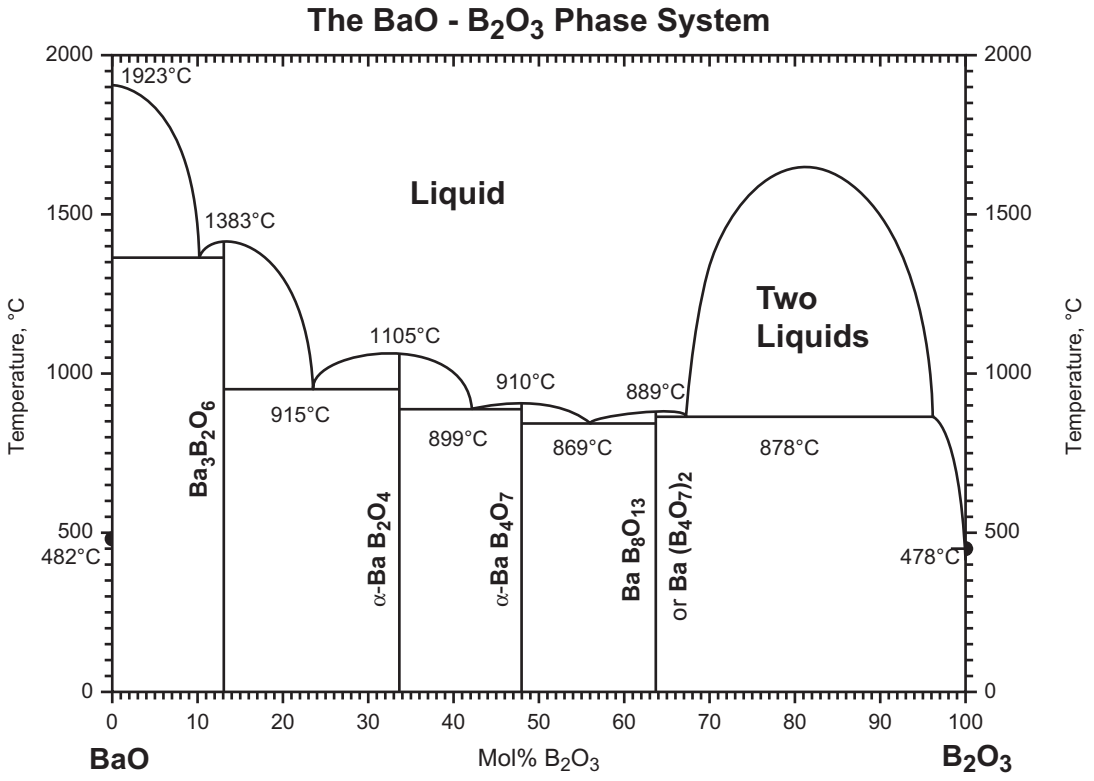

FIGURE 6.39

600–800 °C causes complete conversion to β-BBO. BBO prepared by this method does not contain trace amounts of BaB_2O_2. β-BBO is a nonlinear optical material which is used as a crystal to double the frequency of many lasers.

Barium metaborate can also be prepared by a soluble barium compound and sodium metaborate. Barium borate monohydrate is prepared at 20 °C from the solution of $BaCl_2$ and $Na_2B_2O_4$. The solution is evaporated to obtain crystals. It is a white powder. It is used as an additive to paints as a flame retardant, mold inhibitor and corrosion inhibitor. It is also used as a white pigment. The solubility of barium borate is a disadvantage when used as a pigment. Silica-coated powders are available. The alkaline properties and the anodic passivity properties of the borate ion enhance the anticorrosion performance. Commonly available barium metaborate pigment comes in three grades; Grade I is a barium metaborate itself, grade II is compounded with 27% zinc oxide, and grade III is compounded with 18% of zinc oxide and 29% calcium sulfate. Barium borate shows synergistic performance with zinc borate as a pigment.

Alpha barium metaborate, α-BaB_2O_4, the high-temperature phase, is an optical material with high birefringence and very wide optical transmission window from about 189 to 3500 nm. It has good mechanical properties and is a suitable material for high-power UV polarization optics. It has, in many cases, replaced calcite, TiO_2, $LiNbO_3$ in Glan–Taylor prisms, beam splitters and other similar optical elements. It is not hygroscopic and its MOHs hardness is 4.5. Its damage threshold is high at 1 GW/cm^2 at 1064 nm and 500 MW/cm^2 at 355 nm. Its density is 3.85 g/cm^3.

The low-temperature form of BaB_2O_4 crystallizes in the trigonal crystal system, space group R3c, with six formula units in the cell of dimensions $a = 8.380(4)$ Å and $\alpha = 96.65(4)^\circ$ (hexagonal cell: $a = 12.519$ Å, $c = 12.723$ Å). The structure is closely related to the high-temperature form, α-BaB_2O_4, containing nearly planar $[B_3O_6]^{3-}$ anions. Different is the coordination of the barium atom. In this case, it is surrounded by eight oxygen atoms in an irregular polyhedron.

Barium metaborate dihydrate can be prepared from the solution of $BaCl_2$ and $Na_2B_2O_4$ at 90–95 °C. After cooling to room temperature, a white powder is precipitated. Barium metaborate dihydrate loses water at above 140 °C. It is used as a flame retardant for paints, textiles, and paper.

Vapor formation in the BaO–B_2O_3 system was studied by high-temperature mass spectrometry. The equilibrium reactions with participation of gaseous barium metaborates were determined. The standard enthalpies of formation of gaseous BaB_2O_4(gas) and $BaBO_2$(gas) of -1424 ± 28 and 598 ± 15 kJ/mol, respectively, were evaluated.

Thin films of BBO can be prepared by MOCVD (Metal oxide-chemical vapor deposition) from barium(II) hydro-tri(1-pyrazolyl)borate. Different phases can be obtained depending on deposition temperatures. Thin films of β-barium metaborate can be prepared by a sol–gel synthesis. Alpha (and to less degree beta) barium metaborate crystals can be used as radiative neutron detectors.

Barium metaborate is used as a flux in some $BaTiO_3$ and $PbZrO_3$ EIA-Class 2 dielectric ceramic formulations for ceramic capacitors in an amount of about 2%. The barium–boron ratio is critical for flux performance; BaB_2O_2 content adversely affects the performance of the flux.

Transparent crystalline crystal materials can exhibit different kinds of optical nonlinearities that are associated with a nonlinear polarization. Such media with a nonlinearity are mainly used for parametric optical frequency conversion and other electro-optic modulators, including those which exhibit the Kerr effect, the Raman effect and four-wave mixing. In essentially all cases, artificial (rather than naturally occurring) crystals are used. There are a number of borates, the most important ones being lithium triborate (LiB_3O_5 = LBO), cesium lithium borate (CLBO, $CsLiB_6O_{10}$), β-barium borate (β-BaB_2O_4 = BBO), strongly hygroscopic, often used in Pockels cells. These can be used for generating and frequency-converting laser light. Less frequently used are strontium beryllium borate ($Sr_2Be_2B_2O_7$ = SBBO) and $K_2Al_2B_2O_7$ (KAB), because their band gap energy is relatively high, the crystals are relatively resistant to UV light, and there are suitable phase-matching options. Borates such as LBO and BBO also work well in broadly tunable optical parametric oscillators and optical parametric chirped pulse amplification.

DTA and visual polythermal analysis are used to study phase equilibria in the BaO–BaB_2O_4 system. The following compounds are formed in the system: $Ba_5B_4O_{11} = 5BaO \cdot 2B_2O_3$ (which melts peritectically at 1170 ± 10 °C), $Ba_3(BO_3)_2$ (which melts congruently at 1390 ± 10 °C), and $Ba_4B_2O_7 = 4BaO \cdot B_2O_3$ (which decomposes in the solid state at 1190 ± 10 °C).

Barium orthoborate has the formula of $Ba_3(BO_3)_2$. A mass spectrometric Knudsen effusion method has been used for the study of the vaporization behavior of $Ba_3B_2O_6$(solid) in the temperature range 1434 to 1630 K. Vapor species of Ba(gas), $BaBO_2$(gas), BO(gas), B_2O_2(gas), and B_2O_3(gas) have been found. From their partial pressures, the molar enthalpies of formation and dissociation for $BaBO_2$(gas) have been determined to be:

$$\Delta_f H^0_m(BaBO_2,\ \text{gas},\ 298.15\ \text{K}) = -(633 \pm 21)\text{KJ/mol}$$

$$\Delta_f H^0_m(\text{Ba, gas, } 298.15\ \text{K}) + \Delta_f H^0_m(BO_2, \text{gas}, 298.15\ \text{K}) -$$

$$\Delta_f H^0_m(BaBO_2, \text{ gas}, 298.15\ \text{K}) = (524 \pm 18)\text{KJ/mol},$$

The molar enthalpies of formation for $Ba_3B_2O_6$(s) from the elements and from the constituent oxides were found to be:

$$\Delta_f H^0_m(Ba_3B_2O_6,\ \text{solid}, 298.15\ \text{K}) = -(3469 \pm 50)\text{KJ/mol}$$

$$\Delta_f H^0_m\{(\text{BaO}, \text{solid}, 298.15\ \text{K}) - \Delta_f H^0_m(B_2O_3, \text{solid}, 298.15\ \text{K})\} = -(552 \pm 50)\text{KJ/mol},$$

A novel anhydrous, noncentrosymmetric orthoborate, $Ba_3(BO_3)_2$, has been prepared and its crystal structure determined by XRD of a single crystal (Fig. 6.40).

The material crystallizes in the orthorhombic system with $a = 15.068(2)$, $b = 8.720(2)$, and $Z = 8$; the space group is $Pca2_1$. The structure is composed of layers of BaO_4 tetrahedra and BO_3 triangles connected through shared oxygen vertices; these layers are connected by additional interleaving BO_3 triangles and barium atoms. This structure is identical to that of strontium orthoborate.

If a mixed crystal of Ba^{2+} and Sr^{2+} orthoborates is grown, the composition then varies from the normal orthoborate composition. Single crystals of barium strontium orthoborate, $(Ba_{1.64},Sr_{1.36})_3(B_3O_6)_2$, were grown by a high-temperature solution growth technique, and a detailed structure analysis was carried out. The orthoborate, $(B_3O_6)^{3-}$ anion planar groups in this compound form infinite layers parallel to (001) plane, and Sr and Ba atoms are alternatively placed between the layers and are octahedrally coordinated by six O(2) atoms in the neighboring anion rings. In this structure, a metaborate molecule, $(B_3O_6)^{3-}$ anion ring, is completed by three BO_2 groups related by threefold rotation symmetry along the *c*-axis perpendicularly passing through the center of the molecular plane. The ring plane is planar within 0.078 Å with O_1-B = 1.410 Å, O_1-B_{ix} = 1.397 Å, and O_2-B = 1.306 Å showing double-bond character, whose geometry is very similar to that of $Sr_xBa_{3-x}(B_3O_6)_2$. The strontium atom is octahedrally coordinated by two O atoms in the anion groups with a $Sr\cdots O_2 = 2.5100$ Å, and the barium atom is also octahedrally coordinated by the same two O atoms but with two different coordination bond lengths $Ba\cdots O_2 = 2.7964$ Å and $Ba\cdots O_{2vi} = 2.738$ Å so that the two O atoms are participating in three coordinations with $Sr\cdots O_2\cdots Ba = 90.39°$, $Sr\cdots O_2\cdots Ba_{viii} = 131.05°$, $Ba\cdots O_2\cdots Ba_{viii} = 103°$ (Fig. 6.41).

The sixfold coordination bond lengths of SrO_2 and $Ba\cdots O_2$ are very close to the respective 2.5801 Å and 2.76 Å lengths shown in International tables for X-Ray Crystallography Vol. III.7). Therefore, the three-dimensional infinite molecular network is formed by the O_2 atom in the $(B_3O_6)^{3-}$ anion ring which plays a bridging role among Sr, Ba atoms, and the metaborate molecule.

Barium pyroborate can be prepared by the reaction of the oxides at high temperature:

$$2\text{BaO} + B_2O_3 + \text{heat} \Rightarrow Ba_2B_2O_5$$

Crystals can be grown from a mixture containing appropriate amounts of $BaCO_3$ and H_3BO_3, using KFB_4 as a flux. The mixture is thoroughly milled, heated in a platinum crucible in air to 1193 K (920 °C), and kept at that temperature for 15 h. The temperature is then

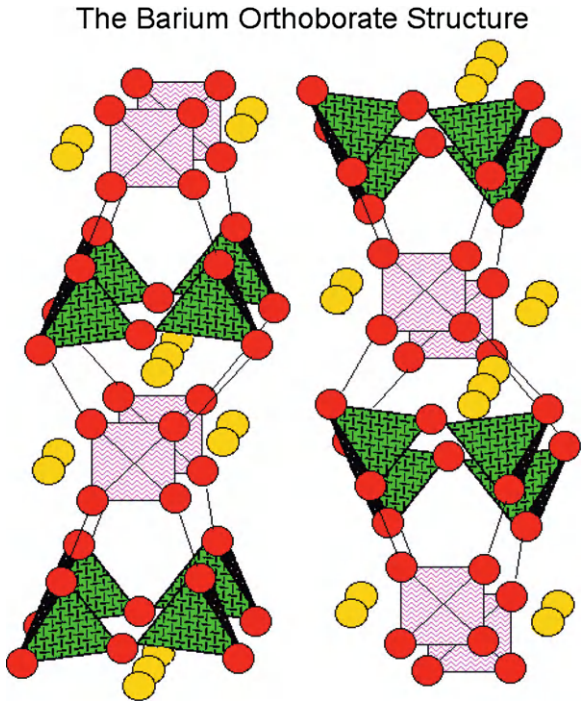

FIGURE 6.40

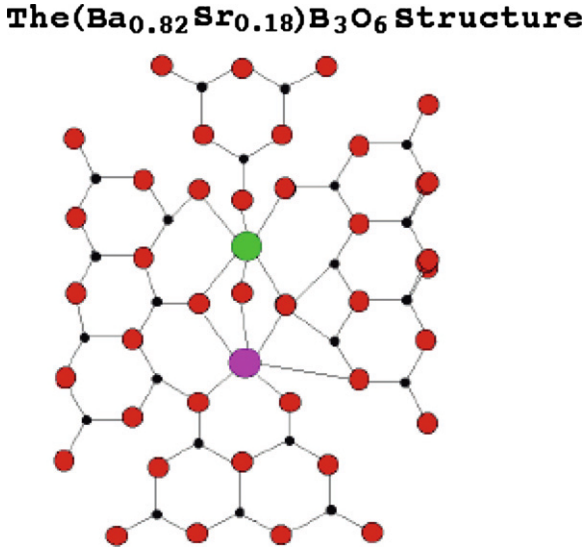

FIGURE 6.41

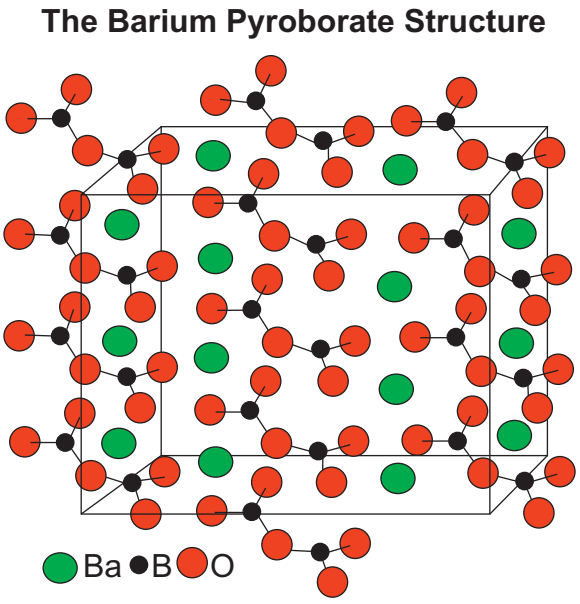

FIGURE 6.42

quickly quenched to 1053 K (880 °C) and slowly cooled from 1053 to 973 K (700 °C) at a rate of 0.011 K/h and then air quenched to room temperature. Colorless crystals are obtained. The structure is monoclinic (Fig. 6.42).

This structure is identical to that of the Sr-homologue. The noncentrosymmetric pyroborate $Ba_2B_2O_5$ crystallizes in the monoclinic space group C2 with a cell of dimensions $a = 6.485$ Å, $b = 9.165$ Å, $c = 3.971$ Å, and $\beta = 96.14°$. It is composed of highly distorted $[BaO_4]$ squares and double-triangular $[B_2O_5]$ groups that are connected to form infinite two-dimensional layers. The layers are stacked parallel to (001), and the Ba atoms interleave successive layers. Parallel alignment of the pyroborate groups is conductive to high efficiency for optical frequency conversion. The magnetic moment at 22 °C is $1.69 \pm 0.03\ \mu_B$.

Barium perborate was prepared by the reaction of boric acid in solution with barium peroxide as early as 1875:

$$BaO_2\ (aq) + H_2BO_3\ (aq) \Rightarrow BaB_2O_6 \cdot 3H_2O\ (solid)$$

The heptahydrate was also reported in 1898. Undoubtedly, the difference is in the solution temperature used to prepare this salt. It is unstable and decomposes to the metaborate plus oxygen gas:

$$BaB_2O_6 \cdot 3H_2O \Rightarrow BaB_2O_4 + 3H_2O\ (gas) + O_2\ (gas)$$

In order to obtain a usable product that is stable and not subject to slow degradation, it is necessary to maintain a reaction temperature not lower than 40 °C or over 60 °C. At lower temperatures, the product tends to decompose readily whereas at higher temperatures,

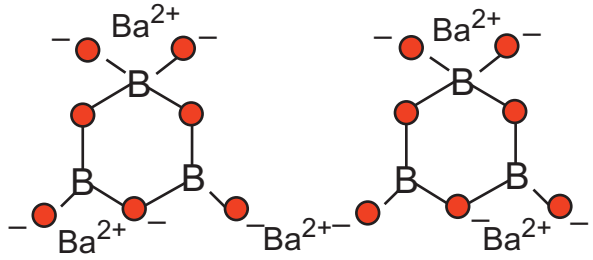

FIGURE 6.43

the peroxide grouping, $(BO_3)_2^{2-}$ tends to decompose in solution. Thus, at $T > 60$ °C, it is difficult to obtain a product having a suitable amount of active oxygen.

Perhaps this is the reason why barium perborate has not found usage as an oxidizing agent in industry. Both the Mg- and Ca-homologues are much more stable, are cheaper, and have found various niches of usage.

The compound, barium triborate, involves the anion $B_3O_7^{5-}$ and would have the formula, $5BaO \cdot 3B_2O_3 = Ba_5B_6O_{14}$ or $Ba_5(B_3O_7)_2$. This would have the Lewis structure shown in Fig. 6.43.

Single crystals of the noncentrosymmetric barium borate, $Ba_2B_{10}O_{17}$, have been grown by slowly cooling a stoichiometric melt. The material crystallizes in the triclinic space group P1 with cell parameters $a = 9.858(1)$, $b = 9.990(1)$, $c = 6.706(1)$ Å, $\alpha = 96.79°$, $\beta = 106.64°$, and $\gamma = 76.89°$. The structure is a new type characterized by a condensation of B_3O_7 rings and BO_3 triangles. A calculation of the second-order nonlinear susceptibility coefficients on the basis of the orientations of the tetrahedral and triangular borate groups in the rings and triangles has yielded a maximum coefficient of $d_{11} = 0.2$ pm/V. This result is consistent with the measured second-harmonic signal—0.5 × KDP. A partial solid solubility of Sr in the host—$Ba_{2-x}Sr_xB_{10}O_{17}(0 < x \leq 0.25)$—has also been observed.

$B_3O_7^{5-}$ rings are also noted in bismuth-containing barium borate compositions. Bismuth, Bi^{3+}, is present as a "bismuthate". Single crystals of a the compound, $BaBi_2B_4O_{10}$, were grown by cooling a melt having a stoichiometric composition. The crystal structure of the compound has been solved by direct methods. It is monoclinic, space group $P2_1/c$, $a = 10.150$ Å, $b = 6.362$ Å, $c = 12.485$ Å, $\beta = 102.87°$, $V = 786.0$ Å^3, $Z = 4$. The structure is based upon anionic thick layers that are parallel to (001). The layers can be described as built from alternating novel borate $[B_4O_{10}]_\infty^{8-}$ chains and bismuthate $[Bi_2O_5]_\infty^{4-}$ chains extended along *b*-axis. The borate chains are composed of $[B_3O_7]^{5-}$ triborate groups of three tetrahedra and single triangles with a $[BO_2]^-$ radical. The borate chains are interleaved along the *c*-axis with rows of the Ba^{2+} cations so that the Ba atoms are located within the layers. The layers are connected by two nonequivalent Ba–O bonds as well as

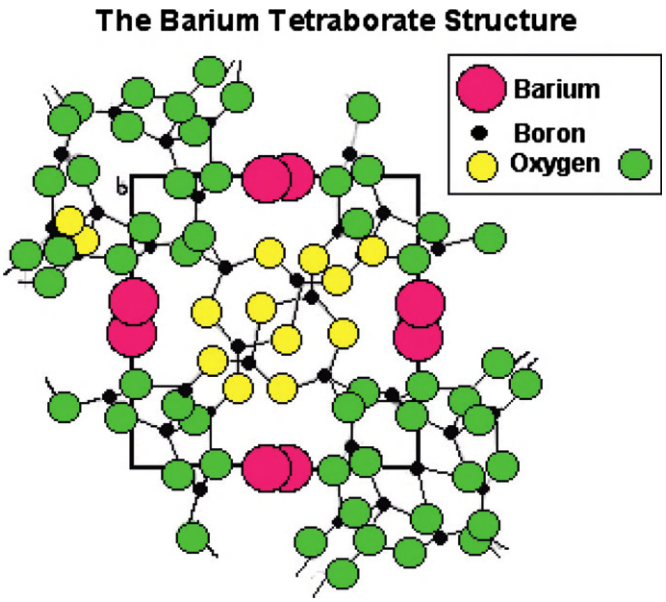

FIGURE 6.44

Atomic positional parameters

	x	*y*	*z*
Ba	0	0.4718	0
O(1)	0.450	0.550	0.125
O(2)	0.278	0.370	0.159
O(3)	0.763	0.212	0.219
O(4)	0.529	0.261	0.136
O(5)	0.237	0.169	0.292
O(6)	0.965	0.189	0.345
O(7)	0.011	0.284	0.192
B(1)	0.680	0.320	0.125
B(2)	0.120	0.120	0.375
B(3)	0.412	0.368	0.142
B(4)	0.185	0.272	0.219
B(5)	0.927	0.238	0.250

FIGURE 6.45

by two equivalent Bi–O bonds with bond valences in the range of 0.2–0.3 e.u.

Thermal expansion of $BaBi_2B_4O_{10}$, studied by high-temperature X-ray powder diffraction in the temperature range of 20–700 °C (temperature step 30–35 °C), shows that it is highly anisotropic. While the *b* and *c* unit-cell parameters increase almost linearly on heating, temperature dependencies of α parameter and β monoclinic angles show nonlinear behavior. As a result, on heating, orientation of the thermal expansion tensor changes, and bulk thermal expansion increases from $20 \times 10^{-6}/°C$ at the first heating stage up to $57 \times 10^{-6}/°C$ at 700 °C that can be attributed to the increase of thermal mobility of heavy Bi^{3+} and Ba^{2+} ions.

Barium tetraborate has been studied extensively. The structure of BaB_4O_7 has been determined from the use of three-dimensional X-ray data (Fig. 6.44).

The structure contains two separate interlocking three-dimensional networks, each of which consists of alternating triborate and pentaborate groups as building blocks. This structure is quite similar to those found in other tetraborates The two kinds of oxygen atoms linked in the triborate and pentaborate groups are clearly delineated. This is a projection along the pseudo-tetragonal axis of one of the networks in barium tetraborate. The four types of atoms are shown. The pentaborate groups are at the corners of the unit cell whereas the triborate groups are at the center. Unit-cell parameters are: $a = 8.562$ Å, $b = 5.78$ Å, $c = 13.201$ Å, space group = $P4_122$. Positional parameters for the lattice are shown in Fig. 6.45.

The unit-cell parameters are: $a = 10.56$ Å, $b = 8.20$ Å, $c = 13.01$ Å, $\beta = 104°$, and $Z = 8$, space group = $P2_1/c$. The borate network can also be described as a three-dimensional linkage of alternating six-membered single rings containing two tetrahedral B atoms and one triangular B atom, and double rings containing two tetrahedral B atoms, one of them being common to both rings, and three triangular B atoms. Each single ring is directly linked only to double rings and each double ring directly links to only to single rings. The Ba atoms fit into channels of this network. Another view of barium tetraborate is shown in the following Fig. 6.46.

This is a view showing the relation of the triborate groups to each other, as shown in the middle of the above view of the structure. In barium tetraborate, two different bond valence sums of the two crystallographic different barium positions are observed.

The thermal behavior of BaB_4O_7 was investigated using high-temperature X-ray powder diffraction analysis. The components of the thermal expansion tensor and the tensor orientation with respect to the crystallographic axes are calculated. Thermal deformation was analyzed in relation to the crystal structure. The thermal expansion of the BaB_4O_7 borate was studied in three high-temperature XRD experiments (two experiments with heating and one experiment with cooling). The thermal expansion of this compound is strongly anisotropic; the expansion is maximum in the *ac* monoclinic plane, whereas a contraction is observed along the *b*-axis.

Activation of barium tetraborate by divalent Europium has been studied. A phosphor peaking at 350 nm was obtained whose spectrum is shown in the following diagram. Although the wavelength is suitable for use in "black-light" lamps, the intensity of the Sr homologue is

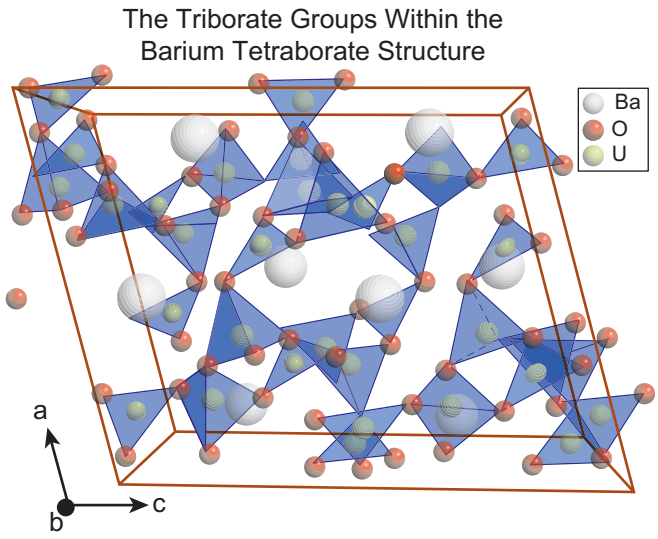

FIGURE 6.46

greater at 370 nm. Thus, this composition has not found use in the lamp industry. Barium tetraborate has the CAS number of 12007-55-5 (Fig. 6.47).

Bismuth-containing barium borates have been studied as frequency-converting crystals. Phase equilibria in the $BaO–Bi_2O_3–B_2O_3$ system have been investigated by X-ray powder diffraction analysis and DTA. Quasi-binary sections have been determined, and an isothermal section of the system in the subsolidus region has been constructed. The $BaO–Bi_2O_3–B_2O_3$ ternary system has been divided into 22 triangles of coexisting phases. It has been found that four bismuth barium borates exist, namely, $Ba_3BiB_3O_9$, $BaBi_2B_4O_{10}$, $BaBiB_{11}O_{19}$, and $BaBiBO_4$. $Ba_3BiB_3O_9$ undergoes a phase transition at 850 °C and exists up to 885 °C, where it decomposes in the solid state. $BaBiB_{11}O_{19}$ and $BaBi_2B_4O_{10}$ melt congruently at 807 and 730 °C, respectively. $BaBiBO_4$ melts incongruently at 780 °C. X-ray powder diffraction data for the low-temperature polymorph of $Ba_3BiB_3O_9$ were presented. $BaBiBO_4$, or $BaBi(BO_3)O$, is a novel borate oxide which has been synthesized by SSR at temperatures below 650 °C and 1 atmosphere pressure. Its crystal structure has been determined from powder XRD data and refined from powder neutron diffraction data (noncentrosymmetric Pna21 space group, $a = 8.5817$ Å, $b = 9.6802$ Å, $c = 5.1505$ Å, $Z = 4$). The structure is built of [001] chains of edge-sharing BO_3 and BiO_5 groups interleaved with Ba^{2+} cations. The measurement of the nonlinear optical properties of the powder sample by the Kurtz–Perry method yielded an efficiency for second-harmonic generation equal to five times that of KH_2PO_4.

A **hydroxylated barium borate**, $Ba_3B_6O_9(OH)_6$, consists of infinite chains of composition of $[B_6O_9(OH)_6]_n^{n6-}$ and Ba^{2+} cations residing between the negatively charged chains. This compound is the first reported chain borate in which the boron atoms are all tetrahedrally coordinated by oxygen atoms (Fig. 6.48).

The structure of this compound contains anionic infinite chains extending along the *a*-direction, with a composition of $[B_6O_9(OH)_6]^{n6-}$ built up from nonplanar six-membered B_3O_6 rings, which are found to join together by sharing B atoms. In each B_3O_6 ring, all the three B atoms are bonded to four oxygen atoms. The B–O bond distances range from 1.444 to 1.523 Å (average—1.479 Å), comparable with the normal average tetrahedral B–O distance observed in many works The negative charges of the polyborate chains are compensated for by the Ba^{2+} cations residing between adjacent chains. Two new borate compounds have been prepared in the presence of amines by

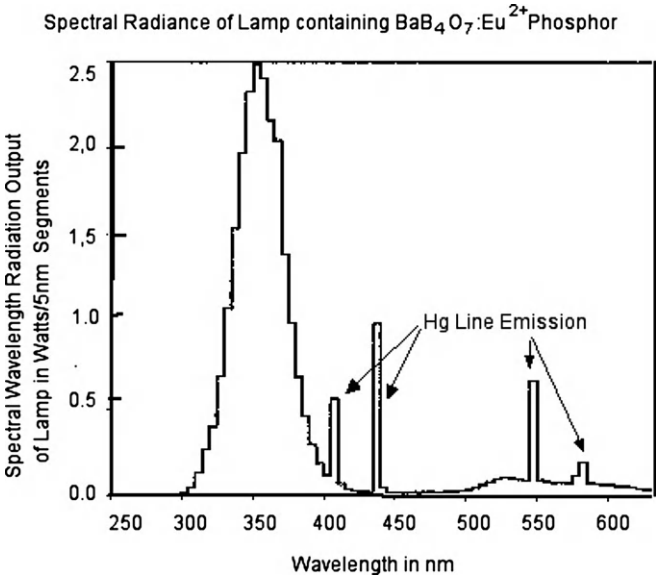

FIGURE 6.47

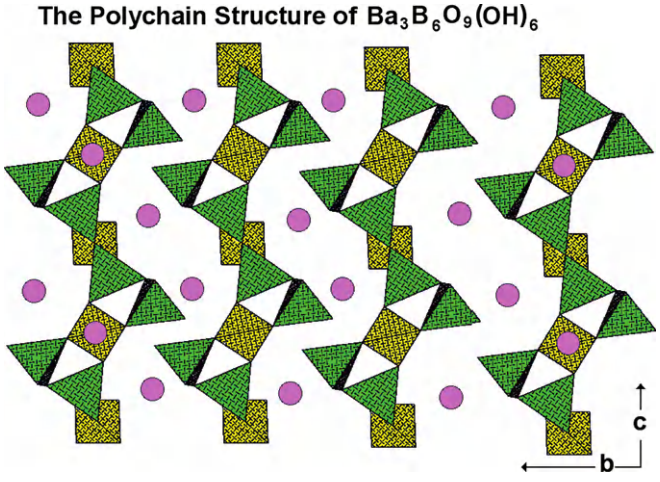

FIGURE 6.48

employing hydrothermal techniques. $Ba_3B_6O_9(OH)_6$ consists of infinite chains of composition of $[B_6O_9(OH)_6]^{n6-}$ and Ba^{2+} cations residing between the negatively charged chains. This compound is the first reported chain borate in which the boron atoms are all tetrahedrally coordinated by oxygen atoms. The SR compound has an identical structure.

The successful synthesis of these two compounds may help in the search for new ways of synthesizing borate crystals with interesting structural features.

Barium borates are widely used in industry and are readily available commercially.

Radium Borates

The scientific literature is devoid of any description of radium borates. They could be prepared by the same methods as those used for barium but there is no record of anyone having done so. The expected, stable, compounds would be RaB_2O_4, $Ra_3(BO_3)_2$, $Ra_2B_2O_5$ and RaB_4O_7. In addition, since barium forms a stable $Ba_3B_6O_9(OH)_6$ compound, there is a strong possibility that radium should also do so.

Perhaps the lack of any description of such salts can be ascribed to the intense radioactivity of the ^{226}Ra atom and the dangers of handling it improperly. Nonetheless, the chemistry of other radioactive cations have been reported so that this explanation does not seem valid. Little interest has been shown in industry or academia for radium plumbates and the corresponding alkaline earth plumbates are much cheaper and easier to handle than the radium salts.

6.4. ALUMINUM COMPOUNDS OF THE ALKALINE EARTHS

Since aluminum is close to the nonmetals in the periodic table, it has some nonmetal characteristics and some metal characteristics. Its oxide is amphoteric. It dissolves in both bases and acids. When dissolved in bases, it forms the aluminate ion. An aluminate can be considered as the neutralization of aluminum oxide with a base, or an adduct of aluminum oxide with the base. The generally accepted form of the aluminate is a mononuclear tetrahedral complex that is negatively charged, $Al(OH)_4^-$ or AlO_2^-. Aluminate can also refer to the polyatomic ion AlO_3^{3-}. Aluminum also forms a series of "aluminides" where the group Al_x^{y-} varies, depending upon the nature of the alkaline earth.

6.4.1. Alkaline Earth Aluminides

An aluminide contains aluminum and one or more electropositive elements. Since aluminum is similar to the nonmetals, it forms compounds with properties intermediate between a metal alloy and an ionic compound. Aluminides have found applications in hydrogen storage technology, the aeronautical industry, and in coatings for furnaces and other high-temperature applications. Many of the alkaline earth aluminides crystallize in the Laves type of cubic to hexagonal lattices. These phases, which form the largest group of intermetallics (with more than 1400 representatives), have the ideal composition AB_2. An intermetallic compound is classified as a Laves phase purely on the basis of the geometry of the crystal structure. The Laves phases crystallize in three structure types, which are named after the representative cubic $MgCu_2$ (C15), hexagonal $MgZn_2$ (C14) and hexagonal $MgNi_2$ (C36). These are represented as shown in Fig. 6.49.

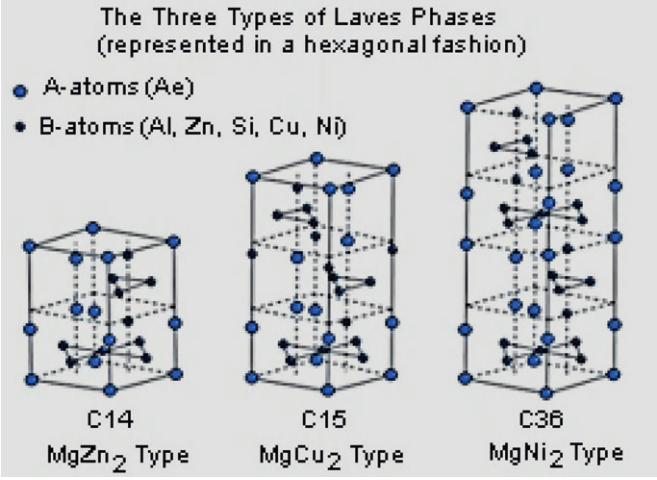

FIGURE 6.49

The B atoms form a series of networks that are distinctive (Fig. 6.50).

Beryllium Aluminides

Beryllium does not form any compounds with aluminum. Instead, it forms a series of alloys whose melting points vary from the melting point of Be (1283 °C) to that of Al (654 °C). However, the melting point line of $Be_{1-x}Al_x$ is not linear but is an "s-shaped" curve as shown in the following diagram. There is a eutectic at 3.1 mol% Be ($Be_{0.031}Al_{0.969}$) of 644 °C so that it is clear that a synergy exists in these alloys (Fig. 6.51).

Al–Be alloys possess physical and mechanical properties that exceed those of standard aluminum alloys in such areas as mechanical stability, dampening, thermal management and reduced weight. "AlBeMet™" combines the high modulus and low density of beryllium with the strength, ductility and fabrication characteristic of aluminum. The use of AlBeMet-AM162,

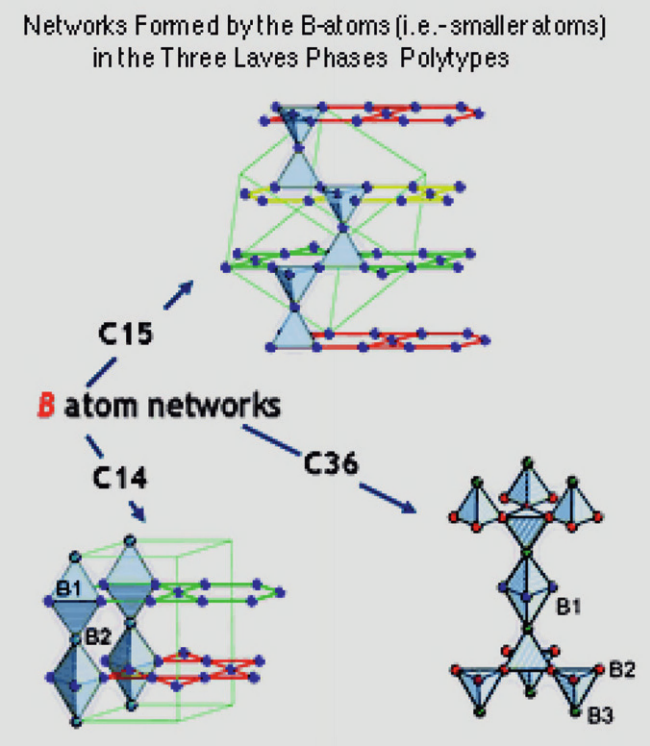

FIGURE 6.50

an aluminum–beryllium metal matrix composite, is an effective way to reduce the size and weight of many structural aerospace components that are currently made out of aluminum and titanium alloys. These savings, which are essential for today's technologies, are primarily due to the material's high modulus and low density combined with its better than average specific strength. The raw material costs are significantly higher than they are for traditional engineering alloys, and the available billet sizes are more limited than they are for aluminum and titanium alloys. Although the material costs are higher for the aluminum–beryllium composite, ease of machining makes it financially competitive when compared to equivalent parts made out of titanium alloys. Due to toxic nature of beryllium, however, debris-generating operations must be strictly regulated to limit worker's exposure to the material and protect them from potentially fatal diseases.

An aluminum–beryllium alloy with a high modulus-to-density ratio (3.8 times that of aluminum or steel) greatly reduces the chance of flexure and mechanical failure (Table 6.4).

These alloys have the following CAS numbers: aluminum–beryllium (Al–Be) alloy CAS number: aluminum = 7429-90-5; beryllium = 7440-41-7.

Magnesium Aluminide

Magnesium aluminide is an intermetallic compound of Mg and Al. Common phases (molecular structures) include the beta phase (Mg_2Al_3) and the gamma phase ($Mg_{17}Al_{12}$). Both have cubic crystal structures. Magnesium aluminides are important constituents of 99.999% aluminum alloys (aluminum–magnesium) and magnesium–aluminum alloys, determining many of their engineering properties. The compound, Mg_2Al_2, has also been investigated for use as a basis for producing metal hydrides for hydrogen storage. Like many

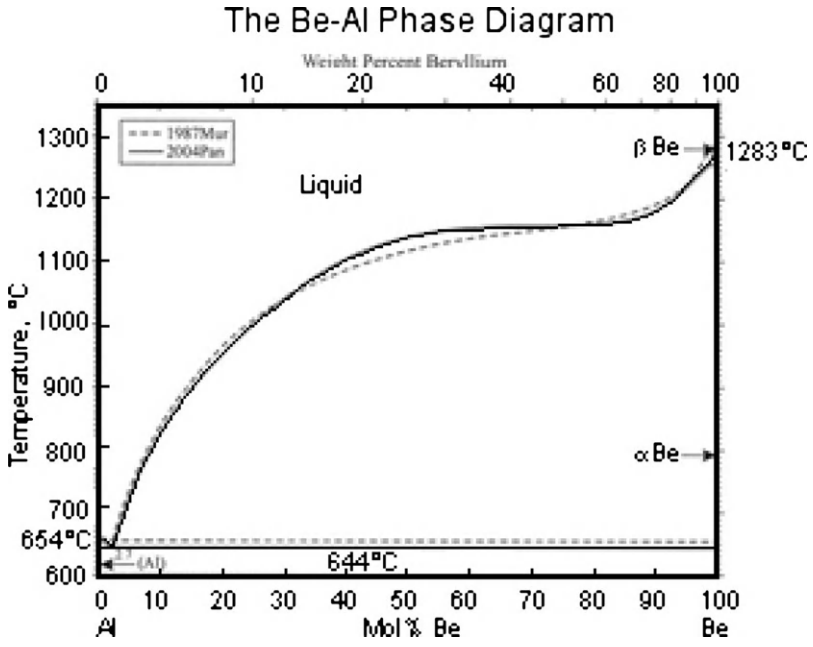

FIGURE 6.51

TABLE 6.4 Aluminum-beryllium (Al–Be) alloy physical constants for alloys available

Nominal density (lb./in^3)	0.076 to 0.086
Yield (KSI)	23 to 40
Melting point (°F)	2010 to 2150
Chemical family	Metal matrix
Ultimate (KS)	34 to 55
Elongation (%)	17 to 7
Modulus (MSI)	19 to 28
Color	Gray

intermetallics, MgAl compounds often have unusual stoichiometries with large and complex unit cells. The phase diagram is given in Fig. 6.52.

Four compounds are formed: Mg_5Al_8, Mg_2Al_3, MgAl, and $Mg_{17}Al_{12}$. Both the 5:8 and the 17:12 compositions melt congruently. The others melt incongruently.

Additionally, there is a compound that forms above 322 °C and is stable only in a very limited range up to 372 °C where it decomposes. This compound, labeled "R", likely has the composition Mg_7Al_9. Thus, the reaction mixture of Mg + Al between the mole ratios of 40.0 and 50.0 At% Mg produces a mixture of Mg_2Al_3 and MgAl. But if the mixture is heated to >322 °C, Mg_7Al_9 becomes stable.

Further heating then forms:

$$3Mg_7Al_3 \Rightarrow 2Mg_2Al_3 + Mg_{17}Al_{12}$$

If an exact mixture containing 42.75 atom% Mg is present, the reaction is:

$$2Mg_2Al_3 + 3Mg_2Al_2 \Rightarrow Mg_7Al_9$$

It is this compound that is stable up to 372 °C where it decomposes to:

$$3Mg_7Al_9 \Rightarrow Mg_{17}Al_{12} + 5Mg_2Al_3$$

However, since the structure of "R" has not been determined, the only basis for its formation has been a change in diffraction pattern at the 42.75 At% composition.

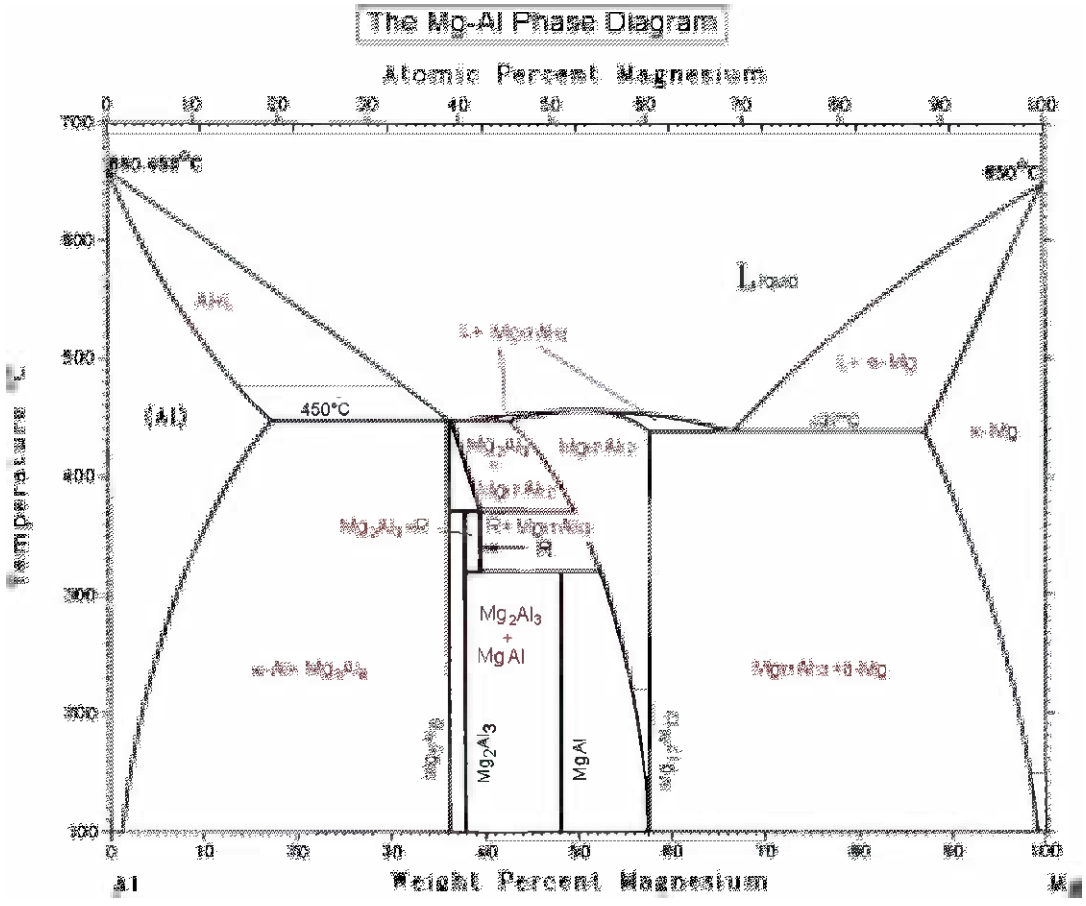

FIGURE 6.52

Pentamagnesium octaaluminide, Mg_5Al_8, is a component of Mg–Al alloys. In Al–Mg alloys with high Mg content (>3% Mg), solid solution is supersaturated with Mg solute atoms, because the Mg content is higher than 1.9% Mg, which is the equilibrium solubility of Mg in Al matrix at room temperature. In that case, Mg solute atoms tend to precipitate out as an equilibrium β-phase (Mg_5Al_8) along the grain boundaries or randomly distributed in the structure. Precipitation sequences of the decomposition of supersaturated solid solution have been reported as follows:

α-Al matrix ⇒ GP zones (β′-phase) ⇒ (β-phase(Mg_5Al_8))

This process occurs slowly even at room temperature, and is significantly accelerated at high temperatures (>65 °C). Since the corrosion potential of β-phase (−1.24 V), is more negative than the potential of Al matrix (−0.87 V), dissolution of anodic (β-phase particles occur in an appropriate solution, such as seawater). Other second phase particles, such as $MnAl_6$, have no influence on the corrosion behavior of Al–Mg alloys, since the corrosion potential of $MnAI_6$ particles (−0.85 V) is as much as the potential of Al matrix.

The presence of Mg_5Al_8 in Mg–Al alloys seriously weakens the strength of low Mg-containing alloys. However, if the alloying step is properly controlled, a major increase in strength and other properties occurs. The generic aluminum alloys derive most of their strength from solution hardening. The Al–Mg phase diagram shows why. At room temperature, aluminum can dissolve up to 1.8 wt% magnesium at equilibrium conditions. In practice, Al–Mg alloys can contain as much as 5.5 wt% Mg in solid solution at room temperature—a super saturation of $5.5 - 1.8 = 3.7$ wt%. In order to obtain this super saturation, the alloy is given the following schedule of heat treatments:

(a) Hold at 450 °C (solution heat treat)

This puts the 5.5% alloy into the single phase (α) field and all the Mg will dissolve in the Al to give a random substitutional solid solution.

(b) Cool moderately quickly to room temperature.

The phase diagram shows that, below 275 °C, the 5.5% alloy has an *equilibrium* structure, that is two phase, $\alpha Al + Mg_5Al_8$. If, then, the alloy is *slowly cooled* below 275 °C, Al and Mg atoms will diffuse together to form precipitates of the intermetallic compound, Mg_5Al_8. However, below 275 °C, diffusion is slow and the C-curve for the precipitation reaction is well over to the right. If the 5.5% alloy is cooled moderately, none of the Mg will be removed from solution as Mg_5Al_8, and the final result will be a supersaturated solid solution at room temperature. This supersaturated Mg gives a substantial increase in yield strength:

Yield strengths of (Al−Mg) alloys

Wt% Mg	Strength in MPa
0.80	40
1.50	55
2.50	90
2.70	120 (SS)
4.50	145 (SS)
5.10	160 (SS)

[SS = superstaurated]

Dimagnesium trialuminide, Mg_2Al_3, has two dimers, each having a unique structure. These have been labeled β-Mg_2Al_3 and β″-Mg_2Al_3. The former is cubic and the latter rhombohedral. A determination of the crystal structure of the phase commonly referred to as β-Mg_2A1_3 has been carried out and the structure has been refined by three-dimensional, least-squares techniques. The final agreement index R is 0.061 for 1215 reflections. The crystals are cubic, space group Fd3m (07) with $a_0 = 28.239$ Å. There are approximately 1168 atoms in the unit cell. These are distributed over 23 crystallographically different positions that, as a result of partial disorder, describe 41 different polyhedra. An interesting feature of the disorder is that it results in an increase in the number of icosahedra in the unit of structure, over that found in the idealized ordered model. The unit cube contains 672 icosahedra, 252 Friauf polyhedra, and 244 miscellaneous, more or less irregular polyhedra of ligancy of 10–16.

An analysis of cross-sections perpendicular to the main diagonal of a cubic elementary cell of a Samson structure such as β-Mg_2Al_3 has been conducted. It has been proven that all skeleton atoms, i.e. which occupy their positions with probability of 100%, form a framework of hexagonal planes. These planes are a part of three domains shifted with respect to each other by one-third of the length of cube's diagonal. Space between domains is filled up by clusters with partially occupied atomic positions. For hexagonal domains, the elementary cell and positions of decorating atoms have been determined. Thus, a specific arrangement of the atoms comprising the structure cannot be given since the disorder is so great. However, the general shape of these structural units have been defined.

The Samson structure of β-Mg_2Al_3 occurs as a cubic elementary cell (Fd-3m, no. 227 space group) that contains 1168 atoms which are distributed over 1832 atomic positions. About 75% of atoms (879 to be exact) form the framework of the structure (skeleton atoms). The framework is made up of Samson's positions which are occupied by atoms with SOF equal to 1. The remaining 289 (25%) atoms partially occupy 953 positions with the average

occupation probability of 30%. They form clusters arranged in an elementary cell in a hexagonal lattice. Their structure can be illustrated as shown in Fig. 6.53.

The lattice constant of the Samson structure is gigantic: $a = 28.242(1)$ Å. At a temperature of 214 °C, the structure undergoes a phase transformation to the rhombohedral β′-Mg_2Al_3 (space group R3m, no. 160, which is a subgroup of the Fd-3m group—index 4) with $a = 19.968(1)$ Å, $c = 48.9114(8)$ Å. It should be pointed out that the constant c of a rhombohedral structure is practically equal to the length of the diagonal of the cubic structure cubic rhomb $a_{cubic}\sqrt{3} = 48.9166$ Å $\approx c_{rhomb}$. The near equivalence in length between the c-axis of the rhombohedral β′-Mg_2Al_3 structure and the diagonal of the cubic β-Mg_2Al_3 is a consequence of lattice transformation connecting the hR cell of the β′-phase to the F cell of the β-phase. Comparison of two different types of Mg_2Al_3 structure, i.e. the β–cubic phase and rhombohedral β′ one, leads to the conclusion that all skeleton atoms of a Samson structure do not change their position during the phase transformation. The skeleton atoms of a Samson phase lie within hexagonal layers.

These layers form three structural domains shifted with respect to each other by 1/3 of the length of the main diagonal of the cubic unit structure. Besides within a hexagonal layer the length of every shift vector is a multiple of about 1/7 of the distances characteristic for hexagonal structures. Once the shift vectors were found, one could then describe the structure as

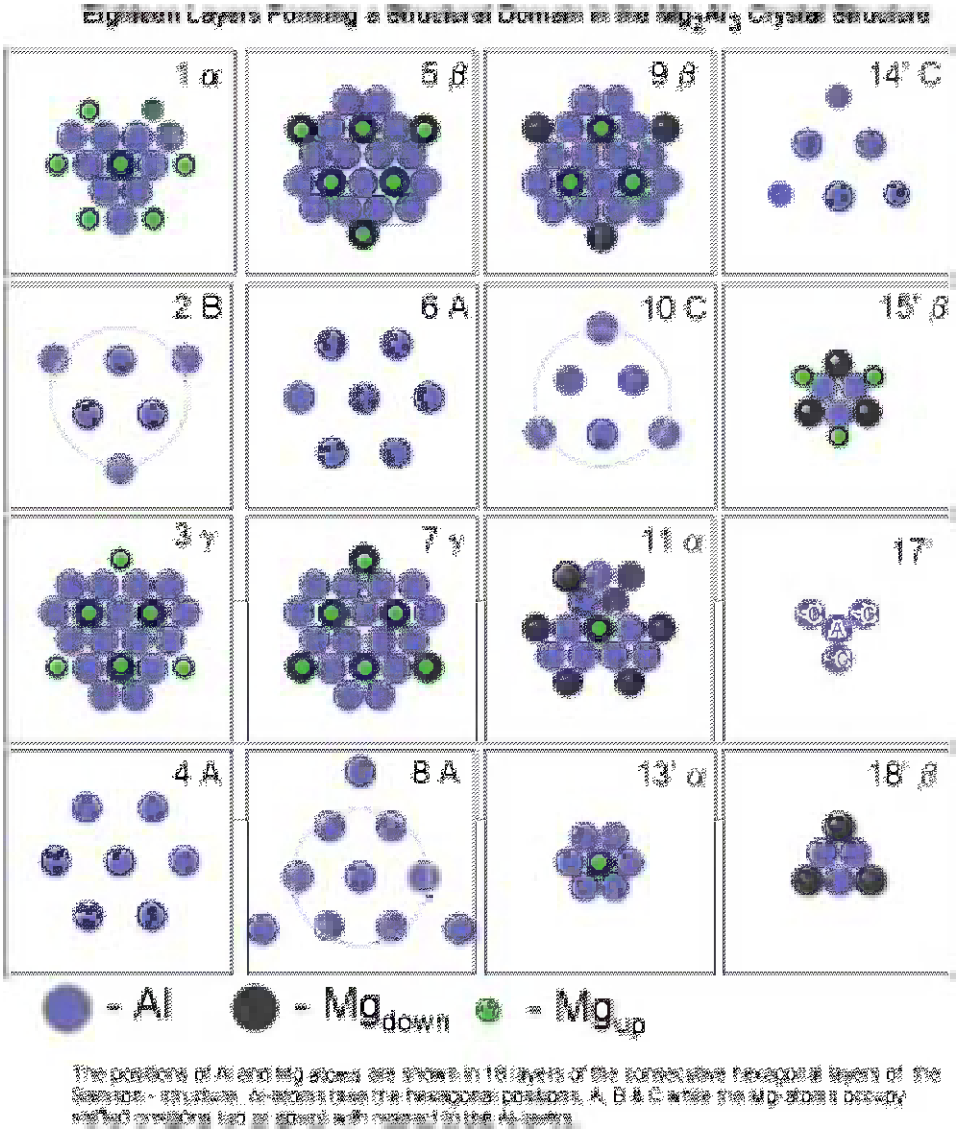

FIGURE 6.53

a modulated one. Thus, the stability range of the Samson phase, β-Mg_2Al_3 can be summarized as:

> "For the composition $Mg_{38.5}Al_{61.5}$, the cubic phase, space group *Fd*-3*m* (no 227), $a = 28.242(1)$ Å, $V = 22526(2)$ Å^3, undergoes at 214 °C a first-order phase transition to rhombohedral β′-Mg_2Al_3, $a = 19.968(1)$ Å, $c = 48.9114(8)$ Å, $V = 16{,}889(2)$ Å^3 (i.e. 22519 Å^3 for the equivalent cubic unit cell), with a space group *R*3*m* (no 160), a subgroup of index 4 of *Fd*-3*m*. The structure of the β-phase has been redetermined at ambient temperature as well as in situ at 400 °C. It essentially agrees with Samson's model, even in most of the many partially occupied and split positions. The structure of β′-Mg2Al3 is closely related to that of the β-phase. Its atomic sites can be derived from those of the β-phase by group-theoretical considerations. The main difference between the two structures is that all atomic sites are fully occupied in case of the β′-phase".

Unusual electronic transport properties have been found in the rhombohedral β′-phase of the complex metallic alloy Mg_2Al_3. The magnetoresistance (MR) is 2 orders of magnitude larger than in the related cubic β-Mg_2Al_3-phase and Kohler's rule is strongly violated in the β′-phase at higher temperatures. Above about 100 K, the Hall coefficient R_H of the β- and β′-phases are similar and free-electron-like, while in the β′-phase, R_H changes sign with decreasing temperature at low fields. These transport anomalies have not been clearly identified. Several conventional mechanisms for a large MR have been examined, and found not to be applicable. The different properties in the β- and the β′-phases are puzzling since the magnitudes of the electrical resistivities are similar and cyclotron frequency-scattering time is equally small in both phases. The similar temperature range in which anomalies occur in the β′-phase in the resistivity, the Hall effect, and the MR indicates an electronic transition or a change of the electron structure in this phase below about 100 K.

Magnesium monoaluminide, MgAl, has been investigated as a storage medium for liquid hydrogen with little success. It is available for sale commercially but does not have a CAS number. The structure remains unknown. The interaction of hydrogen with a 50:50 Mg–Al alloy pre-exposed to air has been studied with in situ time resolved X-ray powder diffraction. The experimental setup allowed recording of full diffraction patterns within 150 s, allowing the study of structural changes during kinetic investigations. Phase fractions as a function of time were derived from series of consecutive diffraction patterns. The apparent activation energy for dehydrogenation of the Mg–Al alloy is found to be approximately 160 kJ/mol. This is not significantly higher than for pure and fully activated Mg. It is suggested that the addition of Al improves the resistance toward oxygen contamination. Furthermore, it was found that Mg–Al is hydrogenated to $MgH_2 + Al$ and upon dehydrogenation an Mg–Al alloy is reformed. Pure Mg is not observed during dehydrogenation, suggesting that the formation of Mg–Al is fast compared to the liberation of hydrogen from MgH_2. From thermodynamical calculations using the semiempirical Miedema model, a slight lowering of the heat of hydride formation is found compared to that of pure Mg.

Heptadeca-magnesium dodeca-aluminide, $Mg_{17}Al_{12}$, is probably the most stable compound of the Mg–Al series of compounds. The γ-phase is an intermetallic compound with a stoichiometric composition of $Mg_{17}Al_{12}$ (at 43.95 wt.% Al) and an α-Mn–type cubic unit cell. The electronic structure of γ phase in the system $Mg_{17}Al_{12}$ contains 58 atoms per unit cell with space group I43m. Magnesium alloys are light metallic structural materials with a unique combination of properties, which are very attractive in applications such as the automobile, aerospace and electronic industries. The use of magnesium alloys has become significant due to a one-third lower density of magnesium compared with aluminum, improved damping ability, a higher resistance to corrosion and better mechanical properties. The presence of γ-$Mg_{17}Al_{12}$ contributes significantly o improved properties over the usage of aluminum alloys in these applications. Young's modulus of the γ-phase is about 80 GPa whereas for magnesium only 45 GPa. The maximum solid solubility of aluminum in magnesium is reasonably high at 12.9 wt.% Al at an eutectic temperature of 710 K (437 °C) whereas the equilibrium concentration at 473 K (200 °C) is about 2.9 wt.% Al. The volume diffusion coefficient (DV) for aluminum in magnesium can be determined using Fig. 6.54.

Precipitates with the Burgers OR [Burgers method of order (or disorder)] in the structure show such order parallel to the basal plane of the matrix, i.e. $(0001)_\alpha$ whereas precipitates with optional ORs lie on the prism plane of the magnesium, i.e. $(1\bar{1}00)_\alpha$ and they are perpendicular to the basal plane of the matrix. The strain caused by the γ phase, $Mg_{17}Al_{12}$ precipitate may be seen clearly from its eigenstrain matrix. In this case, the hcp α phase must be transformed to a regular cubic γ-phase. During transformation, the coordinates system of matrix x^α_1-x^α_2-x^α_3 must be changed to the coordinates of precipitate, ξ^γ_1-ξ^γ_2-ξ^γ_3. The following figure shows a scheme of the transformation of the α phase to the γ precipitate according to the Burgers OR and the Crawley OR methods of disorganization (Fig. 6.55).

In a "as-cast", microstructure of a magnesium alloy, the γ-phase, is the main constituent of the more or less divorced eutectic, but it should also be noted that in slow cooled castings, it may also create discontinuous

$$D_V = 12 \times 10^{-4} \exp\left\{\frac{144 \times 10^3}{RT}\right\} m^2/sec$$

FIGURE 6.54

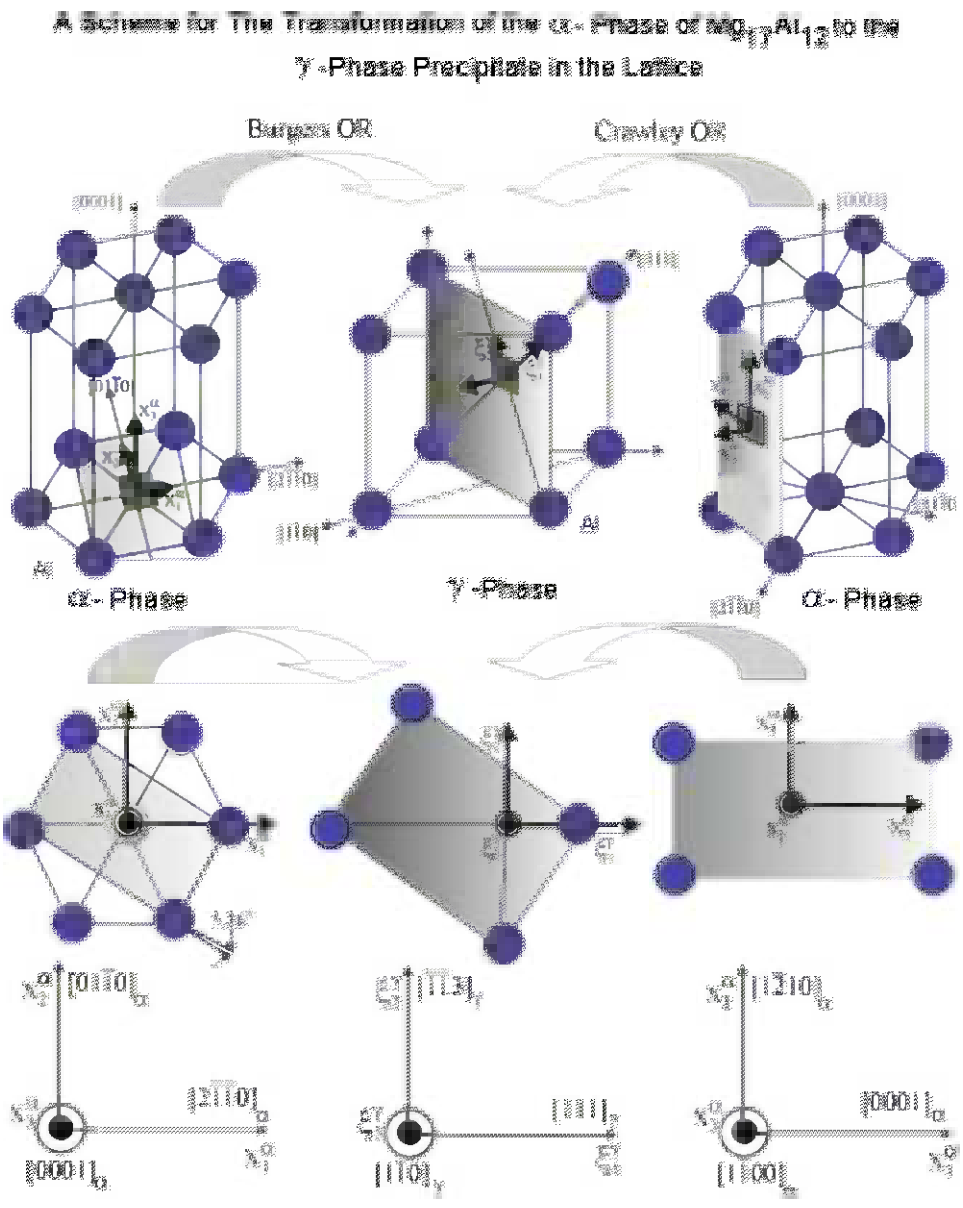

FIGURE 6.55

precipitates. After ageing of a supersaturated solid solution at 423 K, only discontinuous precipitates have been observed whereas at 623 K only continuous ones are were revealed in the microstructure. At intermediate ageing temperatures, both discontinuous and continuous precipitates of the γ-phase occur. The spherical shape of γ-precipitates can be obtained if the correct precipitation and magnesium matrix deformation processes are carefully controlled. The following illustrates the entire process to obtain spherical precipitates of $Mg_{17}Al_{12}$ particles in a metal matrix of magnesium alloys (Fig. 6.56).

The hydriding behavior of the $Mg_{17}Al_{12}$ intermetallic compound was studied in detail. It was found that the $Mg_{17}Al_{12}$ compound can initially react with hydrogen to form Mg_2Al_3, MgH_2 and Al at 573 K (300 °C). Increasing the hydrogenation temperature to 623 K (350 °C), further hydriding leads to the decomposition of Mg_2Al_3 into the hydride MgH_2 and the Al-based solid solution $Al_{0.9}Mg_{0.1}$.

The reactions are:

$$2Mg_{17}Al_{12} + H_2 \Rightarrow 8Mg_2Al_3 + MgH_2 + 2Al$$

$$3Mg_2Al_3 + H_2 \Rightarrow MgH_2 + MgAl_9$$

$$2Mg_{17}Al_{12} + 2H_2 \Rightarrow 5Mg_2Al_3 + 2MgH_2 + 2Al$$

Heating the hydrided mixture to about 650 °C causes the reverse reactions to occur.

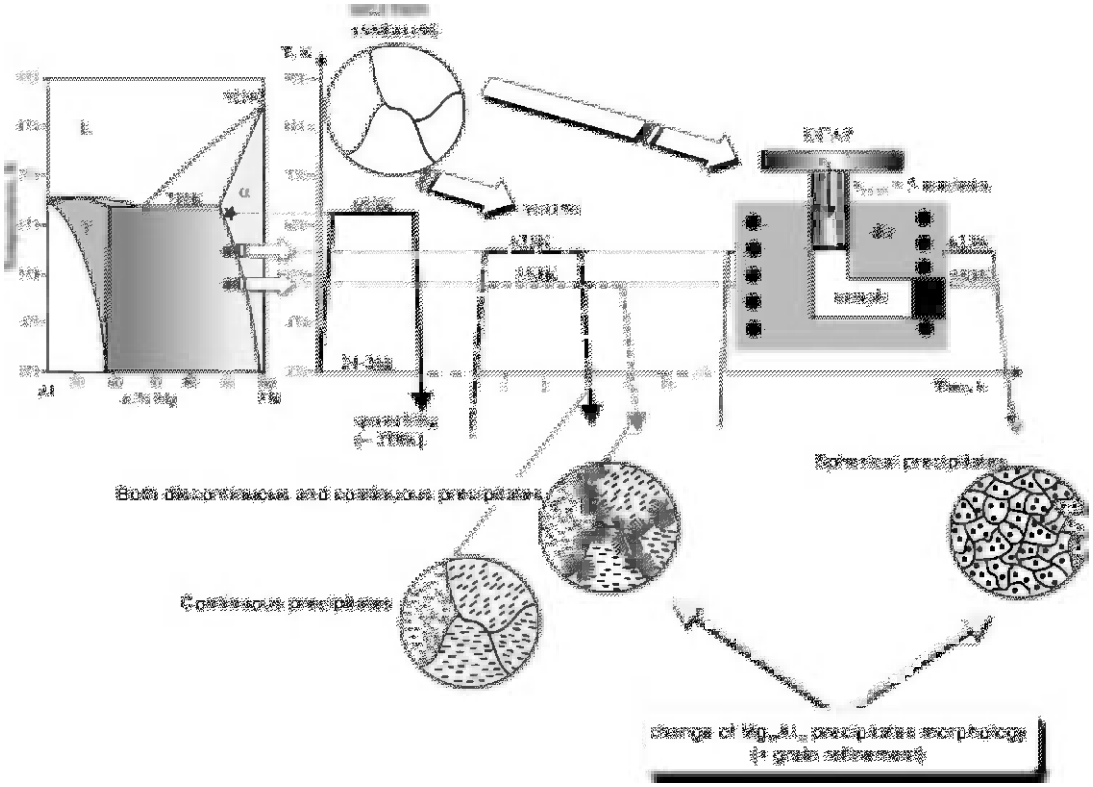

FIGURE 6.56

The crystallization behavior of the Mg–Al alloy (initial ratio Mg:Al = 17:12) prepared by ball milling (BM) was studied by means of XRD, differential scanning calorimetry (DSC), SEM and TEM. In the case of a short BM time (18 ks), we could prepare the mixture of nano-sized Mg and Al grains and the post annealing of the mixtures at even $T < 373$ K yielded formation of the fine and low-strained $Mg_{17}Al_{12}$ phase. In fact, the DSC analysis showed that only the sample after 18 ks of BM had a distinct exothermic peak at 373 K, corresponding to the formation of the $Mg_{17}Al_{12}$ and consisted of the compound from nano Mg and Al grains. The samples prepared for longer BM (144 ks) did not show equivalent the formation peak time. These samples were composed of nano-sized $Mg_{17}Al_{12}$ phase with heavy strained due to mechanical energy. In addition, the $Mg_{17}Al_{12}$ synthesized from the sample after 18 ks of BM is superior in hydrogen properties to the sample after 144 ks of BM. The synthesis of $Mg_{17}Al_{12}$, an intermetallic compound, by both mechanical alloying based on the high-energy BM, and bulk mechanical alloying based on the repeated forging process has been studied. These two processing techniques resulted in alloys with different crystal structures. After MA of up to 20 h, XRD peaks from the intermetallic $Mg_{17}Al_{12}$ with unalloyed Mg and Al were observed. On the other hand, the elemental Mg and Al powders were completely mechanically alloyed resulting in $Mg_{17}Al_{12}$ after 2000 cycles of BMA. (It should be emphasized that 2000 BMA cycles correspond to 4.4 h of processing time.) Compared with MA, BMA has a great advantage on processing time. From the pressure–composition (*P*–*C*) isotherm of BMA powder at 523 K, a plateau corresponding to the hydride formation clearly appeared at 0.06 and 0.04 MPa during absorption and desorption, respectively. It was confirmed that the alloy is able to absorb hydrogen up to 3.2 wt.% at 5.3 MPa, and is also able to desorb hydrogen at 523 K. When the hydriding starts, $Mg_{17}Al_{12}$ decomposed into $Mg_2Al_3 + MgH_2 + Al$. This reaction proceeds to $MgH_2 + Al$, as reported earlier. Then, these separated phases were recombined to $Mg_{17}Al_{12}$ phase upon dehydriding.

Magnesium aluminides are not generally available in the commercial marketplace.

Calcium Aluminides

Calcium forms four compounds in the Ca–Al system when the two elements are heated together. These are $CaAl_4$, $CaAl_2$, CaAl, and Ca_8Al_3. The phase diagram is presented as shown in Fig. 6.57.

Crystal structure data are given in the following table shown below. Only $CaAl_4$ and Ca_8 melt congruently with eutectics at 5.5, 66.3 and 79.8 atom% calcium. The other two melt incongruently (Table 6.5).

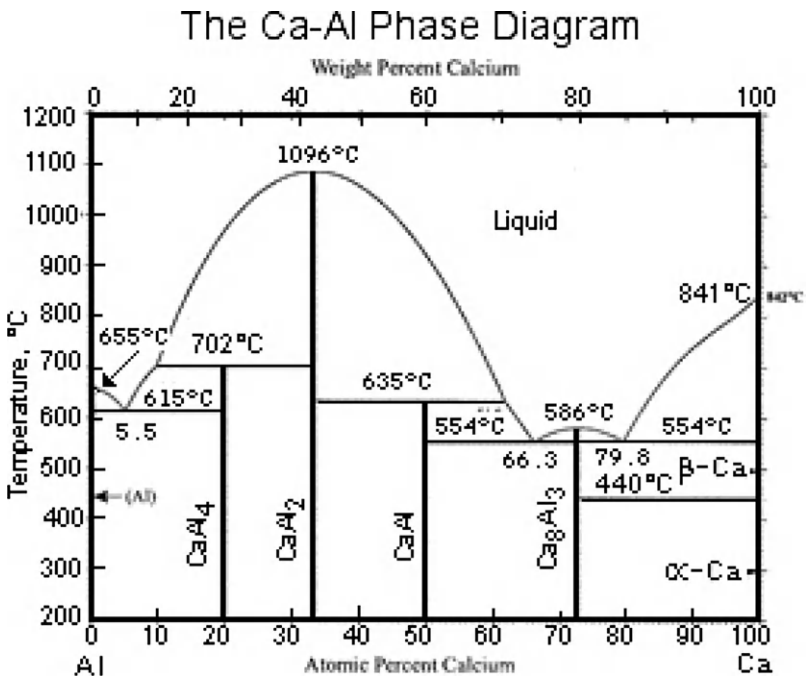

FIGURE 6.57

Calcium tetra-aluminide is dimorphic. The transition from the high-temperature tetragonal $CaAl_4$ structure (space group I4/mmm) to the low-temperature monoclinic (C2/m, $Z = 2$) phase is a slow process at room temperature. This compound has the structure shown in Fig. 6.58.

This is a top and side view of the monoclinically distorted body-centered tetragonal unit cell of $CaAl_4$ containing two formula units. This compound has been investigated as an electron-emitting electrode for a cathode in various devices. Cathodes are used in many devices ranging from microwave ovens, CRTs, to organic light-emitting diodes (OLEDs). Crucial materials properties are a low work function (Φ) and a (relatively) stable surface. In CRTs, a thin layer of a low-Φ metal is often present on top of a cathode made from a structurally stable material to enhance its electron-emitting properties. Electron injection into OLEDs strongly depends on the cathode work function. The lifetime of the device, on the other hand, derives from a subtle interplay between high voltages and reaction of the cathode with the organic material. OLEDs with single-element cathodes can be greatly improved, in terms of lifetime and luminosity, by first evaporating a small layer of a low-Φ metal on the polymer. The work function is defined as the amount of energy it takes to extract electrons from a metal, i.e. bring them from the Fermi level (E_F) to the vacuum V_{vac}.

$$\Phi = V_{Fermi} - V_{vac}$$

At locations that are microscopically far from the material, but macroscopically near it, Φ is surface dependent. $CaAl_4$ has been found to possess one of the lowest work functions known to date and is increasingly being used as a coating on emissive cathodes.

Reactions in the SrH_2–Al–H_2 system were studied by hydrogenation $\Leftrightarrow$ dehydrogenation of a $2SrH_2 + Al$ mixture prepared by BM of SrH_2 alloy under hydrogen. It was found that SrH_2 and Al can react with hydrogen to form Sr_2AlH_7 at 553 K (280 °C) when

TABLE 6.5

Cpd.	At% Ca	Entalpy-ΔH_f kJ/mol	Space group	Crystal structure	Prototype
$CaAl_4$	20	−27.2	I4/mmm	Body-centered tetragonal	$BaAl_4$
$CaAl_2$	33.3	−40.6	Fa1m	Face-centered cubic	$MgCu_2$
CaAl	50.0	—	—	Monoclinic	$(Ca_{13}Al_{14})$
Ca_8Al_3	72.7	−13.7	P**1**	triclinic	Ca_8In_3

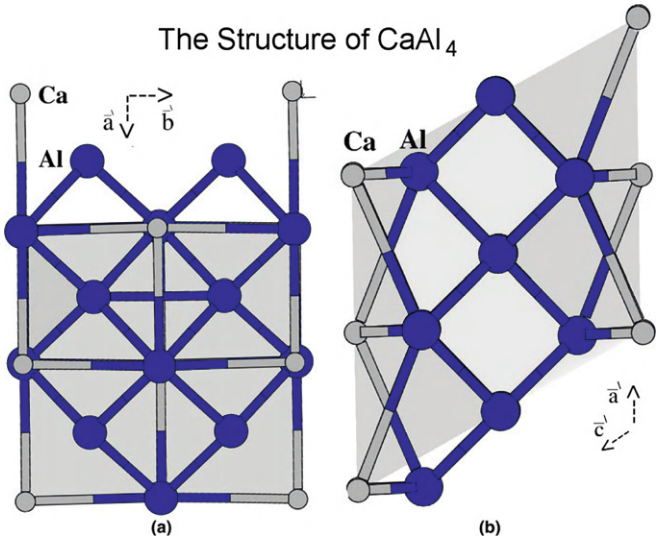

FIGURE 6.58

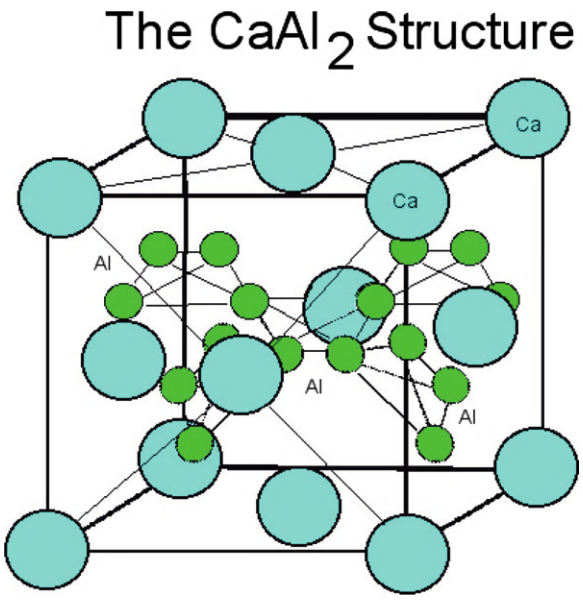

FIGURE 6.59

the hydrogen pressure is above 2.93 MPa. This reaction is reversible. The enthalpy change for the formation of Sr_2AlH_7 from $SrH_2 + Al + H_2$ is about -51 kJ/mol H_2. When the hydrogen pressure is below 1.76 MPa and the temperature is 553 K, $SrAl_2$ reacts with Al to form $SrAl_4$ and H_2 with an enthalpy change of 48 kJ/mol H_2. This reaction is irreversible. Similarly, Sr_2AlH_7 also decomposes into SrH_2, $SrAl_4$ and H_2 when the hydrogen pressure is below the equilibrium pressure of the irreversible reaction.

Calcium dialuminide, $CaAl_2$, has a cubic structure with $a_0 = 8.03$ Å and $Z = 4$. The structure is shown in the following Fig. 6.59.

The Ca atoms are located at (0,0,0) and in face-centered positions while the four Al_4 groups are located at $(\frac{5}{8},\frac{5}{8},\frac{5}{8})$ positions. $CaAl_2$ offers the possibility of high hydrogen storage capacity with extraordinary low material cost. However, $CaAl_2$ does not absorb as much hydrogen at near room temperatures, probably because, according to the Westlakeís empirical law, the distance between interstitial sites (T_{sites}) atoms is too large for simultaneous occupation of hydrogen to form an unstable hydride.

The addition of Si to $CaAl_2$ to form $CaAl_{1-x}Si_x$ produces a compound with superconductivity at $T_c = 7.7$ K. The $CaAl_{1-x}Si_x$ alloy, has been recently synthesized in the C_{32} structure in a wide composition range (x), and shown to be superconducting at all values of x. It has been shown that superconductivity is of electron–phonon type, and that the lower critical temperature with respect to MgB_2 can be understood because the electronic and vibrational states involved in the superconducting pairing are different. $CaAl_2$ is isoelectronic and isostructural to MgB_2, and thus represents an ideal candidate for the observation of superconductivity.

The hydriding behavior of pseudobinary $CaAl_{2-x}M_x$ (M = B, Si) where $0 < x < 1$ alloys with the C_{15} Laves phase structure was examined in the search for new metal hydrides for hydrogen storage. The initial activation for hydriding proceeded at an H_2 pressure of 3 MPa and at temperatures between 300 and 400 °C without changing their phase structure or decomposing thermally. The $CaAl_{1.8}B_{0.2}$ alloy absorbed the largest amount of hydrogen among these alloys, forming $CaAl_{1.8}B_{0.2}H_{0.6}$ at an H_2 pressure of 1 MPa at 60 °C.

Trideca-calcium tetradeca-aluminide, $Ca_{13}Al_{14}$, can be obtained by fusion of the appropriate mixture of the elements in Ta containers at 1100 °C followed by annealing at 600 °C or slow cooling. The structure was determined by single-crystal X-ray means. $Ca_{13}Al_{14}$ crystallizes with monoclinic symmetry (space group C2/m (no. 12), $Z = 2$, $a = 15.551$ Å, $b = 9.873$ Å, $c = 9.726$ Å, $\beta = 108.09°$), $Ca_{13}Al_{14}$ contains a two-dimensional Al network structure composed of planar hexagonal six-membered rings, planar rhombus (four-membered) rings, and trigonal three-membered rings. An electron count on the basis of the simple Zintl–Klemm formalism for three- and four-bonded Al in $Ca_{13}Al_{14}$ suggests that the phase is closed shell. However, full band structure calculations within the extended Huckel formalism indicate that it is metallic, with considerable Ca–Al covalency and, characterically, with all the Al–Al bonding states just filled at EF. The descriptor "metallic Zintl phase" is apt (Fig. 6.60).

The ladder-like structure of the Al atoms is clearly evident.

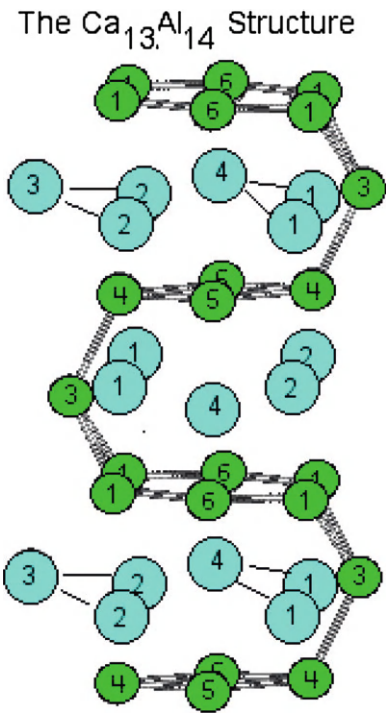

FIGURE 6.60

Octa-calcium tri-aluminide, Ca_8Al_3, can be prepared as the pure Ca_8Al_3 intermetallic compound by induction melting of appropriate amounts of pure metals and subsequent annealing. Ca_8Al_3 has the triclinic Ca_8In_3-type structure (Pi (no. 2), $Z = 2$, $a = 9.484$ Å, $b = 9.592$ Å, $c = 9.671$ Å, $\alpha = 99.02°$, $\beta = 101.13°$, $\gamma = 119.55°$). Ca_8Al_3 contains isolated Ca and Al atoms and is slightly electron rich relative to classical valence rules. This compound is a good metallic conductors with Pauli-paramagnetic-like properties.

The hydrogenation behavior of the Ca_8Al_3 compound was studied in detail. It was found that the Ca_8Al_3 compound can react with hydrogen to form CaH_2 and Al starting from 373 °K, but the process is very sluggish at this low temperature. Prior to the decomposition, the lattice parameters of Ca_8Al_3 do not change, indicating that the compound does not absorb hydrogen to form a solid solution. By increasing the hydrogenation temperature to 523 °K, the hydrogen-induced decomposition of Ca_8Al_3 occurs entirely.

Calcium aluminides are not generally available commercially. There have been no CAS numbers assigned.

Strontium Aluminides

The strontium aluminum and barium–aluminum systems have been examined by thermal, micrographic and X-ray methods. Compounds corresponding to the following compositions were observed: $SrAl_2$ (936 °C), $SrAl_4$ (1040 °C); Sr_8Al_7 (667 °C). Only $SrAl_4$ melts congruently. Eutectic points occur at 81.75 atom% Sr (590 °C) in this system (Fig. 6.61).

The crystal parameters are shown in Table 6.6.

Strontium tetra-aluminide, $SrAl_4$, has the $BaAl_4$ type of structure shown in Fig. 6.62.

Two types of this Zintl structure are shown in which cubic Al_4^{-2} or pentagonal Al_5^{2-} clusters predominate. In this structure, four groups are present in the unit cell.

The synthesis, structural characterization and the properties of the Zintl hydrides, AeE_2H_2 and AeAlSiH (Ae = Ba, Ca, Sr; E = Al, Ga, In), have been reported. The first hydride in this class of compounds is $SrAl_2H_2$ that was discovered under an experiment by Gingl, who hydrogenated $SrAl_2$ at various temperatures (Gingl et al. 2000). The intention was to form alanates, e.g. AlH_4, by terminating the three-dimensional four-connected aluminum network in $SrAl_2$. The new hydride, $SrAl_2H_2$, has a partially conserved aluminum network. The three-dimensional anionic network in $SrAl_2$ is reduced to two dimensions in the hydride, with aluminum bonded to both aluminum and hydrogen. This type of bonding configuration has not been observed before.

Strontium dialuminide, $SrAl_2$, has the structure shown as follows. In $SrAl_2$, the aluminum atoms are arranged three dimensionally in a negatively charged net. When Gingl did an in situ X-ray measurement while heating a sample of strontium aluminide under hydrogen pressure, he discovered a new type of hydride with most of the aluminum structure conserved (Fig. 6.63).

The three-dimensional network had been reduced to a two dimensional one with hydrogen atoms attached in the vacant positions. Orthorhombic $SrAl_2$, $SrZn_2$ and $BaIn_2$ crystallizes in the space group *Imma* ($CeCu_2$ structure type). Their structure consists of puckered hexagon layers of Al atoms, which are stacked on top of each other. The Al atoms have a distorted tetrahedral environment: they are linked to three neighbors within a puckered layer and to a fourth one in the adjacent layer either above or below, thus forming a three-dimensional polymer Zintl anion. The Al–Al atom distances within a layer are considerably shorter than the one linking layers. The difference is about 0.1 Å for $SrAl_2$ and $BaIn_2$. The positive ions are located between the nets, slightly displaced from the centers of the hexagons. According to the Zintl concept, Al atoms are formally reduced by electropositive Sr. In- and Al-atoms isolectronic to Si and, thus, the formation of a polyanionic three-dimensional four-connected network in these compounds is reasonable. However, the Al–Al distances in $SrAl_2$ are rather large (2.78 and 2.88 Å) and much closer to the Al–Al nearest neighbor distance in fcc-Al (2.86 Å) than to the distance expected

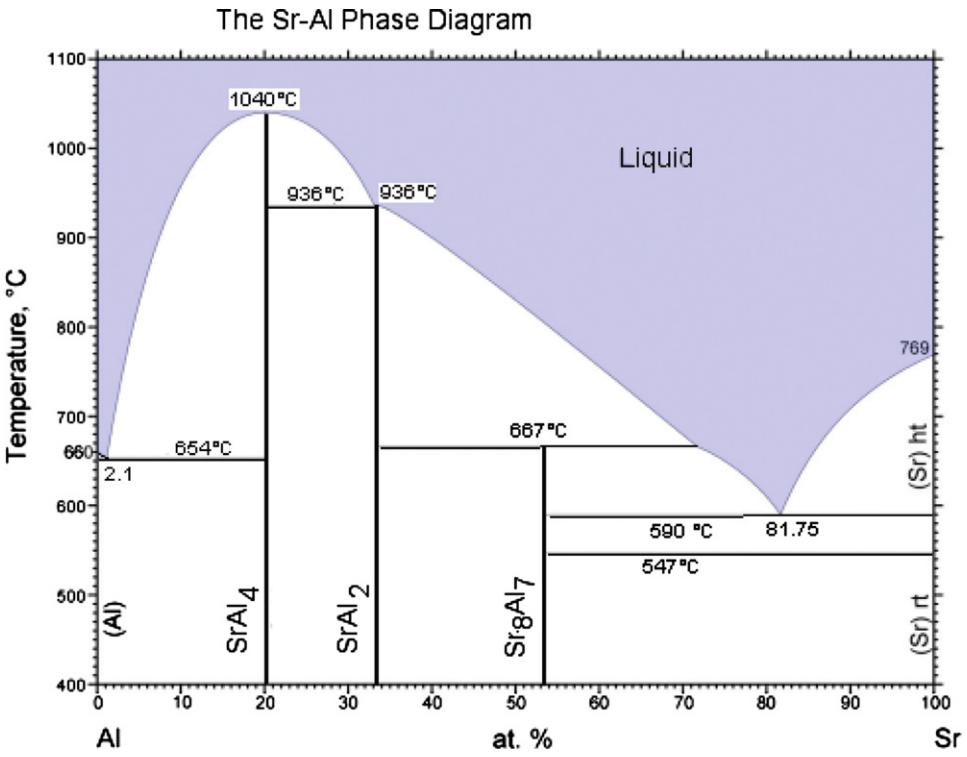

FIGURE 6.61

for a pair of two-electron two-center-bonded Al atoms (around 2.6 Å).

The hydrogenation of $SrAl_2$ is clear-cut, 190 °C and 50 bar, compared to the difficult synthesis of alanates and alane, AlH_3. The latter synthesis uses aluminum in its zero oxidation state in contrast to the synthesis of $SrAl_2H_2$ from $SrAl_2$. (In the $SrAl_2$ precursor, aluminum is reduced by the electropositive metal to −1.) Hence, this discovery shows a different route to alanates by using precursors with aluminum in a reduced state. If $SrAl_2H_2$ is further hydrogenated at 250 °C, the two-dimensional network breaks and Sr_2AlH_7 forms. The hydride, $SrAl_2H_2$, decomposes around 300 °C at 1 atm (Fig. 6.64).

The hydride, Sr_2AlH_7, decomposes into SrH_2, $SrAl_4$, and H_2 when the H_2 pressure is below the equilibrium pressure of the irreversible reaction. Sr_2AlH_7 has a very interesting structure (Fig. 6.65).

The monoclinic structure consists of isolated $[AlH_6^{3-}]$ octahedra and $[HSr_4]^{7+}$ units. The $[HSr_4]^{7+}$ tetrahedra are connected via shared edges and form infinite one-dimensional twisted chains. The heavy atom structure and hydrogen positions were determined, respectively, by X-ray powder diffraction and time-of-flight neutron powder diffraction. They crystallize with a new monoclinic structure in space group I2 (No. 5); cell parameters: $a = 12.575$ Å, $b = 9.799$ Å, $c = 7.991$ Å, $\beta = 100.270(4)°$ (hydride), $a = 12.552$ Å, $b = 9.7826$ Å, $c = 7.9816$ Å, $\beta = 100.286°$ (deuteride), $Z = 8$. Sr_2AlH_7 is the first example that consists of isolated $[AlH_6]$ units and infinite one-dimensional twisted chains of edge-sharing $[HSr_4]$ tetrahedra along the crystallographic c-axis.

Octa-strontium Hepta-Aluminide, Sr_8Al_7, is cubic and has the cell parameters of: $a = 12.76$ Å and a cell volume of 207.755 $Å^3$, $Z = 8$ (Fig. 6.66).

TABLE 6.6

Lattice parameters, Å					
Compound	**Space group**	***a***	***b***	***c***	**Type**
$SrAl_4$	D_{4h}^{17}-I4/mmm	4.463		11.023	$BaAl_4$
$SrAl_2$	D_{2h}^{28}-Imma	4.793	7.922	7.937	$CeCu_2$
Sr_8Al_7	Pm2	12.753			Cubic

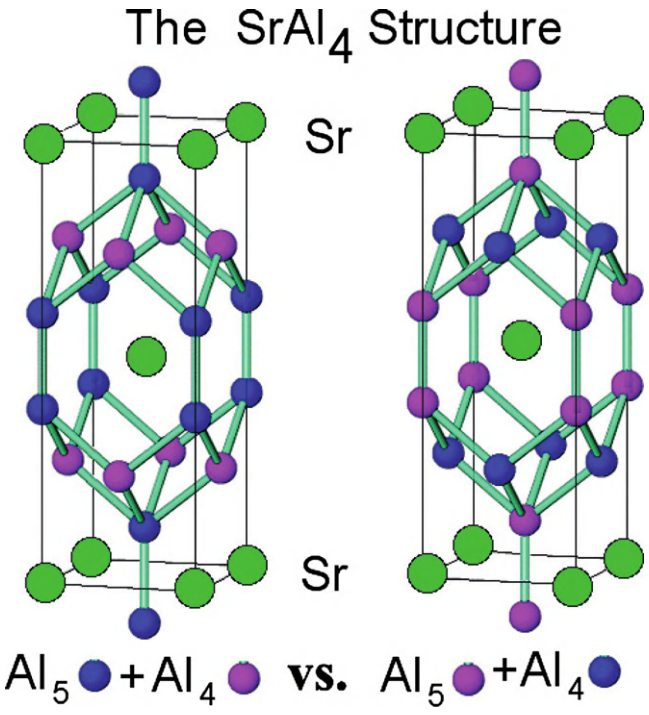

FIGURE 6.62

The structure is composed of Al_7^{16-} units, surrounded by eight Sr^{2+} atoms. The atom coördinates for this structure is shown in Table 6.7.

The Al-building block consists of a tetragonal unit attached to a triangular unit (Fig. 6.67).

Little usage has been found for this compound.

In addition to the above described compounds shown in the phase diagram, the compound, **pentastrontium nona-aluminide**, Sr_5Al_9, has been characterized. It is rhombohedral with: $a = 5.88$ Å, $c = 35.71$ Å, space group = R**3**m, $Z = 4$ and melts at 835 °C. The structure can be visualized as being composed of two building blocks as shown in the following Fig. 6.68.

The structure is composed of Sr_4Al_6 and Sr_6Al_9 building blocks, arranged in an alternating fashion. Little research has been accomplished on the physical properties of this compound other than its melting point that is congruent.

Strontium aluminides are not generally available commercially. However, a "strontium aluminide" is offered for sale with the assigned CAS number of 53169-53-2. No details concerning its composition were forthcoming.

Barium Aluminides

Barium and aluminum can form several compounds as can be determined from examination of the phase diagram. A CAS number of 12253-23-5 has been assigned for a "barium aluminide" product but the specific composition is not generally specified. The phase diagram shows five compounds formed when the two elements are melted together. The specific composition of the compound depends upon the atom ratio used to form the melt (Fig. 6.69).

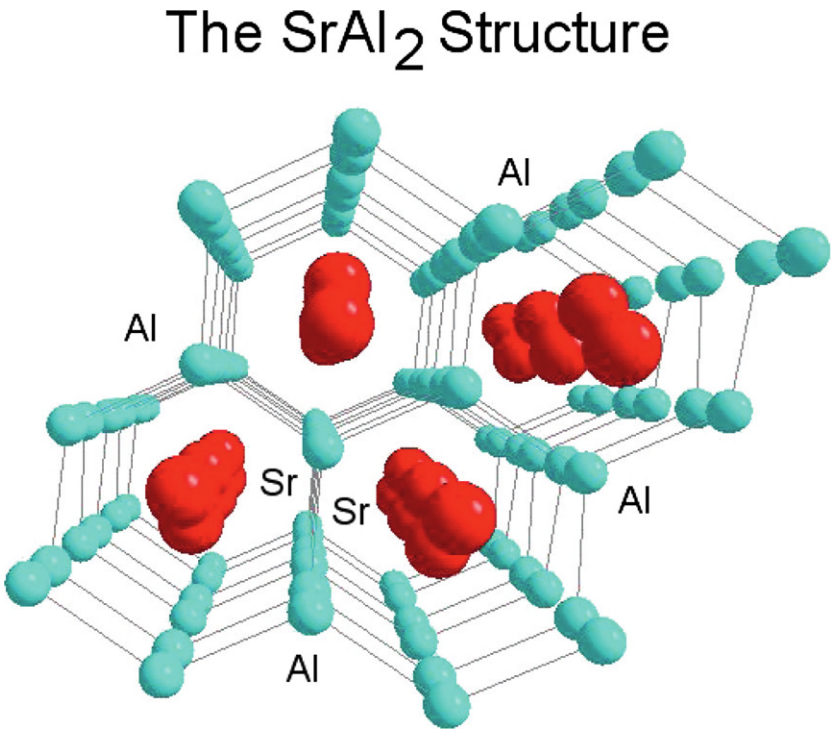

FIGURE 6.63

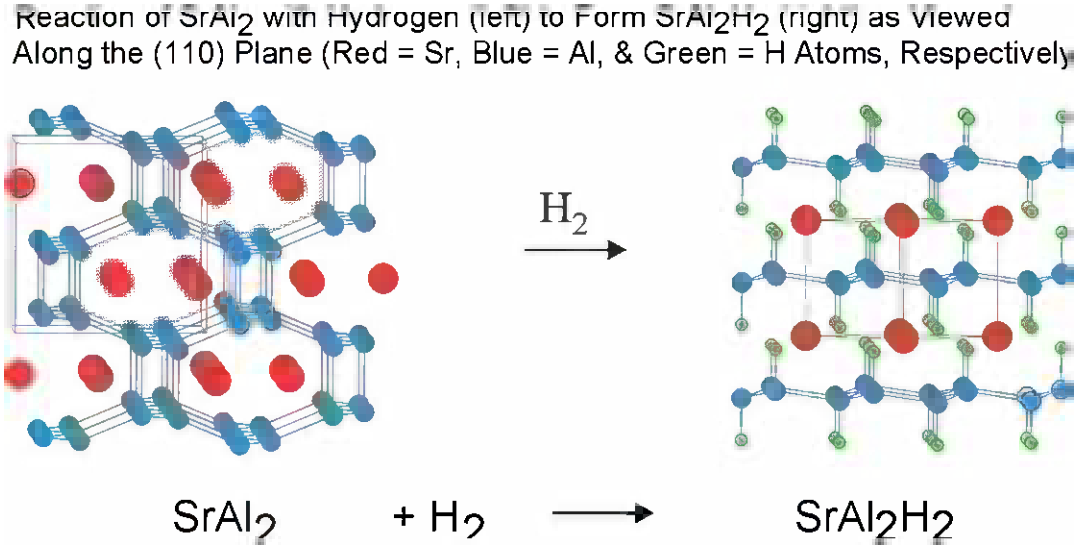

FIGURE 6.64

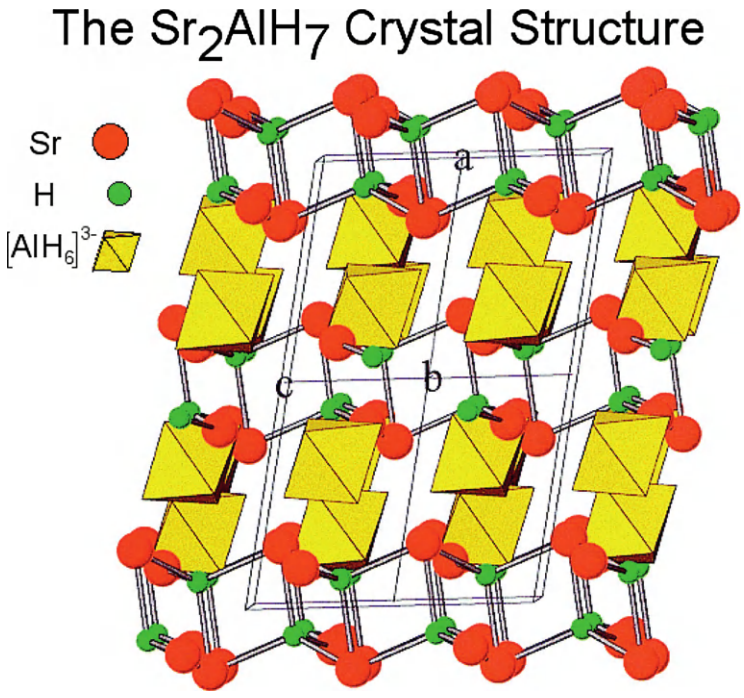

FIGURE 6.65

The unit-cell parameters of these compounds are shown in Table 6.8.

Ba_7Al_{13} was originally mistaken for $Ba_{21}Al_{40}$ but a comparison is given in the table.

Barium tetraaluminide, $BaAl_4$, has a unique structure adopted by many other compounds. It was the first of its kind to have the structure elucidated (Fig. 6.70).

Two types of this Zintl structure are shown in which cubic Al_4^{-2} or pentagonal Al_5^{2-} clusters predominate. In this structure, four groups are present in the unit cell. The Al atoms form groups of two different types of clusters.

These clusters can alternate in succession as shown in the Fig. 6.71 diagram:

Six unit cells are shown along with the possible alternate packing schemes. Ternary $BaAl_4$-type derivative structures are frequently found with silicide and germanide compounds.

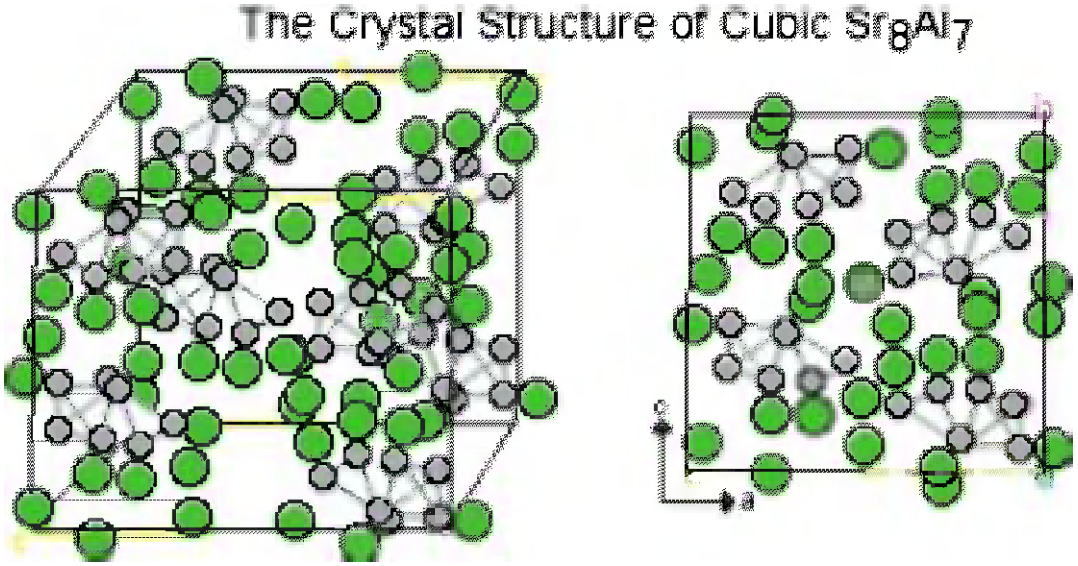

FIGURE 6.66

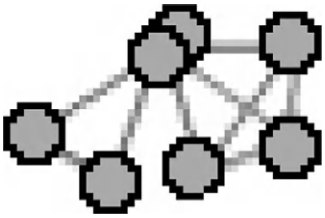

FIGURE 6.67

The Ba atoms occupy two kinds of sites at the center of an almost regular 16-atom coordination polyhedron. All Ba atoms on the tetrahedral site are surrounded by a tetrahedron of Al atoms while those on the pyramidal site are surrounded by five Al atoms in the form of a square pyramid. Another view of this structure is shown in Fig. 6.72.

The $BaAl_4$–tI10 structure, having a general composition MN_2X_2, is not only the most populous of all known structure types, being adopted by some 400 phases, but is representative of a new group of metallurgically important structures that do not adhere to classifications of Cu-type close packings or tetrahedral close packings. The structure can be described by a square pyramidal framework of N and X atoms which by edge-sharing from slabs in (001) planes, the slabs being interconnected by X–X bonds along [001] (in perhaps 10% of the phases no [001] X–X bonds exist). This framework creates tetragonal hexagonal prismatic voids, that enclose the large M atoms. The average observed distances of N–X and [001] X–X can be interpreted in a model that shows that the framework, that is responsible for structural stability, accounts for almost all of the valency electrons provided by N and X. The M atoms (diameters 3.1–5.1 Å) are accommodated in the voids of the framework according to the principles of geometrical packing, apparently without size restriction. In some cases, M–N or M–X interactions are shown to control the variable a, c, and z_X structural parameters, but they only very

TABLE 6.7

1	Sr1	Sr	12	b	1	0.0011	0.2987	0.4421	1.0
2	Sr2	Sr	12	b	1	0.0613	0.5186	0.2025	1.0
3	Al1	Al	12	b	1	0.0760	0.2390	0.1941	1.0
4	Al2	Al	12	b	1	0.2467	0.3133	0.5831	1.0
5	Al3	Al	4	a	.3.	0.0689	0.0689	0.0689	1.0
6	Sr3	Sr	4	a	.3.	0.3127	0.3127	0.3127	1.0
7	Sr4	Sr	4	a	.3.	0.6852	0.6852	0.6852	1.0
1	Sr1	Sr	12	b	1	0.0011	0.2987	0.4421	1.0

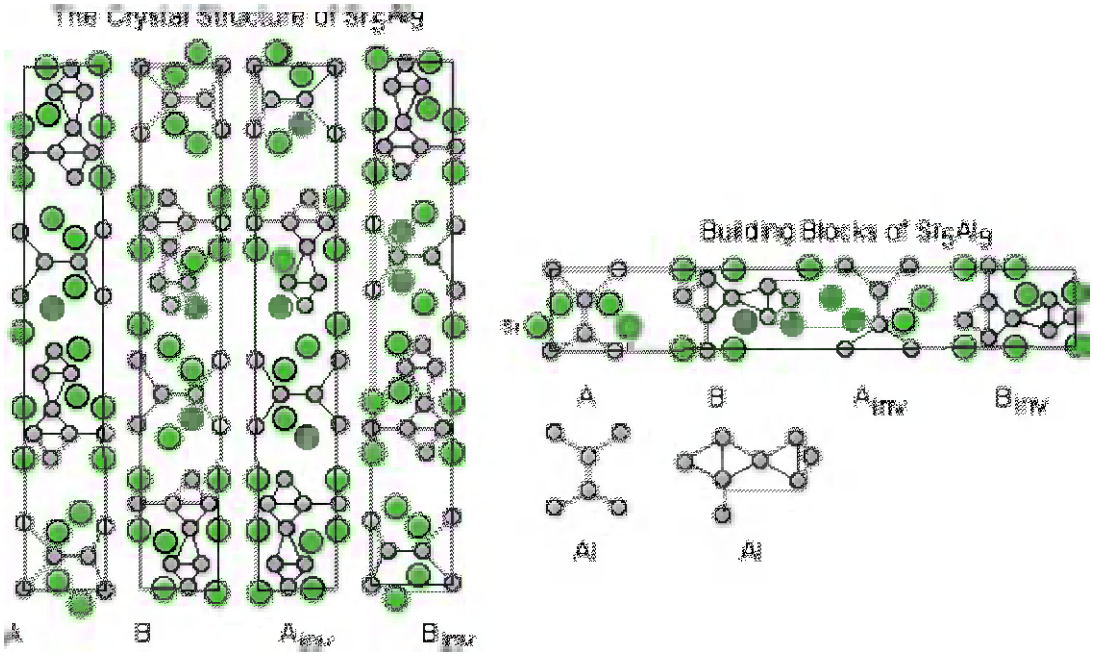

FIGURE 6.68

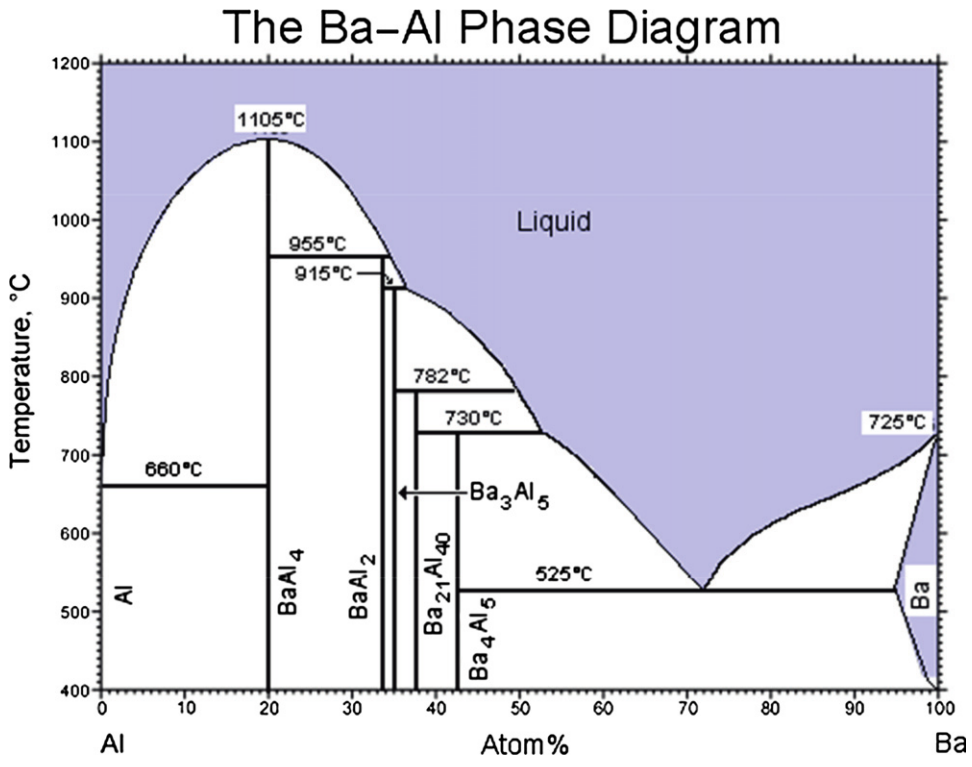

FIGURE 6.69

modestly influence the N–X distances of the framework. A comparison with the Cu_2Sb–tP6 structure was made.

A recent work (2002) has presented a detailed, combined experimental and theoretical study on the structural stability of s–p bonded compounds with the $BaAl_4$ structure type (space group I4/mmm, $Z = 2$) as part of a broad program to investigate the complex questions of structure formation and atomic arrangements in polar intermetallics. From ab initio calculations employing pseudo-potentials and a plane wave basis set,

TABLE 6.8

Group			Lattice parameters (Å)					
Compound	Point	Space	*a* (α)	*b* (β)	*c* (γ)	Z	V (Å^3)	Type
$BaAl_4$	D_{4h}^{17}-T1$_{10}$	I4/mmm	4.566 (111°)	4.566 (111°)	6.487 (90°)	2	117.27	$BaAl_4$
$BaAl_2$	O_h^7	Fd3m	6.153 (60°)	6.153 (60°)	6.153 (60°)	2	164.7	Face-centered cubic
Ba_3Al_5	hP16	P6$_3$/mmm	6.066 (90°)	6.066 (90°)	6.066 (90°)	2		Hexagonal
$Ba_{21}Al_{40}$	hP61	P31m	6.105 (90°)	6.105 (90°)	17.252	2	555.9	Tetragonal
Ba_4Al_5	hP16	P6$_3$/mmm	6.103 (90°)	6.103 (90°)	17.501 (120°)	2	574.2	Tetragonal
Ba_7Al_{13}		P3m1	6.100		17.25			Trigonal

extracted optimized structural parameters, binding energies, and the electronic structure of the systems $AeX(III)_4$, $AeX(II)_2X(IV)_2$, $AeX(II)_2X(III)_2$ (Ae = Ca, Sr, Ba; X(II) = Mg, Zn; X(III) = Al, Ga; X(IV) = Si, Ge) were determined. For all systems, a pronounced pseudo-gap in the density of states separating network X_{42}- bonding from antibonding electronic states that coincides with the Fermi level for an electron count of 14 electrons per formula unit, the optimum value for stable $BaAl_4$-type polar intermetallics. However, the synthesis and structural characterization (from X-ray single-crystal and powder diffraction data) of the new compounds $AeZn_2$–Al^{2+}, $AeZn_2$–$\delta Ga_{2+\delta}$ (Ae = Ca, Sr, Ba; $\delta = 0$–0.2) and $AeMg_{0.9}Al_{3.1}$, $AeMg_{1.7}Ga_{2.3}$.

(Ae = Sr, Ba) manifested that electron deficiency is quite frequent for $BaAl_4$-type polar intermetallics. The site preference for different "X" elements in the ternary systems was quantified by calculating "coloring energies", which, for some systems, was strongly dependent on the size of the electropositive Ae component. The Ae^{2+} cations decisively influence the nearest neighbor distances in the encapsulating polyanionic networks X_4^{2-} and the structures of these networks are surprisingly flexible to the size of the Ae component without changing the overall bonding picture. A monoclinically distorted variant of the $BaAl_4$ structure occurs when the

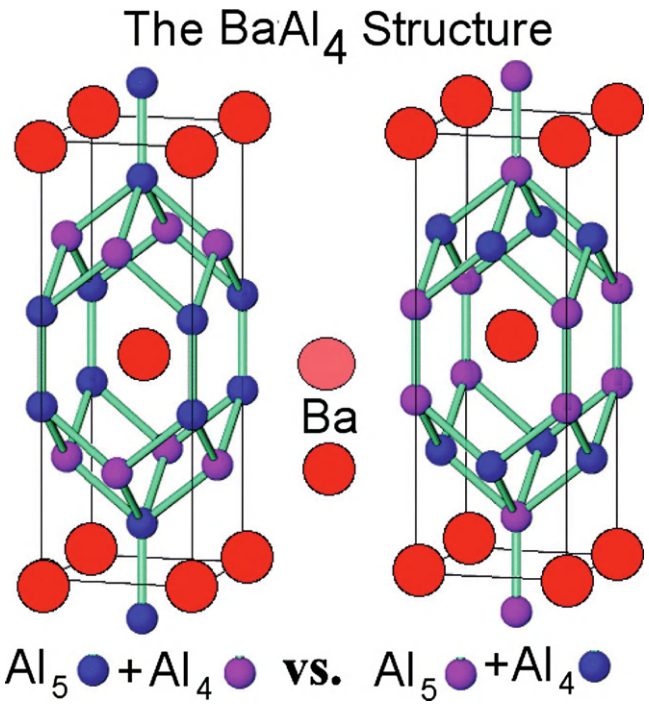

FIGURE 6.70

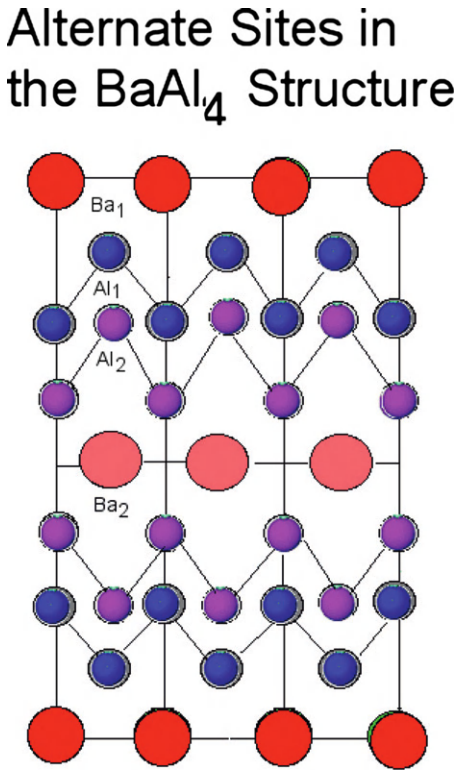

FIGURE 6.71

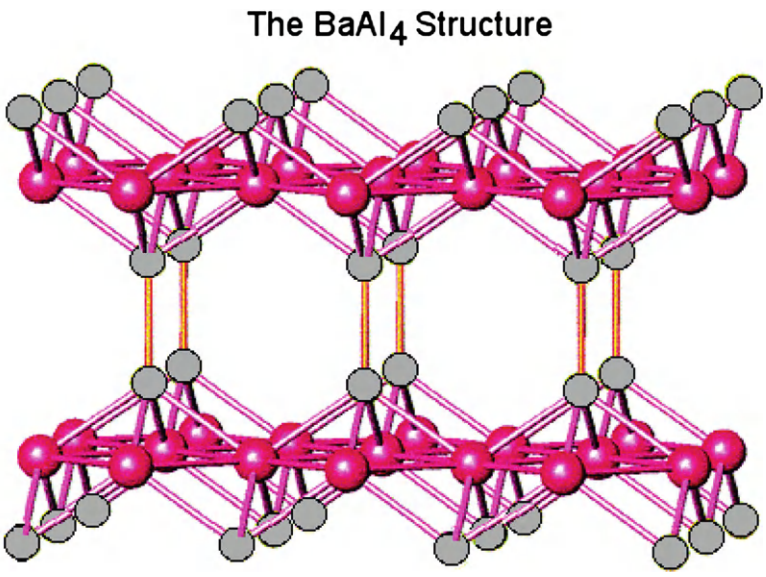

FIGURE 6.72

cations become too small for matching the size of encapsulating X_4^{2-} cages. An even larger size mismatch leads to the formation of the $EuIn_4$ structure type.

$BaAl_4$ has been studied in regard to its work function. The relationship between the work function (Φ) and the surface stability of compounds is not exactly known but is very important for applications such as OLEDs. This relation was studied using first-principles calculations on various surfaces of crystal $BaAl_4$. The most stable surface [Ba-terminated (001)] has the lowest Φ (1.95 eV), which is lower than that of any elemental metal including the metal, Ba. Adding barium to this surface neither increases its stability nor lowers its work function. $BaAl_4$ is also strongly bound. These results run counter to the common perception that stability and a low Φ are incompatible. In addition, a large anisotropy and a stable low-work function surface has been predicted for intermetallic compounds with polar surfaces.

Barium dialuminide, $BaAl_2$, is cubic and crystallizes in the Laves $MgCu_2$ (C15) face-centered structure (Fig. 6.73).

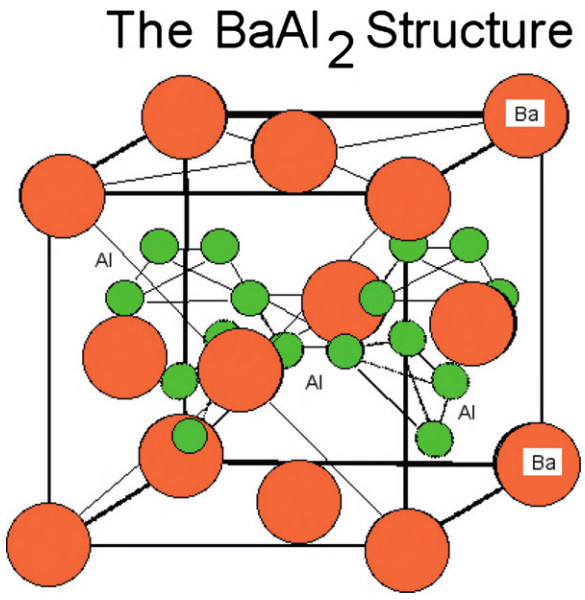

FIGURE 6.73

The Ba atoms are located at (0,0,0) and in face-centered positions while the four Al_4-groups are located at $(\frac{5}{8},\frac{5}{8},\frac{5}{8})$ positions. These Al_4 groups have the configuration shown in Fig. 6.74.

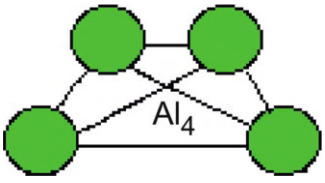

FIGURE 6.74

The atom arrangement in the structure is shown in Table 6.9.

$BaAl_2$ offers the possibility of high hydrogen storage capacity with extraordinary low material cost. However, $BaAl_2$ does not absorb as much hydrogen at near room temperatures, probably because, according to the Westlakeís empirical law, the distance between interstitial

TABLE 6.9

No	Site notation	Atom	Multiplicity	Wyckoff	Site symmetry	*x*	*y*	*z*	Occupancy
1	Al	Al	16	c	.-3m	0	0	0	1.0
2	Ba	Ba	8	b	-43m	3/8	3/8	3/8	1.0

sites (T_{sites}) atoms is too large for simultaneous occupation of hydrogen to form an unstable hydride. According to one source, Ba does not form $BaAl_2$ with Al but forms Ba_7Al_{13}. A new type of hydride, $BaAlH_5$, was formed by hydrogenation of Ba_7Al_{13} under a hydrogen pressure of 7 MPa at 513 K for 5 days (Fig. 6.75).

It crystallizes with a novel orthorhombic structure in the space group Pna21, cell parameters: $a = 9.194$ Å, $b = 7.0403$ Å and $c = 5.1061$ Å.

The crystal structure of $BaAlH_5$ contains Al-centered hydride octahedra [AlH_6], which share one-corner and form one-dimensional zigzag chains along the crystallographic *c*-axis. Because of this interesting arrangement of hydrogen atoms, $BaAlH_5$ has a larger H/M ratio than $NaAlH_4$ and Na_3AlH_6. If some light elements can be used as substitutes for Ba, the weight percent of hydrogen will increase considerably.

$BaAlH_5$ and Ba_2AlH_7 were successfully synthesized through reactive BM commercially available BaH_2 and Al powders for the first time. The effects of the mole ratios of BaH_2/Al on the phase formation and structural properties were investigated by means of an x-ray diffraction method and a subsequent Rietveld refinement. For different BaH_2/Al mole ratios (0.5, 1.0 and 2.0), the main phases were $BaAlH_5$, Ba_2AlH_7 and BaH_2, respectively. Ba_2AlH_7 can also be prepared by

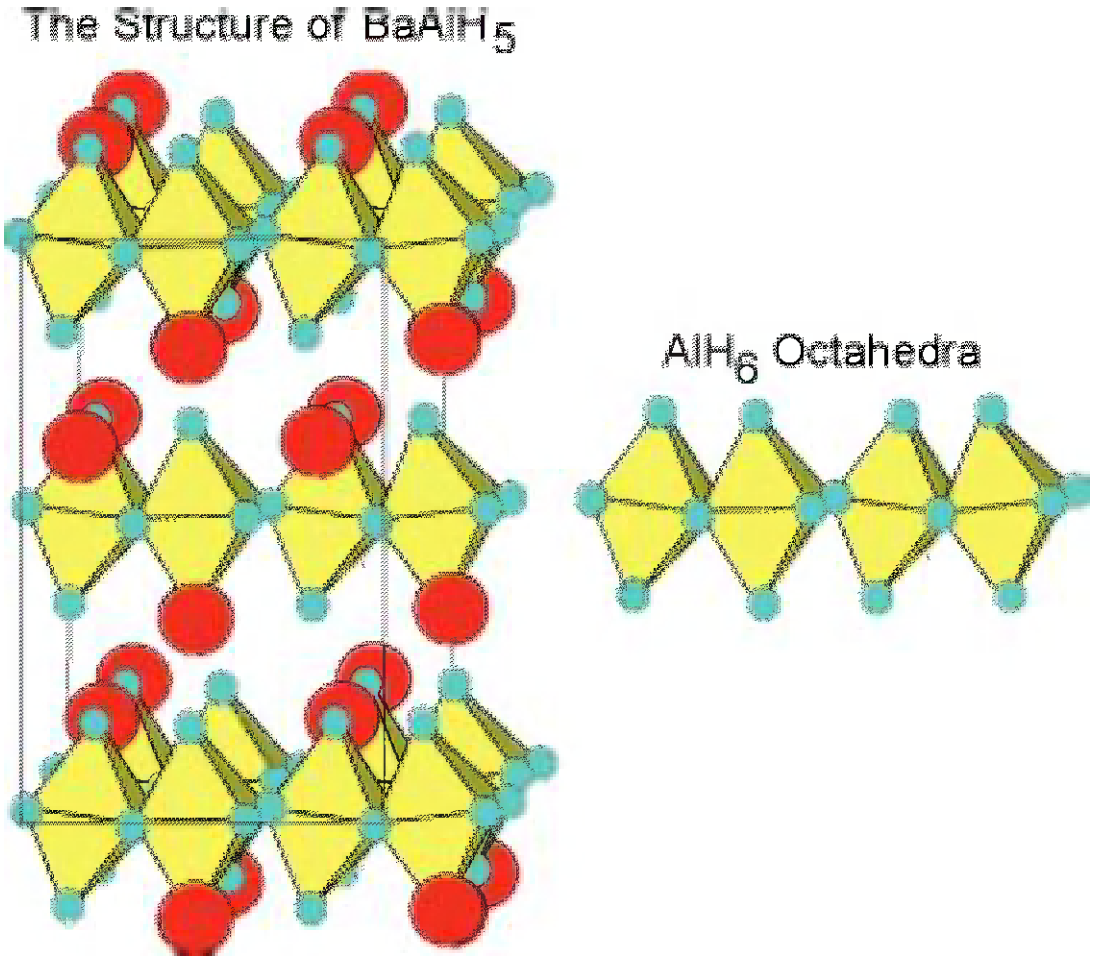

FIGURE 6.75

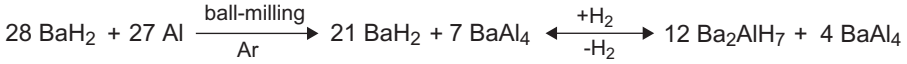

FIGURE 6.76

BM BaH_2/Al (1:1) under Ar and a subsequent hydrogenation. The phase transition and hydriding/dehydriding characteristics of the ball-milled BaH_2/Al (1:1) system under Ar were investigated using in situ DSC under H_2 atmosphere and pressure–composition isotherms (PCI). The mechanochemistry-induced phase transformation of the BaH_2/Al (1:1) mixture to a BaH_2/$BaAl_4$ (3:1) mixture during BM under Ar was first observed. The hydrogenation enthalpy of BaH_2/$BaAl_4$ (3:1) to form Ba_2AlH_7 was determined to be −20.0 kJ/mol from a van't Hoff plot. The phase transitions during BM under Ar and PCT measurements were proposed as shown in Fig. 6.76.

High-pressure forms of intermetallic compounds with the composition $CaZn_2$, $SrZn_2$, $SrAl_2$, and $BaAl_2$ were synthesized from $CeCu_2$-type precursors ($CaZn_2$, $SrZn_2$, $SrAl_2$) and $Ba_{21}Al_{40}$ by multianvil techniques and investigated by X-ray powder diffraction ($SrAl_2$ and $BaAl_2$), X-ray single-crystal diffraction ($CaZn_2$), and electron microscopy ($SrZn_2$). Their structures correspond to that of Laves phases. Whereas the dialuminides crystallize in the cubic $MgCu_2$ (C15) structure, the dizincides adopt the hexagonal $MgZn_2$ (C14) structure. This trend is in agreement with the structural relationship displayed by *sp*-bonded Laves phase systems (face-centered cubic) at ambient conditions.

Tribarium pentaaluminide, Ba_3Al_5, is cubic. The structure has a sequence of layers similar to that of the $MgZn_2$ type of Laves phases, but with a slightly different arrangement of the Al_4 tetrahedra. In Ba_3Al_5, isolated pairs of tetrahedra are joined, instead of the infinite columns present in many Laves phases. Segments of the Ba_3Al_5 are also present in the Ba_4Al_5 phase. The Laves phases crystallize in three structure types, which are named after the representatives cubic $MgCu_2$ (*C15*), hexagonal $MgZn_2$ (*C14*) and hexagonal $MgNi_2$ (*C36*). The "A" and "B" parts (Ae = Mg, Ca, Sr and Ba) (B = Al, Si and others) exhibit distinctive structures as shown in the following Fig. 6.77.

They are polytypes with a common underlying structure principle. In the first half of the last century, it was shown by J.B. Friauf, F. Laves, G.E.R. Schulze, F.C. Frank and J.S. Kasper that the Laves phases can be regarded as tetrahedrally close-packed structures from atoms A and B with ideal ratio of the radii of rA/rB = (3/2)1/2. The A atoms are surrounded by a Z16 Frank–Kasper polyhedron (16 vertices decorated with 12 B atoms and 4 A atoms) and the smaller B atoms are surrounded by an icosahedron formed by six A atoms and six B atoms. Many ternary and multiparty representatives of the Laves phases have been observed with A or B in excess. In addition, ternary Laves phases are known in systems with no corresponding binary Laves phases. Laves phases can be formed by main group metallic elements, transition metals as well as by lanthanides and actinides. The large variety of possible components for both A and B as well as the large interval of experimentally observed enthalpies of formation (0 down to −350 kJ/mol) indicate a considerable diversity in the chemical bonding situation.

The structure of the C15 phase of Ba_3Al_5 is shown in Fig. 6.78.

Only one sheet of the arrangement is shown. The barium atoms form a ladder-like structure along the *c*-axis. The two types of Al atoms are shown. One is above the plane of the Ba atom sheet while the other is slight below. The unit-cell arrangement in the structure is presented in Table 6.10.

A three-dimensional structure, showing the arrangement of the Al_5 groups is shown in the following Fig. 6.79.

Tetrabarium penta-aluminide, Ba_4Al_5, has a similar structure to Ba_3Al_5 as shown in the single sheet Fig. 6.80.

The unit-cell arrangement in the structure is shown in Table 6.11.

Again the "up" and "down" Al atoms are clearly shown. Three aluminides of the series Ba_xAl_5($x = 3$, 3.5, 4) were synthesized from stoichiometric ratios of the elements in Ta crucibles. The crystal structure of the new compound Ba_7Al_{10} was determined using single-crystal X-ray data (space group R**3**m, $a = 6.0423$ Å, $c = 4.8790$ Å, $Z = 3$, $R_1 = 0.0325$). The compound exhibits Al-Kagomé (3.6.3.6.) nets in which half of the triangles form the basis of trigonal bipyramids Al_5. The apical Al are thus three bonded assuming a charge of −2 (^{27}Al-NMR chemical shift $\delta = 660$ pm), whereas the Al atoms of the basal triangle (i.e. of the Kagomé net) are four bonded and thus of formal charge −1($\delta = 490$ ppm). The total charge of the anion is thus exactly compensated by the Ba cations, i.e. the compound can be interpreted as an electron-precise Zintl phase, exhibiting a distinct pseudo-band gap at the Fermi level of the calculated tDOS. According to the total formula, the structure displays a combination of the stacking sequences of Ba_3Al_5 and Ba_4Al_5, the structures of which have been redetermined with current methods (both hexagonal with space group P6/mmc; Ba_3Al_5: $a = 6.0655$ Å, $c = 14.618$ Å, $Z = 2$, $R_1 = 0.0239$; Ba_4Al_5: $a = 6.0921$ Å, $c = 17.758$ Å, $Z = 2$, $R_1 = 0.0300$). These three compounds with slightly different electron counts but similar polyanions allows

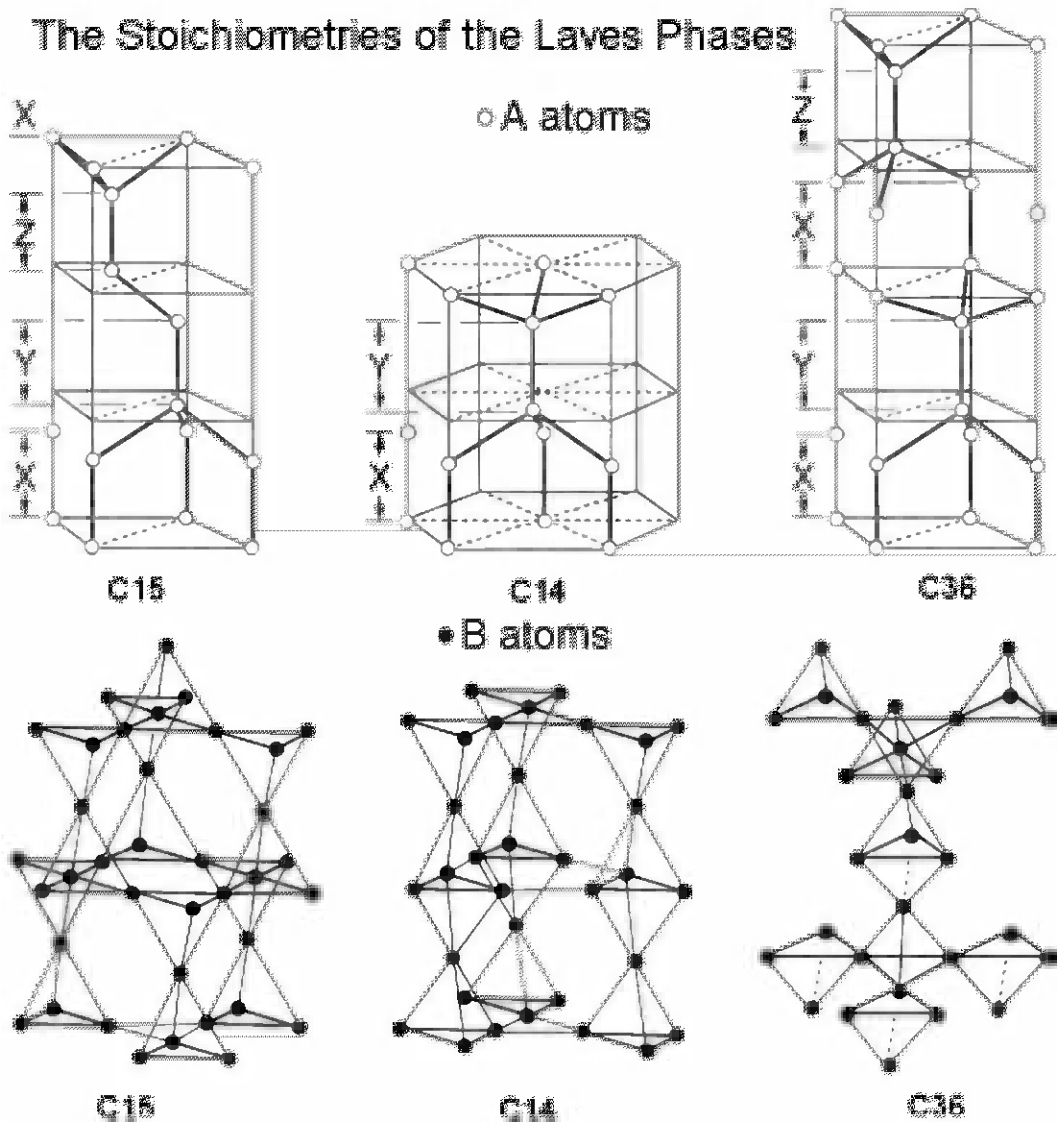

FIGURE 6.77

one to compare the bond lengths, the electronic structures and the overall bonding situation in dependence of positive or negative deviation of the electron count in relation to the novel formally electron-precise Zintl compound Ba_7Al_{10}.

Tetrabarium pentaaluminide, Ba_4Al_5, has been studied as a hydrogen-storing agent. The formation and decomposition behaviors of $BaAlH_5$ and Ba_2AlH_7 were investigated by means of XRD and pressure–composition isotherms (PCT). The phase transitions, phase compositions, and lattice parameters were determined by Rietveld refinement. Significantly pure $BaAlH_5$ with a purity of 99.1% was obtained through hydriding of Ba_4Al_5 alloy at 100 °C under 5 MPa H_2. When the hydrogenation temperature increased to 250 °C, the main phase became Ba_2AlH_7 with some impurity phases of $BaAl_4$ and BaH_2. PCT measurements of Ba_4Al_5 showed that the plateau pressure at 150 °C was about 0.5 MPa, and the maximum absorption H_2 content was 2.15 wt%. The final products obtained after PCT measurements of Ba_4Al_5 at 150 °C, 280 and 350 °C were $BaAlH_5$, a mixture of Ba_2AlH_7, BaH_2 and $BaAl_4$, a mixture of BaH_2 and $BaAl_4$, respectively. Independent decomposition experiments showed that $BaAlH_5$ partly desorbed H_2 to form a mixture of $BaAlH_5$, Ba_2AlH_7, BaH_2, and $BaAl_4$ at 280 °C, whereas both $BaAlH_5$ and Ba_2AlH_7 completely decomposed into BaH_2 and $BaAl_4$ at 350 °C. In addition, a new binary electron-precise *Zintl* compound, $Ba_{3.5}Al_5$, was found to contain Al_5 layers of Kagomé nets, that are also found in Ba_3Al_5 and Ba_4Al_5.

Undodecabarium tetradeca-aluminide, $Ba_{21}Al_{40}$, is a Zintl structure derived from Laves phases. The

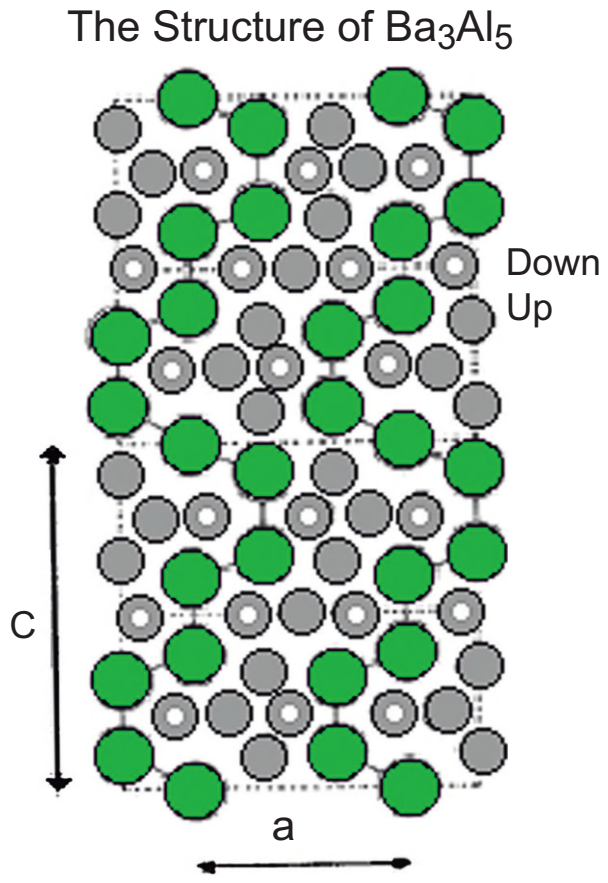

FIGURE 6.78

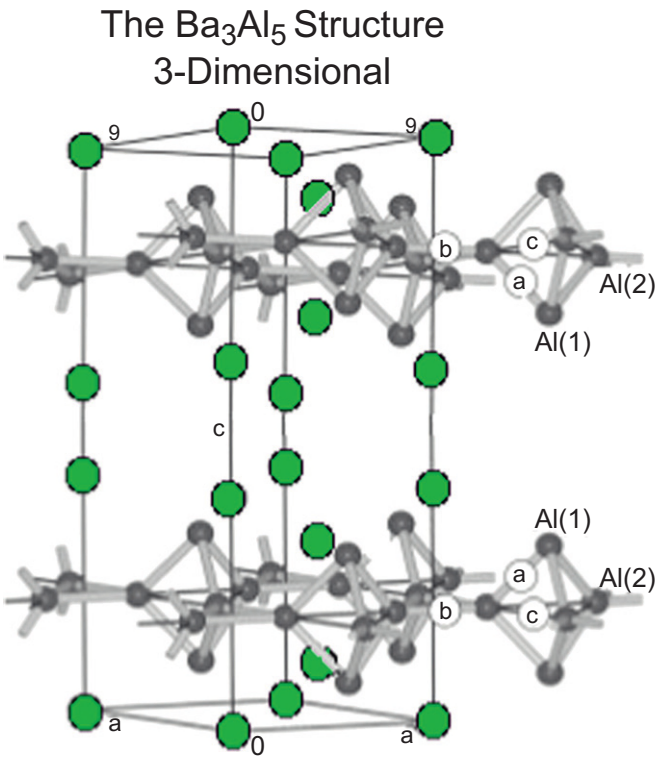

FIGURE 6.79

compound, Ba_7Al_{13}, has been mistaken for $Ba_{21}Al_{40}$. For Ae = Ba in AeB_2 Laves phases, the binary compound $BaAl_2$ does not exist, but the more Ba-rich compound, $Ba_{21}Al_{40}$, forms. The reinvestigation of the crystal structure of $Ba_{21}Al_{40}$ by selected area and convergent beam electron diffraction in a transmission electron microscope revealed a superstructure, which subsequently could be refined from single XRD data. The formula unit of the superstructure is $Ba_{21}Al_{40}$ (space group P31m, $Z = 1$, $a = 10.568$ Å, $c = 17.205$ Å). In $Ba_{21}Al_{40}$, a size match problem between Ba and Al present in Ba_7Al_{13} is resolved. The structure of $Ba_{21}Al_{40}$ can be considered as a Ba excess variant of the hexagonal $MgNi_2$ Laves phase-type structure. An incommensurately modulated variant of the $MgNi_2$ structure is obtained for phases $BaAl_2$–xMg_x with $x = 0.8$–1. At even higher Mg concentrations, a structural change to the proper $MgZn_2$-type structure takes place.

The idealized structure is shown as a C36 Laves structure in the following Fig. 6.81.

The atom arrangement in the structure is shown in Table 6.12.

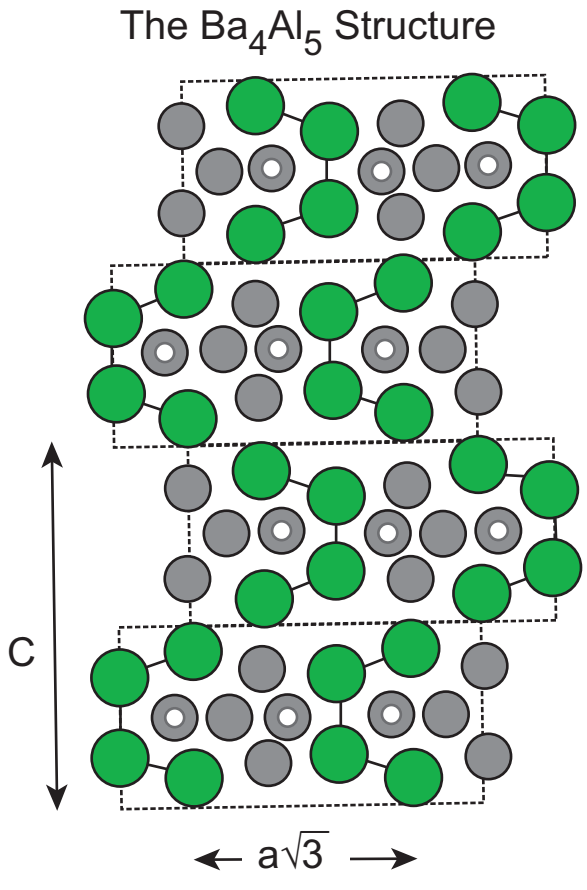

FIGURE 6.80

TABLE 6.10

No	Site notation	Atom	Multiplicity	Wyckoff	Site symmetry	*x*	*y*	*z*	Occupancy
1	Al1	Al	6	h	mm2	0.1547	0.3094	1/4	1.0
2	Al2	Al	4	f	3m.	1/3	2/3	0.1137	1.0
3	Ba1	Ba	4	f	3m.	1/3	2/3	0.6251	1.0
4	Ba2	Ba	2	a	-3m.	0	0	0	1.0

TABLE 6.11

No	Site notation	Atom	Multiplicity	Wyckoff	Site symmetry	*x*	*y*	*z*	Occupancy
1	Al1	Al	6	i	.m.	0.1565	0.8435	0.2873	1.0
2	Al2	Al	3	e	.2/m.	1/2	0	0	1.0
3	Al3	Al	2	d	3m.	1/3	2/3	0.1638	1.0
4	Al4	Al	2	d	3m.	1/3	2/3	0.4038	1.0

TABLE 6.12

No	Site notation	Atom	Multiplicity	Wyckoff	Site symmetry	*x*	*y*	*z*	Occupancy
1	Al1	Al	6	i	.m.	0.1565	0.8435	0.2873	1.0
2	Al2	Al	3	e	.2/m.	1/2	0	0	1.0
3	Al3	Al	2	d	3m.	1/3	2/3	0.1638	1.0
4	Al4	Al	2	d	3m.	1/3	2/3	0.4038	1.0
5	Ba1	Ba	2	d	3m.	1/3	2/3	0.6058	1.0
6	Ba2	Ba	2	d	3m.	1/3	2/3	0.8208	1.0
7	Ba3	Ba	2	c	3m.	0	0	0.1080	1.0
8	Ba4	Ba	1	b	-3m.	0	0	1/2	1.0

The difference manifests itself in the Kagomé network of the Al_{40}^{42-} groups (Fig. 6.82).

Convergent-beam electron diffraction in combination with selected-area diffraction has been used to determine uniquely the space group symmetry of the respective phases formed. The crystal structure of $Ba_{21}Al_{40}$ and $Ba_{14}Al_{22+x}Zn_{5-x}$ are derived from Laves-type structures by omitting and modifying some of the triangular and Kagomé layers. In the case of $Ba_{21}Al_{40}$, intergrowth of motifs from the crystal structures of Ba_3Al_5 and Ba_4Al_5 were observed, whereas for $Ba_{14}Al_{22+x}Zn_{5-x}$ the bulk phase displays a domain structure. Adjacent domains are misoriented by −120°, the specific angle resulting from the pseudo-trigonal symmetry of the Ba net. Therefore, only the (Al, Zn)-net is disordered.

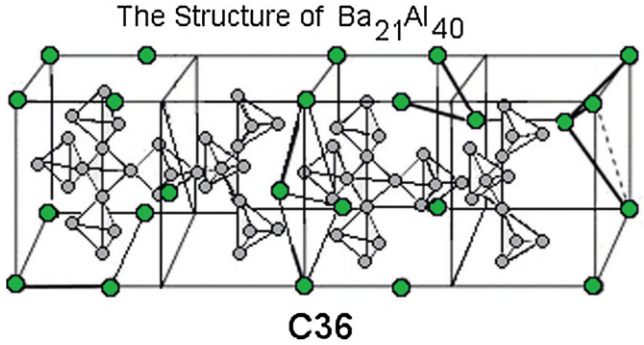

FIGURE 6.81

The hydrogenation characteristics of $Ba_{21}Al_{40}$ have been studied under a hydrogen pressure of 7 MPa at different temperatures for 5 days. $Ba_{21}Al_{40}$ reacts with hydrogen to form $BaAlH_5$ and Al between 373 and 553 K. When the temperature is in the range from 553 to 603 K, $Ba_{21}Al_{40}$ is hydrogenated to Ba_2AlH_7 and Al. However, further increasing the temperature leads to the hydrogen-induced decomposition of $Ba_{21}Al_{40}$ into

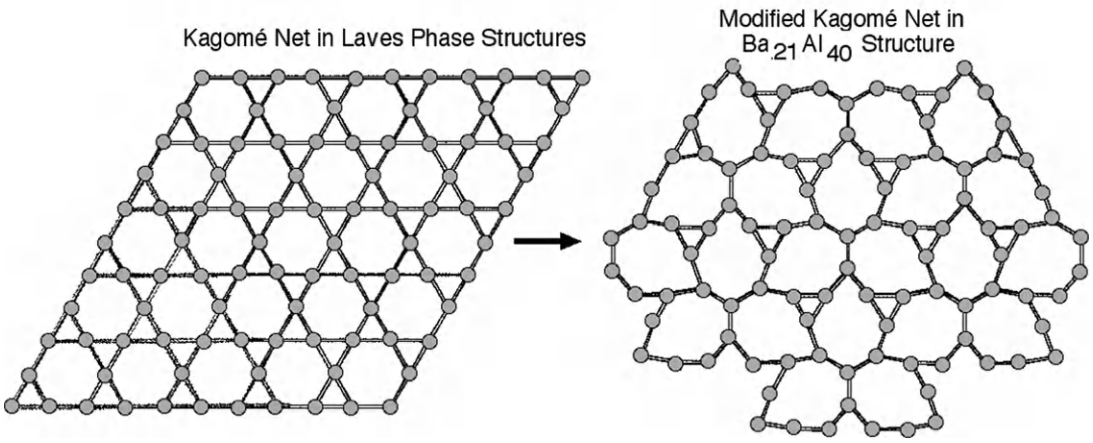

FIGURE 6.82

Ba_2AlH_7 and $BaAl_4$. The crystal structure of Ba_2AlD_7 was also studied by neutron powder diffraction. Ba_2AlD_7 is isostructural to Sr_2AlD_7, crystallizing with a monoclinic structure in space group $I2/a$. The lattice parameters were determined as $a = 13.197$ Å, $b = 10.237$ Å, $c = 8.509$ Å, $\beta = 101.290°$.

The only barium aluminide that has been assigned a CAS number is $BaAl_4$ (CAS 12672-79-6). It is available commercially.

Radium Aluminides

The literature is devoid of any mention of radium aluminides. Apparently, there have been no attempts to characterize such compounds as:

$RaAl_4$
Ra_3Al_5
Ra_3Al_5

This may be due to lack of demand for these compounds in industry and lack of interest in academia because of the intense radioactivity of ^{226}Ra.

6.4.2. Oxy-Aluminum Compounds of the Alkaline Earths

Beryllium Aluminates

Beryllium aluminate is readily formed by heating the oxides together at about 900 °C:

$$BeO + Al_2O_3 + \text{heat} \Rightarrow BeAl_2O_4$$

Three compounds appear in the phase diagram, the 3:1, 1:1 and 1:3 $BeO \cdot Al_2O_3$ combinations (Fig. 6.83).

Note that the 3:1 compound melts incongruently. The $BeAl_2O_4$ compound exists in nature as "crysoberyl" and is used as a gemstone. The thermodynamic constants determined for the above reaction are shown in Table 6.13.

Its CAS number is 120041-06-7 and it melts at 1873 °C. Beryllium aluminate, $BeAl_2O_4$, has the molecular weight of 126.9734 g/mol and it has a density of 3.65 g/cc. Chrysoberyl is orthorhombic with space group Pnma. The gemstone "chrysoberyl", not to be confused with "beryl" (which is an "alumino-silicate"), is an aluminate of Be with the formula $BeAl_2O_4$. The name chrysoberyl is derived from the Greek words Χρυσζ—*chrysos* and βηρνλλοç-*beryllos*, meaning "a gold-white spar". Despite the similarity of their names, chrysoberyl and beryl are two completely different gemstones. Chrysoberyl is the third-hardest frequently encountered natural gemstone and lies at 8.5 on the hardness scale. Only diamond and sapphire are harder.

"Alexandrite", a strongly pleochroic (trichroic) gem, will exhibit emerald green, red and orange-yellow colors depending on the viewing direction in partially polarized light. However, its most distinctive property is that it also changes color in artificial (tungsten/halogen) light compared to daylight. The color change from red to green is due to strong absorption of light in a narrow yellow portion of the spectrum, while allowing large bands of blue-green and red wavelengths to be transmitted. It, too, has the chemical formulation of $BeAl_2O_4$, is orthorhombic but has the space group of Pca2. The colors displayed by alexandrite are the result of impurities in its crystal structure. They are Cr^{3+} and Cu^{2+}, chromium and copper. The alexandrite unit cell can be visualized as being approximately hexagonal close packed (hcp) and composed of four molecules, with eight Al^{3+} ions occupying distorted octahedral sites, and four Be^{2+} ions, located at tetrahedral distorted sites, in addition to oxygen ions located in planes perpendicular to *c*-axis. Distortions from a precise hcp structure of oxygen ions originate from two sites of distinct symmetries: one is called Al_1, located at an inversion site and the other is called

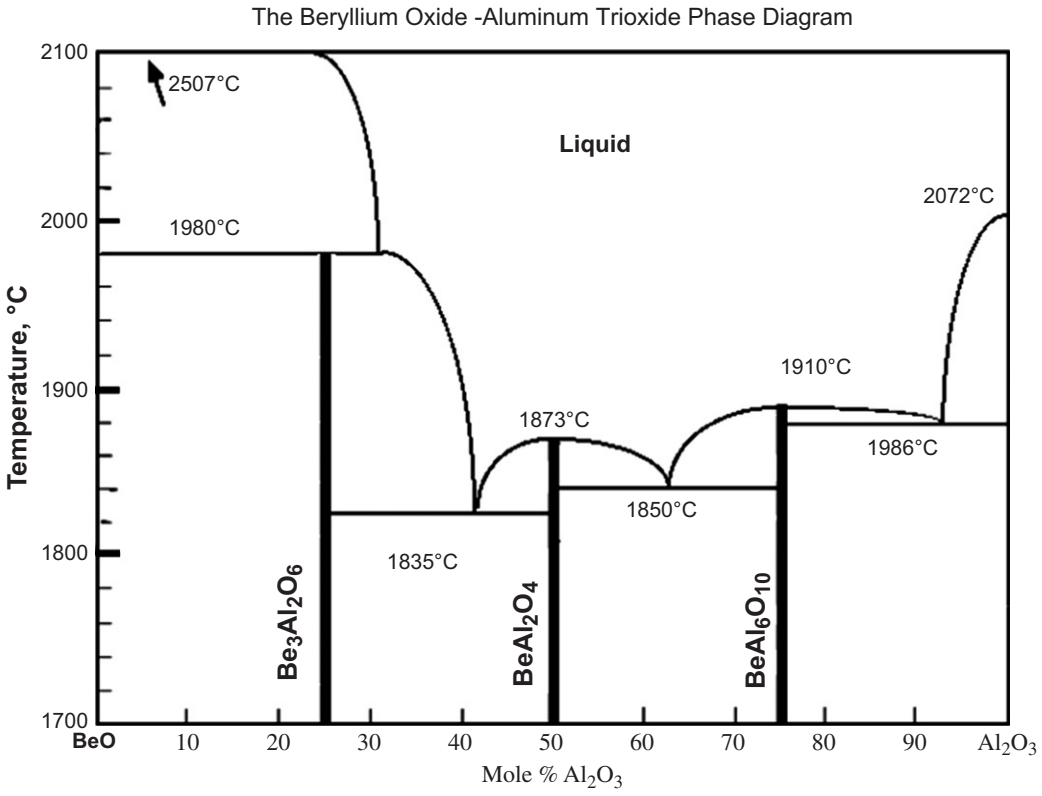

FIGURE 6.83

TABLE 6.13

Enthalpy of formation		Entropy of formation		Gibbs free energy	
(kcal/mol)	(kJ/mol)	(cal/K)	(J/K)	(kcal/mol)	(kJ/mol)
−549.9	−2300.7816	15.84	66.27456	−520.7	−2178.6088

Al_2, located at a reflection site. Both Al sites are octahedrally coordinated. The Al_2 coordination octahedron has a larger Al–O average bond length (1.938 Å) when compared to the Al1 octahedron (1.890 Å) resulting in a larger polyhedral volume.

Another gemstone, "taffeite", has the formulation: $BeMg_3Al_8O_{16}$ (which is a solid solution: $Mg_3Al_2O_6 \cdot BeAl_6O_{10}$). It is hexagonal but the unit-cell dimensions have not been recorded.

The major use in industry for these compounds has been as laser crystals.

Because $Be_3Al_2O_6$ melts incongruently, little use has evolved for this composition. Both $BeAl_2O_4$:Cr^{3+} and $BeAl_6O_{10}$:Cr^{3+} have been grown by Czochralski techniques for use as "tunable" lasers. It was determined that only crystals of $BeAl_2O_4$:Cr^{3+}, grown along the *a*- and *c*-axis showed laser activity. Later work then formed $BeAl_6O_{10}$:Cr^{3+} which was not subject to this limitation. The optical absorption–emission properties of these two crystals is shown in the Fig. 6.84 and the crystal structure of $MgAl_2O_4$ is shown in Fig. 6.85.

The major difference noted was in the tunability of the laser output, the $BeAl_6O_{10}$:Cr^{3+} being superior in this aspect. Comparative studies were performed for "alexandrite" crystals, Al_2BeO_4:Cr^{3+}, employed in solid-state lasers and grown by the horizontal-oriented crystallization (HOC) technique (one-dimensional) and alexandrite crystals grown by the Czochralski (Cz) method (two-dimensional). It was shown that the structural quality and possibilities of generation of stimulated emission for HOC crystals are similar to Cz crystals, and that their damage threshold is about three times higher.

The obtained results and considerably lower cost of HOC-alexandrite crystals proved their advantageous application in powerful laser systems, which require large laser rods with a higher resistance to internal heating caused by generation of the laser beam. It was

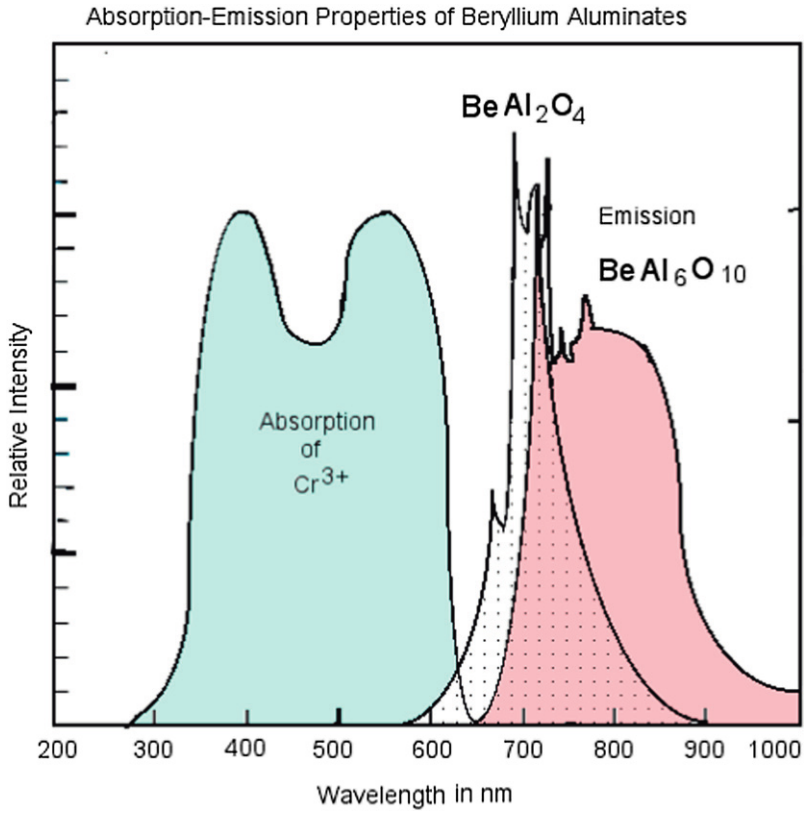

FIGURE 6.84

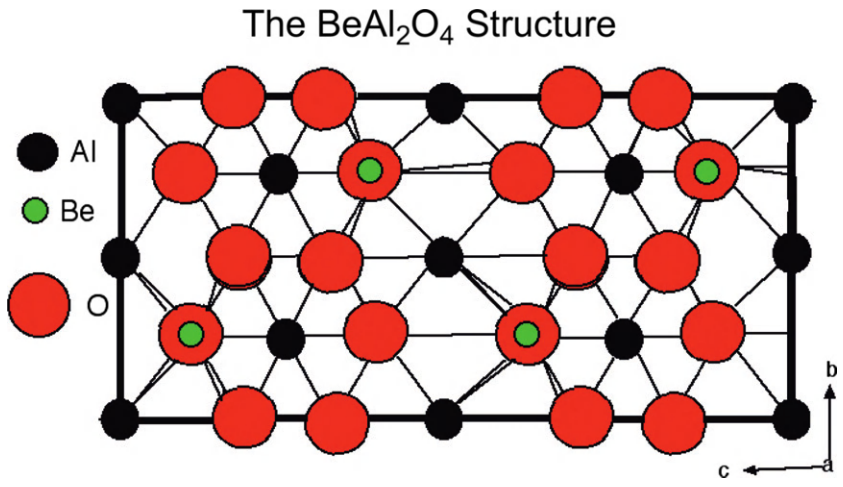

FIGURE 6.85

emphasized that application of HOC technique is promising for growth of laser crystals of other high-temperature oxide compounds. These crystals have a density of 3.74 g/cc, a Mohs hardness of 7.5, a thermal capacity of 0.8 J/kg K, a thermal conductivity of 12.5 W/m K, a Young's modulus of 109 N/m^2 and a Poisson modulus of 0.24.

The stratified hydrodynamic structure of melt in the boat-like crystallization container that predetermines major features of crystal growth was revealed by model experiments. Patterns of (120), (130), and (100) growth sectors of crystal volume and zones of preferred entrapment of gas–melt inclusions as well as efficient distribution coefficient of chrome on crystallization (inversion

included) and distribution behavior of dopant along the grown crystals was shown to be superior to Cz crystals. Occurrence of metal microinclusions of crystallization from the molybenum container (Mo) in grown alexandrite crystals was also analyzed.

A comparison of these two crystals as lasers is shown in Table 6.14.

The absorption spectra of $BeAl_6O_{10}$ are shifted toward the IR range as compared with the alexandrite spectra to be, consequently, superior for using diode pumping as the excitation medium for crystal lasers. $BeAl_6O_{10}$ absorbs 70% at $\lambda = 650$ nm of the maximum, whereas alexandrite is only 35% at the same wavelength.

The structure of alexandrite (crysoberyl) is shown in the following diagram. Only one layer of the three-dimensional structure is shown in Fig. 6.86.

Crystals of alexandrite (crysoberyl) and the beryllium hexa-aluminate are readily available commercially.

Magnesium Aluminates

Spinel is the magnesium aluminum member of the larger spinel group of minerals. It has the formula $MgAl_2O_4$. The cubic spinel structure is very flexible with respect to the cations it can incorporate. There are over 100 known compounds. The formula can be written as $Mg^{2+}(Al_2^{3+})O_4$. This compound can be formed by the SSR of the oxides at ca. 700–1200 °C:

$$MgO + Al_2O_3 + \text{heat} \Rightarrow MgAl_2O_4$$

Magnesium aluminate, $Mg(AlO_2)_2$, has the CAS number of 12068-51-8, a molecular weight of 142.2664 g/mol and a density of 3.55 g/cc. It is

TABLE 6.14

Crystal	Mohs' hardness	Heat conduct, W/mkm*	Density, g/cm^3	Heat cap, J/kg K	Young's modulus, 10^9 N/m^2	Poisson modulus	Fluores, range, mkm*	Fluores, peak, mkm*	Lifetime, mks	Cross-section, 10^{-20} cm^2	Lasing maximum
$BeAl_2O_4$	7.5	23	3.74	0.83	469	0.3	0.7–0.82	0.71	260	0.7	0.75
$BeAl_6O_{10}$	8	12.5	3.7	0.8	381	0.24	0.7–1.1	0.77	13.5	6.0	0.83

* *0.7 mkm = 700 nm*

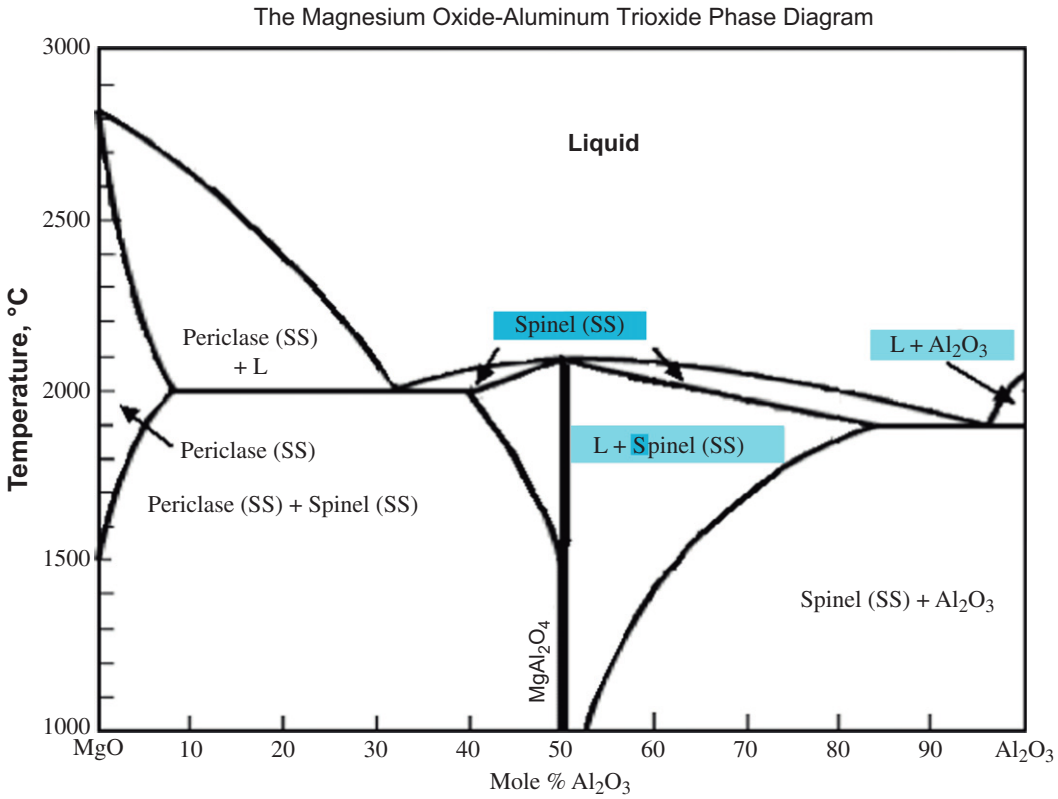

FIGURE 6.86

a colorless, cubic crystal that melts at 2105 °C. The Gibbs free energy involved in this process is:

$$MgO(solid) + Al_2O_3(solid) = MgAl_2O_4(solid)$$

$$\Delta G_{973\ K}^{\circ} = -7.69\ Kcal/mol$$

Most spinel structures can be formed in this way. In general, the use of soluble sodium aluminate, Na_3AlO_3, cannot be used to form the metaaluminate because it forms a double salt, $MgO{\cdot}Na_2O{\cdot}5Al_2O_3$. This compound is sometimes called "β-alumina". Formation of the salt $(Mg, Na)_3(AlO_3)_2{\cdot}xH_2O$, can also occur. In addition, this salt is hydrated and can contain up to 10 water molecules.

The use of several Mg compounds that decompose to form the oxide so as to react with Al_2O_3 has been studied. Little or no difference was noted in the product produced, the initial temperature required, or the rate of reaction that occurred. The exception was γ-Al_2O_3, a compound with a high-specific surface area that reacted much faster with the MgO produced by the decomposition of the various compounds tried.

The phase diagram, shown as follows, presents but one compound, the Spinel. In contrast, the other alkaline earths exhibit a number of other stoichiometries. Spinels have a number of applications in industry. Spinels crystallize in the cubic system, forming octahedral crystals. Owing to its high-melting point (2100 °C), high hardness (16.1 GPa), resistance to chemical attack, and chemical compatibility with alumina, zirconia, and mullite, spinel ($MgAl_2O_4$) is an attractive matrix material for ceramic matrix composites (Fig. 6.86).

A selection of spinels is also presented in Table 6.15.

Monolithic, transparent spinel is also used in optical applications, such as windows for pressure vessels and bulletproof vehicles. The structure of $MgAl_2O_4$ is shown in the following Fig. 6.87.

Among the crystalline compounds, the spinel oxides present a large range of interesting electrical, magnetic and optical properties. The magnesium–aluminum spinel, $MgAl_2O_4$, in particular has been comprehensively studied and previous works point out a high melting point (2135 °C), a high hardness (7.5–8 Mohs), and interesting thermal and optical properties. $MgAl_2O_4$ can crystallize in the "normal" or "inverse" spinel structure. This structure may be described as a cubic closest-packed array of oxygen atoms, with one-eighth of the tetrahedral sites and one-half of the octahedral sites filled. The space group is $Fd\bar{3}$ m (O_H^7) and the lattice parameter "*a*" is equal to 8.08435 Å. In the case of a "normal" spinel structure, Mg^{2+} ions are located in tetrahedral sites and the Al^{3+} ions are in octahedral sites.

As $MgAl_2O_4$ is one of major components of both the spinel phase and the calcium ferrite phase in the Earth's mantle, many researchers have studied its high-pressure phase relations. However, the high-pressure, high-temperature phase relation has been unclear at temperatures higher than 2000 °C. By performing high-pressure experiments, it was determined that $MgAl_2O_4$ spinel decomposes to $Mg_2Al_2O_5$ and Al_2O_3 at 20–25 GPa and temperatures higher than 2000 °C:

$$2\ MgAl_2O_4 + (Heat\ and\ Pressure) \Rightarrow Mg_2Al_2O_5 + Al_2O_3$$

This is the first report of a compound with the composition of $Mg_2Al_2O_5$. The powder XRD pattern cannot be explained by the crystal structures of already known high-pressure phases like the "Brownmillerite"-type $Ca_2Al_2O_5$. In this study, a crystal structure model of this $Mg_2Al_2O_5$ phase was constructed. The obtained structure model was used for structure refinement by a Rietveld analysis. In addition, the $Mg_2Al_2O_5$ phase for a powder XRD measurement was synthesized using a Kawai-type multianvil high-pressure apparatus. The starting material of a mixture of $MgO{:}Al_2O_3 = 2{:}1$ (in molar ratio) was held at 23 GPa and 2500 °C for 10 min. After quenching, the sample was recovered at ambient pressure. The sintered polycrystalline sample was crushed by a die and ground into powder. The powder XRD profile

TABLE 6.15

A selection of spinels

Compound	Characteristics
$MgAl_2O_4$	Spinel itself, base for natural gemstones
$ZnAl_2O_4$	Gahnite, a transparent diamagnetic spinel
$FeAl_2O_4$	Hercynite, a classical paramagnet
γ-Fe_2O_3	Maghemite, a natural material for magnetic recording
$FeCr_2O_4$	Chromite, the chrome ore of Rhodesia
Mn_3O_4	Hausmannite, a natural tetragonal spinel
Fe_3O_4	Magnetite, the ancient navigator's lodestone
Fe_3S_4	Greigite, a ferrimagnetic semimetal
$NiFe_2O_4$	Trevorite, a ferrimagnetic semiconductor
$ZnFe_2O_4$	Franklinite, the paramagnetic ferrite
$CuCo_2S_4$	Carrollite, a natural metallic spinel
Fe_2TiO_4	Ulvùspinel, with giant magnetostrictive properties
Mg_2SiO_4	The high-pressure spinel polymorph of forsterite (olivine) thought to comprise the Earth's inner mantle
LiV_2O_4	A heavy fermion transition metal oxide
$Fe_{1-x}Cu_xCr_2S_4$	A chalcogenide with colossal magnetoresistive properties

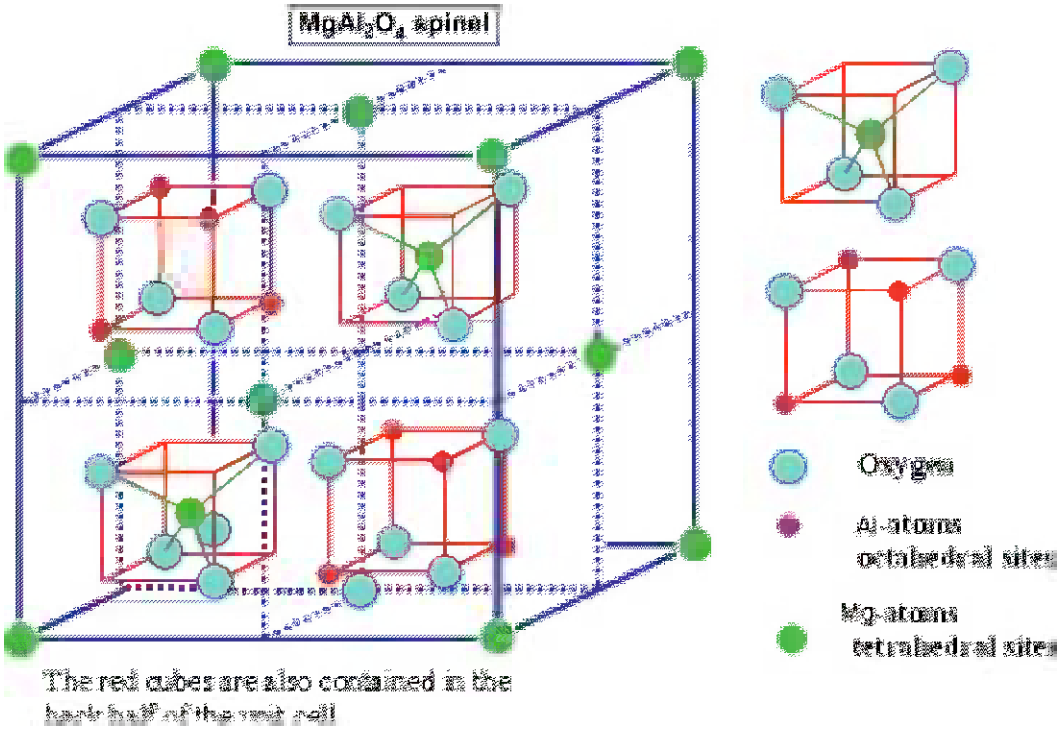

FIGURE 6.87

was measured, showing that crystal symmetry of the $Mg_2Al_2O_5$ phase is orthorhombic. The extinction rules of the powder XRD peaks suggested the space group of Pba2 or Pbam. Since it was found that the XRD pattern is close to that of (Mg, Fe^{2+})$_2$(Fe^{3+}, Al)(BO_3)O_2 (Ludwigite), a structure model of the $Mg_2Al_2O_5$ phase, based on it, was constructed. It should be noted that planar three-coordinated sites in this quasi-Ludwigite was adapted by moving the boron sites by 0.50 Å in atomic coordinate along *c*-axis, because interatomic distances between cation and oxygen in the planar three-coordinated sites are too short for Mg^{2+} and Al^{3+} ions. In this structure model, (Mg,Al)O_6 octahedra were connected by edge sharing and corner sharing to form triangular tunnels along the *c*-axis. Cation sites occupied by only Mg^{2+} are placed in the tunnels. The sites have a coordination environment of trigonal prism-type MgO_6. By the Rietveld analysis, lattice parameters were determined as $a = 9.3710(6)$ Å, $b = 12.1952(6)$ Å, $c = 2.7916(2)$ Å. The calculated density of 3.801(1) g/cm^3 is consistent with the high-pressure phase relations. The *R* factor by adopting the space group of Pbam is smaller than that by Pba2. Therefore, it is suggested that the space group of the $Mg_2Al_2O_5$ phase is Pbam.

In another study, phase transitions in $MgAl_2O_4$ were examined at 21–27 GPa and 1400–2500 °C using a multi-anvil apparatus. A mixture of MgO and Al_2O_3 (corundum), that are high-pressure dissociation products of $MgAl_2O_4$ spinel, was found to combine into calcium ferrite-type $MgAl_2O_4$ at 26–27 GPa and 1400–2000 °C. Below 2000 °C, the calcium ferrite-type $MgAl_2O_4$ is stable above about 26 GPa, and below that pressure a mixture of MgO, periclase and Al_2O_3 corundum is stable. At temperature above 2000 °C and at pressure below 25.5 GPa, a mixture of Al_2O_3 and a new phase with $Mg_2Al_2O_5$ composition is stable. The transition boundary between the two fields has a strong negative pressure–temperature slope. Structure analysis and Rietveld refinement on the basis of the powder XRD profile of the $Mg_2Al_2O_5$ phase indicated that the phase represented a new structure type with orthorhombic symmetry (Pbam), and the lattice parameters were determined as $a = 9.3710$ Å, $b = 12.1952$ Å, $c = 2.7916$ Å, $V = 319.03$ Å^3, $Z = 4$. The structure consists of edge-sharing and corner-sharing (Mg,Al)O_6 octahedra, and contains chains of edge-sharing octahedra running along the *c*-axis. A part of Mg atoms are accommodated in six-coordinated trigonal prism sites in tunnels surrounded by the chains of edge-sharing (Mg,Al)O_6 octahedra. The structure is related with that of Ludwigite (Mg,Fe^{2+})$_2$(Fe^{3+},Al)(BO_3)O_2. The molar volume of the $Mg_2Al_2O_5$ phase is smaller by 0.18% than sum of molar volumes of 2MgO and Al_2O_3 corundum. High-pressure dissociation to the mixture of corundum-type phase and the phase with ludwigite-related structure has been found only in $MgAl_2O_4$ among various $A^{2+}B_3 + 2O_4$ compounds.

Metal matrix composites have been extensively studied, in particular, Spinel and Al metal. If Al_2O_3 particles are introduced into a metal melt consisting of 96%Al–4 wt% Mg by the "vortex" method, aluminum oxide plus a metal matrix results. After being cast, Al_2O_3-(Al–4 wt% Mg) composites were remelted at 700, 750, 800 and 850 °C for different residence times to investigate the formation of $MgAl_2O_4$ (spinel). The results showed that $MgAl_2O_4$ is the unique interface of the Al_2O_3-(Al–Mg) composites held at 700–850 °C. Fine $MgAl_2O_4$ crystals grew on the surface of the Al_2O_3 particle but, as the holding temperature and the residence time increase, some spinels grew into a pyramidal shape. The $MgAl_2O_4$ grew not only at the matrix–particle interface but also on the surface of the composite specimens. The formation reactions of interfacial $MgAl_2O_4$ are as follows:

$$Mg(liq) + 2Al(liq) + 2O_2(gas) \Rightarrow MgAl_2O_4(solid)$$

$$3Mg(liq) + 4Al_2O_3(solid) = 3MgAl_2O_4(solid) + 2Al(liq)$$

Both reactions are equally important. The mechanism of reaction was determined to be governed by diffusion of Al and Mg ions through the layers of reaction products composed of $MgAl_2O_4$ and Al_2O_3 phases. It was found that during the process, the composition of the reaction products changed as the concentration of Mg in the boundary layer diminished.

In another study, the interfacial reactions between Al_2O_3 particles and 50:83 Al–Mg alloys during fabrication by compo-casting and subsequent remelting at 800 °C for 0.5 and 4 h have been studied using analytical TEM and SEM. It was found that the reaction product was changed with increasing remelting time. MgO was the main reaction product after casting and remelting for 0.5 h. The MgO crystals are then very small (about 5–20 nm in size) and the reaction zone is about 50–80 nm thick for the as-cast material and about 100–150 nm after remelting for 0.5 h. However, after remelting for 4 h, MgO is transformed into $MgAl_2O_4$ and the interfacial region is then constituted of large $MgAl_2O_4$ crystals of about 1 μm in size. This transformation indicates that the nature of the reaction products is controlled by the Mg content in the matrix.

The feasibility of fabricating near net-shaped spinel, $MgAl_2O_4$, by the oxidation of solid Mg–Al_2O_3-bearing precursors has been demonstrated. Porous Al_2O_3 preforms were fabricated by uniaxial pressing of Al_2O_3 powder having a mean particle size of 7 microns. The alumina disks and bars were then sintered in air at 1500 °C for 5–12 h so as to produce 65–70% dense preforms. Dense disk-shaped and bar-shaped precursors were fabricated by the pressure-less infiltration of molten Mg into the porous (65–70% dense) Al_2O_3 preforms at 680–700 °C. The shaped, solid MgO–Al_2O_3-bearing precursors were then oxidized in pure, flowing oxygen at 430 °C/40 h to 700 °C/6 h. The resulting mixtures of MgO and Al_2O_3 were converted into $MgAl_2O_4$ within 15 h of annealing in oxygen at 1200 °C. A subsequent 10-h sintering treatment at 1700 °C in flowing Ar yielded shaped spinel-bearing bodies with densities of 92.5% of theoretical. Various shapes could be fabricated.

As a refractory material, $MgAl_2O_4$ spinel has some unique applications in the form of sintered ceramics or coatings. It is considerably more resistant to slags and fluxes, especially alkalis, than alumina. This spinel, including various chemical variations, can be used to coat crucibles and dish nozzles for improved resistance to molten metals and slag. It is usable as an impact resistant optical window and as an infrared radiation lens. As this oxide is practically inert to cold concentrated mineral acids and even boiling acids of moderate concentration, it would be serviceable as a dense coating for chemical reactors. Some variants of this oxide include $MgAl_2O_4/Al_2O_3$ and $MgAl_2O_4$/MgO composites and $MgAl_2O_4/MgCr_2O_4$ solid solutions. Such chemical alterations permit modification of properties such as thermal expansion and corrosion resistance. These materials can be thermally sprayed using flowable, fully reacted powders to give thick dense coatings having properties near to that of bulk ceramics.

Optical absorption of magnesium aluminate spinel single crystals of different compositions $MgO \cdot nAl_2O_3$ ($n = 1.0$ and 2.5) were investigated after irradiation with neutrons, X-rays and the UV light to elucidate existence of specific absorption bands related to lattice defects. The radiation-induced absorption envelope is shifted to higher energy and is larger in intensity in nonstoichiometric spinel in comparison with the stoichiometric one at the same irradiation conditions. Deconvolution of different optical spectra of irradiated crystals shows the shift of the F-type centers from 4.75 and 5.3 eV in stoichiometric crystals to 5.08 and 5.63 eV in $MgO \cdot 2.5Al_2O_3$ for F^+ and F^- centers, respectively. The absorption bands at 3.1 (400 nm) and 3.78 eV (328 nm) are present in both stoichiometric and nonstoichiometric crystals and are identified as V-type centers. By changing the irradiation time and using isochronal annealing, it was revealed that additional bands appear in optical absorption spectra at 4.15 eV (299 nm) for $MgO \cdot 1.0Al_2O_3$ crystals and at 4.46 eV (278 nm) for $MgO \cdot 2.5Al_2O_3$ crystals. From the shift of the band energy position and the high intensity of this band in nonstoichiometric spinel crystals, these wavelengths could be identified with electronic centers related to lattice defects.

Recent studies have demonstrated that cerium containing magnesium aluminate spinels such as $MgAl_2O_4$ and $Mg_2Al_2O_5$ are very effective SO_x reduction catalysts for Fluid catalytic cracking (FCC) units in oil refineries. These magnesium aluminate spinels can be prepared

by three different techniques: (i) thermal co-condensation (ii) coprecipitation and (iii) co-gel formation. Some of the important physical and chemical properties of a spinel, synthesized for this purpose, were found to depend on the preparative route used. The preparation methods and characterization techniques utilized for these spinels were discussed concerning how the SOx abatement activity of these spinels were related to the preparative route employed.

Refractory oxide melts of the binary system MgO–Al_2O_3 have been studied by a molecular dynamics simulation using an advanced ionic interaction model derived from first principles. The simulations reproduced values close to experimental densities, structure factors, and transport properties. Anomalous behavior of the latter was observed as a function of melt composition. The minimum in the Al self-diffusion and the respective maximum in the shear viscosity around the $MgAl_4O_7$ composition were explained by structural changes in the melt. It was concluded that when $MgAl_2O_4$ is melted and excess Al_2O_3 is added, a structural change occurs in the melt:

$$MgAl_2O_4\ (liq) + Al_2O_3(solid) \Leftrightarrow MgAl_4O_7 + (liq)$$
$$+ Al_2O_3(solid) \Leftrightarrow MgAl_6O_{10}\ (liq)$$

However, as the melt cools, the reaction reverted to a mixture of the spinel plus Al_2O_3.

It was found possible to grow a good crystal of $MgAl_6O_{10}$ by a Czochralski method. $Mg_{0.4}Al_{2.4}O_4$ single crystals with good optical quality were successfully grown. The transmission spectrum indicated that the absorption edge of the crystal was at 220 nm, while no apparent absorption peaks were found. The XRD and DSC curve analysis showed that the $MgAl_6O_{10}$ crystal was stable at room temperature. However, after annealing in the air and hydrogen atmosphere at about 1200 °C, $MgAl_6O_{10}$ decomposed into Al_2O_3 and $MgAl_4O_7$. The reaction mainly occurred on the crystal surface, barely inside.

Magnesium aluminate (spinel) is available commercially worldwide in large quantities.

Calcium Aluminates

Calcium aluminate can be formed by heating the oxides together at about 900–1250 °C:

$$CaO + Al_2O_3 + \text{heat} \Rightarrow CaAl_2O_4$$

Calcium aluminate as $CaAl_2O_4$ has the CAS number of 12042-68-1 and a molecular weight of 158.0392 g/mol. It is a white powder and exhibits a monoclinic crystalline form. Its density is 2.98 g/cc and its melting point is 1605 °C. The formation of $CaAl_2O_4$ from $CaCO_3 \cdot Al_2O_3$ powder mixtures has been intensely studied by varying holding times between 1.0 and 40 h and temperatures between 1300 and 1500 °C. Phase formation was studied in samples both quenched from the holding temperatures and in samples slowly cooled. Samples were characterized by X-ray powder diffraction (XRPD), using Guinier-Hägg film data and the Rietveld method, and SEM and TEM. Samples for TEM with very high-site accuracy were produced using focused ion beam microscopy.

In addition to $CaAl_2O_4$, (CA), the samples contained major amounts of CA_2 ($CaAl_4O_7$), $C_{12}A_7$ ($Ca_{12}Al_{14}O_{33}$) and minor amounts of unreacted A (Al_2O_3). Trace amounts of C_3A ($Ca_3Al_2O_6$) were observed only for samples heated to 1500 °C. The amount of the Ca-rich phase $C_{12}A_7$ was found to decrease with time as it reacts with A and, to a less degree, CA_2 to form CA, the most stable phase. In agreement with previous studies, the amount of CA_2 formed decreases comparatively slowly with time. Its unreactivity is due to the fact that it is concentrated in isolated porous regions of sizes up to 100 μm. The formation of the Ca aluminates is found to be in response to local equilibriums within small inhomogeneous regions, with no specific phase acting as an intermediate phase. Samples quenched from 1500 °C were found to contain smaller amounts of poorly crystallized phases. A reaction between C and A takes place as low as 900 °C, forming a metastable orthorhombic modification of CA. The orthorhombic unit cell with $a = 8.732(2)$ Å, $b = 8.078(2)$ Å, $c = \sqrt{3}, \cdot a = 15.124(4)$ Å was verified by electron diffraction, revealing frequent twinning and disorder of the crystallites.

The phase diagram contains five compounds as shown in Fig. 6.88.

The stable phases shown in the phase diagram (formed at atmospheric pressure under an atmosphere of normal humidity) are:

- Tricalcium aluminate, $3CaO \cdot Al_2O_3$ (C3A) = 3:1
- Dodeca-calcium hepta-aluminate, $12CaO \cdot 7Al_2O_3$ (C12A7) = 12:7

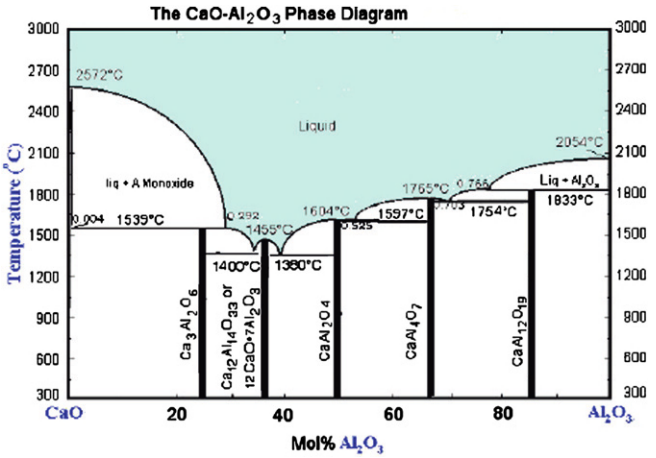

FIGURE 6.88

- Monocalcium aluminate, $CaO \cdot Al_2O_3$ (CA) = 1:1
- Monocalcium dialuminate, $CaO \cdot 2Al_2O_3$ (CA2) = 1:2
- Monocalcium hexa-aluminate, $CaO \cdot 6Al_2O_3$ (CA6) = 1:6

In addition, other phases include:

- Dicalcium aluminate, $2CaO \cdot Al_2O_3$ (C2A) = 2:1, which exists only at pressures above 2500 Mpa. The crystal is orthorhombic, with density 3.480 g/cc.
- Penta-calcium tri-aluminate, $5CaO \cdot 3Al_2O_3$ (C5A3) = 5:3, that forms only under an anhydrous and oxygen-free atmosphere. The crystal is orthorhombic, with a density of 3.067 g/cc. It reacts rapidly with water.
- Tetra-calcium tri-aluminate, $4CaO \cdot 3Al_2O_3$ = 4:3, is a metastable phase formed by dehydrating $4CaO \cdot 3Al_2O_3 \cdot 3H_2O$ (C4A3H3).

The major use found for $CaAl_2O_4$ has been as a hydrous cement. Alternative names are "aluminous cement", "high-alumina cement" (HAC) and "Ciment fondu". They are used in a number of small-scale, specialized applications. The method of making cement from limestone and bauxite was patented in France in 1908 by J. Bied of the Pavin de Lafarge Co. The initial development was as a result of the search for a cement offering sulfate resistance. The cement was called in the French "Ciment fondu". Subsequently, its other special properties were discovered, and these guaranteed its future in niche applications. The main active constituent of calcium aluminate cements is $CaAl_2O_4$, or $CaO \cdot Al_2O_3$, or CA (in the parlance of "cement-chemists"). The cement is prepared by fusing together a mixture of a calcium-bearing material (normally limestone) and an aluminum-bearing material (normally bauxite for general purposes, or refined alumina for white and refractory cements). The liquefied mixture cools to a basalt-like clinker that is ground to produce the finished product. Because complete melting usually takes place, raw materials in lump form can be used. The calcined material drops into the "cool-end" of the melt bath. The melt overflows the hot end of the furnace into molds in which it cools and solidifies. The hydration reactions of calcium aluminate cements are very complex. The strength-developing phases are monocalcium aluminate (CA), dodeca-calcium hepta-aluminate (12C7A) and "belite" = dicalcium silicate, Ca_2SiO_4. A typical composition is $Ca_{0.93}Al_{1.94}Fe_{0.11}Si_{0.02}O_4$. It reacts rapidly with water, forming the metastable hydrate $CaO \cdot Al_2O_3 \cdot 10H_2O$, or a mixture of $2CaO \cdot Al_2O_3 \cdot 8H_2O$, $3CaO \cdot Al_2O_3 \cdot 6H_2O$ and $Al(OH)_3$ gel. These reactions form the first stage of strength development in calcium aluminate cements. The reactive aluminates react with water initially to form a mixture of:

$$CaO \cdot Al_2O_3 \cdot 10H_2O$$

$$2\ CaO \cdot Al_2O_3 \cdot 8\ H_2O,$$

$$3CaO \cdot Al_2O_3 \cdot 6H_2O,$$

$$Al(OH)_3\ \text{gel}$$

The amounts of each present depends upon the curing temperature. The first two hydrates subsequently decompose to a mixture of 3 $CaO \cdot Al_2O_3 \cdot 6H_2O$, $Al(OH)_3$ gel and water, this process being called "conversion". Because of the loss of water, conversion causes an increase in porosity, which can be accompanied by a decrease in strength. This need not be a problem in structural concrete provided that a sufficiently high cement content and a sufficiently low water/cement ratio are employed.

The structures of these compounds and their hydrates have been investigated because of their involvement in the "setting" of Portland cement as well as HAC. There are three fundamental calcium aluminate hydrates that are formed during the course of hydration of HAC. These involve two metastable phases, CAH_{10} ($CaAl_2O_4 \cdot 10H_2O$) and C_2AH_8 ($Ca_2Al_2O_6 \cdot 8H_2O$). Additionally, the stable phase C_3AH_6 ($Ca_3Al_2O_6 \cdot 6H_2O$ = hydrogarnet or Katoite) appears. Further to these species, alumina trihydrate phases often occur during the course of hydration, these being either as an amorphous gel or the crystalline phase Gibbsite.

The major compounds found in these hydrous cements are shown in the following Fig. 6.89.

The purple-tetrahedra are AlO_4 groups but only a part of the red-oxygen atoms are shown (for clarity). The blue spheres are Ca^{2+} cations.

Calcium monoaluminate (CA) is the principal hydraulic mineral present in calcium alumina cement. Its hydration contributes to the high early strength of CA cements. Calcium monoaluminate is a monoclinic phase, pseudo-hexagonal, and its space group is $P2_1/n$, with $Z = 12$ and $D_x = 2.945$ g/cc. It resembles the structure of β-tridymite with an infinite three-dimensional framework of AlO_4 tetrahedra-sharing corners. However, the large ionic radius of the Ca^{2+} cation distorts the tridymite network and a section of the calcium atoms has an irregular coordination polyhedra with oxygen. Under the optical microscope, CA appears as irregular colorless grains, with interference colors less than that of CA2. Some of the Al^{3+} ions in the AlO_4^+ tetrahedra can be partially replaced by iron. CA has a monoclinic unit cell. Figure 1 shows a model of its crystal structure. In calcium aluminate cements, it exists as a solid solution in which the amount of minor elements depends upon the bulk composition of the cement. A typical cement composition is $Ca_{0.93}Al_{1.94}Fe_{0.11}Si_{0.02}O_4$. It reacts rapidly with water, forming the metastable hydrate $CaO \cdot Al_2O_3 \cdot 10H_2O$, or a mixture of $2CaO \cdot Al_2O_3 \cdot 8H_2O$, $3CaO \cdot Al_2O_3 \cdot 6H_2O$ and $Al(OH)_3$

gel. These reactions form the first stage of strength development in calcium aluminate cements.

Grossite or calcium di-aluminate (CA2) has a monoclinic structure with the space group C2/c, $Z = 4$ and $D_x = 2.920$ g/cc. Its structure is based upon a framework of AlO_4 tetrahedra. Some of the oxygen atoms are shared between two tetrahedra and the rest distributed between the other three. The CA2 phase tends to be more refractory in nature than CA. However, it is less reactive, chemocally. CA2, hydrating on its own, will impart a lower strength than CA to the cement after 24 h of curing. However, the hydration of CA2 has been reported to be accelerated by higher temperatures and also by the presence of CA. Grossite's crystal structure is shown in Fig. 2 (presented below).

Dodeca-calcium hepta-aluminate (C12A7) or "Mayenite", $Ca_{12}Al_{14}O_{33}$, is a rare mineral of cubic symmetry, originally reported from the Eifel volcanic complex in Germany. It is also found at pyrometamorphic sites: e.g. in the Hatrurim Formation (Israel) and in some burned coal dumps. Mayenite is also found as an aluminate in aluminate cement where its formula is also written as $12CaO{\cdot}7Al_2O_3$, or C12A7 in the "cement-chemist notation". It has the space group $I_4\bar{3}d$. Its respective crystal structure is composed of Ca^{2+} ions with irregular sixfold coordination with oxygen, which has an incomplete framework of corner-sharing AlO_4 tetrahedra that has the empirical composition, $Al_7O_{16}^{11-}$. In each formula unit, one of the O^{2-} ions is distributed between 12 sites, which increases two of the AlO_4 groups to AlO_5. The calcium ions in mayenite have a highly balanced shell of oxygen atoms, that are roughly distributed on the surface of a hemisphere. These coordinating hemispheres occur in pairs along the axes of crystal symmetry, so that the planar faces are defined by vacancies among the 12-fold positions. Mayenite is the most reactive of all calcium aluminate species occurring in "high-alumina cements" (HACs), and will hydrate very rapidly in contrast to CA. Due to this fact, the amount of mayenite contained in calcium aluminate is very carefully regulated by manufacturers. Its structure is shown in Fig. 3.

Calcium hexa-aluminate (CA6) forms as a result of the sintering of CA2. It is nonhydraulic and more refractory than the other phases, having a melting point of 1870 °C. CA6 is formed in refractory castable products when they are heated to high temperatures. The C3A phase is very reactive and is only present in Portland cements.

Tricalcium aluminate, $Ca_3Al_2O_6$, often formulated as $3CaO{\cdot}Al_2O_3$ to highlight the proportions of the oxides from which it is made, is the most basic of the calcium aluminates. It does not occur in nature, but is an important mineral phase in Portland cement. Pure tricalcium aluminate is formed when the appropriate proportions of finely-divided calcium oxide and aluminum oxide are heated together above 1300 °C. The pure form is cubic, with unit-cell dimension 15.263 Å and has density 3.064 g/cc. It melts with decomposition at 1542 °C. The unit cell contains eight cyclic $Al_6O_{18}^{18-}$ anions, which can be considered to consist of six corner-sharing AlO_4 tetrahedra.

In Portland cement clinker, tricalcium aluminate occurs as an "interstitial phase", crystallizing from the melt. Its presence in clinker is solely due to the need to obtain liquid at the peak kiln processing temperature (1400–1450 °C), facilitating the formation of the desired silicate phases. Apart from this benefit, its effects on cement properties are mostly undesirable. It forms an impure solid-solution phase, with 15–20% of the aluminum atoms replaced by silicon and iron, and with variable amounts of alkali metal atoms replacing calcium, depending upon the availability of alkali oxides in the melt. The impure form has at least four polymorphs whose structure depend upon the amount of impurities present: two types of cubic, one-orthorhombic and one monoclinic crystal form. In keeping with its high basicity, tricalcium aluminate reacts most

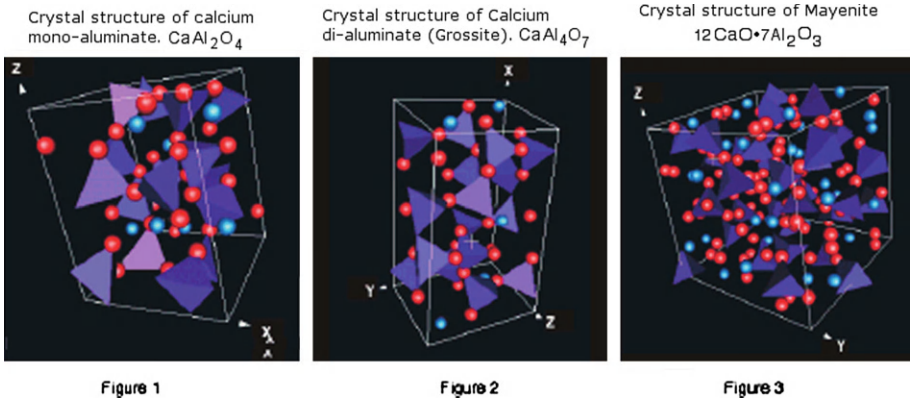

FIGURE 6.89

strongly with water of all the calcium aluminates, and it is also the most reactive of the Portland clinker phases. Its hydration to phases of the form $Ca_2AlO_3(OH)\cdot nH_2O$ leads to the phenomenon of "flash set" (instantaneous set), and a large amount of heat is generated. To avoid this, Portland-type cements include a small addition of calcium sulfate (typically 4–8%). Sulfate ions in solution lead to the formation of an insoluble layer of Ettringite ($3CaO\cdot Al_2O_3\cdot 3CaSO_4\cdot 32H_2O$) over the surface of the aluminate crystals, passivating them. The aluminate then reacts slowly to form the AFm phase, $3CaO\cdot Al_2O_3\cdot CaSO_4\cdot 12H_2O$. These hydrates contribute little to strength development.

Tricalcium aluminate is associated with three important effects that can reduce the durability of concrete: heat release, which can cause spontaneous overheating in large masses of concrete. Where necessary, tricalcium aluminate levels are reduced to control this effect. Sulfate attack, in which sulfate solutions to which the concrete is exposed react with the AFm phase to form Ettringite. This reaction is expansive, and can disrupt mature concrete. Where concrete is to be placed in contact with, for example, sulfate-laden ground waters, either a "sulfate-resisting" cement (with low levels of tricalcium aluminate) is used, or slag is added to the cement or to the concrete mix. The slag contributes sufficient aluminum to suppress formation of Ettringite. Delayed formation, where concrete is cured at temperatures above the decomposition temperature of Ettringite (about 65 °C) has also been employed to obtain stable concrete formations. On cooling, expansive Ettringite formation takes place, which strengthens the cured concrete.

Dodecacalcium hepta-aluminate ($12CaO\cdot 7Al_2O_3$) occurs rarely in nature as the mineral "mayenite" (see above for its structure). It is an important mineral phase in calcium aluminate cements and is an intermediate in the manufacture of "Portland" cement. Its composition and properties have been the subject of much debate, because of variations in composition that can arise during its high-temperature formation. The mineral as normally encountered is a solid-solution series with end-members $Ca_{12}Al_{14}O_{33}$ and $Ca_6Al_7O_{16}(OH)$. The latter composition loses water only at high temperature, and has lost most of it by the melting point (around 1400 °C). If material heated to this temperature is rapidly cooled to room temperature, the anhydrous composition is obtained. The rate of reabsorption of water to form the hydrous composition is negligible below 930 °C. The mineral is cubic. The crystal of $Ca_{12}Al_{14}O_{33}$ has cell dimension 11.983 Å and a density of 2.680 g/cc, while that of $Ca_6Al_7O_{16}(OH)$ has a cell dimension of 1.1976 nm and 2716 kg/m^3. A confusion regarding composition contributed to the mistaken assignment of the composition $Ca_5Al_3O_{33}$. Studies of the system have shown that the solid solution series extends also to the accommodation of other species in place of the hydroxyl group, including halides, sulfide and oxide ions. The mineral as normally encountered is a solid solution series with end-members $Ca_{12}Al_{14}O_{33}$ and $Ca_6Al_7O_{16}(OH)$. The latter composition loses water only at high temperature, and has lost most of it by the melting point (around 1400 °C). If material heated to this temperature is rapidly cooled to room temperature, the anhydrous composition is obtained. The rate of reabsorption of water during cooling to form the hydrous composition is negligible below 930 °C. The mineral is cubic. The crystal of $Ca_{12}Al_{14}O_{33}$ has cell dimension 1.1983 nm and density 2680 kg/m^3 while that of $Ca_6Al_7O_{16}(OH)$ has 1.1976 nm and 2716 kg/m^3. The confusion regarding composition contributed to the mistaken assignment of the composition $Ca_5Al_3O_{33}$. Studies of the system have shown that the solid solution series extends also to the accommodation of other species in place of the hydroxyl group, including halides, sulfide and oxide ions.

Dicalcium aluminate, $2CaO\cdot Al_2O_3$ or $Ca_2Al_2O_5$, was prepared in a piston cylinder apparatus at 1250 °C and 2.5 GPa. The compound is orthorhombic with space group symmetry I2*mb*, $a = 5.2281(1)$ Å, $b = 14.4686(2)$ Å, $c = 5.4004(1)$ Å ($Z = 4$, $D_{calc} = 3.481$ g/cm^3), and belongs to the "Brownmillerite" structure family. Main building units of this structure are (1) layers of perovskite type corner-connected AlO_6 octahedra lying perpendicular to [010], and (2) Zweier single chains of AlO_4 tetrahedra running parallel to the [100] plane. The alternate stacking of the layers and sheets of single chains results in a three-dimensional network in which the calcium ions are incorporated for charge compensation. This structure is the first known example for an alkaline earth aluminate with Zweier single chains of tetrahedra.

Penta-calcium tri-aluminate, $5CaO\cdot 3Al_2O_3$ or $Ca_5Al_6O_{14}$, (C5A3), forms only under an anhydrous and oxygen-free atmosphere. The crystal is orthorhombic, with a density of 3.067 g/cc. It reacts rapidly with water. This unstable form has the space group Cmc2 with $a = 11.253$ Å, $b = 10.996$ Å, $c = 10.290$ Å, $Z = 4$. It consists of alternating sheets of distorted AlO_4 tetrahedra and layers of Ca^{2+} atoms which lie parallel to the (001) plane. The tetrahedra are linked through corners to form a network of five-membered rings. The arrangement of the Ca atoms is unusual in that very short distances of Ca–Ca (~3.200 to 3.267 Å) result in face sharing of the Ca polyhedra.

Tetra-calcium tri-aluminate, $4CaO\cdot 3Al_2O_3$ (C4A3) or $Ca_4Al_6O_{13}$, is a metastable phase formed by dehydrating $4CaO\cdot 3Al_2O_3\cdot 3H_2O$ (C4A3H3). The crystal structure of tetracalcium trialuminate ($Ca_4Al_6O_{13}$), synthesized at 1250 °C and 2.5 GPa, has been determined from single-crystal X-ray data by direct methods [space group

Pcan, $Z = 8$, $a = 5.3002(2)$ Å, $b = 17.7610(5)$, $c = 21.0887(9)$ Å] and refined to $R1 = 6.42\%$. The unit-cell parameters of $Ca_4Al_6O_{13}$ exhibit a relationship to those of perovskite: $a \approx \sqrt{2}\, a_P$, $b \approx 5a_{Pv.}$ and $c \approx 4\sqrt{2}\, a_{Pv}$. The diffraction data showed the typical features of a pseudo-translational symmetry: all reflections (*hkl*) with *l* equal to 4*n* (*n* is an integer) had significantly higher intensity than the reflections with $l \neq 4n$. Furthermore, diffuse streaks parallel to *b** were observed. This compound exhibits Al^{3+} in three different kinds of coordination polyhedra: octahedra, tetrahedra, and trigonal bipyramids. One of the two main building units involves slightly corrugated sheets of perovskite-type corner-sharing AlO_6 octahedra perpendicular to the [010] direction. The octahedral sheets are connected by layers containing tetrahedral Zweier single chains. Within these layers, the tetrahedral chains are linked by two different kinds of rods containing distorted trigonal bipyramids sharing common corners and edges, respectively. The tetrahedral chains and the bipyramidal rods are parallel to [100]. Charge compensation is achieved by the Ca ions, which are coordinated by 9 or 10 oxygen cations.

If $CaSO_4$ (Gypsum) is added to the mix, the mineral, "ettringite" results. It is a hexacalcium aluminate trisulfate hydrate, of general formula:

$$(CaO)_6(Al_2O_3)(SO_3)_3 \cdot 32H_2O,$$

or;

$$(CaO)_3(Al_2O_3)(CaSO_4)_3 \cdot 32H_2O.$$

"Rapid Set® Cement" is an advanced, high-performance, hydraulic cement, that provides structural strength in 1 h, reduced shrinkage, and superior resistance to chemical attack. The chemistry of Rapid Set® Cement is primarily composed of hydraulic tetracalcium trialuminate sulfate (C4A3) and dicalcium silicate (C2S). The C4A3 compound, often referred to as calcium sulfoaluminate, hydrates to form beneficial "ettringite". Ettringite is a strong, needle-like crystal that forms very quickly to give Rapid Set® its high performance. Another significant aspect of the chemistry is the absence of tricalcium aluminate (C3A). C3A is present in Portland cement and makes it susceptible to sulfate attack. The fact that Rapid Set® has little or no C3A makes it very durable in sulfate environments.

Ettringite, a naturally occurring mineral, is formed in the hydrated Portland cement system as a result of the reaction of tricalcium aluminate with calcium sulfate, both present in Portland cement:

$$Ca_3Al_2O_6 + 3CaSO_4 \rightarrow \text{Ettringite}$$

In the cement system, the presence of Ettringite depends on the ratio of calcium sulfate to tri-calcium aluminate (C3A). When this ratio is low, ettringite forms during early hydration and then converts to the calcium aluminate monosulfate (AFm phase or (Al_2O_3–Fe_2O_3–monoaluminate)). When the ratio is intermediate, only a portion of the Ettringite converts to AFm and both can coexist, while ettringite is unlikely to convert to AFm at high ratios. Ettringite is named after Ettringen, Germany, the place where it was discovered in 1874.

Another mineral, Mayenite (after Mayen, Germany), $Ca_{12}Al_{14}O_{33}$, is a rare cubic mineral of cubic symmetry, originally reported from Eifel volcanic complex (Germany). It is also found at pyrometamorphic sites: e.g. in the Hatrurim Formation (Israel) and in some burned coal dumps as "Mayenite". The formula can be written as $[Ca_{12}Al_{14}O_{32}]O$, which refers to the unique feature: anion diffusion process. Mayenite is also found as calcium aluminate in cement where its formula is also written as $12CaO \cdot 7Al_2O_3$, or C12A7 in the "cement-chemist" notation.

The hydrates involved in the setting of these cements are:

Calcium aluminate decahydrate (CAH_{10}) is a metastable hydrate, which is typically formed when calcium aluminates are mixed with water at temperatures below 20 °C. CAH_{10} forms hexagonal platelets of poorly crystallized material making its interrogation by XRD often difficult. Upon heating, CAH_{10} will dehydrate at between 120 and 130 °C with an endothermic reaction which can easily be detected using DTA. CAH_{10} has a unit cell that is deformed orthorhombic. Its structure is shown in Figure 4, shown above in Fig 6.90.

Dicalcium aluminate octahydrate (C_2AH_8) is another metastable calcium aluminate hydrate. It tends to precipitate out of solution as a thin hexagonal platelet similar to CAH_{10}. C_2AH_8 occurs in the temperature range 21–30 °C. It dehydrates in the region of 210–230 °C with a characteristic endothermic peak.

Tri-calcium aluminate hexahydrate (C_3AH_6) or hydrogarnet (Katoite) is the most stable of all calcium

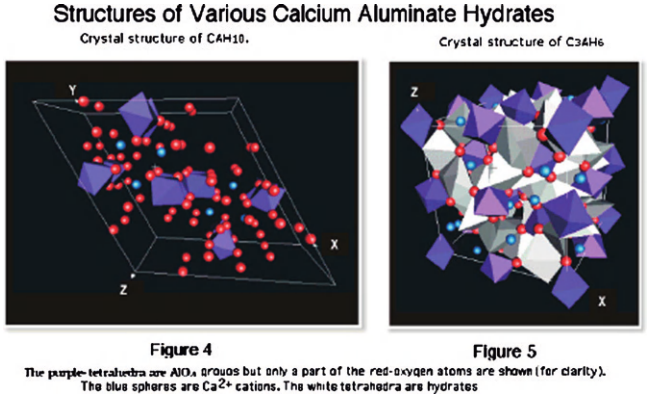

FIGURE 6.90

aluminate hydrates. It has a cubic unit cell. It is formed at higher ambient temperatures. It will not undergo transformation into other hydrates as with CAH_{10} and C_2AH_8. It dehydrates at between 300 and 350 °C forming first of all $C_3AH_{1.5}$ before undergoing complete dehydration around 500 °C. Its crystal structure is shown as shown in Figure 5 of Fig. 6.90.

In addition, several other hydrates have been discovered. Several modifications of the "hexagonal" tetracalcium and dicalcium aluminate hydrates have been obtained. Only a newly established $4CaO \cdot Al_2O_3 \cdot 19H_2O$ hydrate, and an α-form and a β-form of a $2CaO \cdot Al_2O_3 \cdot 8H_2O$ hydrate have been found to occur in the aqueous system at 25 °C. Other modifications are produced on drying under various conditions.

The $4CaO \cdot Al_2O_3 \cdot 19H_2O$ hydrate, characterized in the X-ray patterns by a long basal spacing of 10.62 Å, is dehydrated relatively easily to give a mixture of α-and β-forms of a $13H_2O$ hydrate, characterized by the basal spacings of 8·224 Å and 7·926 Å, respectively (basal here means the longest spacing between the two positions in the crystal structure).

There is little difference in stability between the two forms and it appears to be a matter of chance as to the relative amount of each that may be formed.

Two other tetracalcium aluminate hydrates have been obtained with water contents of $11H_2O$ and $7H_2O$, both of which give basal spacings of 7·42 Å. The α- and β-forms of $2CaO \cdot Al_2O_3 \cdot 8H_2O$ are characterized by basal spacings of 10·728 Å and 10·447 Å, respectively. The α-form appears to be more stable than the β-form. Three other states of hydration of the dicalcium compound exist, having water contents of $7.5H_2O$, $5H_2O$ and $4H_2O$, with basal spacings of 10.642 Å, 8.714 Å, and 7.443 Å, respectively. With various preparations of the compound $3CaO \cdot Al_2O_3 \cdot CaSO_4$,aq., basal spacings of 10·332 Å, 9·621 Å, 8·943 Å, 8·234 Å, and 8·034 Å have also been observed.

The basic nature of "concrete" formed from $CaAl_2O_4$ (CA) in Portland cement has also been elucidated. For CA, the anhydrous grains react immediately upon their addition to water, dissolving congruently to yield calcium ions and aluminate ions. As a consequence of this, the resulting solution appears to increase in both conductivity and pH until a point of super saturation is attained. The dissolution process is typically thought of as being congruent, yet there is often more lime than alumina present in solution:

$$CaAl_2O_4\ (\text{solid}) + 4\,H_2O \Rightarrow Ca^{2+}\ (\text{aq}) + 2\,Al(OH)^-\ (\text{aq})$$

It was reported that this observation is due to the fact that small quantities of alumina gel precipitate out of solution during hydration via the equation:

$$Al(OH)^- \Rightarrow Al(OH)_3\ (\text{gel}) + OH^-$$

This initial stage in the hydration reaction is exothermic and associated heat evolution can be detected easily by calorimetric methods. Once a state of super saturation of Ca^{2+} and $Al(OH)^{4-}$ (aq) species is reached, the reaction reaches a dormant stage prior to the nucleation stage.

In the second stage of the hydration reaction (nucleation), the solution remains supersaturated with ions. Dissolution and hydrate formation occur at a very slow rate, wherein a very high concentration of Ca^{2+} and $Al(OH)^{4-}$ (aq) species is maintained. Thus, the pH and conductivity of the solution will remain constant.

At the end of the nucleation phase of the reaction, massive precipitation and growth of the hydrate species will occur. This immediately results in a reduction in the amount of ions present in the solution, so that if any reacted CA is present, it will quickly be redissolved to attain super saturation once again. However, this will precipitate almost instantaneously to yield hydrated species. Dissolution and hydrate reprecipitation now proceeds simultaneously, though eventually the rate of the reaction will become infinitely large as the anhydrous CA diminishes. At this point, the conductivity will drop sharply corresponding to the drop of inorganic ionic species present in solution. Mass precipitation of species of this nature in the hydration reaction is accompanied by a considerably large exotherm (which can be detected to determine the end-point of the hardening reaction).

The hydration pathway for CA (monocalcium aluminate) in the hardening sequence of chemical reactions for this cement is shown as shown in Fig. 6.91.

Thus, it should be apparent that the hydration of the CA phase is temperature dependent. At lower temperatures, CAH_{10} will form (typically below 20 °C). In the intermediate temperature ranges between 21 and 30 °C, C_2AH_8 will form. Under conditions of elevated temperature C_3AH_6 will form, which is the most thermodynamically stable and the least soluble of the calcium aluminate hydrates. In addition to the hydrates

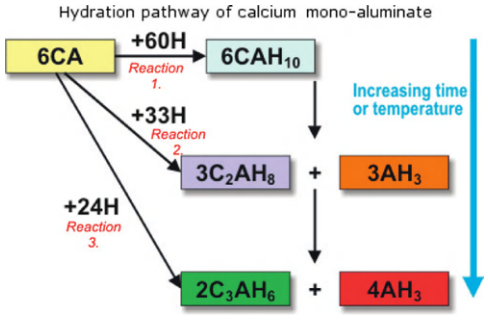

FIGURE 6.91

formed at intermediate temperatures, crystalline Gibbsite (AH_3) will form. Due to the metastable nature of CAH_{10} and C_2AH_8 over long periods of time or at elevated temperatures, both phases will undergo a transformation into the hydrogarnet phase (C_3AH_6.) This reaction is known as *"conversion"*. Conversion is initiated by the nucleation of C_3AH_6 and takes place in solution. As well as obvious changes in the chemistry during conversion, there are accompanying changes in the physical properties. In the transformation from CAH_{10} to C_3AH_6, a 52.5% reduction takes place, and during the change from C_2AH_8 to C_3AH_6 there is a 33.7% reduction in size. This results in an increase in the porosity of the concrete. Another effect of conversion is the release of water from the hydrates. A major impact of this increase in porosity and shrinkage is a decrease in mechanical strength. Conversion is a very topical subject in the field of calcium aluminate cements and the phenomena has been responsible for the failure of many buildings and bridges.

Because of their relatively high cost, calcium aluminate cements are used in a number of restricted applications:

- in construction concretes, rapid strength development is achieved, even at low temperatures.
- in construction concretes, high chemical resistance is possible.
- in refractory concretes, strength is maintained at high temperatures.
- as a component in blended cement formulations, various properties such as ultrarapid strength development and controlled expansion can be obtained.

However, calcium aluminates cements are no longer widely used in building construction because they are not stable enough over time. Incorrect use of calcium aluminate cements has led to widespread construction problems, especially during the third quarter of the twentieth century when this type of cement was used because of its faster hardening properties. After several years, some of the buildings and structures collapsed due to degradation of the cement and many had to be torn down or reinforced. Heat and humidity accelerate the degradation process called "conversion"; the roof of a swimming pool was one of the first structures to collapse in Britain. In Madrid, Spain, a large housing block nicknamed Korea (because it was built to house Americans during the Korean war), built 1951~1954 was affected and had to be torn down in 2006. Also in Madrid, the Vicente Calderón soccer stadium was affected and had to be partially rebuilt and reinforced.

Calcium aluminates are readily available commercially worldwide.

Strontium Aluminates

Strontium aluminate can be prepared by reaction of the oxides at about 700–900 °C:

$$SrO + Al_2O_3 + \text{heat} \Rightarrow SrAl_2O_4$$

The crystals of $SrAl_2O_4$ are monoclinic, with unit-cell parameters: $a = 5.1497$ Å, $b = 8.836$ Å, $c = 8.442$ Å, $\beta = 93.43°$; space group $P2_1$ or $P2_1/m$.

The $SrO \cdot Al_2O_3$ system is of interest in industry because of the use of the intermediate compounds for hydraulic cements, laser matrices, and long-duration photoluminescence or thermoluminescence pigments. But, compared to the information developed for the magnesium and calcium counterparts, the knowledge of the phase diagram of strontium aluminates has been quite limited. The only complete phase diagram of this system was reported in 1979. However, differences in melting and eutectic temperatures have found their way into the literature. The compounds and phase relations are essentially the same as shown by Massazza (1959), except for the differences in the various melting and inversion temperatures reported. The metastable compound, $Sr_4Al_2O_7$, was synthesized by several authors, but was not shown in any of the earlier phase diagrams. The following phase diagram is that which is believed to be the most representative of this phase system (Fig. 6.92).

The $SrO–Al_2O_3$ system shown has five binary phases: $3SrO \cdot Al_2O_3$, $SrO \cdot Al_2O_3$, $SrO \cdot 2Al_2O_3$, $4SrO \cdot Al_2O_3$ and $SrO \cdot 6Al_2O_3$. Liquidus temperatures drop rapidly upon addition of Al_2O_3 to SrO. Thus, $SrO \cdot 6Al_2O_3$ melts incongruently to Al_2O_3 at 1690 °C.

The minimum melting compositions are the eutectics between:

(i) $SrO \cdot 2Al_2O_3$ and $SrO \cdot 6Al_2O_3$ located at 1780 °C.
(ii) $SrO \cdot Al_2O_3$ and $SrO \cdot 2Al_2O_3$ located at 1760 °C.

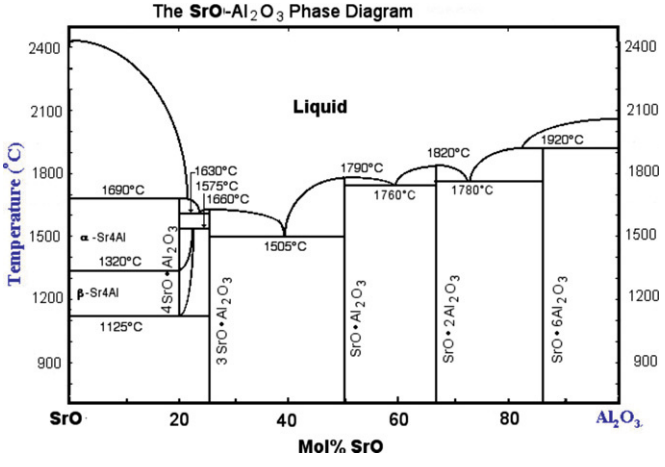

FIGURE 6.92

(iii) 3 SrO Al_2O_3 and SrO·Al_2O_3 located at 1505 °C.
(iv) 4 SrO Al_2O_3 and 3SrO Al_2O_3 located at 1630 °C.

Several of these compounds are difficult to synthesize. Up to about 1999, strontium dialuminate, $SrAl_4O_7$ (SA2), could be synthesized only by solidification from the high-temperature liquid state.

Strontium hexa-aluminate, $SrAl_{12}O_{19}$, has the magnetoplumbite structure. The magnetoplumbite-structured $SrAl_{12}O_{19}$ may be expected to accommodate a diverse chemistry because of the variety of crystallographic sites within the unit cell (Fig. 6.93).

It has a hexagonal structure, with space group *P*63/*mmc*. There are three types of Al^{3+} ions in the lattice. The unit cell is composed of spinel-structured slabs containing Al^{3+} cations separated by mirror planes which contain one Sr^{2+} and three oxygen ions per unit cell. The spinel blocks have the usual IV and VI coordinated sites for cations, whereas the interspinel layers have rather unusual V-fold sites for small cations. The interspinel layers also provide XII-fold sites to accommodate large cations, which may be monovalent, divalent, or trivalent with balancing charge substituents either in the interspinel layer (i.e. $Na_{0.5}$+ $La_{0.5}$) or in both the interspinel layer and the spinel block (e.g. La and Mg replacing Sr and Al, respectively). The latter reaction can be expressed as:

$$SrAl_{12}O_{19} + (x/2)\ La_2O_3 + x\ MgO \Rightarrow Sr_{1-x}La_xAl_{12-x}Mg_xO_{19} + x\ SrO + (x/2)\ Al_2O_3$$

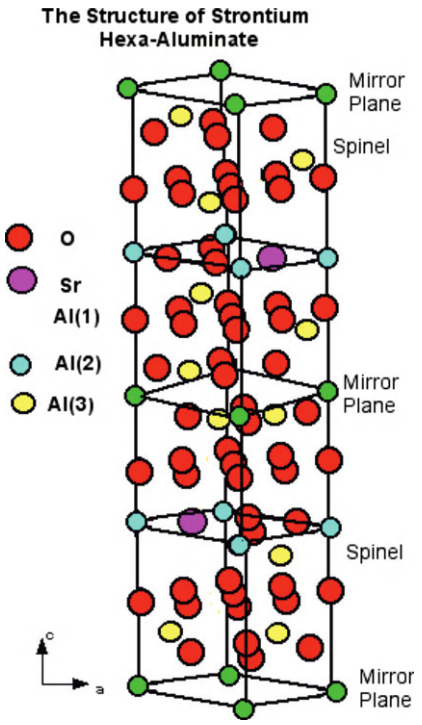

FIGURE 6.93

The defect reaction energy for this process is:

$$E = E(La_{Sr}) + E(Mg_{Al}) + E_{lat}(SrO) + 0.5E_{lat}(Al_2O_3) - 0.5E_{lat}(La_2O_3) - E_{lat}(MgO)$$

Some lattice energies and defect energies related to this question have been calculated and are given in Table 6.16.

"Frenkel" and "Schottsky" lattice defects are: Fr = interstitual + vacancy and Sch = cation vacancy + anion vacancy, respectively. For a comprehensive discussion of lattice defects in solids, see "Chapter 2—The Point Defect" in "Luminescence and the Solid State"—2nd Ed. by R. C. Ropp, Elsevier (2004) ISBN-0-444-51661-1.

The reaction enthalpy is calculated to be −1.02 eV when the binding energy of the two point defects is considered. This negative enthalpy indicates that the defect process is energetically favorable. This results in the following lattice energies (Table 6.17).

Strontium dialuminate, $SrAl_4O_7$ (SA_2), could only be synthesized in the past by solidification from the high-temperature liquid state. However, its synthesis from

TABLE 6.16

Ion	Type	Energy in eV
Sr^{2+}	Vacancy	19.29
Sr^{2+}	Interstitial	−5.00
Al^{3+}	Vacancy	55.23
Al^{3+}	Interstitial	−43.75
O^{2-}	Vacancy	22.64
O^{2-}	Interstitial	−15.10
Sr^{2+}	Frenkel =	7.14
	Frenkel =	5.74
O^{2-}	Frenkel =	3.77
SrO	Schottsky =	4.09
Al_2O_3	Schottsky =	3.94
—	Schottsky =	3.89

= Energy per constituent defect.

TABLE 6.17

SrO = −33.75 eV
MgO = −40.44 eV
Al_2O_3 = −158.78 eV
La_2O_3 = −124.14 eV
$SrAl_{12}O_{19}$ = −987.62 eV
$LaMgAl_{11}O_{19}$ = −977.73 eV

a spray-dried amorphous precursor can be obtained if its stability domains are maintained during synthesis. Its kinetics of formation is very low. It can be crystallized in the 900–1000 °C temperature range either directly with a low heating rate or via two metastable solid solutions [hexagonal strontium monoaluminate, $SrAl_2O_4$ (SA) and β-alumina] by annealing at 950–1000 °C. As the temperature is raised beyond 1100 °C, SA_2 becomes metastable, its formation is no longer possible, and the crystallization of $Sr_4Al_{14}O_{25}$ (S_4A_7) is favored. The latter compound, whose composition is close to that of SA_2, is stable up to 1500 °C. At higher temperature, it decomposes into SA and SA_2, which in its turn decomposes into SA and SA_6 ($SrAl_{12}O_{19}$). There is again another stability domain for SA_2, restricted to a narrow temperature scale close to its melting point (~1800 °C). The behaviors at crystallization from amorphous precursors at low temperature and from liquid at very high temperature are symmetrical: low heating or cooling rates produce pure SA_2 while too rapid kinetics result in mixtures of phases. Strontium dialuminate ($SrAl_4O_7$) can also be synthesized by crystallization of amorphous spray-dried precursors via the ethylenediaminetetraacetic acid precursor route. Differential thermal analysis, thermogravimetric, Fourier transform infrared spectroscopy, and XRD were used to characterize the precursors and the oxide powders derived. XRD analysis showed that single-phase $SrAl_4O_7$ was obtained from pulverized resin at a temperature of 1050 °C for 2 h and $SrAl_4O_7$ can be stable at least up to 1200 °C. Single-phase $SrAl_4O_7$ was not obtained from the citrate acid route.

Strontium dialuminate has two polymorphs, the α-phase being stable at STP but the β-phase can only be prepared at a high pressure and temperature. A mixture of α-$SrAl_4O_7$ and water was used in a cubic anvil type apparatus to prepare β-$SrAl_4O_7$. Pressure was maintained at 5.0 MPa and temperature at 1473 K (1200 °C) for 60 min. If water was not present, unknown phases were obtained. Upon cooling to 800 °C, single crystals of β-$SrAl_4O_7$ were obtained. This crystal is orthorhombic with space group Cmma, $a = 8.085$ Å, $b = 11845$ Å, $c = 4.407$ Å, Dens = 4.84 (calc) and $Z = 2$. The lattice consists of a three-dimensional (Al_4O_7) network of $Al(1)O_6$ octahedra and $Al(2)O_4$ and $Al(3)O_4$ tetrahedra. The bond lengths for the octahedra were 1.795 to 1.968° for the octahedra and 1.449 to 1.537 Å for the tetrahedra. The structure has certain similarities to that of the tetrastrontium aluminate structure. Each Sr atom is surrounded by 10 O atoms with distances ranging from 2.503 to 2.664 Å.

Tetrastrontium aluminate is also very unstable and can only be formed in a narrow temperature range. This can be determined from the phase diagram given above. It does not form at temperatures <1125 °C and when mixtures of $4SrO \cdot Al_2O_3$ are calcined, $Sr_3Al_2O_6$ results. If the mixture is heated above 1100 °C, S3A becomes metastable, and its formation is no longer possible since the crystallization of $Sr_4Al_2O_7$ (Sr4A) is favored. The latter compound, whose composition is close to that of SA2, is stable up to 1690 °C. At higher temperature, it decomposes into SA and SA2, which in its turn decomposes into SA and SA6 ($SrAl_{12}O_{19}$). The behaviors at crystallization from amorphous precursors at low temperature and from liquid at very high temperature are symmetrical: low heating or cooling rates produce pure SA_2 while too rapid kinetics result in mixtures of phases. The phase [$Sr_3Al_2O_6$] has been observed at 1000 °C as a stable phase. This phase was found to be transformed into [$SrAl_2O_4$] at 1250 °C. All of this thermal behavior is the result of the instability of S4A.

The reactions observed were shown in Table 6.18.

Thus, it should be clear that the stable compounds in this system are SA ($SrAl_2O_4$) and SA6 ($SrAl_{12}O_{13}$). X-ray powder diffraction data for $SrAl_2O_4$ have been obtained from the pure synthesized compound. The crystals of $SrAl_2O_4$ are monoclinic, with unit-cell parameters: $a = 5.1497$ Å, $b = 8.836$ Å, $c = 8.442$ Å, $\beta = 93.43°$; space group $P2_1$ or $P2_1/m$.

The major use for **strontium aluminate** (SA) has been as a long-term phosphorescent material when activated by Eu^{2+}. It is labeled as $SrAl_2O_4$:Eu^{2+}. It acts as a photoluminescent phosphor with long persistence of phosphorescence. Its CAS number is 12004-37-4. Strontium aluminate is a vastly superior phosphor than its predecessor, copper-activated zinc sulfide; it is about 10 times brighter, 10 times longer glowing, and 10 times more expensive than ZnS:Cu. It is frequently used in "glow-in-the-dark" toys, where it displaces the cheaper and less efficient ZnS:Cu and it is less toxic. However, the material has high hardness, causing abrasion to the machinery handling it; coating the particles with a suitable lubricant is usually used when strontium aluminate is added to plastics. Strontium aluminate (SA) phosphors produce green and aqua hues, where green gives the highest brightness and aqua the longest glow time. The excitation wavelengths for strontium aluminate range from 200 to 450 nm, i.e. it is "daylight" excited. The emission wavelength for its green formulation is 520 nm, its blue-green version emits at 505 nm, and the blue one emits at 490 nm. Colors with longer

TABLE 6.18

$$S3A + S \xrightarrow{1100°C} Sr4A\{Sr_3Al_2O_6 + SrO \Rightarrow Sr_4Al_2O_7\}$$

$$Sr4A + 4A \xrightarrow{1690°C} 3SA + SA2$$

$$4SA2 + A \xrightarrow{>1690°C} 3SA + SA6$$

$$S3A \xrightarrow{>1690°C} SA + 2S$$

wavelengths can be obtained from the strontium aluminate as well, though at the cost of some loss of brightness. The wavelengths produced depend on the internal crystal structure of the material. Slight modifications in the manufacturing process (the type of reducing atmosphere, small variations of stoichiometry of the reagents, addition of carbon or rare earth halides) can significantly influence the emission wavelengths.

Strontium aluminate phosphor is fired at about 1250 °C. Subjecting it to temperatures above 1090 °C is likely to cause loss of its phosphorescent properties. The glow intensity depends on the particle size; generally, the bigger the particles, the better the glow.

All of the possible phase compositions of the strontium aluminates have been explored for this application. Among them, $Sr_3Al_2O_6$, $SrAl_2O_4$, $SrAl_4O_7$, and $SrAl_{12}O_{19}$ crystals that have been doped with Eu^{2+} and Dy^{3+} ions were found worthy of investigation for determining the phosphorescence mechanism and the development of a new phosphor with a variety of colors. It is noteworthy that the addition of a trivalent cation like Dy^{3+} promotes the formation of electron traps in the lattice via formation of a cation vacancy:

$$DySr^{3+} + VSr^{+} \Leftrightarrow 2Sr_{Sr}^{2+}$$

Dy^{3+} is routinely added to the lattice composition because it causes a loss of photoluminescence and promotes phosphorescence. The luminescent properties of $SrAl_2O_4$ doped with Eu^{2+} and codoped with the rare earths ($Ln^{3+} = Eu^{3+}$, Er^{3+}, Sm^{3+} and Dy^{3+}) have been studied. The materials were synthesized by a reflux method and fired up to 900 °C for 16 h. The XRD pattern confirmed that the synthesized material consists of $SrAl_2O_4$ as main phase. The photoluminescence study gives a clear evidence of europium stabilizing in trivalent form and surprisingly with a lack of presence of europium in the divalent state. The addition of Dy^{3+} as co-dopant in the $Sr_3Al_2O_6$:Eu^{3+} matrix shows a quenching effect in the photoluminescence (PL) spectra. The photoluminescence intensity of Eu^{3+} falls gradually on increasing the concentration of the co-dopant in the range from 0.1 to 2.0 mol%. A significantly intense thermoluminescence (TL) glow peak was obtained for $Sr_3Al_2O_6$:Eu^{3+}:Dy^{3+} (1% and 0.1%) at around 194 °C when irradiated with 10 kGy dose from Sr-90 β-source.

A long-decay strontium aluminate (SrA)-based phosphor has been prepared by a solid state reaction technique. The dependence of initial brightness and observed afterglow characteristics on various thermal processing parameters such as heating rates, time of constant heating and cooling rates have been investigated. It has been found that heating rates (>625 °C/h), time of constant heating (<2 h at around 1200 °C) and cooling rates (>250 °C/h) resulted in nonuniform luminescent samples which are not excited under daylight but were excited under UV (365 nm). When proper heating rates (<300 °C/h), time of constant heating (>4 h at 1200 °C) and cooling rates (<100 °C/h) were employed, high-density ceramic compact (3100 kg/m^3) samples resulted. These phosphors had very low initial brightness but a quite long afterglow under room light and UV excitation. An optimum of both fast rise and long afterglow under room light excitation was been achieved for the SrA samples fired with the heating rates of 300–625 °C/h, time of constant heating of 2–4 h at around 1200 °C and cooling rates of about 100–250 °C/h. The decay characteristics of SrA were much superior to the established ZnS:Cu long-decay phosphor.

The mechanoluminescence (ML) of Eu,Dy co-doped strontium aluminates has been studied (ML is luminescence induced by force or stress on the crystal lattice). The compositions, $SrAl_2O_4$ and $Sr_3Al_2O_6$, showed a high degree of ML capacity, which is clearly visible to the naked eye in the air (One merely presses on the powder to obtain emission.). $SrAl_2O_4$:Eu:Dy shows the highest ML intensity and has many filled traps, high-quantum efficiency and moderate stiffness. On the other hand, $Sr_3Al_2O_6$:Eu:Dy does not have many filled traps and has a high relative quantum efficiency. But it does show a relatively high ML intensity. It has many filled traps and high relative quantum efficiency, but $SrAl_4O_7$:Eu,Dy shows very little ML capacity. The ML properties of $SrAl_2O_4$:Eu,Dy indicates that the lattice is capable of promoting high thermoluminescence because of the stiffness of the lattice. This suggests that "stiffness" is an important factor for obtaining ML intensity within the Eu,Dy co-doped strontium aluminate system.

Discussion of the applicability of long-duration (phosphorescent) phosphors has been based on optical measurements. $Sr_3Al_2O_6$, $SrAl_2O_4$, $SrAl_4O_7$, and $SrAl_{12}O19$ crystals were grown by a floating-zone technique for application as long-duration phosphors. Long-duration phosphorescence with a variety of colors has been observed in $Sr_3Al_2O_6$, $SrAl_2O_4$, $SrAl_4O_7$, and $SrAl_{12}O_{19}$ crystals. The peak wavelength of the phosphorescence is 520 nm for $SrAl_2O_4$, 480 nm for $SrAl_4O_7$, and 400 nm for $SrAl_{12}O_{19}$. The phosphorescence is characterized by decay times that have been analyzed by a curve-fitting technique. It is the green-emitting phosphor, $SrAl_2O_4$:Eu^{2+}:Dy^{3+} that has found the most usage commercially.

As is well-known, the effect of crystal-field symmetry upon the excitation state of the activator is the main cause of differences in the wavelength position of the emission of any phosphor. A variety of different compositions have been tried in an effort to improve both emission intensity (brightness) and decay time (persistence) of the strontium aluminate phosphorescence. The

following table summarizes some of these attempts in terms of crystal structure (Table 6.19).

Divalent europium, Eu^{2+}, emits mostly in the blue region of the spectrum in most lattices. The following is a summary of the peak wavelength of the strontium aluminate phosphors:

$$\text{Sr2A3} = 4600\ \text{Å} \qquad \text{SrA6} = 3950\ \text{Å}$$
$$\text{BaMgAl5} = 4500\ \text{Å} \qquad \text{SrMgA5} = 4650\ \text{Å}$$
$$\text{BaA} = 5050\ \text{Å} \qquad \text{SrA} = 5200\ \text{Å}$$

These structures can be described as "stuffed tridymite" lattices. In $BaAl_2O_4$, there are two different Ba^{2+}-sites, one occurring three times more frequently than the other. Both Ba sites are coordinated by nine oxygen ions. One Ba site is less regular than the other. The structure of $SrAl_2O_4$, which is the monoclinic low-temperature form, has two sites available for Sr^{2+} cations. Both occur in equal amounts in the lattice and are coordinated by nine oxygen ions. The coordination of Sr by oxygen is less regular than that of Ba in these monoaluminates. Due to the existence of the hexagonal form of $SrAl_2O_4$ at higher temperatures, mixed crystals of $Sr_{1-x}Ba_xAl_2O_4$ can be obtained.

In recent years, the **tetrastrontium hepta-aluminate**, $Sr_4Al_{14}O_{25}$, doped with divalent europium, has been regarded as another excellent phosphor host and has attracted considerable research efforts. This compound has been prepared by a solid-state method in which excess alumina was added to the 4:1 mix. Eu^{2+}, Dy^{3+} co-doped strontium aluminate ($Sr_4Al_{14}O_{25}$) phosphor with high brightness and persistent luminescence was also prepared via a combustion process using $SrAl_2O_4$ as a precursor, followed by heating the precursor at 1300 °C in a protective atmosphere of N_2. The result showed that the single-phase $Sr_4Al_{14}O_{25}$ was formed at 1300 °C. The phosphor powders have two main peaks near 403 and 482 nm, respectively, which are ascribed to two types of Eu^{2+} that exist in the $Sr_4Al_{14}O_{25}$ matrix crystal. The average particle size of the $Sr_4Al_{14}O_{25}:Eu^{2+},Dy^{3+}$ phosphor nanoparticles ranges from 20 to 40 nm. These nanometer phosphors exhibit a bright luminescence and a long duration of phosphorescence. The main excitation peak of the samples occurred at 360 nm and the main emission peak at 490 nm, respectively. The material heat treated at a rate of 10 °C/min and soaked at 920 °C for 10 min in an active carbon atmosphere possessed the best performance of luminescence and longest afterglow. The afterglow time allowed it to be visually recognized for over 20 h at darkness after removal of the excited light source. Compared with sulfide long-decay phosphors, $Sr_4Al_{14}O_{25}:Eu^{2+},Dy^{3+}$ phosphors possess safe, chemically stable, very bright and long-lasting phosphorescence in addition to not requiring external radiation from radioactive agents like that used for the sulfide phosphors. Note that a vacancy will exist in the crystal due to the trivalent ion, Dy^{3+}, i.e. $Dy^{3+}_{Sr} + V^{+}_{Sr} \Leftrightarrow 2Sr^{2+}_{Sr}$. This has resulted in a wide field of applications, such as luminous paints in highway, airport, building and ceramics, as well as in textile, dial plate of glowing watch, warning signs and escaping routeway applications.

The effect of trap level in the europium-doped strontium aluminate ($SrAl_2O_3:Eu^{2+}$) phosphors has been evaluated for a fiber-optic thermometer application. Sensitivity and temperature range of the $SrAl_2O_3:Eu^{2+}$ phosphor sensor head vary strongly with the trap depth and the trap density of the phosphors. In the temperature range of 273 to 353 K, $SrAl_2O_3:Eu^{2+}$ co-doped with Dy^{3+} or Nd^{3+}, which has a trap depth at around $E_t = 0.5$ eV, was found to be a powerful sensor

TABLE 6.19

Code	Composition	Structure*	*a*	*c*	Space group
CA6	$CaAl_{12}O_{19}$	Mp	5.564	21.892	P63/mmc
CAM-I	$Ca_2Mg_2Al_{28}O_{46}$	2Mp, Sp	5.571	79.770	R3m
CAM-II	$CaMg_2Al_{16}O_{27}$	Mp, Sp	5.599	31.297	P6m2
SA6	$SrAl_{12}O_{19}$	Mp	5.562	21.972	P63/mmc
SAM-I	$Sr_2MgAl_{22}O_{36}$	Mp, Sp	5.583	22.225	P6m2
SAM-II	$SrMgAl_{10}O_{17}$	bA	5.620	22.400	P63/mmc
BA6-I	$0.82BaO.6Al_2O_3$	bA	5.588	22.769	P63/mmc
BA6-II	$1.32BaO.6Al_2O_3$	bA	5.600	22.922	P6m2
BAM-I	$BaMgAl_{10}O_{17}$	bA	5.627	22.658	P63/mmc
BAM-II	$BaMg_3Al_{14}O_{25}$	bA, Sp	5.638	31.988	P6m2

** Mp, magnetoplumbite block; Sp, spinel block; bA, β-alumina block.*

material having a large temperature coefficient. Persistent luminescence of Eu^{2+}-doped calcium aluminate, $CaAl_2O_4$: Eu^{2+}, was studied under UV and visible illumination. Broadband luminescence was observed in the blue region ($\lambda_{max} = 440$ nm) due to the $4f^6 5d^1 \Rightarrow 4f^7$ transition of Eu^{2+}. The threshold for the visible excitation was found at about 530 nm, which is not high enough in energy to create the monovalent Eu^+ ion required by the mechanisms presented by various authors previously. A new mechanism proposed involves the excited state absorption of two 530-nm photons via deep traps followed by trapping of electrons in shallow traps. The persistent luminescence is observed after a temperature-controlled electron–hole recombination and subsequent energy transfer to the Eu^{2+} luminescent center

Tristrontium aluminate, $Sr_3Al_2O_6$, has also been studied as a long-persistence phosphor. A detailed preparation process involving Eu^{2+} and Dy^{3+} ion co-doped $Sr_3Al_2O_6$ phosphor powders with red long afterglow by sol–gel combustion method in a reducing atmosphere was reported. XRD, SEM and photoluminescence spectroscopy were used to investigate the effects of synthesis temperature on the crystal characteristics, morphology and luminescent properties of the as-synthesized $Sr_3Al_2O_6$:Eu^{2+}:Dy^{3+} phosphors. The results revealed that $Sr_3Al_2O_6$ crystallizes completely when the combustion ash was sintered at 1200 °C. The excitation and the emission spectra indicated that the excitation broadband lies chiefly in visible range and the phosphor powders emit strong light at 618 nm under the excitation of 472 nm. The light intensity and the duration time of $Sr_3Al_2O_6$:Eu^{2+}:Dy^{3+} phosphors were increased when the calcination temperature was increased from 1050 to 1200 °C. The afterglow of $Sr_3Al_2O_6$:Eu^{2+}:Dy^{3+} phosphors sintered at 1200 °C lasts for over 600 s when the excited source is cut off. The red emission mechanism was discussed in terms of the effect of nephelauxetic and crystal field on the $4f^6 5d^1 \Rightarrow 4f^7$ transition of the Eu^{2+} ions.

In another report, a red luminescent $Sr_3Al_2O_6$:Eu^{2+} phosphor was synthesized via a sol–gel route assisted by microwave irradiation in a reducing atmosphere. The phosphor powders were characterized by XRD, SEM and a fluorescence spectrophotometer. The results reveal that the $Sr_3Al_2O_6$:Eu^{2+} phosphor powders calcined above 1150 °C possessed a $Sr_3Al_2O_6$ single cubic phase. The $Sr_3Al_2O_6$:Eu^{2+} particles at 1100 °C showed primarily rod-like morphology. However, the particles at 1150 to 1200 °C showed a flower-like and diffuse morphology. The average flower-like crystallite sizes were between 0.5 and 3 μm. The $Sr_3Al_2O_6$:Eu^{2+} powders exhibited a broad excitation band chiefly in visible range and a red abroad emission band of main peak at 612 nm under the excitation of 472 nm. Particularly, the $Sr_3Al_2O_6$:Eu^{2+} powders prepared at 1200 °C exhibited the strongest luminescent and phosphorescent intensity, which was due to the higher crystallinity and homogeneous flower-like particle morphology.

The luminescent properties of $Sr_3Al_2O_6$:Ln^{3+} doped and co-doped with the rare earths ($Ln^{3+} = Eu^{2+}$ and/or Dy^{3+}) have been studied. The material was synthesized by reflux method and fired up to 900 °C for 16 h. The XRD pattern confirms that the synthesized material consists of $Sr_3Al_2O_6$ as main phase. The photoluminescence study gives a clear evidence of europium stabilizing in trivalent form and surprisingly with no presence of europium in the divalent state. The addition of Dy^{3+} as co-dopant in the $Sr_3Al_2O_6$:Eu^{3+} matrix shows the quenching effect in the photoluminescence (PL) spectra. The photoluminescence intensity of Eu^{3+} falls gradually on increasing the concentration of the co-dopant in the range from 0.1 to 2.0 mol%. The significantly intense thermoluminescence (TL) glow peak was obtained for $Sr_3Al_2O_6$:Eu^{2+}:Dy^{3+} (1% and 0.1%) at around 194 °C when irradiated with 10 kGy dose from Sr-90 β source.

Tri-strontium aluminate has a "stuffed-tridimite" structure as shown in the following diagram. The structure, shown as follows, is based upon $(AlO_3)_6$ rings. It is cubic with a space group of Pa3. The noteworthy feature of this structure is the puckered six-membered tetrahedral AlO_4 rings. There is a front layer and a back layer in this structure, each running parallel to the other. This structure is typical of the strontium aluminates where either tetrahedral, AlO_4, or octahedral AlO_6 groups are present (or sometimes both). The lattice parameters are: $a = 15.8556$ Å, $V = 3986.3$ Å^3, $Z = 24$, $d_{calc} = 4.126$ g/cc (Fig. 6.94).

Only one layer within the cubic structure is shown, for the sake of clarity. Two layers are actually present in the unit cell.

Because of the red emission of trivalent chromium in Al_2O_3 as a laser, the ion, Cr^{3+}, has been added to the mix in long-decay aluminate phosphors. Cr^{3+} activated, red-emitting, long-persistence phosphorescence through

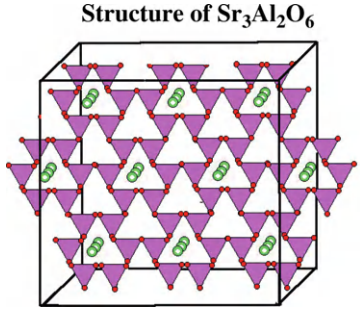

FIGURE 6.94

energy transfer from Eu^{2+} to Cr^{3+} has been reported in strontium aluminates co-doped with Cr^{3+}, Eu^{2+} and Dy^{3+}. The decay processes of the red long-persistent phosphorescence at 693-nm emission show signs of the f–d band of Eu^{2+}, indicating the occurrence of energy transfer from Eu^{2+} to Cr^{3+}. Lifetime measurements of the blue band show that the energy transfer rates increase with increase in Cr^{3+} concentration. There are several phases observed in the strontium aluminates. Energy transfer occurs only for the Eu^{2+} and Cr^{3+} ions that located in the same phase in the host. In $SrAl_{12}O_{19}$ phase, the Eu^{2+} ions emit blue light centered at 400 nm but prefer to transfer energy to the Cr^{3+} site that yields 688-nm emission. In the $Sr_2Al_6O_{11}$ and $Sr_4Al_{14}O_{25}$ phases, the Eu^{2+} ions emit at 460 and 490 nm, respectively, and transfer energy to the Cr^{3+} ions that produce emission at 693 nm. Persistent phosphorescence only occurred in the 490 and 693 nm bands, indicating that efficient phosphorescence comes from the $Sr_4Al_{14}O_{25}$ phase. It is possible to synthesize this phosphor by a cheap, easy and efficient combustion method. Persistent phosphorescence in blue–green (495 nm) by Eu^{2+} and in red (695 nm) by Cr^{3+} was observed in this phosphor. The persistence time for blue–green emission is over 10 h but for red emission, it was comparatively short. Red phosphorescence can be obtained through the persistent energy transfer from Eu^{2+} to Cr^{3+}, converting the blue–green to red. The energy transfer rate increases when the Cr^{3+} ions concentration increases and reaches maximum at 4 at%. The comparative results revealed that the relatively regular morphology, smaller particle size and narrow size distribution can be achieved for the phosphor synthesized by this combustion method but the emission intensity is somewhat less, probably due to lower crystallinity. However, the phosphor after post annealing at 1300 °C showed a higher emission intensity.

In another paper, Cr^{3+} activated red long-persistence phosphorescence through continuous energy transfer from Eu^{2+} to Cr^{3+} has been reported in strontium aluminates co-doped with Cr^{3+}, Eu^{2+} and Dy^{3+}. The decay processes of the red long-persistent phosphorescence at 693-nm emission show the same strong phosphorescence behavior of f–d band of Eu^{2+}, indicating the occurrence of energy transfer from Eu^{2+} to Cr^{3+}. Lifetime measurements of the blue band showed that the energy transfer rates increased with increase of the Cr^{3+} concentration. There are several phases observed in the strontium aluminates. Energy transfer occurs only for the Eu^{2+} and Cr^{3+} ions that located in the same phase in the host. In the $SrAl_{12}O_{19}$ phase, the Eu^{2+} ions emit blue light centered at 400 nm and prefer to transfer energy to the Cr^{3+} sites that yields 688-nm emission. In the $Sr_2Al_6O_{11}$ and $Sr_4Al_{14}O_{25}$ phases, the Eu^{2+} ions emit at 460 and 490 nm, respectively, and transfer the energy to the Cr^{3+} ions that produce emission at 693 nm. It was found that the efficient phosphorescence only occurs in the 490 and 693 nm bands, indicating the best phosphorescent matrix is that based on ions in the $Sr_4Al_{14}O_{25}$ phase.

A novel compound, $12SrO{\cdot}7Al_2O_3$, can be formed from an amorphous material prepared by the simultaneous hydrolysis of strontium and aluminum alkoxides. It has a cubic unit cell with $a = 12.325$ Å. The structure contains tetrahedral AlO_4 groups and octahedral AlO_6 groups. This compound decomposes into $3SrO{\cdot}Al_2O_3$ and $SrO{\cdot}Al_2O_3$ at higher temperatures. A new crystal structure of an aluminate having the formula, $Sr_6[Al_{12}O_{24}]{\cdot}Bi_2O_3$, was obtained as a side phase in the study of Bi–Ca–Sr–Cu–O system. This occurred as a result of a melt interaction with the Al_2O_3 crucible material. This aluminate has a trigonal unit cell with $a = 17.720$ Å, $c = 7.107$ Å, $V = 1933$ Å^3, space group $R3$, $Z = 3$, $d_{calc} = 4.38$ g/cm^3. In the framework of AlO_4 tetrahedra, a 12-atomic block of a new 3-6-3 type as a secondary building unit was found. The block consists of a corrugated sixfold ring and six triple rings. The blocks are stacked according to the rhombohedral law to form elongated sixfold and eightfold rings. A distinctive feature of the structure was the presence of a trigonal-bipyramidal "molecular" Bi_1O_3 group not observed before.

In another application to produce a cement, a strontium monoaluminate was produced by firing the oxides together in air. Some $SrAl_{12}O_{19}$ may be present. When formulated as a high-temperature cement, it hydrates slowly to produce $SrO{\cdot}Al_2O_3{\cdot}7–10H_2O$. In the later course of its hydration, it slowly transforms to $SrAl_6O_{10}{\cdot}6H_2O$, with a loss of strength. The cement can be used in the production of refractory cement that is useful in temperatures up to 2000 °C.

Strontium aluminates are readily available commercially as powders or as long-persistence paints.

Barium Aluminates

Barium aluminate (BA) has the formulation $BaAl_2O_4$, and the CAS number of 12004-04-5. Its molecular weight is 255.2884 g/cc. It is hexagonal in structure and melts at 1827 °C. Various barium aluminates can be synthesized by varying the BaO/Al_2O_3 molar ratio and firing the oxides at elevated temperatures of 800–1200 °C. The phase diagram of the $BaO–Al_2O_3$ system is shown in the following diagram, presented as shown in Fig. 6.95.

Four compounds are evident, $Ba_4Al_2O_7$, $Ba_3Al_2O_6$, $BaAl_2O_4$, and $BaAl_{12}O_{10}$. Barium hexa-aluminate ($BaO{\cdot}6Al_2O_3$) is the most refractory aluminate in the series and melts at 1915 °C. Three compounds melt congruently but the tetra-barium aluminate melts incongruently at 1425 °C to form the tribarium aluminate plus BaO.

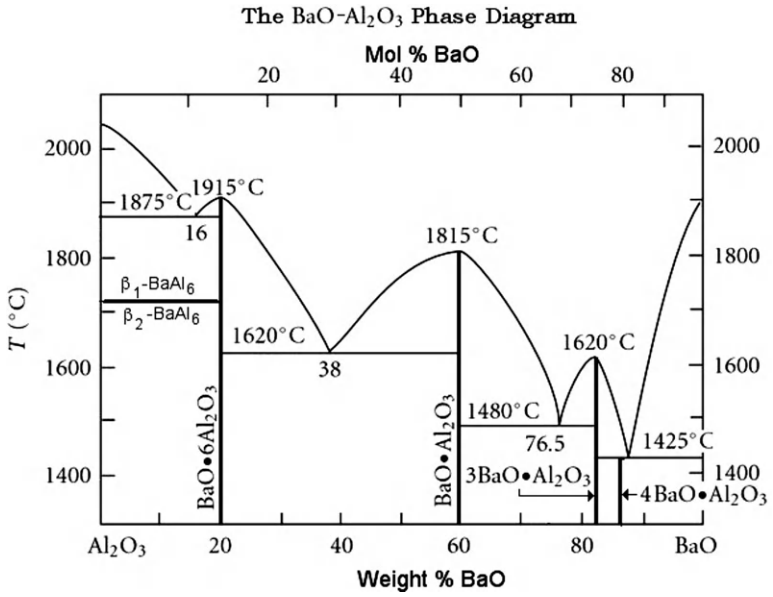

FIGURE 6.95

Barium aluminate, $BaAl_2O_4$ (BA), synthesis by solid–solid reaction at 900 °C between powdered reactants of barium carbonate and alumina in stoichiometric proportions has been studied. During the synthesis and under particular gaseous atmospheres, the aluminate BA, as it forms, reacts with the carbonate to form an intermediate product $Ba_3Al_2O_6$ (B_3A). When the barium carbonate has completely disappeared, B_3A and remaining alumina lead to the barium aluminate, BA. The mechanisms for this reaction synthesis at 900 °C, using pellets made of each reactant $BaCO_3$ and Al_2O_3 as starting materials, involve diffusion of Ba^{2+} through the Al_2O_3 matrix and the diffusion of Al^{3+} through the BaO matrix in opposite directions. The rate of "hopping" of Ba^{2+} ions is much faster than that of Al^{3+} so that the reaction: $3Ba^{3+} + Al_2O_3 \Rightarrow Ba_3Al_2O_6$ builds up first. The later reaction involves $Ba_3Al_2O_6 + 2Al^{3+} \Rightarrow 3BaAl_2O_4$. The ionic diffusion mechanisms described include two kinds of oxygen transfer, either in the solid state, or from the gaseous atmosphere. Kinetic developments corresponding to the most probable rate determining steps in each case were carried out and summarized. The importance of the various chemical parameters that modify the reaction process was discussed and the influence of the gaseous atmosphere was particularly followed. In addition, diffusion experiments using BaO and alumina were studied. This work follows up a kinetic study previously published on the synthesis of $BaAl_2O_4$ from stoichiometric $BaCO_3 + \beta\text{-}Al_2O_3$ powder mixtures, with formation of an intermediate compound. In that study, the formation of other barium aluminates was shown, as the distances of diffusion greatly increase in the lattice. Isothermal sintering of monobarium aluminate ($BaAl_2O_4$) was carried out by measuring shrinkage on firing of compacted pellets of ~45 micron size powder samples at temperature of 1300, 1350, 1400 and 1450 °C. The time dependence of linear shrinkage reveals volume diffusion as dominant mechanism of sintering. The apparent diffusion coefficient (D) of sintering was calculated and its temperature dependence can be represented by the equation:

$$D = 8.04 \times 10^{-9}\ (-188{,}000/\mathrm{RT})/\mathrm{cm}^2/\mathrm{s}$$

In another study, nanosized (10–30 nm particle size) hexagonal barium monoaluminate, having a high surface area of ~30 m^2/g, was synthesized by calcination of hydrothermally prepared precursors. The precursors were obtained by hydrolytic precipitation, using a mixed solution of barium and aluminum nitrates in the presence of aqueous urea at 180 °C. Based on the results of XRD, FTIR, SEM/EDS, TEM, and TG-DTA studies, the most probable sequence of reactions leading to the formation of barium monoaluminate was:

- Conversion of aqueous barium and aluminum nitrates in the presence of urea by hydrothermal precipitation to crystalline orthorhombic barium carbonate and boehmite,
- Formation of an interim form consisting of amorphous fibrillar aluminum oxide(s) interlaced with crystalline barium carbonate in the calcination temperature range of 500–800 °C,
- Initiation of formation of barium monoaluminate at 1000 °C, and
- Formation of a near monophase nanosized barium monoaluminate at 1200 °C.

In another study, pure barium monoaluminate and β_1-β_2-barium hexa-aluminate were prepared by keeping Ba/Al ratio as 1:2 and 1:12, respectively. Similar to the strontium system, these were found to be the most stable phases in the $BaO–Al_2O_3$ system.

The effect of varying Ba/Al ratio from 1:4 to 1:10 on the formation of barium aluminates was also studied. The samples obtained during hydrothermal precipitation contained mixtures of $BaCO_3$ and γ-AlOOH. The mean crystallite diameter (MCD) values along (1 1 1) plane corresponding to $BaCO_3$ phase for these precursors were in the range of 70–99 nm whereas the MCD values along (0 2 0) plane corresponding to γ-AlOOH were in the range of 10–12 nm. The precursors, when calcined at 400 °C, did not show any crystalline phases of alumina and most of the peaks corresponded to barium carbonate with diminished peaks of γ-AlOOH when compared to the precursor. At 800 °C, some peaks for $(Al_2O_3)\underline{O}$ were observed along with major phase of $BaCO_3$. At 1200 °C, irrespective of the Ba/Al ratio, formation of major phase of $BaAl_2O_4$ along with minor phases of α-Al_2O_3 and Ba-$\beta_1\beta_2$-$Al_{12}O_{19}$ were observed. At 1400 °C, $BaAl_2O_4$ remained the major phase at all Ba/Al ratios along with crystalline phase of α-Al_2O_3. Typical peaks corresponding to Ba-$\beta_1\beta_2$-$Al_{12}O_{19}$ aluminate became more prominent when the Ba/Al ratio was ≥1:6. No other intermediate phases such as tri-barium mono-aluminate, barium tetra aluminate or nonstoichiometric barium aluminates were formed.

The effect of high-energy BM and subsequent annealing on a mixture of Al_2O_3 and $BaCO_3$ was also investigated. DTA results show that the initiatory decomposition temperature of $BaCO_3$ decreases with increase of ball milling time duration. XRD measurement indicated that a nanocrystalline powder mixture was produced and that no $BaAl_2O_4$ is formed during a high-energy BM process after milling for 30 h. Significant crystallization of $BaAl_2O_4$ from the nanocrystalline powder mixture milled for 5, 15 and 30 hwas observed after annealing at 900 °C, although a trace of $BaCO_3$ remained at this temperature. Single-phase $BaAl_2O_4$ can be obtained for the sample milled for 5 h at 1000 °C, which is at least 200 °C lower than that used in the traditional solid-state method, while the secondary crystalline phases, $Ba_5Al_2O_8$ and $BaCO_3$, exist within the physical mixture at 1000 °C. No significant gain was observed when the milled powders were annealed at 1000 °C with different milling times and the average size of the particles produced was about 0.3–0.5 μm.

Barium monoluminate is also easily hydrated. A number of studies have been made because of the potential of using barium aluminates in a "fast-setting" cement. A new layered barium aluminate hydrate was synthesized from a hydrothermal system. γ-$BaAl_2O_3(OH)_2\cdot H_2O$ is orthorhombic, Fdd2, with $a = 20.70$ Å, $b = 8.977$ Å, $c = 6.426$ Å, $Z = 8$. It contains chains of composition $[AlO(OH)_2^{-1}]_\infty$, made-up of tetrahedra-sharing corners. Its formula is therefore better written as γ-$Ba[AlO(OH)_2]_2$.

A hydrolysis study was made of the following compounds:

$BaO\cdot Al_2O_3$,
$3BaO\cdot Al_2O_3$,
$BaO\cdot Al_2O_3\cdot H_2O$
$BaO\cdot Al_2O_3\cdot 2H_2O$,
$BaO\cdot Al_2O_3\cdot 4H_2O$,
$BaO\cdot Al_2O_3\cdot 7H_2O$,
$7BaO\cdot 6Al_2O_3\cdot 36H_2O$
$2BaO\cdot Al_2O_3\cdot 5H_2O$
$A1_2O_3\cdot 3H_2O$

From this, together with a study of precipitation from supersaturated barium aluminate solutions, a diagram of phase equilibria (stable and metastable) at 30 °C was drawn. All the barium aluminates are hydrolyzed by water. The stable solid phases in the system $BaO–Al_2O_3–H_2O$ at 30 °C are $A1_2O_3\cdot 3H_2O$ (gibbsite), $Ba(OH)_2\cdot 8H_2O$, and, over a narrow range, probably $2BaO\cdot Al_2O\cdot 5H_2O$. On the basis of the experiments performed and subject to the experimental conditions, the following conclusions were presented:

1. Monobarium aluminate is hydrolyzed by water, with **precipitation of** hydrated alumina.
2. Monobarium aluminate dissolves in barium hydroxide solutions with precipitation first of $7BaO\cdot 6Al_2O_3\cdot 36H_2O$, which subsequently forms $BaO\cdot Al_2O_3\cdot 7HO$ in less basic and $BaO\cdot Al_2O_3\cdot 4H_2O$ in the more basic solutions.
3. Tribarium aluminate is rapidly hydrolyzed by water, with precipitation of $Ba(OH)_2\cdot 8H_2O$, $BaO\cdot Al_2O_3\cdot 7H_2O$, and, subsequently, $2BaO\cdot Al_2O_3\cdot 5H_2O$.
4. All the hydrated barium aluminates dissolve in water and are hydrolyzed, with precipitation of hydrated alumina.
5. The hydrated barium aluminates dissolve in barium hydroxide solutions with eventual precipitation of the equilibrium solid phases, but frequently with preliminary separation of metastable intermediate solid phases.
6. The stable phases in the system $BaO–Al_2O_3–H_2O$ at 30 °C are: (a) gibbsite ($Al_2O_3\cdot 3H_2O$) over a range from approximately zero concentration to about 52 g of BaO and 2.8 g of Al_2O_3 per liter; (b) $Ba(OH)_2\cdot 8H_2O$ from 52.9 g of BaO and zero Al_2O_3 to about 55.5 g of BaO and 2.7 g of Al_2O_3 per liter; (c) probably 2BaO. $Al_2O_3\cdot 5H_2O$ (but possibly $BaO\cdot Al_2O_3\cdot 4H_2O$ or gibbsite) over the short range from 52BaO and $2.8Al_2O_3$ to 55.5BaO and $2.7Al_2O_3$.

7. $7BaO \cdot 6Al_2O_3 \cdot 36H_2O$ is a metastable phase, not sufficiently stable to permit an accurate determination of its solubility.
8. $BaO \cdot Al_2O_3 \cdot 7H_2O$ is also metastable, but it may exist in contact with solution for several months.
9. $BaO \cdot Al_2O_3 \cdot 4H_2O$ is likewise metastable over the **greater** part, if not **all**, of its range. Its stability is greater than that of the higher hydrates.

Supersaturated solutions of alumina in barium hydroxide were prepared and allowed to stand, with occasional shaking, at 30 °C. The precipitates were observed under the microscope from time to time, and changes in concentration of the solutions were determined by analysis. Various methods were used for preparation of the supersaturated solutions. The most satisfactory treatment of anhydrous barium aluminate was to add sufficient water to cause practically complete hydrolysis and precipitation of hydrated alumina, followed by boiling the mixture with barium hydroxide solution to dissolve the alumina. The solution was then filtered promptly while still hot. The anhydrous aluminate used for the purpose was either $BaO \cdot Al_2O_3$ or $3BaO \cdot Al_2O_3$ or a mixture of the two, as desired, prepared by heating a mixture of barium carbonate and gibbsite ($Al_2O_3 \cdot 3H_2O$), in the desired proportions, at about 1300 °C. The final compound, $3BaO \cdot Al_2O_3$, crystallizes in the orthorhombic space group $Pna2_1$ with $M = 291.33$ g/mol, $a = 5.642$ Å, $b = 9.887$ Å, $c = 10.449$ Å, $V = 582.9$ Å^3, $Z = 4$, $R = 0.0288$. The structure of the compound consists of aluminate sheets stacked in an ABAB sequence. Each individual sheet contains six-membered rings formed by corner-sharing $AlO_2(OH)_2$ tetrahedral units with the terminal OH groups pointing toward the interlayer region in one direction. There are Ba^{2+} cations and water molecules located between the adjacent aluminate sheets. On the basis of powder XRD, the as-synthesized compound converts to the $BaAl_2O_4$ phase by thermal treatment at elevated temperatures. The phase transition was also been monitored by infrared spectroscopy.

Formation of $CaAl_2O_4$ in a 1:1 molar mix of CaO and Al_2O_3 occurs at higher temperature through formation of mainly lime-rich phases such as C_3A and $C_{12}A_7$. In the $BaO–Al_2O_3$ mix, however stoichiometric formation of $BaAl_2O_4$ occurs at relatively higher temperatures due to larger ionic size of barium ions. The rate of $BaAl_2O_4$ formation is faster and the interdiffusion coefficient values calculated for $BaO–Al_2O_3$ system were found to be much higher than in $CaO–Al_2O_3$ system. Sintering studies showed a slower rate of densification in $BaAl_2O_4$ powder compacts and were thought to be due to the higher molecular weight of $BaAl_2O_4$ though the values of apparent diffusion coefficients calculated were found to be comparable in both the systems.

In another study, the Ba system was compared to the Mg system. The formation kinetics of monobarium aluminate, $BaO \cdot Al_2O_3$, (BA) in the temperature range of 1100–1380 °C was studied. Activation energy of its formation from barium and aluminum oxide was calculated to be 68.6 Kcal/mol. In the presence of MgO, its formation is accelerated and the activation energy of reaction is found to be 47.3 Kcal/mol. The activation free energies of the reaction were found to increase in the presence of MgO (1.5% by weight). Diffusion coefficients (D) of these reactions have also been calculated and the temperature dependence obeys the relationships:

$$D = 9.596 \times 10^{-4}(-24{,}800/\mathrm{RT})/\mathrm{cm}^2/\mathrm{s}$$

$$D = 9.552 \times 10^{-4}(-20{,}900/\mathrm{RT})/\mathrm{cm}^2/\mathrm{s}$$

without and with MgO, respectively.

Methods of preparation, optical properties, and XRD data were also reported for six barium aluminate hydrates. Three of these were obtained successively by precipitation from supersaturated barium aluminate solutions at 30 °C. The first, designated by the empirical formula $BaO \cdot Al_2O_3 \cdot 6H_2O$, is metastable with respect to the second, $BaO \cdot Al_2O_3 \cdot 7H_2O$, which in turn is metastable with respect to $BaO \cdot Al_2O_3 \cdot 4H_2O$. Two lower hydrates, $BaO \cdot Al_2O_3 \cdot 2H_2O$ and $BaO \cdot Al_2O_3 \cdot H_2O$, were also prepared hydrothermally. $2BaO \cdot Al_2O_3 \cdot 5H_2O$ was obtained from boiling the barium aluminate solutions.

If a molar ratio of 2:5 $Ba(OH)_2$ and AlO(OH) is held under hydrothermal conditions at 618 K (°C) for 3 weeks, well-formed hexagonal prisms form. These have the chemical formula of barium aluminate hydrate, $2BaO \cdot 5Al_2O_3 \cdot H_2O$ or $Ba_2Al_{10}O_{16}(OH)_2$, $[BaAl_5O_8(OH)]$. This compound is hexagonal with space group $P6_3mmc$. Lattice parameters determined were: $a = 5.635$ Å, $c = 13.489$ Å, $V = 371.0$ Å^3, $Z = 4$, $D_{calc} = 3.773$ g/cc. Its structure is related to the well-known β-alumina compound, $Na_2O \cdot 11Al_2O_3$. The only difference is the absence of two oxygen layers from the spinel block.

The density and the ferroelectric, ferrielectric and pyroelectric properties of ceramics derived from $BaAl_2O_4$ have been investigated. The XRD patterns and the variation of the density are consistent with the presence at 300 K of nonstoichiometric materials in the 44.4–50.0 mol% BaO range. They appear to be ferrielectric like $BaAl_2O_4$. The Curie temperature varies from 396 (50% BaO) to 275 K (44.4% BaO) due to the composition change of the solid solution. The value of the spontaneous polarization, P_s, is relatively small and shows anomalous behavior: the thermal variation presents a maximum but there is no structural change. The unit-cell volume increases with decreasing BaO content. A substitution mechanism based on the

replacement of two Ba^{2+} for an $[Al–O–Al]^{4+}$ link, and a model accounting for the ferrielectricity was proposed.

The paraelectric–ferroelectric (PE-FE) phase transition in stuffed tridymite $BaAl_2O_4$ was studied in situ by TEM. Electron diffraction revealed that the PE and FE phases have hexagonal symmetry. The PE-FE phase transition is accompanied by a doubling of the cell dimensions in the *a–b* plane. The transition is reversible, takes place over a wide temperature range (400–670 K) and the interfaces related to the transition have a fluctuating character. The crystal structure of the high-temperature PE phase was determined by high-resolution electron microscopy (HREM). The structures of the PE phase (space group $P6_322$, $a = 5.224$ Å, $c = 8.843$ Å) and of the FE phase (space group $P6_3$, $a = 10.447$ Å, $c = 8.793$ Å) differ mainly by the configuration of the Al–O strings oriented along the *c*-axis. In the PE phase, all the strings are equivalent whereas straight and corrugated strings alternate in an ordered manner in the FE phase resulting in doubling of the *a* and *b* cell parameters. Translation and orientation domains due to the decrease of the translation and point symmetry were frequently observed. $BaAl_2O_4$ has the same structure as that of its Sr homologue and is shown in the following Fig. 6.96.

The structure consists mostly of isolated AlO_4 tetrahedra offset by the large Ba^{2+} ions. Not all of the oxygen atoms are shown, for the sake of clarity.

Tetra-barium aluminate has a unique structure that involves AlO_4 tetrahedra and two types of BaO_6 octahedra, as shown on the next page. This type of structure is common among the alkaline earth aluminates and involves mixed tetrahedra and octachedra. But here, the octahedra are connected and tilted away from each other. Crystal growth experiments in the system $BaO–Al_2O_3$ yielded single crystals of an oxo-aluminate with composition $Ba_4Al_2O_7$. **Tetra-barium aluminate** is orthorhombic, with cell parameters of: $a = 11.3126(5)$, $b = 11.7045(9)$, $c = 27.1850(14)$ Å , space group *Cmca*. The crystal structure is shown in Fig. 6.97.

The structure was solved by direct methods followed by difference Fourier synthesis from X-ray single-crystal diffraction data ($R1 = 0.048$ for 1213 independent observed reflections and 135 parameters). The main building units of tetrabarium aluminate are Al_3O_{10} trimers and isolated AlO_4 tetrahedra. Seven crystallographically different Ba sites crosslink between the tetrahedral groups and are coordinated by six to nine oxygen ligands. The structure is closely related to the mineral "kilchoanite" ($Ca_6[SiO_4][Si_3O_{10}]$) and is the first known alkaline earth representative of an unbranched oligoaluminate with triple tetrahedra.

Tetrabarium aluminate is not very stable, due, perhaps, to the size of the Ba^{2+} cation. It readily decomposes to the tribarium aluminate compound upon heating to elevated temperatures.

It forms a series of solid solutions with its calcium homologues as shown in the following ternary phase Fig. 6.98.

In addition to the solid solutions like $Ba_3A–Ca_3A$, two separate compounds are formed: $BaCaAl_2O_4$ and $BaCaAl_8O_{14}$. Although some authors include Ba_8A, the instabliity of $Ba_4Al_2O_7$ precludes the physical and chemical stability of a compound having a stoichiometry like $Ba_8Al_2O_{11}$.

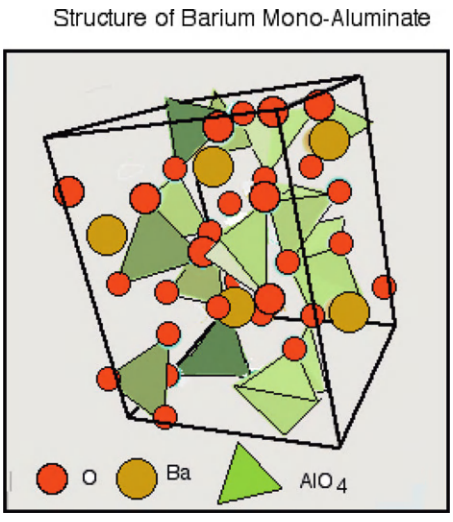

FIGURE 6.96

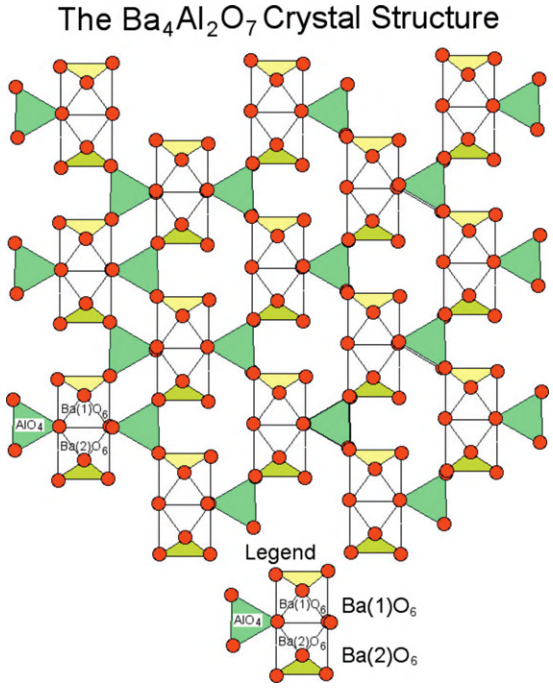

FIGURE 6.97

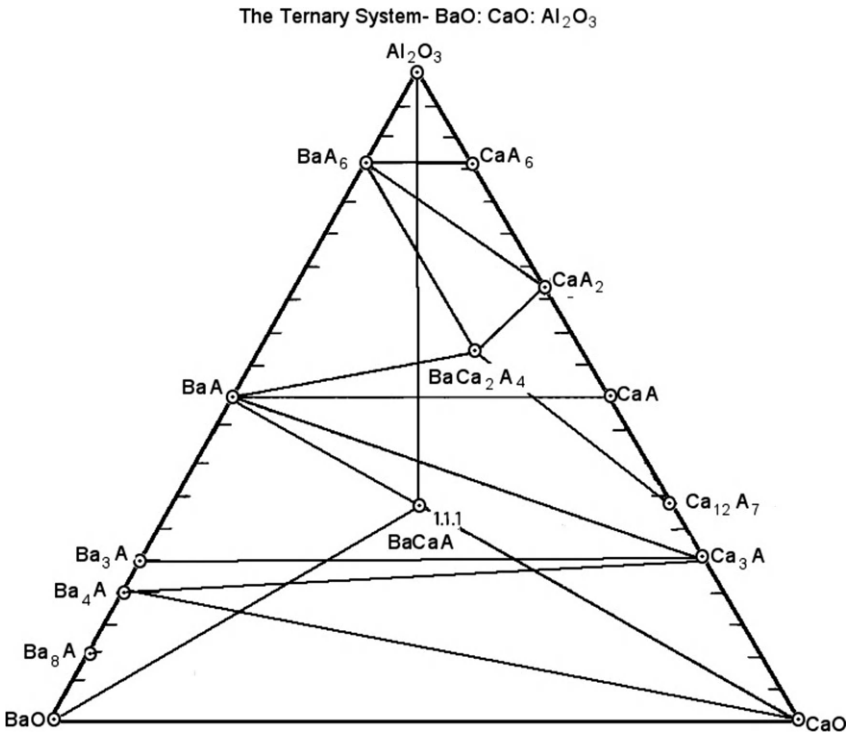

FIGURE 6.98

Single crystals of **tribarium aluminate** have been synthesized from the melt at 1480 °C. The compound adopts a space group $P2_13$, with $a = 16.4984$ Å and $Z = 24$ formula units per unit cell. The principal building units of $Ba_3Al_2O_6$ are highly corrugated 12-membered rings of AlO_4 tetrahedra that are cross-linked via Ba cations. Alternatively, the compound can be derived from the ABO_3 perovskite-type, representing a defect structure with vacancies on the B- and the O-positions. The relationship with perovskite can be expressed by the following formula: $Ba(Al_{3/4}Ba_{1/8}V_{1/8})(O_{3/4}V_{1/4})_3$. The structure shows a pronounced degree of pseudo-symmetry. Apart from one Ba position, all atoms in the structure approximately conform to the symmetry requirements of a perovskite. Nevertheless, the whole structure adopts the cubic subgroup $P2_13$. This investigation was said to correct earlier studies describing $Ba_3Al_2O_6$ in either too low or too high symmetry. The characterization of tribarium aluminate was completed by Raman spectroscopy.

Tri-barium aluminate, $Ba_3Al_2O_6$, has the structure shown in Fig. 6.99.

Where the AlO_4 tetrahedra are tied together in a puckered 12-membered rings. The barium ions surround each tetrahedron in an ordered pattern.

The compound, **barium di-aluminate**, $BaAl_4O_7$, apparently cannot be formed. A simple process, based on the solvothermal reaction of alkaline earth precursors

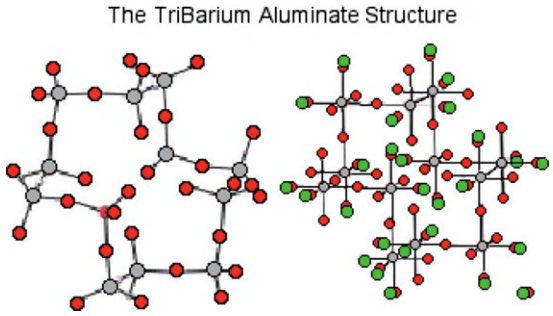

FIGURE 6.99

with aluminum isopropoxide in benzyl alcohol, leads to crystalline complex nanostructures of alkaline earth aluminates, which, up to now, could only be obtained by SSR at temperatures above 1100 °C or by sol–gel and further calcination at temperatures only slightly lower (800 °C). When this nonaqueous route was used, it led to crystalline complex nanostructures of $BaAl_2O_4$, $CaAl_4O_7$, and $SrAl_4O_7$ but $BaAl_4O_7$ could not be obtained.

Barium hexa-aluminate powder with a high surface area (22 m^2/g) and micro-sized (0.3–2 μm) particles was prepared by the calcination (at 1400 °C, for 2 h) of hydrothermally prepared precursors of orthorhombic barium carbonate and boehmite. The precursors were obtained by a hydrothermal treatment (at 180 °C, for

1 h) of aqueous solutions of barium and aluminum nitrates of appropriate compositions in the presence of aqueous urea as the neutralizing precipitant. Results of XRD, TG-DTA and SEM measurements suggested that the most probable reaction sequence for the preparation of barium hexa-aluminate ceramic powder was:

(i) The hydrothermal precipitation of orthorhombic $BaCO_3$ and boehmite (γ-AlOOH) precursors from the aqueous Ba and Al nitrates in the presence of urea,

(ii) The formation of an interim mixture of β-Al_2O_3, $BaCO_3$ and Ba–β_1-β_2- alumina in the temperature range of 800–1200 °C,

(iii) The formation of a ceramic powder corresponding to the composition $BaO{\cdot}6Al_2O_3$ having a –β_1-β_2-alumina type structure at 1400 °C.

The final material did not show presence of any other crystalline phases like alumina, baria, barium mono-aluminate and tri-barium mono-aluminate phases.

In another study, barium hexa-aluminate ($BaO{\cdot}6Al_2O_3$) aerogels were prepared using a supercritical drying method and their properties examined. A barium hexa-aluminate aerogel prepared from a double alkoxide of barium and aluminum showed a high specific surface area of 421 m^2/g. Monolithic barium hexa-aluminate formed. No $BaO{\cdot}Al_2O_3$ or alumina was observed, as is often the case in powder processing. The specific surface area of the monolithic barium hexa-aluminate fired at 1400 °C for 2 h was 12 m^2/g, while that of the barium hexa-aluminate xerogel was only 0.8 m^2/g. A barium hexa-aluminate aerogel was also prepared using barium by using a chelating agent. This aerogel showed a specific surface area of 454 m^2/g, as-dried. In the case of the chelating agent, $BaO{\cdot}Al_2O_3$ was also detected along with barium hexa-aluminate after firing.

The crystal structure of barium hexa-aluminate phase I ($BaAl_{12}O_{19}$) was determined by single-crystal X-ray reflection data. The refinements were carried out by the least-square method to give a final *R*-value of 0.023. The structure was revealed to be essentially of a β-alumina type and the Ba ion was detected only at the 6*h* site near the Beevers-Ross site (2*d* site). The charge compensation for nonstoichiometry was found to be principally effected by the interstitial oxygen due to Frenkel defects of Al^{3+} ions. From the structural point of view, phase-I was referred to as "barium β_1-aluminate." This compound has the same structure as its strontium homologue (Fig. 6.100).

Three types of Al^{3+} ions are present, dividing the structure into mirror planes and a spinel block. Upon calcination at 1200 °C, a marked drop in surface area value was observed associated with the formation of the final $BaO{\cdot}6Al_2O_3$ phase. This compound is hexagonal

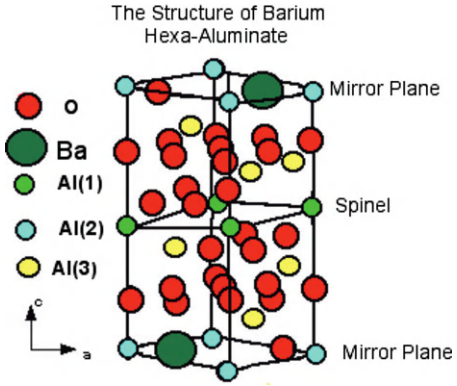

FIGURE 6.100

with $a = 5.582$ Å, $c = 22.715$ Å, $V = 612.9$ Å^3, $Z = 2$ and $D_{calc} = 3.662$ g/cc. The space group is $P6_3/mmc$.

Barium hexa-aluminate is a well-defined refractory compound. Barium hexa-aluminate refactories are strong (MOR ~ 600 MPa). Possible industrial uses are in the glass and metallurgical industries, and also as molds and cores for metal casting. A gel precursor of barium hexaaluminate can be prepared from a solution of a barium salt mixed with a solution of an aluminum salt, to give the oxide stoichiometry $BaO{\cdot}6Al_2O_3$. This is followed by heating to remove volatiles or by adding a separate gelling agent such as ammonium acetate. The gelling agent can also be a salt already present, for instance barium acetate, which gives better control of gelation. The gel is dried and fired to form barium hexaaluminate. Filaments which convert on firing to a barium hexa-aluminate ceramic fiber can be drawn as the gel is forming or extruded from a semi-rigid gel. Refractory components can be prepared from a suitably graded refractory grain mix bonded with the gel. The aluminum salt may be replaced by an aluminum alkoxide. Alkaline gelation is desirable to obtain a rigid coherent gel or a ceramic fiber. FT-IR, XRD and Al-NMR studies showed that barium was not incorporated directly into the gel structure, no barium aluminum oxides being formed before the barium species liquefy. A powder mixture suitable for firing to form barium hexa-aluminate was prepared from alumina and barium carbonate or barium hydroxide. Strong ceramic shapes have been made from a sintered powder mix. XRD studies showed that rapid firing to 1600–1700 °C gives barium hexaaluminate directly. Slow firing to 1600-1700 °C gives barium mono-aluminate as one intermediate phase. Chromium (III) addition reduces the temperature required to form an aluminum–barium oxide, and ultimately, the temperature of formation of barium hexaaluminate.

Although **dodeca-barium hepta-aluminate**, $12BaO{\cdot}7Al_2O_3 = Ba_{12}Al_{14}O_{33}$, does not appear in the phase diagram, it has been prepared via a sol–gel process. Optical and electrical properties of B12A7 films were

investigated. The films were coated on soda lime float glass by a dip coating process, and annealed in air and hydrogen (H_2) at 450 °C for 2 h. The UV absorption edge was red shifted for films annealed in H_2 atmosphere. The B12A7 films had a high transparency of about 90% over a wide visible range with maximum of 95% at 575-nm wavelength. The sheet resistance of the 300-nm films corresponding to 90.57 and 0.974 kΩ per cm^2 has been observed for air and H_2-annealed films, respectively. Such thin films have been tested thermoluminescent dosimeter. A thermoluminescent dosimeter in the form of reusable solid chip was prepared using an acid-catalyzed sol-gel process, with tetramethoxysilane (TMOS) and $BaAl_2O_4$ powder as precursors. In comparison with the manufacturing process of typical lithium fluoride-based dosimeters, the method optimizes the manufacturing process. The new dosimeter has a dose response over a dose range varying from 0.1 to ~160 Gy and can be used to detect higher doses using the typical commercial TLD readers without special adjustments. Furthermore, the process may be used for the preparation of other TLDs using a simple chemical processing. However, the literature is devoid of any other supposed usages of this compound.

Dibarium aluminate, $Ba_2Al_2O_5$, does not exist, in spite of several attempts to synthesize it from the oxides or by a sol–gel synthesis.

Oxides containing aluminum and barium, optionally with chromium, are refractories with several possible industrial uses. A gel precursor of an oxide having the formula $BaO{\cdot}n(Al_{2x}Cr_{2y}O_3)$, where $1 < n < 6.6$, $(x + y = 1)$ and $0 < y < 0.5$ was prepared by mixing a solution of a barium salt with a solution of an aluminum salt or a solution of an aluminum salt and a chromium III salt, then forming a gel which was fired to obtain the desired oxide. Filaments could be drawn as the gel was forming or extruded from a semi-rigid gel. FT-lR, XRD and ^{27}Al NMR studies showed that barium is not incorporated directly into the gel structure. Barium aluminum oxides were obtained only after liquefaction of barium species. A powder mixture suitable for firing to an oxide of the formula $BaO{\cdot}m\ [Al_{2x}Cr_{2y}\ O_3]$ where $4.6 < m < 6.6$, $(x + y) = 1$ and $0 < y < 0.5$ was prepared from source materials barium hydroxide, barium oxide, barium carbonate and barium monoaluminate, alumina and/or a hydrated alumina and chromium III oxide, the relative amounts being varied to give the desired values of m and y on firing. A preferred oxide has the formula $BaO{\cdot}6Al_2O_3$ ($m = 6$ and $y = 0$). Strong ceramic shapes have been prepared from this. XRD studies of oxide compositions (n or $m = 6$ and $y = 0$) sintered at high temperature showed that barium monoaluminate is a low-temperature intermediate phase. Chromium III reduces the temperature required to form a barium aluminum oxide.

$BaAl_{12}O_{19}$–$BaAl_2O_4$ doped with Eu^{2+}, Cr^{3+} and $(Eu^{2+} + Cr^{3+})$ are prepared by SSR. The spectra of $BaAl_{12}O_{19}$–$BaAl_2O_4$:Eu^{2+}, Cr^{3+} shows that the f–d emission bands from Eu^{2+} are centered at 442 and 495 nm and the Cr^{3+} yields the emission lines at 694 and 700 nm. Photoluminescence study demonstrates that the red photoluminescence and energy transfer occurs only in the phase of $BaAl_{12}O_{19}$ not $BaAl_2O_4$ though the samples are mixed phases. The fluorescence lifetime measurements indicate efficient energy transfer from Eu^{2+} to Cr^{3+} in $BaAl_{12}O_{19}$: Eu^{2+}, Cr^{3+}. The energy transfer rate and efficiency are calculated. The results show that the energy transfer rate and efficiency increase following the increase in Cr^{3+} concentration.

$BaMgAl_{10}O_{17}$:Eu^{2+} (BAM) is currently used as the blue-emitting phosphor in most display devices, including color television and computer screens. It is not very stable over time and degrades much faster than the green or red-emitting phosphors. The effect is much sooner in cathode ray tubes or plasma-discharges tubes. The thermal degradation was investigated by forcibly annealing BAM particles in air at temperatures of 500–1300 °C. Rietveld analysis with powder XRD revealed novel lattice deformations in the thermally degraded BAM. The lattice constants c and a changed monotonically as annealing temperature increased, while the unit-cell volume V showed no change with annealing up to 900 °C, then abruptly expanded at 1100 °C annealing. In addition, peak profile analysis revealed increasing lattice strain being induced in the host lattice. The main cause of the thermal degradation of BAM appears to be due to generation of a lattice vacancy like the Schottky defect.

Barium aluminate cements have been synthesized by using barium carbonate, alumina, kaolin and colloidal silica as starting materials. The effects of the source of SiO_2 and of firing temperature on phase formation and physical properties of the fired cements have been studied. Cement samples were characterized using XRD, SEM, EDX. The setting time and heat of hydration of cements were also evaluated. The barium aluminate cements were mixed in castables. Cold crushing strengths evaluated, and values compared to those obtained using calcium aluminate cement (Secar 71). Mixtures of $BaCO_3$ and Al_2O_3 were targeted to produce $BaAl_2O_4$ which had a fast set-time, expansive behavior and lower strength compared to samples with SiO_2 additions. SiO_2 additions, regardless of source, resulted in $BaAl_2Si_2O_8$ (celsian) formation. The prepared samples had short setting times and higher mechanical properties in comparison with standard calcium aluminate cement.

Radium Aluminates

The scientific literature is lacking in any references to radium aluminates. Perhaps this is due to the intense

radioactivity of the isomer ^{226}Ra but is more likely due to lack of interest of those in industry who have usage of such compounds. It is anticipated that various radium aluminates could be prepared, using the same methods as those developed for the barium aluminate series of compounds. Thus, one would expect to be able to obtain:

$RaO \cdot Al_2O_3$,
$3RaO \cdot Al_2O_3$,
$RaO \cdot 6Al_2O_3$
$2RaO \cdot Al_2O_3$,
$RaO \cdot Al_2O_3 \cdot 4H_2O$
$RaO \cdot Al_2O_3 \cdot 7H_2O$,
$7RaO \cdot 6Al_2O_3 \cdot 36H_2O$,
$2RaO \cdot Al_2O_3 \cdot 5H_2O$,
$RaO \cdot Al_2O_3 \cdot H_2O$,
$RaO \cdot Al_2O_3 \cdot 2H_2O$,
$RaO \cdot Al_2O_3 \cdot 4H_2O$
$RaO \cdot Al_2O_3 \cdot 7H_2O$,
$7RaO \cdot 6Al_2O_3 \cdot 36H_2O$,
$2RaO \cdot Al_2O_3 \cdot 5H_2O$.

However, there is no record of such syntheses in the literature.

6.5. ALKALINE EARTH GALLIUM COMPOUNDS

Gallium does not exist in free form in nature, and the few high-gallium minerals such as "gallite" ($CuGaS_2$) are too rare to serve as a primary source of the element or its compounds. Its abundance in the Earth's crust is approximately 16.9 ppm. It has but one stable valence state: Ga^{3+}. The +1 oxidation has also been attested in some compounds, but they tend to disproportionate into elemental gallium and gallium(III) compounds. What is sometimes referred to as gallium(II) compounds may actually be mixed-oxidation state compounds containing both gallium(I) and gallium(III).

Gallium is amphoteric. Strong acids dissolve gallium, forming gallium(III) salts such as $Ga_2(SO_4)_3$ and $Ga(NO_3)_3$. Aqueous solutions of gallium(III) salts contain the hydrated gallium ion, $[Ga(H_2O)_n]^{3+}$, where n is usually 6 because gallium prefers an octahedral coordination. Gallium hydroxide, $Ga(OH)_3$, may be precipitated from gallium(III) solutions by adding NH_4OH or NH_3 (gas) to a solution containing Ga^{3+} ions. Dehydrating $Ga(OH)_3$ at 100 °C produces gallium oxide hydroxide, GaO(OH).

Additionally, it forms anionic species with oxygen. Alkaline solutions dissolve gallium, forming *gallate* salts containing the $Ga(OH)_4^-$ anion. Gallium hydroxide, which is amphoteric, also dissolves in alkali to form gallate salts. Although earlier work suggested $Ga(OH)_6^{3-}$ as another possible gallate anion, this species has not been confirmed in later works.

In general, alkaline earth gallates are prepared by a SSR of the oxides rather than by solution methods because of the formation of hydroxy-dominated compounds and/or hydrated compounds.

6.5.1. Alkaline Earth Gallide Compounds

The alkaline earths form "gallide" compounds with specific lattice structures when the elements are melted together in the proper atomic ratios.

Beryllium Gallide

Beryllium does not form any compounds with gallium. Instead, it forms a continuous solid solution as shown in Fig. 6.101.

The structural characteristics are shown in the following table:

Compound	Structure type	Point group	Space group	Melting point
(Be) rt	Mg	hP2	194	1270 °C
(Be) ht	W	cI2	229	30 °C
(Ga)	Ga	oS8	64	30 °C

Gallium is not used to alloy beryllium in industry because of lack of useful properties over that of Be metal alone.

Magnesium Gallide

The metal, Mg, forms a series of compounds with gallium as shown in Fig. 6.102.

Five compounds are known and their structural characteristics are presented in the following table, along with their melting temperatures (Table 6.20).

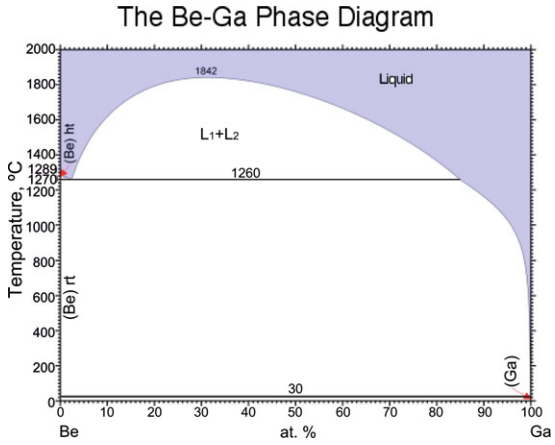

FIGURE 6.101

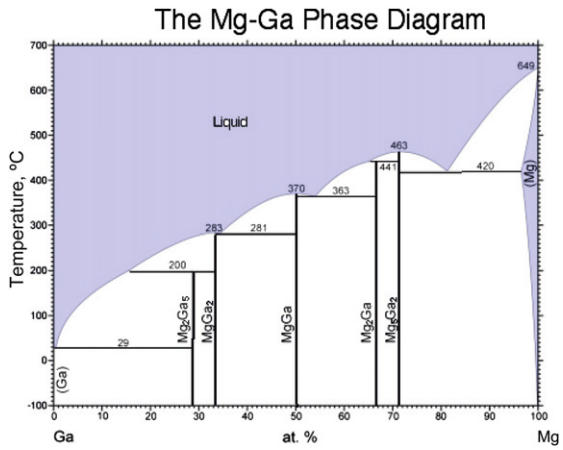

FIGURE 6.102

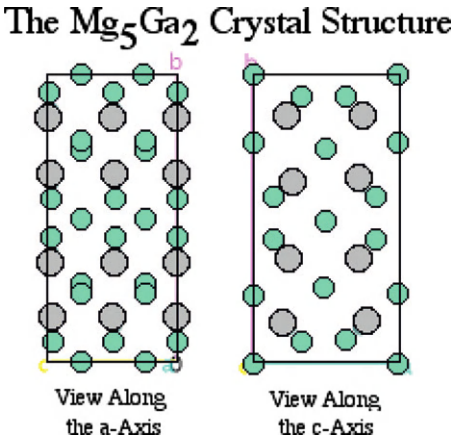

FIGURE 6.103

$MgGa_2$, MgGa, and Mg_5Ga_2 melt congruently, and the others melt incongruently. Note that the crystal types are all distinctive and are "one-of-a-kind".

Penta-magnesium di-gallide, Mg_5Ga_2, is orthorhombic and has the unit-cell parameters of: $a = 6.02$ Å, $b = 7.04$ Å, $c = 8.27$ Å, $\alpha = 115.042°$, $\beta = 111.348°$, $\gamma = 90°$, cell volume $= 289.08$ Å^3. The three-dimensional structure is difficult to depict on a flat surface so that the following structure is shown in two views, one along the *a*-axis of the structure and the other along the *c*-axis[1] (Fig. 6.103).

If these two views are placed at 90° to each other, then the three-dimensional character of the structure can be visualized. This structure is not formed by any other species other than Mg_5Ga_2. The location of the 28 atoms in the unit-cell lattice is shown in Table 6.21.

This compound can be prepared by reaction of a 5:3 mixture of the elements. It has been used to prepare base-free trimethylgallium by reaction of methyl iodide with the intermetallic compound [Mg_5Ga_2] in a high-boiling ether. If Mg_5Ga_2 is hydrided, microparticles of MgH_2 grow at the expense of the compound:

$$Mg_5Ga_2 + 5H_2 \Rightarrow 5MgH_2 + 2Ga$$

TABLE 6.20

Compound	Crystal type	Point group	Space group	Melting temperature	Crystal type
(Mg)	Mg	hP2	194	469 °C	—
(Ga)	Ga	oS8	64	30 °C	—
Mg_5Ga_2	Mg_5Ga_2	tI28	_Ibam _	463 °C	Mg_5Ga_2
Mg_2Ga	Mg_2Ga	hP18	_Pbam	441 °C	Mg_2Ga
$MgGa_2$	$MgGa_2$	oP24	_P62c	283 °C	$MgGa_2$
MgGa	MgGa	tI32	_ $I4_1/a$_	370 °C	MgGa
Mg_2Ga_5	Mg_2Ga_5	tI28	_ I_4_/_m_m_m __	200 °C	Mg_2Ga_5

TABLE 6.21

No	Site notation	Atom	Multiplicity	Wyckoff	Site symmetry	*x*	*y*	*z*	Occupancy
1	Mg3	Mg	8	j	..m	0.155	0.423	0	1.0
2	Ga	Ga	8	j	..m	0.255	0.122	0	1.0
3	Mg2	Mg	8	g	.2.	0	0.24	1/4	1.0
4	Mg1	Mg	4	a	222	0	0	1/4	1.0

[1]For a three-dimensional view, controllable by mouse, visit "NIMS Data Base.com" to observe these structures.

One of the most interesting characteristics of the Mg–Ga system is the existence of a glass-forming concentration range around the eutectic of 70–80 mol% Ga. This encompasses the Mg_5Ga_2 compound which has been studied as a "glassy-metal" and its physical properties examined.

Very little usage of this compound has resulted in industry and the only interest in academia has been the determination of its crystal structure.

It has been assigned the CAS number of 12064-14-1.

Dimagnesium gallide, Mg_2Ga, is hexagonal with cell parameters of: $a = 0.7.794$ nm, $b = 0.7.794$ nm, $c = 0.6.893$ nm, $\alpha = 90°$, $\beta = 90°$, $\gamma = 120°$, cell volume = 362.63 Å^3. The structure is shown in Fig. 6.104.

The location of the 18 atoms in the unit-cell lattice is shown in the following Table 6.22.

This compound has been assigned the CAS number of 12422-88-7. Although this compound has been assessed as a hydrogen-storage media, it did not compare in such properties with other, more efficient materials.

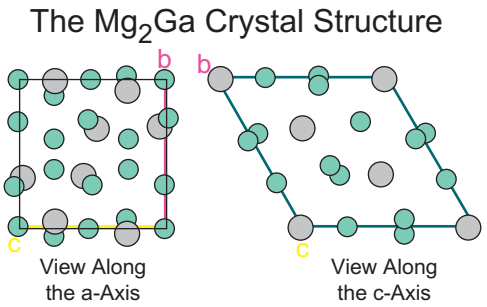

FIGURE 6.104

Magnesium digallide, $MgGa_2$, has the cell parameters of: $a = 0.4.111$ Å, $b = 6.802$ Å, $c = 16.346$ Å, $\alpha = 90°$, $\beta = 90°$, $\gamma = 90°$, cell volume = 457.08 Å^3. The structure is shown in Fig. 6.105.

Again, the three-dimensional structure can be visualized by placing the *c*-axis at 90° to the *a*-axis. The location of the 24 atoms in the unit-cell lattice is shown in the following Table 6.23.

No data can be found in the technical literature concerning its properties except that of structure.

Magnesium gallide, MgGa, has the cell parameters of: $a = 5.5331$ Å, $b = 7.9426$ Å, $c = 7.9426$ Å, $\alpha = 83.039°$, $\beta = 69.628°$, $\beta = 69.628°$, cell volume = 306.58 Å^3. The structure is orthorhombic as shown in the following Fig. 6.106.

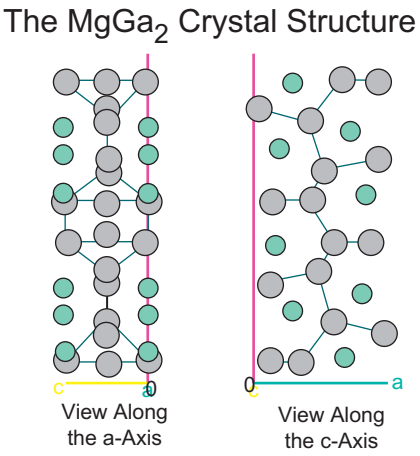

FIGURE 6.105

TABLE 6.22

No	Site notation	Atom	Multiplicity	Wyckoff	Site symmetry	*x*	*y*	*z*	Occupancy
1	Mg2	Mg	6	h	m..	0.399	0.380	1/4	1.0
2	Mg1	Mg	6	g	.2.	0.289	0	0	1.0
3	Ga2	Ga	4	f	3..	1/3	2/3	0.038	1.0
4	Ga1	Ga	2	b	-6..	0	0	1/4	1.0

TABLE 6.23

No	Site notation	Atom	Multiplicity	Wyckoff	Site symmetry	*x*	*y*	*z*	Occupancy
1	Ga2	Ga	4	h	..m	0.0903	0.3098	1/2	1.0
2	Ga3	Ga	4	h	..m	0.3555	0.0625	1/2	1.0
3	Ga4	Ga	4	h	..m	0.4713	0.3420	1/2	1.0
4	Ga1	Ga	4	g	..m	0.0987	0.0665	0	1.0
5	Mg1	Mg	4	g	..m	0.1759	0.4230	0	1.0
6	Mg2	Mg	4	g	..m	0.2981	0.2196	0	1.0

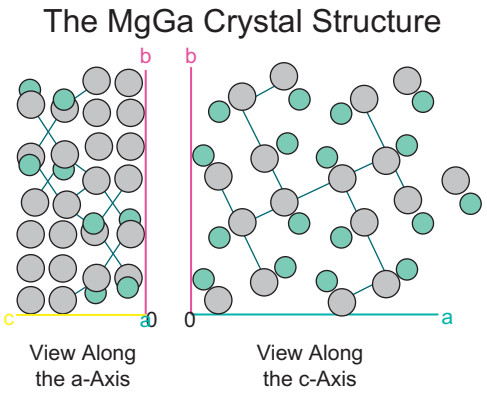

FIGURE 6.106

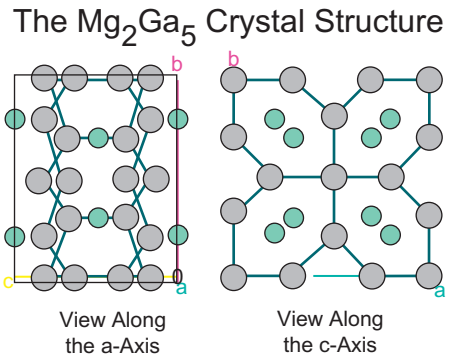

FIGURE 6.107

A three-dimensional structure may be visualized by placing the *c*-axis at 90° to the *a*-axis.

The location of the 32 atoms in the unit-cell lattice is shown in the following Table 6.24.

No data or usage of this compound has arisen in industry or the technical literature.

Dimagnesium penta-gallide, Mg_2Ga_5, crystallizes in an orthorhombic cell with the space group Ibam. The unit-cell parameters are: $a = 0.7.0607$ Å, $b = 7.0607$ Å, $c = 7.0607$ Å, $\alpha = 104.689°$, $\beta = 104.689°$, $\gamma = 119.529°$, cell volume $= 264.61$ Å^3, $Z = 4$. The structure is presented as shown in Fig. 6.107.

Again, this structure can be visualized in three dimensions by placing the *c*-axis at 90° to the *a*-axis. It consists of Ga_2 dumbbells, spaced within the orthorhombic lattice.

The arrangement of the 28 atoms in the unit-cell lattice is shown in Table 6.25.

Commercial usage of these compounds is virtually nil because of their instability to heating a prime requisite for stable and reversible hydrogen-storage purposes.

Calcium Gallides

Calcium forms a number of compounds with gallium metal, even though Ga melts around 30 °C and Ca metal melts at 842 °C. The phase diagram is shown as shown in Fig. 6.108.

Nine compounds are apparent in this diagram. The system, Ca–Ga, forms the most numerous crystalline compounds of any of the alkaline earths.

The lattice parameters are given in the Table 6.26.

The gallium-rich region of the Ca–Ga system (64.9–84.6 atom% Ga) was examined by X-ray methods. In addition to the $CaGa_2$ phase with the $CaIn_2$ structure

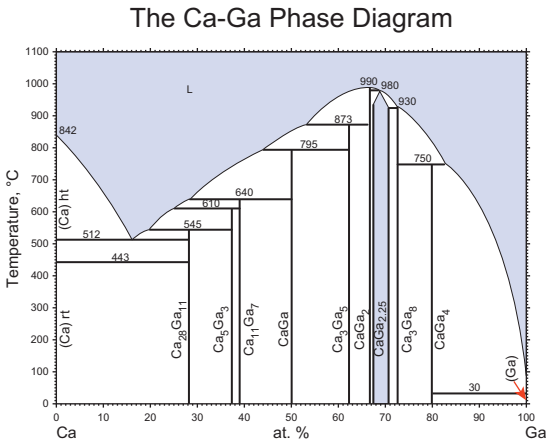

FIGURE 6.108

TABLE 6.24

No	Site notation	Atom	Multiplicity	Wyckoff	Site symmetry	*x*	*y*	*z*	Occupancy
1	Mg	Mg	16	f	1	0.07	0.126	0.371	1.0
2	Ga	Ga	16	f	1	0.302	0.144	0.121	1.0

TABLE 6.25

No	Site notation	Atom	Multiplicity	Wyckoff	Site symmetry	*x*	*y*	*z*	Occupancy
1	Ga1	Ga	16	n	.m.	0	0.2982	0.3190	1.0
2	Mg	Mg	8	h	m.2m	0.2004	0.2004	0	1.0
3	Ga2	Ga	4	e	4mm	0	0	0.2117	1.0

TABLE 6.26

Phase	Structure type	Pearson symbol	Space group	Melting point, °C	Physical parameters
(Ca) rt	Cu	cF4	225	443	No data
(Ca) ht	W	cI2	229	842	No data
CaGa	TlI	oS8	63	795	No data
$CaGa_2$	$CaIn_2$	hP6	194	990	No data
$CaGa_{2.25}$	$Ca_{0.96}Ga_{2.24}$	hP9	191	980	No data
Ca_5Ga_3	Cr_5B_3	tI32	140	610	No data
$CaGa_4$	$CaGa_4$	mS10	12	750	No data
Ca_3Ga_8	Eu_3Ga_8	oI22	71	930	No data
$Ca_{11}Ga_7$	$Ca_{11}Ga_7$	cF144	225	640	No data
$Ca_{28}Ga_{11}$	$Ca_{28}Ga_{11}$	oI78	44	545	No data
Ca_3Ga_5	Ca_3Ga_5	oS32	63	873	No data
(Ga)	Ga	oS8	64	29	No data

type, another phase, $CaGa_{2+x}$, was found in a limited homogeneity range, being $0.1 < x < 0.4$, with crystal structure derived from the AlB_2 type. The mechanism of solid solubility formation was clarified by single-crystal refinement. A new phase Ca_3Ga_8 was identified by powder diffraction data as isotypic with Eu_3Ga_8. The structure of $CaGa_4$, determined by single-crystal methods, can be described as a new monoclinic distortion of the $BaAl_4$ type, related to the low temperature form of $CaAl_4$.

By focusing on the alkaline earth metal Ca, a high flexibility of Ga with respect to the chemical bonding situation was observed. In the Ga-rich part of the systems Ca–Ga, the intermetallic phase $Ca_{1-x}Ga_{2+3x}$ was described. This compound crystallizes in a substitution variant of the AlB_2 type of structure. Due to a substitution of the cations by triangular Ga_3 units, three types of Ga atoms in nonequivalent chemical environments can be assigned using single-crystal X-ray investigation methods. With respect to the first coordination sphere three-bonded Ga atoms form the AlB_2 typical honeycomb-like six-membered rings and are labeled as Ga(3b). Throughout the formation of a chemical bond between the substituting Ga3 units with the atoms of the hexagonal Ga layers, these atoms have to be assigned as Ga(4b) and Ga(4b'), respectively. This structure is shown in Fig. 6.109.

The cation substitution leads to a formation of a homogeneity range between $0.056 \le x \le 0.115$ ($T = 880$ °C) for $Ca_{1-x}Ga_{2+3x}$ and $0 \le x \le 0.056$ ($T = 400$ °C) for $Sr_{1-x}Ga_{2+3x}$, respectively. For $x = 0.115$, the formation of a $Ca_{1-x}Ga_{2+3x}$ super lattice structure was also revealed.

Another view shows the Zintl structure of the Ga atoms (Fig. 6.110).

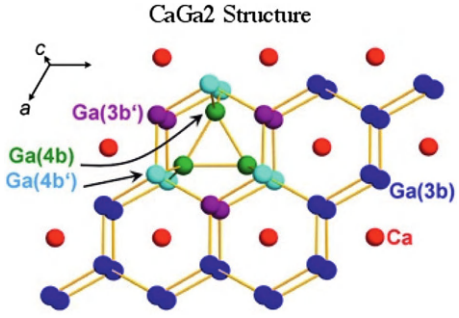

FIGURE 6.109

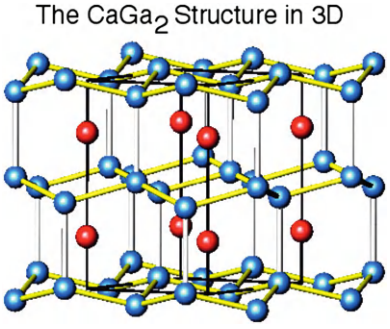

FIGURE 6.110

This structure is fairly simple in composition and arrangement of atoms in three-dimensional space and can be illustrated in two dimension as well. However, the more complicated structures are nearly impossible to decipher. It is for this reason that the structures of the Ca–Ga compounds have been shown as "views along the *a*-axis" which show the first sheet of atom

arrangements and those "views along the *c*-axis" which show the number of sheets within the three-dimensional volume and the arrangement of atoms on each sheet. Where the three-dimensional atom arrangement can be illustrated in two dimension adequately, the diagram will be included. In the more complicated structures, a table, showing the locations of the various atoms, is included.

Calcium digallide, $CaGa_2$, has the $CaIn_2$ structure. It has the unit-cell parameters of: $a = 4.467$ Å, $b = 4.467$ Å, $c = 7.393$ Å, $\alpha = 90°$, $\beta = 90°$, $\gamma = 120°$, cell volume = 127.76 Å. The structure is shown in Fig. 6.111.

The *c*-axis diagram shows four layers present but does not show the hexagonal arrangement of the Ga atoms relative to the Ca atoms. A three-dimensional structure shows this in a much better fashion (Fig. 6.112).

The "yellow" flags show the arrangement of the Zintl dumbbells. The arrangement of the atoms in this structure is shown in the following Table 6.27.

Calcium digallide is a superconductor at 4.3 K. The electronic states of the intermetallic compound $CaGa_2$ were investigated with the empirical local pseudopotential method. The band structure shows the existence of interlayer states which are similar to those recently found in graphite, hexagonal boron nitride, and LiC_6. The chemical binding in the Ga planes consists of strong σ bonds between Ga sp^2 hybrids while the interlayer cohesion mostly results from the overlap between Ga $4p_z$ orbitals.

Calcium mono-gallide, CaGa, has been synthesized by either arc melting or direct reactions in sealed Ta containers. The CrB structures of this binary phase have been identified by Guinier powder diffraction, and the MoB-type structure of the new ternary line phase $Y(Ga_{0.8}Zn_{0.2})$ has been refined by single-crystal means: $I4_1/amd$, $Z = 8$, $a = 4.1787$ Å, $c = 21.856$ Å. Resistivity and magnetic susceptibility measurements on the CrB-type CaGa compound demonstrates its metallic properties and the nonapplicability of a literal Zintl phase assignment of oxidation states. CaGa has the unit-cell parameters of: $a = 4.191$ Å, $b = 4.387$ Å, $c = 6.0997$ Å, $\alpha = 90°$, $\beta = 110.093°$, $\gamma = 90°$, cell volume = 105.32 $Å^3$. The structure is illustrated as shown in Fig. 6.113.

The arrangement of the eight atoms in the structure is shown in Table 6.28.

A better view of this structure can be seen in a three-dimensional view (Fig. 6.114).

No physical data concerning the CaGa compound is available in the literature other than structural data.

Calcium tetra-gallide, $CaGa_4$, is one of the least complicated of the species. It has the lattice parameters of: $a = 4.3544$ Å, $b = 4.3544$ Å, $c = 6.1223$ Å, $\alpha = 69.93°$, $\beta = 69.93°$, $\gamma = 89.516°$, cell volume = 101.59 $Å^3$.

The lattice structure is illustrated as a two- and a three-dimensional model in the following diagram. The three-dimensional lattice model does not

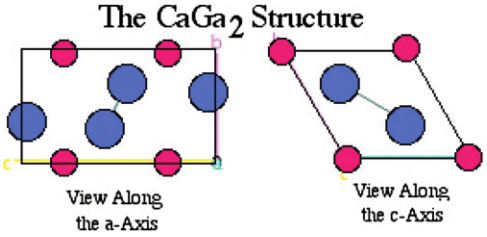

FIGURE 6.111

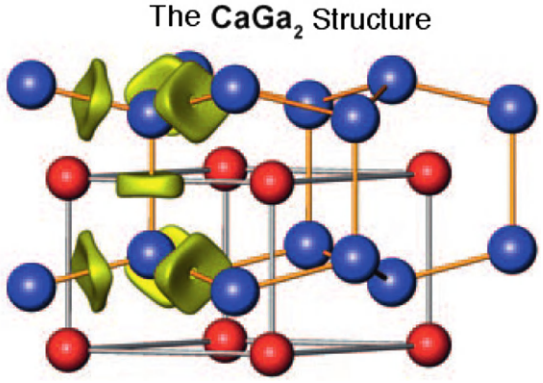

FIGURE 6.112

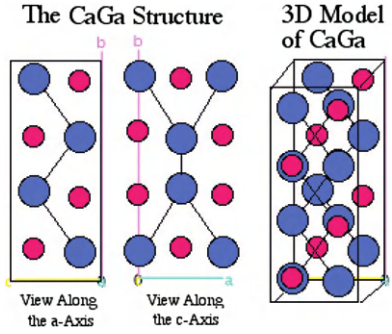

FIGURE 6.113

TABLE 6.27

No	Site notation	Atom	Multiplicity	Wyckoff	Site symmetry	*x*	*y*	*z*	Occupancy
1	Ga1	Ga	4	f	3m.	1/3	2/3	0.045	1.0
2	Ca1	Ca	2	b	-6m2	0	0	1/4	1.0

TABLE 6.28

No	Site notation	Atom	Multiplicity	Wyckoff	Site symmetry	*x*	*y*	*z*	Occupancy
1	Ga1	Ga	4	c	m2m	0	0.108	1/4	1.0
2	Ca1	Ca	4	c	m2m	0	0.367	1/4	1.0

TABLE 6.29

No	Site notation	Atom	Multiplicity	Wyckoff	Site symmetry	*x*	*y*	*z*	Occupancy
1	Ga1	Ga	4	i	m	0.5950	0	0.2308	1.0
2	Ga2	Ga	4	h	2	0	0.2328	1/2	1.0
3	Ca1	Ca	2	a	2/m	0	0	0	1.0

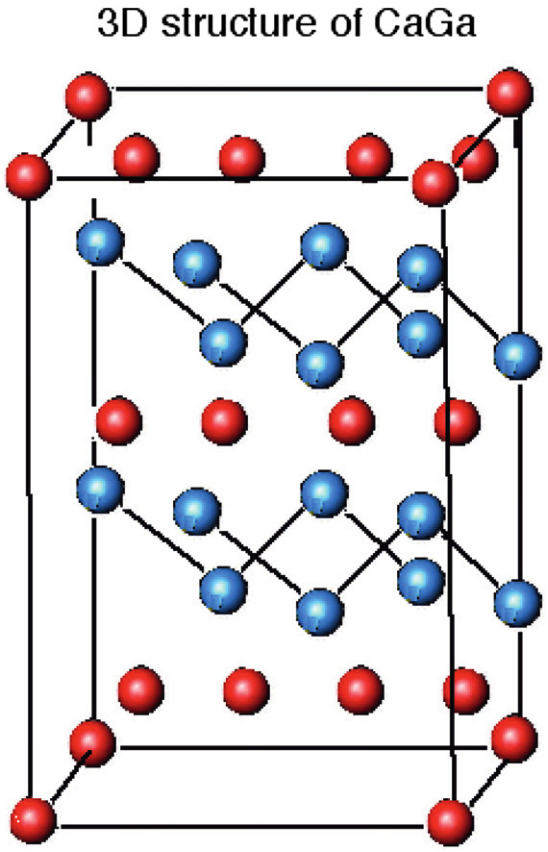

FIGURE 6.114

adequately show the three layers shown along the *c*-axis. The structure is trigonal, not cubic (Fig. 6.115).

The arrangement of the 10 atoms in the structure is shown in Table 6.29.

The structure of $CaGa_4$, determined by single-crystal methods, can be described as a new monoclinic distortion of the $BaAl_4$ type, related to the low temperature form of $CaAl_4$. A better representation is shown as shown in Fig. 6.116.

Here, the Zintl structure is clearly evident.

The enthalpies of formation of $CaGa_4$ at 988 K was determined, using precipitation calorimetry, to be -28.2 ± 1.7 kJ/(g-atom). The integral enthalpy of mixing of the (Ca–Ga) liquid alloys (ΔH_0) measured at 1309 K are described by the following Redlich–Kister equation:

$$\Delta H_0 = x_{Ca}(1 - x_{Ca})\, f(y)$$

$$f(y) = 48y^2 - 8.34y - 161.16$$

$$y = x_{Ca} - x_{Ga}$$

$$\Delta H^0_{Ca} = -104.8 \pm 1.7 \text{ kJ (g-at\%)}^{-1}$$

Calcium di-gallide, $CaGa_{2.25}$, is a much more complicated structure which is a variant of $Ca_{1-x}Ga_{2+x}$. $CaGa_{2.25}$ has the cell parameters of: $a = 4.315$ Å, $b = 4.315$ Å, $c = 4.315$ Å, $\alpha = 90°$, $\beta = 90°$, $\gamma = 120°$, cell volume $= 69.58$ Å^3.

The structure is illustrated as shown in Fig. 6.117.

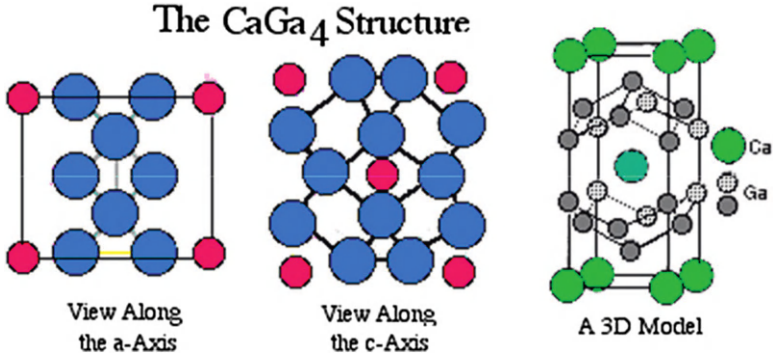

FIGURE 6.115

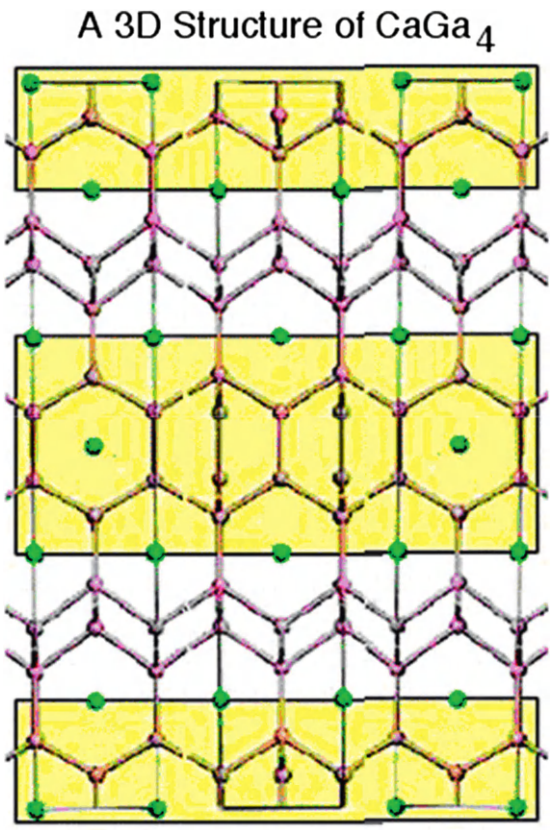

FIGURE 6.116

There are two Ga atoms that are hidden in this representation.

The location of the nine individual atoms in this structure is shown in Table 6.30.

A better representation shows the two hidden Ga atoms in the following Fig. 6.118.

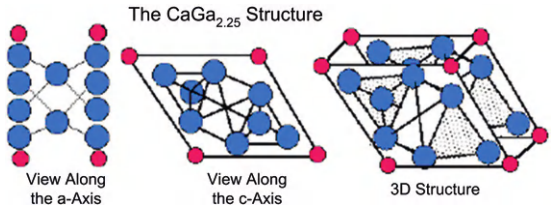

FIGURE 6.117

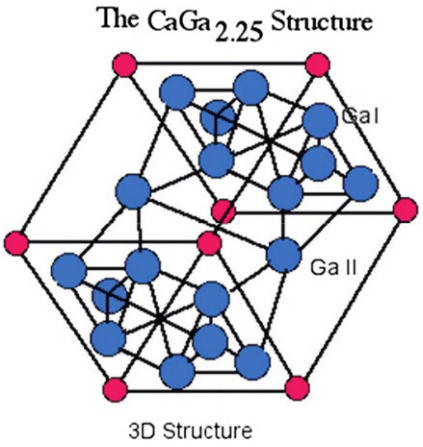

FIGURE 6.118

Undeca-calcium hepta-gallide, $Ca_{11}Ga_7$, has the cell parameters of: $a = 11.3908$ nm, $b = 11.3908$ nm, $c = 11.3908$ nm, $\alpha = 60°$, $\beta = 60°$, $\gamma = 60°$, cell volume $= 104.508$ Å^3, $Z = 8$. Its structure may be represented as shown in Fig. 6.119.

The locations of the various 144 atoms in the lattice are shown in the following Table 6.31.

The actual structure has 25 of these plates of Ca–Ga atoms, with the actual arrangement of Ca and Ga atoms

TABLE 6.30

No	Site notation	Atom	Multiplicity	Wyckoff	Site symmetry	*x*	*y*	*z*	Occupancy
1	Ga1	Ga	6	l	mm2	0.197	0.394	0	0.044
2	Ga2	Ga	2	d	-6m2	1/3	2/3	1/2	1.0
3	Ca1	Ca	1	a	6/mmm	0	0	0	0.956

TABLE 6.31

No	Site notation	Atom	Multiplicity	Wyckoff	Site symmetry	*x*	*y*	*z*	Occupancy
1	Ca1	Ca	48	h	m.m2	0	0.1664	0.1664	1.0
2	Ga1	Ga	32	f	.3m	0.1913	0.1913	0.1913	1.0
3	Ca2	Ca	32	f	.3m	0.371	0.371	0.371	1.0
4	Ga2	Ga	24	e	4m.m	0.2825	0	0	1.0
5	Ca4	Ca	4	b	m-3m	1/2	1/2	1/2	1.0
6	Ca3	Ca	4	a	m-3m	0	0	0	1.0

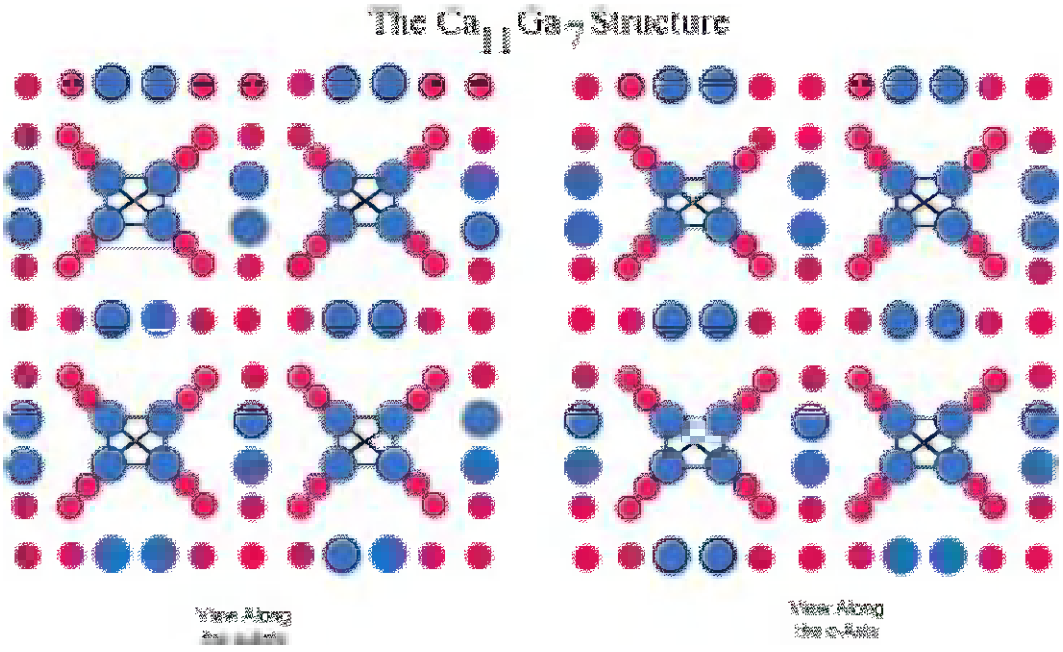

FIGURE 6.119

as shown here. There are five plates in the *b*-direction and five in the *c*-direction. In one unit cell, there are 88 Ca atoms and 56 Ga atoms for a total of 144. Thus, this structure encompasses 1152 atoms in eight unit cells.

The binary alkaline earth triclides $Ca_{11}Ga_7$ and $Sr_{11}In_7$ crystallize with a singular structure type (cubic, space group, Fm3m, $Z = 8$). The Ca- and Sr-mixed triclides forming this structure type were synthesized from stoichiometric mixtures of the elements and were characterized by single-crystal XRD. The structures exhibit isolated M(1) atoms (M(2) = Al, Ga, In, Sn, Pb) together with tetrahedral units $[M(1)_4]$, which are formed by the triel elements exclusively. Remarkably, one of the four crystallographically independent A^{II} positions is—as in the pure element—coordinated by A^{II} partners in a cuboctahedral arrangement. In the mixed M^{III}/M^{IV} compounds, a maximum phase range up to a maximum composition limit: $Ca_{11}[Ga_1^{3-}]_4[Ga_2^{4-}]_3$ is observed, which nearly corresponds to an ionic description according to the Zintl concept (tetrahedral anions isoelectronic to white phosphorus P_4 besides isolated noble gas isosteric tetra-elide anions $[Ga^{IV}]^{4-}$). Thus, this structure encompasses triangular Ga_3^{3-} units tied to tetrahedral Ga_4^{4-} units in a regular fashion.

Dodeca-octa calcium undeca-gallide, $Ca_{28}Ga_{11}$, has the cell parameters of: $a = 5.324$ Å, $b = 7.488$ Å, $c = 31.0641$ Å, $\alpha = 96.922°$, $\beta = 94.916°$, $\gamma = 90°$, cell volume = 1224.79 Å^3. The structure is depicted as shown in Fig. 6.120.

The actual structure has about 78 atoms. The locations of the different Ca and Ga atoms in the lattice are shown in the following Table 6.32.

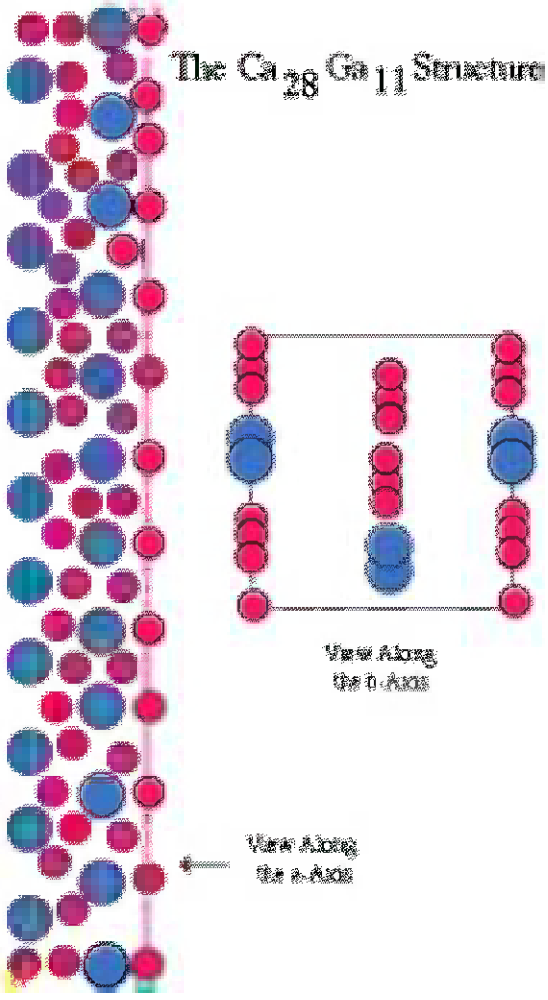

FIGURE 6.120

TABLE 6.32

No	Site notation	Atom	Multiplicity	Wyckoff	Site symmetry	*x*	*y*	*z*	Occupancy
1	Ca2	Ca	4	d	m.	0	0.0436	0.620	1.0
2	Ca7	Ca	4	d	m.	0	0.0599	0.066	1.0
3	Ga2	Ga	4	d	m.	0	0.0908	0.408	1.0
4	Ca8	Ca	4	d	m.	0	0.1168	0.760	1.0
5	Ca1	Ca	4	d	m.	0	0.1374	0.211	1.0
6	Ca13	Ca	4	d	m.	0	0.1760	0.825	1.0
7	Ga5	Ga	4	d	m.	0	0.1804	0.423	1.0
8	Ca4	Ca	4	d	m.	0	0.2241	0.218	1.0
9	Ca9	Ca	4	d	m.	0	0.2380	0.746	1.0
10	Ga3	Ga	4	d	m.	0	0.2729	0.453	1.0
11	Ca11	Ca	4	d	m.	0	0.2942	0.070	1.0
12	Ca3	Ca	4	d	m.	0	0.3175	0.652	1.0
13	Ca6	Ca	4	d	m.	0	0.3533	0.030	1.0
14	Ga1	Ga	4	d	m.	0	0.3605	0.439	1.0
15	Ca12	Ca	4	d	m.	0	0.4034	0.663	1.0
16	Ca5	Ca	4	d	m.	0	0.4171	0.135	1.0
17	Ga4	Ga	4	d	m.	0	0.4560	0.388	1.0
18	Ca10	Ca	4	d	m.	0	0.4700	0.788	1.0
19	Ca15	Ca	2	b	mm2	0	1/2	0.196	1.0
20	Ca14	Ca	2	a	mm2	0	0	0.0	1.0
21	Ga6	Ga	2	a	mm2	0	0	0.414	1.0

The structure of $Ca_{28}Ga_{11}$ is characterized by three types of calcium polyhedra surrounding the Ga atoms: tri-capped trigonal prisms, distorted cubes and distorted cuboicosahedra (10-vertex polyhedra similar to those found around Si in CO_2Si). The linkage of these polyhedra give rise to columns or slabs that alternate along the greatest axis of the cell. No Ga–Ga contacts are present.

No other data is available concerning the physical properties of this compound or its potential usage in industry.

Tricalcium penta-gallide, Ca_3Ga_5, has the unit-cell parameters of: $a = 4.463$ Å, $b = 5.8424$ Å, $c = 15.025$ Å, $\alpha = 90°$, $\beta = 90°$, $\gamma = 112.454°$, cell volume $= 362.07$ Å. The structure may be represented as shown where a unit of 10 Ga atoms are joined in a unique structure, surrounded by six Ca atoms (Fig. 6.121).

This unit is then inverted to form the full structure (Fig. 6.122).

The 32 atoms are located in the lattice in Table 6.33.

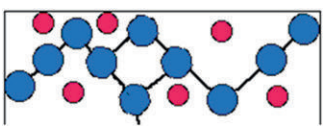

FIGURE 6.121

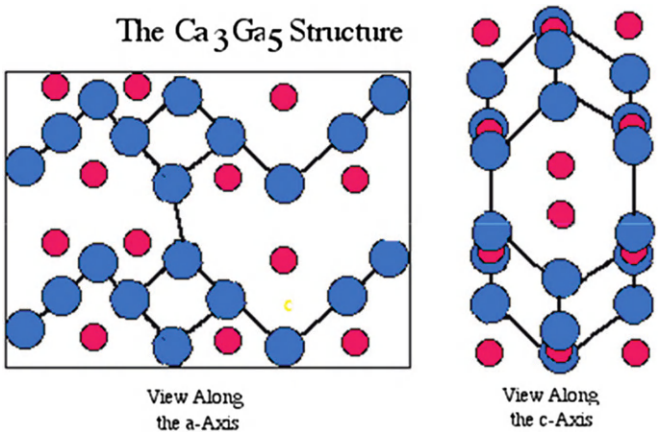

FIGURE 6.122

TABLE 6.33

No	Site notation	Atom	Multiplicity	Wyckoff	Site symmetry	x	y	z	Occupancy
1	Ca1	Ca	8	f	m	0	0.0881	0.1105	1.0
2	Ga2	Ga	8	f	m	0	0.2079	0.5995	1.0
3	Ga3	Ga	8	f	m..	0	0.3846	0.0341	1.0
4	Ca2	Ca	4	c	m2m	0	0.3699	1/4	1.0
5	Ga1	Ga	4	c	m2m	0	0.6633	1/4	1.0

TABLE 6.34

No	Site notation	Atom	Multiplicity	Wyckoff	Site symmetry	x	y	z	Occupancy
1	Ga1	Ga	4	j	mm2	1/2	0	0.047	1.0
2	Ga2	Ga	4	j	mm2	1/2	0	0.251	1.0
3	Ga3	Ga	4	i	mm2	0	0	0.095	1.0
4	Ga4	Ga	4	i	mm2	0	0	0.190	1.0
5	Ca1	Ca	4	i	mm2	0	0	0.352	1.0
6	Ca2	Ca	2	d	mmm	1/2	0	1/2	1.0

A better view of the lattice can be seen in the following diagram. Here, the Zintl arrangement of the Ga atoms is more readily apparent (Fig. 6.123).

Tricalcium octa-gallide, Ca_3Ga_8, has the unit-cell parameters of: $a = 4.323$ Å, $b = 4.323$ Å, $c = 13.2782$ Å, $\alpha = 99.369°$, $\beta = 99.369°$, $\gamma = 90°$, cell volume = 241.48 Å^3. The structure is shown in Fig. 6.124.

The enthalpies of formation of the intermetallic compounds $CaGa_4$, Ca_3Ga_8, and $CaGa_2$, at 298.15 K, were determined by high-temperature liquid gallium solution calorimetric measurements to be -24.9 ± 4.9 kJ/(g-atom), -25.4 ± 2.4 kJ/(g-atom), and -38.8 ± 4.8 kJ/(g-atom), respectively.

The 22 atoms in the lattice are located in Table 6.34.

There are three layers of the atom arrangement of the a-axis to form the three-dimensional structure (Fig. 6.125).

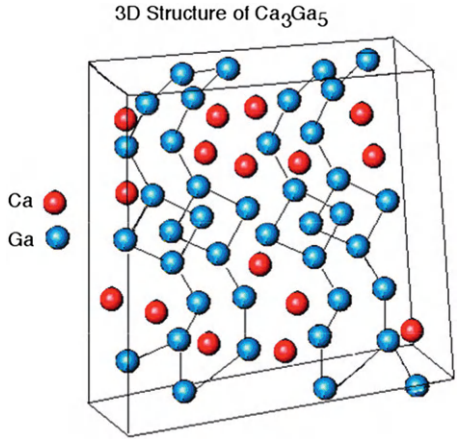

FIGURE 6.123

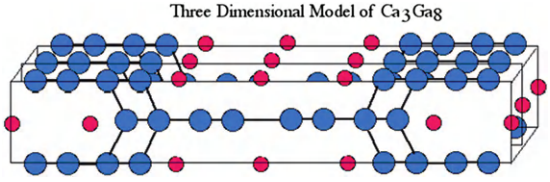

FIGURE 6.125

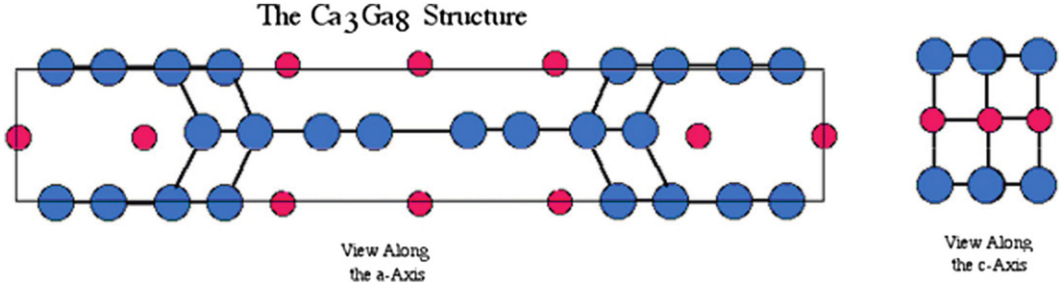

FIGURE 6.124

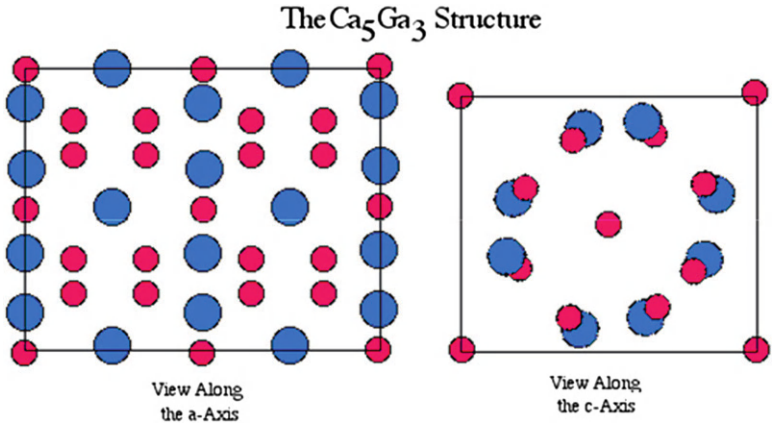

FIGURE 6.126

TABLE 6.35

No	Site notation	Atom	Multiplicity	Wyckoff	Site symmetry	x	y	z	Occupancy
1	Ca1	Ca	16	l	m	0.166	0.666	0.15	1.0
2	Ga1	Ga	8	h	m2m	0.625	0.125	0	1.0
3	Ca2	Ca	4	c	4/m.	0	0	0	1.0
4	Ga2	Ga	4	a	422	0	0	1/4	1.0

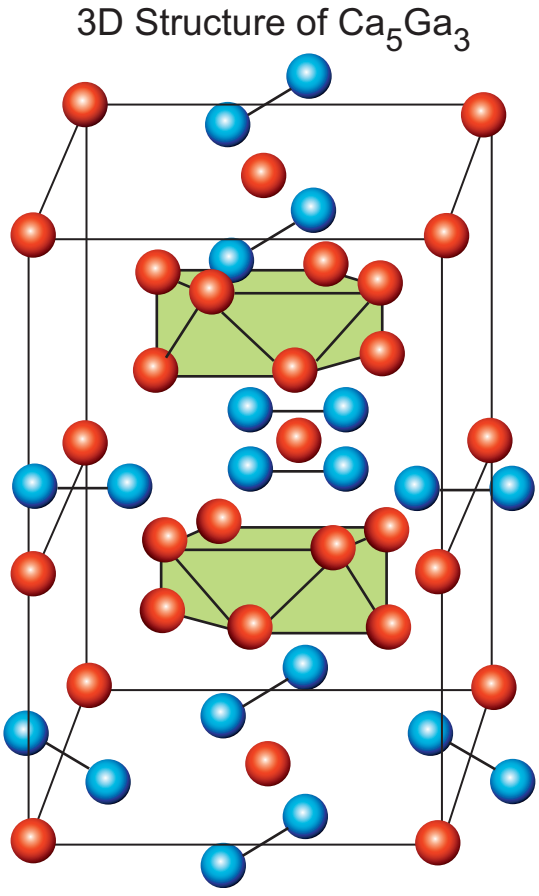

FIGURE 6.127

Penta-calcium tri-gallide, Ca_5Ga_3, has the unit-cell parameters of: $a = 7.954$ Å, $b = 7.954$ Å, $c = 9.4082$ Å, $\alpha = 115.006°$, $\beta = 115.006°$, $\gamma = 90°$, cell volume = 477.15 Å^3. The structure is illustrated as shown in Fig. 6.126.

The location of the 32 individual atoms in this structure is shown in Table 6.35.

A three-dimensional structure is shown in the following Fig. 6.127.

The unit-cell consists of gallium dumbbells surrounding calcium atoms, as well as two skewed octahedron of Ca atoms opposite the center of the cell. Calcium gallides are available in limited quantities commercially. No specific usage of any of them has arisen in industry.

Strontium Gallides

Strontium metal and gallium metal, when melted together, forms a limited number of compounds as can be seen in the following Fig. 6.128.

The crystal parameters are shown in the following Table 6.36.

Strontium digallide, $SrGa_2$, has the AlB_2 structure. The unit-cell structure parameters are: $a = 4.345$ Å, $b = 4.345$ Å, $c = 4737$ Å, $\alpha = 90°$, $\beta = 90°$, $\gamma = 120°$, cell volume = 77.45 Å^3. The structure can be represented by Fig. 6.129.

An analysis of the electron localization function (ELF) shows honeycomb-like 6_3 nets of the Ga atoms as the

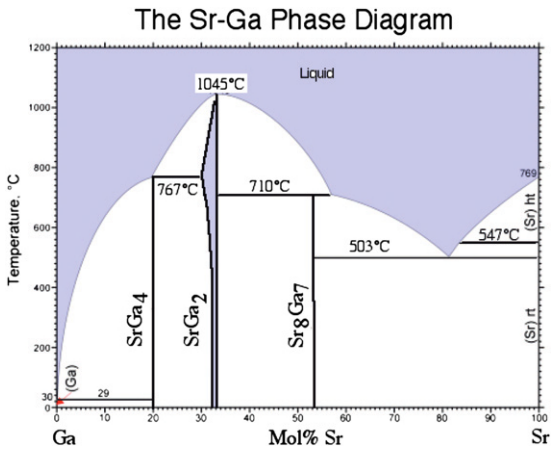

FIGURE 6.128

most prominent structural features in $SrGa_2$ and $BaGa_2$. The location of the individual atoms in this structure is shown in the following Table 6.37.

The layered structure is readily seen in the following Fig. 6.130.

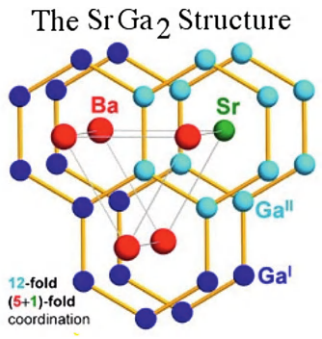

FIGURE 6.129

The hydrogenation behavior of the polar intermetallic systems AeE_2 (Ae = Ca, Sr, Ba; E = Al, Ga, In) has been investigated systematically and afforded the new hydrides $SrGa_2H_2$ and $BaGa_2H_2$. The structure of these hydrides was characterized by X-ray powder diffraction and neutron diffraction of the corresponding deuterides.

Both compounds are isostructural to previously discovered $SrAl_2H_2$ (space-group Pm1, Z = 1, $SrGa_2H_2$/

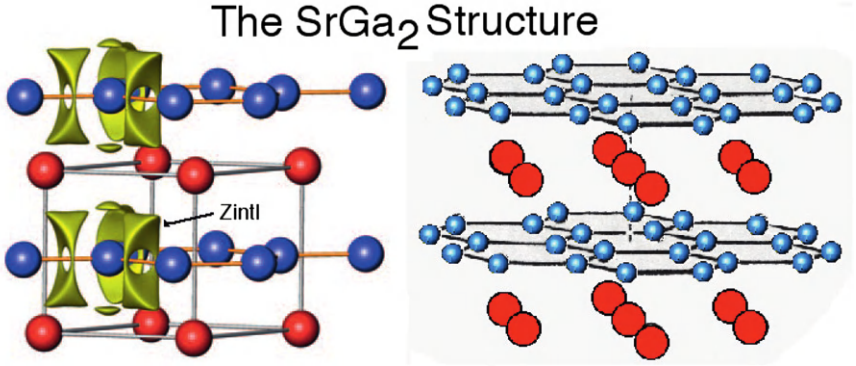

FIGURE 6.130

TABLE 6.36

Compound	Type	Point group	Space group	Melting point, °C	Physical data
(Sr) rt	Cu	cF4	225		No data
(Sr) ht	W	cI2	229		No data
$SrGa_2$	AlB_2	hP3	191	1045	
$SrGa_4$	$BaAl_4$	tI10	139	767	No data
Sr_8Ga_7	Ba_8Ga_7	cP60	198	710	No data
(Ga)	Ga	oS8	64	29	No data

TABLE 6.37

No	Site notation	Atom	Multiplicity	Wyckoff	Site symmetry	*x*	*y*	*z*	Occupancy
1	Ga	Ga	2	d	-6m2	1/3	2/3	1/2	1.0
2	Sr	Sr	1	a	6/mmm	0	0	0	1.0

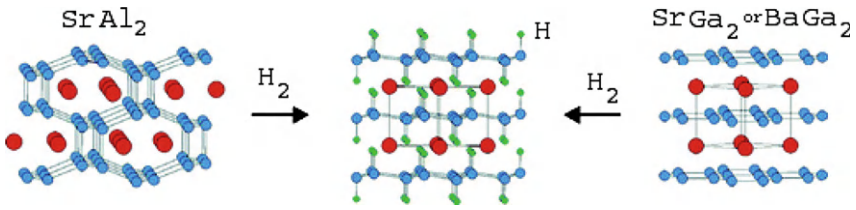

FIGURE 6.131

D_2: $a = 4.4010/4.3932$ Å, $c = 4.7109/4.699$ Å; $BaGa_2H_2/D_2$: $a = 4.5334/4.5286$ Å, $c = 4.9069/4.8991$ Å). The two hydrides, $SrGa_2H_2$ and $BaGa_2H_2$, decompose at around 300 °C at atmospheric pressure. First-principles electronic structure calculations reveal that H is unambiguously part of a two-dimensional polyanion $[E_2H_2]^{2-}$ in which each E atom is tetrahedrally coordinated by three additional E atoms and H. The compounds AeE_2H_2 are classified as polyanionic hydrides. The peculiar feature of polyanionic hydrides is the incorporation of H in a polymeric anion where it acts as a terminating ligand. Polyanionic hydrides provide unprecedented arrangements with both E–E and E–H bonds. The hydrogenation of AeE_2 to AeE_2H_2 takes place at low-reaction temperatures (around 200 °C), which suggests that the polyanion of the polar intermetallics ([E2]2-) is employed as precursor. The structure of these hydrides is shown in Fig. 6.131.

Octa-strontium hepta-gallide, Sr_8Ga_7, has a unique structure similar to that of its Ba homologue (Fig. 6.132).

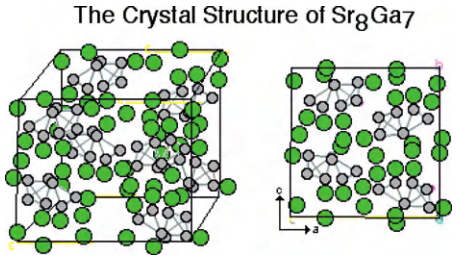

FIGURE 6.132

The structure is composed of Al_7^{16-} units, surrounded by eight Sr^{2+} atoms. It is cubic. Cell parameters are: $a = 12.484$ Å, $b = 12.484$ Å, $c = 12.484$ Å, $\alpha = 90°$, $\beta = 90°$, $\gamma = 90°$, cell volume = 194.64 Å^3. The various atoms are located in Table 6.38.

Two- and three-bonded Ga atoms forming molecular units are observed in Sr_8Ga_7 and Ba_8Ga_7. Three-dimensional frameworks are formed by four- and five-bonded Ga atoms in $SrGa_4$, or $BaGa_4$.

Strontium tetra-gallide, $SrGa_4$, has the cell parameters of: $a = 4.43$ nm, $b = 4.43$ nm, $c = 6.2039$ nm, $\alpha = 110.918°$, $\beta = 110.918°$, $\gamma = 90°$, cell volume = 105.09 Å^3. The structure can be represented as shown in Fig. 6.133.

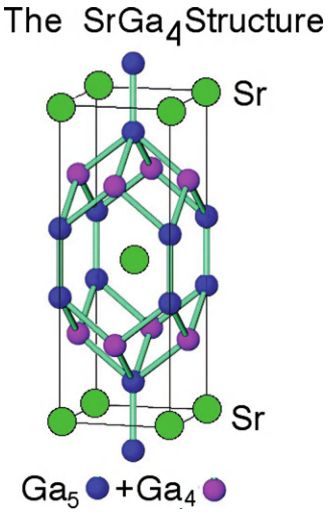

FIGURE 6.133

TABLE 6.38

No	Site notation	Atom	Multiplicity	Wyckoff	Site symmetry	x	y	z	Occupancy
1	Sr(1)	Sr	12	b	1	0.0035	0.304	0.4429	1.0
2	Sr(2)	Sr	12	b	1	0.0622	0.5203	0.2021	1.0
3	Ga(1)	Ga	12	b	1	0.0741	0.2441	0.1946	1.0
4	Ga(2)	Ga	12	b	1	0.2516	0.3137	0.5785	1.0
5	Ga(3)	Ga	4	a	.3.	0.0669	0.0669	0.0669	1.0
6	Sr(4)	Sr	4	a	.3.	0.3146	0.3146	0.3146	1.0
7	Sr(3)	Sr	4	a	.3.	0.6859	0.6859	0.6859	1.0

The various atoms are located in Table 6.39.

Single crystals of $SrGa_4$, were synthesized from the corresponding elements using molten Sn metal as a solvent. The structure determination showed the product to be a binary phase with composition $SrGa_4$, which crystallizes with the $BaAl_4$ type in the body-centered tetragonal space group I4/mmm (No. 139). The three atoms in the asymmetric unit lie on special positions with Wyckoff symbols 2a (Sr), 4d and 4e for the Ga atoms.

Strontium gallides are not generally available commercially.

Barium Gallides

Barium gallides can be prepared by heating the metals in proper atom ratios to form various compounds. The phase diagram shows four compounds, as shown in the Fig. 6.134.

Two- and three-bonded Ga atoms forming molecular units are observed in Sr_8Ga_7 and Ba_8Ga_7. Three-dimensional frameworks are formed by four- and five-bonded Ga atoms in MGa_4 with M = Ca, Sr, or Ba.

The crystal parameters are shown in the following Table 6.40.

Barium tetra-gallide, $BaGa_4$, has the cell parameters of: $a = 4.5661$ Å, $b = 4.5661$ Å, $c = 6.2822$ Å, $\alpha = 111.31°$, $\beta = 111.31°$, $\gamma = 90°$, cell volume = 112.36.

Its structure is unique but identical to that of its Sr homologue (Fig. 6.135).

The positions of the various atoms in the structure is given in the following Table 6.41.

This compound has been studied extensively as to its physical properties. $BaGa_4$ possesses the most popular structure type in solid-state chemistry. More

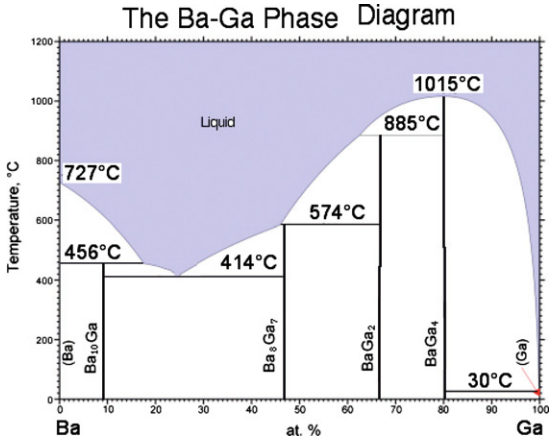

FIGURE 6.134

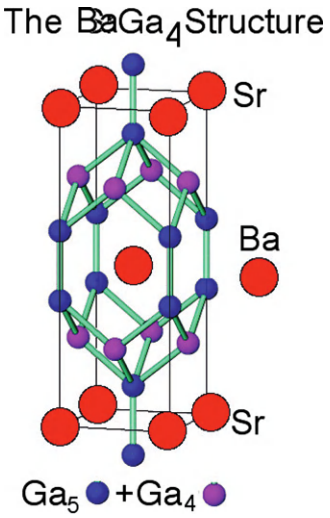

FIGURE 6.135

TABLE 6.39

No	Site notation	Atom	Multiplicity	Wyckoff	Site symmetry	*x*	*y*	*z*	Occupancy
1	Ga1	Ga	4	e	4mm	0	0	0.380	1.0
2	Ga2	Ga	4	d	-4m2	0	1/2	1/4	1.0
3	Sr1	Sr	2	a	4/mmm	0	0	0	1.0

TABLE 6.40

Compound	Type	Point group	Space group	Melting point, °C	Physical data
(Ba)	W	cI2	229	727	No data
$BaGa_4$	$BaAl_4$	tI10	139	1015	No data
$Ba_{10}Ga$	VAl_{10}	cF176	227	456	No data
$BaGa_2$	AlB_2	hP3	191	885	No data
Ba_8Ga_7	Ba_8Ga_7	cP60	198	414	No data
(Ga)	Ga	oS8	64	30	No data

TABLE 6.41

No	Site notation	Atom	Multiplicity	Wyckoff	Site symmetry	x	y	z	Occupancy
1	Ga(II)	Ga	4	e	4mm	0	0	0.3799	1.0
2	Ga(I)	Ga	4	d	-4m2	0	1/2	1/4	1.0
3	Ba	Ba	2	a	4/mmm	0	0	0	1.0

TABLE 6.42

No	Site notation	Atom	Multiplicity	Wyckoff	Site symmetry	x	y	z	Occupancy
1	Ga	Ga	2	d	-6m2	1/3	2/3	1/2	1.0
2	Ba	Ba	1	a	6/mmm	0	0	0	1.0

than 600 compounds crystallize in this structure. Many compounds of this family exhibit interesting physical properties such as superconductivity, unusual magnetic behavior, valence fluctuation and heavy fermion phenomena.

Barium digallide, $BaGa_2$, has the cell parameters of: $a = 4.429$ Å, $b = 4.429$ Å, $c = 5.076$ Å, $\alpha = 90°$, $\beta = 90°$, $\gamma = 120°$, cell volume $= 86.23$ Å^3. The structure can be represented as shown in Fig. 6.136.

The alternating layers of Ba and Ga are readily seen. The individual atoms in the unit cell are located in Table 6.42.

An analysis of the ELF shows honeycomb-like 6_3 nets of the Ga atoms as the most prominent structural features in $SrGa_2$ and $BaGa_2$. A three-dimensional structure is shown in the following Fig. 6.137.

Octa-barium hepta-gallide, Ba_8Ga_7, has the $P2_13$ space group and the cell parameters of: $a = 1.2.99$ nm, $b = 1.2.99$ nm, $c = 1.2.99$ nm, $\alpha = 90°$, $\beta = 90°$, $\gamma = 90°$, cell volume $= 219.93$ Å^3. Its structure can be represented by Fig. 6.138.

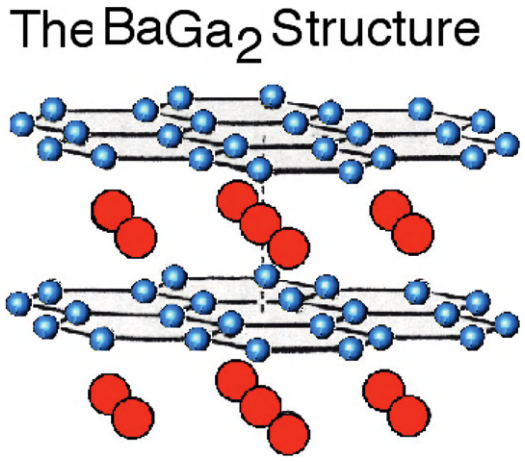

FIGURE 6.136

This compound is isotypic with the Ca and Sr compounds and is characterized by the presence of isolated tetrahedral and triangular clusters of Ga atoms included in cages of 16 Ba atoms. The location of the Ba and Ga atoms in the unit cell is shown in the following Table 6.43.

Penta-barium hexagallide, Ba_5Ga_6, has the cell parameters: $a = 7.771$ Å, $b = 7.771$ nm, $c = 14.376$ nm, $\alpha = 90°$, $\beta = 90°$, $\gamma = 120°$, cell volume $= 751.83$ Å^3.

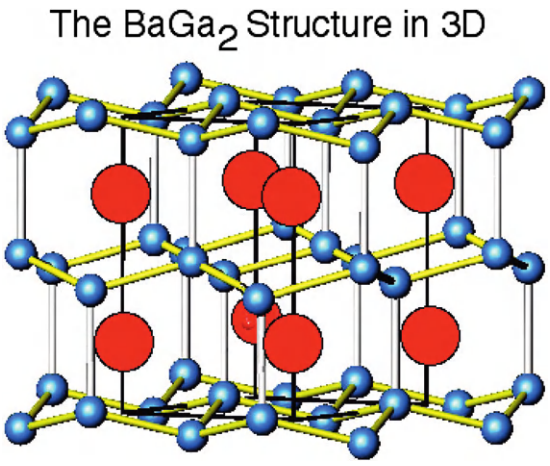

FIGURE 6.137

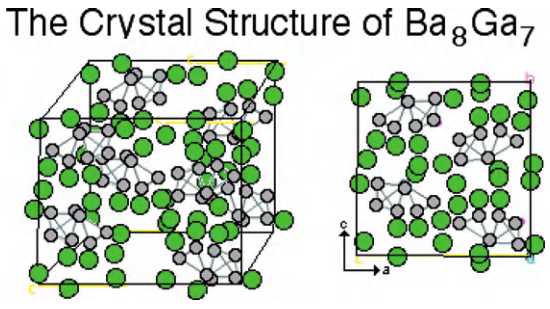

FIGURE 6.138

TABLE 6.43

No	Site notation	Atom	Multiplicity	Wyckoff	Site symmetry	*x*	*y*	*z*	Occupancy
1	Ba1	Ba	12	b	1	0.0011	0.2987	0.4421	1.0
2	Ba2	Ba	12	b	1	0.0613	0.5186	0.2025	1.0
3	Ga1	Ga	12	b	1	0.0760	0.2390	0.1941	1.0
4	Ga2	Ga	12	b	1	0.2467	0.3133	0.5831	1.0
5	Ga3	Ga	4	a	.3.	0.0689	0.0689	0.0689	1.0
6	Ba4	Ba	4	a	.3.	0.3127	0.3127	0.3127	1.0
7	Ba3	Ba	4	a	.3.	0.6852	0.6852	0.6852	1.0

TABLE 6.44

No	Site notation	Atom	Multiplicity	Wyckoff	Site symmetry	*x*	*y*	*z*	Occupancy
1	Ga	Ga	12	l	1	0.46513	0.33077	0.078	1.0
2	Ba1	Ba	6	k	m..	0.02663	0.33457	1/4	1.0
3	Ba2	Ba	4	h	3..	1/3	2/3	0.0284	0.48
4	Ba3	Ba	2	a	3.2	0	0	0	1.0

This compound does not appear in the phase diagram. The crystal structure of Ba_5Ga_6 was determined by single-crystal diffractometry. It is hexagonal, hP22, space group P6c2 (n.188), and contains a disordered Ba position with partial occupation. The structure is characterized by octahedral Ga_6 clusters, isolated and surrounded by a cuboctahedron of 12 Ba atoms. The barium cubo-octahedra, by sharing of edges and faces, are condensed in a tridimensional framework. Application of Wade's rules to the Ga_6-naked cluster gives an excess of two electrons per formula unit.

The compound Ba_5Ga_6 replaces the phase "BaGa" given in the original Ba–Ga phase diagram that was later refined to exclude the BaGa compound. Its structure can be represented by Fig. 6.139.

The atoms are located in Table 6.44.

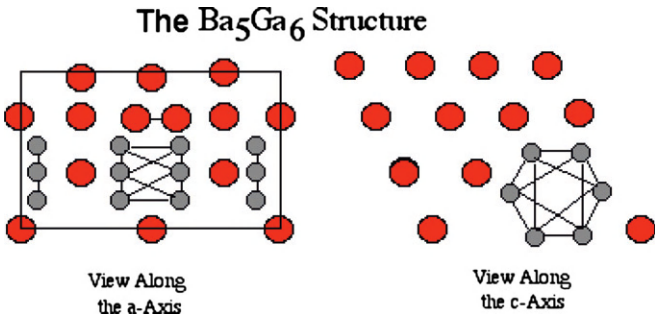

FIGURE 6.139

A unique structure of Ga atoms is shown within the unit cell. This dodecahedron has the general form has shown in Fig. 6.140, and is located at approximately 1/3 of the *c*-direction in the unit cell. There are three of these entities present.

Deca-barium gallide, $Ba_{10}Ga$, has the cell parameters: $a = 14.5098$ nm, $b = 14.5098$ nm, $c = 14.5098$ nm, $\alpha = 60°$, $\beta = 60°$, $\gamma = 60°$, cell volume $= 216.01$ Å^3. It is cubic but has a unique structure consisting of 40 Ba atoms, combined with a tetrahedron of Ga_4 atoms. The structure may be represented by Fig. 6.141.

The locations of the various atoms are shown in Table 6.45.

No data or research appears to exist concerning this compound.

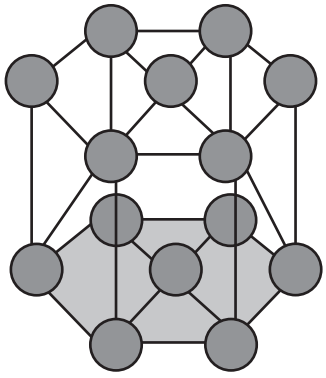

FIGURE 6.140

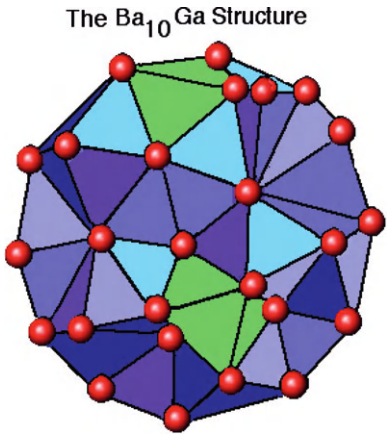

FIGURE 6.141

Barium gallides are available commercially in limited quantities for selected compositions.

Radium Gallides

The scientific literature is lacking in any references to radium gallides. Perhaps this is due to the intense radioactivity of the isomer ^{226}Ra but is more likely due to lack of interest of those in industry who have usage of such compounds. It is anticipated that various radium gallides could be prepared, using the same methods as those developed for the barium gallides series of compounds. Thus, one would expect to be able to obtain:

RaGa,
$RaGa_4$,
$RaGa_2$,
$RaGa_2$.

However, there is no record of such syntheses in the literature.

6.5.2. Alkaline Earth Gallate Compounds

Beryllium Gallates

Beryllium gallate, $BeO{\cdot}Ga_2O_3 = BeGa_2O_4$, can be formed by the SSR of the oxides at about 900 °C.

$$BeO + Ga_2O_3 + \text{heat} \Rightarrow BeGa_2O_4$$

X-ray powder diffraction data for $BeGa_2O_4$ have been obtained from the synthesized compound. The space group was determined by using a hexagonal prismatic single crystal obtained from a lead pyrophosphate flux by slow cooling. The crystal of $BeGa_2O_4$ belongs to the hexagonal system, with unit-cell parameters: $a = 7.7525$ Å, $c = 2.9817$ Å, $V = 155.19$ Å^3; space group $P6_3$ or $P6_3/m$, $Z = 2$. The crystal lattice is isomorphous with β-Si_3N_4. $BeGa_2O_4$ melts at 2013 K and has fairly small thermal expansion coefficients: $\alpha_{//}a = 3.29 \times 10^{-6}$/K, $\alpha_{//}c = 2.95 \times 10^{-6}$/K (298–1173 K average). $D_m = 4.511$ g/cm^3 (323 K) and $D_x = 4.546$ g/cm^3 (298 K).

High-pressure phase transformation of beryllium gallium oxide ($BeGa_2O_4$) has been studied. Applying high pressure at elevated temperatures to the original hexagonal $BeGa_2O_4$ (β–Si_3N_4-type structure), results in a high-pressure modification with orthorhombic structure (olivine-type structure), i.e. o-$BeGa_2O_4$. Lattice parameters of the new phase were determined to be $a = 0.5698$, $b = 0.9759$, and $c = 0.4551$ nm. The pressure and temperature ranges of the stable high-pressure phase observed were 3.5 to 7.5 GPa and 800 to 1600 °C, respectively. A tentative pressure–temperature phase diagram for $BeGa_2O_4$ was proposed. The transformation was not straightforward. Decomposition of the original phase into single oxides and their recombination to form o-$BeGa_2O_4$ was observed to be necessary. This process seems to apply to both formation and decomposition of the high-pressure phase. The stability of the high-pressure phase was explained in terms of the total molar volume for the phase, i.e. the result of summing up molar volumes of constituent compounds. This was said to be the first known report on transformation of the β–Si_3N_4 type structure into a denser structure.

$BeGa_2O_4$ is unique in that it can coexist with the oxides that are used to form it. Thus, the phase diagram exhibits only the beryllium monogallate (Fig. 6.142).

Beryllium gallate has been used as a flux to form high-strength sintered articles of chemical substances having the β-silicon nitride-type crystal structure. Sintered articles formed preponderantly of Si_3N_4 enjoy the properties of high thermal resistance, high strength, and a low thermal expansion coefficient but have proven very difficult to manufacture. Owing to these properties, they have drawn keen interest and have found utility in applications to automobile engine parts, gas turbine parts, cutting tools, etc. Such compositions can be

TABLE 6.45

No	Site notation	Atom	Multiplicity	Wyckoff	Site symmetry	*x*	*y*	*z*	Occupancy
1	Ba(1)	Ba	96	g	..m	0.3051	0.3051	0.1735	1.0
2	Ba(2)	Ba	48	f	2.mm	0.2543	1/8	1/8	1.0
3	Ba(3)	Ba	16	d	.-3m	1/2	1/2	1/2	1.0
4	Ga	Ga	16	c	.-3m	0	0	0	1.0

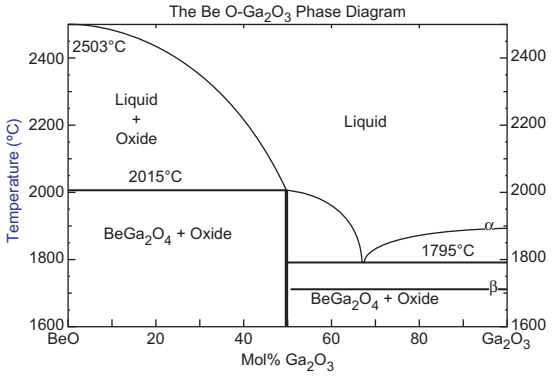

FIGURE 6.142

more easily formed by blending 50 to 99.9 wt% of a β-silicon nitride and/or β′-sialon and 50 to 0.1 wt% of a mixture, as a sintering aid, consisting of $BeGa_2O_4$, and Al_2O_3 in respective amounts so as to have a Ga_2O_3 / BeO ratio in the range of from 2.8 to 9.4, an Al_2O_3/BeO ratio in the range of from 0.0 to 2.6, and an Al_2O_3 /Ga_2O_3 ratio in the range of from 0.0 to 1.1, all ratios being ratios by weight and sintering the resultant blend.

Beryllium monogallate is available in limited quantities commercially. It has no CAS number.

Magnesium Gallates

Although Ca, Sr and Ba form a number of compounds when the molar ratios of MO to Ga_2O_3 are varied in the SSR:

$$xMO + yGa_2O_3 \Rightarrow M_x(Ga_2O_3)_y = M_xGa_{2y}O_{3y}$$

the magnesium cation, Mg^{2+}, forms only the magnesium monogallate, $MgGa_2O_4$. This compound, $MgO{\cdot}Ga_2O_3 = MgGa_2O_4$, can be formed by the SSR of the oxides at about 1200 °C:

$$MgO + Ga_2O_3 + \text{heat} \Rightarrow MgGa_2O_4$$

It has the molecular weight of 227.764 g/mol. Its density is 5.298 g/cc. It has a modified Spinel structure. The phase diagram is similar to that of the BeO–Ga_2O_3 system, except that MgO melts at 2852 °C.

The diffusion of trivalent gallium into the rock salt lattice of MgO has been investigated. This study concerned a diffusion process, with a moving interface, which involves both defect formation and the formation of a new phase, $MgGa_2O_4$. The study was performed on presintered MgO and β-Ga_2O_3 pellets. The Wagner treatment of Fick's second law was used in the analysis and it was subjected to certain boundary conditions and approximations. The diffusion coefficient was determined from the slope of the linear region of the inverse complementary error function of the concentration as a function of penetration. The departure from linearity in the region of greatest penetration indicates that, initially, diffusion takes place in the grain boundaries. The region of linear dependence takes place in the later states of diffusion when bulk diffusion predominates. The mean diffusion coefficient as determined from three different anneal times at 1500 °C was $7.53 \pm 0.25 \times 10^{-10}$ cm^2/s.

In another study, the SSR of single crystals of MgO and β-Ga_2O_3 to form the spinel $MgGa_2O_4$ at 1600 °C was investigated. Three sets of reaction couples consisting of the (100), (110) and (111) planes of MgO contacting the (001) plane of β-Ga_2O_3 were studied. All the reaction products were $MgGa_2O_4$ in single-crystal form. The Wagner mechanism of counter diffusion across the reaction interface was verified. In each instant where Spinel was formed, it adhered strongly to the host crystal. Spinel formed by vapor transport was also observed on the MgO crystal.

Spinelloid phases (which are mixed solid solutions of two differing compositions) of germanate–gallate have been observed and characterized by powder XRD and HREM. $Mg_3Ga_2GeO_3$(III), with a narrow composition range of approximately 3 mol% Mg_2GeO_4, is stable at atmospheric pressure up to about 1420° C, and is isostructural with β-Mg_2SiO_4 and the spinelloid Phase III of the $NiAl_2O_4$–Ni_2SiO_4 system. This represents the first occurrence of a β-phase structure stable at 1 atm pressure. Above 1420 °C (1 atm), $Mg_3Ga_2GeO_8$ (III) decomposes reversibly into a mixture of spinel and olivine. At high pressures (around 30 kbar at 1100 °C), it transforms into another spinelloid phase, $Mg_3Ga_2GeO_8$ (IV), isostructural with Phase IV of the $NiAl_2O_4$–Ni_2SiO_4 system. In terms of crystal structures and phase relations, there exists a close analogy between the magnesium gallo-germanate and nickel alumino-silicate systems, the former being a lower pressure analog of the latter. The results of investigation of a number of other pseudo-binary spinel–olivine oxide systems suggests that the formation of spinelloid phases can be associated with the inverse character of the spinel component.

Magnesium gallate, when activated by divalent manganese, Mn^{2+}, is a phosphor that has a cubic spinel structure and was used in electrostatic copy machines. The spectral properties of the fluorescent lamp were shown in Fig. 6.143.

The characterization and optical properties of luminescent $MgGa_2O_4$:Eu^{3+} powders has also been investigated. Nanograined phosphors of Eu^{3+}-activated $MgGa_2O_4$ crystallites were prepared by a sol–gel technique. The dried sol–gel powders were calcined in air at different temperature from 600 to 1000 °C for 5 h. The XRD profiles showed that the $MgGa_2O_4$:Eu^{3+} powders began to crystallize around 600 °C and formed a stable $MgGa_2O_4$ phase in the temperature range of 600–900 °C. The TEM morphology observations

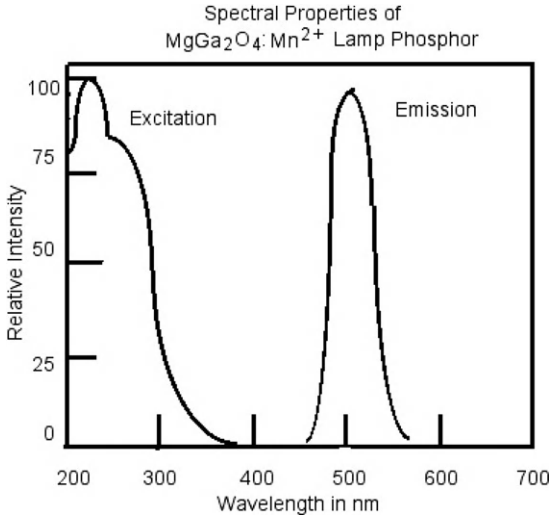

FIGURE 6.143

revealed that the fired powders exhibit small grain size less than 20 nm. In the PL studies, under ultraviolet (394 nm) excitation, the calcined powders emitted bright red luminescence (615 nm, $5D_0 \Rightarrow 7F_2$), and the powders fired at 900 °C were found to have the maximum photoluminescence intensity. The quenching concentration of Eu^{3+} in $MgGa_2O_4$ crystallites was also indicated to be about 5~6 mol%.

Magnesium monogallate is a partially inverted spinel with space group Fdpm and $a = 8.286$ Å. There are two possible sites in the lattice for metal ions, the A and B sites. Because magnesium is divalent and gallium is trivalent, these ions distribute themselves among these sites unequally. Mg^{2+} ions are distributed in about 16% in a tetragonal site and 84% in an octahedral site in the lattice, as shown in the following Fig. 6.144.

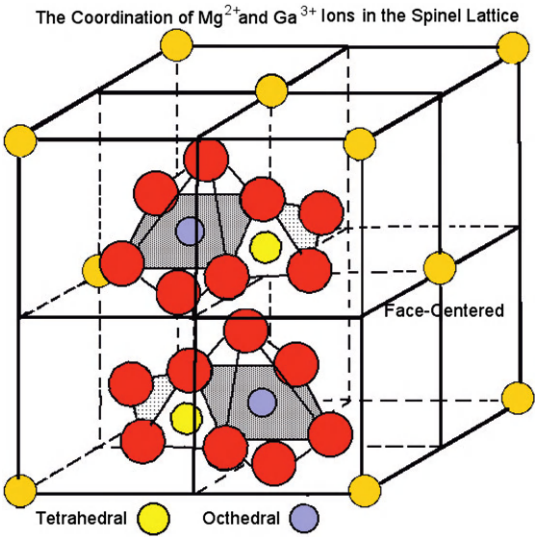

FIGURE 6.144

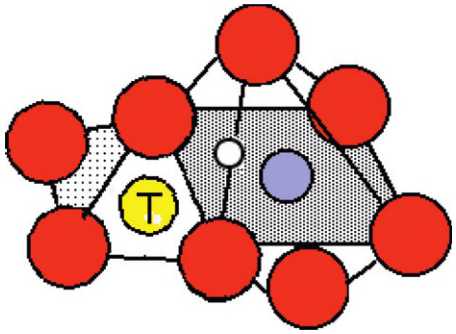

FIGURE 6.145

The oxygen atoms occupy a set of special positions. One or the other of the O- or T-Mg^{2+} or Ga^{3+} atoms is in a face-centered position between four unit cells. The separate tetrahedral and octahedral positions are better seen in the following Fig. 6.145.

Thus, there are two special positions for the Mg^{2+} and Ga^{3+} ions. There are 14 face-centered Ga^{3+} or Mg^{2+} sites that are shared in eight unit cells. The front faces of tetrahedral and octahedral positions of the Mg^{2+} and Ga^{3+} ions in two of the eight unit cells are clearly shown. The Mg^{3+} ions occupy the other positions in these lattice cells. The tetrahedral and octahedral groups are joined by a central oxygen atom in the structure. This structure is unique among the known cubic spinel compounds.

Other gallates of magnesium have not been discovered. Magnesium monogallate is available commercially in limited quantities. It has no CAS number.

Calcium Gallates

Monocalcium gallate can be prepared by firing the oxides together at 1200 °C for 8 h. The reaction is:

$$CaO + Ga_2O_3 + \text{heat} \Rightarrow CaGa_2O_4$$

Its structure has been described as a "stuffed-tridymite" which is a modification of silica. The phase diagram at room temperature is shown in the following Fig. 6.146.

The phase diagram has been determined as consisting of four compounds, although it is possible to form other stoichiometries by varying the formation conditions.

The system, $CaO–Ga_2O_3$, forms four compounds: $Ca_3Ga_2O_6$, $Ca_3Ga_4O_9$, $CaGa_2O_4$ and $CaGa_4O_7$. $3CaO–Ga_2O_3$ melts incongruently to CaO plus liquid at 1263 °C; $CaO·Ga_2O_3$ and $CaO·2Ga_2O_3$ melt congruently at 1369 and 1504 °C, respectively. Eutectics are located at the following temperatures and compositions (in mol% Ga_2O_3): between $3CaO·Ga_2O_3$ and $CaO·Ga_2O_3$, 1245 °C and 37.5%; between $CaO·Ga_2O_3$ and $CaO·2Ga_2O_3$, 1323 °C and 57.0%; and between $CaO·2Ga_2O_3$ and β-Ga_2O_3, 1457 °C and 68.0%. There is

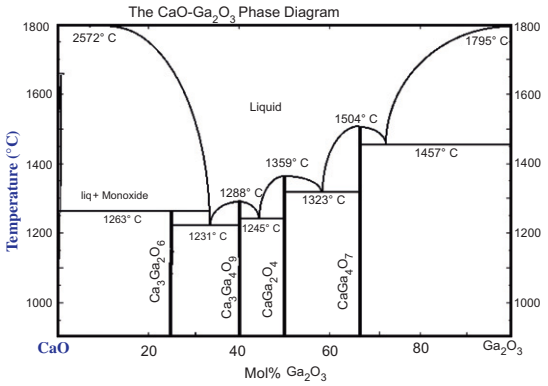

FIGURE 6.146

a peritectic at 1263 °C and 36.0%. Three polymorphs of $CaO{\cdot}Ga_2O_3$ have been described. Compositions from approximately 35 to 70 mol% Ga_2O_3 can be quenched to yield homogeneous glasses.

In another report, this system was reexamined using the methods of X-ray and differential thermal analysis. Four compounds $Ca_3Ga_2O_6$, $Ca_3Ga_4O_9$, $CaGa_2O_4$, and $CaGa_4O_7$ were found in the subsolidus region of the phase diagram of the $CaO–Ga_2O_3$ system. The existence of the gallate, $Ca_3Ga_4O_9$, discovered for the first time, was confirmed by measuring the e.m.f.'s of galvanic cells. Changes in Gibbs energy, enthalpy, and entropy for the reactions of formation of all four calcium gallates from oxides have been determined by the e.m.f. method with a solid $|F^-|$-ionic electrolyte in the range of 1100–1400 K (825–1125 °C). On the basis of the data obtained, the relative stabilities of the compounds were analyzed and the activity of calcium oxide in the system was calculated.

Monocalcium gallate ($CaO{\cdot}Ga_2O_3$) is polymorphic. Single crystals of the three polymorphs of $CaGa_2O_4$ have been studied. $CaGa_2O_4$-I is orthorhombic, with $a = 7.73$, $b = 9.14$, $c = 10.36$ Å; $CaGa_2O_4$-II is orthorhombic with $a = 5.32$, $b = 14.38$, $c = 16.82$ Å; *m*-$CaGa_2O_4$ is monoclinic with $a = 7.86$, $b = 8.90$, $c = 10.55$ Å, $\beta = 93°$. These cell dimensions do not resemble any of those previously reported for other $MO{\cdot}Ga_2O_3$ compounds.

The structure of calcium monogallate involves a series of tetrahedra–octahedra which share both corners and edges of octathedra. A high-pressure modification of calcium monogallate ($CaGa_2O_4$) has been prepared in a piston cylinder apparatus at 700 °C and 4.0 GPa. The compound is orthorhombic (space group *Pnam*, $a =$ 9.12476 Å, $b = 10.56093$ Å, $c = 2.98547$ Å, $V = 287.70$ Å^3, $Z = 4$, $D_{calc} = 5.62$ g/cm^3) and belongs to the $CaFe_2O_4$-type structure family. The structure was refined by the Rietveld method using laboratory X-ray powder diffraction data. Two crystallographically-independent GaO_6 octahedra forming edge-sharing double chains could be distinguished. The shared edges exhibit a considerable shortening. The chains are running parallel to the *c*-axis and are linked by corner sharing. They enclose tunnels in which the calcium atoms are located for charge compensation. Each calcium cation has eight nearest oxygen neighbors. The coordination environment can be described as a bicapped trigonal prism.

The SSRs (solid-state reactions) and the phase relations in the $CaAl_2O_4{\cdot}CaGa_2O_4$ system, of which both end-members have the stuffed tridymite structure, were examined by using three kinds of starting materials:

$$A = CaCO_3 + (Al,Ga)_2O_3$$

$$B = CaAl_2O_4 + CaGa_2O_4$$

$$C = CaCO_3 + Al_2O_3 + Ga_2O_3$$

When using the starting material B, a very low rate of SSR between $CaAl_2O_4$ and $CaGa_2O_4$ was found, which seemed to be due to very slow interchange of Al^{3+} and Ga^{3+} ions located in the tetrahedra of this structure. In order to obtain the probable equilibrium phase relations, it was necessary to use the starting material A. In using the A system, a new stable phase was found over a wide range of composition, which was proposed to have the same structure as so-called metastable phase of $CaGa_2O_4$ but a different array of tetrahedra from either $CaAl_2O_4$ or $CaGa_2O_4$.

In another paper, the modifications of $CaAl_2O_4$ and $CaGa_2O_4$ with the stuffed tridymite structure were examined under high temperatures (600 to 1500 °C) and high pressures (10 to 40 kbar). Calcium monoaluminate $CaAl_2O_4$ was found to transform to three kinds of high-pressure modifications. The original $CaAl_2O_4$ (CA-I) changed to the phase CA-II that had an m-$CaGa_2O_4$ type of structure with a different array of tetrahedra in the six-membered rings of the tetrahedron. The phase CA-II transformed either to the phase CA-IV with $CaFe_2O_4$-type structure or to an unknown phase (CA-III) under high pressures. The phase CA-IV was obtained under the pressures above 30 kb and at the temperatures above 1000 °C. In contrast, calcium monogallate, $CaGa_2O_4$, transformed to the $CaFe_2O_4$-type structure above 30 kb and 700 °C. No phases such as CA-II and CA-III were found. The structural relations among these modifications were discussed.

Dicalcium monogallate, $2CaO{\cdot}Ga_2O_3 = Ca_2Ga_2O_5$, was synthesized as a single crystal in a piston cylinder apparatus at 1250 °C/2.5 GPa from precursors prepared by SSRs. The crystal structure was investigated by XRD methods. The compound crystallizes in the orthorhombic space group *I*2*mb* ($a = 5.3525$ Å, $b = 14.6666$ Å, $c = 5.5651$ Å, $V = 436.88$ Å^3, $Z = 4$, $D_{calc} = 4.56$ g/cm^3)

and is isotypic with Ca_2FeAlO_5 (Brownmillerite) and $Ca_2Al_2O_5$. Basic building units of $Ca_2Ga_2O_5$ are:

(1) Layers of perovskite type corner-connected GaO_6 octahedra.
(2) Sheets comprised of Zweier single chains of GaO_4 tetrahedra (Fig. 6.147).

The alternate stacking of the two building units results in a three-dimensional framework in which the calcium cations are incorporated for charge compensation. Dicalcium gallate is the first structurally characterized representative of a double oxide in the system $CaO{\cdot}Ga_2O_3$ showing a sixfold coordination of Ga^{3+}. The stacking pattern is perhaps better seen in the following diagram where two layers are shown in Fig. 6.148.

A high-temperature XRD study revealed that Brownmillerite-type $Ca_2Al_2O_5$ transforms to an incommensurately modulated structure at elevated temperatures. Single crystals of $Ca_2Al_2O_5$ were synthesized in an end-loaded piston cylinder press at 2.5 GPa and 1273 K. The diffraction pattern observed at 1090 K by in situ single-crystal diffraction experiments was indexed by an *I*-centered orthorhombic cell and a modulation wave vector of $\mathbf{q} = 0.595\ \mathbf{c}$. A $(3+1)$ dimensional model in superspace group *Imma*(00)*s*00 was used to refine the modulated structure. The structure is assembled from two building units: (i) layers of corner-sharing $[AlO_6]$ octahedra, stacked along **b** alternate with (ii) layers of *Zweier* single chains of $[AlO_4]$ tetrahedra running along **a**. The modulated structure arises from an aperiodic sequence of two different configurations of the chains within the tetrahedral layers. The modulated high-temperature phase of $Ca_2Al_2O_5$ is isotypic to the modulated high-temperature modification of $Ca_2Fe_2O_5$. A large hysteresis was found in the phase-transition temperature. On heating, the transition occurs at ca. 1075 K (800 °C); on cooling, satellite reflections can be observed down to 975 K (700 °C). The characterization of $Ca_2Al_2O_5$ was completed by Raman spectroscopy, including a partial interpretation of the spectra.

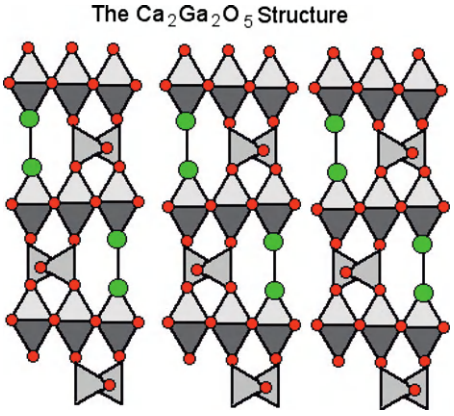

FIGURE 6.147

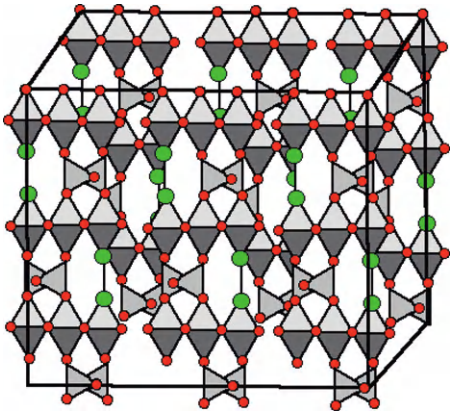

FIGURE 6.148

The compound, **mono-calcium digallate**, $CaGa_4O_7 = CaO{\cdot}2Ga_2O_3$, was prepared and its structure determined by single-crystal X-ray investigations. $CaGa_4O_7$ crystallizes as a monoclinic structure in the space group C_6^2/c with the lattice constants $a = 13.065$, $b = 9.079$, $c = 5.600$ Å; $\beta = 105.15°$. Calcium has an unusual coordination, which can be regarded as a distorted trigonal bipyramid. Its five nearest oxygen neighbors form a trigonal bipyramid. The gallium, however, is tetrahedrally coordinated. Four compounds were found to give significant Mn^{2+}-activated luminescence; $MgO{\cdot}Ga_2O_3$, $ZnO{\cdot}Ga_2O_3$, $K_2O{\cdot}5Ga_2O_3$, and $CaO{\cdot}2Ga_2O_3$. These have characteristic peak emissions at 512, 513·5, 507 and 587 nm, respectively.

Penta-calcium trigallate can be prepared by heating the oxides in the proper molar proportions at 1200 °C:

$$5CaO + 3Ga_2O_3 + \text{heat} \Rightarrow Ca_5Ga_6O_{14}$$

A direct current ($j = 20$ to $80\ mA/cm^2$) passing in vacuum ($P = 0.1$ Pa) at 1275 K (1002 °C) through $Ca_5Ga_6O_{14}$ single crystals led to a change of electrophysical and luminescent properties of samples. Specifically, this procedure induces the ionic component of electrical conductivity of $Ca_5Ga_6O_{14}$ and the red (1.83 eV = 678 nm) luminescence of F-centers. Using the obtained results, it was predicted that the ionic conduction is due to the transport of Ca^{2+} ions.

A novel $Ca_6Mn_3(Ga_{0.80}Al_{0.20})_5O_{18}$ compound was discovered in the Ca–Mn–Al–Ga–O system as a product of the reduction of the $Ca_2Mn(Ga_{0.8}Al_{0.2})O_5$, "Brownmillerite" and then prepared as a single-phase material. The structure consists of a tetrahedral $[(Ga_{0.59}Mn_{0.24}Al_{0.17})_{15}O_{30}]^{18-}$ framework stabilized with the embedded $[(Ca_{0.9}Mn_{0.1})_{14}MnO_6]^{18.24+}$ polycations. A high degree of disorder in the structure can be attributed to the random orientation of the tetrahedra around the Ga3 and Ga4 atoms in order to achieve proper bonding

conditions for the O2 atoms placed at the centers of the tetrahedral clusters. The joint occupation of the tetrahedrally coordinated positions in the framework by Ga and Al is not a necessary condition for the stability of this structure type. This indicates a large ability of this structure type in adapting to changes in the chemical composition.

The structure, in terms of octahedra and tetrahedra is shown in the following Fig. 6.149.

Here, the Ca^{2+} atoms, Ca1, Ca2, Mn and O3 atoms are omitted for clarity. Ga1, Ga2, Ga3 and Ga4 atoms are located at the yellow, brown, green and blue tetrahedra, respectively. The O3 atoms do not participate in the tetrahedral framework and form octahedra around the Mn atoms. The Mn–O3 octahedra together with the Ca1 and Ca2 atoms fill the cages in the tetrahedral framework. The MnO_6 octahedra are isolated from each other and from the tetrahedral framework. The $Ca_{6.3}Mn_3Ga_{4.4}Al_{1.3}O_{18}$ compound exhibits an onion skin-like structure where the Mn atom, chosen as a central point, is surrounded by the enclosed O_6,(Ca, $Mn)_{14}$ and (Ga, Al, $Mn)_{42}O_{104}$ shells (Fig. 6.150).

The full structure is shown in the following where positions of the MnO6 octahedra (red), Ca1 and Ca2 atoms (brown spheres) in the unit cell. The F23-ordered structure is shown for simplicity (Fig. 6.151).

From this point of view, the $Ca_6Mn_3(Ga_{0.80},Al_{0.20})_5O_{18}$ compound demonstrates a certain similarity to the structural organization of the ''Fullerenoid'' $Sr_{33}Bi_{24+d}Al_{48}O_{141+3d/2}$ oxide, where the onion skin-like structure is also present, and the largest sphere in this structure has a geometry virtually identical to that of D2d isomer of the C84 fullerene. However, the analogy with fullerene is based on pure geometrical resemblance since the bonding in complex oxides is essentially more ionic than that in carbon materials. The tetrahedral framework of the $Ca_6Mn_3(Ga_{0.80},Al_{0.20})_5O_{18}$ structure can be described as a three-dimensional $[(Ga_{0.59}Mn_{0.24}Al_{0.17})_{15}O_{30}]^{18-}$ anion stabilized with the embedded $[(Ca_{0.9}Mn_{0.1})14\ MnO_6]^{18+}$ polycations.

Another complex oxide $Ca_7Mn_2Ga_6O_{18}$ was synthesized by the SSR in a sealed evacuated quartz tube at 1000 °C. Its crystal structure was determined by electron diffraction and X-ray powder diffraction. The structure can be represented as a tetrahedral framework, viz., the polyanion $[(Mn_{0.285},Ga_{0.715})_{15}O_{30}]^{19-}$ stabilized by the incorporated cation $[Ca_{14}GaO_6]^{19+}$. The polycation consists of the GaO6 octahedra surrounded by the Ca atoms, which are arranged to form a cube capped at all places. The tetrahedral framework is partially

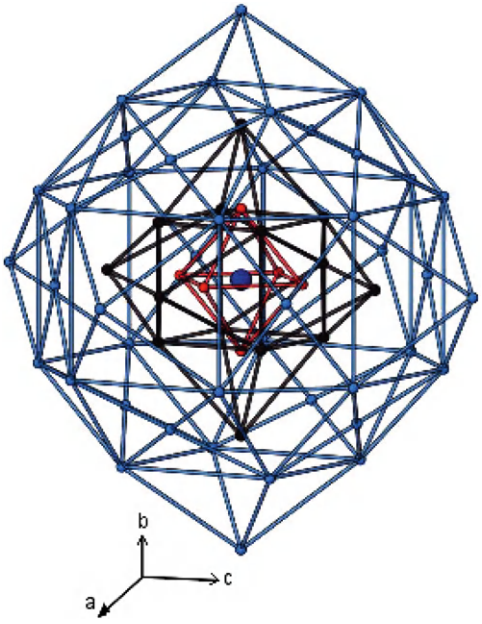

FIGURE 6.150

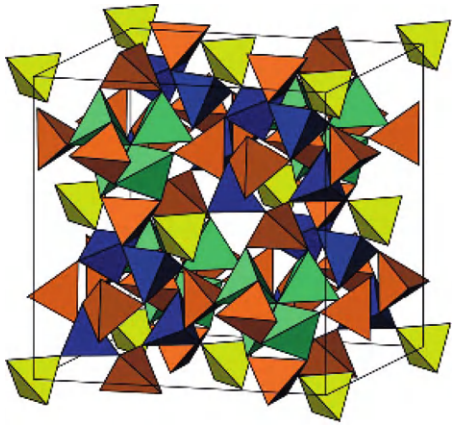

FIGURE 6.149

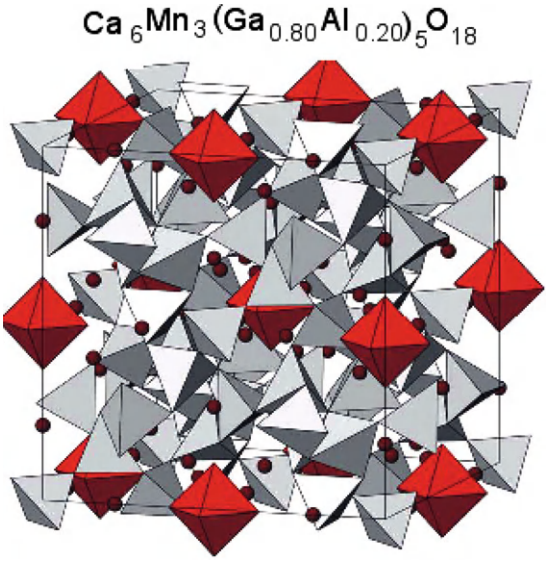

FIGURE 6.151

disordered due to the presence of tetrahedra with two possible orientations in the positions (0, 0, 0) and (x, x, x) with $x \approx 0.15$ and 0.17. The relationship between the $Ca_7Mn_2Ga_6O_{18}$ structures and related-ordered phases with the symmetry $F2_3$, as well as the influence of the oxygen content on the ordering in the tetrahedral framework, was discussed.

The magnetoplumbite family of materials exhibit properties that make them suitable to be used as substrates materials for microwave or luminescent applications. Four members of the family studied in this work are $LaMgAl_{11}O_{19}$, $NdGaMgAl_{10}O_{19}$, $CaGa_6Al_6O_{19}$ and $CaGa_{12}O_{19}$. Dielectric studies have been carried out over a temperature range of 4–300 K (−269 to 27 °C) and a wide frequency range. All four exhibit a low dielectric constant with good temperature stability, low dielectric loss and favorable frequency dependence characteristics.

The luminescence of $Sr(Ga_{12-x}Al_x)_{12}O_{19-y}:Eu^{2+}$ phosphors can be quenched by substitution of a small amount of Mg for Al, or by preparing samples with excess Al_2O_3. It is most probable that oxygen vacancies near the Eu^{2+} activator ions act as the radiationless sinks of the excitation energy. In $CaAl_{12}O_{19}:Eu^{2+}$, the quenching of the luminescence by the introduction of defects is much less effective, so that less oxygen vacancies are supposed to be formed. In view of the fact that the stability of $CaAl_{12}O_{19}$, with respect to less oxygen-containing phases, is higher than that of $Sr(Ga_{12-x}Al_x)_{12}O_{19-y}$, this is a reasonable assumption. The homogeneity range of $La_{1-x}A1_{11+x}0_{19}$: Eu^{2+} is at such values of x that a large number of Al vacancies exist. Quenching of its luminescence by the introduction of oxygen vacancies was not observed. In $LaMgAl_{11}O_{19}:Eu^{2+}$ phosphors, Al^{3+} interstitials, rather than oxygen defects, seem to play a dominate role in achieving charge neutrality.

Calcium gallates are available in limited quantities commercially.

Strontium Gallates

The strontium gallates may be formed by a SSR of the oxides:

$$x\mathrm{SrO} + y\mathrm{Ga_2O_3} + \text{heat} \Rightarrow \mathrm{Sr}_x\mathrm{Ga}_{2y}\mathrm{O}_{3y+x}$$

where x or y can vary from 1, 2, 3, 4, 6 and 7.

In the early literature, it was stated that the system, $SrO{\cdot}Ga_2O_3$, forms three compounds in the SSR of SrO and Ga_2O_3 ($4SrO{\cdot}Ga_2O_3$, $3SrO{\cdot}Ga_2O_3$, and $SrO{\cdot}Ga_2O_3$).

A phase diagram was published in 1969 that shows four compounds (Fig. 6.152).

These are: 1:1 = $SrGa_2O_4$, 4:1 = $Sr_4Ga_2O_7$, 3:2 = $Sr_3Ga_4O_9$, 1:2 = $SrGa_4O_7$, 1:6 = $SrGa_{12}O_{19}$. All were said to melt incongruently except $SrGa_2O_4$ which melts congruently at 1580 °C.

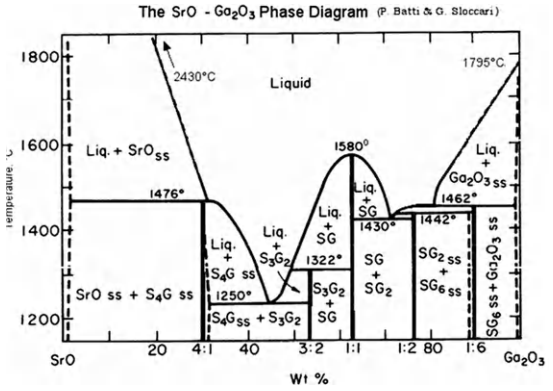

FIGURE 6.152

According to later phase equilibrium studies, at least seven different strontium gallates have to be distinguished: $Sr_4Ga_2O_7$, $Sr_7Ga_4O_{13}$, $Sr_3Ga_2O_6$, $Sr_3Ga_4O_9$, $SrGa_2O_4$, $SrGa_4O_7$ and $SrGa_{12}O_{19}$. In contrast, the $CaO{\cdot}Ga_2O_3$ system shows but four compounds. Furthermore, for strontium monogallate, different polymorphic forms have been reported. However, the space groups and the crystal structures of many of these compounds remain to be solved; to date only the more gallium-rich compounds $SrGa_{12}O_{19}$, $SrGa_2O_4$ and $SrGa_4O_7$ have been completely characterized by structure analysis. $SrGa_{12}O_{19}$ is isotypic with magnetoplumbite. The different polymorphs of $SrGa_2O_4$ belong to the group of stuffed tetrahedral frameworks (similar to the calcium monogallate isotypes). $SrGa_4O_7$ also belongs to the group of framework structures with sixfold tetrahedral rings, though the structure is more complex and not a simple derivative of high tridymite. For $Sr_3Ga_2O_6$, an indexed X-ray powder diffraction pattern based on a cubic unit cell with $a = 16.095$ Å has been published, indicating that this phase may be isostructural with $Ca_3Al_2O_6$. However, there may exist a second tetragonal polymorphic form for this compound. In the case of $Sr_3Ga_4O_9$, only an unindexed powder pattern has been reported by Kobzareva et al. so that the existence of a phase having this composition has remained uncertain. In addition, a compound having a 10:3 molar ratio has recently been discovered in this phase system so that the phase diagram for the strontium gallates remains to be firmly established.

Strontium monogallate has two isomorphs that have been investigated by single-crystal XRD. A β-phase corresponding to the stable modification at room temperature and γ-$SrGa_2O_4$, a quenched high-pressure polymorph prepared at 1250 °C and 2.5 GPa. β-$SrGa_2O_4$ is monoclinic, space group $P12_1/c1$, $a = 8.3770$ Å, $b = 8.9940$ Å, $c = 10.6800$ Å, $\beta = 93.932°$, $V = 802.8$ Å^3, $Z = 8$, $D_{calc} = 4.82$ g/cm^3; γ-$SrGa_2O_4$ is monoclinic as well, space group $P12_1/n1$, $a = 8.1100$ Å, $b = 10.7610$ Å, $c = 9.0570$ Å, $\beta = 91.569°$, $V = 790.1$ Å^3, $Z = 8$,

$D_{calc} = 4.89\ g/cm^3$. The structures of both phases are characterized by layers of six-membered rings of GaO_4 tetrahedra perpendicular to the *a*-axis. The stacking of the layers parallel to the *a*-axis results in a three-dimensional framework containing channels that are occupied by the Sr cations for charge compensation. The two modifications differ with respect to the relative orientation of up (U) and down (D) pointing apices of adjacent tetrahedra within a single ring. The sequence of directedness is UUUDDD for γ-$SrGa_2O_4$ and UUDUDD for β-$SrGa_2O_4$, respectively. γ-$SrGa_2O_4$ belongs to the zeolite ABW-type structures and is apparently the only member with space group symmetry $P12_1/n1$ in combination with a doubled *b*-axis compared to the ABW-aristotype (space group *Jmma*). It is the first member of this structure family with exclusively trivalent tetrahedral ions of only one chemical species and divalent nonframework cations within the channels. The compound is isotypic with the monoclinic modification of $CaGa_2O_4$. The structure is shown in the following diagram. The main structural features of γ-$SrGa_2O_4$ are layers of GaO_4 tetrahedra perpendicular to the *a*-axis (Fig. 6.153).

The stacking of the layers parallel to [100] results in a three-dimensional framework containing tunnels, where the strontium cations are located. Individual layers can be described as being built by the condensation of ditrigonally-shaped six-membered tetrahedral rings. The sequence of up (U) and down (D) pointing apices within a single ring is UUUDDD. This structure of γ-$SrGaO_4$ belongs to the family of the zeolite ABW-type structures and is the first zeolite-type compound with exclusively gallium occupying the tetrahedral positions of the framework.

Strontium monogallate can be made as a "self-activated" phosphor. Gallium has the electron configuration of: Ar $3d^{10}$ $4s^2$ $4p^1$. The trivalent state is thus a closed-shell and can function as an activator (see "Luminescence and the Solid State" by R.C. Ropp (2004—Elsevier, NY) for a more complete explanation in Chapter 6—Design of Phosphors—p. 462).

A tunable blue to blue-white $SrGa_2O_4$ phosphor was prepared with a SSR method by varying the composition concentration of source materials. The decomposition temperature and weight loss of Ga_2O_3 and $SrCO_3$ were evaluated by thermogravimetric analysis. Gallium trioxide has a tendency to sublime so that a slight deficiency of Ga^{3+} ions may occur in the final product. The deficiency of Ga^{3+} in the $SrGa_2O_4$ phosphor is attributed to this sublimation and may be compensated by increasing the molar ratio of $Ga_2O_3/SrCO_3$ in the reaction. Photoluminescence measurements show that Ga^{3+} is the luminescent center of this strontium monogallate phosphor. When the molar ratio of $Ga_2O_3/SrCO_3$ is 1, the emission wavelength of $SrGa_2O_4$:Ga^{3+} phosphor is ~402 nm, which is caused by the $^4T_1 \Rightarrow {}^4A_2$ transition of electrons in Ga^{3+} d-orbits. Crystallization of $SrGa_4O_7$ was observed as the phosphor was prepared at a higher molar ratio of $Ga_2O_3/SrCO_3$. The ligand field and the electron-transferring mechanism in Ga was observed to be modulated by the development of the crystal, $SrGa_4O_7$. Thus, the emission wavelength of phosphor is altered from 402 to 430 nm where the electron is transferred from $^4T_{2A}$ exciting state to the emitting state, $^4T_1$ to the $^4A_2$ ground state and the emission spectrum is broadened in the latter crystal.

If Ce^{3+} is added to $SrGa_2O_4$, the self-activation is restricted. Ce^{3+}-activated $SrGa_2O_4$ phosphor was synthesized by a method of citric gel, wherein citric acid served as the chelate agent, and the as-synthesized powder was calcined in a slightly reduced ambient. The crystallization characteristics of the sample varied with the calcining temperature. Compared with the phosphor prepared by the SSR, the phosphor synthesized by citric gel was calcined at a relatively lower temperature. Consequently, the volatilization of Ga_2O_3 during high-temperature calcining process was avoided. The typical

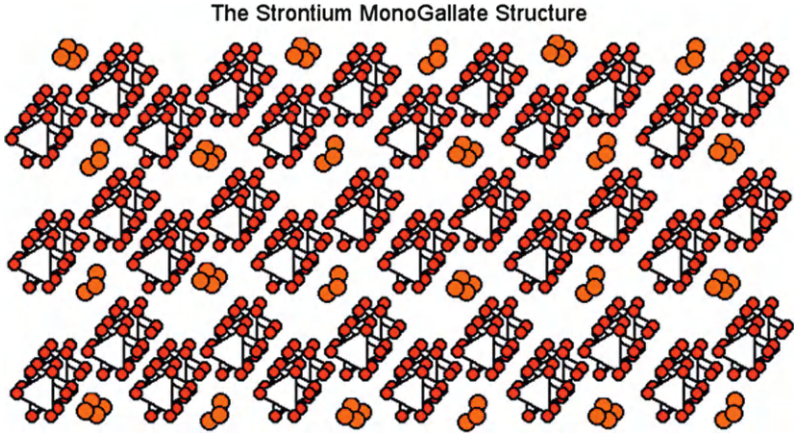

FIGURE 6.153

double-peak emission of Ce^{3+} originated from $^2D(5d) \Rightarrow {}^4F_{5/2}(4f)$, and $^2D(5d) \Rightarrow {}^4F_{7/2}(4f)$ was observed, and the intrinsic emission of $SrGa_2O_4$ host was much restricted. The emission intensity varied with the calcining temperature because the different crystallinity and the optimal concentration of Ce dopant was determined at 3 mol%. Charge compensation was employed, using Li^+ cations:

$$(Ce^{3+} + Li^+)_{Sr} \Leftrightarrow (2Sr^{2+})_{Sr}$$

A bright-blue luminescence was observed with the double-peaks characteristic of Ce^{3+} emission.

Distrontium gallate, $Sr_2Ga_2O_5$, has been prepared by reaction of strontium carbonate with gallium trioxide for 1 hour at 1200 °C:

$$2\,SrCO_3 + Ga_2O_3 + \text{heat} \Rightarrow Sr_2Ga_2O_5 + 2\,CO_2\ (\text{gas})$$

The reaction of the oxides is extremely slow and since $Sr_2Ga_2O_5$ melts as low as 1230 °C, the "oxide reaction" cannot be used effectively. This compound has not appeared in the phase diagrams published to date because of the very slow reaction rates of the oxides. The main usage for this compound has been as a sintering aid. When ceramics with a high melting point (>1500 °C) need to be joined (such as sealing of "end-caps" to form a high-pressure sodium lamp for street lighting), it is not practical to melt the ends together, particularly if they are metallic and do not wet the edges of the ceramic. Furthermore, the lattice parameters do not match, leading to an imperfect join and a weak joint. Distrontium gallate performs admirably in this aspect.

Ceria-based ceramics have been considered as one of the most promising electrolytes for intermediate temperature solid-oxide fuel cells, because its electrical conductivity is higher than that of yttria-stabilized zirconia (YSZ) (ZrO_2:Y^{3+}). The densification behavior and grain growth of $Ce_{0.8}Gd_{0.2}O_{1.9}$ ceramics were investigated with the strontium gallate concentration ranging from 0 to 5 mol%. Both the sintered density and grain size were found to increase rapidly up to 0.5 mol% $Sr_2Ga_2O_5$, and then to decrease with further addition. Dense $Ce_{0.8}Gd_{0.2}O_{1.9}$ ceramics with 97% of the theoretical density could be obtained for a 0.5 mol% $Sr_2Ga_2O_5$-added specimen sintered at 1250 °C for 5 h, whereas pure $Ce_{0.8}Gd_{0.2}O_{1.9}$ ceramics needed to be sintered at 1550 °C in order to obtain an equivalent theoretical density. The addition of $Sr_2Ga_2O_5$ was found to promote the sintering properties of Gd_2O_3-doped CeO_2. Other ceramics that have been sintered and/or joined by the use of $Sr_2Ge_2O_5$ include: $Ce_{0.8}Sm_{0.2}O_{1.9}$ ceramics and $La_{0.8}Sr_{0.2}Ga_{0.83}Mg_{0.17}O_3$ ceramics.

Strontium di-gallate, $SrGa_4O_7$ was prepared, and studied by single-crystal X-ray investigations. It is isotypic with $CaAl_4O_7$ and $CaGa_4O_7$; space group C^6_{2h} – C2/c ($a = 13.46$, $b = 9.19$, $c = 5.69$ Å, $\beta = 105.8°$). Sr^{2+} as well as Ca^{2+} is surrounded by five oxygen ions in a trigonal bipyramidal array.

Strontium digallate ($SrGa_4O_7$) can be synthesized by crystallization of amorphous spray-dried precursors or solidification from the liquid. $SrGa_4O_7$ was prepared via the ethylenediaminetetraacetic acid precursor route. Differential thermal analysis, thermogravimetric, Fourier transform infrared spectroscopy, and XRD were used to characterize the precursors and the oxide powders derived. XRD analysis showed that single-phase $SrGa_4O_7$ was obtained from pulverized resin at a temperature of 1050 °C for 2 h and $SrGa_4O_7$ can be stable at least up to 1200 °C. Single-phase $SrGa_4O_7$ was not obtained from the citrate acid route.

Boron may be substituted into the $SrGa_4O_7$ lattice. A novel borogallate, $SrGa_2B_2O_7$ (M = Sr, Ba), has been synthesized and structurally characterized. The structure of $SrGa_2B_2O_7$ (*Cmcm*, $a = 11.7260$ Å, $b = 8.3745$ Å, $c = 5.7062$ Å, $Z = 4$) has been determined by single-crystal XRD. $BaGa_2B_2O_7$ (*Cmcm*, $a = 11.7434(6)$ Å, $b = 8.7076(4)$ Å, $c = 5.8038(3)$ Å, $Z = 4$) has been shown to be isostructural by ab initio structure determination and Rietveld refinement using powder X-ray data. The $SrGa_2B_2O_7$ structure, formulated as $SrGa_2(B_2O_5)O_2$, consists of a framework of corner-sharing tetrahedral (GaO_4) chains and pyroborate (B_2O_5) groups with the Sr atoms filling eight-coordinated framework cavities. It represents a new structure type for anhydrous borogallates and, in particular, is structurally distinct from the $SrAl_2B_2O_7$ aluminoborate analogs.

Tristrontium monogallate = $Sr_3Ga_2O_6$, a perovskite-related Ga oxide, was synthesized and characterized in order to design new diluted magnetic perovskites for spin electronics. The crystal structure was investigated by powder XRD and Rietveld analysis. Strontium gallate, $Sr_3Ga_2O_6$ (SGO) is a novel cubic structure with a GaO_4 tetrahedral unit, space group P3a, and $a = 16.095$ Å.

In another study, the cubic structure of Tristrontium monogallate, $Sr_3Ga_2O_6$, has been refined from powder diffraction data using the Rietveld method (space group *P3a*, $a = 16.1049$ Å, $V = 4177.1$ Å^3, $Z = 24$, $D_{calc} = 4.75$ g/cm^3). The compound is isostructural with tricalcium aluminate and contains highly puckered, six-membered $[Ga_6O_{18}]^{18-}$ rings. The rings are linked by nine strontium cations having six to nine nearest oxygen neighbors. The structure of the rings is shown in the following diagram presented on the next page.

Thus, the overall formulation can be written as: $Sr_9Ga_6O_{18}$. This may be contrasted to the $(Ga_6O_{19})^{19-}$ rings found in the $Sr_{10}Ga_6O_{19}$ compounds as shown in Fig. 6.154.

The nine Sr^{3+} atoms are arranged in groups of three along the *b*-axis.

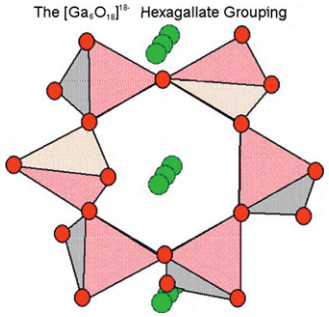

FIGURE 6.154

A novel compound $Sr_3(Al_{0.36}Ga_{0.64})_2O_6$ can be synthesized and was studied by single-crystal XRD. The material crystallizes in the cubic space group Pa3 (No. 205) with $Z = 24$ and a lattice constant $a = 16.0195$ Å. The structure is isotypic with $Ca_3Al_2O_6$ and is characterized by isolated, highly puckered, six-membered $(Al,Ga)O_6$ rings. The rings are linked by strontium cations which are coordinated by six to nine oxygen ligands. Alternatively, the structure can be regarded as an example for a defect ABO_3-perovskite with 12.5% vacancies in the A-sublattice and 25% oxygen vacancies:

$$(Sr_{7/8\text{-}1/8})((Al,Ga)_{3/4}Sr_{1/4})(O_{9/4\text{-}3/4})$$

The ternary systems La_2O_3–SrO–Ga_2O_3, La_2O_3–MgO–Ga_2O_3, and the quaternary system La_2O_3–SrO–Ga_2O_3–MgO were studied at 1350–1400 °C in air with emphasis on the solid solubility of Sr and Mg in $LaGaO_3$. In both ternary systems, the solid solubility of Sr substituting for La and that of Mg substituting for Ga, respectively, is rather small. However, when Sr and Mg are present simultaneously, the solid solubility of Sr and Mg in $LaGaO_3$ increases significantly. In addition, several phases of the quaternary system exhibit a pronounced variation of their La:Sr ratio and a high solid solubility of Mg, as for example $LaSrGa_3O_7$ and $LaSrGaO_4$. The structure $LaGaO_3$ containing Sr and Mg has been determined to be orthorhombic, space group *Pbnm*, $a = 5.53443$ Å, $b = 5.49523$ Å, and $c = 7.78320$ Å. In the quaternary system, extended four phase regions exist between $LaGaO_3$, MgO and the La–Sr–Ga–O compounds. Quaternary phases were not observed.

Tristrontium digallate, $Sr_3Ga_4O_9$, is triclinic, space group $P1_c$ ($a = 6.7490$ Å, $b = 8.0494$ Å, $c = 9.7295$ Å, $\alpha = 85.01(2)$o, $\beta = 72.71(2)$o, $\gamma = 74.24(2)$o, $V = 485.7$ Å^3, $Z = 2$, $D_{calc} = 4.69$ g/cm^3). The compound belongs to the group of tetrahedral single-layer structures. Individual sheets are parallel to (100), thus producing a prominent cleavage. The stepped layers can be described as being built by the condensation of six tetrahedra-wide bands. The bands in turn consist of two open-branched Dreier single chains connected via common corners and they contain tertiary and quaternary tetrahedra Q^3 and Q^4 in the ratio 1:1. The stacking of the layers containing four-, six- and eight-membered rings results in a three-dimensional structure in which the strontium cations reside in the voids between the layers and are coordinated by six to seven oxygen neighbors. The structure is shown in the following Fig. 6.155.

$Sr_3Ga_4O_9$ belongs to the group of tetrahedral single-layer structures. Individual sheets containing GaO_4 tetrahedra extend along (100). The main building unit of the layers are chains of corner-connected tetrahedra that can be classified as open-branched Dreier single chains. These chains run parallel to [010] (see Fig. 6.156a).

Therefore, the translation period along the direction of the chains is about 8.1 Å. Condensation of two neighboring chains, which are related by inversion centers, produces a six tetrahedra-wide band, see Fig. 6.156b.

This ribbon is characterized by the presence of four- and six-membered rings of corner-connected tetrahedra.

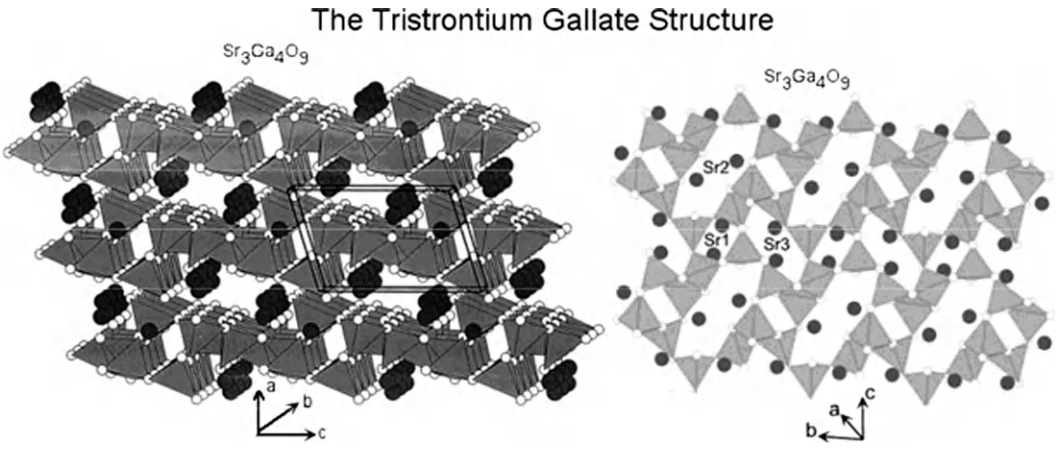

FIGURE 6.155

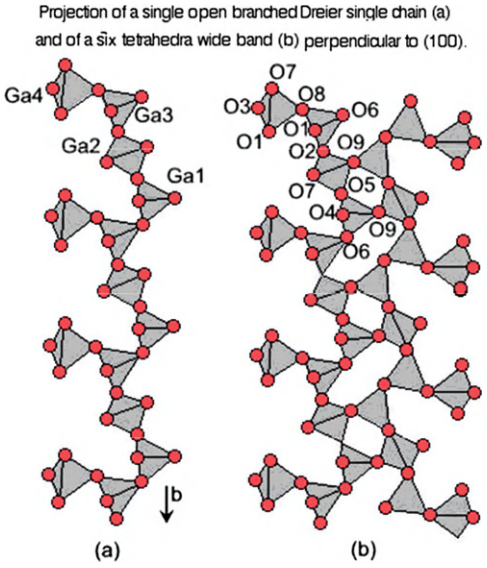

FIGURE 6.156

Further condensation of the bands via the bridging oxygen atoms O1 and O7 results in the stepped sheets mentioned above. Three of the four crystallographically different Ga tetrahedra provide linkage between the neighboring bands: Ga2, Ga3 and Ga4. The Ga2- and Ga3 sites belong to the linear part of the chain whereas Ga4 represents the branched tetrahedron. The tetrahedron around Ga1 is only connected to tetrahedra within the same band. At the interface between two adjacent bands, puckered eight-membered rings are formed containing four tetrahedra of each ribbon.

In a study of **tetrastrontium gallate**, crystal growth experiments yielded single crystals of $Sr_4Ga_2O_7$. This compound is monoclinic, space group $P1c1$, $a = 13.0822$ Å, $b = 15.7967$ Å, $c = 15.8586$ Å, $\beta = 90.643°$, $Z = 16$. The crystals showed twinning by pseudo-merohedry. Furthermore, the diffraction data exhibited the typical features of a superstructure. $Sr_4Ga_2O_7$ can be classified as a mixed anion gallate comprising insular $[GaO_4]$ groups and $[Ga_3O_{10}]$ trimers. Both anion groups are located in layers perpendicular to [100]. There are 32 symmetrically independent Sr cations that cross-link between the tetrahedral anion groups. Alternatively, the compound can be described as a 3-4-4 superstructure of ABO_3 perovskite, with 22.2% vacancies in the oxygen sublattice. The relationship with perovskite can be expressed in the following crystal chemical formula: $Sr(Ga_{2/3}Sr_{1/3})(O_{7/9\text{-}2/9})_3$. A discussion of the structure in the context with other similar defect perovskites is presented.

Decastrontium trigallate, $Sr_{10}Ga_6O_{19}$, occurs in two similar but distinct modifications: a monoclinic as well as an orthorhombic phase. Both compounds are based on noncyclic tetrahedral $[Ga_6O_{19}]$ units. From a structural point of view, the two polymorphs differ with respect to the conformation of these groups as well as their packing. The crystal structures of $Sr_{10}Ga_6O_{19}$, have been characterized using XRD techniques. The structure was determined from a single-crystal diffraction data set. Two phase transitions were identified: (1) between 453 and 503 K, the incommensurate superstructure is replaced by a doubling of the a and b lattice constant, and (2) between 503 and 673 K, a phase with the basic cell is formed, identical to α-$Sr_{10}Ga_6O_{19}$. The compound is monoclinic with space group $C12/c1$ ($a = 34.973$ Å, $b = 7.934$ Å, $c = 15.943$ Å, $\beta = 103.55°$, $V = 4300.7$ Å^3, $Z = 8$, D_{calc}=4.94 g/cm^3) and can be classified as an oligogallate (Fig. 6.157).

It is the first example of an inorganic compound where six $[GaO_4]$ tetrahedra of only one chemical species occupy the tetrahedral centers that are linked via bridging oxygen atoms to form $[Ga_6O_{19}]$ groups. The hexamers are not linear, but are highly puckered. Eleven symmetrically different Sr cations located in planes parallel to (100) cross-link between the oligo groups. They are coordinated by six to eight oxygen ligands.

The early phase diagram studies of the system SrO–Ga_2O_3 do not show a phase of the composition $Sr_{10}Ga_6O_{19}$. The diagram published by Kobzareva et al. contains three phases which are close to $Sr_{10}Ga_6O_{19}$: they are listed as (I) $Sr_4Ga_2O_7$ (20 mol% Ga_2O_3), (II) $Sr_7Ga_4O_{13}$ (22.2 mol% Ga_2O_3) and (III) $Sr_3Ga_2O_6$ (25 mol% Ga_2O_3). The structures of I and III have been resolved. As already mentioned by Kobzareva et al., the structures show a perovskite-related subcell. Phase II has not been determined yet, which leaves room for speculation as to whether it exists at all.

Crystal data are included in the following Table 6.46.

The composition of $Sr_{10}Ga_6O_{19}$ (23.1 mol% Ga_2O_3) is very close to the proposed phase of $Sr_7Ga_4O_{13}$. Possibly, decastrontium hexagallate was misinterpreted as heptastrontium tetragallate. The same assumption was made in a more recent work. However, we cannot exclude that both of them are stable phases. Including the results of this work, at least four polymorphs are known for $Sr_{10}Ga_6O_{19}$: α and β[5] as well as the presented superstructures.

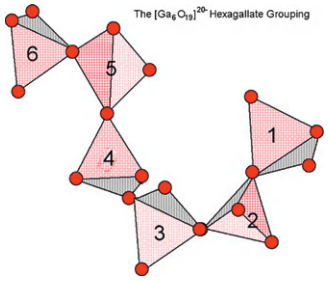

FIGURE 6.157

TABLE 6.46

Chemical formula	α-$Sr_{10}Ga_6O_{19}$	$Sr_{10}Ga_6O_{19}$
Molecular weight	271.847 g/mol	271.847 g/mol
Space group	C2 = c(0βO)	C2 = c
a (Å)	34.9145	35.0481
b (Å)	7.9369	7.9732
c (Å)	15.9450	16.0077
β	103.551°	103.492°
V (Å^3)	4287.5	4349.8

In another study, the crystal structure of $Sr_{10}Ga_6O_{19}$ was investigated by in situ single-crystal XRD in the temperature range 298–673 K. At ambient conditions, the compound shows a (3 + 1)-dimensional modulated structure in the superspace group $C2/c(00)s0$ [a = 34.9145 Å, b = 7.9369 Å, c = 15.9150 Å and = 103.551°] with a modulation wave vector of $\mathbf{q} = 0.4288\ (2)\mathbf{b}^*$. Whereas the presented structural model uses first-order harmonic modulation functions only, some features of the modulations are discussed utilizing an electron density derived by the maximum entropy method. Furthermore, two phase transitions were identified: between 453 and 503 K, the incommensurate superstructure is replaced by a doubling of the a and b lattice constants, and between 503 and 673 K, a phase with the basic cell is formed, identical to α-$Sr_{10}Ga_6O_{19}$. Under some cooling conditions, crystals showing a combined diffraction pattern of both superstructures can be obtained.

Mono-strontium hexagallate, $SrGa_{12}O_{19}$, is triclinic with cell parameters of: a = 5.794 Å, b = 5.794 Å, c = 22.816°, α = 90°, β = 90°, γ = 120°, V = 663.3 Å^3, $D_{(calc)}$ = 6.15 g/cc, Z = 2. The structure is unique in that it is composed of a network of $Ga_6O_{18}^{-2}$ units charge compensated by a single Sr^{2+} cation (Fig. 6.158).

These units are arranged in a triclinic pattern. Two directions along the lattice axes are shown. Structures of magnetoplumbite-type crystals $SrGa_{12}O_{19}$ (M = Al, Fe, Ga) have been refined by the single-crystal XRD method. The space group is $P6_3/mmc$ with Z = 2. The cell dimensions are a = 5.7929 Å and c = 22.8123 Å for $SrGa_{12}O_{19}$ at 22 °C. Four structural models were tested with respect to the states of gallium atoms at trigonal bipyramidal sites: central atom and split atom models with and without anharmonic thermal vibrations. The simple split atom model gave lower R_w values than the central atom model with anharmonic thermal vibrations $SrGa_{12}O_{19}$, whereas it gave an R_w value approximately equal to that given by the central atom model with anharmonic vibration for $SrFe_{12}O_{19}$. The present study suggested that the potential around the Ga atom with trigonal bipyramidal coordination has double minima in all the magnetoplumbite-type crystals at lower temperatures.

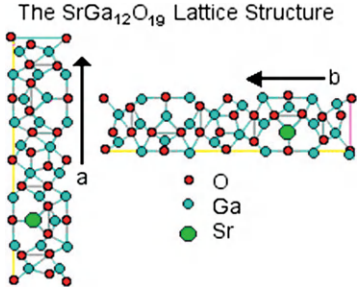

FIGURE 6.158

Hepta-strontium digallate, $Sr_7Ga_4O_9$, has no homologues in the other alkaline earth gallates. It is difficult to prepare and the SSR of the oxides takes >45 h to form a stable compound. However, if the tristrontium gallate is reacted with the tetragallate, the reaction proceeds rapidly:

$$7SrO + 2Ga_2O_3 \Rightarrow Sr_7Ga_4O_{13}\ (46\ h\ at\ 1100\ ^\circ C)$$

$$Sr_4Ga_2O_7 + Sr_3Ga_2O_6 \Rightarrow Sr_7Ga_4O_{13}\ (1.0\ h\ at\ 950\ ^\circ C)$$

It is for this reason that this compound has not been studied as extensively as the other strontium gallates and its structure remains unknown.

A number of red-emitting phosphors have been developed, based upon various strontium gallates for use as electroluminescent (EL) display materials. Bright red EL has been obtained in amorphous and crystalline alkaline earth gallates doped with Eu^{3+}. Powder targets of compositions, $Sr_4Ga_2O_7$, $Sr_7Ga_4O_{13}$, $Sr_3Ga_2O_6$, $Sr_3Ga_4O_9$, $SrGa_4O_7$, $SrGa_{12}O_{19}$, doped with 1–2% Eu, were RF magnetron sputtered onto $BaTiO_3$ substrates. Both annealed and as-deposited films yielded bright EL emission in the red part of the visible spectrum with peaks characteristic of the Eu^{3+} ion. Relative outputs of EL emission are shown as follows:

Compound	fL at 400 VDC
$Sr_4Ga_2O_7$ =	40.0
$Sr_7Ga_4O_{13}$ =	15.0
$Sr_3Ga_2O_6$ =	80.0
$Sr_3Ga_4O_9$ =	0.0 (45.0 at 650 VDC)
$SrGa_4O_7$ =	17.0
$SrGa_{12}O_{19}$ =	0.0 (6.5 at 500 VDC)

Strontium gallates have no CAS number and are not offered for sale commercially.

Barium Gallates

The system, $BaO \cdot Ga_2O_3$, forms at least three compounds—the $4BaO \cdot Ga_2O_3 = Ba_4Ga_2O_7$, $3BaO \cdot Ga_2O_3 = Ba_3Ga_2O_6$, and $BaO \cdot Ga_2O_3 = BaGa_2O_4$ compositions. The SSR is:

$$xBaO + yGa_2O_3 \Rightarrow Ba_xGa_{2y}O_{3y+x}$$

This system is subject to oxygen deficiencies so that the formula,

$$Ba_xGa_{2y}O_{(3y+x)-\delta}$$

sometimes applies. The phase diagram of $BaO–Ga_2O_3$ has not been published and is not available in the current technical literature.

Barium monogallate, $BaGa_2O_4$, belongs to the group of stuffed tetrahedral framework structures AB_2O_4 (A = Ca, Sr, Ba; B = Al, Ga), which are known to show interesting ferroelectric properties and a great variety of different polymorphic forms. They consist of a three-dimensional framework of corner-sharing BO_4 tetrahedra, the cavities of which are filled with alkaline earth metal atoms. $BaGa_2O_4$ is known to have at least four polymorphs, three of which (β-, γ- and δ-phases) are ferroelectric because of the symmetry properties. The paraelectric α-phase is reported to be stable above the ferroelectric–paraelectric phase transition temperature of 770 °C. The three polymorphs of $BaGa_2O_4$ (α-, β- and δ-phases) have a hexagonal structure and one (δ-phase) has a monoclinic structure.

Polymorphism in barium gallate, $BaGa_2O_4$, was studied using electron diffraction and HREM. Three modifications of $BaGa_2O_4$ with structures closely related to the high-temperature γ-form were observed. The phase transitions from α-$BaGa_2O_4$ ($a_\gamma = 18.6143$ Å $= \sqrt{2}\sqrt{3}a$, $c_\gamma = 8.6544$ Å $= c_\alpha$, S.G. $P6_3$) to β-$BaGa_2O_4$ ($\mathbf{a}_\beta = 2\mathbf{a}_\alpha$, $\mathbf{c}_\alpha = \mathbf{c}_\alpha$, S.G. $P6_3$) and to the new δ-polymorph having a monoclinic structure ($\mathbf{a}_\delta = \mathbf{c}_\alpha$, $\mathbf{b}_\delta = 2\mathbf{a}_\alpha + \mathbf{b}_\alpha$, $\mathbf{c}_\delta = 2\mathbf{b}_\alpha$ and $\beta = 92°$, S.G. $P2_1/c$) were induced by electron beam irradiation. HREM observations allow one to establish the close similarity between the structures of δ-$BaGa_2O_4$ and β-$SrGa_2O_4$. The γ ⇒ β and β ⇒ δ transitions involve a rearrangement of oxygen atoms in the BaO layers together with a tilting distortion of the tetrahedral framework. The microstructure of the δ-phase is characterized by the presence of numerous translation and orientation domains. The structure is shown in Fig. 6.159.

This structure is isotypic with the other alkaline earth monogallates, except for the unit-cell dimensions. However, $BaGa_2O_4$ and $SrGa_2O_4$ do not form solid solutions. If these compounds are heated together, they form an entirely different structure from the SSR:

$$BaGa_2O_4 + SrGa_2O_4 + \text{heat} \Rightarrow BaSrGa_4O_8$$

The structure is entirely different from either of the components, as shown in the diagram presented on the next page. A Rietveld refinement of the $BaSrGa_4O_8$ reveals that GaO_4 tetrahedra form the six-membered rings with sharing corners and the Ba and Sr atoms lie at the large cavities of the six-membered rings. The structure has space group $P6_3$ (No. 173) with cell parameters $a = 9.196$ Å, $c = 8.6465$ Å. One of the positions of O atoms splits to the O4 and O5 sites (Fig. 6.160).

In these projections, there are two layers of connected tetrahedra that form the six-membered rings.

In another study, crystals of barium monogallate were obtained by growth from a stoichiometric melt at 1350 °C. The hexagonal crystals belong to space group $P6_3$, $a = 18.6403$ Å and $c = 8.6801$ Å, $V = 2611.9$ Å^3, $Z = 24$, $D_{calc.} = 5.20$ g/cm^3. The structure was solved by Patterson techniques using a single-crystal diffraction data set. Merohedral twinning of the crystal (twin element $2_{[110]}$) was accounted for in the refinement calculations. The main structural features of $BaGa_2O_4$ are layers of six-membered rings of GaO_4 tetrahedra perpendicular to the *c*-axis. The stacking of the layers parallel to *c* results in a three-dimensional framework containing tunnels, where the barium cations are located. Within a single layer, two different types of ditrigonal-shaped six-membered rings are

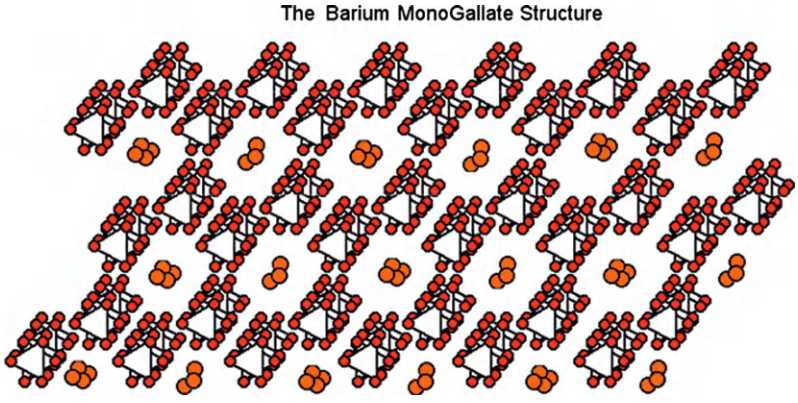

FIGURE 6.159

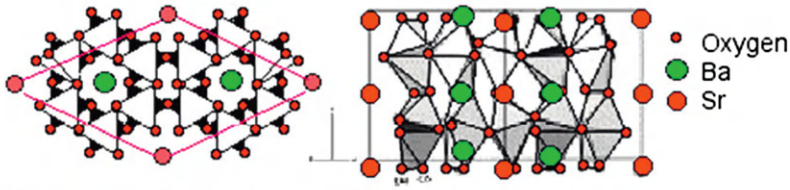

(a) [001] projection of the structure of $BaSrGa_4O_8$. (b) [110] projection of the structure of $BaSrGa_4O_8$

FIGURE 6.160

distinguished on the basis of relative orientation of up (U) and down (D) pointing apices of adjacent tetrahedra: one-fourth of the rings have an UDUDUD topology, whereas the sequences of directedness of the remaining rings is UUUDDD. The structure is isotypic with $KAlGeO_4$. It is the first member of this structure family containing exclusively trivalent tetrahedral ions of only one chemical species and divalent nonframework cations within the channels.

Differential thermal analysis and high-temperature single-crystal diffraction of monobarium gallate indicate that there is a reversible paraelectric–ferroelectric phase transition at about $T_c = 770$ °C. The crystal structure of the previously unknown paraelectric high-temperature modification α-$BaGa_2O_4$ was solved from a single-crystal data set collected at 800 °C. The compound is isotypic with β-$BaAl_2O_4$ and closely related with hexagonal high-Kalsilite, adopting a space group $P6_322$ ($a = 5.3925$, $c = 8.9739$ Å, $V = 226.0$ Å^3, $Z = 2$, $D_{calc} = 5.01$ g/cm^3). The main building elements of the structure are GaO_4^{5-}tetrahedra which are corner linked to form sheets normal to the *c*-axis. These layers are in turn connected to build up a three-dimensional framework enclosing cavities that are occupied by Ba^{2+}. The bridging oxygen atoms between the layers are statistically distributed over three positions displaced 0.56 Å from the ideal position on the threefold axis. The off-centering reduces the Ga–O–Ga bond angle from an energetically unfavorable 180 to 145.0°. Within a single layer of the high-temperature phase, the tetrahedra are arranged in six-membered rings with an UDUDUD conformation. A different framework topology is found in the low-temperature modification β-$BaGa_2O_4$ which is based on two different ring configurations, UUUDDD and UDUDUD. Due to the differences between the sequences of upward and downward pointing tetrahedra in both phases, the α–β transformation is a first-order transition showing a pronounced thermal hysteresis between heating and cooling. The transition is also reflected in the evolution of the lattice parameters where significant discontinuities are observed at T_c.

Dibarium gallate, $Ba_2Ga_2O_5$, apparently does not exist. There are no references to this substance in the available literature and no structure determinations, if it exists at all, have been made. In contrast, distrontium has been prepared and used as a "sintering aid" in lowering the temperature of densification required in the preparation of intermediate temperature solid oxide fuel cells. The possibility that the dibarium gallate has a lower melting point than that of the strontium analog makes it a promising candidate for the sealing and densification of many ceramic devices.

Single crystals of **tribarium gallate** ($Ba_3Ga_2O_6$) have been synthesized from a melt with composition 70 mol % BaO and 30 mol.% Ga_2O_3 in the temperature range between 1200 and 1400 °C. The compound adopts space group *Pa* with $a = 16.746(9)$ Å and $Z = 24$ formula units per unit cell. $Ba_3Ga_2O_6$ belongs to the group of cyclogallates and is closely related to $K_4SrGe_3O_9$. Main building elements are isolated, highly puckered, 12-membered rings built by $[GaO_4]^{5-}$ tetrahedra. Charge balance is achieved by incorporation of Ba ions in the voids between the rings. The coordination number of the alkaline earth atoms is six, eight and nine, respectively.

Preparation of a $Ba_3Ga_2O_6$ powder and its sintering characteristics were investigated in Ar or air. This sintered body with perovskite-related structure was synthesized by reaction sintering, using mixed powders in the atomic ratios of Ba/Ga = 1.5. The order–disorder transition temperatures of the $Ba_3Ga_2O_6$-sintered bodies was 1230 °C. By comparison to other sintered compositional bodies, it was found that the order–disorder transition temperatures were influenced by the ionic radius of cations in B sites, and the transition temperatures decreased with increasing ionic radius.

Tribarium gallate has been investigated as a solid-state ionic conductor for use in high-temperature fuel cells. Oxide ion conductivity of Ga-based perovskite-type oxides, $LnGaO_3$ (Ln = Nd, La) and its related oxide, $A_3Ga_2O_6$ (A = Ba and Sr) was investigated. Oxide ion transference number t_{ion} is almost 1.0 for $Ba_3Ga_2O_6$. However, electrical conductivity of this system of oxides was lower than log σS/cm of −3 of the doped perovskite-type oxide of $NdGaO_3$ and $LaGaO_3$, due to the low solubility of the aliovalent cations. The latter compounds exhibited a high electrical conductivity and the transference number of oxide ion was higher

than 0.9 in the oxygen partial pressure range from $P_{O2} = 1$ to 10 atm. In particular, Ca and Mg doped $NdGaO_3$, exhibited a high oxide ion conductivity similar to the $LaGaO_3$-based oxide.

Single crystals of **tetrabarium gallate**, $Ba_4Ga_2O_7$, were obtained by growth from a melt at 1500 °C. The compound is monoclinic, with cell parameters $a = 17.7447$ Å, $b = 10.6719$ Å, $c = 7.2828$ Å, $\beta = 98.962°$, $V = 1362.3$ Å^3. The diffraction pattern shows systematic absences corresponding to the space group $P12_1/c1$. The structure was solved by direct methods followed by Fourier syntheses. The chemical composition derived from structure solution is $Ba_4Ga_2O_7$, with a unit-cell content of $Z = 6$. Main building units of the structure are GaO_4 tetrahedra sharing one oxygen atom to form Ga_2O_7 groups. The Ga–O–Ga bridging angle of one of the two symmetrically independent groups is linear by symmetry. The dimers are cross-linked by barium cations coordinated by six to eight oxygen ligands.

Single crystals of **barium hexagallate**, $BaGa_{12}O_{19}$, have been grown in a Na_2O–Ga_2O_3 flux. The compound is hexagonal: $a = 5.859$ Å, $c = 23.192$ Å. The crystal structure was determined by single-crystal X-ray reflection data and refined to a final R-value of 0.018. The structure was revealed to be of β-alumina type, with a formula $Ba_{0.65}Ga_{10.80}O_{16.84}$ ($BaGa_{16.7}O_{26}$), and not of magnetoplumbite type as it was conventionally considered. The Ba^{2+} ion is located only in a 6h site, near the Beevers-Ross one. The charge compensation mechanism is that of gallium vacancies in the tetrahedra of the middle of the spinel block instead of that of Frenkel defects. In another study, the following unit-cell parameters were derived. Single-crystal X-ray analysis verified preparation of an ideal magnetoplumbite-type phase in the ternary barium hexagallate system. X-ray refinement was carried out by the full-matrix least squares on F^2 method. Microanalysis data yielded a composition of $Ba_{1.07}Ga_{11.95}O_{19}$. The crystal chemistries of the barium hexagallate and barium hexaaluminate systems were compared and discussed. Crystal data for $BaGa_{12}O_{19}$: $M = 1277.98$, space group $P6_3/mmc$ (No.194), $a = 5.8140$ Å, $c = 23.038$ Å, $V = 674.4$ Å^3, $Z = 2$, $D_{calc} = 6.293$ g/cm^3.

An X-ray-induced F^+ center was used as a paramagnetic probe to study sintered powders of barium hexaaluminates phases I and II (referred to as Ba(ϕ_I) and Ba(ϕ_{II})) and mixed barium-lanthanum hexaaluminate (referred to as BLA). This F^+ center was previously shown to exist only in β-alumina-type mirror planes containing interstitial oxygen ions as charge-compensating defects, so that its study yields information about the local structure of this type of mirror plane. By comparison of the EPR spectra of Ba(ϕ_I) and Ba(ϕ_{II}), it is shown that the latter contains only one type of F^+ center with a reduced hf interaction. This indicates that there is only one type of mirror plane containing interstitial oxygen in Ba(ϕ_{II}) and that the separation between spinel blocks is larger in Ba(ϕ_{II}) than in Ba(ϕ_I). This result agrees with models proposed by other authors for barium-lead hexaaluminate and barium hexagallate. Investigation of the F^+ center in mixed barium-lanthanum hexaaluminate ceramics clearly supports the hypothesis of segregation of Ba^{2+} ions in β-alumina-type mirror planes. It is also shown that the structure of these planes is very similar to that of Ba(ϕ_{II}) defect planes.

Crystallographic data of aluminate and gallate β-aluminas and magnetoplumbites are reviewed. For the $XAl_{11}O_{17}$ and $XGa_{11}O_{17}$ compounds (X = Ba, Sr, Ca), c/a increases as the cationic size increases. The magnetoplumbites have c/a values ranging between 3.915 and 3.954 with the exception of $BaAl_{12}O_{19}$ and $BaGa_{12}O_{19}$. These compounds seem to have strongly distorted magnetoplumbite-derived structures. Upon activation of the $MeAl_{12}O_{19}$ (Me = Ca, Sr or Ba) lattices with Eu^{2+} and Ce^{3+}, the luminescence properties of Ba-containing compounds deviate from the other compounds. This seems to be due to different coordinations of the activator ions. Substitution of Mg^{2+} for Al^{3+} in magnetoplumbite phases results in the case of $SrAl_2O_{19}$ in changes of the c/a ratio, of diffraction intensities and of the luminescence properties. The various data suggest a close similarity of this type of phases and $BaAl_{12}O_{19}$. In the $MeGa_{12}O_{19}$ series (Me = Sr or Ba), the quantum efficiency of $BaGa_{12}O_{19}$: Mn^{2+} was found to be anomalously low.

$BaAl_{12}O_{19}$–$BaAl_2O_4$ doped with Eu^{2+}, Cr^{3+} and ($Eu^{2+} + Cr^{3+}$) were prepared by SSR. The spectra of $BaAl_{12}O_{19}$–$BaAl_2O_4$:Eu^{2+}:Cr^{3+} shows that the f ⇒ d emission bands from Eu^{2+} are centered at 442 and 495 nm and the Cr^{3+} yields the emission lines at 694 and 700 nm. Photoluminescence study demonstrates that the red photoluminescence and energy transfer occurs only in the phase of $BaAl_{12}O_{19}$ not $BaAl_2O_4$ though the samples are mixed phases. The fluorescence lifetime measurements indicate efficient energy transfer from Eu^{2+} to Cr^{3+} in $BaAl_{12}O_{19}$: Eu^{2+}, Cr^{3+}. The energy transfer rate and efficiency are calculated. The results show that the energy transfer rate and efficiency increase following the increase in Cr^{3+} concentration.

Dibarium trigallate, $Ba_2Ga_6O_{11}$, has been investigated as a phosphor for fluorescent lamps. When activated by both Eu^{2+} and Cr^{3+}, it emits both deep-red and blue-green emission bands as shown in the following diagram. When combined with a green-emitting phosphor, a "white" lamp was obtained (Fig. 6.161).

Barium gallates do not have an assigned CAS number and are not offered for sale commercially.

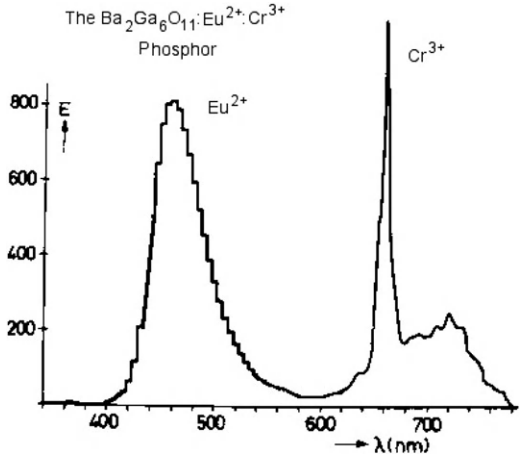

FIGURE 6.161

Radium Gallates

The scientific literature is lacking in any references to radium gallates. Perhaps this is due to the intense radioactivity of the isomer ^{226}Ra but is more likely due to lack of interest of those in industry who may have usage of such compounds. It is anticipated that various radium gallates could be prepared, using the same methods as those developed for the barium gallate series of compounds. Thus, one would expect to be able to obtain:

$RaO \cdot Al_2O_3$,
$3RaO \cdot Al_2O_3$,
$RaO \cdot 6Al_2O_3$,
$2RaO \cdot Al_2O_3$.

However, there is no record of such syntheses in the literature.

6.6. ALKALINE EARTH INDIUM-COMPOUNDS

Indium has but one valence state—In^{3+}. As such, indium is too electropositive and forms a limited number of "indates", i.e. $In_xO_{3x}^{2x-}$. One example is $MgIn_2O_4$ which is a 1:1 compound. For the most part, In^{3+} tends to form cationic species rather than anionic ones. These indium-containing compounds are more like "solid-solutions" in which InO_3^{2-} has a degree of electronegative character. In the case of the alkaline earths, the number of compounds formed goes from zero to five. That is the $MO–In_2O_3$ system forms shown in Table 6.47.

TABLE 6.47

Cation	Be	Mg	Ca	Sr	Ba
# of Cpds	0	1	1	2	5

Additionally, forms a series of "indides" as separate crystalline compounds, M_xIn_y, where x and y can vary from 1 to as many as 28 in the unit cell.

6.6.1. Alkaline Earth Indides

The term "indides" is not used generally in the scientific literature but indicates a binary compound of indium metal with certain alkaline earth metals.

Beryllium Indides

Beryllium does not form any compounds with In metal as shown in the following phase Fig. 6.162.

Indium metal melts at 157 °C and forms an alloy if the two metals are "ball milled" together at room temperature. The room-temperature form of Be (Be_{rt}) appears and is stable at all compositions until 1270 °C where the high-temperature form (Be_{rt}) appears. The latter melts at 1285 °C to form two separate liquids, L_{Be} and L_{In}.

No alloy of Be–In has found usage in industry because of lack of interesting properties other than the appearance of liquid indium combined with particles of Be metal. No CAS number has been assigned.

Magnesium Indides

Magnesium metal forms several compounds with In metal as may be seen in the following phase Fig. 6.163.

The crystal parameters are shown in the following Table 6.48.

For the most part, Mg and In form solid solutions of a specific composition with each other. The melting points of the compositions, like $Mg_{0.1}In_{0.9}$, varies according to its indium content. It has been found that the direct transition of one phase (called β_1) to another phase (called β' phase), as the Mg/In atom ratio is varied, is prevented by the two-phase regions of the whole composition range. The location of the unstable Mg_5In_3 phase, called β_3, has been finally established in

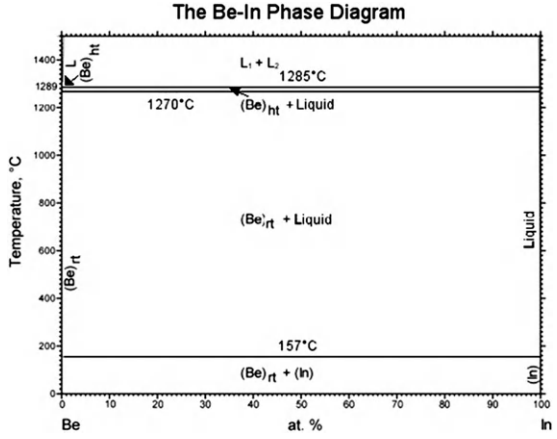

FIGURE 6.162

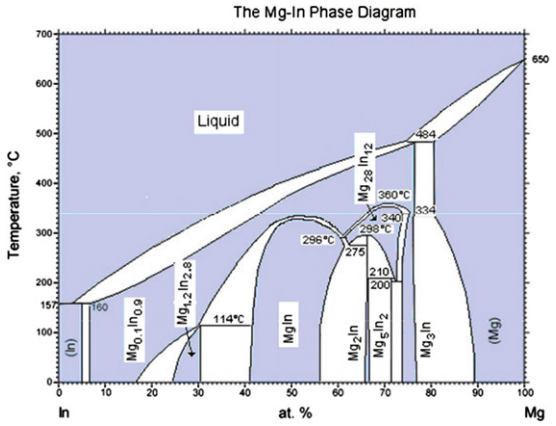

FIGURE 6.163

the phase diagram. β_3-phase is stable only below 210 °C and decomposes into β′ and β_2 phases above this temperature. In addition to this, Mg_3In changes its structure from an ordered 12R symmetry to a disordered f.c.c. structure through an ordered 3R symmetry as the temperature increases. The transformation energy associated with the change in the stacking sequence (12R ⇒3R) and that associated with the order–disorder phase change has been estimated to be ~120 cal/mol and ~340 cal/mol, respectively. Thus, the phase diagram presented above is accurate to the limits of estimation of the phase changes that occur with temperature at any given mole-ratio of Mg/In. These factors account for the departure of the Mg–In phase diagram from the standard phase diagrams of other binary metal systems.

The equilibrium phase diagram of the indium–magnesium system in the range up to 40 atom% Mg has been established by XRD and thermal analysis. The solid solubility of magnesium in indium does not exceed about 5 atom%. An intermediate solid solution, β_1, with a face-centered cubic structure exists over a wide range of composition. An ordered phase, β′, with the superstructure of Cu_3Au type, is formed near 28 atom% Mg at temperatures below 114 °C.

These compounds are not stable and have found little usage in industry. The corrosion process of InMg alloy and the conversion of corrosion products by annealing in vacuum have been investigated by X-ray powder diffraction and energy-dispersive spectroscopy methods. The crystalline indium phase and an amorphous phase with a composition corresponding to the formula of the mineral perovskite ($Mg(OH)_2MgCO_3 \cdot 0.5H_2O$) were found as corrosion products. Their further conversion during annealing in vacuum at various temperatures was examined. Nevertheless, the crystal structure of the various Mg–In compounds have been thoroughly examined.

Dimagnesium indide, Mg_2In, has the unit-cell parameters of: $a = 3.42$ Å, $b = 8.27$ Å, $c = 8.27$ Å, $\alpha = 120°$, $\beta = 90°$, $\gamma = 90°$, cell volume = 202.57 Å^3. The structure can be represented by Fig. 6.164.

The two types of In atoms are shown. In2 is in the center of the unit cell at (1/3, 2/3, 13) and is connected to all of the Mg atoms.

The location of the atoms in the unit cell is shown in Table 6.49.

Mg_2In crystallizes in the orthorhombic space group Pnma ($Z = 4$; Co_2Si-type structure). This indide, Mg_2In, has the lattice parameters of: $a = 7.275$, $b = 5.371$, $c = 9.990$ Å, $Z = 4$, $R1 = 0.0252$). It was synthesized from stoichiometric melts of the elements. The crystal structure exhibits isolated In atoms coordinated by seven to 10 alkaline earth atoms. The electronic structures of the less elaborate compound, Mg_2In, was discussed in comparison with those of the closely related, nominally electron precise Zintl compounds Ca_2Sn and Sr_5Sn_3.

Trimagnesium indide, Mg_3In, has the cell parameters of: $a = 6.323$ Å, $b = 6.323$ Å, $c = 10.9781$ Å, $\alpha = 73.263°$, $\beta = 73.263°$, $\gamma = 60°$, cell volume = 258.47 Å^3. The structure can be represented as shown in Fig. 6.165.

A unit cell is composed of the unit seen in the "*c*-direction" view. As shown in the "diagonal vsiew" part of the diagram, these 18-atom units

TABLE 6.48

Compound	Crystal type	Pearson	Space group	Melting point, °C	Physical properties
(In)	In	tI2	I4/mmm	157	—
$Mg_{0.04}In_{0.96}$	Cu	cF4	Fm-3m	Varies	No data
$Mg_{1.2}In_{2.8}$ (Mg_6In_{14})	Cu3Au	cP4	$P6_3/mmc$	114	No data
MgIn	CuAu	tP2	P·62m	Varies	No data
Mg_2In	Mg_2In	hP9	Ibam	298	No data
Mg_3In	Mg_3In	hR48	P4/mmm	484	No data
Mg_5In_2	Mg_5Ga_2	oI28	R·3m	210	No data
(Mg)	Mg	hP2	Pm·3m	651	Search

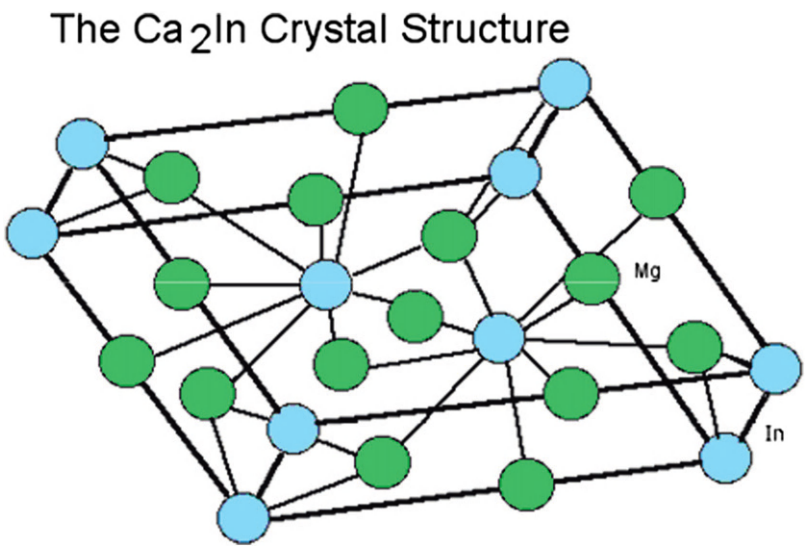

FIGURE 6.164

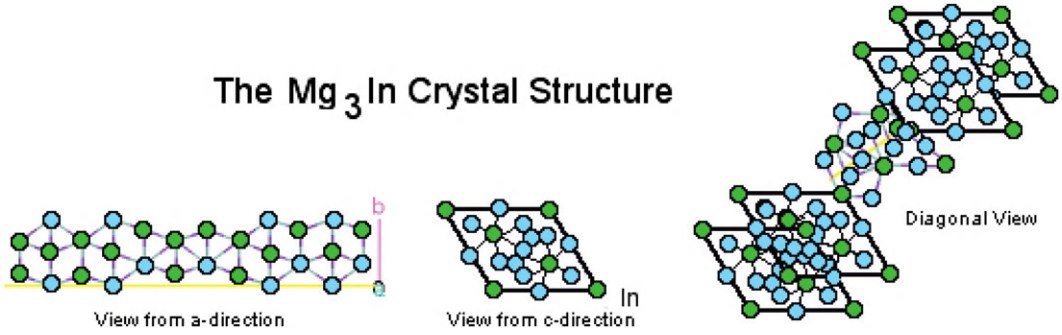

FIGURE 6.165

form two connected units at each end of the lattice, separated by an eight-unit configuration. The location of the atoms in the lattice structure is shown in Table 6.50.

The volume of the primitive cell of Mg_3In increases when pressure is applied. Samples of the alloy Mg_3In were annealed at 200–250 °C in the Bridgman anvil-type press under pressures between 20 and 100 kbar.

TABLE 6.49

No	Site notation	Atom	Multiplicity	Wyckoff	Site symmetry	*x*	*y*	*z*	Occupancy
1	Mg1	Mg	3	g	m2m	0.25	0	1/2	1.0
2	Mg2	Mg	3	f	m2m	0.59	0	0	1.0
3	In2	In	2	d	-6..	1/3	2/3	1/2	1.0
4	In1	In	1	a	-62m	0	0	0	1.0

TABLE 6.50

No	Site notation	Atom	Multiplicity	Wyckoff	Site symmetry	*x*	*y*	*z*	Occupancy
1	Mg1	Mg	18	h	.m	0.5	0.5	0.125	1.0
2	Mg2	Mg	18	h	.m	0.5	0.5	0.29167	1.0
3	In1	In	6	c	3m	0	0	0.125	1.0
4	In2	In	6	c	3m	0	0	0.29167	1.0

TABLE 6.51

No	Site notation	Atom	Multiplicity	Wyckoff	Site symmetry	*x*	*y*	*z*	Occupancy
1	Mg1	Mg	8	j	..m	0.155	0.423	0	1.0
2	In1	In	8	j	..m	0.255	0.122	0	1.0
3	Mg2	Mg	8	g	.2.	0	0.24	1/4	1.0
4	Mg3	Mg	4	a	222	0	0	1/4	1.0

TABLE 6.52

No	Site notation	Atom	Multiplicity	Wyckoff	Site symmetry	*x*	*y*	*z*	Occupancy
1	Mg	0.86Mg + 0.14In	1	d	4/mmm	1/2	1/2	1/2	1.0
2	In	In	1	a	4/mmm	0	0	0	1.0

After being quenched to ambient pressure and temperature, the crystal structure was studied by XRD. The number of close-packed layers in one repeating unit of the alloy structure is 12 with the stacking sequence (3) 3 when annealed under the atmospheric pressure, but at 20, 35 and 55 kbar it increases to 18 with the sequence (31)3, and at 75 and 100 kbar a 24-layered structure with the sequence (311)3 has been found to form. The pressure-induced change in the layer-stacking sequence in Mg3In is similar to the change with the decrease in the electron-atom ratio previously observed for the ternary alloys $Mg_3(In_{1-x},Cd_x)$. The change is about 13.7%.

Pentamagnesium tri-indide, Mg_5In_3, has the crystal cell parameters of: $a = 6.19$ Å, $b = 7.36$ Å, $c = 8.59$ Å, $\alpha = 115.374°$, $\beta = 111.125°$, $\gamma = 90°$, cell volume = 324.15 Å^3. The structure can be represented by Fig. 6.166.

The locations of the various atoms in the lattice are shown in Table 6.51.

This structure is tetragonal in nature. Mg_5In_3 is not stable above 210 °C and no literature describing its physical properties (other than structure) is available in the literature.

Magnesium indide, MgIn, has the unit-cell parameters of: $a = 3.2555$ Å, $b = 3.2555$ Å, $c = 4.413$ Å, $\alpha = \beta = \gamma = 90°$, cell volume = 46.77 Å^3. The structure is body-centered cubic (Fig. 6.167).

The locations of the individual atoms are shown in Table 6.52.

A pressure dependence of the lattice parameters of MgIn having the tetragonal Ll_0-type structure has been measured by an XRD method using a diamond anvil-type squeezer up to 14 GPa. The rate of decrease in the *a* parameter is larger than that of the *c* parameter and, consequently, the axial ratio increases from the value 0.957 at atmospheric pressure to 0.97 at about 8 GPa. On further increasing pressure, however, it remains almost constant. Change in the volume can be described by a Birch–Murnaghan equation with an initial bulk modulus of 38 GPa. Experimental results were discussed taking into account the theory of lattice stability of alloys developed by Mrosan, John and Eschrig.

Magnesium tri-indide, $MgIn_3$, has cell parameters of: $a = 4.589$ Å, $b = 4.589$ Å, $c = 4.589$ Å, $\alpha = \beta = \gamma = 90°$, cell volume = 96.64 Å^3. The structure is face-centered cubic (Fig. 6.168).

The locations of the atoms in this structure are shown in Table 6.53.

The **composition**, $Mg_{0.04}In_{0.96}$, has the cell parameters of: $a = 3.2718$ Å, $b = 3.2718$ Å, $c = 3.3498$ Å, $\alpha = 119.233°$,

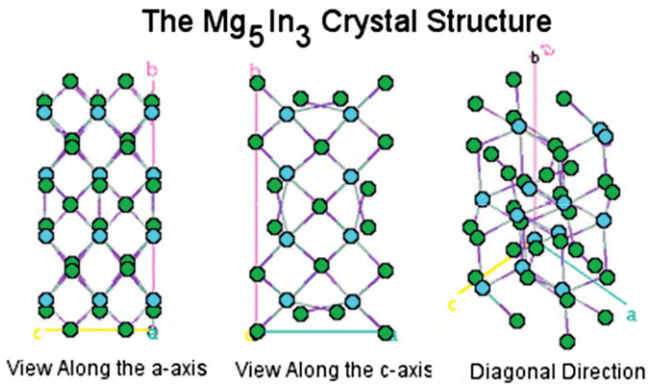

FIGURE 6.166

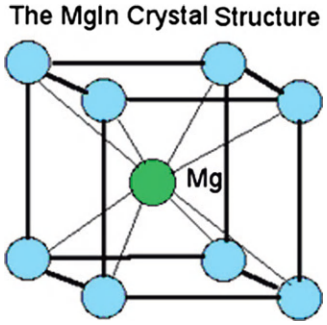

FIGURE 6.167

TABLE 6.53

No	Site notation	Atom	Multiplicity	Wyckoff	Site symmetry	*x*	*y*	*z*	Occupancy
1	In	In	3	c	4/mm.m	0	1/2	1/2	1.0
2	Mg	Mg	1	a	m-3m	0	0	0	1.0

$\beta = 119.233°$, $\gamma = 90°$, cell volume = 25.93 Å^3. The structure may be represented by the following, where a hypothetical view is presented. Nevertheless, the structure is not that of solid indium metal but is a specific structure when Mg metal is allowed to diffuse into In. The **composition**, $Mg_{0.928}In_{0.072}$, has a similar structure with cell parameters of: $a = 3.2003$ Å, $b = 3.2003$ Å, $c = 5.2128$ Å, $\alpha = 90°$, $\beta = 90$ °, $\gamma = 120°$, cell volume = 46.24 Å^3 (Fig. 6.169).

The substitution of Mg for In can be random in this face-centered lattice up to about $Mg_{0.75}In_{0.25}$ which had the lattice parameters of: $a = 3.1912$ Å, $b = 3.1912$ Å, $c = 3.1912$ Å, $\alpha = 60°$, $\beta = 60°$, $\gamma = 60°$, cell volume = 22.98 Å^3. The structure can be illustrated as shown in Fig. 6.170.

This behavior is a singular aspect of the Mg–In crystal system.

The occupation of the atoms in such structures is given in the following Table 6.54.

Calcium Indides

Calcium forms at least three compounds with In metal as may be seen in the following phase Fig. 6.171.

Crystal parameters are shown in Table 6.55.

Calcium diIndide, $CaIn_2$, is known to crystallize in the orthorhombic space group Pnma ($Z = 4$; Co_2Si-type structure). The structure is shown in Fig. 6.172.

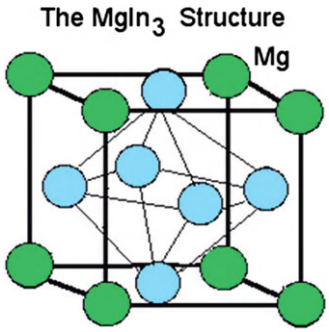

FIGURE 6.168

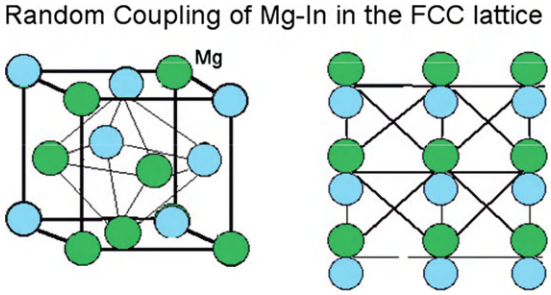

FIGURE 6.170

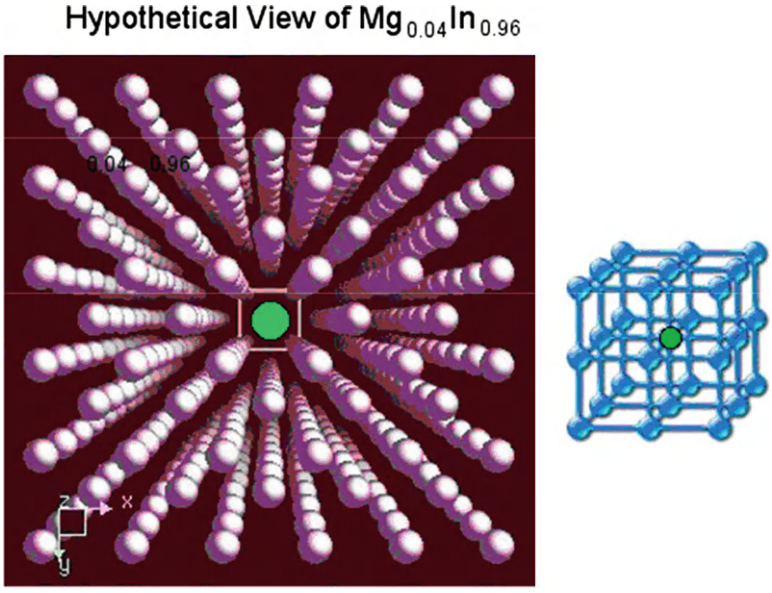

FIGURE 6.169

TABLE 6.54

No	Site notation	Atom	Multiplicity	Wyckoff	Site symmetry	x	y	z	Occupancy
1	Mg	0.75Mg + 0.25In	4	a	m-3m	0	0	0	1.0

TABLE 6.55

Compound	Crystal type	Pearson	Space group	Melting point, °C	Physical properties
(Ca) rt	Cu	cF4	225	443	No data
(Ca) ht	W	cI2	229	842	No data
CaIn	$(Ag_{0.75}In_{0.25})La$	cP2	Pm-3m	895	No data
$CaIn_2$	$CaIn_2$	hP6	$P6_3/mmc$	835	No data
Ca_8In_3	Ca_8In_3	aP22	P-1	765	No data
(In)	In	tI2	139	157	No data

The crystal structures of the known di-indides $A^{II}In_2$ (A^{II} = Ca/Sr: hexagonal, space group $P6_3/mmc$, $a = 4.892/5.009$, $c = 7.739/8.03.6$ Å, $Z = 2$, $R1 = 0.0254/0.0277$, $CaGa_2$ type; A^{II} = Ba: orthorhombic, space group *Imma*, $a = 5.220$, $b = 8.504$, $c = 8.520$ Å, $Z = 4$, $R1 = 0.0265$, KHg_2 type) contain three-dimensional indium tetrahedral networks. In accordance with their interpretation as classical Zintl compounds, the calculated density of states show pseudo band gaps. Among the tetraindides, only $BaIn_4$ (tetragonal, space group $I4/mmm$, $a = 4.970$, $c = 11.983$ Å, $Z = 2$, $R1 = 0.0187$, $BaAl_4$ type) can be explained with the extended Zintl concept. The electron-deficient isotypic alkaline metal indides, KIn_4 and $RbIn_4$ ($a = 4.928$, $c = 12.575$ Å, $R1 = 0.0289$) show the structural consequences of the depopulation of the highest occupied states.

$CaIn_2$ has also observed to have the tetragonal structure with cell parameters of: $a = 4.895$ Å, $b = 4.895$ Å, $c = 7.75$ Å, $\alpha = 90°$, $\beta = 90°$, $\gamma = 120°$, cell volume = 160.82 $Å^3$ (Fig. 6.173).

The site occupancy is shown in Table 6.56.

Additionally, the binary alkaline earth-rich indide compound, **dicalcium indide**, Ca_2In, has the Co_2Si structure type that is orthorhombic, space group Pnma, with $a = 7.275$ Å, $b = 5.371$ Å, $c = 9.990$ Å, $Z = 4$,

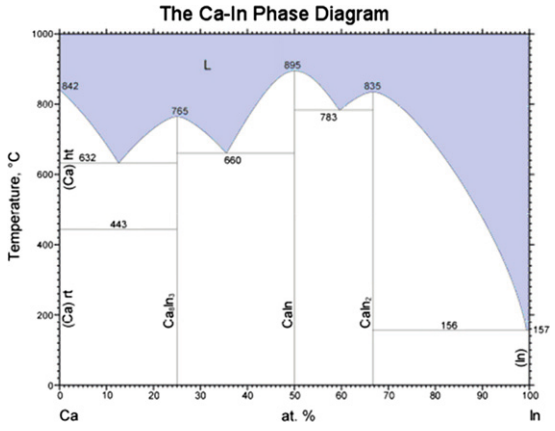

FIGURE 6.171

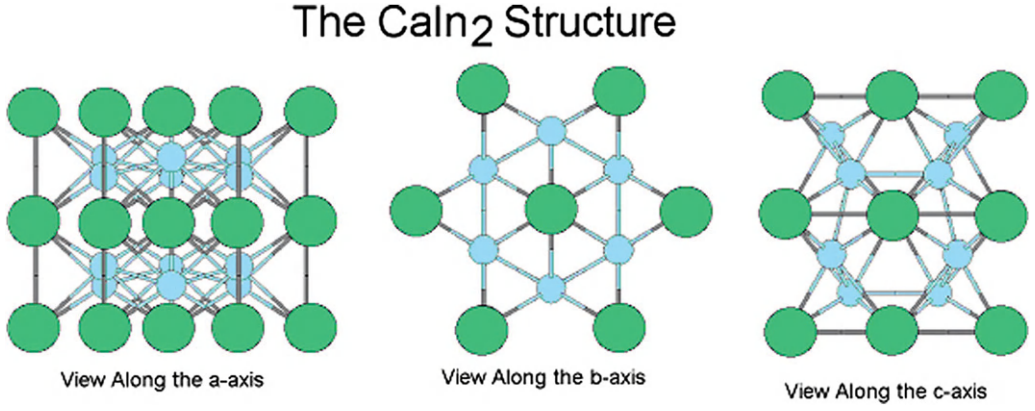

FIGURE 6.172

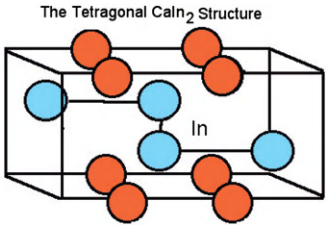

FIGURE 6.173

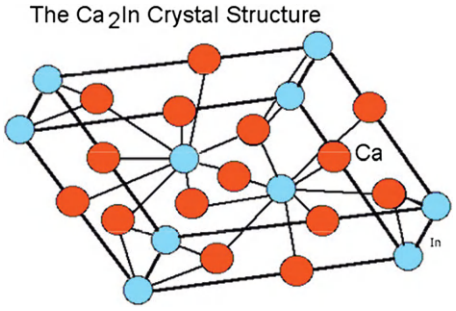

FIGURE 6.174

$R1 = 0.0252$. The structure may be represented as shown in Fig. 6.174.

The coördinates in the lattice are shown in Table 6.57.

Octa-**calcium tri-Indide**, Ca_8In_3, has the triclinic structure with cell parameters of: $a = 9.606$ Å, $b = 9.712$ Å, $c = 9.782$ Å, $\alpha = 99.01°$, $\beta = 101.15°$, $\gamma = 119.6°$, cell volume $= 742.74$ Å^3. The structure can be represented by Fig. 6.175.

The site occupancy is shown in Table 6.58.

The Ca_8In_3 structure is derived by distortion of the face-centered cubic type-like BiF_3. It can be described as a three-layered structure along the *a*-axis, the atoms being located at (0, 1/3, 2/3). Three different coördination polyhedra are found around the In atoms: distorted cubicoahedra (10 vertex polyhedra) for In1, In2, In4,and In6, cubes for In3, and icosahedra for In5. Distorted cubicohedra centered by In at $x = 0$ and $x = 1/3$ are alternately joined by an edge and by a face to form parallel rows. Cubes and icosahedra centered by In at $x = 2/3$ are joined by an edge and also form parallel rows.

Calcium mono-indide, CaIn, has the cell parameters of: $a = 0.3.8191$ nm, $b = 0.3.8191$ nm, $c = 0.3.8991$ nm, $\alpha = \beta = \gamma = 90°$, cell volume $= 55.70$ Å^3. The structure is tetragonal (Fig. 6.176).

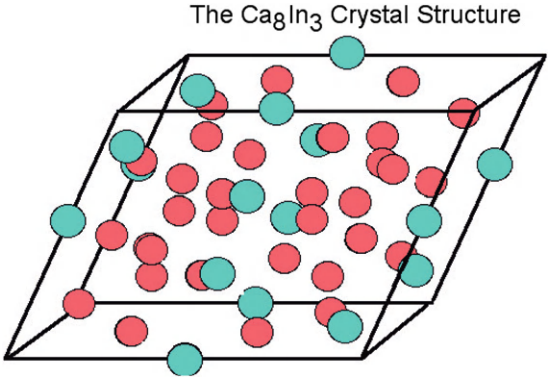

FIGURE 6.175

The mono-indides, AIn, of Ca, Sr and Ba crystallize with three different new structure types: In CaIn (tetragonal, space group $I4/mmm$, $a = 7.37$, $c = 8.40.1$ Å, $Z = 8$, $R1 = 0.0825$), isolated squares of In_4 are present. In contrast, SrIn (orthorhombic, space group $Fdd2$, $a = 10.23$, $b = 26.14$, $c = 8.40$ Å, $Z = 32$, $R1 = 0.1185$) and

TABLE 6.56

No	Site notation	Atom	Multiplicity	Wyckoff	Site symmetry	*x*	*y*	*z*	Occupancy
1	In1	In	4	f	3m.	1/3	2/3	0.045	1.0
2	Ca1	Ca	2	b	-6m2	0	0	1/4	1.0

TABLE 6.57

Atom lattice coordinates			
Atom	***a***	***b***	***c***
Ca	0.00000000	0.00000000	0.25000000
Ca	0.00000000	0.00000000	0.75000000
In	0.33333333	0.66666667	0.04500000
In	0.66666667	0.33333333	−0.04500000
In	0.33333333	0.66666667	0.45500000
In	0.66666667	0.33333333	0.54500000

TABLE 6.58

No	Site notation	Atom	Multiplicity	Wyckoff	Site symmetry	x	y	z	Occupancy
1	Ca3,4	Ca	2	i	1	0.0310	0.2013	0.6507	1.0
2	Ca11,15	Ca	2	i	1	0.0433	0.2101	0.2980	1.0
3	In2,6	In	2	i	1	0.1761	0.3402	0.0272	1.0
4	Ca2,6	Ca	2	i	1	0.2013	0.0002	0.1098	1.0
5	Ca12,16	Ca	2	i	1	0.2744	0.6531	0.2998	1.0
6	In1,4	In	2	i	1	0.3269	0.1621	0.4999	1.0
7	Ca13,14	Ca	2	i	1	0.5425	0.4390	0.3301	1.0
8	Ca1,8	Ca	2	i	1	0.5787	0.7291	0.1078	1.0
9	Ca5,10	Ca	2	i	1	0.6201	0.0981	0.3521	1.0
10	Ca7,9	Ca	2	i	1	0.8339	0.3783	0.1094	1.0
11	In5	In	1	g	-1	0	1/2	1/2	1.0
12	In3	In	1	d	-1	1/2	0	0	1.0

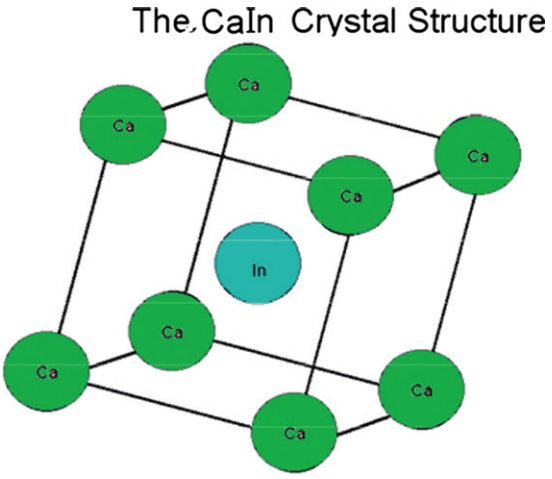

FIGURE 6.176

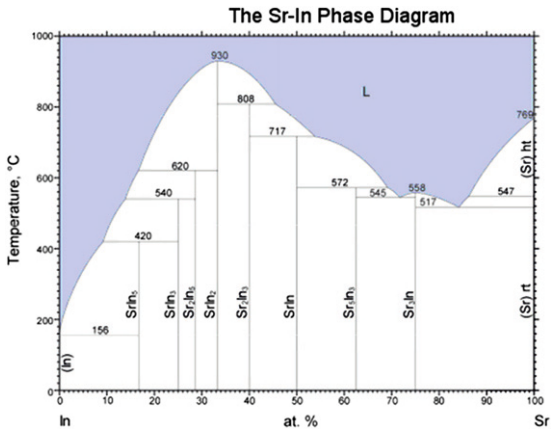

FIGURE 6.177

BaIn (orthorhombic, space group *Cmcm*, $a = 8.158$, $b = 12.481$, $c = 5.578$ Å, $Z = 8$, $R1 = 0.0623$) show—in accordance with the Zintl counting rules—three-bonded In^{2-} atoms, which are connected to form layers (SrIn) and ladders (BaIn), respectively. Both compounds can be structurally regarded as reduced $BaIn_2$, their total density of states like those of the diindide, exhibit pseudo band gaps.

Calcium indides are not very stable in the air or in moisture and are not used.

Commercially, no CAS numbers have been issued for any of them.

Strontium Indides

Strontium forms a number of compounds with In metal as may be seen in Fig. 6.177.

The crystal parameters are shown in Table 6.59.

Eight compounds are shown in the phase diagram but only six are listed in the structural diagrams. The two lists may be compared (Table 6.60).

In one paper, the binary system strontium–indium was investigated using thermal, metallographic and X-ray analysis. The compounds Sr_3In, Sr_3In_2, SrIn, Sr_2In_3, $SrIn_2$, $SrIn_3$, $SrIn_5$ were found. However, the existence of Sr_2In_5 is doubtful and it has not been discussed in the scientific literature.

Strontium indide, SrIn, has the cell parameters of: $a = 3.8191$ Å, $b = 3.8191$ Å, $c = 3.8191$ Å, $\alpha = \beta = \gamma = 90°$, cell volume $= 56.75$ Å^3. The structure is a body-centered cubic lattice (Fig. 6.178).

Site occupancy in this structure is given in the following Table 6.61.

SrIn has found little usage in industry and is regarded as a novelty compound.

TABLE 6.59

Compound	Crystal type	Pearson	Space group	Melting point, °C	Physical properties
$Sr_{28}In_{11}$	$Ca_{28}In_{11}$	o178	Imm2	—	No data
Sr_5In_3	Cr_5B_3	tI32	I4/mcm	572	No data
SrIn	SrIn	oF64	Fdd2	717	No data
$SrIn_2$	$CaIn_2$	hP6	$P6_3/mmc$	930	No data
$SrIn_3$	Mg_3Cd	hP8	$P6_3/mmc$	540	No data
$SrIn_5$	$CaCu_5$	hP6	P6/mmm	420	No data

TABLE 6.60

Phase diagram	Structural diagrams
—	$Sr_{28}In_{11}$
$SrIn_5$	$SrIn_5$
$SrIn_3$	$SrIn_3$
Sr_2In_5	No data
$SrIn_2$	$SrIn_2$
Sr_2In_3	No data
SrIn	SrIn
Sr_5In_3	Sr_5In_3
Sr_3In	No data

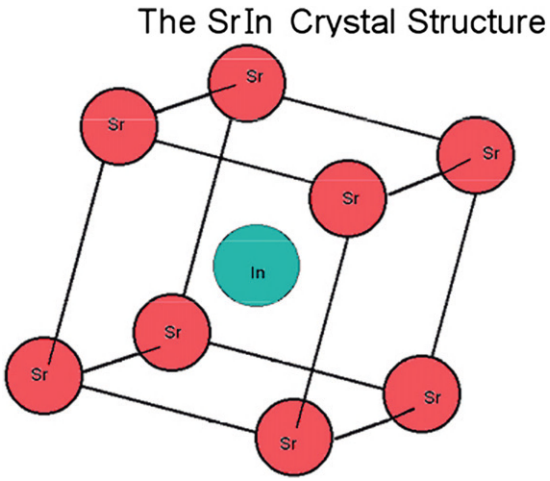

FIGURE 6.178

Strontium di-indide, $SrIn_2$, has the cell parameters of: $a = 5.001$ Å, $b = 5.001$ Å, $c = 8.021$ nm, $\alpha = 90°$, $\beta = 90°$, $\gamma = 120°$, cell volume $= 173.66$ Å^3, $Z = 2$. The structure can be illustrated as shown in Fig. 6.179.

Here, the In atoms adopt a "chair pattern". The site occupation is shown in Table 6.62.

$SrIn_2$, has the $CaIn_2$ structure. In $SrIn_2$, the In-bond distances are increased to 2.98 Å (3) and 3.30 Å. As the cation radius increases from Ca^{2+} (0.99 Å) to Sr^{2+} (1.12 Å), the long In–In bond in the net expands from 3.13 Å ($CaIn_2$) to 3.30 Å ($SrIn_2$). Therefore, one can

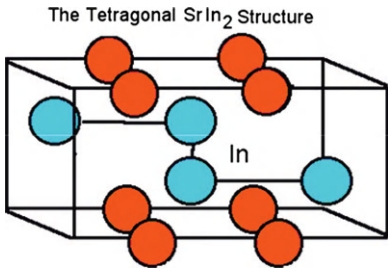

FIGURE 6.179

TABLE 6.61

No	Site notation	Atom	Multiplicity	Wyckoff	Site symmetry	x	y	z	Occupancy
1	In	In	1	b	m-3m	1/2	1/2	1/2	1.0
2	Ca	Ca	1	a	m-3m	0	0	0	1.0

TABLE 6.62

No	Site notation	Atom	Multiplicity	Wyckoff	Site symmetry	x	y	z	Occupancy
1	In	In	4	f	3m.	1/3	2/3	0.046	1.0
2	Sr	Sr	2	b	-6m2	0	0	1/4	1.0

TABLE 6.63

No	Site notation	Atom	Multiplicity	Wyckoff	Site symmetry	x	y	z	Occupancy
1	In1	In	6	h	mm2	0.16667	0.33333	1/4	1.0
2	Sr1	Sr	2	d	-6m2	1/3	2/3	3/4	1.0

TABLE 6.64

No	Site notation	Atom	Multiplicity	Wyckoff	Site symmetry	x	y	z	Occupancy
1	In2	In	3	g	mmm	1/2	0	1/2	1.0
2	In1	In	2	c	-6m2	1/3	2/3	0	1.0
3	Sr	Sr	1	a	6/mmm	0	0	0	1.0

TABLE 6.65

No	Site notation	Atom	Multiplicity	Wyckoff	Site symmetry	x	y	z	Occupancy
1	Sr1	Sr	16	l	..m	0.166	0.666	0.15	1.0
2	In1	In	8	h	m.2m	0.625	0.125	0	1.0
3	Sr2	Sr	4	c	4/m..	0	0	0	1.0
4	In2	In	4	a	422	0	0	1/4	1.0

estimate (taking $Ba^{2+} = 1.34$ Å) a value of at least 3.40 Å for the long bond distance of $BaIn_2$ in the $CaIn_2$ type of structure. This bond distance is too long for a In–In single bond and $BaIn_2$ apparently does not form.

Strontium tri-indide, $SrIn_3$, has the cell parameters of: $a = 5.481$ Å, $b = 6.769$ Å, $c = 6.769$ Å, $\alpha = 120°$, $\beta = 90°$, $\beta = 90°$, cell volume $= 217.49$ Å^3, $Z = 2$. The structure may be represented as shown in Fig. 6.180.

The locations of the atoms in the lattice is shown in Table 6.63.

Strontium penta-indide, has the cell parameters of: $a = 4.827$ Å, $b = 5.937$ Å, $c = 5.937$ Å, $\alpha = 120°$, $\beta = 90°$, $\gamma = 90°$, cell volume $= 147.35$ Å^3, $Z = 2$. The structure can be represented as shown in Fig. 6.181.

Site occupancy in this structure is shown in Table 6.64.

Penta-strontium tri-indide, Sr_5In_3, has the cell parameters of: $a = 8.738$ Å, $b = 8.738$ Å, $c = 10.284$ Å, $\alpha = 115.14°$, $\beta = 115.14°$, $\gamma = 90°$, cell volume $= 627.69$ Å^3. The structure has the form shown in Fig. 6.182.

Site occupancy in this structure is shown in Table 6.65.

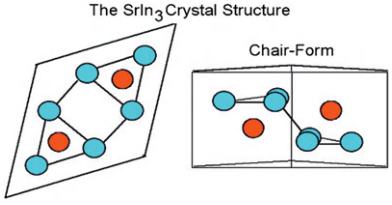

FIGURE 6.180

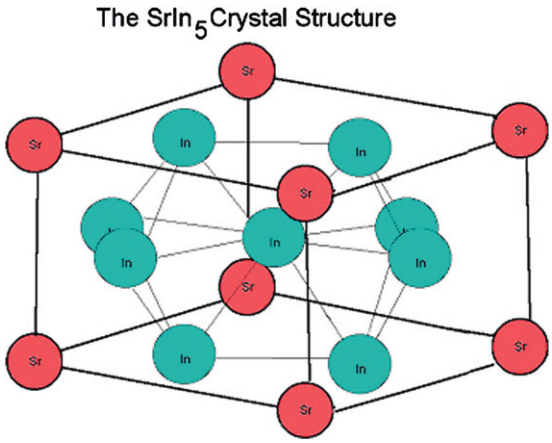

FIGURE 6.181

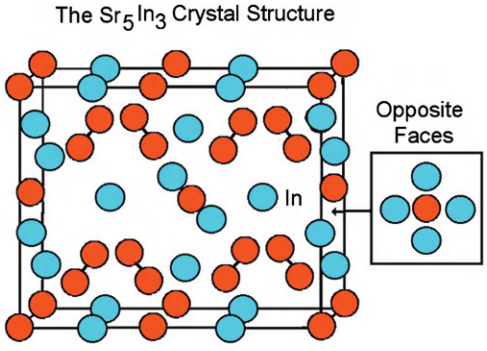

FIGURE 6.182

In the crystal structure of Sr_5In_3 (tetragonal, space group 14/mcm, $a = 8.744$, $c = 16.429$ Å, $Z = 4$, $R1 = 0.0347$, Cr^5B^3 structure type), isolated In atoms coexist with In_2 dumbbells exhibiting short In–In contacts (2.844 Å). The electronic structures of the less elaborate compounds Ca^2In and Sr^5In^3 are discussed in comparison with those of the closely related, nominally electron precise Zintl compounds Ca^2Sn and Sr_5Sn_3.

Octadodeca-strontium undeca-indide, $Sr_{28}In_{11}$, crystallizes in the ortho-rhombic space group Imm2 ($Z = 24$). The cell parameters are: $a = 8.36$ Å, $b = 8.36$ Å, $c = 8.36$ Å, $\alpha = 90°$, $\beta = 90°$, $\gamma = 90°$, cell volume = 581.28 Å^3.

Another paper found that the binary alkaline earth-rich indide, $Sr_{28}In_{11}$, has the orthorhombic, space group Imm2, with $a = 5.826$ Å, $b = 66.878$ Å, $c = 8.235$ Å, $Z = 2$, $R1 = 0.0571$. It was said to have the $Ca^{28}Ga^{11}$ structure type when synthesized from stoichiometric melts of the elements. The crystal structure displays isolated In atoms coordinated by seven to 10 alkaline earth atoms. The compound exhibits a complex three-dimensional network built of four- and five-bonded indium atoms in fused and interbonded pentagons that sandwich the strontium atoms. Both electronic band structure calculations and property measurements show that the compound is metallic. A detailed band structure analysis indicates that the compound is hypoelectronic with a one-electron deficiency, but the In–In bonding is effectively optimized in the structure.

Binary alkaline earth (A^{II}) triclides, **undeca-Ae hepta-indides**, $Ca_{11}Ga_7$ and $Sr_{11}In_7$ have been stated to crystallize with a singular structure type (cubic, space group, $a = 16.02$ Å ($A^{II} = Ca$) and 17.06 Å ($A^{II} = Sr$), $Z = 8$). They were synthesized from stoichiometric mixtures of the elements and characterized by single-crystal XRD. The structures exhibit isolated $A^{II}(1)$ atoms with B(2) atoms = In, together with tetrahedral units $[B(2)]_4$, which are formed by the triel elements exclusively. Remarkably, one of the four crystallographically independent A^{II} positions is—as in the pure element—coordinated by A^{II} partners in a cuboctahedral arrangement. The stabilities and phase ranges of the compounds, which are influenced by geometric and electronic factors (investigated by FP-LAPW band structure calculations), are discussed.

The binary compound, **tri-strontium undeca-indide**, Sr_3In_{11}, was synthesized and structurally characterized by XRD experiments. It crystallizes in the orthorhombic La_3Al_{11} structure type (space group Immm, $Z = 2$; $a = 4.9257$, $b = 14.247$, $c = 11.212$ Å).

The crystal structure of Sr_3In_{11} bears features of the monoclinic $EuIn_4$ structure, which is adopted by $SrIn_4$, and the prominent tetragonal $BaAl_4$ structure, as shown in the Fig. 6.183.

Two types of Sr atoms ($Sr_{I\ and\ II}$) are shown as well as three types of In atoms ($In_{I,II\ and\ III}$) in the structure. Sr_3In_{11} is stable until 550 °C. At higher temperatures, it decomposes peritectically into $SrIn_2$ and In. Structural stability and bonding properties of Sr_3In_{11} were

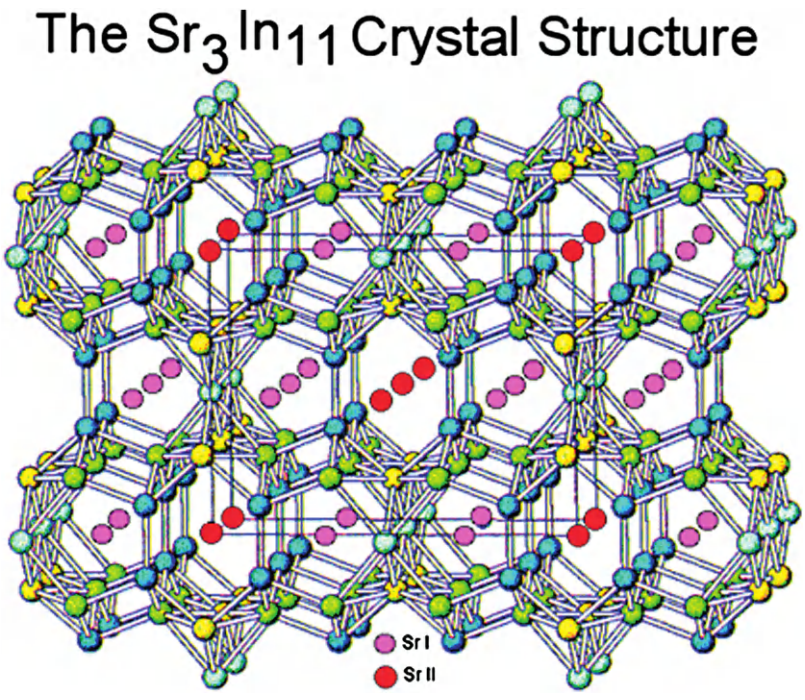

FIGURE 6.183

investigated by first-principles calculations and compared to $SrIn_4$ in the monoclinic $EuIn_4$ and the tetragonal $BaAl_4$ structure. All three structures consist of a three-dimensional, polyanionic, network formed by In atoms and Sr cations encapsulated in cages. The crystal structure of Sr_3In_{11}, isomorphous with the La_3Al_{11} structure, features two types of tunnels along the *a*-axis that are formed by indium pentagons and hexagons.

Strontium tetra-indide, $SrIn_4$, In–In network bonding is perfectly optimized. In contrast, the networks of $EuIn_4$-type $SrIn_4$ and Sr_3In_{11} appear hypo- and hyperelectronic, respectively. The formation of Sr_3In_{11} with a composition close to 1:4 and the nonexistence of $BaAl_4$-type $SrIn_4$ is explained by a delicate interplay of size and electronic factors governing structural stability in the In-rich part of the Sr–In system.

In the **tri-strontium penta-indide** structure, Sr_3In_5 (Cmcm), 4- and 2-bonded indium atoms in a 4:1 ratio form a three-dimensional classical network that encapsulates strontium atoms in its narrow channels. The electrical conductivity of the compound shows typical metallic behavior. The detailed electronic structure analysis suggests that the electron hole is mainly localized on a nonbonding p-orbital on the 2-bonded indium atoms, and that these orbitals, stacked in a σ-type way along the *a*-axis (4.97 Å), interact only weakly with each other to form highly one-dimensional bands.

The compounds, Sr_2In_3 and Sr_3In, have not been studied in the scientific literature. Although the structures of Sr_3In_5, $SrIn_4$, $Sr_{11}In_7$, and $Sr_{28}In_{11}$ have been reported with some detail, no crystal structure diagrams are presented herein.

Strontium indides have found no usage in industry and have no CAS numbers assigned.

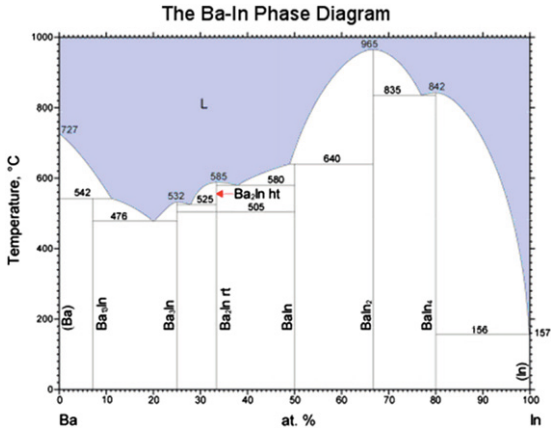

FIGURE 6.184

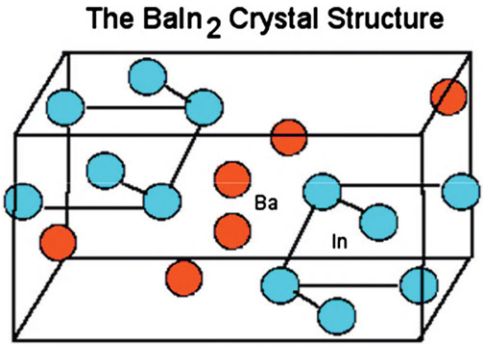

FIGURE 6.185

points of these compounds, the technical literature has few references to any of the properties of these compounds (and certainly not of their structures). Thus, the known crystal parameters are:

Compound	Number of elements	Type	Pearson symbol	Space group	Group #	Melting point, °C
$BaIn_2$	2	KHg_2	oI12	Imma	74	965
$BaIn_4$	2	$BaAl_4$	tI10	I4/mmm	139	842

Barium Indides

Barium forms a number of compounds with In metal as may be seen in the following phase Fig. 6.184.

The binary system of barium–indium has been investigated using thermal, metallographic and X-ray analysis. The six compounds, $Ba_{13}In$, Ba_3In, Ba_2In (two modifications), BaIn, $BaIn_2$ and $BaIn_4$ have been found. Note that the combinations of Ba:In atom ratios, Ba_xIn_y, vary from $x = 3$, 2, 1 (+13) (for $y = 1$) and $y = 1$, 2, 4 for $x = 1$. Although the phase diagram shows the melting

Barium di-indide, $BaIn_2$, has more than one structure. The cell parameters of one form is: $a = 5.225$ Å, $b = 6.5141$ Å, $c = 6.5141$ Å, $\alpha = 80.744°$, $\beta = 66.356°$, $\beta = 66.356°$, cell volume $= 186.05$ Å^3. One structure has the form shown in Fig. 6.185.

The cell occupancy is given in the following Table 6.66.

Barium dilndide, $BaIn_2$, also forms the $CeCu_2$ structure. Following the Zintl concept, the In ions in $BaIn_2$ are isoelectronic with group IV tin and should adopt

TABLE 6.66

No	Site notation	Atom	Multiplicity	Wyckoff	Site symmetry	x	y	z	Occupancy
1	In	In	8	h	m..	0	0.07	0.17	1.0
2	Ba	Ba	4	e	mm2	0	1/4	0.55	1.0

a four-connected structure. In contrast to R-tin, which has a cubic diamond structure, the indium ions in $BaIn_2$ build up an orthorhombic three-dimensional four-connected net containing distorted tetrahedra and ladder polymers of four-membered rings. In the $CeCu_2$ structure (space group Imma), two bond angles in these distorted tetrahedra are fixed at 90°. $BaIn_2$ abandons the $CaIn_2$ structure and favors the orthorhombic 3D4C net of the $CeCu_2$ structure. The structure has been presented as shown in Fig. 6.186.

Here, the In–In bonds are shorter than those in $SrIn_2$ ($CaIn_2$ structure): 2.97 Å (1), 3.03 Å (2), and 3.12 Å (1). However, the bond angles within the "tetrahedra" are distorted to 118.1°, 118.5°, 112.8°, and 90°. At the price of creating two 90° bond angles, relatively short In–In bonds and large cavities for the Ba^{2+} ions are formed in the four-connected net. In comparison to black phosphorus, the puckering of the indium layers in the orthorhombic 3D4C net of $BaIn_2$ is reduced. Otherwise the cavities in the net would be too small for two Ba^{2+} counter ions to be well accommodated.

The indium ions in $BaIn_2$ build up an orthorhombic three-dimensional four-connected net containing distorted tetrahedra and ladder polymers of four-membered rings. In the $CeCu_2$ structure (space group Imma), two bond angles in these distorted tetrahedra are fixed at 90°. The four-connected net in the $CeCu_2$ structure is topologically related to the layers in black phosphorus (space group Cmca). The ladder structure has the form shown in Fig. 6.187.

In CaPtSn (TiNiSi structure), the orthorhombic four-connected net is formed by $(PtSn)^{2-}$ ions in an ordered arrangement. Calculations on $BaIn_2$ and CaPtSn show that the four-connected nets are increasingly stabilized as the valence electron count is increased from 16 to 30 valence electrons per four formula units. For more

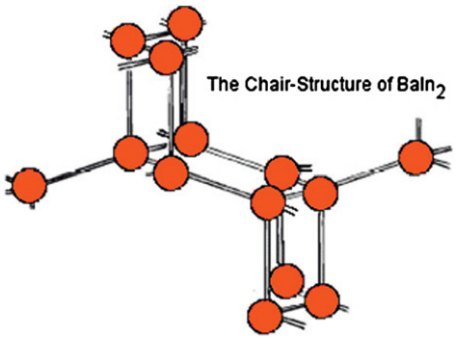

FIGURE 6.187

than 30e, the nets are destabilized due to filling of M⇒E antibonding states. Structural data obtained by precise single-crystal investigations for the TiNiSi series CaPdIn (20e), CaPdSn (24e), CaPdSb (28e), and CaAgSb (32e), confirm the results of the extended Hückel calculations. An interesting and understandable angular asymmetry of the tetrahedral sites in these ternary compounds is apparent.

Barium tetra-indide, $BaIn_4$, has the cell parameters of: $a = 0.4.93$ nm, $b = 0.4.93$ nm, $c = 0.6.896$ nm, $\alpha = 110.944°$, $\beta = 110.944°$, $\gamma = 90°$, cell volume = 144.61 $Å^3$. The structure has the form shown in Fig. 6.188.

Cell occupancy is shown in Table 6.67.

The important role of cation size in the structure choice has been noted in a comparative study of $BaIn_4$, which has the closely related $BaAl_4$-type structure in which barium atoms are sandwiched by six-membered rings.

A novel binary compound, **nona-barium tetra-indide** in the system Ba–In has been synthesized and structurally characterized. According to single-crystal XRD data, Ba_9In_4 crystallizes with the tetragonal symmetry

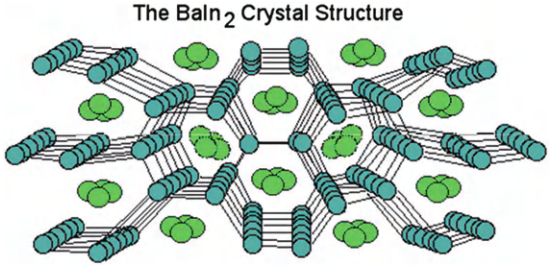

FIGURE 6.186

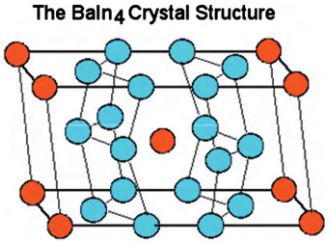

FIGURE 6.188

TABLE 6.67

No	Site notation	Atom	Multiplicity	Wyckoff	Site symmetry	x	y	z	Occupancy
1	In2	In	4	e	4mm	0	0	0.382	1.0
2	In1	In	4	d	-4m2	0	1/2	1/4	1.0
3	Ba	Ba	2	a	4/mmm	0	0	0	1.0

(I4/m, $a = 13.948$, $c = 5.888$ A°, $V = 1145.5$ Å^3, $Z = 2$, $R1 = 0.037$, w$R2 = 0.071$). This very moisture-sensitive compound could only be obtained as a single phase by reaction of metallic barium and indium at 350 °C. Thus, it was not reported in the phase diagram, as presented above.

A new indide hydride, $Ba_9[In]_4[H]$, was synthesized from the elements in stoichiometric proportions using the inherent hydrogen content of commercial elemental barium as hydrogen source. Its structure, constituting a new type, was determined using single-crystal X-ray data (tetragonal, space group $I4/m$, $a = 13.973$ Å, $c = 5.918$ Å, $Z = 2$) in sufficient quality ($R1 = 0.0261$) to allow identification and location of the hydride ion as well as the refinement of its thermal parameter. The crystal structure of $Ba_9[In]_4[H]$ exhibits isolated indium atoms, which are coordinated by 10 barium cations in a cubicosahedral arrangement. The hydride anions are octahedrally surrounded by six Ba^{2+} cations. According to $[HBa_4Ba_{2/2}]$, these octahedra are connected by opposite corners to form chains running along the *c*-axis. The presence of the hydride ion was determined by solid-state NMR spectroscopy, where the chemical shift of the ^{1}H-MAS-NMR signal of –9.0 ppm nicely corresponds to the values in BaH_2 and other metallic hydrides. As in the other binary alkaline earth indides, the band structure calculated using the frame of the FP-LAPW methods shows a pseudo band gap slightly above the Fermi level, associated with the electron-precise valence-electron count of Zintl-type (isolated In^{5-}) components. This compound was compared to other hydrides and indides, both according to the structural as well as the bonding features.

A series of ternary barium triel(M^{III})/tetrel(M^{IV})-ides have been prepared from melts of the elements. They all crystallize with the Pu_3Pd_5-type structure (orthorhombic, space group *Cmcm*) and exhibit isolated M_5 clusters of slightly distorted *nido* shape components (square pyramids). A comparable situation is found for the corresponding germanides, where 0.7 atoms of In ($Ba_3In_{0.7}Ge_{4.3}$: $a = 10.513$ Å, $b = 8.6405$ Å, $c = 10.547$ Å, $R1 = 0.0248$) or Ga ($Ba_3Ga_xGe_{5-x}$: $a = 10.351$ Å, $b = 8.615$ Å, $c = 10.368$ Å, $R1 = 0.0148$) are necessary to stabilize a Ge-rich compound of this structure type. For the stannides, the situation is somewhat different, because the binary phase Ba_3Sn_5 itself forms the Pu_3Pd_5 type. In this case, the structure type remains stable up to a Ga content of 0.5 Ga/f.u. ($Ba_3Ga_{0.5}Sn_{4.5}$: $a = 11.0041$ Å, $b = 8.9619$ Å, $c = 11.1182$ Å, $R1 = 0.0169$) and also with a substantial In content ($Ba_3In_xSn_{5-x}$: $x \approx 0.9$; $a = 11.105$ Å, $b = 9.000$ Å, $c = 11.207$ Å, $R1 = 0.0262$). As the five-atom *nido* cluster requires only 24 valence electrons per formula unit according to *Zintl* and *Wade*, an excess of electrons can be assumed for the binary tetrelides such as Ba_3Sn_5 (26 v.e./f.u.) that even the maximal amount of triel substitution 0.7 M^{III}/f.u. attained in the title compounds cannot sufficiently compensate for. An assessment of the geometric influence of varied valence electron counts however, coupled with a detailed analysis of the calculated electron densities and the partial densities of states in the energy region above the pseudo band gap at 24 v.e./f.u. clearly shows that these excess electrons populate π-bonding M-*p*/Ba-*d* states and actually contribute to a stabilization of the structure. In the range above 25.3 v.e./f.u. predominantly antibonding M-*p* states are populated, resulting in a widening of the base of the cluster.

Barium indides have not found usage in industry due to primarily their instability in the presence of moisture and air.

Radium Indides

The chemistry of radium indides should follow the solid-state chemistry of the Ca, Sr and Ba indides. However, there is absolutely no mention of such compounds in the scientific literature up to the present time.

6.6.2. Alkaline Earth Oxy-Indium Compounds

Indium has but one oxidation state, In^{3+}, and so does not form any other compounds except that of "indates".

Beryllium Indates

It would appear, at first glance, that beryllium indate could be prepared by the reaction of the oxides:

$$BeO + In_2O_3 + \text{heat} \Rightarrow BeIn_2O_4$$

However, there are no reports of the properties of this compound or of any other beryllium indate compounds. No CAS numbers exist. It is likely that the system

$BeO–In_2O_3$ has never been studied in any detail. Only one reference to $BeIn_2O_4$ is to be found, that of "Physical Properties of Adsorbants" by Marek Kosmulski (© 2001 Marcel Dekker, Inc.). This compendium is a listing of known crystallographic data. However, this compound is listed but no unit-cell data are given. Thus, the final conclusion is that $BeIn_2O_4$ does not exist per se.

Magnesium Indates

Magnesium indate can be prepared by the reaction of the oxides at 1100 °C:

$$MgO + In_2O_3 + \text{heat} \Rightarrow MgIn_2O_4$$

However, the reaction is very slow and as long as 10 days of heating is required for complete reaction of these oxides. A much better method, which has been used in general to prepare the alkaline earth indate compounds, is the so-called "combustion synthesis" (CS) method. In the CS method, the nitrates of Mg and In are mixed in proper proportion and a calculated amount of urea ($(NH_2)_2CO$) is added to the solution as a fuel. The solution is placed in a furnace at 500 °C. An exothermic reaction occurs, producing a fluffy white powder. This is then heated for 36 h at 900 °C and then reheated at 1050 °C for 36 h to form a highly crystalline material.

$MgIn_2O_4$ is a transparent conducting oxide. Such materials, due to their high transparency in the visible region of the electromagnetic spectrum and conductivity in the order of 10^2 S/cm, are candidates for a variety of technologically important devices such as liquid-crystal displays, computer monitors, iPods, iPhones, "Blackberries", etc. It has been reported that $MgIn_2O_4$ has a high electrical conductivity and is capable of higher UV transmission than indium tin oxide (ITO). It is a cubic spinel with space group Fd3m and $a = 0.8864$ Å. The spinel structure is basically constituted of closed-packed oxygen ions forming NO_4 or NO_6 polyhedra that run parallel to the (110) direction. The chains are connected to each other by cations like Mg^{2+} in tetrahedral sites. There are 64 equivalent tetrahedral cation sites and 32 octahedral sites in the unit cell. Out of these, 7/8 of the tetrahedral and 1/2 of the octahedral sites are not occupied. A $MgIn_2O_4$ film prepared by a magnetron-sputtering technique, was found to have a resistivity of 3.9×10^{-4} Ω cm. The structure of $MgIn_2O_4$ is shown in the above diagram. It consists of isolated MgO_4 tetrahedra and isolated InO_6 octahedra (Fig. 6.189).

Magnesium ions are distributed over the tetrahedral and octahedral sites of the inverted spinel structure with preferential orientation along (3,1,1) Miller plane. The possible mechanism that promotes conductivity in this system is the charge transfer between the resident divalent (Mg^{2+}) and trivalent (In^{3+}) cations in addition to the available oxygen vacancies in the lattice. A room

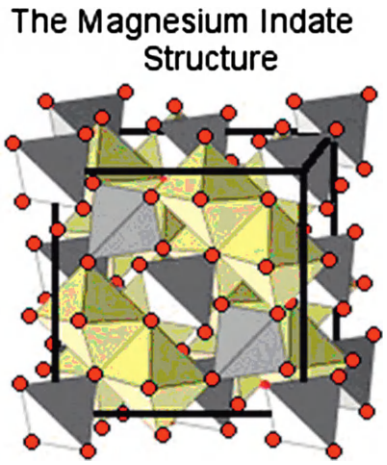

FIGURE 6.189

temperature electrical conductivity of 1.59×10^{-5} S/cm and an average optical transmittance >75% have been achieved. Hall measurements showed *n*-type conductivity with electron mobility value 0.95×10^{-2} $cm^2/V/s$ and carrier concentration $2.7 \times 10^{19}/cm^3$. Smoothness of the film surface observed through atomic force microscope measurements favors this material for gas sensing and opto-electronic device development.

$MgIn_2O_4$ has been adopted as the primary transparent material in optoelectronic device fabrication due to its high optical transparency and electrical conductivity. Such a technologically important material was prepared by the spray pyrolysis technique. Precursors prepared for the cationic ratio $Mg/In = 0.5$ were thermally sprayed onto glass substrates at 400 and 450 °C. The films were characterized by XRD, energy-dispersive absorption X-ray spectroscopy (EDAX), and atomic force microscopy. The XRD results showed the single-phase formation of the material that revealed the presence of Mg^{2+} and In^{3+} in the inverse spinel-related structure. The FTIR and EDAX results further confirmed that the nanocrystalline films were mainly composed of magnesium, indium, and oxygen, in agreement with XRD analysis. For a 423-nm thick magnesium indium oxide films grown at 400 °C, the electrical conductivity was 1.56×10^{-3} S/cm and the average optical transmittance was 63% in the visible range (400–700 nm). Similar $MgIn_2O_4$ films deposited at 450 °C have a conductivity value of 0.95×10^{-3} S/cm and an average transmittance of 75%. Hall coefficient observations showed *n*-type electrical conductivity and high-electron carrier concentration of $2.7 \times 10^{19}/cm^3$. From the diffuse reflectance spectral measurement of $MgIn_2O_4$, the band gap was found to be 4.3 eV which is higher than that of ITO. The conductivity of as-prepared sample and that of the H_2-annealed sample of $MgIn_2O_4$ was and 5.57×10^0 S/cm.

Magnesium indium oxide films ($MgIn_2O_4$), manifesting high transparency were prepared by metal organic chemical spray pyrolysis technique. Precursors prepared for various cationic ratios of $Mg/In = 0.35$, 0.40, 0.45 and 0.50 were thermally sprayed onto quartz substrates, decomposed at 450 °C and the spinel phase evolution was studied. XRD, Rutherford backscattering and X-ray photoelectron spectroscopy studies have been conducted to confirm the formation of single-phase $MgIn_2O_4$ films with Mg/In ratio 0.50. From optical transmission studies, the observed optical band gaps varied from 3.18 to 3.86 eV (321–389 nm) ($0.35 < Mg/In < 0.5$). The electrical conductivity variations of these films were measured in the temperature range between 30 and 150 °C by four-probe technique ($34.07–1.44 \times 10^{-5}$ S/cm) and the Hall coefficient showed *n*-type electrical conduction and high carrier concentration (0.16×10^{20}–$0.89 \times 10^{17}/cm^3$).

Magnesium forms a series of spinels with Al^{3+}, Ga^{3+} and In^{3+}, namely normal magnesium aluminate, $MgAl_2O_4$, half-inverse magnesium gallate, $MgGa_2O_4$, and inverse magnesium indate, $MgIn_2O_4$. The response of each of these oxides for energies of up to 10 keV for the initial knock-on event was analyzed and compared. Defect production was characterized mainly by split interstitials/crowd ions and cation antisite or disorder defects. The results show that cation interstitials preferentially occupy octahedral sites in all three materials. In the normal spinel, subcascade branching occurs and the defects at the end of the cascade are generally isolated, whereas in the half-inverse spinel, the higher energy cascades show a core damage region some of which consists of a partial rearrangement of atoms to the normal spinel structure and a partial transformation to a disordered rock salt structure. In the fully inverse spinel, a more connected region of the disordered rock salt structure with the cascade core is evident. Temperature accelerated dynamics (TAD) was used to characterize the kinetics of defects in these three spinel oxides: magnesium aluminate $MgAl_2O_4$, magnesium gallate $MgGa_2O_4$, and magnesium indate $MgIn_2O_4$. These materials have varying tendencies to disorder on the cation sublattices. In order to understand chemical composition effects, defect kinetics in perfectly ordered, or normal, spinels were studied, focusing on point defects on each sublattice so as to examine the role that cation disorder has on defect mobility. Using TAD, it was found that disorder creates local environments that strongly trap point defects, effectively reducing their mobility. The consequences of this trapping via kinetic Monte Carlo simulations on the oxygen vacancy (V_O) in $MgGa_2O_4$, shows that V_O mobility is directly related to the degree of inversion in the system. Thus, the indate compound is likely to be the best material to replace ITO as a transparent conductive film.

An epitaxially grown magnesium indium oxide ($MgIn_2O_4$) thin film was prepared by pulsed laser deposition (PLD) on an YSZ-buffered Si substrate at 300 °C. Although there is a large lattice mismatch exists (72.5%) between $MgIn_2O_4$[100] and YSZ[100], epitaxial growth, with cube-on-cube relations, was achieved. A room-temperature electrical conductivity of 29.0 S/cm and a transmittance >80% were achieved above 530 nm. The optical band gap measured for a $MgIn_2O_4$ thin film deposited on a glass substrate showed 4.2 eV. On this $MgIn_2O_4$/YSZ/Si(001) substrate, a $BaTiO_3$-$NiFe_2O_4$ composite film was deposited at 700 and 750 °C by PLD. Although the partial decomposition of $MgIn_2O_4$ into In_2O_3 was observed, both $BaTiO_3$ and $NiFe_2O_4$ were simultaneously epitaxially grown on $MgIn_2O_4$ with cube-on-cube relationship. These findings indicate that $MgIn_2O_4$ can be used as a bottom electrode for multiferroic composite films such as $BaTiO_3$ and $NiFe_2O_4$.

Magnesium indate has no CAS number and is not offered for sale commercially.

Calcium Indates

Calium indate may be prepared by the reaction of the oxides:

$$CaO + In_2O_3 + \text{heat} \Rightarrow CaIn_2O_4$$

However, the reaction is slow at 950 °C and may take up to 10 days to obtain a complete reaction. Calcium indate melts above 1500° C. It is more easily prepared by a CS method. In the CS method, the nitrates of Ca and In are mixed in proper proportion and a calculated amount of urea ($(NH_2)_2CO$) is added to the solution as a fuel. The solution is placed in a furnace at 500 °C. An exothermic reaction occurs, producing a fluffy white powder. This is then heated for 36 h at 900 °C and then reheated at 1050 °C for 36 h to form a highly crystalline material.

Employing the following solid oxide galvanic cells with a zirconia electrolyte, i.e. [Ni, NiO-O^{2-}-$In + In_2O_3$] and [Ni, NiO-O^{2-}, +In, CaO, $CaIn_2O_4$], the Gibbs free energies of formation of solid In_2O_3, and $CaIn_2O_4$ were determined to have the form $\Delta G^0_{\text{f, } In_2O_3} = -909.425 + 307.49T$ kJ/mol and $\Delta G^0_{\text{f, } CaIn_2O_4} = -952.550 + 342.797T$ kJ/mol. Consequently, the Gibbs free energy change for the formation of $CaIn_2O_4$ from the respective oxides $CaO + In_2O_3 \Rightarrow CaIn_2O_4$ was established as $\Delta G^0_{\text{f,oxides}} = -43.126 + 35.3T$ kJ/mol over the temperature range 923–1123 K (650–850 °C).

The development of visible light-induced photocatalysts has been found to be of great importance for the efficient utilization of solar energy or indoor artificial light in the photocatalytic degradation of organic pollutants and splitting of water. It has been demonstrated that the metal oxides of MIn_2O_4 (M = Ca, Sr, Ba) have

good photocatalytic activity for degrading organic pollutants such as methylene blue (MB) under visible light irradiation or the splitting of water into hydrogen and oxygen by dispersion of RuO_2 under UV irradiation. These p-block metal oxides are electronically composed of octahedrally coordinated metal ions having the d^{10} configuration. Among these oxides, $CaIn_2O_4$ shows the highest photocatalytic activity. Because Ca^{2+} has the smallest ionic radii, combined with a similar InO_6 octahedra network structure, it probably is more efficient in the photoelectronic transfer of electrons. The activity order under visible light irradiation was $CaIn_2O_4 > SrIn_2O_4 > BaIn_2O_4$. The general structure of these indates is shown in the following Fig. 6.190.

Two types are known. In one, the structure consists of a series of joined tetrahedra–octahedra to form a tetragonal structure with: $a = 5.0348$, $c = 14.0688$ Å, unit cell with *I4cm* (#108) space group symmetry. In the other, a series of edge-joined octahedra are the major feature. $CaIn_2O_4$, $CdIn_2O_4$, $SrIn_2O_4$ and $BaIn_2O_4$ can be prepared by heating the mixed metal oxides in the temperature range 880–1400 °C. These compounds have been reported to be distorted spinels; however, powder and single-crystal X-ray photographs show that they are related to $CaFe_2O_4$ and contain six-coordinated In^{3+}. The general occurrence of spinel, stuffed silica and ferrite-type AB_2O_4 compounds can be correlated with the radius ratio of the cations. Originally, it was thought that all of the alkaline earth monoindates adopted a tetragonal structure but it has been shown that the Sr and Ba compounds differ markedly in structure. Perhaps, this accounts for the enhanced activity of calcium monoindate as a photocatalytic compound. Note that the structure of $CaIn_2O_4$ differs from those of the analogous compounds, $SrIn_2O_4$ and $BaIn_2O_4$. Perhaps it is this difference that accounts for the increased capacity of the calcium compound toward the highest photocatalytic activity (Fig. 6.191).

SSR is the conventional method widely used for preparing these materials, during which the oxides of the starting materials are mixed together, followed by being calcined at high temperature for a sufficient length of time. Due to the evaporation of In_2O_3 above 1273 K (1000 °C), it is difficult to synthesize and obtain pure-phase $CaIn_2O_4$ using the SSR method. Furthermore, this method does not mix the various components at the molecular level so that agglomeration and formation of a pure phase may occur. This more often produce large particles with an extremely low-surface area and a higher degree of lattice defects. These effects are deleterious to the photocatalylitic activity. Using a coprecipitation method, Inoue et al. synthesized a kind of $CaIn_2O_4$ particles with better photocatalytic activity than that of a sample prepared by the SSR method.

The CS method was found to be successful in preparing many metastable phases and also conventional materials at low temperature. A mixed composition of $CaIn_2O_4$ was prepared by a combustion method using the urea as fuel. However, the resulting $CaIn_2O_4$

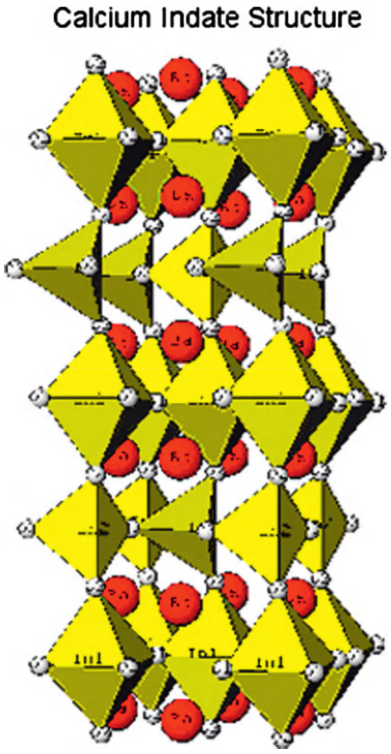

FIGURE 6.190

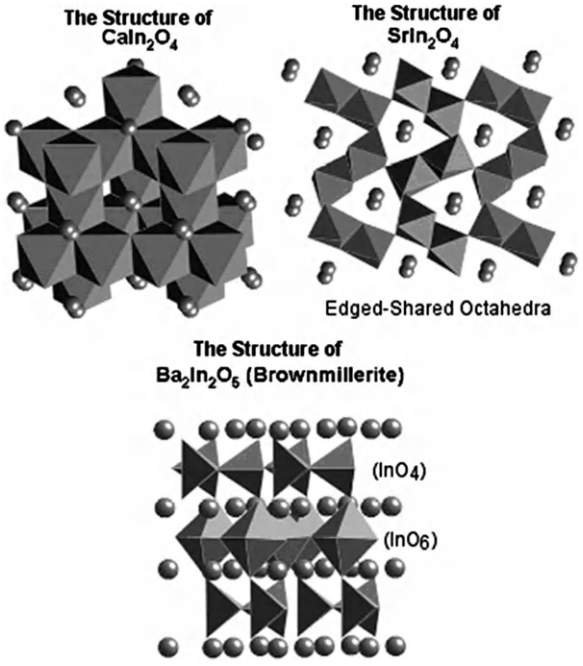

FIGURE 6.191

was impure with a small amount of CaO and In_2O_3 still remaining after calcination at 1323 K (1200 °C) for 6 h (likely due to decomposition of In_2O_3 at that temperature). In another study, a pure $CaIn_2O_4$ particle was prepared at a relatively low temperature by a modified solution–combustion method in which the nitrates were dissolved in water with ethyl nitrate. The mixed solution was kept at 473 K (200 °C) for 30 min to form a solid, which was then slowly heated to 573 K (300 °C) in 30 min (3.3°/min). During this period, a spontaneous combustion took place and a fluffy powder was formed. A following high-temperature treatment made the nanometric particles grow into regular $CaIn_2O_4$ rods. Due to the high crystallization, low impurity level and large surface area, the $CaIn_2O_4$ rods showed significantly higher photocatalytic activity for MB degradation and toluene oxidation under visible light irradiation compared with the sample synthesized by the conventional SSR method. Furthermore, with the dispersion of Pt, the $CaIn_2O_4$ rods exhibited an excellent photocatalytic activity for water decomposition under visible light and UV irradiation.

In the process of preparing a visible light photocatalyst $CaIn_2O_4$, a novel core shell-like composite In_2O_3 at $CaIn_2O_4$ was observed at intermediate calcination temperatures, during the SSR between ball-milled powders of $CaCO_3$ and In_2O_3. The composition, crystallinity and photo absorption of the coupled phases obtained in the temperature range 873–1323 K (600–1050 °C), were characterized by powder XRD, TEM and UV–Vis diffused reflectance spectroscopy. The coupled composite phases In_2O_3 at $CaIn_2O_4$ showed superior visible light-induced photocatalytic degradation of MB compared to single-phase $CaIn_2O_4$. Selective charge separation and efficient charge transport at the interface when illuminated are considered to be the possible reasons for the enhanced photocatalytic performance of this composite catalyst.

The photocatalytic activities of In_2O_3 at $CaIn_2O_4$ composite photocatalysts were investigated based on the decomposition of methyl orange under visible light irradiation ($\lambda > 400$ nm). Different In_2O_3 at $CaIn_2O_4$ contents can be obtained by controlling the synthesis temperature. The photocatalytic tests indicated that the composite samples demonstrated high visible light activity for decomposition of methyl orange. The significant enhancement of the In_2O_3 at $CaIn_2O_4$ photoactivity under visible light irradiation can be ascribed to the efficient separation of photo-generated carriers in the In_2O_3- and $CaIn_2O_4$-coupled semiconductors.

In another study, the photocatalytic properties for water decomposition of RuO_2-dispersed alkaline earth metal and lanthanum indates with an octahedrally coordinated In^{3+} ion of d^{10} configuration were studied. The influences of preparation methods, calcination temperature, and the amount of RuO_2 on the activity of RuO_2-dispersed $CaIn_2O_4$ were examined, and it was shown that the combination of well-crystallized $CaIn_2O_4$ with highly dispersed RuO_2 particles led to the highest photocatalytic performance: hydrogen and oxygen were stably produced at nearly the stoichiometric ratio under UV irradiation. The photocatalytic activity of RuO_2-dispersed $Sr_{1-x}Ca_xIn_2O_4$ ($x = 0.25$, 0.50, 0.75) increased monotonically with increasing x. The activity of RuO_2-dispersed Sr_{1-x} $Ba_xIn_2O_4$ was similar to that of RuO_2-dispersed $SrIn_2O_4$, whereas RuO_2-dispersed $LaInO_3$ had much lower activity. The photocatalytic properties of different kinds of indates were compared.

Terbium-activated $(M_{1-x}Tb_x)In_2O_4$ (M = Ca and Sr, $x = 0.12$, 0.5, 1.0, 1.5 and 2.0 mol%) phosphors have been synthesized by combustion route using urea as a fuel in a pre-heated furnace at 500 °C. The characteristics of the phosphors, such as photoluminescence, crystallinity and particle morphology, were investigated with different levels of Tb^{3+} doping. The green luminescence was attributed to the transition from the $^5D_4$ excited state to $^7F_5$ ground state of Tb^{3+} ions. Qualitative analysis of the phosphors has been performed by energy-dispersive analysis (EDAX). The powder XRD of the phosphor was also studied and reported.

In a like manner, $CaIn_2O_4$:Eu^{3+} phosphors were prepared by a Pechini sol–gel process. XRD, field emission scanning electron microscopy (FE-SEM), photoluminescence (PL), cathodoluminescence (CL) spectra as well as lifetimes were utilized to characterize the samples. The XRD results reveal that the samples begin to crystallize at 800 °C, and the crystallinity increases upon raising the annealing temperature. The FE-SEM images indicate that the $CaIn_2O_4$:Eu^{3+} samples consist of fine and spherical grains with size around 200–400 nm. Under the excitation of ultraviolet light and low-voltage electron beams, the $CaIn_2O_4$:Eu^{3+} phosphors show the characteristic emissions of Eu^{3+} ($^5D \Rightarrow {}^7F_J$ $J, J' = 0, 1, 2, 3$ transitions). The luminescence color can be tuned from white to orange to red by adjusting the doping concentration of Eu^{3+}.

The hitherto unknown compound, **tricalcium monoindate**, $Ca_3In_2O_6$ was prepared and investigated by X-ray single-crystal methods. $Ca_3In_2O_6$ is orthorhombic ($a = 10.908$, $b = 16.45$, $c = 3.228$ Å, space group D^9_{2h}-Pbam) and has a partial statistically distribution of Ca and In. One of the metal positions is occupied only by Ca. The crystal structure of $Ca_3In_2O_6$ is similar to the $CaFe_2O_4$ type which occurs as a mineral, "delafossite". The structure is shown in the following Fig. 6.192.

This structure is characterized by a layer of linearly coordinated Ca^{2+} ions, stacked between edge-shared octahedral layers (InO_6).

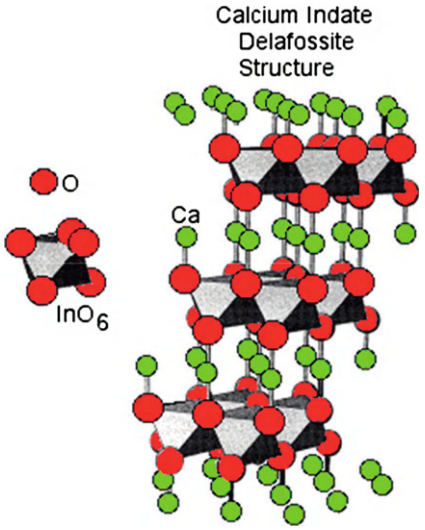

FIGURE 6.192

Four calcium indate compounds are said to be known:

Calcium mono-indate = $CaIn_2O_4$ = 1:1 = 50 mol% indate
Dicalcium tri-indate = $Ca_3In_6O_{11}$ = 2:3 = 60 mol% indate
Tricalcium indate = $Ca_3In_2O_6$ = 3:1 = 25 mol% indate
Tricalcium tetra-indate = $Ca_3In_8O_{15}$ = 3:557 mol% indate

However, the scientific literature is practically devoid of any mention of the properties of these materials other than about one or two authors. Other than the 1:1 and 3:1 compounds, no melting points or other characteristics for the other two have been recorded.

Calcium indate has no CAS numbers and is not offered for sale commercially.

Strontium Indates

Strontium indate, $SrIn_2O_4$, can be prepared by reaction of the oxides at about 1200 °C:

$$SrO + In_2O_3 + \text{heat} \Rightarrow SrIn_2O_{4\neq}$$

Strontium monoindate melts only above 1600° C. $SrIn_2O_4$ was investigated by X-Ray single-crystal methods (space group $D^{16}{}_{2h}$-Pnam; $a = 9.809$, $b = 11.449$, $c = 3.265$). The similarity of the crystal structure of $SrIn_2O_4$ with $Ca_3In_2O_6$ was discussed (see above for the unit-cell structure).

The sintered indate $(Sr,Ca)In_2O_4$ is outstandingly suitable as a crucible material for the SSR of the oxides of bismuth, strontium, calcium and copper to form phases having HT superconductivity, and generally for producing ceramics having a content of Bi, In or Tl. This is of interest in as much as the formation of the superconductive phase in the Bi–Sr–Ca–Cu–O system, which has a transition temperature of 110 K, takes place only at temperatures just below the melting point of the mixture. When such sintering experiments are carried out in crucibles or on carrier plates of Al_2O_3, the latter are strongly attacked and contaminated products of unsatisfactory quality, i.e. a low content of the 110 K phase, are obtained. If, however, the reaction is carried out on a substrate of sintered strontium indate, calcium indate or a Sr–Ca indate, the content of the desired 110 K phase is increased, under otherwise identical conditions. Furthermore, it becomes possible to work at higher sintering temperatures. It is not necessary for the carrier to be composed of solid indate. Preferably, it is composed of a ceramic, for example, Al_2O_3, to which a thin layer of indate has been applied, for example by plasma spraying or by screen printing.

$SrIn_2O_4$ can be prepared by heating the mixed metal oxides in the temperature range 880–1400 °C. These compounds have been reported to be distorted spinels; however, powder and single-crystal X-ray photographs show that they are related to $CaFe_2O_4$ and contain six-coordinated In^{3+}. The general occurrence of spinel, stuffed silica and ferrite-type AB_2O_4 compounds can be correlated with the radius ratio of the cations. $SrIn_2O_4$ was investigated by X-ray single-crystal methods (space group D^{16}_{2h}-Pnam; $a = 9.809$, $b = 11.449$, $c = 3.265$ Å). The similarity of the crystal structure of $SrIn_2O_4$ with $Ca_3In_2O_6$ was striking. In an effort to explain the photoelectric activity of $CaIn_2O_4$, the geometric structures of InO_6 octahedral units were compared among the indates, and it was shown that the photocatalytically active indates possessed distorted InO_6 octahedra having a dipole moment, and that there was a correlation between the photocatalytic activities and the dipole moment. A plane wave density function theory was applied to calculate the density-of-state and band energy diagram for $CaIn_2O_4$. The valence band was composed of the O-2p orbital, whereas the conduction band consisted of the hybridized indium 5s5p orbitals having a large dispersion, indicative of a substantial mobility of photoexcited electrons in the conduction band. The electronic feature of $SrIn_2O_4$ was compared with that of a representative transition metal oxide of $BaTi_4O_9$ with an octahedrally coordinated d^0 metal ion. On the basis of the electronic and geometric consideration, a mechanism was proposed: "Internal fields due to the dipole moment promote the charge separation, while the broad sp conduction bands with large dispersion permit photoexcited electrons to move to RuO_2 particles dispersed as a promoter."

The green-emitting phosphors, $SrIn_2O_4$:xTb ($x = 0.125$, 0.5 and 2%), have been prepared by SSR at 1200 °C. With different levels of Tb^{3+} doping, the XRD, photoluminescent properties, integrated fluorescence

intensity, fluorescence decay lifetime and chromatic characteristics of the phosphors have been systematically investigated.

In another reference, a single-crystal investigation of strontium monoindate, $SrIn_2O_4$, indicated that it had a structure similar to $Ca_3In_2O_6$, the tricalcium monoindate. The space group was Pnam (D^{16}_{2h}) with $a = 9.809$, $b = 11.449$, $c = 3.265$ Å.

Distrontium indate, $Sr_2In_2O_5$, on the other hand, belongs to the orthorhombic space group, Ibm2 (C^{22}_{2v}) with $a = 6.049$, $b = 15.84$, $c = 3.265$ Å and is isostructural with "Brownmillerite", Ca_2FeAlO_5. Half of the In^{3+} atoms are tetrahedrally and half octahedrally coordinated (as in the $CaIn_2O_4$ structure). The ability of trivalent indium to adopt various coordinations—tetrahedral, octahedral, pyramidal—is an interesting feature for the generation of oxygen-deficient perovskites and relatives. In the indates $Sr_2In_2O_5$ and $Ba_2In_2O_5$, the ordering of the oxygen vacancies leads to a Brownmillerite structure with alternating sheets of InO_6 octahedra and InO_4 tetrahedra. A sheet-like element of the Brownmillerite structure is shown in the following Fig. 6.193.

Note that the tetrahedra are isolated from each other but attached to the octahedra. The trivalent In^{3+} ions are half in octahedral and half in tetrahedral coordination.

Only the two compounds listed above are known in the SrO–In_2O_3 system. They do not have a CAS number and are not listed for sale commercially. No uses have arisen in industry, a fact that may explain the lack of interest for such compounds in academia.

The Perovskite-Brownmillerite Structure contains two Octahedra and one Tetrahedra Layers. These Polyhedra contain Indium Coordinated to Oxygen atoms which are tied to the Stountium Atoms in the Structure

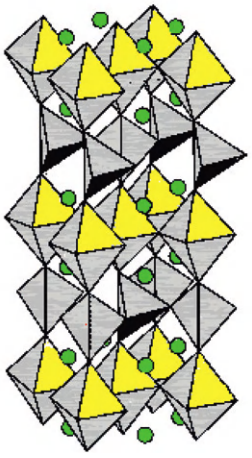

FIGURE 6.193

Barium Indates

The general occurrence of spinel-, stuffed silica- and ferrite-type AB_2O_4 compounds can be correlated with the radius ratio of the cations. Such compounds as $CaIn_2O_4$, $CdIn_2O_4$, $SrIn_2O_4$ and $BaIn_2O_4$ have been reported to be distorted spinels. However, powder and single-crystal X-ray patterns show that they are related to $CaFe_2O_4$ and contain six-coordinated In^{3+} ions. They can be prepared by heating the mixed metal oxides in the temperature range 880–1400 °C. In the BaO–In_2O_3 system, there are five reported compounds. In addition to the known compounds, $BaIn_2O_4$ and $Ba_4In_6O_{13}$, three other compounds have been found: $Ba_2In_2O_5$, $Ba_3In_2O_6$ and $Ba_5In_2O_8$. $Ba_2In_2O_5$ has a simple, perovskite-like X-ray structure, which was not indexed. $Ba_3In_2O_6$ and $Ba_5In_2O_8$ have tetragonal body-centered unit cells with $a = 4.1913$ Å, $c = 21.6693$ Å and $a = 4.1741$ Å, $c = 29.431$ Å, respectively. $Ba_3In_2O_6$ reacts with most air to form a hydrogarnet: $Ba_3In_2(OH)_{12}$. Of the five compounds, only $BaIn_2O_4$ and $Ba_2In_2O_5$ melt congruently, as shown in the following phase Fig. 6.194.

Most of these compounds melt or decompose between 1400 and 1500 °C. Of the binary and ternary compounds in this system, as reported in the literature, only a few of them have been confirmed as stable at 930 °C, namely; $Ba_5In_2O_8$ and $Ba_4In_2O_7$. These two have been identified as a single phase of variable composition $Ba_{5-x}In_{2+x}O_{8+0.5x}$ (α-phase) with $0 \leq x \leq 0.45$, and $Ba_2In_3O_{6.5}$, the latter denoted as $Ba_{1.6}In_{2.4}O_{5.2}$ to reflect its "doubled" perovskite structure (which is different from that reported to date for the $Ba_2In_3O_{6.5}$ compound and identical to the already described series of $Ba_2In_{2-x}Cu_xO_{4+\delta}$ type).

Barium indium oxides ($BaIn_2O_4$, $Ba_4In_6O_{13}$, $Ba_2In_2O_5$, $Ba_3In_2O_6$, and $Ba_5In_2O_8$) were synthesized by a citric process and characterized by powder XRD. The optical absorption properties of these compounds were investigated by UV-visible diffuse reflectance spectroscopy. It was found that, with the increase of the mole ratio of In_2O_3 in the formula, the optical absorption edges of

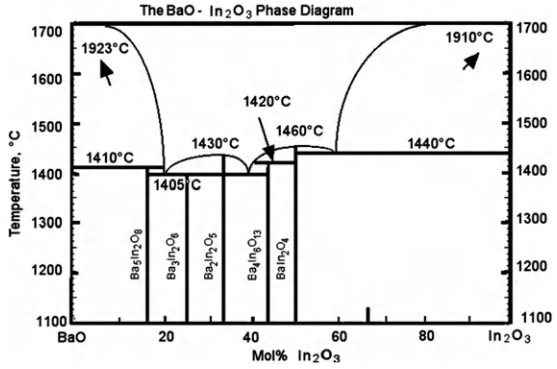

FIGURE 6.194

these oxides shift to the longer wavelength side monotonically. The photocatalytic H_2 and O_2 evolutions under visible light irradiation ($\lambda > 420$ nm) from aqueous CH_3OH/H_2O and $AgNO_3/H_2O$ solutions were performed. Among these oxides, $BaIn_2O_4$ was the most stable compound. The other compounds were not stable chemically in the case of water and visible light irradiation. The structure of $BaIn_2O_4$ is shown in the following Fig. 6.195.

Barium monoindate, $BaIn_2O_4$, has the unit-cell parameters of: monoclinic symmetry; space group C^5_{2h}-$P2_1/a$; $a = 14.432$ Å, $b = 5.833$ Å, $c = 20.792$ Å, $\beta = 110.02°$, $Z = 16$. $BaIn_2O_4$ represents a new structure type with relationships to $BaSc_2O_4$. The crystal structure of $BaIn_2O_4$ is clearly different from $CaIn_2O_4$ and $SrIn_2O_4$.

A variation of barium monoindate is also formed in which the lattice parameters are doubled. $Ba_3In_6O_{12}$ is not very stable but the addition of Ca forms a stable $(Ba,Ca)_3In_6O_{12}$ compound. The tunnel structure of the oxide $(Ba_{0.85}Ca_{2.15})_3In_6O_{12}$ has been revisited. A mono-incommensurate modulation was evidenced by electron diffraction. The simultaneous refinement of X-ray and neutron powder diffraction patterns has allowed a complete determination of the incommensurate structure [$P3_1$]. The existence of a modulated disorder, affecting Ba and Ca atoms, has been pointed out. The occupancy modulation concerning Ba and Ca atoms located on the hexagonal tunnel axis induces a modulation of the Ba–O bond lengths. The HREM study has shown the existence of twinning domains and of crystal regions possessing a defective arrangement of the modulation.

Dibarium indate, $Ba_2In_2O_5$, is a high-temperature semiconductor. At 700 °C, its conductivity, σ, was measured at 5.1×10^{-3} S/cm while that at 900 °C was 1.2×10^{-1} S/cm. This one of the highest oxygen-ion transport conductivities measured for this type of compound. The structure is shown in the following diagram. In situ neutron and XRD experiments were used to determine the crystal structure of $Ba_2In_2O_5$ as related to temperature. $Ba_2In_2O_5$ has a Brownmillerite-type crystal structure from room temperature to 900 °C, consisting of an orthorhombic unit cell with lattice parameters $a = 6.0864(3)$, $b = 16.7903(7)$, $c = 5.9697(3)$ Å and *Icmm* (74) space group symmetry (Fig. 6.196).

At 900 °C, oxygen vacancies begin to disorder. By 925 °C, barium indate recrystallizes in a tetragonal, $a = 6.0348(4)$, $c = 17.0688(22)$ Å, unit cell with *I4cm* (108) space group symmetry. This oxygen vacancy order–disorder transition is associated with an evolution to fast oxide-ion conduction. At 1040 °C, $Ba_2In_2O_5$ becomes a cubic oxygen-deficient perovskite, $a = 4.2743$ Å, in the *Pm3m* space group. At 1080 °C, $Ba_2In_2O_5$ begins to decompose.

The oxygen and proton conductor $Ba_2In_2O_5$ is known to undergo a structural transformation in humid atmosphere at about 300 °C. The resulting phase, $Ba_2In_2O_5 \cdot H_2O$, was investigated by in situ high-temperature XRD. During the transformation, a transient structure existing near 320 °C in a narrow temperature interval is formed. $Ba_2In_2O_5 \cdot H_2O$ is stable from ≈300 °C down to room temperature and may be characterized by S.G. P4/mmm, No. 123, tetragonal, with $a = 4.1827$ Å, $b = 4.1827$ Å and $c = 8.9617$ Å. The atomic rearrangement during the transformation together with the change of the coordination of one-half of the In atoms from tetrahedral to octahedral symmetry reduces the unit-cell volume of $Ba_2In_2O_5 \cdot H_2O$ to one-quarter of the initial value. Linear thermal expansion coefficients of both phases show a strong anisotropy. The interactions among H_2O vapor, CO_2 and $Ba_2In_2O_5$ solid were investigated by thermogravimetry–mass spectroscopy (TG-MS) and XRD measurements. XRD revealed that the crystal structure of as-prepared $Ba_2In_2O_5$ was Brownmillerite-type orthorhombic. However, incorporation of H_2O and CO_2 into the specimen was also confirmed by TG-MS measurement. Weight decrease observed at around 100 and 300 °C in TG curve of as-prepared $Ba_2In_2O_5$ could be attributed to the secession of H_2O by using mass spectroscopy. It

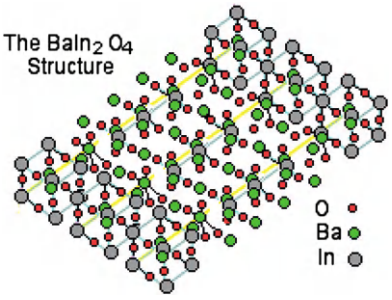

FIGURE 6.195

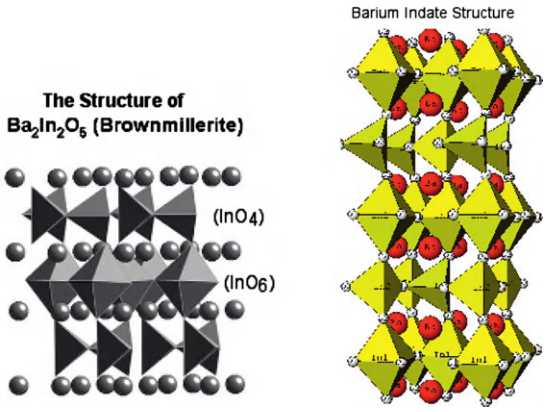

FIGURE 6.196

was suggested that H_2O adsorbed on the surface of the specimen was released at around 100 °C, whereas H_2O incorporated in the crystal was released from the specimen at around 300 °C. The weight of the specimen also decreased at around 700 °C, at which temperature CO_2 secession was confirmed. By annealing the specimen in humid Ar at 250 °C, the amount of H_2O incorporated in the crystal increased from $Ba_2In_2O_5 \cdot 0.34H_2O$ to $Ba_2In_2O_5 \cdot 0.98H_2O$ involving structural transformation from Brownmillerite-type orthorhombic system to tetragonal one other than Brownmillerite.

$Ba_2In_2O_5$ exhibits a dramatic increase in electrical conductivity as the "trapped" oxygen vacancies become partially disordered. On further heating, the vacancies become completely disordered so that the structure reverts to that of a highly defective cubic perovskite. The following diagram illustrates this factor (Fig. 6.197).

Oxygen Frenkel pairs were found to be the most energetically favorable intrinsic defects and are responsible for oxide ion conductivity in the orthorhombic structure. Formation energies of electronic species suggest that $Ba_2In_2O_5$ will oxidize readily to produce positive holes. Energies of proton incorporation reveal that $Ba_2In_2O_5$ should also exhibit reasonable proton conductivity in moist atmospheres.

Network of Oxygen Octahedra and Tetrahedra in $Ba_2In_2O_5$ Showing Interstitial Sites (Squares) and Crystallographically Distinct Oxygen Sites. Indium Ions sit at the Centers of the Octahedra and Tetrahedra, while the Larger Barium Cations Occupy the Open Spaces between the O(2) Ions.

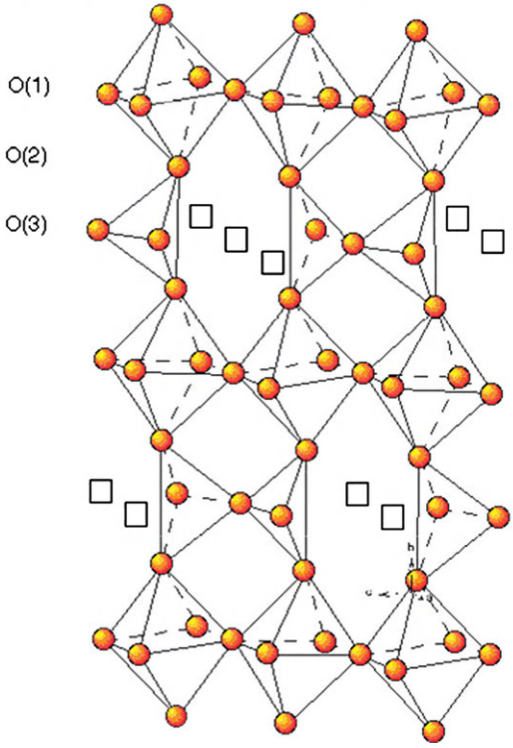

FIGURE 6.197

Attempts to stabilize the disordered phase at lower temperatures by selective doping of A and/or B sites have met with some success, but oxide ion conductivities are not significantly improved compared to fluorite-structured oxides such as YSZ.

In addition, $Ba_2In_2O_5$ has been reported to display both electronic conductivity under variable redox conditions [and proton conductivity due to water incorporation in its low temperature form].

A review of results of experimental studies of ionic conductivity in Brownmillerite and related oxides has been compiled by Kendall et al. The positions found is shown in the following Fig. 6.198.

The 3:1 compounds based on **tribarium indate**, (I) $Ba_2SrIn_2O_6$ and (II) $Sr_{0.93}Ba_{0.07}In_2O_4$, were prepared and investigated by single-crystal X-ray technique. I crystallizes with tetragonal symmetry, space group D–I4/mmm, $a = 4.168$; $c = 21.290$ Å; $Z = 2$; II belongs to the orthorhombic space group D–Pnma, $a = 9.858$; $b = 3.273$; $c = 11.520$ Å; $Z = 4$. I shows in respect to the formerly investigated compound $BaSr_2In_2O_6$ an unexpected statistically distribution of Ba^{2+} and Sr^{2+} with the $La_2SrCu_2O_6$ type. II marks the range of existence of the calcium ferrite type within the alkaline earth oxoindates in direction of large radii of M^{2+} ions.

The proton compounds $Ba_2In_{2(1-x)}Ti_{2x}O_{4+2x}(OH)_y$ $[0 \le x \le 1;\ y \le 2(1-x)]$ were prepared by reacting $Ba_2In_{2(1-x)}Ti_{2x}O_{5+x(1-x)}$ $(0 \le x \le 1)$ phases with water vapor at 200 °C. For $0 \le x \le 0.20$, the filling of oxygen vacancies by protons is almost complete. For larger x values, it decreases significantly down to 30% at $x = 0.7$. The crystal structure of the end-member $Ba_2In_2O_4(OH)_2$ $(x = 0)$ was reinvestigated by a combination of techniques including ^1H and ^2D NMR and electron, X-ray and neutron diffraction. The actual cell is eight

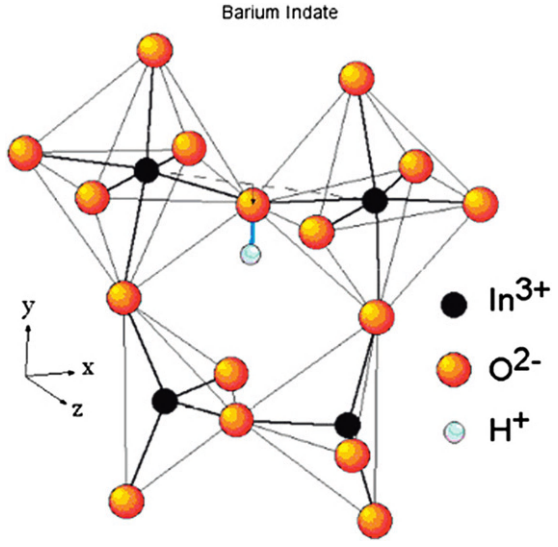

FIGURE 6.198

times larger than that previously published. The structure analysis confirms that the sheet consisting of parallel chains of $In(2)O_4$ tetrahedra and parallel rows of oxygen vacancies in the parent structure of $Ba_2In_2O_5$ has been converted into a $In(2)O_6$ octahedral perovskite-like sheet. It demonstrates that the protons are bonded only to the O atoms around this In(2) site. When x increases, the change in reduced perovskite cell volume, concomitant with the water uptake, remains small for $x < 0.25$ and negligible for larger x values.

The proton conductivity was measured between room temperature and 180 °C. The highest conductivity at 180 °C, $\sigma_{180} \approx 10^{-6}$ S/cm, is observed for $x = 0.3$.

The compound, **tetrabarium triïndate**, $Ba_4In_6O_{13}$, has had limited coverage in the open scientific literature. The crystal structure of $Ba_4In_6O_{13}$ was determined by the single-crystal XRD method using a single crystal grown by the floating zone method. $Ba_4In_6O_{13}$ is isostructural with $Sr_4Fe_6O_{13}$ and crystallizes in the noncentrosymmetric space group *Iba2* with the unit-cell parameters $a = 11.460(6)$, $b = 20.95(3)$, $c = 5.944(2)$ Å. The structure is classified as one of the perovskite derivatives consisted of $Ba_2In_2O_6$- and $Ba_2In_4O_7$-slabs arranged perpendicular to the *b*-axis, as shown in the following Fig. 6.199.

The In(3)-polyhedron in the perovskite-type $Ba_2In_2O_6$-slab is a distorted octahedron, whereas In(1)- and In(2) polyhedra in the $Ba_2In_4O_7$-slab are described as strongly distorted square pyramids. Each polyhedron of In(1) and In(2) shares edges with each other. The sharing scheme of the In(1) polyhedra is similar to the cases for V atoms in CaV_3O_7 and CaV_4O_9, whereas that of the In(2) polyhedra is uncommon.

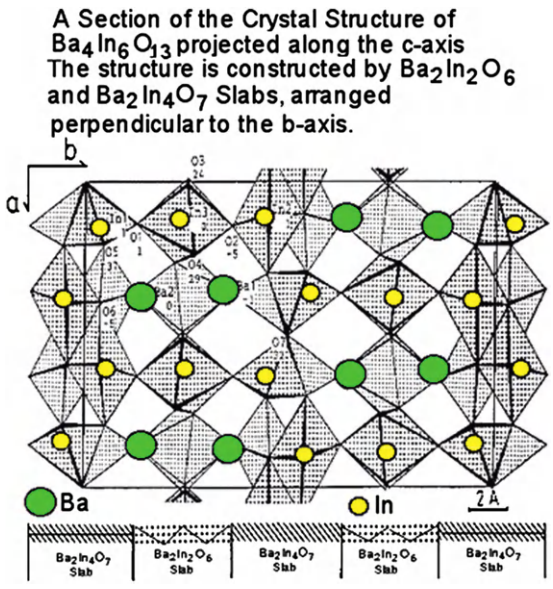

FIGURE 6.199

Although **penta-barium indate** ($Ba_5In_2O_8$) has been prepared, little work has been accomplished concerning its structure or usage either academically or industrially. It melts incongruently at 1410 °C.

Barium indates have no CAS numbers and are not available commercially.

Radium Indates

The scientific literature is lacking in any references to radium indates. Perhaps this is due to the intense radioactivity of the isomer ^{226}Ra but is more likely due to lack of interest of those in industry who may have usage of such compounds. It is anticipated that various radium indates could be prepared, using the same methods as those developed for the barium indate series of compounds. Thus, one would expect to be able to obtain:

$RaO \cdot In_2O_3$,
$3RaO \cdot In_2O_3$,
$5RaO \cdot In_2O_3$,
$2RaO \cdot In_2O_3$,
$3RaO \cdot 3In_2O_3$.

However, there is no record of such syntheses in the literature.

6.7. ALKALINE EARTH THALLIUM COMPOUNDS

The two main oxidation states of thallium are +1 and +3. In the oxidation state +1, most compounds closely resemble the K or Ag compounds. (The ionic radius of thallium(I) is 1.47 Å while that of potassium is 1.33 Å and that of silver is 1.26 Å.). For example, the water-soluble and very basic thallium(I) hydroxide reacts with CO_{2+} forming water-soluble thallium carbonate. This carbonate is the only water-soluble heavy metal carbonate known. The similarity with silver compounds is observed with the halide, oxide, and sulfide compounds. TlBr is a photosensitive yellow compound very similar to the AgBr, while the black TlO and TlS are very similar to AgO and AgS. Tl(I) does not form compounds with the alkaline earths. The compounds with oxidation state +3 resemble the aluminum(III) compounds. They are moderately strong oxidizing agents, as illustrated by the reduction potential of +0.72 V for $Tl^{3+} + 3\ e^- \Rightarrow Tl(s)$. Thallium(III) oxide is a black solid which decomposes above 800 °C, forming thallous(I) oxide and oxygen. In general, thallium is too electropositive to form oxy-thalium compounds in solution. However, for the Ca, Sr and Ba compounds, they can be prepared by solid-state methods.

Thallium also forms a series of intermetallic compounds with the alkaline earths.

6.7.1. Alkaline Earth Thallide Compounds

A series of crystalline compounds can be formed when the various alkaline earth metals are melted together with thallium metal. By varying the atomic ratios of the two components, specific compositions are attained.

Beryllium Thallides

Beryllium metal does not form any compounds with thallium metal. In contrast to the Be–In system where a phase diagram exists showing that Be and In for a solid solution of alloys, no phase diagram for the Be–Tl system exists. If such a diagram exists, it undoubtedly would appear as shown in Fig. 6.200.

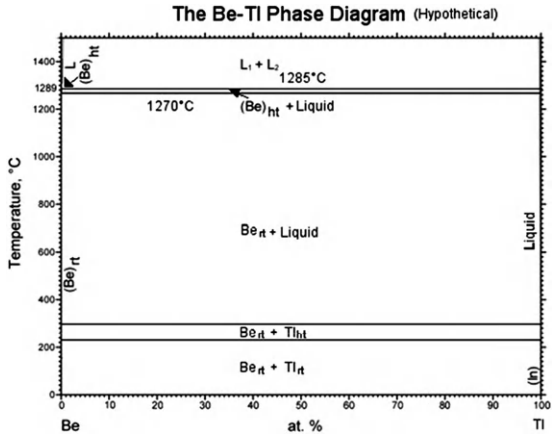

FIGURE 6.200

Magnesium Thallides

Mg metal forms a series of compounds as shown in the phase diagram for the Mg–Tl system (Fig. 6.201).

The crystal parameters are shown in Table 6.68.

Dimagnesium thallide, Mg_2Tl, has a unique crystal structure as shown in the following Fig. 6.202.

The cell parameters are: $a = 3.6796$ Å, $b = c = 8.0828$ Å, $\alpha = 120°$, $\beta = \gamma = 90°$, cell volume $= 208.19$ Å^3, $Z = 4$. The cell occupancy is shown in Table 6.69.

Magnesium mono-thallide, MgTl, has the CsCl type of structure as shown in the following Fig. 6.203.

The cell parameters are: $a = b = c = 3.628$ Å, $\alpha = \beta = \gamma = 90°$, cell volume $= 47.75$ Å^3 and $Z = 1$. The cell occupancy is shown in Table 6.70.

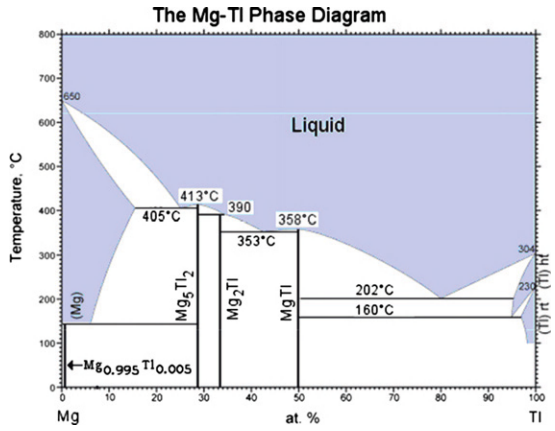

FIGURE 6.201

TABLE 6.68

Compound	Structure type	Pearson symbol	Space group	Melting temperature, °C	Physical parameters
(Mg)	Mg	hP2	194	650	No data
$Mg_{0.995}Tl_{0.005}$	Mg	hP2	$P6_3/mmc$	~150	
Mg_2Tl	Mg_2In	hP9	189	390	No data
Mg_5Tl_2	Mg_5Ga_2	oI28	72	412	No data
MgTl	CsCl	cP2	221	358	No data
(Tl) rt	Mg	hP2	194	230	No data
(Tl) ht	ZnO	hP4	186	304	No data

TABLE 6.69

No	Site notation	Atom	Multiplicity	Wyckoff	Site symmetry	*x*	*y*	*z*	Occupancy
1	Mg1	Mg	3	g	m2m	0.25	0	1/2	1.0
2	Mg2	Mg	3	f	m2m	0.59	0	0	1.0
3	Tl1	Tl	2	d	-6..	1/3	2/3	1/2	1.0
4	Tl2	Tl	1	a	-62m	0	0	0	1.0

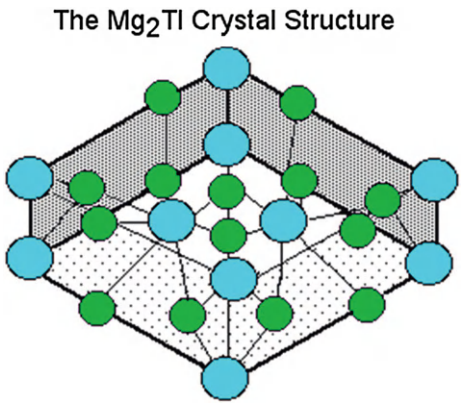

FIGURE 6.202

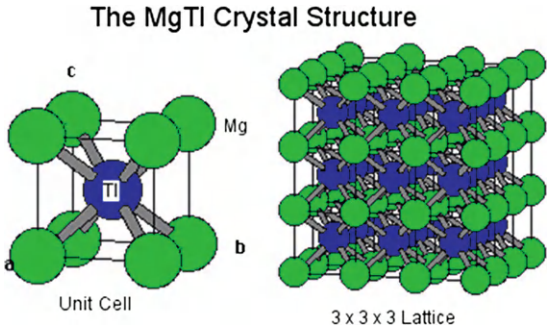

FIGURE 6.203

Penta-magnesium di-thallide, Mg_5Tl_2, has the structure shown in Fig. 6.204.

Cell parameters are: $a = 6.197$ Å, $b = 7.328$ Å, $c = 8.605$ Å, $\alpha = 115.202°$, $\beta = 111.11°$, $\gamma = 90°$, cell volume $= 324.35$ Å^3, $Z = 4$. Cell occupancy is shown in Table 6.71.

The compound, $Mg_{0.995}Tl_{0.005}$, has been found to have a hexagonal structure. Tl atoms are allowed to diffuse

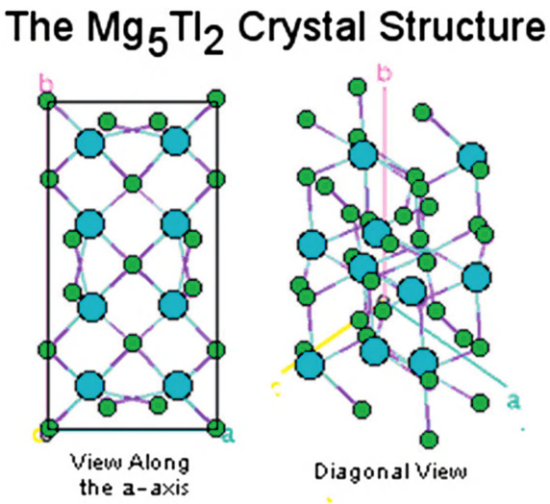

FIGURE 6.204

within the Mg metal structure to change the crystal lattice. A hypothetical structure is thought to consist of Fig. 6.205.

The larger Tl atom substitutes on a Mg atom site, changing the local structure. This mechanism has certain advantages in "hardening" of Mg alloys and is used in Mg metallurgy. The cell parameters are: $a = b = 3.2057$ Å, $c = 5.2122$ Å, $\alpha = \beta = \gamma = 90°$, cell volume $= 46.93$ Å^3.

Magnesium thallides are not used in industry due, in part, to the toxicity of Tl metal in the human body. They are not available commercially.

Calcium Thallides

This series of compounds can be formed by melting the metals under an inert atmosphere. A series of compounds has been obtained as shown in the phase

TABLE 6.70

No	Site notation	Atom	Multiplicity	Wyckoff	Site symmetry	*x*	*y*	*z*	Occupancy
1	Tl	Tl	1	b	m-3m	1/2	1/2	1/2	1.0
2	Mg	Mg	1	a	m-3m	0	0	0	1.0

TABLE 6.71

No	Site notation	Atom	Multiplicity	Wyckoff	Site symmetry	*x*	*y*	*z*	Occupancy
1	Mg1	Mg	8	j	..m	0.155	0.423	0	1.0
2	Tl1	Tl	8	j	..m	0.255	0.122	0	1.0
3	Mg2	Mg	8	g	.2.	0	0.24	1/4	1.0
4	Mg3	Mg	4	a	222	0	0	1/4	1.0

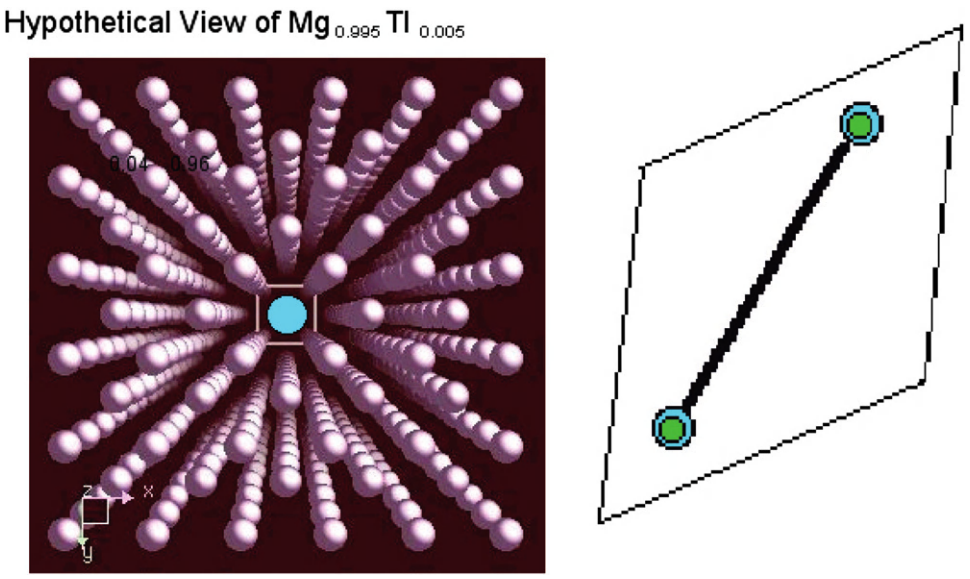

FIGURE 6.205

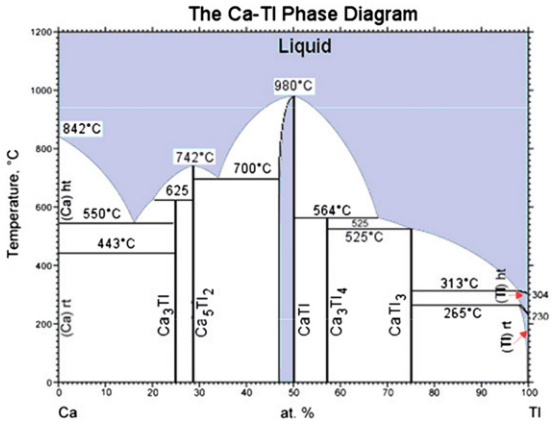

FIGURE 6.206

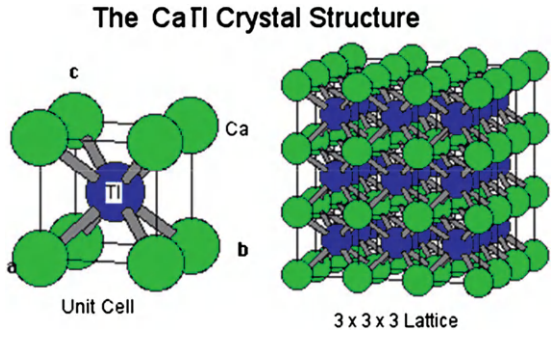

FIGURE 6.207

diagram presented as follows for the Ca–Tl system (Fig. 6.206).

The crystal parameters are:

Calcium mono-thallide, CaTl, has the CsCl structure, which is identical to that of its homologue, MgTl, as shown in the following Fig. 6.207.

Compound	Crystal type	Pearson group	Space group	Melting temperature, °C	Physical properties
(Ca) rt	Cu	cF4	225	443	No data
(Ca) ht	W	cI2	229	550	No data
Ca_3Tl	BiF_3	cF16	225	525	No data
Ca_5Tl_2	Mg_5Ga_2	TI28	Ibam	742	No data
CaTl	CsCl	cP2	221	980	No data
Ca_3Tl_4	—	—	—	564	No data
$CaTl_3$	Cu_3Au	cP4	221	625	No data
(Tl) ht	ZnO	hP4	186	304	No data
(Tl) rt	Mg	hP2	194	230	No data

TABLE 6.72

No	Site notation	Atom	Multiplicity	Wyckoff	Site symmetry	x	y	z	Occupancy
1	Tl	Tl	1	b	m-3m	1/2	1/2	1/2	1.0
2	Ca	Ca	1	a	m-3m	0	0	0	1.0

TABLE 6.73

No	Site notation	Atom	Multiplicity	Wyckoff	Site symmetry	x	y	z	Occupancy
1	Ca2	Ca	8	c	-43m	1/4	1/4	1/4	1.0
2	Ca1	Ca	4	b	m-3m	1/2	1/2	1/2	1.0
3	Tl	Tl	4	a	m-3m	0	0	0	1.0

TABLE 6.74

No	Site notation	Atom	Multiplicity	Wyckoff	Site symmetry	x	y	z	Occupancy
1	Tl	Tl	3	c	4/mm.m	0	1/2	1/2	1.0
2	Ca	Ca	1	a	m-3m	0	0	0	1.0

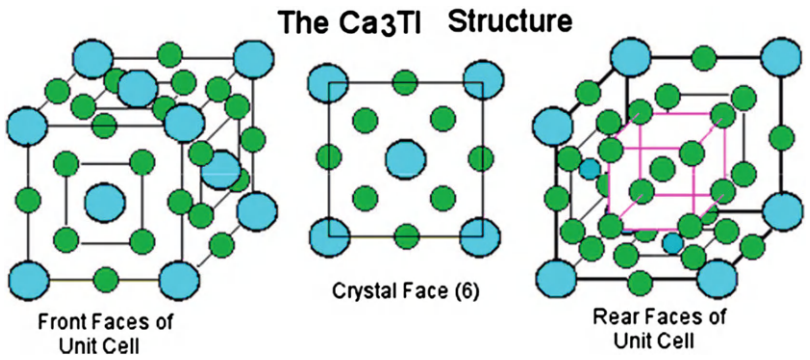

FIGURE 6.208

The structure is cubic and the cell parameters are: $a = b = c = 3.8522$ Å, $\alpha = \beta = \gamma = 90°$, $Z = 57.14$ Å^3, $Z = 1$. Site occupation of the atoms in the structure is shown in Table 6.72.

Tri-calcium thallide, Ca_3Tl, has the BiF_3 type of structure (Fig. 6.208).

The structure consists of Tl atoms at the corners of the unit cell with a face-centered configuration. There are Ca atoms are located in a tilted square at specific locations on any given face (of which there are six for a total of five per face). Many of the Tl atoms are hidden within the lattice. There is a body-centered configuration of nine Tl atoms within the unit cell. Site occupancy is shown in Table 6.73.

Cell parameters for this lattice are: $a = b = c = 5.5508$ Å, $\alpha = \beta = \gamma = 60°$, cell volume $= 120.93$ Å^3, $Z = 10$.

Calcium tri-thallide, $CaTl_3$, has the lattice structure of the Cu_3Au type of crystal (Fig. 6.209).

This structure is identical to that of $MgIn_3$. The structure is a face-centered cubic with cell parameters of: $a = b = c = 4.803$ Å, $\alpha = \beta = \gamma = 90°$, cell volume is 110.80 Å^3 (Site occupation is shown in Table 6.74).

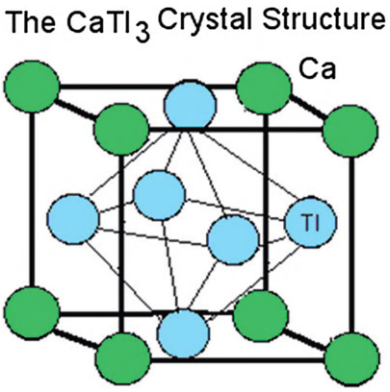

FIGURE 6.209

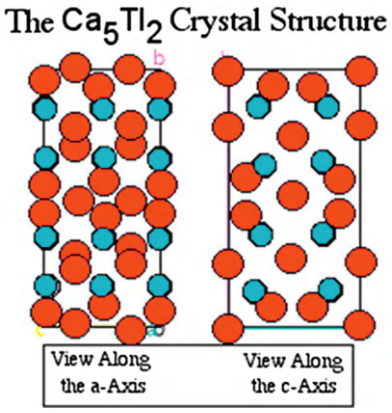

FIGURE 6.210

The compound, **penta-calcium di-thallide**, Ca_5Tl_2, is known to have the Mg_5Ga_2 structure as shown in the following Fig. 6.210.

This structure contains a number of Ca atoms that lie within the center of the lattice. The structure has not been finalized and no lattice parameters are available. Site occupancy is shown in Table 6.75.

Tri-calcium tetra-thallide, Ca_3Tl_4, is almost unknown. Very little data are available for this compound and its discovery was not assessed by determination of its crystal structure. The following is a description of the manner of its discovery:

"When Tl metal was melted and Ca metal added to the melt, a small series of crystals separated. Then, the compound, $CaTl_3$, was formed (deduced by the prolongation of the eutectic at 310 °C). Further addition of Ca metal causes the intermediate melt temperature to rise until 556 °C is reached where Ca_3Tl_4 is formed as crystals at 43.7 atom% Ca. Further addition of Ca metal causes the intermediate melt temperature to rise to 969 °C where the compound CaTl is dominant".

All of these alloys are unstable in air. It is this fact that no usage has arisen for any of the compounds established in the Ca–Tl system. No CAS numbers have been issued. They are not available commercially.

Strontium Thallides

Strontium thallides can be formed by melting the metals together under an inert atmosphere. A series of compounds can be formed by varying the atom ratios in the original melt as shown in the following phase diagram of Fig. 6.211.

At least six compounds are known. Strontium thallides resemble those of the Ca analogues but also form 5:3, 2:3 and 1:2 compounds.

The structure parameters are shown in Table 6.76.

Strontium mono-thallide, SrTl, has the CsCl structure as shown in the following Fig. 6.212.

It is body centered with the Tl atom at the center of the lattice. Cell occupancy is shown in Table 6.77.

Lattice parameters are: $a = b = c = 4.038$ Å and $\alpha = \beta = \gamma = 90°$, cell volume = 65.48 Å^3.

Tri-strontium thallide, Sr_3Tl, has the structure shown in the following diagram. Cell parameters are: $a = 5.771$ Å, $b = 8.073$ Å, $c = 23.723$ Å, $\alpha = \beta = \gamma = 90°$, cell volume = 110.524 Å^3 (Fig. 6.213).

This structure is almost identical to its homologue, Ca_3Tl, except for the lengths of the lattice parameters. Cell occupancy is shown in Table 6.78.

Strontium tri-thallide, $SrTl_3$, has the face-centered cubic type of structure as shown in the following Fig. 6.214.

Cell parameters are: $a = b = c = 4.992$ Å, $\alpha = \beta = \gamma = 90°$, cell volume = 115.43 Å^3. Cell occupation is shown in Table 6.79.

Penta-strontium tri-thallide, Sr_5Tl_3, has the Mg_5In_2 structure and the lattice parameters of: $a = 8.635$ Å, $c = 10.210$ Å, $\alpha = \beta = 114.99°$, $\gamma = 90$ °, cell

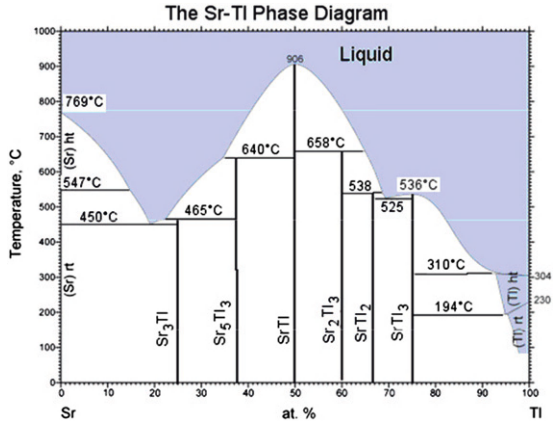

FIGURE 6.211

TABLE 6.75

No	Site notation	Atom	Multiplicity	Wyckoff	Site symmetry	x	y	z	Occupancy
1	Sr3	Mg	8	j	..m	0.155	0.423	0	1.0
2	Ga	Ga	8	j	..m	0.255	0.122	0	1.0
3	Sr2	Mg	8	g	.2.	0	0.24	1/4	1.0
4	Sr1	Mg	4	a	222	0	0	1/4	1.0

TABLE 6.76

Compound	Structure type	Pearson symbol	Space group	Melting point, °C	Physical properties
(Sr) ht	W	cI2	229	769	No data
(Sr) rt	Cu	cF4	225	547	No data
Sr_5Tl_3	Cr_5B_3	tI32	140	640	No data
SrTl	CsCl	cP2	221	906	No data
$SrTl_2$	$CaIn_2$	hP6	194	538	No data
Sr_3Tl	*	oP*		465	No data
$SrTl_3$	$SrPb_3$	tP4	123	536	No data
(Tl) rt	Mg	hP2	194	230	No data
(Tl) ht	ZnO	hP4	186	304	No data

TABLE 6.77

No	Site notation	Atom	Multiplicity	Wyckoff	Site symmetry	*x*	*y*	*z*	Occupancy
1	Tl	Tl	1	b	m-3m	1/2	1/2	1/2	1.0
2	Sr	Sr	1	a	m-3m	0	0	0	1.0

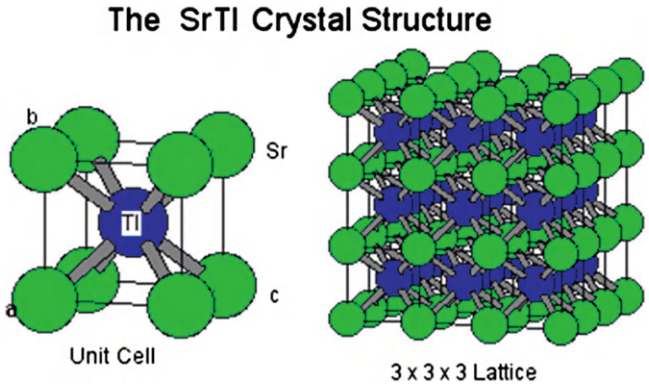

FIGURE 6.212

volume = 611.01 Å^3, $Z = 4$. It is a Zintl structure with Tl–Tl dumbbells predominating in the structure. Each face of the *a*-axis and *c*-axis consists of alternating Sr and Tl atoms and the opposite end faces have a distinctive arrangement of atoms (Fig. 6.215).

Strontium di-thallide, $SrTl_2$, has the structure shown in Fig. 6.216.

It is tetragonal with cell parameters of: $a = b =$ 5.076 Å, $c = 8.231$ Å, $\alpha = \beta = 90°$, $c = 120°$, $Z = 2$, cell volume = 183.26 Å^3. Cell occupancy is shown in Table 6.80.

The compounds, Ca_3Tl_5 (**III**), and Sr_3Tl_5 (**IV**), have been obtained by direct fusion of the elements in sealed

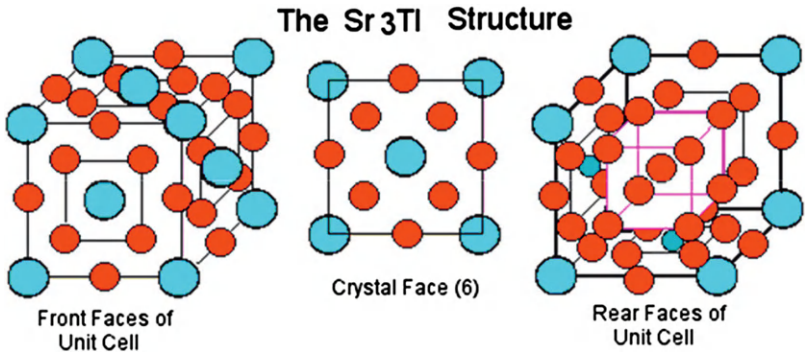

FIGURE 6.213

TABLE 6.78

No	Site notation	Atom	Multiplicity	Wyckoff	Site symmetry	*x*	*y*	*z*	Occupancy
1	Sr2	Sr	8	c	-43m	1/4	1/4	1/4	1.0
2	Sr1	Sr	4	b	m-3m	1/2	1/2	1/2	1.0
3	Tl	Tl	4	a	m-3m	0	0	0	1.0

TABLE 6.79

No	Site notation	Atom	Multiplicity	Wyckoff	Site symmetry	*x*	*y*	*z*	Occupancy
1	Tl2	Tl	2	e	mmm.	0	1/2	1/2	1.0
2	Tl1	Tl	1	c	4/mmm	1/2	1/2	0	1.0
3	Sr	Sr	1	a	4/mmm	0	0	0	1.0

TABLE 6.80

No	Site notation	Atom	Multiplicity	Wyckoff	Site symmetry	*x*	*y*	*z*	Occupancy
1	Tl1	Tl	4	f	3m.	1/3	2/3	0.045	1.0
2	Sr1	Sr	2	b	-6m2	0	0	1/4	1.0

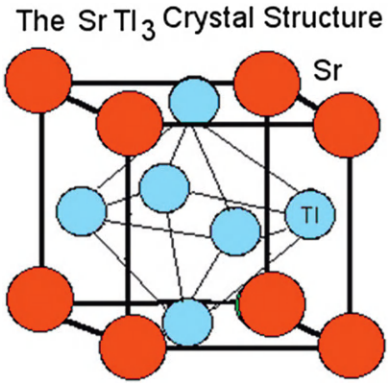

FIGURE 6.214

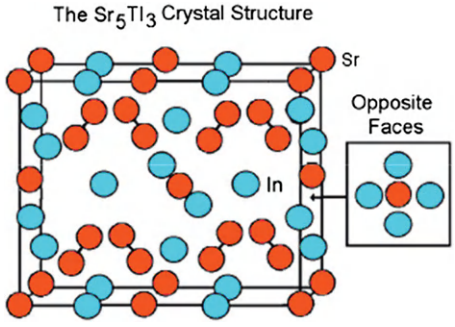

FIGURE 6.215

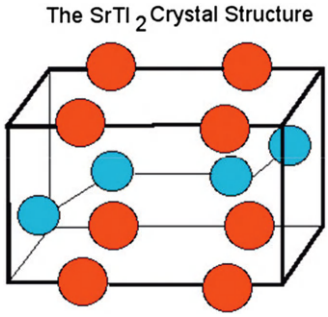

FIGURE 6.216

Nb ampoules at high temperature. Their structures were determined by single-crystal X-ray diffraction studies and the bonding was investigated by *TB–LMTO–ASA* calculations. These binary compounds **III** and **IV** crystallize in the Pu3Pd5-structure type; space group *Cmcm* (No. 63); $Z = 4$ with $a = 10.231(2)$, $b = 8.362(2)$, $c = 10.623(2)$ Å for **III** and $a = 10.592(5)$, $b = 8.667(5)$, $c = 10.973(6)$ Å for **IV**. The structure is shown in the following Fig. 6.217.

Both structure types consist of zigzag chains of distorted square pyramidal clusters, Tl_5^{6-}. In the these structures, the clusters are aligned parallel and show a considerably high degree of polymerization. The electronic band structure for Sr_3Tl_5 and Ca_3Tl_5 show metallic properties and strong participation of the cations in the bonding.

Strontium thallides have not found a usage in industry due, in part, to the toxicity of Tl metal in the human body. No CAS numbers has been assigned. They are not available commercially.

Barium Thallides

Barium forms a series of thallide compounds with Tl as shown in the following phase Fig. 6.218.

Six compounds are seen when the atom ratio of Ba:Tl is varied 13:1, 2:1, 1:1, 1:2, 1:3, and 1:4. The structure factors are partially known (Table 6.81).

Barium tri-thallide, $BaTl_3$, has the structure shown in Fig. 6.219.

This compound was synthesized and characterized by physical property measurements and electronic structure calculations. Its structure (Cmcm) is a new intermediate in the Ni_3Sn family (P63/mmc), and consists of thallium layers formed from two-center bond formation between the parallel chains of face-sharing octahedral clusters. The valence electron concentration (VEC) of the thallium layers is consistent with their two-dimensional nature, in comparison with those in other AX_3-type compounds with one- or three-dimensional anionic networks with the same building blocks and different VECs. The unique geometric features of the anionic thallium layers bring on an unusual competition between inter- and intra-cluster bonds. Detailed studies of the energetics of $BaTl_3$ reveal for the first time the important role of cation–anion interactions in the bonding competition in such an anionic substructure.

Barium di-thallide, $BaTl_2$, has the tetragonal structure shown in Fig. 6.220.

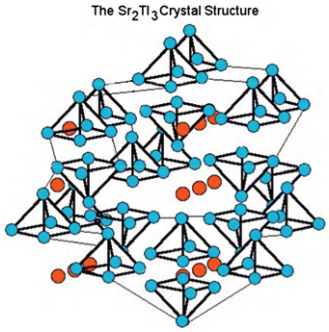

FIGURE 6.217

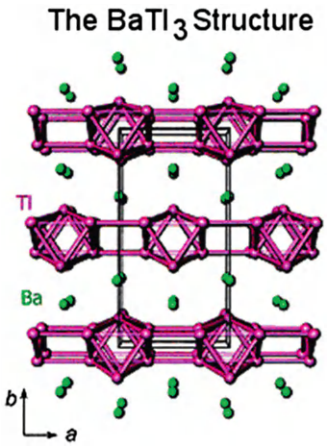

FIGURE 6.219

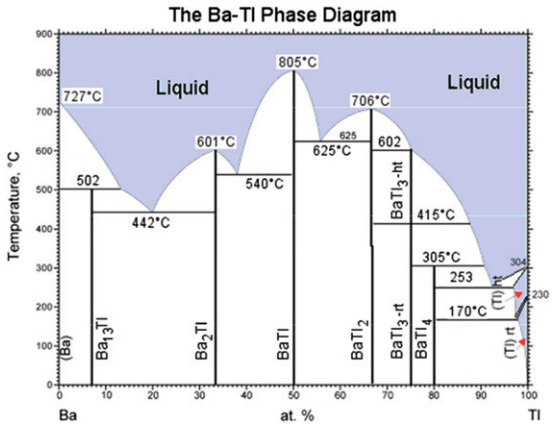

FIGURE 6.218

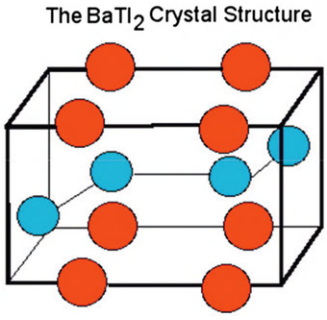

FIGURE 6.220

TABLE 6.81

Compound	Structure type	Pearson symbol	Space group	Melting point, °C	Physical properties
(Ba)	W	cI2	229	727	**No data**
$BaTl_2$	$CaIn_2$	hP6	194	706	**No data**
(Tl) rt	Mg	hP2	194	230	**No data**
(Tl) ht	ZnO	hP4	186	304	**No data**

This is identical to $SrTl_2$ compound except for lattice parameters: $a = b = 5.217$ Å, $\alpha = \beta = 90°$, $c = 120°$, cell volume = 198.82 Å^3. Cell occupancy is shown in Table 6.82.

Barium tetra-thallide, $BaTl_4$, has the following structure shown in Fig. 6.221.

The synthesis and bonding of $BaTl_4$ can be described as: space group = C2/m, $Z = 4$, $a = 12.408$, $b = 5.351$, $c = 10.383$ Å, $\beta = 116.00°$. Pairs of edge-sharing Tl pentagons are condensed to generate a network of pentagonal biprisms along b that encapsulate Ba atoms. Alternating levels of prisms along c afford six more bifunctional Tl atoms about the waists of the biprisms, giving Ba a coordination number of 16. Each Tl atom is bonded to five to seven other Tl atoms and to three to five Ba atoms. There is also strong evidence that Hg substitutes preferentially in the shared edges of the Tl biprisms in $BaHg_{0.8}0Tl_{3.20}$ to generate more strongly bound Hg_2 dimers. Cations that are too small relative to the dimensions of the surrounding polyanionic network make this $BaTl_4$ structure (and for $SrIn_4$ and perhaps $EuIn_4$ as well) one stable alternative to tetragonal $BaAl_4$-type structures in which cations are bound in larger hexagon-faced nets, as for $BaIn_4$ and $SrGa_4$. Characteristic condensation and augmentation of cation-centered prismatic units are common among many relatively cation- and electron-poor, polar derivatives of Zintl phases gain stability. At the other extreme, the large family of Frank–Kasper phases in which the elements exhibit larger numbers of bonded neighbors are sometimes referred to as "orbitally rich".

Barium mono-thallide has the structure (Fig. 6.222).

Lattice parameters are: $a = b = c = 4.341$ Å and $\alpha = \beta = \gamma = 90°$, cell volume = 81.82 Å^3. Site occupancy is shown in Table 6.83.

Di-barium thallide, Ba_2In, is known from phase diagram surveys but has not been studied extensively as to structure. Both Ca and Sr do not form such compounds and the existence of Ba_2Tl remains uncertain.

The major usage of Ba, combined with Tl, has been in the formation of superconducting compounds. A general formula is $Tl_2Ba_2CuO_6$, whose critical temperature, T_c, is 82 K. The formula, $Tl_2Ba_2Ca_2Cu_3O_{10}$, has a T_c of 122 K, one of the highest known for these "high-temperature" superconductors.

Superconducting materials conduct electricity with little or no resistance. Apart from the potential use of such materials in applications such as magnetic propulsion and the storage of magnetic energy, being able to distribute energy along power lines without energy loss through resistance is one of the holy grails of efficient power transmission. Since 1986, when the superconductivity of lanthanum–barium–copper oxide at

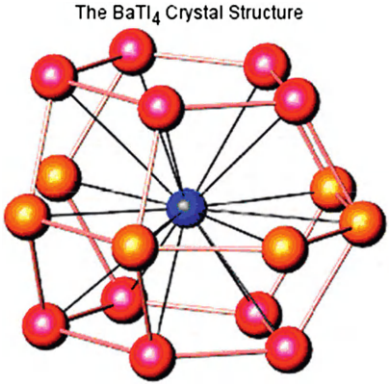

FIGURE 6.221

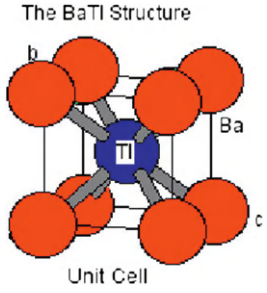

FIGURE 6.222

TABLE 6.82

No	Site notation	Atom	Multiplicity	Wyckoff	Site symmetry	x	y	z	Occupancy
1	Tl1	Tl	4	f	3m.	1/3	2/3	0.045	1.0
2	Ba1	Ba	2	b	-6m2	0	0	1/4	1.0

TABLE 6.83

No	Site notation	Atom	Multiplicity	Wyckoff	Site symmetry	*x*	*y*	*z*	Occupancy
1	Tl	Tl	1	b	m-3m	1/2	1/2	1/2	1.0
2	Ba	Ba	1	a	m-3m	0	0	0	1.0

35 K (−396.67 F) was discovered by Bednorz and Müller, research has continued in the development of HTS materials, particularly in places like Oak Ridge National Laboratory, as part of the U.S. Department of Energy's national effort on HTS' electrical power applications. In 1993, researchers discovered the superconductivity of thallium-doped mercury-barium-calcium-copper oxide at the even higher temperature of 138 K (−211.27 F), a temperature higher even than that for the compound thallium-barium-calcium-copper oxide.

HTS materials are now used in electronic filters for cell phones and in a few superconductor power cables.

In summary, thallium metal forms a number of compounds with the alkaline earths. The atom ratios vary with the nature of the Ae atom and its atomic radius, as shown in the following Table 6.84.

Radium Thallides

The scientific literature is lacking in any references to radium thallides. Perhaps this is due to the intense radioactivity of the isomer ^{226}Ra but is more likely due to lack of interest of those in industry who may have usage of such compounds. It is anticipated that various radium thallides could be prepared, using the same methods as those developed for the barium thallide series of compounds. Thus, one would expect to be able to obtain:

Ra·Tl
3Ra·Tl
5Ra·Tl
2Ra Tl
3Ra·2Tl

However, there is no record of such syntheses in the literature.

6.7.2. Alkaline Earth Thallates

Thallium forms a number of oxygen-dominated compounds with certain of the alkaline earths. The exceptions are beryllium and magnesium.

Beryllium Thallates

A perusal of the literature reveals that no references to beryllium thallates exist. There are no reports of the properties of such compounds or that any beryllium thallate compounds exist. No CAS numbers exist. It is likely that the system BeO–Tl_2O_3 has never been studied in any detail. Both of these elements are harmful and poisonous to the human body and no incentive to discover the properties of such compounds exists.

Magnesium Thallates

Although it might appear, at first glance, that magnesium thallate could be prepared by the reaction of the oxides:

$$MgO + Tl_2O_3 + \text{heat} \Rightarrow MgTl_2O_4$$

However, there are no reports of the properties of this compound or of any other magnesium thallate compounds. No CAS numbers exist. It is likely that the system MgO–In_2O_3 has never been studied in any detail. This is surprising since CaO, SrO and BaO form a number of compounds with Tl_2O_3. One concludes that, in view of the large ionic size of Tl^{3+} in thallate anions, the Mg^{2+} cation is too small to form stable compounds. A search of the available scientific literature concerning the various 1:1, 1:2, 2:1 MgO/Tl_2O_3, etc compounds revealed that a description does not exist. Therefore, one concludes that no such compounds can be formed.

TABLE 6.84

Atom-ratio	Be	Mg	Ca	Sr	Ba
1:1	—	X	X	X	X
1:2	—	—	—	X	X
1:3	—	—	X	X	X
1:4	—	—	—	—	X
2:1	—	X	—	—	—
2:3	—	—	—	X	—
3:1	—	—	X	X	—
5:2	—	X	X	—	—
5:3	—	—	—	X	—
99.5-0.5	—	X	—	—	—
13:1	—	—	—	—	X

The trends, already described above, that certain compositions do not form, because of size prohibitions in stable crystal lattices, is carried out here where no beryllium gallate is stable but one magnesium **gallate** can be formed (five gallates in the CaO–, SrO–, and $BaO–Ga_2O_3$ systems) as compared to the thallate system, $MO–Tl_2O_3$, where no BeO– or $MgO–Tl_2O_3$ compounds have been obtained or characterized.

Calcium Thallates

The phases present in the Tl_2O_3–CaO system have been synthesized and characterized using powder neutron diffraction data. The structures of the phases known to exist in the $Ca_nTl_2O_{3+n}$ system with n =1, 1.5, 2 and 3 have been refined and the oxycarbonate phase with composition $Ca_4Tl_2O_6CO_3$ has been identified. Four compounds are found in the phase Fig. 6.223.

The only stable compound with a congruent melting point is $Ca_3Tl_2O_6$ (3:1). The others, $Ca_2Tl_2O_5$ (2:1), $Ca_3Tl_4O_9$ (3:2), and $CaTl_2O_4$ (1:1) all have incongruent melting points and decompose to the oxides.

The $Ca_nTl_2O_{3+n}$ phases with $n = 1$ or 3 are related to the lillianite structure while the $n = 2$ compound is an oxycarbonate that has been found to crystallize in $I4/mmm$ symmetry for M = Ca. The relationships between these structures have been discussed and comparisons were made to the previously published structures determined from X-ray powder diffraction data.

The structure of **tri-calcium thallate**, $Ca_3Tl_2O_6$, is shown in the following diagram. It consists of alternating chains of TlO_6 octahedra which form channels in which the Ca^{2+} cations reside. Two layers of chains are shown but not all of the oxygen atoms are visible. The structure consists of Tl_6^{6-} octahedra in which Ca^{2+} ions fit into channels between the thallate groupings (Fig. 6.224).

The salt, tricalcium thallate, $Ca_3Tl_2O_6$ (3:1) has been found to crystallize in the space group *Pbam* with

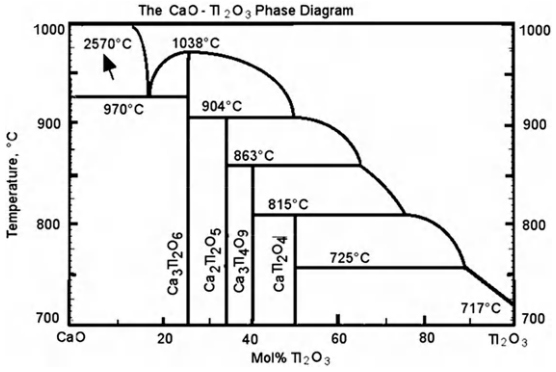

FIGURE 6.223

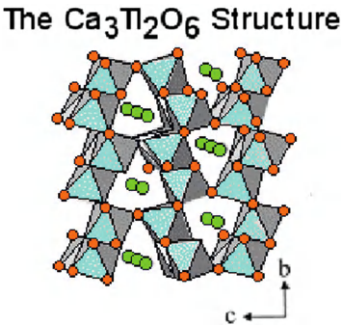

FIGURE 6.224

$a = 11.248$ Å, $b = 16.513$ Å, and $c = 3.333$ Å. The ab initio determination of its structure from powder X-ray data shows that it consists of zigzag rock salt-type layers $[Ca_4Tl_4O_{14}]_\infty$ parallel to (010), built up from quadruple ribbons of TlO_6 octahedra running along c, interconnected with single and double ribbons of CaO_6 octahedra. Along b, these rock salt-type layers share the corners of their octahedra forming tunnels approximately similar to those observed in $CaTi_2O_4$, where calcium ions are located with a monocapped trigonal prismatic coordination. This oxide represents the third member of the series $CanTl_2On_{+3}$; its relationships with the two $n = 1$ and 2 members $CaTl_2O_4$ and $Ca_2Tl_2O_5$, that correspond to a chemical twinning of the rock salt structure, are discussed. In fact, $Ca_3Tl_2O_6$ is isostructural with $Ca_3In_2O_6$.

A **tricalcium dithallate**, $Ca_3Tl_4O_9$ (3:2) has been isolated. It crystallizes in a monoclinic cell, space group $C2/m$, with $a = 11.118(3)$ Å, $b = 3.341(1)$ Å, $c = 12.287(3)$ Å, and $\gamma = 102.88(2)°$. The ab initio determination of this structure shows that it consists of a regular intergrowth of the first two members of the calcium thallate family $CanTl_2O_{3+n}$: $CaTl_2O_4$ ($n = 1$) and $Ca_2Tl_2O_5$ ($n = 2$). Intergrowth defects have been characterized by electron microscopy. Among all oxides and sulfides that belong to the lillianite family, $Ca_3Tl_4O_9$ is the only one that exhibits the ^{2,3}L structure, i.e. where layers are built up from ribbons of two and three edge-sharing octahedra alternately. The ab initio determination of this structure shows that it consists of a regular intergrowth of the first two members of the calcium thallate family $CanTl_2O_{3+n}$: $CaTl_2O_4$ ($n = 1$) and $Ca_2Tl_2O_5$ ($n = 2$). Intergrowth defects have been characterized by electron microscopy. Among all oxides and sulfides that belong to the lillianite family, $Ca_3Tl_4O_9$ is the only one that exhibits the ^{2,3}L structure, i.e. where layers are built up from ribbons of two and three edge-sharing octahedra alternately.

Two calcium thallates, $CaTl_2O_4$ and $Ca_2Tl_2O_5$, i.e. (1:1 and 2:1) have been isolated that crystallize in the *Cmcm* space group with $a = 3.3255$ Å, $b = 11.022$ Å,

and $c = 10.479$ Å for the first and $a = 3.3431$ Å, $b = 11.159$ Å, and $c = 13.499$ Å for the second. The ab initio determination of their structure from powder X-ray data shows that they are closely related and that they represent the first two members of a series with the generic formula $Can Tl_2O_{n+3}$. In fact, the first member, $CaTl_2O_4$, is isotypic to $CaTi_2O_4$ and can be described as a chemical twin of $[Tl_2O_4]_\infty$ rock salt layers, whereas the second member, $Ca_2Tl_2O_5$, is derived from the first by increasing the thickness of the rock salt layers, i.e. by replacing double ribbons of edge-sharing octahedra by triple ribbons. In both structures, the chemical twinning is induced by the ability of calcium to adopt the trigonal prismatic coordination in prismatic tunnels; the direction of rock salt layer is invariable, i.e. parallel to the (113) plane of the cubic rock salt structure.

No calcium thallates have found usage in industry and no CAS numbers have been issued.

Strontium Thallates

The reaction of SrO with Tl_2O_3 is expected to form strontium mono-thallate:

$$SrO + Tl_2O_3 + \text{heat} \Rightarrow SrTl_2O_4$$

In the $Sr_nTl_2O_{3+n}$ system, the structures of the phases with $n = 1$, 2 and 3 have also been refined. Three different modifications have been found with space groups $P4/mmm$, $I4/mmm$ and $Pmmm$ for M = Sr, depending on the ordering of the thallium groups. However, a detailed phase diagram for the SrO–Tl_2O_3 system is not available.

The crystal structure of the **strontium mono-thallate**, $SrTl_2O_4$, has been determined using powder XRD. This oxide is isostructural with $CaFe_2O_4$, i.e. it crystallizes in the space group Pnam with $a = 10.041$ Å, $b = 11.697$ Å and $c = 3.409$ Å (Fig. 6.225).

The $[Tl_2O_4]\infty$ framework is built up from double rutile chains of TlO_6 octahedra forming five-sided tunnels where the strontium cations are located. The semimetallic properties of this phase are once more in favor of the existence of a proximity effect-induced superconductivity in the $[TlO]\infty$ layers of layered thallium cuprates.

A new thallium oxide and strontium compound, **di-strontium thallate**, was prepared by direct interaction in the solid state of SrO with Tl_2O_3 at 900 ° C. Its composition, $Sr_2Tl_2O_5$, was determined by combining chemical analysis and physical methods. The microscopic studies and XRD show that the symmetry of the lattice is orthorhombic with the parameters: $a = 3.502$ (2) Å, $b = 11.506$ (9) Å, $c = 13.798$ (9) Å. Three space groups are compatible with the results: $CMC2_1$, Cc2m, or Cmcm.

The compound, **tetra-strontium thallate**, $Sr_4Tl_2O_7$, was prepared and investigated by X-ray single-crystal methods. $Sr_4Tl_2O_7$ crystallizes in the tetragonal space group $CP4_2nm$ ($a = 5.006$, $c = 18.73$ Å). Sr^{2+} has a trigonal prismatic surrounding whereas Tl^{3+} shows 2 + 2 oxygen neighbors. The crystal structure is completely described as a tetragonal lattice. The golden yellow $Sr_4Tl_2O_7$ appears to be an insulator.

The system, SrO–Tl_2O_3, has not been thoroughly studied as evidenced by lack of a reliable phase diagram. Mention of several compounds has been available in the literature but structure reports are not widely available.

Strontium thallates are not available commercially, due in part to the toxic nature of thallium in the human body.

Barium Thallates

Thallium oxide, Tl_2O_3, forms several compounds with BaO as may be seen in the phase diagram for this system that is shown in Fig. 6.226.

FIGURE 6.225

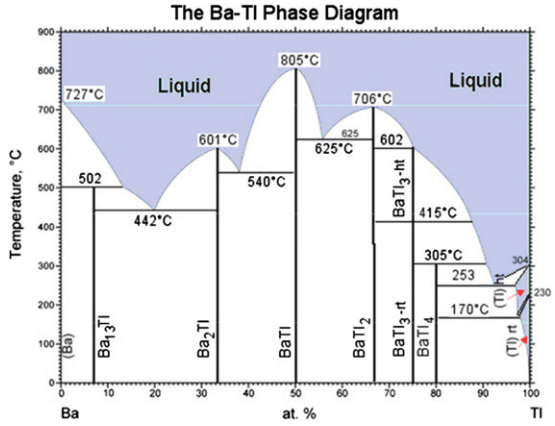

FIGURE 6.226

TABLE 6.85

Cell parameters				
Compound	**Crystal**	***a***	***b***	***c***
$BaTl_2O_4$	Orthorhombic	10.45	11.93	3.476
$Ba_4Tl_6O_{13}$	Orthorhombic	5.748	7.164	9.572
$Ba_2Tl_2O_5$	Orthorhombic	6.264	17.258	6.05
$Ba_4Tl_2O_7$	Tetragonal	5.33		23.04

Crystal cell parameters for this system are given in the Table 6.85.

The 1:1 compound melts incongruently at 840 °C as does the 4:3 compound at 865 °C and the 4:1 compound at 1050 °C. Only the 2:1 compound melts congruently at 1110 °C.

Di-barium thallate, $Ba_2Tl_2O_5$, has been investigated by a combination of XRD, electron diffraction, and energy dispersive X-ray spectroscopy. A monoclinic unit cell was observed with $a = 5.836$, $b = 6.226$, $c = 17.342$ Å, and $\gamma = 91.34°$, cell volume = 651.02 Å^3. The impurity phase coexisting with $Ba_2Tl_2O_5$ was determined to be $Ba_4Tl_6O_{13}$, having an orthorhombic unit cell with $a = 5.748$, $b = 7.221$, and $c = 9.361$ Å.

The structure may be represented by Fig. 6.227.

An oxygen-deficient perovskite, **di-barium thallate**, $Ba_2Tl_2O_{5-x}$, was successfully prepared by a SSR technique. Orthorhombic unit-cell dimensions refined from a powder diffraction pattern are $a = 6.257 \pm 0.0001$, $b = 6.038 \pm 0.0001$, and $c = 17.232 \pm 0.0003$ Å, $\alpha = \beta = \gamma = 90$ °, cell volume = 651.02 Å^3, Pearson symbol = oP36, space group = Pnma.

The perovskite, $Ba_2Tl_2O_5$, was found to be a semiconductor. $Ba_2Tl_2O_5$ was reinvestigated by a combination of XRD, electron diffraction, and energy dispersive X-ray spectroscopy. A new monoclinic unit cell was observed with $a = 5.736$, $b = 6.126$, $c = 17.342$ Å, and $\gamma = 91.34°$. The impurity phase coexisting with $Ba_2Tl_2O_{5-x}$ was determined to be **tetra-barium tri-thallate**, $Ba_4Tl_6O_{13}$, having an orthorhombic unit cell with $a = 5.748$, $b = 7.221$, and $c = 9.361$ Å. The possible mechanism of solid–solid reaction of Ba, Tl oxides was discussed.

The structure of barium monothallate has been determined as shown in the following Fig. 6.228.

In another paper, the same two perovskite-related phases in the Tl_2O_3–BaO system have been synthesized and investigated by X-ray powder diffraction and high-resolution electron microscopy. A solid solution phase was found to exists with the compositions between $BaTl_2O_4$ and $Ba_4Tl_{10}O_{19}$. The typical composition, $Ba_6Tl_{14}O_{27}$, has an orthorhombic unit cell with $a = 17.724$, $b = 6.890$, and $c = 10.235$ Å. The compound $Ba_2Tl_{10}O_{17}$ has a $1 \times 3.5 \times 1$ superstructure derived from the $Ba_6Tl_{14}O_{27}$ phase, being also orthorhombic with unit-cell dimensions of $a = 17.676$, $b = 24.167$, and $c = 10.110$ Å. The relationships between both these new structures, the recently discovered $Ba_4Tl_6O_{13}$ and the perovskite-like basic structures, are discussed. Cell parameters for this composition were found to be: $a = 5.748$ Å, $b = 7.221$ Å, $c = 9/361$ Å, $\alpha = \beta = \gamma = 90°$, cell volume = 388.54 Å^3.

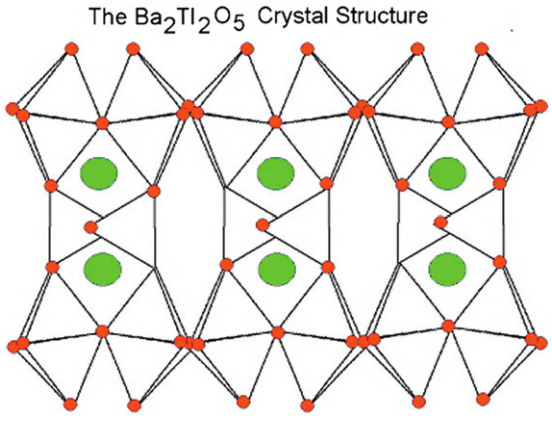

FIGURE 6.227

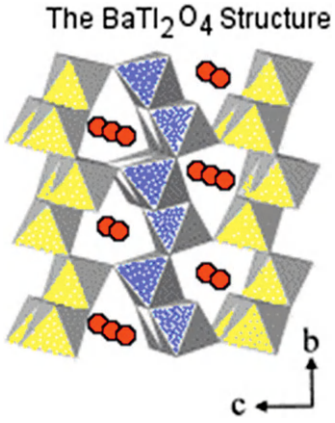

FIGURE 6.228

Barium thallates have not found any uses in industry and are not available commercially. No CAS numbers have been issued, due in part to the toxic nature of thallium in the human body.

Radium Thallates

The scientific literature is lacking in any references to radium thallates. Perhaps this is due to the intense radioactivity of the isomer ^{226}Ra but is more likely due to lack of interest of those in industry who may have usage of such compounds. It is anticipated that various radium thallates could be prepared, using the same methods as those developed for the barium thallate series of compounds. Thus, one would expect to be able to obtain:

$RaO \cdot Tl_2O_3$,
$3RaO\ Tl_2O_3$,
$5RaO \cdot Tl_2O_3$,
$2RaO\ Tl_2O_3$,
$3RaO \cdot 3Tl_2O_3$.

However, there is no record of such syntheses in the present literature.

CHAPTER

7

Group 3 (Sc, Y, and La) Alkaline Earth Compounds

OUTLINE

7.1. Group 3 Transition Metals and Alkaline Earth Compounds **637**
7.1.1. Alkaline Earth—Scandium Compounds 638
Beryllium—Scandium System 638
Magnesium—Scandium System 639
Calcium—Scandium System 640
Strontium—Scandium System 641
Barium—Scandium System 641
Radium—Scandium System 643
7.1.2. Alkaline Earth—Yttrium Compounds 643
Beryllium—Yttrium System 643
Magnesium—Yttrium Compounds 643
Calcium—Yttrium Compounds 645
Strontium—Yttrium Compounds 649
Barium—Yttrium Compounds 650
Radium—Yttrium Compounds 652
7.1.3. Alkaline Earth—Rare Earth Compounds 652

7.1. GROUP 3 TRANSITION METALS AND ALKALINE EARTH COMPOUNDS

This is the first chapter in which the compounds formed from the d-shell elements and the alkaline earths are described. More specifically, these elements involve d-electron shells that are not filled. We have already described the compounds formed from Groups 13 to 17 (Periods 2 to 6) that contain p-electron shells and possess a degree of electronegativity. The modern IUPAC definition of such transition elements states that a transition metal is "an element whose atom has an incomplete d subshell, or which can give rise to cations with an incomplete d subshell". Thus, Group 12 elements within this definition are not transition metals within this definition. All elements in the d-block are metals. Y, Sc and La do not easily form compounds like "yttrides or yttrates $[YO_n^{(2n-1)-}]^{n-}$" because they exhibit significant electropositive characteristics, i.e. they are too metallic. This includes the Lanthanides and Actinides. The number of compounds formed are few and far between as shown in the following table:

Be^{2+}	Mg^{2+}	Ca^{2+}	Sr^{2+}	Ba^{2+}
-	$MgSc_2O_4$	$CaSc_2O_4$	$SrSc_2O_4$	$Ba_3Sc_4O_9$
Y_2BeO	-	$Ca_3Y_2O_6$	SrY_2O_4	$Ba_3Y_4O_9$
$La_2Be_2O_5$	-	-	$Sr_3La_4O_9$	$BaLa_2O_4$
-	-	$CaGd_4O_7$	-	$BaGd_2O_4$
-	-	$Ca_3Yb_2O_6$	-	-
-	-	$CaLu_2O_4$	-	$Ba_3Lu_4O_9$

Note that only the larger of the alkaline earths form a series of compounds. Such compounds cannot be considered as a "barium scandate" nor as a "scandium barate", since the actual composition is a mixed oxide solid-solution arrangement, i.e. $BaO{\cdot}Sc_2O_3$. Thus, the occurrence of compounds in the system $BaO–Sc_2O_3$ has not been thoroughly investigated. It is for this reason that this chapter is short. Although lanthanides (represented by La here) do form a series of compounds, including mixed lanthanide compounds, we will not describe them here because they are not truly relevant to the intent of this book.

Encyclopedia of the Alkaline Earth Compounds
http://dx.doi.org/10.1016/B978-0-444-59550-8.00007-7

Copyright © 2013 Elsevier B.V. All rights reserved.

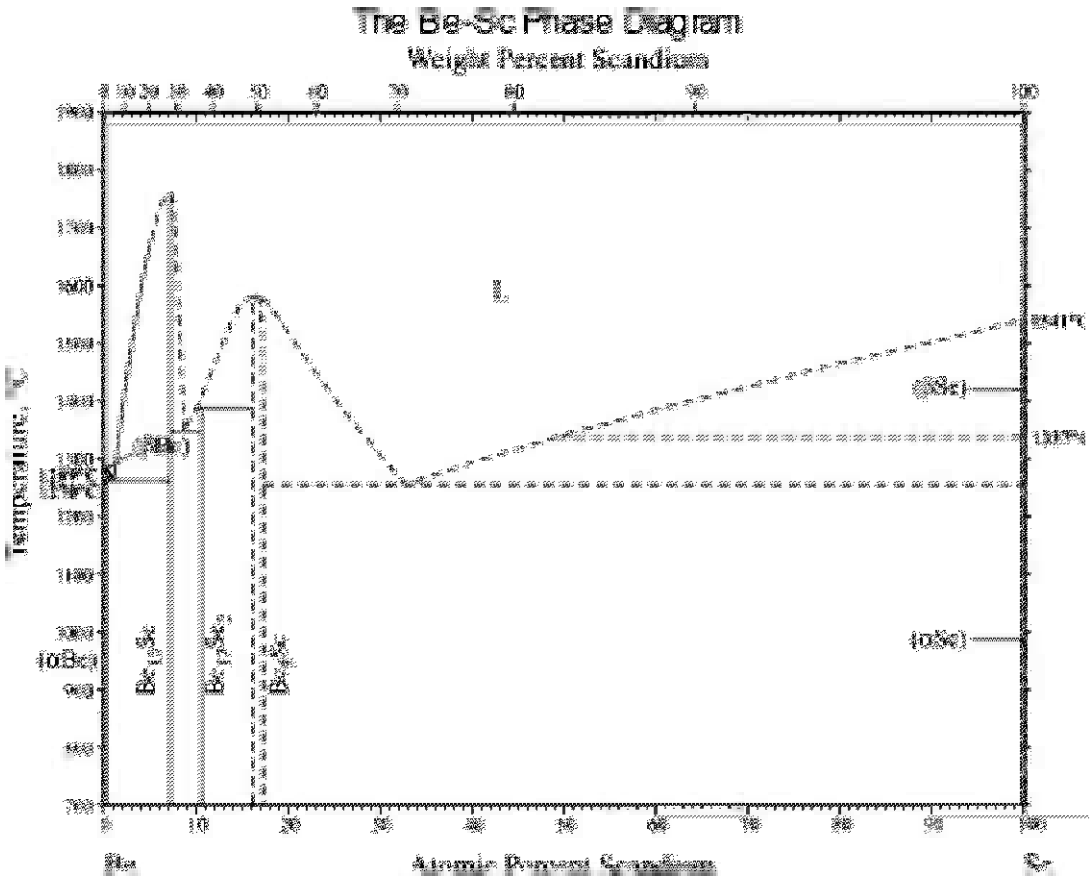

FIGURE 7.1

7.1.1. Alkaline Earth—Scandium Compounds

Since scandium is more expensive than gold, lack of data generated by Academia or Industry perhaps accounts for the scarcity of information concerning these compounds.

The phase diagrams of the **intermetallic** series, Ae–Sc (where Ae is one of the alkaline earths) have been studied. Excluding Be, only one compound is known in this series, that of MgSc. All of the other phase diagrams exhibit a continuous intermetallic solid solution and the larger alkaline earths, when combined with Sc metal, melt to form two liquids. Thus, the only significant feature is that of the polymorphic changes of the alkaline earths, i.e. $\alpha\text{-Ae}_0 \Rightarrow \beta\text{-Ae}_0 \Rightarrow \gamma\text{-Ae}_0$ (where Ae represents any or all of the alkaline earths). It is for this reason that the phase diagrams, in general, are not presented here.

Beryllium–Scandium System

The system, Be^0–Sc^0, forms a few intermetallic compounds, as shown in Fig. 7.1

These intermetallic compounds have the following structural characteristics, shown as follows. Very little data concerning beryllium–scandium compounds have appeared in the technical literature until about 2008 when this data became available (Fig. 7.2).

Be-Sc Crystal Structure Data

Phase	Composition, at % Sc	Point Group	Space Group	Structure Prototype
β Be	0	c/2	Im3m	W
α Be	0	hP2	$P6_1/mmc$	Mg
$Be_{13}Sc$	7.2	cF12	Fm-3c	$NaZn_{7.2}$
$Be_{17}Sc_2$	16.5	hP38 hP19	$P6_1/mmc$ R3m	$Ni_{17}Th_2$ Th_2Zn_{17}
Be_5Sc	16.7	hP6	$P6_1/mmc$	CaCu5
β Sc	100	c/2	Im3m	W
α Sc	100	hP2	$P6_1/mmc$	Mg

FIGURE 7.2

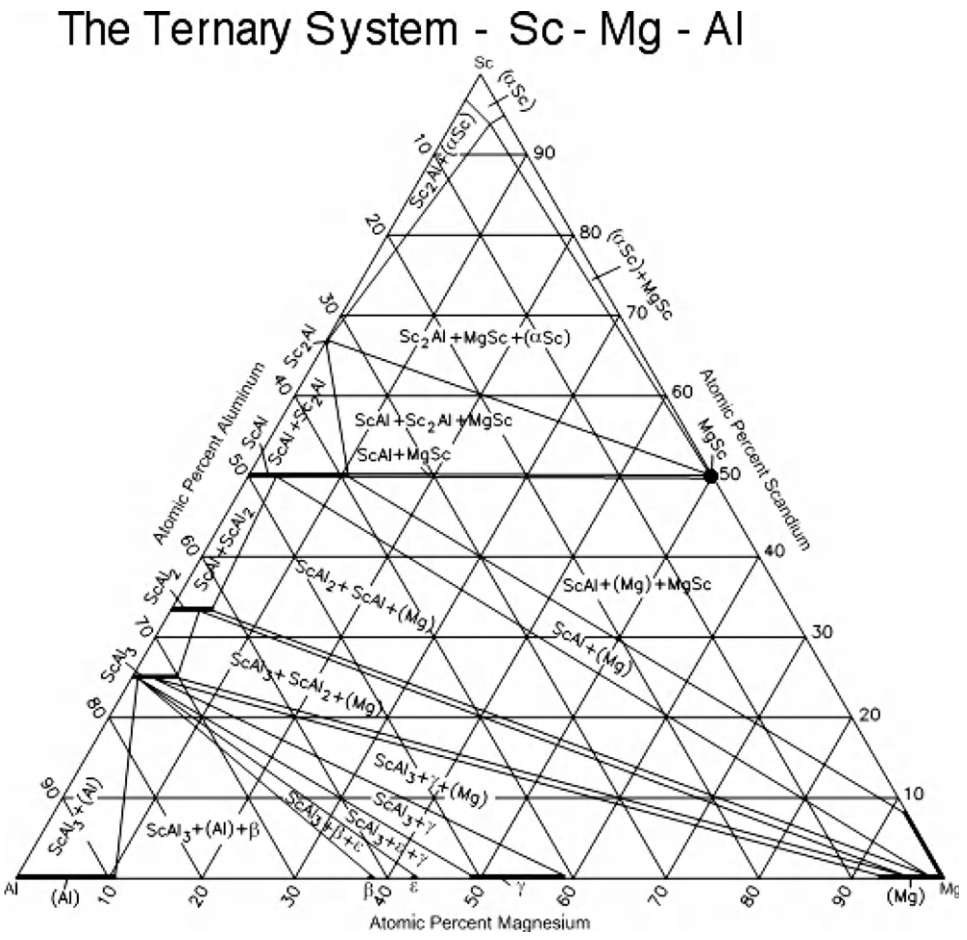

FIGURE 7.3

The oxy-system, $BeO \cdot Sc_2O_3$, does not form any compounds.

There are no uses that have appeared in the Industry and none of these compounds appear to be destined for further consideration.

Magnesium–Scandium System

The intermetallic system, Mg·Sc, has been studied. Whereas, Sc forms many compounds with the metal, Al, it only forms one as shown in the ternary system (Mg-Sc-Al) of Fig. 7.3.

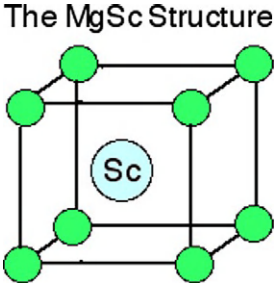

FIGURE 7.4

The one compound, MgSc, has the cubic CsCl structure with $a = 3.436$ Å. It is a body-centered structure with a cell volume of 40.57 Å^3. The Sc atom is located at (1/2/,1/2,1/2) in the unit cell as shown in Fig. 7.4.

It is a body-centered structure with a cell volume of 40.57 Å^3.

The only known binary system is shown in Fig. 7.5. The same compound, MgSc is indicated but the scope and width of the peritectics remain questionable. However, the eutectic points are clearly visible.

As of this date, no complete phase diagram of the system, $MgO–Sc_2O_3$, has been created. The Sc_2O_3–MgO system has been partially studied and found to consist of one liquid and two solid solutions. A relatively simple approach was used to model the solution phases, which were treated as the regular and the subregular solutions of the end-members. The solution parameters were derived from the phase equilibrium data. The thermodynamic calculations using the model allowed the determination of the liquidus, solidus, solvus, and metastable liquid miscibility gaps. Also the lattice stabilities of the components were evaluated.

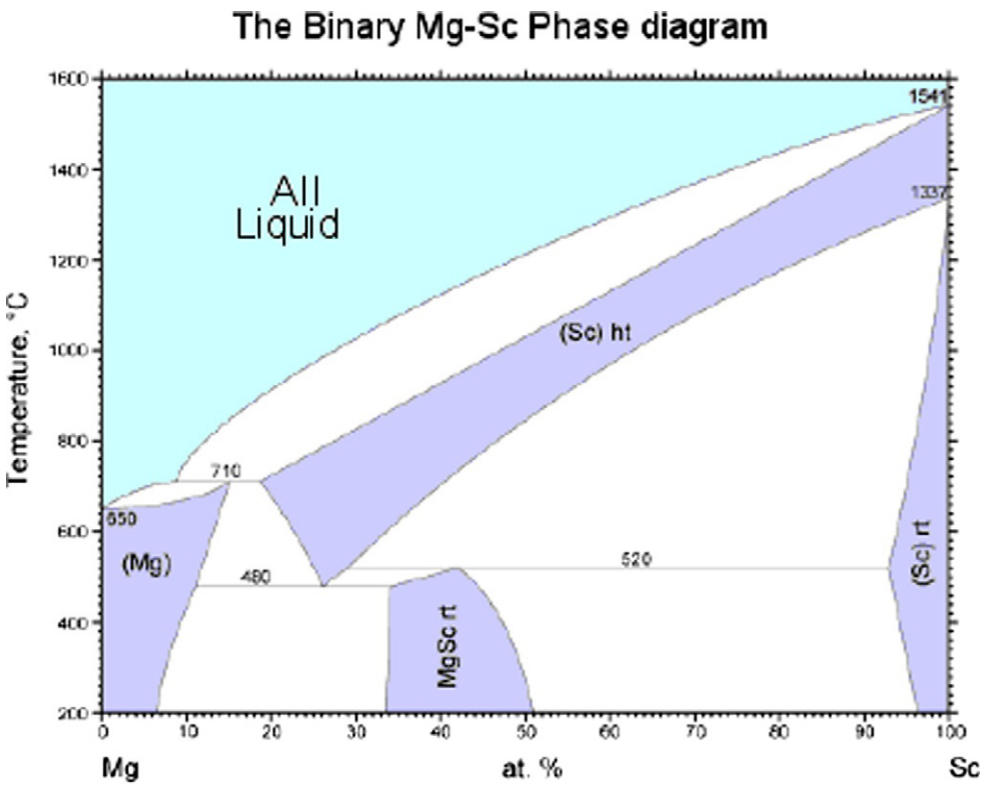

FIGURE 7.5

The hitherto unknown compound $MgSc_2O_4$ was prepared at temperatures above 2000 °C. It crystallizes orthorhombic with the space group D_{2h}^{16}-*Pnam* and is isotypic with $CaSe_2O_4$ and $CaFe_2O_4$. A statistical distribution of Mg^{2+} and Sc^{3+} was found to occupy the metal positions. This is confirmed regarding the distances occurring with the trigonal prismatic coordination (Me^{2+} positions) and with the octahedral coordination (Me^{3+} positions). The $(Sc_2O_4)^{2-}$ framework is rigid as can be shown in the case of the scandates of alkaline earth metals. Thus, analogous compounds with large Me cations cannot be prepared.

The oxy-scandium compound, magnesium scandate, $MgSc_2O_4$, has the CAS number of 12032-33-6 and is offered for sale commercially.

Calcium–Scandium System

The intermetallic system, Ca^0–Sc^0, does not form any compounds but forms intermetallic solid solutions at all compositions (0–100%).

The system, $CaO{\cdot}Sc_2O_3$, has not been studied intensively. A paper describing the 1:1 compounds of $CaO{\cdot}Sc_2O_3$ was published. Therein, it was stated that the compounds $CaSc_2O_4$ and $SrSc_2O_4$ were synthesized by solid-state reaction of the component oxides at temperatures ranging from 950 to 1400 °C. Both calcium and strontium monoscandates are orthorhombic and analogous to $CaFe_2O_4$. Lattice parameters for $CaSc_2O_4$ are: $a_o = 9.461$, $b_o = 11.122$, $c_o = 3.143$ Å and for $SrSc_2O_4$, $a_o = 9.698$, $b_o = 11.302$, $c_o = 3.185$ Å. Based on four molecules per unit cell, the X-ray density for $CaSc_2O_4$ was determined to be 3.89 g/cm^3 and that for $SrSc_2O_4$ is 4.59 g/cm^3. The structure consists of face-shared tetrahedra of ScO_6^{3-} octahedra joined to form rigid $(ScO_6)_2^{6-}$ units. These are arranged in a zigzag pattern in the crystal (see Fig. 7.6).

Both $CaSc_2O_4$ and $SrSc_2O_4$ are isostructural with $CaFe_2O_4$ and have the space group of *Pnam*. Cell parameters are listed in Table 7.1.

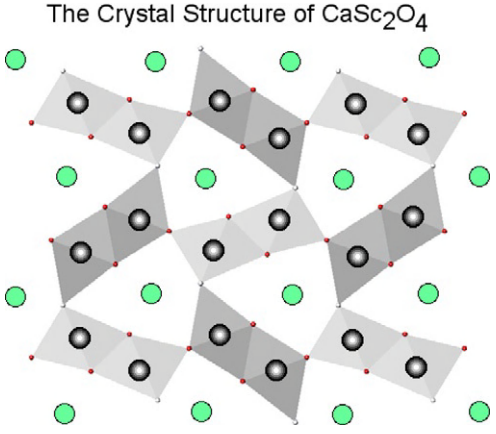

FIGURE 7.6

TABLE 7.1

Pnam	$CaSc_2O_4$	$SrSc_2O_4$
a(Å)	9.461	9.698
b(Å)	11.122	11.302
c(Å)	3.143	3.185
V(Å^3)	330.6	349.1
Z	4	4
MW (g/mol)	193.99	241.53
Density (g/cm^3)	3.90	4.60

In this structure, the octahedra form a rigid three-dimensional (3D) structure with two distinct Sc sites as part of the structure. This organization allows the alkaline earths to occupy the long cavities that exist in the *ab*-plane of the structure.

None of these compounds are available commercially.

Strontium–Scandium System

The system, SrO–Sc_2O_3, has not been studied intensively. Although $Ba_3Sc_2O_5$ is known, the corresponding strontium compound has not been documented. This suggests that the compound, tri-strontium scandate, is not very stable. There are no reports of its synthesis or of its physical properties.

The compound, $SrSc_2O_4$, has the same structure as its homologue, $CaSc_2O_4$, whose structure is presented above.

However, a layered oxysulfide, $Sr_3Cu_2Sc_2O_5S_2$, has been formulated as $Sr_3Sc_2O_5{\cdot}Cu_2S_2$. It is composed of anti-PbO-like Cu_2S_2 slabs alternating with perovskite-like $Sr_3Sc_2O_5$ slabs, and was systematically studied as a p-type transparent conducting material. This material has a wide energy gap of 3.1 eV and a p-type electrical conductivity of 2.8 S/cm at room temperature. A hole mobility of $+150\ cm^{-2}/V/S$ at room temperature was found, which is much higher than the typical value of 10^{-1} to $10\ cm^{-2}/V/S$ found in other copper compounds. The performance of bulk undoped $Sr_3Cu_2Sc_2O_5S_2$ shows the promise of copper oxysulfides as a class of p-type transparent conductive materials that could be essential for optoelectronic applications.

Although a study of the barium scandate (BaO–Sc_2O_3) system has been published, the literature concerning SrO–Sc_2O_3 is almost nonexistent. No compounds are offered for sale commercially and no CAS numbers have been issued to date.

Barium–Scandium System

Information concerning the BaO–Sc_2O_3 system has been scanty in the scientific literature. Compound formation in the BaO–Sc_2O_3 binary system has been examined. Early work established the existence of the compounds $Ba_3Sc_4O_9$ and $BaSc_2O_4$. A later worker then studied compositions ranging from 3–30 mol% of Sc_2O_3 (with the balance consisting of BaO) and then with Sc_2O_3 ranging up to 66% in the temperature range of 900–1400 °C. This resulted in the discovery of a low temperature barium-rich phase, $BaSc_2O_5$. This worker determined that BaO was soluble in $BaSc_2O_5$. Above 1000 °C, excess BaO reacted and the $BaSc_2O_5$ appeared to decompose to form $Ba_3Sc_4O_9$. The compounds were noted to be relatively stable in the ambient atmosphere. The most accurate phase diagram was presented in 1988. This is presented in Fig. 7.7.

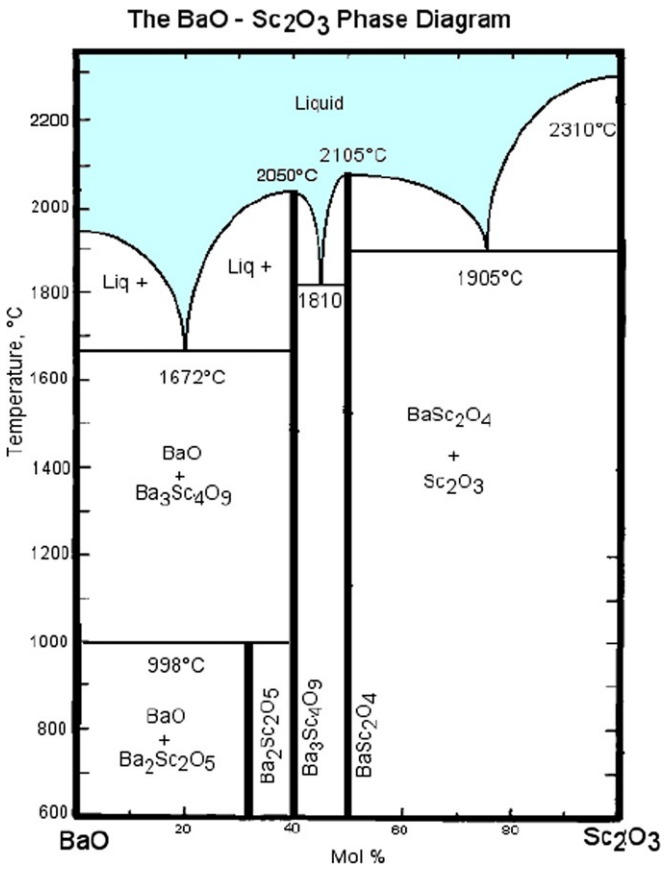

FIGURE 7.7

$Ba_2Sc_2O_5$ decomposes into $Ba_3Sc_4O_9$ and BaO at temperatures greater than 1000 °C. $Ba_3Sc_4O_9$ and $BaSc_2O_4$ were reported to melt congruently at 2050 and 2100 °C, respectively. Another discrepancy between two prior reports involved the low temperature range. It was reported that $Ba_3Sc_4O_9$ and $BaSc_2O_4$ were not stable below 1200 °C whereas others reported that both of these compounds were stable to 900 °C. In addition, some experiments were undertaken utilizing aqueous salts of barium and scandium as starting materials.

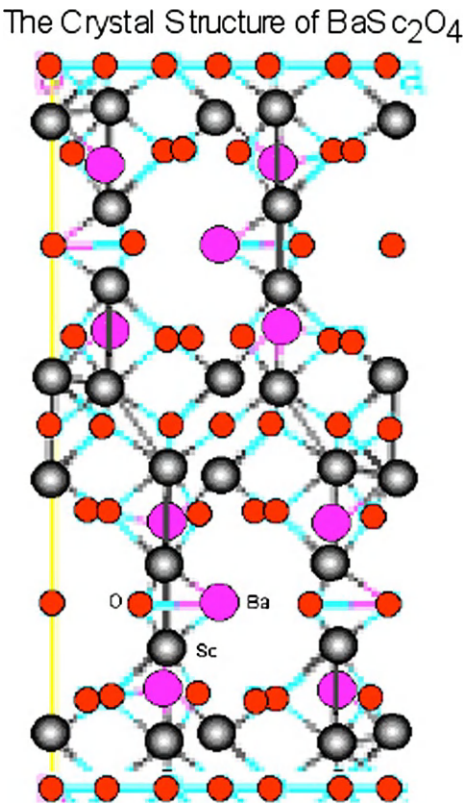

FIGURE 7.8

(Other experiments were conducted using scandium oxide and barium carbonate as the raw materials.) At 1000 °C a different compound was observed, having a composition close to $Ba_3Sc_4O_9$ but with a unit cell dimension decreased along the *c*-axis by a factor of 6. This led others to suggest the existence of yet another barium scandate phase, $Ba_6Sc_6O_{15}$. The results of this investigation provided a somewhat incomplete description for the stability of compounds in the subsolidus region.

The $BaSc_2O_4$ compound was observed to crystallize as a perovskite type structure, in the tetragonal system, with lattice constants $a = 4.160$ Å and $c = 3.994$ Å, The crystal structure of the $Ba_3Sc_4O_9$ compound was determined to be hexagonal with lattice constants of $a = 5.873$ Å and $c = 23.69$ Å. Finally, the crystal structure of the $BaSc_2O_4$ compound was identified as monoclinic, with lattice parameters $a = 9.836$ Å, $b = 20.578$ Å, $c = 5.187$ Å and $\gamma = 89°$. The structure has the form shown in Fig. 7.8.

It consists of a series of ScO_4 tetrahedra, corner-attached to form a series of chains parallel to the *c*-axis The associated cell parameters are: $a = b = 5.7136$ Å, $c = 20.563$Å, $\alpha = \beta = 90°$, $\gamma = 118.881°$, cell volume = 587.71 Å^3, $Z = 4$. Cell occupancy is shown in Table 7.2.

After considerable deliberation, it has been agreed that the structure of $BaSc_2O_4$ is a type between that of calcium ferrite and a "filled" tridymite. The "filled" tridymite structure was thought to be the stable structure formed when only tetrahedral coordination of the R^{+3} ion was possible, usually due to the large ionic size. The crystal structure of $BaSc_2O_4$ has been confirmed using single crystals. The crystal symmetry is monoclinic ($C2/c$, $Z = 12$) with a pseudo-orthorhombic unit cell. The relationship with parent perovskite structure was discussed in terms of coordination polyhedra and bond lengths.

The hydration behavior of the barium scandates with oxygen-deficient perovskite-related structures of tetragonal $Ba_2Sc_2O_5$ and cubic $BaScO_{3-\delta}$ ($\delta = 0.5$) was studied. Both the tetragonal $Ba_2Sc_2O_5$ and cubic $BaScO_{3-\delta}$ absorbed water and formed $Ba_2Sc_2O_5 \cdot 0.60H_2O$ and

TABLE 7.2

No.	Site notation	Atom	Multiplicity	Wyckoff	Site symmetry	*x*	*y*	*z*	Occupancy
1	O3	O	8	f	1	0.065	0.339	0.123	1.0
2	O4	O	8	f	1	0.103	0.144	0.621	1.0
3	O6	O	8	f	1	0.153	0.443	0.0025	1.0
4	Sc2	Sc	8	f	1	0.164	0.119	0.053	1.0
5	Ba2	Ba	8	f	1	0.1656	0.109	0.3615	1.0
6	Sc1	Sc	8	f	1	0.1662	0.108	0.1969	1.0
7	O2	O	8	f	1	0.236	0.373	0.252	1.0
8	O5	O	8	f	1	0.336	0.153	0.121	1.0
9	Sc3	Sc	8	f	1	0.5028	0.117	0.0697	1.0
10	O1	O	4	e	2	0	0.07	1/4	1.0
11	Ba1	Ba	4	e	2	0	0.609	1/4	1.0

$BaScO_{3-\delta}\cdot 0.37H_2O$, respectively, during cooling in a humidified atmosphere. The hydration and the dehydration temperatures for the barium scandates were ~533 and 553 K, respectively; these temperatures were 30–70 K lower than that for $Ba_2In_2O_5$. A distinct difference in the hydration behavior of the structurally different tetragonal $Ba_2Sc_2O_5$ and cubic $BaScO_{3-\delta}$ was not observed. The $Ba_2Sc_2O_5$ types of compounds show protonic conduction below 673 K and p-type conduction above 773 K in a humidified atmosphere.

$Ba_3Sc_4O_9$ has a structure similar to perovskite with cell parameters of: $a = b = 6.873$ Å, $c = 8.5939$ Å, $\alpha = \beta = 70.2°$, $\gamma = 80°$, $Z = 2$, cell volume = 235.88 Å^3.

In addition, it has been determined that the systems (CaO–SrO–BaO)ScO_4 can form mixed cation compounds. In the CaO···SrO···Sc_2O_3 and BaO···SrO···Sc_2O_3 systems, complete series of mixed crystals were found for (Ca,Sr)Sc_2O_4 and (Sr,Ba)$_3Sc_4O_9$, respectively. In the BaO···CaO···Sc_2O_3 system a new ternary phase with composition $Ba_x(Ca_{2x}Sc_{2-2x})Sc_6O_{12}$ was detected having an incommensurate structure which may be described with a basic hexagonal unit cell ($a = 9.739$ Å, $c = 3.1274$ Å) and a second hexagonal cell having the same basic a-axis. The c-axis of the second cell is x-dependent: $c^x = 3.13/x$, x varying from 0.782 to 0.736, corresponding to the region from $BaCa_2Sc_8O_{15}$ with $c^x = 4.00$ Å, to $BaCa_2Sc_9O_{16.5}$ with $c^x = 4.25$ Å.

Radium–Scandium System

Both Ra and Sc, as metals, are too expensive {^{226}Ra = >$1 million/oz and Sc = $1250/oz} and it is unlikely that any radium–scandium compounds will ever be investigated.

7.1.2. Alkaline Earth—Yttrium Compounds

The same limitations exist for the Ae–Y intermetallic and oxy-yttrium dominated compounds of the alkaline earths, as for the Ae–Sc system (Ae = alkaline earths). Thus, Y metal only forms one intermetallic compound with Be metal. Y metal forms three compounds with Mg metal but no compounds are known for the systems: Y–Ca, Y–Sr or Y–Ba. All of these latter combinations show an intermetallic solid solution from >0 to <100% of the alkaline earth combinations. These solid solutions then melt to form two liquids. Although the phase diagrams have been published and are available for the Ca–Y, Sr–Y and Ba–Y systems, only one is shown here.

Beryllium–Yttrium System

The system, Be–Y, as metals, forms just one compound, $Be_{13}Y$, as shown in the following phase diagram (Fig. 7.9).

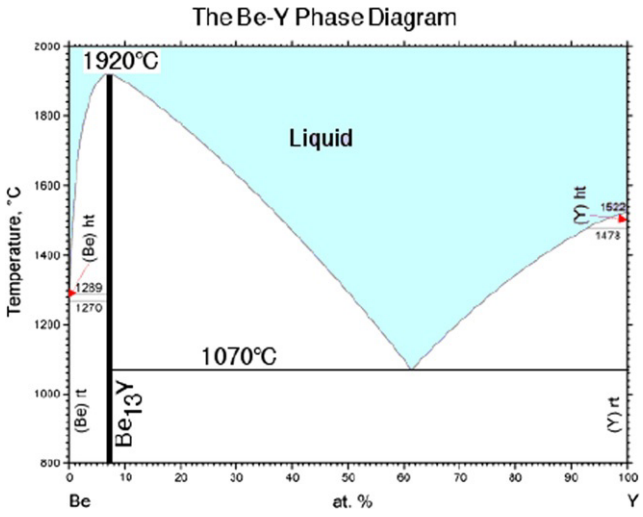

FIGURE 7.9

It melts at 1920 °C, which is about 50% higher than either of its components. Studies were made on the Be–Y system in order to establish the existence of intermetallics in it and to systematize the compounds of type Ae–Be_{13} according to their formula volumes. The existence of a cubic phase YBe_{13}, isomorphous with $NaZn_{13}$ and with a lattice period $a = 10.238$ Å, was established. It was concluded that the known ABe_{13} beryllides can be divided into three groups according to their volume relationships to the volume of the A component:

Sc, Hf, Zr
Mg, Er, Y, Ca, Am
Np, U, Pu, Th, Ce, La

BeO forms but one oxy-dominated compound with Y_2O_3. No other compounds in this system are known.

BeY_2O_4 has the structure shown in Fig. 7.10.

It consists of YO_4 tetrahedra, attached in a zigzag chain with Be^{2+} atoms interspersed along the chains.

Cell parameters are: $a = 3.5315$ Å, $b = 9.8989$ Å, $c = 1.0443$ Å, $\alpha = \beta = \gamma = 90°$, cell volume = 363.56 Å^3, $Z = 4$. Cell occupancy is shown in Table 7.3.

Although $Be_2Y_2O_5$ is listed in one reference as an oxy-yttrate compound of Be, there are no further references that address this composition. Its existence remains in doubt.

No uses for any of these compounds have arisen in Industry and they are not available commercially.

Magnesium–Yttrium Compounds

Mg metal forms three compounds with yttrium metal as shown in the following phase diagram in Fig. 7.11.

The structure of MgY is body-centered cubic as shown in the following diagram in Fig. 7.12.

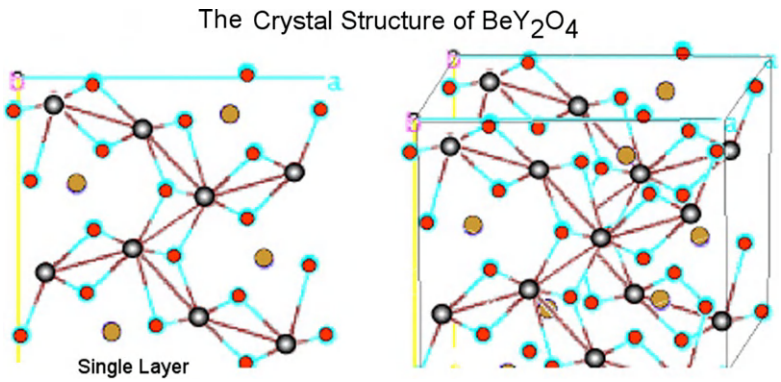

FIGURE 7.10

TABLE 7.3

No.	Site notation	Atom	Multiplicity	Wyckoff	Site symmetry	x	y	z	Occupancy
1	O4	O	4	c	.m.	0.04453	1/4	0.35344	1.0
2	Y1	Y	4	c	.m.	0.09028	1/4	0.67664	1.0
3	Y2	Y	4	c	.m.	0.11738	1/4	0.08626	1.0
4	Be	Be	4	c	.m.	0.19369	1/4	0.37329	1.0
5	O2	O	4	c	.m.	0.24956	1/4	0.51841	1.0
6	O1	O	4	c	.m.	0.27699	1/4	0.24361	1.0
7	O3	O	4	c	.m.	0.51297	1/4	0.61518	1.0

TABLE 7.4

No.	Site notation	Atom	Multiplicity	Wyckoff	Site symmetry	x	y	z	Occupancy
1	Y	Y	1	b	m-3m	1/2	1/2	1/2	1.0
2	Mg	Mg	1	a	m-3m	0	0	0	1.0

The cell parameters are: $a = b = c = 3.797$ Å and $\alpha = \beta = \gamma = 90°$. Cell volume is 74.64 Å^3. The cell occupancy is shown in Table 7.4.

The compound, Mg_2Y, has the structure shown in Fig. 7.13.

Cell parameters are: $a = b = 6.018$ Å, $c = 9.734$ Å, $\alpha = \beta = 90°$, $c = 120°$, cell volume = 305.30 Å^3. Cell occupancy is shown in Table 7.5.

These two compounds are the only structures known. The structure of MgY_5 has not been published. However, an additional compound, $Mg_{24}Y_5$, has been discovered and has the structure shown in Fig. 7.14.

Cell parameters are: $a = b = c = 9.7434$ Å, $\alpha = \beta = \gamma = 109.71°$, cell volume = 712.05 Å^3, $Z = 4$. Cell occupancy is shown in Table 7.6.

In addition, it has been found that Ce^{3+} is able to substitute for Y^0 in these compounds. The structural and magnetic properties of a series of novel compounds in the ternary Ce–Mg–Y system have been studied by X-ray diffraction, SQUID magnetometry and XAS spectroscopy. The crystal structures of the compounds $Ce_{0.34}Y_{0.67}Mg_2$ and $Ce_{0.49}Y_{0.51}Mg_{4.7}$ have been refined. Magnetic data are consistent with a tri-positive ground state $^2F_{5/2}$ for the cerium atom (not tetrapositive). The XAS measurements confirm this result. Crystal field effects are apparent in the magnetic data at temperatures below about 50 K in the compounds with higher Ce concentration.

However, substitution of Zn^0 for Mg^0 in the Mg_2Y compound results in a complete change in crystal structure (Fig. 7.15).

MgO forms oxy-dominated compounds with Y_2O_3. The structure of MgY_2O_4 has the form shown in Fig. 7.16.

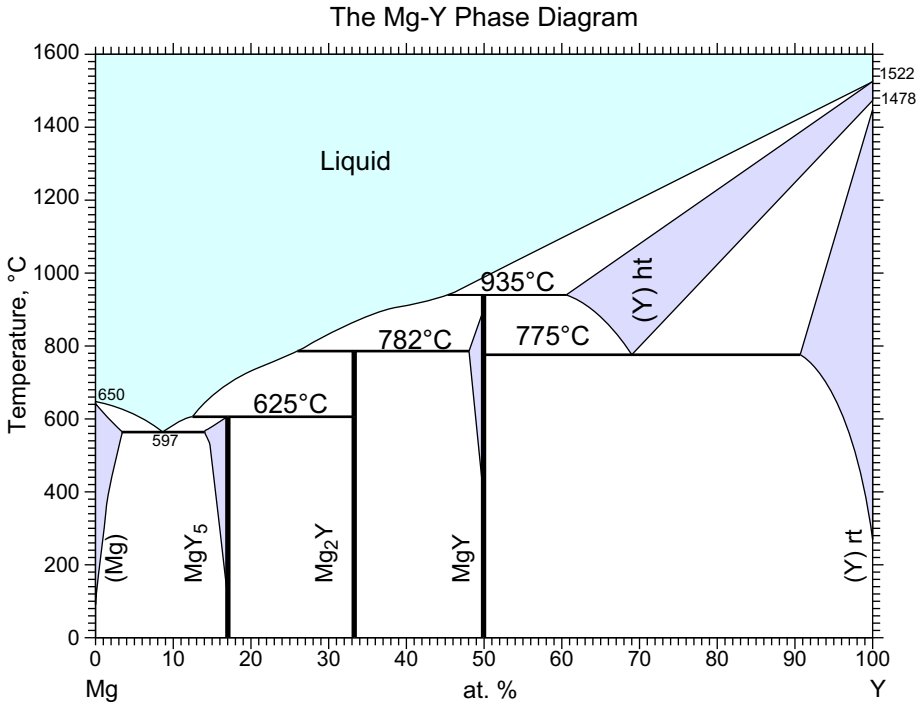

FIGURE 7.11

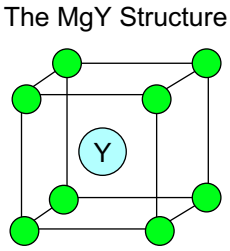

FIGURE 7.12

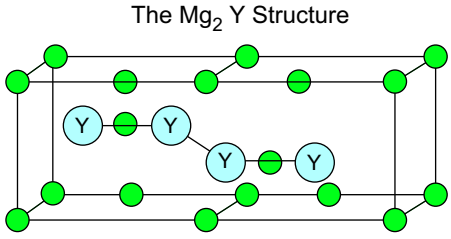

FIGURE 7.13

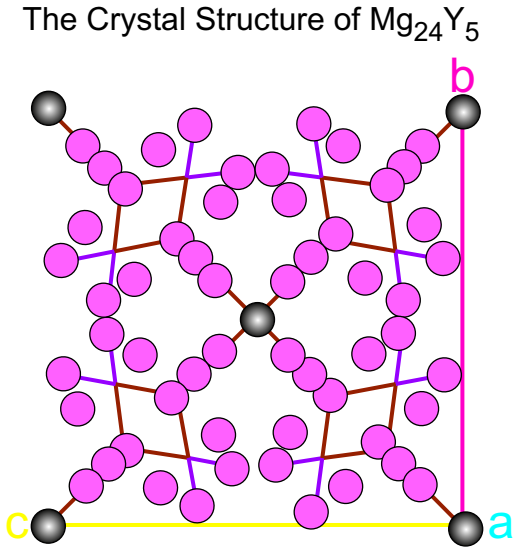

FIGURE 7.14

It is nearly identical to the Be homologue. Cell parameters are: $a = 3.5315$ Å, $b = 9.799$ Å, $c = 10.452$ Å, $\alpha = \beta = \gamma = 90°$. Cell occupancy is shown in Table 7.7.

Other than structure, little is known concerning this compound.

No uses have appeared for these compounds in the Industry and little interest in Academia has been forthcoming at this date and time.

Calcium–Yttrium Compounds

Calcium metal does not form any specific **intermetallic** compounds with yttrium metal. The phase diagram

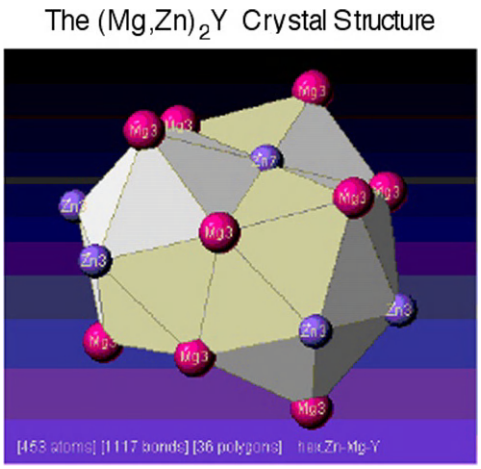

FIGURE 7.15

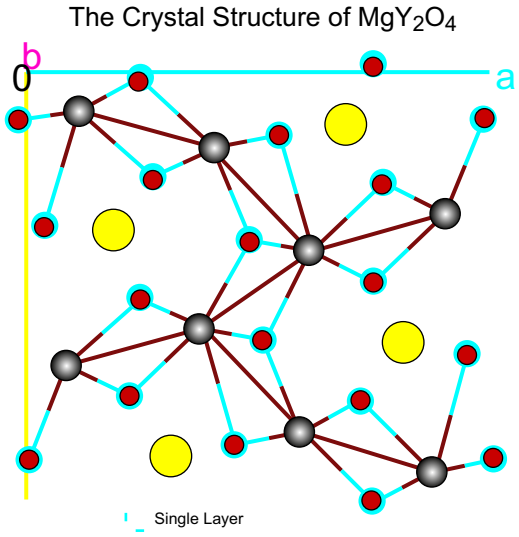

FIGURE 7.16

TABLE 7.5

No.	Site notation	Atom	Multiplicity	Wyckoff	Site symmetry	*x*	*y*	*z*	Occupancy
1	Mg1	Mg	6	h	mm2	0.1697	0.3394	1/4	1.0
2	Y1	Y	4	f	3m.	1/3	2/3	0.5629	1.0
3	Mg2	Mg	2	a	−3m.	0	0	0	1.0

TABLE 7.6

No.	Site notation	Atom	Multiplicity	Wyckoff	Site symmetry	*x*	*y*	*z*	Occupancy
1	Mg2	Mg	24	g	..m	0.091	0.091	0.281	1.0
2	Mg1	Mg	24	g	..m	0.358	0.358	0.036	1.0
3	M	0.679Y + 0.321Mg	8	c	.3m	0.314	0.314	0.314	1.0
4	Y	Y	2	a	43m	0	0	0	1.0

TABLE 7.7

No.	Site notation	Atom	Multiplicity	Wyckoff	Site symmetry	*x*	*y*	*z*	Occupancy
1	O4	O	4	c	.m.	0.04453	1/4	0.35344	1.0
2	Y1	Y	4	c	.m.	0.09028	1/4	0.67664	1.0
3	Y2	Y	4	c	.m.	0.11738	1/4	0.08626	1.0
4	Mg	Mg	4	c	.m.	0.19369	1/4	0.37329	1.0
5	O2	O	4	c	.m.	0.24956	1/4	0.51841	1.0
6	O1	O	4	c	.m.	0.27699	1/4	0.24361	1.0
7	O3	O	4	c	.m.	0.51297	1/4	0.61518	1.0

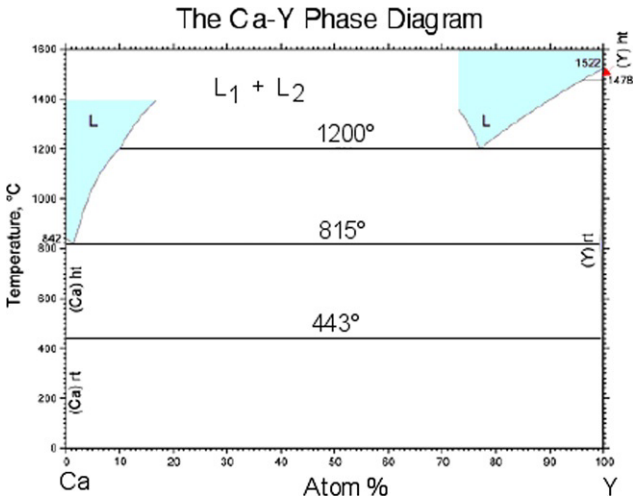

FIGURE 7.17

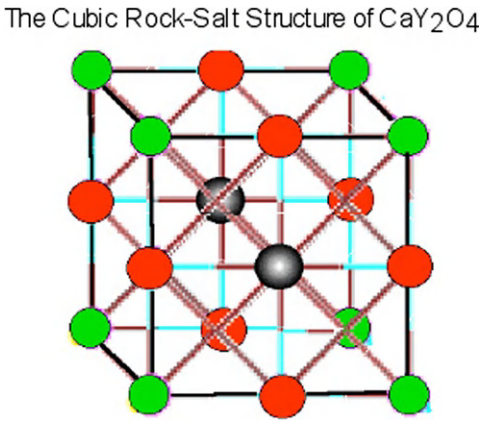

FIGURE 7.18

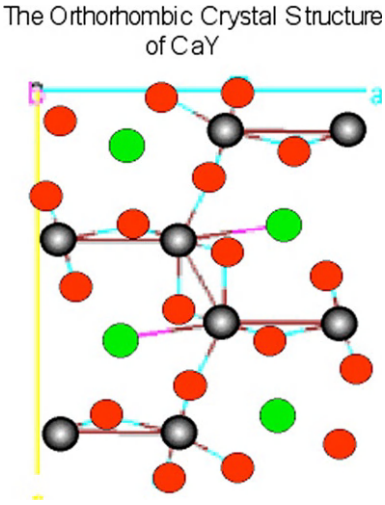

FIGURE 7.19

is devoid of any compounds and shows only the polymorphic transformation of the individual metals. A sample phase diagram has been presented in Fig. 7.17.

The system, $CaO–Y_2O_3$, forms few compounds as well. CaY_2O_4 is a 1:1 compound with the rock salt structure. 0.11 atom% of the cation positions are occupied by Y and 0.89% atom% by Ca in the $Ca_{0.89}Y_{0.11}O_2$ structure (Fig. 7.18).

Cell parameters of $Ca_{0.89}Y_{0.11}O_2$ are: $a = b = c =$ 3.3976 Å, $\alpha = \beta = \gamma = 60°$, cell volume is 27.73 Å^3, $Z = 4$. Cell occupancy is shown in Table 7.8.

Although it may appear that this compound could be related to the CaY_2O_4 composition, the CaY_2O_4 compound has a completely different structure (Fig. 7.19).

It is closely related to that of BeY_2O_4. Cell parameters are: $a = 3.38$ Å, $b = 10.09$ Å, $c = 11.96$ Å, $\alpha = \beta = \gamma = 90°$, cell volume is 407.89 Å^3, $z = 2$. Cell occupancy is shown in Table 7.9.

A $CaO–Y_2O_3$ phase diagram was first made in 1964. This researcher who stated that a eutectic type was prevalent. Later work (1987) also showed the same lack of crystalline compounds. A diagram illustrating this shown in Fig. 7.20.

Both of these authors claimed that only mixtures and a solid solution existed in this system. Yet, others had already reported three compounds to be present in this system, CaY_2O_4, CaY_4O_7 and $Ca_3Y_2O_7$. Later work (1991) also indicated that no compounds exist in the $CaO–Y_2O_3$ system, only separate oxides up to the eutectic temperature. These researchers:

> "The degree of solid solubility between yttria and calcia was measured, in the yttria-rich region, over the temperature range 1200 to 2000 °C. X-ray diffraction results indicate that as much as 12.4 mol% calcia can be dissolved in yttria at 2000 °C. No solid solution between the two oxides was observed below 1400 °C. In addition, ex-solution kinetics was measured. Kinetic data were compared to a number of solid

TABLE 7.8

No.	Site notation	Atom	Multiplicity	Wyckoff	Site symmetry	x	y	z	Occupancy
1	O	O	4	b	m-3m	1/2	1/2	1/2	1.0
2	M	0.89Ca + 0.11Y	4	a	m-3m	0	0	0	0.94

TABLE 7.9

No.	Site notation	Atom	Multiplicity	Wyckoff	Site symmetry	x	y	z	Occupancy
1	O1	O	4	c	.m.	0.071	1/4	0.078	1.0
2	Y1	Y	4	c	.m.	0.077	1/4	0.394	1.0
3	Sr1	Sr	4	c	.m.	0.242	1/4	0.65	1.0
4	O2	O	4	c	.m.	0.289	1/4	0.352	1.0
5	O3	O	4	c	.m.	0.387	1/4	0.016	1.0
6	O4	O	4	c	.m.	0.47	1/4	0.775	1.0
7	Y2	Y	4	c	.m.	0.568	1/4	0.609	1.0

state models with the 3D nucleation model providing the best correlation. The Hulbert model was further used to characterize the growth mechanism. It suggested that growth is phase-boundary controlled between 1200 and 1500 °C and that the nucleation rate either drops to zero or that growth becomes two-dimensional above 1600 °C. Although undoped yttria is both a p- and n-type semiconductor, yttria-calcia solutions are ionic conductors below about 10^{-10} atm oxygen (t_i >0.99) with no trace of n-type conductivity being observed. The activation energy for ionic conduction in yttria-5 mol% calcia is 125 kJ/mol". The only caveat was that the temperature may have not been high enough in their experiments.

It has been observed that the compound, CaY_4O_7, is obtained as a decomposition product from CaY_2O_4:

$$2\ CaY_2O_4 + \text{heat} \Rightarrow CaY_4O_7 + CaO$$

CaY_4O_7, CaY_2O_4, and $Ca_3Y_2O_6$ compounds were found to be stable above temperatures of 1200 °C and could not be quenched to room temperature. $Ca_3Y_2O_6$, CaY_2O_4, and CaY_4O_7 exist up to 1960, 1760 but 2140 °C, respectively. In view of this observation and other results (see above), the phase diagram has been modified to the diagram shown in Fig. 7.21.

No CAS numbers have ever been assigned and no calcium–yttrium compounds are offered for sale commercially. Although the possibility of sulfur-dominated compounds like $CaS{\cdot}Y_2S_3$ exists, no studies of such compounds are available in the scientific literature as well.

In view of the instability of these compounds (which were measured using high temperature XRD equipment), coupled with the fact that they have not been obtained as stable compounds at room temperature, it

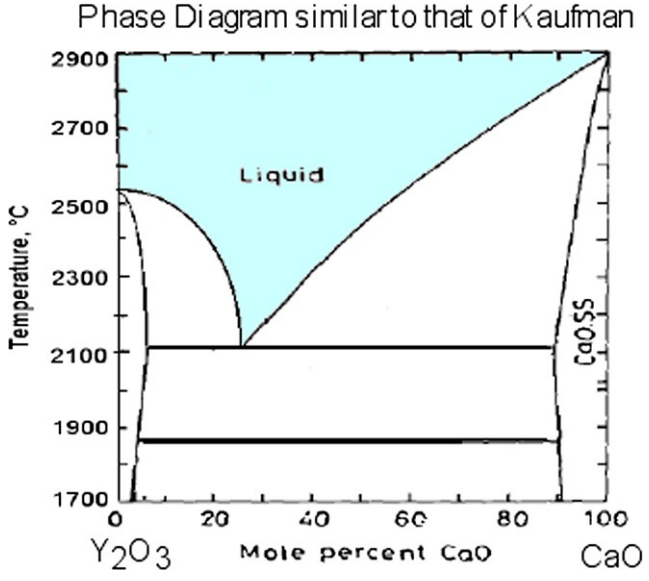

FIGURE 7.20

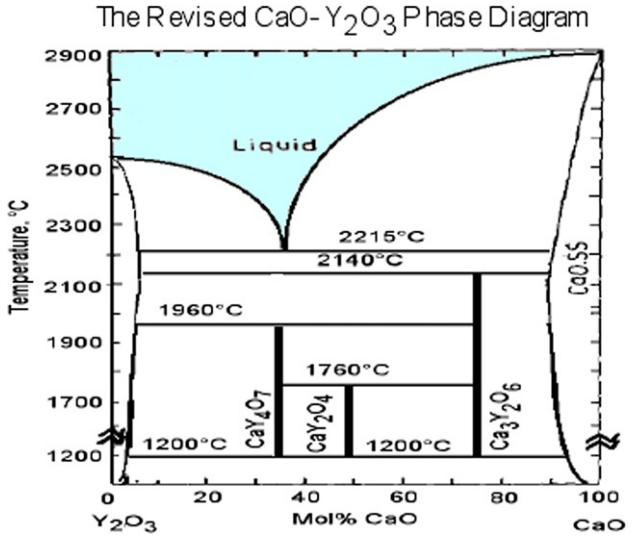

FIGURE 7.21

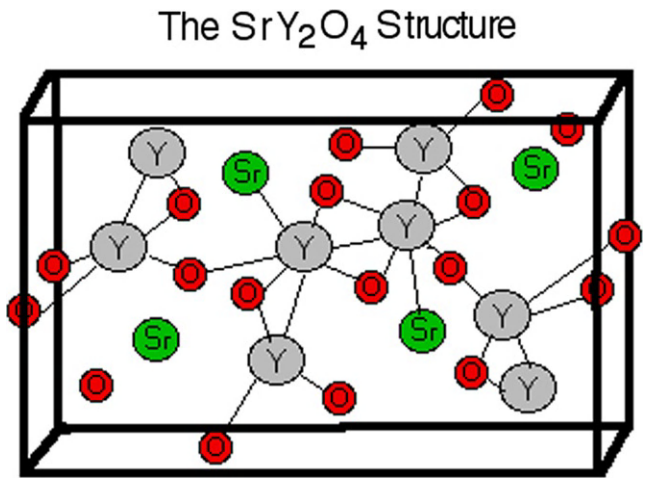

FIGURE 7.22

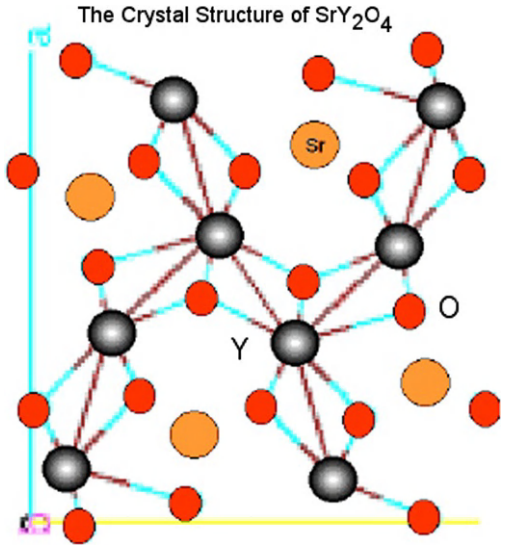

FIGURE 7.23

is not surprising that the scientific literature is very limited. Few papers concerning data relating to these compounds can be found and they present little interest to those in the Industry. They are not offered for sale commercially.

Strontium–Yttrium Compounds

Strontium metal does not form any specific **intermetallic** compounds with Yttrium metal. The phase diagram is devoid of any compounds and shows only the polymorphic transformation of the individual metals (like that shown above for MgO–Y_2O_3).

The system, SrO–Y_2O_3, has not been thoroughly investigated. It was originally stated that no compounds exist. Nonetheless, a recent patent (2009) has described novel red emitting phosphors for use in fluorescent lamps resulting in superior color rendering index values compared to conventional red phosphors. Also disclosed is a fluorescent lamp including a phosphor layer comprising blends of one or more of a blue phosphor, a blue-green phosphor, a green phosphor and a red phosphor selected from the group consisting of SrY_2O_4:Eu^{3+}. This compound has the structure shown in Fig. 7.22.

It is tetragonal with cell parameters of: $a = 3.38$ Å, $b = 10.09$ Å, $c = 11.96$ Å, $\alpha = \beta = \gamma = 90°$, cell volume = 407.89 $Å^3$. Cell occupancy is shown in Table 7.10.

Another view of the same structure is shown in Fig. 7.23.

The applicability of SrY_2O_4 as a thermal barrier coating was investigated. A polycrystalline sample of SrY_2O_4 was prepared and measured concerning its thermophysical properties. The melting temperature (T_m) of SrY_2O_4 is 2413 K (2140 °C). The longitudinal and shear sound velocities were measured by an ultrasonic pulse-echo method at room temperature in air. This enabled the evaluation of the elastic moduli and Debye temperature. The heat capacity (C_P) was measured by using a differential scanning calorimeter in high purity argon atmosphere. The relationships between the

TABLE 7.10

No.	Site notation	Atom	Multiplicity	Wyckoff	Site symmetry	x	y	z	Occupancy
1	O1	O	4	c	.m.	0.071	1/4	0.078	1.0
2	Y1	Y	4	c	.m.	0.077	1/4	0.394	1.0
3	Sr1	Sr	4	c	.m.	0.242	1/4	0.65	1.0
4	O2	O	4	c	.m.	0.289	1/4	0.352	1.0
5	O3	O	4	c	.m.	0.387	1/4	0.016	1.0
6	O4	O	4	c	.m.	0.47	1/4	0.775	1.0
7	Y2	Y	4	c	.m.	0.568	1/4	0.609	1.0

thermophysical properties of SrY_2O_4 were studied. It was concluded that this compound was suitable as a thermal barrier material.

The only interoxide, SrY_2O_4 in the Y_2O_3–SrO system was synthesized at a low temperature of 1120 K (850 °C) by a hybrid polymeric gel cum auto-combustion method. For determining the high temperature stability of SrY_2O_4 the emf of the galvanic cell:

$$\text{-Pt, SrO, } SrF_2\text{, } O_2 \,|SrF_2|\, O_2\text{, } SrF_2\text{, } Y_2O_3\text{, } SrY_2O_4\text{, Pt-}$$

was studied over the temperature range from 935 to 1080 K (660–810 °C) which yielded the least squares expression:

$$E \pm 0.76(\text{mV}) = 236.46 - 0.16198T\ (\text{K})$$

From this, the standard Gibbs energy of formation $\Delta G^{o}_{f,ox}$ of SrY_2O_4 from its constituent binary oxides Y_2O_3 and SrO was derived to be:

$$\Delta G_{f,ox^o}(\text{kJ/mol}) = -45.63 + 0.03126T\ (\text{K})$$

A value of 0.58 could be derived for the activity of SrO, a_{SrO}, in the SrY_2O_4/Y_2O_3 mixture at an extrapolated temperature of 1273 K, which was used for assessing the compatibility of 15 mol% $YO_{1.5}$ stabilized zirconia (YSZ) electrolyte with SrO-bearing components of solid oxide fuel cells.

In the last few years, a growing interest for luminescent-doped nanoparticles has arisen because of the observed modification of their significant properties as compared to the bulk materials. Small crystalline particles exhibit many novel physical properties not found in bulk materials. The nanocrystals are of considerable importance for both technological applications and fundamental studies. Oxide-based luminescent materials have been widely used due to their thermal and chemical stability. SrY_2O_4 is a good host material because it has a wide band gap. In one work, attention was focused on their structural and electronic properties and the calculated results by chemical bond method and density functional method were reported within the scheme due to Perdew–Burke–Ernzerhof. SrY_2O_4 was predicted to be a direct-gap material because the top of the valence band and the bottom of the conduction band are to be along the same direction at G. The bond length and bond covalency were also calculated by chemical bond method. Compared with the SrY_2O_4 bulk crystal, the bond covalency of nanocrystal has a decreasing trend; its band gap also is narrower; the bond lengths of SrY_2O_4 nanocrystal become longer, which is responsible for the change of the covalency and band gap.

Crystals of SrY_2O_4 (space group *Pnam*) were examined by high-temperature powder X-ray diffractometry to determine the changes in unit-cell dimensions with temperature. The individual cell dimensions linearly increased with increasing temperature up to 1473 K. The expansion coefficients (K^{-1}) were 1.263×10^{-5} along the *a*-axis, 7.46×10^{-6} along the *b*-axis, and 9.93×10^{-6} along the *c*-axis. The coefficient of mean linear expansion was 1.001×10^{-5}/K.

No other compounds involving combinations of SrO-Y_2O_3 are known at this time. There are no strontium–yttrium compounds available commercially and none are offered for sale.

Barium–Yttrium Compounds

Barium metal does not form any **intermetallic** specific compounds with yttrium metal. The phase diagram is devoid of any compounds and shows only the polymorphic transformation of the individual metals. The situation differs in the BaO–Y_2O_3 system.

Starting with BaO and Y_2O_3, four compounds have been found in the BaO–Y_2O_3 system. At high temperatures (above 1200 °C) two compounds, mentioned in the literature, are found: $Ba_3Y_4O_9$ and BaY_2O_4. Heating the oxide mixtures at 900 °C results in the formation of a new compound $Ba_2Y_2O_5$. This compound is transformed at 1000 °C into another new compound: $Ba_4Y_2O_7$. X-ray data of the four compounds have been given in detail. The reactions are:

$$\text{BaO} + Y_2O_3 + \text{heat} \Rightarrow BaY_2O_4 (>1200\ ^\circ\text{C})$$

$$3\ \text{BaO} + 2\ Y_2O_3 + \text{heat} \Rightarrow Ba_3Y_4O_9 (>1200\ ^\circ\text{C})$$

$$\text{BaO} + Y_2O_3 + \text{heat} \Rightarrow Ba_2Y_2O_5 (<1000\ ^\circ\text{C})$$

$$2\ Ba_2Y_2O_5 + \text{heat} (>1000\ ^\circ\text{C}) \Rightarrow Ba_4Y_2O_7 + Y_2O_3$$

Although the system, BaO–Y_2O_3–CuO–O, has been evaluated as to its phase diagram because it is a superconductor at 90 K, little work has been accomplished on the system, BaO–Y_2O_3. The final phase diagram has not yet been established. The problem is similar to that of the CaO–Y_2O_3 system where the relevant compounds are stable only over a limited temperature range. The lower limit for a-BaO·and b-Y_2O_3 compounds seems to be 800 °C. However, since the melting points of these compounds are not available, a phase diagram cannot be constructed.

BaY_2O_4 has the same structure as its strontium homologue with cell parameters of: $a = 3.452$ Å, $b = 10.404$ Å, $c = 12.121$ Å. $\alpha = \beta = \gamma = 90^\circ$, cell volume $= 435.12$ Å^3. Cell occupancy is shown in Table 7.11.

The structure of $Ba_3Y_4O_9$ has not been completely established. It has the cell parameters of: $a = b = 6.114$ Å, $c = 9.115$ Å, $\alpha = \beta = 70.403^\circ$, $\gamma = 60^\circ$, cell volume $= 272.04$ Å^3.

In the binary system BaO–Y_2O_3 it has been stated that the compounds "$Ba_4Y_2O_7$" and "$Ba_2Y_2O_5$" are

TABLE 7.11

No.	Site notation	Atom	Multiplicity	Wyckoff	Site symmetry	x	y	z	Occupancy
1	O1	O	4	c	.m.	0.071	1/4	0.078	1.0
2	Y1	Y	4	c	.m.	0.077	1/4	0.394	1.0
3	Ba1	Ba	4	c	.m.	0.242	1/4	0.65	1.0
4	O2	O	4	c	.m.	0.289	1/4	0.352	1.0
5	O3	O	4	c	.m.	0.387	1/4	0.016	1.0
6	O4	O	4	c	.m.	0.47	1/4	0.775	1.0
7	Y2	Y	4	c	.m.	0.568	1/4	0.609	1.0

oxycarbonates with composition $Ba_4Y_2O_7{\cdot}CO_2$ and $Ba_2Y_2O_5{\cdot}2CO_2$. Thus, their existence remains in doubt.

In another study, the coexisting phases in the pseudo-binary system $BaO–Y_2O_3$ have been identified by equilibrating samples containing different amounts of component oxides at 1173, 1273 and 1373 K (900, 1000 and 1100 °C). Only two ternary oxides, BaY_2O_4 and $Ba_3Y_4O_9$, have been found to be stable in the temperature range of investigation. Solid-state galvanic cells:

$$\mathrm{Pt}, O_2 + BaO + BaF_2 || BaF_2 + 2\ \text{mol\%}\ Al_2O_3 || BaF_2 + BaY_2O_4 + Y_2O_3 + O_2, \mathrm{Pt}$$

$$\mathrm{Pt}, O_2 + BaO + BaF_2 || BaF_2 + 2\ \text{mol\%}\ Al_2O_3 || BaF_2 + BaY_2O_4 + Ba_3Y_4O_9 + O_2, \mathrm{Pt}$$

have been employed for determining the Gibbs' energies of formation of BaY_2O_4 and $Ba_3Y_4O_9$ from the component oxides in the range 850–1250 K. A composite solid electrolyte incorporating Al_2O_3-dispersed BaF_2 was used in the cells. To prevent interaction between the Al_2O_3 powder and electrode materials, the solid electrolyte was coated with pure BaF_2. The Gibbs' energies of formation of BaY_2O_4 and $Ba_3Y_4O_9$ from component oxides are given by: ΔG_f^0 (BaY_2O_4, s) = −128,310 +5.211T (±580) J/mol, (850 ≤ /T ≤ /1250 K) and ΔG_f^o ($Ba_3Y_4O_9$, solid) = −317,490 − 24.704T J/mol, (850 ≤ T ≤ 1250 K).

Proton conducting ion transport membranes are required to extract absolutely pure hydrogen from mixed gas streams in the processing of fossil fuels and other petroleum and petrochemical processes. Ceramic materials are required to withstand these high-temperature processes. Yttrium-doped barium cerate ($BaCe_{0.80}Y_{0.20}O_{3-\delta}$) is currently one of the best materials when considering only proton conductivity. However, this material is very sensitive to the carbon dioxide (CO_2) and sulfur (e.g. H_2S) contamination found in the fossil fuel process stream. Barium cerate will decompose into barium carbonate ($BaCO_3$) and ceria (CeO_2) in the presence of CO_2; and CeO_2 reacts with H_2S to produce a sulfide phase, particularly in the highly reducing fuel environment. Two approaches for improving the stability of barium cerate are examined: manipulation of the A- to B-site (in this case, Ba and Ce/Y/Zr, respectively).

Recent work shows, through both experimental results and thermodynamic modeling, that $Ba(Ce,Y)O_{3-\delta}$ is ill-suited for use in environments containing CO_2. Despite efforts to improve the stability of $Ba(Ce,Y)O_{3-\delta}$ through partial ZrCe substitution and adjusting the A-site to B-site cation ratio, the perovskite phase is shown to be unstable in the presence of CO_2 at temperatures below ca. 1000 °C.

It should be noted that the reaction time for the $BaCO_3 + Y_2O_3$ mixture to come to completion is much longer than that of the $BaO–Y_2O_3$ mixture. Thus, the $Ba_4Y_2O_7$ and $Ba_2Y_2O_5$ compounds have proved to be carboxy compounds. Even those compounds annealed in oxygen gas proved to be identical. The stability of these compounds proved to be poor in air containing moisture, with the exception of BaY_2O_4. All compounds, with the exception of BaY_2O_4 decomposed immediately. Only $Ba_3Y_4O_9$ exists at a high temperature but cannot be quenched for measurement at room temperature. This accounts for the fact that these two compounds are the only ones for which ΔG_f^0 has been measured. The temperature ranges of stability for these compounds are shown in Fig. 7.24.

The $BaO–Y_2O_3$ system has been studied more often than any other of the alkaline earth systems. The major interest in the $BaO–Y_2O_3$ system stems from the fact that these two components are the chief oxide components in the high-temperature superconductor series of compounds like $Ba_2YCu_3O_{6+x}$. However, there are no separate commercial uses of these compounds and they are not offered for sale. No CAS numbers have been issued.

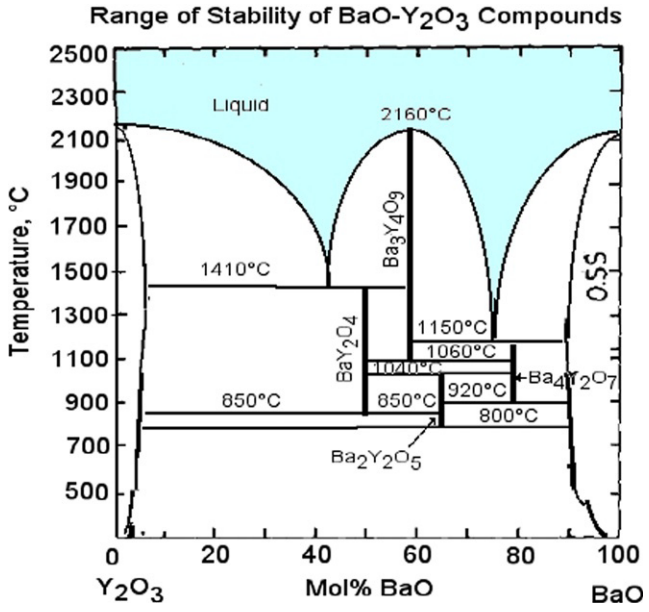

FIGURE 7.24

Radium–Yttrium Compounds

Although compounds similar to those of the barium precursor could be studied, there is no record on any such research papers. Nor are there any examinations of Ra–Y intermetallic compounds available in the published literature. This is probably due to the high cost of Ra metal.

7.1.3. Alkaline Earth—Rare Earth Compounds

The rare earths comprise 14 elements, La to Lu. All of these elements, as oxides, form compounds with the oxides of the alkaline earths. As shown in a recent paper, the type of compounds formed include AeO–Ln_2O_3 in various mole ratios, similar to the Ae–Y_2O_3 system.

The paper describes the interactions of rare earth element (REE) oxides with magnesium, calcium, strontium, and barium oxides in a wide range of concentrations and temperatures from 1000 to 2450 °C. The most typical binary phase diagrams found for these oxide systems are illustrated in the paper. The existence of six types of compounds, i.e. $MeLn_4O_7$, $MeLn_2O_4$, $Me_5Ln_8O_{17}$, $Me_3Ln_4O_9$, $Me_2Ln_2O_5$, has been established. It has been shown that the compounds formed resemble other classes of compounds with REE oxide participation; this is demonstrated by spasmodic property changes in a given series of compounds of a single type (process of formation, X-ray and petrographic characteristics) and by changes of the composition of the compounds. These facts indicate an appreciable role of the 4f electrons of the REE atoms resulting in changes in the nearest environment of the REE atoms; in turn this leads to property and compositional changes of the compounds formed and, hence, to variations of the type of phase diagrams in the La–Lu series. Phase transformations in REE oxides (1800 °C) have been investigated and the regularities observed in the effects of oxides of elements of the IIA subgroup on the transformations are discussed.

The nature and kinetics of decomposition of magnesium oxide-based solid solutions have been studied in the $Sc_2O_3 \cdots MgO$ system. It is suggested that the regularities observed may be valid for other oxide systems having a eutectic type of liquids where the decomposition of the solid solution occurs into the starting components or into solid solutions on their base, without the formation of intermediate compounds. Theoretical calculations of the phase-field boundaries of some types of phase diagrams of the systems studied have been carried out, assuming ideal or regular solution models.

No further description of these compounds will be presented here.

CHAPTER

8

Group 4 (Ti, Zr and Hf) Alkaline Earth Compounds

OUTLINE

8.1. Alkaline Earth Titanium Compounds 653
- *8.1.1. Beryllium Titanates* 653
- *8.1.2. Beryllium Titanides* 654
- *8.1.3. Magnesium Titanides* 656
- *8.1.4. Magnesium Titanates* 656
- *8.1.5. Calcium Titanides* 662
- *8.1.6. Calcium Titanates* 662
- *8.1.7. Strontium Titanides* 667
- *8.1.8. Strontium Titanates* 667
- *8.1.9. Barium Titanides* 669
- *8.1.10. Barium Titanates* 669
- *8.1.11. Radium Titanates* 672

8.2. Alkaline Earth Zirconium Compounds 672
- *8.2.1. Beryllium—Zirconium Compounds* 672
- *8.2.2. Beryllium Zirconides* 672
- *8.2.3. Magnesium Zirconide Compounds* 674
- *8.2.4. Magnesium Zirconate Compounds* 675
- *8.2.5. Calcium Zirconide Compounds* 675
- *8.2.6. Calcium Zirconate Compounds* 675
- *8.2.7. Strontium Zirconides* 679
- *8.2.8. Strontium Zirconates* 679
- *8.2.9. Barium Zirconides* 684
- *8.2.10. Barium Zirconates* 684
- *8.2.11. Radium Zirconates* 686

8.3. Alkaline Earth Hafnium Compounds 687
- *8.3.1. Beryllium Hafnate Compounds* 687
- *8.3.2. Beryllium Hafnide Compounds* 687
- *8.3.3. Magnesium Hafnide Compounds* 690
- *8.3.4. Magnesium Hafnate Compounds* 690
- *8.3.5. Calcium Hafnide Compounds* 692
- *8.3.6. Calcium Hafnate Compounds* 692
  - $BaTiO_3$ Type 692
  - $BaBiO_3$ Type 693
  - $GdFeO_3$ Type 693
  - $LaAlO_3$ Type 693
  - $CaTiO_3$ Type 693
- *8.3.7. Strontium Hafnide Compounds* 695
- *8.3.8. Strontium Hafnate Compounds* 695
  - $GdFeO_3$ Type 695
  - $BaTiO_3$ Type 695
  - $CaTiO_3$ Type 695
- *8.3.9. Barium Hafnide Compounds* 698
- *8.3.10. Barium Hafnate Compounds* 698
- *8.3.11. Radium Hafnium Compounds* 700

8.1. ALKALINE EARTH TITANIUM COMPOUNDS

8.1.1. Beryllium Titanates

Available data on the system BeO–TiO_2 are contradictory and the question as to the existence of any beryllium titanates is still open. In 1960, a paper stated:

"Mixtures of BeO-TiO_2 with stoichiometric ratios of 1:1, 2:1, and 3:1 were heated at temperatures of 450 to 1750 °C. Whether using oxides or hydroxides as starting materials, no evidence of interaction could be observed to indicate the formation of beryllium titanate. X-ray analysis showed only the lines of the starting components. The densities of the calcined product were close to the densities of the corresponding mixtures of BeO-TiO_2. Selective leaching with HCl (1:1) and H_2SO_4 (1:5) left a residue in which only BeO and TiO_2 could be detected by x-ray analysis. The results of thermographic

Encyclopedia of the Alkaline Earth Compounds
http://dx.doi.org/10.1016/B978-0-444-59550-8.00008-9

Copyright © 2013 Elsevier B.V. All rights reserved.

analysis indicated the absence of any interaction between the oxides. Microscopic analysis showed only the presence of two phases, one of which (BeO) fluoresced in ultraviolet light. Additions of up to 5% of Li_2O, Na_2O, MgO, ZnO, Al_2O_3, Fe_2O_3, B_2O_3, SiO_2 and P_2O_5 showed up only the starting components on x-ray analysis. It must be concluded that beryllium titanate is not formed in the system BeO-TiO_2".

However, by 1986, it was concluded that:

> "Be_2TiO_4 (mol weight 129.92) can be obtained by sintering a mixture of beryllium hydroxide and titanium dioxide, using a molar ratio of 2:1. This orthotitanate of beryllium is a light yellow crystalline powder. When heated to 1780 °C, it melts congruently. Permittivity 30. It decomposes in boiling hydrochloric acid. $BeTiO_3$ (mol weight 104.91) is formed in the system BeO-TiO_2. It is a yellowish crystalline powder. It melts at 1720 °C congruently. The powder is water insoluble, but decomposes in boiling hydrochloric acid".

A so-called "beryllium titanate" was found to be piezoelectric. However, a 1993 paper stated:

> "A mixed BeO:TiO_2 ceramic showing a high electrical conductivity has been the subject of preliminary investigation with respect to its application in TSEE and TL dosimetry. The results clearly indicate that the two oxides involved do construct independent substructures in the mixed ceramic. The TiO_2 substructure provides electrical conductivity, and is passive from the TL and TSEE point of view, whereas the BeO substructure is fully responsible for the dosimetric signals. Although the title question cannot be definitely answered yet the results encourage further studies".

Further work has shown that, although Wartenburg et al. included two congruently melting compounds—$2BeO \cdot TiO_2$ at about 1800 °C and BeO–TiO_2 at about 1720 °C, the results were faulty. They concluded that the system contained no compounds. They also concluded that a single eutectic exists at about 85 wt% of TiO_2 and 1670 ± 3 °C and that a narrow region of TiO_2 mixed crystals (an area of solid solution) extends from just beyond the eutectic to pure titania. Early in the study, seven mixtures, ranging in composition from about 55 to 94% of TiO_2, were specially heat treated for X-ray diffraction (XRD) examination. Each of the mixtures was heated to about 10–15 °C above the melting point of the mixture as given by Wartenburg, cooled to the reported solidus temperatures, that temperature maintained for about 2 h, and the mixture then cooled fairly rapidly (about 400 °C/h to about 1000 °C). A phase diagram was presented as shown in Fig. 8.1.

Thus, the current understanding is that BeO does not form any "titanates" when reacted with TiO_2 at high temperatures.

8.1.2. Beryllium Titanides

Be metal does form a series in intermetallic alloys with Ti metal that have distinctive structures. The phase diagram is shown in Fig. 8.2.

The crystal parameters are listed in Table 8.1.

$Be_{12}Ti$ has the structure shown in Fig. 8.3.

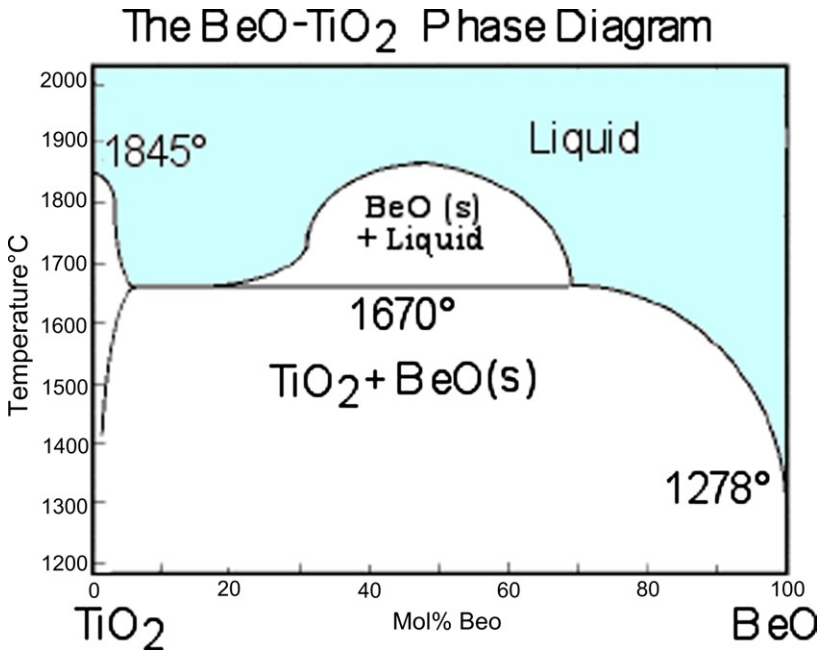

FIGURE 8.1

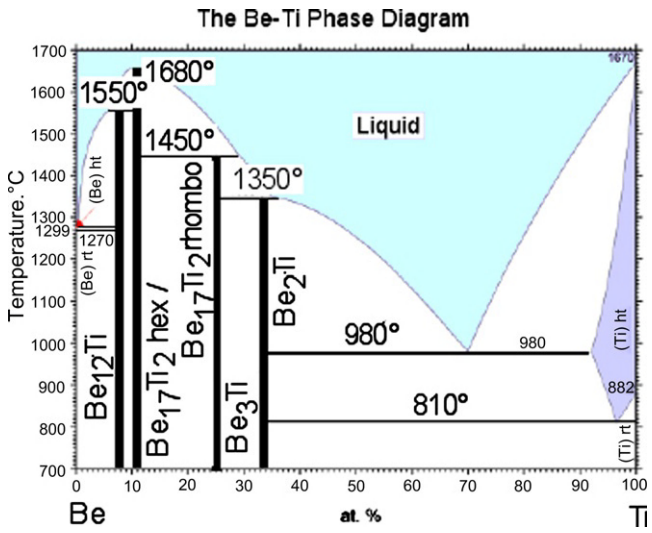

FIGURE 8.2

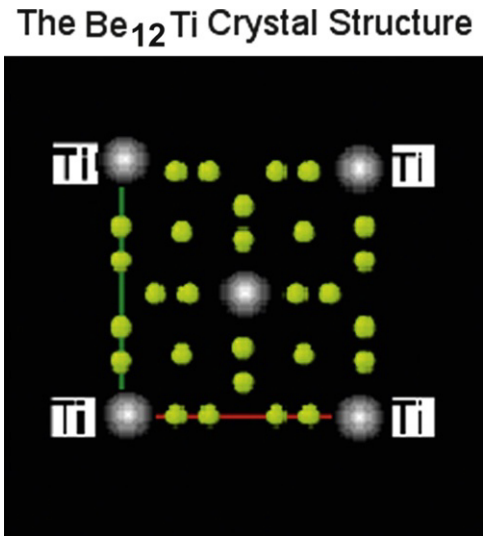

FIGURE 8.3

Unit cell parameters are: $a = 4.195$ Å, $b = 5.6111$ Å, $c = 5.6111$ Å, $\alpha = 81.967°$, $\beta = 68.049°$, $\gamma = 68.049°$, cell volume = 113.62 Å^3. Cell occupancy is listed in Table 8.2.

$Be_{17}Ti_2$ has the structure shown in Fig. 8.4.

Cell parameters are: $a = b = c = 5.5812$ Å, $\alpha = \beta = \gamma = 82.939°$, cell volume = 170.020 Å^3. Cell occupancy is listed in Table 8.3.

Be_2Ti has the structure shown as follows. It consists of a double layer of interconnected Ti tetrahedra, surrounded by cubic patterns of Be atoms. The unit cell contains eight formula units (Fig. 8.5).

Cell parameters are: $a = b = c = 4.5635$ Å, $\alpha = \beta = \gamma = 60°$, cell volume = 67.20 Å^3. Cell occupancy is listed in Table 8.4.

Be_3Ti has the structure shown in Fig. 8.6.

It consists of a series of "Ti ladders" that are connected three-dimensionally. Unit cell parameters are: $a =$

TABLE 8.1

Compound	Type	Point group	Space group	Melting point (°C)	Physical properties
(Be) rt	Mg	hP2	194	1270	No data
(Be) ht	W	cI2	229	1289	No data
$Be_{17}Ti_2$ hex	Th_2Ni_{17}	hP38	194	1660	No data
$Be_{17}Ti_2$	$Zn_{17}Th_2$	hR57	166	1660	No data
$Be_{12}Ti$	$ThMn_{12}$	tI26	139	1550	No data
Be_3Ti	$PuNi_3$	hR36	166	1450	No data
Be_2Ti	$MgCu_2$	cF24	227	1350	Search
(Ti) rt	Mg	hP2	194	882	No data
(Ti) ht	W	cI2	229	1670	No data

TABLE 8.2

No	Site notation	Atom	Multiplicity	Wyckoff	Site symmetry	x	y	z	Occupancy
1	Be1	Be	8	j	m2m.	0.277	1/2	0	1.0
2	Be2	Be	8	i	m2m.	0.361	0	0	1.0
3	Be3	Be	8	f	..2/m	1/4	1/4	1/4	1.0
4	Ti1	Ti	2	a	4/mmm	0	0	0	1.0

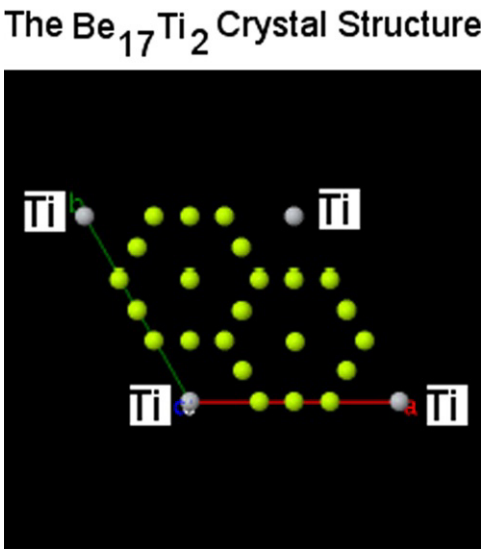

FIGURE 8.4

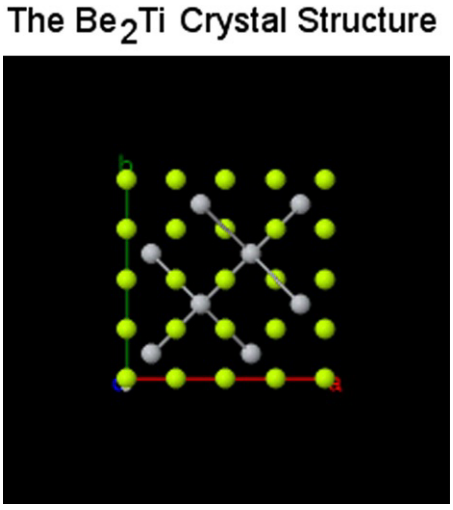

FIGURE 8.5

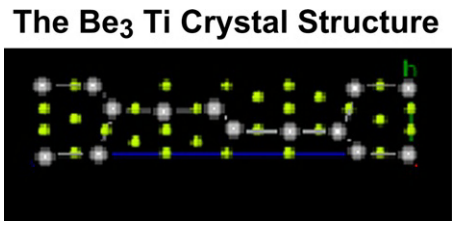

FIGURE 8.6

$b = c = 4.49$ Å, $\alpha = \beta = 75.736°$, $\gamma = 60°$, cell volume $= 124.08$ Å^3. Cell occupancy is listed in Table 8.5.

BeTi has the structure shown in Fig. 8.7, presented on a following page.

Unit cell parameters are: $a = b = c = 2.941$ Å, $\alpha = \beta = \gamma = 90°$, cell volume $= 25.41$ Å^3. Cell occupancy is listed in Table 8.6.

None of these compounds has found usage in Industry and they have not evolved any interest in Academia due to unusual physical or chemical properties. They are not available commercially.

8.1.3. Magnesium Titanides

There are no known intermetallic compounds found in the system, Mg–Ti. A phase diagram has been published but shows only polymorphic transitions of the two metals.

8.1.4. Magnesium Titanates

In the oxygen-dominated system MgO–TiO_2, several compounds are known such as $MgTi_2O_5$, Mg_2TiO_4 and $MgTiO_3$. $MgTi_2O_5$ (Armalcolite) has a pseudobrookite structure with cell parameters of $a = 9.72$ Å, $b = 1.04$ Å and $c = 3.73$ Å (space group *Bbmm*), while Mg_2TiO_4 (Quandilite) has either a cubic structure with $a = 8.40$ Å at 700 °C (space group *Fd3m*, spinel) or

TABLE 8.3

No	Site notation	Atom	Multiplicity	Wyckoff	Site symmetry	*x*	*y*	*z*	Occupancy
1	Be1	Be	18	h	.m	0.5	0.5	0.16667	1.0
2	Be2	Be	18	f	.2	0.33333	0	0	1.0
3	Be3	Be	9	d	.2/m	1/2	0	1/2	1.0
4	Be4	Be	6	c	3m	0	0	0.097	1.0
5	Ti1	Ti	6	c	3m	0	0	0.33333	1.0

TABLE 8.4

No	Site notation	Atom	Multiplicity	Wyckoff	Site symmetry	*x*	*y*	*z*	Occupancy
1	Be	Be	16	c	.-3m	0	0	0	1.0
2	Ti	Ti	8	b	-43m	3/8	3/8	3/8	1.0

TABLE 8.5

No	Site notation	Atom	Multiplicity	Wyckoff	Site symmetry	x	y	z	Occupancy
1	Be1	Be	18	h	.m	0.5002	0.4998	0.0829	1.0
2	Ti1	Ti	6	c	3m	0	0	0.1414	1.0
3	Be2	Be	6	c	3m	0	0	0.3336	1.0
4	Be3	Be	3	b	-3m	0	0	1/2	1.0
5	Ti2	Ti	3	a	-3m	0	0	0	1.0

TABLE 8.6

No	Site notation	Atom	Multiplicity	Wyckoff	Site symmetry	x	y	z	Occupancy
1	Be	Be	1	b	m-3m	1/2	1/2	1/2	1.0
2	Ti	Ti	1	a	m-3m	0	0	0	1.0

a tetragonal structure with $a = 5.94$ Å and $c = 8.42$ Å (space group $P4122$, spinel) at 500 °C. $MgTiO_3$ (Geikielite) has a rhombohedral ilmenite structure with $a = 5.05$ Å and $c = 13.89$ (space group $R3$).

Mg_2TiO_4 has attracted attention because of its optical properties to be used in integrated optics and as a dielectric material. Epitaxial layers of Mg_2TiO_4 grown by solid-state reaction between (001) MgO single crystals and TiO_2 have been used as buffer layers for growing high-temperature superconducting thin films. In contrast, $MgTiO_3$ is known as a dielectric material that has good dielectric properties at high frequencies as well as a high thermal stability. Bulk $MgTiO_3$ is used to construct microwave (MW) ceramic capacitors and resonators. $MgTiO_3$ has a refractive index of 1.95, a value that lies between that of $LiNbO_3$ (2.2) and Al_2O_3 (1.7). Thus, $MgTiO_3$ thin films can be used as a cladding layer. For the most part, $MgTiO_3$ has been produced and studied in bulk ceramic form. However, there have been some reports on fabrication and properties of $MgTiO_3$ thin films. Spinel-forming topotaxial solid-state reactions like:

$$2AO + BO_2 \Rightarrow A_2BO_4 \text{ or } AO + B_2O_3 \Rightarrow AB_2O_4$$

are prototypes of chemical reactions in complex oxides. Previously, a series of topotaxial reactions with (100) MgO single crystals were studied. Different spinels, such as Mg_2TiO_4, Mg_2SnO_4, $MgIn_2O_4$, $MgAl_2O_4$, $MgCr_2O_4$ and $MgFe_2O_4$, with different values of spinel/MgO lattice misfit were considered. In such cases of cube-on-cube orientation, the structure of the reaction fronts and the mechanism of the interfacial reaction were determined by the sign and amount of the lattice misfit. At positive misfit, the Burgers vector of the misfit dislocations present at the reaction front points out of the interface, enabling the dislocations to glide, when coping with the movement of the advancing reaction front. At negative misfit, the Burgers vector lies in the interface plane, so that a climb process is required for the movement of the dislocations. At very low misfit (<0.2%/Å), no misfit (interfacial) dislocations form and the misfit is accommodated by point defects and antiphase boundaries.

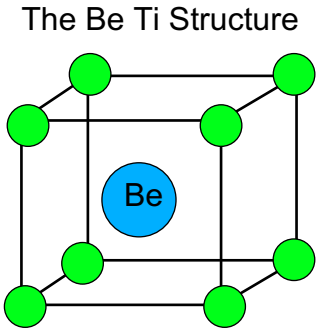

FIGURE 8.7

Three compounds have been established in the phase diagram of MgO–TiO_2, as shown in Fig. 8.8.

These include the orthotitanate, the metatitanate and the dititanate. Thermochemical and crystallographic properties of $MgTi_2O_5$, $MgTiO_3$, and Mg_2TiO_4 have been studied to characterize stability relations, structural variations, and order–disorder phenomena.

Enthalpies of formation, decomposition, and order–disorder transitions were determined by high-temperature solution calorimetry and transposed-temperature-drop calorimetry on synthetic powders.

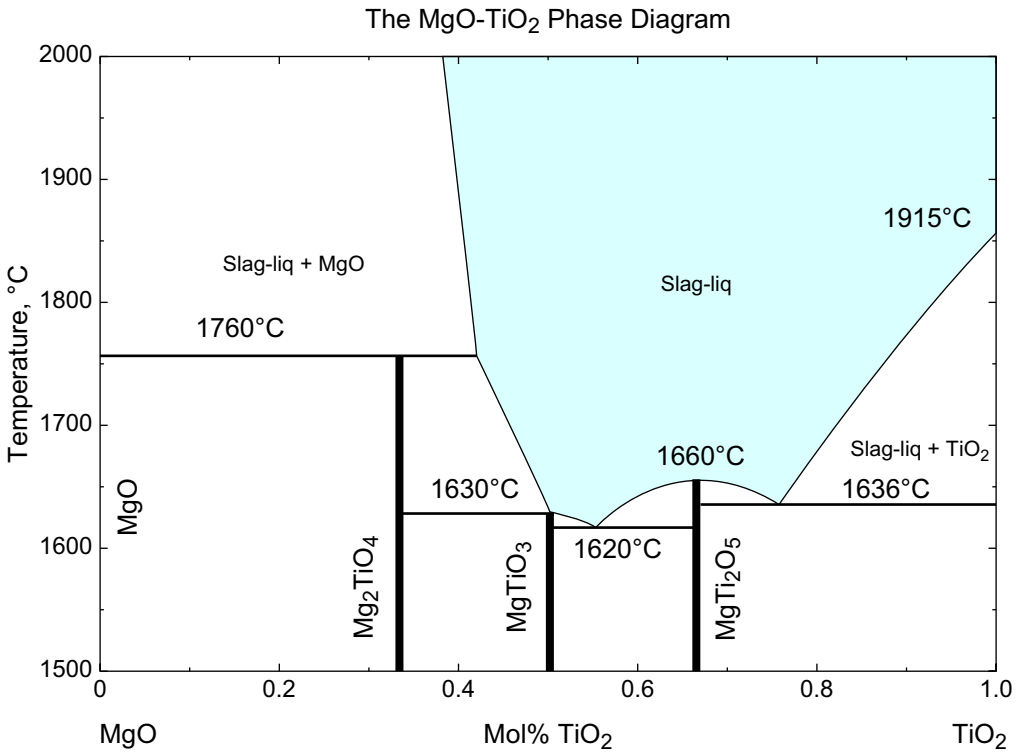

FIGURE 8.8

X-ray lattice parameter measurements and Rietveld refinements of neutron diffraction data were used to evaluate intracrystalline cation distributions and their variation with quenching temperature. $MgTiO_3$ is the most stable phase and apparently retains a fully ordered Mg···Ti distribution to at least 1673 K. Both $MgTi_2O_5$ and Mg_2TiO_4 are stable only at high temperature because of the configurational entropy arising from cation disorder. The disorder in $MgTi_2O_5$ appeared to vary continuously throughout the range of 773–1373 K and was accompanied by changes in lattice parameters. Mg_2TiO_4 undergoes a cubic tetragonal transition at 933 ± 20 K involving the appearance of long-range order on octahedral sites. However, thermochemical evidence suggests that Mg···Ti octahedral short-range order changes gradually, perhaps over an interval of several hundred degrees.

Ilmenite is a weakly magnetic titanium–iron oxide mineral which is iron black or steel gray. It is a crystalline iron titanium oxide ($FeTiO_3$). It crystallizes in the trigonal system, and it has the same crystal structure as corundum and hematite. $MgTiO_3$ has the same structure shown in Fig. 8.9.

Another view of the octahedra is shown in Fig. 8.10.

The compound, Mg_2TiO_4, crystallizes in the cubic system, with a $[Mg(MgTi)O_4]$ inverse structure, where Mg^{2+} occupies part of the Ti^{4+} sites in the lattice.

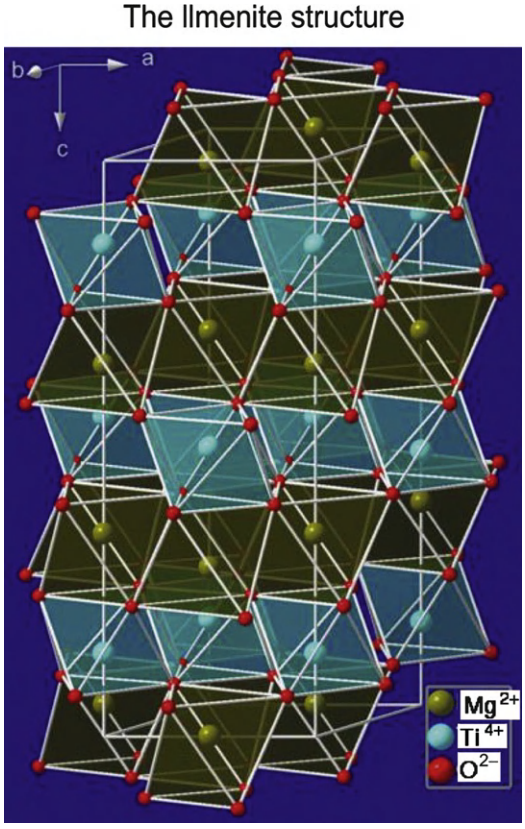

FIGURE 8.9

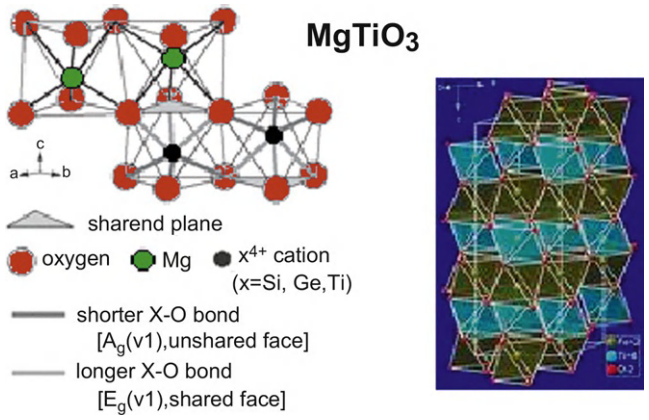

FIGURE 8.10

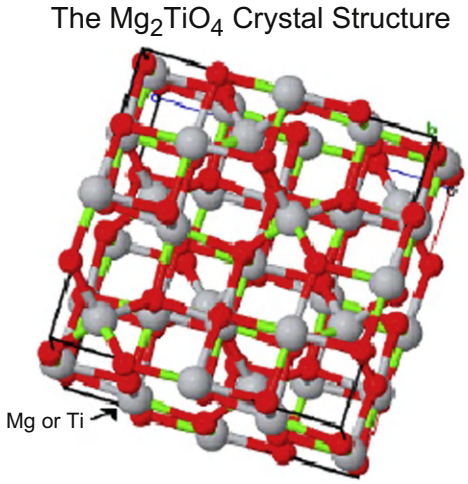

Polyhedra · Edge · Sharing MgO_6 and TiO_6 Octahedra, combined with MgO_4 Tetrahedra, are joined Through Neighboring Octahedra through Vertices

FIGURE 8.11

Synthetic Qandilite (Mg_2TiO_4) is an inverse spinel in which random mixing of Mg and Ti on the octahedral site should give rise to a configurational entropy of 11.5 J/K/mol. The structure can be represented as shown in Fig. 8.11.

The free energy of formation of Mg_2TiO_4 has been determined from the location of the univariant reaction $MgTiO_3 + MgO \Rightarrow Mg_2TiO_4$ in pressure–temperature space between 0 and 20 kbar. The use of literature data for $MgTiO_3$ and MgO, together with the results gave S_o (298 K) = 111.2 ± 0.6 J/K/mol for Mg_2TiO_4. This entropy is only 7.6 ± 0.9 J/K/mol more than the calorimetrically determined value of 103.6 ± 0.7 J/K/mol. The discrepancy implies either considerable short-range order of Mg and Ti in Mg_2TiO_4, or perhaps an error in the high-temperature heat-capacity data for $MgTiO_3$ caused by disordering in this substance. The transformation ranges as a function of pressure are shown in Fig. 8.12.

The electron density distribution in magnesium titanium oxide spinel [composition Mg_2TiO_4 tetrahedral site T = Mg, octahedral site X = Mg, Ti (equal amounts) for general formula TX_2O_4] has been studied with single-crystal XRD methods through scattering factor refinement procedures. In the refinement with harmonic parameters, a positive residual region up to +0.25 e/Å^3 in height encircles oxygen in the hemisphere directed toward the T-site, along with weak residuals assuming octahedral arrangements around the X-site. These

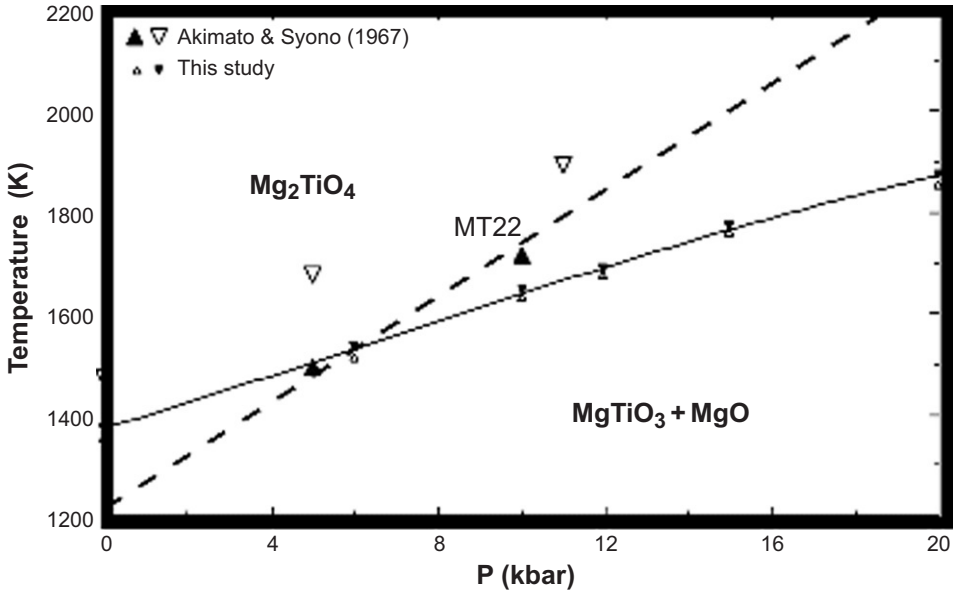

FIGURE 8.12

residuals almost completely disappear with anharmonic refinement. Another residual $+0.20\,e/Å^3$ in height is situated near the X_4O_4 cuboidal unit. [153 equivalent-averaged reflexions, $R = 0.0077$ (harmonic refinement), $R = 0.0059$ (anharmonic refinement).]

In relation to modern telecommunication systems, much attention has been paid to the dielectric properties of materials at MW and millimeter frequencies for wireless communication technologies such as mobile phones, intelligent transport systems, and wireless LAN. Also, the utilized frequency has increased from the MW to millimeter-wave range due to the large quantities of information being relayed and the demand for high-speed transportation in telecommunication systems. Dielectric materials applicable to millimeter-wave frequencies should have a high-quality factor (Q_f) and relatively low dielectric constant (K), as these properties affect the broadness and stability of the resonant frequency. Magnesium metatitanate ($MgTiO_3$) ceramics have been investigated due to their excellent dielectric properties, that is, a high-quality factor ($Q_f = 110{,}000$ GHz) and low dielectric constant ($K = 17$), which are applicable to millimeter-wave frequencies. It has been reported that the origin of the high Q_f value of $MgTiO_3$ specimens is related to the sharing type of MgO_6 and TiO_6 octahedra as well as the absence of 3d electrons which induce electrical conductivity. However, secondary phases such as inverse spinel Mg_2TiO_4 and pseudobrookite $MgTi_2O_5$ are detected during the conventional sintering process of ilmenite, $MgTiO_3$, due to the low solidus limit of the $MgTiO_3$ system. Moreover, these secondary phases affect the MW dielectric properties of $MgTiO_3$ ceramics. A single phase of $MgTiO_3$ showed a dielectric constant (K) of 18.2, a quality factor (Q_f) of 198,000 GHz, and a temperature coefficient of resonant frequency (TCF) of -51 ppm/°C. However, the dielectric properties of the specimens with a secondary phase of $MgTi_2O_5$ ($K = 19.9$, $Q_f = 48{,}000$ GHz) and/or Mg_2TiO_4 ($K = 15.6$, $Q_f = 56{,}000$ GHz) were worsened. Dependence of the MW dielectric properties on the secondary phase of the MgO–TiO_2 system was also discussed in terms of dielectric mixing rules.

Nanocrystalline magnesium titanate materials were synthesized at low temperatures by the sol–gel method, using butyl titanate and magnesium nitrate as precursors. Thermal decomposition behavior of the gel was analyzed by thermogravimetry (TG)–differential thermal analysis (DTA). Crystallinity of $MgTiO_3$ powders was examined by transmission electron microscopy (TEM). The surface morphology was observed by scanning electron microscopy (SEM). The average grain size of $MgTiO_3$ crystals was between 10 and 30 nm at 600 °C and $MgTi_2O_5$ disappeared completely at 700 °C. At the sintering temperature of 1200 °C, the $MgTiO_3$ ceramics which made from the nanopowders calcined at 600 °C achieved excellent dielectric properties: $K_r = 16.6$, $Q_f = 42{,}600$ GHz ($f = 7$ GHz), $\Delta f = -41$ ppm/°C.

Pseudobrookite-type $MgTi_2O_5$ (Karroite) is a synthetic crystalline phase with the *Bbmm* structure and a component in orthorhombic oxide solid solutions, $R^{2+}Ti_2O_5$–$R_2^{3+}TiO_5$, which are present as accessory minerals in lunar and terrestrial rocks. $MgTi_2O_5$ (Karroite) exhibits cation exchange between the two nonequivalent octahedral M1 and M2 sites. The temperature dependence of Ti–Mg disorder has been determined using in situ time-of-flight powder neutron diffraction to establish the cation population of each site. The equilibrium Ti–Mg exchange commences above 700–800 °C, and continues up to 1300 °C. At ~1350 °C, $MgTi_2O_5$ appears to undergo a reversible, displacement phase transition, although the structure can still be refined in space group 63. This transition shows discontinuities in the degree of order, the c cell parameter, and in the M–O bond lengths, quadratic elongation, and bond angle variance for the M1 octahedron, which becomes pseudo-tetrahedral. In contrast, the M2 octahedron shows no significant change. An Arrhenius plot, exhibiting linear behavior from 750 to 1300 °C, gives an exchange enthalpy of ordering of 33.6 kJ/mol, and a value of 10.7 kJ/mol for the entropy of disordering. A value of 5.92 cm^3/mol was deduced for the V of the high-temperature reaction of Geikielite ($MgTiO_3$) + Rutile (TiO_2) to form fully disordered $MgTi_2O_5$ at an extrapolated temperature of 1860 °C.

The crystal structure of $MgTi_2O_5$ projected upon [001] is shown in Fig. 8.13.

All atoms lie in the a–b plane at either c or $c/2$. All MO_6 octahedra share edges in the pseudobrookite-type structure. M1 (2*mm*) and M2 (*m*) sites are labeled.

The magnesium titanates $MgTiO_3$, Mg_2TiO_4 and $MgTi_2O_5$ can be synthesized by the wet chemical peroxide route at low temperatures. The first step of the preparation is the precipitation of peroxo-precursors of definite stoichiometry which are transformable into the corresponding titanates by thermal decomposition. The resulting ultrafine, phase-pure magnesium titanate powders have only a low impurity content. They are very easily sintered above 1200 °C. The rate of densification during sintering of compacts is improved in the order $MgTi_2O_5 < Mg_2TiO_4 < MgTiO_3$, including the green densities, the densities at a given time and the theoretical densities of the titanates for the calculations. The Mg_2TiO_4 formation occurs via the inverse spinel phase of Mg_2TiO_4 in a metastable state at low temperatures and $MgTiO_3$ and MgO as intermediates.

In addition to the Ti^{4+} compounds described above, a compound based on Ti^{3+} is known. The structure has the form shown in Fig. 8.14.

At room temperature, $MgTi_2O_4$ has a cubic ($Fd\bar{3}m$) spinel structure, based on corner-sharing distorted

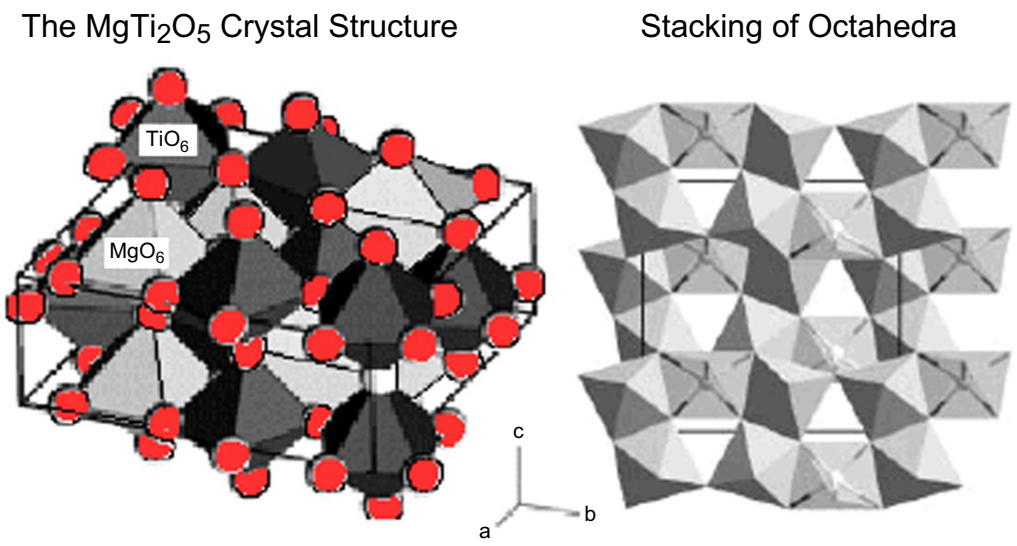

FIGURE 8.13

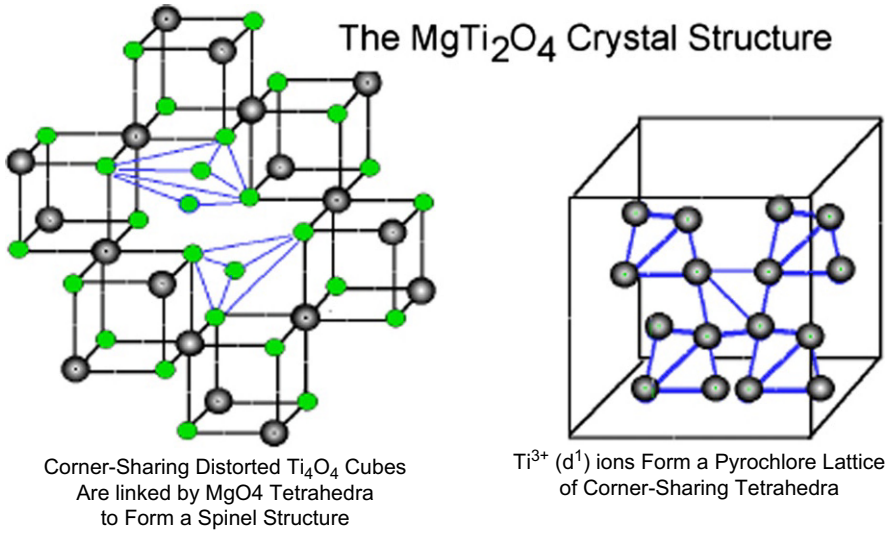

FIGURE 8.14

Ti_4O_4 cubes are linked by MgO_4 tetrahedra. Ti^{3+} (d1) ions form a pyrochlore lattice of corner-sharing tetrahedra. Only a highly reductive sintering atmosphere gives a possibility for the preparation of stoichiometric $MgTi_2O_4$, based on Ti^{3+}. $MgTi_2O_4$ thus obtained shows a metal to spin singlet insulator transition accompanied by the structural change from cubic to tetragonal. Introduction of Ti^{3+} (d^1, $S = 1/2$) to the nonmagnetic insulator $Mg_2Ti^{4+}O_4$ acts partly as doping of carrier dopants and partly as a source of localized electrons. Increasing content of Ti^{3+} leads to their delocalization, resulting in the metallic $MgTi_2O_4$ at $x = 1.0$. The Peierls-like transition observed in the stoichiometric $MgTi_2O_4$ rapidly smears out with the content of Ti^{3+} ion decrease, suggesting an important role of orbital degree of freedom as an effective mechanism for the transition, which seems to be significantly influenced by the randomness associated with the appearance of Ti^{4+} ions.

The transition metal spinel $MgTi_2O_4$ undergoes a metal–insulator transition on cooling below *TM-I* = 260 K. A sharp reduction of the magnetic susceptibility below *TM-I* suggests the onset of a magnetic singlet state. This phenomenon, typically observed in one-dimensional systems, is very rare in cubic compounds, such as the spinels, and is thought to arise because of the interplay between the "frustrated" geometry of the lattice and the orbital occupancy of the Ti sites. Using high-resolution synchrotron and neutron powder diffraction, the low-temperature crystal structure of $MgTi_2O_4$ has been solved. It was found to contain

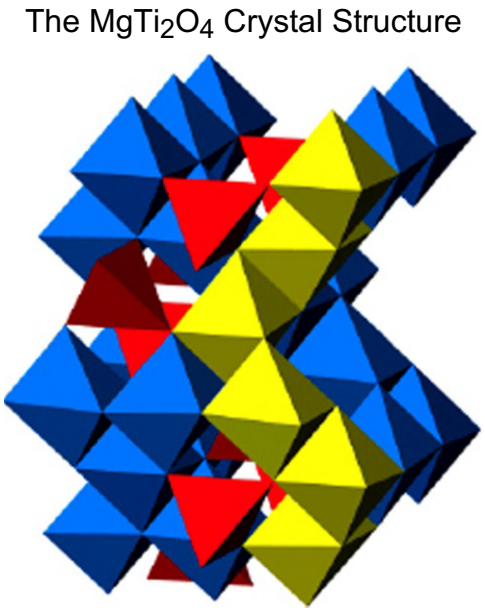

FIGURE 8.15

dimers with short Ti–Ti distances (the locations of the spin singlets) alternating with long bonds to form helices. Band structure calculations based on hybrid exchange density functional theory show that, at low temperatures, $MgTi_2O_4$ is an orbitally ordered band insulator. This structure is shown in Fig. 8.15.

This figure shows one such helix in the context of the spinel structure. Band structure calculations based on hybrid exchange density functional theory show that, at low temperatures, $MgTi_2O_4$ is an orbitally ordered band insulator, whereby the short bonds are associated with doubly occupied *xz* or *yz t2g* orbitals. This interpretation provides an excellent explanation of the structural, transport and magnetic properties.

In general, magnesium titanates are available commercially in limited quantities. $MgTiO_3$ is the composition that is advertised for sale most often. However, no CAS numbers have been assigned to date.

8.1.5. Calcium Titanides

There are no known intermetallic compounds to be found in the system, Ca–Ti. A phase diagram has been published but shows only the polymorphic transitions of the two metals.

8.1.6. Calcium Titanates

The Ti^{4+} system, $CaO–TiO_2$, has been studied intensely. In one study, phase relations in the system Ca–Ti–O were established by equilibration of several samples at 1200 K for prolonged periods and identification of phases in quenched samples by optical and Scanning Electron Microscope (SEM), X-Ray Diffraction (XRD) and Energy-Dispersive X-ray Spectroscopy (EDS). Samples

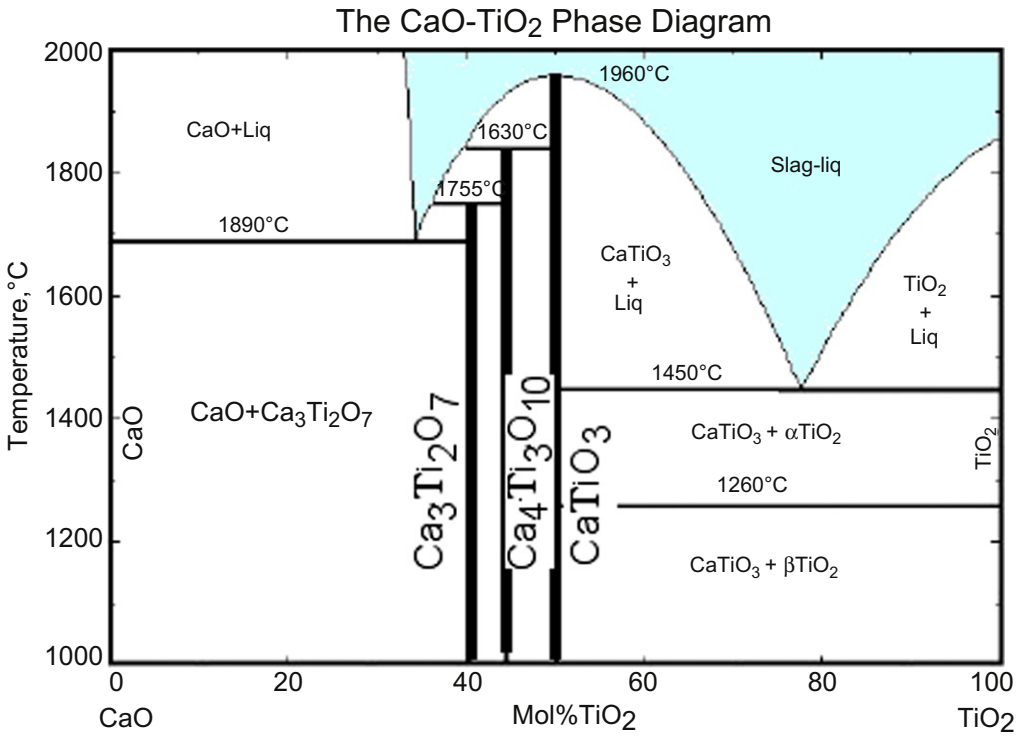

FIGURE 8.16

representing 20 compositions in the ternary system were analyzed, resulting shown in Fig. 8.16.

There was negligible solid solubility of Ca in the phases along the binary Ti–O, and of Ti^{4+} in CaO. Four ternary oxides were identified: $CaTiO_3$, $Ca_4Ti_3O_{10}$ and $Ca_3Ti_2O_7$ containing tetravalent titanium, and $CaTi_2O_4$ containing trivalent titanium. Tie-lines link calcium titanite ($CaTi_2O_4$) with the three calcium titanates ($CaTiO_3$, $Ca_4Ti_3O_{10}$ and $Ca_3Ti_2O_7$), CaO, oxygen excess $TiO_{1+\delta}$ and stoichiometric TiO_2. Tie-lines connect $CaTiO_3$ with TiO_{2-x}, Magneli phases Ti_nO_{2n-1} ($28 \geq n \geq 4$), Ti_3O_5, Ti_2O_3 and $TiO_{1+\delta}$.

CaO was found to coexist with TiO, and Ti–O solid solutions α and β. This phase diagram was found useful for understanding the mechanisms and kinetics of direct calciothermic reduction of TiO_2 to metal and electrochemical reduction of TiO_2 using a graphite anode and molten $CaCl_2$ electrolyte.

A study of mixtures of CaO and TiO_2 fired at 1773 K (1500 °C) with various heating rates confirmed the presence of three binary compounds in the system as: CaO–TiO_2, $CaTiO_3$, $Ca_3Ti_2O_7$, and $Ca_4Ti_3O_{10}$. Mixtures of CaO and TiO_2 of the same composition but fired at different rates were found to develop calcium titanates that are stoichiometrically different. With a heating rate of 50 K/h, Ca_3TiO_7 and $Ca_4Ti_3O_{10}$ are formed and at 300 K/h, mainly calcium monotitanate, $CaTiO_3$, was found, with a small amount of $Ca_3Ti_2O_7$ also present.

All of these calcium titanate compositions may be regarded as variations of the basic perovskite layer in which CaO may be interleaved, as shown in Fig. 8.17.

The features of the crystallochemical structure of calcium titanate indicates that the structure of $Ca_3Ti_2O_7$ and $Ca_4Ti_3O_{10}$ can be perceived as consisting of alternating layers of the perovskite, $CaTiO_3$, and CaO. This means that it can be assumed that the first crystal phase developing in the solid-phase sintering in mixtures

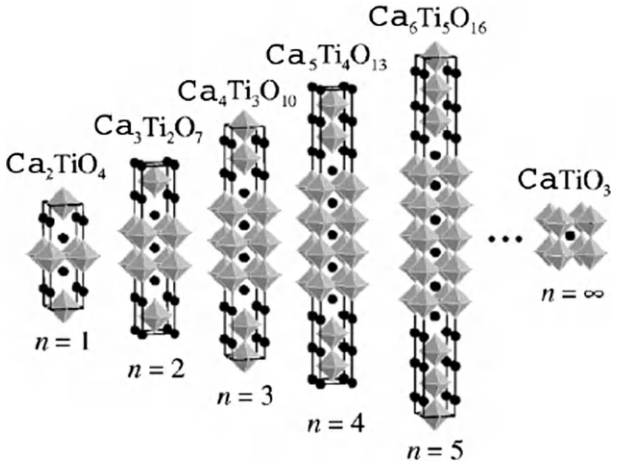

FIGURE 8.17

$CaO–TiO_2$ is $CaTiO_3$. Subsequently, during a slow heating rate, a gradual ordering of the structure of calcium trititanates and tetratitanates occurs, leading to an equilibrium wherein a high concentration of CaO (>88%) is in association with $Ca_3Ti_2O_7$ and $Ca_4Ti_3O_{10}$. With increase in the CaO content in calcium monotitanate, there should be an increase in the resistance of lime refractories to atmospheric hydrolysis. The sintering schedule of lime refractories and especially lime clinker should therefore ensure the formation of titanates and solid solutions most highly enriched with CaO. This has resulted in an increase in hydrolysis resistance for refractory forms based upon lime.

The chemical potentials of CaO in two-phase field ($TiO_2 + CaTiO_3$), ($CaTiO_3 + Ca_4Ti_3O_{10}$), and ($Ca_4Ti_3O_{10} + Ca_3Ti_2O_7$) of the pseudo-binary system ($CaO + TiO_2$) have been measured in the temperature range (900–1250 K), relative to pure CaO as the reference state, using solid-state galvanic cells incorporating single-crystal CaF_2 as the solid electrolyte. The cells were operated under pure oxygen at ambient pressure. The standard Gibbs free energies of formation of calcium titanates, $CaTiO_3$, $Ca_4Ti_3O_{10}$, and $Ca_3Ti_2O_7$, from their component binary oxides were derived from the reversible e.m.f.s. The results can be summarized by the following equations:

$$CaO(solid) + TiO_2(solid) \Rightarrow CaTiO_3(solid)$$

$$\{\Delta G^\circ \pm 85/(J/mol) = -80{,}140 \text{ to } 6.302(T/K)\}$$

$$4CaO(solid) + 3TiO_2(solid) \Rightarrow Ca_4Ti_3O_{10}(solid)$$

$$\{\Delta G^\circ \pm 275/(J/mol) = -243{,}473 \text{ to } 25.758(T/K)\}$$

$$3CaO(solid) + 2TiO_2(solid) \Rightarrow Ca_3Ti_2O_7(solid)$$

$$\{\Delta G^\circ \pm 185/(J/mol) = -164{,}217 \text{ to } 16{,}838(T/^\circ K)\}$$

The reference state for solid TiO_2 is the rutile form. The results of this study were in good agreement with thermodynamic data for $CaTiO_3$ reported in the literature. For $Ca_4Ti_3O_{10}$, Gibbs free energy of formation obtained in this study differed significantly from that reported by Taylor and Schmalzried at $T = 873$ K. For $Ca_3Ti_2O_7$, experimental measurements are not available in the literature for direct comparison with the results obtained in this study. Nevertheless, the standard entropy for $Ca_3Ti_2O_7$ at $T = 298.15$ °K estimated from the results of this study using the Neumann–Koop rule is in fair agreement with the value obtained from low-temperature heat-capacity measurements.

Several investigations of the bulk phase diagram of the system CaO–TiO_2 predicted the existence of three stable compounds such as $Ca_3Ti_2O_7$, $Ca_4Ti_3O_{10}$ and $CaTiO_3$. The first two phases peritectically decompose at 1750 and 1840 °C, respectively, whereas the $CaTiO_3$ phase melts congruently at 1960 °C. There is also a eutectic at 1450 °C between $CaTiO_3$ and TiO_2. $Ca_3Ti_2O_7$ has an

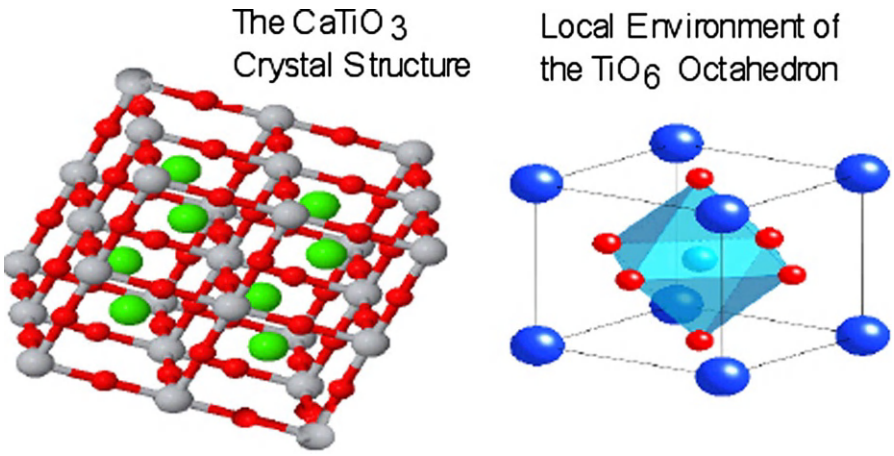

FIGURE 8.18

orthorhombic structure with $a = 5.41$ Å, $b = 19.42$ Å and $c = 5.42$ Å (space group $Ccm21$), while $Ca_4Ti_3O_{10}$ has also an orthorhombic structure with $a = 5.43$ Å, $b = 27.14$ Å and $c = 5.43$ Å (space group $Pcab$). The mineral, perovskite = $CaTiO_3$, has an orthorhombic structure at room temperature with $a = 5.38$ Å, $b = 5.44$ Å and $c = 7.654$ Å (space group $Pbnm$). The orthorhombic distortion of $CaTiO_3$ decreases with increasing temperature. The phase transitions from the room temperature orthorhombic structure to a tetragonal ($a = b = 5.49$ Å and $c = 7.78$ Å, space group $I4/mcm$) polymorph occur at temperatures between 1373 and 1423 K, followed by transformation to the cubic phase ($a = 3.83$ Å, space group $Pm\bar{3}m$) at 1523 K.

$CaTiO_3$ is mostly prepared by a solid-state reaction of CaO or $CaCO_3$ with TiO_2 at high temperatures. The undoped $CaTiO_3$ is an incipient ferroelectric with potential applications in MW-tunable devices. Upon doping with Pb^{2+}, it becomes a true ferroelectric. The versatility of calcium titanate extends to its suitability as a material for the immobilization of radioactive waste and as a biocompatible coating for medical Ti implants. Calcium metatitanate, $CaTiO_3$ has a cubic perovskite structure with $a = 3.795$ Å and $\alpha = \beta = \gamma = 90°$, as shown in Fig. 8.18.

The cell parameters are listed in Table 8.7.

Ceramic solid solutions involving $CaTiO_3$ are among the candidate systems for high-quality MW dielectric materials. Pure $CaTiO_3$ has a dielectric constant of about 180 at room temperature. The dielectric constant increases monotonically as temperature decreases over the measured range from 4.2 to 430 K, and extrapolates to a value greater than 300 at zero temperature. Associated with the trends in dielectric constant is a large positive TCF ($\gamma_f = \partial f/\partial T$) for dielectric resonators made from $CaTiO_3$.

Calcium metatitanate is also orthorhombic with: $CaTiO_3$: SG = $Pbnm$ (No. 62): $a = 5.380$ Å, $b = 5.440$ Å, $c = 7.639$ Å. The structure can be represented as shown in Fig. 8.19.

In order to make this distinction, the following diagram is presented as shown in Fig. 8.20.

TABLE 8.7

Atom	Wyckoff	x	y	z
Ca	4c	0.0065	0.0356	1/4
Ti	4b	0	1/2	0
O1	4b	0.5711	−0.0161	1/4
O2	8d	0.2897	0.2888	0.0373

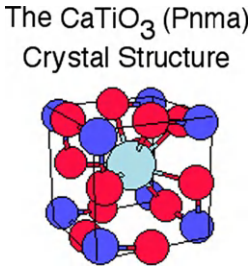

FIGURE 8.19

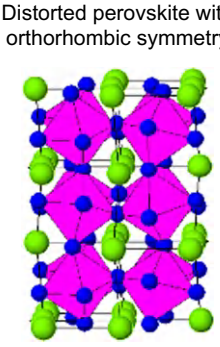

FIGURE 8.20

The distorted octahedra are clearly present and cause the cubic form to disappear entirely. Once formed, the orthorhombic form remains stable, even if high pressure is applied.

Some other unique properties that set perovskites apart and make them ideal for technological applications include:

(1) it is the only crystal structure that is ferroelectric (spontaneous alignment of the electric dipoles caused by interactions between them) not because of an external magnetic field but due to its crystal structure,

(2) it has unique ferro-, pyro-, and piezoelectric properties, and structural properties such as durability and chemical flexibility.

In the $CaTiO_3$–CaO system, two polytypic phases have been reported, $Ca_3Ti_2O_7$ ($n = 2$) and $Ca_4Ti_3O_7$ ($n = 3$). Due to a different Ca/Ti ratio, the phase, Ca_2TiO_4 is not stable. $Ca_3Ti_2O_7$ and $Ca_4Ti_3O_{10}$ consist of coherent intergrowths of **n** perovskite blocks with a single CaO layer having a distorted rock salt configuration. In both structures, the TiO_6 octahedra are tilted and distorted in a fashion like that of $CaTiO_3$. In $Ca_4Ti_3O_{10}$, there are two types of octahedra. Those in the middle of perovskite blocks are designated as "type 1" and those at the edges of the block as "type 2". The mean Ca–O bond lengths in this compound indicate that there are two distinct Ca^{2+} sites in this polytype structure where the Ca_1 sites are larger in the middle of the $CaTiO_3$ blocks and the Ca_2 sites are smaller in the CaO layers (Fig. 8.21).

The calcium titanates, $CaTiO_3$, $Ca_3Ti_2O_7$ and $Ca_4Ti_3O_{10}$, can be synthesized by the wet chemical peroxide route. The first step of the preparation is the precipitation of peroxo-precursors of definite stoichiometry which are transformable into the corresponding titanates by thermal decomposition. The resulting ultrafine, phase-pure calcium titanate powders have only a small impurity content. They are very sinter active above 1200 °C. The rate of densification during sintering of compacts is improved in the sequence $Ca_3Ti_2O_7 < Ca_4Ti_3O_{10} < CaTiO_3$, considering the green densities, the densities at a given time and the theoretical densities of the titanates for the calculations. The phase $CaTi_4O_9$ can be obtained after thermal degradation of a corresponding peroxo-precursor at temperatures below 700 °C. There are also indications of the formation of the phase $CaTi_2O_5$ below 700 °C. A phase in which titanium appears as Ti^{3+} in Ca_2TiO_4 cannot be synthesized using the peroxide route.

Calcium titanate is supplied in large quantities commercially as $CaTiO_3$ with a CAS number of 12049-50-2.

A symmetry analysis of the zero temperature instabilities of the tetragonal phase of tricalcium dititanate, $Ca_3Ti_2O_7$, which is stable at high temperature, has been performed. Order parameters were used to characterize each of the possible lattice distortions in order to construct a Landau free energy that elucidates the proposed group–subgroup relations for structural transitions in these systems. The coupling between the unstable distortion modes and the macroscopic strain tensor was also included. It was shown that in this phase the weak ferromagnetic moment and the spontaneous ferroelectric polarization are coupled, so that rotating one of these ordering by applying an external electric or magnetic field one can rotate the other ordering. A number of different domains (including phase domains) exist in each of the phases and indicate how these may be observed. The structure is shown in Fig. 8.22.

Ruddlesden–Popper (RP) systems are compounds of the form $A_{2+n}B_{1+n}C_{4+3n}$, where n is an integer, and the

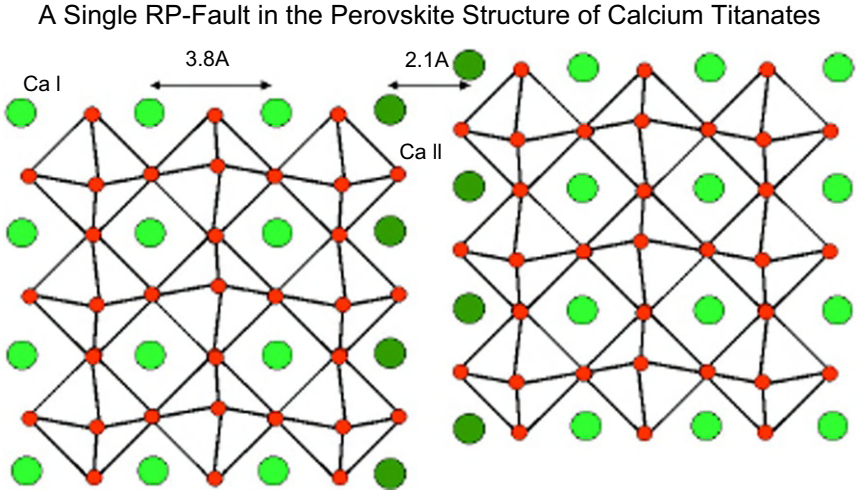

FIGURE 8.21

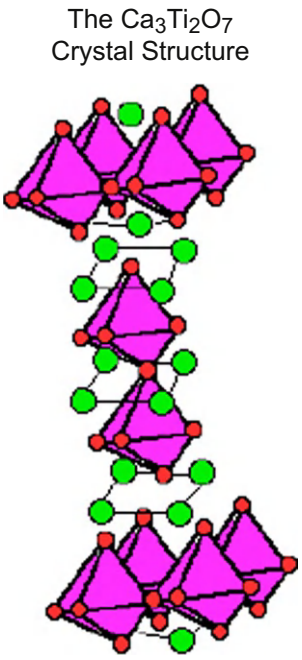

FIGURE 8.22

valences of the ions are usually $A = +2$, $B = +4$ and C (oxygen) $= -2$. They are essentially a series of tetragonal or hexagonal conformations.

Systems like $CaTiO_3$ can be regarded as being $n = \infty$. At high temperatures $T \geq 800$ K, their crystal structure is tetragonal, consisting of n-layer units, each layer consisting of vertex sharing oxygen octahedra at whose center sit a B ion, as shown in Fig. 8.22. As the temperature is lowered, these systems can undergo structural phase transitions into orthorhombic structures. These structural transitions usually involve reorientation of oxygen octahedra. One reason for the continuing interest in octahedral reorientations lies in the fact that they are important for many interesting electronic properties such as high-Tc superconductivity, colossal magnetoresistance, metal–insulator transitions and magnetic ordering.

Compounds concerning Ti^{2+} are also known. In an academic study of a "defect perovskite" structure of stoichiometry $AeTiO_2$ (AE = alkaline earth metal, Be, Mg, Ca, Sr, and Ba), we find substantial Ti–Ti bonding tuned by the size of the Ae^{2+} cation. The bonding is one-dimensional, partially σ, partially π. These formal d2 systems are expected to be nonmagnetic and metallic. A competing (for same Ae) structural alternative, an ordered rock salt structure, is magnetic shown in Fig. 8.23.

The photoactivity of this catalyst, containing Ti^{2+} ions, was evaluated by photocatalytic degradation of an azo dye, acid red 1 (AR1), using UV light irradiation. The results of the investigations revealed that the

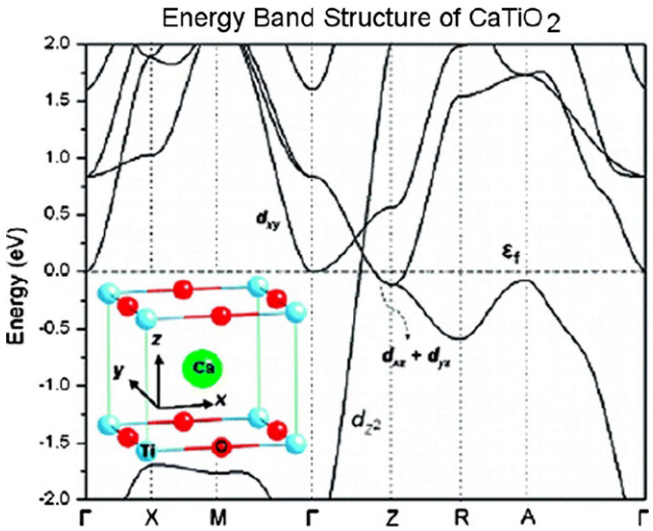

FIGURE 8.23

samples calcined at 300 °C for 3.6 h in a cyclic (2 cycles) mode had the best performance. Lower percentage dopant, 0.3–1.0 wt%, enhanced the photocatalytic activity of TiO_2, with the best at 0.5 wt% $CaTiO_2$. The performance of 0.5 wt% $CaTiO_2$ in the degradation of AR1 was far superior to that of a commercial Anatase TiO_2 Sigma product CAS No. 1317-70-0. The effect of pH on the degradation of AR1 was studied, and the pH of the dye solution exerted a great influence on the degradation of the dye. In contrast, the 2:1 compound, Ca_2TiO_3, was not photocatalytic at all.

Both 1:1 and 1:2 compounds in the $CaO–Ti_2O_3$ system occur as minerals, either Kassite, $CaTi_2O_4(OH)_2$ or Cafetite, $CaTi_2O_5(H_2O)$. The structure of Kassite is shown in Fig. 8.24.

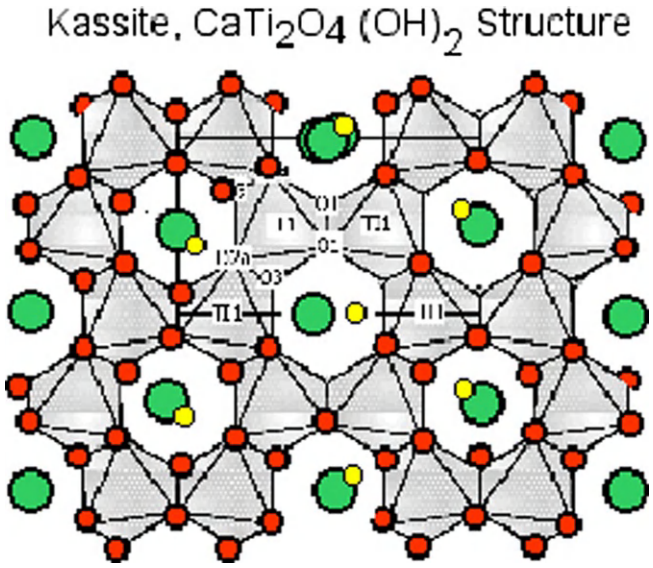

FIGURE 8.24

A related homologue, $Ca_2Ti_2O_6$ has also been studied. Ca–Ti–O films were prepared on quartz substrates by MoCVD (Metal oxide-chemical vapor deposition) using the precursors of $Ti(O\text{-}i\text{-}Pr)_2(dpm)_2$ and $Ca(dpm)_2$. The effects of deposition conditions on the crystal structure and microstructure of Ca–Ti–O films were investigated. The deposition temperatures (T_{dep}) were changed from 787 to 1187 K and the total pressure in the reaction chamber (P_{tot}) was kept at 0.8 kPa. The molar ratio of Ca to Ti precursors ($R_{Ca/Ti}$) was changed from 0.34 to 0.95. At temperatures higher than 1073 K (800 °C), $CaTiO_3$ perovskite films in a single phase were obtained. Mixtures of $Ca_2Ti_2O_6$ in a pyrochlore structure and $CaTiO_3$ in a perovskite structure were obtained at 787–1073 K and the content of $Ca_2Ti_2O_6$ phase increased with decreasing $R_{Ca/Ti}$. $Ca_2Ti_2O_6$ pyrochlore films in a single phase were obtained at $T_{dep} = 1073$ K and $R_{Ca/Ti} = 0.38$. $Ca_2Ti_2O_6$ is a face-centered cubic structure with $a = 9.90$ Å. Pyrochlore showed a granular microstructure about 500 nm in grain size. The transmittance of the $Ca_2Ti_2O_6$ films in a single phase was 50–70% in the wavelength range of 500–2500 nm. The band gap of pyrochlore was about 3.3 eV that calculated by the transmittance. The permittivity of $Ca_2Ti_2O_6$ films was about 100 from room temperature to 700 K.

Calcium titanates are readily available commercially.

8.1.7. Strontium Titanides

There are no known intermetallic compounds in the system, Sr–Ti. A phase diagram has been published but shows only the polymorphic transitions of the two metals.

8.1.8. Strontium Titanates

In the bulk phase diagram of the system SrO–TiO_2, several compounds are known and include compositions such as Sr_2TiO_4, $Sr_3Ti_2O_7$ and $SrTiO_3$. There is a eutectic at 1440 °C between $SrTiO_3$ and TiO_2, as shown in Fig. 8.25.

In the Ti^{4+} system of SrO–TiO_2, Sr_2TiO_4 has a tetragonal structure with $a = b = 3.88$ Å and $c = 12.62$ Å (space group $I4/mmm$), while $Sr_3Ti_2O_7$ has also a tetragonal structure with $a = b = 3.94$ Å and $c = 20.38$ Å (space group $I4/mmm$). $SrTiO_3$ has a cubic perovskite structure with $a = 3.91$ Å (space group $Pm3m$) at room temperature and higher, as shown in Fig. 8.26.

Strontium titanate is commonly produced by a solid-state reaction of $SrCO_3$ with TiO_2 at high temperatures (>1000 °C):

$$SrCO_3(solid) + TiO_2(solid) \Rightarrow SrTiO_3(solid) + CO_2(gas)$$

No intermediate products were observed during $SrTiO_3$ synthesis by Tagawa and Igarashi as well as by Chang and Liu. However, further investigation has suggested that the above reaction resulted via an intermediate Sr_2TiO_4 compound. $SrTiO_3$ is of technical significance. Owing to its high dielectric constant and large dielectric breakdown field, $SrTiO_3$ is a potential candidate for storage capacitor cells in dynamic random access memories. $SrTiO_3$ single crystals and thin films are extensively used as substrates for high-Tc superconducting, ferroelectric and multiferroic thin films. Suitably doped $SrTiO_3$ single crystals have been considered for nonvolatile memories based on resistive switching. Strontium titanate or $SrTiO_3$ single crystal provides a good lattice match to most materials with perovskite structure. At room temperature it exists in the cubic form, but transforms into the tetragonal structure at temperatures less than 105 K. At very low temperatures, $SrTiO_3$ exhibits piezoelectric and superconducting characteristics. It also exhibits a very large dielectric constant.

Strontium titanate ($SrTiO_3$) is currently the most widely used high-temperature superconducting

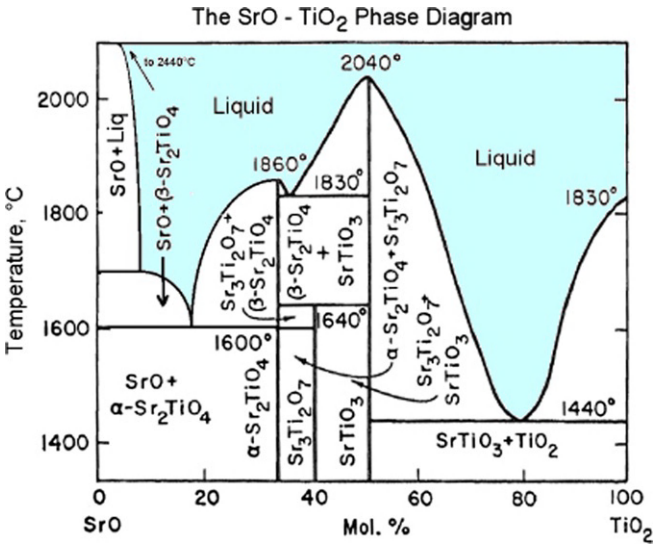

FIGURE 8.25

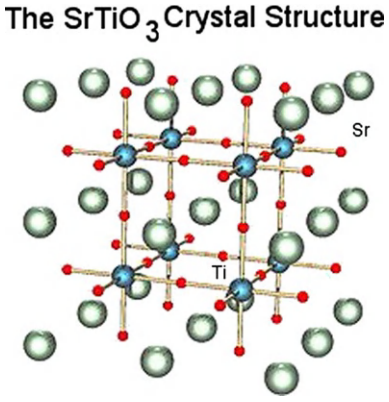

FIGURE 8.26

single-crystal substrate and is superior in this regard. It is compatible with $YBaCuO_3$ high-temperature superconducting materials with advantages such as lattice matching, and lack of twin structure, physical and mechanical properties when the film is formed. Film technology using a variety of systems (such as magnetic sputtering, pulsed laser deposition, laser molecular beam epitaxy, etc.) produced by a variety of high-temperature superconducting thin films (Y-system, Bi-system, La-system, etc.) can be TCO $\geq$ 90 K, JCO $\geq$ 106 A/cm^2 and other indicators. $SrTiO_3$ is also used in high-temperature superconducting junction technology (using double-crystal substrate or the step-like substrate) and is the preferred single-crystal material at the level of substrate (at a specific point of the miter and heat treatment).

In the $SrTiO_3$–SrO system, three polytypic phases have been reported, Sr_2TiO_4 ($n = 1$), $Sr_3Ti_2O_7$ ($n = 2$) and $Sr_4Ti_3O_7$ ($n = 3$). The phase, Sr_2TiO_4 can be described as the ordered sequence of a single SrO fault and a single $SrTiO_3$ perovskite block, while the $Sr_4Ti_3O_{10}$ structure is a sequence of one planar fault and three perovskite layers. These RP phases are completely ordered only when an exact stoichiometry is achieved. For this phase, the Sr/Ti ratio should be 1.33 of coherent intergrowths of **n** perovskite blocks with a single SrO layer having a distorted rock salt configuration. In both structures, the TiO_6 octahedra are tilted and distorted in a fashion like that of $SrTiO_3$. In $Sr_4Ti_3O_{10}$, there are two types of octahedra. Those in the middle of perovskite blocks are designated as "type 1" and those at the edges of the block as "type 2". The mean Sr–O bond lengths in this compound indicated that there are two distinct Sr^{2+} sites in this polytype structure wherein the Ca_1 sites are larger in the middle of the $SrTiO_3$ blocks and the Sr_2 sites are smaller in the SrO layers. An RP defect in the perovskite type of structure was given for the Ca homologue.

Although a 1:2 compound in the CaO–TiO_2 system has been reported, there are no reports of an equivalent $SrTi_2O_5$ phase.

Figure 8.27 shows the structures of the unit cells of the artificially layered phases ($m = 1$–5).

Only $SrTiO_3$ appears in the phase diagram. The strontium (light- and dark-green spheres), titanium (centered in the octahedra), and oxygen (apices of the octahedra) ions are assumed to arrange in the same manner as in the related $SrTiO_3$, Sr_2TiO_4, and SrO ($m = 1, 2, \infty$) phases. Based on these principles, the c lattice parameter of the unit cells for the odd m phases was made equal to the spacing between TiO_2 planes, whereas c is twice for the even m phases owing to a body-centering translation.

Although these phases are easily envisioned, the question was asked as to whether or not they can be formed and whether or not they are stable with respect to large-scale phase separation into the equilibrium

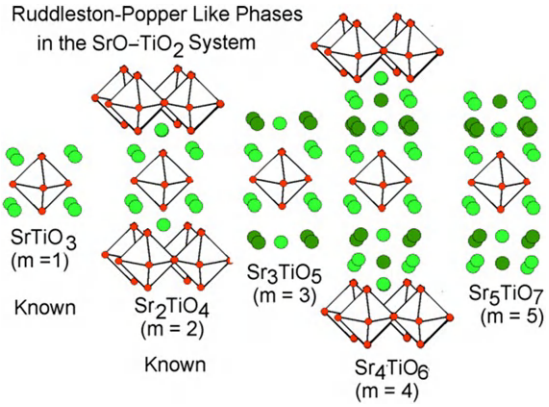

FIGURE 8.27

bulk phases Sr_2TiO_4 and SrO. The epitaxial films were grown on $LaAlO_3$(001) substrates using a molecular beam epitaxy (MBE) system for crystal growth system. The single-crystal substrates were etched in 3:1 HCl:HNO_3 ultrasonically cleaned in acetone and ethanol and annealed prior to the growth of films. Growth was controlled to the monolayer level by first calibrating the flux rates of both sources ex situ. Deposition was carried out by alternating the open elemental source between Sr and Ti (while the other was shuttered) in a manner to deposit m monolayers of SrO followed by a single TiO_2 monolayer. These layers have been valuated as dielectric films for MW applications.

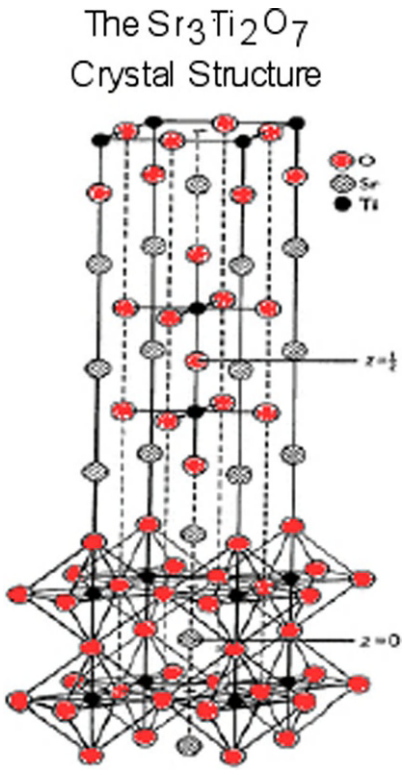

FIGURE 8.28

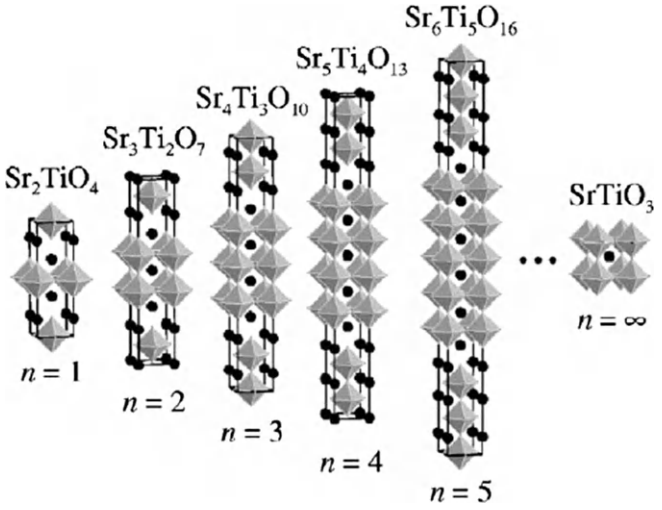

FIGURE 8.29

The compound, tristrontium dititanate, $Sr_3Ti_2O_7$, has the structure shown in Fig. 8.28. It is tetragonal but related to the cubic perovskites, as may be seen by closer examination of the structure diagram shown in Fig. 8.28.

It was formed by firing a mixture of $SrCO_3$ and TiO_2 at a molar ration of 3:2. Its structure is intermediate to Sr_2TiO_4 (K_3NiF_4 type) and perovskite, $SrTiO_3$. Whereas in Sr_2TiO_4, perovskite layers are interleaved with SrO layers, forming a tetragonal, body-centered unit with an axial ratio of about 3:2, double perovskite layers are interleaved with SrO layers in $Sr_3Ti_2O_7$, the axial ratio being increased to about 5:2. The unit cell contains about two formula units. This is better illustrated as shown in Fig. 8.29. The increase in layers for various strontium titanate compositions is more easily seen in Fig. 8.29.

The main usage for $SrTiO_3$ has been as a gemstone. A sample is shown in Fig. 8.30.

Strontium titanate is both much denser (space group = 4.88 for natural, 5.13 for synthetic) and much softer (Mohs hardness = 6–6.5 for natural, 5.5 for synthetic) than diamond. Its refractive index (2.41—as measured by sodium light, 589.3 nm) is nearly identical to that of diamond, but the dispersion (the optical property responsible for the "fire" of the cut stones) of strontium titanate is over four times higher, at 0.19 (B–G interval). This results in an excess of "fire" when compared to diamond.

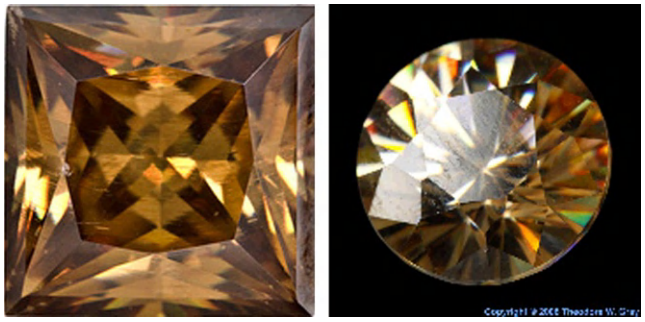

FIGURE 8.30

The strontium titanates $SrTiO_3$, Sr_2TiO_4, $Sr_3Ti_2O_7$ and $Sr_4Ti_3O_{10}$ can be synthesized to a good quality by a wet chemical peroxide route. At first, peroxo-precursors of definite stoichiometry are formed during the preparation. These are then transformed into the titanates by thermal decomposition. The resulting strontium titanate powders are of ultrafine nature and have a high purity. They show high sintering activity at temperatures >1200 °C. The densification behavior during sintering improved in the sequence $Sr_2TiO_4 < Sr_3Ti_2O_7 < Sr_4Ti_3O_{10} < SrTiO_3$.

Vacancy-ordered $Sr_2Ti_2O_5$ (110) epitaxial films in situ deposited on $YBa_2Cu_3O_{7-\delta}$ (YBCO) (103) epitaxial films were studied for insulating layers in high-Tc superconducting heterostructures. The ordered structure is interpreted by a $2 \times 2 \times 2$ superstructure with a long-range ordered arrangement of oxygen vacancies in the film and a 2:1 surface superstructure with an ordered arrangement of surface oxygen vacancies on it. The resistivity of the $Sr_2Ti_2O_5$ film sandwiched between Au and YBCO films was measured as a function of the thickness and temperature, and discussed with respect to electron scattering induced by a deficiency of oxygen in the film and at the film boundary.

In the Ti^{3+} system of SrO–Ti_2O_3, the crystal structure of the strontium thallate $SrTl_2O_4$ was determined using powder XRD. This oxide is isostructural with $CaFe_2O_4$, i.e. it crystallizes in the space group *Pnam* with $a = 10.041$ Å, $b = 11.697$ Å and $c = 3.49$ Å. The $[Tl_2O_4]\infty$ framework is built up from double rutile chains of TlO_6 octahedra forming five-sided tunnels where the strontium cations are located. The semimetallic properties of this phase are once more in favor of the existence of proximity effect induced superconductivity in the $[TlO]\infty$ layers of layered thallium cuprates.

Strontium titanates are available commercially, in the form of gemstones, single-crystal slices and powders.

8.1.9. Barium Titanides

There are no known intermetallic compounds that occur in the system, Ba–Ti. A phase diagram has been published but shows only the polymorphic transition temperatures of the two metals.

8.1.10. Barium Titanates

A number of compounds form by reaction between BaO and TiO_2 at elevated temperatures. Some of these compounds are of great interest and technological importance. Statton first tried to establish phase relations in the BaO–TiO_2 system. Later, this phase diagram was restudied and improved by many other workers.

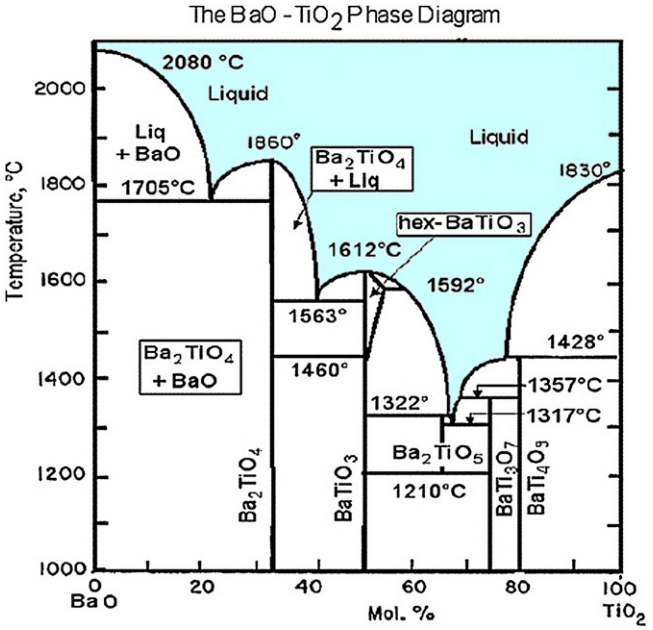

FIGURE 8.31

A high-temperature phase diagram constructed for the system BaO–TiO_2 is shown in Fig. 8.31.

The determination of the phase relationships was based on XRD and microscopic visual analyses of the samples quenched from high temperature. In the Ti-rich region, the results of Kirby et al. are in general agreement with those of Negas et al. and O'Bryan et al. As can be seen from the phase diagram, the formation of Ti-rich barium titanates depends on the ratio of Ba to Ti as well as temperature. The stable Ti-rich barium titanates which exist at high temperatures are: $Ba_6Ti_{17}O_{40}$, $Ba_4Ti_{13}O_{30}$, $BaTi_4O_9$ and $Ba_2Ti_9O_{20}$. The latter two Ti-rich phases are used in MW industry. Other supposedly possible Ti-rich barium titanates such as $BaTi_5O_{11}$ and $BaTi_6O_{13}$ have not been observed in these studies. A compound, $BaTi_2O_5$, was found in a sample containing 65 mol% TiO_2, when quenched from the liquid state. However, heating of this sample at 1320 °C for 64 h resulted in a mixture of $BaTiO_3$ and $Ba_6Ti_{17}O_{40}$ with no evidence of any remaining $BaTi_2O_5$.

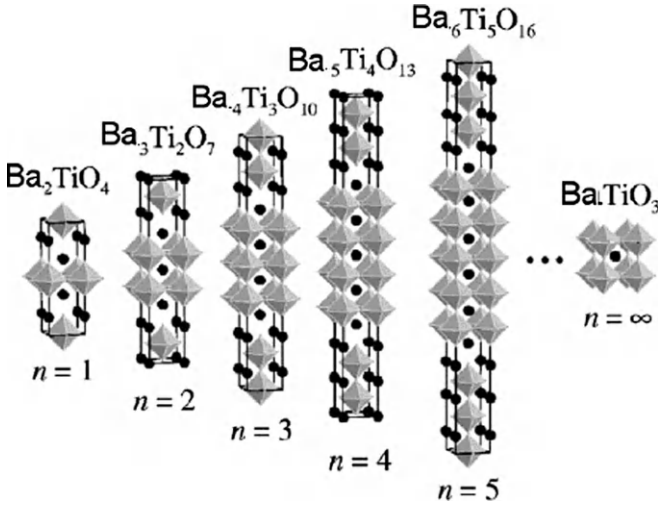

FIGURE 8.32

It was noted that these three Ti-rich barium titanates form only through a liquid intermediate. However, Ritter et al. obtained $BaTi_2O_5$ and $BaTi_5O_{11}$ phases by using low-temperature alkoxide synthesis techniques. In this diagram, both $BaTi_2O_5$ and $BaTi_5O_{11}$ phases crystallize at ~700 °C. $BaTi_2O_5$ decomposes into $Ba_6Ti_{17}O_{40}$ and $BaTiO_3$ at ~1150 °C, while $BaTi_5O_{11}$ decomposes to TiO_2, $Ba_2Ti_9O_{20}$ and/or $BaTi_4O_9$ at ~1200 °C. Thus, we can conclude that both these phases ($BaTi_2O_5$ and $BaTi_5O_{11}$) are either low-temperature stable phases or metastable phases obtained by crystallization of an amorphous precursor. This can be better appreciated by perusal of the following diagram that shows such phases originate from the cubic perovskite phase and are di-, tri-, tetra-, penta- or hexa-perovskites (Fig. 8.32).

The types of barium titanate compounds investigated and their crystalline parameters are shown in Table 8.8 ("*n*" is the number of layers present).

TABLE 8.8

Phase	Space group	*a* (Å)	*b* (Å)	*c* (Å)	*α* (°)	*β*	*γ*	*n*
$BaTi_2O_5$	*A*2/*m*—monoclinic	9.409	3.93	16.92	90	103.5	90	—
$BaTi_4O_9$	*Pmmm*—orthorhombic	14.52	3.79	16.93	90	90	90	—
$BaTi_5O_{11}$	$P2_1n$—monoclinic	7.67	14.02	7.52	90	98.33	90	6
$BaTi_6O_{13}$	*P*1—triclinic	7.51	9.85	7.46	105.38	118.9	72.58	4
$Ba_2Ti_5O_{12}$	*Ammm*—orthorhombic	9.90	11.41	23.54	90	90	90	10
$Ba_2Ti_9O_{20}$	*P*1—triclinic	7.47	14.08	14.34	89.94	79.43	84.45	6
$Ba_2Ti_{13}O_{22}$	*Bmab*—orthorhombic	11.65	14.10	10.05	90	90	90	6
$Ba_4Ti_{13}O_{30}$	*Cmca*—orthorhombic	17.06	9.86	14.05	90	90	90	6
$Ba_6Ti_{17}O_{40}$	*C*2/*c*—monoclinic	9.88	17.08	18.92	90	98.42	90	8

These crystal structures of Ti-rich barium titanates have been extensively studied. $BaTi_4O_9$ and $BaTi_2O_5$ have structures which can be described as cubic close-packed arrangements of Ba and O atoms. Both these compounds have one short cell constant of about 4.0 Å. These structures have often been referred to as Wadsley–Andersson type phases (also called tunnel structures). The structures of other Ti-rich barium titanates, i.e. $BaTi_6O_{13}$, $BaTi_5O_{11}$, $Ba_4Ti_{13}O_{30}$, $Ba_2Ti_9O_{20}$, $Ba_2Ti_{13}O_{22}$ and $Ba_6Ti_{17}O_{40}$, are more complex but can be described as close packing of Ba and O atoms in which some of the octahedral O_6 interstices are occupied by Ti atoms. These structures can be illustrated as being made up of Ba–O close-packed layers with 4, 6, 8 or 10 layers per unit cell. The unit cell dimensions of Ti-rich barium titanates as well the number of layers per unit cell are given in Table 8.8.

The mean thickness of each close-packed layer of the Ti-rich barium titanates is ≈0.234 nm which is similar to the (111) interplanar spacing of $BaTiO_3$. The orientation of the close-packed layer is usually derived from the morphology of the crystals or from the diffraction pattern. For example, in the case of $Ba_6Ti_{17}O_{40}$, the lattice constant $c = 18.92$ Å (≈8 Å ~ 0.234 nm) leads to the conclusion that the unit cell contains eight close-packed layers perpendicular to the *c*-axis. Despite one unit cell repeating itself after 8 layers, the real crystallographic identity period of the packing of the complete structure is 24 layers. This arises because the direction of packing is [103]. The angle between the [103] direction and the (001) plane in $Ba_6Ti_{17}O_{40}$ is ≈1.3. The compositions of other Ti-rich barium titanates can be derived by analogy to the layers in $Ba_6Ti_{17}O_{40}$ and $Ba_4Ti_{13}O_{30}$ as was shown by Roth et al. for the phases $Ba_6Ti_{14}Nb_2O_{39}$, $Ba_{14}Ti_{40}Nb_2O_{99}$ and $Ba_{18}Ti_{54}Nb_2O_{132}$. Recently, a topotaxial orientation relationship between $BaTiO_3$ and $Ba_6Ti_{17}O_{40}$ as well as between $BaTiO_3$ and $Ba_4Ti_{13}O_{30}$ has been established. Despite the different procedure of sample preparation (solid-state reaction of $BaCO_3$ and TiO_2 at high temperatures in air or chemical reaction of SiO_2 film with $BaTiO_3$ single crystals). Thus, the close-packed planes of $Ba_6Ti_{17}O_{40}$ and $Ba_4Ti_{13}O_{30}$ lie parallel to the close-packed planes of $BaTiO_3$. Crystallographically, Krasevec et al. explained the orientation relationship between $Ba_6Ti_{17}O_{40}$ and $BaTiO_3$ phases by the similarity of the stacking sequence of (111) planes of $BaTiO_3$ and (001) planes of $Ba_6Ti_{17}O_{40}$, if the larger unit cell of the monoclinic $Ba_6Ti_{17}O_{40}$ phase was appropriately cut. On the base of the above relationship, a model of a topotactic boundary between $Ba_6Ti_{17}O_{40}$ and $BaTiO_3$ phases was constructed.

In the preparation of $BaTiO_3$ from $BaCO_3$ and TiO_2, it was noted that formation of pseudo-cubic $BaTiO_3$ free from $BaCO_3$ and TiO_2 occurred when the barium–titanium polymeric precursor was heat treated in air at 500 °C for 8 h or at 600 °C for 2 h. However, the Raman spectra of the same powders indicated the formation of tetragonal (rather than cubic) $BaTiO_3$, with traces of high-temperature hexagonal $BaTiO_3$ stabilized at room temperature, XRD of a pyrolyzed product at 500 °C for 2 h revealed a simple mixture of $BaTiO_3$ and an intermediate phase, $Ba_2Ti_2O_5 \cdot CO_3$. The solid-state reaction between $BaCO_3$ and TiO_2 was concluded as not being responsible for the $BaTiO_3$ formation; rather, $BaTiO_3$ formed directly by thermal decomposition of the intermediate $Ba_2Ti_2O_5 \cdot CO_3$ phase at temperatures >500 °C. In addition, by Raman scattering measurements, the intermediate $Ba_2Ti_2O_5 \cdot CO_3$ phase was found to be unstable in ambient air, yielding $BaCO_3$ as one of the decomposed products.

Barium titanate ($BaTiO_3$) is well known to have several phase transitions, depending on temperature. Above the Curie temperature (≈120 °C), it has the cubic perovskite structure (with Ba^{2+} as A and Ti^{4+} as B, $a \approx 4.01$ Å, space group $Pm3m$). This is a centrosymmetric cubic structure with Ba at the corners, Ti at the center and the oxygen atoms at the face centers (Fig. 8.33).

The ions are in the following positions: Ba at (0,0,0), Ti at (1/2,1/2,1/2) and three oxygen ions at (1/2,1/2,0), (1/2,0,1/2), (0,1/2,1/2). The titanium ion is surrounded by six oxygen ions in octahedral configuration and lies in octahedral holes of the Ba–O packing. Each barium ion has 12 oxygen neighbors. However, there are two high-temperature forms of $BaTiO_3$: cubic and hexagonal ($a = 5.74$ Å and $c = 14.05$ Å, space group $C6/mmc$). At temperatures above 1432 °C, the cubic form of $BaTiO_3$ transforms into the hexagonal form. These two modifications are built from close-packed (111) layers of composition BaO_3. In cubic $BaTiO_3$, there is repetition after every third layer as ABC … in the hexagonal form repetition occurs along the *c*-axis after every sixth layer as ABCACB …. As the temperature is lowered, cubic $BaTiO_3$ goes through phase transitions to three different ferroelectric phases: cubic to tetragonal at 393 K, tetragonal to

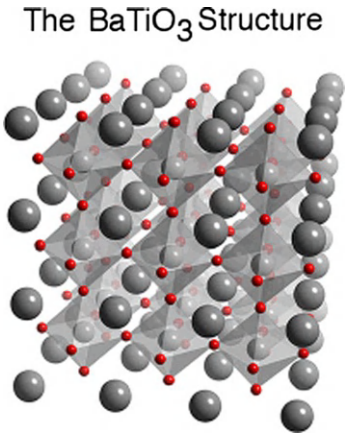

FIGURE 8.33

orthorhombic at 278 K, and orthorhombic to rhombohedral at 183 K. These three phases involve small distortions from the cubic symmetry. At room temperature, $BaTiO_3$ is usually considered as tetragonal with $a = 3.994$ Å, and $c = 4.038$ Å (space group $P4mm$).

The electrical properties of titania and its compounds indicate the suitability of these materials not only as substitutes for condenser grade mica but also for a number of other electrical applications where it is not possible or convenient to use other dielectrics. Of these, barium titanate is far superior. The oxides and carbonates of beryllium, magnesium, cerium, zinc, strontium, cadmium and barium were heated with titanium oxide to a temperature of about 1500 °C. The dielectric constants of the orthotitanates thus obtained were: for beryllium titanate 70, for magnesium 17, for calcium 115, for zinc 30, for strontium 155, for cadmium 62, >1000 for barium. The measurements were carried out at room temperature at a frequency of 1 MHz.

Barium strontium titanate (BST) powders of the formula $Ba_{1-x}Sr_xTiO_3$ ($0 \le x \le 1$) have been prepared by the polymeric precursor route using citric acid and ethylene glycol. Pure BSTs were obtained at 500 °C. These oxides were found to have the cubic structure, which is retained even after heating at 800 °C. Detailed X-ray studies on samples sintered at 1100 °C show weak tetragonal distortion for $BaTiO_3$, while the other BSTs retain their cubic structure. The particle size of the sintered oxides increases from 55 nm for $BaTiO_3$ to 88 nm for $SrTiO_3$, from X-ray line-broadening studies. The nano-sized grains are reasonably stable to sintering (the particle size for $BaTiO_3$ changes from 25 nm at 500 °C to 55 nm at 1100 C). The dielectric constant of the sintered oxides decreases from 510 for $BaTiO_3$ ($x = 0$) to 190 for $SrTiO_3$ ($x = 1$) at 100 kHz. The dielectric loss decreases from 0.05 for $BaTiO_3$ to 0.001 for $SrTiO_3$ at 100 kHz. No ferroelectric transition was observed either in the dielectric studies or by differential scanning calorimetry (Fig. 8.34).

Ba_2TiO_4 (barium orthotitanate) is the most Ba-rich compound in the system $BaO–TiO_2$. It is formed as an intermediate phase during the synthesis of $BaTiO_3$ by solid-state reaction between $BaCO_3$ and TiO_2. Ba_2TiO_4 exists in monoclinic and orthorhombic modifications. The orthorhombic form is stable at high temperatures, while the monoclinic phase is stable at room temperature. The orthorhombic Ba_2TiO_4 was observed to be a chemically unstable compound and it decomposed when exposed to air. Monoclinic Ba_2TiO_4 has a β-Ca_2SiO_4 type structure. Its unit cell has the dimensions: $a = 6.12$ Å, $b = 7.72$ Å, $c = 10.53$ Å and $\beta = 92.99°$. The orthorhombic modification of Ba_2TiO_4 has a distorted β-K_2SO_4 structure. Its unit cell has the dimensions: $a = 7.65$ Å, $b = 10.55$ Å, $c = 0.6.11$ Å (space group $Pnam$). The orthorhombic structure consists of tetravalent titanium cations in an unusual tetrahedral coordination.

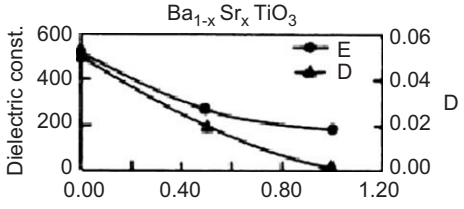

FIGURE 8.34

In the Ti^{3+} system of $BaO–Ti_2O_3$, the compound, $BaTi_2O_4$, remains unknown.

Barium titanates are readily available commercially in several forms.

8.1.11. Radium Titanates

There are no references the study of radium titanates. It is doubtful whether any such compounds can be formed. The literature is devoid of any mention of such compounds similar to those of the barium titanate series of compounds.

The high cost of radium is also a significant deterrent to work in Academia.

8.2. ALKALINE EARTH ZIRCONIUM COMPOUNDS

In contrast to titanium, only a few zirconate compounds of the alkaline earths are known. Additionally, only Be metal forms any intermetallic compounds with Zr metal.

8.2.1. Beryllium–Zirconium Compounds

There are no known compounds based on the $BeO–ZrO_2$ system. A phase diagram is available but shows only polymorphic temperature transitions of the individual oxide components.

8.2.2. Beryllium Zirconides

The intermetallic system, Be–Zr, has been studied and a phase diagram has been published (Fig. 8.35).

At least four compounds are known. With the exception of Be_2Zr, nearly all of the compounds are formed in the Be-rich part of the phase diagram.

$Be_{13}Zr$ has the structure shown in Fig. 8.36.

This lattice consists mostly that of the Be metal as modified by a few Zr atoms. The lattice structure changes in the vicinity of the Zr atoms. Cell parameters are: $a = b = c = 7.102$ Å, $\alpha = \beta = \gamma = 60°$, cell volume = 253.30 $Å^3$, $Z = 8$. Cell occupancy is listed in Table 8.9.

The compound, $Be_{17}Zr_2$, has similar features and the crystal structure shown in Fig. 8.37.

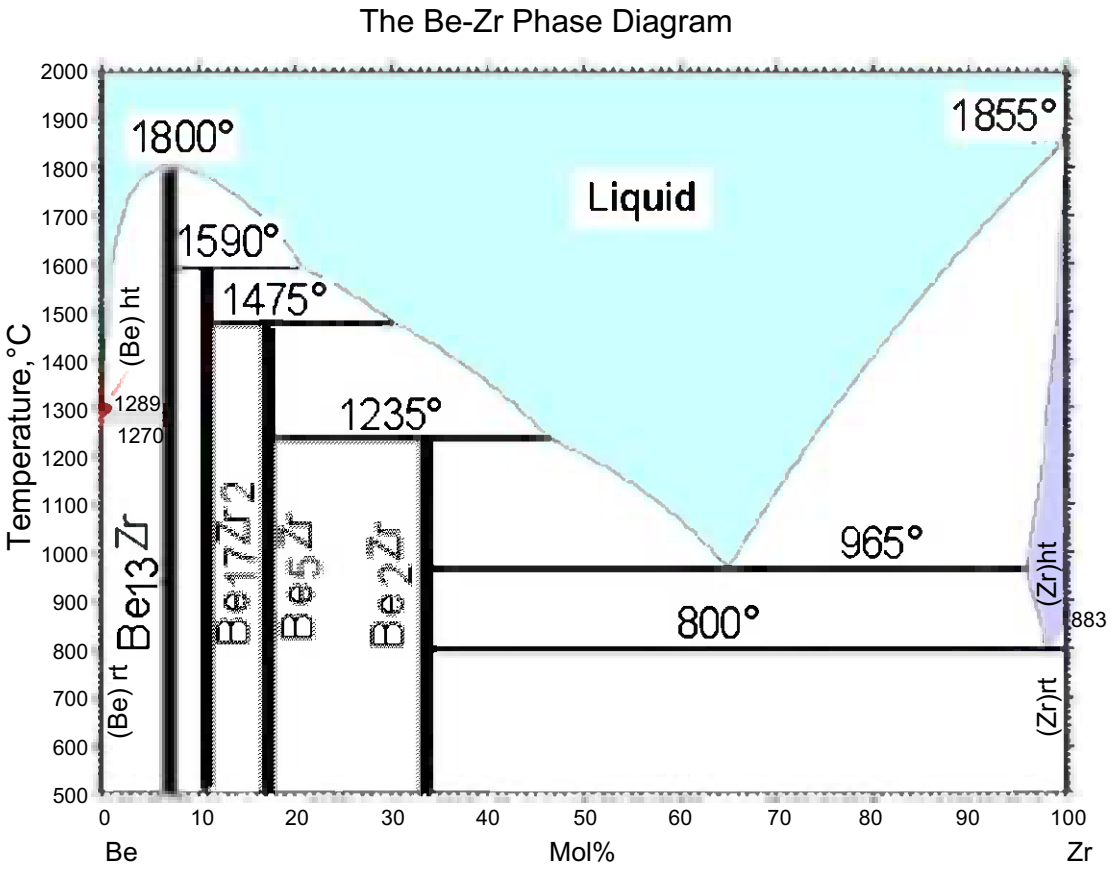

FIGURE 8.35

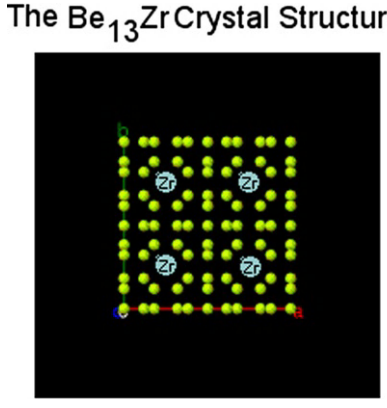

FIGURE 8.36

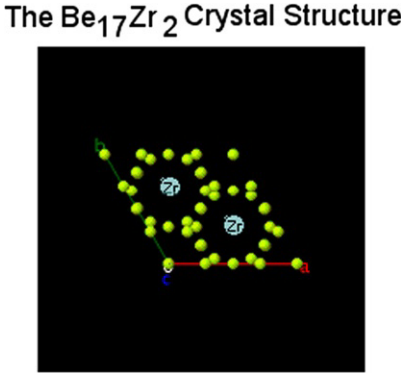

FIGURE 8.37

TABLE 8.9

No	Site notation	Atom	Multiplicity	Wyckoff	Site symmetry	*x*	*y*	*z*	Occupancy
1	Be1	Be	96	i	m..	0	0.11924	0.18063	1.0
2	Be2	Be	8	b	m-3.	0	0	0	1.0
3	Zr1	Zr	8	a	432	1/4	1/4	1/4	1.0

TABLE 8.10

No	Site notation	Atom	Multiplicity	Wyckoff	Site symmetry	*x*	*y*	*z*	Occupancy
1	Be(3)	Be	18	h	.m	0.49896	0.50104	0.1585	1.0
2	Be(4)	Be	18	f	.2	0.2875	0	0	1.0
3	Be(2)	Be	9	d	.2/m	1/2	0	1/2	1.0
4	Be(1)	Be	6	c	3m	0	0	0.0966	1.0
5	Zr	Zr	6	c	3m	0	0	0.3373	1.0

TABLE 8.11

No	Site notation	Atom	Multiplicity	Wyckoff	Site symmetry	*x*	*y*	*z*	Occupancy
1	Be	Be	2	d	-6m2	1/3	2/3	1/2	1.0
2	Zr	Zr	1	a	6/mmm	0	0	0	1.0

TABLE 8.12

No	Site notation	Atom	Multiplicity	Wyckoff	Site symmetry	*x*	*y*	*z*	Occupancy
1	BeII	Be	3	g	mmm	1/2	0	1/2	1.0
2	BeI	Be	2	c	-6m2	1/3	2/3	0	1.0
3	Zr	Zr	1	a	6/mmm	0	0	0	1.0

Cell parameters are: $a = b = c = 5.694$ Å, $\alpha = \beta = \gamma = 82.894°$, cell volume = 180.68 Å^3. Cell occupancy is listed in Table 8.10.

Be_2Zr has the crystal structure shown as follows. Cell parameters are: $a = 3.23$ Å, $b = c = 3.814$ Å, $\alpha = 120°$, $\beta = \gamma = 90°$, cell volume = 40.69 Å (Fig. 8.38).

Cell occupancy is listed in Table 8.11.

Be_5Zr has the crystal structure shown in Fig. 8.39.

Cell parameters are: $a = 3.485$ Å, $b = c = 4.584$ Å, $\alpha = 120°$, $\beta = \gamma = 90°$, cell volume = 62.87 Å^3. Cell occupancy is listed in Table 8.12.

These intermetallic compounds are not available commercially nor have any uses developed in Industry. No CAS numbers have been assigned.

8.2.3. Magnesium Zirconide Compounds

There were no known intermetallic compounds established in the system, Mg–Zr. A phase diagram has been published but showed only the polymorphic transition temperatures of the two metals.

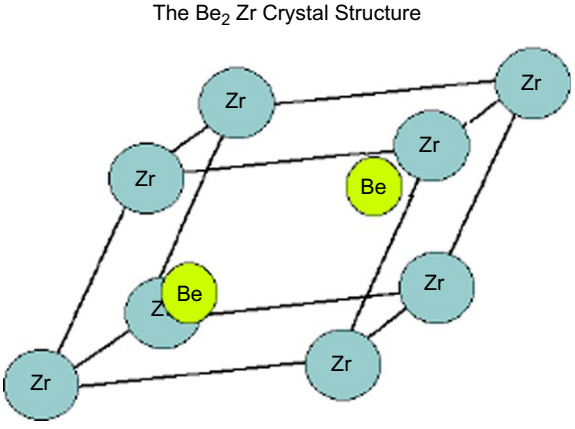

FIGURE 8.38

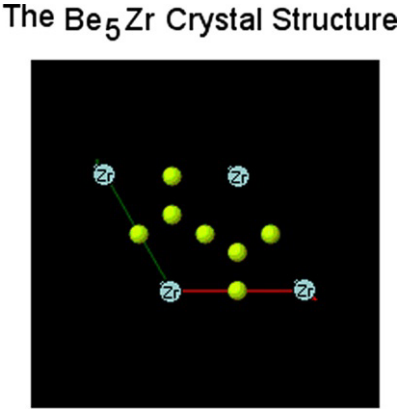

FIGURE 8.39

8.2.4. Magnesium Zirconate Compounds

The system, $MgO–ZrO_2$, has also been studied. A phase diagram is available but shows only the polymorphic temperature transitions of the individual oxide components.

It has been determined that the probable perovskite structure of $MgO–ZrO_2$, i.e. $MgZrO_3$, is difficult to prepare. $MgZrO_3$ melts at 2060 °C. The heat of formation is:

$$\Delta_f H = -3.34 \times 10^2 \text{ kJ/mol, 298 K, MgZrO}$$

This low value accounts for the lack of interest in this compound since it is difficult to create.

$MgZrO_3$ has been used as a thermal barrier material. Because of difficulty in formation of this material from the oxides, a plasma-spray technique has been used. Functionally gradient coatings are widely used at high temperatures in order to improve performances of materials in automotive, aircraft and aerospace industries, etc. These coating systems contain a steel substrate, bonding layer, cermet layer and ceramic coating, respectively. Furthermore, the composition and morphology of the coatings change gradually from ceramic to metal. In a recent work, 304 L stainless steel substrates were coated by functionally gradient coatings consisting of bond coat NiCrAl, 70% NiCrAl + 30% $MgZrO_3$, 50% NiCrAl + 50% $MgZrO_3$, 30% NiCrAl + 70% $MgZrO_3$ as the cermet layer and 100% $MgZrO_3$ as the top coat.

No other known compounds occur in this system. Although the other alkaline earths form a 1:1 compound having a perovskite-like structure, $MgZrO_3$ has the CAS number of 12032-31-4.

8.2.5. Calcium Zirconide Compounds

No known intermetallic compounds have been discovered in the system, Ca–Zr. A phase diagram has been published but showed only the polymorphic transition temperatures of the two metals.

8.2.6. Calcium Zirconate Compounds

The system, $CaO–ZrO_2$, has been studied and a phase diagram has been published. It has the form shown in Fig. 8.40.

Originally, only the 1:1 compound, $CaZrO_3$, was known but later work showed the existence of $CaZr_4O_9$ to be present. However, the existence of the $CaZr_4O_9$ compound remains contentious. Calcium zirconate, $CaZrO_3$, has at least two polymorphs. One structure

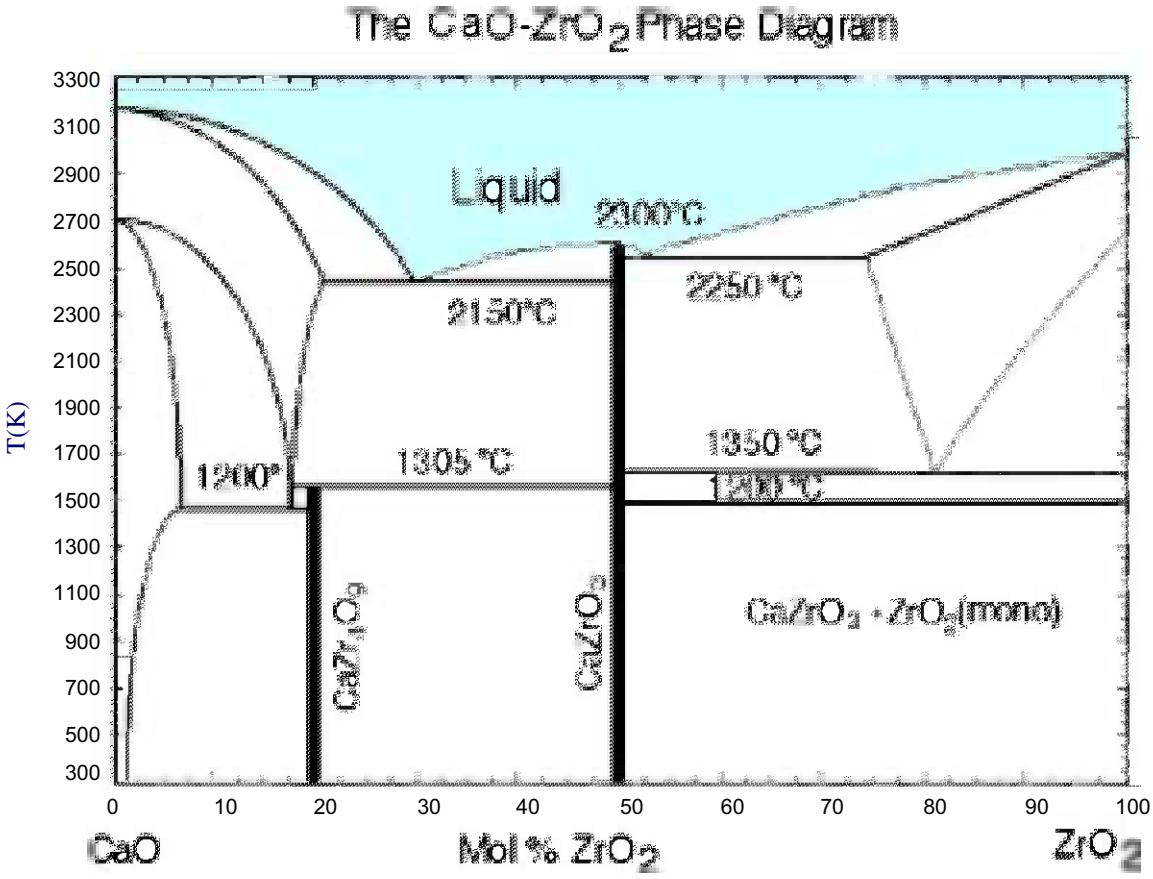

FIGURE 8.40

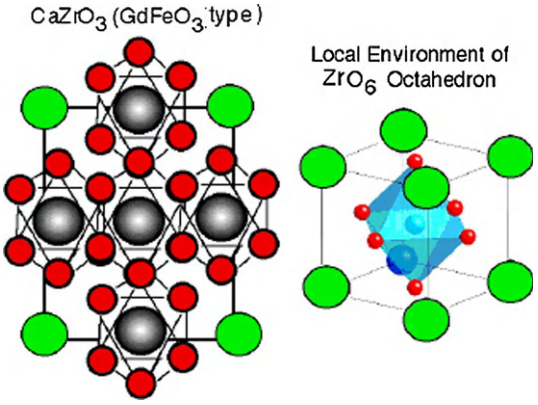

FIGURE 8.41

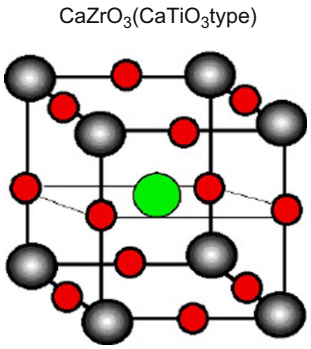

FIGURE 8.42

has the $GdFeO_3$ structure and the cell parameters of $a = b = 5.736$ Å, $c = 8.052$ Å, $\alpha = \beta = \gamma = 90°$, cell volume = 248.62 Å^3. The three-dimensional $GdFeO_3$ polymorph consists of ZrO_6 octahedra (one per cell) interspersed with Ca^{2+} cations. The structure is shown in Fig. 8.41.

Cell occupancy is listed in Table 8.13.

The other polymorph has the structure of $CaTiO_3$ and the cell parameters are: $a = b = c = 4.12$ Å, $\alpha = \beta = \gamma = 90°$, cell volume = 69.93 Å^3 (Fig. 8.42).

Cell occupancy is listed in Table 8.14.

Two other structures have been reported. One form has a cubic structure with point group = hP30, $a = b = c = 5.774$ Å, $\alpha = \beta = \gamma = 60.6°$, cell volume = 137.96 Å^3, while the other was stated to have cell parameters of: $a = b = 4.039$ Å, $c = 4.098$ Å, $\alpha = \beta = \gamma = 90°$. However, no corroborating evidence has emerged and these structures remain doubtful.

Calcium zirconate is readily available commercially and has the CAS number of 12013-47-7. It occurs as a mineral, Lakargiite, $CaZrO_3$—the zirconium analog of perovskite [*Pbnm*, $a = 5.556(1)$, $b = 5.715(1)$, $c = 7.960(1)$ Å, $V = 252.7(1)$ Å^3, $Z = 4$]. Lakargiite was discovered as an accessory mineral in high-temperature skarns in carbonate–silicate rocks occurring as xenoliths in ignimbrites of the Upper Chegem (Verkhniy Chegem) volcanic structure, the North Caucasus, Kabardino-Balkaria, Russia. Lakargiite forms pseudocubic crystals up to 30–35 μm in size and aggregates up to 200 μm. Lakargiite is associated with spurrite, larnite, calcio-olivine, calcite, cuspidine, rondorfite, reinhard-braunsite, wadalite, perovskite, and minerals of the ellestadite group.

$CaZrO_3$ has been studied as a thermal blanket for corrosion resistance to extreme agents like liquid lithium metal. Mixed oxide phases as candidates for a magneto-hydrodynamics-coating material in a liquid lithium blanket concept were investigated by immersing in liquid lithium. $CaZrO_3$ showed a better compatibility than $MgTiO_3$, $MgZrO_3$ and $CaTiO_3$ with respect to mass and thickness changes and electrical resistance. With increasing density of $CaZrO_3$ sample, better compatibility at 823 K was observed. In case of a low-density sample, Li introduced inside of the sample through the opening channel removed the grains itself

TABLE 8.13

No	Site notation	Atom	Multiplicity	Wyckoff	Site symmetry	*x*	*y*	*z*	Occupancy
1	O1	O	8	d	1	0.1984	0.0506	0.3043	1.0
2	Ca1	Ca	4	c	.m.	0.4372	1/4	0.0156	1.0
3	O2	O	4	c	.m.	0.5328	1/4	0.6005	1.0
4	Zr1	Zr	4	a	-1	0	0	0	1.0

TABLE 8.14

No	Site notation	Atom	Multiplicity	Wyckoff	Site symmetry	*x*	*y*	*z*	Occupancy
1	O	O	3	d	4/mm.m	1/2	0	0	1.0
2	Ca	Ca	1	b	m-3m	1/2	1/2	1/2	1.0
3	Zr	Zr	1	a	m-3m	0	0	0	1.0

to increase the corrosion rate to 30 μm/year, while the rate was 11 μm/year in the case of a high-density sample. $CaZrO_3$ samples containing excess of ZrO_2 showed significant decrease of their compatibility at 673 K. The micro-ZrO_2 phase, which is unstable in lithium, may be corroded selectively. Thus, the fabrication of high-density coating, with a Ca to Zr composition ratio 1:1, is considered the key ingredient for the corrosion–resistance in this instance.

Two oxide systems, yttria and calcium zirconate ($CaZrO_3$), have been systematically studied for their potential use as thermistor materials, usable above 1000 °C. Both oxides have a sensitivity (temperature coefficient of resistance) of about 1.5%/°C or higher. Doping yttria with zirconia results in a slight decrease in sensitivity, but enables the system to be used in a humid environment without a protective coating. The electrical response of calcium zirconate was found to be sensitive to methane, but was practically unaffected by humidity and carbon monoxide. The use of a calcium zirconate-based thermistor is, therefore, limited to atmospheres without methane and/or possibly other hydrocarbon gases. The results of feasibility tests of a.c.-powered thermistors based on yttria and calcium zirconate suggest that an excitation circuitry can be used for designing a thermistor display device.

There is a growing interest in calcium–zirconium-based oxides for potential sensor/device applications at elevated temperatures. In particular, several studies have been reported on the use of calcium zirconate-based systems for monitoring oxygen, humidity and hydrogen. $CaZrO_3$ has also been studied for its potential use as high-temperature thermistor material. The electrical response of calcium zirconate (prepared by the solid-state firing of $CaCO_3$ and ZrO_2 powders at 1400 °C) was found to be sensitive to methane, but was practically unaffected by humidity and carbon monoxide.

Stoichiometric calcium zirconate and calcium zirconate with calcia or zirconia excess sintered bodies have been prepared. Electrical properties of these materials were investigated at 950 °C using the dc four-probe and ac impedance spectroscopy methods. XRD analysis was used to determine the changes of cell parameters. The Rietveld method was used to refine the calcium zirconate structure. The e.m.f. measurements of galvanic cells were used to determine the ionic transference numbers in the selected samples. Stoichiometric calcium zirconate appeared to be a rather poor and mixed electron–oxygen ion conductor, whereas calcium zirconate samples with excess of calcia or zirconia exhibit purely oxygen ion conductivity. In both cases, introduction of a respective cation excess led to the significant enhancement in conductivity. A simple point defect model for calcium zirconate with calcia or zirconia excess was proposed.

The preparation of perovskite-based calcium zirconate titanates ($Ca[Zr_xTi_{1-x}]O_3$) via an acetic acid-modified sol–gel process, two different alkoxide sol–gel routes, and the direct reaction of oxides and carbonates was explored. X-ray absorption spectroscopy measurements on xerogels prepared using alkoxides indicated the presence of zirconium and titanium with coordination numbers >6 and <6, respectively. The use of acetic acid as a modifier changes the local structure around zirconium in the xerogel. A calcium-rich phase was observed at low heat treatment temperatures regardless of the sample preparation route. Many of the initially prepared xerogels contained perovskite and the higher titanium content samples more readily crystallized to perovskite upon heating. None of the processing routes led to a clean formation of perovskite at low temperatures. At intermediate temperatures, a fluorite-related phase was always formed in addition to perovskite, and the fluorite-like material transformed to perovskite at higher temperatures. The average composition of the perovskite present in the fluorite–perovskite mixture did not change as more of the fluorite was converted to perovskite by heating, suggesting that the two phases have the same zirconium-to-titanium ratio. The EXAFS analyses indicated that the average Zr–O and Ti–O bond lengths are only weakly dependent upon solid solution composition, even though the average M–O bond length depends strongly on composition. The EXAFS data also suggest that the cation distribution in the solid solution is to some extent dependent upon the sample preparation method.

The wet chemical synthesis of $CaZr_{0.9}In_{0.1}O_3$ powders via a peroxo-oxalate complexation method has been studied in detail using different techniques, i.e. TG-DTA, XRD, FT-IR, BET, SEM, EDX, and non-isothermal densification. Using these techniques, the different reaction steps in the calcination process have been clarified. After drying the precipitated complex at 150 °C for 3 h, a mixture of calcium oxalate and an amorphous zirconia phase was found. Between 200 and 450 °C, the calcium oxalate decomposes into calcium carbonate. In the temperature range 450–800 °C, the calcium carbonate decomposes into CaO, while a crystalline zirconia phase appears ($CaZr_4O_9$). In this temperature range, the formation of $CaZrO_3$ is already observed. Further increasing the calcination temperature to 1000 °C leads to a binary mixture of $CaZrO_3$ and $CaIn_2O_4$. When the calcination temperature is increased to around 1500 °C, the $CaIn_2O_4$ phase dissolves into the calcium zirconate to form the desired $CaZr_{0.9}In_{0.1}O_{3-2\delta}$. All compacts sintered at 1550 °C for 10 h show single-phase $CaZr_{0.9}In_{0.1}O_{3-2\delta}$, independent of the calcination temperature. The morphology of the sintered compacts, however, varies with the calcination temperature, due to the presence or absence of a reactive sintering step around 1300 °C. Powders calcined at 1000 °C show

The $CaZr_4O_9$ Structure

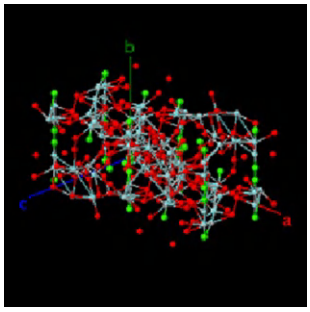

FIGURE 8.43

a larger grain size in the sintered compact than powders calcined at 1450 or 1550 °C.

The precise crystal structure of $CaZr_4O_9$ has not been reported in the literature. The compound, $CaZr_4O_9$, has the cell parameters of: $a = b = 11.5685$ Å, $c = 12.127$ Å, $\alpha = \beta = 86.29°$, $\gamma = 79.141°$, cell volume = 1339.17 $Å^3$.

Cell occupation consists of 30 locations as shown on the next page. Thus, a three-dimensional structure is too complicated to show here. A two-dimensional representation of the structure is shown in Fig. 8.43.

Site symmetry reinforces this observation as listed in Table 8.15.

TABLE 8.15

No	Site notation	Atom	Multiplicity	Wyckoff	Site symmetry	*x*	*y*	*z*	Occupancy
1	O12	O	8	f	1	0.04375	0.06425	0.49611	1.0
2	O16	O	8	f	1	0.06871	0.41337	0.37786	1.0
3	Zr6	Zr	8	f	1	0.09362	0.0655	0.04661	1.0
4	O6	O	8	f	1	0.06338	0.21924	0.37554	1.0
5	Zr3	Zr	8	f	1	0.09944	0.1896	0.55024	1.0
6	Zr4	Zr	8	f	1	0.11459	0.31225	0.05689	1.0
7	Zr7	Zr	8	f	1	0.10273	0.55303	0.05925	1.0
8	O11	O	8	f	1	0.13002	0.04026	0.22999	1.0
9	O1	O	8	f	1	0.10319	0.3262	0.21733	1.0
10	O13	O	8	f	1	0.20312	0.02584	0.05948	1.0
11	O9	O	8	f	1	0.19339	0.20135	0.13796	1.0
12	Ca3	Ca	8	f	1	0.19954	0.18788	0.35255	1.0
13	Zr9	Zr	8	f	1	0.19834	0.43488	0.34996	1.0
14	O3	O	8	f	1	0.22296	0.34065	0.01778	1.0
15	O18	O	8	f	1	0.20292	0.42785	0.18083	1.0
16	O5	O	8	f	1	0.28224	0.33568	0.42415	1.0
17	O15	O	8	f	1	0.28707	0.0429	0.46437	1.0
18	Zr5	Zr	8	f	1	0.31012	0.18338	0.1648	1.0
19	Zr8	Zr	8	f	1	0.30235	0.4402	0.13741	1.0
20	O10	O	8	f	1	0.36243	0.05298	0.24459	1.0
21	O2	O	8	f	1	0.36847	0.33015	0.26309	1.0
22	O7	O	8	f	1	0.362	0.1811	0.37258	1.0
23	O17	O	8	f	1	0.42553	0.41225	0.1321	1.0
24	O8	O	8	f	1	0.41687	0.21023	0.15576	1.0
25	O14	O	8	f	1	0.46262	0.07279	0.01135	1.0
26	O4	O	8	f	1	0.47428	0.28971	0.01633	1.0
27	Ca2	Ca	4	e	2	0	0.06647	1/4	1.0
28	Zr1	Zr	4	e	2	0	0.31615	1/4	1.0
29	Ca1	Ca	4	e	2	0	0.5614	1/4	1.0
30	Zr2	Zr	4	e	2	0	0.81229	1/4	1.0

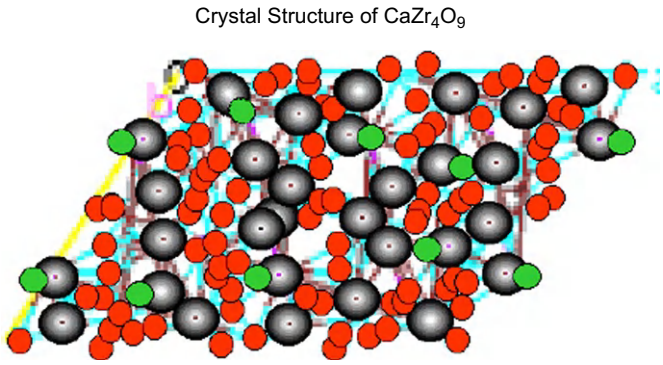

FIGURE 8.44

Vacancy and cation ordering in the δ_1-phase $CaZr_4O_9$ in ZrO_2–CaO system has been investigated. A sample with precipitates of the δ_1 phase has been prepared by annealing a cubic stabilized zirconia single crystal ($Zr_{0.85}Ca_{0.15}O_{1.85}$) at 1300 K for 1 month in air.

Another view of the same structure is shown in Fig. 8.44.

Using powdered material, the structure has been determined by analyzing X-ray and neutron diffraction data by the Rietveld method. The δ_1 phase has the monoclinic space group, $C2/c$. The relation of its lattice parameters to the lattice parameter of the cubic phase was confirmed. The ordering of the calcium ions along the fluorite (110) direction and the ordering of the vacancies separated by δ along the fluorite (111) direction were obtained from the X-ray and neutron data, respectively. All calcium ions are 8-fold coordinated by oxygen ions, while 12 zirconium ions are 6-, 40 zirconium ions 7-, and 12 zirconium ions 8-fold coordinated. The high B-factors (up to 0.18 nm^2) and some anomalous small Zr···O distances (down to 0.169 nm) indicate incomplete order of the δ_1 phase. The chemical equilibrium for the system ZrO_2–CaO was redetermined for temperatures above 1000 °C by heating the reactive powders for extended periods of time. The eutectoid decomposition of the cubic solid solution was found to occur at 1140 ± 40 °C and 17.0 ± 0.5 mol% CaO. Decomposition reactions in sintered cubic solid solutions were studied using electron diffraction and transmission techniques. Decomposition follows metastable extensions of the boundary lines which separate two-phase region from the adjacent cubic solid solution region. The appearance of the diffuse diffraction features in the electron-diffraction patterns of cubic solid solutions seems to be associated with short-range ordering of oxygen vacancies. "Duo-ordered" phases, $CaZr_4O_9$ and $Ca_6Zr_{19}O_{44}$, were synthesized and their upper limits of stability were determined to be 1235 ± 15 and 1355 ± 15 °C, respectively.

The point group and space group symmetry of the controversial fluorite-based stoichiometric superlath phase of $ø_1$ ($CaZr_4O_9$: $Z = 16$), considered to be

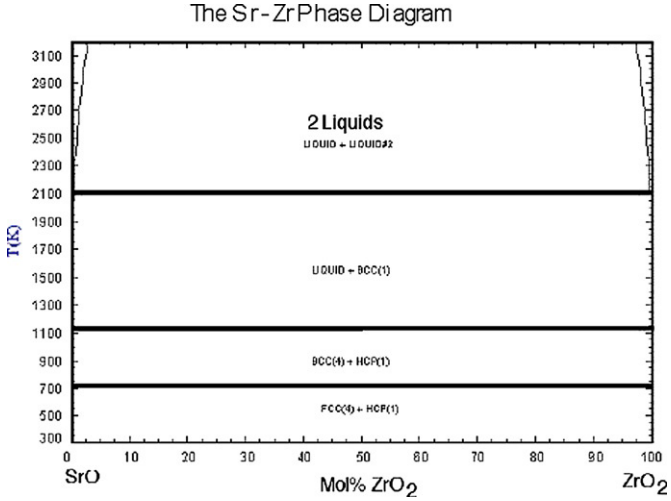

FIGURE 8.45

a coherently intergrown subphase of lime-stabilized zirconia, was examined. Using convergent-beam and selected-area electron diffraction, it was determined that the space group of $ø_1$ is $C2/c$, in apparent agreement with earlier studies utilizing other diffraction techniques.

In view of the fact that the tetrazirconate, $CaZr_4O_9$, is the stable phase, it is not surprising that information concerning the dizirconate, $CaZr_2O_5$, is lacking in the technical literature.

Calcium zirconate, as $CaZrO_3$, is readily available commercially in large quantities.

8.2.7. Strontium Zirconides

There were no known intermetallic compounds determined in the system, Sr–Zr. A phase diagram has been published but showed only the polymorphic transition temperatures of the two metals. This is representative of the Ae–Zr intermetallic forms determined for all of the alkaline earth systems (Fig. 8.45).

8.2.8. Strontium Zirconates

In the oxide system, SrO–ZrO_2, four compounds are known: $SrZrO_3$, Sr_2ZrO_4, $Sr_3Zr_2O_7$, and $Sr_4Zr_3O_{10}$. The formation at 1450 °C of the strontium zirconates, $SrZrO_3$, $Sr_4Zr_3O_{10}$, $Sr_3Zr_2O_7$ and Sr_2ZrO_4, was investigated by X-ray powder diffraction and DTA. Three different routes of synthesis were tested. In the Sr zirconate system, single-phase orthorhombic $SrZrO_3$ and somewhat impure, tetragonal Sr_2ZrO_4 were observed, whereas the formation of ordered RP phases, $Sr_nZr_{n-1}O_{3n-2}$, where $n = 4$ and 3, was not verified. The conductivity of the Sr zirconates increases with increasing Sr/Zr ratio. Samples with a nominal composition corresponding to Sr_2ZrO_4 have a conductivity of 7.5×10^{-5} and 5.9×10^{-4} S/cm^2 at 750 and 1000 °C, respectively. For

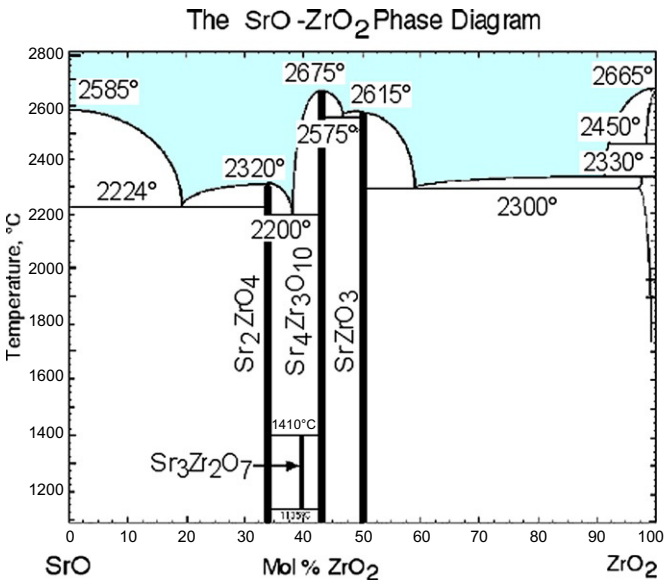

FIGURE 8.46

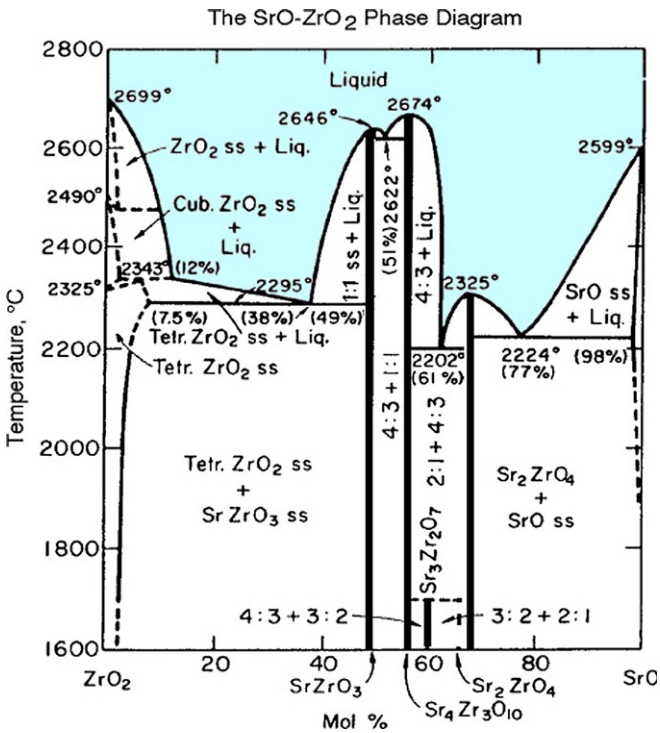

FIGURE 8.47

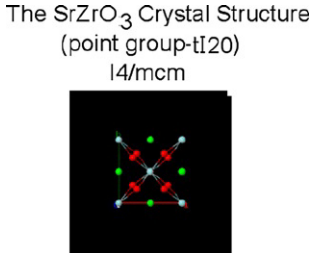

FIGURE 8.48

all samples one observes low activation energies for ionic conduction (~0.5 to 0.65 eV).

The phase diagram of SrO–ZrO_2 is shown in Fig. 8.46.

Another view of the SrO–ZrO_2 system is shown in Fig. 8.47.

In this diagram (dated 1989), more detail is available but the data concerning $Sr_3Zr_2O_7$ has since been modified. Thus, this diagram is regarded as the more accurate of the two diagrams.

In general, it is better to prepare these zirconate compounds by a solid-state reaction of the oxides (or compounds that decompose to form oxides while being heated), then to employ a hydrothermal method. Zirconium compounds, in solution, tend to form hydroxylated gels that are very difficult to decompose to form anhydrates, free of water. Furthermore, alkali ions tend to be incorporated in the product as well. The use of nitrates, i.e. the precursors $Sr(NO_3)_2$ and $ZrO(NO_3)_2 \cdot xH_2O$, has been reported as a superior method. However, disposal of NO_x gases is a problem in this process.

$SrZrO_3$ is dimorphic. One isomer has the point group—tI20 point group and the other cP40 (both with space group = *I*4/*mcm*). The structures of $SrZrO_3$ have been studied in five temperature steps, from room temperature to 1230 °C, by very high-resolution neutron powder diffraction. It was concluded that orthorhombic $SrZrO_3$, with space group *Pnma* at room temperature, changes by a continuous transition to a pseudo-tetragonal structure with space group *Imma* at about 750 °C. It further changes by a discontinuous transformation to tetragonal *I*4/*mcm* at about 840 °C, and finally, continuously, to cubic at 1070 °C. Unit cell parameters are: $a = b = c = 5.8506$ Å, $\alpha = \beta = 119.955°$, $\gamma = 90°$, cell volume = 141.99 $Å^3$ (Fig. 8.48).

Cell occupancy is listed in Table 8.16.

TABLE 8.16

No	Site notation	Atom	Multiplicity	Wyckoff	Site symmetry	*x*	*y*	*z*	Occupancy
1	O2	O	8	h	m.2m	0.2177	0.7177	0	1.0
2	Zr	Zr	4	c	4/m..	0	0	0	1.0
3	Sr	Sr	4	b	-42m	0	1/2	1/4	1.0
4	O1	O	4	a	422	0	0	1/4	1.0

TABLE 8.17

No	Site notation	Atom	Multiplicity	Wyckoff	Site symmetry	*x*	*y*	*z*	Occupancy
1	O1	O	12	b	1	0.0	0.205	0.205	1.0
2	O2	O	12	b	1	0.205	0.205	0.5	1.0
3	Sr1	Sr	4	a	.3.	0.0	0.0	0.0	1.0
4	Zr1	Zr	4	a	.3.	0.25	0.25	0.25	1.0
5	Sr2	Sr	4	a	.3.	0.5	0.5	0.5	1.0
6	Zr2	Zr	4	a	.3.	0.75	0.75	0.75	1.0

TABLE 8.18

Compounds that adopt the strontium zirconate structure						
No	**Compound**	**Number of elements**	**Structure type**	**Point group**	**Space group**	**Space group #**
1	$BaThO_3$	3	$SrZrO_3$	CP40	*P*213	198
2	$CaTiO_3$	3	$SrZrO_3$	tI20	*I*4/*mcm*	140
3	$CeAlO_3$	3	$SrZrO_3$	tI20	*I*4/*mcm*	140
4	$CeVO_3$	3	$SrZrO_3$	tI20	*I*4/*mcm*	140
5	$CaCsCl_3$	3	$SrZrO_3$	tI20	*I*4/*mcm*	140
6	$KMnF_3$	3	$SrZrO_3$	tI20	*I*4/*mcm*	140
7	$LaVO_3$	3	$SrZrO_3$	tI20	*I*4/*mcm*	140
8	$RbAgF_3$	3	$SrZrO_3$	tI20	*I*4/*mcm*	140
9	$SrTiO_3$	3	$SrZrO_3$	tI20	*I*4/*mcm*	140
10	$SrZrO_3$	3	$SrZrO_3$	tI20	*I*4/*mcm*	140
11	$SrZrO_3$	3	$SrZrO_3$	cP40	*P*213	198
12	$Ba_{0.11}Sr_{0.89}SnO_3$	4	$SrZrO_3$	cP40	*P*213	198
13	$Ba_{0.72}Sr_{0.28}CeO_3$	4	$SrZrO_3$	cP40	*P*213	198
14	$La_{0.75}Sm_{0.25}VO_3$	4	$SrZrO_3$	tI20	*I*4/*mcm*	140
15	$Sr_{0.45}Ca_{0.55}SnO_3$	4	$SrZrO_3$	cP40	*P*213	198
16	$SrMn_{0.5}Sb_{0.5}O_3$	4	$SrZrO_3$	tI20	*I*4/*mcm*	140
17	$SrMn_{0.5}Sb_{0.5}O_3$	4	$SrZrO_3$	tI20	*I*4/*mcm*	140

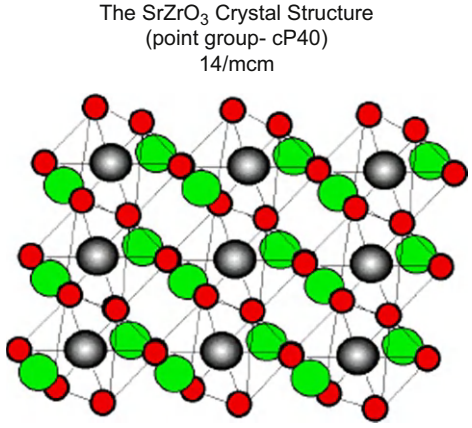

FIGURE 8.49

For the point group structure, cP40 (space group = *I*4/*mcm*), the cell parameters are: $a = b = c = 5.513$ Å, $\alpha = 90°$, $\beta = \gamma = 119.978°$, cell volume = 118.52 Å^3 (Fig. 8.49).

Site occupancy is listed in Table 8.17.

The differences in these two polymorphs may be more discernable shown in Fig. 8.50.

A large number of compounds adopt these $SrZrO_3$ structures as shown in Table 8.18.

The perovskite type of $SrZrO_3$ was investigated as an alternative to yttria-stabilized zirconia (YSZ) material for thermal barrier coating (TBC) applications. Three-phase transformations (orthorhombic ⇔ pseudo-tetragonal ⇔ tetragonal ⇔ cubic) were found only by

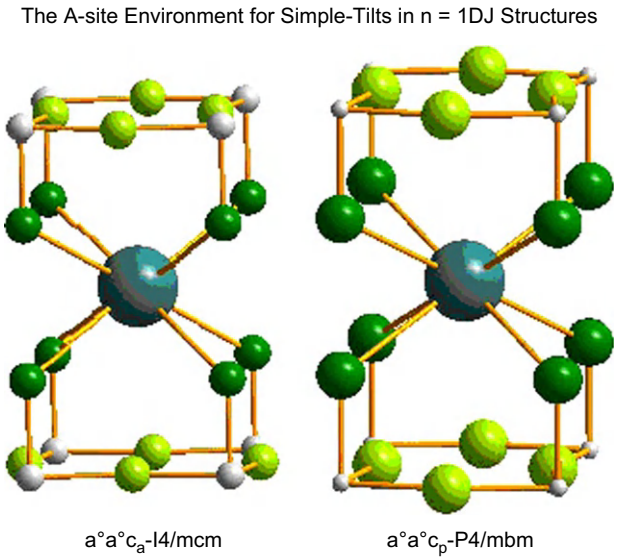

FIGURE 8.50

heat-capacity measurement, whereas the phase transformation from orthorhombic to pseudo-tetragonal was found using thermal expansion measurements. The thermal expansion coefficients (TECs) of $SrZrO_3$ coatings were at least 4.5% larger than YSZ coatings up to 1200 °C. Mechanical properties (Young's modulus, hardness, and fracture toughness) of dense $SrZrO_3$ showed lower Young's modulus, hardness, and comparable fracture toughness with respect to YSZ. The "steady-state" sintering rate of a $SrZrO_3$ coating at 1200 °C was 1.04×10^{-9}/s, which was less than half that of YSZ coating at 1200 °C. Plasma-sprayed coatings were produced and characterized. Thermal cycling with a gas burner showed that at operating temperatures ~1250 °C the cycling lifetime of $SrZrO_3$/YSZ double-layer coating (DLC) was more than twice as long as $SrZrO_3$ coating and comparable to YSZ coating. However, at operating temperatures >1300 °C, the cycling lifetime of $SrZrO_3$/YSZ DLC was comparable to the optimized YSZ coating, indicating $SrZrO_3$ might be a promising material for TBC applications at higher temperatures compared with YSZ.

Elastic behavior associated with the hierarchy of tilting transitions in $SrZrO_3$ has been examined using resonant ultrasound spectroscopy on a ceramic sample at temperatures between 153 and 1533 K (−120 and 1250 °C). Changes in slope of the evolution of resonance frequencies with temperature indicate that phase transitions occur at 1038 K (*Pnma* ⇔ *Imma*), 1122 K (*Imma* ⇔ *I4/mcm*), and 1367 K (*I4/mcm* ⇔ *Pm3m*). Strain analysis of previously recorded neutron diffraction data shows that the *I4/mcm* ⇔ *Pm3m* and *Imma* ⇔ *I4/mcm* transitions are close to triacritical in character, and that *Imma* ⇔ *I4/mcm* is first order.

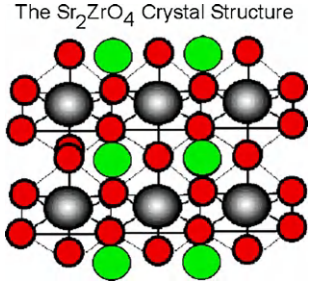

FIGURE 8.51

Deviations from the form of the elastic behavior predicted by Landau theory are found. In particular, elastic softening in the vicinity of the transition suggests that local dynamical fluctuations between individual tilt systems occur rather than a discontinuous switch from one phase to another. Determinations of the mechanical quality factor, *Q*, show that SrZrO3 in the *Pm3m* phase is a classically high-*Q* (i.e. non-dissipating) cubic material. *I4/mcm* and *Imma* phases both have much greater dissipation (low *Q*), which is tentatively attributed to the mobility of twin walls. The room temperature *Pnma* phase is unexpectedly much stiffer than both *I4/mcm* and *Imma* phases and has high *Q*. It appears that when two separate tilt systems operate, as in *Pnma*, they can interact to reduce strain/order parameter relaxations.

The composition Sr_2ZrO_4 has been reported to be in the tetragonal crystal system in space group *I4/mmm* with all parameters $a = 4.103$, $c = 12.82$ and has the K2NiF4 structure. It has the CAS number 12036-39-4. It consists of a series of ZrO_6 octahedra, interspersed with Sr^{2+} cations (Fig. 8.51).

However, it most likely has the structure of Sr_2CeO_4. Whereas, the phosphor, Sr_2ZrO_4 is an efficient phosphor like $MgWO_4$, with an excitation peak at 354 nm and a broad emission peak at about 385 nm, $SrZrO_3$ shows no luminescence at all at room temperature. The luminescence of other Zr compounds is too weak to be seen at room temperature. The reason is that the octahedra of Zr^{4+} in the host lattice, i.e. ZrO_6, are isolated from each other. In the case of Sr2ZrO4, they share oxygen ions along an edge and form a linear chain structure, so that efficient charge-transfer luminescence appears, i.e. it is "self-activated".

The formation of the compound, $Sr_3Zr_2O_7$, is difficult when reactions between the oxides are employed because it is stable only in the temperature range of 1180–1430 °C. Its structure may be represented as shown in Fig. 8.52.

Cell parameters are: $a = b = 4.103$ Å, $c = 10.865$ Å, $\alpha = \beta = 100.848°$, $\gamma = 90.188°$, cell volume = 175.28 Å^3. Cell occupancy is listed in Table 8.19.

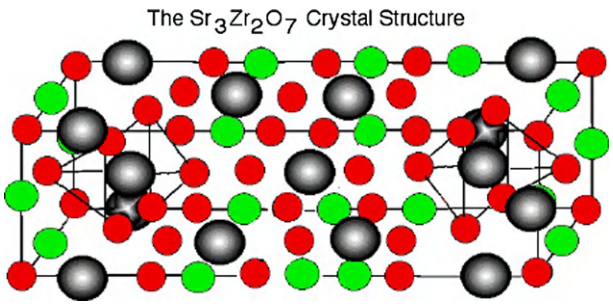

FIGURE 8.52

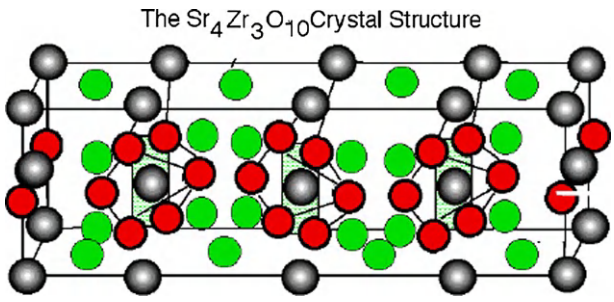

FIGURE 8.53

The compound $Sr_3Zr_2O_7$ is not stable and dissociates in the solid state at about 2300 °C to form $Sr_4Zr_3O_{10}$ and Sr_2ZrO_4:

$$2\,Sr_3Zr_2O_7 + \text{heat} \Rightarrow Sr_4Zr_3O_{10} + Sr_2ZrO_4$$

The Standard molar Gibbs energies of formation of $Sr_3Zr_2O_7$(s) have been determined by measuring Sr(g) pressures over the three-phase system: $\{x_1Sr_4Zr_3O_{10}(s) + x_2Sr_3Zr_2O_7(s) + (1 - x_1 - x_2)Zr_{1-x}O_x(s)\}$ using a Knudsen effusion mass-loss technique employing a Sartorius® microbalance model 4410. The values of the mole fractions x_1 and x_2 in the three-phase mixture are 0.3795 and 0.5391, respectively. The value of $\Delta_fG^0_m(Sr_3Zr_2O_7,s,T)$ has been calculated and is given by:

$$\Delta_fG^0_m(Sr_3Zr_2O_7,s,T)/(kJ/mol) = \{-4229 + 0.7357(T/K)\} \pm 15,$$

where $(1349° \leq K/T \leq 1466°)$.

The $\Delta_fH^0_m(Sr_3Zr_2O_7,s,298.15\,K)$ value was calculated from the known values of $\Delta_fG^0_m(Sr_3Zr_2O_7,s,T)$, and molar heat capacities of Sr(s,l), Zr(s), and O_2(g) as taken from the literature using the values of $Sr_4Zr_3O_{10}$(s) from previously published work. The resulting value was:

$$\Delta_fH^0_m(Sr_3Zr_2O_7),s = -(4186 \pm 38)\ kJ/mol.$$

A corresponding value of $\Delta_fH^0_m(Sr_3Zr_2O_7,s,298.15\,K) = -(4163 \pm 42)$ kJ/mol has also been calculated using the third law. In this method, $\Delta G^0_m = (\delta^T{}_0S^0_m - \eta^T{}_{298.15K}H^0_m/T)$ values for $Sr_4Zr_3O_{10}$(s), Sr(g), $Zr_{0.72}O_{0.26}$(s), $Sr_3Zr_2O_7$(s), and Sr(g) pressure over the three-phase system have been used for the calculation of $\Delta_fH^0_m(Sr_3Zr_2O_7,s,298.15\,K)$ at each experimental temperature.

The compound, $Sr_4Zr_3O_{10}$, has the structure as follows. It is related to the $Sr_3Zr_2O_7$ structure. Cell parameters are: $a = b = 5.812$ Å, $c = 29.361$ Å^3, $\alpha = \beta = \gamma = 90°$, cell volume = 901.52 Å^3 (Fig. 8.53).

Cell occupancy is listed in Table 8.20 and Table 8.21.

Enthalpy increment measurements on $Sr_3Zr_2O_7$(s) and $Sr_4Zr_3O_{10}$(s) were carried out using a Calvet microcalorimeter. The enthalpy increment values were least squares analyzed with the constraints that $H^0(T) - H^0(298.15\,K)$ at 298.15 K equals to 0 and $C^0_p(298.15\,K)$ equals to the estimated value. The dependence of enthalpy increment with temperature can be given as:

$$\Delta H_0(T) - H^0\ (25\ °C)\ (J/mol) = 427.85\ T\ (°C) + 36.502 \times 10^{-3}T^2\ (°C) + 81.67 \times 10^5/T\ (°C) - 158{,}203\ (Sr_4Zr_3O_{10}(s),\ [365.4 \leq T\ (°C) \leq 980.6]$$

$$\Delta H_0(T) - H^0\ (25\ °C)(J/mol) = 349.62\ T\ (°C) + 7.621 \times 10^{-3}T^2\ (°C) + 89.814 \times 10^5/T\ (°C) - 135{,}041\ (Sr_3Zr_2O_7(s),\ [365.4 \leq T\ (°C) \leq 980.6]$$

The first differential of the above equations with respect to temperature gives $C^0_p(T)$. Gibb's functions were evaluated using estimated S^0 (298.15 K) values.

Standard molar Gibbs energies of formation of $Sr_4Zr_3O_{10}$(s) have been determined by measuring Sr(g) pressures over the three-phase mixture: $\{Sr_4Zr_3O_{10}(s) +$

TABLE 8.19

No	Site notation	Atom	Multiplicity	Wyckoff	Site symmetry	*x*	*y*	*z*	Occupancy
1	O1	O	16	j	..2	1/4	1/4	0.1003	1.0
2	Zr1	Zr	8	i	mm2	0	0	0.0967	1.0
3	O2	O	8	i	mm2	0	0	0.2074	1.0
4	Sr1	Sr	8	i	mm2	0	0	0.3154	1.0
5	Sr2	Sr	4	b	mmm	0	0	1/2	1.0
6	O3	O	4	a	mmm	0	0	0	1.0

TABLE 8.20

No	Site notation	Atom	Multiplicity	Wyckoff	Site sym	x	y	z	Occupancy
1	Zr1	Zr	8	C	1	0.0027	0.0	0.1426	1.0
2	Sr1	Sr	8	C	1	0.0079	0.0238	0.2947	1.0
3	O1	O	8	C	1	0.0548	0.4858	0.2882	1.0
4	O2	O	8	C	1	0.0668	0.0142	0.0708	1.0
5	O3	O	8	C	1	0.2099	0.2115	0.49	1.0
6	O4	O	8	C	1	0.2125	0.2115	0.3679	1.0
7	O5	O	8	C	1	0.2125	0.2885	0.1499	1.0
8	Sr2	Sr	8	C	1	0.4962	0.4665	0.4307	1.0
9	Zr2	Zr	4	A	-1	0	0	0	1.0

TABLE 8.21

No	Site notation	Atom	Multiplicity	Wyckoff	Site symmetry	x	y	z	Occupancy
1	O	O	3	d	4/mm.m	1/2	0	0	1.0
2	Ba	Ba	1	b	m-3m	1/2	1/2	1/2	1.0
3	Zr	Zr	1	a	m-3m	0	0	0	1.0

$SrZrO_3(s) + Zr_{1-}xOx(s)\}$ using the Knudsen effusion mass-loss technique employing a Sartorius microbalance, model 4410, and are given as:

$$\Delta_f G_m(Sr_4Zr_3O_{10},s,T) \pm 20(kJ/mol) = -5946.8 + 1.0076(T/K),\ (1157.5 \le T/K \le 1370.5).$$

Using the molar heat capacities for Sr(s,l), Zr(s), and O_2(g) from literature and that for $SrZrO_3$(s) from previous work, $\Delta_f H^0_m(Sr_4Zr_3O_{10},s,298.15\ K)$ has been calculated as $-(5985.4 \pm 49)$ kJ/mol. A value of $\Delta_f H^0_m(Sr_4Zr_3O_{10},s,298.15\ K) = -(5972.8 \pm 44)$ kJ/mol has also been calculated using the values for the function: $\delta = (\eta^\circ TS_m - \eta^T_{298.15K}H_m/T)$ for $SrZrO_3$(s), Sr(g), $Zr_{0.72}O_{0.28}$(s), and $Sr_4Zr_3O_{10}$(s) from literature. The value of $-(5972.8 \pm 44)$ kJ/mol (the third-law value) is recommended for $\Delta_f H^0_m(Sr_4Zr_3O_{10},s,298.15\ K)$.

Strontium zirconates are readily available commercially in small to large quantities worldwide.

8.2.9. Barium Zirconides

The intermetallic system Ba^0–Zr^0 does not form any compounds. Only the polymorphic changes with temperature are apparent in the phase diagram.

8.2.10. Barium Zirconates

In contrast to the Ca and Sr homologues, the system, BaO–ZrO_2, does not form many compounds. The phases formed have not been well researched and the only phase diagram known to date shows only the cubic perovskite, $BaZrO_3$ (Fig. 8.54).

$BaZrO_3$ has the perovskite structure shown in Fig. 8.55.

Cell parameters are: $a = b = c = 4.182$ Å, $\alpha = \beta = \gamma = 90°$, cell volume $= 73.14$ Å^3. Cell occupancy is listed in Table 8.22.

A thermodynamic description of the ZrO_2–BaO system was developed using all available experimental

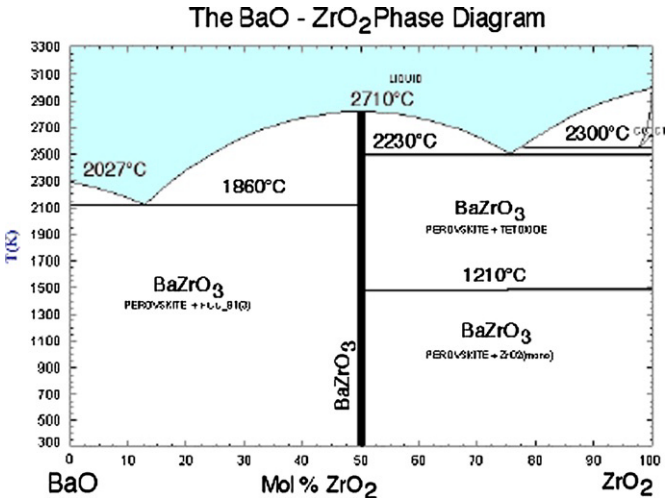

FIGURE 8.54

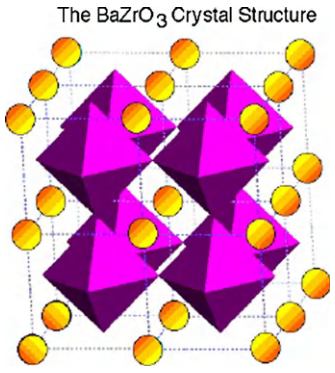

FIGURE 8.55

information. Special attention was paid to the modeling of the perovskite phase $BaZrO_3$ by a temperature-dependent polynomial to fit the experimental thermodynamic properties. The liquid phases, Css (cubic ZrO_2 solid solution) and Tss (tetragonal ZrO_2 solid solution), were modeled by use of the Redlich–Kister formula. The hypothetical compounds Ba_2ZrO_4 and $Ba_3Zr_2O_7$ were treated as stoichiometric phases and the BaOss and Mss (halite BaO and monoclinic ZrO_2 solid solutions) were treated as pure compounds. Comparisons between the calculated and the measured phase diagram as well as the thermodynamic quantities indicate that the most reliable experimental information is satisfactorily accounted for by the present thermodynamic calculation.

The formation of $BaZrO_3$ from very fine (70–90 nm) ZrO_2 powders and coarser (~1 μm) $BaCO_3$ powders has been studied in dry and humid air up to 1300 °C using TGA/DTA, XRD, SEM, TEM, and EDS microanalysis. In the temperature range 900–1100 °C, barium is rapidly transported at the surface of the ZrO_2 particles and reacts, forming $BaZrO_3$. The compound grows as a concentric layer with gradual consumption of the central ZrO_2 particle. The overall formation kinetics of $BaZrO_3$ is well described by a diminishing core model, and the most likely rate-determining step is a phase-boundary process at the ZrO_2–$BaZrO_3$ moving interface. The size and shape of the final particles is generally determined by the morphology of the starting ZrO_2 particles and not by that of the $BaCO_3$. The reaction is faster in humid air than in dry air, and the activation energy decreases from 294 kJ/mol (dry air) to 220 kJ/mol (humid air). When the fraction reacted is >80–90 mol%, the reaction rate rapidly decreases.

In another paper, zirconia–baria solid solutions were obtained by sintering powders produced by coprecipitation from solutions of zirconyl chloride hydrate and barium nitrate. The fired materials had monoclinic, cubic or tetragonal structure depending of composition which ranged from 4 to 16 mol% BaO. The pure cubic phase could be retained at room temperature for compositions from 10 to 12, whereas materials containing 16 mol% BaO were tetragonal; for lower baria content a mixture of monoclinic and cubic phase was detected. The double-phased materials can be fully transformed into the monoclinic form by grinding while for pure cubic or tetragonal samples the transformation is not full. Samples fired at 1450 °C had coarse microstructures and the grains dimension is of several microns just after 1 h of sintering, but materials containing 10, 12 and 16 mol% BaO remain cubic or tetragonal, their transformability being the same as that of materials sintered at lower temperature. The grains growth kinetic during the sintering process is similar to that of the $BaZrO_3$, and the resulting microstructures showed coarser grains than those observed in sintered tetragonal zirconia materials stabilized with other oxides. The crystal structures of cubic or tetragonal BaO stabilized zirconia seem to be isostructural to $BaZrO_3$ as they have similar cell parameters.

Solid oxide fuel cells (SOFCs) are particularly attractive because of their high efficiencies (especially when integrated with thermal energy conversion devices that utilize the high-quality waste heat available from SOFCs), their fuel flexibility, and their operability in the absence of precious metal catalysts. One of the most promising such alternatives is the family of proton conducting perovskites. These materials have particularly high conductivity, but the most promising compositions in terms of electrical properties, Y-doped $BaCeO_3$, readily react with CO_2 and suffer from other long-term stability problems. A promising candidate for proton ceramic SOFC (PC-SOFC) applications is Y-doped $BaZrO_3$ (BYZ). It has desirable properties such as high protonic conductivity and excellent chemical and mechanical stability. The current limitation for application of BYZ in PC-SOFCs is the extremely high grain boundary resistance, which leads to the relatively poor

TABLE 8.22

No	Site notation	Atom	Multiplicity	Wyckoff	Site symmetry	*x*	*y*	*z*	Occupancy
1	O	O	3	d	4/mm.m	1/2	0	0	1.0
2	Ba	Ba	1	b	m-3m	1/2	1/2	1/2	1.0
3	Zr	Zr	1	a	m-3m	0	0	0	1.0

total conductivity. The key to obtaining high conductivity in BYZ is to enhance grain growth and/or increase conductivity across grain boundaries. While these challenges are not directly amenable to theoretical approaches, computational studies of proton transport through bulk perovskites might help to solve the above-mentioned problem and/or to develop alternative materials that may not suffer from the same microstructural drawbacks.

Barium mono-zirconate has been used in the solution growth of single crystals of $YBa_2Cu_3O_{7-\delta}$ and $PrBa_2Cu_3O_{7-\delta}$ in a new type of homemade crucible, namely made of $BaZrO_3$, which has the advantage that it does not react with the occurring melts which are commonly used as a flux. These new crucibles have several advantages: not only the crystals obtained after the growth experiment contain no impurities from the crucible material, but also an important problem is solved, e.g. the corrosion of the crucible does no longer change the composition of the melt during the growth experiment, thus avoiding uncontrollable growth conditions. Hence, due to this novel inert crucible material the use of more sophisticated crystal growth techniques such as top seeded solution growth are now possible.

Polycrystalline perovskite type oxides, $BaZrO_3$ and $BaCeO_3$, have been prepared by mixing the appropriate amounts of ZrO_2, CeO_2, and $BaCO_3$ followed by reacting at 1273 K and sintering at 1773 K. The thermophysical properties, viz. the TEC, melting point, elastic moduli, Debye temperature, and Vickers hardness, of $BaZrO_3$ and $BaCeO_3$ have been measured. The harmonic and dilatational terms of the heat capacity have been evaluated by using the values of the TEC, compressibility, and Debye temperature measured. The relationships between several properties of $BaZrO_3$ and $BaCeO_3$ show the typical characteristics of the perovskite type oxides.

Specific heat capacities (C_p) of polycrystalline samples of $BaCeO_3$ and $BaZrO_3$ have been measured from about 1.6 K up to room temperature by means of adiabatic calorimetry. Experimental data for the heat capacity of $BaCeO_3$ in the range $T < 10$ K were given and experimental data below 53 K for $BaZrO_3$ were provided. Applying Debye's T^3 law for $T \Rightarrow 0$ K, thermodynamic functions as molar entropy and enthalpy were derived by integration. The values obtained were:

$$Cp = 114.8\ (\pm 1.0)\ \text{J/mol/K}^1;\ S^0 = 145.8\ (\pm 0.7)\ \text{J/mol/K for } BaCeO_3$$

$$Cp = 107.0\ (\pm 1.0)\ \text{J/mol/K};\ S^0 = 125.5\ (\pm 0.6)\ \text{J/mol/K for } BaZrO_3$$

at 298.15 K. These results are in overall agreement with previously reported studies but slightly deviating, in both cases. Evaluations of $C_p(T)$ yield Debye temperatures and identify deviations from the simple Debye theory due to extra vibrational modes as well as anharmonicity. The anharmonicity turns out to be more pronounced at elevated temperatures for $BaCeO_3$. The characteristic Debye temperatures determined at $T = 0$ K are $\delta_0 = 365$ (± 6) K for $BaCeO_3$ and $\delta_0 = 402$ (± 9) K for $BaZrO_3$.

The formation of solid solution composition $BaTi_{0.6}Zr_{0.4}O_3$, from $BaCO_3$, TiO_2 and ZrO_2 powders has been studied through solid oxide reaction using TGA/DSC, XRD. $BaCO_3$ decomposes at much lower temperature in the mixture due to the presence of TiO_2. $BaTiO_3$ and $BaZrO_3$ start forming from the temperature range 700–800 °C without intermediate formation of BaO or other titanate/zirconate phases. The rate of $BaTiO_3$ formation is higher than $BaZrO_3$ formation due to the lower activation energy (34.3 kcal/mol) required for titanate formation than zirconate (48.4 kcal/mol). Solid solution then forms by diffusion of $BaTiO_3$ into $BaZrO_3$ from 1300 °C onwards. Lattice parameter of initial SS phase is higher, indicating the phase has a coherent interface with zirconate and higher in Zr concentration than final product. Activation energy for the SS formation (133 kcal/mol) indicates that Ba and/or O diffusion through SS layer may limit the reaction.

Although it does not appear in the phase diagram, the di-barium zirconate, Ba_2ZrO_4, has been characterized (Fig. 8.56).

It has the K_2NiF_4 structure with cell parameters of: $a = b = 4.182$ Å, $c = 7.3451$ Å, $\alpha = \beta = 106.5°$, $c = 90°$, $Z = 4$. Cell volume is: 117.59 Å^3. Cell occupancy is listed in Table 8.23.

This structure contains a body-centered ZrO_6 octahedra with 1/2 of an octahedra at both ends of the tetragonal unit cell. Barium ions are interspersed on the edges of the tetrahedral unit.

With the exception of structural parameters, no other information is available concerning d-barium zirconate. As of 2011, the formation of other phases like Ba_2ZrO_4 and $Ba_3Zr_2O_7$ has not been observed.

Barium zirconate is available commercially in small quantities but no CAS number has been issued.

8.2.11. Radium Zirconates

In view of the high cost and strong radioactivity of ^{226}Ra metal, it is not surprising that the formation of

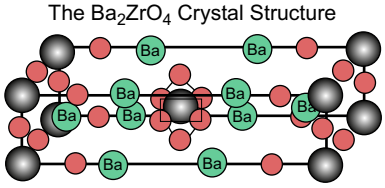

FIGURE 8.56

TABLE 8.23

No	Site notation	Atom	Multiplicity	Wyckoff	Site symmetry	*x*	*y*	*z*	Occupancy
1	O(2)	O	4	e	4mm	0	0	0.172	1.0
2	Ba	Ba	4	e	4mm	0	0	0.3524	1.0
3	O(1)	O	4	c	mmm.	0	1/2	0	1.0
4	Zr	Zr	2	a	4/mmm	0	0	0	1.0

radium zirconates by reaction of the oxides, RaO and ZrO_2, has not been documented in the technical literature. It is not likely that any possible compounds like $RaZrO_3$ will ever be studied.

8.3. ALKALINE EARTH HAFNIUM COMPOUNDS

Hafnium and zirconium form a nearly identical sequence of chemical compounds. Its major valence state is Hf^{4+}, but Hf^{2+} is also known. The white hafnium oxide (HfO_2), with a melting point of 2812 °C and a boiling point of roughly 5100 °C, is very similar to zirconia, but slightly more basic. Hafnium(IV) oxide is quite inert. It reacts with strong acids such as concentrated H_2SO_4 and with strong bases like NaOH. It dissolves slowly in HF to give fluorohafnate anions.

Of all of the alkaline earths, only Be^0 forms intermetallic compounds with Hf^0.

A phase diagram of the system Mg–Hf has been published and is representative of the systems, Mg–Hf, Ca–Hf, Sr–Hf and Ba-Hf.

The oxide-based compounds based on the system, AeO–HfO_2, are few and resemble those found in the AeO–ZrO_2 system. In addition to the great analogy between binary systems with hafnia and zirconia, the main interest in hafnium-containing compounds has been prompted by their higher melting temperatures compared with those of zirconia-based compounds and by several peculiar physicochemical properties characteristic of hafnia-based compounds and solid solutions. Early work in the HfO_2–AeO systems has shown that strontium forms the greatest number of compounds: $SrHfO_3$, Sr_2HfO_4, $Sr_3Hf_2O_7$ and $Sr_4Hf_3O_{10}$; calcium forms two compounds: $CaHfO_3$ and $CaHf_4O_9$; barium and magnesium each produce one compound: $BaHfO_3$ and $Mg_2Hf_5O_{12}$, respectively. Beryllium forms none. Most of these compounds are stable only over a certain temperature range and transform into disordered F-type cubic solid solutions at elevated temperatures. In addition, there exist limited regions of solid solutions based on the monoclinic (M) and tetragonal (T) modifications of HfO_2. Later work has shown that some quite complicated compounds like $Ca_6Hf_{19}O_{44}$ and $Ca_2Hf_7O_{16}$ also exist.

8.3.1. Beryllium Hafnate Compounds

There are no known compounds based on the BeO–HfO_2 system. A phase diagram is available but shows only polymorphic temperature transitions of the individual oxide components.

8.3.2. Beryllium Hafnide Compounds

A phase diagram of the intermetallic compounds formed when Be metal is heated with Hf metal is shown in Fig. 8.57. Both metals are high melting with melting points of 1821 °C for Hf and 1289 °C for Be.

By comparison of the Be–Zr and Be–Hf phase diagrams, it is easily seen that the same type of compounds occurs for Hf as for Zr (Fig. 8.57).

Five compounds are shown, Be_2Hf, Be_5Hf, $Be_{17}Hf_2$, $Be_{13}Hf$ and BeHf. The only compound that melts congruently is $Be_{17}Hf_2$. It is trimorphic. The compound, $Be_{13}Hf$, is only stable between the temperatures of 1400 and 1620 °C, and was difficult to establish in terms of crystal structure, i.e. it is "metastable". It is, however,

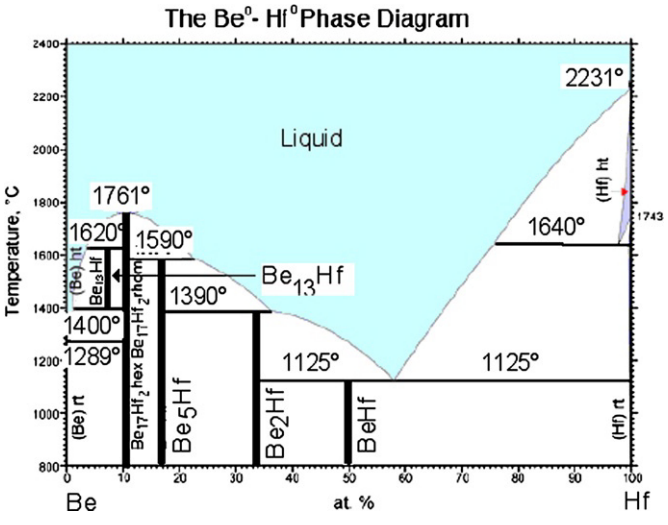

FIGURE 8.57

TABLE 8.24

#	Compound	#Elements	Type	Point group	Space group	Space number
1	$Be_{13}Hf$	2	$NaZn_{13}$	cF112	*Fm*-3*c*	226
2	$Be_{17}Hf_2$	2	$Zn_{17}Th_2$	hR57	*R*-3*m*	166
3	$Be_{17}Hf_2$	2	$Zn_{17}U_2$	hP114	*P*63/*mmc*	194
4	$Be_{17}Hf_2$	2	Th_2Ni_{17}	hP38	*P*63/*mmc*	194
5	Be_2Hf	2	AlB_2	hP3	*P*6/*mmm*	191
6	Be_5Hf	2	$CaCu_5$	hP6	*P*6/*mmm*	191
7	BeHf	2	TlI	oS8	*Cmcm*	63

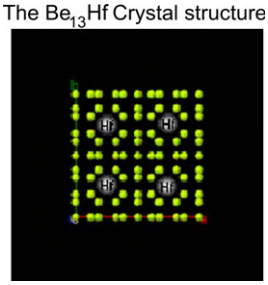

FIGURE 8.58

stable at room temperature once it has been formed. Nonetheless, any applied heat causes it to decompose into the two metal forms.

The crystal data are shown in Table 8.24.

The compound, $Be_{13}Hf$ has the same structure as its Zr counterpart. Cell parameters are: $a = b = c = 7.0711$ Å, $\alpha = \beta = \gamma = 80°$, cell volume = 250.00 Å^3.

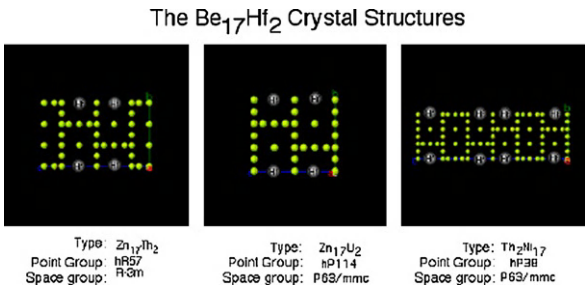

FIGURE 8.59

Cell occupancy of the 112 atoms is also given in Fig. 8.58. The unit cell contains eight formula units, i.e. $Z = 8$.

Cell occupancy is listed in Table 8.25.

The two-dimensional structure shown here can be morphed into a three-dimensional structure by extending 3 units in the "c-direction" of the lattice.

The compound, $Be_{17}Hf_2$, is trimorphic (Fig. 8.59).

The difference lies in the local arrangement of the Hf atoms as surrounded by Be atoms in each structure. Cell parameters are presented as follows:

Type: $Zn_{17}Th_2 - hR57 - R\text{-}3m$: $a = b = c = 5.6563$ Å, $\alpha = \beta = \gamma = 82.973°$, cell volume = 177.20 Å^3. Cell occupancy is listed in Table 8.26.

Type: $Zn_{17}Th_2 - hP38 - P6_3/mmc$: $a = b = c = 7.44$ Å, $\alpha = 120°$, $\beta = \gamma = 90°$, cell volume = 353.78 Å^3. Cell occupancy is listed in Table 8.27.

Type: $Zn_{17}Th_2 - hP114 - P6_3/mmc$: $a = b = c = 7.499$ Å, $\alpha = \beta = 90°$, $c = 120°$, cell volume = 1066.79 Å^3. Cell occupancy is listed in Table 8.28.

The compound, Be_2Hf, has the same crystal structure as Be_2Zr as shown in Fig. 8.60.

TABLE 8.25

No	Site notation	Atom	Multiplicity	Wyckoff	Site symmetry	*x*	*y*	*z*	Occupancy
1	Be1	Be	96	i	m..	0	0.1192	0.1806	1.0
2	Be2	Be	8	b	m-3.	0	0	0	1.0
3	Hf1	Hf	8	a	432	1/4	1/4	1/4	1.0

TABLE 8.26

No	Site notation	Atom	Multiplicity	Wyckoff	Site symmetry	*x*	*y*	*z*	Occupancy
1	Be1	Be	18	h	.m	0.5	0.5	0.1667	1.0
2	Be2	Be	18	f	.2	0.33333	0	0	1.0
3	Be3	Be	9	d	.2/m	1/2	0	1/2	1.0
4	Be4	Be	6	c	3m	0	0	0.097	1.0
5	Hf1	Hf	6	c	3m	0	0	0.3333	1.0

TABLE 8.27

No	Site notation	Atom	Multiplicity	Wyckoff	Site symmetry	*x*	*y*	*z*	Occupancy
1	Be1	Be	12	k	.m.	0.1667	0.3334	0.0	1.0
2	Be2	Be	12	j	m..	0.0	0.3333	1/4	1.0
3	Be3	Be	6	g	.2/m.	1/2	0	0	1.0
4	Be4	Be	4	f	3m.	1/3	2/3	0.61	1.0
5	Hf1	Hf	2	c	-6m2	1/3	2/3	1/4	1.0
6	Hf2	Hf	2	b	-6m2	0	0	1/4	1.0

TABLE 8.28

No	Site notation	Atom	Multiplicity	Wyckoff	Site symmetry	*x*	*y*	*z*	Occupancy
1	Be1	Be	24	l	1	0.0	0.3333	0.0833	1.0
2	Be2	Be	12	k	.m.	0.1667	0.3333	0.0	1.0
3	Be3	Be	12	k	.m.	0.1667	0.3333	0.1667	1.0
4	Be4	Be	12	k	.m.	0.1667	0.3333	0.6667	1.0
5	Be5	Be	12	k	.m.	0.5	0.0	0.1667	1.0
6	Be6	Be	12	j	m..	0.0	0.3333	1/4	1.0
7	Be7	Be	6	g	.2/m.	1/2	0	0	1.0
8	Be8	Be	4	f	3m.	1/3	2/3	0.034	1.0
9	Be9	Be	4	f	3m.	1/3	2/3	0.132	1.0
10	Hf1	Hf	4	f	3m.	1/3	2/3	0.5833	1.0
11	Hf2	Hf	4	e	3m.	0	0	0.0833	1.0
12	Be10	Be	4	e	3m.	0	0	0.201	1.0
13	Hf3	Hf	2	d	-6m2	1/3	2/3	3/4	1.0
14	Hf4	Hf	2	c	-6m2	1/3	2/3	1/4	1.0

TABLE 8.29

No	Site notation	Atom	Multiplicity	Wyckoff	Site symmetry	*x*	*y*	*z*	Occupancy
1	Be	Be	2	d	-6m2	1/3	2/3	1/2	1.0
2	Hf	Hf	1	a	6/mmm	0	0	0	1.0

TABLE 8.30

No	Site notation	Atom	Multiplicity	Wyckoff	Site symmetry	*x*	*y*	*z*	Occupancy
1	Be2	Be	3	g	mmm	1/2	0	1/2	1.0
2	Be1	Be	2	c	-6m2	1/3	2/3	0	1.0
3	Hf	Hf	1	a	6/mmm	0	0	0	1.0

TABLE 8.31

No	Site notation	Atom	Multiplicity	Wyckoff	Site symmetry	x	y	z	Occupancy
1	Be1	Be	4	c	m2m	0	0.108	1/4	1.0
2	Hf1	Hf	4	c	m2m	0	0.367	1/4	1.0

Cell parameters are: $a = b = c = 3.159$ Å, $\alpha = 120°$, $\beta = \gamma = 90$, cell volume $= 39.23$ Å^3. Cell occupancy is listed in Table 8.29.

The compound, Be_5Hf, has the same crystal structure as Be_5Zr (Fig. 8.61).

Cell parameters are: $a = 3.465$ Å, $b = c = 4.519$ Å, $\alpha = 120°$, $\beta = \gamma = 90°$, cell volume $= 61.28$ Å^3. Cell occupancy is listed in Table 8.30.

The compound, BeHf, has the structure shown in Fig. 8.62.

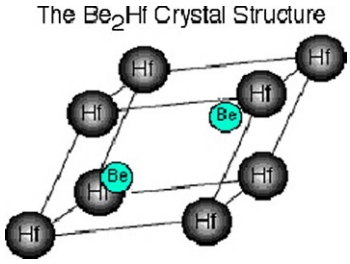

FIGURE 8.60

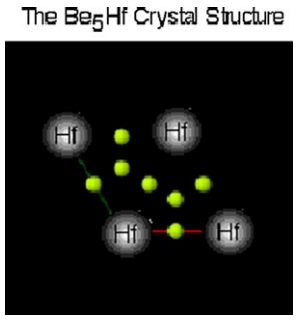

FIGURE 8.61

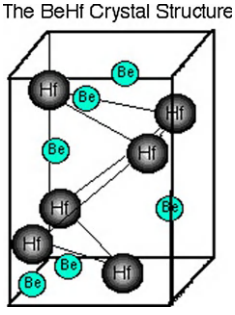

FIGURE 8.62

Unit cell parameters are: $a = 3.34$ Å, $b = 3.72$ Å, $c = 5.27$ Å, $\alpha = \gamma = 90°$, $\beta = 108.45°$, cell volume $= 62.12$ Å^3. Cell occupancy is listed in Table 8.31.

The technical literature is devoid of any papers concerning beryllium–hafnium intermetallic or oxy-hafnium compounds. None of these compounds are commercially available.

8.3.3. Magnesium Hafnide Compounds

The system, Mg–Hf, does not form any intermetallic compounds. A phase diagram has, however, been presented which is typical of the alkaline earths. The only difference in the Ca–Hf, Sr–Hf and BaHf systems lies in the transition temperatures of the individual metals (Fig. 8.63).

8.3.4. Magnesium Hafnate Compounds

The oxy-hafnium system, $MgO–HfO_2$, has been said to form but one compound. The HfO_2–MgO quasi-binary system has been assessed thermodynamically by means of the CALPHAD method. A phase diagram consistent with experimental information was obtained with an optimized set of 10 parameters for different phases. Further information is necessary on the lower limit of fluorite-type solid solution as well as the stability

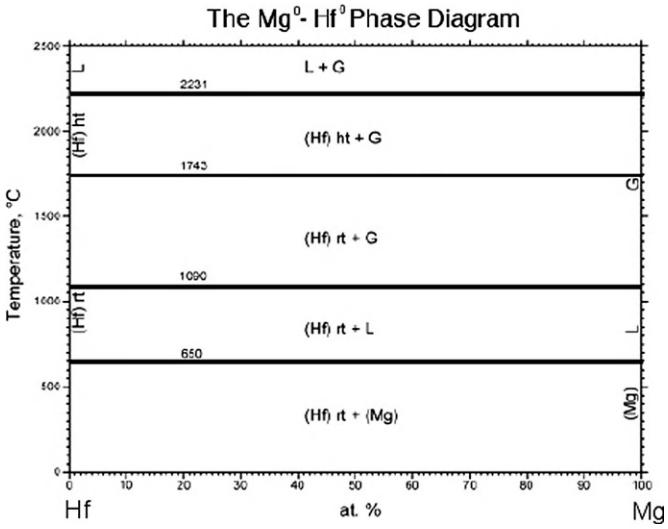

FIGURE 8.63

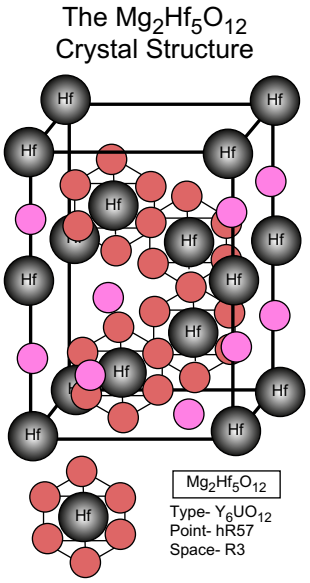

FIGURE 8.64

range of the ordered phase $Mg_2Hf_5O_{12}$ in order to present the full diagram.

This compound has the structure shown in Fig. 8.64.

Cell parameters are: $a = b = c = 6.1494$ Å, $\alpha = \beta = \gamma = 99.651°$, cell volume = 221.59 Å^3. It has the Y_6UO_{12} type structure with point group hR57 and space group = *R*-3.

Cell occupancy is listed in Table 8.32.

This structure consists of 3-HfO_6 octahedra interspersed within the unit cell with Mg^{2+} cations along the edges of the unit cell, which contains three formula units on the average. Two-thirds of the Hf atoms reside on the M1 site and 1/3 is occupied by the Mg atoms.

One study reported on the dielectric and leakage current properties of $Mg_2Hf_5O_{12}$ thin films deposited at room temperature by radio frequency magnetron sputtering. Polycrystalline $Mg_2Hf_5O_{12}$ thin films showed a reasonably high dielectric constant ($\varepsilon_r = 22$) and greatly enhanced leakage current characteristics ($<2 \times 10^{-7}$ A/cm^2) compared to the leakage current ($<2 \times 10^{-5}$ A/cm^2) of HfO_2 thin films at 0.4 MV/cm. A band-edge spectroscopic analysis revealed lower conduction band-edge defect states and a greater p-type-like Fermi energy level of $Mg_2Hf_5O_{12}$ compared to the HfO_2 thin films. The suitability of $Mg_2Hf_5O_{12}$ films as gate insulators for low-voltage operating $InGaZnO_4$ thin film transistors (TFTs) was investigated. All room temperature processed $InGaZnO_4$ TFTs on plastic substrates exhibited a high-field effect mobility of 27.32 cm^2/Vs and a current on/off ratio of 4.01×10^6. The threshold voltage and subthreshold swing were 2 V and 440 mV/dec, respectively. The fabrication and compositional manipulation method of the $Mg_2Hf_5O_{12}$ films described in this work was simple and versatile, providing fascinating opportunities for new high-*k* gate dielectrics.

Another compound, $Mg_{0.2}Hf_{0.6}O_{1.8}$, has been reported to possess the CaF_2 (cubic) structure (Fig. 8.65).

Cell parameters are: $a = b = c = 3.2638$ Å, $\alpha = \beta = \gamma = 60°$, cell volume = 32.01 Å^3. Site occupancy is listed in Table 8.33.

However, this compound can also be regarded as a "mixed oxide".

Although one paper stated that, the decomposition of magnesium hafnyl oxalate, $MgHfO(C_2O_4)_2 \cdot 7H_2O$, when heated formed $MgHfO_3$, there is no corroborating evidence that such a compound exists. According to these authors, the thermal decomposition of these oxalates was investigated employing TGA, DTA,

TABLE 8.32

No	Site notation	Atom	Multiplicity	Site sym	*x*	*y*	*z*	Occupancy
1	M1	0.670Hf + 0.330Mg	18	1	0.1224	0.417	0.0235	1.0
2	O1	O	18	1	0.191	0.032	0.117	1.0
3	O2	O	18	1	0.1933	0.2197	0.39867	1.0
4	Hf1	Hf	3	-3.	0	0	0	1.0

TABLE 8.33

No	Site notation	Atom	Multiplicity	Wyckoff	Site symmetry	x	y	z	Occupancy
1	O	O	8	c	-43m	1/4	1/4	1/4	0.9
2	M	0.8Hf + 0.2Mg	4	a	m-3m	0	0	0	1.0

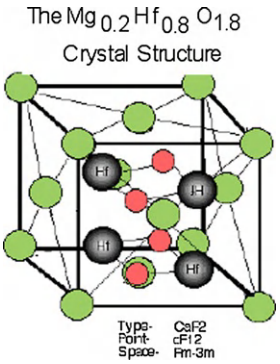

FIGURE 8.65

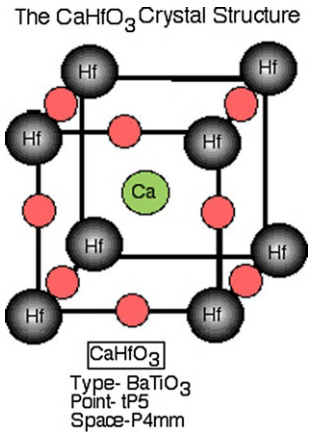

FIGURE 8.66

infrared spectral and chemical analysis techniques. The decomposition proceeds through three major steps, viz. the dehydration of the hydrated oxalate, the decomposition of the anhydrous oxalate to the carbonate and, finally, the decomposition of the carbonate to the oxide. Pure hafnium oxide, HfO_2, was the product in the thermal decomposition of simple hafnyl oxalate and ammonium hafnyl oxalate, while for magnesium hafnyl oxalate, $MgHfO_3$ was isolated as the final decomposition product.

Magnesium hafnates have been found to be unstable when used in high-temperature applications and have not found usage in Industry. They are not available commercially.

8.3.5. Calcium Hafnide Compounds

The intermetallic system, Ca–Hf does not form any compounds.

8.3.6. Calcium Hafnate Compounds

The complete phase diagram of the system, CaO–HfO_2, has not been thoroughly studied. It is known that two compounds are formed from these oxides: $CaHfO_3$ and $CaHf_4O_9$ However, a complete phase diagram has not been published.

The chemical equilibrium for the system HfO_2–$CaHfO_3$ was determined for temperatures above 1200 °C by heating reactive powders for extended periods. The eutectoid decomposition of the cubic solid solution was found to occur at 19.0 ± 0.5 m/o CaO and 1415 ± 7 °C. The solid solubility of CaO in tetragonal hafnia is very low. The tetragonal solid solution was shown to form from monoclinic hafnia solid solution at a eutectoid temperature of 1775 ± 50 °C. Three ordered compounds exist in this system. The ordered compound $CaHf_4O_9(\Phi_1)$ was found to be unstable at all temperatures investigated. It does, however, form metastably. The compound $Ca_2Hf_7O_{16}(\Phi)$ is stable with an upper limit of 1473 ± 5 °C. No lower limit of stability for this compound could be determined. The compound $Ca_6Hf_{19}O_{44}(\Phi_2)$ is stable from 1350 ± 50 °C to its upper limit of 1463 ± 5 °C.

The compound, $CaHfO_3$, crystallizes in several polymorphous modifications, including the cubic and rhombic perovskite type of structures.

$BaTiO_3$ Type

This form has the structure shown in Fig. 8.66.

This is a simple cubic structure with hafnium occupying the corners of the unit cell. The cell is unique in that it contains only 1/2 of the possible oxygen sites filled.

Cell parameters are: $a = b = c = 4.0496$ Å, $\alpha = \beta = \gamma = 90°$, cell volume $= 67.15$ Å^3. Site occupancy is listed in Table 8.34.

TABLE 8.34

No	Site notation	Atom	Multiplicity	Wyckoff	Site symmetry	x	y	z	Occupancy
1	O1	O	2	c	2mm.	1/2	0	0.0329	1.0
2	Ca1	Ca	1	b	4mm	1/2	1/2	0.5224	1.0
3	Hf1	Hf	1	a	4mm	0	0	0.0	1.0
4	O2	O	1	a	4mm	0	0	0.5468	1.0

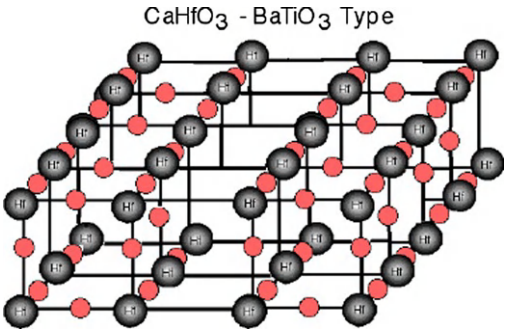

FIGURE 8.67

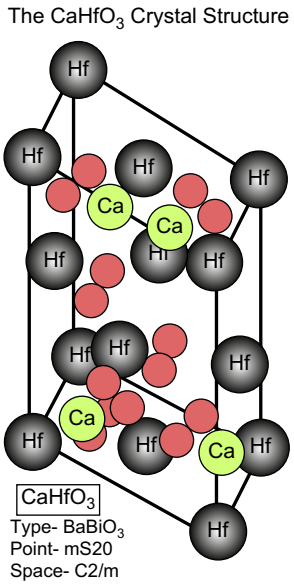

FIGURE 8.68

A three-dimensional structure is also shown as follows, where just the Hf and O ions are shown in Fig. 8.67.

$BaBiO_3$ Type

This structure can be represented as shown in Fig. 8.68. Cell parameters are: $a = 7.998$ Å, $b = 8.001$ Å, $c = 9.038$ Å, $\alpha = 91.52°$, $\beta = \gamma = 90°$, cell volume = 578.16 Å^3. Site occupancy has not been documented.

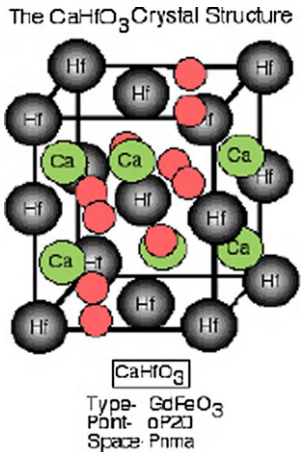

FIGURE 8.69

$GdFeO_3$ Type

This form has the structure shown in Fig. 8.69. Cell parameters are: $a = 5.631$ Å, $b = 5.737$ Å, $c = 8.066$ Å, $\alpha = \beta = \gamma = 90°$, cell volume = 260.57 Å^3.

Site occupancy is listed in Table 8.35.

$LaAlO_3$ Type

This form has the structure shown in Fig. 8.70.

Cell parameters are: $a = b = c = 5.788$ Å, $\alpha = \beta = \gamma = 60.6°$, cell volume = 138.97 Å^3. Site occupancy has not been documented.

This structure consists of 4 HfO_6 octahedra which are joined on an edge and occupy the center of the unit cell. They are surrounded by Ca^{2+} cations located on the edges of the unit cell.

$CaTiO_3$ Type

This structure has the form shown in Fig. 8.71. Cell parameters are: $a = b = c = 4.091$ Å, $\alpha = \beta = \gamma = 90°$, cell volume = 68.47 Å^3.

Site occupancy is listed in Table 8.36.

The three-dimensional structure shown in Fig. 8.72 may be compared to the $BaTiO_3$ type shown above.

Other calcium hafnate compositions have been studied. Three ordered fluorite-related phases occurred in the system CaO–HfO_2 and their crystal structures

TABLE 8.35

No	Site notation	Atom	Multiplicity	Wyckoff	Site symmetry	*x*	*y*	*z*	Occupancy
1	O1	O	8	d	1	0.1984	0.0506	0.3043	1.0
2	Ca1	Ca	4	c	.m.	0.4372	1/4	0.0156	1.0
3	O2	O	4	c	.m.	0.5328	1/4	0.6005	1.0
4	Hf1	Hf	4	a	-1	0	0	0	1.0

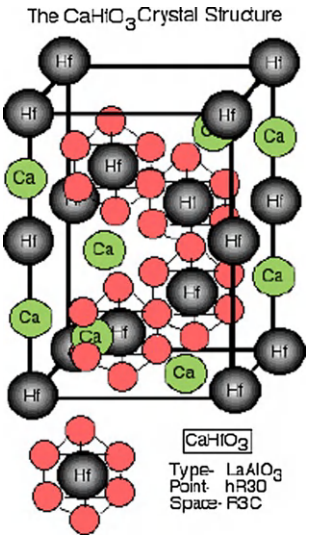

FIGURE 8.70

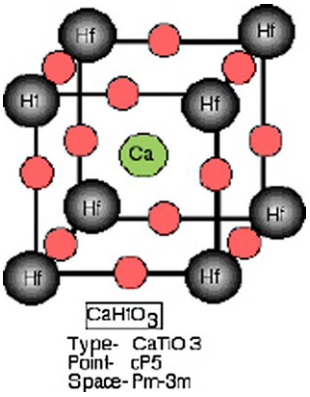

FIGURE 8.71

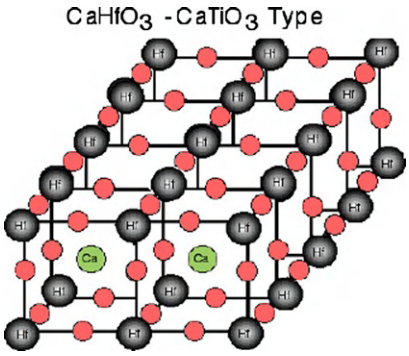

FIGURE 8.72

have been described. $Ca_2Hf_7O_{16}$ (Φ) is rhombohedral, with $a = b = c = 9.527$ Å, $\alpha = \beta = \gamma = 38.80°$. $CaHf_4O_9$ (Φ_1) is monoclinic, with $a = 17.698$ Å, $b = 14.500$ Å, $c = 12.021$ Å, $\beta = 199.47°$. $Ca_6Hf_{19}O_{44}$ (Φ_2) is rhombohedral, with $a = b = c = 12.059$ Å, $\alpha = \beta = \gamma = 98.31°$.

The chemical equilibrium for the system HfO_2-$CaHfO_3$ was determined for temperatures above 1200 °C by heating reactive powders for extended periods. The eutectoid decomposition of the cubic solid solution was found to occur at 19.0 ± 0.5 m/o CaO and 1415 ± 7 °C. The solid solubility of CaO in tetragonal hafnia is very low. The tetragonal solid solution was shown to form from monoclinic hafnia solid solution at a eutectoid temperature of 1775 ± 50 °C. Three ordered compounds exist in this system. The ordered compound $CaHf_4O_9(\Phi_1)$ was found to be unstable at all temperatures investigated. It does, however, form metastably. The compound $Ca_2Hf_7O_{16}(\Phi)$ is stable with an upper limit of 1473 ± 5 °C. No lower limit of stability for this compound could be determined. The compound $Ca_6Hf_{19}O_{44}(\Phi_2)$ is stable from 1350 ± 50 °C to its upper limit of 1463 ± 5 °C.

The atomic arrangement in the fluorite-related phase, $Ca_2Hf_7O_{16}$, has been determined by powder XRD. The unit cell is rhombohedral, R3, with $a = 9.5273$ Å, $\alpha = 38.801°$, and $Z = 1$, and its volume is 2.5 times that of the fluorite subcell from which it is derived. The cations are ordered on the cation sites of the fluorite structure with the calcium ions segregated into discrete layers parallel to the (111) fluorite plane: there is some evidence that the formal anion vacancies are also ordered.

Crystal structures for the fluorite-related phases $CaHf_4O_9$ (Φ_1) and $Ca_6Hf_{19}O_{44}$ (Φ_2) have been determined from X-ray powder diffraction data. Φf_1 is monoclinic, $C2/c$, with $a = 17.698$ Å, $b = 14.500$ Å, $c = 12.021$ Å, $\beta = 119.47°$ and $Z = 16$. Φf_2 is rhombohedral, with $a = 12.058$ Å, $\alpha = 98.31°$ and $Z = 2$.

Both phases are superstructures derived from the defect fluorite structure by ordering of the cations and of the anion vacancies. The ordering is such that the

TABLE 8.36

No	Site notation	Atom	Multiplicity	Wyckoff	Site symmetry	*x*	*y*	*z*	Occupancy
1	O	O	3	d	4/mm.m	1/2	0	0	1.0
2	Ca	Ca	1	b	m-3m	1/2	1/2	1/2	1.0
3	Hf	Hf	1	a	m-3m	0	0	0	1.0

calcium ions are always 8-coordinated by oxygen ions, while the hafnium ions may be 6-, 7-, or 8-coordinated. The closest approach of anion vacancies is a 1/2(111) fluorite subcell vector, and in each structure vacancies with this separation form strings.

Luminescence of Pr from two sites was observed. About 85% of Pr ions occupy on Ca site (A site of perovskite ABO_3) and 15% of Pr ions stay on Hf site (B site). Pr(A) shows an excitation band at 240 nm from the 4f5d state, and gives strong UV emission bands peaking at 294 and 337 nm. Emission at 490 nm from $^3P_0$ is dominant. In contrast, Pr(B) shows 5d excitation band at 275 nm, and gives a weak and broad emission band near 390 nm. Emission from its $^1D_2$ at 610 nm is stronger than the emission from $^3P_0$ state (484 nm). Codoping with Na^+, In^{3+}, or Al^{3+} for the purpose of charge compensation could change distribution of Pr on both sites. Na^+ tends to reduce, but In and Al tend to increase the population of Pr on Hf (B) site.

Calcium hafnates are not very stable at high temperatures, a factor that has led Industry to abandon any potential uses of these compounds. No CAS numbers have been issued to date.

8.3.7. Strontium Hafnide Compounds

The system, Sr–Hf, does not form any intermetallic compounds.

8.3.8. Strontium Hafnate Compounds

In the SrO–HfO_2 system, four compounds, $SrHfO_3$, Sr_2HfO_4, $Sr_3Hf_2O_7$ and $Sr_4Hf_3O_{10}$, are known and their crystal structures have been described. However, the phase diagram is not available.

Studies were made of the synthesis and sintering of strontium hafnate. Ceramics were obtained from $SrHfO_3$ with a density of about 95% of the theoretical, and characterization was made of its basic properties, which suggest the possibility of using $SrHfO_3$ ceramics at elevated temperatures in air and in inert gas. Ceramics made from $SrHfO_3$ cannot be used at high temperatures over a prolonged period in vacuum because of the marked volatilization and change in their phase composition and basic properties.

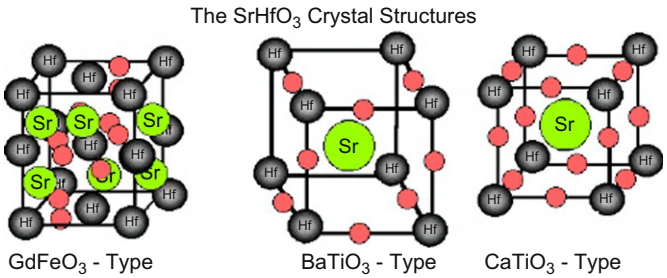

FIGURE 8.73

$SrHfO_3$ is trimorphic. Crystal structures are the same as those for $CaHfO_3$, except for cell parameters. The following diagram compares these structures shown in Fig. 8.73.

The cell parameters and cell occupancies are as follows:

$GdFeO_3$ Type

Unit cell parameters are: $a = 5.7569$ Å, $b = 5.780$ Å, $c = 9.130$ Å, $\alpha = \beta = \gamma = 90°$, cell volume = 271.43 Å^3.

Cell occupancy is listed in Table 8.37.

$BaTiO_3$ Type

Cell parameters are: $a = 4.105$ Å, $b = c = 4.114$ Å, $\alpha = \beta = \gamma = 90°$, cell volume = 69.4 Å^3.

Cell occupancy is listed in Table 8.38.

$CaTiO_3$ Type

Cell parameters are: $a = b = c = 4.121$ Å, $\alpha = \beta = \gamma = 90°$, cell volume = 69.93 Å^3.

Cell occupancy is listed in Table 8.39.

Sr_2HfO_4 has the K_2NiF_4 structure and the form shown in Fig. 8.74.

This structure contains a body-centered HfO_6 octahedra with 1/2 of an octahedra at both ends of the tetragonal unit cell. Strontium ions are interspersed on the edges of the tetrahedral unit. Cell parameters are: $a = b = c = 4.079$ Å, $\alpha = \beta = 107.03°$, $\gamma = 90°$, cell volume = 105.65 Å^3. Cell occupancy is listed in Table 8.40.

The compound, $Sr_3Hf_2O_7$, has the same form as the Sr_2HfO_4 compound except that two HfO_6 octahedra are present in the unit cell (Fig. 8.75).

TABLE 8.37

No	Site notation	Atom	Multiplicity	Wyckoff	Site symmetry	*x*	*y*	*z*	Occupancy
1	O1	O	8	d	1	0.1984	0.0506	0.3043	1.0
2	Sr1	Sr	4	c	.m.	0.4372	1/4	0.0156	1.0
3	O2	O	4	c	.m.	0.5328	1/4	0.6005	1.0
4	Hf1	Hf	4	a	-1	0	0	0	1.0

TABLE 8.38

No	Site notation	Atom	Multiplicity	Wyckoff	Site symmetry	x	y	z	Occupancy
1	O1	O	2	c	2mm.	1/2	0	0.0329	1.0
2	Sr1	Sr	1	b	4mm	1/2	1/2	0.5224	1.0
3	Hf1	Hf	1	a	4mm	0	0	0.0	1.0
4	O2	O	1	a	4mm	0	0	0.5468	1.0

TABLE 8.39

No	Site notation	Atom	Multiplicity	Wyckoff	Site symmetry	x	y	z	Occupancy
1	O	O	3	d	4/mm.m	1/2	0	0	1.0
2	Sr	Sr	1	b	m-3m	1/2	1/2	1/2	1.0
3	Hf	Hf	1	a	m-3m	0	0	0	1.0

TABLE 8.40

No	Site notation	Atom	Multiplicity	Wyckoff	Site symmetry	x	y	z	Occupancy
1	O1	O	4	e	4mm	0	0	0.1533	1.0
2	Sr1	Sr	4	e	4mm	0	0	0.3538	1.0
3	O2	O	4	c	mmm.	0	1/2	0	1.0
4	Hf1	Hf	2	a	4/mmm	0	0	0	1.0

Cell parameters are: $a = b = 4.083$ Å, $c = 10.856$ Å, $\alpha = \beta = 100.839°$, $\gamma = 90°$m cell volume $= 174.46$ Å^3. Cell occupancy is listed in Table 8.41.

The compound, $Sr_4Hf_3O_{10}$, has the structure shown in Fig. 8.76. It has the structure type of $Ca_4Ti_3O_{10}$, point group = oP68, space group = *Pcba*.

Unit cell parameters are: $a = b = 6.783$ Å, $c = 29.235$ Å, $\alpha = \beta = \gamma = 90°$, cell volume = 974.33 Å^3.

Cell occupancy is listed in Table 8.42.

Another structure type of this compound has the structure type of $Sr_4Ti_3O_{10}$, point group = tl34, space group = *I*4/*mmm*, and is shown in Fig. 8.77.

Cell parameters are: $a = b = 4.088$ Å, $c = 14.923$ Å, $\alpha = \beta = 97.873°$, $\gamma = 90°$, cell volume = 244.36 Å^3. Cell occupancy is listed in Table 8.43.

The compound, $SrHfO_3$, has been used as a base for fast-decay phosphors. Luminescence spectra of $SrHfO_3$:Ce^{3+} and $BaHfO_3$:Ce^{3+} consist of a broad band due to Ce^{3+} emission peaking at 410 and 400 nm, respectively. The light yield of $BaHfO_3$:Ce^{3+} and $SrHfO_3$:Ce^{3+}, as a transparent optical ceramic, is approximately 40,000 photons/MeV when compared to a crystal of BGO. The principal decay time constant for $SrHfO_3$:Ce^{3+} and $BaHfO_3$:Ce^{3+} is 15 and 16 ns, respectively. A timing resolution of 276 ps (FWHM) was obtained with a transparent optical ceramic of $SrHfO_3$:Ce^{3+}.

There are only few published studies regarding dielectric properties of the $SrHfO_3$. Most recently, epitaxial $SrHfO_3$ was investigated on Si(100) substrates. There

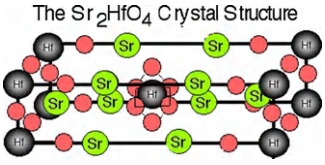

FIGURE 8.74

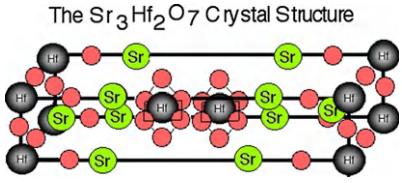

FIGURE 8.75

TABLE 8.41

No	Site notation	Atom	Multiplicity	Wyckoff	Site symmetry	*x*	*y*	*z*	Occupancy
1	O1	O	16	n	.m.	0	0.3957	0.404	0.500
2	Hf1	Hf	4	e	4mm	0	0	0.0974	1.0
3	O2	O	4	e	4mm	0	0	0.1939	1.0
4	Sr1	Sr	4	e	4mm	0	0	0.3128	1.0
5	Sr2	Sr	2	b	4/mmm	0	0	1/2	1.0
6	O3	O	2	a	4/mmm	0	0	0	1.0

TABLE 8.42

No	Site notation	Atom	Multiplicity	Wyckoff	Site symmetry	*x*	*y*	*z*	Occupancy
1	Hf1	Hf	8	c	1	0.0027	0.0	0.1426	1.0
2	Sr1	Sr	8	c	1	0.0079	0.0238	0.2947	1.0
3	O1	O	8	c	1	0.0548	0.4858	0.2882	1.0
4	O2	O	8	c	1	0.0668	0.0142	0.0708	1.0
5	O3	O	8	c	1	0.2099	0.2115	0.49	1.0
6	O4	O	8	c	1	0.2125	0.2115	0.3679	1.0
7	O5	O	8	c	1	0.2125	0.2885	0.1499	1.0
8	Sr2	Sr	8	c	1	0.4962	0.4665	0.4307	1.0
9	Hf2	Hf	4	a	−1	0	0	0	1.0

TABLE 8.43

No	Site notation	Atom	Multiplicity	Wyckoff	Site symmetry	*x*	*y*	*z*	Occupancy
1	O1	O	8	g	2mm.	0	1/2	0.136	1.0
2	O2	O	4	e	4mm	0	0	0.068	1.0
3	Hf1	Hf	4	e	4mm	0	0	0.136	1.0
4	O3	O	4	e	4mm	0	0	0.204	1.0
5	Sr1	Sr	4	e	4mm	0	0	0.296	1.0
6	Sr2	Sr	4	e	4mm	0	0	0.432	1.0
7	O4	O	4	c	mmm.	0	1/2	0	1.0
8	Hf2	Hf	2	a	4/mmm	0	0	0	1.0

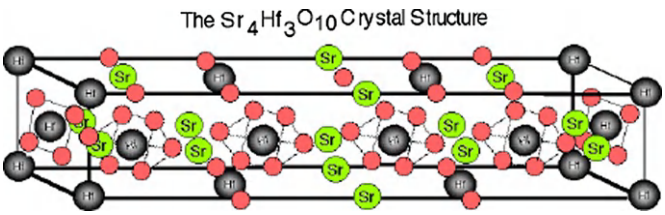

FIGURE 8.76

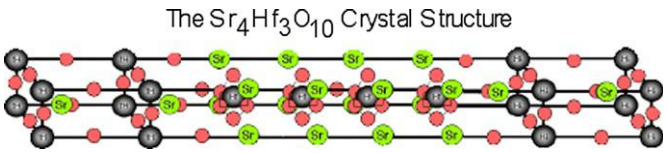

FIGURE 8.77

are, however, no reports on thin $SrHfO_3$ layers deposited onto metal electrodes inevitable in storage capacitors. In this work, $SrHfO_3$ was deposited onto 20 nm layers of magnetron sputtered TiN on Si wafers. The dielectric films were formed by coevaporation of HfO_2 and SrO in a molecular beam deposition chamber. Substrate temperature during evaporation was kept at 400 °C. It was found that "As-deposited" layers are amorphous and show a dielectric constant of $\kappa = 21$. During RTA, the amorphous material crystallizes in the cubic $SrHfO_3$ perovskite phase and the dielectric constant increases to around 35. Low leakage currents, 10^{-7} A/cm^2 at 1.0 V were measured down to CETs of 1.2 nm. $SrHfO_3$ layers have similar properties to $BaHfO_3$ films. In both cases, postdeposition RTA at 800 °C was necessary to convert 10- to 15-nm-thick As-deposited amorphous layers into polycrystalline films with improved κ. The measured dielectric constant of polycrystalline $BaHfO_3$ films is slightly higher than those of $SrHfO_3$. Breakdown fields are also similar: 3.3 and 2.8 MV/cm for amorphous and crystalline films. This is significantly lower than for pure HfO_2 (5.8 MV/cm). For both materials, leakage currents below 10^{-7} A/cm^2 at 1 V were measured for 1.2 nm CET. They are due to point defects, possibly associated with Ti contamination.

Strontium hafnates have not found usage in Industry because their physical and electrical properties have not been found to be superior to the materials presently being used in specific applications.

8.3.9. Barium Hafnide Compounds

The system, Ba–Hf, does not form any intermetallic compounds.

8.3.10. Barium Hafnate Compounds

In the $BaO–HfO_2$ system, one compound is known ($BaHfO_3$). $BaHfO_3$ has the same structure as $BaZrO_3$, as shown in Fig. 8.78.

Cell parameters are: $a = b = c = 4.161$ Å, $\alpha = \beta = \gamma = 90°$, cell volume = 72.00 Å^3. Cell occupancy is listed in Table 8.44.

Barium hafnate ($BaHfO_3$) precursor can be prepared by mixed barium nitrate and hafnium (IV) chloride

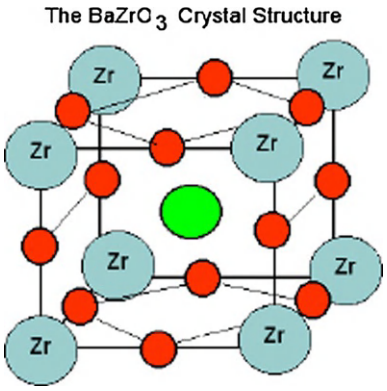

FIGURE 8.78

with ammonium oxalate aqueous solution. Barium hafnate powders were obtained by decomposition of the precipitate precursor at 800 °C for 2 h. As a dispersant, polyethylene glycol (PEG6000) was used in the precipitation reaction and the influence of dispersant dosage on particle size was studied. XRD analysis showed the powders was pure cubic $BaHfO_3$ without impurities. SEM and TEM demonstrated that the size distribution was uniform, and the average grain size was about 50 nm.

The crystal structure and MW dielectric properties of $BaHfO_3$ ceramics prepared by the solid-state route have been investigated. X-ray and electron diffraction show $BaHfO_3$ to be an untilted cubic perovskite ($a^0a^0a^0$, space group), whereas $SrHfO_3$ and $CaHfO_3$ are both orthorhombic-distorted perovskites ($a^-b^+a^-$, space group *Pnma*). $AeHfO_3$ ceramics with a relative density ~90% of the theoretical X-ray density and microstructures were prepared by firing at 1750 °C for 6 hrs. The product consisted of randomly oriented equiaxial grains. Conventional TEM revealed the occurrence of long parallel ferroelastic domains in the subgrain microstructure of $CaHfO_3$ and $SrHfO_3$. At room temperature and MW frequencies, $AeHfO_3$ ceramics, where Ae = Ba, Sr, and Ca, have $\varepsilon_r \sim 24.2$, $Qxf_r \sim 14{,}250$ GHz (at 8.9 GHz) and $\tau_f \sim +111$ ppm/K; $\varepsilon_r \sim 23.5$, $Qxf_r \sim 33{,}534$ GHz (at 9.3 GHz), and $\tau_f \sim 63$ ppm/K; and $\varepsilon_r \sim 21.4$, $Qxf_r \sim 15{,}950$ GHz (at 8.9 GHz), and $\tau_f \sim 33$ ppm/K, respectively. The ion polarizability for Hf^{4+} in a cubic perovskite environment was calculated to be 3.32 Å^3, whereas in a noncubic environment it increased to

TABLE 8.44

No	Site notation	Atom	Multiplicity	Wyckoff	Site symmetry	*x*	*y*	*z*	Occupancy
1	O	O	3	d	4/mm.m	1/2	0	0	1.0
2	Ba	Ba	1	b	m-3m	1/2	1/2	1/2	1.0
3	Hf	Hf	1	a	m-3m	0	0	0	1.0

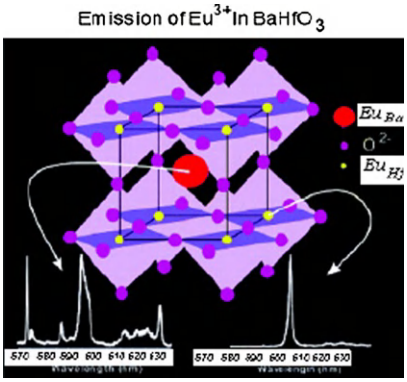

FIGURE 8.79

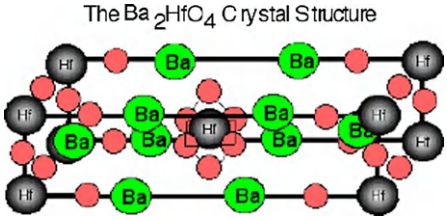

FIGURE 8.80

4.36–4.47 Å^3. The dielectric properties of $AeHfO_3$ (Ae = Ba, Sr, and Ca) were compared with their titanate and zirconate counterparts.

$BaHfO_3$ is a scintillator. The emission properties of $BaHfO_3$:Ce^{3+} consist of a broad band due to Ce^{3+} emission peaking at 400 nm. The light yield of $BaHfO_3$:Ce^{3+} is approximately 40,000 photons/MeV when compared to a crystal of BGO. The principal decay time constant for $BaHfO_3$:Ce^{3+} is 25 ns. A timing resolution of 276 ps (FWHM) was obtained with transparent optical ceramic of $BaHfO_3$:Ce^{3+}. Analysis of the band structure showed that perovskite-type $BaHfO_3$ is a wide gap indirect semiconductor. The band gap was predicted to be 3.94 eV within the screened exchange local density approximation (sX-LDA). The calculated equilibrium lattice constant of this compound was in good agreement with the available experimental and theoretical data reported in the literatures. The independent elastic constants (C_{11}, C_{12}, and C_{44}), bulk modulus B and its pressure derivatives, B', compressibility, β, shear modulus G, Young's modulus Y, Poisson's ratio, Y, and Lamé constants (μ, Å) were obtained and analyzed in comparison with the available theoretical and experimental data for both the single-crystalline and polycrystalline $BaHfO_3$. The bonding-charge density calculation made it clear that the covalent bonds exist between the Hf and O atoms and that ionic bonds exist between the Ba atoms and HfO_3 ionic groups in $BaHfO_3$.

Barium hafnate, $BaHfO_3$ is a valuable host lattice for X-ray phosphors, especially due to its high absorption for ionizing radiation, which results mainly from the presence of two heavy ions, Ba^{2+} and Hf^{4+} in the lattice and density reaches 8.5 g/cm^3. What is also advantageous is that $BaHfO_3$ crystallizes in cubic structure, which allows for transparent ceramics fabrication. These are potentially attractive replacements for monocrystalline materials.

Most of the research on $BaHfO_3$ was has been concentrated on Ce-doped powders, because of its fast luminescence decay, so important in dynamic medical techniques. Doping with Eu^{3+} as its red luminescence fits perfectly the region of the highest efficiency of CCDs, and is presently considered a detector of choice for digital planar X-ray imaging (Fig. 8.79).

In this technique the relatively slow decay of the Eu^{3+} luminescence is not an obstacle. Two series of $BaHfO_3$ powders activated with Eu^{3+} ions were prepared with a ceramic method. By stoichiometric variations, the dopant was forced to enter either Ba^{2+} or Hf(IV) sites. XRD analysis proved that Eu^{3+} ions preferred substitution of Hf(IV) in $BaHfO_3$, while replacement of Ba^{2+} encountered difficulties and led finally to separation of a foreign phase, $Eu_2Hf_2O_7$. Yet, it was shown that the host always incorporated the activator both into Hf(IV) and Ba^{2+} positions, and the two sites, $Eu_{Hf\cdot}$ and $Eu_{Ba\cdot}$, were spectroscopically characterized. From photoluminescence spectra, it appeared that $Eu_{Ba\cdot}$ gave emissions at 573.6, 595, and 626.0 nm, while luminescence from $Eu_{Hf\cdot}$ was practically limited to just one line peaking at 595.6 nm.

Luminescence and excitation spectra taken under synchrotron radiation showed that energy from the excited host is preferentially transferred to Eu_{Hf} compared to $Eu_{Ba\cdot}$. At 10 K, the latter was not capable of intercepting any energy upon excitation above the fundamental absorption of $BaHfO_3$, which limited

TABLE 8.45

No	Site notation	Atom	Multiplicity	Wyckoff	Site symmetry	x	y	z	Occupancy
1	O1	O	4	e	4mm	0	0	0.1533	1.0
2	Ba1	Ba	4	e	4mm	0	0	0.3538	1.0
3	O2	O	4	c	mmm.	0	1/2	0	1.0
4	Hf1	Hf	2	a	4/mmm	0	0	0	1.0

the luminescence in such conditions to a single line peaking at 595.6 nm. Also, under excitation with X-rays, practically only the Eu_{Hf}^{-} was able to produce luminescence.

The compound, Ba_2HfO_4, has the same structure as its Sr counterpart shown in Fig. 8.80.

Cell parameters are: $a = b = 4.191$ Å, $\alpha = \beta = 107.631°$, $\gamma = 90°$. Cell occupancy is listed in Table 8.45.

Although the crystal structure of this compound has been elucidated, it has found little usage in Industry and does not have a CAS number. The usage of $BaHfO_3$ is just beginning to be used in Industrial applications but it does not have a CAS number. These are the only two barium hafnate compounds known to date.

8.3.11. Radium Hafnium Compounds

Although radium could be used to form at least two compounds, $RaHfO_3$ and Ra_2HfO_4, the high cost and radioactive nature of ^{228}Ra has precluded any investigations of this system. Nor is it likely that Ra^0 forms any intermetallic compounds with Hf^0.

CHAPTER

9

Group 5 (V, Nb and Ta) Alkaline Earth Compounds

OUTLINE

9.1. Alkaline Earth Vanadium Compounds 701
9.1.1. Beryllium Vanadium Compounds 701
9.1.2. Magnesium Vanadium Compounds 702
9.1.3. Calcium Vanadium Compounds 709
9.1.4. Strontium Vanadium Compounds 715
9.1.5. Barium Vanadium Compounds 722
9.1.6. Radium Vanadates 728

9.2. Alkaline Earth Niobium Compounds 728
9.2.1. Beryllium Niobium Compounds 729
9.2.2. Magnesium Niobium Compounds 731
9.2.3. Calcium Niobium Compounds 736
9.2.4. Strontium Niobium Compounds 741
9.2.5. Barium Niobium Compounds 752
9.2.6. Radium Niobates 760

9.3. Alkaline Earth Tantalum Compounds 760
9.3.1. Beryllium Tantalum Compounds 760
9.3.2. Magnesium Tantalum Compounds 761
9.3.3. Calcium Tantalum Compounds 767
9.3.4. Strontium Tantalum Compounds 775
9.3.5. Barium Tantalum Compounds 785
9.3.6. Radium Tantalates 794

9.1. ALKALINE EARTH VANADIUM COMPOUNDS

The relation of ion-types of vanadium oxy-ions in solution with pH is shown in the following diagram: Fig. 9.1.

The decavanadate ion is shown in the following Fig. 9.2.

The major valence state is +5 and V_2O_5 is an oxide with slightly basic tendencies.

Vanadium forms a number of different compounds with the alkaline earths. Due to the amphoteric nature of vanadium, these compounds can be formed by either a solution method or solid-state reaction of the oxides. Most often, the latter method is employed.

9.1.1. Beryllium Vanadium Compounds

Be^0 forms only two intermetallic compounds with V^0. A phase diagram has been presented in Fig. 9.3.

Structure parameters are shown in Table 9.1.

Be_2V has the $MgZn_2$ structure with space group $P6_3/mmc$ as shown in Fig. 9.4.

Unit cell parameters are: $a = b = 4.384$ Å, $c = 7.131$ Å, $\alpha = \beta = 90°$, $\gamma = 120°$, cell volume = 118.73 Å^3. Cell occupancy is shown in Table 9.2.

In addition, the compound, $Be_{12}V$, has the structure of the $ThMn_{12}$ type where the V-atoms are arranged on the corners of the cubic cell, and is body-centered (as shown in the following diagram and the *a*-axis diagram): Fig. 9.5.

The Be-atoms are arranged in five internal-layers as shown in the *c*-axis diagram. The point group is tl26, and the space group is $I4/mmm$. The unit cell parameters are: $a = 4.212$ Å, $b = c = 5.5606$ Å, $\alpha = 81.75°$, $\beta = \gamma = 67.744°$, cell volume = 111.55 Å^3.

Note that layers one and five have only two atoms in them. Site occupancy is shown in Table 9.3.

The structure of the $Be_{17}V_2$ compound has not been elucidated. These are the only known Be–V compounds.

Encyclopedia of the Alkaline Earth Compounds
http://dx.doi.org/10.1016/B978-0-444-59550-8.00009-0

Copyright © 2013 Elsevier B.V. All rights reserved.

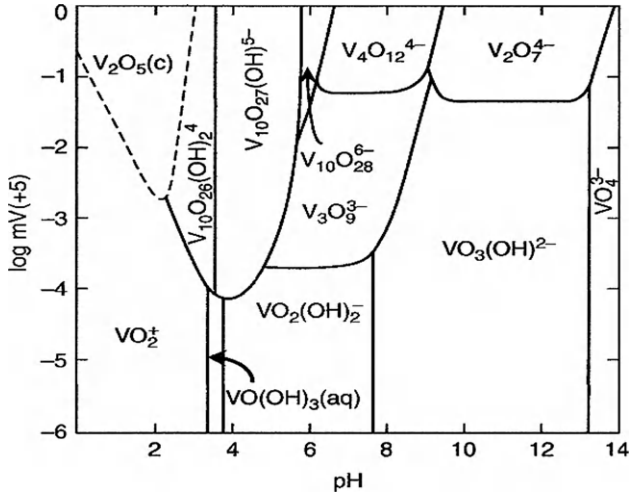

FIGURE 9.1

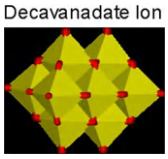

FIGURE 9.2

Beryllium (Be) metal is used as a reference material for a neutron multiplier in the fusion blanket design. However, Be metal may have problems such as high reactivity and large swelling at high temperature-high neutron dose in the DEMO fusion blanket. Beryllium alloys such as Be–Ti and Be–V are promising candidates for advanced neutron multipliers from the viewpoints of high melting point, high beryllium content, low radioactivation, and good chemical stability. In one study, the compatibility between structural material F82H steel and Be-7 atom%/V that included a Be^0 phase was investigated. After annealing, reaction products, at the surface of a F82H steel and Be-7 atom%/V specimen, were analyzed by X-ray diffraction (XRD) analysis and EPMA/SEM (electron probe micro analyzer/scanning electron microscopy) analysis. The thickness and rate constant of reaction layer at the surface of the F82H steel was evaluated and good compatibility between Be–V and F82H was clearly identifiable.

There are no known oxy-vanadium compounds of Be. As early as 1916, it was stated, "It was evident that a normal **beryllium vanadate** was not to be obtained … It has been shown that basic mixtures and not compounds are obtained by the addition of soluble vanadates to solutions of beryllium salts". Note that this involved aqueous solutions. However, the results of heating the oxides together have not been reported in the literature.

No beryllium–vanadium compounds are available commercially and no CAS numbers have been issued.

9.1.2. Magnesium Vanadium Compounds

Magnesium metal, Mg^0, does not form any intermetallic compounds with V^0. A phase diagram has been

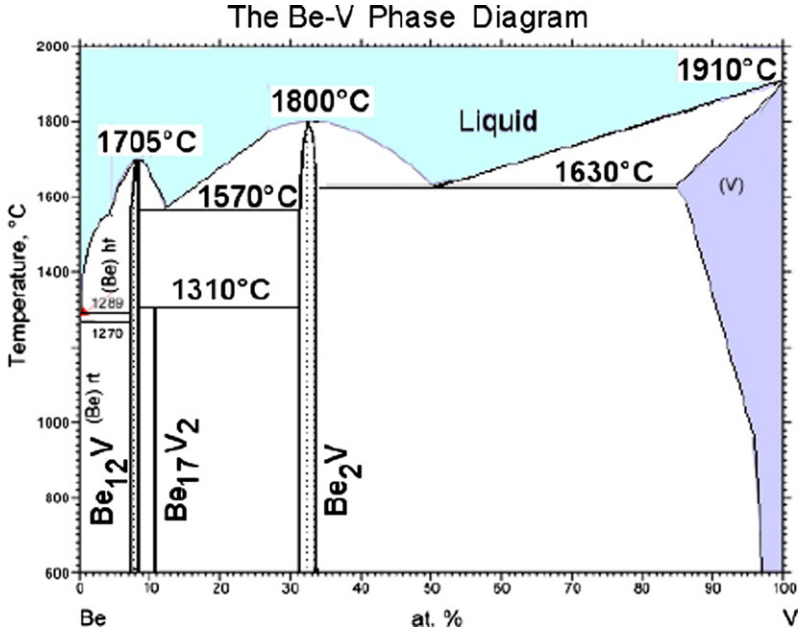

FIGURE 9.3

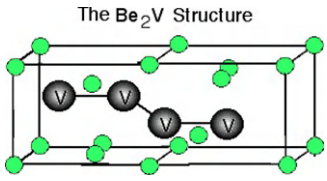

FIGURE 9.4

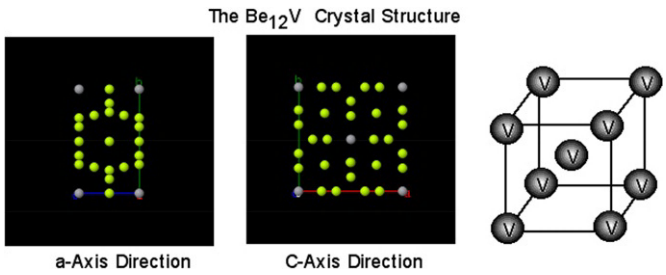

FIGURE 9.5

published showing the various polymorphic stages of both metals as a function of temperature as shown in Fig. 9.6.

This diagram is typical of all of the other alkaline earths (Ca, Sr and Ba) with V-metal and those phase diagrams will not be presented herein.

MgO forms a series of compounds with V_2O_5 when those oxides are heated at high temperatures at various molecular ratios. The solution method is almost unknown. An investigation was made of solid–solid reactions in MgO/V_2O_5 mixtures of various stoichiometric ratios. Three compounds were obtained, viz., $Mg_3V_2O_8$, $Mg_2V_2O_7$, and MgV_2O_6; no evidence was obtained to indicate the formation of other $MgO–V_2O_5$ compounds, as reported in the early literature. DTA data were listed for the three compounds and some observations were made on the mechanism of formation of the compounds. A new polymorph of $Mg_2V_2O_7$ was prepared, and its space group and cell parameters were deduced from the powder XRD pattern. This polymorph undergoes

TABLE 9.1

Compound	Structure type	Point group	Space group	Melt temperature °C	Physical properties
(V)	W	cI2	*Im3m*	1910	No Data
(Be) rt	Mg	hP2	$P6_3/mmc$	1270	No Data
(Be) ht	W	cI2	*Im3m*	1289	No Data
$Be_{12}V$	$ThMn_{12}$	tI26	*I4/mmm*	1705	No Data
Be_2V	$MgZn_2$	hP12	$P6_3/mmc$	1800	No Data
$Be_{17}V_2$	—	—	—	1310	No Data

TABLE 9.2

No	Site notation	Atom	Multiplicity	Wyckoff	Site symmetry	*x*	*y*	*z*	Occupancy
1	Be2	Be	6	h	mm2	0.167	0.334	1/4	1.0
2	V	V	4	f	3m.	1/3	2/3	0.553	1.0
3	Be1	Be	2	a	-3m.	0	0	0	1.0

TABLE 9.3

No	Site notation	Atom	Multiplicity	Wyckoff	Site symmetry	*x*	*y*	*z*	Occupancy
1	Be1	Be	8	j	m2m.	0.277	1/2	0	1.0
2	Be2	Be	8	i	m2m.	0.361	0	0	1.0
3	Be3	Be	8	f	..2/m	1/4	1/4	1/4	1.0
4	V1	V	2	a	4/mmm	0	0	0	1.0

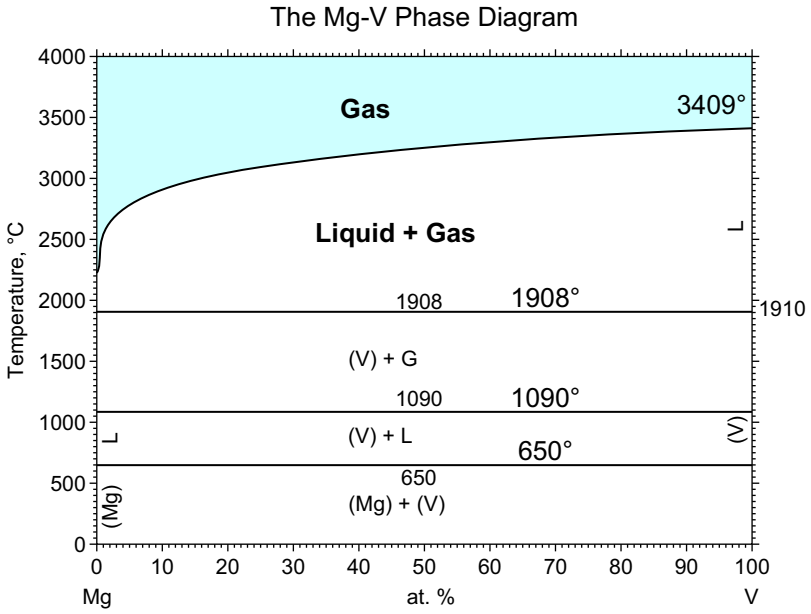

FIGURE 9.6

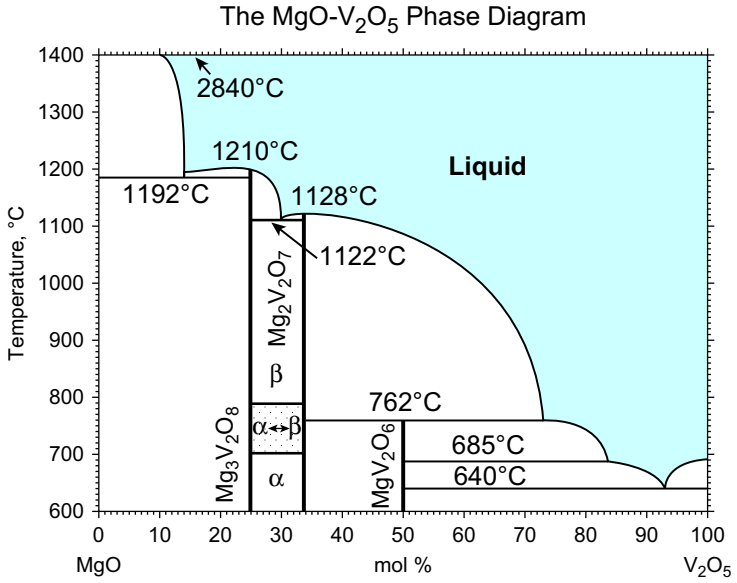

FIGURE 9.7

a transition, reversible with difficulty, at 980–990 K. (700–790 °C).

The above figure presents the phase diagram of this system: Fig. 9.7.

The compound, MgV_4O_5, contains V^{2+} as the vanadium ion. The structure is of the rock-salt type with lattice parameters of: $a = b = c = 4.128$ Å, $\alpha = \beta = \gamma = 90°$, cell volume = 7.03 Å^3, $Z = 4$. Cell occupancy is shown in Table 9.4.

The $MgVO_2$, Mg_2VO_3, and Mg_3VO_4 compounds remain unknown.

In the V^{3+} containing compounds in the $MgO–V_2O_3$ series of compounds, the MgV_2O_4 compound has been studied. The structure has a cubic form, described as a "stuffed trigonal" structure, shown as follows in Fig. 9.8.

The unit cell is usually taken to be cubic with eight molecules of MgV_2O_4 and the space group is $Fd\bar{3}$Å.

TABLE 9.4

No	Site notation	Atom	Multiplicity	Wyckoff	Site symmetry	x	y	z	Occupancy
1	O	O	4	b	m-3m	1/2	1/2	1/2	1.0
2	M	0.8V + 0.2Mg	4	a	m-3m	0	0	0	1.0

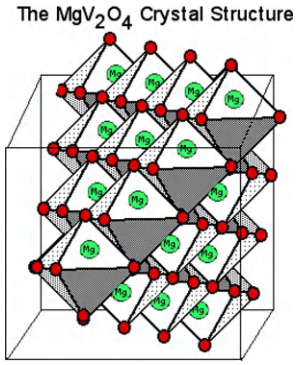

FIGURE 9.8

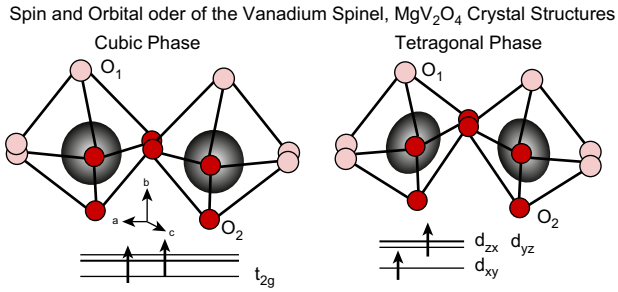

VO6 octahedra along the chain direction in both the cubic and tetragonal phases (distortions have been exaggerated). The trigonal distortion slightly splits the t_{2g} levels in the cubic phase. In the tetragonal phase, the oxygen octahedra are compressed causing large splitting of the t_{2g} levels

FIGURE 9.9

The Mg and V ions are located at the oxygen tetrahedral A(8*a*) and octahedral B(16*d*) sites, respectively. The VO_6 octahedra share edges and three arrays of the V ions cross at each site. Each V ion has six neighboring ones. MgV_2O_4 possesses highly coupled spin, lattice, and orbital degrees of freedom and a distortion from spinel at room temperature (space group $F\bar{4}3m$), which allows for a greater trigonal distortion of the VO_6 octahedra and a low-temperature space group ($I\bar{4}m2$) that maintains the mirror plane symmetry.

In one study of this compound, a unique report of the frustrated spinel, MgV_2O_4, (which possesses highly coupled spin, lattice and orbital degrees of freedom) was presented. Using large single-crystal and powder samples, a distortion from spinel at room temperature (space group *F*-43*m*), which allows for a greater trigonal distortion of the VO_6 octahedra and a low-temperature space group (*I*-4*m*2) that maintains the mirror plane symmetry was discovered.

The magnetic structure that develops below 42 K consists of antiferromagnetic (AFM) chains with a strongly reduced moment while inelastic neutron scattering reveals one-dimensional behavior and a single band of excitations. The implications of these results were discussed in terms of various orbital ordering scenarios. It was concluded that although spin-orbit coupling must be significant to maintain the mirror plane symmetry, the trigonal distortion is large enough to mix the 3d levels leading to a wave function of mixed real and complex orbitals as shown in Fig. 9.9.

The electronic configuration of V^{3+} is $3d^2$, leading to a single-ion spin $S = 1$. Each V^{3+} ion is located at the center of edge sharing VO_6 octahedra which creates a crystal field that splits the d-orbitals and lowers the energy of the three-t_{2g} orbitals by approximately 2:5 eV. These levels are usually assumed to be degenerated (ignoring the small trigonal distortion) so that the two d-electrons of V^{3+} randomly occupy the three-t_{2g} orbitals, thereby introducing an orbital degree of freedom. This class of compounds undergoes a structural transition (TS) from cubic to tetragonal, which partially lifts the orbital degeneracy. A magnetic transition to long-rangeAFM order occurs at a lower temperature (T_N).

The magnetic properties MgV_2O_4 and $Mg(V_{0.85}Al_{0.15})_2O_4$ were also studied. Both compounds are normal cubic spinels having a highly frustrated magnetic lattice. Around $T_2 = 65$ K, MgV_2O_4 has a magnetic order associated with the cubic-tetragonal transition. Below T_2, the susceptibility shows complex behavior. In $Mg(V_{0.85}Al_{0.15})_2O_4$, the spin-glasslike state appears. The ^{51}V-Knight shift of MgV_2O_4 has anomalous temperature dependence. MgV_2O_4 occurs as a mineral called "Magnesiumcoulsonite".

In the V^{4+} system of MgO–VO_2, the compound, $MgVO_3$ has been studied. Its structure is shown in Fig. 9.10.

Cell parameters are: $a = 5.239$ Å, $b = 5.291$ Å, $c = 5.665$ Å, $\alpha = 117.84°$, $\beta = \gamma = 90°$, cell volume = 138.85 Å^3, $Z = 4$. Cell occupancy is shown in Table 9.5.

The magnetic susceptibility and the electron spin resonance in the X-band of the transition metal oxide

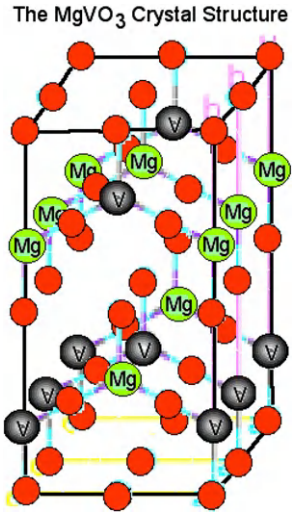

FIGURE 9.10

compound $MgVO_3$ showed that this compound, made of weakly coupled infinite chains of VO_5 pyramids, behaves as a $S = 1/2$ one-dimensional Heisenberg AFM.

In the V^{4+} system of MgO–VO_2, two phases have been investigated at 900 °C. $MgVO_3$ crystallizes in the orthorhombic system, space group $Cmc2_1$, with $a = 5.243$ Å, $b = 10.028$ Å, and $c = 5.290$ Å. The structure is built up from square pyramids VO_5 and MgO_5 sharing edges and forming sheets connected through oxygen atoms. Its structure is related to the ReO_3 and Mg_2NF structures. MgV_2O_5 is orthorhombic with $a = 3.696$ Å, $b = 9.965$ Å, and $c = 11.019$ Å, the space group is $Cmc2_1$, $Cmcm$, or $C2cm$.

The preparation of a high-pressure form of $MgVO_3$ has been accomplished utilizing two independent synthesis methods. The triclinic, ilmenite-type phase has been characterized by its crystallographic, magnetic, and electrical properties. Its structure is believed to be similar to that previously observed for other ilmenite-type AVO_3 derivatives ($CoVO_3$, $NiVO_3$, and $MnVO_3$). The properties of $MgVO_3$ appear to be intermediate between the localized electron model found in $MnVO_3$, $CoVO_3$, and $NiVO_3$, and the delocalized electron regime observed in $CuVO_3$. Related structures, ilmenite and perovskite type $Mg^{2+}V^{4+}O_3$ were newly synthesized at high pressures and high temperatures. The low-pressure form of $MgVO_3$ I is supposed to have a triclinic symmetry and to be isomorphous with the vanadate type of ilmenites $MnVO_3$ I and $CuVO_3$ I. Unit cell dimensions determined were: $a = 5.072$ Å, $b = 5.550$ Å, $c = 5.023$ Å, $\alpha = 90°0'$, $\beta = 118°38$, $\gamma = 63°4$ and $V = 106.3$ Å^3. The high-pressure form of $MgVO_3$ II, stabilized above about 45 kbar, has the orthorhombic perovskite structure with the possible space group of D_{2h}^{16}-$Pbnm$ or C_{2v}^{9}-$Pbn2_1$. Unit cell dimensions were $a = 5.106$ Å, $b = 5.265$ Å, $c = 7.387$ Å and $V = 198.6$ Å^3. It was stated that $MgVO_3$ II is the first perovskite containing Mg^{2+} ions in the larger cationic sites in the ilmenite structure.

In another study, the magnetic susceptibility and the electron spin resonance in the X-band of the transition metal oxide compound $MgVO_3$ was reported. This compound, made of weakly coupled infinite chains of VO_5 pyramids, behaves as an $S = 1/2$ one-dimensional Heisenberg AFM. From the ESR and magnetic experiments it was deduced that the Néel temperature K, the in-chain coupling constant K and the g-factor values $gx = gz = 1.972(2)$, $gy = 1.946(1)$ for V^{4+} ions in $MgVO_3$.

Powder samples of MgV_2O_5, which has a structure similar to the spin ladder compound CaV_2O_5, were synthesized and the magnetic properties were investigated. The magnetic susceptibility shows a broad maximum around 100 K and below about 15 K, it decreases more rapidly with decreasing temperature. The magnetization curves in high fields up to 17 T at 1.5 K and 30 T at 1.7 K show a change of slope around $H_c \sim 12.5$ T, which can be considered to be a transition from a singlet ground state to a gapless magnetic state. The excitation gap Δ was evaluated as $\Delta/k_B \sim 17$ K in agreement with the energy gap of about 2 meV from the inelastic neutron scattering. The results strongly suggest that MgV_2O_5 is a spin ladder system with a spin gap. Magnetic-susceptibility measurements on MgV_2O_5, a compound in which the vanadium oxide planes has the same topology as in CaV_2O_5. The most striking property is that there is an energy gap of about

TABLE 9.5

No	Site notation	Atom	Multiplicity	Wyckoff	Site symmetry	x	y	z	Occupancy
1	O(1)	O	8	m	..2	1/4	1/4	0.248	1.0
2	Mg	Mg	4	j	m2m	0	0.3113	1/2	1.0
3	V	V	4	i	m2m	0	0.1737	0	1.0
4	O(3)	O	2	c	mmm	1/2	0	1/2	1.0
5	O(2)	O	2	a	mmm	0	0	0	1.0

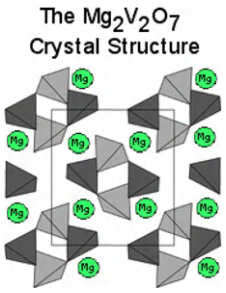

FIGURE 9.11

15 K, much smaller than in CaV_2O_5, where the values reported are of the order of 500 K. It was shown that this might be understood naturally in terms of the phase diagram of the frustrated coupled ladder system. This analysis led to the prediction that MgV_2O_5 should have incommensurate dynamic spin fluctuations. The compound, MgV_3O_7, is not known.

The liquidus–solidus regions of the V^{5+} system MgO–V_2O_5 were investigated over the entire composition range, with the following principal findings: There are two congruently melting compounds: $2MgO \cdot V_2O_5$ melting at 1128 °C, and $3MgO \cdot V_2O_5$ melting at 1210 °C. A third compound, $MgO \cdot V_2O_5$, is thought to have an incongruent melting point at 762 °C. There are three eutectics: one at approximately 15 mol% V_2O_5 melting at 1192 °C, one at approximately 30 mol% V_2O_5 melting at 1122 °C, and one at approximately 75 mol% V_2O_5 melting at 658 °C. These compounds are sometimes called "metavanadate = MgV_2O_6", "pyrovanadate = $Mg_2V_2O_7$" and "orthovanadate = $Mg_3(VO_4)_2$".

The crystal structure of the low-temperature form of magnesium pyrovanadate (α-$Mg_2V_2O_7$) has been determined from synchrotron powder XRD data using Rietveld refinement as shown in Fig. 9.11.

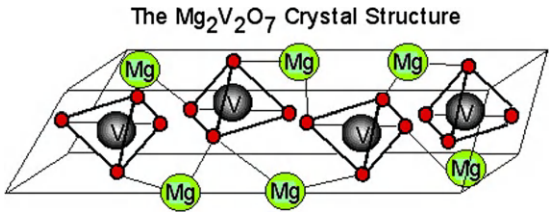

FIGURE 9.12

α-$Mg_2V_2O_7$, grown from a melt of MgO and V_2O_5, is triclinic with space group = $P1$. Another view of this structure is shown in Fig. 9.12.

Cell parameters are: $a = 13.767$ Å, $b = 5.414$ Å, $c = 4.912$ Å, $\alpha = 81.42°$, $\beta = 106.83°$, $\gamma = 130.33°$, $Z = 2$. The structure has chains of $V_2O_7^{4-}$-groups with long V–O bridges between these groups. The average terminal V–O bond length is 1.694 Å. Cell occupancy is shown in Table 9.6.

α-$Mg_2V_2O_7$ is isostructural with $Co_2V_2O_7$ and $Ni_2V_2O_7$. The Mg^{2+} ions are octahedrally coordinated to oxygen atoms in a distorted arrangement while the pyrovanadate anion has an approximately eclipsed conformation of non-bridging oxygen atoms. The ^{51}V MAS NMR spectra of the central and satellite transitions for the two distinct ^{51}V sites in α-$Mg_2V_2O_7$ allow determination of the magnitudes and relative orientations of the ^{51}V quadrupole coupling and chemical shift tensors. The crystal structure data are used to calculate the principal elements of the ^{51}V electric field gradient tensors employing the point-monopole approach. A good correlation between these elements and the experimental ^{51}V quadrupole tensor elements is observed, which allows assignment of the quadrupole coupling constants of $C_Q = 4.80$ MHz and $C_Q = 3.33$ MHz to the crystallographic V(1) and V(2) sites, respectively.

TABLE 9.6

No	Site notation	Atom	Multiplicity	Wyckoff	Site symmetry	x	y	z	Occupancy
1	Mg1	Mg	2	i	1	0.0095	0.2907	0.5837	1.0
2	Mg2	Mg	2	i	1	0.0771	0.2850	0.0831	1.0
3	O6	O	2	i	1	0.1364	0.4507	0.2877	1.0
4	O4	O	2	i	1	0.1956	0.0772	0.4334	1.0
5	O7	O	2	i	1	0.2109	0.053	0.9386	1.0
6	O5	O	2	i	1	0.2648	0.6137	0.0412	1.0
7	O2	O	2	i	1	0.2911	0.583	0.5477	1.0
8	O3	O	2	i	1	0.3135	0.2591	0.7349	1.0
9	V2	V	2	i	1	0.3593	0.286	0.3614	1.0
10	O1	O	2	i	1	0.3945	0.1186	0.2075	1.0
11	V1	V	2	i	1	0.4629	0.1511	0.8606	1.0

The formation process and microwave dielectric properties of the $Mg_2V_2O_7$ ceramics have been investigated. The MgV_2O_6 phase that was formed at around 450 °C interacted with remnant MgO above 590 °C to form a homogeneous monoclinic $Mg_2V_2O_7$ phase. Finally, this monoclinic $Mg_2V_2O_7$ phase was changed to a triclinic $Mg_2V_2O_7$ phase for the specimen fired at 800 °C. Sintering at 950 °C for more than 5 h produced high-density triclinic $Mg_2V_2O_7$ ceramics. In particular, the $Mg_2V_2O_7$ ceramics sintered at 950 °C for 10 h exhibited good microwave dielectric properties of $\varepsilon_r = 10.5$, $Q \times f = 58\ 275$ GHz, and $\tau_f = -26.9$ ppm/°C. Thus, it was concluded that magnesium pyrovanadate is trimorphic.

Propene is an important chemical that can be used to produce polypropylene, acrolein, acrylic acid, propylene oxide, etc. The oxidative dehydrogenation of propane (ODP) to propene is being intensively investigated to produce olefins. The ODP reaction is an exothermic process favored by thermodynamics. Among these catalysts, the V–Mg–O catalyst system is one of the most important. The catalytic oxidation of ethane, propane, 2-methylpropane, butane, pentane, and cyclohexane has been studied using $Mg_3(VO_4)_2$–MgO, $Mg_2V_2O_7$, and $(VO)_2P_2O_7$ as catalysts. These reactions produced a wide range of products ranging from alkenes, dienes, anhydrides, acids, and carbon oxides. Broadly speaking, the major products were dehydrogenation products over $Mg_3(VO_4)_2$, combustion products over $Mg_2V_2O_7$, and oxygen-containing organic products over $(VO)_2P_2O_7$, although there are exceptions to this broad generalization. From the product selectivity, the moles of oxygen consumed per mole of alkane reacted could be calculated. These were the average oxygen stoichiometries for the reactions. They had values of about unity for ethane oxidation over VPO, about two when oxidative dehydrogenation was the predominant reaction, and about four for the other reactions studied. The selectivity patterns in terms of the formation of dehydrogenation products versus oxygen-containing products including carbon oxides were explained by assuming that there existed a selectivity-determining step, which could be the reaction of the surface alkyl species or the adsorbed alkene before its desorption. The formation of oxygen-containing products would be facilitated if the surface alkyl or adsorbed alkene could interact with the vanadium ions in two adjacent VO_x units such that it could easily react with the reactive oxygen in the V–O–V bridge. The results of ethane oxidation, however, could not be explained simply by this model, and other factors, not elucidated, were considered to be affective.

In another paper, the three meta-, pyro-, and ortho-magnesium vanadate phases were synthesized, characterized, and tested as catalysts in the oxy-dehydrogenation of propane. *In situ* electrical conductivity measurements have clearly indicated that these solids behave as intrinsic semiconductors in oxygen at the reaction temperature (520 °C), with band gap energies equal to twice the corresponding activation energies of conduction, in good agreement with the values determined by UV–visible spectroscopy. In the presence of propane, the electrical conductivity of the samples increased instantaneously at a variation rate and to an extent which both changed in the following order: pyro-$Mg_2V_2O_7$ > meta-MgV_2O_6 > ortho-$Mg_3V_2O_8$. The increase in conductivity observed has been attributed to the consumption of surface lattice oxygen anions by propane, leading to the formation of propene, water, and ionized anionic vacancies. The existence of these vacancies were supported by the study of their filling, using either dioxygen, O_2 or nitric oxide, NO, as sources of dissociated oxygen species. It was proposed that pure magnesium vanadates act as redox relays in the oxy-dehydrogenation of propane according to the Mars and van Krevelen mechanism. The higher catalytic activity of pyrovanadate, $Mg_2V_2O_7$, was directly connected with the lability of its surface O^{2-} ions, as detected by conductivity. The high reoxidation rate implied that the solids are working in a surface state close to stoichiometry, i.e. close to the oxidized state. This could explain why the reaction kinetic order with respect to oxygen was equal to zero. The electrical properties of the three V–Mg–O phases could explain why pyrovanadate $Mg_2V_2O_7$ was the most active and the most selective phase for oxidative dehydrogenation of propane into propene.

In another paper, periodic oscillations of oxygen activity of a $Mg_2V_2O_7$ catalyst during the oxidative dehydrogenation of propane were investigated by solid electrolyte potentiometry (SEP). Among the catalysts tested, $Mg_3(VO_4)_2$, prepared with a (Mg + V)/citric acid molar ratio of 1:1.2 and calcined at 823 K for 6 h, exhibited the best catalytic performance and had an excellent thermal stability. The catalytic active-phase was identified as containing $Mg_3(VO_4)_2$, $Mg_2V_2O_7$ and MgV_2O_6 as pure magnesium vanadates. The results of characterization and evaluation showed that $Mg_2V_2O_7$ had the isolated active sites, weakly basic surface and best reducibility of these compositions, and could be recognized as the catalytic active phase.

In another study, two pure magnesium vanadate phases, $Mg_2V_2O_7$ and $Mg_3V_2O_8$, were prepared and tested in the dehydrogenation of n-pentane in the presence of oxygen. Both magnesium vanadates are effective catalysts, with $Mg_3V_2O_8$ exhibiting higher selectivity to form dehydrogenation products. Testing of mechanical mixtures, consisting of each one of the magnesium vanadates and antimony oxides, indicated that the latter had a positive effect especially on the selectivity to dehydrogenation with the $Mg_3V_2O_8$ containing samples. The main products of the reaction were pentenes,

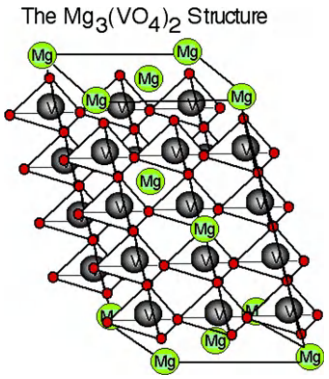

FIGURE 9.13

pentadienes and carbon oxides. Characterization of the samples prior to and after catalytic tests revealed that all catalysts remained practically unchanged during the reaction. The mixtures consisted of separate magnesium vanadate and antimony oxide phases and no formation of new phases was detected. The study of oxidative dehydrogenation of propane was carried out over V–Mg–O catalysts. The citrate method was used to prepare catalysts with the Mg/V atomic ratio varying from 1/4 to 9/1. Three pure Mg vanadates and the corresponding biphasic catalysts were obtained from very homogeneous Mg–V–citrate precursors after calcination at 550 °C.

Among the three pure Mg vanadates, α-$Mg_2V_2O_7$ (pyrovanadate) was found to be the most selective, while MgV_2O_6 (metavanadate) was the worst one. Interestingly, the catalytic behavior of biphasic catalysts is quite different from that of pure Mg vanadate phases. For example, the selectivity of $Mg_3V_2O_8$ (orthovanadate) can be promoted by a coexisting pyrovanadate phase or excess magnesium oxide in intimate contact. These differences were discussed in terms of the different specific activities of phases and possible synergy effects between the phases.

An unusual MgV_2O_6 phase having a Brannerite ($ThTi_2O_6$) related structure was obtained by solid-state reaction and its powder XRD and thermal studies were discussed. Those studies confirmed a structural transition at 833 K (560 °C) for non-stoichiometric magnesium metavanadate.

Magnesium ortho-vanadate has the structure shown in Fig. 9.13.

Cell Parameters are: $a = 6.953$ Å, $b = 11.428$ Å, $c = 8.318$ Å, $\alpha = \beta = \gamma = 80°$, $Z = 57.54$ Å^3. Cell occupancy is shown in Table 9.7.

Reduction of polycrystalline and crystalline magnesium orthovanadate $Mg_3V_2O_8$ by hydrogen was investigated in the temperature range of 560–920 °C. A single crystal of orthorhombic $Mg_3V_2O_8$ with a cation-deficient-spinel structure (25% of the magnesium atoms on octahedral sites are vacant) was transformed into cubic $Mg_3V_2O_6$ which has a cation-stuffed-spinel structure (8*a* and 16*c* sites were partially occupied by magnesium and 16d sites were fully occupied by magnesium and vanadium) at 560 °C in 7% H_2 in N_2. This cubic phase, $Mg_3(VO_3)_2$, has the space group $Fd3m/2$ and the cell parameters of: $a = b = c = 8.409$ Å, $\alpha = \beta = \gamma = 90°$, cell volume = 594.61 Å^3.

Single-crystals of the polar compound, magnesium hydrogen vanadate(V), $Mg_{13.4}(OH)_6(HVO_4)_2(H_{0.2}VO_4)_6$, were synthesized hydrothermally. It represents the first hydrogen vanadate(V) among inorganic compounds. Its structure was determined by single-crystal XRD [space group $P\ 6_3mc$, $a = 12.9096(2)$, $c = 5.0755(1)$ Å, $V = 732.55(2)$ Å, $Z = 1$]. The crystal structure of $Mg_{13.4}(OH)_6(HVO_4)_2(H_{0.2}VO_4)_6$ consists of well separated, vacancy-interrupted chains of face sharing Mg_2O_6 octahedra, with short Mg_2–Mg_2 distances of 2.537(1) Å, embedded in a porous magnesium vanadate 3D framework having the topology of the zeolite, "Cancrinite". All three hydrogen positions in the structure were confirmed by FTIR spectroscopy.

Magnesium vanadate is offered for sale as the metavanadate composition. Its CAS number is 210909-46-9.

9.1.3. Calcium Vanadium Compounds

The metal, Ca^0, does not form any intermetallic compounds with V^0. The system, CaO–V_2O_5, forms

TABLE 9.7

No	Site notation	Atom	Multiplicity	Wyckoff	Site symmetry	*x*	*y*	*z*	Occupancy
1	O1	O	16	g	1	0.263	0.121	0.005	1.0
2	O2	O	8	f	m..	0	0.001	0.241	1.0
3	O3	O	8	f	m..	0	0.249	0.233	1.0
4	V1	V	8	f	m..	0	0.376	0.12	1.0
5	Mg1	Mg	8	e	.2.	1/4	0.131	1/4	1.0
6	Mg2	Mg	4	a	2/m..	0	0	0	1.0

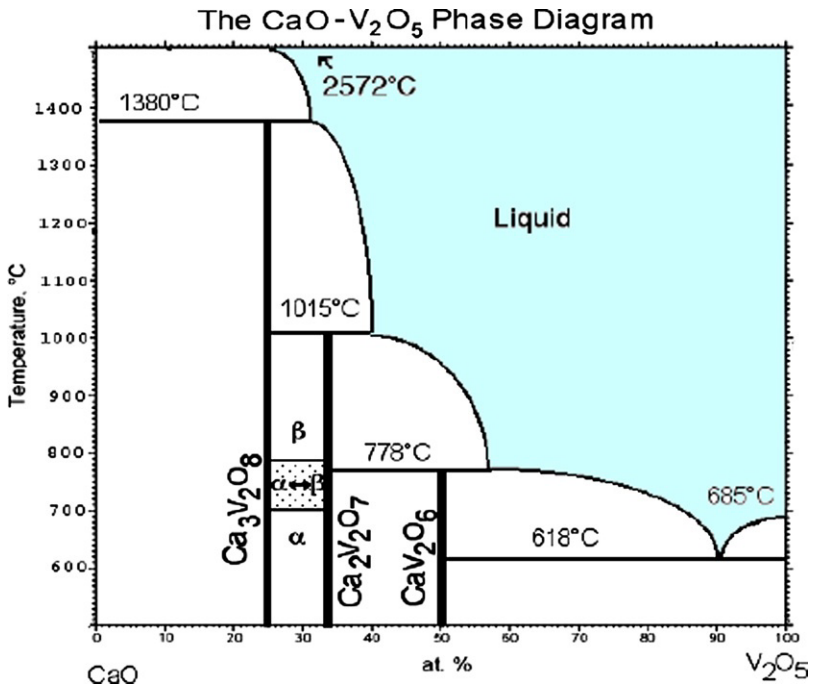

FIGURE 9.14

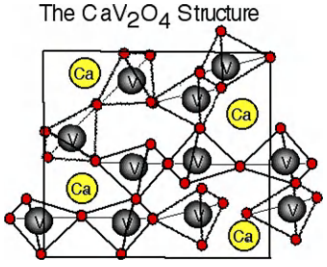

FIGURE 9.15

a series of compounds. The only published phase diagram shows the meta-, pyro- and ortho-vanadate compositions as shown in Fig. 9.14.

However, other compositions have been reported. All three compounds shown in the phase diagram melt incongruently.

In the V^{2+} system of CaO–VO, the compound, $CaVO_2$ is unknown, as is Ca_2VO_3 and Ca_3VO_4.

In the V^{3+} system of CaO–V_2O_3, the compound, CaV_2O_4 has the structure shown on the next page. The lattice parameters are: $a = 6.053$ Å, $b = 6.466$ Å, $c = 8.318$ Å, $\alpha = \beta = 90°$, $\gamma = 83.18°$, cell volume $= 287.69$ Å^3 as shown in Fig. 9.15.

Cell occupancy is shown in Table 9.8.

In the V^{4+} system of CaO–VO_2, the compound, $CaVO_3$ is known to be dimorphic. In the $3d(t2g)^1$ perovskites series, $SrVO_3$–$CaVO_3$–$LaTiO_3$–$YTiO_3$, the transition-metal *d* electron becomes increasingly localized and undergoes a Mott transition between $CaVO_3$ and $LaTiO_3$. By defining a low-energy Hubbard Hamiltonian in the basis of Wannier functions for the *t2g* LDA band and solving it in the single-site dynamical mean-field

TABLE 9.8

No	Site notation	Atom	Multiplicity	Wyckoff	Site symmetry	*x*	*y*	*z*	Occupancy
1	O4	O	4	c	.m.	0.063	1/4	0.087	1.0
2	V2	V	4	c	.m.	0.072	1/4	0.395	1.0
3	Ca	Ca	4	c	.m.	0.241	1/4	0.654	1.0
4	O1	O	4	c	.m.	0.291	1/4	0.355	1.0
5	O2	O	4	c	.m.	0.383	1/4	0.0	1.0
6	O3	O	4	c	.m.	0.47	1/4	0.775	1.0
7	V1	V	4	c	.m.	0.572	1/4	0.605	1.0

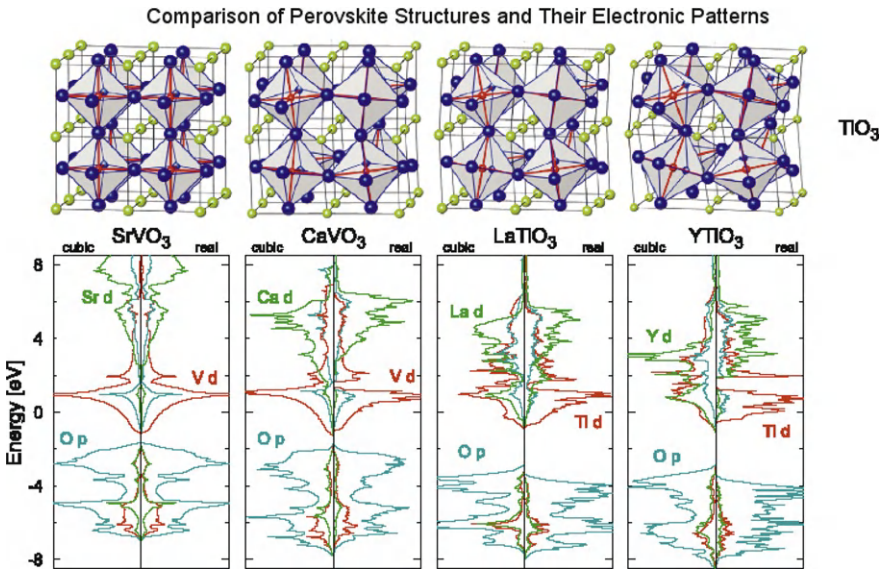

FIGURE 9.16

(DMFT) approximation, it has been shown that together with the Mott transition there occurs a strong suppression of orbital fluctuations due to splitting of the *t*2*g* levels.

A comparison of structures including $CaVO_3$ is shown in the diagram: Fig. 9.16.

A stoichiometric calcium vanadium (IV) oxide with formula $CaVO_3$ has been prepared by soft-chemistry procedures, followed by annealing under reducing conditions (H_2/N_2 flow). This material has been studied by XRD and neutron powder diffraction (NPD), thermal analysis, magnetic and magneto-transport measurements. $CaVO_{3.0}$ perovskite crystallizes in the orthorhombic *Pbnm* (No. 57) space group, with the $GdFeO_3$-type structure. The unit-cell parameters are $a = 5.3219$ Å, $b = 5.3427$ Å and $c = 7.5472$ Å. In this distorted perovskite the VO_6 octahedra are tilted by 10.1° in order to optimize the Ca–O bond-lengths. A bond valence study from NPD data confirms the tetravalent oxidation state for V cations. The perovskite is fully oxygen stoichiometric, as demonstrated from thermal analysis and the refinement of the oxygen occupancy factors. The magnetic susceptibility is predominantly Pauli paramagnetic-like, although a non-negligible temperature-dependent component due to isolated V^{4+} spins is patent at low temperatures. The transport measurements show a metallic behavior between 2 and 300 K; at low temperatures a positive magneto-resistance as large as 14% for $H = 9$ T is interpreted as the result of quantum interference effects.

Four vanadates (IV) have been synthesized by solid-state reactions and characterized in the $CaO–VO_2$ systems as: $CaVO_3$, CaV_2O_5, CaV_3O_7, and CaV_4O_9 (1:1, 1:2, 1:3, 1:4). Structural data have been given. The structural evolution of the series CaV_nO_{2n+1} is described as follows. As n increases from $n = 1$ to $n = 4$, the vanadium +4 compounds show only a five-fold square pyramid coordination. As the Ca/V ratio increases, the Ca_2VO_4 and Ca_3VO_4 compounds can be formed. A chemical potential diagram of the V–Ca–O system was constructed. A V–Ca–O catalyst used in the oxidative dehydrogenation of n-butane was prepared by the impregnation method and was characterized by in-situ XRD. $Ca_3V_2O_8$ and CaO were detected on the in-situ XRD pattern under the oxygen pretreatment at 600 °C, and the XRD measurements under working conditions showed that $Ca_3V_2O_8$ is reduced to CaV_2O_4, having a cubic spinel structure with a lattice constant of $a = 8.427$ Å. The observed reduction of V^{5+} in $Ca_3V_2O_8$ to V^{3+} in CaV_2O_4 under the working conditions were well characterized through the use of the chemical potential diagram.

Among perovskite-type light-3d oxides, $CaVO_3$ has attracted considerable attention because of its metallic conductivity. This behavior is opposed to the insulating one observed in $LaTiO_3$. It was reported for $CaVO_3$ that oxygen defects induced insulating conductivity, while oxygen excess induced metallic conductivity. Another important point concerning CaVO3 is that the magneto-resistance is positive in the stoichiometric samples and is negative in non-stoichiometric samples. In addition, there has been no report on the anisotropic properties of $CaVO_3$. The magnetic properties of perovskite $CaVO_3$ single crystals have been studied by means of magneto-resistance $p(T, H)$ and magnetization $M(H)$ measurements in fields up to 18 T. At 2 K, the magneto-resistance is positive and a maximum value of $\Delta p((18\text{ T})/p_0) = 16.5\%$ is found for $H//a$. The

magnetization exhibits a smooth increase at 2 K, reaching values of $M(18\ \mathrm{T}) = 0.03, 0.05, 0.17\ \mu\mathrm{B/f.u.}$ for $H//a$, $H//b$, and $H//c$, respectively. This anisotropy found in $M(H)$ is consistent with that observed for $\Delta p(H//a) > \Delta p(H//b) > \Delta p(H//c)$. These results can be interpreted in terms of the field-dependent scattering mechanism of $CaVO_3$.

Non-stoichiometric $CaVO_{3-\delta}$ with a well-controlled oxygen content was synthesized at a $\delta = 0.01$ step by reducing stoichiometric $CaVO_{3.00}$ using a Zr sheet. The relations between oxygen deficiency and structure were investigated. Three new phases, phase A ($0.04 < \delta < 0.08$), phase B ($\delta = 0.14$), and phase C ($\delta = 0.2$), appear in the sequence of δ's. Each phase has a vacancy-ordered structure with a much larger unit cell than the primitive one. These oxygen-deficient phases are unstable in air at room temperature and are easily oxidized to stoichiometric $CaVO_{3.00}$. All of the phases are metallic but magnetic susceptibilities of phases B and C with high oxygen deficiencies show Curie–Weiss behaviors, while stoichiometric $CaVO_{3.00}$ and phase A are Pauli paramagnets. In phases B and C there exist at least two distinct V sites in electronic state, that is, localized V sites with $S^{=}$ and itinerant V sites. There are two structures in the photoemission spectra of $CaVO_{3-\delta}$ and $SrVO_{3-\delta\delta}$ in the d-band region. One peak is within ~1 eV of the Fermi level and has a sharp Fermi cutoff. The other is a broad peak centered at ~1.6 eV. From our photoemission spectra of $CaVO_{3-\delta}$ and $SrVO_{3-\delta}$ both with oxygen vacancies ($\delta = \sim 0.1$) and without vacancies ($\delta = 0$), it is shown that the relative intensity of the peak near the Fermi level for $CaVO_{3=\delta}$ drastically decreases with decreasing oxygen vacancy concentration (δ). In contrast, no such drastic change in intensity is observed for $SrVO_{3-\delta}$. This difference in the effect of oxygen vacancies between $SrVO_{3-\delta}$ and $CaVO_{3-\delta}$ reflects the fact that a metal-insulator phase transition induced by bulk oxygen vacancies takes place in $CaVO_{3-\delta}$ but not in $SrVO_{3-\delta}$.

Cavoite, CaV_3O_7 occurs at the Gambatesa mine (Liguria, Italy) filling micro-cavities in massive bands of caryopilite + calcium rhodochrosite and quartz. Cavoite has been found as very rare radiated-aggregates of strongly elongated prismatic to acicular crystals. The crystals vary in color from colorless to olive green-brown. The powder-diffraction data give the refined cell parameters $a = 10.42$ Å, $b = 5.28$ Å, $c = 10.34$ Å and $V = 568.2$ Å^3 in the space group *Pnam*. Cavoite is the natural analog of the synthetic CaV_3O_7, whose structural study is reported in literature together with that of the isostructural phases SrV_3O_7 and CdV_3O_7. A discontinuous change of muon-spin precession frequencies in CaV_3O_7 is observed at $T \sim 0.2$ K, indicating a possible spin reorientation. These results suggest that CaV_3O_7 possesses the identical spin direction as isostructural

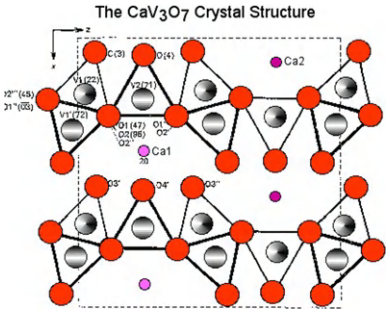

FIGURE 9.17

SrV_3O_7 below ~0.2 K, although the spin directions in the two compounds are different at higher temperatures as determined by elastic neutron scattering. The structure of CaV_3O_7 is shown as Fig. 9.17.

The layered vanadates, CaV_2O_5, MgV_2O_5, CaV_3O_7, and CaV_4O_9, have been thoroughly studied. The uniform susceptibility of the Heisenberg model with these exchange couplings was calculated by the quantum Monte Carlo method; it agrees well with the experimental measurements. These results were stated to naturally explain the unusual magnetic properties of these materials, especially the huge difference in spin gap between CaV_2O_5 and MgV_2O_5, the unusual long range order in CaV_3O_7, and the "plaquette resonating valence bond" spin gap in CaV_4O_9. Muon spin relaxation measurements of CaV_4O_9, CaV_3O_7 and CaV_2O_5 have been made. The sub-lattice magnetization in the AFM state of CaV_3O_7 agrees well with spin wave theory. In CaV_4O_9 and CaV_2O_5, it was observed that spin-freezing occurred below 15 and 50 K, respectively, which indicates that a substantial fraction of the vanadium magnetic moment is not in a spin-singlet state at low temperatures in either materials.

In the $CaO–V_2O_5$ system containing V^{5+}, CaV_2O_6, has the structure shown in Fig. 9.18.

The VO_4 tetrahedra form a series of chains along the a-axis of the unit cell. The unit cell parameters are: $a = 3.671$ Å, $b = 5.3502$ Å, $c = 7.025$ Å, $\alpha = 103.32°$, $\beta = 90°$, $\gamma = 110.06°$, cell volume $= 125.64$ Å^3. In another

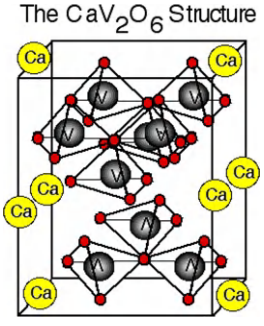

FIGURE 9.18

TABLE 9.9

No	Site notation	Atom	Multiplicity	Wyckoff	Site symmetry	x	y	z	Occupancy
1	O1	O	4	i	m	0.1434	0	0.1182	1.0
2	O2	O	4	i	m	0.2535	0	0.6066	1.0
3	V1	V	4	i	m	0.2658	0	0.3309	1.0
4	O3	O	4	i	m	0.4126	0	0.2781	1.0
5	Ca1	Ca	2	b	2/m	0	1/2	0	1.0

study, MgV_2O_6 was found to crystallize in the monoclinic space group $C2/m$ with lattice parameters $a = 9.279$ Å, $b = 3.502$ Å, $c = 6.731$ Å and $\beta = 111.77°$ with $Z = 2$. The structure was refined, at room temperature, utilizing 593 symmetry independent reflections, by full matrix least squares to a final R-value of 0.032.

The structure consists of Ca^{2+} lying at a site of $2/m$ symmetry octahedrally coordinated to oxygen atoms with a mean separation of 2.140 Å. All the remaining atoms lie in crystallographic mirror planes with the V ion coordinated to six oxygen atoms with bond distances ranging from 1.666 to 2.671 Å. Site occupancy in the unit cell is shown in Table 9.9.

The crystal structure of a high-pressure modification of calcium divanadium (V^{+5}) hexoxide, CaV_2O_6, was refined from X-ray single-crystal data. It contains zigzag chains of corner-sharing VO_4 tetrahedra. Tetrahedra in adjacent chains share corners and form corrugated layers. Tetrahedrally coordinated Ca atoms, which lie on two-fold axes, are situated between the layers. The columbite-like structure results in a strong distortion of the CaO_6 octahedra, which may be stabilized only at high pressure.

If the metavanadate compound, CaV_2O_6, is heated in a hydrogen atmosphere, a loss of oxygen occurs:

$$CaV_2O_6 + 2H_2 \Rightarrow CaV_2O_4 + 2H_2O$$

However, instead of the formation of $O^{=}$ vacancies to form $CaV_2O_{6-\delta}$, a change in the valence state from V^{5+} to V^{3+} occurs. This results in a "vanadite" compound that is stoichiometric and has the formula of CaV_2O_4. Another V^{5+} containing composition, the ortho-vanadate, $Ca_3(VO_4)_2$ has the structure as shown in Fig. 9.19.

Unit-cell parameters are: $a = b = 10.817$ Å, $c = 59.36$ Å, $\alpha = \beta = 67.492°$, $\gamma = 60°$, cell volume $= 1284.20$ Å^3. The crystal structure of $Ca_3(VO_4)_2$ is rhombohedral with space group $R3c$ and with equivalent hexagonal axis lengths of $a = 10.809(1)$ and $c = 38.028(9)$ Å. The rhombohedral cell contains seven formula units. Cell occupancy is shown in Table 9.10.

It is isomorphous with $Ca_3(AsO_4)_2$. The structure was refined by full-matrix least squares utilizing 1252 symmetry-independent reflections to a final R-value of 0.049. One formula unit lies on the three-fold axis with one of the calcium-ion sites on this axis half-occupied and another site octahedrally coordinated to oxygen atoms. The remaining calcium ions are coordinated to 8, 7 and 8 oxygen atoms with Ca–O bond lengths of 2.525, 2.442 and 2.570 Å respectively. The mean V–O bond length for the three crystallographically independent VO_4 groups are within 0.01 Å of 1.69 Å. The structure is related to that of $Ba_3(VO_4)_2$ but with a formula-unit density 7/8 as large, due to the loss of one formula unit per cell from chains along the threefold axis. This change in structure follows from the smaller average cation-oxygen bond length in the calcium salt. R-values as low as 0.041 can be obtained with models that allow for differences in the environment of the half-occupied cation site, presumably dependent upon whether it is filled or empty.

A novel polymorph of calcium orthovanadate $Ca_3(VO_4)_2$ was synthesized at 11 GPa and 1373 K and

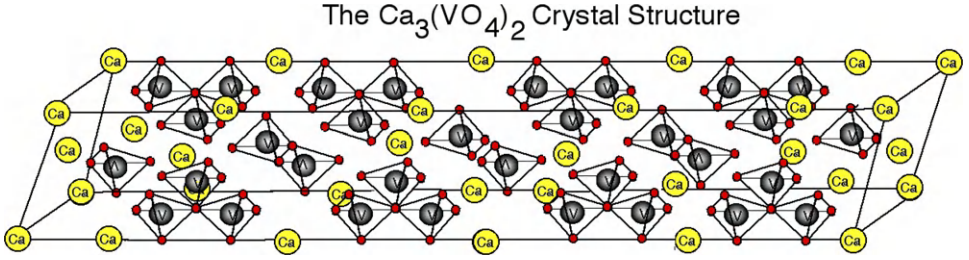

FIGURE 9.19

TABLE 9.10

No	Site notation	Atom	Multiplicity	Wyckoff	Site symmetry	x	y	z	Occupancy
1	O1	O	18	b	1	0.0503	0.3887	0.0547	1.0
2	O2	O	18	b	1	0.0903	0.1797	0.0397	1.0
3	O3	O	18	b	1	0.1373	0.2827	0.1787	1.0
4	V1	V	18	b	1	0.1373	0.3189	0.1346	1.0
5	O4	O	18	b	1	0.151	0.003	0.248	1.0
6	V2	V	18	b	1	0.1619	0.3571	0.0322	1.0
7	O5	O	18	b	1	0.174	0.077	0.455	1.0
8	O6	O	18	b	1	0.2183	0.2367	0.1147	1.0
9	O7	O	18	b	1	0.227	0.219	0.379	1.0
10	O8	O	18	b	1	0.27	0.077	0.325	1.0
11	Ca1	Ca	18	b	1	0.2702	0.1501	0.1741	1.0
12	Ca2	Ca	18	b	1	0.274	0.1391	0.0688	1.0
13	O9	O	18	b	1	0.2953	0.0347	0.1247	1.0
14	Ca3	Ca	18	b	1	0.3827	0.1753	0.2675	1.0
15	Ca4	Ca	6	a	3.	0	0	0.0	1.0
16	O10	O	6	a	3.	0	0	0.19	1.0
17	V3	V	6	a	3.	0	0	0.233	1.0
18	Ca5	Ca	6	a	3.	0	0	0.316	0.50

recovered to ambient conditions. It crystallizes in a monoclinic cell (space group $C2/m$, $Z=2$) with $a=9.6715(2)$, $b=5.43276(7)$, $c=7.0713(1)$ Å, $\beta=116.949(1)^\circ$. The crystal structure was solved by ab initio methods from powder XRD data using direct categorization. The oxygen atoms form a hexagonal close packing. The VO_4^{3-} tetrahedra are radially and angularly distorted. The two crystallographically independent Ca atoms are in deformed octahedral and 10-fold coordinations. Unlike in the palmierite-derived parent $Ba_3(VO_4)_2$ (Rm, $Z=1$) and $Ca_3(VO_4)_2$ ($R3c$, $Z=7$), this network is three-dimensional. The new monoclinic structure of calcium orthovanadate was discussed in relation to those of related orthophosphates and orthovanadates. It was suggested that the pressure-induced amorphously-formed $Ca_3(VO_4)_2$ ($R3c$, $Z=7$) at 10 GPa and room temperature could be due to kinetically inhibited changes in the dimensionality of the crystal structure.

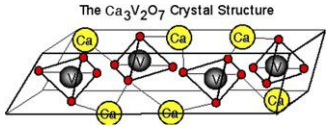

FIGURE 9.20

The pyrovanadate, $Ca_2V_2O_7$, is homologous to $Mg_2V_2O_7$ and has the same structure as shown in the following diagram: Fig. 9.20.

The unit cell parameters are: $a=6.667$ Å, $b=6.921$ Å, $c=7.018$ Å, $\alpha=96.39\cdot$, $\beta=63.84^\circ$, $\gamma=83.64^\circ$, cell volume $=288.83$ Å^3. Cell occupancy is shown in Table 9.11.

Investigations of the CaO–V_2O_3–VO_2–V_2O_5 system under various oxygen pressures and with addition of sodium in starting mixture have been described. A diagram of CaV_4O_9 and CaV_3O_7 stability and the reaction:

$$CaV_3O_7 + VO_2 \Rightarrow CaV_4O_9$$

was studied by variation of temperature and oxygen partial pressure. In this case, the vanadium ion is in the V^{4+} valence state. As a result, single-phase CaV_4O_9 and CaV_3O_7 ceramics were prepared, and plate-like single crystals of CaV_4O_9 were grown. Magnetic susceptibility data confirmed the existence of a disordered spin liquid state with spin gap $\beta=100\pm15$ K in CaV_4O_9 and of an AFM order below $T_N=22$ K in CaV_3O_7.

Muon spin relaxation measurements of CaV_4O_9, CaV_3O_7 and CaV_2O_5 were performed. The sub-lattice magnetization in the AFM state of CaV_3O_7 agrees well with spin wave theory. In CaV_4O_9 and CaV_2O_5, spin

TABLE 9.11

No	Site notation	Atom	Multiplicity	Wyckoff	Site symmetry	x	y	z	Occupancy
1	O2	O	4	i	m	0.1198	0	0.1269	1.0
2	Ca2	Ca	4	i	m	0.1865	0	0.4985	0.4
3	V2	V	4	i	m	0.2903	0	0.1526	0.97
4	O5	O	4	i	m	0.3269	0	0.3326	1.0
5	O4	O	4	i	m	0.4385	0	0.1039	1.0
6	V1	V	4	i	m	0.5916	0	0.1557	0.97
7	O1	O	4	i	m	0.6203	0	0.3363	1.0
8	O3	O	4	i	m	0.754	0	0.1062	1.0
9	Ca1	Ca	2	c	2/m	0	0	1/2	0.4

freezing below 15 and 50 K, respectively was observed, which indicated that a substantial fraction of the vanadium magnetic moment is not in a spin-singlet state at low temperatures in either material.

Another compound, $Ca_{0.6}V_2O_5$, has been discovered. It was prepared by heating the metavanadate with VO_2 in a hydrogen atmosphere. The structure is shown in Fig. 9.21 as follows:

The formula may be construed, as $Ca_3V_5O_{25}$ but is actually composed of three molecular units: $CaV_2O_4 \cdot CaVO_3 \cdot CaV_2O_6$ in which the vanadium atom has the +3, +4 and +5 valence states, respectively. The structure is actually composed of VO_3 triangles, a double tetrahedra and a triangle-tetrahedra unit. Cell parameters are: $a = 3.709$ Å, $b = 6.187$ Å, $c = 9.27$ Å, $\alpha = \gamma = 101.317°$, $\beta = 90°$, cell volume $= 198.60$ Å^3.

The $CaO–V_2O_5$ system has not received the attention that other compounds in the $MgO–V_2O_5$ system have found and calcium vanadate compounds are not used in industry. Certain compounds are available commercially. No CAS numbers have been assigned to date.

9.1.4. Strontium Vanadium Compounds

The metal, Sr^0, does not form any intermetallic compounds with V^0.

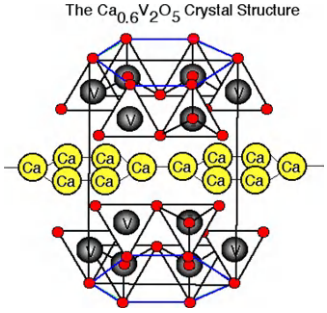

FIGURE 9.21

The system, $SrO–V_2O_5$, forms a series of compounds. The structure of many binary oxides can be predicted on the basis of the relative sizes of the metal and oxide ions and filling of holes in a close packed oxide lattice. Such predictions of structure are more difficult for ternary phases. The combination of two or more metals in an oxide generates a wealth of structural possibilities dependent on the relative sizes of the two metal ions and the oxide ion. In addition the stoichiometry of the ternary oxide may be changed by varying the proportions of the two component oxides and, for transition and lanthanide elements, the oxidation state. For example, at least twenty ternary oxide phases are formed between strontium and vanadium including $Sr_2V_2O_5$, (V-III) & (V-IV), $SrVO_3$ (V^{4+}) Sr_2VO_4 (V^{4+}) and SrV_2O_6 (V^{5+}). The structural chemistry of ternary and more complex oxides is, thus, an extensive subject, there are, however, a few structures which are widely adopted by ternary oxides and many materials from these structural classes have important technological applications. These ternary oxide structures are also used as units in building more complex oxides, such as the high-temperature superconductors.

In the V^{2+} system of SrO–VO, no compounds are known. A modification of Sr_2VO_3 has been found to be a super-conductor. The new superconducting system $Sr_2VO_{3-\delta}$–FeAs has been fabricated at different oxygen contents. It is found that the superconducting transition temperature drops monotonically with the increase of oxygen deficiency and the residual resistivity, indicating an anomalous pair breaking effect by disorders. Magneto-transport measurements reveal that the superconducting transition evolves from one-step-like at low field to two-step-like at high field. The first step corresponds to the upper critical field, while the second one is related to the irreversibility line. A vortex phase diagram is thus derived, which shows a large area of vortex liquid state. This indicates a high anisotropy of

the system. To conclude, the specific heat of the optimally doped sample ($\delta \approx 0.1$) with $T_c = 40$ K was presented. A high residual specific heat coefficient appeared in the superconducting state, suggesting the existence of large amount of unpaired electrons, which may derive from the V-band. Superconductivity at 33 K in $Sr_2VO_{3-\delta}$–FeAs is completely suppressed by small amounts of V-doping in $Sr_2VO_3[Fe_{0.93}(+/-0.01)V_{0.07}(+/-0.01)]As$. The crystal structures and exact stoichiometries are determined by combined NPD and powder XRD. $Sr_2VO_{3-\delta}$–FeAs is shown to be very sensitive to Fe/V mixing, which interferes with or even suppresses superconductivity. This inhomogeneity may be intrinsic and explains scattered reports regarding T_c and reduced superconducting phase fractions in $Sr_2VO_{3-\delta}$–FeAs. Neutron diffraction (ND) data collected at 4 K indicates incommensurate magnetic ordering of the V-sub-lattice with a propagation vector $q = (0,0,0.306)$ suggests that strongly correlated vanadium does not contribute significantly to the Fermi surface of $Sr_2VO_{3-\delta}$–FeAs.

In another study, $(Sr_2ScO_3)_2Fe_2As_2$ and $(Sr_2VO_3)_2Fe_2As_2$ with the spacing distance between FeAs layers as large as 15.66 Å was synthesized and a T_c of 37.2 K was found in the latter compound. Density-functional calculations indicated that the ground states of $(Sr_2ScO_3)_2Fe_2As_2$ and $(Sr_2VO_3)_2Fe_2As_2$ were stripe AFM and checkerboard AFM, respectively. The band structure and Fermi surface of $(Sr_2ScO_3)_2Fe_2As_2$ are similar to those of LaOFeAs, while those of $(Sr_2VO_3)_2Fe_2As_2$ show a significant difference. In $(Sr_2VO_3)_2Fe_2As_2$, both Fe 3*d* and V 3*d* states contribute to the Fermi surfaces, which implies that the V 3*d* states may play important roles in the superconductivity.

The superconducting Fe pnictide, $Sr_2VFeAsO_3$, has been found to be composed of alternating stacks of FeAs and Sr_2VO_3 perovskite-like block layers. The superconducting transition temperature T_c is 37 K. For this system, several band calculations have pointed out that both FeAs and V layers seem to have conduction electrons, and that the Fermi surfaces (FS's) do not have a significant nesting feature. This implies that $Sr_2VFeAsO_3$ gives an opportunity to examine whether Fermi-surface nesting is important for the occurrence of superconductivity of Fe pnictides. On this point, it has been reported that, because the FS's are constructed only by the Fe orbitals of $Sr_2VFeAsO_3$ are similar to those expected in other Fe pnictides; the nesting condition is also satisfied in this system.

In the V^{3+}-containing system, $SrO–V_2O_3$, the compound, SrV_2O_4 is unknown. The phase relationship of Sr–V–O system that contains low-valent V^{3+} oxide has been investigated. The phase identification was performed by XRD. The resistivities of constituent phases were measured by standard four-probe technique at 100–1000 K. The results indicate that low-valent V compounds in the system exist as hexagonal $Sr_8V_8O_{25}$ and cubic $Sr_2V_2O_5$ as well as V_2O_3, which show an electronic resistivity of <100–101 Ω cm at >150 K. The V_2O_3 phase exhibits a steep enhancement in resistivity with a magnitude of order of 105 Ω cm at <150 K, showing a transition from electronic conductor to insulator. These materials are useful for battery cathodes. The structure of $Sr_2V_2O_5$ is one of the "rock-salt" structure types where the Sr^{2+} and V^{3+} ions (as $V_2O_{6-\delta}$) are substituted on the cation and anion sites. Cell parameters are: $a = b = c = 7.656$ Å, $\alpha = \beta = \gamma = 90°$, cell volume = 777.64 Å^3. Cell occupancy has not been given.

In the V^{4+} system of $SrO–VO_2$, the $SrVO_3$ has the structure as shown in Fig. 9.22.

Lattice parameters are: $a = b = c = 3.842$ Å, $\alpha = \beta = \gamma = 90°$, cell volume = 56.71 Å^3, $Z = 1$.

Cell occupancy is shown in Table 9.12.

$SrVO_3$ is a metal-insulator compound. The changes occurring in the electronic structure of digitally controlled $SrVO_3$ ultra-thin films across the metal-insulator transition (MIT) by control of the film thickness using in situ photoemission spectroscopy was investigated. With decreasing film thickness, a pseudogap is formed at E_F through spectral weight transfer from the coherent part to the incoherent part. The pseudogap finally evolves into an energy gap that is

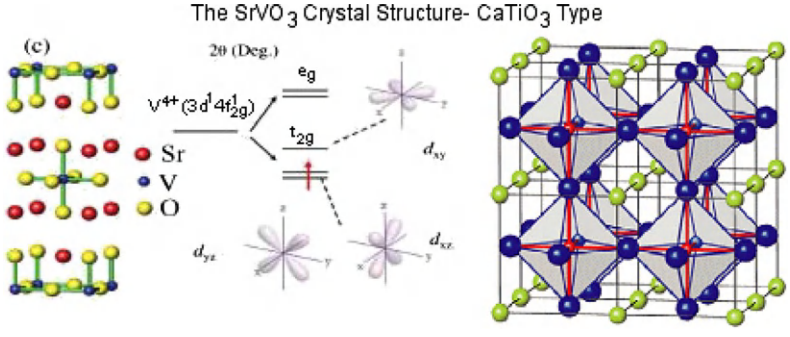

FIGURE 9.22

TABLE 9.12

No	Site notation	Atom	Multiplicity	Wyckoff	Site symmetry	x	y	z	Occupancy
1	O	O	3	d	4/mm.m	1/2	0	0	1.0
2	Sr	Sr	1	b	m-3m	1/2	1/2	1/2	1.0
3	V	V	1	a	m-3m	0	0	0	1.0

indicative of the MIT in an $SrVO_3$ ultra-thin film. The observed spectral behavior is reproduced by layer dynamical-mean-field-theory calculations, and it indicates that the observed MIT is caused by the reduction in the bandwidth due to the dimensional crossover. LDA + DMFT (local density approximation + dynamical mean field theory) results for the many-body spectra of cubic $SrVO_3$ and orthorhombic $CaVO_3$ were measured. Both systems are found to be strongly correlated metals, but not on the verge of a metal-insulator transition. In spite of the considerably smaller V–O–V bonding angle in $CaVO_3$, the LDA + DMFT photoemission spectra of the two systems are very similar, their quasi-particle parts being almost identical. The calculated X-ray absorption spectra show more pronounced, albeit still small, differences. This is in contrast to earlier theoretical and experimental conclusions, but in agreement with recent bulk-sensitive photoemission and X-ray absorption experiments.

Physical properties of the MVO_3 (M = Sr and Ca) perovskite systems and the related compound $Sr_8V_8O_{25}$ have been studied by electrical resistivity, magnetic susceptibility and NMR measurements. It has been pointed out that the magnetic properties of $SrVO_3$ are almost explained with a free electron model, where the electron–electron correlation seems to be small, and the electron transport is possibly due to the orbital mixing between the d^1 and oxygen $p\pi$.

In another study, the influence of local Coulomb correlations on the surface electronic structure of $SrVO_3$, a strongly-correlated metal in a perovskite structure, is investigated for both the SrO-layer and VO_2-layer-terminated (001) surfaces. The electronic structure within the local density approximation of a semi-infinite surface is determined using the embedded Green-function approach, and the resultant density of states projected on the V t_{2g} orbitals is used as an input to a subsequent many-body calculation within the DMFT and the multi-orbital quantum Monte Carlo technique. Qualitatively, the present study confirms the conclusion of recent photoemission experiments and tight-binding DMFT calculations which both indicate that the electronic structure at the surface is more strongly correlated than in the bulk. On a quantitative level significant differences are obtained as a function of orbital polarization at the surface, surface layer relaxation, and SrO vs VO_2 surface termination.

The Mott–Hubbard series $SrVO_3$–$CaVO_3$–$LaVO_3$–YVO_3 present a distinct metal-insulator transition. The microscopic origin of this transition can be related to the correlation effects in the electronic structure. The valence band photoemission results show very interesting trends across these Mott–Hubbard series. These results suggest that the O 2*p* states play an important role in the Mott–Hubbard transition. Some of the changes in the spectra are unexpected and cannot be explained by the current Mott–Hubbard theories as shown in Fig. 9.23.

Another compound containing the V^{4+} ion, $Sr_3V_2O_7$, has the structure as shown in Fig. 9.24.

The cell parameters are: $a = b = 3.8399$ Å, $c = 10.4765$ Å, $\alpha = \beta = 100.56°$, $c = 90°$, cell volume = 149.20 Å^3, $Z = 2$. Cell occupancy is shown in Table 9.13.

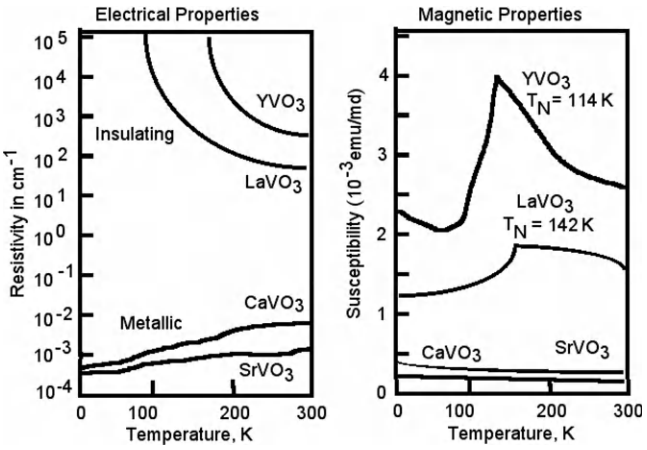

FIGURE 9.23

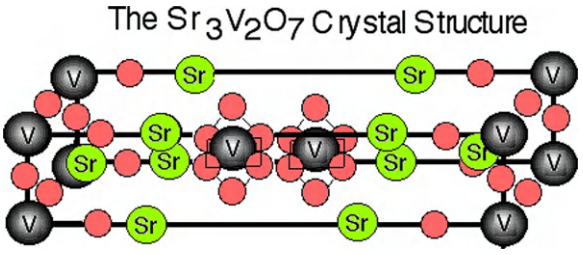

FIGURE 9.24

TABLE 9.13

No	Site notation	Atom	Multiplicity	Wyckoff	Site symmetry	*x*	*y*	*z*	Occupancy
1	O2	O	8	g	2mm.	0	1/2	0.094	1.0
2	V	V	4	e	4mm	0	0	0.099	1.0
3	O3	O	4	e	4mm	0	0	0.193	1.0
4	Sr2	Sr	4	e	4mm	0	0	0.3146	1.0
5	Sr1	Sr	2	b	4/mmm	0	0	1/2	1.0
6	O1	O	2	a	4/mmm	0	0	0	0.88

Synthesis, electrical, and magnetic properties of a layered perovskite-related compound, $Sr_3V_2O_7$, has been reported. Powder XRD analysis confirmed the body-centered tetragonal ($I4/mmm$) structure as proposed earlier. The electrical resistivity of the sample is 0.054 Ω cm at room temperature and decreases with temperature down to 15 K, with T^2 dependence in the range 15–150 K. The temperature-dependent magnetic susceptibility shows a small cusp at 110 K. Spin-glass-like behavior is observed in the temperature range 5–26 K as evidenced by irreversibility of the zero-field-cooled and field-cooled magnetization curves. The spin-glass dynamics of the sample was confirmed via the measurement of the AC susceptibility. The observed electrical and magnetic properties suggest disorder-induced localization of the defects at low temperatures. Two types of metal-insulator transitions in $Sr_3V_2O_7$ have been observed. A transition from the metallic state to the insulating state took place by substituting Cr for V, and this transition was interpreted as the result of the band splitting from the XPS data. The other transition occurred when the oxygen content was decreased in $Sr_3V_2O_{7-\delta}$, and the insulator exhibits variable range hopping conduction and spin freezing properties, which denotes that this transition is considered as the disorder-induced Anderson localization. The electrical and magnetic properties of the $Sr_3V_2O_{7-\delta}$ system have been studied in detail. Electrical resistivity changes from metallic to semiconducting with decreasing oxygen content. Transport is governed by variable-range hopping of the electrons since the resistivity obeys the $\exp(AT^{-1/4})$ law at low temperature. Oxygen-deficient $Sr_3V_2O_{7-\delta}$ exhibits different temperature magnetic susceptibility curves for zero-field-cooled and field-cooled measurements below about 15 K. A measurement of the field dependence of the magnetic susceptibility and the long-time relaxation of thermo-remanent magnetization, which obeys the relationship $M_{TRM} = At^{-\alpha}$. The magnetic properties in the $Sr_3V_2O_7$-d system was therefore interpreted to be spin-glass-like caused by the localized V spins introduced by the disorder-induced localization.

The presence of intergrowths in the $Sr_3V_2O_7$ compound has been elucidated by means of high resolution transmission electron microscopy (HRTEM) and several types of atomic stacking sequence of the intergrowths, i.e. a stacking irregularity along the *c* direction of $Sr_3V_2O_7$, have been clarified. The intergrowths were composed of the $Sr_4V_3O_{10}$ phase, i.e. one of the related compounds $Sr_{n+1}V_nO_{3n+1}$. The presence of such intergrowths are considered to be produced by matrix compositional fluctuations.

The layered perovskite compound, $Sr_3V_2O_{7.01}$, was synthesized by heating mixtures of the constituent oxides at 1110 °C in flowing hydrogen atmosphere. Rietveld analysis based on powder XRD data shows that the compound has a tetragonal structure ($I4/mmm$). The resistivity of the compound is 4.8 mΩ cm at room temperature (300 K) and decreases with decreasing temperature down to 2 K. The magnetic susceptibility can be represented by a summation of temperature-independent and Curie–Weiss terms. The effective number of Bohr magnetons per vanadium atom is 0.37, which is considerably smaller than the free-ion value of 1.73 for V^{4+}.

The V^{4+} containing compound, Sr_2VO_4, shows a temperature-dependent DC susceptibility. Powder XRD on a pure tetragonal sample of Sr_2VO_4 shows an AFM orbital-ordering transition at $T_{OO} = 97$ K, in which the occupied orbitals lie along the *c* axis. The unusual broadening of the X-ray Bragg peaks throughout the orbital-ordering transition temperature region indicates that this process occurs in stages, and the onset of short-range orbital ordering occurs at $T_1 \approx 122$ K. The study of the order parameter associated with this transition by analyzing the spontaneous strain results in a critical exponent $\beta = 0.35$ consistent with 3D Heisenberg behavior. These results experimentally confirm the orbital-ordering state in Sr_2VO_4 predicted by first-principles calculations using combinations of the local-density approximation and the *GW* method.

A sample $Sr_4V_2O_9$ was first prepared by solid-state reaction in air of the appropriate mixture of $SrCO_3$ and

V_2O_5 at 1073 K (800 °C) for 60 h. Polycrystalline Sr_2VO_4 compound was made by reduction of $Sr_4V_2O_9$ under a H_2 flow at 1323 K for 100 h, with several grindings of the sample. The resulting compound contains V^{4+} ions. It has the structure shown in Fig. 9.25 as follows:

Temperature-dependent dc susceptibility and powder XRD on a pure tetragonal sample of Sr_2VO_4 show an antiferromagnetic orbital-ordering transition at $T_\infty = 97$ K, in which the occupied orbitals lie along the c axis. The unusual broadening of the X-ray Bragg peaks throughout the orbital ordering transition temperature region indicates that this process occurs in stages, and the onset of short-range orbital ordering occurs at $T_1 = 122$ K.

Strontium Vanadite, or Sr_2VO_4, is an interesting compound in the family of layered perovskites. A perovskite is a class of materials which generally form in a cubic structure and in most often contain oxygen as a major chemical component. Perovskite materials exhibit lot of interesting and intriguing properties both from theoretical point of view as well as in its applications. Some of these are colossal magnetoresistance, charge ordering, spin dependent transport, interplay of structural, as well as magnetic and transport properties. These compounds are used as catalyst electrodes in certain types of fuel cells and are candidates for memory devices and spintronics applications. In this specific case however, Sr_2VO_4 is of interest because it is similar to La_2CuO_4, i.e.lanthanum cuprate. La_2CuO_4 is a parent compound to high T_c superconductors, and has many correlations with Sr_2VO_4. Both have spin $= 1/2$ layered magnetic atoms, but the La_2CuO_4 case orders antiferromagnetically. Sr_2VO_4 on the other hand, has an unusual orbital ordering. This strange electronic state is not well understood and may be related to the superconductivity in the parent compound.

Neutron powder diffraction experiments were performed for SrV_3O_7, which is characterized by the 1/4 depleted $V^{4+}(S = 1/2)$ square lattice model. An AFM 3D long-range order was observed below $T_N = 34.3$ K. The 'Stripe Order' spin structure, which is not expected from a classical Heisenberg model, is realized. This spin structure is the same as found in CaV_3O_7, but the spin direction here is parallel to the a(stacking)-axis, instead of the c-axis for CaV_3O_7 as shown in Fig. 9.26.

In addition to the four compounds listed above, a mixed valence compound of strontium vanadate has been found. The compound $Sr_2V_3O_9$ contains three kinds of vanadium ions in the unit cell. Two of them are nonmagnetic V^{5+} ions located in VO_4 tetrahedra, and the rest is V^{4+} ions with $S = 1/2$ located in VO_6 octahedra. The VO_6 octahedra are connected with each other by sharing oxygen at the corner along the [101] direction, as shown in the following Fig. 9.27.

The magnetic properties of these mixed valence-state vanadium compounds have been intensely studied. If $Sr_2V_2O_7$ is fired with VO_2, a new compound is obtained:

$$Sr_2V_2O_7 + 5V_2O_3 \Rightarrow 2\,SrV_6O_{11}$$

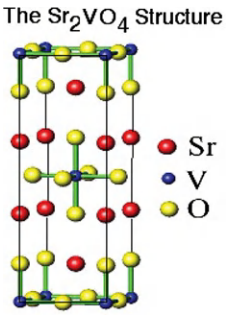

FIGURE 9.25

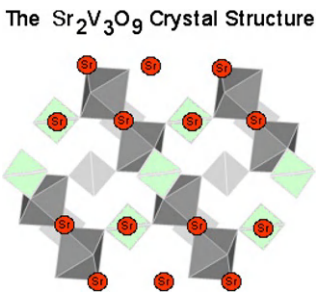

FIGURE 9.27

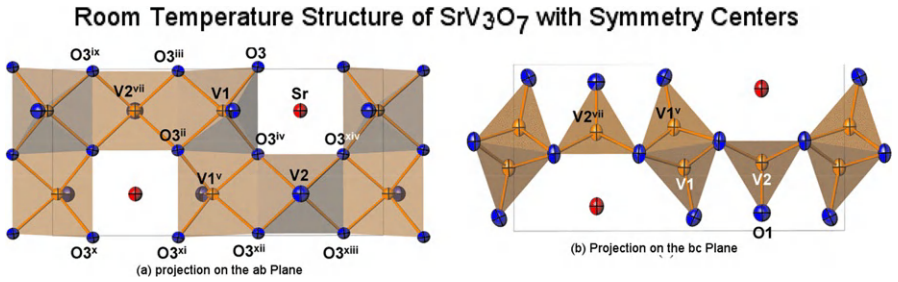

FIGURE 9.26

Single crystals and polycrystals of this compound were synthesized by a solid-state reaction. Four-circle X-ray structural analysis discovered a structural transition at a temperature range between room temperature and 353 K. This transition corresponds to that of NaV_6O_{11} at 245 K. Specific heat measurement of SrV_6O_{11} was performed between 20 and 150 K and two anomalies were observed at 42 and 73 K. These anomalies are consistent with the two peaks in the temperature dependence of magnetization. Below 42 K, SrV_6O_{11} shows metamagnetism and its critical field is about 4 T at 5 K. Its basic magnetic structure at 73 K is considered to be an AFM state formed by the localized electron system.

The *ac*-plane with the magnetic network is weakly stacked along the *b*-axis. The magnetic properties are understood in terms of the $S = 1/2$ 1D-AF chain model with the exchange interaction between the nearest spins, $J = 82$ K, estimated from the susceptibility measurements. However, it has been suggested from ESR measurements and a theory by Koo and Whangbo that the spin-chain direction is not the [101] direction but the [101] direction, along which VO_6 octahedra are connected via a VO_4 tetrahedron. Note that V^{5+} ions and V^{4+} ions are located in VO_4 tetrahedra and VO_6 octahedra, respectively.

The V^{5+}-containing $SrO–V_2O_5$ boundary system contains 4 compounds at SrO to V_2O_5 molar ratios of 4:1, 3:1, 2:1, and 1:1. A fifth compound with a molar composition of 10:3 with the apatite crystal structure was also found. The phase diagram is shown as follows in Fig. 9.28.

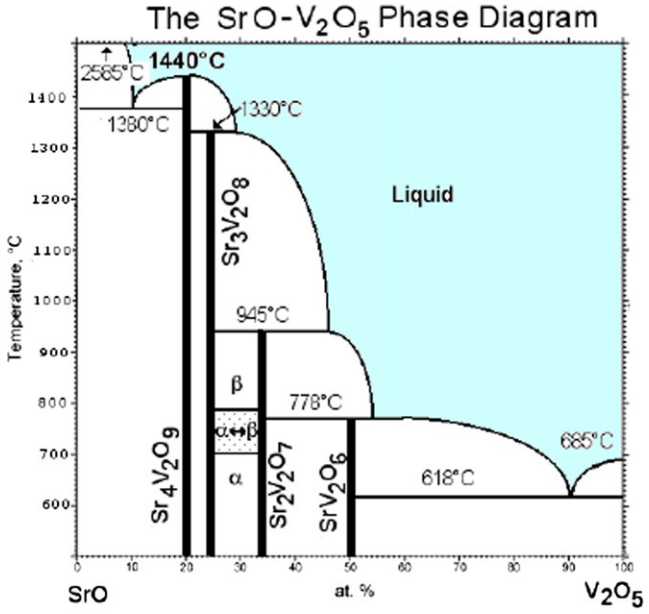

FIGURE 9.28

The phase evolution and properties of the **strontium orthovanadate**, $Sr_3V_2O_8$, were investigated using different methods of preparation: solid-state reaction and two wet-route techniques (colloidal route and sol-gel method-polymerized complex route). DTA/TG study showed decomposition temperatures of starting materials and helped to choose processing temperatures. XRD analysis was used to determine phase evolution. Solid-state reaction sample contained a small amount of $Sr_3V_2O_8$ as soon as after the first calcinations, but 100% of $Sr_3V_2O_8$ did not appear until whole procedure was finished. The colloidal route turned out as an inconvenient method for preparation of pure phase. The final colloidal route sample contained 80% of $Sr_3V_2O_8$, and the residual volume corresponded to $Sr_{10}V_6O_{25}$, which is related to apatite. The most progressive phase evolution was detected in the sol-gel route. Raman and FTIR spectroscopy detected evolution of the first amount of $Sr_3V_2O_8$ after gel heating at 250 °C for 2 h. The pure strontium orthovanadate was prepared after heating at 800 °C for 2 h. The structure is identical to its calcium isomorph as shown in Fig. 9.29.

Cell parameters are: $a = b = 5.619$ Å, $c = 7.4441$ Å, $\alpha = \beta = 67.83°$, $\gamma = 60.0°$, cell volume = 1832.05 Å^3.

Cell occupancy is shown in Table 9.14.

The **pyrovanadate**, $Sr_2V_2O_7$, has the same structure as its calcium homolog as shown in Fig. 9.30.

Cell parameters are: $a = 7.051$ Å, $b = 7.099$ Å, $c = 12.983$ Å, $\alpha = 99.97°$, $\beta = 96.77°$, $\gamma = 90.89°$, cell volume = 636.45 Å^3.

This compound is dimorphic. Single crystals of the high-temperature phase of strontium pyrovanadate, α-$Sr_2V_2O_7$, were grown from a melt. The structure can be described as the packing of four $Sr_2V_2O_7$ layers that are approximately normal to the *b* axis or as the stacking of two zigzag chains. Two different types of $(V_2O_7)^{4-}$ anions are present. Three reported X-ray powder

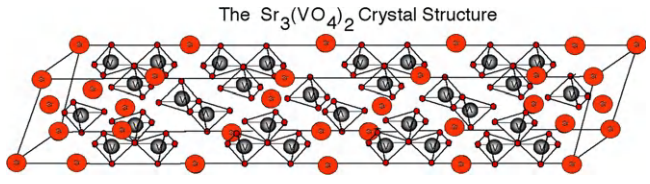

FIGURE 9.29

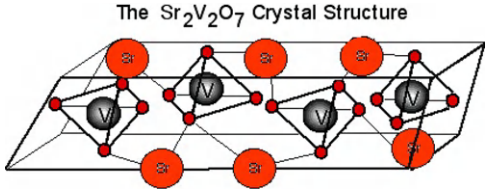

FIGURE 9.30

TABLE 9.14

No	Site notation	Atom	Multiplicity	Wyckoff	Site symmetry	*x*	*y*	*z*	Occupancy
1	O2	O	18	h	.m	0.4996	0.5004	0.2319	1.0
2	Sr2	Sr	6	c	3m	0	0	0.2022	1.0
3	O1	O	6	c	3m	0	0	0.3218	1.0
4	V1	V	6	c	3m	0	0	0.4061	1.0
5	Sr1	Sr	3	a	-3m	0	0	0	1.0

patterns are indexed with the cell parameters from this work. The α to β polymorphic transition temperature is about 645 °C. β-$Sr_2V_2O_7$ is tetragonal, space group $P4_1$ with eight formula units per unit cell and $a = 7.055$ Å, $c = 25.64$ Å. The compound is isomorphous with β-$Ca_2P_2O_7$. The structure was determined from three-dimensional data collected on an automatic diffractometer with both Cu$K\alpha$ and Mo$K\alpha$ radiation. It was solved by comparing a Patterson section with a difference Fourier map. The phases for the latter were calculated from the Ca and P coordinates of β-$Ca_2P_2O_7$. The oxygen atoms were subsequently located from successive difference Fourier maps, and the structure was refined by full-matrix least squares with isotropic temperature factors. The two different sets of data were refined separately, and the final *R* is 0.058 and 0.046 for data using Cu and Mo radiation, respectively. The compound has the dichromate-type structure with nearly eclipsed V_2O_7 groups. The bond distances for the two independent pyrovanadate anions are separable into two sets: the bridging bonds whose lengths are 1.81 Å and the non-bridging bonds whose lengths range between 1.63–1.77 Å. The bond angles are 123°. The coordination number of strontium ranges from 7 to 9.

The formation process and microwave dielectric properties of the $R_2V_2O_7$ (R = Ba, Sr, and Ca) ceramics were investigated. Transient RV_2O_6 phases, which were formed at 300 °C similar to 500 °C by the reaction of RCO_3 and V_2O_5, interacted with remnant RCO_3 to form the homogeneous triclinic $R_2V_2O_7$ phases at 600 °C –700 °C . The $Sr_2V_2O_7$ and $Ca_2V_2O_7$ ceramics sintered at 1000 °C and 950 °C, respectively, for 10 h showed a dense microstructure with the microwave dielectric properties of $\varepsilon_r = 10.4$–12.1, $Q \times f = 15{,}200$–19,520 GHz, and $\tau_f = -30.9$–34.8 ppm/°C. However, the $Ba_2V_2O_7$ ceramic was well sintered at 900 °C for 10 h and it showed good microwave dielectric properties of $\varepsilon_r = 10.1$, $Q \times f = 51{,}630$ GHz, and $\tau_f = -26.5$ ppm/°C.

The addition of Li_2CO_3 to $Sr_2V_2O_7$ ceramics decreased their sintering temperature and time. A dense microstructure was developed for the specimens sintered at 750°–850 °C due to the melting of Li_2CO_3 during the sintering. For the specimens sintered at 800 °C, the grain size was considerably increased when the Li_2CO_3 content exceeded 1.0 mol%. The $Q \times f$ value was increased by the Li_2CO_3 addition due to the increased density and grain size. In particular, a high $Q \times f$ value of 73,800 GHz with ε_r and τ_f values of 9.94 and −28.8 ppm/°C, respectively, was obtained for the specimen containing 3.0 mol% Li_2CO_3 sintered at 800 °C for 2 h.

The compound, **tetrastrontium vanadate**, $Sr_4V_2O_9$, has not been studied thoroughly due, in part, to the tendency of the compound to vaporize or possibly to decompose above its optimal temperature of preparation. There is quite a series of alkaline-earth compounds having the same general formula as tetracalcium vanadate. The phosphate, $4CaO \cdot P_2O_5$, and tetracalcium arsenate, $4CaO \cdot As_2O_5$, are not well known. The preparation of these and the compounds $4CaO \cdot V_2O_5$, $4SrO \cdot P_2O_5$, $4SrO \cdot As_2O_5$, $4BaO \cdot V_2O_5$, and $4BaO \cdot As_2O_5$ by thermal synthesis has been described. Being metastable at room temperature, most of these compounds must be quenched. X-ray powder diagrams show that all these compounds are isostructural and the dimensions of their orthorhombic unit cells have been tabulated.

The **metavanadate**, SrV_2O_6, has a structure similar to the calcium analog. Cell parameters are: $a = 7.656$ Å, $b = 8.26$ Å, $c = 12.297$ Å, $\alpha = \beta = \gamma = 90°$, cell volume = 777.46 Å^3 as shown in Fig. 9.31.

The structure involves VO_4 octahedra that are connected with each other along the [101] direction by

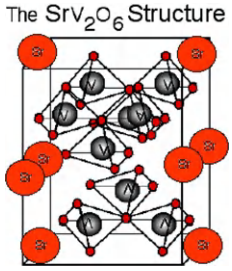

FIGURE 9.31

sharing oxygen at the corner and are also connected via a VO_4 tetrahedron along the [101] direction.

In the V^{6+} system of SrO–VO_3, the compound, $Sr_2VO_{5-\delta}$ has been synthesized. The effects of the oxygen deficiency on the electrical and magnetic properties of $Sr_2VO_{4-\delta}$ were investigated. Single-phase samples of polycrystalline $Sr_2VO_{5-\delta}$ with $\delta = 0.18$, 0.29 and 0.38 were synthesized by the solid-state reaction in flowing hydrogen atmosphere. The crystal structure was determined by Rietveld analysis of XRD data. All the samples were tetragonal at 298 K. With increase of δ, the lattice constant 'a' decreased and the lattice constant 'c' increased. Electrical resistivity measurements showed that all the samples were semiconductive with resistivity of about 1 Ω cm at 298 K. Magnetic measurements showed that the magnetic properties of $Sr_2VO_{5-\delta}$ system were strongly dependent on the oxygen deficiency δ. It was suggested that the non oxygen-deficient compound Sr_2VO_5 ($\delta = 0$) had no magnetic long-range order. As δ was increased, spin-glass-like behavior became evident at low temperatures and was overlapped by a long-range magnetic order with a transition temperature of 35 K for $\delta = 0.2$. It was suggested that the long-range magnetic order was a canted antiferromagnetism with a small net magnetization.

Strontium vanadates are offered commercially in small quantities for research purposes. No Industry uses have yet emerged.

9.1.5. Barium Vanadium Compounds

The metal, Ba^0, does not form any intermetallic compounds with V^0. Like the other alkaline earths, barium forms a number of compounds with vanadium. However, these are limited to the oxo-vanadate types of compounds since intermetallic compounds of Ba^0 and V^0 do not exist.

In the V^{2+} system of BaO–VO, no compounds like $BaVO_2$, Ba_2VO_3 or BaV_2O_3 have been reported.

In the V^{3+} system of BaO–V_2O_3, in contrast to the other alkaline earth MV_2O_4 compounds, Ba does not form BaV_2O_4 when the oxides are heated together in a reducing atmosphere. Apparently, the radius of Ba^{2+} is too large to accommodate it in a perovskite lattice. No other BaO–V_2O_3 compounds have been reported in the current literature.

In the V^{4+} system of BaO–VO_2, the vanadite compound, $BaVO_3$, has been studied. A 5-layer mixed valence oxide, $BaVO_{2.8}$, has been synthesized by reducing $Ba_2V_2O_7$ in high-purity hydrogen gas at 1350 °C. $BaVO_{2.9}$ has been obtained by room temperature oxidation of $BaVO_{2.8}$ in air and $BaVO_{3.0}$ obtained by annealing $BaVO_{2.8}$ or $BaVO_{2.9}$ at 200 °C in air. The structures of this series of novel compounds have been refined by the Rietveld method using ND and XRD data. Magnetic and electrical properties were examined down to 5 K. All three compounds crystallize in the hexagonal system, space group $P\bar{3}m1$ and $Z = 5$. Lattice parameters (Å) derived from Si-calibrated Guinier XRD data are: $BaVO_{2.8}$, $a = 5.7800(2)$, $c = 11.8969(6)$; $BaVO_{2.9}$, $a = 5.7215(5)$, $c = 11.685(2)$; and $BaVO_{3.0}$, $a = 5.6650(3)$, $c = 11.4629(6)$. The $BaVO_{2.8}$ structure consists of face-sharing VO_6^{8-} and VO_6^{9-} octahedra that form VO_{12}^{14-} trimers and of VO_4^{4-} tetrahedra that share corners with the trimers. The $BaVO_{2.9}$ and $BaVO_{3.0}$ structures are similar to $BaVO_{2.8}$, except that the VO_4^{4-} tetrahedra in the latter are replaced by VO_6 octahedra in the former compounds. The previously reported 24R $Ba_8V_7O_{22}$ was found to be an intergrowth product of 5H $BaVO_{2.8}$ ($Ba_5V_5O_{14}$) and 9R $Ba_3V_2O_8$. The hydrogen reduction mechanism of $Ba_2V_2O_7$ is examined and the initial formation of $Ba_3V_2O_8$ in the temperature range 650 to 1200 °C has been proven by ND. The low stability of $BaVO_{2.8}$ is analyzed in terms of stress relief of the face-sharing octahedra and the mobility of the unshared tetrahedron corner oxygen atoms. The electrical conductivity increases dramatically with increasing oxygen content in the $BaVO_{3-\delta}$ series ($\delta = 0.2$, 0.1, and 0.0). $BaVO_{2.8}$ and $BaVO_{2.9}$ are semiconductors with room temperature resistivities of about 30 and 0.14 Ω cm, respectively. $BaVO_{3.0}$ is metallic with a room temperature resistivity of 0.013 Ω cm. The magnetic susceptibility of $BaVO_{2.8}$ shows a broad maximum at about 20 K, indicative of short-range order. The susceptibility of $BaVO_{2.9}$ has both temperature-independent and Curie–Weiss type paramagnetic contributions, and $BaVO_{3.0}$ primarily exhibits Pauli paramagnetism.

A comparison of the alkaline earth vanadites was presented. AVO_3 ($A = Ba^{2+}$, Sr^{2+}, La^{3+}, Gd^{3+}) oxides have been prepared by hydrogen reduction of suitable vanadium(V) ternary oxides. The oxidation state of vanadium in the reduction products seems to be controlled by the nature of other cations. In the presence of strongly basic alkaline-earth metal ions, Ba^{2+} and Sr^{2+} as in $Ba_2V_2O_7$ and $Sr_2V_2O_7$, vanadium is reduced to +4 state. But when A is a trivalent lanthanide ion, as in $LnVO_4$ (Ln = La or Gd), the reduction of vanadium proceeds to the +3 state to yield $LnVO_3$ phases. The products have been characterized by XRD. $BaVO_3$ crystallizes in a hexagonal structure related to $Ba_3V_2O_8$ while $SrVO_3$, $LaVO_3$ and $GdVO_3$ crystallize in $GdFeO_3$ type structure. Electrical transport measurements indicate that $BaVO_3$, $LaVO_3$ and $GdVO_3$ are p-type semiconductors while $SrVO_3$ is metallic.

Another V^{4+} containing vanadite, Ba_2VO_4 has been produced. Phase-pure Ba_2VO_4 has been synthesized by hydrogen reduction of a mixture of $Ba_3V_2O_8$ and 20% excess $BaCO_3$ at 1200–1250 °C, and its crystal structure, designated as β-Ba_2VO_4, refined using a combination

of NPD and XRD data. It is monoclinic, space group $P2_1/n$ (no. 14), with $a = 6.0191$ Å, $b = 7.6494$ Å, $c = 10.465$ Å, $\beta = 92.39(1)°$, and $V = 481.4$ Å^3 from Guinier XRD data. β-Ba_2VO_4 is isostructural with β-Ca_2SiO_4. The structure is closely related to β-K_2SO_4 and consists of isolated VO_4^{4-} tetrahedra and loosely bonded Ba(1)O_{10} and Ba(2)O_9 polyhedra. Its magnetic behavior can be approximated as an $S =$ infinite Heisenberg linear chain. The crystal structure and magnetic properties of the β-Ba_2VO_4 are compared with those of the structurally related high-temperature form of Sr_2VO_4 (β-Sr_2VO_4). Reexamination of the crystal structure of the latter discloses that one of the V^{4+} atoms has rare trigonal bipyramidal coordination and that this atom is weakly bonded to a VO_4^{4-} tetrahedron forming a $V_2O_8^{8-}$ dimer. The formation mechanism of β-Ba_2VO_4 and the possible existence of an orthorhombic form isostructural with β-K_2SO_4 are also discussed.

A new spin 1/2-V^{4+} barium oxovanadate BaV_4O_9 was synthesized and studied by means of single-crystal XRD. Its room-temperature structure is monoclinic, space group $P2/c$. The temperature evolution of the crystal structure and thermal expansion tensor of the material between 293 and 100 K was measured and discussed.

The crystal structure at room temperature is shown in the following Fig. 9.32.

A new preparation route has been developed for 5H $BaVO_{2.8}$ using an induction furnace. It was determined that addition of 4% to 8% molar excess of vanadium in the reaction produced a pure material. In a study of $BaVO_{2.8}$ using NPD, peaks due to long-range magnetic order were not detected. The possibilities of either a spin-glass or super-paramagnetic ground state remain. Transport property measurements on BaVO2.8 suggest that two-dimensional variable range hopping is occurring at low temperatures. With oxidation, the dominant carrier type changes from holes ($BaVO_{2.8}$) to electrons ($BaVO_{3.0}$).

A novel vanadium arsenate $BaAsVO_6$ has been synthesized hydrothermally and structurally characterized by single-crystal XRD, IR spectroscopy, and magnetic susceptibility measurements. It crystallizes in the monoclinic system, space group $P21/c$ with unit cell parameters $a = 5.645(1)$ Å, $b = 10.243(1)$ Å, $c = 8.945(1)$ Å, $\beta = 90.60(1)°$, and $Z = 2$. The layered structure is built up from $V_2O_4^{2+}$ units and AsO_4^{3-} anions, the AsO_4^{3-} ligands being coordinated to two $(V_2O_4^{2+})$ units in both, terminal and bridging μ_2−AsO_4^{3-} fashion. The $[VO_2(AsO_4)]^{2-}$ layers are separated by Ba^{2+} cations. The $V_2O_4^{2+}$ unit has no precedence in oxo-vanadium chemistry.

In the V^{5+} containing sub-solidus region of the BaO–V_2O_5 system, the phase diagram has been determined. Previously reported binary phases of $Ba_3V_2O_8$, $Ba_2V_2O_7$, $Ba_3V_4O_{13}$ and BaV_2O_6 have all been confirmed. (Fig. 9.33).

The metavanadate, BaV_2O_6, has been studied. Single crystals of barium metavanadate BaV_2O_6 have been grown in a hydrothermal system of $VO(OH)_2 + Ba(NO_3)_2$ at 280 °C. The heat of formation is −440 kcal/mol. The compound crystallizes in the orthorhombic system, $C222$, $a = 8.482$ (1), $b = 12.610$ (1), $c = 7.916$ (2) Å, $\alpha = \beta = \gamma = 90°$, $Z = 6$. The structure has since been re-investigated and refined to $R/R_w = 0.029/0.041$ using 1458 unique reflections. An identical structure was derived but the atomic positions were greatly improved. The structure consists of chains of vertex-shared VO_4 tetrahedra running along the (120) directions and Ba atoms located interstitially between the chains.

Soluble barium and strontium bromides, when treated with ammonium metavanadate, precipitate barium or strontium as the metavanadate is shown in Fig. 9.34.

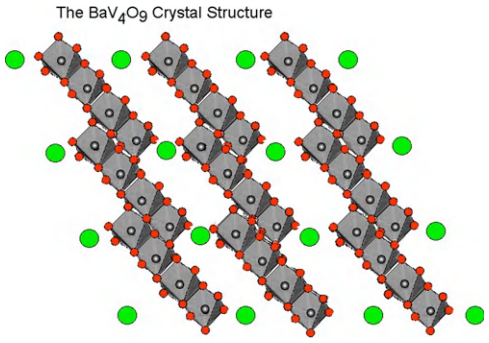

FIGURE 9.32

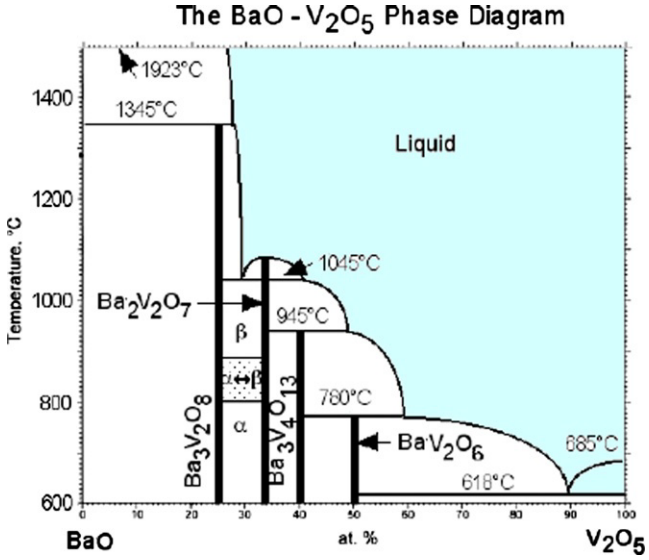

FIGURE 9.33

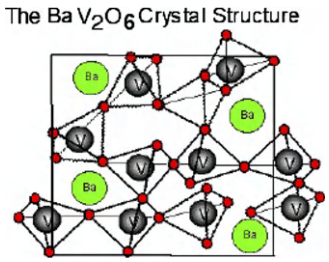

FIGURE 9.34

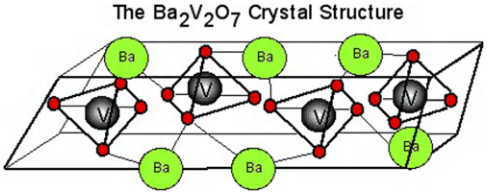

FIGURE 9.35

$Ba(VO_3)_2 \cdot H_2O$ is orthorhombic with $a = 8.997$ Å, $b = 9.728$ Å, $c = 7.409$ Å, $V = 648.7$ Å^3, $Z = 4$. Each V-atom is coordinated by four O atoms to form a tetrahedron. Each atom is connected to the others to form a twisted spiral parallel to the *c*-direction. The Ba atom is coordinated by nine O atoms and one water molecule and the whole is very similar to the diagram given above.

Very little data concerning the metavanadate is available in the literature other than structural data. Most of the research papers are concerned with the pyrovanadate or the orthovanadate. The pyrovanadate, $Ba_2V_2O_7$, has the same structure as the strontium homolog as shown in Fig. 9.35.

$Ba_2V_2O_7$ is triclinic with $a = 13.571$, $b = 7.320$, $c = 7.306$ Å, $\alpha = 90.09(1)$, $\beta = 99.48(1)$, $\gamma = 87.32°$, $V = 715.12$ Å^3, $Z = 4$, and space group *P*1. The crystal structure was solved by Patterson and Fourier methods and refined by full-matrix least-squares analysis to a R_w of 0.034 ($R = 0.034$) using 2484 reflections measured on a Syntex P1 automatic four-circle diffractometer. The structure has two unique divanadate groups that are repeated by the *b* and *c* lattice translations to form sheets of divanadate groups parallel to (100). These sheets are linked by four unique Ba atoms that lie between these sheets. Ba(1) and Ba(3) are coordinated by eight oxygen atoms arranged in a distorted biaugmented triangular prism and a distorted cubic antiprism, respectively. Ba(2) is coordinated by 10 oxygen atoms arranged in a distorted gyro-elongated square dipyramid and Ba(4) is coordinated by nine oxygen atoms arranged in a distorted triaugmented triangular prism. These coordination numbers are substantiated by a bond strength analysis of the structure, and the variation in <Ba–O> distances are compatible with the assigned cation and anion coordination numbers. Both divanadate groups are in the eclipsed configuration with <V–O(br)> bond lengths of 1.821 and 1.824 Å and V–O(br)-V angles of 125.6 and 123.7°, respectively. Examination of the divanadate groups in a series of structures allows certain generalizations to be made. Longer <V–O(br)> (br = bridge) bond lengths are generally associated with smaller V–O(br)–V angles. When V–O(br)–V <140°, the divanadate group is generally in an eclipsed configuration; when V–O(br)–V >140°, the divanadate group is generally in a staggered configuration. Non-tetrahedral cations with large coordination numbers require more oxygen atoms with which they bond, and hence O(br) is more likely to have three coordinates, with the divanadate group in the eclipsed configuration. In the eclipsed configuration, decrease in V–O(br)–V promotes bonding between O(br) and non-tetrahedral cations, and hence smaller non-tetrahedral cations are generally associated with smaller V–O–(br)–V angles.

Li_2CO_3 was added to $Ba_2V_2O_7$ ceramics at various contents up to 20 mol% to decrease their sintering time and temperature. The Li_2CO_3-added $Ba_2V_2O_7$ ceramics sintered at 750 °C for 2 h had a dense microstructure with a high density. A liquid phase, which existed as an amorphous phase after cooling, was formed during the sintering due to the melting of Li_2CO_3 and aided the densification of the specimens. The 6.0 mol% Li_2CO_3-added ceramic sintered at 750 °C showed good microwave dielectric properties of $\varepsilon_r = 10.93$, $Q \times f = 74{,}513$ GHz, and $\tau_f = -19.86$ ppm/°C, indicating that the Li_2CO_3-added $Ba_2V_2O_7$ ceramic is a good candidate material for low-temperature cofired ceramics.

The **orthovanadate**, $Ba_3(VO_4)_2$, has the structure as shown in Fig. 9.36.

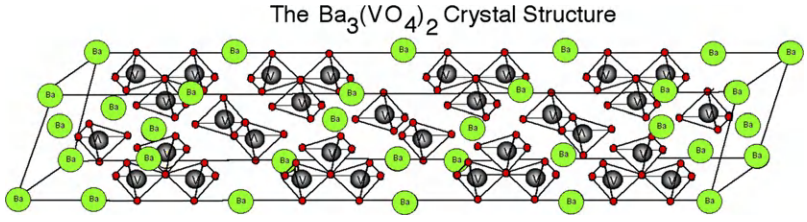

FIGURE 9.36

TABLE 9.15

No	Site notation	Atom	Multiplicity	Wyckoff	Site symmetry	x	y	z	Occupancy
1	O2	O	18	h	.m	0.4955	0.5045	0.2309	1.0
2	Ba2	Ba	6	c	3m	0	0	0.2053	1.0
3	O1	O	6	c	3m	0	0	0.328	1.0
4	V1	V	6	c	3m	0	0	0.4076	1.0
5	Ba1	Ba	3	a	-3m	0	0	0	1.0

Cell parameters are: $a = 5.7842$ Å, $b = 5.7842$ Å, $c = 7.8519$ Å, $\alpha = 68.387°$, $\beta = 68.387°$, $\gamma = 60°$, cell volume $= 205.90$ Å^3. Site occupancy is shown in Table 9.15.

The vanadium is tetrahedrally surrounded by oxygen atoms. There are two kinds of barium atoms, one with distorted octahedral coordination, and the other with 10-fold coordination. Pairs of three barium atoms, Ba(2), Ba(1), Ba(2), share a common triangular face of their respective coordination polyhedra; these three thus form a connected linear cluster. There are two kinds of oxygen atoms; one has two-fold linear coordination, the other, five-fold trigonal-dipyramidal coordination. Pauling's electrostatic-valence rule is perfectly satisfied but some of the bond strengths are unexpected.

The pressure-induced transitions and structural changes in isostructural strontium and barium orthovanadates, $Sr_3(VO_4)_2$ and $Ba_3(VO_4)_2$, via Raman spectroscopy (RS) has been studied. The spectral changes in $Ba_3(VO_4)_2$ can be interpreted as being due to condensation of VO_4^{3-} units into edge- or corner-shared octahedra with little or no hysteresis on decompression. For $Sr_3(VO_4)_2$, there is a pressure-induced first-order phase change at about 150 kbar, with large hysteresis on decompression, which can be rationalized as a transition into a spinelloid series of structures, retaining the tetrahedral coordination of the V atoms.

$Ba_3(VO_4)_2$ and $Ba_3(VO_4)_2$:Nd^{3+} crystals were grown successfully by the Czochralski technique. Powder XRD and transmission spectrum of $Ba_3(VO_4)_2$ crystal were measured at room temperature. Spontaneous Raman scattering spectra of $Ba_3(VO_4)_2$ and $SrWO_4$ crystals were presented, and both larger integral Raman scattering cross-section and stronger peak line intensity were observed in $Ba_3(VO_4)_2$ crystal. In addition, polarized absorption spectra of Nd^{3+}:$Ba_3(VO_4)_2$ crystals were measured at room temperature.

A flower-shaped nano-crystalline barium vanadate has been obtained by the composite hydroxide mediated (CHM) method from V_2O_5 and $BaCl_2$ at 200 °C for 13 h. XRD and XPS spectrum of the as-synthesized sample indicate it is hexagonal $Ba_3V_2O_8$ with a small amount of $Ba_3VO_{4.8}$ coexisting. SEM and TEM display that the flower-shaped crystals are composed of nanosheets with thickness of 20 nm. The UV–Visible spectrum shows that the barium vanadate sample has two optical gaps (3.85 eV and 3.12 eV). Photoluminescence spectrum of the barium vanadate flowers exhibits a visible light emission centered at 492 and 525 nm, which might be attributed to VO_4 tetrahedron with T_d symmetry in $Ba_3V_2O_8$.

Ferromagnetic behavior of the barium vanadate nanoflowers has been determined with a saturation magnetization of about 83.50×10^{-3} emu/g, coercivity of 18.89 Oe and remnant magnetization of 4.63×10^{-3} emu/g, which is mainly due to the presence of a non-orthovanadate phase with spin $S = 1/2$.

Reactions of the alkaline earth metal vanadates such as $Ba_2V_2O_7$ and $Ba_3V_2O_8$ with hydrogen and ammonia have been investigated by TG analysis and in a flow reactor. Reactions in ammonia do not lead to the formation of oxynitride phases, in contrast with the formation of $LaVO_{3-x}N_x$ from $LaVO_4$ under similar conditions as shown in Fig. 9.37.

Both hydrogen reduction and ammonia reactions of the $Ba_2V_2O_7$ compounds are dominated by the formation of the corresponding $A_3V_2O_8$ phases. $Ba_3V_2O_8$ and $Sr_3V_2O_8$ do not react easily in ammonia at temperatures below 1000 °C and $Ca_3V_2O_8$ converts to CaO and VN or to CaO, VN and $CaVO_3$. In contrast, reaction with hydrogen at elevated temperatures produces $BaVO_3$. Reduction of $Ba_2V_2O_7$ by hydrogen yields the compounds $Ba_6V_6O_{19}$ and $BaVO_3$. Their x-ray diagrams show relations to the structure of $Ba_3V_2O_8$. Measurements of the density, electrical conductivity and NMR-spectra in comparison to other corresponding compounds result to a coordination number 4 for the vanadium atoms of $BaVO_3$. The structure of $BaVO_3$ differs widely form the perovskite-type. The relation to the $Ba_3V_2O_8$-structure was discussed.

The syntheses and the results of unit-cell determinations of $Ba_3V_4O_{13}$ and the two forms (low- and high-temperature) of $Ba_3P_4O_{13}$ have been presented. $Ba_3V_4O_{13}$ crystallizes in the monoclinic system, space group Cc or $C2/c$ with unit-cell dimensions $a = 16.087$, $b = 8.948$, $c = 10.159$ Å, $\beta = 114.52°$ Low-$Ba_3P_4O_{13}$ crystallizes in the triclinic system, space group $P1$ or $P\bar{1}$ with unit-cell dimensions $a = 5.757$, $b = 7.243$, $c = 8.104$ Å, $\alpha = 82.75°$, $\beta = 73.94°$, $\gamma = 70.71°$. Low-$Ba_3V_4O_{13}$

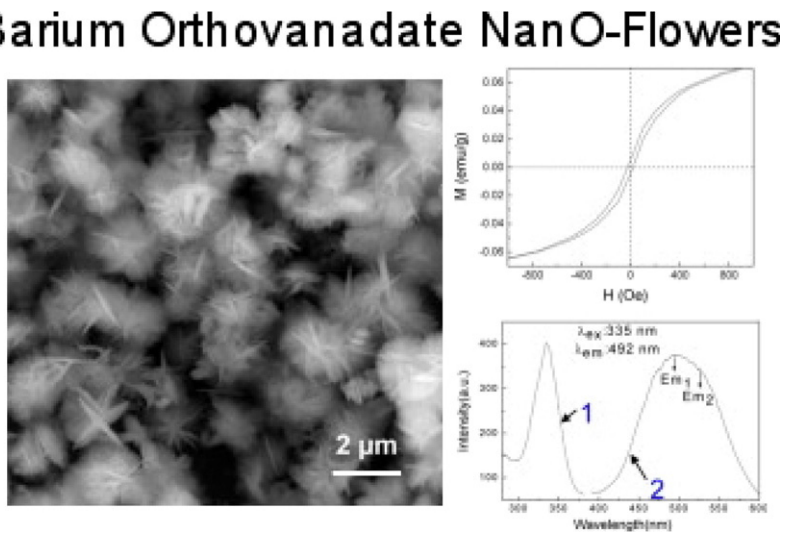

FIGURE 9.37

transforms at 870 °C into high-$Ba_3V_4O_{13}$ which crystallizes in the orthorhombic system, space group *Pbcm* (No. 57) (or *Pbc*2, No. 29) with unit-cell dimensions $a = 7.107$, $b = 13.883$, $c = 19.219$ Å. No relations have been found between the structures of the tribarium tetravanadate and the tribarium tetraphosphate. The compound, $Ba_3V_4O_{13}$ (3:2 $BaO \cdot V_2O_5$) and related compounds, $Ba_5V_5O_{14}$, $Ba_8V_7O_{22}$ have been synthesized. A comparison of their structures is given in the following Fig. 9.38.

Cell parameters are:

$Ba_3V_4O_{13}$-mS80-C2/*m* typex

$a = 8.9418$ Å, $b = 9.2053$ Å, $c = 10.1622$ Å, $\alpha = 111.16°$, $\beta = \gamma = 90°$, $c = 119.06$ Å, cell volume $= 666.94$ Å^3, cell occupancy is shown in Table 9.16.

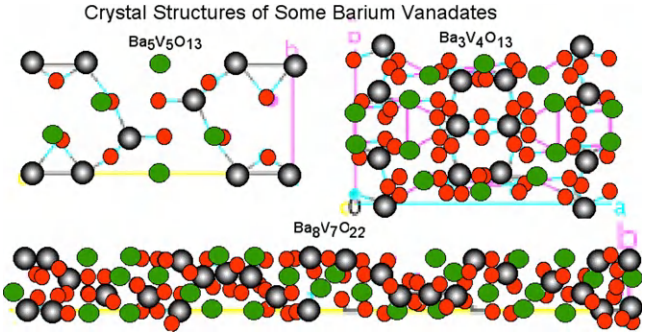

FIGURE 9.38

TABLE 9.16

No	Site notation	Atom	Multiplicity	Wyckoff	Site symmetry	*x*	*y*	*z*	Occupancy
1	V1	V	8	f	1	0.092	0.3136	0.0027	1.0
2	V2	V	8	f	1	0.1147	0.0115	0.3688	1.0
3	O1	O	8	f	1	0.1273	0.1199	0.0062	1.0
4	O2	O	8	f	1	0.1455	0.3664	0.1771	1.0
5	O3	O	8	f	1	0.1645	0.1717	0.4408	1.0
6	Ba1	Ba	8	f	1	0.2944	0.1639	0.3018	1.0
7	O4	O	8	f	1	0.3326	0.4442	0.2269	1.0
8	O5	O	8	f	1	0.3723	0.0811	0.0996	1.0
9	O6	O	8	f	1	0.5202	0.1669	0.0463	1.0
10	O7	O	4	e	2	0	0.063	1/4	1.0
11	Ba2	Ba	4	e	2	0	0.3814	1/4	1.0

TABLE 9.17

No	Site notation	Atom	Multiplicity	Wyckoff	Site symmetry	*x*	*y*	*z*	Occupancy
1	O2	O	6	i	.m.	0.1662	0.8338	0.3096	1.0
2	O3	O	6	i	.m.	0.8469	0.1531	0.1001	1.0
3	Ba3	Ba	2	d	3m.	1/3	2/3	0.0824	1.0
4	V2	V	2	d	3m.	1/3	2/3	0.3703	1.0
5	O1	O	2	d	3m.	1/3	2/3	0.5104	1.0
6	Ba2	Ba	2	d	3m.	1/3	2/3	0.7376	1.0
7	V1	V	2	c	3m.	0	0	0.2006	1.0
8	Ba1	Ba	1	b	-3m.	0	0	1/2	1.0
9	V3	V	1	a	-3m.	0	0	0	1.0

TABLE 9.18

No	Site notation	Atom	Multiplicity	Wyckoff	Site symmetry	*x*	*y*	*z*	Occupancy
1	O2	O	18	h	.m	0.4953	0.5047	0.1913	1.0
2	O3	O	18	h	.m	0.4992	0.5008	0.3974	1.0
3	O1	O	18	h	.m	0.514	0.486	0.3123	1.0
4	V1	V	6	c	3m	0	0	0.0435	1.0
5	Ba2	Ba	6	c	3m	0	0	0.1047	1.0
6	Ba3	Ba	6	c	3m	0	0	0.1812	1.0
7	O4	O	6	c	3m	0	0	0.2272	1.0
8	V3	V	6	c	3m	0	0	0.2565	1.0
9	Ba1	Ba	6	c	3m	0	0	0.3172	1.0
10	Ba4	Ba	6	c	3m	0	0	0.3891	1.0
11	O5	O	6	c	3m	0	0	0.4356	1.0
12	V2	V	6	c	3m	0	0	0.4653	1.0
13	V4	V	3	a	-3m	0	0	0	1.0

$Ba_5V_5O_{14}$-hP24-*P*-3m*l* type

$a = b = 5.78$ Å, $c = 11.897$ Å, cell volume $= 344.21$ Å^3, cell occupancy is shown in Table 9.17.

$Ba_8V_7O_{22}$-hR111-*R*-3*m* type

$a = b = 5.784$ Å, $c = 19.316$ Å, $\alpha = \beta = 81.389°$, $\gamma = 60°$, cell volume $= 551.21$ Å^3. Cell occupancy is shown in Table 9.18.

A similar compound, $BaV_{10}O_{15}$ exhibits a first-order structural phase transition in the temperature range 105 K–135 K, depending upon the sample. The variation in transition temperature has been correlated with the variation in the lattice parameters and degree of sample oxidation. Crystal symmetry decreases from *Cmca* in the high-temperature phase, to *Pbca* in the low-temperature phase. Single crystal work has shown a decrease in certain V–V distance, which has been attributed to metal–metal bond formation. A cooperative magnetic transition occurs near 42 K that contains features of both spin glass behavior and long-range magnetic order. NPD has shown that the moment is much lower than the expected value of 2.2 μB. Furthermore, the magnetic entropy released below 70 K is less than 15% of the entropy release expected for this moment value.

In addition to the four compounds shown in the phase diagram, other compositions have been discovered as well. The crystal structure of $Ba_2V_3O_9$ has been determined and refined to final R and R_w values of 0.025 and 0.028 from 1562 independent single crystal reflections. It crystallizes in the space group $P2_1/m$

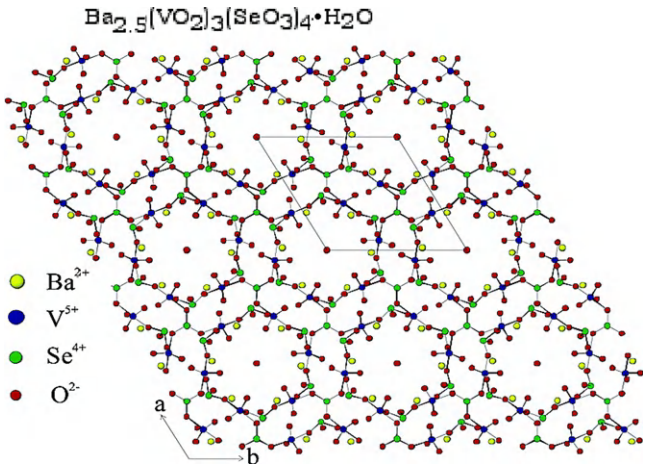

FIGURE 9.39

with $a = 9.302$ Å, $b = 5.969$ Å, $c = 8.118$ Å, and $\beta = 113.96°$. The structure consists of one-dimensional rutile-type chains of edge-sharing VO_6 octahedra parallel to the *b*-axis. The VO_4 tetrahedra share corners with VO_6 octahedra of a single rutile-type chain to form one-dimensional $[V_3O_9]^{4-}_{\infty}$ columns which are held together by Ba^{2+}ions. In this mixed valence compound, V^{4+} and V^{5+} ions are distributed in an ordered way in octahedra and tetrahedra, respectively. In the almost perfect O_6 octahedron, the vanadium atom is off-centered so that it forms a short vanadyl V=O bond of 1.686 Å, typical of a V^{4+} ion. This compound is a barium vanadyl vanadate $Ba_2(VO)(VO_4)_2$. It is the first example of isolated rutile-type chains found with V^{4+} ions. Magnetic susceptibility measurements show that this phase is an anti-ferromagnet with $T_N = 58$ K. At about 20 K. magnetic anisotropy causes a canted spin arrangement.

A novel vanadate, $Ba_{2.5}(VO_2)_3(SeO_3)4 \cdot H_2O$, has been synthesized by hydrothermal methods using $BaCO_3$, $Ba(OH)_2 \cdot H_2O$, V_2O_5, TeO_2, and H_2SeO_3 as reagents. The structure was determined by single-crystal XRD as shown in Fig. 9.39.

$Ba_{2.5}(VO_2)_3(SeO_3)_4 \cdot H_2O$ exhibits a two-dimensional layered structure consisting of VO_5 square pyramids and SeO_3 polyhedra. Infrared spectroscopy (IR) and RS, UV–Vis diffuse reflectance spectroscopy, and thermogravimetric (TG) analysis were also presented. Crystal data: $Ba_{2.5}(VO_2)_3(SeO_3)4 \cdot H_2O$, trigonal, space group *P* (No. 147) with $a = b = 12.8279$ Å, $c = 7.2631$ Å, $V = 1035.1$ Å^3, and $Z = 2$

Barium vanadate is available commercially as the orthovanadate. Its CAS number is 39416-30-3.

9.1.6. Radium Vanadates

Although some radium vanadates could undoubtedly be prepared and studied, no dissertations or papers have appeared in the scientific literature. According to R.T. Lawson (Environmental Science Division, Australian Atomic Energy Commission-1985): "There are no reports on the preparations of **radium vanadate** and no estimates have been reported for the thermodynamic properties of this compound". This is probably due to the high-cost of Ra salts as well as the intense radioactivity of ^{226}Ra itself.

9.2. ALKALINE EARTH NIOBIUM COMPOUNDS

Niobium forms oxides with the oxidation states +5 (Nb_2O_5), +4 (NbO_2), and +3 (Nb_2O_3). The most common state is +5, those of +4 are rare and those of +3 are almost non-existent. The list of alkaline earth niobates is similar to that of the vanadates. The compounds $BeNbO_3$, $CaNbO_3$, $Ca_2Nb_2O_7$, $SrNbO_3$, $BaNbO_2$, $BaNbO_3$ and $BaNb_2O_5$ have been discovered. The trend seems to be related to the size of the alkaline earth cation, zero (0) oxide compounds being formed by beryllium, four (4) definitive compounds by Mg^{2+} and Ca^{2+}, five (5) by Sr^{2+}, and nine (9) by Ba^{2+}. In addition, Nb-metal, Nb^0, forms a series of compounds with Be^0 but none with the other alkaline earths.

Niobium was originally called "Columbium" by Charles Hatchett (1801) who found a new element in a sample of mineral sent to England from Massachusetts in 1734 by John Winthrop. He named the mineral "Columbite" and the new element after "Columbia", the poetical name for "America". However, his results were subsequently disputed because the "element" that Hatchett separated was actually a mixture of Nb^0 and Ta^0. Heinrich Róse (1846) argued that the oxide from the mineral, originally named "Tantalite", actually contained Nb plus Ta. He therefore renamed the elemental metals after the children of Tantalus who were called "Niobe" and "Pelops". The former name remained but the latter became known as "Tantalum" (who was the ruler of a city in western Phrygia, located in Asia Minor or contemporary Turkey). This confusion arose because of the minimal observed chemical differences between tantalum and niobium. It was not until the early 20th century that niobium was first used commercially in incandescent-lamp filaments. This use quickly became obsolete through the replacement of niobium with tungsten, which has a higher melting point and thus is preferable for use in incandescent lamps. The discovery that niobium improves the strength of steel was made in the 1920s, and this application remains its predominant use today. Currently, a number of uses are emerging for alkaline earth niobates, notably the use of single-crystal calcium pyroniobate, $Ca_2Nb_2O_7$, as a frequency-doubler for high-power

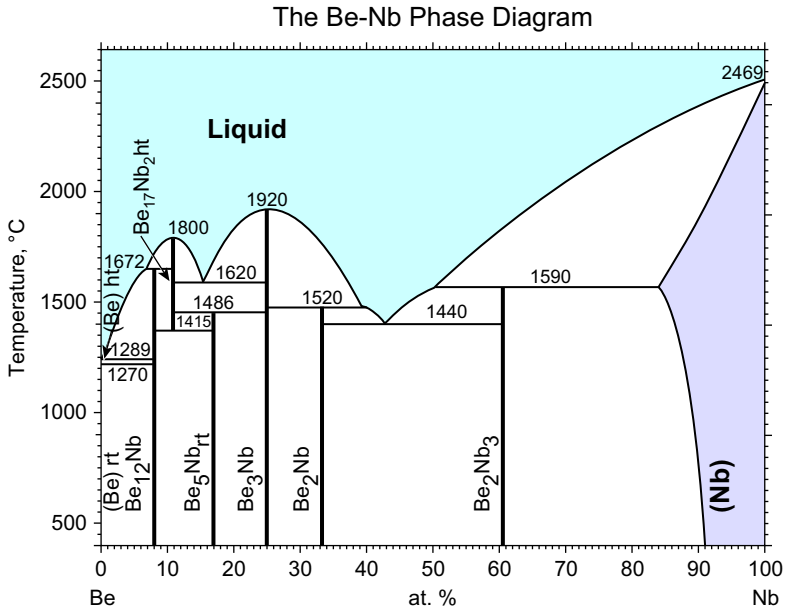

FIGURE 9.40

YAG-lasers. Its response is five (5) times that of KDP (KH_2PO_4) commonly used for second-harmonic generation of 1064 nm (Nd^{3+}) laser beams.

9.2.1. Beryllium Niobium Compounds

Beryllium metal, Be^0, forms a series of intermetallic compounds with Nb^0 as shown in the above phase diagram: Fig. 9.40.

Nearly all of the Be^0–Nb^0 compounds melt peritectically with the exception of Be_3Nb and $Be_{17}Nb_2$ (the latter is stable only between 1415 °C and 1800 °C). These compounds melt congruently. The crystal phase factors are shown in Table 9.19 as follows:

Be_2Nb has the crystal structure as shown in Fig. 9.41.

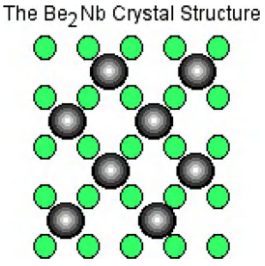

FIGURE 9.41

Here the Be_2Nb arrangement, is repeated in all three directions in the lattice. Cell parameters are: $a = b = c = 4.6259$ Å, $\alpha = \beta = \gamma = 60°$, cell volume = 70.01 Å^3, cell occupancy is shown in Table 9.20.

TABLE 9.19

Compound	Structure type	Point group	Space group	Melting temp, °C	Physical data
(Be) rt	Mg	hP2	194	1270	No Data
(Be) ht	W	cI2	229	1289	No Data
Be_2Nb	$MgCu_2$	cF24	227	1520	No Data
Be_3Nb	$PuNi_3$	hR36	166	1920	No Data
Be_2Nb_3	U_3Si_2	tP10	127	1590	No Data
$Be_{12}Nb$	$ThMn_{12}$	tI26	139	1672	No Data
$Be_{17}Nb_2$ ht	$Zn_{17}Th_2$	hR57	166	1800	No Data
(Nb)	W	cI2	229	2469	No Data

TABLE 9.20

No	Site notation	Atom	Multiplicity	Wyckoff	Site symmetry	x	y	z	Occupancy
1	Be	Be	16	c	.-3m	0	0	0	1.0
2	Nb	Nb	8	b	-43m	3/8	3/8	3/8	1.0

TABLE 9.21

No	Site notation	Atom	Multiplicity	Wyckoff	Site symmetry	x	y	z	Occupancy
1	BeIII	Be	18	h	.m	0.504	0.496	0.0818	1.0
2	NbII	Nb	6	c	3m	0	0	0.1402	1.0
3	BeII	Be	6	c	3m	0	0	0.3344	1.0
4	BeI	Be	3	b	-3m	0	0	1/2	1.0
5	NbI	Nb	3	a	-3m	0	0	0	1.0

TABLE 9.22

No	Site notation	Atom	Multiplicity	Wyckoff	Site symmetry	x	y	z	Occupancy
1	Nb2	Nb	4	h	m.2m	0.1794	0.6794	1/2	1.0
2	Be	Be	4	g	m.2m	0.617	0.117	0	1.0
3	Nb1	Nb	2	a	4/m..	0	0	0	1.0

Be_3Nb has the structure shown as follows in Fig. 9.42.

Cell parameters are: $a = b = 4.561$ Å, $c = 7.4945$ Å, $\alpha = \beta = 72.285°$, $\gamma = 60°$, cell volume $= 125.41$ Å^3. Cell occupancy is shown in Table 9.21.

Be_2Nb_3 has the structure as shown in Fig. 9.43.

Cell parameters are: $a = 3.35$ Å, $b = 6.49$ Å, $c = 6.49$ Å, $\alpha = \beta = \gamma = 90°$, cell volume is 141.10 Å^3. Cell occupancy is shown in Table 9.22.

The compound, $Be_{12}Nb$, has the structure shown as follows in Fig. 9.44.

The cubic lattice contains a body-centered cube of Nb-atoms (see below) but there are three (3) inner layers of Be-atoms in the structure.

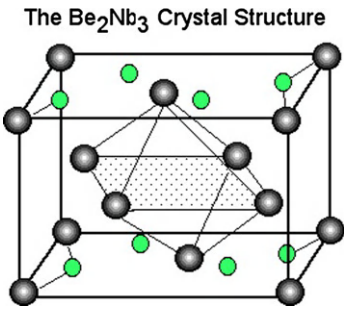

FIGURE 9.43

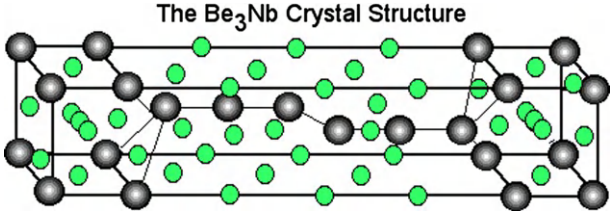

FIGURE 9.42

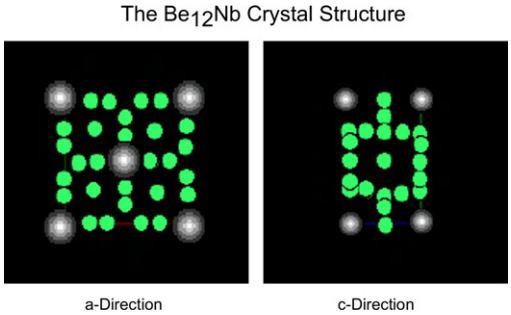

FIGURE 9.44

TABLE 9.23

No	Site notation	Atom	Multiplicity	Wyckoff	Site symmetry	x	y	z	Occupancy
1	Be1	Be	8	j	m2m.	0.277	1/2	0	1.0
2	Be2	Be	8	i	m2m.	0.361	0	0	1.0
3	Be3	Be	8	f	..2/m	1/4	1/4	1/4	1.0
4	Nb1	Nb	2	a	4/mmm	0	0	0	1.0

TABLE 9.24

No	Site notation	Atom	Multiplicity	Wyckoff	Site symmetry	x	y	z	Occupancy
1	M	0.85Nb+0.15Be	2	a	m-3m	0	0	0	1.0

Cell parameters are: $a = 4.244$ Å, $b = c = 5.6209$ Å, $\alpha = 81.806°$, $\beta = \gamma = 67.52°$, cell volume = 114.68 Å^3.

Cell occupancy is shown in Table 9.23.

Another compound, described as $Be_{0.15}Nb_{0.85}$, has been discovered. In this intermetallic compound, 15% of the sites in a semi-cubic body-centered lattice are occupied by Be atoms while the other 85% are randomly occupied by Nb atoms. The structure is shown in Fig. 9.45.

This compound does not appear in the phase diagram. Cell parameters are: $a = b = c = 2.8484$ Å, $\alpha = \beta = \gamma = 109.471°$, cell volume = 17.79 Å^3. Site occupancy is shown in Table 9.24.

Sputter deposition of Be–Nb alloys at low temperatures (30 °C) produces an amorphous phase for compositions of greater than 5 atom% Nb. A metastable crystalline phase, which can be considered a highly faulted form of the $Be_{12}Nb$ occurs at higher deposition temperatures or by low temperature annealing of the amorphous phase. Because of structural similarities, this metastable phase is a precursor to the formation of either $Be_{12}Nb$ or $Be_{17}Nb_2$ upon high temperature annealing. There was no evidence of the Be_5Nb phase that has been postulated on some phase diagrams.

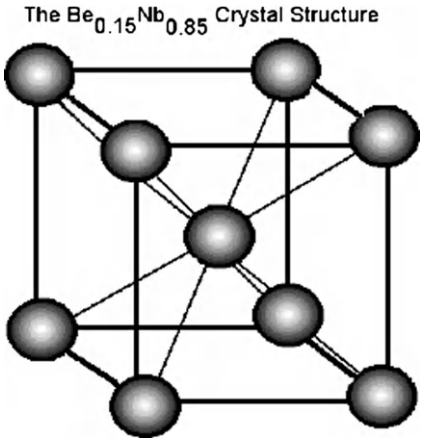

FIGURE 9.45

The system, BeO–Nb_2O_5, does not seem to form any compounds. Reference is made to $BeNb_2O_6$ in one or two papers but no description of its properties has been documented.

No Industrial uses for Be-Nb intermetalic compounds have yet emerged.

9.2.2. Magnesium Niobium Compounds

No intermetallic compounds are formed between Mg^0 and Nb^0 as metals.

In the Nb^{2+} system of MgO–NbO, no compounds like Mg_2NbO_2 have been found.

In the Nb^{3+} system of MgO–Nb_2O_3, no compounds like $MgNb_2O_4$ have been discovered. Nor have the possible compounds like $Mg_2Nb_2O_5$ or $MgNb_2O_7$ been revealed. Thus Nb^{3+} is not a viable valence-state for combination with MgO to form compounds. This behavior may be contrasted to that of MgO and vanadium oxides (which are easily formed).

In the Nb^{4+} system of MgO–NbO_2, the compound, $MgNbO_3$ has not been synthesized. Nor are the possible compounds, Mg_2NbO_4, Mg_3NbO_5, $MgNb_2O_5$, or $MgNb_3O_7$, known to date. Thus, Nb^{3+} is not a viable valence-state for combination with MgO to form compounds. This behavior may be contrasted to that of MgO and vanadium oxides (which readily do so).

In the Nb^{5+} system of MgO–Nb_2O_5, four compounds are thought to exist as shown in Fig. 9.46.

$MgNb_2O_6$ is said to be congruently melting at 1570°C while the compounds (Mg,Nb)$O_{2.42}$, $Mg_5Nb_4O_{15}$ and

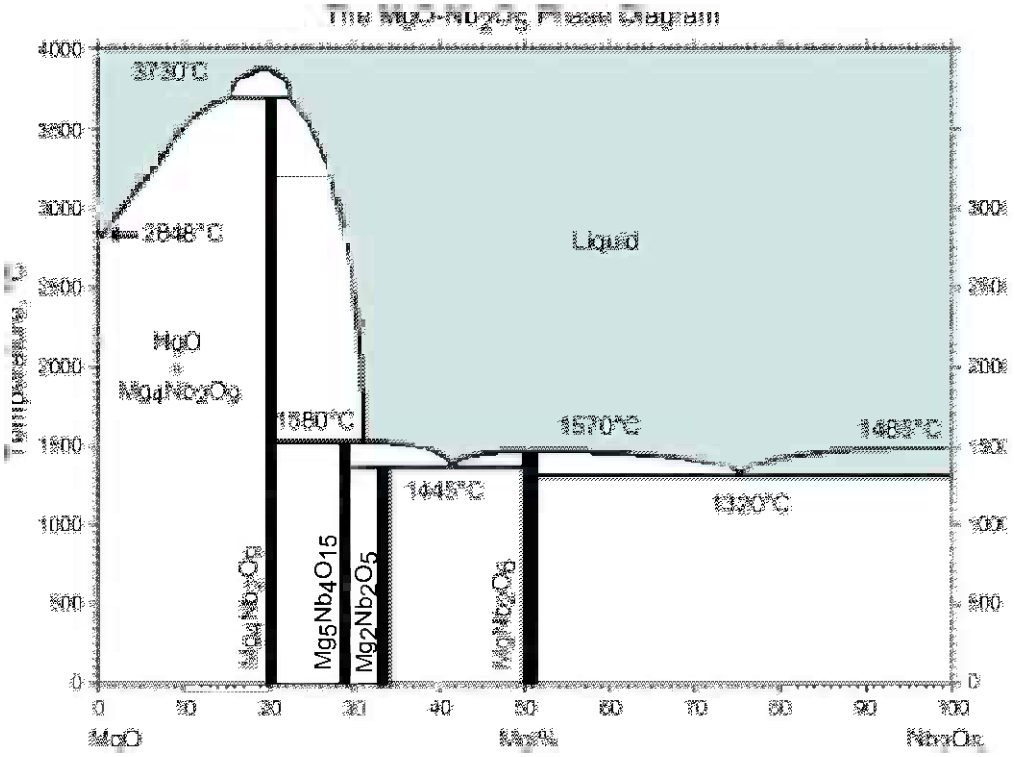

FIGURE 9.46

$Mg_4Nb_2O_9$ decompose peritectically at 1445, 1580 and 3730°C, respectively. Small crystals of all four compounds were grown by the laser-heated pedestal growth (LMPG) method. The Nb_2O_5-rich compounds showed some tendency to partial reduction of Nb^{5+} even when grown in an O_2 atmosphere, resulting in a bluish-black color in the as-grown crystals. In Figure 9.46 (Mg,Nb) $O_{2.42}$ is shown as $Mg_2Nb_2O_{5-\delta}$, where the more likely composition where δ is a small number >2.

The magnesium niobate system (MgO–Nb_2O_5) and its solid solutions have been studied. At least four possible magnesium niobate oxides have been studied: $MgNb_2O_6$, $Mg_4Nb_2O_9$, $Mg_5Nb_4O_{15}$, and $Mg_{0.66}Nb_{0.33}O_{2.9}$. It was reported that $MgNb_2O_6$ and $Mg_4Nb_2O_9$ are the only stable phases that can be found at room temperature. Although magnesium niobate $MgNb_2O_6$ was identified as a potential candidate to be used as a microwave dielectric material, it has not found such usage. However, it has been widely used as a precursor for the synthesis of single-phase relaxor perovskite $Pb(Mg_{0.66}Nb_{0.33}O_3)$ (PMN) since the success of the route, known as the "Columbite method" was proposed. $PbMg_{0.66}Nb_{0.33}O_3$ (PMN) is a relaxor whose dielectric constant can reach 25,000 at high frequencies (100 Hz) and decrease at lower frequencies. Its temperature of maximum dielectric constant (T_m) is −40°C and it loses its spontaneous polarization around −10°C (T_d). With the additions of about 28% of $PbTiO_3$, the T_m shifts to higher temperatures, allowing its use as a piezoelectric at room temperature. In general, production of single-phase $MgNb_2O_6$ is not straightforward, as minor concentrations of the phase $Mg_4Nb_2O_9$ and/or MgO are sometimes formed along side the major phase of $MgNb_2O_6$. The solid-state reaction among constituent oxides of MgO and Nb_2O_5 at an elevated temperature always results in inhomogeneous composition, irregular grain shape, and larger grain size with broad distribution. Moreover, the formation of magnesium niobate phases requires long heat treatment. Use of a niobium ethylate is one way to prepare pure $MgNb_2O_6$ by a sol-gel method:

$$Mg(NO_3)_2 + 2\,Nb(OC_2H_5)_5 \Rightarrow Mg(OC_2H_5)_{10} + 2\,NO_{3^-} + 2\,H^+$$

Addition of citric acid forms the gel, which is heated to 500–800 °C for 3 h to decompose the organic ethylate and form a crystalline $MgNb_2O_6$ compound.

The compounds $MgNb_2O_6$ and $Mg_4Nb_2O_9$ are known to exhibit luminescence in the blue-green region (self-activated). The excitation–emission spectra are shown in Fig. 9.47.

Layers of these compounds were grown by evaporating Nb_2O_5 on the heated surface of a crystal of MgO in order to establish the stability of these compounds. The following Table 9.25 shows typical samples in terms of their deposition temperature and identified phase.

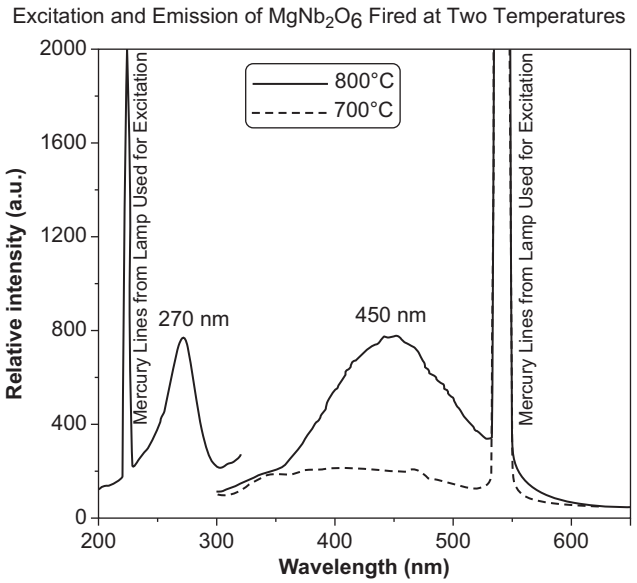

FIGURE 9.47

The reaction begins ~750 °C and both compounds are formed. Above 1050 °C, only $Mg_4Nb_2O_9$ is stable.

The lattice parameters found were:

$Mg_4Nb_2O_9$

$a = b = 5.1624$ Å, $c = 14.024$ Å, $\alpha = \beta = 90°$, $\gamma = 120°$

$MgNb_2O_6$

$a = 5.71$ Å, $b = 14.19$ Å, $c = 5.03$ Å, $\alpha = \beta = \gamma = 90°$

Crystals of $MgNb_2O_6$ have the orthorhombic columbite-type structure. The compound $MgNb_2O_6$ melts congruently at about 1570 °C. $MgNb_2O_6$ has the crystal structure as shown in Fig. 9.48.

The groups are part of the NbO_6 octahedrons, which are distributed in three (3) dimensions in the

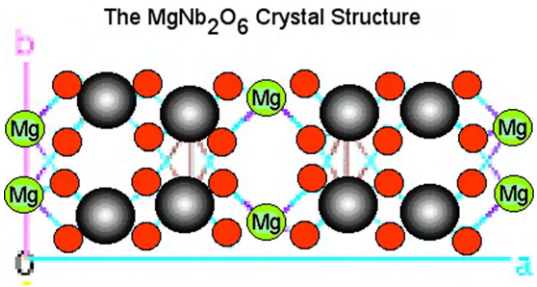

FIGURE 9.48

structure. The Mg^{2+} cations are tetrahedrally coordinated by the oxygen atoms of two (2) octahedra. Cell occupancy is shown in Table 9.26.

Magnesium niobate ($MgNb_2O_6$) powders in orthorhombic form have been successfully prepared via an oxalate synthetic route. Solutions of magnesium chloride hexahydrate and niobium pentachloride were used as the starting materials in the synthesis of $MgNb_2O_6$ powders. The formation mechanism of $MgNb_2O_6$ was clarified by TGA–DTA, FT-IR and XRD. Crystals of $MgNb_2O_6$ may also be grown from a $Na_2Mo_2O_7$ flux by a slow cooling method. The major advantage of this flux method is that crystals grow at a temperature well below the melting point. Another advantage is that well-formed crystals are obtained. The morphology, density and lattice parameters of the resulting crystals were examined. The morphology of the formed powders was examined by (SEM). The following Fig. 9.49 shows the morphology of such crystals as grown from the melt.

It was found that the second phases of MgO, Nb_2O_5 and $Mg_{0.66}Nb_{1.33}O_{2.9}$ tend to form together with $MgNb_2O_6$, depending on calcination conditions. However, single-phase $MgNb_2O_6$ powders consisting

TABLE 9.25

Deposition temp, °C	470	700	800	900	1000	1100
Phase identified	Nb_2O_5	Nb_2O_5	$MgNb_2O_6$	$Mg_4Nb_2O_9$	$MgNb_2O_6$	$Mg_4Nb_2O_9$
			$Mg_4Nb_2O_9$	$MgNb_2O_6$	$Mg_4Nb_2O_9$	

TABLE 9.26

No	Site notation	Atom	Multiplicity	Wyckoff	Site symmetry	*x*	*y*	*z*	Occupancy
1	O1	O	8	d	1	0.0963	0.1041	0.0727	1.0
2	O2	O	8	d	1	0.244	0.1236	0.4207	1.0
3	Nb1	Nb	8	d	1	0.3389	0.3191	0.2506	1.0
4	O3	O	8	d	1	0.4189	0.1163	0.099	1.0
5	Mg1	Mg	4	c	.2.	0	0.3311	1/4	1.0

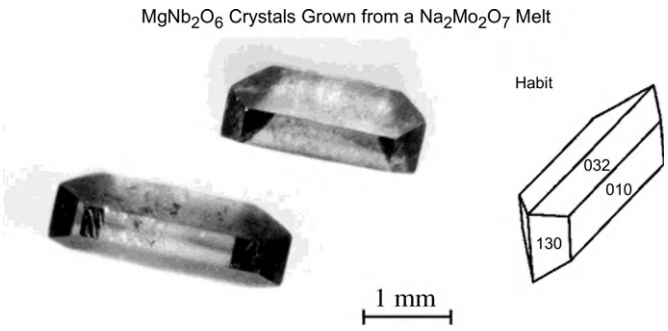

FIGURE 9.49

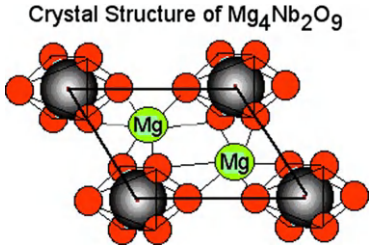

FIGURE 9.50

of nanoparticles ~100–300 nm were successfully obtained for a calcination temperature of 750 °C for 13 h with the introduction of pre-firing (750 °C/2 h) and remixing processes.

$MgNb_2O_6$ single crystals of several cubic centimeters have been grown by the Czochralski technique. The as-grown black crystals were annealed in oxygen at high temperature and became transparent. The process was reversible by high temperature vacuum annealing. The optical absorption observed in as-grown samples has been attributed to oxygen deficiency of the crystal. The grown crystals were resistant against strong mineral acids.

Mainly, two product phases were found in each of the two systems $MgO–Nb_2O_5$ and $MgO–Ta_2O_5$, viz. $Mg_4Nb_2O_9$ and $MgNb_2O_6$, and $Mg_4Ta_2O_9$ and $MgTa_2O_6$ phases, respectively. Details on phase formation and on the $MgNb_2O_6$ and $MgTa_2O_6$ phases have been published. $Mg_4Nb_2O_9$ and $Mg_4Ta_2O_9$ were stated to be hexagonal (space group $P3c1$, No. 165) with the lattice parameters $a = b = 5.1624$ Å and $c = 14.024$ Å for $Mg_4Nb_2O_9$ [JCPDS 38–1459], and $a = b = 5.1611$ Å and $c = 14.0435$ Å for $Mg_4Ta_2O_9$ [JCPDS 38–1458]. The crystal structure of $Mg_4Ta_2O_9$ has a distorted hexagonal close-packed stacking of oxygen ions along the c-axis. It is isotypic with the corundum-type (α-Al_2O_3) structure, with cations occupying two thirds of the octahedral interstices of the oxygen frame. The structure of $Mg_4Nb_2O_9$ is quite similar to that of $Mg_4Ta_2O_9$, with a very small difference in the lattice parameters. Due to this fact, the results obtained on $Mg_4Nb_2O_9$ and $Mg_4Ta_2O_9$ were most similar to each other. Thus the obtained results presented in this paper on the example of either one or the other of the two materials is nearly the same. The structure may be represented as shown in Fig. 9.50.

In another paper, magnesium niobate ($Mg_4Nb_2O_9$) powders have been prepared and characterized by TG–DTA, XRD, SEM and EDX techniques. The effect of calcination temperature, dwell time and heating/cooling rates on phase formation, morphology and chemical composition of the powders were examined. The calcination temperature and dwell time have been found to have a pronounced effect on the phase formation and morphology of the calcined magnesium niobate powders. It has been found that the minor phases of nano-sized MgO inclusion and the columbite-type $MgNb_2O_6$ phase tend to form together with the corundum-type $Mg_4Nb_2O_9$ phase, depending on calcination conditions. It is seen that optimization of calcination conditions can lead to a single-phase $Mg_4Nb_2O_9$ in a hexagonal phase.

Synthesis of $MgTiO_3$ and $Mg_4Nb_2O_9$ phases having an ordered corundum type structure by reacting MgO and TiO_2 or Nb_2O_5 together with the addition of excess MgO has been investigated. When MgO and TiO_2 or Nb_2O_5 are reacted with 1:1 and 4:1 stoichiometry, $MgTiO_3$ and $Mg_4Nb_2O_9$ phases having an ordered corundum type structure are formed. Moreover, a minor amount of $MgTi_2O_5$ and $MgNb_2O_6$ phases are frequently observed along with the ordered corundum type phases. It has been shown that the formation of these additional phases can be suppressed by the addition of stoichiometrically excess of MgO, which can subsequently be removed after the reaction by treating with dilute mineral acid, thus forming pure $MgTiO_3$ and $Mg_4Nb_2O_9$. Another representation of the structure is shown in Fig. 9.51.

Cell occupancy is shown in Table 9.27.

The sintering temperature of $Ba(Mg_{1/3}Nb_{2/3})O_3$ (BMN) ceramic occurs at about 1450 °C. When B_2O_3 was added, BMN sintered at 900 °C and it had a 1:2 ordered hexagonal structure. A liquid phase, which could be responsible for the decrease in sintering temperature, was observed in B_2O_3-added BMN. $Mg_4Nb_2O_9$ and $Ba_2B_2O_5$ second phases were found in

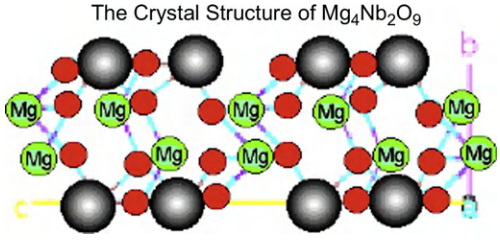

FIGURE 9.51

TABLE 9.27

No	Site notation	Atom	Multiplicity	Wyckoff	Site symmetry	x	y	z	Occupancy
1	O1	O	12	g	1	0.336	0.308	0.086	1.0
2	O2	O	6	f	.2.	0.276	0	1/4	1.0
3	Mg1	Mg	4	d	3..	1/3	2/3	0.019	1.0
4	Mg2	Mg	4	d	3..	1/3	2/3	0.3034	1.0
5	Nb1	Nb	4	c	3..	0	0	0.1426	1.0

the specimens and the $Ba_2B_2O_5$ second phase might be related to the liquid phase. The dielectric constant (ε_r) and Q value increased with increasing sintering temperature and it is due to the increase in bulk density. However, they decreased with increasing B_2O_3 content, which can be explained by the existence of the second phases. Good microwave dielectric properties of $Q \times f = 8500$ GHz, $\varepsilon_r = 27.5$ and temperature coefficient of resonance frequency $(\tau_f) = 27.0$ ppm/°C were obtained for BMN with 2.0 mol% B_2O_3 sintered at 930 °C for 2 h.

In another study, the columbites $MgNb_2O_6$, $MgTa_2O_6$ and corundum-type $Mg_4Nb_2O_9$ ceramics were prepared by a conventional solid-state ceramic route. The structure and microstructure of the sintered samples were investigated by XRD and SEM techniques. The microwave dielectric properties of the samples were measured by the resonance method in the frequency range 4–6 GHz. The dielectric properties were tailored by forming a solid solution between $MgNb_2O_6$ and $MgTa_2O_6$ and by the substitution of TiO_2 for Nb_2O_5 in both $MgNb_2O_6$ and $Mg_4Nb_2O_9$ ceramics. The $Mg(Nb_{0.7}Ta_{1.3})O_6$ composition has $\varepsilon_r = 29$, $Q_u \times f = 67{,}800$ GHz, and $\tau_f = 0.8$ ppm/°C and the $MgO\{(0.5)Nb_2O_5–(1.5)TiO_2\}$ composition has $\varepsilon_r = 34.5$, $Q_u \times f = 81{,}300$ GHz, and $\tau_f = -2$ ppm/°C.

The binary niobate ceramics, with the formula $M^{2+}Nb_2O_6$ where $M^{2+} = Ca$, Mg, or a transition metal (TM), have the orthorhombic columbite structure. The best-known members of this group are zinc niobate ($ZnNb_2O_6$) and magnesium niobate ($MgNb_2O_6$), but Ca, Co, Ni, Mn, Cu, Cd, and Fe $^{2+}$ cations can also be included in the columbite structure. The TM columbite niobates have been found to sinter at temperatures of 1100 °–1200 °C, much lower than the complex perovskites, and this can be lowered even more when Cu^{2+} is used. The best columbite niobates have $Q \times f$ values similar to those of $BaZn_{0.33}Nb_{0.67}O_3$, and all have ε_r between 17 and 25 and negative τ_f values of <-80 ppm/°C. There is a growing interest in the columbites as microwave dielectric ceramics, due to their lower processing temperatures, less complicated processing due to the simple chemistry of the binary compounds, and the lower cost of niobium compared with tantalum, and with incorporation of Cu^{2+} they are approaching low-temperature co-fired ceramics (LTCC) temperatures. They have also been investigated combined with other dielectric ceramics (to compensate for the negative τ_f values), and with additives to lower sintering for LTCC. Furthermore, $MgNb_2O_6$ is in wide use as a precursor to synthesize single phase PMN ($Pb(Mg_{1/3}Nb_{2/3})O_3$) in the "columbite" process, and $NiNb_2O_6$ is being increasingly investigated as a catalyst for splitting water and organic compounds. $CoNb_2O_6$ and other columbites have interesting magnetic properties, and $CaNb_2O_6$ and $CdNb_2O_6$ have useful optical properties.

In another study, single crystals of a magnesium niobium oxide $Mg_5Nb_4O_{15}$ were prepared at 1673 K (1400 °C). This compound has an orthorhombic pseudo-brookite-type structure (space group *Cmcm*). The single-crystal structure refinement was carried out in the temperature range from 293 to 1173 K. The final *R*-factors were $R = 0.025$–0.038 and $R_w = 0.031$–0.044. The lattice parameters were $a = 3.806$, $b = 10.057$ and $c = 10.260$ Å at 293 K and $a = 3.810$, $b = 10.188$ and $c = 10.398$ Å at 1117 K. The linear thermal expansion coefficients were $ß_a = 1.28 \times 10^{-6}$, $ß_b = 15.8 \times 10^{-6}$ and $ß_c = 16.3 \times 10^{-6}$/K. Thermal expansion anisotropy in the bond distances and angles is consistent with the thermal expansion anisotropy in the lattice parameters. $Mg_5Nb_4O_{15}$ in the $MgO–Nb_2O_5$ system and is stable between 1200°C and its incongruent melting point at 1580°C. In an analyysis of the structure of both compounds with the help of ND, it was determined that the compounds are isostructural with pseudo-brookite Fe_2TiO_5, and the presence of any superstructure could not be noticed. The compounds crystallize with the orthorhombic structure within the space group D_2-*Cmcm* with $Z = 4$. The structure consists of double chains of (Mg, Nb)0_6 units, sharing edges of the plane, interconnected through common oxygen along the *a*-axis to give a three dimensional array. Because of the instability of this compound, no applications in Industry have emerged.

$MgNb_2O_6$ has the CAS number of 12163-26-7 and is available commercially.

9.2.3. Calcium Niobium Compounds

No intermetallic compounds are known in the Ca^0–Nb^0 system.

In the Nb^{2+} system of CaO–NbO, no compounds are known.

In the Nb^{3+} system of CaO–Nb_2O_3, the $CaNb_2O_4$ compound has been synthesized. Single crystals of a new reduced calcium niobium oxide, $CaNb_2O_4$, were prepared in an evacuated quartz tube at 1100 °C. The calcium niobium oxide crystallizes in the orthorhombic space group *Pbcm* with $a = 5.054$ Å, $b = 11.904$ Å, and $c = 5.839$ Å, $Z = 4$, and the final R factors are $R = 0.027$ and $R_w = 0.029$ for 799 unique reflections. The crystal structure has the layer built up by edge-sharing of NbO_6 trigonal prisms to form infinite metal–metal bonding as seen in $ANbO_2$ (A = Li, Na). The Ca^{2+} ion is located at the trigonal prism site in the interlayer. No evidence for superconductivity was found down to 2.0 K.

In the Nb^{4+} system of CaO–NbO_2, electrically conducting ABO_x titanates and niobates of the $A_nB_nO_{3n+2}$ type have been synthesized and investigated with respect to their physical and structural properties. Work was initiated on the $LaTiO_x$, $SrNbO_x$ and $CaNbO_x$ systems (where the value of x was found to be variable and controllable, depending upon the synthesis conditions). $CaNbO_3$ belongs to the perovskite-related title compounds of the $A_nB_nO_{3n+2}$ type but their crystal structures were not well known. They belong to the so-called Ruddlesden–Popper phases $A_{m+1}B_mO_{3m+1}$ series. A large number of compositions can be prepared by varying both the cation molecular ratios and the anion ones as well. The thickness of the layers rises with m. For $m = \infty$, the three-dimensional perovskite structure ABO_3 is realized. It has the structure shown on the next page. The $m = 1$ member is also known as the K_2NiF_4 crystal structure type. The metaniobite, $CaNbO_3$, has the structure as shown in Fig. 9.52.

Cell parameters are: $a = 5.56$ Å, $b = 5.77$ Å, $c = 8.016$ Å, $\alpha = \beta = \gamma = 90°$, cell volume = 257.16 Å^3, $Z = 2$. Cell occupancy is shown in Table 9.28.

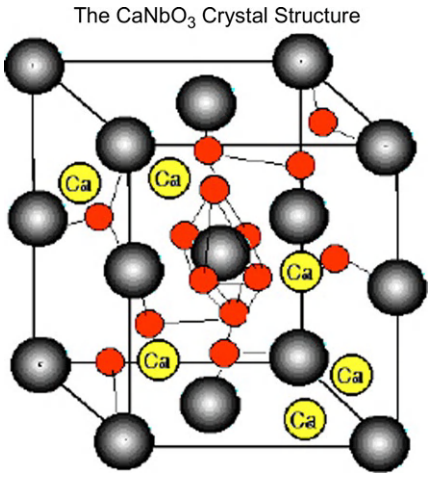

FIGURE 9.52

$CaNbO_x$ system involves a mixed valence Nb^{4+}/Nb^{5+} for $x = 3.5$ and therefore a high electrical conductivity can be expected. The physical properties were not investigated. Among the fully oxidized insulating titanates and niobates there are compounds with remarkable structural and physical properties. Some fully oxidized $n = 4$ type compounds such as $CaNbO_{3.50}$, $SrNbO_{3.50}$ and $LaTiO_{3.50}$ display extraordinary dielectric properties. They are ferroelectric up to extremely high temperatures. Their ferroelectric transition temperatures T_c lie in the range of 1615 K to 1850 K (1342 and 1577 °C). No other ferroelectric materials with such high T_c are known.

Three-dimensional titanium and niobium oxides are superconducting at temperatures considerably lower than layered copper oxides. Single crystals of isostructural niobium oxides, $CaNbO_x$ and $SrNbO_x$ were prepared with the floating zone melting technique. In common with $LaTiO_x$ they have the following properties. For $x \leq 3.4$, its layered perovskite-related structure of a known type is derived from the layered highest-T_c (>1600 K) ferroelectrics, $CaNbO_{3.5}$ and $SrNbO_{3.5}$. In the range $3.42 \leq x \leq 3.50$ well- ordered-intergrowth takes place between the $x = 3.5$ structure and the $x = 3.4$ structure. This intergrowth was found to be representative of the bulk and the stacking sequence is

TABLE 9.28

No	Site notation	Atom	Multiplicity	Wyckoff	Site symmetry	x	y	z	Occupancy
1	O1	O	8	d	1	0.1984	0.0506	0.3043	1.0
2	Ca1	Ca	4	c	.m.	0.4372	1/4	0.0156	1.0
3	O2	O	4	c	.m.	0.5328	1/4	0.6005	1.0
4	Nb1	Nb	4	a	-1	0	0	0	1.0

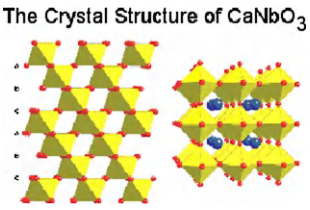

FIGURE 9.53

dependent on x. For x <3.5, magnetic and resistivity measurements were performed between room temperature and 4.2 K. The temperature dependence of the magnetic susceptibility along the layers displays a minimum. Semiconducting behavior was found along the c-axis and perpendicular to the layers. At low temperatures, the resistivity exhibits thermally activated behavior with unexpectedly small activation energies in MeV range. It consists of layers of inter-locking NbO_6 octahedra as shown in Fig. 9.53.

ABO_x niobates and titanates belonging to the homologous series $A_nB_nO_{3n+2}$ are a special group of perovskite-related layered materials. These oxides comprise the highest-T_c ferroelectrics such as $CaNbO_{3.50}$ and $LaTiO_{3.50}$, as well as thermodynamically stable bulk compounds involving well-ordered stacking sequences of layers with different thickness such as $SrNbO_{3.45}$. These belong to the so-called Ruddlesden–Popper phases $A_{m+1}B_mO_{3m+1}$. The thickness of the layers rises with m, for $m = \infty$, the three-dimensional perovskite structure ABO_3 is realized. The $m = 1$ member is also known as the K_2NiF_4 crystal structure type. A crystallographic study on $CaNbO_x$ ($3.4 \leq x \leq 3.5$) was made. This $CaNbO_x$ system involves a mixed valence Nb^{4+}/Nb^{5+} for x <3.5 and therefore a high electrical conductivity was to be expected. However, the physical properties were not investigated.

A related compound, Ca_2NbO_4 is a superconductor. From DC magnetization and powder XRD measurements of the defect-perovskitc-type reduced niobate $Ca_2Nb_{1+x}O_y$, at least two kinds of broad superconducting phases with the critical temperatures of about 9.2 K (for $0 \leq x \leq 1.0$) and 8.3 K (for $1.2–1.5 \leq x \leq 5.0$) were found that covered almost the whole valence state of Nb from Nb^{1+} to Nb^{5+} in the Ca system. The highest shielding effect in this phase is attained for samples prepared from the starting mixtures having the initial mean Nb valence between 1+ and 2+.

In the binary system containing Nb^{5+}, $CaO–Nb_2O_5$ has been shown to include three compounds: $CaO \cdot Nb_2O_5$, which melts congruently at 1560 °C; $2CaO \cdot Nb_2O_5$, which melts congruently at 1576 °C; and $3CaO–Nb_2O_5$, which melts incongruently at 1560 °C. Three eutectic compositions occur at 6% CaO (1362 °C), 23% CaO (1492 °C), and 34% CaO (1535 °C).

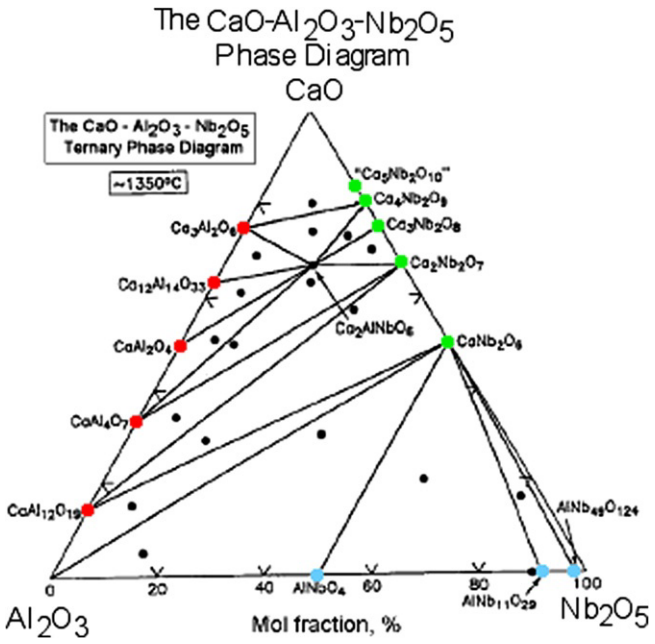

FIGURE 9.54

In addition, $4CaO–Nb_2O_5$ and what was described as "$5CaO–Nb_2O_5$" have been included in a ternary diagram of $CaO–Nb_2O_5$ and Al_2O_3. This is shown as follows in Fig. 9.54.

The binary phase diagram is shown as follows. Note that the compounds formed are based on the molar ratio of x CaO:1.0 Nb_2O_5, where x varies from one (1) to five (5) as shown in Fig. 9.55.

Subsolidus phase equilibria in the $CaO:Al_2O_3:Nb_2O_5$ system at 1325 °C in air have been determined. Only one ternary phase forms, Ca_2AlNbO_6 that exhibits a perovskite-related structure with 1:1 or NaCl-type ordering of Al^{3+} and Nb^{5+} on the B sites. Indexed powder XRD data for this monoclinic compound were given: ($P2_1/n$ (No. 11); $a = 5.3780(1)$, $b = 5.4154(1)$, $c = 7.6248(2)$ Å, $\beta = 89.968(2)°$). The subsystem $CaO–Nb_2O_5$ was reexamined at CaO contents above 70 mol % to clarify inconsistencies in the literature. Two phases were confirmed to form in this region: the polymorphic-ordered perovskite, $Ca_4Nb_2O_9$, with solid solution ranging from approximately 17 to 20.5 mol% Nb_2O_5, and the compound referred to as $Ca_3Nb_2O_8$, which was shown at this time to occur as essentially a point compound at the composition 75.25:24.75 $CaO:Nb_2O_5$.

The perovskite-related structure of the $Ca_3Nb_2O_8$-type phase was shown to be non-cubic. Capacitance methods at 1 MHz were used to determine the dielectric constants and associated temperature coefficients for eleven compounds in the $CaO:Al_2O_3:Nb_2O_5$ system. It was determined that Ca_2AlNbO_6 and $Ca_3Nb_2O_8$ coexist in equilibria and exhibit temperature coefficients of permittivity with opposite signs. Five compositions in

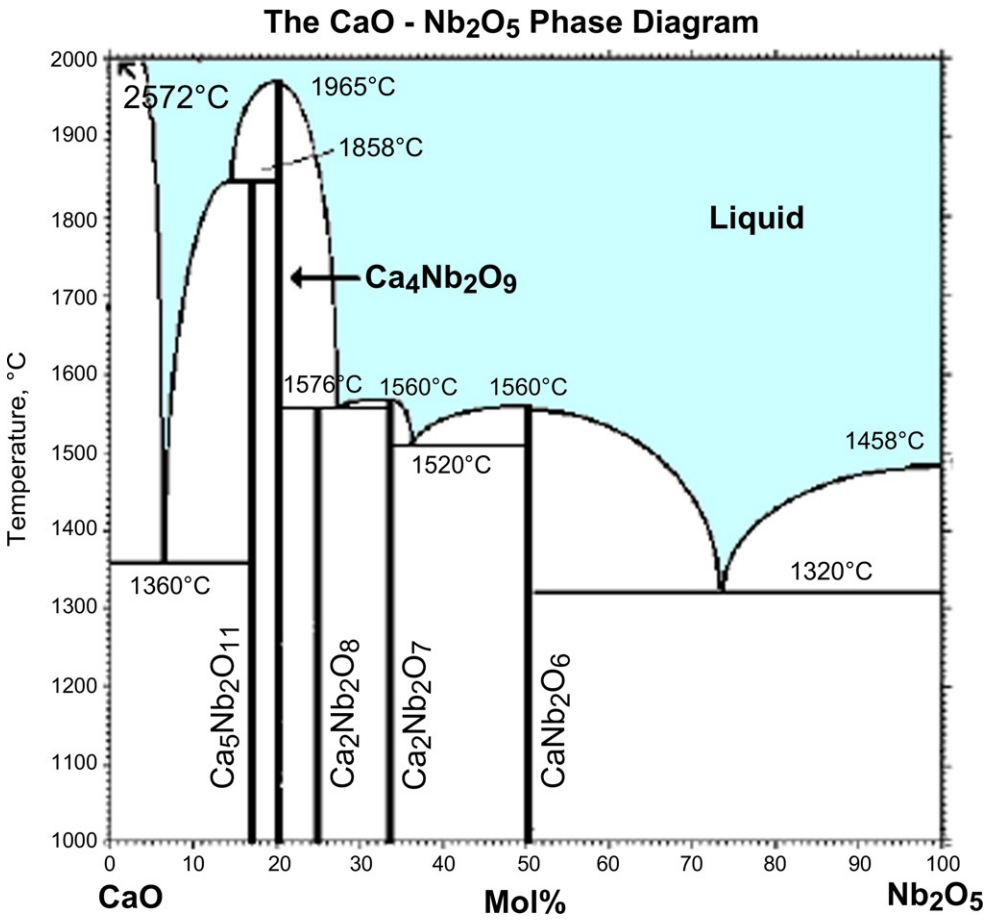

FIGURE 9.55

the $x Ca_2AlNbO_6$:$(1-x)Ca_3Nb_2O_8$ system were prepared and their dielectric properties measured by dielectric resonator methods at 5–7 GHz. The relative permittivities and temperature coefficients of resonant frequency obtained for the end members Ca_2AlNbO_6 and $Ca_3Nb_2O_8$ were 30, −88 ppm/°C, and 45, +113 ppm/°C, respectively. Temperature compensation of the resonant frequency was obtained near $x = 0.67$ with a permittivity of 32; no solid solution was detected by powder XRD.

Liquidus temperatures have been determined in the high-lime part of the system CaO–Nb_2O_5 with the high-temperature hot-stage microscope. The existence of a compound having the composition, $11CaO \cdot 2Nb_2O_5$, and melting congruently at 2105 °C was indicated. The probable existence of a compound with the composition $5CaO \cdot Nb_2O_5$, melting incongruently at 2065°C was announced. Phase relations below 1600°C of compositions near $4CaO \cdot Nb_2O_5$ were interpreted from the results of differential thermal analyses and XRD patterns of samples quenched from various temperatures.

Calcium niobate has the formula of $CaNb_2O_6$ and the structure is shown in Fig. 9.56.

It consists of interconnected niobate octahedrons and the cell constants: $a = 5.219$ Å, $b = 5.752$ Å, $c = 14.96$ Å, $\alpha = \beta = \gamma = 90°$, cell volume = 449.09 $Å^3$. Cell occupancy is shown in Table 9.29.

The pyro-niobate, $Ca_2Nb_2O_7$, is trimorphic. A comparison of the three forms is shown in the following diagram: Fig. 9.57.

Cell parameters are:

$Ca_2Nb_2O_7$ type
cF38-*Fd*-3*m*

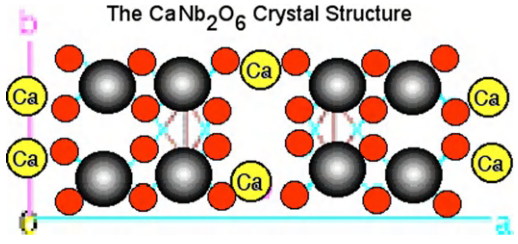

FIGURE 9.56

TABLE 9.29

No	Site notation	Atom	Multiplicity	Wyckoff	Site symmetry	*x*	*y*	*z*	Occupancy
1	O1	O	8	d	1	0.0963	0.1041	0.0727	1.0
2	O2	O	8	d	1	0.244	0.1236	0.4207	1.0
3	Nb1	Nb	8	d	1	0.3389	0.3191	0.2506	1.0
4	O3	O	8	d	1	0.4189	0.1163	0.099	1.0
5	Ca1	Ca	4	c	.2.	0	0.3311	1/4	1.0

TABLE 9.30

No	Site notation	Atom	Multiplicity	Wyckoff	Site symmetry	*x*	*y*	*z*	Occupancy
1	O1	O	48	f	2.mm	0.4286	1/8	1/8	1.0
2	Nb1	Nb	16	d	.-3m	1/2	1/2	1/2	1.0
3	Ca1	Ca	16	c	.-3m	0	0	0	1.0
4	O2	O	8	a	-43m	1/8	1/8	1/8	1.0

$a = b = c = 7.3574$ Å, $\alpha = \beta = \gamma = 60°$, cell volume = 281.62. Cell occupancy is shown in Table 9.30.

$Sr_2Nb_2O_7$ type
o*S*44-*Cmc*21
$a = 3.83$ Å $b = 5.48$ Å, $c = 13.3085$ Å, $\alpha = \gamma = 90°$, $\beta = 98.273°$, cell volume = 276.42 Å^3, $Z = 8$. Cell occupancy is shown in Table 9.31.

$La_2Ti_2O_7$ type
*mP*44-*P*21
$a = 5.502$ Å, $b = 7.697$ Å, $c = 13.385$ Å, $\alpha = 98.62°$, $\beta = \gamma = 90°$, cell volume = 560.85 Å^3, $Z = 8$. Cell occupancy is shown in Table 9.32.

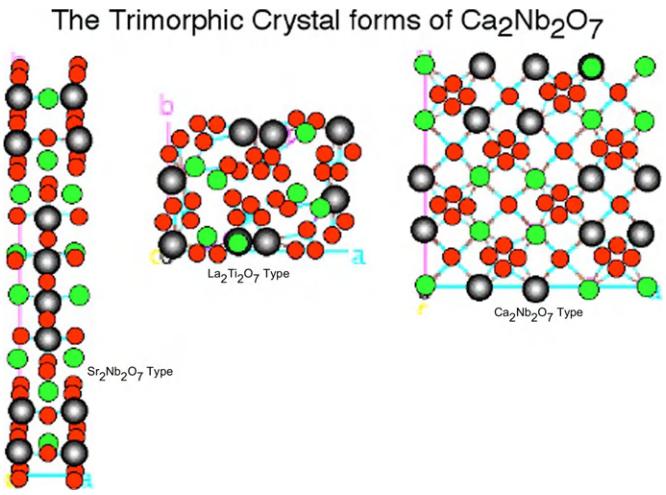

FIGURE 9.57

These structures consist of a series of connected NbO_6 octahedra as partially shown in the above diagram. This arrangement of Ca–Nb–O atoms is identical in the a ⇒ b and a ⇒ c direction in the unit cell. Minus the oxygen-atoms, each face consists of the above arrangement of Ca–Nb atoms, as shown in the following diagram. Only one octahedron is shown in Fig. 9.58.

This structure is the prototype for 441 compounds such as: $Ce_2Zr_2O_7$, $Cd_2Sb_2O_7$, $Ce_2Zr_2O_7$, $Ca_2Os_2O_7$, $La_2Hf_2O_7$, $Mn_2In_2O_7$, $Sr_2Mn_2O_7$, $Sr_2V_2O_7$, $Ce_2Zr_2O_7$, $Ce_2Zr_2O_7$, $Ce_2Zr_2O_7$, $Ce_2Zr_2O_7$, and the like. A complete list is available on NIMS Materials Database (MatNavi).com.

Calcium pyroniobate ($Ca_2Nb_2O_7$) has been discovered as a new nonlinear optical crystal by the Kurtz power method, and the intensity of second harmonic

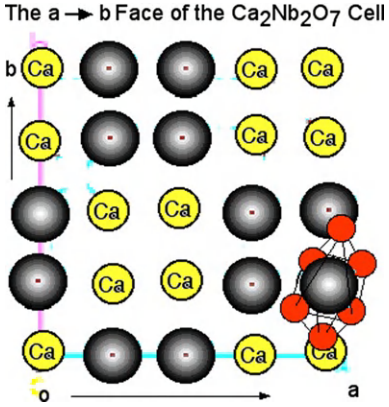

FIGURE 9.58

TABLE 9.31

No	Site notation	Atom	Multiplicity	Wyckoff	Site symmetry	*x*	*y*	*z*	Occupancy
1	O1	O	4	a	m..	0	0.0070	0.0452	1.0
2	Nb1	Nb	4	a	m..	0	0.0578	0.7934	1.0
3	O2	O	4	a	m..	0	0.0932	0.4939	1.0
4	O3	O	4	a	m..	0	0.1099	0.0	1.0
5	Nb2	Nb	4	a	m..	0	0.162	0.323	1.0
6	O4	O	4	a	m..	0	0.1995	0.5869	1.0
7	O5	O	4	a	m..	0	0.2141	0.1082	1.0
8	Ca1	Ca	4	a	m..	0	0.2941	0.3528	1.0
9	O6	O	4	a	m..	0	0.4509	0.2742	1.0
10	Ca2	Ca	4	a	m..	0	0.5519	0.2896	1.0
11	O7	O	4	a	m..	0	0.6509	0.2959	1.0

TABLE 9.32

No	Site notation	Atom	Multiplicity	Wyckoff	Site symmetry	*x*	*y*	*z*	Occupancy
1	O8	O	2	a	1	0.0472	0.353	0.0197	1.0
2	O13	O	2	a	1	0.0183	0.765	0.1801	1.0
3	Nb3	Nb	2	a	1	0.0323	0.0782	0.1154	1.0
4	Nb4	Nb	2	a	1	0.0783	0.5984	0.3229	1.0
5	O14	O	2	a	1	0.0721	0.872	0.4028	1.0
6	O9	O	2	a	1	0.1155	0.274	0.2247	1.0
7	O10	O	2	a	1	0.1326	0.381	0.427	1.0
8	Ca2	Ca	2	a	1	0.1405	0.6602	0.5681	1.0
9	O5	O	2	a	1	0.1734	0.0	0.6973	1.0
10	Ca1	Ca	2	a	1	0.2285	0.0769	0.9106	1.0
11	O11	O	2	a	1	0.2717	-0.018	0.0862	1.0
12	Ca3	Ca	2	a	1	0.2816	0.567	0.1202	1.0
13	O12	O	2	a	1	0.3263	0.664	0.3018	1.0
14	Ca4	Ca	2	a	1	0.3572	0.0937	0.3974	1.0
15	O7	O	2	a	1	0.3684	0.393	0.6148	1.0
16	Nb2	Nb	2	a	1	0.4124	0.1028	0.6744	1.0
17	O6	O	2	a	1	0.4294	0.262	0.8214	1.0
18	O1	O	2	a	1	0.4636	0.351	0.02	1.0
19	O2	O	2	a	1	0.4985	0.271	0.2275	1.0
20	Nb1	Nb	2	a	1	0.5257	0.0772	0.1169	1.0
21	O3	O	2	a	1	0.5889	0.4	0.4375	1.0
22	O4	O	2	a	1	0.7763	0.142	0.1083	1.0

of a Nd:YAG laser generated by this crystal is 5.2 times that of KDP crystal. Following this discovery, attempts to obtain large $Ca_2Nb_2O_7$ single crystals of improved optical quality have been undertaken. A reasonably good quality crystal of 25 mm diameter and 35 mm length has been grown by the Czochralski method. Its optical transparency range has been measured and found to span from 370 to 5500 nm.

The **tricalcium niobate** compound, $Ca_3Nb_2O_8 = 3CaO–Nb_2O_5$, has been shown to exist in two forms: type I, face-centered cubic with $a = 7.978$ Å, having a superlattice with $a = 23.934$ Å, and type II, orthorhombic (pseudo-tetragonal, distorted cubic) with $a = 11.51$ Å, $b = 11.10$ Å, $c = 15.98$ Å, having a pseudocell with $a = 5.754$ Å, $b = 5.551$ Å, and $c = 7.990$ Å. The perovskite-related phase, $Ca_3Nb_2O_8$, when grown as single crystals from a calcium vanadate flux, incorporates a small amount of vanadium from the flux to form the composition $Ca_3Nb_{2-x}V_xO_8$ with $x = 0.025$. The crystals have pseudo-cubic symmetry with $a = 6a_c$ (perovskite). The actual symmetry is rhombohedral, space group $R3$, with $a_h = 16.910(1)$ Å, $c_h = 41.500(2)$ Å. The structure was solved using a combination of single-crystal methods together with constrained refinements of powder X-ray and neutron powder data. The unit-cell composition is $[Ca_{138}\square_{24}]_A\,[Ca_{42}Nb_{117}V_3]_B[O_{480}\square_6]$, with vacancies (indicated by the boxes in the formula) in both the anion sites and *A*-cation sites. The Ca and Nb atoms are fully ordered in the *B*-sites such that (001) layers containing only Nb-centered octahedra alternate with layers containing both Nb-centered and Ca-centered octahedra. At the origin *B*-site, ordered oxygen vacancies result in the octahedron being transformed to a tetrahedron, which, in the single crystals, is occupied by vanadium. The structure displays a new type of octahedral tilt system in which $3 \times 3 \times 3$ blocks of $(a^+a^+a^+)$ tilts are periodically twinned on the pseudo-cubic $\{100\}_c$ planes.

The tetracalcium niobate, $Ca_4Nb_2O_9$, is polymorphic. Four $Ca_4Nb_2O_9$ polymorphs with perovskite-related $A(B'_{1/3}B'_{2/3})O_3$ structures and different arrangements of *B*-site cations were identified and characterized by powder XRD and TEM. The *B*-cation ordering in three of these phases is combined with $b^-b^-c^+$ octahedral tilting. Two high-temperature forms of $Ca_4Nb_2O_9$ are separated by a displacement phase transition which involves octahedral tilting and occurs between 1500 and 1600 °C. Above this transition, the structure is either disordered or exhibits chemical 1:1 ordering (ordering vector $1/2[111]^*_c$) of Ca and Nb cations on the *B*-sites; the correct structural model has yet to be determined. Below the transition, the structure exhibits 1:1 ordering combined with octahedral tilting. Upon cooling, the 1:1 ordered structure transforms to a metastable P1 triclinic structure with lattice parameters $\sqrt{6}a_c \times \sqrt{2}a_c \times 2\sqrt{2}a_c$, $\alpha \sim \gamma \sim 90°$, $\beta \sim 125°$ (a_c refers to cubic perovskite) and ordering vector $1/4[111]^*_c$. This transformation occurs by reordering of cations on (111) planes.

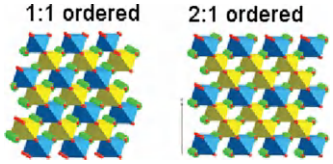

FIGURE 9.59

The metastable P1 structure transforms upon annealing to a stable 2:1 ordered $P2_1/c$ structure with lattice parameters $\sqrt{6}a_c \times \sqrt{2}a_c \times 3\sqrt{2}a_c$, $\beta = 125°$ (ordering vector $1/3[1,1,1]^*_c$). This first-order transition occurs by precipitation and growth of the 2:1 ordered phase, which is stable below 1400 °C.

The related structures are shown as follows. For $Ca_3Nb_2O_9$, the cell parameters are; $a = 5.538$ Å, $b = 9.816$ Å, $c = 14.115$ Å, $\alpha = 91.03°$, $\beta = \gamma = 90°$, cell volume $= 767.18$ Å^3. (Fig. 9.59).

These octahedra are tilted in the disordered phases.

The pentacalcium niobate, $Ca_5Nb_2O_{10}$, has been postulated and the melting temperature has been given (see phase diagram). However, there is no substantiating data in the literature for its actual existence.

Calcium niobates are not offered for sale commercially. No CAS numbers have been assigned.

9.2.4. Strontium Niobium Compounds

No intermetallic compounds of Sr^0 and Nb^0 are known. However, a number of oxide compounds are known.

No compounds are known where niobium has the +2 valence state.

In the Nb^{3+} system of $SrO–Nb_2O_3$, the compound, $SrNb_2O_4$, has never been synthesized. No compounds containing Nb^{3+} have been reported.

In the Nb^{4+} containing system of $SrO–NbO_2$, the compound, $SrNbO_3$, has the perovskite structure shown on the next page. Stoichiometric $SrNbO_3$, with a $GdFeO_3$ type structure, was synthesized between 1300 and 1550 °C in Ar-filled and sealed niobium ampoules. Its crystal structure was refined using time-of-flight ND data. Space group *Pnma*: $a = \sqrt{2}\cdot a_p = 5.6894$ Å; $b = 2\cdot a_p = 8.0684$ Å; $c = \sqrt{2}\cdot a_p = 5.6944$ Å; $R_F^2 = 0.020$; and $R_P = 0.034$. High-resolution electron microscopy (HREM) and ED studies frequently revealed structural defects in $SrNbO_3$. XRD and ED studies showed cubic symmetry for $SrNbO_3$ synthesized below 1300 °C and for compounds with nominal composition $Sr_{0.8}NbO_3$ synthesized between 1200 and 1550 °C. $SrNbO_3$ was found to be temperature independently paramagnetic. No other Nb^{4+} compounds are known. (Fig. 9.60).

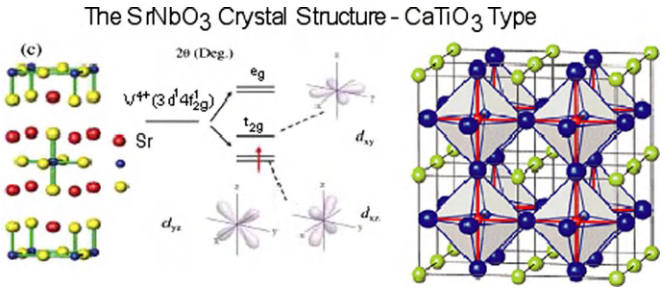

FIGURE 9.60

The Nb^{5+} containing system of $SrO–Nb_2O_5$ forms a number of compounds. The following ternary diagram shows that at least six (6) compounds have been discovered. The binary diagram, based on $SrO–Nb_2O_5$ is also shown as follows on the next page. Of the six (6) compounds displayed only two melt congruently. The 6:1 compound is stable only at high temperatures (>1260 °C) and the 4:1 compound is stable only up to 1260 °C. (Fig. 9.61).

$SrNb_2O_6$ is a potential candidate for ferroelectric and electro-optic applications. It has been prepared at low temperatures from hydroxide precursors.

The simple procedure of mixing commercially purchased strontium hydroxide and niobium (or tantalum) hydroxide thoroughly together and heating at a low temperature (<400 °C) produced pure $SrNb_2O_6$ in a powder form. This is the lowest temperature so far reported for the formation of these phases. The reaction sequence and evolution of the phase formation were investigated by X-ray methods. The phase diagram has the form as shown in Fig. 9.62.

Strontium niobate, $SrNb_2O_6$, has a crystal structure consisting of a series of interconnected NbO_6 octahedra. The structure is shown in Fig. 9.63.

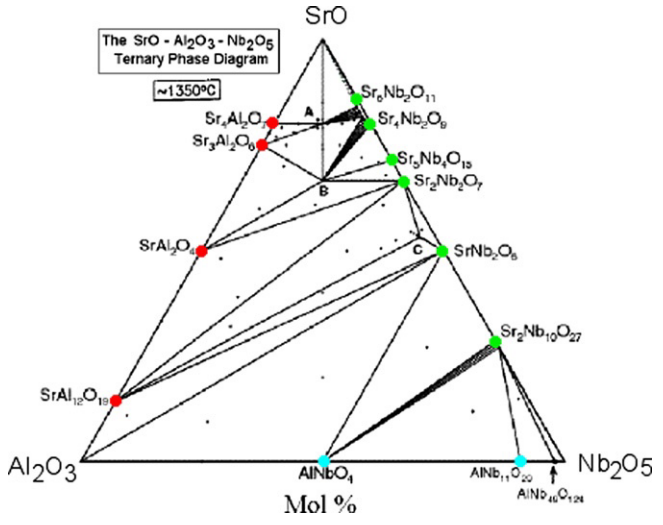

FIGURE 9.61

Cell parameters are: $a = 5.592$ Å, $b = 7.722$ Å, $c = 10.989$ Å, $\alpha = 90.36°$, $\beta = \gamma = 90°$, cell volume = 474.31 $Å^3$. Cell occupancy is shown in Table 9.33.

A general approach to synthesize niobium-containing nano-structured photo-catalysts such as $SrNb_2O_6$, via a facile hydrothermal-electrolytic process has also been demonstrated. This method is based on reactions between soluble/insoluble metallic compounds and metallic oxides in the aqueous solution without using any organic dispersants or capping agents. The one-step technique is controllable and provides a simple, convenient, and innovative strategy for the preparation of niobate nanostructures and basically can be easily expanded to synthesize other materials of a similar structure.

Nanocrystalline rods of $SrNb_2O_6$ powders were successfully prepared by this simple electrochemical method, and the influences of electrolytic solution ingredients, electrolyte concentration, and applied electric current intensity on the electrochemical process and products were systemically studied as shown in Fig. 9.64.

It was found that the formation of strontium niobates is strongly determined by the basic or acidic condition of the electrolytic solution. When $Sr(OH)_2 \cdot 8H_2O$ or the mixed solution, $Sr(OH)_2 \cdot 8H_2O$ plus $SrCl_2 \cdot 6H_2O$, was used as an electrolyte, $Sr_5Nb_4O_{15}$ and $SrNb_2O_6$ phases would simultaneously form, and the relative ratio of $Sr_5Nb_4O_{15}$ to $SrNb_2O_6$ declined with increase of the $SrCl_2 \cdot 6H_2O$ content in electrolytic solution. The higher the basicity of electrolytic solution, the more favored was the crystallization and development of the $Sr_5Nb_4O_{15}$ phase. Only the monoclinic phase $SrNb_2O_6$ was obtained in neutral $SrCl_2 \cdot 6H_2O$ solution or acidic solution of $SrCl_2 \cdot 6H_2O$ with the addition of hydrochloric acid. A lower concentration of $SrCl_2 \cdot 6H_2O$ ($\leq$0.50 M) was beneficial to the formation of the $SrNb_2O_6$ phase and stable anodic sparks could be observed. Moreover, the crystallization and development of the nanocrystalline $SrNb_2O_6$ powders are not sensitive to the applied electric current intensity, and their similar particle size and morphology ultimately result in the loss of UV–Vis absorption and subsequent photo degradation. They show a slight red shift of light absorption onset and better photocatalytic performance compared with that prepared by the solid-state reaction.

It has been shown that these as-synthesized one-dimensional niobate nanostructures with larger BET surface areas possess higher photocatalytic activities for splitting pure water under UV light irradiation than those samples from the solid-state route as shown in Fig. 9.65.

$SrNb_2O_6$ having a rhombic nanotubular structure with a diameter of 300 nm, average length of 3 μm and wall thickness of 50 nm was synthesized via a facile

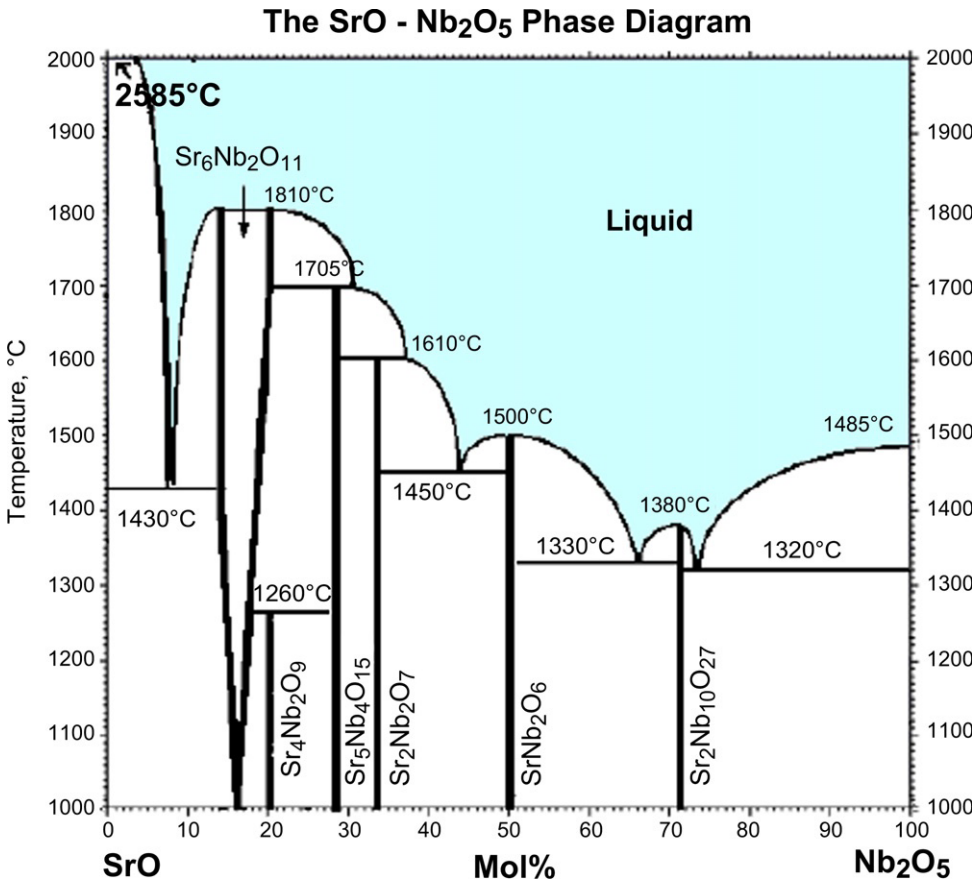

FIGURE 9.62

hydrothermal route. Compared to the same material prepared by the solid-state reaction method, the rhombic nanotubes of $SrNb_2O_6$ exhibited enhanced photocatalytic activity for the production of H_2 from pure water, which was mainly attributed to their higher surface area. The following results shown on the next page were obtained. Thus, $SrNb_2O_6$ is 60 times more effective as TiO_2 in the catalytic splitting of water into O_2 and $2H_2$ gases at room temperature. Moreover, the increased optical absorption properties resulting from the variation of the crystal structure are also attributed to their higher photo-catalytic activity.

The heat capacity and the enthalpy increments of strontium metaniobate $SrNb_2O_6$ were measured by the relaxation method (2–276 K), micro DSC calorimetry (260–320 K) and drop calorimetry (723–1472 K). The

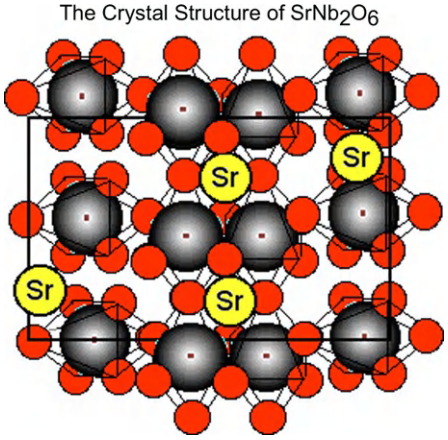

FIGURE 9.63

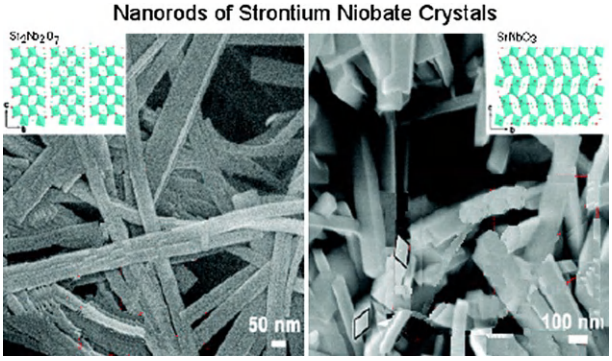

FIGURE 9.64

TABLE 9.33

No	Site notation	Atom	Multiplicity	Wyckoff	Site sym	x	y	z	Occupancy
1	Nb1	Nb	4	e	1	0.0144	0.0271	0.1438	1.0
2	O1	O	4	e	1	0.0329	0.2815	0.4744	1.0
3	O3	O	4	e	1	0.0474	0.3648	0.2122	1.0
4	O5	O	4	e	1	0.25	0.5308	0.6475	1.0
5	Sr	Sr	4	e	1	0.2499	0.534	0.0387	1.0
6	O4	O	4	e	1	0.4493	0.3581	0.2133	1.0
7	O2	O	4	e	1	0.4676	0.2801	0.4745	1.0
8	Nb2	Nb	4	e	1	0.5254	0.0358	0.1423	1.0
9	O6	O	4	e	1	0.7515	0.139	0.1294	1.0

temperature dependence of the molar heat capacity in the form $C_{pm} = (200.47 \pm 5.51) + (0.02937 \pm 0.0760)T - (3.4728 \pm 0.3115) \cdot 106/T^2$ J/K/mol (298–1500 K) was derived by the least-squares method from the experimental data. The standard molar entropy at 298.15 K as Sm^0 (298.15 K) = 173.88 ± 0.39 J/K/mol was evaluated from the low temperature heat capacity measurements. The standard enthalpy of formation ΔH_f (298.15 K) = −2826.78 kJ/mol was derived from total energies obtained by full potential LAPW electronic structure calculations within density functional theory.

Ultrathin strontium niobate films were processed by water-based chemical solution deposition, an approach that offers significant environmental benefits. $SrNb_2O_6$ shows high-k values, a factor that is important for applications such as alternative gate dielectrics in integrated circuits. The study of ultra-thin films (thickness <30 nm) is crucial as this is the thickness range for the application envisaged, and as film properties depend strongly on the film thickness. $SrNb_2O_6$ had a lower crystallization temperature, less interfacial silicate, lower carbonate content, and higher roughness compared to other dielectrics used. The k values of amorphous films were limited (k = 12–14). Crystallization and complete removal of organics or carbonates was accomplished by high-temperature annealing, but increased the roughness and leakage current in the composite.

A novel solution-phase route using $Nb_2O_5 \cdot nH_2O$ as precursor was developed to selectively synthesize single-crystalline $Sr_{0.4}H_{1.2}Nb_2O_6 \cdot H_2O$ nanopolyhedrons and $SrNb_2O_6$ nanorods as photocatalysts via simply adjusting pH values of the reactive solutions as shown in Fig. 9.66.

Strontium barium niobate ($Sr_xBa_{1-x}Nb_2O_6$ = SBN), where ($0.25 \leq x \leq 0.75$) is currently being investigated as a potential ferroelectric material for many micro-device applications, such as pyroelectric infrared detectors, electro-optic modulators, holographic storage, and beam steering, because of its large pyroelectric coefficient, excellent piezoelectric and electro-optic properties, and photorefractive sensitivity. Compared with other well-known ferroelectric materials, SBN has an extremely high electro-optic coefficient. For example, the figure of merit is more than 50 times higher than that of $LiNbO_3$,

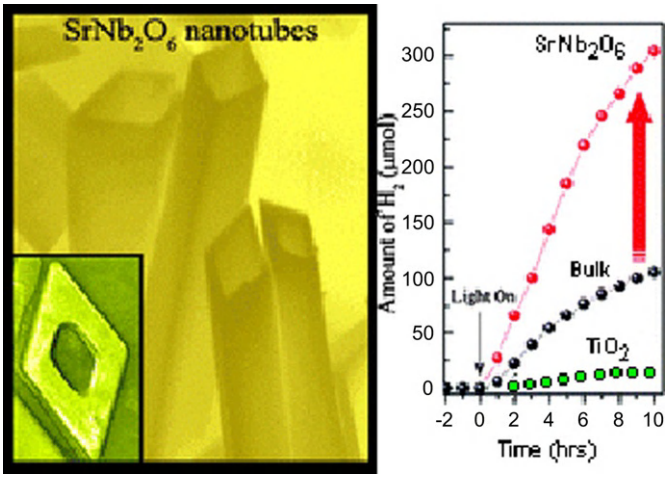

FIGURE 9.65

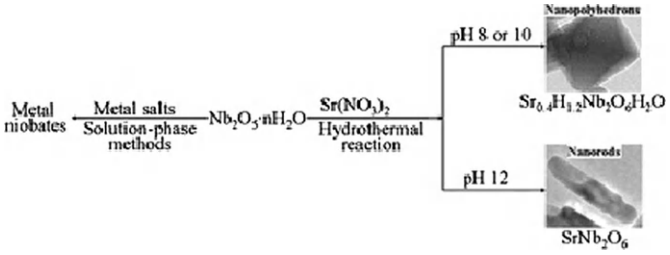

FIGURE 9.66

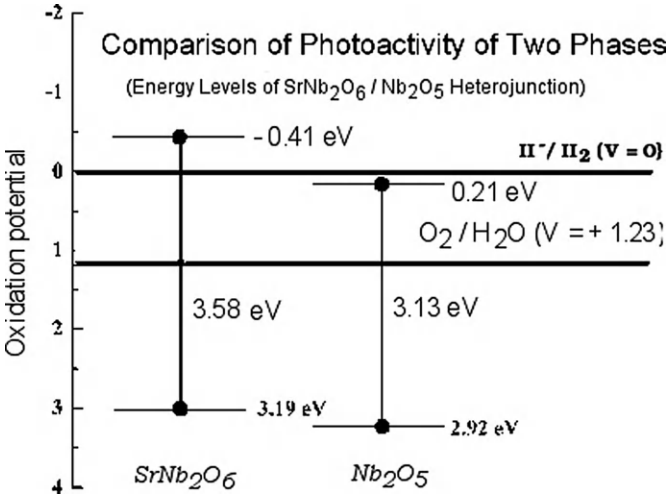

FIGURE 9.67

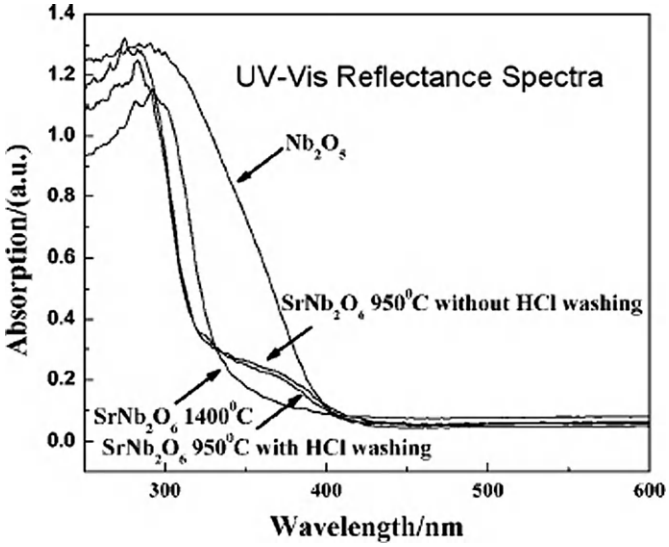

FIGURE 9.68

offering the possibility of much smaller devices. 3 SBN is a solid solution between $BaNb_2O_6$ and $SrNb_2O_6$ phases with a tetragonal tungsten bronze (TTB) structure, wherein its physical properties vary with its composition. These properties and their applications have been investigated mainly for both single crystals and polycrystalline ceramics. Moreover, the demand for thin film processing has increased due to the development of electronic and optical integrated devices. SBN thin films, especially highly *c*-axis-oriented SBN thin films, are desired for optical applications, such as electro-optic properties, photorefractive, and nonlinear optical applications because these applications can take full advantage of the high ferroelectricity of the fabricated SBN films.

$SrNb_2O_6$ powders were prepared by a conventional solid-state method and characterized by powder XRD and UV-Vis diffuse reflection spectra. Their photocatalytic activities were investigated on the degradation of methyl orange. The results show that the photocatalytic activity of pure phase $SrNb_2O_6$ calcined at 1400 °C is lower than that of the impure phase $SrNb_2O_6$ calcined at 950 °C. The hetero-junction model is used to explain that the impure sample can improve the photocatalytic activity due to the interface interaction of Nb_2O_5 and $SrNb_2O_6$ as shown in Fig. 9.67.

Nb_2O_5 has a differing UV-Vis reflectance spectrum than $SrNb_2O_6$ and is believed to contribute electrons to the hole-conductivity of the latter so that the overall photocatalytic efficiency is vastly improved as shown in Fig. 9.68.

The **pyroniobate**, $Sr_2Nb_2O_7$, exhibits at least two separate types of structures. One is that of the calcium homolog (Point group = oP88, space group = $Pna2_1$) and the other is distinctive to the $Sr_2Nb_2O_7$ composition (Point group = oS44, space group = $Cmc2_1$) as shown in Fig. 9.69.

Another view of the Ca-type is presented in the following diagram: Fig. 9.70.

Cell parameters for the Ca-type are: $a = 5.64$ Å, $b = 7.91$ Å, $c = 26.18$ Å, $\alpha = \beta = \gamma = 90°$, cell volume = 1166.48 Å^3.

Cell occupancy is shown in Table 9.34.

Cell parameters for the Sr-type are: $a = 3.958$ Å, $b = 5.704$ Å, $c = 13.540$ Å, $\alpha = \gamma = 90°$, $\beta = 98.04°$, cell volume = 302.41 Å^3. Cell occupancy is shown in Table 9.35.

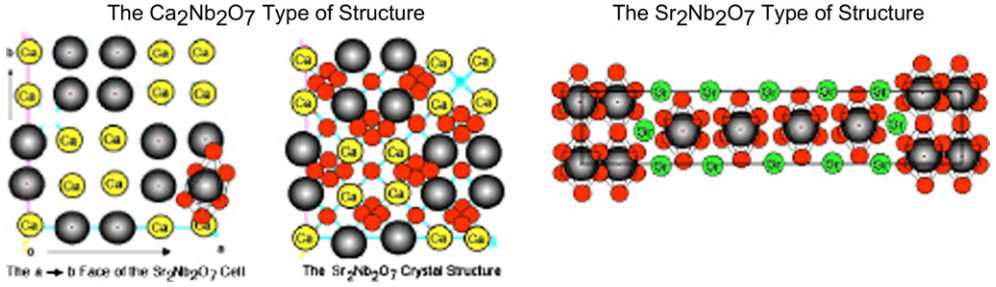

FIGURE 9.69

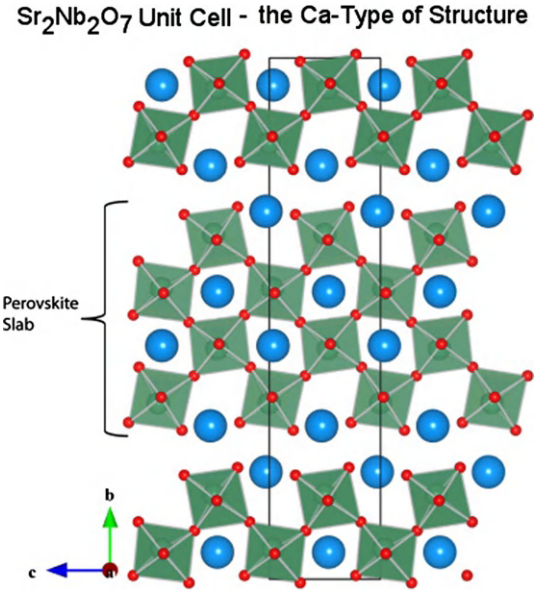

FIGURE 9.70

$Sr_2Nb_2O_7$ belongs to the homologous series of $A_nB_nO_{3n+2}$ type of compounds with A = Sr, B = Nb and $n = 4$. Its Curie temperature is 1342 °C, below which it is ferroelectric and possesses interesting piezoelectric and electro-optic properties. $Sr_2Nb_2O_7$ with certain substitutions, e.g. in the form of important solid solutions such as, $Sr_2(Nb,Ta)_2O_7$ and $(Sr,Ba)_2Nb_2O_7$, is used for ferroelectric memory storage devices based on field effect transistors (FET) and capacitors . The structure of $Sr_2Nb_2O_7$ comprises slabs, each slab extending parallel to {010} planes and consisting of $4NbO_6$ octahedra with Sr atoms occupying the space between them. These NbO_6 octahedra are known to distort and tilt upon cooling and consequently $Sr_2Nb_2O_7$ undergoes three phase transitions from $Cmcm \Leftrightarrow Cmc21 \Leftrightarrow Pbn21 \Leftrightarrow Pb11$ at 1342 °C, 215 °C and −156 °C respectively.

The $Sr_2Nb_2O_7$ (SNO) compound has been determined to be suitable for use as a ferroelectric material for ferroelectric memory FETs, because this substance has a low

TABLE 9.34

No	Site notation	Atom	Multiplicity	Wyckoff	Site symmetry	*x*	*y*	*z*	Occupancy
1	O1	O	4	a	1	0.031	0.104	0.2075	1.0
2	Sr1	Sr	4	a	1	0.0342	0.3748	0.4432	1.0
3	O2	O	4	a	1	0.036	0.657	0.2245	1.0
4	O3	O	4	a	1	0.056	0.161	0.7095	1.0
5	Nb1	Nb	4	a	1	0.0872	0.1262	0.0	1.0
6	Nb2	Nb	4	a	1	0.0885	0.618	0.0043	1.0
7	O4	O	4	a	1	0.098	0.375	0.1025	1.0
8	O5	O	4	a	1	0.136	0.07	0.3355	1.0
9	O6	O	4	a	1	0.138	0.681	0.3305	1.0
10	Nb3	Nb	4	a	1	0.1915	0.1205	0.5265	1.0
11	O7	O	4	a	1	0.196	0.375	0.4615	1.0
12	Sr2	Sr	4	a	1	0.2051	0.3739	0.0267	1.0
13	O8	O	4	a	1	0.239	0.087	0.2505	1.0
14	O9	O	4	a	1	0.24	0.666	0.2485	1.0
15	O10	O	4	a	1	0.293	0.377	0.1235	1.0
16	Nb4	Nb	4	a	1	0.3075	0.1281	0.0245	1.0
17	Sr3	Sr	4	a	1	0.31	0.3741	0.5367	1.0
18	O11	O	4	a	1	0.341	0.103	0.3415	1.0
19	O12	O	4	a	1	0.341	0.645	0.3405	1.0
20	O13	O	4	a	1	0.401	0.377	0.4405	1.0
21	Sr4	Sr	4	a	1	0.4489	0.3788	0.01	1.0
22	O14	O	4	a	1	0.452	0.096	0.2355	1.0

TABLE 9.35

No	Site notation	Atom	Multiplicity	Wyckoff	Site symmetry	x	y	z	Occupancy
1	O1	O	4	a	m..	0	0.0070	0.0452	1.0
2	Nb1	Nb	4	a	m..	0	0.0579	0.7935	1.0
3	O2	O	4	a	m..	0	0.0932	0.4939	1.0
4	O3	O	4	a	m..	0	0.1099	0.0	1.0
5	Nb2	Nb	4	a	m..	0	0.162	0.323	1.0
6	O4	O	4	a	m..	0	0.1996	0.5869	1.0
7	O5	O	4	a	m..	0	0.2141	0.1082	1.0
8	Sr1	Sr	4	a	m..	0	0.2941	0.3528	1.0
9	O6	O	4	a	m..	0	0.4509	0.2742	1.0
10	Sr2	Sr	4	a	m..	0	0.5518	0.2896	1.0
11	O7	O	4	a	m..	0	0.6509	0.2959	1.0

dielectric constant, low coercive field and high heat resistance. In one study, operation was successful for $Sr_2(Ta,Nb)_2O_7$ (STN) capacitors on polycrystalline silicon (poly-Si). Using secondary ion mass spectroscopy (SIMS) profiles, the lack of interdiffusion of ions in the STN metal ferroelectric metal insulator semiconductor (MFMIS) structure was confirmed. C–V and I_D–V_G hysteresis curves, dependent on ferro-electric polarization, were obtained. These capacitors were applied to floating gate type ferroelectric random access memory (FFRAM) cells. The degradation in ferroelectric properties of STN capacitors during FFRAM cell fabrication process was not observed. These FFRAM cells can be operated with a lower voltage than that required for PZT.

The lattice images of oxygen-deficient $SrNbO_{3.5-x}$ have been studied by HRTEM observations. The results indicate that loss of oxygen from $SrNbO_{3.5-x}$ eventually results in the formation of an intergrowth of $Sr_5Nb_5O_{17}$, a member of $n=5$ in the perovskite-related family $A_nB_nO_{3n+2}$. The microstructure of $SrNbO_{3.5-x}$ can be considered as a disordered intergrowth between $Sr_2Nb_2O_7$ and $Sr_5Nb_5O_{17}$.

Pulsed laser deposited films (from a $Sr_2Nb_2O_7$ target) obtained in both oxygen and nitrogen atmospheres upon various substrates were characterized with XRD, EDX, atomic force microscopy(AFM), and TEM. In oxygen atmospheres, films adopted the (110)-layered perovskite structure of the target. Higher temperatures, lower pressures of oxygen, and the use of (110)-oriented $SrTiO_3$ substrates lead to highly crystalline, epitaxial films of $Sr_2Nb_2O_7$. The use of nitrogen atmospheres resulted in cubic perovskite $SrNbO_3$ formation: epitaxial, textured, or polycrystalline films were obtained depending on the substrate; no nitrogen incorporation could be observed on the anion sub-lattice. On $SrTiO_3$, the cubic perovskite films followed a cube-on-cube epitaxy and planar defects were observed to occur on the (110) perovskite planes. In oxygen, films adopt the $Sr_2Nb_2O_7$ (110)-layered perovskite structure (left). In nitrogen, films adopt the cubic perovskite $SrNbO_3$ structure (right), as shown in the following diagram: Fig. 9.71.

The films' microstructure depends, however, on the substrate type and temperature. Recently, a number of ternary transition metal oxide catalysts have been discovered to dissociate water more efficiently than conventional materials such as titania. These new materials all have anisotropic structures made up of layers or tunnels. It has been hypothesized that these materials have high efficiencies because the layers and tunnels somehow separate the photo generated charge carriers and, therefore, the locations of the oxidation and reduction half reactions. If such a separation were to occur, it

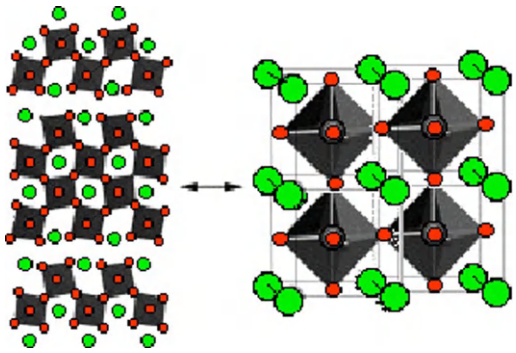

FIGURE 9.71

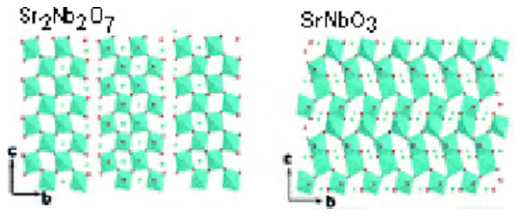

FIGURE 9.72

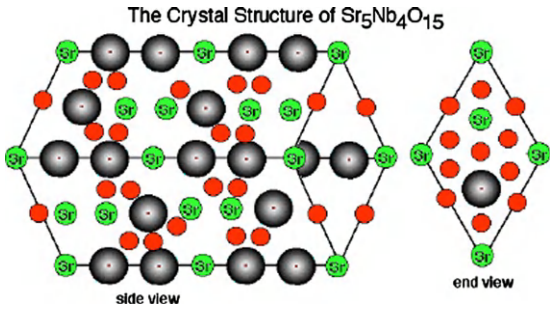

FIGURE 9.73

would suppress carrier recombination and the rate of the back reaction. Two such materials are $Sr_2Ta_2O_7$ and $Sr_2Nb_2O_7$. Both of the structures are made up of corner sharing MO_6 octahedra that are arranged in (110) perovskite type slabs parallel to (010), and separated by Sr_2O layers. The main difference between these materials is the distortion of the NbO_6 octahedra in $Sr_2Nb_2O_7$, which makes it ferroelectric ($Ps \| c$-axis). The role that the layer structure plays in the superior photochemical properties of these compounds is currently unclear.

A comparison between the octahedra structure of in $SrNb_2O_6$ and $Sr_2Nb_2O_7$ shows that the somewhat disordered arrangement of the former becomes ordered as a molecule of SrO is added to former the latter is shown in Fig. 9.72.

The thermal properties of highly textured and polycrystalline samples of 0.5 mol% La-doped $Sr_2Nb_2O_7$ have been measured from just above room temperature 351 °C to 1000 °C. The thermal conductivity was found to be very low (~1 W/mK), temperature independent, and strongly anisotropic parallel and perpendicular to the layered structure up to 1000 °C. The phase transition between the room temperature *IC* orthorhombic phase and the normal orthorhombic phase above 215 °C has a negligible effect on thermal conductivity.

Nanostructured $Sr_2Nb_2O_7$ powders with different morphologies were synthesized via a hydrothermal reaction at 200 °C for 24 h in an Sr^{2+}–$Nb_2O_5 \cdot nH_2O$–KOH system. Powder XRD characterization indicated that 0.3–5 M KOH solutions favored the formation of an $Sr_2Nb_2O_7$ pure phase. On increasing the concentration of KOH from 0.3 to 5 M, the morphology of $Sr_2Nb_2O_7$ samples changed from nanoneedles to nanorods, nanosheets, and finally nano-sized flakes, and their aspect ratios gradually reduced. Ultraviolet–Visible diffuse reflectance spectra analyses showed that the nanostructured $Sr_2Nb_2O_7$ powders had good light absorption properties in the ultraviolet light region.

The ortho-niobate, $Sr_3(NbO_4)_2$, has never been synthesized. However, more complex compounds like $Sr_5Nb_4O_{15}$, $Sr_5Nb_5O_{16}$ and $Sr_3Nb_5O_{15}$ have been discovered.

The compound, $Sr_5Nb_4O_{15}$, has the structure shown as follows: Fig. 9.73.

Cell parameters are: $a = b = 5.659$ Å, $c = 11.459$ Å, $\alpha = \beta = 90°$, $\gamma = 120°$, cell volume = 317.80 Å^3. Cell occupancy is shown in Table 9.36

The strontium niobate compounds $Sr_4Nb_2O_9$ and $Sr_5Nb_4O_{15}$ were prepared by solid-state reactions and studied by high-resolution powder XRD measurements. The structures of the two systems $Sr_4Nb_2O_9$ and $Sr_5Nb_4O_{15}$ were obtained by Rietveld analysis, indicating triclinic and monoclinic unit cell parameters, respectively. Both structures reveal a layering of Sr···O planes. The Nb ions are located in octahedral holes between the Sr···O layers. Another view of the $Sr_5Nb_4O_{15}$ crystal structure is shown in Fig. 9.74.

TABLE 9.36

No	Site notation	Atom	Multiplicity	Wyckoff	Site symmetry	*x*	*y*	*z*	Occupancy
1	O1	O	6	i	.m.	0.1695	0.8305	0.1916	1.0
2	O2	O	6	i	.m.	0.8368	0.1632	0.3864	1.0
3	O3	O	3	e	.2/m.	1/2	0	0	1.0
4	Nb1	Nb	2	d	3m.	1/3	2/3	0.1035	1.0
5	Sr1	Sr	2	d	3m.	1/3	2/3	0.4282	1.0
6	Sr2	Sr	2	d	3m.	1/3	2/3	0.7837	1.0
7	Nb2	Nb	2	c	3m.	0	0	0.3127	1.0
8	Sr3	Sr	1	a	-3m.	0	0	0	1.0

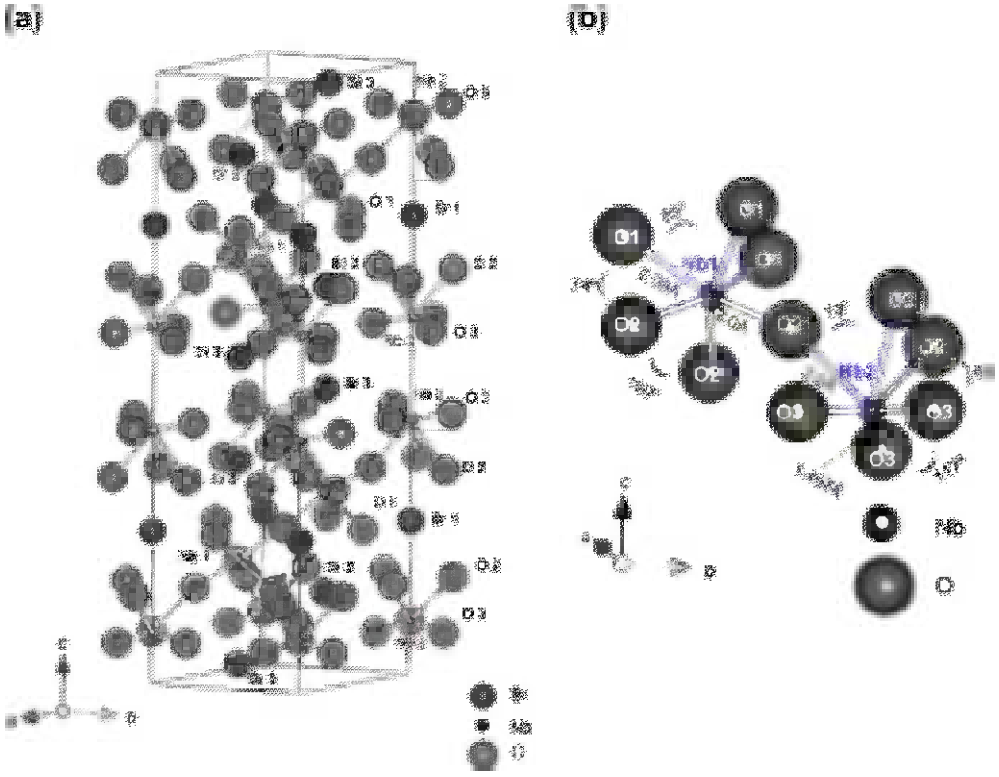

FIGURE 9.74

In the phase diagram, strontium niobate $Sr_4Nb_2O_9$ has a perovskite derivative structure, as well as its neighboring phase $Sr_6Nb_2O_{11}$. At least two researchers, one Russian and the other French, considered the part of the $SrO–Nb_2O_5$ phase diagram between $Sr_4Nb_2O_9$ and $Sr_6Nb_2O_{11}$ as a continuous $Sr_4Nb_2O_9$ base solid solution whose end member is $Sr_6Nb_2O_{11}$. However, one found the $Sr_4Nb_2O_9$ phase to be stable as a solid at room temperature while the other did not. A final conclusion was finally agreed upon. Accordingly, there is a very narrow two-phase field within 1–3 mol between the $Sr_4Nb_2O_9$ and $Sr_6Nb_2O_{11}$ phases.

$Sr_5Nb_4O_{15}$ (SN) and $Ba_5Nb_4O_{15}$ (BN) microwave ceramics prepared by a reaction-sintering process were investigated. Without any calcination involved, the Nb_2O_5 mixture of $BaCO_3$ and $SrCO_3$ was pressed and sintered directly. BN and SN ceramics could be obtained after 2–6 h sintering at 1350–1500 °C. A density 6.13 g/cm^3 (97.3% of theoretical value) was obtained in BN for 4 and 6 h sintering at 1450 °C. The sintering temperature was 200 °C lowered with the addition of 1 wt.% CuO. For SN, low densification 86.9% was obtained at 1500 °C and became dense with 96% of the theoretical density at 1430 °C after 1 wt.% CuO was added. Dielectric constants 39.5 and 38.1 could be obtained in BN and SN. $Q \times f$ values 22,700 GHz at 7.2 GHz and 10,500 GHz at 7.47 GHz are observed in BN and SN.

The investigation of the electrical properties of metal rich alkaline earth niobates was pioneered as early as the 1980's. Even then, the high conductivity of these niobates was related to oxygen ion migration by means of exchange of positions between an ion residing in a regular position of the oxygen sub-lattice and structural oxygen vacancies, as:

$$O^{x_0} + (V^{s_0}) \Leftrightarrow (V^{s_0})^{x} + O^{x_0}(V^{s_0})$$

In parallel to publications of Russian researchers, French workers published a set of works concerning electrical conductivity measurements as a function of temperature and oxygen partial pressure. They chose to study samples containing 81–85 mol% SrO and considered these samples as solid solutions of general formula $Sr(Sr_{1/3+x}Nb_{2/3-x})O_{3-3/2x}$ $(0 \leq x \leq 1/6)$. Discussion was in terms of the point defect model. Later studies of samples of these compositions involved the comparison of the measured (pycnometer) density with densities calculated for various dissolution models. These later studies showed that the model of $Sr_6Nb_2O_{11}$ base solid solution is characterized by the general formula $Sr_{6-2x}Nb_{2+2x}$ O_{11+3x} $(0 \leq x \leq 0.28)$; this formula suggests partial substitution of niobium ions for octahedrally coordinated Sr^{2+} ions. The $Sr_6Nb_2O_{11}$ phase and the related $Sr_4Nb_2O_9$ phase both have dominant oxygen conductivity. The phase $Sr_4Nb_2O_9$ is a non-stoichiometric phase with a disordered perovskite structure.

The complex structural behavior of the perovskite-related compound $Sr_4Nb_2O_9$ ($Sr(Sr_{1/3}Nb_{2/3})O_3$) has been investigated using ED, XRD, and NPD. Analysis of well-equilibrated specimens annealed at various temperatures indicated that two thermodynamically stable polymorphs occur above and below $T = 1250\,^{\circ}C$. The high-temperature (HT) polymorph exhibits an average cubic structure (*Fm* 3*m*, *a* 2*ac*, where 'c' refers to the cubic ~4 perovskite unit cell) with 1:1 (NaCl-type) partial ordering of Sr^{2+} and Nb^{5+} on the *B*-sites. The low-temperature (LT) phase is monoclinic (*P*21/*n*, *a* 6*ac* 3, *b* 2*ac* 2, *c ac* 6, *b* 90) with a distant, yet unknown, *B*-cation arrangement. Examination of the HT cubic polymorph using ED revealed diffuse intensity contours that were consistent with additional local ordering/cluster formation on the sites of the mixed (Sr/Nb) fcc cubic sublattice of the 1:1 ordered *B*-cation array. Concentration of intensity observed at certain points within the diffuse intensity contours was attributed to superstructure formation. Additionally, refinements of the HT structure using XRD and NPD data indicated local displacements of both oxygen and *A*-site Sr atoms, which resembled those associated with octahedral tilting. HT-$Sr_4Nb_2O_9$ specimens subsequently annealed at 900 °C exhibited remarkably complex chemical and structural behavior: The contours of diffuse intensity were replaced by arrays of sharp superlattice reflections corresponding to at least four distinct metastable superstructures, all derived from the 1:1 *B*-cation arrangement. Compositional analysis indicated that these phases exhibit Sr/Nb ratios slightly different from 2/1; that is, they are not true polymorphs, but rather a series of structurally distinct phases with compositions near $Sr_4Nb_2O_9$. The metastable superstructures were attributed to ordering of Sr and Nb on the mixed *B*-sites in the 1:1 ordered array, possibly combined with either *A*-site or oxygen vacancy ordering, depending on the Sr/Nb ratio in the particular phase. The metastable phases transform to the stable LT-$Sr_4Nb_2O_9$ phase upon annealing in the 1100 °C–1200 °C temperature range. The dielectric properties of HT- and LT-$Sr_4Nb_2O_9$ were measured by capacitive methods at 1 MHz. HT-$Sr_4Nb_2O_9$ exhibited an ambient permittivity of 40 with a non-monotonic temperature dependence, while that for LT-$Sr_4Nb_2O_9$ was 30 with near-linear temperature dependence. The peculiar dielectric behavior of HT-$Sr_4Nb_2O_9$ was ascribed to the competitive responses of nanodomains having somewhat different structures and compositions.

Barium and strontium niobates have been prepared by means of an economic and ecologic aqueous solution-gel route with high compositional flexibility. The synthesis of precursor solutions and gels, and thermal analysis of the gels are presented. The crystallization of the different oxides was studied in situ using high-temperature X-ray diffraction measurements (HT-XRD). The crystallization behavior of strontium niobates was strongly dependent on the Sr:Nb ratios, as observed in HT-XRD. Phase pure $SrNb_2O_6$ was obtained at low temperature (600 °C). $Sr_2Nb_2O_7$ and $Sr_5Nb_4O_{15}$ were formed at 900 °C from an intermediate phase, with a minor secondary phase. $Nb_2Sr_4O_9$ crystallized at 600 °C, but transformed to a mixture of phases at high temperature (1000 °C). By off-line furnace annealing, phase pure strontium niobates of all four compositions were obtained. The presented work demonstrated the high compositional flexibility of the aqueous solution-gel route, allowing fast synthesis of different multi metal oxides with high purity.

The possibility that the structure of the novel semiconducting perovskite-related material strontium niobium oxide, $Sr_5Nb_5O_{17}$, refined in space group *Pnn*2, might instead belong to space group *Pnnm* has been investigated. This followed an analysis of the atomic coordinates that indicated the latter space group to be more likely. All I_{obs} were carefully remeasured, first those within a hemisphere containing *c**, then all that lay within the full sphere of reflection. Refinement was undertaken, with each of two different sets of weights, in each space group. Each data set was used under three limiting intensity conditions: $I_{obs} > 4(I_{obs})$, $I_{obs} > 2(I_{obs})$ and finally with *all* reflections, but setting magnitudes with I_{obs} 0 equal to 0. Fourteen separate tests based only upon the XRD data may be used to distinguish between *Pnn*2 and *Pnnm*. Nine tests favored the latter choice, four were indeterminate and one was not used. Seven further tests were made on the basis of physical measurement; of these, three strongly indicated *Pnnm*, one was indeterminate and three could not be used. The evidence clearly suggests the space group is *Pnnm*. The use of all reflections, including those with negative magnitude set equal to zero, is essential to avoid ambiguity in the XRD tests and achieve the highest reliability. Refinement with weights based on variances of Type *A* and Type *B* resulted in improved reliability compared with that obtained from a popular empirical weighting scheme. The revised structure differs in several respects from that published previously.

New oxide compounds with large thermal expansion coefficients and low thermal conductivities are being sought by means of a material calculation technique. Among the thousands of compounds in the databases, there are some materials with low thermal conductivities and large thermal expansion coefficients in the group of strontium–niobium oxides. For example, $Sr_4Nb_2O_9$ has a thermal expansion coefficient of 14.5×10^{-6} /°C and a thermal conductivity of 1.0 W/mK, although a slight amount of other phases appear during long-term annealing. These thermal properties are better than those of yttria-stabilized zirconia, which is the standard material for thermal barrier coatings.

TABLE 9.37

Mol Ratio of Component oxides				
Composition	**SrO**	**Nb_2O_5**	**NbO_2**	**NbO_3**
$Sr_3Nb_5O_{15}$	3	2	1	
$Sr_6Nb_2O_{11}$	6	1		
$Sr_5Nb_5O_{16}$	5	2		1
$Sr_6Nb_{34}O_{91}$	6	16		2
$Sr_7Nb_6O_{21}$	7	1	3	1

Phase relations have been investigated within the $Sr_4Nb_4O_{14}$–$Sr_5Nb_4O_{15}$–$SrTiO_3$ region of the SrO–Nb_2O_5–TiO_2 system with a view to clarifying the occurrence of perovskite-related phases. Most samples were prepared from oxide or carbonate powders heated in air at 1350 °C but some samples were also prepared by argon arc melting. The overall phase analysis was carried out by powder XRD. Two-phase lines contain a homologous series of layered perovskite phases. These are the $Sr_n(Nb,Ti)_nO_{3n+2}$ $(4 \leq n \leq 7)$ series on the $Sr_4Nb_4O_{14}$–$SrTiO_3$ line and $Sr_n(Nb,Ti)_{n-1}O_{3n}$ $(5 \leq n \leq 7)$ on the $Sr_5Nb_4O_{15}$–$SrTiO_3$ line. The microstructures in these homologous series were clarified by TEM. This revealed both ordered and disordered intergrowths of the perovskite homologs and allowed the defect microstructure of $SrTiO_3$ in contact with the layered perovskites to be determined.

In addition to the compounds described above, a series of stable compounds has been synthesized. The composition can only be described as a combination of niobium oxides in which various states of oxidation of the Nb-atom appear. These compositions are all part of the layered perovskite type of compound but with varying stages of oxidation state of the Nb = atom in the structure. The above Table 9.37 lists strontium niobate compounds whose composition is made up of various niobium oxides.

All of these compounds belong to the Ruddlesden–Popper series of layered compounds. Their structures have been solved and are available. It is notable that only the strontium and barium analogs of these alkaline earth niobates form such compounds with Nb^{4+}, Nb^{5+} and Nb^{6+} states of ionization in the same compound. A comparison of such structures is presented in the following diagram: Fig. 9.75.

The green spheres show the Sr^{2+}atom positions in the lattice, the gray spheres are those of the Nb^{5+} atoms and the red spheres are those of the oxygen atoms. For the

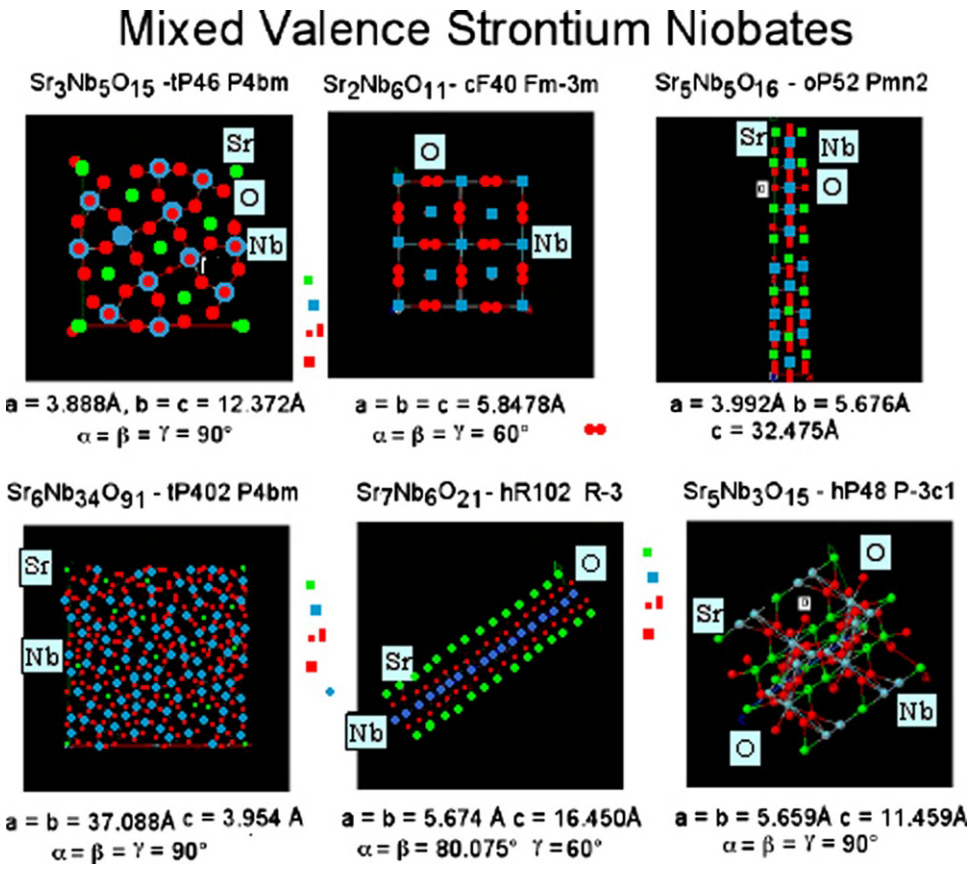

FIGURE 9.75

most part, a view along the *c*-axis is shown, i.e. the *a*–*c* plane of the unit cell. A number of atoms are only partially visible. To visualize a three dimensional view of each lattice, the *a*–*c* plane is doubled and set at the corresponding plane at the angles specified.

Strontium niobate is available commercially as the $SrNb_2O_6$ composition with the CAS number of 12034-89-8.

9.2.5. Barium Niobium Compounds

The system, BaO–Nb_2O_5, resembles the SrO–Nb_2O_5 system in many ways. The structures of many compounds are isomorphic. However, BaO forms up to 16 compounds compared to the eight (8) seen in the SrO family of compounds.

Similar to the SrO family of niobates, no compounds are known where niobium has the +2 valence state.

In the Nb^{3+} system of BaO–Nb_2O_3, the compound, $SrNb_2O_4$ has never been synthesized. No compounds containing Nb^{3+} have been reported.

In the Nb^{4+} system of BaO–NbO_2, the compound $BaNbO_3$ is known. Heating a mixture of NbO_2 and $BaO{\cdot}3B_2O_3$ to 1100 °C (10^{-6}–10^{-7} Torr), followed by slow cooling (8 °C/h) produces golden crystals of the niobate $Ba_2Nb_{15}O_{32}$ (average Nb oxidation state 4+), as well as crystals of $Ba_3Nb_5O_{15}$ ($Nb^{4.8+}$) and $BaNb_8O_{14}$ [8] ($Nb^{3.25+}$) which form in a disproportionate side-reaction. The structure of $Ba_2Nb_{15}O_{32}$ contains a layer (A) of isolated octahedral $[Nb_6O_{12}]O_6$ metal–metal bound clusters, interconnected by Nb-atoms in octahedral holes in the lattice. These layers are separated by layers of Nb_3O_{13} groups (B), and layers with Ba-ions and isolated NbO_6 octahedra (C). Single crystal resistivity measurements indicate semiconducting behavior, with a semiconductor-to-semiconductor transition at 170 K. This coincides with a magnetic transition from a weakly paramagnetic state to diamagnetism below the transition temperature.

In another reference, single crystals of the reduced niobate $Ba_2Nb_{15}O_{32}$ were produced by heating NbO_2 in $BaO{\cdot}3B_2O_3$ under high-vacuum conditions. The borate acts both as a source of BaO and as a flux for crystallization. The compound $Ba_2Nb_{15}O_{32}$ crystallizes in space group *R*3 ($a = 7.777$ Å, $c = 35.518$ Å) and contains isolated $[Nb_6O_{12}]O_6$ clusters arranged in layers. As side products, single crystals of the following phases were observed to be formed:

$Ba_3Nb_5O_{15}$ (space group $P4/mbm$), $a = 12.598$ Å, $c = 3.9774$ Å with a tetragonal tungsten bronze-type structure.

$BaNb_8O_{14}$ (space group *Pcab*, $a = 9.4222$ Å, $b = 10.3649$ Å, $c = 23.716$ Å).

These contain $[Nb_6O_{12}]O_6$ clusters in a three-dimensional arrangement, interconnected by three different modes of oxygen sharing. This compound, $Ba_2Nb_{15}O_{32}$, exhibits a semiconductor-to-semiconductor transition at 170 K, coinciding with a transition from a weakly paramagnetic state to diamagnetism. Single-crystal resistivity measurements on $Ba_3Nb_5O_{15}$ indicate a significant anisotropy ($\rho \perp c = 55$, $\rho \| c$ at 300 K) and small band gap semiconducting behavior.

The phase diagram is shown as follows in Fig. 9.76.

Of the nine (9) compounds shown, only three (3) melt congruently. The other six (6) melt incongruently. The 4:1, 3:1, 5:2, 5:6 and 1:2 compounds have not been studied very extensively. These incongruently melting compounds, $Ba_4Nb_2O_9$, $Ba_3Nb_2O_8$, $Ba_5Nb_4O_{15}$, $Ba_5Nb_{12}O_{35}$, and $BaNb_4O_{11}$, have been documented through study of their crystal structures but only $Ba_5Nb_4O_{15}$ has received any commercial attention.

The **metaniobate**, $BaNb_2O_6$, is polymorphic and has five differing crystal structures. Three (3) are unique to the metaniobate and the others are isomorphous to a ferrate, $NdFeO_6$ and a tantalate, $BaTa_2O_6$, as shown in the following Fig. 9.77.

These three isomorphic structures are shown as the low temperature α-type, and the β-type or γ-type. They are merely specific arrangements of NbO_6 octahedra and can be transposed one into the other by temperature changes as shown in Table 9.38.

Cell parameters and cell occupancies are given as follows:

α-type

$a = 3.952$ Å, $b = 6.059$ Å, $c = 10.434$ Å, $\alpha = \gamma = 90°$, $\beta = 90.35°$, Cell volume = 149.43 Å^3. Cell occupancy is shown in Table 9.39.

β-type

$a = \beta = 7.268$ Å, $\gamma = 10.292$ Å, $\alpha = \beta = 90°$, $\gamma = 114.35°$, cell volume = 495.33 Å^3. Cell occupancy is shown in Table 9.40.

γ-type

$a = 3.946$ Å, $b = 6.034$ Å, $c = 10.461$ Å, $\alpha = \beta = \gamma = 90°$, cell volume = 248.91 Å^3.

Cell occupancy is shown in Table 9.41.

The metaniobate also has the Nd_2FeO_6-type of structure as shown in the Fig. 9.78.

Cell parameters are: $a = 5.12$ Å, $b = 5.84$ Å, $c = 13.82$ Å, $\alpha = \beta = \gamma = 90°$, Cell volume = 413.23 Å^3. Cell occupancy is shown in Table 9.42.

$BaTa_2O_6$ type

This compound has the structure shown in Fig. 9.79. Unit cell parameters are: $a = 3.94$ Å, $b = c = 12.05$ Å, $\alpha = 120°$, $\beta = \gamma = 90°$, cell volume = 495.45 Å^3. Cell occupancy has not been given.

Crystals of the high-temperature form of $BaNb_2O_6$ were grown from a BaB_2O_4 flux. The symmetry of the crystals is orthorhombic and the structure consists of a zigzag pattern of edge-sharing pairs of NbO_6-octahedra joined at corners at nearly 60° and 120°

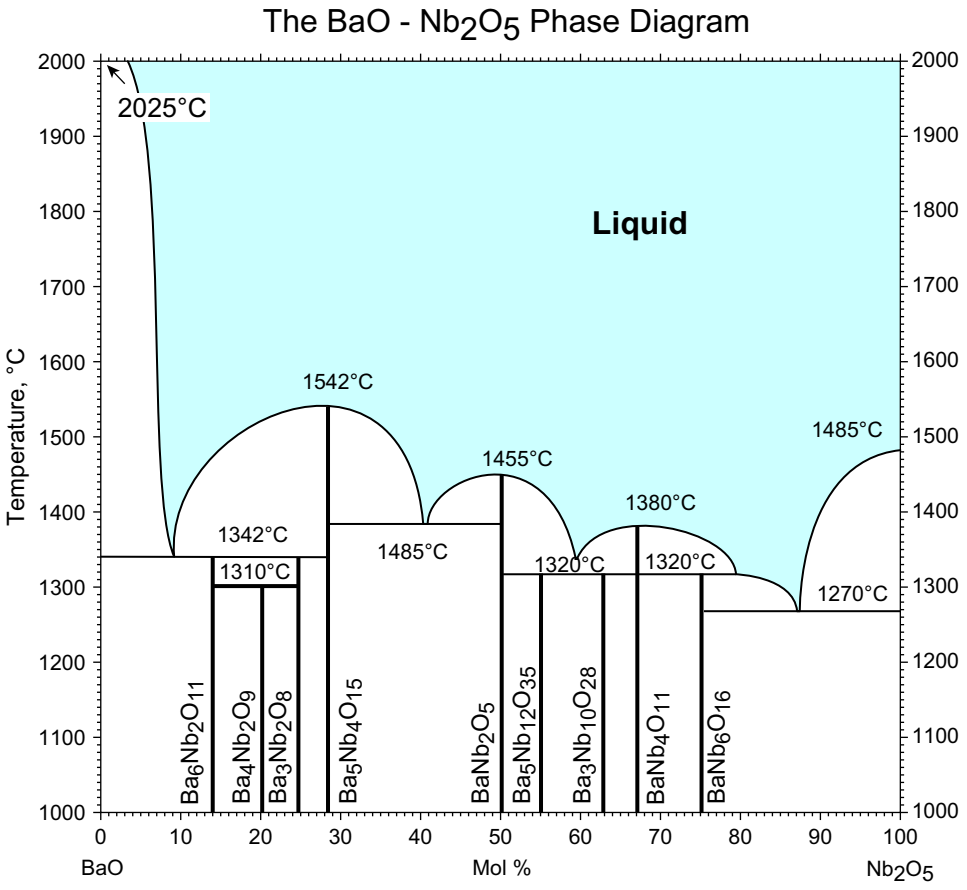

FIGURE 9.76

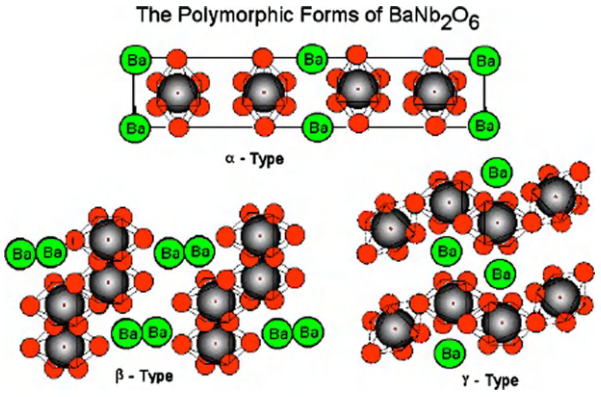

FIGURE 9.77

TABLE 9.38

Structure Parameters of Barium Metaniobate

	Structure type	Point group	Space group
1	α-$BaNb_2O_6$	mP18	$P2_1/c$
2	β-$BaNb_2O_6$	oS72	$C222_1$
3	γ-$BaNb_2O_6$	oP18	*Pmma*
4	$NdFeO_6$	oP36	*Pbcn*
5	$BaTa_2O_6$	hP108	*P6/mmm*

TABLE 9.39

No	Site notation	Atom	Multiplicity	Wyckoff	Site symmetry	*x*	*y*	*z*	Occupancy
1	O3	O	4	e	1	0.007	0.416	0.15	1.0
2	O1	O	4	e	1	0.499	0.198	0.464	1.0
3	O2	O	4	e	1	0.501	0.116	0.197	1.0
4	Nb	Nb	4	e	1	0.531	0.4535	0.1504	1.0
5	Ba	Ba	2	a	-1	0	0	0	1.0

TABLE 9.40

No	Site notation	Atom	Multiplicity	Wyckoff	Site symmetry	x	y	z	Occupancy
1	O4	O	8	c	1	0.008	0.12	0.034	1.0
2	O3	O	8	c	1	0.209	0.298	0.114	1.0
3	O1	O	8	c	1	0.212	0.082	0.257	1.0
4	Nb1	Nb	8	c	1	0.2219	0.1401	0.4259	1.0
5	O7	O	8	c	1	0.243	0.296	0.401	1.0
6	Nb2	Nb	8	c	1	0.2735	0.1418	0.0755	1.0
7	O2	O	8	c	1	0.525	0.159	0.114	1.0
8	Ba1	Ba	4	b	.2.	0	0.4258	1/4	1.0
9	Ba2	Ba	4	b	.2.	0	0.8755	1/4	1.0
10	O6	O	4	a	2..	0.296	0	0	1.0
11	O5	O	4	a	2..	0.686	0	0	1.0

TABLE 9.41

No	Site notation	Atom	Multiplicity	Wyckoff	Site symmetry	x	y	z	Occupancy
1	O1	O	4	j	.m.	0.08	1/2	0.25	1.0
2	Nb1	Nb	4	i	.m.	0.08	0	0.25	1.0
3	O2	O	4	i	.m.	0.1	0	0.6	1.0
4	Ba1	Ba	2	f	mm2	1/4	1/2	0.812	1.0
5	O3	O	2	e	mm2	1/4	0	0.13	1.0
6	O4	O	2	a	.2/m.	0	0	0	1.0

TABLE 9.42

No	Site notation	Atom	Multiplicity	Wyckoff	Site symmetry	x	y	z	Occupancy
1	O1	O	8	d	1	0.0963	0.1041	0.0727	1.0
2	O2	O	8	d	1	0.244	0.1236	0.4207	1.0
3	Nb1	Nb	8	d	1	0.3389	0.3191	0.2506	1.0
4	O3	O	8	d	1	0.4189	0.1163	0.099	1.0
5	Ba1	Ba	4	c	.2.	0	0.3311	1/4	1.0

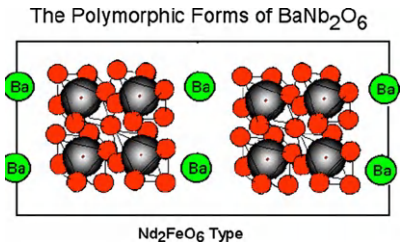

FIGURE 9.78

angles to produce rings of six octahedra. The barium atoms are situated in the cages formed by the rings. Pure hexagonal $BaNb_2O_6$ crystallizes at 640° to 700 °C from an amorphous material prepared by simultaneous hydrolysis of barium and niobium alkoxides. This structure is characterized by layer networks of NbO_6 octahedra. Crystallization isotherms are described by the Avrami equation: $\ln(1-f) = -kt^n$ with $n = 2$; the activation energy is

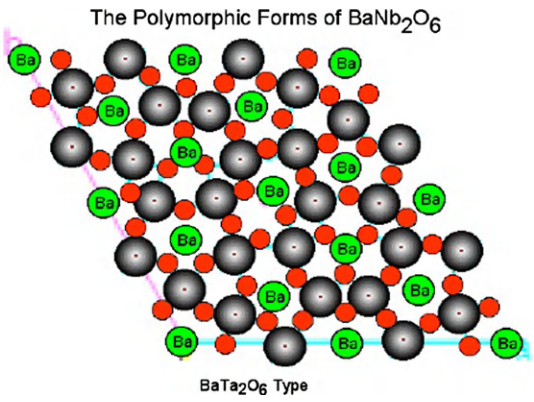

FIGURE 9.79

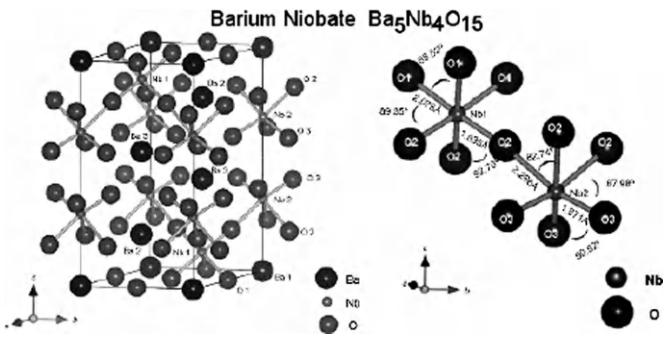

FIGURE 9.80

268 kJ/mol. Hexagonal $BaNb_2O_6$ transforms to the orthorhombic modification at 1250° to 1310 °C.

Barium metaniobate, $BaNb_2O_6$ with polymorphic orthorhombic and hexagonal forms was also prepared by solid-state reaction. Hexagonal α-$BaNb_2O_6$ is the low temperature phase, and can be transformed to the orthorhombic phase over a broad temperature range above 1150 °C. It was observed that the hexagonal-to-orthorhombic phase transition is reversible due to the structural similarity of these two polymorphs. The difference in transition kinetics and associated mechanisms could be confirmed from the analysis of time dependence of transformed phase. It was also found the dielectric properties of each phase was significantly different. In particular, orthorhombic β-$BaNb_2O_6$ has good microwave dielectric properties:

$$Q \times f = 43,000\ \text{GHz}, \quad \varepsilon_r = 30, \quad \tau_f = -45\ \text{ppm/°C}.$$

$Ba_{1-x}Sr_xNb_2O_6$ ceramics, where $0.25 \le x \le 0.75$, are ferroelectric materials with tungsten bronze structures, and have excellent electro-optic, pyroelectric, photorefractive, and piezoelectric properties.

The compound, **penta-barium di-niobate**, $Ba_5Nb_4O_{15}$, its structures and properties, has been well studied. This compound has a hexagonal structure and crystallizes in the $P3m1$ space group with one formula unit per cell ($Z = 1$). The compound has a five-layer closest packing of oxygen and barium ions. The niobium ions are located in the octahedral holes between layers with one layer of octahedral holes are missing niobium ions to accommodate the charge neutrality. The $Ba_5Nb_4O_{15}$ compound is a hexagonal polytype i.e., the (5H) member of a series of polytypes containing 4, 5, 6, 8, 10 and 12 layered (4H, 5H, 6H, 8H, 10H, and 12H) species. The structure has the form as shown in Fig. 9.80

Cell parameters are; $a = 3.878$ Å, $b = 20.86$ Å, $c = 36.27$ Å, $\alpha = \beta = \gamma = 90°$, cell volume = 2934.06 Å^3.

The addition of B_2O_3 to a mixture of $Ba_5Nb_4O_{15}$-$BaNb_2O_6$ significantly lowered the sintering temperature to about 900 °C in comparison to about 1250 °C for B_2O_3-free samples. A B_2O_3-rich intra-granular phase in the sample was attributed to the presence of a liquid phase during sintering. This barium metaniobate, $BaNb_2O_6$ has five polymorphs, with orthorhombic and hexagonal forms. A major contributor to good microwave dielectric properties of low-fired samples is the low-temperature phase, hexagonal $BaNb_2O_6$. A small amount of hexagonal $BaNb_2O_6$ apparently tunes the temperature coefficient of resonant frequency (τ_f) of $Ba_5Nb_4O_{15}$. Therefore the mixture, $Ba_5Nb_4O_{15}$–$BaNb_2O_6$ with B_2O_3 is suitable for preparation of a low-temperature co-fired ceramic (LTCC), due to its reduced sintering temperature and good microwave dielectric properties: $Q \times f = 28{,}000$ GHz; ε_r and τ_f are 42 and 0 ppm/°C, respectively.

A barium niobium oxide displaying bronze characteristics was found by the reaction of niobium metal with mixtures of barium and niobium oxides to form $Ba_5Nb_4O_{15}$. It is a red compound with the cubic perovskite-type structure $a_0 = 4.080$ Å, a good electrical metallic conductor and paramagnetic with Curie–Weiss behavior.

The low-temperature, far-infrared reflectivity, and Raman-scattering measurements for the layered compound, $Ba_5Nb_4O_{15}$, was reported. This material is characterized by a strong anharmonic lattice where the symmetric stretching vibration of the empty octahedra, a singular feature of this layer compound, splits into two narrow Raman-active bands. These differences were assigned to the same phonon in a slightly different environment, and suggested the existence of a small local departure from the reported centro-symmetric $D^3_{3d} - P3m1$ space group. It was concluded that the infrared and mainly the Raman band profiles indicated that the lattice of $Ba_5Nb_4O_{15}$ is close to collapsing into a lower symmetry structure.

A study was carried out of the microwave dielectric properties of the five-layered compound $Ba_5Nb_4O_{15}$ prepared by conventional solid-state synthesis. Results show that $Ba_5Nb_4O_{15}$ has excellent microwave dielectric characteristics; $\varepsilon_r = 38$, $Q \times f = 7500$ at 10 GHz, and $\tau_f = +50$ ppm/K. Since this compound has a high dielectric constant, high Q and sufficiently stable

characteristics, it is perceived as useful for applications at microwave frequencies.

The effect of B_2O_3 on the sintering temperature and microwave dielectric properties of $Ba_5Nb_4O_{15}$ was reinvestigated using powder XRD, SEM, and a network analyzer. Interactions between $Ba_5Nb_4O_{15}$ and B_2O_3 led to the formation of second phases, $BaNb_2O_6$ and BaB_2O_4. The addition of B_2O_3 to $Ba_5Nb_4O_{15}$ resulted in lowering the sintering temperature from 1400° to 925 °C. Low-fired $Ba_5Nb_4O_{15}$ could be interpreted by measuring changes in the quality factor ($Q \times f$), the relative dielectric constant (ε_r), and the temperature coefficient of resonant frequency (τ_f) as a function of B_2O_3 additions. More importantly, the formation of $BaNb_2O_6$ provided temperature compensation. The microwave dielectric properties of low-fired $Ba_5Nb_4O_{15}$ had good dielectric properties: $Q \times f = 18700$ GHz, $\varepsilon_r = 39$, and $\tau_f = 0$ ppm/°C.

$Ba_5Nb_4O_{15}$ ultrafine powders were prepared by a hydrothermal method using $Ba(NO_3)_2$ and Nb_2O_5 precursors. The synthesis characteristics were influenced by the chemical form of precursors, reaction temperature, mole ratio of Ba/Nb and pH value. The chemical form of the precursors has a strong influence on the products of $Ba_5Nb_4O_{15}$. There was no requisite compound in the final product when Nb_2O_5 powder was used as Nb-precursor. In addition, the reaction completeness was also dependent on the synthesis temperature. The best single-phase $Ba_5Nb_4O_{15}$ ultrafine powders were obtained at a temperature of 230 °C. The most appreciate Ba/Nb molar ratio was 3/2. The reactions were only carried out in a solution with pH value between 12 and 14. When pH was equal or larger than 14, there was no product of $Ba_5Nb_4O_{15}$ powder in the reactor.

The effects of a forming atmosphere on the stability, the sintering and the dielectric properties of $Ba_5Nb_4O_{15}$, $BaNb_2O_6$, $ZnNb_2O_6$ and $Zn_3Nb_2O_8$ ceramics were investigated, because of the primary importance of the sintering atmosphere in relation to copper sintering. These Nb-based materials were sintered in air and in Ar/H_2 (10%). Zn-containing samples are very sensitive to the reductive atmosphere. ZnO volatilizes at 800–850 °C and the resulting compound does not exhibit the expected properties. $BaNb_2O_6$ and $Ba_5Nb_4O_{15}$ are more stable in terms of relative weight loss. A phase analysis revealed that a modification of the $BaNb_2O_6$ phase was formed during reduction that induced degradation of the dielectric property stability as a function of temperature. In contrast, the properties of $Ba_5Nb_4O_{15}$ are not modified by a sintering in a reductive atmosphere. A relative permittivity of 38.8, a permittivity temperature coefficient of −150 ppm/°C and an insulating resistivity of $10^{10.9}$ V/cm were obtained for the latter.

A related compound, $Ba_3Nb_5O_{15}$, has the structure as shown in Fig. 9.81

Lattice parameters are: $a = 3.945$ Å, $b = c = 12.362$ Å, $\alpha = \beta = \gamma = 90°$, cell volume = 595.99 Å^3, $Z = 4$. Cell occupancy is shown in Table 9.43.

Little is known concerning this compound other than its crystal structure.

Two related compounds, tribarium niobate and tetrabarium niobate, $Ba_3Nb_2O_8$ and $Ba_4Nb_2O_9$, have received

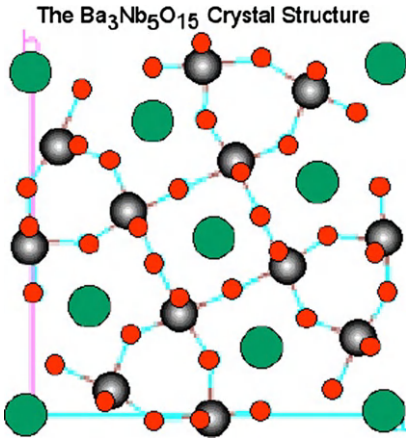

FIGURE 9.81

TABLE 9.43

No	Site notation	Atom	Multiplicity	Wyckoff	Site symmetry	x	y	z	Occupancy
1	O1	O	8	d	1	0.012	0.346	0.484	1.0
2	O2	O	8	d	1	0.071	0.144	0.487	1.0
3	Nb1	Nb	8	d	1	0.2155	0.0748	0.53	1.0
4	O3	O	8	d	1	0.224	0.063	0.001	1.0
5	O4	O	4	c	..m	0.223	0.723	0.484	1.0
6	Ba1	Ba	4	c	..m	0.672	0.172	0.009	1.0
7	Nb2	Nb	2	b	2.mm	1/2	0	0.535	1.0
8	O5	O	2	b	2.mm	1/2	0	0.98	1.0
9	Ba2	Ba	2	a	4..	0	0	0.0	1.0

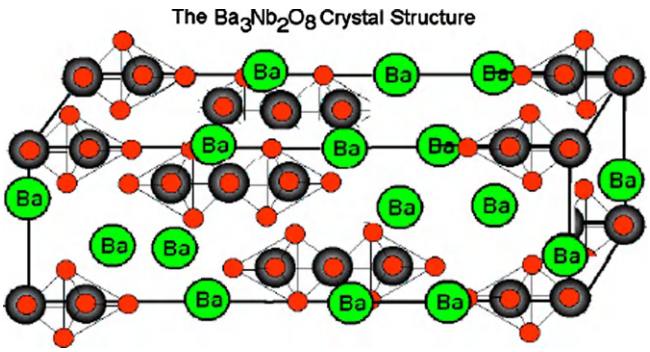

FIGURE 9.82

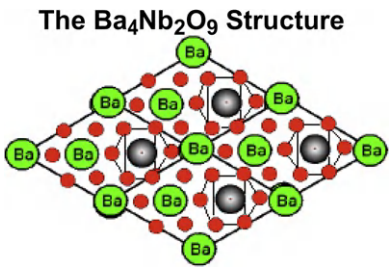

FIGURE 9.83

extensive attention in the literature. They differ by one BaO molecule but have quite differing structures. The **tribarium niobate** compound, $Ba_3Nb_2O_8$, has the structure as shown in Fig. 9.82.

Cell parameters are: $a = b = 6.045$ Å, $c = 7.903$ Å. $\alpha = \beta = 67.513°$, $\gamma = 60°$. Cell volume $= 224.37$ Å^3. Cell occupancy is shown in Table 9.44.

According to one study, the structural investigations performed by powder XRD, selected area ED, and high-resolution electron microscopy(HREM) on $Ba_3Nb_2O_8$ clearly showed that the palmierite structure previously reported for this compound is not adopted. The presence of Nb in the *B* sub-lattice induces a change in symmetry from rhombohedral to hexagonal, and a 9H unit cell is formed. The two possible layer stacking sequences, (*ccchhhhhh*) (*Pm*1) and (*cchhchhhh*) (*Pm*1), was discussed in terms of ordering of both anionic and cationic vacancies.

The crystal structure given above is that which is regarded as most relevant to the actual structure of this compound. Very little information or studies of this 3:1 compound have appeared in the literature and it is clearly inferior in dielectric properties, compared to other barium niobate compositions.

The addition of another BaO molecule to form the compound $Ba_4Nb_2O_9$ changes the NbO_4 tetragonal unit of $Ba_3Nb_2O_8$ to an octagonal unit, NbO_6, in the crystal structure, shown in Fig. 9.83.

Cell parameters are: $a = b = 6.11$ Å, $c = 8.04$ Å, $\alpha = \beta = 90°$, $\gamma = 120°$, cell volume $= 257.80$ Å^3. Cell occupancy is shown in Table 9.45.

TABLE 9.44

No	Site notation	Atom	Multiplicity	Wyckoff	Site symmetry	*x*	i	*z*	Occupancy
1	O2	O	18	h	.m	0.5	0.5	0.2778	1.0
2	Nb1	Nb	6	c	3m	0	0	0.101	0.925
3	O1	O	6	c	3m	0	0	0.167	1.0
4	Ba2	Ba	6	c	3m	0	0	0.298	1.0
5	Ba1	Ba	3	b	-3m	0	0	1/2	1.0
6	Nb2	Nb	3	a	-3m	0	0	0	0.15

TABLE 9.45

No	Site notation	Atom	Multiplicity	Wyckoff	Site symmetry	*x*	*y*	*z*	Occupancy
1	O1	O	6	i	.m.	0.1667	0.833	0.3333	1.0
2	O2	O	3	e	.2/m.	1/2	0	0	1.0
3	Nb1	Nb	2	d	3m.	1/3	2/3	0.1667	1.0
4	Ba1	Ba	2	d	3m.	1/3	2/3	0.6667	1.0
5	Ba2	Ba	1	b	-3m.	0	0	1/2	1.0
6	Ba3	Ba	1	a	-3m.	0	0	0	1.0

Polymorphic phase transitions in $Ba_4Nb_2O_9$ were studied by thermal analyses, HTTEM and powder XRD. Two stable polymorphs were isolated, a low-temperature α-modification and a high-temperature γ-modification, with an endothermic phase transition at 1176 °C. The alpha ⇔ gamma transformation is accompanied by the formation of a 120° domain structure, which is a consequence of the hexagonal ⇔ orthorhombic unit cell reconstruction. Reheating the pre-sintered γ-$Ba_4Nb_2O_9$ results in the formation of a metastable γ′-modification (formerly known as β-polymorph) in the temperature range between 360 °C and 585 °C, before the α ⇒ γ transformation above 800 °C occurs. Above about 1490 °C, $Ba_4Nb_2O_9$ becomes moderately sensitive to a loss of BaO. In air, the surface of the $Ba_4Nb_2O_9$ grains decomposes to nano-crystalline $Ba_5Nb_4O_{15}$ and BaO, which instantly reacts with atmospheric CO_2 to form $BaCO_3$. Surface reaction delays the α ⇒ γ transformation up to 866 °C in air. In vacuum the loss of BaO is even more enhanced and consequently the formation of minor $Ba_3Nb_2O_8$ phase is observed above 1150 °C.

In another study, $Ba_4Nb_2O_9$ was shown to have two basic polymorphs: a high-temperature γ phase, which represents a differing structure type and a low-temperature α phase, which has the rare $Sr_4Ru_2O_9$ structure type. The phases can be rearranged into one or the other by a reconstructive phase transition close to 1370 K. The kinetics is sufficiently slow that the γ phase can easily be quenched to room temperature. Below 950 K, both α and γ phases absorb significant amounts of water. In the case of the γ phase, protons from absorbed water occupy ordered positions in the structure, giving rise to a stoichiometric phase, γ-III-$Ba_4Nb_2O_9 \cdot 1/3H_2O$, at room temperature. γ-III-$Ba_4Nb_2O_9 \cdot 1/3H_2O$ partially dehydrates close to 760 K to give another stoichiometric phase γ-II-$Ba_4Nb_2O_9 \cdot 1/3H_2O$, which completely dehydrates at 950 K to γ-I-$Ba_4Nb_2O_9$. The hydrated γ phases exhibit faster protonic and oxide ionic transport than the hydrated α phases because of the presence in the γ phases of 2D layers containing Nb^{5+} cations with unusually low oxygen coordination numbers (4 or 5) separated by discrete OH groups. Hydration appears to play an important role in stabilizing the γ phases at low temperatures, and the γ ⇔ α transition caused by reheating a quenched sample occurring at a higher temperature in humid atmospheres.

The structure of γ-$Ba_4Nb_2O_9$, having the $Sr_4Ru_2O_9$ structure is shown in the following diagram Fig. 9.84.

In addition to being sensitive to moisture adsorption, this compound also absorbs CO_2. Powder XRD, HRTEM, ED, IR, TG and mass spectroscopy (MS) were performed to investigate the composition and the crystal structure of tetra-barium niobate (V) $Ba_4Nb_2O_9$. The TG, MS and IR studies revealed that the compound is a hydrated oxycarbonate. Assuming that the carbonate

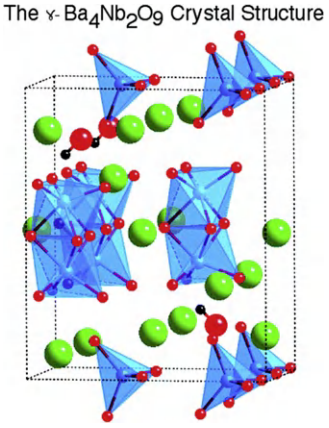

FIGURE 9.84

stoichiometrically replaces oxygen, it was found that the composition of the low-temperature α-modification, obtained by slow cooling from 1100 °C, corresponds to $Ba_4Nb_2O_{8.8}(CO_3)_{0.2} \cdot 0.1H_2O$, while the quenched high-temperature γ-modification has the $Ba_4Nb_2O_{8.42}(CO_3)_{0.58} \cdot 0.38H_2O$ composition. The α-phase has an incommensurately composite-modulated structure consisting of two mutually interacting $[Ba]_\infty$ and the $[(Nb,)O_3]_\infty$ subsystems (where the vacancy is clearly seen). The composite-modulated crystal structure of the α-phase can be described with the lattice parameters $a = 10.2688$ Å, $c = 2.82426$ Å, $q = 0.66774c^*$ and a superspace group $R\bar{3}m(00\gamma)0s$. The HRTEM analysis demonstrates the nanoscale twinning of the trigonal domains parallel to the {100} crystallographic planes. The twinning introduces a one-dimensional disorder into the $[(Nb,)O_3]_\infty$ subsystem, which results in an average $P62c$ crystal structure of the α-phase. Possible places for the carbonate group in the structure were discussed using a comparison with other hexagonal perovskite-based oxycarbonates. It has been concluded that the preparation of $Ba_4Nb_2O_9$ from the oxides in air does not result in the anhydrous compound but cools to a perovskite-based hydroxy-carbonate.

The polymorphic phase transitions and the stability of the individual polymorphs of tetra-barium niobate ($Ba_4Nb_2O_9$) were studied at different temperatures. $Ba_4Nb_2O_9$ ceramics were prepared via a conventional solid-state reaction route. Three $Ba_4Nb_2O_9$ polymorphs were isolated. These include a hexagonal (α) and two orthorhombic (β, γ) modifications. TEM revealed an intergranular BaO-rich amorphous phase and nano-crystalline $Ba_5Nb_4O_{15}$ in all the polymorphs, most abundantly in the α-modification. Superstructure ordering in the γ-modification was confirmed by ED methods. The α-$Ba_4Nb_2O_9$ was observed to be stable in the temperature range 560–1160 °C; below 560 °C the stable polymorph is β-$Ba_4Nb_2O_9$, while above 1160 °C the only stable polymorph is γ-$Ba_4Nb_2O_9$.

Other than phase-transitions and structural data, little information concerning these compounds has appeared in the scientific or technical literature.

The structure of the compound, **barium tri-niobate**, $BaNb_6O_{16}$, has the cell parameters of: $a = 3.98$ Å, $b = 12.47$ Å, $c = 19.72$ Å, $\alpha = 107.44°$, $\beta = \gamma = 90°$, cell volume $= 92.74$ Å^3. An exact structure has not been published. This compound appears as a reaction product of the oxides at high temperatures but does not appear to be stable at room temperature. When the sintering temperature was 1400 °C, a homogeneous phase with a 1:3 ordered structure was found in the specimens. At lower temperatures, a disordered structure and $BaNb_6O_{16}$ second phase were found. The main phase of this system was a cubic perovskite with a small quantity of a second phase like $Ba_5Nb_4O_{15}$, as determined by XRD analysis.

The 5:6 compound, **penta-barium hexa-niobate**, $Ba_5Nb_{12}O_{35}$, has the cell parameters of: $a = 3.878$ Å, $b = 20.86$ Å, $c = 36.27$ Å, $\alpha = \beta = \gamma = 90°$, cell volume $= 2{,}934.04$ Å^3. As with other compounds in this series, the exact structure published is subject to question and is not included here. It is cubic with a complicated structure.

The existence of the compound, **tri-barium penta-niobate**, $Ba_3Nb_{10}O_{28}$, is doubtful. No structural data is available nor are any descriptions of its chemical or physical properties appeared in the scientific literature. Yet, this compound is listed as a component in a ternary phase diagram. The only known compound similar to this composition is $BaNb_4O_6$, which contains Nb^{3+} and Nb^{4+}ions. Although the compound, $Ba_3Nb_{10}O_{28}$, is listed in the phase diagram, no information is available in the scientific or technical literature. It is said to be tetragonal and have the tetragonal tungsten–bronze structure. However, specific data is not available in the scientific or technical literature.

The compound, barium di-niobate, $BaNb_4O_{11}$ has the structure shown as follows in Fig. 9.85.

Cell parameters are: $a = b = 3.182$ Å, $c = 8.212$ Å, $\alpha = \beta = \gamma = 90°$, cell volume is 143.62 Å^3.

Cell occupancy is shown in Table 9.46.

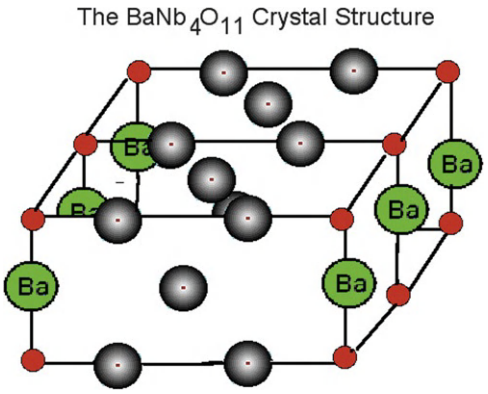

FIGURE 9.85

Little information is available for this compound other than its structure. $BaNb_4O_{11}$ has not been thoroughly studied and little to no data can be found in the open literature.

The compound, **hexa-barium niobate**, $Ba_6Nb_2O_{11}$, has been found to form oxygen-vacancy lattices as well as stoichiometric ones. The perovskite-related phases, $Ba_6Nb_2O_{11}(V_o^s)_1$ and $Ba_4Ca_2Nb_2O_{11}$, where V_o^s stands for "oxygen structural vacancies", have been studied by TG, AC-conductivity and IR and/or RS. A correlation between water uptake and nominal V_o^s concentrations was established, but it was determined that the nature of the alkaline earth metal atom influences the oxygen sub-lattice: $Ba_6Nb_2O_{11}(V_o^s)_1$ has zero water uptake. The relationship between short-range disorder and water uptake is clear; only compounds having a strong oxygen and cation lattice disorder exhibit maximal water uptake. In $Ba_4Ca_2Nb_2O_{11}$, the protonic species change during cooling–heating.

Single crystals of $BaNb_4O_6$ (I) and $Ba_2Nb_5O_9$ (II), containing Nb in various valence states, have been prepared by heating pellets containing $Ba_5Nb_4O_{15}$, NbO_2, Nb_2O_3 Nb (Ba:Nb:O = 1:7:9 for I and 4:14:23 for II) together with 10% BaF_2 as a mineralizer for 24 h in a sealed niobium ampoule at 1600 °C. The crystal structures of I and II were refined using single-crystal data (CAD 4: I, 128 unique reflections, $R = 1.91\%$, $R_w = 1.70\%$, **II**, 223

TABLE 9.46

No	Site notation	Atom	Multiplicity	Wyckoff	Site symmetry	*x*	*y*	*z*	Occupancy
1	O(2)	O	4	i	2mm.	0	1/2	0.2431	1.0
2	Nb(2)	Nb	2	g	4mm	0	0	0.2531	1.0
3	Nb(1)	Nb	2	e	mmm.	0	1/2	1/2	1.0
4	O(1)	O	1	d	4/mmm	1/2	1/2	1/2	1.0
5	Ba	Ba	1	c	4/mmm	1/2	1/2	0	1.0
6	O(3)	O	1	a	4/mmm	0	0	0	1.0

unique reflections, $R = 2.75\%$, $R_w = 2.55\%$). I crystallizes in space group $P4/mmm$ with $a = 4.182$ Å and $c = 8.212$ Å and II in $P4/mmm$ with $a = 4.172$ Å and $c = 12.224$ Å. The atomic positions are slightly different from those previously obtained from powder data. The structures of I and II contain Nb_6O_{12} clusters linked to two-dimensional sheets and can be ascribed to terms of an intergrowth between slabs of perovskite- and NbO-type structures. I and II are metallic in conductivity and exhibit a weak temperature-independent paramagnetism.

A reduced barium niobate, $Ba_2Nb_5O_9$, has been found in the course of an investigation of the Ba–Nb–O system. It has been characterized by means of XRD and high resolution electron microscopy(HREM). The space group is $P4/mmm$ and its unit cell parameters are $a = 4.1696(2)$ and $c = 12.228$ Å. The structure that has been refined by profile fitting of XRD data is an ordered intergrowth between $BaNbO_3$ and NbO, giving rise to two-dimensional layers of corner-sharing octahedral Nb_6-clusters.

A new crystalline form, hitherto unsuspected in the $Ba_xSr_{1-x}Nb_2O_6$ solid-solution zone, has been found to exist for $x = 0.15$, 0.20, 0.25 and 0.29. It has a monoclinic symmetry and belongs to the $P21/a$ space-group. For $x = 0.29$ its lattice parameters are: $a = 10.997$ Å, $c = 5.666$ Å and $\gamma = 90°$ 30/100.

$Ba_{3-x}Sr_xLaNb_3O_{12}$ ($x = 0$ to 3) ceramics were prepared by the conventional solid-state reaction route. All of them adopt $A_4B_3O_{12}$ cation-deficient hexagonal perovskite structure. The substitution of Sr for Ba effectively enhances quality factor and modifies τ_f of $Ba_3LaNb_3O_{12}$. The $Q \times f$ value increases significantly from 16 000 to 45 327 GHz, τ_f improves from −96 to −9 ppm/°C and the dielectric constant (ε_r) varies gradually from 44.8 to 35.8 with the increase of Sr content.

Barium niobates are not used commercially and most of the scientific studies have concentrated upon mixed alkaline earth niobates, including addition of selected rare earths like La^{3+} and Ce^{3+}. Cobalt as Co^{3+} is also another additive that has received intense study in efforts designed to improve the dielectric properties of barium niobates for use in electrical-insulating layer structures in high-frequency capacitors and insulating layers in the construction of integrated circuits.

9.2.6. Radium Niobates

The high cost of Ra-metal and its intense radioactivity has precluded any investigation of any radium niobate compounds. Undoubtedly, the same type of compounds could be formed from RaO and Nb_2O_5 as those that exist in the BaO–Nb_2O_5 system. However, no data is known nor is any expected because of the lack of interest in Academia and Industry in such compounds.

9.3. ALKALINE EARTH TANTALUM COMPOUNDS

Tantalum has the valence states: 5, 4, 3, 2, −1, with the most important one being Ta^{5+}. Only the Ta^{4+} ion appears in the solid-state, the others appear in solution chemistry. Thus, the major system with the alkaline earths involves AeO–Ta_2O_5. Tantalum forms the same type of compounds, with almost identical crystal structures, as the niobates. Indeed, many of the published papers involve both the same type of compositions and the solid-state solution compositions that are formed.

9.3.1. Beryllium Tantalum Compounds

Beryllium does not form any oxygen-dominated tantalate compounds. But, it does form a series of intermetallic compounds similar to that of the Be–Nb system. The intermetallic phase diagram shows six (6) compounds, all of which melt congruently as shown in Fig. 9.86.

The structure factors are shown as follows in Table 9.47.

The structure types are varied. The $BeTa_2$ structure has the form as shown in Fig. 9.87.

The Ta-atoms form a distinctive pattern in the unit-cell. Cell parameters are: $a = 4.89$ Å, $b = c = 4.902$ Å, $\alpha = 75.6°$, $\beta = \gamma = 60.087°$, cell volume = 88.32 Å^3. Cell occupancy is shown in Table 9.48.

In contrast, the Be_2Ta structure has a different form as shown in Fig. 9.88.

A two-dimensional layer is shown. The three dimensional form is shown as well as the arrangement of the individual Be and Ta atoms along one plane of the structure. Here, the four (4) Ta-atoms have adopted a slightly different pattern in the cell, almost akin to an octahedral pattern. Cell parameters are: $a = b = c = 4.6011$ Å, $\alpha = \beta = \gamma = 60°$, cell volume = 68.88 Å^3.

Site occupancy is shown in Table 9.49.

The next compound in the series, Be_3Ta, has the structure as shown in Fig. 9.89.

Here, the Ta-atoms have adopted a slightly distorted Ta_5 pattern. Cell parameters are: $a = b = 4.53$ Å, $c = 7.457$ Å, $\alpha = \beta = 72.318°$, $\gamma = 80°$, cell volume = 124.11 Å^3. Cell occupancy is shown in Table 9.50.

The 2:3 compound, Be_2Ta_3, has the structure as shown in Fig. 9.90.

Where the Ta-atoms dominate the unit cell. Cell parameters are: $a = 3.32$ Å, $b = c = 6.52$ Å, $\alpha = \beta = \gamma = 90°$, cell volume = 140.27 Å^3. Cell occupancy is shown in Table 9.51.

When the Ta-atom content is low, as in $Be_{17}Ta_2$, the following structure results as shown in Fig. 9.91.

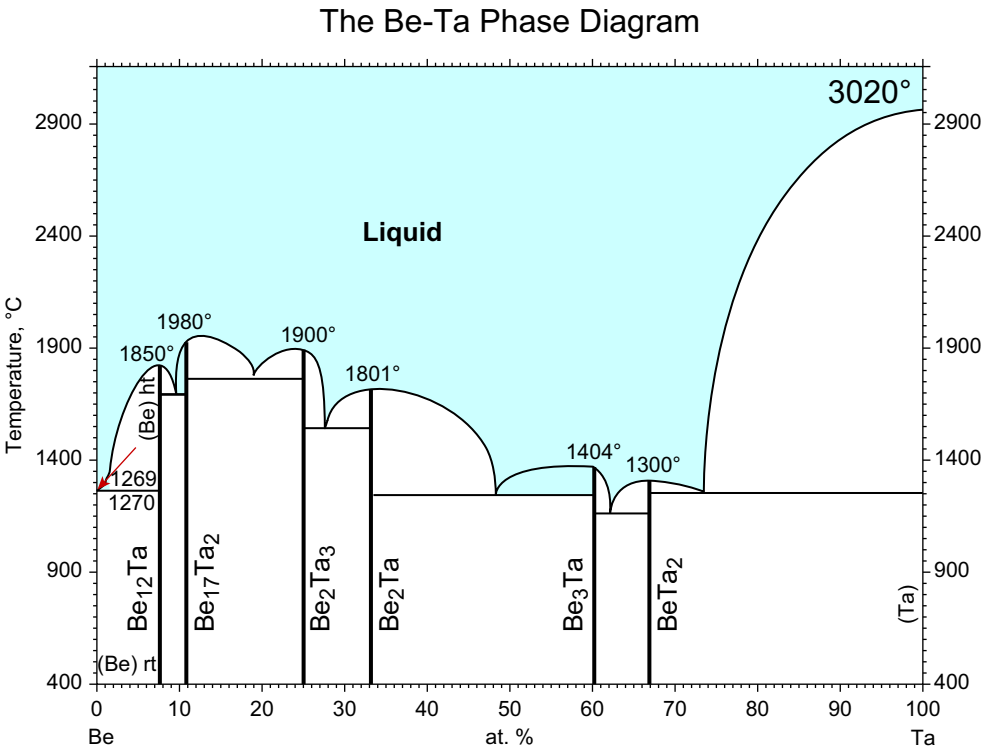

FIGURE 9.86

Note that the Ta-atoms are no longer connected in the unit cell. Cell parameters are: $a = b = c = 5.5687$ Å, $\alpha = \beta = \gamma = 83.112°$, cell volume = 169.23 Å^3. Cell occupation is shown in Table 9.52.

The final composition in the series is $Be_{12}Ta$, which has the structure as shown in Fig. 9.92.

Cell parameters are: $a = 4243$ Å, $b = c = 5.6129$ Å, $\alpha = 81.787°$, $\beta = \gamma = 67.792$ Å, cell volume = 114.58 Å^3. Cell occupancy is shown in Table 9.53.

There are no compounds formed within the BeO–Ta_2O_5 system.

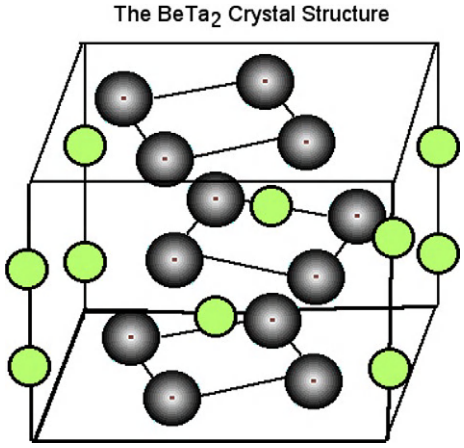

FIGURE 9.87

9.3.2. Magnesium Tantalum Compounds

The system Mg^0–Ta^0 does not form any intermetallic compounds.

TABLE 9.47

No.	Phase	# atoms	Structure type	Point group	Space group
1	$Be_{12}Ta$	2	$ThMn_{12}$	Tl26	*I*4/*mmm*
2	$Be_{17}Ta$	2	$MgCu_2$	HR57	*R*-3*m*
3	Be_2Ta	2	$MgCu_2$	CF24	*Fd*-3*m*
4	Be_2Ta_3	2	U_3Si_2	TP10	*P*4/*mbm*
5	Be_3Ta	2	$PuNi_3$	HR36	*R*-3*m*
6	$BeTa_2$	2	$CuAl_2$	TL12	*I*3/*mcm*

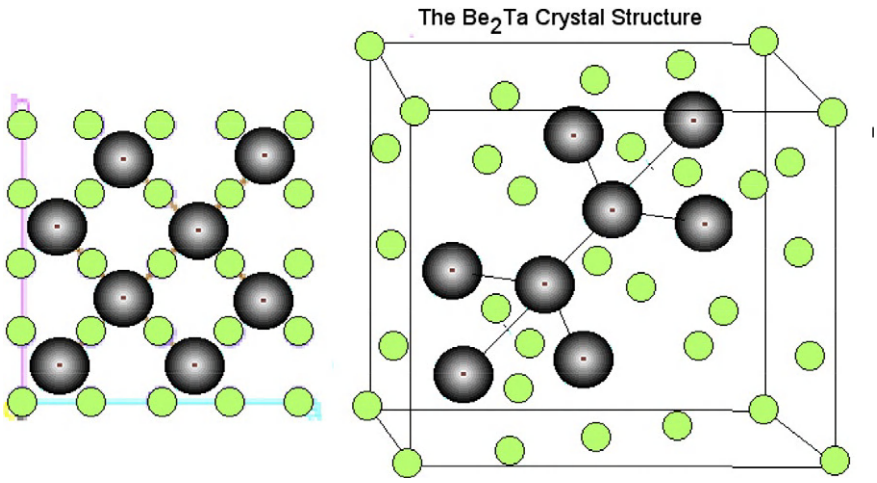

FIGURE 9.88

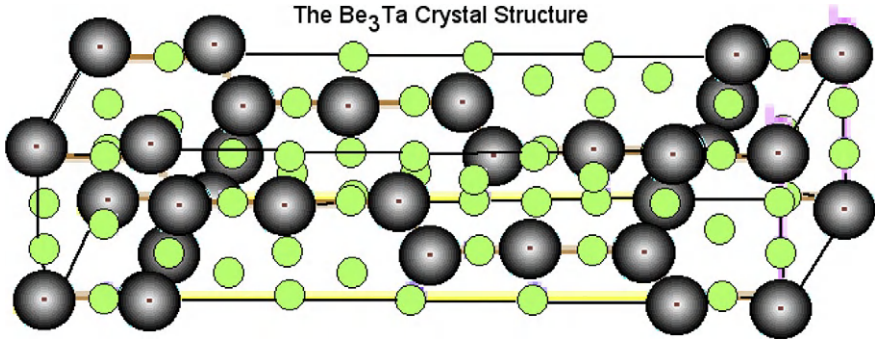

FIGURE 9.89

TABLE 9.48

No	Site notation	Atom	Multiplicity	Wyckoff	Site symmetry	*x*	*y*	*z*	Occupancy
1	Ta	Ta	8	h	m.2m	0.1608	0.661	0	1.0
2	Be	Be	4	a	422	0	0	1/4	1.0

TABLE 9.49

No	Site notation	Atom	Multiplicity	Wyckoff	Site symmetry	*x*	*y*	*z*	Occupancy
1	Be	Be	16	c	.-3m	0	0	0	1.0
2	Ta	Ta	8	b	-43m	3/8	3/8	3/8	1.0

TABLE 9.50

No	Site notation	Atom	Multiplicity	Wyckoff	Site symmetry	*x*	*y*	*z*	Occupancy
1	Be1	Be	18	h	.m	0.5002	0.499	0.0829	1.0
2	Ta1	Ta	6	c	3m	0	0	0.1414	1.0
3	Be2	Be	6	c	3m	0	0	0.3336	1.0
4	Be3	Be	3	b	-3m	0	0	1/2	1.0
5	Ta2	Ta	3	a	-3m	0	0	0	1.0

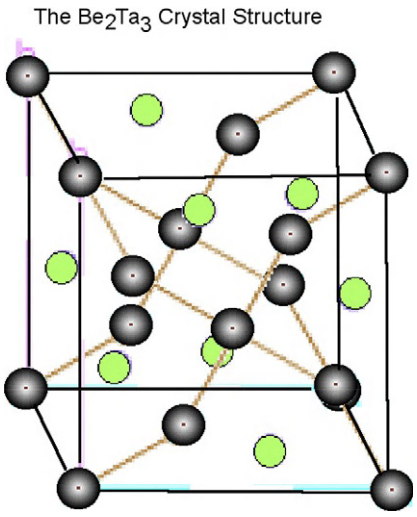

FIGURE 9.90

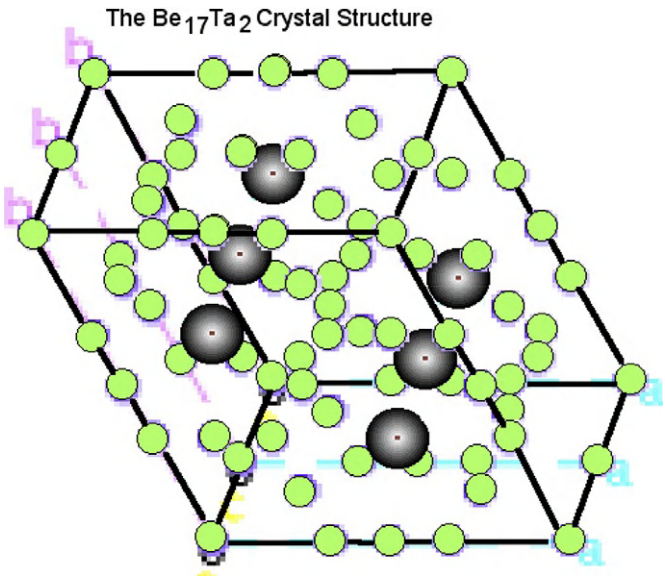

FIGURE 9.91

As stated above, the valence states of $Ta^{2+}$and Ta^{3+} are found only in solution.

The valence state of Ta^{4+} is extremely limited and no studies of synthesis have resulted in a xMgO-yTaO$_2$ compound of any sort.

The Ta^{5+} containing system MgO–Ta_2O_5 shows that MgO and Ta_2O_5 form three compounds: $Mg_4Ta_2O_9$, $Mg_3Ta_2O_8$, and $MgTa_2O_6$. $Mg_4Ta_2O_9$ and $MgTa_2O_6$ are stable up to their melting points, whereas $Mg_3Ta_2O_8$ is stable only between 1475° and about 1675 °C. XRD and density data have been presented for the three compounds as shown in Fig. 9.93.

The structure factors are shown in the following Table 9.54.

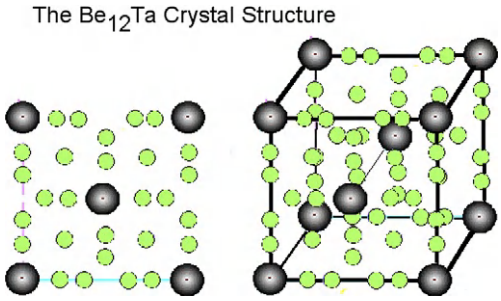

FIGURE 9.92

TABLE 9.51

No	Site notation	Atom	Multiplicity	Wyckoff	Site symmetry	*x*	*y*	*z*	Occupancy
1	Ta1	Ta	4	h	m.2m	0.1821	0.682	1/2	1.0
2	Be1	Be	4	g	m.2m	0.6159	0.116	0	1.0
3	Ta2	Ta	2	a	4/m..	0	0	0	1.0

TABLE 9.52

No	Site notation	Atom	Multiplicity	Wyckoff	Site symmetry	*x*	*y*	*z*	Occupancy
1	Be1	Be	18	h	.m	0.5	0.5	0.1667	1.0
2	Be2	Be	18	f	.2	0.3333	0	0	1.0
3	Be3	Be	9	d	.2/m	1/2	0	1/2	1.0
4	Be4	Be	6	c	3m	0	0	0.097	1.0
5	Ta1	Ta	6	c	3m	0	0	0.3333	1.0

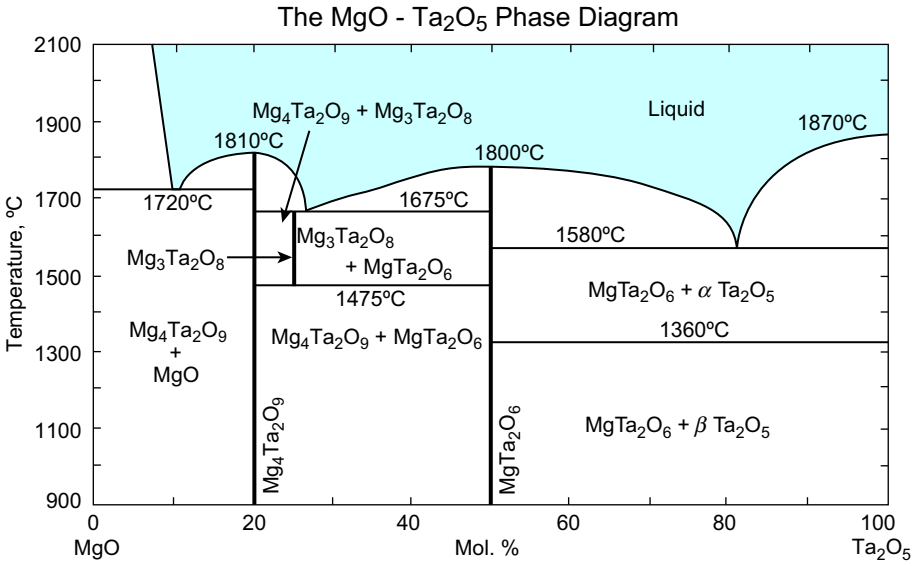

FIGURE 9.93

In one investigation, vapor-phase reactions were investigated using a solid MgO surface and thin-film solid-state reactions. In the system MgO–Nb_2O_5, MgO (001) substrates were subjected to Nb–O vapor at different temperatures in high vacuum. Thin films containing the phases $Mg_4Nb_2O_9$ and $MgNb_2O_6$ were formed by a vapor–solid reaction between the Nb–O vapor and the substrate. The crystallographic orientations of these phases were studied by XRD including pole figure analysis. $Mg_4Nb_2O_9$ grows (114)-, (116)-, and (119)-oriented, whereas $MgNb_2O_6$ grows with a preferential (241) orientation.

The **tetramagnesium tantalate**, hP30 type, has the structure as shown in Fig. 9.94.

The positions of Mg^{2+} in the structure are shown as well as the positions of the octahedra and the tilting of each to the other. Cell parameters are: $a = b = 5.1611$ Å, $c = 14.0435$ Å, $\alpha = \beta = \gamma = 90°$, cell volume = 323.96 Å^3. Cell occupancy is shown in Table 9.55.

Its dielectric behavior is shown in the following diagram, presented on the next page as Fig. 9.95.

Another view of the tetra-magnesium tantalate structure is shown in Fig. 9.96.

Single crystals of (A) $Mg_4Ta_2O_9$ and (B) $Mg_2Ni_2Ta_2O_9$ were prepared by recrystallization of a CO_2-Laser-beam heated flux. Single crystal X-ray structure analysis lead to a trigonal symmetry, space group *D-P3c*1 with: $a = 5.1654$; $c = 14.0463$ Å; B: $a = 5.1362$; $c = 14.0577$ Å; $Z = 2$. Both compounds crystallize with a corundum related structure type. In B, the metal positions are occupied statistically by Mg^{2+} and Ni^{2+}.

$MgTa_2O_6$ has the structure as shown in Fig. 9.97.

TABLE 9.53

No	Site notation	Atom	Multiplicity	Wyckoff	Site symmetry	*x*	*y*	*z*	Occupancy
1	Be1	Be	8	j	m2m.	0.277	1/2	0	1.0
2	Be2	Be	8	i	m2m.	0.361	0	0	1.0
3	Be3	Be	8	f	..2/m	1/4	1/4	1/4	1.0
4	Ta1	Ta	2	a	4/mmm	0	0	0	1.0

TABLE 9.54

#	Formula	# of elements	Structure type	Point group	Space group
1	$Mg_4Ta_2O_9$	3	$Nd_2Mn_4O_9$	hP30	*P*-3*c*1
2	$MgTa_2O_6$	3	Ta_2FeO_6	tP18	$P4_2/mmm$

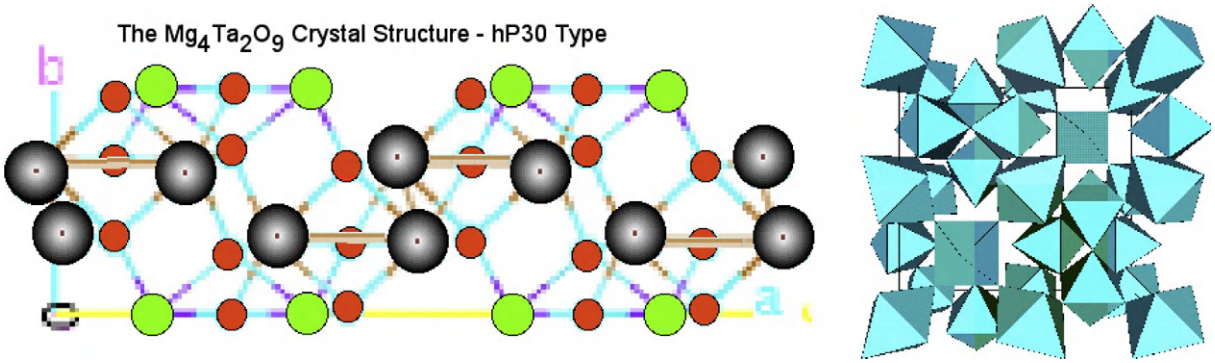

FIGURE 9.94

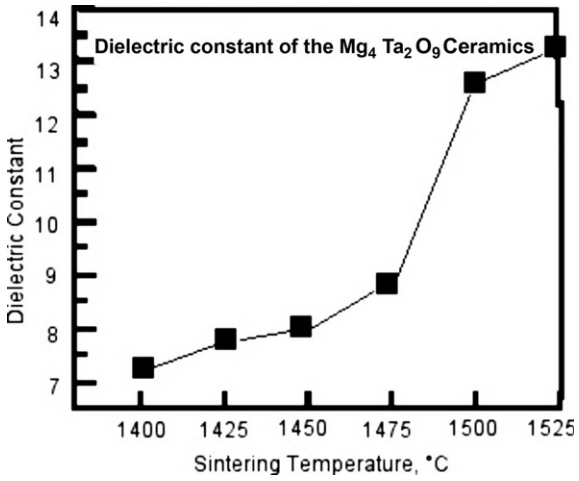

FIGURE 9.95

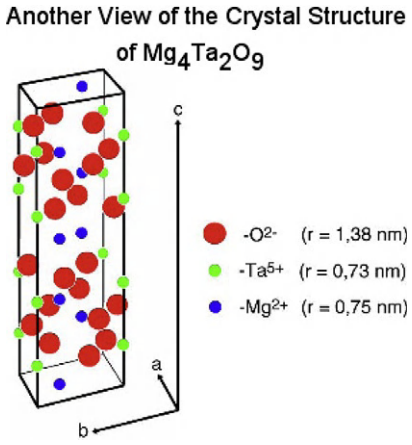

FIGURE 9.96

This is a layered structure. Cell parameters are: $a = b = 4.72$ Å, $c = 9.22$ Å, $\alpha = \beta = \gamma = 90\pm°$, cell volume = 205.71 Å^3. Cell occupancy is shown in Table 9.56.

Two different chemical methods have been applied to prepare $MgTa_2O_6$ (MT_2) and $Mg_4Ta_2O_9$ (M_4T_2) powders. A gel was formed when an aqueous solution of $Mg(NO_3)_2$, TaF_5 and citric acid in stoichiometric ratio is heated on a water bath. This gel on decomposition at 750 °C produced the fine crystallites of a binary oxide, M_4T_2. A simple co-precipitation technique was also successfully applied for the preparation of pure ultrafine single phase MT_2. Ammonium hydroxide was used to precipitate Mg^{2+} and Ta^{5+} cations as hydroxides simultaneously. This precursor, on heating at 750 °C, produces MT_2 powders.

$MgTa_2O_6$ is an interesting dielectric material and has uses in the microwave frequency range. It has been reported to crystallize in the trirutile structure with space group of $P42/mnm$ and tetragonal lattice parameters of $a = 4.7189$ Å and $c = 9.2003$ Å. The structure is made up of strings of edge-shared octahedra, extending along the 'c' direction and these strings are linked to

TABLE 9.55

No	Site notation	Atom	Multiplicity	Wyckoff	Site symmetry	x	y	z	Occupancy
1	O1	O	12	g	1	0.336	0.308	0.086	1.0
2	O2	O	6	f	.2.	0.276	0	1/4	1.0
3	Ta1	Ta	4	d	3..	1/3	2/3	0.019	1.0
4	Ta2	Ta	4	d	3..	1/3	2/3	0.3034	1.0
5	Mg1	Mg	4	c	3..	0	0	0.1426	1.0

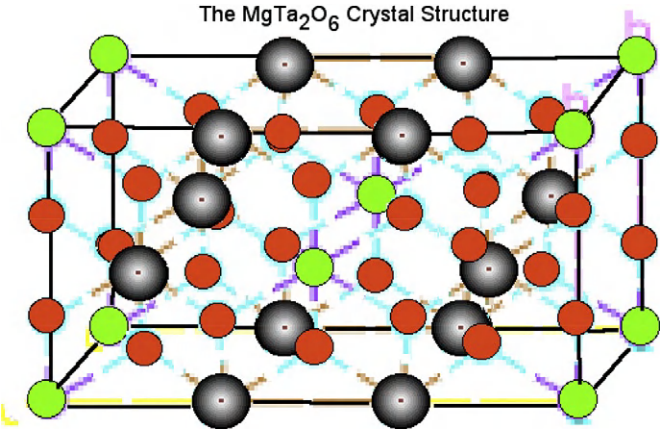

FIGURE 9.97

each other by sharing corners. The edge-sharing occurs at opposite edges in each octahedron and leads to linear octahedral strings in the trirutile structure. Normally the synthesis of $MgTa_2O_6$ by the ceramic route is carried out at high temperatures of 1200 °C to 1400 °C. This structure can be obtained by the ceramic route by heating $Mg(NO_3)_2 \cdot 6H_2O$ and Ta_2O_5 at temperatures of 1200 °C. It may be noted that using MgO as the starting material leads to a biphasic mixtures of $MgTa_2O_6$ and Ta_2O_5 at 1200 °C. The trirutile structure of tetragonal $MgTa_2O_6$ is made up of strings of edge-shared octahedra, extending along the '*c*' direction and these strings are linked to one another by sharing corners. Edge-sharing occurs at opposite edges in each octahedron and leads to linear octahedral strings extending infinitely.

The phase relation in the BaO–MgO–Ta_2O_5 system equilibrated at 1450 °C was reported. Three ternary phases, namely 3:1:1 perovskite $Ba_3MgTa_2O_9$, 9:1:7 TTB (tetragonal tungsten bronze)-type $Ba_9MgTa_{14}O_{45}$ and 4:1:5 $Ba_4MgTa_{10}O_{30}$ closely related to the tungsten bronze structure. Another ternary phase, $Ba_{10}Mg_{0.25}Ta_{7.9}O_{30}$, with a 10 layer hexagonal perovskite structure can be only obtained after equilibration at 1600 °C. MgO solubility in the TTB-like $Ba_4Ta_{10}O_{29}$, $BaTa_4O_{11}$ and $Ba_{6.63}Ta_{34.95}O_{95}$ does not exceed 2.0 mol%. Only the hexagonal polymorph of the $BaTa_2O_6$ phase was found along the $Mg_4Ta_2O_9$–$BaTa_2O_6$ join. Measurements of dielectric properties in the 20 Hz–2 MHz range revealed that $Ba_9MgTa_{14}O_{45}$ has a dielectric constant of 99 with no frequency dispersion and low dielectric loss. The authors also claimed that they had clarified several contradictory reports related to the ternary and binary phases in the BaO–MgO–Ta_2O_5 composition field.

A compound with the formula, $Mg_4Ta_6O_{19} \cdot 9H_2O$, reported in 1893, was obtained by precipitation from solution, using $Na_8Ta_6O_{19}$ and $MgCl_2$. The material was said to be amorphous and gelatinous but has never been confirmed.

The compound, $Mg_5Ta_4O_{15}$, does not appear in the phase diagram but has been studied extensively. The crystal structure of the isomorphous phases $Mg_5Nb_4O_{15}$ and $Mg_5Ta_4O_{15}$ was refined from neutron powder diffraction data. These compounds are isostructural with pseudobrookite, Fe_2TiO_5. The two kinds of metal sites of this structure are randomly occupied by Mg(II) and Nb(V) or Ta(V). The structure consists of double chains of $(Mg,M)O_6$ units (where M = Nb or Ta), sharing edges on the *bc* plane, interconnected through common oxygen atoms along the *a* axis to give a three-dimensional array. The $(Mg, M)O_6$ polyhedra at both metal positions can be described as exceptionally distorted octahedra, with (Mg, M)–O distances ranging from 1.93 to 2.22 Å. The crystallographic formulas can be written as $(Mg_{0.73(2)}Nb_{0.27(2)})_{4c}(Mg_{0.94(2)}Nb_{1.06(2)})_{8f}O$ and $(Mg_{0.66(2)}Ta_{0.34(2)})_{4c}(Mg_{1.01(2)}Ta_{0.99(2)})_{8f}O_5$ respectively, where 4*c* and 8*f* are the Wyckoff sites of the two metal positions of the structure. The space group is *Cmcm* (orthorhombic) and $Z = 4$. Unit cell parameters, cell volume, R_{wp} and *R*, values obtained were $a = 3.8068$ Å, $b = 10.0561$ Å, $c = 10.2566$ Å, $V = 392.64$ Å^3, and 6.72% and 2.94% for the niobium compound; and $a = 3.81884$ Å, $b = 10.0574$ Å, $c = 10.2343$ Å, $V = 393.07$ Å^3, and 4.46%, and 2.36% for the tantalum compound, third and the fourth layers. The crystal structure of $Mg_5Ta_4O_{15}$ is completely different from similar Ca, Sr or Ba compounds and is isostructural with pseudobrookite Fe_2TiO_5. The space group is orthorhombic D_{2h}, *Cmcm* with $Z = 4$. The structure consists of double chains of $(Mg,Ta)O_6$ units, sharing edges of the *bc* plane,

TABLE 9.56

No	Site notation	Atom	Multiplicity	Wyckoff	Site symmetry	*x*	*y*	*z*	Occupancy
1	O1	O	8	j	..m	0.297	0.297	0.322	1.0
2	O2	O	4	f	m.2m	0.307	0.307	0	1.0
3	Ta1	Ta	4	e	2.mm	0	0	0.333	1.0
4	Mg1	Mg	2	a	m.mm	0	0	0	1.0

interconnected through common oxygen along the *a* axis to give a three-dimensional array.

In another study, the structural and microwave dielectric properties of the various $Mg_5Ta_4O_{15}$ ceramics were investigated. The ceramics were prepared by the solid-state ceramic route. Specimens sintered at a temperature of 1400° ~ 1450 °C formed both the $Mg_4Ta_2O_9$ phase and $MgTa_2O_6$ phase. In another range of sintering temperatures, the $Mg_5Ta_4O_{15}$ phase appeared. Bulk density and quality factor were increased with sintering temperature in 1400° ~ 1450 °C, but these were decreased in the range of 1475° ~ 1500 °C. Dielectric constant was increased continuously by increasing the sintering temperature. In the case of the $Mg_5Ta_4O_{15}$ ceramics sintered at 1450 °C for 5 h, the dielectric constant, ε_r, quality factor, τ_f, and temperature coefficient, $Q \times f$, of the resonant frequency were 8.2, 259,473 GHz and −10.91 ppm/°C, respectively. $MgTa_2O_6$ as a secondary phase in $Mg_5Ta_4O_{15}$ caused an increase in ε_r and the positive τ_f of $MgTa_2O_6$ favorably shifts the τ_f of the nonhomogeneous $Mg_5Ta_4O_{15}$ to 17 ppm/°C according to the mixing rule. $MgTa_2O_6$ has $\varepsilon_r = 21.4$, $Q \times f = 93{,}800$ GHz, and $\tau_f = 70$ ppm/°C. Again, the presence of $MgTa_2O_6$ as the secondary phase in $Mg_5Ta_4O_{15}$ is the reason for the increased ε_r, $Q \times f$, and τ_f of the $Mg_5Ta_4O_{15}$ prepared using the raw MgO. $Mg_5Nb_4O_{15}$ is stable above 1400 °C and $Mg_5Ta_4O_{15}$ above 1475 °C.

The compound, di-magnesium tantalate, $Mg_2Ta_2O_7$, is also known. $Mg_2Ta_2O_7$ crystallizes in the cubic pyrochlore structure and is stable in the temperature range from 1400 °C to its melting point. The phase formation in the $Mg_2Ta_2O_7$–Nd_3TaO_7 system in the temperature range from 1300 °C to the melting point has been studied. The formation of $Mg_2Ta_2O_7$-based cubic solid solutions extending to 35-mol% Nd_3TaO_7 has been established. A phase of varying composition with a fluorite-like structure stable to 1500–1550 °C in the concentration range of 43 to 67 mol% Nd_3TaO_7 has also been identified.

Magnesium tantalate is available commercially with the CAS number of 206991-05-1. However, it is described as $Mg_2Ta_2O_7$, even though such a compound has not been characterized crystallographically.

9.3.3. Calcium Tantalum Compounds

Calcium (Ca^0) does not form any metallographic compounds with the metal Ta^0.

No compounds are known in the Ta^{2+} or Ta^{3+} containing systems of CaO–TaO_2 or CaO–Ta_2O_3.

In the Ta^{4+} system of CaO–TaO_2, the compound, $CaTa_2O_5$ has been observed. The reduction of Ta_2O_5 in molten $CaCl_2$ at about 950 °C first forms the stable compounds, $CaTa_2O_4$ and $CaTa_4O_{11}$ during the reaction of the reduced phase, TaO_2 and the Ca^{2+} ion. These compounds are then further reduced to TaO or δ-TaO to form metal particles of ~300 nm in size. The current efficiency and energy consumption was ~78% and ~2.4 kWh/kg of Ta produced. Oxygen content was about 1200 ppm. The specific capacitance of the Ta-powder was about 40 kμFV/g. No attempt was made to isolate these compounds and no structural determinations have been made.

The Ta^{5+}-containing system, CaO–Ta_2O_5, is known to form four (4) compounds. A phase diagram for the CaO–Ta_2O_5 binary system has been plotted from results obtained using sub-solidus sintering, DTA, hot-stage microscopy and an iridium-strip furnace. The compound $CaO \cdot 2Ta_2O_5$ melts incongruently at 1730 °C and the compounds β-CaO Ta_2O_5 and $2CaO \cdot Ta_2O_5$ melt congruently at 1958° and 1896 °C, respectively. The $\alpha \Rightarrow$ β-$CaO \cdot Ta_2O_5$ polymorphic transition occurs at 1558 ± 5 °C. X-ray data were given for two previously unreported calcium tantalates having the stoichiometric compositions $4CaO \cdot Ta_2O_5$ and $5CaO \cdot Ta_2O_5$, respectively. These two compounds formed a solid-solution area in the phase diagram at temperatures above 1590 °C and this single-phase region is postulated to terminate at 1990 °C, i.e., the incongruent melting point of $4CaO \cdot Ta_2O_5$. The phase diagram is shown as follows in Fig. 9.98.

Structure factors are shown in Table 9.57.

Calcium di-tantalate, $CaTa_4O_{11}$, has the structure as shown in Fig. 9.99.

Cell parameters are: $a = b = 6.215$ Å, $c = 12.226$ Å, $\alpha = \beta = \gamma = 90°$, cell volume = 401.31 Å^3. Cell occupancy is shown in Table 9.58.

Very little information is available concerning this compound other than its structure. It has not found usage in Industry nor has it been studied to any great extent.

Dicalcium tantalate, $Ca_2Ta_2O_7$, is polymorphic with existence of four modifications with slightly distorted pyrochlore structures and a high-temperature modification with a perovskite-type layer structure. The high temperature form has the structure as shown in Fig. 9.100.

Unit cell parameters are; $a = 3.86$ Å, $b = 5.52$ Å, $c = 13.51$ Å, $\alpha = \gamma = 90°$, $\beta = 98.16°$, cell volume = 283.22 Å^3. Cell occupancy is shown in Table 9.59.

One view of the low-temperature form of the structure is shown in Fig. 9.101, shown on the next page. It consists of TaO_6 octahedra attached at the corners to form an ordered three-dimensional structure in which the Ca^{2+} ions fit into the channels made by the rows of octahedra.

A better view of the high and low types of Weberite structures of $Ca_2Ta_2O_7$ is afforded in the Fig. 9.101.

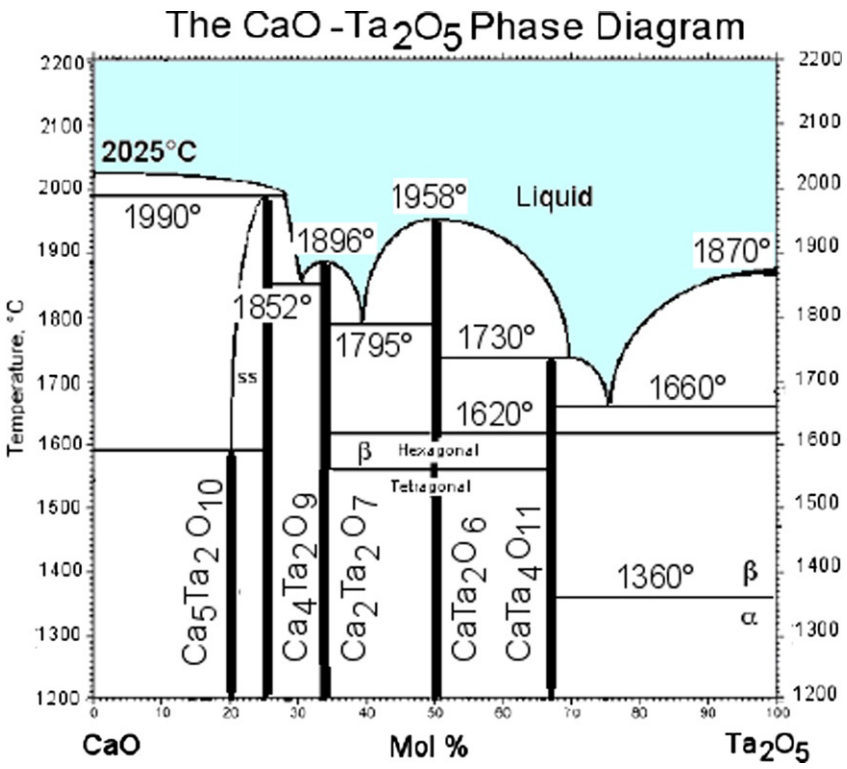

FIGURE 9.98

The main difference is that the niobate-type octahedra are tilted in respect to one-another whereas the tantalate octahedra are aligned perfectly as shown in Fig. 9.102.

Single crystals of the 8O hexagonal modification of $Ca_2Ta_2O_7$ were grown by an optical floating zone melting and their structure was solved by XRD. 8O-$Ca_2Ta_2O_7$ crystallizes in space group $C222_1$ with $a = 7.3690$ Å, $b = 12.7296$ Å, $c = 48.263$ Å. The structure is related to the weberite structure type and can be described as a stacking of 8 basic building units per unit cell. Each building unit consists of one Ta_3Ca and one Ca_3Ta layer with a cubic close packed arrangement.

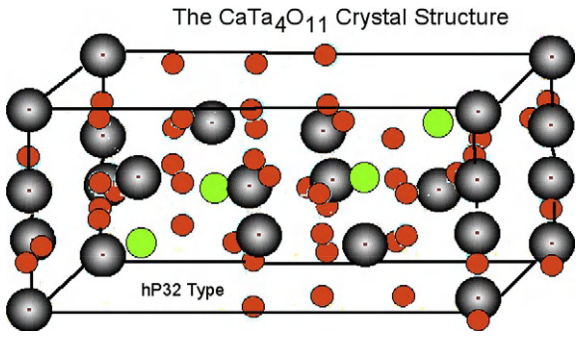

FIGURE 9.99

TABLE 9.57

#	Formula	# of elements	Structure type	Point group	Space group
1	$Ca_{0.09}Ta_{1.94}O_{4.69}$	3	??	oP336	$Pna2_1$
4	$CaTa_2O_6$	3	$(Ce_{0.67}Nd_{0.33})(Ti0.5_{0.5}Nb_{0.5})_2O_6$	hP36	$P6_322$
2	$Ca_2Ta_2O_7$	3	$Ca_2Ta_2O_7$	mS308	$C2$
6	$Ca_2Ta_2O_7$	3	??	—	—
3	$Ca_4Ta_2O_9$	3	??	mP60	$P2_1$
5	$CaTa_4O_{11}$	3	$CaTa_4O_{11}$	hP32	$P6_322$

TABLE 9.58

No	Site notation	Atom	Multiplicity	Wyckoff	Site symmetry	x	y	z	Occupancy
1	O1	O	12	i	1	0.43	0.059	0.344	1.0
2	O2	O	6	g	.2.	0.25	0	0	1.0
3	Ta1	Ta	6	g	.2.	0.6411	0	0	1.0
4	O3	O	4	f	3..	1/3	2/3	0.038	1.0
5	Ta2	Ta	2	d	3.2	1/3	2/3	3/4	1.0
6	Ca1	Ca	2	c	3.2	1/3	2/3	1/4	1.0

TABLE 9.59

No	Site notation	Atom	Multiplicity	Wyckoff	Site symmetry	x	y	z	Occupancy
1	O1	O	4	a	m..	0	0.0072	0.0452	1.0
2	Ta1	Ta	4	a	m..	0	0.0581	0.7935	1.0
3	O2	O	4	a	m..	0	0.0931	0.4939	1.0
4	O3	O	4	a	m..	0	0.1098	0.0	1.0
5	Ta2	Ta	4	a	m..	0	0.162	0.323	1.0
6	O4	O	4	a	m..	0	0.199	0.5869	1.0
7	O5	O	4	a	m..	0	0.21409	0.1082	1.0
8	Ca1	Ca	4	a	m..	0	0.29413	0.3528	1.0
9	O6	O	4	a	m..	0	0.45098	0.2742	1.0
10	Ca2	Ca	4	a	m..	0	0.55185	0.2896	1.0
11	O7	O	4	a	m..	0	0.65089	0.2959	1.0

Transmission measurements in the UV–Vis and IR regions of the spectrum revealed a high transparency in a wide energy range from 0.2–3.5 eV. Dielectric measurements yielded a high ε_r value of 60 at room temperature.

Two calcium tantalate polytypes have also been prepared in the system $Ca_2Ta_2O_7$–$Ca_2Nb_2O_7$. Their structures have been determined and refined using single-crystal XRD data and NPD data, and their dielectric properties have been measured in the 100 kHz to 10 GHz frequency range. The 7M polytype of pure $Ca_2Ta_2O_7$ has monoclinic symmetry with $a = 12.726$, $b = 7.380$, $c = 42.538$ Å, $\beta = 95.771°$, $Z = 28$, space group $C2$. The 7M $Ca_2Ta_{1.9}Nb_{0.1}O_7$ is isostructural, with $a = 12.7170$, $b = 7.3728$, $c = 42.464$ Å, $\beta = 95.755°$. The 5M $Ca_2Ta_{1.8}Nb_{0.2}O_7$ is monoclinic with $a = 12.7528$, $b = 7.3492$, $c = 30.2442$ Å, $\beta = 94.245°$, $Z = 20$, space group $C2$. The two polytypes have in common the closest packing of (001) metal atom layers that alternately have the composition Ca_3Ta and Ta_3Ca. The polytypes have mixed hexagonal-cubic stacking sequences of the metal atom layers: 7M = *hccccchccccccch*…, 5M = *hccchccccch*… The cubic-stacked blocks have weberite-type structures in both polytypes, in which

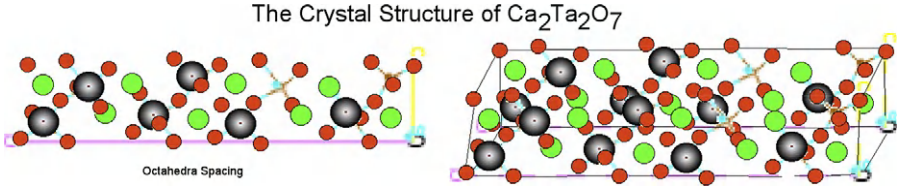

FIGURE 9.100

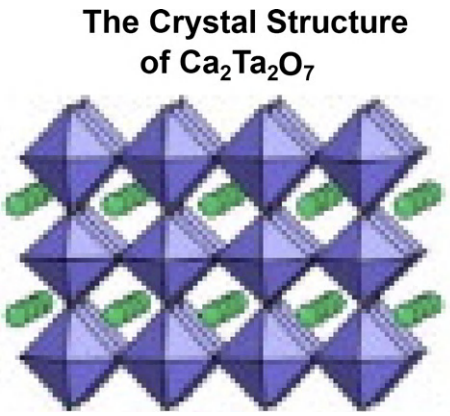

FIGURE 9.101

hexagonal tungsten bronze type layers of corner-connected octahedra are interconnected via corner linking to isolated TaO_6 octahedra in the Ca_3Ta layers to give a $[Ta_2O_7]^{4-}$ framework within which the eight-coordinated calcium atoms are distributed. The polytypes display a broad resonance at about 8 GHz, with relative permittivities of 25 and with $Q \times f$ values of about 200.

The weberite structure ($A_2B_2X_7$) is an anion-deficient fluorite related superstructure. Compared with fluorites, the reduction in the number of anions leads to a decrease in the coordination number of the B cations (VI coordination) with respect to the *A* cations (VIII coordination), thus allowing the accommodation of diverse cations. As a result, weberite compounds have a broad range of chemical and physical properties and great technological potential. $Ca_2Ta_2O_7$-based compounds are important in the weberite family since for N >4, only $Ca_2Ta_2O_7$-based compounds have been reported.

The "B-chains" are illustrated in the diagram shown in Fig. 9.103.

It has been shown that $Ca_2Ta_2O_7$ compounds can crystallize into 3T, 4M, 5M, 6T, 6M and 7M forms by using different doping or synthesis methods. It was also shown that an 8ϕ $Ca_2Ta_2O_7$ single crystal could be grown by using the optical floating zone method.

It is important to note that the close-packed cation layers are stacked the same as fcc (face-centered cubic) stacking in which the stacking sequence is ABCABC… in 2ϕ, 2M, 3T, 4M and 6T polytypes. The cation layers in 5M, 6M, 7M and 8ϕ polytypes ($Ca_2Ta_2O_7$-based compounds) are a mixture of cubic stacking and hexagonal stacking. The hexagonal stacking layers act as mirror glide planes for the cations, for example, the stacking sequence of 5M is *ABCACBACAB* in a unit cell (the underline letters indicate a hexagonal stacking). Therefore, 5M, 6M, 7M and 8ϕ polytypes are not pure weberite. The weberite-blocks are separated by h-stacking layers. A simpler approach is to describe the stacking of *c* as cubic and *h* as hexagonal. The stacking sequence is *ccchccchcc* for 5M [simplified as (3*c*)*h*(3*c*) *h*(2*c*), the integers indicating the number of *c* stacking layers], (5*c*)*h*(5*c*)*h* for 6M, (5*c*)*h*(7*c*)h for 7M and (4*c*) *h*(7*c*)*h*(3*c*) for 8ϕ.

A significant difference between 2ϕ and non-2ϕ weberites is that the AB3 and A3B layers are parallel to the (011) planes for 2ϕ and parallel to the (001) planes for other weberites, The lattice parameter difference between 2M, 4M, 5M, 6M and 7M is mainly on the c axis. The lattice parameters for *n*M ($n = 2$, 4, 5 and 7) are approximately $6_{1/2}$a, $2_{1/2}$a and $[n(6)_{1/2}/2]$a and they are nearly $2_{1/2}$a, $6_{1/2}$a and $3(6)_{1/2}$/a for 6M. The 8ϕ weberite is closely related to a monoclinic variant rather than 2ϕ in both the orientations of the AB_3 and A_3B layers and the lattice parameters. The lattice parameters are nearly $2_{1/2}$a, $6_{1/2}$a and $4(6)_{1/2}$/a. As for 3T, the [100], [0.5, 0.5, 0.5] and [012] vectors in 2ϕ are transformed into the basal vectors. The resulting lattice parameters are approximately $2_{1/2}$a, $2_{1/2}$a and $2(3)_{1/2}$a.

The 7M polytype of pure $Ca_2Ta_2O_7$ has monoclinic symmetry with $a = 12.726$, $b = 7.380$, $c = 42.538$ Å, $\beta = 95.77°$, $Z = 28$, space group *C*2. The 5M $Ca_2Ta_2O_7$ is monoclinic with $a = 12.7528(4)$, $b = 7.3492(2)$, $c = 30.2442(8)$ Å, $\beta = 94.245(2)°$, $Z = 20$, space group *C*2. The two polytypes have in common a close packing of

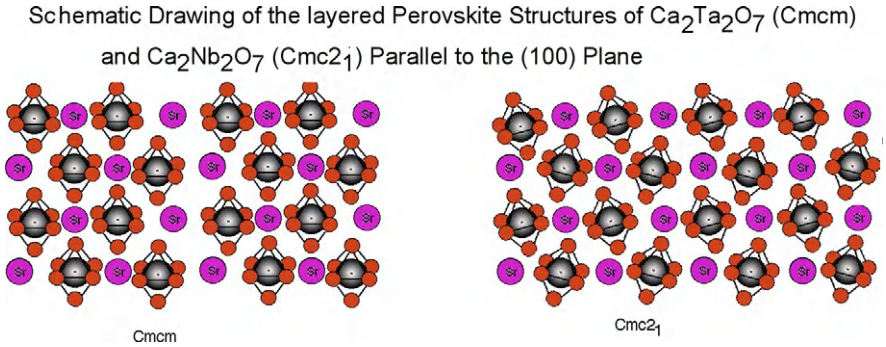

FIGURE 9.102

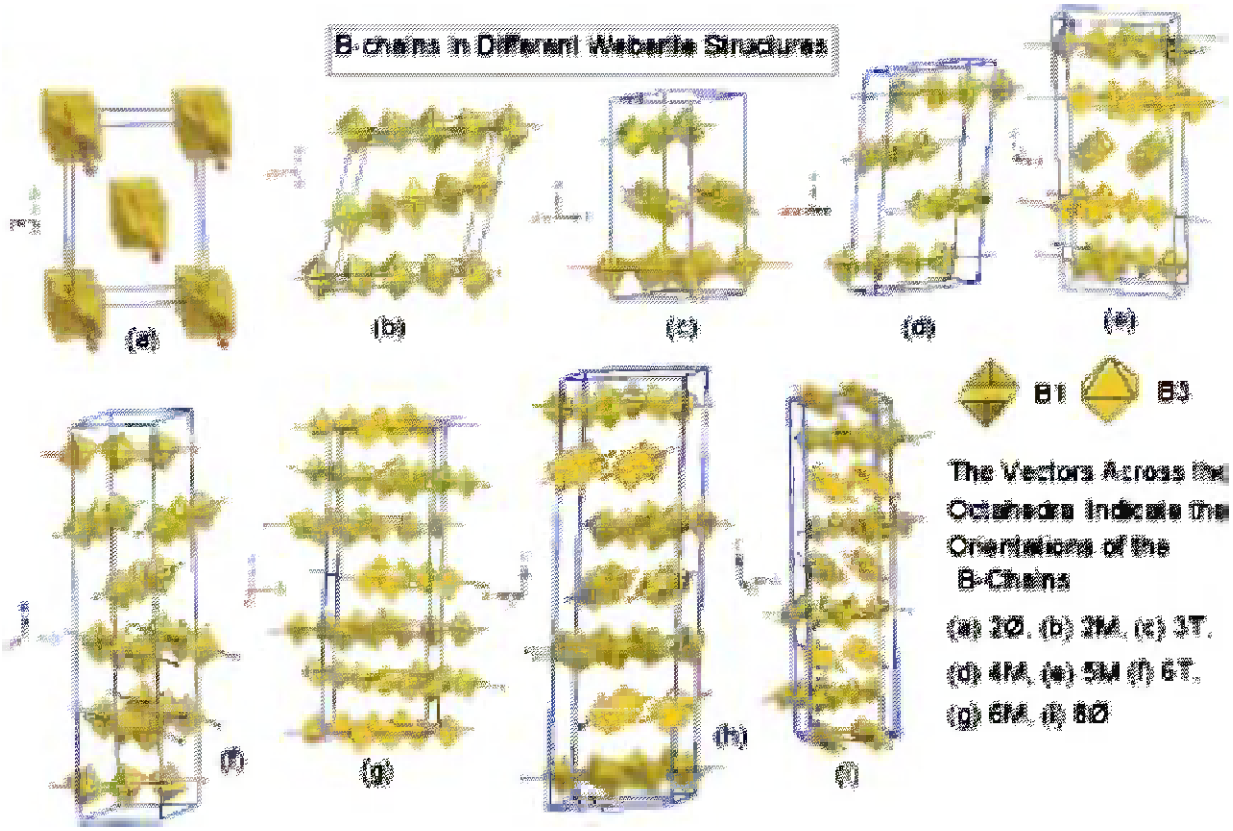

FIGURE 9.103

(001) metal atom layers that alternately have the composition Ca_3Ta and Ta_3Ca. These polytypes have mixed hexagonal-cubic stacking sequences of the metal atom layers: 7M = *hccccchccccccch*…, 5M = *hccchccccch*…. The cubic-stacked blocks have weberite-type structures in both polytypes, in which hexagonal tungsten bronze type layers of corner-connected octahedra are interconnected via corner linking to isolated TaO_6 octahedra in the Ca_3Ta layers to give a $[Ta_2O_7]^{4-}$ framework within which the eight-coordinated calcium atoms are distributed. The polytypes display a broad resonance at about 8 GHz, with relative permittivities of 25 and with Q values of about 200.

The mixed metal oxides $Ca_2B_2O_7$ (B = Nb, Ta) have been synthesized with the pyrochlore structure. The oxides were prepared by hydrolysis of Nb and Ta alkoxides and subsequent crystallization in the presence of the divalent cation in alkaline solution at temperatures up to 100 °C. The reactions yield crystalline phases directly, though with small particle size and high-surface area. The pyrochlore oxide $Ca_2B_2O_7$ was also found to undergo ion exchange in acid under mild conditions to form the hydrated oxide $HnbO_3 \cdot xH_2O$, also with small particle size and high-surface area. Confirmation of the structures of $Ca_2Nb_2O_7$ and $HnbO_3 \cdot xH_2O$ was obtained by Rietveld analysis of the XRD data.

New calcium tantalate polytypes with weberite-related structures have been prepared by doping $Ca_2Ta_2O_7$ with $Sm_2Ti_2O_7$. Trigonal 6-layer (6T) and monoclinic 5-layer (5M) polytypes containing 6 and 10 mol%, respectively of the $Sm_2Ti_2O_7$ component were prepared and the structures were determined and refined using X-ray data on flux-grown single crystals. The 6T phase, $Ca_{1.89}Ta_{1.86}Sm_{0.16}Ti_{0.10}O_7$, has $a = 7.353(1)$, $c = 36.264(1)$ Å, $Z = 12$, space group $P3_1$, and the 5M phase, $Ca_{1.80}Ta_{1.80}Sm_{0.24}Ti_{0.17}O_7$, has $a = 12.763$, $b = 7.310$, $c = 30.190$ Å, $\beta = 94.09°$, $Z = 20$, space group $C2$. The 6T structure is related to the 3T weberite structure, having a cubic close packed metal atom array as in fluorite and a stacking of (001) metal atom layers ($\{111\}_f$) that alternately have the composition Ta_3Ca and Ca_3Ta. Hexagonal tungsten bronze type layers of corner-connected octahedra are interconnected by isolated TaO_6 octahedra in the Ca_3Ta layers, giving an octahedral framework of composition $[Ta_2O_7]^{4-}$ in which the eight-coordinated calcium atoms are distributed. The octahedra in the Ca_3Ta layers have only four anions involved in corner sharing. The different weberite polytypes are distinguished by the geometry of the

two terminal anions, cis- or trans. In the 6T structure there is an alternation of cis- and trans- octahedra in successive Ca_3Ta layers. The 5M polytype differs from the weberite polytypes in having regular twinning of the metal atom lattice on (001), giving a stacking sequence *hccchccccc*…. The *c*-stacked blocks alternatively have the weberite and pyrochlore structures, with ordering of Sm into the Ca sites in the pyrochlore blocks.

In another study, single crystals of the 8O modification of $Ca_2Ta_2O_7$ were grown by an optical floating zone melting and their structure was solved by XRD. 8O $Ca_2Ta_2O_7$ crystallizes in space group $C222_1$ with $a = 7.3690$ Å, $b = 12.7296$ Å, $c = 48.263$ Å. The structure is related to the weberite structure type and can be described as a stacking of eight basic building units per unit cell. Each building unit consists of one Ta_3Ca and one Ca_3Ta layer with a cubic close packed arrangement. Transmission measurements in the UV–Vis and IR region reveal a high transparency in a wide energy range from 0.2–3.5 eV. Dielectric measurements yield a high ε_r value of 60 at room temperature.

New weberite-type $Ca_2Ta_2O_7$ polytypes have been prepared by doping with Nd/Zr respectively. Their structures have been refined using single crystal XRD intensity data. The 4M $Ca_2Ta_2O_7$ polytype has approximately the same composition, from microprobe analyses, as the 3T polytype, with the refined formula of $Ca_{l.92}Ta^{Nd}_{l.92O.08}Zr_{O.08}0_7$ The cell parameters are $a = 12.761$, $b = 7.358$, $c = 24.565$ Å, $\beta = 100.17°$, space group = $C2$, $Z = 16$. $Ca_2Ta_2O_7$ weberite-type polytypes maintain a fluorite-like fcc packing of metal atoms; the fluorite-type topology of edge-shared OM_4 tetrahedra is not maintained. One of the oxygen atoms moves from a tetrahedral Ta_3Ca interstice to an adjacent Ta_2Ca_4 octahedral interstice.

It has been determined that the structure of pure $Ca_2Ta_2O_7$ is 3T weberite up to 1673 K, where it transforms to the 7M polytype. The structure can be easily modified by doping different synthesis routines. One of the most interesting dielectric properties of $Ca_2Ta_2O_7$ is that the temperature coefficient of the dielectric constant (TC″r) is 0 when mixing with 18-mol% of $Ca_2Ta_2O_7$, meeting the requirement for the application of microwave dielectrics. TC″r′ 0 can be easily understood because TC″r is negative for $Ca_2Ta_2O_7$ (444 ppm/K at 295 K) and positive for $Ca_2Nb_2O_7$ (231 ppm/K at 295 K). Extensive studies on the structure of the $(1-x)$ $Ca_2Ta_2O_7 \cdot xCa_2Nb_2O_7$ system have been performed by powder and single-crystal XRD, and NPD. The system forms 7M weberite solid solutions up to $x = 0.1$ and $Ca_2Nb_2O_7$-type solid solutions from $x = 0.2$–1. When $x = 0.1$, the structure transforms into 5M. The solubility limit is reached when the substitution of $Ca_2Nb_2O_7$ increases to 15 mol% and $Ca_2Nb_2O_7$ forms as a second phase. The presence of $Ca_2Nb_2O_7$ thus results in TC″r compensation, making it approximately zero. Another interesting aspect is that most of the $(1-x)Ca_2Ta_2O_7 \cdot xCa_2Nb_2O_7$ compounds have higher dielectric constants (above 30) than pure $Ca_2Ta_2O_7$ and $Ca_2Nb_2O_7$ at 1 MHz. However, another set of published dielectric constants of 5M $Ca_2Ta_{1.8}Nb_{0.2}O_7$ and 7M $Ca_2Ta_{1.9}Nb_{0.1}O_7$ are approximately 18 and 20 at 1 MHz, respectively, which are lower than the previous publication. It is not clear what causes the discrepancy in dielectric constant measurement. It may be due to different firing conditions and measurement methods. Dielectric properties at radio frequency have also been investigated. The dielectric constants of 3T $Ca_{1.6}Nd_{0.4}Ta_{1.6}Zr_{0.4}O_7$, 5M $Ca_2Ta_{1.8}Nb_{0.2}O_7$ and 7M $Ca_2Ta_{1.9}Nb_{0.1}O_7$ are approximately stable (18–19) from 100 kHz up to 5 GHz and reach a maximum (22, 24.5 and 26.1, respectively) at 8 GHz. The dielectric constant is comparable for some important microwave dielectrics, such as $BaMg_{1/3}Ta_{2/3}O_3$ (~24). However, the problem with these systems is that they have low quality factors ($Q \times f \sim 200$) for technical applications. It is interesting to see that 8O $Ca_2Ta_2O_7$, which is synthesized by the optical floating zone melting method from 3T $Ca_2Ta_2O_7$ powder, has a relatively high dielectric constant (~60) at room temperature. And ε_r increases to 90 at 50 K. The high dielectric constant may result from a net dipole created by the off-center Ta^{5+} in the TaO_6 octahedra of the Ca_3Ta layers. The shifting of Ta^{5+} also produces two short Ta–O bonds and two long Ta–O bonds, leading to the distortion of TaO_6 octahedra. The high dielectric constant and the ability to tailor it are interesting for scientific study and possible electronic applications. In addition, the crystallographic study of $Nd_2Zr_2O_7$ and $Sm_2Ti_2O_7$ doping $Ca_2Ta_2O_7$ has been conducted. The resulting phases include 3T, 4M, 5M and 6T weberites. The great structural flexibility of $Ca_2Ta_2O_7$-based compounds is interesting in a crystallographic study and may have potentials in several technical applications.

Mono-calcium tantalate, $CaTa_2O_6$, is dimorphic. The high temperature form, β-$CaTa_2O_6$ has the structure shown as follows. Cell parameters are: $a = 5.37$ Å, $b = 7.501$ Å, $c = 11.071$ Å, $\alpha = \beta = \gamma = 90°$, cell volume = 445.94 Å^3 as shown in Fig. 9.104.

Cell occupancy is shown in Table 9.60.

Single crystals of cubic-$CaTa_2O_6$ were prepared with a CO_2-Laser-technique. X-ray investigations lead to a cubic symmetry (space group $Pm3T^1_h$, $a = 7.78$ Å, $Z = 4$). Ta^{5+} and O^{2-} occupy nearly the positions of these ions in the Perovskite structure. For this reason there is a similarity to $Ca_{0.5}TaO_3$. The decisive difference to the $Ca_{0.5}TaO_3$ is an ordered distribution of Ca^{2+} ions.

The low-temperature form, α-$CaTa_2O_6$, has the cubic perovskite structure with $a = b = c = 3.88$ Å. It exists

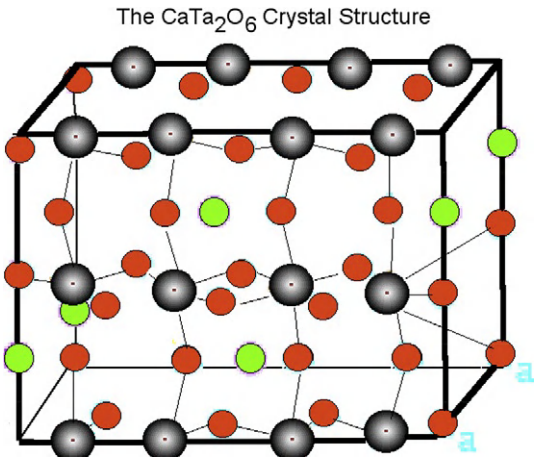

FIGURE 9.104

up to 1558 °C. Above this temperature, the β-form exists with the orthorhombic structure as shown above. The structure of this modification has been studied in detail and it is not perovskite. It has been concluded that $MgTa_2O_6$ has the trirutile structure while $CaTa_2O_6$ has the Eschynite structure as shown in Fig. 9.105.

A similar view of the arrangement of the octahedra is afforded in the following diagram: Fig. 9.106.

Transparent, colorless 30 mm long, (705 ± 11) μm diameter $CaTa_2O_6$, single crystal fibers with a cubic crystalline structure ($Pm3$) were grown by the Laser Heated Pedestal Growth (LHPD) technique. The lattice parameter determined was: $a = 7.757 \pm 0.002$ Å, as obtained from the Rietveld refinement. The fiber growth direction was determined to be [101] by XRD. The growth temperature was 2040 °C and the axial temperature gradient measured at the crystallization interface was 7.5×10^3 C/cm. The fiber/pedestal-pulling ratio was equal to 1.20. Undoped samples were characterized by optical microscopy, XRD patterns, infrared transmission and Raman scattering methods. The structural and spectroscopic results indicate that this crystal may have potential as a host for photo-active ions such as neodymium and erbium that have interesting emissions in the near-infrared region for use in cable and telephonic applications.

The successful growth of undoped and neodymium doped $CaTa_2O_6$ single crystal fibers by the LHPG technique, as well as the fibers' structural and spectroscopic characterizations, has been studied. The 700-μm diameter and 3-cm length fibers present high optical quality and excellent transparency, and XRD measurements indicate that they crystallize in the cubic structure ($Pm3$). The extensive transmission window of the host crystal fibers enables the study of rare-earth ion emission in the near-infrared region with several technological applications. Neodymium doped fibers (0.5–2.5 mol%) were characterized by ground and excited state absorptions, luminescence and lifetime measurements. Stimulated emissions were measured at 1.06 μm ($^4F_{3/2} \Rightarrow {}^4I_{11/2}$ transition) and around 1.34 μm ($^4F_{3/2} \Rightarrow {}^4I_{13/2}$ transition). Because $CaTa_2O_6$:Nd^{3+} fibers can be grown with excellent optical quality at low cost and in processes that are much faster than those usually used to grow bulk crystals, they might become an interesting material for the construction of compact optical devices such as diode pumped miniature lasers.

High optical quality Er^{3+}-doped $CaNb_2O_6$ and $CaTa_2O_6$ single crystal fibers having a 700-mm diameter and 1–2-cm length were grown by the LHPG technique. The fibers present the respective single-phase orthorhombic and cubic structures, and successful incorporation of the dopant ions, as confirmed by their light pink coloration, and characteristic absorption and luminescence spectra. Intense emission was observed at 1550 nm for both compositions, with slightly larger inhomogeneous spectral broadening for Er:CT fibers. These results associated with the fairly low phonon energies, and extensive transmission windows of the fibers, indicate they are potential laser active media for compact optical devices, in the near-infrared, or even in the green and red spectral regions, via up conversion processes.

A rare mineral occurrence of orange-brown manganotantalite lamellae (visible in a hand specimen), intergrown with microlite $[(Ca,Na)_2(Ta,Nb)_2(O,OH,F)_7]$,

TABLE 9.60

No	Site notation	Atom	Multiplicity	Wyckoff	Site symmetry	x	y	z	Occupancy
1	O1	O	8	d	1	0.023	0.538	0.264	1.0
2	O2	O	8	d	1	0.29	0.567	0.378	1.0
3	Ta1	Ta	8	d	1	0.356	0.008	0.04	1.0
4	Ca1	Ca	4	c	.m.	0.042	1/4	0.042	1.0
5	O3	O	4	c	.m.	0.145	1/4	0.375	1.0
6	O4	O	4	c	.m.	0.395	1/4	0.167	1.0

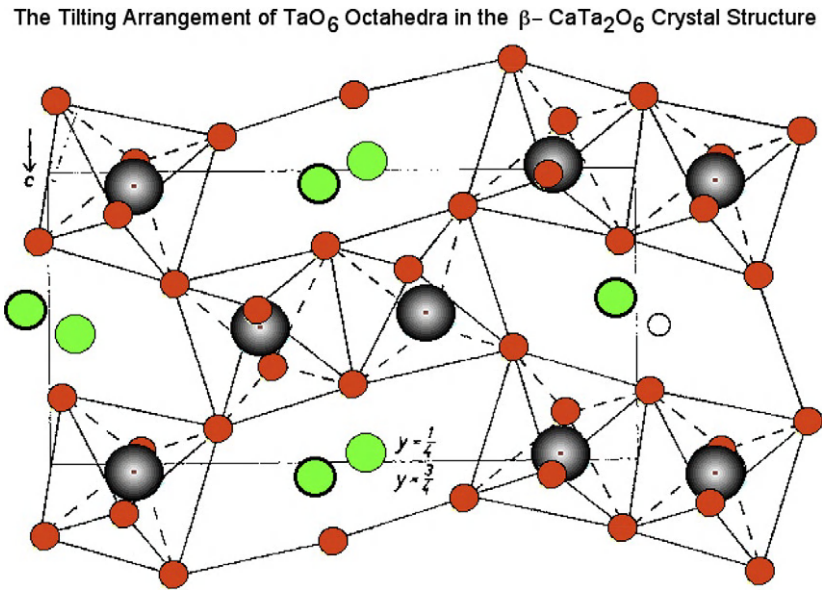

FIGURE 9.105

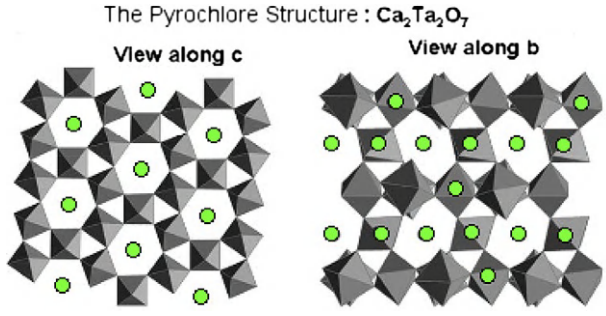

FIGURE 9.106

aggregates of ferrotapiolite, bismuth minerals and apatite was analyzed to understand more about the mechanisms of crystal growth and secondary modification in Ta-rich minerals. The intergrowth occurs within amblygonite/montebrasite nodules near the quartz core of the highly fractionated rare-metal Li/Be/Ta pegmatite that is found at Rubicon, Karibib, Namibia. Electron microprobe analysis showed that manganotantalite lamellae are variable in composition. Primary microlite (Ta_2O_5 82%, 1.97 Ta a.p.f.u.) forms the matrix mineral between the lamellae. In this context, Nb always equals 2 but Ta is in terms of Atoms per formula unit (a.p.f.u.) but less than 2. Textural relations suggest an ex-solution origin for the lamellae. Manganotantalite is represented by three generations in geology: (1) primary late magmatic; (2) disequilibrium ex-solution lamellae; and (3) sub-solidus replacement. Crystallization commenced with primary microlite and likely simultaneous intergrowth between ferrotapiolite and a first generation of late-magmatic primary manganotantalite with low Ta (1.1–1.5 a.p.f.u.). On cooling this was followed by ex-solution of manganotantalite lamellae, generation (2) with low–medium Ta (1.27–1.7 a.p.f.u.). The replacement of microlite by a highly fractionated late-stage melt rich in Mn^{2+}, Ca^{2+} with low Na^{+} finally produces a third generation (3) of manganotantalite with high Ta (1.72–1.99 a.p.f.u.) at the contact with microlite. Native bismuth and bismutite cut across microlite and pseudomorph lamellae as a final hydrothermal replacement. Apatite is ubiquitous at the contact with amblygonite. The stability field of microlite may be extended by incorporation of $CaTa_2O_6$–rynersonite and $Ca_2Ta_2O_7$ -idealized, components in solid solution. However, Rynersonite–$CaTa_2O_6$ with distorted octahedra has some structural templates, which are similar to the structure of pyrochlore (microlite). Hence, via the perovskite/pyrochlore analogy, hypothetical ex-solution of manganotantalite-type structures may occur from a microlite (pyrochlore) host by solid-state diffusion via metastable Rynersonite-type intermediates. Such a mechanism has the potential to explain the crystallographically controlled intergrowth textures and the compositional heterogeneity.

The compound, **tricalcium tantalate**, $Ca_3Ta_2O_8$, has been used as a matrix to develop a green-emitting phosphor for cold-cathode fluorescent lamps used as a backlight in display applications. The purpose of this study was to develop green phosphors with high stability, high luminescent efficiency, excellent color purity and optimum color gamut. The solid-state reaction method was used to synthesize Tb^{3+} activated tantalate phosphors, which are regarded as potential CCFL green phosphors. In Tb^{3+} activated tantalate, $Ca_{3-y}Tb_yTa_2O_8$, the optimum Tb^{3+} content is $y = 0.05$. It emitted green

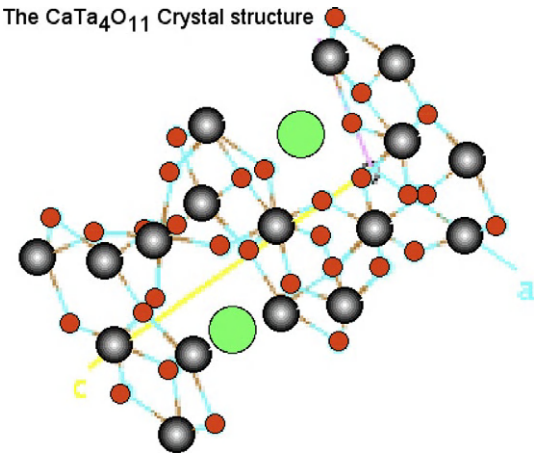

FIGURE 9.107

light due to the $^5D_4 \Rightarrow {}^7F_5$ transition of Tb^{3+} at 548 and 542 nm under excitation with 254 nm light. The emission intensity was higher than that of $Zn_{2.997}Tb_{0.002}Ta_2O_8$ phosphor (which has been reported before) but not for $La_{0.95}Tb_{0.05}TaO_4$ phosphor, which was the brightest in the series. The optimum calcining temperature was 1450 °C for the phosphor. The cross-relaxation and non-radiative relaxation which is related to the $^5D_3$ and $^5D_4$ energy level in Tb^{3+} ions was also discussed.

The compound, **tetra-calcium tantalate**, $Ca_4Ta_2O_9$, has been shown in the phase diagram and one structure has been published. One version gave the unit cell dimensions as: $a = 5.545$ Å, $b = 9.812$ Å, $c = 14.116$ Å, $\alpha = 90.00°$, $\beta = \gamma = 90.0°$. The penta-calcium tantalate, $Ca_5Ta_2O_{10}$, is unknown in structure. The analogous compounds, $Ca_5Nb_4O_{15}$ and $Ca_5Ta_4O_{15}$ are not known as well.

However, the calcium di-tantalate, $CaTa_4O_{11}$, has the structure as shown in Fig. 9.107.

Cell parameters are: $a = b = 6.215$ Å, $c = 12.266$ Å, $\alpha = \beta = 90°$, $\gamma = 120°$, $Z = 2$, cell volume is 410.23 Å^3. Cell occupancy is shown in Table 9.61.

Calcium tantalate is offered commercially as the pyro-tantalate, $Ca_2Ta_2O_7$, and its CAS number is 12049-50-2.

9.3.4. Strontium Tantalum Compounds

Strontium metal does not form any intermetallic compounds with Ta-metal.

No compounds are known in the SrO–TaO system or SrO–Ta_2O_3 system.

In the Ta^{4+}-containing system of SrO–TaO_2, the only reference to a strontium tantalite is a mixed strontium bismuth tantalite (SBT), $SrBi_2Ta_2O_9$. A number of these materials are useful in a broad range of device applications. Various factors that influence the material properties such as particle size, stresses, stoichiometry, compositional homogeneity and their effects on phase transition were investigated. The processing conditions, A- and B-site substitution, size-dependent Raman spectra and the structure-property correlations are discussed in the bulk, thin film and nano-crystalline forms of these materials. Film thickness dependence stress study on lead titanate (PT) and lead zirconate titanate (PZT) films indicated that the nature of stress depends strongly on the lattice parameters of the film and substrate. The size effect was found to decrease the ferroelectric transition temperature in lead-based perovskite materials. Both ionic charge and radii induced changes in the Raman spectra of A- and B-site substituted perovskites and layered compounds were studied. A-site substitution in strontium bismuth tantalite (SBT) was found to induce a relatively linear variation of transition temperature compared with the B-site substituted SBT.

The system, SrO–Ta_2O_5 is known to form five compounds. All are dimorphic except $SrTa_2O_6$, $Sr_3Ta_6O_{16}$ and $Sr_5Ta_5O_{15}$. The phase diagram is shown as follows in Fig. 9.108.

Structure factors are shown in Table 9.62.

$SrTa_2O_6$ is trimorphic while $Sr_2Ta_2O_7$ is dimorphic. Other known strontium tantalates not included in the phase diagram are $Sr_4Ta_2O_9$, and $Sr_6Ta_2O_{11}$.

Three polymorphic forms of **mono-strontium tantalate**, $SrTa_2O_6$ have been recognized. The monoclinic form has also been prepared and studied by powder XRD techniques and DTA. The sequence of formation

TABLE 9.61

No	Site notation	Atom	Multiplicity	Wyckoff	Site symmetry	*x*	*y*	*z*	Occupancy
1	O1	O	12	i	1	0.43	0.059	0.344	1.0
2	O2	O	6	g	.2.	0.25	0	0	1.0
3	Ta1	Ta	6	g	.2.	0.6411	0	0	1.0
4	O3	O	4	f	3..	1/3	2/3	0.038	1.0
5	Ta2	Ta	2	d	3.2	1/3	2/3	3/4	1.0
6	Ca1	Ca	2	c	3.2	1/3	2/3	1/4	1.0

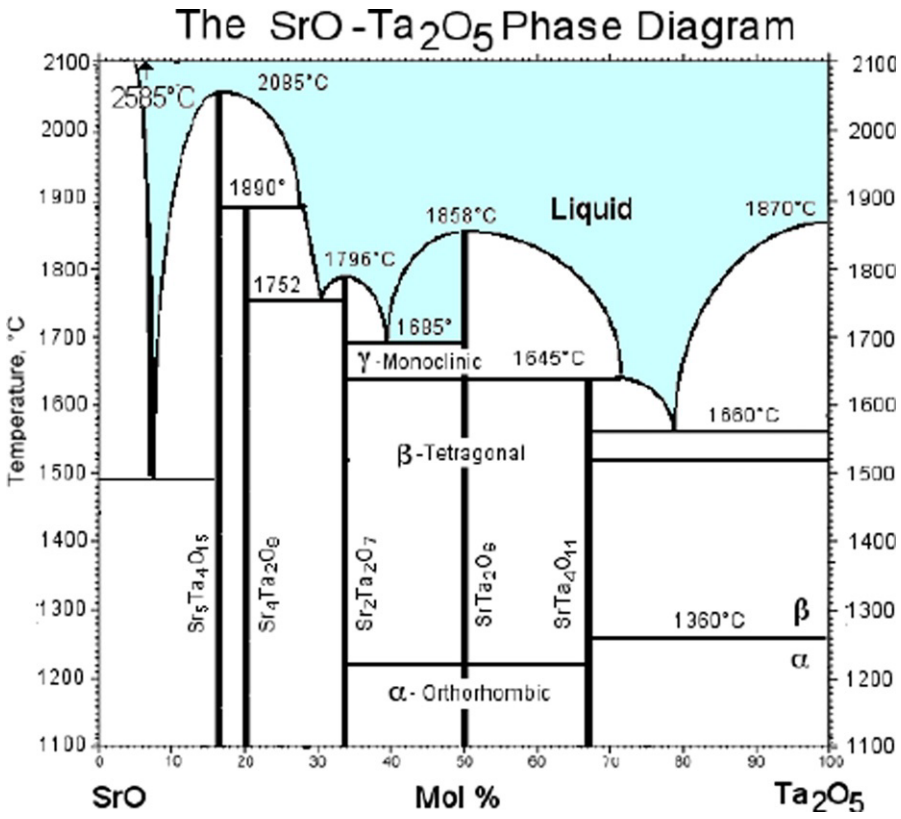

FIGURE 9.108

of these polymorphs has been found to follow a series of temperature changes:

α-Orthogonal (1220 °C) ⇒ β-tetragonal (1645 °C) ⇒ γ-monoclinic

The results of X-ray analysis show that α-$SrTa_2O_6$ crystallizes in a pseudo-orthorhombic unit cell with $a = 5.621$ Å, $b = 7.632$, $c = 5.621$ Å, $\alpha = \beta = \gamma = 90°$.

The structure is identical to the Ca-homolog except for lattice parameters as shown in Fig. 9.109.

Cell occupancy is shown in Table 9.63.

Orthorhombic $SrTa_2O_6$ is a low temperature modification related to orthorhombic $CaTa_2O_6$. $SrTa_2O_6$(orth.) was obtained when the well known modification $SrTa_2O_6$(TTB) which is related to the tetragonal tungsten bronzes was heated in the presence of a transporting agent (chlorine) or a mineralizer (melt of B_2O_3) at temperatures below 1150 °C. It could be prepared by the reaction of a 1:1 mixture of $Sr(NO_3)_2$ or $SrCO_3$ with Ta_2O_5 in a sealed quartz glass tube as well. $SrTa_2O_6$(orth.) also occurred as an intermediate phase

TABLE 9.62

No	Compound	# of elements	Structure type	Point group	Space group
1	$Sr_2Ta_2O_7$	3	$Sr_2Nb_2O_7$	oS44	$Cmc2_1$
2	$Sr_2Ta_2O_7$	3	$Sr_2Ta_2O_7$	oS44	*Cmcm*
3	$SrTa_4O_{11}$	3	$(K_{0.5}Pb_{0.5})_2Nb_6PbO_{16}$	tP46	*P*4/*mbm*
4	$Sr_6Ta_2O_{11}$	3	$BaBiO_3$	cF40	*Fm*-3*m*
5	$Sr_5Ta_4O_{15}$	3	$Ba_5Ta_4O_{15}$	hP24	*P*-3*m*1
6	$SrTa_2O_6$	3	$SrTa_2O_6$	oP26	*Pnma*
7	$SrTa_2O_6$	3	$(Ce_{0.67}Nd_{0.33})(Ti_{0.5}Nb_{0.5})_2O_6$	oP36	*Pnma*

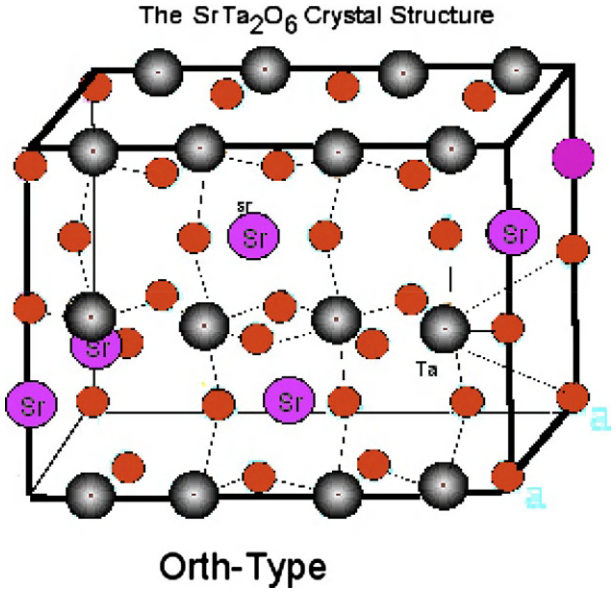

FIGURE 9.109

of the reaction of the corresponding 1:2 mixture at temperatures below 900 °C (e.g. 840 °C). Indexing of Guinier powder patterns led to the following unit cell: $a = 11.006$ Å, $b = 7.638$ Å, $c = 5.622$ Å. At temperatures above 1220 °C, $SrTa_2O_6$(orth.) changes (in air) to $SrTa_2O_6$(TTB). A reversal of this transition could not be achieved without the presence of a mineralizer or a transporting agent. $Ca_xSr_{1-x}Ta_2O_6$ solid solutions of the low temperature form could not definitely be established. However, at 1300 °C solid TTB solutions of $Ca_xSr_{1-x}Ta_2O_6$ were formed. For $x > 0.05$ the TTB unit cells are orthorhombically distorted. For $x \geq 0.85$ the X-ray powder patterns of the solid solutions looked like the one of $CaTa_2O_6$(orth.) and no TTB-structure was observed at 1300 °C. Above 1645 °C, the monoclinic (γ-form) was obtained.

These forms are related to the well-known transition involving the Ruddlesden–Popper change of perovskite to TTB phases, as shown in the following diagram where the original compound was isostructural $K_2SrTa_2O_7$ that is first ion-exchanged to the corresponding acid form and then topo-chemically dehydrated to yield metastable perovskite phase, $SrTa_2O_6$as shown in Fig. 9.110.

The β-form has the structure as shown in Fig. 9.111.

The two lattices may be better compared by the following diagram as shown in Fig. 9.112.

$SrTa_2O_6$ is a promising candidate for gate oxide applications because of its high dielectric constant and low leakage current. The structural and electrical properties of a MOS-derived $SrTa_2O_6$(SrTaO)/n-$In_{0.53}GaAs_{0.47}$(InGaAs)/InP structure, where the SrTaO was grown by atomic vapor deposition, was investigated.

The MOS structure has the form as shown in Fig. 9.113.

A study using TEM (transmission microscopic microscope) revealed a uniform, amorphous SrTaO film having an atomically flat interface with the InGaAs substrate with an SrTaO film thickness of 11.2 nm. The amorphous SrTaO films (11.2 nm) exhibit a dielectric constant of 20, and a breakdown field of >8 MV/cm. A capacitance equivalent thickness of 1 nm is obtained for an SrTaO thickness of 3.4 nm, demonstrating the scaling potential of the SrTaO/InGaAs MOS system. Thinner SrTaO films (3.4 nm) exhibited increased nonuniformity in thickness. From the capacitance–voltage response of the SrTaO (3.4 nm)/n-InGaAs/InP structure, prior to any post deposition annealing, a peak interface state density of $2.3 \times 10^{13}/cm^2$ eV is obtained located at 0.28 eV (±0.05 eV) above the valence band energy (E_v) and the integrated interface state density in range $E_v + 0.2$ to $E_v + 0.7$ eV is $6.8 \times 10^{12}/cm^2$. The peak energy position (0.28 ± 0.05 eV) and the energy distribution of the interface states are similar to other high-k layers on InGaAs, such as Al_2O_3 and $LaAlO_3$, providing further evidence that the interface defects in the high-k/InGaAs system are intrinsic defects related to the InGaAs surface.

$SrTa_2O_6$ thin films with thickness between 6 and 150 nm were also deposited by metal-organic chemical vapor deposition in a multiwafer planetary reactor. The monomolecular precursor, strontium-tantalum-(methoxyethoxy)-ethoxide, was dissolved in toluene

TABLE 9.63

No	Site notation	Atom	Multiplicity	Wyckoff	Site symmetry	x	y	z	Occupancy
1	O(2)	O	8	d	1	0.025	0.533	0.28	1.0
2	O(1)	O	8	d	1	0.285	0.549	0.359	1.0
3	Ta	Ta	8	d	1	0.35741	0.00421	0.0362	1.0
4	Sr	Sr	4	c	.m.	0.0387	1/4	0.0377	1.0
5	O(3)	O	4	c	.m.	0.143	1/4	0.469	1.0
6	O(4)	O	4	c	.m.	0.371	1/4	0.141	1.0

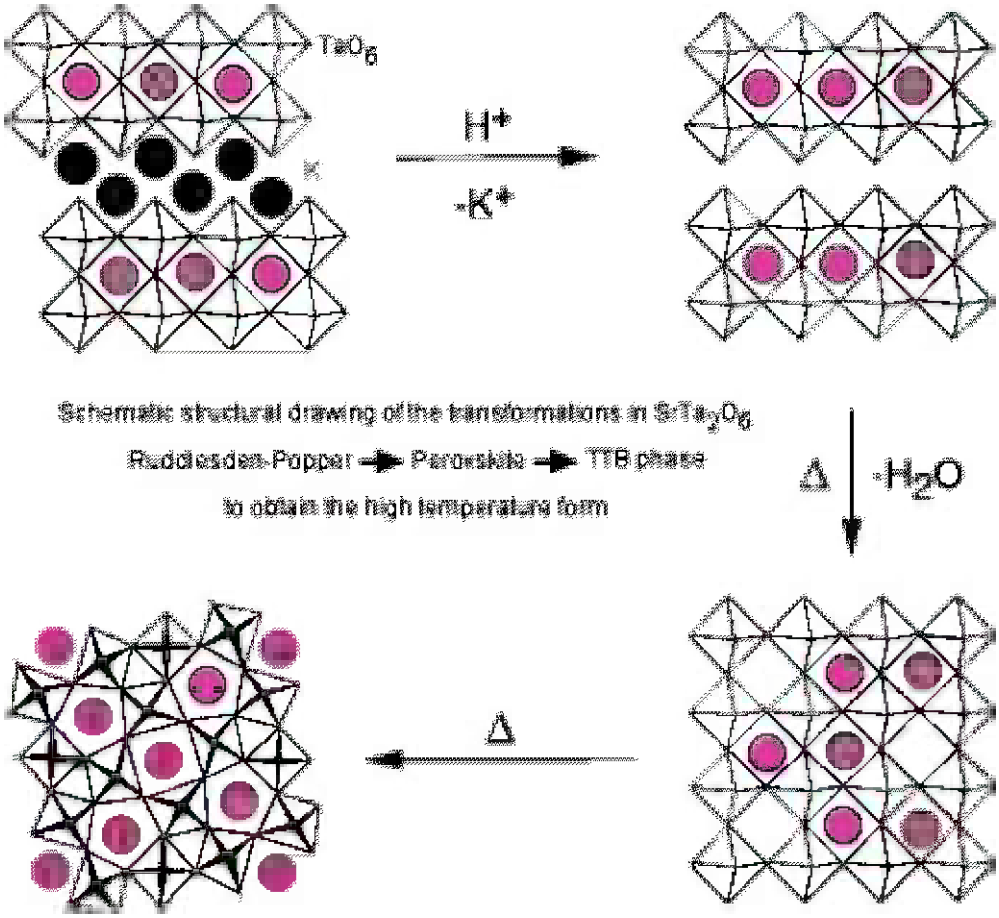

FIGURE 9.110

and injected by a liquid delivery system. A rather narrow process window for the deposition of stoichiometric $SrTa_2O_6$ was found for this precursor at low pressures and a susceptor temperature around 500 °C. Films were grown on $Pt/TiO_2/SiO_2/Si$, TiN_x/Si, and SiO_2/Si substrates. The as-deposited films were X-ray amorphous but could be crystallized by post-annealing at a temperature $\geq$700 °C. The distorted tetragonal tungsten bronze phase of $SrTa_2O_6$ dominated within a broad range of compositions (Sr/Ta: 0.4–0.7) and a perovskite-type phase was additionally observed for Sr/Ta~0.7 and predominated for Sr/Ta~1. The electrical properties have been investigated with metal-insulator-metal and metal-insulator-semiconductor capacitors after sputter

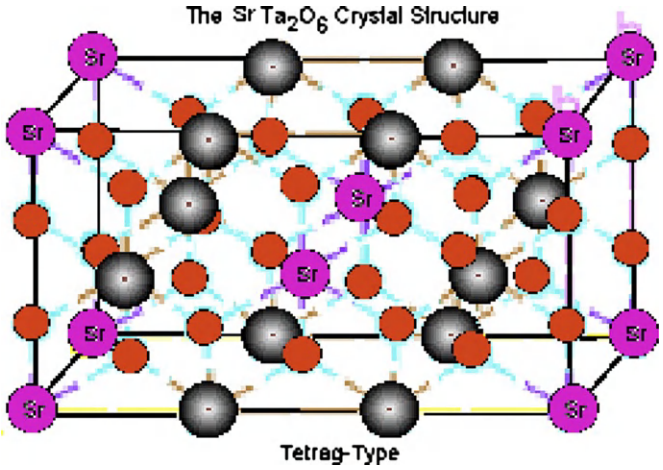

FIGURE 9.111

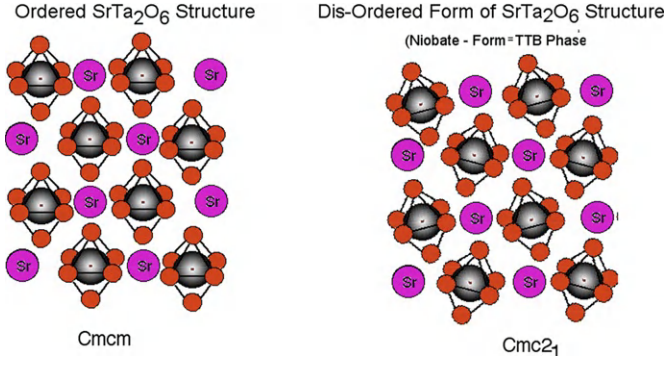

FIGURE 9.112

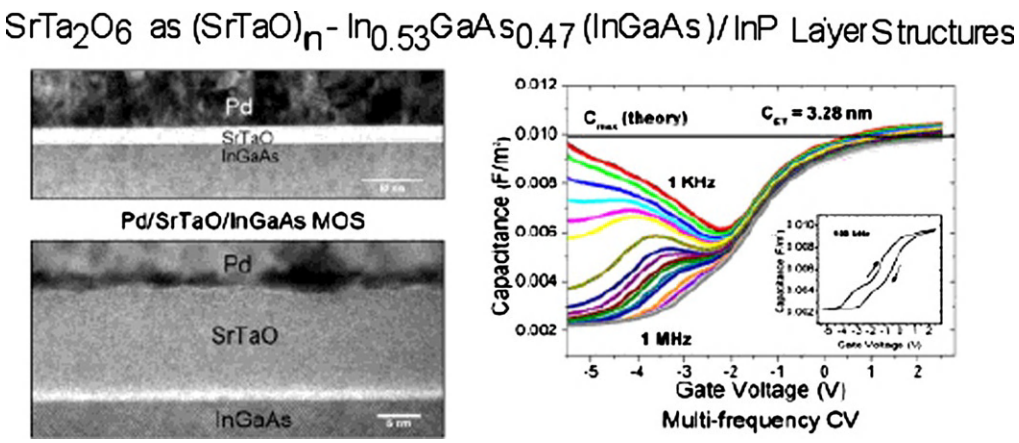

FIGURE 9.113

deposition of Pt top electrodes. The amorphous films had a dielectric constant K in the range of 35–45 and low leakage currents. For stoichiometric $SrTa_2O_6$ the dielectric permittivity reached values of $K = 100$–110, but the leakage currents were increased. Remarkably, the permittivity is not very sensitive to deviations from the exact stoichiometry of the $SrTa_2O_6$ phase (Sr/Ta: 0.4–0.7), but a decrease to values of $K = 30$–40 is observed along with the transition to the perovskite phase at high Sr contents.

$SrNb_2O_6$ (SN) or $SrTa_2O_6$ (ST) compounds can also be prepared at low temperatures from hydroxide precursors. A simple procedure of mixing commercially purchased strontium hydroxide and niobium (or tantalum) hydroxide thoroughly together and heating at a low temperature (<400 °C) produced $SrNb_2O_6$ (SN) or $SrTa_2O_6$ (ST) powders. This is the lowest temperature so far reported for the formation of these phases. These materials are potential candidates for ferroelectric and electro–optic applications.

The compound, **strontium tetra-tantalate**, $SrTa_4O_{11}$, has received some attention in the literature. It has the structure shown as follows in Fig. 9.114.

The structure consists of layers of TaO_7 pentagonal bipyramids, sharing edges as found in U_3O_8. Between the layers lie Sr atoms with distorted cubic coordination geometry and Ta(1) atoms with distorted octahedral coordination geometry. The dimorphism of $SrTa_4O_{11}$ may be described as a step from the tetragonal structure of bronzes to the structure of $CaTa_4O_{11}$. Hexagonal $SrTa_4O_{11}$ is a new modification and isostructural with $CaTa_4O_{11}$. It was obtained by heating the already known $SrTa_4O_{11}$ in a chlorine atmosphere at 1000–1100 °C.

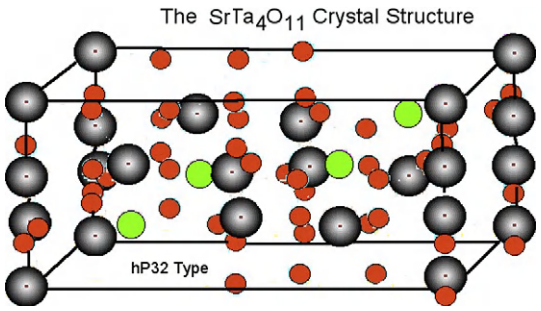

FIGURE 9.114

The Guinier powder pattern could be indexed with the following hexagonal unit cell: $a = 6.25$ Å; $c = 12.33$ Å. In air at 1180 °C, $SrTa_4O_{11}$ (hex.) changes into the well-known TTB-modification (corresponding to the tetragonal tungsten bronzes). The transition of $SrTa_4O_{11}$ (TTB) to $SrTa_4O_{11}$ (hex.) was only observed in the presence of a transporting agent (Cl_2) or a mineralizer (melt of B_2O_3) at temperatures below 1100 °C. This transition could not be achieved by means of a solid-state reaction. In a (Ca, Sr)Ta_4O_{11} solid solution, with at least 78 At% Ca, the hexagonal form could be stabilized even at temperatures where otherwise the TTB-modification occurred.

Very little information is available for this compound other than the structural data. No uses for it have evolved in Industry.

The **pyro-tantalate** compound, $Sr_2Ta_2O_7$, has the structure as shown in Fig. 9.115.

Cell parameters are: $a = 3.95$ Å, $b = 5.68$ Å, $c = 13.76$ Å, $\alpha = \gamma = 90°$, $\beta = 98.251°$. Cell volume = 305.58 Å^3. Cell occupancy is shown in Table 9.64.

The other polymorph is related to the niobate structure as shown in Fig. 9.116.

The cell parameters are: $a = 3.94$ Å, $b = 5.692$ Å, $c = 13.717$ Å, $\alpha = \gamma = 90°$, $\beta = 98.27°$, cell volume = 304.44 Å^3. Cell occupancy is shown in Table 9.65.

The arrangement of the octahedra is more easily seen in the following diagram where the pyro-antimonate is shown in Fig. 9.117.

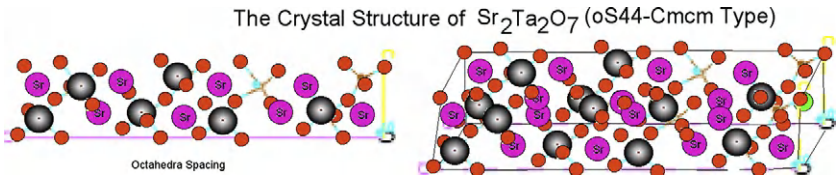

FIGURE 9.115

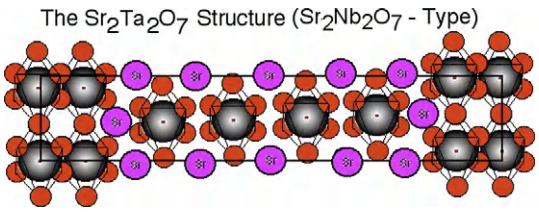

FIGURE 9.116

Recently, a number of ternary transition metal oxide catalysts have been discovered to dissociate water more efficiently than conventional materials such as Titania. These materials all have anisotropic structures made up of layers or tunnels. It has been hypothesized that these materials have high efficiencies because the layers and tunnels somehow separate the photo generated charge carriers and, therefore, the locations of the

TABLE 9.64

No	Site notation	Atom	Multiplicity	Wyckoff	Site symmetry	*x*	*y*	*z*	Occupancy
1	O1	O	8	f	m..	0	0.0991	0.008	1.0
2	O2	O	8	f	m..	0	0.207	0.01	1.0
3	Ta1	Ta	4	c	m2m	0	0.1601	1/4	1.0
4	Sr1	Sr	4	c	m2m	0	0.2884	1/4	1.0
5	O3	O	4	c	m2m	0	0.4524	1/4	1.0
6	Sr2	Sr	4	c	m2m	0	0.5532	1/4	1.0
7	O4	O	4	c	m2m	0	0.6525	1/4	1.0
8	Ta2	Ta	4	c	m2m	0	0.9447	1/4	1.0
9	O5	O	4	a	2/m..	0	0	0	1.0

TABLE 9.65

No	Site notation	Atom	Multiplicity	Wyckoff	Site symmetry	*x*	*y*	*z*	Occupancy
1	O1	O	4	a	m..	0	0.002	0.028	1.0
2	Ta1	Ta	4	a	m..	0	0.05524	0.773	1.0
3	O2	O	4	a	m..	0	0.099	0.5	1.0
4	O6	O	4	a	m..	0	0.1	0.013	1.0
5	Ta2	Ta	4	a	m..	0	0.16012	0.2752	1.0
6	O3	O	4	a	m..	0	0.205	0.514	1.0
7	O7	O	4	a	m..	0	0.209	0.037	1.0
8	Sr2	Sr	4	a	m..	0	0.28808	0.278	1.0
9	O4	O	4	a	m..	0	0.454	0.231	1.0
10	Sr1	Sr	4	a	m..	0	0.55298	0.266	1.0
11	O5	O	4	a	m..	0	0.649	0.238	1.0

FIGURE 9.117

oxidation and reduction half reactions. If such a separation were to occur, it would suppress carrier recombination and the rate of the back reaction. Two such materials are $Sr_2Ta_2O_7$ (*Cmcm*, $a = 3.937$ Å, $b = 27.198$ Å, $c = 5.692$ Å) and $Sr_2Nb_2O_7$ (*Cmc*21, $a = 3.933$ Å, $b = 26.726$ Å, $c = 5.683$ Å). Both of the structures are made up of corner sharing MO_6 octahedra that are arranged in (110) perovskite type slabs parallel to (010), and separated by Sr_2O layers. The main difference between these materials is the distortion of the NbO_6 octahedra in $Sr_2Nb_2O_7$ that makes it ferroelectric (Ps||*c*-axis). The role that the layer structure plays in the superior photochemical properties of these compounds is currently unclear.

Three compounds, $SrTa_2O_6$, $Sr_4Ta_2O_9$, and $Sr_5Ta_4O_{15}$, were synthesized by a polymerizable complex method. Their photocatalytic activities for water splitting into H_2 and O_2 were tested and compared against previously published results for $Sr_2Ta_2O_7$. It was found that the efficiency of the catalysts decreases in the following order:

$$Sr_2Ta_2O_7 > Sr_5Ta_4O_{15} > SrTa_2O_6 > Sr_4Ta_2O_9$$

The relationship between photocatalytic activities and crystal structures was discussed in this paper.

Strontium tantalate, $Sr_2Ta_2O_7$, and strontium niobate, $Sr_2Nb_2O_7$, are ferroelectric crystals with a layered perovskite structure. The space group of the prototype structure is *Cmcm*. The ferroelectric phase transition temperature, T_2, of $Sr_2Ta_2O_7$ is 155 °C and that of $Sr_2Nb_2O_7$ is 1615 °C. The spontaneous polarization of each crystal appears along the *c*-axis in the layer. The transition temperature T_2 of the mixed solid-solution niobate-tantalate crystals, i.e.- $Sr_2(Ta_{1-x}Nb_x)_2O_7$, changes steeply with Nb concentration. The mixed crystals exhibit a superlattice phase transition with twice the lattice constant along the *a*-axis around $T_1 = 443$ °C in the region $x < 0.4$. It has an incommensurate phase transition around 488 °C in the region $x > 0.6$. The transition temperature T_1 of the mixed crystal changes continuously with x from 443 °C to 488 °C. The dielectric anomaly of the single crystals along the *c*-axis around T_1 and T_2 in the mixed crystals reveal the characteristics of the phase transitions of the layered perovskite ferroelectrics. Additionally, the low-frequency dielectric dispersion in $Sr_2Ta_2O_7$ observed at the temperatures from 60 K to 150 K was reported. The dielectric dispersion in the mixed crystal may relate to the dynamical properties of Nb center. The ferroelectric phase transition temperature was found to change sensitively with the Nb concentration from 155 °C for $x = 0$ to 480 °C for $x = 0.081$. A cusp-like dielectric anomaly appears in each sample around 443 °C. The low frequency dielectric dispersion is observed in the temperature range from 60 °C to 150 °C in each sample. The soft mode frequency for the ferroelectric phase transition at 20 °C increases with x.

$Sr_2Ta_2O_7$ and $Sr_2Nb_2O_7$ have a (110) layered perovskite structure and are efficient photolysis catalysts. Aqueous silver and lead cations were photo-chemically reduced and oxidized, respectively, on the surfaces of $Sr_2Ta_2O_7$ and $Sr_2Nb_2O_7$ crystals with a wide range of orientations. AFM has been used to observe the distribution of photo chemically reduced and oxidized products and determine the orientation dependence of the reactivity. On surfaces with the same orientation, reaction products frequently had a non-uniform distribution. The reactivity of both compounds proved to be only weakly anisotropic, with the highest relative reactivity for both oxidation and reduction occurring for surfaces oriented between (010), (110), and (011). These low index orientations have structures similar to the ideal {110} and {100} planes in the perovskite structure, respectively.

$Sr_2Ta_2O_7$ nanosheets have been synthesized by a hydrothermal method without using any template. The thickness, widths, and lengths of $Sr_2Ta_2O_7$ nanosheets are about 10–50 nm, 50–150 nm, and 500 nm, respectively. The optimum conditions for the formation of the nanosheets are maintaining the reactants at 260 °C for 7 days. On basis of the experimental data, a possible formation mechanism of the nanosheets under the hydrothermal conditions was proposed. The photocatalytic activity for water splitting was investigated under ultraviolet irradiation. It has been found that $Sr_2Ta_2O_7$ nanosheets, compared to the bulk $Sr_2Ta_2O_7$ sample, showed a higher photocatalytic activity even in the absence of a co-catalyst. The higher activity of the hydrothermally synthesized sample is attributed to its larger surface areas and nanoscale structure.

Thin films of nanoscale ribbons derived from the layer perovskite $H_2SrTa_2O_7$ were grown and characterized as solid-state proton conductors. The ribbons, made by exfoliation of the parent solid with tetra(n-butyl)ammonium hydroxide, were typically 500 nm long, 40 nm wide, and 3 nm thick, with the short axis corresponding to the layer axis of $H_2SrTa_2O_7$. Powder XRD and HRTEM confirmed that the ribbons had similar *a*-axis unit cell

parameters (3.98 ± 0.05 Å) to $H_2SrTa_2O_7$ (3.87 Å) and the defect perovskite $CaTa_2O_6$ (3.92 Å) which is the dehydration product of $H_2SrTa_2O_7$. By using inductively coupled plasma atomic emission spectroscopy, X-ray photoelectron spectroscopy, and EDX spectroscopy, the ribbons were found to have a lower Sr/Ta ratio than $H_2SrTa_2O_7$. Thin films of these ribbons were grown by layer-by-layer assembly and by spin-coating, and in both cases the long axis had a preferred orientation parallel to the substrate. Electrochemical impedance measurements were done on pellets of $H_2SrTa_2O_7$ and $CaTa_2O_6$ and on films of oriented ribbons measured perpendicular and parallel to the plane of their long axis. At 25 °C, the proton conductivities in humidified air were 1.5×10^{-4} and 1.7×10^{-5} S/cm^2 for pellets containing randomly oriented grains of $H_2SrTa_2O_7$ and $CaTa_2O_6$. The measured conductivities of oriented films of the ribbons were 1.3×10^{-9} and 2.4×10^{-2} S/cm^2 in the perpendicular and parallel directions, respectively, indicating a high proton conductivity along the ribbon axis and very high conductivity anisotropy.

The structural phase transition in $Sr_2Ta_2O_7$ at 170 °C has been investigated by Raman scattering measurements. A low-lying mode of the *Ag* symmetry softens significantly toward T_{tr}. Anomalous increase in the damping constant of this mode has been observed in the vicinity of T_{tr}. The structural phase transitions of $Sr_2Ta_2O_7$ single crystals have also been studied by the modulated temperature differential scanning calorimetry (MDSC), Brillouin scattering and dielectric spectroscopy. The specific heat (C_p) was measured over a wide temperature range from −150 °C to 25 °C and from 100 °C to 210 °C. The C_p curve showed an anomaly at $T_0 = 166.7$ °C, indicating the phase transition $Cmcm \Rightarrow P21/m$. The transition enthalpy ΔH, the transition entropy ΔS and specific heat jump ΔC_p at T_0 were estimated to be 0.465 J/g, 1.01 mJ/g/K and 9.78 mJ/g/K, respectively. The C_p anomaly associated with the ferroelectric phase transition at $T_c = -107$ °C has not been detected. However, both Brillouin and dielectric data showed the anomalies corresponding to the ferroelectric phase transition from $P21/m$ to $P21$.

$Sr_2Ta_2O_7$ nanosheets have been synthesized by a hydrothermal method without using any template. The thickness, widths, and lengths of $Sr_2Ta_2O_7$ nanosheets are about 10–50 nm, 50–150 nm, and 500 nm, respectively. The optimum conditions for the formation of the nanosheets are maintaining the reactants at 260 °C for 7 days. On basis of the experimental data, a possible formation mechanism of the nanosheets under the hydrothermal conditions was proposed. The photocatalytic activity for water splitting was investigated under ultraviolet irradiation. It has been found that $Sr_2Ta_2O_7$ nanosheets, compared to the bulk $Sr_2Ta_2O_7$ sample, showed a higher photocatalytic activity even in the absence of a co-catalyst. The higher activity of the hydrothermally synthesized sample is attributed to its larger surface areas and nanoscale structure.

A comparison of the catalyst activity of some compounds that split water into hydrogen and oxygen under photo-activity of UV light is shown in the following Table 9.66. The conditions used were: room temperature; catalyst 0.3 gm; water 500 cc; 450 W medium-pressure Hg lamp. Work continues in the investigation of this aspect.

A single-source $Sr[Ta(OEt)_5(Me)]_2$ precursor was utilized to form dielectric layers on 200-mm Si(100)/TiN substrates within a thermal budget of BEOL (400 °C). The Sr/Ta ratio in the products was controlled by varying the process pressure. Two stoichiometries, namely, $Sr_2Ta_2O_{7-\delta}$ and $Sr_5Ta_4O_{15-\delta}$, were intensively characterized, to show that $Sr_2Ta_2O_{7-\delta}$ based MIM capacitors offer better electrical performance. The best results, achieved at an $Sr_2Ta_2O_{7-\delta}$ layer thickness of 30 nm, have a capacitive density of 5.5 fF/μm^2 in combination with a linearity coefficient of 80 ppm/V^2 and quality factor of 52 at 10 kHz. The corresponding leakage current density at 2 V is 7×10^{-9} A/cm^2, and the determined breakdown strength is 3.2 MV/cm.

The **penta-strontium di-tantalate** compound, $Sr_5Ta_4O_{15}$, has been well studied. This compound has a hexagonal structure and crystallizes in the $P\bar{3}m1$ space group with one formula unit per cell ($Z = 1$). The compound has a five-layer closest packing of oxygen and strontium ions. The tantalum or niobium ions are located in the octahedral holes between layers with one layer of octahedral holes missing tantalum or niobium ions to accommodate the charge neutrality. The $Sr_5Ta_4O_{15}$ structure is a hexagonal polytype i.e., the (5H) member of a series of polytypes characterized by Hutchison and co-workers containing 4, 5, 6, 8, 10 and 12 layered (4H, 5H, 6H, 8H, 10H, and 12H) species. Whiston and Smith have reported the existence of $Sr_5Ta_4O_{15}$ isostructural with the niobium analog. Two structures have been reported for $Sr_5Nb_4O_{15}$, monoclinic and trigonal.

TABLE 9.66

Perovskite	Structure	Cation valency	Activity (μmol H_2/g catalyst/hr	Quantum yield
$SrTiO_3$	Bulk	+6	8	—
$Sr_3Ti_2O_7$	Layered	+6	11	—
$Sr_2Nb_2O_7$	Layered	+7	402	23
$Sr_2Ta_2O_7$	Layered	+7	796	36
$La_2Ti_2O_7$	Layered	+7	474	12
$LaTiO_3$	Bulk	+7	137	—

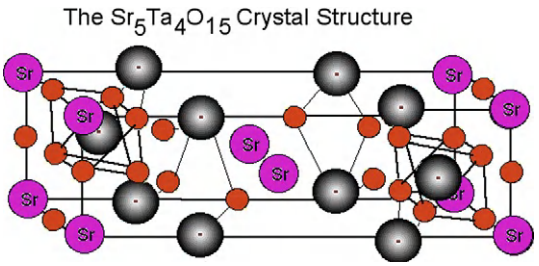

FIGURE 9.118

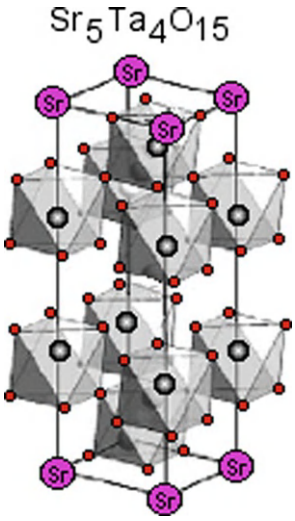

FIGURE 9.119

The trigonal $Sr_5Ta_4O_{15}$ has the structure as shown in Fig. 9.118.

Cell parameters are: $a = b = 5.66$ Å, $c = 11.47$ Å, $\alpha = \beta = 90°$, $\gamma = 120°$, cell volume $= 318.12$ Å^3. Cell occupation is shown in Table 9.67.

The arrangement of the octahedra in the monoclinic form may be more easily seen in the following diagram shown in Fig. 9.119.

Recent progress in microwave (MW) telecommunications has demanded the need for good quality ceramic dielectric resonators. The important characteristics required for dielectric resonators are high permittivity, ε_r (the size of resonators is proportional to $1/\sqrt{\varepsilon_r}$), a high quality factor $Q = \varepsilon_r'/\varepsilon_r''$, and a low temperature coefficient of resonant frequency τ_f. $Sr_5Ta_4O_{15}$ exhibits unusual low frequency heavily damped excitation at 15 cm. This mode is partially seen in the reflectivity and is very well evident in both THz and FTIR transmission spectra. The low frequency excitation observed at 15 /cm in $Sr_5Ta_4O_{15}$ suggests a ferroelectric soft mode; however, more low temperature measurements are needed. The IR spectrum of $Sr_5Nb_4O_{15}$ does not support the previously published report of monoclinic symmetry with $Z = 2$. The spectrum is similar to that for the three related samples with trigonal symmetry and $Z = 1$.

Due to the drive for miniaturization of devices, B-site deficient hexagonal perovskites like $Sr_5Ta_4O_{15}$ have become an area of growing research for their dielectric properties and application in this area, as they display promising properties. The following Table 9.68 shows the measured dielectric properties.

Current work continues on this compound and its homologs concerning improvement in dielectric and photoactive properties.

The mechanism and kinetics of water incorporation into the double perovskite, **hexa-strontium tantalate**, $Sr_6Ta_2O_{11}$, has been investigated in the range 300 to 500 °C and $H_2O = (1 \times 10^{-3}$ atm.). The formation of hydration products $Sr_6Ta_2O_{11}$ xH_2O $(0.2 < x < 0.50)$ was limited by the diffusion of H_2O. It has been found that the concentration dependences of D_2O are the same. With increasing x, the temperature dependences of the chemical diffusion coefficients of water for a composition of $Sr_6Ta_2O_{11} \cdot 0.35H_2O$ could be described with an activation energy of $E_a = 0.49 \pm 0.03$ eV. The chemical diffusion coefficients of water are nearly one order of magnitude lower for the barium tantalate

TABLE 9.67

No	Site notation	Atom	Multiplicity	Wyckoff	Site symmetry	x	y	z	Occupancy
1	O1	O	6	i	.m.	0.1695	0.8305	0.1916	1.0
2	O2	O	6	i	.m.	0.8368	0.1632	0.3864	1.0
3	O3	O	3	e	.2/m.	1/2	0	0	1.0
4	Ta1	Ta	2	d	3m.	1/3	2/3	0.1035	1.0
5	Sr1	Sr	2	d	3m.	1/3	2/3	0.4282	1.0
6	Sr2	Sr	2	d	3m.	1/3	2/3	0.7837	1.0
7	Ta2	Ta	2	c	3m.	0	0	0.3127	1.0
8	Sr3	Sr	1	a	-3m.	0	0	0	1.0

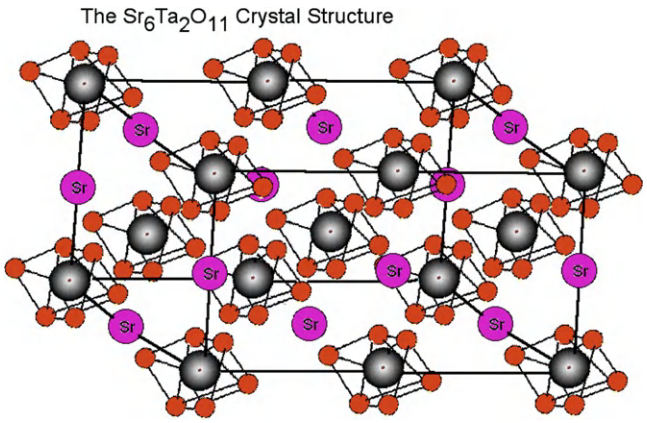

FIGURE 9.120

$Ba_6Ta_2O_{11}$. This result correlates with lower oxygen and proton conductivities in $Sr_6Ta_2O_{11}$ as the consequence of lower mobility. It has the structure as shown in Fig. 9.120.

Cell parameters are: $a = b = c = 5.8739$ Å, $\alpha = \beta = \gamma = 60°$, cell volume = 143.31 Å^3. Cell occupancy is shown in Table 9.69.

The structural transformations of $Sr_6Ta_2O_{11}$ and $Sr_{5.92}Ta_{2.08}O_{11.12}$ oxygen-deficient cryolites with variations in the partial pressures of oxygen $p(O_2)$ and water vapor $p(H_2O)$ have been investigated using XRD, TG, and electrical conductivity measurements. It was found that a change in the oxygen partial pressure leads to a phase transition accompanied by the transformation of the cubic cell into the tetragonal cell, most probably due to ordering of oxygen vacancies. The intercalation of water into the matrix of the complex oxides under investigation results in a structural-chemical transformation during which the solid solution undergoes a transition to an oxyhydrate phase of variable composition and the cubic cell transforms into the orthorhombic cell.

In another study, evolution of the structure and phase relations of the oxygen-deficient cryolite $Sr_6Ta_2O_{11}$ and phase $Sr_{5.92}Ta_{2.08}O_{11.12}$ from homogeneity range have been investigated during water intercalation by gravimetry, dilatometry and XRD measurements. Intercalation of H_2O up to 0.50 and 0.30 mol H_2O per formula units $Sr_6Ta_2O_{11}$ and $Sr_{5.92}Ta_{2.08}O_{11.12}$, respectively, takes place without change in the crystal structure, which could be described under the cubic space group *Fmm* with a cell parameter of approximately 8.32 Å. Further intercalation of water leads to structure transformation to the orthorhombic space group *Fmmm*. The temperature of phase transition increases with increasing pH_2O. It is around 475–450 °C in open air. ($pH_2O \approx 0.02$ atm.). This phase transition is induced by change in pH_2O (T = constant) and temperature (pH_2O = constant) and can be observed as a jump when TG curves are obtained vs. pH_2O or T. At 200 °C, the most hydrated phases correspond to the compositions $Sr_6Ta_2O_{11}\cdot 0.96H_2O$ (H_2O stoichiometry close to the theoretical value of 1.0) and $Sr_{5.92}Ta_{2.08}O_{11.12}\cdot 0.6H_2O$ (70% of the theoretical value).

The systems $Sr_6Ta_2O_{11}$–H_2O and $Sr_{5.92}Ta_{2.08}O_{11.12}$–$H_2O$ were investigated. At high temperatures, both compounds are normal proton conductors but at lower temperatures show the formation of hydrate phases (here labeled β-phases). The latter are deleterious if the above compounds were to be used in fuel cells, sensors and pumping devices. The phase diagrams of the 2 systems were determined using thermogravimetry. The solubility of water vapor in the α-phases was measured. Considering 2-phase mixtures of α and β, the plateau vapor pressures were determined as well as the pertinent thermodynamic parameters. The $\alpha \Rightarrow a + \beta$ solvus was also investigated.

Conductivity of the $Sr_{6-2x}\ Ta_{2+2x}O_{11+3x}$ ($0 \le x \le 0.33$) solid solutions with the cryolite structure was studied in an atmosphere with high content of water vapors with temperature and oxygen activity variation in the gas phase. Appearance of the protonic conductivity component was proved at the temperatures below

TABLE 9.68

Compound	ε_r	τ_f	$Q \times f$
$Ba_5Ta_4O_{15}$	38	31,600	12
$Ba_5Nb_4O_{15}$	39	23,700	78
$Sr_5Ta_4O_{15}$	41	24,000	Too large to detail
$Sr_5Nb_4O_{15}$	40	19,400	55

TABLE 9.69

No	Site notation	Atom	Multiplicity	Wyckoff	Site symmetry	x	y	z	Occupancy
1	O1	O	24	e	4m.m	0.21	0	0	0.920
2	Sr1	Sr	8	c	-43m	1/4	1/4	1/4	1.0
3	Sr2	Sr	4	b	m-3m	1/2	1/2	1/2	1.0
4	Ta1	Ta	4	a	m-3m	0	0	0	1.0

700 °C. It was found that protonic conductivity increases when a decrease in the parameter x occurs in the composition series. This is related to an increase of both the concentration of protonic defects formed in the structure and their mobility. In the case of compositions with $x < 0.15$ at the temperatures below 550 °C, the protonic transport becomes predominant.

The mechanism and kinetics of water incorporation in the double perovskite $Sr_6Ta_2O_{11}$ has been investigated ($T = 300$–500 °C and $aH_2O = 1 \times 10^{-3}$ (300 °C) which varies up to 2.2×10^{-2} at 500 °C). The formation of hydration products $Sr_6Ta_2O_{11} \cdot xH_2O$ ($0.2 < x < 0.50$) was limited by the diffusion of H_2O. It has been found that the concentration dependences of $\tilde{D}_{H2O}$ are the same for both samples: small increasing of $\tilde{D}_{H2O}$ with increasing x. The temperature dependences of the chemical diffusion coefficients of water for compositions of $Ba_4Ca_2Nb_2O_{11} \cdot 0.35H_2O$ and $Sr_6Ta_2\ O_{11} \cdot 0.35H_2O$ could be described with close activation energies of $E_a = 0.38 \pm 0.03$ eV and $E_a = 0.49 \pm 0.03$ eV, respectively. The chemical diffusion coefficients of water are nearly one order of magnitude smaller for the tantalate, $Sr_6Ta_2O_{11}$. This result correlates with lower oxygen and proton conductivities in $Sr_6Ta_2O_{11}$ as the consequence of lower mobilities.

In another study, The perovskite-related phases $Sr_6Ta_2O_{11}$, $Sr_{5.92}Ta_{2.08}O_{11.12}$ (V-o(s))(0.88), and $Sr_{5.46}Ta_{2.54}O_{11.81}$(V-o(s))(0.19), where V-o(s) stands for 'oxygen structural vacancies', have been studied by TG, AC-conductivity and IR and RS. A correlation between water uptake and nominal V-o(s) concentration was established, but the nature of the alkaline earth metal atom influences the oxygen sub-lattice: The relationship between short-range disorder and water uptake is clear: only compounds having a strong oxygen and cation lattice disorder exhibit maximal water uptake: $Sr_6Ta_2O_{11}$. The protonic species were observed to change during cooling–heating.

The compound, **tetra-strontium tantalate**, $Sr_4Ta_2O_9$, has a phase with a completely occupied oxygen sublattice that also exhibits insignificant sensitivity to exposure to water. It has the general crystal structure related to the Ba-homolog in which two octahedra are tilted and surrounded by Sr^{2+} ions as shown in the following diagram: Fig. 9.121.

$Sr_4Ta_2O_9$ and HfO_2 films were prepared on 200 mm TiN/Si(100) substrates by Atomic Vapor Deposition (AVD). Depositions were carried out within a thermal budget of CMOS via back-end of line. Electrical properties have been investigated in metal-insulator-metal capacitors after sputter deposition of Au top electrodes. Both $Sr_4Ta_2O_9$ and HfO_2 dielectrics show excellent electrical performances. Oxides possess high capacitance densities of 3.5 fF/μm^2 (HfO_2) and 4.5 fF/μm^2 ($Sr_4Ta_2O_9$) in combination with high voltage linearity ($\leq$100ppm/V^2).

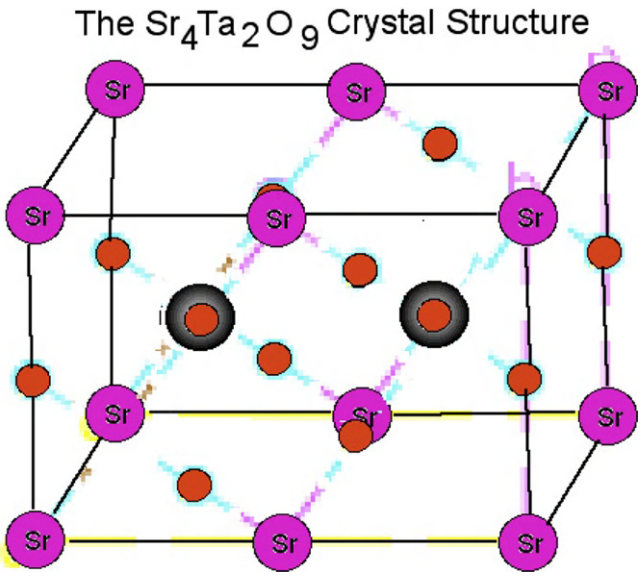

FIGURE 9.121

$Sr_4Ta_2O_9$ MIM capacitors provide lower leakage currents at 2 V, while HfO_2 MIMs offer higher operating voltage values for 10 years lifetime than $Sr_4Ta_2O_9$ based capacitors. The dielectric breakdown fields of HfO_2 (5.8 MV/cm) and $Sr_4Ta_2O_9$ (3.2 MV/cm) were obtained from IV-characteristics.

The conductivities of $Sr_2Ta_2O_7$, $Sr_6Ta_2O_{11}$, Sr_2LaTaO_6 and $Sr_3LaTa_3O_{12}$, both doped and undoped, were measured by the ac complex impedance technique over a temperature range of approximately 400–800 °C. The conductivity of $Sr_2Zr_{2x}Ta_{2-2x}O_{7-x}$ at 800 °C increased from 5.4×10^{-6} S/cm for the undoped compound to 3.0×10^{-4} S/cm at $x = 0.1$, and the activation energy correspondingly decreased from 0.98 to 0.63 eV. $Sr_3TaO_{5.5}$ and Sr_2LaTaO_6 were found to be the endpoints of a solid solution, which can be described by $Sr_{2+x}La_{1-x}TaO_{6-x/2}$ where x ranges from 0 to 1. It has the $(NH_4)_3FeF_6$-type fcc structure. There was a maximum in conductivity at $x = 0.75$ with an oxygen vacancy concentration of 6.25%. The corresponding conductivity at 800 °C was 6.2×10^{-3} S/cm, nearly identical to 15% CaO-stabilized ZrO_2. The conductivities at 800 °C of Sr_2LaTaO_6 and $Sr_3LaTa_3O_{12}$ were 3.6×10^{-5} and 1.0×10^{-6} S/cm, and the activation energies over the 400–800 °C temperature range were 1.41 and 0.84 eV, respectively.

Strontium tantalate is offered for sale commercially as the mono-strontium compound with the CAS number of 12065-74-6.

9.3.5. Barium Tantalum Compounds

The metal, Ba^0, does not form any intermetallic compounds with Ta^0.

Similar to the strontium system, no compounds are known in the Ta^{2+} or Ta^{3+} containing systems of BaO–TaO_2 or BaO–Ta_2O_3.

In the Ta^{4+} containing system of BaO–TaO_2, the compound, $BaTaO_3$ is not known. However, a mixed composition has been prepared and studied. Multiferroic super-lattice thin films of $BaFeO_3/BaTaO_3$ were fabricated by the pulsed laser deposition method for the first time. XRD and dielectric hysteresis measurements were carried out at room temperature. Temperature dependences of dielectric constant, magnetization and second harmonic generation intensities were also measured. Ferroelectricity and weak ferromagnetism were confirmed at room temperature.

In another publication, modeling of the system $A(B'_{1/3}B''_{2/3})O_3$ perovskites where B′ is Zn, B″ is Ta and A is Ba, was studied.

Ionic model (SSCAD) calculations were performed for 36 different cation ordered super cell configurations in the pseudo-binary perovskite related system $BaTaO_3$–$BaZnO_3$. $Ba(Zn_{1/3}Ta_{2/3})O_3$ (BZT) in a $P3m1$ ordered structure is the only single phase compound that is observed experimentally, and the one that SSCAD calculations predict as having lowest formation energy. It is therefore the presumed ground state at the BZT composition. The SSCAD results are supported by first principles VASP pseudo potential calculations which were performed for $BaTaO_3$, $BaZnO_3$, $Ba(Zn_{1/3}Ta_{2/3})O_3$, and $Ba(Zn_{1/2}Ta_{1/2})O_3$ with NaCl type ordering of Zn and Ta. Finite temperature calculations that are based on the SSCAD results, predict a strongly first-order $P3m1$–>$Pm3m$ transition, but the predicted T_C appears to be about an order of magnitude too high. The structure of $BaTaO_3$ is unknown since it is most likely unstable in bulk but probably stabilized by oxygen vacancies. It is likely a cubic perovskite with the formula of $BaTaO_{3-\delta}$ where δ is an array of scattered holes in the cubic lattice.

A similar compound, $BaTa_2O_5$ has been studied. A new lead-free ferroelectric material was developed. Ferroelectric materials are widely used for capacitors and piezoelectric devices. In those applications, "lead-free" is an important keyword due to environmental issues. The newly developed material is a Ba–Ta–O double oxide, $BaTa_2O_5$. The compound was synthesized in single crystal by a floating zone (FZ) method. Excellent ferro electricity was discovered in a particular direction of the crystal plane.

The Ta^{5+} containing system of BaO–Ta_2O_5 is known to form six (6) compounds as shown in the phase diagram: Fig. 9.122.

Three compounds melt congruently: $BaTa_2O_6$, $Ba_5Ta_4O_{15}$ and $Ba_6Ta_2O_{11}$. The others melt incongruently. A single report is available describing a systematic study of phase relations in the BaO–Ta_2O_5 system. Six binary phases were reported to form at 6:1, 4:1, 3:1, 5:2, 1:1, and 1:2 BaO:Ta_2O_5 molar ratios. The three latter compounds are well established: $Ba_5Ta_4O_{15}$ is isostructural with $Ba_5Nb_4O_{15}$ and exhibits a five-layer hexagonal structure derived from perovskite.

Structure factors included are shown in Table 9.70.

$BaTa_2O_6$ exhibits three polymorphs: a low-temperature orthorhombic form isostructural with $BaNb_2O_6$, an intermediate form with a tetragonal tungsten bronze type structure, and a high-temperature hexagonal form; all of the structures are of the framework type with octahedrally coordinated Ta^{5+} and channels accommodating barium. $BaTa_4O_{11}$ occurs with a tetragonal tungsten bronze related structure. The occurrence and crystal chemistry of the higher-BaO compounds at 3:1, 4:1, and 6:1 BaO:Ta_2O_5 have not been well established; however, $Ba_4Ta_2O_9$ has been reported to exist in polymorphic forms with perovskite-related structures. Ceramics have good microwave dielectric properties, including high relative permittivity (ε_r), high quality factor (Q), and low temperature coefficient of resonator frequency (τ_f). The ceramics show ε_r in the range of 11–51, $Q \times f = 2400$–$88{,}000$ GHz and τ_f in the range −73–+232 ppm/°C. This type of materials is called cation-deficient perovskites if written in the perovskite form (ABO_3), and $A_5B_4O_{15}$ is reduced to $AB_{0.8}O_3$. There is a vacancy of 0.2B cation per 1A cation, i.e., overall 1B cation vacancy per 5A cations. Galasso et al. showed that these compounds have hexagonal structure and crystallized them in the $P\bar{3}m1$ space group. They also have the closest packing of oxygen and barium ions into five layers. The tantalum or niobium ions are located in the octahedral holes between layers. One layer of the octahedral hole does not have tantalum or niobium ions to obtain the charge neutrality. Therefore, there is an empty octahedrum, which results in the loss of face sharing on the NbO_6 sub-lattice, and this structure implies strong anharmonicity. The $Ba_5Nb_4O_{15}$ shows a hexagonal structure where the dielectric values are: $\varepsilon_r = 39$, $Q \times f = 23{,}700$ and $\tau_f = 78$ ppm/°C. The $Ba_5Ta_4O_{15}$ has a lower $\varepsilon_r = 28$ than that of $Ba_5Nb_4O_{15}$, even though its tantalum has larger ionic polarizability. This arises because the lattice of $Ba_5Ta_4O_{15}$ is stable whereas that of $Ba_5Nb_4O_{15}$ could collapse to a lower symmetry. Lattice anharmonicity causes a relatively higher permittivity for $Ba_5Nb_4O_{15}$ compound.

Mono-barium tantalate is trimorphic. There are three space groups involved:

$C222_1$, $P3m_1$ and $P3m_1$

The polymorphism of $BaTa_2O_6$ has been described by Layden. Below about 1150 °C, a modification isostructural with orthorhombic $BaNb_2O_6$ forms, between ~1150 °C and 1300 °C a tetragonal tungsten bronze type structure forms, and above 1300 °C a hexagonal modification occurs. For the latter form, a structural

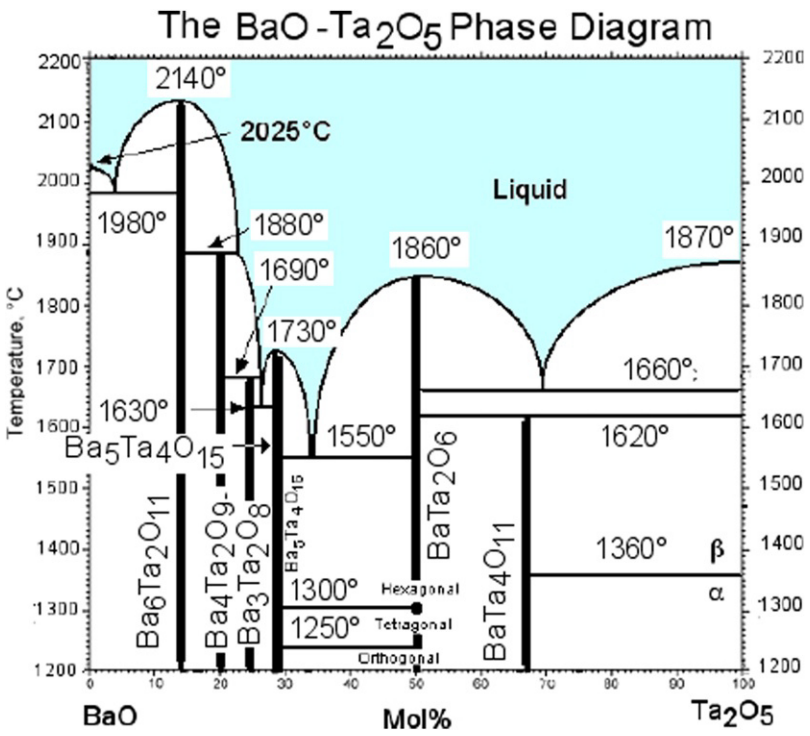

FIGURE 9.122

model has been proposed that was consistent with powder XRD data (*P6/mmm*; $a = 21.14$ Å, $c = 3.917$ Å; $Z = 12$). In the BaO–Nb_2O_5 system, the same hexagonal structure was found to form at the composition $Ba_{0.9}Nb_2O_{5.9}$. Single crystals of all three forms of $BaTa_2O_6$ have been obtained using a BaO:V_2O_5 flux. Completed structural refinements results indicate that: 1) for the hexagonal structure, one of the Ba sites originally placed at $Z = 0$ is actually at $Z = 0.28$, changing the coordination number from an unlikely 18 to a more reasonable 12; and 2) the tetragonal form crystallizes in the non-polar space group $P\bar{4}b2$ rather than the more commonly found *P4bm*. Mixtures prepared along the $BaTa_2O_6$ –$Ba_5Ta_4O_{15}$ join and annealed at temperatures above 1300 °C (e.g. 1550 °C) were found to contain the tetragonal tungsten bronze type form of $BaTa_2O_6$, indicating that this polymorph is kinetically stabilized in this region. The hexagonal form has the sub-lattice as shown in Fig. 9.123.

Lattice parameters are: $a = 6.14$ Å, $c = 8.05$ Å, $\alpha = 90°$, $\gamma = 120°$, cell volume = 259.41 Å^3. Site occupancy is shown in Table 9.71.

Phase equilibria studies in the compound, $BaTa_2O_6$, disclosed three modifications: a low temperature modification isomorphous with orthorhombic $BaNb_2O_6$ which forms below about 1150 °C, a tetragonal modification having the potassium tungsten bronze structure which forms between about 1150 °C and 1300 °C, and

TABLE 9.70

No	Compound	# of Atoms	Structure type	Point group	Space group
1	$Ba_3Ta_2O_8$	3	*	mS26	$C222_1$
2	$Ba_4Ta_2O_9$	3	*	oS240	$P\text{-}3m_1$
3	$Ba_4Ta_2O_9$	3	*	hP15	$P\text{-}3m_1$
4	$Ba_4Ta_2O_9$	3	$Ba_3SrTa_2O_9$	hP15	$P\text{-}3m_1$
5	$Ba_5Ta_4O_{15}$	3	$Ba_5Ta_4O_{15}$	hP24	$P\text{-}3m1$
6	$BaTa_2O_6$	3	$BaTa_2O_6$	tP45	$P4/mbm$
7	$BaTa_2O_6$	3	*	hP105	$P6/mmm$

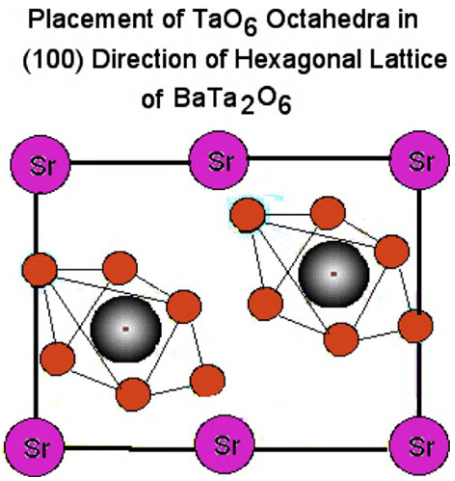

FIGURE 9.123

a hexagonal modification stable from 1300 °C to its melting point at about 1850–1900 °C. The high-temperature hexagonal form of $BaTa_2O_6$ has a *P6/mmm* symmetry with unit-cell parameters of $a = 21.116$ Å, and $c = 3.9157$ Å. Single crystal X-ray structure refinements for both phases are generally consistent with a previously proposed model, except for displacements of some Ba atoms from high-symmetry positions.

Another view of these three structures is presented in Fig. 9.124.

The orientation of the barium ions is better seen in Fig. 9.125

The structures are based on a framework of corner- and edge-connected Nb/Ta-centered octahedra, with barium atoms occupying sites in four different types of [001] channels with hexagonal, triangular, rectangular and pentagonal cross-sections. The refinements showed that the non-stoichiometry in the niobate phase is due to barium atom vacancies in the pentagonal channels and to extra niobium atoms occupying interstitial sites with tri-capped trigonal prismatic coordination. The origin of the non-stoichiometry is attributed to minimization of non-bonded Ba–Ba repulsions. The hexagonal structure is related to the structures of the low-temperature forms of $BaNb_2O_6$ and $BaTa_2O_6$, through a 30° rotation of the hexagonal rings of octahedra centered at the origin. Crystals of the orthorhombic and hexagonal modifications have been grown from this system by the slow-cooling technique.

The tetragonal form could only be obtained as a very fine precipitate. Attempts were made to grow the hexagonal modification from the melt using the Czochralski technique; it was found that not only the hexagonal, but the orthorhombic and tetragonal forms as well, could be grown in this fashion. The phase transformation of crystal fragments was investigated. Only transformations from the orthorhombic and tetragonal forms to the hexagonal form were observed to occur in times less than 100 h in the appropriate temperature ranges.

The hexagonal form of $BaTa_2O_6$ differs considerably from its Sr-homolog, as shown in Fig. 9.126. Yet, it readily forms solid solutions with the strontium homolog.

The proposed structure for hexagonal $BaTa_2O_6$ has one twelfth of the barium atoms located in tunnels, which run in the *c* direction through the Ta-oxygen framework. A relaxation polarization process is observed to occur when an alternating electric field is imposed across single crystal samples in the *c* direction, but is not observed when the field is perpendicular to the *c* direction. This is attributed to the motion of barium atoms in the tunnels.

This compound has been studied as a dielectric film for use in high-frequency capacitors. The characteristics of radio-frequency magnetron sputtered $BaTa_2O_6$ thin films with aluminum (Al) top and indium tin oxide (ITO) bottom electrodes have been investigated as a function of applied field and temperature. The optical transmittance in the visible range was in range of 80–90% regardless of the substrate temperature. The dielectric constant increased from 20 to 30 with increasing the substrate temperature and nearly independent of the frequency in the range of 0.3–100 kHz but the loss factors increased with increasing the substrate temperature at high frequency. The leakage currents of $BaTa_2O_6$

TABLE 9.71

No	Site notation	Atom	Multiplicity	Wyckoff	Site symmetry	*x*	*y*	*z*	Occupancy
1	O1	O	6	i	.m.	0.1667	0.833	0.3333	1.0
2	O2	O	3	e	.2/m.	1/2	0	0	1.0
3	Ta1	Ta	2	d	3m.	1/3	2/3	0.1667	1.0
4	Ba1	Ba	2	d	3m.	1/3	2/3	0.6667	1.0
5	Ba2	Ba	1	b	-3m.	0	0	1/2	1.0
6	Ba3	Ba	1	a	-3m.	0	0	0	1.0

Representation of the Polyhedral Forms of Nano-Barium Tantalate, Viewed Along the Channel Axes, of: (a) Low Temperature Form of $BaTa_2O_6$ with Orthorhombic $CaTa_2O_6$ Structure; (b) Low Temperature form of $BaTa_2O_6$; (c) Hexagonal structure of $BaTa_2O_6$ Obtained by 30° Rotation of the hexagonal rings of the TaO_6 Octahedra

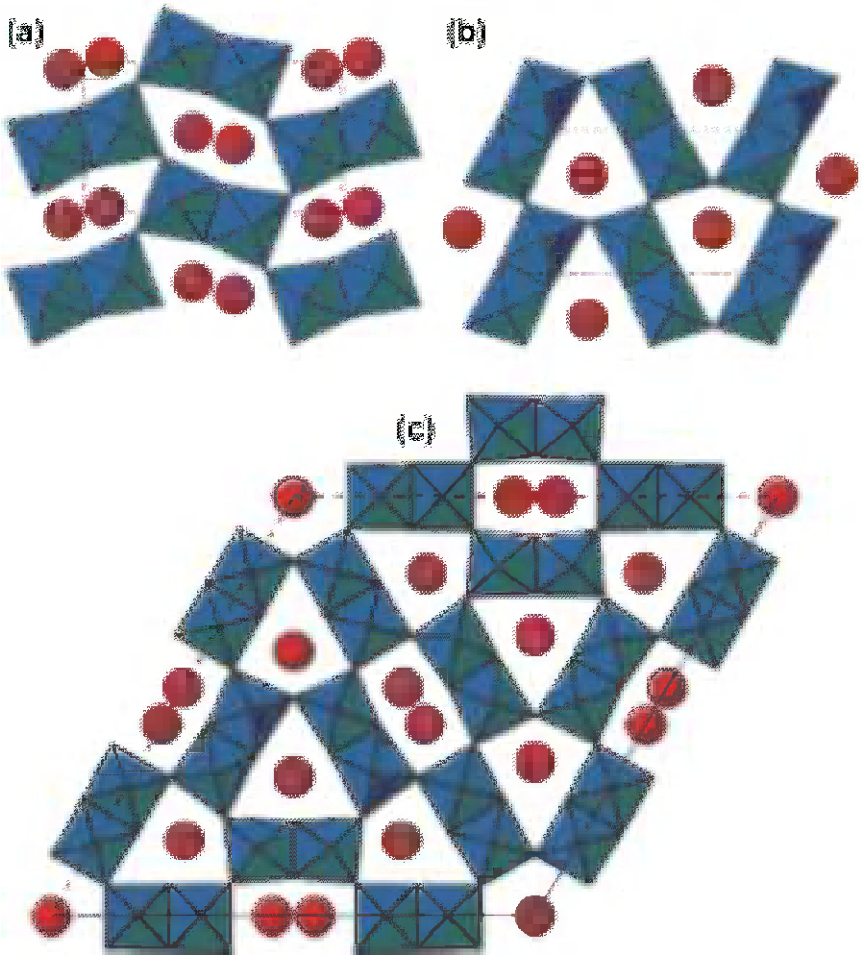

FIGURE 9.124

thin film are in the order of 10^{-6}–10^{-7} A/cm^2 at the applied field of 1 MV/cm and the charge storage capacitance ($E_{breakdown}$) are 5.64 (100 °C), 10.6 (200 °C) and 11.8 (300 °C) μC/cm^2. From the deposition temperature, voltage polarity and thickness dependence of leakage current, we can conclude that the dominant conduction mechanism is ascribed to Schottky emission at high electric field (>1 MV/cm) and hopping conduction at low electric field (<1 MV/cm). The Schottky barrier heights measured are 1.14 eV at Al(+) and 0.8 eV at Al(−).

Hexagonal barium tantalate ($BaTa_2O_6$) nanorods were synthesized by a hydrothermal method based on the reaction of concentrated $Ba(OH)_2$ solution and Ta_2O_5. $BaTa_2O_6$ samples show a uniform cylindrical structure with diameters of 5–30 nm and the lengths of 50–200 nm. The formation of $BaTa_2O_6$ nanorods follows a dissolution–recrystallization mechanism and is governed by hydrothermal temperature and time. $BaTa_2O_{6-\delta}$ nanorod samples prepared at 270 °C for 72 h have exhibited the highest photocatalytic activity in the degradation of Rhodamine B (RhB) in aqueous solution under UV radiation. Hydrogen-related defects were detected in $BaTa_2O_{6-\delta}$ nanorods, which originate from the oxygen octahedron. The number of defects was dependent on the hydrothermal temperature, and the photocatalytic activities of $BaTa_2O_{6-\delta}$ nanorods increase with the decrease of defect amounts. On the basis of the experiment results, the difference in photocatalytic activities for samples is mainly caused by lattice defects, which can act as inactivation centers.

Single crystal of a novel compound, $K_{1.83}Ba_{4.17}Nb_{12.18}O_{36}$, has been synthesized in the course of investigation on the K_2O–BaO–Nb_2O_5 system. The crystal structure was determined by single crystal XRD

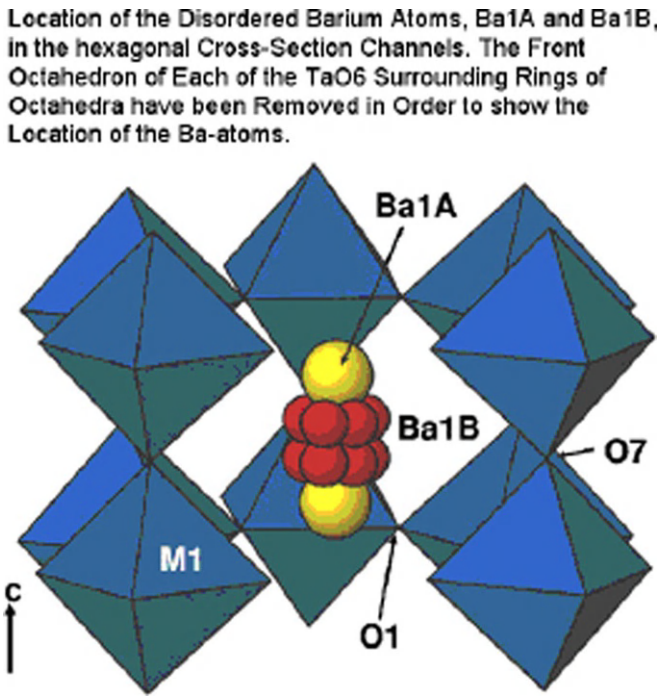

FIGURE 9.125

data. The space group of this compound was found to be $P6/mmm$ (#191) with the lattice parameters of $a = 21.109(4)$ and $c = 3.967(1)$ Å. The final R-factors were $R = 0.039$ and $R_w = 0.042$ for unique 508 reflections. The crystal structure had the same tunnel structure as that of hexagonal $BaTa_2O_6$ (H-$BaTa_2O_6$), which is the highest temperature form in three modifications of $BaTa_2O_6$. The chemical composition of $K_{1.83}Ba_{4.17}Nb_{12.18}O_{36}$ was close to that of the tetragonal tungsten bronze (TTB) type $KBa_2Nb_5O_{15}$ and the powder samples within this composition were prepared so as to clarify the boundary between H-$BaTa_2O_6$ and TTB-type structures. The H-$BaTa_2O_6$-type structure appears in $(K + Ba)/Nb \leq 0.500$ and the TTB-type structure is in $(K + Ba)/Nb \geq 0.575$. The dielectric constants of these samples were measured from room temperature to 500 °C for sintered body. The TTB-type compounds exhibited ferroelectric temperature dependence with the Curie points of 284–372 °C and the H-$BaTa_2O_6$-type compounds were not ferroelectrics as predicted from the crystal structure analysis.

The compound, **barium di-tantalate**, $BaTa_4O_{11}$, appears in the phase diagram as an incongruently melting structure. Although the TTB-type of $BaTa_4O_{11}$ (33 mol% BaO) was previously reported as a line compound, a recent study found an extensive solid solution in this region of the binary system. This solid solution is similar to that found in the BaO:Nb_2O_5 system, and again demonstrates the remarkable stability of tetragonal tungsten bronze related structures over a wide range of stoichiometry. In the region from 43 to 39 mol% BaO, no superstructure formation was observed and powder patterns could be indexed on the basis of tetragonal 12 Å × 4 Å TTB-type unit cells. Although the formula for the solid solution in this region can be written with oxygen-deficiency as $Ba_{5-y}Ta_{10}O_{30-y}$, with $1.2 \leq y \leq 1.8$, there is no logical crystal chemical model to account for the possible oxygen vacancies. Alternatively, and preferably, if one assumes that the strongly bonded octahedral framework (denoted in the following by square brackets) remains intact, the formula for the TTB-type solid solution from 43 to 39 mol% BaO can be expressed as $Ba_xTa_{(10-2x)/5}[Ta_{10}O_{30}]$, with $x = 3.93$ to 3.40. In this model, Ba and the excess Ta occupy disordered sites within the channels, with Ta^{5+} lowering its coordination number by moving from the centers of the channels. In the region from 38 to 31 mol% BaO, superstructures formed with a- and b-parameters related to those of the TTB structure by a factor of $\sqrt{2}$, yielding tetragonal or orthorhombic super cells similar to those observed in a number of other systems. If one assumes that the formation of a super cell with a doubled unit-cell

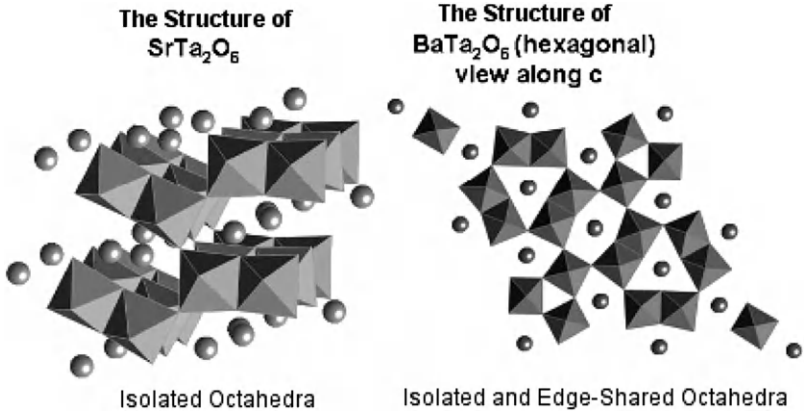

FIGURE 9.126

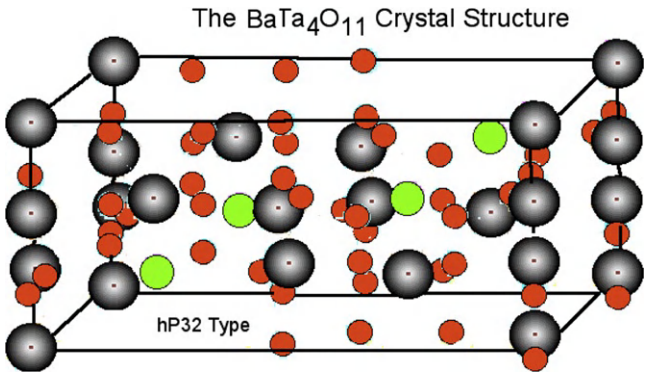

FIGURE 9.127

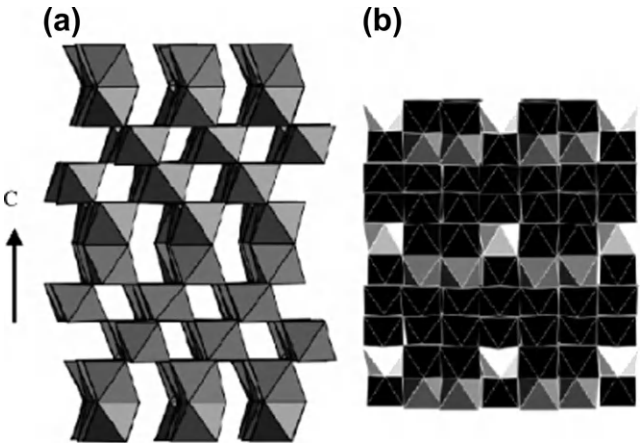

FIGURE 9.128

volume is caused by the ordering of 2[TaO_6] units per super cell in sites within the pentagonal channels, in a manner analogous to the formation of tripled superstructures in TTB-related $Nb_8W_9O_{47}$ or $Sr_2Nb_{10}O_{27}$, and $SrTa_4O_{11}$, then a possible general formula for the $\sqrt{2}$-type solid solution from 38 to 31 mol% BaO is $Ba_xTa_{(14-2x)/5}[Ta_{22}O_{62}]$, with $x = 6.77$ to 5.11, respectively. This model would not require the formation of oxygen vacancies; Ba and excess Ta not associated with the framework would occupy disordered sites within the channels. In the region from 30 to 26 mol% BaO, tripling of the TTB *b*-parameter was observed, resulting in a unit cell with a tripled cell volume. As in $Nb_8W_9O_{47}$ [42,38], the formula for the framework of the tripled TTB structure is [$M_{34}O_{94}$], which includes the 4 [MO] units occupying ordered pentagonal channel sites. Therefore, a possible general formula for the tripled-cell-type solid solution from 30 to 26 mol% BaO is $Ba_xTa_{(18-2x)/5}[Ta_{34}O_{94}]$, with $x = 7.42$–6.17, respectively. As above, this model does not require the formation of oxygen vacancies, and Ba and excess Ta not associated with the [$M_{34}O_{94}$] framework would occupy disordered sites within the channels. Detailed structural determinations have not yet been carried out to confirm these suggested mechanisms accommodating the variable stoichiometry and leading to the formation of the different superstructures.

The compound, barium di-tantalate, $BaTa_4O_{11}$, is believed to have the same structure as the strontium di-tantalate. It would then have the form as shown in Fig. 9.127.

However, the exact structure has not been published to date.

The **tri-barium tantalite** compound, $Ba_3Ta_2O_8$, is hexagonal. Cell parameters are: $a = b = 5.8445$ Å, $c = 7.3832$ Å, $\alpha = \beta = 67.388°$, $\gamma = 60.167°$, cell volume = 194.41 Å^3, $Z = 2$. Although this barium compound has not found usage in Industry, a modification of this structure is beginning to be used in the wireless communication sector. The complex perovskite compounds of barium-zinc tantalates, that exhibit a high relative permittivity, good quality factor (Q), and a near zero temperature coefficient of resonant frequency (τ_f), have been used in manufacturing dielectric resonators in the wireless communication system. A barium zinc niobate ($Ba(Zn_{1/3}Nb_{2/3})O_3$) (BZN) complex perovskite has been reported to have special microwave dielectric properties with close relation of its ordered structure. The tantalate modification has also been studied. The hexagonal perovskite, $Ba_8ZnTa_6O_{24}$, was prepared in single-phase form and was found to be a stable secondary phase, formed as a result of the loss of ZnO from $Ba(Zn_{1/3}Ta_{2/3})O_3$ microwave dielectrics. The experimental and calculated X-ray patterns of $Ba_8ZnTa_6O_{24}$ indicate it is isostructural with $Ba_8ZnNi_6O_{24}$ with an 8H $(CCHC)^2$ close-packed BaO_3 stacking sequence and the lattice parameters, $a = 5.100825$, $c = 5.190587$ Å . The structure has the form as shown in Fig. 9.128.

Here, the structure models of $Ba_8ZnTa_6O_{24}$ are projected along: (a) the (110) direction to highlight the corner and face-shared octahedra and (b) along the [110] direction to highlight the ordering of Ta, Ni, and vacancies in the face-shared octahedra (Ta = black, vacancy = white, Zn-rich = gray). In both the figures, Ba atoms are omitted for clarity.

High-density ceramics of $Ba_8ZnTa_6O_{24}$ could be prepared at temperatures considerably lower (1400 °C) than those used to sinter pure $Ba(Zn_{1/3}Ta_{2/3})O_3$, and exhibit very good microwave dielectric properties with $\varepsilon_r = 530.5$, $Q \times f = 562\ 300$, and $\tau_f = 5136$ ppm/°C at 8.9 GHz. Dense ceramic samples of B $Ba_8ZnTa_6O_{24}$, formed at 1400 °C via a two-stage sintering process, have excellent microwave dielectric properties with $\varepsilon_r = 30.5$, and $Q \times f = 62{,}300$ at 8.9 GHz; however, additives will be needed to lower the temperature coefficient $\tau_f = +36$ ppm/°C.

The **tetra-barium tantalite**, $Ba_4Ta_2O_9$, is dimorphic with space groups of o*S*240-*C*222$_1$ and *hP*15-*P*-3m_1. Cell parameters are: (1) low temperature phase: $a = 12.15$ Å, $b = 12.20$ Å, $c = 16.07$ Å, $\alpha = \beta = 90°$, $\gamma = 119.86°$, cell volume = 2065.76 Å^3, $Z = 16$. The other form (2) has the parameters: $a = 4.253°$, $b = c = 5.952$ Å, $\alpha = 120°$, $\beta = \gamma = 90°$, cell volume = 130.48 Å^3, $Z = 1$. The polymorphic phase transitions and the stability of the individual polymorphs of tetra-barium di-niobate (V) ($Ba_4Nb_2O_9$) were studied at different temperatures. $Ba_4Nb_2O_9$ ceramics were prepared via a conventional solid-state reaction route. Three $Ba_4Nb_2O_9$ polymorphs were isolated. These include a hexagonal (α) and two orthorhombic (γ, β) modifications. TEM revealed an intergranular BaO-rich amorphous phase and nano-crystalline $Ba_5Nb_4O_{15}$ in all the polymorphs, most abundantly in the α-modification. Superstructure ordering in the α-modification was confirmed by ED methods. The α-$Ba_4Nb_2O_9$ was observed to be stable in the temperature range 560–1160 °C; below 560 °C the stable polymorph is β-$Ba_4Nb_2O_9$, while above 1160 °C the only stable polymorph is γ-$Ba_4Nb_2O_9$.

Low-temperature α-$Ba_4Ta_2O_9$ is isostructural with β-$Ba_4Nb_2O_9$ ($Sr_4Ru_2O_9$ type), and it undergoes a reconstructive phase transition at approximately the same temperature (1400 K) to a γ-form that can easily be quenched to room temperature. However, the γ forms of the two compounds are completely different. Whereas γ-$Ba_4Nb_2O_9$ represents a unique structure type, γ-$Ba_4Ta_2O_9$ adopts a more conventional 6H-perovskite type. The α ⇒ γ transition is virtually irreversible in the tantalate, unlike the niobate, which can be converted back to the α form by annealing slightly below the transition temperature. Quenched γ-$Ba_4Ta_2O_9$ is highly strained due to the extreme size mismatch between Ba^{2+} (1.35 Å) and Ta^{5+} (0.64 Å) cations in the perovskite B-sites, and undergoes a series of symmetry-lowering distortions from $P63/mmc \Rightarrow P63/m \Rightarrow P21/c$; the second of these transitions has not previously been observed in a 6H perovskite. Below 950 K, both α-$Ba_4Ta_2O_9$ and γ-$Ba_4Ta_2O_9$ hydrate to a greater extent than the corresponding phases of $Ba_4Nb_2O_9$. Both hydrated forms show significant mixed proton and oxide ionic conductivity, and electronic conductivity upon dehydration.

The low-temperature form has the structure shown as follows. The low-temperature form of $Ba_4Ta_2O_9$ is isostructural with that of $Ba_4Nb_2O_9$ and undergoes a reconstructive phase transition at a similar temperature as shown in Fig. 9.129.

However, the high-temperature forms are different. The tantalates hydrate to a greater extent than the niobates, but show slightly lower protonic and oxide ionic conduction. The structure contains isolated Ta_2O_9 face-sharing octahedral dimers, separated by very large voids.

The compound, **hexa-barium tantalite**, $Ba_6Ta_2O_{11}$, has the highest melting point of all of the barium tantalites, as shown in the phase diagram presented above. It is said to possess a five-layered structure similar to the penta-barium di-tantalate which has a double-layer structure as shown in Fig. 9.130.

This diagram is expanded in order to show the octahedra in the internal structure. The actual structure is more compact. Very little information is available for this compound other than structure. It has proven difficult to prepare and is unstable at room temperature.

The compound penta-barium di-tantalate, $Ba_5Ta_4O_{15}$, has the structure as shown in Fig. 9.131.

Cell parameters are: $a = b = 5.783$ Å, $c = 11.81$ Å, $\alpha = \beta = 90°$, $\gamma = 120°$, cell volume = $a = 0.5783$ nm, $b = 0.5783$ nm, $c = 1.182$ nm, cell volume = 342.34 Å^3, $Z = 1$. Cell occupancy is shown in Table 9.72.

Monomolecular-layer perovskite $Ba_5Ta_4O_{15}$ nanosheets with hexagonal structure have been synthesized by a hydrothermal method. The thickness of the nanosheets was about 1.1 nm, which corresponded to a monolayer of $Ba_5Ta_4O_{15}$ molecules, with the lateral size ranging from 50 to 200 nm. The optimal conditions for the formation of the nanosheets were found to be maintaining the reactants above 270 °C for 24 h. A dissolution recrystallization mechanism was suggested based on observations of the factors that influence nanosheet formation, such as reaction time, temperature, and basicity. Formation of $Ba_5Ta_4O_{15}$ nanosheets took precedence over other nanostructures under high

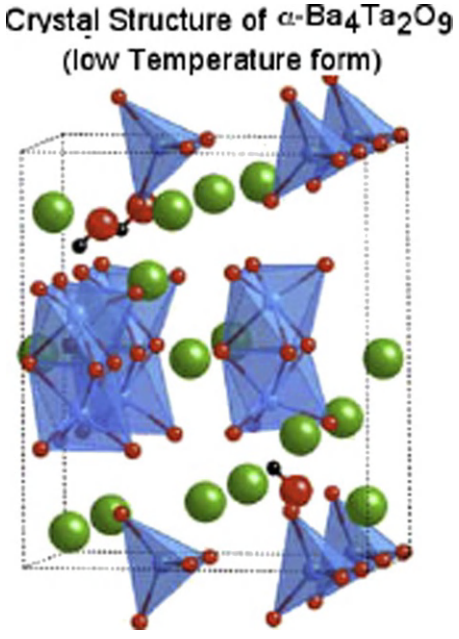

FIGURE 9.129

TABLE 9.72

No	Site notation	Atom	Multiplicity	Wyckoff	Site symmetry	*x*	*y*	*z*	Occupancy
1	O1	O	6	i	.m.	0.1695	0.835	0.1916	1.0
2	O2	O	6	i	.m.	0.8368	0.163	0.3864	1.0
3	O3	O	3	e	.2/m.	1/2	0	0	1.0
4	Ta1	Ta	2	d	3m.	1/3	2/3	0.1035	1.0
5	Ba1	Ba	2	d	3m.	1/3	2/3	0.4282	1.0
6	Ba2	Ba	2	d	3m.	1/3	2/3	0.7837	1.0
7	Ta2	Ta	2	c	3m.	0	0	0.3127	1.0
8	Ba3	Ba	1	a	-3m.	0	0	0	1.0

concentrations of OH^- because the hindering effect of OH^- ions on the *c*-axis growth is strong. Thus, the extended growth rate of polyhedrons on one monolayer was much faster than the superposition rate of the monolayer, and the crystal grows more easily along the *a*- and *b*-planes. The $Ba_5Ta_4O_{15}$ nanosheets showed a high photocatalytic activity in the degradation of Rhodamine B and gaseous formaldehyde. The layered perovskite probably affects the photocatalytic activity by promoting the charge separation and delocalization of photo generated electrons and holes. A better view of this crystal structure is shown in the following Fig. 9.132.

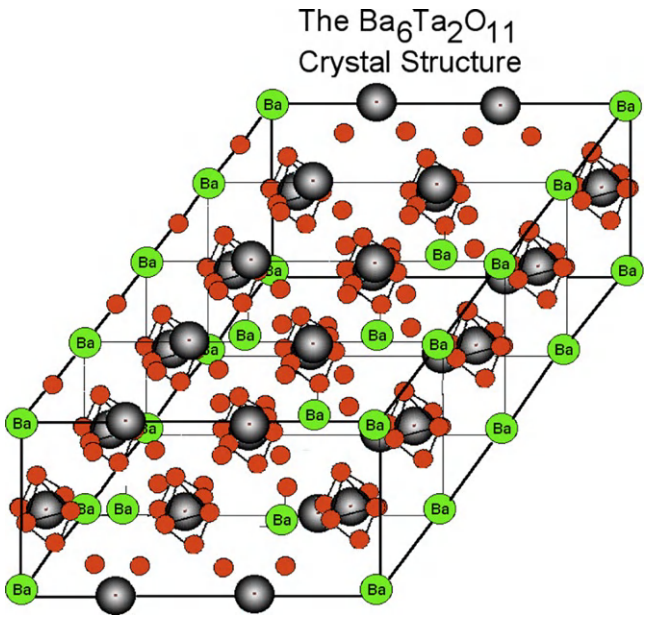

FIGURE 9.130

It is homologous with penta-strontium di-tantalate. Barium, as BaO, forms a number of distinct and unusual tantalate compounds with other members of the alkaline earth family including Mg, Ca, and Sr.

The phase relations in the BaO–MgO–Ta_2O_5 system equilibrated at 1450 °C were reported. Three ternary phases, namely 3:1:1 perovskite $Ba_3MgTa_2O_9$, 9:1:7 TTB (tetragonal tungsten bronze)-type $Ba_9MgTa_{14}O_{45}$ and 4:1:5 $Ba_4MgTa_{10}O_{30}$ closely related to the tungsten bronze structure were reported. Another ternary phase, $Ba_{10}Mg_{0.25}Ta_{7.9}O_{30}$, with a 10 layer hexagonal perovskite structure can be only obtained after equili bration at 1600 °C. MgO solubility in the TTB-like $Ba_4Ta_{10}O_{29}$,

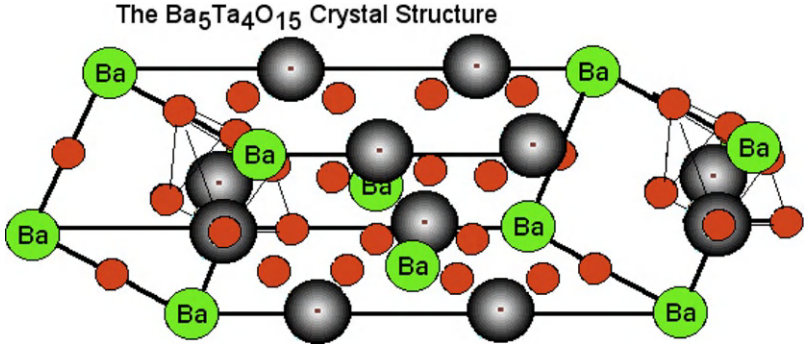

FIGURE 9.131

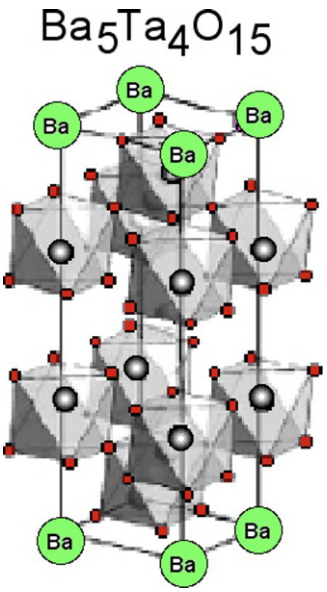

FIGURE 9.132

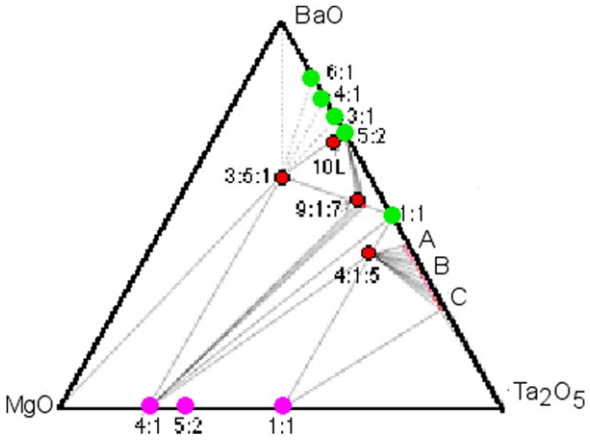

FIGURE 9.133

$BaTa_4O_{11}$ and $Ba_{6.63}Ta_{34.95}O_{95}$ does not exceed 2.0 mol%. Only the hexagonal polymorph of the $BaTa_2O_6$ phase was found along the $Mg_4Ta_2O_9$–$BaTa_2O_6$ join. Measurements of dielectric properties in the 20 Hz–2 MHz range revealed that $Ba_9MgTa_{14}O_{45}$ has a dielectric constant of 99 with no frequency dispersion and low dielectric loss.

The ternary diagram appears as shown in Fig. 9.133.

The photocatalytic activities of strontium pyrotantalate are improved by forming solid solutions with the barium compound, i.e.-$(Sr_{1-x}Ba_x)_2Ta_2O_7$. However, the detailed reason why such an increase in the photo catalytic performance by barium doping occurs has not yet been explained. In this study, Rietveld analysis of the powder XRD data was performed to reveal the structural changes induced by barium doping. The powder samples were prepared by the polymerized complex method with the molar ratio of Sr:Ba:Ta = 1−*X*:*X*:1. Existing phases in the prepared samples were identified and the mass fraction for each phase was estimated by the result of Rietveld analysis. The photocatalytic activity of a mixture of Sr:Ba increases up to $X = 0.2$, where the sample containing Ba-doped $Sr_2Ta_2O_7$ exhibits the highest photocatalytic performance, 5700 μmol/h, in the photolytic decomposition of H_2O into H_2. On the other hand, the sample of $X = 0.8$ composed of mainly Sr-doped $Ba_5Ta_4O_{15}$ shows the next highest activity, 4800 μmol/h. The high photocatalytic activities of strontium–barium tantalate solid solutions can be explained in terms of distortion in the crystal lattice, based on the result of Rietveld analysis.

Barium tantalate is offered for sale commercially as $BaTa_2O_6$ with the CAS Number: 12047-34-6.

9.3.6. Radium Tantalates

Although radium is expected to form the same type of compounds as its barium homolog, such as $RaTa_2O_6$, $Ra_5Ta_4O_{15}$ and $Ra_6Ta_2O_{11}$, the high cost of radium and the high level of radioactivity of ^{226}Ra have likely precluded any studies being made. It is unlikely that any examination of such compounds will occur in the future because of the non-existent demand in Industry for these materials.

CHAPTER

10

Group 6 (Cr, Mo and W) Alkaline Earth Compounds

OUTLINE

10.1. Alkaline Earth Chromium Compounds **795**
10.1.1. Alkaline Earth Chromide Compounds *796*

10.2. Alkaline Earth Oxy-Chromium Compounds **798**
10.2.1. Beryllium Chromates *798*
10.2.2. Magnesium Chromium Compounds *798*
10.2.3. Calcium Chromium Compounds *802*
10.2.4. Strontium Chromium Compounds *809*
10.2.5. Barium Chromium Compounds *813*
10.2.6. Radium Chromium Compounds *819*

10.3. Alkaline Earth Molybdenum Compounds **819**
10.3.1. Beryllium Molybdenum Compounds *820*
10.3.2. Magnesium Molybdenum Compounds *823*
10.3.3. Calcium Molybdenum Compounds *826*
10.3.4. Strontium Molybdenum Compounds *829*
10.3.5. Barium Molybdates *835*
10.3.6. Radium Molybdenum Compounds *841*

10.4. Alkaline Earth—Tungsten Compounds **841**
10.4.1. Beryllium Tungsten Compounds *842*
10.4.2. Magnesium Tungsten Compounds *844*
10.4.3. Calcium Tungstates *846*
10.4.4. Strontium Tungsten Compounds *851*
10.4.5. Barium Tungstates *858*
10.4.6. Radium Tungstates *868*

10.1. ALKALINE EARTH CHROMIUM COMPOUNDS

In the important oxidation state of +3, chromium's extensive chemistry is dominated by the formation of stable complexes in which chromium is dodecahedrally six-coordinate. Dichromium trioxide [CAS 1308-3-91] (also chromium sesquioxide, chromium (+3) oxide), Cr_2O_3, is an important green pigment. Compounds of the type $Ae^{2+}Cr_2O_4$ are mixed oxides, with the chromium occupying the octahedral holes in a closed-packed lattice of oxide ions. The Ae^{2+} oxides are largely spinels and the ore, chromite, is an important example of the class.

Chromium(IV) oxide, chromium dioxide, CrO_2, is obtained by hydrothermal reaction of Cr(VI) or Cr(III) compounds in the presence of oxygen or hydrogen. The stability of chromium dioxide has been studied. It has a tetragonal lattice similar to rutile, TiO_2. Although Cr(IV) does not form anions in aqueous solution, compounds such as dibarium chromate (1:1) Ba_2CrO_4, prepared from the oxides and containing discrete CrO_2 groups, have been prepared (the other Ae_2CrO_4 compounds are unknown). The chemistry of chromium in oxidation state +5 is quite similar to that of the +4 state. There are more ionic chromium(V) compounds, but disproportionation in aqueous systems prevents their isolation from water solution.

Chromium pentoxide, chromium(V) oxide (2:5), Cr_20_5, like CrO_2 can be prepared by the decomposition of CrO_3. A nearly complete series of salts containing the $Cr0_4^{3-}$ ion has been prepared. They resemble the corresponding phosphates structurally and are generally green in color. The alkali metal salts M_3CrO_4 are hygroscopic and unstable in moist air. The barium, strontium, and calcium chromates(V) are also known. The calcium chromite–chromate, $Ca_{0.4}CrO_3 \cdot Cr_2O_3$, reported from the roasting of chromite with lime and

Encyclopedia of the Alkaline Earth Compounds
http://dx.doi.org/10.1016/B978-0-444-59550-8.00010-7

Copyright © 2013 Elsevier B.V. All rights reserved.

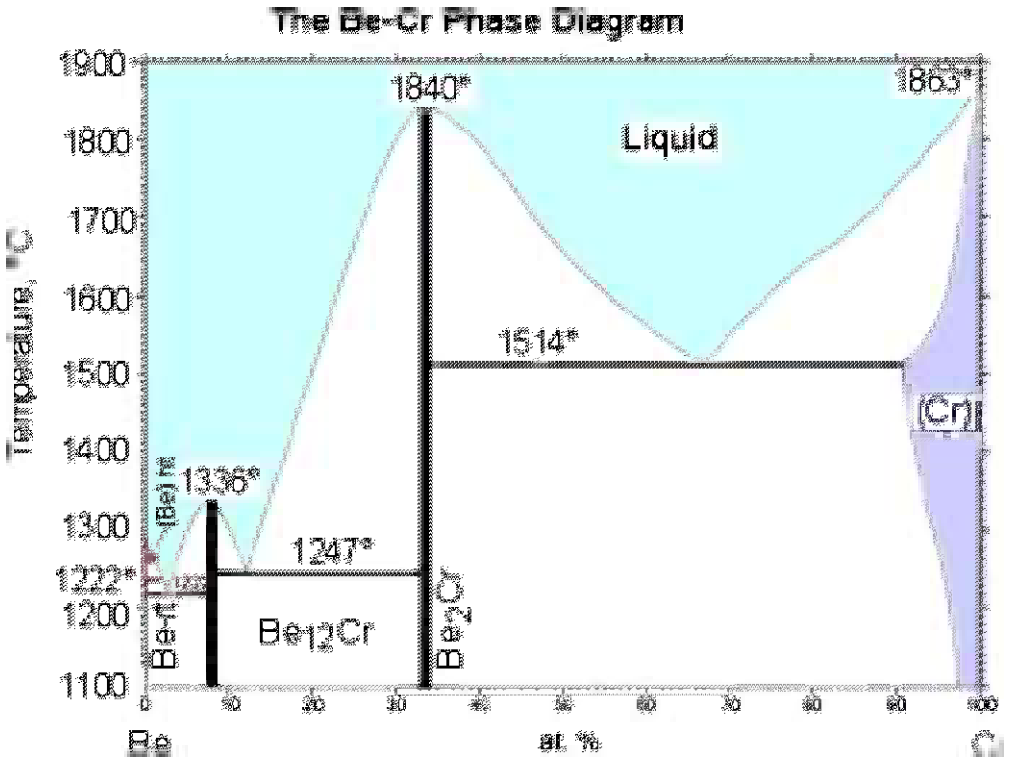

FIGURE 10.1

soda ash, is more properly formulated as $Ca_3(CrO_4)_2$. This compound is readily prepared by heating CaO and $CaCrO_4$ to about 1150 °C. Hydroxy-compounds, such as $Ba_5(CrO_4)_3(OH)$ analogous to apatite also exist.

Chromium(VI) bears a strong structural resemblance to hexavalent sulfur. The principal differences are to be found in the oxidizing nature of chromium(VI). The weaker acidity of H_2CrO_4, the nonexistence of solid dichromates containing the $HCrO_3^-$ ion, the existence of polychromates, particularly dichromates, and the much less energetic hydration of the oxide CrO_3 also contribute to this characteristic. The softer nature of the acid, e.g. the polarizabilty of the CrO_4^{2-} ion, is also a factor. In solution, at pH 6, the tetrahedral yellow CrO_4^{2-} ion is the principal species; at pH 2–6, the orange $HCrO_4^-$ and $Cr_2O_7^{2-}$ ions predominate at moderate concentrations. At very low pH, the principal species is $HCr_2O_7^{2-}$. In heavy concentrated solutions, $Cr_3O_{10}^{2-}$ and $Cr_4O_{13}^{2-}$ ions exist. Chromium trioxide (chromic anhydride, chromium(VI) oxide), CrO_3, is the chromic acid of commerce. It is a red solid, melting at 197 °C with slow decomposition. The decomposition becomes rapid and exothermic at about 220 °C, forming largely impure Cr_2O_5.

Thus, it is the +3 and +6 states of chromium that are most important in the chemical reaction of alkaline earth oxides with oxy-chromium compounds to form "chromites" and "chromates". The dichromates of the alkaline earths have also been characterized. In aqueous solution, chromate and dichromate anions can exist in a chemical equilibrium:

$$2CrO_4^{2-} + 2H^+ \Leftrightarrow Cr_2O_7^{2-} + H_2O$$

Further condensation reactions can occur in strongly acidic solutions with the formation of trichromates, $Cr_3O_{10}^{2-}$, and tetrachromates, $Cr_4O_{13}^{2-}$. All poly-oxyanions of chromium(VI) have structures made up of tetrahedral CrO_4 units sharing corners.

10.1.1. Alkaline Earth Chromide Compounds

The metal, Cr^0, forms a limited number of "chromides" with the alkaline earth metals. Only Be forms any specific compounds and these are limited to two. These intermetallic compounds have found no usage in industrial applications.

The phase diagram of the system, Cr–Be, is shown in Fig. 10.1.

The structural data are shown in Table 10.1.

The compound, Be_2Cr, has the structure shown in Fig. 10.2.

Cell parameters are: $a = b = 4.26$ Å, $c = 6.988$ Å, $\alpha = \beta = 90°$, $\gamma = 120°$, cell volume = 109.23 Å^3. Cell occupancy is shown in Table 10.2.

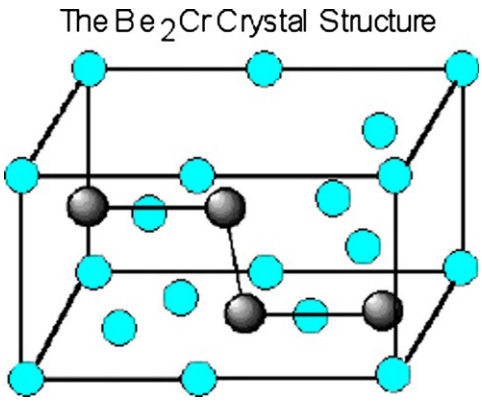

FIGURE 10.2

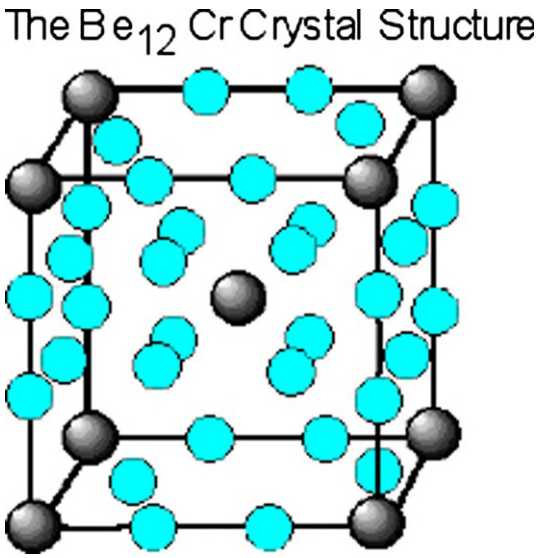

FIGURE 10.3

The compound, $Be_{12}Cr$, has the structure shown in Fig. 10.3.

Cell parameters are: $a = 4.174$ Å, $b = c = 5.5277$ Å, $\alpha = 81.803$ Å, $\beta = \gamma = 67.816$ Å, cell volume $= 109.34$ Å^3, $Z = 2$. Cell occupancy is shown in Table 10.3.

In Be–Cr alloys that are in equilibrium, there is a phase based on $CrBe_{12}$, which is formed by the peritectic reaction: $Liq + CrBe_2 \Leftrightarrow CrBe_{12}$. The composition of the compound is evidently close to the composition at the peritectic point on the phase diagram. Further work on the position of the eutectic point on the phase diagram determined more precisely its value from the beryllium side. Eutectic solidification occurs at 1240 ± 10 °C in the alloy containing 13.8% Cr. Binary beryllium alloys containing up to 13% Cr have relatively low strength, not

TABLE 10.1

Compound	Structure type	Point group	Space group	Melting point, °C	Physical properties
Be_2Cr	$MgZn_2$	hP12	194	1840	No data
(Be) rt	Mg	hP2	194	1220	No data
(Be) ht	W	cI2	229	1289	No data
$Be_{12}Cr$	$ThMn_{12}$	tI26	139	1338	No data
(Cr)	W	cI2	229	1863	No data

TABLE 10.2

No.	Site notation	Atom	Multiplicity	Wyckoff	Sitesymmetry	*x*	*y*	*z*	Occupancy
1	Be1	Be	6	h	mm2	0.1697	0.339	1/4	1.0
2	Cr1	Cr	4	f	3m.	1/3	2/3	0.5629	1.0
3	Be2	Be	2	a	−3m.	0	0	0	1.0

TABLE 10.3

No.	Site notation	Atom	Multiplicity	Wyckoff	Site symmetry	*x*	*y*	*z*	Occupancy
1	Be3	Be	8	j	m2m.	0.293	1/2	0	1.0
2	Be2	Be	8	i	m2m.	0.3624	0	0	1.0
3	Be1	Be	8	f	..2/m	1/4	1/4	1/4	1.0
4	Cr	Cr	2	a	4/mmm	0	0	0	1.0

exceeding 10–11.6 kgf/mm^2. When nickel or vanadium is added to the alloy of beryllium with chromium, the strength rises to 14–17 kgf/mm^2. The ductility of these alloys is low. They have not found usage in industry.

The other alkaline earths, Mg, Ca, Sr, Ba and Ra do not form chromide-type compounds.

10.2. ALKALINE EARTH OXY-CHROMIUM COMPOUNDS

Based on the known stability of the oxygen-dominated chromium ions, we would expect to find: chromites, $Cr_2O_4^{2-}$, CrO_4^{4-}, CrO_3^{2-}, $Cr_2O_6^{2-}$, $Cr_2O_7^{4-}$, $CrO_4^{2-}$and $Cr_2O_7^{2-}$. These are based upon the oxides: Cr_2O_3, CrO_2, Cr_2O_5, and CrO_3.

10.2.1. Beryllium Chromates

Beryllium oxide forms a number of compounds with the chromium oxides. The exact composition depends, to a great extent, on the oxidation state of the chromium ion, $Cr^{3,\ 4,\ 5\ or\ 6+}$.

For the system of BeO–CrO, no compounds are known.

For the trivalent Cr(III) oxide system only $BeCr_2O_4$ is known. One form of this compound is the chrysoberyl ($BeAl_2O_4$) structure shown in Fig. 10.4.

The purple BeO_4 tetrahedra sit at the apex of groups of three edge-connected green Cr(III)O_6 octahedra. In the BeO/Cr_2O_3 system, besides $BeCr_2O_4$ and the starting oxides, only small amounts of $BeCr(VI)O_4$ occur which, however, is supposed to catalytically activate the formation of a spinel-like $MgCrO_4$.

$BeCr_2O_4$ also has the Mg_2SiO_4 structure shown in Fig. 10.5.

Cell parameters are: $a = 4.555$ Å, $b = 5.663$ Å, $c = 9.792$ Å, $\alpha = \beta = \gamma = 90°$, cell volume $= 252.58$ Å^3, $Z = 4$. Cell occupancy is shown in Table 10.4.

The other valence states of chromium do not allow the formation of compounds with BeO. Neither of the compounds shown above has been used in Industry, perhaps due to the lack of interest in Academia concerning their physical and chemical properties.

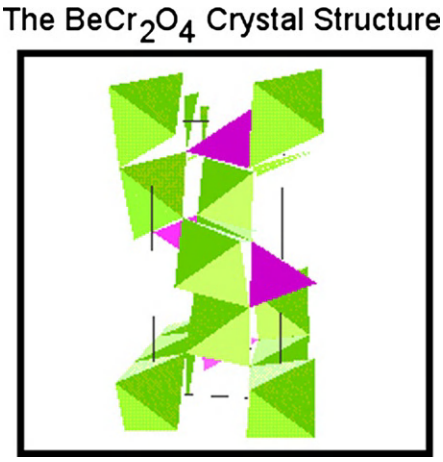

FIGURE 10.4

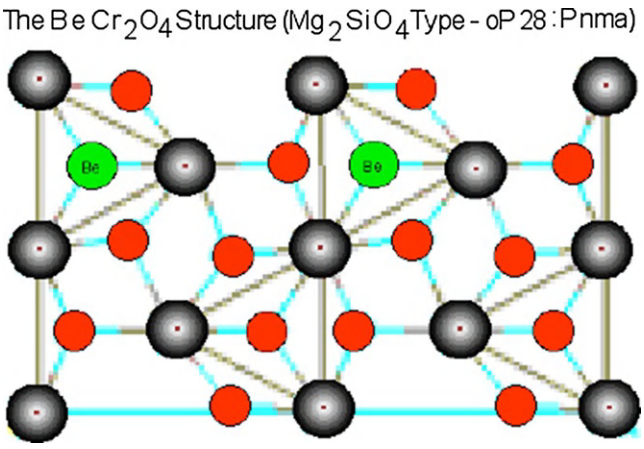

FIGURE 10.5

10.2.2. Magnesium Chromium Compounds

Magnesium oxide forms a limited number of compounds with the chromium oxides. The exact composition depends, to a great extent, on the oxidation state of the chromium ion, $Cr^{3,\ 4,\ 5\ or\ 6+}$.

TABLE 10.4

No.	Site notation	Atom	Multiplicity	Wyckoff	Site symmetry	*x*	*y*	*z*	Occupancy
1	OIII	O	8	d	1	0.338	0.022	0.243	1.0
2	OII	O	4	c	.m.	0.061	1/4	0.269	1.0
3	CrII	Cr	4	c	.m.	0.232	1/4	0.505	1.0
4	Be	Be	4	c	.m.	0.406	1/4	0.069	1.0
5	OI	O	4	c	.m.	0.407	1/4	0.723	1.0
6	CrI	Cr	4	a	−1	0	0	0	1.0

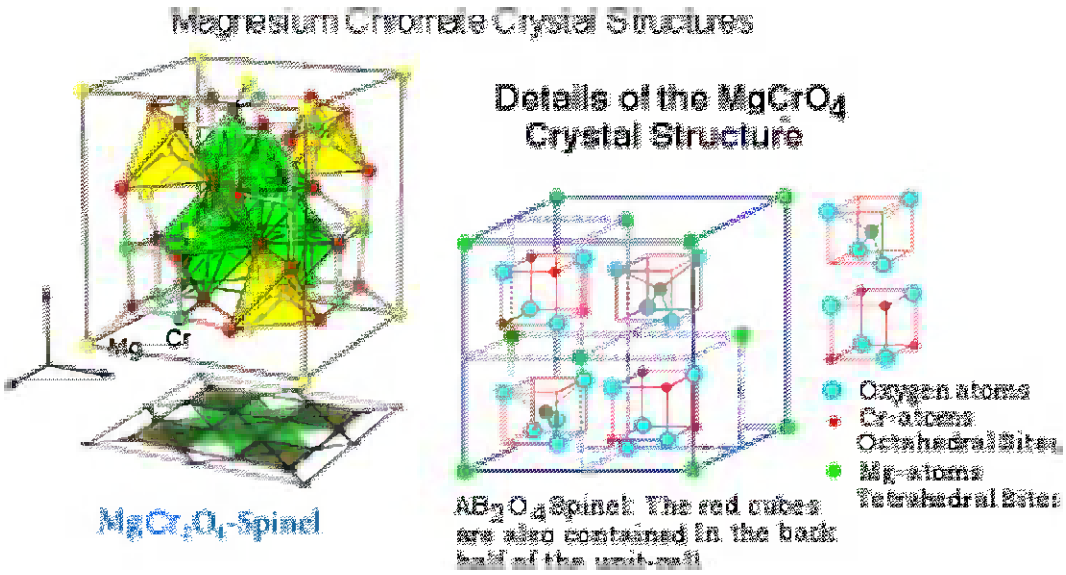

FIGURE 10.6

In the MgO–CrO system, no compounds are known.

In the Cr^{3+}-containing MgO–Cr_2O_3 system, only the compound, $MgCr_2O_4$ is known. The heat capacity of synthetic Eskolaite, Cr_2O_3, and of the synthetic spinel magnesiochromite, $MgCr_2O_4$, was measured from 1.5 K to 340 K. For $MgCr_2O_4$, a substantial magnetic contribution to the entropy is revealed by a sharp peak in the heat capacity curve at 12.55 ± 0.05 K, which indicates the transition to antiferromagnetic long-range order. Integration of the heat capacity curve yields a value of 118.3 ± 1.2 J/(mol K) for the standard entropy at 298.15 K, which is in excellent agreement with that calculated from phase equilibria studies on the reaction $MgCr_2O_4 + SiO_2 = Cr_2O_3 + MgSiO_3$. The new calorimetric results for Cr_2O_3 indicate standard entropy at 298.15 K of 82.8 ± 0.8 J/(mol K).

This compound has the cubic spinel structure as shown in Fig. 10.6.

Cell parameters are: $a = b = c = 5.8513$ Å, $\alpha = \beta = \gamma = 60°$, cell volume $= 141.66$ Å^3, $Z = 8$. Cell occupancy is shown in Table 10.5.

The $MgCr_2O_4$ spinel belongs to the class of normal spinels and is the only compound in the MgO–Cr_2O_3 system that crystallizes in a face centered cubic structure (space group *Fd*3*m*). The unit cell parameter for this compound is equal to 8.329 Å, the melting temperature is 2350 °C, and the density amounts to 4.43 g/cm^3. The magnesium–chromium spinel is a chemically stable compound that does not decompose into oxides up to the melting temperature, but does react with concentrated mineral acids. The high melting temperature of the $MgCr_2O_4$ spinel compound allows one to use it as a refractory material.

The heat capacity of synthetic "Eskolaite", Cr_2O_3, that of the synthetic spinel magnesium chromite, $MgCr_2O_4$, and the chromite, $FeCr_2O_4$, was measured from 1.5 K to 340 K. For $MgCr_2O_4$, a substantial magnetic contribution to the entropy was revealed by a sharp peak in the heat capacity curve at 12.55 ± 0.05 K. This indicates a transition to antiferromagnetic long-range order. Integration of the heat capacity curve yields a value of 118.3 ± 1.2 J/molK for the standard entropy at 298.15 K, which is in excellent agreement with that calculated from phase equilibria studies on the reaction: $MgCr_2O_4 + SiO_2 = Cr_2O_3 + MgSiO_3$. The calorimetric results for Cr_2O_3 indicated standard entropy at 298.15 K of 82.8 ± 0.8 J/mo lK. The measurements for $FeCr_2O_4$ show three distinct heat capacity anomalies, one of which (peaking at 36.5 ± 0.2 K). This was missed by prior low-temperature heat capacity measurements, which only extended down to 53 K. Integration of the heat capacity curve yielded a value for the standard

TABLE 10.5

No.	Site notation	Atom	Multiplicity	Wyckoff	Site symmetry	*x*	*y*	*z*	Occupancy
1	O1	O	32	e	.3m	0.238	0.238	0.2378	1.0
2	Cr1	Cr	16	c	.-3m	0	0	0	1.0
3	Mg1	Mg	8	b	-43m	3/8	3/8	3/8	1.0

entropy at 298.15 K of 152.2 ± 3.0 J/molK for $FeCr_2O_4$, some 6 J/molK greater than the previous calorimetric value.

Magnesium chromite, $MgCr_2O_4$, undergoes a structural transition from a cubic spinel structure [space group $Fd3^{-}m$, $a = 58.32768$ Å at 16 K] into a tetragonal distorted structure [space group $I41/amd$, $a = 55.89199$ Å, $c = 58.31677$ Å at 10 K], isotypic with Hausmannite, Mn_3O_4. This phase transition is unstable and takes place very close to or at the antiferromagnetic ordering temperature.

The vaporization of the system $MgO–Cr_2O_3$ was studied in a vacuum of 10^{-5} torr (10^{-3} N/m^2) at 1500–1700 °C using the Langmuir and Knudsen methods. It was found that the phases in the system vaporize nearly congruently and the logarithm of the vaporization coefficient, η_V, of $MgCr_2O_4$ increases linearly with increasing reciprocal temperature. The α-phase tends to unity at a temperature near the melting point (2525 ± 23 °C). The additivity rule can be applied to the Langmuir vaporization rates on the basis of the surface area ratios of the phases in the two-phase system $MgO–Cr_2O_3$. The enthalpies of vaporization of $MgCr_2O_4$ were 695.0 and 549.2 kcal/mol for the activated and equilibrium processes, respectively.

The rate of formation of single-crystal $MgCr_2O_4$ from single-crystal MgO and polycrystalline Cr_2O_3 in air can be described by the expression $k = 16.3 \exp(80{,}000 \pm 9000/RT)$ cm^2/s. The single crystal of $MgCr_2O_4$ grew by the advancement of (110) planes at the $MgCr_2O_4/Cr_2O_3$ interface. Two different methods were used for the calculation of interdiffusion coefficients of Cr^{3+} in MgO in the temperature range 1340–1640 °C. Wagner's analysis was applied for the calculation of interdiffusion coefficients in the $MgO–Cr_2O_3$ system where an intermediate spinel phase exists. A different mathematical treatment was derived for the calculation of interdiffusion coefficients at the saturation concentration of Cr_2O_3, in MgO single crystal.

In a similar study, the interdiffusion coefficients increased linearly with increasing mole fraction of Cr^{3+} cations and with increasing mole fraction of cation vacancies. For the concentration of 1-mol% Cr_2O_3 diffusing into MgO, the interdiffusion coefficient can be expressed as $D = 5 \cdot 50 \times 10^{-3} \exp(67{,}000 \pm 2000/RT)$ /cm^2/s. The enthalpy of activation was independent of cation vacancy concentration while the entropy of activation increased with increasing vacancy concentration. The measured interdiffusion coefficients were deduced to be the intrinsic diffusion coefficients for Cr^{3+} cations in MgO. Interdiffusion coefficients were in the range of $10^{-12} \times 10^{-9}$ /cm^2/s for the temperatures and concentrations studied. Theoretical formation energy of the Cr vacancy in $MgCr_2O_4$ showed negative values in the case of the oxidation limit of β-$MgCr_2O_4$, in good agreement with experimental results showing abundance of Cr vacancies when annealed in air. On the other hand, the formation energy of the Al vacancy in $MgAl_2O_4$ under the same condition is as large as 4.76 eV. This also corresponds well to the experimental fact that Al vacancy does not form alone when $MgAl_2O_4$ is processed in air.

Polycrystalline $MgCr_2O_4$ and $CuCr_2O_4$ samples were investigated by X-ray and neutron diffraction methods before and after irradiation by fast neutrons ($E_n \geq 1$ MeV) of effluence 2×10^{24}/m^2. It was found that, under irradiation of cubic magnesium and tetragonal copper chromites having the corresponding space groups O^7_h–$Fd3m$ and D^{19}_{4h}–$I4/amd$, different types of cations were redistributed over "allowed" and "forbidden" sites of the initial spinel lattice. As a result, the lattice periods and crystal symmetries were changed. The structures of the irradiated chromites may then be described in terms of the space group O^7_h–$Fm3m$. When annealed, the irradiated samples restored their initial crystal structures. The structural changes occurring on different stages of annealing were analyzed using X-rays.

This compound is a naturally occurring mineral and is found as black crystalline grains in Serpentinite (Fig. 10.7).

Small amounts of metal atom non-stoichiometry are possible in the $ZnCr_2O_4$ and $MgCr_2O_4$ spinels. The non-stoichiometry, though less than 2%, significantly impacts T_N and the nature of the magnetic correlations above T_N. The $Zn_{1+x}Cr_{2-x}O_4$ spinel is particularly sensitive. While stoichiometric $ZnCr_2O_4$ displays antiferromagnetic short-range correlations in the susceptibility above T_N, ferromagnetic correlations are observed in non-stoichiometric, hole-doped $Zn_{1+x}Cr_{2-x}O_4$. The $Mg_{1+x}Cr_{2-x}O_4$ spinels are less profoundly affected by non-stoichiometry, though significant changes are also observed. We contrast the magnetic properties of $Zn_{1+x}Cr_{2-x}O_4$ and $Mg_{1+x}Cr_{2-x}O_4$ ($x = 0$, 0.02, 0.04) with those of materials with the equivalent amounts of isovalent nonmagnetic Ga^{3+} substituted on the Cr^{3+} site to separate the effects of static site disorder and hole doping.

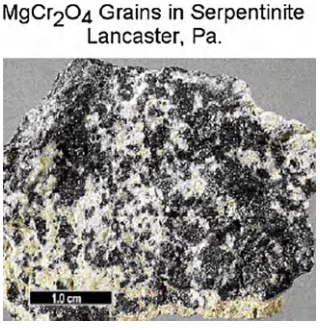

FIGURE 10.7

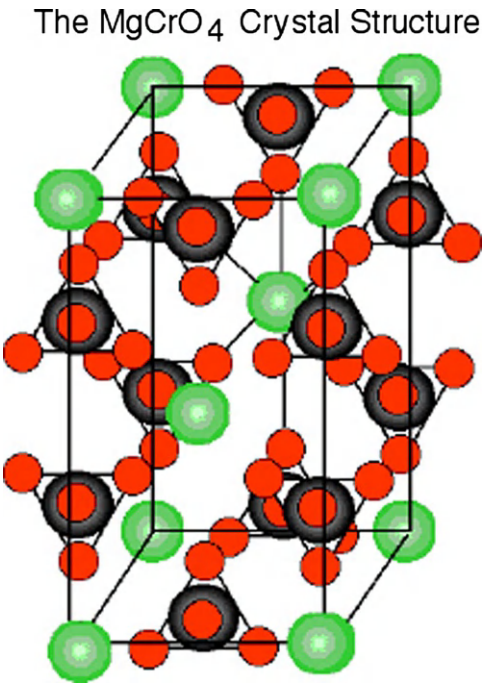

FIGURE 10.8

Magnesium chromite, $MgCr_2O_4$, undergoes a structural transition from a cubic spinel structure [space group $Fd\bar{3}m$, $a = 58.32768(4)$ Å at 16 K] into a tetragonal distorted structure [space group $I41/amd$, $a = 55.8919$ Å, $c = 58.31677$ Å at 10 K], isotypic with Hausmannite, Mn_3O_4. This phase transition takes place very close or at the antiferromagnetic ordering temperature. The structural and magnetic transitions are coincident and their order parameters (the tetragonal strain and Cr moment) scale with each other. The structural transition partially relieves magnetic frustration in the Cr network, although remaining frustration is evident from the low value (1.63 μbar) of the saturated Cr^{3+} moment.

No Cr^{4+}-containing compounds have been found in the $MgO–CrO_2$ system. It is expected that $MgCrO_3$ would have a perovskite structure, but this compound has never been synthesized. The possible +4 chromates, $MgCrO_3$, Mg_2CrO_4, Mg_3CrO_5, $MgCr_2O_5$, and the +5 chromates $MgCr_2O_6$, $Mg_2Cr_2O_7$ and $Mg_3Cr_2O_8$ remain unknown.

Magnesium chromate, $MgCrO_4$, containing Cr(VI) is dimorphic. Phase equilibria were determined for the systems $MgO–Cr_2O_3–O_2$, and $CdO–Cr_2O_3–O_2$ from 450 to above 850 °C and at oxygen pressures of from 2 to 3500 atm. The system, $MgO–CrO_3$, was not studied because of the low melting point of CrO_3. The magnesium and cadmium systems show three analogous phases: the low-temperature α-$MgCrO_4$ and α-$CdCrO_4$ (both with the $CrVO_4$ structure), the high-temperature β-$MgCrO_4$ and β-$CdCrO_4$ (both with the β-$MnMoO_4$ structure), and the spinels $MgCr_2O_4$ and $CdCr_2O_4$. The cadmium system contains an additional phase, Cd_2CrO_5, which is primitive monoclinic (Fig. 10.7).

This is a low-temperature form. The tetrahedra units are clearly seen. Cell parameters of α-$MgCrO_4$ are: $a = b = 5.0032$ Å, $c = 6.324$ Å, $\alpha = \beta = 90°$, $c = 113.396°$, cell volume = 145.28 Å^3, $Z = 4$. Cell occupancy is shown in Table 10.6.

IR spectra have been determined for $NiCrO_4$, α-$MgCrO_4$, α-$CdCrO_4$ (all crystallizing with the $CrVO_4$ structure); β-$MgCrO_4$, β-$CdCrO_4$ (both with the α-$MnMoO_4$, structure); and Cd_2CrO_5. The number of bands does not exceed the predictions of factor group analysis. It was shown that a dichromate-like spectrum can arise from chromate anions if the CrO_4 tetrahedron is sufficiently distorted.

β-$MgCrO_4$ is a high temperature dimorph with the structure of paramagnetic β-$MnMoO_4$, the stable phase at STP. It is monoclinic with lattice constants $a = 10.469 \pm 0.005$, $b = 9.516 \pm 0.005$, $c = 7.143 \pm 0.005$ Å, and $\beta = 106°17 \pm 6$, and space group $C2/m$. This crystal structure has been solved and refined by a combination of three-dimensional (3D) Patterson and Fourier series and by the method of least squares. Thousand eight hundred and seventy three independent integrated intensities were measured by PEXRAD; the final agreement factor between measured and calculated structure factors is 0.0574. Two crystallographically independent Mg atoms are surrounded by highly distorted oxygen octahedra; the Mg–O distance varies between 2.091 ± 0.006 and 2.252 ± 0.003 Å, with average length 2.164 Å. Two crystallographically independent Mg atoms are surrounded by slightly distorted oxygen tetrahedra, with Mg–O distances ranging from 1.724 ± 0.005 to 1.851 ± 0.004 Å, the average being 1.761 Å. The thermal vibrations were found to be significantly anisotropic.

TABLE 10.6

No.	Site notation	Atom	Multiplicity	Wyckoff	Site symmetry	*x*	*y*	*z*	Occupancy
1	O1	O	8	g	..m	0.251	0.475	1/4	1.0
2	O2	O	8	f	m..	0	0.241	0.026	1.0
3	Cr1	Cr	4	c	m2m	0	0.355	1/4	1.0
4	Mg1	Mg	4	a	2/m..	0	0	0	1.0

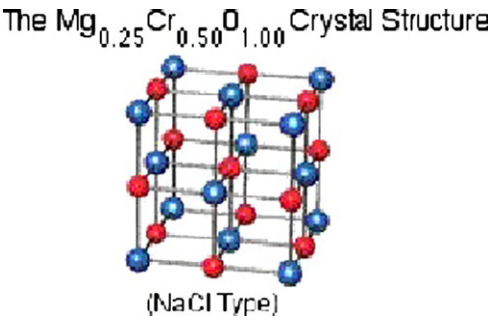

FIGURE 10.9

Another form of $MgCrO_4$ has the NaCl structure where a portion of the Mg^{2+} sites is occupied by divalent Mg-ions and the rest of the metal sites are occupied by $Cr^{6+} + Mg^{2+}$ ions.

The structure is shown in Fig. 10.9.

Cell parameters are: $a = b = c = 2.9338$ Å, $\alpha = \beta = \gamma = 60°$, cell volume = 17.86 Å^3, $Z = 8$. Cell occupancy is shown in Table 10.7.

α-$MgCrO_4$ is not stable and decomposes at 525–645 °C to form magnesium chromite: $4MgCrO_4 \Rightarrow 2MgCr_2O_4 + 2MgO + 3O_2$. The conclusive phase diagram has not been presented in the literature.

The effects of cobalt and manganese oxide doping on the surface and catalytic properties of Cr_2O_3/MgO system have been reinvestigated. The dopant concentration was changed between 1 and 5 mol% cobalt and manganese oxides. Pure and variously doped solids were subjected to heat treatment at 400 and 700 °C. The analytical techniques employed were XRD, nitrogen adsorption at −196 °C, catalytic conversion of isopropanol at 200–400 °C using flow technique and catalytic decomposition of H_2O_2 at 20–40 °C. The results revealed that the doping process of the system, processed at 400 or 700 °C, enhanced the solid–solid reactions between the catalyst constituents, yielding α-$MgCrO_4$, β-$MgCrO_4$ and $MgCr_2O_4$, respectively. Additionally, manganese and cobalt oxide doping for Cr_2O_3/MgO system increased its catalytic activity significantly in the decomposition of H_2O_2. The increase was found to be more pronounced in the case of manganese doping. Opposite results were observed in the case of isopropanol conversion, a mechanism which proceeds via dehydrogenation and dehydration reactions. The S_{BET} of the investigated system was found to decrease by increasing the dopant concentration. The doping process did not modify the activation energy of the catalyzed reaction, but rather changed the concentration of the catalytically active constituents without changing their energetic nature.

These chromate compounds have not yet found usage in Industry. Magnesium chromate is available commercially with the CAS number of 13423-61-5.

10.2.3. Calcium Chromium Compounds

No intermetallic compounds are known. Calcium oxide forms a limited number of compounds with the chromium oxides. The exact composition depends, to a great extent, on the oxidation state of the chromium ion, $Cr^{3,\ 4,\ 5\ or\ 6+}$. For the calcium chromate system, CaO–Cr_nO_m, only three crystal structures are readily available (Table 10.8).

Only those based on CaO–Cr_2O_3 have been investigated. The reason is that the trivalent chromium oxide melts at 2435 °C whereas CrO_3 melts at 197 °C and boils at 251 °C. The phase diagram for the CaO–Cr_2O_3 system is shown in Fig. 10.10.

In the solid-state reaction between CaO and Cr_2O_3, only the $CaCrO_4$ and $Ca_5(CrO_4)_3$ compounds can be produced. The former melts incongruently at 1073 °C to form $CaCr_2O_4$ and the latter melts congruently at 1275 °C, respectively. Only the latter compound is stable

TABLE 10.7

No.	Site notation	Atom	Multiplicity	Wyckoff	Site symmetry	*x*	*y*	*z*	Occupancy
1	Mg	Mg	8	c	-43m	1/4	1/4	1/4	0.04
2	O	O	4	b	m-3m	1/2	1/2	1/2	1.0
3	M	0.75Cr + 0.25Mg	4	a	m-3m	0	0	0	0.67

TABLE 10.8

No.	Compound	No. of elements	Structure type	Point group	Space group
1	$Ca_5(CrO_4)_3$	3	$Ca_5(CrO_4)_3$	oP80	*Pnma*
2	$CaCr_2O_4$	3	CaV_2O_4	oP28	*Pnma*
3	$CaCrO_4$	3	$CrVO_4$	oS24	*Cmcm*

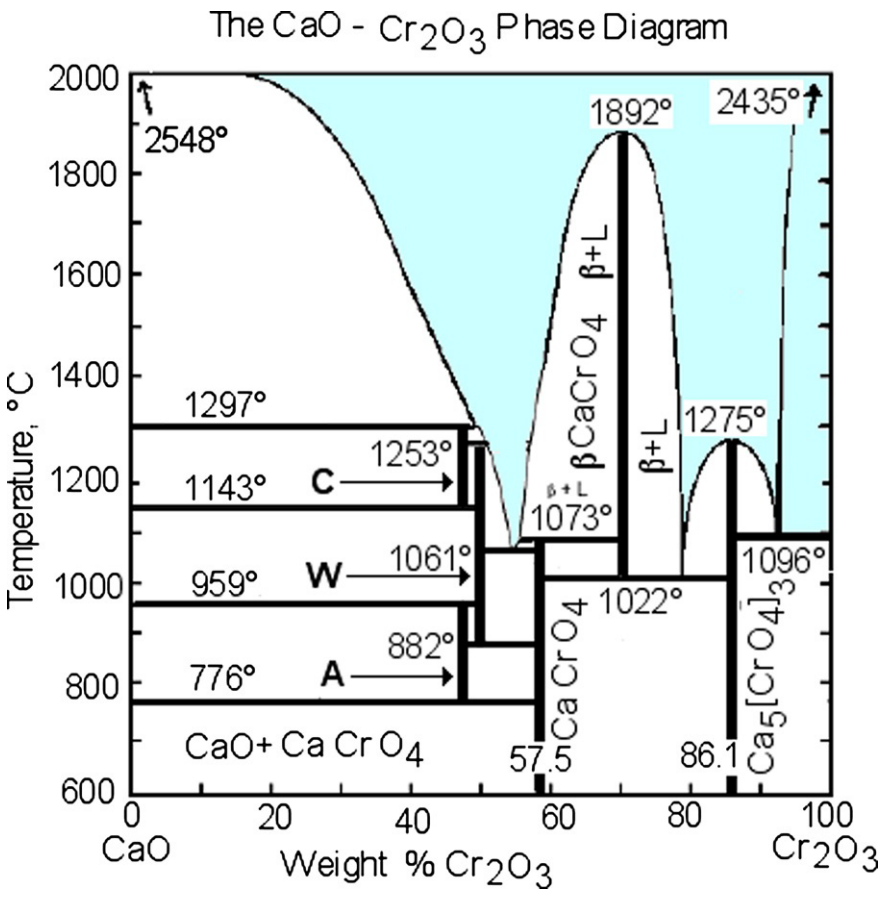

FIGURE 10.10

at room temperature while the other compounds (herein labeled as "a", "w" and "c") are metastable at rather low temperatures 776 ⇒ 959 °C, 882 ⇒ 1253 °C and 1143 ⇒ 1297 °C, respectively. Their structures have not been thoroughly investigated. (**N.B.**-these results have not been verified but are those of a specific investigation published in 1995).

Note that $CaCrO_4$ contains Cr^{6+} ions whereas $Ca_5(CrO_4)_3$ contains Cr^{3+} ions. The reactions that form these compounds are:

$$5CaO + 3Cr_2O_3 \Rightarrow Ca_5(CrO_4)_3 \text{ (neutral atmosphere)}$$

$$4CaO + 6Cr_2O_3 + 3O_2 \Rightarrow 4CaCrO_4 \text{ (oxidizing atmosphere)}$$

At 1073 °C, $CaCrO_4$ decomposes to form:

$$4CaCrO_4 + \text{heat} \Rightarrow 2\beta\text{-}CaCr_2O_4 + 2CaO + 3O_2$$

The high temperature form, β-$CaCr_2O_4$ contains the Cr^{3+} ion. For the trivalent Cr(III) oxide system, only **calcium chromite**, $CaCr_2O_4$, has been meticulously studied. It is dimorphic and the structure of the high temperature form, β-$CaCr_2O_4$ is shown in Fig. 10.11. Two unit cells are shown. It consists of four chromium tetrahedra, two of which are joined by face-sharing (edge-sharing) and the other two joined by point-sharing.

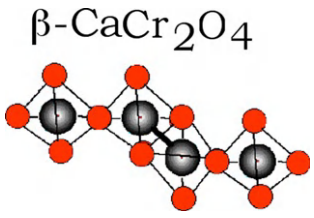

FIGURE 10.11

Cell constants are: $a = 2.99$ Å, $b = 9.07$ Å, $c = 10.61$ Å, $\alpha = \beta = \gamma = 90°$, cell volume $= 287.74$ Å^3, $Z = 4$ (Fig. 10.12).

Cell occupancy is shown in Table 10.9.

In another study, single crystals of high temperature modification, β-$CaCr_2O_4$, were investigated by X-ray goniometer data ($a = 11.059$, $b = 5.836$, $c = 5.114$ Å, space group *D–Pmmn*). β-$CaCr_2O_4$ is isotypic with $SrCr_2O_4$. A mass of residue including needle-like β-$CaCr_2O_4$ crystals was obtained by heating a powder mixture consisting of $CaCO_3$ and Cr_2O_3 on graphite powder in an alumina crucible with holes. The needle-like β-$CaCr_2O_4$ crystals were separated from the mass by hydrochloric acid. The yield of the crystals increased with increasing temperature above 1500 °C and reached about 41 wt%

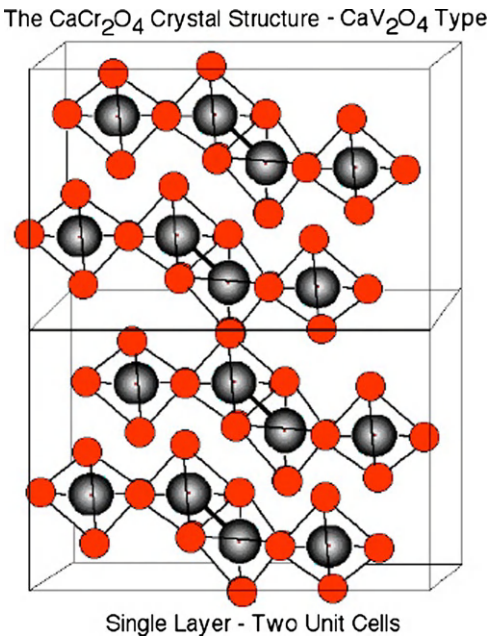

FIGURE 10.12

when heated at 1700 °C for 4 h. Then the average length and diameter of the crystals were 2.5 mm and 118 μm, respectively; the largest crystal was 3.8 mm in length and 187 μm in diameter. Needle axis of the crystals was the *c*-axis. The low temperature form, α-$CaCr_2O_4$, has the structure shown in Fig. 10.13.

CrO_6 octahedra are shown in blue and green colors for the inequivalent Cr1 and Cr2 sites. The Ca^{2+} ions are shown as light gray spheres. The red thin line marks the crystallographic unit-cell. The middle section shows the projection of the CrO_2 layer onto the *bc*-plane. Colored thick lines shows the connectivity between first-neighbor Cr ions. The corresponding interatomic distances are shown. On the right is a depiction of the face-sharing octahedra and their relationship in the structure.

In this compound, in which the unusual topology of the Cr^{3+} magnetic lattice can be described as a network of triangular "zigzag" ladders with legs parallel to *c*, a complex antiferromagnetic ordering with an unequal propagation vector $\mathbf{k} = (0, 0, q)$ ($q \sim 0.477$ at 1.5 K) is evidenced below $T_N = 21$ K. This complex magnetic ordering can be described as a honeycomb-like arrangement of cycloids, running along *c*, and presenting a unique pattern

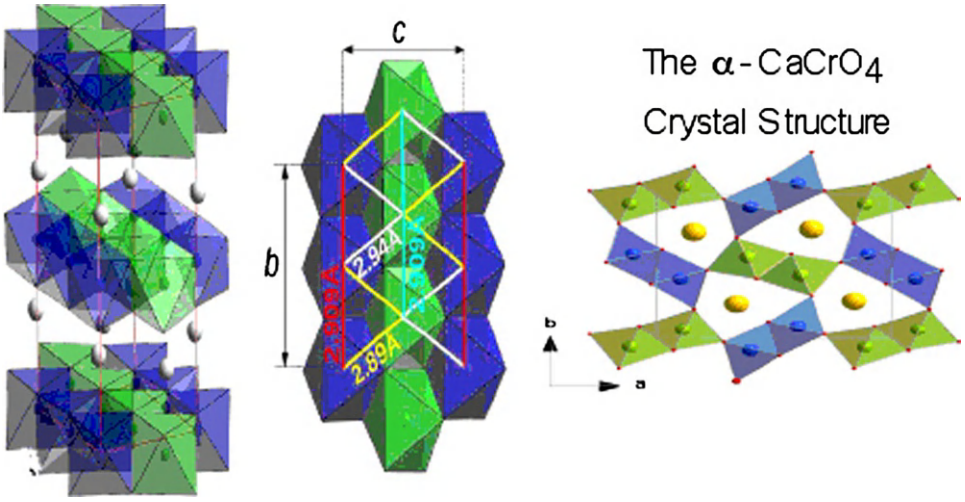

FIGURE 10.13

TABLE 10.9

No.	Site notation	Atom	Multiplicity	Wyckoff	Site symmetry	*x*	*y*	*z*	Occupancy
1	O1	O	4	c	.m.	0.071	1/4	0.078	1.0
2	Cr1	Cr	4	c	.m.	0.077	1/4	0.394	1.0
3	Ca1	Ca	4	c	.m.	0.242	1/4	0.65	1.0
4	O2	O	4	c	.m.	0.289	1/4	0.352	1.0
5	O3	O	4	c	.m.	0.387	1/4	0.016	1.0
6	O4	O	4	c	.m.	0.47	1/4	0.775	1.0
7	Cr2	Cr	4	c	.m.	0.568	1/4	0.609	1.0

of staggered chirality. The crystal structure of α-$CaCr_2O_4$ was first reported by Pausch et al. It crystallizes with orthorhombic symmetry, in the space group *Pmmn*. There are two inequivalent Cr sites, Cr1 located at (0,0,0), having a single symmetry and Cr2 at position (0.5047,0,0.497) located on a mirror plane, each site possessing a multiplicity of 4. The Cr ions are six-coordinated by oxygen in a distorted octahedral configuration. The octahedra share edges to form CrO_2 layers in the *bc*-plane, leaving a weakly distorted triangular lattice as shown by the different interatomic distances marked in Fig. 10.13. The CrO_2 layers, separated by Ca^{2+} ions, are stacked along the *a*-axis of the orthorhombic unit-cell. The in-plane magnetic interactions between Cr can be mediated either by direct exchange through the t_{2g} orbitals or by Cr–O–Cr superexchange interactions. The interactions between layers can be mediated by super–super exchange interactions through two oxygen atoms, but are expected to be much weaker due to the large interatomic Fe–Fe distance (5.52 Å at 1.5 K). This compound shows a weak inverse magnetic susceptibility with a quasi-linear regime above 250 K. A linear fit of the data with a Curie–Weiss law in the temperature range 250 K to 350 K under 3.0 T yields the following diagram (Fig. 10.14).

In another paper, the ferroelectricity of α-$CaCr_2O_4$ in the incommensurate helical magnetic phase (i.e. below T_N, 43 K) has been confirmed by pyroelectric measurements. Magnetoelectric and magnetodielectric coupling exist below T_N and are proportional to the square of magnetic field. From symmetry analysis, it was suggested that the presence of an external electric field destabilizes the symmetrical 2221′ phase and stabilizes 21′ symmetry. This provides a unique system in which the polarization varies as the *fourth-degree* of the order-parameter amplitude and exhibits a vanishingly small value below the first-order transition at T_N, as observed experimentally. This compound crystallizes in an orthorhombic-layered structure with triangular sheets of CrO_2 separated by Ca^{+2} and mostly resembles "Delafossite-$CuCrO_2$" with a small distortion.

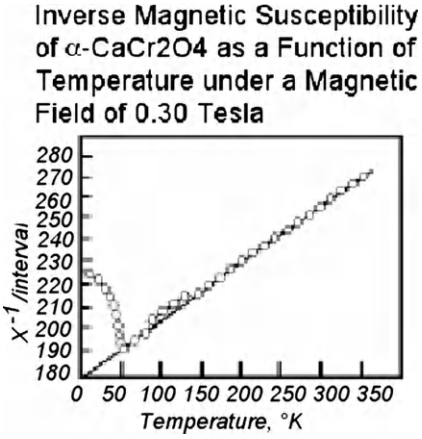

FIGURE 10.14

Recently, the magnetic properties of α-$CaCr_2O_4$ have been investigated in detail. It exhibits a long-range antiferromagnetic incommensurate helical magnetic phase below $T_N = 43$ K that has a magnetic propagation wave vector value of $q = (0,0.3317,0)$. Neutron diffraction data show that the plane of rotation of spins is perpendicular to the wave vector. In materials with incommensurate phases, the lattice modulation is generally connected with a spatially varying electric polarization (e.g. Rb_2ZnCl_4, $NH_4)_2BeF_4$ and K_2SeO_4). At low temperature, these materials exhibit a first-order phase transition to a ferroelectric phase. Similarly, ferroelectricity has been reported in $TbMnO_3$, $YBaCuFeO_5$ and $CuFeO_2$ in the incommensurate magnetic phase. It has been determined that α-$CaCr_2O_4$ fits into this category of quasi-magnetic materials.

In the CaO–CrO_2 system, compelling evidence that $CaCrO_3$ is a rare case of a metallic and antiferromagnetic transition-metal oxide with a 3D electronic structure was revealed. Local spin density approximation calculations correctly describe the metallic behavior as well as the anisotropic magnetic ordering pattern of *C* type. The high Cr valence state induces via sizable pd hybridization remarkably strong next-nearest-neighbor interactions stabilizing this ordering. The subtle balance of magnetic interactions gives rise to magnetoelastic coupling, explaining pronounced structural anomalies observed at the magnetic ordering transition. The electronic structure of the perovskite oxide $CaCrO_3$ using valence-band, core-level, and Cr 2p-3d resonant photoemission spectroscopy (PES) was examined. Despite its antiferromagnetic order, a clear Fermi edge characteristic of a metal with dominant Cr 3d character is observed in the valence-band spectrum. The Cr 3d single-particle density of states are spread over 2 eV, with the photoemission spectral weight distributed in two peaks centered at ~1.2 and 0.2 eV below *EF*, suggestive of the coherent and incoherent states resulting from strong electron–electron correlations. Resonant PES across the Cr 2p-3d threshold identifies a "two-hole" correlation satellite and yields an on-site Coulomb energy $U \sim 4.8$ eV. The metallic DOS at *EF* is also reflected through the presence of a well-screened feature at the low binding energy side of the Cr 2p core-level spectrum. X-ray-absorption spectroscopy at Cr $L_{3,2}$ and 0 K edges exhibits small temperature-dependent changes that point toward a small change in Cr–O hybridization. The Cr 2p core-level spectrum can be reproduced using cluster model calculations that include a charge transfer from the metallic screening channel at *EF*. The overall results indicate that $CaCrO_3$ is a strongly hybridized antiferromagnetic metal, lying

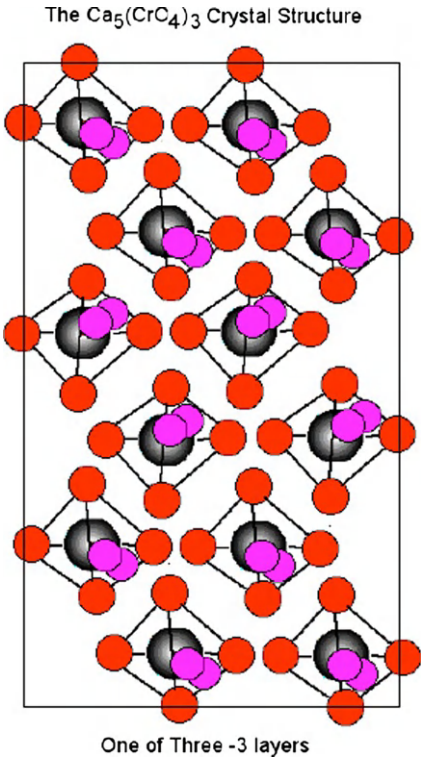

FIGURE 10.15

in the regime intermediate to Mott–Hubbard and charge-transfer systems.

The compound, penta-calcium tri-chromate, $Ca_5(CrO_4)_3$, has an apatite-like structure. The arrangement of atoms in the unit cell is shown in Fig. 10.15.

The structure consists of isolated CrO_4 tetrahedra associated with pairs of Ca^{2+} cations. Cell parameters are: $a = 6.733$ Å, $b = 10.334$ Å, $c = 16.097$ Å, $\alpha = \beta = \gamma = 90°$, cell volume = 1,120.01 Å^3, $Z = 4$.

Cell occupancy is shown in Table 10.10.

The crystal structures of similar compounds, $Ca_5Cr_3O_{12}$ and $Ca_5Cr_{1.8}Si_{1.2}O_{12}$, the chromium analogues of silicocarnotite, $Ca_5P_2SiO_{12}$, have been determined. Both compounds were grown at 1250 °C and analyzed by electron microprobe analysis. Diffraction data collection was accomplished on spherically ground crystals that were both orthorhombic with space group *Pnma*. The charge-balance requirements as well as site-occupancy refinement of the Si-containing compound pointed strongly to the presence of both tetravalent and hexavalent chromium in tetrahedral sites. The Si is located together with tetravalent Cr in a general position, whereas the hexavalent Cr ion is situated on a mirror plane. The calcium atoms are located in seven-, eight-, and nine-coordinated sites. The presence of vacant channels of 3.5 Å diameters perpendicular to (100) is a feature of this structural type. Its relation to the apatite and glaserite structures was also shown.

The system CaO–CrO, processed in air, has been reinvestigated and the existence of intermediate phases with chromium in the oxidation state $\geq 3^+$ (such as $Ca_5Cr_3O_{12}$, $Ca_3(CrO_4)_2$, and $Ca_5(CrO_4)_3$) were confirmed. Under reducing conditions these phases are not stable. A metastable, polymorphic form of calcium chromite, δ-$CaCr_2O_4$, has been observed.

In the CaO-rich section of the CaO–Al_2O_3–Cr_2O_3 system, a ternary intermediate phase, "Chromehaüyne", $Ca_4[(Al,Cr^{3+})_6O_{12}](Cr^{6+}O_4)$, coexists with the calcium chromate and calcium aluminate phases. In air, low melting temperatures are preserved in all assemblages containing the calcium chromate phases. Under

TABLE 10.10

No	Site notation	Atom	Multiplicity	Wyckoff	Site symmetry	*x*	*y*	*z*	Occupancy
1	O5	O	8	d	1	0.039	0.119	0.0343	1.0
2	O7	O	8	d	1	0.044	0.658	0.355	1.0
3	Ca3	Ca	8	d	1	0.179	0.608	0.1668	1.0
4	O3	O	8	d	1	0.187	0.034	0.4858	1.0
5	O4	O	8	d	1	0.271	0.151	0.2742	1.0
6	TET1	Cr	8	d	1	0.361	0.0713	0.3709	1.0
7	Ca2	Ca	8	d	1	0.375	0.092	0.0673	1.0
8	O6	O	8	d	1	0.427	0.508	0.268	1.0
9	TET2	Cr	4	c	.m.	0.025	1/4	0.5773	1.0
10	Ca1	Ca	4	c	.m.	0.035	1/4	0.1745	1.0
11	O1	O	4	c	.m.	0.274	1/4	0.5839	1.0
12	O2	O	4	c	.m.	0.425	1/4	0.0709	1.0

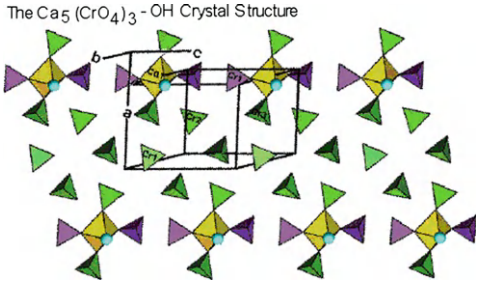

FIGURE 10.16

reducing conditions a new ternary phase, $Ca_6Al_4Cr_2O_{15}$, coexists with CaO, $CaCr_2O_4$, chrome-haüyne, and calcium aluminate phases. The influence of chromium oxide additions on the solidus temperatures of the $CaO–Al_2O_3$ system is insignificant.

The calcium chromate hydroxyl apatite, $Ca_5(CrO_4)_3OH$, was synthesized, and its electrical conductivity and chemical stability were investigated. It has the structure shown in Fig. 10.16.

Lanthanum chromite, $La_2Cr_2O_6$, has been used as a separator in solid oxide fuel cells.

Based on experimental results, detrimental effects of the apatite formation on the surface of lanthanum chromite separators in solid oxide fuel cells have been discussed. The mean Cr–O distance for tetrahedral coordination is 1.66 Å. In an attempt to replace the OH-group with chlorine, a new phase with the composition of Ca_2ClCrO_4 and the unit cell dimensions of $a = 6.237$ Å, $b = 7.122$ Å and $c = 11.045$ Å (orthorhombic) was found. Unit cell dimensions of $Sr_3(CrO_4)_2$, $Ba_3(CrO_4)_2$, $Sr_5Cl(CrO_4)_3$, $Ba_5Cl(CrO_4)_3$, and Sr_2ClCrO_4 were also given.

Calcium chromate ($CaCrO_4$) is a bright yellow solid. It normally occurs as the dihydrate. Calcium chromate loses water at 200 °C. Calcium chromate reacts with organic matter or reducing agents to form Cr(III). Calcium chromate will react explosively with hydrazine. If mixed with boron and ignited, calcium chromate will burn violently. It occurs naturally as the mineral "Chromatite". The compound, $CaCr(VI)O_4$ is metastable as shown in the above phase diagram which was constructed from studies of CaO and Cr_2O_3. No phase diagram for $CaO–CrO_3$ is known (CrO_3 melts at 197 °C). $CaCrO_4$ is an important cathode material in thermally activated electrochemical cells, and it is also often used in many industrial process as an intermediate compound formed in the system of Ca–Cr–O.

$CaCrO_4$ crystallizes into a zircon-type structure of tetragonal lattice with space group $I41/amd$ ($Z = 4$) at ambient conditions. The structure of zircon-type $CaCrO_4$ is built from isolated and slightly distorted CrO_4 tetrahedral units, which are connected with CaO_8 dodecahedra by edge- and corner-sharing. Both these units are shown in Fig. 10.17.

The infrared spectra of the chromates (V) of calcium, strontium and barium have been measured from 2000 to 400/cm. The results, and those for the corresponding chromates (VI), are interpreted in terms of the site symmetry of the anion. It has been shown that, in the chromates(VI), the anion is not strongly perturbed. For the chromate (V) ion, the stretching force constant of the chromium (V)—oxygen bond is 4·94 mdyn/Å and the stretch–stretch interaction constant is 0·22 mdyn/Å. The effect of the non-bonding d electron of chromium (V) on the metal to oxygen bonding was discussed. Pressure-related structural characteristics of $CaCrO_4$ with the zircon-type structure ($I41/amd$) were investigated at ambient pressure in a diamond anvil cell (DAC) up to 29.1 GPa at room temperature. The electromagnetic sources were synchrotron radiation and XRD in an energy-dispersive mode. A sluggish first-order structural phase transition to a scheelite-type phase ($I41/a$) was observed at 5.7 GPa. The lattice parameters of both phases at different pressures were calculated.

Heat capacities of calcium chromate ($CaCrO_4$) and calcium chromite (β-$CaCr_2O_4$) were measured at elevated temperatures using the differential scanning calorimetry. The measured heat capacities of $CaCrO_4$ and β-$CaCr_2O_4$ as a function of temperature (measured in J/mol K) are expressed as C_p ($CaCrO_4$) =

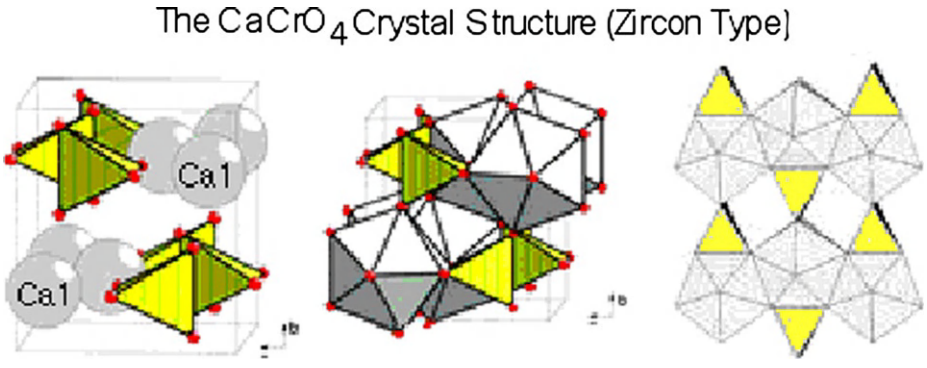

FIGURE 10.17

$127.92 + 35.73 \times 10^{-3}T - 2.257 \times 10^{6}/T^{-2}$ (298–1123 K), $C_p(\beta\text{-}CaCr_2O_4) = 166.69 + 18.33 \times 10^{-3}T - 2.92 \times 10^{6}T^{-2}$ (298–1203 K), respectively.

It is known, for example, that trivalent chromium Cr(III) compounds are generally insoluble, whereas hexavalent chromium Cr(VI) forms soluble compounds. The latter are extremely poisonous to the human body. It is also well established that the most damaging ingestion pathway for Cr(VI) is inhalation. Consequently, Cr(VI)-contaminated wastes should not be incinerated. Another method of disposing of such wastes would be to place them in landfills, but, in time, they are likely to leach and may contaminate ground water resources. A better solution is to contain the wastes in ordinary Portland cement, where heavy-atom contaminants are typically immobilized in a high-strength monolithic cement waste matrix. Depending on the type of the metal ions, stabilization can be through chemisorption, precipitation, chemical-incorporation in the hydrated cement phases, physical entrapment, or a combination of these. In an effort to dispose of such compounds, it was found that when Cr(VI) solution is added to the Portland cement, soluble $CaCrO_4 \cdot 2H_2O$ forms within the first day of reaction. However, as more calcium comes into the pore solution from dissolution of the tricalcium silicate component of the Portland cement, the new stable product formed is $Ca_2CrO_5 \cdot 3H_2O$. In the cement–Cr(VI) waste matrix, $Ca_2CrO_5 \cdot 3H_2O$ is formed according to:

$$Ca(OH)_2 + CaCrO_4 \cdot 2H_2O \Rightarrow Ca_2CrO_5 \cdot 3H_2O$$

The 3D structure is shown in Fig. 10.18.

It consists of double layers CrO_4 tetrahedra and CaO_8 polyhedra that run parallel to the (001) face of the unit cell. Within each double layer, the distance between the Ca and the Cr planes is 3.0858 Å. Each chromium atom is coordinated with four oxygen atoms, forming tetrahedra whose O1–O3–O1 base is oriented (quasi), parallel to the (001) face of the unit cell.

The coordination sphere of Ca, including the values of the Ca–O bond lengths, is shown in Fig. 10.19. Oxygen O4, O5, and O6 correspond to the water molecules and are coordinated with calcium atoms as hydroxyls, whose presence was previously verified by infrared OH stretching vibrations. The presence of Ca–O–H bonds might explain the incongruent dissolution of dicalcium chromate.

The fact that $CaCrO_4$ decomposes with loss of volatile CrO_3 if heated too high in temperature has been utilized to prepare interconnects [one of the key components for solid oxide fuel cells (SOFCs)]. The perovskite lanthanum chromite ($LaCrO_3$) substituted with alkaline earth metals (Ae = Ca or Sr) has been widely accepted as the major candidate for fabricating interconnect material in present generation SOFCs. It satisfies most of the requirements for construction of SOFC, such as high electronic and negligible ionic conductivity, chemical stability at both oxidizing and reducing atmospheres at high temperatures as well as chemical and thermomechanical compatibility with other cell components under operating conditions.

The compound, $La_{0.7}Ca_{0.3}Cr_{0.97}O_3$, with a slight Cr deficiency of 0.03 was prepared by an auto-ignition process. Relatively low-temperature (1150–1300 °C) sintering characteristics and electric conductivities were achieved. The material reached 94.3% relative density when heated at 1200 °C for 5 h in air, which is about 200 °C lower than that of with no Cr deficiency. XRD results indicated that a pure perovskite phase was formed after sintering within the temperature range of 1150–1300 °C. The sample sintered at 1250 °C had the maximum conductivity of 62.0 S/cm at 850 °C in air, which is about 2.6 times as high as that of $La_{0.7}Ca_{0.3}CrO_3$ with no Cr deficiency. When sintered in pure H_2, it achieved the maximum electrical conductivity of 3.3 S/cm at 850 °C compared to a sample sintered at >1200 °C. The TEC of the material was about 11.4×10^{-6} /K, which is very much

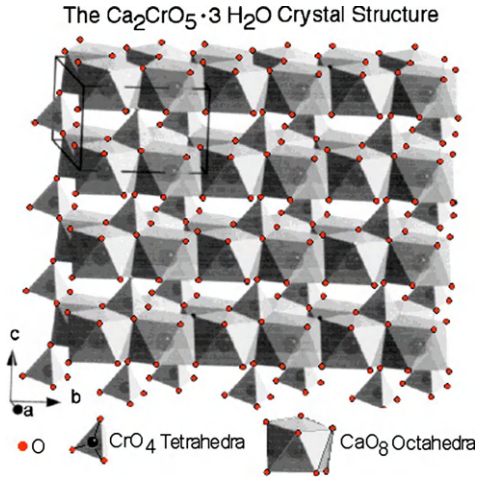

FIGURE 10.18

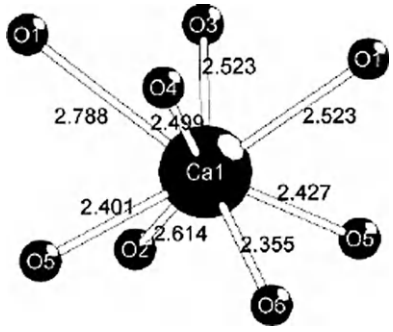

FIGURE 10.19

comparable to that of the other commonly used SOFC components.

Calcium chromate is supplied commercially with CAS No. 12013-31-9, calcium dichromium tetraoxide.

10.2.4. Strontium Chromium Compounds

Strontium oxide forms a number of compounds with the chromium oxides. The exact composition depends, to a great extent, on the oxidation state of the chromium ion, $Cr^{3,\ 4,\ 5\ or\ 6+}$. For the strontium chromite–chromate system, only two crystal structures are found as shown in Table 10.11.

For the trivalent Cr(III) oxide system, under neutral conditions, only $SrCr_2O_4$ is known.

For the $SrO–Cr_2O_3–O_2$ system, four compounds have been found to be stable in air at ambient temperature. However, a permanent phase diagram has not been established since these compounds are metastable and the melting points determined depend, to a great extent, upon the conditions under which they are being melted. However, several compositions involving the $SrO–CrO_2$ system are known. Some are antiferromagnetic.

The phase relations involving various oxides in the system Sr–Cr–O at 1250 K in air have been determined by equilibrating samples representing 17 compositions inside the ternary and subsequent phase identification in quenched samples. Optical and scanning electron microscopes (SEM) were used in conjunction with XRD to identify phases; the composition of each phase was verified using energy dispersive analysis of X-rays (EDX). Four stable ternary oxides, $SrCrO_4$, $Sr_3Cr_2O_8$, Sr_2CrO_4, and $SrCr_2O_4$, were identified. All the compounds, except $Sr_3Cr_2O_8$, were found to be stoichiometric within the accuracy of EDX. X-ray absorption near-edge structure (XANES) analysis showed that the average valence of Cr in $Sr_3Cr_2O_8$ is +5.2, suggesting the presence of mixed valence states in this compound. Only one of the ternary oxides, $SrCr_2O_4$, was found to coexist with Cr metal since it contains Cr^{3+}. The compounds containing Cr^{6+}, $SrCrO_4$ and $Sr_3Cr_2O_8$, were stable in pure oxygen.

The standard Gibbs energy of formation of $SrCrO_4$ was determined as a function of temperature in the range from 950 to 1280 K using a solid-state cell incorporating single-crystal SrF_2 as the electrolyte. The oxygen potential corresponding to the three-phase equilibria involving $SrCrO_4$, $Sr_3Cr_2O_8$, and Cr_2O_3 was measured from 1080 to 1380 K using a cell with yttria-stabilized zirconia as the solid electrolyte and pure oxygen gas at a pressure of 0.1 MPa as the reference electrode. The standard Gibbs energy of formation of $Sr_3Cr_2O_8$ was derived from the oxygen potential. The results can be represented by the following equations:

$$4SrO + 2Cr_2O_3 + O_2 \Rightarrow 4SrCr_2O_4$$

$$\Delta G^0\,(J/mol) = -273.825 + 131.57\,T/K$$

$$3SrO + Cr_2O_3 + O_2 \Rightarrow Sr_3Cr_2O_8$$

$$\Delta G^0\,(J/mol) = -472.345 + 184.20\,T/K$$

In another study, seven (7) compounds, $SrCrO_4$, $SrCr_2O_7$, $Sr_3Cr_2O_8$, $SrCrO_3$ Sr_2CrO_4, $Sr_2Cr_2O_5$, Sr_2CrO_4 and $SrCr_2O_4$ have been reported in the system Sr–Cr–O. The structure of $SrCrO_4$ belongs to the monoclinic system. Space group $= P2_1/n$ ($lt4$) with $a = 7.083$ Å, $b = 7.388$ Å, $c = 6.771$ Å, $\beta = 103.43°$. It is isostructural with $PbCrO_4$. The compound, $SrCr_2O_7$, is in isomorphism with $PbCr_2O_7$ and belongs to the tetragonal system, space group $P4_3/nmc$ (137), with $a = 11.193$ Å, and $c = 9.480$ Å. It is a low temperature phase in this system. The phase, $Sr_3Cr_2O_8$ is trigonal with space group $R\bar{3}m$ and has the hexagonal cell parameters of $a = 5.569$ Å, $c = 20.171$ Å. It is isostructural with $Ba_3(PO_4)_2$. It contains the unusual ion, Cr^{5+}. $SrCrO_3$ is a high-pressure phase formed from SrO and CrO_3 with Cr^{4+} in an octahedral coordination. The compound, Sr_2CrO_4, is orthorhombic, space group $P2_1nb$ (33) with $a = 10.007$ Å, $b = 14.194$ Å, $c = 5.809$ Å at ambient temperature. Under high pressure of 6.6×10^5 Pa and 1000 °C, this structure transforms to the K_2NiF_4 type with $a = 3.821$ Å and $c = 12.422$ Å. This transformation is accompanied by a 12% decrease in cell volume and a change in Cr-coordination of tetragonal to octahedral, i.e. $CrO_4 \Rightarrow CrO_6$. The reaction of Sr_2CrO_4 and CrO_3 at high pressure forms $Sr_2Cr_2O_7$. This compound has a body-centered tetragonal cell with $a = 3.822$ Å and $c = 20.124$ Å.

Strontium chromate ($SrCrO_4$) melts in pure oxygen (0.1 MPa) at 1556 K (1283 °C) and is of interest as an additive to $LaCrO_3$ for use in current-day SOFCs. The thermodynamic stabilities of $CaCrO_4$, $BaCrO_4$ and $SrCrO_4$ are of interest to materials scientists and also in nuclear technology because these are the possible compounds of fission product-cladding chemical interaction under conditions of accident in fast nuclear reactors. Though there are some reports on the thermodynamic stabilities of $CaCrO_4$ and $BaCrO_4$ obtained by the fluoride electrolyte electromotive force (e.m.f.)

TABLE 10.11

No.	Compound	No. of elements	Structure type	Point group	Space group
1	Sr_2CrO_4	3	Sr_2CrO_4	oP56	$Pna2_1$
2	$SrCrO_3$	3	$CaTiO_3$	CP5	$Pm\text{-}3m$

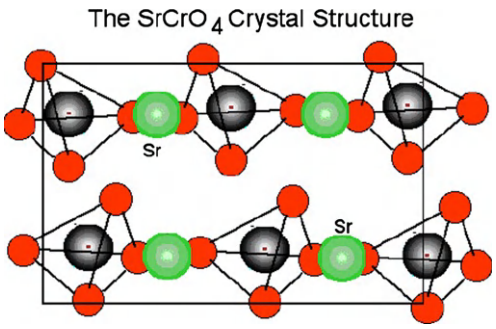

FIGURE 10.20

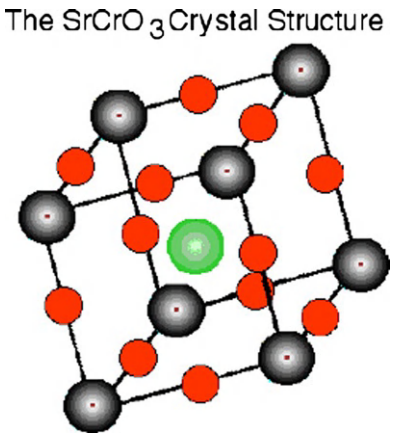

FIGURE 10.21

method, there is no reliable thermodynamic information on $SrCrO_4$. Hence the e.m.f. of the galvanic cells Pt, $O_2(g)/CaO$, $CaF_2/CaF_2/AF_2$, $ACrO_4$, Cr_2O_3/Pt, $O_2(g)$ was studied under an atmosphere of pure oxygen at a pressure of 0.1 MPa over the ranges 788–1070, 851–1116 and 850–1168 K where A is Ca, Sr and Ba, respectively. From the cell e.m.f. data, the standard Gibbs energies of formation ΔG_f^0 of the chromates, according to the reaction $AO(s) + Cr_2O_3(s) + O_2(g) \Rightarrow ACrO_4(s)$ were derived to be:

$$\Delta G_f^0(CaCrO_4) = -1356.6 + 0.31641T(\pm 0.63)\text{kJ/mol},$$
$$\Delta G_f^0(SrCrO_4) = -1359.1 + 0.32998T(\pm 0.30)\text{kJ/mol},$$
$$\Delta G_f^0(BaCrO_4) = -1323.7 + 0.31159T(\pm 0.34)\text{kJ/mol}$$

Both $SrCrO_4$ and $BaCrO_4$ have the structure shown in Fig. 10.20.

It consists of CrO_4 tetrahedra aligning in the "*ab*" direction of lattice (a single layer is shown here). Lattice parameters are: space group $P2_1/n$, $Z = 4$; $a = 7.065$ Å, $b = 7.375$ Å; $c = 6.741$ Å; $\beta = 103.08°$. In $SrCrO_4$ the average Cr–O bond is 1.626 Å. The largest bond length distortions within the XO_4 tetrahedra were found in $SrCrO_4$. α-$PbSeO_4$ (Rooseveltite), $BiPO_4$, $PbCrO_4$ (Crocoite), α-$PbSeO_4$, $SrCrO_4$, $SrSeO_4$, and $ThSiO_4$, exhibit a nine-coordination geometry. This geometric form is best described as a pentagonal interpenetrating tetrahedral polyhedron.

A number of compounds based upon the system SrO–CrO_2 are known in which the Cr^{4+} ion is involved. An overview of a series of experiments involving increasingly complex oxides synthesized from CrO_2, under high-pressure and high-temperature conditions, having a space group of Cl in octahedral coordination was published. Although the emphasis was on the structure and microstructure of the compounds as obtained from XRD and transmission electron microscopy (TEM) and diffraction, attention was also given to their interesting electronic and magnetic properties. The study was complemented with an electron energy loss spectroscopic analysis of the different phases. These are the cubic perovskite $SrCrO_3$, the orthorhombic perovskite $CaCrO_3$, the solid solution $Sr_{1-x}Ca_xCrO_3$, the Ruddlesden–Popper-type $Sr_3Cr_2O_7$, the family $CrSr_2RECu_2O_8$ (RE = rare earth), a compositionally modulated perovskite $PbCrO_3$, and the misfit layer oxide $Sr_2O_2[CrO_2]_{1.85}$. The compound, strontium chromite, $SrCrO_3$, containing tetravalent chromium, Cr^{4+}, has the $CaTiO_3$ structure shown in Fig. 10.21.

It contains Sr^{2+} cations in a body-centered cubic lattice, surrounded by CrO_3 units that are shared by other unit cells.

The structure and magnetic properties of Sr_2CrO_4 and Ba_2CrO_4 were compared with their vanadium analogues β-Sr_2VO_4 and β-Ba_2VO_4. Unlike isostructural β-Sr_2VO_4 that contains the $V_2O_8^{8-}$ dimer, Sr_2CrO_4 contains truly isolated CrO_4^{4-} tetrahedra and its magnetic behavior can be best described as a dimerized chain. Ba_2CrO_4 and Ba_3CrO_5 also contain isolated CrO_4^{4-} tetrahedra. Ba_2CrO_4 is paramagnetic down to 5 K. Ba_3CrO_5 undergoes long-range magnetic order at 8 K, a temperature range significantly higher than that of isostructural Rb_3CoCl_5 and Cs_3CoX_5 (X = Cl, Br).

The strontium chromium oxide $[Sr_2O_2][CrO_2]_{1.85}$ "misfit-layer" compound has been synthesized at high-pressure and high-temperature conditions. Electron diffraction (ED) patterns and high-resolution TEM images along [001] showed the misfit character of the different layers composing the structure with a super cell along the incommensurate parameter, as shown in Fig. 10.22.

In this figure, the average structure of $[Sr_2O_2][CrO_2]_{1.85}$ is shown as

(a) Projection along the common axis.
(b) Projection along the incommensurate *b*-axis.
(c) [010] projection of the Fourier map of the composite crystal summed up along the x_2 and x_4 coordinates.

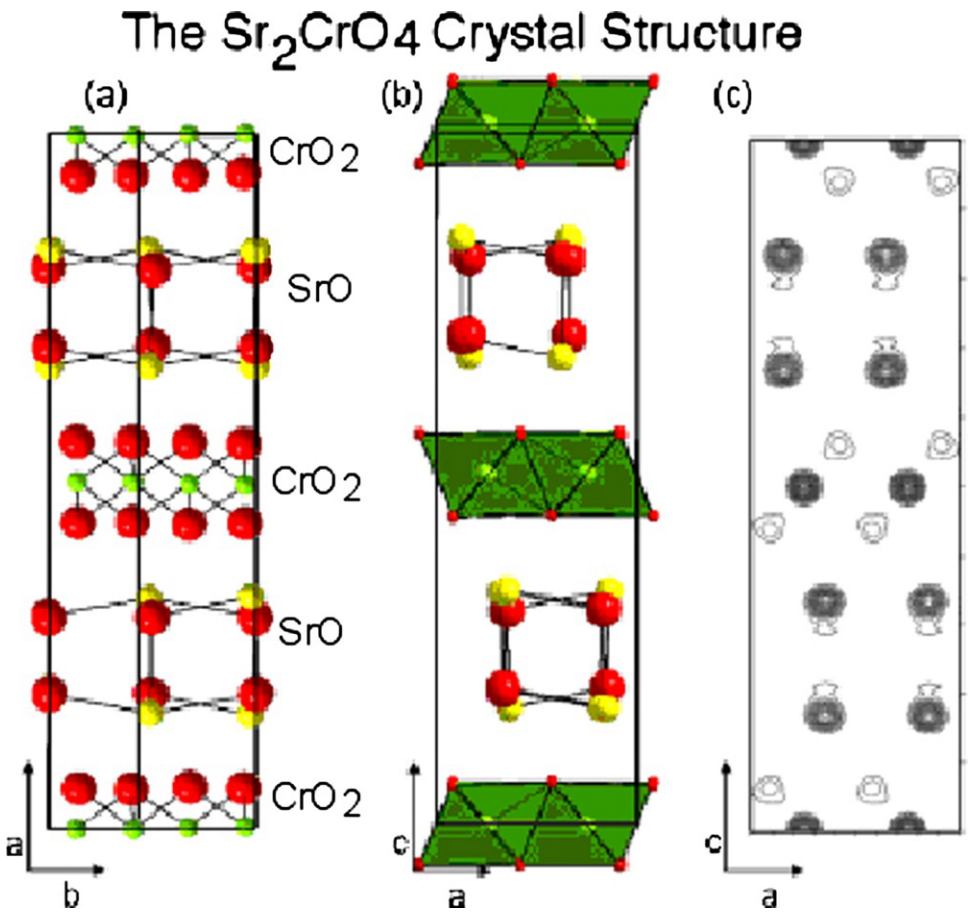

FIGURE 10.22

Yellow and green spheres represent strontium and chromium atoms, respectively, and red spheres for oxygen.

This incommensurately modulated structure has been successfully solved by means of single-crystal XRD with the super space group $C_0nmb(0s20)00s$. This orthorhombic structure corresponds to the stacking of two SrO and one CrO_2 layer and their mirror. The atoms of the Sr–O layer present the larger displacement modulation, especially the Sr atoms have the largest displacements, and are correlated with large modulations in the thermal parameters so as to accommodate the structural mismatch. The intersubsystem bond is particularly strong, in the whole system, which results in an underbonded Cr atom with an estimated valence of 3.48.

The compound, **tristrontium ortho-chromate**, $Sr_3(CrO_4)_2$, contains the Cr^{5+} ion. $Sr_3Cr_2O_8$ is an interesting structure for a number of reasons. It is a dimerized quantum magnet with gapped excitations and displays Bose–Einstein condensation in an applied magnetic field. Furthermore it displays substantial magnon phonon coupling at low temperatures. $Sr_3Cr_2O_8$ consists of triangular bilayers of chromium ions in the **ab** plane that are stacked along the **c** direction in an ABCABC sequence. The magnetic ions are paired into dimers by the dominant antiferromagnetic bilayer coupling and the system can therefore be viewed as a frustrated triangular network of dimers. The chromium ions are in the unusual 5^+ valence state resulting in one electron in the 3d shell and a spin value of 1/2 while the tetrahedral crystal field ensures that this electron occupies the doubly degenerate e_g orbitals. At 285 K, $Sr_3Cr_2O_8$ undergoes a cooperative Jahn–Teller distortion that lifts the orbital degeneracy so that only the $3z^2$-r^2 orbital is occupied. This low-temperature phase is characterized as having monoclinic crystal symmetry and antiferro-orbital ordering. Single crystals of $Sr_3Cr_2O_8$have been prepared. DC susceptibility measurements, high-field magnetization and powder and single-crystal inelastic neutron scattering were utilized. The data reveal a singlet ground state and gapped triplet excitations consisting of three modes arising from the three twins.

In another study, magnetic susceptibility, φ and specific heat C_p versus temperature T measurements on polycrystalline samples of $Sr_3Cr_2O_8$ and the isostructural, nonmagnetic compound $Sr_3V_2O_8$ were reported. A Curie–Wiess fit to the high-T $X(T)$ data for $Sr_3Cr_2O_8$ indicates that the Cr atoms are in the rare Cr^{5+} (spin $S = 1/2$)

valence state as expected from the compositional state. The ground state was found to be a spin singlet with an excitation gap $\Delta/k_B = 61.9$ K to the magnetic triplet states, and a weak interdimer coupling of 6.2 K was inferred.

The **distrontium chromite** compound, Sr_2CrO_4, plus Ba_2CrO_4, and Ba_3CrO_5, have been prepared. The characterization of these three Cr^{4+} compounds by X-ray and magnetic susceptibility experiments has been conducted. The magnetic moments for Sr_2CrO_4, Ba_2CrO_4, and Ba_3CrO_5 were determined to be in good agreement with the calculated value expected for a tetrahedral Cr^{4+} ion. Weak antiferromagnetic ordering for all three compounds is indicated from the small paramagnetic Weiss constants determined from the susceptibility data in the temperature region 80–300 K. Distortions of the tetrahedra from ideality, as determined from the structural features, further cause a reduction in the magnetic moments from the theoretical values.

The compound, **strontium dichromite**, $SrCr_2O_4$, has received moderate study. α-$SrCr_2O_4$ has a triangular planar lattice of d-containing Cr^{3+} made from edge-sharing CrO_6 octahedra. The plane shows a very small orthorhombic distortion from hexagonal symmetry. With a Curie–Weiss temperature of -596 K and a 3D magnetic ordering temperature of 43 K, the magnetic system is quasi two-dimensional and frustrated. Neutron powder diffraction shows that the ordered state is an incommensurate helical magnet, with an in-plane propagation vector of k = (0,0.3217,0). Temperature-dependent synchrotron powder diffraction characterization of the structure shows an increase in the inter-plane spacing on cooling below 100 K and an inflection in the cell parameters at the magnetic ordering temperature. These anomalies indicate the presence of a moderate degree of magneto-structural coupling. The structure has been presented in Fig. 10.23.

Here, the polyhedra are aligned in rows parallel to each other in the lattice.

Phase equilibria were determined in the complete composition range of the SrO–Cr_2O_3–La_2O_3 system in air at 1223 K and under low oxygen pressure (high vacuum, $p(O_2) \approx 10^{-9}$ bar). The (La, Sr)CrO_3 perovskite phase is the only quasi ternary oxide phase stable in air. The quasi ternary Ruddlesden–Popper phases $(La,Sr)_{n+1}Cr_nO_{3(n+1)}$ ($n = 1,2,3$) were identified in addition to the perovskite phase in the samples annealed under low oxygen pressure. The solubility limit of strontium in the $La_{1-x}Sr_xCrO_3$ phase was determined at 1223 K as $x = 0.10 \pm 0.02$ in air and at 1873 K as $x = 0.31 \pm 0.02$ under low oxygen pressure. The crystal lattice parameters of the Ruddlesden–Popper phase $LaSrCrO_4$ were obtained by the analysis of XRD patterns.

Solid-state reaction between $SrCO_3$, Cr_2O_3 and SrF_2 has produced the apatite phase $Sr_{10}(CrO_4)_6F_2$ and

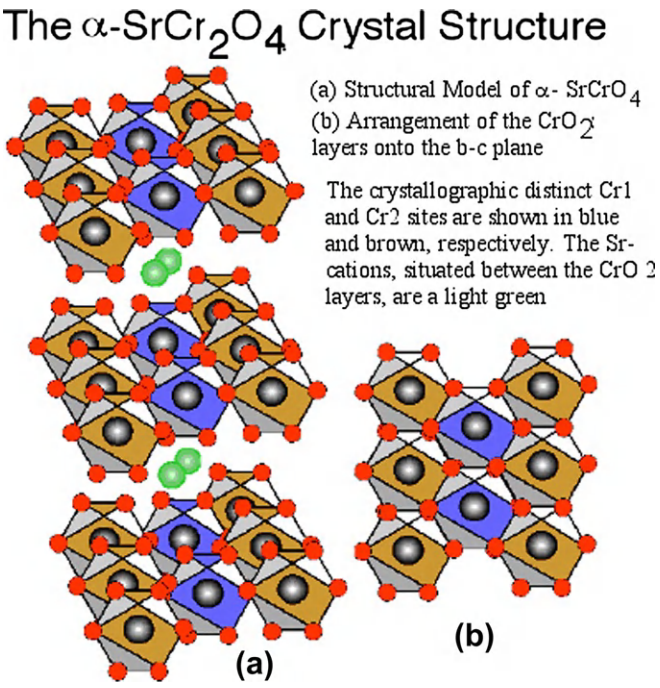

FIGURE 10.23

Sr_2CrO_4 which adopts the K_2NiF_4-type structure. The structure has the form as shown in Fig. 10.24.

The reaction outcome was very sensitive to the heating rate, with rapid rise times favoring the formation of Sr_2CrO_4, which has been synthesized at ambient pressure for the first time. Powder XRD (PXRD) and ED confirmed that Sr_2CrO_4 adopts a body-centered tetragonal cell (space group $I4/mmm$) with lattice parameters $a = 3.8357$ Å and $c = 12.7169$ Å, while a combination of neutron and XRD verified $Sr_{10}(CrO_4)_6F_2$ as hexagonal (space group $P6_3/m$) with lattice parameters: $a = 9.9570$ Å and $c = 7.4292$ Å. X-ray photo-electron spectroscopy (XPES)and magnetic measurements were used to characterize the oxidation states of chromium contained within these phases. PXRD and ED confirmed that Sr_2CrO_4 is body-centered tetragonal, while a combination of neutron and XRD verified $Sr_{10}(CrO_4)_6F_2$ is hexagonal. XPES and magnetic measurements identified the oxidation states of chromium in these phases.

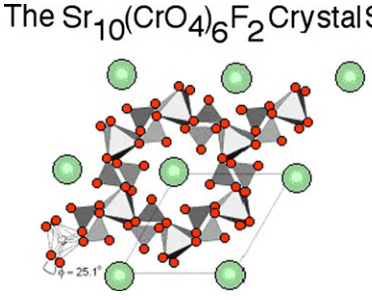

FIGURE 10.24

High pressure and temperature was used to synthesize perovskite-related phases in the Sr–Cr(IV)–O system. The $n = 1$, 2 and ∞ members of the $Sr_{n+1}Cr_nO_{3(n+1)}$ family have been obtained. Another new member, $n = 3$ as well as a hexagonal layered perovskite have also been observed by TEM and ED. The average structure of $Sr_3Cr_2O_7$ as determined by XRD has space group $I4/mmm$, whereas its microstructure includes a large amount of defects both in the layer stacking and within the layers. 2D magnetism and a large electrical resistance in $Sr_3Cr_2O_7$ are observed as opposed to the nonlocalized electronic behavior of $SrCrO_3$.

$SrCrO_4$ is offered for sale commercially with the CAS number of 7789-06-2.

10.2.5. Barium Chromium Compounds

No intermetallic compounds are known. Barium oxide forms a number of compounds with the chromium oxides. The exact composition depends, to a great extent, on the oxidation state of the chromium ion, $Cr^{3,\ 4,\ 5\ or\ 6+}$. In contrast to the other alkaline earth chromite–chromate systems, a number of barium chromate structures are known as shown in Table 10.12.

For the trivalent Cr(III) oxide system only $BaCr_2O_4$ and $Ba_3Cr_2O_6$ are known. The occurrence and products of solid/solid interactions in equimolar-mixed $BaCO_3$ and Cr_2O_3 powders were examined isothermally (700–1000 °C) and non-isothermally (25–1200 °C) under different gas atmospheres, employing thermogravimetry, X-ray diffractometry, infrared and Raman spectroscopy (RS), SEM, and energy dispersive X-ray spectroscopy (EDX). Irrespective of the gas atmosphere, a noncatalytic decomposition of the barium carbonate commenced at 570 °C, a temperature that is much less than the decomposition temperature (~970 °C) of $BaCO_3$ itself. The characteristics and distribution of the yielding products were found to be quite sensitive to the surrounding gas atmosphere. Under N_2 atmosphere, the interactions were thermochemical in nature, leading eventually to the formation of barium chromite ($BaCr_2O_4$) spinel as the sole detectable product. Under O_2 atmosphere, however, the oxygen molecules contributed oxidatively to the chromite thermal genesis course, thus imposing a topochemical nature to the reaction, leading to the formation of $BaCrO_4$, as the major product, and barium chromites ($BaCr_2O_4$ and $Ba_3Cr_2O_6$), as minor products. Proposed reaction pathways and characteristics of products have been presented and discussed. The phase diagram has the form as shown in Fig. 10.25.

Only the two phases appear in the diagram, both containing Cr^{3+}. The photophysical and photocatalytic properties of $BaCr_2O_4$ synthesized with normal spinel-type crystal structure were studied. It was found that H_2 could be photocatalytically evolved from the aqueous CH_3OH solution suspended with Pt(0.2 wt %)/$BaCr_2O_4$ powder under irradiation of both ultraviolet (UV) and visible lights. The wavelength dependence of H_2 evolution under visible light irradiation showed a maximum activity for $\lambda \geq 540$ nm. A possible electronic band structure and corresponding photoexcitation modes of $BaCr_2O_4$ under irradiation of UV and visible lights were proposed in regard to the complicated photophysical and photocatalytic properties.

It has the structure shown in Fig. 10.26.

The two types of Cr^{3+} are clearly shown. Chromium(III) oxide reverses the sequence of dehydration of barium perchlorate trihydrate (BP). Between 223 and 310 °C, the oxide reacts with anhydrous BP in a 1:1 molar ratio to give the yellow barium dichromite $BaCr_2O_4$. Between 350 and 430 °C, this material reacts in a 1:1 stoichiometry with BP, to give barium chromate $BaCrO_4$. The fact that $Ba_3Cr_20_6$ is only detected at low temperatures (<400 °C) has precluded any extensive determination of its physical characteristics.

Single crystals of $BaCr_2O_4$ were prepared as a high temperature compound of the $SrCr_2O_4$-type. It crystallizes with orthorhombic symmetry, space group $D—Pmmn$, $a = 12.286$ Å; $b = 5.921$ Å; $c = 5.146$ Å, $Z = 4$.

TABLE 10.12

No.	Compound	No. of elements	Structure type	Point group	Space group	Chromium valence
1	$BaCrO_4$	3	$BaSO_4$	oP24	*Pnma*	+6
2	$BaCrO_3$	3	Cs_3CoCl_2	oP28	*Pnma*	+4
3	$BaCrO_3$	3	$BaMnO_3$	tl36	*I4/mcm*	+4
4	$BaCrO_3$	3	$BaCrO_3$	hP20	*P6$_3$/mmc*	+4
5	$BaCrO_3$	3	$BaCrO_3$	hP70	*P6$_3$/mmc*	+4
6	Ba_2CrO_4	3	K_2SO_4	hR144	*R-3m*	+4
7	$Ba_4Cr_{13}O_{28}$	3	$Ba_4Cr_{13}O_{28}$	hR69	*R-3m*	+4

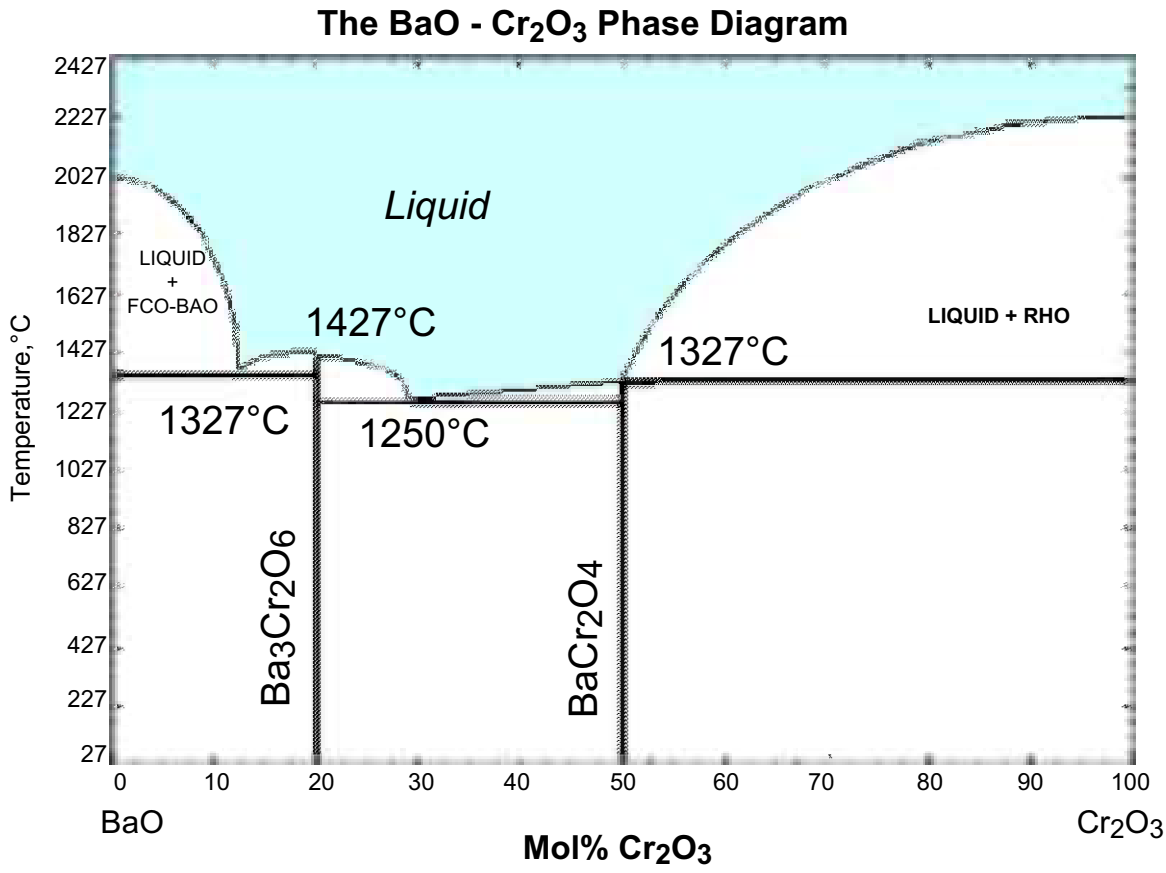

FIGURE 10.25

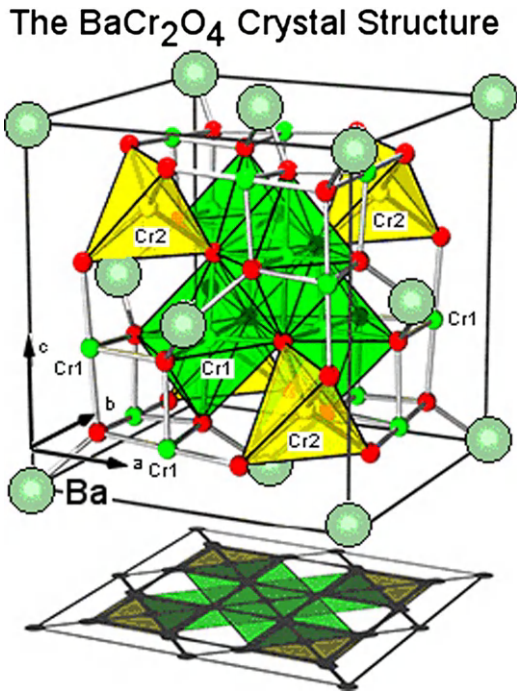

FIGURE 10.26

The crystal structure was described and the relationship to the metastable compounds α-$CaCr_2O_4$ and $SrCr_2O_4$ was discussed.

A number of compounds containing the Cr^{+4} ions are known as shown in Table 10.12 presented above. These include: $BaCrO_3$ (tetramorphic), Ba_2CrO_4, $Ba_4Cr_{13}O_{28}$, and $Ba_3Cr_2O_6$ (which contains +4 and +5 ions).

The structures determined for the four tetramorphic forms of $BaCrO_3$ are shown as follows. The first two forms are shown in Fig. 10.27.

$BaSO_4$ type: Cell parameters are: $a = 5.528$ Å, $b = 7.336$ Å, $c = 9.113$ Å, $\alpha = \alpha \Rightarrow \beta = \gamma = 90°$, cell volume is 369.56 $Å^3$, $Z = 4$.

Cell occupancy is shown in Table 10.13.

$BaCrO_3$ type (hP70): Cell parameters are: $a = b = 5.653$ Å, $c = 32.467$ Å, $\alpha = \beta = 90°$, $\gamma = 120°$, cell volume = 897.57 $Å^3$. Cell occupancy is shown in Table 10.14.

The other two types have the lattice form shown in Fig. 10.28.

$BaCrO_3$-hP20 type: Cell parameters are: $a = b = 5.66$ Å, $c = 9.357$ Å, $\alpha = \beta = 90°$, $\gamma = 120°$, cell

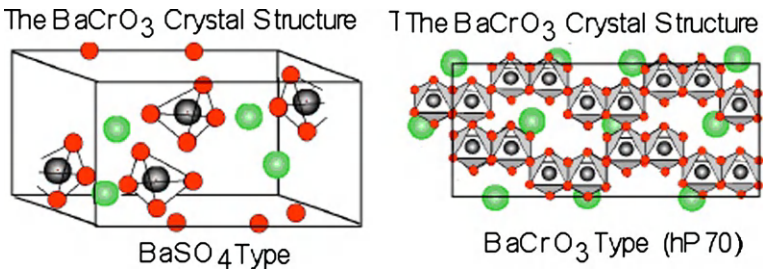

FIGURE 10.27

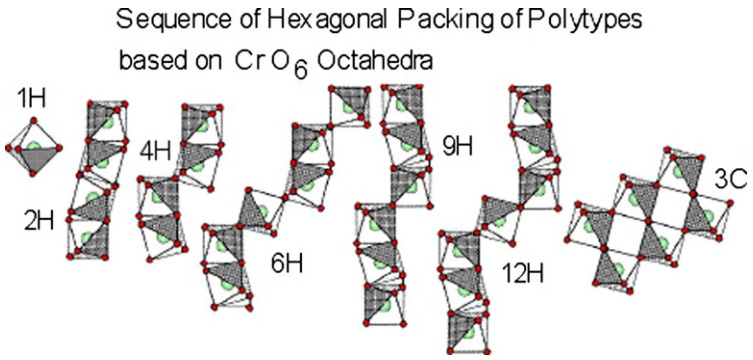

FIGURE 10.28

TABLE 10.13

No.	Site notation	Atom	Multiplicity	Wyckoff	Site symmetry	*x*	*y*	*z*	Occupancy
1	O3	O	8	d	1	0.0847	0.011	0.3223	1.0
2	Cr	Cr	4	c	.m.	0.0574	1/4	0.1943	1.0
3	O2	O	4	c	.m.	0.1792	1/4	0.0324	1.0
4	Ba	Ba	4	c	.m.	0.183	1/4	0.6553	1.0
5	O1	O	4	c	.m.	0.39	1/4	0.3837	1.0

TABLE 10.14

No.	Site notation	Atom	Multiplicity	Wyckoff	Site symmetry	*x*	*y*	*z*	Occupancy
1	O3	O	12	k	.m.	0.1664	0.333	0.6779	1.0
2	O1	O	12	k	.m.	0.1676	0.335	0.5344	1.0
3	O2	O	12	k	.m.	0.5179	0.036	0.1061	1.0
4	O4	O	6	h	mm2	0.1511	0.302	1/4	1.0
5	Ba3	Ba	4	f	3m.	1/3	2/3	0.0390	1.0
6	Ba4	Ba	4	f	3m.	1/3	2/3	0.1733	1.0
7	Cr3	Cr	4	f	3m.	1/3	2/3	0.5649	1.0
8	Cr4	Cr	4	f	3m.	1/3	2/3	0.6451	1.0
9	Ba2	Ba	4	e	3m.	0	0	0.1050	1.0
10	Cr2	Cr	4	e	3m.	0	0	0.2089	1.0
11	Ba1	Ba	2	d	-6m2	1/3	2/3	3/4	1.0
12	Cr1	Cr	2	a	-3m.	0	0	0	1.0

TABLE 10.15

No.	Site notation	Atom	Multiplicity	Wyckoff	Site symmetry	*x*	*y*	*z*	Occupancy
1	O2	O	6	h	mm2	0.1852	0.370	1/4	1.0
2	O1	O	6	g	.2/m.	1/2	0	0	1.0
3	Cr	Cr	4	f	3m.	1/3	2/3	0.1105	1.0
4	Ba2	Ba	2	d	-6m2	1/3	2/3	3/4	1.0
5	Ba1	Ba	2	A	-3m.	0	0	0	1.0

volume = 269.60 Å^3, $Z = 4$. Cell occupation is shown in Table 10.15.

$BaCrO_3$-hR144 type: Cell parameters are: $a = b = 5.652$ Å, $c = 21.1697$ Å, $\alpha = \beta = 82.329°$, $\gamma = 60°$, cell volume = 578.67 Å^3, $Z = 24$. Cell occupation is shown in Table 10.16.

The structure of the four-layer hexagonal $BaCrO_3$ polytype (hP20 type), prepared at high temperature and high pressure, was determined utilizing a Picker FACS-I diffractometer. The hexagonal black crystal was found to crystallize with a four-layer stacking sequence in space group $P6_3/mmc$ having unit cell parameters $a = 5.660(1)$ and $c = 9.357(1)$ Å. The structure was determined from 668 independent reflections of which 605 were considered observed. Equivalent reflections were averaged and this operation yielded 130 unique, observed reflections. Refinement of the structure by least-squares methods gave a conventional *R*-value of 3.0%. The structure consists of a four-layer stacking sequence of close-packed BaO_3 layers containing tetravalent chromium in all the octahedral oxygen interstices. The compound was found to be isostructural with β-$BaMnO_3$ and the recently reported $BaRhO_3$ and $SrMnO_3$.

In another study, a product from the reaction between CrO_2 and Ba_2CrO_4 at 900 °C under 60–65 kbar was found to be the six-layer polytype of $BaCrO_3$ from powder diffraction studies. A hexagonal black crystal obtained from this reaction was isolated for single-crystal studies and structure determination. The crystal

TABLE 10.16

No.	Site notation	Atom	Multiplicity	Wyckoff	Site symmetry	*x*	*y*	*z*	Occupancy
1	O4	O	18	h	.m	0.4812	0.519	0.4450	1.0
2	O2	O	18	h	.m	0.4833	0.517	0.2960	1.0
3	O3	O	18	h	.m	0.4999	0.500	0.0743	1.0
4	O5	O	18	h	.m	0.5008	0.499	0.1487	1.0
5	O1	O	9	e	.2/m	1/2	0	0	1.0
6	Ba1	Ba	6	c	3m	0	0	0.0044	0.5
7	Ba3	Ba	6	c	3m	0	0	0.0748	0.5
8	Ba4	Ba	6	c	3m	0	0	0.0779	0.5
9	Ba6	Ba	6	c	3m	0	0	0.1464	1.0
10	Cr4	Cr	6	c	3m	0	0	0.2001	1.0
11	Cr3	Cr	6	c	3m	0	0	0.2416	1.0
12	Ba2	Ba	6	c	3m	0	0	0.2957	1.0
13	Cr1	Cr	6	c	3m	0	0	0.3497	1.0
14	Cr2	Cr	6	c	3m	0	0	0.3919	1.0
15	Ba5	Ba	6	c	3m	0	0	0.4456	1.0
16	Cr5	Cr	3	b	-3m	0	0	1/2	1.0

was found to possess a six-layer stacking sequence of BaO_3 layers with space group $P6_3/mmc$ and had unit cell parameters $a = 5.629(2)$, $c = 13.698(6)$ Å, and $Z = 6$. The structure was determined from 936 independent reflections of which 693 were considered observed. Averaging equivalent reflections yielded 163 unique, observed reflections. Refinement of the structure by least-squares methods gave a conventional R value of 4.8% ($R_w = 6.2\%$). The structure consists of a six-layer stacking sequence of close-packed BaO_3 layers containing tetravalent chromium in all the octahedral oxygen interstices. The compound was found to be isostructural with previously reported $BaMnO_3$ phases.

Twenty-seven-layer barium chromium oxide, $BaCrO_3$-hR144 type, was prepared at 1200 °C and 60–65 kbar by reaction of CrO_2 and Ba_2CrO_4. The compound crystallizes in space group $R3m$ with hexagonal cell dimensions $a = 5.652 \pm 0.002$ Å, $c = 62.75 \pm 0.02$ Å. The structure was determined from 1070 independent reflections, of which 811 were considered observed, collected by automated counter methods, and refined by least-squares methods to a conventional R-value of 4.1%. The structure consists of a 27-layer stacking sequence of close-packed BaO_3 layers. Zhdanov notation for the sequence is (3)2(2)2, with all of the O_6 octahedral sites occupied by Cr. Strings of four pairs of face-sharing octahedra in which the pairs are linked to each other by corner sharing are in turn joined to each other by octahedra sharing only corners. The structure is thus closely related to the four-layer and six-layer polytypes of $BaCrO_3$. Bariums in two of the five crystallographic positions showed large thermal anisotropy and are better described in terms of half atom occupancy in split sites.

Under the local-spin density approximation method plus on-site coulomb interaction U correction (LSDA+U), the $BaCrO_3$-hP70 type, in the perovskite structure is found to be half-metallic ferromagnet with an integral magnet moment of 2.000 Bohr magnetons (μ_B) per unit. The feasibility of constructing the $BaCr_{0.5}Ti_{0.5}O_3$ superlattice to stabilize the perovskite phase for the $BaCrO_3$ is theoretically explored. Additionally, the influence of screened parameters U on the electronic structures and magnet moments of the perovskite $BaCrO_3$ and $BaCr_{0.5}Ti_{0.5}O_3$ superlattice is expounded.

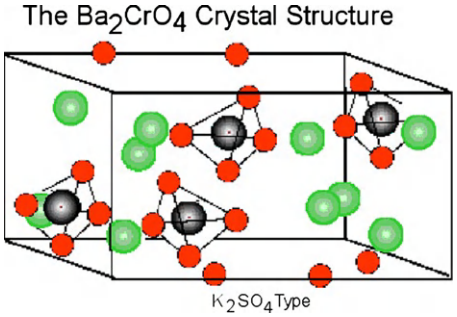

FIGURE 10.29

One of the products of the reaction of CrO_2 and Ba_2CrO_4 at 1300 °C is a 14-layer polytype of $BaCrO_3$. Cell parameters are space group = $P6_3/mmc$ with $a = 5.650$ Å and $c = 32.467$ Å, $Z = 14$. It consists of a 14-layer stacking sequence of closed-packed BaO_3 layers with all of the octahedral sites occupied by Cr^{4+} ions. The Zhdanov notation for the sequence is: {2(3)2|2(3)2}. In each cell, there are strings of three pairs of face-sharing octahedra in which pairs are linked to each other by corner-sharing. The strings are in turn joined to each other by octahedra-sharing-only corners. Thus, the structure is closely related to the four-layer, six-layer and twenty-seven layer polytypes of $BaCrO_3$. In order to clarify what is being discussed, consider the following diagram: Fig. 10.28

It shows the sequence of polytype layers from the aspect of the joined octahedra.

The compound, **dibarium chromite**, Ba_2CrO_4, contains the Cr^{4+} ion and has a structure related to $BaCrO_3$, except for the number of Ba^{2+} ions present in the unit cell. One form has the structure of K_2SO_4 while that of the other is of the $BaSO_4$ type as shown in Fig. 10.29.

The cell parameters are: $a = 5.967$ Å, $b = 7.611$ Å, $c = 10.496$ Å, $\alpha = \beta = \gamma = 90°$, $Z = 4$. Cell volume = 475.99 Å^3. Cell occupancy is shown in Table 10.17.

TABLE 10.17

No.	Site notation	Atom	Multiplicity	Wyckoff	Site symmetry	x	y	z	Occupancy
1	O1	O	8	d	1	0.3017	0.041	0.1478	1.0
2	O2	O	4	c	.m.	0.0368	1/4	0.0838	1.0
3	Ba1	Ba	4	c	.m.	0.1739	1/4	0.4107	1.0
4	Cr1	Cr	4	c	.m.	0.2330	1/4	0.0802	1.0
5	Ba2	Ba	4	c	.m.	0.4892	1/4	0.7045	1.0
6	O3	O	4	c	.m.	0.7976	1/4	0.5585	1.0

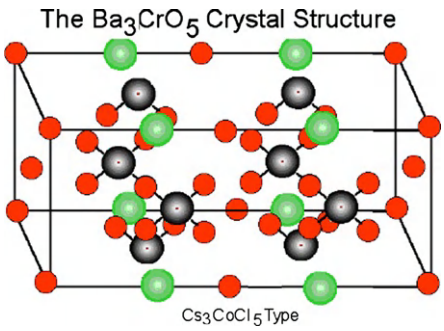

FIGURE 10.30

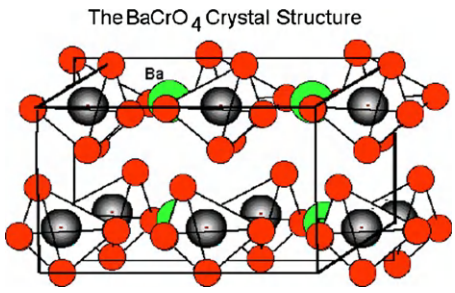

FIGURE 10.31

The preparation of the compounds Ba_2CrO_4, and Ba_3CrO_5 has been described. However, the exact structure of Ba_3CrO_5 has not been published except to state that it has the structure of Cs_3CoCl_5 with point group - = *tI*36 and space group = *I*4/*mcm*. The structure may be represented in Fig. 10.30.

Cell parameters are: $a = b = 9.123$ Å, $c = 9.7041$ Å, $\alpha = \beta = 118.038°$, $\gamma = 90°$, $Z = 4$, cell volume = 603.37 Å^3. Cell occupancy is shown in Table 10.18.

The characterization of these two Cr^{4+} compounds by X-ray and magnetic susceptibility experiments has been conducted. The magnetic moments for Ba_2CrO_4, and Ba_3CrO_5 were determined to be in good agreement with the calculated value expected for a tetrahedral Cr^{4+} ion. Weak antiferromagnetic ordering for both compounds was indicated from the small paramagnetic Weiss constants determined from the susceptibility data in the temperature region 80–300 K. Distortions of the tetrahedra from ideality, as determined from the structural features, further caused a reduction in the magnetic moments from the theoretical values.

The compound, **barium chromate**, $BaCrO_4$, contains the ion, Cr^{6+}, and has the CAS number of 10294-40-3 and the structure is shown in Fig. 10.31.

Cell parameters are: $a = 5.528$ Å, $b = 7.336$ Å, $c = 9.113$ Å, $\alpha = \beta = \gamma = 90°$, cell volume = 369.56 Å^3, $Z = 4$.

Cell occupancy is shown in Table 10.19.

$BaCrO_4$ was studied at high pressure up to 25 GPa in a diamond-anvil cell using both RS and XRD methods. The results showed that $BaCrO_4$ exhibits a phase transition near 9 GPa from both Raman and XRD measurements. The new high-pressure phase ($BaCrO_4$-II) is suggested as a monoclinic ($P2_1/m$) structure, different from other high-pressure forms of ABO_4-type compounds. Moreover, the high-pressure phase of $BaCrO_4$ is found to be reversible; the low-pressure phase is recovered at ~8 GPa upon decompression. The

TABLE 10.18

No.	Site notation	Atom	Multiplicity	Wyckoff	Site symmetry	*x*	*y*	*z*	Occupancy
1	O2	O	16	l	..m	0.142	0.642	0.157	1.0
2	Ba2	Ba	8	h	m.2m	0.663	0.163	0	1.0
3	O1	O	4	c	4/m..	0	0	0	1.0
4	Cr1	Cr	4	b	-42m	0	1/2	1/4	1.0
5	Ba1	Ba	4	a	422	0	0	1/4	1.0

TABLE 10.19

No.	Site notation	Atom	Multiplicity	Wyckoff	Site symmetry	*x*	*y*	*z*	Occupancy
1	O3	O	8	d	1	0.085	0.011	0.3223	1.0
2	Cr	Cr	4	c	.m.	0.057	1/4	0.1943	1.0
3	O2	O	4	c	.m.	0.179	1/4	0.0324	1.0
4	Ba	Ba	4	c	.m.	0.183	1/4	0.6553	1.0
5	O1	O	4	c	.m.	0.39	1/4	0.3837	1.0

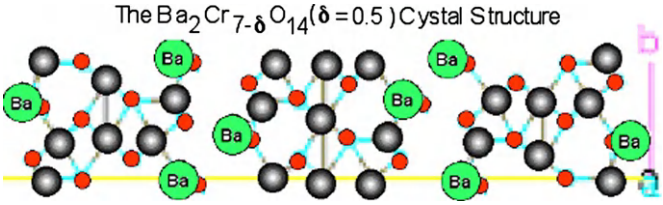

FIGURE 10.32

pressure–volume data of $BaCrO_4$ fitted to a third-order Birch–Murnaghan equation of state yield a bulk modulus of 53(1) GPa and a pressure derivative of 6.8(5), in agreement with the theoretical prediction. For the high-pressure phase $BaCrO_4$-II, the bulk modulus is 117(10) GPa and the pressure derivative is 3(1).

Refinement of the crystal structures of Ba_2CrO_4 and Ba_3CrO_5 using powder neutron diffraction data has confirmed that the former is isostructural with β-K_2SO_4 and the latter is isostructural with Cs_3CoCl_5. Ba_2CrO_4 is orthorhombic, *Pnma* (No. 62), $Z=4$ with $a=7.6285(5)$ Å, $b=5.9136(5)$, $c=10.4639(8)$, and $V=472.04(5)$ Å^3. Ba_3CrO_5 is tetragonal, *I*4/*mcm* (No. 140), $Z=4$ with $a=7.3033(3)$ Å, $c=11.6704(6)$, $V=622.48(4)$ Å^3 from powder Guinier XRD data. Magnetic properties of Sr_2CrO_4, Ba_2CrO_4, and Ba_3CrO_5 were examined down to 2–5 K. The structures and magnetic properties of Sr_2CrO_4 and Ba_2CrO_4 are compared with their vanadium analogues β-Sr_2VO_4 and β-Ba_2VO_4. Unlike isostructural β-Sr_2VO_4, which contains the $V_2O_8^{8-}$ dimer, Sr_2CrO_4 contains truly isolated CrO_4^4 tetrahedra and its magnetic behavior can be best described as a dimerized chain. Ba_2CrO_4 and Ba_3CrO_5 also contain isolated CrO_4^{4-} tetrahedra. Ba_2CrO_4 is paramagnetic down to 5 K. Ba_3CrO_5 undergoes long-range magnetic order at 8 K, a temperature range significantly higher than that of isostructural Rb_3CoCl_5 and Cs_3CoX_5 (X = Cl, Br).

The compound, $Ba_4Cr_{13}O_{28}$ has the structure as shown in Fig. 10.32.

Cell parameters are: $a=b=5.652$ Å, $c=9.815$ Å, $\alpha=\beta=73.266°$, $\gamma=60°$, cell volume = 256.09 Å^3. Cell occupancy is shown in Table 10.20.

Little is known concerning this compound other than its structure, which is that of a 12-layered perovskite.

Barium chromate is offered for sale commercially as $BaCrO_4$ with the CAS number of 10294-40-3.

10.2.6. Radium Chromium Compounds

Although it is likely that radium chromite or chromate compounds could be prepared and studied by the same methods used to characterize the homologous barium compounds, no such information has appeared in the technical literature. This is likely due to the high cost of RaO and its high radioactive intensity.

10.3. ALKALINE EARTH MOLYBDENUM COMPOUNDS

Molybdenum occurs as two oxides MoO_2 and MoO_3 having the Mo^{4+} and Mo^{6+} valence states. Molybdenum trioxide forms *n*- and *p*-type semiconductor phases which are of technological interest. Molybdenum dioxide is produced by roasting molybdite ore (MoS_2). It is colorless to yellowish-white. It is quite soluble in hot water and slightly soluble in cold water. Comparative crystal structures are shown in Fig. 10.33.

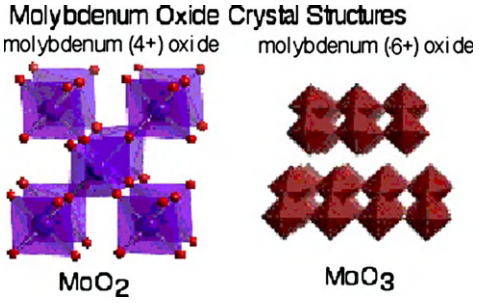

FIGURE 10.33

TABLE 10.20

No	Site notation	Atom	Multiplicity	Wyckoff	Site symmetry	*x*	*y*	*z*	Occupancy
1	O1	O	18	h	.m	0.505	0.495	0.2834	1.0
2	O2	O	18	h	.m	0.506	0.494	0.1281	1.0
3	Cr1	Cr	9	d	.2/m	1/2	0	1/2	1.0
4	Cr3	Cr	6	c	3m	0	0	0.0655	0.75
5	O3	O	6	c	3m	0	0	0.1269	1.0
6	Ba	Ba	6	c	3m	0	0	0.2933	1.0
7	Cr2	Cr	6	c	3m	0	0	0.4264	1.0

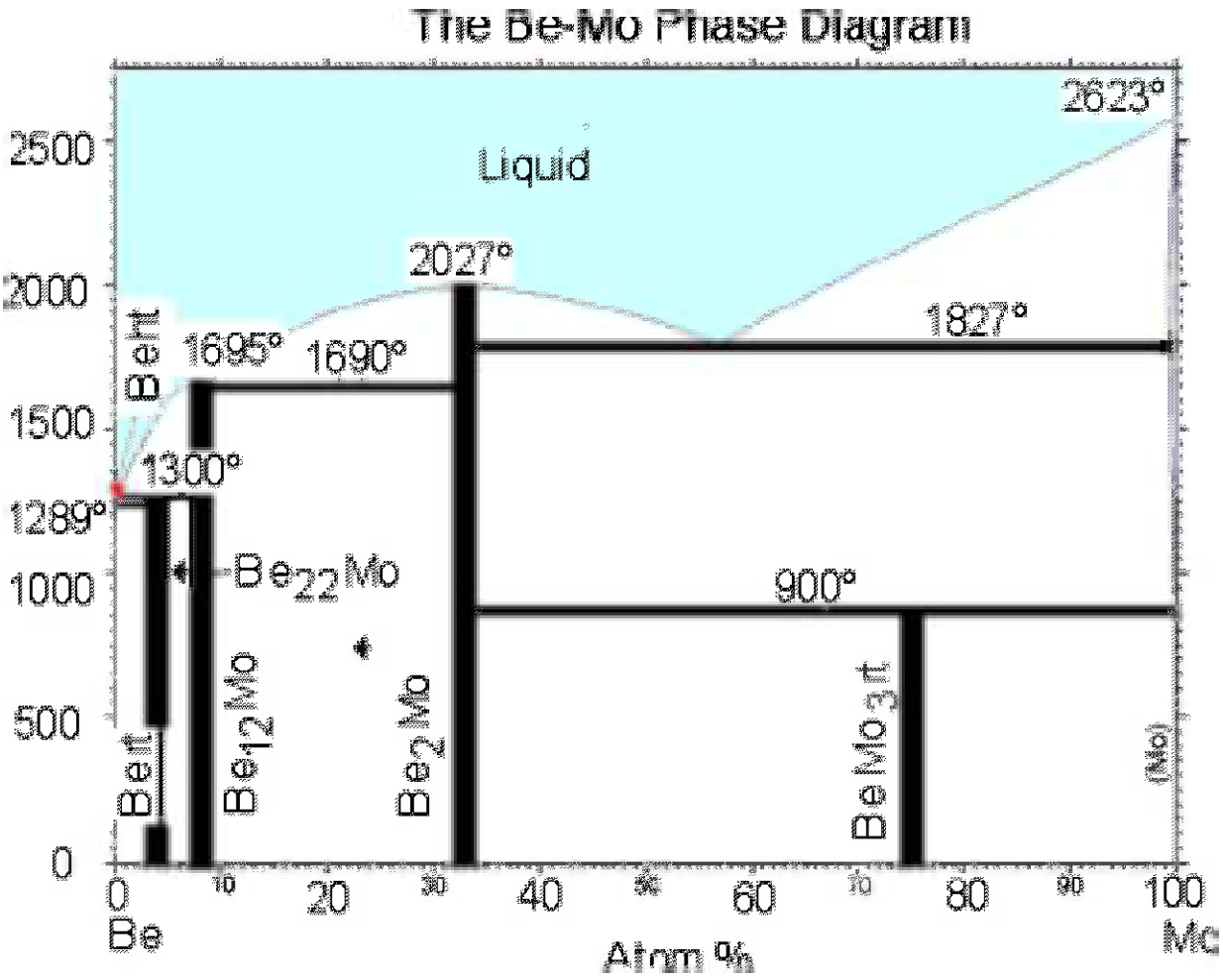

FIGURE 10.34

Both the structures are composed of MoO_6 octahedra, the dioxide having a point-shared structure while the trioxide is composed of separated or point-coordinated octahedra in most cases.

10.3.1. Beryllium Molybdenum Compounds

Only Be forms intermetallic compounds with Mo metal. The phase diagram has been presented in Fig. 10.34.

Structure factors are shown in Table 10.21.

The other alkaline earth metals do not form intermetallic compounds with Mo metal.

The compound, Be_2Mo, has the structure. Cell parameters are: $a = 4.448$ Å, $c = 7.312$ Å, $\alpha = \beta = \gamma = 90°$, cell volume $= 125.26$ Å^3, $Z = 4$.

The reaction between single crystal 99.99% Mo with YBe_{13} [CAS #-12010-31-0] was studied at 1000–1400 °C. A hexagonal-closed-packed Be_2Mo [CAS #-12232-43-8]

TABLE 10.21

Compound	Structure type	Point group	Space group	Melting temperature, °C
(Be) ht	W	cI2	229	1289
(Be) rt	Mg	hP2	194	1270
$Be_{22}Mo$	$Zn_{22}Zr$	cF184	*Fd-3m*	1300
$Be_{12}Mo$	$ThMn_{12}$	tI26	*I4/mmm*	1695
$BeMo_3$ rt	Cr_3Si	cP8	*Pm-3n*	900
Be_2Mo	$MgZn_2$	hP12	$P6_3/mmc$	2027
(Mo)	W	cI2	229	2683

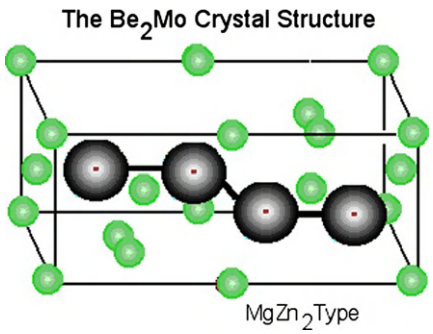

FIGURE 10.35

layer was formed in the contact zone. The activation energy for $MoBe_2$ formation was 42.5 kcal/mol. Cell occupancy is shown in Table 10.22.

The feasibility of producing composites containing nickel or molybdenum fibers in a beryllium matrix was investigated. The composites studied were fabricated by powder metallurgical techniques. The 1-mil-diameter nickel fibers reacted completely below 900 °C, converting the fibers from nickel to Ni_5Be_{21}. As the hot-pressing temperature was raised above 1100 °C, the nickel diffused outward from the beryllide fibers. The solid solubility of nickel in beryllium was about 20 wt% at the 1100 °C pressing temperature at the zone-fiber interface. The 1.5-mil-diameter molybdenum fibers showed no evidence of reaction and little evidence of diffusion after pressing at 900 °C. Between 1000 and 1050 °C pressing conditions, the fibers began to react, producing layers of $MoBe_2$ and $MoBe_{12}$, respectively, surrounding the molybdenum core. The structure remained the same at 1100 °C with no evidence of solid solubility of the molybdenum in the beryllium or vice versa.

The compound **Mo_3Be** was prepared and found to be isomorphous with Mo_3Si, a compound that is cubic. The compound, Be_3Mo, has the crystal structure as shown in Fig. 10.36.

This compound is a "Zintl" phase with Be atoms in body-centered positions and Mo–Mo barbells situated at face-centered positions. Cell parameters are: $a = b = c = 4.892$ Å, $\alpha = \beta = \gamma = 90°$, cell volume = 116.93 Å^3, $Z = 2$. Cell occupancy is shown in Table 10.23.

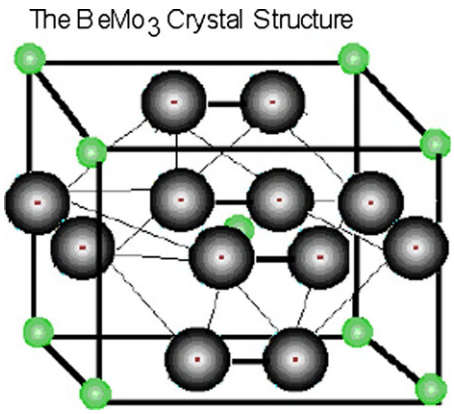

FIGURE 10.36

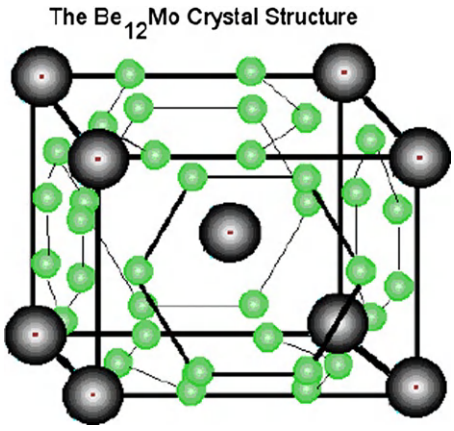

FIGURE 10.37

The compound, $Be_{12}Mo$, has the structure as shown in Fig. 10.37.

TABLE 10.22

No.	Site notation	Atom	Multiplicity	Wyckoff	Site symmetry	*x*	*y*	*z*	Occupancy
1	Be1	Be	6	h	mm2	0.170	0.339	1/4	1.0
2	Mo1	Mo	4	f	3m.	1/3	2/3	0.5629	1.0
3	Be2	Be	2	a	-3m.	0	0	0	1.0

TABLE 10.23

No.	Site notation	Atom	Multiplicity	Wyckoff	Site Symmetry	*x*	*y*	*z*	Occupancy
1	Mo	Mo	6	c	4m.2	1/4	0	1/2	1.0
2	Be	Be	2	a	m-3.	0	0	0	1.0

It consists of two (2) sub-units: a body-centered lattice of Mo atoms and six (6) hexagonal units of Be (Be_6) arranged on the faces of the tetragonal lattice. The unit cell parameters are: $a = b = 5.5471$ Å, $c = 4.3342$ Å, $\alpha = \beta = 67.565°$, $\gamma = 81.625°$, $Z = 2$, cell volume $= 111.31$ Å^3. Cell occupancy is shown in Table 10.24.

The intermetallic compound $MoBe_{12}$ has been found to be ferromagnetic at low temperatures. The ferromagnetic and paramagnetic Curie temperatures are each about 50 K, and at 1.4 K; the saturation moment is approximately 0.2 Bohr magnetons per chromium atom. In contrast, the compounds Nb_2Be_{17}, $NbBe_{12}$, Ta_2Be_{17}, $TaBe_{12}$, $MoBe_{12}$, $ZrBe_{13}$, and $CaBe_{13}$ were found to be nonmagnetic and non-superconducting above 1.4 K.

Although the compound, $Be_{13}Mo$ has been reported, there is no corroborating evidence to confirm its existence in the Be–Mo system.

An intermetallic compound, $Be_{22}Mo$, is also known. It has the structure as shown in Fig. 10.38.

Unit cell parameters are: $a = b = c = 8.2265$ Å, $\alpha = \beta = \gamma = 60°$, cell volume $= 393.67$ Å^3, $Z = 8$. Cell occupancy is shown in Table 10.25.

This compound, $Be_{22}Mo$, has been found to be superconducting with a critical temperature of $T_c = 4.14$ K. No other intermetallic compounds have been discovered to date. None of these compounds have found usage in Industry.

The only reference to beryllium molybdates has been the determination of the heat of formation when BeO was evaporated from Mo metal crucibles. When heated to a sufficiently high temperature, BeO evaporates as a BeO-molecule, $(BeO)_n$ where $n = 1$–5.

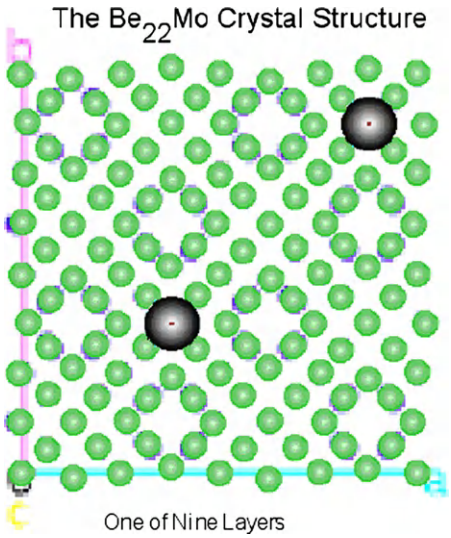

FIGURE 10.38

If a Mo metal crucible is used, then beryllium molybdate molecules are detected in the vapor phase. Gas-phase reactions involving beryllium molybdates and tungstates were studied by high-temperature mass spectrometry. The standard enthalpies of formation and atomization of $BeMoO_3$, $BeWO_3$, $BeWO_4$, and Be_2WO_4 were determined. The following values were determined:

Heat of formation (vapor phase): ΔH_f^0 (2175–2450 °C)

$$Be_3O_3 + 3\,MoO_2 \Rightarrow 3\,BeMoO_3, \quad \Delta H_f^0 = -432 \text{ kJ/mol}$$

$$Be_3O_3 + 3\,WO_2 \Rightarrow 3\,BeWO_3, \quad \Delta H_f^0 = -424 \text{ kJ/mol}$$

TABLE 10.24

No.	Site notation	Atom	Multiplicity	Wyckoff	Site symmetry	x	y	z	Occupancy
1	Be(j)	Be	8	j	m2m.	0.291	1/2	0	1.0
2	Be(i)	Be	8	i	m2m.	0.351	0	0	1.0
3	Be(f)	Be	8	f	..2/m	1/4	1/4	1/4	1.0
4	Mo	Mo	2	a	4/mmm	0	0	0	1.0

TABLE 10.25

No.	Site notation	Atom	Multiplicity	Wyckoff	Site symmetry	x	y	z	Occupancy
1	Be4	Be	96	g	..m	0.0584	0.058	0.325	1.0
2	Be3	Be	48	f	2.mm	0.4843	1/8	1/8	1.0
3	Be1	Be	16	d	.-3m	1/2	1/2	1/2	1.0
4	Be2	Be	16	c	.-3m	0	0	0	1.0
5	Mo	Mo	8	a	-43m	1/8	1/8	1/8	1.0

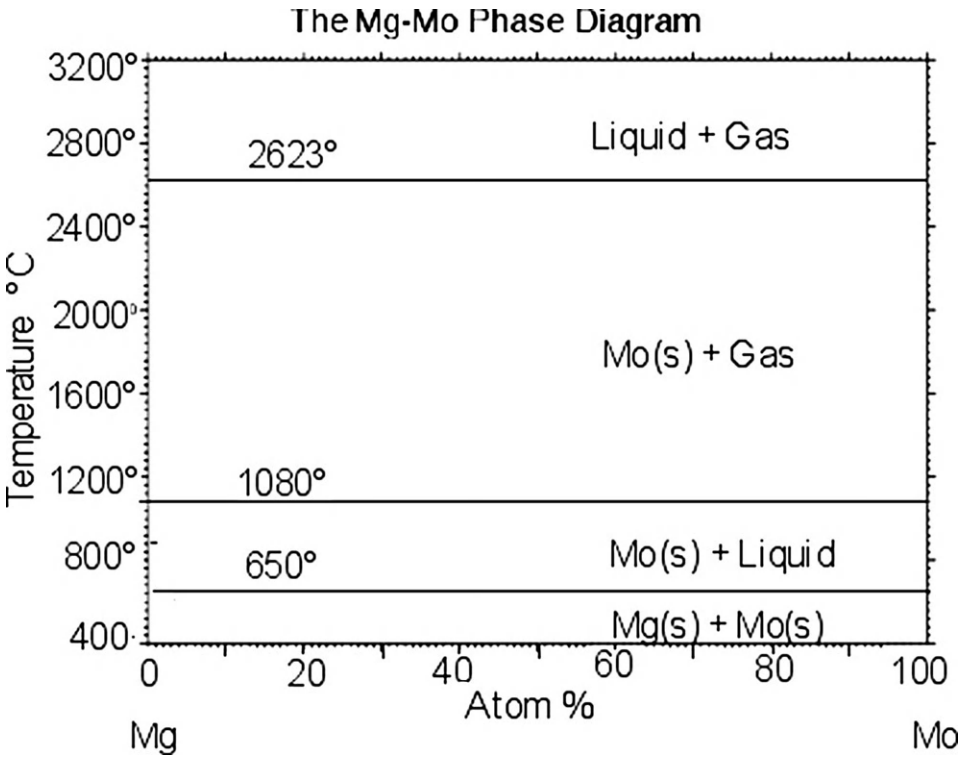

FIGURE 10.39

$$Be_3O_3 + 3\,WO_3 \Rightarrow 3\,BeWO_4, \quad \Delta H_f^0 = -794 \text{kJ/mol}$$

$$2\,Be_3O_3 + 3\,WO_2 \Rightarrow 3\,Be_2WO_4, \quad \Delta H_f^0 = -974 \text{ kJ/mol}$$

However, when the vapors were cooled to room temperature, only a mixture of oxides was obtained. No other Be–Mo compounds are known to date.

10.3.2. Magnesium Molybdenum Compounds

Magnesium does not form any intermetallic compounds with molybdenum. All of the Ae–Mo systems have been investigated and a typical phase diagram has the form as shown in Fig. 10.39.

Except for the temperatures, the other alkaline earths exhibit the same behavior with Mo metal in that no compounds or solid solutions are formed.

MgO forms a limited number of compounds with molybdenum oxides.

No compounds are known where the valence state of Mo is 3+. In the Mo^{4+} system of MgO–MoO_2, the compound, $MgMoO_3$ is expected to belong to the cubic perovskite structure, but this compound has never been synthesized. The possible +4 molybdates, $MgMoO_3$, Mg_2MoO_4, Mg_3MoO_5, $MgMo_2O_5$, and the +5 molybdates $MgMo_2O_6$, $Mg_2Mo_2O_7$ and $Mg_3Mo_2O_8$ remain unknown.

The solid-state reaction of MgO and MoO_3 produces three compounds as shown in Table 10.26.

The phase diagram of MgO–MoO_3 has been presented in Fig. 10.40.

$MgMoO_4$ is trimorphic. Although the compound, dimagnesium tri-molybdate, $Mg_2Mo_3O_{11}$, was identified in early works along with $MgMo_2O_7$, the pyromolybdate, subsequent work has established that this compound is actually the low temperature form of the pyromolybdate in the system, MgO–MoO_3. The

TABLE 10.26

	Compound	Structure type	Point group	Space group	Melting temperature
1a	$MgMoO_4$	$MgWO_4$	mP12	$P2/c$	
1b	$MgMoO_4$	—	aP36	$P1$	
1c	$MgMoO_4$	$MnMoO_4$	aP36	$C2/m$	
2	$MgMo_2O_7$	$MgMo_2O_7$	mP40	$P2_1/c$	
3	$Mg_2Mo_3O_8$	$Zn_2Mo_3O_8$	hP26	$P6_3mc$	830°-Incong

TABLE 10.27

No.	Site notation	Atom	Multiplicity	Wyckoff	Site symmetry	*x*	*y*	*z*	Occupancy
1	O1	O	4	g	1	0.244	0.123	0.603	1.0
2	O2	O	4	g	1	0.284	0.393	0.063	1.0
3	Mo1	Mo	2	f	2	1/2	0.682	1/4	1.0
4	Mg1	Mg	2	e	2	0	0.174	1/4	1.0

transition temperature was established at 840 °C, the point where the X-ray pattern changes into the α-$MgMo_2O_7$ pattern.

Magnesium molybdates, prepared from an aqueous solution of magnesium nitrate and ammonium paramolybdate under various pH conditions, produce the same compositions. The difference is that those compounds formed from solution are catalytic and have been used for the selective oxidation of propane and isobutane with gaseous oxygen under atmospheric pressure in the temperature range of 360–520 °C. The structure analyses by XRD and FT-IR showed the formation of three phases, α-$MgMoO_4$, β-$MgMoO_4$ and $Mg_2Mo_3O_8$, in the catalysts calcined below 550 °C. The catalyst prepared at pH = 5.7 showed the highest activity for the oxidative dehydrogenation of the alkanes as well as the strongest acidity. By XPES measurements, an excess amount of Mo compared to Mg was observed over the active catalysts. It is likely that the excess molybdenum species is present as molybdate and creates acidic sites over the catalyst surface. Low coordinated molybdates are present in $MgMo_2O_7$ (dimer of MoO_3 and $MgMoO_4$) and in $NaMo_2O_7$ (chain of alternating MoO_4 and MoO_6 units). Isolated MoO_4 coordination is, however, rather common for ortho-molybdates (e.g. K_2MoO_4, Na_2MoO_4, $CaMoO_4$, $MgMoO_4$, $MnMoO_4$, $CuMoO_4$, etc.).

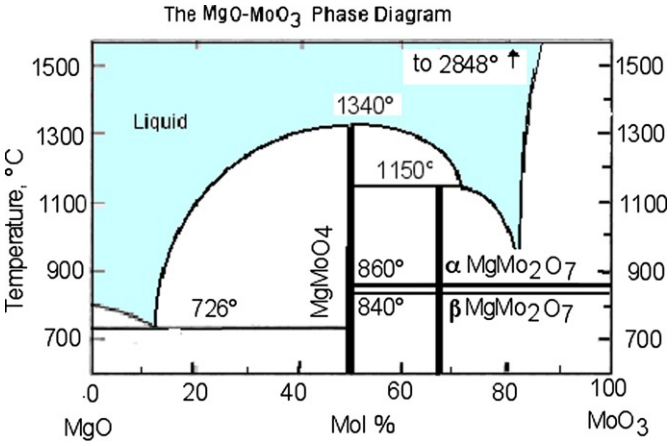

FIGURE 10.40

Note that $MgMoO_4$ is trimorphic, as shown in Fig. 10.41 and $MgMo_2O_7$ is dimorphic (see Fig. 10.42). The former melts congruently whereas the latter melts incongruently (see Fig. 10.40).

$MgWO_4$ type: Cell parameters are: $a = 4.964$ Å, $b = 4.900$ Å, $c = 5.689$ Å, $\alpha = \beta = 90°$, $\gamma = 90.35°$, cell volume = 130.85 Å^3, $Z = 2$. Cell occupancy is shown in Table 10.27.

$MnMoO_4$ type: Cell parameters are: $a = b = 6.9246$ Å, $c = 7.025$ Å, $\alpha = \beta = 77.504°$, $\gamma = 84.235°$, cell volume = 320.57 Å^3, $Z = 4$. Cell occupancy is shown in Table 10.28.

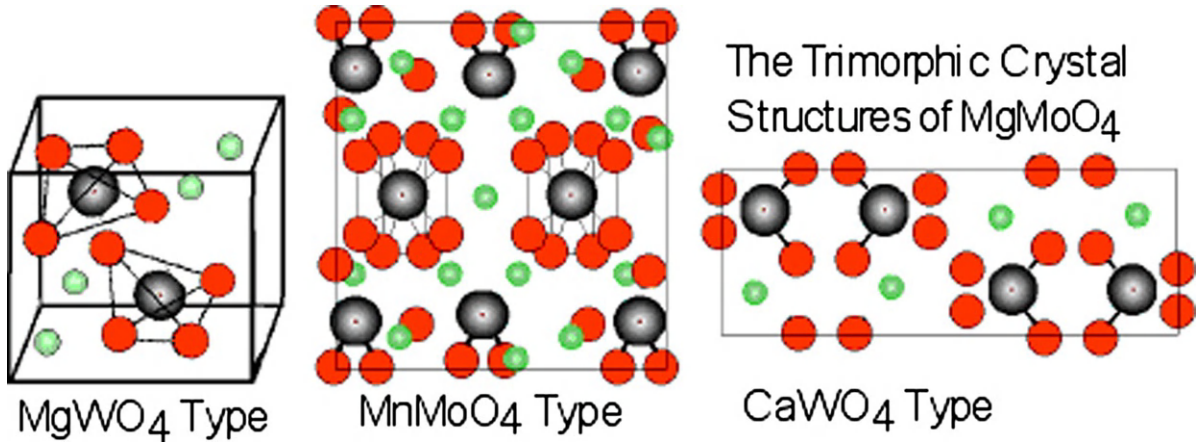

FIGURE 10.41

TABLE 10.28

No.	Site notation	Atom	Multiplicity	Wyckoff	Site symmetry	x	y	z	Occupancy
1	O1	O	8	j	1	0.0415	0.153	0.304	1.0
2	O4	O	8	j	1	0.1337	0.345	0.028	1.0
3	O2	O	8	j	1	0.3587	0.1439	0.3912	1.0
4	O3	O	4	i	m	0.1413	0	0.039	1.0
5	O5	O	4	i	m	0.2017	0	0.645	1.0
6	Mg2	Mg	4	i	m	0.2004	0	0.357	1.0
7	Mo2	Mo	4	i	m	0.7291	0	0.096	1.0
8	Mo1	Mo	4	h	2	0	0.251	1/2	1.0
9	Mg1	Mg	4	g	2	0	0.178	0	1.0

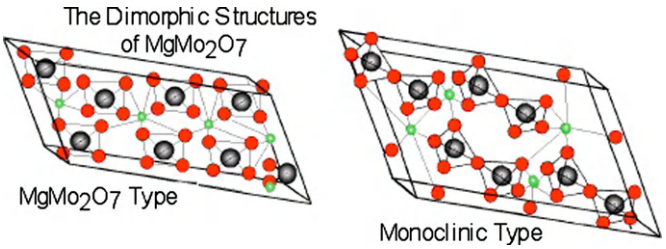

FIGURE 10.42

$MgMoO_4$ type: Cell parameters are: $a = 0.6.92$ Å, $b = 0.8.354$ Å, $c = 0.9.651$ Å, $\alpha = 96.48°$, $\beta = 106.9°$, $\gamma = 101.7°$, cell volume $= 513.87$ Å^3. Cell occupation has not been given.

The importance of luminescent tungstates and molybdates in several technological applications motivated the study of the structural, luminescence and scintillation properties of the $MgWO_4$–$MgMoO_4$ system. XRD studies allowed the identification of three main types of structures in the pseudo-binary system: $MgWO_4$–$MgMoO_4$ system (Sanmartinite = β-$MgMoO_4$, Cuproscheelite = α-$MgMoO_4$, and Wolframite = $MgWO_4$) and the refinement of the parameters of the crystal lattice. It was found that the single-phase solid solution $MgMo_{1-x}W_xO_4$ with the β-$MgMoO_4$ structure is created only at $x < 0.10$, while for higher tungsten content a mixture of different phases is formed. The X-ray luminescence spectra of a series of samples of the $MgWO_4$–$MgMoO_4$ system was measured at $T = 8$ K. The principal emission bands were assigned to the main structural phases as follows: β-$MgMoO_4$, 520 nm; α-$MgMoO_4$, 590 nm; $MgWO_4$ (Wolframite), 480 nm. The phase composition of the sample determined the actual shape of the observed spectra. Possible relations between the crystal structure and luminescence properties of different phases were discussed in terms of a configuration coordinate model. Of all the compounds under test, $MgWO_4$ was found to have the best scintillation response for particle excitation (0.90 ± 0.15 that of $ZnWO_4$ at $T = 295$ K). Further, the light yield also remained high with decreasing temperature, which makes this material potentially useful for cryogenic applications.

The dimorphic compound, magnesium dimolybdate, $MgMo_2O_7$, has the structure shown in Fig. 10.42.

One structure is monoclinic with space group $P2_1/c$ and $a = 8.111$ Å, $b = 5.700$ Å, $c = 15.002$ Å, $\beta = 115.32°$, $Z = 4$, $V = 627.54$ Å^3. The $Mo_2O_7^{2-}$ pyro-anion consists of two corner-sharing MoO_4 tetrahedra which are twisted from the ideal eclipsed configuration by an average of 12.3°. These Mo_2O_7−groups form anionic sheets parallel to the (100) plane. Mg^{2+} ions are situated between the anionic sheets in a distorted-octahedral arrangement of O atoms. The MgO_6 octahedra share one edge, forming Mg_2O_{10} units. The other structure consists of two MoO_4 tetrahedra arranged within the unit cell by 2 units and surrounded by MgO_8 octahedra. Cell parameters for this phase are: $a = 5.711$ Å, $b = 8.111$ Å, $c = 13.6748$ Å, $\alpha = 97.18°$, $\beta = \gamma = 90°$, cell volume $= 627.27$ Å^3, $Z = 4$. Cell occupancy is shown in Table 10.29.

The compound di-magnesium tri-molybdate, $Mg_2Mo_3O_8$, was obtained by solid-state reaction of MgI_2 and MoO_3 (1:1) at 200 °C and subsequent crystallization at 800 °C. Its formula is actually $MgO{\cdot}(MoO{\cdot}2MoO_3)$ where both Mo^{4+} and MoO^{6+} are present in the lattice structure. Under the same conditions, ZnI_2 and MoO_3 only yielded rather impure $Zn_2Mo_3O_8$; however, when ZnI_2 or CdI_2 and MoO_3 were taken in a molar ratio of 1:2, well-crystallized α-Mo_4O_{11} was obtained. The known crystal structures of $Mg_2Mo_3O_8$ and α-Mo_4O_{11} were refined

TABLE 10.29

No.	Site notation	Atom	Multiplicity	Wyckoff	Site symmetry	x	y	z	Occupancy
1	O4	O	4	e	1	0.0069	0.125	0.109	1.0
2	O7	O	4	e	1	0.1452	0.678	0.249	1.0
3	Mo2	Mo	4	e	1	0.2074	0.634	0.371	1.0
4	Mo1	Mo	4	e	1	0.2526	0.126	0.136	1.0
5	O3	O	4	e	1	0.2995	0.381	0.090	1.0
6	O1	O	4	e	1	0.3045	0.609	0.578	1.0
7	O5	O	4	e	1	0.3208	0.368	0.402	1.0
8	O2	O	4	e	1	0.391	0.113	0.261	1.0
9	Mg	Mg	4	e	1	0.5155	0.126	0.410	1.0
10	O6	O	4	e	1	0.6381	0.365	0.067	1.0

with new XRD data ($R = 0.030$ and 0.059, respectively) (Fig. 10.43).

The compound, $MgMoO_3$, does not exist. The structures of the oxidized and reduced phases in the system $MgO–MoO_3$ were characterized by XRD. With $SrMoO_4$, reduction resulted in the formation of $SrMoO_3$; however, each of the other oxides underwent a reversible decomposition. $MgMoO_4$ formed a mixture of crystalline MgO and $Mg_2Mo_3O_8$. For $MgMoO_4$, removal of one O/Mo occurred at a $p(O_2)$ of 10^{-6} atm., corresponding to a ΔG of oxidation of -100 kJ/mol-O_2; however, the equilibrium between $SrMoO_4$ and $SrMoO_3$ occurred at 10^{-26} atm. of O_2, corresponding to a ΔG of oxidation equal to -375 kJ/mol of O_2. These thermodynamic properties differ significantly from oxidation of MoO_2 to MoO_3, for which ΔG is -220 kJ/mol-O_2 at 873 K. All of the mixed oxides were essentially inactive for the selective oxidation of methanol, with specific rates that were much lower than that observed for MoO_3.

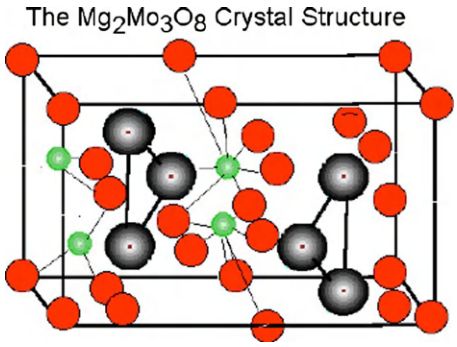

FIGURE 10.43

A compound of the formula $Fe_3Mg_2Mo_2V_3O_{20}$ has been obtained as a result of a reaction between $FeVO_4$ and $MgMoO_4$ taken at a molar ratio of 3:2. This compound crystallizes in the monoclinic system and its unit cell parameters are the following: $a = 6.971$ Å, $b = 9.055$ Å, $c = 1.2.542$ Å, $\gamma = 102.00°$, $Z = 2$.

There have been no uses developed in Industry for any of these magnesium molybdates. $MgMoO_4$ has the CAS number of 12013-21-7.

10.3.3. Calcium Molybdenum Compounds

Calcium oxide forms but few compounds with the molybdenum oxides. In the $CaO–Mo_2O_3$ system, a different strain-relaxation mechanism takes place in ultrathin CaO films grown on Mo(001). Whereas CaO films are amorphous at low growth temperature due to a substantial lattice mismatch with the support, a crystalline phase develops upon annealing to 1000 K. This phase is characterized by a sharp (2×2) pattern in low-energy ED and displays wide, atomically flat terraces in scanning tunneling microscopy (STM) images. The phase transition is initiated by the diffusion of Mo from the support into the film, where it replaces 25% of the Ca ions. The resulting rock salt-type Ca_3MoO_4 structure has a negligible lattice mismatch with the Mo(001), enabling the growth of extended, defect-free oxide patches. The oxidation of Mo atoms from the support provides a second, thermodynamic stimulus for the phase transition. For MgO films grown on the same Mo(001) surface, no relevant intermixing is revealed at the interface, most likely because of the smaller lattice mismatch between both systems.

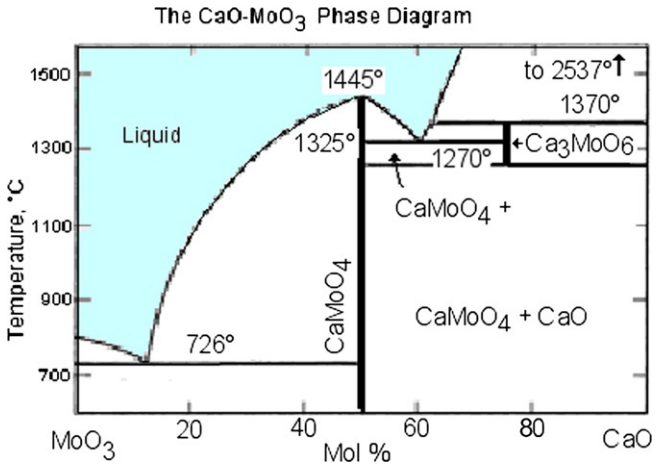

FIGURE 10.44

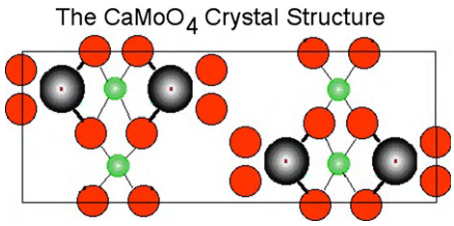

FIGURE 10.45

In the $CaO–Mo_2O_3$ system, no compounds like $CaMoO_4$ or $Ca_3Mo_2O_6$ are known.

The phase diagram is shown in Fig. 10.44.

Structure factors are shown in Table 10.30.

$CaMoO_3$ is the sole member of the $CaO–MoO_2$ family of compounds. The tri-calcium molybdate, Ca_3MoO_6 is meta-stable and only appears between the temperatures of 1270 and 1370 °C. It decomposes below 1270 °C into $CaMoO_4$:

$$Ca_3MoO_6 \Rightarrow CaMoO_4 + 2CaO$$

Calcium molybdate is a white tetragonal crystal with the CAS number of 7789-82-4. Its molecular weight is 200.02 g/mol. It melts at 1446 °C.

The compound, calcium molybdate, $CaMoO_4$, has the crystal structure shown in Fig. 10.45.

In this scheelite structure, the Ca^{2+} exists as a bisdisphenoid polyhedron with eight oxygen atoms forming a CaO_8 polyhedron, whereas the molybdenum (Mo) ions are surrounded by four oxygen atoms forming a tetrahedral unit. The CaO_8 polyhedron shares four of its edges with four other CaO_8 polyhedra extending in the *c*-directions. Each oxygen atom of the CaO_8 polyhedron is connected to one Mo atom. In particular, Mo-containing scheelite type ABO_4 compounds has been of interest for decades, not only because of its excellent optical properties suitable for phosphors, lasers, optical fibers, and electrochromic materials, but also due to its mixed conducting properties for negative electrode materials in Li-ion batteries. Single-phase tetragonal scheelite $CaMoO_4$ (space group, *Pmmm*) can be easily prepared via a conventional solid-state reaction method.

The refined unit cell parameters for $CaMoO_4$ at ambient temperature were: $a = 5.222$ Å, $b = 5.222$ Å, and $c = 11.425$ Å ($V = 311.55$ Å^3). The oxidation state of the transition metal species for the as-sintered $CaMoO_4$ was analyzed by XPS. The two well resolved spectral lines at 232.6 and 235.8 eV were assigned to the binding energies of an electron in Mo-$3d^{5/2}$ and Mo-$3d^{3/2}$, spin-orbit components, respectively. The average thermal expansion coefficient was about 11×10^{-6}/K over the temperature range 303–1273 K. This compound is not stable when heated to elevated temperatures because of the volatility of molybdenum trioxide:

$$CaMoO_4 + \text{heat} \Rightarrow CaO + MoO_3\Uparrow$$

It has been found that pure MoO_3 sublimes above 973 K, but the evaporation rate becomes much more significant beyond the melting point of MoO_3 at 1068 K. To investigate the relationship between evaporation rate and system composition changes, isothermal holding experiments were carried out in the case of $CaMoO_4$ at temperatures 1573, 1723, 1773 and 1823 K. All the mass decreases were assumed to be caused only by MoO_3 evaporation. The molar fraction of MoO_3 in the system was calculated for each time step based on the measured mass decrease. The following Fig. 10.46 shows the variation of evaporation rate as a function of MoO_3 remaining in the system, for $CaMoO_4$ at: (1) 1573 K, (2) 1723 K, (3) 1773 K, and (4)

TABLE 10.30

Compound	Structure type	Point group	Space group	Melting point, °C
$CaMoO_4$	$CaWO_4$	tl24	$I4_1/a$	1445
Ca_3MoO_6	—	—	—	1325
$CaMoO_3$	$GdFeO_3$	OP20	*Pnma*	

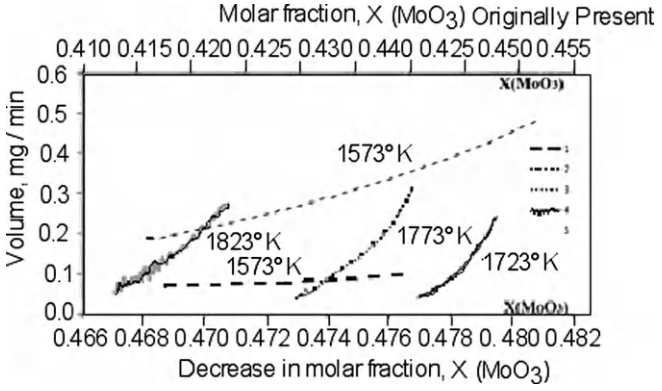

FIGURE 10.46

1823 K (lower *x*-axis) and (5) for $MgMoO_4$ at 1573 K (upper *x*-axis).

It can be seen from the figure that a considerable decrease in evaporation rate is observed for $CaMoO_4$ at each temperature (and to a lesser extent in the case of $MgMoO_4$) even after a small decrease in MoO_3 molar fraction. The X-ray studies showed that the calcium molybdate is formed from the oxide mixture in the temperature interval 773–873 K, which precedes the beginning of evaporation of MoO_3. Results of thermogravimetric (TG) studies with mixtures CaO and MgO with MoO_3 as well as the compounds $CaMoO_4$ and $MgMoO_4$ confirm the above results. In the vapor phase, MoO_3 is known to exist as a mixture of clusters like $(MoO_3)_2$, $(MoO_3)_3$, etc.

It was found, after TGA experiments with $CaMoO_4$ at 1573 and 1673 K were performed, that the substance remained solid and had a faint yellow color probably due to the partial evaporation of MoO_3 from the top of the layer. The sample was found, after the experiment at 1723 K, to have partially melted. In the case of the experiments at 1733, 1773 and 1823 °K, the formation of liquid phase seems to be complete. Hence, line 1 in the above Fig.10.46 should correspond to the evaporation from solid phase, while line 2 is for partially melted powder. These observations are in accordance with the results that reported that pure $CaMoO_4$ has melting point 1719 ± 5 K. Ca_3MoO_6 forms an eutectic with $CaMoO_4$ (60% of molar fraction of CaO with a melting temperature 1598 K). However, Ca_3MoO_6 is unstable below 1543 K and decomposes into CaO and $CaMoO_4$ which would result in only solid products on cooling. Considerable shrinkage and sintering were reported as a result of Ca_3MoO_6 formation from the solid mixture of CaO and MoO_3 above 1543 K. Even these are in accordance with the present results in the case of $CaMoO_4$ samples after treatment at 1573 and 1673 °K. It was found that MoO_3 can be stabilized by mixing with CaO, MgO or $CaCO_3$ and heating the mixtures as the result of appropriate molybdates formation. The formation of $CaMoO_4$ from the mixtures of MoO_3 with CaO or $CaCO_3$ starts after 773 K (as confirmed by high-temperature XRD studies) and is completed around 973 K. The structure of calcium molybdate was also studied by means of synchrotron-based high-resolution powder diffraction methods in the temperature range 12–300 K. The scheelite structure type was confirmed for $CaMoO_4$ in the temperature region investigated and no structural anomalies were observed.

A related compound, di-calcium molybdate, Ca_3MoO_6, can be formed at high temperatures. However, it is not stable below 1543 K and decomposes into $CaMoO_4$:

$$Ca_3MoO_6 \Rightarrow CaMoO_4 + CaO$$

The phase change is reversible. The reported transition appeared to be a ferroelastic second-order transformation producing a structure that is a monoclinic distortion of the low-pressure phase and was previously observed in compounds isostructural to $CaMoO_4$.

Single-crystalline thin films of $CaMoO_3$ and $SrMoO_3$ with a Mo^{4+} state perovskite structure have been epitaxially grown by pulsed-laser deposition from Mo^{6+} state ceramic targets. Phase-pure films were obtained on nearly lattice-matched perovskite substrates using argon gas flow during the deposition. Transport properties of the films are consistent with those of paramagnetic and metallic phases, whereas the residual resistivities are far lower than those reported previously for films and bulk polycrystals. These results indicate that this growth method can be useful for exploring the interfaces and junction properties of 4d and 5d transition metal oxides that are unstable in a conventional oxidative atmosphere.

The compound, **calcium molybdite**, $CaMoO_3$, has been prepared as a polycrystalline perovskite by soft-chemistry procedures, followed by controlled annealing under reducing conditions (H_2/N_2 flow). The crystal structure, studied from neutron powder diffraction data, can be described in an orthorhombic unit cell, space group *Pbnm* (No. 62). The lattice parameters were $a = 5.4510(1)$ Å, $b = 5.5821(1)$ Å and $c = 7.7803(2)$ Å. In the perovskite network, the MoO_6 octahedra are tilted by 13.5° in order to optimize the Ca–O bond lengths; the tilting scheme corresponds to a $GdFeO_3$-like superstructure. It has the form as shown in Fig. 10.47.

The perovskite is fully oxygen stoichiometric, as demonstrated from the refinement of the oxygen occupancy factors. Resistivity and transport measurements indicated that $CaMoO_3$ behaves as a metal; at low temperatures (5 K) a small positive magnetoresistance is observed, reaching a maximum value of

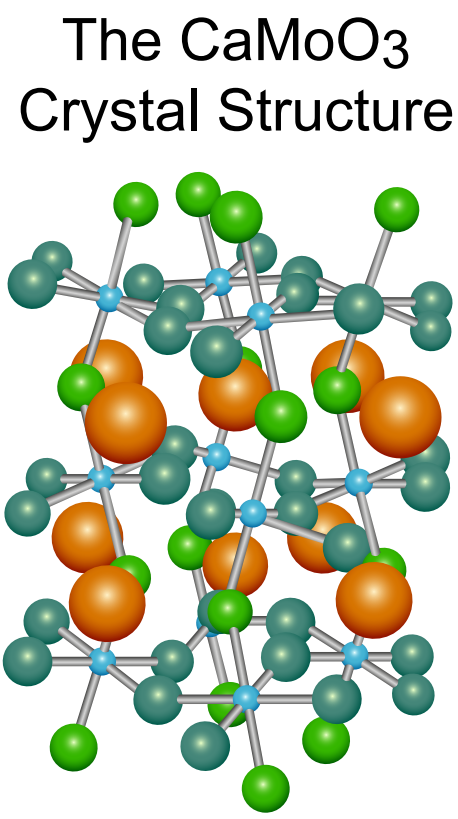

FIGURE 10.47

1.4% at 9 T. The magnetic susceptibility is predominantly Pauli paramagnetic-like, although a non-negligible temperature-dependent component due to isolated Mo^{4+} spins is patent at low temperatures. $CaMoO_3$ is an orthorhombic perovskite (*Pbnm*) where the MoO_6 octahedra are tilted by 13.5°. It was shown that:

(a) It is a Pauli paramagnet
(b) At low temperatures (5 K), it presents a small positive magnetoresistance

Reactions of $CaMoO_4$ and $CaMoO_3$ with ammonia were investigated at temperatures of $873\ K < T < 1123\ K$ with the particular intention to synthesize novel oxynitride perovskites of the general composition $AMo(O,N)_3$ and to study their crystal structure. $CaMo(O,N)_3$ and $BaMo(O,N)_3$ were prepared by thermal ammonolysis of the corresponding $CaMoO_3$ and $BaMoO_3$ precursors at $T = 898$ and 998 K, respectively. The structural parameters of the oxynitrides were obtained from Rietveld refinements of XRD and neutron powder diffraction data. $CaMo(O,N)_3$ crystallizes in the $GdFeO_3$ distorted perovskite structure with orthorhombic space group *Pbnm* and $a = 5.5029(1)$ Å, $b = 5.5546(1)$ Å, $c = 7.8248(1)$ Å as determined by XPRD. Its O/N content refined from the neutron diffraction data corresponds to the composition $CaMoO_{1.7(1)}N_{1.3(1)}$. $BaMo(O,N)_3$ crystallizes in the cubic perovskite structure with space group $Pm\bar{3}m$ and $a = 4.0657(1)$ Å as determined by XPRD. TEM reveals a complex microstructure for both $CaMoO_3$ and $CaMoO_{1.7}N_{1.3}$ represented by twin domains of different orientation.

Calcium molybdate, $CaMoO_4$, has the CAS number 7789-82-4. It is available commercially in tonnage lots.

10.3.4. Strontium Molybdenum Compounds

Strontium oxide forms a limited number compounds with the molybdenum oxides. The systems, SrO–MoO and Sro–Mo_2O_3 do not form any stable compounds.

In the system, SrO–MoO_2, single crystals of a highly conductive oxide $SrMoO_3$ have been grown by a floating-zone method under argon atmosphere with ultralow oxygen partial pressure $p(O_2) \sim 10^{-25}$ atm. The obtained single crystals of $SrMoO_3$ reveal quite low resistivity at 300 K $\rho(300\ K) = 5.1\ \mu\Omega\,cm$, which is the lowest to date in the values of $\rho(300\ K)$ of all the oxides. Resistivity and specific heat data suggest that electrons in $SrMoO_3$ behave as the Fermi liquid (correlated electron), and that its low resistivity is due to the extremely small electron–phonon interaction in $SrMoO_3$.

In another publication (2010) highly conductive $SrMoO_3$ thin films with a smooth surface were grown on $SrTiO_3$ substrates by pulsed-laser deposition. The substrate temperature ranged from 560 °C to 640 °C. Oxygen pressure below 10^{-3} Pa is necessary to obtain high-quality $SrMoO_3$ thin film. The film shows metal-like conducting behavior with low electrical resistivity on the order of 10 μΩ cm between 10 K and room temperature. The smooth surface, good conductivity and optical transparency in ultraviolet region suggest that $SrMoO_3$thin film can be used as a new electrode material and a favorable candidate in a variety of oxide device applications.

The compound, strontium molybdite, $SrMoO_3$, has the general structure as shown in Fig. 10.48.

An RF magnetron reactive sputtering method was used to prepare a $SrMoO_3$ thin film on a silica glass substrate so as to evaluate its optical properties. The reflectivity of the blue-colored film showed a cutoff due to plasmon at ~1.7 eV. From a Kramers–Kronig analysis of the reflectivity, the spectral dependence of dielectric constants and optical constants was obtained. They agreed in tendency with the constants determined by spectroscopic ellipsometry. The plasma frequency due to free carriers (4.5 eV) was obtained by application of a Drude model to reflectivity values, which showed that the effective mass of the

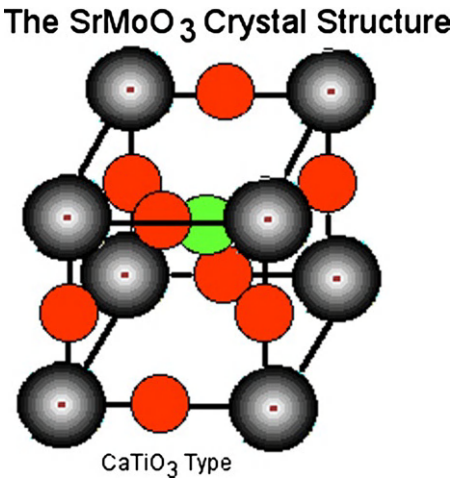

FIGURE 10.48

conduction carrier was $m^+ = 2.1m_0$, where m_0 is the free electron mass.

The structure of a polycrystalline sample of $SrMoO_3$ has been investigated using powder neutron diffraction from 5 to 300 K, to reveal two structural phase transitions, the first from the cubic structure with $a = 3.97629(3)$ Å to a tetragonal structure in *I4/mcm* near 266 K and the second to an orthorhombic *Imma* phase below 125 K. The average Mo–O distance is essentially independent of temperature. The temperature dependence of the octahedral tilting appears typical of a tri-critical phase transition (Fig. 10.49).

Variable temperature neutron diffraction measurements of $SrMoO_3$ from 5 K to room temperature show the presence of two-phase transitions associated with tilting of the octahedra. On cooling, the structure transforms from cubic to tetragonal (*I4/mcm*) and ultimately orthorhombic (*Imma*).

In addition, the enthalpy increment values ($HT^\circ\Delta H^\circ_{298.15\,K}$) of the compounds $SrMoO_3$(solid) and $BaMoO_3$(solid) were measured in the temperature range 426.2 to 1010.8 K (±0.1 K) and 477.8 to 1010.8 K (±0.1 K), respectively, using a high-temperature Calvet calorimeter. The data were least-square fitted with respect to temperature and are given by the following polynomials:

$$\underline{SrMoO_3(solid)}$$

$$\Delta H^\circ_{298.15\,K}\,(J/mol) = -29291 + 91.942\,T(K) + 0.0264\,T^2(K)$$

$$\underline{BaMoO_3(solid)}$$

$$\Delta H^\circ_{298.15\,K}\,(J/mol) = -31427 + 97.977\,T(K) + 0.0275\,T^2(K)$$

Heat capacities of the compounds calculated from the above equations were compared with estimated heat capacity values obtained by Neumann Kopp's rule. Standard entropy ($S_m^\circ(298.15\,K)$), standard enthalpy of formation ($\Delta_f H^\circ(298.15\,K)$) and free energy functions of the compounds were calculated using heat capacities obtained from present experiments, Gibbs free energy of formation of the compounds reported in the literature and elemental thermodynamic data.

In another work, it was determined that $SrMoO_4$ reduced to $SrMoO_3$ at ~800 °C in $4\%H_2/Ar$ and $SrMoO_3$ was found to oxidize to $SrMoO_4$ around 450 °C in air. After performing several redox cycles at 800 °C, no secondary phases were detected with XRD. Secondary phases were also not detected for SMO–YSZ composites sintered up to 1200 °C indicating good chemical compatibility. At 800 °C, the bulk conductivity of $SrMoO_4$ was of order 10^{-3} S/cm. Upon reduction to $SrMoO_3$ the bulk conductivity increased six orders of magnitude to ~103 S/cm. For the infiltrated SMO–YSZ composites, SMO appeared to reach the percolation threshold at loadings between 9% and 14%. An SMO loading of 20% resulted in a conductivity of 20 S/cm, which exceeds the electron conductivity requirement of SOFC anodes.

The system, $SrO–MoO_3$, when heated to elevated temperatures, forms two compounds, $SrMoO_4$ and Sr_3MoO_6. Structure factors for these known compounds are shown in Table 10.31.

Note that Sr_3MoO_6 is dimorphic. The phase diagram for the hexavalent compounds in the system, $SrO–MoO_3$ is shown in Fig. 10.50. The phase diagram of $SrO–MoO_2$ is not known.

Compound formation and compatibility relations have been studied for a portion of the system Sr···Mo···O at 1200 °C. The following binary compounds were prepared: $SrMoO_4$ with the tetragonal scheelite structure, $SrMoO_3$ with the cubic perovskite structure and Sr_3MoO_6. This last compound gave x-ray

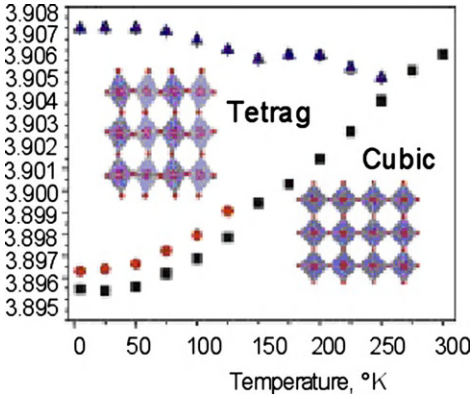

FIGURE 10.49

TABLE 10.31

No.	Compound	Mo valence	Structure type	Point group	Space group	Melting temperature, °C
1	α-Sr_3MoO_6	Mo^{6+}	$(NH_4)_3FeF_6$	cF40	*Fm*-3*m*	1650
2	β-Sr_3MoO_6	Mo^{6+}	$GdFeO_3$	oP20	*Pnma*	1050
3	$SrMoO_4$	Mo^{6+}	$CaWO_4$	tI24	$I4_1/a$	1457
4	$SrMo_5O_8$	Mo^{+4}	$LaMo_5O_8$	mP56	$P2_1/c$	
5	$SrMoO_3$	Mo^{4+}	$CaTiO_3$	cP5	*Pm*-3*m*	

powder data which could be indexed on a cubic unit cell with $a_0 = 16{\cdot}39(1)$ Å. It appeared to have a structure related to that of $(NH_4)_3FeF_6$. X-ray powder data have been determined for $SrMoO_3$ and Sr_3MoO_6. A previously reported fourth compound, Sr_2MoO_4, could not be prepared at 1000, 1200 or 1400 °C. The stable phase assemblage at its bulk composition was (Sr_3MoO_6 + Mo).

However, in later studies, this compound has been evaluated based upon its superconducting properties. In systematic study of polycrystalline Sr_2MoO_4 as an electronic analogue to the spin-triplet superconductor Sr_2RuO_4, the Pauli paramagnetic susceptibility and metallic behaviors of specific heat and electrical resistivity have been observed. The relevant structure has the form shown in Fig. 10.51.

The density of states at the Fermi level $D(E_F)$ deduced from the results is about three times smaller than that of Sr_2RuO_4. Any indication of superconductivity intrinsic to Sr_2MoO_4 has not been observed down to 25 mK, which may correspond to the smaller $D(E_F)$ used to discuss the origin of the difference in electronic states between Sr_2MoO_4 and Sr_2RuO_4.

The crystal structure of $SrMoO_4$ has the form shown in Fig. 10.52.

$SrMoO_4$ was studied under compression up to 25 GPa by angle-dispersive XRD. A phase transition was observed from the scheelite-structured ambient phase to a monoclinic fergusonite phase at 12.2 GPa that had cell parameters $a = 5.265$ Å, $b = 11.191$ Å, $c = 5.195$ Å, and $\beta = 90.9°$, $Z = 4$ at 13.1 GPa. There was no significant volume collapse at the phase transition. No additional phase transitions were observed and on release of pressure the initial phase was recovered, implying that the observed structural modifications are reversible. The reported transition appeared to be a ferroelastic second-order transformation producing a structure that is a monoclinic distortion of the low-pressure phase and was previously observed in compounds isostructural to $SrMoO_4$. The two types of structures are shown in Fig. 10.53.

This figure shows: (a) the scheelite structure of $SrMoO_4$ at 0.5 GPa and (b) the fergusonite structure of $SrMoO_4$ at 24 GPa. Large blue circles represent the Sr atoms, middle-size blue circles the Mo atoms and small black circles the O atoms. The unit cell, Sr–O bonds, and

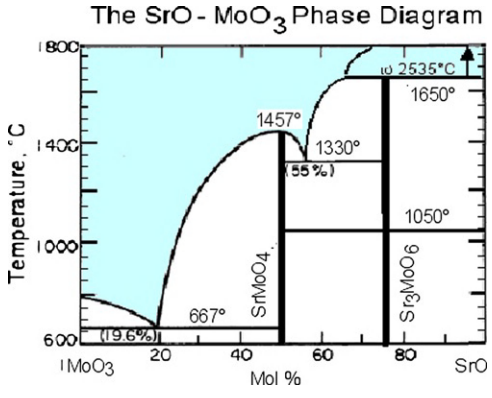

FIGURE 10.50

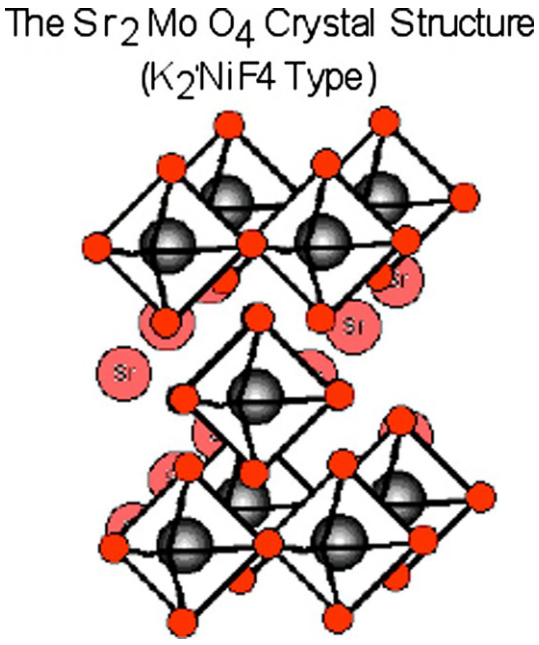

FIGURE 10.51

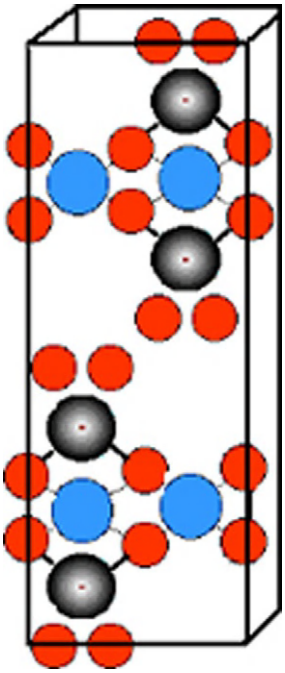

FIGURE 10.52

Mo–O bonds are also shown. In (b), it is illustrated that at high pressure the Mo coordination changes from 4 to 6 with two short bonds (gray), two middle-size bonds (red), and two large bonds (black).

A possible mechanism for the transition has been proposed and its character was discussed in terms of the present data and the Landau theory. Finally, the EOS was reported and the anisotropic compressibility of the studied crystal was discussed in terms of the compression of the Sr–O and Mo–O bonds.

High-temperature mass-spectrometric analysis was used to study the sublimation of $SrMoO_4$(s) at 1570–1800 K. SrMoO ≠ (g) molecules are found to be present in the vapor. The vapor pressure of the SrMoO ≠ (g) molecule was determined to be $\log p = -19980/T + 7.99$. The heat of sublimation ΔH^0_s, $(SrMoO_4(s)) = 480 \pm 40$ kJ/mol was determined using the third law of thermodynamics. The atomization energy of the $SrMoO_4$(g) molecules is calculated to be ΔH^0_{at}, $(SrMoO_4(g)) = 2860 \pm 40$ kJ/mol.

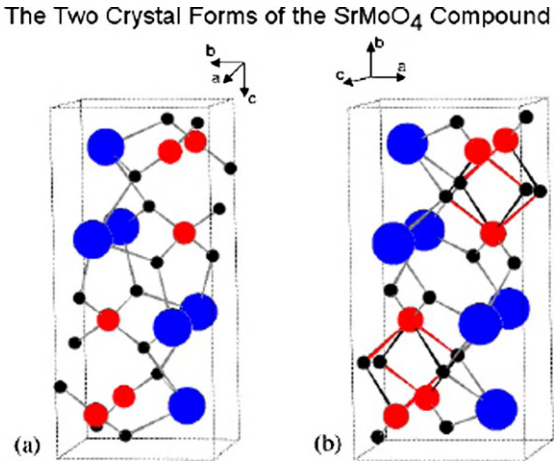

FIGURE 10.53

A fluorescent material for white light emitting diodes (LEDs) involving Eu^{3+} activated molybdate $SrMoO_4$ as a phosphor was fabricated by a solid-state method. XRD showed that the doping of trivalent europium ion reduced the lattice parameters. The excitation and emission spectra indicated that this phosphor could be excited effectively by visible light which then emitted red light with the peaks located at 616 and 624 nm. The influence of Eu^{3+} concentration on the luminescent properties of Eu^{3+} doped $SrMoO_4$ was investigated and the formulation, $(Sr_{0.75}Eu^{3+}_{0.25})$, i.e. 25% mole fraction, was found to be the appropriate molar concentration. The reaction time and temperature had an obvious effect on the luminescent properties. The luminescent intensity reached the strongest when it was sintered at 800 °C for 3 h.

The elemental and phase compositions during the solid-state synthesis of the promising solid oxide fuel cell (SOFC) anode material, Sr_2MgMoO_6, was investigated. It was demonstrated that molybdenum does not notably evaporate under the normal synthesis conditions with temperatures up to 1200 °C due to the formation of $SrMoO_4$ as an intermediate product that occurs at low temperatures, i.e. below 600 °C. However, partial decomposition of the Sr_2MgMoO_6 phase becomes evident at higher temperatures (1500 °C). The effect of $SrMoO_4$ on the electrical conductivity of Sr_2MgMoO_6 was evaluated by preparing a series of Sr_2MgMoO_6 samples with different amounts of additional $SrMoO_4$. Under the reducing operation conditions of an SOFC anode the insulating $SrMoO_4$ phase is apparently reduced to the highly conductive $SrMoO_3$ phase. Percolation takes place with 20–30 wt% of $SrMoO_4$ in an Sr_2MgMoO_6 matrix, with a notable increase in electrical conductivity after reduction. Conductivity values of 14, 60 and 160 S/cm are determined at 800 °C in 5% H_2/Ar for the Sr_2MgMoO_6 samples with 30, 40 and 50 wt% of added $SrMoO_4$, respectively.

For many years, there had been debates over the existence of the compound Sr_2MoO_4 until Lindblom demonstrated that it crystallizes in a K_2NiF_4 type of structure. However, what was actually obtained was a mixture of Sr_2MoO_4 and SrO, and the latter had to be washed away with methanol. Recently, interest in Sr_2MoO_4 has emerged in solid-state physics with the discovery of unconventional superconductivity in

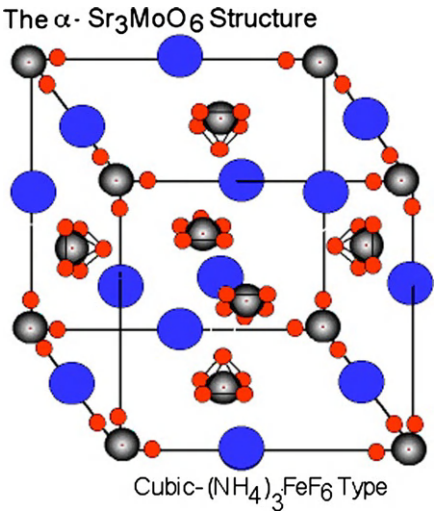

FIGURE 10.54

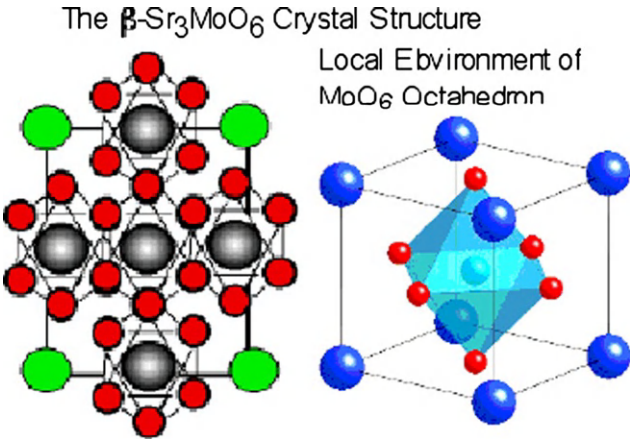

FIGURE 10.55

Sr_2RuO_4. This compound, Sr_2MoO_4, can be prepared using Ti_2O_3 as a catalyst for the reaction:

$$Sr_3MoO_6 + Ti_2O_3 \Rightarrow Sr_2MoO_4 + TiO_2$$

The reaction was first carried out at 840 °C under a flowing Ar atmosphere. The sealed tube was kept at 1150 °C for 1 week. Prior to this, Sr_3MoO_6 had been prepared according to the reaction:

$$3SrCO_3 + MoO_3 \Rightarrow Sr_3MoO_6 + 3CO_2(gas)$$

The mixture of $SrCO_3$ (99.99%) and MoO_3 (99.99%) was heated in flowing Ar atmosphere at 1000 °C for 24 h with two intermittent grindings. This compound is stable in air but if heated to 400 °C, it reverts to the $SrMoO_4$ structure. The layered compound Sr_2VO_4 is an antiferromagnetic insulator with $S = 1/2$, while the isostructural Sr_2MoO_4 is a Pauli paramagnetic metal.

The compound, **tristrontium molybdate**, Sr_3MoO_6, is unstable and melts incongruently. Sr_3MoO_6 was melted in Ar atmosphere under an ultralow oxygen partial pressure (ULOPP) of $p(O_2) = 10'–20'$ Pa by a lamp-image furnace at 1830–1900 K. Sr_3MoO_6 melted in Ar atmosphere was yellow, whereas Sr_3MoO_6 melted under ULOPP changed from yellow to metallic ash-gray luster. XPES analysis showed that the Sr in Sr_3MoO_6 was strongly reduced chemically to a metallic state and that the binding energy of Mo was shifted to the high-energy side. Its structure is shown in Fig. 10.54.

Cell parameters are: $a = b = c = 5.8266$ Å, $\alpha = \beta = \gamma = 60°$, cell volume $= 139.87$ Å^3, $Z = 2$. Cell occupancy is shown in Table 10.32.

The other polymorphic form of Sr_3MoO_6 has the $GdFeO_3$ structure, as shown in Figure 10.55. The heat of formation, $\Delta fG^o_m(Sr_3MoO_6,solid,T)$, has been obtained by measuring equilibrium pressures of CO_2(gas) over the ternary mixture $SrMoO_4$(solid) + $SrCO_3$(solid) + Sr_3MoO_6(solid) in the temperature range 1040–1215 K, using a static manometric method (Fig. 10.55).

The heat of formation, $\Delta_f G^o_m(Sr_3MoO_6,solid,T)$, has been obtained by measuring equilibrium pressures of CO_2(gas) over the ternary mixture $SrMoO_4$(solid) + $SrCO_3$(solid) + Sr_3MoO_6(solid) in the temperature range 1040–1215 K, using a static manometric method. It was found to be given by the equation:

$$\Delta_f G^0_m(Sr_3MoO_6, solid, T)\ (kJ/mol) \pm 0.6 = -2837.9 + 0.6036\,T(K)$$

Using the heat capacity values of Sr(s,1), Mo(solid) and O_2(gas) from the literature, Sr_3MoO_6(solid) from

TABLE 10.32

No.	Site notation	Atom	Multiplicity	Wyckoff	Site symmetry	x	y	z	Occupancy
1	O	O	24	e	4m.m	0.22	0	0	1.0
2	Sr2	Sr	8	c	-43m	1/4	1/4	1/4	1.0
3	Sr1	Sr	4	b	m-3m	1/2	1/2	1/2	1.0
4	Mo	Mo	4	a	m-3m	0	0	0	1.0

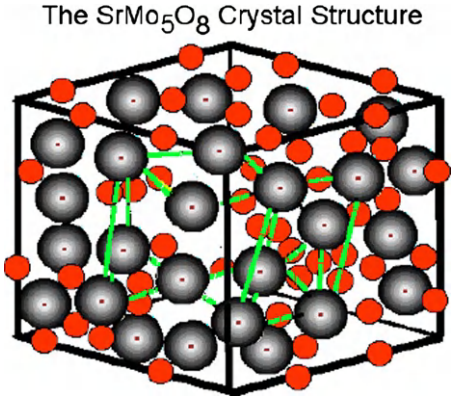

FIGURE 10.56

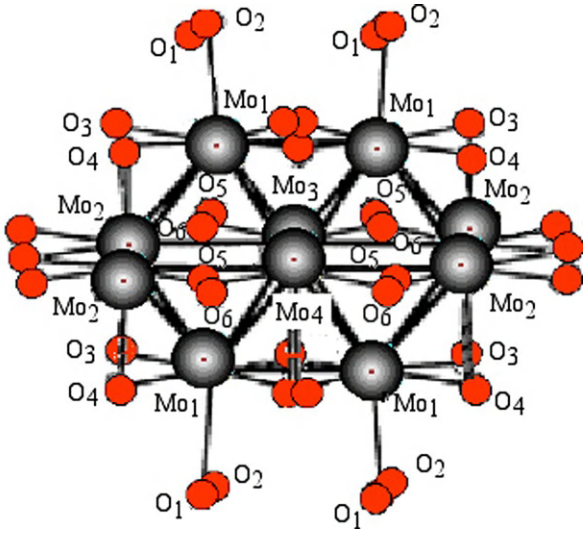

FIGURE 10.57

this work and the variation of $\Delta_f G^{o}_{m}(T)$ with temperature, the value of $\Delta_f H^{0}_{m}$ (at 298.15 K) was calculated as $-(2821.2 \pm 3.0)$ kJ/mol.

A related compound, $Sr_3Mo_2O_7$ has been found. $Sr_3Mo_2O_7$ is a member of the Ruddlesden–Popper type series of $Sr_{n+1}Mo_nO_{3n+1}$ with $n = 2$, a so-called double layered perovskite. This compound has been successfully synthesized to obtain polycrystalline samples of single-phase $Sr_3Mo_2O_7$ with the aid of Ti_2O_3 as $p(O_2)$ buffer. The phase-pure samples allowed us to perform measurements of the electrical resistivity and the magnetic susceptibility on $Sr_3Mo_2O_7$ for the first time. The resistivity revealed that $Sr_3Mo_2O_7$ is a metallic conductor from 300 K to 30 mK. The Pauli-paramagnetic behavior is observed in the susceptibility. This means that $Sr_{n+1}Mo_nO_{3n+1}$ compositions for $n = 1$, 2, and ∞ all show the Pauli-paramagnetic metal behavior, in contrast to $Sr_{n+1}Ru_nO_{3n+1}$ which involves an electronic analogue series.

The compound, strontium penta-molybdate, $SrMo_5O_8$, is a composition and structure unique among the alkaline earth molybdates. It contains Mo^{4+} ions arranged as $Mo_{10}O_{18}$ units so that the average valence is 3.6^{+}. There are 2 units per unit cell, one of which is shared by neighboring cells. The overall structure has the form shown in Fig. 10.56.

Unit cell parameters are: $a = 7.553$ Å, $b = 9.1556$ Å, $c = 9.966$ Å, $\alpha = \gamma = 90°$, $\beta = 109.301°$, cell volume = 650.44 Å^3, $Z = 3$. Cell occupancy is shown in Table 10.33.

This compound is isostructural with $LaMo_5O_8$ and contains bi-octahedral $Mo_{10}O_{18}$ cluster units, strongly linked by Mo···Mo intercluster bonds to form infinite molybdenum oxide chains. Each unit has the form shown in Fig. 10.57.

TABLE 10.33

No.	Site notation	Atom	Multiplicity	Wyckoff	Site symmetry	*x*	*y*	*z*	Occupancy
1	O2	O	4	e	1	−0.0045	0.275	0.064	1.0
2	Mo2	Mo	4	e	1	0.0015	0.378	0.414	1.0
3	O3	O	4	e	1	0.0078	0.501	0.763	1.0
4	Mo3	Mo	4	e	1	0.1781	0.626	0.387	1.0
5	Mo4	Mo	4	e	1	0.187	0.132	0.201	1.0
6	O6	O	4	e	1	0.2018	0.746	0.216	1.0
7	O5	O	4	e	1	0.2017	0.249	0.382	1.0
8	Sr	Sr	4	e	1	0.2533	0.504	0.039	1.0
9	Mo1	Mo	4	e	1	0.3894	0.114	0.017	1.0
10	O1	O	4	e	1	0.395	0.006	0.339	1.0
11	O4	O	4	e	1	0.599	0.256	0.480	1.0

These chains are interconnected through Mo···O···Mo bonds to create four-sided channels in which the Sr^{2+} ions are located. Each Sr^{2+} cation is surrounded by 10 O atoms at distances ranging from 2.529–2.835 Å with the 11th O atom at 3.219 Å in the SrO_{11} cluster in the structure.

Strontium molybdate is available commercially with the CAS number of 13470-04-7. Both $SrMoO_4$ and Sr_3MoO_6 are offered for sale.

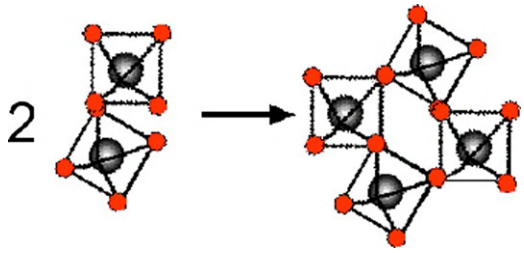

FIGURE 10.58

10.3.5. Barium Molybdates

Barium forms a number of compounds with molydenum oxides. The Mo^{3+}, Mo^{4+} and Mo^{6+} valance states are the most common.

In the BaO–MoO system, no compounds like Ba_2MoO_3 or Ba_3MoO_4 have been reported.

In the BaO–Mo_2O_3 system, the compound $BaMo_2O_4(C_2O_4)_2{\cdot}5H_2O$ was synthesized by the aqueous reaction of $H_2C_2O_4$ and $(NH_4)_2[MoOCl_5]$. This substance contains the binuclear anion, $[Mo_2O_4(C_2O_4)_2(H_2O)_2]^{2-}$ with two octahedrally-coordinated Mo atoms. The octahedra are canted in the middle of the central Mo_2O_2-rings which are formed from the union of two octahedra shown in Fig. 10.58.

However, this compound is not stable and the requisite $BaMo_2O_4$ compound has never been reported. In this Mo^{3+}-containing system, a novel ternary molybdenum oxide, $BaMo_6O_{10}$, was discovered and its crystal structure was determined from single-crystal XRD data. $BaMo_6O_{10}$ crystallizes in the orthorhombic space group *Pnma* with $a = 10.154$ Å, $b = 8.641$ Å, $c = 9.184$ Å, $V = 805.7$ Å^3, $Z = 4$, $R = 0.0438$, $R_w = 0.0401$ for 652 independent reflections with $I > 3.0\sigma(I)$. The structure contains infinite zigzag molybdenum oxide chains built up from M_6O_{12}-type clusters, cross-linked to form channels where Ba^{2+} cations reside. Bond distance analysis results indicate that $BaMo_6O_{10}$ is perfectly bonded with all valence electrons of the Mo atoms in either Mo···Mo or Mo···O bonding states.

In the BaO–MoO_2 system, a ternary oxide, $BaMoO_3$ (Scholder and Brixner, 1955) characterizes this system shown in Fig. 10.59.

$BaMoO_3$ has the $CaTiO_3$ cubic structure (space group *Pm3m*) with $a = 4.0404$ Å.

A polycrystalline sample of perovskite type barium molybdate, $BaMoO_3$, was prepared by a reduction of $BaMoO_4$ under 4% H_2–Ar atmosphere at 1523 K. The thermoelectric properties, viz. the electrical resistivity, Seebeck coefficient, and thermal conductivity of $BaMoO_3$ have been evaluated from room temperature to about 1000 K. The electrical resistivity of $BaMoO_3$ is slightly lower than that of state-of-the-art thermoelectric materials, and has a positive temperature dependence. The Seebeck coefficient of $BaMoO_3$ is negative in the whole temperature range. The thermal conductivity of $BaMoO_3$ at room temperature equals 30 W/m/K, which is very high compared with that of state-of-the-art thermoelectric

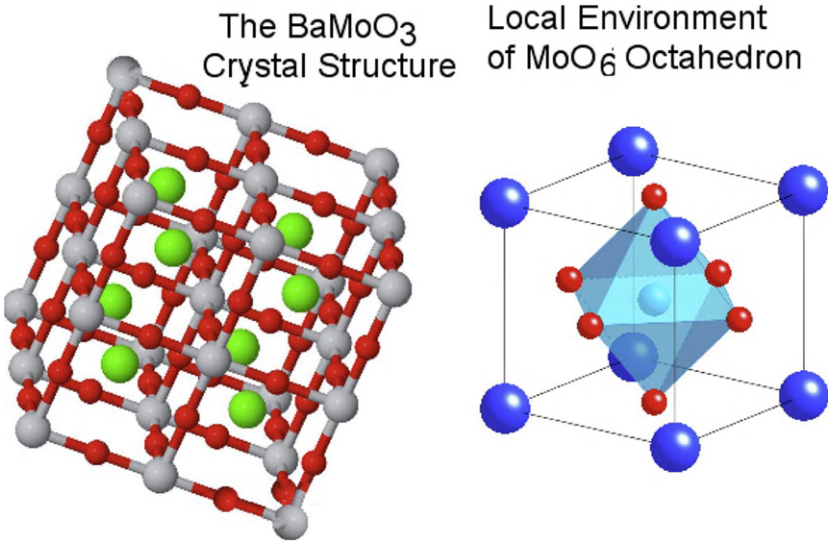

FIGURE 10.59

materials. The maximum value of the thermoelectric figure of merit ZT is 0.015 at around 470 K.

The thermal stability of $BaMoO_3$(solid) was determined by differential thermal analysis (DTA) (solid) and TG methods. A slight gain in weight in the TG curve was attributed to the oxidation of $BaMoO_3$(solid) to $BaMoO_4$(solid) in analytical reagent grade argon at 1050 K. However, the DTA curve did not show any exothermic or endothermic peaks. This confirms the absence of any solid-state phase change in $BaMoO_3$(solid) below 1050 K. It was found by DTA measurements under flowing argon and helium atmospheres that $BaMoO_3$(solid) decomposes at 1653 K into $BaMoO_4$(solid), Mo(solid), and BaO(gas). Mass spectrometric studies reported that barium molybdate salts mainly evaporate as molecular $BaMoO_4$(gas) and $BaMoO_3$(gas). This work identified ternary gaseous oxides, $BaMoO_3$(gas), from the mass spectra of vapor effusing from a molybdenum Knudsen cell containing $BaMoO_4$(solid) and MoO_3(l) at $T > 1900$ K. $BaMoO_3$(gas) was predicted to form as a result of the reaction:

$$BaMoO_4(gas) + MoO_2\ (gas) \Rightarrow BaMoO_3\ (gas) + MoO_3\ (gas)$$

Because the molecular species in this reaction were present in the vapor phase in concentrations of the same order. The enthalpy of formation for the reaction:

$$2BaMoO_3 + O_2 \Rightarrow 2BaMoO_4$$

was measured by oxygen bomb calorimetry, and the Gibbs energy change of the reaction was reported as: $\Delta H_f = -1228$ kcal/mol ($T = 1480$–1580 K).

Perovskite-type oxides, $BaMoO_3$ and $SrMoO_3$, were prepared by reduction of scheelite-type oxides, $BaMoO_4$ and $SrMoO_4$, in H_2 flow at 873 K and characterized by XRD, TG, SEM, TPR, NH_3-TPD, UV–Vis DRS and BET measurement. The catalytic activity of these alkaline earth molybdenum oxide catalysts was tested for oxidation of 2-propanol with gaseous oxygen under atmospheric pressure. Dehydration to propylene was mainly promoted over the scheelite-type with Mo^{6+} ions, while oxidative dehydrogenation to acetone was mainly promoted over the perovskite type with Mo^{4+} ions, and selectivity to acetone was much higher over $BaMoO_3$ than over $SrMoO_3$. Both perovskite-type oxide catalysts underwent oxidation to some degree during the catalytic reaction, so that they also contained some Mo^{6+}. It was concluded that the high selectivity to acetone resulting from oxidative dehydrogenation during 2-propanol conversion was related to the constantly changing oxidation state of the catalyst, resulting in coexistence of Mo^{6+} octahedra and Mo^{4+} octahedra on the $AMoO_3$ oxides.

This system was said to be characterized by nine ternary oxides. This is the only comprehensive listing of compounds available in the literature:

$BaMoO_3(Mo^{4+})$	$BaMoO_4(Mo^{6+})$
$BaMo_2O_7(Mo^{6+})$	$BaMo_3O_{10}(Mo^{6+})$
$BaMo_4O_{13}(Mo^{4+})$	$Ba_2MoO_5(Mo^{6+})$
$Ba_2Mo_5O_{17}(Mo^{6+})$	$Ba_3MoO_6(Mo^{6+})$
	$Ba_3Mo_7O_{24}(Mo^{6+})$

All but two has the 6+-valence state. Although the structure of many of these compounds is known, a finalized phase diagram has not been published. In Fig. 10.60, presented on the next page, the positions of each of these compounds are shown relative to one another along with known melting temperatures (where known). Only $BaMoO_4$ is known to melt congruently.

The exact melting points need to be established with more certainty. The phase diagram shows how these melting points would probably be arranged, given the melting points of the two components, BaO and MoO_3. Nevertheless, this is a representation of how the melting points of this series of compounds ought to appear, but these melting points shown have not yet been firmly established.

In the BaO–MoO_3 system, the system is characterized by these seven ternary oxides. $BaMoO_4$ has a tetragonal structure (space group $I4_1/a$) with $a = 5.56$ Å, $c = 12.76$ Å. Ba_2MoO_5 has an orthorhombic structure with $a = 7.4097$ Å, $b = 11.3906$ Å, $c = 5.7603$ Å and $\alpha = \beta = 65.04°$ and $\gamma = 50.67°$. Lattice parameters of the other barium molybdates have not yet been published in the open literature.

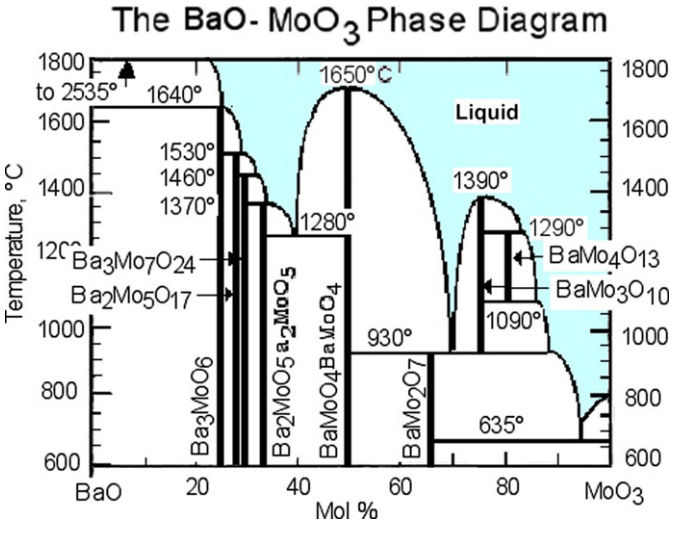

FIGURE 10.60

The structure factors (where known) are shown in Table 10.34.

The structure of barium ortho-molybdate, $BaMoO_4$, has the same structure as the $SrMoO_4$ composition, as shown in Fig. 10.61.

Cell parameters are: $a = b = 5.581$ Å, $c = 7.526$ Å, $\alpha = \beta = 111.76°$, $c = 90°$, cell volume = 199.60 Å^3, $Z = 2$. Cell occupancy is shown in Table 10.35.

Another view of the scheelite-like $BaMoO_4$ structure is shown in Fig. 10.62.

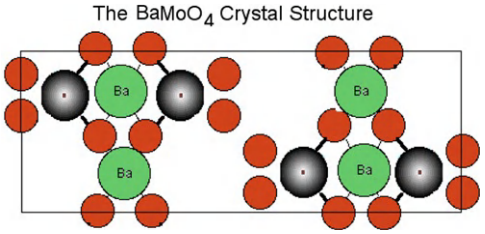

FIGURE 10.61

Scheelite-structured alkaline earth molybdates are technologically important materials as these are used as scintillators, laser host materials or cryogenic detectors for dark matter. These tungstates are also being considered for Raman lasers. $BaMoO_4$ can assume two structures, tetragonal distorted scheelite (b) and cubic (a), depending on the temperature applied during their synthesis. $BaMoO_4$ with a scheelite structure is an important material that has a high application potential in various fields. Recently, crystal structures based on the scheelite type have attracted much interest because of their applications as a scintillating medium and in other electro-optical devices (i.e. solid-state laser and optical fibers). In these scheelite-structured compounds (space group $I41/a$, $Z = 4$), oxygen atoms form a distorted simple cubic arrangement, while the two cations in this structure have fourfold and eightfold coordination with the oxygen atoms. XRD and Raman scattering studies on the scheelite structured barium molybdate show that, at ~5.8 GPa, it undergoes a first-order phase transition to the fergusonite structure ($I2/a$, $Z = 4$)—as also observed in iso-structural barium tungstate. At still higher pressures, barium molybdate transforms to another phase between ~7.2–9.5 GPa. On release of pressure from 15.8 GPa, the initial phase is recovered implying that the observed structural modifications are reversible. The form of the two phases is shown in the diagram as follows. $BaMoO_4$ undergoes structural transformations similar to its strontium homologue as shown in Fig. 10.63.

In the $BaCO_3 \cdot MoO_3$ system with an excess of barium carbonate, $BaMoO_4$ is the stable reaction product up to 1073 K. Above 1073 K, Ba_2MoO_5 and Ba_3MoO_6 can be formed. $BaMo_2O_7$ was formed with an excess of MoO_3. Ustinov et al. (1970) and Yanushkevich and Zhukovskii (1972) gave a partial phase diagram of this system. $BaMoO_4$(s) melts congruently at 1737 K. The compound, $BaMo_2O_7$, melts incongruently at 926 K.

SOFCs have attracted great attention in electrochemical devices because of their high-energy conversion efficiency, little pollution and widely flexible fuel choices. Scheelite type based oxide ion conducting materials like $PbWO_4$, $BaMoO_4$, $SrMoO_4$ possess more ion conductivity and can also be used as an electrolyte for intermediate temperature SOFC (ITSOFC) applications. The development of nanocrystalline Dy^{3+} doped $BaMoO_4$ was pursued in order to increase the ionic conductivity for ITSOFC applications. Nanocrystalline dysprosium doped $BaMoO_4$ samples were prepared by an acrylamide-assisted combustion process. All the samples were characterized by TG/DTA, XRD, FTIR and SEM-EDX techniques and studied concerning their grain and grain boundary conductivities through impedance measurements. XRD patterns of the Dy^{3+} doped $BaMoO_4$ samples and the formation of the crystalline $BaMoO_4$ phase and some mixed phases were

TABLE 10.34

Compound	Structure type	Point group	Space group	Melting point, °C
$BaMoO_4$	$CaWO_4$	tl24	$I4_1/a$	1650
Ba_3MoO_6	$(NH_4)_3FeF_6$	cF40	*Fm-cm*	1325
$BaMoO_3$	$GdFeO_3$	OP20	*Pnma*	

TABLE 10.35

No.	Site notation	Atom	Multiplicity	Wyckoff	Site symmetry	*x*	*y*	*z*	Occupancy
1	O1	O	16	f	1	0.1507	0.009	0.2106	1.0
2	Ba1	Ba	4	b	-4..	0	1/4	5/8	1.0
3	Mo1	Mo	4	a	-4..	0	1/4	1/8	1.0

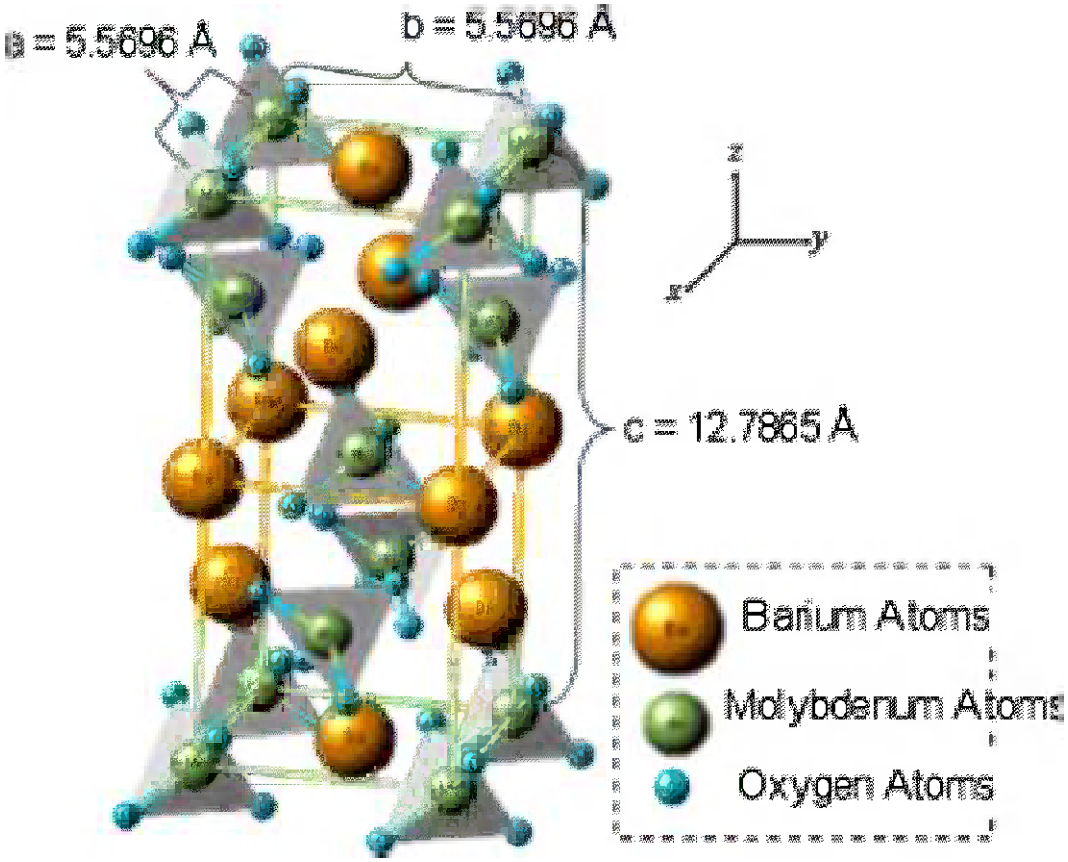

FIGURE 10.62

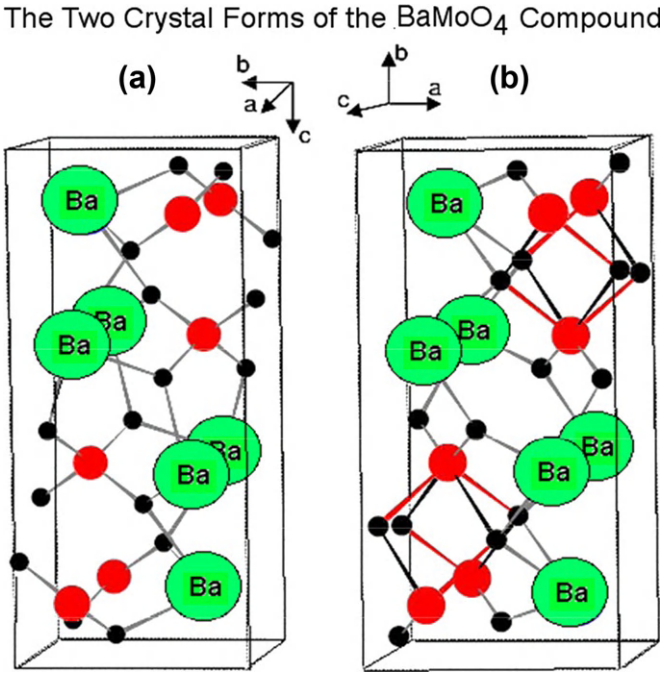

FIGURE 10.63

confirmed by comparing the ICDD data with the observed XRD peaks. The crystallite size was calculated using Scherrer's formula for all the compositions of compounds and found to be less than 100 nm. FTIR spectra results confirm the formation of the MoO_3 structure in Dy^{3+} doped $BaMoO_4$ samples. SEM image of a particular composition of Dy^{3+} doped $BaMoO_4$ sample (BDM4) showed agglomerated spherical particles.

The formation of barium monomolybdate ($BaMoO_4$) in equimolar powder mixtures of $BaCO_3$ and MoO_3 was examined under isothermal and nonisothermal conditions upon heating in air at 25–1200 °C, using thermogravimetry. Concurrence of the observed mass loss (due to the release of CO_2) to the occurrence of the formation reaction was evident. Accordingly, the extent of reaction (x) was determined as a function of time (t) or temperature (T). The x–t and x–T data thus obtained were processed using a well-established mathematical apparatus and methods to characterize the nature of the reaction rate-determining step and derive isothermal and nonisothermal kinetic parameters (rate constant, frequency factor, reaction order, and activation energy). Moreover, the reaction mixture quenched at various temperatures (450–575 °C) in the reaction course was

analyzed by various spectroscopic (X-ray diffractometry, infrared spectroscopy, and laser RS) and microscopic (SEM and XED) techniques for material characterization. The results obtained indicated that the reaction rate may be controlled by unidirectional diffusion of MoO_3 species through the product layer ($BaMoO_4$), which was implied to form on the barium carbonate particles. The nonisothermally determined activation energy (156 kJ/mol) was found to be close to the isothermally determined one (164–166 kJ/mol).

The compound, **barium di-molybdate**, $BaMo_2O_7$, has not been studied intensively. The complex Ba $[Mo_2O_5(C_2O_4)_2(H_2O)_2]\cdot 2H_2O$ (BMO) was prepared and characterized by chemical analysis and IR spectral studies. TG and DTA techniques were used to study the thermal decomposition. The dehydration of BMO takes place in two steps between 115 and 230 °C, two moles of water being lost in each step. The decomposition of anhydrous BMO occurs between 230 and 360 °C in three steps. The first two steps occur in the temperature ranges 230–255 and 255–295 °C to give intermediates having the tentative compositions Ba $[Mo_2O_5(C_2O_4)(CO_3)]$ and $BaMo_2O_7\cdot CO_2$, respectively, the latter then decomposes between 295 and 360 °C to give the end product. The end product consists of $BaMoO_4$, $BaMo_2O_7$ and some other phase which could not be identified.

$\Delta_f G^\circ(BaMo_2O_7,s,T)$ has been determined for barium di-molybdate using the e.m.f. technique. The cell used was:

$$(-)Pt/(BaMo_2O_7(solid) + BaMoO_4(solid) + MoO_2(solid))\ //CSZ//air(p(O_2(gas) = 21.21\,kPa)/Pt(+)).$$

The observed e.m.f.s in the temperature range 828–985 °K could be represented by $E = 0.7663–4.953 \times 10^{-4}T$ *V*. The standard molar Gibbs energy of formation of $BaMo_2O_7$(solid) was evaluated from e.m.f. values and the $\Delta_f G^\circ(T)$ of $BaMoO_4$(solid) and MoO_2(solid). The corresponding expression is given as $\Delta_f G^\circ(BaMo_2O_7,solid,T) = -2269.7 + 0.6173T$ kJ/mol. Using the required literature values, the $\Delta_f H^\circ(BaMo_2O_7,solid,\ 298.15\,K)$ was calculated by the second law method and the corresponding value was found to be −2291.2 kJ/mol. The structure has not been documented but is presumably like that of $SrMo_2O_7$. This is illustrated in Fig. 10.64.

Two types of tetrahedra are shown in the structure. This compound melts incongruently at 655 °C to form $BaMoO_4$ and BaO:

$$BaMo_2O_7 \Rightarrow BaMoO_4 + BaO + O_2$$

Barium di-molybdate has not received much attention in the scientific literature and even less consideration in industry.

The compound, **barium tri-molybdate**, $BaMo_3O_{10}$, is not used in Industry. In Academia, its structure has been elucidated. The crystal structure of $BaMo_3O_{10}$ has been determined from X-ray and neutron powder diffraction data using no prior structural information. Direct methods and combined X-ray and neutron Rietveld refinements were used to solve the structure. There are two Ba, six Mo and 20 O atoms in the asymmetric unit. The crystal symmetry is monoclinic (space group $P2_1$; $Z = 4$), and the unit cell parameters are $a = 14.695$ Å, $b = 7.5704$ Å, $c = 6.9618$ Å, and $\beta = 100.381°$. In a combined Rietveld refinement with 124 variables, the *RF*-values 0.034 and 0.046 were obtained for neutron time-of-flight and X-ray data, respectively, although small oscillations in some parameters could not be avoided in the final refinement cycles. The structure, shown on the next page, is built of layers of $[Mo_3O_{10}^{2-}]$ linked to each other with barium ions. The Mo–O framework contains distorted MoO_6 octahedra interlinked by corner- and edge-sharing as shown in Fig. 10.65.

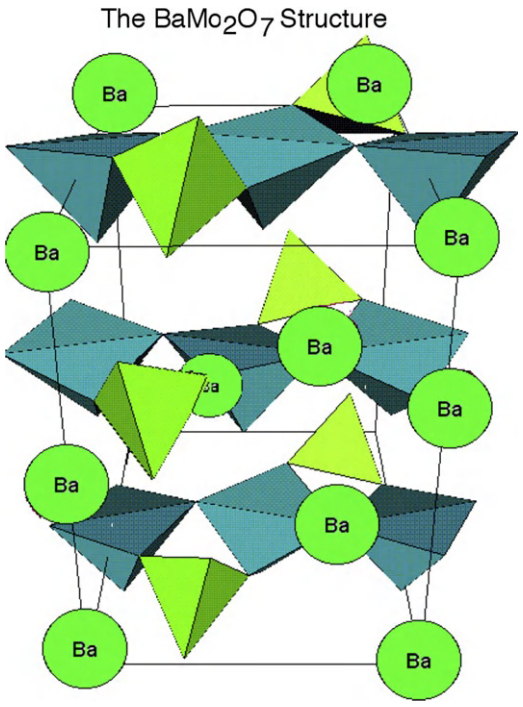

FIGURE 10.64

The compound, **barium tetra-molybdate**, $BaMo_4O_{13}$, has also been prepared hydrothermally as a hydrate. The hydrothermal synthesis, X-ray single-crystal structure, and some properties of the new-layered $BaMo_4O_{13}\cdot 2H_2O$ were described. (Crystal data: $BaMo_4O_{13}\cdot 2H_2O$, $M_\tau = 765.11$, orthorhombic, space group *Pbna* (No. 60), $a = 7.680$ (2) Å, $b = 15.756$ (3) Å, $c = 19.689$ (3) Å, $V = 2382.5$ Å^3, $Z = 8$, $R(F) = 4.00\%$ $R_w(F) = 4.39\%$ [3059 reflections with $I > 3\sigma(I)$]) (Fig. 10.66).

$BaMo_4O_{13}$ $2H_2O$ is the first well-characterized barium molybdate hydrate to be reported, and contains three

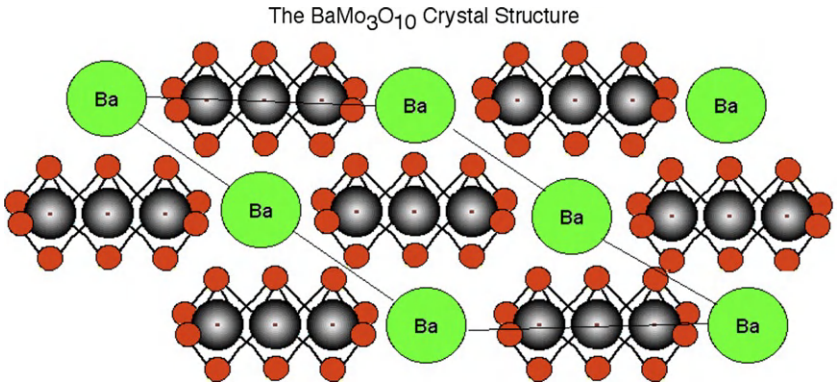

FIGURE 10.65

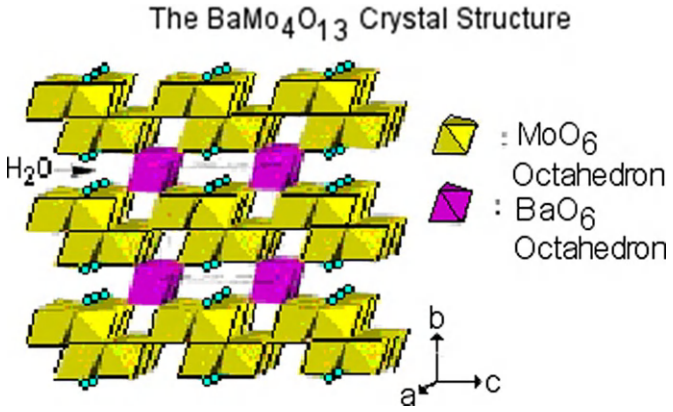

FIGURE 10.66

distinct MoO_6 units and an unusual, distorted, MoO_5 group in its layer structure. The nine-coordinate Ba^{2+} cations and water molecules provide the interlayer packing between the $[Mo_4O_{13}]^{2-}$ sheets. $SrMo_4O_{13}$ $2H_2O$ has also been prepared, and is isostructural with $BaMo_4O_{13}$ $2H_2O$, on the basis of powder X-ray, TGA, and IR data. $BaMo_4O_{13}2H_2O$ is built up from layers of edge- and vertex-sharing MoO_6 and MoO_5 groups. Inter-layer Ba^{2+} cations and water molecules complete the structure. Except for structure, little information has been published concerning this compound. It remains under current investigation as to its catalytic and electrical properties.

The compound, **dibarium molybdate**, Ba_2MoO_5, also has not been studied intensively. Its crystal parameters are: $a = 5.769$ Å, $b = 7.412$ Å, $c = 11.382$ Å, $\alpha = \beta = 65.04°$, $\gamma = 50.67°$, cell volume $= 486.61$ Å^3, $Z = 4$. The structure has the orthorhombic form as shown in Fig. 10.67.

The compound, tribarium molybdate, Ba_3MoO_6, has the structure as shown in Fig. 10.68.

This structure is characterized by MoO_6 groups that are close-packed in the cubic structure and are shared equally by neighboring unit cells. Cell parameters are: $a = b = c = 6.0811$ Å, $\alpha = \beta = \gamma = 60°$, cell volume $= 159.01$ Å^3, $Z = 4$. Cell occupancy is shown in Table 10.36.

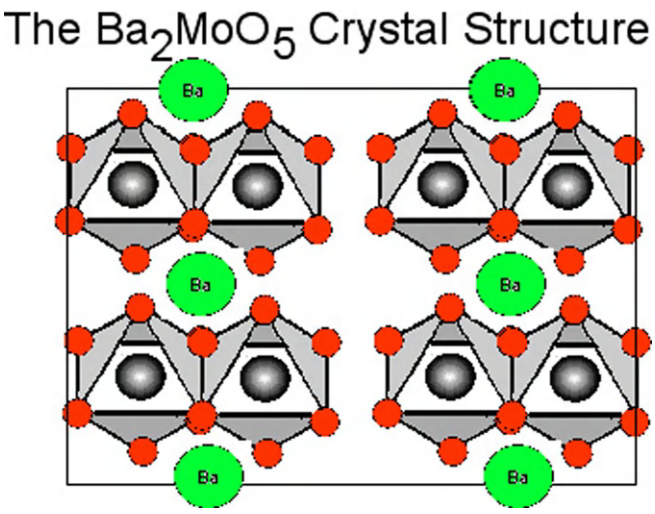

FIGURE 10.67

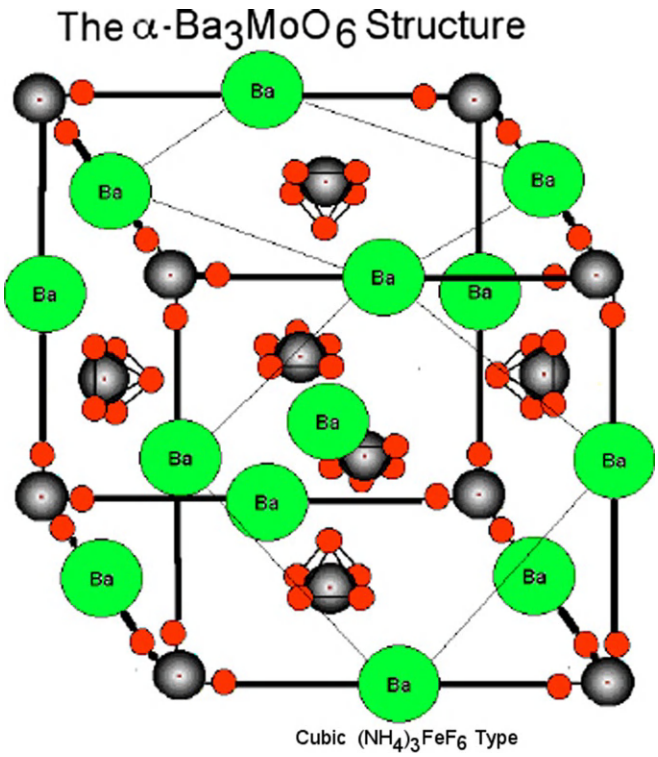

FIGURE 10.68

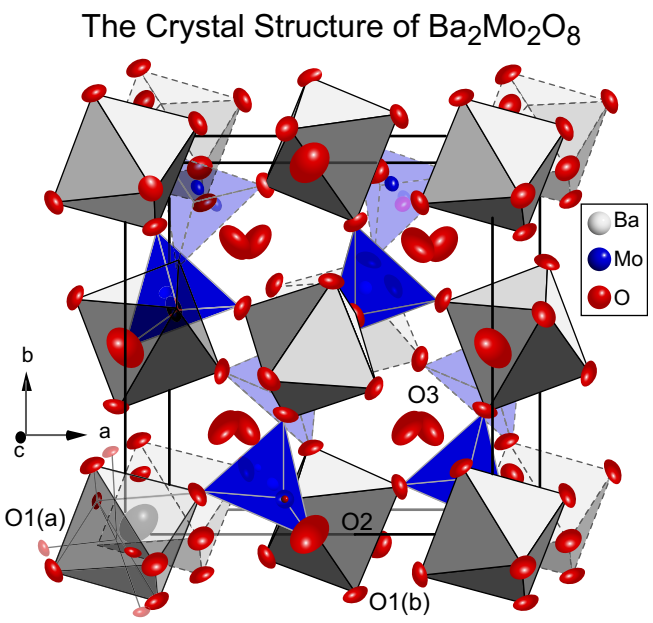

FIGURE 10.69

Neither of these compounds is considered stable at ambient conditions but have been prepared and measured at elevated temperatures.

Little is known concerning the compound, δ-barium di-molybdate, $Ba_2Mo_2O_8$, except for its structure as shown in Fig. 10.69.

Although dibarium penta-molybdate, $Ba_2Mo_5O_{17}$, has been described as a valid component within the family of barium molybdates, only one reference (Dash et al., 2000) lists this compound. No structural data are available nor has there been any description of its physical or chemical properties available in the current literature.

The same may be said concerning the compound, $Ba_3Mo_7O_{24}$. It is significant that reference to this compound (3:7:24) appears in the early literature (~1890–1910) but not in the current scientific sources.

Barium molybdate is offered commercially as $BaMoO_4$-CAS # 7787-37-3 and as Ba_3MoO_6-CAS # 13470-04-7.

10.3.6. Radium Molybdenum Compounds

Radium does not form any compounds with molybdenum or molybdenum oxides,

10.4. ALKALINE EARTH—TUNGSTEN COMPOUNDS

The tungsten-oxide system is mainly composed of three oxides, W_2O_3-tungsten trioxide (W^{3+}), WO_2-tungsten dioxide (W^{4+}), and WO_3-tungsten trioxide (W^{6+}), wherein the valence state of tungsten is indicated. In combination with the alkaline earths, the compounds, $AeWO_3$ and $AeWO_4$ have been termed as "tungstates" and "ortho-tungstates". Although the ammonium ion (NH_4^+) and the alkalis form "polytungstates", the alkaline earths do not.

Some examples of polytungstate ions that have been detected in the solution and/or solid state include:

polymeric $W_2O_7^{2-}$ ions

$[W_7O_{24}]^{6-}$ (paratungstate A)

TABLE 10.36

No.	Site notation	Atom	Multiplicity	Wyckoff	Site symmetry	x	y	z	Occupancy
1	O	O	24	e	4m.m	0.21	0	0	1.0
2	Ba2	Ba	8	c	-43m	1/4	1/4	1/4	1.0
3	Ba1	Ba	4	b	m-3m	1/2	1/2	1/2	1.0
4	Mo	Mo	4	a	m-3m	0	0	0	1.0

$[W_{10}O_{32}]^{4-}$ (tungstate Y)

$[H_2W_{12}O_{42}]^{10-}$ (paratungstate B)

α-$[H_2W_{12}O_{40}]^{6-}$ (metatungstate)

β-$[H_2W_{12}O_{40}]^{6-}$ (tungstate X)

Phase relations in the systems, alkaline earth oxide-orthotungstate (AeO–WO_3), and their stability with metallic tungsten have been investigated by the quenching technique using sealed capsules.

These tungsten oxides and polytungstates form several different types of compounds with the alkaline earths.

In the system BeO–WO_2, no intermediate compounds have been described. Binary mixtures resulted in a eutectic at 1185 °C and 37 mol% BeO.

In the system MgO–WO_3, the 1:1 compound was stable and melted congruently at 1358 °C. There are two crystalline modifications of this compound. The well-known wolframite-type form is stable below 1165 °C. Two eutectics were found: 1120 °C and 28.5 mol% MgO and 1318 °C and 55.0 mol% MgO. In the systems CaO–WO_3, SrO–WO_3, and BaO–WO_3, two binary compounds are stable. The 1:1 compounds with the scheelite-type structure melt, respectively, at 1580, 1535, and 1475 °C, and form eutectics with WO_3 at 1135, 1073, and 935 °C, all with a eutectic composition near 75 mol% WO_3. The 3:1 compounds, having the distorted $(NH_4)_3FeF_6$-type structure, melt at 2250, 2225, and 1795 °C. The eutectics between these two compounds are at 1490 °C and 56.5 mol% CaO, 1410 °C and 57.0 mol% SrO, and 1320 °C and 58.2 mol% BaO. Phase transformations to an ideal $(NH_4)_3FeF_6$-type structure in Sr_3WO_6 and Ba_3WO_6, were observed at 1100 ° and 805 °C, respectively, by application of both high-temperature XRD and DTA. At 1700 °C, metallic tungsten exists in equilibrium with liquid, the alkaline earth oxides, $W_{18}O_{49}$, the 3:1 ternary oxides, and with combinations thereof.

The structural inorganic chemistry of tungsten oxide closely mirrors that of molybdenum oxide. Many orthotungstate compounds possessing isolated WO_4 sites are known. Alkaline earth tungstates rarely form polymeric WO_4 compounds, but one such exception is MgW_2O_7 that consists of a pair of sharing WO_4 units. An isolated WO_5 coordinated site has been determined to be present in the $Ca_3(WO_5)Cl_2$ compound. Isolated WO_6 coordinated units are present in the Wolframite structure.

10.4.1. Beryllium Tungsten Compounds

BeO does not form any compounds with WO_2 or WO_3. However, it does form intermetallic compounds in the Be^0–W^0 system. This system is shown in Fig. 10.70.

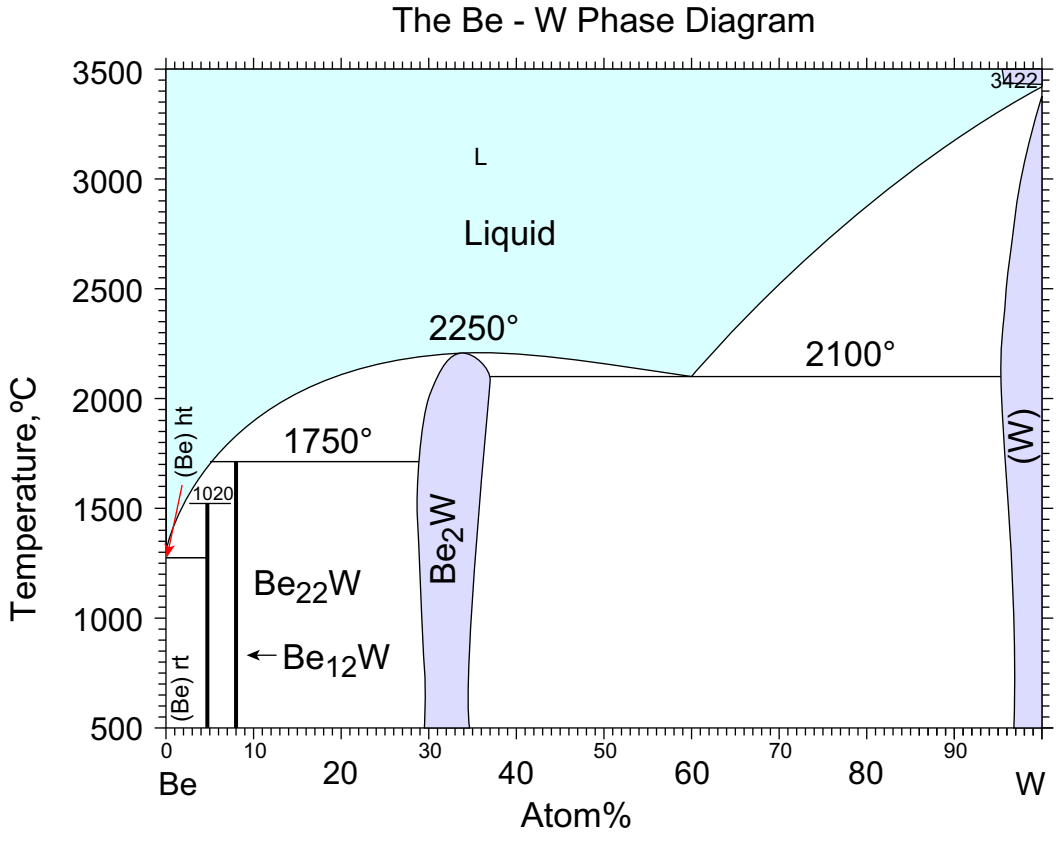

FIGURE 10.70

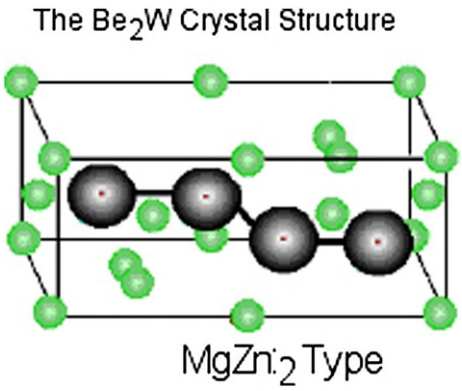

FIGURE 10.71

Only three compounds are known, two of which are modifications of the Be^0 crystal structure.

The structure factors are shown in Table 10.37.

The compound, Be_2W, has the structure shown in Fig. 10.71.

Cell parameters are: $a = b = 4.558$ Å, $c = 7.333$ Å, $\alpha = \beta = 90°$, $\gamma = 120°$, cell volume $= 131.99$ Å^3, $Z = 4$. Cell occupancy is shown in Table 10.38.

The planned application of both metals beryllium and tungsten together as first wall materials of the next step fusion device "ITER" is based on the foreseen advantageous properties of these metals for the respective locations in the plasma vessel. ITER is an international project to design and build an experimental fusion reactor based on the "Tokamak" concept. Erosion, transport, and re-deposition of both materials during operation will lead to transport of elements onto surfaces of different materials. Due to kinetic energy of impinging particles and elevated wall temperatures, alloys and compounds consisting of the present elements will be formed. These "mixed materials" exhibit strongly altered physical and chemical properties compared to the intended properties of the pure elements which were originally installed.

Of all binary systems considered in previous studies, beryllium–tungsten received least attention although Be–W alloys bear the potential of drastically reduced melting temperatures compared to pure W. For the formation of a binary Be–W alloy, two possible scenarios can be envisaged in a fusion device: deposition of tungsten on beryllium surface or vice versa. The intermetallic Be–W system was investigated by analyzing both a W film on polycrystalline Be and the inverse system, Be films on polycrystalline W. The films were annealed up to 1070 K and the alloy formation was investigated by a combination of Rutherford backscattering spectroscopy (RBS) and XPES. For the structure analysis and identification of the formed alloys, XRD measurements were used. In the case of W films on Be, $Be_{12}W$ was identified within the diffusion depth (as expected), whereas Be films on W showed alloy formation restricted to the film–substrate interface. Both XPS and XRD measurements indicate the formation of Be_2W.

The compound, $Be_{12}Mo$, has the structure shown in Fig. 10.72.

Cell occupancy is:

No.	Site notation	Atom	Multiplicity	Wyckoff	Site symmetry	x	y	z	Occupancy
1	Be(j)	Be	8	j	m2m.	0.291	1/2	0	1.0
2	Be(i)	Be	8	i	m2m.	0.351	0	0	1.0
3	Be(f)	Be	8	f	..2/m	1/4	1/4	1/4	1.0
4	Mo	Mo	2	a	4/mmm	0	0	0	1.0

This structure consists of two (2) sub-units: a body-centered lattice of W-atoms and six (6) hexagonal units of Be (Be_6) arranged on the faces of the tetragonal lattice. The unit cell parameters are: $a = b = 5.6163$ Å, $c = 4.216$ Å, $\alpha = \beta = 67.955°$, $\gamma = 81.901°$, $Z = 2$, cell volume $= 114.31$ Å^3.

TABLE 10.37

Compound	Structure type	Point group	Space group	Melting temperature, °C	Physical properties
(W)	W	cI2	229	3422	No data
Be_2W	$MgZn_2$	hP12	194	2250	No data
$Be_{12}W$	$ThMn_{12}$	tI26	139	1750	No data
$Be_{22}W$	$Zn_{22}Zr$	cF184	227	1520	No data
(Be) rt	Mg	hP2	194	1270	No data
(Be) ht	W	cI2	229	1289	No data

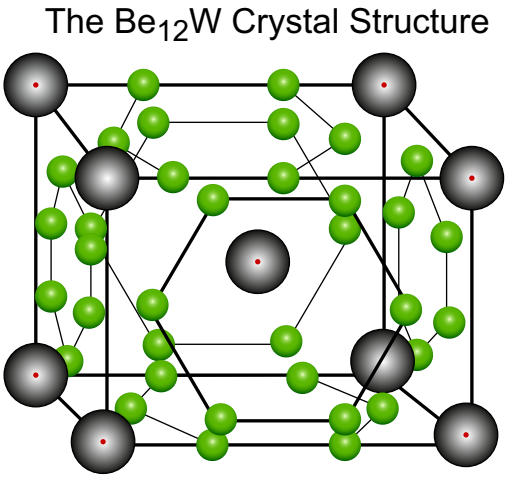

FIGURE 10.72

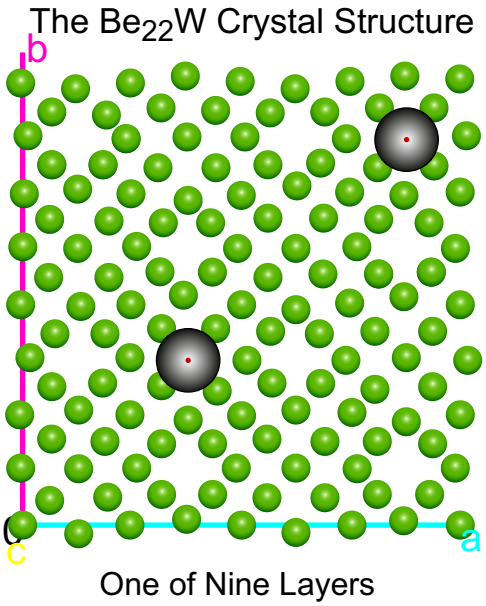

FIGURE 10.73

An intermetallic compound, $Be_{22}Mo$, is also known. It has the structure as shown in Fig. 10.73.

Unit cell parameters are: $a = b = c = 8.2244$ Å, $\alpha = \beta = \gamma = 60°$, cell volume $= 393.37$ Å^3, $Z = 8$. Cell occupancy is shown in Table 10.39.

No other intermetallic compounds have been discovered to date. None of these compounds have found usage in industry at this date (2011).

10.4.2. Magnesium Tungsten Compounds

The system Mg^0–W^0 does not form any intermetallic compounds.

In the divalent WO system, no compounds like Mg_2WO_3 or Mg_3WO_4 have been reported.

In the trivalent system, MgO–W_2O_3, no compounds containing W^{3+} have been reported.

In the W^{4+} system of MgO–WO_2, the expected perovskite formula of $MgWO_3$ has not been reported.

Only one compound, $MgWO_4$, is known to be stable in the MgO–WO_3 system. The phase diagram has the form shown in Fig. 10.74.

The compound, magnesium mono-tungstate, $MgWO_4$, has been stated to be dimorphic. A powder with XRD patterns almost identical with those of the high-temperature phase of $MgWO_4$, reported to exist only above 1065 °C, has been prepared in the temperature range of 200 °C, either by dehydration of $MgWO_4 \cdot H_2O$ or hydrothermally. The unit cell has

TABLE 10.38

No.	Site notation	Atom	Multiplicity	Wyckoff	Site symmetry	x	y	z	Occupancy
1	Be1	Be	8	j	m2m.	0.277	1/2	0	1.0
2	Be2	Be	8	i	m2m.	0.361	0	0	1.0
3	Be3	Be	8	f	..2/m	1/4	1/4	1/4	1.0
4	W1	W	2	a	4/mmm	0	0	0	1.0

TABLE 10.39

No.	Site notation	Atom	Multiplicity	Wyckoff	Site symmetry	x	y	z	Occupancy
1	Be4	Be	96	g	..m	0.0584	0.0584	0.3252	1.0
2	Be3	Be	48	f	2.mm	0.4843	1/8	1/8	1.0
3	Be1	Be	16	d	.-3m	1/2	1/2	1/2	1.0
4	Be2	Be	16	c	.-3m	0	0	0	1.0
5	W	W	8	a	-43m	1/8	1/8	1/8	1.0

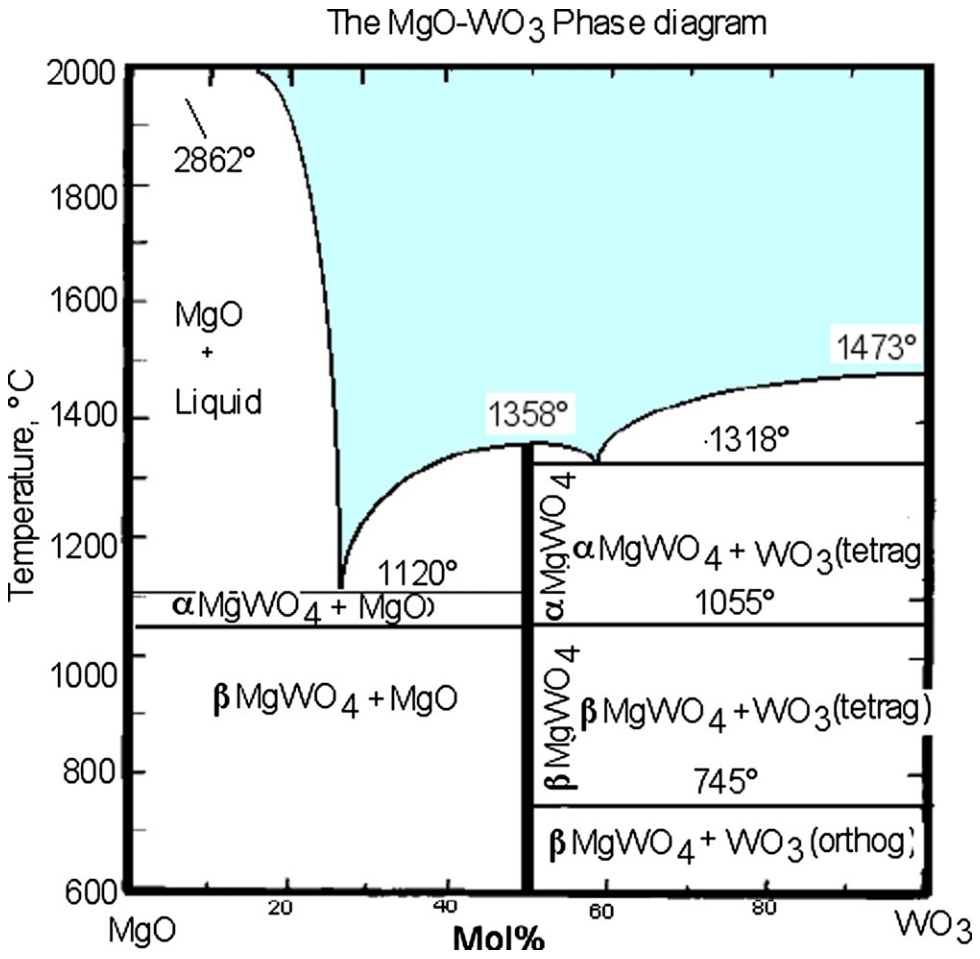

FIGURE 10.74

been determined to be triclinic, with $a = 5.60$ Å, $b = 5.58$ Å, $c = 8.84$ Å, $\alpha = 123.2°$, $\beta = 112.7°$, $\gamma = 101.4°$, $Z = 4$.

By means of results from X-ray powder and selected area ED, infrared spectroscopy and luminescence, and of arguments based on the topotactic nature of the dehydration reaction, as well as on structural relations of "HT"-$MgWO_4$ with both $MgWO_4 \cdot H_2O$ and the wolframite type monoclinic $MgWO_4$, a model for the crystal structure of "HT"-$MgWo_4$ has been derived. The crystal structure models have the form shown in Fig. 10.75. These two dimorphs exhibit similar aspects to their lattice structure as well as that of the hydrates.

The luminescence of $MgWO_4.2H_2O$ contains two emission bands, one due to the tungstate tetrahedron, and another one related to the hydrate group. The former has been compared with the tungstate luminescence of anhydrous $MgWO_4$.

The excitation-emission properties of the $MgWO_4$:W phosphor are shown in Fig. 10.76.

This phosphor is a "self-activated" composition in which the tungstate group is photo-active and probably involves a "charge-transfer" mechanism where a UV-photon is absorbed by the MgO_4 group and the energy is transported to the emitting group, WO_4. It has long been used in fluorescent lamps but not in any other display devices.

$MgWO_4 \cdot 2H_2O$ crystallizes in the monoclinic space group $P21/c$, $a = 5.917$, $b = 10.243$, $c = 8.566$ Å, $\beta = 90.05°$. Its crystal structure consists of individual layers built up from edge-sharing pairs of $MgO_4(H_2O)_2$ octahedra that are corner-linked with WO_4 tetrahedra. Thermal dehydration leads, in a first topotactic step, to

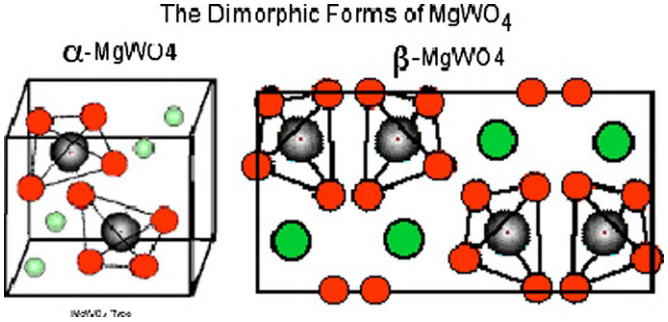

FIGURE 10.75

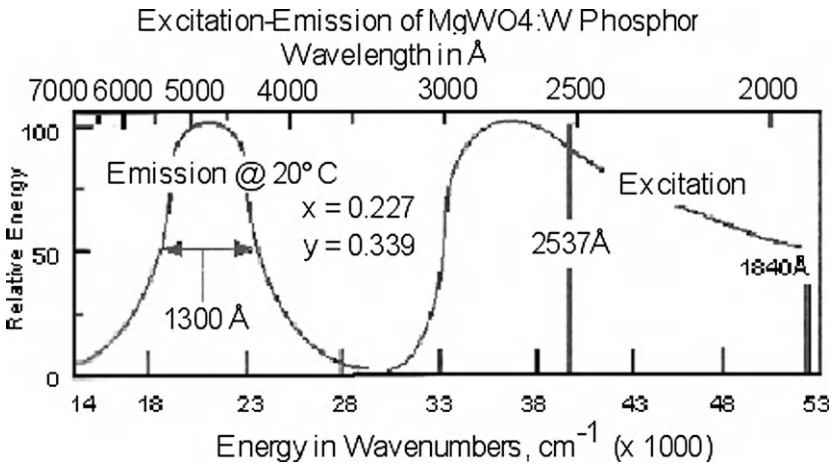

FIGURE 10.76

monoclinic (eventually triclinic) $MgWO_4 \cdot H_2O$, for which a structural model has been deduced, based on its unit cell ($a = 9.246$, $b = 10.773$, $c = 8.564$ Å, $\gamma = 92.43°$) and the relative orientation relations between the two lattices.

It corresponds to an unobserved atomic arrangement, predicted to exist by earlier authors on theoretical grounds. The loss of the remaining water is again topotactic, but leads to a multiple twinned product, which corresponds in its powder diffraction pattern closely to high-temperature $MgWO_4$, reported to exist above 1200 °C only, and is transformed into the stable wolframite structure at 650 °C. These observations are attributed to the topotactic nature of the dehydration process.

The luminescence of $MgWO_4 \cdot 2H_2O$ contains two emission bands, one due to the tungstate tetrahedron, and another one related to the hydrate group. The former is compared with the tungstate luminescence of anhydrous $MgWO_4$.

Magnesium orthotungstate is readily available commercially and has the CAS number of 13573-11-0.

10.4.3. Calcium Tungstates

Like the MgO–W_xO_{x+1} system, CaO does not form many compounds. No intermetallic Ca^0–W^0 compounds are known.

The system, CaO–WO, does not form any compounds nor does the W^{3+} system of CaO–W_2O_3. Compounds like CaW_2O_4, $Ca_2W_2O_5$ and CaW_4O_7 do not exist.

In the CaO–WO_2 system, the wolframite, $CaWO_3$ has not been thoroughly studied. Little work has appeared in the literature concerning this compound. Although, it might appear that $CaWO_3$ should have the perovskite type of lattice, which it does not.

Although the tetra-valent compounds, $Ca_6(WO_3)_5$, $Ca(WO_3)_{10}$, and $Ca_3(WO_3)_{10}$ have been studied in regard to their structure, no papers are available which develop knowledge concerning their physical or electrical properties. For example, $CaWO_3$, in which W^{4+} ions exist, is said to possess the $GdFeO_6$ structure. This is the same as the Sr_3MoO_6 structure where Mo^{6+} ions are present. The structure thus would have the general form, shown as follows. This is typical of perovskite-type compounds as shown in Fig. 10.77.

This may be a form of the so-called "tungsten–bronze" compounds in which the valence of the tungsten atom varies from 4+ to 6+.

However, the compound, $Ca_6(WO_3)_5$, is said to have the $CaTiO_3$ structure as shown in the diagram presented in Fig. 10.78.

These two structures do not seem to be compatible since the latter appears to be a condensation of WO_3^{2-} groups. It is likely that these groups follow the patterns

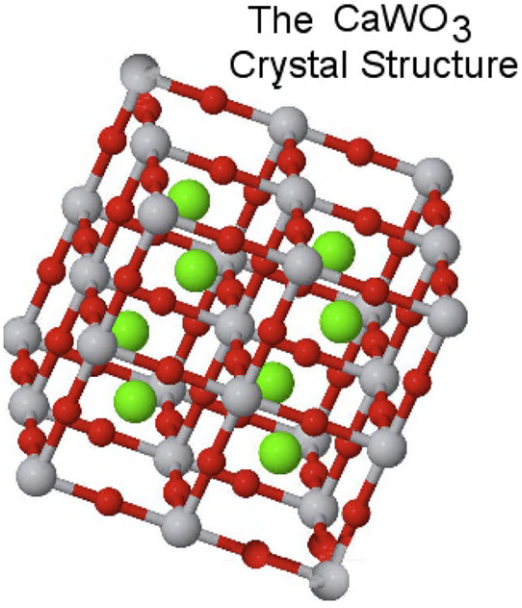

FIGURE 10.77

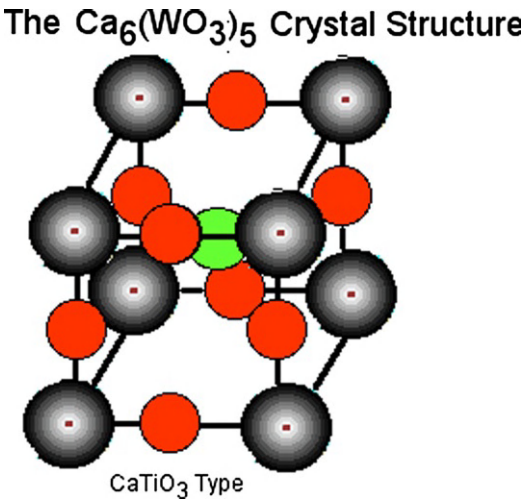

FIGURE 10.78

established by the titanate-group condensations which involve a compound like $Ca_6(WO_3)_5$. If so, then the structures shown for the compounds in the following diagram (Fig. 10.79) would be valid.

This aspect of the chemistry of calcium tungstite compounds needs to be further clarified.

The system, CaO–WO_3, forms two compounds as shown in Fig. 10.80.

Structure factors are shown in Table 10.40.

Alkaline earth tungsten and molybdenum oxides with a scheelite structure have been applied in the past as phosphors, laser hosts and scintillators.

A new field for the application of these materials has emerged a few years ago when a new generation of cryogenic detectors, offering the capability of discrimination between electron and nuclear recoils has been implemented in some particle physics experiments. The increasing interest in using $CaWO_4$ for rare event searches initiated research in the fundamental physical

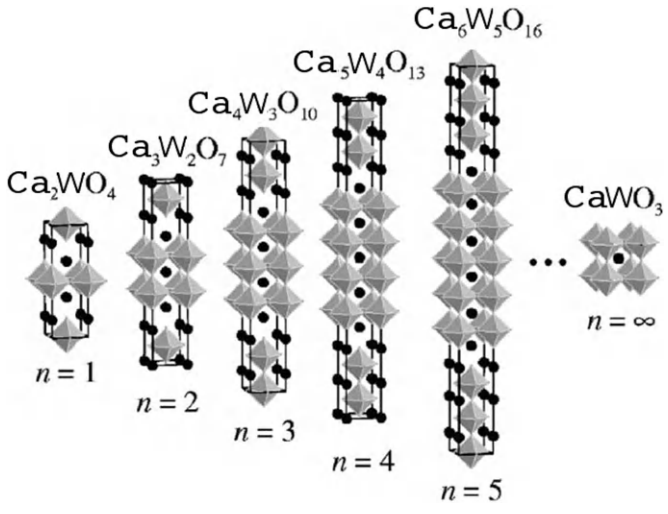

FIGURE 10.79

characteristics of this material over a wide temperature range. The compound, calcium tungstate has the structure shown on the next page. The scheelite structure consists of isolated tetrahedra that form non-touching, one-dimensional (1D) chains. There are two directions that the chains align themselves as shown in Fig. 10.81.

Cell parameters are: $a = b = 5.2444$ Å, $c = 6.7922$ Å, $\alpha = \beta = 112.71°$, $\gamma = 90°$, cell volume $= 156.71$ Å^3, $Z = 9$. Cell occupancy is shown in Table 10.41.

In addition to the scheelite structure, $CaWO_4$ also exhibits a "Fergusonite" structure. $CaWO_4$ is known to have two polymorphs. At high temperatures, it has a tetragonal structure with space group $I41{=}a$ [13] (number 88). This is the so-called the Scheelite structure, referring to the structure of the mineral Scheelite, $CaWO_4$, named in honor of the Swedish chemist, K. W. Scheele (1742–1786). The low-temperature phase is monoclinic with space group C_2/c [5] (number 15). This structure is often called Fergusonite after the Scottish mineral collector Robert Ferguson (1767–1840). The structure may be regarded as a monoclinic distortion of the tetragonal structure. The tetragonal *ct* axis corresponds to the monoclinic *bm* axis. The low temperature phase, β-$CaWO_4$, is sometimes stated to have the $LaNbO_4$ structure which is related to the Fergusonite structure.

The following diagram illustrates these structures (Fig. 10.82).

The (a) scheelite, (b) wolframite, and (c) fergusonite structures of $CaWO_4$ compounds are shown. Large circles represent the A (Ca, Sr) atoms, middle-size circles correspond to the W atoms, and the small circles are the O atoms. The unit cell, A–O bonds and W–O bonds are also shown. As a consequence of the scheelite-to-fergusonite transition two Ca–O and W–O bonds are enlarged; these bonds are showed as dark lines in (c). The CaO_8 and WO_4 polyhedra are also shown. By comparing (a) and (c), the polyhedra distortion caused by the scheelite-to-fergusonite transition is apparent.

(a) Structural site parameters of scheelite $CaWO_4$ at 1.4 GPa: $I41/a$, $Z = 4$, $a = 5.205(5)$ Å, $c = 11.275(7)$ Å (Table 10.42).

(b) Structural site parameters of fergusonite $CaWO_4$ at 11.3 GPa: $I2/a$, $Z = 4$, $a = 5.069$ Å, $b = 10.851$ Å, $c = 5.081$ Å, $b = 90.091$ as shown in Table 10.43.

$CaWO_4$ exhibits a weak luminescence at room temperature but is a very efficient emitter at liquid nitrogen temperatures where it operates as an efficient scintillator. The mechanism of luminescence involves a transition among charge-transfer states since $CaWO_4$ is a direct bandgap insulator. Vibronic coupling of the WO_4^{2-}-center occurs at room temperature but is minimized at LN_2 temperature. The electronic–vibronic

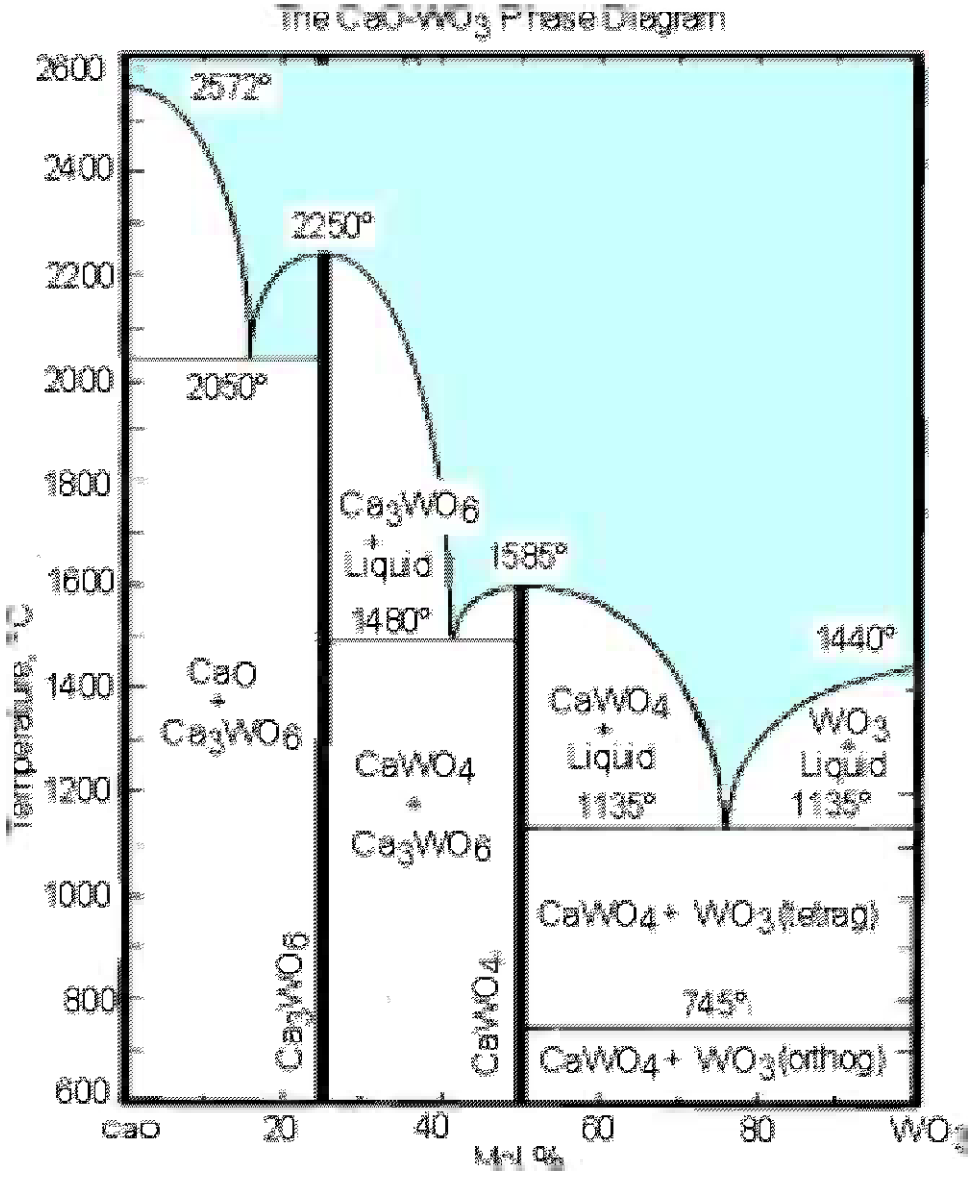

FIGURE 10.80

TABLE 10.40

Compound	Valence	Structure type	Point group	Space group	Melting point, °C
$CaWO_4$	6+	$CaWO_4$	tI24	$I4_1/a$	1545
$CaWO_4$	6+	$LaNbO_4$	mS24	$C2/c$	1075
Ca_3WO_6	6+	$BaBiO_3$	cF40	$Fm\text{-}3m$	2250
$CaWO_3$	4+	$GdFeO_3$	oP20	$Pnma$	
$Ca_6(WO_3)_5$	4+	$CaTiO_3$	cP5	$PM\text{-}3M$	
$Ca(WO_3)_{10}$	4+	WO_3	tP8	$P4/nmm$	
$Ca_3(WO_3)_{10}$	4+	$Rb_{0.81}W_3O_8$	hP12	$P6_3/mcm$	

center of the WO_4^{2-} center has been clarified as shown in Fig. 10.83.

This diagram is a schematic representation of the crystal-field splitting and hybridization of the molecular orbitals of a tetrahedral WO_4^{2-} or MoO_4^{2-} ion with "$*$" indicating the anti-bonding (unoccupied) states. The numbers in parentheses indicate the degeneracy—including spin degeneracy—of each cluster state. The ordering of the molecular orbitals in the diagram approximates the partial density of states analyses. The shaded boxes are included to emphasize the fact that the discrete states are broadened by neighboring cluster interactions in the solid material. The relative positions of the Ca-3d states for $CaWO_4$ and $CaMoO_4$ are also indicated in this diagram.

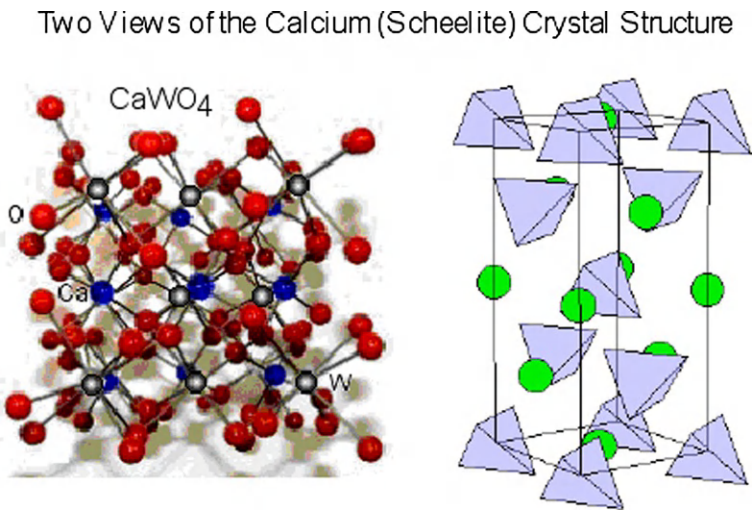

FIGURE 10.81

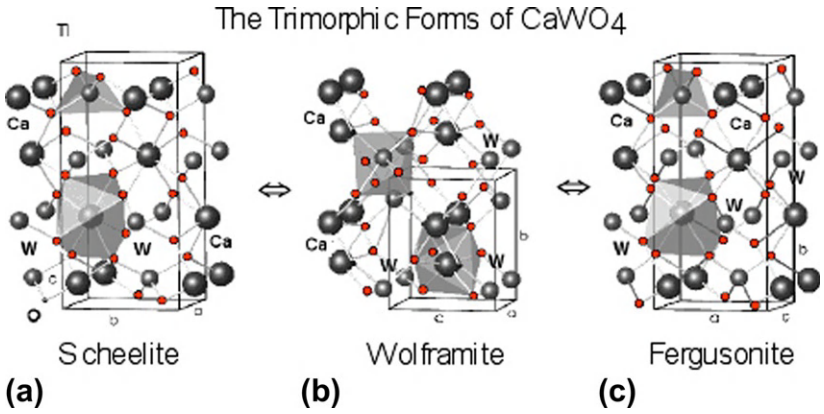

FIGURE 10.82

TABLE 10.41

No.	Site notation	Atom	Multiplicity	Wyckoff	Site symmetry	*x*	*y*	*z*	Occupancy
1	O1	O	16	f	1	0.1507	0.0086	0.2106	1.0
2	Ca1	Ca	4	b	-4..	0	1/4	5/8	1.0
3	W1	W	4	a	-4..	0	1/4	1/8	1.0

$CaWO_4$ was selected as a detector for particle and electron detection in a WIMP (weakly interacting massive particle) apparatus because of its high light yield at low temperatures and the absence of a noticeable degradation of the light yield for events near the crystal surface. Such degradation, often found in coincident phonon-charge measurements with some scintillators, can cause difficulties as it may lead to a

TABLE 10.42

Atom	Site	*x*	*y*	*z*
Ca	4b	0	0.25	0.625
W	4a	0	0.25	0.125
O	16f	0.2289	0.0910	0.0421

TABLE 10.43

	Site	x	y	z
Ca	4e	0.25	0.6100	0
W	4e	0.25	0.1325	0
O1	8f	0.9309	0.9684	0.20421
O2	8f	0.4850	0.2192	0.8637

TABLE 10.44

Atom	Site	x	y	z
Ca1	4e	0.015	0.0589	0.2445
Ca2	2c	0.0	0.5	0.0
O1	4e	0.219	0.171	0.044
O2	4e	0.162	0.224	0.435
O3	4e	0.614	0.050	0.219

misidentification of electron/photon surface events as nuclear recoils.

According to another paper, 1D $CaWO_4$ and $CaWO_4$:Tb^{3+} nanowires and nanotubes have been prepared by a combination method of sol–gel process and electro-spinning. A variety of methods were used to characterize the resulting samples. The results of XRD, FT-IR, TG-DTA indicate that the $CaWO_4$ and $CaWO_4$:Tb^{3+} samples begin to crystallize at 500 °C with the scheelite structure. Under ultraviolet excitation and low-voltage electron beams excitation, the $CaWO_4$ samples exhibit a blue emission band with a maximum at 416 nm originating from the WO_4^{2-} groups, while the $CaWO_4$:Tb^{3+} samples show the characteristic emission of Tb^{3+} corresponding to $^5D_4 \Rightarrow {}^7F_{6,5,4,3}$ transitions due to an efficient energy transfer from WO_4^{2-} to Tb^{3+}. The energy transfer process was further studied by the time-resolved emission spectra as well as kinetic decay curves of Tb^{3+} upon excitation into the WO_4^{2-} groups. Furthermore, the photoluminescence (PL) emission color of $CaWO_4$:x mol%Tb^{3+} can be tuned from blue to green by changing the concentrations (x) of the Tb^{3+} ion. These materials may have potential applications as fluorescent lamps and field emission displays (FEDs).

The compound, tricalcium tungstate, Ca_3WO_6, because of its high melting point, has been explored as a high-temperature resistant coating for space vehicles because of its very high melting point of 2250 °C.

Ca_3WO_6 is monoclinic, $a = 5.5430$ Å, $b = 5.806$ Å, $c = 7.9958$ Å, $\gamma = 90.205(3)°$. The space group $P21/n$ was confirmed by the systematic absences due to the n glide plane. The structure is of the double perovskite-type $A_2\acute{B}\acute{B}\acute{O}_6$ where $A = \acute{B} =$ Ca and $\acute{B}' =$ W. It presents a rock salt type B-cation sub-lattice with alternating CaO_6 and WO_6 octahedra. The tilt of the octahedra can be described as (*a*-*b*-*c*-), in accordance with the Glazer (1972) notation.

Cell occupation is shown in Table 10.44.

The structure has the form shown in Fig. 10.84.

The large octahedra are CaO_6 and small octahedra WO_6. The dark spheres represent Ca atoms, light ones are W and the vertices of the octahedra are O. This compound, Ca_3WO_6, is isostructural with Ca_3UO_6 (space group $P2_1$).

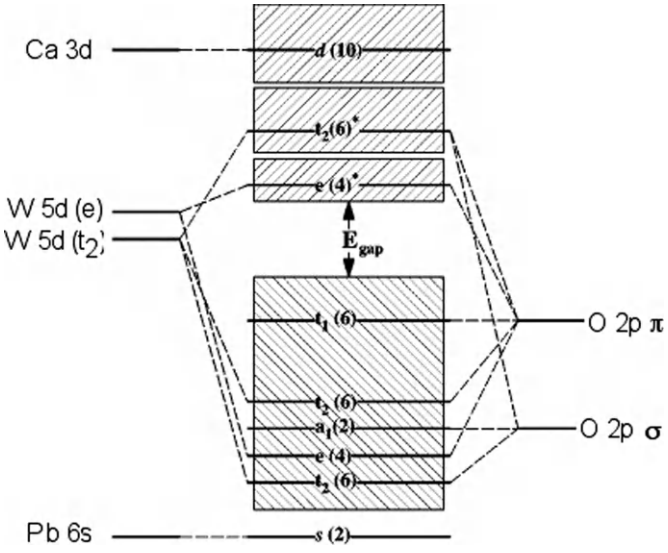

FIGURE 10.83

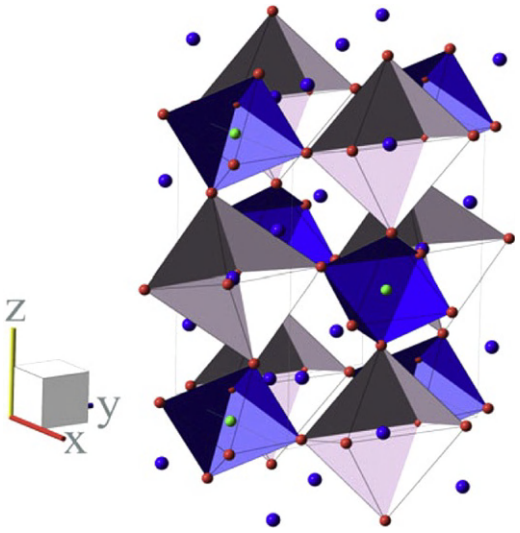

FIGURE 10.84

Thermogravimetry, XRD and SEM methods have been used to study the direct reduction–carburization of $CaWO_4$ with C at 1500 K. The reduction process was studied with solid carbon under an argon atmosphere and under vacuum. CaO, W, WC were the products of the process. Reduction under an atmosphere of CO was then studied and it was found that, compared to argon and vacuum, reduction under CO was very slow and the products were not fully carburized. This led to the conclusion that the first step in the reduction process is a solid–solid reduction reaction with carbon producing tricalcium tungstate (Ca_3WO_6) as an intermediate product. This tricalcium tungstate is then further reduced to W before carburization to WC. The overall rate of the process was found to be controlled by the W–WC stage.

The Ca_3WO_6 ceramic was prepared by solid-state reaction method and was well densified at 1260 °C, or above, for 2 h in air. The sharp Raman vibration mode at 810/cm suggested that long-range order exists in the Ca_3WO_6 structure. The best microwave dielectric properties were obtained in ceramic sample sintered at 1275 °C for 2 h with a permittivity ~15.3, a $Q \times f$ value ~ 29,200 GHz and a TCF value about −30 ppm/°C. Applying the oxide additivity rule, the calculated permittivity agrees well with the measured value. This kind of ceramic may have some potential value for microwave applications in its good microwave dielectric properties.

Calcium tungstate is available as $CaWO_4$ (scheelite) with a CAS number of 7790-75-2.

10.4.4. Strontium Tungsten Compounds

The system Sr^0–W^0 does not form any intermetallic compounds.

In the divalent WO system, no compounds like Sr_2WO_3 or Sr_3WO_4 have been reported.

In the trivalent system, SrO–W_2O_3, the expected compound, SrW_2O_4 has not been reported. There are no other compounds of interest, such as $Sr_2W_2O_5$ or SrW_4O_5, reported as well.

In the W^{4+} system of SrO–WO_2, the cubic perovskite formula of $SrWO_3$ has been reported. The compound, strontium tungstite, $SrWO_3$, has the same structure as the corresponding molybdite as shown in Fig. 10.85.

It is not certain whether these "tungstite or molybdite" compounds follow the trend of the cubic-stacked "perovskite " compounds like the titanates or $CaWO_3$ or whether they follow the "tungsten–bronze" structure motif. The difference is slight with the ratio W:O = 1:3 between perovskite and Sr_2 $(WO_3)_3$ based on the tungsten bronze-type crystal structure with 2×2 perovskite-like unit cells. However, the latter

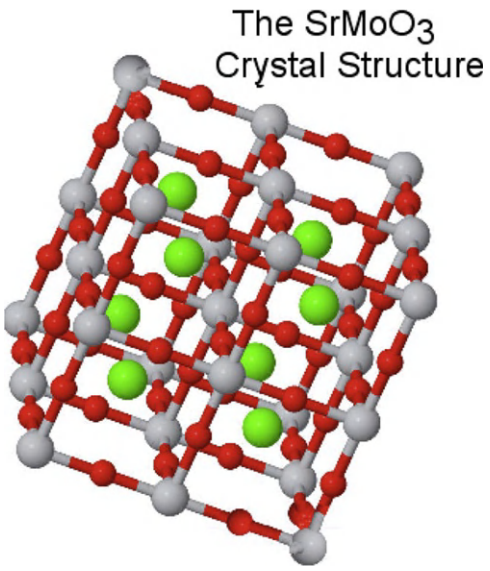

FIGURE 10.85

type of strontium tungstite has not been discovered to date.

The tungsten bronzes are an example of Class II mixed-valence compounds. They have the perovskite AMX_3 crystal structure, with WO_3 forming a supercube lattice, and with various large A cations trapped in the cage-like cavities. The addition of M^{3+} and N^+ ions (NH_4^+ and alkalis) makes an enormous number of tungsten–bronze-based structures possible.

With half of the cavities filled, the tungsten bronze above would have the empirical formula $A_{0.5}WO_3$. The family of tungsten bronzes is very large. Many metallic elements "A" have been inserted into WO_3, although the most widely studied have been the alkali metal tungsten bronzes. In fact, 10 elements are generally considered to form "bronzes": Ti, Zr, V, Nb, Ta, Cr, Mo, W, Re, and U, so the scope of these Class II compounds is very wide.

In contrast to magnetite, the tungsten bronzes can have remarkably high electrical conductivities, which are dependent on the doping level. For example, in the cubic Na_xWO_3 series, when "x" is below 0.3, the compounds are poor semiconductors. The $Na_{0.5}WO_3$ bronze has an ambient electrical conductivity of around 18,000/ohm/cm, and those with higher doping levels of $x > 0.8$ can have conductivities of up to 70,000/ohm/cm, well into the metallic range (Shanks et al., 1963). This arises because the "A" element enters the WO_3 lattice and donates its valence electrons to the tungsten–oxygen p orbitals, creating a π-XO (crystal orbital, metallic bond, conduction band) throughout the W–O lattice. The more "A" element is used to dope the WO_3 lattice, the richer the XO becomes in mobile free electrons and the higher is the compound's electrical

conductivity. The bronzes are all brightly colored solids with a noticeable metallic luster. In Classes I and II the metal cations are separated by anions or other ligands. In Classes IIIA and IIIB, there is direct metal–metal bonding between the cations.

In this system, the hexagonal compound $SrWO_3$, containing W^{4+}, has also been reported. The reaction between SrO(solid) and W(solid) at high temperatures was studied by mass-spectrographic thermal analysis. The vaporization and reactions proceed in three stages. In the first, the gaseous product, Sr(gas), appears above 1285 K:

$$4SrO(solid) + W(solid) \Rightarrow 3Sr(gas) + SrWO_4(solid)$$

In the second stage, vaporization of Sr(gas) is observed above 1580 K from the residual SrO(solid) that was unreacted with W(solid) during the course of the first stage. The third stage overlaps with that of the second stage, producing $SrWO_3$(gas), $SrWO_4$(gas) and a small amount of Sr(gas), all from the vaporization of $SrWO_4$(solid). The reaction is:

$$4SrWO_4(solid) \Rightarrow 2SrWO_3(gas) + SrWO_4(gas) + Sr(gas) + 3O_2(gas)$$

The apparent partial pressure of Sr(gas) and those of $SrWO_4$(gas) and $SrWO_3$(gas) in the third stage was determined from the curve of the mass-spectrometric thermal analysis by a modified integration method and a sensitivity calibration method, respectively. These show that the reactions given above are valid.

The hexagonal compound, $SrWO_3$, can be prepared by the reduction of $SrWO_4$:

$$SrWO_4 + H_2 \Rightarrow SrWO_3 + H_2O$$

The product is stable above 820 °C with $a = 3.842$ Å and $c = 12.623$ Å. However, it is not very stable at room temperature and tends to deoxidize to form the orthotungstate.

$SrWO_3$ has been formed as a thin film on a (100) Si surface. It is amorphous but exhibits intense luminescence under excitation of 433 nm wavelength light.

The emission characteristics are shown in the diagram as follows. Film thickness was of the order of 100–200 μm. This compound could be used in the manufacture of "white-emitting diodes" if its stability during operation can be maintained (Fig. 10.86).

The system, SrO–WO_3 forms two compounds, $SrWO_4$ and Sr_3WO_6. The phase diagram is very similar to the CaO–WO_3 system as shown in Fig. 10.87.

The compound, $SrWO_4$, has the scheelite structure as shown in Fig. 10.88.

It also undergoes structural conformations like the calcium system in which the scheelite ⇔ wolframite ⇔ fergusonite structures are in equilibrium as shown in Fig. 10.89.

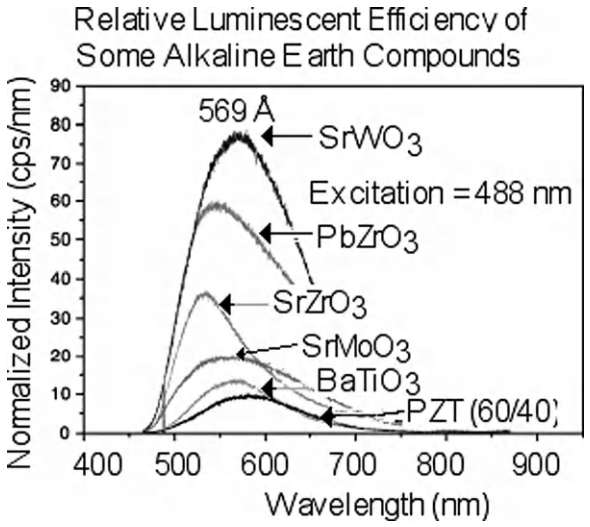

FIGURE 10.86

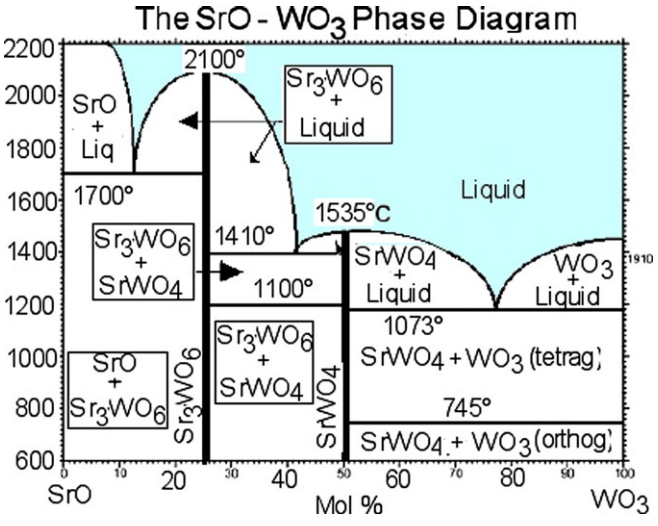

FIGURE 10.87

The (a) Scheelite, (b) Wolframite, and (c) Fergusonite structures of $SrWO_4$ are shown. Large circles represent the A (Ca, Sr) atoms, middle-size circles correspond to the W atoms, and the small circles are the O atoms. The unit-cell, Sr–O bonds and W–O bonds are also shown.

As a consequence of the scheelite-to-fergusonite transition, two Sr–O and W–O bonds are enlarged; these bonds are showed as dark lines in (c). The SrO_8 and WO_4 polyhedra are also shown. By comparing (a) and (c) the polyhedra distortion, caused by the scheelite-to-fergusonite transition, can be seen.

Structural parameters of scheelite $SrWO_4$ at 0.2 GPa are shown in Table 10.45.

Structural parameters of Fergusonite $SrWO_4$ at 10.1 GPa are shown in Table 10.46.

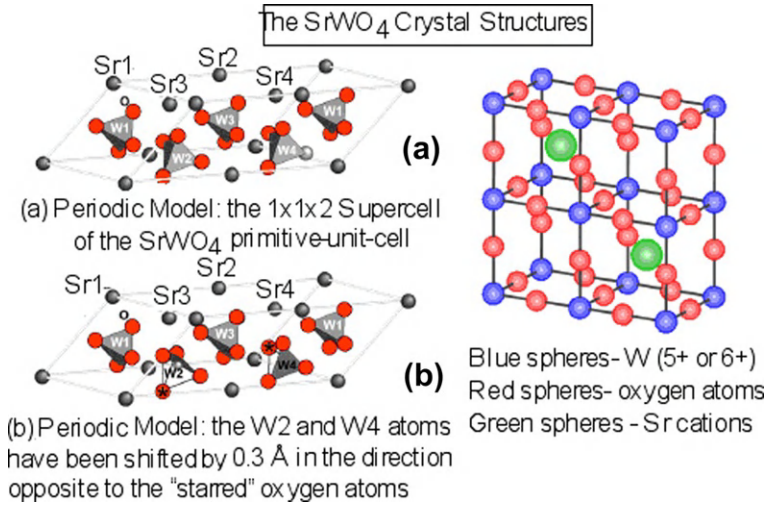

FIGURE 10.88

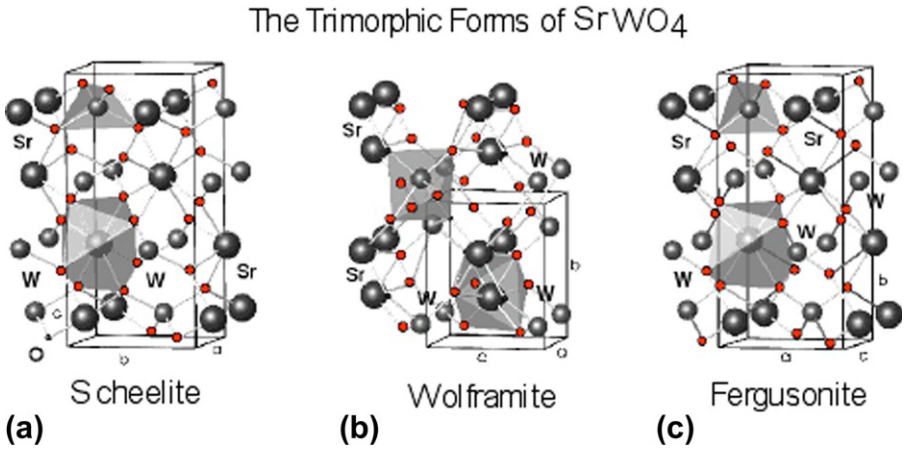

FIGURE 10.89

$SrWO_4$ undergoes a pressure-induced scheelite-to-fergusonite transition around 10 GPa. In particular, $SrWO_4$ has attracted considerable attention for the development of new electro-optics devices due to its efficient blue or green luminescence emission at room temperature. Large sized strontium tungstate ($SrWO_4$) single crystals were grown by a Czochralski method. Raman scattering and infrared absorbance spectra measurements showed that the characteristic lattice vibrational modes of $SrWO_4$ arise mainly from the internal vibrations of the WO_4 tetrahedra and partly by the external SrO_8 polyhedra modes. Thermal properties including thermal expansion, specific heat, thermal diffusion and conductivities of the crystal were investigated to evaluate the thermal properties of $SrWO_4$.

The anisotropy of thermal properties was explained by crystal structure and its correlation with the lattice vibration spectra. The vibronic-coupling and emission

TABLE 10.45 $I4_{1/a}$, $Z = 4$, $a = 5.391(8)$ Å, $c = 11.893(7)$ Å

Atom	Site	x	y	z
Sr	4b	0	0.25	0.625
W	4e	0	0.25	0.125
O	16f	0.2497	0.0925	0.0421

TABLE 10.46 $I2/a$, $Z = 4$, $a = 5.263(9)$ Å, $b = 11.182(6)$ Å, $c = 5.231(6)$ Å, $b = 90.35(1)$

Atom	Site	x	y	z
Sr1	4e	0.25	0.6027	0
W	4e	0.25	0.1243	0
O1	8f	0.9309	0.9598	0.2619
O2	8f	0.4903	0.2278	0.8779

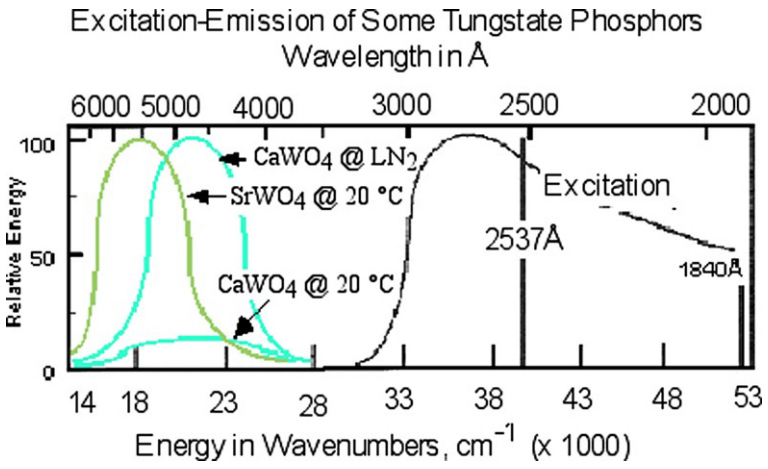

FIGURE 10.90

spectra are similar to those given above for $CaWO_4$, except that $SrWO_4$ is more efficient of the two at room temperature. The emission peak for $CaWO_4$ occurs at 480 nm while that for $SrWO_4$ is situated at 560 nm as shown in Fig. 10.90.

Single crystals of calcium tungstate and strontium tungstate have been grown by double decomposition flux reaction technique using lithium chloride as flux. Growth conditions are optimized to synthesize well faceted crystals. Effect of primary and secondary flux density in the growth charge has been studied. TG study reveals that the grown crystals are highly stable in the temperature range 25–1000 °C. Analysis of optical absorption normal to the *ab*-plane in the spectral range of 200–800 nm reveals the true absorption edge, the nature of transition being the allowed indirect one at 4.56 eV for $SrWO_4$. Well-crystallized $SrWO_4$ products with kayak-like shapes were synthesized by a microemulsion method. In addition, various other morphologies including peanut, dumbbell, and notched sphere shapes were synthesized using a simple precipitation reaction. As the molar ratio of $[WO_4^{2-}]$ to $[Sr^{2+}]$ was increased, the morphology of the $SrWO_4$ crystals evolved from rods, through peanut-like structures and dumbbells, to notched spheres. This morphology evolution of $SrWO_4$ crystals was attributed to a fractal mechanism.

Pure and rare earth (Nd^{3+}, Tm^{3+} and Er^{3+})-doped strontium tungstates of good optical quality with sizes of about 20–50 mm were grown successfully by the Czochralski technique. The (001) orientation was found to be the favorable direction for crystal growth. XRPD, DTA and differential scanning calorimeter (DSC) of pure strontium tungstate were measured. The concentrations of Nd^{3+}, Tm^{3+} and Er^{3+} were measured and their segregation coefficients were also calculated. The absorption and emission spectra of rare earth-doped crystals as a function of the σ and π polarizations were presented and discussed. Favorable values of the absorption cross section centered at about 800 nm suggest that Nd^{3+}- and Tm^{3+}-doped strontium tungstates are promising candidates for laser diode (LD) pumping.

$SrWO_4$ crystals were grown from the melt by the Czochralski method with RF heating. The melting point of $SrWO_4$ is 1535 °C, so it is possible to use a platinum crucible in air atmosphere. A Pt screen was placed above the crucible to provide the needed thermal gradients. Vertical thermal gradient for $SrWO_4$ was less than 50 °C/cm to avoid overheating the crucible. The starting material was synthesized from $SrCO_3$ (purity 5N) and WO_3 (purity 8N). The crystals were grown along direction [100] perpendicular to the optical C4 axis that corresponded to maximal Raman scattering cross-section. Rotation rate was 30 rpm and pulling rate was up to 6 mm/h.

Typical defects observed in as-grown crystals were:

Microscopic scattering centers that caused opalescence due to the evaporation of WO_3 during the growth process

Cracking along the [001] direction, a cleavage plane specific for the crystals with the scheelite structure

These defects were observed in crystals grown with too high crystallization rate or wrong annealing conditions; the "central defect" seems to be bubbles and dendrites, formed due to facet growth on the convex solid–liquid interface. Growth striations are a result of slight deviations in ratio of main components or dopants because of the local variations in crystallization rate. It was shown that $SrWO_4$ crystals grown from the stoichiometric melt had scattering centers and introduction of some excess of WO_3 into the melt allows to decrease

FIGURE 10.91

the number of scattering centers and under definite conditions to eliminate this defect at all. It was determined that excess of 1.5 wt% WO_3 was optimal for the growth of $SrWO_4$:Nd^{3+} and $SrWO_4$:Nd^{3+}:Na^{+} composition series. Optimal excess of WO_3 for series $BaWO_4$:Nd_2O_3 and undoped crystals was 1 wt%. Single crystals of both $SrWO_4$ and $BaWO_4$ are shown in Fig. 10.91.

Raman measurement results on the growth technique, spectral and luminescence characteristics of Nd^{3+} ions in $SrWO_4$ crystals were presented. Optimal conditions to obtain optically homogeneous single crystals free of light scattering centers and growth striations were found. The values of effective segregation coefficients of active Nd and compensating Nb ions were determined. Strontium tungstate crystal exhibits one of the highest Raman gain values (5.0 cm/GW) among Nd-doped Raman host materials. Efficient intracavity Raman self-conversion in Nd^{3+}:$SrWO_4$ laser was demonstrated.

$SrWO_4$ powders were synthesized by co-precipitation method and processed at 140 °C for different times in a microwave hydrothermal (MH) system. XRD patterns revealed that these powders crystallize in a scheelite-type tetragonal structure with space group *I*41/*a*. The small deviations in the lattice parameter values were associated with the effect of microwave radiation. MR and FT-IR spectra showed characteristic modes of these powders. XRD patterns and MR spectra indicated that independent of the processing time in a MH system, $SrWO_4$ powders are ordered at long and short range. FEG-SEM micrographs showed that the processing time is an important factor in the growth mechanism of $SrWO_4$ powders. These micrographs also indicated that the PEG is a surfactant that favors the growth of $SrWO_4$ micro-octahedrons along the [001] direction. A possible growth mechanism for the formation of $SrWO_4$ micro-octahedrons was proposed. UV–Vis absorption spectra showed different optical band gap values, which were associated with the presence of intermediary energy levels within the band gap. PL behavior was explained through distortions on the [WO_4] tetrahedron groups by the microwave radiation. These observations are summarized in Fig. 10.92.

This is a schematic representation of a simple mechanism to explain the PL behavior of $SrWO_4$ powders processed in MH at 140 °C for different times.

(a) Interaction of the microwave radiation on the [WO_4] tetrahedron groups
(b) three possible distortions on [WO_4] tetrahedron groups by the displacement of tungsten atoms along the atomic coordinates (*x*, *y*, and *z*),
(c) proposed model with intermediary energy levels (oxygen 2p and tungsten 5d states) within the band gap,
(d, e) recombination of e and h·pair and
(f) PL spectrum of $SrWO_4$ powders processed in MH at 140 °C for 2 h.

The growth of such crystals was also carefully monitored as shown in Fig. 10.93.

This is a schematic representation of the synthesis and growth mechanism of $SrWO_4$ particles by MH.

(a) Co-precipitation reaction, hydrolysis and addition of surfactant (PEG),

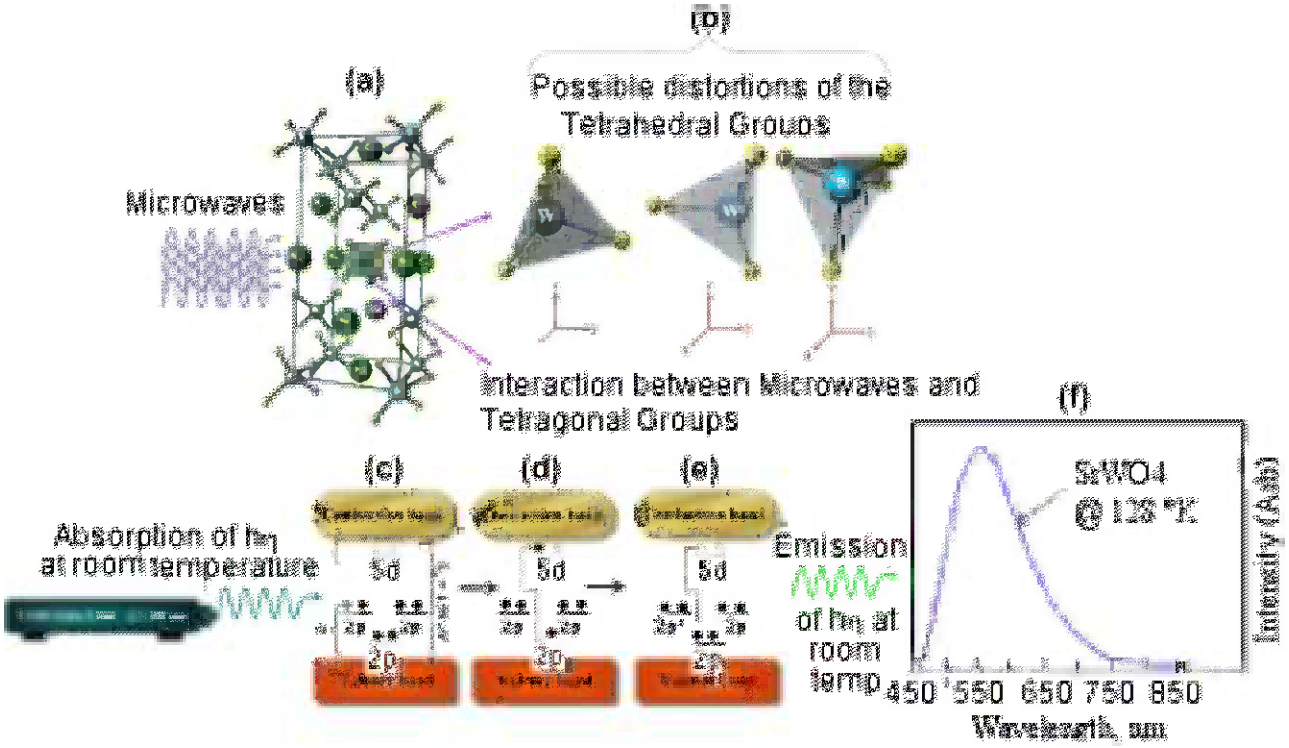

FIGURE 10.92

(b) microwave–hydrothermal system employed in the processing of $SrWO_4$ powders,
(c) aggregation of small particles due to the increase of the effective collision rates by the microwave radiation
(d) formation of a rice grain-like morphology
(e) growth and separation processes of aggregated particles
(f) formation process of small quasi-octahedrons caused by the absorption of PEG on the crystal faces
(g) simultaneous presence of small quasi-octahedrons and faceted micro-octahedrons after 5 h of processing
(h) large micro-octahedrons grown in the preferential (001) direction.

The compound, tristrontium tungstate, Sr_3WO_6, has a double perovskite structure. It exhibits three polymorphs, α, β, and γ. The structure has the general form shown in Fig. 10.94.

The crystal structures of the β and γ polymorphs of Sr_3WO_6 and the γ ⇒ β phase transition have been investigated using ED, synchrotron XRPD, and neutron powder diffraction. The γ-Sr_3WO_6 polymorph is stable above $T_c \approx 470$ K and adopts a monoclinically distorted double perovskite $A_2BB'O_6 = Sr_2SrWO_6$ structure (space group Cc, $a = 10.2363$ Å, $b = 17.9007$ Å, $c = 11.9717$ Å, $\beta = 125.585°$ at $T = 1373$ K, $Z = 12$, ap, bp, cp, lattice vectors of the parent *Fmm* double perovskite structure). Upon cooling it undergoes a continuous phase transition into the triclinically distorted β-Sr_3WO_6 phase (space group $C1$, $a = 10.09497$ Å, $b = 17.64748$ Å, $c = 11.81400$ Å, $\alpha = 89.5470°$, $\beta = 125.4529°$, $\gamma = 90.2889°$ at $T = 300$ K).

Both crystal structures of Sr_3WO_6 belong to a family of double perovskites with broken corner-sharing connectivity of the octahedral framework. A remarkable feature of the γ-Sr_3WO_6 structure is a non-cooperative rotation of the WO_6 octahedra. One-third of the WO_6 octahedra are rotated by 45° about either the *bp* or the *cp* axis of the parent double perovskite structure. As a result, the WO_6 octahedra do not share corners but instead share edges with the coordination polyhedra of the Sr cations at the B positions increasing their coordination number from 6 to 7 or 8. The crystal structure of the β-phase is very close to the structure of the γ-phase; decreasing symmetry upon the γ ⇒ β transformation occurs because of unequal octahedral rotation angles about the *bp* and *cp* axes and increasing distortions of the WO_6 octahedra.

If the metal, W^0, is reacted in air with $SrCO_3$ at temperatures >850 °C, the result is a mixture of Sr_3WO_6 and $SrWO_4$. Metallic Sr then forms according to the equation:

$$2Sr_3WO_6 + W \Rightarrow 3SrWO_4 + 3Sr$$

Thus, it is $SrWO_4$ that is thermodynamically the more stable compound at the higher temperatures.

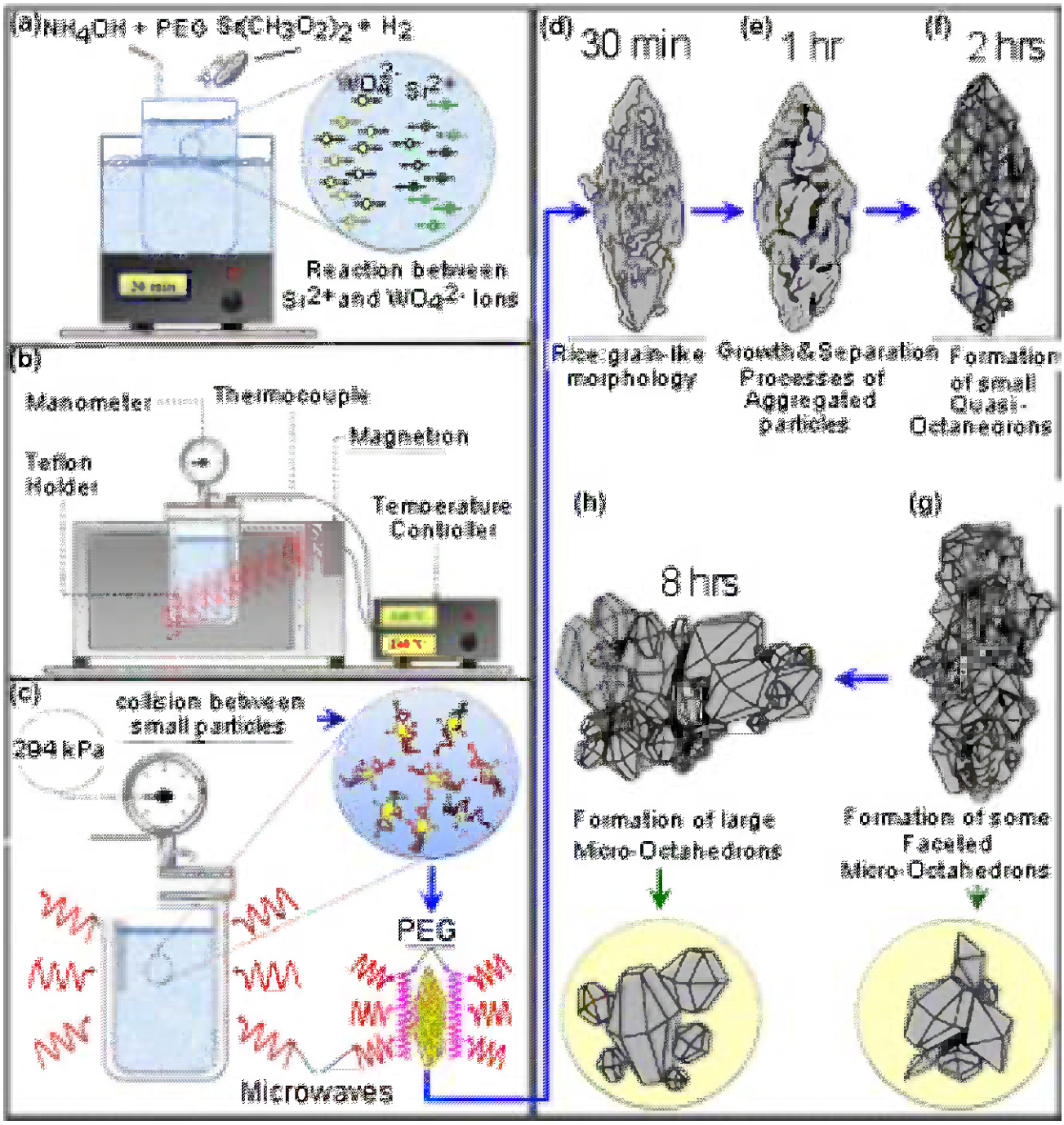

FIGURE 10.93

XRPD measurements of Sr_2CaWO_6 and Sr_2MgWO_6, at different temperatures have been reported. The crystal structures at room temperature of both compounds were determined and results showing the existence of phase transitions in them were presented. For the structure at room temperature of the Ca-containing compound, the space group $P2_1/n$ was obtained, which is different from that previously suggested. The evolution with temperature of the structure of this compound shows the presence of two phase transitions, a discontinuous one at 1130 K and a continuous one at 1250 K, with the following phase transition sequence: $P2_1/n \Rightarrow I4/\mathrm{m} \Rightarrow Fm3M$. The crystal structure of the Mg-containing compound at room temperature has the $I4/m$ space group. The temperature evolution of the structure has revealed a continuous phase transition at 570 K, changing the symmetry from tetragonal ($I4/m$) to cubic ($Fm3m$).

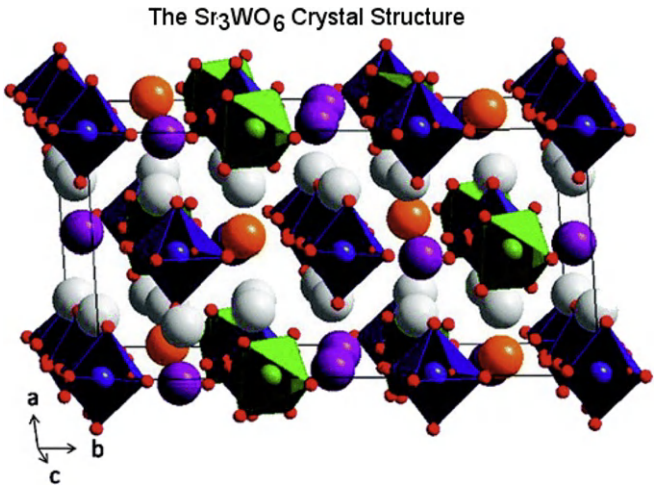

FIGURE 10.94

The compound, distrontium tungstate, Sr_2WO_5, does not appear in the phase diagram. It is tetragonal with unit-cell parameters of $a = 0.5547$ nm, $b = 0.7251$ nm, $c = 1.0896$ nm, $\alpha = 90°$, $\beta = 90°$, $\gamma = 90°$, cell volume = 438.24 Å^3. The structure of Sr_2MoO_5 is unknown, but the pattern of the impurity peaks looked much like those of Sr_2WO_5.

Efficient luminescence at relatively long wavelength was reported for Sr_2WO_5:U, Ba_2WO_5:U and Ba_2TeO_5:U. Excitation and emission bands shift to longer wavelength in this sequence. From vibrational spectroscopy, the hexavalent host lattice ions were shown to be in octahedral coordination. Evidence was given for the substitutional position of the emitting U^{6+} ions. The fine structure of the emission at low temperatures can be ascribed to vibronic interaction with UO_6^{6-} vibrational modes. Due to the presence of radiation-less decay processes in the tungstate group, it is impossible to excite these phosphors in the tungstate group.

Strontium tungstate is available as $SrWO_4$ commercially.

10.4.5. Barium Tungstates

No intermetallic compounds of Ba^0–W^0 are known. In the barium oxide–tungsten oxides series of compounds, a number of compounds have been studied.

In the divalent WO system, no compounds like Ba_2WO_3 or Ba_3WO_4 have been reported.

In the trivalent system, BaO–W_2O_3, the expected compound, BaW_2O_4 has not been reported. There are no other compounds of interest, such as Ba_2W_2O5 or BaW_4O_5, reported as well.

In the W^{4+} system of BaO–WO_2, the cubic perovskite formula of $SrWO_3$ has not been reported. There are no other compounds known to contain the W^{4+} ion.

In earlier work, it was found that the system BaO–WO_3 forms three (3) compounds as shown in a published phase diagram. This diagram indicated that Ba_3WO_6 melts congruently at 1790 °C while Ba_2WO_5 melts incongruently at 1645 °C. $BaWO_4$ melts congruently at 1475 °C. Both the 3:1 and 1:1 compounds are mono-morphic but the 2:1 compound was said to be tri-morphic. This is not consistent with later sources that stated it as the 3:1 compound that is tri-morphic. However, further and more accurate work determined that the trimorphic compound was actually Ba_3WO_6, not Ba_2WO_5. The phase diagram was then corrected and is shown in Fig. 10.95.

One dimorphic, one trimorphic and two other compounds are evident. The tribarium tetratungstate does not appear in the phase diagram, even though it can be formed from BaO and WO_3. It contains W^{5+} ions as part of a Ruddlesden–Popper series.

The structure factors are given in Table 10.47.

In another paper, the 1200 °C isothermal section of the system CaO–BaO–WO_3 was studied in detail. The system contains one ternary compound, Ba_2CaWO_6. It can exist in binary equilibrium with BaO, CaO, Ba_3WO_6, Ba_2WO_5, $BaWO_4$, and Ca_3WO_6. The composition range of solid solutions based on the ternary compound extends from Ba_2CaWO_6 to $Ba_{1.86}Ca_{1.14}WO_6$ at 1200 °C. Solid solubility along the binary join $BaWO_4$–$CaWO_4$ was studied in the interval 1000–1340 °C. Maximum solid solubilities occur at the eutectic temperature (1340 ± 10 °C) and are 18 mol% $CaWO_4$ in $BaWO_4$ and 3.5 mol% $BaWO_4$ in $CaWO_4$. A phase diagram was given for the $BaWO_4$–$CaWO_4$ system. Evidence was presented which shows that Ba_2WO_5 is a stable phase, and the BaO–WO_3 phase diagram was revised accordingly. There are three polymorphs of Ba_3WO_6 related by rapid reversible inversions at 1385 ± 5 and 1490 ± 10 °C. The low-temperature form of Ba_3WO_6 is tetragonal ($a = 8.652$ Å and $c = 16.434$ Å), not cubic as previously reported. The compounds Ca_6WO_9, BaW_2O_7, $BaCa_2WO_6$, $Ba_5CaW_2O_{12}$, and $Ba_{1.5}Ca_{1.5}WO_6$ reported in earlier studies were not confirmed.

The compound, **barium tungstate**, $BaWO_4$, has the same structure as $SrWO_4$, namely the perovskite structure with cell parameters of: $a = b = 5.62$ Å, $c = 7.5024$ Å, $\alpha = \beta = 111.996°$, $\gamma = 90°$, cell volume = 200.99 Å^3, $Z = 4$ as shown in Fig. 10.96.

Cell occupancy is shown in Table 10.48.

Another view of the same structure is shown in Fig. 10.97.

The structure exhibits tetragonal WO_4 units and BaO_6 octahedral units. In-situ high-pressure PXRD studies on $BaWO_4$ show that barium tungstate undergoes a first-order phase transition to a new phase at about 3 GPa.

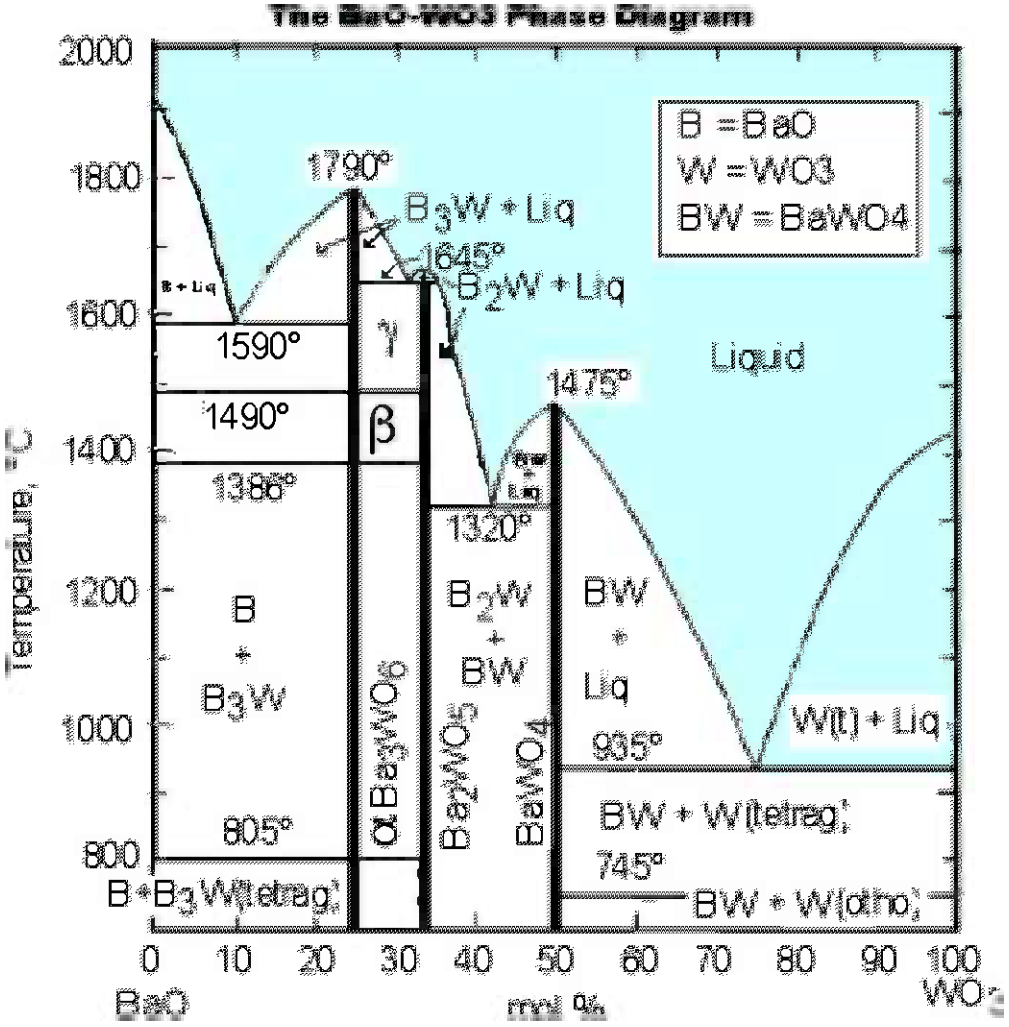

FIGURE 10.95

It has been shown that this new phase could have a structure similar to the monoclinic Fergusonite phase as shown in Fig. 10.98.

At 14 GPa, it further transforms to a new phase which becomes significantly disordered by ~20 GPa. On release of pressure from 20 GPa, the scheelite phase is recovered below 3 GPa, indicating reversible nature of both the transformations.

In another study, at room temperature Raman scattering was measured in barium tungstate ($BaWO_4$) up to 16 GPa. The pressure dependence of all the Raman active first-order phonons of the tetragonal scheelite phase ($BaWO_4$-I, space group $I4_1/a$), is stable at normal conditions. As pressure increases, the Raman spectrum undergoes significant changes around 6.9 GPa due to the onset of the structural phase transition to the monoclinic $BaWO_4$-II phase (space group $P2_1/n$). This transition is only completed above 9.5 GPa. A further change in the spectrum was observed at 7.5 GPa related to a scheelite-to-fergusonite transition. The scheelite, $BaWO_4$-II, and fergusonite phases coexist up to 9.0 GPa due to the sluggishness of I ⇒ II phase transition. Further to the experimental study, ab initio lattice dynamics calculations were performed that helped in

TABLE 10.47

Compound	Structure type	Point group	Space group	Melting point, °C
$BaWO_4$	$CaWO_4$	Tl24	$I4_1/a$	1475
$BaWO_4$	$BaWO_4$	MP48	$P2_1/c$	"
Ba_3WO_6	Ba_3WO_6	AP22	$P1$	1790
Ba_3WO_6	*	CP320	Pm-3m	"
Ba_3WO_6	$(NH_4)_3FeF_6$	CF40	Fm-3m	"
Ba_2WO_5	Ba_2ReO_5	OP32	$Pnma$	1645
$Ba_3(WO_3)_4$	*	OP26	$Pmma$	?
$BaWO_3$	$TlWO_3$	HP34	$P6_3/mcm$	?

* = Not known

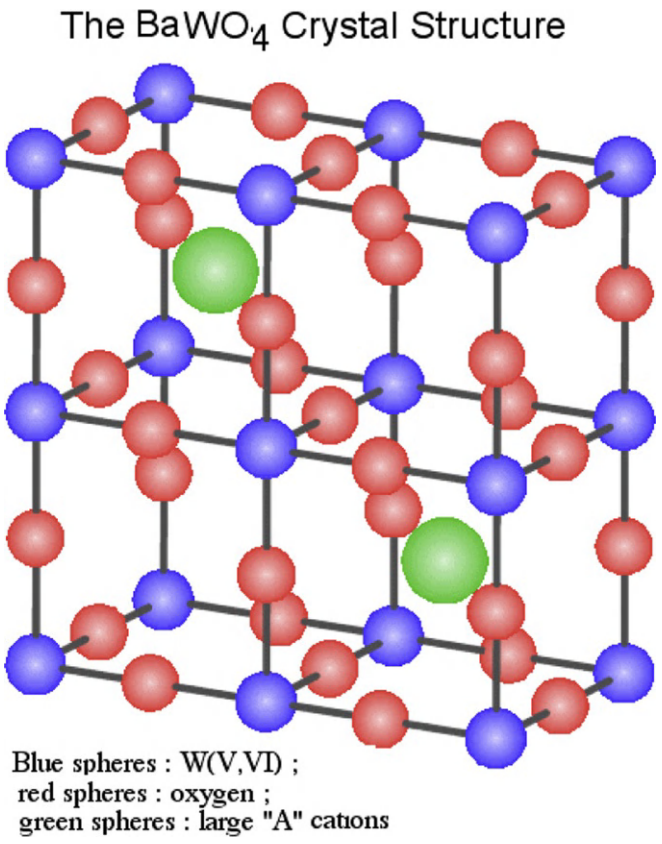

FIGURE 10.96

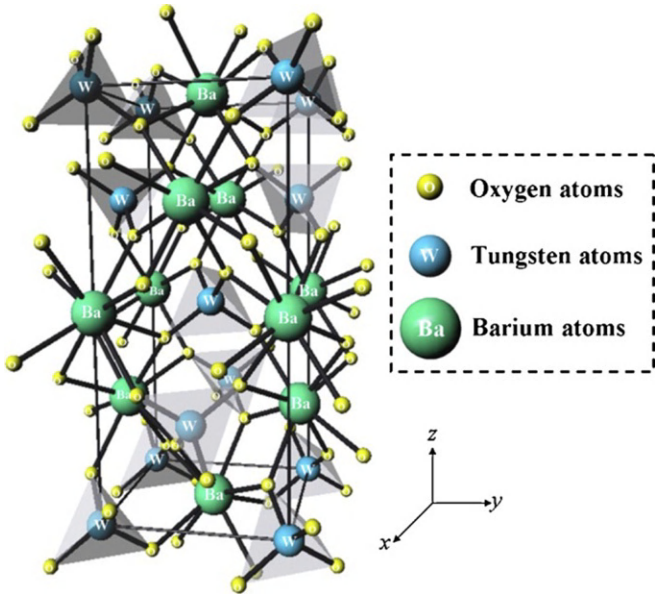

FIGURE 10.97

assigning and discussing the pressure behavior of the observed Raman modes of the three phases as shown in Table 10.49.

Beyond 14 GPa, this compound undergoes another phase transformation to a significantly disordered structure. Both the phase transitions were found to be reversible. This high-pressure phase, $BaWO_4$-II has been found to possess the structure shown Fig. 10.99.

It is monoclinic with $a = 13.159$ Å, $b = 7.161$ Å, $c = 7.499$ Å, $\beta = 93.76°$, $Z = 8$ and space group $= P2_1/n$. This structure has no direct resemblance to either the scheelite or wolframite structures. It consists of dense packed layers of WO_6 octahedra that are connected by edge- or corner-sharing. Barium ions are located between them. The coordination number of Ba^{2+} has increased in this compound, compared to the ordinary type of barium tungstate such as the scheelite structure.

Quantum-mechanical calculations indicated that the disorder at short range consists only of Ba atoms in the $Ba_{1-x}WO_{4-x}$ lattice. This has a very important role in the charge transfer mechanism involved in the intense green PL emission. This indication was detected and confirmed by means of FT RS measurements. The experimental and theoretical results are in good agreement, both demonstrating the specific type of structural disorder that is the best favorable condition for generating the most intense green PL emission in the scheelite lattice structure.

Mass spectrometric studies indicate that barium molybdate and barium tungstate salts evaporate mainly as molecular $BaMoO_4$(gas) and $BaWO_4$(gas), respectively. The importance of ion fragmentation processes occurring in the mass spectrometer was established from appearance potential measurements and the variations in relative ion intensities with condensed phase composition. Third law calculations give for the dissociation reactions:

$$BaMoO_4(gas) \Rightarrow BaO(gas) + MoO_3(gas),$$
$$\Delta G_0^0 = 129.7 \pm 4.0 \text{ kJ/mol}$$

TABLE 10.48

No.	Site notation	Atom	Multiplicity	Wyckoff	Site symmetry	x	y	z	Occupancy
1	O1	O	16	f	1	0.1507	0.009	0.211	1.0
2	Ba1	Ba	4	b	-4..	0	1/4	5/8	1.0
3	W1	W	4	a	-4..	0	1/4	1/8	1.0

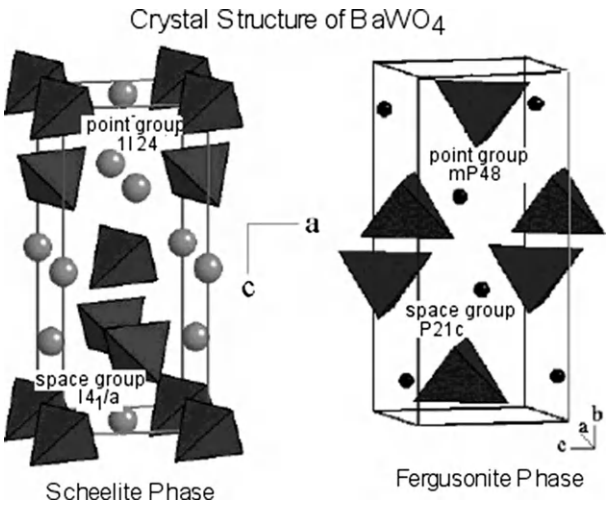

FIGURE 10.98

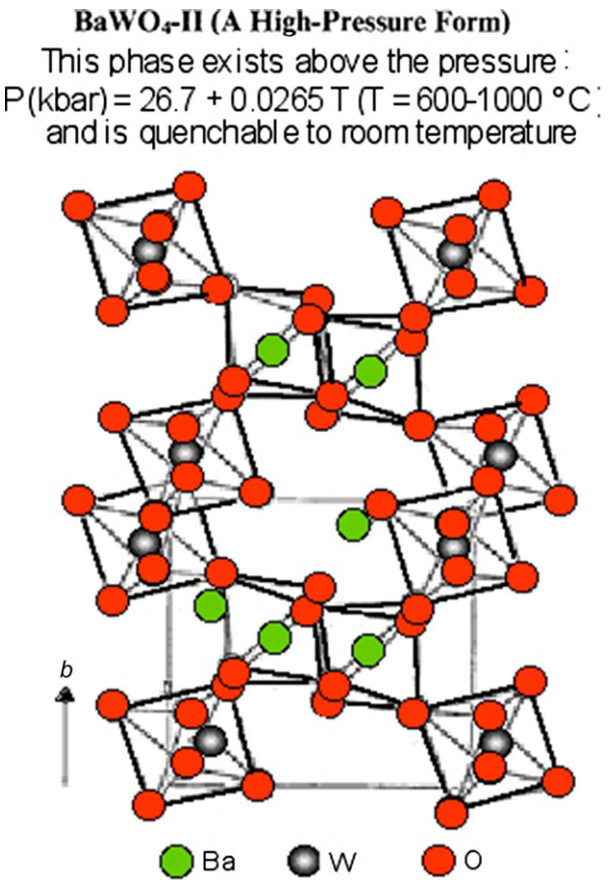

FIGURE 10.99

TABLE 10.49

a. Structural parameters of the scheelite, $BaWO_4$, at 1.0 GPa: $I41/a$, $Z = 4$, $a = 5.603(4)$ Å, $c = 12.693(7)$ Å

Atom	Site	x	y	z
Ba	4b	0	0.25	0.625
W	4a	0	0.25	0.125
O	16f	0.2336	0.0976	0.0499

b. Structural parameters of scheelite $BaWO_4$ at 6.9 GPa: $I41/a$, $Z = 4$, $a = 5.460(4)$ Å, $c = 12.138(7)$ Å

Atom	Site	x	y	z
Ba	4b	0	0.25	0.625
W	4a	0	0.25	0.125
O	16f	0.2222	0.1087	0.0499

c. Structural parameters of scheelite $BaWO_4$ at 7.3 GPa: I2/a, $Z = 4$, $a = 5.465(7)$ Å, $b = 12.109(3)$ Å, $c = 5.439(7)$ Å, $b = 90.087(9)°$

Atom	Site	x	y	z
Ba	4e	0.25	0.6131	0.0
W	4e	0.25	0.1282	0.0
O_1	8f	0.9493	0.9765	0.2538
O_2	8f	0.4666	0.2225	0.8826

$$BaMoO_3(gas) \Rightarrow BaO(gas) + MoO_2(gas),$$
$$\Delta G_0^0 = 132.2 \pm 6.0 \text{ kJ/mol}$$

$$BaWO_4(gas) \Rightarrow BaO(gas) + WO_3(gas),$$
$$\Delta G_0^0 = 148.3 \pm 4 \text{ kJ/mol}$$

The heats of vaporization of $BaMoO_4$(liq) and $BaWO_4$(liq) at 2000 K are 83.5 and 93.7 ± 4 kcal/mol, respectively.

$BaWO_4$ crystals were grown from the melt by the Czochralski method with RF heating. The melting point of $BaWO_4$ is 1475 °C, $SrWO_4$ is 1535 °C, so it is possible to use platinum crucibles and melt in an air atmosphere. A Pt screen was placed above the crucible to provide the needed thermal gradients. Vertical thermal gradient for $BaWO_4$ growth was 60–100 °C/cm; the thermal gradient for $SrWO_4$ was less than 50 °C/cm to avoid crucible overheating. The starting material was synthesized from $BaCO_3$ or $SrCO_3$ (purity 5N) and WO_3 (purity 8N). Crystals were grown along direction [100] perpendicular to the optical C_4 axis that corresponded to maximal Raman scattering cross-section. Rotation rate was 30 rpm and pulling rate was up to 6 mm/h. Typical defects observed in as-grown crystals were: microscopic scattering centers that cause opalescence, due to the evaporation of WO_3 during the growth process; cracking along [001] direction, caused by a cleavage plane specific for the crystals with scheelite structure. These defects were observed in crystals grown with too high crystallization rate or the wrong annealing conditions; the

"central defect" seems to be bubbles and dendrites that are formed due to facet growth on the convex solid–liquid interface. Growth striations are a result of slight deviations in ratio of main components or dopants because of the local variations in crystallization rate. It was shown that $BaWO_4$ crystals grown from a stoichiometric melt had scattering centers and introduction of some excess of WO_3 into the melt allows a decrease in the number of scattering centers obtained and, under certain conditions, to eliminate this defect entirely. It was determined that an excess of 1.5 wt.% WO_3 was optimal for growth of BaWO4:Nd^{3+}:Nb^{5+} and $BaWO_4$:Nd^{3+}:Na^{+}. Optimal excess of WO_3 for the series, $BaWO_4$:Nd_2O_3, and/or undoped crystals was 1.0 wt%. (See the strontium tungstate section above for pictures of some of the crystals).

Thin (~10 nm) BaO films on tungsten substrates (prepared at specific coverage from multilayer Langmuir–Blodgett precursor films) were heated at different temperatures between 200 and 1200 °C in a vacuum environment. The chemical changes occurring at the BaO/W interface were characterized by XPES, infrared reflection spectroscopy, spectroscopic ellipsometry, and XRD analyses. The results showed that a $BaWO_4$ phase forms above an approximate threshold temperature of 800 °C and, contrary to previous observations reported for heterogeneous reactions in powders, no evidence for a Ba_3WO_6 phase was seen. These data form a fundamental basis for understanding the regulation of the emission work function in the operation of an alkaline earth-coated tungsten cathode fluorescent lamp.

One explanation was expanded as follows:

> "Thermionic emitters, consisting of barium oxide dispersed throughout a body of porous tungsten, can be successfully made if suitable compounds of barium are employed as the source of the oxide. Compounds such as the carbonate, which can oxidize tungsten and react to form Ba_3WO_6: $3BaCO_3 + W \Rightarrow Ba_3WO_6 + 3CO$, are unsuitable. However, if by various means, BaO is dispersed in tungsten, reaction occurs at operating temperature of the cathode to slowly generate free barium: $6BaO + W \Rightarrow Ba_3WO_6 + 3Ba$, which diffuses to the surface and lowers the work function. Cathodes consisting of approximately 5 percent of BaO in W are capable of supplying continuous emission in excess of 100 amp/cm^2, give equivalent dc and pulsed emission, and are highly resistant to damage by arcing, temporary poor vacuum, ion bombardment, and high temperatures. Emission current of approximately 8 amp/cm^2 was obtained at an operating temperature of 1000 °C from a typical cathode of this type. The life of this cathode, at 1100 °C, was in excess of 650 h. Constants of the Richardson equation for a relatively inactive cathode were $\eta = 1.56$ eV, $A = 0.6$ amp/cm^2/deg^2".

Barium tungstate ($BaWO_4$) crystals were employed to achieve efficient stimulated Raman scattering conversion in a compact diode-pumped actively Q-switched Nd:YAG laser. With an incident pump power of 9.2 W, 1.56 W of 1181 nm first-Stokes average output power was generated at a pulse repetition rate of 20 kHz, corresponding to an optical-to-optical conversion efficiency of 16.9%.

The generation of multi-watt continuous-wave (CW) yellow (5865 Å) laser emission from an intra-cavity diode-pumped Nd:$GdVO_4$/$BaWO_4$ Raman laser was reported, utilizing a high-Q resonator (for fundamental and first-Stokes wavelengths) and intra-cavity frequency-doubling in LBO. CW output power of 2.9 W was achieved with a high overall diode-to-yellow conversion efficiency of 11% and with good beam quality (M^2 ~2.5).

Properties of the laser operation and simultaneously stimulated Raman scattering in SRS-active neodymium doped $SrWO_4$ and $BaWO_4$ crystals were studied. They were coherently end-pumped at wavelength 752 nm by a pulsed free-running alexandrite laser radiation. The Nd^{3+} ion emission at wavelength 1.065 μm corresponded to a $^4F_{3/2} \Rightarrow {}^4I_{11/2}$ transition. The shortest generated pulse (1.3 ns FWHM) and highest peak power (615 kW) was obtained with a Nd:$BaWO_4$ Raman laser, Q-switched by LiF crystal, with an initial transmission $T_0 = 60\%$. Up to 0.8 mJ was registered at the first-Stokes wavelength 1169 nm. The Q-switched Nd:$SrWO_4$ laser higher energy in Raman emission obtained (1.23 mJ) was longer (2.9 ns FWHM) but resulted in lower peak power (430 kW).

$BaWO_4$, prepared as a single crystal, has been widely used in electro-optical industry due to its emission of blue luminescence. Its intrinsic emission is due to transitions in the tetragonal $(WO4)^{2-}$ molecular ions. Phosphors formed from $BaWO_4$ doped with rare earth ions (RE = Eu, Tb, Tm) were prepared by the polyol method. The crystal structure and morphology of the powders were investigated using XRD, field emission SEM and Fourier transform spectroscopy. The as-prepared $BaWO_4$-based phosphors processed as low as 160 °C show mono-dispersive and crystalline nanostructures. The optical characteristics of the phosphors were investigated using low-voltage cathodoluminescence (CL). Efficient energy transfer between the host and RE ions was revealed in the spectra. No broad-band emission was seen. Red, green and blue CL was observed corresponding to sharp dominant emission peaks located at 616 nm, 545 nm and 473 nm for Eu^{3+}, Tb^{3+} and Tm^{3+} doped phosphors, respectively.

The low-voltage CL spectra obtained are shown in Fig. 10.100.

Although $BaWO_4$ and $CaWO_4$ crystal structures have been reported to be identical with similar optical properties, it is evident that they possess different emission behaviors.

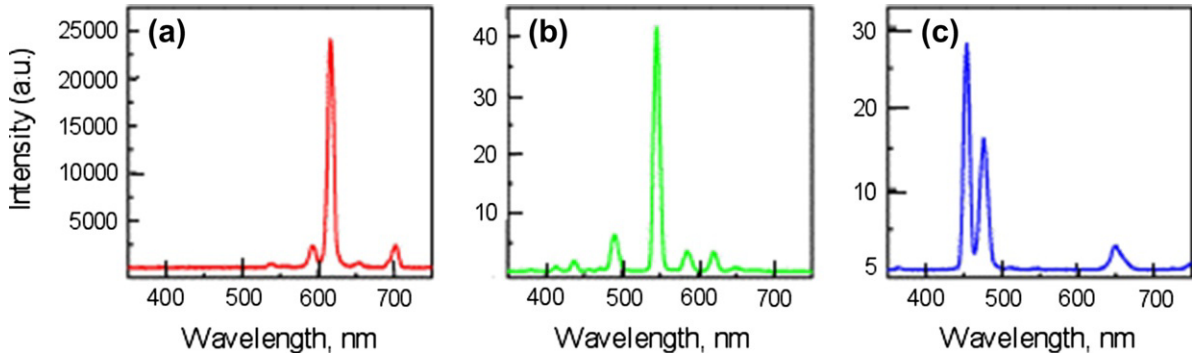

FIGURE 10.100

For $CaWO_4$: Eu^{3+} phosphors, both broad emission of $(WO_4)^{2-}$ ions and sharp line emissions correspond to Eu^{3+} ions were reported.

In $BaWO_4$:Ln^{3+} phosphors, only sharp line emissions were observed free from any broad emission. A recent result of Eu^{3+} doped $ZnWO_4$:Eu^{3+} phosphors also showed spectra similar to those of $CaWO_4$:Eu^{3+}. These differences can be explained by the symmetry of the sites (crystal field effect) in which the rare earth ions located there are significantly affected by changing the host structure cations even though the scheelite structure is maintained. This in turn affects the efficiency of energy transfer.

Since $BaWO_4$ is a weak emitter at room temperature, it was unforeseen that the $Ba_2WO_3F_4$ compound would turn out to be a strong emitter at room temperature. $Ba_2WO_3F_4$ crystallizes in an acentric monoclinic symmetry, space group *Ia* with $a = 9.281(2)$, $b = 9.361(2)$, $c = 7.183(1)$ Å and $\beta = 92.48(2)°$. It exhibits broad band fluorescent emission peaking at 475 nm both under UV and X-ray excitation.

TABLE 10.50

Compound	Luminescent peak produced when excited in short-wave excitation band (nm)	Luminescent peak produced when excited in long-wave excitation band (nm)
Ba_2MgWO_6	412	508
Sr_2MgWO_6	404	520
Ca_2MgWO_6	412	556
Ba_2CaWO_6	468	—
Sr_2CaWO_6	460, 580	—
Ca3WO6	440, 556	—
Ca_3WO_6	440, 556	—
Ba_3WO_6	518	—

The barium and mixed-barium tungstate compounds exhibit a number of interesting emission features, as shown in Table 10.50.

Two emission bands have been observed for the mixed cation compound, Ba_2MgWO_6, that are also present in the spectra of Sr_2MgWO_6 and Ca_2MgWO_6. By selective excitation it is possible to observe the two emission bands separately. The long wavelength emission is observed when the sample is excited by long wavelength UV radiation ($\lambda_{excit} = 320$ to 340 nm) while the short wavelength emission is observed when the sample is excited with radiation of 277 nm. The emission spectra of Ba_3WO_6, Ba_2SrWO_6 and Ba_2CaWO_6 show only one band, the excitation spectrum of which resembles that of the short wavelength emission of Ba_2MgWO_6.

Ce^{4+}-doped Ba_3WO_6 complex oxides were used as catalysts for methane oxidative coupling (MOC), and characterized by XPS and O_2-TPD-MS techniques. The results indicated that the ratio of electrophilic oxygen species O^- and O^{2-} to lattice oxygen on the surface was crucial for C_2 selectivity. By adjusting the relative amount of cations in Ba–W–Ce complex oxides with perovskite superstructure, interstitial oxygen species can be created which benefits C_2 selectivity by raising the relative amount of $(O^- + O^{2-})$ on the surface. The crystal structure of $Ba_3W_2O_9$ contains isolated $W_2O_9^{6-}$ groups. These are reported to luminescence efficiently. This observation shows that clusters of tungstate octahedra emit more efficiently than that of the isolated species.

The compound, dibarium tungstate, Ba_2WO_5, has a structure related to Ba_2ReO_5. Cell parameters are: $a = 5.742$ Å, $b = 7.412$ Å, $c = 11.486$ Å, $\alpha = \beta = \gamma = 90°$, cell volume $= 488.84$ Å^3. The structure is composed of separate dumb-bell like units of $W_2O_{10}^{4-}$, tied together to produce a double-perovskite like structure as shown in Fig. 10.101.

Only one layer is shown here. The actual structure consists of infinite sheets of $Ba_4W_2O_{10}$, laid end-to-end. The Ba_2WO_5 compound is isostructural with Ba_2ReO_5

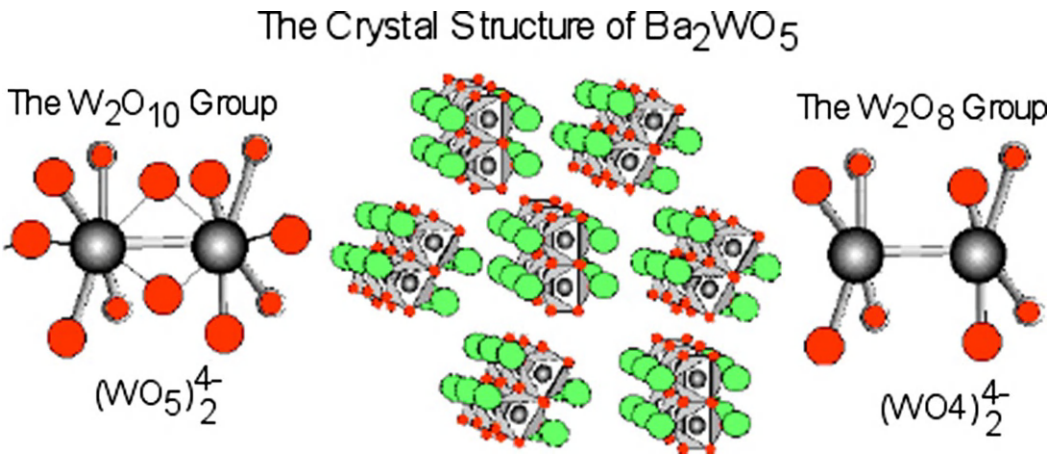

FIGURE 10.101

and contains WO_6 octahedra, which are linked by common corners and form infinite cis-bridged chains, separated by Ba atoms. The W_2O_{10} cluster is known for possessing the average oxidation state of tungstate atoms between +4 and +5.5. The W_2O_8 group on the contrary has been found only in the compounds containing W^{4+}.

NO_x sensing properties of Ba_2WO_5 were investigated in an effort to explore for a new sensor material operative at high temperature. Ba_2WO_5 was prepared from BaO and WO_3, and packed and sintered to fabricate disk-type sensor elements. It was found that the resistance of an element sintered at 800 °C decreased sharply upon exposure to NO_x in air at 500 °C, exhibiting the sensitivity values (defined as the ratio of the resistance in air to that in the sample gas) as large as 47 and 29 to 200 ppm NO and 80 ppm NO_2, respectively. The sensitivity was very dependent on the operating temperature, giving rise to a rather sharp maximum appearing at temperature around 500 °C. In addition, the elements sintered at the other temperatures (750, 850, or 900 °C) failed to exhibit significantly high sensitivity even at 500 °C. The NO_x sensing mechanism of Ba_2WO_5 was briefly discussed. From the response transient to NO and NO_2, a possible reaction occurring on the surface of Ba_2WO_5 in the presence of NO and NO_2 gases is believed to involve the reaction:

$$Ba_2WO_5 + NO(gas) + e^- \Rightarrow NO_2 + BaWO_4(solid) + BaO(solid)$$

Metal tungstates and their composites with carbonates have been investigated for application to semiconductor-type sensors capable of detecting nitrogen oxides at elevated temperatures. Among the metal

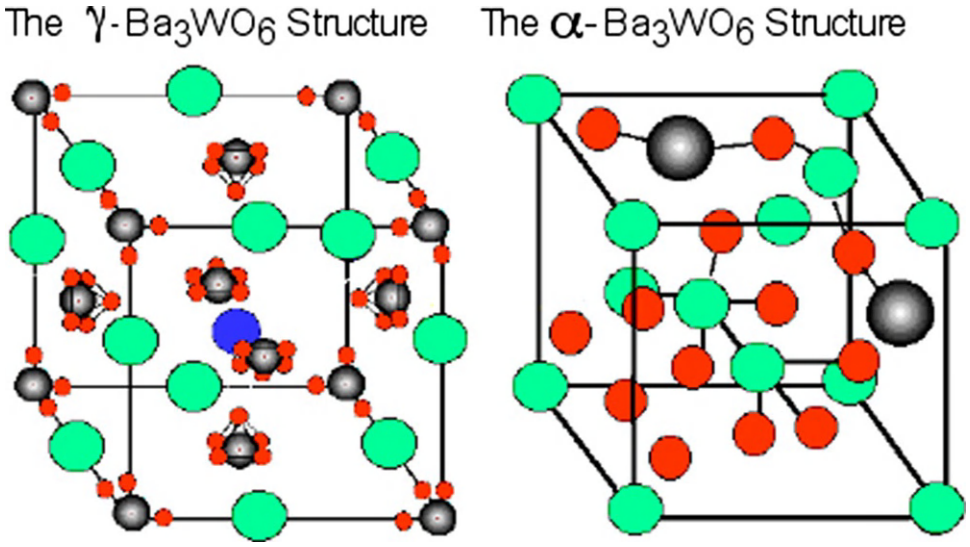

FIGURE 10.102

tungstates tested at 500 °C, $MgWO_4$ and $ZnWO_4$ are highly sensitive to NO_2 only, while $BaWO_4$ is remarkably sensitive to both NO and NO_2. The sensitivity to NO and NO_2 is greatly promoted when $BaWO_4$ is added to $BaCO_3$. The resulting composite, $BaWO_4$–$BaCO_3$ (2:1 in molar ratio) exhibits the most excellent sensing characteristics: its signal output is the same to both NO and NO_2 and increases almost linearly with increasing gas concentration in the range 0–400 ppm NO and 0–200 ppm NO_2 at 600 °C.

The double perovskite, $Ba(Zn_{1/2}W_{1/2})O_3$, is a potential microwave dielectric material. It was studied by using XRD, electron microscopy, and Knudsen effusion combined with mass spectrometry. The results show that above 1200 °C, the perovskite decomposes due to the sublimation of ZnO, which results in the formation of $BaWO_4$, Ba_2WO_5, and amorphous BaO-rich phases. Thus, the dibarium tungstate composition is one of the most stable compounds in this series. The simultaneous presence of $BaWO_4$ and Ba_2WO_5 causes the formation of a liquid phase above 1320 °C, which in the case of ceramics results in a progressive deterioration of the microstructure. As a consequence, the dielectric losses of $Ba(Zn_{1/2}W_{1/2})O_3$-based ceramics strongly depend on the processing parameters.

The structure of $Ba_3W_2O_9$ has been determined from PXRD data and found to be the same as in $Cs_3Tl_2Cl_9$. Two-thirds of the octahedral sites between hexagonal closest-packed BaO_3 layers (ABAB…) are filled by the tungsten atoms. The enneaoxo $W_2O_9^{6-}$ group represents the first crystal chemistry example of tungsten (VI) in a face-sharing arrangement. Infrared and Raman data are consistent with overall 32 (D_3) site symmetry. Crystallographic and spectroscopic evidence supports a covalent bonding model with oxygen pπ-metal dπ stabilization of this tungsten (VI) phase.

Two solid solutions have been obtained in the $Sr_{3-x}Ba_xWO_6$ system. One of them, with $0 \le x \le 0.75$, shows nonlinear behavior. Four transitions have been detected by X-ray, DTA, and dielectric measurements. The HT phase has the structure of cubic $(NH_4)_3FeF_6$, while the other ones are related. Raising x decreases the transition temperatures. At room temperature the obtained phase is piezoelectric and ferroelectric. Ba_3WO_6 is trimorphic. The intermediate structure, β-Ba_3WO_6, is not available. The high- and low-temperature polymorphs have the structure as shown in Fig. 10.102.

Cell parameters are:

HT phase = γ-Ba_3WO_6: $a = b = c = 6.1023$ Å, $\alpha = \beta = \gamma = 60°$, cell volume = 160.68 Å^3, $Z = 4$

β-Ba_3WO_6: $a = b = c = 17.1723$ Å, $\alpha = \beta = \gamma = 90°$, cell volume = 5061.68 Å^3, $Z = ?$

LT phase = α-Ba_3WO_6: $a = b = 6.1072$ Å, $c = 8.671$ Å, $\alpha = \beta = 89.91°$, $\gamma = 89.86°$, cell volume = 323.40 Å^3, $Z = 2$.

The HT-form, α-Ba_3WO_6, has the cell occupancy as shown in Table 10.52.

The cell occupancy of β-Ba_3WO_6 has not been given.

γ-Ba_3WO_6: Cell occupancy is shown in Table 10.53.

It has been known that in the system of BaO–WO_3, there are five compounds $BaWO_4$, $Ba_3W_2O_9$, Ba_2WO_5, Ba_3WO_6 and $Ba_{2.75}WO_{5.75}$. While cubic cryolite A_3BO_6 (or A_2ABO_6) is regarded as a $2 \times 2 \times 2$ superstructure of the simple cubic perovskite ABO_3 with unit cell dimension *ap*, the off-stoichiometric $Ba_{11}W_4O_{23}$ (or $Ba_{2.75}WO_{5.75}$) takes a $4 \times 4 \times 4$ superstructure with $4a_p$ (*Fd*-3*m*), $a = 17.1823$ Å, $Z = 8.23$ °C. (Note that $1X = Ba_3WO_6$ and $4X = Ba_{12}W_4O_{24}$).

The structure, $Ba_{11}W_4O_{23}$, was characterized by two types of asymmetric W ions: one in $W(1)O_6$ octahedra, typical of perovskite, and the other in polyhedra of oxygen and anionic vacancies that are statistically distributed over three divided sites to form 18 partially occupied oxide ions (~30% on average), thus, represented as $W(2)O_{18/3}$. While $W(1)O_6$ octahedra are isolated from each other by Ba1 and Ba2 ions, the W(2) $O_{18/3}$ polyhedra along the (110) direction exhibits a 1D alignment without blocking ions in between, but with the metal vacancies, indicated as V_u and V_d as shown in Fig. 10.103.

In this figure, two views are shown.

(a) A (110) view of $Ba_{11}W_4O_{23}$ unit cell: $W(1)O_6$ are shown as hatched octahedra, and $W(2)O_{18/3}$ as

TABLE 10.52

No.	Site notation	Atom	Multiplicity	Wyckoff	Site symmetry	*x*	*y*	*z*	Occupancy
1	O	O	24	e	4m.m	0.21	0	0	1.0
2	Ba2	Ba	8	c	-43m	1/4	1/4	1/4	1.0
3	Ba1	Ba	4	b	m-3m	1/2	1/2	1/2	1.0
4	W	W	4	a	m-3m	0	0	0	1.0

TABLE 10.53

No.	Site notation	Atom	Multiplicity	Wyckoff	Site symmetry	*x*	*y*	*z*	Occupancy
1	Ba6(2)	Ba	1	a	1	0.0	0.0	0.0	0.5
2	O10	O	1	a	1	0.017	0.055	0.724	1.0
3	O9	O	1	a	1	0.051	0.07	0.287	1.0
4	Ba3	Ba	1	a	1	0.051	0.548	0.789	1.0
5	W2	W	1	a	1	0.057	0.074	0.509	1.0
6	Ba1	Ba	1	a	1	0.091	0.558	0.276	1.0
7	Ba6(1)	Ba	1	a	1	0.103	0.018	0.026	0.5
8	O12	O	1	a	1	0.278	0.85	0.514	1.0
9	O7	O	1	a	1	0.319	0.244	0.508	1.0
10	O5	O	1	a	1	0.35	0.322	0.021	1.0
11	O3	O	1	a	1	0.353	0.763	0.951	1.0
12	O4	O	1	a	1	0.489	0.576	0.809	1.0
13	Ba5(1)	Ba	1	a	1	0.505	0.527	0.547	0.5
14	Ba2	Ba	1	a	1	0.531	0.03	0.76	1.0
15	O2	O	1	a	1	0.552	0.567	0.245	1.0
16	W1	W	1	a	1	0.556	0.559	0.026	1.0
17	Ba4	Ba	1	a	1	0.572	0.053	0.248	1.0
18	Ba5(2)	Ba	1	a	1	0.637	0.506	0.518	0.5
19	O6	O	1	a	1	0.751	0.328	0.98	1.0
20	O1	O	1	a	1	0.764	0.79	0.004	1.0
21	O8	O	1	a	1	0.828	0.281	0.516	1.0
22	O11	O	1	a	1	0.843	0.852	0.496	1.0

white polyhedra. Ba1 and Ba2 are shown as gray spheres, and Ba3 as smaller darker spheres.

(b) Slab of the (001) plane around $Z = 0$ with a thickness of ~5.0 Å.

It has been found that this compound is an oxide ion conductor, over a wide oxygen activity range, but with a moderate ionic conductivity, compared with the conventional electrolyte oxides. The oxide also exhibits a proton conductivity at temperature below 800 °C.

The compound, tribarium di-tungstate, $Ba_3W_2O_9$, has been found to have a structure the same as in $Cs_3Tl_2Cl_9$. The structure of $Ba_3W_2O_9$ has been determined from PXRD data. Two-thirds of the octahedral sites between hexagonal closest-packed BaO_3 layers (ABAB…) are filled by the tungsten atoms. The ennea-oxo $W_2O_9^{6-}$ group represents the first crystal chemistry example of tungsten (VI) in a face-sharing arrangement. Infrared and Raman data are consistent with an overall 32 (D_3) site symmetry. Crystallographic and spectroscopic evidence supports a covalent bonding model with oxygen pπ ⇒ metal dπ stabilization of this tungsten (VI) phase. The structure of $Ba_3Te_2O_9$ has been determined from XPRD data and by profile refinement of neutron diffraction data. $Ba_3W_2O_9$ is octahedrally coordinated as expected and has the face-shared $[B_2O_9]^{6-}$ unit as observed in other similar compositions.

The compound, $Ba_3(WO_3)_4$, has the structure as shown in Fig. 10.104.

It is composed of two octahedra tied together in the *c*-direction (011-section) but two layers of octahedra tied by W–O bonds in the (110) direction. Although the structure of tri-barium tetra-tungstate has been published, there are no studies of its physical or electrical properties available. Nothing has been published concerning its chemical properties as well.

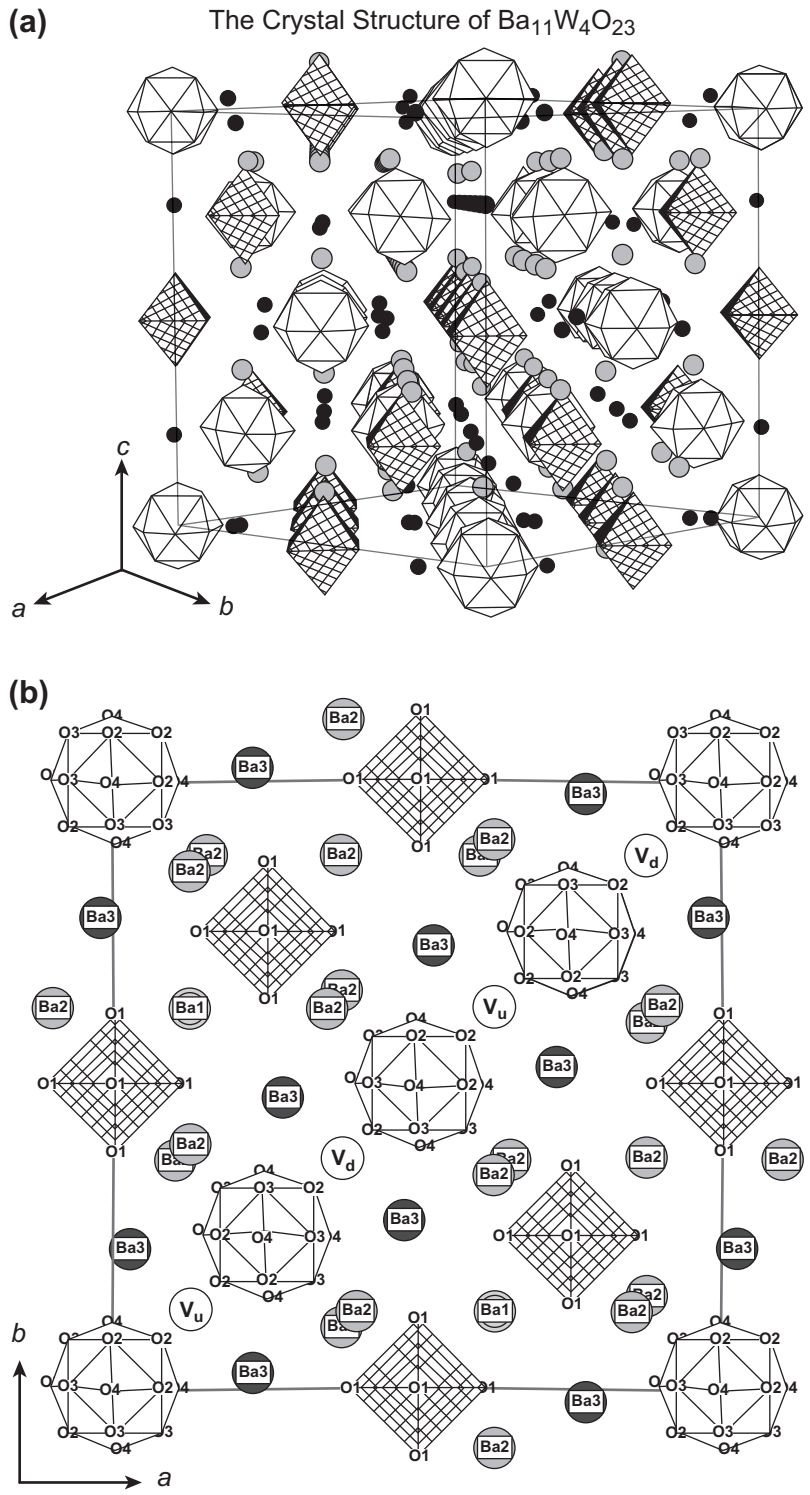

FIGURE 10.103

The compound, $BaWO_3$, barium tungstite, remains unknown, although it has been detected in the gaseous phase when a mixture of BaO and WO_3 are evaporated under neutral or reducing conditions. However, it was stated that measurement or prediction of the free energy of formation proved impossible due to its instability in the gaseous or solid state.

Barium tungstate (CAS 7787-42-0) is available commercially for proteomics research in a pure grade at $53/50 g.

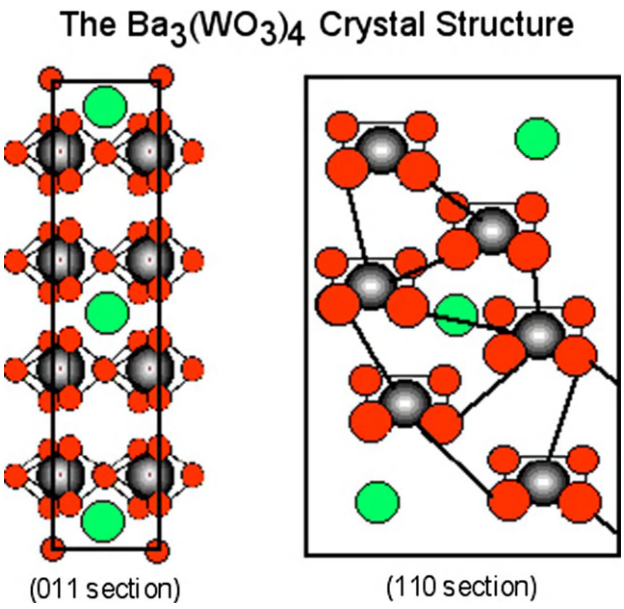

FIGURE 10.104

10.4.6. Radium Tungstates

Although radium tungstates are expected to take the same form as the homologous barium tungstates, the high cost of RaO (~1.0×10^6 USD) and its intense radioactivity have precluded any examination of compounds like $RaWO_4$, Ra_2WO_5 or Ra_3WO_6. It is unlikely these compounds will ever be examined.

CHAPTER

11

Group 7 (Mn, Tc and Re) Alkaline Earth Compounds

OUTLINE

11.1. Alkaline Earth—Manganese Compounds 869
11.1.1. Beryllium—Manganese Compounds 870

11.2. Alkaline Earth—Oxo-Manganese Compounds 870
11.2.1. Beryllium Manganese Compounds 871
11.2.2. Magnesium Manganese Compounds 871
11.2.3. Calcium Manganese Compounds 875
11.2.4. Strontium Manganese Compounds 883
11.2.5. Barium Manganese Compounds 891
11.2.6. Radium Manganese Compounds 895

11.3. Alkaline Earth—Technetium Compounds 895
11.3.1. Beryllium—Technetium Compounds 896
11.3.2. Magnesium Technetium Compounds 896
11.3.3. Calcium Technetium Compounds 897
11.3.4. Strontium Technetium Compounds 898
11.3.5. Barium Technetium Compounds 898
11.3.6. Radium Technetium Compounds 899

11.4. Alkaline Earth—Rhenium Intermetallic Compounds 899

11.5. Alkaline Earth—Oxo-Rhenium Compounds 901
11.5.1. Beryllium Oxo-Rhenium Compounds 901
11.5.2. Magnesium Oxo-Rhenium Compounds 901
11.5.3. Calcium Oxo-Rhenium Compounds 901
11.5.4. Strontium Rhenium Compounds 903
11.5.5. Barium Rhenium Compounds 907
11.5.6. Radium Rhenium Compounds 909

11.1. ALKALINE EARTH—MANGANESE COMPOUNDS

Manganese forms a limited number of intermetallic compounds with the alkaline earths. In addition, a number of "manganites" and "manganates" are known. Many of the so-called "manganites" do not contain discrete oxo-anions, but are mixed oxides with perovskite ($LaMn^{III}O_3$, $CaMn^{IV}O_3$) structures.

Manganese with valence 2–4 enters a wide range of ternary alkaline earth oxides. Just as cuprates are intimately associated with high T_c superconductivity, ternary alkaline earth manganese oxides have attracted considerable attention in the last decade for their **giant-magnetoresistance** properties. Interestingly, this applies not only to the widely studied "manganites" (or rather manganates (III, IV), if we use chemical nomenclature rules), but also to pyrochlore-type $Tl_2Mn_2O_7$ with that has a quite different structures. Manganese ions with valence ≥ 5 form very short, highly covalent Mn–O bonds, resulting in stable, isolated tetrahedral MnO_4^- species. Mn^{5+} and Mn^{6+} are known only in few compounds with very basic cations such as Ba or K.

For manganese ions with valences of 5+, 6+ and 7+, the following names have been designated in Table 11.1.

The manganate(V) anion, MnO_4^{3-}, known trivially as hypomanganate and systematically as tetraoxidomanganate(3−), is a bright blue species with a visible absorption maximum of $\lambda_{max} = 670$ nm.

$$HMnO_4^- \Leftrightarrow MnO_4^{3-} + H;\ pK_a = 13.7 \pm 0.2$$

Encyclopedia of the Alkaline Earth Compounds
http://dx.doi.org/10.1016/B978-0-444-59550-8.00011-9

Copyright © 2013 Elsevier B.V. All rights reserved.

TABLE 11.1

Name	Formula	Oxidation state	Color of solution	Comment
Permanganate	$MnO4^{2-}$	VI	Green	Paramagnetic, strong oxidant, many salts
Hypomanganate	MnO_4^{3-}	V	Blue	Paramagnetic, rarely observed, basic
Manganite	MnO_4^{4-}	IV	Brown	Paramagnetic, rarely observed, basic

TABLE 11.2

No.	Site notation	Atom	Multiplicity	Wyckoff	Site symmetry	*x*	*y*	*z*	Occupancy
1	Be2	Be	6	h	mm2	0.167	0.334	1/4	1.0
2	Mn	Mn	4	f	3m.	1/3	2/3	0.553	1.0
3	Be1	Be	2	a	-3m.	0	0	0	1.0

11.1.1. Beryllium–Manganese Compounds

Beryllium forms two compounds with Mn^0 metal. They are Be_2Mn and $Be_{12}Mn$. These compounds have the $MgZn_2$ and $ThMn_{12}$ structures, respectively. The point groups are tl26 and hP12 while the space groups are $I4/mmm$ and $P6_3/mmc$, respectively (Fig. 11.1).

The phase diagram remains unknown.

The cell parameters are:

Be_2Mn

$a = b = 4.231$ Å, $c = 6.909$ Å, $\alpha = \beta = 90°$, $\gamma = 120°$, cell volume $= 107.11$ Å^3, $Z = 4$. Cell occupancy is shown in Table 11.2.

$Be_{12}Mn$

$a = b = c = 4.1649$ Å, $\alpha = \beta = \gamma = 60°$, cell volume $= 51.09$ Å^3, $Z = 2$. Cell occupancy is shown in Table 11.3.

The only other known phase diagram involves Be–Mn–Al. A ternary phase diagram is shown as follows, illustrating what is known concerning this compound (Fig. 11.2).

The other alkaline earths do not form any intermetallic compounds. They form solid solutions as Ae^0–Mn^0 but no compounds as shown in the phase diagrams of Mg–Mn and Ba–Mn. The phase diagrams are shown in Fig. 11.3.

11.2. ALKALINE EARTH—OXO-MANGANESE COMPOUNDS

It has been observed that manganese, as one of the transition elements, does not form oxo-manganese compounds with the alkaline earths unless the alkaline

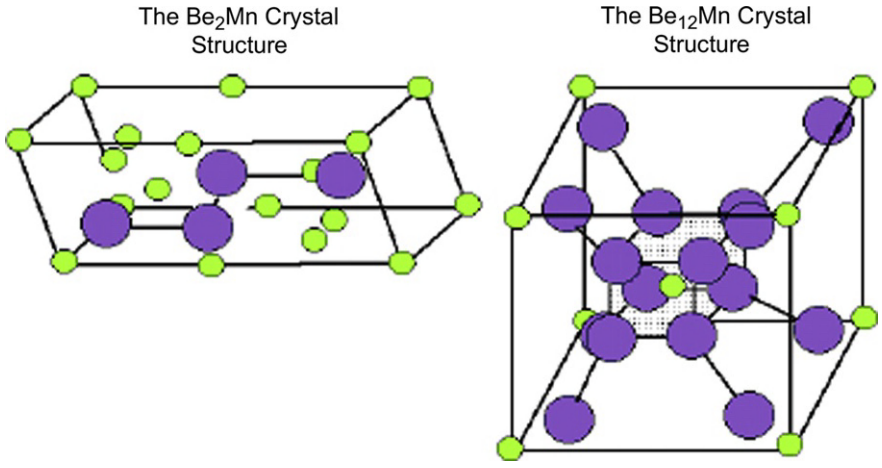

FIGURE 11.1

TABLE 11.3

No.	Site notation	Atom	Multiplicity	Wyckoff	Site symmetry	x	y	z	Occupancy
1	Be	Be	16	c	.-3m	0	0	0	1.0
2	Mn	Mn	8	b	-43m	3/8	3/8	3/8	0.17

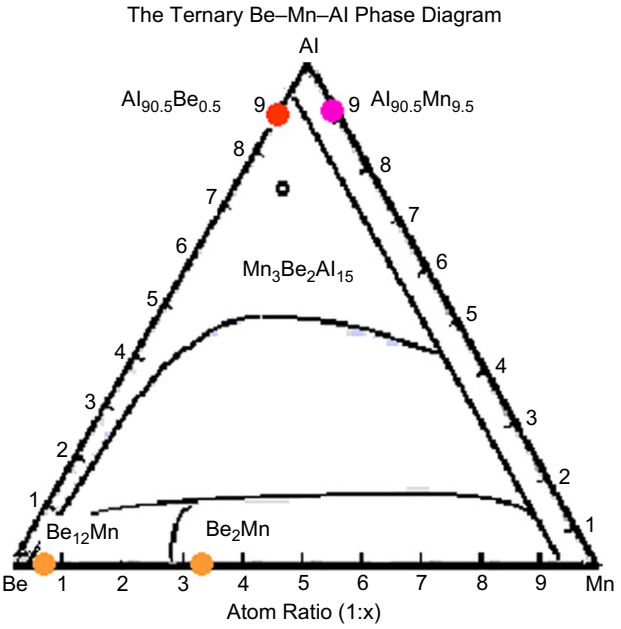

FIGURE 11.2

earth cation is large enough. This seems to be a general rule for all of the transition elements that have the anionic formula of $N_xO_{x+1}^{-x+1}$ for species where x can vary from 2 to 7. What this means in terms of manganese chemistry is that the Mn^{+2} ion in MnO_3^- (manganite) compounds has the largest atomic radius and thus can fit into a structure without undue strain. In contrast, alkaline earth compounds containing the smaller Mn^{6+}, i.e. $Mn_2O_7^{2-}$, are rare (if they exist at all). The ionic sizes of the various Mn ions are: $Mn^{2+} = 0.81$ Å, $Mn^{3+} = 0.72$ Å, $Mn^{4+} = 0.67$ Å, $Mn^{5+} = 0.47$ Å, $Mn^{6+} = 0.395$ Å, and $Mn^{7+} = 0.60$ Å. Thus, the solid-state chemistry of alkaline earth oxide–manganese oxide compounds is generally limited to those based on AeO–MnO, Mn_2O_3 and MnO_2. Seldom is a compound based on MnO_3 or Mn_2O_7 found. And these involve mostly CaO, SrO and BaO. No compounds based on BeO+(MnO, Mn_2O_3 or MnO_2) have been discovered to date. Some compounds based on MgO+(MnO, Mn_2O_3 or MnO_2) or CaO+(MnO, Mn_2O_3 or MnO_2) are very uncommon.

11.2.1. Beryllium Manganese Compounds

A search of the past and current literature does not reveal the existence of any compounds based on oxides of the manganese oxides and BeO.

11.2.2. Magnesium Manganese Compounds

In the MgO–MnO system, no specific compounds are formed from a direct reaction with manganese monooxide, MnO. In this system in air, a periclase-manganosite **solid solution** (approximate composition MgO–MnO) and spinel (approximate composition $MgMnO_2$–$MgMn_2O_4$) are the only phases present in equilibrium with liquids. Liquidus and solidus temperatures increase with increasing MgO content. A peritectic situation exists at 1587 ± 10 °C, with the two phases coexisting in equilibrium with liquid (1 wt% MgO, 99 wt% manganese oxide). This compound, (Mg, Mn)O_2 has

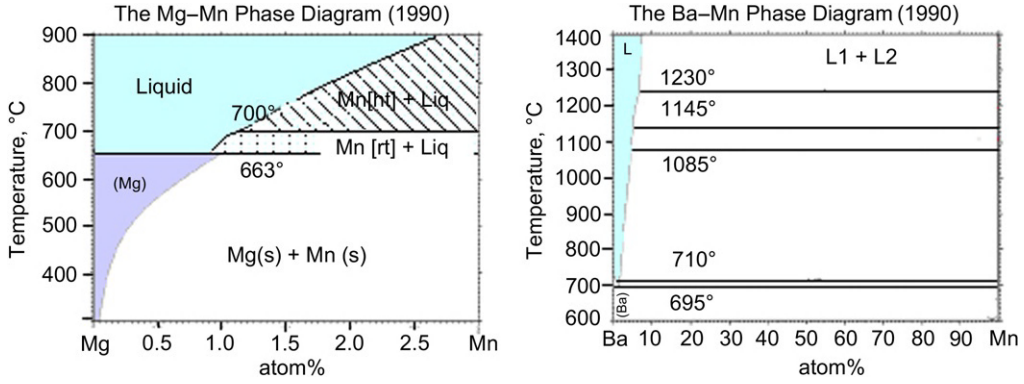

FIGURE 11.3

the NaCl crystal structure with Mg^{2+} and Mn^{2+} occupying 1/2 of the metal sites. The resistivity of $MgMnO_2$ was measured in the temperature range of 290–670 K and it was found to be *p*-type with a negative temperature coefficient of resistance.

In the manganite system, $MgO–Mn_2O_3$, a series of compounds can be formed by the use of Li_2O as a reaction catalyst. The solid–solid interactions between manganese and magnesium oxides in absence and in presence of small amounts of Li_2O have been investigated. The molar ratios between manganese and magnesium oxides in the form of Mn_2O_3 and MgO were varied between 0.05:1 and 0.5:1. The mixed solids were calcined in air at 400–1000 °C. The techniques employed were DTA (differential thermal analysis), X-ray diffraction (XRD) and H_2O_2 decomposition at 20–40 °C. The results obtained revealed that solid–solid interactions took place between the reacting solids at 600–1000 °C yielding magnesium manganates (Mg_2MnO_4, Mg_6MnO_8, $MgMnO_4$ besides unreacted portions of MgO, Mn_2O_3 and Mn_3O_4). Li_2O doping (0.75–6 mol%) of the investigated system followed by calcination at 600 and 800 °C decreased progressively the intensity of the diffraction lines of Mn_2O_3 (Bixbyite) with subsequent increase in the lattice parameter "*a*" of MgO to an extent proportional to the amount of Li_2O added. This finding appeared to suggest that the doping process enhanced the dissolution of Mn_2O_3 in MgO, forming a solid solution. This treatment led also to the formation of Li_2MnO_3. Furthermore, the doping with 3 and 6 mol% Li_2O conducted at 800 °C resulted in the conversion of Mn_2O_3 into Mn_3O_4, a process that took place at 1000 °C in the absence of Li_2O. The produced Li_2MnO_3 phase remained stable by heating at up to 1000 °C. Furthermore, Li_2O doping of the investigated system at 400–1000 °C resulted in a progressive measurable increase in the particle size of MgO. However, it is possible to obtain a pure manganate compound using Mn_2O_3.

Several ternary compounds and solid solutions of the system Mg–Mn–O have been investigated with regard to the dependence of their specific electrical conductivity on the oxygen partial pressure (10^{-19} PO_2–10^5 Pa) at 700–1000 °C. Below 1000 °C the compounds Mg_6MnO_8, Mg_2MnO_4 and $MgMn_2O_4$ are only stable at high-oxygen partial pressures, while the solid solutions $(Mg_{1-x}Mn_x)O$ are only stable at low-oxygen partial pressures ($PO_2 < 10^{-1}$ Pa). Only Mg_6MnO_8 and $Mg_{1-x}Mn_xO$ show a variation of the specific electrical conductivity, σ, with the change of PO_2. Considering the slopes of the plots of log σ versus log PO_2 and the stability of these two compounds, they may be considered as potentially good oxygen sensors.

Solid solutions of tetragonal $MgMn_2O_4$ and cubic $MgAl_2O_4$ have been synthesized and characterized using the XRD technique. Electrical conductivity (σ) and magnetic susceptibility (μ) have been measured over the temperature ranges 25–1000 °C and −195 to 60 °C, respectively. All the compounds were found to be monophasic and crystallized with either tetragonal ($c/a > 1$) or cubic symmetry. The critical concentration of $MgAl_2O_4$, required to stabilize the cubic structure, was found to be only 12.5%. This may be explained as due to migration of a considerable amount of Mn^{3+} to A sites. The values of energy of activation and free energy of activation obtained from $\ln\sigma - 1/T$ and $\ln(\sigma T) - 1/T$ plots were found to be almost identical. All the samples exhibited paramagnetism at $T \geq 195$ °C and indications of antiferromagnetic (AFM) ordering at lower temperatures.

The compound, di-magnesium manganate, Mg_2MnO_4, has the spinel structure shown in Fig. 11.4.

Cell parameters are: $a = b = c = 6.9164$ Å, $\alpha = \beta = \gamma = 60°$, cell volume = 146.44 Å^3, $Z = 4$. Cell occupancy is shown in Table 11.4.

In the $MgO–Mn_3O_3$ system, the compound, $MgMn_2O_4$, also has the magnesium aluminate spinel structure, but with the same positions for the Mg^{2+} and Mn^{4+} ions. This is shown in Fig. 11.5.

Cell parameters are: $a = b = c = 6.0245$ Å, $\alpha = \beta = \gamma = 60°$, cell volume = 154.61 Å^3, $Z = 8$.

Cell occupancy is shown in Table 11.5.

The catalytic activity measurements of these compounds showed that the increase in the molar ratio of Mn_2O_3 in the samples precalcined at 400–800 °C was accompanied by a significant increase in the catalytic activity of the treated solids. The maximum increase in the catalytic activity expressed as reaction rate constant measured at 20 °C attained 3.14-, 2.67- and 3.25-fold for the solids precalcined at 400, 600 and 800 °C, respectively. Li_2O doping of the samples having the formula 0.1 Mn_2O_3/MgO conducted at 400–600 °C brought a progressive significant increase in its catalytic activity. The maximum increase in the value of *k* 20 °C due to Li_2O attained 1.93- and 2.75-fold for the samples preheated at 400 and 600 °C, respectively and opposite effect was found for the doped samples preheated at 800 °C.

Single crystals of spinel and Hausmannite having seven different compositions in the $MgAl_2O_4$–$MgMn_2O_4$–$MnMn_2O_4$ system were synthesized and structurally and chemically characterized by XRD and electron microprobe techniques. As predicted, tetrahedral and octahedral bond lengths increased with increasing substitutions of Mn^{2+} for Mg and Mn^{3+} for Al, respectively. A transition from cubic to tetragonal symmetry occurs at a critical concentration of $Mn^{3+} > 1.4$ atoms per formula unit as a result of the Jahn–Teller distortion around octahedrally coordinated Mn^{3+}. The present data in conjunction with data from the literature provide a basis for quantitative analyses

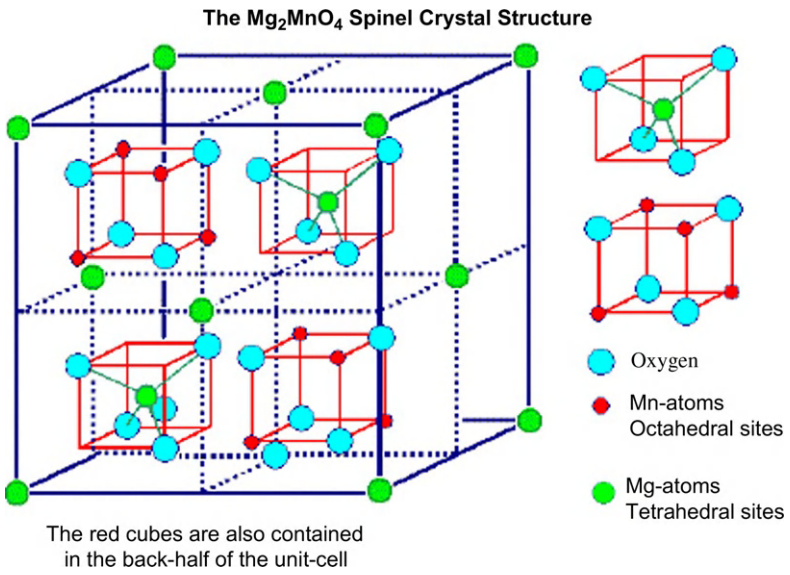

FIGURE 11.4

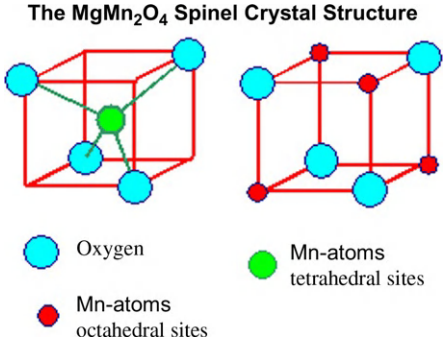

FIGURE 11.5

of the cation polyhedral-distortion parameters and their variations in spinel- and Hausmannite-type structures (*Fdm* and $I4_1/amd$, respectively). In contrast to the linear correlation between $<\sigma_M>$ (octahedral quadratic elongation) and δ^2_M (octahedral bond-angle variance) observed for many silicates and isomorphic structures, these two distortion parameters are not correlated in multiple oxides with spinel- and Hausmannite-type structures. By using a model of multiple linear regression, it was demonstrated that $<\eta_M>$ varies as a function of both δ^2_M and σ_M (octahedral bond-length distortion). The degree of octahedral distortion was significant in the spinel structures and was in fact comparable with that calculated for the Hausmannite-type structures. The degree of octahedral distortion was then related to

TABLE 11.4

No.	Site notation	Atom	Multiplicity	Wyckoff	Site symmetry	*x*	*y*	*z*	Occupancy
1	O1	O	32	e	.3m	0.238	0.238	0.238	1.0
2	M1	0.500 Mg + 0.500Mn	16	c	.-3m	0	0	0	1.0
3	Mg1	Mg	8	b	-4.3m	3/8	3/8	3/8	1.0

TABLE 11.5

No.	Site notation	Atom	Multiplicity	Wyckoff	Site symmetry	*x*	*y*	*z*	Occupancy
1	O	O	32	e	.3m	0.239	0.239	0.239	1.0
2	Mn	Mn	16	c	.-3m	0	0	0	1.0
3	Mg	Mg	8	b	-43m	3/8	3/8	3/8	1.0

steric effects in both spinel- and Hausmannite-type structures, whereas the electronic effects caused by Mn^{3+} accounted for the transition from cubic to tetragonal symmetry.

A novel type of ion-sieve manganese oxide (HMnO(<2Mg)) was prepared by extracting magnesium from Mg_2MnO_4 with aqueous acid. The preparation conditions of HMnO(<2Mg) and its ion-exchange properties were examined. The extraction of magnesium from Mg_2MnO_4 caused a decrease in the lattice constant of a spinel structure. The HMnO(<2Mg) showed a selective adsorption of lithium from seawater when the Mg/Mn ratio of the sample was less than 1. The pH titration curve showed an affinity order of Cs: K < Li above pH 3.5. The lithium-ion uptake increased with increasing solution pH and reached 3 meq/g at pH 12. The selectivity sequence was Na < Li < K < Rb < Cs for alkali metal ions at pH 3.1, while it changed to Na < Rb:Cs < K < Li at pH 8. The selectivity sequences were Mg < Ca < Sr < Ba for alkaline earth metal ions and Ni < Zn < Cu < Co for transition metal ions at pH 3.1. The Li^+-selective property is discussed based on the ion-sieve effect of the protonated octahedral sites at the cubic closed-packed oxygen framework of HMnO(<2Mg).

The phase stability of the $MgMn_2O_4$ spinel has been studied by means of high-pressure XRD for pressures up to 30 GPa. Two samples with different inversion degrees have been considered. Both spinels undergo a phase transition toward an orthorhombic structure ($CaMn_2O_4$ type). As for the more inverted sample the transition pressure is at least 1 GPa lower than that of the less inverted spinel, and the volume contraction, relative compressibility, and density trends are different for the two samples, as well.

In another paper, the influence of the cation migration process on the electrical properties of $MgMn_2O_4$ was investigated. By measuring the temperature dependence of the electrical resistance and thermoelectric power, it is possible to study the migration process of the cations in the spinel lattice, and to establish the temperature range in which the tetragonal-cubic phase change occurs. By using the thermoelectric power data, it was possible to specify the valence formulas of samples that had been quenched or slow-cooled from high temperature. The electrical conduction occurs by a hopping mechanism between the octahedral-site Mn^{3+} and Mn^{4+} ions, and involves very low mobilities.

In the $MgO–MnO_2$ system, two new ilmenites of tetravalent manganese have been prepared at high pressures: $MgMnO_3$: $a = 4.945$ Å, $c = 13.73$ Å and $ZnMnO_3$: $a = 4.965$ Å, $c = 13.80$ Å. The compounds were found to be AFM, and $MgMnO_3$ possessed semiconducting electrical properties.

Synthesis and magnetic properties of nanocrystals (size = 22 nm) of cubic spinel $MgMnO_3$ with the defect structure $[Mg^{2+}][Mg^{2+}_{1/3}Mn^{4+}_{4/3[1/3]}]O_4$ are reported. Analysis of the magnetization M versus T (2–370 K) and M versus H (up to 65 kOe) data shows a blocking temperature $T_B \approx 11$ K and an estimated Néel temperature $T_N \approx 150$ K above which the Weiss temperature $\theta = -7$ K and $\mu = 3.91$ μbar/Mn^{4+}. For $T_B < T < T_N$, fit of the M versus H data to modified Langevin function yields 35 μbar as magnetic moment/particle, resulting from the defect structure.

In the $MgO–Mn_2O_5$ system, no compounds having a composition, $MgMn_2O_6$ or $Mg(MnO_3)_2$ are known. This is likely due to the instability of the Mn^{5+} ion.

In the $MgO–Mn_2O_7$ system, the permanganate is known. It can be prepared by:

$$MgCl_2\ (aq) + Na_2(MnO_4)_2 \cdot H_2O\ (aq) \Rightarrow Mg(MnO_4)_2 \cdot 6H_2O\ (s)$$

This compound has the structure shown in Fig. 11.6.

This compound can be prepared as a molecular sieve by careful control of the initial preparation conditions (Fig. 11.7).

Here, a facile single-step method was developed for synthesizing a Todorokite-type manganese oxide octahedral molecular sieves (OMS-1) and 2 × 4 tunnel-structured manganese oxide (OMS-5) materials. Selection of

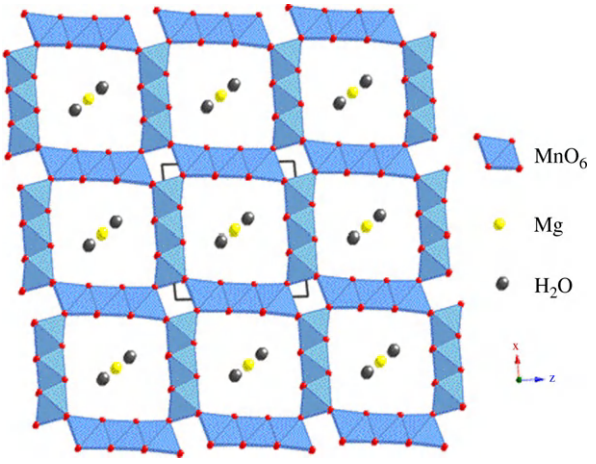

FIGURE 11.6

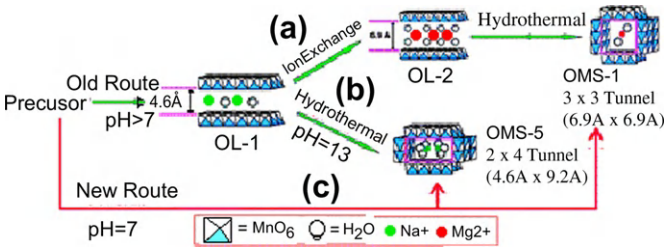

FIGURE 11.7

starting materials and initial pH conditions was crucial to a satisfactory synthesis.

In the $MgO–MnO_3$ system, no known compounds exist.

Magnesium permanganate is offered for sale as $Mg(MnO_4)_2 \cdot 6H_2O$ but little is available concerning its manufacture.

Magnesium permanganate hydrate (CAS 250578-91-7), is a specialty product for proteomics research. Magnesium permanganate (10377-62-5) is also offered for sale commercially.

11.2.3. Calcium Manganese Compounds

In the system, CaO–MnO, no compounds with MnO (hypomanganite) have been found as shown in Fig. 11.8.

This diagram is typical of the other alkaline earth—MnO systems. However, by the use of Li_2O as a molten flux, the crystal structure of $CaMnO_2$ has been determined to be that of the cubic NaCl arrangement.

In the Mn^{2+} system, CaO–MnO, the compound, dicalcium hypomanganite, Ca_2MnO_3, has been prepared. When the precursors $CaMnO_3$ and Ca_2MnO_4 are reduced with any one of a variety of inorganic (H_2, NH_3) or organic (C_2H_4, C_3H_6) reducing agents between 300 and 500 °C, topotactic reaction occurs to produce the ordered oxygen-defect phases $CaMnO_{2.5}$ and $Ca_2MnO_3.5$, respectively. Orthorhombic cell constants for $CaMnO_{2.5}$ are $a = 5.43(1)$, $b = 10.24(1)$, and $c = 3.74(1)$ Å, and for Ca_2MnO_3 are $a = 5.30$, $b = 10.05$, and $c = 12.24$ Å. These compounds were characterized by powder XRD, thermo-gravimetric analysis, magnetic susceptibility, and infrared spectroscopy. The reduced compounds reversibly oxidize to their respective precursor in oxygen at low temperatures.

In another study, an analysis of the electronic and magnetic properties of Ca_2MnO_3 was carried out within local-spin density functional theory using the augmented spherical wave method. From energy differences between the hypothetic magnetic configurations this system was found to be an insulating antiferromagnet in the ground state with a 1 eV gap. An intermediate half metallic ferromagnetic (FM) state was identified with the Hund's rule expected moments for Mn^{III} (4 μBar, high-spin HS configuration). This result of moment magnitude finds support in recent experimental evidence of Mn^{III} bismuth oxides as a ferromagnet in its ground state. This is characterized by a small density of states (DOS) magnitude of itinerant states in spin (⇑) channel pointing to a metallic-like behavior as it is experimentally evidenced.

The Mn^{3+} system, $CaO–Mn_2O_3$, contains the compound, $CaMn_2O_4$ whose structure consists of MO_4^{2-} tetrahedra interconnected facewise is shown in Fig. 11.9.

Cell parameters are: $a = 3.162$ Å, $b = 9.71$ Å, $c = 10.03$ Å, cell volume $= 307.95$ Å^3, $Z = 4$.

Cell occupancy is shown in Table 11.6.

Physical properties including magnetic susceptibility, room-temperature electrical resistivity, thermal conductivity, heat capacity, and thermal expansion have been reported for high-quality single-crystal samples of Marokite, $CaMn_2O_4$. It was determined that $CaMn_2O_4$ is highly electrically insulating and exhibits long-range AFM order below $T_N = 217$ K with easy axis along a. Anisotropic thermal expansion, similar to that of crystallographically layered materials, is observed, suggesting that the crystal structure of $CaMn_2O_4$ is also assembled from previously unexplained layers. An extensive thermodynamic study of the AFM transition was undertaken resulting in a heat-capacity critical exponent $\alpha = 0.082$ and calculated pressure derivative $dT_N/dP = 5.154$ K/GPa.

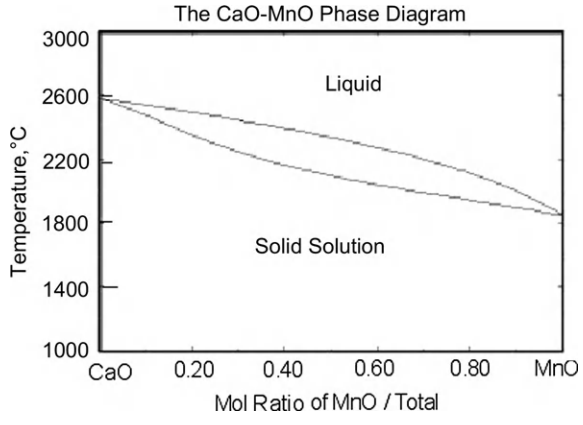

FIGURE 11.8

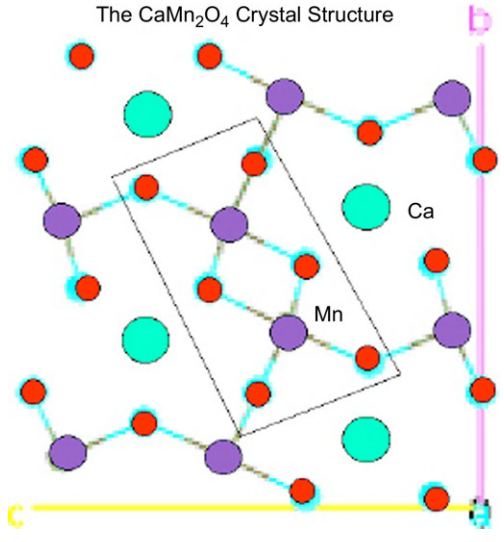

FIGURE 11.9

TABLE 11.6

No.	Site notation	Atom	Multiplicity	Wyckoff	Site symmetry	*x*	*y*	*z*	Occupancy
1	Mn	Mn	8	e	1	0.201	0.3883	0.0682	1.0
2	O3	O	8	e	1	0.193	0.027	0.107	1.0
3	O2	O	4	d	..m	0.181	0.3143	1/4	1.0
4	Ca	Ca	4	d	..m	0.676	0.148	1/4	1.0
5	O1	O	4	c	2..	0.593	1/4	0	1.0

Centimeter-sized single crystals of $CaMn_2O_{4+\delta}$, commonly known as Marokite, were grown using the floating-zone method. The growth conditions are reported along with a discussion of a simple method for polycrystalline rod preparation, which differs from the typical cold isostatic pressure procedure. Crystal characterization was determined by powder XRD, back-reflection Laue diffraction, iodometric titration, energy-dispersive X-ray spectrometry, and vibrating sample magnetometry. Polycrystalline rods, composed of stoichiometric Marokite, were found to produce crystals with $CaMnO_3$ as a secondary impurity phase as revealed by magnetic measurements and powder diffraction. Crystals grown from polycrystalline rods with excess manganese oxide produced single crystals of high quality without impurity phases.

Three structures of $CaMn_2O_4$, $CaFe_2O_4$, and $CaTi_2O_4$ have been proposed as post-spinel phases. Because these structures are very similar, several ambiguities and inconsistencies appear in high-pressure studies, leading to many problems that are yet to be solved. Systematic powder diffraction studies related to these three phases were conducted under high pressure using synchrotron radiation. All three samples have further high-pressure polymorphs. $CaMn_2O_4$ transforms to the $CaTi_2O_4$-type structure at about 30 GPa. The MnO_6 octahedron in the lower pressure structure is distorted by the Jahn–Teller effect. A new phase was observed at pressures above 50 GPa during compression of $CaFe_2O_4$. Rietveld profile fitting analysis of diffraction data at 63.3 GPa demonstrated that the high-pressure structure, with space group *Pnam*, is produced via a martensitic transformation by displacing atoms in every third layer perpendicular to the *c*-axis. $CaTi_2O_4$ also has a new high-pressure polymorph above 39 GPa with space group *Bbmm*. The most probable post-spinel candidate in the mantle is the $CaTi_2O_4$-type structure. The $CaMn_2O_4$-type structure is only formed at high pressure from spinel phases with atoms susceptible to Jahn–Teller distortion.

Mixed calcium manganese(III) oxides (see structure; Ca-green, Mn-red, O-white) with elemental compositions and structures mimicking the active site of photosystem-II were found to be highly active catalysts for the oxidation of water to molecular oxygen. As for PS II, the presence of Ca^{2+} greatly enhances the catalyst performance in comparison to the related manganese-only system Mn_2O_3 (Fig. 11.10).

Calcium manganite $CaMn_2O_4$ is orthorhombic. Susceptibility measurements in weak fields and pulsed fields made on powder and on a single crystal show that this manganite is AFM below $T_N = 225 \pm 5$ K, the moments being parallel to [100]. Neutron diffraction measurements confirm these results and show that the magnetic unit cell is twice the chemical cell (2*a*, *b*, *c* instead of *a*, *b*, *c*). The magnetic ordering has also been determined.

In this Mn^{4+} system, another compound based on the 2:1 ratio, $Ca_2Mn_2O_5$ has been found. It has the structure shown in Fig. 11.11.

It has a layered structure as may ascertained in this figure. The *b*-*c* plane (011) shows the Ca^{2+} ions layered between the MnO_4^{3+} tetrahedra {*a*-*b* plane = (110)}.

Call parameters are: $a = b = 5.183$ Å, $c = 12.6031$ Å, $\alpha = \beta = 101.866°$, $\gamma = 90°$, cell volume = 323.93 Å^3, $Z = 4$. Cell occupancy is shown in Table 11.7.

In the following figure, the ordering of oxygen vacancies in Ca2Mn2O5 having [MnO5] square pyramids is shown (Fig. 11.12).

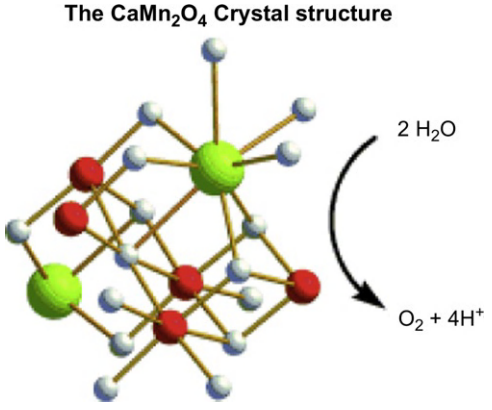

FIGURE 11.10

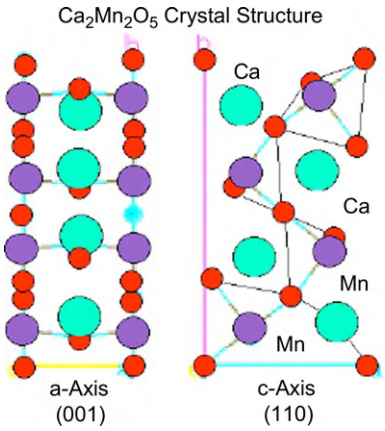

FIGURE 11.11

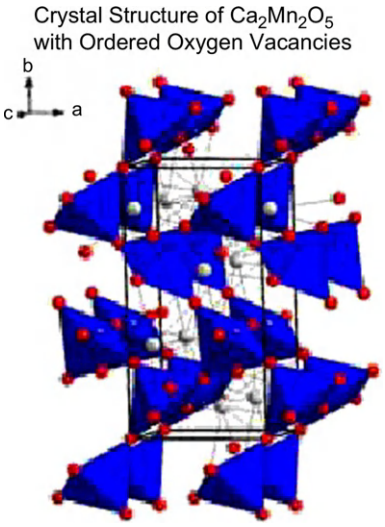

FIGURE 11.12

This is an example of a defect perovskite where the chemistry can be described according to the homologous series $A_nB_nO_{3n-1}$, $n = 2-\infty$. Several types of vacancy orderings are known, including the structure of $Ca_2Mn_2O_5$ having $n = 2$. This structure is related to "Brownmillerite" in which oxygen vacancies cause the perovskite structure to form ordered levels of defects (Fig. 11.13).

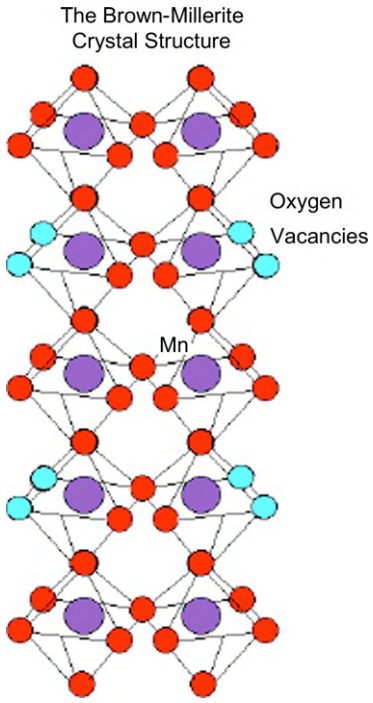

FIGURE 11.13

This is, perhaps more easily seen in the following diagram shown in Fig. 11.14.

This is a schematic representation of the ordered vacancy arrangement respect to (**a**) the perovskite cubic sublattice, (**b**) $Ca_2Mn_2O_5$ and (**c**) Brownmillerite structural types. It has been observed, generally speaking, that the FM fraction in oxygen deficient manganites decreases for high concentration of vacancies, since anionic vacancy introduction breaks the Mn_{4+}–O–Mn_{3+} double exchange interactions avoiding the FM ordering. On the basis of this description two situations can be attained (i) when vacancies are randomly distributed the magnetic behavior of the starting material is lost while (ii) it is partially kept when ordering between octahedral and tetrahedral layers happens. This is possible because the FM interactions remain at the octahedral layers. It is then clear that, together with the more conventional synthetic strategies, chemical

TABLE 11.7

No.	Site notation	Atom	Multiplicity	Wyckoff	Site symmetry	x	y	z	Occupancy
1	O2	O	16	f	..2	0.209_5	0.4595	1/8	1.0
2	Ca	Ca	16	d	2..	0	1/4	0.051	1.0
3	O1	O	16	d	2..	0	1/4	0.294	1.0
4	Mn	Mn	8	a	-4..	0	1/4	3/8	1.0

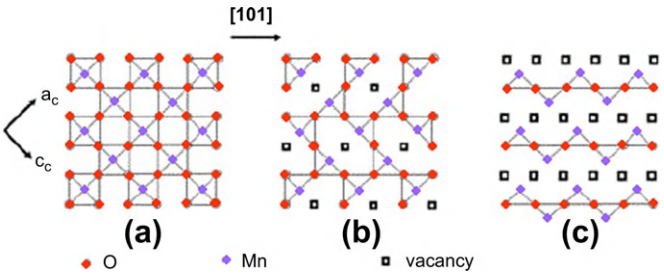

FIGURE 11.14

TABLE 11.8

Composition	Tq (°C)	Mn valence	a (Å)	b (Å)	c (Å)	V (Å^3)
$CaMnO_3$	No quench	3.99	5.2641	5.2782	7.4546	207.13
$CaMnO_{2.94}$	1000	3.88	5.2647	5.2792	7.4601	207.34
$CaMnO_{2.89}$	1100	3.78	5.2644	5.2802	7.4622	207.42

doping and more recently cationic vacancy formation, the anion vacancies can also play an important role in the intriguing structure properties relationships in manganites.

In the Mn^{4+} system, CaO–MnO_2, the manganate compound, $CaMnO_3$, is known. $CaMnO_3$ and $SrMnO_3$ are canonical AF band insulators (Mn^{4+},$t_{2g}^3e_g^0$) with a simple, bi-partite spin arrangement and a small electron density ($\sim 5 \times 10^{18}\,cm^{-3}$) produced by native oxygen vacancies. Oxygen vacancies in transition-metal oxides produce shallow donor states within the band gap that can play a crucial role in determining electronic and magnetic properties through their binding of electrons, hybridization with cation d-states, mediation of exchange interactions, or overlap to form vacancy-derived impurity bands. Such effects are implicated in many novel and unexpected phenomena that are currently the focus of considerable attention within the condensed matter physics community: magnetic polaron formation in manganites and dilute magnetic semiconducting oxides, "d^0 ferromagnetism" in materials like HfO_2 and TiO_2, highly conducting and even magnetic 2D electron gas formation at interfaces between nonmagnetic perovskite insulators. The 3d transition-metal oxides exhibit amazing physical effects such as high-temperature superconductivity. Colossal responses, such as high-temperature superconductivity, colossal magnetoresistance (CMR) and ferroelectricity, have brought doped transition metal oxides into focus during the past two decades.

Two series of manganate phases have been prepared and their magnetic properties measured. The first series consists, in addition to $CaMnO_3$, of three phases having layered structures. In these, tetravalent manganese ions are contained in single or multiple perovskite layers which are separated from each other by nonmagnetic calcium-oxygen layers. Magnetic exchange of the type Mn^{4+}–O–Mn^{4+} is disrupted between layers, and decreased Néel temperatures were expected to result. In a second series of phases, the size of the $CaMnO_3$ unit cell was increased by partial substitution of strontium for calcium. Increased separation of manganese ions produced by this means was expected to reduce Néel temperatures. However, contrary to these expectations, Néel temperatures remained approximately constant for the first series of phases and increased for the second.

$CaMnO_3$ occurs as three forms, two of which are oxygen-defect (holes) compound. The crystal parameters are listed in Table 11.8.

Titration and Mn-K XAS indicate the reduction of Mn(IV) to Mn(III) with increasing δ in the $CaMnO_{3-\delta}$ system by the creation of two five-coordinate Mn(III) sites per O vacancy. The resistivity of the electron doped $CaMnO_{3-\delta}$ decreases as δ increases but remains semiconducting in the range 20–300 K. The superexchange interactions that lead to G-type AFM ordering in the $\delta = 0$, Mn(IV) material still dominate in the O-defect materials. However, the AF-domain canting appears hindered. Evidence of FM intra-cluster Mn(IV)–O–Mn(IV) interactions are found in the Curie constant enhancement with increasing δ. A large 40% MR is demonstrated in $CaMnO_{2.89}$. The difference in spins is illustrated in Fig. 11.15.

The magnetoresistive "electron"-doped materials $CaMnO_{3-\delta}$ ($\delta = 0.06,\ 0.11$) have been investigated by neutron diffraction. While both materials order at $T_N \sim 125$ K, they have unique yet related magnetic structures. The $CaMnO_{2.94}$ sample orders into a simple G-type AFM structure, shown on the left, which is also

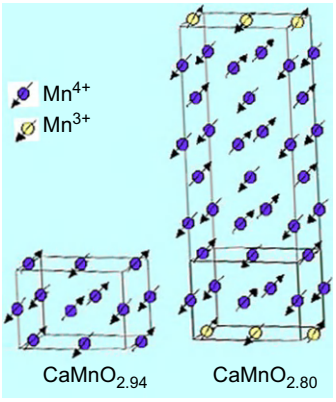

FIGURE 11.15

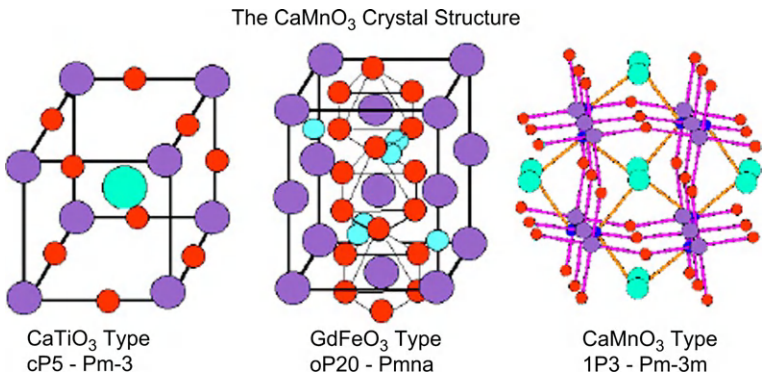

FIGURE 11.16

observed in $CaMnO_3$. The slightly more doped sample $CaMnO_{2.89}$, on the other hand, orders into a magnetic structure which is based upon the G-type, but also involves a Mn^{3+}/Mn^{4+} charge ordering over every four layers in the crystallographic *c* direction (shown on the right). The potential of these kinds of materials as new magnetic recording media is great, but the mechanism for such magnetoresistive behavior is poorly understood. Studies such as this demonstrate how subtle crystal chemistry effects can result in dramatic differences in the properties of materials.

The changes in structure as a function of oxygen defects have been studied. Polarized Raman spectra of oriented finely twinned $CaMnO_3$ thin films and nonpolarized Raman spectra of $CaMnO_3$ ceramics were studied at room temperature using several excitation laser wavelengths. The selection rules for the polarized Raman spectra, obtained from samples consisting of finely twinned orthorhombic domains, were calculated and the symmetry of all observed Raman lines was determined. The relationship between the intensity of the Raman lines and the distortions in the ABO_3 perovskites with $GdFeO_3$-type structure is discussed. These distortions can be described as superposition of four simple basic distortions: two MnO_6 octahedral tilts, Jahn–Teller deformation of $Mn^{3+}O_6$ octahedra, and shift of the A ions from their sites in the ideal perovskite. Twenty of the 24 Raman-allowed modes in the real $GdFeO_3$-type structure have counterparts in only one of the four simpler structures, obtained by a single basic distortion. The assignment of the Raman lines of $CaMnO_3$ to definite atomic vibrations, most of them activated by a single basic distortion, was made in close comparison with the results of lattice dynamical calculations and the Raman spectra of isostructural $LaMnO_3$ and $CaGeO_3$.

The three homologous crystal forms of $CaMnO_3$ are shown in Fig. 11.16.

The cell parameters are:

$GdFeO_3$ type

$a = 5.34$ Å, $b = 5.38$ Å, $c = 7.57$ Å, $\alpha = \beta = \gamma = 90°$, cell volume $= 217.48$ Å^3, $Z = 4$.

Cell occupancy is shown in Table 11.9.

$CaTiO_3$ type

$a = b = c = 3.774$ Å, $\alpha = \beta = \gamma = 90°$, cell volume $= 53.57$ Å^3, $Z = 1$. Cell occupancy is shown in Table 11.10.

$CaMnO_3$ type

$a = b = 5.333$ Å, $c = 7.534$ Å, $\alpha = \beta = \gamma = 90°$, cell volume $= 214.27$ Å^3, $Z = 4$.

Cell occupancy has not been documented.

In addition to the 1:1 compound described above, the $2CaO–3MnO_2$ compound, dicalcium tri-manganate, $Ca_2Mn_3O_8$, is also known. $Ca_2Mn_3O_8$ and $Cd_2Mn_3O_8$, which contain Mn^{4+} monolayers, have also been

TABLE 11.9

No.	Site notation	Atom	Multiplicity	Wyckoff	Site symmetry	*x*	*y*	*z*	Occupancy
1	O1	O	8	d	1	0.198	0.0506	0.3043	1.0
2	Ca1	Ca	4	c	.m.	0.437	1/4	0.0156	1.0
3	O2	O	4	c	.m.	0.533	1/4	0.6005	1.0
4	Mn1	Mn	4	a	-1	0	0	0	1.0

TABLE 11.10

No.	Site notation	Atom	Multiplicity	Wyckoff	Site symmetry	*x*	*y*	*z*	Occupancy
1	O	O	3	d	4/mm.m	1/2	0	0	0.85
2	Ca	Ca	1	b	m-3m	1/2	1/2	1/2	1.0
3	Mn	Mn	1	a	m-3m	0	0	0	1.0

TABLE 11.11

No.	Site notation	Atom	Multiplicity	Wyckoff	Site symmetry	*x*	*y*	*z*	Occupancy
1	O1	O	8	j	1	0.39941	0.27842	0.10829	1.0
2	O2	O	4	i	m	0.09726	0	0.40202	1.0
3	O3	O	4	i	m	0.39615	0	0.53742	1.0
4	Ca	Ca	4	i	m	0.72442	0	0.16593	1.0
5	Mn2	Mn	4	h	2	0	0.25914	1/2	1.0
6	Mn1	Mn	2	a	2/m	0	0	0	1.0

prepared and characterized. Their magnetic susceptibility and electron paramagnetic resonance behavior have been examined in detail. The Mn^{4+} moments in both $Ca_2Mn_3O_8$ and $Cd_2Mn_3O_8$ form an AFM order near 60 and 10 K, respectively. Although the Néel temperature in $Ca_2Mn_3O_8$ is in reasonable agreement with molecular-field theory, that in $Cd_2Mn_3O_8$ is well below its expected value. It is proposed that these results, as well as those in the calcium manganite series $CaMnO_3$–Ca_2MnO_4, may reflect the chemical influence of the divalent cation in modifying the Mn–O covalent mixing. It has the monoclinic structure shown in Fig. 11.17.

Cell parameters are: $a = 4.942$ Å, $b = 5.851$ Å, $c = 6.2358$ Å, $\alpha = 117.98°$, $\beta = 107.35°$, $\gamma = 90°$, $Z = 2$. Cell volume = 149.89 Å^3. Cell occupancy is listed in Table 11.11.

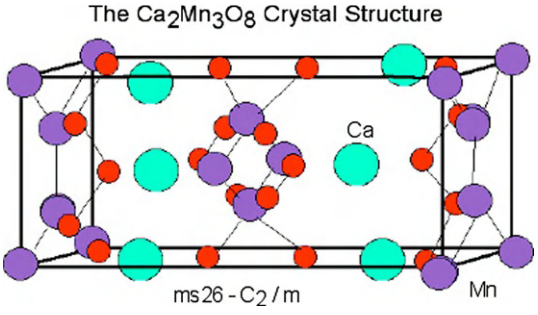

FIGURE 11.17

Another type of structure exists in this system. The dicalcium manganate compound, Ca_2MnO_4 has the structure shown in Fig. 11.18.

Cell parameters are: $a = b = 5.183$ Å, $c = 12.6031$ Å, $\alpha = \beta = 101.866°$, $\gamma = 90°$, cell volume = 323.93 Å^3, $Z = 4$. Cell occupancy is listed in Table 11.12.

The first member of the Ruddlesden–Popper (RP) family, Ca_2MnO_4, has two structures, as has been shown by electron microscopy at room temperature and neutron diffraction data. These are both AFM structures at low temperature. Two forms, with an orthorhombic

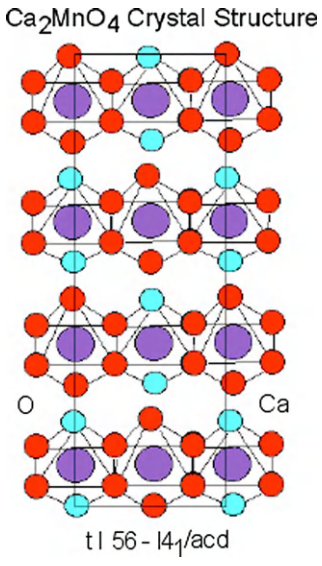

FIGURE 11.18

TABLE 11.12

No.	Site notation	Atom	Multiplicity	Wyckoff	Site symmetry	x	y	z	Occupancy
1	O2	O	16	f	..2	0.2095	0.4595	1/8	1.0
2	Ca	Ca	16	d	2..	0	1/4	0.0510	1.0
3	O1	O	16	d	2..	0	1/4	0.2944	1.0
4	Mn	Mn	8	a	-4..	0	1/4	3/8	1.0

*Aba*2 ($a \approx b \approx \sqrt{2}$ and $c \approx 12$ Å) and a tetragonal $I4_1/cad$ ($a \approx a_p\sqrt{2}$ and $c \approx 24$ Å) symmetry, were found to coexist coherently within the same matrix.

In another study, an analysis of the electronic and magnetic properties of Ca_2MnO_4 and $Ca_2MnO_{3.5}$ was carried out within local-spin density functional theory using the augmented spherical wave method. From energy differences between the hypothetic magnetic configurations both systems were found to be insulating antiferromagnets in the ground state with a 1 eV gap. However, an intermediate half metallic FM state with the Hund's rule expected moments for Mn^{IV} (3 μBar) and Mn^{III} (4 μBar, high-spin HS configuration), respectively. The latter result of moment magnitude finds support in recent experimental evidence of Mn^{III} bismuth oxide as a ferromagnet in its ground state. This is characterized by a small DOS magnitude of itinerant states in spin (⇑) channel pointing to a metallic-like behavior as it is experimentally evidenced. For both Ca_2MnO_4 and $Ca_2MnO_{3.5}$ the chemical bonding characteristics are resolved for the two spin channels.

The enthalpies of oxidation of $Ca_2MnO_{4-\delta}$ have been determined by in situ oxidation in a high-temperature adiabatic calorimeter. Ca_2MnO_4, was synthesized by the EDTA precursor or the ceramic method, and partly reduced materials were prepared by topotactic reduction in diluted H_2 (5–10%) at 290–355 °C. Unit cell dimensions and oxygen stoichiometry of partly reduced and reoxidized materials were determined by powder XRD, thermogravimetry, and iodometric titration. The enthalpy of oxidation of $Ca_2MnO_{4-\delta}$ was more exothermic than for $CaMnO_{3-\delta}$. The enthalpy of oxidation was discussed in terms of basicity of oxides, the Goldschmidt tolerance factor, and the crystal structures of the oxidized and reduced materials.

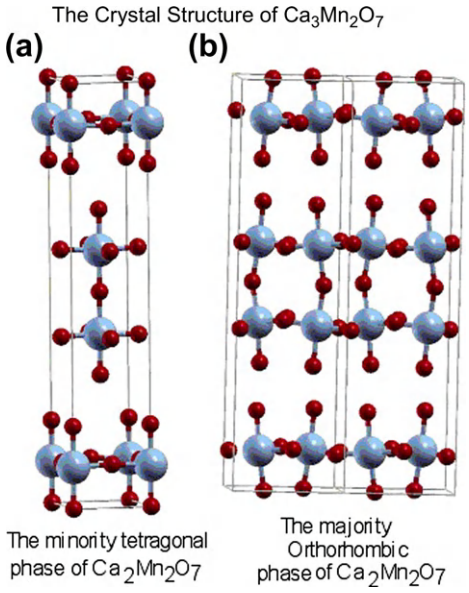

FIGURE 11.19

There is also a 3:1 compound in this system. Tricalcium di-manganate, $Ca_3Mn_2O_7$, is dimorphic. These homomorphs have the structure shown as follows. It consists of a tetragonal lattice and an orthorhombic phase (Fig. 11.19).

On the basis of density functional theory electronic band structure calculations using the augmented spherical wave method, the electronic and magnetic properties of the orthorhombic and tetragonal phases of $Ca_3Mn_2O_7$ were investigated and the spin exchange interactions of the orthorhombic phase were analyzed. The final calculations showed that the magnetic insulating states are more stable than the nonmagnetic metallic state for both polymorphs of $Ca_3Mn_2O_7$, the orthorhombic phase is more stable than the tetragonal phase, and the ground state of the orthorhombic phase is AFM. The total energies calculated for the three spin states of the orthorhombic phase of $Ca_3Mn_2O_7$ led to estimates of the spin exchange interactions $J_{nn} = -3.36$ meV and $J_{nnn} = -0.06$ meV. The accuracy of these estimates was tested by calculating the Curie–Weiss temperature within the mean-field approximation.

A compound, calcium hepta-manganate, $CaMn_7O_{12}$, contains the Mn^{3+} ion and has been found to have the structure as shown in Fig. 11.20.

Cell parameters are: $a = b = c = 5.206$ Å, $\alpha = \beta = \gamma = 60.406°$, cell volume $= 100.69$ Å^3, $Z = 2$. Cell occupancy is listed in Table 11.13.

The structural phase transition in $CaMn_7O_{12}$ has been investigated by using high-resolution synchrotron and neutron powder diffraction. Both measurements show

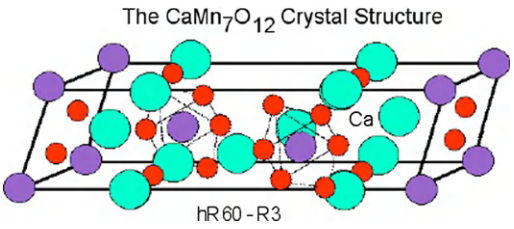

FIGURE 11.20

a phase coexistence phenomenon between 409 and 448 K and two different crystallographic phases coexist in the material. The first one is trigonal and it has a charge ordering (CO) of the Mn^{3+} and Mn^{4+} ions, while the second one is cubic and charge delocalized (CD). The volume fraction of the CD phase increases with temperature from 0 at 400 K up to 100% about 460 K. Both phases have domains of at least 150 nm at each temperature in the PS region. A percolation scenario assuming a growth of the volume of the highly conducting CD regions at the expense of the volume of the insulating CO matrix is discussed and it is found to be in agreement with literature data of the $CaMn_7O_{12}$ resistivity.

In the Mn^{3+} system, $CaO–M_2O_3$, the compound, tetra-calcium di-manganate, has the structure as shown in Fig. 11.21.

The structure encompasses the MnO_5^{5-} group coupled to a MnO_4^{4-} group. Cell parameters are: $a = 5.297$ Å, $b = 6.6598$ Å, $c = 10.053$ Å, $\alpha = \beta = 90°$, $\gamma = 113.434°$, cell volume $= 325.39$ Å^3, $Z = 4$. Cell occupancy is listed in Table 11.14.

In this type of compound, Mn^{2+} lies near the size borderline. It occupies the large site in $A_2Mn_2O_7$

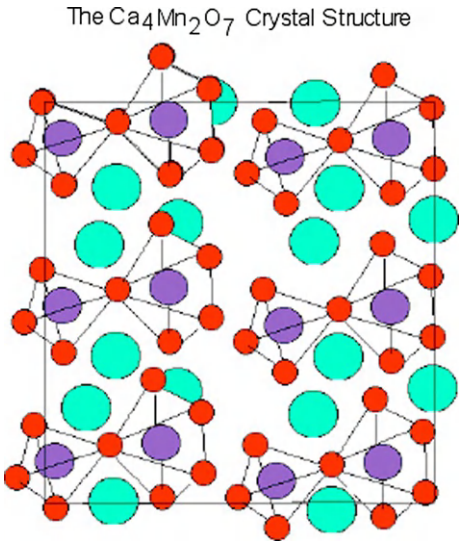

FIGURE 11.21

pyrochlores, contrary to Mn^{4+}, and occupies separate crystallographic sites in known mixed-valent $Mn^{2+}–Mn^{3+}$ or Mn^{4+} oxides. The bond distances, Mn–O–Mn bonding angles and Mn sublattice topology are given for the main Ae–Mn–O structures. Only the perovskite and K_2NiF_4 structures give Mn–O–Mn angles near 180°, while these are close to 90° in spinels, to 135° in pyrochlores and marokites. The magnetic properties of non-perovskite manganese oxides were briefly discussed in view of these structural features. The magnetic properties of oxides with intermediate superexchange angles are complex, especially when the manganese lattice is frustrated. This situation arises in two

TABLE 11.13

No.	Site notation	Atom	Multiplicity	Wyckoff	Site symmetry	*x*	*y*	*z*	Occupancy
1	O1	O	18	e	.2	0.454	0	1/4	1.0
2	Mn1	Mn	6	b	-3.	0	0	0	1.0
3	M1	0.750 Mn + 0.250 Ca	6	a	32	0	0	1/4	1.0

TABLE 11.14

No.	Site notation	Atom	Multiplicity	Wyckoff	Site symmetry	*x*	*y*	*z*	Occupancy
1	O1	O	16	g	1	0.159	0.272	0.121	1.0
2	Ca	Ca	16	g	1	0.347	0.287	0.125	1.0
3	O2	O	8	f	m..	0	0.078	0.297	1.0
4	Mn	Mn	8	f	m..	0	0.268	0.130	1.0
5	O3	O	4	a	2/m..	0	0	0	1.0

important structural families, the spinels and the pyrochlores. As a result, mixed valence in spinels, which is easy to achieve, does not give rise to physical properties comparable to those of the so-called "manganites".

In the Mn^{5+} system of $CaO–Mn_2O_5$, the compound mono-calcium manganate is not known. The dicalcium and tricalcium compounds, $Ca_2Mn_2O_7$ and $Ca_3Mn_2O_8$, have not been discovered. The instability of the Mn^{5+} ion is probably the major contributor to lack of data concerning such compounds.

In the Mn^{6+} system of $CaO–MnO_3$, the electrical, physical and chemical properties of the manganate, $CaMnO_4$, are not described in the technical literature. The dicalcium and tricalcium manganates, Ca_2MnO_5 and Ca_3MnO_6, have never been prepared. It is doubtful if they actually exist.

In contrast, the calcium permanganate (VII) compound, $Ca(MnO_4)_2$ is offered for sale commercially in large lots as an oxidizer and as a bactericide with the CAS number of 10118-76-0. Because manganese is in the +7 state, the permanganate (VII) ion is a strong oxidizing agent. Permanganate solutions are purple in color and are stable in neutral or slightly alkaline media. Calcium permanganate can be prepared in solution by the reaction:

$$CaCl_2\ (aq) + 2NaMnO_4\ (aq) \Rightarrow CaMn_2O_8\ (solid) + 2NaCl$$

This compound is stable and is in common use in qualitative analysis that involves redox reactions (permanganometry). It is a useful reagent with organic compounds, but is not very selective. Manganates(VII) are not very stable thermally and decompose at low temperatures (180–280 °C), releasing oxygen gas.

Calcium manganates are readily available commercially. The calcium permanganate salt is thought to be a "tooth whitener".

11.2.4. Strontium Manganese Compounds

In the Mn^{2+} system of SrO–MnO, the compound, $SrMnO_3$, has not been described in the open scientific literature. The reason is that the stoichiometric compound is not stable while the defect compound, $SrMnO_{2.5+\delta}$, has been established as a stable compound. The compound, strontium hypomanganite, $SrMnO_{2.5}$ has been found to possess a defect structure (Fig. 11.22).

This phase crystallizes with orthorhombic symmetry in the space group *Bbcm* with lattice parameters, $a = 5.30$ Å, $b = 10.05$ Å, $c = 12.23$ Å. The oxygen vacancies form an ordered arrangement in the perovskite block layers to give an equivalent structure to the defect perovskites $SrMnO_{2.5}$ and $CaMnO_{2.5}$ consisting of corner connected MnO_5 square-based pyramids. In these isostructural phases, the manganese ions are in square pyramidal coordination, and are subject to AFM coupling with three neighboring Mn^{3+} ions, and FM coupling with two others. It is shown that the structure of $Sr_2MnO_{3.5-\delta}$ contains Mn–O layers with a different ordering pattern to that reported previously for layers with the same overall composition, $MnO_{1.5}$. As a result of the different packing of the square pyramidal MnO_5 units, a new magnetic structure is formed below the Neel temperature.

The related compounds, dicalcium- and tri-calcium-hypomanganite, Sr_2MnO_3 and Sr_3MnO_4, have also not been synthesized. Their existence remains in doubt.

In the Mn^{3+} system of $SrO–Mn_2O_3$, very little data concerning the compound, $SrMn_2O_4$ is available. The reason is that the stoichiometric compound is not stable while a defect state is more stable. Thus, a compound like $SrMn_2O_{3.5+\delta}$ has been thoroughly studied because it exhibits a large negative magnetoresistance effect while $SrMn_2O_4$ does not. The Mn^{3+} ion is so unstable that, in acidic solution, it disproportionates to Mn^{2+} and MnO_4^{4-} in solution.

However, the related compound, Sr_2MnO_5 has been reported. The crystal and magnetic structure of $SrMn_{0.5}O_{2.5}$ has been investigated by neutron power diffraction from 20 to 425 K. The compound has orthorhombic crystal structure with the unit cell dimensions $a = 5.5307$ Å, $b = 10.7829$ Å, $c = 3.8145$ Å at 425 K, where space group is *Pbam* and $Z = 4$ (Fig. 11.23).

The structure is related to $SrMnO_{2.5+\delta}$ except that the Sr^{2+} ions are ordered, not disordered. Below $T_N = 375$ K, an AFM ordering occurs and the magnetic unit cell is orthorhombic with the dimensions $am = ac$, $bm = bc$, $cm = 2cc$, where ac, bc and cc are the parameters of the crystallographic unit cell. The FM and AFM coupling coexist in the c-plane according to the difference of Mn–O–Mn angle and the coupling between adjacent planes is AFM. The direction of the magnetic moments

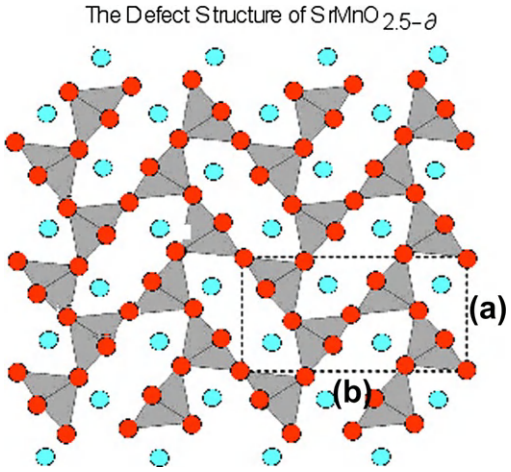

FIGURE 11.22

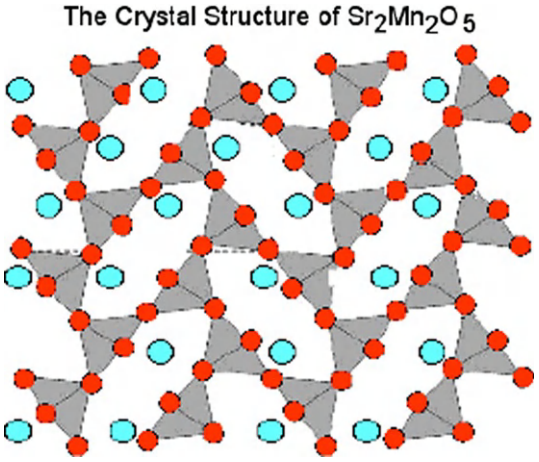

FIGURE 11.23

is along the crystallographic *b*-axis. The magnitude of magnetic moment at 20 K is 3.44 μbar per Mn. The resolution of the magnetic structure at room temperature and 4.2 K shows that the Mn^{+3} ions (d^4) order with a propagation vector $k = (0,0,1/2)$ and a magnetic moment of 3.2 μbar at 4.2 K. Each manganese ion is in square pyramidal coordination, and is coupled antiferromagnetically with three neighbors and ferromagnetically with two others.

Grossly non-stoichiometric perovskite-related $Sr_2Mn_2O_{5-\delta}$ oxide was used to exhibit the distribution of oxygen vacancies in this type of compound. The distribution remains even at high temperatures and is far from random. This behavior occurs with relatively few configurations and is associated with different arrangements of tetrahedral BO_4, square pyramidal BO_5 and octahedral BO_6 entities that are thermally accessible at most temperatures. A plot of this compound in terms of energy versus: degeneracy is given in the following diagram shown in Fig. 11.24.

Since the Sr^{2+} ions are evenly distributed, even at high temperature, the oxygen-vacancies remain evenly distributed as well. This behavior is rarely found in other alkaline earth compounds and most have a randomly distributed vacancy network. In this phase, oxygen vacancies are ordered in lines running along one of the (100) directions of the parent cubic perovskite system. Oxygen-vacancy ordering allows the charge and orbital ordering of the Mn^{3+} and Mn^{4+} cations.

A related compound, $Sr_3Mn_2O_6$, is known to exist. The oxygen-deficient RP phase $Sr_3Mn_2O_6$ crystallizes with an ordered array of oxygen vacancies to afford a structure in which the Mn^{3+} ions exist in a square-pyramidal environment. The MnO_5 polyhedra are linked through their corners to form a structure that is related to that observed for the single-layered material, $Sr_2MnO_{3.5}$. Due to the unique interlayer ordering, both phases have a magnetic structure that consists of FM clusters of four corner-sharing MnO_5 pyramids that are antiferromagnetically ordered relative to each other (Fig. 11.25).

The superstructure is due to the oxygen vacancies ordering in these compounds, an ordering which is different from that in the defect perovskites $SrMnO_{2.5}$ and $Ca_2MnO_{3.5}$. Both $Sr_2MnO_{3.5}$ and $Sr_3Mn_2O_{6+x}$ have an interlayer ordering of the same type of structure with elongated pseudo-hexagonal channels, formed by

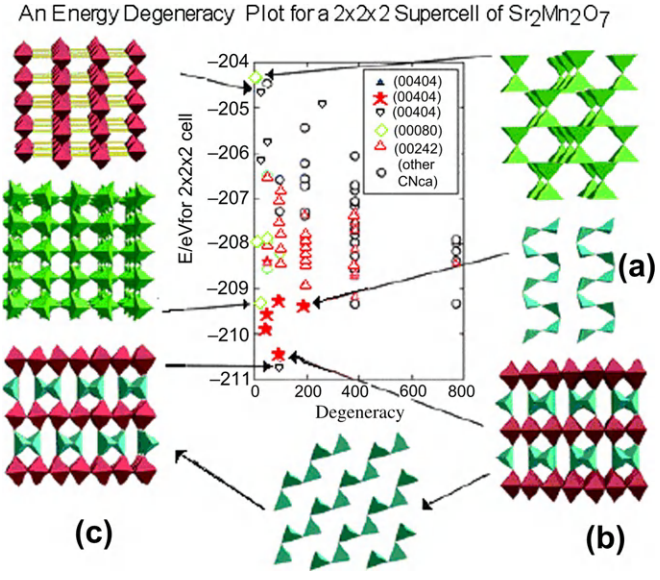

FIGURE 11.24

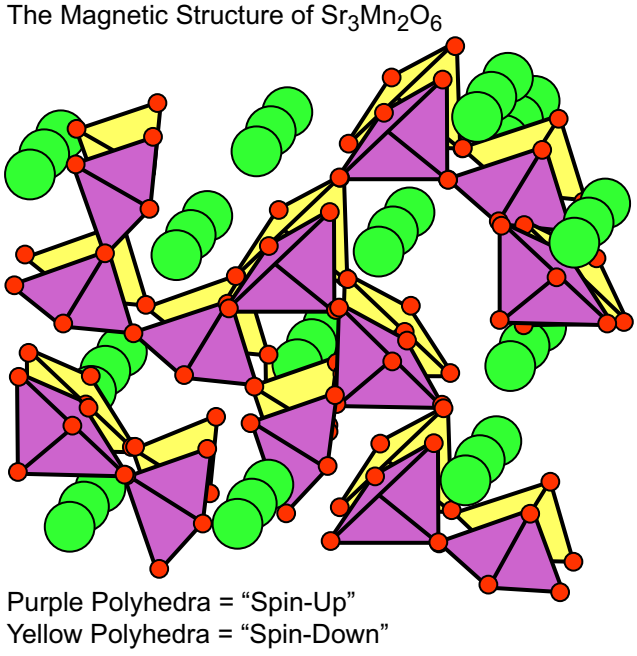

FIGURE 11.25

corner-connected MnO_5 square-based pyramids. The stacking in the two compounds, however, occurs in a different manner, leading to a monoclinic cell in the first case, and a tetragonal one in the second. Neutron powder diffraction refinements confirmed a unique model.

In another paper, the nuclear and magnetic structures of a polycrystalline sample of $Sr_3Mn_2O_6$ have been determined using Rietveld analysis of neutron powder diffraction data and electron diffraction (ED) techniques. The pure Mn^{3+} double-layered phase crystallizes in a superstructure of the simple RP subcell: tetragonal, $P4 = mbm$; $a = 10.8686$ Å and $c = 20.2051$ Å. Magnetic susceptibility studies suggest a transition at 250 K to a canted AFM ordered structure. The magnetic unit cell consists of FM clusters of corner-sharing MnO_5 units, which are antiferromagnetically aligned to other clusters within the layers. The double-layered RP phase $Sr_3Mn_2O_{6+x}$ crystallizes with the oxygen vacancies forming an ordered array in the "MnO_2" layers of the perovskite blocks. The vacancies order to give a similar layer structure to $Sr_2MnO_{3.5}$ consisting of corner connected Jahn–Teller distorted MnO_5 square-based pyramids. The primitive tetragonal structure shows complete oxygen vacancy ordering in the perovskite block layers at $z = 0$ and 1; whereas only partial order is observed in the middle layer at z 1/4 1 2: $Sr_3Mn_2O_{6+x}$ orders antiferromagnetically below ca. 250 K and the magnetic structure contains FM clusters aligned antiferromagnetically to each other within the perovskite block layers.

The Mn^{4+} system involving SrO–MnO_2 has been studied extensively because of its electrical properties. The compound, $SrMnO_3$, is a perovskite. The compound, Sr_2MnO_4, has a body-centered tetragonal structure and a reduced phase $Sr_2MnO_{3.84}$ is reported to contain the oxygen vacancies in the "MnO_2" layers (equatorial positions) in a disordered array. The magnetic structure of Sr_2MnO_4, is analogous to that of K_2NiF_4. The magnetic unit cell shows a doubling along the *a*-axis, with the magnetic moments parallel to the *c*-axis exhibiting AFM ordering with $T_N \approx 170$ K. This contrasts with the magnetic structure of Ca_2MnO_4 where the *c*-axis was doubled for the magnetic cell. A related double-layered oxygen-deficient strontium manganite, $Sr_3Mn_2O_{6.35}$ has also been reported. This RP structure also has the oxygen defects located in the equatorial "MnO_2" layers, but again, similar to $Sr_2MnO_{3.84}$, these vacancies are found to exist in a disordered manner.

Perovskites containing Mn in mixed $Mn^{3+/}Mn^{4+}$ oxidation states have been the focus of much attention owing to their ability to display large negative magnetoresistance effects upon application of magnetic fields of the order of several tesla. The study of these manganese oxides, widely known as manganites, that exhibit the CMR effect is among the main areas of research within the area of Strongly Correlated Electrons. After considerable theoretical effort in recent years, mainly guided by computational and mean-field studies of realistic models, considerable progress has been achieved in understanding the curious properties of these compounds. These recent studies suggest that the ground states of manganite models tend to be intrinsically inhomogeneous due to the presence of strong tendencies toward phase separation, typically involving FM metallic and AFM charge and orbital ordered insulating domains. Calculations of the resistivity versus temperature using mixed states lead to a good agreement with experiments. The mixed-phase tendencies have two origins: (i) electronic phase separation between phases with different densities that lead to nanometer scale coexisting clusters, and (ii) disorder-induced phase separation with percolative characteristics between equal-density phases, driven by disorder near first-order metal-insulator transitions. The coexisting clusters in the latter can be as large as a micrometer in size. In addition, the physics of manganites appears dominated by intrinsic inhomogeneities and its description is quite difficult in purely analytic frameworks that usually assume uniform states.

The field of manganites started with the seminal paper of Jonker and van Santen (1950) where the existence of ferromagnetism in mixed crystals of $LaMnO_3$–$CaMnO_3$, $LaMnO_3$–$SrMnO_3$, and $LaMnO_3$–$BaMnO_3$ was reported. Various types of structures are obtained as a function of preparation temperature. The following diagram illustrates this factor, obtained by ED techniques (Fig. 11.26).

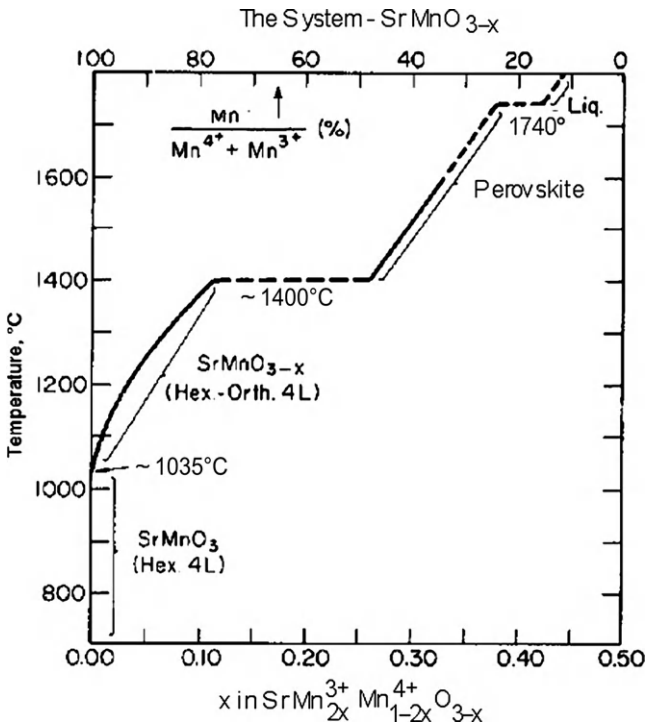

FIGURE 11.26

The pure Mn^{3+} single-layered phase crystallizes in the primitive monoclinic space group $P2_1/c$ with lattice constants $a = 6.8524$ Å, $b = 10.8131$ Å, $c = 10.8068(4)$ Å, $\beta = 113.247°$. The oxygen defects form an ordered superstructure within the perovskite block layers consisting of interconnected MnO_5 square pyramids, slightly different from those observed for the defect perovskites $SrMnO_{2.5}$ and $Ca_2MnO_{3.5}$. Magnetic susceptibility studies show a broad transition at 280 K, which is attributed to an overall AFM ordering of spins, which leads to doubling of the unit cell along [100]. The magnetic unit cell comprises FM clusters of four corner-sharing MnO_5 pyramids, which are antiferromagnetically aligned to other similar clusters within the perovskite block layers.

α-$SrMnO_{3.5-\delta}$ crystallizes in the hexagonal system with unit cell dimensions $a = 5.454$ Å, $c = 9.092$ Å, space group $P6_3/mmc$, $Z = 4$. The structure was solved by the heavy-atom method; of 404 unique reflections measured by counter method, 203 that obeyed the condition $|F_0| \geq 3\sigma$ ($|F_0|$) were used in the refinement to a conventional R value of 0.043. The structure consists of four close-packed SrO_3 layers in an $ABAC$ stacking sequence along the hexagonal c-axis. Oxygen octahedra containing Mn^{4+} are grouped into face-sharing pairs linked by corner sharing within the cubically stacked "A" layer.

Dilatometric measurements were used to determine phase transition temperatures and oxidation temperatures of $Sr_2MnO_{4-\delta}$ and several phases in the system $SrMnO_{3-\delta}$. The use of dilatometry is based on differences among the molar volume of the various phases determined by XRD. Oxidation of $SrMnO_{3-y}$ and $Sr_2MnO_{4-y'}$ proceeded without change in the basic structure of perovskite and K_2NiF_4 type, respectively. Anion vacancies produce lattice expansion in reduced Sr_2MnO_{4-y} and $SrMnO_{3-y}$ compared with $Sr_2MnO_{4.00}$ and β-$SrMnO_{3.00}$. In the case of $SrMnO_{2.58}$, the ratio of lattice constants indicates narrow structural relations to β-$SrMnO_3$.

The nuclear and magnetic structures of polycrystalline $Sr_2MnO_{3.5}$ have been determined by the Rietveld analysis of neutron powder diffraction data and ED techniques. The pure Mn^{3+} single-layered phase crystallizes in the primitive monoclinic space group $P2_1/c$ with lattice constants $a = 6.8524(3)$ Å, $b = 10.8131(4)$ Å, $c = 10.8068(4)$ Å, $\beta = 113.247(4)°$. The oxygen defects form an ordered superstructure within the perovskite block layers consisting of interconnected MnO_5 square pyramids, slightly different from those observed for the defect perovskites $SrMnO_{2.5}$ and $Ca_2MnO_{3.5}$. Magnetic susceptibility studies show a broad transition at ~280 K, which is attributed to an overall AFM ordering of spins, which leads to doubling of the unit cell along [100]. The magnetic unit cell comprises FM clusters of four corner-sharing MnO_5 pyramids, which

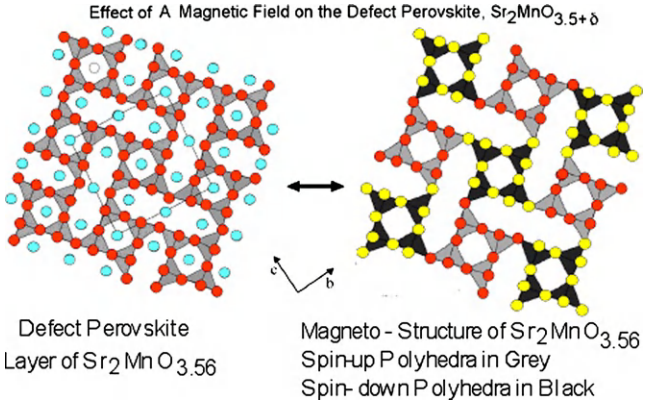

FIGURE 11.27

are antiferromagnetically aligned to other similar clusters within the perovskite block layers. The effect of a magnetic field upon the structure of the defect perovskite, $Sr_2MnO_{3.56}$ composition is shown in Fig. 11.27.

ED (electron diffraction) studies clearly revealed a superstructure implying an ordering of the oxygen vacancies to give a primitive monoclinic cell with $a = 6.85$ Å, $b = 10.28$ Å, $c = 10.26$ Å, $\beta = 104.61°$. Rietveld structure refinement based on various plausible distributions of the oxygen vacancies showed that only one arrangement appeared consistent with such a large unit cell in the bc plane, ca. 10×10 Å. The arrangement, which corresponds to $P2_1/c$ symmetry, is similar to that seen for the ordered perovskite $SrMnO_{2.5}$. The Mn^{3+} ions have the electronic configuration $t_{2g}^3 e_g(dz^2)^1$ and the magnetic exchange between adjacent square-based pyramids can be ascertained by the interactions between the singly occupied dz^2 orbitals, and the perpendicular, empty dx^2-y^2 orbitals. This leads to the prediction of FM exchange when a connecting oxygen anion links a dz^2 orbital with a vacant dx^2y^2 orbital, and an AFM alignment upon interaction of two dz^2 orbitals. Hence, the intralayer magnetic structure was deduced as clusters of four ferromagnetically aligned moments, which are arranged antiferromagnetically to other clusters within the perovskite block layers. This behavior may be summarized as:

> "The single-layered phase $Sr_2MnO_{3.5}$ crystallizes with the oxygen vacancies forming an ordered array in the "MnO_2" layers of the perovskite block. Although the defect structure formed can be compared with that found in the oxygen-deficient perovskite $SrMnO_{2.5}$ and the analogous $Ca_2MnO_{3.5}$, the vacancies order to give a new type of structure of corner connected Jahn–Teller distorted MnO_5 square-based pyramids. $Sr_2MnO_{3.5}$ orders antiferromagnetically below 280 K and the magnetic structure contains FM clusters aligned antiferromagnetically to each other within the perovskite block layers".

The tri-strontium di-manganate is also known. The structure is shown in Fig. 11.28.

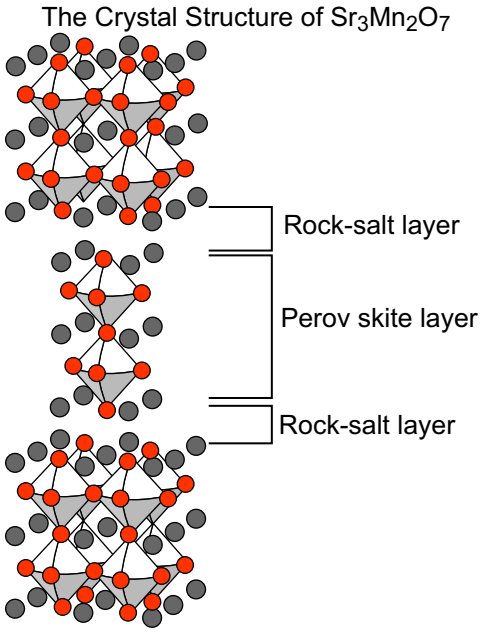

FIGURE 11.28

The crystal and magnetic structures of the bilayer RP phase $Sr_3Mn_2O_{7-\delta}$ ($\delta = 0.0,\ 0.45$). The $\delta = 0.45$ compound exhibits a large number of oxygen vacancies that are disordered in the MnO_2 planes and is a nonmagnetic insulator. $Sr_3Mn_2O_{7.0}(\delta = 0)$ in an AFM insulator whose magnetic structure is analogous to that of the related $SrMnO_3$ perovskite. The stoichiometric layered material has a small distortion of its exclusively $Mn^{4+}O_6$ octahedra as a result of steric influence of the surrounding cations. Thus, it provides a baseline for structural distortions related to electronic and/or magnetic transitions in doped materials.

Polycrystalline $Sr_3Mn_2O_{6.54}$ and $Sr_3Mn_2O_7$ layered manganites were studied at room temperature using Raman spectroscopy. While the phonon spectrum of the stoichiometric $Sr_3Mn_2O_7$ sample is consistent with the group theoretical analysis for the $I4/mm$ structure, three additional modes are observed in the phonon spectrum of the oxygen-deficient $Sr_3Mn_2O_{6.54}$ sample. Based on an analysis of the temperature dependence of the Raman spectrum of $Sr_3Mn_2O_{6.54}$ and a comparison with the Raman spectrum of $LaSr_2Mn_2O_7$, we conclude that the "extra" modes should be viewed as disorder-induced Raman scattering.

The electronic structure of the RP layered perovskite compound $Sr_3Mn_2O_7$ was studied from density functional calculations using the linear muffin-tin orbital method. An AFM, insulating solution is obtained in agreement with the experiments, with a magnetic moment of about 2.52 bar for each Mn atom. The magnetic interactions between the Mn atoms, both within the bilayer and between the bilayers, are shown to arise from superexchange. The intrabilayer interaction involves the three-site Mn–O–Mn superexchange much like the case of the well-known $CaMnO_3$, while the interbilayer exchange, mediated via the longer Mn–O–O–Mn superexchange path, is considerably weaker. Consistent with the layered nature of the compound, a strong out-of-plane to in-plane band-mass anisotropy for $Sr_3Mn_2O_7$ ($mz^*/mx,y^* = 10.9$ for electrons and -4.2 for holes) was found, while for the related compound $LaSr_3Mn_2O_7$, which is a FM metal, a strong anisotropy in the resistivity $\rho c/\rho_{ab}$-40 using kinetic transport theory, in qualitative argument with the experimental value of ~100 was obtained.

Transition metal oxides have been extensively studied due to the complex interactions between the different order parameters. The layered manganites have shown long-range magnetic, charge, orbital and correlated structural distortions. Such order parameters in the RP group, $(La,Sr)_{n+1}Mn_nO_{3n+1}$ have been studied with a variety of techniques. The resonant X-ray scattering results for the bilayer, $n = 2$ member, with $x = 0.7$ is shown in the following figure, Fig. 11.29. This overdoped system has a hole density provided by the doped strontium ions sufficient for the usual half doped CE checkerboard to become unstable. Indeed, this breakdown of the 1:1 checkerboard pattern and associated herringbone orbital order has been observed to collapse with $x \approx 0.575$. Further investigations have suggested that the orbital and charge order are caused to melt through the onset of AFM order. In contrast, no such long-range magnetic order has been observed in $La_{0.6}Sr_{2.4}Mn_2O_7$.

The phase diagram for the bilayer manganite series $La_{2-2x}Sr_{1+2x}Mn_2O_7$ ($0.35 < x < 0.75$) is shown in Fig. 11.30.

Data points marked by X show the onset of charge order (and JT) through the appearance of superlattice reflections, X data points mark the maxima in the intensity of the CO (or JT) reflections, interpreted as the onset of A-type AFM order. The data points marked by symbols are taken from prior publications. The phase diagram for the bilayer manganites, showed a general transition from a FM phase in the underdoped system, to an AFM phase around half doping, to a paramagnetic overdoped system as a function of increasing doping. Charge order and cooperative Jahn–Teller distortions are observed in the half doped and overdoped systems. It has been previously shown that the CE checker board charge order breaks down at $x \approx 0.575$, and through resonant XRD it is suggested that the formation of a charge density wave and associated orbital density wave in the $x = 0.7$ system becomes dominant.

In the Mn^{5+} system of $SrO–Mn_2O_5$, the compound, $SrMn_2O_6$, has been discovered. The structure is illustrated in Fig. 11.31.

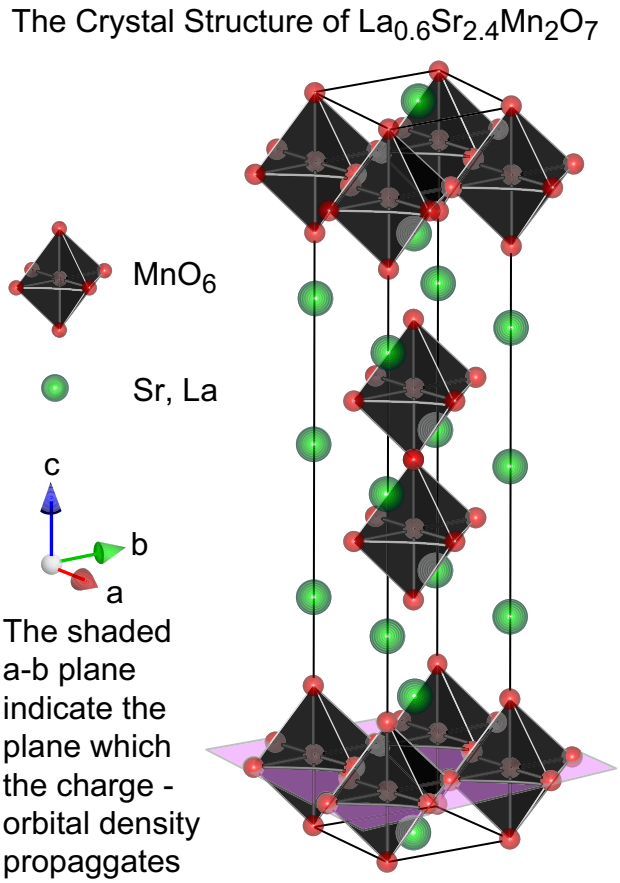

FIGURE 11.29

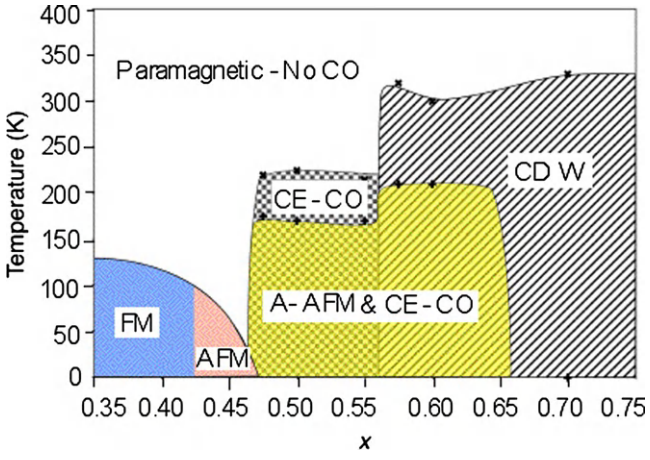

FIGURE 11.30

$SrMn_3O_6$ exhibits an incommensurately modulated structure. This strontium manganate phase has been synthesized and characterized by structural refinement of NPD data using a 4D formalism. The structure can be described by edge-sharing MnO_6 octahedra, which

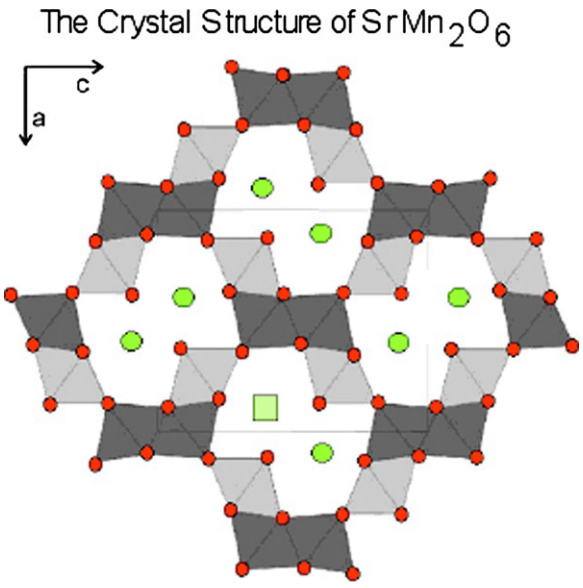

FIGURE 11.31

exist in groups of four, in a distorted z-shape. These z-shaped units form an infinite ribbon along the short *b*-axis of the unit cell, and are corner linked to four other z-shaped units to give double tunnels shaped like a figure of eight. The Sr cations are located in 67% of the available tunnel sites.

$SrMn_3O_6$ exhibits an average distorted tunnel structure with the same basic features as $Na_xFe_xTi_{2-x}O_4$ and $BaPb_{1.5}Mn_6Al_2O_{16}$, but a complicated incommensurate 1D modulation is present with modulation wave-vector components $\mathbf{q} = 0.52a + 0.31b$. The existence of ordered strontium vacancies is implied from the structural refinement and this constitutes the main driving force of the modulation in $SrMn_3O_6$; the slight distortion of the Mn–O framework can be attributed to this ordering of strontium and vacancies. It could therefore be proposed that the $BaPb_{1.5}Mn_6Al_2O_{16}$ may also exhibit a similar type of modulation since the tunnel sites are again only partially occupied. The most intense reflections are the basic reflections, which correspond to the Pnma subcell with $a = 9.1334$ Å, $b = 2.8219$ Å and $c = 12.0959$ Å.

The electronic structure of the RP layered perovskite compound $Sr_2Mn_2O_7$ has been studied from density functional calculations using the linear muffin-tin orbitals method. An AFM, insulating solution was obtained, with a magnetic moment of about 2.52 μbar for each Mn atom. The magnetic interactions between the Mn atoms, both within the bilayer and between the bilayers, were shown to arise from superexchange. The intrabilayer interaction involves the three-site Mn–O–Mn superexchange much like the case of the well-known $CaMnO_3$, while the interbilayer exchange, mediated via

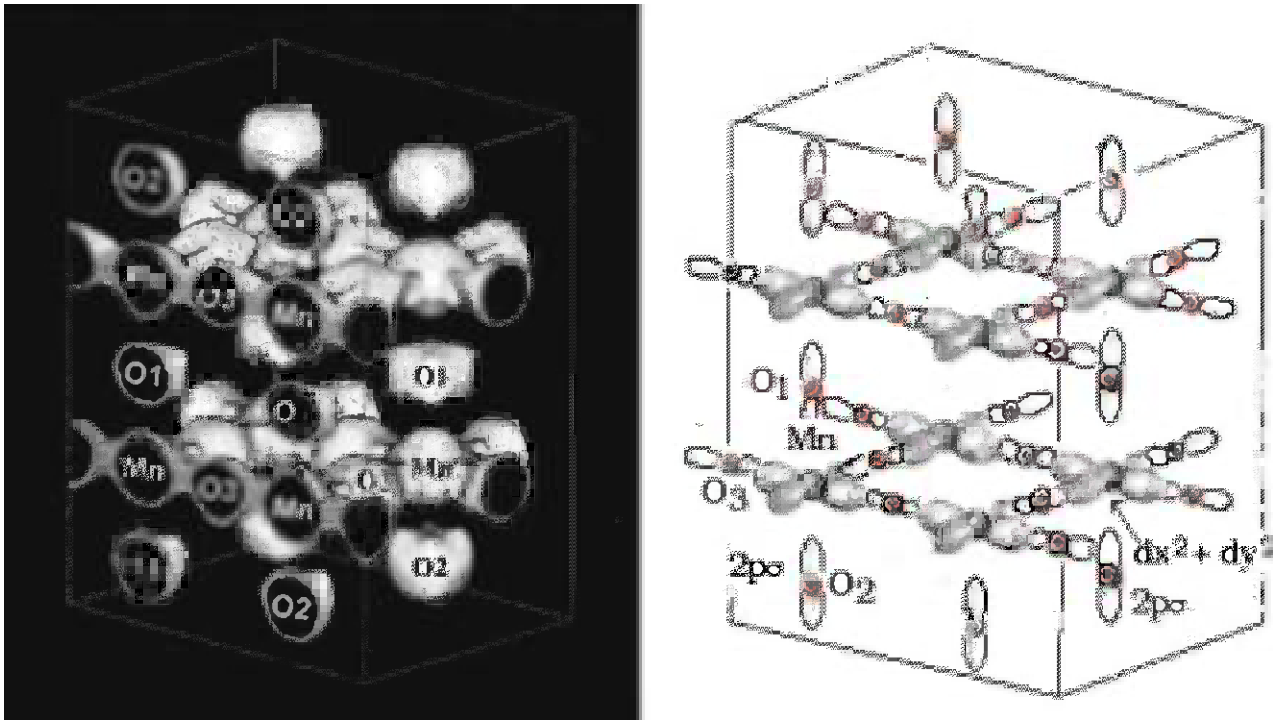

FIGURE 11.32

the longer Mn–O–O–Mn superexchange path, is considerably weaker. Consistent with the layered nature of the compound, a strong out-of-plane to in-plane band-mass anisotropy for $Sr_3Mn_2O_7$ ($mz^*/mx,y^* \sim 10.9$ for electrons and ~4.2 for holes) was seen, while for the related compound $LaSr_2Mn_2O_7$, which is a FM metal, a strong anisotropy in the resistivity $rc/rab \sim 40$, using kinetic transport theory, in qualitative agreement with the experimental value of ~100 was obtained. The following diagram shows contours containing a charge density of 0.4 eÅ^3, obtained by the maximum-entropy analysis of synchrotron-X-ray powder diffraction data for $NdSr_2Mn_2O_7$ at 19 K, showing the MnO_6 double layers. The schematic orbital structure is also shown in Fig. 11.32.

In a study of the composition, $(Nd_{12x}La_x)Sr_2Mn_2O_7$, researchers found a narrow, charge order CE AFM regime to exist on the La-rich end of the series, that dominates in a narrow temperature range between 110 and 220 K. On further cooling, the resistivity of $LaSr_2Mn_2O_7$ first increases sharply at the charge ordering transition, reaches a maximum, and then decreases to a minimum near 100 K. Single-crystal neutron-scattering data provide greater detail. A-type AFM order and CE-type charge order appear simultaneously at 210 K. This coincides with a decrease in diffuse magnetic scattering. Near 120 K, the CE-type charge ordering disappears and a weak, CE-type AFM peak appears.

In the Mn^{6+} system of SrO–MnO_4, the compound $SrMnO_4$ has been used for organic synthesis. Strontium manganate ($SrMnO_4$) in the presence of aluminum chloride ($AlCl_3$) is an efficient reagent for the high-yielding oxidative deprotection of aromatic and aliphatic silyl and pyranyl ethers into their corresponding carbonyl compounds, in solution and under solvent-free conditions (Fig. 11.33).

Yields are in excess of 95% for a great number of compounds.

The oxygen-deficient RP phase Sr_3MnO_6 is a double-layer manganite that crystallizes with an ordered array of oxygen vacancies to give a structure containing $Mn(VI)O_5^{4-}$ square-pyramidal polyhedra. The MnO_5 polyhedra are linked through their corners to form a structure that is related to that observed for the single-layered material, $Sr_2MnO_{3.5}$. At 250 K, there is a transition to a canted AFM ordered structure. The magnetic unit cell consists of FM clusters of corner-sharing MnO_5 units, which are antiferromagnetically aligned to other clusters within the layers.

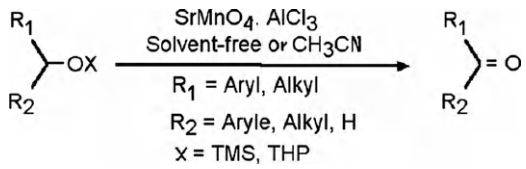

FIGURE 11.33

The crystal and magnetic structures of the bilayer RP phase $Sr_3Mn_2O_{7-\delta}$ ($\delta = 0,0.45$) were investigated. A correlation of these structures with their magnetic and transport properties was made. The $\delta = 0.45$ compound contains a large number of oxygen vacancies that are disordered in the MnO_2 planes. As a result of this disordered vacancy structure, $Sr_3Mn_2O_{6.55}$ is a nonmagnetic insulator. $Sr_3Mn_2O_{7-\delta}$ ($\delta = 0$) is an AFM insulator whose magnetic structure is related to that of the $SrMnO_3$ perovskite. Comparison of this end-member compound to its doped congeners in the $\gamma La_{2-2x}Sr_{1+2x}Mn_2O_7$ series highlights the extreme sensitivity of magnetic structure to dopant concentration in these layered materials.

The magnetic and structural properties of the layered manganite $Sr_7Mn_4O_{15}$ have been studied by powder neutron diffraction and magnetic susceptibility techniques between 5 and 300 K. The structure consists of pairs of face-sharing MnO_6 octahedra to form Mn_2O_9 dimers. The description of the crystal structure has been improved by employing a model in which some of the Sr and O ions are statistically distributed over two different sites. Three different magnetic phases can be distinguished in the temperature region studied. Below ~75 K, the Mn^{4+} sublattice is antiferromagnetically ordered with an antiparallel alignment between all nearest-neighbor manganese ions. Between ~75 and ~150 K extensive quasi two-dimensional (2D) magnetic clusters are present. At temperatures above ~150 K, one can observe correlations related to intradimer spin pairing. Truly paramagnetic behavior is not observed at any temperature below 300 K.

Low-temperature topotactic reduction reactions can exhibit remarkable selectivity. The reaction of the complex Mn(IV) oxide $Sr_7Mn_4O_{15}$ with CaH_2 selectively removes only oxide ions which link MnO_6 octahedra in a corner shared manner, leaving the rest of the anion lattice in place (Fig. 11.34).

The preparation of the Mn(III) phase $Sr_7Mn_4O_{13}$ and further reduction to form $Sr_7Mn_4O_{12}$ allows the controlled removal of all the 180° Mn–O–Mn superexchange pathways present in the material. Thus, we can directly and rationally influence the magnetic coupling interactions in complex oxides.

"Anion-doped" mixed valent Mn(III)/Mn(IV) phases can be prepared by the subsequent partial oxidation of $Sr_7Mn_4O_{13}$. Reaction with a limited stoichiometry of oxygen yields the highly metastable phase $Sr_7Mn_4O_{14}$. Reaction with fluorine gas allows the preparation of $Sr_7Mn_4O_{13}F_2$. Solid-state ^{19}F NMR confirms that the fluoride ions are located in the sites vacated by oxide ions on reduction. This shows that the oxide–fluoride ordering is patterned by the anion vacancy ordering in the reduced intermediate, allowing this feature of the structure to be controlled.

Reaction of $LaSrMnO_4$ with CaH_2 at 420 °C yields $LaSrMnO_{3.67(3)}$. Raising the temperature to 480 °C yields the Mn(II) phase $LaSrMnO_{3.50(2)}$. Neutron powder diffraction data show that both phases adopt body-centered orthorhombic crystal structures ($LaSrMnO_{3.67}$, Immm: $a = 3.7256$ Å, $b = 3.8227$ Å, $c = 13.3617$ Å; $LaSrMnO_{3.50}$, Immm: $a = 3.7810$ Å, $b = 3.7936$ Å, $c = 13.3974$ Å) with anion vacancies located within the equatorial MnO_{2-x} planes of the materials. The origin of the low-dimensional magnetic order and ordering of the anion vacancies in the reduced phases is shown in Fig. 11.35.

Analogous reactivity is observed between $LaBaMnO_4$ and CaH_2 to yield body-centered tetragonal reduced phases ($LaBaMnO_{3.53(3)}$, I4/mmm: $a = 3.8872(1)$ Å, $c = 13.6438(2)$ Å). Low-temperature neutron diffraction and magnetization data show that $LaSrMnO_{3.5}$ and $LaBaMnO_{3.5}$ exhibit three-dimensional (3D) AFM order below 155 K and 135 K, respectively. Above these temperatures, they exhibit 2D AFM order with paramagnetic behavior observed above 480 K in both phases.

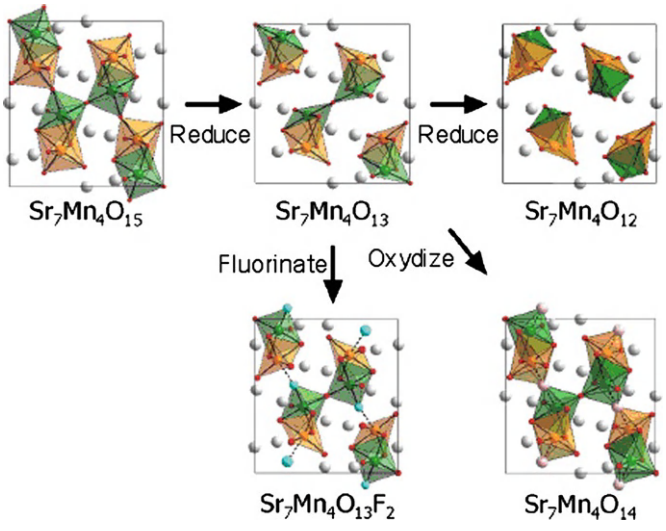

FIGURE 11.34

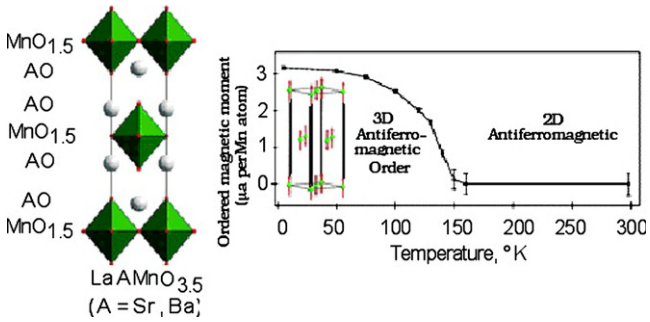

FIGURE 11.35

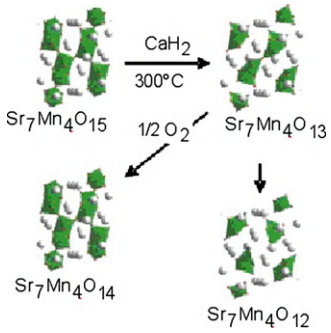

FIGURE 11.36

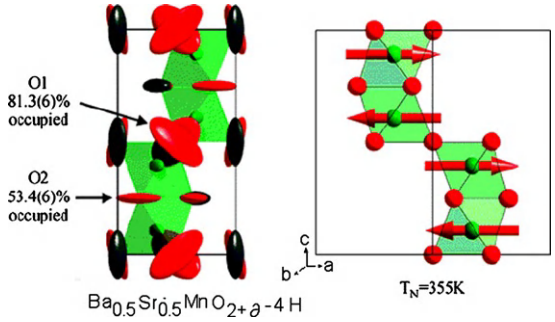

FIGURE 11.37

The synthesis of phases of composition $Sr_7Mn_4O_{15-x}$ $(0 < x < 3)$ is reported via the topotactic manipulation of the anion lattice of $Sr_7Mn_4O_{15}$. In addition the reduced cation substituted phases $BaSr_6Mn_4O_{13}$ and $Sr_6CaMn_4O_{13}$ are described. Structural characterization using powder X-ray and neutron diffraction data reveals that in all phases anions are selectively removed from sites which link the MnO_6 octahedra in the structure in an apex-sharing manner. An explanation based on the total lattice energy of the anion deficient phases is presented to account for this unusual selectivity. Topotactic reduction of $Sr_7Mn_4O_{15}$ selectively removes apex-linked oxide ions, as shown in Fig. 11.36.

Strontium manganate is offered for sale commercially as $SrMnO_4$.

11.2.5. Barium Manganese Compounds

It has been observed that MnO (hypomanganite) will form compounds with the alkaline earths if the cation, like Ba^{2+}, is sufficiently large. The anion-deficient perovskite 4H-$BaMnO_{2+x}$ has been obtained by a topotactic reduction, with LiH, of the hexagonal perovskite 4H-$BaMnO_{3-x}$. The crystal structure of 4H-$BaMnO_{2+x}$ was solved using electron diffraction and X-ray powder diffraction and further refined using neutron powder diffraction (space group—Pnma, $a = 10.375$ Å, $b = 9.466$ Å, $c = 11.276$ Å, at 373 K). The orthorhombic superstructure arises from the ordering of oxygen vacancies within a 4H (chch) stacking of close packed c-type $BaO_{2.5}$ and h-type $BaO_{1.5}$ layers. The ordering of the oxygen vacancies transforms the Mn_2O_9 units of face-sharing octahedra into Mn_2O_7 (two corner-sharing tetrahedra) and MnO_6 (two edge-sharing tetrahedra) groups. The Mn_2O_7 and MnO_6 groups are linked by corner sharing into a 3D framework. The structures of the $BaO_{2.5}$ and $BaO_{1.5}$ layers are different from those observed previously in anion-deficient perovskites providing a new type of order pattern of oxygen atoms and vacancies in close packed structures. Magnetization measurements and neutron diffraction data reveal 4H-$BaMnO_{2+x}$ adopts an antiferromagnetically ordered state below $T_N \sim 350$ K.

The synthesis of the Mn(II) phase 4H-$Ba_{0.5}Sr_{0.5}MnO_{2+\delta}$ via the topotactic reduction of 4H-$Ba_{0.5}Sr_{0.5}MnO_{3-x}$ with the novel reducing agent LiH, has been described. Neutron powder diffraction data show that oxide ions are de-intercalated from the host structure in a disordered manner to yield "tetrahedral" MnO_4 coordination sites. Magnetic susceptibility and neutron powder diffraction data show that the title phase adopts a canted antiferromagnetically ordered state below $T_N = 355$ K, consistent with the strong magnetic coupling expected between d^5 centers. The ordering of defects is shown in Fig. 11.37.

In this system of Mn^{2+} anions, MnO_2^{2-}, the compound, Ba_2MnO_3, could be prepared by solid-state reaction in hydrogen atmosphere. X-ray structure investigations gave a monoclinic unit cell $a = 5.84$ Å, $b = 11.57$ Å, $c = 12.70$ Å, $\beta = 93.74°$, space group CC_c. Mn^{2+} forms isolated tetrahedron chains connected by sevenfold coordinated Ba^{2+}. The crystal structure of Ba_2MnO_3 can be thought of as a heavily distorted rock salt structure.

In the Mn^{3+} system of BaO–Mn_2O_3, the compound, $BaMn_2O_4$, has not been prepared. No compounds based on the Mn^{3+} oxidation state are to be found including compounds like Ba_2MnO_5 and Ba_3MnO_6. As stated before, the Mn^{3+} state is too unstable and disproportionates into Mn^{2+} and Mn^{4+}.

In the Mn^{4+} system of BaO–MnO_2, the compound, barium manganite, $BaMnO_3$ has been studied intensely in regard to its "Gigantic Magnetoresistance" phenomenon. The crystal structure of the 2H perovskite $BaMnO_3$ has been refined from neutron powder diffraction data collected at room temperature and 80 and 1.7 K. The structure consists of chains of face-sharing MnO_6 octahedra, separated by Ba^{2+} cations. At room temperature, $a = 5.6991(2)$, $c = 4.8148(2)$ Å, space group $P63/mmc$. At 80 K, $a = 9.8467(1)$, $c = 4.8075(1)$ Å, space group $P63cm$. The structural phase transition introduces

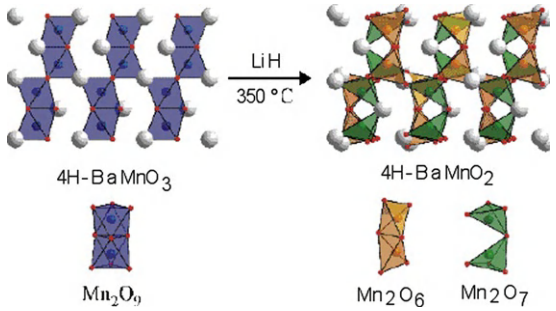

FIGURE 11.38

a displacement of neighboring chains and reduces the coordination number of Ba^{2+}. Long-range AFM ordering is apparent below $T_N = 59$ K, with a magnetic moment of 1.31 μbar per Mn^{4+} cation at 1.7 K. Neighboring spins within each chain are antiferromagnetically coupled and lie in a plane perpendicular to [001]. The spin directions associated with the chains at (1/3, 2/3, z) and (2/3, 1/3, z) are rotated by ±120° with respect to that of the chain at (0, 0, z).

Reaction of LiH with 4H-$BaMnO_3$ reductively deintercalates oxide ions from the host structure resulting in the Mn(II) phase $BaMnO_2$. The anion vacancies in the material are ordered in a complex manner, leading to the formation of Mn_2O_7 and Mn_2O_6 "dimer" units consisting of pairs of edge or corner sharing MnO_4 distorted tetrahedra. Further corner sharing of the dimer units leads to the formation of a novel 3D Mn(II)–O network. This is shown in the following diagram. Strong Mn–O–Mn superexchange coupling leads to the observation of AFM order at room temperature in 4H-$BaMnO_2$ and 4H-$Ba_{0.5}Sr_{0.5}MnO_2$ (Fig. 11.38).

The complex stacking sequences adopted by $BaMnO_{3-x}$ phases are driven by their anion nonstoichiometry. Neutron diffraction data indicate that the anion vacancies in $BaMnO_{3-x}$ phases are located almost exclusively on "hexagonal" sites which link MnO_6 octahedra in a face-sharing manner (Fig. 11.39).

As the vacancy concentration increases additional "cubic" corner-linked layers are incorporated into structures to accommodate the declining structural tolerance factor. Initially these cubic layers maximize their separation (15R, 8H, 9R), however as the anion vacancy concentration increases the stacking sequence changes to incorporate Mn_2O_{9-x} dimer units that specifically stabilize vacant anion sites.

The system $BaMnO_{3-x}$ ($0 \le x < 0.5$) in air has been investigated by gravimetric, quenching, single-crystal and powder XRD studies. Below 1150 °C hexagonal, two-layer $BaMnO_3$ ($a = 5.699$ Å, $c = 4.817$ Å) is stable. Above 1150 °C a series of anion-deficient $BaMnO_{3-x}$ phases exists. With increasing temperature, these include a rhombohedral 15-layer form ($a = 5.681$ Å, $c = 35.377$ Å; hexagonal indexing) and hexagonal 8-layer ($a = 5.699$ Å, $c = 18.767$ Å), 6-layer ($a = 5.683$ Å, $c = 14.096$ Å), 10-layer ($a = 5.680$ Å, $c = 23.373$ Å) and 4-layer ($a = 5.672$ Å, $c = 9.319$ Å) forms. The 6-layer modification is not of the hexagonal $BaTiO_3$-type. A simple orderly structural sequence involving a progressive increase of cubic-type layer stacking with increasing temperature characterizes the phases prepared.

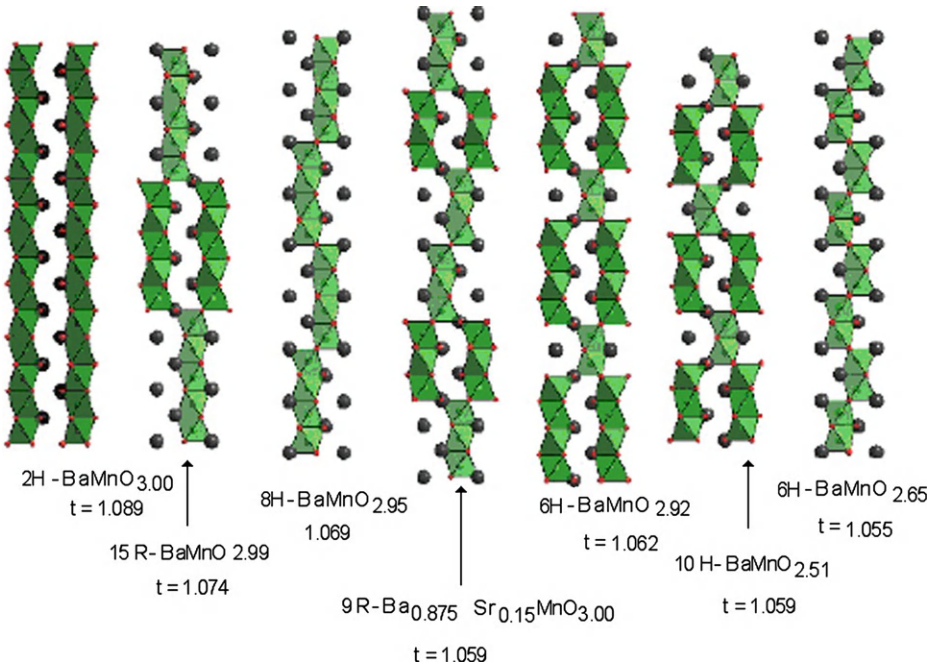

FIGURE 11.39

Influence of anion stoichiometry on phase formation is considered.

Mixed valence Mn(III)/Mn(IV) oxides exhibit strong coupling between charge, spin and lattice degrees of freedom. This leads to strongly correlated behavior and the observation of charge and orbital order, magnetoresistance and a variety of other complex behavior. A number of mixed valency, i.e. Mn(II)/Mn(III), complex oxides have been prepared to see if these phases exhibit analogous complex behavior. The diagram given as follows shows this factor (Fig. 11.40).

Topotactic reduction of cubic perovskite $La_{1-x}Ba_xMnO_3$ phases leads to the formation of the corresponding $La_{1-x}Ba_xMnO_{2.5}$ Brownmillerite phases. The Brownmillerite structure has a series of variants which exhibit different ordering patterns of the twisted tetrahedral chains. Detailed analysis of the structural parameters obtained from the $La_{1-x}Ba_xMnO_{2.5}$ phases has enabled us to construct a plot that rationalizes the different Brownmillerite structural variants as a function of the tetrahedral chain twist angle and tetrahedral layer separation. This plot can be extended to include a wide range of reported Brownmillerite phases enabling the structural variant a particular composition will adopt, to be predicted on the basis of simple structural parameters. In addition this structural analysis has allowed the identification of robust octahedral-site Mn(II)–Mn(III) charge order at room temperature in phases centered on $La_{0.75}Ba_{0.25}MnO_{2.5}$ compositions.

The synthesis and structure determination of 4H-$BaMnO_{3-x}$ ($0x0.35$) and 4H-$Ba_{0.5}Sr_{0.5}MnO_{3-x}$ ($0x0.21$) have been described in another paper. Neutron powder diffraction data unambiguously show the anion vacancies in the oxygen-deficient phases lie in the hexagonal BaO_{3-x} layers, rather than the cubic layers predicted by previous structural models. The localization of anion vacancies in the hexagonal layers is discussed on the basis of the local coordination polyhedra of the metal cations. Low-temperature neutron diffraction data show the oxidized materials adopt AFM ordered structures ($Ba_{0.5}Sr_{0.5}MnO_{2.99}$). Anion-deficient phases do not achieve magnetic order, suggesting that the Mn(III/IV) charge disorder suppresses long-range magnetic order. The following diagram illustrates the type of anion vacancy that occurs in these compounds (Fig. 11.41).

The synthesis and structural characterization of 15R-, 8H-, 6H′-, and 10H-$BaMnO_{3-x}$ and 9R-$Ba_{0.875}Sr_{0.125}MnO_3$ are also described. Neutron powder diffraction data reveal a strong preference for the location of anion vacancies within the face-shared hexagonal layers of these phases. At high-anion vacancy concentrations, Mn_2O_{9-x} dimer units become dominant. Magnetic characterization indicates AFM order in all these phases. Ordering temperatures are in the range $250\ K < T < 270\ K$ and show a dependence on the fraction of cubic layers present in the stacking sequence.

In a following paper, novel phases in the $BaMnO_{3-x}$ system were investigated by high-resolution electron microscopy. A hexagonal cell with two atomic layers (2H, $a = 5.72$ Å, $c = 4.84$ Å) was found to have an oxygen deficiency to some degree, though its X-ray powder pattern gave a single phase of a 2H crystal. Observed structure images showed that a 2H phase was transformed into a 10H (6L + 4L) phase under a low beam intensity and into a 6H (4L + 2L) phase under a very high beam intensity. A mechanism of phase transformation was proposed in that "oxygen deficiency in face-sharing octahedra induces the displacement of the Mn ions which reduce the coordination number and the disruption of face-sharing octahedra. In the reduction process of $BaMnO_3$, the oxygen loss is accompanied with structural changes related to the introduction of

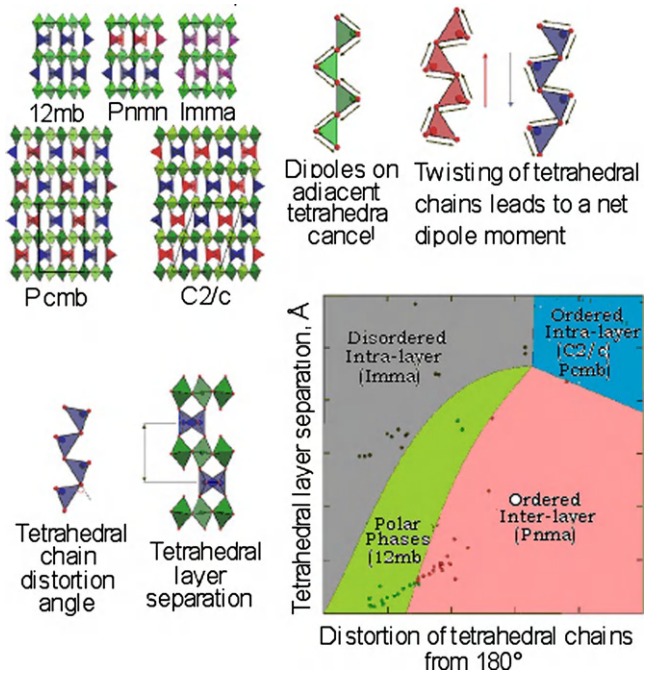

FIGURE 11.40

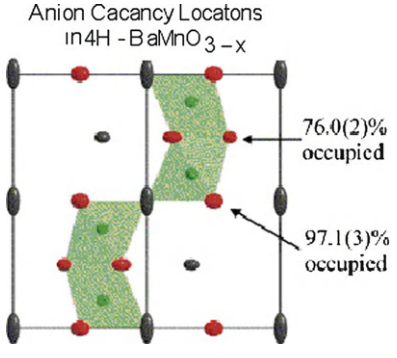

FIGURE 11.41

cubic layers in the starting hexagonal close packing". Several ordered hexagonal types (2H, 15H, 8H, 6H, 10H and 4H) can be obtained, for an explicit oxygen content, as a function of the synthetic route. The synthesis and structural characterization of the 6H type was also described.

The electronic structure and electrical transport properties of the cubic perovskite (E21) oxide barium manganese ($BaMnO_3$) and the $BaMnO_3/BaTiO_3$ superlattice was investigated by the density functional theory in this report. The results show that the cubic $BaMnO_3$ exhibits half-metallic properties with an integral magnetic moment of 3.000 μbar per unit cell in its metastable state, while the $BaMnO_3/BaTiO_3$ superlattice also shows a stable half-metallic ground state with an integral magnetic moment of 12.000 μbar per unit cell. The construction of a $BaMnO_3/BaTiO_3$ superlattice could stabilize the cubic metastable phase of the $BaMnO_3$ compound and provide a stable half-metallic material for potential applications in spintronic devices. In summary, $BaMnO_{3-\delta}$ and lightly Li- and K-doped $BaMnO_{3-\delta}$ possess strong magnetoelectric effects near room temperature. The large dielectric constants of these materials, comparable to those of well-known ferroelectrics, are closely associated with magnetic order and magnetic anisotropy that sensitively hinges on the cubic stacking ratio. These findings provide ***a new paradigm for developing novel, high-temperature magnetoelectrics and, eventually, multiferroic materials*** of technological importance.

Hypomanganate, MnO_4^{3-}, is a blue-colored ion of Mn(V) that forms when MnO_4^{2-} is treated with manganite MnO_4^{4-} at pH > 12. It has also been generated by treatment of $KMnO_4$ in 10 M KOH with H_2O_2. The pK_a of $HMnO_4^{2-}$ is 13.7, which indicates that solutions of hypomanganate contain significant amounts of the protonated form even at high pH's. Oxidations of alkenes by permanganate are proposed to proceed via the intermediacy of "esters" of hypomanganate, that is, species of the type $MnO_2(OR)_2^-$ where R is an alkyl group.

The Mn^{5+}-containing compound, $BaMn_2O_7$ has been reported. It is related to the $BaMnO_{3-\delta}$ type of compounds. The discovery of novel structural and physical properties in the A-site ordered manganite $RBaMn_2O_6$ (R = Y and rare earth elements) has demanded new comprehension about perovskite manganese oxides. In the present study, the A-site disordered form, $R_{0.5}Ba_{0.5}MnO_3$, was successfully synthesized and investigated concerning its structure and electromagnetic properties. $R_{0.5}Ba_{0.5}MnO_3$ has a primitive cubic perovskite cell. The magnetic glassy states are unexpectedly dominant as the ground state of $R_{0.5}Ba_{0.5}MnO_3$ in contrast to the ordinary disordered manganite $R_{0.5}A_{0.5}MnO_3$ (A = Sr and Ca). A peculiar behavior detected was the step-like ultrasharp magnetization and resistivity change observed in $Pr_{0.5}Ba_{0.5}MnO_3$.

The crystal structure and electromagnetic properties of the A-site ordered perovskite manganite, $TbBaMn_2O_6$, have been studied. $TbBaMn_2O_6$ has successive phase transitions; the structural transition at $T_t = 450$ K, the charge/orbital order transition at $T_{CO} = 430$ K and the AFM transitions on Mn ions at $T_N = 210$ K and on Tb ions at $T_N = 12$ K. At T_t, both *a*- and *b*-axis expand by 0.7%, and the *c*-axis shrinks by 1.3% in the low-temperature phase. The magnetic interaction changes from FM (the high-temperature triclinic phase) to AFM (the low-temperature monoclinic phase) across T_t. The electrical resistivity clearly shows anisotropic behaviors at T_t; an increase of resistivity along the *c*-axis and no change within the *ab*-plane. The obtained results strongly suggest the dx^2-y^2-type orbital order at T_t. Comparing to the metal-disordered manganites, two remarkable features are recognized in $RBaMn_2O_6$: (1) relatively high-charge order transition temperature and (2) the presence of structural transition without any charge and magnetic ordering. These features are closely related to the peculiar structure that the MnO_2 square lattice is sandwiched by the rock salt layers of two kinds; RO and BaO with different lattice sizes.

The compound, $Ba_2Mn_2O_7$, is unknown. However, the tri-barium di-manganate, $Ba_3Mn_2O_8$, has been reported. $Ba_3Mn_2O_8$ is a hexagonally coordinated Mn^{5+} $S = 1$ spin dimer system with small uniaxial single-ion anisotropy. [135,137]Ba NMR spectroscopy was used to establish the lower critical field Hc_1 of distinct field-induced phases for *H* parallel to c, *H* perpendicular to c, and to measure the longitudinal (Ml) and transverse (Mt) magnetizations in the vicinity of the quantum critical point (QCP). M_l-parallel (T, Hc_1), M_l-perpendicular (T, Hc_1) points were reproduced by solving a low-energy model for a dilute gas of interacting bosons. M_l-parallel (T goes to 0, $H = Hc_1$) (M_l-perpendicular (T goes to 0, $H = Hc_1$)) follows the expectation for a BEC (Ising-like) QCP.

Single crystals of $Ba_3Mn_2O_8$ were grown by a slow cooling flux method. $Ba_3Mn_2O_8$ is a spin dimer compound based on pairs of $S = 1$, $3d^2$, Mn^{5+} ions arranged on a triangular lattice. AFM intradimer exchange leads to a singlet ground state in zero-field. Specific heat, magnetocaloric effect, and torque magnetometry measurements were performed in magnetic fields up to 32 T and temperatures down to 20 mK. For fields above $H\{c_1\} \sim 8.7$ T, these measurements reveal a single magnetic phase for *H* parallel to c, but two distinct phases (approximately symmetric about the center of the phase diagram) for *H* perpendicular to c. Analysis of the simplest possible spin Hamiltonian describing this system yields candidates for these

ordered states corresponding to a simple spiral structure for *H* parallel to c, and to two distinct modulated phases for *H* perpendicular to c. Both single-ion anisotropy and geometric frustration play crucial roles in defining the phase diagram. The relation between the Ba^{2+} ions and the Mn^{5+} ions is shown in Fig. 11.42.

This schematic diagram shows the arrangement of MnO_4 tetrahedra in the *R*-3*m* structure of $Ba_3Mn_2O_8$. Intradimer (J_0), out-of-plane interdimer (J_1), in-plane direct interdimer (J_2) and in-plane crossed interdimer (J_3) exchange bonds are drawn as thick black, dotted black, thin black and dashed black lines, respectively. Only two of the in-plane crossed interdimer exchange bonds (J_3) were drawn for clarity. $Ba_3Mn_2O_8$ crystallizes in the rhombohedral *R*3*m* structure, and is comprised of pairs of Mn^{5+} $3d^2$ ($S = 1$) ions arranged vertically on hexagonal layers. Each Mn^{5+} ion is coordinated by distorted oxygen tetrahedra, which results in an orbitally non-degenerate ground state. Successive layers are stacked following an "ABC" sequence, such that the dimer units on adjacent planes are positioned in the center of the triangular plaques of the layers above and below. Pairs of ions on each dimer are coupled antiferromagnetically, resulting in a singlet ground state. Initial powder inelastic neutron scattering (INS) indicated an intradimer exchange energy $J_0 \approx 1.61(3)$ meV[14]. The same INS measurements revealed a spin gap of 1.05 meV and a hierarchy of additional exchange energies, in which interdimer coupling between Mn ions in the same plane is characterized by $J_2 - J_3 = 0.112^{+0.015}_{-0.003}$ meV and interdimer coupling between Mn ions residing on adjacent planes is characterized by $J_1 = -0.062^{+0.007}_{-0.006}$ meV.

In the Mn^{6+} system of BaO–MnO_3, the compound $BaMnO_4$ is known. Two convenient methods were developed to transform $KMnO_4$ into barium permanganate, $BaMn_2O_7$ and other permanganate salts via $BaMnO_4$ or Mn_2O_7 intermediates. Pure $BaMnO_4$ was prepared by the reaction of $KMnO_4$ with KI in the presence of $BaCl_2$ and NaOH. Hydrothermal reaction of barium manganate with excess carbon dioxide for 1.5 h at 100 °C led to barium permanganate with almost quantitative yield. $BaMnO_4$, is generated by the reduction of $KMnO_4$ with iodide in the presence of $BaCl_2$. Just like $BaSO_4$, $BaMnO_4$ exhibits low solubility in virtually all solvents. It has the CAS number of 7787-35-1 and is offered for sale commercially. Manganates, particularly the insoluble $BaMnO_4$, have been used as oxidizing agents in organic synthesis. They will oxidize primary alcohols to aldehydes and then to carboxylic acids. Secondary alcohols are easily oxidized to ketones. Barium manganate has also been used to oxidize hydrazones to diazo compounds.

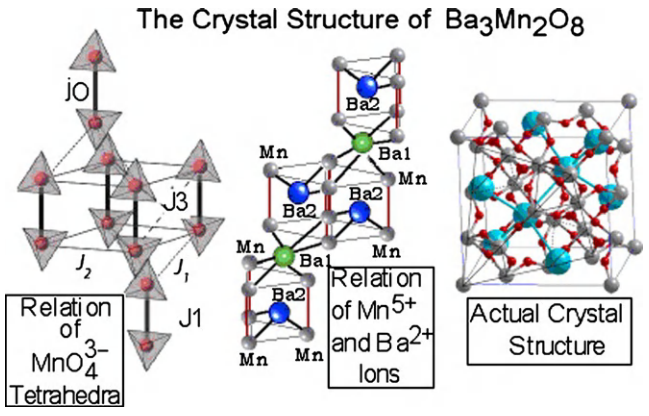

FIGURE 11.42

$BaMnO_4$ has a scheelite-like structure. XRD and Raman scattering studies on the scheelite structured barium molybdate show that, at ~5.8 GPa, it undergoes a first-order phase transition to the fergusonite structure ($I\,2/a, Z = 4$)—as also observed in iso-structural barium tungstate. At still higher pressures, barium molybdate transforms to another phase between ~7.2 and 9.5 GPa. On release of pressure from 15.8 GPa, the initial phase is recovered, implying that the observed structural modifications are reversible.

In the Mn^{7+} system of BaO–Mn_2O_7, the compound, barium permanganate, $BaMn_2O_8$, is known. It has the CAS number of 7787-36-2 and is offered for sale commercially. It is a strong oxidizer and i used in the manner described for $BaMnO_4$. Since this compound, $Ba(MnO_4)_2$ has the tendency to disproportionate into the insoluble $BaMnO_4$:

$$BaMn_2O_8 + \text{heat}\ (T > 280\ ^\circ\text{C}) \Rightarrow BaMnO_4 + MnO_2 + O_2$$

it has not found widespread use in the Industry and has not been extensively researched by Academia.

Barium Manganate (CAS = 7787-42-0) is readily available commercially on a worldwide basis.

11.2.6. Radium Manganese Compounds

No Compounds are known.

11.3. ALKALINE EARTH—TECHNETIUM COMPOUNDS

The element technetium, Tc, does not appear in nature and all of it used commercially is produced synthetically. It is the lowest atomic number element that does not have any stable isotopes. The most common isotope, technetium-99, i.e. $^{99}Tc_{43}$, is a weak beta emitter with a short half-life of $T_{1/2} = 6.0$ h. Because such radiation is blocked by the walls of laboratory glassware, Tc is employed in the medical profession to

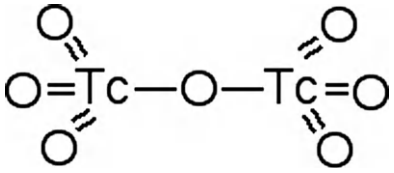

FIGURE 11.43

pinpoint blood flow blockage in the arterial–venous system of the human body.

All isotopes are radioactive. The only known stable oxide is **Technetium(VII) oxide** with the formula, Tc_2O_7. This yellow volatile solid is a rare example of a molecular binary metal oxide, the other examples being RuO_4, OsO_4 and the unstable Mn_2O_7. It adopts a centro-symmetric corner-shared bi-tetrahedral structure in which the terminal and bridging Tc–O bonds are 167 pm and 184 pm, respectively and the O–Tc–O angle is 180°. The Gibbs structure is shown in Fig. 11.43.

The vapor pressure of Tc_2O_7 is much higher than that of Re_2O_7 at low temperatures (e.g. 10^{-1} mm at 100 °C, compared to $\sim 3 \times 10^{-5}$ for Re_2O_7). In contrast to rhenium, technetium (VII) is therefore easily lost upon evaporation of acid solutions unless a reducing agent is present or the evaporation is conducted at a low temperature. This limits the number of alkaline earth—technetium compounds that have been synthesized. The solution chemistry is mostly based upon pertechnetic acid. Pertechnetic and perrhenic acids behave as very strong acids, Ka ~ 10^{-1} s. Their extensive dehydration to M_2O_7 in such media as 7.0 M sulfuric acid complicates a spectrophotometric comparison of acid strengths. Heptavalent technetium, present in aqueous solutions as pertechnetate ion, TcO_4^- can be extracted into a variety of organic liquids, including alcohols, ketones, ethers, organo-phosphorus, and tertiary and quaternary amines dissolved in nonpolar solvents. Good extraction from acid but not from neutral nor alkaline solution was observed with the alcohols, esters of phosphoric acid, and tertiary amines. Ketones and quaternary amines extracted technetium efficiently over a wide pH range. The technetium species transferred between phases was shown to be $HTcO_4$ from acid aqueous media, and to be $MTcO_4$ from neutral alkali metal salt solutions.

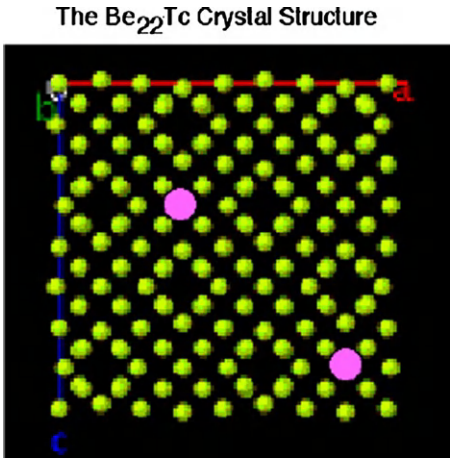

FIGURE 11.44

The crystal chemistry of technetium has been investigated as a series of simple binary and ternary oxide structures. An investigation of the system Tc–O under controlled conditions has revealed only one intermediate compound. Technetium-containing spinels can be synthesized in which technetium lies on the octahedral sites in the lattice. Technetium will enter the B-sites in ABO_3 compounds yielding perovskite, hexagonal $BaTiO_3$, and pyrochlore structures. The radius of the Tc^{4+} is shown to be 0·67 Å.

11.3.1. Beryllium–Technetium Compounds

Be^0 metal forms one known compound with Tc^0 metal. The structure has the $Zn_{22}Zr$-type of structure shown in Fig. 11.44.

Cell parameters are: $a = b = c = 8.1784$ Å, $\alpha = \beta = \gamma = 60°$, cell volume = 386.80 Å^3, $Z = 8$. Cell occupancy is shown in Table 11.15.

Be does not form any oxo-technetium compounds. No structures have been reported and the literature is devoid of any mention of such compounds.

11.3.2. Magnesium Technetium Compounds

Mg^0 metal does not form any intermetallic compounds with Tc^0 metal.

TABLE 11.15

No.	Site notation	Atom	Multiplicity	Wyckoff	Site symmetry	*x*	*y*	*z*	Occupancy
1	Be1	Be	96	g	..m	0.0617	0.06174	0.3192	1.0
2	Be2	Be	48	f	2.mm	0.4867	1/8	1/8	1.0
3	Be3	Be	16	d	.-3m	1/2	1/2	1/2	1.0
4	Be4	Be	16	c	.-3m	0	0	0	1.0
5	Tc1	Tc	8	a	-43m	1/8	1/8	1/8	1.0

In the Mg–Tc–O system, the compound $MgTc_2O_8 \cdot 4H_2O$ has the unit cell dimensions of: $a = 6.46$ Å, $b = 7.03$ Å, $c = 7.195$ Å, $\alpha = 63.06°$, $\beta = 69.88°$, $\gamma = 71.99°$, cell volume = 268.87 Å^3, $Z = 4$. space group = P-1, point group of $aP15$. It is triclinic but no specific structural arrangement has been presented in the literature. It is readily soluble in water.

The compound, $Mg_2(TcO_4)_2$, has been described as a black powder that is cubic with $a = 8.498$ Å, having the spinel type of structure. $Mg_2(TcO_4)_2$ is offered for sale commercially, with the CAS number of 71683-38-0.

No other magnesium technetate compounds have been described in the literature.

11.3.3. Calcium Technetium Compounds

The metal, Ca^0, does not form any compounds with the Tc^0 metal.

In the Ca–Tc–O system, the technetium perovskite, $CaTcO_3$ has been synthesized. Combining synchrotron X-ray and neutron diffraction, it was found that $CaTcO_3$ is an AFM with a surprisingly high Neel temperature of ~800 K. The transition to the magnetic state does not involve a structural change, but there is obvious magnetostriction. Electronic structure calculations confirm the experimental results. The structure of $CaTcO_3$, $SrTcO_3$ and $BaTcO_3$ is shown in Fig. 11.45.

Side (a) and top (b) views of the *Pnma* structure of the distorted perovskite are shown. The Tc atoms (medium-light blue spheres) are surrounded by O_6 atoms to form an octahedron. $AeTcO_3$ compounds adopt the same distorted *Pnma* perovskite structure as $LaMnO_3$, characterized by a $GdFeO_3$-like (GFO) tilting of the TcO_6 octahedra caused by the Ae–O and Ae–Tc covalencies, and a concomitant Jahn–Teller (JT) Tc–O bond length disproportionation, with long (l) and short (s) Tc-O(2) in-plane distances and medium (m) Tc-O(1) vertical ones. When compared to $LaMnO_3$, the experimental values of the JT modes, $Q_2 = 2(l - s)/\sqrt{2}$ and $Q_3 = 2(2m - l - s)/\sqrt{2}$ in $CaTCO_3$ and $SrTCO_3$ are significantly smaller due to the intrinsically different electronic configuration of the transition metal ions. In $LaMnO_3$, the Mn^{3+} ions 3d states are in a $t^3_{2g}e^1_g$ configuration and a strong JT effect is required to release the degeneracy of the e_g orbitals and to form an orbitally ordered state. On the contrary in $AeTcO_3$, the Tc^{4+} ions ($4d^3$: $t^3_{2g}e^0_g$) have completely filled (empty) $t_{2g}(e_g)$ manifolds, similarly to Mn^{4+} ions in $CaMnO_3$, a configuration which inhibits the occurrence of electronic and structural JT instabilities, and leads to an insulating G-type AFM ground state (AFM-G). However, at variance with 3d transition metal (TM) ions in perovskites, where d^3 configurations unavoidably lead to fully polarized $m = 3$ μbar moments on TM (e.g. $CaMnO_3$), a much larger extension of the 4d electrons is observed That, in turn, forms much stronger hybridizations with Op states. A sizable amount of charge fills the 4d minority states as well, with a consequential reduction of magnetic moment and an overtly evident intraatomic violation of Hund's rule.

The structure of $CaTcO_3$ is shown in the following diagram. Cell parameters have not been given (Fig. 11.46).

In other papers, Avdeev et al. and Rodriguez et al. have reported the successful synthesis of the first ever fabricated Tc-based perovskites, namely $CaTcO_3$ and $SrTcO_3$. Furthermore they have shown that these compounds display the anomalously high Neel temperatures (T_N) of 800 K for $CaTcO_3$ and 1000 K for $SrTcO_3$, by far the highest among materials not incorporating 3d transition metals. These results are surprising and challenge the current understanding of the magnetic interaction in perovskites. In particular they pose three fundamental questions: i) Is the origin of such a large magnetic ordering temperature related to the strong Tc 4d-Op hybridization? ii) What is the role played by the structural degrees of freedom? and iii) Is the enhancement of T_N upon Ca/Sr substitution related to the observed increase in unit cell volume and the corresponding modification of the internal atomic positions? These questions remain to be answered.

No other calcium technetate compounds are known to date. No CAS numbers have been issued.

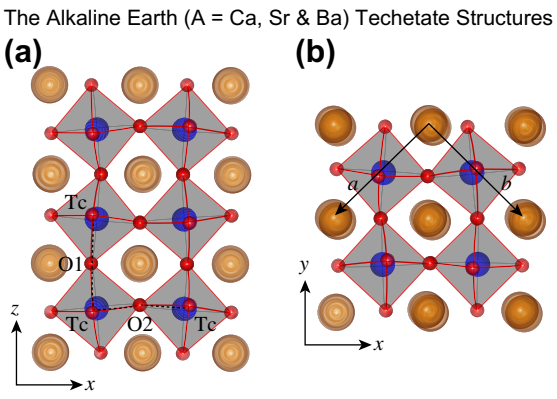

FIGURE 11.45

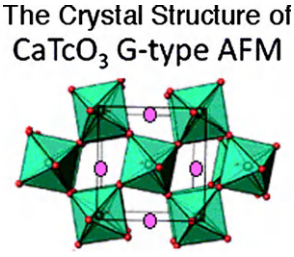

FIGURE 11.46

11.3.4. Strontium Technetium Compounds

The metal, Sr^0, does not form any compounds with the Tc^0 metal.

In the Sr–Tc–O system, the compound, Sr_2TcO_4, has been described as a black tetragonal material having the K_4NiF_4 type of structure with $a = 3.901$ Å, $c = 12.72$ Å.

The compound, $SrTcO_3$, is a perovskite. Strontium meta-technetiate exhibits the highest magnetic transition temperature outside of the first-row 3d-transition elements, as shown below. Magnetic scattering by the Tc cations is substantiated given that the peak intensity and thus magnetic ordering is retained to 750 °C, well above a crystallographic transition of $SrTcO_3$ to the highest possible symmetry group for a perovskite, *Pm*3 *m*, at 500 °C.

The structure of the perovskite $SrTcO_3$ has been investigated using both synchrotron X-ray and neutron powder diffraction. At room temperature $SrTcO_3$ is orthorhombic as a consequence of cooperative tilting of the corner sharing TcO_6 octahedra. The tilts are sequentially removed as the sample is heated with the oxide displaying the sequence of structures *Pnma* ⇒ *Imma* ⇒ *I*4/*mcm* ⇒ *Pmm*. Neutron powder diffraction data collected in the temperature range 4–1023 K indicate that $SrTcO_3$ has G-type AFM structure, in which each Tc moment is antiparallel to its six nearest neighbors, below 1000 K. The magnetic structure is collinear AFM with the technetium moments parallel to *c*-axis and can be described by the propagation vector $\mathbf{k} = [0,0,0]$ and the basis vector $(0,0,A_z)$. The same magnetic structure is observed in each of the four crystal structures. The arrangement of the octahedra is shown in Fig. 11.47.

The structure of $SrTcO_3$ has been presented above, except for the unit cell parameters. They are: $a = 5.543$ Å, $b = 7.854$ Å, $c = 5.576$ Å, cell volume $= 242.74$ Å^3, $\alpha = \beta = 164.74°$, $\gamma = 168.76°$. It is thus a distorted tetragonal structure composed of TcO_6 octahedra. It has been observed that the magnetism in the technetium perovskite, $SrTcO_3$, is unaffected by the phase transitions associated with tilting of the TcO_6 octahedra. The existence of the Tc(VII) compound, $Sr(TcO_4)_2$ has not been established.

No other strontium technetate compounds are known. These compounds are not available commercially and no CAS numbers have been issued.

11.3.5. Barium Technetium Compounds

The metal, Ba^0, does not form any compounds with the Tc^0 metal.

In the Ba–Tc–O system, the compound, Ba_2TcO_4, has been described as a black tetragonal material having the K_4NiF_4 type of structure with $a = 4.401$ Å, $c = 13.40$ Å. It decomposes at 630 °C.

Barium forms a perovskite, $BaTcO_3$, and its structure is isomorphous to the Ca and Sr perovskites as described above. The evolution of the magnetic ordering temperature of the $4d^3$ perovskites $RTcO_3$ (R = Ca, Sr, Ba) and its relation with its electronic and structural properties has been studied by means of hybrid density functional theory and Monte Carlo simulations. When compared to the most widely studied 3d perovskites the large spatial extent of the 4*d* shells and their relatively strong hybridization with oxygen weaken the tendency to form Jahn–Teller like orbital ordering. This strengthens

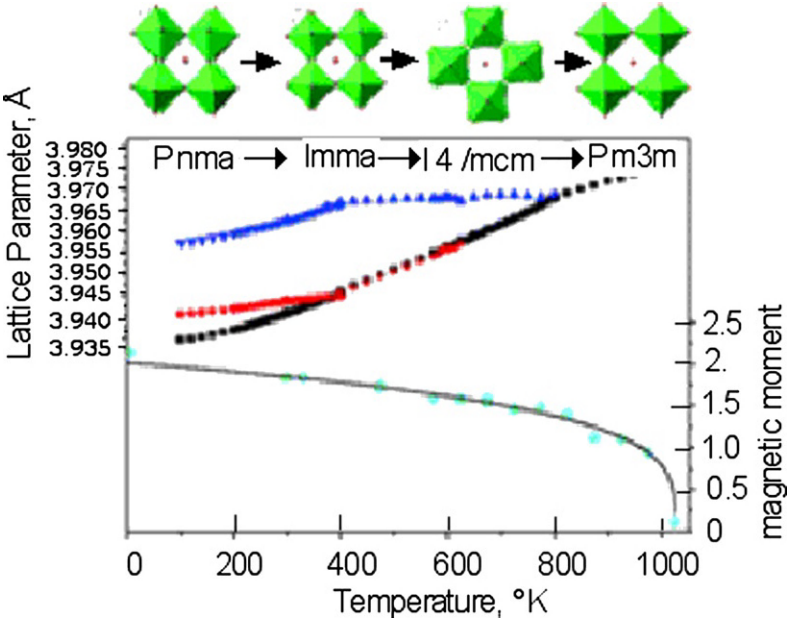

FIGURE 11.47

the superexchange interaction. The resulting insulating G-type AFM ground state is characterized by large superexchange coupling constants (26–35 meV) and Neél temperatures (750–1200 K). These monotonically increase as a function of the R ionic radius due to the progressive enhancement of the volume and the associated decrease of the cooperative rotation of the TcO_6 octahedra.

In the case of technetium, even TcO_3 is not well established. Gerlit claimed evidence for a Tc(VI) intermediate in the hydrazine reduction of alkaline pertechnetate. Rulfs et al. examined the growth of the intermediate spectrophotometrically in order to select an optimum time for precipitation of $BaTcO_4$. But small-scale preparations of this material were too high in Tc/Ba ratio, despite known contamination with $BaCO_3$. These peripheral objectives have led to significant new information, but a (VI) salt of technetium has not been obtained. The existence of the Tc (VII) compound, $Ba(TcO_4)_2$, has not been established.

No barium technetate compounds are offered for sale commercially.

11.3.6. Radium Technetium Compounds

Although radium–technetium compounds like $RaTcO_3$ could be synthesized, the likely of such a synthesis is nil. Both elements are radioactive and the demand for such compounds in the Industry is zero.

11.4. ALKALINE EARTH—RHENIUM INTERMETALLIC COMPOUNDS

The metal, Rhenium, does not form any compounds with the alkaline earth metals, with the exception of beryllium. According to the phase diagram of Be^0–Re^0, three compounds (3) exist shown in Fig. 11.48.

One of these is a slight adjustment of the basic metal, Be^0. Note that Be_2Re exists over a range of Br/Re atom ratios. The structure factors are listed in Table 11.16.

The compound, $Be_{22}Re$, has the following structure shown in Fig. 11.49.

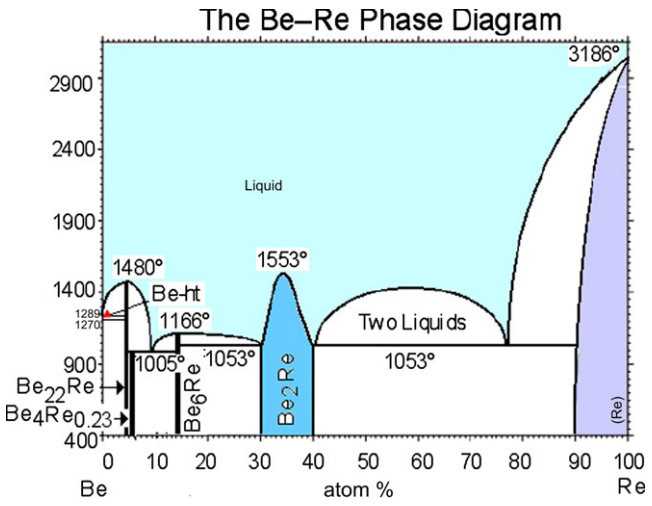

FIGURE 11.48

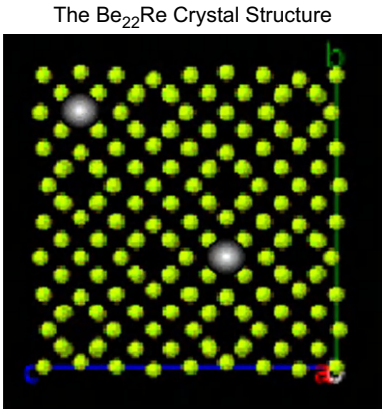

FIGURE 11.49

Cell parameters are: $a = b = c = 8.1742$ Å, $\alpha = \beta = \gamma = 60°$, cell volume $= 386.21$ Å^3, $Z = 6$. Cell occupancy is shown in Table 11.17.

Cell parameters are: $a = b = c = 8.1742$ Å, $\alpha = \beta = \gamma = 60°$, cell volume $= 386.21$ Å^3, $Z = 6$. Cell occupancy is shown in Table 11.18.

TABLE 11.16

Compound	Type	Point group	Space group	MP	Physical
(Be) rt	Mg	hP2	194	1270 °C	No data
(Be) ht	W	cI2	229	1289 °C	No data
$Be_{22}Re$	$Zn_{22}Zr$	cF184	*Fd*-3*m*	1480 °C	No data
$Be_4Re_{0.23}$	Be_5Au	cF24	$P6_3/mmc$	1005 °C	No data
Be_2Re	$MgZn_2$	hP12	*F*-43*m*	1553 °C	No data
(Re)	Mg	hP2	194	3180 °C	No data

TABLE 11.17

No.	Site notation	Atom	Multiplicity	Wyckoff	Site symmetry	x	y	z	Occupancy
1	Be1	Be	96	g	..m	0.0617	0.06174	0.3192	1.0
2	Be2	Be	48	f	2.mm	0.4867	1/8	1/8	1.0
3	Be3	Be	16	d	.-3m	1/2	1/2	1/2	1.0
4	Be4	Be	16	c	.-3m	0	0	0	1.0
5	Re1	Re	8	a	-43m	1/8	1/8	1/8	1.0

TABLE 11.18

No.	Site notation	Atom	Multiplicity	Wyckoff	Site symmetry	x	y	z	Occupancy
1	Be1	Be	96	g	..m	0.0617	0.06174	0.3192	1.0
2	Be2	Be	48	f	2.mm	0.4867	1/8	1/8	1.0
3	Be3	Be	16	d	.-3m	1/2	1/2	1/2	1.0
4	Be4	Be	16	c	.-3m	0	0	0	1.0
5	Re1	Re	8	a	-43m	1/8	1/8	1/8	1.0

TABLE 11.19

No.	Site notation	Atom	Multiplicity	Wyckoff	Site symmetry	x	y	z	Occupancy
1	Be2	Be	6	h	mm2	0.167	0.334	1/4	1.0
2	Re	Re	4	f	3m.	1/3	2/3	0.553	1.0
3	Be1	Be	2	a	-3m.	0	0	0	1.0

TABLE 11.20

No.	Site notation	Atom	Multiplicity	Wyckoff	Site symmetry	x	y	z	Occupancy
1	Be	Be	16	e	.3m	0.622	0.622	0.622	1.0
2	Re(c)	Re	4	c	-43m	1/4	1/4	1/4	0.102
3	Re(a)	Re	4	a	-43m	0	0	0	0.129

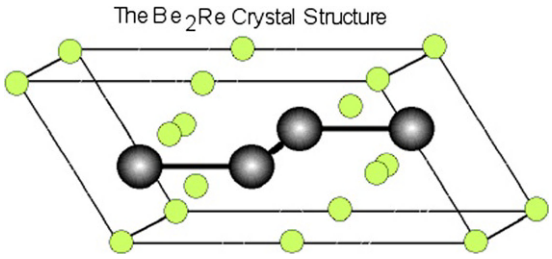

FIGURE 11.50

The structure of Be_2Re has the form shown in Fig. 11.50.

Cell parameters are: $a = b = 4.345$ Å, $c = 7.087$ Å, $\alpha = \beta = 90°$, $\gamma = 120°$, cell volume $= 115.87$ Å^3, $Z = 3$. Cell occupancy is shown in Table 11.19.

The compound, $Be_{4.0}Re_{0.23}$, has the structure shown in Fig. 11.51.

Cell parameters are: $a = b = c = 4.1543$ Å, $\alpha = \beta = \gamma = 60°$, cell volume $= 50.70$ Å^3. $Z = 2$. Cell occupancy is shown in Table 11.20.

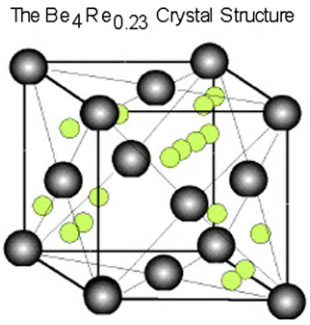

FIGURE 11.51

None of these compounds have found usage in the Industry and they are not offered for sale commercially.

11.5. ALKALINE EARTH—OXO-RHENIUM COMPOUNDS

These compounds are extremely rare and few in number. In fact, Re is reluctant to form any oxides at all. In a recent study of rhenium and its effect upon the Earth's mantle, the following comment was made:

> "Rhenium concentrations have been measured in eight samples from Volcan Alcedo in the Galapagos Archipelago—four basalts, an icelandite, a dacite and a rhyolite (all part of a fractionation trend), and a magnetite phenocryst-rich separate from a rhyolite. This study shows that Re concentrations increase (from 234 to 850 ppt) during the FeO and TiO_2 enrichment trend, and indicates that Re is incompatible in olivine, augite and plagioclase. Once magnetite stabilizes and fractionates, the iron and titanium enrichment trend in the melt reverses, and Re concentration drops from 610 ppt in the icelandite to 36 ppt in the rhyolite. The magnetite-rich separate has an extremely high Re content of 40 ppb–further evidence for compatibility of Re in magnetite. The paucity of sulfides in this suite suggests that magnetite is a significant host phase for Re. Re–SiO_2 trends in the Alcedo suite can be modeled with a magnetite–melt partition coefficient (D) of 20–50 for a sulfide-free system and D of 20–26 for a sulfide-bearing system. Compatibility of Re in magnetite suggests a valence of 3+ or 4+ for Re in terrestrial magmatic processes. The distribution of Re and Os in cubic oxides may be controlled by crystal chemistry".

The conclusion can be reached that Re forms oxides reluctantly.

11.5.1. Beryllium Oxo-Rhenium Compounds

Beryllium does not form any compounds with Rhenium oxide components.

11.5.2. Magnesium Oxo-Rhenium Compounds

No compounds are known in the MgO–ReO or MgO–Re_2O_3 systems.

In the MgO–ReO_2 system, attempts to prepare spinels of the type Mg_2ReO_4, $MgReO_3$ and $MgNiReO_3$ have similarly failed. In all three cases, the products consist of oxides and no diffraction peaks other than those resulting from the mixture of oxides were evident.

In the MgO–ReO_3 system, the compound, $MgReO_4$ apparently has the wolframite structure. But, the structure and crystal parameters have not been readily available. Only sixfold coordination is known for Re^{6+} in magnesium rhenium oxides. Conversely, the octahedral environment varies from the perfect octahedron in ReO_3 to the distorted one in Mg_3ReO_6.

In the MgO–Re_2O_7 system, the crystal structure of $Mg(ReO_4)_2 \cdot 4H_2O$ was determined from single-crystal X-ray diffractometer data. This compound was prepared from solution with $MgCl_2$ and $KreO_4$. The compound is triclinic, space group P1, with lattice parameters $a = 7.692$, $b = 7.026$, $c = 6.469$ Å, $\alpha = 108.279$, $\beta = 92.388$, $\gamma = 120.418°$, $Z = 1$, $dens_{calcd.} = 3.58\ g/cm^3$, $dens_{exp.} = 3.62\ g/cm^3$. The structure was solved in anisotropic approximation from 2990 observed reflections and refined to an index R of 7.4%. The rhenium atom is tetrahedrally coordinated, the magnesium atom octahedrally coordinated.

Magnesium rhenate compounds are not available commercially due, in part, to their very high cost.

11.5.3. Calcium Oxo-Rhenium Compounds

The Ca–Re–O system contains more compounds than the Mg system. This is due, in part, to the size factor where both Mg^{2+} and Be^{2+} are too small to form stable compounds.

No compounds are known in the CaO–ReO or CaO–Re_2O_3 systems.

In the CaO–ReO_2 system, the $CaReO_3$ compound has not been synthesized or described. An increase of the oxidation state of rhenium (>3) is expected to lead to the formation of structures containing cluster groups with different orders of metallic Re–Re bonds. The Re_2O_{10} cluster is known for the average oxidation state of rhenium atoms between +4 and +5.5. The Re_2O_8 group in contrast was found only in the compounds containing Re^{4+} (Fig. 11.52).

The oxidation state of rhenium in such double oxides will influence the charge carrier concentration and, consequently, the electrical and magnetic properties of these compounds. Nevertheless, there are only rare cases of careful structure-properties investigations in these systems. However, in a ternary system, magnetic and electrical properties of the sintered oxides belonging to the $CaIr_xRe_{1-x}O_3$ series were examined ($x = 0.25$; 0.33; 0.50; 0.66; 0.75). These compounds exhibit semiconducting ($x = 0.25$; 0.33) and metallic ($x = 0.66$; 0.75) properties over the temperature range from 77 to 600 K. The d^3 and

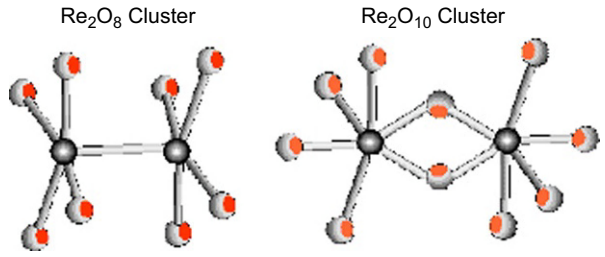

FIGURE 11.52

d^5 low-spin electron configurations for Re^{+4} and Ir^{+4} ions respectively, leads to the strong lowering of the magnetic moments, as the result of the superexchange interactions by the O^{2-} anions.

In the system CaO–Re_2O_5, single crystals of **$Ca_2Re_2O_7$** were synthesized using a flux method under 4 GPa at 973 K in a cubic-anvil type. It has a pyrochlore type of structure. $Ca_2Re_2O_7$ exhibits a unique structural transition characterized by a loss of the inversion symmetry as a metal. A novel effect has been predicted for conductors containing a broken mirror symmetry [e.g. polar metals and asymmetrical quantum well (QW) structures]. If such a conductor is under the direct current, $\mathbf{J}\cdot\mathbf{E}^{d}$, the circular polarized infrared radiation should induce an additional transverse current $\mathbf{J}_H\cdot\mathbf{E}^{d}\mathbf{x}\mathbf{c}$, where $\mathbf{E}^{d}$ is the driving electric field and **c** is a vector directed either along the polar axis or perpendicular to a QW. The sign of the current, $\mathbf{J}_H$, can be reversed by switching the helical nature of the light from right to left handed. Thus the phenomenon is, in fact, something like the Hall effect in which light acts as an external magnetic field. Competition between the FM double-exchange interaction and the superexchange AFM interaction was theoretically studied in the presence of geometrical frustration in the crystal. As the superexchange interaction increases, the FM metal becomes unstable and is taken over by a cooperative paramagnetic metal, in sharp contrast to a discontinuous transition to the AFM insulator in the absence of frustration. In the critical region, the system exhibits a peculiar temperature-independent behavior with highly incoherent transport, suggesting a large residual entropy at low temperatures in pyrochlore oxides.

In the system, CaO–ReO_3, only sixfold coordination is known for Re^{6+} in oxides. However, the octahedral environment varies from the perfect octahedron in ReO_3 to the distorted one in Ca_3ReO_6. The complex oxide Ca_3ReO_6 was synthesized and its crystal structure determined using X-ray powder analysis (space group $P2_1/n$; $a = 5.53664$ Å; $b = 8.80322$ Å; $c = 7.98492$ Å; $\beta = 90.073°$; $R_I = 0.032$, $R_P = 0.069$, $R_{wP} = 0.095$; $Z = 2$). The real symmetry is monoclinic due to a simultaneous tilt and rotation of the CaO_6 and ReO_6 octahedra. Electron diffraction and electron microscopy confirm the X-ray results. Ca_3ReO_6 is isostructural with A_2RRuO_6 oxides. Its structure has the form shown in Fig. 11.53.

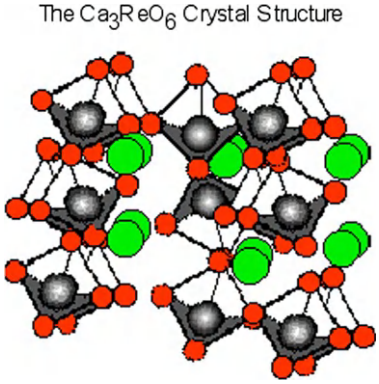

FIGURE 11.53

It consists of pairs of ReO_6 octahedra which are tilted relative to one another. The tilting and distortion of Re(Ca)O_6 octahedra together with B-cation ordering decrease the symmetry from orthorhombic to monoclinic with an angle close to 90°. One may well conclude that Rhenium is limited to different oxidation states from +4 to +7 in oxides. At the present time only compounds containing Re^{7+} are well studied, while the information about reduced Re-containing oxides (i.e. $V_{Re} < +7$) is very limited. In spite of the rich chemistry of rhenium in a low oxidation state, the synthetic problems encountered have discouraged the research in this field: Re cations with ($V_{Re} < +7$) are easily oxidized to Re^{7+} and they have the strong tendency to disproportionate. Such compounds have attracted the attention of many scientists in basic research because of their various interesting physical properties. For example, rhenium bronzes A_xReO_3 (A = Li, K) exhibit superconducting properties at low temperatures. Only one attempt to observe and build a phase diagram for the ternary rhenium oxides was carried out (BaO–Re–Re_2O_7). However, information and phase diagram data for other alkali earth—rhenium–oxygen systems is very scarce.

The $M_5Re_2O_{12}$ (M = Ca, Sr) oxides with Re in the formal oxidation state +7 also crystallizes in a hexagonal perovskite-like structure, where Re and M atoms are in a distorted octahedral oxygen coordination, d(Re–O) = 1.80–1.97 Å. The alkaline earth atoms are situated in the centers of eight- and ninefold polyhedra. The Ca_3ReO_6 compound belongs to the $A_2BB'O_6$ (Ca_2CaReO_6) perovskites with a "rock salt" type distribution of Re and Ca atoms over the B-cation sublattice. The tilting and distortion of Re(Ca)O_6 octahedra together with B-cation ordering decrease the symmetry from orthorhombic to monoclinic with an angle close to 90°.

The thermal decomposition of $Ca_5Re_2O_{12}$ in vacuo yielded single crystals of a perovskite-related phase having the composition $Ca_3ReO_{5.5}$. The $Ca_5Re_2O_{12}$ oxide with Re in the formal oxidation state +7 also crystallizes in a hexagonal perovskite-like structure, where Re and

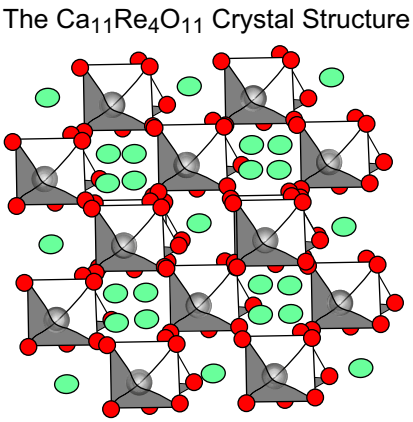

FIGURE 11.54

M atoms are in a distorted octahedral oxygen coordination, d(Re–O) = 1.80–1.97 Å. The alkaline earth atoms are situated in the centers of eight- and ninefold polyhedra. The structure has the form shown in Fig. 11.54.

The crystal structure of the $Ca_{11}Re_4O_{24}$ compound can also be derived from the perovskite structure. The rhenium atoms occupy two crystallographic sites, both with slightly distorted octahedral oxygen coordination. The averaged Re(1)–O distance of 1.931 Å and for Re(2)–O of 1.877 Å clearly reflects the two different oxidation states of rhenium in this compound. The formal oxidation state of $Re^{6.5+}$ in $Ca_{11}Re_4O_{24}$ is actually a consequence of one half Re^{6+} and the other half Re^{7+}. Four of eleven Ca atoms are distributed with Re atoms in the *B*-sublattice in a rock salt manner. The *A*-sublattice is not completely occupied and formally the $Ca_{11}Re_4O_{24}$ formula may be written as $Ca_7 \cdot (Ca_4Re_4)O_{24}$, which emphasizes the cation-deficient vacancies in the *A*-sublattice.

The magnetic susceptibility of $Ca_{11}Re_4O_{24}$ was determined with a Faraday balance in the temperature range between 138 and 296 K. The compound shows Curie–Weiss behavior with a magnetic moment of $\mu_{exp} = 1.2(1)$ μbar per Re(VI) ion. High-temperature treatment led to the formation of the most stable phases in this system, Ca_5ReO_{12} and $Ca(ReO_4)_2$, independent on the choice of precursors. The phases of primary interest are therefore unstable at temperatures above 950 °C.

The following table lists the most stable materials as well as the ranges and products of oxidation or reduction (Table 11.21).

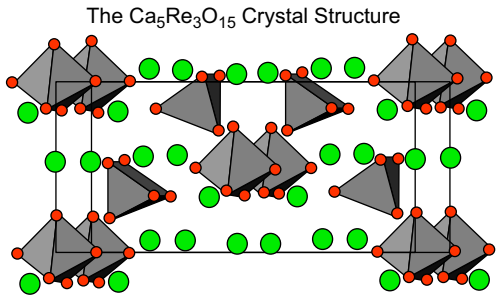

FIGURE 11.55

In the Ca–Re–O system, the stability of the Ca-rich phases was investigated. Two phases, $Ca_{11}Re_4O_{24}$ and $Ca_5Re_3O_{15}$, could be synthesized as single phase. The crystal structures of the complex oxides $Ca_{11}Re_4O_{24}$ and $Ca_5Re_3O_{15}$ were determined recently by X-ray single-crystal diffraction. Some discrepancies between the crystal structures revealed from powder diffraction data and single crystal ones were established. The structure of $Ca_5Re_3O_{15}$ is shown in Fig. 11.55.

Calcium rhenates are not available commercially and demand for these substances is almost nil. The high cost of Rhenium in general has precluded any usage in the Industry.

11.5.4. Strontium Rhenium Compounds

The literature describes many compounds concerning strontium oxy-rhenium compounds.

No compounds are known in the SrO–ReO system or the $SrO–Re_2O_3$ system.

In the $SrO–ReO_2$ system, it was claimed in a little known Czechoslovak thesis publication that a perovskite compound had been observed. However, the crystal parameters were not available. In a later thesis publication, the ternary compound, Sr_2CrReO_6, was studied. It is a double perovskite and the crystal parameters were given. It is dimorphic with the tetragonal form having $a_T = 5.5272$ Å, $c_T = 7.8091$ Å. The pseudo-cubic form has $a_c = b_c = c_c = 2 \cdot a_T/\sqrt{2} = 7.8166$ Å.

In the $SrO–ReO_3$ system, a number of compounds have been discovered. The Sr_3ReO_6 oxide has a monoclinic cell with $a = 8.1177(8)$ Å, $b = 5.9103(6)$ Å, $c = 5.9422(6)$ Å, $\beta = 90.47(1)°$ (space group I_2/m) and adopts a distorted

TABLE 11.21

Phase	Products of reduction	Lower $P(O_2)$ limit, bar	Upper $P(O_2)$ limit, bar	Products of oxidation
Ca_2ReO_6	$Re + CaO$	2.0×10^{-18}	1.0×10^{-3}	$Ca_5Re_2O_{12} + CaO$
$Ca_{11}Re_4O_{24}$	$Ca_3ReO_6 + Ca_5Re_3O_{15}$	5.0×10^{-11}	1.0×10^{-9}	$Ca_5ReO_{12} + CaO$
$Ca_5Re_3O_{15}$	$Re + Ca_3ReO_6 + Ca(ReO_4)_2$	5.0×10^{-11}	1.0×10^{-9}	$Ca_5Re_2O_{12} + CaO$

perovskite structure with Sr and Re ordered on the B-sites in a "rock salt" manner. Formally the Sr_3ReO_6 formula can be written as Sr_2SrReO_6. The Sr_3ReO_6 complex oxide could be considered as a Ba_2SbBiO_6 type of perovskite structure distortion. The ReO_6 and SrO_6 octahedra are cooperatively rotated about the [011] perovskite plane and are tilted with respect to a_0b-b-Glazer notation. The A-sites in a perovskite cell are occupied by the rest of Sr atoms. This compound is stable in the narrow range of partial oxygen pressure of 4.6×10^{-17} to 2.3×10^{-15} bar only. At the higher partial oxygen pressure the Sr_3ReO_6 oxide decomposes to a mixture of SrO and $Sr_{11}Re_4O_{24}$ compounds. The formal Re valence in the Sr_3ReO_6 increases from +6 to +6.5 due to a formation of cation vacancies in the A-sublattice, that leads to changing the coordination number of the Sr atoms in the B-sublattice from 6 to 8. The further increasing of a partial oxygen pressure to 1.1×10^{-3} bar leads to decomposition of the $Sr_{11}Re_4O_{24}$ compound to $Sr_5Re_2O_{12}$ and SrO. In this case the rest of the Re atoms with the oxidation state +6 in the $Sr_{11}Re_4O_{24}$ oxidizes to the Re^{+7} and vacancies in the B-sublattice are formed. This oxidation sequence could be considered as a stepwise increase of the amount of cation vacancies in the A- and B-sublattices from $Sr_6Re_2O_{12}$ through $Sr_{5.5}Re_2O_{12}$ to $Sr_5Re_2O_{12}$.

In the SrO–Re_2O_7 series of compounds, a novel oxide $Sr_2Ru_3O_{10}$ has been prepared under hydrothermal conditions (480–650 °C, 1800–2100 bar) and characterized by X-ray single-crystal diffraction data. The structure was refined in $C2/m$ space group with $a = 10.985(3)$ Å, $b = 5.635(1)$ Å, $c = 6.452(6)$ Å, and $\beta = 105.3(4)°$. The structure refinement converged to $R = 0.032$ and $R_w = 0.042$. The ruthenium atoms with a mean oxidation number of 5.33 occupy two sorts of octahedral sites. The first form infinite rutile-like chains parallel to the *b*-axis, while the second link these chains together to form layers parallel to (100) plane. The average Ru–O bond distance in the two types of octahedra does not allow assignment of an integral oxidation number to individual Ru ions. The Sr^{2+}cations are located in the interlayer space ensuring the stacking cohesion. The $Sr_2Ru_3O_{10}$ structure can also be described by the stacking of SrO_5 layers. The same stoichiometry is encountered in the barium fluorides $Ba_2M_3F_{10}$ (M = Ni, Cu, or Zn) but the stacking sequence is based on BaF_3 and BaF_7 layers. $Sr_2Ru_3O_{10}$ was the first example of strontium ruthenium oxide with Ru/Sr ratio higher than one. The Sr/Ru ratio is allowed by the existence of SrO_5 layers, which creates 1.5 octahedral sites per SrO_5 layer.

The X-ray powder diffraction patterns of annealed samples with $Sr_{2.75}ReO_{5.75}$ bulk composition was completely indexed based on a body-centered tetragonal cell with $a = 11.6779$ Å and $c = 16.1488$ Å (cell volume, $V = 2202.26$ Å^3). The indexing of the XRD pattern was confirmed by an electron diffraction study. The preliminary electron diffraction study did not reveal any superstructural spots corresponding to a decrease in symmetry or a unit cell expansion. Since the reflections with *hkl*: $h + k + l = 2n+1$, *hk*0: h, $k = 2n+1$ and 00*l*: $l = 4n+1$ were systematically absent, space group $I41/a$ was considered for further crystal structure determination The integral intensities of the reflections from the angular range 5°–70° for the diffraction pattern of $Sr_{11}Re_4O_{24}$ were extracted by profile fitting and further used for the calculation of the 3D Patterson distribution. The analysis revealed the positions of Re and for a part of the Sr atoms. The atomic coordinates of the other Sr and oxygen atoms were found by a subsequent Fourier and difference Fourier syntheses.

Re_2O_{10} clusters are connected with each other to form a 3D framework in Sr_xReO_3 ($0.5 \geq x \geq 0.4$) in the same way as in $La_4Re_6O_{19}$. The Sr_xReO_3 compound was synthesized by annealing under high pressure (50 kbar, 900 °C). The Re–Re distance in the Re_2O_{10} group for this structure is 2.429 Å. The only difference between these two structures is filling of the channels in the framework. The Sr atoms are situated in the interstices of the channels statistically (occupation number 0.3) on the 16f position of $Im3$ space group and have a ninefold coordination.

The $Sr_{2.4}Re_6O_{18}$ structure has the same cubic framework formed by the Re_2O_{10} group, and has a distribution of A-cations into the hexagonal channels. This formula can be written as $(Sr_{2.4})(Re_6O_{18})$ to distinguish between atoms belonging to the framework and those located inside the channels. Note that ordering of A-cations occurs with the increasing number of filled interstices and leads to a decrease of symmetry. Accordingly, as the Sr atoms fill the interstices statistically, the $Sr_{2.4}Re_6O_{18}$ structure has $Im\bar{3}$ symmetry and a body-centered cell similar to other compounds with 3D frameworks of Re_2O_{10} clusters.

Three new phases were prepared, Sr_3ReO_6, $Sr_{11}Re_4O_{24}$ and $Sr_7Re_4O_{19}$, and their crystal structures were solved and refined. Only one of these phases, $Sr_{11}Re_4O_{24}$ (the most stable in this system), could be prepared as a single phase without explicit control of the partial oxygen pressure in the sealed silica tube. The synthesis of the two other compounds requires a careful control of the partial oxygen pressure. The structure of $Sr_{11}Re_4O_{28}$ has the form shown in Fig. 11.56.

The following Table 11.22 lists the most stable materials as well as the ranges and products of oxidation or reduction. Formally the $M_{11}Re_4O_{24}$ formula (M = Sr or Ba) can be written as $M_7(M_4Re_4)O_{24}$, which allows the consideration of this compound as a cation-deficient perovskite with vacancies in the A-sublattice. This projection of the $Sr_{11}Re_4O_{24}$ crystal structure along the [001] shows that Re and M(4) atoms both occupy the *B*-position of the perovskite subcell in an ordered manner forming a "rock salt" type cation sublattice.

FIGURE 11.56

The remaining M atoms are placed in the channels of a 3D framework formed by ReO_6 and $M(4)O_8$ polyhedra, connected by corner sharing and edge sharing. Re(1) and Re(2) atoms are located in distorted octahedra ($d_{Re(1)–O} = 1.92–1.97$ Å, $d_{Re(2)–O} = 1.87–1.88$ Å). Since the octahedral coordination is not typical for Sr cations, the perovskite octahedral framework is significantly transformed. So, $Re(1)O_6$ octahedra are only slightly tilted along [110] whereas $Re(2)O_6$ ones are rotated along the same axis by $\approx 45°$. This changes the M(4) oxygen environment from an octahedron to an irregular eightfold polyhedron where Sr(4)–O distances vary in the range of 2.32–2.87 Å, and Ba(4)–O ones in the range of 2.40–2.85 Å. As a result, the $Re(2)O_6$ octahedron is edge shared by the equatorial oxygen atoms O(4) and O(6) to four $M(4)O_8$ polyhedra and connected with two $M(4)O_8$ ones by corner sharing via the apical oxygen atoms O(5). $Re(1)O_6$ octahedra are linked with the M(4) polyhedra only by corner sharing. The rotation of the ReO_6 octahedra leads to two kinds of nonequivalent channels filled by A-cations (see above diagram). In the first one only 3/4 of A-positions are occupied by M(1) and M(2) cations with 12-fold ($d_{Sr(1)–O} = 2.59–3.21$ Å) and 10-fold ($d_{Sr(2)–O} = 2.55–3.26$ Å) coordinations, respectively. The second one contains M(3) atoms surrounded by eight oxygen atoms ($d_{Sr(3)–O} = 2.50–2.97$ Å). The formal oxidation state of Re, calculated from the refined composition, is equal to +6.5. The Re atoms in the $M_{11}Re_4O_{24}$ structure are distributed over two nonequivalent positions and an ordered placement of Re_{+6} and Re_{+7} cations is expected.

The composition $Sr_{11}Re_4O_{24}$ ($Sr_{2.75}ReO_6$) is close to Sr_3ReO_6. An increase of the size of strontium atoms in comparison with the calcium ones in Ca_3ReO_6 results in an essential structural rearrangement of the anion framework and a formation of vacancies in the *A*-sublattice. The type of polyhedra sharing is different for these two structures in spite of the similar *B*-cation "rock salt" arrangement. In most cases the octahedral tilting distortion of the perovskite structure leads to a change of the first coordination sphere around A-cations. At the same time, the coordination environment of *B*-cations remains almost unchanged. The main reason for this distortion is the requirement to optimize the distances between A-cations and oxygen atoms. The geometrical relationship between *A*–O and *B*–O distances is determined by the Goldschmidt factor. In contrast the degree of octahedra tilting in the $M_{11}Re_4O_{24}$ structure significantly exceeds the usual tilt angles (which are approximately equal to 10°) and leads to dramatic changes in the first coordination sphere for half of the *B*-cations. This structural transformation is caused by the large size of M cations (M = Sr, Ba), which have to be surrounded by more than six oxygen atoms.

The crystal structure type of $M_{11}Re_4O_{24}$ (M = Sr, Ba) is closely related to two other structures of the already known compounds with the same stoichiometry, $Ca_{11}Re_4O_{24}$ and $Sr_{11}O_{s4}O_{24}$. The structure of $Sr_{11}O_{s4}O_{24}$ has been refined in the centrosymmetric, monoclinic space group $I2/a$, while for $Ca_{11}Re_4O_{24}$ noncentrosymmetric, the tetragonal space group $I41$ was unambiguously established. Both structures are considered to be derived from the common tetragonal, higher symmetry space group $I41/a$ of $M_{11}Re_4O_{24}$ (M = Sr, Ba) through a "translationengleiche" [(t) transformation]. These minor differences in the $M_{11}Re_4O_{24}$ structures for M = Ca and M = Sr, Ba can be traced to the different space requirements of the calcium and strontium atoms. In $Ca_{11}Re_4O_{24}$ the calcium atoms have coordination of 8 and 9. In contrast, the strontium atoms, occupying the *A*-sublattice, have coordination numbers of 10 and 12.

The compound, $Sr_7Re_6O_{19}$, has the crystal structure form shown as follows. There are two nonequivalent Re positions in the $Sr_7Re_4O_{19}$ crystal structure. The Re atoms are situated in the distorted octahedra. The average Re–O distance is 1.95 Å and 1.94 Å for Re(1) and Re(2) atoms, respectively, in good agreement with

TABLE 11.22

Phase	Products of reduction	Lower $P(O_2)$ limit, bar	Upper $P(O_2)$ limit, bar	Products of oxidation
Sr_3ReO_6	Re + SrO	4.5×10^{-17}	2.3×10^{-15}	$Sr_{11}Re_4O_{24} + SrO$
$Sr_{11}Re_4O_{24}$	Re + SrO	2.3×10^{-15}	1.1×10^{-3}	$Sr_5Re_2O_{12} + SrO$
$Sr_7Re_4O_{19}$	Re + SrO	2.3×10^{-15}	1.3×10^{-9}	$Sr_5Re_2O_{12} + Sr(ReO_4)_2$

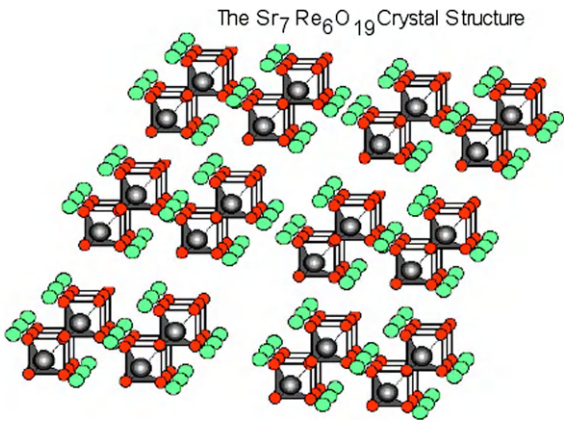

FIGURE 11.57

the ionic radius of Re_{6+} (0.52 Å) for CN = 6. Sr atoms have two different coordinations (Fig. 11.57).

Sr(1) and Sr(4) are 12-fold coordinated, Sr(2) and Sr(3) have 10 neighboring oxygen atoms each. The Sr(4) environment is regular in contrast to other Sr/O-polyhedra and can be described as a four capped cube . Other Sr atoms have irregular oxygen coordination. The $Sr_7Re_4O_{19}$ structure may be considered as an intermediate structure between Ba_2ReO_5 and $Ba_3Re_2O_9$ structures. The Ba_2ReO_5 compound contains ReO_6 octahedra linked by common corners and form infinite *cis*-bridged chains. In contrast, corner-sharing ReO_6 octahedra build infinite layers in the $Ba_3Re_2O_9$ structure. The $Sr_7Re_4O_{19}$ structure consists of two isolated, infinite chains of corner-sharing ReO_6 octahedra connected with each other. A new $Sr_7Re_4O_{19}$ double oxide could be considered as the fourth member of the $A_{4+n}Re_4O_{16+n}$ structure family ($n = 0, 1, 2,\ldots$), where A is an alkaline earth metal.

The compound, Sr_3ReO_6, has been synthesized by annealing in an evacuated silica tube under controlled partial oxygen pressure $p(O_2) = 4.6 \times 10^{-15}$ bar at 740 °C for 24 h. To control partial oxygen pressure a mixture of Ni and NiO was used. The structure investigation of the Sr_3ReO_6 complex oxide was carried out using X-ray powder diffraction. Its cation composition was determined by EDX analysis, Sr: Re = 3.00(4):1.00(4). The powder diffraction pattern of the Sr_3ReO_6 oxide was indexed, based on an *I*-centered monoclinic cell with $a = 8.1177$ Å, $b = 5.9103$ Å, $c = 5.9422$ Å, $\beta = 90.47°$. The structure has the form shown in Fig. 11.58.

The Sr_3ReO_6 complex oxide adopts a distorted perovskite structure with Sr and Re ordered on the *B*-sites in "rock salt" manner. Formally the Sr_3ReO_6 formula can be written as Sr_2SrReO_6. The Sr_3ReO_6 complex oxide could be considered as a Ba_2SbBiO_6 type of perovskite structure distortion. The ReO_6 and SrO_6 octahedra are cooperatively rotated about the [011] axis of the perovskite subcell and a_0b-b tilted with respect to Glazer's

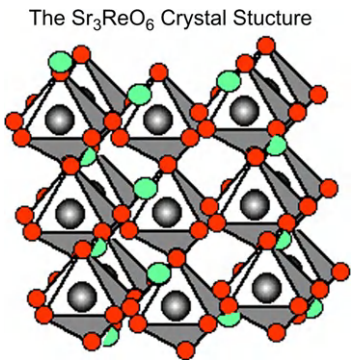

FIGURE 11.58

notation. The A-sites in a perovskite cell are occupied by the remaining Sr atoms. This compound is stable in the narrow range of partial oxygen pressure from 4.6×10^{-17} to 2.3×10^{-15} bar only. At a higher partial oxygen pressure the Sr_3ReO_6 oxide decomposes to a mixture of SrO and $Sr_{11}Re_4O_{24}$. The formal Re valence in Sr_3ReO_6 increases from +6 to +6.5 due to a formation of cation vacancies in the *A*-sublattice, that leads to a change in the coordination number of the Sr atoms in the *B*-sublattice from 6 to 8. A further increase of the partial oxygen pressure to 1.1×10^{-3} bar leads to decomposition of $Sr_{11}Re_4O_{24}$ to $Sr_5Re_2O_{12}$ and SrO. In this case all Re atoms with the oxidation state +6 in $Sr_{11}Re_4O_{24}$ are oxidized to Re_{+7}, and vacancies in the *B*-sublattice are formed. This oxidation sequence can be considered as a stepwise increase of the amount of cation vacancies in the *A*- and *B*-sublattices from $Sr_6Re_2O_{12}$ through $Sr_{5.5}Re_2O_{12}$ to $Sr_5Re_2O_{12}$, as shown in the following equations:

$$Sr_6Re_2O_{12} \Rightarrow Sr_{5.5}Re_2O_{12} + 1/2\ SrO$$
$$Sr_{5.5}Re_2O_{12} + 1/2\ SrO \Rightarrow Sr_5Re_2O_{12} + 1/2\ SrO$$

The compound, $Sr_5Re_2O_{12}$ has the structure form shown in Fig. 11.59.

The structural relations between Sr_3ReO_6 (a) $[A_2ABO_6]$, $Sr_{11}Re_4O_{24}$ (b) $[A_{1.75}ABO_6]$ and $Sr_5Re_2O_{12}$

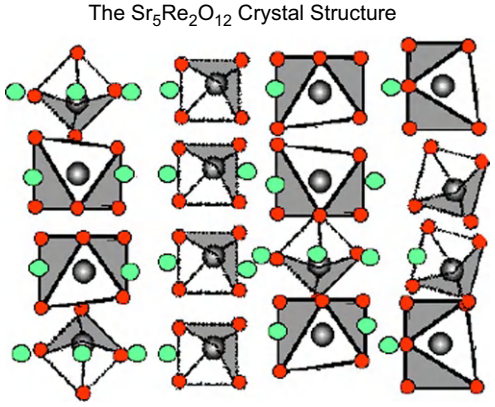

FIGURE 11.59

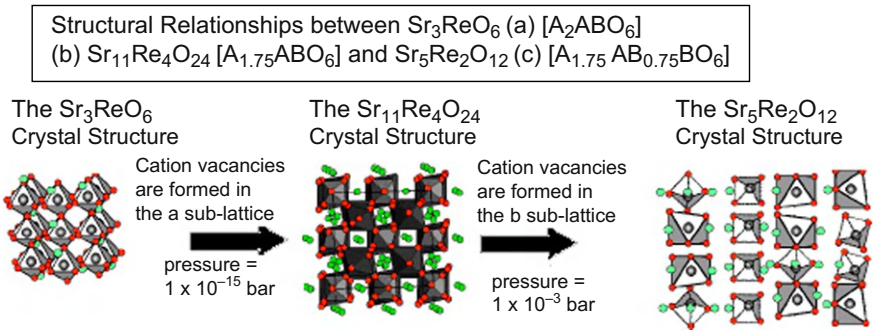

FIGURE 11.60

(c) $[A_{1.75}A_{0.75}BO_6]$ are shown in the following diagram in Fig. 11.60.

It should be clear that control of the oxygen partial pressure has a direct effect upon the nature of the strontium rhenate compound obtained and that cation vacancies and/or anion vacancies are the norm at specific synthesis conditions.

Strontium rhenates are not available commercially and no CAS numbers have been issued. No uses have emerged in the Industry, a fact that may be due to the high cost of Re metal that was $ 10.25/g in 2010.

11.5.5. Barium Rhenium Compounds

The Ba–Re–O system is very like that of the Sr–Re–O system and many of the comments and observations made for the Sr system are directly applicable to the Ba system. There is, however, at least one difference that exists between the systems. Whereas, three (3) compounds that are the most stable are listed in the Sr–Re–O system, only one (1) has been found in the Ba–Re–O system. That compound is $Ba_{11}Re_4O_{24}$. However at oxygen partial pressures of $PO_2 \geq 3 \times 10^{-3}$, it decomposes to $Ba_5Re_2O_{12}$ plus $Ba_3(ReO_5)_2$.

No compounds are known that involve the lower valence state of rhenium. The systems, BaO–ReO, $BaO–Re_2O_3$, $BaO–ReO_2$ and $BaO–Re_2O_5$ are nearly devoid of compounds. Most of the known compounds involve the $BaO–ReO_3$ and $BaO–Re_2O_7$ systems. The $Ba_3Re_2O_9$ oxide has hexagonal perovskite-like structures based on a 9R(*chh*)3 close-packed stacking of the BaO_3 layers where Re atoms are situated in the octahedral interstices. Units of three face-sharing octahedra are linked by corner sharing and form infinite chains along the [001] direction. The middle octahedron of these units is vacant to overcome the electrostatic repulsion between the highly charged neighboring Re^{6+} cations (Fig. 11.61).

For $Ba_3Re_2O_9$, the magnetic data, measured with a Faraday balance, suggest a Curie–Weiss behavior in the temperature region from 80 to 230 K, the magnetic moment is $\mu_{exp} = 1.55$ μbar per Re(VI) ion. Electrical resistivity measurements on $Ba_3Re_2O_9$ and Ba_2ReO_5 have revealed a high-room temperature resistivity ($\rho \sim 10^7$ Ωcm), which is doubtless a consequence of the orthogonality of the Re t_{2g} orbitals involved in the π–bonding to *cis* oxygen atoms.

The Ba_2ReO_5 compound is isostructural with Ba_2WO_5. The Ba_2ReO_5 compound contains ReO_6 octahedra linked by common corners and form infinite *cis*-bridged chains. In contrast, corner-sharing ReO_6 octahedra build infinite layers in the $Ba_3Re_2O_9$ structure shown in Fig. 11.62.

The existence of the compound, Ba_3ReO_6 remains in doubt. Syntheses of samples with controlled partial oxygen pressure and with BaO excess did not lead to a reproducible formation of the early observed compound, "Ba_3ReO_6". The conclusion can be made that the observed compound may be considered as a complex barium–rhenium oxycarbonate, where carbonate groups substitute BaO_6 octahedra partially in the 3D network of the corner-sharing octahedra BaO_6 like in the well-known case of barium–copper oxycarbonate, erroneously denoted as "$BaCuO_2$". This conclusion is supported by geometrical considerations

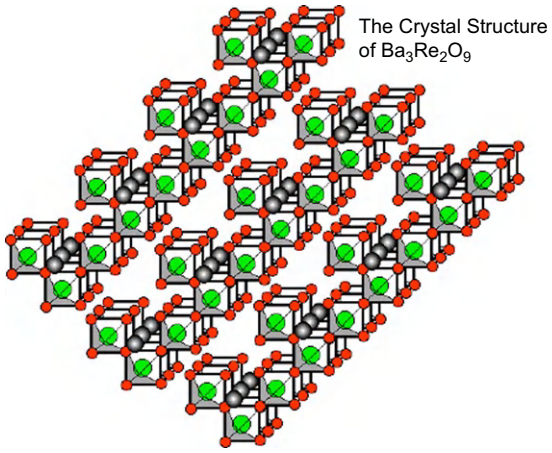

FIGURE 11.61

FIGURE 11.62

for the expected Ba_3ReO_6 complex oxide, which should crystallize in a perovskite-related structure with rock salt ordering of cations in the *B*-subcell, like in the Ca_3ReO_6 and the Sr_3ReO_6 structures. One-third of the Ba atoms would occupy the center of oxygen octahedra, but such an octahedral coordination would be very unusual for the big barium atoms, as the ionic radius of Ba^{2+} is 1.36 Å for sixfold coordination. Even in the case of the analogous strontium compound, Sr_3ReO_6, with $r_{Sr+2} = 1.16$ Å for a sixfold coordination, the occupancy of octahedral sites by Sr atoms results in a considerable restriction of the stability range in comparison to other observed phases in the Sr–Re–O system.

The crystal structure of the recently reported $Ba_{11}Re_4O_{24}$ compound can also be derived from the perovskite structure, designated a_{per} here. The crystal parameters are: $a = 12.2347$ Å and $c = 16.647$ Å ($V = 2496.65$ Å^3 for M = Ba). The cell parameters of $M_{11}Re_4O_{24}$ are clearly connected with the parameters of the perovskite subcell a_{per}: $a = 2\,a_{per}$, $c = 4\,a_{per}$. Formally the $M_{11}Re_4O_{24}$ formula can be written as $M_7(M_4Re_4)O_{24}$, which allows us to consider this compound as a cation-deficient perovskite with vacancies in the *A*-sublattice. This structure is shown in Fig. 11.63.

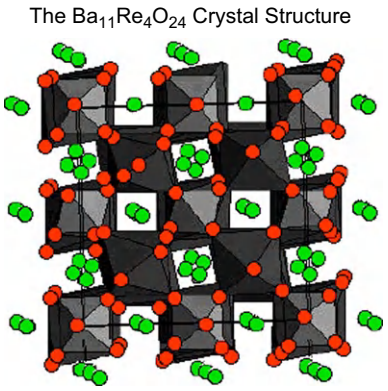

FIGURE 11.63

The rhenium atoms occupy two crystallographic sites, both with slightly distorted octahedral oxygen coordination. The averaged Re(1)–O distance of 1.931 Å and for Re(2)–O of 1.877 Å clearly reflects the two different oxidation states of rhenium in this compound. The formal oxidation state of $Re_{+6.5}$ in $Ca_{11}Re_4O_{24}$ is actually a consequence of one half Re_{+6} and the other half Re_{+7}. Four of eleven Ca atoms are distributed with Re atoms in the *B*-sublattice in a rock salt manner. The *A*-sublattice is not completely occupied and formally the $Ca_{11}Re_4O_{24}$ formula may be written as $Ca_7 \cdot (Ca_4Re_4)O_{24}$, which emphasizes the cation-deficient vacancies in the *A*-sublattice.

The crystal structure type of $Ba_{11}Re_4O_{24}$ is closely related to two other structures of the already known compounds with the same stoichiometry, $Ca_{11}Re_4O_{24}$ and $Sr_{11}O_{s4}O_{24}$. The structure of $Sr_{11}O_{s4}O_{24}$ has been refined in the centrosymmetric, monoclinic space group *I*2/*a*, while for $Ca_{11}Re_4O_{24}$ noncentrosymmetric, the tetragonal space group *I*41 was unambiguously established. Both structures may be deemed to be derived from the common tetragonal, higher symmetry space group *I*41/*a* of $Ba_{11}Re_4O_{24}$ through a translationengleiche (t) transformation.

A spectrophotometric study shows that less than 35% of normal perrhenate converts to a meso form in 15 M base, and $K_f \sim 0.1$. The species absorbs at 260 μm ($\delta = 6400$) and near 310 μm ($\delta \sim 1400$), overlapping the normal perrhenate features. Reflectance spectra on an isolable barium salt, $Ba_3(ReO_5)_2$, confirm this resolution of the curve components. Single crystals of two new barium rhenate compositions, $Ba_{16}Re_6O_{37}$ and $Ba_{10}Re_3O_{16}(OH)_3$, and of one new polymorph, orthorhombic $Ba_5Re_2O_{12}$, were grown out of a barium hydroxide flux in sealed silver tubes. $Ba_{16}Re_6O_{37}$ and $Ba_{10}Re_3O_{16}(OH)_3$ crystallize into the monoclinic *C*2/*m* system, with $a = 20.577$ Å, $b = 5.8897$ Å, $c = 15.438$ Å, $\beta = 92.255°$ and $a = 19.3834$ Å, $b = 5.8172$ Å, $c = 10.2925$ Å, $\beta = 91.7460°$, respectively. The orthorhombic polymorph of $Ba_5Re_2O_{12}$ crystallizes in the space group *Pnma*, with $a = 19.6728$ Å, $b = 5.8491$ Å and $c = 10.4648$ Å. All the three crystal structures are related and consist of a framework of BaO_x polyhedra (where *x* varies from 6 to 12) with inter-penetrating layers of ReO_6 octahedra. The arrangement of these octahedra is shown in Fig. 11.64.

A systematic survey of the BaO–Re–Re_2O_7 phase diagram was reported with emphasis on the reduced ternary oxides. At 800 °C, the previously reported compounds $Ba_3Re_2O_9$, Ba_2ReO_5, and Ba_3ReO_6 were observed, all of which contain Re(VI) in ReO_6 octahedra. The stability of these phases is apparently due to Re–O π-bonding in and between the octahedra.

The previously unknown structure of Ba_2ReO_5 was determined by powder neutron diffraction and found to be isotypic with that of $K_2VO_2F_3$ (space group

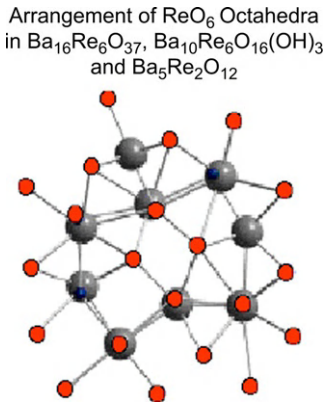

FIGURE 11.64

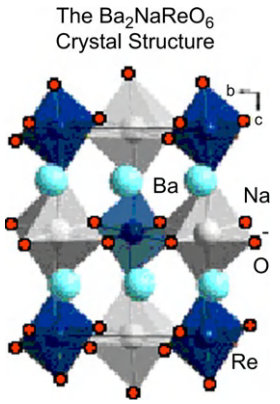

FIGURE 11.65

Pnma), with $a = 7.3233$, $b = 5.7745$, and $c = 11.4124$ Å. ReO_6 octahedra share adjacent corners to produce cis-chains which are held together by 10 coordinated Ba atoms.

Single crystals of the double perovskite rhenates A_2BReO_6 (A = Sr, Ba; B = Li, Na) were grown out of molten hydroxide fluxes. Single crystals of orange/yellow Ba_2LiReO_6, Ba_2NaReO_6 and Sr_2LiReO_6 were solved in the cubic, *Fm*-3*m* space group with $a = 8.1214$ Å, 8.2975 Å, and 7.9071 Å, respectively, while Sr_2NaReO_6 was determined to be monoclinic $P2_1/n$ with $a = 5.6737$ Å, $b = 5.7988$ Å, $c = 8.0431$ Å, and $\beta = 90.02°$. The cubic structure consists of a rock salt lattice of corner-shared ReO_6 and MO_6 (M = Li, Na) octahedra that, in the monoclinic structure, are both tilted and rotated. A discrepancy exists between the symmetry of Sr_2LiReO_6 indicated by the single-crystal refinement of flux-grown crystals (cubic, *Fm*-3*m*) and the symmetry indicated by the powder diffraction data collected on polycrystalline samples prepared by the ceramic method (tetragonal, *I*4/*m*). It is possible that the cubic crystals are a kinetic product that forms in small quantities at low temperatures, while the powder represents the more stable polymorph that forms at higher reaction temperature. The structure is shown in Fig. 11.65.

Single-crystal structure analyses of double perovskite rhenates, Sr_2LiReO_6, Ba_2LiReO_6 and Ba_2NaReO_6 indicate cubic symmetry while that of Sr_2NaReO_6 shows monoclinic symmetry.

In addition a mixed Ba–Mg compound has been synthesized. The XRD patterns of the annealed samples of Ba_2MgReO_6 composition were completely indexed based on a primitive an F-centered cubic cell with $a = 8.0850$ Å. This indexation is only in slight disagreement with the cell parameters reported by Sleight et al. for barium-containing compound. The Ba_2MgReO_6 structure model was taken as from Woodward for the F-centered cubic cell and a BO_6 octahedra tilt system, where $a = b = c = 2\,a_{per}$, a°a°a° tilt system, corresponding to Glazer's notation.

The magnetic properties of Ba_2MgReO_6 were also studied. A similar unexpected behavior as in the case of the $Sr_7Re_4O_{19}$ oxide was observed. The temperature dependence of magnetization shows an anomalous course in the case of Ba-containing samples. The results of the zero-field cooled measurements drastically differed from the field cooled ones, and their observed values are negative until 19 K was reached at the field strength of 100 G for Ba_2MgReO_6. The Ba_2MgReO_6 compound demonstrates a temperature-independent curve of magnetization between 300 and 30 K. Despite this observation, hysteresis loops were observed for both the Ba and for the Sr-containing compound inclusive at 300 K.

Barium oxy-rhenate compounds are not available commercially and no CAS numbers have been issued.

11.5.6. Radium Rhenium Compounds

Although radium rhenate compounds could be synthesized similar to those exhibited by the Ba–Re–O system, it is unlikely that they ever will be due to the high radioactivity of ^{226}Ra and the high cost of rhenium.

CHAPTER

12

Group 8 (Fe, Ru and Os) Alkaline Earth Compounds

OUTLINE

12.1. Alkaline Earth—Iron Intermetallic Compounds 911

12.2. Alkaline Earth—Oxy-Iron Compounds 914
- *12.2.1. Beryllium Oxy-Iron Compounds* 914
- *12.2.2. Magnesium Oxy-Iron Compounds* 914
- *12.2.3. Calcium Oxy-Iron Compounds* 916
- *12.2.4. Strontium Oxy-Iron Compounds* 922
- *12.2.5. Barium Oxy-Iron Compounds* 930
- *12.2.6. Radium Oxy-Iron Compounds* 937

12.3. Alkaline Earth—Ruthenium Compounds 937
- *12.3.1. Beryllium Oxy-Ruthenium Compounds* 937
- *12.3.2. Magnesium Ruthenium Compounds* 939
- *12.3.3. Calcium Ruthenium Compounds* 939
- *12.3.4. Strontium Ruthenium Compounds* 944
- *12.3.5. Barium Ruthenium Compounds* 950
- *12.3.6. Radium Ruthenium Compounds* 953

12.4. Alkaline Earth—Osmium Compounds 954
- *12.4.1. Beryllium Osmium Compounds* 954
- *12.4.2. Magnesium Osmium Compounds* 954
- *12.4.3. Calcium Osmium Compounds* 955
- *12.4.4. Strontium Osmium Compounds* 957
- *12.4.5. Barium Osmium Compounds* 958
- *12.4.6. Radium Osmium Compounds* 960

12.1. ALKALINE EARTH—IRON INTERMETALLIC COMPOUNDS

Only Be^0 metal forms intermetallic compounds with the metal, Fe^0. The others do not form any compounds. The compounds, $Be_{0.2}Fe_{0.8} = BeFe_4$, $Be_{0.56}Fe_{1.44} = BeFe_{2.57}$, $Be_{12}Fe$, $Be_{17}Fe_2$, Be_5Fe and Be_2Fe are known. A phase diagram has not been published.

The compound, Be_5Fe has the structure form shown in Fig. 12.1.

The lattice direction (100), is shown but the (001) direction is identical. The cubic faces are face-centered with Fe atoms and there are five (5) internal rows of Be atoms. It is a cubic material with cell parameters of: $a = b = c = 4.1543$ Å, $\alpha = \beta = \gamma = 60°$, cell volume = 50.70 Å^3, $Z = 4$. Cell occupancy is shown in Table 12.1.

The compound, $Be_{12}Fe$ has a similar structure form, except that the Fe atoms form a body-centered cube (Fig. 12.2).

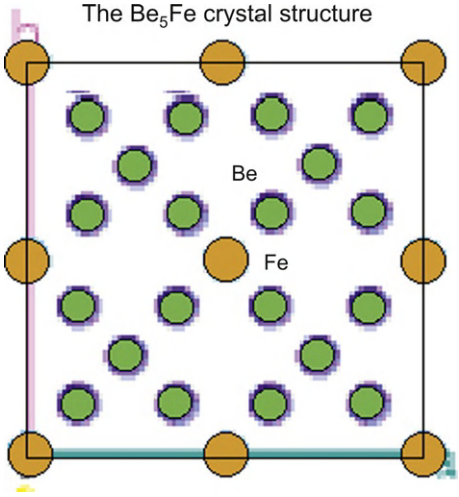

FIGURE 12.1

Encyclopedia of the Alkaline Earth Compounds
http://dx.doi.org/10.1016/B978-0-444-59550-8.00012-0

Copyright © 2013 Elsevier B.V. All rights reserved.

TABLE 12.1

No.	Site notation	Atom	Multiplicity	Wyckoff	Site symmetry	x	y	z	Occupancy
1	Be1	Be	16	e	.3m	0.625	0.625	0.625	1.0
2	Be2	Be	4	c	-43m	1/4	1/4	1/4	1.0
3	Fe1	Fe	4	a	-43m	0	0	0	1.0

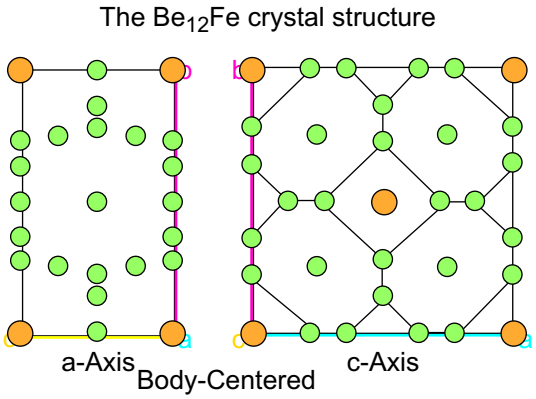

FIGURE 12.2

Both the *a*- and *c*-axes are shown [the (100) and (001) directions in the lattice]. There are three (3) internal arrangements of Be atoms within the unit cell, arranged in a distorted octahedron around a central Be atom. Cell parameters are: $a = 4.232$ Å, $b = c = 5.548$ Å, $\alpha = 81.636°$, $\beta = \gamma = 67.58°$, cell volume $= 111.31$ Å^3, $Z = 2$. Cell occupancy is shown in Table 12.2:

The compound, Be_2Fe has the structure form shown in Fig. 12.3.

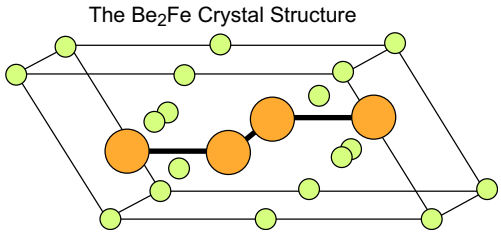

FIGURE 12.3

The lattice direction (100), is shown. The Fe atoms are arranged in a zigzag manner. It is a monoclinic material with cell parameters of: $a = b = 4.215$ Å, $c = 6.853$ Å, $\alpha = \beta = 90°$, $\gamma = 120°$, cell volume $= 105.44$ Å^3, $Z = 4$. Cell occupancy is shown in Table 12.3.

The compound, $Be_{17}Fe_2$, has the structure form shown in Fig. 12.4.

The cell parameters are: $a = b = 4.137$ Å, $c = 10.72$ Å, $\alpha = \beta = 90°$, $\gamma = 120°$, cell volume $= 158.89$ Å^3, $Z = 2$. Cell occupancy is shown in Table 12.4.

The compound, $Be_{0.56}Fe_{1.44}$ has the body-centered cubic structure where the Be atoms and Fe atoms are distributed randomly at the central position in the lattice (Fig. 12.5).

TABLE 12.2

No.	Site notation	Atom	Multiplicity	Wyckoff	Site symmetry	x	y	z	Occupancy
1	Be1	Be	8	j	m2m.	0.277	1/2	0	1.0
2	Be2	Be	8	i	m2m.	0.361	0	0	1.0
3	Be3	Be	8	f	..2/m	1/4	1/4	1/4	1.0
4	Fe1	Fe	2	a	4/mmm	0	0	0	1.0

TABLE 12.3

No.	Site notation	Atom	Multiplicity	Wyckoff	Site symmetry	x	y	z	Occupancy
1	Be1	Be	6	h	mm2	0.1697	0.3394	1/4	1.0
2	Fe1	Fe	4	f	3m.	1/3	2/3	0.5629	1.0
3	Be2	Be	2	a	-3m.	0	0	0	1.0

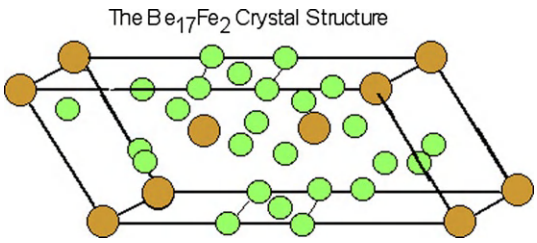

FIGURE 12.4

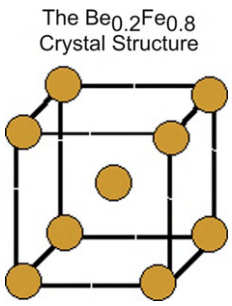

FIGURE 12.6

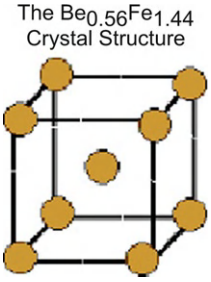

FIGURE 12.5

Cell parameters are: $a = b = c = 2.732$ Å, $\alpha = \beta = \gamma = 90°$. Cell volume = 20.53 Å^3, $Z = 1$. Cell occupancy is shown in Table 12.5.

The compound, $Be_{0.2}Fe_{0.8}$, has a similar body-centered cubic structure shown in Fig. 12.6.

Unit cell parameters are: $a = b = c = 2.4162$ Å, $\alpha = \beta = \gamma = 90°$, cell volume = 10.86 Å^3, $Z = 1$. Cell occupancy is shown in Table 12.6.

Mg, Ca, Sr and Ba do not form intermetallic compounds with Fe. None of these compounds are used in the Industry and they are not offered for sale commercially.

TABLE 12.4

No.	Site notation	Atom	Multiplicity	Wyckoff	Site symmetry	*x*	*y*	*z*	Occupancy
1	Be1	Be	6	n	.m.	0.1665	0.8335	0.1830	1.0
2	Be2	Be	3	k	mm2	0.5045	0.4955	1/2	1.0
3	Be3	Be	2	i	3m.	2/3	1/3	0.0982	1.0
4	Fe1	Fe	2	i	3m.	2/3	1/3	0.3069	1.0
5	Be4	Be	2	h	3m.	1/3	2/3	0.3408	1.0
6	Be5	Be	2	g	3m.	0	0	0.3767	1.0
7	Be6	Be	1	c	-6m2	1/3	2/3	0	0.34
8	Fe2	Fe	1	a	-6m2	0	0	0	0.36

TABLE 12.5

No.	Site	Atom	Multiplicity	Wyckoff	Site symmetry	*x*	*y*	*z*	Occupancy
1	M	0.56Be + 1.44Fe	1	b	m-3m	1/2	1/2	1/2	1.0
2	Fe	Fe	1	a	m-3m	0	0	0	1.0

TABLE 12.6

No.	Site notation	Atom	Multiplicity	Wyckoff	Site symmetry	*x*	*y*	*z*	Occupancy
1	Fe	Fe	1	b	m-3m	0	0	0	1.0
2	M	0.8 Fe + 0.2 Be	1	a	m-3m	1/2	1/2	1/2	1.0

12.2. ALKALINE EARTH—OXY-IRON COMPOUNDS

A large number of compounds are known with iron. The number of compounds that have been synthesized varies from a few with MgO to many with BaO.

12.2.1. Beryllium Oxy-Iron Compounds

Beryllium oxide, BeO, does not form any compounds with the iron oxides.

12.2.2. Magnesium Oxy-Iron Compounds

The system, MgO–FeO, does not form any compounds as shown in the phase diagram presented as follows. Only solid mixtures of oxides appear. A eutectic was found at 1530 °C and 0.5 molar ratios of oxides. No compounds are known in this system (Fig. 12.7).

In the Fe^{3+}-containing system of MgO–Fe_2O_3, the ferrite, $MgFe_2O_4$, is in great demand. The ever expanding electronic industry's need of ferrites, both hard and soft, is evident from the estimated world ferrite production of 5,16,000 metric tons per year (MTPY) in 1990 to 15,00,000 MTPY in the year 2005. The ferrite grade iron oxide, a-Fe_2O_3, required for such production of ferrites in the year 2005 would be of about 10,50,000 MTPY.

The production of ferrites has been on the rise ever since the commercialization of these took place some 60 years ago. The magnesium ferrite, $MgFe_2O_4$, prepared from these synthetic iron oxides, showed a high resistivity of ~108 ohm/cm. All ferrites showed saturation magnetization, $4\pi M_s$, in the narrow range of 900–1200 G. The Curie temperature, T_C, of all these fell within a small range limit of 670 ± 30 K. All ferrites had low dielectric constants (e_c), 12–15, and low dielectric loss, tan δ, which decreased with the increase in frequency indicating a normal dielectric dispersion, as found in ferrites. The presence of an insignificant amount of polarizable Fe^{2+} ions can be attributed to their high resistances and low dielectric constants. Impurities inherent in the samples had no marked influence on the electrical properties of the ferrites prepared from the iron ore rejects, suggesting the possibility of formation of a ferrite of constant composition, $MgFe_2O_4$, of low magnetic and dielectric losses at lower temperatures of 1000 °C by ceramic technique.

Super-paramagnetism is a unique and important aspect of magnetism in nanoparticles. The super-paramagnetic properties of the spinel $MgFe_2O_4$ ferrite nanoparticles with a particle size from about 6 to 18 nm have been studied. The blocking temperature is a function of the particle size and increases with increasing particle size. The coercivity of $MgFe_2O_4$ nanoparticles is also a function of the particle size below the blocking temperature. When the temperature rises above the blocking temperature, the nanoparticles show non-hysteresis magnetization behaviors. With these interesting super-paramagnetic properties, $MgFe_2O_4$ nanoparticles have potentials for applications such as ferro-fluids, magneto-caloric refrigeration, and the contrast agents for magnetic resonance imaging. The structure has the form shown in Fig. 12.8.

The tetrahedral and octahedral cation sites are shown in gray and white, respectively, and the O atoms as small circles. A unit cell is outlined. **$MgFe_2O_4$ is one of the most important ferrites**. The oxides, MgO and Fe_2O_3 were heated together at 900 °C and quenched in

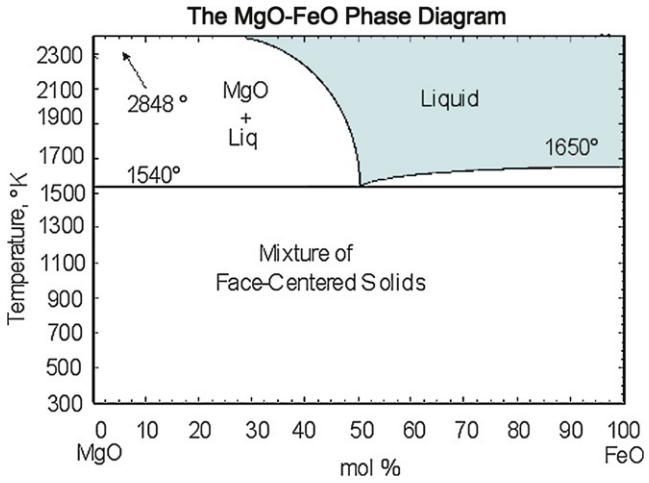

FIGURE 12.7

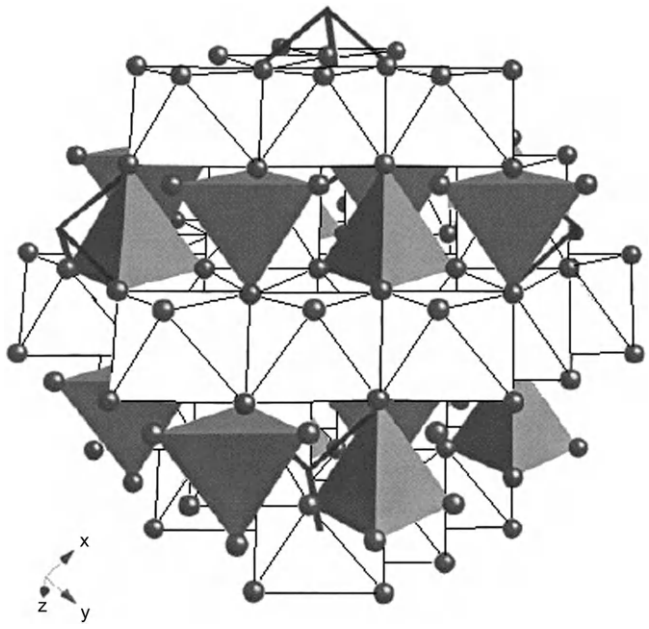

FIGURE 12.8

air. The structural behavior of magnesioferrite was determined from in situ synchrotron X-ray powder diffraction data (SXRD) [$\lambda = 0.92225$ Å] at room pressure and temperatures from 28 to 982 °C on heating and cooling. The "*a*" parameter of the unit cell increases linearly on heating, but deviates to give a discontinuity at 581 °C.

Above 581 °C and on cooling from 982 °C, the "*a*" parameter varies linearly. This parameter at 28 °C before heating [8.39704 Å] and after cooling to 47 °C [8.39514 Å] differs because the cation order, frozen in the structure, is not the same. Cation order, $x,\{^{iv}[Mg_{1-x}Fe_x]^{vi}[Mg_{x/2}Fe_{1-x/2}]_2O_4\}$, analyzed in terms of the inversion parameter, and the order parameter, $Q = 1 - (3/2)x$, show no change on heating until the temperature is high enough to cause exchange of Mg^{2+} and Fe^{3+} cations between the octahedral and tetrahedral sites. This activation barrier is overcome at 581 °C, where the sample achieves the maximum ordered state on heating [$x_{max} = 0.867$] and begins to move toward equilibrium. This relaxation is toward a more ordered configuration and is a kinetically controlled process. Above 581 °C, the cations become continuously disordered along the equilibrium pathway to the maximum temperature studied [$T_{max} = 982$ °C, $x = 0.769$] and reverse along the equilibrium pathway on cooling. At T_B, the maximum equilibrium order is frozen in, and maintained to room temperature, where $x_{max} = 0.895$.

The influence of Sn^{4+} and /or Mo^{6+} ions on the microstructure and humidity sensitivity of the Mg ferrite prepared by a self-combustion method was studied. The sintered compacts have a typical porous structure. The average grain size changes from 500 to 100 nm by partial substituting of Mg ions with Sn ions in $MgFe_2O_4$. The $Mg_{0.9}Sn_{0.1}Fe_2O_4$ porous ceramic exhibits the best humidity sensitivity among the specimens studied. Its electrical resistivity changed remarkably, by three orders of magnitude, when the relative humidity increased from 11 to 98%. Among the studied elements, this composition exhibits a short response time. However, the response time is not yet a satisfactory value. These preliminary results show that the promoting effects of Sn^{4+} ions on humidity sensitivity of Mg ferrite can be related with the changes in porosity and grain size (specific surface area). Further investigations are necessary to shorten the response time, without any decrease in humidity sensitivity, and to explain the role of Sn^{4+} substituent.

In another paper, epitaxial $MgFe_2O_4$ thin films were synthesized by oxide molecular beam epitaxy at 300 °C. Reflection high-energy electron diffraction and transmission electron microscopy (TEM) showed that the films were epitaxial with a (001) orientation. Magneto-optic Kerr effect and superconducting quantum interference device magnetization measurements revealed that films were ferrimagnetic with a saturation ellipticity of 0.005 °C, and saturation magnetization of 120 emu/cm^3. The ferrimagnetism was attributed to the formation of a partially inverted spinel structure with a cation distribution $[Mg^{2+}_{0.2}Fe^{3+}_{0.8}][Mg^{2+}_{0.8}Fe^{3+}_{1.2}]O_4$.

ptMagnesioferrite, $MgFe_2O_4$ was found to undergo a transformation to a high-pressure phase with the suggested $CaMn_2O_4$—structure at around 17 GPa. Thermodynamic calculations, however, postulate the breakdown of $MgFe_2O_4$ into its constituent oxides at high pressure and temperature prior to the formation to the high-pressure phase. This behavior was experimentally observed by use of DAC (Diamond Anvil Cell) technique where synthetic $MgFe_2O_4$ at 26 ± 4 GPa and laser heating between 1500 and 2000 K were employed. The high-pressure phase of $MgFe_2O_4$ was identified and the break down products MgO and Fe_2O_3 by Mössbauer spectroscopy, Raman spectroscopy and synchrotron X-ray diffraction (SXRD). The multiphase assemblage results suggest that inhomogeneous conditions prevailed during the laser annealing in the DAC experiments.

Two different reactions were suggested at high pressure and temperature:

$$T < 1800 \text{ K: } MgFe_2O_4 \Rightarrow Fe_2O_3 + MgO$$
$$T > 1800 \text{ K: } MgFe_2O_4 \Rightarrow \text{hp-}MgFe_2O_4.$$

Magnetic properties, such as Curie temperature (T_C), saturation magnetization (M_s), remanent magnetization (M_r), and coercivity (H_c) of nanoparticles of magnesium ferrites ($MgFe_2O_4$), were studied in a broad range of temperatures varying from room temperature to 800 K. The magnetization decreased with increasing temperature, approaching zero at ~750 K. The Curie temperature, determined by means of the inverse susceptibility versus temperature, was ~738 K. The saturation magnetization, coercivity, and remanence decreased with increasing temperature, being close to zero at temperatures near T_C. However, for temperatures 100 K above room temperature, these magnetic properties were still the same as those at room temperature. The coercivity temperature dependence could be expressed in terms of $T^{3/4}$, indicating that $MgFe_2O_4$ nanoparticles may form a system of random and noninteracting identical particles. The results were discussed in terms of interparticle interactions induced by the thermal fluctuations, cation distribution, and other imperfections that exert fields on Mg^{2+} ions that could increase with temperature.

In the Fe^{2+}- and Fe^{3+}-containing system of MgO–Fe_3O_4, no compounds are known.

In the Fe^{4+}-containing system of MgO–FeO_2, no compounds have been discovered.

In the Fe^{5+}-containing system of MgO–Fe_2O_5, no compounds have been discovered to date.

In the Fe^{6+}-containing system of MgO–FeO_3, a set of samples of Fe/MgO, in the concentration range between 1.5 and 9 wt% of Fe, was prepared by the impregnation method and then calcined at 1073 K. All of them were characterized by XRD and Raman and Mössbauer spectroscopy. The data obtained showed that the solids were made up of **$MgFeO_4$** nanoclusters and Fe^{3+} ions dispersed in the MgO matrix. The size of the clusters and the amounts of each phase were calculated using the XRD and Mössbauer data. No other data were available for this compound and no other Fe^{6+}-containing magnesium ferrates have been synthesized.

In the Fe^{7+}-containing system of MgO–Fe_2O_7, no compounds have been discovered. These compounds are expected to be unstable and to be highly oxidizing to organic compounds. Only alkali-based compounds are known.

$MgFe_2O_4$ is offered for sale commercially with the CAS number of 12068-86-9 by many manufacturers.

12.2.3. Calcium Oxy-Iron Compounds

Several types of compounds are known in the CaO–Fe_xO_y systems.

In the Fe^{2+}-containing system of CaO–FeO, $CaFeO_2$, a material exhibiting an unprecedented layered structure containing $3d^6$ iron atom in a high-spin distorted square-planar coordination, was reported. This phase, obtained through a low-temperature reduction procedure using calcium hydride, was characterized through powder neutron diffraction, synchrotron XRD, Mössbauer spectroscopy, XAS experiments as well as first-principles density functional theory (DFT) calculations. The XAS spectra near the Fe–K edge for the whole solid solution $(Sr_{1-x},Ca_x)FeO_2$ supported the fact that iron is in a square-planar coordination for $0 \leq x \leq 0.8$ but clearly suggests a change of coordination for $x = 1$. The structure reported has the form shown in Fig. 12.9.

This structure contains infinite FeO_2 layers in which the FeO_4 units distort from square planar toward tetrahedra and rotate along the *c*-axis in an unprecedented manner. This is in marked contrast to the well-studied and accepted concept that octahedral rotation in perovskite oxides occurs but the octahedral shape is kept almost regular. This phase exhibits high-spin configuration and G-type antiferromagnetic ordering as in $SrFeO_2$. However, the distortion of the FeO_2 layers leads to only a slight decrease of the Neel temperature with respect to $SrFeO_2$. First-principles DFT calculations have provided a clear rationalization of the structural and physical observations for $CaFeO_2$ and highlight how the nature of the cation influences the structural details of the $AeFeO_2$ family of compounds (Ae = Ca, Sr, Ba). Using the results of these calculations, the driving force for the distortion of the FeO_2 layers in $CaFeO_2$ was also discussed in several articles. The tetrahedral structure of $SrFeO_2$ (space group *P*4/*mmm*) consists of layers of corner-sharing FeO_4 squares with strontium atoms in between. The structure closely resembles the sheet-like lattice geometry of superconducting copper oxides. There is no known structural instability as a function of temperature in $SrFeO_2$ or the similar compound $CaFeO_2$.

In another study, based on DFT with the generalized gradient approximation plus on-site Coulomb repulsion method, a study of the electronic, magnetic, and optical properties in infinite-layer iron oxide $CaFeO_2$ and $BaFeO_2$ was made. $CaFeO_2$ possesses a *P*421/*m* tetragonal symmetry. The single downspin electron of the Fe^{2+} ion occupies a d_z^2 level instead of Jahn–Teller instability from the double degenerated d_{x-y}^{22} and d_z^2 levels predicted in crystal field theory. Magnetic structure shows great contrast between intralayer and interlayer exchange interactions. Linear dielectric function, on the other hand, exhibits obvious anisotropic behavior between in plane and out of plane responses. For the larger ionic size of Ba, $BaFeO_2$ is found to have a *P*4/*mmm* tetragonal symmetry, which is similar to $SrFeO_2$. Together with the previous calculations of $SrFeO_2$, it was found that the anisotropic behaviors in these two dimensional (2D) structures are robust and independent of A-site size.

In the phase diagram of this system, two compounds are shown (Fig. 12.10).

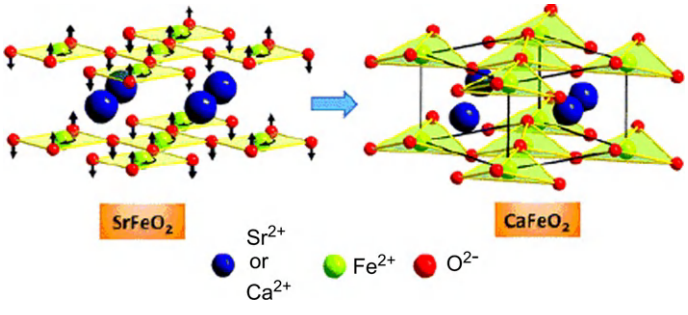

FIGURE 12.9

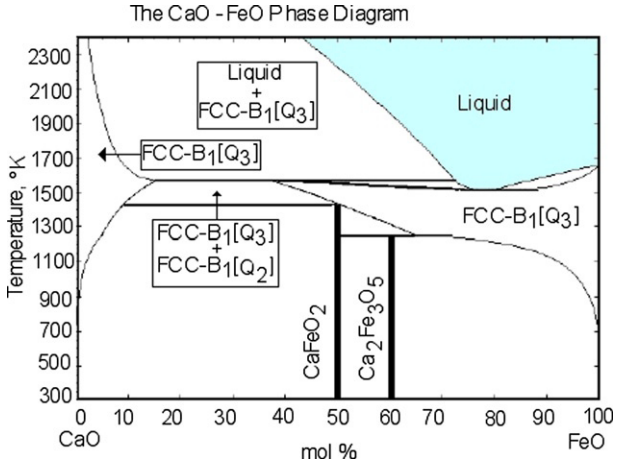

FIGURE 12.10

Little is known concerning the $2CaO \cdot 3FeO$ compound. Dicalcium ferrite, $Ca_2Fe_3O_5$, belongs to the $ABO_{3-\delta}$ perovskite family with $\delta = +0.5$. It presents ordered oxygen vacancies in the (101) directions of the cubic perovskite structure, leading to the orthorhombic distortion ($a_c\sqrt{2} \times 4a_c \times a_c\sqrt{2}$), and to a stacking sequence of planes of Fe^{3+} ions in octahedral and tetrahedral coordination. This compound is said to be antiferromagnetic with $T_n = 725$ K.

In the Fe^{3+}-containing system of $CaO–Fe_2O_3$, the compound, calcium ferrite, $CaFe_2O_4$ is known. It has the general structure shown in Fig. 12.11.

The phase diagram of the system, shown as follows, presents three compounds. These compounds represent the mol ratios (Fig. 12.12).

$2CaO–Fe_2O_3$
$CaO–Fe_2O_3$
$CaO–2Fe_2O_3$

All of these compounds melt incongruently.

The $CaFe_4O_7$ compound is stable only over a limited temperature range of 260 K. This compound decomposes according to:

$$CaFe_4O_7 + \text{heat}\ (T > 1593\ \text{K}) \Rightarrow \alpha\text{-}Fe_2O_3 + CaFe_2O_4$$

Investigations of the iron-rich part of the Ca–Fe–O phase diagram at 1200 °C, have verified the specification of the crystallographic and magnetic characteristics of three compounds, $CaFe_4O_7$, $Ca_4Fe_9O_{17}$ and $Ca_3Fe_{15}O_{25}$. ^{57}Fe Mössbauer spectroscopy studies were made on these compounds. $CaFe_4O_7$ and $Ca_4Fe_9O_{17}$ must be considered as antiferromagnetic, whereas $Ca_3Fe_{15}O_{25}$ is ferrimagnetic. Parallel crystallographic and magnetic analyses indicate that these ferrites can be classified in the hexagonal ferrite family with the magnetoplumbite structure.

The standard Gibbs energy change for the reactions $CaO + Fe_3O_3 \Rightarrow CaFe_2O_4$ and $2CaO + Fe_3O_3 \Rightarrow Ca_2Fe_2O_5$ has been determined from solid-state electromotive force (e.m.f.) measurements, using CaF_2 as solid electrolyte. The temperature dependence of the standard Gibbs energies of formation from the elements is represented by the equations:

$$\Delta G_f\,(CaFe_2O_4) = -1448.4 \times 10^3 + 128.0\,T + 27.95\,T\ln(T)$$
$$(1030 < T/\text{K} < 1280\ \text{K}$$

$$\Delta G_f\,(Ca_2Fe_2O_5) = -2049.9 \times 10^3 = 12.84\,T + 55.91\,T\ln(T)$$
$$(1140 < T/\text{K} < 1340\ \text{K}$$

By applying a "third law" analysis of the experimental data, the standard enthalpy of formation of $CaFe_2O_4$ from constituent oxides at 298 K was evaluated as:

$$\Delta H_{298}\,(CaFe_2O_4) = -17.5 \pm 0.4\ \text{kJ/mol}.$$

In another study, the compositions of the calcium alumino-silicato-ferrite phases in commercial iron-ore sinters, which are solid solutions based on the ferrites $CaFe_4O_7$, $CaFe_2O_4$, and $Ca_2Fe_2O_5$ of the $CaO–Fe_2O_3$ system, were studied. The sequence of the formation of the calcium alumino-silicato-ferrites and their compositions with Ca_2SiO_4 and Ca_3SiO_5 silicates in sinters were found to be analogous to the crystallization of the ferrite and silicate phases in the ternary $CaO–SiO_2–Fe_2O_3$ system. This allows the phase diagram of this system to be used for the explanation of the formation of the mineral binder compositions for ore grains during sintering of commercial superfluxed sinters.

The hemicalcic ferrite $CaFe_4O_7$ crystallizes in the monoclinic system, space group $C2$ with the parameters: $a = 10.409$ Å, $b = 6.005$ Å, $c = 31.640$ Å, $\beta = 96°30$. Its crystalline structure is related to that of the hexagonal ferrite types of compound. It is constructed by an

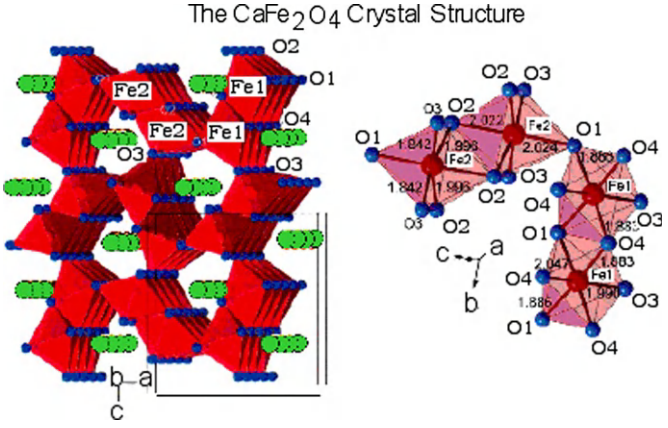

FIGURE 12.11

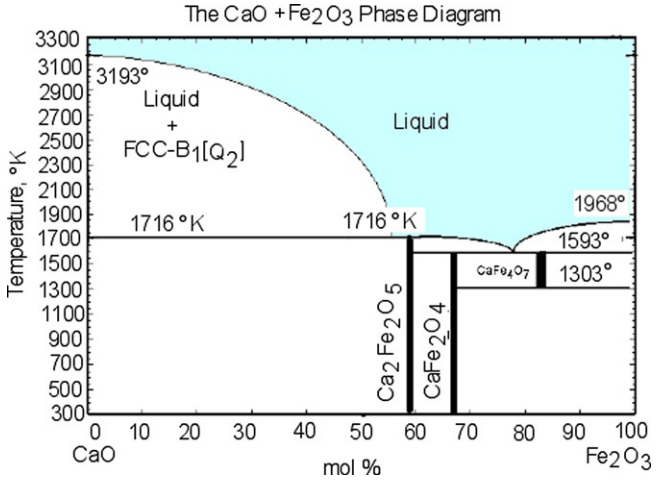

FIGURE 12.12

alternating stacking process along c_0 axis of two structural blocks with the following characteristics:

- A plane of trigonal-based FeO_5 bipyramids surrounded by two mixed Fe···Ca layers
- A triple layer of iron atoms, formed by a plane of mixed tetrahedral and octahedral polyhedra surrounded by two octahedral polyhedra. This type of ordering is also encountered in the spinel structure (mixed and "kagomé" system).

The total conductivity of $CaFe_2O_{4-\delta}$, studied in the oxygen partial pressure range from 10^{-17} to 0.5 atm. at 1023–1223 K, was predominantly *p*-type electronic under oxidizing conditions. The oxygen ion transference numbers determined by the steady-state oxygen permeation and Faraday efficiency measurements varied in the range of 0.2 to 7.2×10^{-4} at 1123–1273 K, increasing with temperature. No evidence of any significant cationic contribution to the conductivity was found. The Mössbauer spectroscopy, thermogravimetry, and XRD measurements showed that the orthorhombic lattice of calcium ferrite is essentially intolerant to the oxygen vacancy formation and to doping with lower valence cations, such as Co and Ni. The oxygen nonstoichiometry (δ) is almost negligible, 0.0046–0.0059 at 973–1223 K and $P(O_2) = 10^{-5}$ to 0.21 atm., and provides a substantial dimensional stability of $CaFe_2O_{4-\delta}$ ceramics. The average linear thermal expansion coefficients, calculated from the controlled atmosphere dilatometry and high-temperature XRD data, were $(9.6–13.9) \times 10^{-6}$/K in the oxygen pressure range from 10^{-8} to 0.21 atm. at 873–1373 K. Decreasing the $P(O_2)$ partial pressure resulted in a modest lattice contraction and in the "p to n" transition indicated by the conductivity and Seebeck coefficient variations. The phase decomposition of $CaFe_2O_{4-\delta}$ occurred at oxygen chemical potentials between the low-$P(O_2)$ stability limit of $CaFe_2O_{5-\delta}$ Brownmillerite and the hematite/magnetite boundary in binary Fe–O system.

An (hk0)-oriented *p*-type $CaFe_2O_4$ (E_g: 1.9 eV) photocathode was prepared, and hydrogen and oxygen gases were produced from a photocell short circuited by connecting the $CaFe_2O_{4-\delta}$ and *n*-type TiO_2 electrodes under illumination without applying an external voltage. The open-circuited voltage was 0.97 V and the short-circuit current was about 200 $\mu A/cm^2$, and the amount of evaluated hydrogen and oxygen gases after 2 days of reaction were about 70 and 4 μmol, respectively. The circuit employed is shown in Fig. 12.13.

The $CaFe_2O_4$ composition was studied, in order to analyze its physical and chemical behavior, in order to verify its stability under industrial conditions, when applied as pigments. The characterization was accomplished using thermal analysis, XRD, nitrogen adsorption, scanning electronic microscopy (SEM) and diffuse reflectance. It was observed that a succession of exothermic reactions occurred, due to the thermal decomposition of the organic material used, and that stability at 700 °C was reached.

The material became completely crystalline at 800 °C. Between 700 and 1100 °C, the color was stabilized, showing an absorption edge in the region of 650 to 750 nm, characteristic of the desired red color.

Single-crystal diffraction data collected for $CaFe_2O_4$ at high pressure reveal that, above 50 GPa, an isosymmetric phase transition (i.e. no change in symmetry) was marked by a volume decrease of 8.4%. X-ray emission spectroscopic data at ambient and high pressure confirmed that the nature of the phase transition was related to the Fe^{3+} high-spin/low-spin transition. The bulk modulus, K_0 , calculated with a Birch–Murnaghan EoS ($K' = 4$) was remarkably different [$K_0 = 159(2)$ GPa for $CaFe_2O_4$ "high-spin" and $K_0 = 235$ GPa for $CaFe_2O_4$ "low-spin"]. Crystal structure refinements revealed a decrease of 12% of the Fe^{3+} crystallographic site volume. The geometrical features of the low-spin Fe^{3+} crystallographic site at high pressure (bond lengths, volume) indicated a relevant decrease of Fe^{3+}–O bond lengths, and the results were in agreement with tabulated values for crystal radii of Fe^{3+} in high- and low-spin state. The reduced crystal size of Fe^{3+} in the low-spin state suggested that in lower Earth mantle assemblages, Fe^{3+} partitioning in crystallographic sites should be strongly affected by the iron spin state.

The 2:1 compound, $Ca_2Fe_2O_5$, has the crystal structure shown in Fig. 12.14.

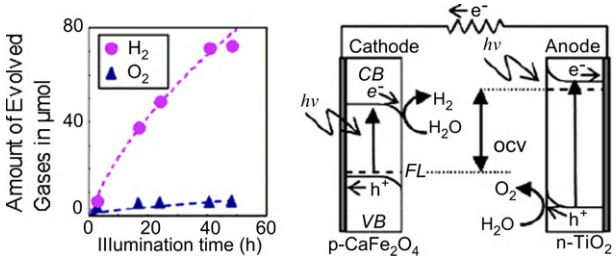

FIGURE 12.13

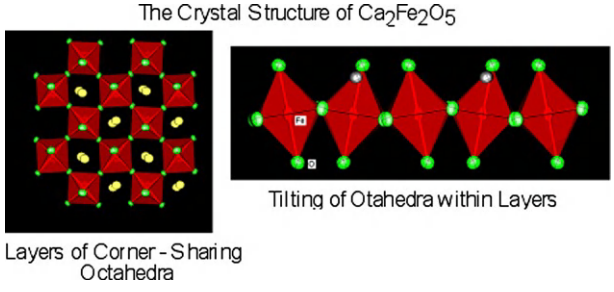

FIGURE 12.14

The transition metal compound, $Ca_2Fe_2O_5$ (CFO), which is an antiferromagnet with a Nëel temperature of 725 K, has been investigated extensively in light of an observed weak ferromagnetism phenomena. Two magnetic transitions at $T_1 \approx 140$ K and $T_2 \approx 60$ K were observed in the CFO crystal. Magnetic measurements indicated that $Ca_2Fe_2O_5$ is an antiferromagnet, with weak parasitic ferromagnetism. The lattice, with the space group *Pcmn*-D_{2h}^{16}, can be considered as an oxygen-deficient perovskite. The magnetic structure as determined from a neutron diffraction study was of G-type, and Fe^{3+} spins are directed approximately along *c*-axis. $Ca_2Fe_2O_5$ showed a first-order phase transition from space group *Pnma* to a modulated structure described by superspace group, *Imma* (00°)s00. The transition starts at 947 K during heating and the reverse transition in cooling conditions starts at 923 K, as determined from differential thermal analysis. In situ high-temperature single-crystal XRD experiments revealed a phase coexistence over a range of ca. 25 K. Data collected in this range showed a good fit to a combined model of the two simultaneously occurring phases, which was refined using the software Jana2006. In situ high-temperature TEM [selected area diffraction (SAED), dark field and high-resolution images] was utilized to prove the existence of *Pnma* and *Imma*(00°) s00 domains within the temperature range of the phase coexistence. Remaining planar defects were observed within the *Pnma* phase at temperatures below the phase transition. From the analysis of high-resolution electron micrographs, these defects were proven to be antiphase boundaries (APBs) with a displacement vector of $\mathbf{R} = 1/2$ [111].

In another paper, calcium ferrite was synthesized in air at 1573 K and thermoelectric properties (direct current electrical conductivity σ, Seebeck coefficient α, thermal conductivity, thermal expansion a_L) were measured from 373 to 1050 K in air. The Seebeck coefficient was positive over all temperatures, indicating conduction by holes, and electrical properties were continuous through the *Pnma* ⇒ *Imma* phase transition. Based on the thermopower and conductivity activation energies as well as estimated mobility, polaron hopping conduction was found to dominate charge transport. The low electrical conductivity, <1 S/cm, limits the power factor ($\alpha^2\sigma$), and thus the figure of merit for thermoelectric applications. The thermal conductivity values of ~2 W/m K and their similarity to Ruddlesden–Popper phases implies the potential of the alternating tetrahedral and octahedral layers to limit phonon propagation through Brownmillerite structures. Bulk linear coefficient of thermal expansion ($\sim 14 \times 10^{-6}$/K) was calculated from volume data based on high-temperature in situ XRPD, and showed the greatest expansion perpendicular to the alternating layers.

The oxygen-deficient perovskite, $Ca_2Fe_2O_5$, which is of the Brownmillerite-type of structure, exhibits a structural phase transition at ca. 970 K from space group *Pnma* ($a = 0.54$ nm, $b = 1.48$ nm, $c = 0.56$ nm) to a modulated structure with an aperiodic sequence of FeO_4 tetrahedral chains, described by the superspace group *Imma*(00)s00. In situ high-temperature TEM (transmission electron micrographs) were was used in order to prove the co-existence of both phases within a coexistence range of ca. 25 K. Polycrystalline material was pulverized, sonicated in ethanol and dispersed on a holey carbon film on a Cu grid. In-situ TEM was performed using a high-voltage atomic resolution microscope operated at 1250 kV (point resolution 0.12 nm) with a high-temperature heating stage and a drift-compensating device. The hypothesis of phase coexistence was proven by dark-field TEM (DF-TEM), selected-area electron diffraction and high-resolution imaging. At 1100 K, the entire grain under observation showed the modulated structure by the presence of satellite reflections in (h01) layer. The modulation wave vector of $\boldsymbol{q} = 0.58c^*$ determined from the diffraction pattern was in good agreement with results from XRD experiments. By carefully lowering the temperature, the two-phase regime was approached where reflections from the primitive lattice (which are not allowed in the HT phase) and satellite reflections show up simultaneously. The DF micrographs show the coexistence of the phases in real space. Domains of the high-temperature (HT) phase were identified by fringes caused by the modulation. The domains of the low-temperature phase (P_L) grow upon lowering the temperature. Within the P_L phase, residual defects are observed which were analyzed to be APBs. Such APBs are formed during the growth of the P phase when two P_L domains get in contact and are shifted by a displacement vector of $\mathbf{R} = 1/2$ [111] (this centering vector is lost during the HT ⇒ P_L transition). An APB can be modeled in a way such that the substructure of octahedral layers stays intact whereas the configuration of the tetrahedral layers changes across the boundary.

The perovskite-related oxide $Ca_2Fe_2O_5$ takes up additional oxygen under high pressure and elevated temperature. The Mössbauer spectra from a number of preparations establish the existence of new phases that are structurally related to the original lattice. The latter features an ordered arrangement of oxygen vacancies that form alternate layers of octahedral and tetrahedral Fe polyhedra. The introduction of oxygen to give $CaFeO_{2.60}$ initially increases the number of octahedral layers to give a sequence [ootot]. Some of the iron, in the double-octahedral layers, undergoes oxidation to the 5+ oxidation state (by a nominal charge-disproportionation of Fe^{4+} at low temperature). At least six distinct iron sites can be identified, and their coordination numbers

established. It is believed that the charge disproportionation (CD) is reversed with increasing temperature. Further uptake of oxygen to give $CaFeO_{2.69}$ produces some layers with five coordination. Mössbauer spectra revealed the existence of unusually complicated and subtle magnetic interactions, which include spin-reorientation effects. It was proposed that this transformation may be triggered by a change in oxidation state of some of the cations. Oxidation can extend to at least $CaFeO_{2.80}$ before any substantial intergrowth of $CaFeO_3$ becomes apparent. It was clear that a wide range of nonstoichiometry can be achieved by the intergrowth of layers of Fe in different coordination, and the extra oxygen is counterbalanced by the generation of Fe^{5+} cations in octahedral coordination. The CD appears to be established within 2D layers of corner-sharing octahedra.

$Ca_2Fe_2O_5$ powder samples, undoped and doped with Na^+, Mg^{2+}, Al^{3+}, Ti^{4+}, Ge^{4+}, were prepared with different synthesis routes to investigate the origin of the weak ferromagnetic component reported in literature for calcium ferrite single crystals. XRPD and EPR measurements have shown the presence of Fe_3O_4 magnetite as impurity phase in all the samples. This ferrimagnetic phase deeply influences the magnetic behavior with features very similar to those reported in literature for $Ca_2Fe_2O_5$, both powders and single crystals. Our results support the hypothesis that the weak ferromagnetic component observed in $Ca_2Fe_2O_5$ can be also due to the presence of magnetite impurity traces (Fe_3O_4) in the samples.

In the CaO–FeO–Fe_2O_3 system, the compound, $CaFe_3O_5$, is known. As in magnetite, Fe_3O_4, calcium ferrite $CaFe_3O_5$ is an oxide in which electron transfer occurs between the iron ions ($Fe^{3+}/Fe^{2+} = 2$). This intervalence exchange process has been studied by ^{57}Fe Mössbauer spectroscopy and by electrical conductivity measurements. In $CaFe_3O_5$, the Fe^{3+} and Fe^{2+} ions occupy different crystallographic sites and have a deformed octahedral coordination. Each $Fe^{2+}O_6$ octahedron shares an edge with two $Fe^{3+}O_6$ octahedra. In the antiferromagnetic region ($T_n = 282 \pm 2$ K), the Fe^{3+} and Fe^{2+} ions are well differentiated. Thermally-activated electron transfer was observed above T_n in the paramagnetic region and was well characterized by the Mössbauer spectra obtained. These were analyzed using the hypothesis of an electron jump limited to a trimer $Fe^{3+}\cdots Fe^{2+}\cdots Fe^{3+}$ which leads to a relaxation time of 180 ns at 298 K and 80 ns at 400 K. Within this temperature interval, the process follows the Arrhenius Law with an activation energy of 0.10 eV. Electrical conductivity measurements led to similar results with an activation energy of 0.09 ± 0.02 eV.

In another study, solid-state calcium ferrite formation reactions between different kinds of iron oxides and CaO under controlled $P(O_2)$ pressures at 1273 K have been investigated. The calcium ferrite formation rates were evaluated, using a thermogravimetric (TG) method. The phase identification and quantification of calcium ferrites in the experiment have been carried out by using XRD method (the Rietveld method). It was found that intermediate calcium ferrite phases of $CaFe_2O_4$ and $CaFe_3O_5$ are formed prior to the $Ca_2Fe_2O_5$ formation when Fe_2O_3 and Fe_3O_4 were used as a starting iron oxide, respectively. When starting from wüstite, intermediate calcium ferrite phases are not formed. The rates of $Ca_2Fe_2O_5$ formation are found to be different depending on the starting reactant iron oxide phases. The $Ca_2Fe_2O_5$ formation rate from wüstite is faster than that from Fe_3O_4, and that from Fe_3O_4 is faster than that from Fe_2O_3. It is also found that the $Ca_2Fe_2O_5$ formation rate starting from Fe_3O_4 decreases with $P(O_2)$, but that starting from wüstite is independent from $P(O_2)$.

In the Fe^{4+}-containing system of CaO–FeO_2, the compound, $CaFeO_3$, is known. Mössbauer spectroscopy of $CaFeO_3$ suggested a "charge disproportion" reaction of Fe^{4+} into Fe^{3+} and Fe^{5+} below 290 K. Crystal structure was investigated at 298 and 113 K (in a "charge disproportionate" state) by using a monochromated synchrotron radiation facility. The crystal structure was found to be similar to $GdFeO_3$ with *Pbnm* at 293 K. At 113 K, two kinds of nonequivalent Fe cations (which could be assigned to Fe^{3+} and Fe^{5+}) form a NaCl-type arrangement on the Fe sublattice; the space group is monoclinic $P2_1/n$ which is one of the subgroups of *Pbnm*. On the difference Fourier map, a residual peak was observed at the center of Fe···O bond; this suggests the strong covalent mixing between e_g(Fe) levels and 2p(O) ones. The Fe···O···Fe bond angle in $CaFeO_3$ was determined to be about 160°, which significantly differs from the 180° angle bonding of $SrFeO_3$. It indicated that the e_g bandwidth in $CaFeO_3$ is narrowed and that eventually the itinerant nature was suppressed. This accounted for the observation that the charge disproportion tends to occur in $CaFeO_3$ with decrease in temperature.

In another paper, stoichiometric $CaFeO_3$ was prepared and was characterized by crystallographic, magnetic and electrical measurements. A slight tetragonal distortion from the ideal cubic perovskite structure was found. The tetra-molecular unit cell has units of: $a = 5.325$ (3) Å and $c = 7.579$ (5) Å. The susceptibility showed a maximum at about 115 K and the temperature dependence of electrical resistivity changed from metallic to semiconductive in the vicinity of the magnetic transition temperature. These indicate a phase transition from the metallic-paramagnetic (the HT phase) to the semiconductive-antiferromagnetic phase. The Mössbauer spectra indicated that a charge-disproportionation (CD) $2Fe^{4+} \Rightarrow Fe^{3+} + Fe^{5+}$ associates with the transition. Using a diamond anvil cell, ^{57}Fe Mössbauer

spectroscopy has been carried out on the perovskite oxide $CaFeO_3$ under high pressures up to 65 GPa at various temperatures.

The critical temperature of the CD (CD reaction: $2Fe^{4+} \Rightarrow Fe^{3+} + Fe^{5+}$) and a magnetic ordering have been determined as a function of pressure. The CD occurs at an almost constant temperature of about 290 K in the pressure range of 0–17 GPa. At an increase of the pressure above 20 GPa, the CD reaction was suppressed and its critical temperature reduced to lower than 6 K. On the other hand, the magnetic ordering temperature of 125 K at an ambient pressure rises to 400 K at 34 GPawithout the occurrence of the CD. This suggests that the different charged particles control the charge and spin order separately in $CaFeO_3$.

In situ ^{57}Fe Mössbauer spectroscopy and XRD on $CaFeO_3$ ($Fe^4{:}t^3{}_2e^1$) under pressure have revealed a first-order high-spin ($S = 2$) to low-spin ($S = 1$) transition near 30 GPa. The spin and structure transition were an alternative manifestation of the electronic instabilities of the σ-bonding Fe–O– ($Fe^{4-} + Fe^{4+}$), $0 < \sigma < 1$, occurs at a $T_t \sim 290$ K. Such instabilities, found at the transition, localized to itinerant σ-band electrons, reflected a sensitivity to interactions with the lattice.

Single crystals of $CaFeO_3$ have been synthesized at high pressure of 4.5 GPa with a mixture of $KClO_4$, NaCl and $CaCl_2$ as flux and oxidizing agent. The temperature dependence of the resistivity showed a metal-insulating transition at 295 K, corresponding to the charge disproportionation. A screw-spin type antiferromagnetic transition was observed at 115 K. These results indicated that the crystals were free from oxygen defect. Energy-dispersive powder XRD study with synchrotron radiation at high pressure revealed that a moisture was necessary to crystal growth of $CaFeO_3$.

In addition, a compound, $CaFe_5O_7$, which is a mixture of Fe^{4+} and Fe^{3+} is known. This compound can be written as: $CaO{\cdot}3FeO_2{\cdot}2Fe_2O_3$. It has the unit cell parameters of: $a = 3.064$ Å, $b = 5.2199$ Å, $c = 17.822$ Å, $\alpha = \beta = 90°$, $\gamma = 107.07$ Å^3, cell volume = 272.46 Å^3.

It was found that $CaFe_5O_7$ does not disappear by decomposition to three solid phases at about 1050 °C, as suggested by previous phase diagrams. Instead it disappears by melting at about 1100 °C. On cooling, part of the liquid solidifies to a eutectic structure, Wustite + $Ca_2Fe_2O_5$. A revision of Turkdogan's oxygen potential–temperature diagram was proposed in order to account for the new information. No other information is available concerning this compound.

In the Fe^{5+}-containing system of $CaO–Fe_2O_5$, no compounds are known.

In the hexavalent iron, Fe^{6+}-containing system of $CaO–FeO_3$, the compound, $CaFeO_4$ is known. $CaFeO_4$ is commonly prepared directly from the reaction between an aqueous solution of the acetate or chloride of the metals and potassium ferrate:

$$K_2FeO_4(aq) + Ca(C_2H_3O_2)_2 \Rightarrow CaFeO_4(s) + 2KC_2H_3O_2(aq)$$

The results showed that the synthesized sample mainly consists of calcium ferrate (VI), and calcium ferrate (VI) hydrate that mainly exists as $CaFeO_4{\cdot}2H_2O$ with the highest obtained purity of 74.9%. Calcium ferrate is a strong oxidizer when acidified. It has the structure form shown in Fig. 12.15.

The structure is orthorhombic with space group *P-nam* and unit cell parameters of: $a = 9.230$ Å, $b = 10{,}706$ Å, $c = 3.024$ Å. The coordination of the oxygen atoms around Fe is that of a distorted octahedron. Around the

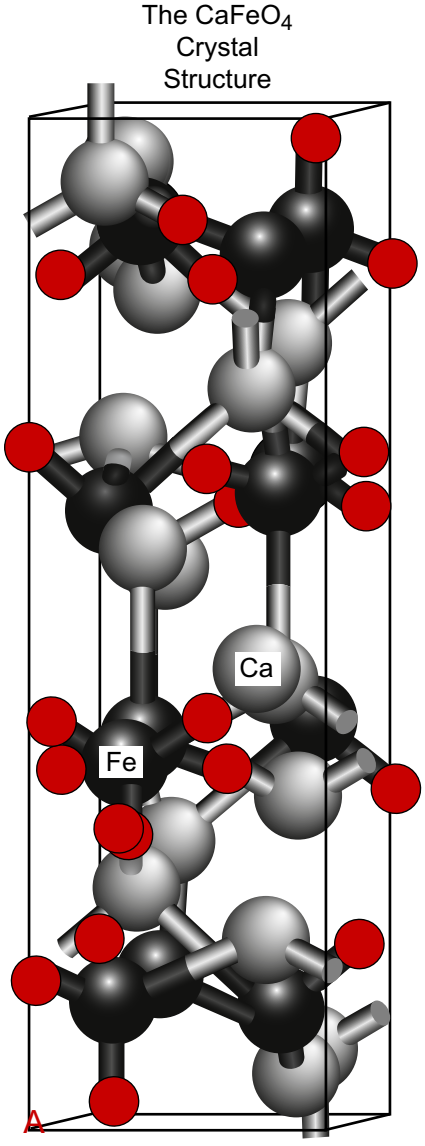

FIGURE 12.15

Ca atoms, there is a coordination of nine oxygen atoms in a configuration first noted for $CaTi_2O_4$, for which $CaFeO_4$ is isomorphous.

Calcium ferrate, $CaFeO_4$, is offered commercially for use as an antibacterial water treatment chemical. Calcium ferrite, $CaFe_2O_4$, is also offered for sale commercially with the CAS number of 12013-33-1.

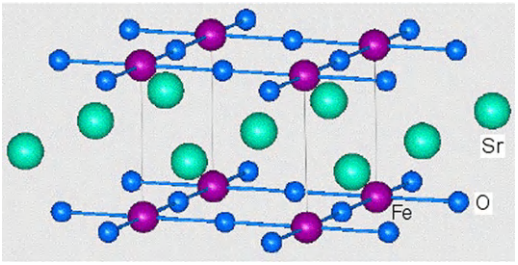

FIGURE 12.17

12.2.4. Strontium Oxy-Iron Compounds

SrO forms a number of ferrites and ferrates with iron oxides.

In the Fe^{2+}-containing system of SrO–Fe, the compound, $SrFeO_2$ is known. Its structure was presented above in the Ca section. One phase diagram presented for the system of SrO–FeO reveals no compounds formed, just a eutectic at 1630 K (Fig. 12.16).

However, $SrFeO_2$ exhibits some exotic magnetic and electronic properties. Neutron diffraction studies show the presence of antiferromagnetic ordering with a very high Nëel temperature ($T_N = 473$ K). The magnetic ordering temperature is very high in spite of the low-dimensional nature of the magnetic structure. Magnetic properties of $SrFeO_2$ have been examined by DFT band structure and total energy calculations. Ab-initio calculation of the zone center phonon modes has also been reported. It is of fundamental and practical importance to understand the stability of $SrFeO_2$ and $CaFeO_2$ as a function of temperature and pressure. Detailed lattice dynamical calculations to understand the phonon properties of these compounds have been carried out.

One view of this structure has the form shown in Fig. 12.17.

A first-principles study of $SrFeO_2$, an infinite-layer oxide with Fe atoms in a perfect square-planar coordination down to essentially 0 K was carried out. The results revealed this striking behavior relies on the double occupation of the $3d_z^2$ orbitals of high-spin Fe^{2+}. Such an electronic state results from the hybridization of iron's $3d_z^2$ and 4s orbitals, which enables a large reduction of the intra-atomic exchange splitting of the $3d_z^2$ electrons. The generality of the phenomenon was discussed.

The magnetic structure has the form shown in Fig. 12.18.

$SrFeO_2$ presents Fe^{2+} ions in a square-planar coordination, forming unprecedented infinite FeO_2 layers that remain undistorted down to at least 4.2 K. As a result of the tetragonal point symmetry at the Fe site, the z^2 orbital is fully symmetric and can hybridize with the formally-empty Fe-4s state. It has been concluded that $SrFeO_2$, an unusual high-spin Fe^{2+} layered phase, is free from structural instabilities and exhibits strong magnetic interactions. The hybridization of iron's $3d_z^2$ and 4s orbitals, which results in a large

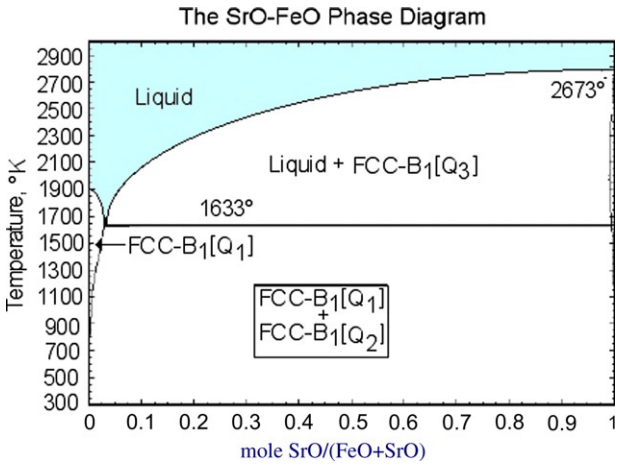

FIGURE 12.16

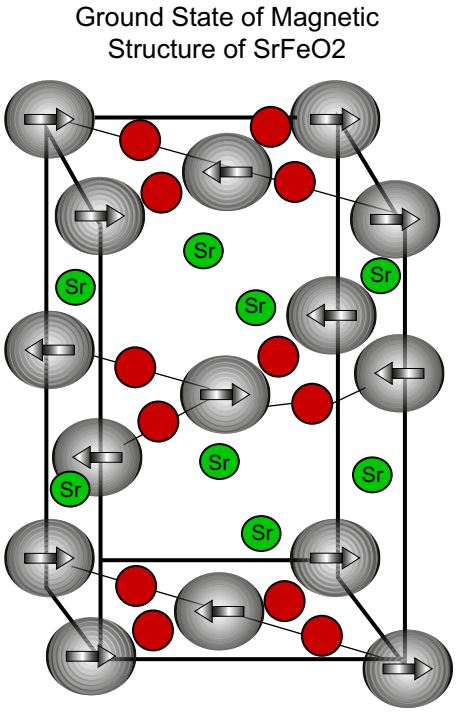

FIGURE 12.18

reduction of the intra-atomic exchange splitting associated to the z^2 electrons, is the key feature to understand the structural stability of the material.

Single-crystal thin films of $SrFeO_2$, which is an oxygen-deficient perovskite with "infinite layers" of $Fe^{2+}O_2$, were prepared by using CaH_2 for low-temperature reduction of epitaxial $SrFeO_{2.5}$ single-crystal films deposited on $KTaO_3$ substrates. This reduction process, removing oxygen ions from the perovskite structure framework and causing rearrangements of oxygen ions, topotactically transforms the Brownmillerite $SrFeO_{2.5}$ to the *c*-axis oriented $SrFeO_2$. The layered oxoferrate(II) $SrFeO_2$ (see scheme: Fe = red, Sr = yellow, O = gray) was synthesized by the reduction of the slightly oxygen-deficient perovskite $SrFeO_{3-x}$ at 400 K with CaH_2 in a form of topotactical reaction (Fig. 12.19).

The square-planar-coordinated iron(II) ions in $SrFeO_2$ exhibit a high-spin d^6 configuration with a doubly occupied d orbital. $SrFeO_2$ orders antiferromagnetically at an unusual high Nëel temperature of $T_N = 473$ K.

In the system, $SrFeO_{3-x}$, an example is the family of compounds, $SrFeO_x$ ($2.5 \leq x \leq 3$). The valency of the Fe ions can be changed by heating a sample in either an oxidizing or a reducing environment. As a result, the oxygen content can vary in between 2.5 and 3. For example, in $SrFeO_{2.875}$, some Fe ions can be assigned to the oxidation state +3 and others to +4. The oxygen vacancies order so that FeO_5 square pyramids are formed. These $SrFeO_x$ compounds are examples of defect perovskites. Their chemistry can be described according to the homologous series $A_nB_nO_{3n-1}$, $n = 2-\infty$.

The ordering of these vacancies is shown in Fig. 12.20. Fe ions are located in both square pyramids and in octahedra.

An infinite-layer structure artificial superlattice thin film, $[CaFeO_2]/[SrFeO_2]$, was prepared by low-temperature reduction of a Brownmillerite-structure artificial superlattice thin film $[CaFeO_{2.5}]/[SrFeO_{2.5}]$ grown on a $SrTiO_3(001)$ substrate. Both the $Ca_2Fe_2O_5$ and $Sr_2Fe_2O_5$ Brownmillerite structures changed to the infinite-layer structures and an unusual square-planar-coordination FeO_2 plane was stabilized in the infinite-layer superlattice. The low-temperature reduction technique is useful for making superlattices that cannot be made by simply depositing a film.

$Sr_3Fe_2O_5$ adopts the *Immm* space group (No. 71), $a = 3.5168$ Å, $b = 3.95405$ Å, $c = 20.91727$ Å, $Z = 2$. Sr(1) on 2*c* (0.5,0.5,0), Sr(2) on 4*i* (0,0,0.31242), Fe on 4*i* (0,0,0.09616(4)), O(1) on 2*a* (0,0,0), O(2) on 4*j* (0.5,0,0.59526), O(3) on 4*i* (0,0,0.19298), with 100% occupancy, $B_{iso}(Sr(1)) = 0.792$ Å^2, $B_{iso}(Sr(2)) = 0.486$ Å^2, $B_{iso}(Fe) = 0.3$ Å^2, $B_{iso}(O(1)) = 0.723$ Å^2, $B_{iso}(O(2)) = 0.791$ Å^2, $B_{iso}(O(3)) = 0.847$ Å^2, $R_p = 2.95\%$, $R_{wp} = 3.76\%$.

The oxidation behavior of $Sr_3Fe_2O_5$ in air has been described. The transformation to $Sr_3Fe_2O_{7-y}$ ($y \leq 1$) phase takes place dramatically above 250 °C. The oxygen content of the sample, using a TG method, was $y \sim 0.4$ as checked by its XRD pattern. It was noted that there is ambiguity in determining the oxygen content by TG because $Sr_3Fe_2O_5$ is highly air sensitive, in contrast to $SrFeO_2$. It was found that if the $Sr_3Fe_2O_5$ sample was exposed to air even for a short period of time for the setup of the TG experiment, a part of it was readily oxidized, absorbed water and was even decomposed (to yield, e.g. $Sr_3Fe_2(OH)_{12}$). Initial decrease in weight below 150 °C was due to the release of water. For this reason, a precise estimation of the oxygen content by TG could be not made. If no reaction of $Sr_3Fe_2O_5$ occurred during the setup, the observed weight gain would give the final composition: $Sr_3Fe_2O_{7-y}$ ($0.5 < y < 0.9$). This is somewhat smaller than the expected composition of $Sr_3Fe_2O_{6.6}$. It was concluded from the TG measurements that the oxygen content of the product is far less than 6 ($y = 1$) that had been thought as the lower limit. The oxygen content of $y = 0.5$ was evident from Neutron diffraction, synchrotron XRD, and Mössbauer spectroscopy measurements.

When the composition of $SrFeO_2$ was changed by the addition of FeO to form $SrFe_2O_3$, a new class of

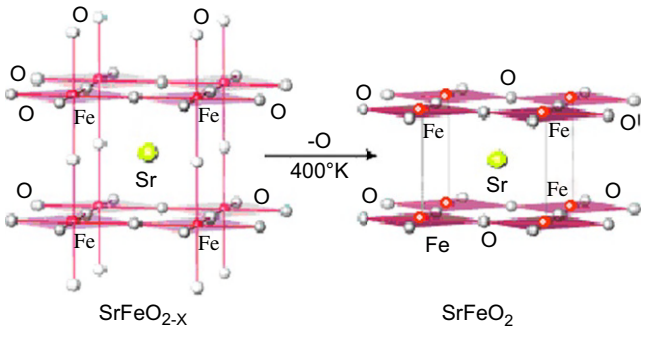

FIGURE 12.19

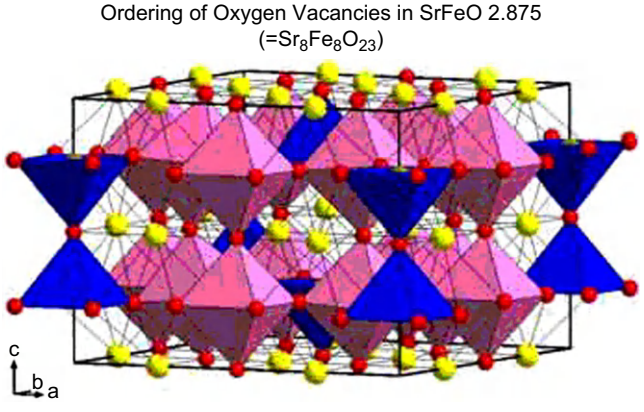

FIGURE 12.20

commercial magnets was born. The birth of this family of magnets was announced in 1952 (isotropic) and 1954 (anisotropic). Also known as Ceramic magnets, they are manufactured in two compositions: Strontium based ($SrFe_2O_3$) and Barium based ($BaFe_2O_3$). The process consists in milling the raw materials compound into single crystals approximating a single domain in size. Then the powder is wet or dry pressed in a dye under the influence of a magnetic field. After that, the pressed compacts are sintered in ovens at high temperatures. Their good coercive force results from the high crystal anisotropy of Barium and Strontium iron oxide. Nowadays, Ceramic magnets are the lowest cost magnetic material available. They are very hard and brittle and must be ground to obtain close mechanical tolerances.

Ferrite has a high resistance against corrosion, acids, salts, lubricants and gases. Ceramic, also known as Ferrite, magnets (general composition $BaFe_2O_3$ or $SrFe_2O_3$) have been commercialized since the 1950s and continue to be extensively used today due to their low cost. Ferrite magnets are stronger than AlNiCo and have much better corrosion resistance than Rare Earth MAGNETS. Ceramic Magnets offer the best value when comparing cost with other type of magnets. Ceramic (Ferrite) magnets are inexpensive, moderate in magnetic strength, and they are easily magnetized in a variety of formats. Ceramic magnets offer good corrosion resistance and generally do not require a coating or plating. Consideration should be given to the grade of alloy when exposing Ceramic magnets to temperature extremes. Ceramic (Ferrite) magnets have good resistance to external demagnetization fields because of its high-Intrinsic Coercive Force (Hci). This resistance and low cost make Ceramic magnets a popular choice for electromechanical applications.

In the Fe^{3+}-containing system of SrO–Fe_2O_3, the phase diagram has the form shown in Fig. 12.21.

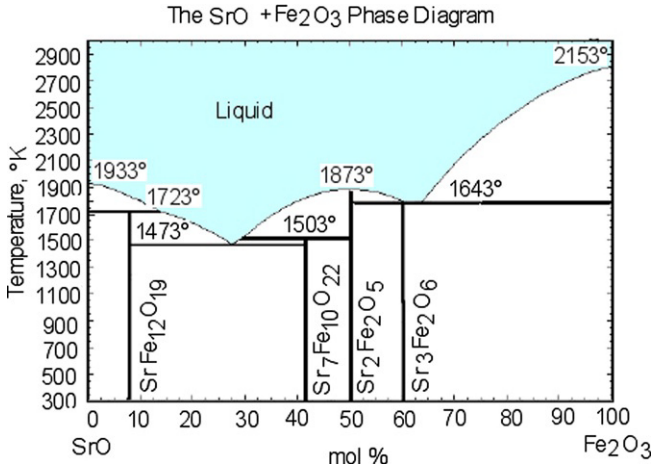

FIGURE 12.21

$Sr_2Fe_2O_{5+x}$ materials have been tested as thin film gas sensors since the reversible uptake of oxygen at elevated temperatures can readily occur.

This is accompanied by significant changes in the electrical conductivity that can be monitored as a sensor transduction signal in a sensing thin film device. Therefore, thermal stability of the sensing thin film system plays an important role in the sensitivity, rapid response and longer term signal reproducibility of the sensors. This arises because the ceramic-based gas sensors are operated at elevated temperature. As a result, the films may react with the underlying substrate changes at $Sr_2Fe_2O_{5+x}/Al_2O_3$ (sapphire and sintered alumina) interface were observed after a further annealing at 850 °C for 5 h. Additional layer appears in the interface indicating that interface reactions occurred.

The change in structure is shown in Fig. 12.22. Single crystals of strontium monoferrite, $SrFe_2O_4$, were obtained by growth from a melt at 1550 °C. The monoclinic crystals belong to space group $P112_1/n$ ($a = 8.1098$, $b = 9.1177$, $c = 10.8495$ Å, $\beta = 91.53°$, $V = 801.96$ Å^3, $Z = 2$, $D_{calc} = 4.36$ g/cm^3).

The structure was solved by direct methods using a single-crystal diffraction data set. The main structural features of $SrFe_2O_4$ are layers of FeO_4 tetrahedra perpendicular to the *a*-axis (Fig. 12.23).

The stacking of the layers parallel to [100] results in a three-dimensional (3D) framework containing tunnels, where the strontium cations are located. Individual

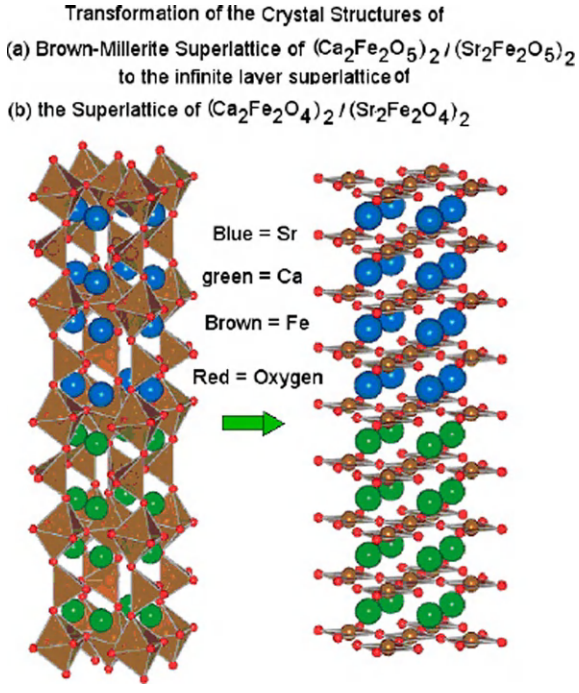

FIGURE 12.22

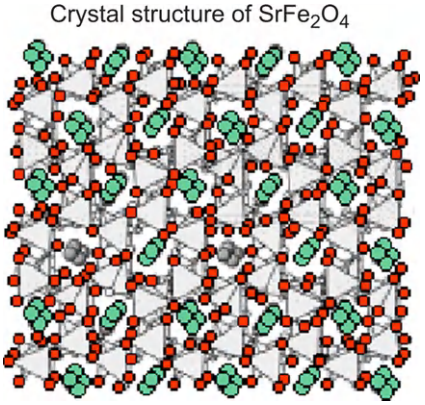

FIGURE 12.23

layers can be described as being built by the condensation of di-trigonally shaped, six-membered, tetrahedral rings. The sequence of up (U) and down (D) pointing apices within a single ring is UUUDDD. The structure belongs to the family of the zeolite ABW-type structures and is the first zeolite type compound with exclusively ferric iron occupying the tetrahedral positions of the framework.

The citrate–nitrate gel combustion route was used to prepare $SrFe_2O_4$(solid), $Sr_2Fe_2O_5$(solid) and $Sr_3Fe_2O_6$(solid) powders and the compounds were characterized by XRD analysis. Different solid-state electrochemical cells were used for the measurement of e.m.f. as a function of temperature from 970 to 1151 K. The standard molar Gibbs energies of formation of these ternary oxides were calculated as a function of temperature from the e.m.f. data and are represented as:

$$\Delta G_f\ (SrFe_2O_4(solid)\ T)/kJ/mol = -1494.8 + 0.3754\ (T/K)\ (970 \le T/K \le 1151)$$

$$\Delta G_f\ (Sr_2Fe_2O_5(solid)\ T)/kJ/mol = -2119.3 + 0.4461\ (T/K)\ (970 \le T/K \le 1151)$$

$$\Delta G_f\ (Sr_3Fe_2O_6(solid)\ T)/kJ/mol = -2719.8 + 0.4974\ (T/K)\ (969 \le T/K \le 1151)$$

Standard molar heat capacities of these ternary oxides were determined from 310 to 820 K using a heat flux type differential scanning calorimeter. Based on second law analysis and using the thermodynamic database–FactSage software, thermodynamic functions such as $\Delta_f H^\circ(298.15\ K)$, $S^\circ(298.15\ K)$ $S^\circ(T)$, $C_p^\circ(T)$, $H^\circ(T)$, $\{H^\circ(T) - H^\circ(298.15\ K)\}$, $G^\circ(T)$, produced the free energy functions, $\Delta_f H^\circ(T)$ and $\Delta_f G^\circ(T)$ for these ternary oxides. These were also recalculated from 298 to 1000 K.

Permanent ferrite magnets are made of **hard ferrites**, which have a high coercivity and high remanence after magnetization. These are composed of iron and Ba and Sr oxides. The high coercivity means the materials are very resistant to becoming demagnetized, an essential characteristic for a permanent magnet. They also conduct a magnetic flux well and have a high magnetic permeability. This enables these so-called *ceramic magnets* to store stronger magnetic fields than iron itself. They are cheap, and are widely used in household products. The maximum magnetic field B is about 0.35 T and the magnetic field strength H is about 30 to 160 kiloampere turns per meter (400–2000 oersteds). The density of ferrite magnets is about 5 g/cm^3. The most common hard ferrites are **Strontium ferrite**, $SrFe_{12}O_{19}$ ($SrO{\cdot}6Fe_2O_3$), a common material for permanent magnet applications. They are used in e.g. subwoofer magnets and as a medium for magnetic recording. The crystal and magnetic structure of strontium ferrite $Sr_4Fe_4O_{11}$ ($SrFeO_{2.75}$) has been investigated using neutron powder diffraction and magnetic susceptibility measurements over the temperature range 1.5–293 K and by Mössbauer spectroscopy at room temperature. $Sr_4Fe_4O_{11}$ is orthorhombic (symmetry group *Cmmm*) over the temperature range 1.5–293 K. Its crystal structure contains two iron sites occupied by trivalent and tetravalent iron. The trivalent magnetic moments order antiferromagnetically below $T_N = 232(4)$ K and the magnetic unit cell coincides with the chemical cell. The ordered moments are parallel to the *b*-axis and the tetravalent iron moments form a magnetically frustrated sublattice. The extrapolated value of the Fe^{3+} moment is 3.55(5) μbar at 0 K. The antiferromagnetic coupling occurs by the superexchange mechanism and is mediated by oxygen ions. There are no signs of long-range magnetic order in the tetravalent sublattice down to 1.5 K.

The crystal structure of the $Sr_2Fe_2O_5$ Brownmillerite compound has been investigated using electron diffraction and high-resolution electron microscopy (HREM). The S–$Sr_2Fe_2O_5$ structure demonstrates 2D order: the tetrahedral chains with two mirror-related configurations (L and R) are arranged within the tetrahedral layers according to the -L-R-L-R- sequence, and the layers themselves are displaced with respect to each other over 1/2[111] or 1/2[11†] vectors of the Brownmillerite unit cell, resulting in different ordered stacking variants. A unified superspace model is constructed for ordered stacking sequences in Brownmillerites based on the average Brownmillerite structure with $a = 5.5298$ Å, $b = 15.5875$ Å, $c = 5.6687$ Å, and $(3+1)$-dimensional superspace group: $I2/m(0\beta\gamma)0s$, $q = \beta b^* + \gamma c^*$, $0 \le \beta \le 1/2$, $0 \le \gamma \le 1$.

In another paper, the evolution of crystal and magnetic structures of $Sr_2Fe_2O_5$ with temperature was studied using neutron powder diffraction. The measurements were made in the temperature range from room temperature up to 1223.15 K and the patterns were analyzed using the Rietveld method. The oxide undergoes two-phase transitions: (i) from the antiferromagnetic to the paramagnetic state and (ii) from the orthorhombic to the cubic structure. The changes in structural parameters

with temperature were discussed and a new structural model was proposed for the cubic phase. The diffraction patterns were refined using *Ib'm'*2, *Ibm*2, and *Fm*3*c* symmetry groups in the antiferromagnetic, the paramagnetic and the cubic state, respectively, with $Z = 4$.

Atomistic simulations of the structures and defect energetics of the two mixed-conducting strontium ferrite materials, $Sr_2Fe_2O_5$ and $Sr_4Fe_6O_{13}$, have been reported. Oxygen Frenkel defects are found to be the predominant intrinsic defects in both materials, with the Frenkel energy in the intergrowth structure, $Sr_4Fe_6O_{13}$, being much less than that in $Sr_2Fe_2O_5$ or other known oxide ion conductors. Formation of electronic defects under oxidizing and reducing conditions is calculated to be more favorable in the $Sr_4Fe_6O_{13}$ intergrowth structure than in $Sr_2Fe_2O_5$. Comparison of solution energies for cobalt incorporation shows $Sr_4Fe_6O_{13}$ has a slight preference for Co^{2+} being located on lower coordination sites, whereas in $Sr_2Fe_2O_5$, Co^{2+} ions located on tetrahedral sites are most favorable. Binding energy calculations suggest the possible formation of Co^{2+}-vacancy clusters with increasing Co^{2+} concentration. The rapid oxide ion conductivity in $Sr_4Fe_{6-x}Co_xO_{13\pm\delta}$ membranes is thought to arise from a combination of factors: a low-oxygen Frenkel energy (to produce an intrinsic population of mobile interstitial oxide ions and vacancies), low-migration energy barriers, and ease of distortion of polyhedra. A comparison of the two structures is shown in Fig. 12.24.

The pressure dependence of the crystal structure of $Sr_2Fe_2O_5$ has been studied at room temperature by angle-dispersive synchrotron XRPD and ^{57}Fe Mössbauer spectroscopy using diamond anvil cell techniques. Between 11 and 14 GPa the low-pressure Brownmillerite-type structure with an equal number of octahedrally and tetrahedrally coordinated Fe^{3+} sites is transformed into a tetragonal perovskite-like structure. The Mössbauer spectra of the high-pressure phase reveal two subspectra with an intensity ratio of about 3:1. The Mössbauer parameters are consistent with two five-coordinated Fe^{3+} sites differing in the degree of structural distortion of the FeO_5 polyhedra. Laser annealing of the high-pressure phase at 15 GPa induces a transformation from the tetragonal perovskite into an orthorhombic phase that is isostructural with $Sr_2Mn_2O_5$. This structure consists of a network of corner-sharing FeO_5 square pyramids. The coordination number of the Sr^{2+} ions has increased from 8 in the Brownmillerite structure to 10 in the $Sr_2Mn_2O_5$-type phase.

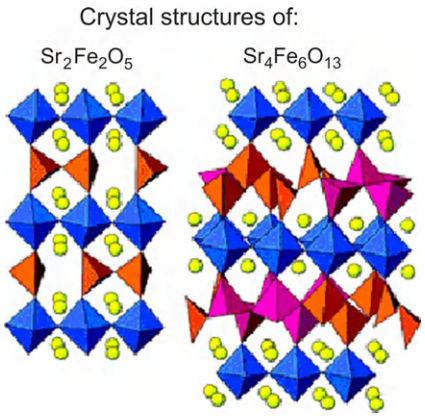

FIGURE 12.24

The electronic structure of strontium ferrite $Sr_3Fe_2O_6$ was calculated using the tight-binding linear muffin-tin orbital method in the local spin density approximation of DFT with Coulomb correlations correction (LSDA + U). The semiconducting character of the spectrum with charge transfer energy gap of 1.82 eV was obtained in reasonably good agreement with experimental data. The iron ions are found to be in the high-spin state. The calculated value of the local spin magnetic moment of Fe^{3+} ion is 3.94 μbar. This is not typical for trivalent iron ion in the high-spin state. It was shown that the strong hybridization between Fe^{3d} and O^{2p} orbitals favors the $d^6\underline{l}$ configuration of Fe^{3+} ion, where $\underline{l}$ is a hole in the oxygen p shell. The mechanism of oxygen transport in ferrite was discussed based on the total energy calculations of the different spatial configurations of oxygen vacancies.

The system $Sr_3Fe_2O_{6.00-6.90}$ forms a single phase of unusual structure, derived from that of perovskite by interleaving nonmagnetic layers of strontium-oxygen ions between pairs of perovskite layers composed of strontium–iron–oxygen ions. It exhibits a broad range of oxygen stoichiometry. As a consequence of this structure and the variable valence of the iron atom, a variety of magnetic interactions are possible. Between 1.4 and 300 K specimens of higher oxygen concentration are antiferromagnetic. The Nëel temperature (130 K for $Sr_3Fe_2O_{6.90}$) approaches 0 K at the composition $Sr_3Fe_2O_{6.50}$. Specimens in this range have positive paramagnetic Curie temperatures, indicative of a ferromagnetic type interaction. Specimens with oxygen content lower than $Sr_3Fe_2O_{6.50}$ exhibit strongly negative $Fe^{3+}\cdots O^{=}\cdots Fe^{3+}$ exchange. At the lower oxygen limit, $Sr_3Fe_2O_{6.00}$, strongly antiferromagnetic ordering appears stable to above room temperature.

The crystal and oxygen defect structure of the $n = 2$ Ruddlesden–Popper phase, $Sr_3Fe_2O_{6+\delta}$, has been studied by in situ high-temperature neutron powder diffraction in the temperature range $20 \leq T \leq 900$ °C in air. The analysis of the neutron diffraction data revealed the presence of structural oxygen vacancies on both the O(1) sites linking the octahedra along the *c*-axis and the O(3) sites in the FeO_2 planes of the perovskite layers. The oxygen vacancies on the O(3) site increase with temperature up to 0.25 per formula unit at $T = 900$ °C. This result supports the previously

proposed oxygen ion diffusion mechanism in $Sr_3Fe_2O_{6+\delta}$ that involves the migration of vacancies from an O(3) site to an adjacent O(1) site. The total linear expansion along the *c*-axis $a_c = 17.7 \times 10^{-6}/K$ mainly affects the perovskite block while the width of the rock salt layers remains stable with temperature. Oxygen defect phases such as $Sr_3Fe_2O_7$, $Sr_3Fe_2O_{6.5}$ and $Sr_3Fe_2O_6$ are antiferromagnetic compounds with semiconductor-like behaviors and thermally activated carriers.

In the Fe^{2+}–Fe^{3}-containing system of SrO–Fe_3O_4 (FeO–Fe_2O_3), the compound, $Sr_2Fe_3O_6$ is known. Different samples of the ferrite "$Sr_4Fe_6O_{13}$" = $(Sr_2Fe_3O_{6+\delta})_2$, synthesized in air, nitrogen, and argon, have been studied by HREM. It was shown that this oxide is oxygen deficient, i.e. $Sr_4Fe_6O_{13-\delta}$, and that its structure is modulated. The electron diffraction study showed that the modulation vector is $pa^* + qc^*$, with $p = (1 - \delta)/2$ varying in the range [0.4–0.5] and q close to one. It was shown that the component of the modulation vector along *c* induces complex modulated structures. It was also demonstrated that oxygen nonstoichiometry corresponds to the generation of the microphases, $[Sr_8Fe_{12}O_{26}]$, $[Sr_2Fe_3O_6]_n$, whose first integral member $n = 1$ (which corresponds to p = 0.4), was isolated for the first time by synthesis under argon. Structural models involving intergrowths of single perovskite $[Sr_2Fe_3O_6]\infty$ layers with complex $[Sr_2Fe_4O_{7-\delta}]\infty$ layers involving two kinds of pyramidal ribbons, FeO_5 trigonal bi-pyramids and FeO_5 distorted tetragonal pyramids, were used to explain the oxygen deficiency.

In the Fe^{4+}-containing system of SrO–FeO_2, reduction with CaH_2 of the double-layered perovskite $Sr_3Fe_2O_7$ yielded the novel two-legged $S = 2$ ladder compound $Sr_3Fe_2O_5$. Together, with the synthesis of $SrFeO_2$, this opens up new avenues for solid-state chemistry and physics of a series of *n*-legged ladders $Sr_{n+1}Fe_nO_{2n+1}$. The $SrFeO_x$ system with $2.5 \leq x \leq 3.0$ was prepared and examined by differential thermal analysis, thermogravimetry, powder XRD, and the ^{57}Fe Mössbauer effect. The following diagram illustrates the structural transformation from FeO_6 octahedra in $Sr_3Fe_2O_7$ to FeO_4 squares in $Sr_3Fe_2O_5$, which occurs via the intermediate $Sr_3Fe_2O_6$ (Sr-blue, O-red, Fe-yellow) (Fig. 12.25).

Four single phases with different structures exist in this system, the typical compositions of which are $SrFeO_3$, $SrFeO_{2.86}$, $SrFeO_{2.73}$, and $SrFeO_{2.50}$.

NB-the latter three compositions can be transposed into formulas with an even number of atoms- that is:

$$SrFeO_{2.50} = Sr_2Fe_2O_5$$
$$SrFEO_{2.73} = Sr_{11}Fe_{11}O_{30}$$

The compounds, $SrFeO_{2.86}$ and $SrFeO_{2.73}$, have tetragonal and orthorhombic structures, respectively. Their unit cells are related to the cubic perovskite cell for $SrFeO_3$ in the manner that $a_t \approx 2 \times 2^{1/2}\ a_c$, $c_t \approx 2a_c$ and $a_o \approx 2c_o \approx 2 \times 2^{1/2}\ a_c$, $b_o \approx 2a_c$, where the suffixes c, t, and o stand for the cubic, tetragonal, and orthorhombic structures, respectively. These single-phase compositions suggest the ideal series of $SrFeO_{3\text{-}1/n}$, where $n = \infty$, 8, 4, and 2 to give an oxygen ratio of $x = 3$, 2.875, 2.75, and 2.50, correspondingly. The vacancy ordered phase of $SrFeO_{2.86}$, $SrFeO_{2.73}$, and $SrFeO_{2.50}$ show first-order transitions to their cubic, disordered structures at 250, 320, and 830 °C, respectively. Formation of the cubic, disordered structure above a temperature depending on the composition is suggested for the whole composition range. The material $Sr_2FeO_{3-\delta}$ is thought to exist in four different oxygen phases within the range of $3 - \delta = 2.5$–3.32.

The cubic $SrFeO_3$ $(3 - \delta = 3)$, tetragonal $Sr_8Fe_8O_{23}$ $(3 - \delta = 2.875)$ and the orthorhombic phases, $Sr_4Fe_4O_{11}$ $(3 - \delta = 2.75)$, and $Sr_2Fe_2O_5$ $(3 - \delta = 2.5)$ have the general structure shown in Fig. 12.26.

Evidence from Mössbauer measurements have suggested that these are the only stable phases that exist in this range and stoichiometries other than these are an inhomogeneous mixture of the four phases.

The cubic phase $SrFeO_3$ has helical antiferromagnetic order at ~140 K and is highly conductive. It consists of well-ordered FeO_6 octahedra where the Fe ions have 4+ valence. By reducing the oxygen content, $Sr_8Fe_8O_{23}$ was obtained. This phase shows antiferromagnetic order at ~70 K and displays an order of magnitude increase in resistivity below this temperature.

The phase is made up of square pyramidal FeO_5 that forms dimers. These are adjacent to distorted FeO_6 and

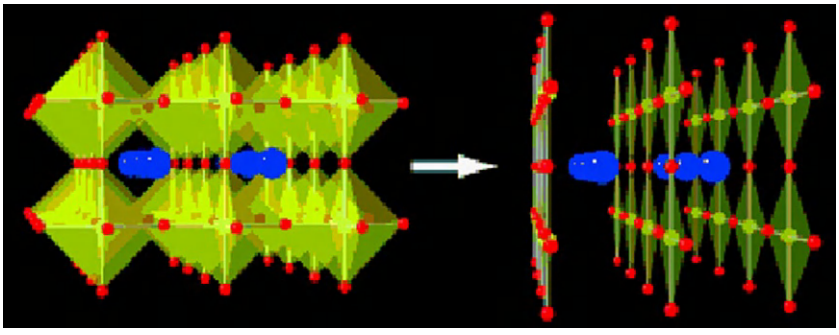

FIGURE 12.25

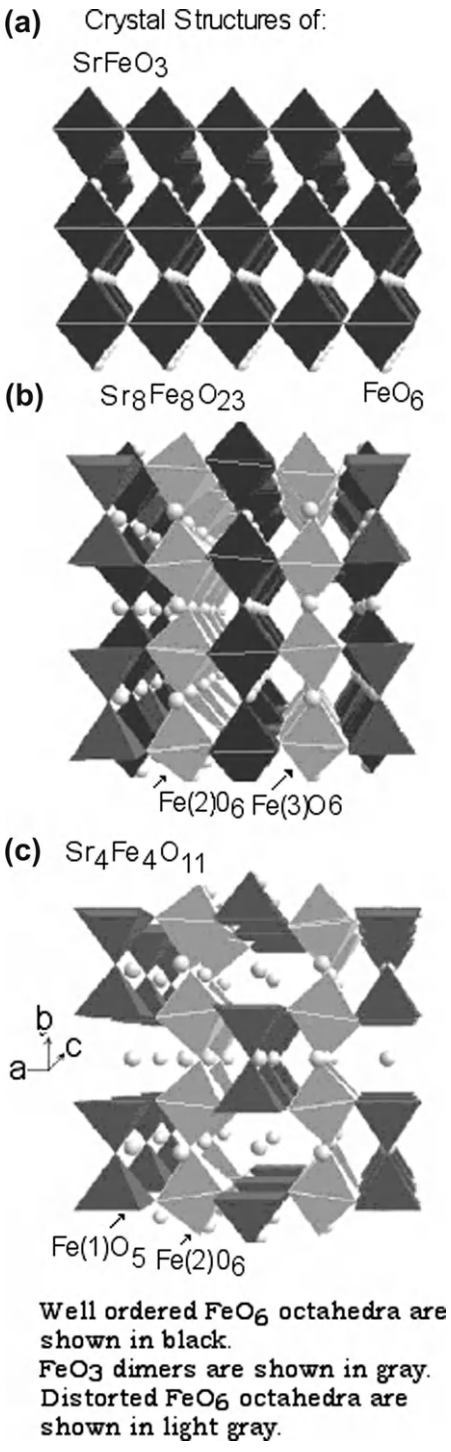

FIGURE 12.26

well-ordered FeO_6 octahedra. It has been argued that the Fe ions in the distorted FeO_6 octahedra have a valence of 3.5+ while the other Fe ions are both 4+. The increase in resistivity was said to be caused by charge ordering of the $Fe^{3.5+}$ ions to Fe^{3+} and Fe^{4+} reminiscent of the partial charge ordering Verwey transition in Fe_3O_4. Further reduction in oxygen content then leads to the $Sr_4Fe_4O_{11}$ phase, that is antiferromagnetic below ~230 K and shows semiconductor-like resistivity. It contains square pyramidal FeO_5 units that form dimers and distorted FeO_6 octahedra. The Fe ions are believed to have valences of 3+ and 4+, respectively.

The Fe^{4+} ions in the FeO_6 octahedra have antiferromagnetic order, while the Fe^{3+} ions are not believed to possess any long-range magnetic order. However, there is evidence that spin frustration in the Fe^{3+} moments can cause weak spin glass behavior below ~50 K. The $Sr_4Fe_4O_{11}$ phase also shows an exchange bias like effect below ~230 K, which is well above the temperature where the spin glass behavior is observed. The magnetic ordering temperature of the Fe^{4+} ions is around 230 K, suggesting they play a key role in the mechanism causing the exchange bias like effect. Finally, there is the oxygen deficient, $Sr_2Fe_2O_5$ phase. It has the Brownmillerite structure and is composed of FeO_4 tetrahedra and distorted FeO_6 octahedra, where the Fe ion is believed to have a valence of 3+.

Evidence has been presented for a novel phase of ideal composition $SrFeO_{2.75}$ in the system $SrFeO_{3-\delta}$ ($0.5 < \delta < 0$). Electron diffraction evidence suggested an orthorhombic or body-centered tetragonal symmetry with lattice parameters related to the cubic perovskite lattice parameter a_c by $a\ 2\sqrt{2}a_c$, $b\ \sqrt{2}a_c$, $c\ 2\sqrt{2}a_c$. A plausible model for the structure was presented which is related to that of $SrFeO_{2.5}$. Powder XRD photographs revealed only a simple cubic perovskite cell for $SrFeO_{2.75}$, presumably because the ordered domains giving rise to the superstructure observed in electron diffraction are small in extent. At other intermediate compositions, slow cooling gave mixtures of the novel phase and either $SrFeO_{2.5}$ or $SrFeO_3$. The two-phase regions narrow at high temperatures and TG studies at 1 atm. pressure of oxygen indicated a single phase between $SrFeO_{2.5}$ and $SrFeO_{2.75}$, stable between 500 and 950 °C.

The compound, Sr_2FeO_4, has the general form shown in Fig. 12.27.

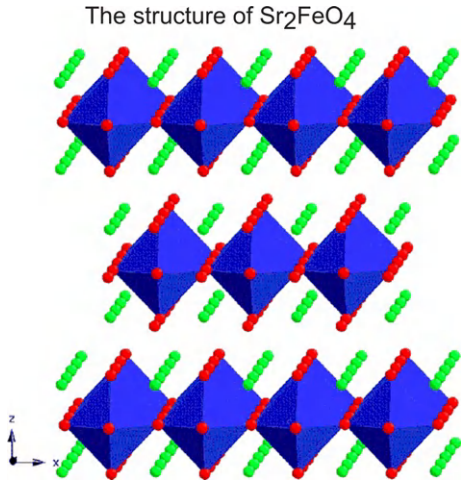

FIGURE 12.27

In order to make clear the phase relationships and non-stoichiometry of the $SrFeO_{2.5}$–$SrFeO_3$ system at elevated temperatures, measurements were made using high-temperature gravimetry and high-temperature powder XRD analysis under the controlled oxygen partial pressure of $1–10^{-5}$ atm. at temperatures above 400 °C. At 400–900 °C, the system was found to consist of the $SrFeO_{2.5+\delta}$ phase of the Brownmillerite-type structure with small oxygen excess-type nonstoichiometry and the $SrFeO_{3-\delta}$ phase of the cubic perovskite-type structure with large oxygen-deficient type nonstoichiometry. At temperatures above 900 °C, the Brownmillerite phase transformed to the perovskite type and the system was composed of only the cubic perovskite-type phase.

In the following diagram, structural changes of a reductive reaction are shown in Fig. 12.28.

In this diagram, reduction of Sr_2FeO_4 (left) to Sr_2FeO_3 (right) to obtain a one-leg spin ladder, i.e. a one-dimensional (1D) spin chain is shown in Fig. 12.28(a); a reductive reaction of $Sr_4Fe_3O_{10}$ (left) to $Sr_4Fe_3O_7$ (right) to obtain a three-leg spin ladder, i.e. a 3D spin chain, is shown in Fig. 12.28(b). These materials all contain iron in the tetravalent ⇒ divalent state, i.e. $Fe^{4+} \Rightarrow Fe^{2+}$. These Fe ions are believed to have valences corresponding to these values.

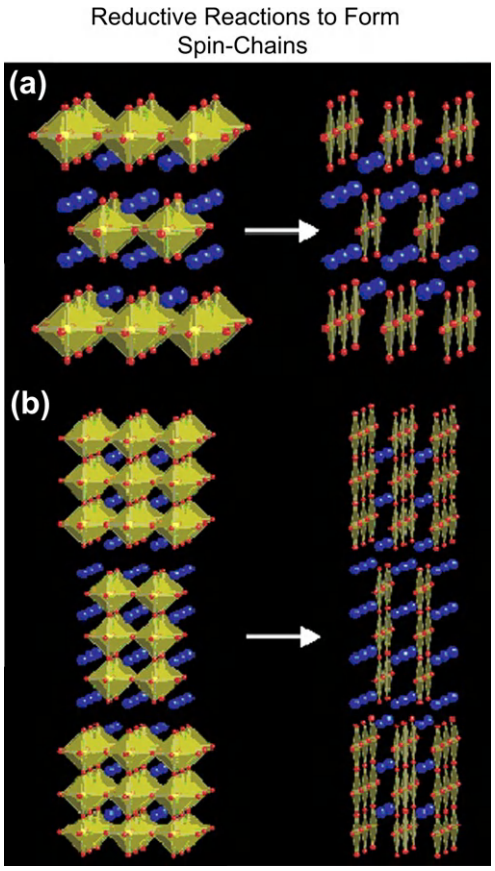

FIGURE 12.28

The solid-state reactions occurring in the system $SrCO_3$–Fe_2O_3 (composition Fe/X (iron cationic fraction) = 0.5–0.923) have been studied. At Fe/X = 0.5, $Sr_2Fe_2O_{5-\delta}$ (Brownmilletite) forms by annealing of the activated mixture at 850 °C under nitrogen while the non-stoichiometric perovskite ($SrFeO_{3-\delta}$) is the equilibrium product when annealing is performed under air.

At Fe/X = 0.66 a mixture of $SrFe_2O_4$ and $SrFe_2O_5$ is the final product no matter what is the annealing atmosphere. The enthalpies of reaction at these compositions have been determined. By increasing iron content (Fe/X = 0.8), the annealing at 850 °C of the activated mixture leads to $SrFe_2O_4$, $SrFe_2O_5$ and $SrFe_{12}O_{19}$ (indicated as the usual term for strontium hexaferrite).

Finally at Fe/X = 0.923, $SrFe_{12}O_{19}$ is produced from the mechanically activated mixture at temperatures lower (approximately 800 °C) than in the case of conventional solid-state route. In the case of the last two compositions, no reaction enthalpy could be determined as the process is too slow.

Strontium ferrate(IV), Sr_2FeO_4, crystallizes with a tetragonal unit cell, $I4/mmm$, $a = 3.8642(1)$, $c = 12.3968(2)$ Å, and $V = 185.1$ Å^3. The structure of this compound is of the K_2NiF_4 type as refined by Rietveld analysis of powder XRD data. This material contains iron(IV) in a very slightly distorted octahedral environment. The behavior of the high-pressure magnetic, structural, and transport properties of Sr_2FeO_4 (Fe^{4+}), an antiferromagnetic ($T_N = 60$ K) insulator, using diamond anvil cells up to $P = 30$ GPa. With the increasing pressure a significant increase in the conductance (σ) is observed and at $P_M = 19$ GPa the compound metallizes as concluded from the onset of a negative slope of $\delta(T)$. Magnetic studies performed with ^{57}Fe Mössbauer spectroscopy showed no evidence of a magnetic moment collapse at P_M and beyond, up to $P = 30$ GPa. No structural phase transition occurs up to 30 GPa. The coexistence of magnetic moments and metallic state in this oxide is clear evidence of an intra-ligand p–p gap as proposed by the XPS data analyses.

Sr_2FeO_4 and $Sr_3Fe_2O_7$ have been studied using low-temperature powder neutron diffraction, magnetometry and ^{57}Fe Mössbauer spectroscopy. Sr_2FeO_4 orders antiferromagnetically at 60 K while the Nëel temperature of $Sr_3Fe_2O_7$ is 110 K. At room temperature the Mössbauer spectrum of $Sr_3Fe_2O_7$ is interpreted in terms of a disproportionation, $Fe^{4+} \leftrightarrow Fe^{3+} + Fe^{5+}$, though neutron diffraction measurements show a single, crystallographic iron site. Neutron diffraction data collected below the Nëel temperatures from Sr_2FeO_4 (4 K) and $Sr_3Fe_2O_7$ (6 and 90 K) only show broad weak magnetic reflections indicative of antiferromagnetic ordering in two dimensions. Mössbauer data collected below T_N from Sr_2FeO_4 indicate the presence of at least four magnetically different Fe^{4+} sites. The pseudobinary system, SrO–Fe_2O_{3+x}, is

known in air to produce $Sr_{m+1}Fe_mO_{3m+1}$ ($m = 1, 2, 3, \infty$) Ruddelsden–Popper phases and the phases, $Sr_4Fe_6O_{14}$ and $SrFe_{12}O_{19}$. Sr_2FeO_4 ($m = 1$) decomposes in air at 930 °C to form SrO and $Sr_3Fe_2O_{7-\delta}$. The $Sr_4Fe_3O_{10-\delta}$ ($m = 3$) is stable in air up to 850 °C. Above this temperature, it disproportionates into $Sr_3Fe_2O_{7-\delta}$ ($m = 2$) and $SrFe_{3-\delta}$ ($m = \infty$). In an oxygen atmosphere, $Sr_3Fe_2O_{7-\delta}$, $SrFeO_{3-\delta}$, $Sr_4Fe_6O_{12-\delta}$ and $SrFe_{12}O_{19}$ are stable to 1520, 1600, 1245 and 1450 °C, respectively. $Sr_3Fe_2O_{7-\delta}$ is tetragonal, $SrFeO_{3-\delta}$ is tetramorphic: (a) cubic perovskite ($\delta = 0$), (b) tetragonal ($\delta = 0.16$–0.24), (c) orthorhombic ($\delta = 0.25$) and (d) Brownmillerite ($\delta = 0.5$). $Sr_4Fe_6O_{12-\delta}$ and $SrFe_{12}O_{19}$ are orthorhombic and hexagonal (magnetoplumbite), respectively.

In the Fe^{5+}-containing system of SrO–Fe_2O_5, no compounds are known. This valence state is not stable and decomposes readily:

$$2Fe^{5+} \Rightarrow Fe^{4+} + Fe^{6+}$$

In the Fe^{6+}-containing system of SrO–FeO_3, the compound of $SrFeO_4$ is known. Cathodes comprised of Fe(VI) salts, and capable of three-electron reduction, have been found to be useful for the formation of energetic super-iron batteries. This study presented a synthesis procedure for $SrFeO_4$ or strontium super-iron cathodic salts, and introduced mixed salts containing barium and strontium cations, $Sr_xBa_{(1-x)}FeO_4$. The XRD and first IR spectra of $SrFeO_4$ were presented, and compared to known spectra of K_2FeO_4 and $BaFeO_4$. The measured solubility of $SrFeO_4$ was found to be low in concentrated KOH electrolytes (0.001 mM in 13.5 M KOH), a factor of use in alkaline cathodic chemistry. AAA batteries were prepared and discharged with this new cathode, and exhibit high discharge energies, approaching, but slightly lower than those previously observed for barium super-iron alkaline batteries. The discharge energy further approaches the barium cell when the mixed cathode salt is employed, particularly for $x = 0.25$–0.5 in $Sr_xBa_{(1-x)}FeO_4$.

The synthesis and analysis of a range of Fe (VI) compounds has been presented. Fe(VI) compounds have also been variously referred to as ferrates or super-iron compounds. Fe(VI) salts with detailed syntheses in this paper include high-purity alkali earth Fe(VI) salts $BaFeO_4$, and $SrFeO_4$. Two conventional, as well as two improved Fe(VI) synthetic routes, were presented.

The conventional syntheses include solution phase oxidation (by hypochlorite) of Fe(III), and the synthesis of less soluble super-irons by dissolution of Fe_4^{2-}, and precipitation with alternate cations. These new routes include a solid synthesis route for Fe(VI) salts and the electrochemical synthesis (include in situ and ex situ synthesis) of Fe(VI) salts. Fe(VI) analytical methodologies summarized were FTIR, ICP, titrimetric, UV/VIS, XRD, Mössbauer and a range of electrochemical analyses. Fe(VI) compounds have been explored as energy storage cathode materials in both aqueous and non-aqueous phase in "super-iron" battery configurations, as well as novel oxidants for synthesis and water treatment purification. Preparation of reversible Fe(VI/III) thin film toward a rechargeable super-iron cathode was also presented. In addition, the preparation of unusual $KMnO_4$ and zirconia coatings on Fe(VI) salts, via organic solvent deposition, was summarized. These coatings can stabilize and activate Fe(VI) salts in contact with alkaline media.

$SrFe_{12}O_{19}$ is offered for sale commercially as a basis for manufacturing ceramic magnets.

12.2.5. Barium Oxy-Iron Compounds

Similar to the SrO system, barium forms a number of oxy-ferrites and oxy-ferrates. No Ba^0–Fe^0 compounds are known.

In the Fe^{2+}-containing system of BaO–FeO, several compounds are known. The compound, $BaFeO_2$ has been thoroughly studied. Based on the DFT with the generalized gradient approximation plus the on-site Coulomb repulsion method, the electronic, magnetic, and optical properties in infinite-layer iron oxide $BaFeO_2$ were elucidated. It was revealed that $BaFeO_2$ possesses a $P4/mmm$ tetragonal symmetry that is similar with $SrFeO_2$. The structure has the general form shown in Fig. 12.29.

Another view of this perovskite structure is shown in the following diagram. The J_{1-4} spin vectors within the lattice are also shown in Fig. 12.30.

It has been demonstrated that the single downspin electron of Fe^{2+} occupies the d^2 level instead of the double degenerate dx^2-y^2 and d^2 levels predicted from Jahn–Teller instability in crystal field theory. Magnetic structure shows great contrast between intralayer and interlayer exchange interactions. Linear dielectric function, on the other hand, exhibits obvious anisotropic behavior between in plane and out of plane responses.

If FeO is added to $BaFeO_2$, the compound, $BaFe_2O_3$ is obtained. This compound has found extensive usage in Industry as a solid-state ceramic magnet. The following

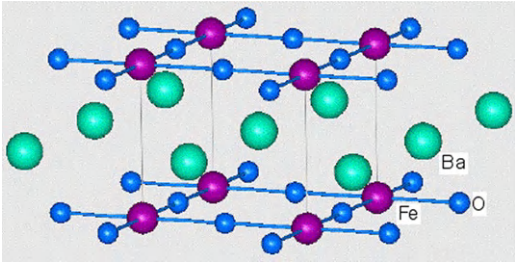

FIGURE 12.29

Perspective View of the Tetragonal Structure of $BaFeO_2$
The Large, Midle and Small Spheres Represent the Ba, Fe and O Ions Respectively. The Spin - Exchange Paths, J1 , J2, J3 and J4 are also Indicated

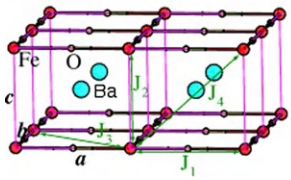

	J_1	J_2	J_3	J_4
$SrFeO_2$ (expt.)	7.04	2.18	0.43	-0.23
$SrFeO_2$ (opt.)	7.91	2.29	0.30	-0.30
$CaFeO_2$ (opt.)	8.90	3.24	0.35	-0.45
$BaFeO_2$ (opt.)	5.81	1.34	-0.29	-0.16

FIGURE 12.30

diagram presents some of the shapes that have been manufactured (Fig. 12.31).

Disc magnets can be pressed into any desired shape or size, then magnetized. They are readily available in various forms, are hard and brittle, but cannot be drilled or machined. They are stable and resistant to demagnetization, cost effective, corrosion resistant. Uses include: Electric motors, Audio speakers, Electronic equipment, Industrial automation systems, Conveyor belts, and Automotive sensors.

In the Fe^{3+}-containing system of $BaO–Fe_2O_3$, the phase diagram shows five (5) compounds. These are the 7:2, 2:1, 1:2, 2:3 and 1:6 compounds in the $BaO–Fe_2O_3$ system (Fig. 12.32).

FIGURE 12.31

Another phase diagram has been published purporting to show the most stable compounds in the $BaO–Fe_2O_3$ system. This is shown as follows for purposes of comparison in Fig. 12.33.

Little is known concerning the $Ba_7Fe_4O_{13}$ compound. Its structure has not been published at this date and no information is readily available.

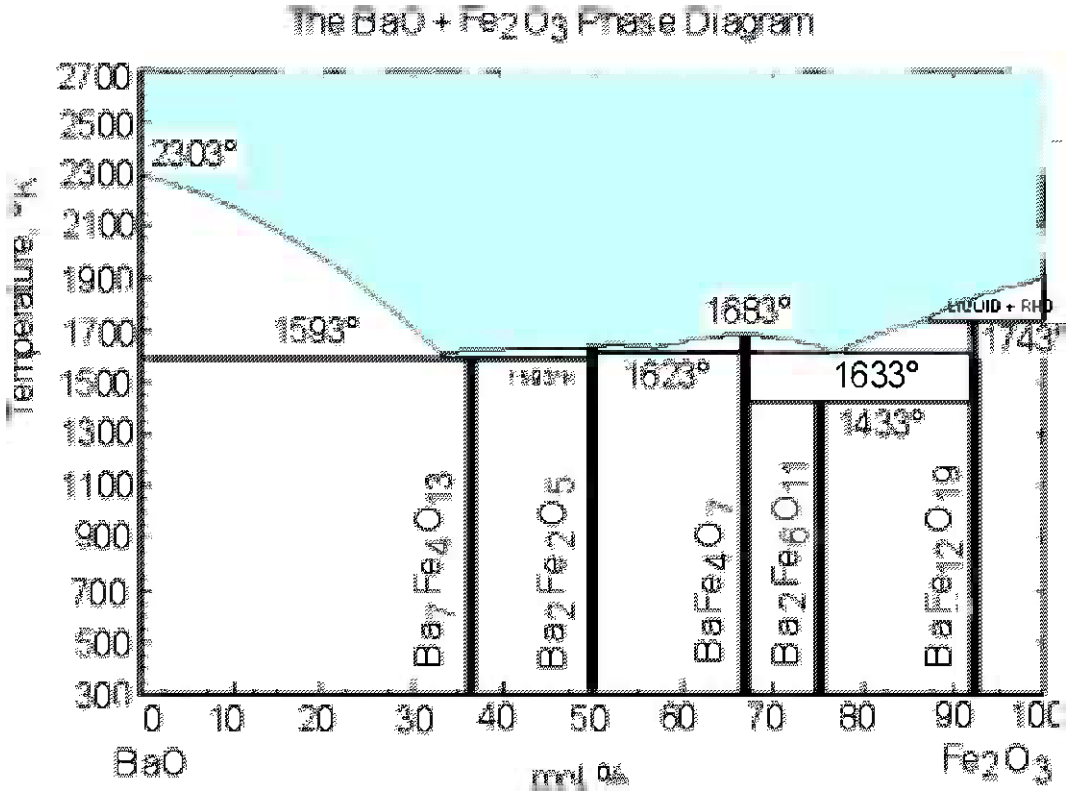

FIGURE 12.32

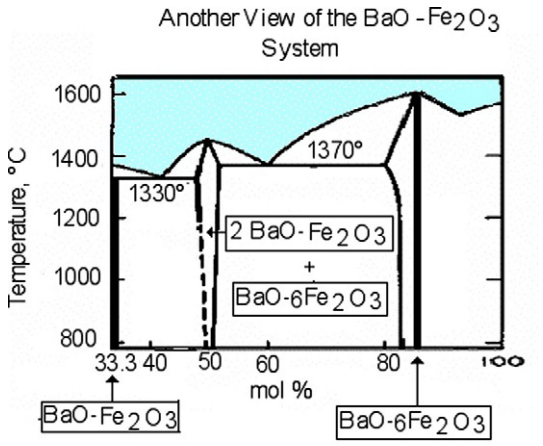

Fig 12-33

FIGURE 12.33

The compounds, $Ba_2Fe_2O_5$, $BaFe_4O_7$, and $BaFe_{12}O_{19}$ will be described below. The $BaO–6Fe_2O_3$ compound has the structure shown in Fig. 12.34.

This compound is also used as a powder for manufacturing ceramic magnets. It is pressed in the desired shape and then magnetized at about 230–330 °C. Upon cooling, the magnet is hard and retains its magnetic remanance. Other compounds that have been tried for this purpose include $BaFe_{15}O_{23}$ and $BaFe_{18}O_{27}$. The only difference between these compounds is the number of Ba^{2+} ions actually incorporated within the unit cell.

The literature concerning the $Ba_2Fe_6O_{11}$ compound is not extensive. $Ba_2Fe_6O_{11}$ has been synthesized in both powder and single-crystal form from the ternary composition 15 B_2O_3–37.5 Fe_2O_3–47.5 BaO (mole ratio). Although a metastable phase, it displays great stability and will not decompose even when subjected to temperatures as high as 1200 °C. When heated to the melting point, this compound recrystallized to $BaFe_{12}O_{19}$ and $BaFe_2O_4$, the equilibrium compounds. A Mössbauer experiment at 300 K revealed that a hyperfine spectrum is present leading to the conclusion that the compound is magnetically ordered. XRD data are given. It crystallizes in the orthorhombic space group *Pnnm*: $a = 23.024(10)$ Å, $b = 5.181(3)$ Å, $c = 8.900(4)$ Å, $Z = 4$. Fe^{3+} ions occur in both octahedral (Fe···O mean distance: 2.02 Å) and tetrahedral (Fe···O mean distance: 1.865 Å) coordination. Two types of Ba^{2+} ions are found, with six and seven neighboring oxygen atoms. The structure consists of sheets of edge-shared FeO_6 octahedra that are connected by means of corner-shared tetrahedra. $Ba_2Fe_6O_{11}$ is a complex antiferromagnet with a Nëel temperature $T_N = 488$ K.

Although it does not appear within the phase diagram, the 1:1 compound, $BaFe_2O_4$ is said to be tetramorphic. However, only two of these structures have been established. This compound undergoes polymorphic transitions at 800 and 1000 °C. The resulting phases are: γ-$BaFe_2O_4$ stable up to 800 °C with an orthorhombic phase, β-$BeFe_2O_4$, stable between 800 and 1000 °C, pseudo orthorhombic phase, crystal parameters of: $a = 5.463$ Å, $b = 9.461$ Å, $c = 8.710$ Å. α-$BaFe_2O_4$, stable above 1000 °C, and hexagonal with $a = 5.158$ Å, $c = 9.016$ Å, space group $P6_322$ with $Z = 2$. If β-$BaFe_2O_4$ is quenched, a metastable form, δ-$BaFe_2O_4$ is obtained with $a = 5.442$ Å, $b = 9.325$ Å and $c = 8.670$ Å, that is stable at room temperature. A comparison of two of these structures is shown in Fig. 12.35.

Numerous studies have been completed on the phase relations in the Ba–Fe–O ternary system. Three stable phases have been reported, $Ba_2Fe_2O_5$, $BaFe_2O_4$ and the hexagonal $BaFe_{12}O_{19}$. In spite of this, many apparently contradictory results have been found, with the hexagonal $BaFe_2O_4$ phase usually being reported as coexisting with $BaFe_{12}O_{19}$ and Fe_2O_3, along with other metastable phases. They are mutually insoluble in each other as solids, and both coexist up to 1000 °C. After this point, a third phase, the metastable hexagonal $BaFe_{12}O_{11}$, can also develop until the ternary mixture reaches its liquid point at 1175 °C. There it reverts to $BaFe_{12}O_{19}$ and α-$BaFe_2O_4$ on cooling. Fine-particle spinel ferrites, such as $BaFe_2O_4$, are useful for the low-temperature preparation of high-density ferrites and as suspension materials for ferromagnetic liquids.

Unit cell parameters of γ-$BaFe_2O_4$ are: $a = 5.387$ Å, $b = 8.458$ Å, $c = 10.4244$ Å, $\beta = 113.934°$, $\alpha = \beta = \gamma = 90°$, cell volume is 434.12 Å^3, $Z = 4$. Cell occupancy is shown in Table 12.7.

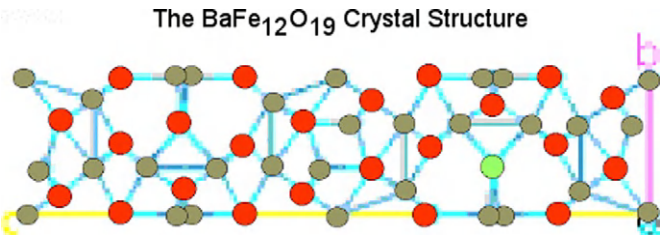

FIGURE 12.34

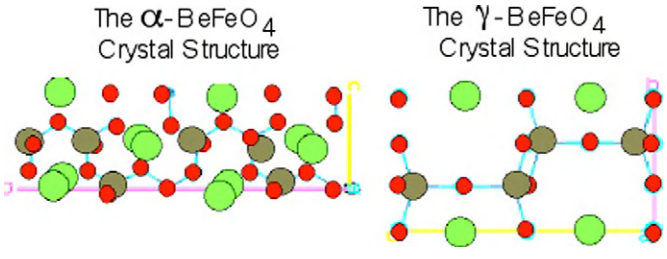

FIGURE 12.35

TABLE 12.7

No.	Site notation	Atom	Multiplicity	Wyckoff	Site symmetry	*x*	*y*	*z*	Occupancy
1	Fe1	Fe	8	b	1	0.209	0.208	0.048	1.0
2	Fe2	Fe	8	b	1	0.222	0.042	0.006	1.0
3	O1	O	8	b	1	0.243	0.463	0.177	1.0
4	O2	O	8	b	1	0.275	0.123	0.191	1.0
5	O3	O	8	b	1	0.281	0.291	0.191	1.0
6	O4	O	4	a	m..	0	0.047	0.0	1.0
7	Ba1	Ba	4	a	m..	0	0.117	0.501	1.0
8	O5	O	4	a	m..	0	0.22	0.0	1.0
9	Ba2	Ba	4	a	m..	0	0.369	0.024	1.0

TABLE 12.8

No.	Site notation	Atom	Multiplicity	Wyckoff	Site symmetry	*x*	*y*	*z*	Occupancy
1	O2	O	6	g	.2.	0.343	0	0	1.0
2	Fe	Fe	4	f	3..	1/3	2/3	0.055	1.0
3	O1	O	2	c	3.2	1/3	2/3	1/4	1.0
4	Ba	Ba	2	b	3.2	0	0	1/4	1.0

δ-$BaFe_2O_4$ has the unit cell parameters of: $a = 5.442$ Å, $b = 8.67$ Å, $c = 9.325$ Å, $\alpha = 90°$, $\beta = 90°$, $\gamma = 90°$, cell volume is: 439.37 Å^3, $Z = 2$. Cell occupancy was not given.

Unit cell parameters for γ-$BaFeO_4$ are: $a = 5.458$ Å, $b = 5.458$ Å, $c = 10.016$ Å, $\alpha = 90°$, $\beta = 90°$, $\gamma = 120°$, cell volume = 232.60 Å^3, $Z = 2$. Cell occupancy is shown in Table 12.8.

Unit cell parameters of δ-$BaFe_2O_4$ are: $a = 5.463$ nm, $b = 8.71$ nm, $c = 9.461$ nm, $\alpha = 90°$, $\beta = 90°$, $\gamma = 90°$, Cell volume = 450.18Å^3, $Z = 2$.

Barium ferrite $Ba_2Fe_2O_5$ has been studied using various techniques. XRD and TEM have shown the phase to crystallize with a monoclinic symmetry, the unit cell being a complex supercell of a cubic perovskite cell. The Mössbauer resonance spectrum exhibits five sextuplets that have been assigned to Fe^{3+} in O*h*, T*d*, and fivefold coordinated sites. Obviously, $Ba_2Fe_2O_5$ does not adopt the Brownmillerite structure of homologous calcium (or strontium) ferrite and the oxygen vacancy ordering is more complex. The compound, $Ba_2Fe_2O_5$ has a complicated structure shown in Fig. 12.36.

Barium ferrite $Ba_2Fe_2O_5$ is a complex perovskite-related structure. The crystal is monoclinic $P2_1/c$, with $a = 6.969$, $b = 11.724$, $c = 23.431$ Å, $\beta = 98.74°$. The composition of one unit cell is $Ba_{28}Fe_{28}O_{70}$. The structure was solved using a combination of HREM, crystallographic image processing (CIP) and electron diffraction. The structure can be described as a perovskite with 14 oxygen positions unoccupied with respect to the ABO_3 stoichiometry in the monoclinic unit cell. These positions can be identified from the potential map obtained by HREM and CIP. They form two linear groups.

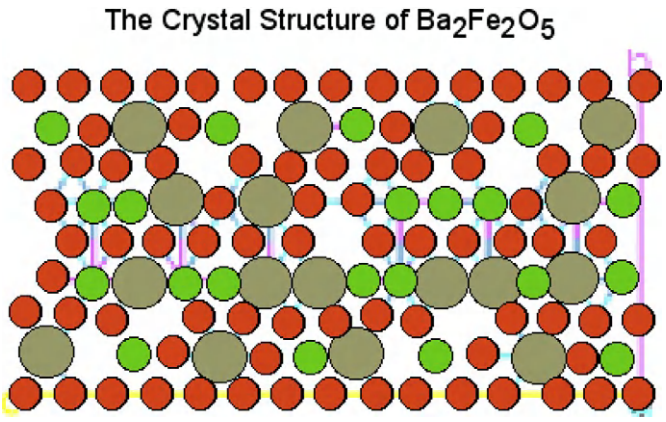

FIGURE 12.36

Seven of them lie on a line along [476]*m* (corresponding to [110]*c* of perovskite), while the seven other symmetry-related positions lie along [46]*m* (corresponding to [101]*c* of perovskite).

Cell occupancy is shown in Table 12.9.

The standard molar Gibbs energy of formation of $BaFe_{12}O_{19}$(solid), $BaFe_2O_4$(solid), $Ba_2Fe_2O_5$(solid), $Ba_3Fe_2O_6$(solid) and $Ba_5Fe_2O_8$(solid) have been determined using solid-state electrochemical technique employing CaF_2(solid) as an electrolyte. The reversible emf values have been measured in the temperature range from 970 to 1151 K. The oxygen chemical potential corresponding to three phase equilibria involving technologically important compound $BaFe_{12}O_{19}$(solid) has

TABLE 12.9

No.	Site notation	Atom	Multiplicity	Wyckoff	Site symmetry	*x*	*y*	*z*	Occupancy
1	O1	O	4	e	1	0.0	0.25	0.0	1.0
2	Fe1	Fe	4	e	1	0.0	0.375	0.25	1.0
3	O2	O	4	e	1	0.071	0.125	0.1071	1.0
4	Ba1	Ba	4	e	1	0.071	0.375	0.1071	1.0
5	Ba2	Ba	4	e	1	0.071	0.625	0.6071	1.0
6	O3	O	4	e	1	0.143	0.0	0.2143	1.0
7	Fe2	Fe	4	e	1	0.143	0.125	0.4643	1.0
8	O4	O	4	e	1	0.143	0.25	0.2143	1.0
9	O5	O	4	e	1	0.143	0.5	0.2143	1.0
10	Fe3	Fe	4	e	1	0.143	0.625	0.4643	1.0
11	Ba3	Ba	4	e	1	0.214	0.125	0.3214	1.0
12	O6	O	4	e	1	0.214	0.375	0.3214	1.0
13	Ba4	Ba	4	e	1	0.214	0.625	0.3214	1.0
14	O7	O	4	e	1	0.286	0.0	0.4286	1.0
15	Fe4	Fe	4	e	1	0.286	0.125	0.1786	1.0
16	O8	O	4	e	1	0.286	0.25	0.4286	1.0
17	O9	O	4	e	1	0.286	0.5	0.4286	1.0
18	Fe5	Fe	4	e	1	0.286	0.625	0.1786	1.0
19	Ba5	Ba	4	e	1	0.357	0.125	0.0357	1.0
20	O10	O	4	e	1	0.357	0.375	0.0357	1.0
21	Ba6	Ba	4	e	1	0.357	0.625	0.0357	1.0
22	O11	O	4	e	1	0.429	0.0	0.1429	1.0
23	O12	O	4	e	1	0.429	0.25	0.1429	1.0
24	Fe6	Fe	4	e	1	0.429	0.375	0.3929	1.0
25	O13	O	4	e	1	0.429	0.5	0.1429	1.0
26	O14	O	4	e	1	0.50	0.125	0.25	1.0
27	Ba7	Ba	4	e	1	0.50	0.375	0.25	1.0
28	O15	O	4	e	1	0.571	0.25	0.3571	1.0
29	Fe7	Fe	4	e	1	0.571	0.375	0.1071	1.0
30	O16	O	4	e	1	0.643	0.375	0.4643	1.0
31	O17	O	4	e	1	0.714	0.25	0.0714	1.0
32	O18	O	2	a	−1	0	0	0	1.0

been determined using solid-state electrochemical technique employing CSZ as an electrolyte from 1048 to 1221 K. The values of $\Delta_f G^0{}_m(T)$ for the above ternary oxides are given by:

$$\Delta_f G^0{}_m(BaFe_{12}O_{19}, (solid)/kJ/mol = -5431.3 + 1.5317 (T/K) \quad (970 \le T/K \le 1151)$$

$$\Delta_f G^0{}_m(BaFe_2O_4, (solid)/kJ/mol = -1461.4 + 0.3745 (T/K) \quad (970 \le T/K \le 1151)$$

$$\Delta_f G^0{}_m(Ba_2Fe_2O_5, (solid)/kJ/mol = -2038.3 + 0.4433 (T/K) \quad (970 \le T/K \le 1149)$$

$$\Delta_f G^0{}_m(Ba_3Fe_2O_6, (solid)/kJ/mol = -2700.1 + 0.6090 (T/K) \quad (969 \le T/K \le 1150)$$

$$\Delta_f G^0{}_m(Ba_5Fe_2O_8, (solid)/kJ/mol = -3984.1 + 0.9300 (T/K) \quad (973 \le T/K \le 1150)$$

The uncertainty estimates for $\Delta_f G^0{}_m$ includes the standard deviation in the e.m.f and the uncertainty of the data taken from the literature. An isothermal oxygen potential diagram for the system Ba–Fe–O was constructed at 1100 K based on the thermodynamic data obtained in this study.

In the FeO–Fe_2O_3-containing system of BaO–Fe_3O_4, no compounds are known.

In the Fe^{4+}-containing system of BaO–FeO_2, various barium orthoferrates over wide Fe^{4+} concentrations have been prepared and their magnetic properties were investigated. The hexagonal phase with large Fe^{4+} concentration is ferromagnetic above the anomaly point. With increasing Fe^{3+}, it tends to be antiferromagnetic. The cubic tetragonal phases are paramagnetic with positive paramagnetic Curie temperature. In these phases, the Fe^{4+}–Fe^4 interaction is ferromagnetic, but the Fe^{3+}–Fe^{4+} and Fe^{3+}–Fe^{3+} interactions are antiferromagnetic. Some of the Fe^{3+} and Fe^{4+} ions in these phases take low-spin states due to strong uniaxial crystalline fields caused by neighboring oxygen vacancies. The triclinic I phase appears to have a magnetic structure of a 1D antiferromagnet. The magnetic structures of the triclinic II and rhombohedral phases resemble that of the triclinic I.

The compound $BaFeO_{3-x}$ exists in many forms, depending on the oxygen deficiency: triclinic ($2.64 < \delta < 2.67$), rhombohedral ($2.62 < \delta < 2.64$), tetragonal ($2.75 < \delta < 2.81$) and hexagonal ($2.63 < \delta < 2.92$). Furthermore, the hexagonal phase is classified into 6H- and 12H-type $BaFeO_{3-}$ The hexagonal phase has a wide range in oxygen content ($BaFeO_{2.63–2.92}$). The other phases have the limited compositions and the distinct structures of perovskite: triclinic I, $BaFeO_{2.50}$; triclinic II, $BaFeO_{2.64–2.67}$; rhombohedral I and II, $BaFeO_{2.62–2.64}$; and tetragonal, $BaFeO_{2.75–2.81}$. The phases contain Fe^{4+} ions correlating with the oxygen content. The hexagonal phase shows a continuous change in oxygen content with temperature down to $BaFeO_{2.63}$. The perovskite-like phases, however, show characteristic transformations. The triclinic I phase oxidizes to the triclinic II form at 320–500 °C and to the hexagonal form at 720–915 °C in oxygen. These transformations are related to oxidation–reduction of iron ions ($Fe^{3+} \Leftrightarrow Fe^{4+}$) as the oxygen content is changed in the crystal structure.

The structure of the mixed valency $Ba_5Fe_5O_{14}$ ($BaFeO_{2.8}$), prepared using a molten KOH-$Ba(OH)_2$ flux, has been determined using single-crystal XRD. $Ba_5Fe_5O_{14}$ forms twinned crystals with the orthorhombic space group *Cmcm*, $a = 5.7615$, $b = 9.9792$ and $c = 24.347$ Å, $Z = 4$. The structure, which is closely related to the 10H $BaFeO_{2.65}$ perovskite, is composed of two oxygen-deficient BaO_2 layers and eight BaO_3 layers with a $(hchhc)_2$ stacking sequence, where h and c denote hexagonal or cubic layers. A displacement of barium and oxygen atoms in the BaO_2 layers from hexagonal special positions lowers the symmetry from hexagonal to orthorhombic. This combination of stacking and vacancies creates trimers of face-sharing FeO_6 octahedra pillared by dimers of corner-sharing FeO_4 tetrahedra. The Fe^{4+} atoms are located in the center of the trimer and in the tetrahedral sites. The magnetism of $Ba_5Fe_5O_{14}$, investigated using SQUID magnetometry, is characteristic of a strongly coupled antiferromagnet.

$BaFeO_{2.8-\delta}$ with a crystal structure different from any of those previously reported in the system $BaFeO_y$ ($2.54 \le y \le 43.0$) was prepared by a low-temperature method of synthesis, based on the oxidative thermal decomposition of $BaFe[(CN)_5NO_2]\cdot 3H_2O$. The structure was solved *ab* initio by a high-resolution synchrotron XRPD method. The compound crystallizes in space group *P63/mmc*, Z"10, unit cell parameters $a = 5.77944$, $c = 24.60871$ Å. The structure consists of 10H close packed $(hchch)_2$ stacking of BaO_n layers (eight BaO_3 layers and two oxygen-deficient BaO_2 layers). Additional oxygen deficiencies are randomly distributed on the h-BaO_3 layers. Six iron ions occupy octahedral sites sharing faces between them along the *c*-axis and four occupy tetrahedral sites (2 T′ and 2 T″) sharing faces with the octahedra and sharing corners between them. This new barium ferrate polytype is believed to be stabilized only at this low temperature (850 °C) and atmospheric oxygen pressure, since it has not been described for samples prepared with other methods of synthesis.

The structure of the mixed-valent $Ba_5Fe_5O_{14}$ ($BaFeO_{2.8}$), prepared using a molten KOH–$Ba(OH)_2$ flux, has been determined using single-crystal XRD. $Ba_5Fe_5O_{14}$ forms twinned crystals with the orthorhombic space group *Cmcm*, $a = 5.7615(8)$, $b = 9.9792(14)$ and $c = 24.347(3)$ Å, $Z = 4$. The structure, which is closely related to the 10H $BaFeO_{2.65}$ perovskite, is composed of two oxygen-deficient BaO_2 layers and eight BaO_3 layers with a $(hchhc)_2$ stacking sequence, where h and c denote hexagonal or

cubic layers. A displacement of barium and oxygen atoms in the BaO_2 layers from hexagonal special positions lowers the symmetry from hexagonal to orthorhombic. This combination of stacking and vacancies creates trimers of face-sharing FeO_6 octahedra pillared by dimers of corner-sharing FeO_4 tetrahedra. The Fe^{4+} atoms are located in the center of the trimer and in the tetrahedral sites. The magnetism of $Ba_5Fe_5O_{14}$, investigated using SQUID magnetometry, is characteristic of a strongly coupled antiferromagnet.

The compound, $BaFe_2O_5$, is a perovskite-based structure. Numerous investigations have shown that it contains the Fe^{4+} ion in a cubic structure. No lower valance states like Fe^{3+} or Fe^{2+} have been detected. It contains octahedral units of FeO_6 interspersed with Ba^{2+} ions. When a trivalent ion like Y^{3+} is added to this compound (or any other divalent cation like Ba^{2+}), it does so be the defect equation:

$$Y_{Ba}^{3+} + V_{Ba}^{-} \Leftrightarrow 2Ba_{Ba}^{2+}$$

The stoichiometry changes from octahedrons of FeO_6 to five-sided pentagons of FeO_5, is shown in the following diagram. Note that both Fe^{3+} and Fe^{2+} have appeared (Fig. 12.37).

Related compounds include $BaFe_2O_5$ and Ba_2FeO_4.

Crystals of Ba_2FeO_4 and Ba_3FeO_5, grown from a "self-sealing" KOH-$Ba(OH)_2$ flux, have been characterized by single-crystal XRD, Mössbauer spectroscopy, and magnetic measurements. Ba_2FeO_4 forms non-merohedral twinned crystals with the monoclinic space group $P21/n$, $a = 6.034$ Å, $b = 7.647$ Å, $c = 10.162$ Å, $\beta = 92.931°$, and $Z = 4$. Ba_3FeO_5 crystallizes in the orthorhombic space group *Pnma*, with $a = 10.301$ Å, $b = 8.151$ Å, $c = 7.611$ Å, and $Z = 4$. Although both compounds feature discrete FeO_4^{4-} tetrahedra, the anion found in Ba_2FeO_4 has shorter Fe–O bonds and is significantly distorted, relative to the Ba_3FeO_5 anion.

An iron valence of 4+ was confirmed by magnetic susceptibility measurements and by the low-temperature isomer shifts of −0.152 and −0.142 mm/s relative to α-iron for Ba_2FeO_4 and Ba_3FeO_5, respectively (Fig. 12.38).

The standard Gibbs Free Energy of the following compounds have been established as shown in Fig. 12.39.

In the Fe^{5+}-containing system of BaO–Fe_2O_5, no compounds are known.

In the Fe^{6+}-containing system of BaO–FeO_3, the ferrate, FeO_4^{2-}, ion is thermodynamically a stronger oxidant than the common oxidants MnO_4^- and CrO_4^{2-}. Thus, it has been used in various fields such as oxidation of organic substrates, water disinfection and degradation of organic synthetic pollutants. Super-iron batteries incorporating Fe(VI) cathodes salts with a higher capacity and energy advantage compared to the conventional alkaline batteries have also been recently introduced.

In one study, the thermal decomposition of solid samples of iron(VI) oxides, $K_2FeO_4 \cdot 0.088\ H_2O$ (**1**) and $BaFeO_4 \cdot 0.25H_2O$ (**2**) in inert atmosphere has been examined using simultaneous thermogravimetry and differential thermal analysis (TG/DTA), in combination with in situ analysis of the evolved gases by online coupled mass spectrometer (EGA–MS). The final decomposition products were characterized by ^{57}Fe Mössbauer spectroscopy. Water molecules were released first, followed by a distinct decomposition step with endothermic DTA peak of **1** and **2** at 273 and 248 °C, respectively, corresponding to the evolution of molecular oxygen as confirmed by EGA–MS. The released amounts of O_2 were determined as 0.42 and 0.52 mol pro formula of **1** and **2**, respectively. The decomposition product of K_2FeO_4 at 250 °C was

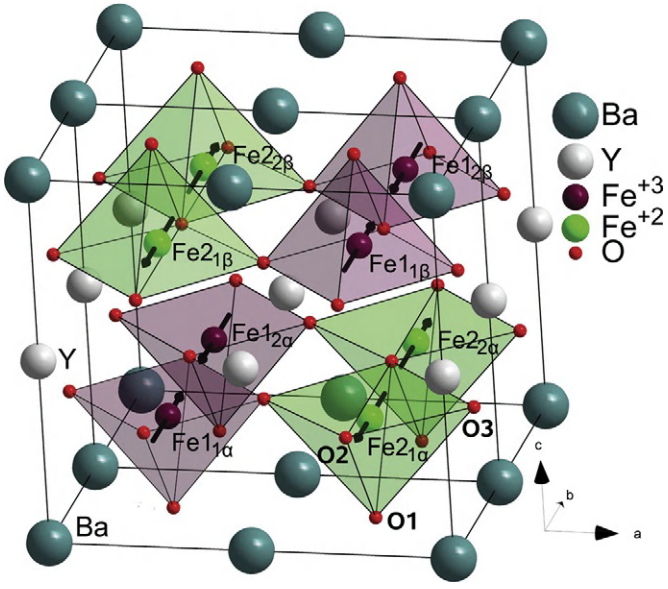

FIGURE 12.37

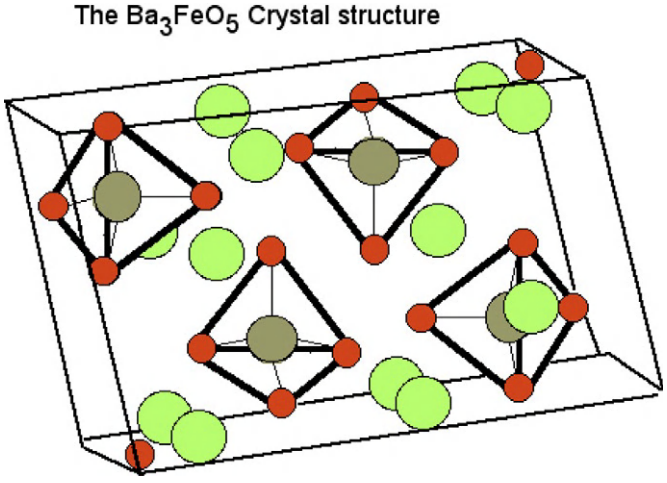

FIGURE 12.38

$$\Delta_f G_m^0(BaFe_{12}O_{19}, s)/kJ\,mol^{-1}(\pm 0.6) = -5431.3 + 1.5317\,(T/K) \quad (970 \leqslant T/K \leqslant 1151)$$

$$\Delta_f G_m^0(BaFe_2O_4, s)/kJ\,mol^{-1}(\pm 1.3) = -1461.4 + 0.3745\,(T/K) \quad (970 \leqslant T/K \leqslant 1151)$$

$$\Delta_f G_m^0(Ba_2Fe_2O_5, s)/kJ\,mol^{-1}(\pm 1.4) = -2038.3 + 0.4433\,(T/K) \quad (970 \leqslant T/K \leqslant 1149)$$

$$\Delta_f G_m^0(Ba_3Fe_2O_6, s)/kJ\,mol^{-1}(\pm 1.5) = -2700.1 + 0.6090\,(T/K) \quad (969 \leqslant T/K \leqslant 1150)$$

and

$$\Delta_f G_m^0(Ba_5Fe_2O_8, s)/kJ\,mol^{-1}(\pm 1.6) = -3984.1 + 0.9300\,(T/K) \quad (973 \leqslant T/K \leqslant 1150)$$

FIGURE 12.39

determined as Fe(III) species in the form of $KFeO_2$. Formation of an amorphous mixture of superoxide, peroxide, and oxide of potassium may be other products of the thermal conversion of iron(VI) oxide **1** to account for less than expected released oxygen. The TG and Mössbauer data suggest that barium iron perovskite with the intermediate valence state of iron (between III and IV) was the product of thermal decomposition of iron(VI) oxide **2**.

Nanocrystalline $BaFeO_4$ was prepared and purified by special measures. Magnetic susceptibility measurements confirmed the existence of Fe(VI). XRD studies indicated that it has an orthorhombic unit cell with space group *Pnma* and lattice parameters $a = 8.880$ Å, $b = 5.512$ Å, $c = 7.214$ Å. High-resolution transmission electron microscopy (HRTEM) and SAED characterization provided further proofs to the accuracy of XRD data.

Higher capacity batteries based on an unusual stabilized iron(VI) chemistry are presented. The storage capacities of alkaline and metal hydride batteries are largely cathode limited, and both use a potassium hydroxide electrolyte. The new batteries are compatible with the alkaline and metal hydride battery anodes but have higher cathode capacity and are based on available, benign materials. Iron(VI/III) cathodes can use low-solubility K_2FeO_4 and $BaFeO_4$ salts with respective capacities of 406 and 313 mA/h/g. Super-iron batteries have a 50% energy advantage compared to conventional alkaline batteries. A cell with an iron(VI) cathode and a metal hydride anode is significantly (75%) rechargeable.

Barium ferrite is available commercially as $BaFe_{12}O_{19}$ with the CAS number of 11138-11-7.

12.2.6. Radium Oxy-Iron Compounds

While radium ferrites or ferrates could undoubtedly be synthesized with properties similar to those of the Ba–Fe–O system, no data exists in the technical literature concerning such compounds. This is undoubtedly due to lack of interest in Industrial and Academic circles.

12.3. ALKALINE EARTH—RUTHENIUM COMPOUNDS

The number of known compounds in the Ae–Ru–O system is much less than the number of Fe compounds in the Ae–Fe–O system. The chemistry of ruthenium consists mostly of complex cations like $[Ru(NH_3)_6]^{3+}$, $[RuCl(NH_3)_5]^{3+}$ or $[Ru(NH_3)_5SH]^{2+}$. In general, Ru_xO_y derived compounds involve only a few of specific valence states of Ru. The alkaline earth ions precipitate soluble RuO_4^{2-} as black $MgRuO_4 \cdot H_2O$, black $CaRuO_4 \cdot H_2O$, red $SrRuO_4 \cdot H_2O$ and red $BaRuO_4 \cdot H_2O$. This was reported in 1893.

12.3.1. Beryllium Oxy-Ruthenium Compounds

Be does not form any oxy-ruthenium compounds in the system, Be–Ru–O. However, it does form intermetallic compounds of varying proportions of Be^0/Ru^0 metals. The phase diagram is shown in Fig. 12.40.

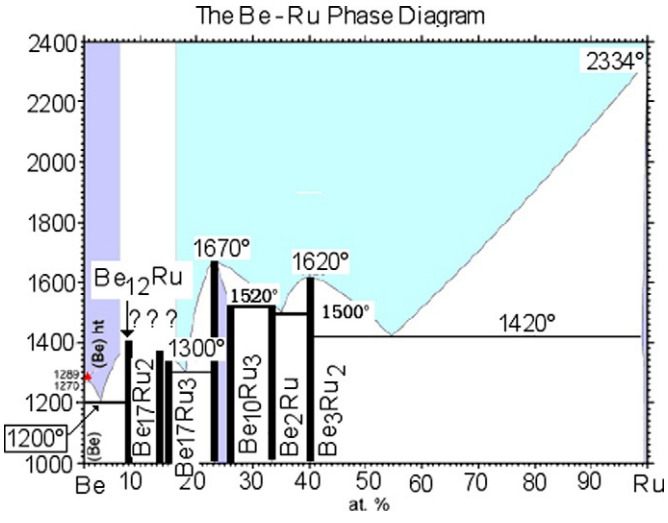

FIGURE 12.40

The Be_2Ru Crystal Structure

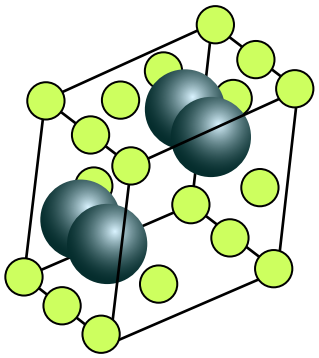

FIGURE 12.41

Six compounds are shown but only three (3) structures have been published. The compound, Be_3Ru_2 is cubic with cell parameters of: $a = b = c = 9.892$ Å, $\alpha = \beta = \gamma = 109.47°$, cell volume = 744.68 Å^3. The exact lattice structure has not been forthcoming.

The compound, Be_2Ru, has the structure shown in Fig. 12.41.

Cell parameters are: $a = b = 5.96$ Å, $c = 9.18$ Å, $\alpha = \beta = \gamma = 90°$, cell volume = 282.40 Å^3, $Z = 4$. Cell occupancy is shown in Table 12.10.

$Be_{17}Ru_3$ has the structure shown in Fig. 12.42.

Cell parameters are: $a = b = c = 9.5523$ Å, $\alpha = \beta = \gamma = 109.471°$, cell volume = 670.97 Å^3, $Z = 1$. Cell occupancy is shown in Table 12.11.

The $Be_{17}Ru_3$ Crystal Structure

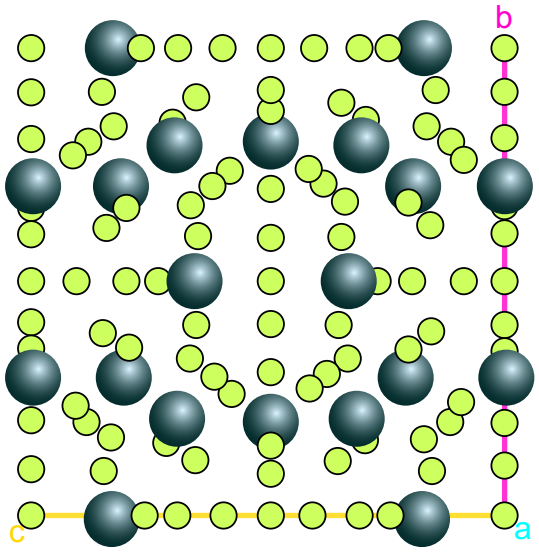

FIGURE 12.42

In contrast, the compound, $Be_{17}Ru_2$, has a structure that is completely different from that of $Be_{17}Ru_3$ (Fig. 12.43).

Cell parameters are: $a = b = 4.203$ Å, $c = 10.94$ Å, $\alpha = \beta = 90°$, $\gamma = 120°$, cell volume = 166.75 Å^3, $Z = 2$. Cell occupancy is shown in Table 12.12

No usage has arisen in the Industry and these compounds remain an Academic oddity.

TABLE 12.10

No.	Site notation	Atom	Multiplicity	Wyckoff	Site symmetry	*x*	*y*	*z*	Occupancy
1	Be1	Be	6	h	mm2	0.169	0.3394	1/4	1.0
2	Ru1	Ru	4	f	3m.	1/3	2/3	0.5629	1.0
3	Be2	Be	2	a	−3m.	0	0	0	1.0

TABLE 12.11

No.	Site notation	Atom	Multiplicity	Wyckoff	Site symmetry	*x*	*y*	*z*	Occupancy
1	Be1	Be	48	h	1	0.114	0.3434	0.201	1.0
2	Ru1	Ru	24	g	m..	0	0.1879	0.3014	1.0
3	Be2	Be	24	g	m..	0	0.2305	0.0914	1.0
4	Be3	Be	24	g	m..	0	0.4055	0.3488	1.0
5	Be4	Be	16	f	.3.	0.1645	0.1645	0.1645	1.0
6	Be5	Be	12	e	mm2..	0.196	0	1/2	1.0
7	Be6	Be	12	d	mm2..	0.406	0	0	1.0

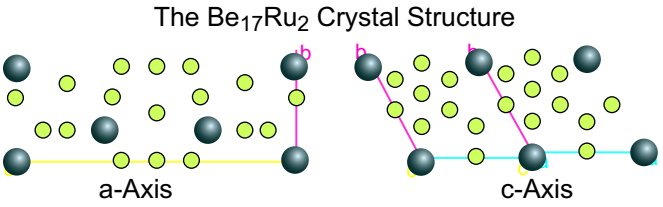

FIGURE 12.43

12.3.2. Magnesium Ruthenium Compounds

No intermetallic compounds in the system, Mg^0–Ru^0, are known.

MgO forms no compounds with the oxides of Ru_xO_y, where x or y can vary from 2 to 8. As a matter of fact, the only available reference is one that dated 1893 where a soluble RuO_4^{2-} compound was used to precipitate insoluble ortho-ruthenates:

$$Ae^{2+} + RuO_4^{2-} \Rightarrow AeRuO_4 \cdot H_2O$$

In the Ru^{2+}-, Ru^{3+}-, Ru^{4+}-, Ru^{5+}-, Ru^{6+}-, Ru^{7+}- or Ru^{8+}-containing systems of Mg–Ru–O (40 possible compounds), no details of synthesized compounds have been published.

Magnesium ruthenates are not offered commercially.

12.3.3. Calcium Ruthenium Compounds

No intermetallic compounds in the system, Ca^0–Ru^0, are known.

In the Ru^{2+}-containing system of CaO–RuO, a complex compound involving two uranyl carbonate **minerals**, "Liebigite", $Ca_2[UO_2(CO_3)_2]\cdot 10H_2O$, and "Andersonite", $CaNa_2[UO_2(CO_3)_2]\cdot 6H_2O$, was found to coexist as a trace, with the presumed formulation $Ca_2[RuO_2(CO_3)_2]\cdot 10H_2O$. No other data has been forthcoming.

In the Ru^{3+}-containing system of CaO–Ru_2O_3, no compounds have been reported.

In Ru^{4+}-containing system of CaO–RuO_2, the compound, $CaRuO_3$ is known. The magnetic ground state of the perovskite structure $CaRuO_3$ has been unexplained for decades. It has been shown that paramagnetic $CaRuO_3$ can be made ferromagnetic by very small amounts of partial substitution of Ru by Ti. Magnetic hysteresis loops were observed at 5 K for as little as 2% Ti substitution. Ti is nonmagnetic and isovalent with Ru, indicating that the primary effect of the substitution of Ti for Ru is the disruption of the magnetic ground state of $CaRuO_3$ through disorder. The data suggested that $CaRuO_3$ is poised at a critical point between ferromagnetic and paramagnetic ground states. The magnetic ground state of $CaRuO_3$ (Ru^{4+}, $4d_4$: t_{2g}^4, e_g^0 with $S = 1$) is controversial. Recent publications indicate that paramagnetic behavior (or exchange enhanced paramagnetism) down to 30 mK, is also supported by the single line shape of a ^{99}Ru Mössbauer spectrum measured at 4.1 K. The high- and low-temperature resistivity results indicate that $CaRuO_3$ is a non-Fermi liquid metal.

Magnetic studies of ceramic and single-crystal $CaRuO_3$ samples have demonstrated that irreversibility appears in the zero-field-cooled and field-cooled curves only when measured at low-applied magnetic fields. A small hysteresis loop opens at low temperatures, and the remanent magnetization decreases with temperature and disappears at 90 and 71 K for the ceramic and crystal samples, respectively. The easy axis for the magnetization is in the [001] direction. Mössbauer studies of 1% ^{57}Fe doped in $CaRuO_3$ show a magnetic sextet at 4.1 K that disappears at 90 K. ^{57}Fe ions experience an exchange field from their magnetic Ru^{4+} neighbors and also become magnetically ordered. $CaRuO_3$ has a perovskite-like structure.

In another paper, it was proposed that $CaRuO_3$ is not paramagnetic, but rather shows the characteristics of short-range magnetic interactions, possibly spin glass behavior, or alternatively, the data are consistent with an itinerant electron picture of ferromagnetism. Neutron diffraction experiments at 10 K showed that no additional magnetic neutron scattering peaks exist, indicating that $CaRuO_3$ is not a canted antiferromagnet. It

TABLE 12.12

No.	Site notation	Atom	Multiplicity	Wyckoff	Site symmetry	x	y	z	Occupancy
1	Be1	Be	6	n	.m.	0.1665	0.8335	0.1830	1.0
2	Be2	Be	3	k	mm2	0.5045	0.4955	1/2	1.0
3	Be3	Be	2	i	3m.	2/3	1/3	0.0982	1.0
4	Ru1	Ru	2	i	3m.	2/3	1/3	0.3069	1.0
5	Be4	Be	2	h	3m.	1/3	2/3	0.3408	1.0
6	Be5	Be	2	g	3m.	0	0	0.3767	1.0
7	Be6	Be	1	c	6m2	1/3	2/3	0	0.34
8	Ru2	Ru	1	a	6m2	0	0	0	0.36

has been well established that the isostructural $SrRuO_3$ is a ferromagnet (FM) with a Curie temperature $T_C = 165$ K. The stark contrast between $SrRuO_3$ and $CaRuO_3$ was unexpected because the closed shells-like character of Sr and Ca do not contribute to the density of states at the Fermi surface and therefore should not be the origin for the different magnetic ground states of these two compounds. Since a common structural feature of the two compounds is that they are composed of an array of corner-shared RuO_6 octahedra, it was assumed that the degree of tilting and rotation of these octahedra within their ideal cubic perovskite structure governs the observed differences in the magnetic ground states. A narrow itinerant 4d band is formed through hybridization of Ru-t_{2g} and O-2p orbitals. The 4d bandwidth thus formed sensitively depends on the degree of hybridization. $CaRuO_3$ is believed to have a narrow itinerant 4d-band width (narrower than for $SrRuO_3$), which is too narrow for long-range magnetic ordering, but not so narrow as to cause $CaRuO_3$ to be nonmetallic. It means that $CaRuO_3$ is on the verge of magnetic ordering and readily evolves into an ordered phase. On the other hand, no long-range magnetism has been observed in the isostructural orthorhombic $LaRuO_3$ down to 4.2 K. The Ru^{3+} ($4d^5$, t_{2g}^5, e_g^0) ions are assumed to be in the low-spin state with ($S = 0.5$). In that sense, $LaRuO_3$ differs from both $CaRuO_3$ and $SrRuO_3$ compounds.

A high-pressure dense phase of $CaRuO_3$ was recently created by high-pressure and high-temperature experiments where it was successfully quenched to room temperature. The crystal structure at ambient conditions was identified to be of the post-perovskite type, which is entirely different from the perovskite structure of the regularly synthesized $CaRuO_3$. A quasi 1D magnetism was discovered in the post-perovskite $CaRuO_3$ (Ru^{4+}: $4d^4$, *Cmcm*), which is iso-compositional with the perovskite $CaRuO_3$ (*Pbnm*). An antiferromagnetic spin chain function with $-J/kB = 350$ K well reproduces the experimental curve of the magnetic susceptibility vs temperature, suggesting long-range antiferromagnetic correlations. The anisotropic magnetism is probably owed to the d_{yz}-2pπ-d_{zx} and d_{zx}-2pπ-dyz superexchange bonds along the *a*-axis. The Sommerfeld coefficient of the specific heat is small, 0.16 mJ/mol/K^2, indicating that the magnetism reflects the localized nature of the 4d electrons. This was the first observation of an integer ($S = 1$) spin chain antiferromagnetism in the 4d electron system.

The shift in structure is shown in Fig. 12.44.

This shows a sketch of the crystal structures of (a) the perovskite and (b) the post-perovskite $CaRuO_3$. The figures used the same drawing scale. The post-perovskite phase is 1.7 % denser in volume than the perovskite phase. Single crystals of $CaRuO_3$ (**1**) and $SrRuO_3$ (**2**) have been

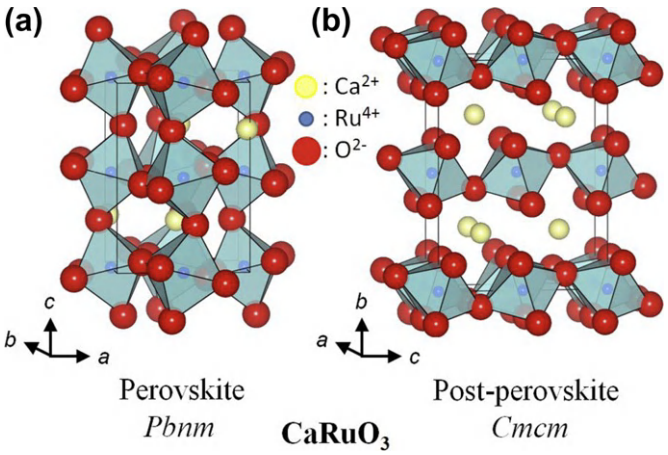

FIGURE 12.44

synthesized by a flux method and their structures have been determined by means of single-crystal XRD techniques. The crystallographic data are (**1**): formula weight fw = 189.15, orthorhombic, space group *Pnma* (No. 62), $a = 5.524$, $b = 7.649$, $c = 5.354$ Å, $V = 226.2$ Å^3, $Z = 4$, $Dx = 5.554$ g/cm^3, $\mu = 81.97$/cm, final $R = 0.031$ for 297 observed reflections. (**2**): formula weight = 236.69, cubic, space group *Pm* (No. 200), $a = b = c$ =3.910 Å, $V = 59.8$ Å^3, $Z = 1$, $Dx = 6.572$ g/cm^3, $\mu = 275.28$/cm, final $R = 0.032$ for 33 observed reflections.

$CaRuO_3$ is a non-Fermi liquid metal near a magnetic instability, as characterized by the following properties: (1) the heat capacity C (T,B) ~ T log T is readily enhanced in low applied fields, and exhibits a Schottky peak at 2.3 K that exhibits field dependence when T is reduced; (2) the magnetic susceptibility diverges as T^{σ} at low temperatures with $1/2 < \delta < 1$, depending on the applied field; and (3) the electrical resistivity exhibits a $T^{3/2}$ dependence over the range . No Shubnikov–de Haas oscillations are discerned at 1.7 K < T < 24 K for applied fields up to 45 T. These properties, which sharply contrast those of the itinerant FM $SrRuO_3$, indicate $CaRuO_3$ is a rare example of a stoichiometric oxide compound that exhibits non-Fermi liquid behavior near a quantum critical point.

The standard Gibbs energy of formation of $CaRuO_3$(s) has been determined using a solid-state galvanic cell with CaF_2(s) as the solid electrolyte referred to as the fluoride cell. The fluoride cell is represented by:

$$-\mathrm{Pt/O_2(gas)}, \{\mathrm{CaO(solid)} + \mathrm{CaF_2(solid)}\}//\mathrm{CaF_2}// \{\mathrm{CaF_2(solid)} + \mathrm{RuO_2(solid)} + \mathrm{CaRuO_3(solid)}\}, \mathrm{O_2(gas)/Pt(+)}$$

The standard Gibbs energy of formation of $CaRuO_3$(s) obtained by the fluoride cell can be represented by:

$$\Delta_f G^\circ(\mathrm{CaRuO_3(solid)})/\mathrm{kJ/mol} = -984.1 + 0.2841 \cdot (T/\mathrm{K}) \quad (815 < T/\mathrm{K} < 1053)$$

The slope and intercept of the above equation correspond to the enthalpy and entropy of formation, respectively, of $CaRuO_3$(solid), from its elements at an average experimental temperature $T_{av} = 934$ K. Using the Neumann–Kopp rule, the heat capacity of $CaRuO_3$(solid) was estimated. The standard enthalpy of formation of the compound at 298.15 K was then calculated by using estimated heat capacity data and the e.m.f. data obtained from fluoride cell and was found to be −995.0 kJ/mol.

The effects of Ru-site metal dopants on the low-temperature magnetization of $CaRuO_3$ have been reported. Dopants of two types were tested: those with closed d shells in their expected oxidation state (Al^{3+}, Zn^{2+}, Ti^{4+}, V^{5+} and Pt^{2+}), and those with unpaired d electrons (Mn^{4+}, Fe^{3+}, Co^{2+}, Ni^{2+} and Cu^{2+}) in their expected oxidation state. The results were consistent with the recent proposal that $CaRuO_3$ is not a classical antiferromagnet, but rather is poised at a critical point between ferromagnetic and paramagnetic ground states. Additions of Ti, Fe, Mn and Ni result in ferromagnetic behavior.

The compounds, $(Ca_{0.5},Mg_{0.5})RuO_3$ and $(Ca_{0.5},Sr_{0.5})RuO_3$, having the $CaTiO_3$ perovskite structure (point group = *oP*20, space group = *Pm*-3*m*) have also been synthesized.

It was discovered that Sr_2RuO_4 has superconductivity at a modest temperature of about 1.0 K. This compound is a perovskite ruthenium oxide and a representative of the Ruddlesden–Popper family, $(Sr,Ca)_{n+1}Ru_nO_{3n+1}$ with $n = 1$. These materials exhibit a rich variety of magnetic phases. There is a strong resemblance in the structure to the cuprate compounds, the role of the RuO_2 plane is analogous to the role of the CuO_2 plane in the cuprates. The mechanism of superconductivity in Sr_2RuO_4 has been widely studied. It was suggested that Sr_2RuO_4 is a possible candidate of a *p*-wave superconductor. The assumption is that the triplet pairing is induced by ferromagnetic fluctuations. Since $SrRuO_3$ is a strong FM, ferromagnetic fluctuations should be present in $Sr_2RuO_{4.2}$. Calculations indicate that Sr_2RuO_4 is a FM.

A summary of the electronic band structure is shown in Fig. 12.45.

The electronic band structure receives its basic character from the 4d-t_{2g} orbitals of the Ru ion: {d_{yz}, d_{zx}, d_{xy}} which disperse dominantly in each RuO_2-plane via the π-hybridization with the O-2p-orbitals. It is easy to see that the d_{yz}- and d_{zx}-orbitals have a very anisotropic dispersion yielding two-quasi 1D bands, that hybridize to form a one electron-like (β-band) and one hole-like (α-band) Fermi surface.

The doping of Ca for Sr introduces a gradual rotation of the RuO_6 octahedra around the *z*-axis and yields a modification in the band structure, which the analysis of the emerging magnetic properties in region III is

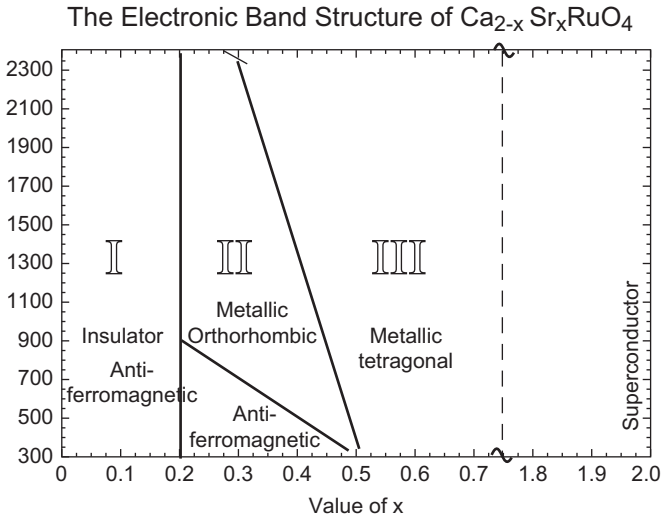

FIGURE 12.45

based on. The region III is metallic, paramagnetic and has tetragonal crystal symmetry. The region II is metallic, at low temperature with presumably antiferromagnetic correlation and has orthorhombic symmetry. In both regions the susceptibility over a certain range of temperature is Curie like with a spin $S = 1/2$. The region I is a Mott insulator with antiferromagnetic long-range order of a spin $S = 1$.

The growth of single crystals of the layered perovskite Ca_2RuO_4 by a floating-zone method was accomplished in another paper. It was confirmed that stoichiometric Ca_2RuO_4 is a Mott insulator. Canted antiferromagnetic (CAF) ordering occurs below 113 K. The development of a short-range CAF order below 150 K was also observed. The origin of the temperature-induced Mott transition in Ca_2RuO_4 was studied. The local density approximation + dynamical mean-field theory was used as a method. The following was shown:

(1) The Mott transition is driven by the change in structure from long to short *c*-axis layered perovskite (L-Pbca to S-Pbca); it occurs together with orbital order, which follows, rather than produces, the structural transition.

(2) In the metallic L-Pbca phase the orbital polarization is ~0.

(3) In the insulating S-Pbca phase the lower energy orbital, ~xy, is full.

(4) The spin-flip and pair-hopping Coulomb terms reduce the effective masses in the metallic phase. These results indicate that a similar scenario applies to $Ca_{2-x}Sr_xRuO_4$ ($x < 0.2$). In the metallic $x < 0.5$ structures, electrons are progressively transferred to the xz/yz bands with increasing *x*. However no orbital-selective Mott transitions were found down to ~30 K.

Application of very modest pressures to pure Ca_2RuO_4 transforms it from an antiferromagnetic Mott insulator to a quasi 2D metal with a ferromagnetic ground state. The smallness of the moment compared with the saturated moment of the localized Ru^{4+} ion reflects the itinerant character of the magnetism.

The structure of Ca_2RuO_4 has been reported. It is a layered perovskite having the localized structure shown in Fig. 12.46.

This structure is made up of RuO_2 layers built up of corner-sharing RuO_6 octahedra. The structure combines a rotation around the *c*-axis with a tilt around the *b*-axis. It is characterized by a long *c*-axis (L-Pbca) at $T_s = 360$ K and by a short one (s-Pbca) below T_s.

This layered perovskite undergoes a paramagnetic metal to paramagnetic insulator transition at $T_M = 360$ K. A similar insulator-to-metal transition also happens when a modest (~0.5 GPa) pressure is applied to this compound. This nature of these transitions is still under question. While it is clear that a Mott-type mechanism makes the 2/3-filled t_{2g} bands insulating, two differing scenarios, with different orbital occupations, have been suggested ($n = n_{xy} + n_{xz} + n_{yz}$) and ($p = -(n_{xy} + n_{xz})/2$). In the first, only the xy-band becomes metallic, i.e. the transition is orbital-selective where n and p jump from (2,2) and 1 in the insulator to (1,3) and $-1/2$ in the metal. In the second, there is a single Mott transition, assisted by the crystal-field splitting, $\Delta = e_{xz/yz} - e_{xy} > 0$, similar to the case of $3d^1$ perovskites. The spin-hop and pair-hopping Coulomb terms reduce the effective masses in the metallic phase. To date, the issue remains open.

Data concerning $Ca_3Ru_2O_7$ has been reported. The laminar perovskite $Ca_3Ru_2O_7$ naturally forms ferromagnetic double layers of alternating moment directions, as in the spin-valve superlattices. The mechanism of huge magnetoresistive effect in the material has been controversial due to a lack of clear understanding of various magnetic phases and phase transitions. In this neutron diffraction study in a magnetic field, we identify four different magnetic phases in $Ca_3Ru_2O_7$ and determine all first-order and second-order phase transitions between them. The spin-valve mechanism then readily explains the dominant magnetoresistive effect in $Ca_3Ru_2O_7$.

Huge magnetoresistive effect has also been observed recently in the double-layered perovskite $Ca_3Ru_2O_7$, which orders antiferromagnetically at $T_N = 56$ K and is isostructural to the manganites. Its behavior at low temperatures is similar to that in the manganites when a magnetic field is applied perpendicular to the easy axis of magnetization. A smaller magnetoresistive effect occurs in a first-order metamagnetic transition when the magnetic field is applied along the easy axis. The spin-valve mechanism has been proposed in both experimental and theoretical studies. However, the situation is complicated by a first-order metal-insulator transition (MIT) at $T_{MIT} \approx 46$ K. In particular, the spin-valve explanation runs into severe difficulty with the recent experimental conclusion that the fully spin-polarized phase is the least favorable for electronic conduction. Thus, alternative mechanisms such as orbital order have been proposed. The field-induced "ferromagnetic" phase (which should be called the paramagnetic phase) as well as the antiferromagnetic phases of $Ca_3Ru_2O_7$, has been deduced from bulk measurements. They form the foundation in current understanding of the novel magnetoresistive phenomena in $Ca_3Ru_2O_7$.

In the following diagram, the crystal structure has the form shown in Fig. 12.47.

$Ca_3Ru_2O_7$ shows perovskite-like structures, with double layers of RuO_6 octahedra that corner share with each other to form planes with Ca–O layers intervening within and between the double-layer planes. The Ca–O layer helps stabilize the perovskite structure without contributing to the total spin of this system. Since no oxygen ions within the intervening Ca–O layer are shared by the Ru ions of the adjacent layers, the exchange

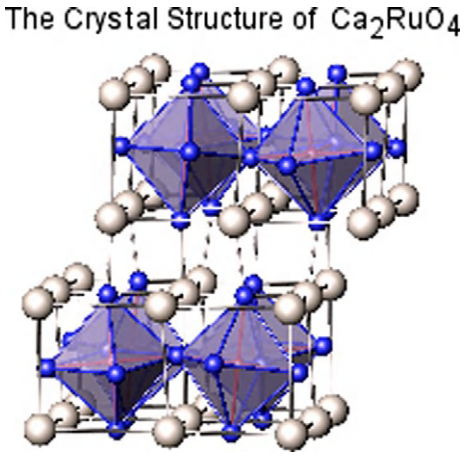

FIGURE 12.46

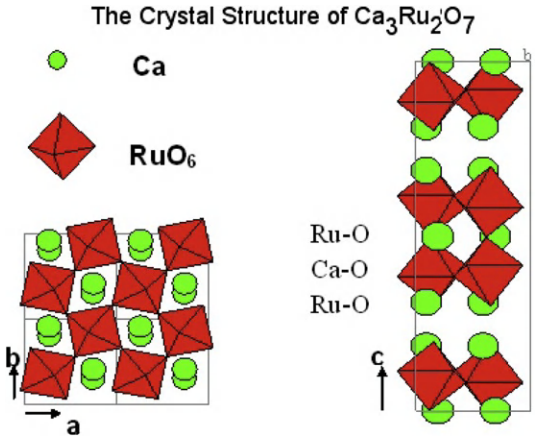

FIGURE 12.47

interactions and conductivity perpendicular to the RuO planes are expected to be weaker compared with those within the RuO planes. Compared with the ionic size of Sr^{2+} (Sr = 1.18 Å) the ionic size of Ca^{2+}(Ca = 1.00 Å) is smaller, resulting in an orthorhombic distortion with $a = 5.3720$ Å, $b = 5.55305$ Å, and $c = 19.572$ Å. This corresponds to a space group of either $A2_1ma$ (with a being the short axis) or $Cmc2_1$ (with a being the long axis).

The distortion exhibits itself as a rotation (around the c-axis) and a tilting (away form the c-axis) of the RuO_6 octahedra as clearly illustrated in the above figure. The tilting projects primarily along the ac plane, giving rise to an orthorhombic structure with anisotropic a- and b-lattice parameters. It is estimated that the Ru–O–Ru bond angles, which reflect the distortion effect, differ considerably from 180°. Within the ab plane, the Ru–O–Ru bond angles alternate between 149.87° and 150.47°, whereas for the Ru ions in the double layers the Ru–O–Ru bond angle is 152.13°. The tilting and rotation of RuO_6 octahedral is so severe that even the individual octahedra are contorted. Within the octahedra, the O–Ru–O bond angle is distorted away from 180°: around 177° for O–Ru–O bond angles along the c-axis, between 179.42° and 179.53° for O–Ru–O bond angles perpendicular to the c-axis. Compared with the Ru–O bond (~1.9910 Å) sandwiched between the RuO_6 planes, the other Ru–O bonds are longer (~1.9914 Å).

The polarized Raman spectra of the layered ruthenate, $Ca_3Ru_2O_7$, has been measured between 5 and 300 K in several exact scattering configurations. All observed Raman lines were assigned to definite phonon modes of A_1 or A_2 symmetry on the basis of their polarization properties and by comparison to the results of lattice dynamical calculations for the orthorhombic $A2_1ma$ structure. It was established that the Fano-shaped A_2 mode, which exhibits a strong anomaly near the metal–nonmetal transition at $T_M = 48$ K, involved mainly in-plane breathing-type oxygen vibrations. Other A_2 modes also exhibit detectable anomalies near T_M.

The magnetic and interplane transport properties of $Ca_3Ru_2O_7$ at high magnetic fields and low temperatures. $Ca_3Ru_2O_7$ with a bilayered orthorhombic structure was determined to be a Mott-like system with a narrow charge gap of 0.1 eV. Of the host of unusual physical phenomena revealed in this study, a few are particularly intriguing:

(1) a collapse of the c-axis lattice parameter at a metal–nonmetal transition, T_{MI} (=48 K), and a rapid increase of T_{MI} with low uniaxial pressure applied along the c-axis;
(2) quantum oscillations in the gapped, nonmetallic state for 20 mK $< T <$ 6.5 K;
(3) tunneling colossal magnetoresistance, which yields a precipitate drop in resistivity by as much as three orders of magnitude;
(4) different in-plane anisotropies of the colossal magnetoresistance and magnetization. All results appear to indicate a highly anisotropic ground state and a critical role of coupling between lattice and magnetism. The implication of these phenomena was discussed.

Only the interoxide phases, Ca_2RuO_4, $Ca_3Ru_2O_7$, and $CaRuO_3$, are present in the pseudo-binary system CaO–RuO_2. The standard Gibbs energies of formation (ΔG_f^0) of the three calcium ruthenates from their component oxides have been measured in the temperature range 925–1350 K using solid-state cells with yttria-stabilized zirconia as the electrolyte and $Ru + RuO_2$ as the reference electrode. The standard Gibbs energies of formation ΔG_f^0 of the compounds can be represented by:

$$Ca_2RuO_4: \Delta G_f^0/\mathrm{J/mol} = -38{,}340 - 6.611\,T$$
$$Ca_3Ru_2O_7: \Delta G_f^0/\mathrm{J/mol} = -75{,}910 - 11.26\,T$$
$$CaRuO_3: \Delta G_f^0/\mathrm{J/mol} = -35{,}480 - 3.844\,T$$

The data for Ca_2RuO_4 correspond to the stoichiometric composition, which has an orthorhombic structure, space group $Pbca$, with short c-axis ("S" form). The structural features of the ternary oxides responsible for their mild entropy stabilization are discussed. A 3D oxygen potential diagram for the system Ca–Ru–O is developed as a function of composition and temperature from the results obtained. Using the Neumann–Kopp rule to estimate the heat capacity of the ternary oxides relative to their constituent binary oxides, the standard enthalpies of formation of the three calcium ruthenates from the elements and their standard entropies at 298.15 K are evaluated.

The 2D ruthenate family $Ca_{2-x}Sr_xRuO_4$ presents a rich phase diagram, evolving as x is varied from the Fermi liquid triplet superconductor Sr_2RuO_4 to the antiferromagnetic (Mott) insulator Ca_2RuO_4. The origin and indeed the nature of some of the phases remain the subject of controversy. Further interest has been added by surface studies, which indicate that (contrary to intuition) the Mott state is less stable on the surface than in the bulk. Bulk $Ca_{1.9}Sr_{0.1}RuO_4$ exhibits a metal to insulator transition as the temperature is decreased below 150 K, whereas surface sensitive probes place the transition at $\approx$125 K. This unexpected result challenges the conventional notion that correlation effects are stronger at surface, and requires explanation.

In the Ru^{5+}-containing system of CaO–Ru_2O_5, the compound, $Ca_2Ru_2O_7$ has been studied. Single crystals of the ruthenate, $Ca_2Ru_2O_7$, were obtained. An XRD study on a single crystal revealed that this material crystallizes in a pyrochlore structure with a lattice parameter, $a = 10.197$ Å. The magnetic susceptibility above 30 K is the summation of a Curie–Weiss contribution

and a constant term independent of temperature. The effective moment per Ru atom is only 0.36 Bohr magnetons, one order of magnitude smaller than that expected from a localized spin model with $S = 3/2$ for Ru^{5+}. Below 23 K, the localized spins freeze in a spin glass state. The resistivity at room temperature is 2×10^{-3} Ohm-cm, comparable to that in metallic, highly correlated oxides. Spin glass properties of the ruthenate, $CaRu_2O_7$, were studied by precise magnetization measurements. The effective moment per Ru atom is only 0.25 μbar, which is one decade smaller than that expected from a localized spin model with $S = 3/2$ for Ru^{5+}. In spite of the small moment, a spin glass transition occurs at $Tg = 25.0$ K, and the nonlinear susceptibility $X_{nl}(\sim X^2)$ diverges negatively at Tg. The value of the critical exponent δ can be estimated as $\delta = 3.7$ from the magnetic field dependence of X_{nl} at Tg, which is comparable to those of other pyrochlore spin glasses and the canonical spin glasses.

The magnetism of a series of ruthenium pyrochlore oxides $A_2Ru_2O_7$ (A = Hg, Cd, Ca), whose electronic properties within a localized ion picture are characterized by non-degenerate t_{2g} orbitals (Ru^{5+}, $4d^3$) and thereby subject to geometrical frustration, has been investigated by a muon spin rotation/relaxation (muSR) technique. The A cation (mostly divalent) was varied to examine the effect of covalency (Hg > Cd > Ca) on their electronic property. In a sample with A = Hg that exhibits a clear metal-insulator (MI) transition below 100 K (which is associated with a weak structural transition), a nearly commensurate magnetic order is observed to develop in accordance with the MI transition. Meanwhile, in the case of A = Cd where the MI transition is suppressed to the level of small anomaly in the resistivity, the local field distribution probed by muon indicates emergence of a certain magnetic inhomogeneity below <30 K. Moreover, in $Ca_2Ru_2O_7$ that remains metallic, it was determined that a highly inhomogeneous local magnetism below >>25 K that comes from randomly oriented Ru moments and thus described as a "frozen spin liquid" state. The systematic trend of increasing randomness and itinerant character with decreasing covalency suggests close relationship between these two characters. As a reference for the effect of orbital degeneracy and associated Jahn–Teller instability, the examination of a tetravalent ruthenium pyrochlore, $Tl_2Ru_2O_7$ (Ru^{4+}, $4d^4$) was conducted, where the result of muSR indicates a nonmagnetic ground state that is consistent with the formation of the Haldane chains suggested by neutron diffraction experiments.

In the Ru^{6+}-containing system of CaO–RuO_3, the compound, $CaRuO_4$ has been studied. It has the structure shown in Fig. 12.48.

For the Mott insulator $CaRuO_4$, it has been observed that the orbital population dramatically changes with temperature. Together, with the finding that a substantial

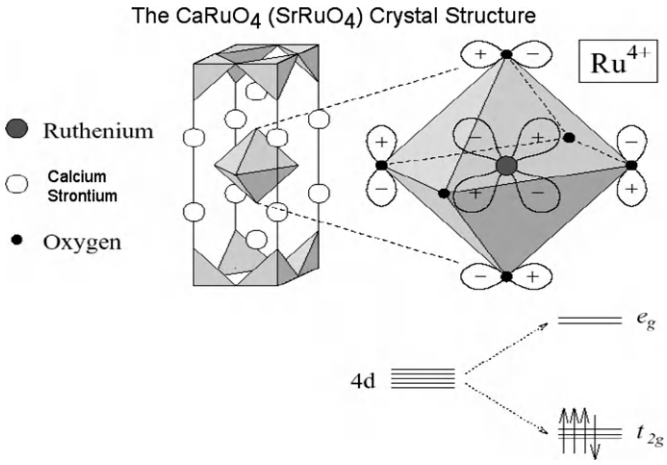

FIGURE 12.48

orbital angular momentum is present in the Ru 4d band, it has been argued that the cooperation between the strong spin-orbit coupling and the small distortion of the RuO_6 octahedra causes the interesting changeover of the spin and orbital anisotropy as a function of temperature. However, the published data concerning this compound are sparse and its properties have not been thoroughly established. $CaRuO_4$ is one of the layered Ruddlesden–Popper series of calcium ruthenates in which $n = 1$. The Sr series is shown below. The Ca series is identical in nature.

In the Ru^{7+}-containing system of CaO–Ru_2O_7, no compounds are known.

In the Ru^{8+}-containing system of CaO–RuO_4, no compounds are known.

Both of these ruthenium oxides are highly oxidizing, unstable, and liable to explode spontaneously. Perhaps this is the reason why no Ru^{7+} and Ru^{8+} compounds are known.

Calcium ruthenates are not available commercially.

12.3.4. Strontium Ruthenium Compounds

No intermetallic compounds in the system, Sr^0–Ru^0, are known.

In the Ru^{2+} series containing of SrO–RuO, the $SrRu_3O_4$ has been studied. It has been reported that this compound is a triplet odd-parity (p- or f-wave) superconductor. However, to date, no further research papers have appeared.

Perovskite ruthenium oxides of the Ruddlesden–Popper type, $(Sr/Ca)_{n+1}Ru_nO_{3n+1}$, have attracted significant attention due, in part, to the recent discovery of superconductivity in $Sr_2Ru_4O_4$. In addition, these materials exhibit a rich variety of magnetic phases, and bear strong structural resemblance to the cuprate superconductors, with RuO_2 planes taking the place of the

CuO_2 planes. Since the discovery of high-temperature superconductivity in layered cuprates, understanding of Mott-Hubbard MIT in a quasi 2D system has been a subject of significant interest. While Sr_2RuO_4 is a good metal and is believed to be well described within a framework of Fermi liquid theory, Ca_2RuO_4 is an insulator. It was suggested that the MIT in $(Sr,Ca)_2RuO_4$ is of the Mott-Hubbard type resulting from lattice distortions caused by the smaller size of the Ca^{2+} ion compared to the Sr^{2+} ion. In this scenario, the lattice distortions lead to a reduction of an electronic orbital overlap, similar to that observed in 3D $RNiO_3$, thus reducing W. A similar effect is expected for $(Sr/Ca)_3Ru_2O_7$, although the structural distortions and the corresponding bandwidth reduction may be smaller in this more rigid two-plane structure. Thus Sr/Ca substitution in layered $(Sr/Ca)_{n+1}Ru_nO_{3n+1}$ $(n = 1,2)$ provides a way for a continuous "tuning" of Mott-Hubbard parameter, U_yW, making it an ideal system for an experimental study of a transition from normal metal to Mott insulator at a constant carrier doping in a quasi 2D system.

In the Ru^{3+}-containing system of $SrO–Ru_2O_3$, the compound, $SrRu_2O_4$ has been found to be superconducting. However, only one paper is known in which it is compared to MgB_2 as a superconductor. The superconducting phase diagram for a 2D, three-band tight-binding model of $SrRu_2O_4$ using the fluctuation exchange approximation (FLEX) method was calculated. Electron interactions were modeled by a local-atom interaction with intraband, interband and exchange terms and an atomically local spin–orbit interaction is included as well. These results suggested that FLEX produces a singlet-pairing state with dx^2/y^2 orbital symmetry, a result that is not in agreement with many experimental results. However, it was determined that the values for the interaction strengths that are required to generate $T_C \sim 1.5$ K lead to normal-state quasi particle line widths that are in reasonable agreement with experimental results. At early stages, $SrRu_2O_4$ was believed to be close to a ferromagnetic instability. Ferromagnetic quantum critical spin fluctuations were believed to be responsible for triplet superconductivity, and even for stabilizing the particular chiral p-wave state. It was later discovered that $SrRu_2O_4$ is actually closer to a material possessing an antiferromagnetic spin-density wave instability (which makes stabilization of a p-wave state rather puzzling). However, it is generally accepted that critical fluctuations are very important for superconductivity in this compound.

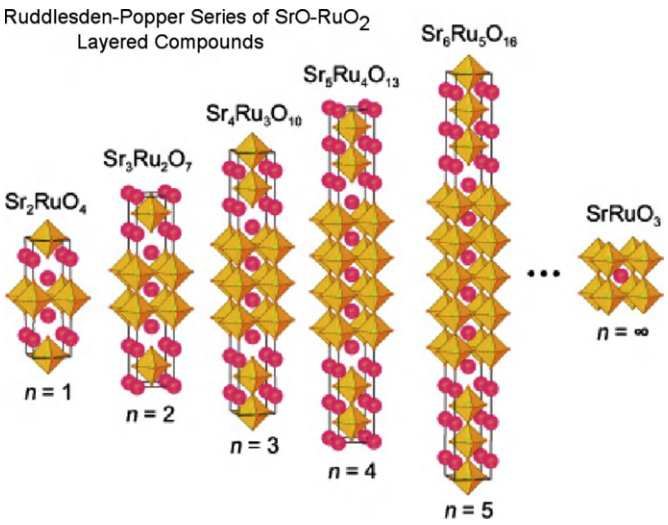

FIGURE 12.49

In the Ru^{3+} system of $SrO–Ru_2O_3$, the only compound mentioned in the literature is $Sr_3Ru_3O_7$. This compound undergoes ferromagnetic transitions below about 105 K and has revealed the existence of a well-defined, magnetically tuned quantum critical point. Only one paper has been published to date.

In the Ru^{4+}-containing system of $SrO–RuO_2$, a number of compounds are known. A Ruddlesden–Popper series $Sr_{n+1}Ru_nO_{3n+1}$ of layered perovskite ruthenate compounds shows that, with increasing number of consecutive RuO_2 layers, there appears to be an empirical trend toward ferromagnetism. This is shown in Fig. 12.49.

The magnetic properties of these compounds are summarized in Table 12.13.

The layered perovskite Sr_2RuO_4 first received widespread attention due to the discovery of superconductivity by Maeno and coworkers in 1994. Since then, a decade of intensive research has established the unconventional nature of that superconductivity, although a host of questions remain open concerning its microscopic origin. In parallel with work on the superconducting state, considerable experimental effort has been expended on understanding the metallic state from which the superconductivity condenses. Sr_2RuO_4 has a critical temperature of $T_c = 1.5$ K (in the clean limit)

TABLE 12.13

N	1	2	3	∞
Compound	Sr_2RuO_4	$Sr_3Ru_2O_7$	$Sr_4Ru_3O_{10}$	$SrRuO_3$
Magnetic properties	Paramagnetic	Metamagnetic transition (98)	Ferromagnetic $T_c = 148$ K	Ferromagnetic $T_c = 165$ K

and originally attracted interest because it possesses a layered perovskite structure like the high Tc cuprates and is therefore one of the very few perovskite oxide superconductors containing no copper. Further studies then indicated that the properties of Sr_2RuO_4 itself deviate strongly from the BCS "standard model" of s-wave superconductivity. There is now good evidence that Sr_2RuO_4:

(1) Shows spin triplet pairing,
(2) Exhibits time-reversal symmetry breaking of the orbital part of the pair wave function,
(3) Possesses line nodes in the gap function.

Sr_2RuO_4 is a layered superconductor with a $T_c \approx 0.95$ K. The electrical resistivity is strongly anisotropic and has an unusual T dependence: $ab \approx T^2$ for $T <$ K and $ab \approx T$ for $T > 100$ K; the ratio c/ab is about 850 around 4 K and 220 around 290 K. The de Haas–van Alphen effect (dHvA) and Shubnikov —de Haas (SdH) experiments show the presence of three anisotropic "Fermi surfaces". Experiments on Sr_2RuO_4 and related oxides indicate that this conductor is close to a spin 1 Mott insulating state. A model has been presented for the insulating and conducting states of these compounds and a mechanism for the MIT. It was claimed that there are two bands of non-Fermi liquids (which are close to half-filled) and an almost full band. The residual Hund's coupling in this (primarily 4d) band was argued to cause triplet correlations among the low-energy spinon excitations of the two bands of non-Fermi liquids below about 100 K. Based on this, it was clear that the experimentally observed superconducting state was likely to be a triplet p-wave type. This prediction has since been verified.

The physics of transition metal oxides is, in a first approximation, mainly the physics of the d-electron shell. If we take strontium and oxygen to have the usual nominal valences Sr^{2+} and O^{2-}, the ruthenium ion Ru^{4+} in Sr_2RuO_4 is left in a $4d^4$ electronic configuration. In the octahedral crystal field environment of the layered perovskite structure of Sr_2RuO_4, the energetically low-lying d levels are the three orbitals—nominally referred to as d_{xy}, d_{xz}, and d_{yz}—that belong to the t_{2g} representation of the octahedral group (see following figure). These orbits can thus accommodate six ($\Downarrow\Uparrow$) paired electrons and are partially filled in the $4d^4$ configuration of Sr_2RuO_4.

In the conventional theories of spin-fluctuation mechanism for superconductivity, the ferromagnetic spin fluctuation leads to triplet pairing, while the antiferromagnetic one causes singlet pairing. However, recently a mechanism leading to spin triplet superconductivity due to antiferromagnetic spin fluctuation has been proposed for Sr_2RuO_4. It was found that the anisotropy in spin fluctuation and the nesting property of the Fermi surface play crucial roles for the Cooper pairing. In the

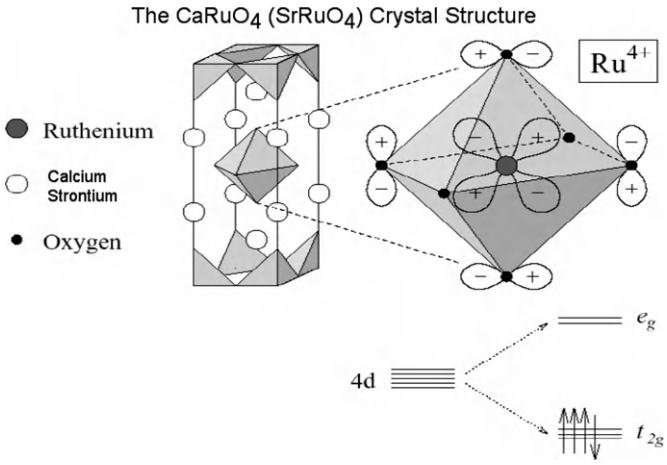

FIGURE 12.50

previous studies, however, the spin anisotropy was assumed phenomenologically. Further study of the origin of the anisotropy, using the more realistic three-band Hubbard model with spin orbit coupling and interband interactions, has been made. Its structure has the form shown in Fig. 12.50.

In this model, an anisotropy is naturally obtained, which becomes large enough, depending on the parameters, to support the superconducting mechanism for triplet pairing. It was found that the Hund coupling between the orbitals plays an important role. In general, metallic behavior is fairly rare among the transition metal oxides, and, more often than not, the d electrons remain localized, frequently forming a magnetic insulating state. This is mainly due to the large on-site (Hubbard) repulsion and the small interatomic overlap, both arising from the small orbital radius of the d electrons, particularly in the 3d series. There are exceptions, though, and Sr_2RuO_4 is one of several ruthenium oxide systems where the d electrons are itinerant. From the simplest point of view, the Fermi surface is then formed in a tight-binding fashion from the d_{xy}, d_{xz}, and d_{yz} atomic orbitals on the ruthenium sites. There is also some antibonding admixture of the oxygen p orbitals that, unlike the situation in most other oxide metals, has significant weight at the Fermi energy level. The layered structure of Sr_2RuO_4 prevents strong overlap of the orbitals along the c-axis, hence the electronic structure is, to a first approximation, 2D.

Density functional calculations have been used to investigate the spin structure of quantum fluctuations (QF), low-lying excitations and their relationship to superconductivity in Sr_2RuO_4. It has been demonstrated how the presence of the Fermi surface nesting in this highly 2D system leads in theory to establishment of antiferromagnetic spin density superstructure in the ground state and therefore in QF. These calculations confirmed the ground state spin structure that

develops in Sr_2RuO_4 upon partial Ti substitution (as found in experiment), even at concentrations typical for additives. The Ti disrupts the Ru–O–Ru chains, leading to an increase in the local density of states, and thereby favors moment formation on the neighboring Ru sites. Supercell calculations and frozen spin wave calculations have shown a marginal antiferromagnetic instability at the Fermi surface-nesting vector. At this wave vector, the magnetocrystalline anisotropy was found to be very small. The spin structure of QF and low-energy excitations are discussed in relation to these results. The nesting leads to the following effects:

(1) development of the spin structure in QFs and related low-lying excitations as a result of enhancement of the intersite exchange,
(2) effect of *lasing* on QFs, which implies selecting and amplifying waves out of the wave packet with nesting vector **qN** only.

The crystalline strontium ruthenate can be viewed as a superconducting liquid crystal, since the triplet nature of superconductivity makes it close to symmetry-broken phases of ^{3}He liquid, whereas the spin and orbital moments are ordered on the scale of spin–spin correlation length.

The oxide superconductor Sr_2RuO_4 has emerged as an archetypal strongly correlated electron system. Quantum oscillation measurements have revealed a Fermi surface consisting of three slightly warped cylinders populated by quasi particles with masses ranging from 3.4 to 14.6 times the bare electron mass. There is strong evidence that Sr_2RuO_4 is a spin triplet superconductor, and the simplicity of the Fermi surface combined with detailed knowledge of the quasi particle properties from quantum oscillation and orbital-specific NMR measurements means that Sr_2RuO_4 may be a key system for understanding unconventional superconductivity. A comparison of Sr_2RuO_4 with 3D nearly ferromagnetic 3d metals has suggested that quasi 2D spin fluctuations may be responsible for the fact that Sr_2RuO_4 is the first nearly ferromagnetic metal to show superconductivity.

In the ternary Sr–Rh–O system, several compounds have already been reported:

$Sr_{0.75}Rh_4O_8$ ($SrRu_{16}O_{32}$)
$SrRh_2O_4$
$Sr_6Rh_5O_{15}$
Sr_2RhO_4
Sr_4RhO_6
$(Sr_{0.5}Ca_{0.5})RuO_3$

The latter compound is dimorphic and has either the structure of $GdFeO_3$ (PG = o*P*20, SG = *Pnma*) or the $CaTiO_3$ structure (PG = *cP*5, SG = *Pm-3m*).

The above compounds were synthesized by rather conventional methods, and appear well characterized. Recently, two new members were added to the rhodate system, which were prepared by a high-pressure method; the perovskite $SrRhO_3$ and the bilayered $Sr_3Rh_2O_7$. At the end of the high-pressure studies, it was clear that the three compounds form a novel perovskite family as expressed by the general formula $Sr_{n+1}Rh_nO_{3n+1}$ (n = 1, 2, and infinity), indicating that this must be a Ruddlesden–Popper series.

$Sr_3Ru_2O_7$ is the bilayered member of the perovskite Strontium Ruthenate series and is the sister compound to the well-known spin triplet superconductor $Sr_2RuO_{4.9}$. It is a Fermi liquid at low temperatures with a large electronic specific heat, σ, of 110 mJ/Ru mol K^2 indicating strong electronic correlations. Its large Wilson ratio of 10 and structural similarity to the tri-layered, ferromagnetic $Sr_4Ru_3O_{10}$ have lead to the generally accepted view that this material is an exchange-enhanced paramagnet on the verge of ferromagnetism. High-pressure and high-temperature heating (6 GPa and 1500 °C) brought about successful preparation of a polycrystalline sample of the expected member at $n = 3$ of $Sr_{n+1}Rh_nO_{3n+1}$. Neutron diffraction studies revealed the orthorhombic crystal structure (*Pbam*) at room temperature and 3.4 K. Local structure distortions rotationally tilt the RhO_6 octahedra ~12° in the perovskite-based blocks along the *c*-axis, and approximately a 20% disorder was found in sequence of the alternating rotational tilt. The sample was also investigated by measurements of specific heat, thermo power, magnetic susceptibility, and electrical resistivity. The data clearly revealed enhanced paramagnetism and electrically conducting character, which reflected the nature of the correlated $4d_5$ electrons of Rh^{4+}. However, no clear signs of magnetic and electrical transitions were observed above 2 K and below 70 kOe, providing a remarkable contrast to the rich electronic phenomena for the significantly relevant ruthenate, $Sr_4Ru_3O_{10}$. Its structure is shown in Fig. 12.51.

This is a structural view of $Sr_4Rh_3O_{10}$. The fine lines signify the orthorhombic unit cell. Cooperative rotations along the *c*-axis of the RhO_6 octahedra are indicated by circular arrows in the diagram. There is approximately a 20 % stacking error, such as A''(B'') at A'(B') blocks, was indicated by the neutron diffraction study. The tilting of each RhO_6 octahedron was ~12° along the *c*-axis. Two-step metamagnetic transitions are additionally observed at 5.8 T and at 6.3 T, which coincide with a range of broad maximum in the magnetoresistance. At low temperatures, these two metamagnetic features each further split in two. Such a behavior of multiple transitions is qualitatively different from the first order transition at 5.1 T and indicate the complexity of such metamagnetic transitions.

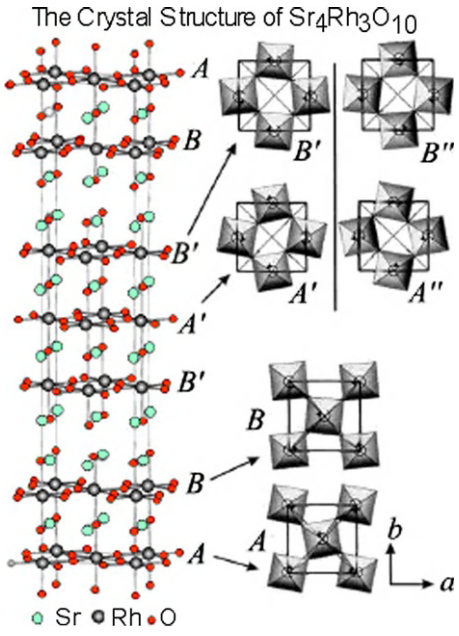

FIGURE 12.51

A novel material was produced by special processing of crystals of Sr_2RuO_4 (which is known to be a triplet superconductor with T_c values ~ 1.0–1.5 K). This material was claimed to be superconductive (zero DC resistance and expulsion of magnetic flux) at temperatures exceeding 200 K, that is at least 20 K higher than the copper-bearing compounds known as "high-temperature" superconductors. The special processing includes laser ablation and deposition of a silver coating and laser micromachining; Ag doping and enhanced oxygen are observed in the resultant surface layer. The transition, whether measured resistively or by magnetic field expulsion, is broad and not abrupt. When the transition was registered by resistive methods, the critical temperature is markedly reduced when the measuring current is increased. The resistance disappeared by about 190 K. The highest value of Tc registered by magneto-optical visualization is about 220 K and even higher values (up to 250 K) were indicated from the SQUID magnetometer measurements.

Laser ablation is one of the non-traditional methods of materials processing that may substantially alter the physical properties of samples. In addition to removing atoms from the surface, it may leave behind a recrystallized surface layer of altered composition and properties. The superconducting layer thickness is estimated to be 4–5 μm. The deeper layers (total thickness of the samples is 25 μm) have also been affected, and demonstrate pronounced ferromagnetism at temperatures as high as room temperature. This is itself also interesting since Sr–Ru–O systems never before demonstrated ferromagnetism at temperatures higher than 150 K.

However, other workers have not been able to reproduce these results and $Sr_2RuO_{6+\delta}$ is not regarded as a superconductor but retains its ferromagnetism. Time will tell if this compound, $Sr_2RuO_{6+\delta}$ ($\delta < 1.0$) proves to be a replacement for the high-temperature cuprate compounds currently under usage in the Industry.

In the Ru^{5+}-containing system of SrO–Ru_2O_5, the $Sr_2Ru_2O_7$ compound has been synthesized. $Sr_3Ru_2O_7$ is the $n = 2$ member of the Ruddlesden–Popper series of layered perovskites $Sr_{n+1}Ru_nO_{3n+1}$ octahedral ruthenium oxide. The four electrons in the ruthenium 4d t_{2g} orbitals hybridize with the oxygen 2p to create metallic bands that are narrow but still sufficiently broad to avoid insulating transitions. Thus, $Sr_3Ru_2O_7$ has a Ru–O bilayer per formula unit and the Ru effective spin has mainly a Heisenberg character. The (*H*,*T*) "crossover" phase diagram is rather similar to that derived for $CeRu_2Si_{21}$ whose properties are dominated by layers of octahedral ruthenium oxide . The four electrons in the ruthenium 4d t_{2g} orbitals hybridize with the oxygen 2p to create metallic bands that are narrow but still sufficiently broad to avoid insulating transitions.

Thus, $Sr_3Ru_2O_7$ has a Ru–O bilayer per formula unit and the Ru effective spin has mainly a Heisenberg character. The (*H*,*T*) "crossover" phase diagram is rather similar to that derived for $CeRu_2Si_2$. There is a rapid super-linear rise in magnetization in a field of 5.5 T for magnetic fields applied in the *ab*-plane. The metamagnetism is broadened as the temperature is raised. Metamagnetism is seen for all temperatures below 10 K, centered on a field of approximately 5.5 T. In metallic systems such as $Sr_3Ru_2O_7$, the change in magnetization is due to a rapid change from a paramagnetic state at low fields to a more highly polarized state at high fields via a crossover or a phase transition. However, some of the basic physics is same in both cases. The observation of itinerant metamagnetism demonstrates the existence of strong ferromagnetic coupling in the system. Thus, experimental results of the metamagnetism in $Sr_2Ru_2O_7$ give strong evidence for a new type of quantum critical behavior, namely a quantum critical end point. This study showed that this behavior can be caused by band structure effects, e.g. by the vicinity of a Van Hove singularity. The phase diagram for the multi-layer ruthenates, developed as a function of magnetic field and band filling, showed the presence of a quantum critical end point that terminates a first-order phase boundary. At the end point, the Fermi level of the majority spin band is precisely located at the Van Hove singularity. Thus, this system is rather susceptible to disorder effects. The possible appearance of Condon-domain like structures in a metamagnetic system was investigated. Condon-domains are the result of the coexistence of two magnetic phases at a first-order phase transition and may influence the motion of carriers via domain-wall scattering.

The magnetization curves are in good qualitative agreement with the observed behavior in $Sr_4Ru_3O_{10}$ for magnetic fields parallel to the *ab*-plane(2). Furthermore, the data are consistent with the experimental findings in $Sr_3Ru_2O_7$, where smooth metamagnetism has been observed at fields that are two to three times larger than the critical field in $Sr_4Ru_3O_{10}$. In the following figure, the resistivity (ρ_{res}) versus magnetic field of $Sr_3Ru_2O_7$ for three samples (of increasing purity) is shown in Fig. 12.52.

The top trace shows the unusual T^3 dependence previously reported for $\rho_{res} = 2.8\ \Omega/cm$. The temperature dependence of ρ_{res} at the MMT (magnetic moment temperature) changes to a negative gradient at low temperatures, with a minimum that increases systematically with temperature, as the sample gets purer. The susceptibility (χ) and resistivity (ρ_{res}) versus magnetic field across the metamagnetic field is shown in the following diagram (Fig. 12.53). The measurements were made at $T = 20$ mK on different crystals, both having $\rho_{res} = 0.5\ \Omega/cm$. The ac excitation field was 0.32 G at a frequency of 83.4 Hz. The temperature of each curve is between 0.06 and 0.1 K and the magnetic field is perpendicular to the RuO_2 planes. As the sample purity increases, the same basic peak remains as the dominant feature, but more structure develops. One observes a pronounced dip at 7.5 T, and the central peak is seen to have very steep sides at 7.8 and 8.1 T. The system's properties appear to be governed by the presence of a metamagnetic QCP (Quantum critical point = magnetically ordered phase).

The magnetic spectrum of $Sr_4Ru_2O_9$, in which the spectral feature from the RuO_6 units is shifted by 1 eV to lower energy upon increasing the Ru valence from Ru(IV) to Ru(V), results in a better separation of the RuO_6^- related state from the SrO band. This shift to lower energy that occurs in a manner fully analogous to the behavior observed in the spectra of 3d-TM oxides due to the increase of covalence with increasing valence.

Thus, the e_g-related peak in $Sr_4Ru_2O_9$ is individually identifiable in the energy range 530.5–532.5 eV. It is evident that the lower energy t_{2g}-related peak at 528.5 eV is narrower than the broad higher energy e_g- related peak as already observed in the Ru $L_{2;3}$ XAS spectrum discussed earlier. This is a direct result of the stronger covalent dp σ-like mixing between the O-2p and Ru-4d(e_g) orbitals. Ru(V) with the $t_{2g}^3e_g$ configuration has been known to possess a high-spin state ($S = 3/2$).

In the Ru^{6+}-containing system of SrO–RuO_3, the compound, $SrRuO_4$, has been described. The rapid suppression of the superconducting temperature, T_c, was the first indication that $SrRuO_4$ is a p-wave superconductor. The spin triplet Cooper pairs satisfy the Spin-Statistics Theorem by having odd orbital angular momentum and comply with the SST by virtue of being odd in time or frequency. The possibility of spin triplet, p-wave pairing in $SrRuO_4$ ($T_c = 1.4$ K) has generated considerable interest. $SrRuO_4$ is a perovskite with strong anisotropy and strong ferromagnetic fluctuations. The latter are expected to favor triplet pairing; measurements show a Knight shift that remains constant down to $T/T_c << 1$, as expected for a spin triplet state for the field orientation used. Bonalde et al. measured the penetration depth down to 40 mK using a tunnel diode oscillator. Several samples were measured. At the lowest temperatures, the superfluid density varied quadratic ally with temperature, suggesting the presence of nodes. However, other experiments in $SrRuO_4$ point to a state with a finite energy gap. One widely considered candidate was the axial state $d(k) = \Delta_0 z(k_x + ik_y)$ where z is perpendicular to the basal plane. The authors ruled out "gapless" behavior from impurities that can give a T^2-dependence even to a superconductor with an energy gap. They concluded that the quadratic dependence may arise from nonlocality. The issue is not settled and several other triplet pairing states have also been investigated for this material. At this point in time, the only known p-wave superconductor is $SrRuO_4$

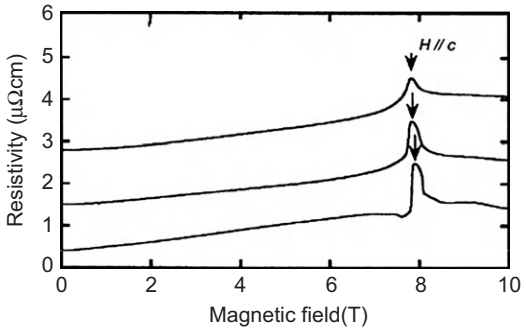

FIGURE 12.52

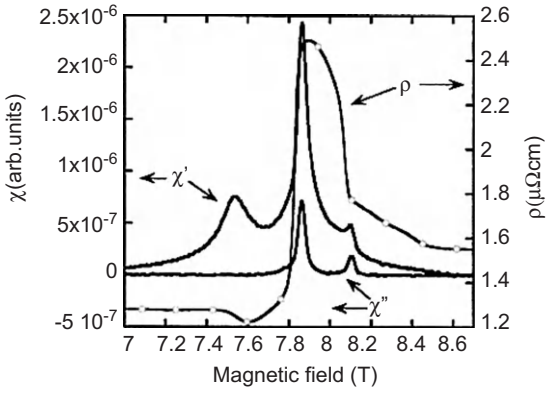

FIGURE 12.53

which with a T_{max} of about 1.5 K for the undoped compound. The known d-wave superconductors include the heavy fermion systems and the cuprates. Both p- and d-wave superconductors exhibit points of zero gap magnitude called nodes. The main difference between the p-wave and d-wave order parameters is the relative phases exhibited by the different lobes of the order parameter.

In the Ru^{7+}-containing system of SrO–Ru_2O, only two papers mention the compounds, $Sr_2Ru_2O_9$ and $Sr_3Ru_2O_{10}$. Little data has been forthcoming concerning these compounds that are described as "itinerant metamagnets", meaning that their degree of magnetism can be easily disrupted by the formation of oxygen vacancies and/or other lattice imperfections.

In the Ru^{8+}-containing system of SrO–RuO_4, no compounds are known.

Strontium ruthenate is available commercially as Sr_2RuO_4.

12.3.5. Barium Ruthenium Compounds

No intermetallic compounds in the system, Ba^0–Ru^0, are known.

In the Ru^{2+}-containing system of BaO–RuO, no compounds are known.

In the Ru^{3+}-containing system of BaO–Ru_2O_3, no compounds are known.

In the Ru^{4+}-containing system of BaO–RuO_2, several compounds are known. $BaRuO_3$ exists in two polytypes (4H and 9R) based on different stacking sequences of close-packed BaO_3 layers. Raman measurements on ceramic samples of both structures and on a 9R single crystal have been performed. The symmetries of most of the 9R modes have been determined from polarization-resolved measurements on the single crystal. A factor group analysis predicts nine Raman modes in the 9R and eight in the 4H structure.

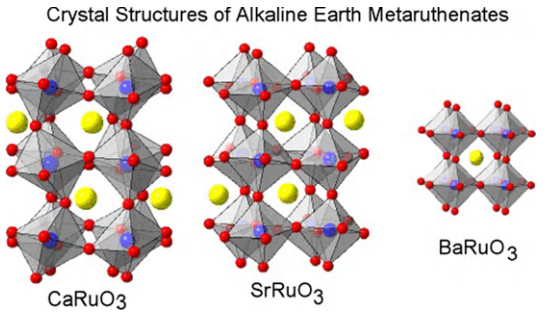

FIGURE 12.55

The $BaRuO_3$ compound falls into the class of hexagonal stacked polytypes known for CrO_6, MnO_6 and FeO_6 compounds (Fig. 12.54).

The cubic perovskite $BaRuO_3$ has been synthesized under 18 GPa at 1000 °C. Rietveld refinement indicates that this compound has a stretched Ru–O bond. The cubic perovskite $BaRuO_3$ remains metallic to 4 K and exhibits a ferromagnetic transition at $T_c = 60$ K, which is significantly lower than the $T_c \approx 160$ K for $SrRuO_3$. The availability of cubic perovskite $BaRuO_3$ not only makes it possible to map out the evolution of magnetism in the whole series of $AeRuO_3$ (Ae = Ca, Sr, Ba) as a function of the ionic size of the A-site r_A, but also completes the known polytypes of $BaRuO_3$.

The crystallography of $ARuO_3$ is shown in the above diagram. This diagram shows a comparison of the structures for these three compounds (Fig. 12.55). (a) Schematic drawing of the three perovskites $CaRuO_3$, $SrRuO_3$, and $BaRuO_3$ where red balls stand for O, gray for RuO_6, and yellow balls for alkaline earths Ca, Sr, and Ba.

In the following diagram, the magnetic spectrum of $Sr_4Ru_2O_9$, in which the spectral feature from the RuO_6 units is shifted by 1 eV to lower energy upon increasing the Ru valence from Ru(IV) to Ru(V), results in a better separation of the RuO_6^- related state from the SrO band (Fig. 12.56).

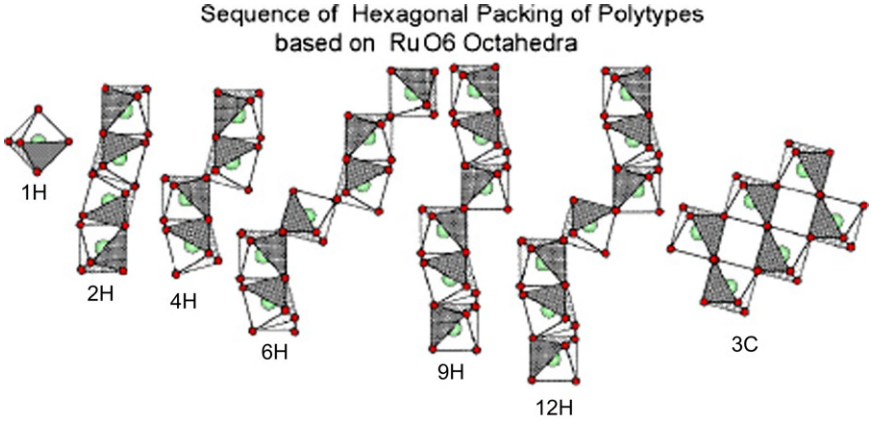

FIGURE 12.54

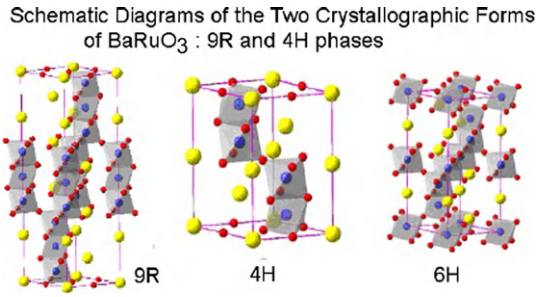

FIGURE 12.56

This shift to lower energy occurs in a manner fully analogous to the behavior observed in the spectra of 3d-TM oxides due to the increase of covalence with increasing valence.

It has been determined that if the 9R form is heated under pressure, it transforms into the other configurations at specific pressures, as shown in Fig. 12.57.

Extension of the plot of T_c versus r_A in perovskites $ARuO_3$ (A = Ca, Sr, Ba) shows that T_c does not increase as the cubic structure is approached, but has a maximum for orthorhombic $SrRuO_3$. Suppressing T_c by Ca and Ba doping in $SrRuO_3$ is distinguished by sharply different magnetic susceptibilities σ(T) of the paramagnetic phase. This distinction has been interpreted in the context of a Griffiths' phase on the (Ca Sr)RuO_3 side and bandwidth broadening on the (Sr,Ba)RuO_3 side.

The phase diagram of the magnetic transition temperatures versus the tabulated average A-site ionic radius r_A for $Sr_{1-y}Ba_yRuO_3$ and $Sr_{1-x}Ca_xRuO_3$ is shown in Fig. 12.58.

Three members in the phase diagram $CaRuO_3$, $SrRuO_3$, and $BaRuO_3$, in which the A-site size variance is 0, are distinguished by the solid symbols. The shaded area in the phase diagram represents the phase having the characteristic x^{-1}(T) of the Griffiths' phase. Letters inside the diagram stand for the crystal structure as determined by XRD at room temperature, O for orthorhombic, T for tetragonal, and C for cubic. The inset shows the temperature dependence of inverse magnetic susceptibility of $Sr_{1-x}Ca_xRuO_3$ measured with a magnetic field $H = 1$ T and of $Sr_{1-y}Ba_yRuO_3$ measured with a magnetic field $H = 0.5$ T in this work.

In another paper, single crystals of $BaRuO_3$ were grown using a $BaCl_2$ flux at ambient pressure. Most of the crystals had the nine-layer rhombohedral structure (9R), a form considered to be the stable form of $BaRuO_3$ at ambient pressure. However, some $BaRuO_3$ crystals in this preparation had the four-layer hexagonal (4H) structure that had been considered as a phase produced only at high pressure (15–30 kbar). The crystal structure of 4H $BaRuO_3$ was refined for the first time. Single-crystal XRD data gave a space group of $P6_3/mmc$ (No. 194), $a = 5.729$ Å, $c = 9.500$ Å, $Z = 4$, a final conventional R(based on F_0) of 2.01%, and a_wR2 (based on F^2_0) of 4.07%. The structure of 4H $BaRuO_3$ may be described as perovskite related with a four-layer stacking of BaO_3 layers in the sequence **hchc**. This led to pairs of face-sharing RuO_6 octahedra that are connected to other octahedra by corner sharing. The Ru–Ru distance in the Ru_2O_9 dimer of 4H $BaRuO_3$

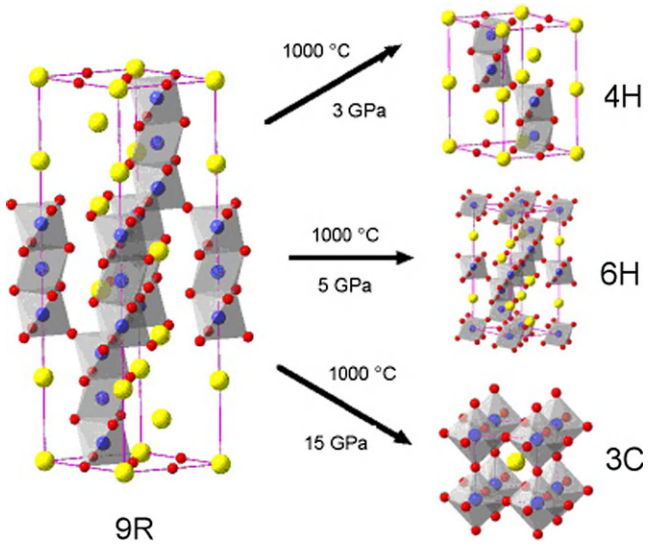

FIGURE 12.57

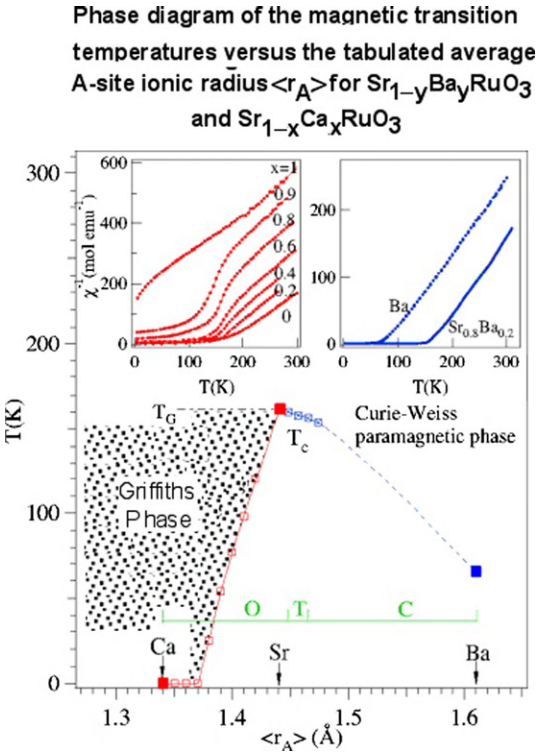

FIGURE 12.58

is 2.537 Å, which indicates the presence of a metal–metal bond.

The single-phase 6H $BaRuO_3$ with the hexagonal $BaTiO_3$ structure was synthesized at 5 GPa and 1000 °C. Rietveld refinement of the powder X-ray data for the 6H phase resulted in the lattice parameters to be $a = 5.7127$ Å and $c = 14.0499$ Å; the average Ru–O distance and direct Ru–Ru distance in the Ru_2O_9 dioctahedron being 1.992 and 2.5658 Å, respectively. The electrical resistivity of the 6H $BaRuO_3$ follows a relationship of σ versus $T^{3/2}$ below 60.0 K, a signature deviation from the Fermi liquid behavior. Both magnetic susceptibility and specific heat data indicate that the 6H $BaRuO_3$ is an exchange-enhanced Pauli paramagnet due to the electron correlation effect with large Wilson ratio R_W and Stoner enhancement factor. The comprehensive evolution of transport and magnetic properties from 9R across 4H to 6H $BaRuO_3$ was discussed.

The results of magnetic susceptibility and electrical resistivity measurements, made on single crystals of the nine-layer and four-layer crystallographic forms of $BaRuO_3$, have been reported. The two forms differ in the relative amounts of corner and face sharing of RuO_6 octahedra. They display qualitatively different properties below approximately 100 K: the four-layer form shows a metallic resistivity down to low temperatures, while the nine-layer shows a crossover to a more resistive state. No local moment magnetism is observed in either phase below 400 K, which is of particular interest in the context of previously observed magnetic and superconducting phases in the Sr–Ru–O system. Resistive measurements to temperatures below 0.1 K reveal no occurrence of superconductivity in either form. Temperature-dependent reflectivity spectra of non-perovskite nine-layer $BaRuO_3$ single crystal and four-layer $BaRuO_3$ epitaxial film was measured. In optical conductivity spectra obtained through Kramers–Kronig transformation, it was observed that both materials show pseudogap formations in their metallic states. A clear development of pseudogap as well as a coherent component as a function of temperature is evidently distinguished from other pseudogap systems, such as high T_c cuprates and heavy electron systems. We suggested that these interesting features should be related to the structural characteristics of the layered structures with face sharing of RuO_6 octahedra, which might induce 1D instability. High electrical conductive $BaRuO_3$ thin films with (110) perovskite orientation have been successfully fabricated on Si(100) substrates by pulsed ArF excimer laser deposition and post-annealing. The resistivity of the films at room temperature is in the range of 10^{-2} to 10^{-3} Ω/cm.

The observation of a modulated structure and a ferromagnetic insulating state in a high-quality single crystal of a nine-layer $BaRuO_3$ was reported. Using X-ray scattering, the modulated satellites were observed to double the unit cell along the *c*-axis at low temperature. The ferromagnetic insulating state is confirmed by magnetic and resistivity measurements. Analyzing the peak profiles from the modulation and host structure respectively, showed a lattice distortion at $T \approx 55$ K. These findings elucidate the intimate relationship between ferromagnetism and lattice distortion in a nine-layer $BaRuO_3$.

The compound, Ba_2RuO_4, has been grown as an epitaxial $Ba_2RuO_{4-\delta}$ film with the K_2NiF_4 structure by pulsed laser deposition on (100) $SrTiO_3$ substrates. XRD and cross-sectional TEM results indicate that the films are *c*-axis oriented, single-domain, and contain relatively few stacking faults and intergrowths. Electrical measurements indicate metallic conductivity to low temperatures, but no evidence of superconductivity. It is significant that films with the composition $BaRuO_3$ could not be prepared.

The study of the solid-state reactions in air or oxygen of the ternary system Ba–Ru–O shows the existence of the new compounds $Ba_4Ru_3O_{10}$ and $Ba_5Ru_3O_{12}$. The crystal symmetry of $Ba_4Ru_3O_{10}$ is monoclinic ($P2_1/a$) with the unit cell constants $a = 5.776(1)$ Å, $b = 13.076(1)$ Å, $c = 7.234(2)$ Å and $\beta = 113.53(3)°$. $Ba_4Ru_3O_{10}$ is isostructural with $Ba_4Ir_3O_{10}$ and the structure consists of trinuclear groups $[Ru_3O_{12}]$ of face-sharing octahedra 2D connected via terminal corners to form $[Ru_3O_{10}]$ zigzag layers. The magnetic properties confirm the oxidation state (Ru^{4+}) of ruthenium. $Ba_5Ru_3O_{12}$ is isostructural with $Ba_5(Ir_{1.5}Ru_{1.5})O_{12}$ with the cell parameters $a = 10.862(1)$ Å, $b = 5.893(1)$ Å and $c = 19.790(2)$ Å ($Pnma$). The crystal structure was refined on the basis of a single crystal in which part of the ruthenium was replaced by platinum. The structure consists of isolated $[Ru_3O_{12}]$ trimeric groups separated by barium atoms. Valence bond calculation confirms that the electronic charges are localized, and the magnetic behavior is interpreted in terms of antiferromagnetic isolated trimeric units.

The compound $Ba_5Nb_2O_9(O_2)$ has been synthesized by solid-state reactions. The crystal structure has been refined from X-ray powder data. $Ba_5Nb_2O_9(O_2)$ is isostructural with $Ba_5Ru_2O_9(O_2)$ with the cell parameters $a = 6.045$ Å, $c = 18.316$ Å ($P6_3/mmc$). Perpendicular to the *c*-axis, the structure is built up by the periodic stacking of three close packed $[BaO_3]$ layers separated by a layer of composition $[Ba_2O_2]$ containing $(O_2)^{2-}$ peroxide ions. The compound $Ba_5Ru_2O_{10}$ has been obtained by thermal decomposition of $Ba_5Ru_2O_9(O_2)$. The structure has been refined from X-ray powder data. The structure is similar to $Ba_5Ru_2O_9(O_2)$ but now the composition of the layer is $[Ba_2O]$. The magnetic properties of $Ba_5Ru_2O_9(O_2)$ and $Ba_5Ru_2O_{10}$ have been interpreted in terms of isolated dimers and confirm the structural results. All these phases belong to a new family of compounds formulated as $[A_2(O_2)][A_nB_{n-1}O_{3n}]$ where *n* represents the number of $[AO_3]$ successive

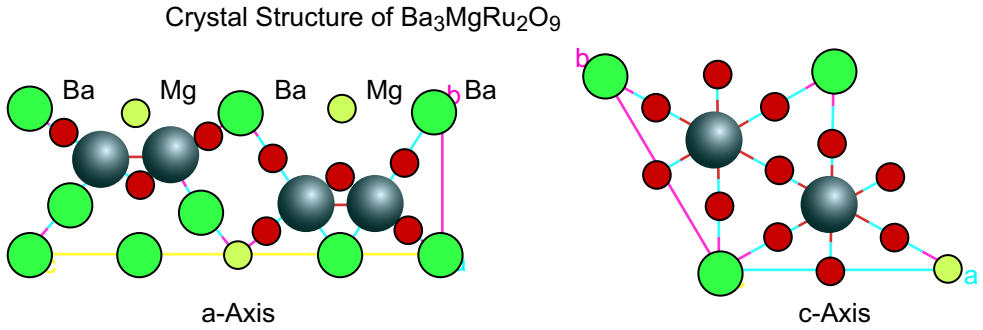

FIGURE 12.59

layers in the hexagonal perovskite slabs. This series can be extended to ternary barium sulfides.

In the Ru^{5+}-containing system of $BaO–Ru_2O_5$, only one compound is known. The compound, $Ba_3MgRu_2O_9$, has the structure shown in Fig. 12.59.

Cell parameters are: $a = b = 5.762$ Å, $c = 14.155$ Å, $\alpha = \beta = 90°$, $\gamma = 120°$, $Z = 2$.

Cell volume = 409.99 $Å^3$. Cell occupancy is shown in Table 12.14.

In the Ru^{6+}-containing system of $BaO–RuO_3$, the compound, $BaRuO_4$ has been synthesized. However, it cannot be formed by solid-state methods since it contains a peroxy-ruthenate grouping, RuO_4^{2-} that is potentially explosive. Because RuO_4 will readily decompose explosively at slightly elevated temperatures, it cannot be synthesized directly, nor is it commercially available through major chemical vendors. However, if K_2RuO_4 in solution is contacted by $BaCl_2$, a barium peroxy-ruthenate hydrate is precipitated:

$$BaCl_2(aq) + K_2RuO_4(aq) \Rightarrow BaRuO_4 \cdot H_2O(solid)$$

The structure of the so-called barium ruthenate monohydrate is more likely $BaRuO_3 \cdot (OH)_2$. This is a hexagonal compound with $a = 5.787$ Å, $c = 8.491$ Å, $Z = 2$, space group = $P6_2/mmc$. In the subcell, partial occupancy can be explained by steric considerations. Refinement of the structure results in a rhombohedral call with $a_0 = a\sqrt{3} = 10.23$ Å, $c_0 = 3c = 25.471$ Å, $Z = 18$, space group = $R3c$. The dihydroxy-trioxo-ruthenate(VI) ions have a trigonal-bipyramid configuration with three-short Ru–O bonds (1.755 Å) and two longer Ru–OH bonds (2.02 Å). They form six layers of $RuO_3(OH)_2^{2-}$ ions, stacked perpendicularly to the c-axis and separated by Ba^{2+} ions. Stacking defects in the succession of layers has led to statistical hexagonal symmetry.

A solution of barium chloride precipitates K_2RuO_4 to form red precipitate $BaRuO_4 \cdot H_2O$. No anhydrides like Ru_2O_7 and Ru_2O_3 are known, but RuO_3 can be formed. No acid like $HRuO_4$ that would form the salts is known, because, when these salts are decomposed with acid, then an unstable RuO_4 and lower oxides result. The latter are the basic oxides and form salts with acids.

In the Ru^{7+}-containing system of $BaO–Ru_2O_7$, no compounds are known.

In the Ru^{8+}-containing system of $BaO–RuO_4$, no compounds are known.

No barium ruthenates compounds are available commercially.

12.3.6. Radium Ruthenium Compounds

No intermetallic compounds in the system, Ra^0–Ru^0, are known. Although radium probably forms the same type of compounds with ruthenium oxides, there have been no mention of such in the scientific literature (to date).

TABLE 12.14

No.	Site notation	Atom	Multiplicity	Wyckoff	Site symmetry	x	y	z	Occupancy
1	O2	O	12	k	.m.	0.1666	0.3333	0.5833	1.0
2	O1	O	6	h	mm2	0.5	0.0	1/4	1.0
3	Ba2	Ba	4	f	3m.	1/3	2/3	0.0912	1.0
4	Ru	Ru	4	f	3m.	1/3	2/3	0.655	1.0
5	Ba1	Ba	2	b	−6m2	0	0	1/4	1.0
6	Mg	Mg	2	a	−3m.	0	0	0	1.0

12.4. ALKALINE EARTH—OSMIUM COMPOUNDS

Osmium has the following valence states: +1, −1, −2 in solution media and 2+, 3+, 4+, 5+, 6+, 7+, and 8+ in solid media. However, the number of compounds actually synthesized is small compared to the other elements in this 8d series.

Thus, not all of the oxide compounds are stable enough to form compounds with the alkaline earths. The most common oxidation states are +2, +3, +4, and +8. The +8 oxidation state is notable for being the highest attained by any chemical element. Osmium tetraoxide, OsO_4, is a very toxic compound, formed when powdered osmium is exposed to air, and is a very volatile, water-soluble, pale yellow, crystalline solid with a strong smell. In basic solution, it forms red osmates $OsO_4(OH)_2^{2-}$. OsO_2, osmium dioxide, is black, non-volatile, and much less reactive and toxic. Only two osmium oxide compounds have major applications: osmium tetroxide—for staining tissue in electron microscopy and the non-volatile osmates for organic oxidation reactions.

12.4.1. Beryllium Osmium Compounds

In the $BeO–Os_xO_{2x+1}$ system, no compounds are formed as the valence of Os is varied from +2 to +8.

It does, however form intermetallic compounds of the nature, $Be^0–Os^0$. Three compounds are known: $Be_{12}Os$, $Be_{17}Os_2$ and $Be_{17}Os_3$. The latter two compounds have structures identical to the Be^0Ru^0 series of compounds. These structures are compared in Fig. 12.60.

The cell parameters for $Be_{17}Os_2$ are: $a = b = 4.224$ Å, $c = 10.95$ Å, $\alpha = \beta = \gamma = 90°$, cell volume $= 139.20$ Å^3, $Z = 6$. Cell occupancy is shown in Table 12.15.

$Be_{17}Os_3$ has the cell parameters of: $a = b = c = 9.8225$ Å, $\alpha = \beta = \gamma = 109.471$ Å, cell volume $= 729.54$ Å^3, $Z = 12$, but an exact structure has not been published. Cell occupancy is shown in Table 12.16.

$Be_{12}Os$ has the following cell parameters but an exact structure has not been published: $a = 8.4803$ Å, $b = 10.628$ Å, $c = 11.305$ Å, $\alpha = 96.546°$, $\beta = \gamma = 90°$, cell volume $= 1012.26$ Å^3, $Z = 6$.

These compounds remain as research oddities and no commercial usage has evolved.

12.4.2. Magnesium Osmium Compounds

Magnesium does not form any intermetallic compounds with osmium metal.

In the system of $MgO–Os_xO_y$, where $x = 1$ or 2 and y varies from 2 to 8, very few compounds are known.

In the Os^{3+}-containing system of $MgO–Os_2O_3$, the compound, $MgOs_2O_4$ has been studied. The 3s

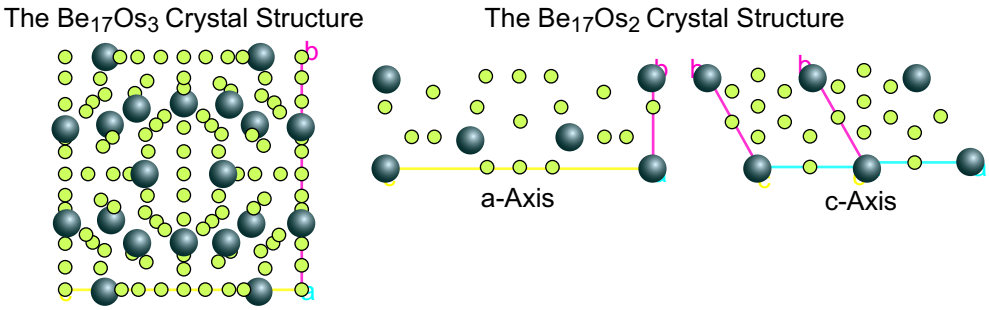

FIGURE 12.60

TABLE 12.15

No.	Site notation	Atom	Multiplicity	Wyckoff	Site symmetry	x	y	z	Occupancy
1	Be1	Be	6	n	.m.	0.1665	0.8335	0.1830	1.0
2	Be2	Be	3	k	mm2	0.5045	0.4955	1/2	1.0
3	Be3	Be	2	i	3m.	2/3	1/3	0.0982	1.0
4	Os1	Os	2	i	3m.	2/3	1/3	0.3069	1.0
5	Be4	Be	2	h	3m.	1/3	2/3	0.3408	1.0
6	Be5	Be	2	g	3m.	0	0	0.3767	1.0
7	Be6	Be	1	c	−6m2	1/3	2/3	0	0.34
8	Os2	Os	1	a	−6m2	0	0	0	0.36

TABLE 12.16

No.	Site notation	Atom	Multiplicity	Wyckoff	Site symmetry	x	y	z	Occupancy
1	Be1	Be	48	h	1	0.114	0.3434	0.201	1.0
2	Os1	Os	24	g	m..	0	0.1879	0.3014	1.0
3	Be2	Be	24	g	m..	0	0.2305	0.0914	1.0
4	Be3	Be	24	g	m..	0	0.4055	0.3488	1.0
5	Be4	Be	16	f	.3.	0.1645	0.1645	0.1645	1.0
6	Be5	Be	12	e	mm2.	0.1956	0	1/2	1.0
7	Be6	Be	12	d	mm2.	0.4065	0	0	1.0

band of Mg is lower in energy than the other alkaline earths, and appears around the Fermi level, which makes $MgOs_2O_4$ always metallic in conductivity. No data concerning structure are available and no other compounds have been described in this system.

In the Os^{6+}-containing system of $MgO–OsO_3$, the compound, $MgOsO_4$, is too unstable to be isolated. However, this compound is formed momentarily by the addition of K_2OsO_4 in solution upon the surface of MgO particles. It then causes the dihydroxylation of various organic olefins with excellent yields. A typical reaction is shown in Fig. 12.61.

New bifunctional catalysts composed of OsO_4^{2-} and WO_4^{2-} designed and prepared by a counter-ionic stabilization technique involving the reactions of K_2OsO_4–Na_2WO_4 with nanocrystalline MgO are well characterized. This bifunctional catalyst, NAP-Mg-OsW, performs tandem Heck asymmetric dihydroxylation and asymmetric dihydroxylation-*N*-oxidation reactions, in the presence of the chiral ligand 1,4-bis(9-*o*-dihydroquinidinyl)phthalazine [$(DHQD)_2PHAL$] in a single pot. It is quite impressive to note that H_2O_2 is used as a terminal oxidant to provide *N*-methylmorpholine *N*-oxide (NMO) in situ by the oxidation of *N*-methylmorpholine (NMM) in the asymmetric dihydroxylation-*N*-oxidation catalyzed by NAP-Mg-OsW. No other compounds are known in this system.

In the Os^{4+}-, Os^{5+}-, Os^{7+}-, and Os^{8+}-containing systems, no compounds are known.

Magnesium osmates are not available commercially and no CAS numbers have been issued.

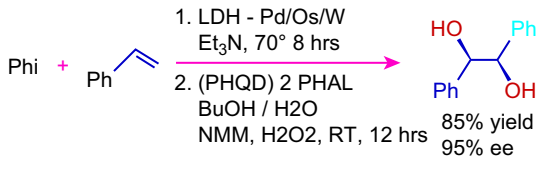

FIGURE 12.61

12.4.3. Calcium Osmium Compounds

Calcium does not form any intermetallic compounds with osmium metal.

In the system of $CaO–Os_xO_y$, where $x = 1$ or 2 and y varies from 2 to 8, no compounds involving the Os^{2+}, Os^{7+} and Os^{8+} ions are known.

In the Os^{3+}-containing system of $CaO–Os_2O_3$, the compound, $CaOs_2O_4$ has been studied from a theoretical standpoint. It is metastable and has not yet been isolated. It is expected to have a spinel structure shown in Fig. 12.62.

Theoretically, determined structure parameters of spinel osmates are shown in Table 12.17. Angle denotes the Os–O–Os bond angle; OsO and Os–Os denote the nearest neighbor Os–O bond length, and Os–Os bond length, respectively.

For comparison, the same parameters for the pyrochlore and iridate, $Y_2Ir_2O_7$, are also listed. It is apparent that the A-site element has a considerable effect on the Os–O bond angle and its length. $CaOs_2O_4$: Its reciprocal lattice (Brillouin Zones) band structure from nonmagnetic LDA + SO calculation was found to be metallic. The energy bands around the Fermi level appear as $J_{eff} = 1/2$ states similar to the ones found in Sr_2IrO_4, and also in $Y_2Ir_2O_7$, where a metal rather than the interesting topological insulator scenario of was obtained due to a 2-4-2 sequence of degeneracy at the ⌜ point.

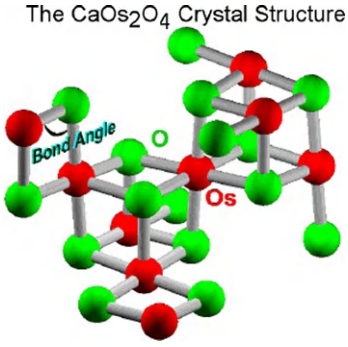

FIGURE 12.62

TABLE 12.17

	Angle	Os–Os	Os–O
$CaOs_2O_4$	98.50 Å	3.07 Å	2.04 Å
$SrOs_2O_4$	94.50 Å	3.12 Å	2.05 Å
$BaOs_2O_4$	103.10 Å	3.28 Å	2.11 Å
$Y_2Ir_2O_4$	129.70 Å	3.60 Å	1.99 Å

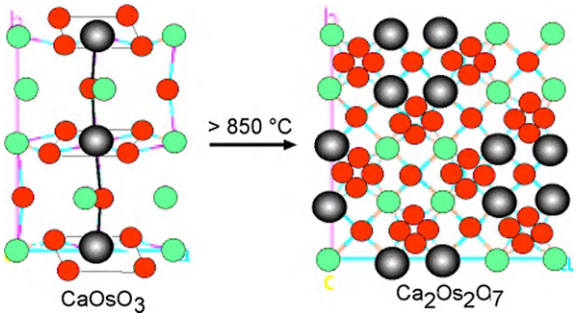

FIGURE 12.63

To date, these compounds have not been isolated in a stable form at room temperature.

In the Os^{4+}-containing system of CaO–OsO_2, the compound, $CaOsO_3$, has been studied. The thermal decomposition of $CaOsO_3$ by differential thermal analyses, thermogravimetry and XRPD has been studied. In nitrogen $CaOsO_3$ decomposes at 880 ± 10 °C into CaO, osmium metal and oxygen due to the reaction $CaOsO_3 \Rightarrow CaO + Os + O_2$. In static air, the decomposition occurs in three stages:

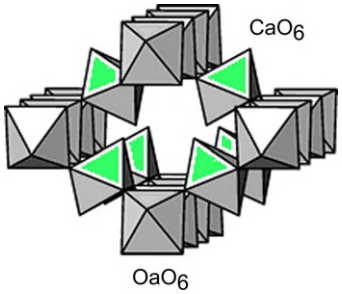

FIGURE 12.64

$$2CaOsO_3(solid) + 0.5O_2(gas) \Rightarrow Ca_2Os_2O_7(solid) \quad [850–808\ °C]$$

$$Ca_2Os_2O_7 \Rightarrow Ca_2Os_2O_{6.5} + 0.25O_2 \quad [850–1000\ °C]$$

$$Ca_2Os_2O_{6.5} \Rightarrow CaO + OsO_4 + 0.25O_2 \quad [>1005\ °C]$$

The first intermediate $Ca_2Os_2O_7$ is isostructural with orthorhombic $Ca_2Nb_2O_7$ and its cell parameters are: $a_0 = 3.745$ Å, $b_0 = 25.1$ Å, $c_0 = 5.492$ Å, $Z = 4$, space group *Cmcm* or *Cmc*2. $Ca_2Os_2O_7$ exhibits metallic conductivity and its electrical resistivity is 4.6×10^{-2} ohm/cm at 296 K. Note that a change in oxidation potential has occurred with $CaOsO_3$(IV) ⇒ $Da_2Os_2O_7$ (V) (Fig. 12.63).

The arrangement of the OsO_6 and CaO_6 octahedra in $Ca_2Os_2O_7$ may perhaps be better seen in Fig. 12.64.

Cell parameters of $CaOsO_3$ are: $a = b = 5.808$ Å, $c = 7.898$ Å, $\alpha = \beta = \gamma = 90°$, cell volume = 263.12 Å^3, $Z = 4$. Cell occupancy is shown in Table 12.18.

Cell parameters for $Ca_2Os_2O_7$ are: $a = b = c = 7.2408$ Å, $\alpha = \beta = \gamma = 60°$, cell volume = 268.44 Å^3, $Z = 2$, Cell occupancy is shown in Table 12.19.

$Ca_2Os_2O_7$ adopts a stoichiometric, orthorhombic weberite structure but the distortion of the OsO_6

TABLE 12.18

No.	Site notation	Atom	Multiplicity	Wyckoff	Site symmetry	*x*	*y*	*z*	Occupancy
1	O1	O	8	d	1	0.1984	0.0506	0.3043	1.0
2	Ca1	Ca	4	c	.m.	0.4372	1/4	0.0156	1.0
3	O2	O	4	c	.m.	0.5328	1/4	0.6005	1.0
4	M1	0.500Ca + 0.500Os	4	a	−1	0	0	0	1.0

TABLE 12.19

No.	Site notation	Atom	Multiplicity	Wyckoff	Site symmetry	*x*	*y*	*z*	Occupancy
1	O1	O	48	f	2.mm	0.4286	1/8	1/8	1.0
2	Os1	Os	16	d	.−3m	1/2	1/2	1/2	1.0
3	Ca1	Ca	16	c	.−3m	0	0	0	1.0
4	O2	O	8	a	−43m	1/8	1/8	1/8	1.0

octahedra and eightfold Ca–O coordinations decrease with increasing temperature indicating that this material lies close to the weberite/pyrochlore phase boundary. No other compounds are known in this system.

In the Os^{5+}-containing system of $CaO–Os_2O_5$, the $Ca_2Os_2O_7$ compound has been described as a decomposition product of $CaOsO_3$. Its structure was presented above. No other compounds have been synthesized in this system to date.

In the Os^{6+}-containing system of $CaO–OsO_3$, the compound, Ca_3OsO_6, has been studied. Single crystals of Ca_3OsO_6 can be obtained from stoichiometric amounts of CaO_2 and Os, Pt capsule, 6 GPa, 1500 °C, 1 h, LiCl, and KCl in a mass ratio of 1:5:2 (Pt crucible, 750 °C, 12 h). The compound is orthorhombic: $a = 14.859$, $b = 7.550$, $c = 5.487$ Å, $Z = 8$. Refinement was achieved in space group $Pna2_1$ by means of conventional least squares and Fourier techniques using intensity data corrected for absorption effects. The final R value is 0.047. Like ferroelectric compounds $BaMF_4$ (M = Zn, Co,…), the structure consists of two octahedra thick slabs with a distorted perovskite structure; theses slabs are linked by Ca^{2+} ions; but, in contrast to these compounds, the corner-sharing OsO_6 octahedra form zigzag chains along the b-axis and the Ca atoms are no longer situated in a mirror plane of this derivative . An attempt to prepare Ca_4OsO_6 by the reaction of four moles of **CaO_2 to OsO_3 met with failure**.

No calcium osmate compounds are offered for sale commercially.

12.4.4. Strontium Osmium Compounds

Strontium does not form any intermetallic compounds with osmium metal.

In the system of $SrO–Os_xO_y$, where $x = 1$ or 2 and y varies from 2 to 8, no compounds involving the Os^{2+}, Os^{7+} systems are known.

In the Os^{3+}-containing system of $SrO–Os_2O_3$, $SrOs_2O_4$ has the same structure as its calcium homologue. Neither of these compounds have been obtained in a pure state at room temperature since they tend to decompose in air to SrO, OsO_4 and oxygen. $SrOs_2O_4$ is metastable and has not yet been isolated. It is expected to have a spinel structure with electrical characteristics of a metal. No other compounds are known in this system.

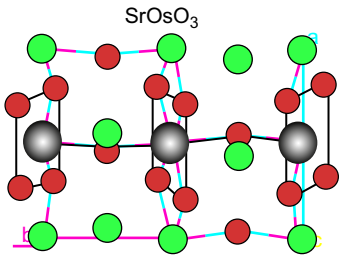

FIGURE 12.65

In the Os^{4+}-containing system of $SrO–OsO_2$, the compound, $SrOsO_3$ has been studied. It has the same structure as the Ca homologue shown in Fig. 12.65.

Cell parameters are: $a = 5.32$ Å, $b = 5.58$ Å, $c = 7.92$ Å. $\alpha = \beta = \gamma = 90°$, cell volume = 234.52 Å^3, $Z = 2$. Cell occupancy is shown in Table 12.20.

Like its calcium homologue, it decomposes to form $Sr_2Os_2O_7$ where a change in valency occurs. The decomposition of orthorhombic $Sr_2Os_2O_7$ depends strongly on the partial pressure of air above the samples investigated. A defect structure can be formed. If the pressure is low, the defect pyrochlore $Sr_2Os_2O_{6.4}$ is obtained. It has the same structure as the pyro-osmate, $Sr_2Os_2O_7$. The thermal decomposition of $SrOsO_3$ in a dynamic airflow has been studied using differential thermal analysis, thermogravimetry and XRPD. It decomposes to the pyro-osmate above 800 °C. After decomposition of the pyro-osmate above 920 °C, a new phase was discovered, which has the formula $SrOsO_4$, a scheelite structure and tetragonal unit cell parameters $a_0 = 5.422$ Å, $c_0 = 11.92$ Å, $Z = 4$, space group $I4_1/a$, and a pycnometric density of 6.46 g/cm^3. Above 1030 °C, $SrOsO_4$ decomposes into SrO, osmium tetroxide and osmium metal.

No other compounds have been found in this system.

In the Os^{5+}-containing system of $SrO–Os_2O_5$, the thermal decomposition of $Sr_2Os_2O_7$ by DTA, thermogravimetry and XRPD has been studied. Orthorhombic

TABLE 12.20

No.	Site notation	Atom	Multiplicity	Wyckoff	Site symmetry	x	y	z	Occupancy
1	O1	O	8	d	1	0.1984	0.0506	0.3043	1.0
2	Sr1	Sr	4	c	.m.	0.4372	1/4	0.0156	1.0
3	O2	O	4	c	.m.	0.5328	1/4	0.6005	1.0
4	Os1	Os	4	a	−1	0	0	0	1.0

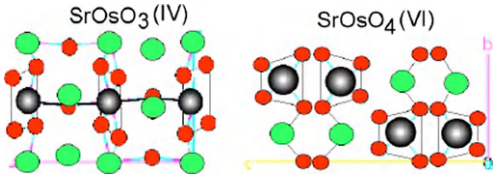

FIGURE 12.66

$Sr_2Os_2O_7$ evolves oxygen slowly above 845 °C transforming into the intermediate orthorhombic $Sr_2Os_2O_{7-x}$ up to $x \leq 0.16$. At $x = 0.16$–0.20 a new cubic phase begins to form. The cubic phase $Ca_2Os_2O_{7-y}$ has a pyrochlore structure type and its homogeneity region is spread to $y \leq 0.60$. Above 1010 °C the pyrochlore, $Sr_2Os_2O_{7-y}$, decomposes completely into SrO, osmium metal, osmium tetroxide and oxygen.

A body-centered cubic structure related to the cubic $KSbO_3$ structure has been found for phases with compositions close to $BaOs_2O_6$, $SrOs_2O_6$, and $SrRe_2O_6$. A primitive cubic structure also related to the cubic $KSbO_3$ structure has been found for phases with compositions close to $NaOsO_3$, $BiPtO_{3.5}$, and $BiOsO_{3.5}$. The ternary oxides $Cd_2Ir_2O_7$, $Ca_2Ir_2O_7$, and $Ca_{1.7}Os_2O_7$ have been prepared with the cubic pyrochlore structure. All iridium phases contain Ir^{5+} and are the first oxide examples of iridium in an oxidation state higher than 4. The osmate compositions contain osmium in a +5 state, i.e. Os^{5+}.

In the Os^{6+}-containing system of SrO–OsO_3, the compound $SrOsO_4$ has the structure shown in Fig. 12.66.

A comparison of the two valence states is shown. The OsO_6 octahedra are connected in the former and isolated in the latter. Cell parameters of $SrOsO_4$ are: $a = b = 5.422$ Å, $c = 7.0867$ Å, $\alpha = \beta = 112.492°$, $\gamma = 90°$, cell volume = 175.21 Å^3, $Z = 4$. Cell occupancy is shown in Table 12.21.

Single crystals of the compound $Sr_3(OsO_4(OH)_2)_2 \cdot H_2O$ were prepared in closed steel tubes under high pressure and investigated by single-crystal X-ray determination. It crystallizes with triclinic symmetry, space group C_1^i–$P1$, $a = 5.7877$ Å, $b = 10.407$ Å, $c = 10.485$ Å, $\alpha = 10.82°$. $\beta = \gamma = 104.30°$, $Z = 2$. $OsO_4(OH)_2$ octahedra are occupied by osmium in the oxidation states Os^{6+} and Os^{8+} in a disordered manner. The crystal chemistry was shown and the statistical distribution of the different valence states of osmium was discussed with respect to calculations of the Coulomb term of lattice energy.

In the Os^{8+}-containing system of SrO–OsO_4, the compound, $SrOsO_5$ has been synthesized. The crystal chemistry of oxides of Osmium shows it to form different oxidation states and generally as anions in the anionic part of the solids. This clear decision in favor of the anionic part of crystal structures is caused with the combination of osmium with large cations like Alkaline Earth– and Rare Earth–metals. Despite different valence states of osmium, the oxygen surrounding is to a great extent octahedral. Besides isolated OsO_6 octahedra, edge shared $^1{}_\infty[Os_2O_{10}]$-double (showing Os–Os interchanges), $^1{}_\infty[Os_2O_{10}]$-chains and 2- or 3D networks oxo-osmates reveal the structures of perovskites, pyrochlores and stacking variants of perovskites. $SrOsO_5$ is a representative for Osmium in an unusual coordination by oxygen. At least two osmium metal clusters are present and the formulation is: $Sr_2[Os_2O_{10}]$.

The crystal structure of a strontium osmate(VIII) compound, $Sr[OsO_5(H_2O)] \cdot 3H_2O$, has been described but details are lacking concerning its preparation. It is likely that this compound was produced in solution by the use of $K_2[OsO_4(OH)_2]$ or $Na_2[OsO_4(OH)_2] \cdot 2H_2O$. Vibrational spectra show the $[OsO_4(OH)_2]^2$-ions to have *cis*-octahedral structures. In addition, the first mixed-valence compound involving an alkaline earth metal tetra-oxodihydroxo-osmate(VI,VIII), $Sr_3(OsO_4(OH)_2)_2 \cdot H_2O$, has been reported.

There are no strontium osmates offered for sale commercially and no CAS numbers have been issued.

12.4.5. Barium Osmium Compounds

Barium does not form any intermetallic compounds with osmium metal.

In the system of BaO–Os_xO_y, where $x = 1$ or 2 and y varies from 2 to 8, no compounds involving the Os^{2+}, Os^{5+}, Os^{7+} or Os^{8+} ions have been synthesized.

In the Os^{3+}-containing system of BaO–Os_2O_3, the compound, $BaOs_2O_4$, has not been isolated. The presumed spinel structure was described above for

TABLE 12.21

No.	Site notation	Atom	Multiplicity	Wyckoff	Site symmetry	*x*	*y*	*z*	Occupancy
1	O1	O	16	f	1	0.151	0.009	0.211	1.0
2	Sr1	Sr	4	b	–4..	0	1/4	5/8	1.0
3	Os1	Os	4	a	–4..	0	1/4	1/8	1.0

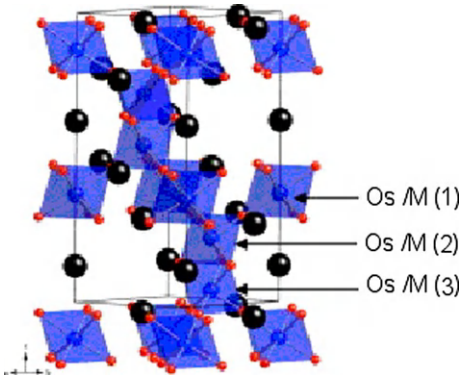

FIGURE 12.67

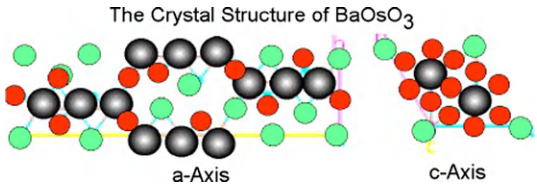

FIGURE 12.68

the Ca and Sr homologs. The bond angles for $BaOs_2O_4$ were presented above. The major difference between the Ba homologue and the others is that the LDA + SO calculation with $U = 0$ gives that at the Γ point the eight $J_{eff} = 1/2$ states have degeneracy 4–2–2 and not 2–4–2 as found in the Ca and Sr cases. These differences significantly affect its band structure. The value of U will induce magnetism, but axion insulator or Dirac metal state for BaOs2O4 is not found for any reasonable U.

Two complex oxide compounds, containing Os^{3+}, have been studied. Two complex oxides of osmium, $Ba_2Fe_{0.92}Os_{1.08}O_6$ and $Ba_2Co_{0.77}Os_{1.23}O_6$, have been prepared as single crystals from molten potassium hydroxide. Both oxides crystallize in the hexagonal space group $P6_3mc$ with $a = 5.7403(1)$ Å and $c = 14.0771(6)$ Å and $a = 5.7745(2)$ Å and $c = 14.0946(7)$ Å for $Ba_2Fe_{0.92}Os_{1.08}O_6$ and $Ba_2Co_{0.77}Os_{1.23}O_6$, respectively. The structure of these compounds is related to the 6H $BaTiO_3$ structure but exhibit mixed occupancy of both metals on the three crystallographically independent metal sites.

The relevant structure is shown in Fig. 12.67. The black spheres represent Ba^{2+} while M(1), M(2) and M(3) represent the MO_6 octahedra where M is $Fe_{0.92}Os_{1.08}O_6$ or $Co_{0.77}Os_{1.23}O_6$.

In the Os^{4+}-containing system of $BaO–OsO_2$, the structure of the compound, $BaOsO_3$ has been determined. It differs from that of the homologues, $CaOsO_3$ and $SrOsO_3$ (Fig. 12.68).

Cell parameters are: $a = b = 6.221$ Å, $c = 8.166$ Å, $\alpha = \beta = 67.69°$, $\gamma = 60°$, cell volume = 244.35 Å^3, $Z = 6$. Cell occupancy is shown in Table 12.22.

Whereas the Ca and Sr homologues decompose to form the $Ae_2Os_2O_7$ type of structure with a change from Os^{4+} to Os^{5+}, the compound, $Ba_2Os_2O_7$ is unknown. One paper states that $BaOsO_3$ decomposes at 835 °C in air and is complete by 890 °C to form $BaOsO_4$. The latter then decomposes at 1060 °C to form BaO and OsO_4.

The crystal structure and magnetic properties of a barium osmate $Ba_{11}Os_4O_{24}$ were investigated. This compound crystallizes in a cation-deficient double perovskite-related structure (space group $I4_1/a$; $Z = 4$), which is isostructural with the strontium rhenate, $Sr_{11}Re_4O_{24}$. This compound shows semiconductive behavior with thermal activation. A weak ferromagnetic transition has been found at 7.5 K through its magnetic susceptibility measurements. At 6.8 K, a λ–type specific heat anomaly has been observed.

No other Os^{4+}-containing compounds are known.

In the Os^{6+}-containing system of $BaO–OsO_3$, the compound, $BaOsO_4$ is known. It is an intermediate product in the decomposition of $BaOsO_3$ in air and has the structure shown in Fig. 12.69.

The compound, Ba_3OsO_6 containing Os(VI) has been thoroughly documented. There is ample evidence in chemical literature that the compound Ba_3OsO_6 is stable up to at least 1300 K.

TABLE 12.22

No.	Site notation	Atom	Multiplicity	Wyckoff	Site symmetry	x	y	z	Occupancy
1	O1	O	18	h	.m	0.4889	0.5111	0.2251	1.0
2	O2	O	9	e	.2/m	1/2	0	0	1.0
3	Ba1	Ba	6	c	3m	0	0	0.2179	1.0
4	Os1	Os	6	c	3m	0	0	0.3829	1.0
5	Os2	Os	3	b	−3m	0	0	1/2	1.0
6	Ba2	Ba	3	a	−3m	0	0	0	1.0

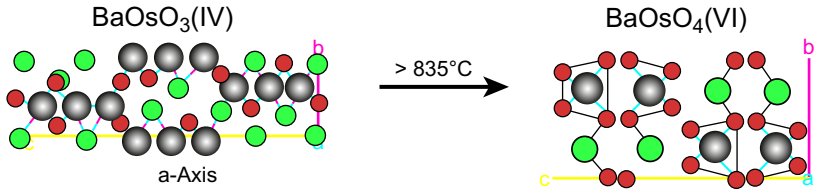

FIGURE 12.69

No other barium osmate compounds are known to date. None of these compounds are available commercially.

12.4.6. Radium Osmium Compounds

Radium does not form any intermetallic compounds with osmium metal. While radium undoubtedly will form Os compounds very similar to those of the Ba system, there is no record of anyone having tried to synthesize such compounds. The lack of interest in the Industry and Academia is probably the major factor for this situation.

CHAPTER

13

Group 9 (Co, Rh and Ir) Alkaline Earth Compounds

OUTLINE

13.1. Alkaline Earth Cobalt Compounds **961**
13.1.1. Beryllium Cobalt Compounds 961
13.1.2. Magnesium Cobalt Compounds 963
13.1.3. Calcium Cobalt Compounds 965
13.1.4. Strontium Cobalt Compounds 971
13.1.5. Barium Cobalt Compounds 978
13.1.6. Radium Cobalt Compounds 984

13.2. Alkaline Earth Rhodium Compounds **984**
13.2.1. Beryllium Rhodium Compounds 984
13.2.2. Magnesium Rhodium Compounds 986
13.2.3. Calcium Rhodium Compounds 988
13.2.4. Strontium Rhodium Compounds 990
13.2.5. Barium Rhodium Compounds 993
13.2.6. Radium Rhodium Compounds 994

13.3. Alkaline Earth Iridium Compounds **994**
13.3.1. Beryllium Iridium Compounds 994
13.3.2. Magnesium Iridium Compounds 995
13.3.3. Calcium Iridium Compounds 997
13.3.4. Strontium–Iridium Compounds 1000
13.3.5. Barium Iridium Compounds 1002
13.3.6. Radium Iridium Compounds 1004

13.1. ALKALINE EARTH COBALT COMPOUNDS

13.1.1. Beryllium Cobalt Compounds

Beryllium, in the system Be–Co–O, does not form any cobaltate type of compounds.

However, it does form a series of intermetallic compound with Co metal. The phase diagram shows four compounds (Fig. 13.1).

However, two of the compounds shown are high-temperature phases only and are not stable at room temperature. The compound, BeCo, has a body-centered structure shown in Fig. 13.2.

Cell parameters are: $a = b = c = 2.625$ Å, $\alpha = \beta = \gamma = 90°$, cell volume = 18.09 Å^3, $Z = 1$. Point group = cP2, space group = Pm-3m. Cell occupancy is shown in Table 13.1.

The structure of the compound, Be_9Co, has not been published. It has the cell parameters of: $a = b = c = 6.5936$ Å, $\alpha = \beta = \gamma = 109.471°$, cell volume = 220.67 Å^3.

The compound, Be_5Co has the structure shown in Fig. 13.3.

The Co^0 atoms occupy face-centered positions. Cell parameters are: $a = b = c = 4.138$ Å, $\alpha = \beta = \gamma = 60°$, cell volume = 50.10 Å^3. $Z = 4$, point group = cF24, space group = F-43m. Cell occupancy is shown in Table 13.2.

The structure of the compound, Be_3Co, has not been published. It has the cell parameters of: $a = b = 8.3783$ Å, $c = 13.7652$ Å, $\alpha = \beta = 90°$, $\gamma = 120°$, cell volume = 836.81 Å^3, $Z = 4$.

The exact structure of the compound, $Be_{21}Co_5$, has not been published. It has the cell parameters of: $a = b = c = 10.781$ Å, $\alpha = \beta = \gamma = 60°$, cell volume = 886.06 Å^3, $Z = 4$.

The structure of the compound, $Be_{17}Co_2$, is shown in Fig. 13.4.

Encyclopedia of the Alkaline Earth Compounds
http://dx.doi.org/10.1016/B978-0-444-59550-8.00013-2

Copyright © 2013 Elsevier B.V. All rights reserved.

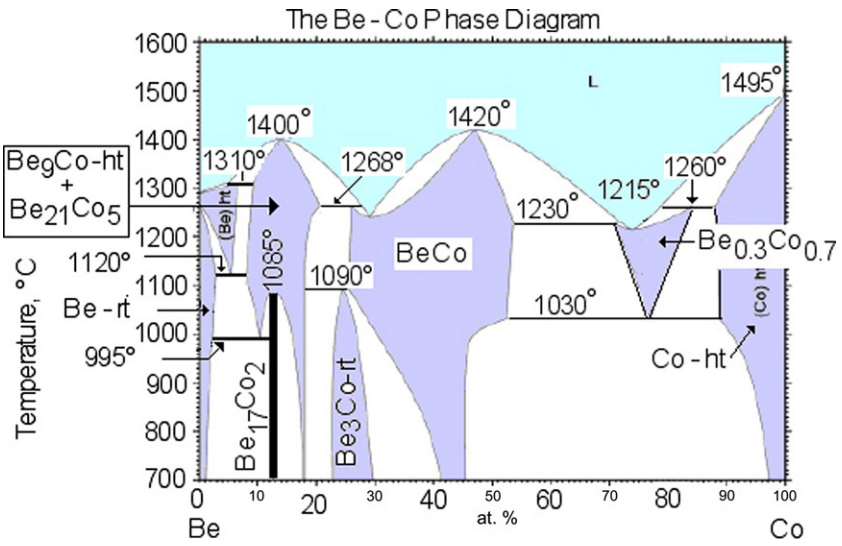

FIGURE 13.1

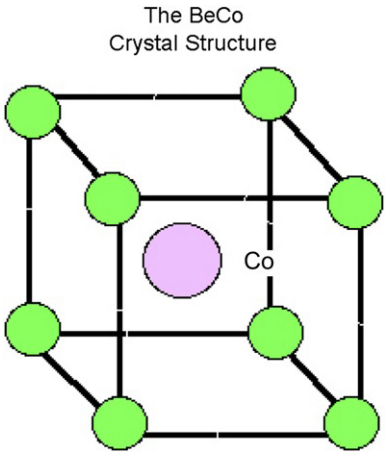

FIGURE 13.2

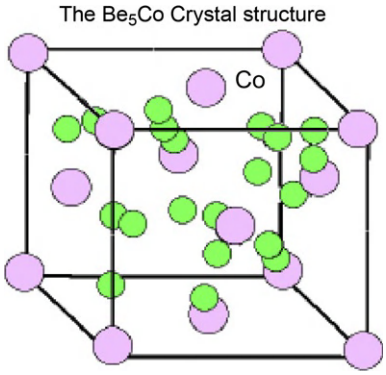

FIGURE 13.3

Cell parameters are: $a = b = 4.115$ Å, $c = 10.9818$ Å^3, $\alpha = \beta = 90°$, $\gamma = 120°$, cell volume = 161.34 Å^3, $Z = 1$, point group = hP19, space group = P-6m2. Cell occupancy is shown in Table 13.3.

$Be_{12}Co$ is body centered with Co atoms and has the structure shown in Fig. 13.5.

The Co atoms occupy a body-centered cube and there are three internal layers of Be atoms, making this structure be made of five layers of Be^0–Co^0 atoms. The cell parameters are: $a = 4.249$ Å, $b = c = 5.5408$ Å, $\alpha = 81.546°$, $\beta = \gamma = 67.454°$, cell volume = 111.47 Å^3, $Z = 2$. Point group = tl26, space group = $I4/mmm$. Cell occupancy is shown in Table 13.4.

Be_2Co has the structure where the body-centered cubic lattice is randomly occupied by Be^0 or Co^0 in the ratio of 2:1 (Fig. 13.6).

Cell parameters are; $a = b = c = 2.2361$ Å, $\alpha = \beta = \gamma = 109.47°$, cell volume = 8.61 Å^3, $Z = 2$, point group = cI2, space group = Im-3m. Site occupancy is shown in Table 13.5.

TABLE 13.1

No.	Site notation	Atom	Multiplicity	Wyckoff	Site symmetry	x	y	z	Occupancy
1	Co	Co	1	b	m-3m	1/2	1/2	1/2	1.0
2	Be	Be	1	a	m-3m	0	0	0	1.0

TABLE 13.2

No.	Site notation	Atom	Multiplicity	Wyckoff	Site symmetry	*x*	*y*	*z*	Occupancy
1	Be1	Be	16	e	.3m	0.625	0.625	0.625	1.0
2	Be2	Be	4	c	-43m	1/4	1/4	1/4	1.0
3	Co1	Co	4	a	-43m	0	0	0	1.0

TABLE 13.3

No.	Site notation	Atom	Multiplicity	Wyckoff	Site symmetry	*x*	*y*	*z*	Occupancy
1	Be1	Be	6	n	.m.	0.167	0.8335	0.183	1.0
2	Be2	Be	3	k	mm2	0.505	0.4955	1/2	1.0
3	Be3	Be	2	i	3m.	2/3	1/3	0.098	1.0
4	Co1	Co	2	i	3m.	2/3	1/3	0.307	1.0
5	Be4	Be	2	h	3m.	1/3	2/3	0.341	1.0
6	Be5	Be	2	g	3m.	0	0	0.377	1.0
7	Be6	Be	1	c	-6m2	1/3	2/3	0	0.34
8	Co2	Co	1	a	-6m2	0	0	0	0.36

None of these compounds have found commercial usage and they are not available for sale.

13.1.2. Magnesium Cobalt Compounds

Magnesium metal does not form any intermetallic compounds with Co metal.

In the Co^{2+}-containing system of MgO–CoO, the compound $MgCoO_2$ is known. It has the structure shown in Fig. 13.7.

Other than its structure, no other references are available concerning its physical and chemical properties. Cell parameters are: $a = b = c = 2.9963$ Å, $\alpha = \beta = \gamma = 60^\circ$, cell volume $= 19.02$ Å^3, $Z = 4$, point group = cF48, space group = *Fm*-3*m*.

The compound, $MgCo_3O_4$, has been mentioned in at least one paper regarding its catalytic activity regarding the decomposition of methane, CH_4. The process of catalytic methane oxidation is very important in Industry as it is directly applicable to the purification of exhaust gases from a large spectrum of industries, vehicles, catalytic heat generators, etc. Unfortunately, this compound was not very active in this capacity, in comparison to other Pt compounds.

In the Co^{3+}-containing system of MgO–Co_2O_3, the compound, $MgCo_2O_4$, has the structure shown in Fig. 13.8.

In one paper, an investigation of the synthesis and electrical properties of the spinel, $MgCo_2O_4$, was made because it was being considered as a candidate of the cathode materials of magnesium ion batteries in the

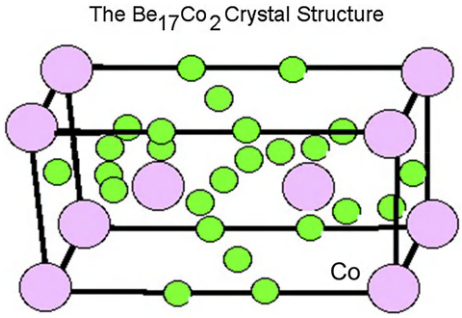

FIGURE 13.4

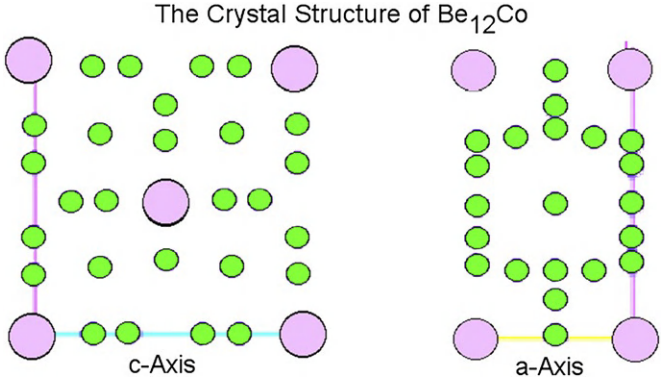

FIGURE 13.5

TABLE 13.4

No.	Site notation	Atom	Multiplicity	Wyckoff	Site symmetry	*x*	*y*	*z*	Occupancy
1	Be1	Be	8	j	m2m.	0.277	1/2	0	1.0
2	Be2	Be	8	i	m2m.	0.361	0	0	1.0
3	Be3	Be	8	f	..2/m	1/4	1/4	1/4	1.0
4	Co1	Co	2	a	4/mmm	0	0	0	1.0

TABLE 13.5

No.	Site notation	Atom	Multiplicity	Wyckoff	Site symmetry	*x*	*y*	*z*	Occupancy
1	M	2/3Be + 1/3 Co	2	A	m-3m	0	0	0	1.0

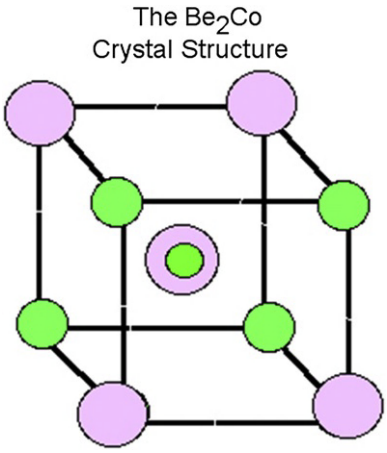

FIGURE 13.6

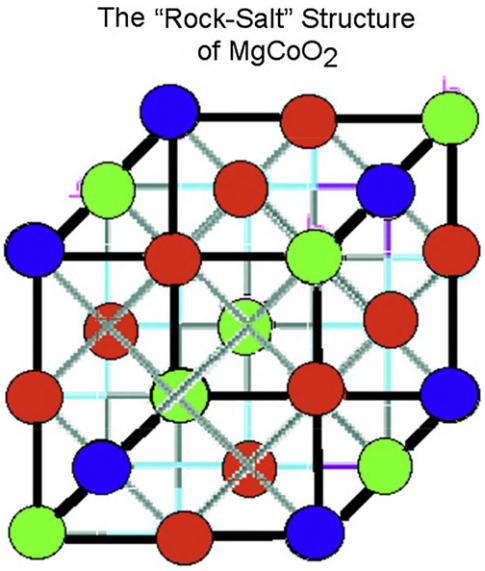

FIGURE 13.7

future. Samples were synthesized using two types of techniques: (1) solid-state reaction and (2) a wet process. The crystal structures of the samples were analyzed by X-ray diffraction (XRD), and their electrical conductivities were obtained through the DC resistance and AC impedance measurements. By solid-state reaction, a sample of a single $MgCo_2O_4$ phase was not obtained. The sample synthesized at 800 °C for 24 h, after milling together of Co_3O_4 and MgO powder, was comprised of dual phases of spinel-type and rock salt-type structures. Samples synthesized at temperatures higher than 880 °C showed a single rock salt-type phase without electrical conductance. The $MgCo_2O_4$ sample showed *p*-type semiconducting behavior similar to the spinel type of Co_3O_4, but its electrical conductivity at room temperature was shown to exceed that of Co_3O_4. In contrast, a sample consisting of a single spinel-type phase was successfully synthesized by wet process, which exhibited an electrical conductivity of the order 102 S/cm, being much higher than those of the samples

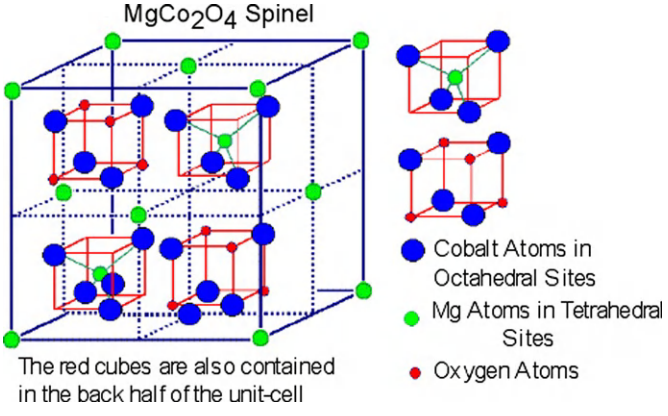

FIGURE 13.8

synthesized by solid-state reaction. Thus, it was concluded that the substitution of Co^{2+} in Co_3O_4 with Mg^{2+} was found to enhance the electrical conductivity of the spinel-type phase.

In another work, the compounds, $FeCo_2O_4$ and $MgCo_2O_4$, were synthesized by the urea combustion and oxalate decomposition method, respectively. Powder XRD, high-resolution transmission electron microscopy (HRTEM), selected area electron diffraction (SAED) and X-ray photoelectron spectroscopy (XPS) have been used to characterize the phases. Scanning electron microscopy (SEM) showed the distinct features in the morphology, submicron size of $FeCo_2O_4$ and needle-shaped particles of $MgCo_2O_4$. Galvanostatic cycling was carried out in the voltage range 0.005–3.0 V vs Li at a current of 60 mA/gm (~0.08 C) up to 50 cycles. The observed first-cycle charge capacities are, $FeCo_2O_4$: 827 mA/h/gm (corresponding to theoretical 7.3 mol of Li per mole of $FeCo_2O_4$) and $MgCo_2O_4$: 736 mA/h/gm (5.7 Li). At the end of 50 cycles, $FeCo_2O_4$ retained ~90% of its first-charge capacity, and a coulombic efficiency of ~99% is noted between 20 and 50 cycles. $MgCo_2O_4$ showed extensive capacity fading and retained only 0.9 mol of cyclable Li in the range 28–50 cycles. These results show that Fe is a better counter ion than Mg. The average charge and discharge voltages are ~2.0 V and ~1.2 V, respectively, for both the compounds. Cyclic voltamperograms, up to 12 cycles on $FeCo_2O_4$, complemented the galvanostatic cycling results. Impedance studies were carried out on $FeCo_2O_4$ at various voltages during the first cycle and after 10 cycles, and the data were interpreted.

$MgCo_2O_4$ spinel catalysts were prepared via the solution combustion synthesis (SCS) and coprecipitation (CP) methods. The produced powder catalysts were characterized by XRD, BET, FESEM, TPD, and XPS. The performance of these catalysts toward the decomposition of N_2O to N_2 and O_2 was evaluated in a temperature programmed reaction apparatus in the absence of and in the presence of oxygen ($W/F = 0.03$ g s/cm^3). The catalyst prepared by the CP method has been found to provide the best activity; the half conversion temperature (T_{50}) of nitrous oxide was 380 and 415 °C in the absence and in the presence of oxygen, respectively. The $MgCo_2O_4$ spinel catalysts were directly deposited, by in situ SCS and CP, over ceramic honeycomb monoliths and tested in a lab-scale test rig. Again, in this case, a prevalent activity of the catalytic monolith prepared by CP was observed. The higher activity of the catalyst prepared by CP could be correlated with its higher surface area and its higher capacity of enriching the surface with the more reactive supra-facial, weakly chemisorbed, oxygen species.

Magnesium ion batteries (MIBs) with a Mg metal-negative electrode are expected to combine high energy density and high electromotive force, owing to the divalent ion careers and its low redox potential. However, it has been reported to date that the cell voltage of MIBs is not high enough (1.5 V), being far below that of lithium ion batteries (LIBs) (4–5 V). In this work, the authors have investigated the potentiality of Mg–Co–O and Mg–Ni–O complex oxides as the positive electrode for MIBs, which are composed of these positive electrodes and a Mg-negative electrode in acetonitrile with $Mg(ClO_4)_2$ salt as an electrolyte. These MIBs exhibited a relatively high open circuit voltage (OCV) and can light a blue diode after charge. However, as the combination of the acetonitrile electrolyte and metal Mg can yield a passivation on the surface of the Mg electrode, these materials were also checked for use in a well-established Li ion battery system. Results confirmed that the charged battery can show a high OCV. In order to attain such a high cell voltage, it would be significant to exploit the unstabilized ion after charge in the host complex oxide. This was not accomplished.

A novel route of low-temperature preparation of Mg, Ni and Zn cobaltite spinel catalysts has been investigated. Cobalt oxalate, co-precipitated with the oxalate of magnesium, nickel or zinc, respectively, in a 2:1 ratio, has been used as starting material. Cobaltite synthesis proceeds during thermal treatment of coprecipitated oxalates in air. It was established that coprecipitated oxalates are solid solutions and the oxidation of Co^{2+} to Co^{3+} during thermal treatment begins at lower temperatures than that of the dissociation onset of the anhydrous product, thus facilitating the synthesis of cobaltites. A preparation procedure that allows avoiding local overheating of the material due to the strongly exothermal processes of oxalate dissociation was developed. The application of this procedure permits the formation of spinel phases of $MgCo_2O_4$, $NiCo_2O_4$ and $ZnCo_2O_4$ with specific surface areas of 63, 94 and 81 m^2/g, respectively, at 250 °C. No other compounds are known in this system.

No other compounds are known in:

(1) the Co^{2+}–Co^{3+}-containing system of MgO–Co_3O_4,
(2) the Co^{4+}-containing system of MgO–CoO_2,
(3) the Co^{5+}-containing system of MgO–Co_2O_5 or
(4) the Co^{6+}-containing system of MgO–CoO_3.

Magnesium cobaltite or cobaltate compounds are not offered commercially and no CAS numbers have been issued.

13.1.3. Calcium Cobalt Compounds

Calcium metal does not form any intermetallic compounds with cobalt metal.

In the Co^{2+}-containing system of CaO–CoO, the compound, $CaCoO_2$ is not stable at room temperature. The existence of gaseous cobaltates of alkaline earth metals has been established by high-temperature mass spectrometry. Gaseous molecules: $CaCoO_2$, $SrCoO_2$ and $BaCoO_2$ were found for the first time. On the basis of the measured constants of the equilibrium of gas-phase reactions the standard enthalpies of formation: -149 ± 19 kJ/mol, -149 ± 20 kJ/mol and -250 ± 16 kJ/mol; standard atomization enthalpies were: 1251 ± 22 kJ/mol, 1233 ± 23 kJ/mol and 1353 ± 20 kJ/mol for $CaCoO_2$, $SrCoO_2$ and $BaCoO_2$, respectively.

The compound, Ca_2CoO_3 (II), has been found to be a slab-layered rock salt type of compound. It is not stable at room temperature but has been found to exist in the CaO–Co_3O_4 series of compounds. Consequently, it has been established as a thin-layer structure on silicon matrices. Thin films of the *p*-type thermoelectric misfit-layered oxide, $[Ca_2CoO_3]_{0.62}[CoO_2]$, were prepared for the first time by means of the atomic layer deposition technique using $Ca(thd)_2$, $Co(thd)_2$, and O_3 as precursors. As deposited films were amorphous; however, with heat treatment in an O_2 gas flow, well-crystallized highly *c*-axis-oriented $[Ca_2CoO_3]_{0.62}[CoO_2]$ films were obtained. The oxygen content of the O_2-annealed film was further controlled through a reductive N_2 annealing. Because the degree of reduction was dependent on the annealing temperature, the choice of N_2-annealing temperature provided a tool for precise tuning of the oxygen content (Fig. 13.9).

With decreasing oxygen content, the lattice parameter (*c*) and the Seebeck coefficient (*S*) were found to increase. The room-temperature S values were 113 and 128 μV/K for the oxygen-richest sample and the most reduced sample, respectively.

Large and high-quality single-crystal flakes of the $[Ca_2CoO_3]_{0.62}[CoO_2]$ compound can also be obtained if the crystals are grown from Co_3O_4 and $CaCO_3$ reagents with chloride flux. Typical single-crystal flake size is about $5 \times 5 \times 0.02$ mm^3. Obtained crystal flakes were consolidated by the spark plasma sintering (SPS) technique at 1100 K for 1 h. Grain alignment was checked by XRD and also was confirmed by SEM observations on the fractured surface. At 1000 K, electrical conductivity of the textured ceramics is about 270 S/cm, twice as high as that of powder sample sintered by the SPS procedure. The Z_T value of the textured sample reaches 0.4 at 1000 K, being 50% improvement relative to the powder-sintered sample, although the thermal conductivity increases simultaneously. The constructed commensurate supercell has the following parameters: $a' = 3 \cdot a = 14.5$ Å, $b' \approx 8 \cdot b_1 \approx 5 \cdot b_2 = 28.2$ Å, $c' = 10.8$ Å and $\beta = 94.3°$.

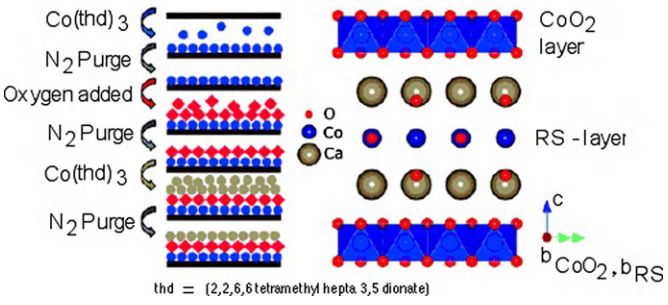

FIGURE 13.9

Electronic transportation and thermodynamic properties of misfit-layered polycrystalline $[Ca_2CoO_3]_{0.62}[CoO_2]$ were measured in order to clarify the nature of metal–semiconductor transition (MST) at $T_{MS} \approx 400$ K. Above this, a simultaneous decrease of resistivity and increase of thermopower with temperature give rise to a great enhancement of thermoelectric power factor up to 1000 K. A first-order phase transition characteristic around T_{MS} was revealed by anomalies of resistivity, differential scanning calorimetry, and thermal expansion. The first-order characteristic of the MST can be rationalized by using the virial theorem via an itinerant to localized electron transition in the narrow eT band within the $[CoO_2]$ plane. Above T_{MS}, the reduction of the retained delocalized states within the matrix of localized states, and the enhancement of charge carrier effective mass with increasing temperature, has been hypothesized to account for the considerable enhancement of the observed thermopower.

Another paper has examined the temperature transition of $[Ca_2CoO_3]_{0.62}[CoO_2]$ in detail. The formation mechanism of thermoelectric $[Ca_2CoO_3]_{0.62}[CoO_2]$ (CCO) on β-$Co(OH)_2$ templates with maintained orientations was investigated by identifying the intermediate phases and specifying the relationship between their crystallographic orientations. β-$Co(OH)_2$ templates were mixed with the complementary reactant $CaCo_3$ and a compact was prepared by tape casting, with the developed (001) plane of the templates aligned along the casting plane. High-temperature XRD of the compact revealed that β-$Co(OH)_2$ decomposed into Co_3O_4 by 873 K, and Co_3O_4 reacted with CaO to form CCO by 1193 K via the formation of the newly detected intermediate phase β-Na_xCoO_2-type Ca_xCoO_2 at 913–973 K. Pole figure measurements and SEM and TEM observations revealed that the relationship between the crystallographic planes was (001) β-$Co(OH)_2$ parallel to the {111} plane of Co_3O_4 that is parallel to the (001) plane of (001) CCO. The crystal structures of the four materials possess the common CoO layer (or similar), which is composed of edge-sharing CoO_6 octahedra, parallel to the planes. The cross-sectional HRTEM analysis of an incompletely reacted specimen showed

transient lattice images from Ca_xCoO_2 into CCO, in which every other CoO_2 layer of Ca_xCoO_2 was preserved. Thus, it was demonstrated that a textured CCO ceramic is produced through a series of in situ topotactic conversion reactions with a preserved CoO_2 layer as its template.

The cobaltite, $Ca_3Co_4O_{9+\delta}$ has shown a large thermoelectric effect and is considered to be a good candidate for use as a thermoelectric material. The composition of $Ca_3Co_4O_{9+\delta}$ is better expressed as $[Ca_2CoO_3][CoO_2]_{b1/b2}$ with the misfit-layered structure featuring different periodicities along the *b*-axis, with b1 referring to the *b*-axis length of the NaCl-type $[Ca_2CoO_3]$ sublattice and b2 referring to the *b*-axis length of the $[CoO_2]$ sublattice. The crystal structure of $Ca_3Co_4O_{9+\delta}$ can be viewed as being of two subsystems, i.e. the distorted NaCl-type Ca_2CoO_3 sublattice and the CdI_2-type $[CoO_2]$ sublattice, alternately stacked along the *c*-axis. In this paper, measurements of the electrical resistivity and Seebeck coefficient for a series of misfit-layered oxides, $Ca_3Co_yO_{9+\delta}$ (where $y = 4$–6), prepared by solid-state reaction, were reported. Structural parameters are refined with the superspace group X2/m(0b0)s0 using powder XRD data. With partial substitution of Si^{4+} for Co^{3+}, the resistivity decreases, while the thermopower increases simultaneously. These results indicate that partial substitution of Si^{4+} improves the thermoelectric characteristics of $Ca_3Co_4O_{9+\delta}$.

The compound, Ca_3CoO_4, has also been reported. It was prepared by reacting Ca metal with Co(2-methoxyethoxide) in 2-methoxyethanol. The resulting clear solution was carefully hydrolyzed with water to obtain a sol. The sol was dried and pyrolyzed at 400 °C to obtain a moisture sensitive powder that showed diffraction peaks due to $CaCO_3$ perhaps due to reaction with atmospheric CO_2. Further sintering at 800 °C furnished crystalline Ca_3CoO_4. However, no further description of this compound has appeared in the current literature.

In the Co^{3+}-containing system of CaO–Co_2O_3, the crystal structure and transport properties of the quasi one-dimensional (1D) cobalt oxide $CaCo_2O_4$ was studied. The $CaCo_2O_4$ phase crystallizes in calcium-ferrite type structure shown in Fig. 13.10.

The structure of $CaCo_2O_4$ belongs to an orthorhombic system (space group: *Pnma*) with lattice parameters, $a = 8.789$ Å, $b = 2.9006$ Å and $c = 10.282$ Å. A Curie–Weiss-like behavior in magnetic susceptibility was seen with the nearly trivalent cobalt low-spin state (Co^{3+}, 3d t_{2g}^6, $S = 0$). A semiconductor-like temperature dependence of resistivity ($p = 3 \times 10^{-1}\ \Omega$ cm at 380 K) with dominant hopping conduction at low temperature, metallic-temperature-dependent large thermoelectric power (Seebeck coefficient: $S = +147\ \mu V/K$ at 380 K), and Schottky-type specific heat with a small

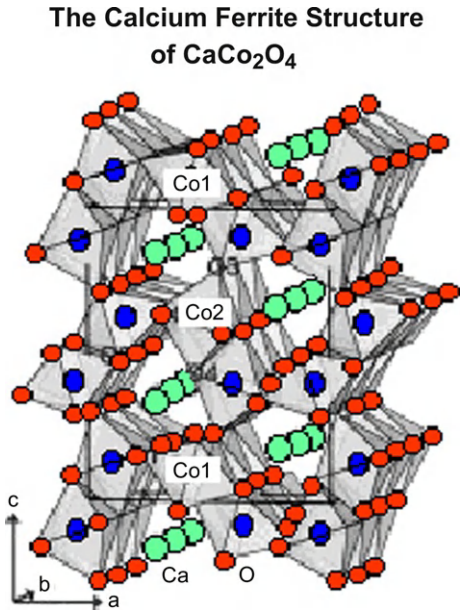

FIGURE 13.10

Sommerfeld constant ($\gamma = 4.48$ mJ/Co mol K^2), were also observed. These results suggested that the compound possesses a metallic electronic state with a small density of states at the Fermi level. The doped holes are localized at low temperatures due to disorder in the crystal. The carriers probably originate from slight off-stoichiometry of the phase. It was also found that *S* tends to increase even more beyond 380 K. The large *S* is possibly attributed to residual spin entropy and orbital degeneracy coupled with charges by strong electron correlation in the cobalt oxides.

Electrospinning is a well-established method for synthesizing micro-dimensional and 1D fibers from a large variety of precursor solutions. Initially, research focused on the production of polymer nanofibers. However, in recent years, a large variety of oxide ceramics have been produced through electrospinning of sol–gel systems. In one study, polycrystalline calcium cobaltite ($Ca_3Co_4O_9$) fibers of diameter 30–100 nm were electrospun from sol–gels based on a novel combination of polyvinyl alcohol, cobalt acetate and calcium acetate precursors. XRD data have showed that, at calcination temperatures of between 250 and 500 °C, metastable CoO and $CaCO_3$ exist as transition phases and that subsequent heating at 650 °C converted these phases to calcium cobaltite. Thermal analysis has confirmed this staged calcination mechanism and also revealed the effect of oxygen starvation on the final structures. Microscopic analysis confirmed the highly crystalline nature of the oxide fibers, and the presence of highly faceted grains, around 20–40 nm in thickness. These are the primary building blocks in these fibers.

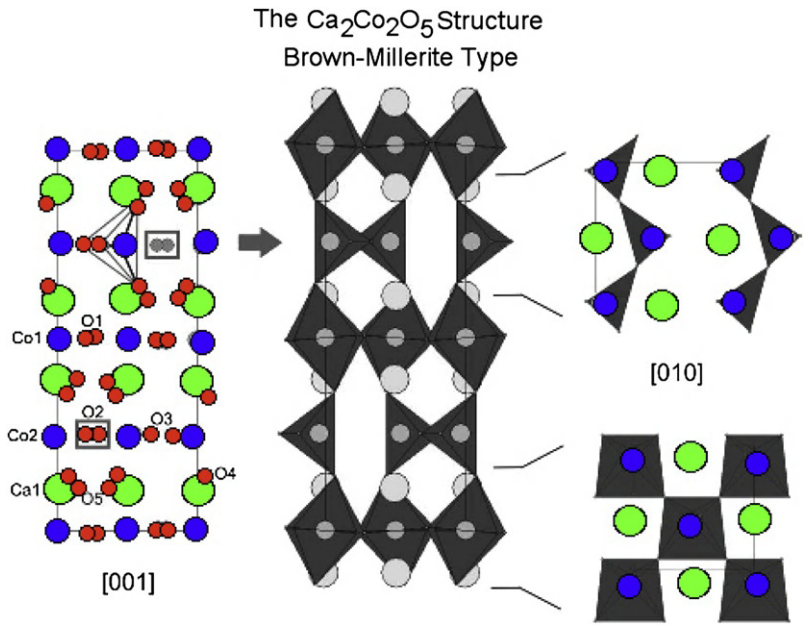

FIGURE 13.11

Furthermore, the material will only exist in fibrous form if calcination is a staged process, rather than a single, high-temperature process. Bulk calcium cobalt oxide is regarded as a competitive thermoelectric material due to its structural complexities associated with a layered structure. Microscopic analysis has shown that this layered structure is preserved when the electrospun nanostructured form is preserved. The measured thermopower in these nanostructures is at least 30% higher than that reported from bulk material at 300 K.

The Co^{3+}-containing compound, $Ca_2Co_2O_5$, has the Brownmillerite type of structure, as shown in Fig. 13.11.

A well-crystallized epitaxial $Ca_2Co_2O_5$ thin film was deposited on a $NdGaO_3$ substrate by the pulsed laser deposition technique. Its average Brownmillerite structure (space group: *Ibm*2 with $a \approx a_p\ 2$, $b \approx 4a_p$ and $c \approx a_p\ 2$) has been determined by direct methods using precession electron diffraction data recorded on a cross-sectional sample.

This compound can also be synthesized by a CP (chemical precipitation) method plus SPS (spark plasma sintering) using cobalt and calcium nitrates as starting materials and sodium hydroxide as a precipitant. Single-phase $Ca_2Co_2O_5$ ceramics can be obtained by SPS at 800 °C for 5 min using the precursor powders calcined at 700–850 °C for 2 h. It is critical to obtain stochiometric precursor by controlling the final pH 13.2 during the CP process. The SPS process is effective in obtaining single-phase $Ca_2Co_2O_5$ ceramics. The thermoelectric properties of the prepared sample were investigated from 100 to 700 °C. At 700 °C, the electrical resistivity, Seebeck coefficient, thermal conductivity and figure of merit of the sample were 9.30×10^{55} Ω/m, 178 μV/K, 1.55 W/mK and 0.21, respectively.

Textured Bi-substituted $Ca_2Co_2O_5$ ceramics have been prepared using a CP method combined with SPS. The Bi substitution is effective in increasing the grain orientation of the $Ca_2Co_2O_5$-based ceramics (from 0.46 to 0.85). Electrical conductivity increases obviously with partial substitution of Bi^{3+} for Ca^{2+} (from 113.9 to 142.4 S/cm at 973 K). The $Ca_{1.92}Bi_{0.08}Co_2O_5$ sample exhibits higher power factor (4.4×10^{-4} W m^{-1} K^{-2}) than that of pure $Ca_2Co_2O_5$ (3.2×10^{-4} W m^{-1} K^{-2}) at 973 K, indicating that the $Ca_2Co_2O_5$ system is another promising *p*-type material for high-temperature thermoelectric applications.

The electrochemical performance of mixed oxides, $Ca_2Fe_2O_5$ and $Ca_2Co_2O_5$ for use in Li-ion batteries was studied in lithium-batteries with Li as the counter electrode. The compounds were prepared and characterized by XRD and SEM. $Ca_2Fe_2O_5$ showed a reversible capacity of 226 mAh/g at the 14th cycle and retained 183 mAh/g at the end of 50 cycles at 60 mA/g in the voltage window 0.005–2.5 V. A reversible capacity in the range, 365–380 mAh/g, which is stable up to 50 charge–discharge cycles is exhibited by $Ca_2Co_2O_5$ in the voltage window, 0.005–3.0 V and at 60 mA/g. This corresponds to recyclable moles of Li of 3.9 ± 0.1 (theoretical: 4.0). Significant improvement in the cycling performance and attainable reversible capacity were noted for $Ca_2Co_2O_5$ on cycling to an upper cutoff voltage of 3.0 V as compared to 2.5 V. Coulombic efficiency for

both compounds is >98%. Electrochemical impedance spectroscopy data clearly indicate the reversible formation/decomposition of polymeric surface film on the electrode surface of $Ca_2Co_2O_5$ in the voltage window, 0.005–3.0 V. Cyclic voltammetry results compliment the galvanostatic cycling data.

When a molten salt method was used to synthesize $Ca_2Co_2O_5$ powder, using Co_3O_4 and $CaCO_3$ as raw materials and $CaCO_3$–$CaCl_2$ as a eutectic salt, the resultant was a ceramic exhibiting the highest thermoelectric behavior ever recorded. The formation process of $Ca_2Co_2O_5$, via molten salt mechanisms, was further investigated by powder XRD and SEM techniques. The results showed that sheet-like particles can be obtained at 963 K. The electrical conductivity and the Seebeck coefficient of the specimen were measured from 323 to 963 K. The measured properties increased with increasing temperature and the highest value of power factor (2.0×10^{-4} W/m/K^2) was obtained at 963 K. This indicates that molten salt synthesis is a promising method to prepare high temperature, high thermoelectric performance materials.

The Co^{3+}-containing compound, $Ca_3Co_2O_6$ is also known. A polycrystalline sample of $Ca_3Co_2O_6$ was prepared by solid-state reaction of $CaCO_3$ and Co_3O_4 at 1243 K in air. The electrical resistivity (γ) of $Ca_3Co_2O_6$ exhibited semiconducting behavior and ranged from 1.6×10^2 to 1.3×10^{-1} Ω/cm at temperatures from 400 to 1170 K. The Seebeck coefficient (S) showed a positive value, and decreased from 660 to 140 μV/K with increasing temperature from 350 to 1170 K. The power factor (S^2/p) tended to increase with increasing temperature, and the maximum value was 1.6×10^{-5} W/(m/K^2) at 1150 K. It has the structure shown in Fig. 13.12.

This diagram shows (a) the $Ca_3Co_2O_6$ hexagonal cell, octahedral Co(I) and trigonal Co(II) sites are shown in light and dark blue, respectively; (b) proposed magnetic exchange pattern between the Co(II) sites; (c)a sketch showing one possible arrangement of the normalized Co(II) magnetic moments in the incommensurate magnetic ground state (μ\\c-axis, shown vertical).

$Ca_3Co_2O_6$ is a very interesting system, characterized by low-dimensional magnetism and topological frustration. The diagram shows the crystallographic structure of the compound is made up of chains of face-sharing polyhedra running along the c-axis, arranged in the ab-plane on a triangular lattice. Due to local symmetry, one half of the Co ions have a magnetic moment (Co(II), μ ~ 5.1 μbar), subject to (antiferro-)ferromagnetic (inter-)intrachain interactions. In this sketch, magnetic sites are located at the center of dark blue polyhedra, representing oxygen cages with trigonal prismatic (TP) coordination. This novel 1D cobaltate, $Ca_3Co_2O_6$, is not a ferromagnetic (FM) half metal but a Mott insulator. Both the octahedral and the trigonal Co ions are formally trivalent, with the octahedral being in the low-spin and the trigonal in the high-spin state. The inclusion of the spin-orbit coupling leads to the occupation of the minority-spin d^2 orbital for the unusually coordinated trigonal Co, producing a giant orbital moment (1.57 μbar). It also results in an anomalously large magneto-crystalline anisotropy (of order 70 meV), elucidating why the magnetism is highly Ising like. The crystal structure of $Ca_3Co_2O_6$ (space group = $R3c$) shown above is highly anisotropic. Along the c-axis, there are chains of alternating CoO_6 TPs and CoO_6 octahedra with a Co–Co spacing of 2.59 Å. In the ab-plane, the CoO_6 chains are arranged in a triangular lattice with a Co–Co separation of 5.24 Å, double that found along the chains. Both the cobalt ions are trivalent with alternate high-spin ($S = 2$) and low-spin ($S = 0$) states

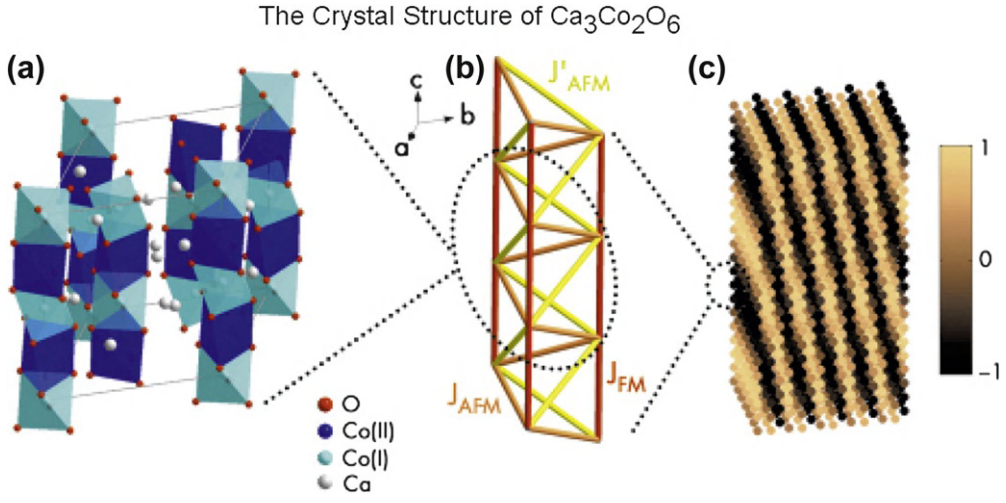

FIGURE 13.12

corresponding to the CoO_6 TPs and the octahedra, respectively. The intrachain coupling is FM while the interchain coupling is antiferromagnetic (AFM). At low temperatures (~8 K), a series of equally spaced steps emerge in the magnetization when a magnetic field is applied along the *c*-axis. Magnetization steps have been observed at 0 T, 1.2 T, 2.4 T, 3.6 T, with possible steps at the higher fields of 4.8 T and 6 T. When the temperature is increased to an intermediate value (~10 K), only the 3.6 T step remains. The hysteresis in the magnetization as a function of magnetic field is then greatly reduced. At these temperatures, the magnetization is saturated above 3.6 T with a value of $M_{Sat} = 5.1$ μbar/f.u, indicating complete FM ordering. Below 3.6 T, the value of the magnetization is $M_{sat}/3$. This latter value is ascribed to two-thirds of the chains having spin up and one-third having spin down.

$Ca_3Co_2O_6$ has been the focus of considerable experimental and theoretical attention due to its peculiar magnetic properties for several years. Below the Neel temperature ($T_N \sim 25$ K), 3D long-range magnetic order is established. At low temperature, an unexpected evolution of the magnetic order parameter versus both temperature and magnetic field has been observed. In particular, diffracted intensities corresponding to antiferromagnetic (AFM) reflections decrease on cooling below 17 K, while the bulk magnetization increases in a series of equally spaced steps versus the magnetic field, instead of smoothly approaching its saturation value. Depending on external conditions, the relaxation of the magnetization toward its equilibrium state can also be dramatically modified. Magnetic ordering occurs below 24 ± 2 K. Above 80 K, the Curie–Weiss law is followed and an effective magnetic moment of 5.7 ± 0.2 μbar was found. $Ca_3Co_2O_6$ is ferrimagnetic at low temperatures, with FM ordering dominating within the Co···O chains. In high magnetic fields, above around 2.7 MA/m, a field-induced transition from ferrimagnetic to FM structure occurs, implying turning of the spins in one of the chains.

In another paper, the magnetic coupling between quasi 1D FM chains in $Ca_3Co_2O_6$ oxide was studied using magnetic measurements under hydrostatic pressures (*P*) up to 12 kbar. It was found that the low-temperature ferrimagnetic phase, resulting from the AFM coupling of FM chains, was stabilized under pressure. Both the critical field for the spin-flip transition of the linear chains (H_{SF}) and the temperature T^* where the long-range ferrimagnetic ordering sets in rise under pressure with the following rates: $dH_{SF}/dP \approx 135$–155 Oe/kbar and $dT^*/dP \approx 0.073$ K/kbar, respectively. It was shown that these variations can be accurately described in terms of the interchain bond-length compression.

In the $Ca_3Co_2O_6$ compound, it has been found that it is an ising magnetic system on a triangular lattice. This compound is isostructural to $Sr_4PtO_{6.9}$, a structure related to the hexagonal perovskites (PVs). The "-A-B-A-B-" hexagonal stacking of the $[AO_3]$ layers yields the 2H hexagonal PV of the $A_3B_3O_9$ formula. This stacking mode creates octahedral crystallographic sites that are occupied by B cations, leading to the oxygen stoichiometric 2H-$BaCoO_3$ compound. By considering an A_3O_9 unit obtained by tripling the $[AO_3]$ layer and also by the removal of three oxygen anions, an A_3O_6 layer can also be built. So, in addition to the octahedral site created by the stacking of A_3O_9 units, the stacking of the A_3O_6 units generates a TP site occupied by a A′ cation. Finally, by mixing of the $[A_3O_9]$ and $[A_3A'O_6]$ blocks, a large family of oxides with general formula $A_{3n+3}mA'nB_{3m+n}O_{9m+6n}$ can be described. There, the ratio between the $[A_3A'O_6]$ and $[A_3O_9]$ blocks is given by $n/m \cdot 10$. For these compounds, the unit cell $a \approx 10$ Å corresponds to $\sim a_h\sqrt{3}$, where a_h is the hexagonal *a* parameter. Along the *c*–*b*-axis, the structures can be described as chains of face-shared octahedra and TPs, occupied by the B and A_h cations, respectively. This is consistent with the needlelike aspect of the crystals.

In the Co^{2+}–Co^{3+}-containing system, i.e. CaO–Co_3O_4, three misfit layer compounds with the same chemical formula $Ca_3Co_{4-x}O_{9-\partial}$ have been isolated. They exhibit either a monoclinic or an orthorhombic symmetry. These crystals are constituted of two interpenetrating Co sublattices showing incommensurate periods along the *b*-axis. The structure of the three crystals can be described as an alternate stacking along [001] of distorted rock salt-type slabs $[Ca_2CoO_3]$ and of $[CoO_2]$ layers displaying a distorted CdI_2-type structure. Relating to the symmetry and the different observed *c* periods, different sequences are found for the $[CoO_2]$ layers running along [001] within the three crystals. Two of them were determined by single XRD using the four-dimensional (4D) superspace formalism. A significant displacement modulation is implied, acting mainly on Ca and O atoms involved in the intersystem bonding scheme. This modulation leads to a noticeable distortion of the CoO_6 octahedra of the $[CoO_2]$ layers. Strong interactions, via Ca–O bonds, are evidenced between the two sublattices. A systematic positional disorder is observed inside the [CoO] layer.

Single crystals of $(Ca_2CoO_3)_{0.7}CoO_2$ with a $Ca_3Co_4O_9$ structure were grown using a modified strontium chloride flux technique, and their electrical and thermal properties were determined. Growth conditions were established for obtaining plate-like single crystals of a relatively large size ($5 \times 10 \times 0.05 \times$ mm^3). At 973 K, thermoelectric power *S* and electrical resistivity ρ of the specimens are ≈ 240 μV/K and $\approx 2.3 \times 10^{-5}$ Ωm, respectively, and their thermal conductivity κ is nearly 3 Wm^1/K, as determined by mathematical extrapolation. The figure of merit $Z_T = S^2T/\rho\kappa$ derived there

was ≈0.87 at 973 K. The relatively low κ is likely the result of a misfit structure between the CoO_2 layer and the Ca_2CoO_3 slab.

The compound, $Ca_2Co_3O_6$, has been mentioned in regard to its magnetic properties relative to $Ca_3Co_2O_6$. This dicalcium compound also has a low-temperature ferrimagnetic phase, resulting from the AFM coupling of FM chains, by stabilization under pressure. Both, the critical field for the spin-flip transition of the linear chains (H_{SF}), and the temperature T^* where the long-range ferrimagnetic ordering sets in rise under pressure, were determined. The compound $Ca_2Co_3O_6$ is a quasi 1D magnetic system made up of spins aligned in chains. Due to the weak AFM interaction between FM chains, it exhibits a 3D transition at low temperatures. This compound adopts a spinel-like structure.

In the Co^{4+}-containing system of CaO–CoO_2, the preparation of $CaCoO_3$ via solid-state methods has not been successful, under ambient or high-pressure conditions. However, the defect material, $SrCoO_{3-\geq}$ is a FM oxide with the cubic PV crystal structure, which can be prepared under high oxygen pressure.

The energy gap of any given PV is usually less than 3.0 eV. Many show good photocatalytic activity in the visible light region and can be used as a photocatalytic agent. In one paper, a PV-type oxide $CaCoO_3$, stable in solution, was prepared by citric complexometry. Photocatalytic degradation experiments, using the $CaCoO_3$ to dispose of a water-soluble dye, were carried out. The conditions of photocatalytic degradation such as photocatalytic time, amount of photocatalyst, the illumination intensity, pH value and additional oxidant (H_2O_2) on photocatalysis were also studied in the research. The results showed that $CaCoO_3$ has a significant photocatalysis-decolorizing effect on the acid red dye. When the concentration of the catalyst is 4 gm/l, the reaction time was 180 min, pH value was 2, the illumination intensity was 60 W, with the dosage of 10% H_2O_2 at 50 ml/l. The degradation ratio of the acid red dye was 97.2%.

No other compounds are known in this system.

In the Co^{5+}-containing system of CaO–Co_2O_5, the compound, $CaCo_2O_6$, has been studied briefly. Hopping conductivity in 1D $CaCo_2O_6$ single crystals (published 2002), with a chain-like structure, has been found to be lower than other similar compounds but no further work has been undertaken.

In the Co^{6+}-containing system of CaO–CoO_3, the results of three-dimensional (3D) numerical simulation of the magnetic structure and magnetization curves of $Ca_3Co_2O_6$ have been presented. The structures of the low-temperature and high-temperature phases differ significantly: the false frustrated low-temperature phase is transformed into a partially disordered AFM honeycomb structure. Two additional magnetization steps at low temperatures are formed at the expense of the domain structure and the ferrimagnetic phase. All fundamental hypotheses used in terms of the 2D model have found their confirmation during the 3D simulation.

No other compounds have been documented.

Calcium cobaltate or cobaltite compounds are not offered for sale commercially nor is a CAS number available.

13.1.4. Strontium Cobalt Compounds

Strontium does not form any intermetallic compounds with Co metal.

In the Co^{2+}-containing system of SrO–CoO, the compound, $SrCoO_2$ is not very stable at room temperature. The existence of gaseous cobaltates of alkaline earth metals has been established by high-temperature mass spectrometry. Gaseous molecules: $CaCoO_2$, $SrCoO_2$ and $BaCoO_2$ have been found for the first time. On the basis of the measured constants of the equilibrium of gas-phase reactions the standard enthalpies of formation: (-149 ± 19) $kJ \cdot mol^{-1}$, (-149 ± 20) kJ/mol and (-250 ± 16) kJ/mol; standard atomization enthalpies obtained were: (1251 ± 22) kJ/mol, (1233 ± 23) kJ/mol and (1353 ± 20) kJ/mol for $CaCoO_2$, $SrCoO_2$ and $BaCoO_2$, respectively.

A study of the Sr···Co···O system concerning Sr_2CoO_3 has allowed the isolation of a new layered cobaltite $[Sr_2CoO_3][CoO_2]_{1.8}$. It was noted that the Co^{3+} ion is present. The structural analysis by transmission electron microscopy shows a composite structure consisting in two substructures related to triple rock salt-type layers and single CdI_2-type layer, respectively. The structure of this compound is similar to that of the well-known misfit cobaltite $[Ca_2CoO_3][CoO_2]_{1.62}$, also called "$Ca_3Co_4O_9$". The latter is intensively studied for thermoelectric power application to convert waste heat energy into electricity at temperature well above 300 K. A large thermoelectric power is also found for this new cobaltite $[Sr_2CoO_3][CoO_2]_{1.8}$, which exhibits a Seebeck coefficient such as $S_{300\ K} \approx 110\ \mu V/K$. This value, lower than that of $[Ca_2CoO_3][CoO_2]_{1.62}$ ($S_{300\ K} \approx 125\ \mu V/K$), shows that the misfit character, quantified by the ratio $b_1/b_2 = 1.8$ and 1.62 for the "Sr-" and "Ca-" based misfit cobaltites, respectively, is directly connected to the thermoelectric properties in these materials.

The stoichiometric compound, Sr_2CoO_3, is not very stable but the alternative strontium-defect compound has been observed. The incommensurate modulated crystal structure of the hexagonal cobalt oxide $Sr_{1.261}CoO_3$ has been studied using a 4D superspace profile analysis of neutron powder diffraction (NPD) data. $Sr_{1.261}CoO_3$ is a composite crystal that consists of $[CoO_3]$ and [2Sr] subsystems. The $[CoO_3]$ subsystem

forms 1D chains that run parallel to the *c*-axis and consist of face-sharing CoO_6 polyhedra with octahedral (O_h) and TP coordinations. The structure analysis reveals that the [CoO_3] chains contain 73.9% O_h and 26.1% TP sites, and that the TP sites have longer Co–O bonds than the O_h sites: $d_{av} = 2.039$ Å (TP) and 1.895 Å (O_h). The averaged Co bond valences are $Co^{3.56+}$ in the O_h sites and $Co^{2.45+}$ in the TP sites, suggesting that a considerable amount of Co^{3+} ions are mixed with Co^{4+}ions in the O_h sites and with Co^{2+} ions in the TP sites. The observed magnetic susceptibility can be well explained assuming that the compound has the Co mixed valence state with the spin configurations of $S = 0$ low-spin state for $Co^{3+}(d^6)$, $S = 1/2$ low-spin state for $Co^{4+}(d^5)$ and $S = 3/2$ high-spin state for $Co^{2+}(d^4s^2)$. The Weiss temperature, approximately 0.8 K, implies that $Sr_{1.261}CoO_3$ naturally assumes a Curie paramagnetic state, probably owing to the obstruction of the intrachain magnetic interaction by the nonmagnetic Co^{3+} ions. These results suggest that the nonmagnetic Co^{3+} ions play an essential role in the magnetism of $Sr_{2-\delta}CoO_3$ systems.

No other compounds are known in this system.

In the Co^{3+}-containing system of SrO–Co_2O_3, the geometric and electronic properties of $SrCoO_{2.5}$ ($Sr_2Co_2O_5$) have been studied using the local-spin density approximation together with the Hubbard method. The geometric optimization shows that the energy of a unit supercell for $SrCoO_{2.5}$ with the space group *Pnma* is at least 1.37 eV lower than the others, so we infer that the *Pnma* structure is the ground state of $SrCoO_{2.5}$ at low temperature. The electronic band structure calculations demonstrate that the paramagnetic ordering $SrCoO_{2.5}$ at high temperature has the character of an indirect band gap semiconductor, while the AFM ordering $SrCoO_{2.5}$ at low temperature has the character of a conductor. The magnetism calculation shows that the magnetic moment of Co is 2.96 μbar, comparable with the experimental measurement at the liquid nitrogen temperature, i.e. 3.30 ± 0.5 μbar.

This compound ($Sr_2Co_2O_5$) has the Brownmillerite-type of structure as determined by NPD measurements at temperatures ranging from 10 to 623 K, across the Néel temperature ($T_N = 537$ K) of this AFM oxide. The study was complemented with differential scanning calorimeter (DSC), DC susceptibility and magnetization measurements. Although the refinement of the crystal structure from NPD data was possible in the orthorhombic *Pnma* and *Ima*2 space groups, the support of ab initio band structure calculations has allowed the selection, without ambiguity, of the *Ima*2 space group as the ground state for $SrCoO_{2.5}$ Brownmillerite structure. In *Ima*2 the crystallographic structure of $SrCoO_{2.5}$ can be described as layers of corner-sharing CoO_6(1) octahedra alternating along the *a*-axis, with layers of vertex-sharing CoO_4(2) tetrahedra, and conforming chains running along the [0,0,1] direction. The magnetic structure below $T_N = 537$ K was determined to be *G*-type with the magnetic moments directed along the *c*-axis. This magnetic arrangement is stable from T_N down to 10 K. At $T = 10$ K, the magnetic moment values for Co1 and Co2 atoms are 3.12(13) μbar and 2.88(14) μbar, respectively, compatible with a $Co^{2+}L①$ state, where L① stands for a ligand hole. The magnetic susceptibility curves show, below 200 K, a divergence of zero-field cooling and field cooling curves, displaying broad maxima which are interpreted as due to the presence of FM clusters embedded into an AFM matrix. This inhomogeneity is inherent to the synthesis process, where, by quenching microcrystalline samples of the $SrCoO_{3-x}$ composition from high temperature, cubic, FM PVs have been identified by diffraction methods.

The electrochemical oxidation of the antiferromagnetically ordered $SrCoO_{2.5}$, with Brownmillerite-type structure, to the cubic ferromagnet $SrCoO_3$, with PV structure, has been investigated in situ by NPD as well as by XAFS spectroscopy, in specially designed electrochemical cells as a function of the charge transfer. One mechanism proffered is shown in Fig. 13.13.

For fuel cells, the operating temperatures are usually about 1000 °C. Under such extreme conditions the mechanical and thermal stability of electrodes are significantly limited. One of the very few exceptions is the $SrCoO_{2.5}$ system, which can be electrochemically oxidized via a reversible topotactic redox reaction, in an aqueous alkaline electrolyte at room temperature, yielding $SrCoO_{3.0}$ as the final reaction product. The reaction can formally be described by:

$$SrCoO_{2.5} + xO^{2-} \Rightarrow SrCoO_{2.5+x} + 2xe^- \quad (0 < x < 0.5)$$

The Co is purely Co^{3+} for the starting compound whereas Co^{4+} is achieved for the final reaction product. From NPD experiments, two intermediate phases, $SrCoO_{2.75}$ and $SrCoO_{2.82}$, have been characterized. Superstructure reflections have been observed for the $SrCoO_{2.82}$ phase only. To investigate the true symmetry of the intermediate phase, an electrochemically prepared sample of $SrCoO_{2.82}$ has been measured ex

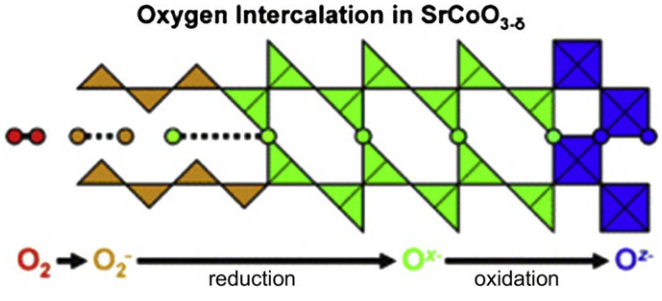

FIGURE 13.13

situ on the high-resolution powder diffractometer at beam line **BM01B**. It was found that reflections, indexed in the averaged cubic PV cell as (h00) or (hh0), are clearly separated into two distinct diffraction peaks, whereas (hhh) reflections were unique, where the profiles of (111), (200), (220) reflections are reported and compared with that of the cubic $SrCoO_3$ PV. This combined NPD and X-ray powder diffraction (XRPD) study represents the first observation of 3D oxygen ordering during an oxygen intercalation reaction. The $SrCoO_{2.82}$ phase can be described as being in a tetragonal unit cell, related to the PV cell by $a = b = 2a\sqrt{2}$ and $c = 2a$. The structure of this intermediate phase confirms the strongly topotactic character of the oxygen intercalation reaction. Overall, the first part of the reaction covers the continuous formation from $SrCoO_{2.5}$ to $SrCoO_{2.7}$ while the second starts from $SrCoO_{2.8}$ to give the fully oxidized $SrCoO_3$ phase. Around $SrCoO_{2.75\pm0.05}$, a plateau is observed leading to the assumption that around this charge transfer a "stand-by" of the Co oxidation takes place.

Temperature-dependent XRD and NPD have been exploited, in complement with DTA–TGA, conductivity and thermal expansion measurements, to revisit the structural evolution of $SrCoO_{2.5}$ Brownmillerite-like phases from room temperature to 1200 °C (Fig. 13.14).

Three different polymorphs have been identified: the orthorhombic "O" Brownmillerite phase between room temperature and 653 °C, the hexagonal "H" phase between 653 and 920 °C, and the cubic PV "C" above 920 °C, which is transformed again, by cooling, into the "H" phase at 774 °C. The metastable "O" Brownmillerite phase can only be obtained by quenching in liquid N_2 from 1000 °C. The refinement of the crystal and magnetic structures of $SrCoO_{2.5}$ from NPD data collected "in situ" as a function of temperature in an air atmosphere led to define structural details of the very distinct coordination polyhedra present in the different polymorphs, which have been correlated with the transport properties. The conductivity shows little dependence up to 250 °C, and it abruptly increases above this temperature, which is concomitant with a contraction of the Co_2–O_3 bonds of the tetrahedral CoO_4 units of the "O" Brownmillerite structure at 350 °C, suggesting the presence of an insulator-to-metal transition in this structural polymorph. The dramatic reduction of conductivity above 500 °C is connected with the transformation to the "H" polymorph, with a complete oxygen sublattice and a face-sharing octahedral framework with a poor 1D electronic conduction. Further heating above 900 °C boosts again the conductivity when the sample is entering the cubic PV region, characterized by a 3D vertex-sharing network of CoO_6 octahedra. The total conductivity displays a maximum value of 150 S/cm at 900 °C and it increases during the cooling run, thus displaying a characteristic metallic

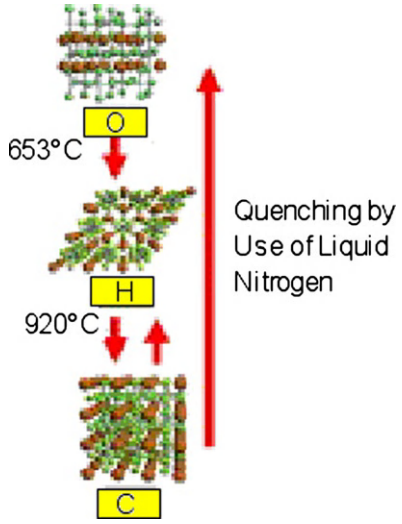

FIGURE 13.14

behavior for the "C" phase. This polymorph presents conductivity values substantially above the required 100 S/cm in solid oxide fuel cells (SOFCs), suggesting that it is a good candidate for cathode materials in energy conversion devices.

In another study, three very distinct polymorphs of overall stoichiometry $SrCoO_{2.5}$ were identified in the temperature range 25–1200 °C, starting from the "O" Brownmillerite phase previously obtained by quenching in liquid N_2 from 1000 °C. A metal–insulator transition was detected in the "O" phase, correlated to subtle structural changes. A drop of conductivity associated to the "H" hexagonal polymorph was followed by a huge increase of σ when entering the cubic "C" phase. These transformations can be seen in Fig. 13.14.

The phase separation and inhomogeneities induced by oxygen non-stoichiometry in $SrCoO_{2.5+x}$ have been examined more thoroughly. In previous work, it has been shown that as oxygen is driven into the $SrCoO_{2.5}$ electrochemically, the material structurally separates into two different phases: one is AFM $SrCoO_{2.5}$, and the other is FM $SrCoO_{2.75}$.

A recent (2010) paper shows that two distinct FM phases appear for $SrCoO_{2.88}$ and $SrCoO_3$, with $T_c = 220$ and 280 K, respectively. These changes may perhaps be better seen in Fig. 13.15.

The phase diagram of $SrCoO_{2.5+x}$ suggests that the four magnetic line phases are the only stable ground states in the system. While AFM $SrCoO_{2.5}$ is orthorhombic, the three FM phases are pseudo-cubic and, unlike the magnetic properties, do not show the coexistence of different structures. The existence of the distinct $T_c = 220$ K and $T_c = 260$ K magnetic phases with no structural differentiation indicates the presence of magnetic phase separation.

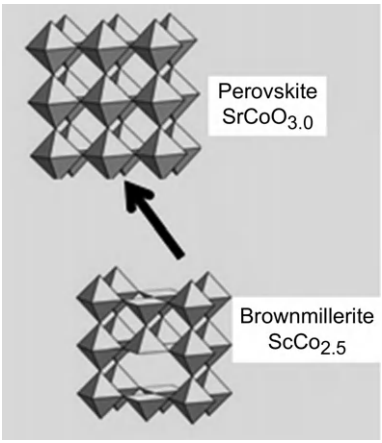

FIGURE 13.15

A dense phase of a post-layered PV $Sr_3Co_2O_6$ was created by a high-pressure and high-temperature synthetic route and quenched to ambient conditions. The structure of $Sr_3Co_2O_6$ was determined by synchrotron XRPD. $Sr_3Co_2O_6$ crystallizes in the K_4CdCl_6-type structure (an infinite chain-type structure), which is 6% denser than the known, iso-compositional layered PV $Sr_3CoO_{7-\delta}$ (δ~1). The K_4CdCl_6 type of $Sr_3Co_2O_6$ shows complex magnetic behavior reflecting the spin-chain nature as well as the analogue oxides $Ca_3Co_2O_6$ and Ca_3CoRhO_6, whose microscopic magnetic origin is still highly debated. Its structure has the form shown in Fig. 13.16.

Under normal preparation conditions, this compound exhibits oxide defects. The structural and magnetic phase diagrams of the bilayer Ruddlesden–Popper phase, $Sr_3Co_2O_x$, was extended beyond previously reported limits of $x \approx 6.1$ to $x = 6.60$. The room temperature crystal structure for the $x = 6.60$ material is orthorhombic with oxygen vacancies located in the apical position that links the two nominally CoO_2 layers

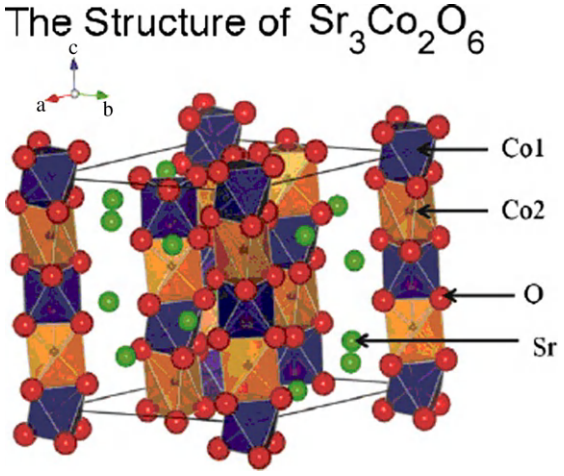

FIGURE 13.16

in the PV block. An antiferromagnetic ground state is converted to FM by moderate magnetic fields and high-temperature magnetic susceptibility data indicate short-range FM order. The oxygen defect structure of $Sr_3Co_2O_x$ in the range $5.64 < x < 5.80$ was also studied. Oxygen vacancies are present in both the in-plane sites, as well as the linking apical site. Critically, this linking site is displaced significantly along z ① from its ideal position, creating a particularly short Co–O bond. Using a combination of NPD data and crystal-chemical considerations, we provide a model of the local Co ion environments. Additionally, low-temperature NPD and magnetization data show that the magnetic ground state of these oxygen-deficient materials is a complex antiferromagnet, with considerable sensitivity to precise oxygen content.

Two low-dimensional cobaltite series in the Sr–Ca–Co–O system have been investigated for their solid solution limit, structure, and compatibility phase relationships (850 °C in air). Thermoelectric properties have been measured for selected members of these solid solutions. In $(Ca,Sr)_3Co_4O_9$, which has a misfit layered structure, Sr was found to substitute in the Ca site to a limit of $(Ca_{0.8}Sr_{0.2})_3Co_4O_9$. Compounds in the homologous series consist of 1D parallel $Co_2O_6^{6-}$ chains that are built from successive alternating face-sharing CoO_6 TPs and "n" units of CoO_6 octahedra along the hexagonal c-axis. In the $Ca_{n+2}Co_nCo'O_{3n+3}$ series, only the $n = 1$ phase ($Ca_3Co_2O_6$) could be prepared under the present synthesis conditions. Sr substitutes in the Ca site of $Ca_3Co_2O_6$ to a limit of $(Ca_{0.9}Sr_{0.1})_3Co_2O_6$. In the $Sr_{n+2}Ca_nCoO_{3n+3}$ series, Ca substitutes in the Sr site of the $n = 2$, 3, and 4 members to a limit of $(Sr_{0.7}Ca_{0.3})_4Co_3O_9$, $(Sr_{0.67}Ca_{0.33})_5Co_4O_{12}$, and $(Sr_{0.725}Ca_{0.275})_6Co_5O_{15}$, respectively. While the members of the $Ca_{n+2}Co_nCo'O_{3n+3}$ and $Sr_{n+2}Ca_nCoO_{3n+3}$ series have reasonably high Seebeck coefficients and relatively low thermal conductivity, the electrical conductivity is not capable of achieving high Z_T values.

No compounds are known in the Co^{2+}–Co^{3+}-containing system of SrO–Co_3O_4.

In the Co^{4+}-containing system of SrO–CoO_2, the compound, $SrCoO_3$ has received some attention. The magnetic ground state of cobalt PV $SrCoO_3$ is under much debate at present due to its complex magnetic properties. To shed further light on this issue, various magnetic structures of enlarged double cells have been examined. The calculation was carried out self-consistently within the unrestricted Hartree–Fock approximation and the real-space recursion method. The results showed that the magnetic ground state mainly depends on the competition between the crystal field strength Dq and Hund's coupling j. For a fixed value of j, it can be either the intermediate-spin state ($t^4_{2g}e^1_g$), the low-spin state coupled with the intermediate-spin state ferromagnetically ($t^5_{2g}e^0_g$-$t^4_{2g}e^1_g$-FM), or the low-spin state ($t^5_{2g}e^0_g$) as Dq

increases. However, the intermediate-spin state is the most probable candidate for the magnetic ground state in view of the experimental photoemission spectra and magnetic moment.

The electrical resistivity of the FM defect structure, $SrCoO_{3-\delta}$ ($0 < \delta < 0.5$) was measured in the temperature range from 77 to 300 K. All samples were good conductors and showed metallic behavior. The magnetic transition was independent of the electrical conductivity in $SrCoO_{3-\delta}$. The logarithm-specific electrical resistivities (log p) at 80 K and 300 K monotonously decreased with increasing the oxygen deficiency. This result was explained by considering the itinerant electron model.

$SrCoO_{3-\delta}$ is a material with multiple phase structures. The influence of Sc^{3+} doping in the B-site of $SrCoO_{3-\delta}$ on its lattice structure/phase stability, electrical conductivity, and cathode performance for intermediate-temperature SOFCs (IT-SOFCs) was investigated by XRD, four-probe DC conductivity and impedance spectroscopy measurements, respectively. The introduction of large size Sc^{3+} (0.745 Å) cation together with the sol–gel synthesis technique, led to a substantial stabilization of the cubic phase of $SrCoO_{3-\delta}$, even at a Sc^{3+} doping amount as low as 5 mol%. Such stabilization resulted in a sharp increase in the electrical conductivity of the material, which was found to be p-type in nature. A maximum electrical conductivity and favorable cubic phase stability of the material were reached at the Sc^{3+} doping concentration of 5–10 mol%. A further increase of Sc^{3+} doping, however, lowered the electrical conductivity due to the blocking effect of Sc^{3+} for the electron conduction. An area-specific resistance as low as 0.25 Ωcm^2 was reached at 600 °C for $SrSc_{0.1}Co_{0.9}O_{3-\delta}$ as a cathode material in IT-SOFCs, based on $Sm_{0.15}Ce_{0.85}O_{1.925}$ as the electrolyte.

Atomic resolution Z-contrast imaging and electron energy-loss spectroscopy (EELS) methods were used to study the defect structure of oxygen-deficient strontium cobaltite ($SrCoO_{3-\delta}$) after repeated oxidation/reduction cycles at elevated temperatures. Ordered microdomains were found in the reduced sample. Z-contrast imaging showed ordering in alternate CoO_2 planes, characteristic for a Brownmillerite-type vacancy ordered structure. EELS showed that the average valence state of cobalt had decreased after testing. In the tested sample, cobalt was found in +3 and +2 valence states, respectively. In addition, cobalt oxide precipitates were found at grain boundaries and in triple pockets in this sample, indicating a cobalt deficiency of the grains.

$SrCoO_{3-\delta}$ forms a PV structure with oxygen vacancies and is FM for $\delta < 0.25$. A study of polycrystalline samples has been made by controlling the oxidation state, using electrochemistry methods. Under these conditions, it was found that, magnetically, the system segregates into separate, stable phases that correspond to $SrCoO_{2.75}$ ($T_C = 165$ K), $SrCoO_{2.875}$ ($T_C = 220$ K), and $SrCoO_3$ ($T_C = 280$ K), with two-phase behavior for intermediate oxygen concentrations.

A large-size single crystal of stoichiometric $SrCoO_{3.00}$ was prepared with a two-step method combining the floating zone technique and subsequent high-oxygen pressure treatment. $SrCoO_3$ crystallizes in a cubic PV structure with space group Pm-3m, and displays an itinerant FM behavior with the Curie temperature of 305 K. The easy magnetization axis is found to be along the [111] direction, and the saturation moment is 2.5 μbar/f.u. in accord with the picture of the intermediate-spin state. The resistivity at low temperatures (T) is proportional to $T2$, indicative of the possible effect of orbital fluctuation in the intermediate spin FM metallic state. Unusual anisotropic magnetoresistance is also observed and its possible origin was discussed.

The Ruddlesden–Popper homologous series of compounds, $Sr_{n+1}Co_nO_{3n+1}$ ($n = 1$, 2, 3, 4, and ∞), were successfully synthesized by a high-pressure and high-temperature technique. Structure refinement revealed that these compounds crystallize in tetragonal structures, while the compound, $n = \infty$, is cubic. These compounds are FM with the Curie temperature decreasing from 255 K for $n = 1$ to about 200 K for $n = 2$ to 4 and down to 175 K for $SrCoO_3$. Co^{4+} ions were present as intermediate spin states for $n = 1$–4, but the low-spin state (coupled electrons) was present in $SrCoO_3$. Negative magnetoresistance was observed for Sr_2CoO_4 and found to be larger than that for $SrCoO_3$ (Fig. 13.17).

In a homologous compound, $Sr_6Co_5O_{15}$ [$=Sr_6(Co^{3+}{}_2,Co^{4+}{}_3)O_{15}$], the crystal structure of the defect compound, $Sr_6Co_5O_{14.3}$ has been analyzed by XRD of a c-axis elongated prismatic single crystal grown by a flux method. $Sr_6Co_5O_{14.3}$ is an oxygen-deficient phase of $Sr_6Co_5O_{15}$ that contains 1D columns of Co–O octahedra and triangular prisms. Oxygen defects are preferentially introduced in an O site shared by the

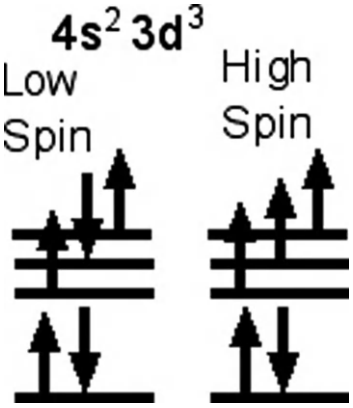

FIGURE 13.17

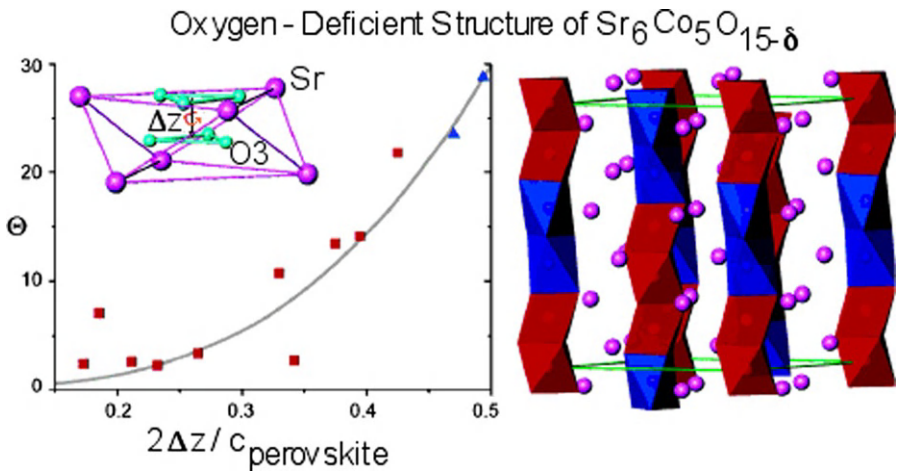

FIGURE 13.18

Co–O triangular prism and octahedron in the structure of $Sr_6Co_5O_{15}$. The average structure of $Sr_6Co_5O_{14.3}$ can be improved by splitting the oxygen defect site with the rhombohedral space group $R3$ ($a = 9.4334$ Å and $c = 12.5156$ Å).

Polycrystalline samples of $Sr_6Co_5O_{15}$ ($m = 1$, $n = 1$) and $Ca_3Co_2O_6$ ($m = 1$, $n = 0$), which are the members of homologous series $(A_3Co_2O_6)m(A'_3Co_3O_9)n$ (A, A′ = Ca, Sr, Ba), were prepared by solid-state reaction in air. The theoretical density ratios of obtained pellets, 89% for $Sr_6Co_5O_{15}$ and 95% for $Ca_3Co_2O_6$, sintered by the SPS method, increased compared to those of $Sr_6Co_5O_{15}$ (60%) and $Ca_3Co_2O_6$ (67%) prepared by solid-state reaction, respectively. Electrical resistivity (ρ) of $Sr_6Co_5O_{15}$ and $Ca_3Co_2O_6$ exhibited semiconducting behavior in the range of 300–1120 K. The temperature dependence of electrical resistivity for $Sr_6Co_5O_{15}$ showed a hysteresis-like behavior. The electrical resistivity of $Sr_6Co_5O_{15}$ (6.1×10^{22} to 4.6 Ω cm) and $Ca_3Co_2O_6$ (4.1×10^{-2} to 1.2×10^{3} Ω cm), sintered by the SPS method, was lower than those of $Sr_6Co_5O_{15}$ (1.3×10^{1} to 8.0 Ω cm) and $Ca_3Co_2O_6$ (1.5×10^{-1} to 4.5×10^{3} Ω cm) when prepared by solid-state reaction. Seebeck coefficients (S) of $Sr_6Co_5O_{15}$ and $Ca_3Co_2O_6$ were positive and were more than 100 μV/K in the range of 300–1120 K. Both compounds showed different temperature dependencies, respectively. The power factor (S^2/p) tended to increase with increasing temperature; the maximum values of the power factor were 1.4×10^{-5} W/(m K^2) for $Sr_6Co_5O_{15}$ and 1.6×10^{-5} W/(m K^2) for $Ca_3Co_2O_6$ prepared by solid-state reaction, and 3.0×10^{-5} W/(m K^2) for $Sr_6Co_5O_{15}$ and 5.2×10^{-5} W/(m K^2) for $Ca_3Co_2O_6$ sintered by the SPS method.

Two selected members of the homologous Ruddlesden–Popper series, $Sr_{n+1}Co_nO_{3n+1}$, were studied because of their potential applications as thermoelectric materials. Both the $n = 3$ member, $(Sr_{0.8}Ca_{0.2})_5Co_4O_{12}$, and the $n = 4$ member, $Sr_6Co_5O_{15}$, have distorted hexagonal PV-related structures that possess 1D cobalt oxide chains separated by alkaline earth cations. The linear chains consist of one unit of CoO_6 TP alternating with n units of CoO_6 octahedra. Crystal structures and reference powder XRD patterns of $(Sr_{0.8}Ca_{0.2})_5Co_4O_{11}$ [$P3c1$, $a =$ 9.4196(2) Å, $c = 19.9857(6)$ Å, $V = 825.83$ Å^3, and $Dx = 5.358$ g/cm^3] and $Sr_6Co_5O_{15}$ [$R32$, $a = 9.497\,64(12)$ Å, $c = 12.3956(2)$ Å, $V = 968.34$ Å^3, and $Dx = 5.455$ g/cm^3] were reported.

The structure has the form shown in Fig. 13.18. Large single crystals of oxygen-deficient $Sr_6Co_5O_{15-\delta}$ compounds, i.e. $Sr_6Co_5O_{14.70}$ and $Sr_6Co_{4.9}Ni_{0.1}O_{14.36}$, were obtained by using K_2CO_3 flux in the presence of additives of transition metal oxides.

The single-crystal structure determination showed that the structures of $Sr_6Co_5O_{14.70}$ and $Sr_6Co_{4.9}Ni_{0.1}O_{14.36}$ crystallize in the space group R and can be described as 1D face-sharing CoO_3 polyhedral chains and Sr cation chains. Unlike the other known 2H-PV-related oxides in which the polyhedral chains consist of octahedra (O_h) and TP, the structure of $Sr_6Co_5O_{14.70}$ and $Sr_6Co_{4.9}Ni_{0.1}O_{14.36}$ contains Oh and intermediate polyhedra (IP). This can be attributed to a general structure formula $A_6A'_2B_3O_\delta$, which is closely related to the known $A_6A'B_4O_{15}$ phases by shifting of a B atom and the O_3 triangle along the c-axis. Further study of the O_3 triangle revealed that this oxygen position splits into two independent positions, corresponding to polyhedral geometry of IP and TP, respectively. Therefore, the polyhedral chain in the structure should be more precisely described as a random composite of the $4O_h + TP$ and $3O_h + 2IP$. This model was used to interpret the magnetic properties, although not quantitatively. A 4D structure analysis was also conducted for both $Sr_6Co_5O_{14.70}$ and $Sr_6Co_{4.9}Ni_{0.1}O_{14.36}$ with a commensurate modulated structure in a 4D superspace group, $R_3m(00y)0s$, $\gamma = p/k = 3/5$. By considering the same 4D superspace group, $Rm(00y)0s$, but different

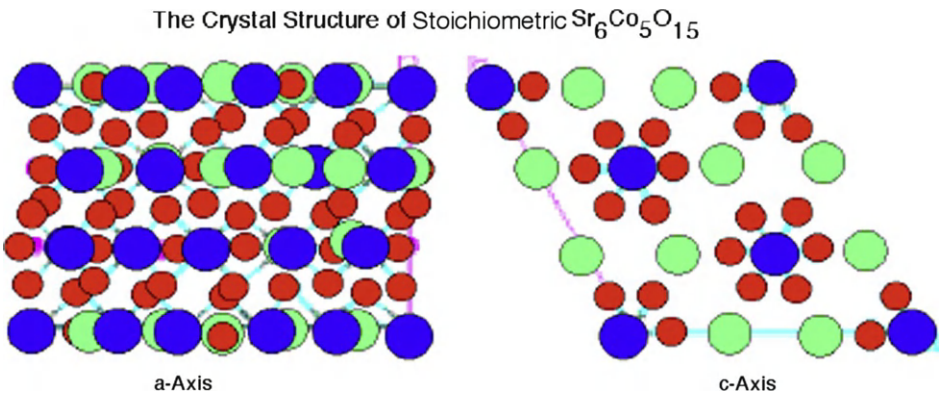

FIGURE 13.19

t-phases, one can understand the structure relationship between $Sr_6Co_5O_{14.70}$ and $Sr_6Rh_5O_{15}$.

The latter has the form shown in Fig. 13.19.

Cell parameters are: $a = b = c = 6.9282$ Å, $\alpha = \beta = \gamma = 86.859°$, cell volume $= 331.11$ Å^3, $Z = 3$. Cell occupancy is shown in Table 13.6.

A single-crystalline film of Sr_2CoO_4 with square-lattice CoO_2 sheets (K_2NiF_4-type structure) was synthesized, and its electronic properties were characterized. The compound exhibited both FM and metallic behaviors, with a fairly high Curie temperature T_C of ~250 K, in contrast to the superconductivity recently found in a triangular-lattice CoO_2-sheet compound. The film's large magnetoresistance with current perpendicular to the CoO_2 plane showed field-hysteretic behavior analogous to tunneling magnetoresistance. The electronic structure of Sr_2CoO_4 was also investigated to characterize the quasi 2D FM metal state in terms of optical spectroscopy and first principles calculation.

Two reports have confirmed that the compound, Sr_2CoO_4 (formal oxidation state Co^{4+}), showed a high Curie temperature (~250 K), but they described different magnetic moments of 1.8 and 1 μbar per Co. Using both commonly used functionalisms in the correlated band approach (designated as LDA + U) as well as the local-spin density approximation (LSDA), the combined effects of correlation and hybridization of the cobalt atom with O $2p$ states were calculated and analyzed. Sr_2CoO_2 is already FM within LSDA ($M = 1.95$ μbar). Increasing U from zero, the two LDA + U schemes affect the moment oppositely out to a critical value $U_c = 2.5$ eV. At this point they transform discontinuously from different states to the same large U state. Fixing U at Uc, spin moment calculations showed a similar behavior out to a minimum at 1 μbar (a half metallic state), beyond which the fully localized limit scheme jumps to a state with energy minimum very near 2 μbar (very close to the LSDA moment). Although the energy minima occur very near to integer values of the moment per cobalt atom (1 μbar, 2 μbar), the strong 3d-2p mixing and resulting 3d orbital occupations seem to preclude any meaningful $S = 1/2$ or $S = 1$ assignment to the Co ion.

The electronic and magnetic properties of Sr_2CoO_4 compound were further studied using ab initio electronic structure calculations. Two kinds of FM solutions: (i)

TABLE 13.6

No.	Site notation	Atom	Multiplicity	Wyckoff	Site symmetry	x	y	z	Occupancy
1	O1	O	18	f	1	0.15157	0.1617	0.3168	1.0
2	O2	O	18	f	1	0.15183	0.0099	0.1225	1.0
3	O3	O	9	e	.2	0.1377	0	1/2	1.0
4	Sr1	Sr	9	e	.2	0.6715	0	1/2	1.0
5	Sr2	Sr	9	d	.2	0.3445	0	0	1.0
6	Co1	Co	6	c	3.	0	0	0.2188	1.0
7	Co2	Co	6	c	3.	0	0	0.4006	1.0
8	Co3	Co	3	a	32	0	0	0	1.0

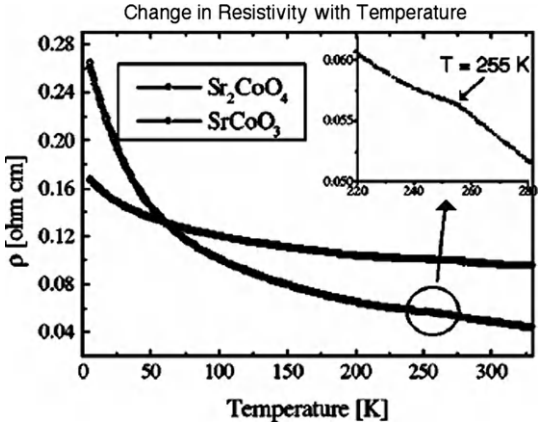

FIGURE 13.20

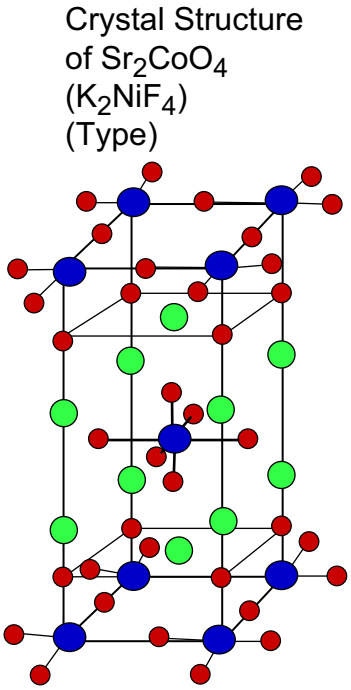

FIGURE 13.21

half-metallic and (ii) metallic were found. The half-metallic solution is a ground state of the system and the metallic one is a metastable state. The strong hybridization between Co-3d and O-2p orbitals decides the electronic and magnetic properties of the compound. The total magnetic moment per formula unit is found to be ~3 μbar ($S = 3/2$). These calculations gave the magneto-crystalline anisotropy energy of ~2.7 meV, which provides a good description of experimentally observed large magnetocrystalline anisotropy. The Heisenberg exchange parameters up to fourth nearest neighbors were also calculated. The mean-field theory gives $T_C = 887$ K. The possible physical implications of the FM half-metallic ground state are also discussed.

Sr_2CoO_4 is not very stable in air at room temperature. However, it was found that by Y doping, the pure Sr_2CoO_4 phase could be obtained. The refined structure of the Y-doped Sr_2CoO_4 was found to be of the K_2NiF_4 type with space group $I4/mmm$. Refinement results indicated that for $x = 0.5$ in $Sr_{2-x}Y_xCoO_4$, the in-plane Co–O (1) bond length 1.876 Å is a bit shorter compared to that for $y = 0$ 1.898 Å, while the Co–O (2) bond distance along the c-axis is longer 2.030 Å compared to $x = 0$ 1.994 Å. This indicated that the Y^{3+} doping caused the Co–O bonds to contract within the ab plane and to elongate along the c-axis, yielding more distortion of the CoO_6 octahedron compared with the undoped Sr_2CoO_4. The resistivity of these two compounds is compared in Fig. 13.20.

Sr_2CoO_4 has a lower room temperature resistivity [0.04 Ω cm] than that of $SrCoO_3$ [0.09 Ω cm]. However, the resistivity of both samples showed a very gradual increase with decreasing of temperature and never tended to reach infinity at low temperature. This result indicates that the resistance of both compounds is dominated by carrier scattering at grain boundaries as is widely seen for polycrystalline samples.

The structure of Sr_2CoO_4 has the form shown in Fig. 13.21.

In addition, the reduced Ruddlesden–Popper phases, $Sr_3Co_2O_{5+\delta}$ with $\delta = 0.91$, 0.64 and 0.38, have been prepared in a nitrogen atmosphere. The crystal structures were determined by powder neutron diffraction. Oxygen vacancies are found both in 0(3) and 0(4) sites but the majority are along one crystallographic axis in the CoO_2 plane, inducing an orthorhombic distortion of the normally tetragonal $n = 2$ Ruddlesden–Popper structure. Superstructures due to oxygen ordering are observed by electron microscopy. The magnetic measurements reveal complex behavior with some FM interactions present for $Sr_3Co_2O_{5.91}$ and $Sr_3Co_2O_{5.64}$.

In the Co^{5+}-containing system of $SrO–Co_2O_5$, no compounds are known to date.

In the Co^{6+}-containing system of $SrO–CoO_3$, the structure of the $SrCrO_4$ compound was determined, crystallizing in the monoclinic space group $P21/n$ (no. 14), with lattice parameters $a = 6.73$ Å, $b = 7.33$ Å, $c = 7.07$ Å, $b = 104°$ and $Z = 4$. The structure is similar to the structure of $SrSeO_4$, as given in the literature.

Strontium cobaltites or cobaltates are not offered for sale commercially and no CAS numbers have been assigned to date.

13.1.5. Barium Cobalt Compounds

Barium metal does not form any intermetallic compounds with cobalt metal.

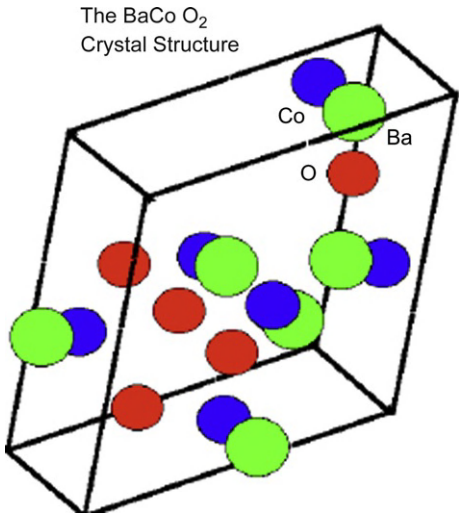

FIGURE 13.22

In the Co^{2+}-containing system of BaO–CoO, the compound, $BaCoO_2$, has been found not to be very stable in air at room temperature. The existence of gaseous cobaltates of alkaline earth metals has been established by high-temperature mass spectrometry. Gaseous molecules, $CaCoO_2$, $SrCoO_2$ and $BaCoO_2$, have been found for the first time. On the basis of the measured constants of the equilibrium of gas-phase reactions the standard enthalpies of formation: (-149 ± 19) kJ/mol, (-149 ± 20) kJ/mol and (-250 ± 16) kJ/mol; standard atomization enthalpies were: (1251 ± 22) kJ/mol, (1233 ± 23) kJ/mol and (1353 ± 20) kJ/mol for $CaCoO_2$, $SrCoO_2$ and $BaCoO_2$, respectively.

By a combination of high pressure and high temperature, high-temperature XRD has allowed the determination of the structure of **stoichiometric** $BaCoO_3$ shown in Fig. 13.22.

Cell parameters are: $a = b = 5.852$ Å, $c = 6.723$ Å, $\alpha = \beta = 90°$, $\gamma = 120°$, cell volume $= 199.46$ Å^3, $Z = 3$. Cell occupation is shown in Table 13.7.

Only one or two references list this compound and no other compounds like $BaCo_2O_4$ or Ba_2CoO_3 are known.

In the Co^{3+}-containing system of BaO–Co_2O_3, the compound, $BaCoO_3$, is not known. However, a carbonato type of compound has been established. The crystal and magnetic structure of $Ba_5Co_5O_{14}$ $\{Ba_5[2Co^{3+}, 3Co^{4+}]_5O_{14}\}$ has been determined by means of X-ray and neutron diffraction. This oxide has trigonal symmetry (space group $P\text{-}3m1$) and lattice parameters $a = 5.6453$ Å and $c = 11.9223$ Å. The main structural feature is the presence of blocks of composition Co_3O_{12}, folded along the c-axis, built up by units of three sharing-faces octahedra connected through their terminal corners to two CoO_4 tetrahedra, which define layers parallel to the basal plane (001). The material shows FM behavior with $T_C \approx 47$ K. As determined from neutron diffraction data, the magnetic moments are aligned parallel lying on the (101) plane (and equivalent), making an angle of 63° with the c-axis. The Curie temperature (T_C) strongly increases with the hydrostatic pressure (1.1 K/GPa) until 6 GPa, and it decreases for higher pressures. From the electronic point of view, $Ba_5Co_5O_{14}$ is a low-dimensional system with an Anderson localization state of the charge carriers. This structure is related to the 2H-ABO_3 by means of the expression $a = a_{2H}(3)^{1/2}$ and $c = 2c_{2H}$. It can be described from the ordered intergrowth of two blocks, $[Ba_2Co_2O_6]^{\delta-}$ and $[Ba(CO_3)_{0.60}]^{\delta+}$, alternating along the a-axis. The first block corresponds to two 2H-like rods and the second one can be related to the $BaCO_3$ aragonite-type structure.

The thermoelectric properties of $Ba_3Co_2O_6(CO_3)_{0.7}$ have been investigated using prismatic single crystals elongated along the c-axis. $Ba_3Co_2O_6(CO_3)_{0.7}$ has a pseudo 1D structure similar to that of 2H PV-type $BaCoO_3$ and contains CoO_6 octahedral columns running parallel to the c-axis. The prismatic crystals are grown by a flux method using a K_2CO_3–$BaCl_2$ flux. The electrical conductivity (σ) along the columns (c-axis) exhibits a metallic behavior (670–320 S/cm in the temperature range of 300–1100 K), whereas the temperature dependence of the electrical conductivity perpendicular to the c-axis is semiconducting. The Seebeck coefficient (S) along the columns is positive and greater than 100 μV/K over the measured temperature range (116–128 μV/K). $Ba_3Co_2O_6(CO_3)_{0.7}$ shows power factors (σS^2) of 5.5×10^{-4}–9.0×10^{-4} W/μm/K^2 above room temperature, relatively high values for an oxide material.

The systematic search of new intermediate phases between 2H-$BaCoO_3$ and $Ba_3Co_2O_6$ structures has shown, for the first time, the existence of polymorphism in mono-dimensional phases of the homologous series $(A_3B_2O_6)$-$(A_3B_3O_9)$. A new $Ba_8Co_7O_{21}$ phase, different

TABLE 13.7

No.	Site notation	Atom	Multiplicity	Wyckoff	Site symmetry	x	y	z	Occupancy
1	O1	O	6	c	1	0.420	0.302	0.2067	1.0
2	Ba1	Ba	3	b	.2.	0.347	0	5/6	1.0
3	Co1	Co	3	a	.2.	0.418	0	1/3	1.0

from the trigonal phase previously reported, has been synthesized. The new material is orthorhombic (space group $Fd2d$) with unit cell parameters $a_o = 1.14$, $b_o = 1.98$, and $c_o = 1.75$ nm. Both orthorhombic and trigonal phases are built up of isolated rows of polyhedra parallel to the c-axis formed by one TP and six octahedra-sharing faces, but with a different spatial arrangement between the chains. The orthorhombic structure can be derived from a hcp stacking of Ba_8O_{24} and $Ba_8Co_2O_{18}$ layers.

The $BaCo_4O_7$ compound provides a novel topology for studying geometric frustration, in which face-sharing tetrahedra of magnetic ions link to form trigonal bipyramids on a Kagomé lattice. Mean-field models of the generic magnetic phase diagram of $BaCo_4O_7$ determined show a variety of magnetic states as a function of two exchange parameters: J_{ab} and J_c, where J_{ab} links Co ions in the Kagom'e planes and J_c links Co ions from the Kagomé plane to the interleaving triangular layer. It has been found that the addition of Y^{3+}–Ca^{2+} to this compound greatly improves the thermoelectric properties of the composite.

$\{Y_{0.5}/Ca_{0.5}\}BaCo_4O_7$ contains Kagomë layers of Co ions, whose spins are strongly coupled according to a Curie–Weiss temperature of −2200 K. At low temperatures, $T = 1.2$ K, a diffuse neutron scattering study with polarization analysis revealed that characteristic spin correlations close to a predicted 2D coplanar ground state with staggered chirality was present. The absence of 3D long-range AF order proved negligible coupling between the Kagomé layers. The scattering intensities are consistent with high-spin $S = 3/2$ states of Co^{2+} in the Kagomé layers and low-spin $S = 0$ states for Co^{3+} ions at interlayer sites.

The average crystal structure of $Y_{0.5}Ca_{0.5}BaCo_4O_7$ is shown in Fig. 13.23. Thicker lines between the Co_2 atoms highlight the Kagomé layers. All Co atoms are tetrahedrally coordinated by oxygen, as shown in the polyhedral representation (left), emphasizing the threefold

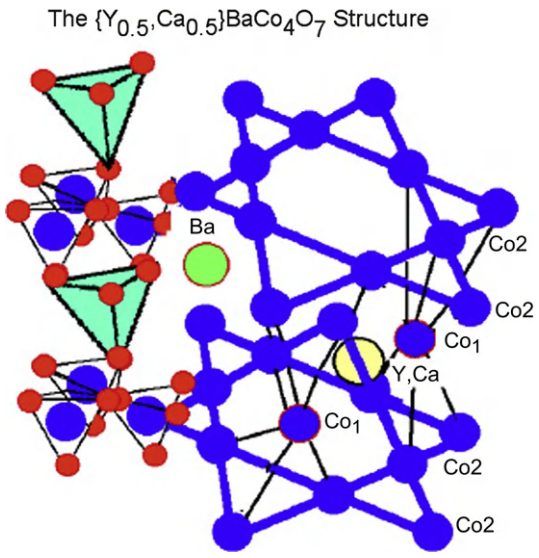

FIGURE 13.23

symmetry axes, going through Co_1(blue), which allow trimerization of Co_2 in the Kagomé substructure.

The above description involves an average of the two compounds, (Ba,Y)Co_4O_7 and (Ba,{Y,Ca})Co_4O_7. A novel mixed valent cobaltite, $CaBaCo_4O_7$, has been synthesized. Its structure, closely related to the $LnBaCo_4O_7$ oxides of the "114" series, differs from the latter by a large orthorhombic distortion, involving a buckling of the CoO_4 tetrahedra of the Kagomé layers. Importantly, this new phase is ferrimagnetic with a $T_C = 70$ K and a very large coercive field of 2 T at 5 K, in contrast to $LnBaCo_4O_7$ oxides, which exhibit magnetic frustration. Neutron diffraction studies have been carried out in the temperature (T) range between 10 and 130 K on a single crystal of $YBaCo_4O_7$, which has the stacking of Kagomé and triangular lattices of CoO_4 tetrahedra along the c-axis. This structure has the form shown in Fig. 13.24.

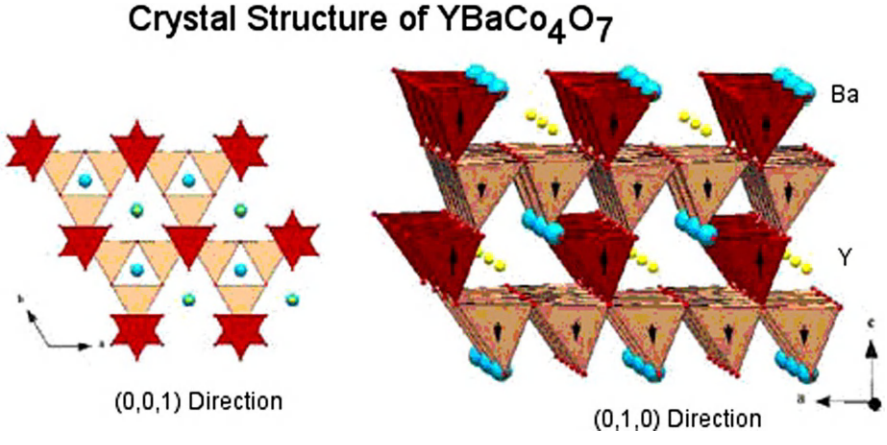

FIGURE 13.24

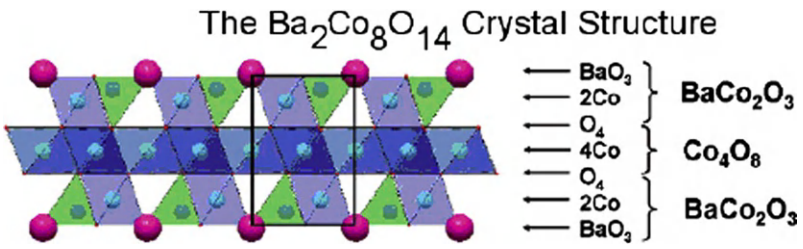

FIGURE 13.25

Structural transitions have been found at two temperatures $T_{c1} \sim 70$ K and $T_{c2} \sim 105$ K. With decreasing T, magnetic order appears along with the transition at T_{c2}, but it does not grow to an ideal long-range order even at the lowest T studied (~10 K). Two groups of magnetic diffuse reflections, which originate from the Co moments of the Kagomé and triangular lattices, are observed separately in the reciprocal space. With further decreasing T, the growth rates of the intensities of these two are enhanced by another transition at T_{c1}. These magnetic behaviors seem to be related to the release of the geometrical frustration. At 10 K, the patterns of the magnetic short-range order have been determined for both sites of the Kagomé and triangular lattices. Extraordinary oxygen ordering and mobility have been found in an oxygen-nonstoichiometric mixed-valence cobalt oxide, $YBaCo_4O_{8.5}$. The excess oxygen atoms appear to be incorporated in an orderly way into the $YBaCo_4O_7$ parent lattice with different configurations as the oxygen content varies. Intense electron beam irradiation was used to observe recurrent oxygen migration in the lattice, causing reversible structural modulation transitions. The oxygen migration can be attributed mainly to the electron beam heating effect.

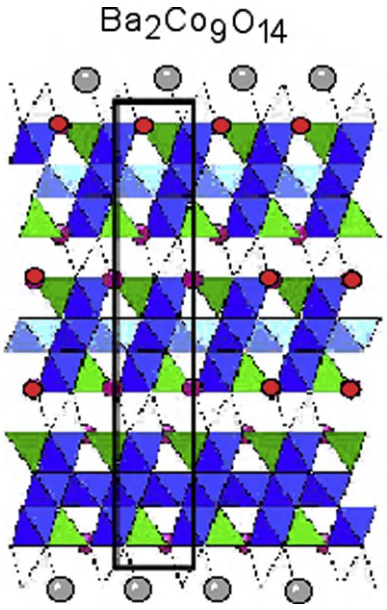

FIGURE 13.26

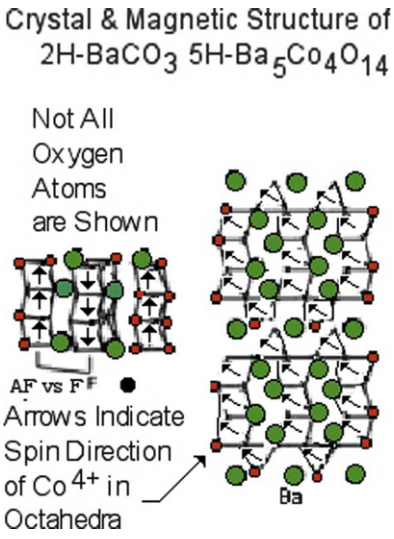

FIGURE 13.27

A complex compound, $Ba_2Co_8O_{14}$ is also known. It has the structure shown in Fig. 13.25.

In the Co^{2+}–Co^{3+}-containing system of BaO–Co_3O_4, the compound $Ba_2Co_9O_{14}$ is known. It has the structure shown in Fig. 13.26.

The formula is perhaps better written: $Ba_2(Co^{3+})_4(Co^{4+})_3O_{14}$. Very little information concerning this compound is available in the literature.

In the Co^{4+}-containing system of BaO–CoO_2, the compound, $BaCoO_3$ has been studied. The stoichiometric compound has a hexagonal-2H pseudo-PV structure with space group $P63/mmc$, and lattice parameters $a = 5.645$ Å and $c = 4.752$ Å. This structure has the form shown in Fig. 13.27.

A series of defect structures are known. In the following diagram, three projections are shown (Fig. 13.28).

The three projections are:

(a) The (ab, cb) projection of the 2H-$BaCoO_3$ structures showing the chains made of face-shared CoO_6 octahedra separated by the Ba^{2+} cations (circles).

(b) Corresponding ($\vec{a}$ $\vec{b}$) projection reveals the triangular lattice of the CoO_6 chains.

(c) Perspective view of the $Ca_3Co_2O_6$ structure showing the chains of face-shared CoO_6 TPs and octahedra.

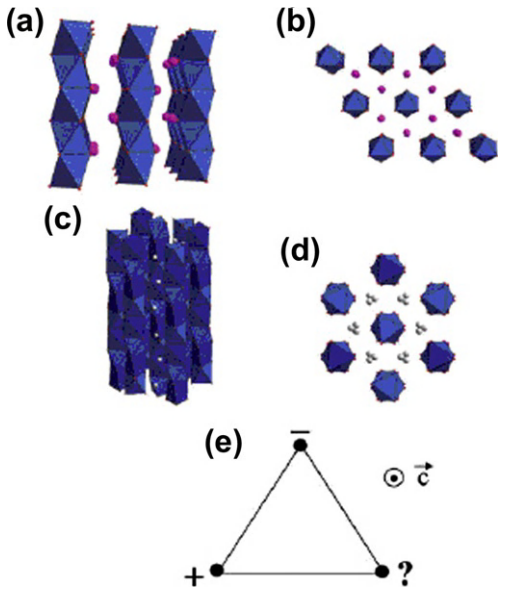

FIGURE 13.28

The circles are for the Ca^{2+} cations separating these chains

(d) The corresponding $(\vec{a}\ \vec{b})$ projection is also shown together with the projection of the chain magnetization (e) to illustrate the magnetic frustration.

The two first members for these cobaltites are 2H-$BaCoO_3$ [(m) 1, n, 0]; (a and b in the Figure) and $Ca_3Co_2O_6$ [(*m*) 0, *n*, 1]; (c and d in the Figure). In the latter, the chains set on a triangular lattice are made of 1:1 alternation of a CoO_6 octahedron (oct) and a TP; these chains are separated by Ca^{2+} cations.

The cubic (c) or hexagonal (h) stacking of $[AO_{3-\delta}]$ layers allows us to describe the so-called hexagonal PVs illustrated for the $BaCoO_{3-\delta}$ phases by the 2H (see above Figure) and 12H terms in Fig. 13.29.

This figure shows the (ab,cb) projection of the 12H-$BaCoO_3$ structure (a) and the corresponding (ab,bb′) projection (b). The (*a*,*b*) plane projection of the former illustrates the triangular array of chains (*P*63/*mmc* space group) made of the face-shared CoO_6 octahedra separated by the Ba^{2+} cations. It must be recalled that this compound is the $(m = 1,\ n = 0)$ term of the $A_{3n+3m}A'_nB_{3m+n}O_{9m+6n}$ series with A = Ba and B = Co. In contrast to the 1D structure of the 2H structure (*a*, *b*), the (*a*, *b*) projection of the 12H structure demonstrates that the units of four face-shared octahedra, reminiscent of the 2H chains, are bridged together by new types of CoO_x polyhedra resulting from the "$O_{2.6}$" oxygen deficiency.

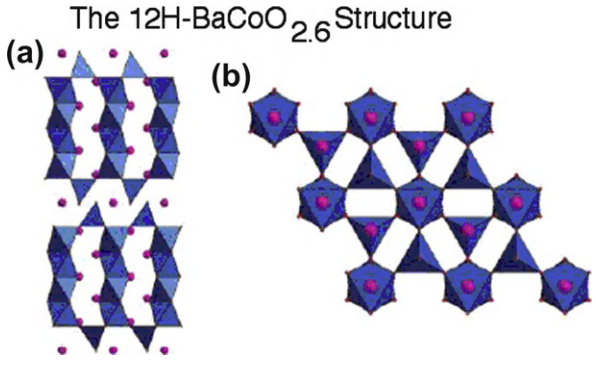

FIGURE 13.29

The magnetic structure of the AFM hexagonal PV $BaCoO_3$ was investigated by neutron diffraction using a powder sample in the temperature range between 60 and 1.5 K. It was found that AF diffraction peaks clearly appear below the Néel temperature ($T_N = 15$ K), which are indexed with the propagation vector k = (1)/(3),(1)/(3),0), indicating that the AF super unit cell is three times larger than the crystallographic unit cell. Data from a parallel muon-spin rotation/relaxation (σ^+SR) measurement allowed the final selection of a unique AF spin structure from several possible spin arrangements compatible with the neutron diffraction pattern. The proposed AF structure is modulated along the (110) direction and described by $m_l = m_0\cos(2\pi kl)$, where m_l is the moment at the Co^{4+} site l and $m_0 = (0,0,0.53\ \mu bar)$ at 1.5 K

Ordering of ionic vacancies in the $BaCoO_{2.94}$ hexagonal-related PV has been studied. An electron diffraction and high-resolution electron microscopy study shows that oxygen vacancies in $BaCoO_{2.94}$ lead to a threefold superstructure along the $(110)_{2H}$ direction, the …hhh… hexagonal sequence characteristic of the 2H type being maintained. According to compositional and structural data, the most probable structural model should be formed by three AO_3-layers intergrowing with one $AO_{2.67}$-layer along the *c*-axis. In such oxygen-deficient layers, one of each six oxygen atoms in every oxygen row is removed, leading to the observed superstructure.

The systematic search of new intermediate phases between 2H-$BaCoO_3$ and $Ba_3Co_2O_6$ structures has shown, for the first time, the existence of polymorphism in monodimensional phases of the homologous series $(A_3B_2O_6)$-$(A_3B_3O_9)$. A new $Ba_8Co_7O_{21}$ phase, different from the trigonal phase previously reported, has been synthesized. The new material is orthorhombic (space group *Fd*2*d*) with unit cell parameters $a_o = 1.14$, $b_o = 1.98$, and $c_o = 1.75$ nm. Both orthorhombic and trigonal phases are built up of isolated rows of polyhedra parallel to the *c*-axis formed by one TP and six octahedra-sharing faces, but with a different spatial arrangement between the chains. The orthorhombic structure can be derived from the hcp stacking of Ba_8O_{24} and $Ba_8Co_2O_{18}$ layers.

The crystal structure of $Ba_3Co_2O_6(CO_3)_{0.60}$ has been determined by means of X-ray, neutron and electron diffraction, and high-resolution electron microscopy. This compound has a hexagonal symmetry (space group P) and lattice parameters $a = 9.683$ and $c = 9.5180$ Å related to the 2H-ABO_3 by means of the expression $a = a\sqrt{H^3}_{1/2}$ and $c = \sqrt{c-2}\sqrt{H}$. It can be described from the ordered intergrowth of two blocks, $[Ba_2Co_2O_6]-$ and $[Ba(CO_3)_{0.60}]+$, alternating along the a-axis. The first block corresponds to two 2H-like rods and the second one can be related to the $BaCO_3$ aragonite-type structure. Neutron diffraction data elucidate the relative orientation of carbonate groups along c-axis in the aragonite-like blocks.

The thermoelectric properties of the modified carbonate-barium cobaltite, $Ba_3Co_2O_6(CO_3)_{0.7}$, have been investigated using prismatic single crystals elongated along the c-axis. $Ba_3Co_2O_6(CO_3)_{0.7}$ has a pseudo 1D structure similar to that of 2H PV-type $BaCoO_3$ and contains CoO_6 octahedral columns running parallel to the c-axis. The prismatic crystals are grown by a flux method using a K_2CO_3–$BaCl_2$ flux. The electrical conductivity (σ) along the columns (c-axis) exhibits a metallic behavior (670–320 S/cm in the temperature range of 300–1100 K), whereas the temperature dependence of the electrical conductivity perpendicular to the c-axis is semiconducting. The Seebeck coefficient (S) along the columns is positive and greater than 100 μV/K over the measured temperature range (116–128 μV/K). $Ba_3Co_2O_6(CO_3)_{0.7}$ shows power factors (σS^2) of 5.5×10^{-4}–9.0×10^{-4} W/μm/K^2 above room temperature, relatively high values for an oxide material.

Single-crystal Ba_2CoO_4 was grown using the floating zone technique. Single-crystal refinement of XRD data indicates that Ba_2CoO_4 has a monoclinic structure with $a = 5.9176$ Å, $b = 7.6192$ Å, $c = 10.3790$ Å, and $\beta = 91.734°$ at room temperature. Magnetic susceptibility, specific heat, and thermal conductivity show anomalies at $T_N = 25$ K, due to AFM ordering. However, the magnitude of the Néel temperature T_N is significantly lower than the Curie–Weiss temperature ($|\Theta| \approx 110$ K), suggesting either reduced-dimensional magnetic interactions and/or the existence of magnetic frustration. The latter may be induced by disorder evident from the variable-range hopping behavior in the electrical resistivity, nonzero T term in the specific heat, and T^2 dependence in the thermal conductivity at low temperatures. A crystal chemical study based on the cation arrays allows the establishment of a new relationship between Ba_2CoO_4 and 2H$\cdots$$BaCoO_3$. Moreover, the Ba subarray seems to be related to the structure of elemental Ba. The structure is shown in Fig. 13.30.

Large single crystals of Ba_2CoO_4 were synthesized. Single crystals were also obtained for Sr doped $Ba_{2-x}Sr_xCoO_4$. Powder and single-crystal XRD results indicate that pure Ba_2CoO_4 has a monoclinic structure at room temperature. With Sr doping, the lattice structure changes to orthorhombic when $x \geq 0.5$ and to tetragonal when $x = 2.0$. In addition, Ba_2CoO_4 and Sr_2CoO_4, have completely different basic building blocks in the structure. One contains the CoO_4 tetrahedron and the latter the CoO_6 octahedron, respectively.

Electronic and magnetic properties were characterized and discussed. The magnetic susceptibility, specific heat and thermal conductivity show that Ba_2CoO_4 has an AFM ground state with an AF ordering temperature $T_N = 25$ K. However, the magnitude of the Neel temperature T_N is significantly lower than the Curie–Weiss temperature ($|\Theta| = 110$ K), suggesting either reduced-dimensional magnetic interactions and/or the existence of magnetic frustration. The AF interaction persists in all the samples with different doping concentrations. The Neel temperature does not vary much in the monoclinic structure regime but decreases when the system enters orthorhombic.

Magnetically, Ba_2CoO_4 has an AF insulating ground state while Sr_2CoO_4 has a FM metallic ground state. Neutron powder refinement results indicate a magnetic structure with the spin mostly aligned along the a-axis. The result from a muon-spin rotation/relaxation (mu + SR) experiment agrees with our refinement. It confirms the AF order in the ab-plane. The spin dynamics and its anisotropy in the AF phase were also studied. The results from inelastic neutron scattering show that spin waves have a clear dispersion along a-axis but not along c-axis, indicating spin anisotropy. This work finds the strong spin-lattice coupling in this novel complex material. However, if Sr^{2+} is substituted in the structure, a radical change is obtained (Fig. 13.31).

The effect of the oxygen content on the magnetic and transport properties of the FM $Eu_{0.9}Ca_{0.1}BaCo_2O_{5.5+\delta}$ has been investigated. Unlike the increase in T_C with calcium content, paradoxically the T_C value decreases as the oxygen content increases, as observed in the undoped phase. Assuming that the Goodenough-Kanamori rules apply to this very complex magnetic system, these experiments suggest that the Co^{3+} disproportionation into Co^{4+} and Co^{2+}, plays an important role in the appearance of ferromagnetism. The magnetic phase separation scenario of FM domains embedded in an AFM matrix plays an important role in the ferromagnetism of the calcium doped "112" cobaltites. All the samples covering a wide range of oxygen content, exhibit p-type conductivity.

In the Co^{5+}-containing system of BaO–Co_2O_5, the compound, $BaCo_2O_6$, remains unknown.

In the Co^{6+}-containing system of BaO–CoO_3, no compounds are known.

Barium cobaltite or coabaltate compounds are not offered for sale commercially.

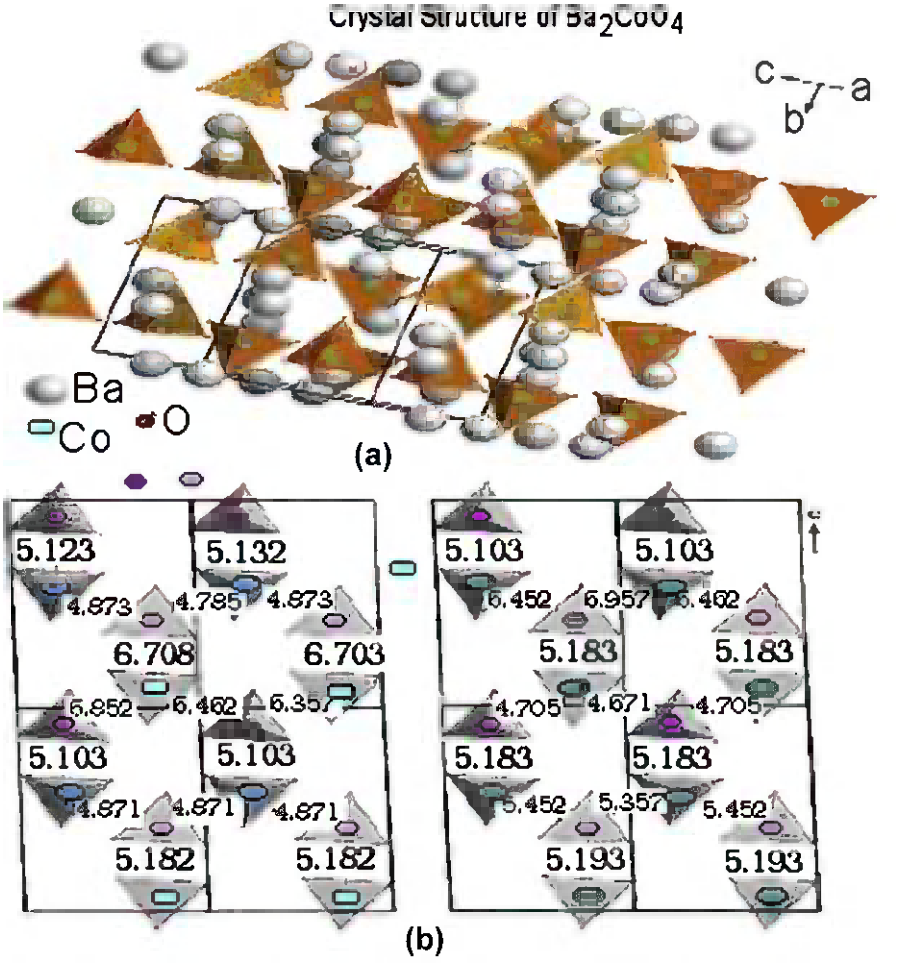

Top: Crystal Structure of $BaCoO_4$- nearest-neighbor network of CoO_4 Tetrahedra
Left Panel: shows distances to the upper plane of neighbors
Right Panel: shows distances to the lower plane of neighbors
The upper plane of each vertical pair of tetrahedra (purple) is the same in both panels

FIGURE 13.30

13.1.6. Radium Cobalt Compounds

Although radium undoubtedly forms the same type of compounds as barium, no reports of such syntheses have reached the literature. This is due to the lack of interest in Industry, coupled with the corresponding one in Academia.

13.2. ALKALINE EARTH RHODIUM COMPOUNDS

Rhodium has the known stable oxides that include Rh_2O_3, RhO_2 and $RhO_2 \cdot xH_2O$. Only Be^0 forms intermetallic compounds with rhodium metal.

13.2.1. Beryllium Rhodium Compounds

The system, Be^0–Rh^0, forms two compounds. There are also two established compounds in the BeO–Rh_xO_y system.

BeRh forms the CsCl type of structure where the Rh^0 atom is in a body-centered lattice. This structure has the form shown in Fig. 13.32.

Cell parameters are: $a = b = c = 2.739$ Å, $\alpha = \beta = \gamma = 90°$, cell volume: 20.55 Å^3, $Z = 2$, cell occupancy is shown in Table 13.8.

$Be_{15.34}Rh_{2.36}$ has the structure shown in Fig. 13.33.

Cell parameters are: $a = b = 4.193$ Å, $c = 10.881$ Å, $\alpha = \beta = 90°$, $\gamma = 120°$, cell volume = 165.42 Å^3, $Z = 1$. Cell occupancy is shown in Table 13.9.

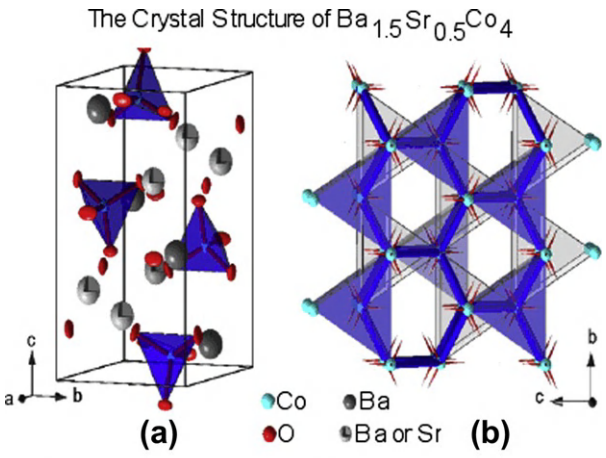

(a) Co-Ions in a Tetrahedral Coordination

(b) Magnetic Network consisting of Inter-penetrating Trigonal Prisms of Co Ions with Spins of 5/2

FIGURE 13.31

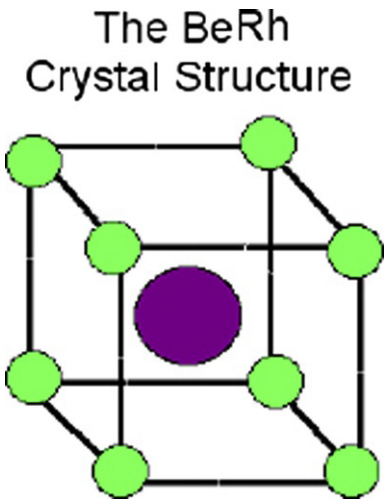

FIGURE 13.32

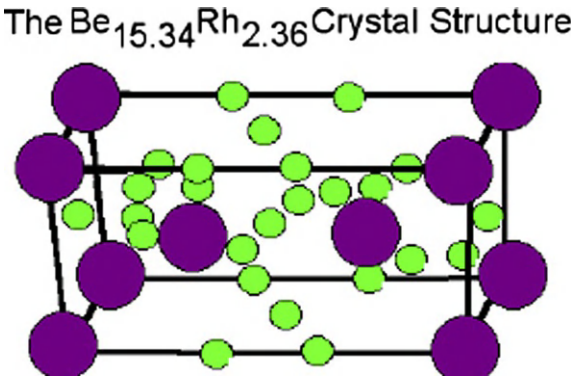

FIGURE 13.33

No other compounds are known in this system.

In the $BeO–Rh_2O_3$ system, beryllium forms only one compound, $BeRh_2O_4$, but it is dimorphic. One form has the $BeAl_2O_4$ structure shown in Fig. 13.34.

Cell parameters are: $a = b = c = 5.9284$ Å, $\alpha = \beta = \gamma = 60°$, cell volume $= 147.23$ Å^3, $Z = 9$. Cell occupancy is shown in Table 13.10.

The other form of $BeRh_2O_4$ is shown in Fig. 13.35.

Cell parameters are: $a = b = c = 5.9256$ Å, $\alpha = \beta = 119.982$ Å, $\gamma = 90°$, cell volume $= 147.38$ Å^3, $Z = 6$. Cell occupancy is shown in Table 13.11.

TABLE 13.8

No.	Site notation	Atom	Multiplicity	Wyckoff	Site symmetry	*x*	*y*	*z*	Occupancy
1	Be	Be	1	b	m-3m	1/2	1/2	1/2	1.0
2	Rh	Rh	1	a	m-3m	0	0	0	1.0

TABLE 13.9

No.	Site notation	Atom	Multiplicity	Wyckoff	Site symmetry	*x*	*y*	*z*	Occupancy
1	Be1	Be	6	n	.m.	0.166	0.8335	0.183	1.0
2	Be2	Be	3	k	mm2	0.505	0.4955	1/2	1.0
3	Be3	Be	2	i	3m.	2/3	1/3	0.098	1.0
4	Rh1	Rh	2	i	3m.	2/3	1/3	0.307	1.0
5	Be4	Be	2	h	3m.	1/3	2/3	0.341	1.0
6	Be5	Be	2	g	3m.	0	0	0.377	1.0
7	Be6	Be	1	c	-6m2	1/3	2/3	0	0.34
8	Rh2	Rh	1	a	-6m2	0	0	0	0.36

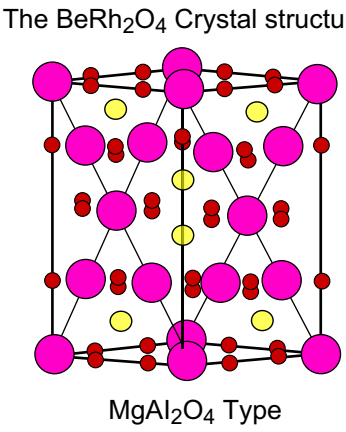

FIGURE 13.34

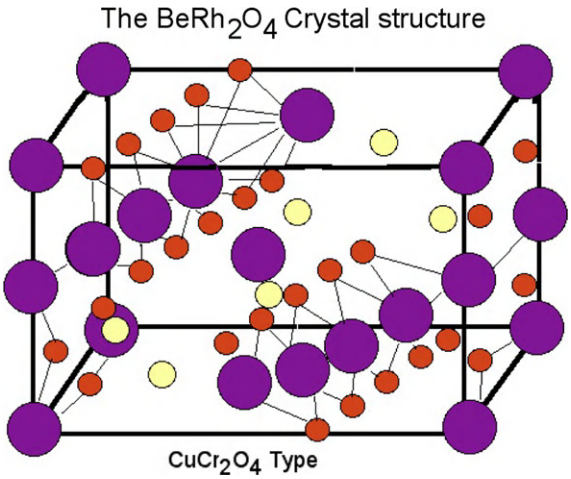

FIGURE 13.35

Little information is available in the literature concerning these compounds. It has been stated the $BeRh_2O_4$ is expected to be semiconducting in its electrical properties (because it contains Rh^{3+}-$4d^5$ electrons) but no specific measurements have been published.

No other compounds are known. Beryllium rhodite or rhodate compounds are not available commercially nor has a CAS number ever been assigned.

13.2.2. Magnesium Rhodium Compounds

Magnesium does not form any intermetallic compounds with rhodium metal.

No compounds are known:

(1) In the Rh^{2+}-containing system of MgO–RhO
(2) In the Rh^{2+}–Rh^{3+}-containing system of MgO–Rh_3O_4,
(3) In the Rh^{4+}-containing system of MgO–RhO_2,
(4) In the Rh^{5+}-containing system of MgO–Rh_2O_5,
(5) In the Rh^{6+}-containing system of MgO–RhO_3.

In the Rh^{3+}-containing system of MgO–Rh_2O_3, only one compound, $MgRh_2O_4$, has been reported. The structure has the form shown in Fig. 13.36.

Cell parameters are: $a = b = c = 6.004$ Å, $\alpha = \beta = \gamma = 60°$, cell volume $= 153.04$ Å^3, $Z = 8$.

Cell occupancy is shown in Table 13.12.

A precise decomposition curve for stoichiometric $MgRh_2O_4$ was determined experimentally to evaluate its thermodynamic properties. The standard state enthalpy and entropy at 298 K for decomposition to Rh, MgO and O are 88.8 ± 1.9 kcal/mol and 59.8 ± 1.4 cal/mol/K, respectively. A third law entropy for $MgRh_2O_4$ was estimated for 298 K as 35.2 ± 1.5 cal/mol/K. Solid solutions between $MgRh_2O_4$ and $MgAl_2O_4$ were prepared that exhibited positive deviations from Vegard's law. Preliminary data on decomposition of the solid solution are consistent with positive deviations

TABLE 13.10

No.	Site notation	Atom	Multiplicity	Wyckoff	Site symmetry	*x*	*y*	*z*	Occupancy
1	O1	O	32	e	.3m	0.238	0.238	0.238	1.0
2	Rh1	Rh	16	c	.-3m	0	0	0	1.0
3	Be1	Be	8	b	-43m	3/8	3/8	3/8	1.0

TABLE 13.11

No.	Site notation	Atom	Multiplicity	Wyckoff	Site symmetry	*x*	*y*	*z*	Occupancy
1	O1	O	16	h	.m.	0	0.533	0.252	1.0
2	Rh1	Rh	8	c	.2/m.	0	0	0	1.0
3	Be1	Be	4	b	-4m2	0	1/4	3/8	1.0

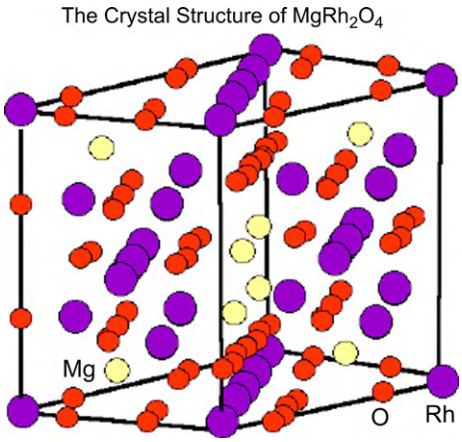

FIGURE 13.36

from ideality becoming negative as $MgAl_2O_4$ is approached.

The Gibbs free energy of formation and heat capacity of α-Rh_2O_3 and $MgRh_2O_4$, the MgO···Rh···O phase diagram, and constraints on the stability of $Mg_2Rh^{4+}O_4$ have been studied. The oxygen potentials of the reactions were measured using electrochemical cells of the type Pt, metal + oxide|CSZ|YDT (air), Pt. Relative to a reference pressure of 1 bar, the following was determined:

$$\mu_{O_2(\beta\text{-}Rh_2O_3)}\ (\pm 63\ \text{J/mol}) = -278{,}500 + 283.8T - 11.69T\ \ln T\ (860\ \text{K} < T < 1355\ \text{K})$$

and:

$$\mu_{O_2(MgRh_2O_4)}\ (\pm 63\ \text{J/mol}) = 297314 + 369.405T - 23.3338T\ \ln T\ (940\ \text{K} < T < 1495\ \text{K})$$

The constant pressure heat capacities of α-Rh_2O_3 and $MgRh_2O_4$ were measured with a DSC operated in step heating mode between 360 and I065 K. Best fits to the data (in J/mol/K with an uncertainty of ±2 J/mol/K) gave:

$$C_p(\beta\text{-}Rh_2O_3) = 123.6 + 0.0141T - 208.8T^{-0.5} - 2{,}312{,}000/T^2$$

and:

$$C_p(MgRh_2O_4) = 174.0 + 0.014T - 4297000/T^2$$

A third law analysis showed satisfactory internal consistency of the Gibbs free energy of formation and heat capacity data of β-Rh_2O_3, but with a much lower value for $S_{298.15,\ \beta\text{-}Rh2O3}$ (71.5 ± 1.5 J/mol/K compared with those made earlier (1989)). This is attributed to the new C_p(β-Rh_2O_3) data that are significantly different from the original measurements of Wöhler and Jochum (1933) and the adjusted values of 1989.

Spinels prepared in the MgO···Rh···O system are solid solutions between $MgRh_2^{3+}O_4$ and $Mg_2Rh^{4+}O_4$ and the interpretation of the data for $\mu_{O_2(MgRh_2O_4)}$ requires an understanding of phase relationships in the MgO···Rh···O system. From an isothermal projection of oxygen potentials onto the Mg···Rh binary at 1373 K, the mole fraction $MgRh_2^{3+}O_4$ in spinel ($X_{MgRh_2O_4}$) in equilibrium with MgO and Rh at 1373 K was estimated to be about 0.92. (i.e. $X_{Mg_2RhO_4} \approx 0.08$). This provides a calibration point for determining the temperature dependence of $a^{spinel}_{MgRh_2O_4}$ in $MgRh_2^{3+}O_4$-$Mg_2Rh^{4+}O_4$ solid solutions, (where "a" is a lattice parameter). A third law analysis showed that, once corrected for $a^{spinel}_{MgRh_2O_4}$, the data for $\mu_{O_2(MgRh_2O_4)}$ and $C_p(MgRh_2O_4)$ become fully consistent. The calculated value for $S_{298.15,\beta\text{-}Rh_2O_4}$ is 105.75 ± 2 J/mol · K. This is in reasonable agreement with the assumption of additive oxide entropies $S_{298.15,\ MgRh_2O_4} \approx 98.4$ J/mol/K, using the value of $S_{298.15,\ \beta\text{-}Rh_2O_3}$. It was concluded that the data for β-Rh_2O_3 and $MgRh_2^{3+}O_4$ are internally consistent.

From the third law analysis, it is also possible to determine the activity of $Mg_2Rh^{4+}O_4$, in $MgRh_2^{3+}O_4$-$Mg_2Rh^{4+}O_4$ solid solutions ($a^{spinel}_{MgRh_2O_4}$) as a function of temperature. The data for $a^{spinel}_{MgRh_2O_4}$ may be combined with the e.m.f. measurements for the spinel + MgO + Rh assemblage to evaluate the Gibbs free energy of formation of $Mg_2Rh^{4+}O_4$:

$$\Delta_f G^{O}{}_{Mg_2RhO_4,T}\ (\pm 6000\ \text{J/mol}) = -100076.3 + 100.0T\ (1008 < T < 1495\ \text{K})$$

It was perceived that $Mg_2Rh^{4+}O_4$ is an important component in rhodate spinels at high temperatures, thus extending the stability field of spinel in the MgO–Rh–O system.

It has been reported that if a thin layer of Rh metal is deposited upon a fresh layer of MgO, the composite is superior to any other catalyst for the conversion of methane to synthesis gas or "syn-gas". This is a mixture of CO and H_2, and is a very important petrochemical feedstock. At high temperature, $MgRh_2O_4$, is formed on the surface that is very stable and acts as a source

TABLE 13.12

No.	Site notation	Atom	Multiplicity	Wyckoff	Site symmetry	x	y	z	Occupancy
1	O1	O	32	e	.3m	0.2378	0.2378	0.2378	1.0
2	Rh1	Rh	16	c	.-3m	0	0	0	1.0
3	Mg1	Mg	8	b	-43m	3/8	3/8	3/8	1.0

of oxygen and electrons, the oxygen atoms being replaced from the MgO substrate.

$$CH_4 + H_2O \Leftrightarrow CO + 3H_2$$
$$\Delta H^0 = +206\ \text{kJ/mol}$$

No other compounds are known. Magnesium rhodites or rhodates are not available commercially and no CAS numbers have been issued.

13.2.3. Calcium Rhodium Compounds

Ca^0 and Rh^0 do not form any intermetallic compounds.

No compounds are known in the systems:

(1) in the Rh^{2+}-containing system of CaO–RhO,
(2) in the Rh^{2+}–Rh^{3+}-containing system of CaO–Rh_3O_4,
(3) in the Rh^{5+}-containing system of CaO–Rh_2O_5,
(4) in the Rh^{6+}-containing system of CaO–RhO_3.

In the Rh^{3+}-containing system of CaO–Rh_2O_3, $CaRh_2O_4$, an insulator, forms a full range solid solution with the metallic conductor, $Na_2Rh_2O_4$. This compound, prepared by solid-state reaction of the oxides, is not very stable at room temperature. It has the structure shown in Fig. 13.37.

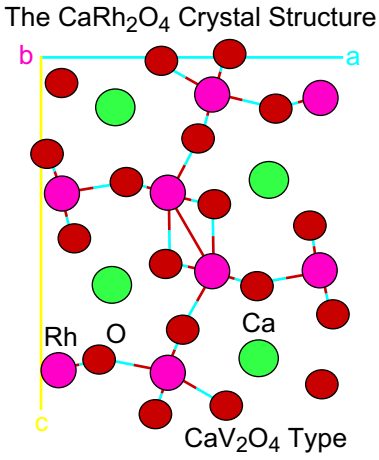

FIGURE 13.37

Cell parameters are: $a = 3.085$ Å, $b = 9.167$ Å, $c = 10.745$ Å, $\alpha = \beta = \gamma = 90°$, cell volume = 303.87 Å^3, $Z = 4$. Cell occupancy is shown in Table 13.13.

The Gibbs free energy of formation of $CaRh_2O_4$(solid) has been determined using two techniques viz., quadrupole mass spectrometer coupled to a Knudsen cell and solid-state cell incorporating CaF_2(solid) as the solid electrolyte. In the former method, equilibrium O_2(gas) pressures were measured over the phase field Rh(solid) + Rh_2O_3(solid), in the temperature range 793.7–909.1 K and over the three-phase mixture $CaRh_2O_4$(solid) + Rh(solid) + CaO(solid) was measured from 862.1 to 1022.7 K.

The Gibbs free energy of formation of Rh_2O_3 (solid) from elements in their standard state has been given in the literature as:

$$\Delta_f G^0\ (Rh_2O_3\ (\text{solid}))\ (\text{kJ/mol} \pm 2.0) = -363.2 + 0.241T\ (\text{K}).$$

The Gibbs free energy of formation of $CaRh_2O_4$(solid) from elements in their standard state was given by:

$$\Delta_f G^0\ (CaRh_2O_4\ (\text{solid}))\ (\text{kJ/mol} \pm 2.0) = -1030.5 + 0.3437T\ (\text{K}).$$

In the electrochemical technique, the cell configuration employed was:

$$(-)Pt/O_2\ (\text{gas}).\ \{CaO(\text{solid}) + CaF_2(\text{solid})\}//CaF_2//\{CaRh_2O_4\ (\text{solid}) + Rh_2O_3(\text{solid}) + CaF_2(\text{solid})\},\ O_2(\text{gas})/Pt(+).$$

The e.m.f. values were measured in the temperature range 879.7–1000 K can be represented by the following expression:

$$E_V\ (\pm 7.63 \times 10^{-4}) = 0.3928 - 2.374 \times 10^{-4}T\ (\text{K})$$

From the measured e.m.f. of the cell and requisite $\Delta_f G^0$ values from the literature, $\Delta_f G^0$ ($CaRh_2O_4$ (solid)) from elements in their standard state has been calculated and can be represented by:

$$\Delta_f G^0\ (CaRh_2O_4\ (\text{solid}))\ (\text{kJ/mol} \pm 2.0) = -1079 + 0.390T\ (\text{K})$$

The two values complement each other. The uncertainty estimates for $\Delta_f G^0$ include the standard deviation

TABLE 13.13

No.	Site notation	Atom	Multiplicity	Wyckoff	Site symmetry	x	y	z	Occupancy
1	O1	O	4	c	.m.	0.071	1/4	0.078	1.0
2	Rh1	Rh	4	c	.m.	0.077	1/4	0.394	1.0
3	Ca1	Ca	4	c	.m.	0.242	1/4	0.65	1.0
4	O2	O	4	c	.m.	0.289	1/4	0.352	1.0
5	O3	O	4	c	.m.	0.387	1/4	0.016	1.0
6	O4	O	4	c	.m.	0.47	1/4	0.775	1.0
7	Rh2	Rh	4	c	.m.	0.568	1/4	0.609	1.0

in the e.m.f. and uncertainty in the data taken from the literature. The slope and intercept of the above equation gives the entropy and enthalpy of formation of the compound at the average experimental temperature $T_{av} = 940$ K.

In the Rh^{4+}-containing system of CaO–RhO_2, the compound, $CaRhO_3$ has been synthesized. High-pressure phase transitions of $CaRhO_3$ PV (perovskite phase) were examined at pressures of 6–27 GPa and temperatures of 1000–1930 °C, using a multi-anvil apparatus. The results indicate that $CaRhO_3$ PV successively transforms to two new high-pressure phases with increasing pressure. Rietveld analysis of powder XRD data indicated that, in the two new phases, the phase stable at higher pressure possesses the $CaIrO_3$-type post-perovskite (PPV) structure (space group *Cmcm*) with lattice parameters: $a = 3.1013$ Å, $b = 9.8555$ Å, $c = 7.2643$ Å, $V_M = 33.43$ cm^3/mol. The Rietveld analysis also indicated that $CaRhO_3$ PV has the $GdFeO_3$-type structure (space group *Pnma*) with lattice parameters: $a = 5.5631$ Å, $b = 7.6308$ Å, $c = 5.3267$ Å, $V_M = 34.04$ cm^3/mol. The third phase stable in the intermediate P, T conditions between PV and PPV have monoclinic symmetry with the cell parameters: $a = 12.490$ Å, $b = 3.1233$ Å, $c = 8.8630$ Å, $\beta = 103.96°$, $V_M = 33.66(1)$ cm^3/mol ($Z = 6$). Molar volume changes from PV to the intermediate phase and from the intermediate phase to PPV are −1.1 and −0.7%, respectively. The equilibrium phase relations determined indicate that the boundary slopes are large positive values: 29 ± 2 MPa/K for the PV–intermediate phase transition and 62 ± 6 MPa/K for the intermediate phase–PPV transition. The structural features of the $CaRhO_3$ intermediate phase suggest that the phase has edge-sharing RhO_6 octahedra and may have an intermediate structure between PV and PPV.

In another study, high-pressure phase transitions of $CaRhO_3$ PV were examined at pressures of 6–27 GPa and temperatures of 1000–1930 °C, using a multi-anvil apparatus. The results indicated that $CaRhO_3$ PV successively transforms to two new high-pressure phases with increasing pressure. Rietveld analysis of powder XRD data indicated that, in the two new phases, the phase stable at higher pressure possesses the $CaIrO_3$-type PPV structure (space group *Cmcm*) with lattice parameters: $a = 3.1013(1)$ Å, $b = 9.8555(2)$ Å, $c = 7.2643(1)$ Å, $V_M = 33.43(1)$ cm^3/mol. The Rietveld analysis also indicated that $CaRhO_3$ PV has the $GdFeO_3$-type structure (space group *Pnma*) with lattice parameters: $a = 5.5631(1)$ Å, $b = 7.6308(1)$ Å, $c = 5.3267(1)$ Å, $V_M = 34.04(1)$ cm^3/mol. The third phase stable in the intermediate P, T conditions between PV and PPV has monoclinic symmetry with the cell parameters: $a = 12.490(3)$ Å, $b = 3.1233(3)$ Å, $c = 8.8630(7)$ Å, $\beta = 103.96(1)°$, $V_M = 33.66(1)$ cm^3/mol ($Z = 6$). Molar volume changes from PV to the intermediate phase and from the intermediate phase to PPV are −1.1 and −0.7%, respectively. The equilibrium phase relations determined indicate that the boundary slopes are large positive values: 29 ± 2 MPa/K for the PV–intermediate phase transition and 62 ± 6 MPa/K for the intermediate phase–PPV transition. The structural features of the $CaRhO_3$ intermediate phase suggest that the phase has edge-sharing RhO_6 octahedra and may have an intermediate structure between PV and PPV.

In another paper, the discovery of the PV to PPV transition in $MgSiO_3$ in a laser-heated anvil apparatus, has led to wide attention being focused on the PPV phase of $MgSiO_3$. This relates to the fact that the PPV phase is likely to play a key role in Earth's lowermost mantle, and because the PV to PPV transition can explain many features of the "D" seismic discontinuity. The PPV phase of $MgSiO_3$ cannot be quenched to ambient pressure/temperature conditions so that further studies must be conducted using analogue compounds of $MgSiO_3$ PPV, like $CaRhO_3$, that are quenchable to ambient pressure/temperature conditions. However, it can only be obtained at high pressure/temperature conditions using a multi-anvil apparatus. Further studies on this material revealed structural phase transitions at high P–T along with a metal–insulator transition caused by hole doping. In the case of $CaIrO_3$, the PPV phase of $CaIrO_3$ synthesized at 2 GPa, 1373 K transforms into a PV phase at 2 GPa, 1673 K. In other words, the PV phase can be synthesized at temperatures higher than those needed for synthesizing the PPV phase. This is also the case for $CaRhO_3$ (6 GPa, 1873 K) and $CaRuO_3$ (23 GPa, 1343 K). Within density functional theory, the equations of state for PV and PPV forms of $CaRhO_3$ have been obtained with equilibrium values of volume in agreement with experiment. Energy magnitudes point to a stabilization of PPV versus PV. This is interpreted by use of analyses of the charge density and the chemical bonding plots, showing that the Rh–0 interactions within two oxygen sublattices are selectively differentiated and reinforced for one of the two oxygen sublattices within the PPV variety with respect to the PV variety that has only one. Investigation of the magnetic properties shows no magnetic order and a metallic character for PV while ferromagnetism occurs in PPV with a tendency to insulating behavior. This long-range order is favored by direct $t_{2g} \leftrightarrow t_{2g}$ interactions through edge-sharing octahedra in PPV $CaRhO_3$, stronger than indirect $t_{2g} \cdot P_\pi \cdot t_{2g}$ ones in the PV variety. The structure is shown in Fig. 13.38.

$CaRuO_3$ PPV undergoes an AFM transition at ~270 K while the PV shows no magnetic transition above 1.0 K. The factor, 1/X, of $CaRuO_3$ PPV is about three times as large as that of the PV at 300 K. The differences in magnetic properties between the PV and PPV of $CaRuO_3$ indicate that the effect of antiferromagnetic interaction on magnetic susceptibility in the PPV is larger than that in the PV. Considering the origins of magnetic properties

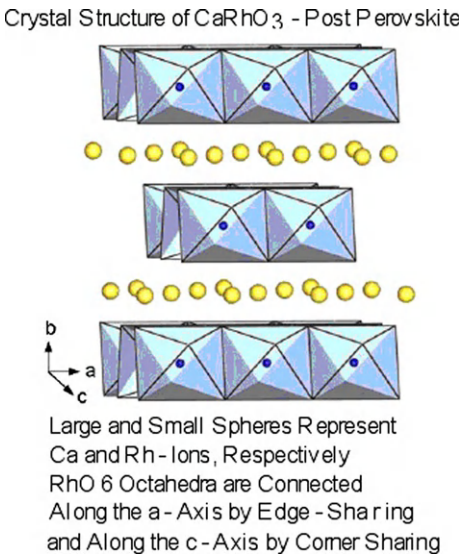

FIGURE 13.38

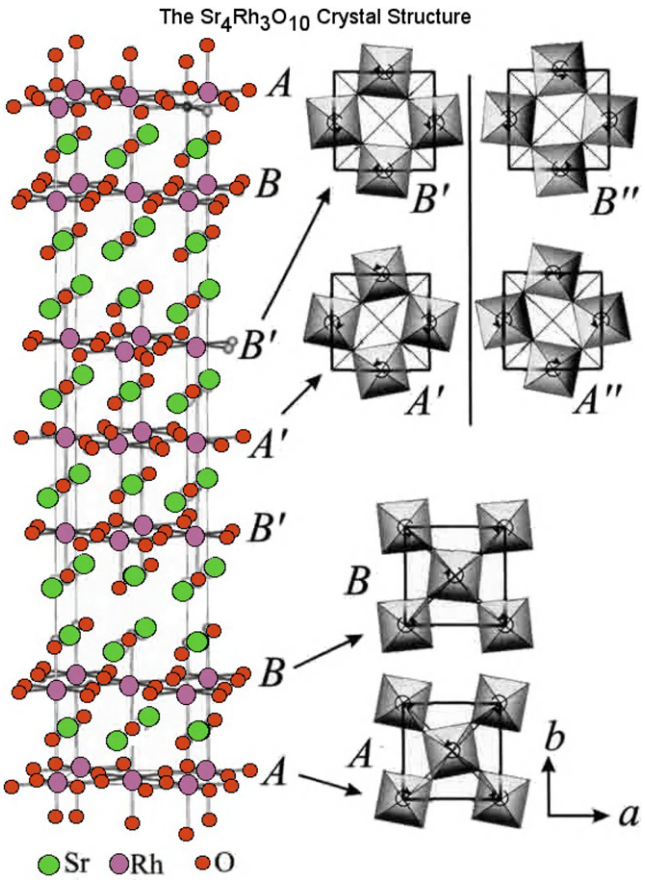

FIGURE 13.39

of those compounds, the difference of effect of antiferromagnetic interaction between the PV and the PPV can be comprehended. It was thought that magnetism of $CaRuO_3$ PV originates mainly from an interaction with itinerant electrons and superexchange interaction for Ru–O–Ru linkages. It was suggested that the difference in magnetic interaction between the PV and the PPV may be caused by the inhibition of itinerant magnetism with decreasing d-band width caused by reduction of the Ru–O–Ru bond angle of corner-sharing octahedra in PPV (139.0°), which is smaller than in PV (151.2°), and by change from a 3D to a quasi 2D Ru–O network.

Calcium rhodate compounds are not offered for sale commercially nor have any CAS numbers been issued.

13.2.4. Strontium Rhodium Compounds

In the ternary Sr–Rh–O system, several compounds have been reported: $Sr_{0.75}Rh_4O_8$, $SrRh_2O_4$, $Sr_6Rh_5O_{15}$, Sr_2RhO_4, and Sr_4RhO_6, which were synthesized by solid-state conventional methods. Recently, two new members were added to the rhodates system, which were prepared by a high-pressure method; the PV $SrRhO_3$ and the bilayered $Sr_3Rh_2O_7$. At the end of the high-pressure studies, it was clear that these compounds form a novel PV family as expressed by the general formula $Sr_{n+1}Rh_nO_{3n+1}$ ($n = 1$, 2, and infinity), indicating this must be a Ruddlesden–Popper series. It was also stressed that all the members were magnetically and electrically active because the oxygen-coordinated rhodium ions were formally tetravalent and had an unpaired electron per each (t^5_{2g}-e^0_g) configuration. Since all compounds in $Sr_{n+1}Rh_nO_{3n+1}$ formally form a spin-1/2 system, an appearance of quantum critical characters could be highly expected in the vicinity of the $Sr_{n+1}Rh_nO_{3n+1}$ composition or at physically extreme conditions. In fact, past studies on the $n = \infty$ compound suggested a substantial influence from quantum critical fluctuations.

A neutron diffraction study produced details of the structure of $Sr_4Rh_3O_{10}$ as shown in Fig. 13.39.

Because the significantly relevant systems, $Sr_3Rh_2O_7$ and $SrRhO_3$, share a common structure model with each corresponding ruthenate, the structurally intermediate $Sr_4Rh_3O_{10}$ was expected to share the tri-layered structure model with the ruthenate, $Sr_4Ru_3O_{10}$. High-pressure and high-temperature heating (6 GPa and 1500 °C) brought about successful preparation of a polycrystalline sample of the expected member at $n = 3$ of $Sr_{n+1}Rh_nO_{3n+1}$. Neutron diffraction studies showed the same orthorhombic crystal structure (*Pbam*) at room temperature and 3.4 K. Local structure distortions rotationally tilt the RhO_6 octahedra ~12° in the PV-based blocks along the *c*-axis, and approximately a 20% disorder was found in sequence of the alternating rotational tilt. The result clearly supported the *Pbam* model for the structure of $Sr_4Rh_3O_{10}$ as well as $Sr_3Rh_2O_7$. These compounds were also investigated by measurements of specific heat, thermopower, magnetic susceptibility, and

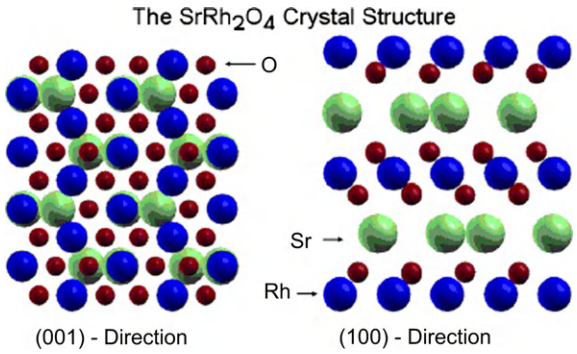

FIGURE 13.40

electrical resistivity. The data clearly revealed enhanced paramagnetism and electrically conducting character, which reflected nature of the correlated 4d5-electrons of Rh^{4+}. However, no clear signs of magnetic and electrical transitions were observed above 2 K and below 70 kOe, providing a remarkable contrast to the rich electronic phenomena for the significantly relevant ruthenate, $Sr_4Ru_3O_{10}$.

No compounds have been found in the Rh^{2+}-containing system of SrO–RhO.

In the Rh^{3+}-containing system of $SrO–Rh_2O_3$, the compound, $SrRh_2O_4$ has the structure shown in Fig. 13.40.

$SrRh_2O_4$ exists as RhO_2 sheets, isostructural to the CoO_2 sheets of Na_xCoO_2, and stacked in the same way. Similar to the Na ions in Na_xCoO_2, the Sr ions are distributed over the two TP (trigonal prismatic) sites in between the layers. The hexagonal crystal structure consists of hexagonal Rh sheets, coordinated above and below (along the *c*-axis) with hexagonal O sheets to produce an octahedral coordination of the Rh. These RhO_2 blocks are stacked in alternating fashion. That is, considering the stacking -O-Rh-O-O-Rh-O., one has a stacking pattern of .ABC·CBA. This yields two different types of TP sites between the one over the Rh ions (B) and the other over the O in the layer on the opposite side of the Rh sheet.

Density functional calculations have been used to obtain the electronic structure of β-$SrRh_2O_4$ in comparison with spinel $ZnRh_2O_4$. Both materials are band insulators, with substantial crystal field-induced band gaps, reflecting a strong transition metal–O hybridization. However, due to the bonding topology in these materials, the valence bands are very narrow. This leads to high thermoelectric powers within standard Boltzmann transport theory, and indicates that they can be the basis of good thermoelectric materials, provided that they can be doped into metallic states with reasonable carrier mobility. In the case of β-$SrRh_2O_4$, scattering due to Sr disorder is important. In addition, again in β-$SrRh_2O_4$, the band gap may be large enough to be of interest for photo-electrochemical H_2 production.

β-$SrRh_2O_4$ was prepared as a black powder by solid-state reaction of $SrCO_3$ with Rh metal in air. The compound crystallizes in the space group $P63c$, $Z = 1$, with $a = 3.0626$ Å and $c = 11.3996$ Å. The structure consists of $Cd1_2$-type layers of edge-sharing RhO_6 octahedra with an AABB oxygen layer sequence. Strontium is found in partial occupation of both available interlayer sites, in TP coordination.

Transport and thermal properties were examined for the layered rhodium oxide β-$Sr_{1-x}Rh_2O_4$. The parent compound $SrRh_2O_4$ is a band insulator. Transport and thermal properties were examined for the layered rhodium oxide β-$Sr_{1-x}Rh_2O_4$. The introduction of Sr^{2+} deficiencies results in an insulator–metal transition around $x \leq 0.2$. The metallic phase for $x > 0.2$ is a strongly correlated Fermi liquid with an enhanced quasi particle mass. The enhanced thermoelectric power of $S = 150\ \mu V/K$ at 1000 K in this metallic phase suggested that $Sr_{1-x}Rh_2O_4$ has great potential as a thermoelectric material.

α-$SrRh_2O_4$ has a triangular planar lattice of d^3 Cr^{3+} made from edge-sharing RhO_6 octahedra; the plane shows a very small orthorhombic distortion from hexagonal symmetry. With a Weiss temperature of ~596 K and a 3D magnetic ordering temperature of 43 K, the magnetic system is quasi 2D and frustrated. NPD shows that the ordered state is an incommensurate helical magnet, with an in-plane propagation vector of k = (0, 0.3217, 0). Temperature-dependent synchrotron powder diffraction characterization of the structure shows an increase in the inter-plane spacing on cooling below 100 K and an inflection in the cell parameters at the magnetic ordering temperature. These anomalies indicate the presence of a moderate degree of magneto-structural coupling. This material has a layered structure with triangular sheets of formula RhO_2 separated by Sr^{2+} in TP co-ordination. No other compounds are known in this system.

Results were presented concerning XRD, electrical resistivity, thermal stability and magnetic susceptibility data of the four phases found in the Rh_2O_3–SrO system within the compositional interval of 0–70 mol% SrO. Only Sr_2RhO_4 was already described in the literature; $Sr_3Rh_2O_{6.5}$, $SrRh_2O_4$ and $SrRh_3O_{5.5}$ are completely new. The first two crystallize in a hexagonal system with the unit cell parameters corresponding to: $a = 9.602$ Å, $c = 8.222$ Å and $a = 3.054$ Å, $c = 11.39$ Å, respectively, while $SrRh_3O_{5.5}$ is monoclinic with $a = 14.554$ Å, $b = 12.193$ Å, $c = 7.903$ Å and $\beta = 98.53°$. It has been found that, in these phases, resistivity strongly depends on oxygen content and whether Rh ions exhibit variable oxidation states. All the Rh_2O_3–SrO binaries represent interesting objects for more detailed studies of the nature of several magnetic anomalies exhibited by them.

Single crystals of $Sr_6Rh_5O_{15}$ were grown from a molten potassium carbonate flux. The structure was solved by both the traditional 3D crystallographic approach and the 4D superspace group approach using JANA2000. Both methods produced an equivalent structure determination, thereby confirming the 4D superspace group approach as an effective structure solution method for 3D commensurate composite structures. $Sr_6Rh_5O_{15}$ corresponds to the $n=1$, $m=1$ member of the $A_{3n+3m}A'_nB_{3m+n}O_{9m+6n}$ family of 2H hexagonal PV-related oxides. This compound is characterized by pseudo 1D polyhedral chains of four face-sharing RhO_6 octahedra followed by one RhO_6 TP. These chains in turn are separated by Sr_∞ chains. Magnetic measurements were carried out on oriented single crystals, and a very large magnetic anisotropy in the magnetic susceptibility was observed. The crystal structure has the form shown in Fig. 13.41.

In this diagram, the structure of $Sr_6Rh_5O_{15}$ consists of chains of four face-sharing RhO_6 octahedra followed by one RhO_6 TP. They are labelled: light gray, RhO_6 octahedra; dark gray, RhO_6 TPs; green spheres, Sr atoms. The compound contains more than one valence of rhodium, namely:

$$Sr_6(2Rh^{3+}, 3Rh^{4+})_5O_{15}$$

In the Rh^{2+}–Rh^{3+}-containing system of SrO–Rh_3O_4, the stoichiometric compound, $SrRh_3O_5$, is not known. No other compounds have been synthesized.

In the Rh^{4+}-containing system of SrO–RhO_2, single crystals of layered PV $Sr_2RhO_{4-\delta}$ ($\delta=0.0$ and 0.1) were successfully grown by the floating zone method. Stoichiometric single crystals ($Sr_2RhO_{4.0}$) were obtained by O_2-annealing the as-grown crystals ($Sr_2RhO_{3.9}$). $Sr_2RhO_{4.0}$ and $Sr_2RhO_{3.9}$ show quasi 2D Fermi liquid behavior at low temperatures, whereas there are large differences in the anisotropy of electrical resistivity $\rho_c(3\text{ K})/\rho_{ab}(3\text{ K})$ and Wilson ratio R_w between $Sr_2RhO_{4.0}$ and $Sr_2RhO_{3.9}$:

$$\rho_c(3\text{ K})/\rho_{ab}(3\text{ K}) = 2400 \text{ for } Sr_2RhO_{4.0};\ R_w = 3.8$$
$$\rho_c(3\text{ K})/\rho_{ab}(3\text{ K}) = 19{,}000 \text{ for } Sr_2RhO_{3.9};R_w = 6.4$$

The differences experienced in the temperature dependence of the in-plane electrical resistivity ($T<15$ K), magnetic susceptibility ($T<300$ K) and specific heat ($T<10$ K) of $Sr_2RhO_{4.0}$ and $Sr_2RhO_{3.9}$ are mainly derived from those differences between the density of states and band structure near the corresponding Fermi level. It was stated that the changes in these physical properties, which are accompanied by oxygen defects in the $Sr_2RhO_{4-\delta}$ system, can be explained by the rigid band model. Moreover, these results also suggest that t_{2g} band filling can be controlled by adjusting the oxygen defect content δ in the $Sr_2RhO_{4-\delta}$ system. Although many similarities are observed in this study between the physical properties of $Sr_2RhO_{4.0}$ and $SrRu_2O_4$, $Sr_2RhO_{4.0}$ does not exhibit superconductivity down to 36 mK.

The bilayered rhodium oxide, $Sr_3Rh_2O_7$, was synthesized by high-pressure and high-temperature heating techniques. The single-phase polycrystalline sample of $Sr_3Rh_2O_7$ was characterized by measurements of magnetic susceptibility, electrical resistivity, specific heat, and thermopower. The structural characteristics were investigated by powder neutron diffraction technique. The rhodium oxide $Sr_3Rh_2O_7$ [*Bbcb*, $a=5.4744$ Å, $b=5.4716$ Å, $c=20.875$ Å] is isostructural to the meta-magnetic metal, $Sr_3Ru_2O_7$, with five 4d electrons per Rh (which is electronically equivalent to the hypothetical bilayered ruthenium oxide, where one electron per Ru is doped into the Ru-327 unit). The present data showed that the rhodium oxide $Sr_3Rh_2O_7$ is metallic with enhanced paramagnetism, similar to $Sr_3Ru_2O_7$. However, neither manifest contributions from spin fluctuations nor were any traces of a meta-magnetic transition found within the studied range from 2 K to 390 K below 70 kOe.

Study of the structural changes occurring during the reduction process of the $Sr_2RhO_{4+\delta}$ (214), i.e. the 2:1:4 atom-ratios, (n = 1 term of the Ruddlesden-Popper series), shows that for $\delta<0.02$ values, this material dissociates into the Sr_4RhO_6 (416) mono-dimensional phase, $\alpha=\infty$, $\beta=0$ compound of the $(A_3B_2O_6)_\alpha\cdot(A_3B_3O_9)_\beta$ family, and Rh metal. During the first stage, this process occurs by the formation of an intergrowth between the (214) and (416) materials which can be only detected by high-resolution electron microscopy and is easily interpreted on the basis of the structural relationship established between them. Further reduction allows the segregation of both phases as separated entities, which coexist with Rh metal. The dissociation

The Crystal Structure of $Sr_6Rh_5O_{15}$

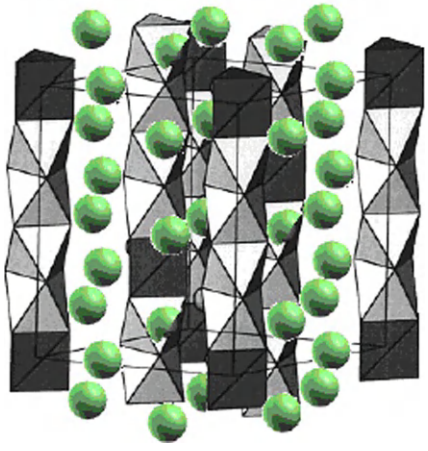

FIGURE 13.41

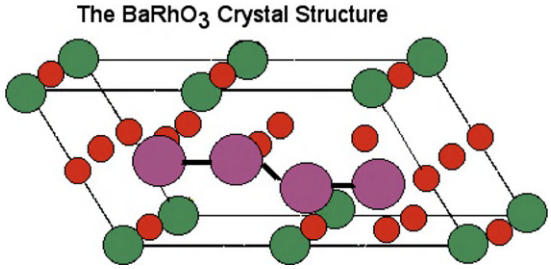

FIGURE 13.42

process is reversible and, under oxidizing conditions, a layered material with anionic composition $\delta = 0.06$ is always obtained. This behavior seems to be a general way of accommodating the compositional changes in layered A_2BO_4 phases where the B-cation is always in an octahedral environment. The structural mechanism of this transformation is proposed, and the structural relationship between these two low-dimensional oxides is established. When heated, transition from the layered Sr_2RhO_4 to the mono-dimensional Sr_4RhO_6 phase occurs:

$$2Sr_2RhO_4 + \text{heat} \Rightarrow Sr_4RhO_6 + RhO_2$$

In the Rh^{5+}-containing system of $SrO–Rh_2O_5$, no compounds are known.

In the Rh^{6+}-containing system of $SrO–RhO_3$, no compounds have been discovered.

Strontium rhodate or rhodite compounds are not available for sale commercially.

13.2.5. Barium Rhodium Compounds

A number of barium rhodate compositions have been reported in the literature.

In the Rh^{2+}-containing system of BaO–RhO, no compounds have been synthesized.

In the Rh^{2+}–Rh^{3+}-containing system of $BaO–Rh_3O_4$, no mention of any of the possible compounds such as $BaRh_3O_5$ or $Ba_2Rh_3O_6$ can be found in the technical literature.

In the Rh^{3+}-containing system of $BaO–Rh_2O_3$, the compound, $BaRh_2O_4$, is expected to have a similar crystal structure as that of $SrRh_2O_4$. However, such a determination has not appeared in the literature at this time. No other compounds have been synthesized in this system.

In the Rh^{4+}-containing system of $BaO–RhO_2$, the compound, $BaRhO_3$ has a crystal structure form shown in Fig. 13.42.

Barium rhodium oxide, $BaRhO_3$, was prepared at 1175 °C and 60–65 kbar by the reaction of BaO_2 and RhO_2. A hexagonal black platelet obtained in the reaction product was found to possess a four-layer stacking sequence in space group $P6_3/mmc$ having hexagonal unit cell parameters $a = 5.744(1)$ and $c = 9.642(1)$ Å. The structure was determined from 707 independent reflections of which 224 were considered observed. Averaging equivalent reflections yielded 132 unique observed reflections. Refinement of the structure by least-squares methods gave a conventional R value of 4.4%. The structure consists of a four-layer stacking sequence of close-packed BaO_3 layers containing tetravalent rhodium in all the octahedral oxygen interstices. The compound was found to be isostructural with previously reported $BaMO_3$ phases. This is the first single-crystal refinement of the 4H polytype using a four-circle X-ray diffractometer.

Cell parameters are: $a = b = 5.772$ Å, $c = 9.641$ Å, $\alpha = \beta = \gamma = 90°$, cell volume = 278.14 Å^3, $Z = 4$.

Cell occupancy is shown in Table 13.14.

Three different phases in the Ba–Rh–O system were prepared under high-pressure/high-temperature conditions. The black crystalline products were studied by XRD techniques and the space groups for several phases were obtained. The first phase, the 4H polytype $BaRhO_3$, was reported in the literature, but in addition two new phases were isolated and their structures determined. The second high-pressure Ba–Rh–O product, previously reported to be an 18R polytype, was observed to be isostructural with $BaIrO_3$. This phase was found to be non-stoichiometric with a deficiency in rhodium in octahedral sites, and a stoichiometry of $BaRh_{0.92}O_3$. The space group is $C2/m$ and the unit cell parameters are $a = 10.005$, $b = 5.764(1)$, $c = 14.937$ Å, $\beta = 102.99°$ and $Z = 12$. The third phase isolated in this study was observed to possess a Hollandite-type structure with space group $I2/m$, where the RhO_6 octahedra share

TABLE 13.14

No.	Site notation	Atom	Multiplicity	Wyckoff	Site symmetry	x	y	z	Occupancy
1	O1	O	6	h	mm2	0.16667	0.3333	1/4	1.0
2	O2	O	6	g	.2/m.	1/2	0	0	1.0
3	Rh1	Rh	4	f	3m.	1/3	2/3	0.11	1.0
4	Ba1	Ba	2	d	-6m2	1/3	2/3	3/4	1.0
5	Ba2	Ba	2	a	-3m.	0	0	0	1.0

edges and vertices. Its unit cell parameters are $a = 9.435$, $b = 3.1041$, $c = 10.399$ Å, $\beta = 94.45°$ and $Z = 1$. Refinement of the structure generated the composition $Ba_{1.72}Rh_8O_{16}$.

The $\alpha = 3$, $\beta = 6$ term of the series $(A_3B_2O_6)_\alpha \cdot (A_3B_3O_9)_\beta$ has been synthesized in polycrystalline form. The structural characterization by powder XRD, electron diffraction and high-resolution electron microscopy indicates that this material is isostructural with $Ba_9Co_8O_{24}$. In the structure, seven face-sharing octahedra alternate with a TP defining chains running parallel to the *c*-axis of a rhombohedral unit cell (*Rc*), with parameters $a = 1.00766(4)$ nm and $c = 4.1571(2)$ nm. The structural refinement shows the presence of a small percentage of Rh vacancies leading to the composition $Ba_9Rh_{7.92}O_{24}$. Pauli paramagnetic behavior is observed.

The structure, 2H-$BaRhO_3$ has not yet been synthesized. Single crystals of two new barium rhodates were grown from a molten potassium carbonate flux. These rhodates, $Ba_{11}Rh_{10}O_{30}$ and $Ba_{32}Rh_{29}O_{87}$, are structurally related to the 2H-hexagonal PV structure and are characterized by pseudo 1D chains of alternating face-sharing TPs and octahedra. The structures of $Ba_{11}Rh_{10}O_{30}$ and $Ba_{32}Rh_{29}O_{87}$ were solved using the 4D superspace group approach in January 2000. $Ba_{11}Rh_{10}O_{30}$, with a repeat of nine RhO_6 octahedra followed by one RhO_6 TP, contains the longest chain sequence of face-sharing octahedra known for this 2H-PV-related family of oxides. A structural analysis of these two compounds revealed clear trends in metal–metal distances and octahedral heights not previously identified for this family of oxides. The application of these trends toward the structure of the all-octahedra-containing end member of the structural series, the hypothetical 2H-$BaRhO_3$, enabled a prediction of its rhodium–rhodium distance, octahedral height, and lattice parameters.

A plot of the interatomic distances between Rh–Rh atoms and the number of Rh atoms in the chain are shown in Fig. 13.43.

No other compounds are known in this system.

In the Rh^{5+}-containing system of BaO–Rh_2O_5, no compounds have appeared in the literature.

In the Rh^{6+}-containing system of BaO–RhO_3, the synthesis and microstructural characterization, by means of selected-area electron diffraction and high-resolution electron microscopy, of $Ba_7Rh_6O_{18}$ was reported. This material, isostructural to $Ba_7Co_6O_{18}$, is formed by rows of one TP and five face-sharing octahedra running parallel to the *c*-axis of a trigonal unit cell, with parameters $a = 10.04(5)$ and $c = 31.65(7)$ Å. The substitution of Sr by Ba is accommodated by means of twin formation due to a rearrangement of the rows of polyhedra. This compound belongs to the 1D oxide of the homologous series $(A_3Rh_2O_6)_\alpha$–$(A_3Rh_3O_9)_\beta$.

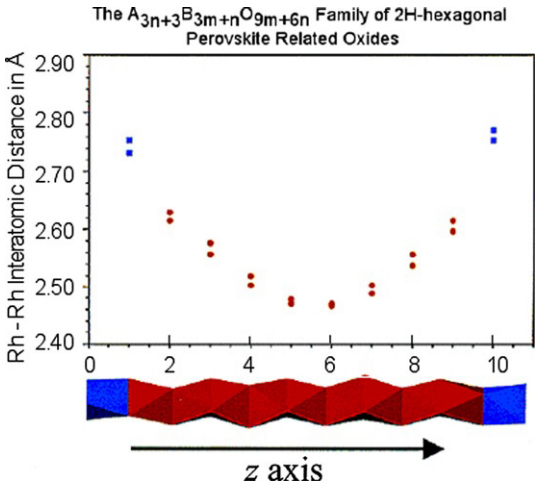

FIGURE 13.43

Barium rhodate or rhodite compounds are not offered for sale commercially and no CAS numbers have been issued.

13.2.6. Radium Rhodium Compounds

Although radium probably forms similar types of compounds as those of barium rhodates, no mention of such is available in the current literature. This is undoubtedly due to the lack of interest in both Academia and Industry. The radioactivity of ^{126}Ra and the high cost of rhodium metal ($1975.00/oz—July 2011) are probably the major factors in this lack of interest.

13.3. ALKALINE EARTH IRIDIUM COMPOUNDS

Iridium has the electron configuration [Xe] $4f^{14}$ $5d^7$ 6 and the valence states of −3, −1, 0, 1, 2, **3**, **4**, 5, 6. The first four states are found only in solution. It is the +3 and +4 states that are the more important. IrO_2, a brown powder, is the only well-characterized oxide of iridium. Ir_2O_3, has been described as a blue-black powder that is oxidized to IrO_2 by HNO_3. Iridium also forms iridates such as K_2IrO_3 and $KIrO_3$ with oxidation states +4 and +5, but no similar compounds have been found with the alkaline earths.

13.3.1. Beryllium Iridium Compounds

The system, Be^0–Ir^0, has been stated to form at least three intermetallic compounds, Be_4Ir, $Be_{44}Ir_7$ and $Be_{13}Ir_3$. However, only one compound, $Be_{17}Ir_2$ has had its structure published. It has the form shown in Fig. 13.44.

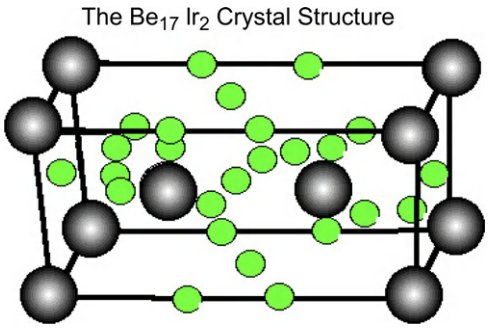

FIGURE 13.44

Cell parameters for $Mg_{17}Ir_2$ are: $a = b = 4.193$ Å, $c = 10.892$ Å, $\alpha = \beta = \gamma = 90°$, cell volume $= 165.34$ Å^3, $Z = 6$. Cell occupancy is shown in Table 13.15.

It is somewhat puzzling that $Be_{17}Ir_2$ does not appear in a published phase diagram. Yet, the structures of the compounds, $Be_{44}Ir_7$, $Be_{13}Ir_3$ and Be_3Ir have not appeared in the open literature. By comparing the published data for the Mg–Ir system, it becomes obvious that the Be–Ir system was misinterpreted and that these three compounds do not exist.

Beryllium oxide(s) does not form any compounds with the iridium oxides.

13.3.2. Magnesium Iridium Compounds

Magnesium metal forms a series of intermetallic compounds with Ir^0 metal, as shown in the partial phase diagram of Fig. 13.45.

The compound, Mg_3Ir, has the structure shown in Fig. 13.46.

TABLE 13.15

No.	Site notation	Atom	Multiplicity	Wyckoff	Site symmetry	*x*	*y*	*z*	Occupancy
1	Be1	Be	6	n	.m.	0.166	0.8335	0.183	1.0
2	Be2	Be	3	k	mm2	0.505	0.4955	1/2	1.0
3	Be3	Be	2	i	3m.	2/3	1/3	0.098	1.0
4	Ir1	Ir	2	i	3m.	2/3	1/3	0.307	1.0
5	Be4	Be	2	h	3m.	1/3	2/3	0.34	1.0
6	Be5	Be	2	g	3m.	0	0	0.377	1.0
7	Be6	Be	1	c	-6m2	1/3	2/3	0	0.34
8	Ir2	Ir	1	a	-6m2	0	0	0	0.36

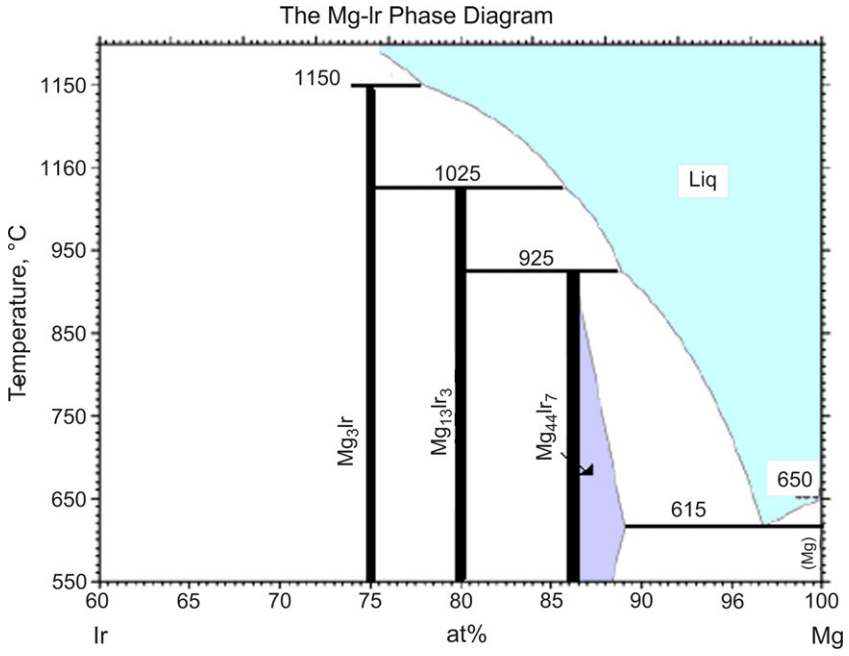

FIGURE 13.45

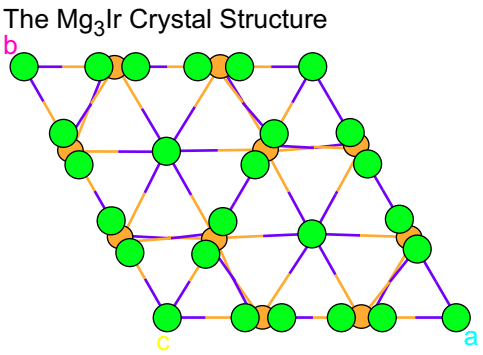

FIGURE 13.46

Cell parameters are: $a = b = 7.927$ Å, $c = 8.194$ Å, $\alpha = \beta = 90°$, $\gamma = 120°$, cell volume = 445.69 Å^3, cell occupancy is shown in Table 13.16.

The other known compound has the form shown in Fig. 13.47.

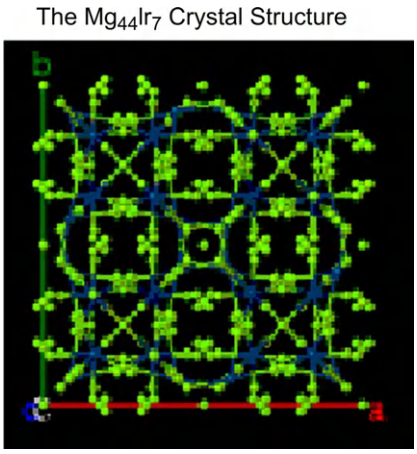

FIGURE 13.47

Cell parameters are: $a = b = c = 14.2233$ Å, $\alpha = \beta = \gamma = 60°$, cell volume = 2034.63 Å^3. Cell occupancy is shown in Table 13.17.

TABLE 13.16

No.	Site notation	Atom	Multiplicity	Wyckoff	Site symmetry	x	y	z	Occupancy
1	Ir	Ir	6	c	..m	0.3274	0	0.0415	1.0
2	Mg(2)	Mg	6	c	..m	0.3663	0	0.3784	1.0
3	Mg(1)	Mg	6	c	..m	0.718	0	0.222	1.0
4	Mg(3)	Mg	4	b	3..	1/3	2/3	0.0997	1.0
5	Mg(4)	Mg	2	a	3.m	0	0	0.0	1.0

TABLE 13.17

No.	Site notation	Atom	Multiplicity	Wyckoff	Site symmetry	x	y	z	Occupancy
1	Mg1	Mg	48	h	..m	0.0516	0.0516	0.1600	1.0
2	Mg2	Mg	48	h	..m	0.0989	0.0989	0.7725	1.0
3	Mg3	Mg	48	h	..m	0.1084	0.1084	0.2812	1.0
4	Mg4	Mg	48	h	..m	0.1548	0.1548	0.5209	1.0
5	Mg5	Mg	48	h	..m	0.1917	0.1917	0.0187	1.0
6	Mg6	Mg	24	g	2.mm	0.1422	1/4	1/4	1.0
7	Mg7	Mg	24	g	2.mm	0.6171	1/4	1/4	1.0
8	Mg8	Mg	24	f	2.mm	0.3211	0	0	1.0
9	Ir1	Ir	16	e	.3m	0.1510	0.1510	0.1510	1.0
10	Ir2	Ir	16	e	.3m	0.4172	0.4172	0.4172	1.0
11	Mg9	Mg	16	e	.3m	0.5524	0.5524	0.5524	1.0
12	Ir3	Ir	16	e	.3m	0.6584	0.6584	0.6584	1.0
13	Mg10	Mg	16	e	.3m	0.9196	0.9196	0.9196	1.0
14	Mg11	Mg	4	a	-43m	0	0	0	1.0

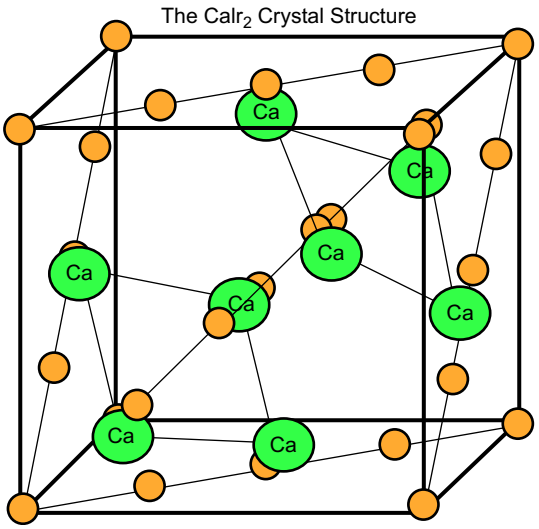

FIGURE 13.48

In the system of MgO–Ir_xO_y, no compounds have been documented. Even the known oxides of Ir_2O_3 and IrO_2 have not been observed to form stable compounds with MgO.

None of these compounds are available commercially.

13.3.3. Calcium Iridium Compounds

In the Ca–Ir system, only one structure has been reported (Fig. 13.48).

Cell parameters are: $a = b = c = 5.3351$ Å, $\alpha = \beta = \gamma = 60°$, cell volume = 107.38 Å^3, cell occupancy is shown in Table 13.18.

No compounds have been reported in the Ir^{2+}-containing system of CaO–IrO, in the Ir^{3+}-containing system of CaO–Ir_2O_3 or in the Ir^{2+}–Ir^{3+}-containing system of CaO–Ir_3O_4.

In the Ir^{4+}-containing system of CaO–IrO_2, the types of compounds formed in the system depends upon the oxygen partial pressure available during the solid-state reaction. The diagram presented as Fig. 13.49 shows this phenomenon.

The diagram shows the minimum partial pressure required during reaction of CaO with Ir metal at 1300 K. This is a constant factor for each of the three compounds (the horizontal lines). Excess Ir metal is present at all times until the pressure is reached where IrO_2 is produced directly. The vertical lines represent a separation of bi-compositional areas of compounds

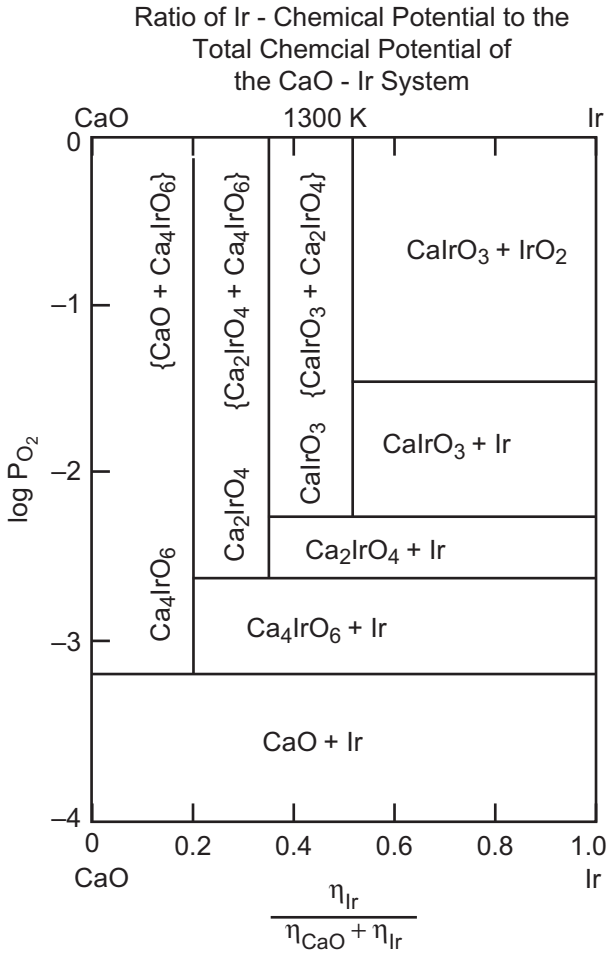

FIGURE 13.49

produced as a function of the ratio of the chemical potential of Ir in terms of the chemical potential of both components. The standard Gibbs energies of formation of the compounds, obtained from the e.m.f. of the cells, can be represented by the equations:

$$IrO_2 \quad \Delta G^0_f/\mathrm{J/mol} = -239{,}230 + 172.19T$$

$$CaIrO_3 \quad \Delta G^0_{f(ox)}/\mathrm{J/mol} = 460 + 1.13T$$

$$Ca_2IrO_4 \quad \Delta G^0_{f(ox)}/\mathrm{J/mol} = -31{,}145 + 0.81T$$

$$Ca_4IrO_6 \quad \Delta G^0_{f(ox)}/\mathrm{J/mol} = -37{,}400 + 2.01T$$

where $\Delta G^0_{f(ox)}$ represents the standard Gibbs energy of formation of the ternary compound from its component binary oxides CaO and IrO_2. Based on the thermodynamic information, this chemical potential diagram for the system Ca–Ir–O was developed. The standard Gibbs

TABLE 13.18

No.	Site notation	Atom	Multiplicity	Wyckoff	Site symmetry	*x*	*y*	*z*	Occupancy
1	Ir	Ir	16	c	.-3m	0	0	0	1.0
2	Ca	Ca	8	b	-43m	3/8	3/8	3/8	1.0

energies of formation of IrO_2, $CaIrO_3$, Ca_2IrO4 and Ca_2IrO_6 were measured in the temperature range 940–1350 K using solid-state cells with $Y_2O_3{\cdot}ZrO_2$ as the electrolyte and pure oxygen gas at a pressure of 0.1 MPa as the reference electrode. For the design of appropriate working electrodes, phase relations in the ternary system Ca–Ir–O were investigated at 1300 K. The only stable oxide detected along the binary Ir–O line was IrO_2. Three ternary oxides, $CaIrO_3$, Ca_2IrO_4, and Ca_4IrO_6, compositions of which fall on the joined $CaO–IrO_2$, were found to be stable. Each of the oxides coexisted with pure metal Ir. Therefore, five working electrodes were prepared, consisting of mixtures of:

$$\mathrm{Ir} + \mathrm{IrO_2},$$
$$\mathrm{Ir} + \mathrm{IrO_2} + \mathrm{CaIrO_3},$$
$$\mathrm{Ir} + \mathrm{CaIrO_3} + \mathrm{Ca_2IrO_4},$$
$$\mathrm{Ir} + \mathrm{Ca_2IrO_4} + \mathrm{Ca_4IrO_6},$$
$$\text{and } \mathrm{Ir} + \mathrm{Ca_4IrO_6} + \mathrm{CaO}.$$

These mixtures unambiguously define unique oxygen chemical potentials under isothermal and isobaric conditions.

When three condensed phases coexist at equilibrium in a ternary system such as Ca–Ir–O, the system is bivariant. At a fixed temperature and total pressure, three condensed phases coexist only at a unique partial pressure of oxygen (as shown above). Therefore, horizontal lines on the diagram represent three-phase equilibria. On reducing the oxygen partial pressure at 1200 K, IrO_2 dissociates first followed by the ternary oxides in the order of decreasing cationic fraction of Ir. The stability domain of each stoichiometric phase is defined by a plane, because the sum of the chemical potentials of the different components weighted by the appropriate stoichiometric coefficients is equal to the Gibbs energy of formation of the phase. Lines, defined by the intersection of the corresponding planes, represent two-phase fields. Points of intersection of three planes identify three-phase equilibria.

The compound, $CaIrO_3$ has the form shown in Fig. 13.50. The structure of the Ca_4IrO_6 has not been elucidated. $CaIrO_3$ dissociates to Ir and Ca_2IrO_4 at 1408 K.

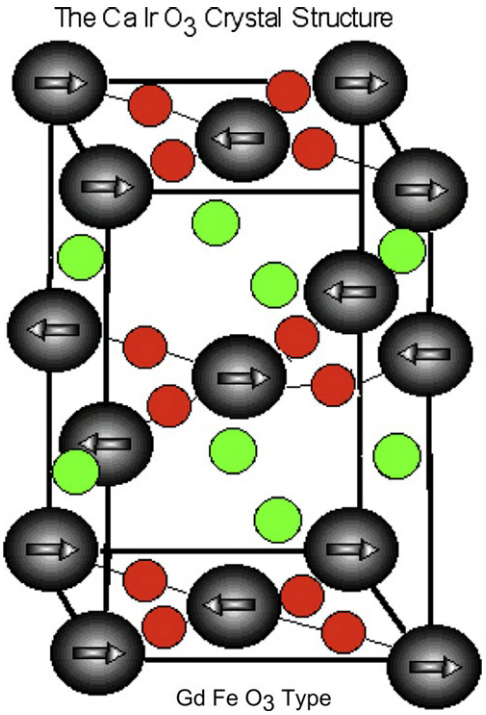

FIGURE 13.50

Cell parameters are: $a = 5.346$ Å, $b = 5.587$ Å, $c = 7.677$ Å, $\alpha = \beta = \gamma = 90°$, cell volume $= 229.30$ Å^3, $Z = 10$. Cell occupancy is shown in Table 13.19.

In another paper, the structure of $CaIrO_3$ (*Cmcm*) was refined at high pressure and at low temperature using time-of-flight NPD data. Evidence supporting deviation from space group *Cmcm* to $Cmc2_1$ has been determined to be inconclusive. As the $CaIrO_3$ (*Cmcm*) unit-cell volume changes, refinements indicated deformation of cation-centered coordination polyhedra, rather than tilting. Structure models demonstrated that Ca^{2+}-centered polyhedra are an order of magnitude more compressible than Ir^{4+}-centered octahedra. Bond valence sums show significant chemical strain (over-bonding) of calcium and oxygen at ambient conditions. Implications for structure change in $CaIrO_3$ PPV were discussed and a method for predicting the Clapeyron slope between PV and PPV phases was proposed based on

TABLE 13.19

No.	Site notation	Atom	Multiplicity	Wyckoff	Site symmetry	*x*	*y*	*z*	Occupancy
1	O1	O	8	d	1	0.198	0.0506	0.304	1.0
2	Ca1	Ca	4	c	.m.	0.437	1/4	0.016	1.0
3	O2	O	4	c	.m.	0.533	1/4	0.601	1.0
4	Ir1	Ir	4	a	-1	0	0	0	1.0

extrapolation of the volume ratio between cation-centered polyhedra.

Further work has included the preparation of single crystals of $CaIrO_3$ via a flux growth method. Crystal structure parameters, including the anisotropic displacement parameters, were determined based on a single-crystal XRD experiment. The unit-cell dimensions are $a = 3.147$, $b = 9.866$, and $c = 7.302$ Å. The structure was found to be a 3D dense structure with small vacant spaces. The $CaIrO_3$ structure can be described as a pseudo 1D oxide and was compared with Ca_4IrO_6 structure. The IrO_6 octahedra are significantly distorted, in contrast to other octahedral Ir^{4+} compounds. The O–O distances for faces and edges shared between polyhedra are shorter than other non-shared edge distances. These effects were explained by Pauling's rules and occurred to decrease the repulsion between the cations. Thermal vibrations of Ca and Ir atoms were found to be significantly anisotropic. Thermal vibrations of Ca and Ir atoms in this structure are restricted in orientation toward the shared face, shared edges, and shortest cation–cation directions. The single-crystal experiment shows that $CaIrO_3$ crystals grow fastest along the *a*-axis and that they assume a prism or needle shape. Strongly preferred orientation of such prism-shaped $CaIrO_3$-type PPV $MgSiO_3$ crystals may develop under the shear flow in the Earth's mantle.

Several calcium iridium oxides were prepared by solid-state reactions and by a hydroxide precipitation technique. These phases were characterized by XRPD data, electrical and magnetic properties. The calcium-rich phase, Ca_4IrO_6, was an insulator exhibiting Curie–Weiss behavior above 77 K with a Weiss constant of −47 K and a magnetic moment of 1.76 μbar.

In contrast, Ca_2IrO_4 is a semiconductor and the temperature-dependent susceptibility above 77 K was analyzed in terms of 1D linear chains of octahedrally coordinated Ir^{4+} ions. Its structure has the form shown in Fig. 13.51.

Single crystals of tetracalcium iridium hexa-oxide, Ca_4IrO_6, tricalcium magnesium iridium hexa-oxide, Ca_3MgIrO_6, and tricalcium zinc iridium hexa-oxide, Ca_3ZnIrO_6, were prepared via high-temperature flux growth and structurally characterized by single-crystal XRD. The three compounds are isostructural and adopt the K_4CdCl_6 structure type, comprised of chains of alternating face-shared $[CaO_6]$, $[MgO_6]$ or $[ZnO_6]$ TPs and $[IrO_6]$ octahedra, surrounded by columns of Ca^{2+} ions. Two $CaIrO_3$ phases were also isolated, but only the orthorhombic PV modification was sufficiently pure for magnetic studies. This compound was Pauli paramagnetic with metallic conductivity.

The pressure–volume–temperature (P–V–T) relation of $CaIrO_3$ and the PPV variety was measured at pressures and temperatures up to 8.6 GPa and 1273 K, respectively, with energy-dispersive synchrotron XRD using a DIA-type, cubic-anvil apparatus. Unit-cell dimensions were derived from the Le Bail full profile refinement technique, and the results were fitted using the third-order Birch–Murnaghan equation of state. The derived bulk modulus K_{T0} at ambient pressure and temperature is 168.3 ± 7.1 GPa with a pressure derivative $K_{0T0} = 5.4 \pm 0.7$. All of the high-temperature data, combined with previous experimental data, are fitted using the high-temperature Birch–Murnaghan equation of state, the thermal pressure approach, and the Mie-Grüneisen-Debye formalism.

The refined thermoelastic parameters for CaIrO3 ppv are:

Temperature derivative of bulk modulus

$$<\text{eth}>oK_T = oT_P = -0.038 \pm 0.011 \text{ GPa/K},$$
$$aK_T = 0.0039 \pm 0.0001 \text{ GPa/K}$$
$$\partial K_T/\partial T_V = -0.012 \pm 0.002 \text{ GPa/K}$$
$$\partial P/\partial T_{2V} = 1.9 \pm 0.3 \times 10^{-6} \text{ GPa}_2/\text{K}^2$$

Using the Mie-Grüneisen-Debye formalism, the Grüneisen parameter $c_0 = 0.92 \pm 0.01$ and its volume dependence $q = 3.4 \pm 0.6$ were obtained. The systematic variation of bulk moduli for several oxide PPVs can be described approximately by the relationship $K_{T0} = 5406.0/\text{V(molar)} + 5.9$ GPa.

A structural, thermodynamic, and transport study of the newly synthesized $Sr_5Rh_4O_{12}$, $Ca_5Ir_3O_{12}$, and Ca_4IrO_6 single crystals was conducted. These quasi 1D insulators consist of a triangular lattice of spin chains running along the *c*-axis, and are commonly characterized by a partial AFM order, a small entropy removal associated with the phase transitions, and a sizable low-temperature specific heat linearly proportional to temperature. $Sr_5Rh_4O_{12}$ is antiferromagnetically ordered below 23 K with strong evidence for an Ising character. Isothermal magnetization of $Sr_5Rh_4O_{12}$ exhibits two-step like transitions leading to a ferrimagnetic state at 2.4 T and a FM state at 4.8 T, respectively. $Ca_5Ir_3O_{12}$ and Ca_4IrO_6 are also

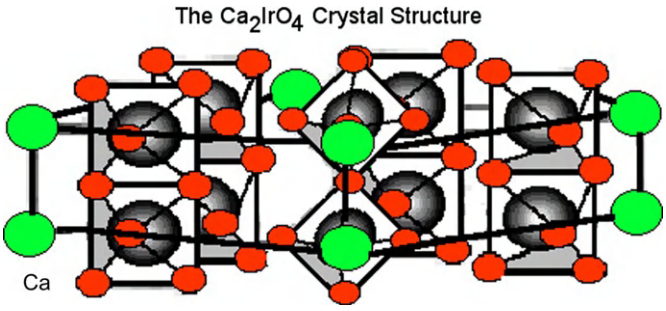

FIGURE 13.51

antiferromagnetically ordered below 7.8 and 12 K, respectively, and show an unusually large ratio of the Curie–Weiss temperature to the Néel temperature. In particular, $Ca_5Ir_3O_{12}$, which includes both Ir^{4+} and Ir^{5+} ions, reveals that only $S = 1/2$ spins of the Ir^{4+} ions are involved in the magnetic ordering, whereas $S = 1$ spins of the Ir^{5+} ions remain disordered. All results suggest the presence of a geometrical frustration that causes incomplete long-range AFM order in these quasi 1D compounds.

In the Ir^{5+}-containing system of CaO–Ir_2O_5, the ternary oxides $Ca_2Ir_2O_7$, $Cd_2Ir_2O_7$, and $Ca_{1.7}Os_2O_7$ have been prepared. They possess the cubic pyrochlore structure. All of these iridium phases contain Ir^{5+} and are the first oxide examples of iridium in an oxidation state higher than 4. A body-centered cubic structure related to the cubic $KSbO_3$ structure has been found for phases with compositions close to $BaOs_2O_6$, $SrOs_2O_6$, and $SrRe_2O_6$. The osmate compositions contain osmium in a +5 state, i.e. Os^{5+}. A primitive cubic structure also related to the cubic $KSbO_3$ structure has been found for phases with compositions close to $NaOsO_3$, $BiPtO_{3.5}$, and $BiOsO_{3.5}$.

No compounds have been documented in the Ir^{6+}-containing system of CaO–IrO_3.

Calcium–iridium compounds are not offered for sale commercially.

13.3.4. Strontium–Iridium Compounds

In the Sr–Ir system, only one compound, $SrIr_2$, has been reported. It has an identical crystal structure to $CaIr_2$ except for the cell parameters: $a = b = c = 7.7351$ Å, $\alpha = \beta = \gamma = 60°$, cell volume = 114.13 Å^3, cell occupancy is shown in Table 13.20.

A number of compositions of several phases in the Sr–Ir–O system have been reported within the past 30 years, and the single-crystal structures of three of these were determined. The formulation for one of these phases, namely the body-centered cubic, has been assigned different ratios of strontium, iridium and oxygen by various workers, which has led to some confusion as to its exact chemical composition. To clarify this situation, a study of the composition of the different Sr–Ir–O phases was carried out by electron microprobe analysis using a Kevex quantum energy dispersive detector, which is readily capable of detecting the K_α X-ray emission from oxygen along with that from heavier elements. Reference standards of pure IrO_2, SiO_2 (quartz), fused $SrCl_2$ and $SrCO_3$ were used for calibration of Ir, O, Cl and Sr contents, respectively. In addition, the Sr to Ir ratio was determined by using known standards such as the well-characterized monoclinic and orthorhombic (high-pressure) forms of $SrIrO_3$, and Sr_2IrO_{4-}. The analysis of the body-centered cubic Sr···Ir···O phase indicates a chemical formula of $Sr_{0.79}IrO_{2.8}Cl_{0.07}$. The trace of chlorine may be necessary to stabilize this structural form of the compound. The standard Gibbs energies of formation of $SrIrO_3$, Sr_2IrO_4 and Sr_4IrO_6 have been determined in the temperature range from 975 to 1400 K using solid-state cells with (Y_2O_3) ZrO_2 as the electrolyte and pure oxygen gas at a pressure of 0.1 MPa as the reference electrode. For the design of appropriate working electrodes, phase relations in the ternary system Sr–Ir–O were investigated at 1350 K. The only stable oxide detected along the binary Ir–O was IrO_2. Three ternary oxides, $SrIrO_3$, Sr_2IrO_4 and Sr_4IrO_6, compositions of which fall on the join SrO–IrO_2, were found to be stable. Each of the oxides coexisted with pure metal Ir. Therefore, three working electrodes were prepared consisting of mixtures of $Ir + SrO + Sr_4IrO_6$, $Ir + Sr_4IrO_6 + Sr_2IrO_4$, and $Ir + Sr_2IrO_4 + SrIrO_3$. These mixtures unambiguously define unique oxygen chemical potentials under isothermal and isobaric conditions. Used for the measurements was a novel apparatus, in which a buffer electrode was introduced between reference and working electrodes to absorb the electrochemical flux of oxygen through the solid electrolyte. The buffer electrode prevented polarization of the measuring electrode and ensured accurate data. The standard Gibbs energies of formation of the compounds, obtained from the e.m.f. of the cells, can be represented by the following equations:

$$SrIrO_3: \Delta G^{o}_{f\,(ox)}/\mathrm{J/mol} = -58{,}860 - 1.23T\ (\pm 650)$$

$$Sr_2IrO_4: \Delta G^{o}_{f\,(ox)}/\mathrm{J\ mol^{-1}} = -82{,}315 - 2.86T$$

$$Sr_4IrO_6: \Delta G^{o}_{f\,(ox)}/\mathrm{J\ mol^{-1}} = -84{,}690 - 6.78T$$

where $\Delta G^{o}_{f(ox)}$ represents the standard Gibbs energy of formation of the ternary compound from its component binary oxides SrO and IrO_2. Based on the thermodynamic information, chemical potential diagrams for the system Sr–Ir–O were developed.

No compounds have been reported in the Ir^{2+}-containing system of SrO–IrO, in the Ir^{3+}-containing system of SrO–Ir_2O_3, or in the Ir^{2+}–Ir^{3+}-containing system of SrO–Ir_3O_4.

TABLE 13.20

No.	Site notation	Atom	Multiplicity	Wyckoff	Site symmetry	x	y	z	Occupancy
1	Ir	Ir	16	c	.-3m	0	0	0	1.0
2	Sr	Sr	8	b	-43m	3/8	3/8	3/8	1.0

In the Ir^{4+}-containing system of $SrO–IrO_2$, $SrIrO_3$ has been found to be a non-Fermi liquid metal near a FM instability, as characterized by the following properties:

(1) small ordered moment but no evidence for long-range order down to 1.7 K;
(2) strongly enhanced magnetic susceptibility that diverges as $T^{-\gamma}$ at low temperatures with $1/2 < \gamma < 1$, depending on the applied field;
(3) heat capacity $C(T,H) \sim -T \log T$ that is readily amplified by low applied fields;
(4) a strikingly large Wilson ratio at $T < 4$ K; and
(5) a $T^{3/2}$ dependence of electrical resistivity over the range $1.7 < T < 120$ K.

A phase diagram based on such data implied that $SrIrO_3$ is a rare example of a stoichiometric oxide compound that exhibits non-Fermi liquid behavior near a quantum critical point ($T = 0$ and $\mu_0 H = 0.23$ T). However, the phase diagram was never published in the open literature.

Single crystals with the composition $Sr_5Ir_3O_{11}$ were found to grow in the system $SrO–IrO_2$. A single-crystal structure determination [tetragonal, space group $I4/mmm$, with $a = 3.890(1)$ and $c = 16.890$ Å, and $R = 0.050$] revealed alternate stacking of single and double IrO_6 PV layers interleaved with SrO layers along the c-axis. Although the refined metal–oxygen distances were quite reasonable, the thermal parameters of one "heavy" atom (iridium) and one "light" atom (oxygen) were non-positive definite. Careful examination of Weissenberg and transmission electron microscopy photographs showed that the single crystals actually contained random distributions of single and double IrO_6 PV layers arising from the intergrowth of Sr_2IrO_24 and $Sr_3Ir_2O_7$ phases.

Single crystals of $Sr_3Ir_2O_7$ were grown for the first time by the $SrCl_2$ flux method using SrO_2 and IrO_2 in a sealed Pt tube under ambient pressure. The compound crystallizes in a tetragonal unit cell [$a = 3.896$ and $c = 10.585$ Å] with space group $I4/mmm$ (No. 139) and $Z = 2$. The crystal structure was solved by means of single-crystal XRD and refined to $R = 0.014$. The structural refinement showed that the IrO_6 octahedra are rotated about the c-axis by about 12°, similar to the rotational distortion recently found in Sr_2IrO_4. However, unlike in Sr_2IrO_4, the IrO_6 rotations in $Sr_3Ir_2O_7$ are not correlated, hence no superlattice reflections appear.

The electronic structures of the 5d Ruddlesden–Popper series $Sr_{n+1}Ir_nO_{3n+1}$ ($n = 1$, 2, and ∞) were studied using optical spectroscopy and first-principles calculations. These included Sr_2IrO_4, $Sr_3Ir_2O_7$ and $SrIrO_3$. As 5d orbitals are spatially more extended than 3d or 4d orbitals, it has been widely accepted that correlation effects are minimal in 5d compounds. However, we observed a bandwidth-controlled transition from a Mott insulator to a metal as we increased n. In addition, the artificially synthesized PV $SrIrO_3$ showed a very large mass enhancement of about 6, indicating that it was in a correlated metallic state. Sr_2IrO_4 should be occupied by five t_{2g} electrons. The large SO coupling can split the degenerate t_{2g} orbitals into $J_{\text{eff},1/2}$ and $J_{\text{eff},3/2}$ bands. The $J_{\text{eff},1/2}$ bands can be very narrow due to a decreased hopping integral caused by the isotropic orbital and mixed spin characters. Bulk $SrIrO_3$ has a hexagonal crystal structure at room temperature and atmospheric pressure. It transforms to the PV structure only at a higher pressure and temperature. The structure of the atmospheric pressure form of $SrIrO_3$ has been shown to be a monoclinic distortion of the hexagonal $BaTiO_3$ structure ($a = 5.604$ Å, $b = 9.618$ Å, $c = 14.172$ Å, $\beta = 93.26°$). The cell dimensions have been studied to 1000 °C and the coefficients of thermal expansion given. The structure transforms at 40 kbar and 1000 °C to an orthorhombic PV ($a = 562$ Å, $b = 5.583$ Å, $c = 7.892$ Å) with a 3% decrease in volume. This high-pressure phase only retransforms slowly at atmospheric pressure and 1200 °C and exhibits metallic conductivity and Pauli paramagnetism.

Schematic band diagrams of 5d $Sr_{n+1}Ir_nO_{3n+1}$ compounds, which are well described by the effective total angular moment J_{eff} states due to strong spin-orbit coupling are shown as follows: (a) Mott insulator, Sr_2IrO_4, (b) barely insulator, $Sr_3Ir_2O_7$, and (c) correlated metal, $SrIrO_3$. E_F represents the Fermi level and the arrow indicates the direction for the bandwidth W increase.

Sr_2IrO_4 has the symmetry of space group $I\,4_1/acd$ and lattice parameters $a = 5.4994$ and $c = 25.7841$ Å. The unit cells of the two compounds are related to one another by the transformation matrix (1, −1, 0/1, 1, 0/0, 0, 2). The main difference between the two structures is that the MO_6 octahedra (M = Ru, Ir) have a regular, undistorted configuration in the ruthenium compound, while they are tilted by about 11° around the c-axis of the unit cell in the iridium compound. The oxygen atoms of the IrO_2 layers were found to be disordered over two sets of positions x, x, 1/4 with $x = 1/4 \pm \delta$. This means that the IrO_6 octahedra assume two configurations and, on a local level, their relative orientation does not obey the symmetry requirements of space group $I4_1/acd$ in all cases. The MO_6 octahedra are elongated along the c-axis, and this distortion is more pronounced in Sr_2RuO_4 than in Sr_2IrO_4. The coordination of the strontium atoms is ninefold in both compounds. Because of the tilting of the IrO_6 octahedra, however, the coordination polyhedra are different in the two cases. No phase transitions have been observed down to 10 K in either compound.

The magnetic structuring of Sr_2IrO_4 is shown in Fig. 13.52.

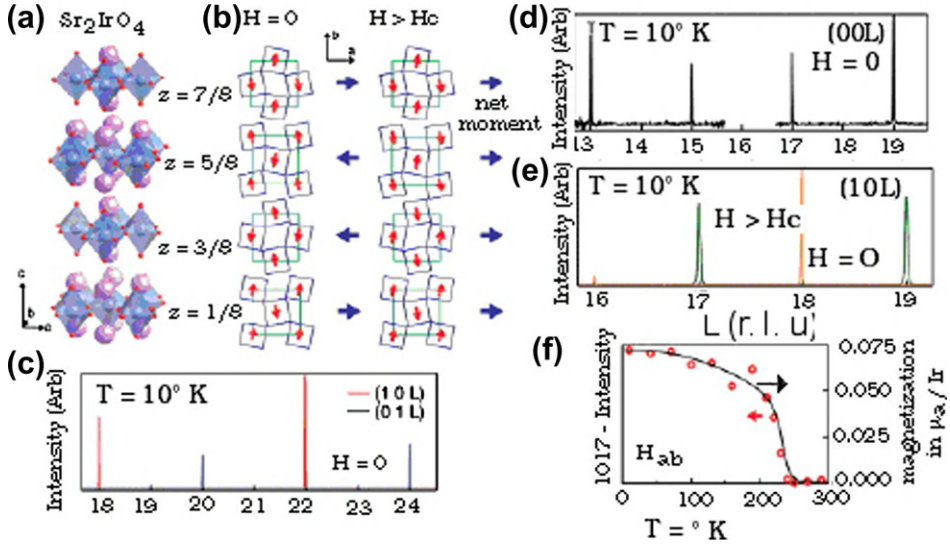

FIGURE 13.52

The following describes these factors:

Magnetic ordering pattern of Sr_2IrO_4: (**a**) Layered crystal structure of Sr_2IrO_4, consisting of a tetragonal unit cell (space group $I4_1/acd$) with lattice parameters $a \approx 5.5$ Å and $c \approx 26$ Å. The blue, red, and purple circles represent Ir, O, and Sr atoms, respectively. (**b**) Canted AFM ordering pattern of $J_{\text{eff}} = 1/2$ moments (arrows) within IrO_2 planes and their stacking pattern along the *c*-axis in zero field and in the weakly FM state, determined from the X-ray data shown in (C) to (E). (**c** and **d**) L-scan profile of magnetic XRD ($\lambda = 1.1$ Å) along the (1 0 L) and (0 1 L) direction (C) and the (0 0 L) direction (D) at 10 K in zero field. The huge fundamental Bragg peak at (0 0 16) and its background were removed in (D), r.l.u., reciprocal lattice unit. (**e**) L-scan of magnetic XRD ($\lambda = 1.1$ Å) along the (1 0 L) direction at 10 K in zero field and in the in-plane magnetic field of ≈ 0.3 T parallel to the plane. (**f**) The temperature dependence of the intensity of the magnetic (1 0 19) peak (red circles) in the in-plane magnetic field $H \approx 0.3$ T. The temperature-dependent magnetization in the in-plane field of 0.5 T is shown by the solid line.

An extremely damage-robust $SrRuO_3/IrO_2$ top electrode (TE) FeRAM, prepared with a Cu BEOL process, was demonstrated for the first time as a promising device for 130 nm CMOS embedded memory. The ferroelectric capacitor with a $SrRuO_3/IrO_2$ TE showed no degradation during the Cu metallization (used to suppress the oxygen and lead vacancies at theTE interface). Switching charge (Qsw) of 40 $\mu C/cm^2$ was achieved for $0.45 \times 0.45\ \mu m^2$ TE size capacitor. The opposite state polarization margin of 90% was retained against imprint at 70 h and 150 °C bake. This high-reliable capacitor, with a large Q_{sw} and a small bit line capacitance of "chain" structure, increased the signal window drastically. A signal window of 730 mV at 1.8 V operation voltage after a three-level Cu metallization was achieved. This technology makes possible future 130 nm embedded FeRAM and other devices beyond.

No compounds have been discovered in the Ir^{5+}-containing system of $SrO–Ir_2O_5$, or in the Ir^{6+}-containing system of $SrO–IrO_3$.

Strontium iridate compounds are not offered for sale commercially, nor have any CAS numbers been issued.

13.3.5. Barium Iridium Compounds

Barium metal does not form any intermetallic compounds with iridium.

No compounds have been discovered in the Ir^{2+}-containing system of BaO–IrO, in the Ir^{3+}-containing system of $BaO–Ir_2O_3$, in the Ir^{2+}–Ir^{3+}-containing system of $BaO–Ir_3O_4$, in the Ir^{5+}-containing system of $BaO–Ir_2O_5$, or in the Ir^{6+}-containing system of $BaO–IrO_3$.

In the Ir^{4+}-containing system of $BaO–IrO_2$, the high-pressure and high-temperature sequence of the Ruddlesden–Popper type of $BaIrO_3$ layered compounds have been studied. The structures have the general form shown in Fig. 13.53.

The high-pressure sequence of the PV polytypes of $BaIrO_3$ has been investigated in the pressure range up to 10 GPa. At ambient pressure, the so-called "9R" polytype has been prepared by solid-state reaction and slow cooling in air to yield an almost fully oxygen-stoichiometric $BaIrO_{2.96}$ composition. The crystal structure has been refined from XRD data in the monoclinic $C2/m$ space group with $a = 10.0046$ Å, $b = 5.75362$ Å, $c = 15.1839$ Å, $\beta = 103.27°$; it contains trimers of face-sharing octahedra

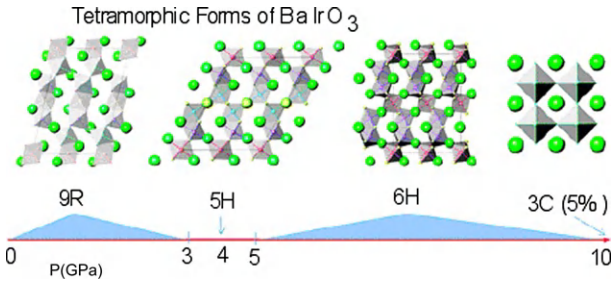

FIGURE 13.53

(or Ir_3O_{12} trioctahedra) that are linked by their vertices to form columns parallel to the *c*-axis with a stacking of layers of corner-sharing (c) and face-sharing (h) IrO_6 octahedra along the sequence hhchhc. This structure is stable up to 3 GPa. At 4 GPa a new 5H polytype of $BaIrO_3$ has been stabilized as a pure phase. The crystal structure has been solved by ab initio procedures from powder XRD data. It is monoclinic with $a = 9.9511$ Å, $b = 5.7503$ Å, $c = 13.71003$ Å, $\beta = 118.404°$, and it was refined in the $C2/m$ space group from NPD data collected at room temperature. This polytype can be described as a stacking of IrO_6 octahedra along the sequence hchcc. The structure contains chains of double dimer units of face-sharing octahedra; the twin dimers are connected to single layers of vertex-sharing octahedra, forming infinite chains along *c*. This is a unique stacking that, with this repetition length, has never been described before among the hexagonal polytypes of ABO_3 PVs. The 5H polytype is stable in a narrow pressure range. At 5 GPa, the 6H structure is formed and is stable up to 10 GPa. The 6H-$BaIrO_3$ polytype is monoclinic, space group $C2/c$, with $a = 5.7483$ Å, $b = 9.9390$ Å, $c = 14.3582$ Å, $\beta = 91.319°$. The structure consists of dimers of face-sharing octahedra separated by single corner-sharing octahedra, showing the sequence hcchcc along the *c*-axis. At 10 GPa the cubic 3C perovskite structure could be identified as a minority phase, with $a = 4.0611$ Å, defined in the *Pmm* space group. The uncertain stability of the 5H polytype, as well as the novel pressure sequence displayed by $BaIrO_3$ (that is distinct from the classical sequence 9R-4H-6H-3C exhibited by many transition metal oxides, for instance $BaRuO_3$) is a result of the commanding stability of the "9R" ambient pressure structure, which is reinforced by a strong Ir–Ir bond across the octahedral faces. The Ir–Ir Coulombic repulsion across shared faces destabilizes the 4H polytype relative to the 6H phase to allow stabilization of the hybrid 5H polytype in a narrow pressure range.

In another study, the 6M-$BaIrO_3$ with the distorted hexagonal $BaTiO_3$ structure was synthesized by high-pressure sintering. Through Rietveld refinement of the powder XRD data, the lattice parameters $a = 5.7459$ Å, $b = 9.9289$ Å, $c = 14.3433$ Å, and $\beta = 91.340°$ were obtained (Fig. 13.54).

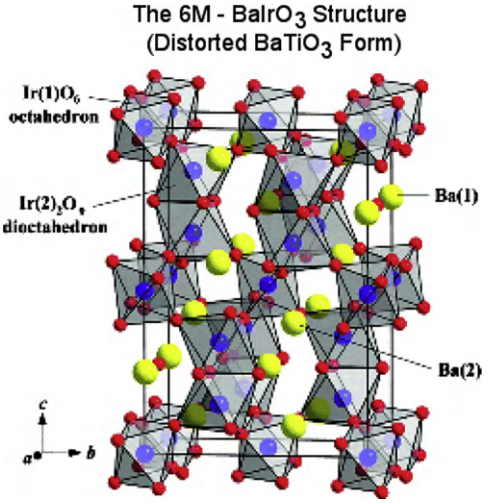

FIGURE 13.54

In the Ir_2O_9 dioctahedron, the average Ir–O distance and direct Ir–Ir distance were equal to 2.067 and 2.719 Å, respectively. The temperature dependence of electrical resistivity shows that the 6M-$BaIrO_3$ is a new metallic iridate. It is an abnormal metal, being deviated from the Fermi liquid behavior, following a linear relationship of μ versus T below 20 K. Both magnetic susceptibility and specific heat data indicate that it is an exchange-enhanced Pauli paramagnet, because of the electron–electron correlation effect.

The crystal structure of 6M-$BaIrO_3$ is monoclinic (space group $C2/m$), and contains zigzag chains of the Ir_3O_{12} trimer with the face-shared IrO_6 octahedra along the *c*-axis. Each trimer is linked to form a corner-shared network along the *c*-axis, and a 2D network perpendicular to the *c*-axis as well. $BaIrO_3$ single crystals exhibit a giant nonlinear conduction as a function of pulsed external current, and shows a negative derivative resistance from 2 to 6 A/cm^2 at 4.2 K. This structure belongs to a new class of collective excitation in solids that are associated with the giant nonlinear conduction.

At ambient pressure, $BaIrO_3$ crystallizes in the distorted 9R-$BaRuO_3$ structure, with the space group $C2/m$, due to a large tolerant factor (about 1.051) as calculated from the ion radii in Shannon Table. $BaIrO_3$ is a weak ferromagnet, with the Curie temperature T_C about 183 K. It is the first known ferromagnet that contains a 5d transition metal cation in a ternary oxide, which originates from spin polarization of Ir cations rather than spin canting. The polycrystalline sample of $BaIrO_3$ is a semiconductor. The obvious kink in the T curve corresponds to the Curie temperature T_C. Below T_C, the electrical resistivity increases more rapidly with the decreasing temperature. For the single crystal,

the temperature dependence of resistivity in the *ab*-plane is similar with that of the polycrystalline $BaIrO_3$, but the electrical resistivity at low temperature is much smaller than the corresponding value of polycrystal at the same temperature. However, along the *c*-axis, that is the high conductivity axis.

$BaIrO_3$ transforms to a more insulating phase below T_C, and then transforms to metallic and insulating states at 80 K and 26 K, respectively, which is different from the *p*-*T* curve of polycrystal. Polycrystalline single-phase samples of $BaIrO_{2.73}$ and $BaIrO_{2.96}$ have been successfully prepared. Superconducting quantum interference device data indicate the magnetic susceptibility of both samples is low and only weakly temperature dependent in the range $180\,K < T < 296\,K$, demonstrating the presence of delocalized electrons. The materials exhibit high electrical conductivity that is dependent on the oxygen stoichiometry. In addition, magnetic susceptibility data for both compositions show that a transition to a ferromagnetically ordered state occurs at 180 K. It is proposed that this ferromagnetism arises from a difference in the relative populations of the α and β spin bands and not from localized electrons.

The 5d-electron-based $BaIrO_3$ is a nonmetallic weak ferromagnet with a Curie temperature at $T_C = 175\,K$. Its largely extended orbitals generate strong electron–lattice coupling, and magnetism and electronic structure are thus critically linked to the lattice degree of freedom. Here we report results of our transport and magnetic study on slightly Sr-doped $BaIrO_3$. It is found that dilute Sr doping drastically suppresses T_C, and instantaneously leads to a nonmetal–metal transition at high temperatures. All results highlight the instability of the ground state and the subtle relation between magnetic ordering and electron mobility. It is clear that $BaIrO_3$ along with very few other systems represents a class of materials where the magnetic and transport properties can effectively be tuned by slight alterations in lattice parameters.

$BaIrO_3$ shares a number of unique features with other iridates such as the layered Sr_2IrO_4 and $Sr_3Ir_2O_7$. They are all characteristically insulating with unusual temperature dependence of resistivity and negative differential resistivity or non-ohmic behavior. These iridates are all weakly FM with high-magnetic ordering temperatures ($T_C = 240\,K$ and 285 K for Sr_2IrO_4 and $Sr_3Ir_2O_7$, respectively) and yet only a fraction of the expected ordered moment ($\mu_S = 0.14\,\mu bar/Ir$ and $0.04\,\mu bar/Ir$ for Sr_2IrO_4 and $Sr_3Ir_2O_7$, respectively). In addition, all these materials often show a simultaneous transition in magnetization and resistivity, but none displays sensitivity of T_C to high magnetic fields and detectable magnetoresistance near and below T_C except at very low temperatures. It is striking that all their counterparts to the ruthenates ($BaRuO_3$, Sr_2RuO_4, and $Sr_3Ru_2O_7$) are metallic or even superconducting and that all these ruthenates are less structurally distorted. Clearly, the lattice degree of freedom plays a critical role in determining the ground state in these systems with extended electron orbitals.

The 5M $BaIrO_3$ variation, which is intervenient in the 9M and 6M forms, was synthesized under high pressure and high temperature, and the physical properties were obtained. The measurement of low-temperature electrical resistivity shows that the 5M-$BaIrO_3$ is a Fermi liquid metal, because of the linear relationship of p versus T^2 at low temperature. The relationships of magnetic susceptibility versus temperature indicate that the 5M $BaIrO_3$ staked variety is a weak ferromagnet, with the Curie temperature T_C about 54.3 K. By calculation of the low-temperature specific heat data, using the Wilson ratio R_W of 1.67 and Stoner enhancement factor *S* of 2.8, a modest electron-electron correlation effect in the 5M-$BaIrO_3$ arrangement was seen.

No barium iridates are offered for sale commercially nor have any CAS numbers been issued.

13.3.6. Radium Iridium Compounds

Although it is likely that radium forms the same type of compounds with iridium oxides, no description of any type of iridate compounds has appeared in the technical literature. The most likely stable compound is expected to be $RaIrO_3$. The lack of interest from Industry and Academia probably stems from the high cost of Ir metal and the radioactivity of ^{226}Ra.

CHAPTER

14

Group 10 (Ni, Pd and Pt) Alkaline Earth Compounds

OUTLINE

14.1. Alkaline Earth Nickel Compounds 1005
14.1.1. Beryllium Nickel Compounds 1005
14.1.2. Magnesium Nickel Compounds 1007
14.1.3. Calcium Nickel Compounds 1009
14.1.4. Strontium Nickel Compounds 1013
14.1.5. Barium Nickel Compounds 1015
14.1.6. Radium Nickel Compounds 1019

14.2. Alkaline Earth Palladium Compounds 1019
14.2.1. Beryllium Palladium Compounds 1019
14.2.2. Magnesium Palladium Compounds 1020
14.2.3. Calcium Palladium Compounds 1022
14.2.4. Strontium Palladium Compounds 1027
14.2.5. Barium Palladium Compounds 1029
14.2.6. Radium Palladium Compounds 1031

14.3. Alkaline Earth Platinum Compounds 1031
14.3.1. Beryllium Platinum Compounds 1032
14.3.2. Magnesium Platinum Compounds 1032
14.3.3. Calcium Platinum Compounds 1035
14.3.4. Strontium Platinum Compounds 1040
14.3.5. Barium Platinum Compounds 1044
14.3.6. Radium Platinum Compounds 1048

14.1. ALKALINE EARTH NICKEL COMPOUNDS

In general, only the Nickel oxides, NiO and Ni_2O_3, form compounds with the alkaline earths. The NiO_2 compound does not appear in most systems.

In the Ae–Ni–O system, the electronic structure of various nickel oxides with nickel valence varying from 1+ to 3+ was investigated with the aim to find similarities and differences to the isoelectronic cuprates. Only if the Ni ions are forced into a planar coordination with the O ions, can a $S = 1/2$ magnetic insulator be realized with the difficult Ni^{1+} oxidation state and possibly doped with low-spin ($S = 0$) Ni^{2+} holes directly analogous to the superconducting cuprates? The more common Ni^{3+} oxidation state cannot be used to make a parent magnetic insulator as it forms rather as localized ($S = 1$) Ni^{2+} embedded in a sea of itinerant O holes. Strong coupling of these holes to the localized spins via 2p-3d hybridization leads to a heavy fermion system with a large Kondo temperature, which was confirmed experimentally for $LaNiO_3$. In both nickelates and cuprates the antibonding e_g shell of the 3d complex is partly occupied with three electrons in Ni^{1+} and Cu^{2+}, two electrons in Ni^{2+} and Cu^{3+}, and one electron in Ni^{3+} and Cu^{4+} (if it exists). The results for a planar coordinated Ni^{3+} oxidation state show that even in this case the Jahn–Teller paradigm does not work and the Fermi energy enters the nonbonding O 2p orbital, a configuration which is not a Jahn–Teller split 3d ion. It was concluded that nickelates cannot be used in a manner directly analogous to the superconducting cuprates. Of the various nickelate compounds possible, it is the perovskite structures that are the most stable (Fig. 14.1(A)).

14.1.1. Beryllium Nickel Compounds

Beryllium metal forms a series of intermetallic compounds with Ni^0 metal. The phase diagram is shown in Fig. 14.1(B).

Encyclopedia of the Alkaline Earth Compounds
http://dx.doi.org/10.1016/B978-0-444-59550-8.00014-4

Copyright © 2013 Elsevier B.V. All rights reserved.

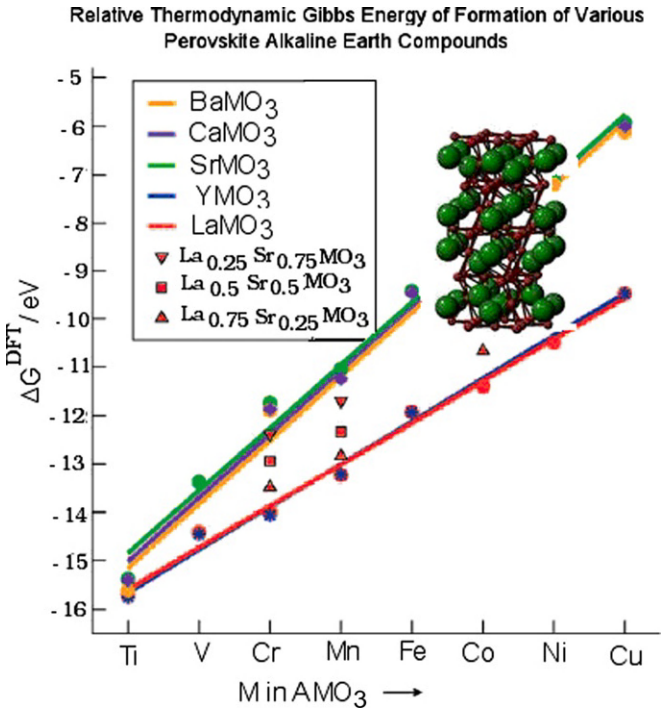
Relative Thermodynamic Gibbs Energy of Formation of Various Perovskite Alkaline Earth Compounds
BaMO3
CaMO3
SrMO3
YMO3
LaMO3
La0.25 Sr0.75MO3
La0.5 Sr0.5 MO3
La0.75 Sr0.25 MO3
ΔG DFT / eV
- 5
- 6
- 7
- 8
- 9
- 10
- 11
- 12
- 13
- 14
- 15
- 16
Ti
V
Cr
Mn
Fe
Co
Ni
Cu
M in AMO3 ⟶

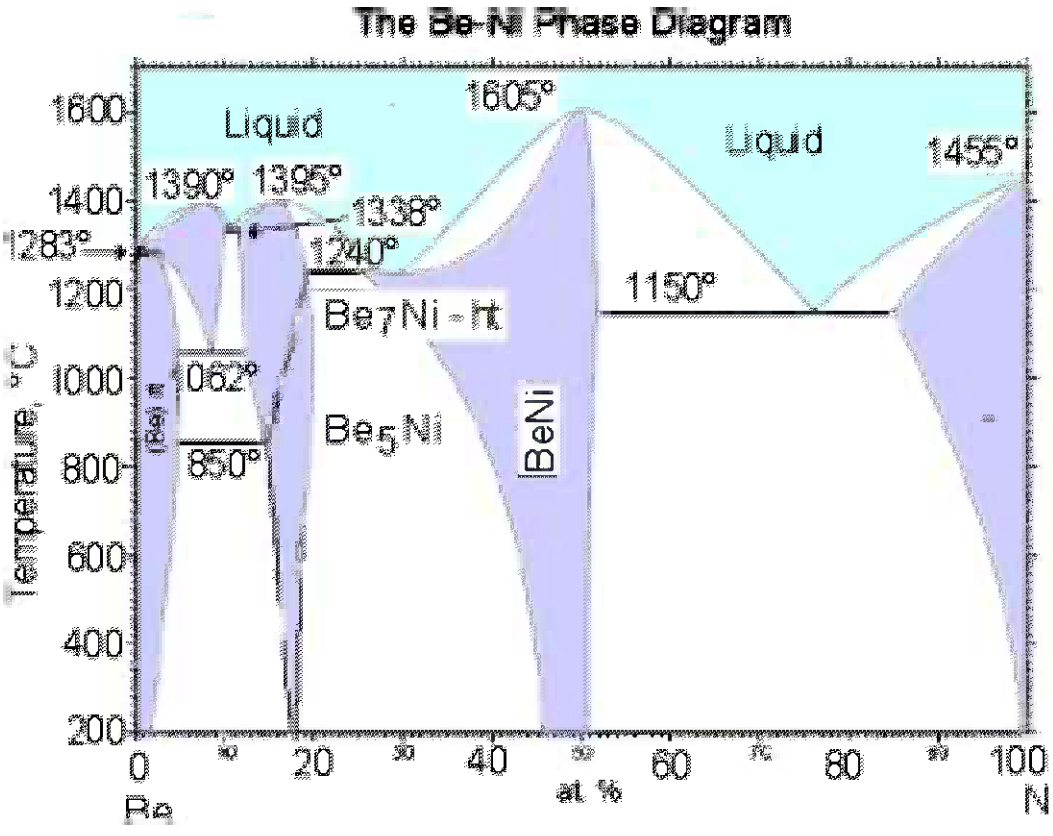
The Be-Ni Phase Diagram
Liquid
1605°
Liquid
1455°
1390°
1395°
1338°
1283°
1240°
1150°
Be7Ni - ht
1062°
Be5Ni
850°
BeNi
1600
1400
1200
1000
800
600
400
200
Temperature, °C
0
20
40
60
80
100
at %
Be
N

FIGURE 14.1

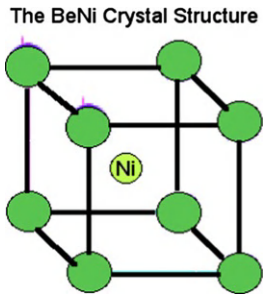

FIGURE 14.2

The compound, BeNi, has the structure form where the Ni atom in the body-centered position of a cubic lattice (Fig. 14.2).

Cell parameters of BeNi are: $a = b = c = 2.604$ Å, $\alpha = \beta = \gamma = 90°$, cell volume $= 17.66$ Å^3, $Z = 1$. Cell occupancy is shown in Table 14.1.

The compound, Be_7Ni, is known but its structure has not yet been finalized. Cell parameters of the cubic lattice are: $a = b = c = 6.6026$ Å, $\alpha = \beta = \gamma = 109.471°$, cell volume $= 221.58$ Å^3, $Z = 2$. It is a high-temperature form.

The compound, $Be_{21}Ni_7$ is also known with the cell parameters of: $a = b = c = 10.8018$ Å^3, $\alpha = \beta = \gamma = 60$, cell volume $= 891.20$ Å^3, $Z = 2$. Its structure has not been finalized. It also is a high-temperature form.

The compound, $BeNi_3$, has also been discovered with cell parameters of: $a = 2.578$ Å, $b = 3.647$ Å, $c = 3.914$ Å, $\alpha = \beta = \gamma = 90°$, cell volume $= 36.80$ Å^3, $Z = 1$. Its exact structure is not available. No other intermetallic compounds are known.

In the beryllium oxy-nickelate systems, i.e. Be–Ni–O, no compounds are known. This includes possible combinations of BeO such as: BeO–NiO, BeO–Ni_2O_3, BeO–Ni_3O_4, BeO–NiO_2, and BeO–Ni_2O_5.

Beryllium nickelate compounds are not offered for sale commercially and no CAS numbers have been assigned to date.

14.1.2. Magnesium Nickel Compounds

Magnesium metal forms a few intermetallic compounds with Ni metal. The phase diagram is shown in Fig. 14.3.

The compound Mg_2Ni is known. It has the structure shown as follows. The cell parameters of Mg_2Ni are:

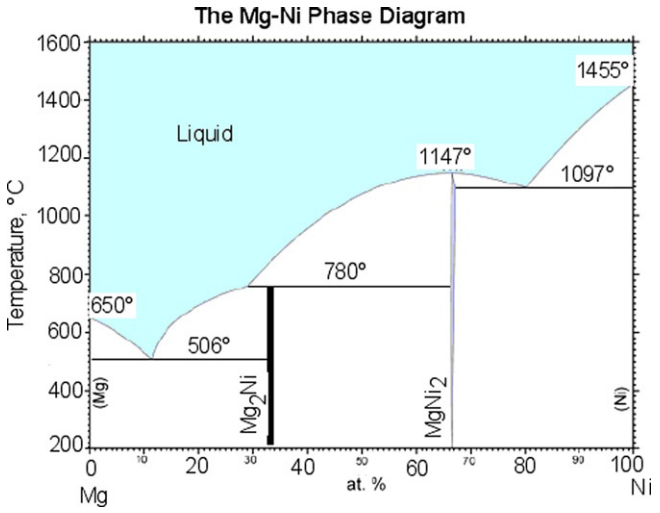

FIGURE 14.3

$a = b = 5.2117$ Å, $c = 13.2538$ Å. $\alpha = \beta = 90°$, $\gamma = 120°$, cell volume $= 311.77$ Å^3, $Z = 6$ (Fig. 14.4).

Cell occupancy is shown in Table 14.2.

The compound, Mg_2Ni is also known. Its structure has the form shown as follows in Fig. 14.5.

Cell parameters are: $a = b = 4.825$ Å, $c = 15.294$ Å, $\alpha = \beta = \gamma = 90°$, cell volume $= 318.35$ Å^3, $Z = 8$. Cell occupancy is shown in Table 14.3.

No other intermetallic compounds are known.

MgO forms a limited number of oxy-nickelate compounds. In the Ni^{2+}-containing system of MgO–NiO, the compound, $MgNiO_2$, has been mentioned in a number of papers. If a bed of nano-sized Ni metal particles is deposited upon a layer of MgO, the composite catalyzes certain organic compounds like CH_4 (or other aliphatics) to form a synthesis gas. When the catalyst bed is heated to a high temperature, the formation of $MgNiO_2$ has been observed. It is not stable at room temperature but its structure has been determined as: $MgNiO_2$ (cubic system, spatial group $Fm3m$, parameter $a = 4.1922$ Å). Its symmetry and unit cell parameter are essentially the same as for those of MgO.

The compound, $MgNi_2O_3$, has been synthesized by an oxalate method in which oxalic acid is added in excess to a solution of the chlorides of the two metals. The thermal decomposition processes taking place in the solid-state mixture of $NiC_2O_4 \cdot 2H_2O$–$MgC_2O_4 \cdot 2H_2O$

TABLE 14.1

No.	Site notation	Atom	Multiplicity	Wyckoff	Site symmetry	x	y	z	Occupancy
1	Ni	Ni	1	b	m-3m	1/2	1/2	1/2	1.0
2	Be	Be	1	a	m-3m	0	0	0	1.0

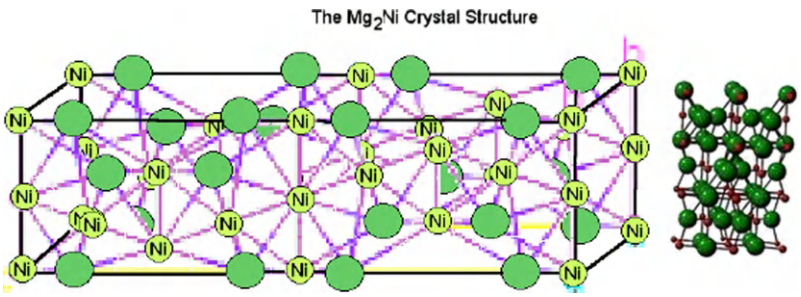

FIGURE 14.4

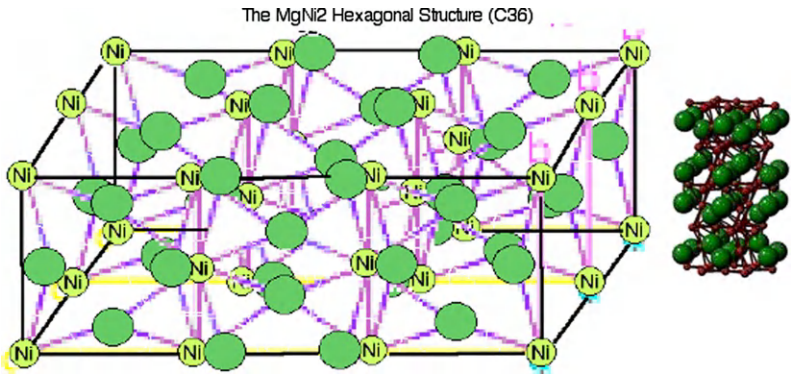

FIGURE 14.5

TABLE 14.2

No.	Site notation	Atom	Multiplicity	Wyckoff	Site symmetry	*x*	*y*	*z*	Occupancy
1	Mg1	Mg	6	j	..2	0.162	0.3240	1/2	1.0
2	Mg2	Mg	6	f	2..	1/2	0	0.381	1.0
3	Ni1	Ni	3	c	222	1/2	0	0	1.0
4	Ni2	Ni	3	a	222	0	0	0	1.0

TABLE 14.3

No.	Site notation	Atom	Multiplicity	Wyckoff	Site symmetry	*x*	*y*	*z*	Occupancy
1	Ni1	Ni	6	h	mm2	0.164	0.3286	1/4	1.0
2	Ni2	Ni	6	g	.2/m.	1/2	0	0	1.0
3	Ni3	Ni	4	f	3m.	1/3	2/3	0.125	1.0
4	Mg1	Mg	4	f	3m.	1/3	2/3	0.656	1.0
5	Mg2	Mg	4	e	3m.	0	0	0.094	1.0

(2:1 mole ratio) have been investigated in air using thermogravimetry or differential-thermogravimetry (TG-DTG), differential scanning calorimeter (DSC) and XRD techniques. The decomposition proceeded through a four well-defined steps while TG curves closely corresponded to the theoretical mass loss. The result of XRD showed that well-crystallized $MgNi_2O_3$ formed in the sample calcined at 600 °C for 2 h. The activation energies for the decompositions of NiC_2O_4 and MgC_2O_4 were calculated through the Ozawa and

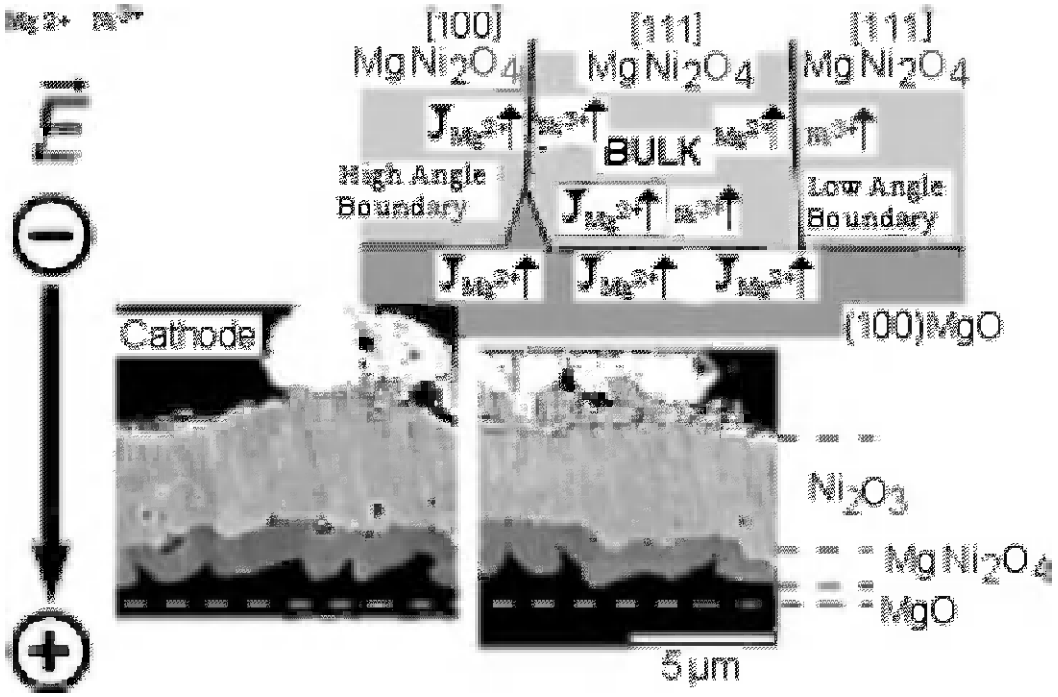

FIGURE 14.6

Kissinger–Akahira–Sunose (KAS) methods, and the possible conversion functions have been estimated through the comparative method. No further data concerning this compound are available and the crystal structure remains unknown.

In the Ni^{3+}-containing system of $MgO–Ni_2O_3$, the compound, $MgNi_2O_4$, has been synthesized. Under working conditions, certain ceramic materials like $MgNi_2O_4$ are often exposed to high electrical fields in addition to high temperatures. For this reason, the investigation of the reaction kinetics and the morphological evolution of the moving interfaces of a spinel-forming solid-state reaction under the influence of an external electric field was conducted. A model, based on linear transport theory and defect thermodynamics was used to analyze the results. This is shown in Fig. 14.6.

Compared to a reference reaction without external electric field, the reaction rate was found to be strongly enhanced by an external field and the morphology of the product layer was significantly changed. Systematic kinetic studies confirmed a linear law with a constant growth rate for the electric field-driven spinel formation. The role of grain boundaries as fast diffusion paths was highly accentuated. A relationship between large angle grain boundaries in the product phase and the local reaction kinetics was pointed out. An analysis of the reaction rate indicates an unusually high transference for the trivalent ions compared to the divalent ions in the grain boundaries of the spinel phase.

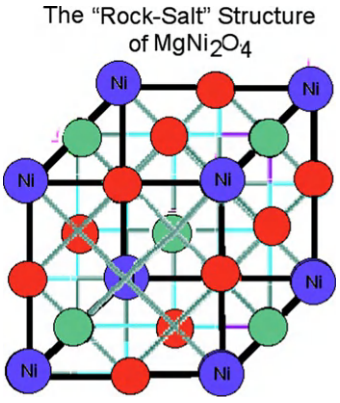

FIGURE 14.7

$MgNi_2O_4$ forms the rock salt structure as shown in the following diagram, with $a = 6.235$ Å (Fig. 14.7).

No compounds are known in the $Ni^{2+}–Ni^{3+}$-containing system of $MgO–Ni_3O_4$, in the Ni^{4+}-containing system of $MgO–NiO_2$, or in the Ni^{5+}-containing system of $MgO–Ni_2O_5$.

Magnesium nickelate compounds are not offered commercially and no CAS numbers have been issued to date.

14.1.3. Calcium Nickel Compounds

Calcium metal forms a series of intermetallic compounds with nickel metal.

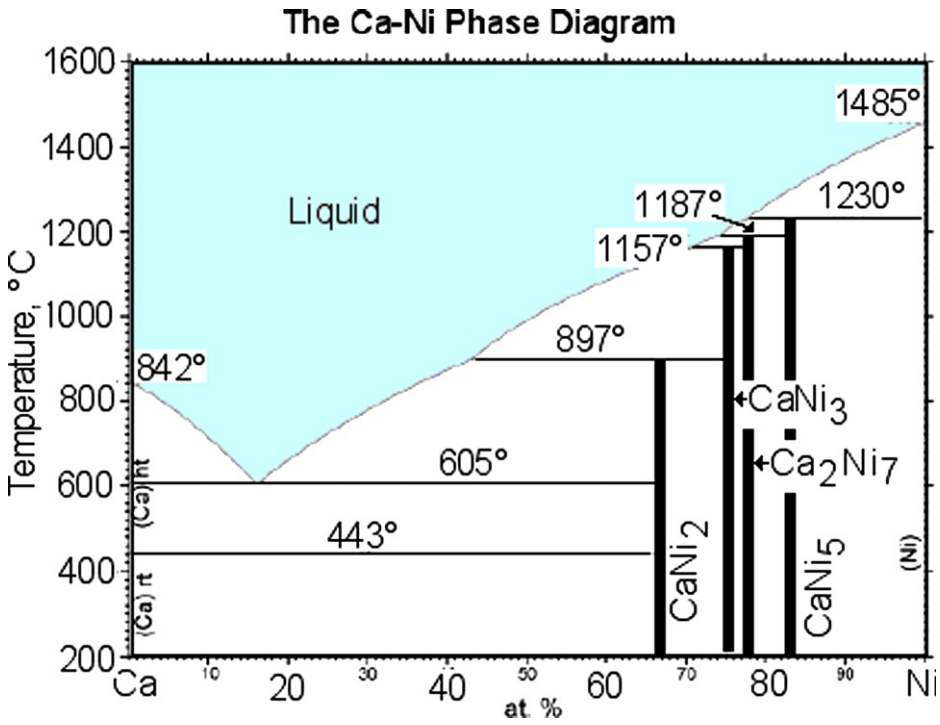

FIGURE 14.8

FIGURE 14.9

The phase diagram is shown in Fig. 14.8:

The compound, Ca_2Ni_7, has the structure shown in Fig. 14.9.

Cell parameters are: $a = b = 5.009$ Å, $c = 12.363$ Å, $\alpha = \beta = 78.31°$, $\gamma = 60°$, cell volume $= 261.18$ Å^3, $Z = 6$. Cell occupancy is shown in Table 14.4.

$CaNi_2$ has the structure shown in Fig. 14.10.

Cell parameters are: $a = b = c = 5.1272$ Å, $\alpha = \beta = \gamma = 60°$, cell volume $= 95.31$ Å^3, $Z = 6$. Cell occupancy is shown in Table 14.5.

The compound, $CaNi_3$, has the structure shown in Fig. 14.11.

Cell parameters are: $a = b = 5.032$ Å, $c = 8.5797$ Å, $\alpha = \beta = 72.954°$, $\gamma = 60°$, cell volume $= 176.90$ Å^3, $Z = 4$. Cell occupancy is shown in Table 14.6.

The compound, $CaNi_5$, has the structure shown in Fig. 14.12.

Cell parameters are: $a = 3.948$ Å, $b = c = 4.962$ Å, $\alpha = 120°$, $\beta = \gamma = 90°$, cell volume $= 84.11$ Å^3, $Z = 1$. Cell occupancy is shown in Table 14.7.

No other compounds are known. Calcium nickelides are not used in the Industry and little interest in their

TABLE 14.4

No.	Site notation	Atom	Multiplicity	Wyckoff	Site symmetry	x	y	z	Occupancy
1	Ni1	Ni	18	h	.m	0.5	0.5	0.111	1.0
2	Ni2	Ni	9	e	.2/m	1/2	0	0	1.0
3	Ca1	Ca	6	c	3m	0	0	0.055	1.0
4	Ca2	Ca	6	c	3m	0	0	0.149	1.0
5	Ni3	Ni	6	c	3m	0	0	0.278	1.0
6	Ni4	Ni	6	c	3m	0	0	0.388	1.0
7	Ni5	Ni	3	b	-3m	0	0	1/2	1.0

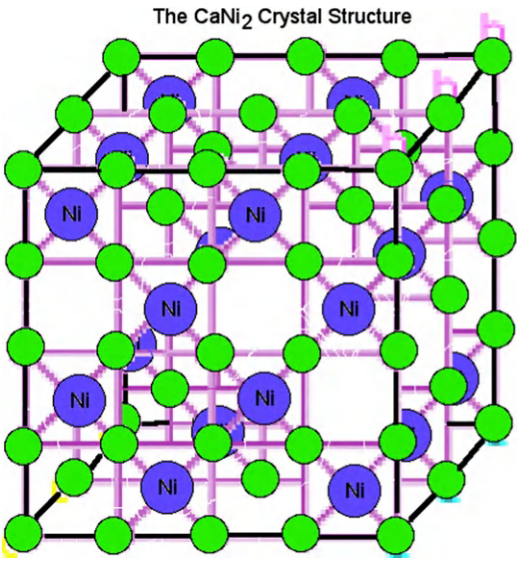

FIGURE 14.10

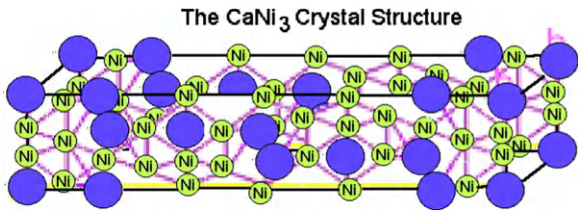

FIGURE 14.11

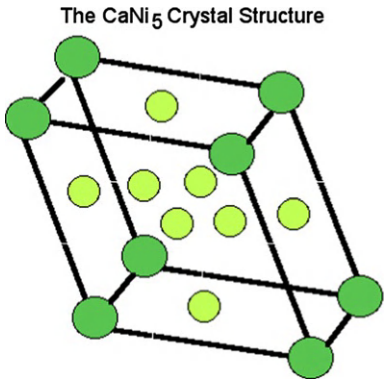

FIGURE 14.12

physical properties has been demonstrated by those in Academia. In the system, Ca–Ni–O, only a few nickelate compounds are known.

In the Ni^{2+}-containing system of CaO–NiO, $CaNiO_2$-based polycrystalline samples were prepared by a solid-state reaction and/or chemical synthesis followed by a hot-pressing and/or sintering procedure. X-ray

TABLE 14.5

No.	Site notation	Atom	Multiplicity	Wyckoff	Site symmetry	*x*	*y*	*z*	Occupancy
1	Ni	Ni	16	c	.-3m	0	0	0	1.0
2	Ca	Ca	8	b	-43m	3/8	3/8	3/8	1.0

TABLE 14.6

No.	Site notation	Atom	Multiplicity	Wyckoff	Site symmetry	*x*	*y*	*z*	Occupancy
1	Ni1	Ni	18	h	.m	0.500	0.499	0.083	1.0
2	Ca1	Ca	6	c	3m	0	0	0.141	1.0
3	Ni2	Ni	6	c	3m	0	0	0.334	1.0
4	Ni3	Ni	3	b	-3m	0	0	1/2	1.0
5	Ca2	Ca	3	a	-3m	0	0	0	1.0

TABLE 14.7

No.	Site notation	Atom	Multiplicity	Wyckoff	Site symmetry	*x*	*y*	*z*	Occupancy
1	Ni2	Ni	3	g	mmm	1/2	0	1/2	1.0
2	Ni1	Ni	2	c	-6m2	1/3	2/3	0	1.0
3	Ca	Ca	1	a	6/mmm	0	0	0	1.0

diffraction and electron microscopy analysis, and measurement of their electrical conductivity, Seebeck coefficient and thermal conductivity were carried out to determine the relative thermoelectric properties of this oxide semiconductor. $CaNi_2$ is inferior to other known thermoelectric materials.

A patent dated 2008 described a process for producing hydrogen comprising reacting at least one hydrocarbon and steam in the presence of a complex metal oxide and a steam-hydrocarbon reforming catalyst in a production step under reaction conditions sufficient to form hydrogen and a spent complex metal oxide. This was entitled: "Use of Mixtures of Calcium Oxide, CaO, and Nickel Oxide, Using NiO with Pt/ZrO".

> "Two mixtures of CaO/NiO with different metal ratios, 1:1, CaO:NiO (nominally "CaNiO2") and 2:1 CaO:NiO (nominally "Ca_2NiO_3") were prepared. Solutions of 0.50 molar (M) $Ca(NO_3)_2$ and 0.50 M $Ni(NO_3)_2$ (0.25 M for Ca_2NiO_3) were co-precipitated with a 1.0 M $NaHCO_3$ solution. The precursors were heated at 750 °C for 10 hours (12 hours for "Ca_2NiO_3") under oxygen flow. The mixtures were shown by powder x-ray diffraction to be physical mixtures of the oxides, not ternary complex metal oxides. A steam-methane reforming reaction was carried out using this 1:1 CaO:NiO mixture and 1% Pt/ZrO_2. The rates of production of hydrogen, carbon dioxide, carbon monoxide, and methane versus time on stream were given. The reaction process can be subdivided into several regions. The temperature profile of the reaction exhibited multiple exothermic and endothermic peaks. Between 10 and 30 minutes after initiation, a region of substantial production of H_2 with little production of carbon monoxide or carbon dioxide by-products was observed.
>
> The regeneration reaction of the spent nominally "$CaNiO_2$" was carried out at 700 °C under 20% oxygen/argon. The carbon dioxide production rate and the temperature changes with time on stream were recorded. In accordance with previous results, an initial exothermic reaction was observed, believed to be due to the oxidation of nickel metal to nickel oxide. This reaction yielded 41.8 kcal per/mole of nickel. This exothermic event, however, only resulted in a relatively small increase in the rate of carbon dioxide production, which quickly reverted back to the initial rate. Consequently, even after more than 8 hours of heating, there was still a substantial rate of CO_2 production ($\approx$0.035 mmol/min.), thus the said "$CaNiO_2$" was still not completely regenerated, demonstrating that this is not a practical oxide mixture for the preparation of hydrogen by the present process.
>
> Similarly, the nominally "Ca_2NiO_3" composition, a physical mixture of 2 parts calcium oxide, CaO, to one part nickel oxide, NiO, and therefore also not a ternary oxide, was also not completely regenerated by heating at 700 °C for 8 hours".

In the Ni^{3+}-containing system of $CaO–Ni_2O_3$, no compounds have been reported.

The Ni^{2+}–Ni^{3+}-containing system of $CaO–Ni_3O_4$ remains unknown.

In the Ni^{4+}-containing system of $CaO–NiO_2$, the compound, $CaNiO_3$ has been studied. Perovskite oxides (ABO_3) are generally stable and exhibit high photocatalytic activity. A series of perovskite oxides was synthesized by means of blend deposition using the nitrate of A and B as the raw materials, and using ammonia or sodium carbonate to cause precipitation. The result of activity evaluation indicates that the effect of A is low while that of B is outstanding. The activity of $CaNiO_3$ is one of the highest among those photocatalysts studied. The test result of XRD and TEM shows that the purity of $CaNiO_3$ is comparatively high and the particle shape is approximately round with a diameter in the range of 150–200 nm. The photocatalytic activity of $CaNiO_3$ and TiO_2 was compared, and showed that the activity of the two photocatalysts is equal under UV irradiation. Under sunlight, the $CaNiO_3$ activity is higher than that of TiO_2, so that that the rate of degradation of acid-red-B is 63% and 47%, respectively. In addition, the compound oxides of $CaFe_xNi_{1-x}O_3$ ($x = 0.1$–0.9) have been synthesized. Among them, the activity of $CaFe_{0.3}Ni_{0.7}O_3$ is one of the highest and under sunlight, the degradation of acid-red-B can reach 91%. Addition of Co and Ag to the $CaFe_{0.3}Ni_{0.7}O_3$ composition showed that Co produces a compound that is much lower in activity, while the activity of $CaFe_{0.3}Ni_{0.7}O_3$ was increased by the addition of Ag so that the rate of degradation of acid-red-B is 96%.

The kinetics of degradation of acid-red-B under UV was studied over $CaNiO_3$ catalyst. The reaction order was defined to be 1.4. The pre-exponential factor of the reaction was $k_o = 1.01 \times 10^7$ mol-0.4 $L_{0.4}$ min^{-1}, and the activation energy was $E_a = 35.5$ kJ/mol. The mechanism of degradation of acid-red-B was analyzed by IR and UV–VIS spectral analysis. According to these results, the double bond of nitrogen in acid-red-B degradation disappeared firstly, then the naphthalene ring was broken and finally the benzene ring was cracked. The photocatalysis is improved by adding H_2O_2 into the solution, and the activity is raised with the increase of the amount of H_2O_2. Increasing the acidity of the solution also aids in the decomposition of acid-red-B.

In another paper, a novel microwave heating method for preparation of $CaNiO_3$ as a photocatalyst material was described. The optimum preparation conditions are that the microwave power is 560 W, the microwave heating time is 30 min, the calcination temperature is 700 °C and the calcination time was 5 h. The compound was measured by X-ray diffraction. In visible light and under the conditions of simulated fuel wastewater, the photocatalytic properties of the catalyst material were studied using acid-red-B. The results show that the photocatalytic material prepared by that microwave heating has a high photocatalytic performance of degradation, and the degeneration rate of the dye may reach 98%.

No compounds in the Ni^{5+}-containing system of $CaO–Ni_2O_5$ have been documented.

Calcium–nickel compounds are not offered commercially nor are calcium nickelates. No CAS numbers have been issued.

14.1.4. Strontium Nickel Compounds

Strontium metal forms just one compound with nickel metal as shown in the following phase diagram in Fig. 14.13.

The structure of the compound, SrNi, has not been published. The structure was said to be orthorhombic with cell parameters of: $a = b = 3.332$ Å, $c = 7.009$ Å, $\alpha = \beta = 90°$, $\gamma = 120°$, cell volume = 67.39 Å^3, $Z = 4$.

No other intermetallic compounds are known.

The constitution of the SrO–NiO system was studied experimentally for the first time. Samples were prepared either from $SrCO_3$ and NiO or from $Sr(NO_3)_2$ and $Ni(NO_3)_2 \cdot 6H_2O$ and characterized by high-temperature X-ray powder diffraction, scanning electron microscopy, thermogravimetric and differential thermal analyses. In the SrO–NiO quasi-binary system an eutectic reaction: liquid (SrO + NiO) was found to occur at 1396 ± 5 °C, while the homogeneity range of terminal solid solutions is negligible. Thermodynamic calculations using the regular solution model for the liquid and rock salt-type phases were employed to predict liquidus and solidus curves. Three ternary compounds, $SrNiO_{2.5}$, $Sr_5Ni_4O_{11}$, and $Sr_9Ni_7O_{21}$ were observed in the samples prepared from nitrate solutions, but only $Sr_9Ni_7O_{21}$ was proved to be thermodynamically stable in air up to 1030 ± 6 °C. When heating in air, $SrNiO_{2.5}$ and $Sr_5Ni_4O_{11}$ were found to transform irreversibly into a mixture of $Sr_9Ni_7O_{21}$ and NiO. Isothermal section of the SrO–NiO–O subsystem, which represents phase equilibria at 950–1030 °C as well as an isobaric section of the Sr–Ni–O system in air were constructed (Fig. 14.14).

In the Ni^{2+}-containing system of SrO–NiO, single crystals of $SrNiO_2$ were prepared by high temperature and oxygen pressure. It is isotypic with $SrCuO_2$ (space group D—$Cmcm$, $a = 3.581$, $b = 16.362$, $c = 3{,}915$ Å). The relationship between $SrNiO_2$ and K_2NiF_4 type was discussed. This compound is not stable at room temperature.

The compound, Sr_2NiO_3, is much more stable in air at room temperature. Sr_2NiO_3 compounds with one-dimensional (1D) Ni–O chains have been successfully synthesized in the form of single-crystalline thin films using a combinatorial approach. The crystal structure was examined using X-ray diffraction and high-resolution TEM (see Fig. 14.15). Polarized absorption spectroscopy and third-harmonic generation

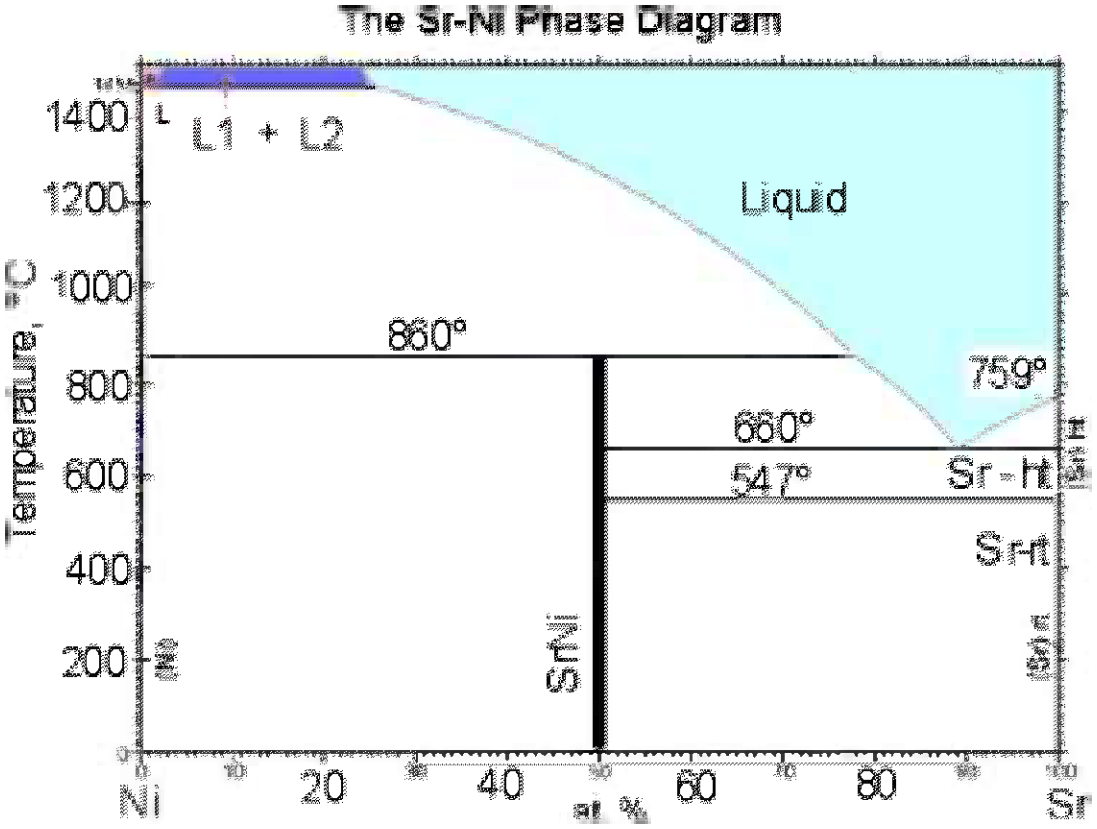

FIGURE 14.13

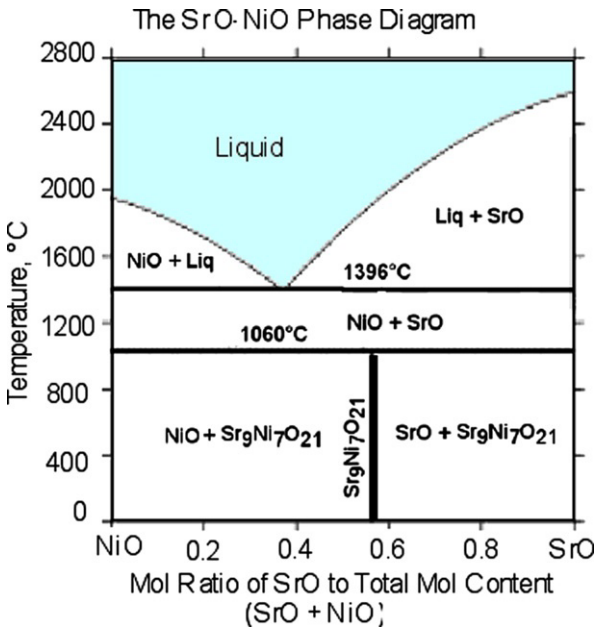

FIGURE 14.14

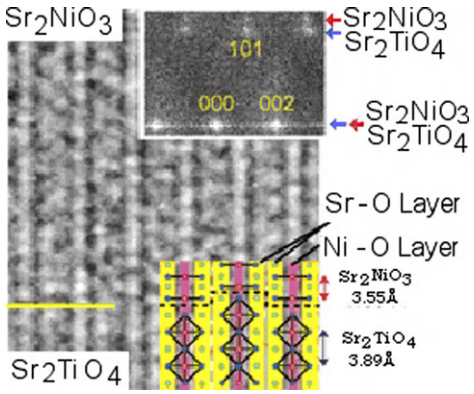

FIGURE 14.15

spectroscopy revealed a 1D electronic structure and sizable nonlinear optical susceptibility, respectively, for Sr_2NiO_3.

In the Ni^{3+}-containing system of SrO–Ni_2O_3, the compound, $SrNi_2O_4$ remains unknown. However, the trivalent Ni^{3+} ion has been observed to exist with Ni^{4+} in various compounds.

No compounds involving the Ni^{2+}–Ni^{3+} ions have been discovered in the system SrO–Ni_3O_4.

In the Ni^{4+}-containing system of SrO–NiO_2, the compound, $SrNiO_3$ is not stable at room temperature. The constitution of the Sr–Ni–O system was studied experimentally for the first time. Samples were prepared either from $SrCO_3$ and NiO or from $Sr(NO_3)_2$ and $Ni(NO_3)_2 \cdot 6H_2O$ and characterized by high-temperature X-ray powder diffraction, scanning electron microscopy, thermogravimetric and differential thermal analyses. In the SrO–NiO quasi-binary system, an eutectic reaction: liquid SrO + NiO was found to occur at 1396 ± 5 °C, while the homogeneity range of terminal solid solutions is negligible. Thermodynamic calculations using the regular solution model for the liquid and rock salt-type phases were employed to predict liquidus and solidus curves. Three ternary compounds, $SrNiO_{2.5}$, $Sr_5Ni_4O_{11}$, and $Sr_9Ni_7O_{21}$ were observed in the samples prepared from nitrate solutions, but only $Sr_9Ni_7O_{21}$ was proved to be thermodynamically stable in air up to 1030 ± 6 °C. When heated in air, $SrNiO_{2.5}$ and $Sr_5Ni_4O_{11}$ were found to transform irreversibly into a mixture of $Sr_9Ni_7O_{21}$ and NiO:

$$36\ SrNiO_{2.5} + O_2 \Rightarrow 4\ Sr_9Ni_7O_{21} + 8\ NiO$$

$$18\ Sr_5Ni_4O_{11} + 3\ O_2 \Rightarrow 10\ Sr_9Ni_7O_{21} + 2\ NiO$$

Isothermal section of the SrO–NiO–O subsystem, which represents phase equilibria at 950–1030 °C as well as an isobaric section of the Sr–Ni–O system in air were constructed.

However, the actual stoichiometry of $Sr_5Ni_4O_{11}$ remains questionable. A crystal structure investigation of the so-called $Sr_5Ni_4O_{11}$ from single-crystal X-ray data has shown that the composition of this oxide is in fact close to $Sr_4Ni_3O_9$. The structure has been solved in the trigonal *P*321 space group. The final refinement gave an *R* factor of 0.045 for 512 independent reflections. The structure contains NiO_3 chains with two NiO_6 octahedra and one NiO_6 trigonal prism alternating and sharing faces. The chains run along the threefold axis and are connected by Sr ions. The Ni–O distances seem to indicate a possible repartition of Ni^{4+} in the octahedral sites and Ni^{2+} in the trigonal prisms.

In another study, two crystal phases of strontium–nickel oxides, $SrNiO_3$ and compounds with composition near $Sr_2Ni_2O_5$, containing tetra- and trivalent nickel ions, respectively, have been synthesized in an oxidizing atmosphere. $SrNiO_3$, synthesized under high pressures of oxygen above 50 atm., has a hexagonal unit cell with $a = 5{\cdot}355 \pm 0{\cdot}001$, $c = 4{\cdot}860 \pm 0{\cdot}001$ Å and is isostructural with $BaNiO_3$ with a perovskite-like structure. The phase with composition near $Sr_2Ni_2O_5$ with hexagonal unit cell has been synthesized above 600 °C and at 1 atm. of wet oxygen gas. The existence of water has a remarkable effect to form both the compounds of $SrNiO_3$ and $Sr_2Ni_2O_5$. The former compound is not stable and decomposes slowly:

$$4\ SrNiO_3 \Rightarrow 2\ Sr_2Ni_2O_5 + O_2$$

The so-called 1D oxides, showing chains of two-times face-shared octahedra and/or trigonal prisms, found in $Sr_3Yb_{0.89}NiO_6$; Sr_3PbNiO_6; $Sr_{12}Ni_{7.5}O_{27}$; $Sr_4Ni_3O_9$; $BaNi_{0.83}O_{2.5}$ and $NaSr_{12}Ni_7O_{23}$ have been thoroughly examined. Large chains of the type, filled by Ni^{3+} and Ni^{4+}, are found in $Sr_9Ni_{6.64}O_{21}$.

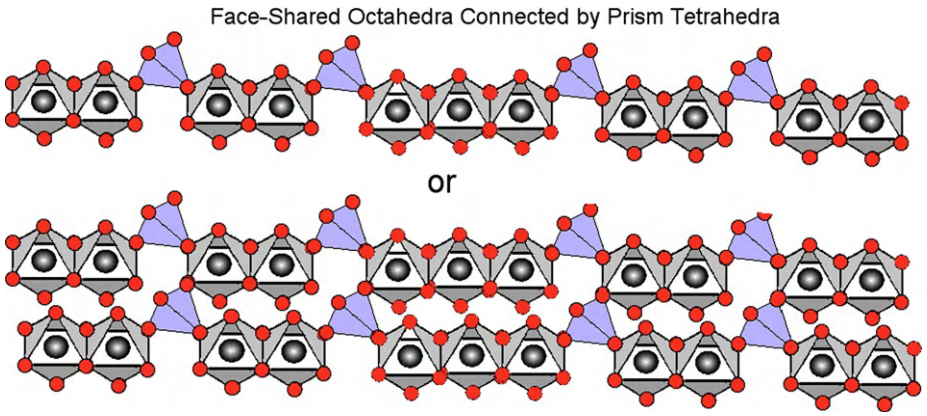

FIGURE 14.16

Crystals of the phase $Sr_9Ni_{6.64}O_{21}$ have been grown. This compound is the $n=2$ member of the $A_{3n+3}A_nB_{n+3}O_{6(n=9)}$ series. The composition and the crystal structure have been established from X-ray single-crystal diffraction data. The structure contains face-shared chains of NiO_6 polyhedra parallel to the *c*-axis and is related to the hexagonal 2H polytype perovskite. $Sr_9Ni_{6.64}O_{21}$ crystallizes in the space group *Rc* (No. 167) with $a=9.467$ Å, $c=35.87$ Å, $V=2784$ Å^3, and $Z=6$ (Fig. 14.16).

Single crystals of $Sr_{12}Ni_{7.5}O_{27}$ were prepared in closed silver tubes using a KO_2 flux. X-ray investigations show trigonal symmetry, space group D_3^2-*P*321, $a=9.474$ Å, $c=7.802$ Å, $Z=1$. It belongs to the modified perovskites, characterized by face-shared Ni_2O_9 double octahedra and under-occupied trigonal NiO_6 prisms. The oxidation state of the nickel ions can be verified by calculations of the Coulomb terms of the lattice energy.

No other strontium nickelates have appeared in the current technical literature. They are not available commercially and no CAS numbers have been assigned to date.

14.1.5. Barium Nickel Compounds

Barium metal does not form any intermetallic compounds with nickel metal as shown in Fig. 14.17.

In the BaO–In_xO_y system, only a few compounds are known.

In the Ni^{2+}-containing system of BaO–NiO, $BaNiO_2$, which is one of the stable phases in the Ba–Ni–O system, is an insulator consisting of zigzag chains of Ni^{2+} ions. Susceptibility measurements have been accomplished by several groups wherein it was reported that $BaNiO_2$ is diamagnetic. This means that Ni^{2+} is in a low-spin state with $S=0$, a state sometimes achieved with ions in square planar d^8 systems. On the other hand, the moment estimated from the Curie constant is fairly large, indicating that Ni^{2+} is in a high-spin state with $S=1$. Using extensive neutron scattering on single crystals of $BaNiO_2$, it was shown that this structure exhibits paramagnetism with full Ni^{2+} moment at each site at room temperature. Since the magnetic-scattering intensity decreases with decreasing temperature, magnetic susceptibility, heat capacity and muon spin relaxation (μSR) measurements were carried out to show that $BaNiO_2$ is, in fact, in a nonmagnetic state at low temperatures. This compound has the form shown in Fig. 14.18.

Cell parameters are: $a=4.732$ Å, $b=c=5.4192$ Å, $\alpha=116.159°$, $\beta=\gamma=90°$, cell volume $=124.67$ Å^3, $Z=4$. Cell occupancy is shown in Table 14.8.

A better view of the relationship of the Ni^{2+} ions and the Ba^{2+} ions is shown in Fig. 14.19.

In this same system, the compound, Ba_3NiO_4, has the structure shown in Fig. 14.20.

The structure of Ba_3NiO_4 involves a co-planar arrangement of O atoms around Ni atoms.

Cell parameters are: $a=b=c=7.1268$ Å, $\alpha=\beta=\gamma=66.836°$. Cell volume $=293.52$ Å^3, $Z=6$. Cell occupancy is shown in Table 14.9.

A recent review describes features of the crystal chemistry of oxo-nickelates containing large cations like alkali-, alkaline earth and rare earth metals. Starting with alkali oxo-nickelates, K_2NiO_2 is the only known oxo-nickelate showing O–Ni–O dumbbells with nickel in the oxidation state Ni^{2+}. The trigonal planar coordination (found within silver-oxo-compounds) is restricted to Ba_3NiO_4 and $K_9Ni_2O_7$. Square planar polygons (NiO_4) are found in $Nd_4Ni_3O_8$; Na_2NiO_2; Ki_2NiO_2; $BaNiO_2$ and $SrNiO_2$ for example. A special quality in the crystal chemistry of connected square planar NiO_4 polygons is the formation of Ni_6O_{12} rings in $Ba_2NaNi_3O_6$. All the other oxo-nickelates exhibit octahedral or trigonal prismatic coordination of nickel by oxygen. Always of interest are the so-called 1D oxides, showing chains of two times face-shared octahedra and/or trigonal prisms, found in $Sr_{12}Ni_{7.5}O_{27}$; $Sr_4Ni_3O_9$ or $BaNi_{0.83}O_{2.5}$. Many of the oxidation states of nickel are published with non-integral valence states like

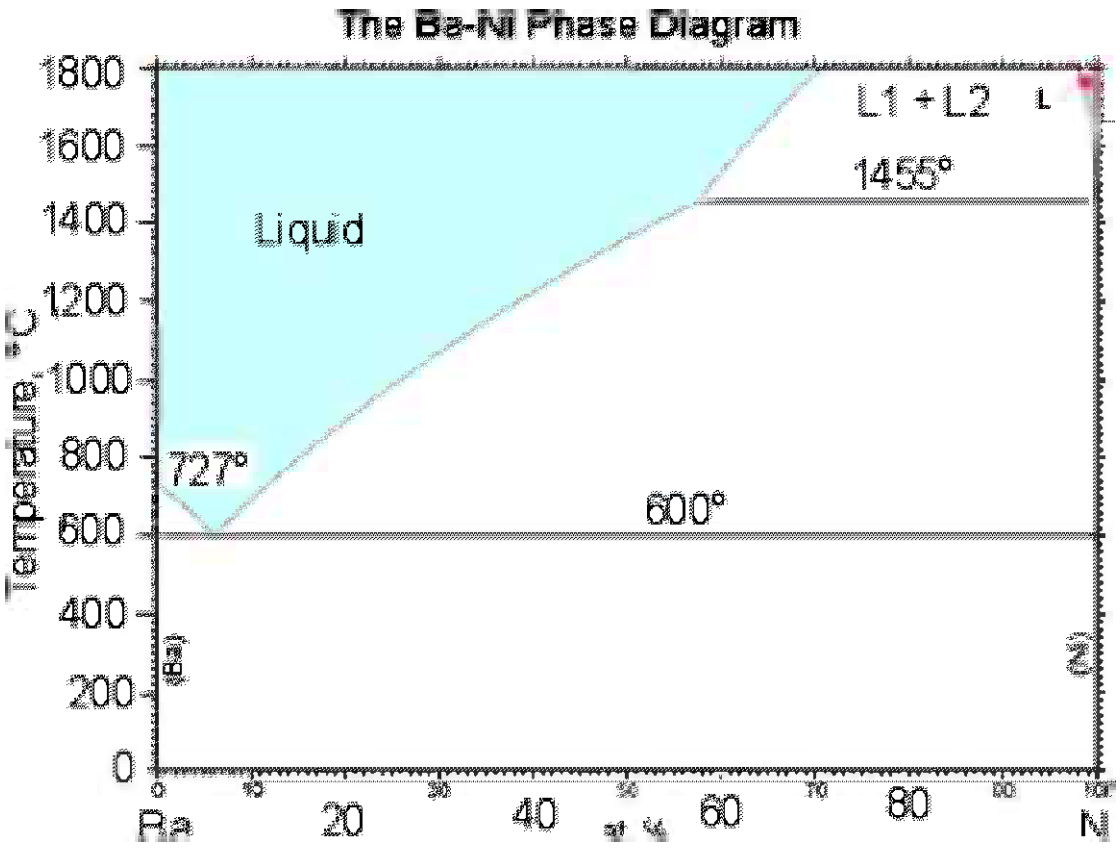

FIGURE 14.17

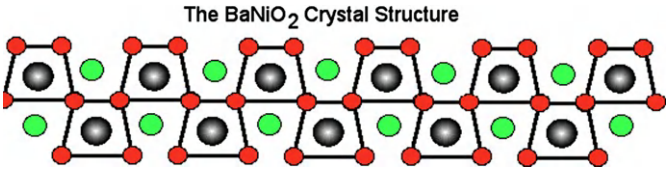

FIGURE 14.18

$Ni^{2.667+}$, $Ni^{2.5+}$, $Ni^{2.292+}$, $Ni^{3.614}$. Using calculations of the Coulomb terms of lattice energy most of the mixed valences could be split up in integral numbers protecting the electro neutrality between metal ions and oxygen, i.e. $Ni^{2.5+} = Ni^{2+} + Ni^{3+}$ and $Ni^{2.667} = Ni^{2+} + 2Ni^{3+}$.

Single crystals of $BaNi_{0.83}O_{2.5}$ were grown from mixtures of $BaCO_3$ and NiO using KOH as a flux. The composition and the crystal structure have been established from X-ray single-crystal diffraction data. $BaNi_{0.83}O_{2.5}$ is stoichiometric and crystallizes in a trigonal structure, space group *R*32, with hexagonal unit cell parameters (Å) $a = 9.8890(4)$ $c = 12.867(4)$, volume 1089.7(3) $Å^3$, and $Z = 18$. $BaNi_{0.83}O_{2.5}$ contains two kinds of Ba atoms both coordinated with 10 oxygen atoms, and three different Ni atoms octahedrally coordinated to oxygen at distances which approximately correspond to Ni_{2+} and to low-spin Ni_{3+} and Ni_{4+}. NiO_6 octahedra share opposite faces giving rise to chains parallel to the *c*-axis, in which some Ni–Ni distances are shorter than in Ni metal. This structure, which is compared with that of $BaNiO_3$, can be considered like a close packing of Ba and oxygen atoms in which almost one-quarter of the octahedral sites are occupied by nickels. $BaNi_{0.83}O_{2.5}$ is an electrical insulator. The results of magnetic measurements from room temperature to 5 K are given.

TABLE 14.8

No.	Site notation	Atom	Multiplicity	Wyckoff	Site symmetry	*x*	*y*	*z*	Occupancy
1	O	O	8	g	..m	0.25	0.083	1/4	1.0
2	Ba	Ba	4	c	m2m	0	0.347	1/4	1.0
3	Ni	Ni	4	a	2/m..	0	0	0	1.0

TABLE 14.9

No.	Site notation	Atom	Multiplicity	Wyckoff	Site symmetry	x	y	z	Occupancy
1	O2	O	18	e	.2	0.250	0	1/4	1.0
2	Ba	Ba	18	e	.2	0.583	0	1/4	1.0
3	O1	O	6	b	-3.	0	0	0	1.0
4	Ni	Ni	6	a	32	0	0	1/4	1.0

Crystals of $NaBa_2Ni^{2+}{}_2Ni^{3+}O_6$ were prepared by either electro synthesis in molten NaOH or controlled cooling in a NaOH flux. They crystallize in an F-centered orthorhombic unit cell, space group *Fmmm*, and are formed from the stacking along the c-axis of compact $[NaNi_3O_6]^{4-}$ blocks that are separated by Barium cations. It appears that, due to a perfect coincidence between the (a, a, c) unit cell constants and the related primitive hexagonal lattice (a, a, c, $\gamma = 120°$), a recurrent twinning mechanism, characterized by a threefold axis from one block to the subsequent one, occurred in the crystals studied. Thus, the coexistence of three independent domains yielded a misleading C-centered orthorhombic false symmetry. After the stacking fault detection from electron diffraction and HREM pictures was realized, a special attention was given to the X-ray data refinement process. This led to the establishment and concept of the existence of three independent domains and to good reliability factors. The composition plane located at the barium layers level was also investigated. It was shown that the barium environment at the twin interface adopts a symmetrical oxygen coordination in agreement with the full coherence of domains boundaries observed in HREM pictures. Therefore, valence bond calculations indicate a D1–D1 interface that is more stable than that of D1–D2 and D1–D3, and confirms the large size of superimposed monodomains. The compounds progressively decompose from 300 °C, forming a mixture of NiO, $BaCO_3$, and $BaNiO_3$. The magnetic susceptibility measured for $NaBa_2Ni_3O_6$ follows a Curie–Weiss law that involves high-spin Ni^{2+} and Ni^{3+} cations. The spin blocks are shown in Fig. 14.21.

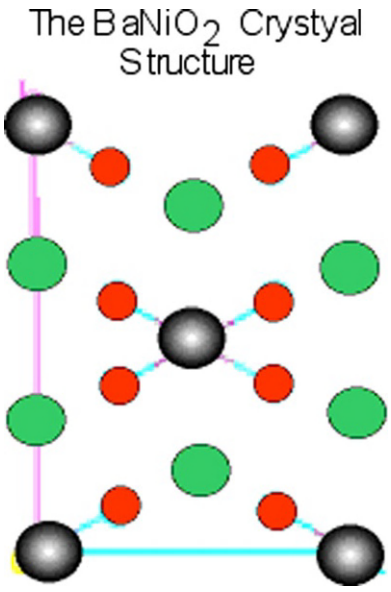

FIGURE 14.19

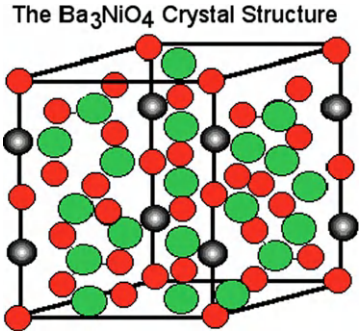

FIGURE 14.20

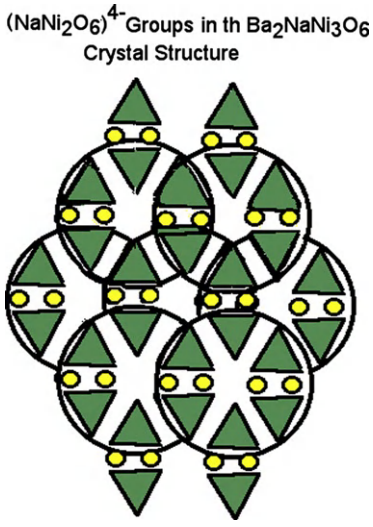

FIGURE 14.21

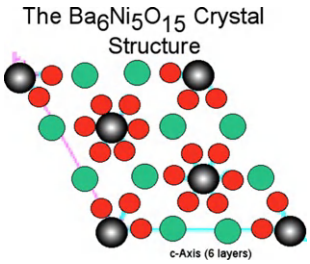

FIGURE 14.22

In the Ni^{2+}–Ni^{4+}-containing system of $BaO–Ni_3O_5$, the compound, $Ba_6Ni_5O_{15}$ has been synthesized. It has the structure shown in Fig. 14.22.

These layers are shown in the *c*-axis direction. If this layer turned 90° in the *b*-direction and then stacked 6-high, the complete structure is revealed. The *a*- and *b*-faces consist of: atoms in a six-layer configuration.

Cell parameters are: $a = b = c = 7.1409$ Å, $\alpha = \beta = \gamma = 87.643°$, cell volume $= 263.23$ Å^3, $Z = 4$. Cell occupancy is shown in Table 14.10.

In the Ni^{3+}-containing system of $BaO–Ni_2O_3$, the compound, $BaNi_2O_4$ remains unknown. No other Ni^{3+}-containing compounds have been synthesized.

In the Ni^{4+}-containing system of $BaO–NiO_2$, the crystal structure of $BaNiO_3$ has been determined using a single crystal. The space group is $P6_3/mmc$ and lattice constants are: $a = 5.629$ Å, $c = 4.811$ Å with $Z = 2$. This structure is characteristic with linear chains of Ni atoms having a Ni–Ni distance of 2.405 Å wherein the NiO_6 octahedron is trigonally distorted.

In another study, $BaNiO_3$ and intermediates with compositions ranging between $Ba_3Ni_3O_8$ $\{Ba_3(Ni^{2+}+2Ni^{4+})O_8\}$ and $Ba_2Ni_2O_5$ $\{Ba_2(2Ni^{3+})O_5\}$ were prepared. $BaNiO_3$ is black, stable in alkali, and has a structure made up of layers identical with the (111) planes of a perovskite but stacked in a close-packed hexagonal fashion. When fired at 730 °C in an atmosphere of 730 mm of oxygen, the structure changes due to loss of oxygen to form one of the series, $Ba_3Ni_3O_8$ or $Ba_2Ni_2O_5$ wherein the oxygen content is a function of the temperature between 730–1200 °C, at which a sharp melting point occurs. These latter materials are black but their crystal structures have not yet seen determined.

Single crystals of $BaNiO_3$ have been synthesized in molten KOH. The enthalpies of formation from the component oxides at 25 °C of $BaNiO_2$, $BaNiO_{2.63}$, and $BaNiO_3$ have been measured using high-temperature reaction calorimetry. As the value of x increases in $BaNiO_{2+x}$, the enthalpy of formation becomes more exothermic. From the enthalpy of formation data, an enthalpy of oxidation of -196 ± 20 kJ/(mole O_2) was obtained. This value is very similar to the values of -202 and -220 kJ/(mole O_2) obtained for $YBa_2Cu_3O_{7-y}$ and $La_{2-x}Ba_xCuO_{4-y}$, respectively, that are related to the high-temperature superconductor compositions. Energetic and structural data were discussed in terms of a model in which the holes have significant oxygen character.

The effect of hole doping into the divalent nickel oxide Y_2BaNiO_5, which provides a good example of 1D electronic structure in the presence of strong d–d interactions, has been examined by means of several techniques including X-ray absorption and electron energy-loss spectroscopy at oxygen K-edges (O_K-edges). The crystal structure of this compound shows 1D chains of vertex-sharing NiO_6 octahedra running along the *z*-axis. Hole doping into this material is realized by substituting Ca^{2+} or Sr^{2+} ions for the Y^{3+} ions. It was suggested that the doped holes have antibonding Ni $3d(3z^2\text{-}r^2)$–$O^{2p}(z)$ character.

The effect of Ba substitution in $LnNiO_3$ (Ln = Pr, Sm, Eu) perovskites on the structural and catalytic properties was studied by means of textural measurements, X-ray and neutron powder diffraction (XRD, NPD), thermogravimetric analysis, temperature-programmed reduction and catalytic activity in CO oxidation to CO_2 were employed. All the samples were prepared using

TABLE 14.10

No.	Site notation	Atom	Multiplicity	Wyckoff	Site symmetry	*x*	*y*	*z*	Occupancy
1	O1	O	18	f	1	0.152	0.1617	0.317	1.0
2	O3	O	18	f	1	0.152	0.0099	0.123	1.0
3	O2	O	9	e	.2	0.138	0	1/2	1.0
4	Ba1	Ba	9	e	.2	0.672	0	1/2	1.0
5	Ba2	Ba	9	d	.2	0.345	0	0	1.0
6	Ni2	Ni	6	c	3.	0	0	0.219	1.0
7	Ni1	Ni	6	c	3.	0	0	0.401	1.0
8	Ni3	Ni	3	a	32	0	0	0	1.0

soft-chemistry procedures, decomposing citrate precursors at 1073 K, and subsequently oxygenating them at 1273 K under a very high oxygen pressure (200 bar). This treatment, necessary for the stabilization of Ni^{3+}–Ni^{4+} mixed valences, resulted in very low specific areas (1–2 m^2/g). The X-ray diffraction profiles indicated pure perovskite phases with orthorhombic distortion, which increased in the order Pr < Sm <Eu. The Rietveld refinement of NPD data for a selected $Pr_{0.95}Ba_{0.05}NiO_3$ sample showed a significant reduction in the Ni–O distances with respect to the undoped compound, concomitant with the hole doping of the d-bands of the solid. Temperature-programmed reduction profiles revealed that the reduction of Ni^{3+} occurs through two consecutive reduction steps ($Ni^{3+/4+} \Rightarrow Ni^{2+} \Rightarrow Ni^0$). Both unsubstituted and Ba-substituted samples were tested in CO oxidation and it was found that the intrinsic activity is enhanced with Ba substitution particularly for the $Pr_{0.95}Ba_{0.05}NiO_3$ sample. This higher activity in CO oxidation appears to be related to the relative ease of oxygen removal from the hole-doped perovskites and to the presence of oxygen vacancies.

In the Ni^{5+}-containing system of $BaO–Ni_2O_5$, no compounds are known.

Barium nickelates are not offered for sale commercially and no CAS numbers have been issued to date.

14.1.6. Radium Nickel Compounds

Although radium probably forms the same compounds as its barium homologue, there is no evidence that such compounds have ever been synthesized. This is undoubtedly due to lack of interest in both Industry and Academia.

14.2. ALKALINE EARTH PALLADIUM COMPOUNDS

Pd forms very few compounds with the alkaline earths. Palladium primarily exists in the 0, +2, +4 oxidation states; the +4 oxidation state is comparatively rare. The +5 or +6 state has not been observed. The known oxides include PdO, PdO_2 and Pd_3O_4.

14.2.1. Beryllium Palladium Compounds

Beryllium forms a number of compounds with Pd metal, as shown in the following phase diagram in Fig. 14.23.

Seven compounds are shown but only the high Be-containing compounds, i.e. =Be > 50 atom%, have had their structures determined. Be_2Pd_3, $BePd_2$, and $BePd_3$ all melt incongruently and Be_3Pd_4 is a

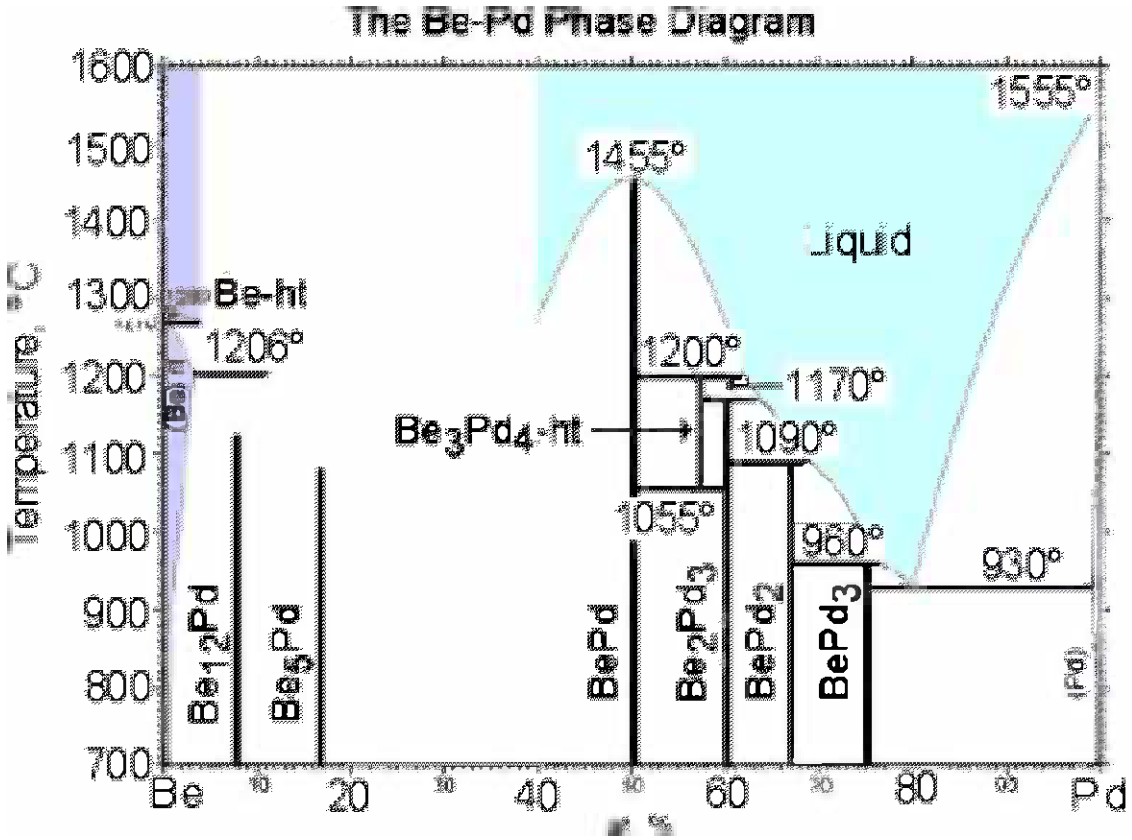

FIGURE 14.23

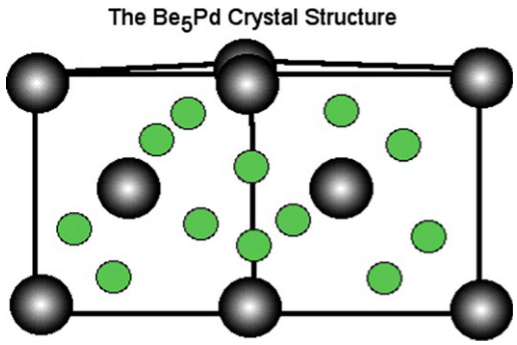

FIGURE 14.24

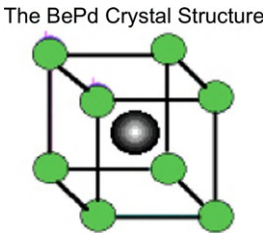

FIGURE 14.25

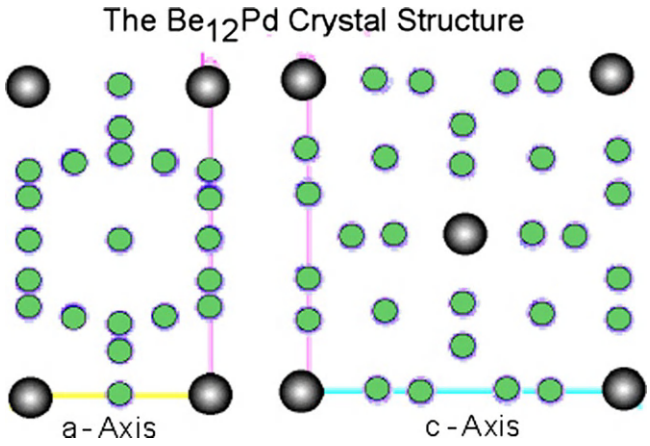

FIGURE 14.26

high-temperature compound, stable only between 1055–1200 °C.

Be_5Pd has the structure shown in Fig. 14.24.

It is cubic with cell constants of: $a = b = c = 4.2299$ Å, $\alpha = \beta = \gamma = 60°$, cell volume = 53.52 Å^3, $Z = 3$. Cell occupancy is shown in Table 14.11.

BePd has the structure shown in Fig. 14.25.

Cell parameters are: $a = b = c = 2.813$ Å, $\alpha = \beta = \gamma = 90°$, cell volume = 22.26 Å^3, $Z = 1$. Cell occupancy is shown in Table 14.12.

$Be_{12}Pd$ has the structure shown in Fig. 14.26.

The cell is body-centered in regard to the Pd atoms. Cell parameters are: $a = 4.251$ Å, $b = c = 5.5634$ Å, $\alpha = 81.607°$, $\beta = \gamma = 67.539°$, cell volume = 112.37 Å^3, $Z = 4$. Cell occupancy is shown in Table 14.13.

BeO does not form any compounds with PdO or PdO_2. A search of the literature revealed no stable compounds.

No beryllium palladates have been reported. They are not offered for sale commercially and no CAS numbers have been issued to date. Perhaps this is due to the lack of interest in Industry and Academia.

14.2.2. Magnesium Palladium Compounds

Mg metal forms a series of intermetallic compounds with Pd metal as shown in the following phase diagram shown as follows. Two of the compounds melt congruently. The other four melt incongruently. Mg_5Pd_2 is dimorphic, as is MgPd. Not all of the crystal structures have been shown. Of the six compounds

TABLE 14.11

No.	Site notation	Atom	Multiplicity	Wyckoff	Site symmetry	x	y	z	Occupancy
1	Be II	Be	16	e	.3m	0.625	0.625	0.625	1.0
2	Be I	Be	4	c	-43m	1/4	1/4	1/4	1.0
3	Pd	Pd	4	a	-43m	0	0	0	1.0

TABLE 14.12

No.	Site notation	Atom	Multiplicity	Wyckoff	Site symmetry	x	y	z	Occupancy
1	Be	Be	1	b	m-3m	1/2	1/2	1/2	1.0
2	Pd	Pd	1	a	m-3m	0	0	0	1.0

TABLE 14.13

No.	Site notation	Atom	Multiplicity	Wyckoff	Site symmetry	x	y	z	Occupancy
1	Be1	Be	8	j	m2m.	0.277	1/2	0	1.0
2	Be2	Be	8	i	m2m.	0.361	0	0	1.0
3	Be3	Be	8	f	..2/m	1/4	1/4	1/4	1.0
4	Pd1	Pd	2	a	4/mmm	0	0	0	1.0

shown here, the structures of the Mg_4Pd and $Mg_{0.9}Pd_{11}$ compounds have not been described in the literature (Fig. 14.27).

$Mg_{85}Pd_{14}$ may better be described as: $Mg_{83}(Mg_{0.51}Pd_{0.49})_4Pd_{12}$. It has the structure shown in Fig. 14.28.

Cell parameters are: $a = b = c = 14.2185$ Å, $\alpha = \beta = \gamma = 60°$, cell volume $= 2032.58$ Å^3, $Z = 4$. Cell occupancy is shown in Table 14.14.

Mg_3Pd is dimorphic. The two crystal structures are shown in Fig. 14.29.

Na_3As type

$a = b = 4.613$ Å, $c = 8.412$ Å, $\alpha = \beta = \gamma = 90°$, cell volume $= 154.99$ Å^3, $Z = 4$. Cell occupancy is shown in Table 14.15.

Cu type

$a = b = c = 2.7719$ Å, $\alpha = \beta = \gamma = 60°$, cell volume $= 15.06$ Å^3, $Z = 4$. Cell occupancy is shown in Table 14.16.

The compound, Mg_5Pd_2, has the structure shown in Fig. 14.30.

Cell parameters are: $a = 8.161$ Å, $b = c = 8.644$ Å, $\alpha = 120°$, $\beta = \gamma = 90°$. Cell volume $= 528.02$ Å^3, $Z = 2$. Cell occupancy is shown in Table 14.17.

The compound, Mg_2Pd, is not shown in the phase diagram but has the structure shown in Fig. 14.31.

Cell parameters are: $a = b = c = 8.5192$ Å, $\alpha = \beta = \gamma = 60°$, cell volume $= 437.20$ Å^3, $Z = 32$. Cell occupancy is shown in Table 14.18.

The compound MgPd is dimorphic with the structures shown in Fig. 14.32.

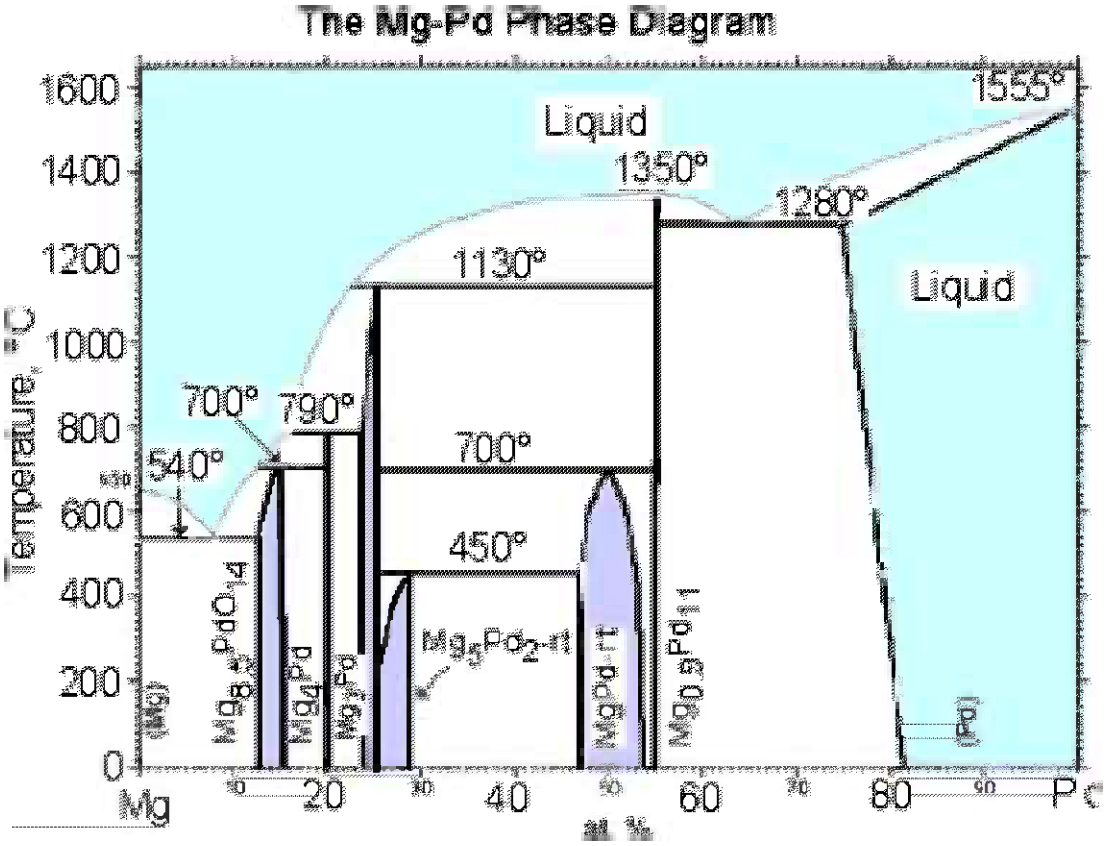

FIGURE 14.27

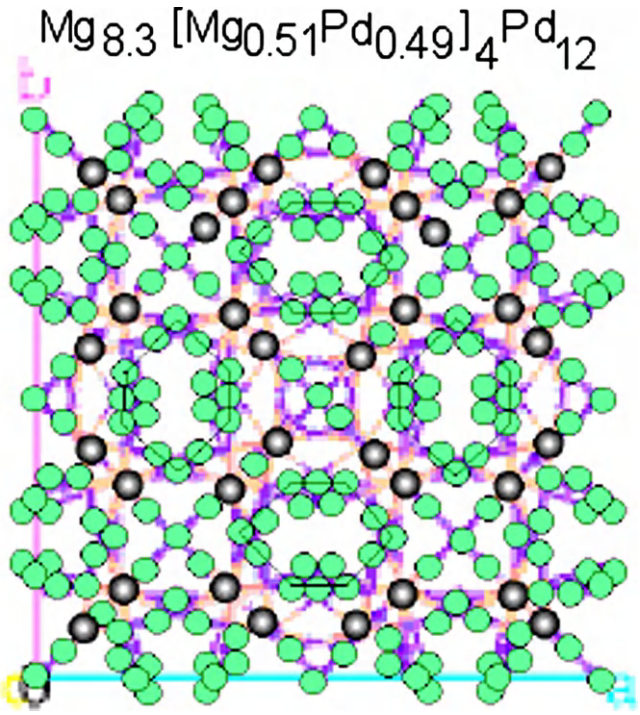

FIGURE 14.28

The two structures are essentially the same except for the *a*-parameter in the CuTi type.

CsCl type

$a = b = c = 3.122$ Å, $\alpha = \beta = \gamma = 90°$, cell volume = 30.37 Å^3, $Z = 1$. Cell occupancy is shown in Table 14.19.

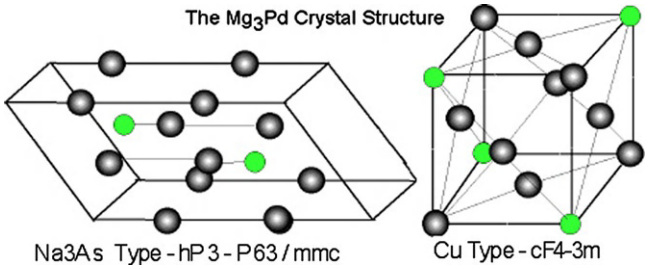

FIGURE 14.29

CuTi type

$a = 3.422$ Å, $b = c = 3.033$ Å, $\alpha = \beta = \gamma = 90°$, cell volume = 31.40 Å^3, $Z = 1$. Cell occupancy is shown in Table 14.20.

No other intermetallic compounds are known.

In the Mg–Pd–O system, only a few compounds are known. No compounds involving: the Pd^{2+}-containing system of MgO–PdO, the Pd^{3+}-containing system of MgO–Pd_2O_3, the Pd^{5+}-containing system of MgO–Pd_2O_5 and the Pd^{2+}–Pd^{3+}-containing system of MgO–Pd_3O_4 have been reported.

In the Pd^{4+}-containing system of MgO–PdO_2, a spinel phase has been synthesized ($a_0 = 8.501$ Å) whose stoichiometry is believed to be Mg_2PdO_4. This is the only reference to be found concerning the Mg–Pd–O system.

Magnesium palladium compounds are not offered for sale commercially and no CAS numbers are known.

14.2.3. Calcium Palladium Compounds

Ca^0 metal forms a series of compounds with Pd^0 metal as shown in the following phase diagram in Fig. 14.33.

TABLE 14.14

No.	Site notation	Atom	Multiplicity	Wyckoff	Site symmetry	*x*	*y*	*z*	Occupancy
1	Mg5	Mg	48	h	..m	0.0498	0.0498	0.1572	1.0
2	Mg3	Mg	48	h	..m	0.0990	0.0990	0.7781	1.0
3	Mg1	Mg	48	h	..m	0.1065	0.1065	0.2840	1.0
4	Mg2	Mg	48	h	..m	0.1561	0.1561	0.5239	1.0
5	Mg4	Mg	48	h	..m	0.1935	0.1935	0.0176	1.0
6	Mg6	Mg	24	g	2.mm	0.1428	1/4	1/4	1.0
7	Mg7	Mg	24	g	2.mm	0.6313	1/4	1/4	1.0
8	Mg8	Mg	24	f	2.mm	0.3148	0	0	1.0
9	Pd13	Pd	16	e	.3m	0.1504	0.1504	0.1504	1.0
10	Pd10	Pd	16	e	.3m	0.4179	0.4179	0.4179	1.0
11	Mg9	Mg	16	e	.3m	0.5525	0.5525	0.5525	1.0
12	Pd11	Pd	16	e	.3m	0.6565	0.6565	0.6565	1.0
13	M12	0.51Mg + 0.49Pd	16	e	.3m	0.9187	0.9187	0.9187	1.0
14	Mg14	Mg	4	a	-43m	0	0	0	0.97

TABLE 14.15

No.	Site notation	Atom	Multiplicity	Wyckoff	Site symmetry	x	y	z	Occupancy
1	Pd1	Pd	4	f	3m.	1/3	2/3	0.583	1.0
2	Mg1	Mg	2	c	-6m2	1/3	2/3	1/4	1.0
3	Pd2	Pd	2	b	-6m2	0	0	1/4	1.0

TABLE 14.16

No.	Site notation	Atom	Multiplicity	Wyckoff	Site symmetry	x	y	z	Occupancy
1	M	0.75Pd + 0.25Mg	4	a	m-3m	0	0	0	1.0

TABLE 14.17

No.	Site notation	Atom	Multiplicity	Wyckoff	Site symmetry	x	y	z	Occupancy
1	Mg″	Mg	12	k	.m.	0.196	0.392	0.061	1.0
2	Mg′	Mg	6	h	mm2	0.533	0.066	1/4	1.0
3	Pd′	Pd	6	h	mm2	0.88	0.76	1/4	1.0
4	Pd	Pd	2	c	-6m2	1/3	2/3	1/4	1.0
5	Mg	Mg	2	a	-3m.	0	0	0	1.0

Six compounds are shown but only CaPd and $CaPd_2$ melt congruently. Incongruently melting compounds include: Ca_9Pd, Ca_3Pd, Ca_5Pd, and Ca_3Pd_2. The compound, CaPd has the CsCl structure shown in Fig. 14.34.

Cell parameters are: $a = b = c = 3.518$ Å, $\alpha = \beta = \gamma = 90°$, cell volume $= 43.54$ Å^3, $Z = 1$. Cell occupancy is shown in Table 14.21.

The compound, Ca_5Pd_2, has the form shown in Fig. 14.35.

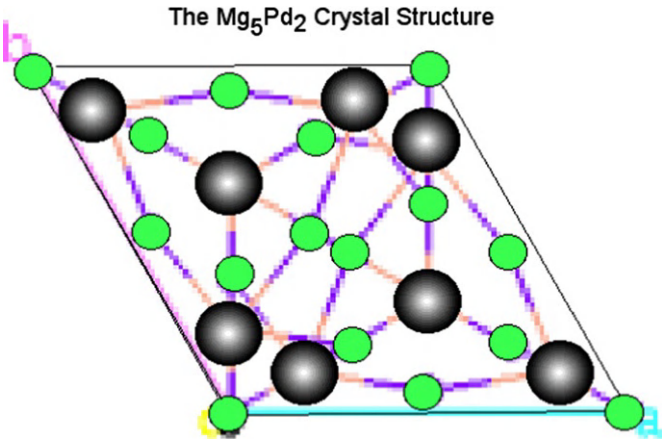

FIGURE 14.30

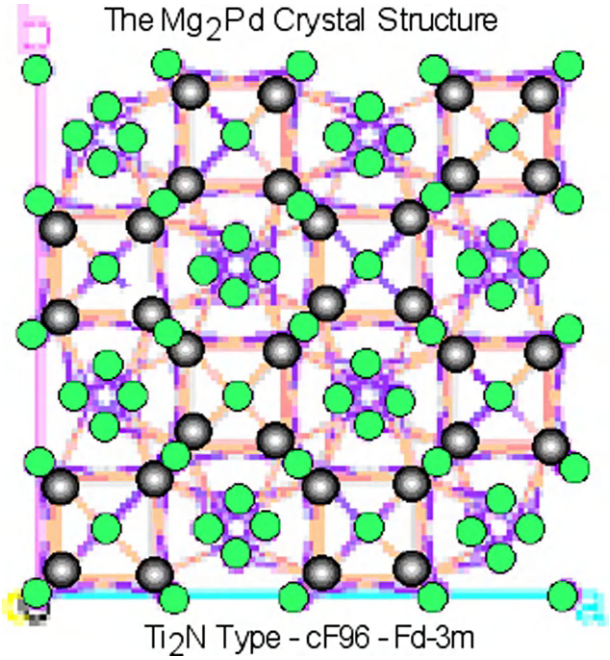

FIGURE 14.31

TABLE 14.18

No.	Site notation	Atom	Multiplicity	Wyckoff	Site symmetry	x	y	z	Occupancy
1	Mg1	Mg	48	f	2.mm	0.43	1/8	1/8	1.0
2	Pd	Pd	32	e	.3m	0.2166	0.2166	0.2166	1.0
3	Mg2	Mg	16	c	.-3m	0	0	0	1.0

TABLE 14.19

No.	Site notation	Atom	Multiplicity	Wyckoff	Site symmetry	x	y	z	Occupancy
1	Mg	Mg	1	b	m-3m	1/2	1/2	1/2	1.0
2	Pd	Pd	1	a	m-3m	0	0	0	1.0

TABLE 14.20

No.	Site notation	Atom	Multiplicity	Wyckoff	Site symmetry	x	y	z	Occupancy
1	M	0.9Mg + 0.1Pd	1	d	4/mmm	1/2	1/2	1/2	1.0
2	Pd	Pd	1	a	4/mmm	0	0	0	1.0

Cell parameters are: $a = 6.708$ Å, $b = 7.704$ Å, $c = 8.996$ Å, $\alpha = 96.77°$, $\beta = 111.89°$, $\gamma = 90°$. Cell volume = 427.87 Å^3, $Z = 4$. Cell occupancy is shown in Table 14.22.

The compound, Ca_3Pd, has the form shown in Fig. 14.36.

Cell parameters are: $a = 6.691$ Å, $b = 7.699$ Å, $c = 9.937$ Å, $\alpha = \beta = \gamma = 90°$, cell volume = 5.11.89 Å^3, $Z = 4$. Cell occupancy is shown in Table 14.23.

The compound, Ca_3Pd_2, has the form shown in Fig. 14.37.

Cell parameters are: $a = b = c = 7.642$ Å, $\alpha = \beta = \gamma = 71.608°$, cell volume = 389.83 Å^3, $Z = 9$. Cell occupancy is shown in Table 14.24.

The compound, $CaPd_2$, has the form shown in Fig. 14.38.

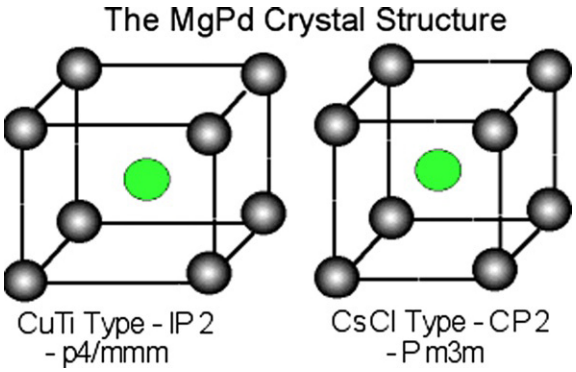

FIGURE 14.32

Cell parameters are: $a = b = c = 5.4108$ Å, $\alpha = \beta = \gamma = 60°$, cell volume = 112.01 Å^3, $Z = 8$. Cell occupancy is shown in Table 14.25.

The compound, $CaPd_5$, has the form shown in Fig. 14.39.

Cell parameters are: $a = 4.224$ Å, $b = c = 5.147$ Å, $\alpha = 120°$, $\beta = \gamma = 90°$, cell volume = 96.91 Å^3, $Z = 1$. Cell occupancy is shown in Table 14.26.

Although the compound, Ca_9Pd is shown in the phase diagram, its structure remains unknown. No other intermetallic compounds have been discovered.

In the Pd^{2+}-containing system of CaO–PdO, three novel black compounds of the $MePd_3O_4$ type have been synthesized. All three have the cubic $Na_xPt_3O_4$ structure with unit cell constants $a_0 = 5.826$ Å for $SrPd_3O_4$, $a_0 = 5.747$ Å for $CaPd_3O_4$, and $a_0 = 5.742$ Å for $CdPd_3O_4$.

The electronic energy band structure for cubic palladium oxides $CaPd_3O_4$ in the $NaPt_3O_4$ structure has been calculated by the full-potential linear augmented-plane-wave method within the local-density approximation. $CaPd_3O_4$ is almost semiconducting, but has a very small number of carriers. It was proposed that this compound would be a good candidate as an excitonic insulator, similar to CaB_6. Furthermore, the bands near the Fermi level have 1D character. The metal-insulator transition in $Ca_{1-x}Li_xPd_3O_4$ has been studied through charge transport measurements. The resistivity, the Seebeck coefficient, and the Hall coefficient have been consistently explained in terms of a simple one-band

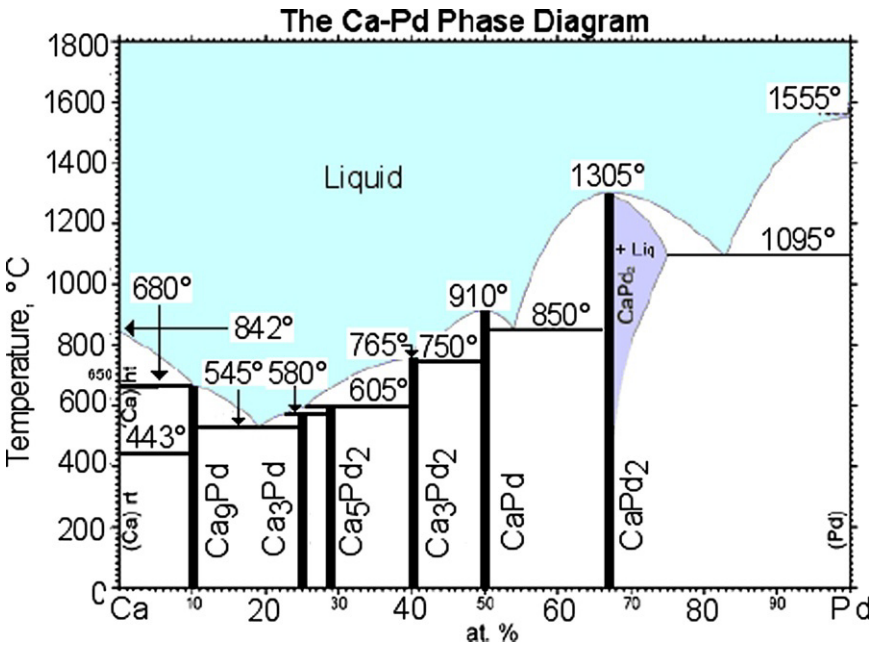

FIGURE 14.33

picture, where a hole with a moderately enhanced mass is itinerant three dimensionally. Contrary to the theoretical prediction presented in the literature [Phys. Rev. B 62, 13 426 (2000)], $CaPd_3O_4$ is unlikely to be an excitonic insulator, and holds a finite carrier concentration down to 4.2 K. Thus, the metal-insulator transition in this system is basically driven by localization effects.

Single crystals of the ternary palladates, $SrPd_3O_4$ and $CaPd_3O_4$, have been grown out of a potassium hydroxide flux. Small cubic crystals can be readily isolated from the soluble flux matrix and characterized by SEM and single-crystal X-ray diffraction. Both $SrPd_3O_4$ and $CaPd_3O_4$ crystallize with the $NaPt_3O_4$ structure and feature square planar coordination of palladium

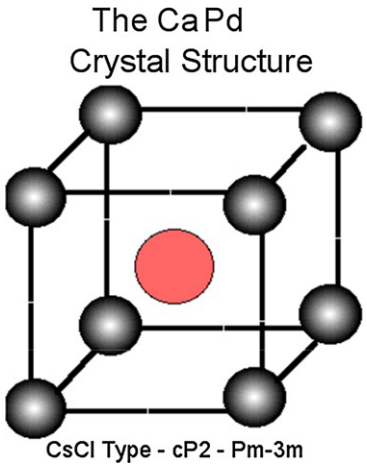

FIGURE 14.34

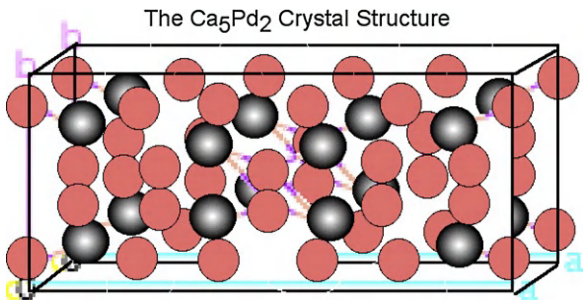

FIGURE 14.35

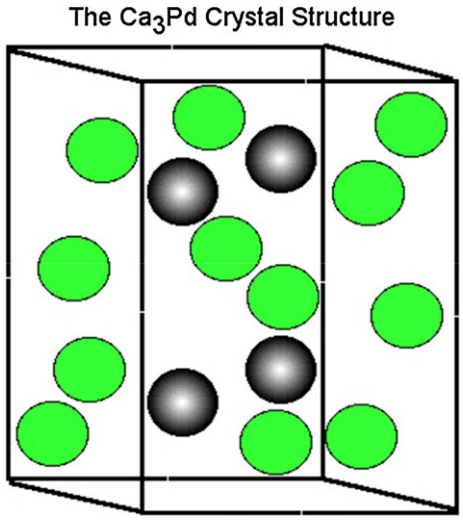

FIGURE 14.36

TABLE 14.21

No.	Site notation	Atom	Multiplicity	Wyckoff	Site symmetry	*x*	*y*	*z*	Occupancy
1	Pd	Pd	1	b	m-3m	1/2	1/2	1/2	1.0
2	Ca	Ca	1	a	m-3m	0	0	0	1.0

TABLE 14.22

No.	Site notation	Atom	Multiplicity	Wyckoff	Site symmetry	*x*	*y*	*z*	Occupancy
1	Pd1	Pd	8	f	1	0.112	0.196	0.574	1.0
2	Ca1	Ca	8	f	1	0.222	0.096	0.300	1.0
3	Ca2	Ca	8	f	1	0.401	0.093	0.064	1.0
4	Ca3	Ca	4	e	2	0	0.091	1/4	1.0

TABLE 14.23

No.	Site notation	Atom	Multiplicity	Wyckoff	Site symmetry	*x*	*y*	*z*	Occupancy
1	Ca1	Ca	8	d	1	0.1834	0.0689	0.1656	1.0
2	Ca2	Ca	4	c	.m.	0.0388	1/4	0.6578	1.0
3	Pd1	Pd	4	c	.m.	0.3764	1/4	0.4426	1.0

TABLE 14.24

No.	Site notation	Atom	Multiplicity	Wyckoff	Site symmetry	*x*	*y*	*z*	Occupancy
1	Ca1	Ca	18	f	1	0.0976	0.4135	0.0735	1.0
2	Pd1	Pd	18	f	1	0.3104	0.2467	0.1037	1.0
3	Ca2	Ca	6	c	3.	0	0	0.2085	1.0
4	Ca3	Ca	3	a	-3.	0	0	0	1.0

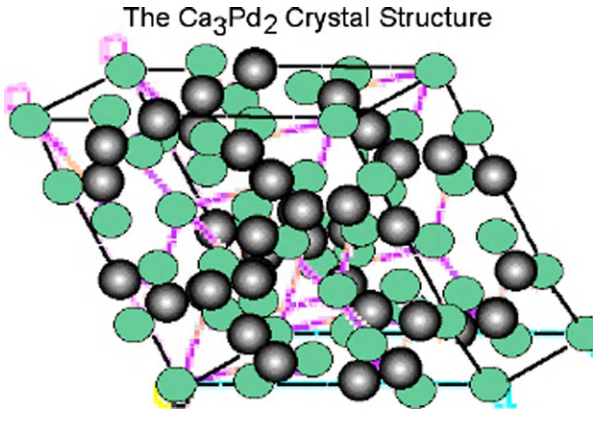

FIGURE 14.37

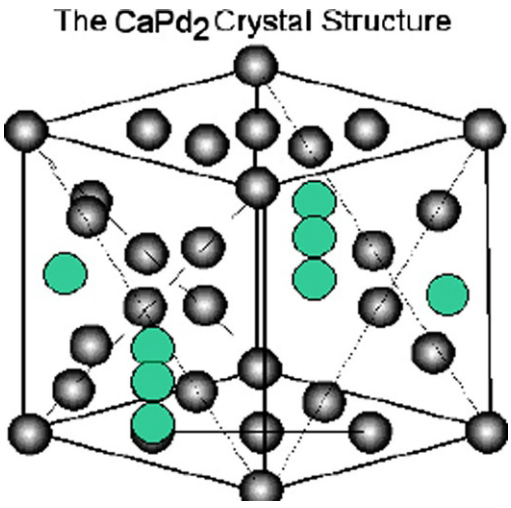

FIGURE 14.38

TABLE 14.25

No.	Site notation	Atom	Multiplicity	Wyckoff	Site symmetry	x	y	z	Occupancy
1	Pd	Pd	16	c	.-3m	0	0	0	1.0
2	Ca	Ca	8	b	-43m	3/8	3/8	3/8	1.0

TABLE 14.26

No.	Site notation	Atom	Multiplicity	Wyckoff	Site symmetry	x	y	z	Occupancy
1	Pd2	Pd	3	g	mmm	1/2	0	1/2	1.0
2	Pd1	Pd	2	c	-6m2	1/3	2/3	0	1.0
3	Ca	Ca	1	a	6/mmm	0	0	0	1.0

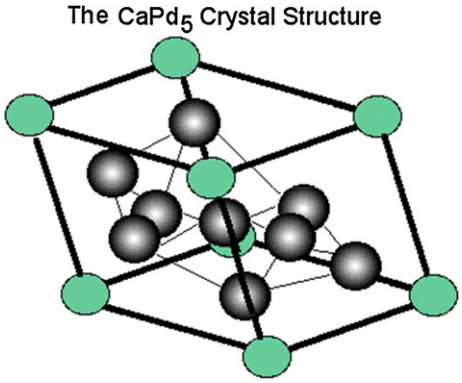

FIGURE 14.39

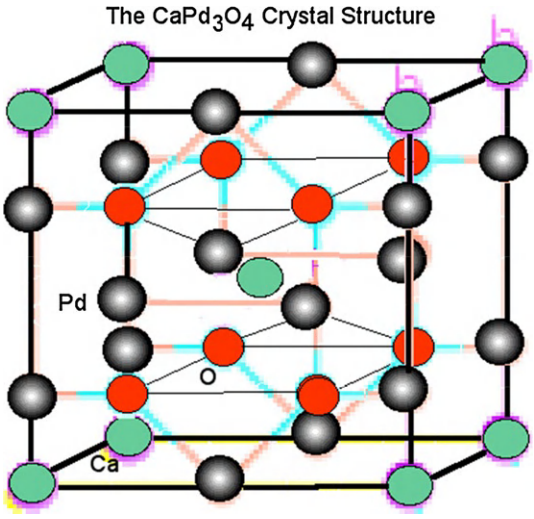

FIGURE 14.40

atoms. $SrPd_3O_4$ and $CaPd_3O_4$ crystallize in space group $Pm3$(no. 223) with $a = 5.8120$ Å, $V = 196.33$ Å^3, $Z = 2$, and $a = 5.7356$ Å, $V = 188.68$ Å^3, $Z = 2$, respectively. It has the structure shown in Fig. 14.40.

A systematic study of the crystal structures of oxopalladates has shown that a change in scale occurs wherein an arrangement of planar PdO_4 polygons link to other isolated PdO_4 units to form $^1_\infty[PdO_3]$- and $^1_\infty[PdO_2]$-chains, square $^1_\infty[Pd_4O_8]$-tubes, and in-plane $^1_\infty[PdO_2]$-nets up to two- and three-dimensional networks. Remarkable is the formation of isolated Pd_6O_{12} rings and cage compounds ($Tl^+Pd_{12}O_{24}$ macropolyhedron) created by the perpendicular crossing of three $Pd_4(gap)_4O_{16}$ rings. PdO_4 polygons in combination with lone pair (LP) active elements produce PdO_4LP_2 octahedra. Pd^{4+} in octahedral coordination corresponds to the expectation but Pd^{4+} inside tetrahedral units and Pd^{2+} inside octahedral units and trigonal prismatic oxygen surrounding Pd^{4+} belong to the abnormal coordination. Mixed valence Pd^{2+} or Pd^{5+} and Pd^{3+} are rarities in palladium chemistry. The metal-rich compounds show a tendency to create clusters.

No compounds are known in the Pd^{3+}-containing system of $CaO–Pd_2O_3$, in the mixed valence of the $Pd^{2+}–Pd^{3+}$-containing system of $CaO–Pd_3O_4$, in the Pd^{4+}-containing system of $CaO–PdO_2$, or in the Pd^{5+}-containing system of $CaO–Pd_2O_5$.

Calcium palladates are not offered for sale commercially and no CAS numbers have been issued.

14.2.4. Strontium Palladium Compounds

Strontium metal forms three intermetallic compounds with Pd. However, the phase diagram has not yet published. The known compounds are: SrPd, $SrPd_3$ and $SrPd_5$.

SrPd has the structure shown in Fig. 14.41.

It consists of Pd–Sr dumb bells tied together into an orthorhombic structure.

Cell parameters are: $a = 4.192$ Å, $b = 4.524$ Å, $c = 6.031$ Å, $\alpha = \gamma = 90°$, $\beta = 110.33°$, cell volume = 107.10 Å^3, $Z = 2$. Cell occupancy is shown in Table 14.27.

TABLE 14.27

No.	Site notation	Atom	Multiplicity	Wyckoff	Site symmetry	x	y	z	Occupancy
1	Pd1	Pd	4	c	m2m	0	0.108	1/4	1.0
2	Sr1	Sr	4	c	m2m	0	0.367	1/4	1.0

TABLE 14.28

No.	Site notation	Atom	Multiplicity	Wyckoff	Site symmetry	x	y	z	Occupancy
1	Pd	Pd	16	c	.-3m	0	0	0	1.0
2	Sr	Sr	8	b	-43m	3/8	3/8	3/8	1.0

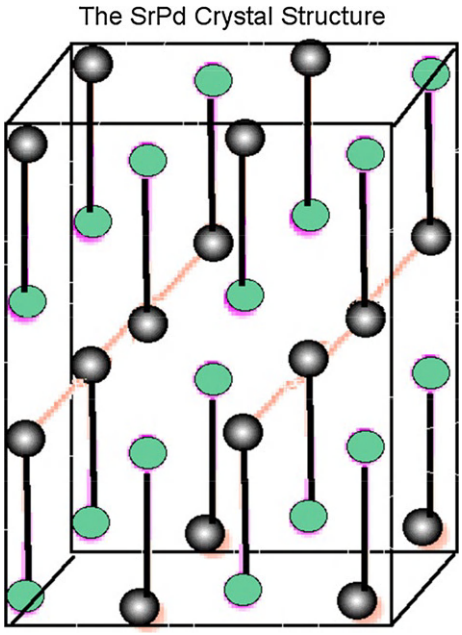

FIGURE 14.41

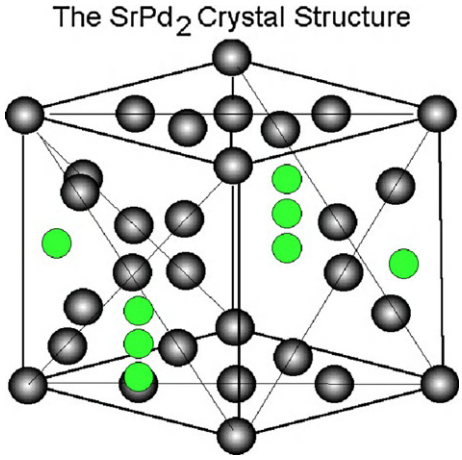

FIGURE 14.42

$SrPd_2$ has the structure shown in Fig. 14.42.

Cell parameters are: $a = b = c = 5.5338$ Å, $\alpha = \beta = \gamma = 60°$, cell volume $= 119.83$ Å^3, $Z = 6$. Cell occupancy is shown in Table 14.28.

$SrPd_5$ has the structure shown in Fig. 14.43.

Cell parameters are: $a = 4.392$ Å, $b = c = 5.383$ Å, $\alpha = 120°$, $\beta = \gamma = 90°$, cell volume $= 110.22$ Å, $Z = 2$. Cell occupancy is shown in Table 14.29.

No other intermetallic compounds are known.

In the Pd^{2+}-containing system of SrO–PdO, Sr_2PdO_3 is body-centered orthorhombic with $a_0 = 3.970$ Å, $b_0 = 3.544$ Å, and $c_0 = 12.84$ Å; the structure proposed for this compound is closely related to the K_2NiF_4 structure.

Three novel black compounds of the $MePd_3O_4$ type have been synthesized. All three have the cubic $Na_xPt_3O_4$ structure with unit cell constants $a_0 = 5.826$ Å for $SrPd_3O_4$, $a_0 = 5.747$ Å for $CaPd_3O_4$, and $a_0 = 5.742$ Å for $CdPd_3O_4$.

A hitherto unknown black $SrPd_3O_4$ [cubic, $a = 5.826$ Å, $NaPt_3O_4$ type] and brown Sr_2PdO_3 [according to X-ray powder patterns orthorhombic, D_{2h}^{25}; $a = 3.977$, $b = 3.530$, $c = 12.82$ Å] were prepared. Single crystals of the ternary palladate $SrPd_3O_4$ were grown out of a potassium hydroxide flux. These small cubic crystals can be readily isolated from the soluble flux matrix and were characterized by SEM and single-crystal X-ray diffraction. $SrPd_3O_4$ features square planar coordination of the palladium atoms. The structure has the form shown in Fig. 14.44.

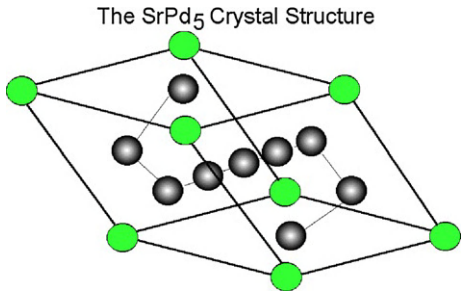

FIGURE 14.43

TABLE 14.29

No.	Site notation	Atom	Multiplicity	Wyckoff	Site symmetry	x	y	z	Occupancy
1	Pd2	Pd	3	g	mmm	1/2	0	1/2	1.0
2	Pd1	Pd	2	c	-6m2	1/3	2/3	0	1.0
3	Sr	Sr	1	a	6/mmm	0	0	0	1.0

TABLE 14.30

No.	Site notation	Atom	Multiplicity	Wyckoff	Site symmetry	x	y	z	Occupancy
1	O	O	8	e	.32	1/4	1/4	1/4	1.0
2	Pd	Pd	6	c	-4m.2	1/4	0	1/2	1.0
3	Sr	Sr	2	a	m-3.	0	0	0	1.0

Cell parameters are: $a = b = c = 5.825$ Å, $\alpha = \beta = \gamma = 90°$, cell volume = 197.65 Å^3, $Z = 2$. Cell occupancy is shown in Table 14.30.

Sr_2PdO_4 has the structure shown in Fig. 14.45.

Call parameters are: $a = 3.652$ Å, $b = 3.972$ Å, $c = 6.949$ Å, $\alpha = 106.61°$, $\beta = 104.76°$, $\gamma = 0°$, cell volume = 0.27 Å^3, $Z = 2$. Cell occupancy is shown in Table 14.31.

The relationship between the two structures is illustrated in Fig. 14.46.

No compounds have been discovered in the Pd^{3+}-containing system of SrO–Pd_2O_3, in the Pd^{2+}–Pd^{3+}-containing system of SrO–Pd_3O_4, or in the Pd^{5+}-containing system of SrO–Pd_2O_5.

In the Pd^{4+}-containing system of SrO–PdO_2, $SrPdO_3$ was prepared by the citrate method. XRD, SEM and TGA characterizations were carried out. The catalytic activity toward hydrogen evolution reaction was investigated, the activation energy, and reaction order and reaction mechanism have been determined using Tafel polarization and impedance techniques. The modified surface showed up to 100 times more efficiency toward electrocatalytic production of hydrogen. Adsorption of hydrogen on the catalyst was the rate-determining step and the reaction order at the surface of the catalyst is 0.86. The molar magnetic susceptibility was measured using Faraday's method and antiferromagnetic character was observed. However, no details of the structure were given and no other confirmation has appeared in the literature.

Strontium palladates are not available commercially for sale nor have any CAS numbers been issued to date.

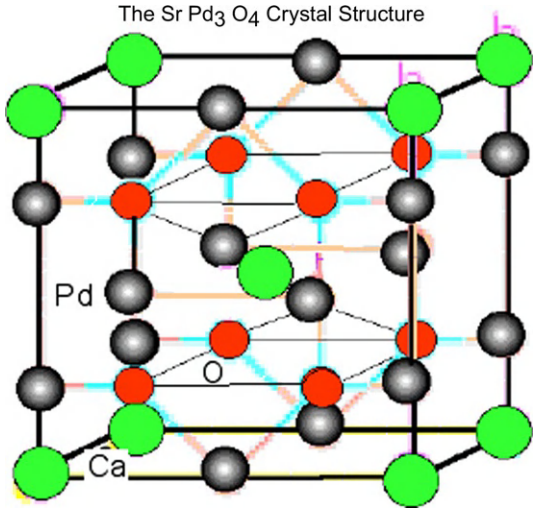

FIGURE 14.44

14.2.5. Barium Palladium Compounds

Barium metal forms a few intermetallic compounds with Pd metal. The phase diagram is incomplete but is shown in Fig. 14.47.

The structure of the compound, BaPd, differs from that of the Ca and Sr homologs (Fig. 14.48).

It consists of two chair forms of (Ba-Pd)$_3$ with the following cell parameters: $a = 4.352$ Å, $b = 4.683$ Å, $c = 6.283$ Å, $\alpha = \gamma = 90°$, $\beta = 110.25°$, cell volume = 120.01 Å^3, $Z = 6$. Cell occupancy is shown in Table 14.32.

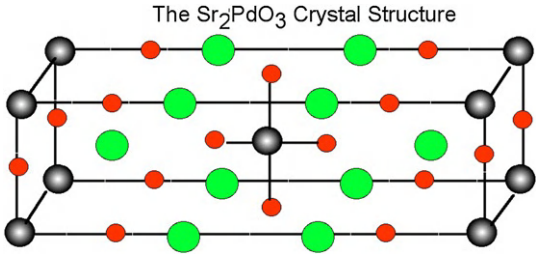

FIGURE 14.45

TABLE 14.31

No.	Site notation	Atom	Multiplicity	Wyckoff	Site symmetry	x	y	z	Occupancy
1	O1	O	4	i	mm2	0	0	0.1547	1.0
2	Sr1	Sr	4	i	mm2	0	0	0.3521	1.0
3	O2	O	2	d	mmm	1/2	0	1/2	1.0
4	Pd1	Pd	2	a	mmm	0	0	0	1.0

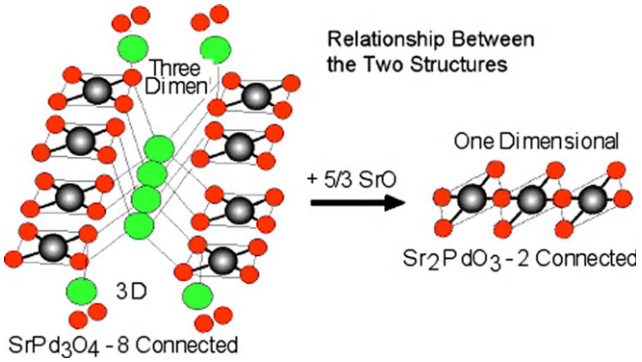

FIGURE 14.46

The compound, $BaPd_2$, has the structure shown in Fig. 14.49.

Cell parameters are: $a = b = c = 5.634$ Å, $\alpha = \beta = \gamma = 60°$, cell volume = 126.42 Å^3, $Z = 4$. Cell occupancy is shown in Table 14.33.

The compound, $BaPd_5$, has the structure shown in Fig. 14.50.

Cell parameters are: $a = 4.332$ Å, $b = c = 5.541$ Å, $\alpha = 120°$, $\beta = \gamma = 90°$, cell volume = 115.09 Å^3, $Z = 2$. Cell occupancy is shown in Table 14.34.

In the Pd^{2+}-containing system of BaO–PdO, the compound, Ba_2PdO_3, has received some attention in the literature. Ba_2PdO_3 is isostructural with Sr_2CuO_3. Its structure has the form shown in Fig. 14.51.

The structural arrangement involves PdO_4 square planes as a 1D chain. The cell parameters are: $a = 3.8362$, $b = 4.080$, $c = 13.335$ Å.

The compounds, $BaPdO_2$ and $BaPd_3O_4$, are unknown in this system, contrary to the CaO–PdO and SrO–PdO systems.

No compounds are known in the Pd^{3+}-containing system of BaO–Pd_2O_3, in the Pd^{2+}–Pd^{3+}-containing system of BaO–Pd_3O_4, in the Pd^{4+}-containing system of BaO–PdO_2, or in the Pd^{5+}-containing system of BaO–Pd_2O_5. It is likely that the lack of formation in these systems is due to the large radius of the Ba^{2+} ion.

Barium palladate compounds are not available commercially nor have any CAS numbers been assigned at this date.

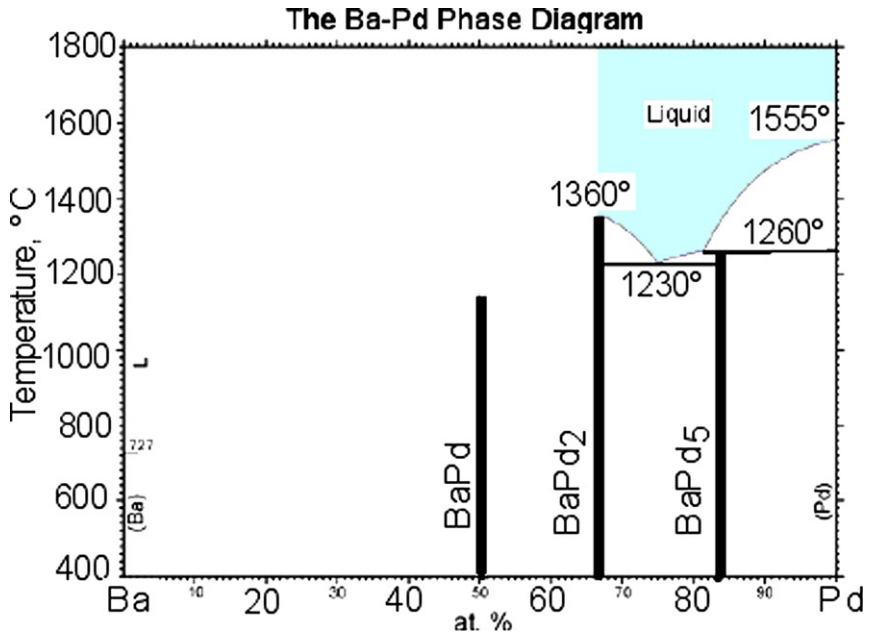

FIGURE 14.47

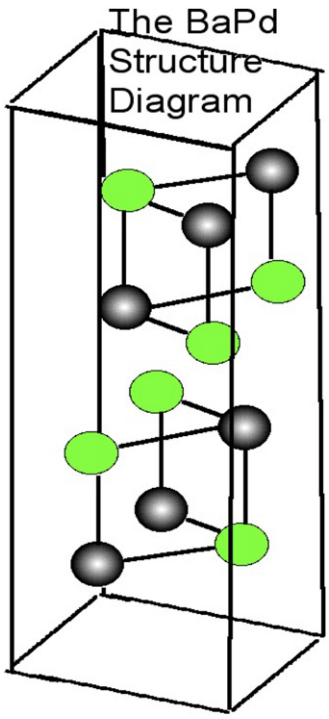

FIGURE 14.48

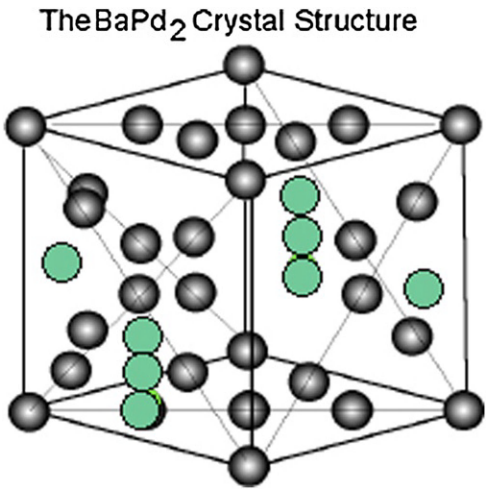

FIGURE 14.49

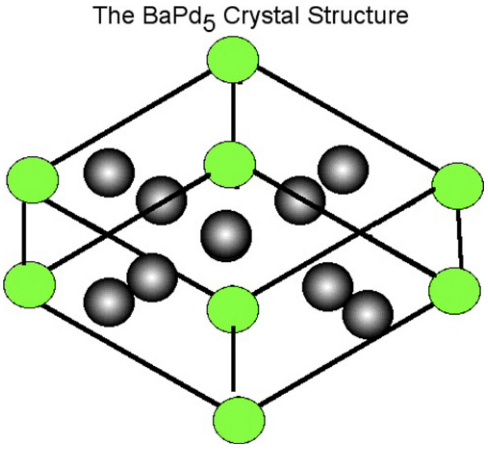

FIGURE 14.50

14.2.6. Radium Palladium Compounds

Because barium forms only one or two compounds with palladium oxides, it is likely that radium does not form any compounds in the systems of $RaO–Pd_xO_y$. However, there is no record of any attempts to form such compounds, due to the high cost and high radioactivity of the $^{226}Ra^{2+}$ ion.

14.3. ALKALINE EARTH PLATINUM COMPOUNDS

Platinum has two major oxidation states, Pt^{2+} and Pt^{4+} which form the oxides, PtO_2 and the less common PtO. These can react to form:

$$2\,PtO + PtO_2 \Rightarrow Pt_3O_4$$

where Pt is in the +4 valence state.

A study has been made concerning the coordination of Pt^{2+} and Pt^{4+} by oxygen wherein the crystal structures of oxo-platinates were systemized. Pt^{2+} exclusively shows,

TABLE 14.32

No.	Site notation	Atom	Multiplicity	Wyckoff	Site symmetry	*x*	*y*	*z*	Occupancy
1	Pd1	Pd	4	c	m2m	0	0.108	1/4	1.0
2	Ba1	Ba	4	c	m2m	0	0.367	1/4	1.0

TABLE 14.33

No.	Site notation	Atom	Multiplicity	Wyckoff	Site symmetry	*x*	*y*	*z*	Occupancy
1	Pd	Pd	16	c	.-3m	0	0	0	1.0
2	Ba	Ba	8	b	-43m	3/8	3/8	3/8	1.0

TABLE 14.34

No.	Site notation	Atom	Multiplicity	Wyckoff	Site symmetry	x	y	z	Occupancy
1	Pd2	Pd	3	g	mmm	1/2	0	1/2	1.0
2	Pd1	Pd	2	c	-6m2	1/3	2/3	0	1.0
3	Ba	Ba	1	a	6/mmm	0	0	0	1.0

in solids, a square and planar coordination well known and typical for Cu^{2+}, Pd^{2+} and Ni^{2+} as well. Often mixed valences (Pt^{2+}/Pt^{4+}) are observed in a square planar oxygen surrounding. Some exceptionally rare coordination is the dumbbell like O–Pt^{2+}–O. The crystal chemistry of Pt^{4+} resembles the countless metal ions showing octahedral coordination by oxygen. Despite different compositions the compounds $BaLn_2PtO_5$, $Ba_3Cu_2Ln_2PtO_{10}$, $Ba_5Ln_8Zn_4O_{21}$, $Ba_{13}Ln_8Zn_4Pt_4O_{37}$ and $Ba_{17}Ln_{16}Zn_8Pt_4O_{57}$ show amazing relationships of polyhedra connections. Additionally was shown that $Ba_4Sm_4Zn_3PtO_{15}$ is isotypic to $Ba_6Nd_2Al_4O_{15}$ and $Ba_4NaCu_{0.5}Pt_{1.5}O_8$ to $Ba_{15}Pt_6O_{27}$. Oxo-platinates containing lone pair active elements show one-side open polyhedra. The positions of the free (s^2) electrons were then calculated using the Coulomb terms of lattice energy. The large size of the Pt ion precludes the formation of stable compounds containing the smaller alkaline earth cations like $Be^{2+}$and Mg^{2+} and possibly Ca^{2+}, if they exist at all.

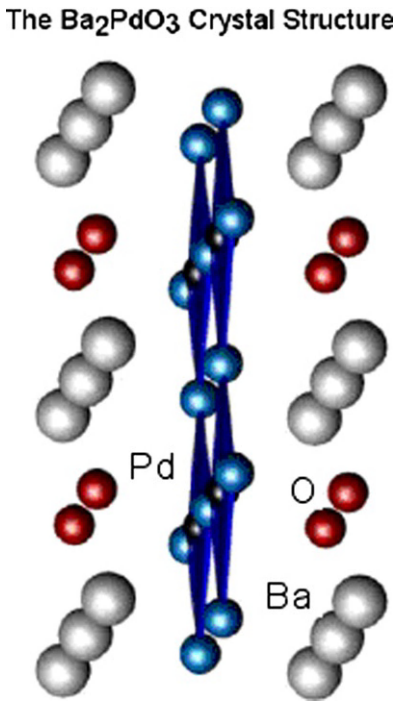

FIGURE 14.51

14.3.1. Beryllium Platinum Compounds

Beryllium forms a few intermetallic compounds with platinum as shown in the phase diagramin Fig. 14.52.

Not all of these compounds have been fully described and only Be_5Pt and $Be_{12}Pt$ have their structure identified. BePt is said to melt congruently but the other melting points have not been clarified.

Be_5Pt has the structure shown in Fig. 14.53.

Cell parameters are: $a = b = c = 4.2271$ Å, $\alpha = \beta = \gamma = 60°$, cell volume $= 53.41$ Å^3, $Z = 4$. Cell occupancy of Be_5Pt is shown in Table 14.35.

$Be_{12}Pt$ has the structure shown in Fig. 14.54.

Cell parameters are: $a = 4.252$ Å, $b = c = 5.5414$ Å, $\alpha = 81.536°$, $\beta = \gamma = 67.44°$, cell volume $= 111.35$ Å^3, $Z = 2$. Cell occupancy is shown in Table 14.36.

The structures of $BePt_{15}$, BePt, and Be_2Pt_5 remain unknown.

In the system, Be–Pt–O, no platinite or platinate compounds are known.

These compounds remain an Academic oddity and no Industry usages have resulted.

14.3.2. Magnesium Platinum Compounds

Magnesium forms a few intermetallic compounds with platinum. However, the phase diagram is the only one in the alkaline earth series that has not been published. At least four compounds are known. Mg_3Pt has the form shown in Fig. 14.55.

Cell parameters are: $a = b = 7.9103$ Å, $c = 8.3223$ Å, $\alpha = \beta = \gamma = 90°$, cell volume $= 450.98$ Å^3, $Z = 6$. Cell occupancy is shown in Table 14.37.

MgPt has the unit cell form shown in Fig. 14.56.

Cell parameters are: $a = b = c = 4.863$ Å, $\alpha = \beta = \gamma = 60°$, cell volume $= 115.00$ Å^3, $Z = 4$. Cell occupancy is shown in Table 14.38.

The compound, $MgPt_3$, is dimorphic and has the structures shown in Fig. 14.57.

$SrPb_3$ type

$a = 3.722$ Å, $b = c = 3.884$ Å, $\alpha = \beta = \gamma = 90°$, $Z = 1$. Cell volume $= 56.00$ Å^3. Cell occupancy is shown in Table 14.39.

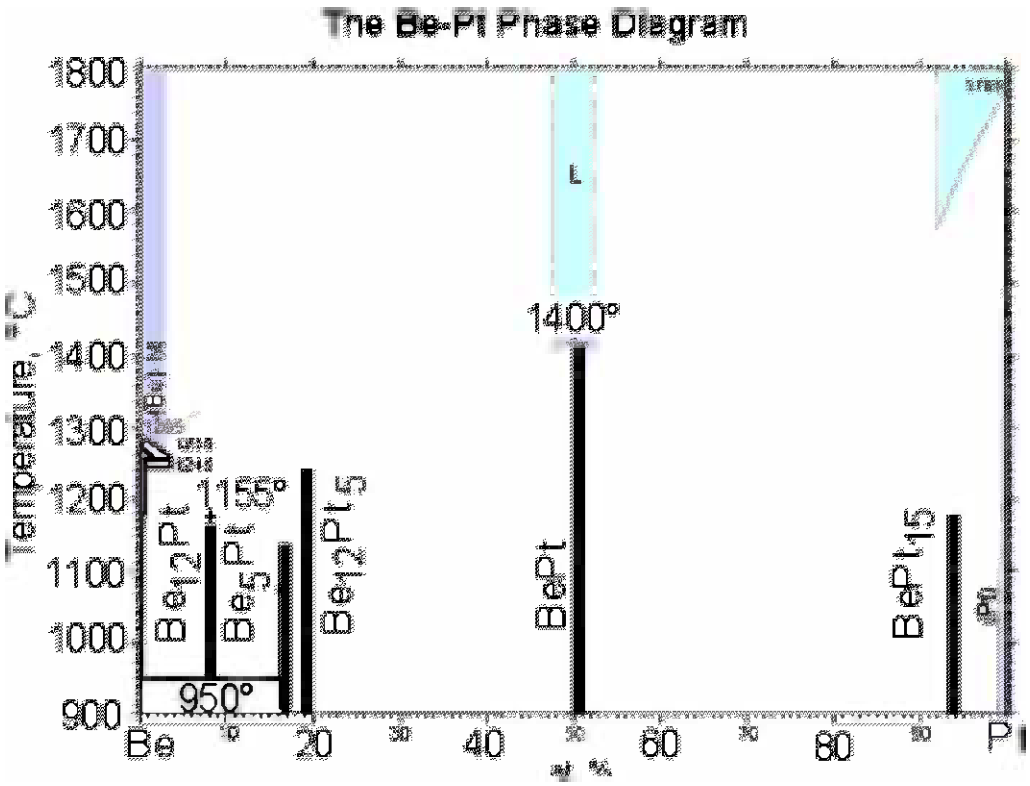

FIGURE 14.52

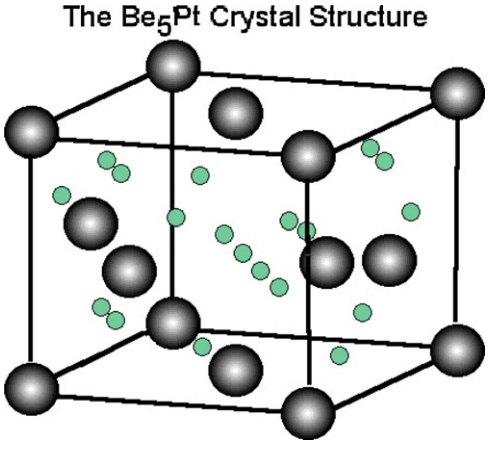

FIGURE 14.53

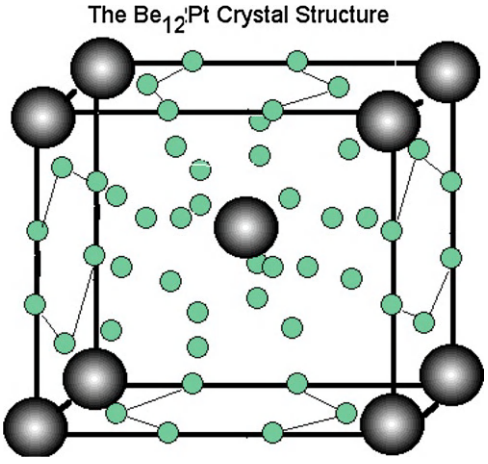

FIGURE 14.54

TABLE 14.35

No.	Site notation	Atom	Multiplicity	Wyckoff	Site symmetry	*x*	*y*	*z*	Occupancy
1	Be2	Be	16	e	.3m	0.625	0.625	0.625	1.0
2	Be1	Be	4	c	-43m	1/4	1/4	1/4	1.0
3	Pt	Pt	4	a	-43m	0	0	0	1.0

TABLE 14.36

No.	Site notation	Atom	Multiplicity	Wyckoff	Site symmetry	x	y	z	Occupancy
1	Be1	Be	8	j	m2m.	0.277	1/2	0	1.0
2	Be2	Be	8	i	m2m.	0.361	0	0	1.0
3	Be3	Be	8	f	..2/m	1/4	1/4	1/4	1.0
4	Pt1	Pt	2	a	4/mmm	0	0	0	1.0

TABLE 14.37

No.	Site notation	Atom	Multiplicity	Wyckoff	Site symmetry	x	y	z	Occupancy
1	Pt	Pt	6	c	..m	0.328	0	0.079	1.0
2	Mg(2)	Mg	6	c	..m	0.376	0	0.396	1.0
3	Mg(1)	Mg	6	c	..m	0.715	0	0.242	1.0
4	Mg(3)	Mg	4	b	3..	1/3	2/3	0.116	1.0
5	Mg(4)	Mg	2	a	3.m	0	0	0.0	1.0

TABLE 14.38

No.	Site notation	Atom	Multiplicity	Wyckoff	Site symmetry	x	y	z	Occupancy
1	Pt1	Pt	4	a	.3.	0.0926	0.0926	0.0926	1.0
2	Mg1	Mg	4	a	.3.	0.3865	0.3865	0.3865	1.0

$AuCu_3$ type

Cell parameters are: $a = b = c = 3.906$ Å, $\alpha = \beta = \gamma = 90°$, cell volume $= 59.59$ Å^3, $Z = 2$. Cell occupancy is shown in Table 14.40.

The compound, $MgPt_7$, has the crystal structure shown in Fig. 14.58.

Unit cell parameters are: $a = b = c = 5.5324$ Å, $\alpha = \beta = \gamma = 60°$, cell volume $= 119.74$ Å^3, $Z = 4$. Cell occupancy is shown in Table 14.41.

No other intermetallic compounds have been discovered.

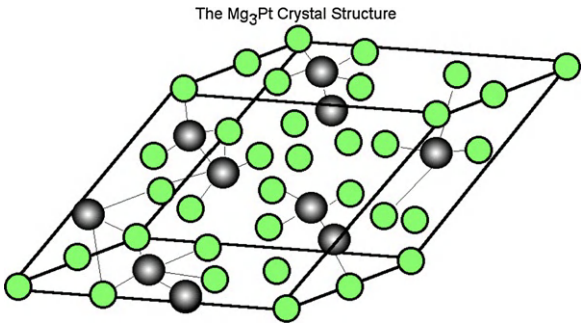

FIGURE 14.55

In the system, Mg–Pt–O, only the +2 and +4 states of Pt form stable compounds. In the Pt^{2+}-containing system of MgO–PtO, the compound, $MgPt_3O_4$, has the structure shown in Fig. 14.59.

Cell parameters are: $a = b = c = 5.642$ Å, $\alpha = \beta = \gamma = 90°$, cell volume $= 179.11$ Å^3, $Z = 2$. Cell occupancy is shown in Table 14.42.

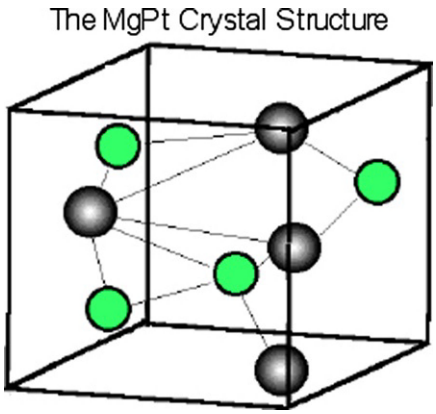

FIGURE 14.56

TABLE 14.39

No.	Site notation	Atom	Multiplicity	Wyckoff	Site symmetry	x	y	z	Occupancy
1	Pt2	Pt	2	e	mmm.	0	1/2	1/2	1.0
2	Mg	Mg	1	c	4/mmm	1/2	1/2	0	1.0
3	Pt1	Pt	1	a	4/mmm	0	0	0	1.0

TABLE 14.40

No.	Site notation	Atom	Multiplicity	Wyckoff	Site symmetry	x	y	z	Occupancy
1	Pt	Pt	3	c	4/mm.m	0	1/2	1/2	1.0
2	Mg	Mg	1	a	m-3m	0	0	0	1.0

Other than its structure, little has been published concerning this compound.

In the Pt^{4+}-containing system of $MgO–PtO_2$, the Mg_2PtO_4 compound has been synthesized. Mg_2PtO_4 and Zn_2PtO_4 can be synthesized at 850–900 °C and oxygen pressures of 150–200 atm. Both oxides are inverse spinels with unit cell constants of $a_0 = 8.521$ Å and $a_0 = 8.549$ Å for Mg_2PtO_4 and Zn_2PtO_4, respectively.

The compound, $MgPtO_3$, is not stable and has only been characterized as an inverse spinel when layered Pt metal is used as a catalyst at 600 °C on a base of $MgAl_2O_4$ to dehydrogenate certain alkanes like n-butane.

No other Pt compounds are known in the MgO–PtO or $MgO–PtO_2$ systems. No magnesium platinate compounds are offered for sale commercially and no CAS numbers have been issued to date.

14.3.3. Calcium Platinum Compounds

Ca metal forms a series of intermetallic compounds with Pt metal as shown in the following phase diagram in Fig. 14.60.

The phase diagram is incomplete and pertinent data like melting points are missing for three of the compounds. At least six compounds are known.

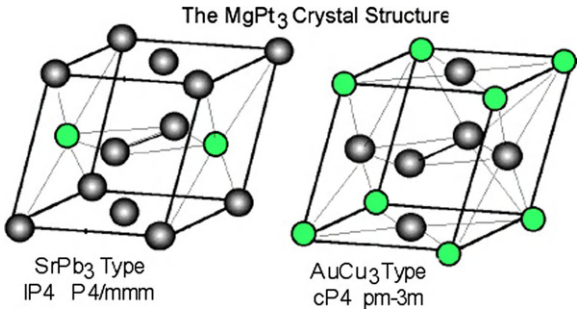

FIGURE 14.57

The Ca_3Pt_2 compound has the structure form shown in Fig. 14.61.

Cell parameters for Ca_3Pt_2 are: $a = b = c = 7.5524$ Å, $\alpha = \beta = \gamma = 71.126°$, cell volume = 374.06 Å^3, $Z = 9$.

Cell occupancy is shown in Table 14.43.

The compound, Ca_5Pt_2, has the crystal form shown in Fig. 14.62.

Cell parameters are: $a = 6.627$ Å, $b = 7.662$ Å, $c = 8.7302$ Å, $\alpha = 96.91°$, $\beta = 112.31°$, $\gamma = 90°$, cell volume = 406.64 Å^3, $Z = 4$. Cell occupancy is shown in Table 14.44.

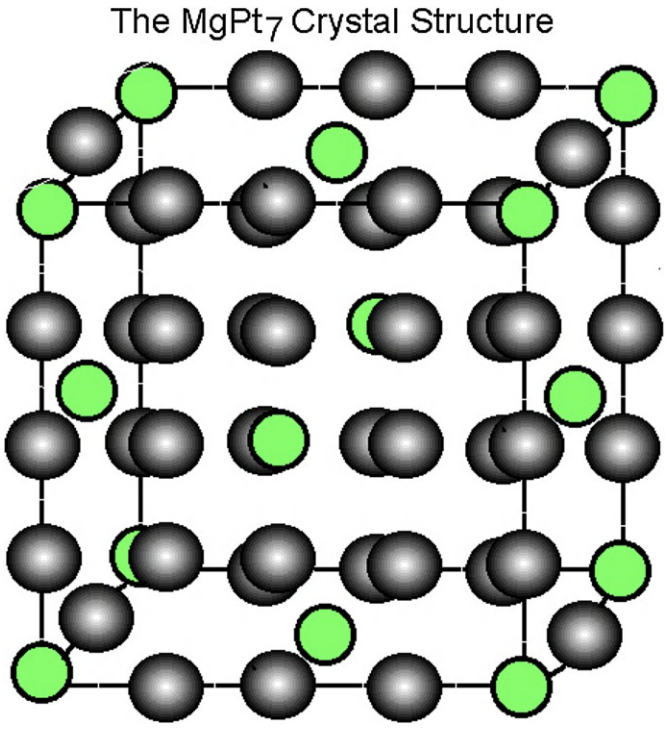

FIGURE 14.58

TABLE 14.41

No.	Site notation	Atom	Multiplicity	Wyckoff	Site symmetry	x	y	z	Occupancy
1	Pt2	Pt	24	d	m.mm	0	1/4	1/4	1.0
2	Pt1	Pt	4	b	m-3m	1/2	1/2	1/2	1.0
3	Mg	Mg	4	a	m-3m	0	0	0	1.0

TABLE 14.42

No.	Site notation	Atom	Multiplicity	Wyckoff	Site symmetry	x	y	z	Occupancy
1	O	O	8	e	.32	1/4	1/4	1/4	1.0
2	Pt	Pt	6	c	-4m.2	1/4	0	1/2	1.0
3	Mg	Mg	2	a	m-3.	0	0	0	1.0

The compound, Ca_5Pt_3, has the crystal form shown in Fig. 14.63.

Cell parameters are: $a = 5.753$ Å, $b = c = 8.6675$ Å, $\alpha = 83.677°$, $\beta = \gamma = 70.628°$, cell volume $= 384.60$ Å^3, $Z = 4$. Cell occupancy is shown in Table 14.45.

The compound, $CaPt_2$, has the crystal form shown in Fig. 14.64.

Cell parameters are: $a = b = c = 5.3945$ Å, $\alpha = \beta = \gamma = 60°$, cell volume $= 111.06$ Å^3, $Z = 8$. Cell occupancy is shown in Table 14.46.

The compound, $CaPt_5$, has the crystal form shown in Fig. 14.65.

Cell parameters are: $a = 4.368$ Å, $b = c = 5.322$ Å, $\alpha = 120°$, $\beta = \gamma = 90°$, cell volume $= 107.14$ Å $\pm 3 \pm$, $Z = 1$. Cell occupancy is shown in Table 14.47.

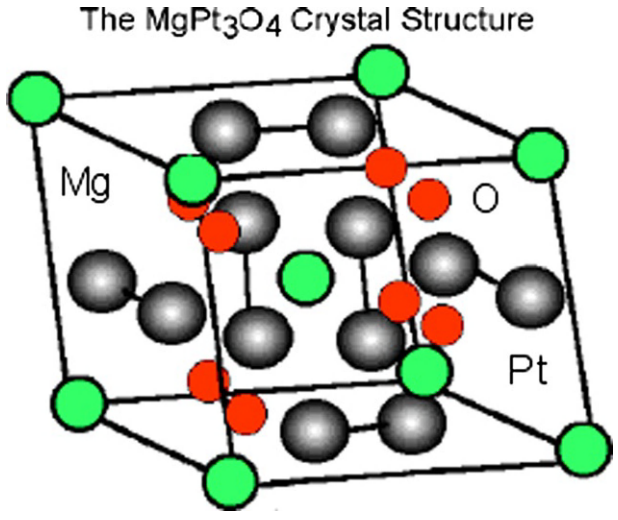

FIGURE 14.59

The compound, Ca_2Pt_7, is known but its structure has not been documented. The thermodynamic properties of this compound include:

Enthalpy of formation: $\Delta H_f = -7.19$ kJ/mol;

Entropy of formation: $S_f = -6.2$ J/K/mol.

No other intermetallic compounds have been discovered.

In the Ca–Pt–O system, a few compounds are known. In the Pt^{2+}-containing system of MgO–PtO, the compound, $CaPt_3O_4$ has been synthesized. It has the structure shown in Fig. 14.66.

Cell parameters are: $a = b = c = 5.743$ Å, $\alpha = \beta = \gamma = 90°$, cell volume $= 189.42$ Å^3, $Z = 2$. Cell occupancy is shown in Table 14.48.

In the Pt^{3+}-containing system of CaO–Pt_2O_3, the compound, $CaPt_2O_4$ has been studied. It has a structure that is a two-dimensional analog of the platinum-bronze structure. It crystallizes in the D^3_{4h}-$P4_2/mmc$ space group of the tetragonal system with two formula groups per unit cell and dimensions of $a = 5.7786$ Å and $c = 5.5987$ Å. The structure is unique in that non-intersecting chains of Pt occur in the x and z directions. One and three dimensions are known and $CaPt_2O_4$ forms the missing link. The unusual formation of Pt^{3+} oxidation state was explained by the metallic bonding between the Pt ions.

A study was made of tight-binding electronic band structures by calculation for the three representative types of ternary platinum oxides with columnar PtO_4 chains, $NaPt_3O_4$, $CaPt_2O_4$, and $CdPt_3O_6$. Despite the dimerization in its columnar PtO_4 chains, $CaPt_2O_4$ is metallic because the upper half of the z^2 band overlaps with the other d-block bands. The dimerization of the columnar PtO_4 chains does not represent a charge density wave instability but is probably caused by the

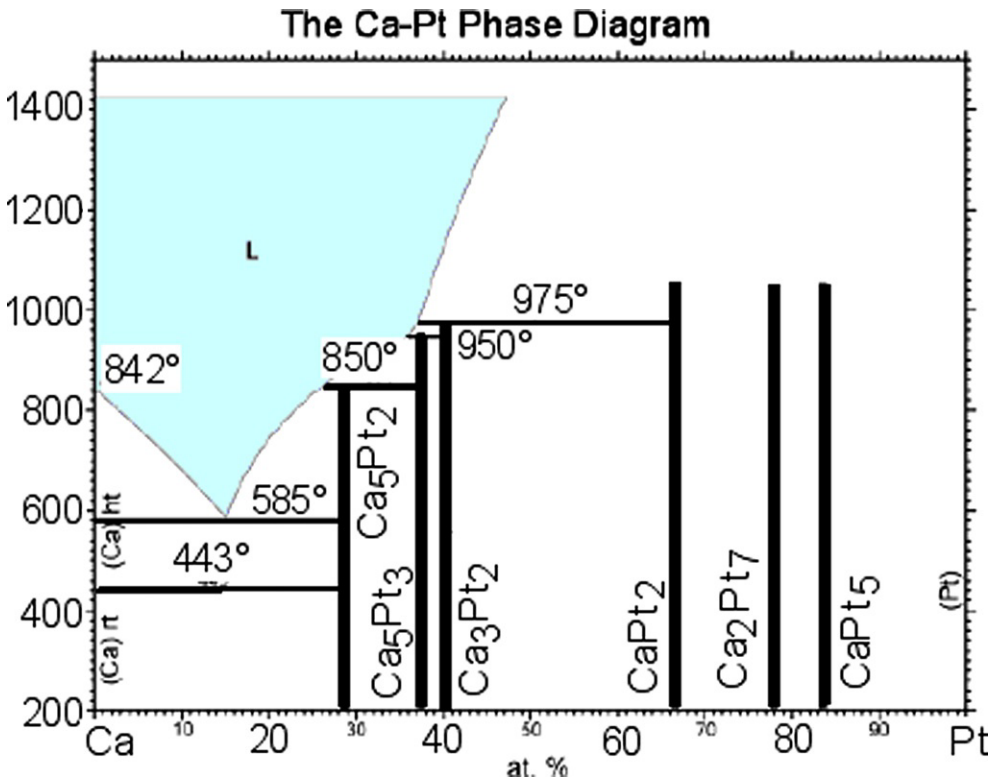

FIGURE 14.60

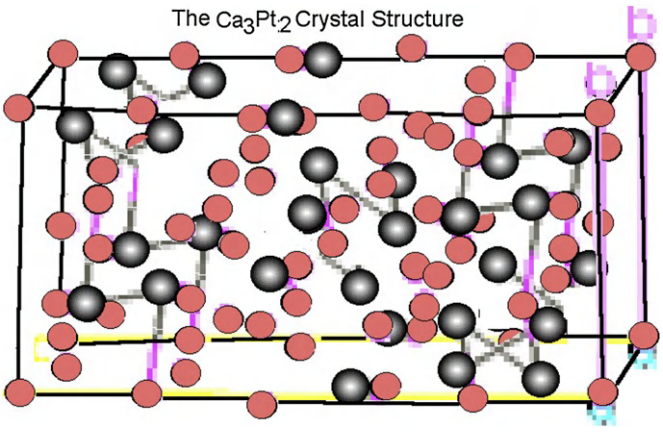

FIGURE 14.61

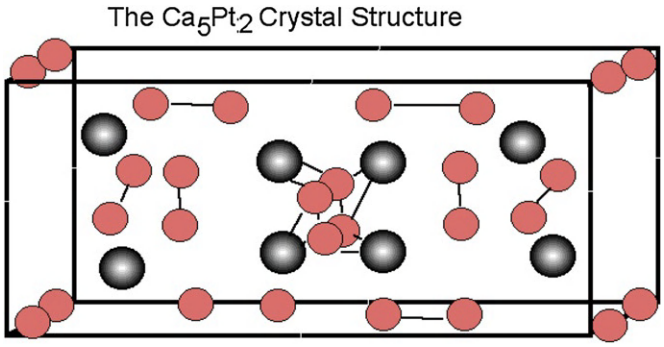

FIGURE 14.62

alternation of filled and unfilled square-prism sites along each chain.

In the Pt^{4+}-containing system of $MgO–PtO_2$, the compound, $CaPtO_3$, has been studied. ABX_3 post-perovskites (or strongly metastable phases at room pressure) are of importance as analogs of post-perovskite $MgSiO_3$, a deep-earth phase stable only at very high pressure. Commonly, $CaIrO_3$ has been used for this purpose, but it has been suggested that $CaPtO_3$ might provide a better analog. The isothermal in compressibility of orthorhombic post-perovskite-structured $CaPtO_3$ to 40 GPa was measured at ambient temperature, by X-ray powder diffraction using synchrotron radiation. A third-order Birch–Murnaghan equation of state fitted to the experimental data yields $V_0 = 228.10$ Å^3, $K_0 = 168.2$ GPa and $K_{-0} = 4.51$. Similar fits to the cube of each axis of the unit-cell shows that the *b*-axis is the most compressible ($b_0 = 9.9191$ Å, $K_0 = 123.3$ GPa, $K_{-0} = 2.37$); the *a*-axis ($a_0 = 3.12777$ Å, $K_0 = 195.7$ GPa, $K_{-0} = 6.63$) and *c*-axis ($c_0 = 7.3551$ Å, $K_0 = 192$ GPa, $K_{-0} = 12.2$) are both more inflexible and have almost identical incompressibility when the material is close to ambient pressure, but the *c*-axis

TABLE 14.43

No.	Site notation	Atom	Multiplicity	Wyckoff	Site symmetry	x	y	z	Occupancy
1	Ca1	Ca	18	f	1	0.0976	0.4135	0.0737	1.0
2	Pt1	Pt	18	f	1	0.3104	0.2467	0.1037	1.0
3	Ca2	Ca	6	c	3.	0	0	0.2085	1.0
4	Ca3	Ca	3	a	-3.	0	0	0	1.0

TABLE 14.44

No.	Site notation	Atom	Multiplicity	Wyckoff	Site symmetry	x	y	z	Occupancy
1	Pt1	Pt	8	f	1	0.1123	0.1960	0.5743	1.0
2	Ca1	Ca	8	f	1	0.222	0.096	0.300	1.0
3	Ca2	Ca	8	f	1	0.401	0.093	0.064	1.0
4	Ca3	Ca	4	e	2	0	0.091	1/4	1.0

TABLE 14.45

No.	Site notation	Atom	Multiplicity	Wyckoff	Site symmetry	x	y	z	Occupancy
1	Ca1	Ca	16	k	m..	0.074	0.223	0	1.0
2	Pt1	Pt	8	h	m.2m	0.17	0.67	0	1.0
3	Ca2	Ca	4	b	-42m	0	1/2	1/4	1.0
4	Pt2	Pt	4	a	422	0	0	1/4	1.0

shows greater stiffening on compression. Comparison of these axial incompressibility with those of $CaIrO_3$ shows that $CaPtO_3$ is slightly less anisotropic under compression (possibly because of the absence of Jahn–Teller distortion), suggesting that $CaPtO_3$ may be a somewhat better analog of $MgSiO_3$. Our sample also contained minor amounts of a cubic four phase, for which the third-order Birch–Murnaghan equation-of-state parameters were found to be: $V_0 = 186.00$ Å^3, $K_0 = 213$ GPa and $K_{-0} = 4.9$.

The structure of one Pt^{4+}-containing compound is known. The Ca_4PtO_6 compound, containing Pt^{4+}, has the structure shown in Fig. 14.67.

Cell parameters are: $a = b = c = 6.5322$ Å, $\alpha = \beta = \gamma = 90.274$ Å, cell volume $= 278.72$ Å^3, $Z = 6$.

Cell occupancy is shown in Table 14.49.

Ca_2PtO_4 is also known. The derivation of the energy-volume equations of state EOS for Ca_2PtO_4 as a Ca_2IrO_4 type, and in K_2NiF_4 type (knf) structures, has led to an energy destabilization at a larger volume for the latter. This led to the proposal that the former is a post-K_2NiF_4—pknf—occurring compound at high pressures having a reduced

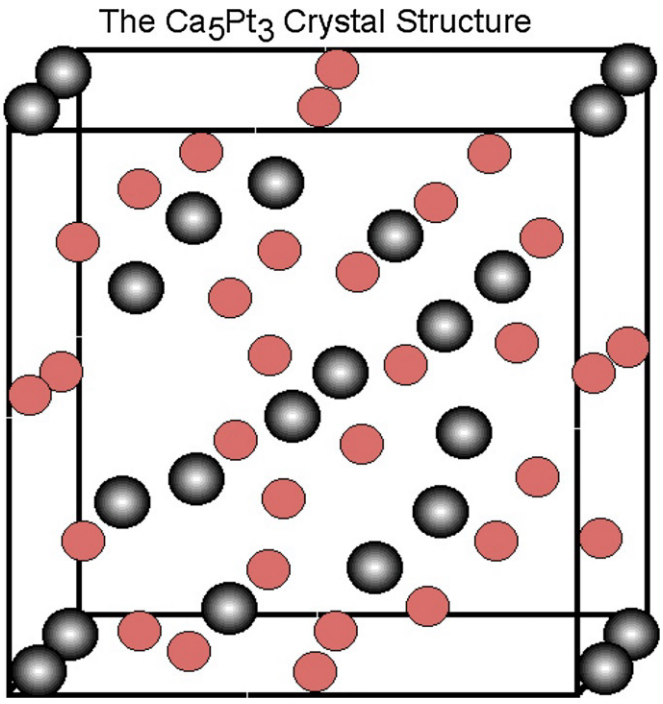

FIGURE 14.63

TABLE 14.46

No.	Site notation	Atom	Multiplicity	Wyckoff	Site symmetry	*x*	*y*	*z*	Occupancy
1	Pt	Pt	16	c	.-3m	0	0	0	1.0
2	Ca	Ca	8	b	-43m	3/8	3/8	3/8	1.0

TABLE 14.47

No.	Site notation	Atom	Multiplicity	Wyckoff	Site symmetry	*x*	*y*	*z*	Occupancy
1	Pt2	Pt	3	g	mmm	1/2	0	1/2	1.0
2	Pt1	Pt	2	c	-6m2	1/3	2/3	0	1.0
3	Ca	Ca	1	a	6/mmm	0	0	0	1.0

TABLE 14.48

No.	Site notation	Atom	Multiplicity	Wyckoff	Site symmetry	*x*	*y*	*z*	Occupancy
1	O	O	8	e	.32	1/4	1/4	1/4	1.0
2	Pt	Pt	6	c	-4m.2	1/4	0	1/2	1.0
3	Ca	Ca	2	a	m-3.	0	0	0	1.0

dimensionality, 2D-knf ⇒ 1D-pknf and a rearrangement of the PtO_6 octahedra from corner sharing in knf to edge sharing in pknf. Bader charge analysis indicated an increased covalence of Pt–O bond with such a transformation. The lowered dimensionality is also illustrated from the density of states (Fig. 14.68).

This diagram illustrates the facts:

- Transformations of 3D perovskite (pv) to 2D post-perovskite (ppv-ABO_3) with pressure *P* are known.
- That, in parallel, the K_2NiF_4 type (knf) is a potential low *P* form of Ca_2IrO_4 type (pknf).
- Pressure transformation of 2D corner-sharing octahedra (knf) to 1D edge-sharing octahedra (pknf) occurs.
- Augmentation based on DFT computations of equation of state, charge density, DOS for the Ca_2PtO_4 case was confirmed.

A novel A-site ordered perovskite $CaCu_3Pt_4O_{12}$ was synthesized under high pressure and high temperature of 12 GPa and 1250 °C. $CaCu_3Pt_4O_{12}$ is the first perovskite in which the B site is fully occupied by Pt^{4+}. The crystal structure refinement based on the synchrotron powder X-ray diffraction data shows that $CaCu_3Pt_4O_{12}$ crystallizes in the space group *Im* (cubic) with a lattice constant of $a = 7.48946$ Å. The magnetic susceptibility data show the antiferromagnetic transition at $T_N = 40$ K, which is attributed to the magnetic ordering

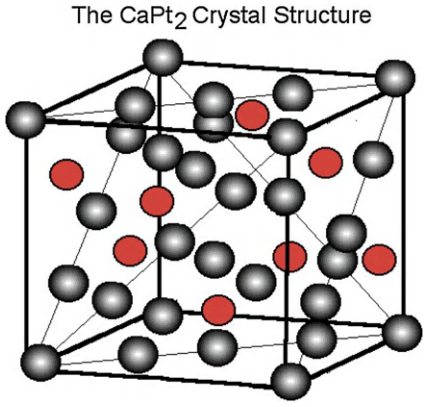

FIGURE 14.64

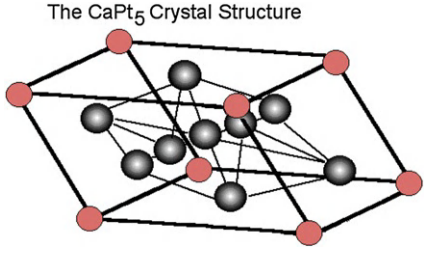

FIGURE 14.65

TABLE 14.49

No.	Site notation	Atom	Multiplicity	Wyckoff	Site symmetry	x	y	z	Occupancy
1	O1	O	36	f	1	0.1911	0.0315	0.1023	1.0
2	Ca1	Ca	18	e	.2	0.3757	0	1/4	1.0
3	Pt1	Pt	6	b	-3.	0	0	0	1.0
4	Ca2	Ca	6	a	32	0	0	1/4	1.0

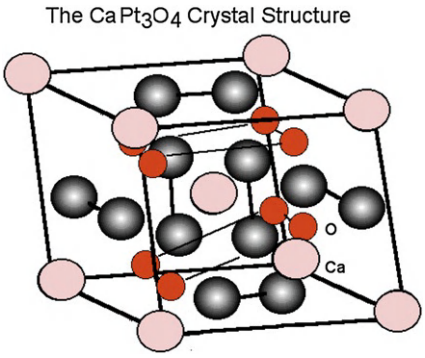

FIGURE 14.66

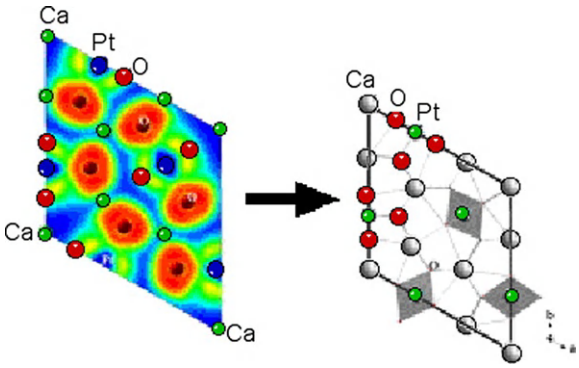

FIGURE 14.68

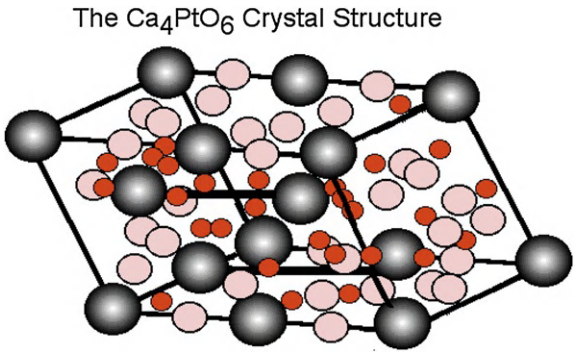

FIGURE 14.67

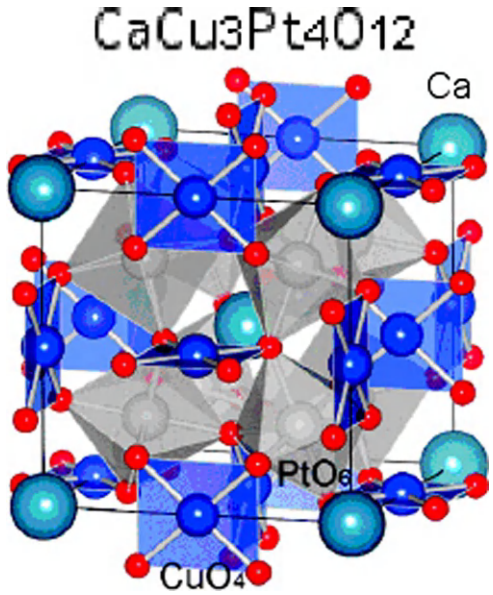

FIGURE 14.69

of Cu^{2+} spins with $S = 1/2$. It has the structure shown in Fig. 14.69.

No other calcium platinate compounds are known. There are no calcium platinates offered for sale commercially.

14.3.4. Strontium Platinum Compounds

Platinum metal forms a small number of intermetallic compounds with strontium metal, as shown in the following phase diagram in Fig. 14.70.

The compound, $SrPt_5$ has the structure shown in Fig. 14.71.

Cell parameters are: $a = 4.364$ Å, $b = c = 5.397$ Å, $\alpha = 120°$, $\beta = \gamma = 90°$, cell volume $= 110.08$ Å^3, $Z = 1$. Cell occupancy is shown in Table 14.50.

$SrPt_2$ has the crystal form shown in Fig. 14.72.

Cell parameters are: $a = b = c = 5.499$ Å, $\alpha = \beta = \gamma = 60°$, cell volume $= 117.59$ Å^3, $Z = 8$. Cell occupancy is shown in Table 14.51.

Although Sr_9Pt is listed as a compound in the phase diagram, its crystal structure has not been finalized. The only data available are the cell parameters of: $a = b = c = 4.307$ Å, $\alpha = \beta = \gamma = 60°$, cell volume $= 56.59$ Å^3, $Z = 2$.

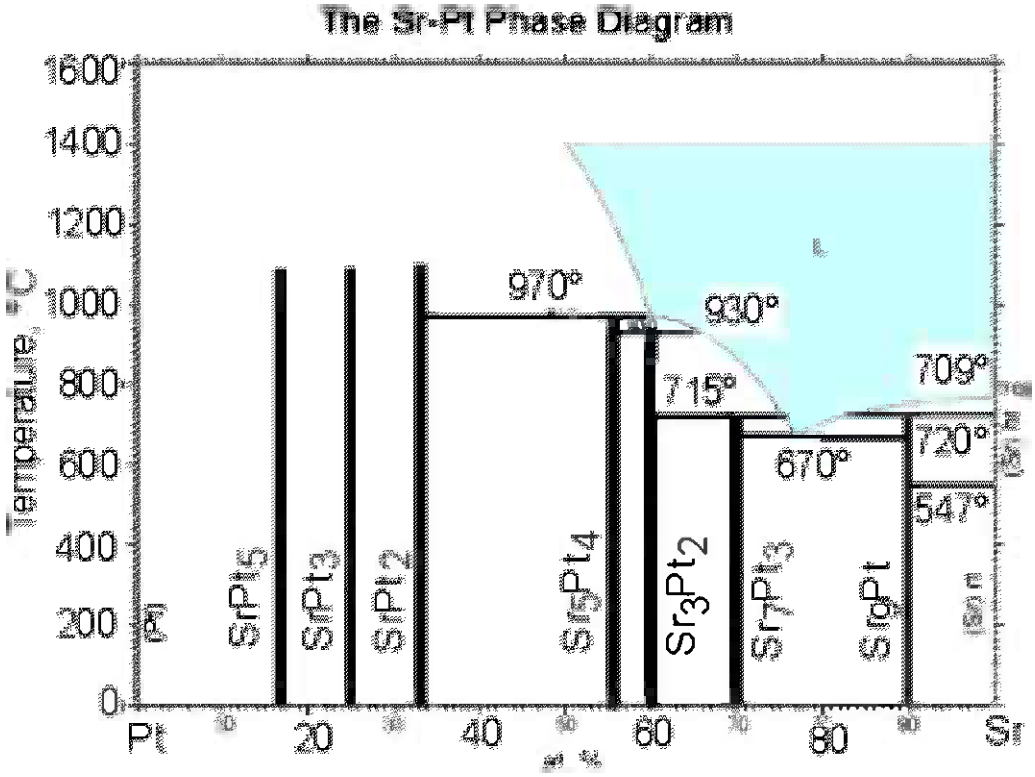

FIGURE 14.70

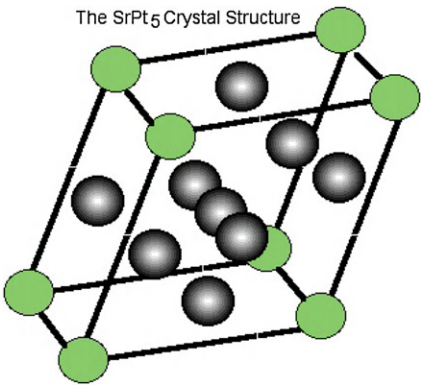

FIGURE 14.71

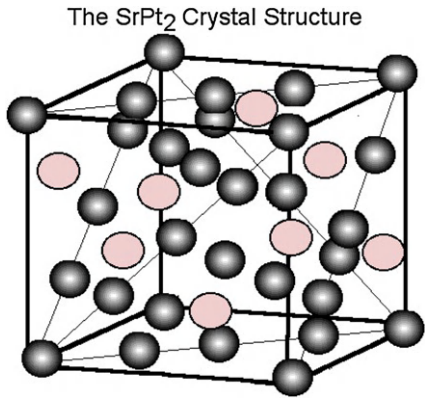

FIGURE 14.72

The compound, Sr_7Pt_3, has the crystal structure shown in Fig. 14.73.

Cell parameters are: $a = 7.134$ Å, $b = 7.929$ Å, $c = 24.326$ Å, $\alpha = \beta = \gamma = 90°$, cell volume = 1359.45 Å^3, $Z = 4$. Cell occupancy is shown in Table 14.52.

The compound, Sr_5Pt_4, has the form shown in Fig. 14.74.

Cell parameters are: $a = 7.879$ Å, $b = 8.147$ Å, $c = 15.606$ Å, $\alpha = \beta = \gamma = 90°$, cell volume = 1001.75 Å^3, $Z = 4$. Cell occupancy is shown in Table 14.53.

The compound, Sr_3Pt_2, has the crystal form shown in Fig. 14.75.

Cell parameters are: $a = b = c = 8.007$ Å, $\alpha = \beta = \gamma = 71.33°$, cell volume = 447.01 Å^3, $Z = 9$. Cell occupancy is shown in Table 14.54.

In the Pt^{2+}-containing system of SrO–PtO, the structure of $SrPtO_2$ has been determined (Fig. 14.76).

Pt forms a square planar structure of PtO_4 units surrounded by layers of four Sr ions, arranged in a cubic lattice.

The structures and electronic properties of a number of real and hypothetical ABX2 compounds sharing (or evolving from) a single $P4/mmm$ structural type were

TABLE 14.50

No.	Site notation	Atom	Multiplicity	Wyckoff	Site symmetry	*x*	*y*	*z*	Occupancy
1	Pt2	Pt	3	g	mmm	1/2	0	1/2	1.0
2	Pt1	Pt	2	c	-6m2	1/3	2/3	0	1.0
3	Sr	Sr	1	a	6/mmm	0	0	0	1.0

TABLE 14.51

No.	Site notation	Atom	Multiplicity	Wyckoff	Site symmetry	*x*	*y*	*z*	Occupancy
1	Pt	Pt	16	c	.-3m	0	0	0	1.0
2	Sr	Sr	8	b	-43m	3/8	3/8	3/8	1.0

TABLE 14.52

No.	Site notation	Atom	Multiplicity	Wyckoff	Site symmetry	*x*	*y*	*z*	Occupancy
1	Sr3	Sr	8	d	1	0.0410	0.6158	0.1514	1.0
2	Pt1	Pt	8	d	1	0.1184	0.0966	0.4615	1.0
3	Sr1	Sr	8	d	1	0.3212	0.1744	0.1829	1.0
4	Sr2	Sr	8	d	1	0.3298	0.0216	0.1808	1.0
5	Pt2	Pt	4	c	.m.	0.0226	1/4	0.0364	1.0
6	Sr4	Sr	4	c	.m.	0.1764	1/4	0.6444	1.0

examined. These include the known $CaCuO_2$ and $SrPtO_2$ phases. A number of variations of this *P*4/*mmm* ABX_2 framework, some obvious, some exotic, all with a chemical motivation, were investigated. Careful attention was given to the d-orbital splitting patterns and magnetic states (ferromagnetic or antiferromagnetic) of these compounds, as well as their stability gaged by phonon dispersions and energetics. $SrPtO_2$, and $LaPtO_2$ have antiferromagnetically coupled ground states.

No other data are available concerning the other possible compounds in this Pt^{2+}-containing system.

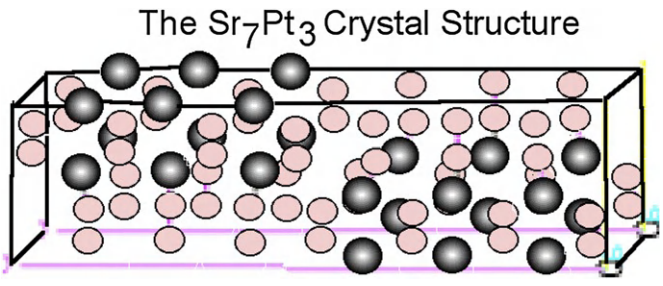

FIGURE 14.73

In the Pt^{4+}-containing system of SrO–PtO_2, the compound, Sr_4PtO_6 has been studied. It has the structure shown in Fig. 14.77.

Cell parameters are: $a = b = c = 6.881$ Å, $\alpha = \beta = \gamma = 90.093°$, cell volume $= 325.89$ Å^3, $Z = 6$. Cell occupancy is shown in Table 14.55.

Another view of the structure is shown in Fig. 14.78.

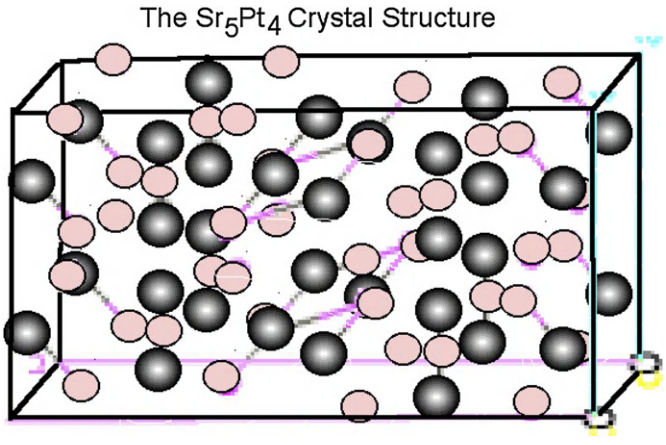

FIGURE 14.74

TABLE 14.53

No.	Site notation	Atom	Multiplicity	Wyckoff	Site symmetry	*x*	*y*	*z*	Occupancy
1	Sr1	Sr	8	d	1	0.0253	0.1004	0.6781	1.0
2	Pt1	Pt	8	d	1	0.2206	0.0449	0.0312	1.0
3	Sr2	Sr	8	d	1	0.3795	0.1157	0.3388	1.0
4	Pt2	Pt	4	c	.m.	0.0868	1/4	0.3885	1.0
5	Sr3	Sr	4	c	.m.	0.212	1/4	0.0024	1.0
6	Pt3	Pt	4	c	.m.	0.3239	1/4	0.6333	1.0

TABLE 14.54

No.	Site notation	Atom	Multiplicity	Wyckoff	Site symmetry	*x*	*y*	*z*	Occupancy
1	Sr1	Sr	18	f	1	0.0976	0.4135	0.0737	1.0
2	Pt1	Pt	18	f	1	0.3104	0.2467	0.1037	1.0
3	Sr2	Sr	6	c	3.	0	0	0.2085	1.0
4	Sr3	Sr	3	a	-3.	0	0	0	1.0

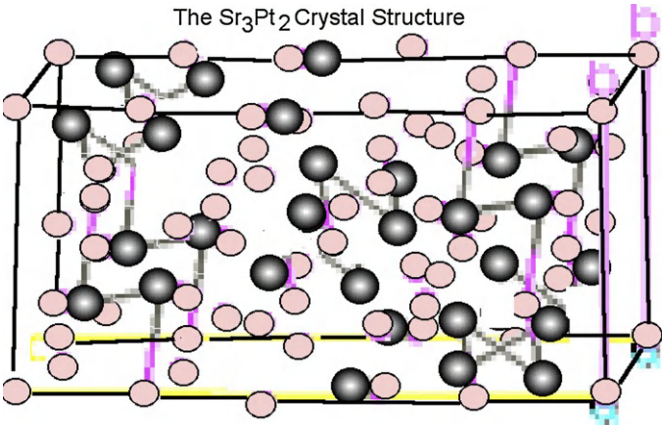

FIGURE 14.75

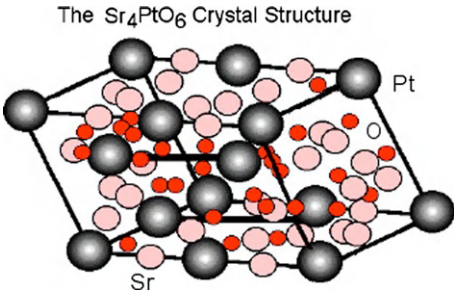

FIGURE 14.77

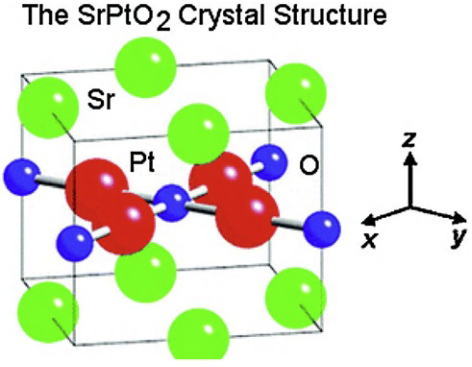

FIGURE 14.76

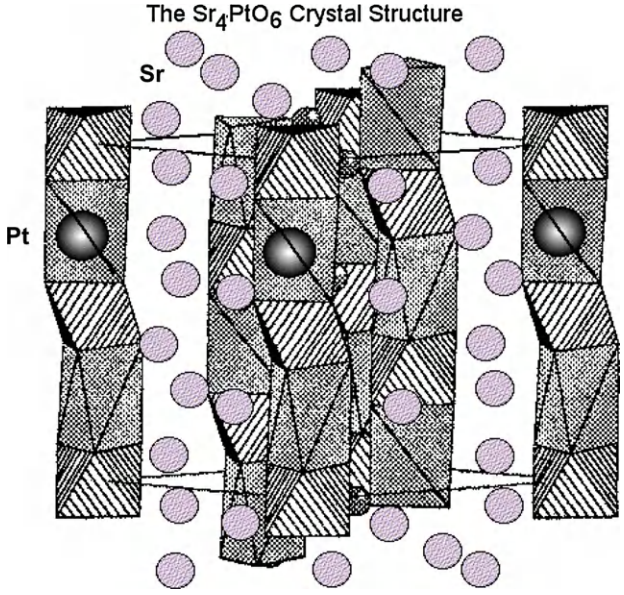

FIGURE 14.78

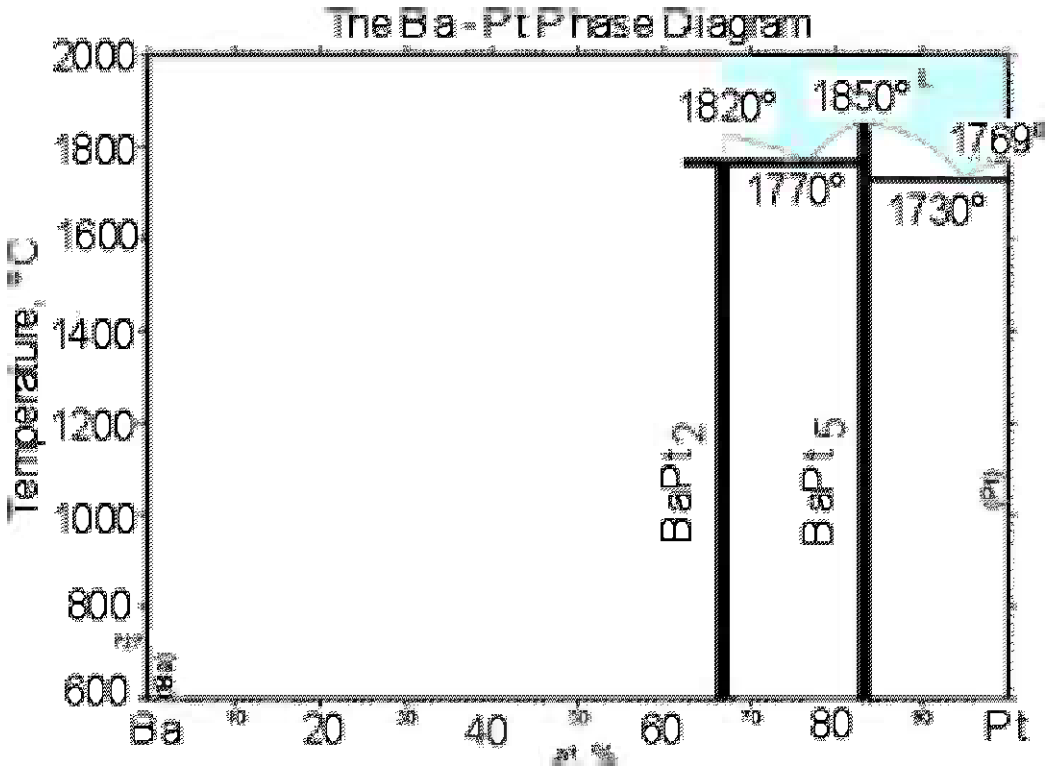

FIGURE 14.79

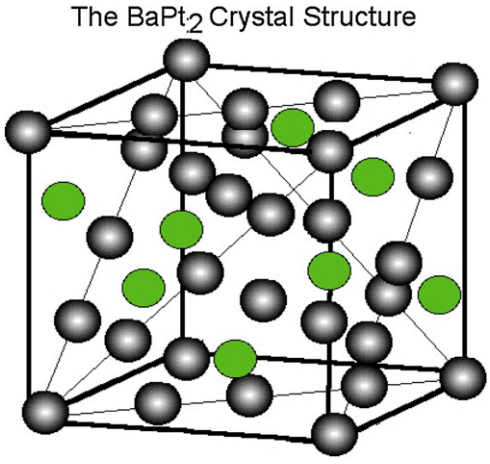

FIGURE 14.80

Here, only two of the PtO_6 octahedra show the Pt atom. The crystals are trigonal with space group *R*3*c*; the triply primitive hexagonal cell dimensions are $a = 9.74$, $c = 11.90$ Å. The platinum ions are octahedrally coordinated with oxygen and are linked in the *c*-direction through strontium ions surrounded by trigonal prisms of oxygen atoms. These strings of coordination polyhedra are connected laterally by strontium atoms in eightfold coordination with oxygen. This structure is of the same type as that reported for K_4CdC_{16}. The isolation of one PtO_6 group from the next is postulated as a reason for the ease of hydrolysis of the compound. Sr_4IrO_6 and Sr_4RhO_6 have the same structure.

No other compounds in the systems, SrO–PtO or $SrO–PtO_2$ have been reported.

Strontium platinate or platinite compounds are available for sale commercially.

14.3.5. Barium Platinum Compounds

Barium metal forms a few intermetallic compounds with Pl metal. The phase diagram is incomplete but lists two compounds, as shown in Fig. 14.79.

The compound, $BaPt_2$, has the structure shown in Fig. 14.80.

Cell parameters are: $a = b = c = 5.6144$ Å, $\alpha = \beta = \gamma = 60°$, cell volume $= 125.14$ Å^3, $Z = 8$. Cell occupancy is shown in Table 14.56.

A better view of $BaPt_2$ is shown in Fig. 14.81.

No other data are available in the literature.

The compound, $BaPt_5$, has the structure shown in Fig. 14.82.

Cell parameters are: $a = 4.337$ Å, $b = c = 5.505$ Å, $\alpha = 120°$, $\beta = \gamma = 90\underline{0}$, cell volume $= 113.82$ Å^3, $Z = 1$. Cell occupancy is shown in Table 14.57.

TABLE 14.55

No.	Site notation	Atom	Multiplicity	Wyckoff	Site symmetry	*x*	*y*	*z*	Occupancy
1	O	O	36	f	1	0.181	0.011	0.093	1.0
2	Sr2	Sr	18	e	.2	0.37	0	1/4	1.0
3	Pt	Pt	6	b	-3.	0	0	0	1.0
4	Sr1	Sr	6	a	32	0	0	1/4	1.0

TABLE 14.56

No.	Site notation	Atom	Multiplicity	Wyckoff	Site symmetry	*x*	*y*	*z*	Occupancy
1	Pt	Pt	16	c	.-3m	0	0	0	1.0
2	Ba	Ba	8	b	-43m	3/8	3/8	3/8	1.0

TABLE 14.57

No.	Site notation	Atom	Multiplicity	Wyckoff	Site symmetry	*x*	*y*	*z*	Occupancy
1	Pt2	Pt	3	g	mmm	1/2	0	1/2	1.0
2	Pt1	Pt	2	c	-6m2	1/3	2/3	0	1.0
3	Ba	Ba	1	a	6/mmm	0	0	0	1.0

No other intermetallic compounds are known. There have been no descriptions of the physical properties of these compounds and they are not offered for sale commercially. No CAS numbers have been issued to date.

In the Pt^{2+}-containing system of BaO–PtO, if $BaCO_3$ is heated with Pt metal in an oxidizing atmosphere, the compound, $BaPtO_2$ is formed:

$$BaCO_3 + Pt + O_2 + \text{heat (600–800 °C)} \Rightarrow BaPtO_2$$

$$5\ BaPtO_2 + \text{heat (>800 °C)} \Rightarrow 5\ BaPtO_{2.38} + O_2$$

However, heating this compound above 800 °C in an oxidizing atmosphere causes oxidation of Pt^{2+} to Pt^{4+} with formation of a defect structure lacking oxygen atoms. Above 1200 °C, this structure looses further oxygen to form compounds of indeterminate compositions. $BaPtO_2$ has the structure shown in Fig. 14.83.

Nonetheless, other than structure, little is known concerning this compound.

The compound, $BaPt_3O_4$, is known. It has the structure shown in Fig. 14.84.

Cell parameters are: $a = b = c = 5.715$ Å, $\alpha = \beta = \gamma = 90°$, cell volume = 186.66 Å^3, $Z = 1$. Cell occupancy is shown in Table 14.58.

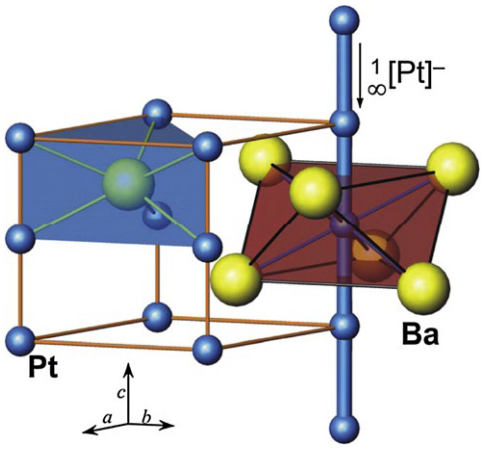

FIGURE 14.81

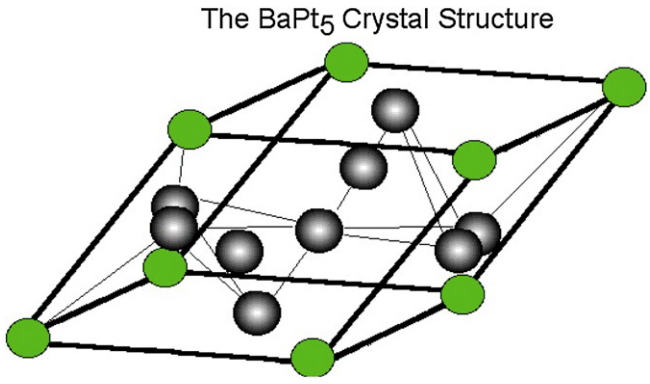

FIGURE 14.82

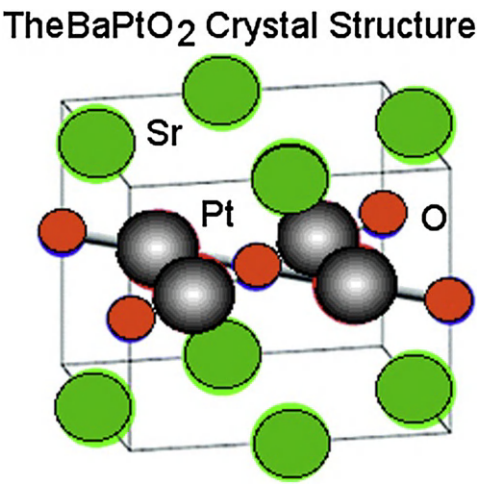

FIGURE 14.83

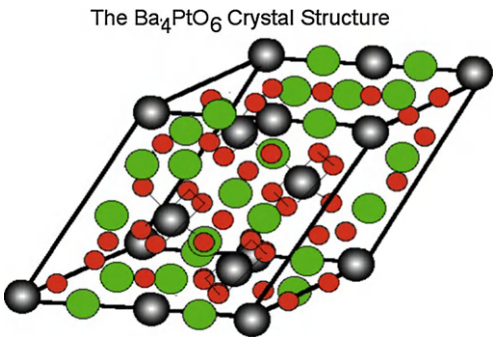

FIGURE 14.85

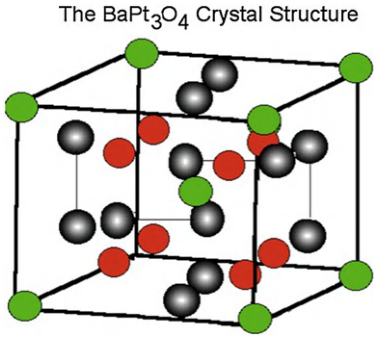

FIGURE 14.84

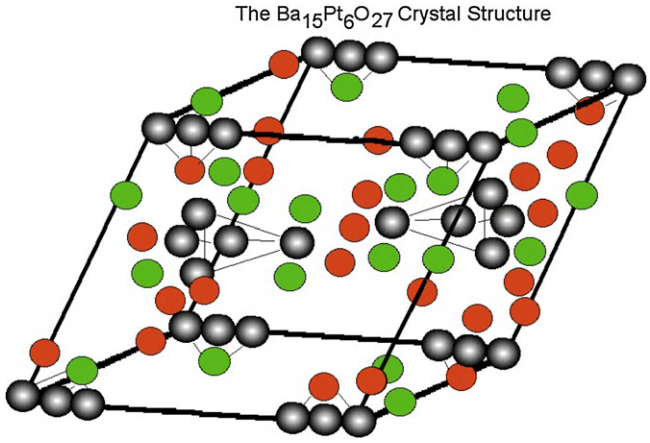

FIGURE 14.86

TABLE 14.58

No.	Site notation	Atom	Multiplicity	Wyckoff	Site symmetry	*x*	*y*	*z*	Occupancy
1	O	O	8	e	.32	1/4	1/4	1/4	1.0
2	Pt	Pt	6	c	-4m.2	1/4	0	1/2	1.0
3	Ba	Ba	2	a	m-3.	0	0	0	1.0

TABLE 14.59

No.	Site notation	Atom	Multiplicity	Wyckoff	Site symmetry	x	y	z	Occupancy
1	O	O	36	f	1	0.1774	0.0218	0.0953	1.0
2	Ba2	Ba	18	e	.2	0.3690	0	1/4	1.0
3	Pt	Pt	6	b	-3.	0	0	0	1.0
4	Ba1	Ba	6	a	32	0	0	1/4	1.0

TABLE 14.60

No.	Site notation	Atom	Multiplicity	Wyckoff	Site symmetry	x	y	z	Occupancy
1	O1	O	12	i	1	0.176	0.512	0.055	1.0
2	O3	O	6	h	m..	0.17	0.14	1/4	1.0
3	Ba1	Ba	6	h	m..	0.3337	0.0192	1/4	1.0
4	Pt3	Pt	6	h	m..	0.3353	0.5975	1/4	0.17
5	O2	O	6	h	m..	0.525	0.357	1/4	1.0
6	O4	O	6	g	.2.	0.156	0	0	0.74
7	Ba2	Ba	6	g	.2.	0.6646	0	0	1.0
8	Pt2	Pt	4	f	3..	1/3	2/3	0.1984	0.25
9	Pt1	Pt	4	f	3..	1/3	2/3	0.5907	1.0
10	Pt5	Pt	4	e	3..	0	0	0.0877	0.18
11	Pt4	Pt	4	e	3..	0	0	0.1554	0.33
12	Pt6	Pt	2	a	32.	0	0	0	0.12

Little data concerning its physical or electrical properties have been published for this compound. The technical literature is devoid of any mention of other BaO–PtO compounds.

In the Pt^4-containing system of $BaO–PtO_2$, the compound, Ba_4PtO_6, is known. It has the structure shown in Fig. 14.85.

Cell parameters are: $a = b = c = 7.241$ Å, $\alpha = \beta = \gamma = 89.66°$, cell volume $= 379.69$ Å^3, $Z = 6$. Cell occupancy is shown in Table 14.59.

The compound, $Ba_{15}Pt_6O_{27}$, has the structure shown in Fig. 14.86.

Cell parameters are: $a = 8.638$ Å, $b = c = 10.108$ Å, $\alpha = 120°$, $\beta = \gamma = 90°$, cell volume $= 764.32$ Å^3, $Z = 4$. Cell occupancy is shown in Table 14.60.

$BaPtO_3$ was prepared by the reaction of $BaO_2 + PtO_2$ at high O_2 pressures and by the thermal decomposition of $BaPt(OH)_6$ at 500–700 °C in O_2 at 1 atm. The powder pattern can be indexed based on a hexagonal cell with $a = 5.64$, $c = 27.44$ Å, corresponding to a 12-layer perovskite structure. The oxygen content of $BaPtO_{3-x}$ materials was determined by firing the samples in H_2 to form $Ba(OH)_2 + Pt$ and calculating x from the weight loss.

The compound, Ba_2PtO_4 is also known but data concerning this compound is sparse. It has the following cell parameters: Ba_2PtO_4. Orthorhombique $a = 17.62$ Å, $b = 10.17$ Å, $c = 8.85$ Å. A related compound, Ba_4PtO_6 is hexagonal, $a = 10.064$ Å, $c = 12.663$ Å.

Other compounds in the Pt^{4+} system of $BaO–PtO_2$ include $Ba_4Pt_3O_9$. It is monoclinic with $a = 17.46$ Å, $b = 10.08$ Å and $c = 8.55$ Å. This compound has the formal arrangement of $Ba_4(Pt^{4+}{}_{1-y}–Ba^{2+}{}_y)O_9$ where $y < 1.0$.

$$3\ Ba_4Pt_3O_9 \Rightarrow Ba_{12}Pt_9O_{27}$$

This composition has a hexagonal structure with $a = 5.83$ Å $\approx a_{hex}\sqrt{3}$ and $c = 4.31$ Å $\approx c_{hex}\sqrt{2}$. A variety of perovskite-type mixed oxides corresponding to the solid solution $Ba_{12-x}[Ba_xPt_{3-x}]Pt_6O_{27}$ (where 0 is less than or equal to x less than or equal to 3) was studied by X-ray photoelectron spectroscopy (XPS). Pt was found to be in two valence states, Pt^{2+} and Pt^{4+} and the quantity of Pt^{2+} decreases when x increases. The intrinsic activity, for catalytic CO oxidation, was found to be dependent on x. At low temperature (below 170 °C), the highest activity is obtained for $Ba^{12}Pt_9O_{27}$ ($x = 0$) and the activity decreased with increasing x. The apparent activation energies increased, from 80 to 110 kJ/mol, when x increased; for a sample of metallic platinum catalyst studied in the same conditions, a value of 120 kJ/mol was found. The partial reaction order/O-2 (in the range of 0.64–0.90) increased with x while the partial order/CO (in the range of −0.34 to −0.70) decreased when x increased. Moreover, for the oxide containing only Pt^{4+} ($Ba_{15}Pt_6O_{27}$) the reaction orders were similar to those determined for the metallic platinum. Hence, there is undoubtedly a correlation between the Pt^{2+}/Pt^{4+} ratio in these oxides and the catalytic activity for CO oxidation. This can be explained by assuming that CO chemisorption on Pt^{2+} is weaker than on Pt^{4+}, which implies a less inhibitor effect of CO at low temperature.

A single-crystal study of $Ba_3Pt_2O_7$ showed that the structure tolerates a variable composition which can be written $Ba_3Pt_{2+x}O_{7+2x}$. The crystal studied had a hexagonal cell of dimensions $a = 10.108 \pm 0.006$ Å and

$c = 8.638 \pm 0.009$ Å, and a probable space group $P62c$, $Z = 4$. The density determined by water displacement was 7.99 g/cm^3; the theoretical density for $Ba_3Pt_2O_7$ is 7.94 g/cm^3. The structure was determined from the set of 401 observed independent reflections obtained from 5189 reflections measured by the automated counter methods. Refinement on F was carried to a conventional R of 8.0%. The structure has barium–oxygen layers with an essentially four-layer stacking sequence of the double hexagonal (ABAB) type. Platinum is found mainly in face-sharing octahedra, but is also distributed over some sites in which the coordination is nearly square planar and other sites in which the coordination is trigonal prismatic with three Pt–O bond lengths of 2.00 Å and three long Pt–O distances of 2.65 Å. The platinum with planar coordination is 0.08 Å from the plane of the four oxygen atoms.

No other barium–platinum compounds are known. Data concerning the electrical properties of these compounds is almost non-existent. They are not offered for sale commercially and no CAS numbers have been assigned to any of these compounds.

14.3.6. Radium Platinum Compounds

Although Ra^{2+} most likely forms the same type of compounds as Ba^{2+}, there is no record of any effort to study such compounds. No such compounds have been reported and the likelihood of anyone doing so is nil. In view of the high cost of both Pt and Ra metals, and the radioactivity of ^{226}Ra, a description of the properties of radium platinates or platinites will never be published.

CHAPTER

15

Group 11 (Cu, Ag and Au) Alkaline Earth Compounds

OUTLINE

15.1. Alkaline Earth Copper Compounds **1049**
15.1.1. Beryllium Copper Compounds *1049*
15.1.2. Magnesium Copper Compounds *1052*
15.1.3. Calcium Copper Compounds *1055*
15.1.4. Strontium Copper Compounds *1061*
15.1.5. Barium Copper Compounds *1070*
15.1.6. Radium Copper Compounds *1079*

15.2. Alkaline Earth—Silver Compounds **1080**
15.2.1. Beryllium Silver Compounds *1080*
15.2.2. Magnesium Silver Compounds *1081*
15.2.3. Calcium Silver Compounds *1083*
15.2.4. Strontium Silver Compounds *1086*
15.2.5. Barium Silver Compounds *1089*
15.2.6. Radium Silver Compounds *1091*

15.3. Alkaline Earth Gold Compounds **1092**
15.3.1. Beryllium Gold Compounds *1092*
15.3.2. Magnesium Gold Compounds *1094*
15.3.3. Calcium Gold Compounds *1098*
15.3.4. Strontium Gold Compounds *1105*
15.3.5. Barium Gold Compounds *1109*
15.3.6. Radium Gold Compounds *1113*

15.1. ALKALINE EARTH COPPER COMPOUNDS

Copper forms both oxidic and intermetallic compounds with the alkaline earths. These compounds have been thoroughly studied after the copper-based high-temperature superconducting compounds like $HgBa_2Ca_2Cu_3O_{8+\delta}$ were announced in 1997. There now exist a large number of papers and books relating to these types of compounds. No description of these superconducting compounds will be given here.

15.1.1. Beryllium Copper Compounds

Only two intermetallic compounds of Be–Cu have been discovered as shown in the following phase diagram. The third compound shown is a high-temperature form not stable at room temperature (Fig. 15.1).

A Be/Cu alloy compound structure has been used as a plasma-facing material for the International Thermonuclear Experimental Reactor (ITER). Bonding of Be to Cu alloy was completed by diffusion bonding or brazing. Methods such as scanning electron microscope (SEM), energy dispersive spectrum (EDS), X-ray diffraction (XRD) and X-ray photoelectron spectroscopy (XPS) analysis were employed to inves tigate the interface structure of joint, fracture mechanism and phases of shear fracture surface were also studied. Be to Cu alloys were formed using Ti as interlayer interface under the bonding 'temperature 850 °C. The formational free energy of the possible intermetallic compounds was calculated by the Castep module of Material Studio, according to "flux-energy principal" to confirm the formation of interface reaction. The atomic population and overlap population of intermetallic compounds were analyzed. The formational energy of vacancy and diffusion migratory energy of Be, Cu, α-Ti and β-Ti were calculated by "Castep", and the atomic population of simple vacancy attachment of atoms to Be, Cu, α-Ti, or β-Ti were analyzed. Intermetallic Ti compounds were the main stable type formed. It was found that $TiBe_2$-αTi, Ti_2Cu, Ti_3Cu_4, Ti_2Cu_3 and $TiCu_4$ layered structures were formed

http://dx.doi.org/10.1016/B978-0-444-59550-8.00015-6

Copyright © 2013 Elsevier B.V. All rights reserved.

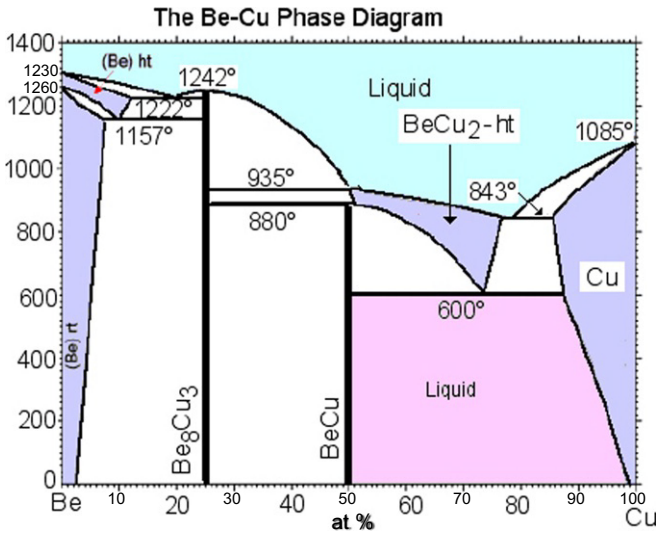

FIGURE 15.1

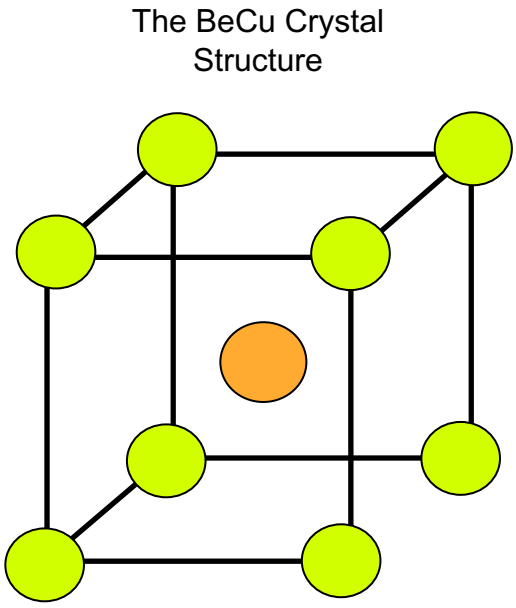

FIGURE 15.2

on the joint interface (there was a segregated Ti_2Cu phase present as well). The shear strength of joints was found to be lower. The fracture was determined to be cleavage–intergranular cracking. The XRD analysis showed that the joints ruptured around the interface between Ti_2Cu layer and Ti_3Cu_4 layers. The use of Ti as an interface has come under question.

Of the known compounds, BeCu has the structural form shown in Fig. 15.2.

In this diagram, Cu is in the body-centered position. Cell parameters are: $a = b = c = 2.702$ Å, $\alpha = \beta = \gamma = 90°$, cell volume $= 19.73$ Å^3, $Z = 1$. Cell occupancy is shown in Table 15.1.

At the vacuum ultraviolet (VUV) free electron laser in Hamburg (FLASH), an infrared (IR) beamline is being built to allow novel pump and probe experiments combining coherent IR pulses with the free electron laser radiation in the VUV spectral range. It provides useful IR radiation generated as a "dedicated" undulator over the wavelength range from 200 μm to 10 μm and possibly even shorter. Another important application of the beamline is electron diagnostics of the longitudinal charge distribution of the electron bunches. One of the most important tasks of the front ends in undulator beamlines is to handle the very intensive photon beam. In treating for such a high heat load, a grazing geometry technique, wherein inclining an irradiated surface to the photon beam to reduce the heat flux level, is very commonly used. In addition to this traditional method, advanced material such as "Glidcop" (copper alloy strengthened by adding alumina) for copper was applied to masks, absorbers and xy-slits in Spring-8 because of its structurally toughness against the thermal stress. From the results of analyses and various evaluation tests, the following conclusions were attained:

(1) The static strength of the brazed joint between low-Z material and a cooling body made of copper, or beryllium/copper (Be/Cu), is about eight times as large as a graphite/copper (G/Cu) joint.
(2) Concerning the vacuum properties, beryllium is much superior to graphite.

$BeCu_2$ has the crystal structure shown in Fig. 15.3.

Cell parameters are: $a = b = c = 4.3364$ Å, $\alpha = \beta = \gamma = 60°$, cell volume $= 53.38$ Å^3, $Z = 8$. Cell occupancy is shown in Table 15.2.

The compound, Be_8Cu_2, has the structure shown in Fig. 15.4.

This compound involves the site occupancy shown at the top (orange) of the diagram where each site is randomly occupied. Cell parameters are: $a = 2.557$ Å, $b = c = 4.179$ Å, $\alpha = 120°$, $\beta = \gamma = 90°$, cell volume $= 38.67$ Å^3, $Z = 2$. Cell occupancy is shown in Table 15.3.

TABLE 15.1

No.	Site notation	Atom	Multiplicity	Wyckoff	Site symmetry	*x*	*y*	*z*	Occupancy
1	Cu	Cu	1	b	m-3m	1/2	1/2	1/2	1.0
2	Be	Be	1	a	m-3m	0	0	0	1.0

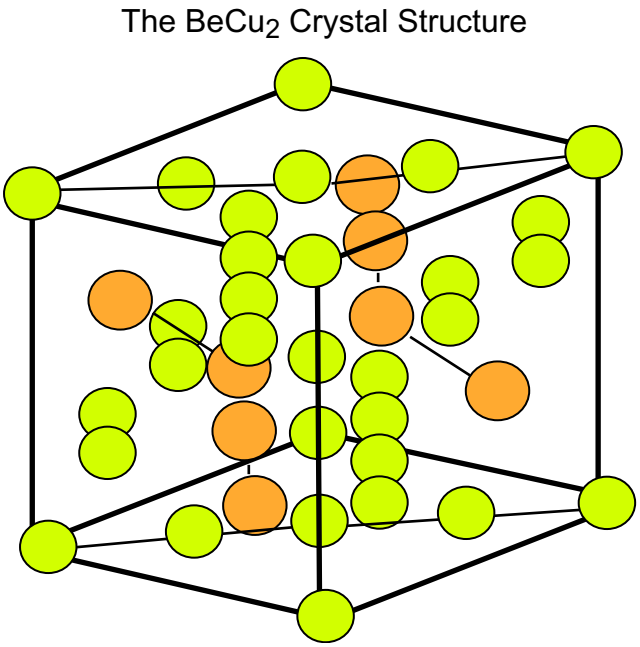

FIGURE 15.3

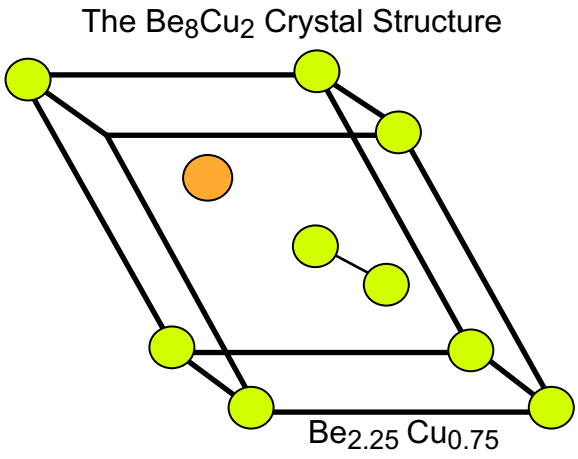

FIGURE 15.4

In contrast, fracture in room temperature tensile bars of Cu–Be occurred in the Be_2Cu–BeCu reaction zone layer at the copper–beryllium interface. This bond exhibited high-fracture strength values (322, 331 MPa). The fracture was a mixed mode consisting of dimple rupture and trans-granular cleavage. A continuous layer of intermetallics is formed between the copper and beryllium at the diffusion bonding temperature (450 °C). These phase(s), although exhibiting high strength, also exhibited poor ductility and fracture toughness.

The compound, BeCu2, has the structure shown in Fig. 15.5.

Cell parameters are: $a = b = c = 2.4162$ Å, $\alpha = \beta = \gamma = 109.47°$, cell volume = 10.86 Å^3, $Z = 2$. Cell occupancy is shown in Table 15.4.

No other intermetallic compounds are known.

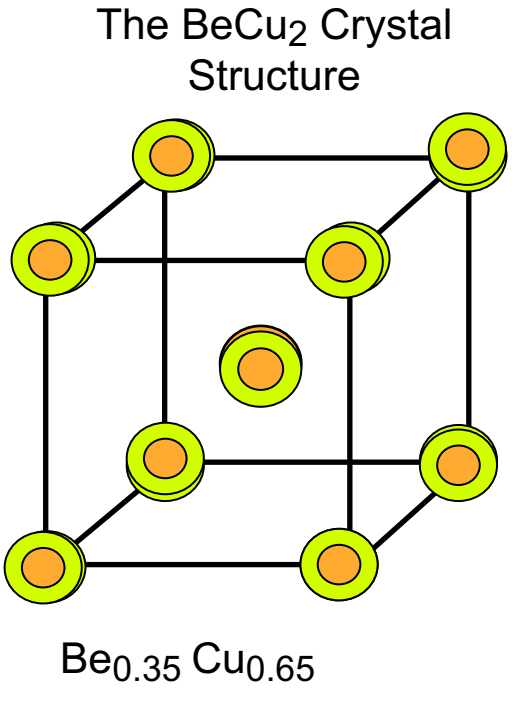

FIGURE 15.5

TABLE 15.2

No.	Site notation	Atom	Multiplicity	Wyckoff	Site symmetry	x	y	z	Occupancy
1	Be	Be	16	c	.-3m	0	0	0	1.0
2	Cu	Cu	8	b	-43m	3/8	3/8	3/8	1.0

TABLE 15.3

No.	Site notation	Atom	Multiplicity	Wyckoff	Site symmetry	x	y	z	Occupancy
1	M	0.75Cu + 0.25Be	1	e	-6m2	2/3	1/3	0	1.0
2	Be1	Be	1	d	-6m2	1/3	2/3	1/2	1.0
3	Be2	Be	1	a	-6m2	0	0	0	1.0

TABLE 15.4

No.	Site notation	Atom	Multiplicity	Wyckoff	Site symmetry	x	y	z	Occupancy
1	M	0.65Cu + 0.35Be	2	a	m-3m	0	0	0	1.0

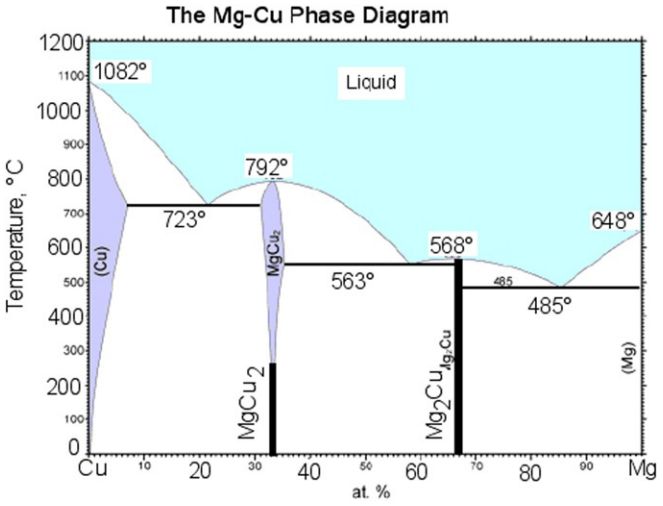

FIGURE 15.6

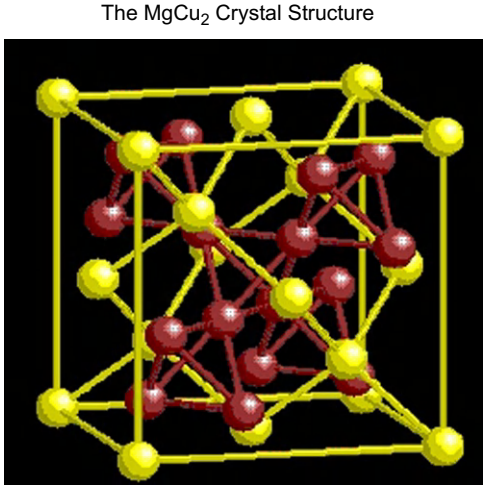

FIGURE 15.7

BeO does not form any compounds with the copper oxides. No compounds have been described in the current literature. Be–Cu alloys are available commercially but no BeO–CuO_x compounds are offered for sale.

15.1.2. Magnesium Copper Compounds

Magnesium forms two intermetallic compounds with Cu as shown in the above phase diagram, as shown in Fig. 15.6.

No other compounds are known. The cell parameters of Mg_2Cu and $MgCu_2$ are not available.

$MgCu_2$ has the structure shown in Fig. 15.7.

This is a typical Laves phase, called the C15 type structure, that belongs to cubic system. Space group is *Fd*3*m*.

A simple comparison of the $MgCu_2$ structure can be made (Fig. 15.8).

It should be clear that this structure is a combination of the two phases.

Magnesium metal is known to easily form hydrides. The addition of copper improves that function. In contrast to Mg_2Cu, the compounds $MgNi_2$ and $MgCu_2$ do not form hydrides under conventional hydrogenation conditions. It is assumed that the hydrogenation does not occur because the enthalpy of formation of the hydride phase is large and positive. Using Miedema's rule, a calculation of the enthalpy of formation of substituted alloys based on these two copper compounds was made. For certain alloy mixtues, the enthalpy of

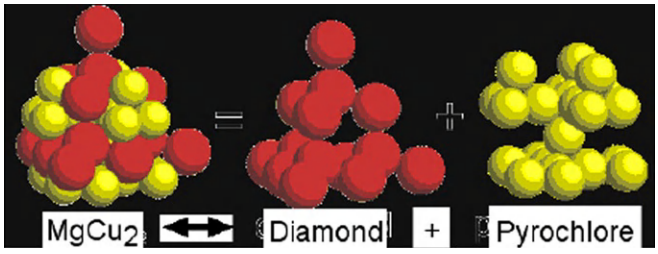

FIGURE 15.8

formation is believed to be 10–20 kJ/mol lower. Synthesized alloys were made with the above calculation as a guide. However no hydride was formed under the conditions used, 4.0 MPa at 573 K. The size of the interstitial holes compared to the hydrogen atomic size was used to explain these results.

The deformation behavior of $MgCu_2$ Laves phase intermetallic compound was studied by compression experiments. $MgCu_2$ was plastically deformed at a temperature above 673 K, where the strain rate was low. The large temperature and strain rate dependences of the stress and small activation volumes obtained over the temperature range 673–873 K suggested that the deformation was rate controlled by the Peierls mechanism. The compounds with stoichiometric composition showed the usual large strain hardening over the temperature range 673–973 K. However, when the compounds included the Cu-rich or Mg-rich composition within the limit of Laves phases, they showed

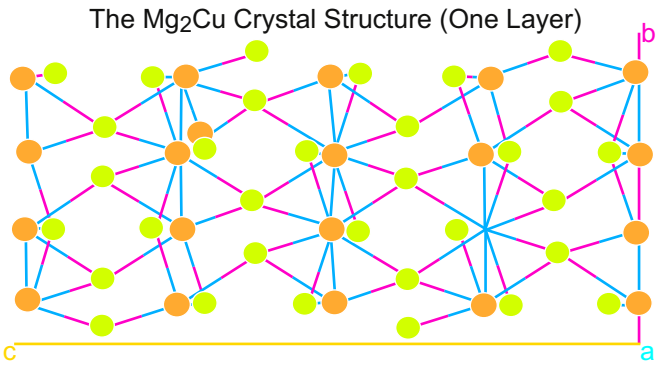

FIGURE 15.9

a mild yield drop (though the type of yield drop varied with composition and the test temperature). The compounds rapidly cooled from the melts showed a gum elastic deformation, which was considered to be due to the stress-induced transformation, at the condition of very low stress and room temperature.

The charge density distribution of the intermetallic compound $MgCu_2$ was obtained by the maximum entropy method (MEM) from the synchrotron powder diffraction data. In the MEM charge density map, the overlap of electron densities was clearly observed between the neighboring Cu atoms. This showed that there is a rather strong covalent bond between Cu–Cu atoms. It was also found that the Cu–Cu bonding occurs along the very well-known Kagomé net, which characterizes the Laves phase structure. At least, in the case of $MgCu_2$, the Kagomé network is the real electronic network in reality, rather than a geometrical concept to represent structural characteristics of Laves phase compounds.

The compound, Mg_2Cu, has the structure shown in Fig. 15.9.

The three-dimensional (3D) structure consists of two layers within a tetragonal cell with no atoms on the corners of the lattice.

Cell parameters are: $a = b = 5.235$ Å, $c = 9.536$ Å, $\alpha = \beta = 98.01°$, $\gamma = 119.49°$, cell volume $= 218.60$ Å^3, $Z = 8$. Cell occupancy is shown in Table 15.5.

Mg_2Cu spontaneously undergoes hydrolysis in water at room temperature, and reacts with water to form $Mg(OH)_2$, Cu and hydrogen. Cu nanoparticles were formed as well as Cu_2O. The hydrolysis behavior of Mg_2Cu was compared to that previously found for Mg_2Ni. The Cu nanoparticles prepared by hydrolysis of Mg_2Cu were spherical in shape with a mean size of about 10 nm.

A mechanical alloying (MA) process was used to synthesize the nanocrystalline Mg_2Cu and the nanocomposite Mg_2Cu/Pd hydrogen storage materials. The structure of these materials has been examined by XRD and SEM. Thermodynamic and electrochemical properties have also been investigated. The MA for 18 h led directly to the formation of the orthorhombic-type structure with a crystallite sizes of about 30 nm. The results show that the maximum absorption capacity reaches 2.25 wt% for nanocrystalline Mg_2Cu alloy. This is lower than in the polycrystalline Mg_2Cu alloy (2.6 wt%) because of a significant amount of strain, chemical disorder and defects introduced into the material during the MA process. On the other hand, mechanically coated Mg_2Cu alloy with palladium has effectively reduced the degradation rate of the studied electrode material. Nano-structured Mg_2Cu shows excellent hydrogen storage properties because nano-structured materials have more surface area and more defects, which means more nucleation sites with hydrogen, and smaller particles, which means shorter diffusion distance for hydrogen in the alloy particles.

The dehydrogenation kinetics of air exposed samples of MgH_2/Mg_2Cu and $MgH_2/MgCu_2$ have been studied with in situ time resolved X-ray powder diffraction. The X-ray setup enabled the recording of full diffraction patterns within 150 s, thereby allowing the study of structural changes combined with simultaneous extraction of kinetic parameters. Phase fractions as a function of time and temperature were derived from series of consecutive diffraction patterns by numerical integration of selected diffraction peaks. The apparent activation energy for the dehydrogenation of the MgH_2/Mg_2Cu, and $MgH_2/MgCu_2$ sample was found to be 108 kJ/mol and 160 kJ/mol, respectively. Furthermore, substantially improved dehydrogenation kinetics of MgH_2 and resistance toward oxidation of Mg due to the presence of $Mg_2Cu/MgCu_2$ are discussed in relation to previous work. In the hydrogenation process for the super-laminates at 573 K, Mg_2Cu is formed through interdiffusion between Mg and Cu metals. Then the Mg_2Cu decomposes into MgH_2 and $MgCu_2$. In the

TABLE 15.5

No.	Site notation	Atom	Multiplicity	Wyckoff	Site symmetry	x	y	z	Occupancy
1	Mg1	Mg	16	g	..2	1/8	1/8	0.0415	1.0
2	Cu	Cu	16	g	..2	1/8	1/8	0.4982	1.0
3	Mg2	Mg	16	f	.2.	1/8	0.4586	1/8	1.0

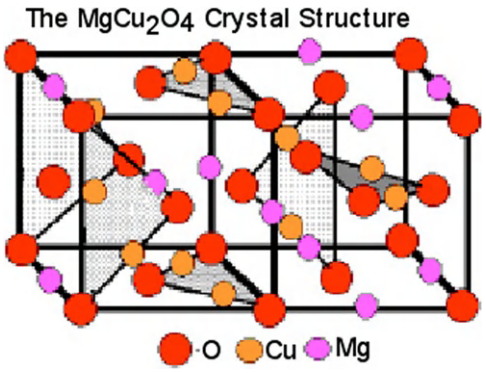

FIGURE 15.10

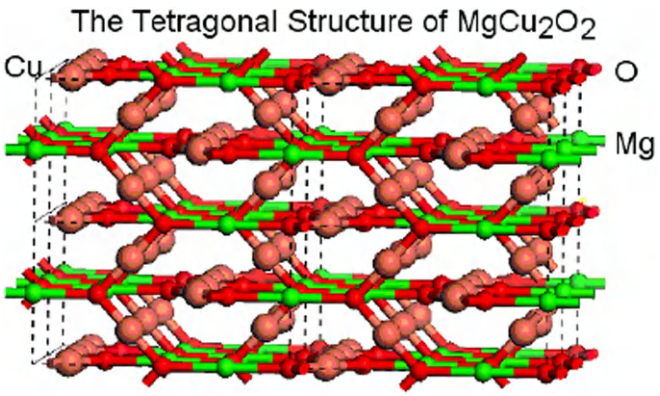

FIGURE 15.11

dehydrogenation process at 573 K, the MgH_2 compound releases hydrogen and returns to metallic Mg. The Mg then reacts with $MgCu_2$, and Mg_2Cu is formed again. Throughout the sequence, Mg_2Cu phase absorbs and desorbs hydrogen reversibly at 473 K.

No other intermetallic compounds are known. Mg–Cu alloys are not available commercially, and no CAS numbers have been issued to date.

In the Cu^+-containing system of MgO–Cu_2O, the compound, $MgCu_2O_2$, is one of the family of compounds that exhibit p-type conductivity and are transparent conductive oxides (TCO) like indium tin oxide. TCOs are used in:

(1) Transparent electrodes in flat panel displays (ITO)
(2) Organic light-emitting diodes
(3) Solar cells
(4) Touch screen panels
(5) Transparent electronic windows
(6) Electrochromic windows
(7) Electromagnetic shielding

$MgCu_2O_2$ has the form shown in Fig. 15.10.

Another view of the $MgCu_2O_2$ lattice is shown in Fig. 15.11.

The lattice constants of the family of MCu_2O_2 are given in Table 15.6

The stability of these oxides has been calculated and rated according to their decomposition into constituent oxides, i.e.

$$\Delta E = E(MCu_2O_2) - [E(Cu_2O) + E(MO)]$$

where $E(MCu_2O_2)$ is the total energy of the bulk alloy and $E(Cu_2O)$ and $E(MO)$ is the total energy of bulk Cu_2O and the bulk alkaline earth oxide in the rock salt structure. The results determined were shown in Table 15.7.

Of these, $MgCu_2O_2$ and $CaCu_2O_2$ are unstable while $SrCu_2O_2$ and $BaCu_2O_2$ are stable. Cation coordination and M–O distances impact on stability:

Mg: 4 coordinate in these compounds
Ba: 6 coordinate in these compounds

In the Cu^{2+}-containing system of MgO–CuO, no data concerning the $MgCuO_2$ compound are available. However, the compound, $MgCu_2O_3$, has received some attention in the literature.

This compound has a ladder-like structure, as shown in Fig. 15.12.

A thermodynamic evaluation of the ternary Mg–Cu–O system has been made and a set of parameters consistently describing the system has been determined. Güggenite is the only ternary solid phase within the system and its stoichiometry is close to $MgCu_2O_3$.

The MgO phase can dissolve a considerable amount of CuO. This can be described by a simple model in which Mg^{2+} substitution by Cu^{2+} occurs. Phase diagrams were given for the MgO–CuO_x system at 0.21 and 1 bar oxygen partial pressures as well as a potential diagram. An isothermal section at 1423 K is also presented. Available experimental data are rather limited and most of them are well described by the calculation. There are still uncertainties concerning the

TABLE 15.6

MCu_2O_2	a [Å]	b [Å]	c [Å]
Mg	5.11	25.11	25.11
Ca	5.25	35.253	9.577
Sr	5.447	5.447	9.871
Ba	5.768	5.768	10.335

TABLE 15.7

MCu_2O_2	ΔE (eV)
Mg	+14
Ca	+7
Sr	−0.8
Ba	−1.0

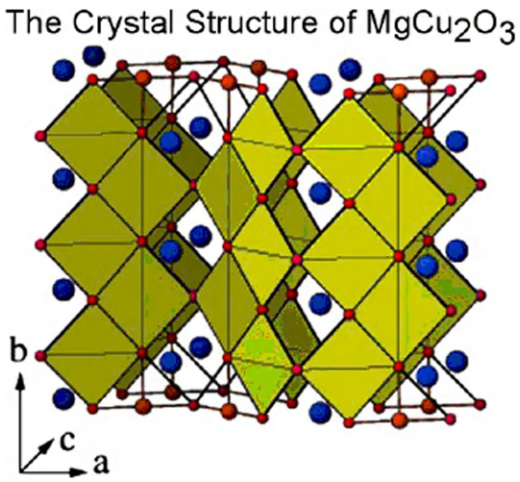

FIGURE 15.12

CuO solubility in MgO and on the Cu^{1+}/Cu^{2+} ratio present in MgO. For this reason, it is not presented here.

The electrical conductivity of $MgCu_2O_3$ was measured on single crystals in the temperature range $180 < T < 300$ K. The compound is a thermally activated semiconductor with a band gap of 0.94 eV and a resistivity of $2.8 \times 10^4\ \Omega$ at 21 °C. Neutron diffraction experiments on powder samples revealed an AFM phase transition at $T_N = 94.5$ K, while the magnetic susceptibility measured in the temperature range $12 < T < 292$ K is atypical for an AFM. The magnetic structure was derived from the neutron experiments. The magnetic moment per Cu^{2+} ion is 0.33 μbar and thus is anomalously small.

In another paper, the magnetic properties of undoped and Li-doped $MgCu_2O_3$ single crystals were studied by magnetic susceptibility and neutron diffraction measurements. The pure compound was found to be a semiconductor with an AFM ground state ($T_N = 95$ K). Above T_N, short-range magnetic correlations within the Cu–O chains of the $MgCu_2O_3$ structure give rise to a predominantly one-dimensional (1D) magnetic behavior. This was revealed by the quantitative interpretation of the susceptibility measurements. Below T_N, the 3D magnetic structure, derived from neutron diffraction experiments, can be described by an essentially, collinear model. A small spin canting, however, exists, because adjacent CuO_6 octahedra are strongly tilted with respect to each other. The magnetic structure can be represented by two independent magnetic sublattices, which, in the mean-field approximation, are not coupled. The topology is similar to the one producing an infinitely degenerate state in AFM face-centered cubic (fcc) lattices. Doping experiments with Li clearly demonstrated the importance of spin fluctuations and fluctuations of the local exchange fields for lifting the degeneracy in such a system. A remarkably small amount of Li (about 2 mol% Li) is sufficient to disturb the magnetic lattice in such a way that the almost collinear spin arrangement changes into an arrangement where the spins of one sublattice are strongly canted with respect to the spins of the other sublattice.

This structure ($MgCu_2O_3$), which is homologous to $BaCu_2O_3$ and $SrCu_2O_3$, can be viewed as stacked buckled Cu_2O_3 planes of the prototypical planar TLL $SrCu_2O_3$ system. These compounds show, in addition to the common AFM-period doubling along the chain (*b*-axis), different magnetic structures in *c*- and *a*-directions. These include ferromagnetic (FM) ordering in *c*-direction and on the kinked PL-rungs for A1/4Mg, and AFM ordering for A1/4Ca. Along the *a*-axis, AFM period doubling and/or an incommensurate spiral-type wave near 3/7 commensurability, respectively, have been observed.

By comparing $SrCu_2O_3$ having straight rungs to the strongly "kinked" rungs in $MgCu_2O_3$ (with decreased buckling (Cu–O–Cu bond) at angle H), it has been determined that there is a transition from a super-exchange dominated AFM to a FM rung (a strengthening crosspiece in the structure of a chair) exchange model. This is governed by Hund's rule coupling at the intermediate O of the ring center that approaches $\Theta = 90°$. It also depends upon the crystalline field strength that caused splitting of on-site energies for differently oriented O-2p orbitals if it is small. Comparing the observed magnetic structures one concludes that this transition occurs at a critical H_c in between those of A1/4Ca and A1/4Mg. Near H_c, the ring exchange J_r is expected to be small.

In another paper, it was claimed that:

> "In the system $Mg_{1-x}Cu_{2+x}O_3$, the phase with $x = 0$, i.e. the compound $MgCu_2O_3$, does not exist. Neutron powder measurements and single-crystal X-ray studies clearly show that the Mg lattice site is partially occupied by Cu^{2+} ions with typical values of $x = 0.1$. This substitutional disorder, best denoted by the formula $(Mg_{1-x}Cu_x)Cu_2O_3$, is surprising, since the coordination polyhedron of the Mg site is a compressed oxygen octahedron, while the Jahn–Teller ion Cu^{2+} usually prefers a tetragonally elongated oxygen octahedron, as it exists on the regular Cu site of the lattice. The local environment of the Cu^{2+} ions on the Mg site was also checked by electron paramagnetic resonance (EPR) measurements".

No other compounds in the MgO–Cu_xO_y system are known. No magnesium cuprate compounds are offered for sale commercially and no CAS numbers have been issued to date.

15.1.3. Calcium Copper Compounds

Ca metal forms at least three intermetallic compounds with copper metal as shown in Fig. 15.13.

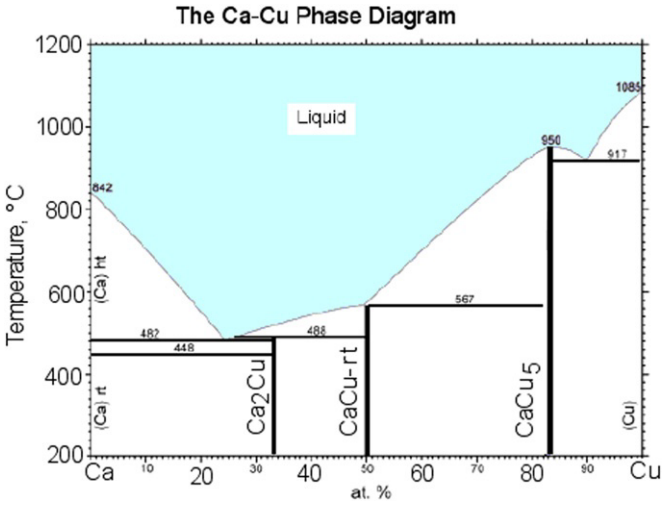

FIGURE 15.13

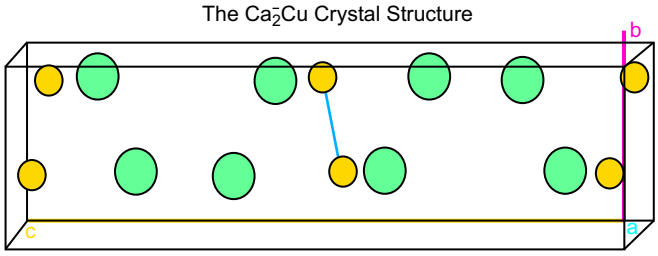

FIGURE 15.14

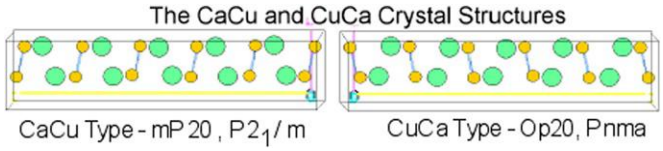

FIGURE 15.15

The compound, Ca_2Cu, has the structural form shown in Fig. 15.14.

Cell parameters are: $a = 4.161$ Å, $b = 6.126$ Å, $c = 14.532$ Å, $\alpha = \beta = \gamma = 90°$, cell volume $= 370.37$ Å^3, $Z = 4$. Cell occupancy is shown in Table 15.8.

X-ray structural analysis shows that Ca_2Cu is orthorhombic, *Pnma*, $a = 6.126$, $b = 4.161$, $c = 14.532$ Å, $Z = 4$, $D = 2.58$ mg/m^3, (Mo K_α) $= 8.4$/mm. The structure comprises stacked Cu-centered trigonal prisms of Ca atoms that share two rectangular faces. This allows the formation of infinite zigzag chains of Cu atoms.

CaCu is dimorphic with the structures shown above in Fig. 15.15.

CaCu type $a = 4.271$ Å, $b = 5.882$ Å, $c = 19.473$ Å, $\alpha = 94.3°$, $\beta = \gamma = 90°$, cell volume $= 487.58$ Å^3, $Z = 10$. Cell occupancy is shown in Table 15.9.

CuCa type $a = 4.271$ Å, $b = 5.894$ Å, $c = 38.822$ Å, $\alpha = \beta = \gamma = 90°$, cell volume $= 976.72$ Å^3, $Z = 10$. Cell occupancy is shown in Table 15.10.

TABLE 15.8

No.	Site notation	Atom	Multiplicity	Wyckoff	Site symmetry	*x*	*y*	*z*	Occupancy
1	Cu	Cu	4	c	.m.	0.109	1/4	0.0147	1.0
2	Ca2	Ca	4	c	.m.	0.134	1/4	0.407	1.0
3	Ca1	Ca	4	c	.m.	0.363	1/4	0.6669	1.0

TABLE 15.9

No	Site notation	Atom	Multiplicity	Wyckoff	Site symmetry	*x*	*y*	*z*	Occupancy
1	Cu2	Cu	2	e	m	0.0472	1/4	0.6118	1.0
2	Ca5	Ca	2	e	m	0.1435	1/4	0.0710	1.0
3	Ca3	Ca	2	e	m	0.2424	1/4	0.4715	1.0
4	Ca1	Ca	2	e	m	0.3450	1/4	0.8724	1.0
5	Cu4	Cu	2	e	m	0.4106	1/4	0.2124	1.0
6	Ca2	Ca	2	e	m	0.5374	1/4	0.6719	1.0
7	Cu5	Cu	2	e	m	0.6110	1/4	0.0129	1.0
8	Cu3	Cu	2	e	m	0.7501	1/4	0.4118	1.0
9	Cu1	Cu	2	e	m	0.8087	1/4	0.8118	1.0
10	Ca4	Ca	2	e	m	0.9485	1/4	0.2721	1.0

TABLE 15.10

No.	Site notation	Atom	Multiplicity	Wyckoff	Site symmetry	x	y	z	Occupancy
1	Cu5	Cu	4	c	.m.	0.0060	1/4	0.6072	1.0
2	Ca1	Ca	4	c	.m.	0.0362	1/4	0.1321	1.0
3	Ca2	Ca	4	c	.m.	0.1348	1/4	0.3735	1.0
4	Cu3	Cu	4	c	.m.	0.2062	1/4	0.1441	1.0
5	Ca3	Ca	4	c	.m.	0.2361	1/4	0.6259	1.0
6	Cu2	Cu	4	c	.m.	0.3052	1/4	0.8503	1.0
7	Ca4	Ca	4	c	.m.	0.3356	1/4	0.3726	1.0
8	Cu1	Cu	4	c	.m.	0.4069	1/4	0.601	1.0
9	Ca5	Ca	4	c	.m.	0.4351	1/4	0.1362	1.0
10	Cu4	Cu	4	c	.m.	0.6066	1/4	0.6057	1.0

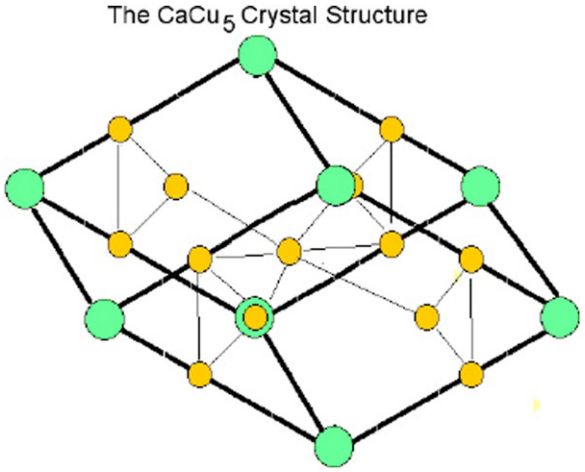

FIGURE 15.16

X-ray photoelectron and ultraviolet photoemission measurements have been made on $Ca_{10}Cu_{90}$ alloys. The core-level XPS spectra of Ca show strong satellites that are discussed in terms of the core-hole screening effects. It was suggested that these spectra are due to the mixing of d^0-, d^1-, and d^2-configurations of calcium in the final state and that band-like effects are important. In the case of the X-ray photoemission valence band only small differences have been observed between the alloy and the noble metal, whereas for ultraviolet photoemission valence bands the corresponding changes are more pronounced. The energy shifts of the X-ray photoemission valence bands are attributed to the enhancement of the p partial density of states just below the Fermi level in the case of the alloy. In addition, linear muffin-tin-orbital band calculations have been performed for the $CaCu_5$ compound by using a super-lattice with and without the Ca 2p core hole. When the core hole is created, the weight of the Ca 3d local partial density of states is increased at the Fermi level, whereas the Cu 3d band remains almost unchanged. The compound, $CaCu_5$, has the form shown in Fig. 15.16.

Cell parameters are: $a = 4.047$ Å, $b = c = 5.074$ Å, $\alpha = 120°$, $\beta = \gamma = 90°$. Cell volume $= 90.83$ Å^3, $Z = 1$. Cell occupancy is shown in Table 15.11.

Another view of the $CaCu_4$ structure is given in Fig. 15.17.

This structure is adopted by a number of other intermetallic compounds. An example is:

Single crystals of dysprosium heptanickel tritin were synthesized from the constituent elements by arc melting. Two of the five Ni atoms are at general sites and all other atoms are at sites with either twofold or m symmetry. The structure contains '$DyNi_5Sn$' and '$DyNi_2Sn_2$' fragments and represents a new member of the $CaCu_5$ series of intermetallics.

TABLE 15.11

No.	Site notation	Atom	Multiplicity	Wyckoff	Site symmetry	x	y	z	Occupancy
1	Cu2	Cu	3	g	mmm	1/2	0	1/2	1.0
2	Cu1	Cu	2	c	-6m2	1/3	2/3	0	1.0
3	Ca	Ca	1	a	6/mmm	0	0	0	1.0

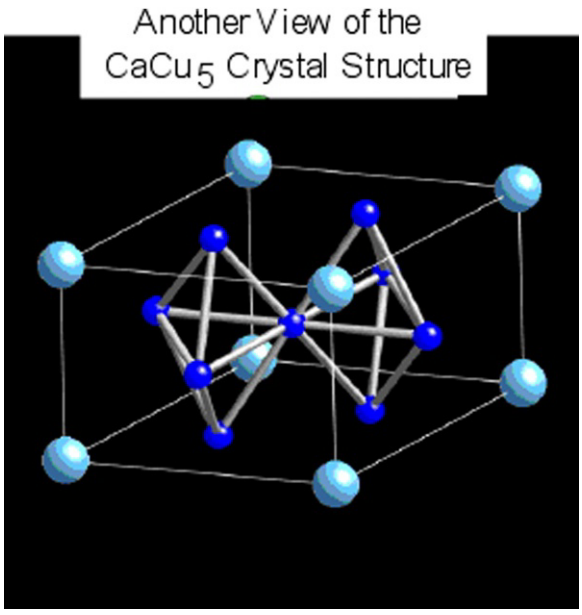

FIGURE 15.17

No other Ca–Cu intermetallic compounds are known. They are not offered for sale commercially and no CAS numbers have been assigned to date.

The system, Ca–Cu–O, forms several stable cuprate compounds with CaO.

In the Cu^{+}-containing system of CaO–Cu_2O, the compound, $CaCu_2O_2$, is known and was discussed in the Mg–Cu–O section presented above. Its structure was given as shown where the larger orange-red balls are Cu^{+}, the smaller red balls are oxygen and the green balls are Ca^{2+} (Fig. 15.18).

Oxides with the structure MCu_2O_2 (M = Ca, Ba, Mg and Sr) are promising materials for the development of new p-type transparent conducting oxide thin films. By using as precursors calcium and copper tetramethyl-heptanedionate dissolved in meta-xylene, mixed calcium copper films have been grown in the temperature range from 450 °C to 550 °C.

At these temperatures, deposited films exhibited a high-mirror reflection effect, good adherence and were reasonably uniform with the cationic composition of the films being easily controlled by adjusting the copper calcium ratio in the precursor solution. In $CaCu_2O_2$, copper is in the Cu^{1+} oxidation state and depending on the oxygen partial pressure used, the films either consisted of $CaCu_2O_3$ or a mixture of CaO, CuO and Cu_2O. Optimization of annealing conditions increased the presence of Cu^{1+} in the film. Films had a maximum transmittance of 50% in the visible range and were highly resistive. Appropriate annealing conditions reduced the resistivity of the films. It has been determined that $CaCu_2O_2$ is not stable in air and moisture and decomposes while $SrCu_2O_2$ is stable. The latter forms a transparent conductive layer on several substrates and remains stable. The conductivity is p-type and is due to Cu^{+} vacancies in the lattice.

In the Cu^{2+}-containing system of CaO–CuO, contrary to $SrCu_2O_3$, the pseudo-ladder two-leg compound $CaCu_2O_3$ does not show a significant spin gap behavior as expected for typical two-leg ladder systems. $CaCu_2O_3$ single crystals (size about 2–3 mm^3) were cut from a boule, grown in an IR furnace by the traveling solvent floating zone method. The crystals were found to be phase pure as confirmed by X-ray diffraction, energy dispersive X-ray (EDX) and thermogravimetric analysis. However, the EDX results indicate a deficiency of Ca, with a balancing excess in Cu, corresponding to a non-stoichiometric composition $Ca_{1-y}Cu_{2+y}O_{3-\delta}$. The lattice constants determined as $a = 9.944$ Å, $b = 4.078$ Å and $c = 3.461$ Å agree well with published values. Note, that $MgCu_2O_3$, referred to above, has the same lattice structure. Magnetic measurements on single crystals have been performed in a SQUID magnetometer for temperatures from 5 K up to 120 K in magnetic fields (m0Hp7T) applied along the different crystallographic axes. The magnetic susceptibility has been determined from magnetization measurements at 1 T. The structure has the form shown in Fig. 15.19.

Experimental and theoretical studies of the unoccupied electronic structure of $CaCu_2O_3$ single crystals

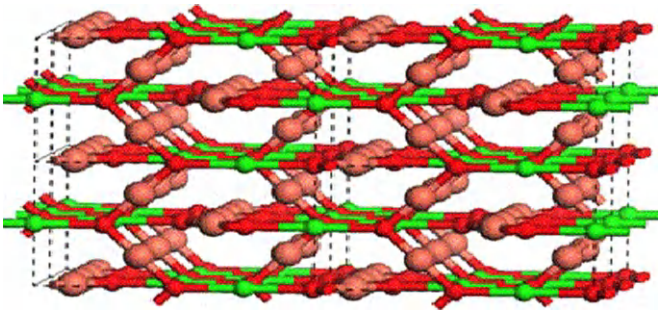

FIGURE 15.18

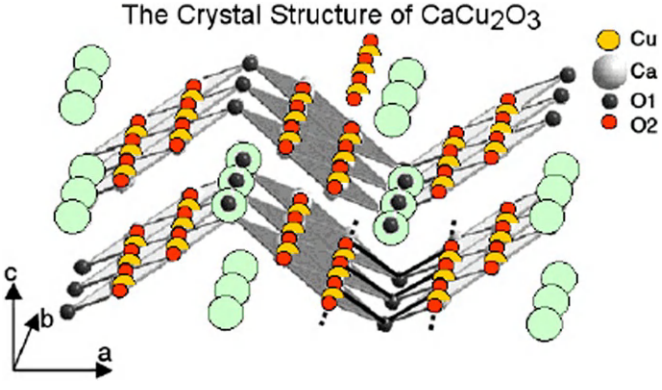

FIGURE 15.19

have been performed using polarization-dependent X-ray absorption spectroscopy and band structure calculations. The measured hole distribution shows an unusual large number of holes in electron orbitals parallel to the interlayer direction which is in agreement with the theoretical analysis. A corresponding strong interlayer exchange was found to be responsible for the missing spin gap which is generic for other two-leg ladder cuprates. It has been shown that strong anisotropy in the electronic spectrum suppresses superconducting temperature in comparison with conventional copper oxide superconductors with square lattices.

Magnetization measurements on single crystals show $CaCu_2O_3$ to be a 3D AFM ($T_N = 27$ K), showing relatively strong magnetic anisotropy and metamagnetic transitions. The 3D behavior is due to exchange between the ladders as deduced from electronic structure calculations within the local density approximation.

In the compounds $MgCu_2O_3$ and $CaCu_2O_3$ the Cu and O atoms are connected topologically in the same way as in the fascinating spin ladder compound $SrCu_2O_3$. In contrast to the latter, the Cu–O–Cu bonding angle corresponding to the "rungs" is significantly less than 180° in $MgCu_2O_3$ and $CaCu_2O_3$. As a consequence, the magnetic susceptibility is quite different compared with that of $SrCu_2O_3$. Single-phase samples of $CaCu_2O_3$ revealed a deficiency of Ca, a balancing excess in Cu, and an oxygen deficiency corresponding to $Ca_{1-x}Cu_{2+x}O_{3-\delta}$. The excess Cu atoms, which are located near the Ca sites, are in the $3d^{10}$ state. The deficiency of oxygen causes a Curie term in the magnetic susceptibility due to the interruption of Cu–O–Cu bonds. From the overall behavior of the susceptibility an antiferromagnetic ordering at a Néel temperature of about 27 K was concluded.

Magnetization and high-field electron spin resonance (ESR) response of the $S = 1/2$ Heisenberg pseudo-ladder magnet $CaCu_2O_3$ is dominated at low temperatures by a few percent of 'extra' Cu spin states arising due to the structural disorder. These 'extra' spins interact with the bulk spins and jointly order in an antiferromagnetical structure at $T_N = 27$ K. At $T \leq T_N$, ESR data reveal a small magnon anisotropy gap of the order of $\sigma \leq 1.0$ MeV. Substitution of 15% of nonmagnetic Zn for Cu reduces the concentration of 'extra' spins and results in the suppression of the magnetic order and closing of the magnon gap. These results support the scenario with a significant role of the 'extra' spins for stabilization of the magnetic order in this frustrated quantum magnet.

In another paper, experimental results for the thermal conductivity kappa (κ) of the pseudo-two-leg ladder material $CaCu_2O_3$ have been presented. The strong buckling of the ladder rungs renders this material a good approximation to $S = 1/2$ Heisenberg chain. Despite a strong suppression of the thermal conductivity of this material (K) in all crystal directions due to inherent disorder, a dominant magnetic contribution (mag) of K-mag along the chain direction was found. K-mag is linear in temperature, resembling the low-temperature limit of the thermal Dried weight Dth of the $S = 1/2$ Heisenberg chain. The comparison of K-mag and Dth yields a magnetic mean-free path of l.0 mag approximately 22 ± 5 Å, in good agreement with magnetic measurements.

The resistivity $\rho(T)$ of the spin-ladder compound $CaCu_2O_3$ measured along the Cu–O–Cu leg (j||b) exhibits a strongly activated character. It increases from ~10^4 to ~10^9 Ωm if T decreases from 350 to 100 K. The charge transfer above $T \approx 200$ K is governed by a quasi-1D nearest-neighbor hopping (NNH) conductivity mechanism characterized by the law $\rho(T) = \exp(E_a/kT)$. Below 200 K, a novel quasi-1D variable-range hopping (VRH) conductivity law $\rho(T) = \exp[(T_0/T)^{3/4}]$ is observed. The NNH activation energy, Ea, and the VRH characteristic temperature, T0, exhibit high sensitivity to the cation (Ca,Cu) content, decreasing by 2.3–2.5 times and by 3.0–3.2 times, respectively, when the composition of Ca is changed from 0.854 to a range of 0.786–0.798 and the composition of Cu from 2.039 to a range of 2.159–2.163. The behavior of E_a and T_0 can be attributed to a corresponding variation of the concentration of intrinsic defects associated with Cu vacancies. On the other hand, no direct dependence of E_a and T_0 to the excess oxygen concentration is observed. A detailed analysis of $K(T)$ demonstrates that conventional d-dimensional models of the hopping conductivity, based on the electron localization in disordered systems, cannot interpret the experimental data at any $d = 1$, 2 or 3, since this leads to the mismatch of the characteristic energies and/or unphysical values of the characteristic length scales. The observed VRH conductivity law on the low-temperature interval, $\ln \rho \sim T^{3/4}$, contradicts the models above, too. Instead, it was found that this law can be substantiated and the correct matching of the energy and length scales can be found within a model of Fogler et al (2004) by treating $CaCu_2O_3$ as a 3D array of quasi-1D electron crystals.

The packing structure of 3 unit cells (a°—3b°—c°) for Ca_2CuO_3 (a) and the model cluster $Ca_{18}Cu_8O_{28}$ (b) used in the *ab initio* calculation of vibrational states are shown in Fig. 15.20.

The enthalpies of reactions between alkaline earth cuprates M_2CuO_3 (M = Ca, Sr) and hydrochloric acid were measured in a hermetic swinging calorimeter at 298.15 K. The M_2CuO_3 samples were prepared by solid-phase synthesis from calcium or strontium carbonate and copper oxide and characterized by X-ray powder diffraction, EDX and wet analysis. The

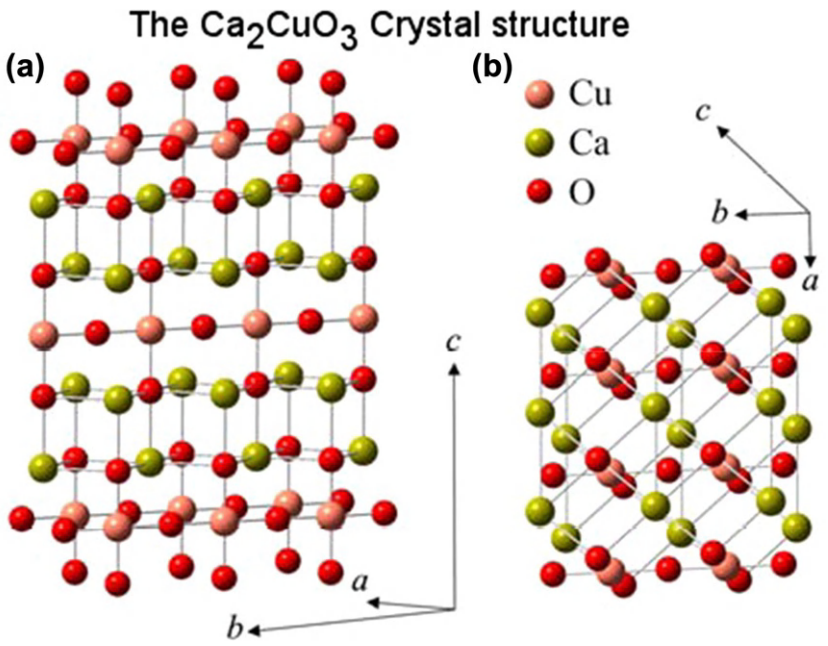

FIGURE 15.20

standard enthalpies of formation obtained for the cuprates, -1431 ± 4 kJ/mol for Ca_2CuO_3 and -1374 ± 3 kJ/mol for Sr_2CuO_3, were discussed and compared with previous experimental and assessed values.

The results were presented using a combined periodic and cluster model approach to the electronic structure and magnetic interactions in the spin chain compounds Ca_2CuO_3 and Sr_2CuO_3. An extended t-J model was presented that includes in-chain and interchain hopping and magnetic interaction processes with parameters extracted from ab initio calculations. For both compounds, the in-chain magnetic interaction was found to be around -240 meV, larger than in any of the other cuprates reported in the literature. The interchain magnetic coupling is found to be weakly antiferromagnetic, i.e. -1 meV. The effective in-chain hopping parameters are estimated to be -650 meV for both compounds, whereas the value of the interchain hopping parameter is 30 meV for Sr_2CuO_3 and 40 meV for Ca_2CuO_3, in line with the larger interchain distance in the former compound. These effective parameters were shown to be consistent with expressions recently suggested for the Néel temperature and the magnetic moments, and with relations that emerge from the t-J model Hamiltonian. Next, the physical nature of the band gap was investigated. Periodic calculations indicated that an interpretation in terms of a charge-transfer insulator is the most appropriate one, in contrast to the suggestion of a covalent correlated insulator recently reported in the literature.

The enthalpies of reactions between alkaline earth cuprates, M_2CuO_3 (M = Ca, Sr), and hydrochloric acid were measured in a hermetic swinging calorimeter at 298.15 K. The M_2CuO_3 samples were prepared by solid-phase synthesis from calcium or strontium carbonate and copper oxide and characterized by X-ray powder diffraction, EDX and wet analysis. The standard enthalpies of formation obtained for the cuprates, ~1431 ± 4 kJ/mol for Ca_2CuO_3 and ~1374 ± 3 kJ/mol for Sr_2CuO_3, were discussed and compared with previous experimental and assessed values.

In situ high-pressure energy dispersive X-ray diffraction measurements on polycrystalline powder of Ca_2CuO_3 with a Cu–O chain structure have been performed in a diamond-anvil cell (DAC) instrument using synchrotron radiation. The resistance versus pressure and capacitance versus pressure relationships up to 20 GPa have been studied simultaneously using the DAC technique at room temperature. The results showed that the structure of Ca_2CuO_3 is stable under pressures up to 34 GPa. According to the Birch–Murnaghan equation of state, assuming $B_0' = 4$, the bulk modulus $B_0 = 165.4 \pm 1.8$ GPa has been obtained. It was found that the resistance decreases continuously with increasing pressure up to 20 GPa. However, a sharp drop in the pressure range of 1.8–6.0 GPa was observed. Meanwhile the capacitance increased all along with the pressure and displayed a steep jump at the same pressure range in which the resistance rapidly changed. This metallization phenomenon may be ascribed to an electronic structure transition induced by the pressure.

The CaO–CuO system has been investigated at high oxygen pressure. Only two ternary compounds, $Ca_{0.83}CuO_2$ and $Ca_{14}Cu_{24}O_{41}$, were found to be stable at

$p(O_2) = 500$ bar. $Ca_{14}Cu_{24}O_{41}$ has been synthesized as a bulk phase for the first time. The formation of this phase occurred only in a very narrow range of temperature and oxygen pressure. Resistivity measurements at high pressure from 3 to 8.5 GPa show a superconducting transition in the whole range of pressures. Magnetic properties of this compound at ambient pressure have been also studied. A study of structural and electrical properties under high pressure and low temperature for $S = 1/2$ Heisenberg two-leg ladder compound $Sr_{0.4}Ca_{13.6}Cu_{24}O_{41+\delta}$ was made. It showed a superconducting transition above 3 GPa with a maximum T_c of 13 K. The $Sr_{0.4}Ca_{13.6}Cu_{24}O_{41+\delta}$ phase survives at least up to 9 GPa and down to 7 K without decomposition or phase transition, indicating that it was responsible for the observed superconductivity. The most important role of high pressure for realizing superconductivity was the fact that enhancement of the interaction between the Cu_2O_3 ladder and the 1D CuO_2 chain which accelerates redistribution of holes via locally formed Cu_{ladder}–O_{chain} hybrid orbitals occurs. Electrical property of the normal state is affected by the carrier density, dimensionality, random potential, and spin scattering which are related to structural modification under high pressure.

In another paper, the low-temperature crystal structure of a 1D chain-ladder composite material $Sr_{0.4}Ca_{13.6}Cu_{24+y}O_{41+z}$ was determined by the Rietveld analysis of neutron diffraction data using a super-space group approach. The hole distribution between the chain and ladder planes was estimated by the bond valence sum (BVS) calculation based on Cu–O interatomic distances. The minimum of the distance between ladder-copper and chain-oxygen atoms [Cu(1)–O(3)] was revealed to expand with lowering temperature. The BVS calculation indicated that such a structural change corresponds to a redistribution of holes from the ladder to the chain and that almost all of the holes are localized in the chain below or near the Néel temperature. By assuming reasonable magnetic interactions between hole-unoccupied Cu sites on the chain plane, we propose a possible magnetic structure model taking into account the distribution of holes and observed magnetic neutron Bragg reflections. The results suggest the presence of spin dimers, spin trimers, and "lone" spins in the chain, of which the latter two have effective magnetic moments. These moments may be an origin of staggered antiferromagnetic spin modulation onto the spin liquid state.

In the Cu^{3+}-containing system of MgO–Cu_2O_3, the compound, $Ca_3Cu_2O_6$, has been studied. The double doped unit cell of $La_{2-\delta}Ca_{1+\delta}Cu_2O_{6+\delta}$ (LCCO-52) consists of two chemical formulas, $La_2CaCu_2O_7$ and $Ca_3Cu_2O_6$ which are responsible for the occurrence of superconductivity with $n = 2$ superconducting CuO_2 planes per chemical formula. The distance x between double doped unit cells projected into a CuO_2 plane

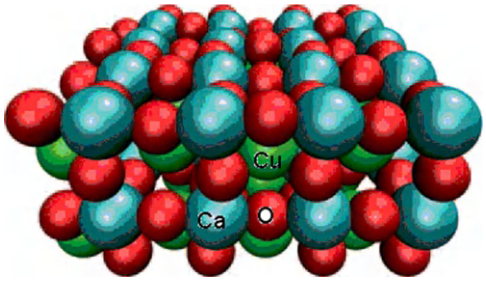

FIGURE 15.21

matches the experimental transition temperature, T_c, quite well. The ternary compound La_2CuO_4 is the parent material for several high-temperature superconductors (HTSC) by doping with an alkaline earth or alkali metal (Ba, Sr, Ca, Na, K, …) and/or introduction of oxygen deficiency or interstitial oxygen excess within the crystal.

In the Cu^{2+}–Cu^{3+}-containing system of MgO–Cu_3O_4, the compound, $CaCu_3O_5$, is mentioned in a patent (1993) but no corroboration has appeared in the literature. The compound, $Ca_2Cu_3O_6$, is also mentioned in the literature concerning the superconductor, $Ba_2Ca_{n-1}+xCu_{n+y}O_z$. It is described as shown in the following:

$Ca_2Cu_3O_6$—Active block

$Ba_2(Ca_{x/2}Ca_{y/2}H_vC_1)_2O_{3+}\delta$—Transformed charge reservoir

---

$Ba_2Ca_2Cu_3(Ca_{x/2}Ca_{y/2}H_vC_1)_2O_{10+\delta}$

In the Cu^{4+}-containing system of MgO–CuO_2, the compound, $CaCuO_3$, is a perovskite with the general structure shown in Fig. 15.21.

Its stability, measured in terms of Gibbs energy of formation, is $\Delta G_f = -6.00$ eV at 298 K for the reaction:

$$CaO + CuO + 1/2O_2 \Rightarrow CaCuO_3$$

$CaCuO_3$ is not mentioned in the open literature except in regard to an additive for preparing high-temperature superconducting compounds, La–Sr–Ca–Cu–O, Ba–Y–Ca–Cu–O, Bi–Sr–Ca–Cu–O, Nd–Ce–Ca–Cu–O, Tl–Ba–Ca–Cu–O, Ba–K–Ca–Bi–O, and Ba–Rb–Ca–Bi–O. Other possible compounds like Ca_2CuO_4 and $CaCu_2O_5$ are only mentioned in the same sense.

The same may be said for compounds in the Cu^{5+}-containing system of MgO–Cu_2O_5.

Calcium cuprate compounds are not offered for sale commercially and no CAS numbers have been issued to date.

15.1.4. Strontium Copper Compounds

Strontium forms two intermetallic compounds with copper metal as shown in the following phase diagram in Fig. 15.22.

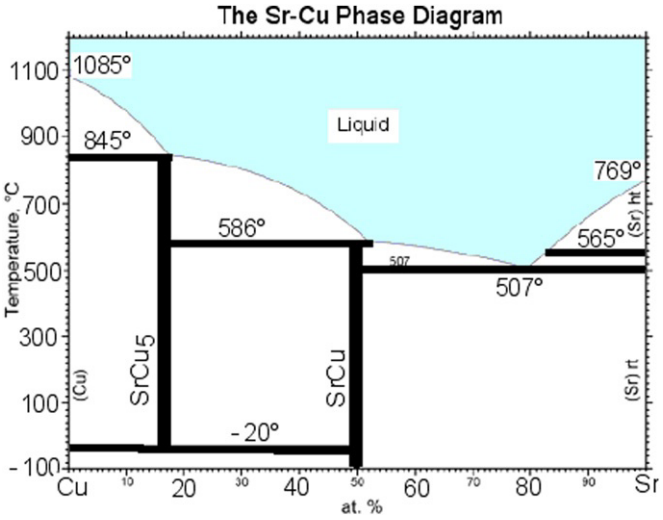

FIGURE 15.22

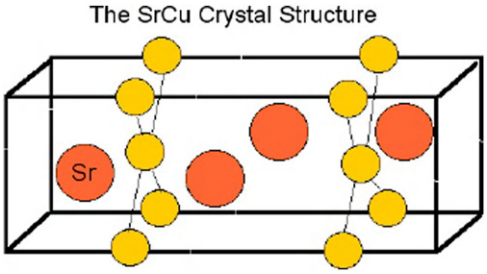

FIGURE 15.23

SrCu has the structure form shown in Fig. 15.23.

Cell parameters for SrCu are: $a = b = 4.341$ Å, $c = 15.384$ Å, $\alpha = \beta = \gamma = 90°$, cell volume $= 251.00$ Å^3, $Z = 4$. Cell occupancy is shown in Table 15.12.

The compound, $SrCu_5$, has the crystal form shown in Fig. 15.24.

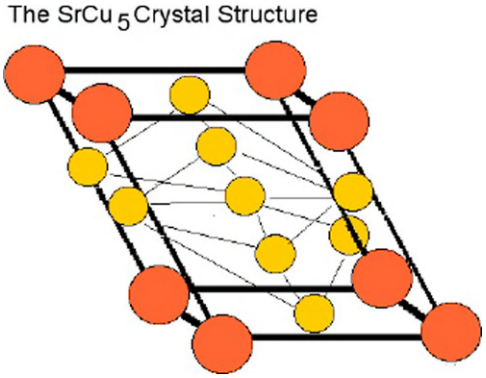

FIGURE 15.24

Cell parameters are: $a = 4.057$ Å, $b = c = 5.2635$ Å, $\alpha = 120°$, $\beta = \gamma = 90°$, cell volume $= 97.10$ Å^3, $Z = 4$. Cell occupancy is shown in Table 15.13.

No other intermetallic Sr–Cu compounds are known. There have been no studies of the physical or electrical properties of these compounds in the recent literature. They are not available commercially and no CAS numbers have been issued to date.

No phase diagrams are available for the Sr–Cu–O system.

In the Cu^+-containing system of $SrO–Cu_2O$, the compound, $SrCu_2O_2$ is known. It is a wide band gap p-type conductive oxide. $SrCu_2O_2$ thin films were prepared on SiO_2 glass substrates by pulsed laser deposition. The film deposited in O_2 atmosphere of 7×10^{-4} Pa at 573 K showed high optical transmission in visible and near-infrared regions. Potassium was doped at the Sr site for substitutional doping. The optical band gap of the K-doped film was estimated to be ~3.3 eV. The DC electrical conductivity of the K-doped film at 300 K was 4.8×10^{-2} S/cm and the activation energy was 0.10 eV. A positive sign of Seebeck and Hall coefficients demonstrated the p-type conduction of the film. Hole

TABLE 15.12

No.	Site notation	Atom	Multiplicity	Wyckoff	Site symmetry	x	y	z	Occupancy
1	Sr1	Sr	4	f	3m.	1/3	2/3	0.6217	1.0
2	Cu1	Cu	2	c	-6m2	1/3	2/3	1/4	1.0
3	Cu2	Cu	2	b	-6m2	0	0	1/4	1.0

TABLE 15.13

No.	Site notation	Atom	Multiplicity	Wyckoff	Site symmetry	x	y	z	Occupancy
1	Cu2	Cu	3	g	mmm	1/2	0	1/2	1.0
2	Cu1	Cu	2	c	-6m2	1/3	2/3	0	1.0
3	Sr	Sr	1	a	6/mmm	0	0	0	1.0

concentration and mobility at 300 K were $6.1 \times 10^{17}/cm^3$ and 0.46 $cm^2/V/s$, respectively.

Preparation of p-type transparent conducting Ca-doped $SrCu_2O_2$ thin films deposited on a quartz glass substrate has been carried out by a pulsed laser deposition technique. X-ray diffraction patterns illustrate that Ca-doped $SrCu_2O_2$ thin films with oriented growth have been obtained at a deposition temperature as low as 350 °C. The film deposition at 350 °C has a conductivity of 8.2×10^{-2} S/cm, carrier concentration of $1.33 \times 10^{17}/cm^3$, hole mobility of 3.82 $cm^2/V/s$ and a band gap of 3.2 eV at room temperature (300 K). A transparent p–n hetero-junction diode was fabricated using *p*-type $SrCu_2O_2$:Ca and *n*-type ZnO:Al thin films on an ITO-coated glass substrate. The junction exhibits nonlinear and rectifying I–V characteristics.

A near-UV emitting diode was fabricated by successive hetero-epitaxial growth of In_2O_3:Sn(ITO), *n*-electrode, *n*-ZnO, and *p*-$SrCu_2O_2$ (SCO) on an extremely flat surface of yttria-stabilized ZrO_2 single crystalline substrate using a pulsed-laser deposition technique. Upon current injection at room temperature, the resulting diode emitted near-UV light with a peak at 382 nm. The threshold voltage for emission was 3 V, which is in agreement with the energy difference between the ZnO donor level and the SCO acceptor level. The epitaxial relationship between SCO and ZnO depends on the deposition temperature of SCO on ZnO. The inhomogeneity of the SCO crystal was improved by raising the deposition temperature from 350 °C to 600 °C. The threshold current for near-UV emission from the diode fabricated by deposition of the SCO film at 600 °C was reduced to 1/5 of that at 350 °C. One reason why this hetero-epitaxial growth occurs for oxides with large lattice misfit is explained in terms of the high ionicity of chemical bonds in oxides.

Photoemission spectra of K-doped $SrCu_2O_2$ excited with vacuum ultraviolet synchrotron radiation have been measured over a range of photon energies between 36 eV and 164 eV. Intensity changes in the spectra with changing photon energy showed that the states at the top of the valence band are of dominant Cu 3d atomic character, although there is evidence for significant hybridization between O-2p and Cu-3d states. The experimental results were compared with partial densities of states derived from calculations using a hybrid exchange approximation to density functional theory.

In another study, transparent oxide p–n hetero-junction diodes based on $SrCu_2O_2$ (SCO) were fabricated by RF-magnetron sputtering. A Zn-terminated polar plane (Zn-face), an O-terminated polar plane (O-face), and a non-polar plane (A-face) of highly oriented polycrystalline ZnO plates were used as substrates to clarify what effect the surface polarity of ZnO has upon the p–n heterojunction characteristics. Highly transparent and very electrically conductive SCO films were obtained by the application of low RF power ($\hat{E} < 0.5$ W/cm^2) under high deposition pressures (8–10 Pa). Although none of the as-prepared p-$SrCu_2O_2$/n-ZnO hetero-junctions showed a very good rectifying I–V characteristics, the junction between SCO and the O-terminated ZnO polar surface exhibited clear rectifying I–V characteristics after post-deposition annealing at 923 K in Ar gas. The origin of the variation in the I–V characteristics that depended on the crystal axis orientation of the ZnO substrates was assumed to be due to the surface polarity of the ZnO surface. It would appear that not only the gas-sensing characteristics but also the diode properties depend on the crystal axis orientations of the ZnO layer. A transparent p-n junction based on zinc oxide (ZnO) was suggested to have the good gas-sensing properties.

Liquid precursors for $SrCu_2O_2$ were made by dissolving copper formate and strontium acetate in water. Bulk single-phase powdered $SrCu_2O_2$ was synthesized through the spray deposition of liquid precursors at 180 °C followed by a 4 h anneal at 775 °C and 2.0×10^{-5} Torr vacuum. Additionally, $CaCO_3$ was successfully added to the precursor solution and subsequently incorporated after annealing. This was a critical demonstration of the ability to perform cation substitutions by this approach. Employing the liquid precursor for thin films resulted in mixed phase $SrCu_2O_2$ and Cu_2O due to Sr loss during annealing. The liquid precursor was also successfully inkjet printed. The deposition-temperature phase diagram presented was shown in Fig. 15.25.

The structure of $SrCu_2O_2$ is based on planar zigzag chains running in orthogonal [100] and [010] directions, shown in Fig. 15.26.

The tetragonal structure of $SrCu_2O_2$ belongs to the space group $I\,41/amd$ with a unit cell containing two formula units and defined by the lattice constants

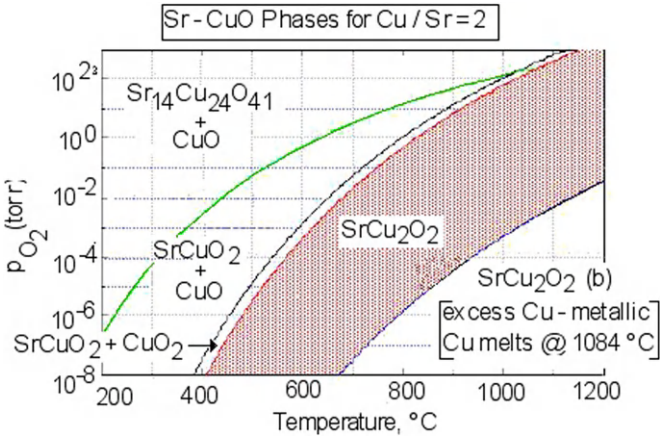

FIGURE 15.25

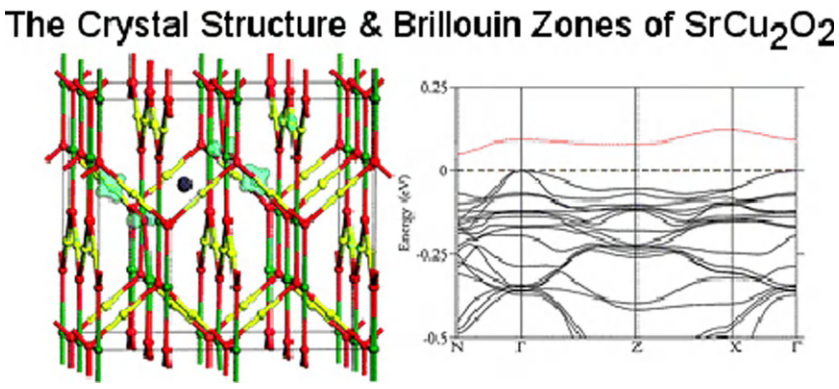

FIGURE 15.26

$a = 5.469$ Å and $c = 9.826$ Å. In the simplest ionic model description $SrCu_2O_2$ is a d_{10} Cu(I) oxide with an upper valence band of filled Cu-3d states that sits above a band of filled O-2p states. The conduction band is derived from empty Cu-4s states.

Within the linear O–Cu–O units the Cu-$3d_{2z}$ orbitals have r-like symmetry, the $3d_{xz}$ and $3d_{yz}$ p-like symmetry and the $3d_{xy}$ and $3d_{x2!y2}$ d-like symmetry. Thus O-2p orbitals can mix with Cu-$3d_{2z}$ via strong r overlap and with $3d_{xz}$ and $3d_{yz}$ via weaker p interactions. However $3d_{xy}$ and $3d_{x2!y2}$ must remain localized on Cu as there are no orbitals on oxygen having the correct d symmetry for covalent mixing. Provided that the oxygen stoichiometry is unchanged, introduction of singly charged K^+ onto Sr^{2+} sites must be accompanied formally by oxidation of a corresponding number of the Cu^+ ions present in the lattice to Cu^{2+}. Of course this introduces holes into the previously full Cu-3d bands. An issue of particular importance is the extent to which the Cu-3d and O-2p states mix, especially at the top of the valence band: it has been suggested that delocalization of hole states off copper and onto oxygen by O-2p/Cu-3d-hybridization at the top of the valence band is a prerequisite for good hole mobility.

A closer view of the structure is shown in Fig. 15.27.

The transparency of $SrCu_2O_2$ to light can be explained by the calculation of dipole transition matrix elements. The calculated effective masses for the conduction band states are found to be larger than those for the valence states for $SrCu_2O_2$, opposite to the trend in conventional semiconductors and *n*-type transparent conductive oxides.

It was predicted that adding a small amount of Ca (~16%) into $SrCu_2O_2$ would increase the band gap and reduce the hole effective mass of $SrCu_2O_2$, therefore increasing the transparency and conductivity.

The electronic structure of $SrCu_2O_2$, a wide gap (~3.3 eV) *p*-type oxide semiconductor, was examined by photoelectron and optical spectroscopy. The spectroscopy results were compared with the energy band structure calculated by the local density approximation method to clarify the origins of *p*-type conductivity in this material. Despite the significant difference in band gap energy, the basic electronic structure around the band gap region was found to be quite similar to that of Cu_2O. Thus, the 3d-4sp orbital of Cu^+ ion is hybridized with the 2p orbital of ligand O^{2-} ions due to the covalence of Cu–O bonds, to form states near the valence band maximum; the conduction band minimum is predominantly composed of the hybridized orbital of Cu-4sp and O-2p, forming the direct band gap at Γ point of the Brillouin zone. A sharp absorption band observed near the fundamental absorption edge is likely attributable to an exciton. Although the corresponding exciton emission was not observed near the absorption edge,

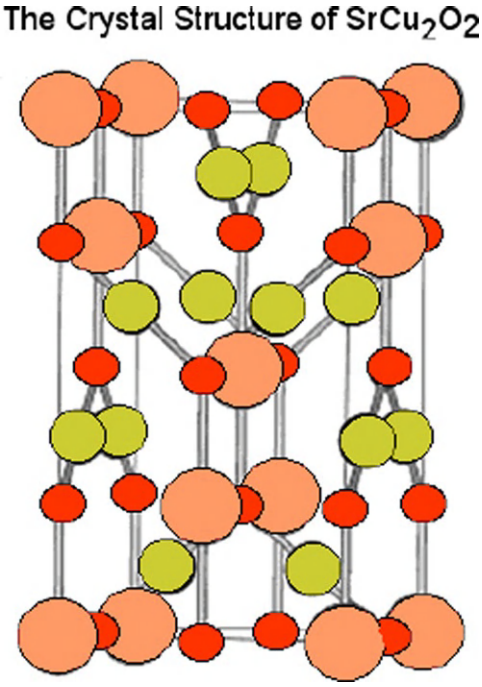

FIGURE 15.27

a blue-green emission band (stokes shift of ~1.0 eV) was observed at −2.47 eV. The emission is presumably attributable to intraatomic transitions of Cu^{+}, partially allowed by p-orbital mixing into s- and d-orbitals.

In another paper, *p*-type $SrCu_2O_2$ (SCO) films were deposited by pulsed laser deposition, from SCO target, on glass and *n*-type Si substrates. SCO films were deposited at two different substrate temperatures, namely 300 °C and 500 °C, while the oxygen pressure was kept constant at 5×10^{-2} Pa and their properties were investigated. Films deposited at 300 °C were single-phase $SrCu_2O_2$, whereas deviation from stoichiometry was observed for films deposited on Si at 500 °C. Both SCO films were *p*-type materials and their resistivity increased with the increase of the substrate temperature (from 142 Ω cm to 10 kΩ cm). Their transparency reached 70% even for films with thickness of 800 nm. SCO films deposited on *n*-type Si showed rectifying behavior and the p-SCO/n-Si hetero-structure formed from low-temperature deposited SCO (300 °C) exhibited better *p*/*n* junction properties than that formed at the substrate temperature of 500 °C. Improvements which can be implemented for enhancing the output performance of the hetero-junction were addressed.

A modulated structure analysis of the mutually incommensurate composite crystal, $(Sr_2Cu_2O_3)_{0.70}CuO_2$ with two-legged spin ladder, has been performed on the basis of a (3+1)-dimensional superspace group approach. It has been found that the symmetry of $(Sr_2Cu_2O_3)_{0.70}CuO_2$ should be described by a centrosymmetric super-space group. In the modulated composite structure of $(Sr_2Cu_2O_3)_{0.70}CuO_2$, displacement modulation of O atoms in the CuO_2 chain was found to be fairly large and played an important role. Structural interaction between the CuO_2 chain and the Cu_2O_3 ladder has been extensively investigated. The crystal structure of the quasi 1D cuprate $Ca_{0.83}CuO_2$, also known as $Ca_4Cu_5O_{10}$, $(Sr_2Cu_2O_3)_{0.70}CuO_2$, ($Sr_{14}Cu_{24}O_{41}$) etc., was determined using a superspace group approach. The compound consists of two interpenetrating subsystems of CuO_2 chains and Ca atoms. Structural parameters were refined with a superspace group of $F2/m(1+\alpha 0)\,\gamma 0s$ using powder X-ray and neutron diffraction data. Lattice parameters were refined to be $a_1 = 2.8043$ Å, $b = 6.3179$ Å, $c_1 = 10.5744$ Å, and $\beta_1 = 90.10°$ for the [CuO_2] subsystem and $a_2 = 3.3652$ Å, $b = 6.3179$ Å, $c_2 = 10.5893$ Å, and $\beta_2 = 93.04(1)°$ for the [Ca] subsystem. The Ca atoms suitably sit in the center of the modulated O_6 octahedra (Fig. 15.28).

A remarkable displacement modulation of the O and Ca atom sites was observed parallel to the *b*-axis and the *c*-axis, respectively. On the other hand, the Cu atom sites deviated mainly in the *a* direction to yield a periodic fluctuation between the nearest Cu–Cu distances.

In another paper, the temperature dependence of atomic modulation in the incommensurate composite crystal structure of $(Sr_2Cu_2O_3)_{0.70}CuO_2$, "$Sr_{14}Cu_{24}O_{41}$" with two-legged Cu_2O_3 ladder and edge-shared CuO_2 chain has been investigated by single-crystal X-ray diffraction method using centrosymmetric (3 + 1)-dimensional superspace group. The displacement modulations of all constituent atoms at 150 K have been compared with those obtained at room temperature. The hole distribution between the Cu_2O_3 ladder plane and the 1D CuO_2 chain has been considered on the basis of: the changes of lattice constants of incommensurate basic structure, the role of the atomic modulation and the interatomic distances between Cu atom in the Cu_2O_3 and O atom in the CuO_2. It was indicated that the small amount of holes doped in the Cu_2O_3 ladder have been back-transferred to the CuO_2 chain and that almost all of the holes in $(Sr_2Cu_2O_3)_{0.70}CuO_2$ are localized in the CuO_2 at low temperature.

Single crystals of $[Sr_2Cu_2O_3][CuO_2]x$ ($x = 1.436$) were obtained by a slow cooling method using KCl as a flux. KCl acted as a good intermediate for the growth of this compound. This compound takes a composite crystal structure. The first subsystem is [$Sr_2Cu_2O_3$] and second subsystem is [CuO_2]. Both subsystems have an

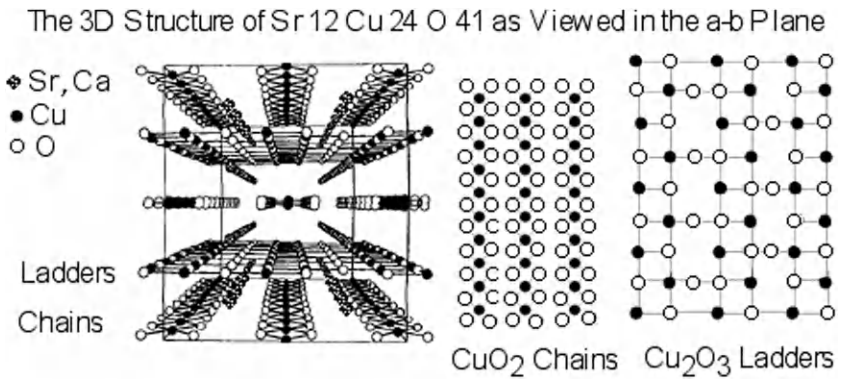

FIGURE 15.28

orthorhombic structure with superspace group $M_{TST}^{Az,ma}$: $M_{TST}^{Az,ma}$. The compound has mutually incommensurate periods along the *c*-axis. The lattice parameters are $a = 11.457$ Å, $b = 13.409$Å, $c_1 = 3.935$ Å and $c_2 = 2.740$ Å. Characteristic features of this compound are found in chains and sheets composed of Cu and oxygen atoms. On the basis of the structural studies of the samples grown by floating zone and flux methods, it was concluded that the phase $(M_2Cu_2O_3)(Cu_{1+}O_{2+})$, described as the $m/n = 1/1$ member, with Cu-deficient Cu–O ribbons in the series $(M_2Cu_2O_3)m(CuO_2)n$ can be treated as an individual structural type intermediate between $SrCu_2O_3$ and incommensurate-type phases $(M_2Cu_2O_3)m(CuO_2)n$ with *m* and *n*. The deficiency of the Cu sites in CuO ribbons is a particular crystal chemistry feature of this structural type, in addition to the geometrical feature ($m = n$). The structural type of the 'Cu-deficient ladder' can transform into the incommensurate-type phases $(M_2Cu_2O_3)m(CuO_2)n$ ($m/n = 5/7, 7/10, 9/13$, etc.) in the presence of free $[CuO_4]^{6-}$ radicals in the melt. A realization of the $(M_2Cu_2O_3)m(CuO_2)n$ phase with a particular m/n value is caused by the type of M cation was concluded. On the basis of recent data, the role of trivalent ions in the chemical composition of the $(M_2Cu_2O_3)m(CuO_2)n$-type compounds was also analyzed. The occurrence of the superconductivity in $(Sr,Ca)CuO_2$ samples was discussed by analogy with cuprates of the infinite-layer structure type.

$Sr_{14-x}Ca_xCu_{24}O_{41}$ crystals at high Ca concentrations are superconducting under pressure and hole pairing was proposed to be a robust feature of doped ladders. The measured dielectric response in the microwave region, the low-energy Raman data, the nonlinear transport properties along with soft X-ray scattering allowed the conclusion that the ground state in $Sr_{14-x}Ca_xCu_{24}O_{41}$ for a wide range of Ca concentrations ($x \leq 12$) is characterized by charge density wave correlations. This state seems to be driven not by phonons but by Coulomb forces and many body effects. The similarity in the finite frequency Raman response as opposed to the very different behavior of the DC resistivity between undoped and doped ladders was highlighted in this discussion. It was found that at high Ca concentrations, although the resistivity shows a crossover between insulating and linear in temperature metallic regime, the carrier relaxation is characterized by the same large activation energy ($\approx$2000 K) which determines the Arrhenius behavior of the CDW compound $Sr_{14}Cu_{24}O_{41}$.

In the Cu^{2+}-containing system of SrO–CuO, the phase diagram shows four compounds in Fig. 15.29.

It has been shown that tetragonal $SrCuO_{2-\delta}$ is superconducting at liquid N_2 conditions. Formation regions of orthorhombic and tetragonal $SrCuO_2$-type compounds in the $Sr_{1-x}Ca_xCuO_2$ system were studied at 1000 °C under both ambient and high pressure

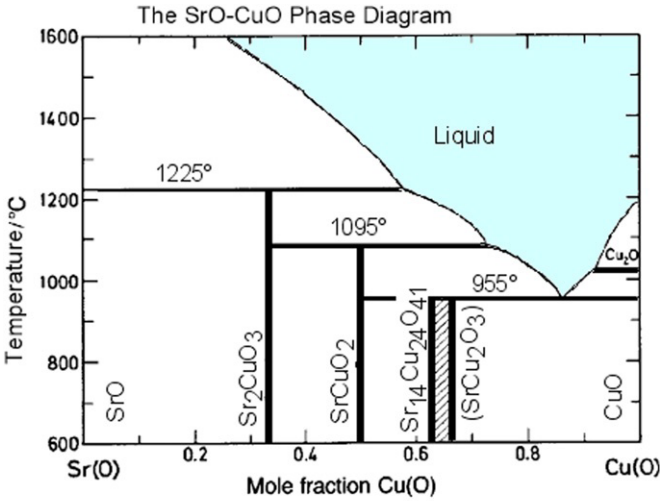

An *x*–*t* diagram for the Sr(O)–Cu(O) system in air

FIGURE 15.29

conditions. Under ambient pressure, single-phase samples of the orthorhombic phase solid solution were formed in the region between $x = 0.0$ and 0.45, mixed-phase samples containing the orthorhombic phase in the region between $x = 0.5$ and 0.65, and the tetragonal phase at $x = 0.9$. The tetragonal phase solid solution was obtained under 2–5 GPa in the compositional region between $x = 0.2$ and 0.8. The tetragonal phase was stabilized under pressure higher than 4 GPa for the samples with $x = 0.0$–0.1. No tetragonal phase was obtained in the samples of Ca content $x = 1.0$. The compound, $SrCuO_2$, has been found to have the structure shown in Fig. 15.30.

The tetragonal phase with $x = 0.9$ obtained under ambient pressure decomposed at above 4 GPa to a mixed phase. The minimum lattice constants for the *a*-axis in both orthorhombic and tetragonal phase were determined to be 0.386 nm. Solid solution limit for both tetragonal and orthorhombic phases was explained by the concept of minimum Cu···O distance (=1.93 Å) to stabilize $[CuO_4]$ coordination. Single crystals of the orthorhombic $SrCuO_2$ were grown by a traveling solvent floating zone (TSFZ) method. It was found that a suitable chemical composition of the traveling solvent for the TSFZ growth was Sr:Cu = 3:7 in molar ratio. Lattice constants of the grown crystal were $a_0 = 3.92$, $b_0 = 16.35$ and $c_0 = 3.57$ Å and the chemical composition was Sr:Cu = 1.00:0.98 in molar ratio. The grown crystal was compressed at 1000 °C and 6 GPa for 1 h.

The orthorhombic crystal was transformed to polycrystalline tetragonal $SrCuO_2$ with $a_0 = 3.93$ and $c_0 = 3.43$ Å by the high-pressure treatment. Preferable orientation of crystalline axis was found in the obtained polycrystalline sample of the tetragonal $SrCuO_2$. The axial relationship between the single crystalline

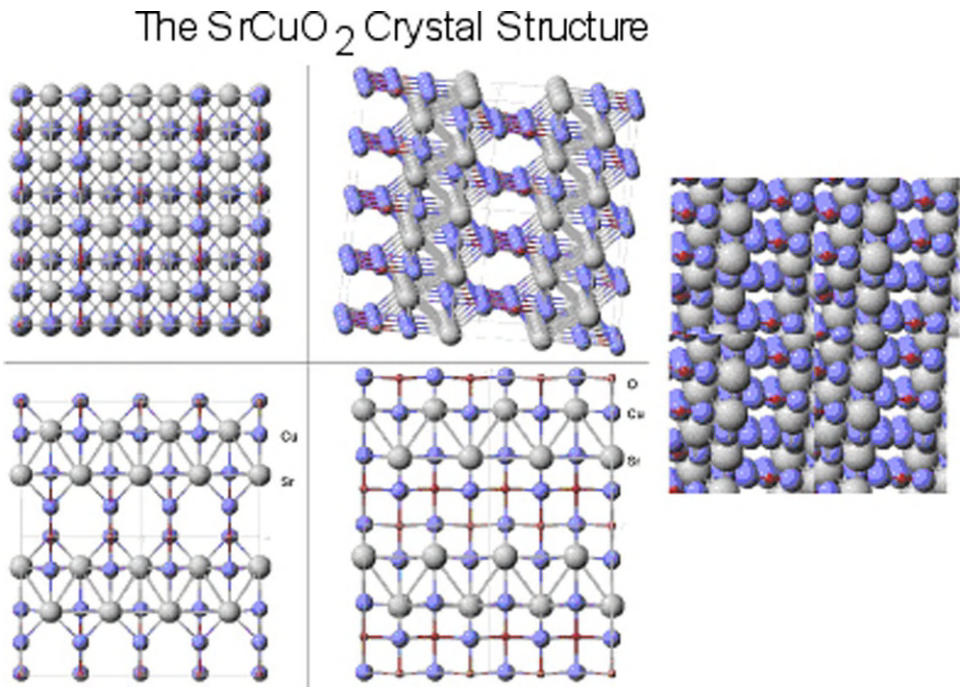

FIGURE 15.30

precursor of the orthorhombic $SrCuO_2$ and the obtained tetragonal $SrCuO_2$ was discussed from the viewpoint of the orientation of the [CuO_4] square planar coordination. A pressure-induced splitting of the Cu–O chains was found in $SrCuO_2$ subjected to pressures >7 GPa compared to room temperature. The high-pressure phase is a superstructure of the infinite-layered tetragonal superconducting phase of $SrCuO_2$ and is not stable under ambient conditions. The Cu–O chains buckle with further increasing pressure, and a new high-density polymorph of $SrCuO_2$ is formed at 34.2 GPa.

Processes of $SrCuO_2$ and Sr_2CuO_3 ceramics decomposition induced by contact with water and carbon dioxide were studied by EPR. The dominant signals in the spectra were found to originate from $Sr_2Cu(OH)_6$ (for Sr_2CuO_3) and $SrCu(OH)_4 \cdot H_2O$ (for $SrCuO_2$) compounds. The thermally induced conversion of $SrCu(OH) \cdot 4H_2O$ into $Sr_2Cu(OH)_6$ was analyzed, and its product CuO was found to exist in a nanocrystalline form. The presence of CO_2, reacting with $Sr(OH)_2$, was shown to modify the decomposition process, leading to the appearance of $SrCu(OH)_4 \cdot H2O$, some hydroxycarbonates and $Cu(OH)_2$ on the surface of ceramics were studied. At temperatures higher than 300 °C CuO reacts back with $Sr(OH)_2$. For the samples in contact with atmospheric moisture, this compound, deposited on a surface of $SrCuO_2$, decomposes to $Sr_2Cu(OH)_6$. The presence of the AFM compounds, $Cu(OH)_2$, CuO, and $Cu_2[(OH)_2CO_3]$, in the samples can influence the results of magnetic measurements of the studied ceramics. The unit cell parameters found for these compounds were shown in Table 15.14.

A comparison of the two crystal structures is shown in Fig. 15.31.

If Sr_2CuO_3 is heated to 1000 °C, it decomposes to form $SrCuO_2$:

$$Sr_2CuO_3 + \text{heat} \Rightarrow SrCuO_2 + SrO$$

The stability of the infinite layer $SrCuO_2$ upon heating in air was investigated by a high temperature X-ray diffraction method. The infinite layer $SrCuO_2$ first reacted gradually with CO_2 in air to form $SrCO_3$ when the temperature was above 300 °C. When the temperature was over 400 °C, the infinite layer $SrCuO_2$ transformed into orthorhombic $SrCuO_2$. The lattice

TABLE 15.14

No.	Site notation	Atom	Multiplicity	Wyckoff	Site symmetry	*x*	*y*	*z*	Occupancy
1	Be	Be	16	c	.-3m	0	0	0	1.0
2	Ag	Ag	8	b	-43m	3/8	3/8	3/8	1.0

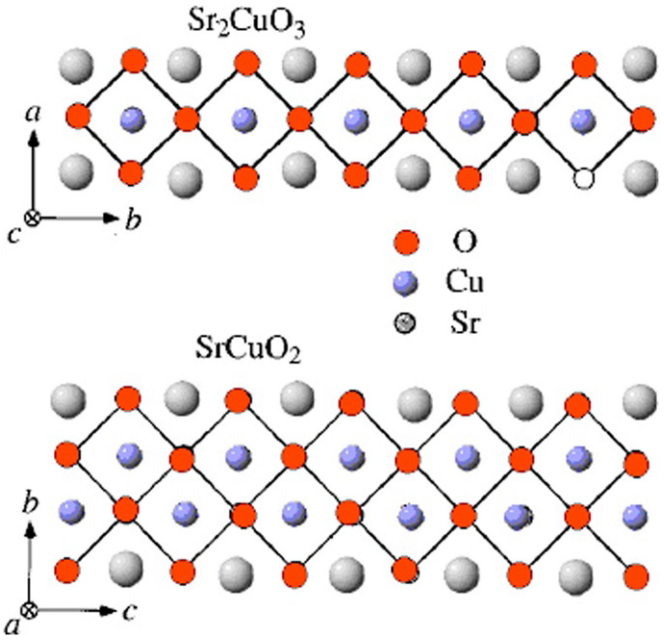

FIGURE 15.31

parameters a and c of the infinite layer $SrCuO_2$ showed different thermal expansion coefficients, i.e. $d\alpha/dT = 3.392 \times 10^{-5}$ Å/°C and $dc/dT = 5.80 \times 10^{-5}$ Å/°C. High-purity samples of the chain cuprate $SrCuO_2$ were investigated and a huge magnetic heat conductivity K_{mag} was observed. An extremely large spinon mean-free path of more than a micrometer demonstrates that K_{mag} is only limited by extrinsic scattering processes which is a clear signature of ballistic transport in the underlying spin model. The standard enthalpy of formation obtained for the cuprate, Sr_2CuO_3 was −1374 kJ/mol.

The crystal structure of the quasi 1D cuprate Sr_2CuO_3 has been studied under high pressure using neutron powder diffraction methods. Full structure refinements were undertaken, using the Rietveld method, with data acquired between room pressure and 0.55(1) GPa at room temperature. The compressibility of Sr_2CuO_3 is anisotropic, a consequence of the ordered nature of the anion vacancies in this material. The effect of high pressure and chemical substitution on the crystal structure of the $Sr_{2-x}Ca_xCuO_3$ system was discussed and it was suggested that the substitution of Sr^{2+} by Ca^{2+} may constitute a "chemical pressure" effect in this solid solution. The availability of accurate bond length compressibility data for Sr_2CuO_3 may now allow an appraisal of the effect of applied pressure on the remarkable electronic properties of this material, through appropriate band structure calculations. Sr_2CuO_3 behaves almost perfectly like a 1D AFM with an exchange coupling of $J = 1700^{+150}_{-100}$ K. For Sr_2CuO_3, $J_a = -119$ meV for the intrachain coupling and $J_b = -0.28$ meV for the interchain coupling was obtained. The experimental Neel temperatures were found to be proportional to the ratio J_b/J_a to a high accuracy. This indicates that the isolated chain is an antiferromagnet with vanishing T_N.

A single-phase $Sr_2CuO_{3+\delta}$ superconductor of $T_c = 75$ K with the K_2NiF_4 structure under high pressure was formed under high pressure to form partially occupied "apical oxygen" sites which also acts as the dopant. Oxygen atoms only partially occupy the apical sites next to the CuO_2 planes and act as hole dopants. After post-annealing the as prepared sample from 150 to 300 °C, the superconducting transition temperature (T_c) could be systematically enhanced up to 95 K. Transmission electron microscopy (TEM) measurements on the $Sr_2CuO_{3+\delta}$ superconductors revealed a series of modulated structure phenomena resulting from dopant ordering. The distribution geometry of dopant such as the partially occupied apical oxygen here can be an additional route to reach further higher T_c.

The copper K-edge EXAFS recorded from the compound Sr_2CuO_3 was best fitted to a first-shell coordination of four oxygen atoms at 1.95 Å. In contrast, the best fit to the data recorded from the oxygen-rich compound $Sr_2CuO_{3.9}$ was to a first shell of two oxygen atoms at 1.75 Å and a second shell of three oxygen atoms at 1.90 Å. These results may be associated with the incommensurate ordering in $Sr_2CuO_{3.9}$ of the anionic sublattice, a fact suggested by powder neutron diffraction as well. The short Cu···O bond distance is also consistent with the high nominal oxidation state of copper, ca + 3.8 in $Sr_2CuO_{3.9}$.

The synthetic conditions of the "$Sr_2CuO_{3+\delta}$" phase (214) in the Sr–Cu–O system were investigated using high-pressure techniques at 5 GPa and 1400 °C. Sr_2CuO_3 powder was used as starting materials, and $KClO_3$ as oxidizer. The effect of the initial amount of $KClO_3$ on the structure and the physical properties was investigated. Two crystallographic domains of the tetragonal fundamental structure: $a \approx 3.76$ Å, $c \approx 12.54$ Å, and $a \approx 3.79$ Å, $c \approx 12.46$ Å, respectively were observed. TEM investigations of the latter have shown evidence of modulations along the [110] direction which leads to a new superlattice with a periodicity of $5a/\sqrt{2} \times 5a/\sqrt{2} \times c$. Moreover, two new phases appeared in this system; one is monoclinic and related to the infinite layer structure with $a = 8.430$ Å, $b = 11.100$ Å, $c = 3.641$ Å, $\beta = 83.2°$, the other suggested a change of the space group from body centered (I) to primary (P). The electrical properties and magnetic behavior observed for these materials were discussed in relation with the synthesis conditions and observed phases. Bulk superconductivity up to 80 K has been obtained.

In another paper, a *single-phase* superconductor $Sr_2CuO_{3+\delta}$ with nominal $\delta = 0.4$ (detected from XRD

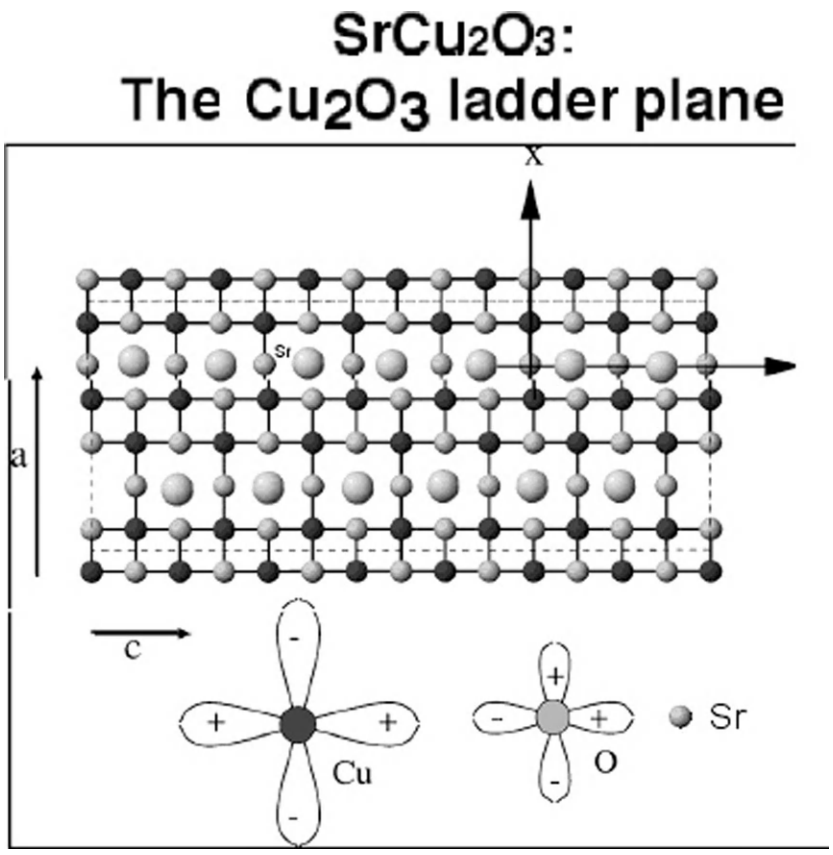

FIGURE 15.32

data) ($T_c = 75$ K) has been synthesized using a high-pressure technique. The structure and microstructure of this material have been carefully studied by means of transmission electron diffraction (ED), high-resolution transmission electron microscopy (HRTEM), electron energy-loss spectroscopy (EELS) and energy dispersive analysis of X-ray (EDX) techniques. Interestingly enough, ED and HRTEM investigations reveal that almost all grains of the tetragonal form $Sr_2CuO_{3+\delta}$ exhibit modulated features. This result strongly suggests that the superconductivity at 75 K in the material is associated with the modulated phases. Two types of modulated phases having different primitive cells but equal in volume are found in the sample. One is the face-centered orthorhombic modulated phase with a space group *Fmmm* and lattice constants of $5\sqrt{2}a_p \times 5\sqrt{2}a_p \times c_p$. The other is the base-centered monoclinic modulated phase with a space group $C2/m$ and unit cell parameters of $a_m = 5\sqrt{2}a_p \times c_p$, $b_m = c_p$, and $\beta = 101.3°$. The relative ratio of the former to the latter phase contents is about 4:1. Oxygen K absorption edges from EELS measurements suggest that the two modulated phases have the same hole intensity. Defects such as twin boundaries, small-angle asymmetrical tilt boundaries and dislocations are frequently observed in the C_2/m monoclinic modulated phase. The compound, $SrCu_2O_3$, has the ladder-like structure shown in Fig. 15.32

A 3D structure is shown in Fig. 15.33.

The temperature-dependent magnetic excitation of the 1D spin-ladder compound $SrCu_2O_3$ was investigated by use of Raman spectra. At low temperatures a two-magnon peak is identified at 3160 ± 10/cm and its temperature dependence analyzed in terms of a thermal expansion model. It was found that the two-magnon peak position must include a cyclic ring exchange of $J_{cycl}/J_{perp} = 0.09$–0.25 with a coupling constant along

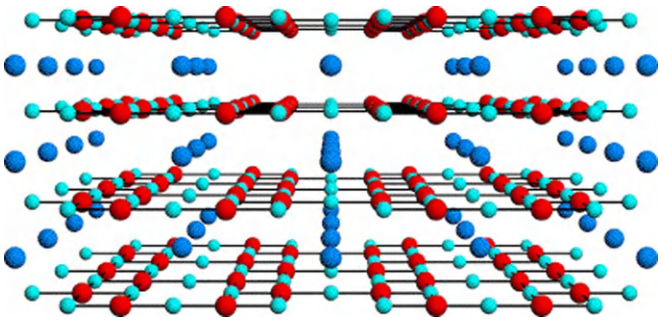

FIGURE 15.33

the rungs of J_{perp} of approximately 1215/cm (1750 K) in order to be consistent with other experiments and theoretical results.

The two-leg ladder $SrCu_2O_3$ belongs to the homologous series $Sr_{n-1}Cu_nO_{2n-1}$ and was first synthesized in 1991. Due to the massive reaction of the sample material with the crucible (Au or Pt), only short reaction times up to 30 min has been used typically. An improved composite crucible with a single-crystalline MgO inset in a sealed Pt capsule was used to demonstrate its capability for single-crystal growth of $SrCu_2O_3$. Experiments with a typical duration of 15 h were conducted at pressures between 3 and 6 GPa at temperatures between 950 and 1500 °C. Slow cooling of the melt effected directed growth of the first $SrCu_2O_3$ millimeter-sized single crystals.

In the Cu^{3+}-containing system of SrO–Cu_2O_3, the compound, $Sr_2Cu_2O_5$, has been studied. These quantum spin ladder materials have attracted much recent interest. The materials consist of ladders made of AFM chains of $S = 1/2$ spins coupled by interchain AFM bonds. Examples of two-leg ladder materials are $SrCu_2O_3$ and $LaCuO_{2.5}$; an example of a three-leg ladder material is $Sr_2Cu_2O_5$. Superconductivity has apparently been discovered in the ladder material $Sr_{0.4}Ca_{13.6}Cu_{24}O_{41}$ under pressure with $T_c = 12$ K at 3 GPa. Part of the interest in quantum-spin ladder materials stems from the fact that they are simple model systems for theories of superconductivity based on magnetic pairing mechanisms.

In the Cu^{2+}–Cu^{3+}-containing system of SrO–Cu_3O_4, the compound, $SrCu_3O_5$, has received some attention in the literature because it fits into the "spin-ladder" class of materials. Only ladders with an even number of legs exhibit a spin gap (i.e. a finite energy scale for triplet excitations) as seen from different characteristic behaviors of the spin susceptibility observed in $SrCu_2O_3$ and $SrCu_3O_5$, typical two-leg and three-leg compounds, respectively.

Other than a comparison to $SrCu_2O_3$, no other data are available for this compound.

In the Cu^{4+}-containing system of SrO–CuO_2, the compound, $SrCuO_3$, has not been described. However, the Sr_2CuO_4 compound has been found to be superconducting. Sr_2CuO_3 (orthorhombic, *Immm*) is converted at about 400 °C under oxygen at 160 bar to $Sr_2CuO_{3.9}$ [tetragonal, $I4/mmm$; $a = 3.7907(7)$, $c = 12.417(2)$ Å], which is structurally related to La_2CuO_4. Although the formal Cu oxidation state in this material appeared to be higher than any previously reported for Cu in an oxide environment (around +3.8), powder neutron diffraction data provided no evidence for O_2^{2-} or O_2^- ions, but are consistent with a highly defective structure containing Sr, Cu, and O vacancies. The cation vacancies are in a 2:1 ratio to maintain the stoichiometry, and the O vacancies are confined to the CuO_2 layers. Additional peaks in the neutron diffraction profile were indicative of an ordering process to give an extended, possibly incommensurate, structure. Cu K-edge EXAFS suggested that the resulting local Cu coordination contains two very short Cu···O bonds (1.755 Å).

The best fit to the data recorded from X-ray analysis to the oxygen loss in the compound, $Sr_2CuO_{3.9}$, is to a first shell of two oxygen atoms at 1.75 Å and a second shell of three oxygen atoms at 1.90 Å. The result may be associated with the incommensurate ordering in $Sr_2CuO_{3.9}$ of the anionic sublattice which had been suggested by powder neutron diffraction. The short Cu···O bond distance was also consistent with the high-nominal oxidation state of copper, ca + 3.8 in $Sr_2CuO_{3.9}$. The superconductivity found in $Sr_2CuO_{4-\delta}$ showed that new physics has occurred in a highly studied region of the cuprate phase diagram. Moreover, evidence was adduced that 30% of the oxygen sites in the CuO_2 layers are vacant, a conclusion which is at odds with the universally made assumption that superconductivity originates in stoichiometric CuO_2 layers. A metastable superconductor with non-stoichiometric CuO_2 layers exists in an unexplored overdoped region of the phase diagram of cuprate superconductors. The enhanced T_c of 95 K found in $Sr_2CuO_{4-\delta}$ for $\delta \approx 0.6$ corresponds to an average copper valence of ~2.8+. New mechanisms are needed to account for the enhanced superconductivity. Two possibilities were suggested. One involves a band of paired electrons formed by the overlap of negative-U oxygen vacancies. The second involves pairing in the CuO_2 layer that is enhanced either by an optimal inhomogeneous distribution of oxygen sites or by a distribution of vacancy-rich/vacancy-poor regions.

The synthesis of new superconducting $Sr_2CuO_{4-\delta}$ thin films ($T_c^{onset} \sim 75$ K) using a molecular beam epitaxial (MBE) method has been reported. This superconductor has a tetragonal structure with an in-plane lattice constant $a_0 = 3.79$ Å and a *c*-axis lattice constant $c_0 = 13.55$ Å. This *c*-axis lattice constant is significantly larger than previously reported for this system. Strong oxidation using ozone gas at a low temperature of around 350\^circC is essential to the realization of phase conversion from the orthorhombic insulating phase (Sr_2CuO_3) to the tetragonal superconducting phase ($Sr_2CuO_{4-\delta}$).

In the Cu^{5+}-containing system of SrO–Cu_2O_5, the compound, $SrCu_2O_6$, is unknown and no other compounds like $Sr_2Cu_2O_7$ or $SrCu_4O_{11}$ have been found.

Strontium–copper compounds are not offered for sale commercially and no CAS numbers have been issued to date.

15.1.5. Barium Copper Compounds

Barium forms but two intermetallic compounds with Cu metal as shown in Fig. 15.34.

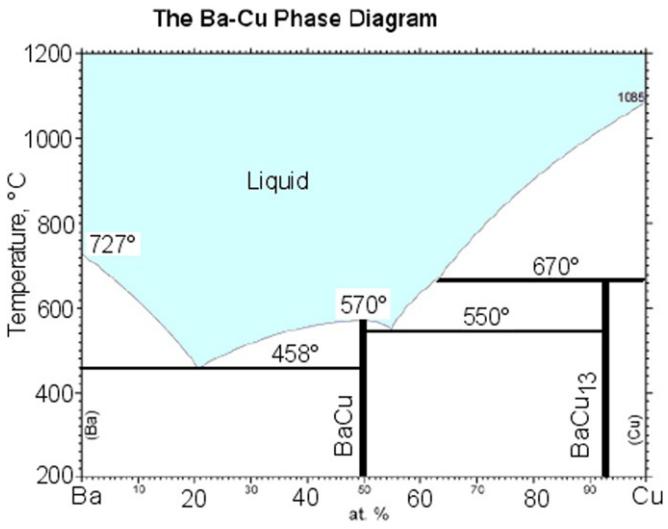

FIGURE 15.34

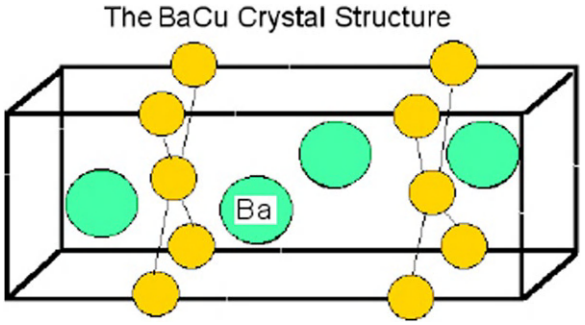

FIGURE 15.35

BaCu has the structure shown in Fig. 15.35.

Cell parameters are: $a = b = 4.496$ Å, $c = 16.232$ Å, $\alpha = \beta = 90°$, $\gamma = 120°$, cell volume $= 284.12$ Å^3, $Z = 4$.

Cell occupancy is shown in Table 15.15.

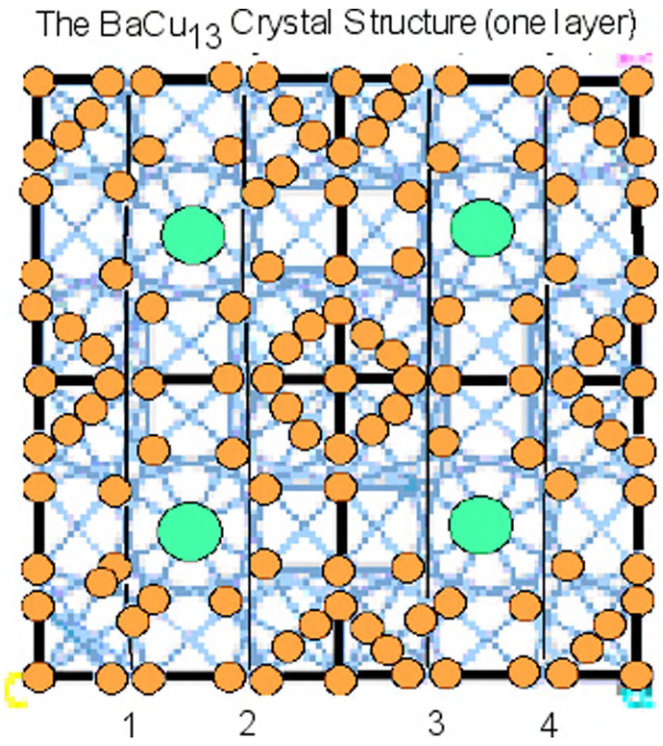

FIGURE 15.36

The compound, $BaCu_{13}$, has the crystal structure form shown in Fig. 15.36.

Only one layer is shown. In the 3D structure, there are two of these layers, separated by the layers of Cu atoms labeled 1 and 2 and 3 and 4.

Cell parameters are: $a = b = c = 8.3113$ Å, $\alpha = \beta = \gamma = 60°$, cell volume $= 405.97$ Å^3, $Z = 8$. Cell occupancy is shown in Table 15.16.

The thermodynamic constants for these compounds (from Johnson et al., 2005) are shown in Fig. 15.37.

TABLE 15.15

No.	Site notation	Atom	Multiplicity	Wyckoff	Site symmetry	*x*	*y*	*z*	Occupancy
1	Be1	Be	8	j	m2m.	0.277	1/2	0	1.0
2	Be2	Be	8	i	m2m.	0.361	0	0	1.0
3	Be3	Be	8	f	..2/m	1/4	1/4	1/4	1.0
4	Ag1	Ag	2	a	4/mmm	0	0	0	1.0

TABLE 15.16

No.	Site notation	Atom	Multiplicity	Wyckoff	Site symmetry	*x*	*y*	*z*	Occupancy
1	Ag	Ag	3	c	4/mm.m	0	1/2	1/2	1.0
2	Mg	Mg	1	a	m-3m	0	0	0	1.0

Thermodynamics of the Ba-Cu System

	BaCu		$BaCu_{13}$	
	ΔH	ΔS	ΔH	ΔS
Calc - 1984	- 19,829	- 18,758	- 4,265	- 3.801
Calc- 1990	- 22,208	- 19705	- 2,885	- 1.856
Calc- 1993	- 2,679.41	- 0.25394	- 1,016.90	0.00
Exp- 1993	- 2597± 3.92			
Calc- 2010	- 2,594	- 0.0	- 924.6	0.00

LIQUID

	A_0	A_1	A_2	A_3	B_0	B_1	B_2	B_3
Calc-1984	-45,121	1,143	0.0	0.0	42.86	0.0	0.0	0.0
Calc-1990	- 764.8	-2595.8	-2879.6	-1970.9	-18.97	16.94	0.0	0.0
Calc-1993	-713.9	-2798.2	-1,905.6	-990.4	-5.799	6.290	3.476	0.0
Calc-2010	-7191	0.0	0.0	0.0	3.363	0.0	0.0	0.0

FIGURE 15.37

No other intermetallic compounds are known in this system. Ba–Cu intermetallic compounds are not offered for sale commercially.

In the Cu^{+}-containing system of BaO–Cu_2O, the compound $BaCu_2O_2$, has been studied because of its relationship to the high-temperature superconducting compound, $YBa_2Cu_3O_{6+x}$. The quaternary phase relations near $YBa_2Cu_3O_{6+x}$ have been investigated using a solid-state ionic technique. Three invariant reactions were discovered. At 850 °C, $YBa_2Cu_3O_{6+x}$ with excess Cu_2O reacts to form Y_2BaCuO_5 and $BaCu_2O_2$ at 1×10^{-3} atm. oxygen pressure, while pure $YBa_2Cu_3O_{6+x}$ decomposes to Y_2BaCuO_5, $BaCu_2O_2$, and $YBa_3Cu_2O_{6.5\pm x}$ at 4×10^{-4} atm. oxygen. These results show that the phase relations near $YBa_2Cu_3O_{6+x}$ change markedly with oxygen pressure.

Although $SrCu_2O_2$ is stable, transparent to light and is a superconductor when oxygen vacancies are formed in the $SrCu_2\ O_{2-\delta}$ composition, Brillouin zone measurements have shown that the Γ-gap of $BaCu_2O_2$ is smaller so that the light transmission properties are much lower than any of the other alkaline earth copper (cuprite) compounds. It has been determined that the cuprite, $BaCu_2O_2$, containing monovalent copper is the only phase stable at reduced partial pressure of oxygen and(or) at high temperatures. $BaCu_2O_2$ (tetragonal with cell parameters of: $a = 5.722$, $c = 10.064$ Å, space group $I41/amd$, $Z = 4$) was identified by X-ray powder diffraction and has the structure shown in Fig. 15.38.

The interaction between components in the system $(BaO)_x$–$(CuO,Cu_2O)_{1-x}$ was investigated experimentally using differential thermal, thermal gravimetric, and X-ray diffraction analyses at temperatures up to 950 °C. It was found that at least three ternary compounds, $Ba_2Cu_3O_5$, $BaCuO_2$, and $BaCu_2O_2$, are formed in the system. $Ba_2Cu_3O_5$ is formed at relatively low temperatures (375–630 °C); $BaCuO_2$ is formed at higher temperatures but is unstable in the presence of excess copper oxide.

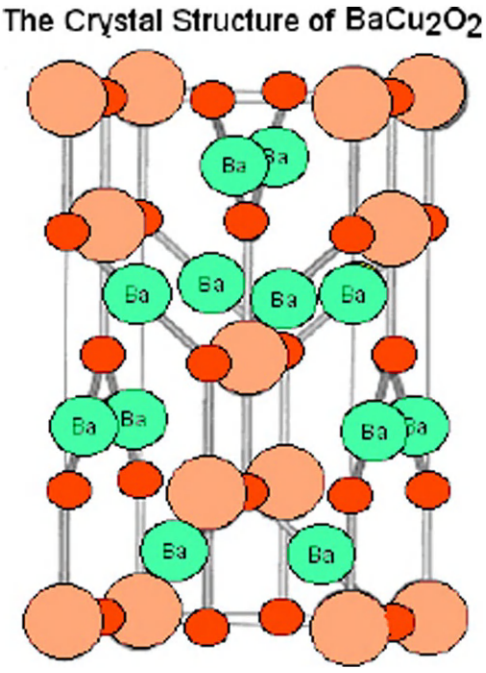

FIGURE 15.38

The compound $BaCu_2O_2$ is a result of $BaCuO_2$ disproportioning in the presence of excess copper oxide at temperatures above 900 °C, i.e.

$$2\ BaCuO_2 + 2\ CuO + \text{heat} \Rightarrow 2\ BaCu_2O_2 + O_2$$

A series of emf measurements were carried out on the electrodes, defined as:

$$BaCuO_2 \| BaCu_2O_2 \| Cu_2O$$

$$Ba_2CuO_3 \| BaCuO_2 \| BaCu_2O_2$$

These were measured over the ranges 1003–1132 K and 1175–1235 K in air. From the results, the Gibbs free

energy of formation of $BaCu_2O_2$ and Ba_2CuO_3 was determined to be:

$$\Delta G^0_{fox}\ (BaCu_2O_2)\ (kJ/mol) = -25.09 + 0.01548\ T\ (K)$$

$$\Delta G^0_{fox}\ (BaCu_2O_3)\ (kJ/mol) = +5.79\ -\ 0.07492\ T\ (K)$$

In contrast, data from another paper gave a differing result when flowing Ar with a partial O_2 pressure of 1.27 Pa was used. A solid-state galvanic cell:

$$Pt,\ Ar\ +\ O_2,\ Cu_2O\ +\ BaCu_2O_2\ +\ BaF_2||BaF_2||BaF_2\ +\ BaO,\ O_2\ +\ Ar,\ Pt$$

was measured as a function of temperature in the range 970–1170 K. Single-crystal BaF_2 was used as the solid electrolyte. The partial pressure of oxygen in the argon gas flowing over the electrodes was 1.27 Pa. The reversible e.m.f. of the cell can be expressed by $E = 224 - 0.016\ T\ (\pm 1.8)$ mV. The Gibbs free energy of formation of barium cuprite from component oxides according to the reaction is:

$$BaO(s)\ +\ Cu_2O(s) \Rightarrow BaCu_2O_2(s)$$

$$\Delta G^0_f\ =\ -43\ 230 + 3.09\ T(\pm 350) J/mol$$

The composition of melt from the crystallization and liquidus regions of the BaO–CuO_x phase diagram was studied within the range 50.0–80.0 mol% CuO at $p(O_2) = 21$ kPa. At 900–1050 °C, melt in the range of the compositions studied was structured and consisted of oxides having cubic structure of $BaCuO_2$; (Ba/Cu = 0.80–0.96), tetragonal structure of $BaCu_2O_2$; (Ba/Cu = 0.50–0.62), and monoclinic structure of CuO. The off-stoichiometry of $BaCu_2O_2$ manifested itself in electron diffraction (ED) patterns taken in a TEM as diffuse scattering streaks extending in the [100] and [010] directions. These data have been explained by considering the existence of clusters having a suggested composition of $Ba_2Cu_3O_{3.5+x}$ that were produced by a $BaCu_2O_{2+x}$ disproportionation, integrated into the $BaCu_2O_2$ structure. Thermal effects observed in the liquidus region, which are accompanied with a change in oxygen content, were also associated with the cluster structure of the melt and its evolution in response to varying temperature.

The Gibbs energy changes for the syntheses of the interceramic compounds of $BaCuO_2$ and $BaCu_2O_2$ were investigated as a basic study in the Y–Ba–Cu–O system that includes the superconductor, $YBa_2Cu_3O_{6.5+x}$. For the compound $BaCuO_2$, thermogravimetry analysis with CO_2–O_2–N_2 gas mixtures was employed, and equilibrium temperatures were determined at which CO_2 partial pressures in the gas mixtures were equilibrated with mixed powder of $BaCuO_2$, CuO, and $BaCO_3$. The Gibbs energy change for the reaction of $BaCO_3 + CuO = BaCuO_2 + CO_2$ was determined from the relation between CO_2 partial pressure and equilibrium temperature, taking into consideration the effect of CO_2 dissolution in $BaCuO_2$. For the study on $BaCu_2O_2$, electromotive force (e.m.f.) measurement using yttria-stabilized zirconia solid electrolyte was conducted. A technique using two cells was applied to the e.m.f. measurement for minimizing the effect of dispersion of oxygen from samples, and the Gibbs energy change for the reaction of $BaCuO_2 + CuO = BaCu_2O_2 + 1/2O_2$ was decided from the measured O_2 partial pressure.

In the Cu^{2+}-containing system of BaO–CuO, the phase diagram shows two compounds. The compound $BaCuO_2$ has received some attention in Academia. In particular, if excess oxygen atoms are added to the overall molecule, $BaCuO_{2+\delta}$, a complex magnetic structure results, as shown in Fig. 15.39.

To clarify the combined magnetic behavior of $BaCuO_{2+x}$, which contains, in the body-centered cubic (bcc) unit cell, two $Cu_{18}O_{24}$ spherical clusters, eight Cu_6O_{12} ring clusters, and six CuO_4 lone units, measurements of magnetization, Cu nuclear magnetic resonance (NMR) near 6 T, and pure quadrupole resonance (PQR) in zero field were made on samples with well-defined oxygen contents $x = 0$ and 0.14. Quantitative analysis of Curie–Weiss-like susceptibility data for $BaCuO_{2.00}$ indicated that Cu spins within the Cu_6 clusters go into a ferromagnetically (FM) ordered ground state with a maximum spin $S_r = 3$ below ~100 K, and those within the Cu_{18} clusters into an FM-like ground state below

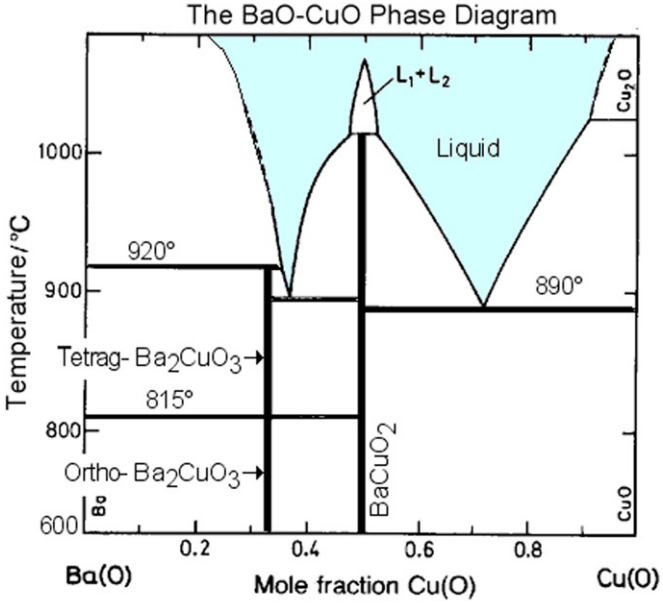

An *x*–*t* diagram for the Ba(O)–Cu(O) system in an Ar–O_2 mixture with p_{O_2} = 21 kPa.

FIGURE 15.39

~20 K with net spin $S_s \sim 5$ that is less than the maximum possible spin $S_s = 9$. For $BaCuO_{2.14}$ the Cu spins within the Cu_6 clusters go into an FM ordered ground state at a lower temperature of ~30 K, and these clusters exhibit no signature of long-range magnetic ordering down to 2 K. The NMR spectra for $BaCuO_{2.00}$ observed below ~12 K have a trapezoidal structure that is known to be a characteristic of long-range magnetic ordering, and is consistent with the AFM ordering of the Cu_6 clusters below $T_N = 15$ K (as predicted previously). On the other hand, the spectrum for $BaCuO_{2.14}$ observed in a temperature range between 1.2 and ~50 K had an electric quadrupole-split powder pattern structure. This provides microscopic evidence that there is no long-range magnetic ordering in $BaCuO_{2.14}$. The addition of 0.14 mol of oxygen atoms resulted in a large suppression of some magnetic entities. However, some anomalies in the NMR and PQR data for $BaCuO_{2.14}$ near ~10 K, which could be associated with short-range ordering of the paramagnetic Cu_{18} clusters, were found.

Phase equilibrium experiments using quantitative energy dispersive X-ray spectrometric analysis (EDS) of a $BaCuO_2$ single crystal grown from a Ba–Cu–O melt were completed. Results showed this phase to be relatively copper rich with a nominal composition of $Ba_{0.94}Cu_{1.06}O_{2+\delta}$. The structure is a "two-ladder" type of compound shown in Fig. 15.40.

The $BaCuO_2$ compound can be deposited as an infinite layer phase, even if the real structure is present in many percents of copper vacancies, $V_{\overline{Cu}}$, in the CuO_2 planes. In addition, it was found that, in the $(BaCuO_2)_2$ layers of the investigated superconducting superlattices, the Cu/Ba ratio obtained by the simulations is less than one. However, in this latter case, the copper vacancies are localized only in the CuO_2 planes between barium atoms. Non-stoichiometric compounds with an excess of oxygen are compatible with the experimental data, indicating the $Ba_2Cu_{2-x}O_{4-y}$ layers as the "reservoir charge blocks" in the superconducting superlattices.

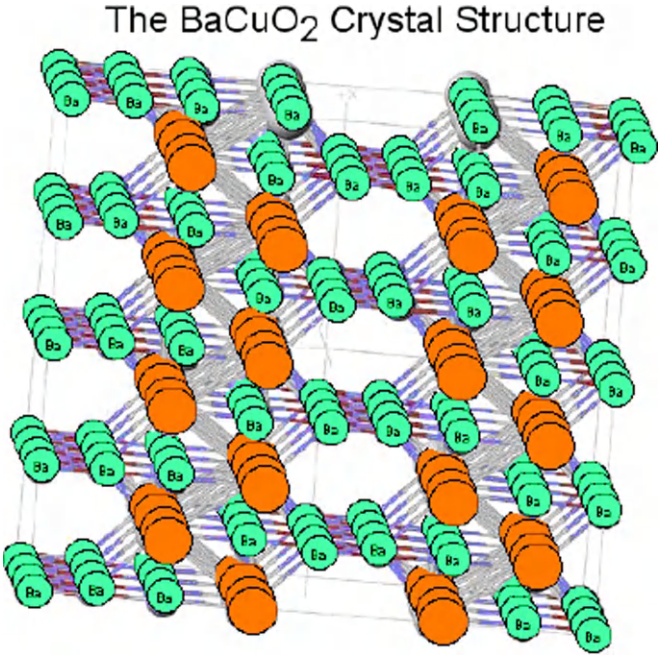

FIGURE 15.40

The interaction between components in the system $(BaO)_x$–$(CuO,Cu_2O)_{1-x}$ was investigated experimentally using differential thermal, thermal gravimetric, and X-ray diffraction analyses at temperatures up to 950 °C. It was found that at least three ternary compounds, $Ba_2Cu_3O_5$, $BaCuO_2$, and $BaCu_2O_2$, are formed in the system. $Ba_2Cu_3O_5$ is formed at relatively low temperatures (375–630 °C); $BaCuO_2$ is formed at higher temperatures but is unstable in the presence of excess copper oxide. This compound has been found to convert to the Ba_2CuO_4 form spontaneously at room temperature if allowed to sit in air:

$$2\,BaCuO_2 \Rightarrow Ba_2CuO_3 + CuO$$

In other words, the stable form of Cu^{2+} in these compounds is Ba_2CuO_3. $BaCuO_2$ melts congruently at 1020 °C. Neutron diffraction experiments have been performed in order to study the magnetic ordering of $BaCuO_{2+\delta}$. In these measurements, unpolarized neutrons and polarized neutrons with full polarization analysis have been utilized. From these measurements, it has been determined that $BaCuO_{2+\delta}$ orders antiferromagnetically below $T_N = 15.0 \pm 0.5$ K with a magnetic propagating vector $\mathbf{k} = [1,1,1]$. This structure is commonly referred to as a $[\pi\pi\pi]$ or a G-structure. The Cu atoms in the Cu_6 ring clusters, located at the (1/4,1/4,1/4) positions, order ferromagnetically within these clusters while the clusters themselves order antiferromagnetically. The ordered magnetic moment of each of these Cu atoms is 0.89 ± 0.05 μbar at $T = 4.2$ K. No evidence of long-range magnetic ordering of the Cu atoms in the Cu_{18} clusters, located at the (0,0,0) and (1/2,1/2,1/2) positions, was found down to a temperature $T = 2.5$ K.

The specific heats of samples of $BaCuO_2$ and $BaCuO_{2+\delta}$, were measured for the temperature range $0.35 \leq T \leq 30$ K in magnetic fields to 7 T. Magnetization and/or neutron diffraction measurements had been made earlier. $BaCuO_{2+\delta}$ has a complex structure with 90 formula units in a bcc unit cell; 6 Cu are "lone spins," 48 are in 8-Cu_6O_{12} "ring clusters," and 36 are in $2Cu_{18}O_{24}$ "sphere clusters". The ring and sphere clusters have ferromagnetically ordered ground states with spins $S = 3$ and 9, respectively. AFM ordering of the ring clusters occurs with a Néel temperature $T_N(0) \sim 15$ K. The specific heat of $BaCuO_2$ shows a cooperative

ordering anomaly associated with the AFM ordering of the ring clusters. Schottky-like anomalies, having maxima at ~5 and ~0.7 K, are identified with the ordering of the sphere clusters and the lone spins, respectively. Only Schottky-like anomalies are observed for the specific heat of $BaCuO_{2+\delta}$. It was suggested that the increase in the Cu oxidation state, due to the addition of 0.14 mol of O, increases Cu–O covalent bonding (spin compensation) and/or produces nonmagnetic Cu^{3+}, which in addition to the known increase in the Cu–O bond lengths, disrupts the superexchange paths that lead to the AFM ordering of the ring clusters in $BaCuO_2$. For $BaCuO_2$ the magnetic entropy was 90% of that predicted for the ordering of the three Cu structures. On the other hand, the magnetic entropy for $BaCuO_{2+\delta}$ was only 65% of that predicted, which suggests a relative large suppression of some magnetic entities due to the addition of 0.14 mol of O. Although $BaCuO_{2+\delta}$ is an insulator, the specific heat has a T-proportional component that is magnetic field dependent and is presumably associated with the magnetic degrees of freedom.

Pulsed laser deposition was used to synthesize artificially layered high-temperature superconductors. Thin-film compounds were formed when the constraint of epitaxy was used to stabilize $SrCuO_2$–$BaCuO_2$ superlattices in the infinite layer structure. Using this approach, two new structural families, $Ba_2Sr_{n-1}Cu_{n+1}O_{2n+2+\delta}$ and $Ba_4Sr_{n-1}Cu_{n+3}O_{2n+6+\delta}$ have been synthesized; these families are superconductors at temperatures as high as 70 K.

In another paper, $(BaCuO_2)_2/(CaCuO_2)n$ superconducting superlattices were grown by pulsed laser deposition for n ranging from 1 to 6. The critical temperature was found to depend strongly on the growth conditions. A maximum Tc value of about 80 K (zero resistance temperature) was found for superlattices grown at high oxygen pressure ($PO_2 \sim 0.8$ mbar) and relatively high temperature ($Tg = 600$ °C). The dependence of Tc on the number n of $CaCuO_2$ layers (for superlattices grown exactly in the same conditions) was investigated. Tc versus n showed the expected behavior with a maximum Tc value of 80 K for $n = 2$–3. However, such values are somewhat lower than that expected for a cuprate structure containing 3–4 CuO_2 planes and having an optimum carrier concentration. Two possible explanations for this effect were envisaged. The first one deals with the chemistry of the "charge reservoir" block, the second one with the special role of interelectron interaction in these highly disordered artificial structures. Finally, it was shown that, taking into account the degree of disorder, a shift of Tc of about 20 K relative to the *bulk* value Tc_0, consistent with the microscopic parameters of these materials, can be foreseen.

Magnetic and electrical transport properties of artificially layered $[(BaCuO_2)_2/(CaCuO_2)_2]N$ superlattices grown by pulsed laser deposition have been investigated. It has been found that these superlattices have a metallic normal-state resistivity with a transition temperature of about 74 K. The concentration of holes, from Hall measurements, is as high as 0.55 carriers per unit cell. From magnetization measurements, a critical current density of about 6×10^5 A/cm^2 was estimated at 10 K. Magnetoresistivity and magnetization decay allowed the measurement of the activation energy for the so-called "fluxons" motion. The observed value is not far from that of $YBa_2Cu_3O_{7-x}$, especially at low temperatures. All these features show that the layer by layer pulsed laser deposition was a viable technique for the synthesis of these new artificially layered high-temperature superconducting materials having interesting electrical and magnetic properties.

The complex ternary system Ba–Cu–O was re-visited using a 0.1 MPa oxygen pressure. It was established that, for such pressure, the $BaO_2 \Rightarrow BaO + 1/2O_2$ reaction has an important role in order to reach the equilibrium state. In this case, the pathway for the phase formation was then described by ternary sections such as BaO_2–BaO–CuO. The temperatures and the reactions that form the three compounds observed in this system have been determined. $Ba_2CuO_{3.04}$ decomposes by a peritectic-like reaction at 1033 °C and shows a structural transition from orthorhombic to tetragonal crystal form at 825 °C; $BaCuO_2$ is a congruent melting compound at 1035 °C and $Ba_2Cu_3O_{5.5}$ undergoes a peritectoid decomposition into $BaCuO_2$ and CuO at 893 °C. The stability of the $BaCuO_x$ ($x \geq 2$) phase was mapped over a wide range of temperature (300–1100 °C) and oxygen pressure (10^{-5}–10^3 bar). At ambient pressure and temperature, $BaCuO_x$ is found to be in a metastable state. Long annealing at 450 °C tends to decompose this phase into $Ba_2Cu_3O_5$ and BaO_2. Having obtained the phase stability domain in the $[T,p(O)_2]$ plane the authors were able to prepare single-phase samples of $BaCuO_x$ with different oxygen contents suitable for precise intrinsic thermodynamical measurements. They showed that the behavior of the low-temperature specific heat ($1.1 \leq T \leq 32$ K) and its dependence on the magnetic field ($0 \leq B \leq 14$ T) may be understood by taking into account a many-level magnetic system directly related to the Cu_6O_{12} and $Cu_{18}O_{24}$ structural blocks of $BaCuO_x$. Depending on the oxygen concentration, competition between AFM ordering and the many-level system was observed. With increasing oxygen content, the Néel temperature decreased whereas amplitude of the many-level system increased. The zero-field AF transition belongs to the 3D isotropic Heisenberg universality class.

The compound, $BaCu_3O_4$, has been observed to form as a "satellite-type" secondary phase when the

superconducting compound, $YBa_2Cu_3O_{7-\delta}$, is heated to >1400 °C. Superconducting single crystals of $YBa_2Cu_3O_{7-\delta}$ displaying a secondary phase pattern superimposed on the orthorhombic bulk phase pattern have been investigated by X-ray diffraction. The crystal structure of the satellite phase material has been solved and shown to correspond to a new alkaline earth oxocuprate (II) $BaCu_3O_4$. It has orthorhombic symmetry. The space group is D^{19}_{2h}-*Cmmm* with $a = 10.986$ Å, $b = 5.503$ Å, $c = 3.923$ Å and $Z = 2$. All the oxygen atoms of the structure are involved in a 2D network of copper–oxygen square planar coordination polyhedra having edge linkage. Short distances d(Cu–Cu) = 2.752 Å are found along infinite 1D copper chains. Structural similarities with $YBa_2Cu_3O_{7-\delta}$ may explain the frequent occurrence of $BaCu_3O_4$ within the host phase, and consequently its possible role as a weak link between superconducting regions. Metastable $BaCu_3O_4$ has been synthesized by MOCVD (metal-organic chemical vapor deposition) techniques on perovskite substrates. Strain effects lead to an epitaxial island growth of micrometer-sized crystallites with two orientations relative to the substrate surface. They were used for a polarized single-crystal analysis by micro-Raman spectrometry. The results can be used to detect $BaCu_3O_4$ as an impurity phase in $YBa_2Cu_3O_{7-\delta}$ thin films with a mole fraction level of less than 1%, a sensitivity which exceeds that of XRD by at least one order of magnitude.

The structure of $BaCu_3O_4$ phase occurring as particles on the surface of (001) $RBa_2Cu_3O_7$ epitaxial films prepared by MOCVD has been investigated using quantitative electron diffraction and HREM. The orthorhombic unit cell is $a = 10.97$ Å, $b = 5.54$ Å, $c = 3.94$ Å with space group *Cmmm*, the values being in agreement with an XRD study. The structure consists of alternating Cu_3O_4 and Ba layers along the *c*-axis. The compound can be stabilized due to the formation of low-energy coherent boundaries with $RBa_2Cu_3O_7$ and/or perovskite substrates.

The compound, Ba_2CuO_3, is said to be dimorphic, forming a orthorhombic crystal structure below 810 °C and a tetragonal form above that temperature, the last being apparently unstable above ~920 °C. This compound is unstable in moisture and CO_2 and so has not been studied intensively. Ba_2CuO_3 was fabricated by solid-state reactions of CuO (99+% purity) or $Cu(NO_3)_2 \times 2.5H_2O$ (98% purity) and $Ba(NO_3)_2$ (99+% purity). The mixtures were calcined in porcelain crucibles in air for 24 h at 920 °C, for Ba_2CuO_3. The oxide $Ba_2CuO_{3+\delta}$ was synthesized and a maximum oxygen content of 3.5 was found corresponding to an orthorhombic structure. The departure from stoichiometry was measured at various temperatures and the experimental results were interpreted in terms of two domains of oxygen vacancies. This system was characterized by the presence of two fundamental mixed crystal fields: the first ($0 \le x \le 0.5$) formed by solids with tetragonal symmetry, deriving from $Ba_2CuO_{3+\delta}$; the second ($0.7 \le x \le 2$) formed by solids with orthorhombic symmetry and structurally related to Sr_2CuO_3 characterized by a preferential presence of oxygen vacancies along b_o. The oxide $Ba_2CuO_{3+\delta}$, where $\delta = 0.3$ has the structure shown in Fig. 15.41.

In contrast, the reaction of BaO + CuO, in flowing argon ($PO_2 = 10^{-6}$ atm.), resulted in two compounds corresponding to the formulas, $Ba_2CuO_{3-\delta}$ and $Ba_3CuO_{4-\delta}$. The cell parameters and structural type were defined. In presence of pure oxygen or CO_2 free air, these formulas were observed.

The latter composition can exist with two modifications characterized by a different distribution of oxygen vacancies. One structure is shown in Fig. 15.42. The structure of this compound has the orthorhombic space group *Cmmm* and the lattice parameters $a = 10.94(2)$ Å, $b = 5.47(1)$ Å, $c = 3.91(1)$ Å

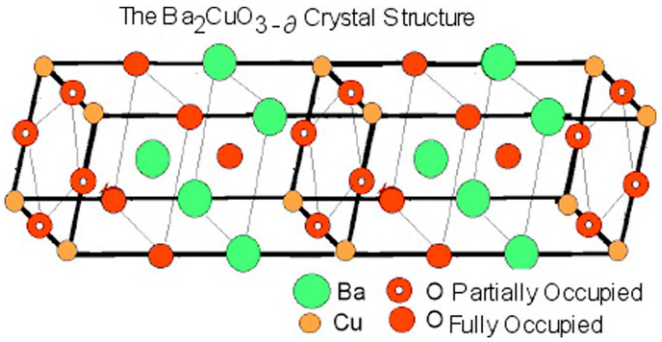

FIGURE 15.41

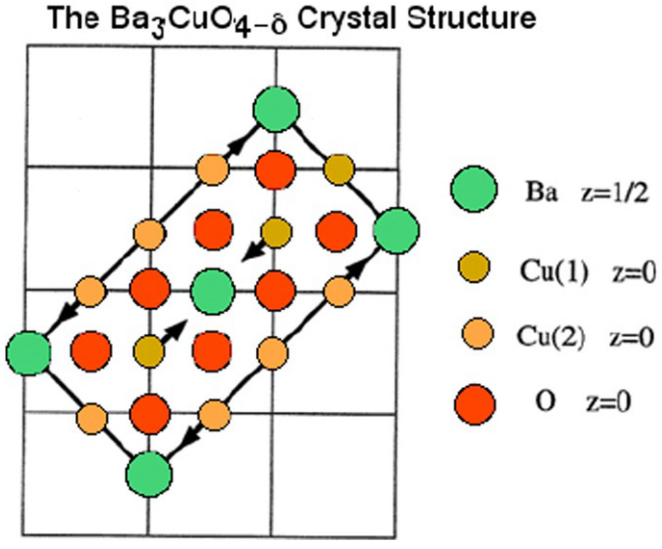

FIGURE 15.42

and is characterized by a stacking of Cu_3O_4 layers connected by barium atoms.

The flat copper–oxygen layers contain ordered vacancies on the copper sites with two vacancies per unit cell. The Cu atoms are displaced by 0.028 Å toward the vacancies as shown by the arrows.

In the Cu^{2+}–Cu^{3+}-containing system of BaO–Cu_3O_4, the compound, $BaCu_3O_5$, is unknown. However, the $Ba_2Cu_3O_6$ compound has been mentioned in the literature. The superconductors, $Ba_4CaCu_3O_{8+\delta}$ and $Ba_6CaCu_3O_{10-\delta}$, have been synthesized and the stability of these two ternary compounds has been investigated by means of X-ray diffraction, differential thermal analysis and thermogravimetry analysis. These phases are metastable at low temperature in atmospheric oxygen, i.e. $p(O_2) = 1$ bar. The DTA/TGA curves indicate an equilibrium recovery between 300 °C and 400 °C corresponding to the decomposition into BaO_2, CaO and $Ba_2Cu_3O_6$ (where Cu is actually in the $\{2Cu^{3+}\text{-}Cu^{2+}\}$ state) while in the superconductor formulation, Cu is in the Cu^{4+} state, i.e. $\{2Cu^{4+}\text{-}Cu^{2+}\}$.

In another publication, spontaneous crystallization from a solution in a melt at a pressure of $(0.8–1) \times 10^{-3}$ Pa was used to obtain single crystals of a novel non-perovskite-like superconducting phase $Ba_2Cu_3O_{6-\delta}$, (space group = *Pccm*, $a = 13.065$, $b = 20.654$, and $c = 11.431$ Å). The superconducting properties of the crystals were investigated by the modulated microwave absorption. The superconducting transition temperatures were 5 (sample No. 1), 7 and 13 K (sample No. 2). The superconductivity in the $Ba_2Cu_3O_{6-\delta}$ crystals is attributed to the presence of CuO_2 chains of edge-sharing copper–oxygen squares. Non-perovskite-like $Ba_2Cu_3O_{6-\delta}$ crystals are a new class of 1D superconductors. It has been observed that, in these compounds, each compound has a unique sequence of layers in the *c*-axis direction:

- **superconducting layers**: $[CuO_2^-]$ and $[-O_2Cu]$
- **insulating layers**: $[Y^{3+}]$ or $[-Ca^{2+}]$
- **hole-donating layers**: [Cu–O_b] or [Bi–O]

Cuprate superconductors have a σ_h horizontal reflection plane ⊥ to the *c*-axis direction at the center of the unit cell. Other reflection planes are at the top and bottom of the unit cell. All atoms (except those in the σ_h plane) thus appear twice in the unit cell.

No further work is available concerning these compounds.

In the Cu^{4+}-containing system of BaO–CuO_2, it has been observed that a Cu analog of $BaTiO_3$, $BaCuO_3$, does not exist because the Cu^{4+} ion does not exist in oxides.

However, complex compounds are formed when the system is formed with the combination of chloride (Cl^-) units in the structure. In crystallography, a structure is often described in terms of geometrical arrangements. The term "low dimensionality" means that building blocks form less than 3D arrangements, typically chains or columns (1D) or layers (2D). New compounds having low-dimensional arrangements of transition metal building blocks have been prepared. The presence of alkaline earth polyhedra induced the formation of low-dimensional transition metal sublattices, as AE frameworks have themselves been seen to make low-dimensional arrangements. If the transition metal (Co_{II}, Ni_{II} or Cu_{II}) sites in a compound form a simple arrangement such as a linear chain, that compound may harbor interesting physical properties e.g. magnetic frustration, high-temperature superconductivity, or anisotropic conductivity. This is illustrated in Fig. 15.43.

A schematic model of "zero to three dimensions" for understanding the connection between crystal structures of varying dimensionalities using the example of carbon is shown here. The C_{60} carbon cage, known as Buckminster-Fullerene, is a closed system, forming a 0D arrangement. Such cages are sometimes found to hold guests inside, such as smaller molecules or metals, but here it is simply described as a model of minimum dimension. Carbon nanotubes are shown as a 1D example. The strong σ/π-bonds between carbon atoms in graphite form sheets, shown as an example of a 2D arrangement; in between the layers there are weak π–π interactions leading to electronic conductivity. The diamond, the hardest material known, is tetrahedrally sp^3-bonded forming a 3D network.

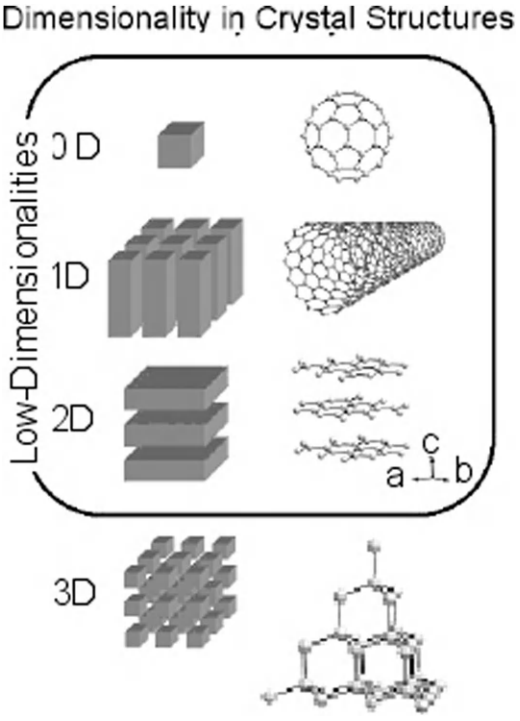

FIGURE 15.43

The addition of halogen ions to the simple $Ba_xCu_yO_z$ compounds shown above (where x, y, z varies from 1 to 8) forms very complex compounds where x, y, and z can vary from 1 to 128.

Ba atoms form a 1D column in the $Ba_9Cu_7O_{15}C_{l2}$ structure (Kipka and Mueller-Buschbaum, 1976) with a rather interesting combination of units, as shown in Fig. 15.44.

One of the units is a Ba_3O_{15} polyhedra ring (a) formed by connecting three BaO_6 irregular polyhedra. Each Ba–Ba distance in the triangular arrangement is 4.26 Å. Another Ba unit forms a $[BaO_4]_3[CuO_2]_3$ ring (b) with three BaO_6 hexagons and three CuO_4 squares connected by edge sharing. Those two distinctive Ba units are connected in the sequence ABAB… to form a 1D column along the [001] direction that has encloses of enough volume to hold Cl atoms inside. Because of this Ba column arrangement, magnetic interactions between Cu cations are limited to occur within Cu_6O_{12} rings. The Cu building blocks are separated. (c) The two Ba arrangements connect in the sequence ABAB… to form a 1D column along the [001] direction. (d) Each CuO_4 square (blue) is a fragment of a Cu_6O_{12} ring.

As an example of a 2D arrangement, a bilayered Ba coordination with a combination of oxygen and halide anions can be seen in the $Ba_2Cu_3O_4X_2$ (X═Cl and Br) structure. A central Ba atom bonds to eight neighboring atoms: four O and four X atoms at the distances 2.74 and 3.14 Å, respectively, to form a square antiprismatic $[BaO_4C_{l4}]$ polyhedron. The $[BaO_4C_{l4}]$ polyhedra are connected through the halides to form a $[BaO_2X]_n$ bilayer in the (110) plane (Fig. 15.45).

In this diagram, the following may be discerned: (a) Ba atomic arrangement in the $Ba_2Cu_3O_4X_2$ (X═Cl and Br) structure is shown. Each Ba atom takes a coordination with four O and four X atoms to form a $[BaO_4X_4]$ polyhedron. (b) View of the $[BaO_2X]_n$ zigzag layer along the [010] direction. (c) The $[BaO_2X]^n$ zigzag layer formed in the (001) plane.

The chain structure of this compound can be more easily seen in Fig. 15.46.

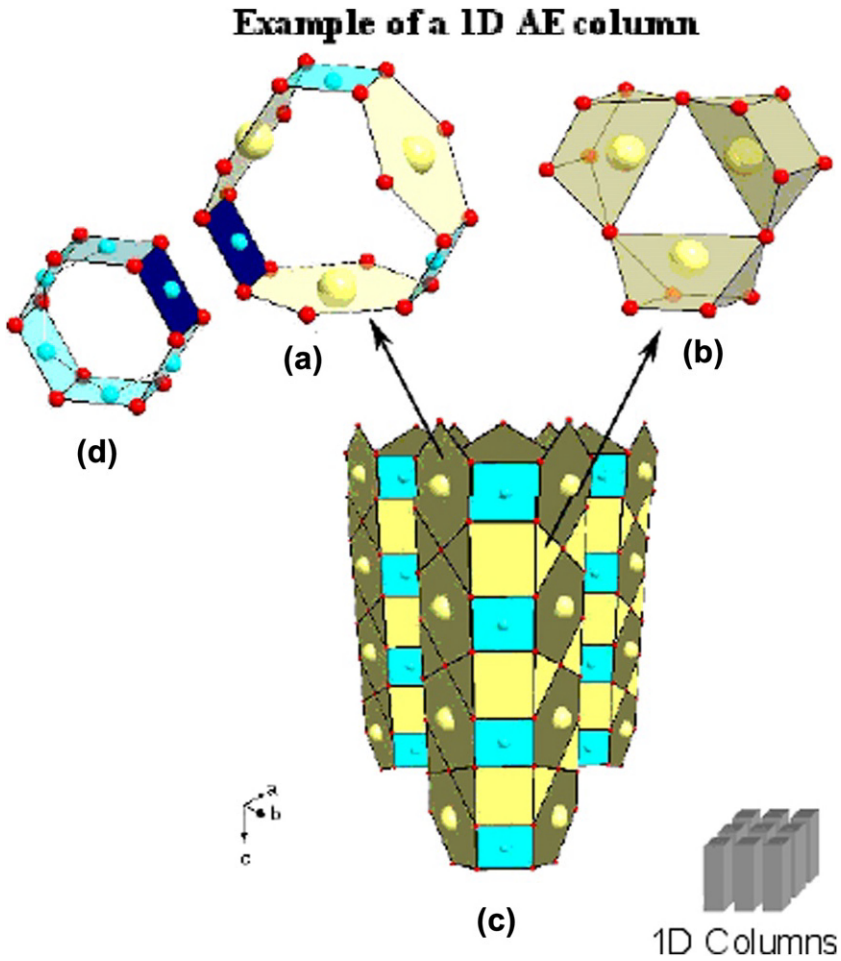

FIGURE 15.44

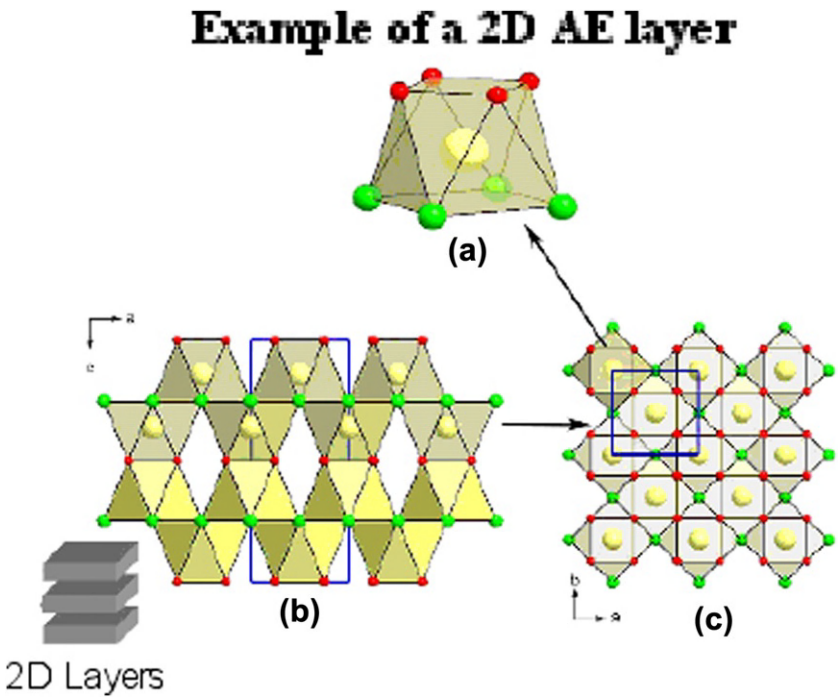

FIGURE 15.45

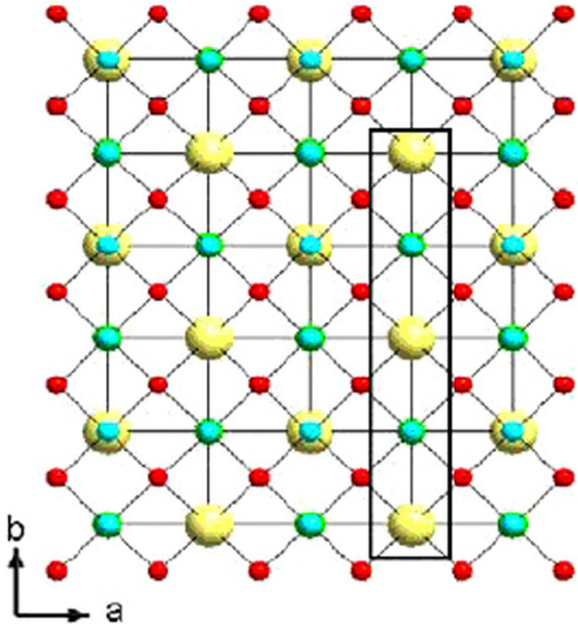

FIGURE 15.46

Here is shown: (a) The [BaCuOCl] layer in the compound $Ba_2Cu_3O_4Cl_2$. Ba atoms (yellow), Cu atoms (light blue), O atoms (red), Cl atoms (light green). The common $[BaCuO_4]_n$ chain arrangement is indicated with a black box.

Examples of alkaline earth 3D networks are mainly found in compounds with Sr or Ba atoms. A Ba cage in the $Ba_{44}Cu_{45}O_{87}Cl_4$ compound (Kipka & Mueller-Buschbaum, 1977) is formed by edge sharing of two hexagonal faces and 24 triangles. The Ba atoms are separated by the distances of 3.9–4.3 Å. This Ba_{20} cage is connected to the six nearest neighboring cages by face sharing to form a 3D cage network. There is a Cu_6O_{12} ring as a guest inside of each Ba_{20} cage, making this structure a vivid example of AE polyhedra blocking interactions between transition metals as shown in Fig. 15.47.

This figure shows Ba_{20} cages in the $Ba_{44}Cu_{45}O_8Cl_{47}$ structure: (a) Each Ba_{20} cage (light yellow) connects to six neighboring Ba_{20} cages by face sharing to form the 3D network arrangement. (b) Each Ba_{20} cage holds a Cu_6O_{12} ring. The same metal arrangement occurs in the $Ba_{41}Cu_{44}O_{84}Cl_2$ and $Ba_{88}Cu_{88}O_{175}Br_2$ structures. (c) The Cu_6O_{12} ring.

Barium cuprite or cuprate compounds are not offered for sale commercially and no CAS numbers have been assigned to date.

15.1.6. Radium Copper Compounds

Although Ra^{2+} undoubtedly forms the same type of compounds as Ba^{2+} with copper oxides, there have been no reports of the synthesis of such compounds. This is undoubtedly due to the high cost of RaO or Ra metal and the lack of interest in Industry and Academia for such compounds.

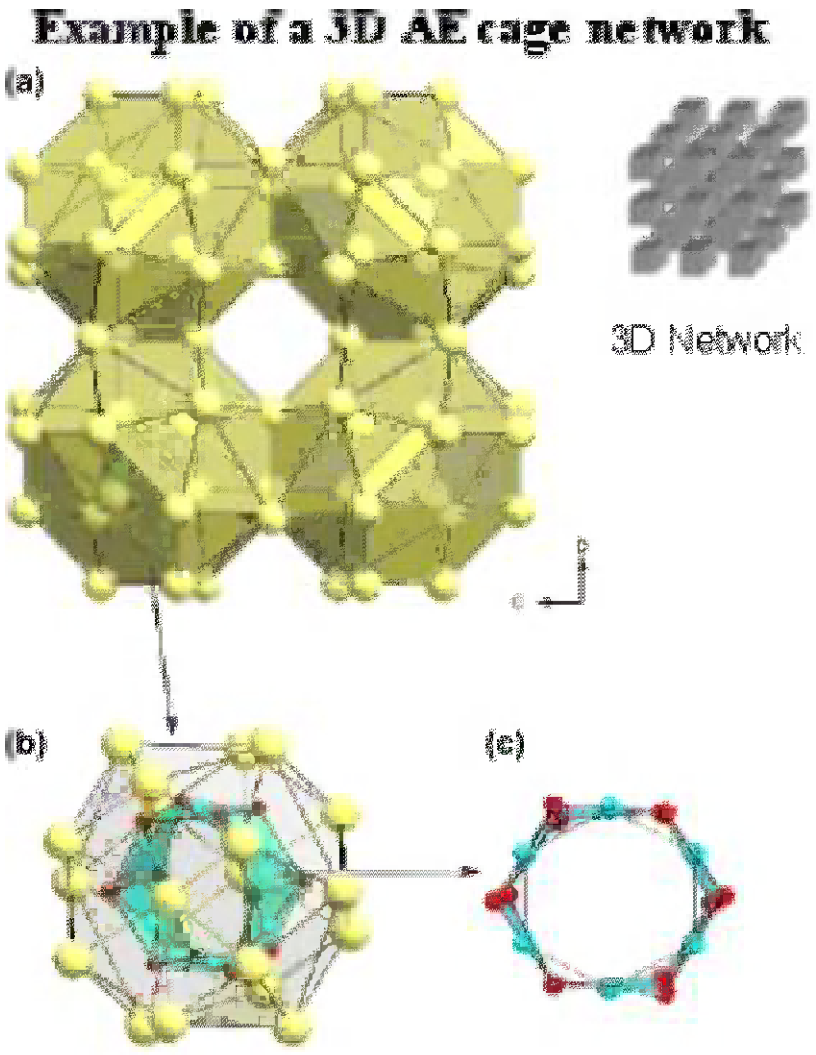

FIGURE 15.47

15.2. ALKALINE EARTH—SILVER COMPOUNDS

Silver has the valence states of: +1, +2, and sometimes +3. The major oxide is Ag^{+} as Ag_2O. It is a fine black or dark brown powder. Silver(I,III) oxide is used as part of the manufacture of silver oxide–zinc alkaline batteries. It has an empirical formula AgO, which might suggest that silver is in the +2 valence state. However, AgO is diamagnetic and X-ray diffraction studies have shown that silver atoms have two different coordination environments, one having two collinear oxide neighbors and the other four coplanar oxide neighbors. AgO is therefore best formulated as $Ag^{I}Ag^{III}O_2$ or $Ag_2O{\cdot}Ag_2O_3$. It is also known as silver peroxide, although it does not have peroxide (O_2^{2-}) anions.

15.2.1. Beryllium Silver Compounds

The metal, Be, forms just one compound with Ag metal as shown in Fig. 15.48.

Be_2Ag has the structure shown in Fig. 15.49.

Cell parameters are: $a = b = c = 4.4456$ Å, $\alpha = \beta = \gamma = 60°$, cell volume $= 62.13$ Å^3, $Z = 8$. Cell occupancy is shown in Table 15.14.

Although it is not shown in the phase diagram, the compound, $Be_{12}Ag$ has the structure shown in Fig. 15.50.

Cell parameters are: $a = 4.246$ Å, $b = c = 5.5709$ Å, $\alpha = 81.55°$, $\beta = \gamma = 67.599°$, cell volume $= 112.64$ Å^3, $Z = 2$. Cell occupancy is shown in Table 15.15.

No other intermetallic compounds are known.

In the system Be–Ag–O, no known compounds have been documented.

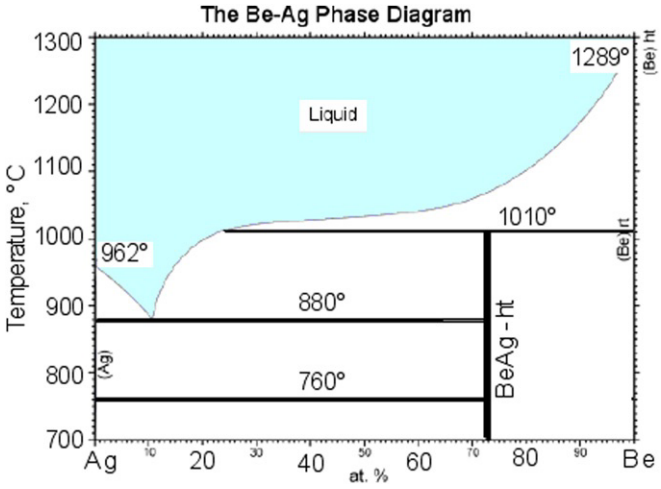

FIGURE 15.48

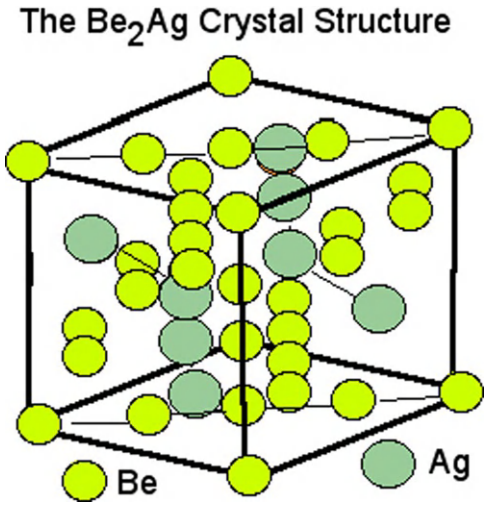

FIGURE 15.49

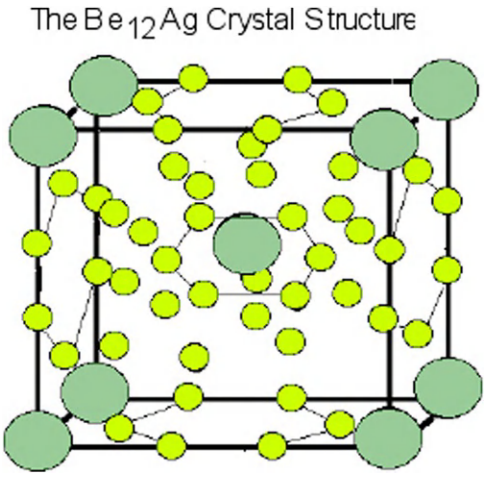

FIGURE 15.50

15.2.2. Magnesium Silver Compounds

Mg metal forms a series of intermetallic compounds with Ag metal as shown in Fig. 15.51.

The structure of the $MgAg_3$ compound is shown in Fig. 15.52.

Cell parameters are: $a = b = c = 4.1111$ Å, $\alpha = \beta = \gamma = 90°$, cell volume $= 69.48$ Å^3, $Z = 1$. Cell occupancy is shown in Table 15.16.

MgAg has the structure shown in Fig. 15.53

Cell parameters are: $a = b = c = 3.3138$ Å, $\alpha = \beta = \gamma = 90°$, cell volume $= 36.39$ Å^3, $Z = 1$. Cell occupancy is shown in Table 15.17.

The compound, $Mg_{54}Ag_{17}$, does not have a published structural arrangement of the atoms in the unit cell. The cell parameters are: $a = b = c = 12.4723$ Å, $\alpha = 107.57°$, $\beta = \gamma = 110.38°$, cell volume $= 1492.43$ Å^3, $Z = 2$.

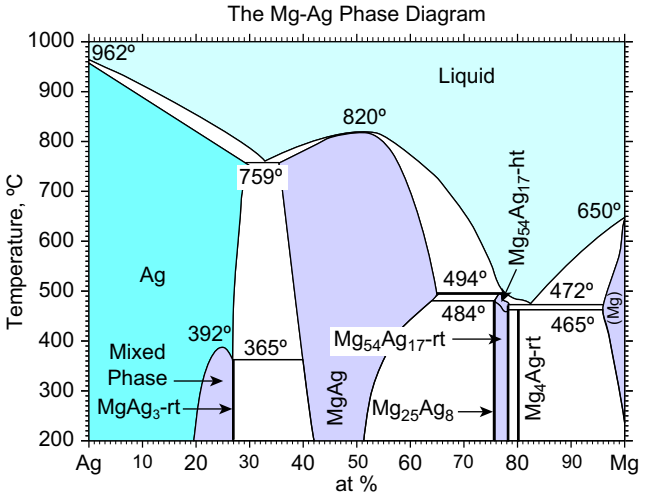

FIGURE 15.51

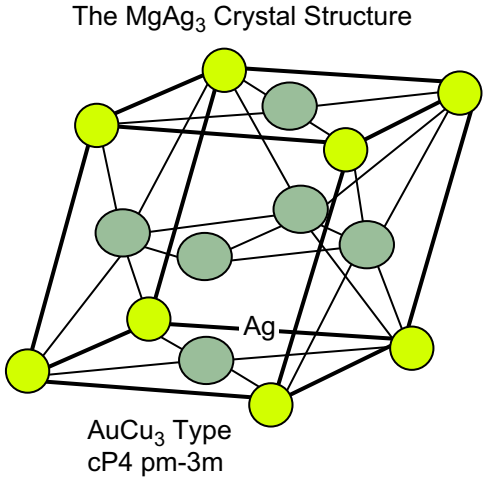

FIGURE 15.52

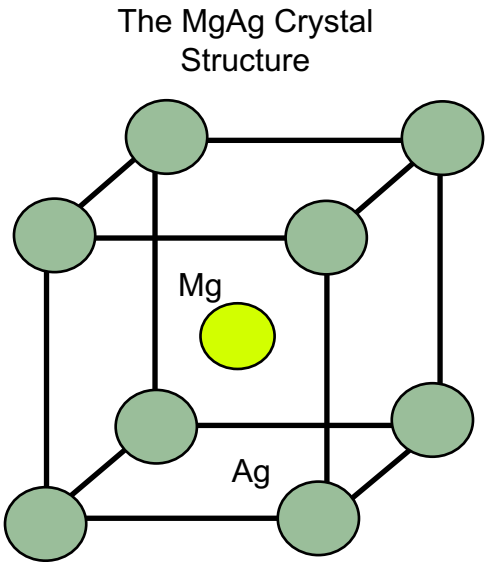

FIGURE 15.53

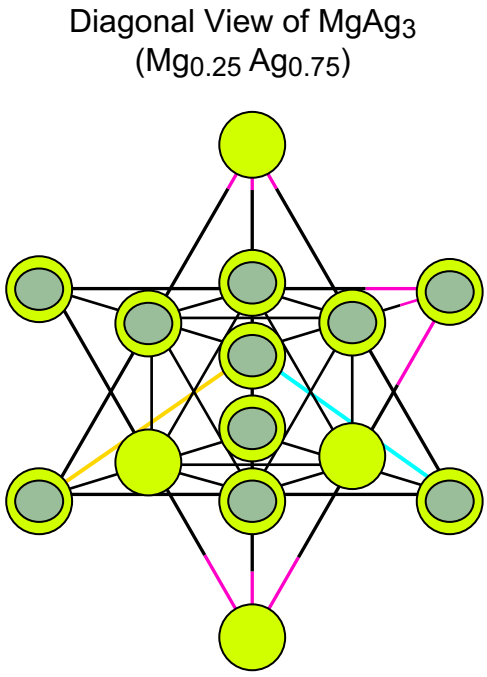

FIGURE 15.54

The hydrolysis behavior of some Mg-rich compounds (Mg_2Cu, $Mg_{54}Ag_{17}$ and Mg_3Au) at room temperature has been systematically investigated. Cu, Ag and Au nanoparticles have successfully been prepared by the hydrolysis of these compounds. The Cu, Ag, and Au nanoparticles obtained by the hydrolysis method are close to spherical in shape with a particle size below 20 nm. A continuous skeleton of magnesium atoms could be the channel for the dissolution of Mg atoms in these Mg-rich compounds, which is helpful in the hydrolysis of these Mg-rich compounds. The hydrolysis of the Mg-rich compounds provides a new and relatively simple method for the production of transition metal nanoparticles.

The compound, $Mg_{25}Ag_8$, does not have a published structural arrangement of the atoms in the unit cell. The cell parameters are: $a = b = c = 12.461$ Å, $\alpha = \beta = \gamma = 60°$, cell volume = 1368.05 Å^3, $Z = 64$. No other information is available.

The compound, Mg_4Ag, was obtained by melting the elements in a sealed Ta-ampoule and heating at 472 °C. Mg_4Ag is formed from $Mg_{54}Ag_{17}$ and δ-Mg. It is hexagonal with space group of $P63/m$ with $a = 12.485$ Å and $c = 14.412$ Å in a unique structure type. It is a hitherto unknown I_3-cluster phase with building blocks of three vertex-connected icosahedra as the fundamental structural units, joined via a small number of connection types: 1.9 icosahedra, 1.3 tri-capped trigonal prisms and 0.4 Frank-Kasper Z15 polyhedra per unit cell.

There are compounds such as $Mg_{0.996}Ag_{0.004}$ and Mg_1Ag_3 cited but no structural data are available. These two compounds appear to be based upon a Mg metal site in the lattice which is randomly sited by Ag atoms to provide the correct ratio of Mg/Ag atoms in the structure shown in Fig. 15.54.

In another paper, MgB_2 with T_c of 37 K could be fabricated through the diffusion reaction between Mg_4Ag and amorphous B at relatively low temperatures above 550 °C. The melting point of Mg_4Ag is 472 °C, much lower than that of pure Mg (650 °C). Therefore the reaction between Mg_4Ag and B is a liquid–solid diffusion reaction. The fabrication of MgB_2 wires through a powder-in-tube method and an in situ reaction process by using Mg_4Ag powder and amorphous B powder as the starting materials was accomplished. The J_c–B properties of the wires depended on not only the size of starting powder but also the reaction temperature. No other intermetallic compounds are known. One of these materials is available commercially and no CAS numbers have been issued to date.

TABLE 15.17

No.	Site notation	Atom	Multiplicity	Wyckoff	Site symmetry	x	y	z	Occupancy
1	Mg	Mg	1	b	m-3m	1/2	1/2	1/2	1.0
2	Ag	Ag	1	a	m-3m	0	0	0	1.0

TABLE 15.18

Compound	ΔH_f (kJ/mol)	ΔS (J/mol)	ΔG_f (kJ/mol)	Temp (K)
Ca_2Ag_9	-15.7	0.49	-15.9	830
Ca_2Ag_7	-19.6	-0.8	-18.9	830
$CaAg_2$	-22.7	-1.01	-18.9	830
CaAg	-23.1	-4.02	-25.0	830
Ca_5Ag_3	-24.3	-2.3	-24.2	830
Ca_3Ag	-16.5	0.71	-16.2	830

In the Ag–O-containing system of $Mg_xAg_yO_z$, where x, y or z can vary from 1 to 8, no compounds have been studied or published in the current or past literature. Magnesium does not form any type of oxygen-dominated compounds with Ag. Such compounds, if they exist, have not been offered commercially for sale nor has any interest been shown in the technical literature to date.

15.2.3. Calcium Silver Compounds

Calcium forms several intermetallic compounds with silver. In one seminal paper, the Ca–Ag binary system has been assessed with CALPHAD approach based on experiment information about phase diagram and thermodynamic properties. The excess Gibbs energies of the solution phases including liquid, bcc and fcc were formulated with Redlich–Kister polynomial functions. The intermetallic compounds Ca_2Ag_9, Ca_2Ag_7, $CaAg_2$, CaAg, Ca_5Ag_3 and Ca_3Ag were treated as stoichiometric phases. Self-consistent thermodynamic parameters have been obtained and the calculated results agree well with literature data (Table 15.18).

The phase diagram presented was shown in Fig. 15.55.

$CaAg_2$ has the structure shown in Fig. 15.56.

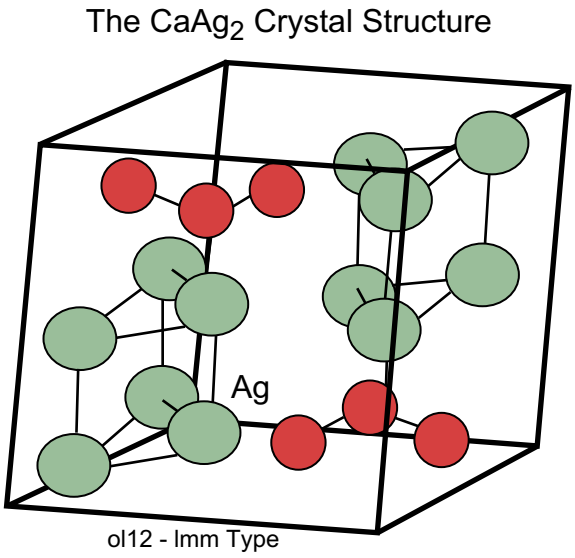

FIGURE 15.56

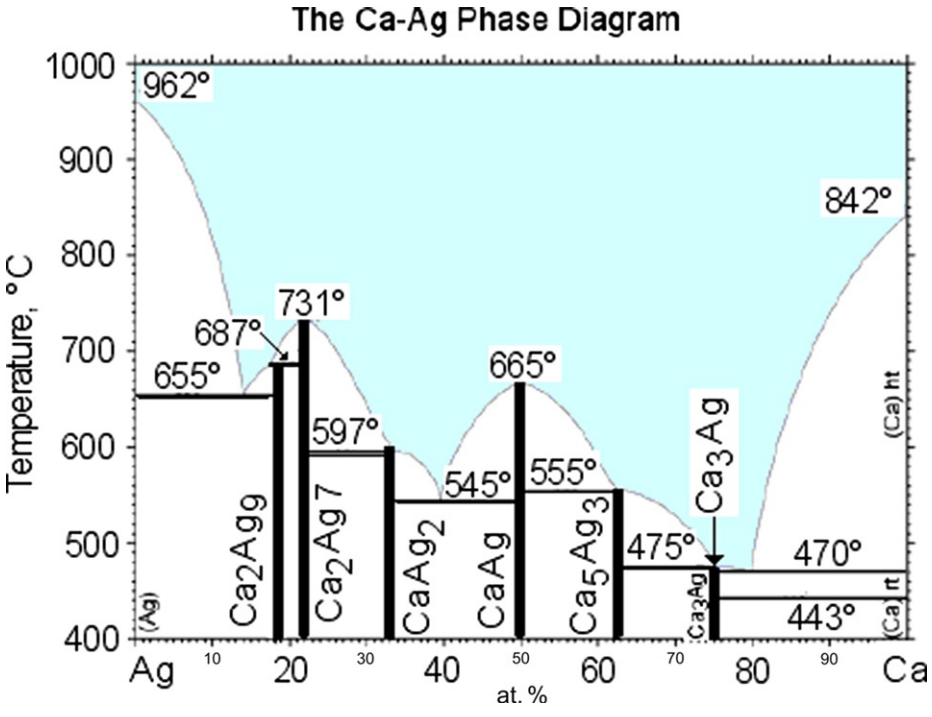

FIGURE 15.55

TABLE 15.19

No.	Site notation	Atom	Multiplicity	Wyckoff	Site symmetry	x	y	z	Occupancy
1	Ag	Ag	8	h	m..	0	0.0499	0.17	1.0
2	Ca	Ca	4	e	mm2	0	1/4	0.605	1.0

TABLE 15.20

No.	Site notation	Atom	Multiplicity	Wyckoff	Site symmetry	x	y	z	Occupancy
1	Ag	Ag	4	c	m2m	0	0.074	1/4	1.0
2	Ca	Ca	4	c	m2m	0	0.3576	1/4	1.0

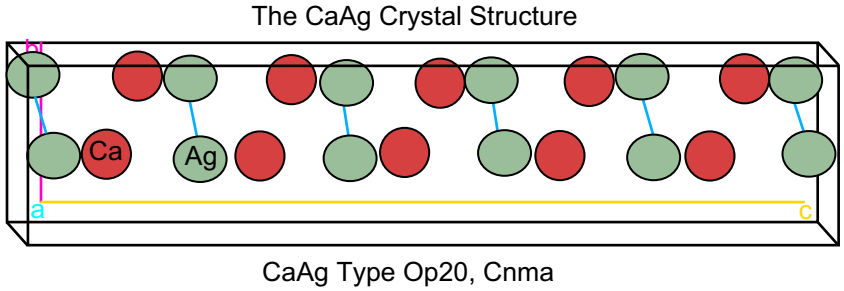

FIGURE 15.57

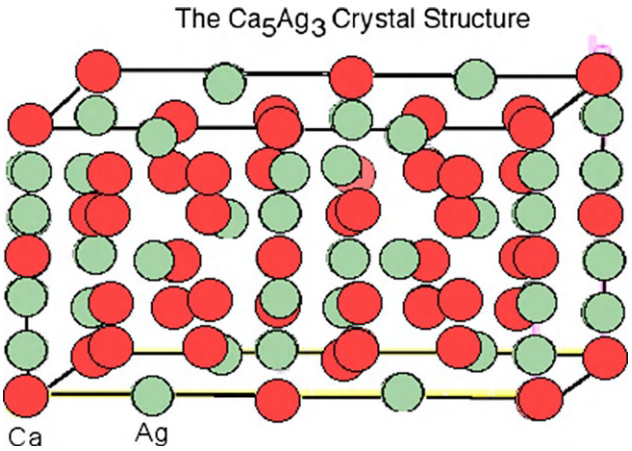

FIGURE 15.58

Cell parameters are: $a = 4.683$ Å, $b = c = 5.934$ Å, $\alpha = 75.42°$, $\beta = \gamma = 66.78°$, cell volume $= 138.28$ Å^3, $Z = 4$. Cell occupancy is shown in Table 15.19.

The $CaAg_2$–$CaZn_2$–$CaAl_2$ pseudo ternary system has been studied by micrographic and X-ray diffraction analyses of 37 alloys, melted and annealed at 973 K or 873 K in tantalum crucibles. Single-crystal and powder X-ray data show a distribution of the phases among four structure types: $MgAg_2$, $MgCu_2$, $MgNi_2$ (the Laves phases) and $CeCu_2$ (for the first time reported as KHg_2). A good separation of the structural domains was obtained by means of a 2D map based on the size and electronic factors. The different volume effects, shown by the $CeCu_2$-type phases compared to those of the Laves phases, were accounted for on the basis of the hard-sphere space-filling model.

CaAg has the structure shown in Fig. 15.57.

Cell parameters are: $a = 4.058$ Å, $b = 4.654$ Å, $c = 6.077$ Å, $\alpha = 90°$, $\beta = 109.50°$, $\gamma = 90°$, cell volume $= 108.19$ Å^3, $Z = 4$. Cell occupancy is shown in Table 15.20.

The compound, Ca_5Ag_3, has the structure shown in Fig. 15.58.

Cell parameters are: $a = b = 8.039$ Å, $c = 9.415$ Å, $\alpha = \beta = 115.27°$, $\gamma = 90°$, cell volume $= 485.05$ Å^3, $Z = 4$.

Cell occupancy is shown in Table 15.21.

The compound, Ca_2Ag_7, has the structure shown in Fig. 15.59.

Only one layer is shown. The actual 3D structure consists of three of the layers in which the Ag atoms are arranged in a cage-like structure three dimensionally. Cell parameters are: $a = b = 5.486$ Å, $c = 14.078$ Å, $\alpha = \beta = 90°$, $\gamma = 119.52°$, cell volume $= 368.65$ Å^3, $Z = 4$. Cell occupancy is shown in Table 15.22.

In one paper, a theoretical method based on electronic packing frustration (EPF) for DFT-calibrated μ2-Hückel calculations in probing these structural pressure (SP)

TABLE 15.21

No.	Site notation	Atom	Multiplicity	Wyckoff	Site symmetry	x	y	z	Occupancy
1	CaII	Ca	16	l	..m	0.164	0.664	0.15	1.0
2	AgII	Ag	8	h	m.2m	0.622	0.122	0	1.0
3	CaI	Ca	4	c	4/m..	0	0	0	1.0
4	AgI	Ag	4	a	422	0	0	1/4	1.0

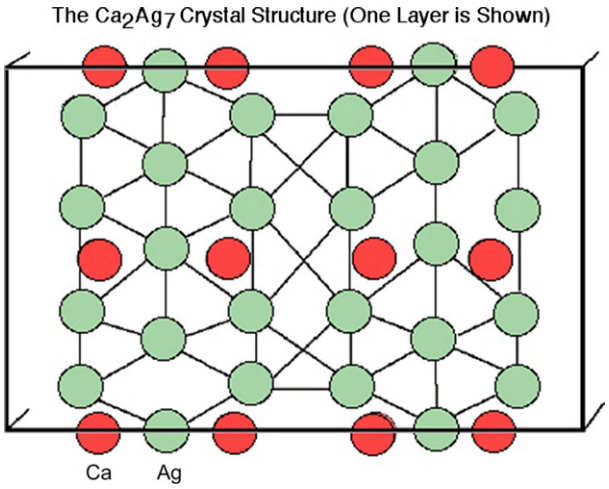

FIGURE 15.59

effects was used. Applying this method to the Ca_2Ag_7 structure, a variant of the $CaCu_5$ type with defect planes, revealed its formation is EPF driven. The defect planes resolve severe SPs surrounding the Ca atoms in a hypothetical $CaCu_5$-type $CaAg_5$ phase.

The compound, Ca_3Ag_8, is not included in the phase diagram presented above. It has the structure shown in Fig. 15.60.

Only one layer of this cage-like structure is seen. The 3D structure exhibits a cage of Ag atoms around 4-Ca atoms, arranged in a flat structure in the center of the unit cell. Cell parameters are: $a = b = c = 8.496$ Å, $\alpha = \beta = \gamma = 109.47°$, cell volume $= 472.04$ Å^3, $Z = 4$. Cell occupancy is shown in Table 15.23.

This cage structure is better seen in Fig. 15.61.

A Z-14 structure is exhibited for the Ca_3Ag_8 structure. Such structures may be regarded as arrangements of

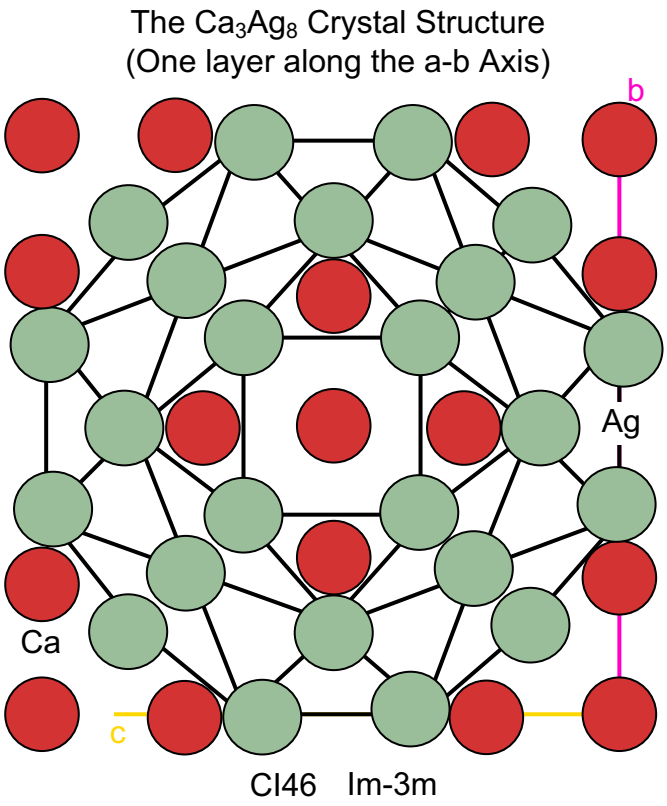

FIGURE 15.60

nested polyhedral units, isolated or linked, centered at sites of high symmetry. Ca_3Ag_8 is a centered unit of 27 atoms having a cubo-octahedron as the outermost polyhedron.

The compounds, Ca_2Ag_9 and Ca_3Ag, are shown in the phase diagram but little concerning their physical,

TABLE 15.22

No.	Site notation	Atom	Multiplicity	Wyckoff	Site symmetry	x	y	z	Occupancy
1	Ag3	Ag	16	h	1	0.1653	0.1707	0.0765	1.0
2	Ag2	Ag	8	g	..m	0.2491	0.4225	1/4	1.0
3	Ca	Ca	8	f	m..	0	0.6781	0.1147	1.0
4	Ag1	Ag	4	c	m2m	0	0.1733	1/4	1.0

TABLE 15.23

No.	Site notation	Atom	Multiplicity	Wyckoff	Site symmetry	*x*	*y*	*z*	Occupancy
1	Ag2	Ag	24	h	m.m2	0	0.347	0.347	1.0
2	Ca	Ca	12	e	4m.m	0.255	0	0	1.0
3	Ag1	Ag	8	c	.-3m	1/4	1/4	1/4	1.0

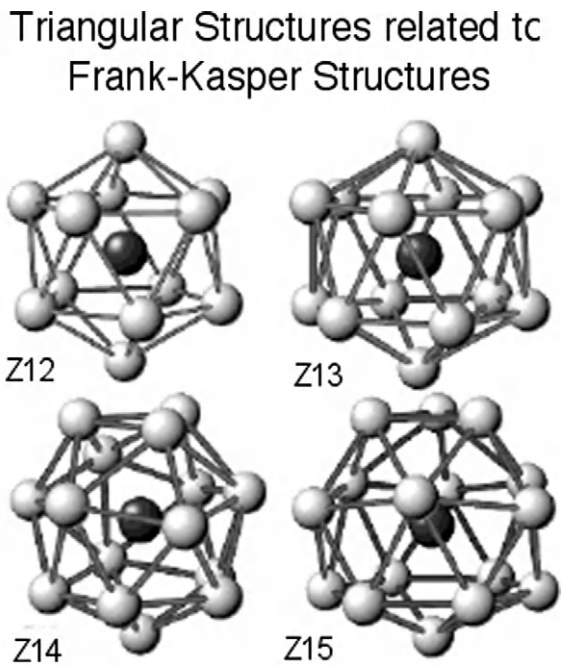

FIGURE 15.61

structural or electrical properties has appeared in the scientific literature. Both are known to exhibit Frank-Kasper type of structural arrangements with Ca_3Ag having 26 of Z-15 type of units, while Ca_2Ag_9 has 36 of $Z = 16$ units in their unit cell structures. No other papers have documented these compounds.

No other intermetallic compounds are known and no calcium–silver compounds are offered for sale commercially. No CAS numbers have been issued to date.

In the Ag^+-containing system of CaO–Ag_2O, no compounds are known. In the systems, CaO–AgO, CaO–Ag_2O_3 and CaO–AgO_2, no compounds have been discovered. It may be concluded that calcium and silver do not form any oxygen-dominated compounds. No such compounds are offered for sale commercially and no CAS numbers have been issued to date.

15.2.4. Strontium Silver Compounds

Strontium metal forms several intermetallic compounds with silver metal as shown in Fig. 15.62.

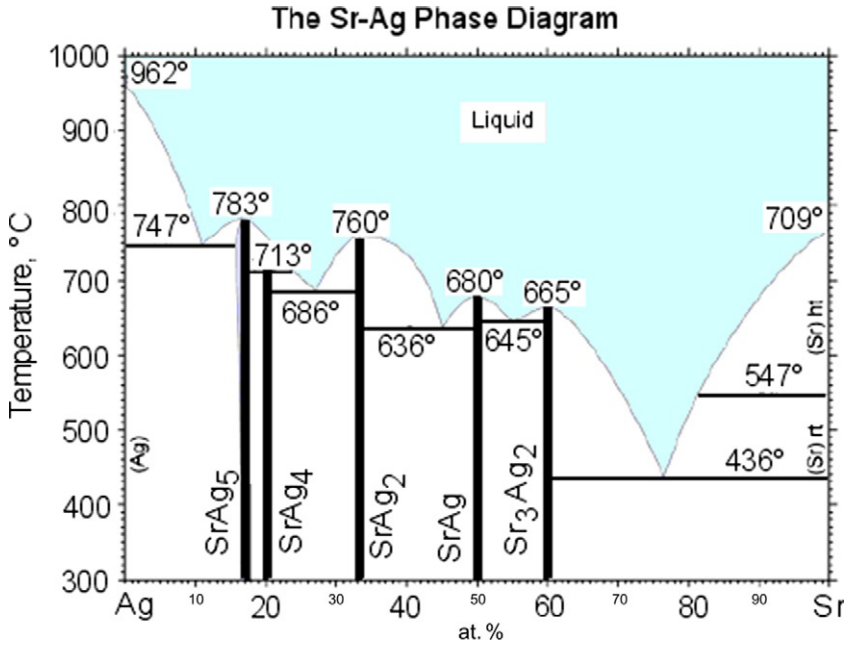

FIGURE 15.62

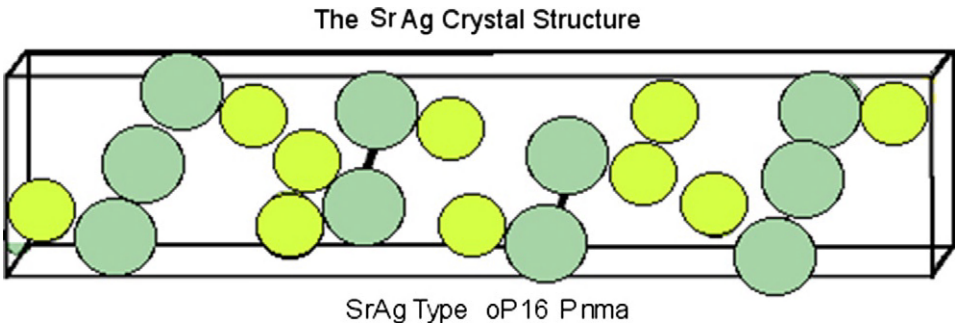

FIGURE 15.63

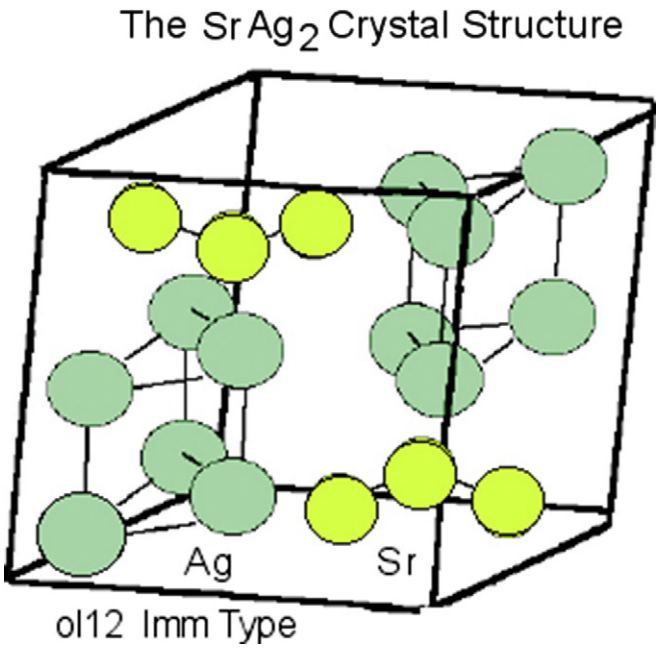

FIGURE 15.64

SrAg (CAS = 11091-79-5) has the structure shown in Fig. 15.63.

Cell parameters are: $a = 4.788$ Å, $b = 6.385$ Å, $c = 16.558$ Å, $\alpha = \beta = \gamma = 90°$, cell volume = 506.20 Å^3, $Z = 8$. Cell occupancy for SrAg is shown in Table 15.24.

The structure of SrAg is a variant of the CrB–FeB type of trigonal-prismatic coordination around the Ag metal and differs from CaAg and BaAg only in the arrangement and sequence of the prisms along the a-axis.

The compound, $SrAg_2$, has the structure shown in Fig. 15.64.

It is identical to that of Ca_2Ag. Cell parameters are: $a = 4.817$ Å, $b = c = 6.115$ Å, $\alpha = 77.788°$, $\beta = \gamma = 66.911°$, cell volume = 153.56 Å^3, $Z = 8$. Cell occupancy is shown in Table 15.25.

No data concerning the $SrAg_2$ compound are available in the current scientific literature.

$SrAg_5$ (CAS-12250-17-8) has the structure shown in Fig. 15.65.

Cell parameters are: $a = 4.631$ Å, $b = c = 5.644$ Å, $\alpha = 120°$, $\beta = \gamma = 90°$, cell volume = 127.66 Å^3, $Z = 1$. Cell occupancy is shown in Table 15.26.

Contrary to expectation, the isotypic phases $SrAg_5$ and $SrPd_5$ ($CaCu_5$-type) do not form a continuous mixed

TABLE 15.24

No.	Site notation	Atom	Multiplicity	Wyckoff	Site symmetry	x	y	z	Occupancy
1	Sr2	Sr	4	c	.m.	0.0349	1/4	0.2467	1.0
2	Ag2	Ag	4	c	.m.	0.1078	1/4	0.7570	1.0
3	Sr1	Sr	4	c	.m.	0.2851	1/4	0.0127	1.0
4	Ag1	Ag	4	c	.m.	0.3574	1/4	0.5027	1.0

TABLE 15.25

No.	Site notation	Atom	Multiplicity	Wyckoff	Site symmetry	x	y	z	Occupancy
1	Ag	Ag	8	h	m..	0	0.05	0.16	1.0
2	Sr	Sr	4	e	mm2	0	1/4	0.55	1.0

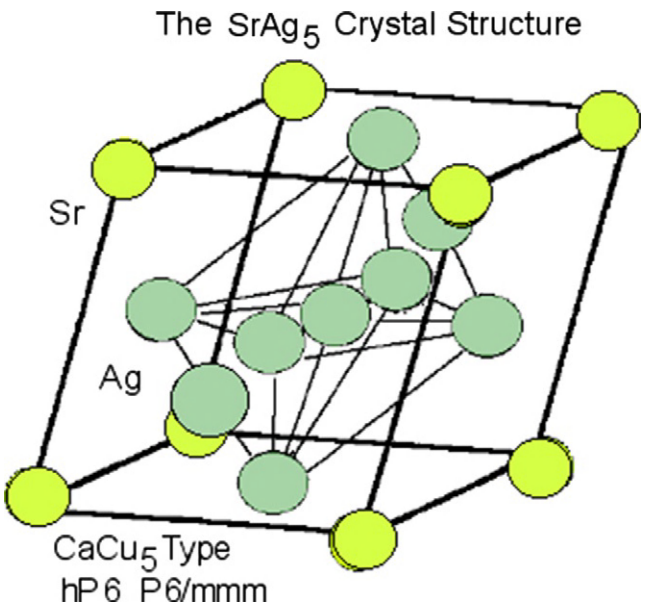

FIGURE 15.65

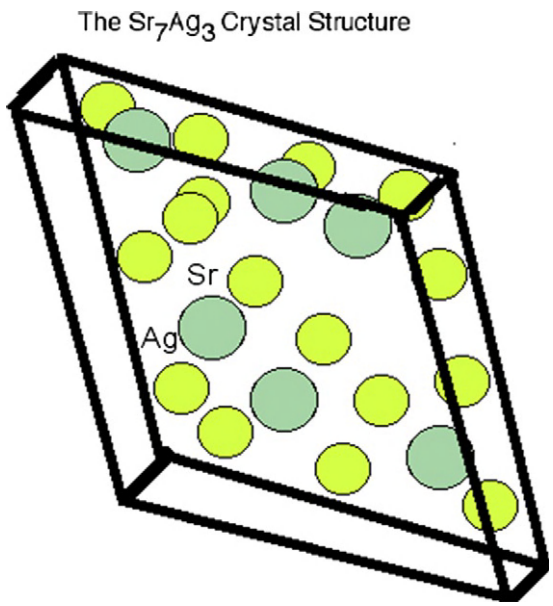

FIGURE 15.66

crystal series. In the range 40% $SrPd_5$ and 90% $SrPd_5$ the mixed crystals have a different structure, which is however closely related to the $CaCu_5$ structure. The diamagnetism of $SrAg_5$ ($\sim 10.9 \times 10^{-6}$ $cm^3/g/atom$) increases linearly on replacing Ag by Pd, attaining a limiting value of $\sim 10.9 \times 10^{-6}$ $cm^3/g/atom$ at 38% $SrPd_5$. In these alloys, palladium is incorporated in a nonvalent state with a completely filled 4d band.

The compound, Sg_7Ag_3, has the structure shown in Fig. 15.66.

Cell parameters are: $a = 7.277$ Å, $b = c = 11.383$ Å, $\alpha = 120°$, $\beta = \gamma = 90°$, cell volume = 816.15 $Å^3$, $Z = 2$.

Cell occupancy is shown in Table 15.27.

The compound, Sr_3Ag_2, has the structural form shown in Fig. 15.67.

Cell parameters are: $a = b = c = 8.4594$ Å, $\alpha = \beta = \gamma = 72.145°$, cell volume = 533.014 $Å^3$, $Z = 9$. Cell occupancy is shown in Table 15.28.

Crystal structure of the phases, strontium-silver (Sr_3Ag_2 CAS number 93509-33-2), calcium-gold (Ca_5Au_3), strontium-gold (Sr_7Au_3), and strontium-silver (Sr_7Ag) was investigated. Sr_3Ag_2 is rhombohedral (Er_3Ni_2-type), space group $R3$, with $a = 9.962$ and $c = 18.935$ Å. Ca_5Au_3 is tetragonal (Cr_5B_3 type), space group $I4/mcm$, with $a = 7.867$ and $c = 14.39$ Å. Sr_7Au_3 is hexagonal (Th_7Fe_3 type), space group $P63/mmc$, with $a = 11.07$ and

TABLE 15.26

No.	Site notation	Atom	Multiplicity	Wyckoff	Site symmetry	x	y	z	Occupancy
1	Ag2	Ag	3	g	mmm	1/2	0	1/2	1.0
2	Ag1	Ag	2	c	-6m2	1/3	2/3	0	1.0
3	Sr	Sr	1	a	6/mmm	0	0	0	1.0

TABLE 15.27

No.	Site notation	Atom	Multiplicity	Wyckoff	Site symmetry	x	y	z	Occupancy
1	Ag1	Ag	6	c	.m.	0.185	0.815	0.25	1.0
2	Sr1	Sr	6	c	.m.	0.544	0.456	0.03	1.0
3	Sr2	Sr	6	c	.m.	0.874	0.126	0.31	1.0
4	Sr3	Sr	2	b	3m.	1/3	2/3	0.0	1.0

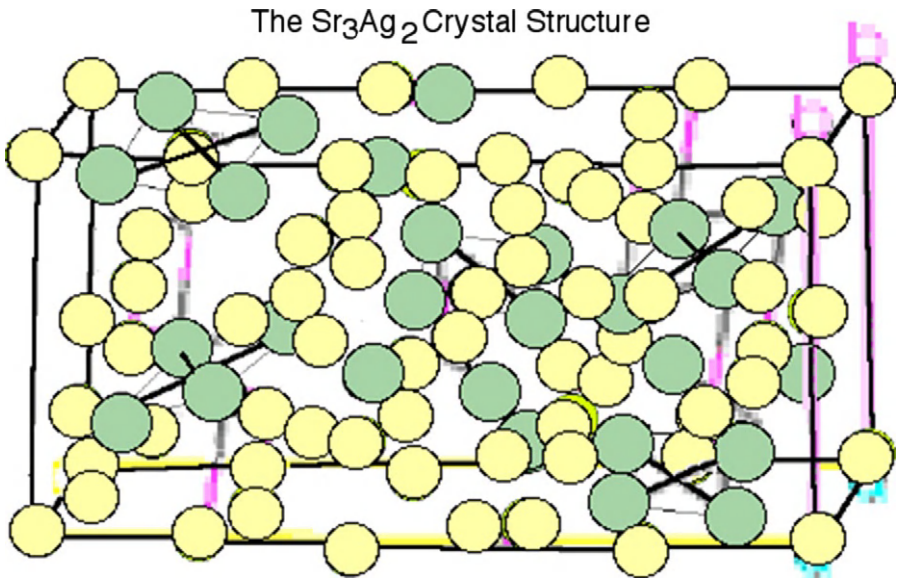

FIGURE 15.67

TABLE 15.28

No.	Site notation	Atom	Multiplicity	Wyckoff	Site symmetry	*x*	*y*	*z*	Occupancy
1	Sr(3)	Sr	18	f	1	0.09393	0.4111	0.0727	1.0
2	Ag	Ag	18	f	1	0.30843	0.2451	0.1037	1.0
3	Sr(2)	Sr	6	c	3.	0	0	0.2072	1.0
4	Sr(1)	Sr	3	a	-3.	0	0	0	1.0

$c = 7.161$ Å. Sr_7Ag_3 has Th_7Fe_3-type structure with $a = 11.38$ and $c = 7.277$ Å.

No other intermetallic compounds are known. Several of these intermetallic compounds are offered for sale commercially and the CAS numbers have been noted above.

In the SrO–Ag_2O and SrO–AgO systems, no compounds like $SrAg_2O_2$ or $SrAgO_2$ have been documented in the current literature. It may be concluded that strontium and silver do not form any oxygen-dominated compounds.

No such compounds are offered for sale commercially and no CAS numbers, involving Sr–Ag–O compounds have been issued to date.

15.2.5. Barium Silver Compounds

Barium metal forms three compounds with Ag metal, as shown in Fig. 15.68.

The Ba···Ag system was studied by thermal analysis, metallography and X-ray diffraction. Four intermediate phases were identified: $BaAg_5$ and $BaAg_2$ which melt congruently at 715 and 770 °C, respectively, and BaAg and Ba_3Ag_2 which form peritectically at 560 and 360 °C, respectively. Three eutectics were formed: between silver and $BaAg_5$ at 700 °C and 86.0 atom% Ag, between $BaAg_5$ and $BaAg_2$ at 655 °C and 76.5 atom % Ag and between Ba_3Ag_2 and barium at 340 °C and 22.0 atom% Ag.

The crystal structures of $BaAg_5$ ($CaCu_5$-type), $BaAg_2$ ($CeCu_2$-type) and BaAg (FeB-type) were confirmed. The phase Ba_3Ag_2 was found to be isotypic with Er_3Ni_2. The $BaAg_5$ phase showed a homogeneity range, the maximum width extending from $BaAg_{4.5}$ to $BaAg_7$ in the high-temperature region. The mechanism of formation for the silver-rich phases of the solid solution was studied by diffractometric investigation of a single crystal of the composition $BaAg_{6.74}$.

$BaAg_5$ has the structural form shown in Fig. 15.69.

Cell parameters are: $a = 4.612$ Å, $b = c = 5.802$ Å, $\alpha = 120°$, $\beta = \gamma = 90°$, cell volume $= 134.50$ Å^3, $Z = 1$. Cell occupancy is shown in Table 15.29.

The selective oxidation of $BaAg_5$ has been examined at 650–680 °C in flowing 3%H_2/Ar ($PO_2 \leq 1.1 \times 10^{-19}$ atm.). Under these conditions, a continuous external barium oxide scale formed. Depletion of Ba from the underlying $BaAg_5$ led to the formation of a continuous

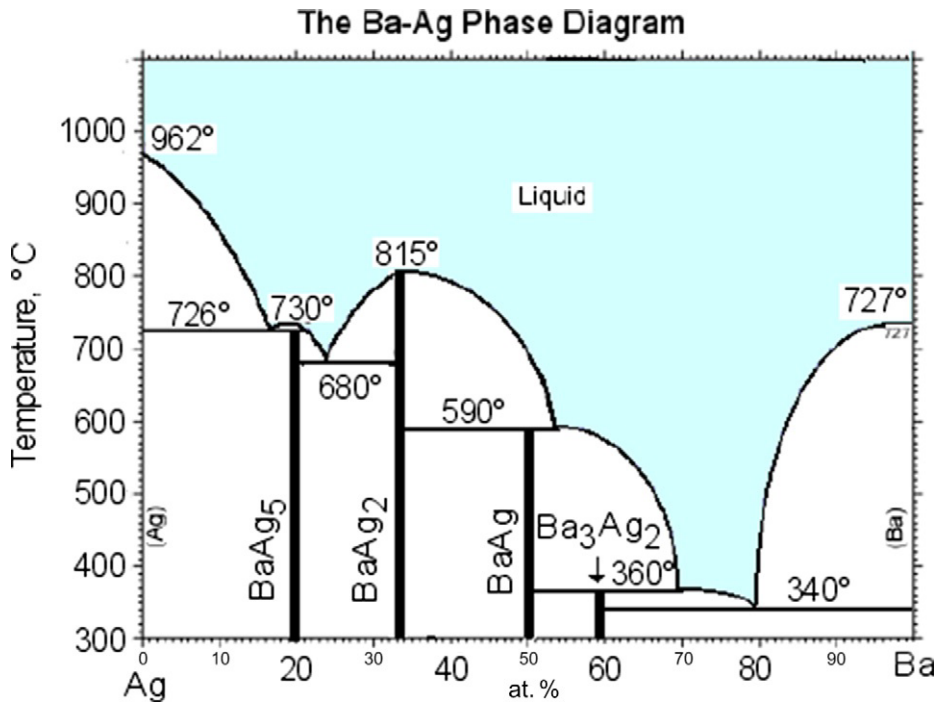

FIGURE 15.68

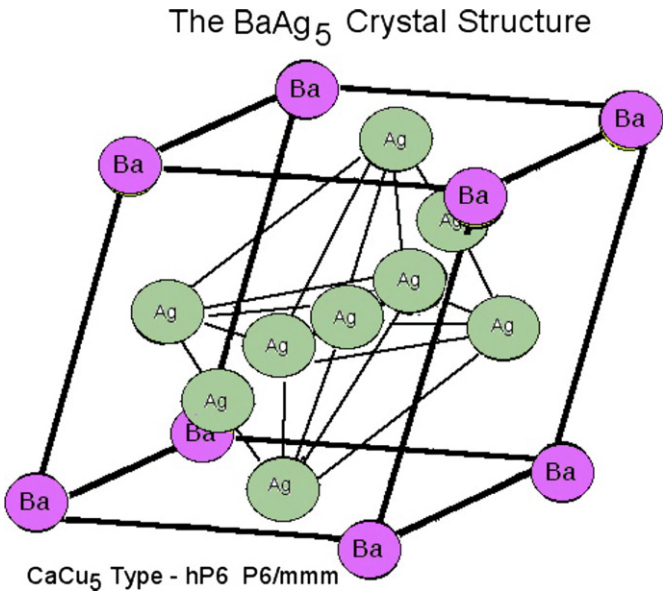

FIGURE 15.69

Ag layer between the oxide scale and the $BaAg_5$. Ba was only detected along grain boundaries in the continuous Ag layer, which was consistent with the negligible solubility reported for Ba in bulk Ag. The local thickness of the continuous Ag layer was inversely correlated to the local Ag grain size. Subsequent experiments with Ag-clad $BaAg_5$ revealed that surface oxide formation commenced at exposed Ag grain boundaries. $BaAg_5$ specimens clad with fine grained Ag foil exhibited more extensive oxide formation in a given time than specimens clad with coarse grained Ag foil. These observations confirmed that outward Ba migration through the continuous Ag layer occurred preferentially along Ag grain boundaries. This work demonstrates that an intermetallic compound may undergo external oxidation even when a continuous metallic (or intermetallic) layer, that possesses a low solubility for the oxidizable element, forms under the oxide scale.

The compound, $BaAg_2$, has the structural form shown in Fig. 15.70.

Cell parameters are: $a = 4.952$ Å, $b = c = 6.3405$ Å, $\alpha = 78.91°$, $\beta = \gamma = 67.014°$, cell volume $= 1368.53$ Å^3, $Z = 4$.

TABLE 15.29

No.	Site notation	Atom	Multiplicity	Wyckoff	Site symmetry	x	y	z	Occupancy
1	Ag2	Ag	3	g	mmm	1/2	0	1/2	1.0
2	Ag1	Ag	2	c	-6m2	1/3	2/3	0	1.0
3	Ba	Ba	1	a	6/mmm	0	0	0	1.0

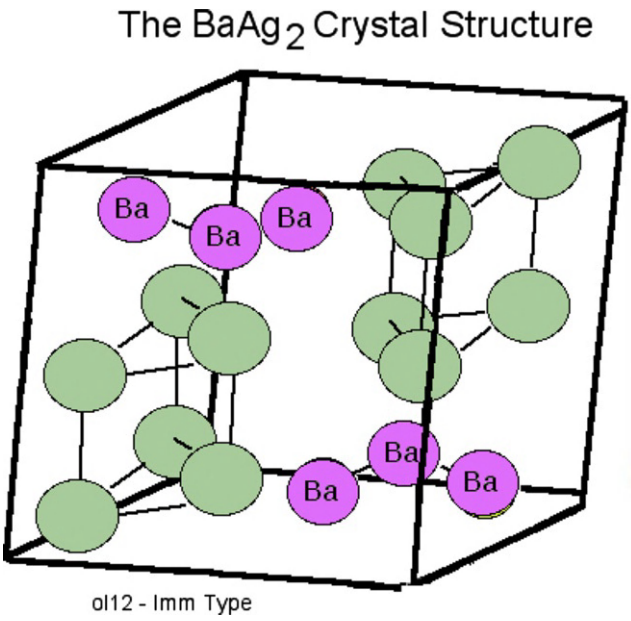

FIGURE 15.70

Cell occupancy is shown in Table 15.30.

Ba_3Ag_2 has the structure shown in Fig. 15.71.

Cell parameters are: $a = b = c = 8.802$ Å, $\alpha = \beta = \gamma = 72.30°$, cell volume $= 601.87$ Å^3, $Z = 9$. Cell occupancy is shown in Table 15.31.

The above two compounds have not been thoroughly researched in the literature and little data concerning their physical and chemical properties can be found in the current literature.

The compound, BaAg has the structural form shown in Fig. 15.72.

Cell parameters are: $a = 4.982$ Å, $b = c = 8.657$ Å, $\alpha = \beta = \gamma = 90°$, cell volume $= 286.85$ Å^3, $Z = 4$. Cell occupancy is shown in Table 15.32.

No other intermetallic compounds are known. None of these intermetallic compounds are offered for sale commercially and no CAS numbers have been issued to date.

The system, $Ba_xAg_yO_z$, where x, y or z can vary from 1 to 8, does not form any barium argentite or argentate compounds. No references were found describing any compositions within this system.

15.2.6. Radium Silver Compounds

Although radium undoubtedly forms the same type of compounds as barium, there are no papers or references describing such work on intermetallics or oxygen-dominated compounds. This is due to lack of interest in Industry and Academia concerning such compounds and the high cost of Ra metal or RaO.

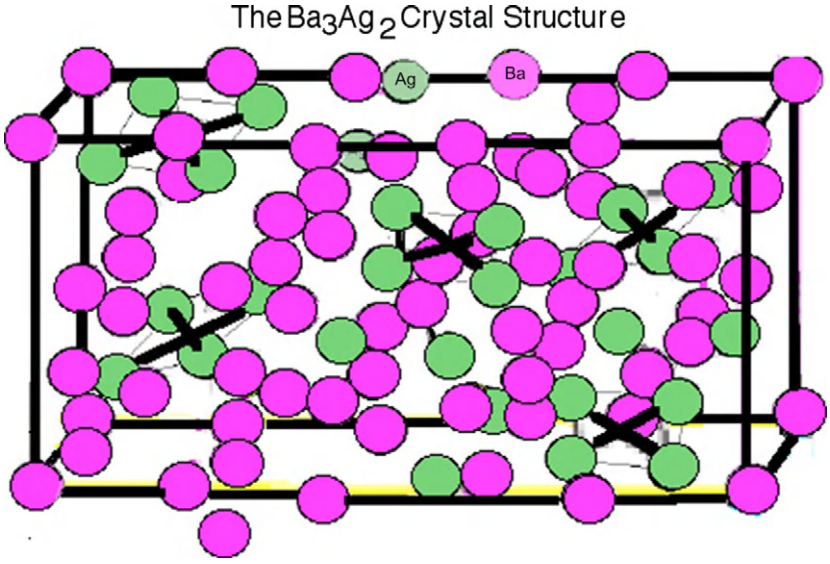

FIGURE 15.71

TABLE 15.30

No.	Site notation	Atom	Multiplicity	Wyckoff	Site symmetry	x	y	z	Occupancy
1	Ag1	Ag	8	h	m..	0	0.06	0.163	1.0
2	Ba1	Ba	4	e	mm2	0	1/4	0.547	1.0

TABLE 15.31

No.	Site notation	Atom	Multiplicity	Wyckoff	Site symmetry	x	y	z	Occupancy
1	Ba1	Ba	18	f	1	0.09763	0.4135	0.0737	1.0
2	Ag1	Ag	18	f	1	0.31043	0.2467	0.1037	1.0
3	Ba2	Ba	6	c	3.	0	0	0.2085	1.0
4	Ba3	Ba	3	a	-3.	0	0	0	1

TABLE 15.32

No.	Site notation	Atom	Multiplicity	Wyckoff	Site symmetry	x	y	z	Occupancy
1	Ag	Ag	4	c	.m.	0.033	1/4	0.131	1.0
2	Ba	Ba	4	c	.m.	0.18	1/4	0.629	1.0

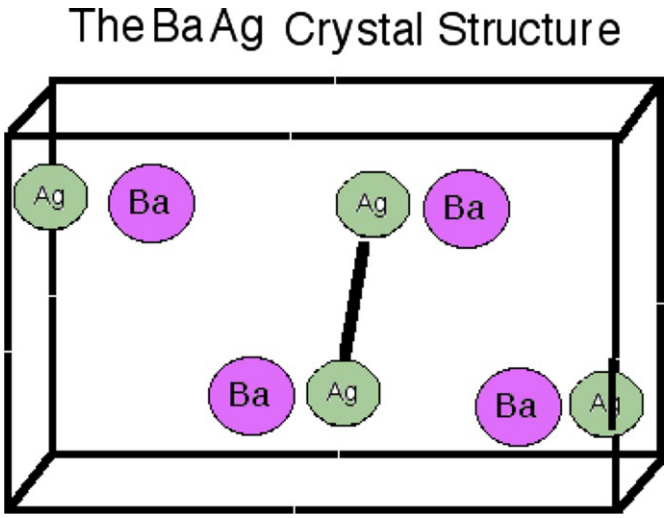

FIGURE 15.72

15.3. ALKALINE EARTH GOLD COMPOUNDS

Gold has the valence states of: −1, 0, +1, + 2, +3, +4 and +5 but Au(I) and Au(III) dominate its chemistry. Au(I), referred to as the aurous ion, is the most common oxidation state. Very few, if any, oxygen-dominated compounds form with the alkaline earths but a few intermetallic compounds are known.

15.3.1. Beryllium Gold Compounds

Be metal forms six compounds with gold metal as shown in Fig. 15.73.

Two of these compounds are not stable at room temperature. In addition, only one of these compounds, BeAu, has structural data available, and its diagram is shown in Fig. 15.74.

Cell parameters are: $a = b = c = 4.668$ Å, $\alpha = \beta = \gamma = 90°$, cell volume = 101.72 Å^3, $Z = 4$. Cell occupancy is shown in Table 15.33.

No further data are available concerning this compound.

A compound not shown in the phase diagram, Be_5Au, is stated to have the structure shown in Fig. 15.75.

The structure is cubic with Au atoms at face-centered positions in the unit cell.

Cell parameters are: $a = b = c = 4.313$ Å, $\alpha = \beta = \gamma = 60°$, cell volume = 56.75 Å^3, $Z = 4$. Cell occupancy is shown in Table 15.34.

A compound, $Be_{12}Au$, is also not listed in the phase diagram but has the structure shown in Fig. 15.76.

Cell parameters are: $a = 4.252$ Å, $b = c = 5.5453$ Å, $\alpha = 81.55°$, $\beta = \gamma = 67.46°$, cell volume = 111.53 Å^3, $Z = 2$. Cell occupancy is shown in Table 15.35.

No structural data are available for the following compounds:

$BeAu_3$
$BeAu_2$
Be_3Au
Be_4Au
Be_3Au_4

The only work concerning these compounds was contained in the paper that illustrated the phase diagram. No further endeavors have appeared in the open literature and these are the only known Be–Au compounds known to date.

In the BeO–Au_xO_y system, where x or y can be 1, 2 or 3, no compounds are known. BeO does not form any stable oxy-aurite compounds and no papers concerning such compounds exist in the current literature.

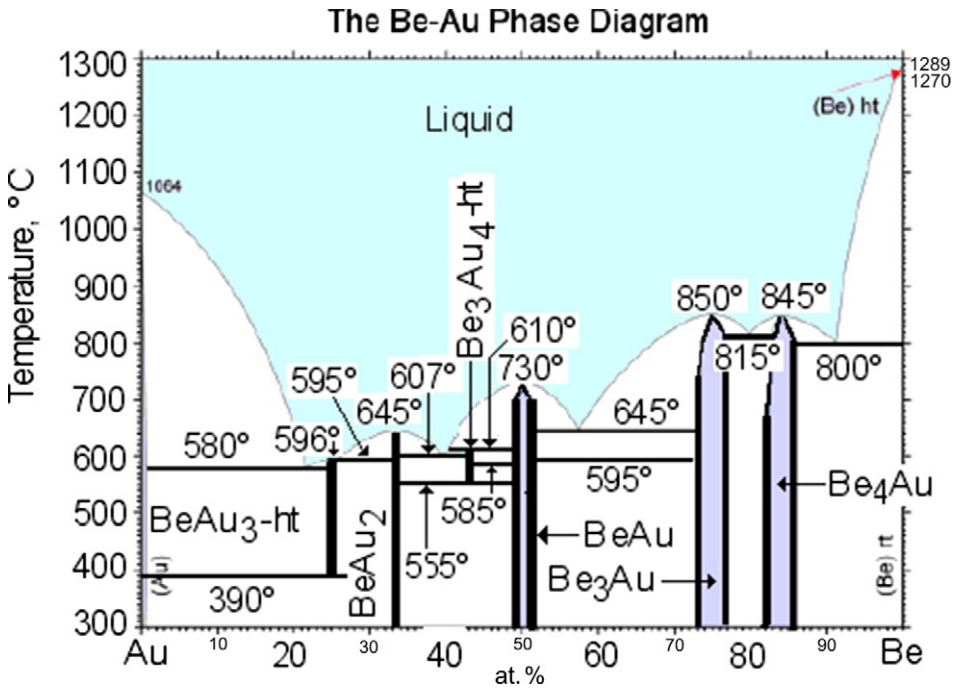

FIGURE 15.73

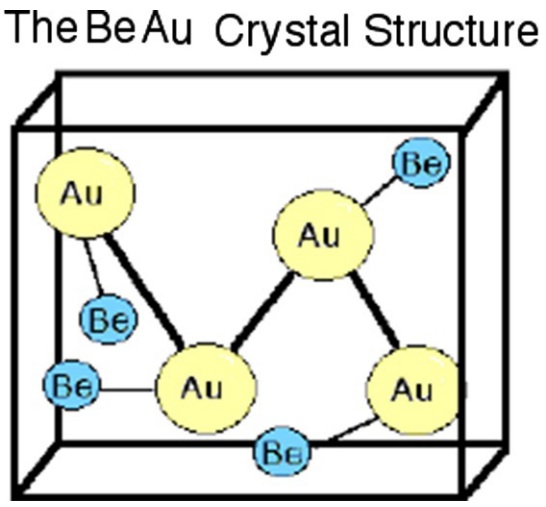

FIGURE 15.74

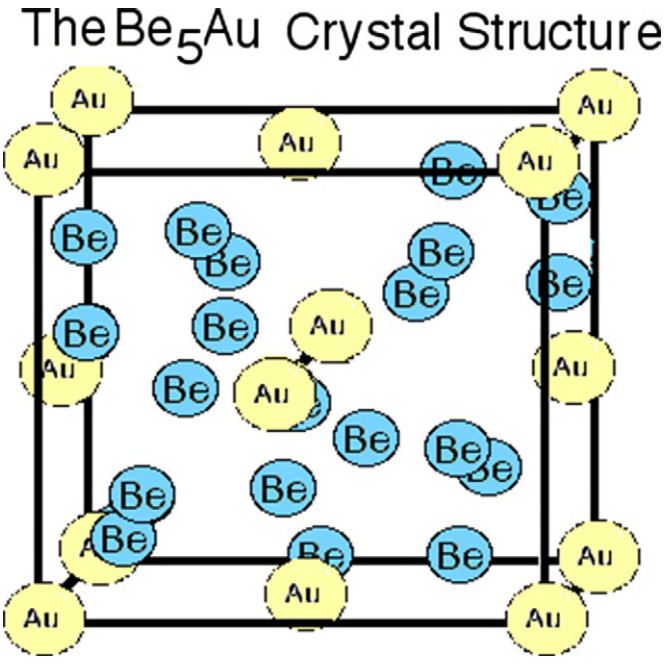

FIGURE 15.75

TABLE 15.33

No	Site notation	Atom	Multiplicity	Wyckoff	Site symmetry	*x*	*y*	*z*	Occupancy
1	Be	Be	4	a	.3.	0.094	0.094	0.094	1.0
2	Au	Au	4	a	.3.	0.35	0.35	0.35	1.0

TABLE 15.34

No.	Site notation	Atom	Multiplicity	Wyckoff	Site symmetry	*x*	*y*	*z*	Occupancy
1	Be2	Be	16	e	.3m	0.625	0.625	0.625	1.0
2	Be1	Be	4	c	-43m	1/4	1/4	1/4	1.0
3	Au	Au	4	a	-43m	0	0	0	1.0

TABLE 15.35

No.	Site notation	Atom	Multiplicity	Wyckoff	Site symmetry	*x*	*y*	*z*	Occupancy
1	Be1	Be	8	j	m2m.	0.277	1/2	0	1.0
2	Be2	Be	8	i	m2m.	0.361	0	0	1.0
3	Be3	Be	8	f	..2/m	1/4	1/4	1/4	1.0
4	Au1	Au	2	a	4/mmm	0	0	0	1.0

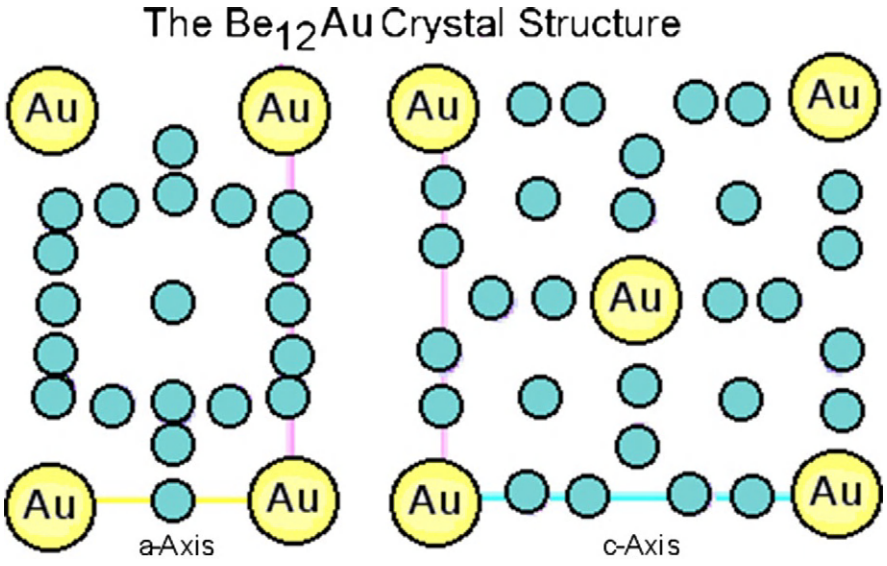

FIGURE 15.76

No Be–Au intermetallic of oxy-gold compounds are offered for sale commercially and no CAS numbers have been issued to date.

15.3.2. Magnesium Gold Compounds

Magnesium metal forms a number of intermetallic compounds with gold. The phase diagram has the form shown in Fig. 15.77. The diagram is incomplete in that the melting points of some of the compounds were not given.

A number of compounds are shown but data regarding these compounds are sparse.

The compound, $MgAu_{16}$, has the structure shown in Fig. 15.78.

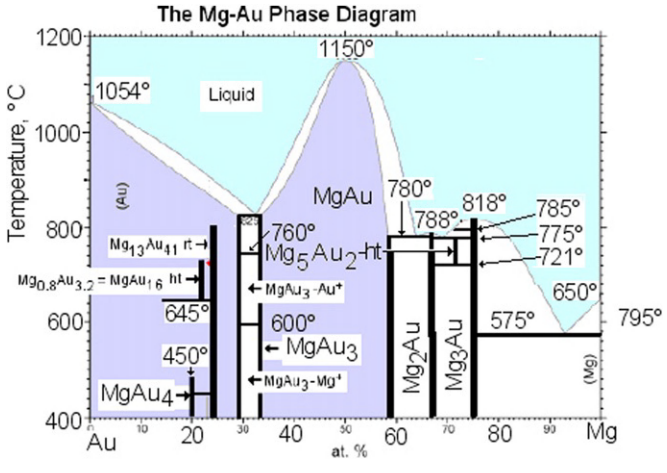

FIGURE 15.77

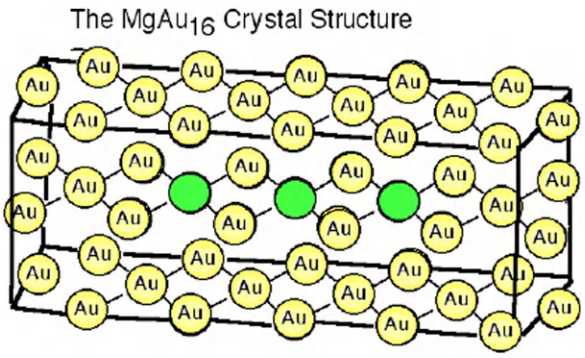

FIGURE 15.78

Although the Mg atoms are shown at specific sites in the unit cell, they actually are scattered randomly throughout the structure.

Cell parameters are: $a = b = 4.073$ Å, $c = 8.644$ Å, $\alpha = \beta = 103.63°$, $\gamma = 90°$, cell volume = 135.20 Å^3, $Z = 4$, cell occupancy is shown in Table 15.36.

The compound, $Mg_{13}Au_{41}$, has the structural form shown in Fig. 15.79.

Cell parameters are: $a = 9.441$ Å, $b = c = 14.927$ Å, $\alpha = 120°$, $\beta = \gamma = 90°$, cell volume = 1,821.77 Å^3, $Z = 2$. Cell occupancy is shown in Table 15.37.

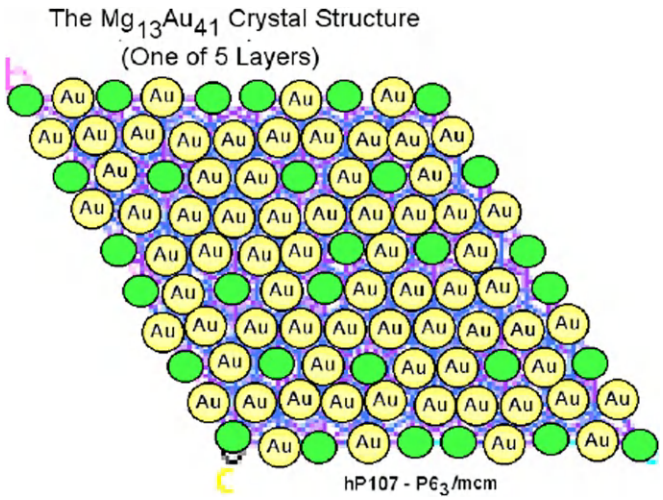

FIGURE 15.79

The compound, Mg_2Au, has the unit-cell structure shown in Fig. 15.80.

Cell parameters are: $a = 8.253$ Å, $b = 13.561$ Å, $c = 18.328$ Å, $\alpha = \beta = \gamma = 90°$, cell volume = 2,051.25 Å^3, $Z = 2$. Cell occupancy is shown in Table 15.38.

The compound, Mg_3Au, has the structure shown in Fig. 15.81.

TABLE 15.36

No.	Site notation	Atom	Multiplicity	Wyckoff	Site symmetry	x	y	z	Occupancy
1	M1	0.800Mg + 0.200Au	4	e	4mm	0	0	0.1189	1.0
2	Au1	Au	4	e	4mm	0	0	0.3749	1.0
3	Au2	Au	4	d	-4m2	0	1/2	1/4	1.0
4	Au3	Au	4	c	mmm.	0	1/2	0	1.0

TABLE 15.37

No.	Site notation	Atom	Multiplicity	Wyckoff	Site symmetry	x	y	z	Occupancy
1	Au1	Au	12	k	..m	0.33	0	0.0	1.0
2	Au2	Au	12	j	m..	0.11	0.33	1/4	1.0
3	Au4	Au	12	j	m..	0.22	0.56	1/4	1.0
4	Au3	Au	12	j	m..	0.33	0.44	1/4	1.0
5	Au6	Au	12	i	..2	0.11	0.22	0	1.0
6	Mg1	Mg	12	i	..2	0.22	0.44	0	1.0
7	Au5	Au	12	i	..2	0.56	0.12	0	1.0
8	Au7	Au	6	g	m2m	0.11	0	1/4	1.0
9	Mg3	Mg	6	g	m2m	0.44	0	1/4	1.0
10	Mg2	Mg	6	g	m2m	0.78	0	1/4	1.0
11	Au8	Au	4	d	3.2	1/3	2/3	0	1.0
12	Mg4	Mg	2	b	-3.m	0	0	0	1.0

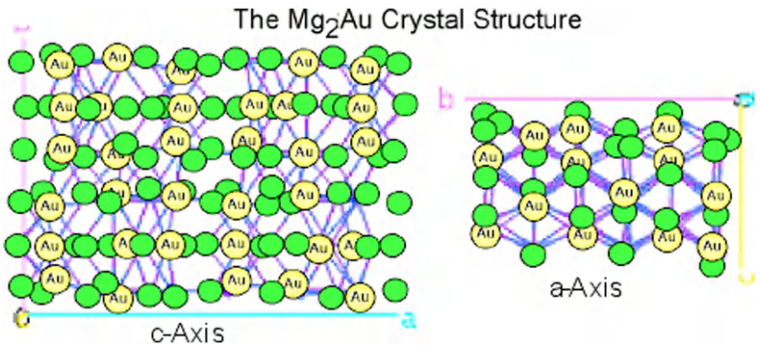

FIGURE 15.80

TABLE 15.38

No.	Site notation	Atom	Multiplicity	Wyckoff	Site symmetry	*x*	*y*	*z*	Occupancy
1	Mg11	Mg	8	d	1	0.005	0.091	0.205	1.0
2	Mg7	Mg	8	d	1	0.052	0.08	0.571	1.0
3	Mg8	Mg	8	d	1	0.094	0.571	0.084	1.0
4	Au4	Au	8	d	1	0.105	0.587	0.427	1.0
5	Mg10	Mg	8	d	1	0.170	0.071	0.287	1.0
6	Au6	Au	8	d	1	0.256	0.577	0.112	1.0
7	Mg9	Mg	8	d	1	0.269	0.588	0.437	1.0
8	Mg12	Mg	8	d	1	0.342	0.066	0.247	1.0
9	Au5	Au	8	d	1	0.424	0.608	0.387	1.0
10	Au1	Au	4	c	.m.	0.081	1/4	0.379	1.0
11	Mg2	Mg	4	c	.m.	0.128	1/4	0.072	1.0
12	Mg6	Mg	4	c	.m.	0.151	1/4	0.709	1.0
13	Mg3	Mg	4	c	.m.	0.237	1/4	0.421	1.0
14	Au3	Au	4	c	.m.	0.289	1/4	0.102	1.0
15	Mg4	Mg	4	c	.m.	0.320	1/4	0.749	1.0
16	Au2	Au	4	c	.m.	0.381	1/4	0.407	1.0
17	Mg1	Mg	4	c	.m.	0.437	1/4	0.075	1.0
18	Mg5	Mg	4	c	.m.	0.483	1/4	0.718	1.0

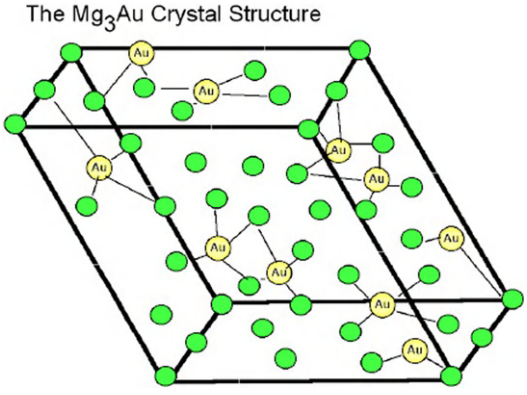

FIGURE 15.81

Cell parameters are: $a = b = c = 8.0594$ Å, $\alpha = \beta = 90°$, $\gamma = 120°$, cell volume $= 477.02$ Å^3, $Z = 6$. Cell occupancy is shown in Table 15.39.

The MgAu compound has the structural form shown in Fig. 15.82.

Cell parameters are: $a = b = c = 3.272$ Å, $\alpha = \beta = \gamma = 90°$, cell volume $= 34.97$ Å^3, $Z = 1$. Cell occupancy is shown in Table 15.40.

The compound, $MgAu_3$, has the structure shown in Fig. 15.83. Only the top and side layers are shown. The full structure consists of a 5 by 5 matrix of these layers.

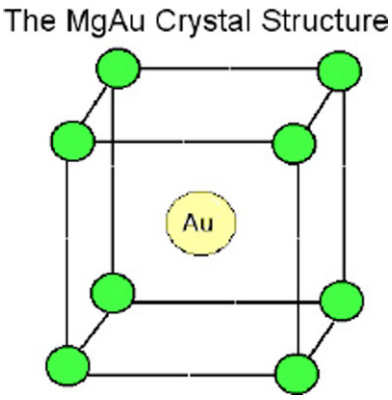

FIGURE 15.82

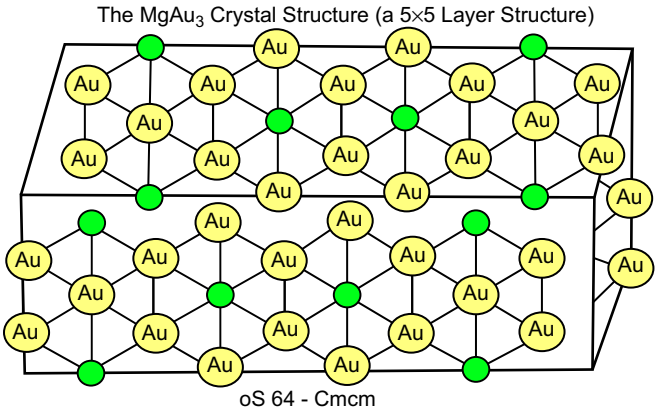

FIGURE 15.83

Cell parameters are: $a = 5.747$ Å, $b = 9.437$ Å, $c = 10.381$ Å, cell volume $= 540.99$ Å^3, $Z = 16$. Cell occupancy is shown in Table 15.41.

Another form of $MgAu_3$ is shown in Fig. 15.84.

These two compounds are probably the $MgAu_3$–Au^+ and $MgAu_3$–Mg^+, respectively, as shown in the phase diagram.

TABLE 15.39

No.	Site notation	Atom	Multiplicity	Wyckoff	Site symmetry	*x*	*y*	*z*	Occupancy
1	Au	Au	6	c	..m	0.3288	0	0.0748	1.0
2	Mg(2)	Mg	6	c	..m	0.3754	0	0.3973	1.0
3	Mg(1)	Mg	6	c	..m	0.7248	0	0.2427	1.0
4	Mg(3)	Mg	4	b	3..	1/3	2/3	0.1147	1.0
5	Mg(4)	Mg	2	a	3.m	0	0	0.0	1.0

TABLE 15.40

No.	Site notation	Atom	Multiplicity	Wyckoff	Site symmetry	*x*	*y*	*z*	Occupancy
1	Au	Au	1	b	m-3m	1/2	1/2	1/2	1.0
2	Mg	Mg	1	a	m-3m	0	0	0	1.0

TABLE 15.41

No.	Site notation	Atom	Multiplicity	Wyckoff	Site symmetry	*x*	*y*	*z*	Occupancy
1	Au2	Au	8	g	..m	0.24	0.42	1/4	1.0
2	Au1	Au	8	g	..m	0.26	0.17	1/4	1.0
3	Mg1	Mg	8	f	m..	0	0.12	0.0	1.0
4	Au3	Au	8	f	m..	0	0.38	0.0	1.0
5	Au4	Au	8	e	2..	0.24	0	0	1.0
6	Au5	Au	8	d	-1	1/4	1/4	0	1.0
7	Au6	Au	4	c	m2m	0	0.04	1/4	1.0
8	Mg2	Mg	4	c	m2m	0	0.29	1/4	1.0
9	Mg3	Mg	4	c	m2m	0	0.54	1/4	1.0

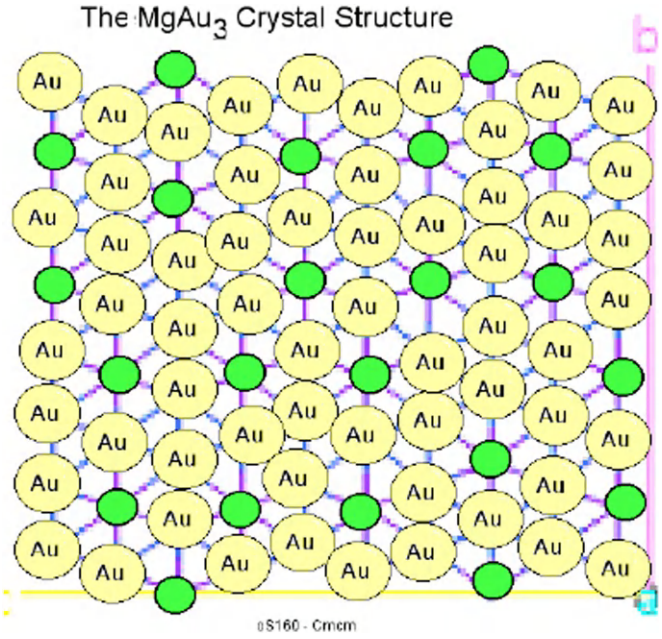

FIGURE 15.84

Cell parameters are: $a = 5.742$ Å, $b = 10.322$ Å, $c = 23.592$ Å, $\alpha = \beta = \gamma = 90°$, cell volume = 1342.55 Å^3, Z = 40. Cell occupancy is shown in Table 15.42.

Although $MgAu_4$ and Mg_2Au_5 are shown in the phase diagram, there are no data concerning their properties or structure in the current technical literature. No other Mg–Au intermetallic compounds are known. Mg_2Au is offered for sale commercially with a CAS number of 12399-98-2.

In the MgO–Au_xO_y system, where x or y can be 1, 2 or 3, no compounds have been discovered or documented in the current literature. No compounds are known. MgO does not form any stable oxy-aurite compounds and no papers concerning such compounds exist in the current literature.

15.3.3. Calcium Gold Compounds

Calcium forms several intermetallic compounds with gold. In one seminal paper, the Ca–Au binary system has been assessed with a CALPHAD approach based on experiment information about phase diagram and thermodynamic properties. The excess Gibbs energies of the solution phases including liquid, bcc and fcc were formulated with Redlich–Kister polynomial functions. The intermetallic compounds $CaAu_5$, $CaAu_3$, $CaAu_2$, CaAu, Ca_4Au_3, Ca_5Au_3 and Ca_2Au were treated as stoichiometric phases. Self-consistent thermodynamic parameters were obtained and the

TABLE 15.42

No.	Site notation	Atom	Multiplicity	Wyckoff	Site symmetry	x	y	z	Occupancy
1	Au4,6	Au	16	h	1	0.25	0.045	0.05	1.0
2	Au1,7	Au	16	h	1	0.25	0.205	0.15	1.0
3	Au3,5	Au	16	h	1	0.25	0.295	0.05	1.0
4	Au2,8	Au	16	h	1	0.25	0.455	0.15	1.0
5	Au9,11	Au	8	g	..m	0.25	0.125	1/4	1.0
6	Au10,12	Au	8	g	..m	0.25	0.375	1/4	1.0
7	Au14,20	Au	8	f	m..	0	0.085	0.15	1.0
8	Au16,17	Au	8	f	m..	0	0.085	0.55	1.0
9	Mg4,5	Mg	8	f	m..	0	0.165	0.05	1.0
10	Mg1,8	Mg	8	f	m..	0	0.165	0.65	1.0
11	Au13,19	Au	8	f	m..	0	0.335	0.15	1.0
12	Au15,18	Au	8	f	m..	0	0.335	0.55	1.0
13	Mg3,6	Mg	8	f	m..	0	0.415	0.05	1.0
14	Mg2,7	Mg	8	f	m..	0	0.585	0.15	1.0
15	Mg9,12	Mg	4	c	m2m	0	0.00	1/4	1.0
16	Mg10,11	Mg	4	c	m2m	0	0.25	1/4	1.0
17	Au22,23	Au	4	c	m2m	0	0.50	1/4	1.0
18	Au21,24	Au	4	c	m2m	0	0.75	1/4	1.0

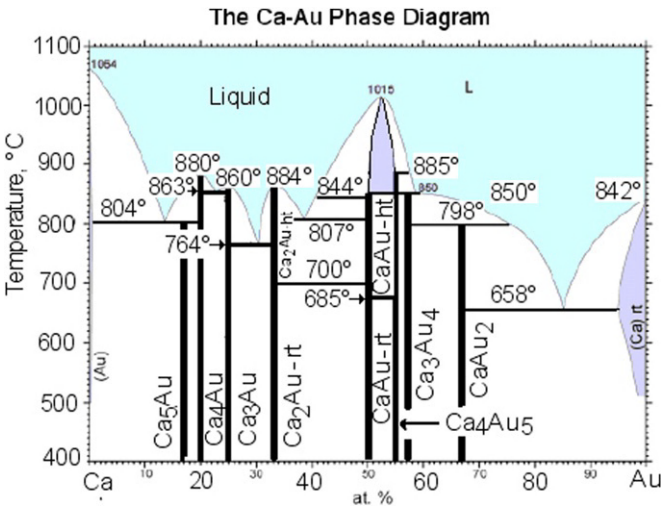

FIGURE 15.85

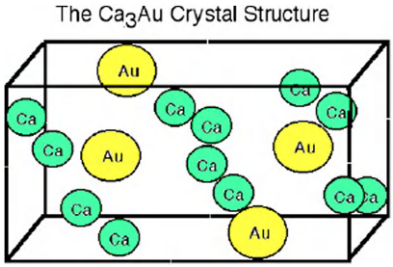

FIGURE 15.86

calculated results agreed well with literature data (Table 15.43).

The phase diagram presented is shown in Fig. 15.85.

A total of 13 compounds have been documented. At least nine structures of these intermetallic compounds have been published while the structures of Ca_2Au, Ca_5Au, Ca_3Au and Ca_4Au_5 have not been solved. Very little literature exists to date concerning these compounds.

Eight appear in the phase diagram while five (Ca_5Au_2, Ca_5Au_3, Ca_5Au_4, Ca_2Au_3 and $CaAu_3$) do not. A total of four appear in both the phase diagram and structural data published in the current literature.

TABLE 15.43

Compound	ΔH_f (kJ/mol)	ΔS (J/mol)	ΔG_f (kJ/mol)	Temp (K)
$CaAu_5$	-41	-4.0	-37.0	900
$CaAu_3$	-66.0	-13.0	-54.0	900
$CaAu_2$	-87.1	-23.3	-68.2	900
CaAu	-105.8	-22.4	-85.8	900
Ca_5Ag_3	—	—	-87.6	900
Ca_4Au_3	—	—	-87.7	900
Ca_2Au	—	—	-86.5	900

The compound, Ca_2Au, has received some attention in the literature. The local meta-GGA exchange correlation density functional (TPSS) with a relativistic effective core potential was employed to systematically investigate the geometric structures, stabilities, and electronic properties of bimetallic Ca_2Au_n ($n = 1$–9) and pure gold Au_n ($n \leq 11$) clusters. The optimized geometries show that the most stable isomers for Ca_2Au_n clusters have 3D structure when $n \geq 2$, and that one Au atom capping the Ca_2Au_{n-1} structure for different-sized Ca_2Au_n ($n = 1$–9) clusters is the dominant growth pattern. The average atomic binding energies and second-order difference in energies show that the Ca_2Au_4 isomer is the most stable among the Ca_2Au_n clusters. The same pronounced even–odd alternations are found in the HOMO–LUMO gaps, VIPs, and hardnesses. The polarizabilities of the Ca_2Au_n clusters show an obvious local minimum at $n = 4$. Moreover, the inverse corrections to the polarizabilities versus the ionization potential and hardness were found for the gold clusters.

Ca_5Au_3 is tetragonal (Cr_5B_3 type), space group $I4/mcm$, with $a = 7.867$ and $c = 14.39$ Å.

Ca_3Au has the structure shown in Fig. 15.86.

Cell parameters are: $a = 6.784$ Å, $b = 7.795$ Å, $c = 10.004$ Å, $\alpha = \beta = \gamma = 90°$, cell volume $= 528.50$ Å^3, $Z = 4$. Cell occupation is shown in Table 15.44.

The compound, CaAu, has the structural form shown in Fig. 15.87.

Cell parameters are: $a = 3.961$ Å, $b = 4.576$ Å, $c = 5.881$ Å, $\alpha = \gamma = 90°$, $\beta = 109.68°$, cell volume $= 100.37$ Å^3, $Z = 4$. Cell occupancy is shown in Table 15.45.

The compound, $CaAu_2$, has the structure shown in Fig. 15.88.

TABLE 15.44

No.	Site notation	Atom	Multiplicity	Wyckoff	Site symmetry	x	y	z	Occupancy
1	Ca(1)	Ca	8	d	1	0.1741	0.0642	0.1632	1.0
2	Ca(2)	Ca	4	c	.m.	0.038	1/4	0.6435	1.0
3	Au	Au	4	c	.m.	0.3786	1/4	0.4483	1.0

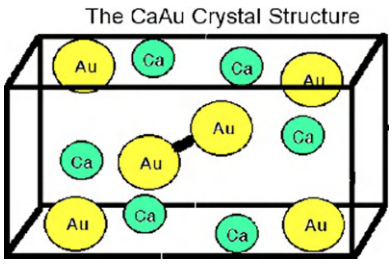

FIGURE 15.87

Cell parameters are: $a = 4.611$ Å, $b = c = 5.841$ Å, $\alpha = 74.45°$, $\beta = \gamma = 66.75°$, cell volume $= 131.63°$, $Z = 2$. Cell occupancy is shown in Table 15.46.

Brittle single crystals of $CaAu_2$ and $SrAu_2$ were synthesized by the reaction of alkaline earth metals and gold powder at 750 °C. The structures were determined from X-ray single-crystal diffractometer data:

$CaAu_2$: *Imma*, $Z = 4$, $a = 4.611(1)$ Å, $b = 7.067(2)$ Å, $c = 8.079(2)$ Å, $R/Rw(w = 1) = 0.069/0.071$ for 248 structure factors with F_o^2 $3(F_o^2)$ and 11 variables.

$SrAu_2$: *Imma*, $Z = 4$, $a = 4.732(2)$ Å, $b = 7.484(2)$ Å, $c = 8.165(3)$ Å, $R/Rw(w = 1) = 0.032/0.038$ for 542 structure factors with F_o^2 $3(F_o^2)$ and 12 variables.

Both compounds crystallize with the KHg_2 ($CeCu_2$) structure type. The structures consist of 3D gold frameworks with a trigonal pyramidal $3 + 1$ coordination for each gold atom. Calcium and strontium occupy channel-like cavities within the gold partial structures.

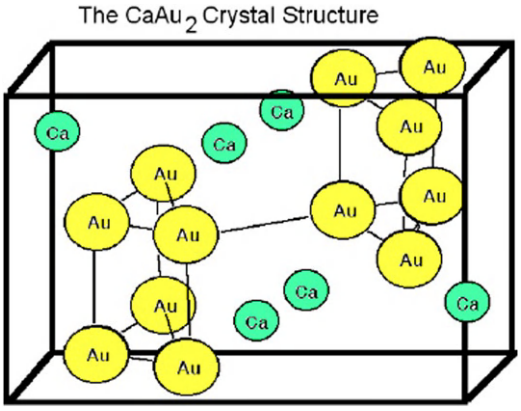

FIGURE 15.88

In contrast, the compound, Ca_3Au_4, has the structure shown in Fig. 15.89.

Cell parameters are: $a = 5.9084$ Å, $b = c = 8.1709$ Å, $\alpha = 114.38°$, $\beta = \gamma = 103.85°$, cell volume $= 321.77$ Å^3, $Z = 6$. Cell occupancy is shown in Table 15.47.

A new intermetallic in the Ca–Au phase field has been synthesized, using an unusual high-pressure route, with the stoichiometry Ca_3Au_4. The structure of the intermetallic compound was investigated using powder X-ray and powder neutron diffraction techniques. Ca_3Au_4 adopts the Pu_3Pd_4 structure type, which crystallizes in the rhombohedral space group R containing 42 atoms in a hexagonal unit cell.

TABLE 15.45

No.	Site notation	Atom	Multiplicity	Wyckoff	Site symmetry	*x*	*y*	*z*	Occupancy
1	Au	Au	4	c	m2m	0	0.08	1/4	1.0
2	Ca	Ca	4	c	m2m	0	0.36	1/4	1.0

TABLE 15.46

No.	Site notation	Atom	Multiplicity	Wyckoff	Site symmetry	*x*	*y*	*z*	Occupancy
1	Au	Au	8	h	m..	0	0.0415	0.164	1.0
2	Ca	Ca	4	e	mm2	0	1/4	0.54	1.0

TABLE 15.47

No.	Site notation	Atom	Multiplicity	Wyckoff	Site symmetry	*x*	*y*	*z*	Occupancy
1	Au3	Au	18	f	1	0.0563	0.2777	0.2208	1.0
2	Ca	Ca	18	f	1	0.2089	0.1645	0.2639	1.0
3	Au1	Au	3	b	-3.	0	0	1/2	1.0
4	Au2	Au	3	a	-3.	0	0	0	1.0

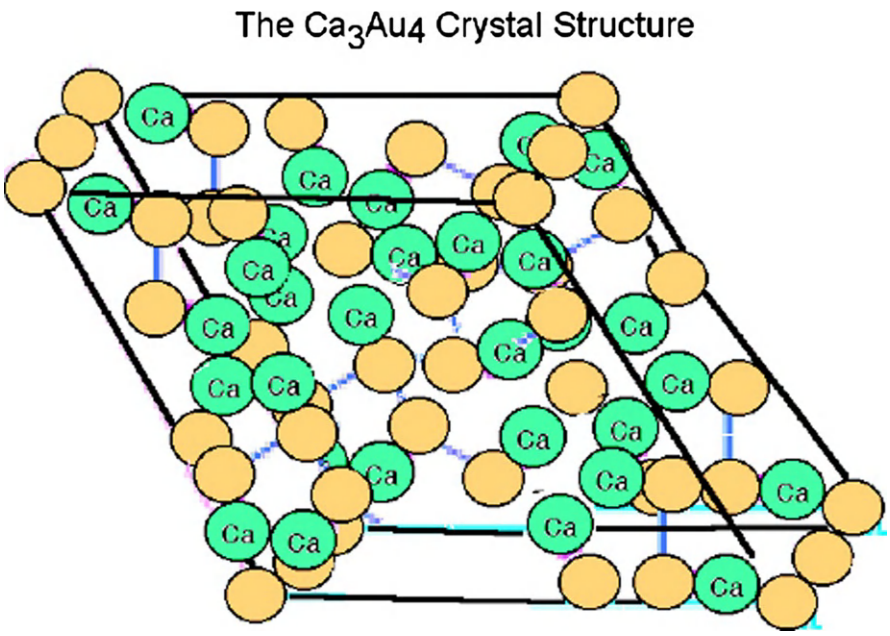

FIGURE 15.89

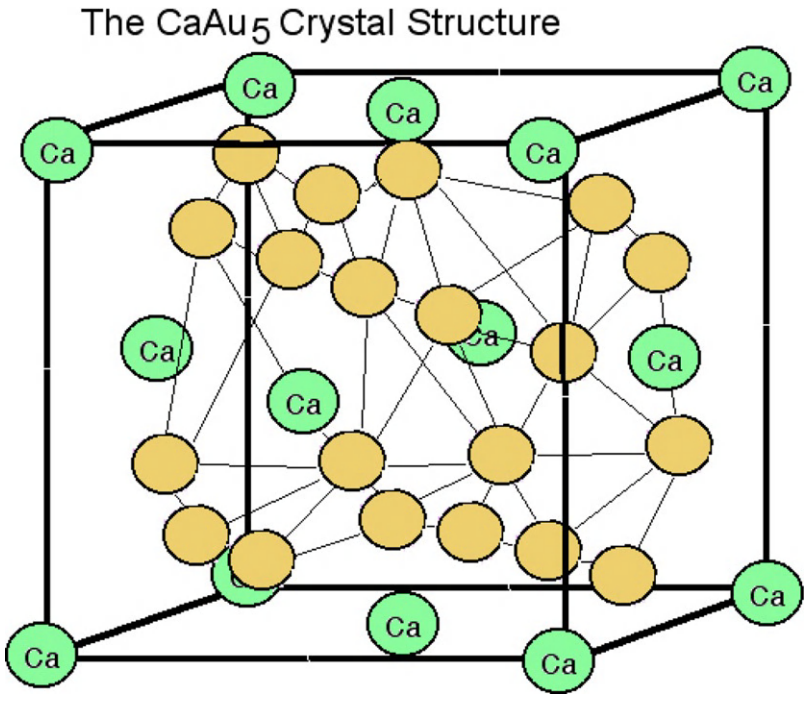

FIGURE 15.90

The following phases appear in the phase diagram but their structures have not been determined:

Ca_2Au, Ca_4Au, Ca_5Au, and Ca_4Au_5

In contrast, the opposite occurs in that following phases do not appear in the phase diagram, but their structures have appeared in the technical literature:

$CaAu_5$, Ca_5Au_2, Ca_5Au_3, Ca_5Au_4 and Ca_7Au_2

$CaAu_5$ has the structure shown in Fig. 15.90.

Cell parameters are: $a = b = c = 5.478$ Å, $\alpha = \beta = \gamma = 60°$, cell volume $= 116.24$ Å^3, $Z = 6$. Cell occupancy is shown in Table 15.48.

The compound, Ca_5Au_2, has the structural form shown in Fig. 15.91.

Cell parameters are: $a = 6.809$ Å, $b = 7.746$ Å, $c = 9.090$ Å, $\alpha = 96.73°$, $\beta = 111.99$ Å, $\gamma = 90°$, cell volume $= 440.98$ Å^3, $Z = 4$. Cell occupancy is shown in Table 15.49.

TABLE 15.48

No.	Site notation	Atom	Multiplicity	Wyckoff	Site symmetry	*x*	*y*	*z*	Occupancy
1	Au2	Au	16	e	.3m	0.625	0.625	0.625	1.0
2	Au1	Au	4	c	-43m	1/4	1/4	1/4	1.0
3	Ca	Ca	4	a	-43m	0	0	0	1.0

TABLE 15.49

No.	Site notation	Atom	Multiplicity	Wyckoff	Site symmetry	*x*	*y*	*z*	Occupancy
1	Au	Au	8	f	1	0.109	0.205	0.5794	1.0
2	Ca(2)	Ca	8	f	1	0.219	0.0788	0.3169	1.0
3	Ca(1)	Ca	8	f	1	0.408	0.1094	0.0791	1.0
4	Ca(3)	Ca	4	e	2	0	0.0783	1/4	1.0

The compound, Ca_5Au_3, has the structure shown in Fig. 15.92.

Cell parameters are: $a = b = 7.867$ Å, $c = 9.095$ Å, $\alpha = \beta = 115.63°$, $\gamma = 90°$, cell volume = 445.30 Å^3, $Z = 4$. Cell occupancy is shown in Table 15.50.

Ca_5Au_3 is tetragonal (Cr_5B_3 type), space group *I*4/*mcm*, with $a = 7.867$ and $c = 14.39$ Å. First principles density functional calculations were carried out to probe the oxidation states of the transition metal and alkaline earth elements in the Cr_5B_3-type compounds which has a general formula AE_5T_3 consisting of T_2 dimers and isolated T atoms. Typical compositions are: Ca_5Au_3, Ca_5Ag_3, Ca_5Hg_3, Sr_5Cd_3, and Ca_5Zn_3. The electronic structures of all these AE_5T_3 compounds are best described as $[(AE^{2+})_5(T–T)^{4–}(T^{2–})]+4e^-$. In the covalent bonding of the AE^{2+} ions with the transition metal anions T^{2-}, the $(n–1)$d orbitals of AE^{2+} contribute more than the *n*s and *n*p orbitals of AE^{2+}.

The compound, Ca_5Au_4, has the structure shown in Fig. 15.93.

Cell parameters are: $a = 7.727$ Å, $b = 8.019$ Å, $c = 8.028$ Å, $\alpha = \gamma = 90°$, $\beta = 109.16°$. Cell volume = 469.88 Å^2, $Z = 2$. Cell occupancy is shown in Table 15.51.

Another view of this structure is shown in Fig. 15.94.

Coordination polyhedron around the M–M dimers in the Ca_5Au_4 structure can be seen in Fig. 15.95.

The dark blue spheres form a trigonal biprism, and the light blue spheres cap its four rectangular faces. The coordination polyhedra surrounding a M_2 dimer are Au_2Ca_{12} in Ca_5Au_4. In the crystal structure of Ca_5Au_4 planar $CaAu(1)_2$ layers, which are isostructural with the $YbAg_2$ layers of Yb_3Ag_2, alternate with $Ca_4Au(2)_2$ slabs. The Au atoms are also present as Au_2 dimers with short interatomic distance, i.e. Au(1)-Au(1)) = 285 pm and Au(2)-Au(2)) = 296 pm.

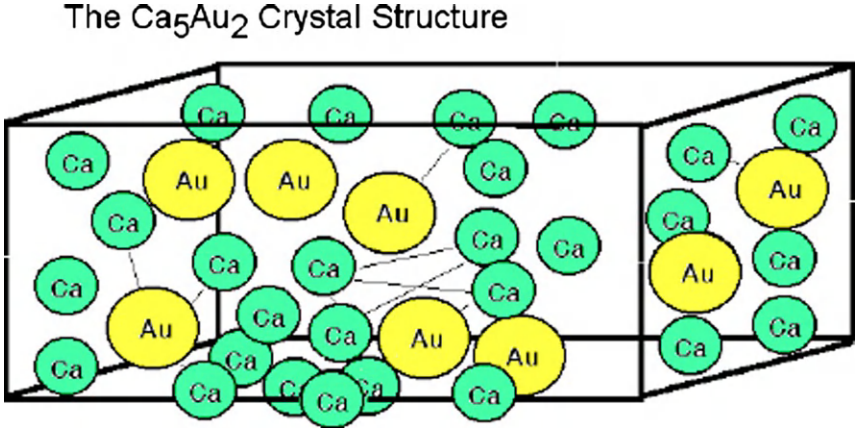

FIGURE 15.91

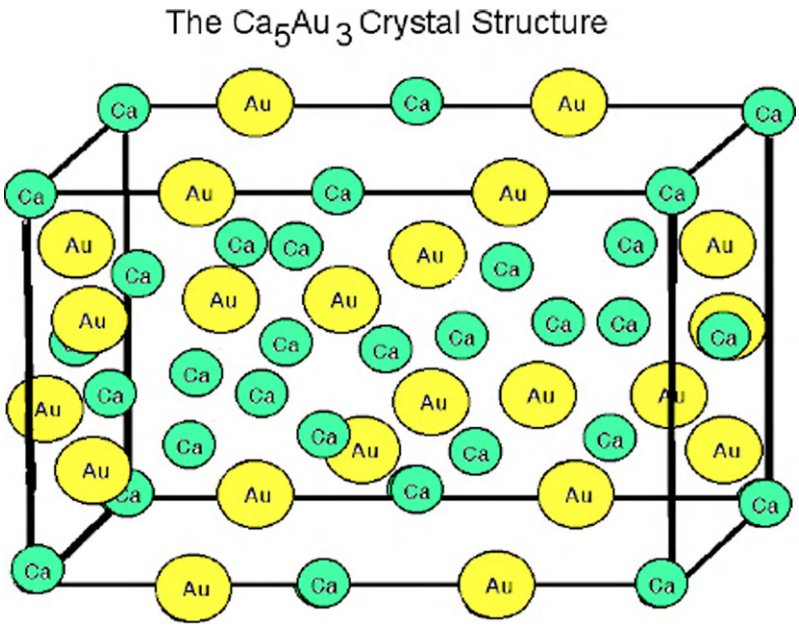

FIGURE 15.92

TABLE 15.50

No.	Site notation	Atom	Multiplicity	Wyckoff	Site symmetry	*x*	*y*	*z*	Occupancy
1	Ca(2)	Ca	16	l	..m	0.165	0.665	0.1452	1.0
2	Au(2)	Au	8	h	m.2m	0.631	0.1306	0	1.0
3	Ca(1)	Ca	4	c	4/m..	0	0	0	1.0
4	Au(1)	Au	4	a	422	0	0	1/4	1.0

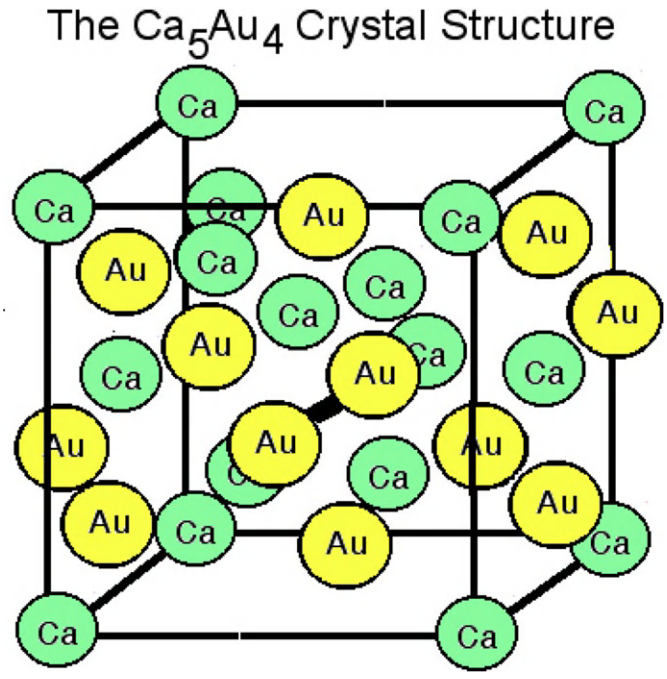

FIGURE 15.93

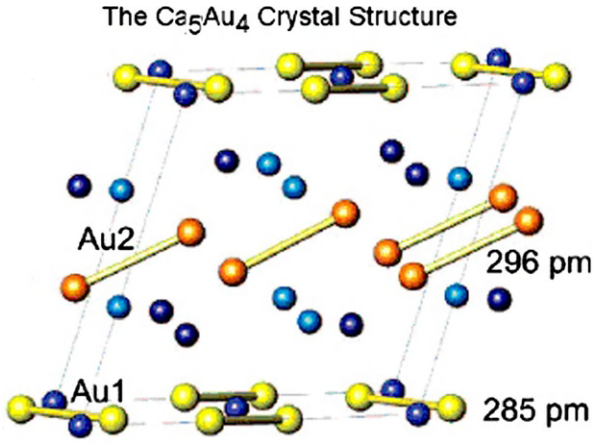

FIGURE 15.94

TABLE 15.51

No.	Site notation	Atom	Multiplicity	Wyckoff	Site symmetry	*x*	*y*	*z*	Occupancy
1	Au1	Au	4	e	1	0.012	0.6301	0.1288	1.0
2	Ca2	Ca	4	e	1	0.255	0.332	0.252	1.0
3	Au2	Au	4	e	1	0.419	0.0329	0.1433	1.0
4	Ca1	Ca	4	e	1	0.692	0.320	0.069	1.0
5	Ca3	Ca	2	a	-1	0	0	0	1.0

The chemical bonding of the M_2 dimers (M = Ag, Au, Hg) present in Yb_3Ag_2, Ca_5Au_4 and Ca_3Hg_2 was examined on the basis of first principles electronic band structure calculations. In these compounds, the 6s- and 5d-block bands of M are completely filled while the frontier levels of M are given by partially filled 6p-block bands such that the transition metal atoms M are best described as anions with electron configuration (5d) 10(6s)2(6p)1. Thus, the M_2 dimers (M = Ag, Au, Hg) of Yb_3Ag_2, Ca_5Au_4 and Ca_3Hg_2 are present as $[Ag–Ag]_4$, $[Au\text{-}Au]_4$, and $[Hg\text{-}Hg]_2$ Zintl anions, respectively. It is these compounds in which the M_2 dimers have a single bond formed by the p–p_4 interaction between the 5p and 6p orbitals of M atoms. The anions of late transition metal elements are different from those of late main group elements in their tendency for covalent bond formation.

Two novel intermetallic compounds have been synthesized and structurally studied by single-crystal diffractometer data: Ca_7Au_3 (*oP*80, space group *Pbca*, $a = 20.742$, $b = 18.036$, $c = 6.665$ Å, $Z = 8$, $R = 0.051$) and Ca_5Au_4 (*mP*18, space group $P21/c$, $a = 8.028$, $b = 8.019$, $c = 7.727$ Å, $\beta = 109.16°$, $Z = 2$, $R = 0.104$). Both atomic arrangements, which represent new structural types, are based on Au-centered Ca trigonal prisms and are geometrically related to the Th_7Fe_3 and Pu_5Rh_4 structures.

The compound, Ca_7Cu_3, has the structure shown in Fig. 15.96. Only one layer is shown. The 3D structure has two layers in the tetragonal structure.

The cell parameters are: $a = 6.665$ Å, $b = 18.036$ Å, $c = 20.742$ Å, $\alpha = \beta = \gamma = 90°$, cell volume = 2493.39 $Å^3$, $Z = 8$. Cell occupancy is shown in Table 15.52.

No other intermetallic compounds have been documented. Several intermetallic compounds like Ca_2Au (CAS = 90992-80-2) are offered for sale commercially.

In the Au^+- or Au^{2+}-containing systems of CaO–Au_2O or CaO–AuO, no compounds are known.

The compound, $CaAu_2O_4$, in the Au^{3+}-containing system of CaO–Au_2O_3, has been reported. The compound was prepared as yellowish-green powder from a 1:1 molar CaO–Au_2O_3 mixture of oxides when heated at high pressure and temperature (>70 MPa and 845 °C). Single crystals of $CaAu_2O_4$ crystallize in

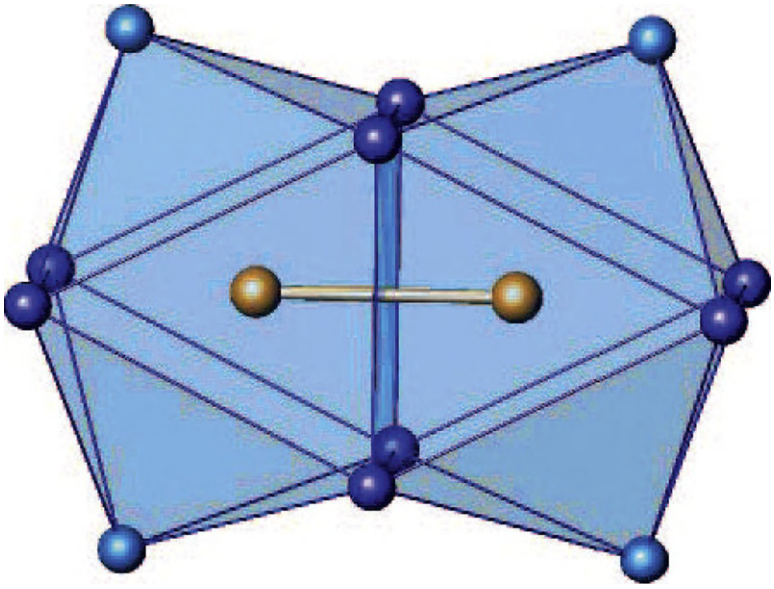

FIGURE 15.95

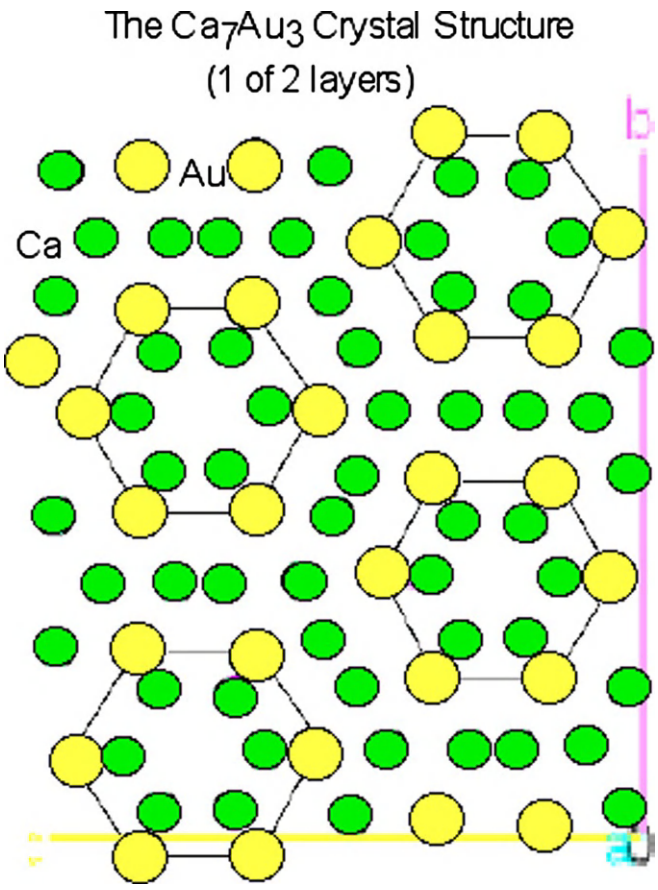

FIGURE 15.96

the tetragonal space group $I41/a$ with $Z = 4$. To date, only two studies have been made of this compound (1995 and 2010).

No other compounds are known in the CaO–Au_xO_y system, where x or y can be 1, 2 or 3. No compounds, such as oxygen-dominated calcium aurite or aurate, are offered commercially and no CAS numbers have been issued to date.

15.3.4. Strontium Gold Compounds

Strontium metal forms several compounds with gold, as shown in Fig. 15.97.

Six compounds are shown. Of these, five have had their structure elucidated and a sixth, Sr_2Au_3, is not shown in the phase diagram but has had its structure established. One compound in the phase diagram, $SrAu_9$, remains to have its structural characteristics documented.

The crystal structure of the phases, strontium–silver (Sr_3Ag_2), calcium–gold (Ca_5Au_3), strontium–gold (Sr_7Au_3), and strontium–silver (Sr_7Ag_3) has been determined. Sr_3Ag_2 is rhombohedral (Er_3Ni_2 type), space group $R3$, with a 9.962 and c 18. 93509-33-2 is the CAS registry number. Sr_7Au_3 is hexagonal (Th_7Fe_3 type), space group $P63mc$, with $a = 11.07$ and $c = 7.161$ Å. Sr_3Ag_2 is rhombohedral (Er_3Ni_2 type), space group $R3$, with a 9.962 and c 18. 93509-33-2 is the CAS registry number of Sr_3Ag_2.

$SrAu_5$ has the structure shown in Fig. 15.98.

Cell parameters are: $a = 4.615$ Å, $b = c = 5.627$ Å, $\alpha = 120°$, $\beta = \gamma = 90°$, cell volume $= 126.55$ Å^3, $Z = 1$. Cell occupancy is shown in Table 15.53.

$SrAu_2$ has the structure shown in Fig. 15.99.

Cell parameters are: $a = 4.732$ Å, $b = c = 6.022$ Å, $\alpha = 76.83°$, $\beta = \gamma = 66.87°$, cell volume $= 144.58$ Å^3, $Z = 1$. Cell occupancy is shown in Table 15.54.

Brittle single crystals of $SrAu_2$ were synthesized by the reaction of alkaline earth metals and gold powder at 750 °C. The structure was determined from X-ray single-crystal diffractometer data. $SrAu_2$: *Imma*, $Z = 4$, $a = 4.732(2)$ Å, $b = 7.484(2)$ Å, $c = 8.165(3)$ Å, $R/Rw(w = 1) = 0.032/0.038$ for 542 structure factors with

TABLE 15.52

No.	Site notation	Atom	Multiplicity	Wyckoff	Site symmetry	*x*	*y*	*z*	Occupancy
1	Au3	Au	8	c	1	0.028	0.0190	0.3453	1.0
2	Ca1	Ca	8	c	1	0.040	0.2826	0.3161	1.0
3	Ca3	Ca	8	c	1	0.042	0.3754	0.1257	1.0
4	Ca2	Ca	8	c	1	0.052	0.4699	0.3127	1.0
5	Ca5	Ca	8	c	1	0.234	0.2168	0.0219	1.0
6	Ca7	Ca	8	c	1	0.245	0.1273	0.4175	1.0
7	Ca6	Ca	8	c	1	0.249	0.0276	0.0210	1.0
8	Ca4	Ca	8	c	1	0.252	0.1267	0.2092	1.0
9	Au1	Au	8	c	1	0.469	0.3805	0.0602	1.0
10	Au2	Au	8	c	1	0.471	0.2320	0.3404	1.0

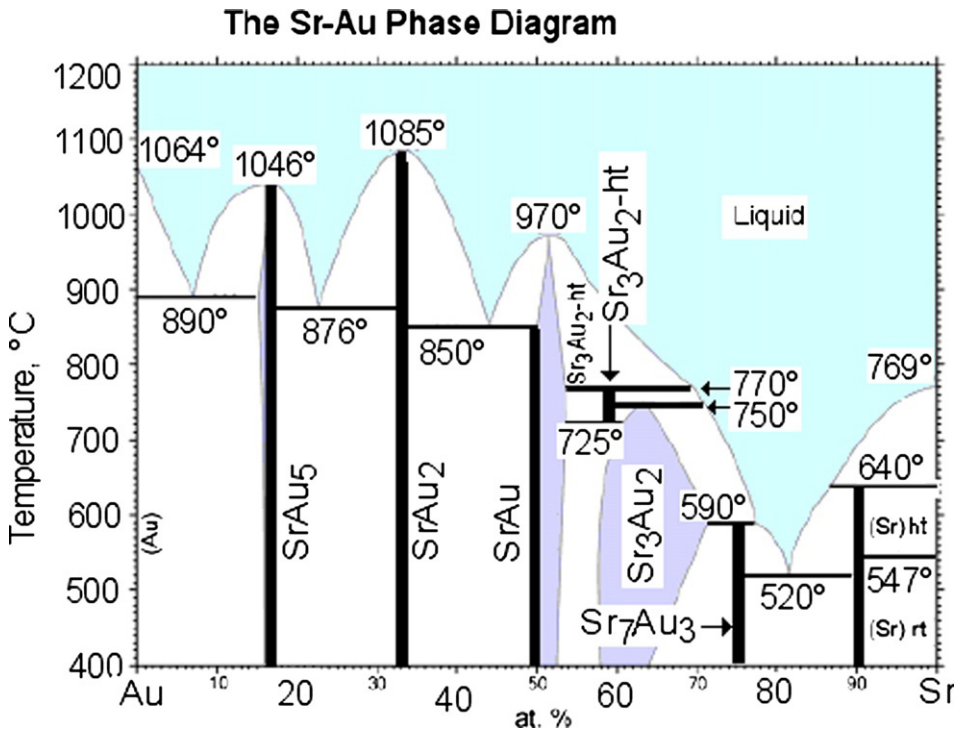

FIGURE 15.97

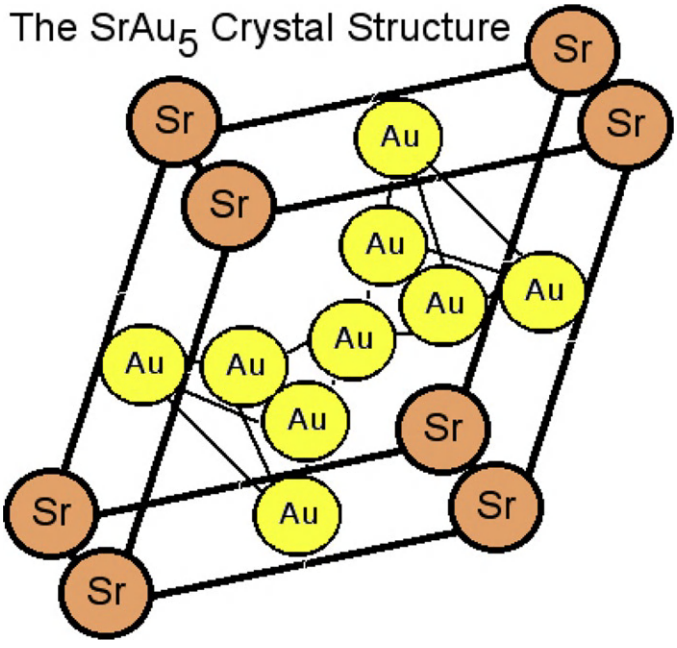

FIGURE 15.98

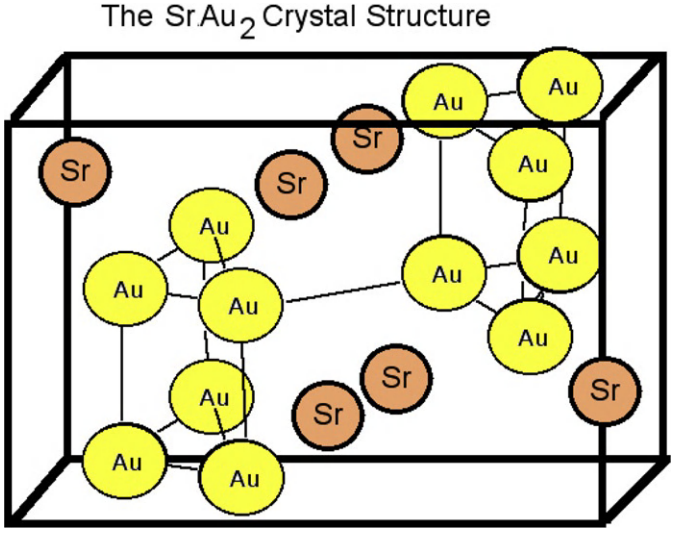

FIGURE 15.99

TABLE 15.53

No.	Site notation	Atom	Multiplicity	Wyckoff	Site symmetry	*x*	*y*	*z*	Occupancy
1	Au2	Au	3	g	mmm	1/2	0	1/2	1.0
2	Au1	Au	2	c	-6m2	1/3	2/3	0	1.0
3	Sr	Sr	1	a	6/mmm	0	0	0	1.0

TABLE 15.54

No.	Site notation	Atom	Multiplicity	Wyckoff	Site symmetry	x	y	z	Occupancy
1	Au	Au	8	h	m..	0	0.0458	0.16356	1.0
2	Sr	Sr	4	e	mm2	0	1/4	0.5395	1.0

TABLE 15.55

No.	Site notation	Atom	Multiplicity	Wyckoff	Site symmetry	x	y	z	Occupancy
1	Au7	Au	2	e	m	0.053	1/4	0.1412	1.0
2	Sr2	Sr	2	e	m	0.066	1/4	0.6135	1.0
3	Sr9	Sr	2	e	m	0.149	1/4	0.3124	1.0
4	Sr4	Sr	2	e	m	0.153	1/4	0.8137	1.0
5	Sr6	Sr	2	e	m	0.261	1/4	0.0149	1.0
6	Sr1	Sr	2	e	m	0.265	1/4	0.5162	1.0
7	Sr8	Sr	2	e	m	0.347	1/4	0.2142	1.0
8	Sr3	Sr	2	e	m	0.358	1/4	0.7143	1.0
9	Sr10	Sr	2	e	m	0.447	1/4	0.4131	1.0
10	Au5	Au	2	e	m	0.499	1/4	0.9419	1.0
11	Sr7	Sr	2	e	m	0.531	1/4	0.1149	1.0
12	Au2	Au	2	e	m	0.581	1/4	0.6437	1.0
13	Au9	Au	2	e	m	0.653	1/4	0.3419	1.0
14	Au4	Au	2	e	m	0.662	1/4	0.8420	1.0
15	Au6	Au	2	e	m	0.774	1/4	0.0401	1.0
16	Au1	Au	2	e	m	0.784	1/4	0.5412	1.0
17	Au8	Au	2	e	m	0.869	1/4	0.2428	1.0
18	Au3	Au	2	e	m	0.873	1/4	0.7433	1.0
19	Au10	Au	2	e	m	0.957	1/4	0.4442	1.0
20	Sr5	Sr	2	e	m	0.985	1/4	0.915	1.0

F_o^2 $3\sigma(F_o^2)$ and 12 variables. This compound crystallizes with the KHg_2 ($CeCu_2$) structure type. The structure consists of 3D gold frameworks with a trigonal pyramidal (3 + 1) coordination for each gold atom. Strontium occupies channel-like cavities within the gold partial structures.

SrAu has the structure shown in Fig. 15.100.

Cell parameters are: $a = 4.697$ Å, $b = 6.192$ Å, $c = 4.013$ Å, $\alpha = 94.21°$, $\beta = \gamma = 90°$, cell volume = 1163.98 Å^3, $Z = 20$. Cell occupancy is shown in Table 15.55.

Sr_3Au_2 has the structure shown in Fig. 15.101.

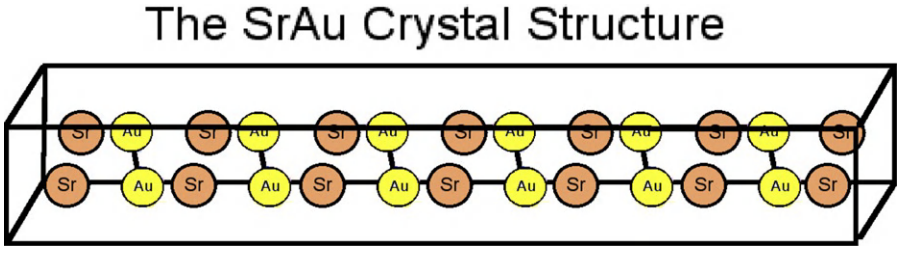

FIGURE 15.100

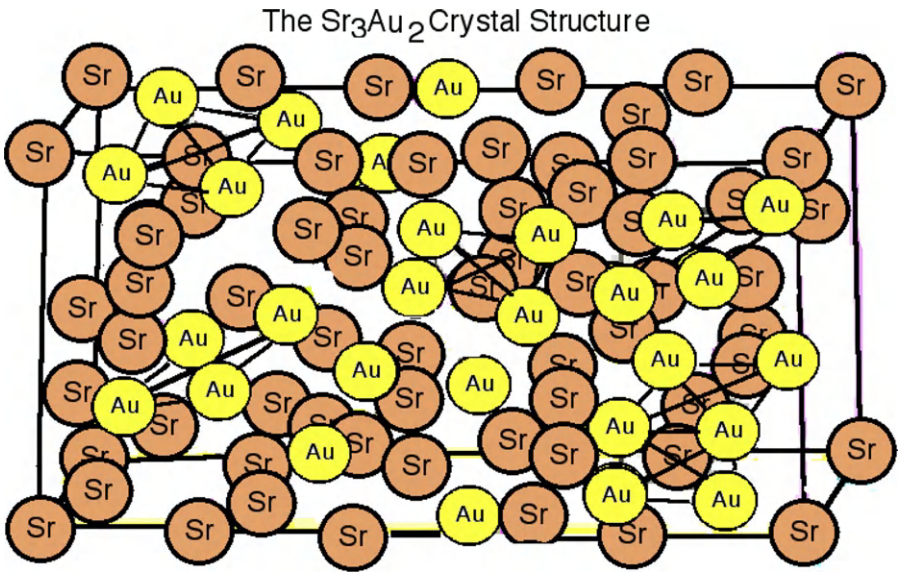

FIGURE 15.101

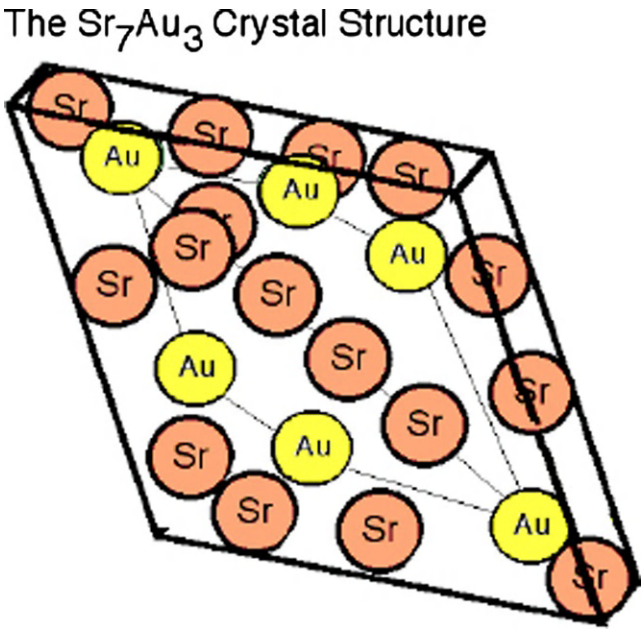

FIGURE 15.102

Cell parameters are: $a = b = c = 8.2583$ Å, $\alpha = \beta = \gamma = 71.11°$, cell volume $= 488.85$ Å^3, $Z = 9$. Cell occupancy is shown in Table 15.56.

The compound. Sr_7Au_3, has the structure shown in Fig. 15.102.

Cell parameters are: $a = 7.161$ Å, $b = c = 11.072$ Å, $\alpha = 120°$, $\beta = \gamma = 90°$, cell volume $= 759.98$ Å^3, $Z = 5$. Cell occupancy is shown in Table 15.57.

No other intermetallic compounds have been discovered or documented.

In the Au^+- or Au^{2+}-containing systems of SrO–Au_2O or SrO–AuO, no compounds have been documented in the literature. The Au^{3+}-containing system of SrO–Au_2O_3 has been studied.

Two aurates, $BaAu_2O_4$ and $SrAu_2O_4$, have been prepared as polycrystalline greenish-brown powders from alkaline earth peroxides and elemental Au by applying an elevated oxygen pressure (gold tubes, $T = 873$–923 K, $p(O_2) = 333$ MPa, 3d). Single crystals of $BaAu_2O_4$ were obtained by adding a 3% aqueous hydrogen peroxide solution and decreasing the temperature to 823 K, with otherwise similar conditions. X-ray single-crystal structure determination on $BaAu_2O_4$ led

TABLE 15.56

No.	Site notation	Atom	Multiplicity	Wyckoff	Site symmetry	*x*	*y*	*z*	Occupancy
1	Sr(1)	Sr	18	f	1	0.0992	0.4171	0.0738	1.0
2	Au	Au	18	f	1	0.3080	0.2482	0.1012	1.0
3	Sr(2)	Sr	6	c	3.	0	0	0.2066	1.0
4	Sr(3)	Sr	3	a	-3.	0	0	0	1.0

TABLE 15.57

No.	Site notation	Atom	Multiplicity	Wyckoff	Site symmetry	*x*	*y*	*z*	Occupancy
1	Au	Au	6	c	.m.	0.1883	0.8117	0.214	1.0
2	Sr(3)	Sr	6	c	.m.	0.5426	0.4574	-0.021	1.0
3	Sr(2)	Sr	6	c	.m.	0.8747	0.1253	0.295	1.0
4	Sr(1)	Sr	2	b	3m.	1/3	2/3	0.0	1.0

to the tetragonal space group $I41/a$ (No. 88) with four formula units per unit cell, which has the dimensions $a = 6.4297$ Å and $c = 10.251$ Å. The crystal structure was determined and refined to a final R value of 1.88% using 240 unique reflections. The crystal structure of the isotypic $SrAu_2O_4$ was refined by full profile analysis of powder X-ray diffraction data ($a = 6.1830$ Å, $c = 10.1704$ Å, $I41/a$, $Z = 4$, $R_I = 5.88\%$, and $R_{Pr} = 8.93\%$). Both aurates(III) are isostructural with $LaPd_2O_4$ and contain square planar AuO_4 units which are stacked along [100] and [001] planes and connected to a 3D framework by common corners. The alkaline earth ions are coordinated by eight oxygen atoms to form slightly distorted dodecahedra. The aurates(III) are diamagnetic and decompose under normal atmosphere at temperatures above 773 K.

The hitherto unknown compound, $Sr_5Au_2O_8$, was prepared by the reaction of an Sr/Au alloy with $Sr(OH)_2$ in closed silver tubes. The crystal structure was determined by means of an X-ray single-crystal investigation. $Sr_5Au_2O_8$ forms orthorhombic crystals: space group D_2^7-$F222$; $a = 11.7449$ Å; $b = 11.7407$ Å; $c = 6.5155$ Å; $Z = 4$. The O^{2-} ions are coordinated in a quadratic planar arrangement around Au^{3+} and as a distorted cube around Sr^{2+}.

No other compounds are known in the $SrO–Au_xO_y$ system, where x or y can be 1, 2 or 3. No compounds, such as oxygen-dominated strontium aurite or aurate, are offered commercially and no CAS numbers have been issued to date.

15.3.5. Barium Gold Compounds

Ba metal forms at least four compounds with gold metal. The phase diagram illustrates the nature of these phases (Fig. 15.103).

$BaAu_5$ has the structure shown in Fig. 15.104.

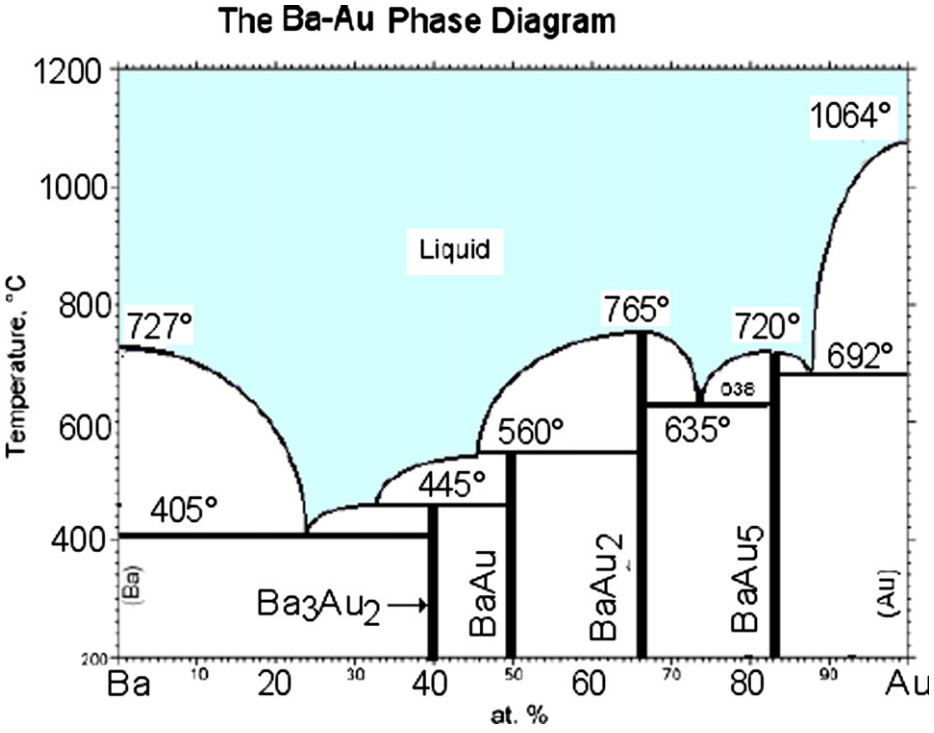

FIGURE 15.103

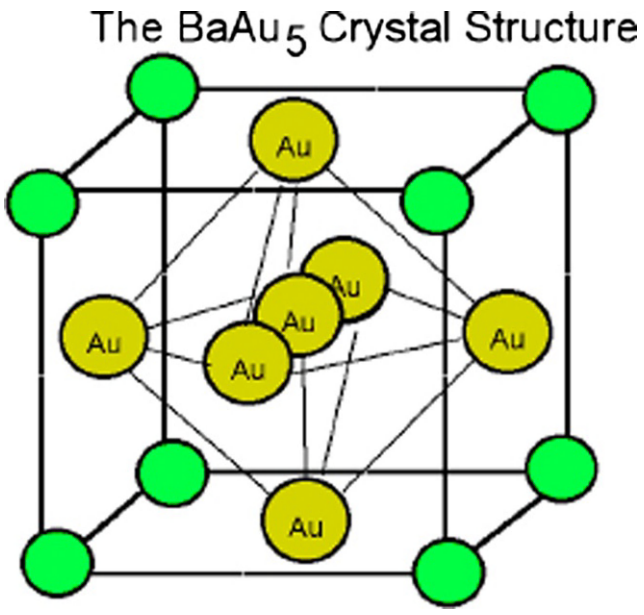

FIGURE 15.104

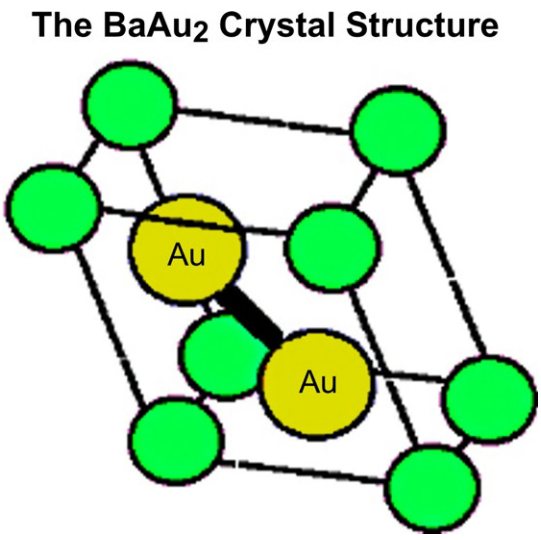

FIGURE 15.105

Cell parameters are: $a = 4.542$ Å, $b = c = 5.693$ Å, $\alpha = 120°$, $\beta = \gamma = 90°$, cell volume $= 127.35$ Å^3, $Z = 1$. Cell occupancy is shown in Table 15.58.

The compound, $BaAu_2$, has the structural form shown in Fig. 15.105.

Cell parameters are: $a = 4.119$ Å, $b = c = 4.804$ Å, $\alpha = 120°$, $\beta = \gamma = 90°$, cell volume $= 82.32$ Å^3, $Z = 1$. Cell occupancy is shown in Table 15.59.

BaAu has the structure shown in Fig. 15.106.

Cell parameters are: $a = 4.925$ Å, $b = 6.392$, $c = 8.338$ Å, $\alpha = \beta = \gamma = 90°$, cell volume $= 262.32$ Å^3, $Z = 4$. Cell occupancy is shown in Table 15.60.

Four of these hitherto unknown Ba–Au phases, $BaAu_5$, BaAu, $BaAu_2$ and Ba_3Au_2 are isotypic with the corresponding silver compounds. Ba_3Au_2 has the structural form shown in Fig. 15.107.

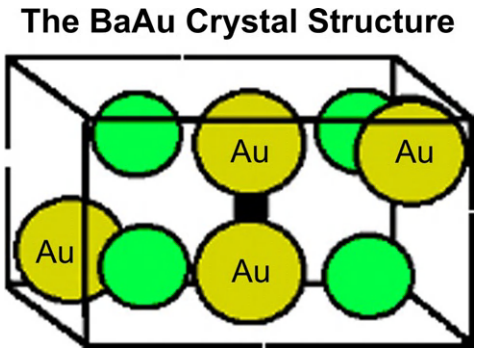

FIGURE 15.106

Cell parameters are: $a = b = c = 8.6056$ Å, $\alpha = \beta = \gamma = 71.052°$, cell volume $= 552.71$ Å^3, $Z = 8$. Cell occupancy is shown in Table 15.61.

TABLE 15.58

No.	Site notation	Atom	Multiplicity	Wyckoff	Site symmetry	x	y	z	Occupancy
1	Au2	Au	3	g	mmm	1/2	0	1/2	1.0
2	Au1	Au	2	c	-6m2	1/3	2/3	0	1.0
3	Ba	Ba	1	a	6/mmm	0	0	0	1.0

TABLE 15.59

No.	Site notation	Atom	Multiplicity	Wyckoff	Site symmetry	x	y	z	Occupancy
1	Au	Au	2	d	-6m2	1/3	2/3	1/2	1.0
2	Ba	Ba	1	a	6/mmm	0	0	0	1.0

TABLE 15.60

No.	Site notation	Atom	Multiplicity	Wyckoff	Site symmetry	x	y	z	Occupancy
1	Au1	Au	4	c	.m.	0.036	1/4	0.11	1.0
2	Ba1	Ba	4	c	.m.	0.18	1/4	0.625	1.0

TABLE 15.61

No.	Site notation	Atom	Multiplicity	Wyckoff	Site symmetry	x	y	z	Occupancy
1	Ba1	Ba	18	f	1	0.0976	0.4135	0.0737	1.0
2	Au1	Au	18	f	1	0.3104	0.2467	0.1037	1.0
3	Ba2	Ba	6	c	3.	0	0	0.2085	1.0
4	Ba3	Ba	3	a	-3.	0	0	0	1.0

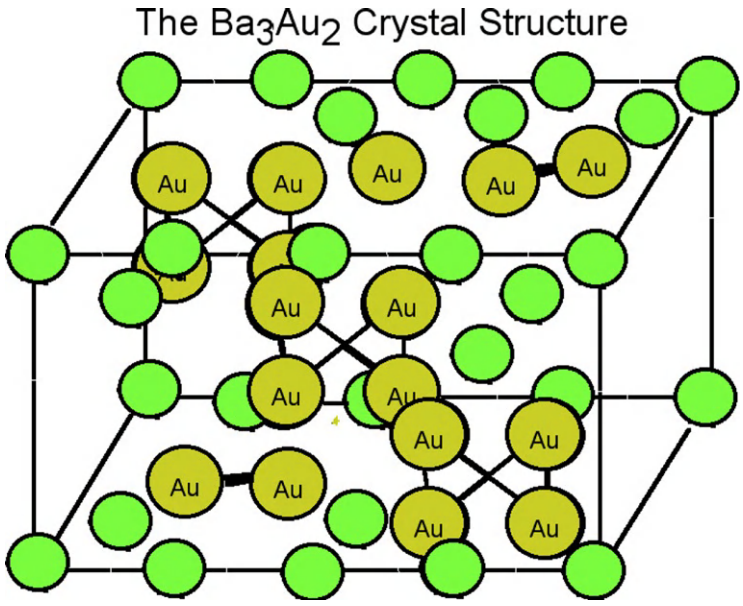

FIGURE 15.107

No other intermetallic compounds are known in the Ba^0–Au^0 system.

Two novel aurates, $BaAu_2O_4$ and $SrAu_2O_4$, have been prepared as polycrystalline greenish-brown powders from alkaline earth peroxides and elemental Au by applying an elevated oxygen pressure (gold tubes, $T = 873$–923 K, $p(O_2) = 333$ MPa, 3d). Single crystals of $BaAu_2O_4$ were obtained by adding a 3% aqueous hydrogen peroxide solution to the tubes and decreasing the temperature to 823 K, with otherwise similar conditions. X-ray single-crystal structure determination on $BaAu_2O_4$ crystals led to the tetragonal space group $I\,41/a$ (No. 88) with four formula units per unit cell with dimensions $a = 6.4297$ Å and $c = 10.251$ Å. The crystal structure was determined and refined to a final R value of 1.88% using 240 unique reflections. The crystal structure of the isotypic $SrAu_2O_4$ was refined by full profile analysis of powder X-ray diffraction data ($a = 6.1830$ Å, $c = 10.1704$ Å, $I41/a$, $Z = 4$, $R_I = 5.88\%$, and $R_{Pr} = 8.93\%$). Both aurates(III) are isostructural with $LaPd_2O_4$ and contain square planar AuO_4 units which are stacked along [100] and [001] planes and connected to a 3D framework by common corners. The alkaline earth ions are coordinated by eight oxygen atoms that form slightly distorted dodecahedra. The aurates(III) are diamagnetic and decompose under normal atmospheric pressure at temperatures above 773 K.

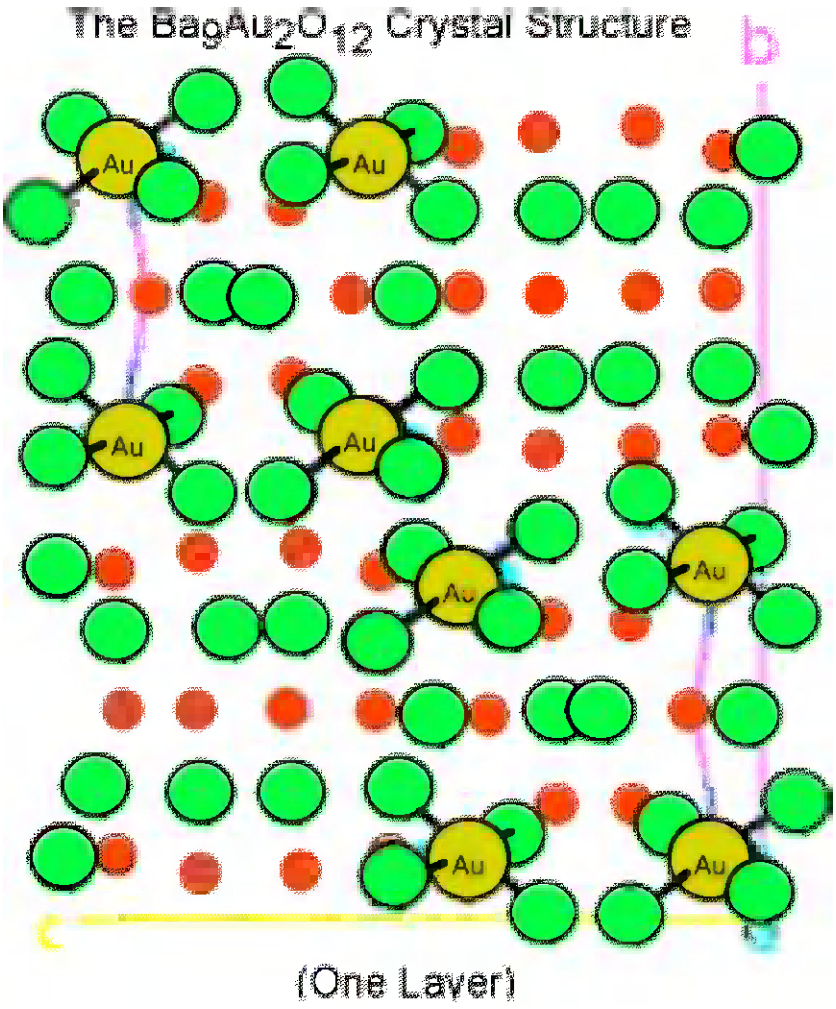

FIGURE 15.108

TABLE 15.62

No.	Site notation	Atom	Multiplicity	Wyckoff	Site symmetry	*x*	*y*	*z*	Occupancy
1	O1	O	8	d	1	0.007	0.151	0.546	1.0
2	O5	O	8	d	1	0.011	0.653	0.2	1.0
3	Ba6	Ba	8	d	1	0.029	0.1393	0.1879	1.0
4	O6	O	8	d	1	0.16	0.075	0.009	1.0
5	Ba4	Ba	8	d	1	0.1678	0.5813	0.0511	1.0
6	O4	O	8	d	1	0.179	0.091	0.376	1.0
7	Ba1	Ba	8	d	1	0.1832	0.5576	0.3226	1.0
8	O3	O	8	d	1	0.326	0.022	0.176	1.0
9	Au	Au	8	d	1	0.4192	0.0838	0.065	1.0
10	Ba5	Ba	4	c	.m.	0.1053	1/4	0.399	1.0
11	Ba2	Ba	4	c	.m.	0.1647	1/4	0.679	1.0
12	O2	O	4	c	.m.	0.295	1/4	0.23	1.0
13	O7	O	4	c	.m.	0.433	1/4	0.463	1.0
14	Ba3	Ba	4	c	.m.	0.6765	1/4	0.5638	1.0

The hitherto unknown compound Ba_4AgAuO_6 was prepared by oxidizing Ba/Au/Ag alloy with BaO_2/$Ba(OH)_2$ mixture in closed Ag tubes. X-ray single-crystal investigation led to orthorhombic symmetry space group *D-Cmcm*; $a = 13.275$, $b = 5.782$, $c = 11.396$ Å, $Z = 4$. Ba_4AgAuO_6 shows distorted pentagonal bipyramidal polyhedra around Ba^{2+} and square planar AuO_4 polygones. Ag^+ shows an unusual $2 + 2$ coordination by O^{2-}.

Another barium aurate compound, $Ba_9Au_2O_{12}$, has been discovered. It has the structure shown in Fig. 15.108.

Only one layer is shown. There are three intermediate layers in the *b*-direction having the same arrangement of atoms. $Ba_9Au_2O_{12}$ was prepared by oxidizing Ba–Au alloy with BaO_2 in sealed gold tubes. X-ray single-crystal investigation indicated orthorhombic symmetry, space group D_{2h}^{16}-*Pnam*, with Au^{3+} coordinated with square planar polygons of O^{2-}. There are five different Ba–O polyhedra.

Cell parameters are: $a = 7.133$ Å, $b = 14.093$ Å, $c = 17.165$ Å, $\alpha = \beta = \gamma = 90°$, cell volume $= 1725.52$ Å^3, $Z = 4$. Cell occupancy is shown in Table 15.62.

No other Ba–Au–O compounds are known. None of the above compounds are offered for sale commercially and no CAS numbers have been issued to date.

15.3.6. Radium Gold Compounds

Although Ra metal or radium oxide probably forms the same type of compounds with Au_2O or Au_2O_3 as Ba^0 or BaO, there is no record in the literature of anyone having done so.

CHAPTER

16

Group 12 (Zn, Cd and Hg) Alkaline Earth Compounds

OUTLINE

16.1. Alkaline Earth Zinc Compounds **1115**
16.1.1. Beryllium Zinc Compounds *1115*
16.1.2. Magnesium Zinc Compounds *1115*
16.1.3. Calcium Zinc Compounds *1122*
16.1.4. Strontium Zinc Compounds *1131*
16.1.5. Barium Zinc Compounds *1136*
16.1.6. Radium Zinc Compounds *1140*

16.2. Alkaline Earth Cadmium Compounds **1140**
16.2.1. Beryllium Cadmium Compounds *1140*
16.2.2. Magnesium Cadmium Compounds *1140*
16.2.3. Calcium Cadmium Compounds *1143*
16.2.4. Strontium Cadmium Compounds *1147*
16.2.5. Barium Cadmium Compounds *1151*
16.2.6. Radium Cadmium Compounds *1156*

16.3. The Alkaline Earth Mercury Compounds **1156**
16.3.1. Beryllium Mercury Compounds *1156*
16.3.2. Magnesium Mercury Compounds *1156*
16.3.3. Calcium Mercury Compounds *1159*
16.3.4. Strontium Mercury Compounds *1163*
16.3.5. Barium Mercury Compounds *1170*
16.3.6. Radium Mercury Compounds *1174*

16.1. ALKALINE EARTH ZINC COMPOUNDS

Zn forms a few intermetallic (IM) compounds with the alkaline earths. There are also a few "zincate" compounds known.

16.1.1. Beryllium Zinc Compounds

Be does not form any IM compounds with Zn metal as shown in Fig. 16.1.

In the Be–Zn–O system, no "zincate" compounds have been documented to date.

16.1.2. Magnesium Zinc Compounds

Mg forms a series of IM compounds with Zn metal as shown in Fig. 16.2.

Five compounds are shown, but only $MgZn_2$ melts congruently. The others melt incongruently at relatively low temperatures.

Phase layer growth and interdiffusion in the binary Mg–Zn system was investigated utilizing solid-to-solid diffusion couples annealed at 295, 315 and 325 °C for 21, 7 and 5 days, respectively. The diffusion microstructure was examined by scanning electron microscopy and concentration profiles were determined using X-ray energy dispersive spectroscopy and electron microprobe analysis. The Mg solid solution, Mg_2Zn_{11}, $MgZn_2$ and Mg_2Zn_3 in all three couples were observed in addition to the high temperature, $Mg_{51}Zn_{20}$ phase at 325 °C. The $MgZn_2$ phase was observed to grow the thickest layer, followed by the Mg_2Zn_3 and the Mg_2Zn_{11} phases. Activation energies for the parabolic growth were calculated to be 105 kJ/mol and 207 kJ/mol for the Mg_2Zn_3 and $MgZn_2$, respectively. Relevant interdiffusion coefficients were calculated for the phases present by analyses of concentration profiles.

In the Mg–Zn binary system, as the composition goes from magnesium- to zinc-side, there are stoichiometric compounds of $Mg_{48}Zn_{52}$, Mg_2Zn_3, $MgZn_2$ and

http://dx.doi.org/10.1016/B978-0-444-59550-8.00016-8

Copyright © 2013 Elsevier B.V. All rights reserved.

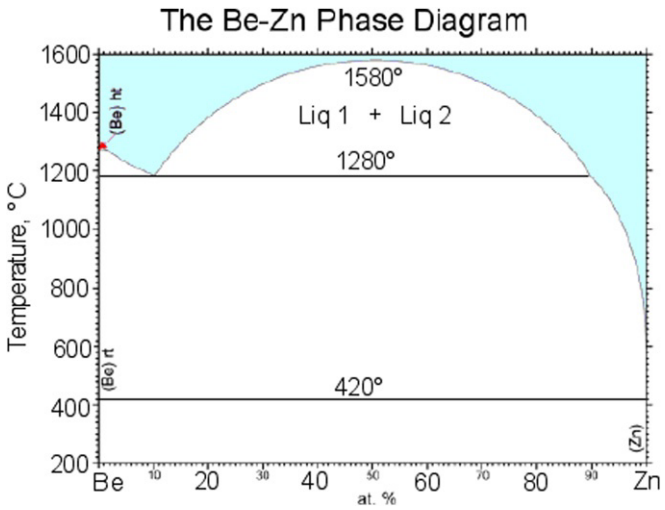

FIGURE 16.1

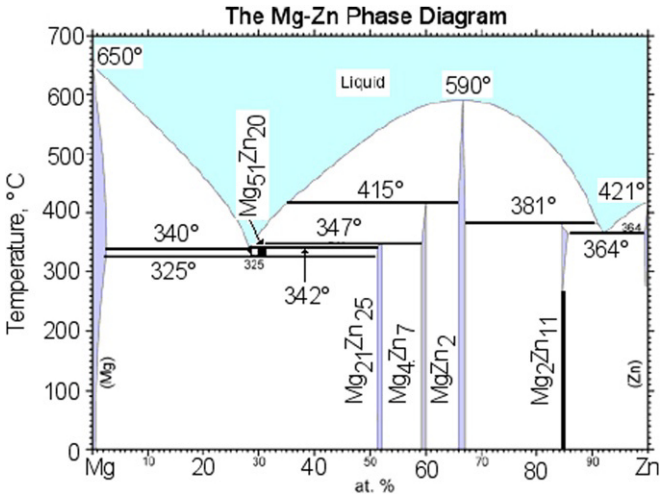

FIGURE 16.2

Mg_2Zn_{11}. Their valence bands are composed of Mg electrons spread over the crystal as if they are nearly free electrons in pure magnesium and localized Zn-3d electrons. The electronic states for the IM compounds, $Mg_{48}Zn_{52}$, Mg_2Zn_3, $MgZn_2$ and Mg_2Zn_{11} in the Mg–Zn binary system were investigated by measuring the coefficients, **g**, of the electronic contribution to the heat capacities and calculating the densities of states (DOS) in the vicinities of the Fermi levels (EF) by the DV-Xa molecular orbital method. The g value of Mg_2Zn_{11} was found to be nearly equal to that of pure Zn while the g value of $Mg_{48}Zn_{52}$ and Mg_2Zn_3 was similar to that of pure Mg. The g value of $MgZn_2$ was comparable to the simple compositional average of the g values of pure Mg and Zn. Such g values probably result from the localization or de-localization of valence electrons, consistent with the DOS theoretically

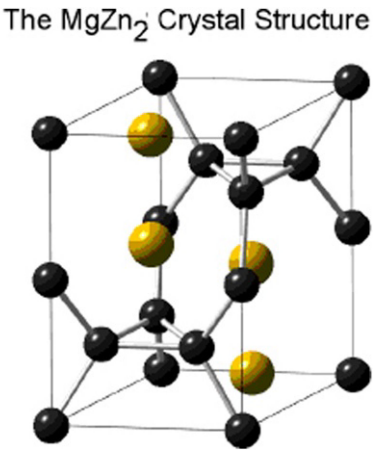

FIGURE 16.3

calculated by the DV-Xa molecular orbital method. The combined use of the measured g and the calculated DOS are expected to provide an important method to clarify electronic states of substances as thermal spectroscopy.

$MgZn_2$ has the structural form shown in Fig. 16.3.

Cell parameters are: $a = b = 5.2234$ Å, $c = 8.5562$ Å, $\alpha = \beta = 90°$, $\gamma = 120°$, cell volume $= 202.17$ Å^3, $Z = 4$. Cell occupancy is shown in Table 16.1.

A considerable amount of work has been accomplished concerning the C16 type of Laves-phase $MgZn_2$ compound because of its formation when steel, corrosion-proofed by zinc plating, is exposed to seawater. In addition, interest in the Laves phases has grown recently due to their promising behavior as solid-state hydrogen storage materials. They also have interesting magnetic and electrical properties. The Laves phase structures ($MgCu_2$, $MgZn_2$ and $MgNi_2$ types) are adopted by a large number of binary IM compounds of composition AB_2. These phases belong to the class of tetrahedral close-packed alloys. Two of the structural features of the Laves phases which have aroused interest are, firstly the dependence of the structure adopted (especially the choice between the cubic $MgCu_2$ and hexagonal $MgZn_2$ types) on the number of valence electrons of the constituent metal atoms and, secondly the structural distortions observed in a number of the hexagonal $MgZn_2$ type phases. By performing extended Hückel band calculations on model, AB_2 compounds with both the cubic and hexagonal structures and on the B sub-nets alone, structure electron count and deformation electron count correlations can be derived. These correlations depend on the highly peaked nature of the DOS of the Laves phases, primarily due to the B network.

The $MgCu_2$ type structure (*Strukturbericht* symbol C15) is face-centered cubic, belonging to the space group $Fd3m$ (O_h^7) with eight formula units per non-primitive

TABLE 16.1

No.	Site notation	Atom	Multiplicity	Wyckoff	Site symmetry	x	y	z	Occupancy
1	Zn2	Zn	6	h	mm2	0.1697	0.3394	1/4	1.0
2	Mg	Mg	4	f	3m.	1/3	2/3	0.563	1.0
3	Zn1	Zn	2	a	-3m.	0	0	0	1.0

cubic unit cell. The *A*-sublattice of the $MgCu_2$ structure defines a cubic diamond net, while the *B*-sublattice can be described in terms of B_4 tetrahedra sharing all of their vertices in such a way that each pair of fused tetrahedra adopts a staggered conformation.

The $MgZn_2$ type structure (*Strukturbericht* symbol C14) is hexagonal, belonging to the space group *P*63/*mmc* (D^4_{6h}) with four formula units per unit cell. The *A*-sublattice of the $MgZn_2$ structure defines a hexagonal diamond net. The *B*-sublattice is composed of B_4 tetrahedra, though their arrangement is distinct to that in $MgCu_2$. The tetrahedra alternately share vertices and faces along the *c*-axis, thereby forming chains of epically fused trigonal bipyramids. These chains are linked together by vertex sharing in the *ab* plane.

The $MgNi_2$ type structure (*Strukturbericht* symbol C36) also belongs to the hexagonal space group *P*63/*mmc* (D^4_{6h}), though it possesses eight formula units per unit cell. The $MgNi_2$ structure is a composite of the $MgCu_2$ and $MgZn_2$ structures.

The $MgZn_2$ crystal was found to have hexagonal axes with $a = 5.15$ and $c = 8.48$ Å. The unit cell contains four molecules. Crystals of the compound were formed by melting together the calculated amounts of magnesium and zinc under a molten mixture of sodium and potassium chlorides to prevent oxidation. The melt was then allowed to cool slowly in the electric furnace, about 4 h being taken to cool from 10° above to 10° below the melting point of the compound, 595 °C. The least distance between two magnesium atoms is 3.16 Å, between two zinc atoms, 2.52 Å, and between a magnesium and a zinc atom, 3.02 Å. The values computed from the atomic radii of magnesium and zinc determined from the crystal structure are respectively 3.22 Å, 2.67 Å, and 2.95 Å.

The single-crystalline elastic constants of the Laves phase $Mg(Cu,Zn)_2$ have been determined by the ultrasonic pulse-echo technique over the temperature range 4.2–298 K and over the composition range 10–51 mol% $MgZn_2$. The compositional dependence of the elastic contents indicates that a changing electron concentration causes initial contact and then a subsequent overlap of a Brillouin zone boundary by the Fermi surface. This contact occurs near 20 mol% $MgZn_2$ and correlates with previous measurements of magnetic susceptibilities and of specific heats. Debye temperatures at 0 K were also determined from the experimental values of the elastic constants.

The C14 Laves-phase $MgZn_2$ was investigated from 30 to 36 atom% Mg. This allowed measurement of chemical disorder that was monitored over a limited concentration range so that the influence on electron properties could be investigated. These studies included thermodynamic calculations of atomic configurations of Mg and Zn at off-stoichiometric compositions, electronic transport measurements, and electronic band structure calculations of $MgZn_2$. The disorder introduced by alloying was found to be substitutional for all C14 alloys, and to have a markedly stronger effect on resistivity and magnetoresistance, $\Delta p(B)/p(0)$, on the Mg-rich side due to strain introduced when Mg substitutes for Zn. $p(T)$ and Hall constant were characteristic for weakly disordered binary alloys. $\Delta p/p$ of $MgZn_2$ was large, reached 6 at 4.2 K and 8 T, and decreased strongly at off-stoichiometric compositions. The results were discussed in view of the band structure results and in terms of relations between atomic order and electronic properties. Several properties were found to resemble pure Zn. An empirical correlation over more than six orders of magnitude in $\Delta p/p$ was found for Zn and Zn-based alloys.

If the compound, $MgZn_2$, is subjected to high temperature and pressure, this Laves phase transforms by diffusion-controlled reaction at the $MgZn_2$ surface of the nanoparticles according to: $8\ MgZn_2 \Rightarrow 2\ Mg_4Zn_7 + O_2$. Isothermal aging of plastically deformed Mg–Zn alloys resulted in precipitation along the {1012} twin boundaries. The bulky precipitates so formed had structures similar to those recently reported for the rod-like β_1 precipitates, but allowed a more detailed study by high-resolution TEM due to their larger size. The core of the precipitates often had the structure of the monoclinic Mg_4Zn_7 phase, and had the orientation, $[0001]_{Mg}//[010]$; $\{1010\}_{Mg}//(201)$, with either the matrix or the twin. On this Mg_4Zn_7 phase, the hexagonal $MgZn_2$ phase grew in two directions, both with $[010]_{Mg4Zn7}//[1120]_{MgZn2}$ orientations. One of these orientations formed a known orientation relationship, $[0001]_{Mg}//[1120]_{MgZn2}$ or $\{1120\}_{Mg}//(0001)_{MgZn2}$ with the matrix. The part of the precipitate with the $MgZn_2$ structure was usually in direct contact with the twin boundary. Both the Mg_4Zn_7 and $MgZn_2$ phases have layered structures that can be described as similar building blocks of

icosahedrally coordinated atoms. The atomic positions of zinc atoms comprise the vertices of these icosahedra and form "thick" rhombic tiles. The orientations of these rhombuses remain unchanged across the interfaces between the two phases. Near the interface with $MgZn_2$, transition structures formed in the Mg_4Zn_7 phase with the Zn:Mg atom ratio between those of the Mg_4Zn_7 and $MgZn_2$ phases. In these transition structures, the unit cell of the Mg_4Zn_7 phase is extended along [100] or [001] by half a unit cell length by continuation of the rhombic tiling.

The compound, $Mg_{51}Zn_{20}$, has the structure shown in Fig. 16.4.

Both the *a*-*c* plane and the *a*-*b* planes of the three dimensional (3D) structure are shown. The black lines show how the structure is divided into parts, with layers of Mg atoms and layers of Zn atoms.

Cell parameters are: $a = b = c = 12.2971$ Å, $\alpha = \beta = 107.828°$, $\gamma = 11046°$, cell volume $= 1430.57$ Å^3, $Z = 2$. Cell occupancy is shown in Table 16.2.

The structure of the pseudo-cubic $Mg_{51}Zn_{20}$ phase, which is related to icosahedral quasicrystals, was interpreted as a modulated crystal. It essentially comprises distorted close-packed layers with ordered atomic vacancies. The basic reciprocal lattice vectors point to the vertices of a distorted icosahedron. The crystal structure of $Mg_{51}Zn_{20}$, a phase designated conventionally as "Mg_7Zn_3" has been determined by the single-crystal X-ray diffraction (XRD) method. It was solved by the examination of a Patterson synthesis, and refined by the ordinary Fourier and least squares method; the *R* value obtained was 4.8% for 1167 observed reflections. The crystal is orthorhombic, space group *Immm*, with $a = 14.083$, $b = 14.486$, $c = 14.025$ Å, and $Z = 2$. There are 18 independent atomic sites, Zn1–Zn6, Mg1–Mg10, A, and B, and the last two sites are statistically occupied by Zn and Mg atoms with the occupancies; 0.46-Zn7 + 0.52-Mg11 and 0.24-Zn8 + 0.74-Mg12, for A and B, respectively. The structure of the crystal is described as an arrangement of icosahedral coordination polyhedra, to which all the atomic sites but Zn3 site belong. In this arrangement, the Zn atoms other than the Zn3 and Zn8(B) center the icosahedral coordination polyhedra with coordination number 12. The Zn3, Zn8 atoms, and all the Mg atoms except Mg11(A) are located at the centers of various coordination polyhedra with the coordination numbers from 11 to 15. The distances between neighboring atoms are 2.71–3.07, 2.82–3.65, and 2.60–3.20 Å for Zn–Zn, Mg–Mg, and Zn–Mg, respectively.

The hydrogen absorption capacity of the $Mg_{51}Zn_{20}$ IM compound was investigated. The equilibrium pressures at 300, 330 and 380 °C were found to be 3.6, 8.05 and 31.0 atm., respectively. The highest hydrogen content in $Mg_{51}Zn_{20}$ corresponds to the nominal composition $Mg_{51}Zn_{20}H_{95}$ (3.62 wt% hydrogen). Evidence of MgH_2 formation in the hydrided material was found.

The atomic structure of amorphous $Mg_{70}Zn_{30}$ alloy and the structural change in the crystallization process under isothermal annealing were studied by EXAFS and XRD. The results of both measurements show that atoms begin to take short-range and long-range order of $Mg_{51}Zn_{20}$ crystal during the crystallization process under isothermal annealing.

The compound, Mg_2Zn_{11}, has the structure shown in Fig. 16.5.

Cell parameters are: $a = b = c = 8.5521$ Å, $\alpha = \beta = \gamma = 90°$, cell volume $= 625.37$ Å^3 $Z = 8$.

Cell occupancy is shown in Table 16.3.

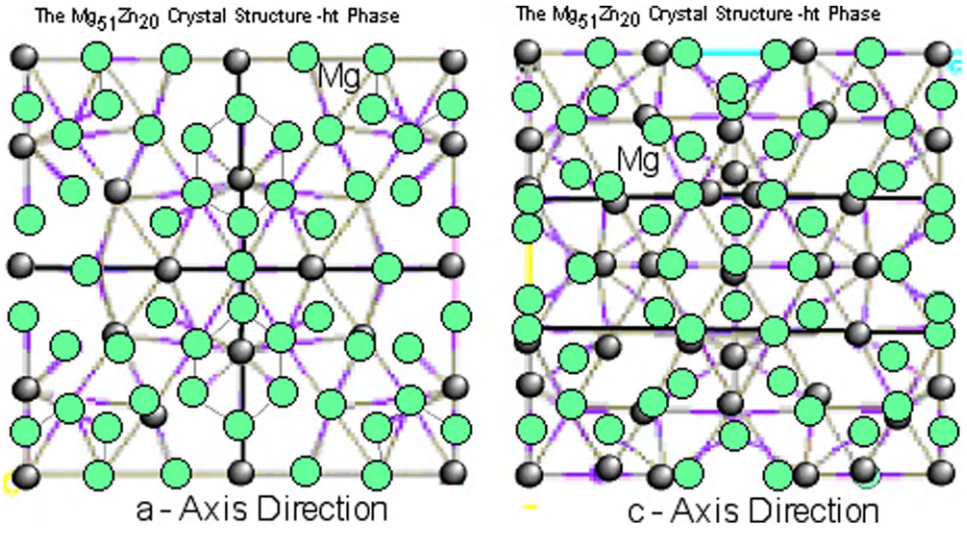

FIGURE 16.4

TABLE 16.2

No.	Site notation	Atom	Multiplicity	Wyckoff	Site symmetry	*x*	*y*	*z*	Occupancy
1	Mg2	Mg	16	o	1	0.1177	0.1815	0.2846	1.0
2	Mg3	Mg	16	o	1	0.1886	0.3074	0.1086	1.0
3	Mg1	Mg	16	o	1	0.3065	0.1116	0.1812	1.0
4	Mg4	Mg	8	n	..m	0.1731	0.1068	0	1.0
5	Zn3	Zn	8	n	..m	0.3323	0.2055	0	1.0
6	Mg5	Mg	8	n	..m	0.3807	0.3903	0	1.0
7	Mg12	Mg	8	m	.m.	0.1095	0	0.1687	0.74
8	Zn8	Zn	8	m	.m.	0.1096	0	0.1698	0.24
9	Zn1	Zn	8	m	.m.	0.2066	0	0.3389	1.0
10	Zn7	Zn	8	m	.m.	0.4002	0	0.3355	0.46
11	Mg11	Mg	8	m	.m.	0.4011	0	0.3463	0.52
12	Mg6	Mg	8	l	m..	0	0.1803	0.1029	1.0
13	Mg7	Mg	8	l	m..	0	0.3170	0.4025	1.0
14	Zn2	Zn	8	l	m..	0	0.3379	0.2131	1.0
15	Zn5	Zn	4	j	mm2	1/2	0	0.1729	1.0
16	Mg9	Mg	4	i	mm2	0	0	0.3521	1.0
17	Mg10	Mg	4	g	m2m	0	0.3852	0	1.0
18	Zn4	Zn	4	f	2mm	0.1949	1/2	0	1.0
19	Mg8	Mg	4	e	2mm	0.3848	0	0	1.0
20	Zn6	Zn	2	a	mmm	0	0	0	1.0

Mg_2Zn_{11} can be seen as an intermediate step in structural complexity between the simple Laves-phase $MgZn_2$ on one side, and the complex 1/1 approximation and quasicrystals Zn(Mg)Al and Zn(Mg)Sc on the other. The structure can be described as a cubic packing of a triacontahedron whose center is partially occupied by a Zn atom. This partially occupied site turned out to play a major role in understanding the lattice dynamics. Data from inelastic neutron scattering demonstrated a Van Hove singularity in the vibrational spectrum of Mg_2Zn_{11} for energy as low as 4.5 meV, which is a unique feature for a nearly close-packed metallic alloy. This

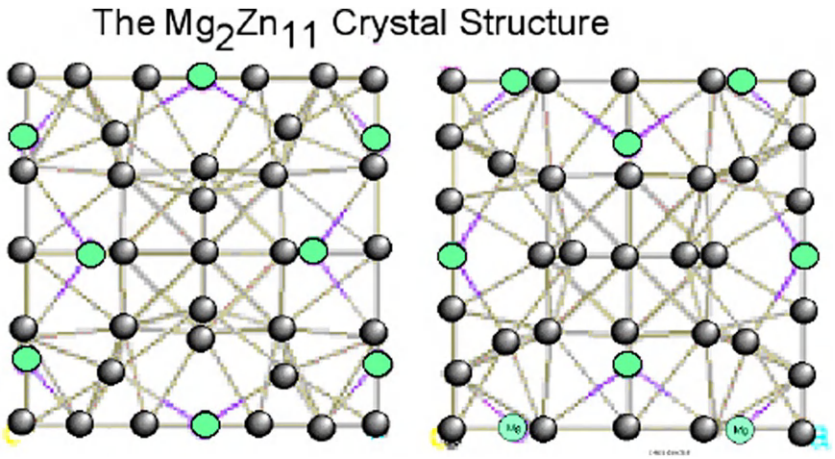

FIGURE 16.5

TABLE 16.3

No.	Site notation	Atom	Multiplicity	Wyckoff	Site symmetry	*x*	*y*	*z*	Occupancy
1	Zn1	Zn	12	j	m..	0	0.157	0.257	1.0
2	Zn2	Zn	8	i	.3.	0.278	0.278	0.278	1.0
3	Zn3	Zn	6	h	mm2..	0.265	1/2	1/2	1.0
4	Zn4	Zn	6	g	mm2..	0.340	1/2	0	1.0
5	Mg	Mg	6	f	mm2..	0.18	0	1/2	1.0
6	Zn5	Zn	1	a	m-3.	0	0	0	1.0
1	Zn1	Zn	12	j	m..	0	0.157	0.257	1.0
2	Zn2	Zn	8	i	.3.	0.278	0.278	0.278	1.0

corresponds to a gap opening at the Brillouin zone boundary and an interaction between a low-lying optical branch and an acoustic one, as could be deduced from the dispersion relation measured by inelastic X-ray scattering. Second, the measured phonon DOS exhibits many maxima, indicating strong mode interactions across the whole energy range. The origin of the low-energy modes in Mg_2Zn_{11} and other features of the vibrational spectra were studied carefully, using both ab initio and empirical potential calculations. A detailed analysis of vibrational eigenmodes was presented, linking features in the vibrational spectrum to atomic motions within the structural building blocks.

The Gibbs–Thomson coefficient and solid–liquid interfacial energy of the solid Mg_2Zn_{11} phase in equilibrium with Zn–Mg eutectic liquid have been determined to be $(3.3 \pm 0.2) \times 10^{-8}$ Km and $(20.8 \pm 2.1) \times 10^{-3}$ J/m^2 from the equilibrated grain boundary groove shapes with a numerical model. The grain boundary energy of the solid Mg_2Zn_{11} phase has been calculated to be $(40.9 \pm 4.5) \times 10^{-3}$ J/m^2 by considering a force balance at the grain boundary grooves. The thermal conductivity ratio of the eutectic Zn–Mg liquid phase to the solid Mg_2Zn_{11} phase has also been found to be 0.81.

The Mg_4Zn_7 compound has the structure shown in Fig. 16.6.

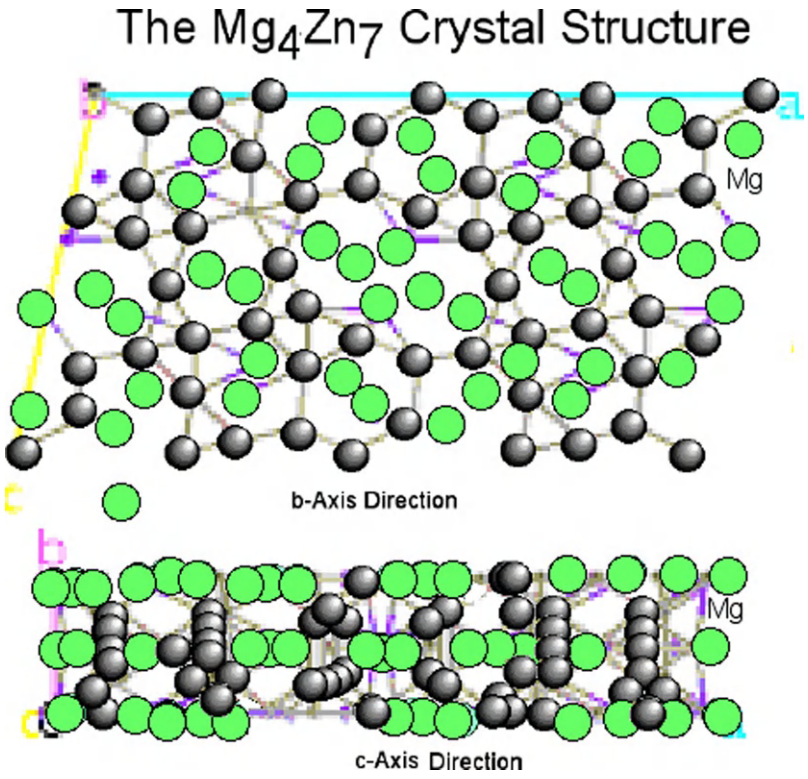

FIGURE 16.6

As shown in the *c*-axis slice of the 3D structure, there are three layers of Mg atoms holding the Zn atoms together. The *b*-axis part of the 3D structure shows the relationship of the Zn atoms to the Mg atoms in the structure.

Cell parameters are: $a = 5.242$ Å, $b = 13.242$ Å, $c = 14.284$ Å, $\alpha = 102.25°$, $\beta = 90°$, $\gamma = 101.41°$, cell volume $= 948.23$ Å^3, $Z = 10$. Cell occupancy is shown in Table 16.4.

The Frank-Kasper family, characterized by tetrahedral close packing, includes the compound, Mg_4Zn_7. Constraints of close packing dictate that only special atomic environments with triangulated coordination shells occur, namely $Z = \{12,14,15,16\}$ with 12–16 nearest neighbors surrounding the central atom. Icosahedral quasicrystal Frank-Kasper phases are represented by prototype $Al_6Mg_{11}Zn_{11}$ (cI162) while the Mg_4Zn_7 (mC110) phase is an approximant of a decagonal quasicrystal. The Laves phase of $MgZn_2$ (hP12) may be viewed as a common approximation for both quasicrystal Frank–Kasper families. The quasicrystal Frank-Kasper structures are pseudo-binary, in that large atoms (e.g. Mg) center highly coordinated polyhedra ($Z = 14$, 15 or 16) while smaller atoms (e.g. Al or Zn) have icosahedral $Z = 12$ coordination. In both icosahedral and decagonal structures about 60% of the atoms are of the smaller $Z = 12$ coordinated type.

The structure of the compound, Mg_2Zn_3, has been examined. However, the finalized structure is not yet documented. This compound was not included in the phase diagram. Cell parameters are: $a = 5.31$ Å, $b = 11.65$ Å, $c = 14.45$ Å, $\alpha = 81.9°$, $\beta = 84°$, $\gamma = 84.0°$, cell volume $= 875$ Å^3, Z is not given.

TABLE 16.4

No.	Site notation	Atom	Multiplicity	Wyckoff	Site symmetry	*x*	*y*	*z*	Occupancy
1	Zn4	Zn	8	j	1	0.086	0.25	0.069	1.0
2	Zn3	Zn	8	j	1	0.108	0.25	0.398	1.0
3	Zn2	Zn	8	j	1	0.268	0.25	0.327	1.0
4	Zn1	Zn	8	j	1	0.430	0.25	0.252	1.0
5	Mg10	Mg	4	i	m	0.008	0	0.403	1.0
6	Mg7	Mg	4	i	m	0.033	0	0.226	1.0
7	Zn5	Zn	4	i	m	0.079	0	0.909	1.0
8	Mg5	Mg	4	i	m	0.129	0	0.608	1.0
9	Mg3	Mg	4	i	m	0.166	0	0.247	1.0
10	Zn6	Zn	4	i	m	0.168	0	0.033	1.0
11	Mg2	Mg	4	i	m	0.177	0	0.821	1.0
12	Mg6	Mg	4	i	m	0.213	0	0.477	1.0
13	Zn7	Zn	4	i	m	0.256	0	0.157	1.0
14	Zn8	Zn	4	i	m	0.313	0	0.638	1.0
15	Zn11	Zn	4	i	m	0.330	0	0.466	1.0
16	Zn10	Zn	4	i	m	0.346	0	0.287	1.0
17	Mg4	Mg	4	i	m	0.361	0	0.070	1.0
18	Mg9	Mg	4	i	m	0.445	0	0.457	1.0
19	Mg8	Mg	4	i	m	0.479	0	0.102	1.0
20	Zn12	Zn	4	i	m	0.521	0	0.322	1.0
21	Zn9	Zn	4	i	m	0.598	0	0.234	1.0
22	Mg1	Mg	4	i	m	0.693	0	0.149	1.0
23	Zn13	Zn	4	e	-1	1/4	1/4	0	1.0
24	Zn14	Zn	2	a	2/m	0	0	0	1.0

The compound, $Mg_{21}Zn_{25}$, is included in the phase diagram, but its structure has not been elucidated.

No other Mg–Zn IM compounds have been discovered to date.

In the Mg–Zn–O system, few compounds have been discovered. For example, the instability of such compounds does not allow the direct preparation of any compounds from the oxides themselves. However, the use of organic complexes has allowed the formation of a semiconducting composition, $Mg_xZn_{1-x}O$. The synthesis and characterization of the first hetero-bimetallic methylzinc–magnesium alkoxide clusters $[Me_6MgZn_6(OR)_8]$ [R = Et (**1-a**), *n*-Pro (**1-b**), *n*Bu (**1-c**)] with a bis-cubane-shaped $MgZn_6O_8$ core has been described. The thermal degradation of 1-a to c and mixtures of 1-a and the homo-metallic MeZn–alkoxide cubane [{MeZnOtBu}$_4$] in dry synthetic air led to wide-band gap semiconducting $Mg_xZn_{1-x}O$ nanoparticles at temperatures below 500 °C. The final materials were characterized by different analytical techniques such as PXRD, REM, TEM, EDX, and IR spectroscopy. The morphology of the as-prepared magnesium-containing ZnO samples is influenced by the different organo groups (alkoxo) in the precursors. EDX mapping showed that magnesium is uniformly distributed in the ZnO matrix. The incorporation of magnesium led to a distortion of the ZnO lattice with an increased *a*-axis and decreased *c*-axis parameters. Room temperature photoluminescence (PL) spectra reveal that the near-band edge emission of Mg^{2+}-doped ZnO is shifted to higher energies relative to that of pure ZnO. Combinations of ZnO with MgO form wurtzite solid solutions for Mg concentrations up to 30%, resulting in an increase in optical band gap to 3.9 eV. At Mg concentrations above 45%, rock salt $Mg_{1-x}Zn_xO$ solid solutions are stabilized for deposited thin films, and can be tailored in band gap in the deep-ultraviolet range between 4.8 eV for x 0.55 up to 7.8 eV for MgO. ZnO is polymorphic and it is known to exist in two cubic structures. Stabilization of a rock salt ZnO phase can be achieved by the application of external pressure.

No other compounds have been documented in the literature. No magnesium zincate compositions are offered for sale commercially and no CAS numbers have been issued to date.

16.1.3. Calcium Zinc Compounds

Calcium forms a number of IM compounds with Zn metal. The phase diagram is shown in Fig. 16.7.

The Ca–Zn system displays eight intermediate compounds, with pronounced maxima in the liquidus at Zn-rich concentrations. The available experimental phase diagram data have been reviewed by Itkin and Alcock. Their reported diagram is based mainly on the DTA measurements of Messing et al., but with

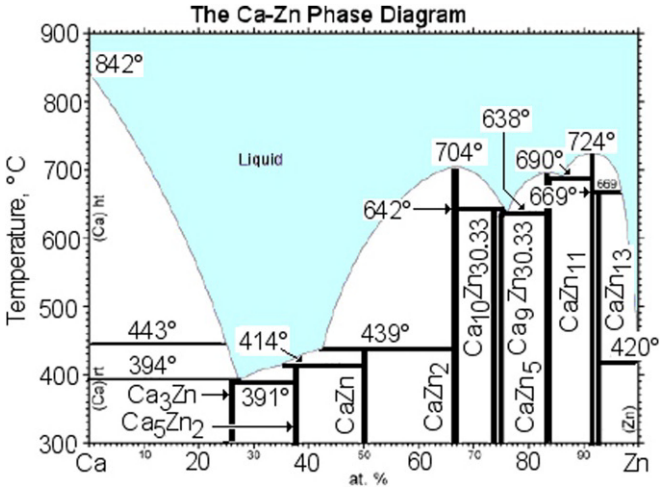

FIGURE 16.7

modification of the compounds, Ca_7Zn_4 and Ca_7Zn_{20} to Ca_5Zn_3 and $CaZn_3$ based on later crystallographic information. Very limited amounts of experimental data have been found in the literature for the Ca–Zn system. Because of the high vapor pressure of the Ca–Zn alloys above 50 atom% Zn, Messing et al. used vapor effusion measurement for compound identification. They reported eight intermediate stoichiometric compounds: Ca_3Zn, Ca_7Zn_4, CaZn, 2, Ca_7Zn_{20}, $CaZn_5$, $CaZn_{11}$ and $CaZn_{13}$. Apart from $CaZn_2$, $CaZn_5$ and $CaZn_{11}$, all compounds undergo peritectic decomposition. Later on, the compounds Ca_7Zn_4 and Ca_7Zn_{20} were replaced with the formulas, Ca_5Zn_3 and $CaZn_3$, respectively, based on the more accurate crystallographic investigations of Bruzzone et al. and Fornasini and Merlo. Thermodynamic data were determined (Table 16.5).

TABLE 16.5

Cpd	ΔH_f^0 (J/mol)	S^0 (J/mol)	Cp(J/mol/K)
Ca_3Zn	−36353	163.85	Cp = 3°—Cp (Ca,FCC-A1) + Cp (Zn,HCP-Zn)
Ca_5Zn_3	−108144	326.10	Cp = 5°—Cp (Ca,FCC-A1) + 3°—Cp (Zn,HCP-Zn)
CaZn	−35605	79.10	Cp = Cp (Ca,FCC-A1) + Cp (Zn,HCP-Zn)
$CaZn_2$	−65952	118.20	Cp = Cp (Ca,FCC-A1) + 2°—Cp (Zn,HCP-Zn)
$CaZn_3$	−83210	154.86	Cp = Cp (Ca,FCC-A1) + 3°—Cp (Zn,HCP-Zn)
$CaZn_5$	−118083	226.35	Cp = Cp (Ca,FCC-A1) + 5°—Cp (Zn,HCP-Zn)
$CaZn_{11}$	−210647	421.70	Cp = Cp (Ca,FCC-A1) + 11°—Cp (Zn,HCP-Zn)
$CaZn_{13}$	−209934	511.72	Cp = Cp (Ca,FCC-A1) + 13°—Cp (Zn,HCP-Zn)

TABLE 16.6

No.	Site notation	Atom	Multiplicity	Wyckoff	Site symmetry	x	y	z	Occupancy
1	Zn	Zn	8	h	m..	0	0.057	0.165	1.0
2	Ca	Ca	4	e	mm2	0	1/4	0.553	1.0

TABLE 16.7

No.	Site notation	Atom	Multiplicity	Wyckoff	Site symmetry	x	y	z	Occupancy
1	Zn1	Zn	96	i	m..	0	0.1192	0.1806	1.0
2	Zn2	Zn	8	b	m-3.	0	0	0	1.0
3	Ca	Ca	8	a	432	1/4	1/4	1/4	1.0

High-pressure forms of IM compounds with the composition $CaZn_2$, $SrZn_2$, $SrAl_2$, and $BaAl_2$ were synthesized from $CeCu_2$-type precursors ($CaZn_2$, $SrZn_2$, $SrAl_2$) and $Ba_{21}Al_{40}$ by multi-anvil techniques and investigated by X-ray powder diffraction ($SrAl_2$ and $BaAl_2$), X-ray single-crystal diffraction ($CaZn_2$), and electron microscopy ($SrZn_2$). Their structures correspond to that of Laves phases. Whereas the dialuminides crystallize in the cubic $MgCu_2$ (C15) Laves structure, the dizincides adopt the hexagonal $MgZn_2$ (C14) structure. This trend is in agreement with the structural relationship displayed by sp bonded Laves phase systems at ambient conditions.

$CaZn_2$ has the structure shown in Fig. 16.8.

Cell parameters are: $a = 4.5911$ Å, $b = c = 5.7813$ Å, $\alpha = 78.773°$, $\beta = \gamma = 66.606°$, cell volume $= 129.17$ Å^3, $Z = 2$. Cell occupancy is shown in Table 16.6.

$CeCu_2$-type polar IMs can be transformed to Laves phases upon simultaneous application of pressure and temperature. The observed structures are controlled by the valence electron concentration, as shown in Fig. 16.9. This trend is in agreement with the structural relationship displayed by sp bonded Laves phase systems at ambient conditions.

$CaZn_{13}$ has the structure shown in Fig. 16.10.

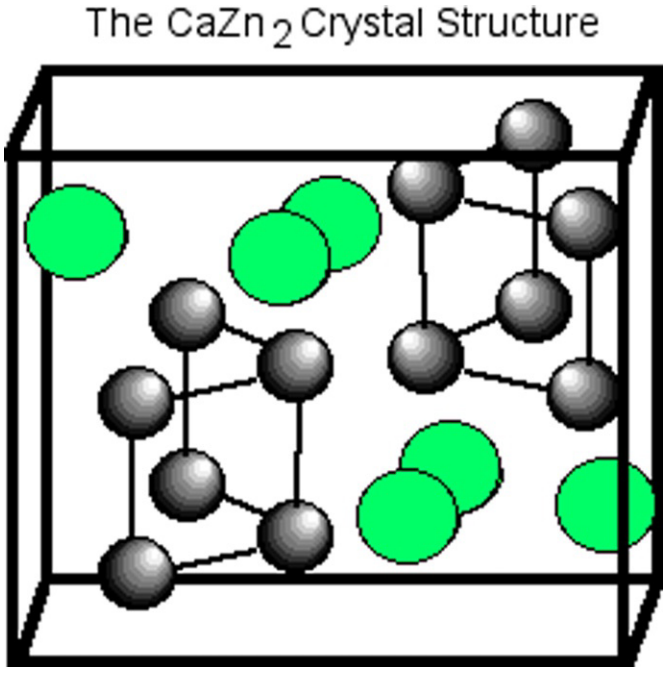

FIGURE 16.8

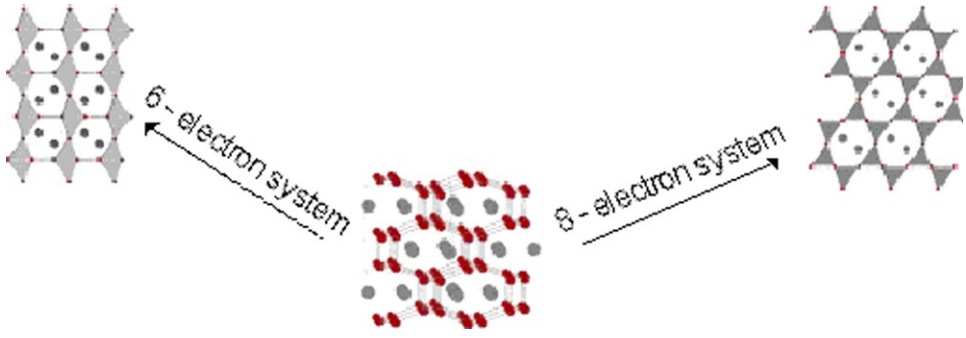

FIGURE 16.9

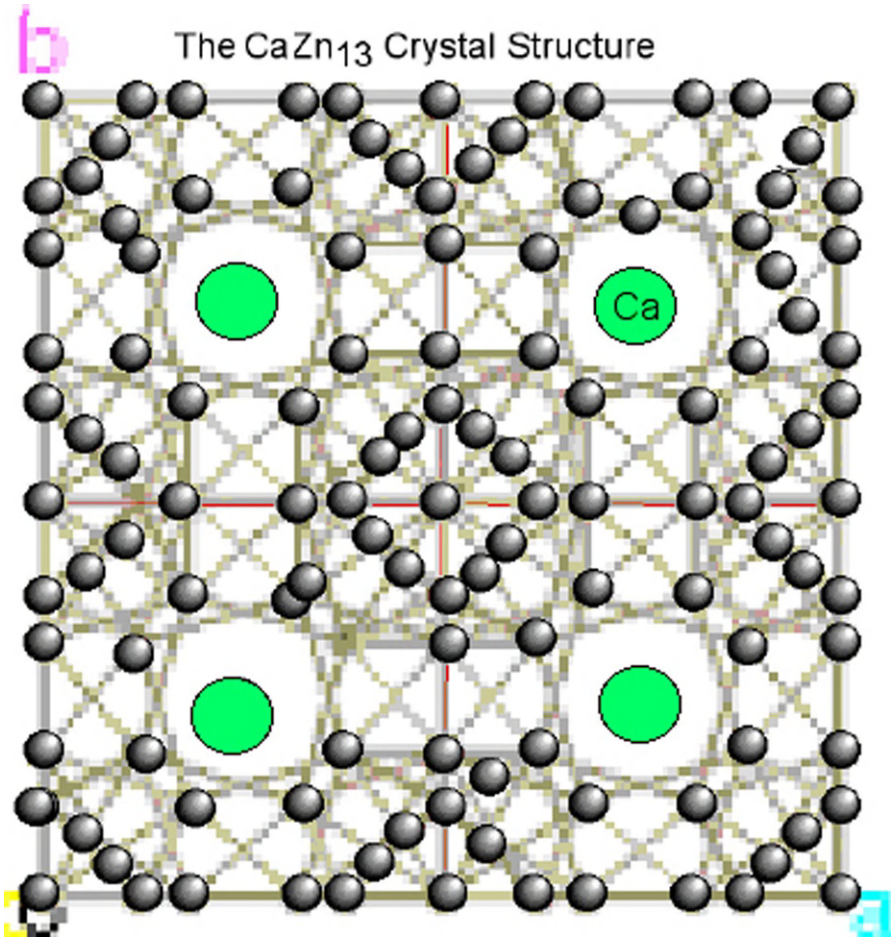

FIGURE 16.10

The Ca atoms lie within channels in the structure, one Ca atom per unit cell. A total of four units are shown here in this *a*-*c* plane. In the *b*-direction, there are layers of Zn atoms between the channels so that this diagram represents eight unit cells in a 3D structure. Cell parameters are: $a = b = c = 8.65641$ Å, $\alpha = \beta = \gamma = 60°$, cell volume = 458.67 Å^3, $Z = 8$. Cell occupancy is shown in Table 16.7.

The compound, $CaZn_5$, has the crystal structure shown in Fig. 16.11.

Cell parameters are: $a = 4.242$ Å, $b = c = 5.370$ Å, $\alpha = 120°$, $\beta = \gamma = 90°$, cell volume = 105.98 Å^3, $Z = 4$. Cell occupancy is shown in Table 16.8.

$CaZn_5$ is supplied commercially with the CAS number: 12258-72-9. The eutectic 7.3:2.7 molar ratio mixture of calcium and zinc metal melts at 394 °C and was explored as a solvent for the growth of new IM phases for potential use as hydrogen storage materials. The reaction of nickel in this molten mixture produces two new phases—the $CaCu_5$-related structure $CaNi_2Zn_3$ ($P6/mmm$, $a = 8.9814$ Å, $c = 4.0665$ Å) and a new cubic structure (Fd–$3m$, $a = 21.5051(4)$ Å). The structure determined was shown in Fig. 16.12.

In this diagram, the features include:

(a) The $CaNi_2Zn_3$ structure type; the $CaCu_5$ substructure is indicated by a dashed unit cell.
(b) The coordination environments of the two calcium sites in this structure.

In contrast, the cubic structure is much more complicated and is shown in Fig. 16.13 and Table 16.9.

TABLE 16.8

No.	Site notation	Atom	Multiplicity	Wyckoff	Site symmetry	*x*	*y*	*z*	Occupancy
1	Zn2	Zn	3	g	mmm	1/2	0	1/2	1.0
2	Zn1	Zn	2	c	-6m2	1/3	2/3	0	1.0
3	Ca	Ca	1	a	6/mmm	0	0	0	1.0

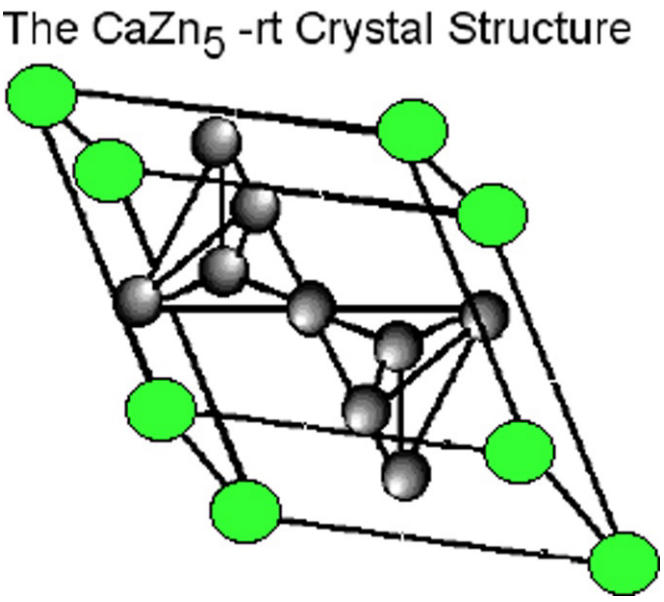

FIGURE 16.11

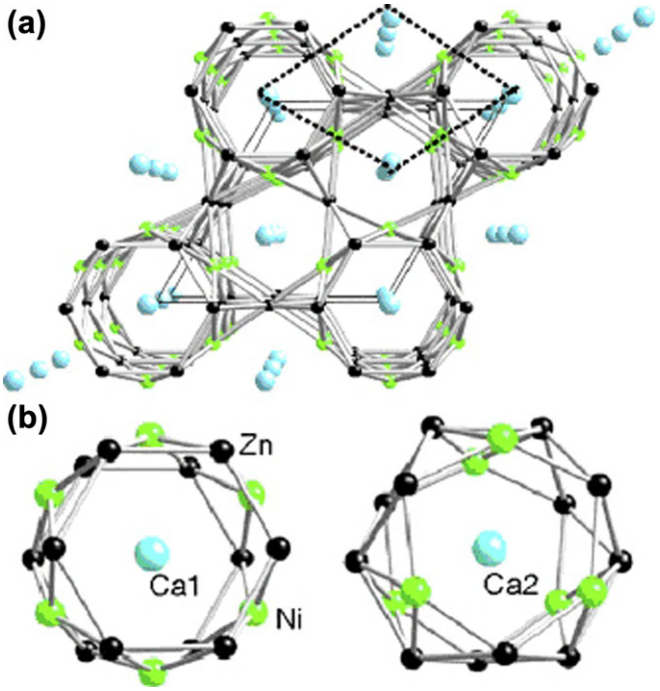

FIGURE 16.12

The zinc-rich compounds in the binary systems with the heavier alkaline earth elements, $CaZn_{11}$ and $CaZn_5$, have been synthesized from melts of the elements. Their crystal structures have been refined based on modern single-crystal X-ray data. $CaZn_5$ (hexagonal, space group $P6/mmm$, $a = 5.3899$, $c = 4.2456$ Å, $Z = 1$, $R1 = 0.0144$) crystallizes with the $CaCu_5$ structure type and exhibits a small but distinct phase width $Ca_{1-x}Zn_{5+2x}$ up to a composition of $Ca_{0.87}Zn_{5.26}$ ($a = 5.3338$, $c = 4.3004$ Å, $R1 = 0.0170$) achieved through a gradual substitution of Ca by Zn_2 dumbbells. The high-temperature form of $SrZn_5$, which was prepared by quenching of melted samples, also adopts the ideal $CaCu_5$ structure type ($a = 5.54.1$, $c = 4.28.2$ Å, $R1 = 0.0314$).

The room temperature modification of $SrZn_5$ (orthorhombic, space group $Pnma$, $a = 13.133$, $b = 5.299$, $c = 6.697$ Å, $Z = 4$, $R1 = 0.0349$) forms a singular structure, whereas the Ba compound of corresponding composition (orthorhombic, space group $Cmcm$, $a = 10.783$, $b = 8.398$, $c = 5.320$ Å, $Z = 4$, $R1 = 0.0281$) crystallizes with a third, also rather uncommon structure. For the compound $CaZn_{11}$ ($BaCd_{11}$ structure type; tetragonal, space group $I41/amd$, $a = 10.6811$, $c = 6.8281$ Å, $Z = 4$, $R1 = 0.0299$) the originally proposed structure type was confirmed and also refined using single-crystal data. The chemical bonding in all these compounds was analyzed using FP-LAPW band structure methods. Together with geometrical criteria and observed valence electron numbers of isotypic compounds, the results were used to compare and discuss the stability of the different structures of the IM phases in the systems AZn_5 and AM_{11} (M = Zn, Cd, Hg).

$CaZn_{11}$ has the structure shown in Fig. 16.14.

Cell parameters are: $a = 6.832$ Å, $b = c = 8.304$ Å, $\alpha = 8.026°$, $\beta = \gamma = 65.31°$, cell volume = 390.98 Å^3, $Z = 4$. Cell occupancy is shown in Table 16.10.

Little is known concerning this compound.

The Ca_3Zn compound has the crystal structure shown in Fig. 16.15.

Cell parameters are: $a = 4.152$ Å, $b = 6.496$ Å, $c = 10.186$ Å, $\alpha = 107.38°$, $\beta = \gamma = 90°$, cell volume = 280.22 Å^3, $Z = 4$. Cell occupancy is shown in Table 16.11.

Ca_3Zn was found to crystallize with the Re_3B type of structure (space group, $Cmcm$ and $Z = 4$). The structure was refined with anisotropic temperature factors using single-crystal diffractometer data to an R value of 0.022. Single-crystal examination showed that CaZn crystallizes with the CrB type of structure (space group, $Cmcm$ and $Z = 4$).

TABLE 16.9

The $Ca_{21}Ni_2Zn_{36}$ structure type

(a) This view highlights the linkages between the nickel-centered icosahedra and additional zinc sites; calcium atoms are shown as non-bonded spheres

(b) This view highlights the clathrate II framework produced by connecting three of the calcium sites

(c) This view highlights the pentagonal dodecahedron of calcium sites, encapsulating the Ni at Zn12 icosahedron

(d) This view highlights the hexakaidecahedron of calcium sites, encapsulating the triangles of Zn3 atoms and the Ca4 site in comparison to the contents of the Mg26 hexakaidecahedron of $Mg_{35}Cu_{24}Ga_{53}$

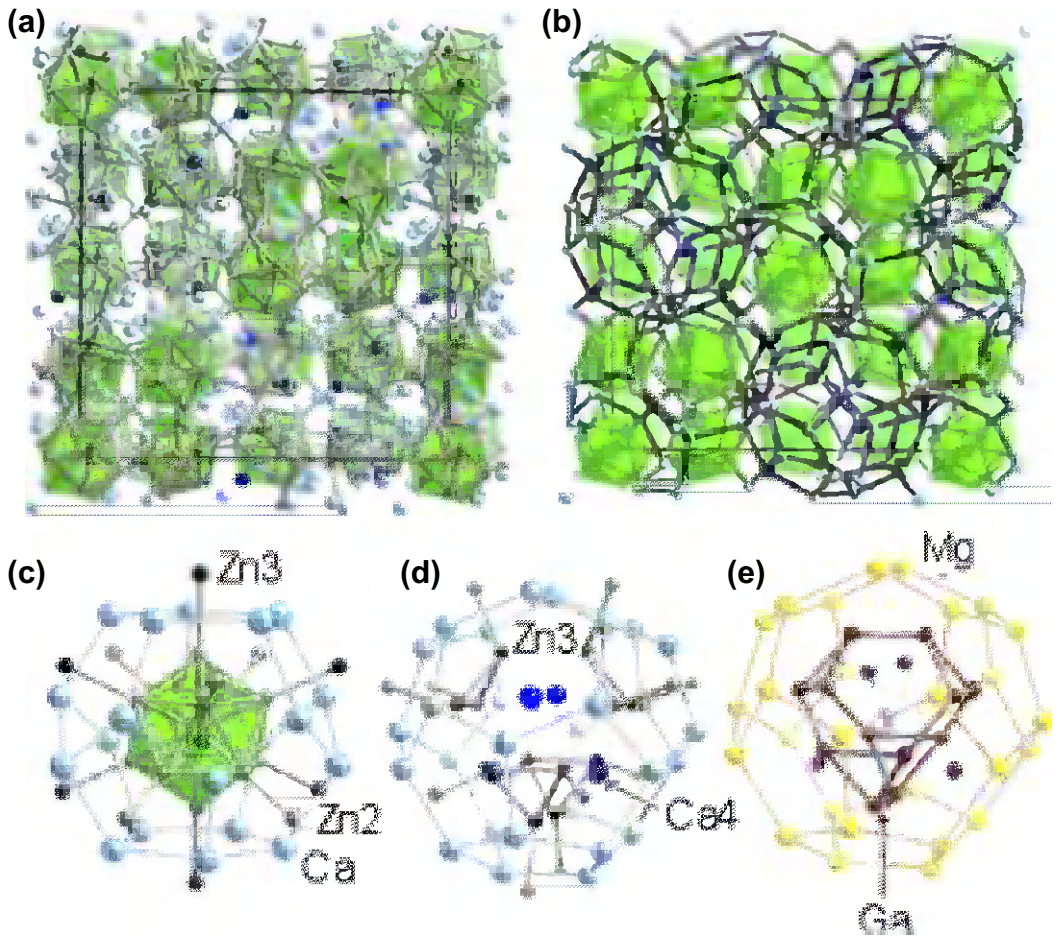

FIGURE 16.13

The compound, Ca_5Zn_3, has the structural form shown in Fig. 16.16.

Cell parameters are: $a = b = 7.962$ Å, $c = 9.539$ Å, $\alpha = \beta = 114.67°$, $\gamma = 90°$, cell volume = 488.12 Å^3, $Z = 4$. Cell occupancy is shown in Table 16.12.

Ca_5Zn_3 has been synthesized from stoichiometric amounts of the pure elements. It crystallizes with the Cr_5B_3 type of structure: space group $I4/mcm$, $a = 7.963$ Å, $c = 15.407$ Å, $c/a = 1.93$, $Z = 4$, $R = 4.05\%$ (all F_o), 3.93%. Around one central calcium atom, distorted rhombic dodecahedra occur that contain all the remaining calcium atoms and all zinc atoms. They build up a 3D infinite network. In the tetragonal *ab*-plane, the rhombic dodecahedra are interconnected as well via common faces as via Zn–Zn dumbbells (Zn–Zn 263 pm), along [001] they share common zinc atoms. This compound is supplied commercially with the CAS number of 67907-40-8.

Density functional calculations were carried out to probe the oxidation states of the transition metal and alkaline earth elements in the Cr_5B_3-type compounds. AE_5T_3 consisting of T_2 dimers and isolated T atoms (i.e. Ca_5Au_3, Ca_5Ag_3, Ca_5Hg_3, Sr_5Cd_3, and Ca_5Zn_3) were studied. The electronic structures of all these AE_5T_3 compounds are best described as $[(AE^{2+})_5(T–T)^{4-}(T^{2-})] + 4e^-$. In the covalent bonding of the AE^{2+} ions with the transition metal anions T^{2-}, the (n–1)

TABLE 16.10

No.	Site notation	Atom	Multiplicity	Wyckoff	Site symmetry	*x*	*y*	*z*	Occupancy
1	Zn1	Zn	32	i	1	0.205	0.127	0.067	1.0
2	Zn2	Zn	8	c	.2/m.	0	0	0	1.0
3	Ca1	Ca	4	b	-4m2	0	1/4	3/8	1.0
4	Zn3	Zn	4	a	-4m2	0	3/4	1/8	1.

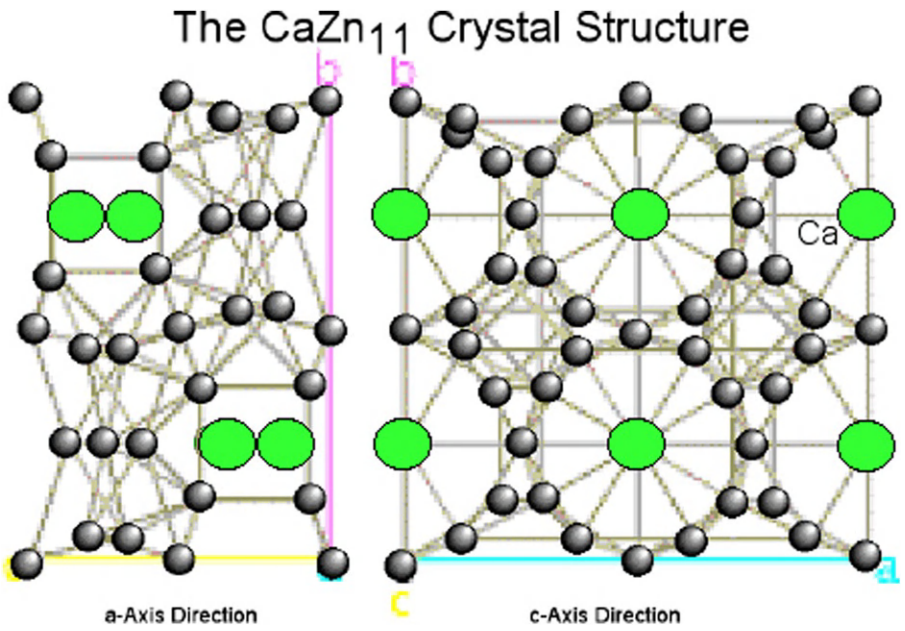

FIGURE 16.14

d orbitals of AE^{2+} contribute more than the ns and np orbitals of AE^{2+}.

The compound, $Ca_{3.33}Zn_{10.11} = Ca_{10}Zn_{30.33}$, has the structural characteristics shown in Fig. 16.17.

Cell parameters are: $a = 7.327$ Å, $b = c = 9.168$ Å, $\alpha = 120°$, $\beta = \gamma = 90°$, cell volume $= 533.34$ Å^3, $Z = 2$. Cell occupancy is shown in Table 16.13.

No data are available for this compound other than the structural data shown above. It has not merited further study of its physical or electronic properties.

CaZn has the structure shown in Fig. 16.18.

Cell parameters are: $a = 4.202$ Å, $b = 4.442$ Å, $c = 6.174$ Å, $\alpha = 90°$, $\beta = 109.90°$. $\gamma = 90°$, cell volume $= 108.34$ Å^3, $Z = 4$. Cell occupancy is shown in Table 16.14.

Single-crystal examination showed that CaZn crystallizes with the CrB type of structure (space group, *Cmcm*, and $Z = 4$).

Nine diffusion couples and 32 key samples were prepared to map the phase diagram of the Ca–Mg–Zn system. Phase relations and solubility limits were determined for binary and ternary compounds using scanning electron microscopy, electron probe microanalysis and XRD. The crystal structure of the ternary

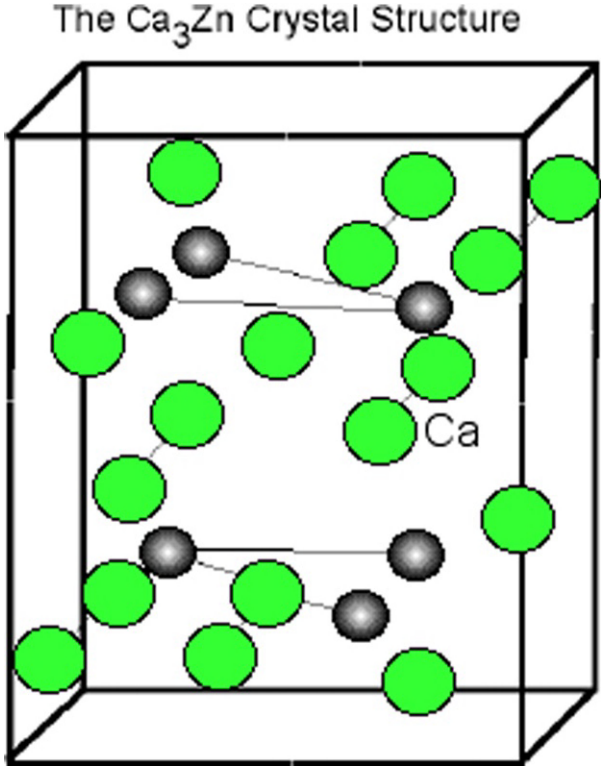

FIGURE 16.15

TABLE 16.11

No.	Site notation	Atom	Multiplicity	Wyckoff	Site symmetry	*x*	*y*	*z*	Occupancy
1	Ca(2)	Ca	8	f	m..	0	0.1414	0.0605	1.0
2	Ca(1)	Ca	4	c	m2m	0	0.4323	1/4	1.0
3	Zn	Zn	4	c	m2m	0	0.7524	1/4	1.0

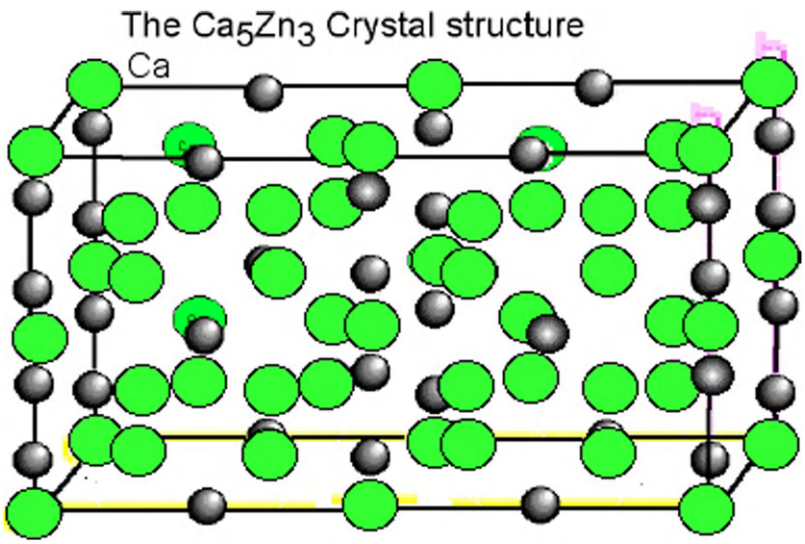

FIGURE 16.16

compounds was studied by XRD and electron backscatter diffraction. Four ternary IM compounds were identified in this system: $Ca_3Mg_xZn_{15-x}$ ($4.6 \leq x \leq 12$ at 335 °C, IM1), $Ca_{14.5}Mg_{15.8}Zn_{69.7}$ (IM2), $Ca_2Mg_5Zn_{13}$ (IM3) and $Ca1_{.5}Mg_{55.3}Zn_{43.2}$ (IM4). Three binary compounds were found to have extended solid solubility into ternary systems: $CaZn_{11}$, $CaZn_{13}$ and Mg_2Ca form substitutional solid solutions where Mg substitutes for Zn atoms in the first two compounds, and Zn substitutes for both Ca and Mg atoms in Mg_2Ca. The isothermal section of the Ca–Mg–Zn phase diagram at 335 °C was constructed based on the obtained experimental results. The morphologies of the diffusion couples in the Ca–Mg–Zn phase diagram at 335 °C were studied.

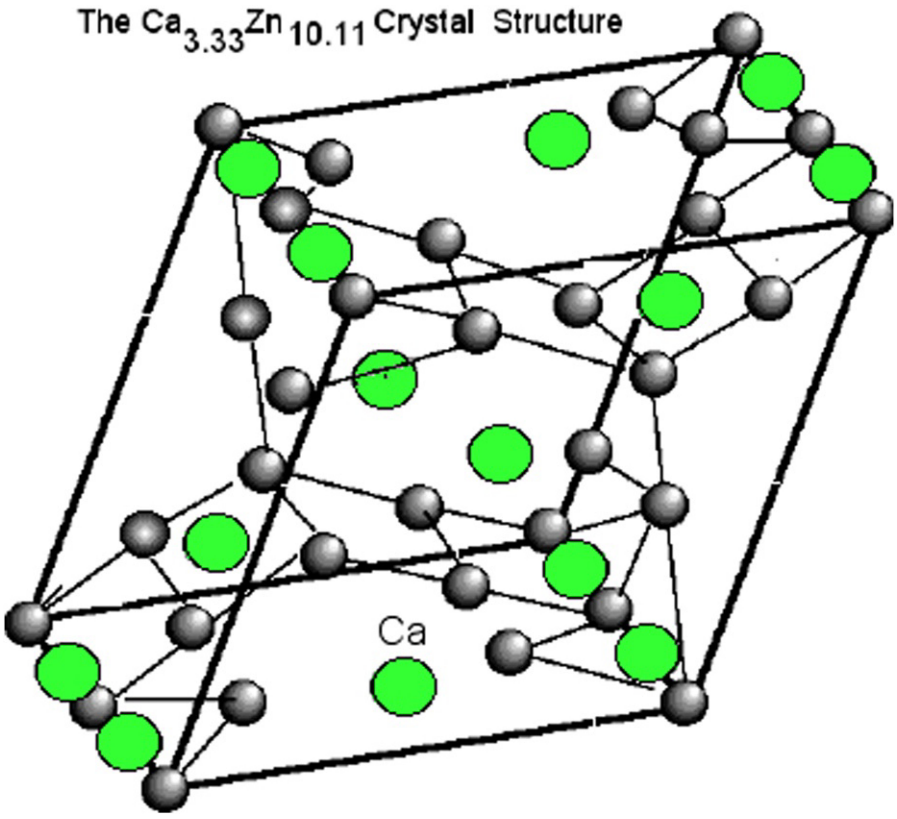

FIGURE 16.17

TABLE 16.12

No.	Site notation	Atom	Multiplicity	Wyckoff	Site symmetry	x	y	z	Occupancy
1	Ca(2)	Ca	16	l	..m	0.1704	0.6704	0.1471	1.0
2	Zn(2)	Zn	8	h	m.2m	0.6169	0.1169	0	1.0
3	Ca(1)	Ca	4	c	4/m..	0	0	0	1.0
4	Zn(1)	Zn	4	a	422	0	0	1/4	1.0

Depending on the terminal compositions of the diffusion couples, the two-phase regions in the diffusion zone have either a tooth-like morphology or contain a matrix phase with isolated and/or dendritic precipitates. The ternary diagram has the form shown in Fig. 16.19.

In the Ca–Zn–O system, few "zincate" compounds are known. One compound, calcium hexahydroxodizincate dihydrate, $CaZn_2(OH)_6 \cdot 2H_2O$ (CZO), is well known in the literature as an active material for secondary Zn electrodes employed in batteries. In principle, this material is able to promote a better charge/discharge reversibility as well as solve the problems of shape change and dendrite formation in the Zn electrodes. It has the structure shown in Fig. 16.20.

The crystalline CZO structure is characterized by the presence of Ca atoms bonded to six oxygen atoms, resulting in $[CaO_6]$ clusters with octahedral coordination. On the other hand, the Zn atoms are coordinated to four oxygens in a tetrahedral configuration, i.e. forming $[ZrO_4]$ clusters. The H_2O molecules are bonded by hydrogen bridges to the hydroxyl groups [OH] for the charge balance of the lattice. Lozenge-like CZO microparticles were obtained by MH processing at 130 °C for 1 and 2 h, respectively. XRD patterns and Rietveld refinement confirmed that the pure CZO phase with monoclinic structure was obtained when the MH conditions were performed at 130 °C for 2 h. UV-Vis absorption spectra showed an increase in the E_{gap} values with the processing time. This phenomenon was mainly attributed to a reduction of intermediary energy levels associated to the ZnO (secondary phase) within the band gap. The origin of the orange PL emission of this material was attributed to the existence of singly ionized oxygen vacancies and/or distortions on the $[ZnO_4]$ clusters into the lattice. FEG-SEM micrographs indicated that the processing time is a key factor in the formation and growth processes of CZO microparticles.

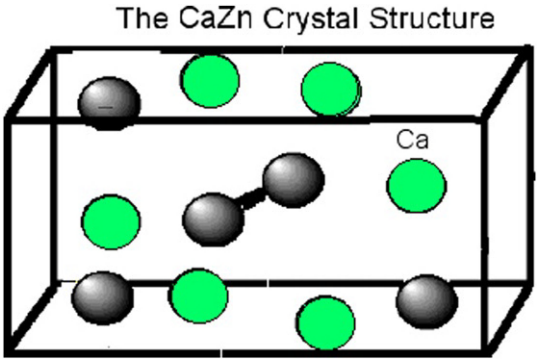

FIGURE 16.18

TABLE 16.13

No.	Site notation	Atom	Multiplicity	Wyckoff	Site symmetry	x	y	z	Occupancy
1	Zn1	Zn	12	k	.m.	0.1692	0.3384	0.0556	1.0
2	Ca1	Ca	6	h	mm2	0.5260	0.0520	1/4	1.0
3	Zn2	Zn	6	h	mm2	0.9022	0.8044	1/4	0.66
4	Zn3	Zn	4	f	3m.	1/3	2/3	0.0715	1.0
5	Ca2	Ca	2	b	-6m2	0	0	1/4	0.33
6	Zn4	Zn	2	a	-3m.	0	0	0	0.13

TABLE 16.14

No.	Site notation	Atom	Multiplicity	Wyckoff	Site symmetry	x	y	z	Occupancy
1	Zn	Zn	4	c	m2m	0	0.065	1/4	1.0
2	Ca	Ca	4	c	m2m	0	0.355	1/4	1.0

Synthesis of $CaZn_2O_2$ was accomplished via a method involving a solution combustion method. The procured calcium nitrate, zinc nitrate, and acetamide (fuel) were used for the synthesis of nanoparticles (1:1 nitrates). They were dissolved in a small quantity of distilled water in a silica crucible, introduced into the muffle furnace, which was preheated to 500 °C. The solution undergoes dehydration and catches fire by spreading throughout the mass, finally yielding calcium zincate. Calcium zincate nanoparticle is formed by the complete combustion of the calcium nitrate and zinc nitrate with acetamide as fuel.

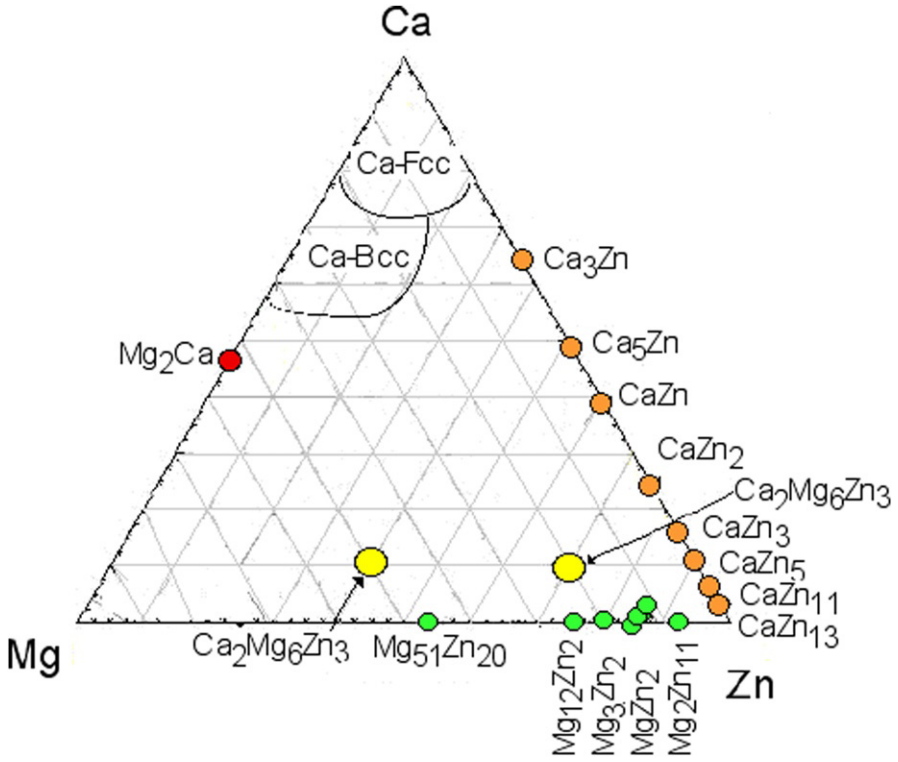

FIGURE 16.19

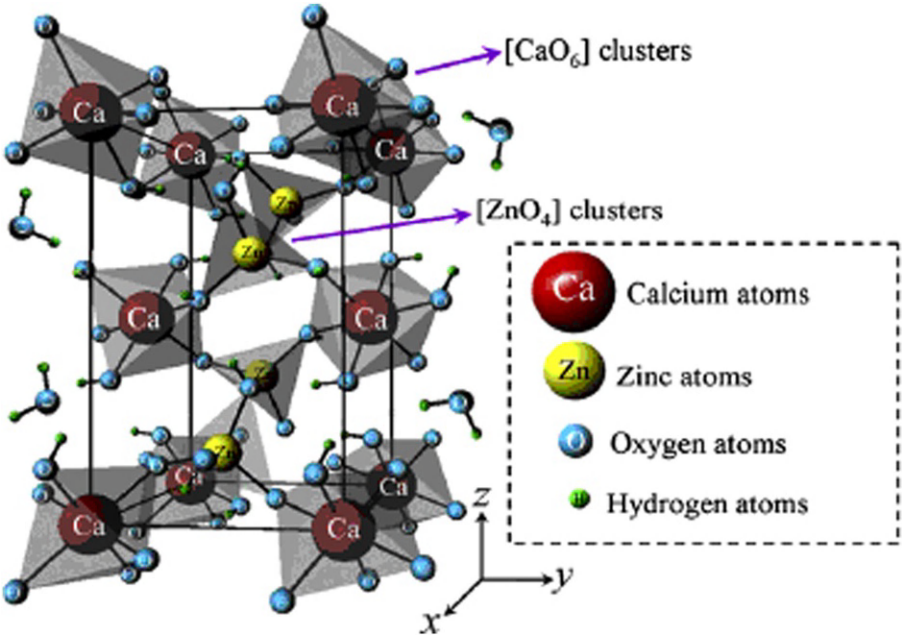

FIGURE 16.20

$$11Ca(NO_3)_2 + 11Zn(NO_3)_2 + 20CH_3CONH_2 \Rightarrow 11CaZnO_2 + 40\,CO_2 + 50H_2O + 32N_2$$

Calcium zincate nanoparticles ($CaZnO_2$) of average crystallite size 43.59 nm were used as a photocatalyst in presence of sunlight against Coralline Dark Red 2B ago dye (30 mg/l). Adsorption studies were carried out at different pH, and photocatalyst dosages. The calcium zincate nanoparticle was found to be an efficient low-cost photocatalyst which degraded Coralline Dark Red 2B dye in presence of sunlight in a relatively short period of time. Best results were obtained when the solution pH was >9.0.

Ca zincate ($CaZn_2(OH)_6 \cdot 2H_2O$) was found to play an important role in the geochemical behavior of Zn in cementation systems. One paper described the determination of a solubility product for Ca zincate and its range of application. Calcium zincate was synthesized and characterized by XRD. Samples were then equilibrated at 25 °C and an ionic strength of 0.1 M in a pH range between 11.4 and 12.7. A solubility product, $\log K_{s0} = 43.9$, was determined for infinite dilution using the Davies equation for the following reaction. The solubility product can be used to successfully interpret the results of experiments in which Zn is equilibrated with C-S-H(I) at pH values between 11.7 and 12.78 at 25 °C and an ionic strength of 0.1 M. However, the solubility product is not able to model both the Zn and Ca concentration at a given pH value because dissolution is incongruent.

Pure, crystalline, fine particulate calcium zincate was prepared. Its chemical composition, $Ca(OH)_2 \cdot 2Zn(OH)_2 \cdot 2H_2O$ was established by chemical analysis, weight loss in thermo gravimetric analysis, and by X-ray powder diffraction pattern. Its solubility in different KOH solutions at 298 K was determined. The solubility data were used to determine the activities of ZnO and H_2O with respect to pure solid ZnO and liquid water, respectively, in calcium zincate. They were also used to determine the vapor pressure of water over calcium zincate and other thermodynamics properties of this system. The equilibrium constant of the reaction $Ca(OH)_2 \cdot 2Zn(OH)_2 \cdot 2H_2O(S) = Ca(OH)_2(s) + 2ZnO(s) + 4H_2O(l)$ was found to be 0.049 ± 0.015. The standard free energy of formation of calcium zincate was found to be -1785 ± 150 cal/mol at 298 K. The standard heat of formation was found to be −665 cal/mol, and the standard entropy of formation was found to be 3.35 cal/°mol.

No other calcium zincate compounds are known.

16.1.4. Strontium Zinc Compounds

Sr metal forms four compounds with Zn metal as shown in Fig. 16.21.

The Sr–Zn system displays the four stoichiometric compounds SrZn, $SrZn_2$, $SrZn_5$, and $SrZn_{13}$. The accepted phase diagram is due mainly to Bruzzone and Merlo who used DTA, metallographic and X-ray methods to determine the phase boundaries. Additional

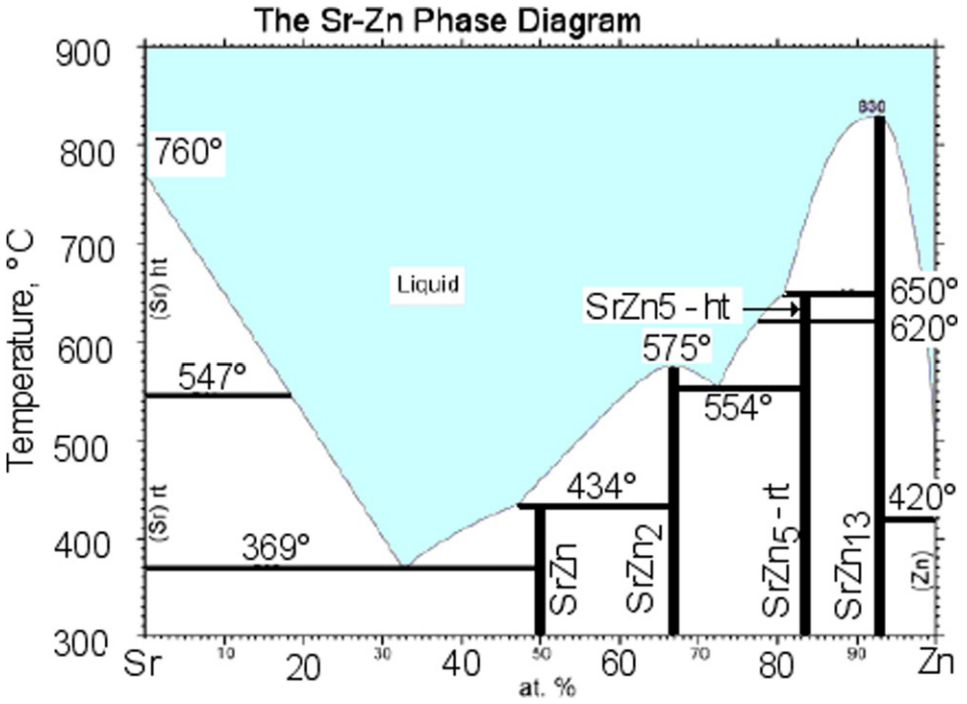

FIGURE 16.21

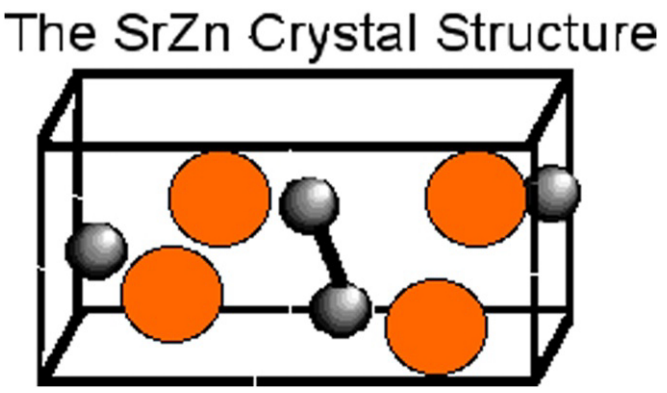

FIGURE 16.22

measurements of the solubility of Sr in liquid Zn have been made by Shunk, using a metallographic method, and by Volkovich et al. using an e.m.f. technique in the range from 0.1 to 4 atom% Sr. Thermodynamic data are shown in Table 16.15.

The compound, SrZn, has the structure shown in Fig. 16.22.

Cell parameters are: $a = 4.607$ Å, $b = 6.417$ Å, $c = 8.714$ Å, $\alpha = \beta = \gamma = 90°$, cell volume $= 257.91$ Å^3, $Z = 4$. Cell occupancy is shown in Table 16.16.

SrZn has the space group, *Pnma*, and crystallizes with the FeB-type structure. The atomic parameters of SrZn were refined using single-crystal diffractometer data. Equi-atomic compounds of calcium, strontium, barium, europium and ytterbium, which crystallize with structures based on the trigonal prismatic coordination of the partner atom, were examined in terms of the shape of the trigonal prism.

The compound, $SrZn_2$ has the structural conformation shown in Fig. 16.23.

Cell parameters are: $a = 4.777$ Å, $b = c = 6.0283$ Å, $\alpha = 80.449°$, $\beta = \gamma = 66.658°$, cell volume $= 146.34$ Å^3, $Z = 4$. Cell occupancy is shown in Table 16.17.

High-pressure forms of IM compounds with the composition $CaZn_2$, $SrZn_2$, $SrAl_2$, and $BaAl_2$ were synthesized from $CeCu_2$-type precursors by multi-anvil techniques and investigated by X-ray powder diffraction ($SrAl_2$ and $BaAl_2$), X-ray single-crystal diffraction ($CaZn_2$), and electron microscopy ($SrZn_2$). Their structures correspond to that of Laves phases. Whereas the dialuminides crystallize in the cubic

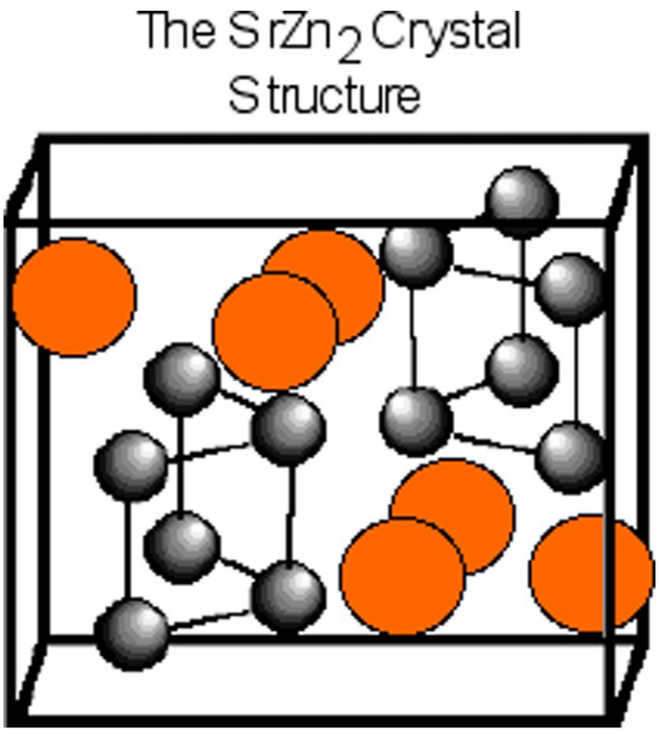

FIGURE 16.23

TABLE 16.15

Cpd	ΔH_f^0 (J/mol)	S^0 (J/mol)	Cp(J/mol/K)
SrZn	−36700	87.30	$Cp = Cp$ (Sr,FCC-A1) + Cp (Zn,HCP-Zn)
SrZn2	−69700	120.46	$Cp = Cp$ (Sr,FCC-A1) + 2°—Cp (Zn,HCP-Zn)
SrZn5	−146500	206.70	$Cp = Cp$ (Sr,FCC-A1) + 5°—Cp (Zn,HCP-Zn)
SrZn13	−250074	514.00	$Cp = Cp$ (Sr,FCC-A1) + 13°—Cp (Zn,HCP-Zn)

TABLE 16.16

No.	Site notation	Atom	Multiplicity	Wyckoff	Site symmetry	x	y	z	Occupancy
1	Zn1	Zn	4	c	.m.	0.036	1/4	0.11	1.0
2	Sr1	Sr	4	c	.m.	0.18	1/4	0.625	1.0

TABLE 16.17

No.	Site notation	Atom	Multiplicity	Wyckoff	Site symmetry	x	y	z	Occupancy
1	Zn1	Zn	8	h	m..	0	0.06	0.163	1.0
2	Sr1	Sr	4	e	mm2	0	1/4	0.547	1.0

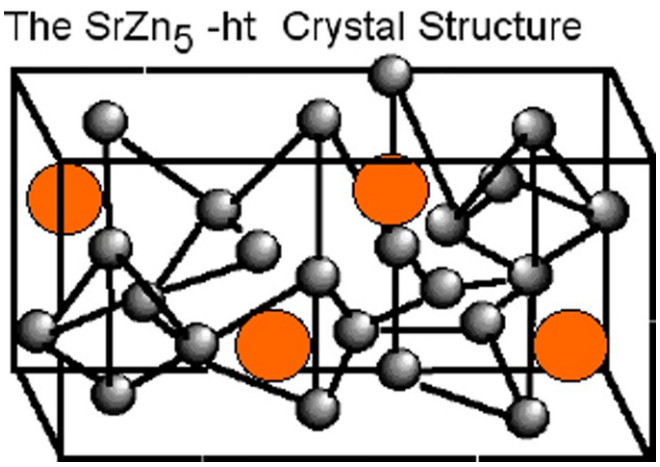

FIGURE 16.24

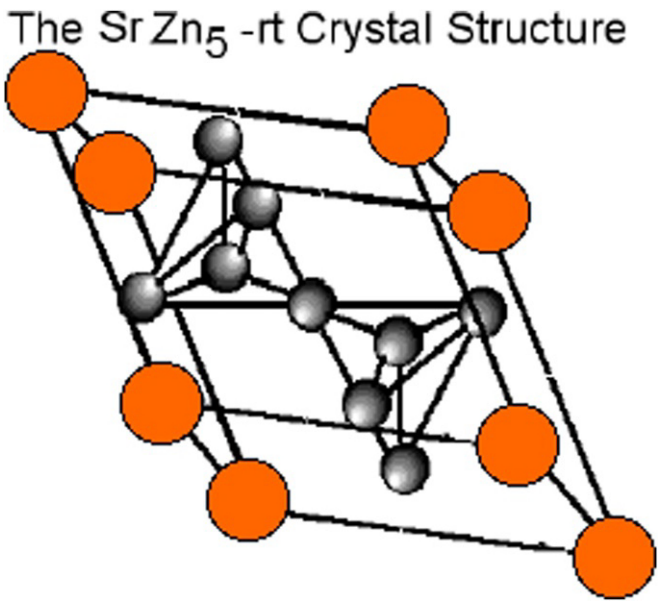

FIGURE 16.25

$MgCu_2$ (C15) structure, the dizincides adopt the hexagonal $MgZn_2$ (C14) structure. This trend is in agreement with the structural relationship displayed by sp bonded Laves phase systems at ambient conditions. $CeCu_2$-type polar IMs can be transformed to Laves phases upon simultaneous application of pressure and temperature. The observed structures are controlled by the valence electron concentration.

If $SrZn_2$ is heated in air, it decomposes. Oxidative decomposition of $SrZn_2$ ($CeCu_2$ type) into SrH_2 and $SrZn_{13}$ ($NaZn_{13}$ type) upon hydrogenation was demonstrated. X-ray powder patterns (Cu-Kα) of the product mixture were shown for synthesis temperatures of 100, 150, and 300 °C (reaction time 24 h, pressure 50 bar).

The compound, $SrZn_5$ has the structure shown in Fig. 16.24.

Cell parameters are: $a = 5.312$ Å, $b = 6.707$, $c = 13.147$ Å, $\alpha = \beta = \gamma = 90°$, cell volume $= 468.44$ Å^3, $Z = 4$. Cell occupancy is shown in Table 16.18(A).

The $SrZn_5$ compound stable at room temperature, has the structure shown in Fig. 16.25.

Cell parameters are: $a = 4.283$ Å, $b = c = 5.549$ Å, $\alpha = 120°$, $\beta = \gamma = 90°$, cell volume $= 114.21$ Å^3, $Z = 1$. Cell occupancy is shown in Table 16.18(B).

The $SrZn_5$ phase undergoes a structural transformation at 620 °C. The high-temperature form of $SrZn_5$, which was prepared by quenching of melted samples, adopts the ideal $CaCu_5$ structure type ($a = 5.541$ Å,

TABLE 16.18A

No.	Site notation	Atom	Multiplicity	Wyckoff	Site symmetry	*x*	*y*	*z*	Occupancy
1	Zn1	Zn	8	d	1	0.144	0.000	0.350	1.0
2	Zn2	Zn	4	c	.m.	0.021	1/4	0.601	1.0
3	Zn3	Zn	4	c	.m.	0.202	1/4	0.045	1.0
4	Zn4	Zn	4	c	.m.	0.215	1/4	0.660	1.0
5	Sr1	Sr	4	c	.m.	0.412	1/4	0.356	1.0

TABLE 16.18B

No.	Site notation	Atom	Multiplicity	Wyckoff	Site symmetry	*x*	*y*	*z*	Occupancy
1	Zn2	Zn	3	g	mmm	1/2	0	1/2	1.0
2	Zn1	Zn	2	c	-6m2	1/3	2/3	0	1.0
3	Sr	Sr	1	a	6/mmm	0	0	0	1.

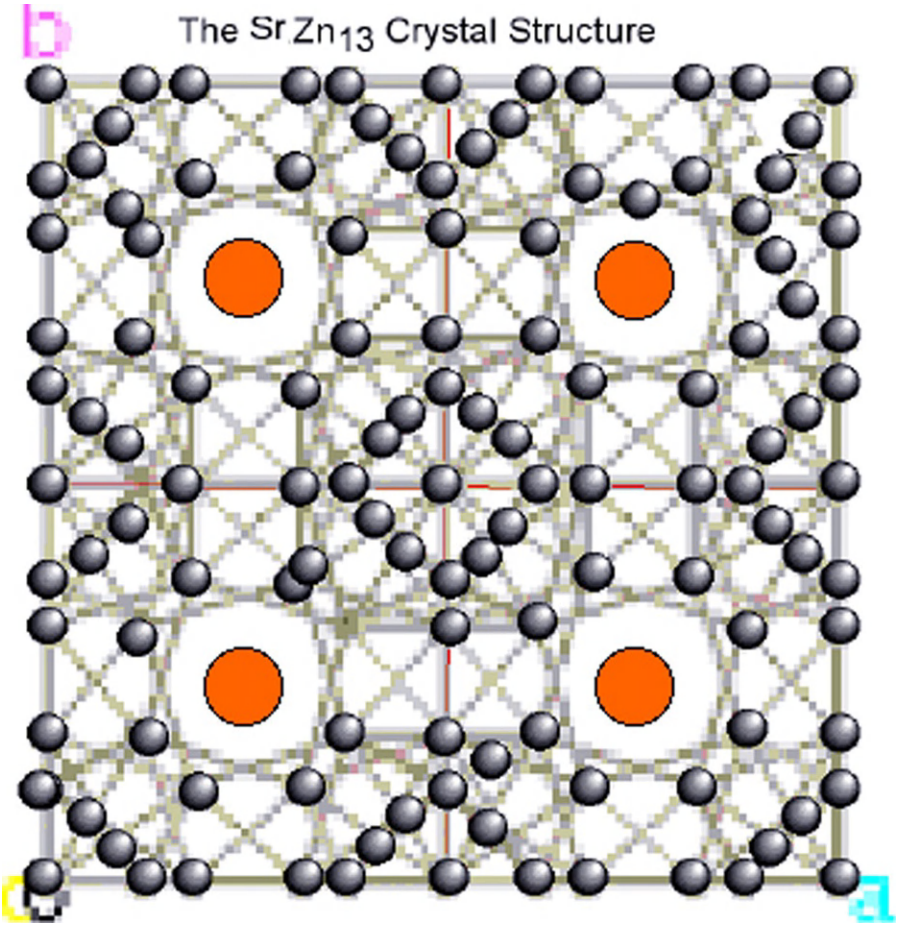

FIGURE 16.26

$c = 4.282$ Å, $R1 = 0.0314$). The room temperature modification of $SrZn_5$ (orthorhombic, space group *Pnma*, $a = 13.133$ Å, $b = 5.2991$ Å, $c = 6.6972$ Å, $Z = 4$, $R1 = 0.0349$) forms a singular structure, whereas the Ba compound of corresponding composition (orthorhombic, space group *Cmcm*, $a = 10.783$, $b = 8.398$, $c = 5.320$ Å, $Z = 4$, $R1 = 0.0281$) crystallizes with a third, also rather uncommon structure.

The compound, $SrZn_{13}$ has the structure shown in Fig. 16.26.

The Sr atoms lie within channels in the structure, one Sr atom per unit cell. A total of four units are shown here in this *ac*-plane. In the *b*-direction, there are layers of Zn atoms between the channels so that this diagram represents eight-unit cell in a 3D structure.

Cell parameters are: $a = b = c = 8.65641$ Å, $\alpha = \beta = \gamma = 60°$, cell volume $= 458.67$ Å^3, $Z = 8$. Cell occupancy is shown in Table 16.19.

Single crystals of strontium undecazinc, $SrZn_{11}$, were obtained when decomposing $SrZn_2$ under conditions of high pressure and high temperature. This novel binary Sr–Zn compound crystallizes in the space group *I*4/*amd* ($BaCd_{11}$ structure type) with one Sr position ($\bar{4}$m2) and three Zn sites ($\bar{4}$m2,·2/m·1). The structure is described in terms of all-face-capped Zn(8) tetrahedra as the central building unit, defined by the Zn atoms on .2/m. and 1. These building units are condensed into chains by the central tetrahedra-sharing edges, and the chains are interconnected by shared capping atoms. The resulting 3D framework of Zn atoms yields channels that are occupied

TABLE 16.19

No.	Site notation	Atom	Multiplicity	Wyckoff	Site symmetry	*x*	*y*	*z*	Occupancy
1	Zn1	Zn	96	i	m..	0	0.1192	0.1806	1.0
2	Zn2	Zn	8	b	m-3.	0	0	0	1.0
3	Sr1	Sr	8	a	432	1/4	1/4	1/4	1.0

by Sr and Zn atoms on the high-symmetry $\bar{4}$m2 positions. For the compound, $CaZn_{11}$, crystal parameters were: (tetragonal, space group $I41/amd$, $a = 10.6811$, $c = 6.8281$ Å, $Z = 4$, $R1 = 0.0299$). The originally proposed structure type was confirmed and also refined by using single-crystal data.

The ternary system, Sr–Mg–Zn, has also been studied and has the form shown in Fig. 16.27.

No other Sr–Zn IM compounds are known.

In the Sr–Zn–O system, few "zincate" compounds are known. In the system, SrO–Zn_2O, no compounds have been reported. In the SrO–ZnO system, two novel blue-emitting phosphors have been synthesized. Two new blue-emitting phosphors, $SrZnO_2$:Pb^{2+} and Ce^{3+} were synthesized using an adipic acid or sucrose-template sol–gel route, respectively. The resulting phosphor particles were fine, nanocrystalline and pure. The optimum activator concentrations were found to be 1 mol% Pb^{2+} and 12 mol% Ce^{3+}. Two excitation bands centered at 283 and 317 nm, plus a weak shoulder at 275 nm, were observed for Pb^{2+}-doped samples. However, only one broad excitation band with a maximum at 294 nm was observed for Ce^{3+}-doped samples fired at 1000 °C for 2 h. The emission spectra of $SrZnO_2$:Pb^{2+} showed a very broad band extending from 374 to 615 nm with a maximum at ~455 nm which was ascribed to the $^3P_1 \Rightarrow {}^1S_0$ transition on the Pb^{2+} ions allowed by the strong spin-orbit coupling. Similarly, $SrZnO_2$:Ce^{3+} showed a broad emission band extending from 374 to 609 nm and centered at 467 nm. This broad emission was attributed to the $5d^1 \Rightarrow 4f^1$ transition of Ce^{3+} ions. The lower level $^2F_{5/2}$ of the $4f^1$ is populated but the level $^2F_{7/2}$ is almost empty at room temperature where all measurements were taken.

In another paper, the $SrZnO_2$:Sm^{3+} phosphor has been synthesized by a gel-combusting method and characterized using X-ray powder diffraction, TEM, TG as well as excitation, and emission spectroscopy. The luminescence properties of this phosphor have been studied. It crystallizes in an orthorhombic structure with *Pnma* space group and unit cell with the lattice parameters: $a = 5.830$ Å, $b = 3.340$ Å and $c = 11.348$ Å. These materials can be efficiently excited in the UV to visible region (350–420 nm, main peaks 413 and 380 nm), making them attractive as conversion phosphors for LED applications. A red emission at 600–730 nm (main peaks 607 and 655 nm) is observed for

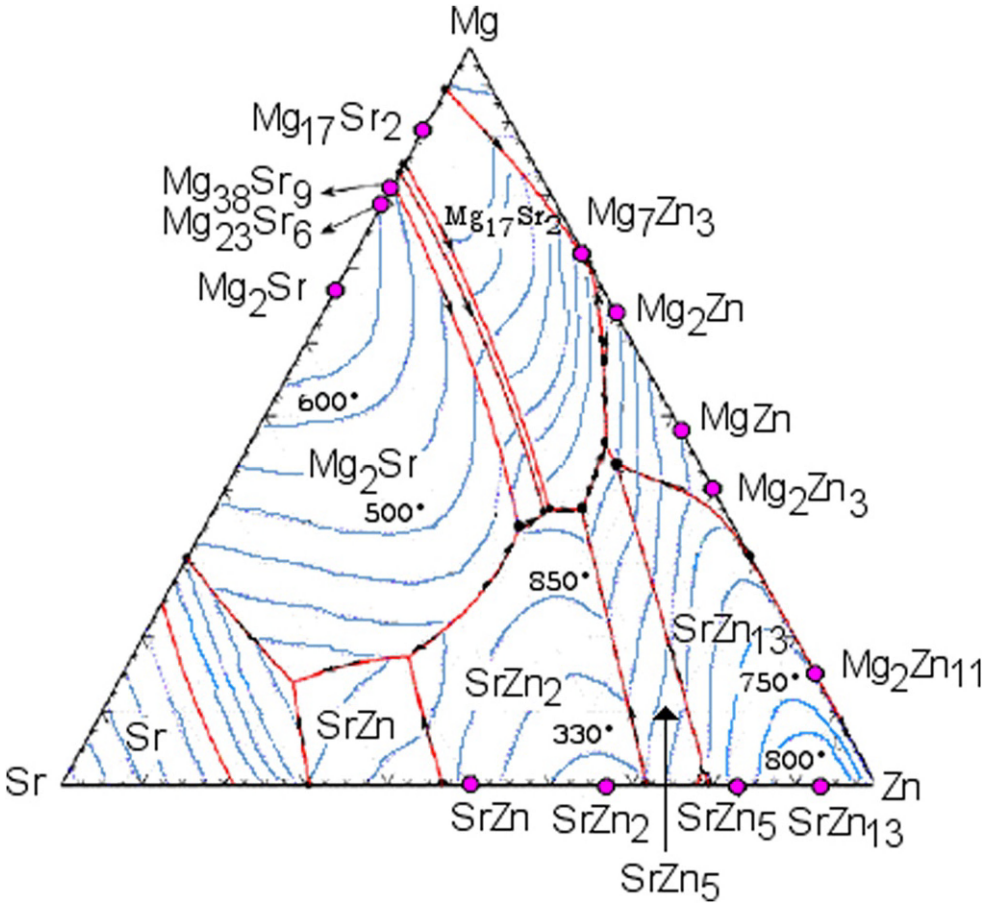

FIGURE 16.27

$SrZnO_2:Sm^{3+}$ which is a promising conversion phosphor for white-light LEDs.

The crystal structure of $SrZnO_2$ has been determined by 3D Patterson- and Fourier syntheses. The space group is $D^{16}{}_{2h}$-*Pmnb*. The orthorhombic unit cell ($a = 3.35$, $b = 5.84$, $c = 11.37$ Å) contains four formula units; $d_x = 5.52$, $d_{pyc} = 5.49$ g/cm^3. With the last refinement, R and R_1 fall to 0.064 and 0.069, respectively (CuKα). The [ZnO_2]-arrangement is a previously unknown two-dimensional (2D) one. It can be derived from the cristobalite arrangement. Sr is situated between the waved layers. In $SrZnO_2$, the ZnO_4 tetrahedra share edges with each other and form waved layers. The Sr atoms are located at the cavity between the layers.

Colorless crystals of $SrZn(OH)_4 \cdot H_2O$ have been obtained by electrochemical oxidation of Zn in a zinc/iron pair in an aqueous ammonia solution saturated with strontium hydroxide. The X-ray crystal structure determination was successful including all hydrogen positions: P1, $Z = 2$, $a = 6.244(1)$ Å, $b = 6.3000$ Å, $c = 7.701$ Å, $\alpha = 90.59(1)°$, $\beta = 112.56(2)°$, $\gamma = 108.66(2)°$, $N(F \geq 3\sigma F) = 1967$, $N(\text{Var.}) = 84$, $R/R_w = 0.020/0.024$. In $SrZn(OH)_4 \cdot H_2O$, Zn^{2+} is tetrahedrally coordinated by four OH^- ions while Sr^{2+} has $6OH^-$ and one H_2O as neighbors. The polyhedra around Sr^{2+} are connected to chains which are linked three dimensionally by isolated tetrahedra [$Zn(OH)_4$]. Hydrogen bonds between H_2O as donor and OH^- were characterized by Raman spectroscopy.

No other SrO–ZnO compounds have been documented to date. Strontium zincate compounds are not offered for sale commercially and no CAS numbers have been issued.

16.1.5. Barium Zinc Compounds

Only a few IM compounds are known in the Ba^0–Zn^0 system as shown in Fig. 16.28.

The Ba–Zn system was investigated by differential thermal, metallographic and X-ray analysis. Among the five intermediate phases identified, the Ba_2Zn, BaZn and $BaZn_{13}$ compounds melt congruently at 360, 340 and 885 °C, respectively. $BaZn_2$ and $BaZn_5$ form peritectics at 380 and 635 °C, respectively. Three eutectics are formed: between Ba and Ba_2Zn at 345 °C (25.0 atom% Zn); between Ba_2Zn and BaZn at 330 °C (46.0 atom% Zn); between BaZn and $BaZn_2$ at 325 °C (53.5 atom% Zn). The crystal structures of BaZn (CsCl type), $BaZn_5$ ($BaZn_5$ type) and $BaZn_{13}$ ($NaZn_{13}$ type) were confirmed. Ba_2Zn, isotypic with Ba_2Cd and Ba_2Hg, belongs to the $MoSi_2$ type. The atomic parameters of $BaZn_2$, which crystallizes in the $CeCu_2$-type structure, have been refined using single-crystal diffractometer data.

The compound, BaZn, has the structural form shown in Fig. 16.29.

Cell parameters are: $a = b = c = 4.093$ Å, $\alpha = \beta = \gamma = 90°$, cell volume = 68.57 Å^3, $Z = 1$. Cell occupancy is shown in Table 16.20.

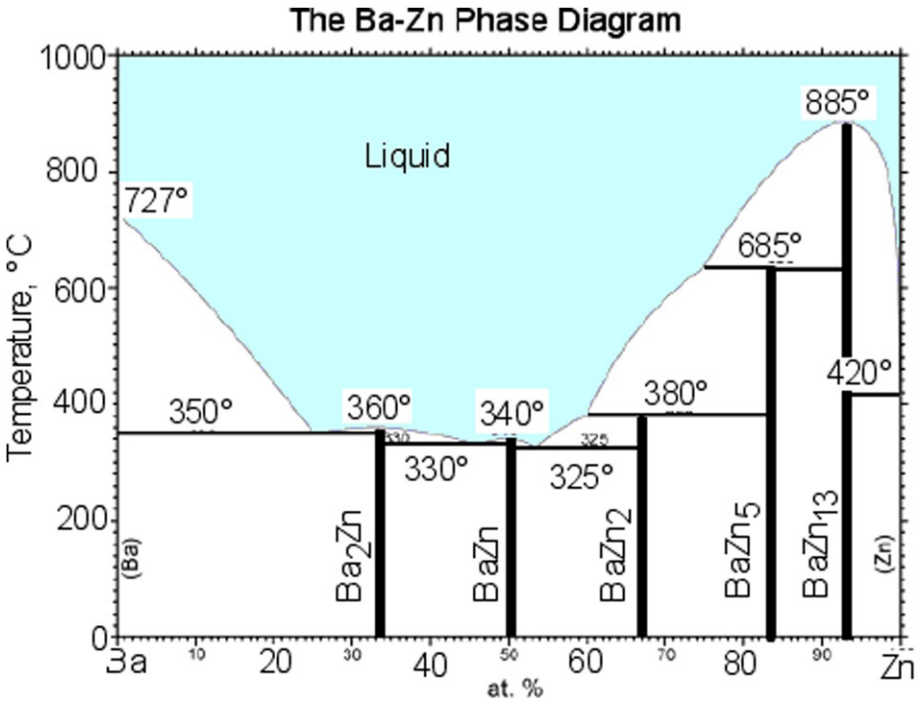

FIGURE 16.28

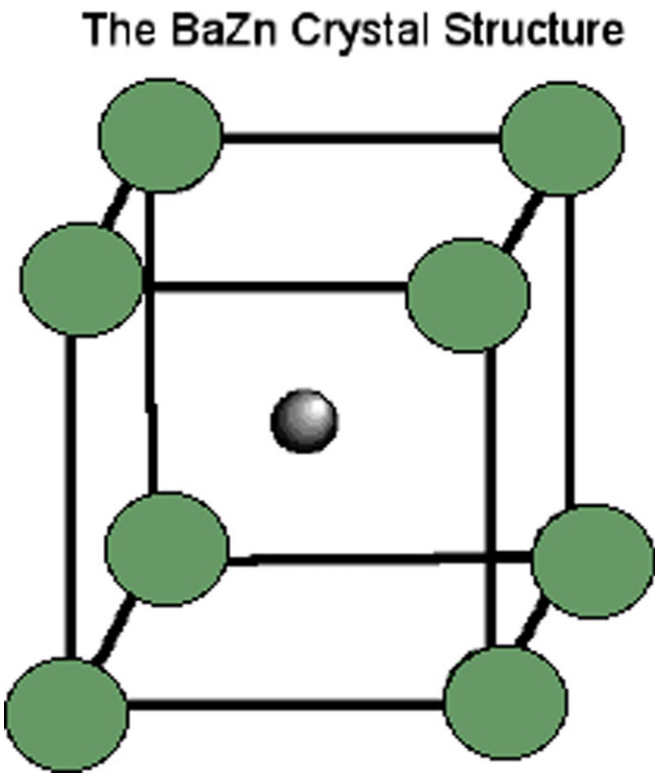

FIGURE 16.29

Very little data concerning this compound are available except for those involving structure.

The compound, Ba_2Zn has the structural form shown in Fig. 16.30.

Cell parameters are: $a = b = 4.175$ Å, $c = 8.0415$ Å, $\alpha = \beta = 105.05°$. $\gamma = 90°$, cell volume $= 130.38$ Å^3, $Z = 1$. Cell occupancy is shown in Table 16.21.

There is no mention of this compound in the technical literature. Structural data are the only references to be found.

The compound, $BaZn_2$, has the structure shown in Fig. 16.31.

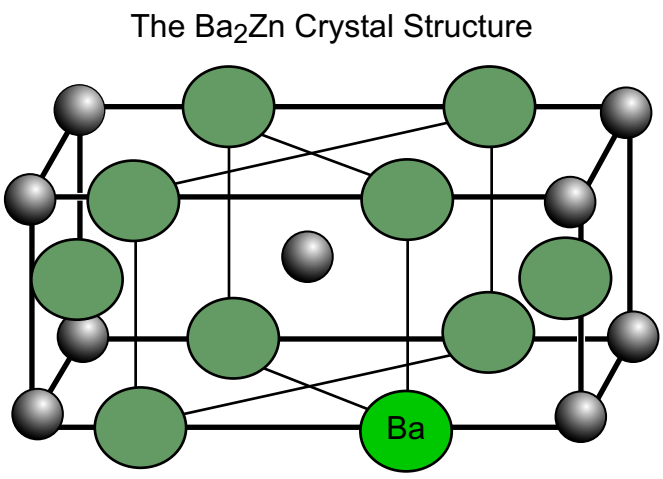

FIGURE 16.30

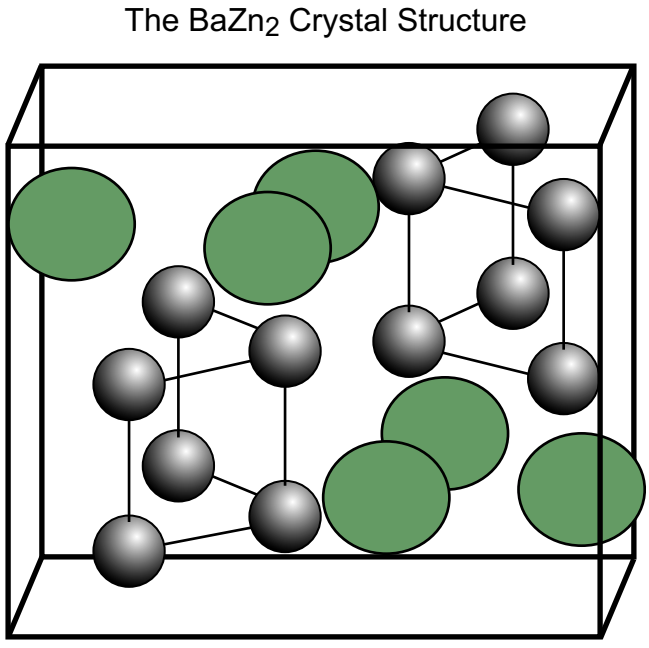

FIGURE 16.31

TABLE 16.20

No.	Site notation	Atom	Multiplicity	Wyckoff	Site symmetry	*x*	*y*	*z*	Occupancy
1	Zn	Zn	1	b	m-3m	1/2	1/2	1/2	1.0
2	Ba	Ba	1	a	m-3m	0	0	0	1.0

TABLE 16.21

No.	Site notation	Atom	Multiplicity	Wyckoff	Site symmetry	*x*	*y*	*z*	Occupancy
1	Ba1	Ba	4	e	4mm	0	0	0.34	1.0
2	Zn1	Zn	2	a	4/mmm	0	0	0	1.0

TABLE 16.22

No.	Site notation	Atom	Multiplicity	Wyckoff	Site symmetry	x	y	z	Occupancy
1	Zn	Zn	8	h	m..	0	0.0772	0.1595	1.0
2	Ba	Ba	4	e	mm2	0	1/4	0.5602	1.0

TABLE 16.23

No.	Site notation	Atom	Multiplicity	Wyckoff	Site symmetry	x	y	z	Occupancy
1	Zn1	Zn	8	g	..m	0.191	0.274	1/4	1.0
2	Zn2	Zn	8	e	2..	0.204	0	0	1.0
3	Zn3	Zn	4	c	m2m	0	0.074	1/4	1.0
4	Ba1	Ba	4	c	m2m	0	0.665	1/4	1.0

Cell parameters are: $a = 5.009$ Å, $b = c = 6.1564$ Å, $\alpha = 78.616°$, $\beta = \gamma = 61.995°$, cell volume $= 158.31$ Å^3, $Z = 4$. Cell occupancy is shown in Table 16.22.

The literature is devoid of any mention of the physical or electrical properties of this material.

The compound, $BaZn_5$, has the structural form shown in Fig. 16.32.

Cell parameters are: $a = 5.318$ Å, $b = c = 6.8489$ Å, $\alpha = 103.92°$, $\beta = \gamma = 90°$, cell volume $= 242.13$ Å^3, $Z = 1$. Cell occupancy is shown in Table 16.23.

No data concerning the physical or electrical properties of this compound are available in the current technical literature.

$BaZn_{13}$ has the structural form shown in Fig. 16.33.

The Ba atoms lie within channels in the structure, one Ba atom per unit cell. A total of four units are shown here in this *ac*-plane. In the *b*-direction, there are layers of Zn atoms between the channels so that this diagram represents eight-unit cell in a 3D structure.

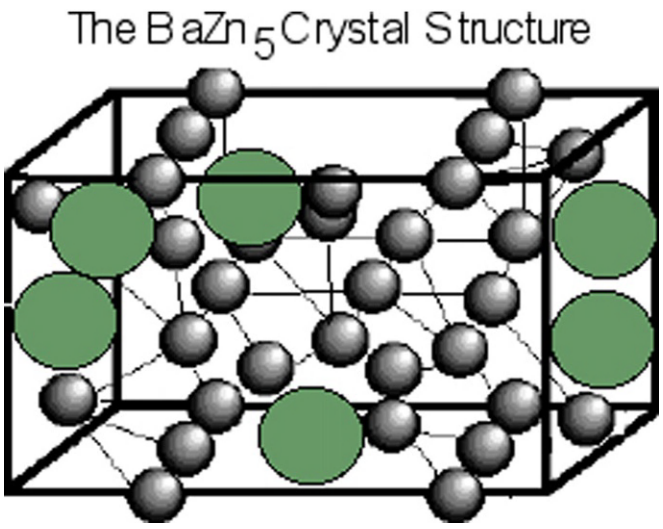

FIGURE 16.32

Cell parameters are: $a = b = c = 8.7391$ Å, $\alpha = \beta = \gamma = 60°$, cell volume $= 471.94$ Å^3, $Z = 8$. Cell occupancy is shown in Table 16.24.

No other IM compounds are known and no barium zincide compounds are offered for sale commercially.

In the Ba–Zn–O system, the magnetic properties of Y–Ba–Zn–O samples in which Y_2O_3, $BaCO_3$ and ZnO powders were mixed at atomic ratios of Y:Ba:Zn = 1:2:3 were explored. Abnormal magnetic behavior has been seen on the M-H and M-T curves. At liquid nitrogen temperature, the samples expelled the permanent magnets but no levitation was observed unlike in type II superconducting samples. The M-H curves were quite dependent on the field direction ($H//ab$ and $H \perp ab$-plane). At low-field regime, ferromagnetism was clearly seen but diamagnetism appeared at fields higher than 1.0 T. Some traces of Meissner-like expulsion up to 500 Oe were also seen.

In the system BaO–ZnO, the crystal structure of $BaZnO_2$ has been determined by Patterson- and Fourier syntheses along the [1,0,0] dimension. The space group is $P3_12$–D_3^4. The hexagonal unit cell ($a = 5.886$ Å, $c = 6.734$ Å, $c/a = 114$) contains three formula units: $d_{calc} = 5.82$, $d_{pyk} = 5.78$ g/cm^3. The last refinement gave $R = 0.075$; $R' = 0.113$ (MoKα-radiation). The ZnO_2 arrangement is very similar to that of low quartz; Ba is situated in interstitial holes. In this sense, $BaZnO_2$ is a stuffed derivative of low quartz.

Single crystals of Ba_2ZnO_3 were prepared by solid-state reaction. It crystallizes monoclinic: space group $C_{2h}^{6=}$, $C12/c1$; $a = 5.833$; $b = 11.376$; $c = 12.585$ Å; $\beta = 93.63°$; $Z = 8$. The crystal structure was characterized by $^{\infty}{}_1[ZnO_3]$ chains along the [100] direction. They are connected by Ba^{2+} in sevenfold oxygen coordination. Ba_2ZnO_3 is an example of *zweier* single chain

TABLE 16.24

No.	Site notation	Atom	Multiplicity	Wyckoff	Site symmetry	*x*	*y*	*z*	Occupancy
1	Zn1	Zn	96	i	m..	0	0.1192	0.1806	1.0
2	Zn2	Zn	8	b	m-3.	0	0	0	1.0
3	Ba1	Ba	8	a	432	1/4	1/4	1/4	1.0

compounds i.e. containing a repeat unit of two tetrahedra. These chains run parallel to [100]. The Ba^{2+}, cation lies on two crystallographic-independent sites, both seven coordinate. A(1) is in distorted pentagonal bipyramidal coordination and A(2) shows monocapped trigonal prismatic coordination.

Photoluminescent properties of novel red-emitting Mn^{2+}-activated MZnOS (M = Mg, Ca, Ba, OS = oxysulfide) phosphors were investigated (Fig. 16.34).

Mn^{2+}-activated MgZnOS phosphors show a single symmetric narrow red emission band in the wavelength range of 550 to 700 nm due to the $^4T_1(^4G) \Rightarrow {}^6A_1(^6S)$ transition of Mn^{2+}. Peak centers are at about 614 nm for M = Ca and 634 nm for M = Ba, regardless of the excitation wavelength and Mn^{2+}-doping concentration.

A comparison was made between the luminescence properties of Mn^{2+} in the Ca versus Ba compound. A similarity between them is that both Mn^{2+}-activated CaZnOS and BaZnOS can be efficiently excited under host lattice excitation in the wavelength range of 250 to 350 nm due to efficient energy transfer between the host lattice (MZnOS) and activator (Mn^{2+}). An unexpected difference is that Mn^{2+}-activated CaZnOS can also be efficiently excited under the excitation of Mn^{2+} itself (d–d transitions) in the wavelength range of 350 to 500 nm. This difference is ascribed to different crystal structures, different coordination

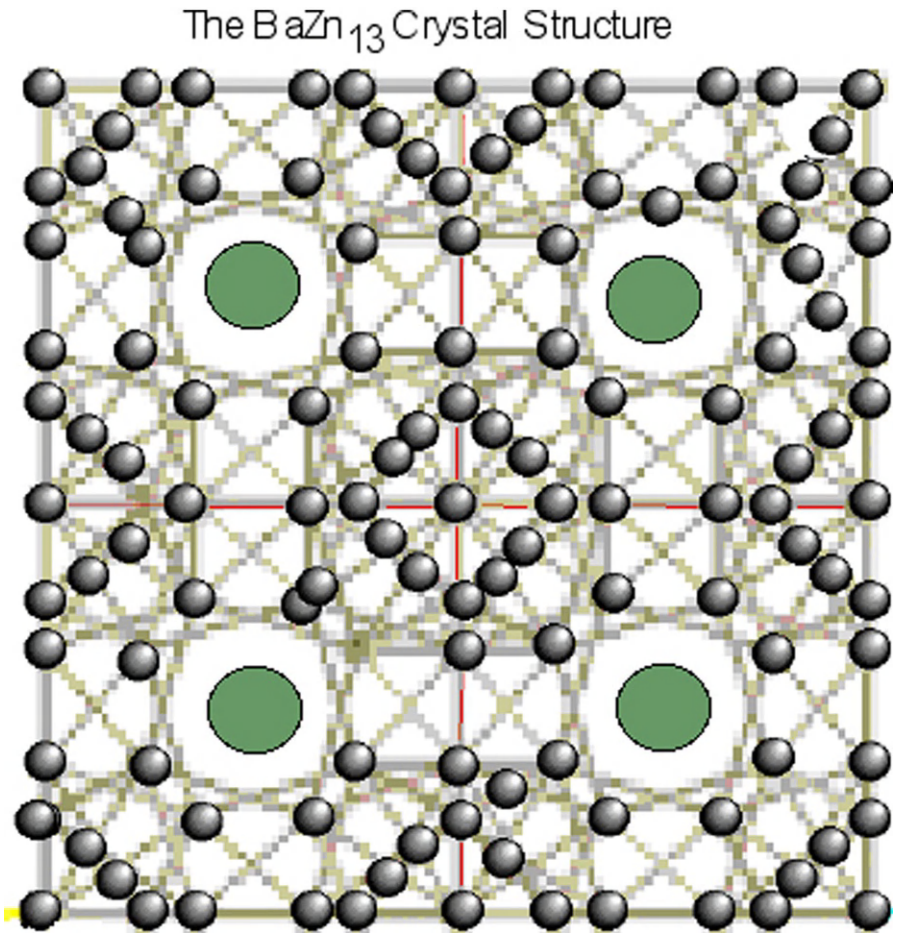

FIGURE 16.33

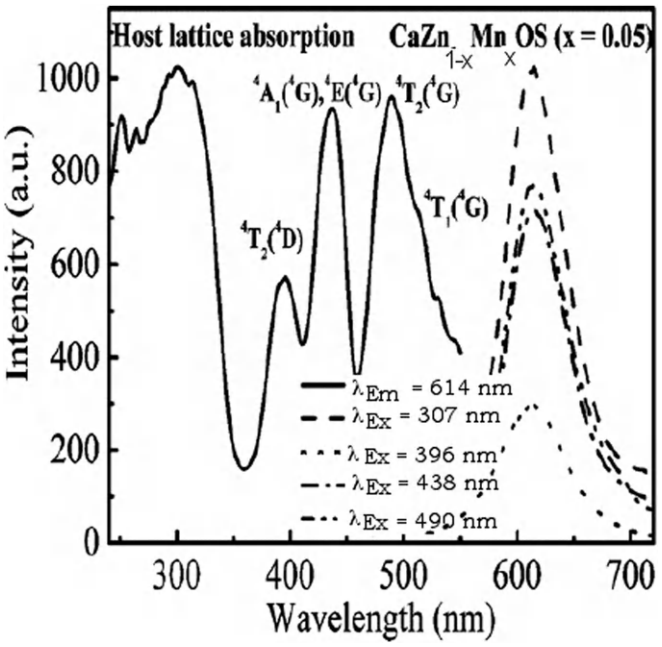

FIGURE 16.34

environments, and point symmetries for Mn^{2+} in these two compounds. The potential applications of these phosphors are pointed out. Among them, Mn^{2+}-activated CaZnOS shows great potential for application as an alternative red-emitting LED conversion phosphor due to its high absorption and strong excitation bands in the wavelength range of 350 to 500 nm.

The wide-band gap oxy-sulfide semiconductor BaZnOS adopts a high-symmetry modification of the $SrZnO_2$ structure type and contains layers of vertex-linked ZnO_2S_2 tetrahedra, which represent a novel coordination environment for zinc in the solid state. BaZnOS: orthorhombic, space group *Cmcm*; $a = 3.9619$ Å, $b = 12.8541$ Å, $c = 6.1175$ Å, $Z = 4$. Diffuse-reflectance spectroscopy measurements reveal a direct band gap of 3.9 eV, consistent with the white color and the results of band structure calculations. The band gap is larger than those observed in ZnO and ZnS, consistent with the more ionic nature of BaZnOS. Attempts to dope this compound electronically have so far not proved possible.

Crystallization from supersaturated sodium hydroxozincate solutions by adding solutions of alkali earth metal hydroxides yields crystals of $Sr_2Zn(OH)_6$ and $Ba_2Zn(OH)_6$. The X-ray structure determination on these crystals was successful including all hydrogen positions:

$Sr_2Zn(OH)_6$: $P2_1/n$, $Z = 2$, $a = 5.794$ Å, $b = 6.160$ Å, $c = 8.141$ Å, $\beta = 91.23°$, $N(F^2{}_0{}^\circ - 2\sigma F^0) = 1127$, $N(\text{Var.}) = 53$, $R_1/wR_2 = 0.047/0.081$,

$Ba_2Zn(OH)_6$: $P2_1/n$, $Z = 2$, $a = 6.043$ Å, $\beta = 6.336$ Å, $c = 8.451$ Å, $\beta = 91.23°$, $N(F^2{}_0{}^\circ - 2\sigma F^0) = 1669$, $N(\text{Var.}) = 54$, $R_1/wR_2 = 0.029/0.067$.

$Sr_2Zn(OH)_6$ and $Ba_2Zn(OH)_6$ crystallize isotypically in a distorted Li_2O type of structure. Sr^{2+} and Ba^{2+} form a cubic primitive arrangement of distorted octahedra of OH^- around Zn^{2+} ions, filling therein alternating cubic gaps in an ordered way.

No other barium zincate materials are known. They are not offered for sale commercially and no CAS numbers have been issued to date.

16.1.6. Radium Zinc Compounds

Although Ra metal or radium oxide probably forms the same type of compounds with Zn or ZnO as Ba^0 or BaO, there is no record in the literature of anyone having done so.

16.2. ALKALINE EARTH CADMIUM COMPOUNDS

Cd metal forms a number of IM compounds with the alkaline earths. Only a few "cadmates" are known.

16.2.1. Beryllium Cadmium Compounds

Be metal does not form any IM compounds with Cd metal.

The systems, BeO–Cd_2O, BeO–CdO and BeO–Cd_2O_3, have not been documented in the past or current technical literature.

16.2.2. Magnesium Cadmium Compounds

Mg metal forms three IM compounds with Cd metal as shown in Fig. 16.35.

These compounds are eutectic over a wide range of temperatures and compositions. Two are dimorphic and exhibit room- and high-temperature modifications of their structure. The compound, Mg–Cd, has the structure shown in Fig. 16.36.

Cell parameters of MgCd are: $a = 3.2217$ Å, $b = 5.0051$ Å, $c = 5.2712$ Å, $\alpha = \beta = \gamma = 90°$, cell volume $= 84.98$ Å^3, $Z = 2$. Cell occupancy is shown in Table 16.25.

Little is known concerning this compound other than its structural data.

The compound, Mg_3Cd, has the structure shown in Fig. 16.37.

Cell parameters are: $a = 5.083$ Å, $b = c = 6.314$ Å, $\alpha = 120°$, $\beta = \gamma = 90°$, cell volume $= 175.17$ Å^3, $Z = 2$. Cell occupancy is shown in Table 16.26.

In contrast, the $MgCd_3$ compound has the structure shown in Fig. 16.38.

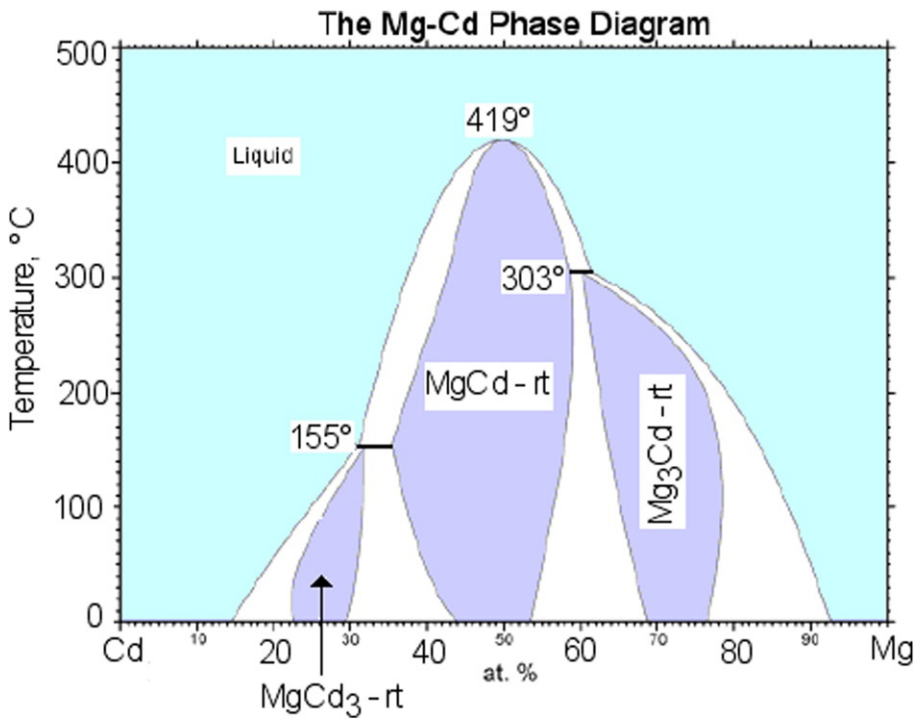

FIGURE 16.35

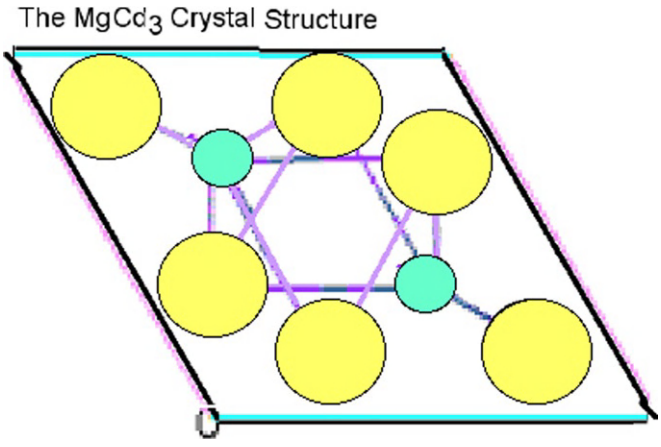

FIGURE 16.36

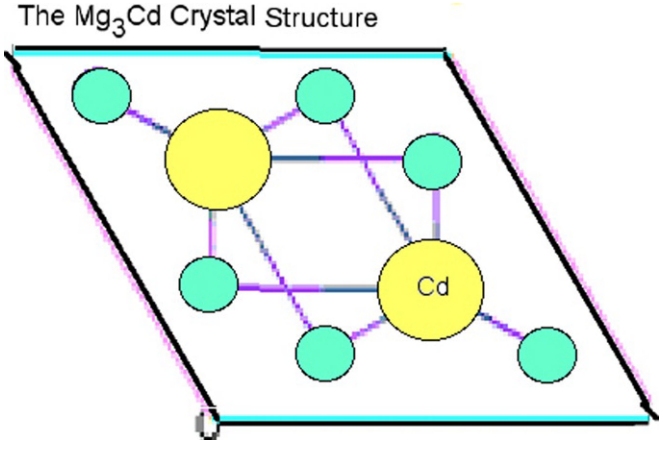

FIGURE 16.37

TABLE 16.25

No.	Site notation	Atom	Multiplicity	Wyckoff	Site symmetry	*x*	*y*	*z*	Occupancy
1	Cd	Cd	2	f	mm2	1/4	1/2	0.677	1.0
2	Mg	Mg	2	e	mm2	1/4	0	0.182	1.0

TABLE 16.26

No.	Site notation	Atom	Multiplicity	Wyckoff	Site symmetry	*x*	*y*	*z*	Occupancy
1	Mg1	Mg	6	h	mm2	0.16667	0.33333	1/4	1.0
2	Cd1	Cd	2	d	-6m2	1/3	2/3	3/4	1.0

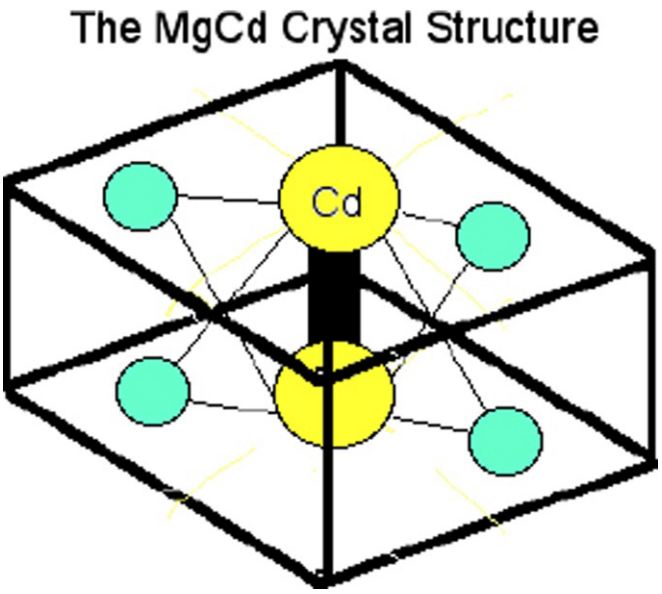

FIGURE 16.38

Cell parameters are: $a = 5.0452$ Å, $b = c = 6.2335$ Å, $\alpha = 120°$, $\beta = \gamma = 90°$, cell volume $= 169.77$ Å^3, $Z = 2$. Cell occupancy is shown in Table 16.27.

The Mg–Cd system has a close-packed hexagonal (c.p.h.) lattice and possesses ordered structures for concentrations corresponding to Mg_3Cd, MgCd and $MgCd_3$. In general, the c.p.h. lattice can be divided into four large hexagonal sublattices (lattice constants of them now become $a' = 2a$ and $c = c$). For ordered MgCd, two of these sublattices are occupied by Mg while the other two by Cd; and for the ordered Mg_3Cd three sublattices are occupied by Mg and the remaining one is occupied by Cd, for the ordered $MgCd_3$ the relation is just the reverse. The order–disorder transformation of these alloys has been measured through temperature dependencies of several physical properties, such as specific heat (C_p), expansion coefficient (β) and electrical resistivity (ρ). For the Mg_3Cd alloy C_p vs temperature curve showed anomalous behavior similar to β-brass, while the presence of latent heats has been confirmed for MgCd and $MgCd_3$ alloys. For Mg_3Cd and MgCd alloys, β vs temperature curves indicated a close parallelism to their C_p vs temperature curves. On the other hand, for $MgCd_3$ alloy, a noteworthy contraction was associated with its disordering, causing the coefficient of thermal expansion to tend toward negative infinity at the Curie point. The ρ vs temperature curves for these alloys have characteristic from of the order–disorder transformation. During the annealing of the previously quenched Mg_3Cd and MgCd alloys, their hardness decreases with time. It is interesting to note that these highly ordered superlattices possess hardness smaller than the random alloys of the same compositions.

In another paper, using XRD studies of the structural state of type Mg_3Cd alloys during the ordering stage accompanied by an increase in their electrical resistivity Ω, the authors analyzed the problem of the admissibility of previously postulated interpretations of the anomalous variation in Ω in the initial stages of ordering of certain investigated alloys. It was tentatively concluded that this anomalous variation may be associated with the non-monotonic character of the dependence of Ω on the degree of order. The kinetics of order–disorder processes in alloys of type Mg_3Cd and $MgCd_3$ in the single-phase and two-phase regions were both investigated by measuring the electrical resistance of the material directly at the temperatures at which tests are carried out. It was shown that in a $MgCd_3$-type alloy the processes involved in an order–disorder transition proceed much more slowly in the two-phase region than in the single-phase region. The Mg_3Cd alloy, on the other hand, exhibited no such delay effects. This difference in the behavior of these alloys investigated was said to be due to lattice distortions, accompanying transitions in the two-phase region, which are greater for $MgCd_3$ than for Mg_3Cd.

Antiphase boundaries (APBs) and stacking faults affect the deformation behavior of many IMs. In an ordered c.p.h. structure of $D0_{19}$ type (e.g. Mg_3Cd, Ti_3Al-based alloys), stable planar faults of two types are possible on the basal plane. These are APBs and complex stacking faults (CSFs), which are a combination of an APB and a stacking fault. The latter can be either of shear or of climb type. If the bounding partial dislocations of a CSF lie in its plane, then it is designated as a shear CSF, otherwise it is called a climb CSF. A mathematical formulation of the theory of diffraction from a $D0_{19}$ structure having a shear or climb type of CSF has been carried out. The diffraction effects owing to the presence of these CSFs have been found. Integrated intensities and widths of the reflections are affected. These have been evaluated in terms of the probability of the occurrence of these faults.

The resolution of lattice fringes in ordered and partially ordered Cu_3Au has been calculated using the dynamical theory of electron diffraction, taking into consideration

TABLE 16.27

No.	Site notation	Atom	Multiplicity	Wyckoff	Site symmetry	*x*	*y*	*z*	Occupancy
1	Cd1	Cd	6	h	mm2	0.16667	0.33333	1/4	1.0
2	Mg1	Mg	2	d	-6m2	1/3	2/3	3/4	1.0

the effects of such variables as foil thickness and orientation, objective lens defocus, degree of order and, for partially ordered alloys, the position of small ordered domains in the foil. The experimental observations were found to be in excellent agreement with these calculations. Lattice defects in ordered Cu_3Au have been studied using this technique. Thus, the domain wall thickness at the translational antiphase domain boundaries was shown to be one or two atomic diameters and the antiphase boundary separating the pair of fundamental lattice dislocations, which constituted a super-dislocation, was revealed. A clear distinction exists between the lattice image contrast of predominantly ordered and disordered regions and this has been utilized to study partial long-range order and short-range order. Short-range order in this system is characterized by a dispersion of small highly ordered domains, ~15 Å diameter, in a predominantly disordered matrix.

The later stages of DO_{19} ordering in Mg_3Cd have been investigated by direct lattice imaging. The DO_{19} structure involves a hexagonal abab … stacking, similar to the LI_2 cubic structure with abcabc … stacking.

Unit cell high steps (5.3 Å) have been clearly resolved in the following interfaces:

- the order–disorder interface,
- translational antiphase boundaries,
- rotational domain boundaries.

These observations are thought to indicate a ledge mechanism for ordering and domain growth. Lattice imaging and corresponding optical diffraction have also been used for phase identification and determination of unit cell dimensions (Fig. 16.39).

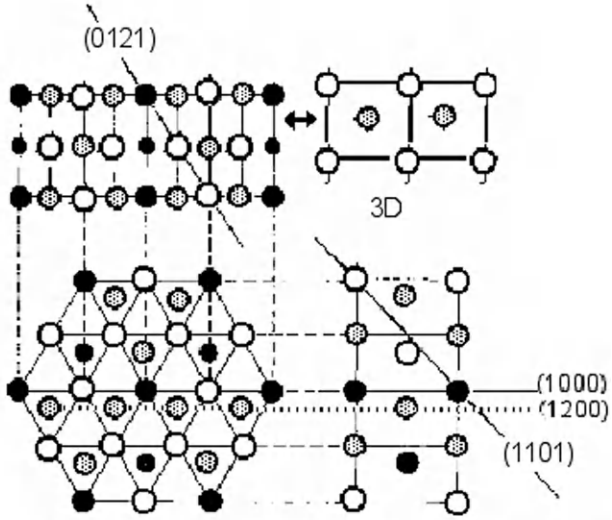

Atomic Configurations of the DO13 Structure, as Viewed from the three Pricipal Axes. Open corcles refer to the Mg-atoms while the black or dotted circles refer to the two Types of Cd-atoms

FIGURE 16.39

In addition, the characteristic domain structure of the DO_{19} phase was been studied in detail, and the unusual multiple domain junctions were explained in terms of the orthorhombic lattice distortion upon transformation. Considerably more information has been discovered by lattice imaging than is possible by conventional electron microscopy. A model for the twinned structure of Mg_3Cd from its ordered, hexagonal state was derived from the classical twin indices for (1012) twinning. Use of these indices transforms the ordered hexagonal Mg_3Cd structure into an ordered orthorhombic structure having identical atom positions as the hexagonal structure, but with a different sequence of magnesium and cadmium occupancy. This different sequence gives rise to additional X-ray super lattice lines.

No other IM compounds are known for this system.

In the Mg–Cd–O system, no known compounds, similar to those in the Mg–Zn–O system have been documented in the available technical literature.

Magnesium cadmates are not available commercially for sale and no CAS numbers have been issued to date.

16.2.3. Calcium Cadmium Compounds

Ca metal forms several IM compounds with Cd metal as shown in Fig. 16.40.

The compound, CaCd has the structural form shown in Fig. 16.41.

Cell parameters are: $a = b = c = 3.8378$ Å, $\alpha = \beta = \gamma = 90°$, cell volume $= 56.53$ Å^3, $Z = 2$. Cell occupancy is shown in Table 16.28.

Other than structural data, little is available concerning the physical or electrical properties of this material in the past or current literature.

The compound,$CaCd_2$, has the structure shown in Fig. 16.42.

Cell parameters are: $a = 4.9242$ Å, $b = c = 6.1772$ Å, $\alpha = 75.32°$, $\beta = \gamma = 66.51°$, cell volume $= 157.03$ Å^3, $Z = 2$. Cell occupancy is shown in Table 16.29.

This is the high-temperature form. The low-temperature form is shown in Fig. 16.43.

Cell parameters are: $a = 9.6542$ Å, $b = c = 5.9964$ Å, $\alpha = \beta = 90°$, $\gamma = 120°$, cell volume $= 157.03$ Å^3, $Z = 2$. Cell occupancy is shown in Table 16.30.

$CaCd_2$ forms the KHg_2 structure at elevated temperatures (orthorhombic, space group $= Imma$) and the $MgZn_2$-type Laves phase at ambient conditions (hexagonal, space group $P63/mmc$, $Z = 4$).

The compound, $CaCd_6$ has the unique structure shown in Fig. 16.44.

Cell parameters are: $a = b = c = 13.5793$ Å, $\alpha = \beta = \gamma = 109.47°$, cell volume $= 1927.58$ Å^3, $Z = 24$. Cell occupancy is shown in Table 16.31.

The $CaCd_6$ structure, also known as the 1/1 cubic approximant, is the pure A-cell, tiling A.cI2. The precise

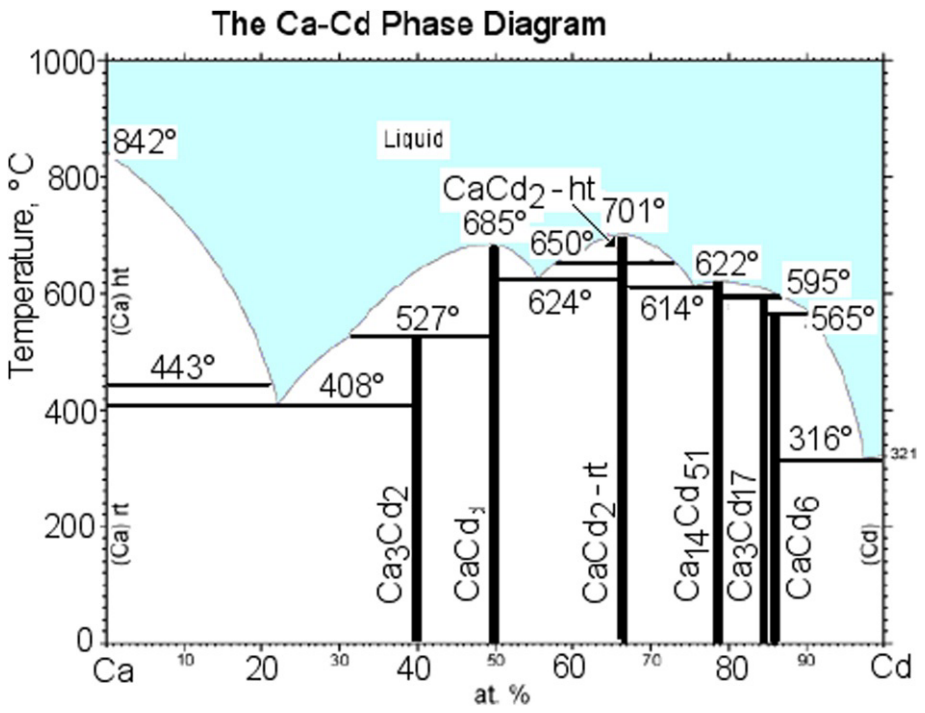

FIGURE 16.40

structure remains controversial since the Pearson type has been given variously as cI160, cI176, cI184 and cI232 as a result of uncertainty regarding the proper orientations of the Cd_4 cluster-center tetrahedra. In fact, there appears to be a low temperature order–disorder phase transition (around $T = 100$ K) in which these tetrahedra lock into specific relative orientations.

Thermodynamically stable binary icosahedral quasicrystals occur in the alloy system, Ca_7Cd_5. In each case, the phase diagram of the binary alloy contains a 1/1 cubic approximant of structure type Cd_6Ca at a close by composition. This Cd_6Ca structure can be represented in a conventional simple cubic unit cell with a lattice parameter of $a = 15.7$ Å. However, the Pearson (point group) symbol for Cd_6Ca is cI176 indicating that it is cubic, body-centered, with 176 atomic positions

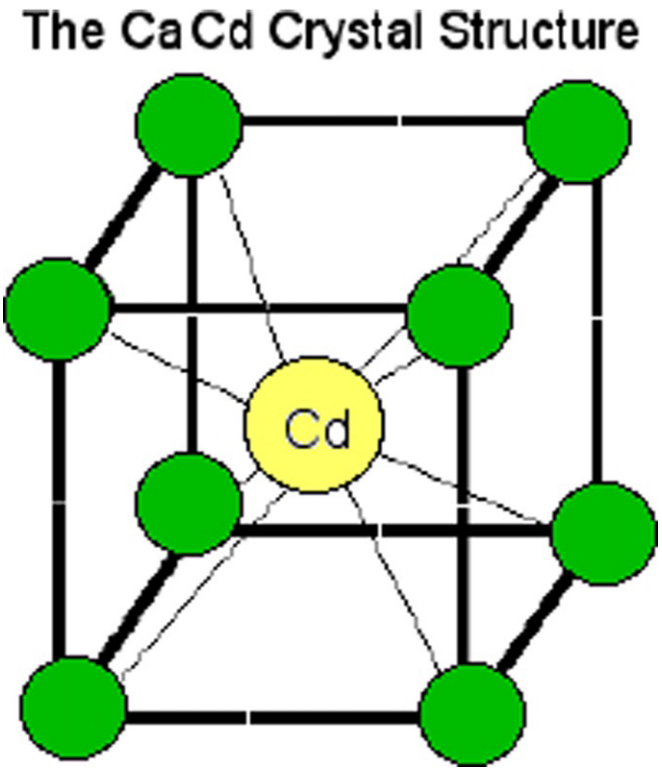

FIGURE 16.41

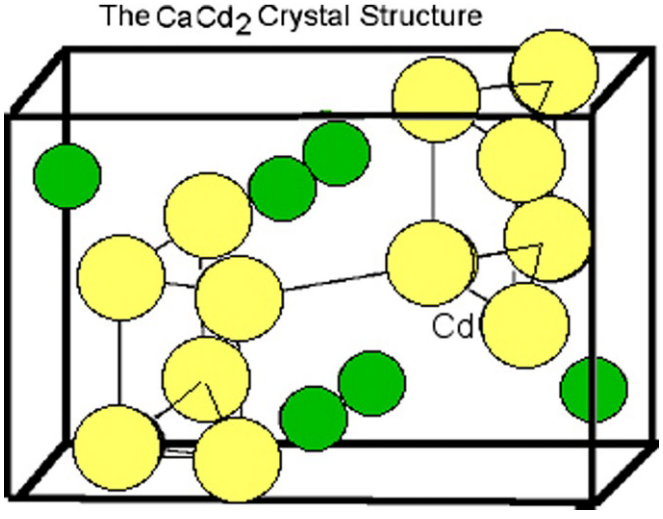

FIGURE 16.42

TABLE 16.28

No.	Site notation	Atom	Multiplicity	Wyckoff	Site symmetry	*x*	*y*	*z*	Occupancy
1	Cd	Cd	1	b	m-3m	1/2	1/2	1/2	1.0
2	Ca	Ca	1	a	m-3m	0	0	0	1.0

TABLE 16.29

No.	Site notation	Atom	Multiplicity	Wyckoff	Site symmetry	*x*	*y*	*z*	Occupancy
1	Cd	Cd	8	h	m..	0	0.06	0.165	1.0
2	Ca	Ca	4	e	mm2	0	1/4	0.55	1.0

TABLE 16.30

No.	Site notation	Atom	Multiplicity	Wyckoff	Site symmetry	*x*	*y*	*z*	Occupancy
1	Cd1	Cd	6	h	mm2	0.1701	0.3394	1/4	1.0
2	Ca1	Ca	4	f	3m.	1/3	2/3	0.5629	1.0
3	Cd2	Cd	2	a	-3m.	0	0	0	1.0

per simple cubic unit cell. Since 176 is not a multiple of the basic 7-atom stoichiometric unit (6 Cd and 1 Ca), there must be a partial occupancy. In fact, the unit cell contains 144 Cd atoms, 24 Ca atoms and 8 vacancies. This is shown in Fig. 16.45.

The structure Ca_2Cd_7-hP68 is based on trigonal prisms, whose triangular faces are Y-faces, but their rectangular faces are not Z-faces, so this structure is not a CCT, and should not be considered a proper approximant. The clusters based at trigonal prism vertices are imperfect basic clusters, and instead of being centered by Cd_4 tetrahedra, they are centered by Cd_3 triangles.

The compound, $Ca_{14}Cd_{51}$, has the structural form shown in Fig. 16.46.

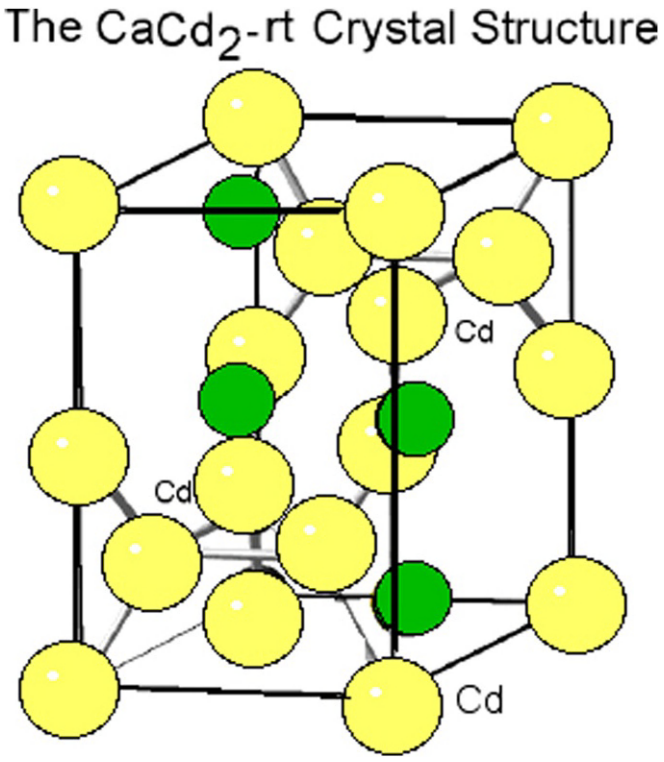

FIGURE 16.43

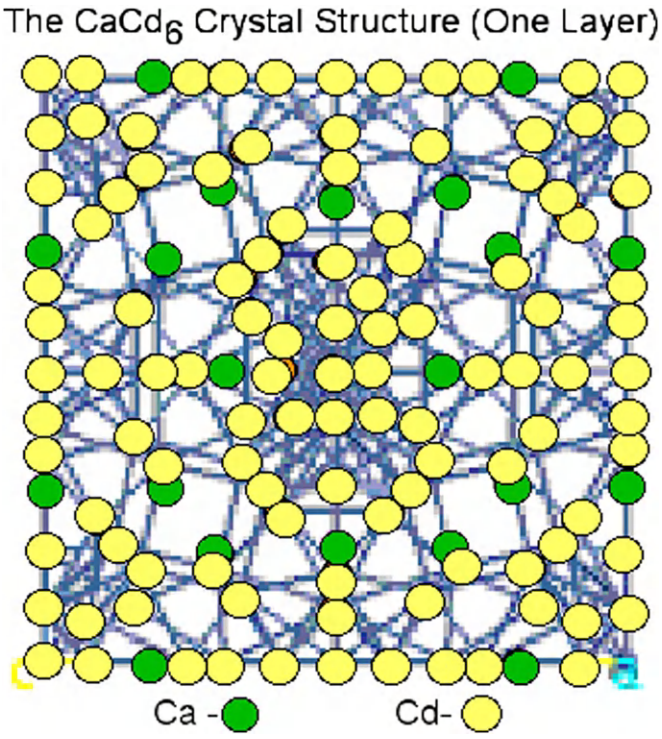

FIGURE 16.44

The Basic Icosahedral Clusters of the CaCd6 - Type of Compound. They Consist of Three Concentric Shells (labelled as b & d). The Internal cluster is in a Tetrahedron (a) while the Ca - atoms involve (c) involve a Hexagonal Pattern.

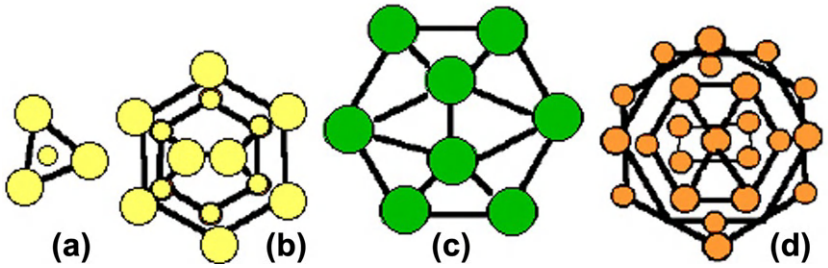

FIGURE 16.45

Cell parameters are: $a = 9.787$ Å, $b = c = 13.465$ Å, $\alpha = 120°$, $\beta = \gamma = 90°$, cell volume $= 1536.71$ Å^3, $Z = 1$. Cell occupancy is shown in Table 16.32.

Only one *a*-*b* face is shown. The 3D model consists of two layers, separated by a layer of Cd atoms.

Thermodynamically stable binary icosahedral quasicrystals occur in the alloy systems, Cd_5Yb_7 and Cd_5Ca_7. Since their discovery, numerous attempts have been made to model their structure. Efforts that rely on "atomic surfaces" and higher dimensional space suffer problems since certain atomic positions appear to be displaced far from any simply represented position. Atomic surface representations also average over disorder phenomena in a manner that probably hides important details of the structure. One approach is to assume that the fundamental building motif of the structure is the large $Ca_{12}Cd_{54}$ atom cluster, as is observed in a 1/1" approximation. This phase, that is stable over a range of Cd-rich systems, is an alternative approach to model the quasicrystal structure to specify how the clusters arrange to fill space quasiperiodically, and to fill some empty regions with "glue" atoms. This approach is modeled in Fig. 16.47.

The compound, Ca_3Cd_2 has the conformational form shown in Fig. 16.48.

Cell parameters are: $a = 8.0236$, $b = c = 8.8642$ Å, $\alpha = \beta = \gamma = 90°$, cell volume $= 630.14$ Å^3, $Z = 1$. Cell occupancy is shown in Table 16.33.

This compound is offered for sale commercially with the CAS number of 37191-29-0.

The closest cubic approximation to the $MCd_{5.7}$ (M = Ca, Yb) quasicrystals known so far, namely $Ca_{13}Cd_{76}$, was obtained by high-temperature reaction of the elements. It exhibits a new type of structure for IM compounds with an unprecedented arrangement of triacontahedral clusters (see following structure), which could prove useful in modeling the structures of the $MCd_{5.7}$ quasicrystals (Fig. 16.49).

No other IM compounds are known. At least one, Ca_3Cd_2, is offered for sale commercially.

In the Ca–Cd–O system, no compounds have been documented in the past or present technical literature. No description of such compounds (if they exist) has been published.

TABLE 16.31

No.	Site notation	Atom	Multiplicity	Wyckoff	Site symmetry	*x*	*y*	*z*	Occupancy
1	Cd1	Cd	48	h	1	0.1184	0.3405	0.2003	1.0
2	Cd2	Cd	24	g	m..	0	0.0741	0.0832	0.3
3	Ca1	Ca	24	g	m..	0	0.1899	0.2997	1.0
4	Cd3	Cd	24	g	m..	0	0.2407	0.0923	1.0
5	Cd4	Cd	24	g	m..	0	0.4043	0.3460	1.0
6	Cd5	Cd	16	f	.3.	0.1608	0.1608	0.1608	1.0
7	Cd6	Cd	12	e	mm2..	0.1902	0	1/2	1.0
8	Cd7	Cd	12	d	mm2..	0.4055	0	0	1.0

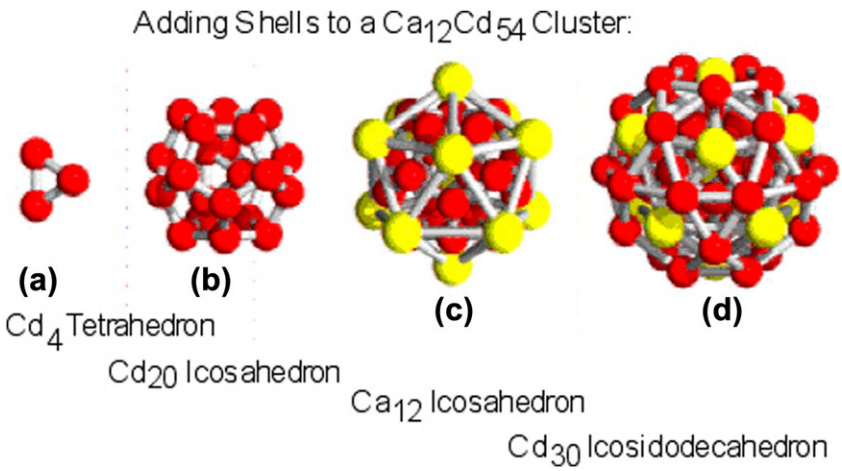

FIGURE 16.47

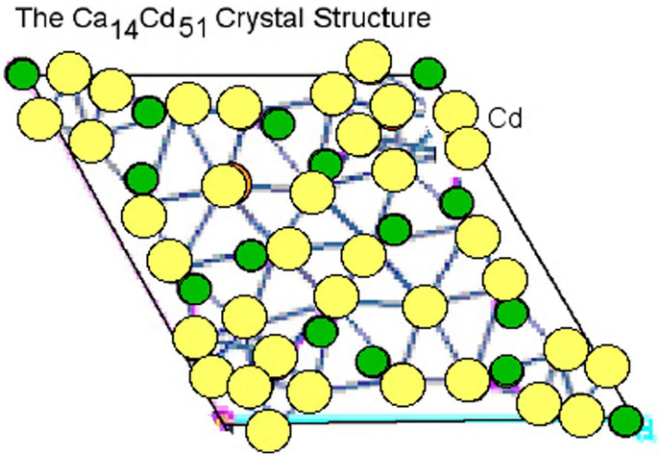

FIGURE 16.46

16.2.4. Strontium Cadmium Compounds

Strontium, metal forms a series of compounds with Cd metal as shown in Fig. 16.50. Six compounds are shown. The structures of all six compounds have been published.

The compound, SrCd, has the conformational form shown in Fig. 16.51.

Cell parameters are: $a = b = c = 4.0251$ Å, $\alpha = \beta = \gamma = 90°$, cell volume $= 65.21$ Å^3, $Z = 1$. Cell occupancy is shown in Table 16.34.

Other than for structural data, no other description of this compound is available in the past or present technical literature.

$SrCd_2$ has the structural form shown in Fig. 16.52.

Cell parameters are: $a = 5.1643$ Å, $b = c = 6.5566$ Å, $\alpha = 79.42°$, $\beta = \gamma = 68.81°$, cell volume $= 84.98$ Å^3, $Z = 2$. Cell occupancy is shown in Table 16.35.

Other than structural data, this compound has not been subjected to any precise studies of its physical or electrical properties.

The $SrCd_6$ compound has the conformational structure shown in Fig. 16.53.

Only one layer is shown. The 3D structure consists of two layers, one at the (100) interface of the *ac*-directions and the other at (010) of the *ac*-interface layer.

Cell parameters are: $a = b = c = 13.8912$ Å, $\alpha = \beta = \gamma = 109.47°$, cell volume $= 2{,}063.39$ Å^3, $Z = 24$. Cell occupancy is shown in Table 16.36.

TABLE 16.32

No.	Site notation	Atom	Multiplicity	Wyckoff	Site symmetry	*x*	*y*	*z*	Occupancy
1	Cd1	Cd	12	l	1	0.1049	0.439	0.3305	1.0
2	Cd2	Cd	12	l	1	0.2662	0.0744	0.2370	1.0
3	Cd3	Cd	12	l	1	0.4944	0.1155	0.1526	1.0
4	Cd4	Cd	6	k	m..	0.0589	0.2383	1/2	1.0
5	Ca1	Ca	6	k	m..	0.4680	0.1394	1/2	1.0
6	Cd5	Cd	6	j	m..	0.0193	0.1324	0	0.500
7	Ca2	Ca	6	j	m..	0.1138	0.3898	0	1.0
8	Cd6	Cd	4	h	3..	1/3	2/3	0.2987	1.0

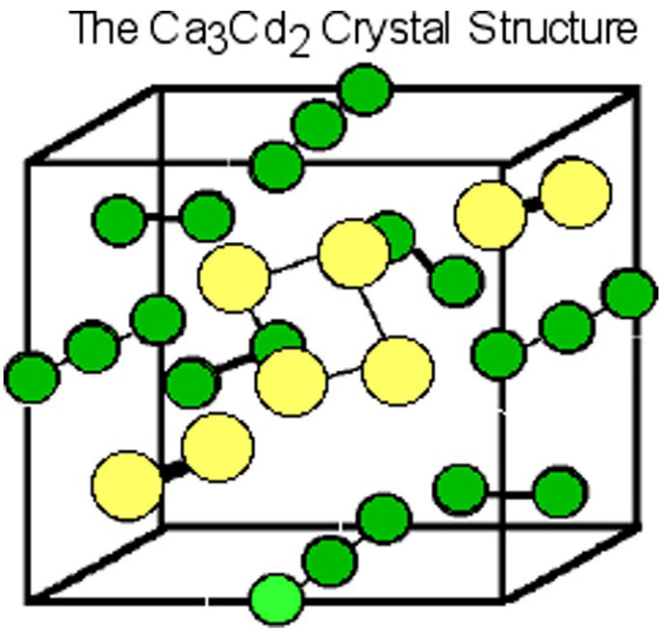

FIGURE 16.48

The basic building block of the $SrCd_6$ phase is shown in Fig. 16.54.

In Fig. 16.54(a) the cluster unit is built up of 12 MCd_{16} polyhedra and eight Cd_8 cubes. In Fig. 16.54(b), we see the alternative representation of the basic building block. The defect triacontahedron is entirely composed of Cd atoms; the pentagonal pyramids seen in the image belong to the 12 underlying MCd_{16} polyhedra. The bright triangular faces indicating missing corner atoms are in fact the planes that bisect the Cd_8 cubes seen in Fig. 16.54(a).

The coordination of Cd atoms around the different *Sr atoms* in the $SrCd_6$ phases can be described with one single polyhedron, the $SrCd_{16}$ polyhedron. It is a monocapped, double, pentagonal antiprism with nearly perfect fivefold symmetry. Twelve of these polyhedra are arranged to form the cluster unit that serves as the basic building block in the MCd_6 and $M_{13}Cd_{76}$ phases. This arrangement of MCd_{16} polyhedra automatically generate cube-shaped interstices (Cd_8 cubes!) that share square faces with the adjacent MCd_{16} polyhedra. Each cluster unit is associated with eight surrounding Cd_8 cubes (Fig. 16.55).

The Cd_{20} pentagonal dodecahedron is seen in Fig. 16.55(a)—the Cd_4 tetrahedron residing inside has been omitted in the image. The Cd_{30} icosidodecahedron is seen in Fig. 16.55(b), where the 12 pentagons in the polyhedron correspond to the intermediate pentagonal planes of the surrounding $SrCd_{16}$ polyhedra. Each of these pentagons has a Sr metal atom situated at their geometrical centers (seen as the large sphere in the magnified $SrCd_{16}$ polyhedron to the left in the figure), but these atoms have been omitted in the image. The defect rhombic triacontahedron is seen in Fig. 16.55(c)—the tips of the $12SrCd_{16}$ polyhedra are seen as pentagonal pyramids.

The $SrCd_{11}$ compound has the structure shown in Fig. 16.56.

Cell parameters are: $a = 7.673$ Å, $b = c = 9.299$ Å, $\alpha = 80.21°\beta = \gamma = 65.94°$, cell volume $= 550.40$ Å^3, $Z = 4$. Cell occupancy is shown in Table 16.37.

The unit cell is a body-centered tetragonal and the space group is $I4/amd$. The positions of the atoms show that Sr has 22 Cd atom neighbors while Cd atoms have 12–14 nearest neighbors.

The compound, $Sr_{13}Cd_{58}$, has a structure related to $Ca_{14}Cd_{51}$ and $Ca_{12}Cd_{54}$. These compounds have icosahedral conformations as shown in Fig. 16.57.

The overall structure of $Sr_{13}Cd_{58}$ has the form shown in Fig. 16.58.

Cell parameters are: $a = 15.912$ Å, $b = c = 16.058$ Å, $\alpha = 120,°\beta = \gamma = 90°$, cell volume $= 3{,}557.33$ Å^3, $Z = 4$. Cell occupancy is shown in Table 16.38.

The compound, Sr_5Cd_3, has the structure shown in Fig. 16.59.

Cell parameters are: $a = b = c = 8.7172$ Å, $c = 10.3388$ Å, $\alpha = \beta = 114.93°$, $\gamma = 90°$, cell volume $= 630.71$ Å^3, $Z = 4$. Cell occupancy is shown in Table 16.39.

Both the incongruently melting compounds, Ca_5Hg_3 and Sr_5Cd_3, have been synthesized from stoichiometric amounts of the pure elements. They crystallize with the Cr_5B_3 type of structure: space group $I4/mcm$, $Z = 4$. The most remarkable fragments are dumbbells X_2, which have interatomic distances only slightly longer than the sum of Pauling's covalent radii: Hg–Hg (Cd–Cd) = 306 (298) pm. The structure can be constructed by rhombic dodecahedra as the only

TABLE 16.33

No.	Site notation	Atom	Multiplicity	Wyckoff	Site symmetry	*x*	*y*	*z*	Occupancy
1	Cd1	Cd	4	c	..m	0.104	0.104	0.439	1.0
2	Cd2	Cd	4	c	..m	0.123	0.123	0.031	1.0
3	Ca1	Ca	4	c	..m	0.295	0.295	0.725	1.0
4	Ca2	Ca	4	c	..m	0.348	0.348	0.251	1.0
5	Ca3	Ca	4	b	2..	0	1/2	0.000	1.0

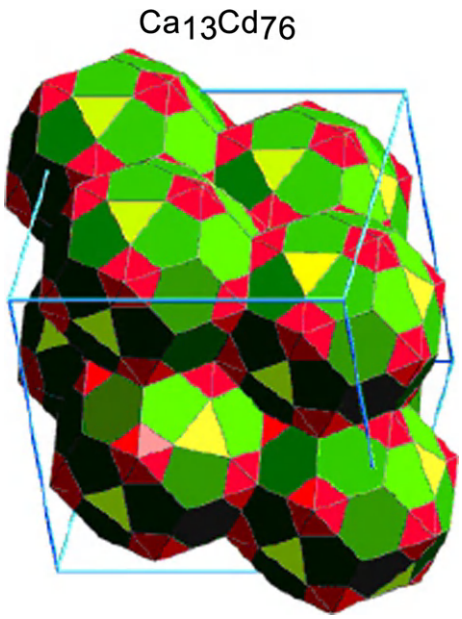

FIGURE 16.49

constituent moieties. These rhombic dodecahedra are built up by eight Ca (Sr) atoms and six Cd atoms and are furthermore centered by an additional Sr atom. Along [001] the rhombic dodecahedra share common vertices, but along [110] they are interconnected via common triangular faces. This kind of face sharing is responsible for the short distances obtained between the polyhedra, which leads to the occurrence of the dumbbells mentioned above.

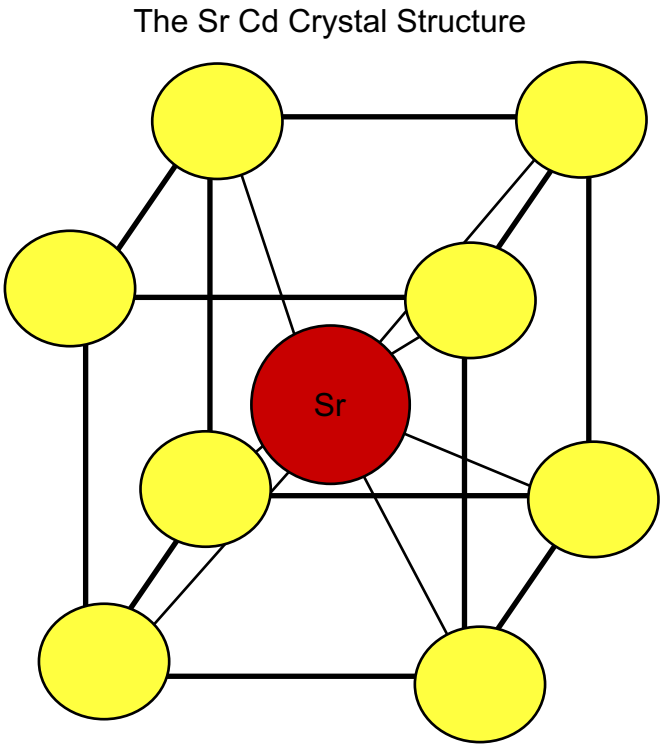

FIGURE 16.51

No other IM compounds are known. No strontium cadmide compounds are offered for sale commercially and no CAS numbers have been issued to date.

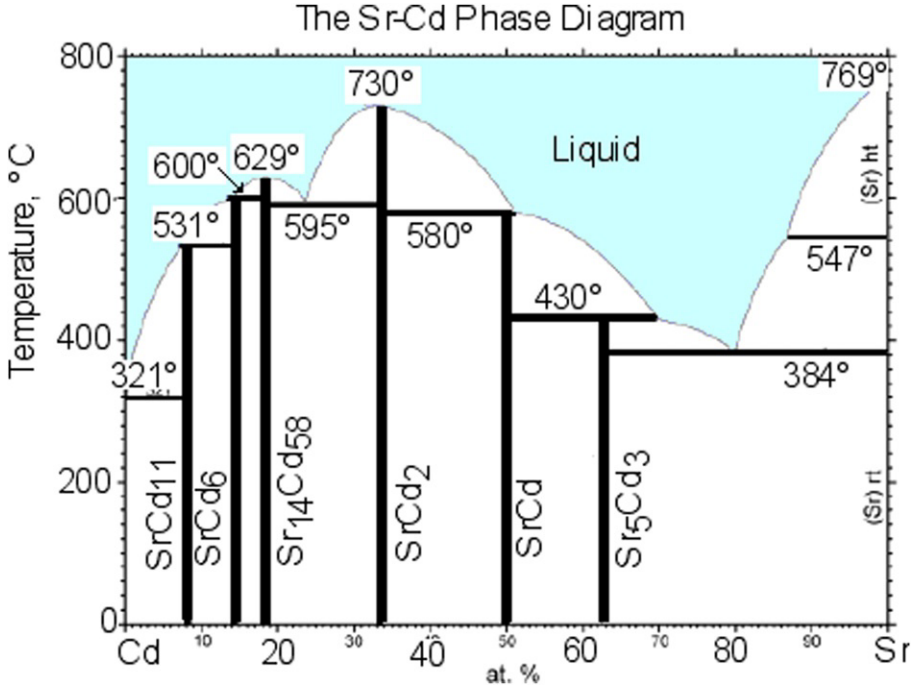

FIGURE 16.50

TABLE 16.34

No.	Site notation	Atom	Multiplicity	Wyckoff	Site symmetry	x	y	z	Occupancy
1	Sr	Sr	1	b	m-3m	1/2	1/2	1/2	1.0
2	Cd	Cd	1	a	m-3m	0	0	0	1.0

TABLE 16.35

No.	Site notation	Atom	Multiplicity	Wyckoff	Site symmetry	x	y	z	Occupancy
1	Cd	Cd	8	h	m..	0	0.055	0.165	1.0
2	Sr	Sr	4	e	mm2	0	1/4	0.55	1.0

TABLE 16.36

No.	Site notation	Atom	Multiplicity	Wyckoff	Site symmetry	x	y	z	Occupancy
2	Cd2	Cd	24	g	m..	0	0.0741	0.0832	0.333
3	Sr1	Sr	24	g	m..	0	0.1899	0.2997	1.0
4	Cd3	Cd	24	g	m..	0	0.2407	0.0923	1.0
5	Cd4	Cd	24	g	m..	0	0.4044	0.3460	1.0
6	Cd5	Cd	16	f	.3.	0.1608	0.1608	0.1608	1.0
7	Cd6	Cd	12	e	mm2..	0.1902	0	1/2	1.0
8	Cd7	Cd	12	d	mm2..	0.4055	0	0	1.0

In the Sr–Cd–O system, no cadmate compounds have been documented. The scientific literature is devoid of any mention of such materials. No strontium cadmate compounds have been offered for sale commercially and no CAS numbers have been issued to date.

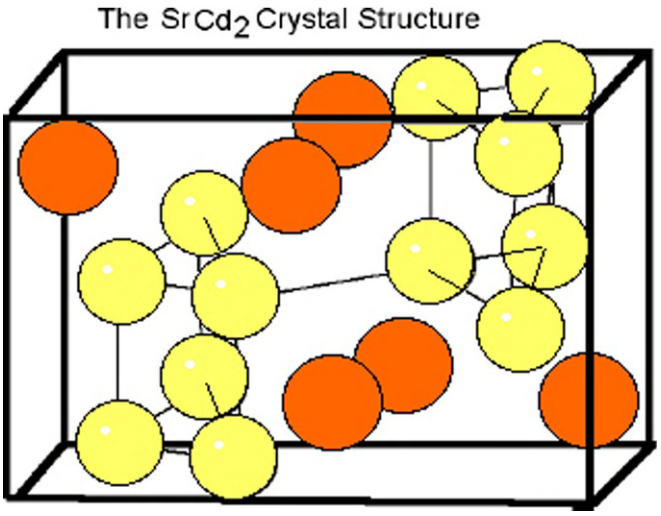

FIGURE 16.52

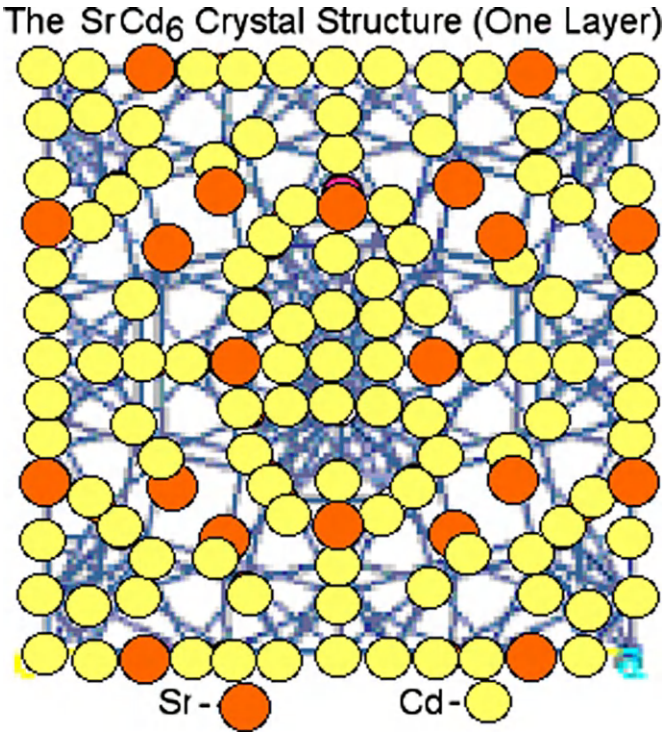

FIGURE 16.53

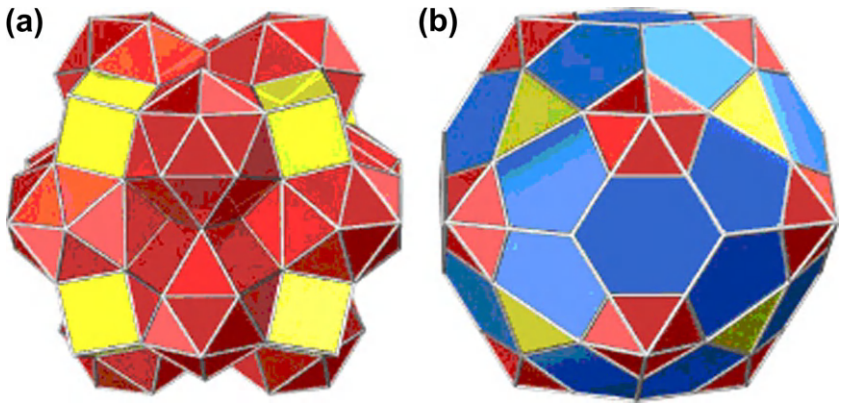

FIGURE 16.54

16.2.5. Barium Cadmium Compounds

Barium forms several IM compounds with cadmium metal as shown in Fig. 16.60.

Five Compounds are shown. All melt congruently except for Ba_2Cd which melts incongruently at 409 °C.

The compound, BaCd has the structure shown in Fig. 16.61.

Cell parameters of BaCd are: $a = b = c = 4.2131$ Å, $\alpha = \beta = \gamma = 90°$, cell volume = 74.78 Å^3, $Z = 1$. Cell occupancy is shown in Table 16.40.

BaCd has hexagonal symmetry with space group = $P6_3/mmc$, $Z = 4$ and is formed by a sequence along the (001) planes of slabs of trigonal prisms in which Bs is centered by Cd atoms and stacked in a close-fitting manner.It is a layered compound.

No further mention of this compound is available in the past or current literature except for those papers dealing with structure.

$BaCd_2$ has the structure shown in Fig. 16.62.

Cell parameters are: $a = 5.1643$ Å, $b = c = 6.5566$ Å, $\alpha = 79.42°$, $\beta = \gamma = 68.81°$, cell volume = 84.98 Å^3, $Z = 2$. Cell occupancy is shown in Table 16.41.

No mention of the physical or electrical properties of this compound is available in the past or current technical literature. It has not been characterized except for its structural characteristics.

In contrast, the Ba_2Cd compound has the structure shown in Fig. 16.63.

Cell parameters are: $a = 4.2722$ Å, $b = c = 8.1783$ Å, $\alpha = \beta = 105.14°$, $\gamma = 90°$, cell volume = 138.70 Å^3, $Z = 1$. Cell occupancy is shown in Table 16.42.

This compound is offered for sale commercially with the CAS number of 37190-20-8. No other description of the physical or electronic behavior of this compound has been documented in the past or current technical literature.

It has not found usage in Industry or interest by the Academic community.

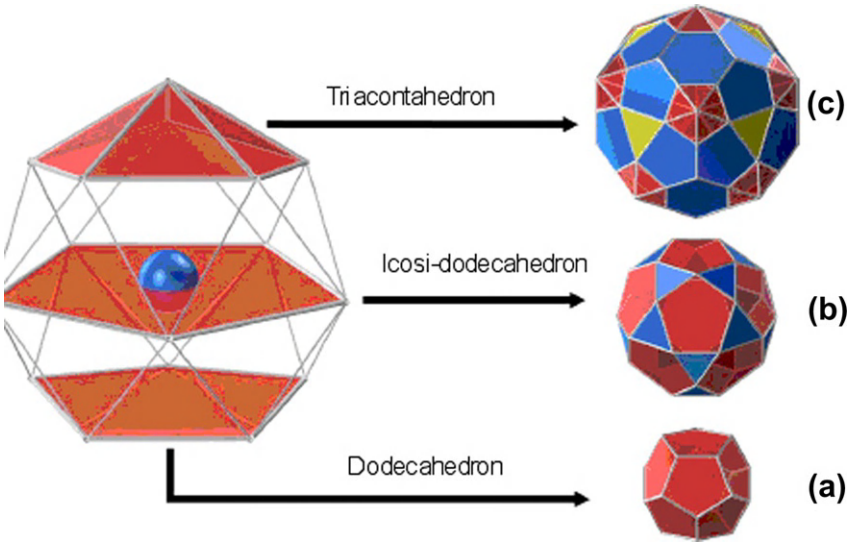

FIGURE 16.55

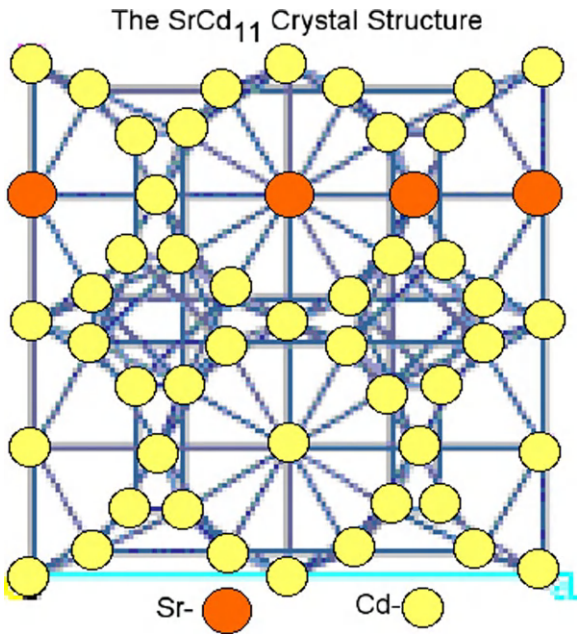

FIGURE 16.56

The compound, $BaCd_{11}$, has the conformational character shown in Fig. 16.64.

Cell parameters are: $a = 7.7455$ Å, $b = c = 9.3519$ Å, $\alpha = 80.14°$, $\beta = \gamma = 65.56°$, cell volume $= 561.00$ Å^3, $Z = 4$. Cell occupancy is shown in Table 16.43.

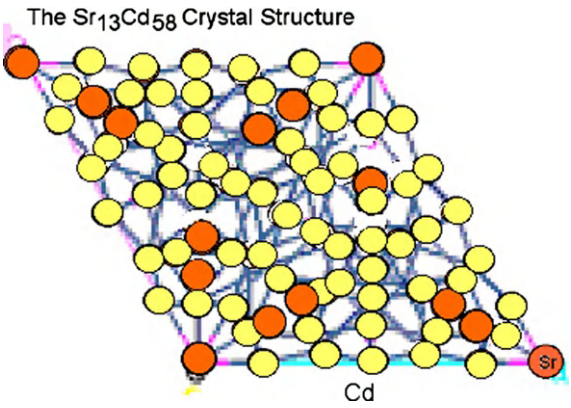

FIGURE 16.58

The $BaCd_{11}$ compound crystallizes in the space group $I41/amd$ with one Ba position (m2) and three Cd sites (m2, .2/m., 1). The structure is described in terms of all-face-capped Cd_8 tetrahedra as the central building unit, defined by the Cd atoms on .2/m. and 1 sites. The building units are condensed into chains by the central tetrahedra-sharing edges, and the chains are interconnected by shared capping atoms. The resulting 3D framework of Cd atoms yields channels that are occupied by Ba and Cd atoms on the high-symmetry $\bar{4}$m2 positions.

The compound, Ba_7Cd_{31}, has the structure shown in Fig. 16.65.

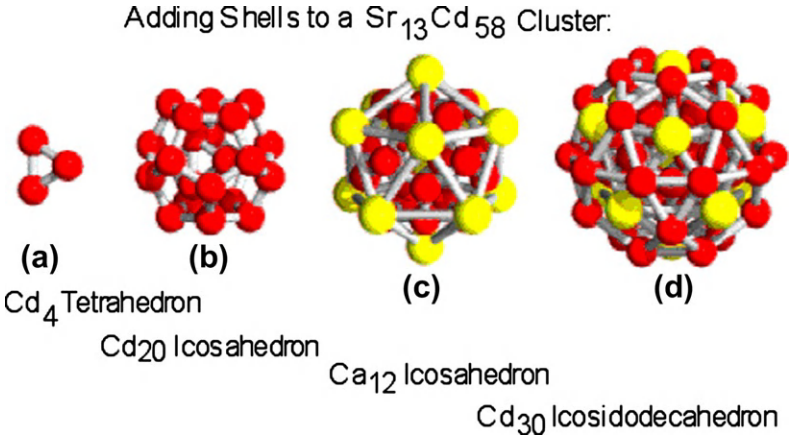

FIGURE 16.57

TABLE 16.37

No.	Site notation	Atom	Multiplicity	Wyckoff	Site symmetry	*x*	*y*	*z*	Occupancy
1	Cd1	Cd	32	i	1	0.205	0.127	0.067	1.0
2	Cd2	Cd	8	c	.2/m.	0	0	0	1.0
3	Sr1	Sr	4	b	-4m2	0	1/4	3/8	1.0
4	Cd3	Cd	4	a	-4m2	0	3/4	1/8	1.0

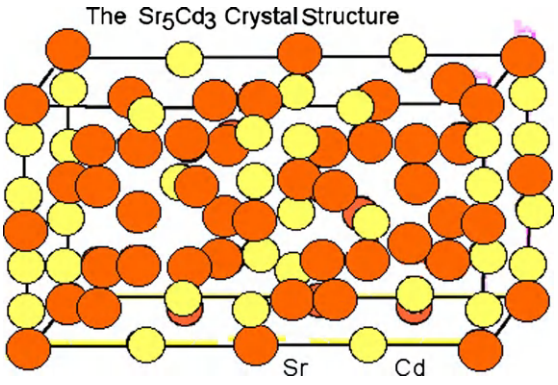

FIGURE 16.59

Cell parameters are: $a = 10.234$ Å, $b = c = 10.744$ Å, $\alpha = 120°$, $\beta = \gamma = 90°$, cell volume $= 1018.92$ Å^3, $Z = 1$. Cell occupancy is shown in Table 16.44.

No other description of the physical or electronic behavior of this compound has been documented in the past or current technical literature. It has not found usage in Industry or interest by the Academic community.

Two Zintl compounds $Ba_2Cd_2As_3$ and $Ba_2Cd_2Sb_3$ have been synthesized and structurally characterized. They crystallize in a novel monoclinic structure type with the space group $C2/m$ (no. 12), featuring poly-anionic layers made of $CdPn_4$ tetrahedra (Pn = As, Sb) and homo-atomic Pn–Pn bonds. The topological relationships between the structure of $Ba_2Cd_2Sb_3$ and those of $BaCd_2Sb_2$ ($CaAl_2Si_2$ type) and $Ba_3Cd_2Sb_4$ (own type) were discussed as well. Based on electronic structures calculations, carried out by the density functional method, and resistivity measurements, pure $Ba_2Cd_2As_3$ was shown to be a small-gap semiconductor and pure $Ba_2Cd_2Sb_3$ to be a poor metal. The structures of these compounds are amenable to doping on both the cation and pnicogen sites, and make them promising materials for thermoelectric applications. A Zintl structure is shown in Fig. 16.66.

TABLE 16.38

No.	Site notation	Atom	Multiplicity	Wyckoff	Site symmetry	*x*	*y*	*z*	Occupancy
1	Cd1	Cd	24	l	1	0.3633	0.0362	0.1012	1.0
2	Cd2	Cd	12	k	.m.	0.0973	0.1946	0.1599	1.0
3	Sr1	Sr	12	k	.m.	0.2065	0.4130	0.0515	1.0
4	Cd3	Cd	12	k	.m.	0.2374	0.4748	0.6606	1.0
5	Cd4	Cd	12	k	.m.	0.5628	0.1256	0.6395	1.0
6	Cd5	Cd	12	k	.m.	0.6011	0.2022	0.0527	1.0
7	Cd6	Cd	12	j	m..	0.0833	0.3666	1/4	1.0
8	Cd7	Cd	12	i	.2.	0.1902	0	0	1.0
9	Cd8	Cd	6	h	mm2	0.2692	0.5384	1/4	1.0
10	Sr2	Sr	6	h	mm2	0.5414	0.0828	1/4	1.0
11	Sr3	Sr	6	h	mm2	0.8715	0.7430	1/4	1.0
12	Cd9	Cd	6	g	.2/m.	1/2	0	0	1.0
13	Cd10	Cd	4	f	3m.	1/3	2/3	0.0949	1.0
14	Cd11	Cd	2	d	-6m2	1/3	2/3	3/4	1.0
15	Cd12	Cd	2	b	-6m2	0	0	1/4	1.0
16	Sr4	Sr	2	a	-3m.	0	0	0	1.0

TABLE 16.39

No.	Site notation	Atom	Multiplicity	Wyckoff	Site symmetry	*x*	*y*	*z*	Occupancy
1	Sr2	Sr	16	l	..m	0.1689	0.6689	0.1472	1.0
2	Cd2	Cd	8	h	m.2m	0.621	0.121	0	1.0
3	Sr1	Sr	4	c	4/m..	0	0	0	1.0
4	Cd1	Cd	4	a	422	0	0	1/4	1.0

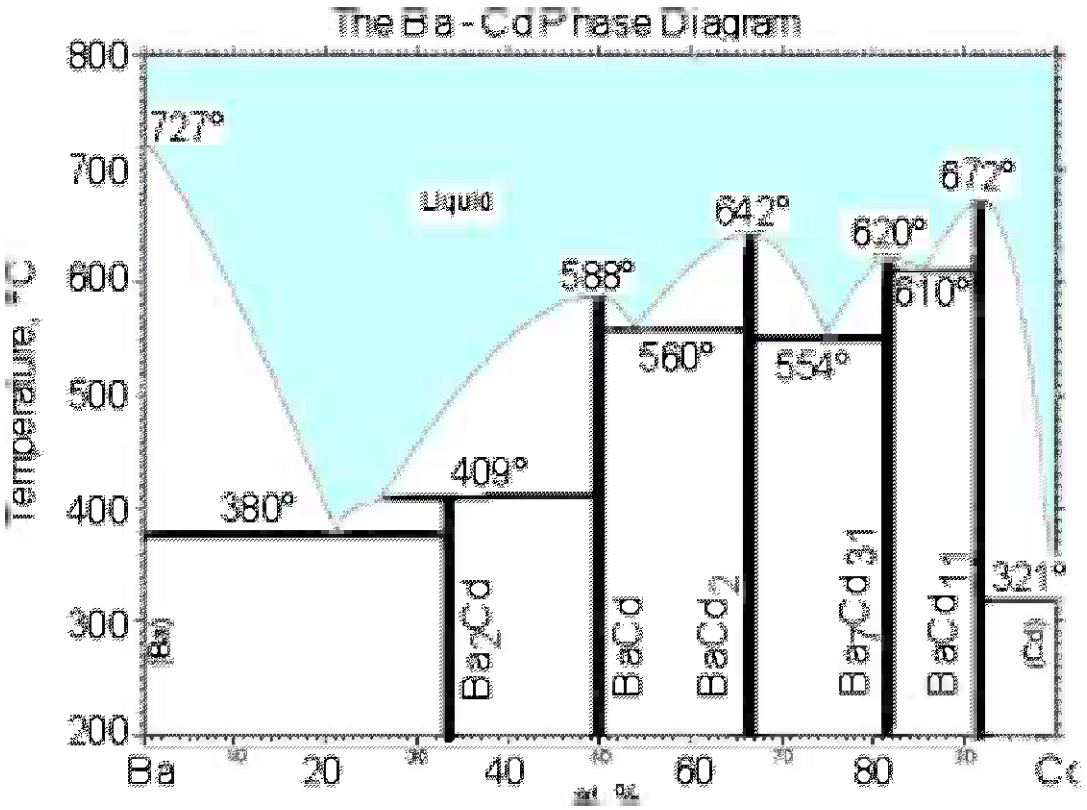

FIGURE 16.60

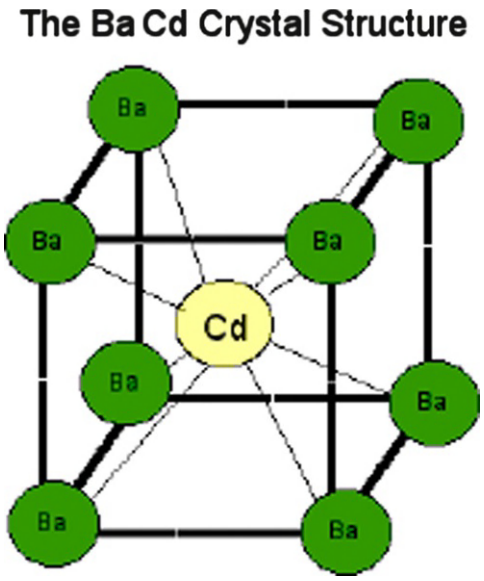

FIGURE 16.61

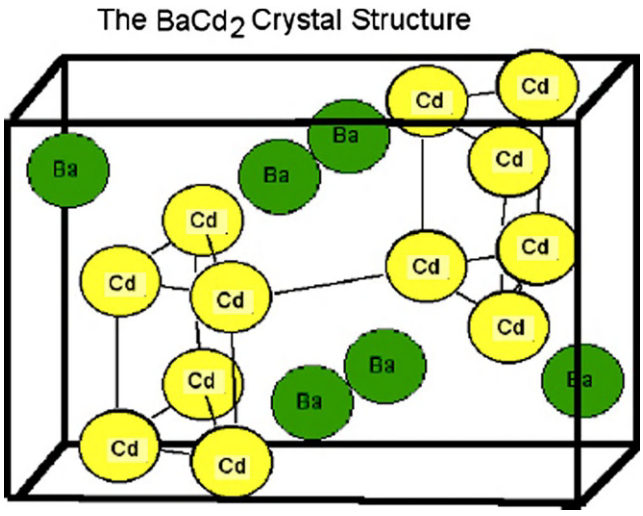

FIGURE 16.62

TABLE 16.40

No.	Site notation	Atom	Multiplicity	Wyckoff	Site symmetry	*x*	*y*	*z*	Occupancy
1	Cd	Cd	1	b	m-3m	1/2	1/2	1/2	1.0
2	Ba	Ba	1	a	m-3m	0	0	0	1.0

TABLE 16.41

No.	Site notation	Atom	Multiplicity	Wyckoff	Site symmetry	*x*	*y*	*z*	Occupancy
1	Cd1	Cd	8	h	m..	0	0.06	0.163	1.0
2	Ba1	Ba	4	e	mm2	0	1/4	0.547	1.0

TABLE 16.42

No.	Site notation	Atom	Multiplicity	Wyckoff	Site symmetry	*x*	*y*	*z*	Occupancy
1	Ba	Ba	4	e	4mm	0	0	0.37	1.0
2	Cd	Cd	2	a	4/mmm	0	0	0	1.0

TABLE 16.43

No.	Site notation	Atom	Multiplicity	Wyckoff	Site symmetry	*x*	*y*	*z*	Occupancy
1	Cd1	Cd	32	i	1	0.205	0.127	0.067	1.0
2	Cd2	Cd	8	c	.2/m.	0	0	0	1.0
3	Ba1	Ba	4	b	-4m2	0	1/4	3/8	1.0
4	Cd3	Cd	4	a	-4m2	0	3/4	1/8	1.0

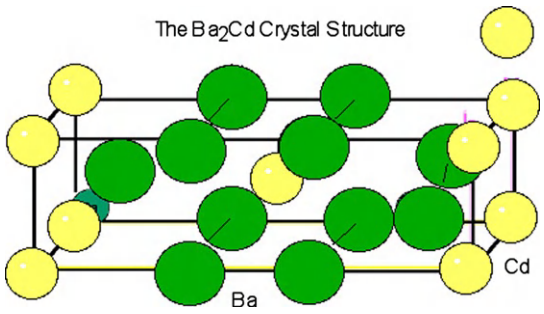

FIGURE 16.63

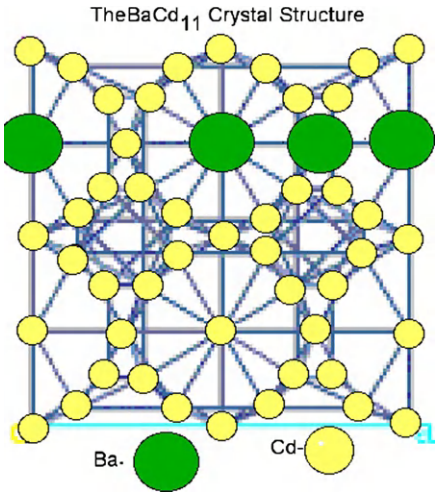

FIGURE 16.64

This compound has shown a high degree of thermoelectric power conversion, but only at very low temperatures, as shown in Fig. 16.67.

No other IM compounds of Ba–Cd metals are known.

In the system, Ba–Cd–O, the crystal structure of $BaCdO_2$ has been determined. The orthohombic unit cell [$a = 3.660$; $b = 6.168$; $c = 11.950$ Å; space group *Pmnb—D*] contains four formula units; $d_x = 6.94$, $d_{pyc} = 6.86$ g/cm^3. With the last refinement, R and R' fall to 0.058 and 0.075, respectively ($\sin\theta/\lambda \leq 0.950$). The total arrangement is related to that of ($SrZnO_2^2$). Here, the Cd atom is surrounded by 5 (4 + 1) O-neighbors [trigonal bipyramidal] while each Zn atom has a tetrahedral arrangement of four O neighbors.

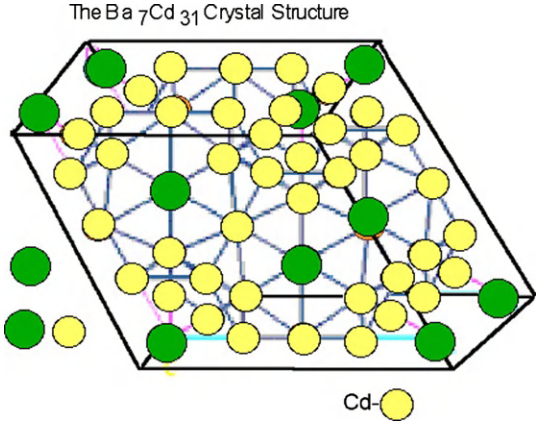

FIGURE 16.65

TABLE 16.44

No.	Site notation	Atom	Multiplicity	Wyckoff	Site symmetry	x	y	z	Occupancy
1	Cd3	Cd	12	o	.m.	0.1852	0.3704	0.2604	1.0
2	Cd5	Cd	6	m	mm2	0.1038	0.2076	1/2	0.5
3	Cd1	Cd	6	j	m2m	0.2708	0	0	1.0
4	Cd2	Cd	6	i	2mm	1/2	0	0.1619	1.0
5	Cd4	Cd	4	h	3m.	1/3	2/3	0.3499	1.0
6	Ba3	Ba	3	g	mmm	1/2	0	1/2	1.0
7	Ba2	Ba	2	e	6mm	0	0	0.2135	1.0
8	Ba1	Ba	2	c	-6m2	1/3	2/3	0	1.0

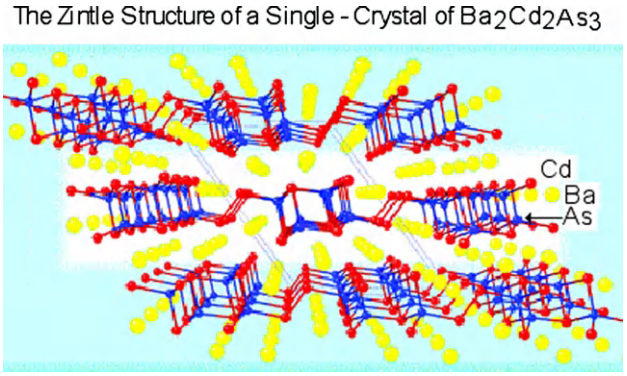

FIGURE 16.66

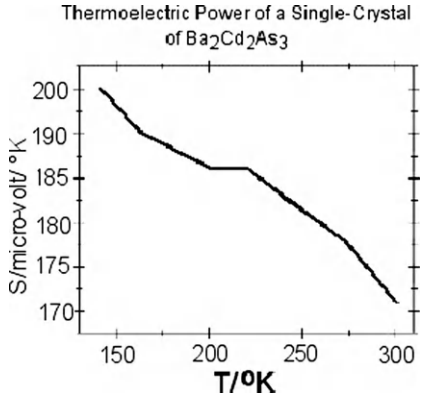

FIGURE 16.67

Therefore, the 2D $[ZnO_2]$-arrangement is replaced by a 3D one. Ba is situated at specific holes in the lattice, being surrounded by seven O atoms.

No other barium cadmate compounds have been documented in the past or present technical literature.

16.2.6. Radium Cadmium Compounds

Although Ra^0 and RaO undoubtedly form the same type of compounds with Cd^0 or CdO, there is no record of anyone having done so in the past or current literature. This is probably due to lack of interest by both Academia and Industry but more likely due to the high cost of either of these components.

16.3. THE ALKALINE EARTH MERCURY COMPOUNDS

Mercury forms several IM compounds with the alkaline earths. However, only a few oxide-based compounds are known.

16.3.1. Beryllium Mercury Compounds

Beryllium does not form any IM compounds with mercury. Nor does it form any compounds in the $BeO–Hg_xO_y$ system, where x and y can vary from 1 to 3.

16.3.2. Magnesium Mercury Compounds

Magnesium metal forms six different IM compounds with Hg metal. This is shown in Fig. 16.68.

The structures of five of these compounds are known and include the 1;1, 1:2, 2:1, 3:1 and 5:3 compounds. Of the six (6) compounds shown in the diagram, two melt congruently. The others melt incongruently. The structure of the compound, Mg_5Hg_2, remains unknown.

The formation enthalpies per mole of the compounds MgHg(solid) and CaHg(solid) have been determined as -28.2 ± 0.8 and -56.8 ± 4.6 kJ/mol, respectively. This was accomplished by studying the vaporization of compounds of the Mg–Hg and Ca–Hg systems, with a novel Knudsen cell–mass spectrometer system. Comparative values of −30 [MgHg(solid)] and −59 kJ/mol [CaHg(solid)] were predicted, using the

volume contraction model, as well as the values of −34.6 [MgHg(solid)] and −1.6 kJ/mol [CaHg(solid)] for the Pauling model of ionic bond, and using the electronegativities of Gordy and Thomas. The enthalpies of formation were compared with those of IM compounds having predominantly ionic bonds. The enthalpies of formation per mole of an atom of the compounds such as BaHg(solid) and SrHg(solid) were predicted as −61.6 and −77.9 kJ/mol, by applying the same Pauling model of ionic bond to the electronegativities of Gordy and Thomas.

The MgHg compound has the form shown in Fig. 16.69.

Cell parameters are: $a = 10.234$ Å, $b = c = 10.744$ Å, $\alpha = 120°$, $\beta = \gamma = 90°$, cell volume = 1018.92 Å^3, $Z = 1$.

Cell occupancy is shown in Table 16.45.

The de Haas–van Alphen effect has been observed in the quadrivalent β-brass compound MgHg. Five frequency groups have been measured in the {110} and {100} planes along with some effective masses at high symmetry points. All five groups observed are well explained by Skriver's relativistic LMTO band calculation. A football-shaped piece predicted in the third band has the size and shape of an observed closed section which was inverted with tetragonal harmonics. The remaining orbits arise from the multi-connected second band surface, a surface formed by connecting pockets at Γ and R with arms along <111> of the Brillouin surface of the crystal structure.

The compound, Mg_2Hg, has the structure shown in Fig. 16.70.

Cell parameters are: $a = 4.618$ Å, $b = 6.224$ $c = 8.843$ Å, $\alpha = \beta = \gamma = 90°$, cell volume = 252.77 Å^3, $Z = 4$. Cell occupancy is shown in Table 16.46.

The compound, $MgHg_2$, has the conformational form shown in Fig. 16.71.

Cell parameters are: $a = b = 3.933$ Å, $c = 5.159$ Å, $\alpha = \beta = 111.79°$, $\gamma = 90°$, cell volume = 64.40 Å^3, $Z = 2$. Cell occupancy is shown in Table 16.47.

The compound, Mg_3Hg, has the structural form shown in Fig. 16.72.

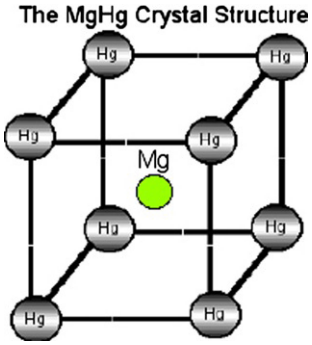

FIGURE 16.69

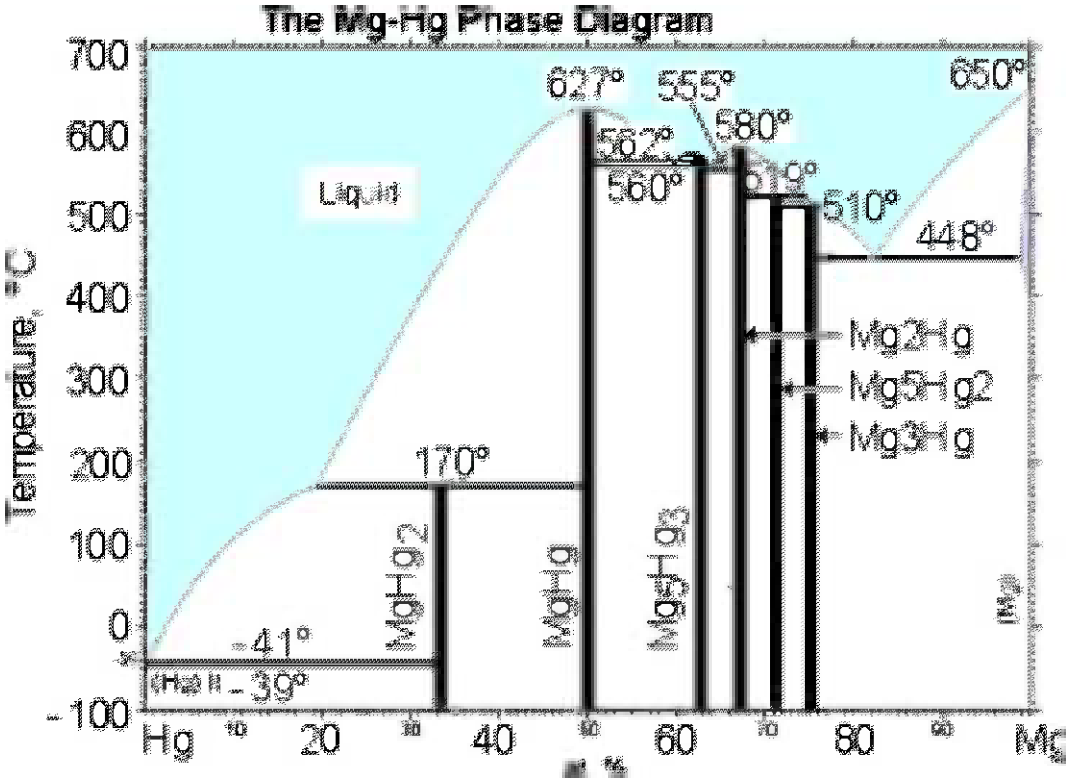

FIGURE 16.68

TABLE 16.45

No.	Site notation	Atom	Multiplicity	Wyckoff	Site symmetry	x	y	z	Occupancy
1	Mg	Mg	1	b	m-3m	1/2	1/2	1/2	1.0
2	Hg	Hg	1	a	m-3m	0	0	0	1.0

TABLE 16.46

No.	Site notation	Atom	Multiplicity	Wyckoff	Site symmetry	x	y	z	Occupancy
1	Mg1	Mg	4	c	.m.	0.038	1/4	0.718	1.0
2	Mg2	Mg	4	c	.m.	0.174	1/4	0.062	1.0
3	Hg1	Hg	4	c	.m.	0.202	1/4	0.389	1.0

TABLE 16.47

No.	Site notation	Atom	Multiplicity	Wyckoff	Site symmetry	x	y	z	Occupancy
1	Hg	Hg	4	e	4mm	0	0	0.333	1.0
2	Mg	Mg	2	a	4/mmm	0	0	0	1.0

Cell parameters are: $a = b = 4.858$ Å, $c = 8.639$ Å, $\alpha = 120°$, $\beta = \gamma = 90°$, cell volume = 1,018.92 Å^3, $Z = 1$. Cell occupancy is shown in Table 16.48.

The compound, Mg_5Hg_3, has the structure shown in Fig. 16.73.

Cell parameters are: $a = 5.919$ Å, $b = c = 8.243$ Å, $\alpha = 120°$, $\beta = \gamma = 90°$, cell volume = 348.30 Å^3, $Z = 2$. Cell occupancy is shown in Table 16.49.

Evaporation of the compounds Mg_5Hg_3(solid), Mg_2Hg(solid), Mg_5Hg_2(solid), and Mg_3Hg(solid) was studied using a Knudsen cell–mass spectrometer system. They evaporate according to the equations:

$$2Mg_5Hg_3(\text{solid}) \Rightarrow Hg(\text{gas}) + 5Mg_2Hg(\text{solid}), \quad (1)$$

$$5Mg_5Hg(\text{solid}) \Rightarrow Hg(\text{gas}) + 2Mg_5Hg_2(\text{solid}), \quad (2)$$

$$3Mg_5Hg_2(\text{solid}) \Rightarrow Hg(\text{gas}) + 5Mg_3Hg(\text{solid}), \text{ and} \quad (3)$$

$$Mg_3Hg(\text{solid}) \Rightarrow Hg(\text{gas}) + 3MgHg(\text{solid}) \quad (4)$$

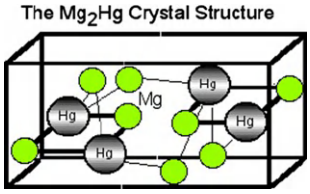

FIGURE 16.70

The Hg partial pressures of (Eqns 1 and 4) are:

$$\log(p\text{Pa}) = (4973.1 \pm 60.3)\text{K}/T + (9.886 \pm 0.12)\ (440 - 540\ \text{K}),$$

$$\log(p\text{Pa}) = (6605.6 \pm 69.1)\text{K}/T + (10.91 \pm 0.11)\ (499 - 7110\ \text{K}),$$

$$\log(p\text{Pa}) = (7118.3 \pm 116.5)\text{K}/T + (10.91 \pm 0.19)\ (548 - 9890\ \text{K}), \text{and}$$

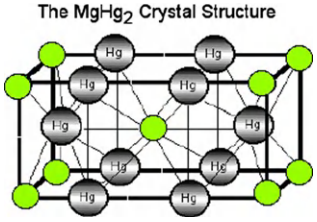

FIGURE 16.71

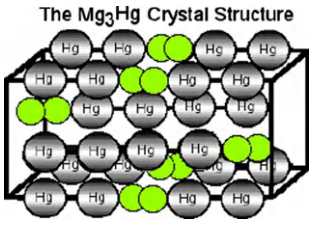

FIGURE 16.72

TABLE 16.48

No.	Site notation	Atom	Multiplicity	Wyckoff	Site symmetry	x	y	z	Occupancy
1	Hg1	Hg	4	f	3m.	1/3	2/3	0.583	1.0
2	Mg1	Mg	2	c	-6m2	1/3	2/3	1/4	1.0
3	Hg2	Hg	2	b	-6m2	0	0	1/4	1.0

TABLE 16.49

No.	Site notation	Atom	Multiplicity	Wyckoff	Site symmetry	x	y	z	Occupancy
1	Mg2	Mg	6	g	m2m	0.25	0	1/4	1.0
2	Hg	Hg	6	g	m2m	0.61	0	1/4	1.0
3	Mg1	Mg	4	d	3.2	1/3	2/3	0	1.0

$$\log(p\text{Pa}) = (7502.3 \pm 58.8)\text{K}/T + (11.29 \pm 0.10)\ (525 - 695\ \text{K})$$

The enthalpy changes of reactions (Eqns 1 and 4) were determined using the second and third Law method.

Formation enthalpies in kJ/mol at 298 K were obtained as:

-60.5 ± 4.3 ($MgHg_2$),
-56.4 ± 1.7 (MgHg),
-217.1 ± 7.3 (Mg_5Hg_3),
-79.8 ± 2.8 (Mg_2Hg),
-166.0 ± 6.8 (Mg_5Hg_2),
-84.2 ± 4.0 (Mg_3Hg).

for the compounds given in parentheses.

The superconducting transition temperatures of several of these Hg–Mg metallic compounds have been determined. The critical temperature decreases monotonically with increasing Mg content, and shows no apparent crystal structure dependence. An attempt was made to extrapolate to the transition temperature of pure Mg. This procedure yielded an estimate (rather uncertain) of between 1.0 and 10.0×10^{-3} K for the T_c of pure Mg. The transition temperatures of Hg_2Mg, HgMg, Hg_3Mg_5, $HgMg_2$ and $HgMg_3$ fall in the range 4·0–0.16 K. The critical temperatures of a few compounds of Hg with Ba and Ca have also been measured above 1.25 K.

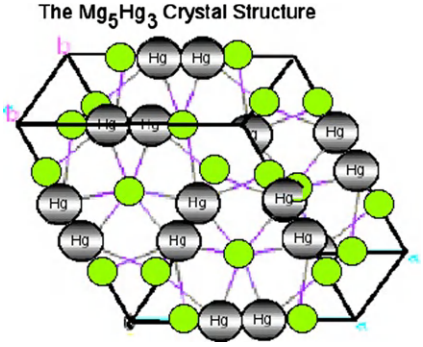

FIGURE 16.73

Magnesium–mercury amalgams are supplied commercially with the CAS numbers of Mg_5Hg_3(solid) [12055-41-3], Mg_2Hg(solid) [12055-30-0], Mg_5Hg_2(solid) [55200-37-8].

In the system, MgO–Hg_xO_y, where x and y can vary from 1 to 3, no compounds have been documented in the past or present literature.

16.3.3. Calcium Mercury Compounds

Calcium metal forms a number of IM compounds with Hg metal as shown in Fig. 16.74.

Nine (9) compounds are shown in the diagram, two of which melt congruently. The others melt peritectically or incongruently. The structures of eight compounds have been documented in the current literature. The structure of Ca_3Hg_2 has not been documented.

The CaHg compound has the structure shown in Fig. 16.75

Cell parameters are: $a = 10.234$ Å, $b = c = 10.744$ Å, $\alpha = 120°$, $\beta = \gamma = 90°$, cell volume $= 1018.92$ Å^3, $Z = 1$. Cell occupancy is shown in Table 16.50(A).

The formation enthalpies per mole of an atom of the compound CaHg(solid) was determined as -56.8 ± 4.6 kJ/mol, by studying the vaporization of compounds of the Ca–Hg system with a novel Knudsen cell–mass spectrometer system. A value of -59 kJ/mol [CaHg(solid)] was predicted using the volume contraction model, and the Pauling model of ionic bonds combined with the electronegativities of Gordy and

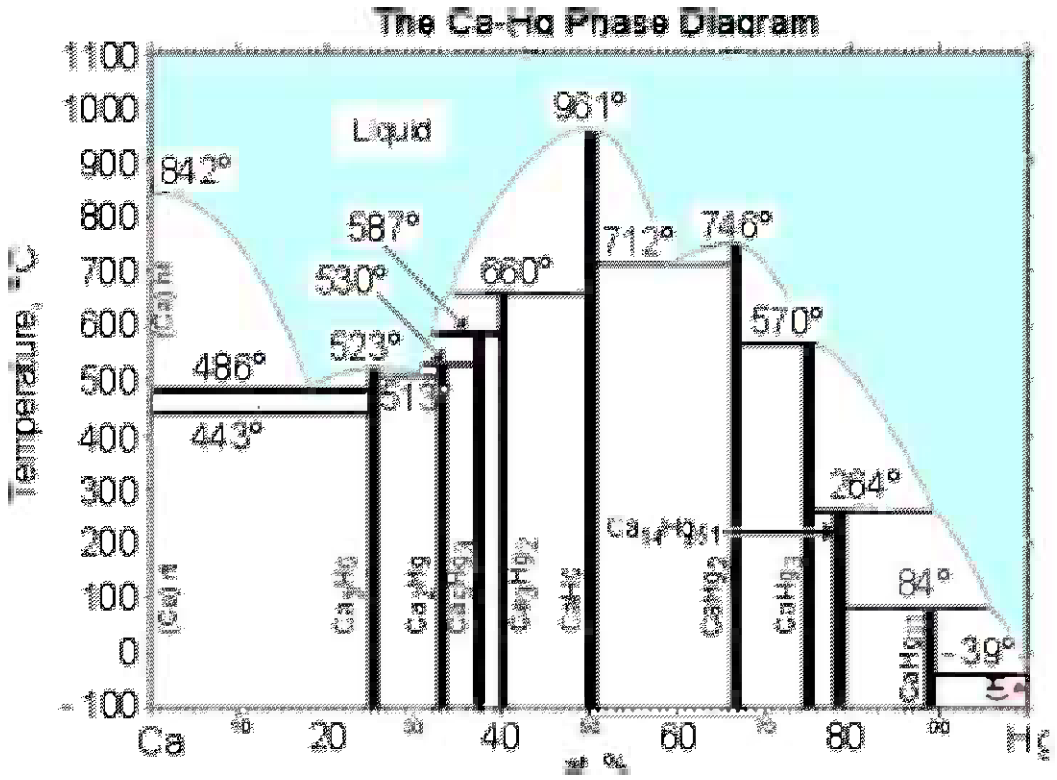

FIGURE 16.74

Thomas. The enthalpy of formation was compared with those of IM compounds with predominantly ionic bond. The enthalpies of formation per mole of an atom of the compounds BaHg(solid) and SrHg(solid) were predicted as −61.6 and −77.9 kJ/mol, by applying the Pauling model of ionic bond with the electronegativities of Gordy and Thomas.

The compound, $CaHg_2$, has the structural form shown in Fig. 16.76.

Cell parameters are: $a = 3.5712$ Å, $b = c = 4.8943$ Å, $\alpha = 120°$, $\beta = \gamma = 90°$, cell volume $= 74.07$ Å^3, $Z = 1$. Cell occupancy is shown in Table 16.50(B).

Vapor pressure measurements in the system Ca–Hg (0–50 atom% Ca) at temperatures between 250 and 500 °C confirmed the existence of the phases $CaHg_5$, $CaHg_3$, $CaHg_2$, and CaHg. No other phases exist in the examined range. $CaHg_3$ crystallizes with a stoichiometric composition without any range of homogeneity, but $CaHg_5$ and $CaHg_2$ have small (0.2 and 0.8 atom%, respectively) homogeneity ranges. The examinations confirm the peritectic decomposition of $CaHg_5$ (263 °C) and the stability of $CaHg_3$, $CaHg_2$ and CaHg up to

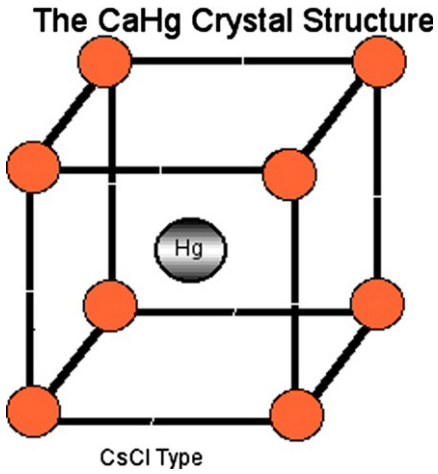

FIGURE 16.75

temperatures above 500 °C. The heats of reaction of the Hg-rich Ca–Hg-compounds formed from CaHg and Hg, as calculated from vapor pressure measurements are relatively small. Further experiments proved that

TABLE 16.50A

No.	Site notation	Atom	Multiplicity	Wyckoff	Site symmetry	*x*	*y*	*z*	Occupancy
1	Hg	Hg	1	b	m-3m	1/2	1/2	1/2	1.0
2	Ca	Ca	1	a	m-3m	0	0	0	1.0

TABLE 16.50B

No.	Site notation	Atom	Multiplicity	Wyckoff	Site symmetry	x	y	z	Occupancy
1	Hg1	Hg	2	d	3m.	1/3	2/3	0.42	1.0
2	Ca1	Ca	1	a	-3m.	0	0	0	1.0

TABLE 16.51

No.	Site notation	Atom	Multiplicity	Wyckoff	Site symmetry	x	y	z	Occupancy
1	Ca1	Ca	4	c	.m.	0.038	1/4	0.718	1.0
2	Ca2	Ca	4	c	.m.	0.174	1/4	0.062	1.0
3	Hg1	Hg	4	c	.m.	0.202	1/4	0.389	1.0

Hg is not soluble in Ca at least at a temperature of 450 °C.

The compound, Ca_2Hg has the structure shown in Fig. 16.77.

Cell parameters are: $a = 4.892$ Å, $b = 7.863$ Å, $c = 9.874$ Å, $\alpha = \beta = \gamma = 90°$, cell volume $= 74.07$ Å^3, $Z = 4$. Cell occupancy is shown in Table 16.51.

The physical or electronic properties of this material have not been documented in the past or present literature. The only related data have been that of its structure determination. Ca_2Hg is offered commercially with a CAS number of 39461-28-4.

The compound, Ca_3Hg, has the structure shown in Fig. 16.78.

Cell parameters are: $a = 6.8282$, $b = 8.1513$, $c = 10.152$ Å, $\alpha = \beta = \gamma = 90°$, cell volume $= 565.29$ Å^3, $Z = 4$. Cell occupancy is shown in Table 16.52.

The chemical bonding of the Hg_2 dimers present in Ca_5Au_4 and Ca_3Hg_2 was examined based on first principles electronic band structure calculations. In these compounds, the 6s- and 5d-block bands of Hg are completely filled while the frontier levels of Hg are given by partially filled 6p-block bands such that the transition metal atoms Hg are best described as anions with electron configuration $(5d)^{10}(6s)^2(6p)^1$. Thus, the Hg_2 dimers in Ca_5Au_4 and Ca_3Hg_2 are present as $[Au\text{-}Au]^{4-}$, and $[Hg\text{-}Hg]^{2-}$ Zintl anions, respectively. In these compounds, the Hg_2 dimers have a single bond formed by the p_σ–p_σ interaction between the 5p and 6p orbitals of Hg atoms. The anions of late transition metal elements are different from those of late main group elements in their tendency for covalent bond formation.

This compound is supplied commercially with the CAS number of 39461-28-4.

The compound, $CaHg_3$, has the structure shown in Fig. 16.79.

Cell parameters are: $a = 5.024$ Å, $b = c = 6.635$ Å, $\alpha = 120°$, $\beta = \gamma = 90°$, cell volume $= 191.39$ Å^3, $Z = 2$. Cell occupancy is shown in Table 16.53.

This compound is supplied commercially with the CAS number of 12049-40-0.

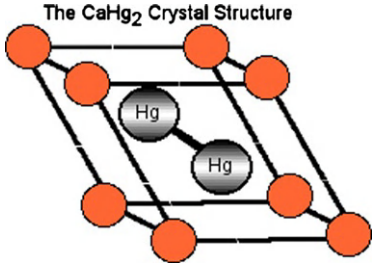

FIGURE 16.76

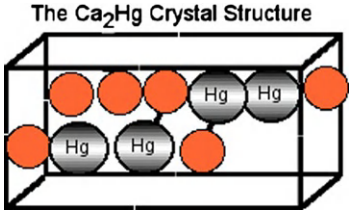

FIGURE 16.77

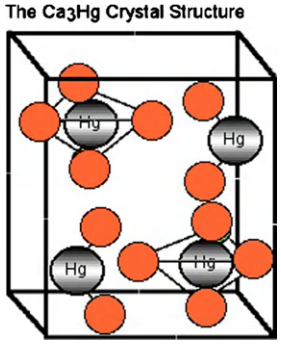

FIGURE 16.78

TABLE 16.52

No.	Site notation	Atom	Multiplicity	Wyckoff	Site symmetry	*x*	*y*	*z*	Occupancy
1	Ca1	Ca	8	d	1	0.1834	0.0689	0.1656	1.0
2	Ca2	Ca	4	c	.m.	0.0388	1/4	0.6578	1.0
3	Hg1	Hg	4	c	.m.	0.3764	1/4	0.4426	1.0

TABLE 16.53

No.	Site notation	Atom	Multiplicity	Wyckoff	Site symmetry	*x*	*y*	*z*	Occupancy
1	Hg1	Hg	6	h	mm2	0.1667	0.3333	1/4	1.0
2	Ca1	Ca	2	d	-6m2	1/3	2/3	3/4	1.0

TABLE 16.54

No.	Site notation	Atom	Multiplicity	Wyckoff	Site symmetry	*x*	*y*	*z*	Occupancy
1	Ca2	Ca	16	l	..m	0.1645	0.6645	0.1467	1.0
2	Hg2	Hg	8	h	m.2m	0.6323	0.1323	0	1.0
3	Ca1	Ca	4	c	4/m..	0	0	0	1.0
4	Hg1	Hg	4	a	422	0	0	1/4	1.0

The compound, Ca_5Hg_3, has the structure shown in Fig. 16.80.

Cell parameters are: $a = 9.3573$ Å, $b = c = 8.1892$ Å, $\alpha = 90°$, $\beta = \gamma = 115.95°$, cell volume = 492.92 Å^3, $Z = 4$. Cell occupancy is shown in Table 16.54.

Both the incongruently melting compounds, Ca_5Hg_3 and Sr_5Cd_3, have been synthesized from stoichiometric amounts of the pure elements. They crystallize with the Cr_5B_3 type of structure: space group $I4/mcm$, $Z = 4$; Ca_5Hg_3 (Sr_5Cd_3): $a = 8.189$ (8.717) Å, $c = 14.701$ (16.601) pm, $c/a = 1.80$ (1.90), $R = 2.33\%$ (2.97%). The most remarkable fragments are dumbbells X_2, which have interatomic distances only slightly longer than the sum of *Pauling's* covalent radii: Hg–Hg (Cd–Cd) = 306 (298) pm. The structure can be visually viewed as rhombic dodecahedra as the only constituent moieties. These rhombic dodecahedra are built up by eight Ca (Sr) atoms and six Hg (Cd) atoms and are furthermore centered by an additional Ca (Sr) atom. Along [001] the rhombic dodecahedra share common vertices, but along [110] they are interconnected via common triangular faces. This kind of face sharing is responsible for the short distances obtained between the polyhedra, which leads to the occurrence of the dumbbells mentioned above.

The compound, $CaHg_{11}$, has the structure shown in Fig. 16.81.

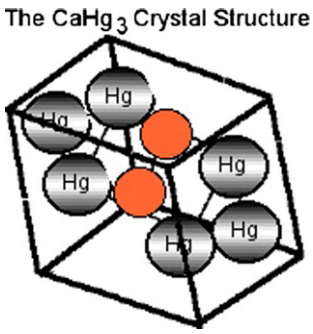

FIGURE 16.79

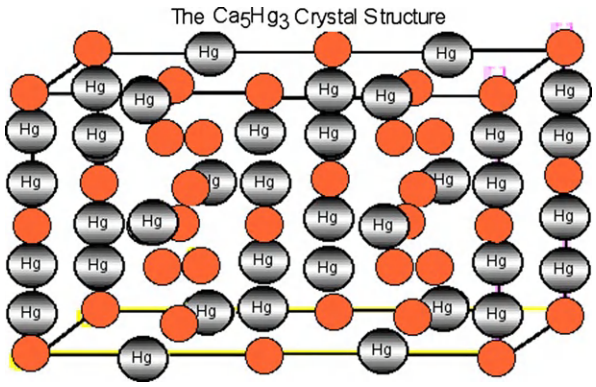

FIGURE 16.80

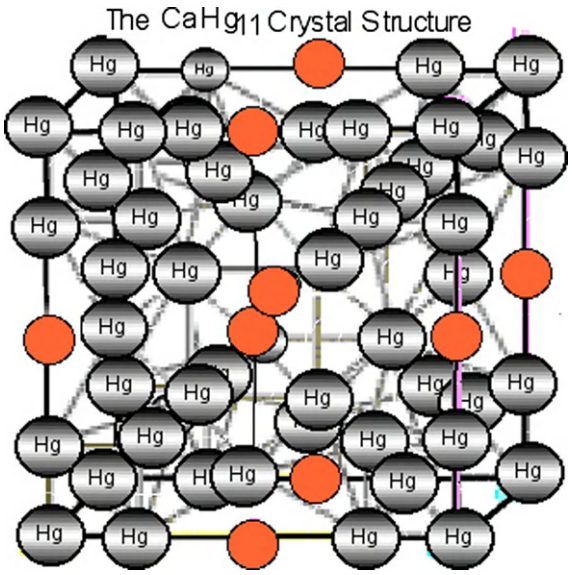

FIGURE 16.81

Cell parameters are: $a = b = c = 9.635$ Å, $\alpha = \beta = \gamma = 90°$, cell volume $= 884.74$ Å^3, $Z = 3$. Cell occupancy is shown in Table 16.55.

This compound has not been the subject of any scientific investigation and the only data relating to it involve structural constants.

The compound, $Ca_{14}Hg_{51}$, has the structure shown in Fig. 16.82.

Cell parameters are: $a = 9.6332$ Å, $b = c = 13.442$ Å, $\alpha = 120°$, $\beta = \gamma = 90°$, cell volume $= 1506.92$ Å^3, $Z = 1$. Cell occupancy is shown in Table 16.56.

This compound has similar structural properties to those of the Ca–Cd system (Fig. 16.83).

It also forms compact icosahedral structures as shown in Fig. 16.83.

The compound, Ca_3Hg_2, has the structure shown in Fig. 16.84.

Cell parameters are: $a = 4.1974$ Å, $b = c = 9.4762$ Å, $\alpha = \beta = \gamma = 90°$, cell volume $= 301.52$ Å^3, $Z = 2$. Cell occupancy is shown in Table 16.57.

The coordination polyhedron around the Hg–Hg dimers in Ca_3Hg_2 is shown in Fig. 16.85.

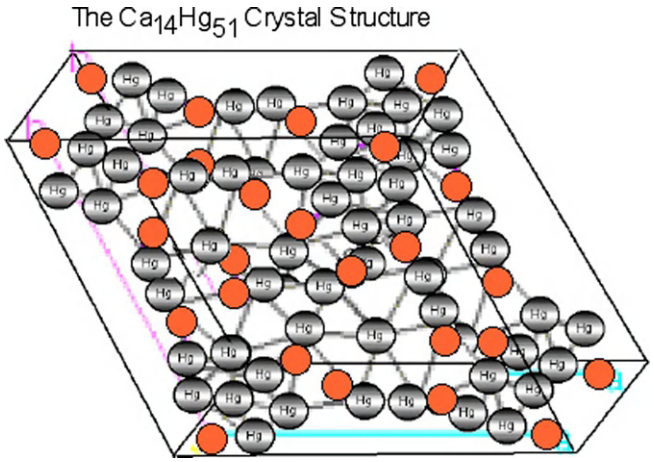

FIGURE 16.82

The dark blue spheres form a trigonal biprism, and the light blue spheres cap its four rectangular faces.

A number of calcium mercuride compounds are offered for sale commercially, as noted above.

In the CaO–HgO system, the only known compound is $CaHgO_2$ that has the structure shown in Fig. 16.86.

Cell parameters are: $a = 6.5391$ Å, $b = c = 3.6482$ Å, $\alpha = \beta = 74.02°$, $\gamma = 60°$, cell volume $= 69.59$ Å^3, $Z = 2$. Cell occupancy is shown in Table 16.58.

No other calcium mercurate compounds are known. No calcium mercurate compounds are offered for sale commercially and no CAS numbers have been issued.

16.3.4. Strontium Mercury Compounds

Strontium metal forms a number of IM compounds with Hg metal as shown in Fig. 16.87.

Nine (9) compounds are known, two of which melt congruently. The others melt incongruently. The structures of all nine compounds have been documented in the current literature.

The strontium–mercury system has been investigated using thermal, micrographic and X-ray methods. Two compounds melt congruently: SrHg (850 °C) and

TABLE 16.55

No.	Site notation	Atom	Multiplicity	Wyckoff	Site symmetry	x	y	z	Occupancy
1	Hg3	Hg	12	j	m.m2	1/2	0.155	0.155	1.0
2	Hg4	Hg	12	i	m.m2	0	0.225	0.225	1.0
3	Hg2	Hg	8	g	.3m	0.345	0.345	0.345	1.0
4	Ca	Ca	3	c	4/mm.m	0	1/2	1/2	1.0
5	Hg1	Hg	1	a	m-3m	0	0	0	1.0

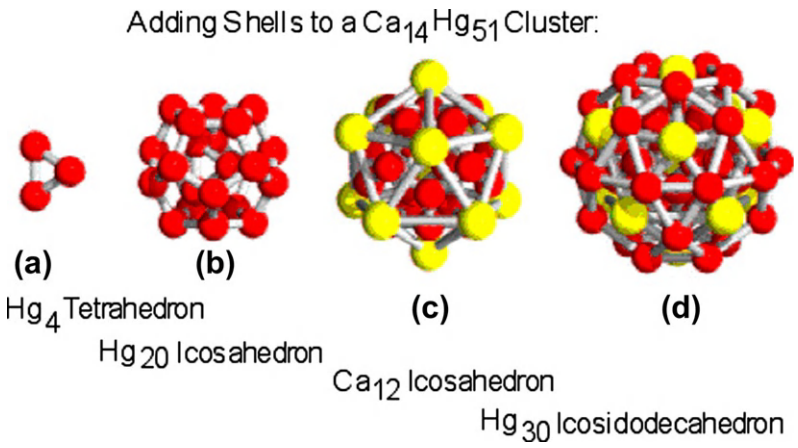

FIGURE 16.83

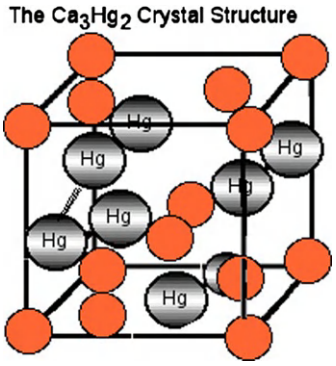

FIGURE 16.84

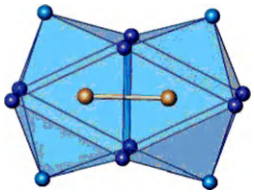

FIGURE 16.85

TABLE 16.56

No.	Site notation	Atom	Multiplicity	Wyckoff	Site symmetry	*x*	*y*	*z*	Occupancy
1	Hg1	Hg	12	l	1	0.1049	0.439	0.3305	1.0
2	Hg2	Hg	12	l	1	0.2662	0.0744	0.2370	1.0
3	Hg3	Hg	12	l	1	0.4944	0.1155	0.1526	1.0
4	Hg4	Hg	6	k	m..	0.0589	0.2383	1/2	1.0
5	Ca1	Ca	6	k	m..	0.4680	0.1394	1/2	1.0
6	Hg5	Hg	6	j	m..	0.0193	0.1324	0	0.50
7	Ca2	Ca	6	j	m..	0.1138	0.3898	0	1.0
8	Hg6	Hg	4	h	3..	1/3	2/3	0.2987	1.0
9	Ca3	Ca	2	e	6..	0	0	0.3060	1.0
10	Hg7	Hg	2	c	-6..	1/3	2/3	0	1.0

TABLE 16.57

No.	Site notation	Atom	Multiplicity	Wyckoff	Site symmetry	*x*	*y*	*z*	Occupancy
1	Ca1	Ca	4	h	m.2m	0.1821	0.6821	1/2	1.0
2	Hg1	Hg	4	g	m.2m	0.6159	0.1159	0	1.0
3	Ca2	Ca	2	a	4/m..	0	0	0	1.0

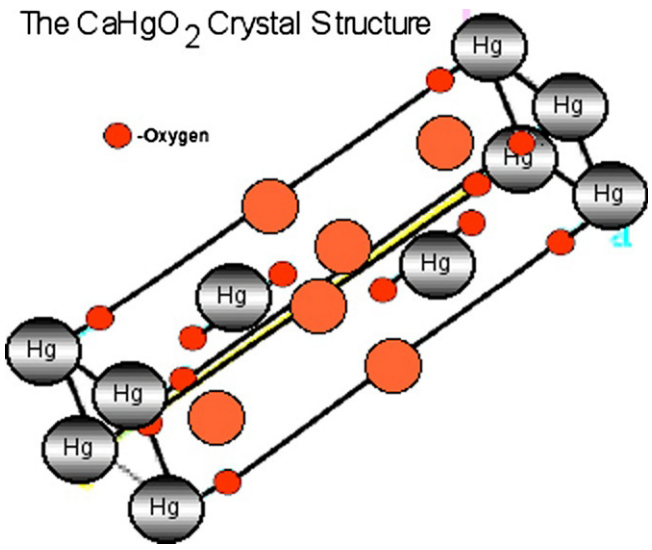

FIGURE 16.86

$SrHg_2$ (772 °C). Eight other compounds form by peritectic reactions:

Sr_3Hg (458 °C)

Sr_2Hg (478 °C)

Sr_3Hg_2 (545 °C)

$SrHg_3$ (512 °C)

$SrHg_{3.6}$ (481 °C)

$Sr_2Hg_{9\sim}$ (427 °C)

$SrHg_{11}$ (289 °C)

$SrHg_x (x \leq 13,\ 62\ °C)$

Two eutectics occur at 82.0 atom% Sr (442 °C) and at 40.5 atom% Sr (694 °C).

The SrHg compound has the structure shown in Fig. 16.88.

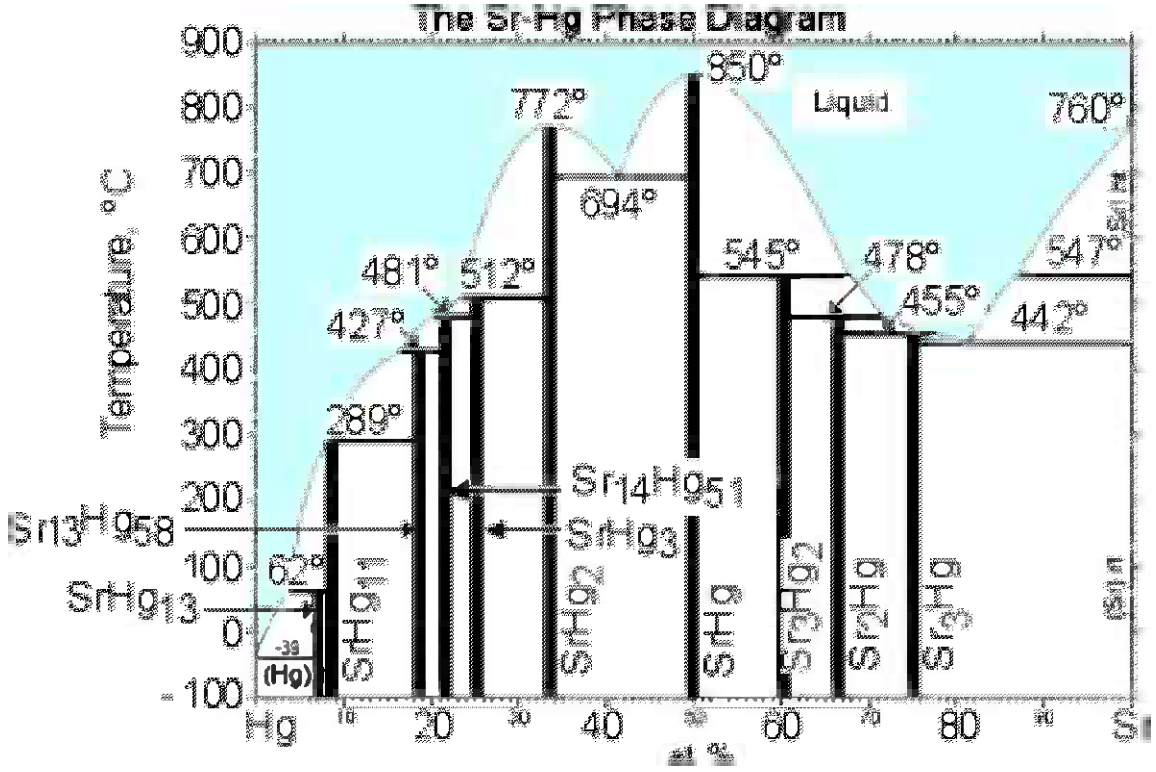

FIGURE 16.87

TABLE 16.58

No.	Site notation	Atom	Multiplicity	Wyckoff	Site symmetry	*x*	*y*	*z*	Occupancy
1	O1	O	6	c	3m	0	0	0.10637	1.0
2	Ca1	Ca	3	b	-3m	0	0	1/2	1.0
3	Hg1	Hg	3	a	-3m	0	0	0	1.0

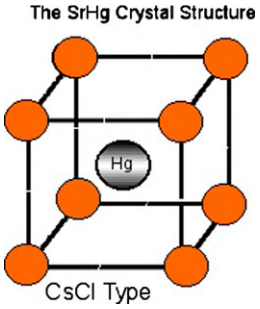

FIGURE 16.88

Cell parameters are: $a = b = c = 3.9552$ Å, $\alpha = \beta = \gamma = 90°$, cell volume = 61.86 Å^3, $Z = 1$. Cell occupancy is shown in Table 16.59.

Other than structural data, this compound has not been the subject of an intensive survey of its physical or electronic properties.

The compound, $SrHg_2$, has the structure shown in Fig. 16.89.

Cell parameters are: $a = 4.9852$ Å, $b = c = 6.2864$ Å, $\alpha = 178.16°$, $\beta = \gamma = 66.64°$, cell volume = 165.24 Å^3, $Z = 4$. Cell occupancy is shown in Table 16.60.

Other than structural data, this compound has not been studied intensively and an intensive survey of its physical or electronic properties remains to be accomplished.

The compound, Sr_3Hg, has the structure shown in Fig. 16.90.

Cell parameters are: $a = 7.4053$ Å, $b = 8.5232$, $c = 11.0824$ Å, $\alpha = \beta = \gamma = 90°$, cell volume = 699.29 Å^3, $Z = 4$. Cell occupancy is shown in Table 16.61.

In contrast, the compound, $SrHg_3$, has the structure shown in Fig. 16.91.

Cell parameters are: $a = 6.1063$ Å, $b = c = 6.9064$ Å, $\alpha = 120°$, $\beta = \gamma = 90°$, cell volume = 210.89 Å^3, $Z = 2$. Cell occupancy is shown in Table 16.62.

Little data concerning this compound are available concerning its physical or electronic properties. A few papers, studying the structural characteristics, have been published

The compound, Sr_3Hg_2, has the structure shown in Fig. 16.92.

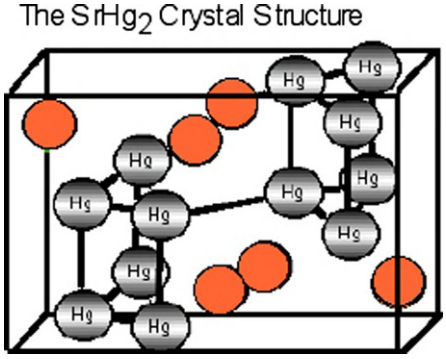

FIGURE 16.89

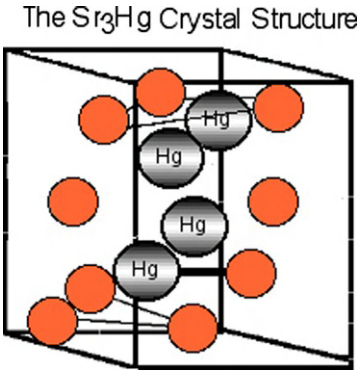

FIGURE 16.90

Cell parameters are: $a = 45.531$ Å, $b = c = 8.8833$ Å, $\alpha = \beta = \gamma = 90°$, cell volume = 359.29 Å^3, $Z = 4$. Cell occupancy is shown in Table 16.63.

Mixtures of strontium and mercury in molar ratios of 7:3 have been annealed for 20 days at 520 °C. From the pure product, Sr_3Hg_2 single crystals have been obtained. Sr_3Hg_2 crystallizes in the U_3Si_2 type of structure (space group $P4/mbm$); the cell constants are $a = 8.883$ (2) and $c = 4.553(1)$ Å. All of the Hg atoms are involved in Hg_2 dumbbells with Hg–Hg distances of 3.41 Å.

The compound, $SrHg_{11}$, has the structure shown in Fig. 16.93.

TABLE 16.59

No.	Site notation	Atom	Multiplicity	Wyckoff	Site symmetry	x	y	z	Occupancy
1	Hg	Hg	1	b	m-3m	1/2	1/2	1/2	1.0
2	Sr	Sr	1	a	m-3m	0	0	0	1.0

TABLE 16.60

No.	Site notation	Atom	Multiplicity	Wyckoff	Site symmetry	x	y	z	Occupancy
1	Hg1	Hg	8	h	m..	0	0.06	0.163	1.0
2	Sr1	Sr	4	e	mm2	0	1/4	0.547	1.0

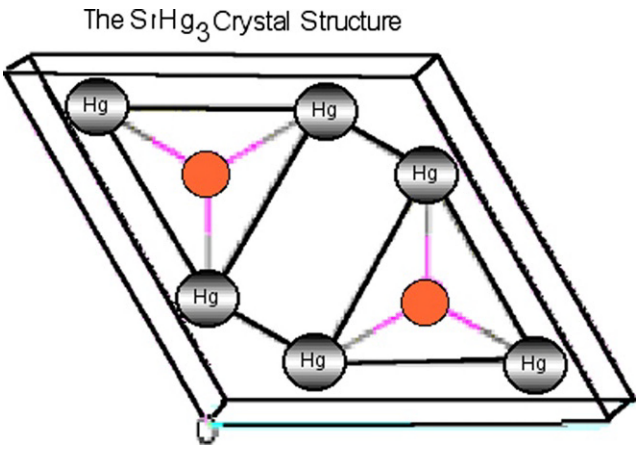

FIGURE 16.91

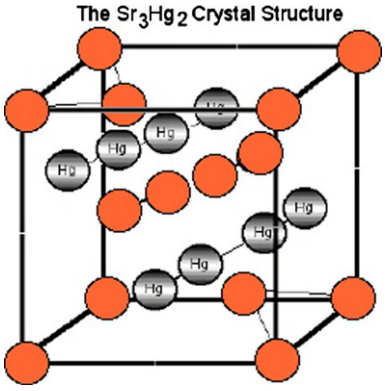

FIGURE 16.92

Cell parameters are: $a = b = c = 9.5102$ Å, $\alpha = \beta = \gamma = 90°$, cell volume = 860.14 Å^3, $Z = 3$. Cell occupancy is shown in Table 16.64.

The silvery metallic air-sensitive $SrHg_{11}$ compound can be prepared as a homogeneous, microcrystalline sample starting directly from stoichiometric mixtures of the elements. It decomposes peritectically and represents the mercury richest thermodynamically stable phases in the binary diagram. It crystallizes isotypically in space group $Pm3m$ ($Z = 3$) with the lattice constants: $SrHg_{11}$: $a = 9.510$ Å (powder), $BaHg_{11}$: 95871(1) pm (powder). Based on a systematical symmetry analysis one can show the relationship between the MHg_{11} structure type, β-Hg and a cubic close packing of spheres.

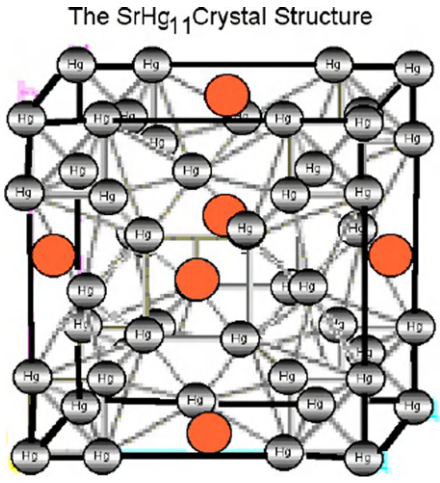

FIGURE 16.93

TABLE 16.61

No.	Site notation	Atom	Multiplicity	Wyckoff	Site symmetry	*x*	*y*	*z*	Occupancy
1	Sr1	Sr	8	d	1	0.1834	0.0689	0.1656	1.0
2	Sr2	Sr	4	c	.m.	0.0388	1/4	0.6578	1.0
3	Hg1	Hg	4	c	.m.	0.3764	1/4	0.4426	1.0

TABLE 16.62

No.	Site notation	Atom	Multiplicity	Wyckoff	Site symmetry	*x*	*y*	*z*	Occupancy
1	Hg1	Hg	6	h	mm2	0.1667	0.3333	1/4	1.0
2	Sr1	Sr	2	d	-6m2	1/3	2/3	3/4	1.0

TABLE 16.63

No.	Site notation	Atom	Multiplicity	Wyckoff	Site symmetry	*x*	*y*	*z*	Occupancy
1	Sr2	Sr	4	h	m.2m	0.1581	0.6581	1/2	1.0
2	Hg	Hg	4	g	m.2m	0.6359	0.1359	0	1.0
3	Sr1	Sr	2	a	4/m..	0	0	0	1.0

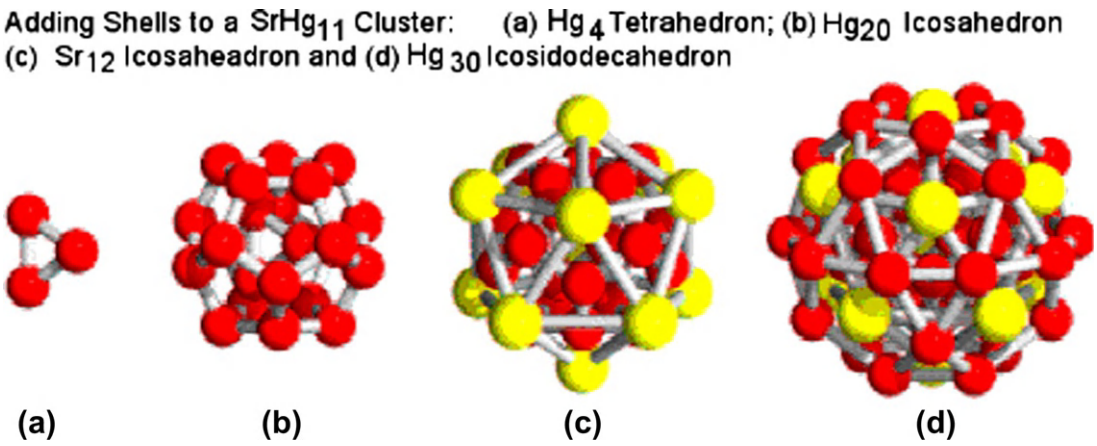

FIGURE 16.94

Furthermore the description of the structure can be based on a 3D arrangement of four capped tetragonal hexagon prisms $SrHg_{20}$, the latter ones being typical for the first coordination sphere of the Hg atoms ($C_N = 20$). Together, with additional, formally isolated Sr atoms these polyhedra constitute the topology of the Cu_3Au structure type. An alternative description emphasizes polyhedra based on three shells around a centering Hg atom in the sense Hg at Hg_{12} at Hg_{32} at Sr_{12}. These endohedral polyhedra, which serve as complex building units, constitute the 3D structure by formal condensation.

Finally, the structure can be regarded as built-up from centered cubo-octahedra $HgHg_{12}$, square planar and cube-shaped Hg_4 and Hg_8 units (Fig. 16.94).

The compound, $Sr_{14}Hg_{51}$, has the structure shown in Fig. 16.95.

This compound is related to the compounds, $Ca_{14}Hg_{51}$ and $Ca_{14}Cd_{51}$. It also forms compact icosahedral structures as shown above.

Cell parameters are: $a = 9.884$ Å, $b = c = 13.783$ Å, $\alpha = 120°$, $\beta = \gamma = 90°$, cell volume = 1,624.75 Å^3, $Z = 1$. Cell occupancy is shown in Table 16.65.

The compound, $Sr_{13}Hg_{58}$, has a structure related to $Ca_{13}Cd_{76}$. This structure is also shown in Fig. 16.96.

Cell parameters are: $a = b = c = 15.9424$ Å, $\alpha = 120°$, $\beta = \gamma = 90°$, cell volume = 3474.47 Å^3, $Z = 2$. Cell occupancy is shown in Table 16.66.

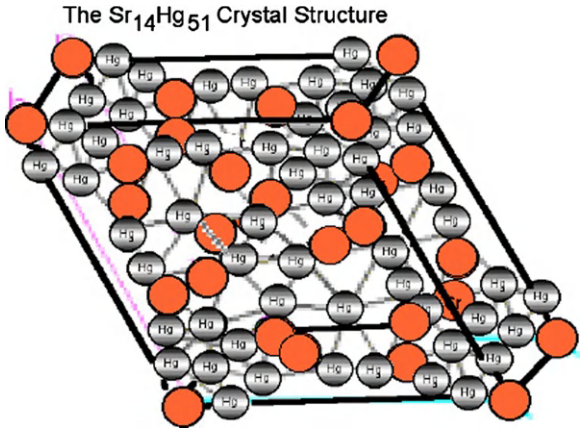

FIGURE 16.95

The compound, $SrHg_8$, does not appear in the phase diagram. However, the mercury-rich IM compound $SrHg_8$ has been prepared by reaction of the elements at 200 °C. Single-crystal XRD analysis revealed that it adopts a new structure type (Pearson symbol *oP*72, space group = *Pnma*, $a = 13.328$ Å, $b = 4.9128$ Å, $c = 26.446$ Å) (Fig. 16.97).

The Sr atoms are centered within two types of 18-vertex Hg polyhedra formed by augmenting pentagonal prisms with octagonal waists. The condensation of these Sr at Hg_{18} clusters is associated with the formation of a complex

TABLE 16.64

No.	Site notation	Atom	Multiplicity	Wyckoff	Site symmetry	*x*	*y*	*z*	Occupancy
1	Hg1	Hg	12	j	m.m2	1/2	0.155	0.155	1.0
2	Hg2	Hg	12	i	m.m2	0	0.225	0.225	1.0
3	Hg3	Hg	8	g	.3m	0.345	0.345	0.345	1.0
4	Sr1	Sr	3	c	4/mmm	0	1/2	1/2	1.0
5	Hg4	Hg	1	a	m-3m	0	0	0	1.0

TABLE 16.65

No.	Site notation	Atom	Multiplicity	Wyckoff	Site symmetry	*x*	*y*	*z*	Occupancy
1	Hg1	Hg	12	l	1	0.1049	0.439	0.3305	1.0
2	Hg2	Hg	12	l	1	0.2662	0.0744	0.2370	1.0
3	Hg3	Hg	12	l	1	0.4944	0.1155	0.1526	1.0
4	Hg4	Hg	6	k	m..	0.0589	0.2383	1/2	1.0
5	Sr1	Sr	6	k	m..	0.4680	0.1394	1/2	1.0
6	Hg5	Hg	6	j	m..	0.0193	0.1324	0	0.50
7	Sr2	Sr	6	j	m..	0.1138	0.3898	0	1.0
8	Hg6	Hg	4	h	3..	1/3	2/3	0.2987	1.0
9	Sr3	Sr	2	e	6..	0	0	0.3060	1.0
10	Hg7	Hg	2	c	-6..	1/3	2/3	0	1.0

TABLE 16.66

No.	Site notation	Atom	Multiplicity	Wyckoff	Site symmetry	*x*	*y*	*z*	Occupancy
1	Hg1	Hg	24	l	1	0.3633	0.0362	0.1012	1.0
2	Hg2	Hg	12	k	.m.	0.0973	0.1946	0.1599	1.0
3	Sr1	Sr	12	k	.m.	0.2065	0.4130	0.0515	1.0
4	Hg3	Hg	12	k	.m.	0.2374	0.4748	0.6606	1.0
5	Hg4	Hg	12	k	.m.	0.5628	0.1256	0.6395	1.0
6	Hg5	Hg	12	k	.m.	0.6011	0.2022	0.0527	1.0
7	Hg6	Hg	12	j	m..	0.0833	0.3666	1/4	1.0
8	Hg7	Hg	12	i	.2.	0.1902	0	0	1.0
9	Hg8	Hg	6	h	mm2	0.2692	0.5384	1/4	1.0
10	Sr2	Sr	6	h	mm2	0.5414	0.0828	1/4	1.0
11	Sr3	Sr	6	h	mm2	0.8715	0.7430	1/4	1.0
12	Hg9	Hg	6	g	.2/m.	1/2	0	0	1.0
13	Hg10	Hg	4	f	3m.	1/3	2/3	0.0949	1.0
14	Hg11	Hg	2	d	-6m2	1/3	2/3	3/4	1.0
15	Hg12	Hg	2	b	-6m2	0	0	1/4	1.0
16	Sr4	Sr	2	a	-3m.	0	0	0	1.0

anionic Hg–Hg bonding network, as supported by electronic structure calculations which reveal strong mixing of Hg 6s and 6p states in highly delocalized bands superimposed with a narrower 5d band below the Fermi level.

No other IM compounds are known. A few Sr–Hg compounds are available for sale commercially, as noted above.

Little work has been reported on simple inorganic compounds containing Sr and Hg in combination. $SrHg_2O_2Cl_2$ has been prepared as reddish brown powder by the solid-state reaction of strontium peroxide

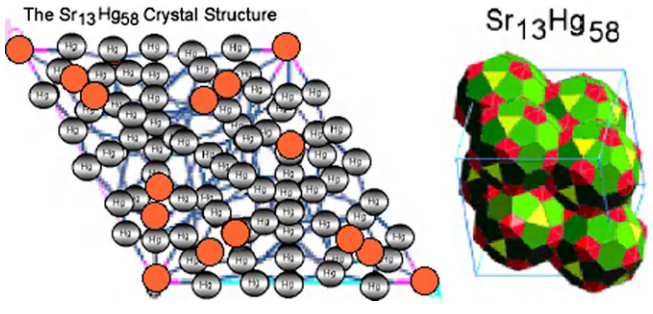

FIGURE 16.96

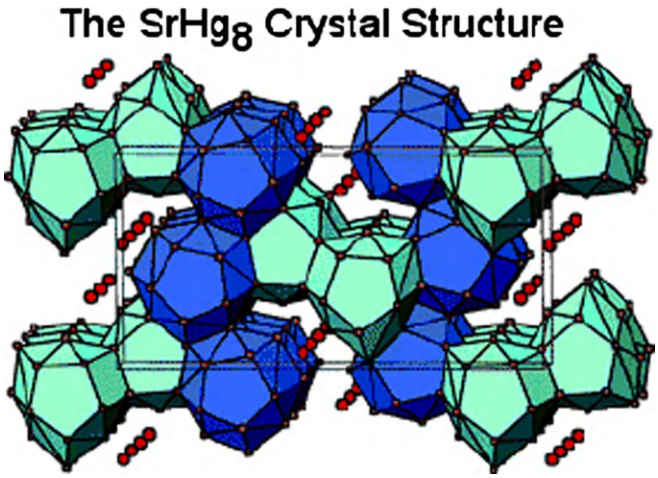

FIGURE 16.97

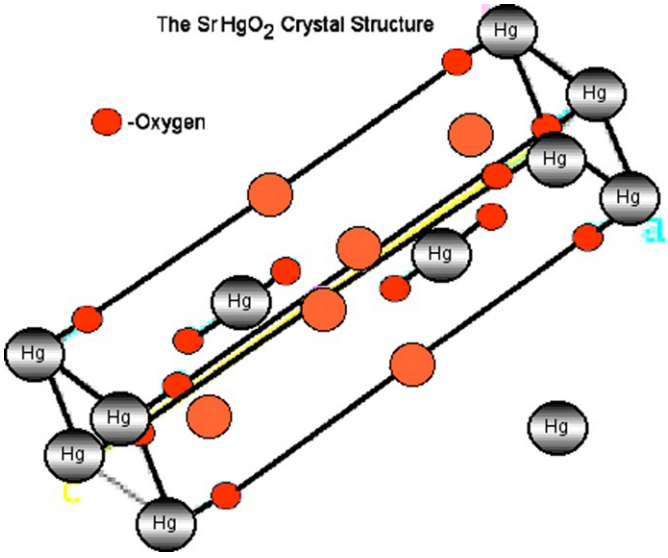

FIGURE 16.98

SrO_2 with calomel, Hg_2Cl_2. The crystal structure of the new phase $SrHg_2O_2Cl_2$ includes an unusual T-shaped HgO_3 grouping as part of infinite $[Hg_2O_2]$-infinity sheets. In the structure of $SrHg_2O_2Cl_2$ ($P\ 21/n$, $a = 9.9432$, $b = 7.0226$, $c = 8.2877$ Å, $= 102.441$, $V = 565.44$ Å^3, $Z = 4$). One can isolate a cationic r-octahedron grouping, SrO_8.

The only known oxy-mercury compound known is $SrHgO_2$ that has the structure shown in Fig. 16.98.

No other compounds are known in the SrO–HgO system.

16.3.5. Barium Mercury Compounds

Barium metal forms a number of IM compounds with Hg metal as shown in Fig. 16.99.

At least eight compounds are shown but only five of these have been studied in regard to their structure. The structure of the compounds, $BaHg_6$, $BaHg_{13}$ and $BaHg_4$ remains unknown at this point in time.

The compound, BaHg, has the structure shown in Fig. 16.100.

Cell parameters are: $a = b = c = 4.1313$ Å, $\alpha = \beta = \gamma = 90°$, cell volume $= 70.50$ Å^3, $Z = 1$. Cell occupancy is shown in Table 16.67.

Other than structural data, this compound has not been the subject of an intensive survey of its physical or electronic properties.

The compound, $BaHg_2$, has the structure shown in Fig. 16.101.

Cell parameters are: $a = 5.1444$, $b = c = 6.4731$, $\alpha = 77.15°$, $\beta = \gamma = 66.59°$, cell volume $= 180.97$ Å^3, $Z = 4$. Cell occupancy is shown in Table 16.68.

In contrast, the compound, Ba_2Hg, has the structure shown in Fig. 16.102.

Cell parameters are: $a = 15.192$ Å, $b = c = 4.202$ Å, $\alpha = \beta = \gamma = 90°$, cell volume $= 267.95$ Å^3, $Z = 4$. Cell occupancy is shown in Table 16.69.

The above two compounds have not been studied intensively and little has been established concerning their physical or electronic properties.

The compound, Ba_7Hg_{31}, has the structure shown in Fig. 16.103.

Cell parameters are: $a = b = 10.778$ Å, $c = 10.189$ Å, $\alpha = 120°$, $\beta = \gamma = 90°$, cell volume $= 1025.03$ Å^3, $Z = 1$. Cell occupancy is shown in Table 16.70.

This compound has not been studied intensively and little has been established concerning its physical or electronic properties.

The compound, $BaHg_{11}$, has the structure shown in Fig. 16.104.

Cell parameters are: $a = b = c = 9.5875$ Å, $\alpha = \beta = \gamma = 90°$, cell volume $= 881.28$ Å^3, $Z = 4$. Cell occupancy is shown in Table 16.71.

This silver-metallic air-sensitive compound can be prepared as a homogeneous, microcrystalline sample starting directly from stoichiometric mixtures of the elements. It decomposes peritectically and represents one of the mercury richest thermodynamically stable phases in the binary diagram. It crystallizes isotypically in space group $Pm3m$ ($Z = 3$) with the lattice constants: $BaHg_{11}$: 9.5871 Å (powder). Based on a systematical symmetry analysis, one can show the relationship between the $BaHg_{11}$ structure type, β-Hg and a cubic close packing of spheres, respectively. Furthermore the description of the structure can be based on a 3D arrangement of four capped tetragonal hexagon prisms $BaHg_{20}$, the latter ones being typical for the first coordination sphere of the Ba-atoms

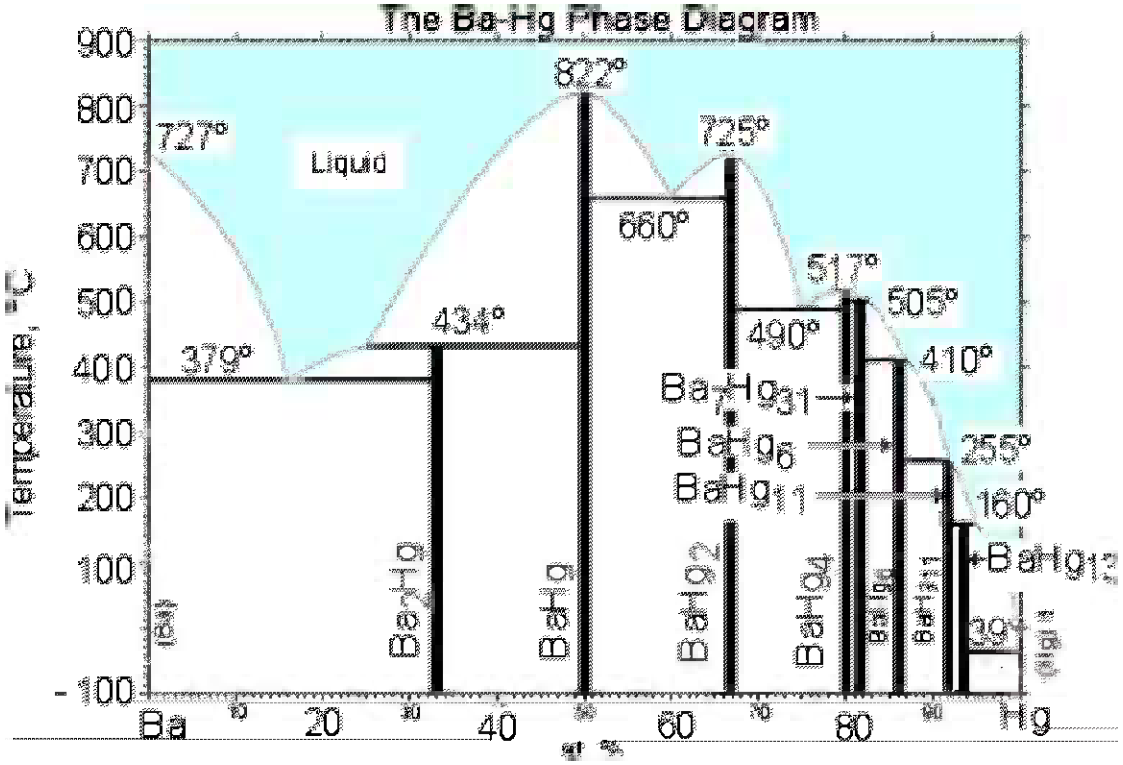

FIGURE 16.99

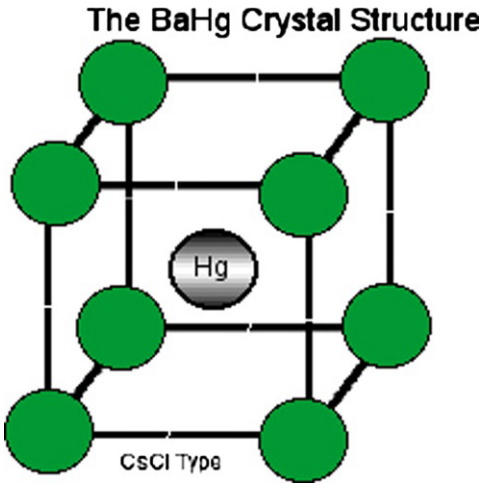

FIGURE 16.100

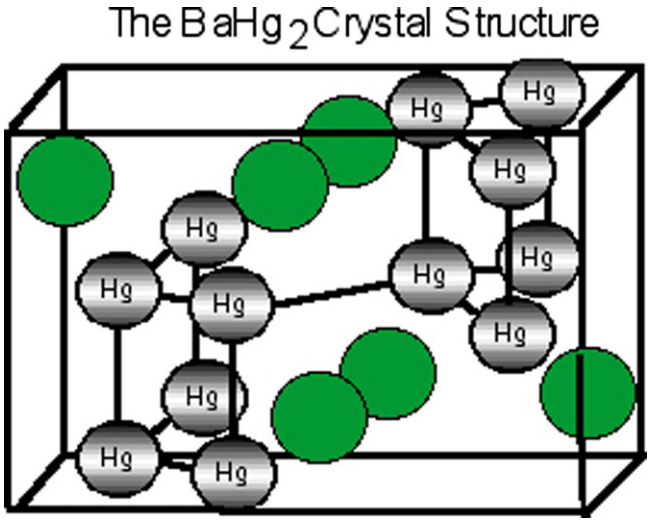

FIGURE 16.101

TABLE 16.67

No.	Site notation	Atom	Multiplicity	Wyckoff	Site symmetry	*x*	*y*	*z*	Occupancy
1	Hg	Hg	1	b	m-3m	1/2	1/2	1/2	1.0
2	Ba	Ba	1	a	m-3m	0	0	0	1.0

TABLE 16.68

No.	Site notation	Atom	Multiplicity	Wyckoff	Site symmetry	*x*	*y*	*z*	Occupancy
1	Hg1	Hg	8	h	m..	0	0.06	0.163	1.0
2	Ba1	Ba	4	e	mm2	0	1/4	0.547	1.0

TABLE 16.69

No.	Site notation	Atom	Multiplicity	Wyckoff	Site symmetry	*x*	*y*	*z*	Occupancy
1	Ba	Ba	4	e	4mm	0	0	0.37	1.0
2	Hg	Hg	2	a	4/mmm	0	0	0	1.0

($C_N = 20$). Together with additional, formally isolated Hg atoms, these polyhedra constitute the topology of the Cu_3Au structure type. An alternative description emphasizes polyhedra based on three shells around a centering Hg atom in the sense Hg at Hg_{12} at Hg_{32} at Ba_{12}. These endohedral polyhedra, which serve as complex building units, constitute the 3D structure by formal condensation. Finally, the structure can be regarded as built-up from centered cubo-octahedra $HgHg_{12}$, square planar and cube-shaped Hg_4 and Hg_8 units. These icosahedra are shown in Fig. 16.105.

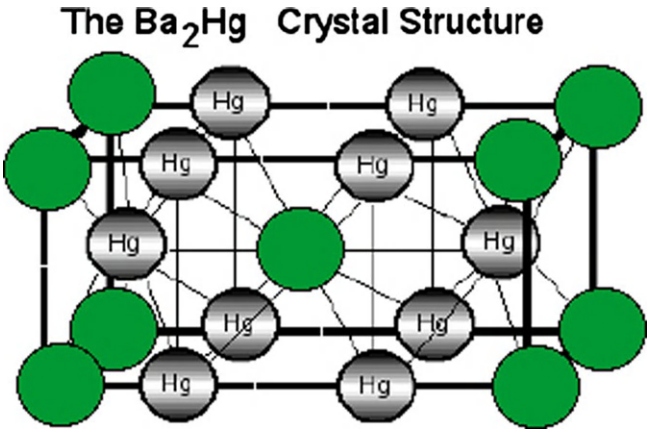

FIGURE 16.102

The compounds, $BaHg_6$, $BaHg_{13}$ and $BaHg_4$ are shown in the phase diagram but their structures have not been elucidated or documented.

No other IM compounds are known. No Ba–Hg compounds are offered for sale commercially and no CAS numbers have been issued to date.

Very few oxymercurate compounds are known. The $BaHg_2O_2$ compound has the structure shown in Fig. 16.106.

$BaHgO_2$ was prepared for the first time by an oxygen-high pressure technique. X-ray investigations of single crystals indicate a hexagonal symmetry, space group D_6^6–$P6_322$ (No. 182); $a = 6.904$ Å; $Z = 6$. Hg^{2+} is coordinated by two oxygen ions and Ba^{2+} by six oxygen

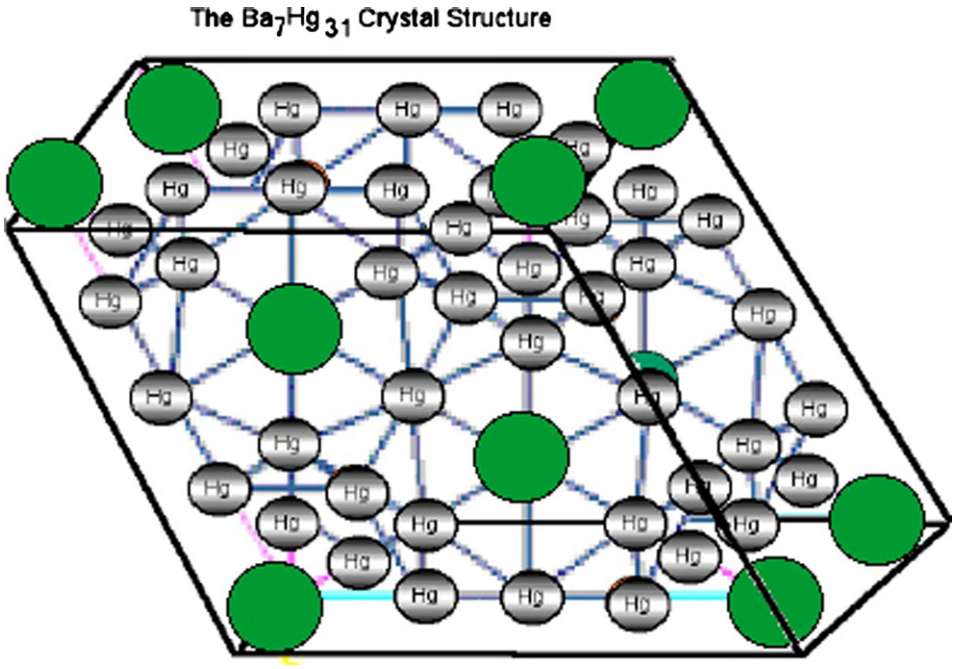

FIGURE 16.103

TABLE 16.70

No.	Site notation	Atom	Multiplicity	Wyckoff	Site symmetry	*x*	*y*	*z*	Occupancy
1	Hg1	Hg	12	o	.m.	0.1852	0.3704	0.2604	1.0
2	Hg2	Hg	6	m	mm2	0.1038	0.2076	1/2	0.50
3	Hg3	Hg	6	j	m2m	0.2708	0	0	1.0
4	Hg4	Hg	6	i	2mm	1/2	0	0.1619	1.0
5	Hg5	Hg	4	h	3m.	1/3	2/3	0.3499	1.0
6	Ba1	Ba	3	g	mmm	1/2	0	1/2	1.0
7	Ba2	Ba	2	e	6mm	0	0	0.2135	1.0
8	Ba3	Ba	2	c	-6m2	1/3	2/3	0	1.0

TABLE 16.71

No.	Site notation	Atom	Multiplicity	Wyckoff	Site symmetry	*x*	*y*	*z*	Occupancy
1	Hg3	Hg	12	j	m.m2	1/2	0.154	0.154	1.0
2	Hg4	Hg	12	i	m.m2	0	0.232	0.232	1.0
3	Hg2	Hg	8	g	.3m	0.3463	0.3463	0.3463	1.0
4	Ba	Ba	3	c	4/mmm	0	1/2	1/2	1.0
5	Hg1	Hg	1	a	m-3m	0	0	0	1.0

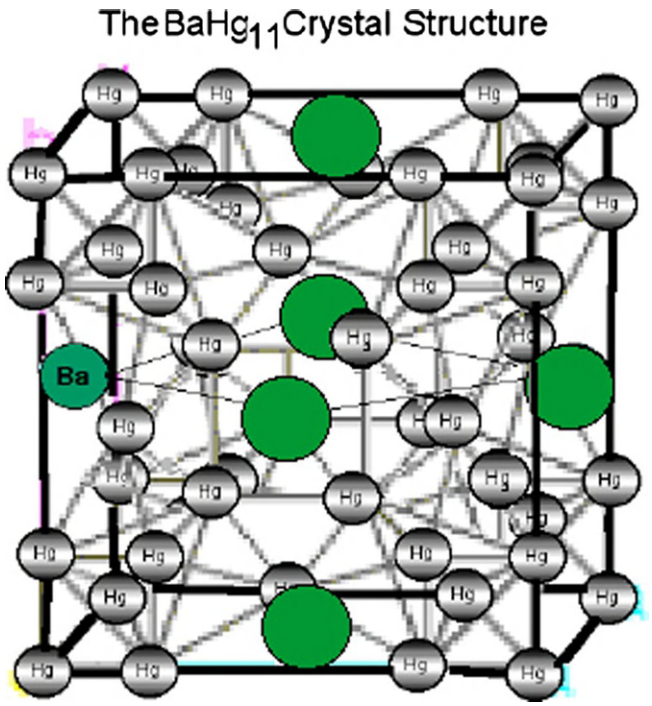

FIGURE 16.104

ions. 2D layers of trigonal BaO_6 prisms are connected by O–Hg–O dumbbells along [001].

During an investigation of the BaO–HgO system, a new polymorph of $BaHgO_2$ was obtained with a rhombic configuration. This phase was characterized by X-ray powder diffraction, scanning electron microscopy, and EDS analysis. Similar to the $SrHgO_2$ and $CaHgO_2$ counterparts, it crystallizes with the 3R delafossite structure with cell parameters $a = 4.097$, $c = 19.348$ Å, space group $R3/m$, and $Z = 3$. It is also shown that the distortion from the 3R delafossite structure, reported for $SrHgO_2$, might be the effect of a merohedral twinning due to stacking faults.

Recent results in the field of oxomercurate(II) chemistry have been reviewed. The methods of preparation and the crystal chemistry of oxomercurates were also discussed. Although only one compound has been documented in the Ba–Hg–O system, a number of oxomercurates (M_2HgO_4), alkaline earth oxomercurates ($MHgO_4$, $CdHgO_4$), rare earth oxomercurates, ternary oxomercurates ($BaAg_2Hg_2O_4$ and $Ba_3Pt_4HgO_{11}$) and the compounds $Ba_2Hg_2Pd_7O_{14}$,

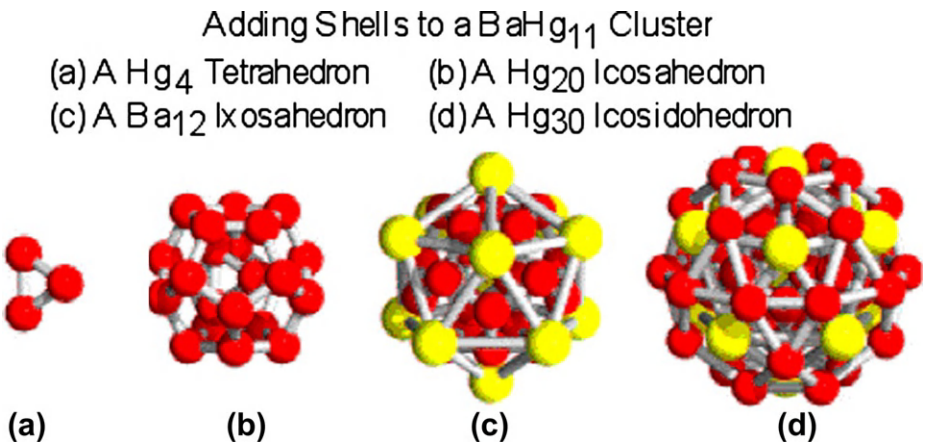

FIGURE 16.105

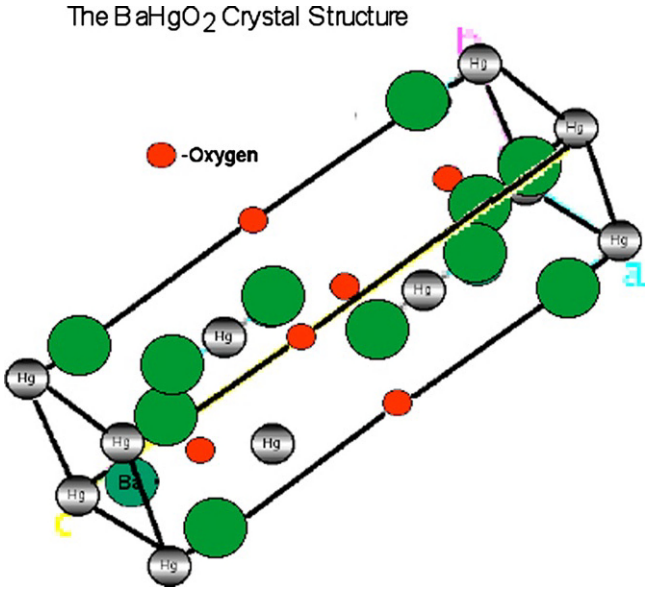

FIGURE 16.106

$HgCr_6$, $Hg_2Nb_2O_7$ and HgV_2O_6 were analyzed. The change in crystal chemical behavior from oxomercurates to mercury-oxometallates was also discussed in this paper.

A novel method of thermogravimetry under controlled mercury and oxygen partial pressures was developed, which allowed the attainment of precise thermodynamic data for the equilibrium:

$$MHgO_2(solid) \Leftrightarrow MO(solid) + Hg(gas) + 1/2O_2(gas) \quad (M = Ca, Sr, \text{ and } Ba)$$

Temperature dependencies of equilibrium constants K_p are described by the equations:

$$\text{Log } K_p(CaHgO_2) = -(9424 + /-540)/T + (10.28 + /-0.57), (888 - 1013\ K)$$

$$\text{Log } K_p(SrHgO_2) = -(10197 + /-890)/T + (10.10 + /-0.83), (1043 - 1118\ K)$$

$$\text{Log } K_p(BaHgO_2) = -(10474 + /-730)/T + (9.94 + /-0.64), (1098 - 1163\ K)$$

Thermal stability of mercurates increases in the order $CaHgO_2 < SrHgO_2 < BaHgO_2$.

16.3.6. Radium Mercury Compounds

While radium undoubtedly forms the same type of compounds as barium, there is no record of anyone having done so. This is probably due to the high cost of radium metal or the oxide, RaO.

General References

The published literature concerning the known alkaline earth compounds is extremely diverse and lengthy. It encompasses a multitude of technical books, journals and scientific chronicles, stretching back at least 100–150 years. In perusing these references, the author has determined that most of the pertinent and reliable data concerning a given alkaline earth compound was published after about the 1930s, a date that marked the beginning of the "Electronic Age," of which we, the public, are experiencing today. Yet, a considerable amount of research and published data, prior to the 1930s, exists concerning such compounds. The best sources for this data are:

1. "Treatise on Inorganic Chemistry" by H. Remy, Vols. I & II, Elsevier Pub. Co. (1936).
2. "The Chemical Elements and Their Compounds" by N.V. Sidgwick, Vol. I & II, Oxford Clarendon Press (1930).
3. "Dana's Manual of Mineralogy" by C.S. Hurlbut—18th Ed., J. Wiley & Sons (1953)
4. "Reference Book of Inorganic Chemistry" by W. M. Latimer & J. H. Hildebrand, The Macmillan Co. (1940)

These volumes cover most of the INORGANIC compounds known at the date of publication including some of the alkaline earth compounds (which are a fraction of all of the inorganic and organo-inorganic materials covered in these references). That is, the number and amount of data pertaining to alkaline earth compounds are a small fraction of the total content. A number of tables, diagrams and figures are included in these references and are, in some cases, the source for some of the figures and tables included in this volume.

Since no reference book exists devoted solely to alkaline earth compounds, the author began to peruse the scientific literature to that end. This book is designed to document all of the alkaline earth compounds known to date in the scientific literature. It is a reference book intended to bring together, in an organized fashion, information difficult to find, or dispersed in many published journals and books. Many of these references are obscure and not easily discovered except by persistent searching. For example, it is easy to find papers and publications relating to $BaGeO_3$, a compound related to $BaSiO_3$. As many as 1490 papers are associated with various aspects of this compound. Yet it is β-$BaGeO_3$, not α-$BaGeO_3$, that has the $BaSiO_3$ crystal structure. The author has sorted through these papers in order to describe, accurately, the known properties of α- and β-$BaGeO_3$.

As such, the previously published subject matter has been the source of information presented here. The author has assembled results and conclusions, published by various researchers in the open literature, regarding a particular compound. He then used his personal knowledge and experience to discuss a variety of viewpoints and judgments reached by diverse authors concerning the physical and chemical properties for each compound presented within this volume. The reader then has a starting point concerning whether a particular compound is known to exist and what properties it may exhibit.

Although there are many other resources for inorganic compounds like the Wiley Encyclopedia, Scifinder, Scopus/Scirus, the Gmelin Handbooks, PubMed, Springer/Link, the NIMS Materials database and the Web of Science, they cover a vast multitude of compounds and are, in some cases, difficult or costly to access. In contrast, the present book is limited to alkaline earth compounds. This is the major worth of this book—a place to determine what alkaline earth compounds are known to exist. The author did not use these sources of information but lists these sources of information for use by the reader:

SciFinder®
A Division of the American Chemical Society

- References from more than 10,000 currently published journals and patents from more than 63 patent authorities
- Important scientific discoveries from the present to the mid-1800s
- The latest scientific breakthroughs almost as soon as they are published with references added

daily and some patent information as recent as 2 days ago
- The world's largest collection of organic and inorganic substance information

What is Scirus—A Scientific Web-based search Engine
– Filters out nonscientific Web pages
– Searches Web Journals
– Searches 300 Million Web Sites
– Searches Digital Archives
– Searches for pdfs and papers

SCOPUS

Scopus, officially named **SciVerse Scopus**, is a bibliographic database containing abstracts and citations from academic journal articles. It covers nearly 18,000 titles from over 5000 international publishers, including coverage of 16,500 peer-reviewed journals in the scientific, technical, medical, and social sciences (including arts and humanities). It is owned by Elsevier and is available online by subscription. Searches in Scopus incorporate searches of scientific web pages through Scirus, another Elsevier product, as well as patent databases.

THE GMELIN HANDBOOK

The eight edition of the *Gmelin Handbook of Inorganic and Organometallic Chemistry* is said to be the most extensive printed compilation of information and data on metallic chemical elements and their compounds and alloys. It was compiled by the Gmelin Institute, part of the Max Planck Institute, and published in over 400 volumes between 1924 and 1998 by Springer-Verlag. All information in the handbook was derived from the primary journal and patent literature of chemistry, physics, and metallurgy, and then critically appraised and organized by chemical element and species. Gmelin is typically used to locate factual information on specific compounds:

History and Occurrence
Formation and Preparation (Bildung und Darstellung)
Physical properties (crystallographic, optical, spectral, electrical, magnetic, mechanical, thermodynamic)
Chemical properties and reactions, electrochemical behavior, etc.
Uses, toxicology, miscellany

MATERIALS DATABASE "MATNAVI"

National Institute for Materials Science, 1-2-1 Sengen, Tsukuba, Ibaraki, 305-0047 JAPAN

The NIMS materials database (MatNavi) gathers useful numerical data from a variety of material databases and academic documents made public. Various MatNavi database sections are composed of the: Polymer Database, Inorganic Material Database, Computational Electronic Structure Database, Metallic Material Database, Diffusion Characteristics Database, and the Superconducting Material records found in the open literature. Structures and phase diagrams may be accessed in these databases if known.

PubMed comprises more than 21 million citations for biomedical literature from MEDLINE, life science journals, and online books. Citations may include links to full-text content from PubMed Central and publisher web sites. PubMed was first released in January 1996.

Springer/Link is an integrated full-text database for journals, books, protocols, e-References, and book series published by Springer. SpringerLink currently offers 2436 fully peer-reviewed journals and 40,153 books online. General and detailed information about their journals, books, software and other products is available in the corporate website.

THOMSON REUTERS

Web of Science ® provides researchers, administrators, faculty, and students with quick, powerful access to the world's leading citation databases. Authoritative, multidisciplinary content covers over 12,000 of the highest impact journals worldwide, including Open Access journals and over 150,000 conference proceedings. You will find current and retrospective coverage in the sciences, social sciences, arts, and humanities, with coverage to 1900.

These sites on the Internet are presented for those Readers who wish to use them to determine the origin of the papers and publications discussed in this book. The author did not use them but consulted directly publications from various journals and published books.

The present volume is modeled upon that of the Gmelin Handbook.

However, the reader will soon discover that references to the scientific literature, including tables, drawings and figures, are not given within the book. There is a good reason for this. Early in the writing of the manuscript, the author assembled known data and results published as papers and books in the open literature. He then described succinctly was known about a particular alkaline earth compound and added references. Since his description was based upon the compilation and personal assessment of what several authors had published in the past, just one compound required 6–8 citations. Many compounds required 8–12 references and sometimes even more. Therefore, the decision was made not to include citations because the reference pages would consume a large part of the book. If the reader wishes to ascertain which authors discovered the properties of a particular compound, a good starting point is the above bibliographic database references available on the Internet.

Concerning figures, the author has drawn all of these, starting with figures published within various articles and books. In many cases, more than one author(s) published essentially the same result, each a refinement of the previous one. The author then formed the figure (such as a crystal structure) according to the latest results known to date. For example, the author redrew many phase diagrams that were not complete and added known data to complete the diagram. Because most of the figures had several contributors, no citations have been included since they, like the information presented for each compound, would consume a considerable space within the manuscript.

Most of the tables are compilations of previously published data derived from books and journals or from the **NIMS Materials database (MatNavi)**. For example, some tables present unit-cell occupancies for a specific crystal structure. These were derived from the literature but have many authors. No specific citations are presented for these tables as well.

Some of the journals and books that were consulted during the creation of this manuscript include the following:

1. Journal of Applied Crystallography—published by International Union of Crystallography, 2 Abbey Square, Chester CH1 2HU, England
2. Journals Published by the American Chemical Society—Washington, D.C.
   - Inorganic Chemistry
   - Accounts of Chemical Research
   - Chemistry of Materials
   - Journal of the American Chemical Society
   - Journal of Physical Chemistry
   - Journal of Chemical Education
   - Industrial and Engineering Chemistry
   - Analytical Chemistry
   - Progress in Inorganic Chemistry, Vols. 21–47
   - Listing of Inorganic Syntheses, Vols. 22–35, J. Am. Chem. Soc 2011, 133(8), pp 2783–2793
3. Journals Published by The Royal Society of Chemistry
   - Journal of the Chemical Society—Dalton Transactions
   - Journal of Applied Crystallography
   - Journal of Biological Inorganic Chemistry
   - Journal of Chemical Crystallography
   - Journal of Chemical Physics
   - Journal of Chemical Technology and Biotechnology
   - Journal of Chemical Thermodynamics
   - Journal of Crystal Growth
   - Journal of Inorganic Biochemistry
   - Journal of Materials Chemistry
   - Journal of Physics and Chemistry of Solids
   - Journal of Solid State Chemistry
   - Journal of Solid State Electrochemistry
4. Handbook of Inorganic Chemicals by Pradyot Patnaik, Ph.D., The McGraw-Hill Companies, Inc, (2003)

5. "Compressibility of α-Ca_3N_2 to 137 Kb Using Synchrotron Radiation and a Diamond Anvil Cell" by Michael J. Bucknum, INIFTA, National University of La Plata, La Plata 1900, Buenos Aires, Argentina (Nature Proceedings: hdl:10101/npre.2008.1771.4 : Posted 8 May 2008)

6. "Information about the electronic structure of $SrTiO_3$, $BaBiO_3$ and $LiNbO_3$ deduced from the XPS satellites and their relevance to optical functions" by B. Mayer, S. M̈ahl, M. Neumann, Fachbereich Physik, Universitåt Osnabrück, Barbarastrasse 7, D-49069 Osnabrück, Germany, Z. Phys. B 101, 85–90 (1996)—Springer-verlag

7. "Phase Equilibria and Crystallography of Ceramic Oxides" by W. Wong-Ng, R. S. Roth, T. A. Vanderah, and H. F. McMurdie, National Institute of Standards and Technology, Gaithersburg, MD 20899-8520, [J. Res. Natl. Inst. Stand. Technol. 106, 1097–1134 (2001)]

8. "Pulsed laser deposition of $BaGa_2O_4$" by M. Kodu, T. Avarmaa, H. Mändar, R. Jaaniso, Appl Phys A (2008) **93**: 801–805

9. "THE CRYSTAL STRUCTURE OF SANBORNITE, $BaSi_2O_5$", Robert M. Douglas, Department of Geological Sciences, University of California, Berkeley 4, THE AMERICAN MINERALOGIST, VOL. 43, MAY–JUNE, 1958.

The above citations are but a small fraction of the references scrutinized by the author in the creation of this manuscript.

Index

Note: Page numbers with "*f*" denote figures; "*t*" tables.

A

Actinium, 104
Adelite, 302
Admontite, 495–496
Aksaite, 496
Alabaster, 153
Alexandrite, 540–542
Alforsite, 264
Alkylation, 32
Aluminates, 483
American Beryllium Inc., 107
Ammonia, 201
Antiferromagnetic (AFM) coupling, 969–970
Antimonate, 309
Antimonite, 309
Antogorite, 394
Apatites of magnesium, 245
Aqua fortis, *See* Nitric acid
Arsenic acid, 286–287, 286f
Arsenious acid, *See* Arsenous acid
Arsenous acid, 286–287, 286f
Asbestine, 395
Aspdin, Joseph, 121

B

BaBiO3 type calcium hafnate compounds, 693
Barium, 18–19
Barium aluminates, 559–566, 560f
Barium aluminides, 529–540, 532f, 533t
Barium antimonate, 315–316
Barium antimonide, 325–328, 326f, 327f
Barium antimonite, 311–312
Barium apatites, 262
Barium arsenates, 306–309
Barium arsenide, 289–290, 290f
Barium arsenites, 295–296, 296f
Barium bismuthate, 333–336, 336t
Barium bismuthides, 347–350, 347f, 348f, 348t, 349f, 349t, 350t
Barium borates, 511–517
Barium borides, 491–492, 491f
Barium boron oxide, *See* Barium metaborate
Barium bromate, 94, 94t
Barium bromide, 65–66, 66f, 66t, 67t
Barium bromite, 91–92
Barium bromoapatite, 264
Barium cadmium compounds, 1151–1156
Barium carbides, 358–359, 358f, 358t
Barium carbonate, 368–370
Barium chlorate, 81–82, 81t, 82f, 83t
Barium chloride, 62–65, 64f, 64t, 65t
Barium chlorite, 78
Barium chloroapatite, 264
Barium chromate, 818–819
Barium chromium compounds, 813–819
Barium cobalt compounds, 978–983
Barium copper compounds, 1070–1079
Barium di-aluminate, 564
Barium dialuminide, 534–536, 534f, 535f, 535t, 536f
Barium diborate, *See* Barium metaborate
Barium digallide, 582, 582f
Barium digermanide, 423, 424f, 425f, 425t
Barium dihydrogen orthoarsenate, 307
Barium di-molybdate, 839, 839f, 841, 841f
Barium di-niobate, 759, 759f
Barium distannide, 442–443, 443f
Barium di-tantalate, 790–791, 791f
Barium di-thallide, 629–630, 629f, 630f, 630t
Barium dithionate, 168–169
Barium dithionite, 168
Barium fluorapatite, 263
Barium fluoride, 60–62, 62f, 62t, 63t, 64t
Barium gallates, 596–598
Barium gallides, 580f, 581–584, 581f, 581t, 582t
Barium germanates, 410–412, 410f, 411f, 412f
Barium germanides, 423–428, 423f, 424t
Barium gold compounds, 1109–1113
Barium hafnate compounds, 698–700, 698f, 698t, 699f, 699t
Barium hafnide compounds, 698
Barium hexa-aluminate, 564–565, 565f
Barium hexagallate, 598
Barium hydride, 30
Barium hydroxide, 123–124, 123t, 124f
Barium hydroxyapatite, 262–263
Barium hyperoxides, 132, 132f
Barium hypobromite, 89, 89f
Barium hypochlorite, 76
Barium hypophosphate, 282
Barium hypophosphite, 237, 237f
Barium indates, 618–621, 618f
Barium indides, 610–612, 610f, 611f, 611t
Barium iodate, 99
Barium iodide, 66–68, 67f, 67t, 68f, 68t, 69t
Barium iodoapatite, 264
Barium iridium compounds, 1002–1004
Barium manganese compounds, 891–895
Barium mercury compounds, 1170–1174
Barium metaborate, 511–512, 511f
Barium metaniobate, 752, 754f, 755, 755f
Barium metaphosphate, 279–280, 279f, 280t
Barium molybdates, 835–841
Barium monogallate, 596–597, 596f, 597f
Barium monogermanide, 423–428, 425f, 426f, 426t, 427f, 427t, 428f
Barium monohydrogen orthoarsenate, 308
Barium monoindate, 619, 619f
Barium monomolybdate, 838–839
Barium monostannide, 442, 443f
Barium nickelates, 1019
Barium nickel compounds, 1015–1019
Barium niobate, 760
Barium niobium compounds, 752–760
Barium nitrate, 221–223, 222f, 222t
Barium nitride, 209–210, 210t
Barium nitrite, 213–215, 213t, 214f
Barium orthoborate, 512–513, 513f
Barium orthophosphates, 259–262
Barium osmium compounds, 958–960
Barium oxide, 113–115, 114t
Barium oxy-iron compounds, 930–937
Barium palladium compounds, 1029–1030
Barium pentastannide, 443, 444f
Barium perborate, 514–515, 514f
Barium perbromate, 95–96, 95f
Barium perchlorate, 86, 87t
Barium periodate, 103–104, 103f
Barium peroxide, 129–130, 129f
Barium peroxodisulfate, 172
Barium peroxy-monosulfate, 171, 171f
Barium peroxyphosphate, 285–286
Barium phosphide, 233–234, 233f, 234f
Barium phosphite, 240–241, 241f
Barium platinum compounds, 1044–1048
Barium plumbates, 476–480, 477f, 479f
Barium plumbides, 469–472, 469f, 470f
Barium polyphosphates, 279–280, 279f, 280t
Barium pyroarsenate, 308
Barium pyroarsenite, 296
Barium pyroborate, 513–514, 514f
Barium pyrophosphate, 271, 271f
Barium pyrosulfate, 162
Barium rhenium compounds, 907–909
Barium rhodium compounds, 993–994
Barium ruthenate monohydrate, 953
Barium ruthenium compounds, 950–953
Barium–scandium system, 641–643, 641f, 642f, 642t
Barium selenate, 184
Barium selenide, 177, 177t, 178f
Barium selenite, 180–181
Barium silicates, 400–403, 400f, 401f, 402f
Barium silicide, 381–386, 382f, 382t, 383t, 384f, 384t, 385f, 386f, 386t, 387f
Barium silver compounds, 1089–1091
Barium stannates, 454–458, 454f, 455f
Barium stannides, 441–446, 442f

Barium sulfate, 156–158, 157f, 157t
Barium sulfide, 141–142, 141f
Barium sulfite, 149
Barium tantalum compounds, 785–794
Barium technetium compounds, 898–899
Barium tellurate, 196–197
Barium telluride, 188–190
Barium tellurite, 193–194
Barium tetraaluminide, 530–534, 533f, 534f
Barium tetraborate, 515–516, 515f, 516f
Barium tetra-indide, 611, 611f, 612t
Barium tetra-molybdate, 839
Barium tetrathionate, 169, 169f, 169t
Barium thallates, 633–635, 633f, 634f, 634t
Barium thallides, 629–631, 629f, 629t
Barium thionates, 168–169
Barium thiosulfate, 160
Barium titanates, 669–672, 670f, 670t, 671f, 672f
Barium titanides, 669
Barium tri-molybdate, 839
Barium tri-niobate, 759
Barium triplumbide, 471–472, 472f
Barium tristannide, 443, 443f, 443t, 444f
Barium tungstates, 858–867
Barium tungstite, 867
Barium vanadium compounds, 722–728
Barium–yttrium compounds, 650–651, 651t, 652f
Barium zinc compounds, 1136–1140
Barium zirconates, 684–686, 684f, 685f, 685t, 686f, 687t
Barium zirconides, 684
Baryte, 38
BaTiO3 type calcium hafnate compounds, 692–693, 692f, 692t
BaTiO3 type strontium hafnate compounds, 695, 696t
Baylis–Hillman reaction, 48
Bémont, G., 21–22
Berthollet, Claude Louis, 75
Berylium arsenite, 291
Berylliosis, 4
Beryllium, 4–8, 702
Beryllium aluminates, 540–543, 541f, 541t, 542f, 543f, 543t
Beryllium aluminides, 517–518, 518f, 519t
Beryllium antimonate, 312–313, 313f
Beryllium antimonide, 317
Beryllium antimonite, 309
Beryllium arsenates, 297–298, 297f, 298f
Beryllium arsenide, 287
Beryllium bismuthates, 328
Beryllium bismuthides, 337, 337f
Beryllium borates, 493–517, 493f
Beryllium boride, 484–485, 484t, 485f, 486f
Beryllium bromate, 92
Beryllium bromide, 40
Beryllium bromite, 89
Beryllium cadmium compounds, 1140
Beryllium carbides, 353–354
Beryllium carbonates, 359–360, 360f
Beryllium chlorate, 79
Beryllium chloride, 39–40
Beryllium chlorite, 76
Beryllium chromates, 798
Beryllium cobalt compounds, 961–963
Beryllium copper compounds, 1049–1052
Beryllium dihydrogen orthoarsenate, 297
Beryllium dithionate, 163–164
Beryllium dithionite, 163
Beryllium–zirconium compounds, 672
Beryllium fluoride, 38–39
Beryllium gallates, 584–585, 585f
Beryllium gallide, 567, 567f
Beryllium germanates, 403–404, 403f
Beryllium germanides, 413, 414f, 414t
Beryllium gold compounds, 1092–1094
Beryllium hafnate compounds, 687
Beryllium hafnide compounds, 687–690, 687f, 688f, 688t, 689t, 690f, 690t
Beryllium hydride, 27, 27f
Beryllium hydroxide, 116–118, 117f, 117t
Beryllium hyperoxides, 130
Beryllium hypobromite, 88
Beryllium hypochlorite, 73–74
Beryllium hypophosphate, 281
Beryllium hypophosphite, 234–235, 235f
Beryllium indates, 612–613
Beryllium indides, 599, 599f
Beryllium iodate, 97
Beryllium iodide, 41
Beryllium iridium compounds, 994–995
Beryllium manganese compounds, 870–871
Beryllium mercury compounds, 1156
Beryllium metabisulfite, 170
Beryllium metaphosphates, 273, 273t
Beryllium molybdenum compounds, 820–823
Beryllium nickel compounds, 1005–1007
Beryllium niobium compounds, 729–731
Beryllium nitrate, 215–216, 215t
Beryllium nitride, 201–202, 201f, 202t
Beryllium nitrite, 210
Beryllium orthoarsenate, 297
Beryllium orthophosphates, 242–243, 242t
Beryllium osmium compounds, 954
Beryllium oxide, 106–108, 107f, 108t
Beryllium oxo-rhenium compounds, 901
Beryllium oxy-iron compounds, 914
Beryllium oxy-ruthenium compounds, 937–938
Beryllium palladium compounds, 1019–1020
Beryllium pentathionate, 164, 164f
Beryllium perbromate, 94–95
Beryllium perchlorate, 83, 83f
Beryllium periodate, 99–100, 99f, 100f
Beryllium peroxide, 125
Beryllium peroxydisulfate, 171
Beryllium peroxyphosphate, 283
Beryllium phosphide, 229–230
Beryllium phosphite, 238
Beryllium platinum compounds, 1032
Beryllium plumbates, 472
Beryllium plumbides, 459
Beryllium polyphosphates, 266, 273, 273t
Beryllium pyrosulfate, 160–161
Beryllium rhodium compounds, 984–986
Beryllium–scandium system, 638–639, 638f
Beryllium selenate, 181–182
Beryllium selenide, 173–174, 173f
Beryllium selenite, 178
Beryllium silicates, 389–392, 392f
Beryllium silicides, 371–372
Beryllium silver compounds, 1080
Beryllium stannates, 447, 447f
Beryllium stannides, 428
Beryllium sulfate, 150
Beryllium sulfide, 137–138, 137f
Beryllium sulfite, 143
Beryllium tantalum compounds, 760–761
Beryllium–technetium compounds, 896
Beryllium tellurate, 194–195, 195f
Beryllium telluride, 186–187, 186f
Beryllium tellurite, 190
Beryllium tetrathionate, 164
Beryllium thallates, 631
Beryllium thallides, 622, 622f
Beryllium thionates, 163–164
Beryllium thiosulfate, 158
Beryllium titanates, 653–654, 654f
Beryllium titanides, 654–656, 655f, 655t, 656f, 656t, 657f, 657t
Beryllium tungsten compounds, 842–844
Beryllium vanadium compounds, 701–702
Beryllium–yttrium system, 643, 643f, 644f, 644t
Beryllium zinc compounds, 1115
Beryllium zirconides, 672–674, 673f, 673t, 674f, 674t
Beryllonite, 243
Berzelius, Jöns Jacob, 162, 482
Bigcreekite, 401–403, 402f
Birnessite, 335
Bismuth, 413
Bisulfite, *See* Calcium sulfite
Blanc fixe, 157
Bleaching, 149
Bleaching powder, 71–72, 74
Bond valence sum (BVS) calculation, 1061
Bone ash, *See* Tribasic calcium phosphate
Boracite, 495–496
Borate, 483
Boric acid, 482–483
Boron, 482
Bottinoite, 313–314
Brandholzite, 313–314
Brassite, 299
Brin, L. D., 129
Brin process, 129
British Alkali Act of 1863, 33
Bromic acid, 87
Bromites, 87
Bromous acid, 87
Brucite, 118
Brush ceramics, 107
Brushite, 246
Burtite, 451
Bussy, A. B., 9, 44
Bystromite, 313

C

Cadmates, 1140
Cadmium compounds, 1140–1156
Calcimine, 120

Calcination, 110
Calcioborite, 503
Calcite, 363, 363f
Calcium, 12–15
Calcium aluminate decahydrate, 551, 551f
Calcium aluminates, 547–553, 547f
Calcium aluminides, 524–527, 525f, 525t
Calcium antimonate, 314
Calcium antimonide, 321–324, 322f, 323f
Calcium antimonite, 310–311
Calcium apatite compounds, 251–252, 251f
Calcium arsenates, 302–304, 303t, 304t
Calcium arsenide, 288–289
Calcium arsenites, 293–295
Calcium bismuthate, 329–330, 330f
Calcium bismuthides, 339–343, 339f, 340f, 340t, 341f, 341t, 342f, 342t
Calcium borates, 498–503, 498f
Calcium boride, 488–490, 488f, 489f
Calcium bromate, 92–93
Calcium bromide, 53–55
Calcium bromite, 89–90, 90f
Calcium bromoapatite, 255
Calcium cadmium compounds, 1143–1146
Calcium carbides, 355–357, 356f, 356t, 357f
Calcium carbonate, 362–366, 362f, 365f, 366f
Calcium chlorate, 79–80, 80t
Calcium chloride, 51–53
Calcium chlorite, 77, 77f
Calcium chloroapatite, 254
Calcium chromate, 807, 807f
Calcium chromium compounds, 802–809
Calcium cobalt compounds, 965–971
Calcium copper compounds, 1055–1061
Calcium dialuminide, 526, 526f
Calcium digallide, 572–574, 572f, 572t, 574f, 574t
Calcium dihydrogen arsenate, 304
Calcium dihydrogen arsenite, 293–294
Calcium diindide, 603–604, 604f, 605f, 605t
Calcium distannide, 435
Calcium di-tantalate, 767, 768f, 775, 775f
Calcium dithionite, 165–166, 166f
Calcium divanadium hexoxide, 713
Calcium ferrate, 922
Calcium fluoride, 49–51
Calcium fluoroapatite, 254
Calcium gallates, 586–590, 587f
Calcium gallides, 570–578, 570f, 571f, 571t
Calcium germanates, 406–409, 406f, 407f
Calcium germanides, 414–419, 416f
Calcium gold compounds, 1098–1105
Calcium hafnate compounds, 692–695
Calcium hafnide compounds, 692
Calcium hepta-manganate, 881
Calcium hexa-aluminate, 549
Calcium hydride, 29–30
Calcium hydrogen arsenate trihydrate, 303
Calcium hydrogen orthoarsenate, 303
Calcium hydroxide, 120–122, 120f
Calcium hydroxyapatite, 252–253, 253f
Calcium hyperoxides, 130–131
Calcium hypobromite, 88
Calcium hypochlorite, 74–76
Calcium hypophosphate, 282
Calcium hypophosphite, 236, 236f
Calcium indates, 614–617, 615f, 617f
Calcium indides, 603–606, 604f, 604t
Calcium iodate, 98, 98f, 98t
Calcium iodide, 55–56, 55t, 56t
Calcium iodoapatite, 255
Calcium iridium compounds, 997–1000
Calcium manganese compounds, 875–883
Calcium manganite, 875f, 876, 876f
Calcium mercury compounds, 1159–1163
Calcium metaärsenite, 294, 294f
Calcium metabisulfite, 170–171
Calcium metaborate, 499–500, 499f
Calcium metaphosphates, 274–278, 275f, 276t, 277f
Calcium molybdenum compounds, 826–829
Calcium molybdite, 828, 829f
Calcium monoaluminate, 548–549
Calcium mono-gallide, 572, 572f, 573f, 573t
Calcium mono-indide, 605–606, 606f
Calcium mono-thallide, 624–625, 624f, 625t
Calcium nickel compounds, 1009–1013
Calcium niobate, 738
Calcium niobium compounds, 736–741
Calcium nitrate, 218–220, 218t, 219t, 220f
Calcium nitride, 205–207, 205f
Calcium nitrite, 211–212, 211f, 211t, 212f
Calcium orthoborate, 500
Calcium orthophosphates, 245–252
Calcium orthosilicate, 397, 397f, 397
Calcium orthovanadate, 713–714
Calcium osmium compounds, 955–957
Calcium oxide, 109–112
Calcium oxo-rhenium compounds, 901–903
Calcium oxy-iron compounds, 916–922
Calcium palladium compounds, 1022–1027
Calcium perborate, 501, 501f
Calcium perbromate, 95
Calcium perchlorate, 84–85, 85f
Calcium periodate, 101–102, 102f, 102t
Calcium peroxide, 126–128, 126f, 127f, 127t
Calcium peroxyphosphate, 283–284
Calcium phosphide, 231–232, 232f
Calcium phosphite, 239, 240f
Calcium platinum compounds, 1035–1040
Calcium plumbates, 473–475, 474f
Calcium plumbides, 461–464, 461f, 462t, 463f, 464f, 465f
Calcium polyphosphates, 274–278, 275f, 276t, 277f
Calcium pyroarsenate, 304
Calcium pyroarsenite, 294
Calcium pyroborate, 500–501, 500f
Calcium pyroniobate, 739–741
Calcium pyrophosphate, 268–270
Calcium pyrosulfate, 161
Calcium rhodium compounds, 988–990
Calcium ruthenium compounds, 939–944
Calcium–scandium system, 640–641, 640f, 641t
Calcium selenate, 183–184, 183t
Calcium selenide, 175–176, 175f
Calcium selenite, 179–180
Calcium silicates, 395–398, 396f
Calcium silicides, 375–377, 375f, 376f, 377f
Calcium silver compounds, 1083–1086
Calcium stannates, 450–452, 452f
Calcium stannides, 432–436, 433f, 433t, 434f, 434t, 435t
Calcium sulfate, 152–155, 153f, 153t
Calcium sulfide, 138–140, 139f
Calcium sulfite, 145–149
Calcium tantalate, 775
Calcium tantalum compounds, 767–775
Calcium technetium compounds, 897
Calcium tellurate, 195–196
Calcium telluride, 187–188, 188f
Calcium tellurite, 190–192
Calcium tetra-aluminide, 525–526, 526f
Calcium tetraborate, 501–502, 501f
Calcium tetra-gallide, 572–573, 573f, 573t, 574f
Calcium tetrathionate, 166–167
Calcium thallates, 632–633, 632f
Calcium thallides, 623–626, 624f
Calcium thionates, 165–167
Calcium thiosulfate, 159
Calcium titanates, 662–667, 662f, 663f, 664f, 664t, 665f, 666f
Calcium titanides, 662
Calcium triborate, 501, 501f
Calcium triplumbide, 461–462
Calcium tristannide, 435
Calcium tri-thallide, 625, 625f, 625t
Calcium tungstates, 846–851
Calcium vanadium compounds, 709–715
Calcium vanadium (IV) oxide, 711
Calcium–yttrium compounds, 645–649, 647f, 647t, 648f, 648t
Calcium zinc compounds, 1122–1131
Calcium zirconate compounds, 675–679, 675f, 676f, 676t, 678f, 678t, 679f
Calcium zirconide compounds, 675
CALPHAD (calculation of phase diagrams) method, 378, 414, 690–691, 1083, 1098
Calsomine, 120
Canted antiferromagnetic (CAF) ordering, 941
Carbonatite, 364
Carbonic acid, 352–353, 353t
Carbonization, 120
Carlfriesite, 191
Carnolite, 44
Caro's acid, *See* Peroxymonosulfuric acid
Castep, 1049–1050
CaTiO3 type calcium hafnate compounds, 693–695, 693f, 694f, 694t
CaTiO3 type strontium hafnate compounds, 695–698, 696t
Cavoite, 712, 712f
Celestite, 155–156
Ceramic magnets, 923–924
Ceramic oxide superconductors, preparation of, 115
Chalcogen apatites, 266
Chalk, 363
Chambersite, 496
Chloric acid, 70, 71t
Chlorous acid, 70, 70t
Chromates, 796
Chromites, 796

Chromium dioxide, 795
Chromium (IV) oxide, 795
Chromium (V) oxide, 795–796
Chromium pentoxide, 795–796
Chrysoberyl, 540
Cobaltates, 961, 965
Cobalt compounds, 961–984
Colemanite, 503
Columbite method, 732
Composite hydroxide mediated (CHM) method, 725
Contact process, 134–135
Copper compounds, 1049–1079
Coprecipitation (CP) method, 965
Covalent hydrides, 26
Covering power, 247–249
Crawford, Adair, 16
Crysotile, 394
Curie, Marie, 21–22, 62–63, 66
Curie, Pierre, 21–22
Curie–Weiss behaviors, 712
Cyclo-triphosphoric acid, *See* Trimetaphosphoric acid
Czochralski Method, 192, 258, 263, 264, 413, 504, 541, 547, 724, 733, 740, 787, 853, 854, 861

D

Dalton, John, 157
Danalite, 138
Davidite, 371
Davy, Humphrey, 2, 9, 16, 18–19, 55, 482
Dead-burned magnesium oxide, 109
Debierne, André-Louis, 22, 104
Deca-barium gallide, 583, 584f, 584t
Decastrontium trigallate, 594–595, 594f, 595t
De Haas–van Alphen effect, 1157
Delbert, Pierre, 45
Diamond-anvil cell (DAC) technique, 1060
Dibarium aluminate, 566
Dibarium chromite, 817
Dibarium gallate, 597
Dibarium germanide, 423, 424f, 424t
Dibarium indate, 619–620, 619f, 620f
Dibarium molybdate, 840, 840f
Dibarium plumbide, 470, 470f
Dibarium stannide, 444–445, 445f, 446f, 446t
Di-barium thallate, 634
Di-barium thallide, 630–631, 631t
Dibarium trigallate, 598, 599f
Dibarium tristannide, 445
Dibarium tungstate, 863, 864f
Dibasic barium phosphate, 259–261, 260f, 261f
Dibasic beryllium arsenate, 297
Dibasic calcium phosphate, 246–249, 247f, 248f, 249f
Dibasic magnesium arsenate, 298–299
Dibasic radium phosphate, 265
Dibasic salt, 243–244
Dibasic strontium phosphate, 255–256
Dicalcium aluminate, 550
Dicalcium aluminate octahydrate, 551
Dicalcium ferrite, 917
Dicalcium germanide, 415–417, 417f, 417t, 418f, 418t
Dicalcium indide, 604–605, 605f, 605t
Di-calcium molybdate, 828
Dicalcium monogallate, 587–588
Dicalcium phosphate dihydrate (DCPD), *See* Brushite
Dicalcium plumbide, 464, 464f
Dicalcium stannide, 433–435
Dicalcium tantalate, 767, 769–770, 769f, 770f, 772
Dichlorine heptoxide, 72–73, 73f
Dichlorine hexoxide, 72
Dichlorine monoxide, 71, 71f, 72f, 72t
Dichlorine pentoxide, 72–73
Dichlorine trioxide, 72, 72t
Dichromium trioxide, 795
Dimagnesium gallide, 569, 569f, 569t
Dimagnesium indide, 600, 601f, 601t
Di-magnesium manganate, 872
Dimagnesium penta-gallide, 570, 570f, 570t
Di-magnesium tantalate, 767
Dimagnesium thallide, 622, 622t, 623f
Dimagnesium trialuminide, 520–522, 521f
Di-magnesium tri-molybdate, 825
Diopside, 394
Diphosphoric acid, *See* Pyrophosphoric acid
Diphosphorous trioxide, 223–224
Dirubidium calcium tetraborate octahydrate, 503
Disilicic acid, 371
Distrontium chromite, 811f, 812
Distrontium gallate, 592
Distrontium germanide, 419–420, 420f
Distrontium indate, 618, 618f
Distrontium plumbide, 464, 466f
Distrontium stannide, 440–441, 441f, 441t
Distrontium triplumbide, 467, 467f
Distrontium tungstate, 858
Disulfuric acid, 136–137, 137f
Dithionic acid, 137, 137f
Dithionite, 162–163, 162f, 170
Di-trontium thallate, 633
Dodeca-barium hepta-aluminate, 565–566
Dodeca-calcium hepta-aluminate, 549–550
Dodeca-octa calcium undeca-gallide, 575–576, 575f, 576t
Dolomite, 10
Dow Chemical Co., 47
Downs Process, 6
Dow Process, 44, 47
Drying, 149
DustGard Liquid, 45

E

Electrolysis, 44
Electron energy-loss spectroscopy (EELS) method, 975
Electronic packing frustration (EPF), 1084–1085
Electrospinning, 967–968
Elektron, 11
Enastite, 393
Epsom salt, 150–152
Epson salt, *See* Magnesium sulfate
Ettringite, 551
Expedition, 149

F

Faraday, Michael, 44
Fe pnictide, 716
Fergusonite, 847
Ferrates, 930
Flocculants, 120
Fluoborite, 496
Fluorapatite, 257–258
Forsterite, 393, 393f
Francolite, 254
Free electron laser in Hamburg (FLASH), 1050

G

Gahn, Johan Gottlieb, 18–19
Gallates, 483
Gay-Lussac, Joseph, 482
GdFeO3 type calcium hafnate compounds, 693, 693f, 693t
GdFeO3 type strontium hafnate compounds, 695, 695t
Germanium serpentine, 406, 406f
Gigantic Magnetoresistance phenomenon, 891–892
Gillespie–Nyholm theory, 56–57
Ginorite, 503
Glasserite, 250
Glasser-Jenkins equation, 251–252
Glidcop, 1050
Glucina, *See* Beryllium oxide
Glucinium (Gl), *See* Beryllium
Gold compounds, 1092–1113
Goodenough-Kanamori rules, 983
Groatite, 303
Grossite, 549
Güggenite, 1054
Gypsum, 152–155

H

Haidingerite, 303
Halogen acids, 31–37
Halurgite, 496
Hambergite, 494
Hard-burned magnesium oxide, 109
Hard ferrites, 925
Hatchett, Charles, 728–729
Hatrurite, 398
Hausmannite, 335
Hayyan, Jabir ibn, 32
Henry's Law, 33
Heptadeca-magnesium dodeca-aluminide, 522–524, 522f, 523f, 524f
Hepta-strontium digallate, 595
Herbert, Dow, 47
Herderite, 243
Hexa-barium niobate, 759
Hexa-barium tantalite, 792, 793f
Hexagonal barium tantalate nanorods, 789
Hexagonal perovskite, 791
Hexa-strontium tantalate, 783–785, 784f
High resolution transmission electron microscopy (HRTEM), 718
Homberg, William, 482
Hope, Thomas, 16
Hornesite, 299

Hoyle, Fred, 5
Hungchaoite, 496
Hydride compounds, of alkaline earths, 26–30
Hydroboracite, 495
Hydrobromic acid, 35–36
Hydrochloric acid, 32–35
Hydrodesulfurization, 133
Hydrofluoric acid, 31–32
Hydrogen phosphide, 224–225
Hydrogen sulfide, 132–133
Hydrogen telluride, 185
Hydroiodic acid, 36–37, 37f
Hydromagnesite, 361
Hydroxyapatite, 257, 258f
Hydroxylated barium borate, 516–517, 516f
Hypobromites, 87
Hypobromous acid, 87
Hypochlorous acid, 70, 70t
Hypomanganate, 894
Hypophosphoric acid, 227–229, 228f, 281, 281f
Hypophosphorous acid, 225, 225f, 229

I

Iceland Spar, 362, 362f
Indates, 483–484
Inderite, 496
Intermediate-temperature solid oxide fuel cells (IT-SOFCs), 975
Intermetallic compounds, 911–913
International Thermonuclear Experimental Reactor (ITER), 1049–1050
Interstitial hydrides, 26
Iodic acid, 96
Iodous acid, 96
Ionic hydrides, 26–30
Iridium compounds, 994–1004
Irtran-5, 109

J

JANA2000, 992
Johachidolite, 503

K

Kaliborite, 498
Kalsomine, 120
Karsten, L. G., 360
Kawasaki process, 144
Kissinger–Akahira–Sunose (KAS) method, 1007–1009
K-mag, 1059
Knudsen effusion technique, 321–322
Kosmulski, Marek, 612–613
Kotoite, 496
Kraft process, 145–147, 145t, 147f

L

LaAlO3 type calcium hafnate compounds, 693, 693f
Lanthanum chromite, 807
Lanthanum chromite, 808
Laser-heated pedestal growth (LMPG) method, 731–732, 773
Lath and plaster, 121
Lautarite, *See* Calcium iodate
Laves phase structures, 1116
Lavoisier, Antoine, 2, 18–19
Lead-champer process, 134
Lead oxides, 458–459
Leblanc process, 33
Liebig method, 81
Light-burned magnesium oxide, 109
Lime burning, *See* Calcination
Limelight, 112
Lime plaster, 121–122
Limestone, 363–364
Lime wash, 121
Lithopone, 157
Local spin density approximation (LSDA), 977
Low-temperature co-fired ceramics (LTCC) temperatures, 735
Ludwig, C. F., 360
Ludwigite, 495

M

Macallisterite, 496
Magnalium, 10
Magnesium, 8–12
Magnesium aluminates, 543–547, 544t, 545f
Magnesium aluminide, 518–524, 519f
Magnesium antimonate, 313–314
Magnesium antimonide, 317–321, 318f, 319f, 320f
Magnesium antimonite, 309–310
Magnesium arsenates, 298–302
Magnesium arsenide, 287–288, 288f
Magnesium arsenites, 291–293, 292f
Magnesium bismuthate, 328–329, 329f
Magnesium bismuthides, 337–339, 337t, 338f, 339t
Magnesium borates, 494–498, 495f, 497f
Magnesium boride, 485–488, 486f, 487f
Magnesium bromate, 92, 93t
Magnesium bromide, 46–47
Magnesium bromite, 89
Magnesium cadmium compounds, 1140–1143
Magnesium carbides, 354–355, 355f
Magnesium carbonates, 360–362, 360t, 361f
Magnesium chlorate, 79, 79t
Magnesium chloride, 10, 43–46
Magnesium chlorite, 76
Magnesium chromate, 801, 801f
Magnesium chromite, 800–801, 800f, 803
Magnesium chromium compounds, 798–802
Magnesium cobalt compounds, 963–965
Magnesium copper compounds, 1052–1055
Magnesium digallide, 569, 569f, 569t
Magnesium dihydrogen orthoarsenate, 300–301
Magnesium dithionate, 164–165
Magnesium dithionite, 164
Magnesium fluoride, 41–43
Magnesium gallates, 585–586, 586f, 632
Magnesium gallide, 567–570, 568f, 568t, 570f, 570t
Magnesium germanates, 404–406, 405f
Magnesium germanides, 413–414, 415f, 415t, 416t
Magnesium gold compounds, 1094–1098
Magnesium hafnate compounds, 690–692, 691f, 691t, 692f
Magnesium hafnide compounds, 690, 690f
Magnesium hexahydroxostannate, 449
Magnesium hydride, 27–29
Magnesium hydroxide, 11, 118–120
Magnesium hyperoxides, 130, 130f
Magnesium hypobromite, 88
Magnesium hypochlorite, 74
Magnesium hypophosphate, 281
Magnesium hypophosphite, 235–236
Magnesium indides, 599–603, 600f, 600t, 602f, 602t
Magnesium iodate, 97–98, 97t
Magnesium iodide, 47–49
Magnesium ion batteries (MIBs), 965
Magnesium iridium compounds, 995–997
Magnesium manganese compounds, 871–875
Magnesium mercury compounds, 1156–1159
Magnesium metabisulfite, 170
Magnesium metaphosphates, 273–274
Magnesium molybdates, 824
Magnesium molybdenum compounds, 823–826
Magnesium monoaluminide, 522
Magnesium monogallate, 586, 586f
Magnesium mono-thallide, 622, 623f, 623t
Magnesium nickel compounds, 1007–1009
Magnesium niobate powders, 733
Magnesium niobate system, 732
Magnesium niobium compounds, 731–736
Magnesium niobium oxide, 735
Magnesium nitrate, 214f, 216–218, 216t, 217f, 217t
Magnesium nitride, 202–205, 203f, 204f
Magnesium nitrite, 210–211
Magnesium orthoarsenite, 292
Magnesium orthophosphates, 243–245
Magnesium orthostannate, 449
Magnesium ortho-vanadate, 709, 709f
Magnesium osmium compounds, 954–955
Magnesium oxide, 108–109, 108f, 110t
Magnesium oxide flue-gas disposal system, 144f
Magnesium oxo-rhenium compounds, 901
Magnesium oxy-iron compounds, 914–916
Magnesium palladium compounds, 1020–1022
Magnesium perborate, 497–498, 498f
Magnesium perbromate, 95
Magnesium perchlorate, 83t, 84, 84t, 85f
Magnesium periodate, 100–101, 100f, 101f
Magnesium peroxide, 125–126, 125f
Magnesium peroxydisulfate, 171–172
Magnesium peroxymonosulfate, 171
Magnesium peroxyphosphate, 283
Magnesium phosphide, 230–231
Magnesium phosphite, 238–239
Magnesium platinum compounds, 1032–1035
Magnesium plumbates, 473
Magnesium plumbides, 459–461, 460f
Magnesium polyphosphates, 273–274

Magnesium pyroarsenate, 300
Magnesium pyroarsenite, 293
Magnesium pyroborate, 497, 497f
Magnesium pyrophosphate, 266–268, 266f
Magnesium pyrosulfate, 161
Magnesium pyrovanadate, 707, 707f, 709
Magnesium rhodium compounds, 986–988
Magnesium ruthenium compounds, 939
Magnesium–scandium system, 639–640, 639f, 640f
Magnesium selenate, 182–183, 182f, 182t
Magnesium selenide, 174–175, 174f
Magnesium selenite, 178–179, 178f, 179f
Magnesium silicate perovskite, 394, 394f
Magnesium silicates, 392–395, 393f
Magnesium silicide, 372–375, 373f, 373t
Magnesium silver compounds, 1081–1083
Magnesium stannates, 447–450, 448f
Magnesium stannides, 428–432, 429f, 429t, 430f, 430t, 431f, 432f
Magnesium sulfate, 10, 150–152
Magnesium sulfide, 138, 138f, 139t
Magnesium sulfite, 143–145, 143f
Magnesium tantalate, 767
Magnesium tantalum compounds, 761–767
Magnesium technetium compounds, 896–897
Magnesium tellurate, 195, 195f
Magnesium telluride, 187, 187f
Magnesium tellurite, 190
Magnesium tetraärsenite, 293
Magnesium tetrathionate, 165
Magnesium thallates, 631–632
Magnesium thallides, 622–623, 622f, 622t
Magnesium thionates, 164–165
Magnesium thiosulfate, 158–159
Magnesium titanates, 656–662, 658f, 659f, 661f, 662f
Magnesium titanides, 656
Magnesium tri-indide, 602–603, 603f, 603t, 604t
Magnesium tungsten compounds, 844–846
Magnesium vanadium compounds, 702–709
Magnesium–yttrium compounds, 643–645, 644t, 645f, 646f, 646t
Magnesium zinc compounds, 1115–1122
Magnesium zirconate compounds, 675
Magnesium zirconide compounds, 674
Magnessium indates, 613–614, 613f
Mag wheels, 11
Manganate (V) anion, 869
Manganotantalite, 773–774
Marble, 364–365, 365f
Maximum entropy method (MEM), 1053
Mcallisterite, 496
Mechanical alloying (MA) process, 1053
Mercury compounds, 1156–1174
Meridianite, 152
Metaborate, 493
Metal-organic chemical vapor deposition (MOCVD) techniques, 1076
Metal–semiconductor transition (MST), 963
Metaniobite, 736, 736f, 737f
Metaperiodic acid, 96
Metaphosphoric acid, 226–227, 229, 272
Metasilicic acid, 371
Metatelluric acid, 186, 186f
Metavanadate, 721, 721f, 723, 724f
2-Methoxyethanol, 967
Mie-Grüneisen-Debye formalism, 999
Milk of magnesia, 10, 118–119
Moissan, H., 55
Molten salt method, 969
Molybdenum dioxide, 819
Molybdenum trioxide, 819
Mono-barium tantalate, 786
Monobasic barium phosphate, 259, 260f
Monobasic calcium phosphate, 245–246
Monobasic radium phosphate, 265
Monobasic salt, 243
Monobasic strontium arsenite, 295
Monobasic strontium phosphate, 255, 255f
Mono-calcium digallate, 588
Monocalcium gallate, 587
Monocalcium plumbide, 463–464
Mono-calcium tantalate, 772, 773f
Mono-strontium hexagallate, 595
Mono-strontium tantalate, 775, 777–779, 777f
Moraesite, 243
Mortar, 121
Morveau, Guyton-de, 18–19
Mroseite, 191
Muriatic acid, *See* Hydrochloric acid
Murray, James, 118

N

Nearest-neighbor hopping (NNH), 1059
Nickel compounds, 1005–1007
Nickel oxides, 1005
Nicol, William, 362–363
Niobium compounds, 728–760
Nitric acid, 201
Nitrogen acids, 201
Nitrous acid, 201
Niveolinite, 360
Nobleite, 503
Nona-barium tetra-indide, 611–612

O

Octa-barium hepta-gallide, 582, 582f, 583t
Octacalcium pentagermanium octadecaoxide, 408–409
Octa-calcium tri-aluminide, 527
Octa-calcium tri-indide, 605, 605f, 606t
Octadodeca-strontium undeca-indide, 609
Octa-strontium hepta-aluminide, 528–529, 531f, 531t
Octa-strontium hepta-gallide, 580, 580f, 580t
Oldhamite, 140
Oligophosphorous acid, 225–226
Orthoborate, 493, 496
Orthoperiodic acid, 96
Orthosilicic acid, 371
Ortho-vanadate, 713, 713f
Osmium compounds, 954–960
Oxidative dehydrogenation of propane (ODP), 708
Oxide of iridium, 994
Oxo-germanium compounds, 413
Oxy-bromine acids, 87
Oxy-chlorine acid anhydrides, 71–73, 71t
Oxy-chlorine acids, 70–71
Oxydisulfuric acid, 170
Oxy-iodine acids, 96
Oxy-iron compounds, 914–937
Oxy-sulfur acids, 132–137

P

Paints, 120–121
Palladium compounds, 1019–1031
Penta-bariumdi-niobate, 754–755, 754f
Penta-barium hexagallide, 582–583, 583f, 583t
Penta-barium hexa-niobate, 759
Penta-barium indate, 621
Pentabarium monoplumbide, 470–471, 471f
Pentabarium triplumbide, 470, 471f
Penta-calcium di-thallide, 626, 626f, 626t
Penta-calcium tri-aluminate, 550
Pentacalcium triborate, 501
Penta-calcium tri-chromate, 806
Penta-calcium trigallate, 588–590, 589f
Penta-calcium tri-gallide, 578, 578f, 578t
Penta-calcium tri-germanide, 417, 418f, 418t, 419, 419f
Pentacalcium triplumbide, 462–463, 463f
Penta-magnesium di-gallide, 568–569, 568f, 568t
Penta-magnesium di-thallide, 623, 623f, 623t, 624f
Pentamagnesium octaaluminide, 520
Pentamagnesium tri-indide, 602, 602f, 602t
Penta-strontium di-tantalate compound, 782, 783f
Pentastrontium nona-aluminide, 529, 532f
Pentastrontium quadro-plumbide, 467–469, 468f, 469f
Penta-strontium tri-germanide, 420–421, 421f, 421t
Penta-strontium tri-indide, 608–609, 608f, 608t
Pentastrontium triplumbide, 467, 468f
Pentastrontium tristannide, 440, 440f, 441t
Penta-strontium tri-thallide, 626–627, 628f
Perbromic acid, 87
Perchloric acid, 70–71, 71t
Periodic acid, 96, 96f
Perovskite, 406, 406f, 1012
Peroxophosphoric acid, 228–229, 228f
Peroxy acids, 170
Peroxydisulfuric acid, 170, 170f
Peroxymonosulfuric acid, 170
Pharmacolite, 303
Phaunouxite, 303
Phillips, Peregrine, 134
Phosphenic acid, 272
Phosphinates, 225, 234
Phosphoric acid, 226, 229
Phosphorous (III) tetraoxide, 224, 224f
Phosphorous (V) pentoxide, 224
Phosphorous acids, 224–229, 225f, 225t
Phosphorous oxide anhydrides, 223–224
Pickling, 32
Pinnoite, 496
Pitchblende, 69
Plaster of paris, 153–155
Platinum compounds, 1031–1048

Polonium-based alkaline earth compounds, 197
Polyphosphides, 231
Portland cement mortar, 121
Portlandite, 120
Power-gated hole burning, 138
Preobrazhenskite, 496
Propene, 708
Pulp screening, 149
Pulp washing, 149
Pyroborate, 493, 493f, 496
Pyrochlore oxide, 771
Pyroniobate, 738, 739f, 744f, 745–746, 745f, 746f, 748f, 770f
Pyrophosphate, 272
Pyrophosphoric acid, 227, 227f, 229
Pyrosilicic acid, 371
Pyrosulfuric acid, 136–137
Pyrovanadate, 712f, 714, 719f, 720, 723f, 724

Q

Quicklime, *See* Calcium oxide

R

Radium, 19–23
Radium aluminates, 566–567
Radium aluminides, 540
Radium antimonate, 316–317
Radium antimonide, 328
Radium antimonite, 312
Radium aptites, 265
Radium arsenates, 309
Radium arsenide, 290
Radium arsenites, 296–297
Radium bismuthate, 336–337
Radium bismuthide, 350
Radium borates, 517
Radium boride, 492
Radium bromate, 94
Radium bromide, 69, 70t
Radium bromite, 92
Radium bromoapatite, 265–266
Radium cadmium compounds, 1156
Radium carbide, 359
Radium carbonate, 370–371
Radium chlorate, 82–83
Radium chloride, 69, 69t
Radium chlorite, 78
Radium chloroapatite, 265
Radium chromium compounds, 819
Radium cobalt compounds, 984
Radium copper compounds, 1079
Radium dithionite, 170
Radium fluorapatite, 265
Radium fluoride, 68–69
Radium gallates, 599
Radium gallides, 584
Radium germanate, 412–413
Radium germanides, 428
Radium gold compounds, 1113
Radium hafnium compounds, 700
Radium hydride, 30
Radium hydrogen phosphate, *See* Dibasic radium phosphate
Radium hydroxide, 124
Radium hydroxyapatite, 265
Radium hyperoxides, 132
Radium hypobromite, 89
Radium hypochlorite, 76
Radium hypophosphate, 282
Radium hypophosphite, 237
Radium indates, 621
Radium indides, 612
Radium iodate, 99
Radium iodide, 70
Radium iodoapatite, 266
Radium iridium compounds, 1004
Radium manganese compounds, 895
Radium mercury compounds, 1174
Radium metaphosphates, 280–281
Radium molybdenum compounds, 841
Radium nickel compounds, 1019
Radium niobates, 760
Radium nitrate, 223
Radium nitride, 210
Radium nitrite, 215
Radium orthophosphates, 264–265
Radium osmium compounds, 960
Radium oxide, 115–116
Radium oxy-iron compounds, 937
Radium palladium compounds, 1031
Radium perbromate, 96
Radium perchlorate, 86
Radium periodate, 104
Radium peroxide, 130
Radium phosphide, 234
Radium phosphite, 241
Radium platinum compounds, 1048
Radium plumbates, 480
Radium plumbides, 472
Radium polyphosphates, 271–272, 280–281
Radium pyrosulfate, 162
Radium rhenium compounds, 909
Radium rhodium compounds, 994
Radium ruthenium compounds, 953
Radium–scandium system, 643
Radium selenate, 184
Radium selenide, 177
Radium selenite, 181
Radium silicates, 403
Radium silicides, 386
Radium silver compounds, 1091
Radium stannates, 458, 458f
Radium stannides, 446
Radium sulfate, 158
Radium sulfide, 142
Radium sulfite, 150
Radium tantalates, 794
Radium technetium compounds, 899
Radium tellurate, 197
Radium telluride, 190
Radium tellurite, 194
Radium tetrathionate, 170
Radium thallates, 635
Radium thallides, 631
Radium thionates, 170
Radium thiosulfate, 160
Radium titanates, 672
Radium tungstates, 868
Radium vanadates, 728
Radium–yttrium compounds, 652
Radium zinc compounds, 1140
Radium zirconates, 686–687
Rankinite, 397–398, 398f
Rare earth compounds, 652
Rauenthalite, 303
Recuperation, 149
Rhodates, 986
Rhodium compounds, 984–994
Rietveld method, 74, 205
Riewelt method, 307
Ringwoodite, 393
Roebuck, John, 134
Roesslerite, 298–299, 299f
Rose, Gustav, 299
Roselite, 299
Rupprecht, Anton, 9
Ruthenium compounds, 937–953

S

Saline hydrides, 26
Sanbornite, 401, 402f
Sassolite, 482
Scheele, Carl Wilhelm, 18–19
Scintillation, 67
Sealants, 120–121
Seebeck coefficient, 983
Selenic acid, 173
Selenides, 172
Selenious acid, *See* Selenous acid
Selenous acid, 173
Sensodyne, 58
Serpentinites, 394–395
Silicic acid, 371
Silver compounds, 1080–1091
Six Framework Program, 11
Smith, Francis Marion, 503
Soda process, 146
Solid electrolyte potentiometry (SEP), 708
Solid oxide fuel cells (SOFCs), 685–686, 808, 832, 837–838
Solution combustion synthesis (SCS), 965
Solvay Process, 51
Sorel-cement, 45
Sorokin, Peter, 51
Spark plasma sintering (SPS), 963
Spirit of nitre, *See* Nitric acid
Spirits of salt, *See* Hydrochloric acid
Sputtering, 113
Stannate, 447
Stannite, 446–447
Stevenson, Mirek, 51
Strontioborite, 509
Strontioginorite, 509
Strontium, 15–18
Strontium aluminates, 553–559, 553f
Strontium aluminides, 527–529, 528f, 528t
Strontium antimonate, 314–315, 315f, 315t
Strontium antimonide, 324–325, 324f, 325f
Strontium antimonite, 311
Strontium apatites, 257
Strontium arsenates, 304–306, 305t
Strontium arsenide, 289
Strontium arsenites, 295, 295f
Strontium barium niobate, 744–745

Strontium bismuthates, 331–333, 331f, 332f
Strontium bismuthides, 343–347, 343f, 343t, 344f, 344t, 345f, 345t, 346f, 346t, 347f
Strontium bismuth tantalite (SBT), 775
Strontium borates, 504–511
Strontium boride, 490–491, 490f
Strontium bromate, 93–94
Strontium bromide, 58–59, 59f, 59t, 60t
Strontium bromite, 90–91
Strontium bromoapatite, 259
Strontium cadmium compounds, 1147–1150
Strontium carbides, 357–358, 358f
Strontium carbonate, 366–368, 367f
Strontium chlorate, 80–81
Strontium chloride, 57–58, 58f, 58t, 59t
Strontium chlorite, 77–78
Strontium chloroapatite, 258–259
Strontium chromate, 809–810, 810f
Strontium chromium compounds, 809–813
Strontium cobalt compounds, 971–978
Strontium copper compounds, 1061–1070
Strontium dialuminate, 554–555
Strontium dialuminide, 527–528, 529f, 530f
Strontium dichromite, 812
Strontium digallide, 578–580, 579f, 579t, 592
Strontium di-germanide, 421–423, 422f, 422t
Strontium dihydrogen orthoarsenate, 306
Strontium dihydrogen phosphate, 255
Strontium di-indide, 607–608, 607f, 607t
Strontium dimetaärsenite, 295
Strontium di-thallide, 627, 628f, 628t, 629f
Strontium dithionate, 167
Strontium dithionite, 167
Strontium ferrite, 925, 929
Strontium fluoride, 56–57, 56t, 57t
Strontium gallates, 590–595, 590f
Strontium gallides, 578–581, 579f, 579t
Strontium germanates, 409–410, 409f, 410f
Strontium germanides, 419–423, 420f
Strontium gold compounds, 1105–1109
Strontium hafnate compounds, 695–698, 695f, 696f, 696t, 697f, 697t
Strontium hafnide compounds, 695
Strontium hexa-aluminate, 554, 554f, 554t
Strontium hydride, 30
Strontium hyperoxides, 122–123, 122t, 131–132
Strontium hypobromite, 88–89
Strontium hypochlorite, 76
Strontium hypophosphate, 282
Strontium hypophosphite, 236–237
Strontium indates, 617–618
Strontium indides, 606–610, 606f, 607f, 607t
Strontium iodate, 98–99
Strontium iodide, 59–60, 60f, 61t, 62t
Strontium iodoapatite, 259
Strontium–iridium compounds, 1000–1002
Strontium manganese compounds, 883–891
Strontium mercury compounds, 1163–1170
Strontium metaborate, 504–505, 504f
Strontium metaphosphate, 278–279, 279f
Strontium molybdenum compounds, 829–835
Strontium monogallate, 588f, 589f, 590–592, 591f
Strontium monogermanide, 420, 421f, 421t
Strontium monohydrogen arsenate, 305–306
Strontium monoindate, 617–618
Strontium monoplumbide, 464–466, 466f
Strontium monostannide, 440, 440f, 440t
Strontium mono-thallate, 633, 633f
Strontium mono-thallide, 626, 627f, 627t
Strontium nickel compounds, 1013–1015
Strontium niobate, 742–743, 743f, 752, 779
Strontium niobate, 781
Strontium niobium compounds, 741–752
Strontium nitrate, 220–221, 220t
Strontium nitride, 207–209
Strontium nitride carbodiimide, 209
Strontium nitrite, 212–213
Strontium orthoarsenate, 305
Strontium orthoborate, 505–506, 505f, 506f, 507t
Strontium orthophosphates, 255–257
Strontium orthovanadate, 720
Strontium osmates, 958
Strontium osmium compounds, 957–958
Strontium oxide, 112–113, 112f
Strontium oxy-iron compounds, 922–930
Strontium palladium compounds, 1027–1029
Strontium penta-indide, 608, 608f, 608t
Strontium penta-molybdate, 834
Strontium perborate, 507–508, 507f
Strontium perbromate, 95
Strontium perchlorate, 85–86, 86t
Strontium periodate, 102–103
Strontium peroxide, 128–129, 128f, 129f
Strontium peroxodisulfate, 172
Strontium peroxymonosulfate, 171
Strontium peroxyphosphate, 284–285
Strontium phosphide, 232–233, 233f
Strontium phosphite, 239–240
Strontium platinum compounds, 1040–1044
Strontium plumbates, 475–476
Strontium plumbides, 464–469, 465f
Strontium polyphosphates, 278–279, 279f
Strontium potassium arsenate octahydrate, 306, 307t, 308f
Strontium pyroarsenate, 306
Strontium pyroarsenite, 295
Strontium pyroborate, 506–507, 507f
Strontium pyrophosphate, 270–271
Strontium pyrosulfate, 161–162
Strontium rhenium compounds, 903–907
Strontium rhodium compounds, 990–993
Strontium ruthenium compounds, 944–950
Strontium–scandium system, 641
Strontium selenate, 184
Strontium selenide, 176–177, 176f
Strontium selenide–samarium–europium phosphor, 176–177
Strontium selenite, 180
Strontium silicates, 398–400, 398f, 399f
Strontium silicide, 377–381, 378f, 378t, 379t, 380f, 381f
Strontium silver compounds, 1086–1089
Strontium stannates, 452–454
Strontium stannides, 436–441, 436f, 437f, 437t, 438t
Strontium sulfate, 155–156, 156f
Strontium sulfide, 140–141, 140f
Strontium sulfite, 149
Strontium tantalate, 779, 780f, 781–782, 785
Strontium tantalum compounds, 775–785
Strontium technetium compounds, 898
Strontium tellurate, 196, 196f
Strontium telluride, 188
Strontium tellurite, 192–193
Strontium tetra-aluminide, 527, 529f
Strontium tetraborate, 508–509, 508f, 509f
Strontium tetra-gallide, 580, 580f, 581t
Strontium tetra-indide, 610
Strontium tetrastannide, 437–439, 439f
Strontium tetra-tantalate, 779, 779f
Strontium tetrathionate, 167–168, 168f
Strontium thallates, 633
Strontium thallides, 626–629, 626f, 627t
Strontium thionates, 167–168
Strontium thiosulfate, 159–160, 160t
Strontium titanates, 667–669, 667f, 668f, 669f
Strontium titanides, 667
Strontium tri-indide, 608, 608f, 608t
Strontium triplumbide, 466–467, 467f
Strontium tristannide, 439, 439f, 439t
Strontium tri-thallide, 626, 628f, 628t
Strontium tungsten compounds, 851–858
Strontium undecazinc, 1134–1135
Strontium Vanadite, 719
Strontium vanadium compounds, 715–722
Strontium–yttrium compounds, 649–650, 649f, 649t
Strontium zinc compounds, 1131–1136
Strontium zirconates, 679–684, 680f, 680t, 681f, 681t, 682f, 683f, 683t, 684t
Strontium zirconides, 679, 679f
Stucco, 154–155
Suanite, 496
Sulfite process, 145–147, 145t
(Sulfo-oxy)sulfonic acid, *See* Disulfuric acid
Sulfuric acid, 133–135
Sulfurous acid, 133
Super-paramagnetism, 914
Swedenborgite, 312–313
Synthesis gas (syn-gas), 987–988

T

Taffeite, 541
Takedaite, 503
Talc, 395
Tantalum compounds, 760–794
Technetium (VII) oxide, 896
Teflates, 197
Telluric acid, 185–186, 185f
Tellurous acid, 185
Tennant, Charles, 75
Teruggite, 496
Tetrabarium aluminate, 563–564, 563f, 564f
Tetrabarium gallate, 598
Tetrabarium niobate, 756–758
Tetrabarium penta-aluminide, 536–537, 538f, 539t
Tetrabarium pentaaluminide, 537
Tetrabarium tantalite, 792
Tetrabarium triïndate, 621, 621f
Tetrabarium tri-thallate, 634
Tetraborate, 482, 494

Tetracalcium niobate, 741
Tetra-calcium tantalate, 775
Tetra-calcium tri-aluminate, 550–551
Tetramagnesium tantalate, 764, 765f
Tetrapolyphosphate, 272
Tetrapolyphosphoric acid, 228–229, 228f
Tetrastrontium aluminate, 555, 555t
Tetrastrontium gallate, 594
Tetrastrontium hepta-aluminate, 557–558
Tetra-strontium tantalate, 785, 785f
Tetra-strontium thallate, 633
Tetrastrontium vanadate, 721
Tetrathionate, 163, 163f
Thallates, 484
Thénard, Louis, 482
Thermal grease, 107
Thiosulfuric acid, 136, 136f
Tilghman, Benjamin C., 146
Transition metal hydrido complexes, 26
Transparent conductive oxides (TCO), 1054
Traveling solvent floating zone (TSFZ) method, 1066
Travertine, 365
Tribarium distannide, 445
Tribarium di-tungstate, 866
Tribarium gallate, 597–598
Tribarium indate, 620–621
Tribarium niobate, 756–757
Tribarium niobate compounds, 756–757
Tribarium pentaaluminide, 536, 537f, 538f, 539t
Tri-barium pentaniobate, 759
Tribarium pentaplumbide, 470, 470f
Tribarium pentastannide, 443–444, 445f, 445t
Tri-barium tantalite compound, 791
Tribasic barium phosphate, 261–262
Tribasic barium arsenite, 295–296
Tribasic calcium arsenate, 304
Tribasic calcium phosphate, 249–251
Tribasic magnesium arsenate, 299, 300f
Tribasic salt, 244–245
Tribasic strontium arsenite, 295
Tribasic strontium phosphate, 256–257, 257f
Triborate, 494
Tricalcium aluminate, 549–550
Tri-calcium aluminate hexahydrate, 551–552
Tricalcium arsenate, 302
Tricalcium distannide, 435
Tricalcium dithallate, 632–633
Tricalcium monoindate, 616, 617f
Tricalcium niobate compound, 741
Tricalcium octa-gallide, 577, 577f, 577t
Tricalcium penta-gallide, 576–577, 576f, 577f, 577t
Tricalcium pentastannide, 435, 435f, 436t
Tricalcium plumbide, 464, 465f
Tricalcium tantalate, 774–775
Tri-calcium tetra-thallide, 626
Tri-calcium thallate, 632, 632f
Tri-calcium thallide, 625, 625f, 625t
Tricalcium tungstate, 850–851
Trideca-calcium tetradeca-aluminide, 526, 527f
Trihydrogen nitride, 201
Trimagnesium indide, 600–601, 601f, 601t
Trimetaphosphoric acid, 272, 272f
Tripolyphosphate, 272
Tripolyphosphoric acid, 228–229, 228f
Tristrontium aluminate, 558–559, 558f
Tristrontium digallate, 593–594
Tri-strontium di-manganate, 886, 887f
Tristrontium molybdate, 833
Tristrontium monogallate, 592–593, 593f
Tristrontium monoplumbide, 466, 466f
Tristrontium ortho-chromate, 811
Tri-strontium penta-indide, 610
Tristrontium pentastannide, 439–440, 439f
Tri-strontium thallide, 626, 627f, 628t
Tristrontium tungstate, 856, 858f
Tri-strontium undeca-indide, 609–610, 609f
Tufa, 365
Tunellite, 509

U

Ulexite, 495, 503
Undeca-Ae heptaindides, 609
Undeca-calcium hepta-gallide, 574–575, 574t, 575f
Undodecabarium tetradeca-aluminide, 537–540, 539f, 539t, 540f

V

Valentine, M. B., 360
Vanadium, 701
Vanadium arsenate, 723
Vanadium compounds, 701–728
Vauquelin, Louis-Nicholas, 6
Veatchite, 509
Vegard's law, 188
Vertical Bridgman (VB) technique, 174–175, 374, 381, 384
Vivianite, 299

W

Wadsleyite, 393
Warwickite, 495
Weberite, 314, 770
Weilite, 303–304
Wet sulfuric acid method, 135
White Sands National Monument, 153
Whitewash, 120
Whitlockite, 249
Wightmanite, 496
Witherite, 38, 369
Wolframite, 846, 846f
Wölhler, Friedrich, 6
Wollastonite, 396–397
Wood chips cooking, 148
Wood chip screening, 148

Z

Z-contrast imaging, 975
Zemannite, 190
Zincates, 1115
Zinc compounds, 1115–1140
Zintl compounds, 1153
Zintl ion, 317
Zintl-Klemm concept, 317